SCHOLARLY PUBLICATIONS

A CURRENT AWARENESS BULLETIN
OF RESEARCH OUTPUT

@DTU

(121st Edition)

JANUARY 2023

BY: CENTRAL LIBRARY

DELHI TECHNOLOGICAL UNIVERSITY
(FORMERLY *DELHI COLLEGE OF ENGINEERING)*
GOVT. OF N.C.T. OF DELHI
SHAHBAD DAULATPUR, MAIN BAWANA ROAD
DELHI 110042

PREFACE

This is the **One Hundred Twenty First** Issue of Current Awareness Bulletin started by Delhi Technological University, Central Library. The aim of the bulletin is to compile, preserve and disseminate information published by the faculty, students and alumni for mutual benefits. The bulletin also aims to propagate the intellectual contribution of Delhi Technological University (DTU) as a whole to the academia.

The bulletin contains information resources available in the internet in the form of articles, reports, presentations published in international journals, websites, etc. by the faculty and students of DTU. The publications of faculty and student which are not covered in this bulletin may be because of the reason that the full text either was not accessible or could not be searched by the search engine used by the library for this purpose.

The learned faculty and students are requested to provide their uncovered publications to the library either through email or in CD, etc. to make the bulletin more comprehensive.

This issue contains the information published during **January, 2023**. The arrangement of the contents is alphabetical. The full text of the article which is either subscribed by the university or available in the web is provided in this bulletin.

Central Library

CONTENTS

1. A bibliometric analysis of cold spray coating process using VOSviewer, ***6.Ayaz Mehmood***, ***3.Mohammad Zunaid*** and ***3.Ashok Kumar Madan***, Mechanical, DTU

2. A Comparative Analysis of Consensus Algorithms for Decentralized Storage Systems, Pratima Sharma, ***3.Rajni Jindal*** and Malaya Dutta Borah, CSE, DTU

3. A comprehensive review on algal nutraceuticals as prospective therapeutic agent for different diseases, ***8.Asmita Kumari***, ***8.Garima*** and ***3.Navneeta Bharadvaja***, Biotechnology, DTU

4. A fusion way of feature extraction for automatic categorization of music genres, ***6.Dhruv Sharma***, ***3.Sachin Taran*** and ***3.Anukul Pandey***, Electronics, DTU

5. A Hybrid Firefly Algorithm Approach for Job Shop Scheduling Problem, ***6.Gayathri Devi K***, ***3.R. S. Mishra*** and ***3.A. K. Madan***, Mechanical and Production Industrial and Automobiles, DTU

6. A literature survey on multimodal and multilingual automatic hate speech identification, ***6.Anusha Chhabra*** and ***3.Dinesh Kumar Vishwakarma***, IT, DTU

7. A novel dual-slope resistance to digital converter with lead resistance compensation, ***7.1.Gopal Singh***, Shiraz Sohail, Umapathy Mangalanathan, Uma Gandhi, and Tarikul Islam, Electrical, DTU

8. A Novel Electrochemical Biosensor Based on Polyaniline-Embedded Copper Oxide Nanoparticles for High-Sensitive Paraoxon-Ethyl (PE) Detection, ***6.Saroj Paneru*** and ***3.Devendra Kumar***, Applied Chemistry, DTU

9. A novel read decoupled 8T1M nvSRAM cell with improved read/write margin, ***7.Damyanti Singh***, ***3.Neeta Pandey*** and Kirti Gupta, Electronics, DTU

10. Acute metabolic alterations in the hippocampus are associated with decreased acetylation after blast induced TBI, ***7.Megha Kumari***, Palkin Arora, Priyanka Sharma, ***3.Yasha Hasija***, Poonam Rana, Maria M. D'souza, Namas Chandra and Richa Trivedi, Biotechnology, DTU

11. ADVERSARIAL ADAPTATION FOR FRENCH NAMED ENTITY RECOGNITION, ***8.Arjun Choudhry***, ***8.Pankaj Gupta***, Maxime Nicol, Marie-Jean Meurs, ***8.Inder Khatri***, ***8.Aaryan Gupta*** and ***3.Dinesh Kumar Vishwakarma***, IT, DTU

12. Ag-doped-CuO nanoparticles supported polyaniline (PANI) based novel electrochemical sensor for sensitive detection of paraoxon-ethyl in three real samples, ***6.Saroj Paneru*** and ***3.Devendra Kumar***, Applied Chemistry, DTU

13. All-Optical N-Bit Reversible Complex Multiplier, ***7.Diksha Ruhela*** and ***3.Rajni Jindal***, CSE, DTU

14. Alzheimer's Disease Detection using Particle Swarm Optimization, ***6.Neha Garg***, ***3.Mahipal Singh Choudhry*** and Rajesh Mungasaji Bodade, Electronics, DTU

15. An Interpretable Network to Thermal Images for Breast Cancer Detection, ***6.Kamakshi Rautela***, ***3.Dinesh Kumar*** and Vijay Kumar, Electronics, DTU

16. Analysis of Personalized tourism recommender systems, ***8.Dipit Sharma***, ***8.Imane Elouaghzani***, ***8.Eklavya*** and ***3.Rahul Katarya***, CSE, DTU

17. Analysis of QD-Si Solar Cell with Efficiency Enhancing Methods using Nano materials, ***8.Ankush***, ***8.Anubhav Singh***, ***3.Yogendra Kr. Meena*** and ***3.Manish Jain***, Applied Physics and Applied Chemistry, DTU

18. Applications of Human Activity Recognition in Different Fields: A Review, ***7.Yash Daga*** and ***3.Shweta Meena***, Software Engineering, DTU

19. Assessment of seasonal groundwater quality variation employing GIS and statistical approaches in Kabul basin, Afghanistan, ***6.Ali Reza Noori*** and ***3.S. K. Singh***, Environmental, DTU

20. Assessment of Water Quality of the River Gomti, India by Water Quality Index, ***6.Amit Krishan***, ***3.Rajeev Kumar Mishra*** and Anwar Khursheed, Environmental, DTU

21. Automated Major Depressive Disorder (AMDD) Detection using Audio-Visual Feature Discriptor and CNN, ***8.Nikhil Singh***, ***3.Rajiv Kapoor***, Ruchirangad Kapoor and Siddharth Arora, Electronics, DTU

22. Biosynthesized rGO@ZnO-based ultrasensitive electrochemical immunosensor for bovine serum albumin detection, ***7.1.Palak Garg***, ***6.Deeksha Thakur***, ***7.Sakshi Verma***, ***6.Owais Jalil***, Chandra Mouli Pandey & ***3.Devendra Kumar***, Applied Chemistry, DTU

23. Cadmium Uptake From Soil by Ornamental Metallophytes: A Meta-analytical Approach, ***6.Deepika*** and ***3.Anil Kumar Haritash***, Environmental, DTU

24. Cavity-Backed Slot Loaded Substrate Integrated Waveguide Self-Diplexing Antenna for C Band Applications, ***3.Sudarshan Kumar*** and ***3.Asok De***, Electronics, DTU

25. Classification and Analysis of Textual data using Naive Bayes with TF-IDF, ***6.Chingmuankim*** and ***3.Rajni Jindal***, CSE, DTU

26. Comparing differences of trust, collaboration and communication between human-human vs human-bot teams: an experimental study, ***6.Ruchika Jain***, ***3.Naval Garg*** and ***3.Shikha N. Khera***, DSM, DTU

27. Convertible Uni-Bike Based on Inverted Pendulum Model and Prototype Using Additive Manufacturing, ***6.Rohit Kumar MISHRA***, ***8.1.Rishabh RATHORE***, ***8.1.Ritesh Kumar JANGID*** and ***8.SAMRAT***, Mechanical, DTU

28. Correlation Between COVID 19 and Selected Risk Factors: An Ecological Study, Deepak Dhamnetiya, Shalini Shalini, ***8.Abhishek Mehra*** and Ravi Prakash Jha, Mathematics and Computing, DTU

29. Cosmological tests of the osculating Barthel-Kropina dark energy model, Amine Bouali, ***7.Himanshu Chaudhary***, Rattanasak Hama, Tiberiu Harko, Sorin V. Sabau and Marco San Mart´ın, Applied Mathematics, DTU

30. DEA based fuzzy portfolio evaluation models integrated with TOPSIS techniques to rank the efficient Portfolios under different risk indicators, Abha Aggarwal, ***3.Anjana Gupta***, Rajkumar Verma and ***6.Reenu Kumari***, Applied Mathematics, DTU

31. Decoding the role of MDM2 as a potential ubiquitin E3 ligase and identifying the therapeutic efficiency of alkaloids against MDM2 in combating Glioblastoma, ***6.Sudhanshu Sharma*** and ***3.Pravir Kumar***, Biotechnology, DTU

32. Design and Analysis of Fabric Antenna for Medical and Wireless Applications, ***7.SHRUTI AWASTHI*** and ***3.Priyanka Jain***, Electronics, DTU

33. Design and analysis of wavelength tunable metamaterial reflector, ***6.Ankit***, ***3.Kamal Kishor*** and ***3.Ravindra Kumar Sinha***, Applied Physics, DTU

34. Design and Implementation of Different Machine Learning Algorithms for Credit Card Fraud Detection, ***8.Aditi Singh***, ***8.Anoushka Singh***, ***8.Anshul Aggarwal*** and ***3.Anamika Chauhan***, IT, DTU

35. Design of an Autonomous UAV for Racing Applications, ***8.Nimish Bahl***, ***8.Pooja Sahu***, ***8.Pranav Sharma***, ***8.Pranshu Gautam***, Arshpreet Singh and ***6.Akanksha Srivastava***, Electronics, DTU

36. Development and deployment of a Hybrid Controller for a Dual-Axis Solar Tracker System, ***8.Yatharth Ahuja***, ***8.Ghanvir Singh***, ***8.Sushrut M. Singh***, Suraj Bhat and Subir Kumar Saha, Electrical and Mechanical, DTU

37. DUAL GATE AlGaN/GaN MOS-HEMT BIOSENSOR FOR ELECTRICAL DETECTION OF BIOMOLECULES-ANALYTICAL MODEL, Ruby Mann, ***3.Sonam Rewari***, Shobha Sharma and R.S. Gupta, Electronics, DTU

38. ECG Signal Feature Extraction and Waveform Representation, Atul Kumar and ***6.1.Dinesh Kumar Atal***, Electrical, DTU

39. Effect of Ce4+→Ce3+ conversion on the structural and luminescence properties of Ce4+ doped Gd2Ti2O7 pyrochlore oxide, ***7.Umang Berwal***, ***3.Vinod Singh*** and ***3.Rinku Sharma***, Applied Physics, DTU

40. Effective Governance Through Crowdsourcing: A Strategic Framework for Empowered Participation, ***6.Divya Mishra*** and ***3.Nidhi Maheshwari***, USME, DTU

41. Evaluating the Robustness of Biomedical Concept Normalization, Sinchani Chakraborty, Srishti Gureja, Atif Hassan, Sayantan Basu, ***8.Harsh Raj*** and ***8.1.Tanmay Jain***, Mathematics and Computer, DTU

42. EXPLORING BEHAVIORAL BIASES IN STOCK MARKET: EVIDENCE FROM INDIA, ***3.Deepali Malhotra***, DSM, DTU

43. Exploring the psychometric properties of the Cyberbullying Attitude Scale (CBAS) and its relation with teasing and gratitude in Indian collegiate, ***6.Suhans Bansal*** and ***3.Naval Garg*** and Jagvinder Singh, USME, DTU

44. Fake News Detection via Graph-Based Markov Chains, ***8.Shashank Parmar***, ***8.Shashank Taneja*** and ***3.Rahul***, Software Engineering, DTU

45. Genetic Landscape of Major Depressive Disorder: Assessment of Potential Diagnostic and Antidepressant Response Markers, Priyanka Singh, Ankit Srivastava, ***7.Debleena Guin,*** Sarita Thakran, Jyoti Yadav, Puneet Chandna, Mamta Sood, Rakesh Kumar Chadda and Ritushree Kukreti, Biotechnology, DTU

46. Graphitic Carbon Nitride-Wrapped Metal-free PoPD-Based Biosensor for Xanthine Detection, ***6.Deeksha Thakur***, Chandra Mouli Pandey and ***3.Devendra Kumar***, Applied Chemistry, DTU

47. Identifying oral microbiome alterations in adult betel quid chewing population of Delhi, India, Mayank Bahuguna, Sunila Hooda, ***7.1.Lalit Mohan***, Rakesh Kumar Gupta and Prerna Diwan, Biotechnology, DTU

48. Investigation of Microstructure and Several Quality Characteristics of AA7075/Al2O3/Coconut Shell Ash Hybrid Nano Composite Prepared through Ultrasonic Assisted Stir-Casting, ***8.Ashish Kumar***, ***3.R.C. Singh***, and ***3.Rajiv Chaudhary***, Mechanical, DTU

49. Localization and Detection of Multiple Attacks in Wireless Sensor Networks Using Artificial Neural Network, ***6.Gebrekiros Gebreyesus Gebremariam***, ***3.J. Panda*** and ***3.S. Indu***, Electronics, DTU

50. Low Voltage Schmitt Trigger Full Adders Design for High Noise Immunity, ***6.1.Bhawanand Jha***, Kirti Gupta and ***3.Rajeshwari Pandey***, Electronics, DTU

51. Mobile Application based Tracking using GPS and GSM, ***8.Mayank Kumar Jarwal***, ***8.1.Abhimanyu Barun***, ***6.Akanksha Srivastava*** and Arshpreet Singh, Electronics, DTU

52. Mul-FaD: attention based detection of multiLingual fake news, ***8.Nishtha Ahuja*** and ***3.Shailender Kumar***, CSE, DTU

53. Negative Capacitance Multiplier Configuration Using Single CFOA Employing Grounded Capacitor, ***6.Meghana Shrivastava***, ***3.Pragati Kumar*** and ***3.D. R. Bhaskar***, Electrical, DTU

54. Nickel complexes bearing ONS chelating ligands: A promising contender for in vitro cytotoxicity effect on human pancreatic cancer MIA-PaCa-2 cells, Deepika Tanwar, Tashmeen Kaur, Robin Kumar, ***6.Deepali Ahluwalia***, Deepika Sharma and Umesh Kumar, Applied Chemistry, DTU

55. On the Approximation of Dam-Break Problems Using a Fuzzified HR-TVD Scheme, ***6.Ruchika Lochab*** and ***3.Vivek Kumar***, Applied Mathematics, DTU

56. Opinion Leaders for Information Diffusion Using Graph Neural Network in Online Social Networks, ***6.LOKESH JAIN***, ***3.RAHUL KATARYA*** and SHELLY SACHDEVA, CSE, DTU

57. Outage probability analysis of RF/FSO System Over Nakagami-m Fading and Fisher-Snedecor Distribution with Pointing Error, ***6.Rekha Rani***, ***3.Dr. Gurjit Kaur***, and Dr. Lakshmanan. M., Sirhan Maheshwari, Vikash Kumar Pandey, Sneha Porwal and Asad, Electronics, DTU

58. Performance Analysis of Cascaded FBGs at 10 Gbps with Different Dispersion Compensation Techniques, ***7.Divya Sisodiya*** and ***3.Deepika Sipal***, Electronics, DTU

59. Personality Detection using Kernel-based Ensemble Model for leveraging Social Psychology in Online Networks, AKSHI KUMAR, ***6.ROHIT BENIWAL*** and ***6.DIPIKA JAIN***, CSE, DTU

60. Post Quantum Public and Private Key Cryptography Optimized for IoT Security, Ajay Kaushik, ***8.Lakshmi Sai Srikar Vadlamani***, ***8.Mohammed Mohsin Hussain***, ***8.Milind Sahay***, ***8.Rahul Singh***, ***8.Ananya Komal Singh***, ***3.S. Indu***, Puneet Goswami, Nalliyanna Goundar Veerappan Kousik, CSE, Electronics and IT, DTU

61. Power Enhancement and Hotspot Reduction of a Rooftop Solar PV Array Using MOSFETs, ***6.Rahma Aman*** and ***3.M. Rizwan***, Electrical, DTU

62. Power Forecasting in Photovoltaic System using Hybrid ANN and Wavelet Transform based Method, ***6.Pooja Singh***, ***3.Anup Kumar Mandpura*** and ***3.Vinod Kumar Yadav***, Electrical, DTU

63. Robust Image Processing based Real-time Optical Mark Recognition System, ***8.Viraj Jain***, Siddharth Malik and Vimal Bhatia, Electrical, DTU

64. Scattering Parameter Analysis of Gate Stack Gate All Around (GS-GAA) FinFET at THz for RF Applications, ***7.Bhavya Kumar***, ***7.Megha Sharma*** and ***3.Rishu Chaujar***, Applied Physics, DTU

65. Secured healthcare monitoring for remote patient using energy-efficient IoT sensors, ***7.1.Bhaskar Kapoor***, Bharti Nagpal and Meshal Alharbi, CSE, DTU

66. Sentiment classification and analysis of twitter data on distance learning using ML classifiers, ***7.Farheen Ajaz***, ***8.Prince*** and ***3.Sumedha Seniaray***, Applied Mathematics, DTU

67. Shifting from traditional engineering education towards competency-based approach: The most recommended approach-review, ***3.Ruchika Malhotra***, ***6.Massoud Massoudi*** and ***3.Rajni Jindal***, Software Engineering and CSE, DTU

68. Single DXCCTA based Charge Controlled Floating Incremental/Decremental Memristor Emulator, ***6.Navnit Kumar***, ***3.Manjeet Kumar*** and ***3.Neeta Pandey***, Electronics, DTU

69. Software defect prediction using hybrid techniques: a systematic literature review, ***3.Ruchika Malhotra***, ***6.Sonali Chawla*** & Anjali Sharma, Software Engineering, DTU

70. SONG: A Multi-Objective Evolutionary Algorithm for Delay and Energy Aware Facility Location in Vehicular Fog Networks, Md. Muzakkir Hussain, Ahmad Taher Azar, Rafeeq Ahmed, Syed Umar Amin, Basit Qureshi, V. Dinesh Reddy, ***6.Irfan Alam*** and Zafar Iqbal Khan, CSE, DTU

71. Stopwatch Method For Assembly Line Production, ***8.S. Wangchuk*** and ***3.A.K Madan***, Production and Industrial and Mechanical, DTU

72. Super Ultra-Wideband Planar Antenna with Parasitic Notch and Frequency Selective Surface for Gain Enhancement, Pankaj Jha, Anubhav Kumar, ***3.Asok De***, and Rakesh Kumar Jain, Electronics, DTU

73. Targeting Y220C mutated p53 by Foeniculum vulgare-derived phytochemicals as cancer therapeutics, ***8.Saksham Garg***, ***8.Japneet Singh*** and ***3.Smita Rastogi Verma***, Biotechnology, DTU

74. The Problematics of Parenthood in the Shiva Trilogy by Amish, ***3.Saroj Bala*** and ***3.Rajiv Ranjan Dwivedi***, Humanities, DTU

75. Unwinding the modalities of necrosome activation and necroptosis machinery in neurological diseases, ***6.Rohan Gupta***, ***6.Smita Kumari***, ***6.Rahul Tripathi***, ***6.Rashmi K Ambasta*** and ***3.Pravir Kumar***, Biotechnology, DTU

1. *Vice Chancellor*
2. *Pro Vice Chancellor*
3. *Faculty*
4. *Teaching-cum-Research Fellow*
5. *Asst. Librarian*
6. *Research Scholar*
7. *PG Scholar*
8. *Undergraduate Student*

1.1. *Ex Vice chancellor*
2.1. *Ex Pro Vice Chancellor*
3.1. *Ex Faculty*
4.1. *Alumni*
5.1 *Others*
6.1. *Ex Research Scholar*
7.1. *Ex PG Scholar*
8.1. *Ex Undergraduate Student*

Materials Today: Proceedings xxx (xxxx) xxx

Contents lists available at ScienceDirect

Materials Today: Proceedings

journal homepage: www.elsevier.com/locate/matpr

A bibliometric analysis of cold spray coating process using VOSviewer

Ayaz Mehmood [a,b,*], Mohammad Zunaid [b], Ashok Kumar Madan [b]

[a] Department of Mechanical Engineering, Mewat Engineering College (Wakf), Nuh, Haryana 122107, India
[b] Department of Mechanical Engineering, Delhi Technological University, Bawana Road, Delhi 110042, India

ARTICLE INFO

Article history:
Available online xxxx

Keywords:
Bibliometric analysis
Cold spray
Deformation
Coatings
VOSviewer

ABSTRACT

Cold spray coating is an Additive Manufacturing technology that is accustomed to amend surfaces of the substrate and improves many benefits in material engineering applications. This is a high-velocity solid state spray technique that uses temperatures sufficiently below the melting point of the products to preserve their chemical and physical properties. A thorough examination of 387 documents found in the Scopus database from 1999 to 2022 was carried out. In this study, we analyzed cold spray research and its evolution using a bibliometric approach and scientometric evaluation using the free tool VOSviewer to create bibliometric maps. These maps help in understanding the overall development, research trends, and major gaps identified in the literature. We identified prolific authors, their work, contribution and collaboration in the field of cold spray research, important publishing sources, and keyword assessment based on co-occurrence using density visualization maps that help in understanding research gaps. Despite several successful experiments, cold spray on brittle materials has received little attention, because of its high specific strength, fatigue resistance, biocompatibility and corrosion resistance, the cold spray has potential applications in aircraft parts, medical implant materials and protective coatings highlighting the need for research in this area.
© 2023 Elsevier Ltd. All rights reserved.
Selection and peer-review under responsibility of the International Conference on Advancements in Manufacturing Engineering – 2022.

1. Introduction

Cold spray is a powder deposition spraying technology that became popular in past years, the 'Institute for Theoretical and Applied Mechanics' introduced it in Russia 1980 s [1]. This method used solid particles that push along with carrier gases towards the substrate that create the thickness of the coating ranging from (100–1500) μm [2]. It has a considerable advantage over others such as plasma spray, HVOF and laser cladding since there is no melting so less chance of oxidation, evaporation, and a mismatch in microstructure and expansion [3,4]. The benefits of multi-component coatings on complex shapes with perfect bonding and tolerances are increasing significantly in many industrial applications [5]. Another technological benefit of cold spray is to mount the substrate on platform additive manufacturing to control the spraying gun with a robot arm to produce intricate structures [6].

Cold spray is especially important when applied to metal ceramics-based coatings that use mixed powders because it improves surface qualities and functionality in corrosive and abrasive conditions [7]. When compared to ductile materials, the effect of ceramic particles on the binding strength of cold spray composite coatings on AZ91 alloy substrates at 65 °C and 125 °C has an increased density and better hardness, and deposition efficiency is around 50 %, resulting in denser and harder coatings that are anticorrosive and wear-resistant, ceramics composite materials using various melting points [8,9]. Metals, ceramics, composites, and polymers, among other materials, can be deposited, providing a wide range of intriguing potential for obtaining specific features [10]. An experimental 2-D model reported size and crystallographic structures, molecular dynamics in the manufacturing of ceramics is the initial step in cold spray this approach used additional deformation techniques as well as more complex 3-D calculating systems [11]. The effect of substrate qualities at temperatures ranging from room temperature to 400 °C sprayed TiO2 on (C1020) and (AA1050), some oxide layer remained even after high jet impingement, oxides layers stuck on metals that annealed, causing plastic deformation of the substrate and pre-

* Corresponding author.
E-mail address: ayaz.amu09@gmail.com (A. Mehmood).

https://doi.org/10.1016/j.matpr.2022.12.135
2214-7853/© 2023 Elsevier Ltd. All rights reserved.
Selection and peer-review under responsibility of the International Conference on Advancements in Manufacturing Engineering – 2022.

Please cite this article as: A. Mehmood, M. Zunaid and A.K. Madan, A bibliometric analysis of cold spray coating process using VOSviewer, Materials Today: Proceedings, https://doi.org/10.1016/j.matpr.2022.12.135

heating increased the bonded area by six times which causes splat adhesion strength by 30 % [12,13].To design and simulate the impact process and particle flows during coatings, FEA and CFD tools are used and the numerical simulation approaches strengthen process parameters towards coatings and modulated porosity and strength [14,15]. Heat transfer properties are deterministic when coatings are simulated to determine bulk heat generation in the coating and substrate using axisymmetric models [16].

Bibliometric analysis is one of the research strategies used to efficiently perform scientific studies and analyze data. It aids in focusing data findings, demonstrates the literature's current trend concerning a particular research subject, and aids in predicting future research and its consequences for everyday life [17]. Bibliometric analysis is a metric analysis that provides the broad contours and overall structure of the research field [18]. The field of bibliometric has recently received a lot of attention from the scientific community. Today, bibliometric is recognised as a practical method for establishing a broad framework for a specific area of scientific inquiry [19]. Although it is primarily concerned with the study of libraries and information, it has been actively applied in a variety of other academic subjects [20,21].

2. Bibliometric data and method

Scientific documents were analyzed and an assessment of literature data globally to establish facts, a bibliometric analysis was conducted [22]. In this study, 23 years of published articles were retrieved from Scopus and bibliographic mapping was performed [23].

The extracted results were downloaded as a comma-separated value format (.csv) file in the collected article's format containing: full records and cited references. Fig. 1, shows a schematic of the bibliometric analysis and methodological process.

Each item selected and only publications based on keywords searched in the Scopus database are as TITLE-ABS-KEY (*"COLD SPRAY" AND "DEFORMATION" AND "COATINGS"*) used. As a result, 387 articles were found and filters were utilised to extract the relevant papers, data collection, and assessment evaluation conducted with relevant bibliometric parameters.

3. Results and discussion

3.1. Annual trends of scientific publications

As depicted in Fig. 2, Material science and engineering are the two leading areas of research with 45 % and 25 % of articles, respectively.

Fig. 3 depicts a research trend analysis based on the number of publications and cumulative publications, as well as publication years. The total number of research papers are 248, and the first literature document was published in 1999. From 2008 the number of publications in each year grew exponentially till the current year. In 2020 maximum number of papers published was around

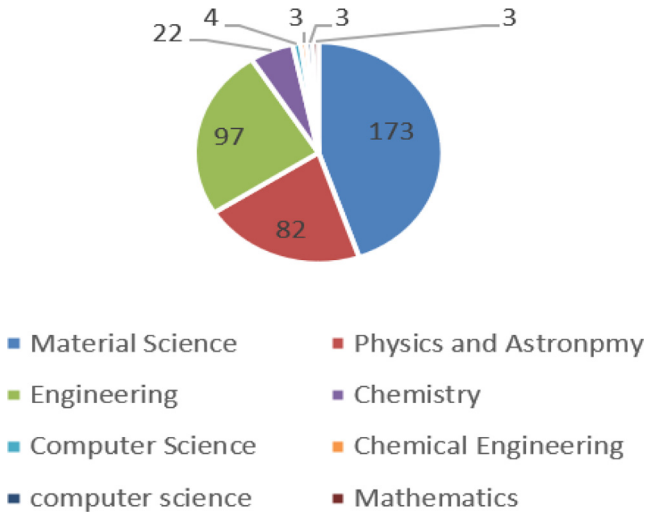

Fig. 2. Subject area of in Cold spray study.

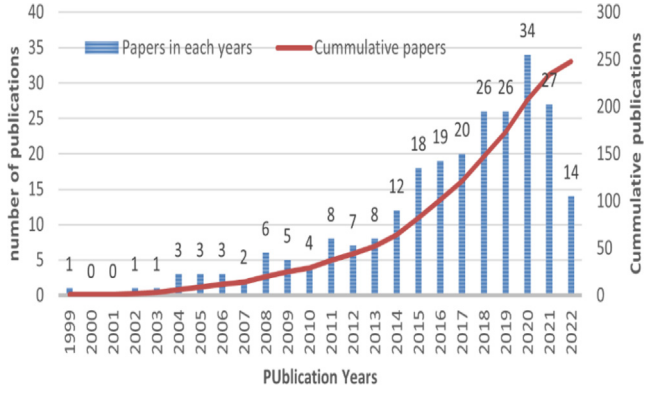

Fig. 3. Level of development of research on cold spray coatings.

34. However, 14 articles published in 2022 so far. Furthermore, the cumulative database suggests attention was given since 2004 and three publications in each year till 2006. From 2008 – 2013, the annual output was less than 10 articles per year. This could be interpreted as an underdeveloped growth and its practical applications [24]. The research advanced after 2013 indicates an improvement in the cold spray structure and physical and chemical properties of powders - substrate [25]. Some innovative papers came in 2014, and afterwards many researchers started interest and broke this false assumption. This trend is likely to continue in the years to come, as cold spray technology progresses and its uses on other engineering materials impact industrial development [26].

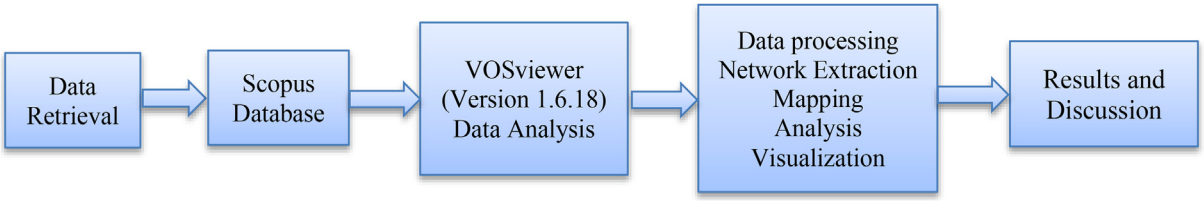

Fig. 1. Steps involved in data assessment and bibliometric analysis.

3.2. Analysis of influential authors and Co-authorship mapping

The influential authors and their pioneer research in a certain academic field can be demonstrated by the number of citations received and collaborated contributions, facilitating knowledge transfer, ideas and concepts [27]. Out of 748 authors, 27 met the requirement of having at least 5 publications. The most publications by authors are Jodoin b. (13) articles, followed by Liao h. (10) and Xie y. (10) articles, Assadi h. and Champagne v.k. (9) articles each respectively. Assadi h. is first with total citations (1347), Gartner f. is at second with (1308) followed by Klassen t. with (465) citations in this field of research. Moreover, when average citations are considered, Assadi h. with nearly (149.7), is at the top followed. by Yue s. second with (55.1), while Li c.-j..at third with (47.1) citations on average as mentioned in Table 1. Liao h, Lic-j., and Yue s. are the top authors in terms of h index > 40 [28]. This shows that most of the authors are inspired in the same direction of research at most stages consisting, of metallic materials powders, composite coatings on materials and analyses of microstructure, bonding, and corrosion behaviour.

Fig. 4 depicts the author and co-author relationship through visualization of citations. However, it is critical to identify developing authors based on their average annual publication with a co-author. It was discovered that the most recent three authors in this discipline were all from China. However, two of them (Sun. w. and Xie. y) from the same institution (National Engineering Laboratory for Modern Materials Surface Engineering Technology) and one author (Chen. c) from (the State Key Laboratory of Advanced Special Steels), whose research is generally around 2016–2021.

3.3. The network visualization of sources

The most prestigious authors share their findings along with citations and source references. Researchers may also quickly and simply select the best sources for their study publishing based on their research, the journal's reputation, and citations [29,30].

Fig. 5 provides statistics for the five main sources of publications from 2015. 'Surface and Coatings Technology' has dramatic increase since 2017 and almost steady publications on average afterwards. With an increase in the number of publications in 'Coatings' and 'Acta Materialia' which are emerging sources and the 'Journal of Thermal Spray Technology' and 'Applied Surface Science' the quantity published is fewer and has shown a declining trend.

Out of 75 sources, 19 met the requirement of having at least 3 documents published. The same cluster journals and node size signifies higher citations [31]. Overall, five sources contributed to 72 % of publications on cold spray, although some of them are not included in Table 2, we identified such sources, and articles and mentioned them in section 3.4. The 'Journal Surface and coatings technology' is at first rank, and is highly popular among researchers followed by 'Journal of Thermal Spray Technology, 'Applied Surface Science' and 'Acta Materialia in terms of the number of publications. Higher citation means a lot of dynamic research on cold spray accepted by particular sources [32].

In this study, we analyzed 'Surface and Coatings technology' at the top in terms of citations (1797). The number of citations per document reveals the importance of the journal articles, it reflects that 'Acta Materialia', 'Scripta Materialia' and 'Applied Surface Science' are the top three journals and their average citations per document are (159.67), (75.4) and (60.38) respectively. Although 'Acta Materialia' comes out as to highly impact source due to the maximum citation per document and large TLS.

In Fig. 6, the journals are divided into seven groups: red (5 journals), green (3 journals), blue (3 journals), yellow (3 journals), violet (3 journals), cyan (1 journal), and orange (1 journal) . The stronger the connection between two journal nodes, the shorter their link [33].

3.4. Most influential publications

In this section, out of 248 documents, 36 met the requirement of having 50 citations for each document. The 10 most cited studies found in the Scopus database are mentioned in Table 3. Most researchers cite documents for academic work with more citations due to work being extremely high and suitable [34].

The most cited paper by Schmidt t. (2006) published in Acta Materialia with total citations of 856, analyzed Adiabatic shear instability (ASI) on Cu and 316L (steel) using particle size (25–50) μm with decreased critical velocity 600 m/s results larger particles, at or beyond 500 m/s caused high-rate deformation due to different material properties and particle size [35]. Three publications before Schmidt t., in (1999), (2002) and (2003) on cold spray focus on the impact of high-velocity powder using ductile materials such as copper/aluminium/stainless steel/silver etc. as shown in Fig. 7., both as powder and substrate characterization.

The second most cited paper is by Assadi h (2016) in again Acta Materialia with a total of citations 432 highlights cold spray is two-fold: (a). surface technology and (b). solid-state additive manufacturing process, offering an alternative to selective laser melting or electron beam melting methods, uses a high-pressure supersonic jet at critical velocities (500–1200) m/s, the kinetic energy rupture surface oxide and deforms particles plastically. This study reveals that ASI may consider a prerequisite for bonding on metals [36]. The third paper is 'Cold-gas dynamic-spray process interfacial bonding between feed-powder particles and the substrate: a computational study' by Grujicic. m (2003) having total citation 411, published in the journal 'Applied Surface Science' studies the impact of Al particle with the incident velocity of 650 m/s and a flat infinite copper substrate at four instant observed plastic deformation under high impact pressure using Cu particles on the steel substrate [37].

We observed that out of the ten most cited papers worldwide, based on the publication year (2015), source (material and design)

Table 1
Leading author of the topic cold spray.

Author	Institutions	Country	Documents	Total citations	Average citations	Total h index
jodoin b.	University of Ottawa	Canada	13	255	19.6	41
liao h.	ICB UMR 6303	France	10	376	37.6	61
xie y.	National Engineering Laboratory	China	10	191	19.1	21
assadi h.	Brunel University London	UK	9	1347	149.7	33
li c.-j.	State Key Laboratory	China	9	424	47.1	64
yin s.	Trinity College Dublin	Ireland	9	379	42.1	35
champagne v.k.	U.S. Army Research Laboratory	USA	9	229	25.4	32
ogawa k.	Tohoku University	Japan	8	207	25.9	24
chromik r.r.	McGill University	Canada	8	170	21.3	36
yue s.	McGill University	Canada	7	386	55.1	56

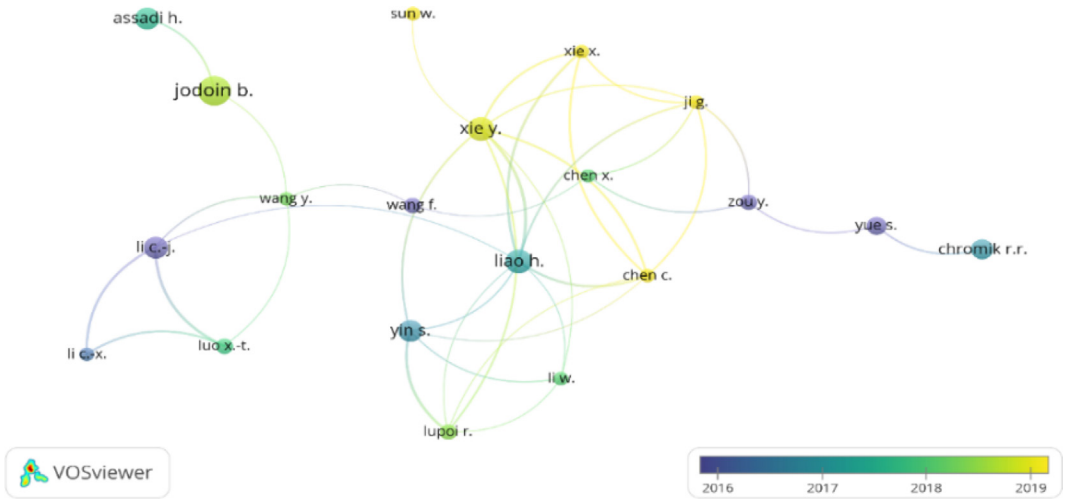

Fig. 4. Overlay Visualization of Co-authorship analysis.

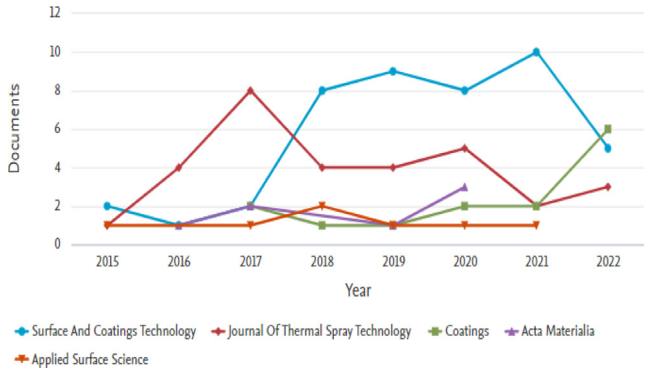

Fig. 5. The number of publications by source.

and the number of citations (130). Luo x.-t, studies on 'Microstructure and mechanical property of Ti and Ti6Al4V prepared by an in-situ shot peening assisted cold spraying' concluded that the shot peening technique on large size particles, showed plastically deform layer enhanced and porosity declined, this is one of the influential studies in cold spray [45]. However many researchers have investigated using metallic materials such as copper, titanium, steel, and high entropy alloy, to develop and optimize the spray parameter feedstock properties and substrate conditions to understand the bonding mechanism of cold spray [46].

3.5. The density visualization of keywords Co-occurrence

Density visualization is interpreted by the font's size, the background of keywords and density colour are used to define TLS. The order of sequence is TLS of yellow > green > blue. The distance between each keyword indicates how closely the research topics are related [47]. Co-occurrence analysis was done in two criteria I: "in the title, abstract, or keyword" and II: "author-provided keywords". In criteria I, All the keywords (2142), out of these selected keywords (341) are threshold based on a minimum of three co-occurrences in Fig. 8(a). Criteria II, keywords (661) are generated and (28) met the threshold of five occurrences in Fig. 8(b). Terms often associated with a cold spray like 'grain refinement', 'spray nozzle', 'substrate' and 'binary alloy' do not appear in Fig. 8(b), due to different occurrences of keywords and TLS. The keyword cold spay is also associated with other parameters such as 'bonding mechanism', 'residual stresses', 'recrystallization', and 'numerical simulation', Fig. 8(b) conclude that the occurrence of these types of keywords are least in terms of their TLS, and research publications in the past years have not diversified yet.

Furthermore, the study is required to identify proper materials selection, powder refinement procedure and its toxicity, and use of CFD for analysis and design of geometries that help this field to reach the highly advanced level and could be suitable in other applications [9,48]. Cold spray process works well on automotive and aircraft material coating and maintenance, however, this method is still not properly investigated in the field of biomedical, so far thermal spray method is only used with limitations [49].

Research Gaps and Potential Future Directions.

Some of the important keywords such as "metal matrix composite", "numerical simulation", "residual stresses", "composite coatings", and "recrystallization" have the lowest TLS of 7, 8, 10, 11, and 12 respectively in section 3.5. The inclusion of these keywords in research could improve the cold spray technology on a wider level and perform coatings on other substrates with the help of different materials and analysis techniques.

Table 2
List of main sources of cold spray research in the period 1999–2022.

Source	Publications	Citations	Citations per documents	Total link strength (TLS)
surface and coatings technology	59	1797	30.46	221
journal of thermal spray technology	37	1346	36.38	194
applied surface science	13	785	60.38	84
acta materialia	12	1916	159.67	215
coatings	11	70	6.36	31
surface engineering	8	154	19.25	32
materials science and engineering	6	197	32.83	29
international journal of advanced manufacturing technology	5	74	14.8	15
scripta materialia	5	377	75.4	64

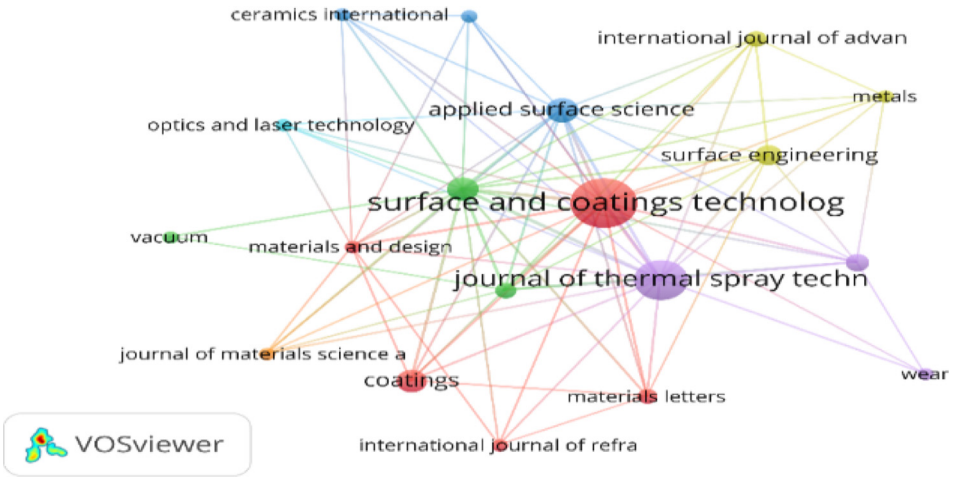

Fig. 6. The Network Visualization of sources.

Table 3
List of top ten influential papers on the topic of cold spray obtained up to July 2022.

Rank	Total citations	Title	Author	Journal	Ref.	Cluster
1	856	A generalized parameter window for cold spray deposition has been developed	Schmidt t. (2006)	Acta Materialia	[35]	2
2	432	Cold spraying – A materials perspective	Assadi h. (2016)	Acta Materialia	[36]	5
3	411	Cold-gas dynamic-spray process interfacial bonding between feed-powder particles and the substrate: a computational study	Grujicic m. (2003)	Applied Surface Science	[37]	6
4	358	High-velocity cold spray particles have an impact	Dykhuizen r. c. (1999)	Journal of Thermal Spray Technology	[38]	3
5	336	Coatings of aluminium using kinetic spray with relatively large powder particles	Steenkiste t. h.v. (2002)	Surface and Coatings Technology	[39]	3
6	180	Electron backscatter diffraction characterization of dynamic recrystallization in the particle/particle interfacial region of cold-sprayed nickel coating	Zou y. (2009)	Scripta Materialia	[40]	2
7	175	Cold spray metal coatings' residual stress and thermomechanical properties	Luzin v. (2011)	Acta Materialia	[41]	7
8	145	Particle Deformation, Coating Microstructure, and Property Relationship in High-Pressure Cold Spray	Rokni m.r. (2017)	Journal of Thermal Spray Technology	[42]	4
9	130	Ti and Ti6Al4V microstructures and mechanical properties prepared by in-situ shot peening assisted cold spraying	Luo x.-t. (2015)	Materials & Design	[43]	5
10	130	The effects of heat treatment on cold-sprayed coatings' mechanical properties	Huang r. (2015)	Surface and Coatings Technology	[44]	7

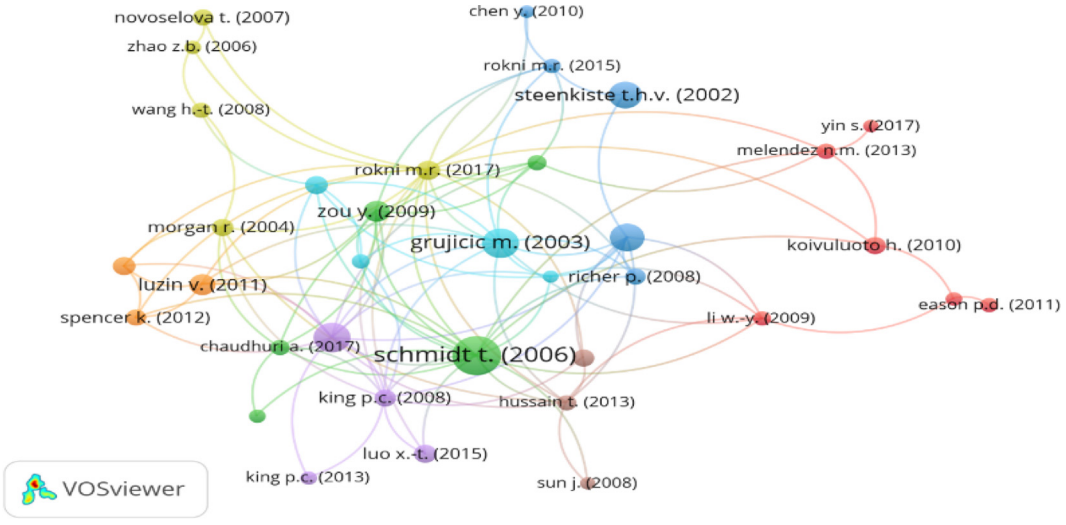

Fig. 7. The Network Visualization of documents based on citations.

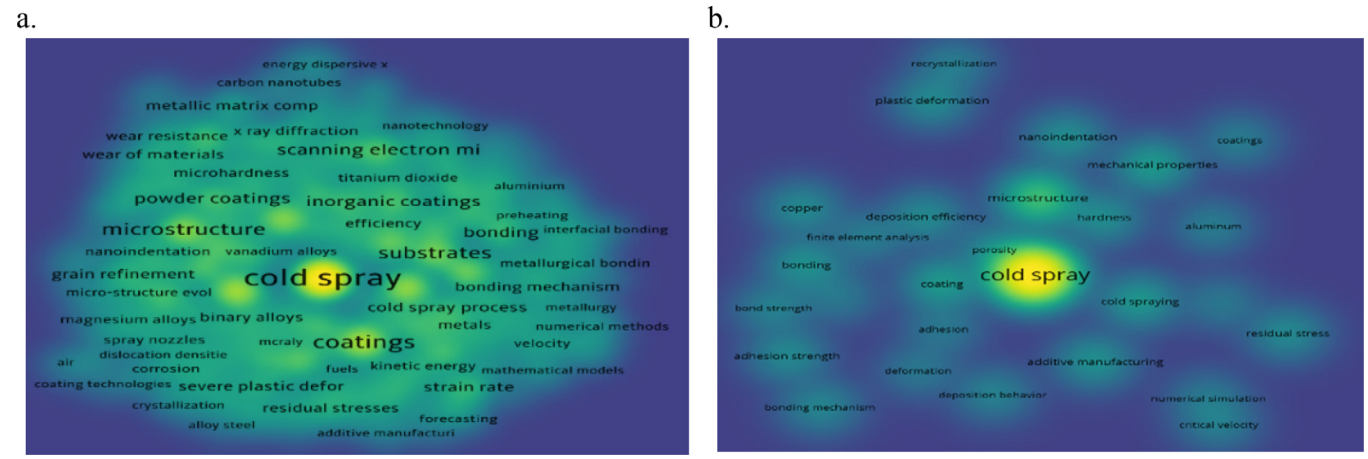

Fig. 8. (a). Density visualization of keywords co-occurrence in the title, abstract co-occurrence in the title, abstract, and keyword list minimum 3 occurrences; (b) Density visualization of keywords co-occurrence in the title, abstract co-occurrence in the title, abstract, and keyword list minimum 3 occurrences.

"Metal matrix composite" is useful for providing favorable properties due to constituent phases such as ductile intermetallic materials and hard ceramic particles that offer thermal and mechanical treatments in coatings to improve properties and macrostructure [50]. "Numerical simulation" consideration in the cold spray is useful to optimize and synthesize coatings on various powder-substrate combinations and would predict cold spray process characteristics, properties, and minimize expensive experiments and save time. Moreover, it can be easy to use and extract maximum, more accurate information from synthesis coating conditions and parameters [15,51].

Another important term to investigate is "residual stresses," which can affect coatings microstructures, bonding mechanism, and repair quality. The evaluation of residual stress would benefit materials in a variety of engineering applications in various environments by improving fatigue life. Residual stresses in Cu and its alloys extend coating life [52].

4. Conclusions and perspectives for future studies

In this study, we performed a comprehensive bibliometric mapping on cold spray by analyzing its relevant literature using VOSviewer and retrieved 387 research articles from the Scopus database. Around 70 % of the relevant documents were published in the area of material science and engineering. The first article was published in 1999, but significant research interest began in 2008, as the trend suggests. The most cited authors were from Canada, France, Germany, China, and the United States, with only a few collaborations with authors from other countries.

Based on publications, average citation, and author's document citations Jodoin. b. having 13 publications followed by (Lio. H, Xie. Y) With 10 each and (Assadi h, Lic. J) with 9 publications. In terms of average citations Assadi h. at rank first, Yue.S. with rank second, and Lic.J. rank third. However, an assessment of the author's document showed that Schmidt t. has received 856 citations. Assadi h and Grujicic m acquired 432 and 411 citations, respectively, they were the leading authors. But the most influential author is Luo x.-t with 130 citations published source is 'material and design' in 2015. Holistic analysis on cold spray reflects Assadi. h is the most influential author in terms of overall assessments. Source publish documents, the assessment showed that "surface and coating technology", "Journal of thermal spray technology", "Applied Surface Science" and "Acta Materialia" are the leading sources, with 59, 37, 13 and 12 articles, respectively. Overall citations show that the leading sources are "Acta Materialia" (1916), "surface and coating technology" (1797), and "journal of thermal spray technology" (1346) citations. The result from the analysis of the keywords co-occurrence density visualization indicates additional research on cold spray is required. Material like ceramics, metallic glasses and WC-metal composites, biomedical materials are rarely used so far. Other keywords such as metal matrix composite, numerical simulation and residual stresses need to be incorporated in cold spray analysis that would help to find improved microstructure, save efforts in time-consuming experiments and offer wider applications of cold spray due to improved coatings life. These gaps provide an opportunity for researchers to advance the field of cold spray coatings. In the future, further research may consider including scientific publications and academic sources in other bibliometric parameters for similar analyses. The findings of this paper will assist specialists in expanding their understanding of the subject and may inspire them to develop new ideas.

Data availability

No data was used for the research described in the article.

Declaration of Competing Interest

The authors declare that they have no known competing financial interests or personal relationships that could have appeared to influence the work reported in this paper.

Acknowledgements

This work was supported by Delhi Technological University, Delhi

References

[1] A. V. B. Fernando Santos da Silva, Nuria Cinca, Sergi Dosta, Irene Garcia Cano, Josep Maria Guilemany, "Cold gas spray coatings: basic principles, corrosion protection and applications," *Eclética Química J.*, vol. 42, pp. 9–32, 2017.

[2] M. Meyer and R. Lupoi, "An analysis of the particulate flow in cold spray nozzles," no. 2013, pp. 127–136, 2015, doi: 10.5194/ms-6-127-2015.

[3] F. Ghadami, A.S.R. Aghdam, Improvement of high velocity oxy-fuel spray coatings by thermal post- treatments : a critical review, Thin Solid Films 678 (February) (2019) 42–52, https://doi.org/10.1016/j.tsf.2019.02.019.

[4] Q. Xu, Y. Zhang, S. Liu, C. Li, C. Li, High-temperature oxidation behavior of CuAlNiCrFe high- entropy alloy bond coats deposited using high-speed laser cladding process, Surf. Coat. Technol. (2020), https://doi.org/10.1016/j.surfcoat.2020.126093.

[5] M. Sathish, N. Radhika, B. Saleh, A critical review on functionally graded coatings : methods, properties, and challenges, Compos. Part B 225 (April 2021), https://doi.org/10.1016/j.compositesb.2021.109278.

[6] K.S. Al-Hamdani, J.W. Murray, T. Hussain, A. Kennedy, A.T. Clare, Cold sprayed metal-ceramic coatings using satellited powders, Mater. Lett. 198 (2017) 184–187, https://doi.org/10.1016/j.matlet.2017.03.175.

[7] P. Petrovskiy, M. Doubenskaia, A. Sova, A. Travyanov, Surface & Coatings Technology Analysis of copper-tungsten cold spray coating : kinetics of coating formation and its thermal properties, Surf. Coat. Technol. 385 (January 2020), https://doi.org/10.1016/j.surfcoat.2020.125376.

[8] Q. Wang, K. Spencer, N. Birbilis, M.X. Zhang, The influence of ceramic particles on bond strength of cold spray composite coatings on AZ91 alloy substrate, Surf. Coat. Technol. 205 (1) (2010) 50–56, https://doi.org/10.1016/j.surfcoat.2010.06.008.

[9] S. Kumar, M. Kumar, N. Jindal, Overview of cold spray coatings applications and comparisons: a critical review, World J. Eng. 17 (1) (2020) 27–51, https://doi.org/10.1108/WJE-01-2019-0021.

[10] A. Moridi, S. Hassani-Gangaraj, ... M. G.-S., and undefined 2014, "Cold spray coating: review of material systems and future perspectives," *Taylor Fr.*, Accessed: Feb. 18, 2022. [Online]. Available: https://www.tandfonline.com/doi/abs/10.1179/1743294414Y.0000000270.

[11] B. Daneshian, F. Gärtner, H. Assadi, M.V. Vidaller, D. Höche, T. Klassen, Features of ceramic nanoparticle deformation in aerosol deposition explored by molecular dynamics simulation, Surf. Coat. Technol. 429 (September 2021) 2022, https://doi.org/10.1016/j.surfcoat.2021.127886.

[12] N.I. Omar, M. Yamada, T. Yasui, M. Fukumoto, Bonding mechanism of cold-sprayed TiO2 coatings on copper and aluminum substrates, Coatings 11 (11) (2021) 1–21, https://doi.org/10.3390/coatings11111349.

[13] R. Ortiz-Fernandez, S. Imbriglio, R. Chromik, B. Jodoin, The role of substrate preheating on the adhesion strength of cold-sprayed soft particles on hard substrates, J. Therm. Spray Technol. 30 (3) (2021) 655–667, https://doi.org/10.1007/s11666-020-01148-w.

[14] T. Yu, M. Chen, Z. Wu, Experimental and numerical study of deposition mechanisms for cold spray additive manufacturing process, Chinese J. Aeronaut. 35 (2) (Feb. 2022) 276–290, https://doi.org/10.1016/j.cja.2021.02.002.

[15] M. Terrone, A. Ardeshiri Lordejani, J. Kondas, S. Bagherifard, A numerical Approach to design and develop freestanding porous structures through cold spray multi-material deposition, Surf. Coat. Technol. 421 (June 2021), https://doi.org/10.1016/j.surfcoat.2021.127423.

[16] O.C. Ozdemir, Q. Chen, S. Muftu, V.K. Champagne, Modeling the continuous heat generation in the cold spray coating process, J. Therm. Spray Technol. 28 (1–2) (2019) 108–123, https://doi.org/10.1007/s11666-018-0794-z.

[17] P. K. Muhuri, A. K. Shukla, and A. Abraham, "Industry 4.0: A bibliometric analysis and detailed overview," *Eng. Appl. Artif. Intell.*, vol. 78, no. December 2018, pp. 218–235, 2019, doi: 10.1016/j.engappai.2018.11.007.

[18] A. Naveau, R. Smirani, S. Catros, and H. De Oliveira, "applied sciences A Bibliometric Study to Assess Bioprinting Evolution," pp. 1–16, 2017, doi: 10.3390/app7121331.

[19] A.M. Moshiul, R. Mohammad, F.A. Hira, N. Maarop, Alternative marine fuel research advances and future trends: a bibliometric knowledge mapping approach, Sustain. 14 (9) (2022) pp, https://doi.org/10.3390/su14094947.

[20] J. M. Merigó, A. Rocafort, and J. P. Aznar-alarcón, "Bibliometric Overview of Business & Economics," vol. 1699, no. June, 2016, doi: 10.3846/16111699.2013.807868

[21] O. Ellegaard, J.A. Wallin, The bibliometric analysis of scholarly production: how great is the impact?, Scientometrics 105 (3) (2015) 1809–1831, https://doiorg/10.1007/s11192-015-1645-z.

[22] G.A. Fordjour, A.Y.M. Chow, Global research trend and bibliometric analysis of current studies on end-of-life care, Int. J. Environ. Res. Public Health 19 (18) (2022) pp, https://doi.org/10.3390/ijerph191811176.

[23] L.F. Cabeza, M. Chàfer, É. Mata, Comparative analysis of web of science and scopus on the energy efficiency and climate impact of buildings, Energies 13 (2) (2020) pp, https://doi.org/10.3390/en13020409.

[24] A. Srikanth, G. Mohammed Thalib Basha, and B. Venkateshwarlu, "A Brief Review on Cold Spray Coating Process," *Mater. Today Proc.*, vol. 22, no. February 2021, pp. 1390–1397, 2019, doi: 10.1016/j.matpr.2020.01.482.

[25] P. Poza, M.Á. Garrido-Maneiro, Cold-sprayed coatings: Microstructure, mechanical properties, and wear behaviour, Prog. Mater. Sci. 123 (2022), https://doi.org/10.1016/j.pmatsci.2021.100839.

[26] D. Guo et al., Cold spray: over 30 years of development toward a hot future, J. Therm. Spray Technol. 31 (4) (2022) 866–907, https://doi.org/10.1007/s11666-022-01366-4.

[27] Y.M. Guo, Z.L. Huang, J. Guo, H. Li, X.R. Guo, M.J. Nkeli, Bibliometric analysis on smart cities research, Sustain. 11 (13) (2019), https://doi.org/10.3390/su11133606.

[28] I. Masic, E. Begic, Scientometric dilemma: is H-index adequate for scientific validity of academic's work?, Acta Inform Med. 24 (4) (2016) 228–232, https://doi.org/10.5455/aim.2016.24.228-232.

[29] T. Liskiewicz, G. Liskiewicz, J. Paczesny, Factors affecting the citations of papers in tribology journals, Scientometrics 126 (4) (2021) 3321–3336, https://doi.org/10.1007/s11192-021-03870-w.

[30] I. Tahamtan, A. Safipour Afshar, K. Ahamdzadeh, Factors affecting number of citations: a comprehensive review of the literature, Scientometrics 107 (3) (2016) 1195–1225, https://doi.org/10.1007/s11192-016-1889-2.

[31] L.H. Handoko, Bibliometric analysis and visualization of islamic economics and finance articles indexed in scopus by Indonesian authors, Sci. Ed. 7 (2) (2020) 169–176, https://doi.org/10.6087/KCSE.213.

[32] L. Huang, Z. Xia, Y. Cao, A bibliometric analysis of global fine roots research in forest ecosystems during 1992–2020, Forests 13 (1) (2022) 1–16, https://doi.org/10.3390/f13010093.

[33] H. A. Alkadhim *et al.*, "Knowledge Mapping of the Literature on Fiber-Reinforced Geopolymers: A Scientometric Review," *Polymers (Basel).*, vol. 14, no. 22, 2022, doi: 10.3390/polym14225008.

[34] L. Bornmann, R. Haunschild, S.E. Hug, Visualizing the context of citations referencing papers published by Eugene Garfield: a new type of keyword co-occurrence analysis, Scientometrics 114 (2) (2018) 427–437, https://doi.org/10.1007/s11192-017-2591-8.

[35] T. Schmidt, F. Gärtner, H. Assadi, H. Kreye, Development of a generalized parameter window for cold spray deposition, Acta Mater. 54 (3) (2006) 729–742, https://doi.org/10.1016/j.actamat.2005.10.005.

[36] H. Assadi, H. Kreye, F. Gärtner, T. Klassen, Cold spraying – a materials perspective, Acta Mater. 116 (2016) 382–407, https://doi.org/10.1016/j.actamat.2016.06.034.

[37] D.H.M. Grujicic, J.R. Saylor, D.E. Beasley, W.S. DeRosset, Computational analysis of the interfacial bonding between feed-powder particles and the substrate in the cold-gas dynamic-spray process, Appl. Surf. Sci. 3–4 (219) (2003) 211–227, https://doi.org/10.1016/S0169-4332(03)00643-3.

[38] R.C. Dykhuizen, M.F. Smith, D.L. Gilmore, R.A. Neiser, X. Jiang, S. Sampath, Impact of high velocity cold spray particles, J. Therm. Spray Technol. 8 (4) (1999) 559–564, https://doi.org/10.1361/105996399770350250.

[39] T.H.V. Steenkiste, J.R. Smith, R.E. Teets, Aluminum coatings via kinetic spray with relatively large powder particles, Surf. Coat. Technol. 154 (2–3) (2002) 237–252, https://doi.org/10.1016/S0257-8972(02)00018-X.

[40] Y. Zou, W. Qin, E. Irissou, J.G. Legoux, S. Yue, J.A. Szpunar, Dynamic recrystallization in the particle/particle interfacial region of cold-sprayed nickel coating: electron backscatter diffraction characterization, Scr. Mater. 61 (9) (2009) 899–902, https://doi.org/10.1016/j.scriptamat.2009.07.020.

[41] V. Luzin, K. Spencer, M.X. Zhang, Residual stress and thermo-mechanical properties of cold spray metal coatings, Acta Mater. 59 (3) (2011) 1259–1270, https://doi.org/10.1016/j.actamat.2010.10.058.

[42] M.R. Rokni, S.R. Nutt, C.A. Widener, V.K. Champagne, R.H. Hrabe, Review of relationship between particle deformation, coating microstructure, and properties in high-pressure cold spray, J. Therm. Spray Technol. 26 (6) (2017) 1308–1355, https://doi.org/10.1007/s11666-017-0575-0.

[43] X.T. Luo, Y.K. Wei, Y. Wang, C.J. Li, Microstructure and mechanical property of Ti and Ti6Al4V prepared by an in-situ shot peening assisted cold spraying, Mater. Des. 85 (2015) 527–533, https://doi.org/10.1016/j.matdes.2015.07.015.

[44] R. Huang, M. Sone, W. Ma, H. Fukanuma, The effects of heat treatment on the mechanical properties of cold-sprayed coatings, Surf. Coat. Technol. 261 (2015) 278–288, https://doi.org/10.1016/j.surfcoat.2014.11.017.

[45] X.T. Luo, Y.K. Wei, Y. Wang, C.J. Li, Microstructure and mechanical property of Ti and Ti6Al4V prepared by an in-situ shot peening assisted cold spraying, Mater. Des. 85 (November 2015) 527–533, https://doi.org/10.1016/j.matdes.2015.07.015.

[46] S. Singh, R. K. S. Raman, C. C. Berndt, and H. Singh, "Influence of cold spray parameters on bonding mechanisms: A review," *Metals (Basel).*, vol. 11, no. 12, 2021, doi: 10.3390/met11122016.

[47] H. He, M. Dyck, and J. Lv, "applied sciences The Heat Pulse Method for Soil Physical Measurements : A Bibliometric Analysis".

[48] S. Chadha, R. Jefferson-Loveday, T. Hussain, Modelling Knudsen number effects in suspension high velocity oxy fuel thermal spray, Int. J. Heat Mass Transf. 152 (2020), https://doi.org/10.1016/j.ijheatmasstransfer.2020.119454.

[49] T.Y. Liao et al., Multifunctional cold spray coatings for biological and biomedical applications: a review, Prog. Surf. Sci. 97 (2) (2022), https://doi.org/10.1016/j.progsurf.2022.100654.

[50] L. He and M. Hassani, *A Review of the Mechanical and Tribological Behavior of Cold Spray Metal Matrix Composites*, vol. 29, no. 7. Springer US, 2020. doi: 10.1007/s11666-020-01091-w

[51] T. Yu, M. Chen, Z. Wu, Experimental and numerical study of deposition mechanisms for cold spray additive manufacturing process, Chinese J. Aeronaut. 35 (2) (2022) 276–290, https://doi.org/10.1016/j.cja.2021.02.002.

[52] R. Fernandez, B. Jodoin, Cold spray aluminum-alumina cermet coatings: effect of alumina content, J. Therm. Spray Technol. 27 (4) (2018) 603–623, https://doi.org/10.1007/s11666-018-0702-6.

A Comparative Analysis of Consensus Algorithms for Decentralized Storage Systems

Pratima Sharma, *Bennett University, Uttar Pradesh, 201310, India*
Rajni Jindal, *Delhi Technological University, Delhi, 110042, India*
Malaya Dutta Borah, *National Institute of Technology Silchar, Silchar, Assam, 788010, India*

Blockchain has emerged as a revolutionary technology for various industrial applications of the next century. One of them is a decentralized storage system enabled by the corporation of Blockchain technology. In this context, Blockchain provides innovation to address traditional storage challenges by securely transmitting files through a fully decentralized network and eliminating the data failure risks that arise from a centralized structure. The decentralized storage system allows people to rent out unused hardware storage space and must prove that they store unaltered files. This study gives general readers an overview of decentralized storage technologies in various aspects, including background and technical details. Then, we explore the different consensus protocols used in the decentralized storage system. Finally, we discuss the various aspects of the Blockchain-based decentralized storage system.

A Blockchain system is a distributed network in which all nodes are connected with the help of different types of networks and are geographically scattered. Santoshi Nakamoto initially implemented the Blockchain concept in 2008.[1] Traditional storage system requires a trusted third party to confirm and store data. It suffers from many disadvantages like security, privacy, efficiency, cost, etc. Decentralization is the primary feature of Blockchain technology that solves the issues mentioned above. Blockchain provides a network where various participants who do not trust each other may share data in a shared network. Bitcoin is the first application of Blockchain technology that brought it into the global picture. Blockchain technology receives tremendous progress in the financial sector and other fields like supply chain, healthcare, Internet of Things, artificial intelligence, and decentralized storage.[2] Peer-to-peer storage systems such as Filecoin, Sia, Swarm, etc., provide an interesting Blockchain application that stores user data in a complete distributed network without involving trusted parties. The decentralized storage system helps us to eliminate the traditional data failures and outages by improving the data's security, privacy, and efficiency. The consensus algorithm plays an essential part in the Blockchain network to provide an efficient and secure system. Some popular decentralized storage system consensus algorithms are Proof-of-Storage, Proof-of-Resource, Proof-of-Retrievability, etc.[3] Till now, the focus is predominantly on the application of Blockchain in different fields. Therefore, this article presents an overview of decentralized storage systems and analyses various consensus algorithms used in these systems. It also presents the advantages and disadvantages of different decentralized storage systems in terms of various performance parameters. The article's main objective is to provide a better understanding of the different consensus algorithms in various decentralized storage systems to the researchers and academicians working in the same field.

1520-9202 © 2023 IEEE
Digital Object Identifier 10.1109/MITP.2022.3215433
Date of current version 11 January 2023.

DECENTRALIZED STORAGE SYSTEMS

Nowadays, marketplaces utilize Blockchain technology to use disk space as a commodity to provide users

Authorized licensed use limited to: DELHI TECHNICAL UNIV. Downloaded on January 19,2023 at 06:25:05 UTC from IEEE Xplore. Restrictions apply.

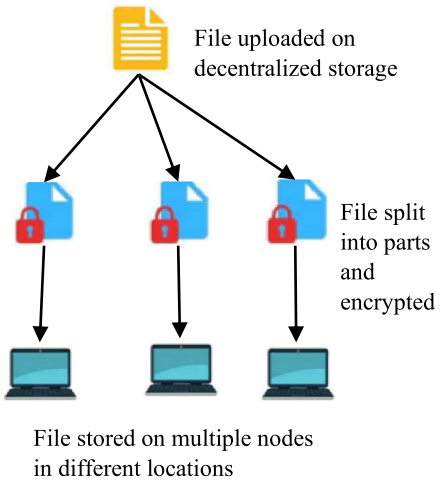

FIGURE 1. Working of decentralized storage systems.

storage services. Figure 1 shows the working of decentralized storage systems in which file is divided into multiple encrypted shared and then distributed on the various systems. This section explores some of the most popular decentralized storage systems.

MaidSafe

The MaidSafe is a peer-to-peer decentralized autonomous system that provides robust data storage and messaging service. It stores data efficiently and reliably by using the content addressable resource identifiers and self-encryption process. The Safe network limits the resource size to 1 MB. The client's data more than 1 MB is first divided into multiple chunks of less than or equal to 1 MB then chunks are distributed on the MaidSafe network. The MaidSafe network maintains resource identifiers of divided files in the form of an encryption datamap record that maintains the privacy feature and is further utilized to retrieve the entire file. It also uses Safecoin to incentivize resource suppliers.[4] The MaidSafe network implements a Proof-of-Resource consensus algorithm for the verification process.

Key Points

Applicability: The MaidSafe network utilizes the 256 bits resource identifiers that are determined by the resource's content. It ensures the immutability feature means that two similar copies will have the same identifier. The resource identifiers are simple, unique, encrypted, and efficient that increase the privacy features and provide secure messaging services. Thus, the MaidSafe network provides web hosting and Safemail services.

Advantages: The Safe network provides reliable data storage and communications services. It utilizes the content-addressable identifier and self-encryption to store data efficiently and effectively in the decentralized network and maintains the immutability, security, privacy, and reliability features.

Disadvantages: The MaidSafe network-based Safecoin is not available using Fait currencies. The user first buys bitcoin and then exchange it to the Safecoin tokens. Thus, this process increases processing time.

Storj

The Storj network is developed based on Ethereum Blockchain to provide a decentralized and trust-based storage system. The user who wants to store a large volume of data and keeps it on the Blockchain may create a bloating problem.[5] Thus, the Storj network only stores the Meta details of each file in the Blockchain network, which may include the details like file location, file hash, etc. It stores the Meta details in the encrypted form and allows the users to access their information anytime. The Storj network uses the Metadisk application that ensures the availability of stored files. The user file is stored in at least three locations because if the original file is destroyed, then also file can be retrieved as per the user's demand. This process is called Proof-of-Redundancy. All files are divided into multiple parts before storing on the Storj network. The divided parts are called shards, and the involved process is called sharding. Sharding ensures that no single node holds a complete copy of an uploaded file. Also, shards maybe blend with unnecessary information to make it hidden when important files are transmitted in the network. The Storj uses the Proof-of-Storage consensus algorithm in which there is a direct relation between the amount of free space available and more influence of the miner in the network. The Storj platform uses a peer-to-peer storage contract to provide an agreement between the space provider and the space renter. The renter represents the person who agrees to rent out the storage space. The storage contract has been built on top of a Distributed Hash Table (DHT).[19] Instead of a central server registry of every node, coordination of all contracts occurs using DHT.

Key Points

Applicability: The Storj provides a decentralized storage system with protection from malicious attacks. It ensures the privacy features using default encryption on every file. The Storj provides a low cost with a high throughput-based decentralized storage network.

Authorized licensed use limited to: DELHI TECHNICAL UNIV. Downloaded on January 19,2023 at 06:25:05 UTC from IEEE Xplore. Restrictions apply.

Advantages: The Storj leverages the advantages of latent storage and underutilized network capacity to incentivize the user worldwide to contribute free storage space to those who demand ultrasecure and private storage.

Disadvantages: The Storj user interface is a bit complicated to understand. It also lacks the software for IOS and Android to use in Mobiles. The Storj requires the hosting side to be simple and scalable for implementing a decentralized network.

Sia: A Decentralized Storage Network

Sia is a decentralized storage system in which nodes rent out disk space. The space providers are known as the node or hosts of the Sia network. The hashes of the file and the original file part are considered as storage proofs and publicly available.[6] Like Storj, the Sia network encrypts and digitally signs the data before uploading it to the Sia network. Also, the Sia network sets up a contract between the clients and hosts that defines the data storage duration and reward for valid and invalid proofs. It also utilizes the Merkle root concept to define the file proof for the hosts. Sia network uses its native currency (Siacoin) and open-source Blockchain network. The developers of the Sia network try to use it in other currency networks.

Key Points

Applicability: Sia focuses on creating a distributed, self-sustaining, and cheap marketplace for cloud users. It provides a full-fledged incentivization program to both customers and storage providers.

Advantages: Sia offers a simple and easy-to-use storage system with content-sharing facilities. It provides a strong solution to data security issues. Sia uses the smart contract concept to deploy the storage proof process between the host and the renter and ensure privacy features.

Disadvantages: The Sia network is not user-friendly for nontechnical users. If users lack the knowledge of using Siacoin and Bitcoin, it will be very hard for them to use the Sia platform.

Interplanetary File System (IPFS)

The IPFS is a distributed file system protocol that shares and stores data in a peer-to-peer network. IPFS connects all computing devices to the same file system with no single point of failure. It uses a content-addressing technique to identify the stored file in a global namespace uniquely. A content identifier, or CID, is a tag used in IPFS to point to the information. It does not reveal where the data are contained, but it forms a kind of content-based address. IPFS distributes information in the network using Distributed Hash Table, allowing any network peer to find and request the content from any node. The DHT allows fast access by representing content in the form of key-value pairs.[7]

Key Points

Applicability: IPFS network allows nodes to store and share data with DHT without a centralized authority. It uses public-key cryptography to ensure authentication and verification of shared data. IPFS utilizes the Merkle Directed Acyclic Graph to maintain the integrity of the stored data. For example, the user first generates the Merkle root of the file before uploading it on the IPFS. Then, store the root value in the block. For the integrity verification purpose, the stored root value is compared with the newly calculated value.[18] If both are the same, then the integrity is maintained. Thus, it provides uniquely marked, tamper-resistant, and secure storage services.

Advantages: IPFS users can communicate with each other even if the wide-area network is not available for some reason. IPFS requires no servers. Thus, users can distribute their work without any cost. It has higher bandwidth and thus provides a faster data loading service.

Disadvantages: IPFS provides a persistent data structure; hence there is no option for deleting or removing action. This is because the content is distributed among IPFS nodes. Also, IPFS does not guarantee that the uploaded content remains on the network.

Filecoin

Filecoin decentralized storage network executes on top of the IPFS network. IPFS is a distributed file system that connects all computing devices in a peer-to-peer network and removes a single point of failure problem. Filecoin helps the clients store data by utilizing the storage space offered by the storage provider without involving any trusted third parties.[8] Filecoin ensures clients that their data are safe throughout the time by using a consensus algorithm. It uses two consensus algorithms that are Proof-of-SpaceTime and Proof-of-Replication. Proof-of-SpaceTime ensures the clients that their data are being stored for a specific period. Proof-of-Replication ensures the clients that their data are not stored on a single node but rather safely distributed in the dedicated storage locations. The Filecoin network uses Filecoin (FIL) token for the reward system.

Authorized licensed use limited to: DELHI TECHNICAL UNIV. Downloaded on January 19,2023 at 06:25:05 UTC from IEEE Xplore. Restrictions apply.

Key Points

Applicability: Filecoin provides a distributed storage system that can be audited, validated, and incentively built. It offers the postal messaging protocol with storing privacy feature using JSON RPC interface.

Advantages: Filecoin has a built-in function to verify the stored files over time. The storage providers generate proof that they are maintaining the user files. Anyone can join the Filecoin network without needing permission. Filecoin resists censorship because no central provider can be coerced into deleting files or withholding service.

Disadvantages: Filecoin requires access confirmation from multiple servers to process transactions by the unification of documents. Thus, the rate becomes slow as servers are not always active.

SWARM

The Swarm platform is designed to manage and store Ethereum network public records in a decentralized manner. The Swarm network uses a counter mode encryption algorithm to encrypt and decrypt the client's data.[9] The Swarm node divides the file into multiple chunks and distributes them in the peer-to-peer network. Swarm supports data-streaming, storage, and payment services in which participants share bandwidth and storage space to provide the necessary infrastructure for the services. The Swarm architecture is divided into three layers. The first layer is the Swarm core, which contains network components and smart contracts to create and manage new services or projects. The second layer is Swarm services, which makes the investment service easier and increases operation facilities. The third layer is the Swarm app, which supports the applications that are not developed on the Swarm platform. The Swarm supports the proof-of-participation consensus algorithm. The participants have a significant share of assets of the Swarm network; for example, coins or tokens have more control in making decisions. Unlike the Proof-of-Work algorithm in which CPU power consumption considers as a deciding factor.

Key Points

Applicability: Swarm provides the infrastructure services for developers of Decentralized Applications. It also offers messaging services, storage insurance, payment channels, and database services to the users.

Advantages: Swarm network uses a hash table that gathers information as key/value sets called as DHT. Information is spread over a network in DHT and organized efficiently to allow fast access and lookup between nodes. Decentralization, fault tolerance, privacy, and scalability are the key benefits of DHT's.

Disadvantages: The encryption feature is nondeterministic in Swarm decentralized network. Due to the random key generated on every file upload, the user should not rely on the result, as uploading the same content with encryption enabled may result in a different result.

Table 1 summarizes the basic building blocks of decentralized storage systems.

DECENTRALIZED CONSENSUS ALGORITHMS

Consensus algorithms are responsible for verifying the transaction in a Blockchain network. This section explains the different consensus protocols using a prover $\mathcal{P}$, which tries to satisfy the verifier $\mathcal{V}$, that prover stores some data $\mathcal{D}$, verifier releases a challenge $\mathcal{C}$ to prover that response with an equivalent proof $\mathcal{T}_{\mathcal{C}}$ accordingly. The proof-based consensus protocols vary in terms of properties and features. Proof-based methods are mainly used in public blockchain networks, where security risks are more. In this method, any node may join the network freely, and nodes need to show they have performed sufficient proof and ready a block to be appended to the Blockchain. For creating proof, they will be rewarded. Some of the most prominent consensus algorithms used in decentralized storage are briefly discussed below.

Proof-of-Resource (PoR)

The PoR scheme allows prover $\mathcal{P}$ to assure verifier $\mathcal{V}$ that $\mathcal{P}$ spends some storage resources. The PoR scheme is based on a Proof-of-Work algorithm in which expended resources are not computation power but rather a storage space. The decentralized network uses PoR to check that suppliers (the nodes that store chunks of encrypted data) follow the network rules. PoR checks the node's ability based on CPU speed, the bandwidth available, online time, and storage space[10] to ensure that all the network nodes follow the network standard. If any node fails to reach the network standard, then the node will be removed automatically.

Proof-of-Storage (PoS)

The PoS algorithm considers an available free external hard drive capacity to select miner nodes. The node having higher free storage space can save multiple solutions to the nonce problem in the mining process. The PoS allows client $\mathcal{U}$ to outsource file $\mathcal{F}$ on server $\mathcal{S}$ and then continuously checks if $\mathcal{S}$ is still saving $\mathcal{F}$.

Authorized licensed use limited to: DELHI TECHNICAL UNIV. Downloaded on January 19,2023 at 06:25:05 UTC from IEEE Xplore. Restrictions apply.

TABLE 1. Decentralized storage systems basic building blocks.

Features	MaidSafe	Sia	Storj	Swarm	Filecoin	IPFS
Distributed Database	Autonomous distributed network for storage and communication	Independent Blockchain-based networks and agreements are built between renter and provider	The distributed contract between the seller and the purchaser of storage space	Offer P2P storage and service solutions	Peer to Peer storage marketplace built on IPFS	Distributed file-sharing system
Pay-per-use	Safecoin	Siacoin	Storj Tokens	—	Filecoin	Free storage
Encryption	Self-Encryption	Twofish Algorithm	—	Counter Mode Encryption	Asymmetric Encryption	Asymmetric Encryption
Consensus Mechanism	Proof-of-Resource	Proof-of-Storage	Proof-of-Retrievability	Proof-of-Participation	Proof-of-Replication and Spacetime	—
Privacy	Resource Identifiers ensure the immutability	Storage proof ensures security	Use Distributed Hash Table	Use Postal for privacy features	Ensures privacy by using DHT	DHT and Merkle DAG increase privacy
Reward System	Safecoin	Siacoin	Storj tokens	Built-in incentive	Filecoin	—
Status	Active	Active	Active	Building	In development	In development

The PoS method improves the Proof-of-Work node complexity issue and simplifies the overall process. Thus, in the PoS consensus, verifiers invest the storage space instead of expensive hardware or burning coins.[12] PoS receives great attention from researchers due to its inherent features and its linkage with digital signatures, proof, and correcting methods.[12]

Proof-of-Retrievability (PoRe)

The PoRe proof is a cryptographic-based method that allows storage providers to prove that a user can access the entire stored file. In simple words, a storage provider, or a prover $\mathcal{P}$ ensures the client $\mathcal{U}$ that a user uploaded file $\mathcal{F}$ is fully available for the access process. The storage system users frequently execute the PoRe algorithm to ensure that their files on the storage system can be retrieved at any time. PoRe algorithm requires less communication overhead; thus, it is used as an attractive consensus algorithm in various storage systems.[10]

Proof-of-Replication (PoRep)

The PoRep algorithms ensure that the prover $\mathcal{P}$ has a dedicated and unique physical storage structure to store $\mathcal{F}$ securely. The algorithm ensures that the prover $\mathcal{P}$ cannot deduplicate and keep $\mathcal{F}$ twice. The PoRep algorithm guarantees the proper replication process in decentralized storage systems. It also ensures that the file replica is saved independently without duplication.[11]

Proof-of-Spacetime (PoSt)

The PoS scheme helps a user see how a storage provider is storing the outsourced data at the challenge. In a PoS system, proving that any data are stored over a period of time is extremely difficult.[12] A natural solution to this problem is to make the consumer submit challenges to the storage provider regularly (e.g., every minute). However, in decentralized systems like Filecoin, where storage providers must upload their proofs to the Blockchain network, the communication difficulty involved in each interaction can be a constraint. To solve this problem, a new proof called Proof-of-Spacetime is implemented. A verifier may verify that a prover has stored the outsourced data they committed to over a period of time.

Table 2 summarizes the basic details of decentralized storage consensus algorithms.

DISCUSSION

This article evaluated various distributed technologies and identified the different consensus algorithms utilized in them with applications, advantages, and disadvantages.

Authorized licensed use limited to: DELHI TECHNICAL UNIV. Downloaded on January 19,2023 at 06:25:05 UTC from IEEE Xplore. Restrictions apply.

TABLE 2. Comparative analysis of decentralized storage consensus algorithms.

Features	PoR	PoS	PoRe	PoRep	PoSt
Blockchain-type	Public	Public	Permissioned	Public	Pubic
Decentralization	Medium	High	Medium	Low	Low
Reward	Safecoin	Siacoin	Storj tokens	Filecoin	Filecoin
Required resources	Storage space	Free disk storage	Free disk storage	Data replication	Storage space
Implementation	Safecoin	Spacemint, Burstcoin	Permacoin, Gochain	Filecoin	Filecoin
Decentralized storage	MaidSafe	Sia	Storj	Filecoin	Filecoin
Advantages	Provide utility to end-users proportional to the growth of network resources.	There is no need for dedicated hardware or constant upgrading of hard drives.	Incurs lower communication complexity.	Resistant to Sybil attacks[13] and provides a transparent, verifiable scheme for storage system.	Prefer storage over computing; thus requires less energy.
Disadvantages	Disbursement of network resources has not yet been formally specified and implemented.	Not many developers have adopted the algorithm.	It is possible for malware to affect mining activities.[15]	Slow encoding process.[14]	Suffers from incremental difficulty adjustment problem.[16]

As a result, we observed that blockchain technology brings enormous benefits, including improvements in the storage process, cost, and security as compared to existing cloud storage methods.[17] Blockchain offers excellent features in this sector, as it substantially lower data storage prices as well as provides additional data security levels due to its decentralized nature.[20]

Furthermore, Blockchain cloud storage systems take user data and split it into tiny chunks. Then, they add a security layer and distribute it across the network. Blockchain technologies such as hashing algorithms, public/private key encryption, and transaction ledgers can be used for this. In a decentralized environment, every chunk of data is stored. When intruders try to break it in, they will first get encrypted data, then only get a chunk of the data and not the whole file—this will protect documents in decentralized storage system.

Moreover, many new consensus algorithms have jumped into this new cloud storage market for Blockchain, and the entire business is taking on a new form. We have identified five consensus algorithms used in the different decentralized storage systems. It is observed that most of the algorithms are proof-based algorithms in which the renter sends the proof of stored data to the user on request or periodically. Any nodes can participate in the decentralized network with enough storage space. Each consensus algorithm has its own positive and negative points. Thus, the developer or researcher may select the algorithm depending on the requirements, such as if the user wants to reduce the communication complexity, then PoRe is the suitable algorithm. Depending on the priority, need, and requirements, the user may consider any decentralized storage system and algorithm.

CONCLUSION

Blockchain technology is a distributed approach that has attracted interest from various dimensions. Decentralized storage is one of the crucial areas that overcome many limitations of the traditional storage system. This article analyzes the various decentralized storage technologies based on different criteria. The consensus algorithm is the central concept of the decentralized storage system, but ongoing research on the decentralized consensus algorithm is still in its initial stage. Thus, a detailed overview of the decentralized storage consensus algorithm has been presented in this article. As a result, we observed that Blockchain could bring enormous benefits, including improvements in the storage process, cost, and security compared to existing methods. We intended to demonstrate that although Blockchain could change many sectors, it should not be seen as a perfect solution despite the excitement of this technology. Thus, we also present the advantages and challenges of various decentralized storage systems to provide a better understanding.

Authorized licensed use limited to: DELHI TECHNICAL UNIV. Downloaded on January 19,2023 at 06:25:05 UTC from IEEE Xplore. Restrictions apply.

REFERENCES

1. S. Nakamoto, "Bitcoin: A peer-to-peer electronic cash system," 2008. [Online]. Available: https://bitcoin.org/bitcoin.pdf
2. P. Sharma, R. Jindal, and M. D. Borah, "A review of blockchain-based applications and challenges," *Wireless Pers. Commun.*, vol. 123, pp. 1201–1243, 2022, doi: 10.1007/s11277-021-09176-7.
3. J. Nijsse and A. Litchfield, "A taxonomy of blockchain consensus methods," *Cryptography*, vol. 4, no. 4, pp. 1–15, 2020, doi: 10.3390/cryptography4040032.
4. N. Lambert, Q. Ma, and D. Irvine, "Safecoin: The decentralized network token," White Paper, 2015. [Online]. Available: https://docs.maidSafe.net/Whitepapers/pdf/Safecoin.pdf
5. S. Wilkinson, T. Boshevski, J. Brandoff, and V. Buterin, "Storj a peer-to-peer cloud storage network," White Paper, 2018. [Online]. Available: https://Storj.io/Storj.pdf
6. D. Vorick and L. Champine, "Sia: Simple decentralized storage," White Paper, 2014. [Online]. Available: https://prod.coss.io/documents/white-papers/Siacoin.pdf
7. J. Benet, "IPFS-content addressed, versioned, P2P file system," White Paper, 2014. [Online]. Available: https://arxiv.org/abs/1407.3561
8. P. Labs, "Filecoin: A decentralized storage network," White Paper, 2018. [Online]. Available: https://Filecoin.io/Filecoin.pdf
9. V. Trón, Á. fischer, N. Johnson, D. A. Nagy, and Z. Felföldi, "Swarm documentation release 0.5," White Paper, 2020. [Online]. Available: https://Swarm-guide.readthedocs.io/_/downloads/en/latest/pdf/
10. K. D. Bowers, A. Juels, and A. Oprea, "Proofs of retrievability: Theory and implementation," in *Proc. ACM Workshop Cloud Comput. Secur.*, 2009, pp. 43–54, doi: 10.1145/1655008.1655015.
11. J. Benet, D. Dalrymple, and N. Greco, "Proof of replication," Protocol Labs, San Francisco, CA, USA, Tech. Rep. 678, 2017.
12. S. Kamara, "Proofs of storage: Theory, constructions, and applications," in *Algebraic Informatics*, vol. 8080, T. Muntean, D. Poulakis, and R. Rolland, Eds., Berlin, Germany: Springer, 2013, doi: 10.1007/978-3-642-40663-8_4.
13. A. Hafid, A. S. Hafid, and M. Samih, "A tractable probabilistic approach to analyze sybil attacks in sharing-based blockchain protocols," *IEEE Trans. Emerg. Topics Comput.*, to be published, doi: 10.48550/arXiv.2104.07215.
14. B. Fisch, "PoReps: Proofs of space on useful data," *Protocol Labs*, 2018. [Online]. Available: https://eprint.iacr.org/2018/678
15. G. T. Nguyen and K. Kim, "A survey about consensus algorithms used in blockchain," *J. Inf. Process. Syst.*, vol. 14, pp. 101–128, 2018, doi: 10.3745/JIPS.01.0024.
16. S. S. Panda, B. K. Mohanta, U. Satapathy, D. Jena, D. Gountia, and T. K. Patra, "Study of blockchain-based decentralized consensus algorithms," in *Proc. IEEE Region 10 Conf.*, 2019, pp. 908–913, doi: 10.1109/TENCON.2019.8929439.
17. P. Sharma, R. Jindal, and M. D. Borah, "Blockchain technology for cloud storage: A systematic literature review," *ACM Comput. Surv.*, vol. 53, no. 4, pp. 1–32, 2021, doi: 10.1145/3403954.
18. P. Sharma, R. Jindal, and M. D. Borah, "Blockchain-based integrity protection system for cloud storage," in *Proc. 4th Int. Conf. Technol. Innov. Manage. Eng. Sci.*, 2019, pp. 1–5, doi: 10.1109/TIMES-iCON47539.2019.9024583.
19. M. Bernardini, D. Pennino, and M. Pizzonia, "Blockchains meet distributed hash tables: Decoupling validation from state storage," *Distrib., Parallel, Cluster Comput.*, vol. 2334, pp. 1–13, 2019, doi: 10.48550/arXiv.1904.01935.
20. S. Namasudra, G. C. Deka, P. Johri, M. Hosseinpour, and A. H. Gandomi, "The revolution of blockchain: State-of-the-art and research challenges," *Arch. Comput. Methods Eng.*, vol. 128, pp. 1497–1515, 2021, doi: 10.1007/s11831-020-09426-0.

PRATIMA SHARMA is working as an assistant professor with Bennett University, Uttar Pradesh, 201310, India. Her research and publication interests include blockchain technology, honeypot, network security, information security, and data mining. She received her Ph.D. degree from Delhi Technological University, India. Contact her at pratima.sharma@bennett.edu.in.

RAJNI JINDAL is working as a professor and the head with Delhi Technological University, Delhi, 110042, India. Her primary area of interest is database systems, data mining, operating systems, and compiler design. She received her Ph.D. in computer engineering from the Faculty of Technology, Delhi University, Delhi. She is a senior member of IEEE and a life member of CSI. Contact her at rajni.jindal@dce.ac.in.

MALAYA DUTTA BORAH is working as an assistant professor grade-I with the National Institute of Technology (NIT) Silchar (An Institute of National Importance), Assam, 788010, India. Her research areas include blockchain technology, data mining, and cloud computing. She is a member of IEEE, CSI, ACM, and MIR Lab. Contact her at malayaduttaborah@cse.nits.ac.in.

Authorized licensed use limited to: DELHI TECHNICAL UNIV. Downloaded on January 19,2023 at 06:25:05 UTC from IEEE Xplore. Restrictions apply.

3 Biotech (2023) 13:44
https://doi.org/10.1007/s13205-022-03454-2

REVIEW ARTICLE

A comprehensive review on algal nutraceuticals as prospective therapeutic agent for different diseases

Asmita Kumari[1] · Garima[1] · Navneeta Bharadvaja[1]

Received: 15 March 2022 / Accepted: 25 December 2022
© King Abdulaziz City for Science and Technology 2023

Abstract

Ongoing research in the food supplement sector provides insightful information regarding algae as a new-generation nutritional supplement and is also referred to as a superfood. Due to the diverse nutritional components, algae have documented numerous health benefits like fighting microbial diseases, hypertension, obesity, and diabetes. Therefore, algae-derived nutraceuticals account for a rapidly expanding market in the food supplements sector. The concept of algal prebiotics and their role in modulating gut microbiota have also been a chief contributor to this. This review evaluates the use of possible algal species and their specific bioactive compounds for the management of several chronic diseases. Proteins, peptides, polysaccharides, phenolics, and vitamins give an insight into the significance of algae in boosting the immune system and improving the body's nutritional makeup. In addition, phyco-compounds such as polysaccharides and polyphenols are also receiving a lot more interest in cosmeceutical applications for protecting skin from photodamage. The incorporation of algae in the diet for the management and prevention of chronic diseases like cancer, lung, and heart disease has been discussed in this review along with their action mechanism. This review provides a brief overview of several bioactive compounds present in micro and macroalgae and their therapeutic effect on lifestyle diseases, gastrointestinal diseases as well as neurodegenerative diseases.

Keywords Nutraceutical · Bioactive compounds · Phycocompounds · Prebiotics · Gut microbiota · Cosmeceutical

Introduction

Algae belong to the plant kingdom's lower phylogenetic tiers, possessing the unique feature of carrying out photosynthesis. The diversity ranges from the microscopic Cyanobacteria to enormous complex kelps. Macroalgae and microalgae are the two major sub-divisions of algae. Macroalgae also known as "seaweeds" are massive, multi-cellular marine organisms resembling big plants. It is further divided into three categories based on colour; Rhodophyta, Chlorophyta, and Phaeophyta also called red algae, green algae, and brown algae, respectively. Phytoplanktons are examples of microalgae and are single-celled photosynthetic organisms. Its two main groups are diatoms and dinoflagellates (Koyande et al. 2021; Radmer 1996). Algae form the basis of the food chain and cover more than 70% of the world's total living mass. Approximately 300,000 algal species have been discovered to date. Owing to their bioactive molecules and their effect on human health, algae are an extensively desired product for use in nutraceuticals. Protein, carbohydrates, and lipids are among the important substances derived from these algae for pharmacological and nutraceutical purposes. *Chlorella* was the first commercially cultivated microalgae for nutraceuticals, which began in Japan in 1960 (Nilesh Hemantkumar and Ilza Rahimbhai 2020). Because these microalgae grow at a rapid rate, they produce a substantial amount of protein-rich biomass and are a rich source of single-cell protein. Apart from its high-value food product algae can be used as additives, antioxidants, dyes, and feed for aquaculture. These are also used in cosmetics and the preparation of biofilm (Mendis and Kim 2011).

The exponential population surge threatens to reduce levels of food security as time progresses. Meeting the current demands of high nutritional value food is a challenge for the agricultural sector as well as the food industry. Because of the decreasing nutritional food quality, there has been a

✉ Navneeta Bharadvaja
navneetab@dce.ac.in

[1] Plant Biotechnology Laboratory, Department of Biotechnology, Delhi Technological University, Shahbad Daulatpur, Main Bawana Road, Delhi 110042, India

Published online: 11 January 2023

rise in lifestyle diseases and certain nutritional deficiency diseases. To attenuate this problem studies are being done on algae to be used as a nutritional supplement and have been widely accepted as a functional food. Microalgae *Spirulina* is regarded as a superfood as it contains 60–70% protein weight; it also contains vitamin B, phycocyanin, omega-6 fatty acid, vitamin E, and many minerals. It is highly effective in diabetes, hypertension, and weight loss. It helps to manage cholesterol metabolism by raising HDL levels which promotes better cardiovascular health. C-phycocyanin pigment found in *Spirulina* has anti-oxidant and anti-inflammatory properties (Bishop and Zubeck 2012). Another microalgae *Chlorella*was utilized as an ideal food in space journeys. It has detoxicant action and helps in the stimulation of the immune system (Nicoletti 2016). It consists of > 50% protein, ~ 5% chlorophyll, ~ 20% dietary fibre, carbohydrates, lipids, provitamin A, thiamin B1, riboflavin, niacin, vitamin E, B6, B12, biotin, folic acid, and pantothenic acid. It is known to regulate high blood pressure, and relieve fibromyalgia, and ulcerative colitis (Naguib 2000).

Chlorella is being marketed as a tablet by different companies. It also shows inhibitory action on aortic atheromatous lesions. *Haematococcus* is a unicellular green alga that is used for pharmaceuticals and cosmetics as well. It is the largest source of astaxanthin. Astaxanthin is a carotenoid that has 10 times the antioxidant potential than β-carotene and 1000 times the antioxidant potential of vitamin E (Naguib 2000). It shows important gastroprotective effects, neuroprotective, ocular protective, anticancer, and hepatoprotective effects and also helps in kidney function impairment (Yuan et al. 2011b). It also aids in some important metabolic functions like immune response, protection against UV radiation, reproductive behavior and anti-inflammatory effects. Astaxanthin extracted from *Haematococcus* was tested on humans for 8 weeks to study the efficacy as well as any toxicity of algal-derived astaxanthin. No significant toxicity was observed (Satoh et al. 2009). Moreover, it showed positive results for treating and preventing neurological damage relating to age-related macular degeneration.

Aphanizomenon is a prokaryotic cyanobacterium and is being used as a food source since ancient times. A significant amount of C-phycocyanin is present in *Aphanizomenon* and is known to promote liver function and boost bile output. Apart from this, it exhibits antioxidant, anti-inflammatory, and high hypo cholestrolemic activity. A large amount of omega 3 and omega 6 (i.e., polyunsaturated fatty acid) are also present in *Aphanizomenon* which helps in the prevention of immunosuppressive and cardiovascular diseases. Furthermore, it also helps to prevent mental health issues and dermatological problems (dos Santos et al. 2021). Recent studies have also found its ability to promote the activity of natural killer cells that trigger apoptosis in cancer or cells infected with the virus (Hart et al. 2007). *Dunaliella salina*is dominantly used in nutraceutical production. Protein, glycerol, and beta-carotene can be extracted in large amounts from its thin cell wall. A smaller amount of alpha-carotene can also be extracted. These beta carotenes are highly effective free radical scavengers that help restore enzyme activity by decreasing levels of lipid peroxidation and enzyme inactivation (Marino et al. 2020). This antioxidant activity of beta carotene also helps in slowing the ageing process and preventing cancer in various organs. *Dunaliella* also has hepatoprotective properties and reduces the incidence of liver lesions (Hsu et al. 2008; Al-obaidi et al. 2021).

Recent trends in the food industry demand a more sustainable switch in food products. This plant-based food supplement is preferred over animal-derived products and is considered to be more healthy. In comparison with terrestrial crops, algal biomass possesses more nutritional value and further its production is more sustainable. Food and herbs have been used as medicines in traditional Asian cultures. Therefore, the idea of incorporating seaweeds has been adopted in the modern approach. This not only meets the current demand for more sustainable and healthy food but also acts as a therapeutic agent for the treatment and prevention of certain deadly diseases (Shannon and Abu-Ghannam 2019; Katiyar and Arora 2020). In comparison with modern treatment methods such as radiotherapy or chemotherapy that have several side effects on the body, these phycocompounds are being used as a substitute by the pharmaceutical industries. Furthermore, worldwide availability, diversity, and productivity make it the best substitute for integral utilization where specifically refined phycocompounds are used or even whole alga can be used as a target product. Improvements in technical conditions and the development of advanced biorefineries have made it possible to exploit every fraction of algal biomass for beneficial byproducts. In addition, intensive research and current studies are making use of genetic engineering tools to increase the value of these phycocompounds (Domínguez 2013; Martins et al. 2018).

Current challenges and market of Algal products

Although the potential of algal biomass is known and thousands of algal species have been identified to date, very few of them are being used at the industrial level production. Production of macroalgae is still limited to countries in Europe like France, Ireland and Spain contributing to 32% of macroalgae production, while the rest 68% of macroalgae harvesting is still done from wild stocks (Araújo et al. 2021). The small market size in certain countries, variability in annual biomass supply, and current technological development are responsible for the slow expansion of algal

industries. Besides the lack of large-scale outdoor locations for the cultivation and processing of the algae, the ack of optimum growth conditions isa vital reason for a lower rate of expansion of algal products (Araújo et al. 2021). Cultivation of algae also requires precautionary measures such as prevention from contamination and predators. On a wider level of commercial production, insufficient utilization and recycling of resources add to high manufacturing costs. The lack of production of valuable co-products also adds to the high manufacturing cost of algal products (Sharma and Sharma 2017).

Steadfastly increasing interest in the use of algae in food industries and new improved technologies for hygienic cultivation limits the constraints of algae production (Kratzer and Murkovic 2021). In a study conducted by Araújo et al. (2021) about the current status of algae production, the results showed that algae-producing sectors in Europe account for 67% of macroalgae production and 33% of microalgae production at industrial levels. 222 Spirulina-producing companies are spread across 22 countries in Europe. In 2019 Norway has reported as the third largest seaweed harvesting company whereas France, Ireland, Portugal, the Faroe Islands, and Iceland were also significant producers (Kratzer and Murkovic 2021). In comparison to algae-producing companies in Europe in the last decade, there has been an increase of 150% in the number of new algae-producing companies. There is an ongoing increase in macroalgal production in a total of 13 countries in Europe (Araújo et al. 2021). Owing to the raising demands from the pharmaceuticals and nutraceutical industries, the global market for algae is targeted to reach USD 3318 million by 2022 (Balasubramaniam et al. 2021). Seaweed has been an integral part of Asian cuisine since ancient times and therefore Asia accounts for major seaweed production in the world (Balasubramaniam et al. 2021). In 2019, Asia contributed 97.4% of world seaweed production whereas America and Europe contributed 1.4% and 0.8%, respectively. In 2019, worldwide cultivation of brown seaweed reached 16.4 million tonnes and there has been an increase of 10.9% annual growth rate in its production since 1950–2019 (Cai et al. 2021). Red seaweed cultivation across the globe was estimated to be 18.3 million tonnes in 2019. In terms of quantity and value, red seaweed accounted for 52.6% and 47.6%, respectively, of worldwide seaweed cultivation. Production of green seaweed contrarily showed a stunted growth rate with 16,696 tonnes of global annual production. Production of microalgae accounts for 25,000 tonnes which has a current market value of 50 million Euros and is targeted to reach 70 million Euros by 2025 (Fernández et al. 2021). Since there is a rapid and consistent increase in world population, by 2050 food production and alternative dietary source needed to be increased by 60%The algal nutraceuticals and pharmaceutical industry is estimated to reach a market value of 1131 million Euros by 2027 (Mendes et al. 2022). Algae as meat substitute in the food industry raised its value to 223.65 million Euros. The use of algae in the form of dietary supplements and nutraceuticals has increased globally and it accounted for 30 billion Euros in 2020 and is also expected to grow at a rate of 50.6% by 2026. Sales of algal vitamins and nutraceuticals in the western market are threefolds to the eastern market and are expected to reach a value of 182 billion Euros by 2022 (Mendes et al. 2022). Table 1 describes a list of industries involved in the production of algal products.

Algae for lifestyle diseases

Diabetes mellitus

Diabetes mellitus is the most prevalent metabolic condition with the highest growth rate in the world, characterized by persistent hyperglycemia. Based on its causes it can be classified into two types, 1) insulin-dependent diabetes mellitus and non-insulin-dependent diabetes mellitus also called type 1 and type 2 respectively. In particular, type 2 diabetes mellitusis characterized by insulin resistance induced by an unbalanced diet, and low physical activity, with which obesity being the primary reason for its exponential rise worldwide. Due to insulin resistance, there is excess production of glucose by the liver but due to its insufficient utilization by muscle and adipose tissues, a condition of hyperglycemia arises and is characterized by polyuria, polydipsia, and polyphagia (Gunathilaka et al. 2020).

Bioactive compounds present in algal species include phlorotannins, polysaccharides such as fucoidans, alginates, laminarins, carotenoids such as fucoxanthin, sterol–fucosterol have proved to have high antidiabetic potential. Therapeutic targets for these bioactive compounds and their mechanisms are:

(i) Inhibitory activity of α-Amylase and α-Glucosidase enzymes: In the cell's metabolic pathway, α-amylase and α-glucosidase enzymes play a vital role in the formation of glucose. Inhibition of these enzymes helps in lowering postcibal blood glucose levels. The presence of several phlorotannins in marine algae such as eckol, phloroglucinol, dieckol, 7-phloroeckol and 6,6′-bieckol, phlorofucofuroeckol-A and methanol extracts have shown to have an inhibitory effect on these enzymes. Compared to regular acarbose, algal phlorotannins show strong antidiabetic activity (Lee and Jeon 2013).
(ii) Inhibitory activity of Aldose Reductase (AR): Aldose reductase is an enzyme that converts glucose to sorbitol, which is a key step in the polyol pathway. A high amount of this can cause diabetic neuropathy. Phlorotannins found in ethanol extract, hexane, and aque-

ous fractions extracted from the brown alga *Ecklonia stolonifera* exhibit inhibitory action on the enzyme AR (Jung et al. 2008). Jung et al. investigated the inhibitory action of algae on aldose reductase. Fucosterol, a substance derived from *Ecklonia stolonifera*, was found to block aldose reductase activity in rat lenses as well as human recombinant aldose reductase enzyme (Gunathilaka et al. 2020). Similar activity was also shown by dichloromethane fraction extracted from *Saccharina japonica* and fucoxanthin extracted from *Eisenia bicyclis*and *Undaria pinnatifida* (Jung et al. 2012).

(iii) Inhibitory activity of angiotensin-converting enzymes: Activation of rennin–angiotensin–aldosterone causes an increase in the blood pressure in diabetic patients that further leads to microvascular and macrovascular complications. Phlorotannins prevent this condition by having an inhibitory role on angiotensin-converting enzyme (ACE) (Paiva et al. 2017). *Ecklonia stolonifera* was examined for its anti-diabetic properties and was found to have significant amounts of phlorotannins, which inhibited the angiotensin-converting enzyme (ACE). These phlorotannins include eckol, phlorofucofuroeckol-A and dieckol, among which dieckol inhibited ACE non-competitively. Other seaweeds such as *Sargassum fusiforme, Sargassum horneri* and *Ecklonia cava* have been shown to have similar ACE (Jung et al. 2006).

(iv) Inhibitory activity of protein tyrosine phosphatase (PTP) 1B: Inhibition of the enzyme PTP 1B increases insulin sensitivity thus decreasing the blood glucose levels. Eckol, 7-phloroeckol, phlorofucofuroeckol-A isolated from several species of brown algae blocks the activity of PTP 1B enzyme through a non-competitive inhibitory mechanism (Lopes et al. 2017). Among these phlorofucofuroeckol-A possess the highest inhibitory efficiency. In a study by Ali et al. *Sargassum serratifolium* was explored for the inhibitory activity of the PTP 1B enzyme. The results showed the highest inhibitory effect with hexane fraction than ethanol extract.

(v) Inhibitory activity of dipeptidyl peptidase-4 Enzyme: The enzyme DPP-4 regulates glucose metabolism by lowering the GLP-1 levels thus leading to the hyperglycemic condition. Ethyl acetate fractions and sulfated polysaccharide fractions of algae have been shown to have an inhibitory effect on the DPP-4 enzyme (Yang et al. 2019). In a dose-dependent manner, *Turbinaria conoides, S. binderi* and *Padina sulcata* are known to have significant DPP-4 inhibitory action. *Turbinaria ornata* possess a high content of sulphated polysaccharides which are known to block the DPP-4 enzyme (Sharifuddin et al. 2015). Figure 1 represent the target

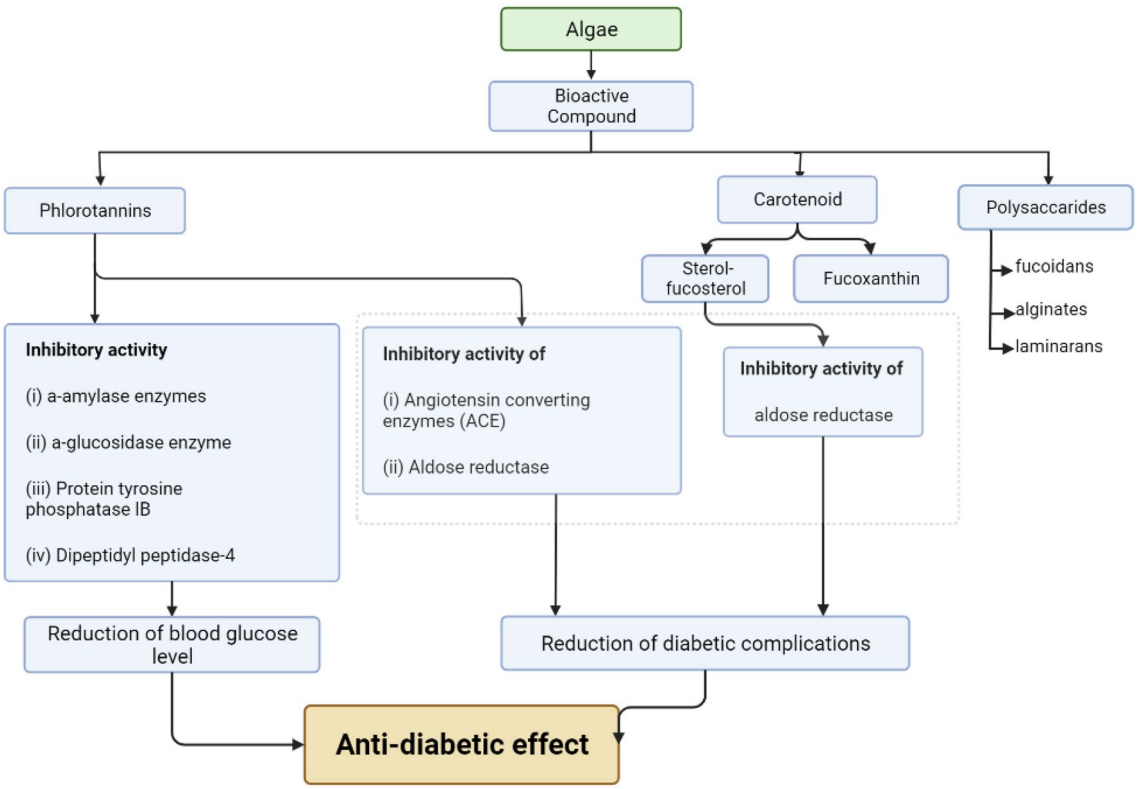

Fig. 1 Target mechanism of algal bioactive compounds for management of diabetes mellitus

mechanism of algal bioactive compounds for the management of diabetes mellitus.

Hypertension

Among the diverse functions of algae comes the anti-hypertensive effect. Apart from the abundance of bioactive compounds present in algae, it is also rich in dietary fibre and nitrate content which accounts for the hypotensive effect and leads to a decrease in blood pressure (Ismail et al. 2020). Certain peptides from macroalgae possess hypotensive potential on the human circulatory system and promote a healthy heart by preventing lethal illnesses including peripheral vascular disease and atherosclerosis (Fitzgerald et al. 2011). Nori-peptides a secondary metabolite extracted from seaweed *Porphyraye zoensis* show an important antihypertensive activity and also regulate blood cholesterol levels, inhibit hepatic cholesterol biosynthesis, and prevent hyperplasia (Toblli et al. 2002). Peptides, phlorotannins and polysaccharides are the chief bioactive compounds that target to regulate hypertension. Calcium channel blockers and diuretics are also some of the other common treatments for hypertension while, renin–angiotensin system inhibitors are the most widely used effective approach. In its working mechanism renin transforms angiotensinogen into activated angiotensin I, a potent vasodilator. Upon action of angiotensin-I converting enzyme, this angiotensin-I is further transformed to angiotensin II. This angiotensin II is a potent vasoconstrictor, that leads to hypertension. Therefore, blocking the reaction at the initial stage of the formation of angiotensin II or directly inhibiting angiotensin I synthesis are the two main approaches to lower blood pressure (Seca and Pinto 2018). ACE I inhibitors have a twofold mode of action. The first is they reduce the quantity of salt retained in the kidneys and the second is, they block the hormone angiotensin II from being produced (a hormone that causes blood vessels to narrow) (Reis et al. 2020). The reduced level of this hormone causes the blood to flow more efficiently through the arteries by helping the blood vessels to dilate and contract and thus regulating high blood pressure (Seca and Pinto 2018). Figure 2 represents a working mechanism of the anti-hypertensive effect of algal bioactive compounds.

Commercialized hypotensive peptides extracted from *Porphyrayezoensis, Pyropiayezoensis, Undaria pinnatifida, and Gracilariopsis lemaneiformis*are commonly available for consumption. Macroalgae *Ecklonia stolonifera and Ecklonia cava* are the largest sources of antihypertensive phlorotannins (Seca and Pinto 2018). In a study by Suetsuna et al., ten amino acids were extracted from the brown algae *Undaria pinnatifida*, which comprises 15% protein. These ten isolated amino acids were sequenced and studied for their hypotensive effect. It was found that these ten dipeptides followed the mechanism

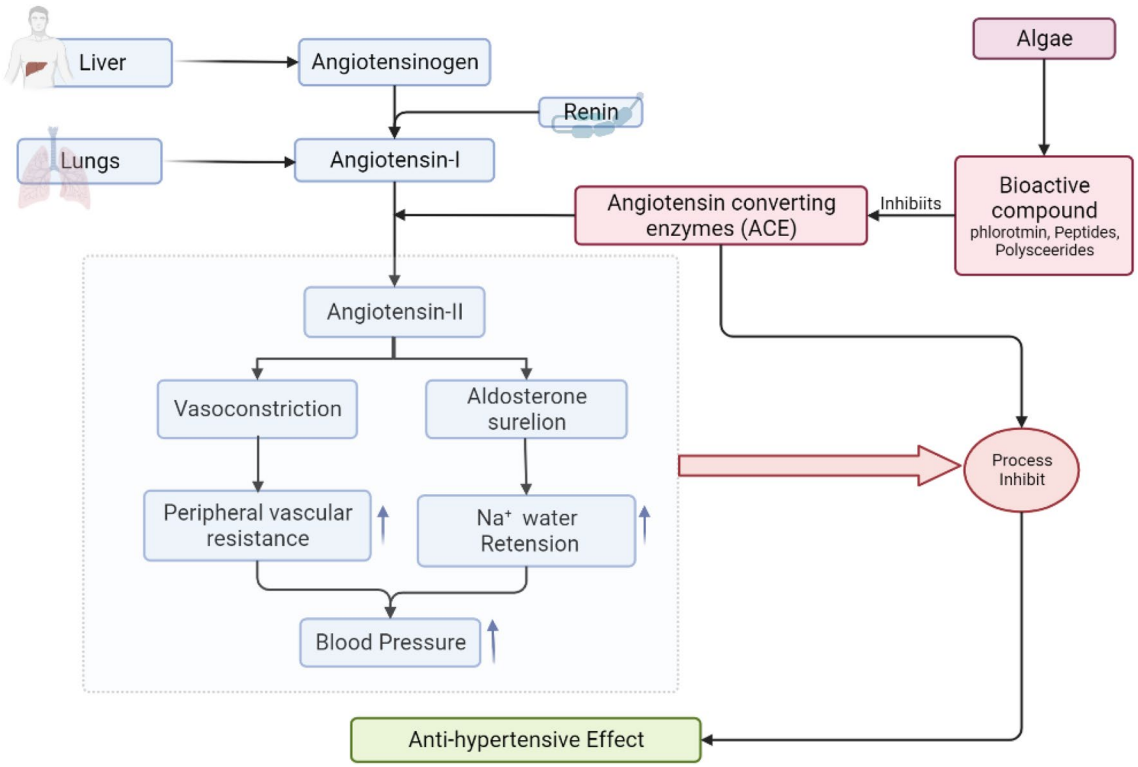

Fig. 2 Mechanism of anti-hypertensive effect of algal bioactive compounds

of ACE I inhibition to lower blood pressure (Seca and Pinto 2018). D-Polymannuronic sulphate is the prime polysaccharide isolated from *Pelvetiacanaliculata* (Linnaeus) and have been shown to possess acute and prophylactic hypotensive activity in vivo. It shows an antihypertensive effect by increasing the level of NO contents and lowering the levels of Angiotensin II and Endothelin 1 hormone (Seca and Pinto 2018).

Obesity

Obesity refers to the building-up of extra fat in the body and is linked to having adverse effects on the body such as hypertension, cardiovascular complications, and diabetes. Macro and microalgae have shown positive results for obesity treatment pressure (Ismail et al. 2020). Key bioactive compounds found in algae such as alginates, fucoidan, phlorotannins, fucoxanthin, fucosterol, and indole derivatives have been shown to have a role in digestion and are regarded as potential agents for obesity treatment. Changes in lipoprotein breakdown, repression of inflammation, reduction of adipogenesis, and a delay in stomach emptying are all part of these drugs' mechanisms of action (Wan-Loy and Siew-Moi 2016).

Fucoxanthin is abundantly found in *Undaria pinnatifida, Laminaria digitata, Hijikia fusiformis, tricornutum,*and *Isochrysisgalbana.* It increases β-oxidation and decreases lipogenesis in epididymal adipose tissue as well as enhances the activity of 5′ adenosine monophosphate-activated protein kinase along with acetyl-coenzyme A carboxylase (Hu et al. 2012). Alginates present in seaweed improve satiety and assist intestinal transit through their bulking capacity, providing an anti-obesity effect. These are commonly extracted from the genera *Lessonia, Macrocystis, Laminaria* and *Ascophyllum. Laminaria* and *Lessonia* are the primary sources. The mechanisms by which they exert their effect include delay in stomach clearance, activation of gastric stretch receptors, and restricted nutrient absorption by the cells (El Khoury et al. 2014). Phlorotannins such as phloroglucinol, and dioxinodehydroeckol extracted from brown algae *Ecklonia stolonifera* works as anti-obesity agents by preventing the differentiation of adipocytes. 1*H*-indole—carbaldehyde and 6-Formylindole are the chief indole derivative compounds that show adipogenesis inhibition. Another compound isolated from *Ecklonia stolonifera* that acts as an anti-obesity agent is sterols. Sterols block the expression of PPARγ and CCAAT proteins which are marker proteins of adipocyte expression (Seca and Pinto 2018).

Algae for cardiovascular diseases

Hypertension, hyperglycemia, and hyperlipidemia further give rise to achronic risk of cardiovascular disease (CVD). CVD includes conditions such as atherosclerosis, arteriosclerosis, thrombosis, myocardial infarction, and stroke in some cases. Damage to cells by free radicals is a crucial factor underlying CVD and stroke. Algal carotenoids have proved to have a beneficial role in treating CVD. This effect is attributed to the antioxidant activity of carotenoids. Carotenoids protect against oxidative stress by activating genes that regulate enzymes including superoxide dismutase (SOD), and catalase which protect against oxidative degradation of lipids and consequent damage to nucleic acid and proteins. Beta-carotene also helps to prevent oxidative stress by inhibiting lipid free radicals, scavenging reactive oxygen species, and absorbing UV radiation. *Dunaliella* being a rich source of Beta-carotene helps in the reduction of lipid peroxidation thus lowering plasma cholesterol levels (Raposo and De Morais 2015). A study by Hussein et al. (2005) showed the correlation between astaxanthin and low-density lipoprotein (LDL). It showed the inhibitory action of astaxanthin on low-density lipoprotein and thereby lowering the risk of atherosclerosis. Clinical trials on astaxanthin oral administration for 14 days showed positive results in regulating hypertension and a long-term dose of 5 weeks could reduce the risk of stroke (Sathasivam and Ki 2018). In humans, astaxanthin helps to increase adiponectin levels in the body and improve triglyceride levels along with high-density lipoprotein cholesterol (Ambati et al. 2014).

Genera *Haematococcus* is the largest producer of carotenoids, producing ~ 3.8% of astaxanthin of its dry weight. Other algal species include *Ulva lacuta*, and *Catenella repens* (O'Sullivan et al. 2010). Microalgae *Arthrospira* was studied by Miranda et al. for its effect on cardiovascular diseases. It was found that extracts from *Arthrospira* mainly phenolic components showed antioxidant effects and inhibited LDL cholesterol peroxidation. Microalgae are a rich source of vitamin C, B complex and provitamin A. These vitamins can counteract endothelial dysfunction that is mainly caused by the formation of free radicals and also prevent stroke in patients with cardiovascular disease (Raposo and De Morais 2015).

Algae for gastrointestinal diseases

The algal prebiotic concept has proved to be beneficial for the modulation of intestinal microbiota. Polysaccharides are major constituents of seaweeds and microalgae and act as prebiotics. These algal polysaccharide compounds that act as prebiotics include alginates, fucoidans, laminarin, and carrageenan. They act as roughage as they do not get metabolized in the upper gastrointestinal system. These dietary fibres delay stomach emptying due to their viscosity and regulate the transit time, thus improving nutrient and mineral absorption. The colon is heavily colonized with genera "*Bacteroides, Prevotella, Eubacterium, Clostridium*

and Bifidobacterium, Lactobacillus, Staphylococcus, Enterococcus, Streptococcus, Enterobacter and Escherichia" (Besednova et al. 2020). These prebiotics provide a selective fermentation substrate for beneficial microbes to flourish thus changing the microflora profile of the human gut thus aiding in better digestion and preventing diseases caused by harmful bacteria (Besednova et al. 2020; Zheng et al. 2020).

Inflammatory bowel disease (IBD) are chronic inflammatory intestinal conditions that occur majorly due to an imbalanced immune system and interaction with microbes. The two most prevalent kinds of IBD are Crohn's disease and ulcerative colitis which are characterized by persistent diarrhoea, abdominal pain, and rectal bleeding. Furthermore, immunological dysregulation also occurs in IBD, when regulatory cells of innate acquired immunity fail to function properly, resulting in T-cell activation. As a result, soluble inflammatory mediators are released (Besednova et al. 2020). Immunosuppressants, antibiotics, and anti-inflammatory drugs are the current recommendations for the treatment of IBD. However, their usage is frequently harmful to the body and can also cause negative side effects. Some common side effects include osteoporosis, hypertension, and gastrointestinal ulcer aggravation from corticosteroids. Headache and nausea might occur due to amino salicylates. As a result, novel therapy options are being developed that target therapeutic targets which include potent natural compounds that can inhibit leukocyte adherence and migration into inflamed gut walls and inhibit the activity of cytokines and restore gut microflora, thus stimulating the healing of gastric mucosal layer. Algal polysaccharides such as alginates, fucoidans, carrageenans, agars, porphyrin, xylan, and ulvan are being used as nutraceuticals for the treatment of IBD (Besednova et al. 2020; Christaki et al. 2013). *Helicobacter pylori* colonize the gastric mucosa affecting the microbiota of the gut and can cause gastritis and peptic ulcer. Algal polysaccharides mainly fucoidans are used for the eradication of *H. pylori* by targeting the cell receptors of gastric mucosa and thus preventing its binding to the intestinal wall. Fucoidans possess potent anti-inflammatory and immunomodulatory effects which further enhance with increasing degree of sulfation in its structure. Therefore, besides protecting intestinal mucosa, fucoidans also protect against stomach infection and gastric cancers (Zheng et al. 2020).

Algae for microbial diseases

Antibacterial effects

Brown algae *Ecklonia kurome* are a rich source of phlorotannins and has antibacterial effects by interacting with bacterial proteins which results in bactericidal effect. It shows bactericidal action on multiresistant Gram-negative and Gram-positive bacteria. *S. enteritidis, S. typhimurium*, and *V. parahaemolyticus* are some of the Gram-negative strains while *S. aureus*, and *B. cereus* are the Gram-positive strains. Bromoditerpenes extracted from red algae *Sphaerococcus coronopifolius* exhibit antibacterial action on Gram-positive bacteria. Other marine seaweed having antibacterial effects include *Ulva fasciata*, and *Hypneamusci formis* (Ismail, Alotaibi and EL-Sheekh 2020). Bioactive compounds in these algae modify the cell porousness of the pathogen, disrupting the function of the membrane and finally leading to the destruction of pathogen cells. Red algae *Laurencia luzonesis* contain sesquiterpenes which have a strong bactericidal effect. *Bacillus megaterium* also acts as an antifungal agent (Arvinda Swamy 2011). Elatol and iso-obtusol are halogenated furanones which can be extracted from *Laurencia majuscule.* The human pathogenic bacterium *Staphylococcus epidermis* is susceptible to elatol, while iso-obtusol works against *Salmonella* species. Both of these halogenated compounds work by interfering with the biosynthetic pathway AI-2 of bacteria. They bind covalently with the LuxS enzyme which leads to the production of autoinducers-2 which in turn has bactericidal action (Arvinda Swamy 2011). In humans, urinary tract infection (UTI) is most of the most frequent and concerning infection caused by bacteria, and methanol extracts of seaweeds effectively kill bacterial pathogens *E. coli* and *S. aureus* causing UTI (Arvinda Swamy 2011).

Antiviral effects

Macroalgal polysaccharides are a potent source for treating viral diseases, such as HIV, hepatitis C, herpes simplex virus, and genital warts. Sulphated polysaccharides are found abundantly in algal cell walls and these include carrageenan, agar, ulvan, fucoidan, laminarin. By interfering with distinct phases of viral infection, these polysaccharides have antiviral efficacy against a wide range of viruses (Hans et al. 2021; Besednova et al. 2021). Sulfated polysaccharides have a distinctive structure that disrupts the virus life cycle at various stages. They either cause the inactivation of virions before infection or block their replication inside the host cell. They are also capable of attaching to immunomodulators that stimulate Natural Killer cells and trigger immunological responses. Polyphenolic compounds derived from algae also resist the replication of enveloped as well as non-enveloped viruses (Sami et al. 2021). Figure 3 describes the possible antiviral mechanism exhibited by algal nutraceuticals.

Algae as a novel approach have been developed to treat the present outburst of acute respiratory disease coronavirus disease 19 (COVID-19). The spike (S) proteins of the SARS-CoV-2 virus are the structural proteins that contain recombinant receptor-binding domain (RBD) which binds to ACE2 protein and help in viral invasion into the host cell (Sami

et al. 2021). Currently, studies are being done to combat the spread of the SARS-CoV-2 virus by developing effective and harmless drugs using algal bioactive compounds. Coronavirus proteins are translated from a single polyprotein, simultaneously releasing two proteases: major proteases (Mpro) and papain-like protease (PLpro). The protein's active site contains a dyad of Cys145 and His41 which are promising targets for the inhibitory drugs. Besides polysaccharides, algal polyphenols are potential therapeutic compounds that exhibit antiviral activity. They inhibit the activity of PLpro and S protein of coronavirus, thus blocking viral entry. Phlorotannins extracted from *E. cava* block the activity of PLpro of the SARS-CoV virus (Sami et al. 2021; Vo and Kim 2010). Griffithsin and cyanovirin-n are the most studied algal lectins for antiviral application. They are widely used to counteract HIV infection besides the SARS-CoV-2 virus (Pagarete et al. 2021). Table 2 summarizes the different bioactive compounds targeting different diseases.

Neuroprotective effects of algae

Neurodegeneration is defined as damage or reduction in the count of neurons in certain areas of the central nervous system over time. The term neuroinflammation refers to the activation of glial cells mostly microglia and astrocytes into a provocative inflammatory condition which is an efficient innate defense mechanism that protects the nervous system and also maintains homeostasis (Barbalace et al. 2019). The long-term inflammatory events in the neuronal cells, on the other hand, can trigger a cascade of events that culminate in the gradual destruction of nerve cells, as seen in Alzheimer's disease, multiple sclerosis, Parkinson's and Huntington's disease (Barbalace et al. 2019; Glass et al. 2010). Overstimulation of glial cells leads to the production of cytokines and oxygen radicals which cause synaptic impairment and neuronal death culminating in CNS damage (Barbalace et al. 2019). An increasing number of studies have emphasized the critical role of the immune system in the onset and development of neurodegeneration activity. Immune cell growth and migration are caused by alterations in cytokine signalling, further, impaired phagocytosis and nonspecific reactive change in glial cells are also typical characteristics of neurodegeneration (Tarozzi et al. 2013). The main molecular events that trigger the development of Alzheimer's disease are oxidative stress and protein deposition. Marine algae prevent neuroinflammation by blocking the action of pro-inflammatory enzymes such as cyclooxygenase-2 and inducible nitric oxide synthase, regulating mitogen-activated protein kinase (MAPK) or ERK pathways and activating NF-κB (Yu et al. 2015). Figure 4 describes the bioactivities of algal compounds to prevent neurodegeneration.

Alzheimer's disease (AD)

AD was originally recognized and reported in 1906 by Dr Alois Alzheimer and is the most prevalent type of neurodegenerative disease. This is marked by the gradual loss of nerve cells, resulting in brain atrophy, particularly in cognition centers. It is the most prevalent cause of dementia which

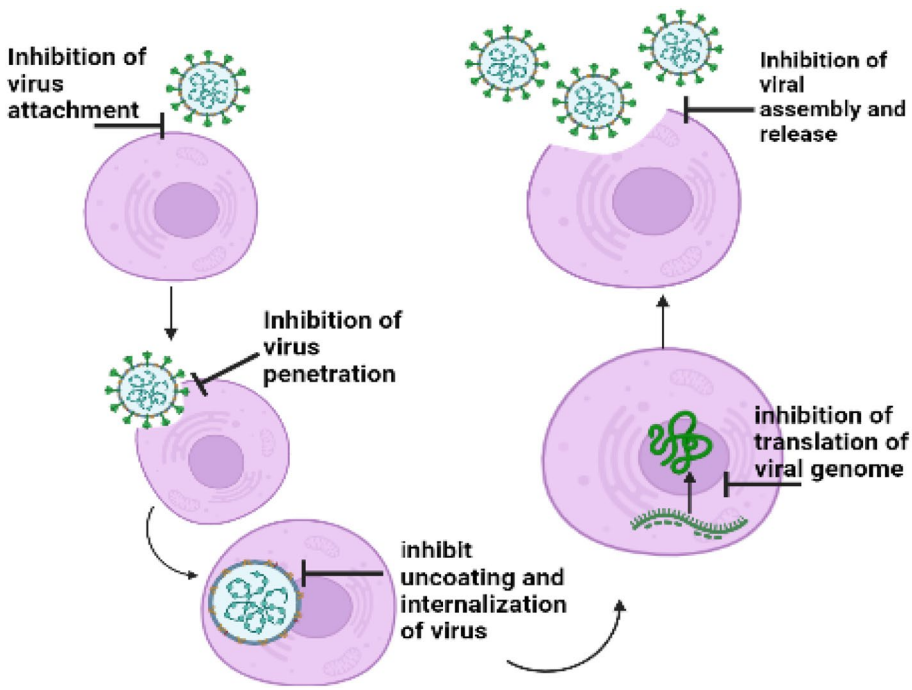

Fig. 3 Possible antiviral mechanism exhibited by algal nutraceuticals

is a progressive mental condition that leads to impairment of critical brain processes and leads to memory loss and cognitive deficit (Silva et al. 2021). The characteristic feature of AD is the dysregulation in the levels of beta-amyloid (Aβ), neurofibrillary tangles, and high concentration of unubiquitinated tau. AD is often referred to as tauopathy due to the presence of a greater percentage of misfolded and insoluble tau protein. The misfolding of Aβ leads to the appearance of senile plaques and misfolding of tau protein makes it insoluble and leads to its build-up due to the prevention of its release by the blood–brain barrier (Bauer et al. 2021; Bertsch et al. 2021). The involvement of reactive oxygen species also adds to neuronal damage. These subsequent events lead to altered levels of neuromodulators such as acetylcholine (ACh) and butyrylcholine (BCh). Principle therapeutic strategy against AD is the blocking of the binding of acetylcholinesterase enzyme (AChE) and butyrylcholinesterase enzyme (BuChE). Both of these enzymes are responsible for the hydrolysis of Ach and BCh (Pangestuti and Kim 2011; Silva et al. 2021). Seaweed being the recently discovered potent inhibitor of AChE and BuChE also improves the cholinergic deficit in patients. *Ochtodessecundiramea, Hypneamusciformis, Pterocladiacapillacea, Gelidiumpristoides*, and *Gracilariacorticata* exhibit inhibitory potency of these enzymes (Alghazwi et al. 2020). Besides this fucoidan extracts inhibit the aggregation of amyloid-beta and the production of ROS and significantly improve hydrogen peroxide toxicity (Li et al. 2017a). Seaweed polysaccharides inhibit lipid peroxidation and erythrocyte hemolysis leading to the control of neuroinflammation that prevents neuronal damage and helps in the repair of brain tissue (Silva et al. 2019).

Parkinson's disease (PD)

It is a type of neurological illness that impairs the mobility of the elderly. It is marked by the formation of Lewy bodies (deposits of a protein named alpha-synuclein), loss of dopaminergic (DAergic) neuronsin the "*substantia nigra* of *pars compacta* (SNpc)" and decline in the levels of dopamine (Ramkumar et al. 2017; Alves et al. 2016). Nerve cells and black substance which is a portion of the basal ganglia deteriorate. Though the basal ganglia do not convey connections directly to the CNS, they are essential structures connected to movement. Some other distinguishable symptoms of Parkinson's disease include resting tremors of muscles, muscular stiffness, and postural instability. Alves et al. verified the antioxidant potential of *Bifurcaria bifurcata.* Its methanolic and dichloromethane extracts work by scavenging the free radicals and protecting against neuronal damage (Li et al. 2017a; Hannan et al. 2020). Several extracts of macroalgae showed neuroprotective effects in human neuroblastoma cells from 6-hydroxydopamine (6-OHDA). *Laminaria japonica, Ecklonia cava, Fucus vesiculosus, Saccharina japonica, Turbinaria*, and *decurrens* are the other algal species used to produce dichloromethane extracts to cure PD (Rodriguez-Pallares et al. 2007). The other possible mechanisms associated with the treatment of PD include the prevention of alteration in mitochondrial membrane potential thus regulating oxidative phosphorylation. Decrease in level of H_2O_2 thus preventing oxidative stress (Valado et al. 2017). Decrease in the activity of Caspase-3 that mediate cell death by apoptosis. DNA staining with DAPI (4′,6-diamidino-2-phenylindole) probe unveiled that treatment with algal bioactive compounds decreased karyopyknosis and fragmentation of chromatin which are hallmarks of apoptosis (Pereira and Valado 2021).

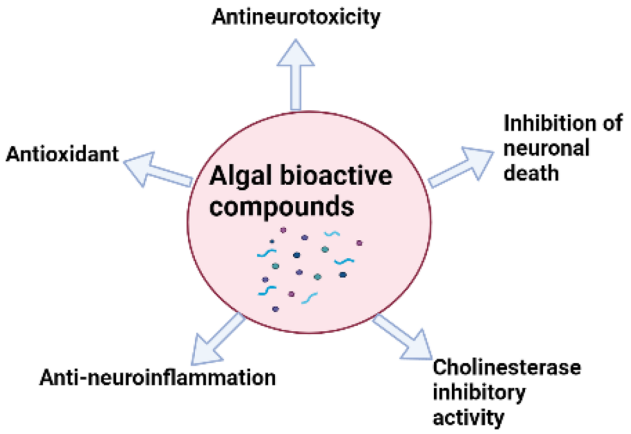

Fig. 4 Bioactivities of algal compounds to prevent neurodegeneration

Multiple sclerosis (MS)

It is an autoimmune-related neurological demyelination disorder of the CNS. Common symptoms of MS include muscular weakness, the disturbed balance of motor coordination, fatigue, joint ache, depression, and changes in visual acuity. Since this disease cannot be cured, algal compounds are employed to reduce the symptoms of this disease (Wahls et al. 2019; Saadaoui et al. 2020). Since lifestyle factors and food quality affects the course and seriousness of the disease, dietary recommendations for people diagnosed with MS can minimize the symptoms of the disease. Algal bioactive compounds induce epigenetic alteration in gene transcription and improve the composition of gut microbiota, which further results in decreased inflammation. This also provides for nutrient sufficiency needed for neuronal structure (Larsen and Minna 2011). PUFAs form a significant component of algal cell membranes and are pioneers of eicosanoids which are crucial bioregulators of a variety of cellular processes. PUFAs have been shown to effectively lower the risk of MS development (Saadaoui et al. 2020). Furthermore, vitamin deficiencies add to the severity of the

multiple sclerosis symptoms, the most significant of which are vitamins A and D which act as response modifiers of the immune system. Vitamin C, E and B_{12} play a vital role in myelinogenesis and some of the algal species rich in these vitamins are *Porphyra* spp., *Ulva* spp., and *Laminaria* spp. (Pereira and Valado 2021).

Algae for treatment of cancer

Cancer is a worldwide critical health challenge. Mutations, tumor suppressor gene inactivation, and overexpression of growth-promoting oncogenes are among the genetic and epigenetic changes that cause cancer. The overstimulated oncogenes include EGFR, ERBB2, KRAS, CDK4, BCL2 (Hanahan and Weinberg 2011; Morgillo et al. 2016). Multiple molecular anomalies have been linked to the pathogenesis of human cancer, leading to increased angiogenesis, resistance to apoptosis, sustained proliferative signalling, inactivation of tumour suppressor genes, and stimulation of metastasis of cancer cells (Fan et al. 2014). Among the proposed mechanisms for cancer progression resistance to EGFR inhibitors is the most prevalent cause. Algal compounds are effective in different types of cancer such as breast cancer, colorectal cancer, and lung cancer (Gantar et al. 2012). Owing to their effectiveness and low toxicity, phycobiliproteins extracted from Rhodophyta species play an essential role as antitumor drugs. They can boost the effectiveness of traditional anticancer drugs while reducing their negative effects. Phycocyanin in particular has an antitumor effect, preventing cancer cells from multiplying and killing infected cells, these are some of its effects making it a viable source for anticancer drugs (Ismail et al. 2020). Inhibition of tumors via xenobiotic metabolism, which lowers the rate of carcinogenesis, or disruption of mitosis at the telophase stage of cell division are two ways macroalgal phenolic chemicals inhibit tumor progression. They also reduce the levels of cellular proteins and certain flavonoids can even block the activity of aromatase, which helps in the progression of cancer cells (Ismail et al. 2020).

The algal bioactive compounds that exhibit anti-inflammatory and anti-tumor activity include peptides from *Chlorella vulgaris*, *Chlorella pyrenoidosa* (Guedes et al. 2013), phycobiliproteins extracted from red microalgae (Somasekharan et al. 2016), polysaccharides such as carrageenan from *Betaphycusgelatinum, Eucheuma denticulatum, K. alvarezii, Kappaphycus striatus*, fucoidan from *F. vesiculosus, U. pinnatifida, S. cichorioides* and laminarin from brown algae such as *Saccharina* species and *Laminaria* (Vishchuk et al. 2013; Zainal Ariffin et al. 2014; Ouyang et al. 2012). Among other tetraterpenoids such as canthaxanthin and β-carotene, astaxanthin extracted from *H. pulvialis* exhibits mitotic arrest and promotes apoptosis thus, inhibiting tumor cells in human colon cancer (Ambati et al. 2014). Figure 5 describes the action of phenolic compounds in the treatment of cancer.

Mechanism of anti-tumor activity

I. Apoptosis

Apoptosis causes cell cycle block and ultimately leads to cell death. The anticancer effect of the medications is centered on the interruption of these two phenomena. The concept of cell death caused by a cell cycle block has gotten a lot of interest since it might be utilized to minimize pharmacological resistance and reduce mutagenesis and toxicity. Upon treatment of tumor cells, Caco-2 and HepG2 with degraded κ-carrageenans at adequate concentrations, hallmarks of apoptosis such as detachment of adherent cells, externalization of phosphatidylserine, karyopyknosis, and formation of apoptotic bodies (ApoBDs) were observed. Furthermore, transcription of cell proliferation markers like PCNA, and MKI67 decreased in apoptotic cancer cells (Kim et al. 2010; Katoh 2017). Fucoidans increase the activation of Caspase-3 that are central effector of apoptosis. Fucoidans increase the porosity of the mitochondrial inner membrane and secretion of cytochrome c and Smac/Diablo

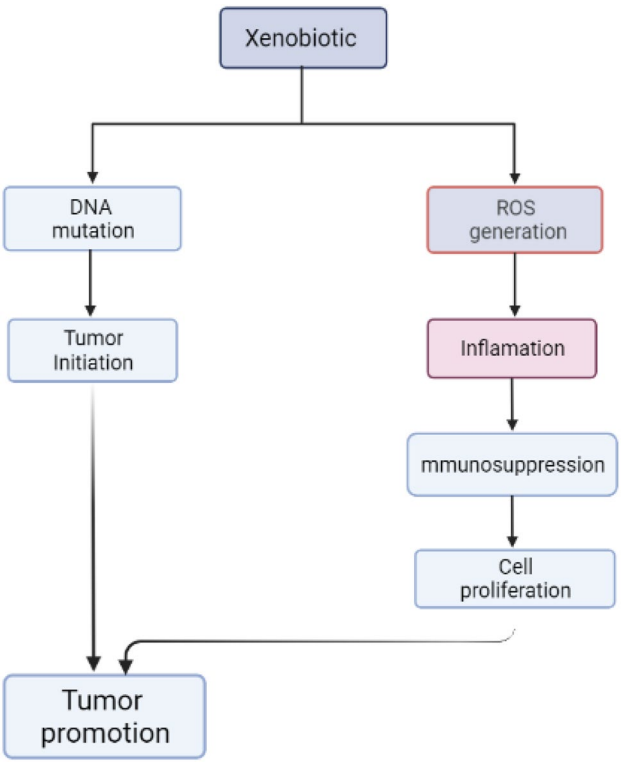

Fig. 5 Action of phenolic compounds in treatment of cancer

that promotes the activation of caspases (Dijksterhuis et al. 2014; Khotimchenko et al. 2020).

II. Wnt-cascade role in antiproliferation

The Wnt-cascade is one of the most essential cellular signalling pathways which is also involved in embryonic development and stem cell phenotypic maintenance. Mutation in this pathway leads to the formation of malignant tumors. Wnt comprises secreted glycolipoproteins that activate the signalling pathway that controls cell differentiation and the mitotic rate of cells. If the activity of Wnt is blocked, Axin, casein kinase 1 (CK1) and glycogen synthase 3β kinase (GSK3β) form a complex with cytoplasm β-catenin (Tabatabai et al. 2017). After the formation of this complex, CK1 and GSK3β then collectively phosphorylate β-catenin, which is subsequently identified and ubiquitinated followed by proteasome degradation (Yuan et al. 2011a; Li et al. 2017b). In the activated state, Wnt binds to its target Frizzleds (Fr) receptors which further activates the Dishevelled (Dvl) protein. The Dishevelled protein stabilizes a "destructing complex-Wnt/Fr/LRP/Dvl/Axin" and also inhibits GSK3 thus maintaining the levels of β-catenin (Khotimchenko et al. 2020).

III. Immune mechanism

Humoral and cell-mediated immunity inhibits tumour growth through activation of the complement system, proliferation of immune cells, and synthesis of immune cell factors. Enhanced NK cell activity and macrophage phagocytosis are observed in oligo-carrageenan-treated cancer cells (Yao et al. 2014). It also accelerated the maturation of Dendritic cells (DC) stimulating MHCII expression on DC. This stimulates the secretion of cytokines IL-12, IL-1β, and TNF-α. In a study by Li et al. (2017b), it was discovered that λ-carrageenan aids in DC maturation and cytokine production leading to the death of cancer cells by using the inhibitor for Toll-like receptors-TAK-242 and determining the phosphorylation status of components in the MAPK and NF-κB signalling pathways. Furthermore, the anticancer effects of λ-carrageenan have been linked to the suppression of Tregs (regulatory T-cells) and myeloid-derived suppressor cells (MDSC), both of which reduce the immune response to a foreign antigen (Khotimchenko et al. 2020).

IV. Anti-angiogenic mechanism

The term angiogenesis refers to the building up of new blood vessels on the foundation of preexisting blood vessels that aid in the progression of solid tumors by supplying nutrients to these cells. Since cancer is marked by increased vessel permeability, it also contributes to the greater metastatic potential of cancer cells. Algae-derived oligosaccharides possess the capability to hinder angiogenesis and reduce the levels of intracellular matrix metalloproteinase production inside endothelial cells further limiting endothelial cell invasion and migration. Yao et al. studied dose-dependent inhibition of vein endothelial cell proliferation by κ-carrageenan. It was found that under in vitro circumstances, it also decreased ECV304 cell migration triggered by human breast cancer cells (MCF-7) and fully blocked the development of capillaries in collagen gel at a dosage of 200 g/mL (Li et al. 2017b). Anti-angiogenic effects are induced by inhibiting cytokine mRNA production and receptors for vascular endothelium growth factor 1 (VEGF 1), basic fibroblast growth factor (bFGF), and CD105 (Khotimchenko et al. 2020). Figure 6 describes a detailed mechanism for the anti-cancer effect of algal bioactive compounds.

Algae for skin photoprotection

Ultraviolet radiation (UVR) wavelength ranges from 200 to 400 nm and is a part of the electromagnetic spectrum of solar radiation. UV-A and UV-B a component of UVR having a wavelength above 290 nm cause skin damage (Conde et al. 2000; Oren and Gunde-Cimerman 2007). Mycosporine-like amino acids (MAAs) commonly called "microbial sunscreens" are aromatic amino acids involved in photoprotection. The capacity of these chemicals to disperse hazardous UV radiations into heat energy that scatters into the environment without producing reactive photoproducts protects the cell (Misonou et al. 2003). In vitro, MAAs can also prevent UVR-induced thymine dimer formation (Chrapusta et al. 2017). Other phycocomponents such as carbohydrates, phenolic compounds, terpenoids, and carotenoids also show anti-oxidative photoprotection (Oren and Gunde-Cimerman 2007). Brown algae phycocomponents have a strong inhibitory action on the expression of UV-induced MMP-1 (Matrix-metalloprotein complex) resulting in photodamage. Dieckol and eckolare the two compounds from *Ecklonia stolonifera* that can suppress the expression of MMP-1 in the human dermal fibroblast cell line (Kalasariya et al. 2020). Furthermore, phlorotannins which are found in many algal species promote the expression of NF-κB and AP-1 (activator protein-1) which decreases the activity of MMP-1. A high level of expression of MMP can cause extracellular deterioration and algal polysaccharides can reduce the threat of photodamage by interacting with fibroblast growth factors (FGF) produced by macrophages and protecting them from proteolysis (Kalasariya et al. 2020; Joe et al. 2006).

Besides photoprotection, phycocomponents are also helpful in skin curation, and treating dehydration. Natural humectants containing MAAs, and polysaccharides improve the water-holding capacity of the stratum corneum preventing skin dryness and dehydration and maintaining the elasticity of the skin (Kalasariya et al. 2020).

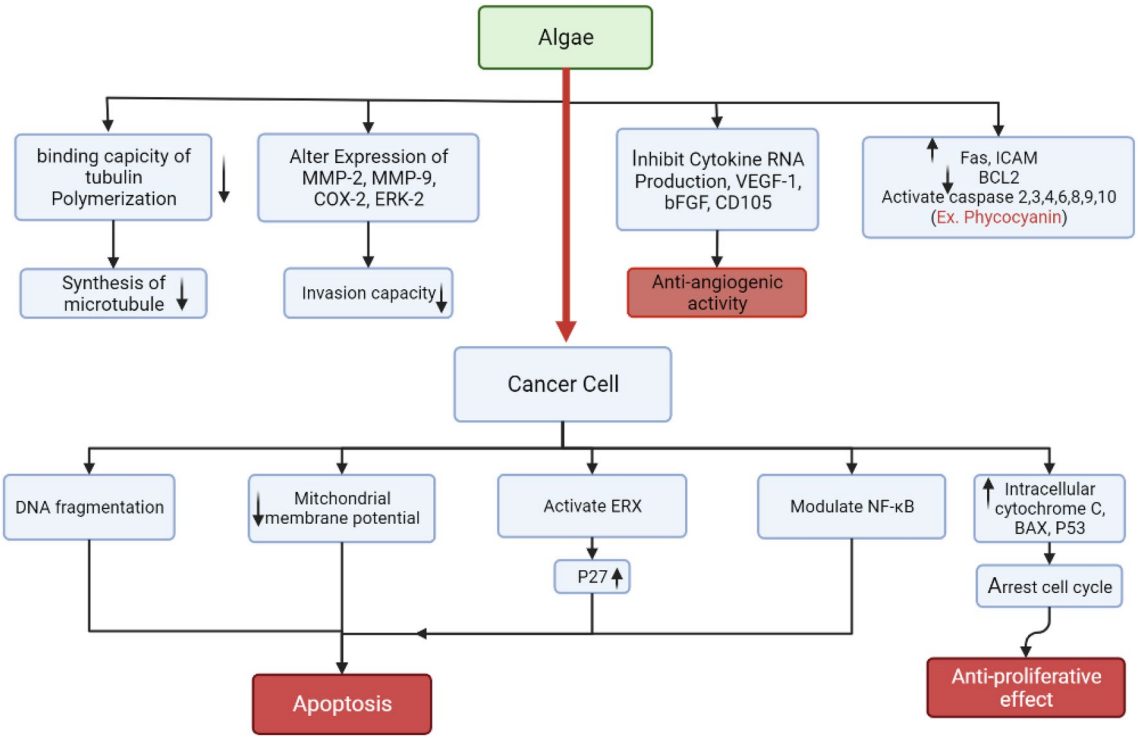

Fig. 6 Detailed mechanism for anti-cancer effect of algal bioactive compounds

Table 1 List of manufacturing companies involved in production of algal products

Company	Country	Algal species used	Key products	Annual revenue in 2021	References
Earthrise Nutritionals, LLC	California, USA	*Spirulina*	*Spirulina* based products	$ 22 million	Sharma and Sharma (2017), Araújo et al. (2021)
Cyanotech Corporation	Hawaii, USA	*Haematococcus pluvialis, Spirulina*	Bioastin astaxanthin and spirulina products	$ 32.3 million	Sharma and Sharma (2017)
BlueBioTech Int. GmbH	Germany	*Spirulina platensis, Haematococcus Pluvialis*	phycocyanin, astaxanthin, and microalgae powder	$ 5.9 million	Mehta et al. (2018)
Algatechnologies Ltd	Israel, USA	*Haematococcus pluvialis*	AstaPure, a natural astaxanthin	$ 15 million	Balasubramaniam et al. (2021)
E.I.D.—Parry (India) Limited	India	*Chlorella*, *Spirulina*	Nutraceuticals from micro algae	$ 22.7 million	Ratledge (2013), Kratzer and Murkovic (2021)

Conclusion

This review summarizes the medicinal importance of some algal-derived nutraceuticals. These bioactive compounds are not only potentially effective but also eco-friendly and safe. Furthermore, the cultivation of algae is sustainable as it has the ability for carbon dioxide sequestration. These algal bioactive compounds are being employed in food as stabilizers, thickening agents, emulsifiers, and texture modifiers. They serve in fulfilling various human dietary requirements and also have a significant role in combating serious health problems like cardiovascular, and neurodegenerative diseases, immune disorders, atherosclerosis, stroke, and carcinomas. Owing to the greater diversity in the biochemical composition of algae, it is now considered a potential functional food or superfood. Algal biomass possesses a significant variability in terms of biochemical composition and technological improvements about its incorporation as a food supplement has favored its

Table 2 Algal species and their bioactive compounds for different diseases

Algal species	Type of nutraceutical	Bioactive compounds	Target disease	References
Ecklonia cava, Fucus spp., *Ascophyllum*	Polyphenols	Phlorotannins	HIV	Vo and Kim (2010)
Porphyridum cruentum	Polysachharides	Lectins	Myeloid tumor	Gardeva et al. (2009)
Chlorella zofingiensis, Muriellopsis	Carotenoid	Lutein	Stroke and Cardiovascular disease	Liu et al. (2017), Ku et al. (2013)
Skeletonema costatum, Crypthecodinium cohnii	PUFA	Omega 3- fatty acid	Coronary heart disease, inflammatory disease	Shahidi (2012)
Saccharina latissima, Porphyra tenera	Amino acid, carotenoid	Taurine, Fucoxanthin	Obesity, hypocholestrolemic effect	Maeda (2015)
Gracilaria blodgettii, Gracilaria lemaneiformis,Ulva lacuta	Polyphenols, polysaccharide	Phlorotannins, porphyran, alginic acid	Allergy, asthama, inflammatory diseases	Cheong et al. (2021), Jaswir and Monsur (2011)
Aphanizomenon	Carotenoid	c-Phycocyanin	Artheritis, dermatological problems	Bishop and Zubeck (2012)
Hematococcus	Carotenoid	Astaxanthanin	Age related muscular degeneration	Bishop and Zubeck (2012)
Chondrus crispus, Gelidium cartilagrinum	Carbohydrates	Carrageenan	STD (genital warts, gonorrhea, herpes,simplex virus)	Mendis and Kim (2011)
Laminaria digitata, Laminaria phyperborea	Polysaccharides	Alginic acid	Gastritis, gastroduodenal ulcers	Besednova et al. (2020)
Laminaria japonica	Vitamins	Iodine	Goiter	Mendis and Kim (2011)
Spirulina, Porphyra yezoensis, Chlorella vulgaris	Protein	Nori-peptides	Cardiovascular diseases, hypertension	Ambati et al. (2014), Toblli et al. (2002)
Wollea saccata, Phormedium fragile, Spirulina plantensis	Phenols, alkaloids	Alginates	Plant fungal diseases	Righini et al. (2019)
Laurencia spp.	Phytochemicals	Halogenated compounds	Tuberculosis, antimicrobial	Cabrita et al. (2010)
Gracilaria spp., *Microcystis aeruginosa*	Protein	MAAs	Skin cancer	Lawrence et al. (2017)
Ecklonia kurome, Ulva fasciata, Hypnea musciformis	Pigments, phenols	Astanxanthin, Phlorotannins,	Bacterial diseases	Arvinda Swamy (2011)
Ecklonia cava	Sulfated polysaccharides	Ulvan, fucoidan	Viral diseases	Pujol et al. (2012)
Sargassum polycystum *Ecklonia stolonifera,* Ishige okamurae	Phlorotannins, polysachacrides sterol	Fucoidans, alginates, laminarans, fucosterol	Diabetes mellitus	Shimada et al. (2016)
Pterocladia capillacea, Gelidium pristoides, Gracilaria corticata	Polysaccharides, phenols	Fucoidan, phlorotannins	Alzheimer's disease	Silva et al. (2019)
Laminaria japonica, Ecklonia cava, Fucus vesiculosus, Saccharina japonica, Turbinaria, decurrens	Polysaccharides, phenolic compounds	Fucoidan, dieckol	Parkinson's disease	Jha et al. (2017)
Palmaria palmate, Saccharina latissima, Saccorhiza polyschides	PUFAs, phenols	Omega 3-fatty acids, bromophenol	Multiple sclerosis	Yuan et al. (2011a, b)
Haematococcus pluvialis	Carotenoid	Astanxanthin	Kidney function impairment	Bajpai et al. (2014)
Sarcothalia crispata, Mazzaella laminarioides, Chondrus crispus	Polyphenols, carotenoids, polysaccharides	Astanxanthin, carrageenan, laminarin, fucoidan	Cancer	Fan et al. (2014)

commercial production. Multinational food companies and pharmaceutical industries are bringing these nutritional innovations to customer consumption products (like breakfast cereals, probiotics, and soft drinks). Due to the increasing rate of inflation in recent years, the future seems more promising for the commercial application of algae in the food, cosmetic, and pharmaceutical industries as well as feedstock for energy. The challenge yet remains to modify seaweeds into more palatable functional food for increasing the consumption demand. Apart from these basic aspects, the amount of production must be increased so that raw seaweed demands may be satisfied at competitive costs and more attempts must be made to discover new sources of algae that have previously been overlooked.

Acknowledgements We are grateful to Vice Chancellor of Delhi Technological University, Delhi, India for constant support and guidance.

Author contributions The authors have equally contributed. All the authors have read the final manuscript.

Data availability The authors confirm that the data supporting the findings of this study are available within the article.

Declarations

Conflict of interest The authors declare that they have no conflict of interest in the publication.

Research involving human participants and/or animals No.

Informed consent Yes, we know every aspect of our participation.

References

Alghazwi M et al (2020) Impact of Ecklonia radiata extracts on the neuroprotective activities against amyloid beta (Aβ1-42) toxicity and aggregation. J Funct Foods 68(August 2019):103893. https://doi.org/10.1016/j.jff.2020.103893

Al-obaidi JR et al (2021) Uncovering prospective role and applications of existing and new nutraceuticals from bacterial, fungal, algal and cyanobacterial, and plant sources. Sustainability (switzerland). https://doi.org/10.3390/su13073671

Alves C et al (2016) 'Bifurcaria bifurcata: a key macro-alga as a source of bioactive compounds and functional ingredients. Int J Food Sci Technol 51(7):1638–1646. https://doi.org/10.1111/ijfs.13135

Ambati RR et al (2014) Astaxanthin: Sources, extraction, stability, biological activities and its commercial applications—a review. Mar Drugs 12(1):128–152. https://doi.org/10.3390/md12010128

Araújo R et al (2021) Current status of the algae production industry in Europe: an emerging sector of the blue bioeconomy. Front Mar Sci 7(January):1–24. https://doi.org/10.3389/fmars.2020.626389

Arvinda Swamy ML (2011) Marine algal sources for treating bacterial diseases 1st edn, advances in food and nutrition research, 1st edn. Elsevier Inc., Amsterdam. https://doi.org/10.1016/B978-0-12-387669-0.00006-5

Bajpai A et al (2014) Oxidative stress and major depression. J Clin Diagn Res 8(12):CC04–CC07. https://doi.org/10.7860/JCDR/2014/10258.5292

Balasubramaniam V et al (2021) Isolation of industrial important bioactive compounds from microalgae. Molecules 26(4):1–45. https://doi.org/10.3390/molecules26040943

Barbalace MC et al (2019) Anti-inflammatory activities of marine algae in neurodegenerative diseases. Int J Mol Sci. https://doi.org/10.3390/ijms20123061

Bauer S et al (2021) The application of seaweed polysaccharides and their derived products with potential for the treatment of Alzheimer's disease. Mar Drugs. https://doi.org/10.3390/md19020089

Bertsch M et al (2021) A sensitivity analysis of a mathematical model for the synergistic interplay of amyloid beta and tau on the dynamics of Alzheimer's disease. Brain Multiphys 2(June 2020):100020. https://doi.org/10.1016/j.brain.2020.100020

Besednova NN et al (2020) Extracts and marine algae polysaccharides in therapy and prevention of inflammatory diseases of the intestine. Mar Drugs 18(6):1–18. https://doi.org/10.3390/md18060289

Besednova NN et al (2021) Antiviral effects of polyphenols from marine algae. Biomedicines 9(2):1–23. https://doi.org/10.3390/biomedicines9020200

Bishop MW, Zubeck MH (2012) Evaluation of microalgae for use as nutraceuticals and nutritional supplements. J Nutr Food Sci. https://doi.org/10.4172/2155-9600.1000147

Cabrita MT, Vale C, Rauter AP (2010) Halogenated compounds from marine algae. Marine Drugs 8(8):2301–2317. https://doi.org/10.3390/md8082301

Cai J, Lovatelli A, Aguilar-Manjarrez J, Cornish L, Dabbadie L, Desrochers A, Diffey S, Garrido Gamarro E, Geehan J, Hurtado A, Lucente D, Mair G, Miao W, Potin P, Przybyla C, Reantaso M, Roubach R, Tauati M, Yuan X (2021) Fisheries and seaweeds and microalgae: an overview for unlocking. FAO Fisheries and Aquaculture Circular, Rome

Cheong RCT et al (2021) Otolaryngologic manifestations in pediatric inflammatory multisystem syndrome temporally associated with COVID-19. JAMA Otolaryngol - Head and Neck Surg 147(5):482–484. https://doi.org/10.1001/jamaoto.2020.5698

Chrapusta E et al (2017) Mycosporine-like amino acids: potential health and beauty ingredients. Mar Drugs 15(10):1–29. https://doi.org/10.3390/md15100326

Christaki E et al (2013) Functional properties of carotenoids originating from algae. J Sci Food Agric 93(1):5–11. https://doi.org/10.1002/jsfa.5902

Conde FR, Churio MS, Previtali CM (2000) The photoprotector mechanism of mycosporine-like amino acids. Excited-state properties and photostability of porphyra-334 in aqueous solution. J Photochem Photobiol B 56(2–3):139–144. https://doi.org/10.1016/S1011-1344(00)00066-X

Dijksterhuis JP, Petersen J, Schulte G (2014) WNT/Frizzled signalling: Receptor-ligand selectivity with focus on FZD-G protein signalling and its physiological relevance: IUPHAR review 3. Br J Pharmacol 171(5):1195–1209. https://doi.org/10.1111/bph.12364

Domínguez H (2013) Algae as a source of biologically active ingredients for the formulation of functional foods and nutraceuticals. Funct Ingred Algae Foods Nutraceuticals. https://doi.org/10.1533/9780857098689.1

dos Santos MAZ et al (2021) Rhodophyta, Ochrophyta and Chlorophyta macroalgae from different sub-Antarctic regions (Chile) and their potential for polyunsaturated fatty acids. Revista Brasileira De Botanica 44(2):429–438. https://doi.org/10.1007/s40415-021-00712-0

El Khoury D et al (2014) Effect of sodium alginate addition to chocolate milk on glycemia, insulin, appetite and food intake in healthy adult men. Eur J Clin Nutr 68(5):613–618. https://doi.org/10.1038/ejcn.2014.53

Fan X et al (2014) Marine algae-derived bioactive peptides for human nutrition and health. J Agric Food Chem 62(38):9211–9222. https://doi.org/10.1021/jf502420h

Fernández FGA et al (2021) The role of microalgae in the bioeconomy. New Biotechnol 61:99–107. https://doi.org/10.1016/j.nbt.2020.11.011

Fitzgerald C et al (2011) Heart health peptides from Macroalgae and their potential use in functional foods. J Agric Food Chem 59(13):6829–6836. https://doi.org/10.1021/jf201114d

Gantar M, Dhandayuthapani S, Rathinavelu A (2012) Phycocyanin induces apoptosis and enhances the effect of topotecan on prostate cell line LNCaP. J Med Food 15(12):1091–1095. https://doi.org/10.1089/jmf.2012.0123

Gardeva E et al (2009) Cancer protective action of polysaccharide, derived from red microalga porphyridium cruentum—a biological background. Biotechnol Biotechnologic Equip 23:783–787 https://doi.org/10.1080/13102818.2009.10818540

Glass CK et al (2010) Mechanisms underlying inflammation in neurodegeneration. Cell 140(6):918–934. https://doi.org/10.1016/j.cell.2010.02.016

Guedes ÉAC et al (2013) Cytotoxic activity of marine algae against cancerous cells. Rev Bras 23(4):668–673. https://doi.org/10.1590/S0102-695X2013005000060

Gunathilaka TL et al (2020) Antidiabetic potential of marine brown algae—a mini review. J Diabetes Res. https://doi.org/10.1155/2020/1230218

Hannan MA et al (2020) Neuroprotective potentials of marine algae and their bioactive metabolites: pharmacological insights and therapeutic advances. Mar Drugs. https://doi.org/10.3390/md18070347

Hans N, Malik A, Naik S (2021) Antiviral activity of sulfated polysaccharides from marine algae and its application in combating COVID-19: mini review. Bioresour Technol Rep 13(December 2020):100623. https://doi.org/10.1016/j.biteb.2020.100623

Hart AN et al (2007) Natural killer cell activation and modulation of chemokine receptor profile in vitro by an extract from the cyanophyta Aphanizomenon flos-aquae. J Med Food 10(3):435–441. https://doi.org/10.1089/jmf.2007.401

Hsu YW et al (2008) Protective effects of Dunaliella salina—a carotenoids-rich alga, against carbon tetrachloride-induced hepatotoxicity in mice. Food Chem Toxicol 46(10):3311–3317. https://doi.org/10.1016/j.fct.2008.07.027

Hu X et al (2012) Combination of fucoxanthin and conjugated linoleic acid attenuates body weight gain and improves lipid metabolism in high-fat diet-induced obese rats. Arch Biochem Biophys 519(1):59–65. https://doi.org/10.1016/j.abb.2012.01.011

Hussein G et al (2005) Antihypertensive and neuroprotective effects of astaxanthin in experimental animals. Biol Pharm Bull 28(1):47–52. https://doi.org/10.1248/bpb.28.47

Ismail MM, Alotaibi BS, EL-Sheekh MM (2020) Therapeutic uses of red macroalgae. Molecules 25(19):1–14. https://doi.org/10.3390/molecules25194411

Jaswir I, Monsur HA (2011) Anti-inflammatory compounds of macro algae origin: a review. J Med Plant Res 5(33):7146–7154. https://doi.org/10.5897/JMPR11.018

Jha A et al (2017) Functional connectivity of the pedunculopontine nucleus and surrounding region in Parkinson's disease. Cerebral Cortex 27(1):54–67. https://doi.org/10.1093/cercor/bhw340

Joe MJ et al (2006) The inhibitory effects of eckol and dieckol from Ecklonia stolonifera on the expression of matrix metalloproteinase-1 in human dermal fibroblasts. Biol Pharm Bull 29(8):1735–1739. https://doi.org/10.1248/bpb.29.1735

Jung HA et al (2006) Angiotensin-converting enzyme I inhibitory activity of phlorotannins from Ecklonia stolonifera. Fish Sci 72(6):1292–1299. https://doi.org/10.1111/j.1444-2906.2006.01288.x

Jung HA et al (2008) Inhibitory activities of extracts from several kinds of seaweeds and phlorotannins from the brown alga Ecklonia stolonifera on glucose-mediated protein damage and rat lens aldose reductase. Fish Sci 74(6):1363–1365. https://doi.org/10.1111/j.1444-2906.2008.01670.x

Jung HA et al (2012) Promising antidiabetic potential of fucoxanthin isolated from the edible brown algae Eisenia bicyclis and Undaria pinnatifida. Fish Sci 78(6):1321–1329. https://doi.org/10.1007/s12562-012-0552-y

Kalasariya HS et al (2020) Beneficial effects of marine algae in skin moisturization and photoprotection. Int J Pharm Sci Health Care. https://doi.org/10.26808/rs.ph.i10v5.01

Katiyar R, Arora A (2020) Health promoting functional lipids from microalgae pool: a review. Algal Res 46(January):101800. https://doi.org/10.1016/j.algal.2020.101800

Katoh M (2017) Canonical and non-canonical WNT signaling in cancer stem cells and their niches: cellular heterogeneity, omics reprogramming, targeted therapy and tumor plasticity (review). Int J Oncol 51(5):1357–1369. https://doi.org/10.3892/ijo.2017.4129

Khotimchenko M et al (2020) Antitumor potential of carrageenans from marine red algae. Carbohydr Polym 246(June):116568. https://doi.org/10.1016/j.carbpol.2020.116568

Kim EJ et al (2010) Fucoidan present in brown algae induces apoptosis of human colon cancer cells. BMC Gastroenterol. https://doi.org/10.1186/1471-230X-10-96

Koyande AK et al (2021) Emerging algal nanotechnology for high-value compounds: a direction to future food production. Trends Food Sci Technol 116(February):290–302. https://doi.org/10.1016/j.tifs.2021.07.026

Ku CS et al (2013) Health benefits of blue-green algae: prevention of cardiovascular disease and nonalcoholic fatty liver disease. J Med Food 16(2):103–111. https://doi.org/10.1089/jmf.2012.2468

Larsen JE, Minna JD (2011) Molecular biology of lung cancer: clinical implications. Clin Chest Med 32(4):703–740. https://doi.org/10.1016/j.ccm.2011.08.003

Lawrence BJ et al (2017) Cognitive training and noninvasive brain stimulation for cognition in Parkinson's disease: a meta-analysis. Neurorehabilitation Neural Repair 31(7):597–608. https://doi.org/10.1177/1545968317712468

Lee SH, Jeon YJ (2013) Anti-diabetic effects of brown algae derived phlorotannins, marine polyphenols through diverse mechanisms. Fitoterapia 86(1):129–136. https://doi.org/10.1016/j.fitote.2013.02.013

Li H et al (2017a) Food-derived antioxidant polysaccharides and their pharmacological potential in neurodegenerative diseases. Nutrients. https://doi.org/10.3390/nu9070778

Li J et al (2017b) λ-Carrageenan improves the antitumor effect of dendritic cellbased vaccine. Oncotarget 8(18):29996–30007. https://doi.org/10.18632/oncotarget.15610

Liu T et al (2017) NF-κB signaling in inflammation. Signal Transduct Targeted Ther. https://doi.org/10.1038/sigtrans.2017.23

Lopes G, Andrade PB, Valentão P (2017) Phlorotannins: towards new pharmacological interventions for diabetes mellitus type 2. Molecules 22(1):1–21. https://doi.org/10.3390/molecules22010056

Maeda H (2015) Toward a full understanding of the EPR effect in primary and metastatic tumors as well as issues related to its heterogeneity. Adv Drug Deliv Rev 91:3–6. https://doi.org/10.1016/j.addr.2015.01.002

Marino T et al (2020) Natural beta-carotene: a microalgae derivate for nutraceutical applications. Chem Eng Trans 79(April):103–108. https://doi.org/10.3303/CET2079018

Martins AP et al (2018) Biotechnological potential of benthic marine algae collected along the Brazilian coast. Algal Res 33(May):316–327. https://doi.org/10.1016/j.algal.2018.05.008

Mendes M et al (2022) Algae as food in Europe: an overview of species diversity and their application. Foods 11(13):1871. https://doi.org/10.3390/foods11131871

Mendis E, Kim SK (2011) Present and future prospects of seaweeds in developing functional foods. 1st edn, advances in food and nutrition research, 1st edn. Elsevier Inc., Amsterdam. https://doi.org/10.1016/B978-0-12-387669-0.00001-6

Misonou T et al (2003) UV-absorbing substance in the red alga Porphyra yezoensis (Bangiales, Rhodophyta) block thymine photodimer production. Mar Biotechnol 5(2):194–200. https://doi.org/10.1007/s10126-002-0065-2

Morgillo F et al (2016) Mechanisms of resistance to EGFR-targeted drugs: lung cancer. ESMO Open 1(3):1–10. https://doi.org/10.1136/esmoopen-2016-000060

Naguib YMA (2000) Antioxidant activities of astaxanthin and related carotenoids. J Agric Food Chem 48(4):1150–1154. https://doi.org/10.1021/jf991106k

Nicoletti M (2016) Microalgae nutraceuticals. Foods 5(3):1–13. https://doi.org/10.3390/foods5030054

Nilesh Hemantkumar J, IlzaRahimbhai M (2020) Microalgae and its use in nutraceuticals and food supplements. Microalgae Physiol Appl. https://doi.org/10.5772/intechopen.90143

Oren A, Gunde-Cimerman N (2007) Mycosporines and mycosporine-like amino acids: UV protectants or multipurpose secondary metabolites? FEMS Microbiol Lett 269(1):1–10. https://doi.org/10.1111/j.1574-6968.2007.00650.x

O'Sullivan L et al (2010) Prebiotics from marine macroalgae for human and animal health applications. Mar Drugs 8(7):2038–2064. https://doi.org/10.3390/md8072038

Ouyang L et al (2012) Programmed cell death pathways in cancer: a review of apoptosis, autophagy and programmed necrosis. Cell Prolif 45(6):487–498. https://doi.org/10.1111/j.1365-2184.2012.00845.x

Pagarete A et al (2021) Antiviral potential of algal metabolites—a comprehensive review. Mar Drugs 19(2):1–23. https://doi.org/10.3390/md19020094

Paiva L et al (2017) Angiotensin I-converting enzyme (ACE) inhibitory activity, antioxidant properties, phenolic content and amino acid profiles of *Fucus spiralis* L. protein hydrolysate fractions. Mar Drugs. https://doi.org/10.3390/md15100311

Pangestuti R, Kim SK (2011) Neuroprotective effects of marine algae. Mar Drugs 9(5):803–818. https://doi.org/10.3390/md9050803

Pereira L, Valado A (2021) The seaweed diet in prevention and treatment of the. Mar Drugs 19:1–25

Pujol CA et al (2012) Antiviral activity against dengue virus of diverse classes of algal sulfated polysaccharides. Int J Biologic Macromol 51(4):412–416. https://doi.org/10.1016/j.ijbiomac.2012.05.028

Radmer RJ (1996) Algal diversity and commercial algal products. Bioscience 46(4):263–270. https://doi.org/10.2307/1312833

Ramkumar M et al (2017) Neuroprotective effect of Demethoxycurcumin, a natural derivative of Curcumin on rotenone induced neurotoxicity in SH-SY 5Y Neuroblastoma cells. BMC Complement Altern Med 17(1):1–11. https://doi.org/10.1186/s12906-017-1720-5

Raposo MFDJ, De Morais AMMB (2015) Microalgae for the prevention of cardiovascular disease and stroke. Life Sci 125:32–41. https://doi.org/10.1016/j.lfs.2014.09.018

Ratledge C (2013) Microbial oils: an introductory overview of current status and future prospects. OCL - Oilseeds and fats, crops and lipids, 20(6). https://doi.org/10.1051/ocl/2013029

Reis SE et al (2020) Influence of sulfated polysaccharides from *Ulva lactuca* L. upon Xa and IIa coagulation factors and on venous blood clot formation. Algal Res 45(December 2019):101750. https://doi.org/10.1016/j.algal.2019.101750

Righini H et al (2019) Different antifungal activity of Anabaena sp., Ecklonia sp., and Jania sp. Against Botrytis cinerea. Marine Drugs 17(5):15–17. https://doi.org/10.3390/md17050299

Rodriguez-Pallares J et al (2007) Mechanism of 6-hydroxydopamine neurotoxicity: the role of NADPH oxidase and microglial activation in 6-hydroxydopamine-induced degeneration of dopaminergic neurons. J Neurochem 103(1):145–156. https://doi.org/10.1111/j.1471-4159.2007.04699.x

Saadaoui I et al (2020) Algae-derived bioactive compounds with anti-lung cancer potential. Mar Drugs. https://doi.org/10.3390/md18040197

Sami N, Ahmad R, Fatma T (2021) Exploring algae and cyanobacteria as a promising natural source of antiviral drug against SARS-CoV-2. Biomed J 44(1):54–62. https://doi.org/10.1016/j.bj.2020.11.014

Sathasivam R, Ki JS (2018) A review of the biological activities of microalgal carotenoids and their potential use in healthcare and cosmetic industries. Mar Drugs. https://doi.org/10.3390/md16010026

Satoh A et al (2009) Preliminary clinical evaluation of toxicity and efficacy of a new astaxanthin-rich Haematococcus pluvialis extract. J Clin Biochem Nutr 44(3):280–284. https://doi.org/10.3164/jcbn.08-238

Seca AML, Pinto DCGA (2018) Overview on the antihypertensive and anti-obesity effects of secondary metabolites from seaweeds. Mar Drugs. https://doi.org/10.3390/md16070237

Shahidi F (2012) Nutraceuticals, functional foods and dietary supplements in health and disease. J Food Drug Anal 20(SUPPL.1):226–230. https://doi.org/10.38212/2224-6614.2144

Shannon E, Abu-Ghannam N (2019) Seaweeds as nutraceuticals for health and nutrition. Phycologia 58(5):563–577. https://doi.org/10.1080/00318884.2019.1640533

Sharifuddin Y et al (2015) Potential bioactive compounds from seaweed for diabetes management. Mar Drugs 13(8):5447–5491. https://doi.org/10.3390/md13085447

Sharma P, Sharma N (2017) Industrial and biotechnological applications of algae: a review. J Adv Plant Biol 1(1):1–25. https://doi.org/10.14302/issn.2638-4469.japb-17-1534

Shimada SL et al (2016) Sustained use of patient portal features and improvements in diabetes physiological measures. J Med Int Res. https://doi.org/10.2196/jmir.5663

Silva J et al (2019) Antioxidant and neuroprotective potential of the brown seaweed bifurcaria bifurcata in an in vitro Parkinson's disease model. Mar Drugs 17(2):1–16. https://doi.org/10.3390/md17020085

Silva M, Seijas P, Otero P (2021) Exploitation of marine molecules to manage alzheimer's disease. Mar Drugs 19(7):1–26. https://doi.org/10.3390/md19070373

Somasekharan SP et al (2016) An aqueous extract of marine microalgae exhibits antimetastatic activity through preferential killing of suspended cancer cells and anticolony forming activity. Evid-Based Complement Altern Med. https://doi.org/10.1155/2016/9730654

Tabatabai R et al (2017) Targeting the Wnt pathway in cancer: a review of novel therapeutics. Target Oncol 12(5):623–641. https://doi.org/10.1007/s11523-017-0507-4

Tarozzi A et al (2013) Sulforaphane as a potential protective phytochemical against neurodegenerative diseases. Oxid Med Cell Longev. https://doi.org/10.1155/2013/415078

Toblli JE et al (2002) P-487 effects of losartan on cavernous tissue in spontaneously hypertensive rats P-489 plasma renin activity and aldosterone level in patients with essential P-488 antihypertensive effect of nori-peptides derived from red alga porphyra yezoensis different. J Hum Hypertens 15(4):2002

Valado A et al (2017) Multiple sclerosis: association of gelatinase B/matrix metalloproteinase-9 with risk and clinical course the

disease. Mult Scler Relat Disord 11(Decemeber 2016):71–76. https://doi.org/10.1016/j.msard.2016.12.003
Vishchuk OS, Ermakova SP, Zvyagintseva TN (2013) The fucoidans from brown algae of Far-Eastern seas: anti-tumor activity and structure-function relationship. Food Chem 141(2):1211–1217. https://doi.org/10.1016/j.foodchem.2013.03.065
Vo TS, Kim SK (2010) Potential anti-HIV agents from marine resources: an overview. Mar Drugs 8(12):2871–2892. https://doi.org/10.3390/md8122871
Wahls TL, Chenard CA, Snetselaar LG (2019) Review of two popular eating plans within the multiple sclerosis community: low saturated fat and modified paleolithic. Nutrients 11(2):1–34. https://doi.org/10.3390/nu11020352
Wan-Loy C, Siew-Moi P (2016) Marine algae as a potential source for anti-obesity agents. Mar Drugs 14(12):1–19. https://doi.org/10.3390/md14120222
Yang HW et al (2019) Anti-obesity and anti-diabetic effects of ishige okamurae. Mar Drugs 17(4):1–11. https://doi.org/10.3390/md17040202
Yao Z et al (2014) Enzymatic preparation of κ-carrageenan oligosaccharides and their anti-angiogenic activity. Carbohyd Polym 101(1):359–367. https://doi.org/10.1016/j.carbpol.2013.09.055
Yu DK et al (2015) Phlorofucofuroeckol B suppresses inflammatory responses by down-regulating nuclear factor κB activation via Akt, ERK, and JNK in LPS-stimulated microglial cells. Int Immunopharmacol 28(2):1068–1075. https://doi.org/10.1016/j.intimp.2015.08.028
Yuan H et al (2011a) Enhanced immunostimulatory and antitumor activity of different derivatives of κ-carrageenan oligosaccharides from Kappaphycus striatum. J Appl Phycol 23(1):59–65. https://doi.org/10.1007/s10811-010-9536-4
Yuan JP et al (2011b) Potential health-promoting effects of astaxanthin: a high-value carotenoid mostly from microalgae. Mol Nutr Food Res 55(1):150–165. https://doi.org/10.1002/mnfr.201000414
Zainal Ariffin SH et al (2014) Cytotoxicity effect of degraded and undegraded kappa and iota carrageenan in human intestine and liver cell lines. BMC Complement Altern Med 14(1):1–16. https://doi.org/10.1186/1472-6882-14-508
Zheng LX, Chen XQ, Cheong KL (2020) Current trends in marine algae polysaccharides: the digestive tract, microbial catabolism, and prebiotic potential. Int J Biol Macromol 151:344–354. https://doi.org/10.1016/j.ijbiomac.2020.02.168
Hanahan D, Weinberg R (2011) Hallmarks of cancer: supplement. Cell Press
Kratzer R, Murkovic M (2021) Food ingredients and nutraceuticals from microalgae: main product classes and biotechnological production. Foods. https://doi.org/10.3390/foods10071626

Springer Nature or its licensor (e.g. a society or other partner) holds exclusive rights to this article under a publishing agreement with the author(s) or other rightsholder(s); author self-archiving of the accepted manuscript version of this article is solely governed by the terms of such publishing agreement and applicable law.

Multimedia Tools and Applications
https://doi.org/10.1007/s11042-023-14371-8

A fusion way of feature extraction for automatic categorization of music genres

Dhruv Sharma[1] · Sachin Taran[1] · Anukul Pandey[1]

Received: 13 June 2022 / Revised: 1 September 2022 / Accepted: 10 October 2022
© The Author(s), under exclusive licence to Springer Science+Business Media, LLC, part of Springer Nature 2023

Abstract
Over the past decade, the invention of streaming services has led to the magnification of the music industry. With a plethora of available song choices, there is a dire need for recommendation techniques to help listeners discover music genres complementing their palate. This makes a vital need for automatic music genre categorization systems. With this objective, in this work fusion of direct and indirect features is introduced for the automatic categorization of music genres. In direct Feature Extraction (FE), the physical characteristics of music genres are assessed by timbral, chroma, and source separation-based features. In indirect FE, tunable Q-Wavelet transform and Teager energy operator are used to explore the non-linear characteristics of music signals. The proposed algorithm is examined on the GTZAN dataset, primarily focusing on the four-class classification problem. The introduced features are tested with multiple machine learning techniques to explore the best for music genre categorization. The wide neural network classifier with a single fully connected layer churned out optimal performance fetching an overall accuracy and F1 score of 95.8% and 95.82%, respectively. The proposed algorithm also outperforms most of the state-of-the-art techniques for the given dataset.

Keywords Music genres · Feature extraction · Feature fusion · Tunable Q-wavelet transform · Teager energy operator · Neural network

1 Introduction

The immense growth and disruption of the global music industry in the past few decades has exposed humans to various music genres [7], making the need to classify them essential. This in

✉ Sachin Taran
taransachin2@gmail.com

Anukul Pandey
anukul66@gmail.com; anukul.pandey@dtu.ac.in

[1] Delhi Technological University (DTU), Delhi, Shahbad Daulatpur, New Delhi 110042, India

Published online: 19 January 2023

turn, would help structure extensive music archives [2]. The Internet age has brought a widespread use of online music listening; various streaming giants require music genre classification to recommend songs to the listeners [43]. From Drinkify to playlisting, genre classification has diverse applications. As a classification problem, this system consists of the following steps: a) Features' selection and extraction from original music signals; b) To automatically categorize music into its genres; c) selected features are trained on machine learning or deep learning models [18, 35]. Feature extraction is relevant in the field of signal processing and artificial intelligence which includes medical applications [3, 4], image classification [6], etc.

Different features and techniques have been used in the literature to categorize music signals. Sugianto et al. [47] proposed a voting based system to improve upon the performance of their genre categorization model. They used Melspectrogram for FE and Convolutional Neural Network (CNN) for genre categorization. Tzanetakis et al. proposed an automatic genre classifier method where they evaluated timbral/short frame features, rhythmic/significant frame features, and pitch content-based features on the GTZAN dataset [53]. They used the Gaussian mixture model and Support Vector Machine (SVM) for automatic classification. Holzapfel et al. used timbral features to drive Non-negative Matrix Factorization (NMF) [23]. Furthermore, factorizing in the time-frequency plot is achieved through Short Time Fourier Transform (STFT), also known as a spectrogram. Consequently, a characteristic spectral basis was deduced for further classification.

Nanni et al. [39] amalgamated the visual and handcrafted features based on acoustic aspects of the musical data for its different genres categorization. These features were separately classified and fused to make it to the end decision. For visual aspects, spectrograms, Harmonic/Percussive Source Separation (HPSS) images, and time-frequency images based on Q-transform were taken into account. Textural descriptors for the above included the usage of Gabor filtering and binarized picture aspects based on statistical measures. They used various classifier techniques, of which CNN yielded optimal results. Liu et al. [37] developed a novel block of CNN for categorization. The model displayed strong capabilities to segregate genres while decision-making distinctively. It dived into low-level aspects of Cepstral Coefficients and utilized them to the optimum. This method also suggested a solution to the challenge of managing the entire learning process of the model with scarce data, ensuring robustness simultaneously. In [33], Lee et al. proposed a method that used Mel-Frequency Cepstral Coefficients (MFCCs) and octave-based contrast in the spectral domain. It also evaluated envelop for signals in the spectral domain.

Haggblade et al. [22] also used MFCC and statistical measures to extract features and yielded optimal categorization results using a neural network. Yu et al. [55] expressed the limitations of the usage of spectrogram for genre categorization. They disregarded the myth that spectrums with distinctively varied temporal steps have the same significance. Considering this, they incorporated variations in the spectrum to propose a novel deep learning method for which they infused the mechanism based on attention over bidirectional Recurrent Neural Networks (RNN). Further, this mechanism was broadened into serialized and paralleled forms of which the latter portrayed greater flexibility and superior results. J. Li et al. [36] proposed to use the extracted spectrograms for each music signal and train them on their proposed improved deep learning model based on combined Angular Margin and Cosine Margin Softmax. In [10], Cai et al. infused the auditory-based image aspects that go in sync. The human auditory system has low-level traditional spectral features and acoustically sound aspects for categorizing genres. The best results were obtained using Support Vector Machine (SVM) as their categorization model. Panagakis et al. [41] proposed music signal classification via a joint sparse matrix, a low-rank representation.

They used cortical-based representation for feature extraction. Cortical extraction involves the computation of Q-transform, followed by compression of magnitude. After that, Discrete Wavelet Transform and time averaging are done to obtain cortical representation. It also used MFCC and chroma features.

In [30], Kumaraswamy et al. proposed an evolved model of deep CNN. A self-adaptive algorithm was used for training. The Sea-Lion method for optimization was used for weight update and optimization. For feature extraction, STFT and pitch-oriented features were used in addition to NMF. Individually, Kumaraswamy [29] also worked on the improved moth-flame methodology for the same set of features to solve the optimization issues of model parameters. Using this method, the association between the extracted aspects can be strengthened by multiplying a weight function with each feature. A contrastive divergence method was used in the classifier model to reconstruct the visible states before updating weights. Abdoli et al. [1] proposed a single-dimensional convolutional network as the classifier against the usual 2-dimensional one. As opposed to the quintessential image classifier that a regular CNN classifier is, their proposed model is capable of direct learning from the music signals of the database. Splitting of signal into its overlapped frames was done via a sliding window. It yielded better performance than the traditional model. Lee et al. [31] proposed a novel method of multi-scale feature extraction method and fed the extracted features to the CNN model for music genre categorization. In [38], K. Markov et al. employed various Gaussian processes to categorize music into genres. They also used the same method for music emotion detection. For Gaussian processes, gram matrices and kernel functions were used. However, its accuracy declined by 11% compared to conventional models like SVM.

Costa et al. [13] proposed using representation learning, replacing the direct feed of texture-based descriptions with the music-related image classifier. In this method, downscaling of images with high resolution was performed. These were then split into smaller patches. In the representation learning method, their key focus was on global-level features. Actions using this method are restricted to the same monotonous level. Hence, W.Y. Ng et al. [40] proposed a novel method to infuse the Network Vector of Locally Aggregated Descriptors (NetVLAD) model, a way for local representation and self-attention. The former is used to capture data across various levels, and the latter is used for learning their chronic dependencies. These were combined with CNN, and a meta classifier was used. Castillo et al. [12] proposed a method to directly extricate tracks from an online streaming platform YouTube via a web-oriented application. Region-based Convolutional Neural Network (RCNN) as long-short-term memory churned out the highest accuracy of all the used models. MFCC features were changed into 128-dimensional embedding areas before being fed to categorization models. In [42], Pelchat et al. reviewed various neural network techniques used for genre categorization. They utilized spectrograms extracted from time frames of clips as mere inputs. Six convolutional layers were used.

To identify distinct textures within each track, Foleis et al. [19] proposed a novel method to pick up textures based on the K-Means method. Multitude representation of textural aspects improved accuracy. Wang et al. [54] proposed an algorithm based on cross-view to act upon multiview data. They aimed at the derivation of optimal measure of distance for the same multiview data or, in other words, deriving an identical metric. Its corresponding graph structure was determined for the data, which was utilized in learning the distance measure. The main advantage of this method is that a balance can be achieved for multiview data. This also brought the challenge of possibilities of over smoothness of the metric. This could be

avoided by heuristically manipulating iterations in the process of fusion. Ceparrini et al. [11] proposed a method for subgenre categorization over electronic dance music. It contains newly released songs. Their main idea was to categorize such new music into music subgenres and test their ability to distinguish themselves from others. They used various Tree-based classifiers were used for implementation. In their proposed method, Elbir et al. [16] improved upon the STFT for feature extraction by integrating them over it to obtain the power frequency distribution and finally fuse them before passing over the features to the classifier. RBF and SVM and Polynomial SVM models were integrated to execute the categorization. Sawhney et al. [44] proposed latent features that were extracted directly from the raw music data and fed the features to a classifier based on autoencoder based on deep Softmax to categorize music signals into genres.

The differentiable features play a key role in the categorization of music signals into genres. This work proposes a new fusion way of Feature Extraction (FE) where direct and indirect features are combined to improve the performance of music genre categorization. Direct features including the Timbral, Chroma, and Harmonic-Percussive components (TCHP) are used to explore the frequency-related characteristics of music signals, and indirect features based on Tunable Q-Wavelet Transform (TQWT) and Teager Energy Operator (TEO) are suggested to assess the non-linear characteristics of music signals. The introduced feature set is tested on different machine learning algorithms to explore the best classifier in the multiclass classification problems of music genres. The key contributions are as follows:

- A novel feature extraction algorithm has been proposed that involves a fusion of signal decomposition features and TCHP features.
- The effect of the number of TQWT provided sub-bands on the categorization of music signal genres has been explored.
- The proposed features have been tested against several classifiers to reconnoitre the best-suited model in music genre recognition applications.
- The proposed method has obtained a better music genre categorization performance as compared to existing studies.

The proposed method based on **T**QWT-**T**EO and TCHP has been named as TT-TCHP.

The rest of the sections are arranged as follows. Sections 2 and 3 introduce the methods of TQWT and TEO, respectively. The proposed methodology is covered thoroughly in section 4. Experimental results and discussion have been covered in sections 5 and 6, and the work has finally been concluded in section 7.

2 Tunable Q-wavelet transform (TQWT)

TQWT is a transform based on wavelets meant for discrete-time signals. The characteristic that makes it unique is its ability to be tunable as per the input's oscillatory behavior. In the literature, TQWT is explored for the analysis of multicomponent signals like electroencephalogram, electromyogram, etc. [28, 50]. The music signal also shows the multi-component oscillatory nature [15]. The separation of these components into a range of frequencies can avail the deeper characteristics of the music signals. In this regard, TQWT is explored for the decomposition of music signals into their underlying components or Sub-Bands (SBs). TQWT

is parameter dependent and can be tuned as per the nature of signals. This characteristic makes it unique to tune as per the input's oscillatory behavior of the music signal. Another conspicuous aspect of TQWT is that signals undergoing this transformation are perfectly reconstructable, so information loss is minimum [45]. TQWT is parameter-dependent; it depends on several aspects, including the utmost important Q-factor. It further depends upon redundancy, also known as oversampling rate r, and total decomposition levels j [45]. The TQWT signals decomposition uses a multi-rate filter bank. It involves low and high pass and low pass filtering. These filters are devoid of rational transfer functions). Hence, their specification lies in the frequency domain. Figure 1 shows the decomposition and reconstruction processes. Unitary Discrete Fourier Transform is applied to the inputs. The frequency responses of filters $H_0(w)$ and $H_1(w)$ are Low Pass Scale (LPS) and High Pass Scale (HPS).

In LPS, only low-frequency information is passed. It has a scaling parameter a. If f is the sampling rate of an input signal, then the sampling rate of LPS output is af. While on the other hand, HPS only permits high-frequency information. It uses scaling parameter b. Hence, its output sampling rate will be bf [25]. For reconstruction, sampling rates are inverted. To limit the redundancy of TQWT, one must ensure, as per [45] that,

$$0 < b <= 1 \; and \; 0 < a < 1 \tag{1}$$

And, for perfect reconstruction of signal, $a + b > 1$, always. This ensures the localization of responses in the time domain. $H_0(w)$ and $H_1(w)$ are mathematically defined as [45]:

$$|H_0(w)| = 1, \qquad |w| <= (1-b)\pi \tag{2}$$

$$H_0(w) = 0, \qquad a\pi <= |w| <= \pi \tag{3}$$

$$H_1(w) = 0, \qquad |w| <= (1-b)\pi \tag{4}$$

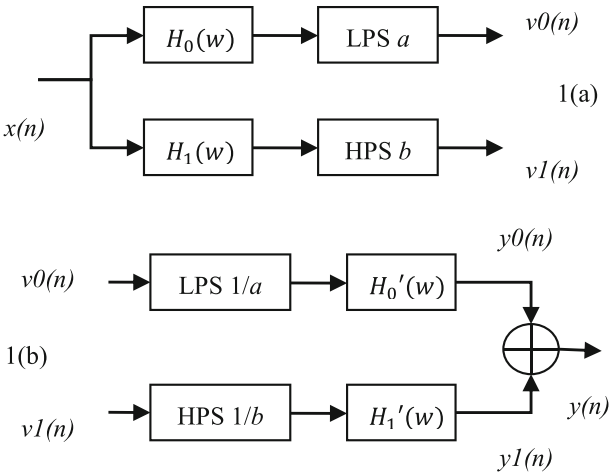

Fig. 1 TQWT filter banks for (**a**) Decomposition and (**b**) Reconstruction

$$|H_1(w)| = 0, \qquad a\pi <= |w| <= \pi \tag{5}$$

It is to be noted that the sum of squares of the magnitudes of both the filter responses must be unity for perfect reconstruction. Various parameters of this wavelet transform can be expressed in terms of sampling parameters as follows [25]:

$$\text{Redundancy, r} = \frac{b}{1-a} \tag{6}$$

$$\text{Q-factor, Q} = \frac{2-b}{b} \tag{7}$$

Similarly, for a given Q-factor and redundancy value, as per [25], these parameters can be evaluated as

$$b = \frac{2}{Q+1}, \quad a = 1- \frac{b}{r} \tag{8}$$

The previous scenario was for single-stage decomposition. For the j^{th} stage decomposition, there will be a total of $j+1$ SBs resulting from decomposition. Figure 2 shows the TQWT decomposition of an input signal x up to j stages. In this figure, only the SBs resulting from LPF are decomposed further iteratively up to J levels, adding up to a total of $j+1$ SBs. The sampling rate for the j^{th} SB will be $ba^{J-1}f$ and a^Jf for HPS and LPS, respectively.

Figure 3 shows the TQWT SBs of a music signal for 2-level decomposition. Here, the input signal is denoted by blue colour.

3 Teager energy operator (TEO)

The TEO is primarily used for determining the energies of complex signals that can be broken into products of simplified functions. It is a nonlinear operator [27]. Introduced by H.M. Teager [51, 52], TEO was further analyzed, developed, and simplified by J. Kaiser [26, 27] in his works. He derived formulae for TEO for both

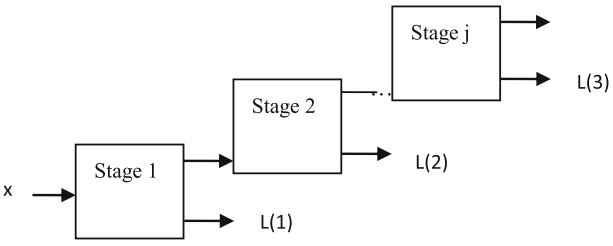

Fig. 2 J-stage filter bank of TQWT

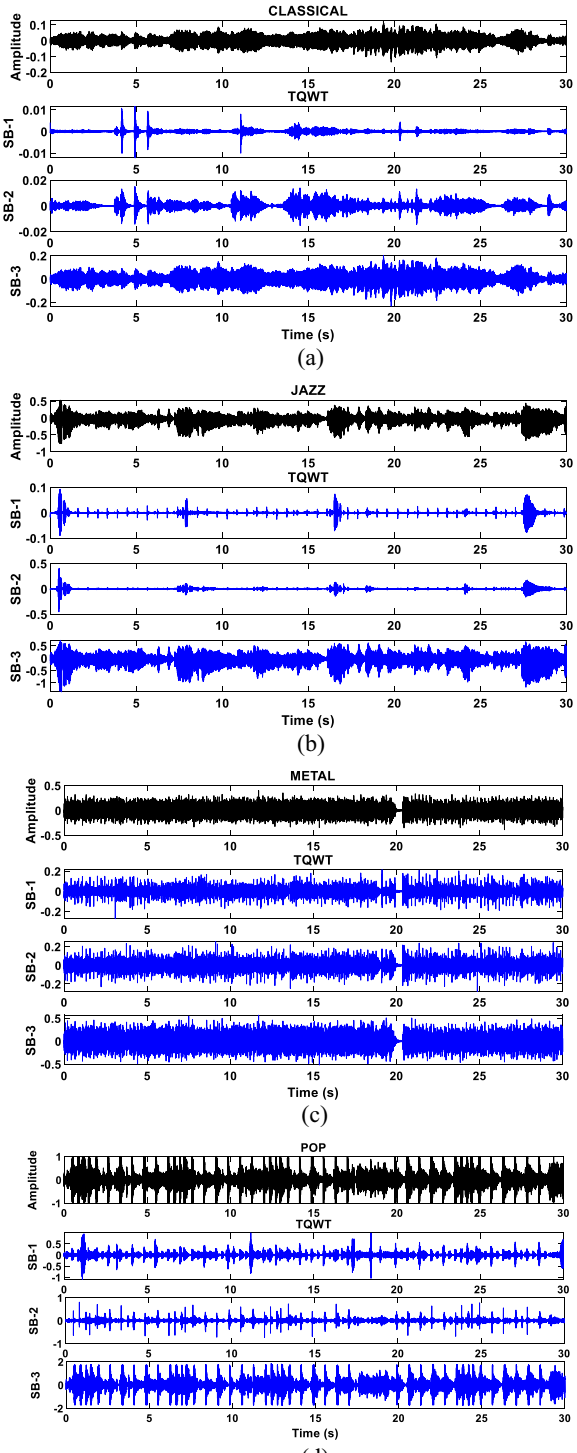

Fig. 3 TQWT plot for music signal for $j = 2$ (levels) (**a**) Classical (**b**) Jazz (**c**) Metal (**d**) Pop

continuous as well as discrete signals. For a continuous signal *x(t)*, the TEO is defined as per [8] as:

$$\Psi[x(t)] = \left(\frac{d}{dt}x(t)\right)^2 - x(t)\left(\frac{d^2}{dt^2}x(t)\right) \tag{9}$$

Teager-Kaiser energy operator for a discrete signal *x(n)* as defined in [26] is given as:

$$\Psi[x(n)] = x^2(n) - x(n+1)\,x(n-1) \tag{10}$$

Here, *x(n)*, *x(n-1)* and *x(n + 1)* are the present, past, and future values of signal sample.

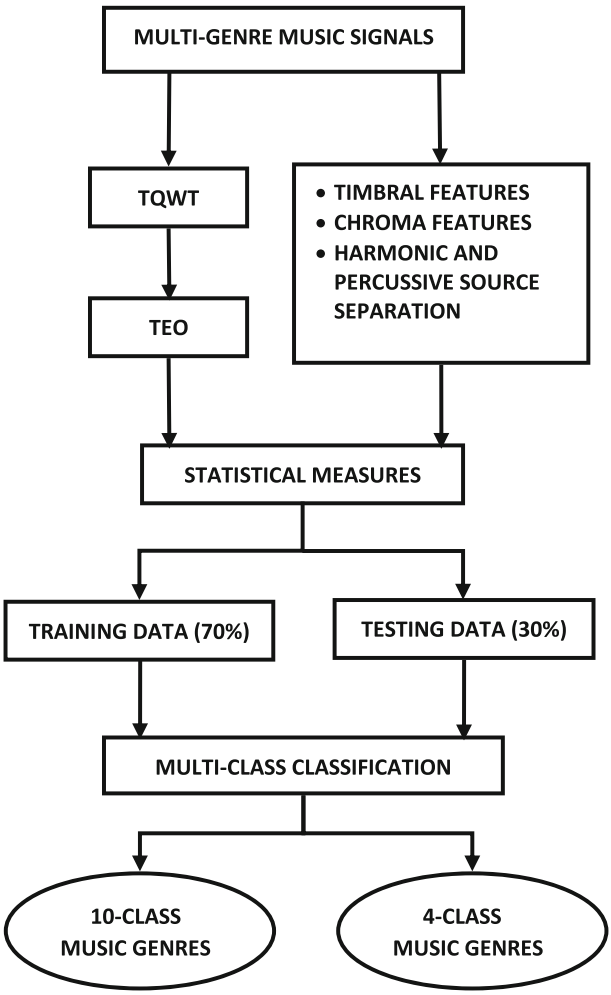

Fig. 4 Block Diagram of Proposed Methodology

Hence, it is observed that TEO operates on three adjacent values, the past one, the present one, and the future value. The TEO energy product of two-time functions yields a simple and symmetrical result. This indicates that TEO is a good measure for modulation and product methods. If there are n samples in the music signal, TEO will extract *n-2* feature values from it.

4 Proposed methodology

The proposed music genre system comprises a FE module and a classification module. The FE involves TT-TCHP based features from the GTZAN dataset which is followed by genre classification model. The block diagram summarizing the proposed method is shown in Fig. 4.

4.1 Feature extraction Level-1

At FE level-1 music signals are transformed into the non-linear Teager Energy (TE) by TQWT-TEO and frequency-related variations by the TCHP.

TQWT-TEO based transformation. A novel method of TQWT-TEO-based features has been proposed in this work. The input music signal is first decomposed into SBs dependent on its oscillatory behavior. This is achieved by the application of TQWT to the music signal. Then, the non-linear Teager energy operator is applied to each SB to extract the features for further classification. The algorithm for TQWT-TEO-based feature extraction is given in A1.

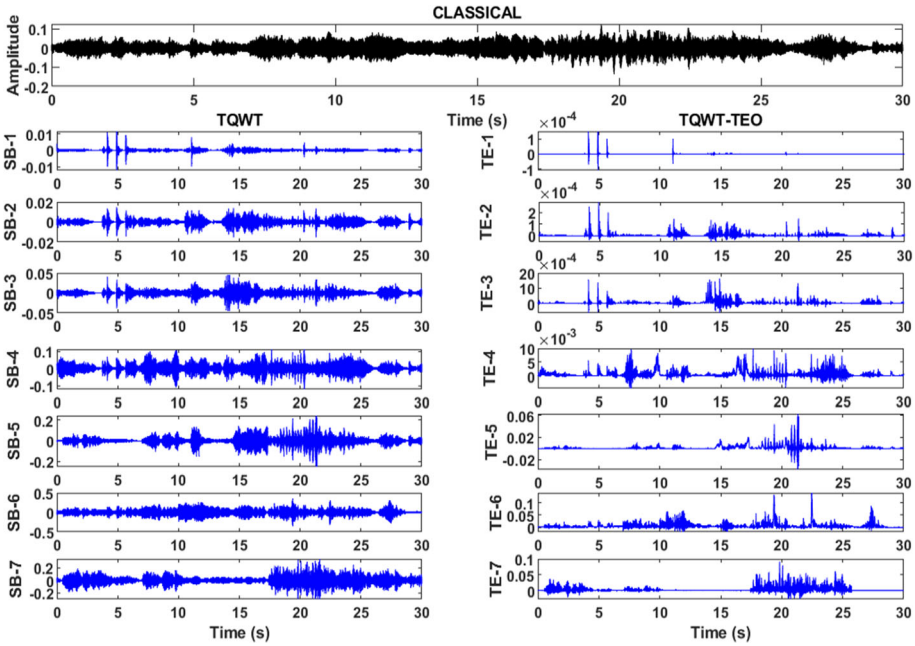

Fig. 5 TQWT-TEO plot for 7-Sub-band Decomposition of Classical Music Signal

Figure 5 shows non-linear energies of different TQWT-provided SBs. It is observed that TEO extracts the major energies of the sub-bands which are represented by sudden peaks and high intensities. The resulting energy is non-linear in nature and called Teager Energy (TE). It is also observed that TEO provides differentiable energy distribution for all SBs, which is extremely useful in extracting sparse features from the music signals.

Algorithm A1 TQWT-TEO based Transformation

```
Input: x(n)

Output: Teag_feat
Initialize J,Q and r.
tqw = tqwt(x(n),r,Q,J)
for   i = 1 to J
        m = length(tqw({1,J}))
        Teag_signal(1) = 0;
        Teag_signal(m) = 0;

        for     k = 2 to length(tqw{1,i})-1
                Teag_feat(i,k-1) = tqw(i,k)^2 - (tqw(i,k-1).*tqw(i,k+1));

        end
End
```

TCHP based Transformation: At this stage, the different genre music signal characteristics are explored by timbral, chroma, harmonic, and percussive components.

Timbral Features. These are the frequency domain features with shorter frames [21]. Music signals are non-stationary. Hence, evaluating timbral features over the entire duration is not feasible. Hence, small frames are taken, and features are repeatedly extracted within these frames. The usual length of the frame for these features ranges from 10 to 100 ms. If frame size exceeds 100 ms, non-stationary behavior might likely be observed within the frame, and hence features will not be accurately extracted. If it's less than 10 ms, the extracted values have higher chances of redundancy. Also, it would not make sense from an acoustic perspective if the frame size is kept below 10 ms because the time resolution of human hearing is 10 ms. Hence, below 10 ms, humans cannot appreciate the features of acoustic events. Various timbral features used in this paper are explained below.

Spectral Centroid. Spectral centroid is a frequency domain feature. It represents the point of the centre of gravity of the frequencies in the frequency bin of the corresponding signal frame. In Fig. 6, the spectral centroid has been extracted for a Jazz music clip of 30 sec. The frame size of 10 ms has been taken.

Mathematically [47], centroid is given as:

$$Ct = \frac{\sum_{n=1}^{N} Mt[n] * n}{\sum_{n=1}^{N} Mt[n]} \tag{11}$$

Where *Mt[n]* is the magnitude of the FT corresponding to *t* and *n* is the frequency bin.

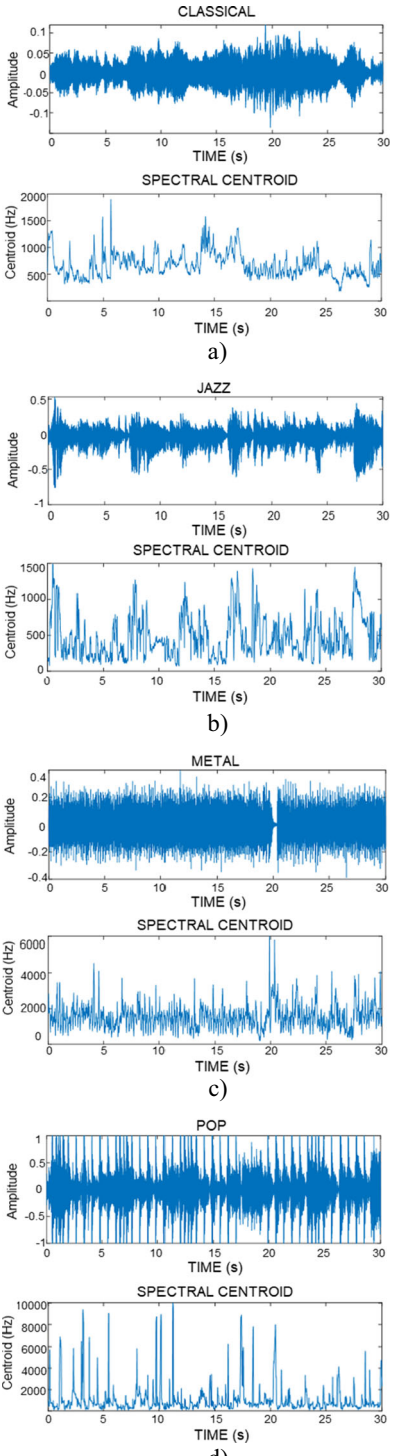

Fig. 6 Spectral Centroid Extraction from Music Signals (**a**) Classical (**b**) Jazz (**c**) Metal (**d**) Pop

Spectral Rolloff. When the low-frequency power values of a signal frame add up to reach 85% of the overall power, the corresponding normalized frequency is referred to as spectral roll-off. In Fig. 7, spectral roll-off has been extracted for a Jazz music clip of 30-sec belonging to the GTZAN dataset. Mathematically [47], roll-off is given as:

$$R = 0.85 * \sum_{n=1}^{N} Mt[n] \tag{12}$$

Chroma Features: Chroma features project the complete spectrum of a music signal into corresponding pitch classes. These are referred to as chroma or tonal height. These are twelve in number. Inspired by the musical octaves, these help in distinguishing distinct pitches. So, the entire input can project itself as 12 semitones or chroma of the octave [17].

Harmonic and Percussive Source Separation: It involves the extraction of harmonic and percussive features of a music signal. Harmony is a consequence of a series of chords played sequentially. It captures vertical data concerning the music signal. Harmonic components possess a certain pitch. It is perceivable by human ears. While on the other hand, percussive components are generated out of a collision between two objects. They do not possess any pitch, unlike in the former case. However, they do have a coherent time localization [49]. Figure 8 shows the harmonic and percussive components of the music signals. Here, the harmonic component is represented in black and percussive in blue.

4.2 Feature extraction Level-2

Statistical measures, including mean and variance, are then evaluated over the music signal transformation done at FE level-1. The mean and variance features are defined as [46]:

$$\mu = \frac{1}{P} \sum_{p=1}^{P} x(p) \tag{13}$$

$$\sigma^2 = \frac{1}{P} \sum_{p=1}^{P} (x(p) - \mu)^2 \tag{14}$$

Here P is the number of samples, and $x(p)$ refers to the previously extracted feature values. Hence, the feature count increases to 10. Extracted features based on TT-TCHP are summarized in Table 1, with j being the decomposition level.

4.3 Classification

Classification helps in categorizing input into different classes. Firstly, training and testing data features have been separated into a ratio of 70:30. This division has been done randomly, which gives better results. Training data is further divided for the training and validation process. Cross-validation folds are applied, and in this scenario, its value was taken as 13 as it helped to achieve optimal results. Further, training data features were trained on three different classifiers, and then testing data features were sent to each classifier to evaluate the system accuracy.

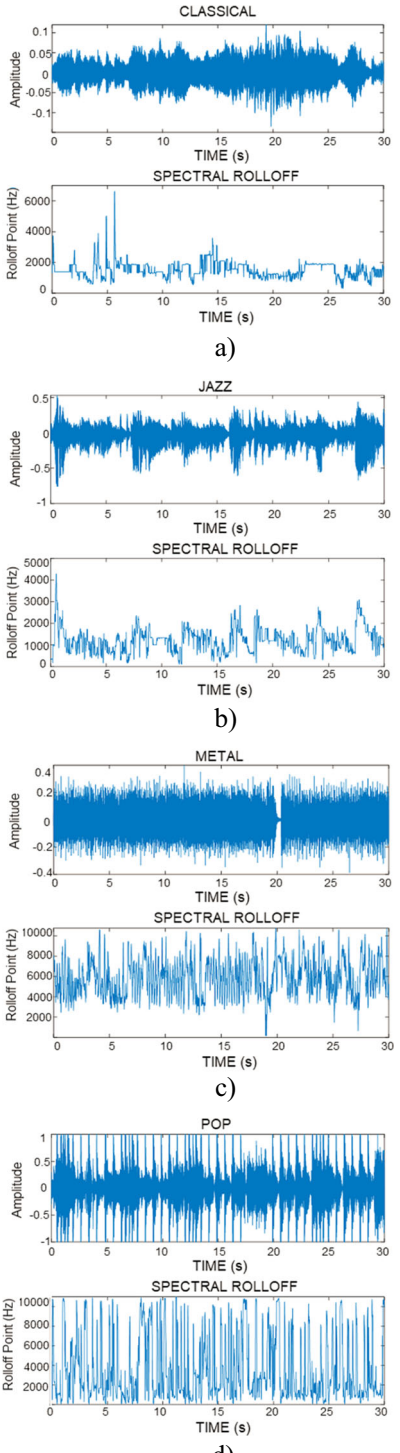

Fig. 7 Spectral Rolloff Extraction from Music Signals (**a**) Classical (**b**) Jazz (**c**) Metal (**d**) Pop

These classifiers include Cubic SVM [24], Wide Neural Network, and Ensemble Bagged Trees. An ensemble tree is a combination of distinct and diverse yet accurate classifiers. Bagging manipulates the instability of the basic categorization algorithm [14]. The proposed vast neural network is a deep learning method with one fully connected layer [34].

5 Experimental results

5.1 Dataset

GTZAN dataset has been used for classification [53]. It covers different music genres with 100 audio files in each category, each being a 22,050 Hz – 16 bit, .wav format audio clip lasting for 30-sec. This database has been used to create a four-class problem covering four music genres: Classical, Jazz, Metal, and Pop. The reason for choosing these genres is that in the last few years, there has been a gradual fusion of a large number of less distinctive music genres [9], and hence it does not make much sense to include them as individual classes in the current times [20]. These trends have been synchronized with literature regarding each genre's accuracy. The selected classes have mostly recorded the highest accuracies in [22]. These are synchronized with the current trends in the music industry in terms of their abilities to be distinguished.

5.2 Performance metrics

Accuracy enjoys wide popularity when it comes to performance metrics [32]. It includes both normal and abnormal observations during evaluation. On the other hand, sensitivity and specificity focus on abnormal and normal observations, respectively [56]. These metrics use True Positive (TP), False Negative (FN), True Negative (TN), and False Positive (FP). Mathematically [56],

$$Accuracy = \frac{TP + TN}{TP + TN + FP + FN} \tag{15}$$

$$True\ Positive\ Rate\ (TPR) = \frac{TP}{TP + FN} \tag{16}$$

$$Predictive\ Positive\ Value\ (PPV) = \frac{TP}{TP + FP} \tag{17}$$

$$F1{-}score = 2\frac{TPR \times PPV}{TPR + PPV} \tag{18}$$

The TPR and PPV are also known as recall and precision, and the F1-score is calculated as per Eq. (18).

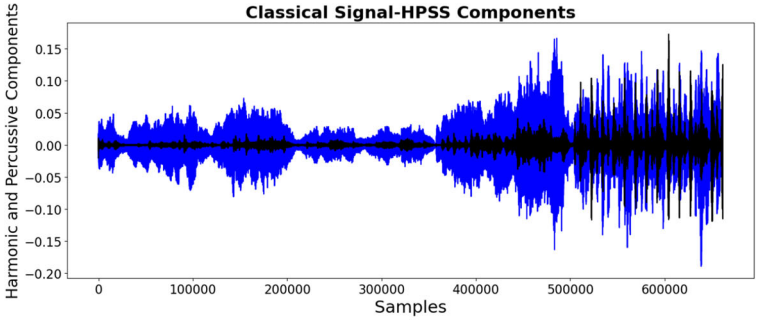

a)

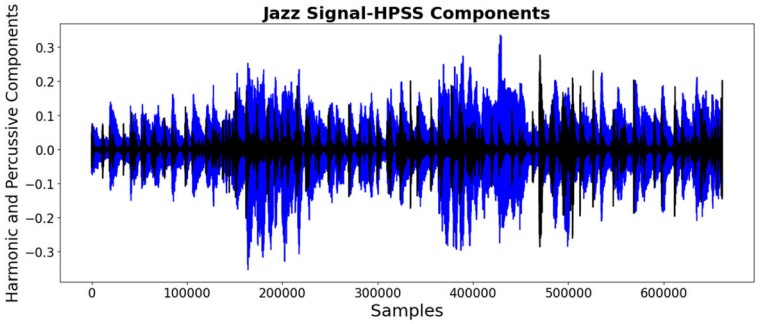

b)

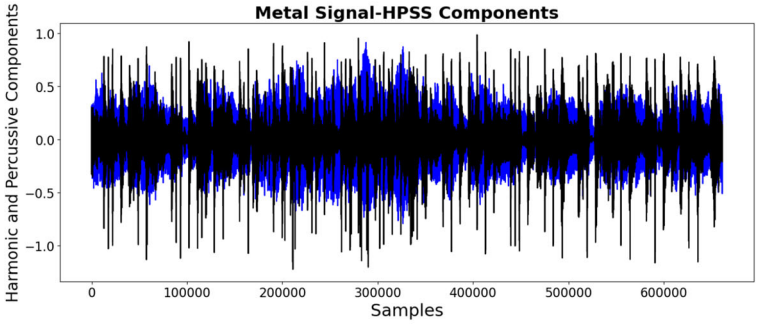

c)

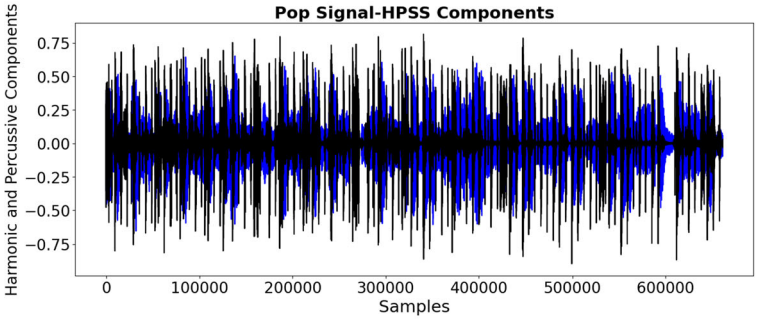

d)

Fig. 8 Harmonic/Percussive Source Separation of Music Signals (**a**) Classical (**b**) Jazz (**c**) Metal (**d**) Pop

Table 1 List of Extracted Features

Feature Vector	Description
TQWT-TEO Mean (j+1)	Mean of non-linear energies of each decomposed SB tuned to signal's oscillatory behaviour.
TQWT-TEO Variance (j+1)	Variance of non-linear energy values of each decomposed SB tuned to signal's oscillatory behaviour.
Spectral Centroid Mean	Mean of centre of gravities of frequency bins corresponding to the frames of music signals.
Spectral Centroid Variance	Variance of centre of gravities of frequency bins corresponding to the frames of music signals.
Spectral Rolloff Mean	Mean of a set of values that represent normalized frequencies for each frame, corresponding to which, sum of low-frequency power values add up to 85% of total power.
Spectral Rolloff Variance	Variance of a set of values that represent normalized frequencies for each frame, corresponding to which, sum of low-frequency power values add up to 85% of total power.
Chroma Mean	Mean of 12 frequency bin octave representations of music signal frames.
Chroma Variance	Variance of 12 frequency bin octave representations of music signal frames.
Harmony Mean	Mean of harmonic components of music signal frames.
Harmony Variance	Variance of harmonic components of music signal frames
Percussive Mean	Mean of percussive components of music signal frames.
Percussive Variance	Variance of percussive components of music signal frames.

5.3 Results

In the proposed method TT-TCHP, the TQWT-TEO decomposes music signals into non-linear Teager energies of different SBs. The mean and variance are computed over them to obtain the required features. The statistical measures of TCHP transformation are also evaluated as features. Raw data has been taken from GTZAN dataset, where each music signal sampled at 22050 Hz. The extracted features for each data file are stored in the .csv format. Training and testing data are then shuffled randomly at the 70:30 ratio. The training data is then split into K groups/folds. The first fold is taken as a holdout or validation set of the data to perform the cross-validation. The rest of the groups or folds are treated as training data. The selected model is then trained and fitted over the training set, that is, on the leftover k-1 sets. Evaluation of the model is done using the validation set. After validating the training model, the remaining 30% of the testing data is tested against the trained models to evaluate their performance. The 13 -fold cross-validation has been utilized, which churned out optimum results for the given features upon testing.

The overall length of each signal is 661,794 samples. In the proposed algorithm TQWT is parameter dependent. TQWT uses key parameters including redundancy (r), decomposition levels (j), and the Q-factor for extraction of sub-bands from the music signals. The selected parameters and their effect were thoroughly studied and analyzed as follows. Redundancy (r) has been kept as 2 because with a further increase in r leads to more overlapping of adjacent frequency responses which declines the efficiency of classification. Similarly, Q-factor has been set to 2 as with its further increase, the corresponding frequency response becomes narrower and increases the number of oscillatory wavelets. This reduces the accuracy of the classification model and requires a greater number of decomposition levels to cover the signal range. The decomposition levels are varied from 2 to 6 levels. Beyond the sixth level, the

information becomes rather irrelevant and causes poor performance of the classification algorithm.

The histograms for all four classes corresponding to the novel feature of fused TQWT-TEO are shown in Fig. 9. These have been used to represent the distribution of features for each class. It is observed that most of the resulting histograms are skewed right and unimodal, with a variable degree of skewness. This means that outliers, in general, are present in the right or at higher feature values for each class. It is further observed that, out of all the classes, classical data shows maximum skewness while pop data shows the least amount of skewness. Hence, the TQWT-TEO feature vectors are concentrated towards the left within the lower frequency bin for classical data.

The features have been trained against three different classifier models. MATLAB 2021a has been to implement these machine learning algorithms. The comprehensive neural network model used here has a single fully-connected layer keeping a layer size of 100 neurons. ReLU activation function has been used here. For the SVM, the cubic kernel function has been used. Further, it has a one versus one multiclass algorithm implemented for categorization. The third model, the bagged ensemble tree, uses the learner-type Decision trees using a total number of thirty learners. The peak value of the number of splits turned out to be 278. Bagging has been used as the ensemble method.

The four-class problem involving classical, jazz, metal, and pop is of keen interest. The accuracies of the three described models for variable SB size are summarized in Table 2. Here, 13-fold cross-validation has been taken as it churned out the highest accuracy with minimum training and testing price. It is observed that Wide Neural Network (WNN) yields the highest accuracy of 95.8%. It is quite conspicuous that with an increase in the number of SBs of the TQWT, the categorization accuracy while using the WNN model also increases. Another noteworthy observation is that using 7 sub-band decompositions results in maximum accuracy for each model.

While decomposition of music signals into three and four SBs records the same accuracy in the case of WNN, it is interesting to note that three sub-band decompositions yield higher accuracy for the other two models compared to the four sub-band models as opposed to the regular trend in the table. The ensemble method is weak when detecting metal genre music clips compared to the other four genres. On the other hand, WNN has shown more consistency towards all the genres for higher-level sub-band decompositions. In Table 2, latency parameters Training Time (TT) and prediction speed have also been presented. The average TT varies from 3 to 5 sec for cubic SVM and 3–6 sec for WNN. Ensemble bagged trees have taken longer in the training process as compared to SVM and WNN, with their training time varying between 7 and 9 sec for all the sub-band combinations. Moving on to the prediction speeds, the maximum prediction speed is offered by the WNN model in the range of 3300–4000 Observations (Obs)/s. While on the other hand, prediction speeds of cubic SVM and ensemble bagged trees varies between 1100 and 1700 Obs/s and 500–600 Obs/s, respectively.

The confusion matrix for the four-class problem when the Wide Neural Network model is used, where music signals are decomposed into seven SBs, is shown in Table 3. The confusion matrix shows that the Classical genre has the highest TPs, followed by Jazz. The performance metrics for individual classes for the case of optimal performer, i.e., the seven sub-band-based WNN model, are shown in Table 4. The maximum accuracy of 100% has been observed for Classical genre class. This model not only provides higher accuracy than the other two models but is also relatively more consistent in terms of individual genre accuracies.

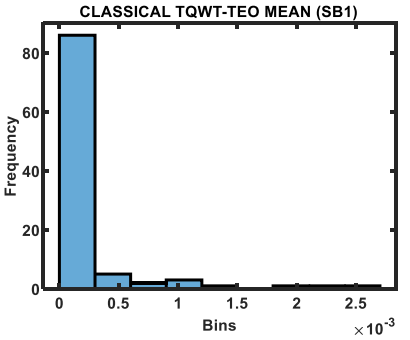
CLASSICAL TQWT-TEO MEAN (SB1)
Frequency
Bins
×10^-3

(a)

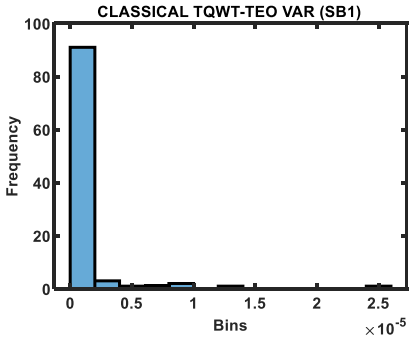
CLASSICAL TQWT-TEO VAR (SB1)
Frequency
Bins
×10^-5

(b)

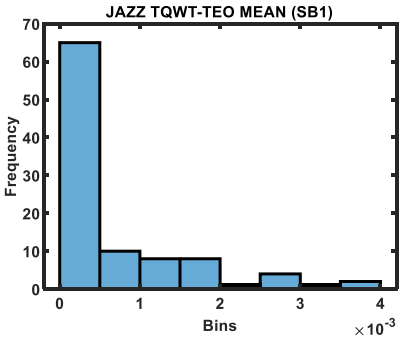
JAZZ TQWT-TEO MEAN (SB1)
Frequency
Bins
×10^-3

(c)

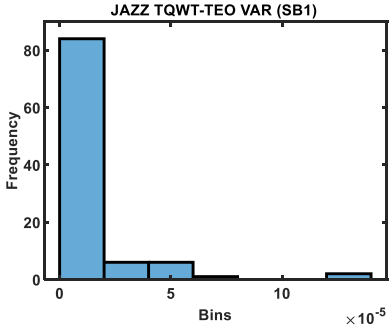
JAZZ TQWT-TEO VAR (SB1)
Frequency
Bins
×10^-5

(d)

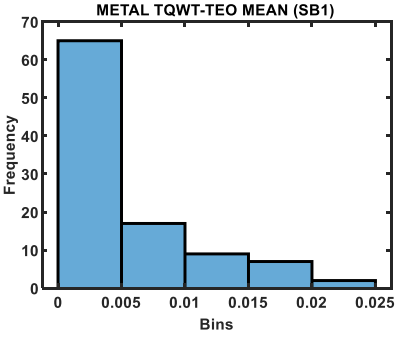
METAL TQWT-TEO MEAN (SB1)
Frequency
Bins

(e)

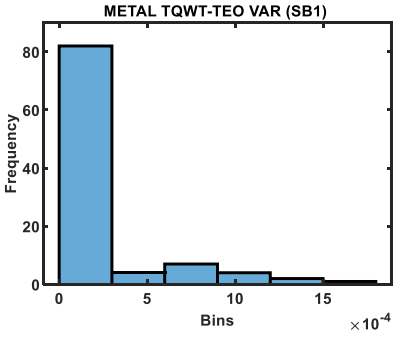
METAL TQWT-TEO VAR (SB1)
Frequency
Bins
×10^-4

(f)

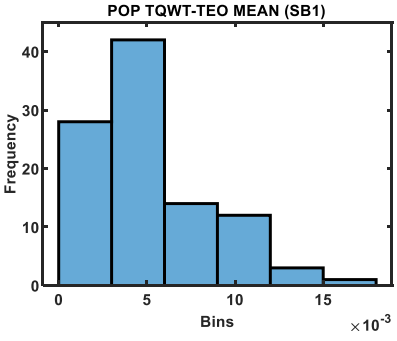
POP TQWT-TEO MEAN (SB1)
Frequency
Bins
×10^-3

(g)

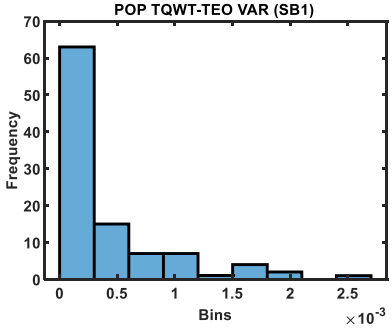
POP TQWT-TEO VAR (SB1)
Frequency
Bins
×10^-3

(h)

Fig. 9 Histogram representation of first TQWT-TEO sub-band-based features for each class (**a**) Mean values of Classical signal; (**b**) Variances of Classical signal; (**c**) Mean values of Jazz signal; (**d**) Variances of Jazz signal; (**e**) Mean values of Metal signal; (**f**) Variances of Metal signal; (**g**) Mean values of Pop signal; (**h**) Variances of Pop signal

A ten-class problem has also been taken into consideration. Table 5 presents the summary of 10- music genres problem. In this table, TT-TCHP feature set with ensemble bagged tree model are obtained highest accuracy 72.7%. In Table 5, the average TT for WNN and ensemble bagged tree models is found to be around 10s. For cubic SVM, it is a little over 13 s, that is, the maximum TT of the three models, unlike in the four-class problem. The prediction speed for WNN is the highest out of the three models which is 6700 Obs/sec. Ensemble bagged tree and cubic SVM followed with 1100 and 920 Obs/sec, respectively.

Performance metrics for individual matrices in the case of the ensemble bagged trees model for the exact specifications are summarized in Table 6. The model churned out the highest F1 score of 94.74% for the classical genre, followed by 83.65% for jazz genre. On the other hand, the lowest F1 score was observed in the case of the Hip-Hop genre.

6 Discussion

The proposed method (TT-TCHP) is the fusion of TQWT-TEO (TT) features and TCHP features. It is tested on the GTZAN dataset having four classes and ten classes of music signal genres. In this section, the results of proposed method have been compared with the existing state-of-art methodologies on same dataset where accuracy is the evaluation criterion for music genre categorization. The overall performance validation of proposed method is presented in Table 7.

This work mainly focuses on classification of four classes classical, jazz, metal, and pop because it enables sociological and psychological research to construct efficient correlation among musical similarities with homunculus sensors. These classes show efficient mapping with human sensory system correction. Each genre of the four classes stimulates a different

Table 2 Performance Metrics of music genre classification for various models (4 classes)

Classifier	SBs	Accuracy	TPR	PPV	F1	TT (s)	Prediction Speed (Obs/s)
Wide Neural Network	1–3	87.5%	87.63%	87.58%	87.6	4.96 s	4000
	1–4	87.5%	87.51%	87.42%	87.46	5.45 s	3900
	1–5	91.7%	91.6%	91.83%	91.71	5.485 s	3300
	1–6	91.7%	91.67%	91.93%	91.79	4.437 s	3600
	1–7	95.8%	95.83%	95.82%	95.82	3.672 s	3700
Cubic SVM	1–3	91.7%	91.75%	91.98%	91.86	3.369 s	1100
	1–4	86.7%	86.65%	86.82%	86.73	3.346 s	1500
	1–5	90.0%	90.00%	90.25%	90.12	3.814 s	1700
	1–6	90.8%	90.83%	90.85%	90.84	4.485 s	1300
	1–7	95.0%	95.00%	95.05%	95.02	4.039 s	1700
Ensemble Bagged Trees	1–3	89.2%	89.32%	89.70%	89.50	7.227 s	580
	1–4	88.3%	88.35%	89.13%	88.73	8.443 s	520
	1–5	90.0%	90.1%	90.47%	90.28	7.52 s	580
	1–6	90.8%	90.85%	91.65%	91.25	7.051 s	600
	1–7	90.8%	90.83%	91.55%	91.18	7.035 s	500

Table 3 Confusion Matrix for Wide Neural Network (7 SBs)

Confusion Matrix		Predicted Class			
		Classical	Jazz	Metal	Pop
True Class	Classical	30	0	0	0
	Jazz	0	28	1	1
	Metal	0	0	29	1
	Pop	0	2	0	28

emotional response based on its reception by the sensory system [48]. The classical genre evokes peace, and calmness brings ease and communicates deep emotions. Jazz brings out nostalgia, depth, and melancholy. On the other hand, metal stimulates feelings of joy and aggression, while the pop genre boosts adrenaline. Music signals belonging to four classes of genres may find their applications in digital watermarking [5] of tracks in context to digital security and copyrights.

Table 7 presents the four-class classification performance comparison report of proposed work. It is observed that the proposed algorithm based on TT-TCHP yields accuracy 95.8% which overperforms the past work. Li et al. [35] also reduced the dataset to a four-class problem and tested the features based on spectrograms against various deep learning models. They achieved the maximum accuracies of 80.19% and 83.58% in the case of the Residual neural Network (ResNet50) and balanced and trusted version of the Residual neural Network (ResNet50_trust) models, respectively. Sawhney et al. [44] proposed to use latent features extracted directly from the raw music data. They achieved a recognition accuracy of 65% upon using an autoencoder based on deep Softmax. J. Li et al. [36] extracted spectrograms for each music signal, fed them to newly improved deep learning models, and achieved accuracies of 91.7% and 93.75% for CosFace CNN and combined angular margin and cosine margin softmax, respectively.

Additionally, in Table 7, the 10-class classification comparison is also summarized. Elbir et al. [16] worked on the ten-class problem using the GTZAN dataset. They not only improved upon the STFT for feature extraction but also integrated them over it to obtain power frequency distribution and finally fuse them before feeding features to the classifier. RBF and SVM were integrated to execute the categorization. An accuracy of 72.7% was achieved. Like them, [10, 31, 35] also dealt with the database and categorization as a ten-class problem. Lee et al. [31] used multi-scale feature extraction and fed the extracted features to CNN model to obtain an overall accuracy of 72%. Sugianto et al. [47] used Melspectrogram for FE and CNN for genre categorization and churned out an accuracy of 71.84% using the voting scheme. Li et al. [35] also used STFT and spectrogram to extract features for the ten-class music signals. These features were tested against various deep learning models, and an optimal

Table 4 Performance Metrics of individual genres for WNN (7 SBs)

Genre	Accuracy	TPR	PPV
Classical	100.0%	100.0%	100.0%
Jazz	96.67%	93.3%	93.3%
Metal	98.33%	96.7%	96.6%
Pop	96.67%	93.3%	93%

Table 5 Comparison of different Models for 10 Genre Classification

Classifier Model	Accuracy	TT (s)	Prediction Speed (Obs/s)
Wide Neural Network	71.7%	10.096 s	6700
Ensemble Bagged Tree	72.7%	10.537 s	1100
Cubic SVM	70.7%	13.264 s	920

Table 6 Performance Metrics for 10 Classes based on Ensemble Bagged Trees Model

Genre	Recall	Precision	F1 Score
Blues	73.3%	91.7%	81.47
Classical	90.0%	100.0%	94.74
Country	80.0%	61.5%	69.54
Disco	73.3%	68.8%	70.98
Hip-Hop	60.0%	56.2%	58.04
Jazz	76.7%	92.0%	83.65
Metal	83.3%	69.4%	75.71
Pop	56.7%	85.0%	68.02
Reggae	60.0%	66.7%	63.17
Rock	73.3%	59.7%	65.80

accuracy of 71.56% was achieved for the ResNet50_trust. The model also has an improved loss function. In comparison, the proposed model achieved an accuracy of 72.7% for ensemble bagged trees. Although it is higher than most of the previous methods, it is relatively much lower than the four-class classification accuracy.

7 Conclusion

TQWT is a unique wavelet transform tunable as per the input's oscillatory characteristic and henceforth has been used on music signals for decomposition. Due to its ability to deal with complex signals, TEO has been used on the decomposed SBs. This provides a vital aid in the feature extraction of music signals and exemplary non-stationary complex signals. These

Table 7 Comparison with past techniques for GTZAN Dataset

Authors [Ref.] {Year}	Features	Classes	Classifier	Accuracy
Elbir et al. [16] (2018)	Improved STFT, Power Frequency Distribution	10	SVM (Polynomial)	71.3%
Lee et al. [31] (2017)	Multi-scale features	10	CNN	72%
Sugianto et al. [47] (2019)	Melspectrogram	10	CNN	71.84%
Li et al. [35] (2022)	STFT, Spectrogram	10	ResNet50_trust	71.56%
		4	ResNet50	81.09%
		4	ResNet50_trust	83.58%
Sawhney et al. [44]	Latent features	4	Deep Softmax Autoencoder	65%
Li et al. [36]	Spectrogram	4	AMCM-Softmax	93.75%
		4	CosFace CNN	91.7%
Proposed Method	TQWT-TEO, Timbral and HPSS (TT-TCHP)	10	Ensemble Bagged Tree	72.7%
		4	Wide Neural Network	95.8%

features, along with Timbral/Spectral, Chroma features, and Harmonic/Percussive components, were further analyzed statistically, and the resulting features were used for classifying signals into four prominent music genres, i.e., Classical, Jazz, Metal, and Pop, as a four-class problem. The Wide Neural Network classifier when applied on TT-TCHP features performed the best for the given GTZAN dataset and yielded an accuracy of 95.8%, outperforming all the state-of-the-art techniques. The ten-class problem achieved an optimal accuracy of 72.7% when the ensemble bagged tree model was used for categorization.

In the future scope, the outcome of the proposed algorithm can be synchronized with physical music genre rating systems to improve the belongingness of a particular music genre. Nowadays, various artists fuse multiple genres into a single track. However, the proposed system is only capable of detecting single genre per music signal. Hence, the proposed algorithm could be further evolved by introducing a multiple-genre weight assignment for each signal to enable mapping more than one genre with a fusion track. The number of data samples can be increased by setting a smaller frame size of the music signal to improve the classification performance of the ten-class music genre system.

Funding This work is not funded in any funding agencies.

Data availability The dataset that support the findings of this study is belongs to [GTZAN] and it is available on Kaggle.

Declarations

Conflict of interest To the best of our knowledge, this work does not have any financial and/or non-financial conflict of interest.

References

1. Abdoli S, Cardinal P, Lameiras Koerich A (2019) End-to-end environmental sound classification using a 1D convolutional neural network. Expert Syst Appl, Elsevier 136:252–263
2. Baniya BK, Lee J (2016) Importance of audio feature reduction in automatic music genre classification. Multimed Tools Appl, Springer 75:3013–3026
3. Bhatti UA, Huang M, Wang H, Zhang Y, Mehmood A, Di W (2017) Recommendation system for immunization coverage and monitoring. Human Vacc Immun, Taylor and Francis 14(1):165–171
4. Bhatti UA, Huang M, Wu D, Zhang Y, Mehmood A, Han H (2018) Recommendation system using feature extraction and pattern recognition in clinical care systems. Enterprise Inform Syst Taylor and Francis 13(3): 329–351
5. Bhatti UA, Yuan L, Yu Z, Li J, Nawaz SA, Mehmood A, Zhang K (2020) Hybrid watermarking algorithm using Clifford algebra with Arnold scrambling and chaotic encryption. IEEE Access 8:76386–76398
6. Bhatti UA, … Mehmood A (2022) Local similarity-based spatial–spectral fusion hyperspectral image classification with deep CNN and Gabor filtering. IEEE Trans Geosci Remote Sens 60:1–15
7. Borjian N, Kabir E, Seyedin S, Masehian E (2018) A query-by-example music retrieval system using feature and decision fusion. Multimed Tools Appl, Springer 77:6165–6189
8. Boudraa A, Salzenstein F (2018) Teager–Kaiser energy methods for signal and image analysis: a review. Digital Signal Process, Elsevier 78:338–375
9. Brisson R, Bianchi R (2020) On the relevance of music genre-based analysis in research on musical tastes. Psychol Music, SAGE J 48:777–794
10. Cai X, Zhang H (2022) Music genre classification based on auditory image, spectral and acoustic features. Multimed Syst, Springer 28:779–791

11. Caparrini A, Arroyo J, Pérez-Molina L, Sánchez-Hernández J (2020) Automatic subgenre classification in an electronic dance music taxonomy. J New Music Res, Taylor and Francis 49:269–284
12. Castillo JR, Flores MJ (2021) Web-based music genre classification for timeline song visualization and analysis. IEEE Access 9:18801–18816
13. Costa YMG, Oliveira LS, Silla CN (2017) An evaluation of convolutional neural networks for music classification using spectrograms. Appl Soft Comput J, Elsevier 52:28–38
14. Dietterich TG (2000) An experimental comparison of three methods for constructing ensembles of decision trees: bagging, boosting, and randomization. Mach Learn, IEEE 40:139–157
15. Doelling KB, Assaneo MF, Bevilacqua D, Pesaran B, Poeppel D (2019) An oscillator model better predicts cortical entrainment to music. Proc Natl Acad Sci 116(20):10113–10121
16. Elbir A, Ilhan HO, Serbes G, Aydin N (2018) Short time Fourier transform based music genre classification. In: Proceedings of the electric electronics. Computer Science, Biomedical Engineerings' Meeting. IEEE, pp 1–4
17. Ellis DPW, Poliner GE (2007) Identifying `cover songs' with Chroma features and dynamic programming beat tracking. In proceedings of the IEEE international conference on acoustics, speech and signal processing, 4:1429-1432.
18. Ferretti S (2018) On the complex network structure of musical pieces: analysis of some use cases from different music genres. Multimed Tools Appl, Springer 77:16003–16029
19. Foleis JH, Tavares TF (2020) Texture selection for automatic music genre classification. Appl Soft Comput J, Elsevier 89:106–127
20. Fredriksson D (2019) Pathways of pop: arts and education policy, studieförbund and genre hierarchies. In: Marija Dumnić Vilotijević, Ivana Medić (Ed) contemporary Popular Music studies, 19th edition, springer VS, Wiesbaden, Germany.
21. Fu Z, Lu G, Ting KM, Zhang D (2011) A survey of audio-based music classification and annotation. IEEE Trans Multimedia 13:303–319
22. Haggblade M, Hong Y, Rao K (2011) Music Genre Classification. Stanford University, pp:1–5.(online) (https://citeseerx.ist.psu.edu/viewdoc/download?doi=10.1.1.375.204&rep=rep1&type=pdf)
23. Holzapfel A, Stylianou Y (2008) Musical genre classification using nonnegative matrix factorization-based features. IEEE Trans Audio Speech Lang Process 16:424–434
24. Jain U, Nathani K, Ruban N et al (2018) Cubic SVM classifier based feature extraction and emotion detection from speech signals. In proceedings of the 2018 international conference on sensor networks and signal processing. IEEE, 386–391
25. Jha CK, Kolekar MH (2020) Cardiac arrhythmia classification using tunable Q-wavelet transform based features and support vector machine classifier. Biomedical signal processing and control, Elsevier 59(101875).
26. Kaiser JF (1990) On a simple algorithm to calculate the "energy" of a signal. In Proceedings of the IEEE International Conference on Acoustics, Speech, and Signal Processing, pp:381–384
27. Kaiser JF (1993) Some useful properties of Teager's energy operators. IEEE Int Conf Acoustics Speech Signal Process 3:149–152
28. Kiran PU, Abhiram N, Taran S, Bajaj V (2018) TQWT based features for classification of ALS and healthy EMG signals. Am J Compt Sci Inform Technol 6(2):19
29. Kumaraswamy B (2022) Optimized deep learning for genre classification via improved moth flame algorithm. Multimedia Tools Appl, Springer 81:17071–17093
30. Kumaraswamy B, Poonacha PG (2021) Deep convolutional neural network for musical genre classification via new self Adaptive Sea lion optimization. Applied soft computing, Elsevier, 108.
31. Lee J, Nam J (2017) Multi-level and multi-scale feature aggregation using Pretrained convolutional neural networks for music auto-tagging. IEEE Signal Process Lett 24:1208–1212
32. Lee MC, Nelson SJ (2008) Supervised pattern recognition for the prediction of contrast-enhancement appearance in brain tumors from multivariate magnetic resonance imaging and spectroscopy. Artif Intell Med, Elsevier 43:61–74
33. Lee CH, Shih JL, Yu KM, Lin HS (2009) Automatic music genre classification based on modulation spectral analysis of spectral and cepstral features. IEEE Trans Multimedia 11:670–682
34. Li CB, Choung J, Noh M-H (2018) Wide-banded fatigue damage evaluation of catenary mooring lines using various artificial neural networks models. Marine Struct, Elsevier 60:186–200
35. Li J, Han L, Li X, … Gou Z (2022) An evaluation of deep neural network models for music classification using spectrograms. Multimed Tools Appl, Springer 81:4621–4647
36. Li J, Han L, Wang Y, … Yan H (2022) Combined angular margin and cosine margin softmax loss for music classification based on spectrograms. Neural Comput Appl, Springer 34:10337–10353
37. Liu C, Feng L, Liu G, … Liu S (2021) Bottom-up broadcast neural network for music genre classification. Multimedia Tools Appl, Springer 80:7313–7331

38. Markov K, Matsui T (2014) Music genre and emotion recognition using Gaussian processes. IEEE Access 2:688–697
39. Nanni L, Costa YMG, Aguiar RL, … Brahnam S (2018) Ensemble of deep learning, visual and acoustic features for music genre classification. J New Music Res, Taylor and Francis 47:383–397
40. Ng WWY, Zeng W, Wang T (2020) Multi-level local feature coding fusion for music genre recognition. IEEE Access 8:152713–152727
41. Panagakis Y, Kotropoulos CL, Arce GR (2014) Music genre classification via joint sparse low-rank representation of audio features. IEEE/ACM Trans Audio Speech Language Process 22:1905–1917
42. Pelchat N, Gelowitz CM (2020) Neural network music genre classification. Can J Electr Comput Eng 43(3): 170–173
43. Pichl M, Zangerle E (2021) User models for multi-context-aware music recommendation. Multimed Tools Appl, Springer 80:22509–22531
44. Sawhney A, Vasavada V, Wang W (2018) Latent feature extraction for musical genres from raw audio. Stanford University
45. Selesnick IW (2011) Wavelet transform with tunable Q-factor. IEEE Trans Signal Process 59:3560–3575
46. Seo JS, Lee S (2011) Higher-order moments for musical genre classification. Signal Process, Elsevier 91: 2154–2157
47. Sugianto S, Suyanto S (2019) Voting-Based Music Genre Classification Using Melspectogram and Convolutional Neural Network. In Proceedings of the 2019 International Seminar on Research of Information Technology and Intelligent Systems (ISRITI), IEEE, pp:330–333
48. Swaminathan S, Schellenberg EG (2015) Current emotion research in music psychology. Emotion Rev, Sage 7(2):189–197
49. Tachibana H, Ono N, Sagayama S (2014) Singing voice enhancement in monaural music signals based on two-stage harmonic/percussive sound separation on multiple resolution spectrograms. IEEE/ACM Trans Audio, Speech Language Process 22:228–237
50. Taran S, Bajaj V (2019) Motor imagery tasks-based EEG signals classification using tunable-Q wavelet transform. Neural Comput Appl, Springer 31:6925–6932
51. Teager HM (1980) Some observations on oral airflow during phonation. IEEE Trans. Acoustics, Speech, Signal Process 28:599–601
52. Teager HM, Teager SM (1983) A phenomenological model for vowel production in the vocal tract. Speech Science, Recent Advances, pp 73–109
53. Tzanetakis G, Cook P (2002) Musical genre classification of audio signals. IEEE Trans Speech Audio Process 10:293–302
54. Wang Y, Zhang W, Wu L, … Zhao X (2017) Unsupervised metric fusion over Multiview data by graph random walk-based cross-view diffusion. IEEE Trans Neural Networks Learn Syst 28:57–70
55. Yu Y, Luo S, Liu S, … Feng L (2020) Deep attention-based music genre classification. Neurocomputing, Elsevier 372:84–91
56. Zou Q, Jiang H, Dai Q, … Wang Q (2020) Robust lane detection from continuous driving scenes using deep neural networks. IEEE Trans Veh Technol 69:41–54

Publisher's note Springer Nature remains neutral with regard to jurisdictional claims in published maps and institutional affiliations.

Springer Nature or its licensor (e.g. a society or other partner) holds exclusive rights to this article under a publishing agreement with the author(s) or other rightsholder(s); author self-archiving of the accepted manuscript version of this article is solely governed by the terms of such publishing agreement and applicable law.

ResearchGate

See discussions, stats, and author profiles for this publication at: https://www.researchgate.net/publication/357465437

A Hybrid Firefly Algorithm Approach for Job Shop Scheduling Problem

Article · December 2021

DOI: 10.22214/ijraset.2021.39536

CITATIONS
0

READS
21

1 author:

Gayathri Devi Ka
Delhi Technological University
8 PUBLICATIONS **4** CITATIONS

SEE PROFILE

Some of the authors of this publication are also working on these related projects:

optimisation for scheduling in FMS View project

All content following this page was uploaded by Gayathri Devi Ka on 22 June 2022.

The user has requested enhancement of the downloaded file.

iJRASET
International Journal For Research in Applied Science and Engineering Technology

INTERNATIONAL JOURNAL FOR RESEARCH

IN APPLIED SCIENCE & ENGINEERING TECHNOLOGY

Volume: 9 **Issue:** XII **Month of publication:** December 2021

DOI: https://doi.org/10.22214/ijraset.2021.39536

www.ijraset.com

Call: 08813907089 | E-mail ID: ijraset@gmail.com

International Journal for Research in Applied Science & Engineering Technology (IJRASET)
ISSN: 2321-9653; IC Value: 45.98; SJ Impact Factor: 7.538
Volume 9 Issue XII Dec 2021- Available at www.ijraset.com

A Hybrid Firefly Algorithm Approach for Job Shop Scheduling Problem

Gayathri Devi K [1], R. S. Mishra [2], A. K. Madan [3]
[1]*Research Scholar,* [2]*Professor & Dean,* [3]*Professor, Department of Mechanical and Production Industrial and Automobiles Engineering, Delhi Technological University, Delhi, India*

Abstract: ***Job shop scheduling has always been one of the most sought out research problems in Combinatorial optimization. Job Shop Scheduling problems (JSSP) are categorized under NP hard problems. In recent years the meta heuristic algorithms have been proved effective to solve hardcore NP problem. Firefly Algorithm is one of such meta heuristic techniques which is nature inspired from firefly characteristic. Its potential can be enhanced further by hybridizing it with other known evolutionary algorithms and thereby getting improved results in less computational time. In this paper we have proposed a new hybrid technique christened as HyFA, by hybridizing Firefly algorithm(FA) with simulated annealing (SA) and Greedy heuristics approach (GHA). The hybrid technique has the advantages of all three algorithms and are combined in such a way that a quicker and better optimal solution is obtained. Our proposed HyFA is coded in Matlab with an objective to minimize the makespan (C_m). The novel hybrid technique is then used to evaluate 1-25 Lawrence problems taken from literature. The results show the proposed technique is more effective not only in getting optimal results but has significantly reduced computational time.***

Keywords: Scheduling, Optimisation, Job shop scheduling, Meta-heuristics, Firefly, Simulated Annealing, Greedy heuristics Approach.

I. INTRODUCTION

Scheduling is a decision making process and is one of the hardcore NP problem. The job-shop scheduling problem (JSSP) consists of ‘n’ jobs and ‘m’ machines. Each job must go through m machines to complete its work. We consider one job consists of m operations. Each operation uses one of ‘m’ machines to complete one job’s work for a fixed time interval. Once one operation is processed on a given machine, it cannot be interrupted before it finishes the job’s work. The sequence of operations of one job should be predefined and maybe different for any job.

Scheduling is allocation of resources efficiently to perform collective tasks. Most of the scheduling problems are combinatorial in nature and solving such problems requires making distinct choices of an optimal solution from number of alternatives. Since the scheduling problems are NP hard, simultaneous optimization of multiple objectives are necessary and it is difficult to find an optimal solution with the use of traditional algorithms. Combinatorial optimization problems are always difficult to solve, due to its high complexity and the computational time increases exponentially.

In the recent years, a lot of research has been carried out on the combinatorial problems and many methods were proposed to overcome the high computational time and the results were being proven that less computational time is required when we use meta heuristics techniques. Meta heuristics has gained popularity in the last decade and it continues to prove that it’s the best technique to get better optimal solutions.

When we hybridize different Meta heuristic approaches the optimal solutions are much more better and effective and efficient with computational time reducing drastically. One such attempt has been made in this paper. An attempt has been made to hybridize three different meta heuristics approach such as Firefly Algorithm (FA), Simulated Annealing (SA), Greedy Heuristics Approach (GHA), thereby developing a new novel technique named as HyFA.

II. LITERATURE REVIEW

There has been a number of research works focused on the Job Shop Scheduling Problem (JSSP) reported in the literature. Over the decades of research, JSSP has undergone extensive research from mathematical approaches to meta heuristic approaches. Table 1 briefly summarizes some of the recent published research works related to JSSP and other recently developed meta heuristics.

©IJRASET: All Rights are Reserved

Table 1 Brief Literature study on the recent JSSP articles

Authors	Approaches	Problem	Results
Crama et al[1]	Review paper	A review paper that described several combinatorial optimization problems. Serves as a good base paper to understand the basics of Scheduling problems in combinatorial nature	Serves as a good base paper to understand the basics of Scheduling problems in combinatorial nature
Mishra et al [2]	Review paper	A review paper on recent advancements done in non traditional optimization techniques	This paper also serves as a good base paper.
Marichelvam et al [3]	Improved PSO technique + dispatching rule	Addressed the multi-stage hybrid flow shop problem with identical parallel machines at each stage by considering the effect of human factors	A statistical analysis was performed to analyze the results and found their technique is effective
Reddy [4]	Hybrid genetic algorithm	Simultaneous scheduling of machines and AGVs in FMS. Tested on Lawrence instances.	The algorithm presented a good number of diversified and non-dominated solutions
Lin et al [5]	Particle swarm optimization, simulated annealing technique and multi-type individual enhancement scheme	To solve the job-shop scheduling problem for 43 benchmark instances, designed by Fisher and Thompson and instances of LA01–LA40 Lawerence	The proposed algorithm was found to be more robust and efficient than the existing algorithms. The authors also proved that MPSO can reach the optimal area in the search space with smaller population size and iterations than other existing algorithms
Sankar et al [6]	Multi-objective evolutionary algorithm (MOEA) based on GA	Solve the scheduling problem of an FMS with combined objective function of minimizing penalty cost and maximizing machine utilization.	Two versions of the migration model has been constructed and the performance of two parallel GAs has been compared and found it to be effective.
Batur & Erol [7]	A simulated annealing based algorithm has been proposed.	Worked on two-machine flexible robotic cells consisting of CNC machines in which sets of multiple part-types are produced.	Experimental results showed that their approach gave satisfactory results.
Nidish Mathew [8]	NSGA	Benchmark problem of Jerald 43x16 has been attempted to solve multi objectives.	Procedures developed in this work can be suitably modified to any kind of FMS with a large number of components and machines
Kumar et al [9]	Genetic Algorithm and Differential Evolution	Scheduling of FMS systems for 43x16 problem setup.	The results of the proposed approach has been compared with conventional scheduling rules and found to be effective.
Xinyu Li & Gao [10]	Hybrid algorithm (HA) which hybridizes the genetic algorithm (GA) and tabu search (TS)	To minimize the make span. Tested on 201 open problems for FJSP.	The proposed algorithm combines the advantages of evolutionary algorithm and LS method thereby solving the FJSP effectively.
Scaria et al[11]	Artificial Bee Colony (ABC)	Objective to minimize the makespan. Benchmark problems provided by E. Taillard has been solved using this approach	The proposed method found to be more effective than other meta heuristics.

Xiaofeng Li & Zhao [12]	Greedy Algorithm	Flexible flow shop scheduling problem	The authors simplified FFSP into SFFS (Simple FFS) problem for simulation implementation. And found that greedy algorithm to be less complex and effective.
Karthikeyan, Asokan, Nickolas, & Page [13]	Hybrid discrete firefly algorithm (HDFA)	To minimize a combined objective function. Kacem benchmark instances has been used to test the algorithm	Discrete firefly algorithm (DFA) combined with local search (LS) method enhanced the searching accuracy and information sharing among fireflies, thereby making their algorithm more effective.
Mati, Rezg & Xie [14]	Greedy heuristic	Integrated approach with the geometric approach for solving a two-job shop problem, one is flexible job and the second job is a job shop job. Lawrence instanes has been used to test the algorithm	The results obtained by the Greedy heuristic approach on benchmark instances are effective and better.
Sreekara Reddy et al [15]	Multi-objective teacher learning-based optimization algorithm (MOTLBO)	Addresses the multi-objective model for a flexible job shop scheduling problem (FJSSP)	The proposed algorithm has been found to be less complex with less parameter hence effective.
Sun et al [16]	Genetic Algorithm	Problem of penalty function for the job shop scheduling problem. Lawrence instances have been used to test the validity of the proposed approach.	An adaptive penalty function has been designed to search in both feasible and infeasible regions of the solution space. Thereby making the proposed algorithm more effective.
Narendhar, S Amudha, T [17]	Hybrid Bacterial Foraging Algorithm(HBFO)	To minimize makespan for job shop problem. And the algorithm has been tested on Lawrence instances.	The authors compared the HBFO with classic BFO and found their approach gives better make span.
Roshanaei Et al [18]	Artificial Immune and Simulated Annealing (AISA) Algorithms	Position and sequence based mixed integer linear programming (MILP) models have been developed. Case study was used to study the performance of the proposed algorithm.	Parametric size complexities of the proposed models under partial and total cases of F-JSSP were investigated. The proposed AISA found five new best solutions in a benchmark of 20 instances for the make-span optimization criterion.
Yuan and Xu [19]	Hybrid differential evolution (HDE)	To solve flexible job shop scheduling problem (FJSP) to minimize the makespan. Four sets of well known benchmark instances in the FJSP literature are considered.	A novel conversion mechanism has been developed. Also, a local search algorithm based on the critical path is embedded in the DE framework which made the proposed HDE more efficient by finding new best known solutions.

Firefly algorithm (FA) is one of the recently developed swarm intelligence technique which has been proving to be more effective in obtaining optimal solutions. Though Firefly is effective it has a limitation of pre mature convergence. To overcome this problem we have used Simulated Annealing and Greedy Heurustic as local search technique in order to avoid the local optima entrapment. Hence the classic FA is hybridized with SA and GHA and new algorithm Hybrid Firefly Algorithm (HyFA) is proposed. The present work is an attempt to minimize makespan in Job shop scheduling by proposed hybrid technique HyFA . The remainder of this paper is organized as follows. The problem formulation of JSSP with assumpations and constriants are introduced in Section 3. Section 3 also describes the proposed methodolgy to solve the FJSP. Section 4 shows the computational results. Finally, Section 5 provides conclusions and further research.

III. PROBLEM FORMULATION

JSSP are widely known as NP-Hard problem. The JSSP is an operation-sequencing problem on multiple machines subject to some precedence constraints among the operations. The JSSP can be described as a set of n jobs denoted by J_i where i =1,2…n which have to be processed on a set of m machines denoted by M_k where k =1,2….m. Operation of i^{th} job on the k^{th} machine will be denoted by O_{ik} with the processing time P_{ik} . For an n x m JSSP, the problem can be modeled by a set of m machines, denoted by M_k k = (1, 2, ...,m) to process a set of O_{ik} operations.Each job should be processed through the machines in a particular technological order also known as precedence constraint. Once a machine starts to process a job, processing of an operation cannot be interrupted. The required time to complete all operations for their processes is called make-span. Another constraint known, as capacity constraint is that each machine can process only one job at a time. The time span required to complete all operations of all the jobs is known as make span (C_m) and is the most important objective of JSSP.

Minimize Make span C_m = max of [C1, C2, C3,…….Cn] (1)

Where C1, C2, C3 are completion times of Jobs 1,2 and 3

$$O_q \leq O_i - t_i \qquad i = 0,1,2,\ldots, n \qquad q \in P_i \tag{2}$$

$$\sum_{m \in M(i)} \omega_{im} \leq 1 \quad m \in M, \quad t \geq 0 \tag{3}$$

$$O_i \geq O, \quad i = 0,1,2,3\ldots k \tag{4}$$

The objective fitness function in Eq.(1) is to minimize make span that is the completion time of the last operation. The constraint of precedence relationship is defined by Eq. (2). In Eq.(3), it indicates that one machine can process at most one operation at a time. The finish time must be positive by the constraint stated in Eq. (4).

A. Assumptions

The following assumptions and constraints are to be considered in solving of job shop scheduling problem such as i) all jobs are independent. ii) Machine time includes Job setup time also iii) Job descriptions are known in advance. iv) All machines should be available throughout the process. v) All jobs have to be processed without break. vi) Machine cannot process the parallel job at a time. vii) Each machine will process one job. viii) Each job requires m machines to complete the required process. ix) No Pre-emptions are allowed. The order of processing is not the same and x) Operations cannot be interrupted.

B. HyFA-The hybrid approach implementation

A new hybrid technique HyFA is proposed for solving JSSP with an objective to minimize make-span, which is a combination of Firefly Algorithm(FA), Simulated Annealing (SA) and Greedy Heuristic Approach (GHA). The proposed hybrid HyFA is effective because it's taking advantage of global search and local search as well. We have used two local search methods so that there will be diversity in population when searching for optimal results. The simulated annealing acts as both global and local search method thereby preventing the results to get trapped in local optima. Greedy heuristics resolves the intricacies of sequencing. We therefore expect that the said HyFA will be able give good results for the combinatorial optimization. The flow process for HyFA implementation is exhibited through Figure1.

1) *Firefly Algorithm:* A firefly algorithm is a swarm intelligence optimization technique. A firefly algorithm is applied on the basis of firefly. A firefly is attracted to another firefly based on the brightness of its light [20]. In this algorithm, all the fireflies are assumed to be unisexual. The attractiveness depends upon the brightness, and hence, the node which is less bright is attracted to a node which is brighter and merges together. If there isn't a node nearby, it will move randomly until brightness is detected. It has been used in lots of applications for computational solutions to optimize the process. From the review of the literature it is found that this scheme is used for mostly problem dependent process. In this regards, a new hence, the node that is less bright is attracted to a node that is brighter and merges together. If there isn't a node nearby, it will move randomly until brightness is detected. It has been used in lots of applications for computational solutions to optimize the process. In essence, FA uses the following three idealized rules:[21][22] (1).Fireflies are unisexual so that one firefly will be attracted to other fireflies

regardless of their sex.(2).The attractiveness is proportional to the brightness and they both decrease as their distance increases. Thus, for any two flashing fireflies, the less brighter one will move toward the more brighter one. If there is no brighter one than a particular firefly, it will move randomly.(3).The brightness of a firefly is determined by the landscape of the objective function. The implementation of FA starts with initialization of swarm of fireflies, with flashing light intensity. At each step, pairwise of light intensity is compared and the firefly with lower light intensity will move toward the higher one. The moving distance depends on the attractiveness. After moving, the new firefly is evaluated and updated for the light intensity. During pairwise comparison loop, the best-so-far solution is iteratively updated. The comparison of pair of fireflies is repeated until termination criteria are satisfied. Finally, the best-so-far solution is visualized. The main processes are described in the following subsections.

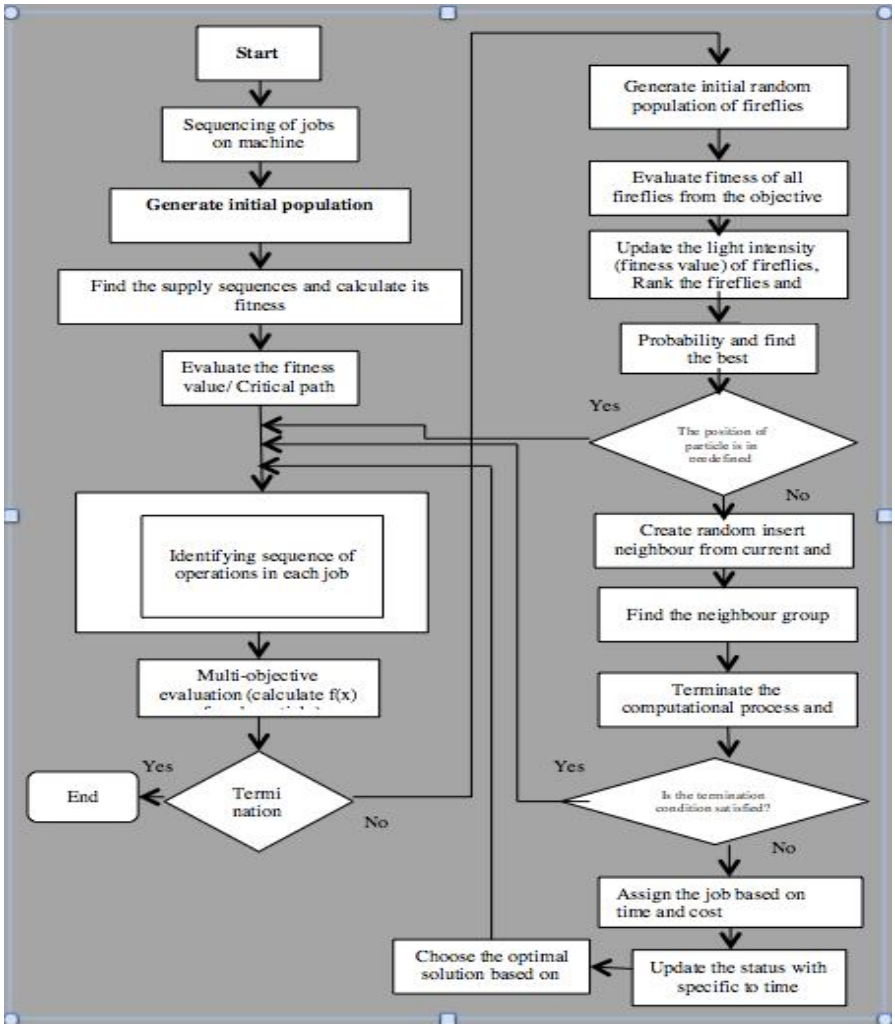

Fig.1. Flow process for HyFA

2) *Solution Procedure*: A random population is introduced initially, for example, every firefly of the underlying populace has been produced utilizing the easy going stage of both the part types to be assigned and the accessible machine on which these part types can be allotted. Alphanumeric strings are used to encode the operations that produce jobs. Each encoded operation is randomly selected and sequenced until all the operations are arranged in order to create a firefly. Here firefly is the candidate solution. So by this random generation we introduce a swarm of fireflies. The length of slots in a firefly is equal to the total number of operations to be performed. The size of the firefly population determines the number of candidate solutions or the amount of search in the solution space. Each firefly is attracted to other firefly based on the objective function in order to achieve optimal solutions. In this paper we are considering minimization problem, so the brightness will be the reciprocal of the Objective Function. The population of the firefly is further evolved when the firefly moves to next attractive firefly (solution).

The distance amongst 2 generic fireflies (e.g. “i" and “j”) is expressed by means of Cartesian distance as follows:

$$r_{ij} = \|pi - pj\| = \sqrt{\sum_{k=1}^{n} (p_{ik} - p_{jk})^2} \quad (5)$$

where pi and pj are spatial co-ordinates.

In the traditional FA the light intensity perceived of each firefly relies on the value of r as stated above and it directly relates to the magnitude of objective function. In line with a formulation provided by Yang (2009), it can be expressed as:

$$I = I_0 e^{\gamma r^2} \quad (6)$$

Here, I_0 - original light intensity γ - Coefficient of light absorption.

Attractiveness (β) represents a relative measure of the light perceived by beholders and other fireflies. Therefore the formulation of the attractiveness is expressed as:

$$\beta = \beta_0 e^{-\gamma r^2} \quad (7)$$

Here, $\beta_0$denotes the attractiveness when the distance r is equal to zero.

Movement: This factor of the generic firefly “i" that is appealed through a brighter one, can be expressed as:

$$p_i(t+1) = p_i + \beta_0 e^{-\gamma r^2 ij}(p_i(t) - p_i(t)^2) + \alpha \epsilon_i \quad (8)$$

In this equation

$p_i(t)$ represents the position of the firefly at the time t;

$\beta_0 e^{-\gamma r^2 ij}(p_i(t) - p_i(t)^2)$ represents the attraction between fireflies;

$\alpha \epsilon_i$ represents the randomness of the process where the vector ϵ_i includes random numbers extracted from a normal distribution and α is a random parameter.

3) *Simulated Annealing:* Simulated annealing is a Meta heuristic technique, which gained popularity due to its ability to be both local search and global search. It was introduced by Kirkpatrick. The algorithm is technically a hill-climbing process except instead of picking the best move, it picks a random move. If the selcted random move provides an improved solution then, the solution will be updated and accepted. Otherwise, the algorithm makes the move but with some probability less than 1. The algorithm also accepts some new solutions by accepting worse neighbours even if it raises the objective. This provides the way to avoid being trapped in local minima and is able to explore global solutions. The success rate of this technique is decided through how effectively and qualitatively the neighbours have been created with this model. From the review of the literature it is found that this scheme is used for mostly problem dependent process. In this regards, a new feasible solution is produced by the random exchange of operation sequence and machine sequence. The process is repeated as many times as possible until the search terminates. The optimal solution is found out in the iteration number below 100.This searching has been done with a maximum of 100 repetitive steps/ iterations. In SA the neighbourhood and annealing rate function and temperature plays an important role to get better performance.

4) *Neighbourhood Structure:* To create a set of feasible solutions, neighbourhood structures are needed. In general, the disjunctive graph is used to describe the neighbourhood structure. In the neighbourhood structures, the neighbourhoods are generated in terms of neighbourhood strategies. As local search efficiency is directly affected by neighborhood structure proper care has to be taken. Random neighbor insert is adopted in our paper. Any two vectors are selected and the larger position number is inserted into previous position of the smaller position number and smaller position number and the subsequent number sequence is postponed. According to the characteristic of the annealing temperature function, it can be obtained that its decreased amplitude becomes faster at a high temperature level, while its decreased amplitude becomes slower at a low temperature level. It is likely to result in an insufficient search in the solution space. In order to enhance the exploitation ability of the SAA, an improved annealing rate function inspired by the Hill function is developed as

$$T(t) = \beta \times \frac{T_0^n}{T_0^n + t^n} \quad (9)$$

5) *Greedy Heuristics:* The greedy heuristics are commonly used to speed up research. This heuristic is one of the popular methods to solve combinatorial optimization and Operations Research problems (i.e. generally NP-hard). The greedy heuristics are used because they are fast, they produce solutions good quality, they are easy to implement and can easily be expanded: in addition, they can be easily randomized [23]. Undeniably, for many cases, this algorithm has proved to lessen the complexity of polynomial time period. In addition, its application has given a lead to avoid the issue called "local optimum". This is the most prevalent method in answering the combinatorial kind of optimizing difficulties and the operational researching issues of NP-hard nature. The particular benefits that are harvested through this approach include the rapidity, solutions with excellence, ease of execution, possibility for expansion, and easier randomization. At the moment which it feels better is picked for selection by this algorithm and hence it derives this name. More precisely, it chooses local optimum point on confidence/ hope and proceeds with an assumption that the chosen point will offer an optimal solution in global manner. Based on the SA and GHA, the mutation, fitness of current state and optimal solution are found. Reiterate the steps until termination criteria are achieved.

The parameters used in HyFA are given in Table 2.

Table 2. Parameters used in HyFA

Parameter	Value
Firefly size in population	30
Annealing function	Fast annealing
Initial temperature and annealing function	100
The total number of generations	200
Initial attractiveness between two fireflies	0.1
Absorption coefficient of the least intensity firefly	1
The maximum iteration size	800

IV. RESULTS AND DISCUSSIONS

This section is devoted to the computational experiments done to evaluate the performance of the proposed HyFA algorithm. The proposed algorithm have been implemented and tested by using Matlab R2016b, computing environment on an Intel Core™i7, with Windows 10. It is aimed to specify with the results that recommended algorithm is an able approach for the scheduling problems involved with flexibility for job shop applications. LA1-25 Benchmark instances were taken from Operations Research (OR) Library to test the efficiency of proposed HyFA with best known solutions (Benchmark datasets) and the obtained datasets are compared with other researcher's experimental research datasets (obtained by using of other algorithms). Our program is editable, we can change number of flies and number of iteration as well, to preset the parameters. The HyFA was run for 20 times inorder to evaluate its consistency and efficacy. Performance comparison of HyFA with other algorithms taken from literature are given in Table 3. Column 1 shows the problem number, column 2 & 3 shows the 'n' jobs 'm' machines , column 4 shows BKS best known solutions, column 5-8 shows the Cm values of other techniques found in literature.

©IJRASET: All Rights are Reserved

Table 3 Performance Comparison of HyFA with other techniques

Problem	n	m	BKS	GRASP[24]	DE[25]	BFOA[17]	FA[26]	HyFA
LA 1	10	5	666	666	666	693	666	666
LA 2	10	5	655	655	655	683	658	656
LA 3	10	5	597	604	597	634	597	597
LA 4	10	5	590	590	590	624	604	590
LA 5	10	5	593	593	593	593	593	593
LA 6	15	5	926	926	926	926	926	926
LA 7	15	5	890	890	890	903	890	890
LA 8	15	5	863	863	863	873	863	863
LA 9	15	5	951	951	951	951	951	951
LA 10	15	5	958	958	958	958	958	958
LA 11	20	5	1222	1222	1222	NA	1222	1222
LA 12	20	5	1039	1039	1039	NA	1039	1039
LA 13	20	5	1150	1150	1150	NA	1150	1159
LA 14	20	5	1292	1292	1292	NA	1295	1295
LA 15	20	5	1207	1207	1207	NA	1207	1207
LA 16	10	10	945	946	945	NA	945	945
LA 17	10	10	784	784	784	NA	784	784
LA 18	10	10	848	848	848	NA	848	848
LA 19	10	10	842	842	842	894	842	842
LA 20	10	10	902	907	902	NA	902	902
LA 21	15	10	1046	1091	NA	1207	1046	1046
LA 22	15	10	927	960	NA	NA	929	928
LA 23	15	10	1032	1032	NA	NA	1032	1032
LA 24	15	10	935	978	NA	1102	935	935
LA 25	15	10	977	1028	NA	1131	977	977

V. CONCLUSIONS AND FUTURE SCOPE

The proposed hybridized algorithm HYFA is used to minimize the make-span of JSSP. The program coding was done in Matlab 2016b and above and the coding can be edited to suit as per the requirement for any combination of machines and jobs. The experimental results have demonstrated a remarkable decrease in computing time and getting better optimal operation and machine sequence for solving the JSSP. The contributions of this research paper are:

1) A novel hybridized evolutionary algorithm HyFA is done by combining three Meta heuristics namely FA, SA, GHA.

2) The proposed algorithm showed an effective result and successfully solved the scheduling problem. Twenty-Five test instances of Lawrence with different size are taken to conduct experimental studies. The objective of minimizing make span have been attempted and the optimal results were found in very less computational time.

3) In the future, attempts can be made further, to hybridize other evolutionary algorithms to construct an effective hybrid algorithm. Also we can consider other objectives and multi-objectives and try to reduce the constraints and solve the other branches of JSSP like FJSP. Not all benchmark problems have optimal solutions. We hope this technique will help to achieve that.

BIBLIOGRAPHY

[1] Crama Y (1997) Combinatorial optimization models for production scheduling in automated manufacturing systems. Eur J Oper Res 99:136–153. https://doi.org/10.1016/S0377-2217(96)00388-8
[2] Mishra R, Devi GK, Madan A (2019) Non-traditional optimization techniques of scheduling in FMS: A Review. Int J Res Eng Innov 3:157–164
[3] Marichelvam MK, Geetha M, Tosun Ö (2020) An improved particle swarm optimization algorithm to solve hybrid flowshop scheduling problems with the effect of human factors – A case study. Comput Oper Res 114:104812. https://doi.org/10.1016/j.cor.2019.104812
[4] Reddy BSP, Rao CSP (2006) A hybrid multi-objective GA for simultaneous scheduling of machines and AGVs in FMS. Int J Adv Manuf Technol 31:602–613. https://doi.org/10.1007/s00170-005-0223-6
[5] Lin TL, Horng SJ, Kao TW, et al (2010) An efficient job-shop scheduling algorithm based on particle swarm optimization. Expert Syst Appl 37:2629–2636. https://doi.org/10.1016/j.eswa.2009.08.015
[6] Sankar SS, Ponnanbalam SG, Rajendran C (2003) A multiobjective genetic algorithm for scheduling a flexible manufacturing system. Int J Adv Manuf Technol 22:229–236. https://doi.org/10.1007/s00170-002-1464-2
[7] Batur GD, Erol S (2016) Using simulated annealing for flexible robotic cell scheduling. Gazi Univ J Sci 29:573–582
[8] Nidhish Mathew Nidhiry DRS (2012) A COMBINED OBJECTIVE GENETIC ALGORITHM FOR SCHEDULING OF MACHINES IN FMS. Int J Eng Res Appl ISSN 3:
[9] Kumar AVSS, Veeranna V, Durgaprasad B, Sarma BD (2013) Combined Objective Optimization Of FMS Scheduling With Non-Traditional Optimization Techniques. Int J Eng Res Technol (IJERT 2:1420–1428
[10] Li X, Gao L (2016) An effective hybrid genetic algorithm and tabu search for flexible job shop scheduling problem. Int J Prod Econ 174:93–110. https://doi.org/10.1016/j.ijpe.2016.01.016
[11] Scaria A, George K, Sebastian J (2016) An Artificial Bee Colony Approach for Multi-objective Job Shop Scheduling. Procedia Technol 25:1030–1037. https://doi.org/10.1016/j.protcy.2016.08.203
[12] Li X, Zhao H (2009) Greedy Algorithm Solution of Flexible Flow Shop Scheduling Problem. Int J Comput Sci Netw Secur 9:9–12
[13] Karthikeyan S, Asokan P, Nickolas S, Page T (2015) A hybrid discrete firefly algorithm for solving multi-objective flexible job shop scheduling problems. Int J Bio-Inspired Comput 7:386. https://doi.org/10.1504/IJBIC.2015.073165
[14] Mati Y, Rezg N, Xie X (2001) An integrated greedy heuristic for a flexible job shop scheduling problem. Proc IEEE Int Conf Syst Man Cybern 4:2534–2539. https://doi.org/10.1109/ICSMC.2001.972939
[15] Sreekara Reddy MBS, Ratnam C, Rajyalakshmi G, Manupati VK (2018) An effective hybrid multi objective evolutionary algorithm for solving real time event in flexible job shop scheduling problem. Meas J Int Meas Confed 114:78–90. https://doi.org/10.1016/j.measurement.2017.09.022
[16] Sun L, Liang YY, Cheng X (2010) Solving Job Shop Scheduling Problem Using Genetic Algorithm with Penalty Function. Int J Intell Inf Process 1:65–77. https://doi.org/10.4156/ijiip.vol1.
[17] Narendhar S, Amudha T (2012) A Hybrid Bacterial Foraging Algorithm For Solving Job Shop Scheduling Problems. Int J Program Lang Appl 2:1–11
[18] Roshanaei V, Azab A, Elmaraghy H (2013) Mathematical modelling and a meta-heuristic for flexible job shop scheduling. Int J Prod Res 51:6247–6274. https://doi.org/10.1080/00207543.2013.827806
[19] Yuan Y, Xu H (2013) Flexible job shop scheduling using hybrid differential evolution algorithms. Comput Ind Eng 65:246–260. https://doi.org/10.1016/j.cie.2013.02.022
[20] Lindfield G, Penny J (2017) The Firefly Algorithm. In: Introduction to Nature-Inspired Optimization. Elsevier, pp 85–100
[21] Fister I, Yang XS, Brest J (2013) A comprehensive review of firefly algorithms. Swarm Evol Comput 13:34–46. https://doi.org/10.1016/j.swevo.2013.06.001
[22] Yang XS, Karamanoglu M (2013) Swarm Intelligence and Bio-Inspired Computation: An Overview. In: Swarm Intelligence and Bio-Inspired Computation. Elsevier, pp 3–23
[23] El-Ghazali Talbi (2009) Metaheuristics. University of Lille
[24] Binato S, Hery WJ, Loewenstern DM, Resende MGC (2002) A grasp for job shop scheduling. Oper Res Comput Sci Interfaces Ser 15:59–79. https://doi.org/10.1007/978-1-4615-1507-4
[25] Shilpa P, Balaraju G (2018) Job shop scheduling using differential evolution algorithm. Int J Mech Prod Eng Res Dev 8:327–338. https://doi.org/10.24247/ijmperdjun201837
[26] Udaiyakumar KC, Chandrasekaran M (2014) Application of firefly algorithm in job shop scheduling problem for minimization of Makespan. Procedia Eng 97:1798–1807. https://doi.org/10.1016/j.proeng.2014.12.333

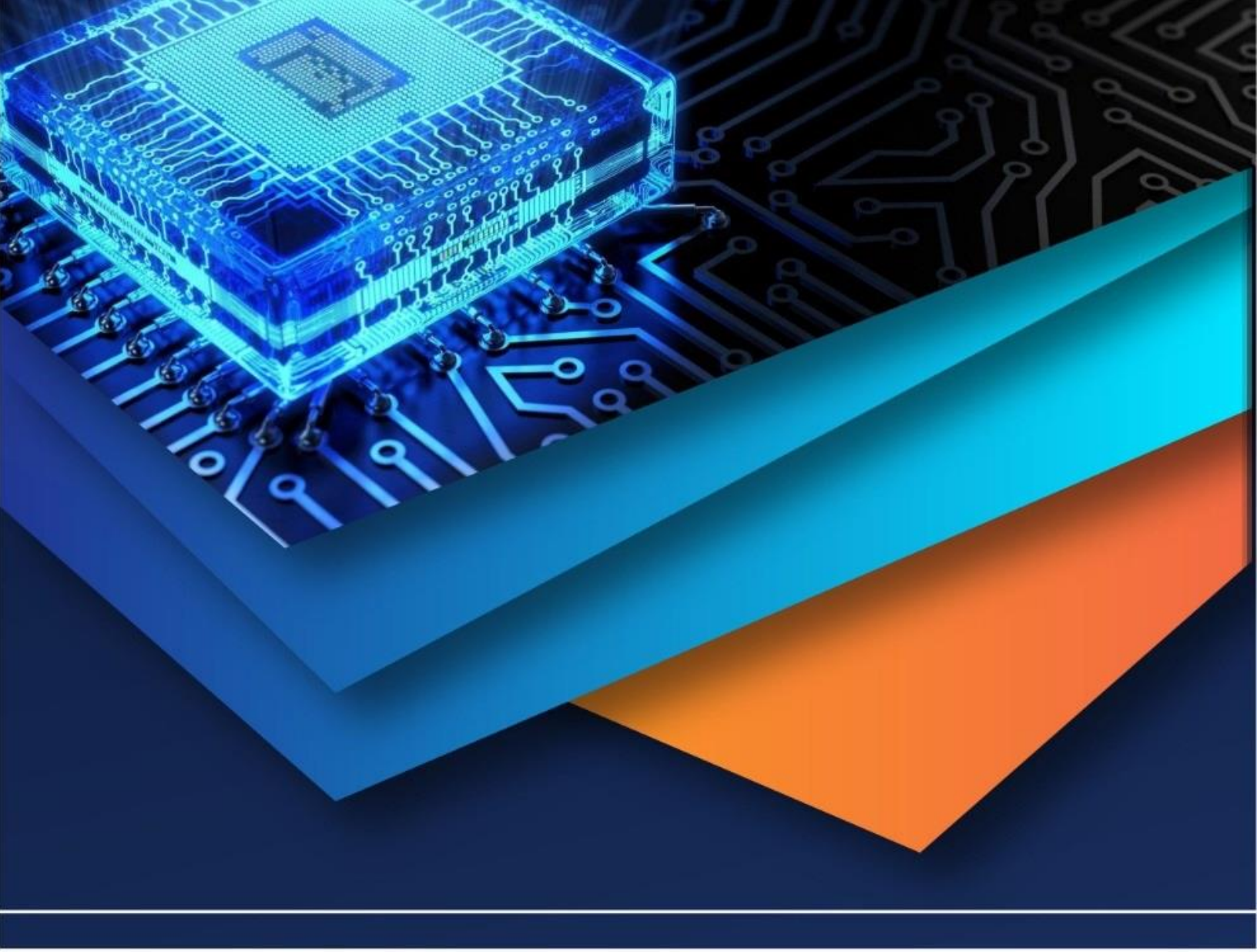

10.22214/IJRASET

45.98

IMPACT FACTOR: 7.129

IMPACT FACTOR: 7.429

INTERNATIONAL JOURNAL FOR RESEARCH

IN APPLIED SCIENCE & ENGINEERING TECHNOLOGY

Call : 08813907089 (24*7 Support on Whatsapp)

View publication stats

Multimedia Systems
https://doi.org/10.1007/s00530-023-01051-8

REGULAR PAPER

A literature survey on multimodal and multilingual automatic hate speech identification

Anusha Chhabra[1] · **Dinesh Kumar Vishwakarma**[1]

Received: 19 September 2022 / Accepted: 9 January 2023
© The Author(s), under exclusive licence to Springer-Verlag GmbH Germany, part of Springer Nature 2023

Abstract
Social media is a more common and powerful platform for communication to share views about any topic or article, which consequently leads to unstructured toxic, and hateful conversations. Curbing hate speeches has emerged as a critical challenge globally. In this regard, Social media platforms are using modern statistical tools of AI technologies to process and eliminate toxic data to minimize hate crimes globally. Demanding the dire need, machine and deep learning-based techniques are getting more attention in analyzing these kinds of data. This survey presents a comprehensive analysis of hate speech definitions along with the motivation for detection and standard textual analysis methods that play a crucial role in identifying hate speech. State-of-the-art hate speech identification methods are also discussed, highlighting handcrafted feature-based and deep learning-based algorithms by considering multimodal and multilingual inputs and stating the pros and cons of each. Survey also presents popular benchmark datasets of hate speech/offensive language detection specifying their challenges, the methods for achieving top classification scores, and dataset characteristics such as the number of samples, modalities, language(s), number of classes, etc. Additionally, performance metrics are described, and classification scores of popular hate speech methods are mentioned. The conclusion and future research directions are presented at the end of the survey. Compared with earlier surveys, this paper gives a better presentation of multimodal and multilingual hate speech detection through well-organized comparisons, challenges, and the latest evaluation techniques, along with their best performances.

Keywords Hate speech · Multilingual · Multimodal · Machine learning · Deep learning · Online social media

1 Introduction

With the growing internet and technology, a large amount of information content is present on online community networks as multimodal data (Text, Pictures, and videos). If we look at the statistics, we can visualize that a large number of people using social media is escalating at a very great speed, and people can easily present their views to each other via various social media platforms. The type of content on the online social media stages contributes to the propagation of hate speech and misleading people. Right now, controlling this kind of media information is very important. Therefore, hate speeches harm individuals and impact society by raising hostility, terrorist attacks, child pornography, etc. Figure 1 shows a portion of hate speech and offensive expressions posted on social media or the web. Figure 1(a) shows a clear example of encouraging violence during huge fights against CAA, NRC, and NPR across India in Jan 2020 [1]. Figure 1(b) shows the tweet released under #putsouthafricansfirst, a person openly tweeting to attack the foreigners working in South Africa. Figure 1(c) shows a tweet posted in 2014 advocating killing Jewish people for fun after the synagogue shooting in Pittsburg [2]. Figure 1(d) shows a post posted in Jan 2018 that a supreme leader is giving a genuine threat statement to the US for war [3].

The recent instances of high-profile politicians making speeches were an apparent attempt at inciting violence, which led to large-scale violence. These instances are yet to be dealt with by law enforcement agencies. Hence, the integrity of identifying hate instances is one of the most significant challenges in social media stages, and research-based analysis of this type of content is necessary. The following

✉ Dinesh Kumar Vishwakarma
dinesh@dtu.ac.in

Anusha Chhabra
anusha.chhabra@gmail.com

[1] Biometric Research Laboratory, Department of Information Technology, Delhi Technological University, Delhi 110042, India

Published online: 20 January 2023

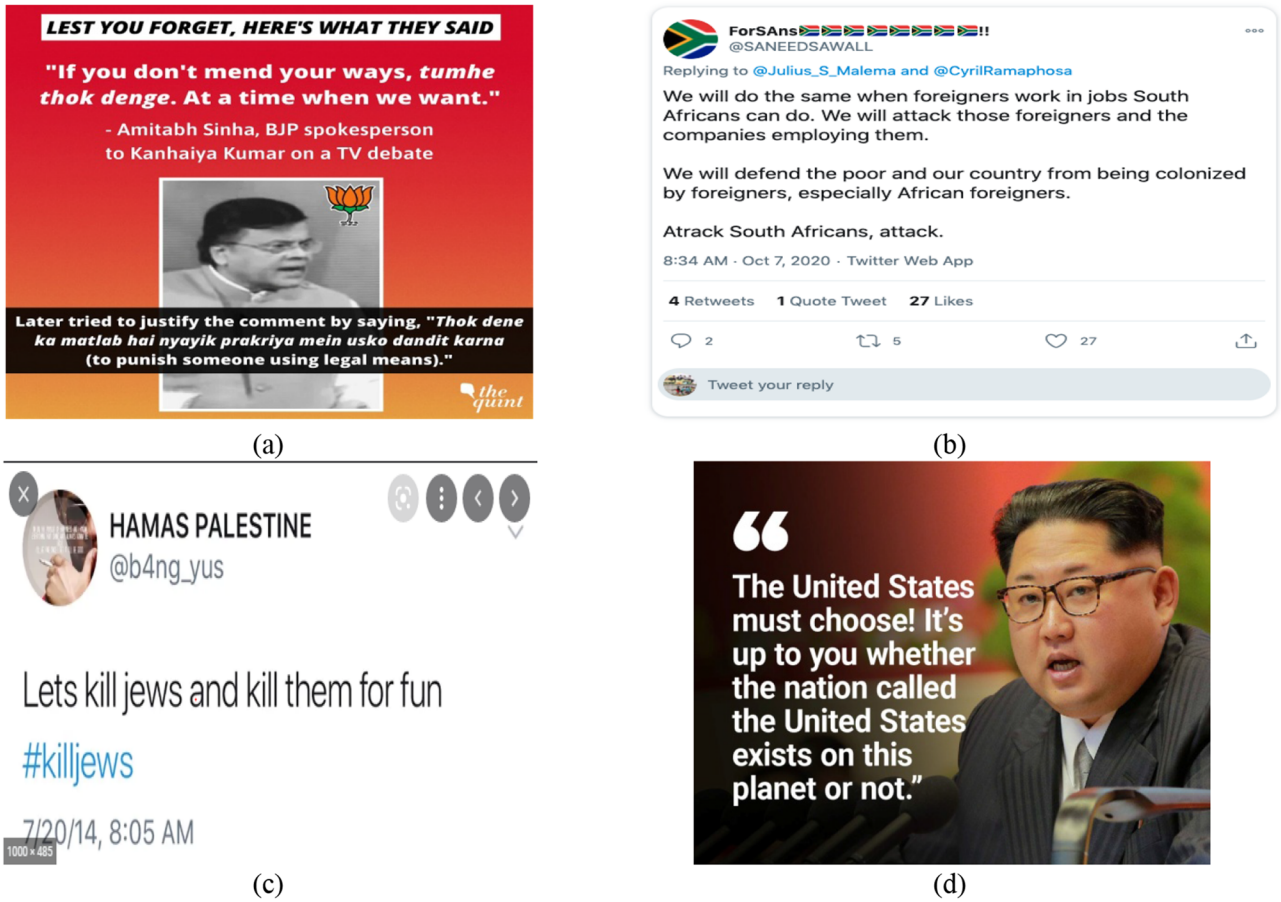

Fig. 1 Examples of hate speech and offensive expressions present over social media

section describes the definition analysis of hate speech from various sources.

1.1 Hate speech: definition perspective and analysis

There is a general agreement among researchers to define hate speech, and researchers have described it as a language that attacks an individual or a society dependent on characteristics like race, shading, nationality, sex, or religion [4]. This section provides some state-of-the-art definitions of hate speech (Table 1). Although many authors and social media platforms have given their purposes for hate speech, researchers are following them to understand the forms and classifications of hate speech. The definitions from the various sources are as follows:

- Some of the scientific definitions include the community's perspective.
- Major social networking sites like Facebook, YouTube, and Twitter are the most used platforms where hate speech occurs regularly.

The definition analysis (Table 2) mainly relies on various sources like multiple definitions from scientific papers and powerful social media platforms. The dimensions used for analysis are "violence," "attack," "specific targets," and "status."

After a thorough definition analysis, we have also portrayed the definition of Hate Speech as follows:

> "Hate Speech is a toxic speech attack on a person's individuality and likely to result in violence when targeted against groups based on specific grounds like religion, race, place of birth, language, residence, caste, community, etc."

1.2 Hate speech: forms and related words

Figure 2 shows significant hate forms of speech like Cyberbullying, Toxicity, Flaming, Abusive Language, Profanity, Discrimination, etc., and Table 3 presents the definitions of the above forms of hate speech found in the literature with their distinction from hate speech.

Table 1 Some of the prominent definitions by some state-of-the-art

References	Hate speech definitions
[5]	An antagonistic, malevolent speech focused on an individual or a social event of people taking into account a part of their genuine or intrinsic qualities. It communicates unfair, scary, objecting, hostile, or potentially biased perspectives toward those attributes, including sex, race, religion, identity, shading, public beginning, incapacity, or sexual direction
[6]	Hate speech is a conscious and hardheaded public assertion expected to slander a gathering of individuals
[7]	Hate speech is a quick attack on individuals subject to race, identity, sex, character, and veritable sickness or impediment. We portray assail as horrible or dehumanizing talk, clarifications of deficiency, or calls for dismissal or seclusion
[8]	Hate speech alludes to content that advances viciousness or scorn against the public dependent on specific ascribes, like ethnic or race beginning, religion, inability, sex, age, veteran reputation, and sexual direction/sex personality
[9]	Content that attacks people based on actual or perceptual race, ethnicity, country of origin, religion, gender, sexual orientation, disability, or illness is not permitted. It is considered a potential threat or attack for the content that many people find offensive (jokes, Stand-up comedy, lyrics of popular songs, etc
[10]	Hate speech attacks an individual or get-together depending on characteristics like religion, race, ethnicity, insufficiency, sexual heading, or sex character
[11]	Hate speech attack others dependent on racism, ethnicity, public start, sexual bearing, sex, character, age, handicap, or genuine illness
[12]	The language used to convey hate speech towards a selected bunch
[13]	Hate Speech is a purposeful attack on a specific social occasion of people motivated by the pieces of the group's character
[14]	Hate Speech assails or prompts malignance against gatherings in light of explicit qualities like actual looks, religion, ethnicity, sexism, and many more. Moreover, individuals with diverse phonetic styles in unobtrusive construction can happen

Table 2 Definition Analysis

Ref	Dimensions			
	Specific targets	Status	Violence	Attack
[5]	Yes	No	Yes	No
[6]	Yes	No	Yes	No
[7]	Yes	Yes	No	Yes
[8]	Yes	No	Yes	No
[9]	Yes	Yes	Yes	No
[10]	Yes	No	No	Yes
[11]	Yes	No	No	Yes
[12]	Yes	No	Yes	No
[13]	Yes	Yes	Yes	Yes
[14]	Yes	Yes	Yes	No

Hence, analyzing hate speech on the web is one of the critical areas to study due to the following reasons:

- Reduce conflicts and disputes created among human beings due to toxic language and offensive expressions.
- The broad availability and notoriety of online web-based media, like Facebook, Twitter, Instagram, web journals, microblogs, assessment sharing sites, and YouTube, boost communication and allow people to freely share information in the form of their thoughts, emotions, and feelings among strangers.
- Moreover, click baiting takes massive attention and encourages visitors to click on the link, harming readers' emotions.

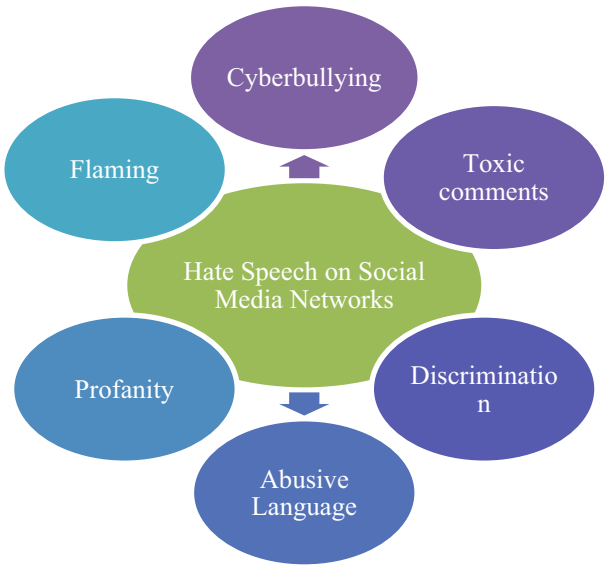

Fig. 2 Forms of Hate speech

- Hate speeches can incite violence and cause irreparable loss of life and money.
- The latest incident was triggered by online hate speech in the Philippines, citing the example of the Christchurch mosque shooting in 2019 [20].
- To forestall bigot and xenophobic viciousness and separation spread among Asians and individuals of Asian drop uniquely in this pandemic. As per the report distributed by US Today in May 2021, more than 6600 hate

Table 3 Comparison between Hate speech and its various forms

Forms	Definitions of forms	Distinction from hate speech
Cyberbullying	Characterized as a deliberate demonstration completed by a social occasion or individual using electronic stages [15]	Hate speech is abusive speech explicitly directed toward a unique, non-controllable attribute of a group of people
Discrimination	Interaction via a distinction and afterward utilized as the premise of unreasonable treatment [16]	Hate speech is a virulent form of discrimination
Flaming	Flaming describes antagonistic, profane, and threatening remarks that can upset and offend other members of the forums, generally called trolls [17]	Unlike flaming, hate speech can occur in any context
Abusive Language	The term abusive language seeks to diminish or humiliate some person or group [18]	Hate Speech is a type of abusive language
Profanity	Hostile or indecent words or expressions	Hate speech can use profane words but not always
Toxic language	Conveying content that is disrespectful, abusive, unpleasant, and harmful [19]	Not all toxic comments contain hate speech

and offensive incidences against Asian- Americans and Asians have been accounted for [6].
- To save our society from being gravely damaged.

From the points mentioned above, it has been observed that detecting and restraining hate speech at an initial stage is very crucial and, indeed, a challenging task. Major online media stages like Facebook, Twitter, and YouTube are trying to eliminate hate speeches and other harmful content at an initial step as part of their ongoing projects, using advanced AI techniques. However, keeping an eye on an individual is vital to have hate off platforms. Social media platforms and an individual can adopt the following suggestions:

- The most significant source of hate speech on the internet is trolls. A person should block, mute, or report these trolls instead of giving recognition.
- A person should do a proper data analysis and facts before forwarding the posts.
- Social media firms should follow strong policy rules against abusive behavior.

The following section describes the general framework of hate speech detection adopted by several researchers.

1.3 Motivation

Recently, it has been observed that the number of users are actively involving on social media in the forms of WhatsApp post, Facebook posts, YouTube shorts, reviews, comments etc. on various topics. People are sharing their views resulting in tremendous amount of data on the web. The data should be analyzed for further research. Giving the various hate form definitions, their analysis and to highlight the motivation behind the hate content detection in every aspect, we briefly discuss the recent works in this area in terms of various methodologies, modalities, performances, benchmarks etc. The further future trends are also highlighted giving the motivation to researchers for detecting hate content.

1.4 General framework of hate speech detection

Figure 3 provides a framework for the process of hate speech identification. The foremost step is to search the powerful source platform where most hate speech/ offensive languages occur. Most state-of-the-art adopted significant social media firms like Facebook and Twitter. The second step is to collect data either in the form of posts or tweets. Gathering a great measure of information from web-based media stages nowadays is one of the significant research challenges for researchers and academia. The platforms provide a simple and quick approach to gathering and storing information through inbuilt APIs [21]. Figure 4 shows the types of data accessible and non-accessible via social media, respectively.

A large amount of hate speech data collection is from two powerful social media platforms: Twitter, Instagram, Facebook, and these two platforms are actively working on combating hate speeches. The next phase includes data normalization and feature extraction for training a model, and the last step performs classification to classify the problem.

Most literature surveys ([14, 25–27, 4, 28–31]) have been published till now. Table 4 compares our survey with related surveys in various aspects like definition analysis, comparison with other hate forms, NLP aspect in terms of modalities, and explanation of models and datasets. This paper also gives an itemized portrayal of hate speech identification in multimodal information by considering major phases like data collection, text mining approaches in automatic hate speech detection, and different machine and deep learning approaches. This paper is a more detailed and systematic survey considering various parameters in terms of datasets, methods, etc. as follows:

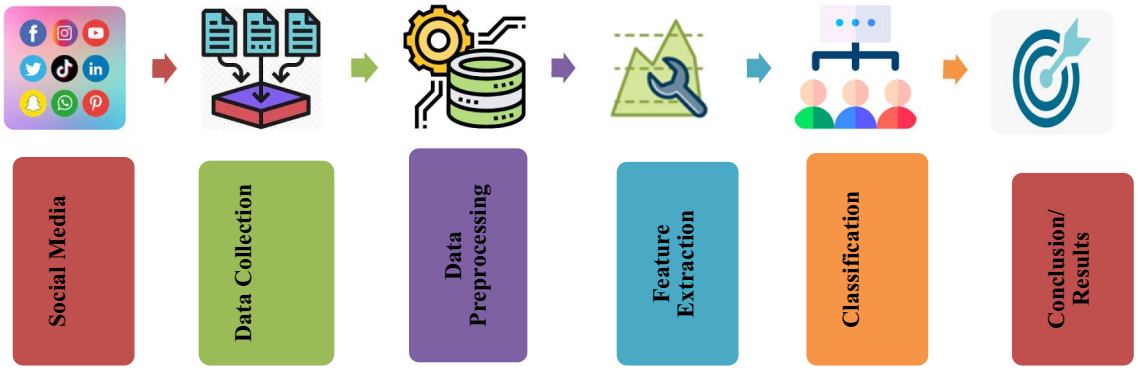

Fig. 3 General framework of hate speech detection

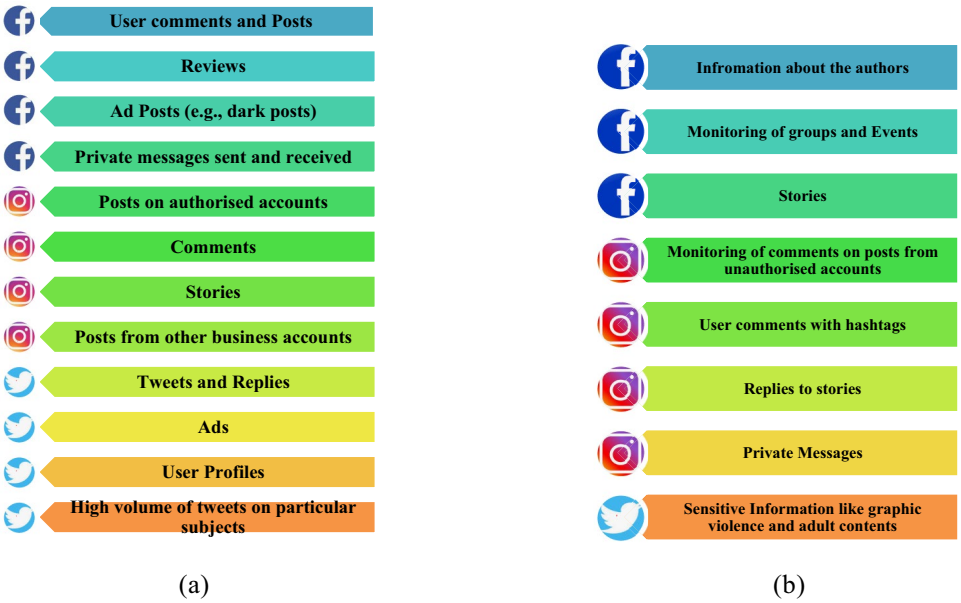

Fig. 4 **a** Type of data accessible via some social media networks and **b** Type of data not accessible via some social media networks [22–24]

Table 4 Comparison table of related surveys

Ref	Definition analysis	Comparison with other hate forms	Feature Extraction (NLP Aspect)	Modality (text-T, images- I, videos – V)	Linguistic aspect	Models aspect	Datasets
[4]				T	Monolingual		
[14]				T	Monolingual		
[25]				T	Multilingual		
[26]				T	Multilingual		
[27]				T	Multilingual		
[28]				T	Monolingual		
[29]				T	Multilingual		
[30]				T	Multilingual		
[31]				T	Monolingual		
Our survey				T + I + V	Multilingual		

- The study of detecting online hate content has been growing only in the last few years, and machine learning is more prominent. This survey covers the job done in deep and hybrid architectures to determine the issue of recog-

nizing hate speech. This survey also covers the feature extraction methods used in automatic hate speech detection.

- The beauty of this literature covers possible identified merits and demerits of the recent state-of-the-art works, their fundamental aspects, and techniques used in tabular form.
- Another beauty of this survey is that it covers publicly available datasets, dataset challenges, and benchmark models.
- Most previous surveys are on textual data, and limited literature is particularly for detecting hate speech in multimodal information. Therefore, this review paper also considers multimedia data (such as text, images, and videos) to highlight the detection process and the previous works on multilingual hate speech detection. However, this survey incorporates some famous works done for multilingual and multimodal data in this field.
- The survey also considers the current challenges and possible future directions; which researchers can view as further work in this area.

1.5 Review technique

However, various investigations have been distributed in earlier years identifying hate speech, yet this survey contains some noticeable works in this field. We considered influential journals, conferences, and workshops from various online databases such as IEEE Xplore, Science Direct, Springer, ACM Digital Library, MDPI, CEUR Proceedings, etc. The comprehensive survey contains a review of more than 120 articles based on keywords like "hate speech detection," "offensive language detection," "multilingual," "images," "videos," etc. It has been observed from Fig. 5 that the number of articles published on hate speech detection seemed to increase yearly in the last five years.

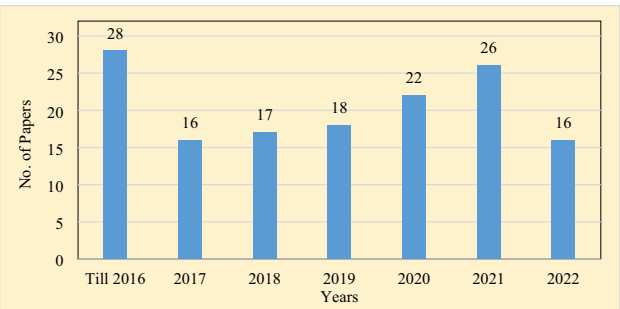

Fig. 5 Year-wise contribution of a research article on Hate Speech Detection over the last five years

This survey presents a comprehensive analysis of hate speech detection research arena as shown in Fig. 6. It breaks down the hate speech detection into several meaningful categorizations such as types of hate speeches, approaches, datasets, feature extraction methodologies etc. Special attention has been paid in the exploration of multimodal and multilingual approaches of better classification capabilities. Specifically, feature extraction methods such as Bag-of-Words, N-grams, Lexicon & Sentiment based features, TF-IDF, part of speech, word references and rule based are analyzed and also presented visually in Fig. 7. Next, hate speech detection methods are discussed in great detail categorizing them into traditional machine learning based and deep learning based approaches. A separate section elaborates the merits and demerits of the same. Special analysis of publicly available multimodal hate speech datasets is also presented that dives into the challenges posed by each of the multimodal hate speech datasets. Evaluation metrics and performance benchmarks are presented to highlight the effectiveness of current state-of-the-art approaches for hate speech detection.

This survey is organized as follows. The introduction is discussed in Sect. 1, whereas Sect. 2 describes possible feature extraction techniques in context with NLP Aspect for automatic hate speech detection. Section 3 covers the most vital work using different methodologies like machine and deep learning and the conversation on multilingual work. Section 4 highlights the challenges related to hate speech datasets and their benchmark models. In contrast, Sect. 5 depicts the various evaluation metrics and performance measures. Finally, Sects. 6 and 7 portrays the conclusion and further future directions respectively.

2 Feature extraction techniques in automatic hate speech detection

A feature is the closed characteristics of an entity or a phenomenon. [32] Focus on natural language processing (NLP) to explore the automation of understanding human emotions from texts. This section provides various text features used to extract hate content (Fig. 7). Word references and lexicons are the most straightforward and basic approaches for feature extraction in text analysis. Identifying the appropriate features for classification is more tedious when using machine learning. The fundamental step in traditional and deep learning models is tokenization, in which the primary and straightforward approach is dictionaries/ lexicons. Dictionary is a method that generates a set of words to be looked at and included in the text. Frequencies of terms are used directly as features. Features play an essential role in machine learning models. Machine learning approaches cannot work on raw data, so feature extraction techniques are needed to convert text into vectors of features. Many

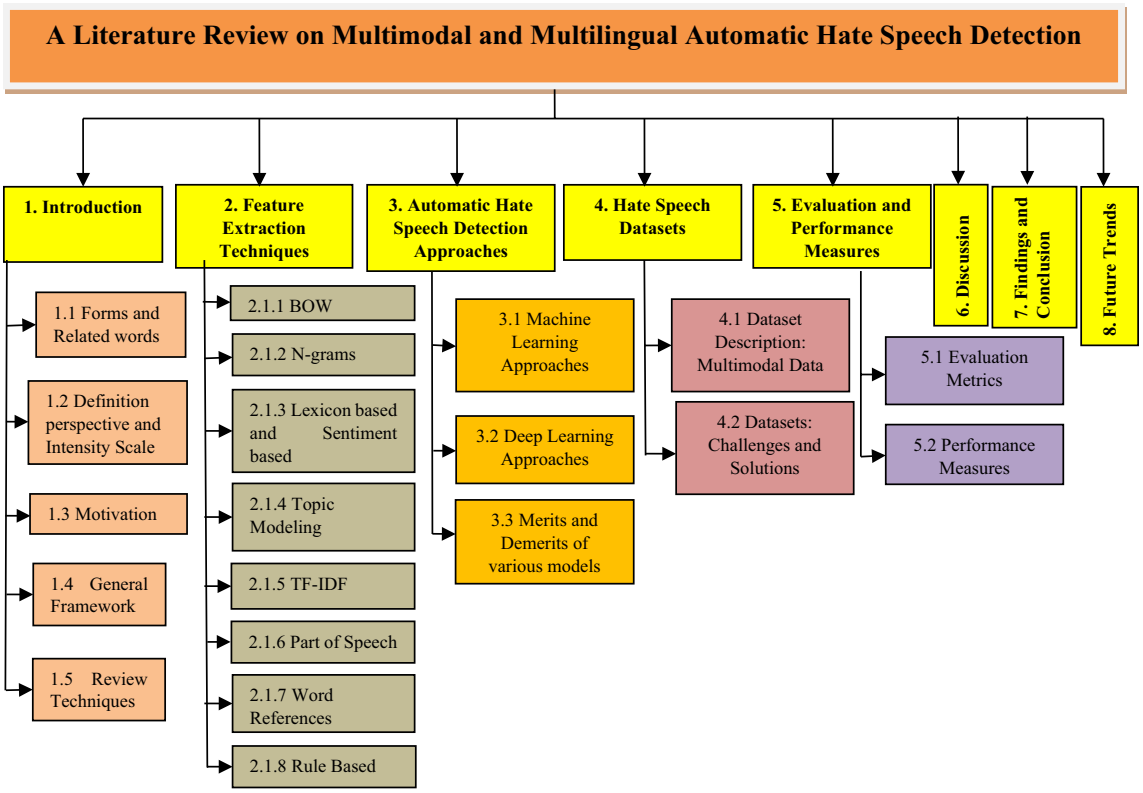

Fig. 6 Organization of the survey

basic features like BOW, Term Frequency- inverted Term Frequency, Word references, etc., are used.

2.1 Bag-of-words (BOW)

BOW is an approach like word references extensively used for document classification ([14, 33–35]). The frequency of each word is used as a characteristic for training a classifier after gathering all the words. The burden of this technique is that the sequencing of words is disregarded, whether it is syntactic or semantic information. Both pieces of information are crucial in detecting hate content. [36] Used BOW to represent Arabic hate features as text pre-processing before applying various machine learning classifiers. [37] Derived a method for detecting Arabic religious hate speech using different features with the machine and deep learning models. Consequently, it can prompt misclassification of whether the terms are utilized in multiple contexts. N-grams were executed to overcome the issue.

2.2 N-grams

The N-grams approach is the most utilized procedure in identifying hate speech and offensive language ([12, 18, 33, 38–41]). The most widely recognized N-grams approach combines the words in sequence into size N records. The objective is to enumerate all size N expressions and check their events. It further increases the performance of all classifiers since it incorporates each word context [42]. Rather than utilizing words, it is additionally conceivable to use the N-grams approach along with characters. [43] Proved character N-gram features are more predictive in detecting hate speech than token N-gram features, whereas it is not valid in the case of identifying offensive language. Although N-grams also have limitations, like all the related words have maximum distance in a sentence [33], an answer for this issue lies in incrementing the N value. However, it lowers the processing speed [15]. [39] Proved that greater *N* values perform better than lower *N*-values (unigrams and trigrams). The authors [4, 38] observed that character N-gram features

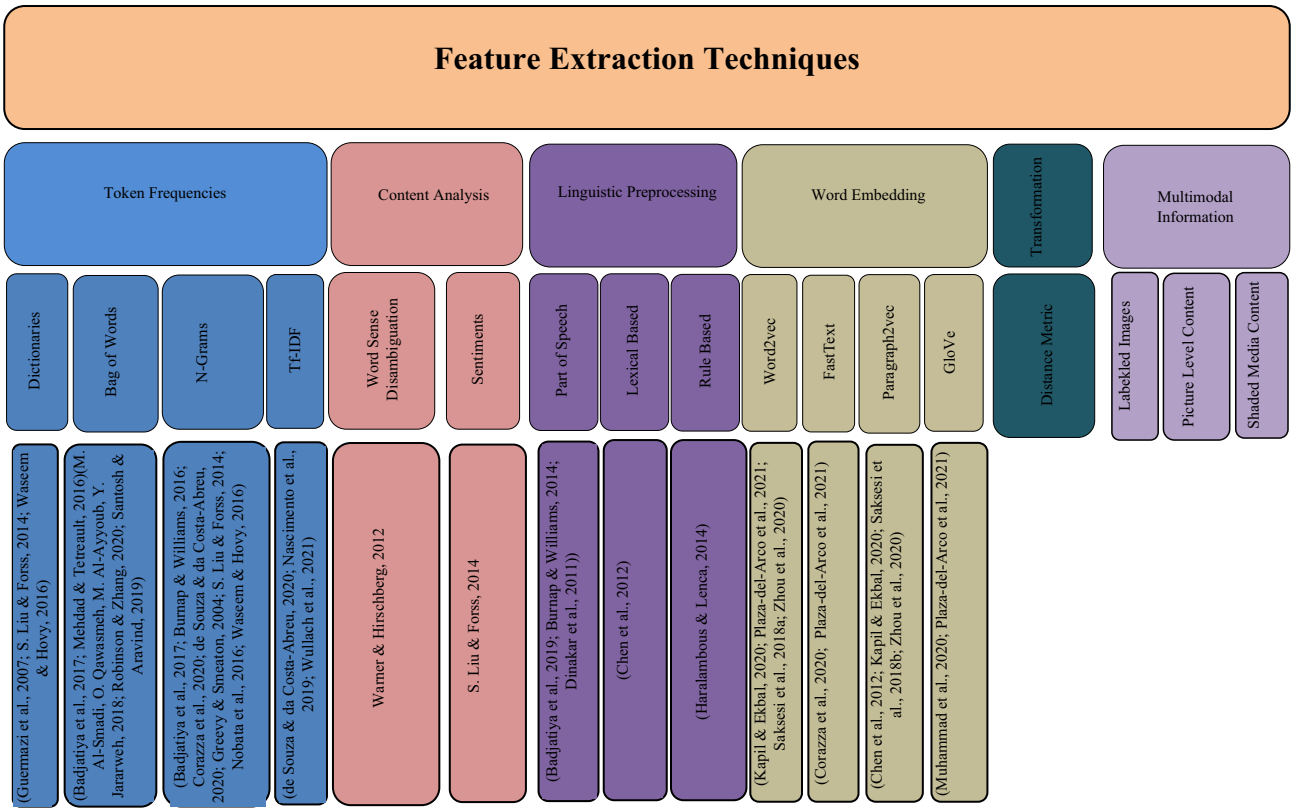

Fig. 7 Common feature extraction techniques

perform better when combined with extra-linguistic features. The authors generated one hot N-gram and N-gram embedding feature to train the model and analyzed better performance by N-gram embedding [44].

2.3 Lexicon-based and sentiment based

Lexical features use unigrams, and bigrams of the target word, whereas syntactic features include POS tags and various components from a parse tree. The parser used in NLP, proposed by the Stanford NLP Group [45], was used to catch the linguistic conditions inside a sentence [15]. Lexicon-based methods are crucial in identifying the sentiments of speech. For example, nigga is an offensive word and must be prohibited in ordinary language [46]. Hateful speech on a social stage cannot be a positive polarity because awful grammar provides a negative inclination by the speaker to the listeners and readers. Authors in ([12, 39, 47–50]) [51]) consider sentiments as a characteristic for identifying hate speech. Some authors [39] used the sentiment features in combination with others, which proved in result enhancement. [52] Presents metaheuristic approach for sentiment analysis and proved that the optimization methods can be alternatively used against machine leaning models with promising results.

2.4 Topic modeling

This method is also famous for topic classification, which focuses on extracting topics that occur in a corpus. Topic modeling is also used for detecting hateful comments from central social media platforms like Youtube [53]. [54]) used the Latent Dirichlet Allocation model ([55]) to discover abstract topics and use them in classifying multimodal data. [56] Derived text clusters from LDA for multilingual hate speech detection and proved that topic modeling is not giving any major incite for classification.

2.5 TF-IDF

TF-IDF is a scoring measure broadly used in information retrieval and is planned to reflect how important a term is in a given record. TF-IDF is the most common feature extraction technique used by traditional classification methods for hate speech identification ([35, 57, 58]). TF-IDF differs from a bag of words technique or N-gram technique because the word recurrence offsets the frequency of each term in the corpus, which clarifies that a few words show up more often than expected (for example,

stop words). [59] Used N-grams and TF-IDF values to perform a comparative analysis of the machine learning models to detect hate speech and offensive language and claimed that the L2 normalization of TF-IDF outperforms the baseline results.

2.6 Part-of-speech

POS tagging is a well-known task in NLP. This approach refers to the technique of classifying words into their parts of speech. Moreover, it improves the value of the context and identifies the word's role in the context of a sentence [60]. Some authors [40] used this approach to classify racist text. PoS tagging with TF-IDF gives a better result in Indonesian Hate Speech Detection [61].

2.7 Word embedding

The most widely recognized technique in text analysis of hate content is the utilization of word references. This methodology comprises all words (the word reference) that are looked at and included in the message. The frequencies are utilized straightforwardly as features and for calculating scores. In NLP, Word embedding is used for representing of words while performing text analysis [62]. Uses word2vec embedding for extracting hate content features for grouping the semantically related words. [63] Applies attention based neural networks and word embedding feature extraction methods for classification. Hate speech detection in Spanish language [64] uses word embedding methods like Word2Vec, Glove, FasText for feature extraction.

Another procedure used in text analysis of hate content is the distance metric, which can be used to supplement word reference-based methodologies. A few investigations have called attention when the negative words are obscured with a purposeful incorrect spelling [65]. Instances of these terms are @ss, sh1t [18], nagger, or homophones, for example, joo [65].

2.8 Rule-based approach

Text analysis uses a rule-based feature selection technique for finding the regularities in data, for example, IF–THEN clauses. [66] Proves that rule-based methods do not include learning but depends on word reference of subjectivity pieces of information. This particular approach is used to extract subjective sentences to generate hate content classifiers for unlabeled corpus [48]. [67] works on the combination of dictionary-based classifiers along with rule-based classifiers to generate the semantic features for hate speech classification.

3 Automatic hate speech identification approaches

This segment describes the research on hate speech identification using various models by establishing a thorough subjective and quantitative examination of what specifies multilingual hate speech. This section compares different machine and deep learning models for detecting hate speech in multiple languages, along with the labels/classification and datasets used**.** Authors also compares the deep learning based models with shallow based [68] learning models. Figure 8 shows various traditional and deep learning models used to identify hate speeches. It has also been observed that in the past few years, most work has been done on the general English language using various machine-learning models. It has also been seen that the results of deep learning and hybrid learning models outperformed using precision and recall. Following two Sects. 3.1 and 3.2, describes the sub-domain AI approaches to multilingual data.

3.1 Machine learning approaches to hate speech detection

Several machine learning models are being created to perform tasks like classification, prediction, clustering, etc. Machine learning models are also able to take advantage of data availability. Labeled data, which is utilized for training the model to achieve reliable accuracy, comes under the classification task. The machine learning algorithms performance directly depends on how accurately the features are identified or extracted. Classification algorithms perform detection tasks after normalizing the text. The efficacy of a model on a combination of several datasets is always better than training on a specific dataset [69]. Machine-learning algorithms are categorized as supervised, semi-supervised, and unsupervised methods. Researchers used these methods to detect online hate data in various languages**.** Out of different machine learning models, researchers primarily use SVM to classify social media data as hate or non-hate. Random Forest holds the second position, and so forth [70]. From Table 5, it has been clearly seen that most research is being conducted on the general English language using supervised machine learning methods. Some authors investigated the impact of pre-processing techniques [36] to improve text quality and mainly to retain the features without losing information [71] for better performance. A piece of research on multi-class classification on some datasets [18] carried out a machine learning-based approach for classifying online user comments into four classes (Clean, Hate, Derogatory, and Profanity) on the Amazon dataset. As Supervised, the

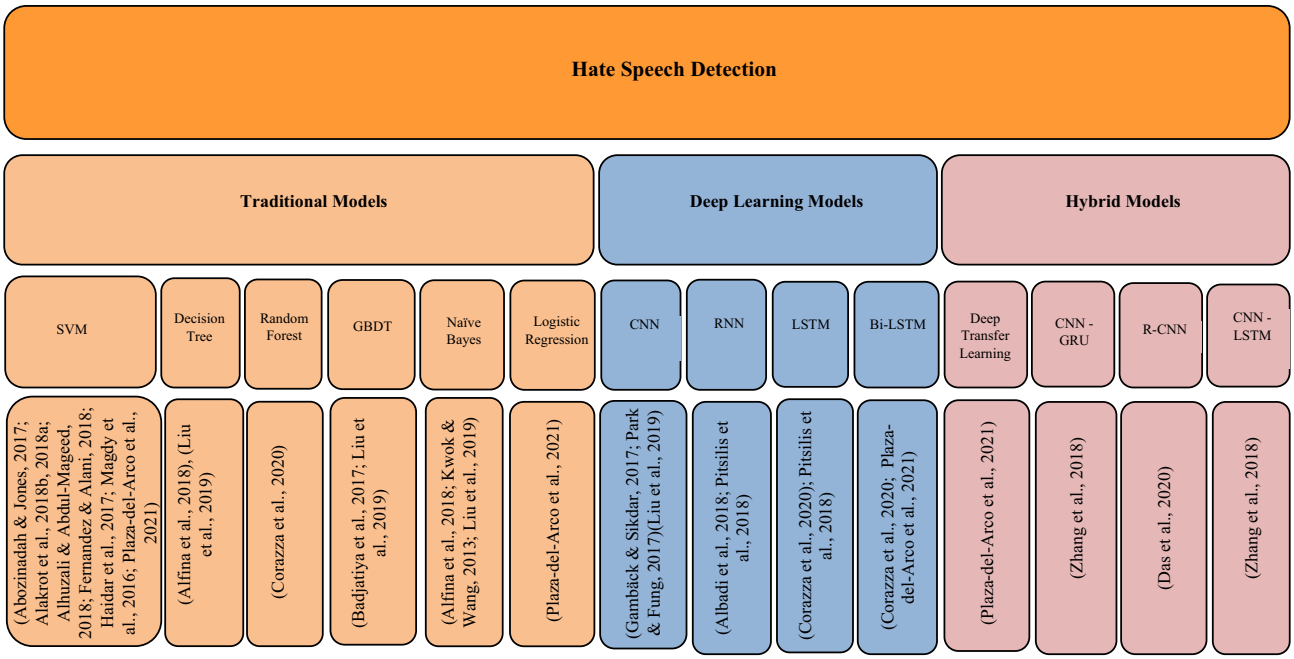

Fig. 8 Taxonomy of Hate Speech Detection considering various models

learning approach is area subordinate since it depends on manually marking a massive volume of information.

The advantage of manual labeling is its efficiency for domain-dependent tasks, while limitation occurs in execution time. The authors trained a supervised machine learning text classifier and used human-annotated data from the Twitter dataset to train and test the classifiers [72]. [72] The Bayesian logistic regression model is used to classify twitter data into hateful and antagonistic labels. Authors [73] focus on South Asian Languages for evaluating and comparing the effectiveness of various supervised techniques for hate speech detection. Semi-supervised learning algorithms are prepared to utilize both labeled and unlabeled information. Labeling information related to unlabeled information can viably upgrade efficiency. [74] Analyzed that unsupervised learning has a limited capacity to deal with limited-scale events, whereas supervised learning can adequately catch small-scale events; however, manually labeling the informational collection lowers the model scalability. [75] Utilized several choices of machine learning classifiers with various vector representations like TF-IDF, Count Vectorizer, and Word2vec as baselines with their own created Urdu dataset. KNN is the most widely used choice when a classification task is considered in a supervised learning approach [76], [77]. [78] Build an ensemble system utilizing various traditional machine learning (LR, SVM, RF, MNB, and XGB) for detecting sentiments.

When working with a particular language, the task can be considered an area-dependent task. The first racial-oriented research was carried out by [34], who carried out a supervised model to distinguish bigoted tweets [72]. Trained a supervised machine learning text classifier and used human-annotated data from Twitter to train and test the classifiers. [50] Proposed an approach for distinguishing hate speech for the Italian language on Facebook.

Authors [79] explored the capacity to recognize hate in the Indonesian language. The best outcomes from [48] were acquired when they consolidated semantic hate and theme-based components. SVM outperformed CNN and the ensemble approach in all subtasks of HaSpeeDe [80], using hate-rich embeddings [81]. Due to the many users available worldwide, multilingual hate speeches are spreading across the continent in different forms.

3.2 Deep learning approach to hate speech detection

Deep learning architectures (Table 6) represent a promising future in text analysis tasks. It relies totally upon artificial neural networks to investigate the patterns in the text with extra depth. In a couple of years, deep learning methods have outperformed machine learning methods in terms of performance due to the availability of large datasets. From the previous works, RNN and CNN are the most generally utilized deep learning models for NLP tasks. The execution of these two profound neural networks is a bit troublesome because of their intricate architectures. RNN has two sorts: LSTM and GRU, which upholds sequential architectures

Table 5 Recent state-of-the-artwork for detecting hate speech in various languages using machine learning models

Machine learning				
Methods	Ref	Models/Algorithms	Classification	Dataset
Supervised ***Methods***	General (English)			
	[82]	Fasttext	__	Youtube
				Myspace
				Slashdot
	[83]	SVM	__	Twitter
				Wikipedia
				Usenet
	[58]	SVM	(Sexuality, Race, Intelligence)	YouTube
	[84]	Multinomial- Naïve Bayes	__	Formspring
		Stochastic gradient descent		
	[72]	Bayesian logistic regression	(Hateful, Antagonistic)	Twitter
	[85]	Logistic regression	(Hateful, Clean)	Yahoo
	[86]	Logistic regression	(Hate, Not Hate)	Twitter
	[87]	SVM	(Hate, Offensive, OK)	Twitter
	[18]	NLP	(clean, hate, derogatory, profanity)	Amazon
	[12]	SVM	(Hate, Offensive, and Neither)	Twitter
		Naïve Bayes		
		Decision tree		
		Random forest		
	[88]	SVM	(Benevolent, Hostile, and others)	Twitter
		Fasttext		
	General (Roman-Urdu)			
	[75]	Logistic regression	(Hate, Offensive, and Neutral)	Twitter
		SVM		
		Random forest		
	General (Hindi-EnglisH Coded Mixed)			
	[89]	BoW	(Hate and Non-Hate)	Twitter
		Character n-grams		
		Word n-grams		
		Negation words		
		Punctuation Marks		
	Cyberbullying (Turkish)			
	[90]	Multinomial- Naïve Bayes	__	Twitter
				Instagram
	Radicalisation (English)			
	[91]	SVM	(Pro-ISIs, Non-Pro-ISIs, both, None)	Twitter
	Racial (English)			
	[34]	Naïve Bayes	(Racist, Non-Racist)	Twitter

Table 5 (continued)

Machine learning				
Methods	Ref	Models/Algorithms	Classification	Dataset
	Religious (English)			
	[65]	SVM	(Anti-Semitic, Not Anti-Semitic)	Yahoo news group
	General (Italian)			
	[50]	SVM	(Hate, Non-Hate)	Face Book
	General (Indonesian)			
	[79]	Random forest	(Hate, Non-Hate)	Twitter
		Decision tree		
	Abusive (Arabic)			
	[92]	Naïve Bayes	(Abusive, Normal)	Twitter
	[93]	SVM	(Abusive, Non- Abusive)	Twitter
	[94, 95]	SVM	(Offensive, In-Offensive)	Youtube
	Adult (Arabic)			
	[96]	SVM	(Adult, Normal)	Twitter
	Cyberbullying (Arabic)			
	[97]	SVM	(Hate, Non-Hate)	Facebook
				Twitter
	Terrorism (Arabic)			
	[98]	SVM	(Pro-ISIs, Anti-ISIs)	Twitter
Semi-Supervised	General (Spanish)			
	[64]	Logistic regression	(Hate and non-Hate)	HaterNet and HatEval
		SVM		
		LSTM		
		Bi- LSTM		
		Transfer learning		
	General (English)			
	[99]	Logistic regression	(Profane, Non-Profane)	Twitter
	[48]	Rule-based	(No Hate, Weak Hate, Strong Hate)	Blog
	Cyberbullying (English)			
	[100]	Fuzzy SVM	—	MySpace
				Slashdot
	Radicalisation (EnglisH)			
	[101]	LibSVM	(Hate, Extremism Promoting)	Twitter
	Terrorism (Arabic)			
	[102]	AdaBoost	(Jihadism, Anti-Jihadism)	Twitter
Unsupervised	General (English)			
	[15]	Match Rules	(Pejorative/ Profanities, Obscenities)	YouTube
	Cyberbullying (English)			
	[103]	K-Means	—	YouTube
				Formspring
				Twitter
	ViolenT (Arabic)			
	[104]	K-Means	(Violence, Non-Violence)	Twitter

Table 6 Generic deep learning architectures

Architectures	Key features	Merits	Demerits
Multi- layer Perceptron (MLP)	It consists of more than 2- hidden layers Widely applicable for classification and regression	High success rate	The learning process is deficient
Recurrent neural networks (RNN)	Useful where output depends on previous results Share the same weight for each step Mainly used for sequence learning problems The capability of analyzing the data stream	Good response Can memorize sequential events	Learning issue due to gradient problem
Convolution Neural Networks (CNN)	Highly applicable to visual data Every hidden layer filter transforms the inputs to the 3D output volume	Few neuron connections required	Requires large labeled datasets
Auto-encoder	The exact number of Input/output nodes Mainly used for feature extraction and space dimensionality reduction	No need for labeled data	Error-prone training
Deep belief network (DBN)	The hidden layer of each network is visible to the next layer Allows supervised and unsupervised learning	Use a greedy learning approach to initialize the stack Maximizing the likelihood inferences directly	Expensive training due to the sampling process
Deep boltzmann machine (DBM)	Uses Stochastic MAX likelihood method to maximize the lower bound of likelihood	Robust interface for indefinite output	Interfacing demands high-time complexity Parameter optimization is tedious for large datasets

though CNN has a hierarchical architecture. The efficacy of deep learning methods is directly based on the right choice of algorithms, the number of hidden layers, feature representation techniques, and learning high-level features from the data. Due to the exclusive performance factors, deep learning approaches are not better in every case than conventional methods. For hate speech identification,

[105] Utilized RNN model with word frequency and their outcomes beat the present state-of-the-art deep learning methods for hate speech identification. Deep learning techniques like automatic prediction, sentiment analysis, and classification are now being used to process hate images. [106] is a collection of memes from various social media platforms like Reddit, Facebook, Twitter and Instagram. The dataset is prepared from the 2016 U.S. Presidential Election Event, a collection of manually annotated image URLs and text embedded in the images, resulted in 743 memes. With respect to the classification of hateful memes, [107–109] presents various deep learning models to classify on memes dataset. Out of the researches done so far, [109] presents a visio-linguistic model (VILIO) for hateful memes detection and yields benchmark results. Deep learning strategies are recently being utilized in message characterization and sentiment analysis with maximum exactness [110]. Authors [78] used deep learning and transfer-based models (DNN, DNN with Embedding, CNN, LSTM, Bi-LSTM, m-BERT, distil-BERT, XML-RoBERTa, MuRIL) to reduce misclassification rate and to improve prediction rate for understanding code-mixed Dravidian languages. Table 7 shows the recent state-of-the-art for identifying hate speech using deep and hybrid learning methods while considering multiple languages like English, Italian, Arabic, Spanish, etc. As seen in Table 7, deep and hybrid learning models are evolving for classification tasks. Most works have been done on the Twitter dataset in the general English language using supervised approaches ([41, 105, 111–113]). Authors [114] show that LSTM is the most effective machine learning method for hate speech identification. [115] uses rule-based clustering methods which outperform the other baseline and state-of-the-art methods like Naive Bayes, BERT, Logistic Regression, RNN, LSTM, CNN-Glove, GRU-3-CNN in terms of AUC, Accuracy, Precision, Recall and F1-Score. [54] Performs semi-supervised multi-task learning utilizing a fuzzy ensemble approach in which they generated sequential and constructive rules to be added to the rule set and Latent Dirichlet Allocation [55] for implementing topic extraction and identifying hate speech forms

Table 7 Recent state-of-the-art for detecting hate speech in various languages via deep and hybrid learning models

Deep and Hybrid Learning				
Methods	Ref	Models/Algorithms	Classification	Dataset
Supervised methods	General (English)			
	[111]	CNN	(Hate, Non-Hate, Racism, Sexism)	Twitter
	[41]	LSTM	(Sexism, Racism, None)	Twitter
		GBDT		
	[105]	LSTM	(Sexism, Racism, None)	Twitter
		RNN		
	[113]	CNN + GRU	(Sexism, Racism, Both, Non-Hate, and Hate)	Twitter
	Religious (Arabic)			
	[119]	GRU based RNN	(Hate and Non-Hate)	Twitter
	Roman Urdu			
	[73]	Naive Bayes	(Neutral-Hostile, Simple-Complex, Offensive- Hate Speech)	Twitter
		Logistic regression		
		Random forest		
		SVM		
		CNN		
Semi-Supervised ***Methods***	[54]	Fuzzy ensemble approach	(Religious, Race, Disability, Sexual Orientation)	Twitter
		CNN		
		LSTM		
		GBT		
		SVM		
		Naive Bayes		
		Decision Tree		

for four classes from the Twitter dataset. The authors also proved that the fuzzy-based approach [54], metaheuristic approaches ([116, 117]) and Interpretable approach [118] had outperformed other techniques with high detection rate. [119] performs a supervised hybrid learning approach for classifying hate speech into two labels, specifically in the Arabic dialect. Moreover, Baysian attention networks, which follow the architecture of transformer models, are implemented for multilingual (English, Croatian and Slovene) contexts [120].

3.3 Merits and demerits of various models

Hate speech identification is a very much prevalent research field now a day. Researchers worldwide are experimenting with various models for specific field detection with numerous advantages and disadvantages. [121] implemented CNN and BERT models and proved efficient accuracy with intra-domain and cross-domain datasets. ([122, 123]) used FCM, SCM, and TKM for concatenating/combining features extracted from CNN and R-CNN, respectively, on textual and visual Twitter data, giving an advantage resulting in good accuracy compared to other baseline models. [124] used ELMO, BERT, and CNN to improve classification results but with higher time complexity. [125] also have a limitation of higher computational complexity, yet they created their detection system and implemented a deep belief network on labeled and unlabeled data. [116] presents two metaheuristic optimization algorithms (Ant Lion Optimization and Moth Flame Optimization) for the first time to solve Hate Speech Detection Problem with an efficient accuracy of above 90%. [117] implemented enhanced seagull optimization algorithm on CrowdFlower and StormFront datasets claiming the outperforming scores of above 98%. The pros and cons of the latest state-of-the-art works on hate speech detection are shown in Table 8.

4 Hate speech datasets

Social media platforms are prevalent nowadays, and users are increasing tremendously. Due to this, hate speech contents in various forms are at its peak. The presence of a massive amount of data on the web and collecting a good and relevant amount of data is challenging for researchers. Social media stages provide simple and easy approaches to gathering data using their APIs [21]. However, data assortment is not confined to APIs only. Figure 9 shows various ways of accessing data from social media.

Table 8 Merits and demerits depicted from the latest state-of-the-art works in hate speech detection

Refs	Objective	Features	Models	Merits	Demerits
[126]	To include the diacritics in detecting Vietnamese hate content	One hot embedding	● RNN ● LSTM ● GRU ● BERT	Results from models with diacritics generation outperformed others without diacritics generation	Only character-level feature is applied for implementation
[63]	Sentiment knowledge-based hate speech detection	● Word Embedding ● N-grams	Attention-based neural network	Including sentiments increases the overall performance	Small-scale datasets ate chosen for system generation can lead to uncovering bias
[115]	To propose a method for dealing with the problem of hate speech classification	●Tri-gram ●Wordngram	Rule-based clustering	Robustness to data imbalance	Complexity is directly proportional to the size of the dataset
[127]	To extract multimodal information	Character embedding	● CNN ● Attention-based Bi-GRU	High attention score for social context feature	Misclassification due to a few instances of hate words in the dataset
[128]	Hate content detection on textual data, along with image processing	TF-IDF	● CNN ● VGG ● RNN ● LSTM	Good performance on the combination of image, text, and captions	_
[129]	Cross-Lingual hate speech detection using capsule network	FastText	● CNN ● LSTM ● Bi-LSTM	Capsule network learning outperforms the other state-of-the-art models for multiple language pairs	Non-translation of words used in hashtags
[116]	Metaheuristic Optimization based Automatic detection of hate content	● BoW ● TF-IDF ● Word2vec	● Ant-Lion Optimization ● Moth- Flame Optimization	Metaheuristic Optimization-based approach has shown the overall increased performance	Higher time complexity
[130]	Abusive context detection in Greek contents on Refugees and Migrants	● Unigram ● Bigram ● Trigram	● BERT ● Resnet	Good accuracy achieved for specific domain content	Social-based information is missing
[131]	To identify Arabic hate content using multi-task learning	Word Embedding	● BERT	The proposed model outperformed existing models already applied to Arabic datasets	Contextual representation is not good while generating outcomes
[121]	To analyze a large dataset of about 1 million realistic hate and non-hate sequences and highlight the problems that may occur when training a hate speech classifier on small datasets	● POS ● Sentiment features ● TF-IDF	● CNN ● BERT	Good accuracy with intra-domain as well as cross-domain datasets	Implemented on textual tweets only
[64]	Hate speech detection for the Spanish language	● Word2vec ● GloVe ● FastText ● TF-IDF	● Logistic Regression ● SVM ● LSTM ● CNN ● Bi-LSTM ● Transfer Learning	Transfer Learning achieves the best results	Limited to training the model on monolingual language only

Table 8 (continued)

Refs	Objective	Features	Models	Merits	Demerits
[132]	To detect hate speech with their proposed system that classifies the text into three classes with 98.71% accuracy	●Sentimental ● Unigram ● Pattern	● Deep classifiers ● Gradient Descent Process ● Ensemble Classifiers ● Logistic Regression	● Proposed method gives good accuracy with minimum loss function values ● Used ensemble approach for the proposed system results in improving the overall hate speech recognition rate	The proposed system is designed and implemented on textual data only
[124]	To improve the results of the classification	Word2vec	● Elmo ● BERT ● CNN	Provides comparable suitability on feature sets	Time complexity is high
[133]	Identification of multilingual (English, Italian, and German) hate speech	● Word Embedding ● N-grams ●Social network- specific feature ● Emoji Embedding ● Emotion Lexica ● FastText	● LSTM ● GRU ● Bi-LSTM	LSTM yields better results on limited length of tweets than Bi-LSTM	Adding unigram and bigram as features with LSTM decreases the performance of all three languages
[125]	To create a system detecting Hate Speech	GloVe	Deep belief network	Deep learning includes supervised and unsupervised algorithms that take both labeled and unlabeled data	The process is expensive due to the sampling technique
[122]	To distinguish hate content in three data sources: the tweet picture, the tweet text, and the text showing up in the image	● Feature Concatenation Model (FCM) ● Spatial Concatenation Model (SCM) ● Textual Kernels Model (TKM)	● CNN ● LSTM	Multi-domain detection with good accuracy	● Multimodal data mainly contains textual processing ● Relations between textual and visual elements are very complex
[123]	To fetch the actual caption and then combine it with multimodal representation to perform binary classification, mainly focused on textual and visual modality	● Feature Concatenation Model (FCM) ● Spatial Concatenation Model (SCM) ● Textual Kernels Model (TKM)	R-CNN	Good accuracy when compared to baseline models	Establishing relations between textual and visual elements is very complex
[134]	To propose a multi-task model for catching the standard features and task-specific features from five labels (Sexism, Racism, Hate, Offensive, Harassment)	● Word Embedding ● CBOW ● Character embedding ● Word2vec	● LSTM ● CNN ● GRU	● Removes the data scarcity problem ● Achieves performance improvement statistically over single task-based systems	Domain-specific embedding is missing

Table 8 (continued)

Refs	Objective	Features	Models	Merits	Demerits
[54]	Setting multiple tasks for classifiers training	_	● Fuzzy Ensemble approach ● CNN ● LSTM ● LDA	● Proposed fuzzy methodology is appropriate for dealing with the diversity as shown by topic detection ● Proposed approach gives an intensity score for each kind of hate speech from a tweet ● Enables the analysis of the correlation between various labels	Approval of fuzzy-based approaches requires comprehensive testing
[135]	To identify hate speech in long archives	● TF-IDF ● Char quad-gram ● Word unigram ● Lexicon Features	● Naive Bayes ● SVM	Accuracy achievement is suitable even for long documents	● Data set is too small ● The features that ascertain the number of words with a positive and negative opinion, ignoring the negative opinions, drive the framework to recognize the sentiment of the words inaccurately
[89]	To automatically detect hateful content on Twitter from code-mixed text	● BoW ● Character n-grams ● word n-grams ● Negation words ● Punctuation marks	● Sub-word level LSTM ● Hierarchical LSTM	Character n-grams feature gives better results	Word and document features do not give better results
[136]	Focus on bias seriousness rather than bias removal from unstructured text data	● PoS ● WordNet ● Centroid Embedding	● Logistic regression ● Multi-layer Perceptron (MLP) ● CNN	Centroid embedding helps in getting bias-free vector representations by calculating the centroid of an adequate number of words, consequently giving improved performance	Bias mitigation ordinarily doesn't prompt any significant change in the ROC-AUC esteems, and it only decreases bias in the learning
[137]	Brazilian Portuguese text classification for detecting hate speech	TF-IDF	● Multinomial Naïve Bayes ● Random Forest ● SVM	SVM is giving the highest performance of about 95%	No relationship between semantics
[138]	To characterize whether a message in the sentence contains components of hate speech or not	Word2vec	Deep learning with RNN (LSTM Based)	● LSTM can conquer the vanishing gradient on standard RNN from long-haul conditions learning ● LSTM is proven to be more viable than standard RNN	Training parameters like learning rate affect the performance of the overall system
[41]	Handling the complexity of natural language constructs with multiple deep learning architectures	● Char n-grams ● TF-IDF ● BOW	● CNN ● LSTM ● Logistic Regression ● Random Forest ● SVM ● GBDT	● comparable words obtained using deep neural network learned embeddings clearly show the hatred towards the objective words ● Minimization of bogus negatives	Concatenations of CNN, LSTM, and FastText embedding as components for GBDTs didn't prompt better outcomes

Table 8 (continued)

Refs	Objective	Features	Models	Merits	Demerits
[139]	Capturing the biases in data annotations and detecting hate content with efficient accuracy	● Word Embedding	● BERT ● Bi-LSTM ● CNN	Enhancing the performance of hate speech detection system	Time complexity may be high

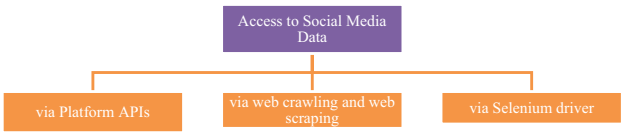

Fig. 9 Prominent ways to access data from social media

4.1 Dataset description

Hate speech identification has become a crucial task in many languages and fields. Recordings play a fundamental role in disseminating content as they can contact a vast crowd, including little youngsters. Appraisals say that 1 billion hours of videos are observed every day on YouTube alone. Detecting hate speech is important to give youngsters a protected climate and a healthy environment for clients in general. Until now, the text has been the most famous configuration utilized by researchers working on it. Subsequently, most current works summarize recognizing hate speech in the text (social platform posts, news remarks, tweets, and so on). While hate speech detection methods primarily use textual inputs, few research contributions exist toward multimodal hate speech detection. Several authors have generated multi-class/ multi-label datasets in various languages for curbing hate content on social media. Hate speech detection (HaSpeeDe) is the prevalent shared task organized within Evalita 2018 [80] and consists of manually annotating Italian messages taken from Twitter and Facebook. This shared task was further categorized into three sub-tasks: HaSpeeDe-FB, HaSpeeDe-TW, and Cross-HaSpeeDe.

4.2 Datasets challenges

- The available and widely used datasets ([38, 140]) have issues in their subjectiveness which introduces bias in the performances. Hate Speech datasets are affected mainly by social, behavioral, racial, temporal, and content production biases [141]. Data imbalance due to bias may lead to misclassification [142].
- One of the significant issues is the unlabeled non-English datasets. Few manually annotated labeled datasets were released for detecting offensive language and hate speech [78]. Moreover, Multilingual hate speech datasets can also share the writing of other languages. For example, a dataset can contain Farsi and Arabic tweets while creating an Urdu hate speech and offensive language dataset [75]
- The problem also arises when the web address of datasets changes [143]. Authors who create a new dataset do not publish those [73].

- Twitter (Lenient data usage policies) is the most prevalent platform. However, the Twitter resources are significant because of the exceptional classification of the Twitter posts, which is limited to short text. Henceforth, contents from other media stages are longer and can be a piece of more extensive conversation in hate speech.
- Datasets differ in their size, degree, and features of the data annotated, which prompts the issue of irregularity in the quantity of hate and non-hate texts within datasets. For example, on a social stage like Twitter, hate speech occurs at a shallow rate contrasted to non-hate. Therefore, researchers can gather data from social media platforms with no character length limit.

Given the above challenges, making data available in a superior arrangement for demand research is essential. Table 9 represents various benchmark models on multiple datasets. Commonly used datasets ([12, 38], Gomez et al., 2020)) benchmarks are also shown in the table.

The overall description of datasets regarding modalities (T-Text, I-Images, V-Videos), classes/ labels, languages, etc., are tabulated in Table 10.

5 Evaluation and performance measures

As datasets play a significant role in testing the performance of hate speech detection. The better-normalized dataset is the best performance an algorithm will give. In this section, metrics for evaluation of machine and deep learning techniques used are F_1-Score, Recall, and Precision, and performance measurement metrics are accuracy and AUC (Area under Curve).

5.1 Evaluation metrics

Most state-of-the-art have utilized accuracy, F_1-Score, Precision, Recall Metrics, and ROC to assess performance metrics. [132] represents several loss functions like mean MSE, cross-entropy, and likelihood loss to anticipate hate speech in the most used dataset, such as Twitter. The loss function is the difference between the predicted value denoted by ŷ and labeled value denoted by y. [143] use four different strong performances indicators (KPIs), which are the percentage of True Positive, the precision, the recall, & F_1- Score defined using Eq. 1:

$$F_1 - Score = 2 \times \frac{P - R}{P + R} \tag{1}$$

[132] uses several loss functions such as Mean Square Error Rate (MSE) [163], given in Eq. 2, Cross-Entropy Loss (CEL) [164] as in Eq. 3, and Likelihood Loss (L) [165] in Eq. 4 to approximate the accuracy of the proposed model in identifying hate speech on the Twitter dataset.

$$MSE = \frac{1}{N}\sum_{i=1}^{N}\left(y_i - \hat{y}_i\right)^2 \tag{2}$$

Where,

N denoted the quantity of information relative to the predicted value ŷ and labeled y.

$$CEL = \sum_{c=1}^{M} y_{o,c} Log\left(P_{o,c}\right) \tag{3}$$

where,

M represents classes and related features,

O denotes the observed value of the particular class-related feature,

P represents the prediction probability value relevant to O,

Log is the logarithmic function, and.

Y gives the output value as binary values of a specific class.

Table 9 Benchmark models on datasets

Dataset	Refs	Benchmark models	F1-score	Accuracy	Precision	AUC- ROC
Ethos_binary	[144]	Bi-LSTM + Static BE	0.7971	0.8015	0.8037	_
Maha-Hate	[145]	BERT	_	0.909	_	_
HateXplain	[146]	BERT + HateXplain [Attn]	0.687	0.698	_	0.851
APEACH	[147]	BERT	0.8424	_	_	_
Told-Br	[148]	Multilingual BERT	0.75	_	_	_
Hateful memes	[109]	Vilio	_	_	_	0.825
OffVidPT-2/ OffVidPT-3	[149]	M-CNN	0.74	_	_	0.78
MMHS150K	[122]	TKM	0.70	68.2	_	0.731
t-Davidson	[12]	BERTbase + CNN	0.92	_	0.92	_
WaseemHavoy	[38]	BERTbase + CNN	0.88	_	0.89	_

Table 10 Dataset description in terms of size, labels, languages, and modalities

Source	Name of the dataset	Refs	Size	Classes/ labels	Language	Modality
Youtube and Reddit comments	Multi-labEl haTe speecH detectiOn dataSet (ETHOS)	[144]	998	Ethos_Binary ● Hate ● Non-Hate Ethos_Multi-Label ● Violence ● Non-Violence ● Gender ● Race ● National origin ● Disability ● Religion ● Sexual Orientation	English	T
Line today	Hate speech	[46]	~12 K and ~1 M	● Hate ● Offensive ● Normal	Taiwan	T
Twitter	ToxiGen	[150]	~2 M	● Toxic ● Benign	English	T
Twitter	Slovenian twitter Dataset 2018–2020 1.0	[151]	~12 M	● Acceptable ● Inappropriate ● Offensive ● Violent	Slovenian	T
Crowd sourcing platforms	APEACH	[147]	~11 K	● Hate ● Non-Hate	Korean	T
Twitter	Maha-Hate	[145]	25 K	● Hate ● Offensive ● Profane ● Not	Marathi	T
Twitter	Urdu hate speech and offensive language	[75]	~11 K	● Hate ● Offensive ● Neutral	Roman-Urdu	T
Twitter and GAB	HateXplain	[146]	9055 twitter posts, 11,093 GAB posts	● Hate ● Offensive ● Normal	English	T
Handcrafted	HatemojiCheck	[152]	~4 K Test cases	● Hateful ● Not Hateful	English	I
Youtube and Facebook	HS-BAN	[153]	50 K	● Hate ● Non-Hate	Bangla	T
Twitter	ToLD-Br	[148]	21 K	● Toxic ● Non- Toxic	Portuguese	T
Facebook	Hateful Memes	[108]	10 K	● Hateful ● Not Hateful	English	I+T
Youtube	OffVidPT-2/ OffVidPT-3	[149]	400	● Offensive ● Non- offensive	Portuguese	V
Twitter	MMHS150K	[122]	150 K	● No attack ● Racism ● Sexism ● Homophobic ● Religion-based attacks ● Any community attacks to other attacks	English	I+T
Bengali wikipedia dump and Bengali news articles	Bengali_hate_speech v1.0	[154]	3418 Samples	● Personal hate ● Political hate ● Religious hate ● Geopolitical hate ● Gender Abusive hate	Bengali	T

Table 10 (continued)

Source	Name of the dataset	Refs	Size	Classes/ labels	Language	Modality
Youtube	Hate_speech_dataset_videos	[155]	300	● Normal ● Hateful (Racist, Sexist)	English	V
Wikipedia comments + Civil comments	Detoxify	_	~55 K	● Very toxic ● Toxic ● Hard to say ● Non- toxic	English, French, Spanish, Italian, Portuguese, Turkish, Russian	T
Twitter	OffensEval2020	[156]	~9 M	● Offensive ● Non-Offensive	Arabic, Danish, English, Greek, and Turkish	T
Twitter	OffensEval2019	[157]	~14 K	● Offensive ● Non-Offensive	English	T
Facebook and YouTube	T-HSAB	[158]	~6 K	● Normal ● Abusive ● Hate	Tunisian Arabic	T
Twitter	L-HSAB	[159]	~6 K	● Normal ● Abusive ● Hate	Levantine Arabic	T
Twitter	HatEval19	[140]	19 K	● Hate ● Non-Hate	Spanish, English	T
Twitter	Peer-to-Peer Hate	[160]	28 K	● Hate ● Non-Hate	English	T
Twitter and Facebook	Evalita2018	[80]	4 K posts	● No-Hate ● Weak- Hate ● Strong- Hate	Italian	T
Twitter	Twitter Abusive Behaviour	[161]	80 K	● Normal ● Spam	English	T
Twitter	t-Davidson	[12]	25 K	● Hate ● Offensive ● Neither	English	T
News articles	BEEP	[161]	9381 Human Labeled comments & 2,033,893 Unlabeled comments	● Hate ● Offensive but not hate ● None	Korean	T
Twitter	Arabic offensive	[162]	1.1 K and 32 K	● Obscene ● Offensive ● Clean	Modern Standard Arabic	T
Twitter	WaseemHavoy	[38]	~17 K	● Racist ● Sexist ● Neither	English	T

$$L = -\frac{1}{n}\Sigma_{i=1}^{n} \log(\hat{Y}_{(i)}) \tag{4}$$

where,

n gives the number of classes.

y denotes the output.

5.2 Performance of popular hate speech detection methods

Most state-of-the-art on hate speech detection used precision, recall, and F_1-score for evaluation; others used AUC and accuracy for performance measures due to some imbalanced datasets. Table 11 gives evaluation and performance measures from some state-of-the-art works based on accuracy, precision, recall, F_1 score, and AUC. As seen in Table 11, Precision, Recall, and F_1-score are the metrics used by most authors as they provide better insights into the prediction than accuracy and AUC. Deep-learning models have outperformed machine-learning models with high-performance metrics, as presented in Table 11.

Table 11 Performance comparison

Ref	Algorithms	Accuracy	Precision	Recall	F1-Score	AUC
[115]	Rule-based clustering	0.94	0.92	0.91	0.92	0.96
[64]	BERT, XLM, BETO	–	–	–	0.772	–
[149]	BERT, CNN, Random forest, Naive bayes	–	–	–	0.74	0.78
[132]	Deep learning	0.9873	–	–	–	–
[166]	Linear SVM classifier	0.90	0.88	1.0	0.90	–
	Naive bayes classifier	0.92	0.899	0.964	0.924	–
[167]	BERT	–	0.86	0.94	0.77	–
[143]	Random forest, SVM, and J48graft [168]	–	0.88	0.87	0.87	–
[41]	Logistic regression, SVM, DNN, CNN, Random forest, GBDT	–	0.93	0.93	0.93	–
[12]	Logistic regression, SVM	–	0.91	0.90	0.90	–
[50]	SVM, LSTM	-	0.83	0.87	0.85	–
[49]	One-class classifiers, Decision tree, Naïve bayes, Random forest	–	0.73	0.86	–	–
[18]	Skip bigram model	–	0.83	0.83	0.83	–
[110]	Deep learning	0.91	–	–	–	–
[38]	Logistic regression	–	0.72	0.77	0.73	–
[33]	SVM, Random forest, Decision tree	–	0.79	0.59	0.68	–
[169]	SVM	–	0.49	0.43	0.46	–
[170]	Random forest, Decision tree, SVM, Bayesian LR	–	0.89	0.69	0.77	–
[85]	Logistic regression	–	–	–	–	0.80
[39]	Naïve Bayes	–	0.97	0.82	–	–
[72]	Decision tree, Random Forest, SVM	–	0.89	0.69	0.77	–
[34]	Naïve bayes	0.73	–	–	–	–
[65]	SVM	0.94	0.68	0.60	0.63	–

6 Discussion

Hate speech is an emerging issue in social media sites now days. The identification of hate content is one of the major concern and challenge for the researchers. The proposed article shows a systematic order of state-of-the-art works done so far. Feature extraction methods such as distance metric and multimodal information, especially related to hate content detection, are not used to the best of my knowledge. Both directional models such as RNN and LSTM, and non-directional models such as Transformers ad BERT are utilized in identifying hate content. Although machine learning has shown its growth in the last decade, but NLP has also shown the steepest growth by including the evolutionary models such as BERT and Transformers. The variants of BERT like ALBERT, RoBERTa, DistilBERT etc. are used increasingly in solving real life problems because of their self-attention mechanism. The researchers also use LSTM model as it yields subsequently higher results than BERT on small datasets does. The pros and cons of various models are described in detail in the Sect. 3.3. From the last two years, the metaheuristic optimization algorithms such as Ant Lion optimization, Flame Moth optimization, Seagull optimization are also considered in this area with the promising results.

7 Findings and conclusion

Hate speech attempts to marginalize different classes and groups of persons already in the minority due to their race, language and religion. This article reviewed the most outstanding work on automatic hate speech identification. Firstly, we introduced some state-of-the-art hate speech definitions and analysis on the basis of some specific dimensions. This survey also highlights some of the NLP aspects in this area. There is also a good comparison between hate speech definition and definitions of various hate forms. Then, we presented a taxonomy of automatic hate speech detection, including sub-domains of AI approaches. Metaheuristic algorithms which are very new with context of hate speech detection are also mentioned in this manuscript. Paper also covers various works done in multilingual and multimodal hate speech detection along with various datasets description.

8 Future trends

Our studies recommend some future trends from the following angles:

- We have explored some standard hate speech datasets along with their key features, classifications, objectives, and types of data format available. Most datasets are available in textual form. Very few datasets like (MultiOFF, MMHS150K) are found on hateful memes. No video dataset is found publicly as per the best of my knowledge. So, creating a new dataset of images and videos can be further seen as a future task. Moreover, numerous analysts look at the significant challenge of the datasets availability as few publicly available datasets exist. Authors do not use them, and if they create a new dataset, they do not publish them, making it too difficult to compare results and conclusions.
- Choosing informative, independent, and discriminating features are crucial in classification problems. This paper covers commonly used text analysis features for hate classification tasks. Hence, automatic feature engineering for generating specific hate features can be a future aspect.
- For the last few years, authors have been focusing on multilingual hate speech identification by creating their datasets. But very few labeled datasets are found in non-English languages. Various benchmark models can be applied to non-English labeled datasets also.
- We have also covered important work for hate speech identification in various languages. Hence, the models that understood only the English language are not efficient in processing the input from different Indian languages [78]. So, building a system for code-mixed languages can be considered a future aspect.
- Nowadays, emojis are also used to show feelings and attitudes in users minds [36], and they are vital elements in delivering hate or offensive content over social media. Hence, pre-processing emojis text can be seen as a different area so that there can be an improvement in aggression detection.
- There are significantly fewer works on neutral tagged content [75]. So, devising a new method for handling neutral tagged contents in multi-label datasets in a better way can be considered a future job.
- In our systematic survey, we tracked that most work portrays techniques, separated features, and models utilized. In any case, it is uncommon to discover jobs with available public repositories. More sharing of code, calculations, measures for feature extraction, and stages can assist the area with advancing rapidly.
- In this article, some of the metaheuristic optimization approaches are also coined to solve hate speech detection. Apart from the mentioned metaheuristic approaches such as ALO and FMO, Parameter Optimization approach can also be implemented in future for solving the hate content detection.

Author contributions Anusha Chhabra: Software, Validation, Investigation, Data Curation, Writing – Original Draft, Visualization.Dinesh Kumar Vishwakarma: Conceptualization, Methodology, Formal Analysis, Resources, Writing – Review & Editing, Supervision, Project Administration, Funding Acquisition.

Declarations

Conflict of interest The authors declare no competing interests.

References

1. M. Bose, "South Asia Journal," 2020. http://southasiajournal.net/india-senior-bjp-leaders-are-giving-india-a-free-tutorial-in-hate-speech/
2. R. E. Brannigan, J. L. Moss, and J. Wren, "The conversation," *Fertility and Sterility*, 2015. https://theconversation.com/hate-speech-is-still-easy-to-find-on-social-media-106020.
3. M. Suster, "Business Insider," *Amazon's Game-Changing Cloud Was Built By Some Guys In South Africa*, 2010. https://www.businessinsider.com/736-of-all-statistics-are-made-up-2010-2?r=US&IR=T%0Ahttp://www.businessinsider.com/amazons-game-changing-cloud-was-built-by-some-guys-in-south-africa-2012-3.
4. A. Schmidt and M. Wiegand, "A Survey on Hate Speech Detection using Natural Language Processing," *Soc. 2017 - 5th Int. Work. Nat. Lang. Process. Soc. Media, Proc. Work. AFNLP SIG Soc.*, no. 2012, pp. 1–10, 2017, doi: https://doi.org/10.18653/v1/w17-1101.
5. Cohen-Almagor, R.: Freedom of Expression v. Social Responsibility: Holocaust Denial in Canada. J. Mass Media Ethics Explor. Quest. Media Moral. **28**(1), 42–56 (2013). https://doi.org/10.1080/08900523.2012.746119
6. Delgado, R., Stefancic, J.: Images of the outsider in American law and culture: can free expression remedy deeply inscribed social Ills? Fail. Revolutions **77**(6), 3–21 (2019). https://doi.org/10.4324/9780429037627-2
7. Techterms.com, "Facebook Definition," 2008. http://www.techterms.com/definition/facebook.
8. Youtube, "YouTube hate policy," 2019. https://support.google.com/youtube/answer/2801939?hl=en.
9. Facebook, "What does facebook consider hate speech?," 2013. https://www.facebook.com/help/135402139904490.
10. Nockleby, J.T.: Hate Speech. In: Levy, L.W., Karst, K.L., et al. (eds.) Encyclopedia of the American Constitution, pp. 1277–1279. Macmillan, New York (2000)
11. Twitter, "Twitter_Hate Definition [online]," 2017. https://support.twitter.com/ articles/.
12. Davidson, T., Warmsley, D., Macy, M., Webe, I.: Automated hate speech detection and the problem of offensive language. Proc. 11th Int. Conf. Web Soc. Media, ICWSM **11**(1), 512–515 (2017)
13. de Gibert, O., Perez, N., García-Pablos, A., Cuadros, M.: Hate Speech Dataset from a White Supremacy Forum. arXiv preprint arXiv (2019). https://doi.org/10.18653/v1/w18-5102
14. Fortuna, P., Nunes, S.: A survey on automatic detection of hate speech in text. ACM Comput. Surv. (2018). https://doi.org/10.1145/3232676
15. Chen, Y., Zhou, Y., Zhu, S., Xu, H.: Detecting offensive language in social media to protect adolescent online safety. Proc. - 2012 ASE/IEEE Int. Conf. Privacy, Secur. Risk Trust 2012 ASE/IEEE Int. Conf. Soc. Comput. Soc (2012). https://doi.org/10.1109/SocialCom-PASSAT.2012.55

16. Thompson, N.: Equality, Diversity and Social Justice. Sixth, PALGRAVE MACMILLAN (2016)
17. Guermazi, R., Hammami, M., Ben Hamadou, A.: Using a semi-automatic keyword dictionary for improving violent web site filtering. Proc. - Int. Conf. Signal Image Technol. Internet Based Syst. SITIS (2007). https://doi.org/10.1109/SITIS.2007.137
18. Nobata, C., Tetreault, J., Thomas, A., Mehdad, Y., Chang, Y.: "Abusive language detection in online user content." 25th Int World Wide Web Conf. WWW **2016**, 145–153 (2016). https://doi.org/10.1145/2872427.2883062
19. Google and Jigsaw, "Perspective API," 2017. https://perspectiveapi.com.
20. Asia Centre, "Hate speech in Southeast Asia. New forms, old rules," 2020. [Online]. Available: https://asiacentre.org/wp-content/uploads/2020/07/Hate-Speech-in-Southeast-Asia-New-Forms-Old-Rules.pdf.
21. Lomborg, S., Bechmann, A.: Using APIs for data collection on social media. Inf. Soc. **30**(4), 256–265 (2014). https://doi.org/10.1080/01972243.2014.915276
22. Facebook, "Facebook [Online]," 2022. https://www.facebook.com/about/privacy/update.
23. Lindsey, "Instagrams-Api," 2022. https://rapidapi.com/blog/how-to-navigate-and-connect-to-instagrams-api/ (accessed Mar. 09, 2022).
24. Twitter_Rules, "https://help.twitter.com/en/rules-and-policies/twitter-api," 2022. https://help.twitter.com/en/rules-and-policies/twitter-api.
25. M. S. Jahan and M. Oussalah, "A systematic review of Hate Speech automatic detection using Natural Language Processing," arXiv:2106.00742v1, 2021, [Online]. Available: http://arxiv.org/abs/2106.00742.
26. Dhanya, L.K., Balakrishnan, K.: "Hate speech detection in asian languages: a survey", ICCISc 2021–2021 Int. Conf. Commun. Control Inf. Sci. Proc. (2021). https://doi.org/10.1109/ICCISc52257.2021.9484922
27. Poletto, F., Basile, V., Sanguinetti, M., Bosco, C., Patti, V.: Resources and benchmark corpora for hate speech detection: a systematic review. Lang. Resour. Eval. **55**(2), 477–523 (2021). https://doi.org/10.1007/s10579-020-09502-8
28. N. Naaz, Y. Malik, and K. P. Adhiya, "Hate Speech Detection in Twitter-A Survey," *Int. J. Manag. Technol. Eng.*, vol. 9, no. 1, pp. 1272–1277, 2019, [Online]. Available: http://www.ijamtes.org/gallery/147-jan19.pdf.
29. Robinson, D., Zhang, Z.: Detection of hate speech in social networks: a survey on multilingual corpus. Comput. Sci. Inf. Technol. (2020). https://doi.org/10.5121/csit.2019.90208
30. Alrehili, A.: Automatic hate speech detection on social media: A brief survey. Proc. IEEE/ACS Int. Conf. Comput. Syst. Appl. AICCSA (2019). https://doi.org/10.1109/AICCSA47632.2019.9035228
31. Mohiyaddeen and Dr: Shifaulla Siddiqui, "Automatic hate speech detection: a literature review." Int. J. Eng. Manag. Res. **11**(2), 116–121 (2021). https://doi.org/10.31033/ijemr.11.2.17
32. Araque, O., Iglesias, C.A.: An Ensemble Method for Radicalization and Hate Speech Detection Online Empowered by Sentic Computing. Cognit. Comput (2022). https://doi.org/10.1007/s12559-021-09845-6
33. Burnap, P., Williams, M.L.: Us and them: identifying cyber hate on Twitter across multiple protected characteristics. EPJ. Data Sci. (2016). https://doi.org/10.1140/epjds/s13688-016-0072-6
34. Kwok, I., Wang, Y.: Locate the hate: Detecting tweets against blacks. Proceedings of the 27th AAAI Conference on Artificial Intelligence, AAAI (2013). https://doi.org/10.1609/aaai.v27i1.8539
35. Baydoğan, V.C., Alatas, B.: Çevrimiçi Sosyal Ağlarda Nefret Söylemi Tespiti için Yapay Zeka Temelli Algoritmaların Performans Değerlendirmesi. Fırat Üniversitesi Mühendislik Bilim. Derg. **33**(2), 745–754 (2021). https://doi.org/10.35234/fumbd.986500
36. Husain, F., Uzuner, O.: "Investigating the Effect of Preprocessing Arabic Text on Offensive Language and Hate Speech Detection", *ACM Trans*. Asian Low-Resource Lang. Inf. Process. **21**(4), 1–20 (2022). https://doi.org/10.1145/3501398
37. Chowdhury, A.G.: ARHNet - Leveraging Community Interaction For Detection Of Religious Hate Speech In Arabic". Proc. 57th Annu. Meet. te Assoc. Comput. Linguist. **2019**, 273–280 (2019)
38. Z. Waseem and D. Hovy, "Hateful Symbols or Hateful People? Predictive Features for Hate Speech Detection on Twitter," pp. 88–93, 2016, doi: https://doi.org/10.18653/v1/n16-2013
39. Liu, S., Forss, T.: Combining N-gram based similarity analysis with sentiment analysis in web content classification. KDIR 2014 - Proc. Int. Conf. Knowl. Discov. Inf. Retr (2014). https://doi.org/10.5220/0005170305300537
40. Greevy, E., Smeaton, A.F.: Classifying racist texts using a support vector machine. Proc. Sheff. SIGIR - Twenty-Seventh Annu. Int. ACM SIGIR Conf. Res. Dev. Inf. Retr (2004). https://doi.org/10.1145/1008992.1009074
41. Badjatiya, P., Gupta, S., Gupta, M., Varma, V.: Deep learning for hate speech detection in tweets. 26th Int. World Wide Web Conf. 2017, WWW 2017 Companion **2**, 759–760 (2017). https://doi.org/10.1145/3041021.3054223
42. Katona, E., Buda, J., Bolonyai, F.: Using N-grams and Statistical Features to Identify Hate Speech Spreaders on Twitter. CEUR Workshop Proc. **2021**, 2025–2034 (2021)
43. Mehdad, Y., Tetreault, J.: "Do Characters Abuse More Than Words? Dialogue. SIGDIAL 2016 - 17th Annual Meeting of the Special Interest Group on Discourse and Dialogue, Proceedings of the Conference (2016). https://doi.org/10.18653/v1/w16-3638
44. Mulki, H., Ali, C.B., Haddad, H., Babao, I.: Tw-StAR at SemEval-2019 Task 5: N-gram embeddings for Hate Speech Detection in Multilingual Tweets. Proc. 13th Int Work. Semant. Eval. **2019**, 503–507 (2019)
45. S. N. Group, "Stanford NLP Group," 2005. https://nlp.stanford.edu/.
46. Wang, C., Day, M., Wu, C.: Political Hate Speech Detection and Lexicon Building : A Study in Taiwan. IEEE Access **10**, 44337–44346 (2022). https://doi.org/10.1109/ACCESS.2022.3160712
47. Liu, S., Forss, T.: "New classification models for detecting hate and violence web content Knowl. IC3K 2015 - Proc. 7th Int. Jt. Conf. Knowl. Discov. Knowl. Eng. Knowl. Manag **1**, 487–495 (2015). https://doi.org/10.5220/0005636704870495
48. Gitari, N.D., Zuping, Z., Damien, H., Long, J.: A lexicon-based approach for hate speech detection. Int. J. Multimed. Ubiquitous Eng. **10**(4), 215–230 (2015). https://doi.org/10.14257/ijmue.2015.10.4.21
49. S. Agarwal and A. Sureka, "Characterizing Linguistic Attributes for Automatic Classification of Intent Based Racist/Radicalized Posts on Tumblr Micro-Blogging Website," 2017, [Online]. Available: http://arxiv.org/abs/1701.04931.
50. Del Vigna, F., Cimino, A., Dell'Orletta, F., Petrocchi, M., Tesconi, M.: Hate me, hate me not: Hate speech detection on Facebook. CEUR Workshop Proc. **1816**, 86–95 (2017)
51. Ali, M.Z., Rauf, S., Javed, K., Hussain, S.: Improving hate speech detection of urdu tweets using sentiment analysis. IEEE Access **9**, 84296–84305 (2021). https://doi.org/10.1109/ACCESS.2021.3087827
52. Baydogan, C., Alatas, B.: Sentiment analysis in social networks using social spider optimization algorithm. Teh. Vjesn. **28**(6), 1943–1951 (2021). https://doi.org/10.17559/TV-20200614172445

53. Pablo, J., Jiménez, J.: Topic modelling of racist and xenophobic YouTube comments. Analyzing hate speech against migrants and refugees spread through YouTube in Spanish. TEEM'21 Ninth Int. Conf. Technol. Ecosyst. Enhancing Multicult **2021**, 456–460 (2021)
54. Liu, H., Alorainy, W., Burnap, P., Williams, M.L.: Fuzzy multi-task learning for hate speech type identification. Web Conf. 2019 - Proc. World Wide Web Conf. WWW (2019). https://doi.org/10.1145/3308558.3313546
55. Blei, D.M., Ng, A.Y., Jordan, M.I.: Latent Dirichlet allocation. J. Mach. Learn. Res. **3**(4–5), 993–1022 (2003). https://doi.org/10.1016/b978-0-12-411519-4.00006-9
56. V. Mujadia, "IIIT-Hyderabad at HASOC 2019 : Hate Speech Detection," *CEUR Workshop Proc.*, 2019.
57. Kumar, P.M.A., Pradesh, A.: Hate Speech Detection using Text and Image Tweets Based On Bi-directional Long Short-Term Memory. 2021 Int. Conf. Disruptive Technol. Multi-Disciplinary Res. Appl **2021**, 158–162 (2021)
58. Dinakar, K., Reichart, R., Lieberman, H.: Modeling the detection of textual cyberbullying. AAAI Work. - Tech. Rep. **11–02**, 11–17 (2011)
59. Gaydhani, A., Doma, V., Kendre, S., Bhagwat, L.: Detecting Hate Speech and Offensive Language on Twitter using Machine Learning : An N-gram and TFIDF based Approach. IEEE Int. Adv. Comput. Conf **1809**, 08651 (2018)
60. Gambino, G., Pirrone, R., Ingegneria, D.: CHILab @ HaSpeeDe 2: Enhancing Hate Speech Detection with Part-of-Speech Tagging. CEUR Workshop Proc. **2020**, 165 (2020)
61. Erizal, E., Setianingsih, C.: "Hate Speech Detection in Indonesian Language on Instagram Comment Section Using Maximum Entropy Classification Method." 2019 Int Conf. Inf. Commun. Technol. **2019**, 533–538 (2019)
62. Bilal, M., Khan, A., Jan, S., Musa, S.: Context-Aware Deep Learning Model for Detection of Roman Urdu Hate Speech on Social Media Platform. IEEE Access **10**, 121133–121151 (2022). https://doi.org/10.1109/ACCESS.2022.3216375
63. Zhou, X., et al.: "Hate Speech Detection based on Sentiment Knowledge Sharing." Proc. 59th Annu. Meet. Assoc. Comput. Linguist. 11th Int Jt. Conf. Nat. Lang. Process. **2021**, 7158–7166 (2021)
64. Plaza-del-Arco, F.M., Molina-González, M.D., Ureña-López, L.A., Martín-Valdivia, M.T.: Comparing pre-trained language models for Spanish hate speech detection. Expert Syst. Appl. **166**, 114120 (2021). https://doi.org/10.1016/j.eswa.2020.114120
65. W. Warner and J. Hirschberg, "Detecting hate speech on the world wide web," in *Proceeding LSM '12 Proceedings of the Second Workshop on Language in Social Media*, 2012, no. Lsm, pp. 19–26, [Online]. Available: http://dl.acm.org/citation.cfm?id=2390374.2390377.
66. Haralambous, Y., Lenca, P.: Text classification using association rules, dependency pruning and hyperonymization. CEUR Workshop Proc. **1202**, 65–80 (2014)
67. Abro, S., Shaikh, S., Ali, Z.: Automatic Hate Speech Detection using Machine Learning : A Comparative Study. Int. J. Adv. Comput. Sci. App. **11**(8), 484–491 (2020)
68. Baydogan, C., Alatas, B.: Deep-Cov19-Hate: A Textual-Based Novel Approach for Automatic Detection of Hate Speech in Online Social Networks throughout COVID-19 with Shallow and Deep Learning Models. Teh. Vjesn. **29**(1), 149–156 (2022). https://doi.org/10.17559/TV-20210708143535
69. Chiril, P., Wahyu, E., Farah, P., Véronique, B., Viviana, M., Patti, V.: Emotionally Informed Hate Speech Detection : A Multi - target Perspective. Cognit. Comput. (2022). https://doi.org/10.1007/s12559-021-09862-5
70. Mullah, N.S., Zainon, W.M.N.W.: Advances in machine learning algorithms for hate speech detection in social media: a review. IEEE Access **9**, 88364–88376 (2021). https://doi.org/10.1109/ACCESS.2021.3089515
71. Naseem, U., Razzak, I., Eklund, P.W.: "A survey of pre-processing techniques to improve short-text quality : a case study on hate speech detection on twitter. Multimed Tools Appl (2020). https://doi.org/10.1007/s11042-020-10082-6
72. P. Burnap and M. Williams, "Hate Speech, Machine Classification and Statistical Modelling of Information Flows on Twitter: Interpretation and Communication for Policy Decision Making," in *Internet, Policy & Politics*, 2014, pp. 1–18, [Online]. Available: http://orca.cf.ac.uk/id/eprint/65227%0A.
73. Khan, M.M., Shahzad, K., Malik, M.K.: "Hate speech detection in Roman Urdu", *ACM Trans*. Asian Low-Resource Lang. Inf. Process. **20**(1), 1–19 (2021). https://doi.org/10.1145/3414524
74. Hua, T., Chen, F., Zhao, L., Lu, C.-T., Ramakrishnan, N.: STED: semi-supervised targeted-interest event detection". Knowledge Discov. Data Mining **2013**, 1466–1469 (2013)
75. Ali, R., Farooq, U., Arshad, U., Shahzad, W., Omer, M.: Computer speech & language hate speech detection on Twitter using transfer learning. Comput. Speech Lang. **74**, 101365 (2022). https://doi.org/10.1016/j.csl.2022.101365
76. Ma, C., Du, X., Cao, L.: Improved KNN algorithm for fine-grained classification of encrypted network flow. Mdpi Electron (2020). https://doi.org/10.3390/electronics9020324
77. Ferreira, P.J.S., Cardoso, J.M.P.: k NN prototyping schemes for embedded human activity recognition with online learning. Mdpi Comput (2020). https://doi.org/10.3390/computers9040096
78. Kumar, P., Bhawal, S.: Computer speech & language hate speech and offensive language detection in Dravidian languages using deep ensemble framework. Comput. Speech Lang. (2022). https://doi.org/10.1016/j.csl.2022.101386
79. Alfina, I., Mulia, R., Fanany, M.I., Ekanata, Y.: 2018 "Hate speech detection in the Indonesian language: a dataset and preliminary study. 2017 Int. Conf. Adv. Comput. Sci. Inf. Syst. ICACSIS **2018**, 233–237 (2017). https://doi.org/10.1109/ICACSIS.2017.8355039
80. Bosco, C., Orletta, F.D., Poletto, F., Tesconi, M.: Overview of the EVALITA 2018 hate speech detection task. CEUR Workshop Proc. (2018). https://doi.org/10.4000/books.aaccademia.4503
81. Bai, X., Merenda, F., Zaghi, C., Caselli, T., Nissim, M.: RuG EVALITA 2018: hate speech detection in Italian social media. CEUR Workshop Proc. **2263**, 1–5 (2018)
82. Chen, H., McKeever, S., Delany, S.J.: Abusive text detection using neural networks. CEUR Workshop Proceedings, 2086(2), 258–260.ction using neural networks. CEUR Workshop Proc. **2086**(2), 258–260 (2017)
83. M. Wiegand, J. Ruppenhofer, A. Schmidt, and C. Greenberg, "Inducing a lexicon of abusive words ? a feature-based approach," NAACL HLT 2018 - 2018 Conf. North Am. Chapter Assoc. Comput. Linguist. Hum. Lang. Technol. - Proc. Conf., vol. 1, pp. 1046–1056, 2018, doi: https://doi.org/10.18653/v1/n18-1095.
84. Pawar, R., Agrawal, Y., Joshi, A., Gorrepati, R., Raje, R.R.: "Cyberbullying detection system with multiple server configurations. IEEE Int. Conf. Electro Inf. Technol. (2018). https://doi.org/10.1109/EIT.2018.8500110
85. N. Djuric, J. Zhou, R. Morris, M. Grbovic, V. Radosavljevic, and N. Bhamidipati, "Hate speech detection with comment embeddings," in WWW 2015 companion—proceedings of the 24th international conference on World Wide Web, 2015, pp. 29–30, doi: https://doi.org/10.1145/2740908.2742760.
86. W. Z, "Are you a racist or am i seeing things? Annotator influence on hate speech detection on twitter.," in proceedings of the first

workshop on NLP and computational social science. Association for computational linguistics, 2016, pp. 138–142.
87. Malmasi, S., Zampieri, M.: Detecting hate speech in social media. Int. Conf. Recent. Adv. Nat. Lang. Process. RANLP. **2017**, 467–472 (2017). https://doi.org/10.26615/978-954-452-049-6-062
88. M. R. Jha A, "When does a compliment become sexist? analysis and classification of ambivalent sexism using twitter data. In:," In proceedings of the second workshop on NLP and computational social science. Association for Computational Linguistics, 2017, pp. 7–16.
89. Santosh, T.Y.S.S., Aravind, K.V.S.: Hate speech detection in Hindi-English code-mixed social media text. ACM Int. Conf. Proc. Ser. (2019). https://doi.org/10.1145/3297001.3297048
90. Özel, S.A., Akdemir, S., Saraç, E., Aksu, H.: "Detection of cyberbullying on social media messages in Turkish", *2nd Int*. Conf. Comput. Sci. Eng. UBMK **2017**, 366–370 (2017). https://doi.org/10.1109/UBMK.2017.8093411
91. M. Fernandez and H. Alani, "Contextual semantics for radicalisation detection on Twitter," *CEUR Workshop Proc.*, vol. 2182, 2018.
92. Abozinadah, E.A., Mbaziira, A.V., Jones, J.H.J.: Detection of abusive accounts with Arabic tweets. Int. J. Knowl. Eng. **1**(2), 113–119 (2015). https://doi.org/10.7763/ijke.2015.v1.19
93. Abozinadah, E.A., Jones, J.H.: A statistical learning approach to detect abusive twitter accounts. ACM Int. Conf. Proceeding Ser (2017). https://doi.org/10.1145/30932413093281
94. Alakrot, A., Murray, L., Nikolov, N.S.: Dataset construction for the detection of anti-social behaviour in online communication in Arabic. Procedia Comput. Sci. **142**, 174–181 (2018). https://doi.org/10.1016/j.procs.2018.10.473
95. Alakrot, A., Murray, L., Nikolov, N.S.: Towards accurate detection of offensive language in online communication in Arabic. Procedia Comput. Sci. **142**, 315–320 (2018). https://doi.org/10.1016/j.procs.2018.10.491
96. A. A. E. M. B. N. H. Alhuzali and M. Abdul-Mageed, "Think Before Your Click: Data and Models for Adult Content in Arabic Twitter," *Proc. Elev. Int. Conf. Lang. Resour. Eval. (LREC 2018)*, 2018.
97. Haidar, B., Chamoun, M., Serhrouchni, A.: A multilingual system for cyberbullying detection: Arabic content detection using machine learning. Adv. Sci. Technol. Eng. Syst. **2**(6), 275–284 (2017). https://doi.org/10.25046/aj020634
98. Magdy, W., Darwish, K., Weber, I.: Failed revolutions: using Twitter to study the antecedents of ISIS support. First Monday (2016). https://doi.org/10.5210/fm.v21i2.6372
99. Xiang, G., Fan, B., Wang, L., Hong, J., Rose, C.: "Detecting offensive tweets via topical feature discovery over a large scale twitter corpus. ACM Int. Conf. Proceeding Ser (2012). https://doi.org/10.1145/23967612398556
100. V. Nahar, S. Al-maskari, X. Li, and C. Pang, "Databases Theory and Applications - 25th Australasian Database Conference, {ADC} 2014, Brisbane, QLD, Australia, July 14–16, 2014. Proceedings," vol. 8506, 2019, 2014, doi: https://doi.org/10.1007/978-3-319-08608-8.
101. Agarwal, S., Sureka, A.: 'Using KNN and SVM based one-class classifier for detecting online radicalization on twitter.' Int. Conf. Distributed Comput. Internet Technol. (2015). https://doi.org/10.1007/978-3-319-14977-6_47
102. Kaati, L., Omer, E., Prucha, N., Shrestha, A.: Detecting multipliers of Jihadism on Twitter. Proc 15th IEEE Int. Conf. Data Min. Work. ICDMW (2015). https://doi.org/10.1109/ICDMW.2015.9
103. Di Capua, M., Di Nardo, E., Petrosino, A.: Unsupervised cyber bullying detection in social networks. Proc. Int. Conf. Pattern Recognit. (2016). https://doi.org/10.1109/ICPR.2016.7899672
104. Abdelfatah, K.E., Terejanu, G., Alhelbawy, A.A.: "Unsupervised Detection of Violent Content in Arabic Social Media. Comput. Sci.Info Technol. (2017). https://doi.org/10.5121/csit.2017.70401
105. Pitsilis, G.K., Ramampiaro, H., Langseth, H.: Effective hate-speech detection in Twitter data using recurrent neural networks. Appl. Intell. **48**(12), 4730–4742 (2018). https://doi.org/10.1007/s10489-018-1242-y
106. S. Suryawanshi, B. R. Chakravarthi, M. Arcan, and P. Buitelaar, "Multimodal Meme Dataset (MultiOFF) for Identifying Offensive Content in Image and Text," *Proc. Second Work. Trolling, Aggress. Cyberbullying*, vol. 2020-Decem, no. May, pp. 32–41, 2020, [Online]. Available: https://www.aclweb.org/anthology/2020.trac-1.6.
107. T. Deshpande and N. Mani, *An Interpretable Approach to Hateful Meme Detection*, vol. 1, no. 1. Association for Computing Machinery, 2021.
108. D. Kiela *et al.*, "The Hateful Memes Challenge: Detecting Hate Speech in Multimodal Memes," pp. 1–17, 2020, [Online]. Available: http://arxiv.org/abs/2005.04790.
109. N. Muennighoff, "Vilio: State-of-the-art Visio-Linguistic Models applied to Hateful Memes," arXiv:2012.07788v1, pp. 1–6, 2020, [Online]. Available: http://arxiv.org/abs/2012.07788.
110. Yuan, S., Wu, X., Xiang, Y.: A two phase deep learning model for identifying discrimination from tweets. In Adv. Database Technol. EDBT (2016). https://doi.org/10.5441/002/edbt.2016.92
111. Gambäck, B., Sikdar, U.K.: "Using Convolutional Neural Networks to Classify Hate-Speech. In Proceed First Workshop Abusive Language Online (2017). https://doi.org/10.18653/v1/w17-3013
112. F. P. Park JH, "One-step and two-step classification for abusive language detection on twitter.," 2017.
113. Zhang, Z., Robinson, D., Tepper, J.: "Detecting hate speech on twitter using a convolution gru based deep neural network. In Lecture Note. Comput. Sci. **10843**, 745–760 (2018)
114. Erico, C., Salim, R., Suhartono, D.: A systematic literature review of different machine learning methods on hate speech detection. Int. J. Info. Vis. **4**, 213–218 (2020)
115. Ayo, F.E., Folorunso, O., Ibharalu, F.T., Osinuga, I.A., Abayomi-Alli, A.: "A probabilistic clustering model for hate speech classification in twitter. Expert Syst. Appl. (2021). https://doi.org/10.1016/j.eswa.2021.114762
116. Baydogan, C., Alatas, B.: Metaheuristic ant lion and moth flame optimization-based novel approach for automatic detection of hate speech in online social networks. IEEE Access **9**, 110047–110062 (2021). https://doi.org/10.1109/ACCESS.2021.3102277
117. Asiri, Y., Halawani, H.T., Alghamdi, H.M., Abdalaha Hamza, S.H., Abdel-Khalek, S., Mansour, R.F.: enhanced seagull optimization with natural language processing based hate speech detection and classification. Appl. Sci. (2022). https://doi.org/10.3390/app12168000
118. Y. G. and X. L. Pengfei Du,: Towards an intrinsic interpretability approach for multimodal hate speech detection. Int. J. Pattern Recognit. Artif. Intell. (2022). https://doi.org/10.1142/S0218001422500409
119. N. Albadi, M. Kurdi, and S. Mishra 2018 "Are they our brothers? Analysis and detection of religious hate speech in the Arabic Twittersphere. *Proc. 2018 IEEE/ACM Int. Conf. Adv. Soc. Networks Anal. Mining, ASONAM. Doi:* https://doi.org/10.1109/ASONAM.2018.8508247.
120. Miok, K., Škrlj, B., Zaharie, D., Robnik-Šikonja, M.: To ban or not to ban: bayesian attention networks for reliable hate speech detection. Cognit. Comput. **14**(1), 353–371 (2022). https://doi.org/10.1007/s12559-021-09826-9
121. Wullach, T., Adler, A., Minkov, E.: Towards hate speech detection at large via deep generative modeling. IEEE Internet

Comput. **25**(2), 48–57 (2021). https://doi.org/10.1109/MIC.2020.3033161
122. Gomez, R., Gibert, J., Gomez, L., Karatzas, D.: "Exploring hate speech detection in multimodal publications. Proc. - 2020 IEEE Winter Conf. Appl. Comput. Vision, WACV (2020). https://doi.org/10.1109/WACV45572.2020.9093414
123. A. Das, J. S. Wahi, and S. Li, "Detecting Hate Speech in Multimodal Memes," 2020, [Online]. Available: http://arxiv.org/abs/2012.14891.
124. Zhou, Y., Yang, Y., Liu, H., Liu, X., Savage, N.: Deep learning based fusion approach for hate speech detection. IEEE Access **8**, 128923–128929 (2020). https://doi.org/10.1109/ACCESS.2020.3009244
125. Muhammad, I.Z., Nasrun, M., Setianingsih, C.: Hate speech detection using global vector and deep belief network algorithm. 2020 1st Int. Conf. Big Data Anal. Pract. IBDAP (2020). https://doi.org/10.1109/IBDAP50342.2020.9245467
126. Le-hong, P.: Knowledge-based systems diacritics generation and application in hate speech detection on vietnamese social networks. Knowledge-Based Syst. (2021). https://doi.org/10.1016/j.knosys.2021.107504
127. P. Vijayaraghavan, H. Larochelle, and D. Roy, "Interpretable Multi-Modal Hate Speech Detection," *Int. Conf. Mach. Learn.*, 2021.
128. G. Sahu, R. Cohen, and O. Vechtomova, "Towards A Multi-agent System for Online Hate Speech Detection," *Proc. 20th Int. Conf. Auton. Agents Multiagent Syst.*, 2021.
129. A. Jiang, Aiqi; Zubiaga, *Cross-lingual Capsule Network for Hate Speech Detection in Social Media*, vol. 1, no. 1. Association for Computing Machinery, 2021.
130. Perifanos, K.: Multimodal hate speech detection in greek social media. Mdpi Multimed. Technol. Interact. (2021). https://doi.org/10.3390/mti5070034
131. Aldjanabi, W., Dahou, A., Al-qaness, M.A.A., Elaziz, M.A., Helmi, A.M., Damaševi, R.: Arabic offensive and hate speech detection using a cross-corpora multi-task learning model. Mdpi inform. (2021). https://doi.org/10.3390/informatics8040069
132. Al-Makhadmeh, Z., Tolba, A.: Automatic hate speech detection using killer natural language processing optimizing ensemble deep learning approach. Computing **102**(2), 501–522 (2020). https://doi.org/10.1007/s00607-019-00745-0
133. Corazza, M., Menini, S., Cabrio, E., Tonelli, S., Villata, S.: A multilingual evaluation for online hate speech detection. ACM Trans. Internet Technol. (2020). https://doi.org/10.1145/3377323
134. Kapil, P., Ekbal, A.: A deep neural network based multi-task learning approach to hate speech detection. Knowledge-Based Syst. (2020). https://doi.org/10.1016/j.knosys.2020.106458
135. Aulia, N., Budi, I.: Hate speech detection on Indonesian long text documents using machine learning approach. ACM Int. Conf. Proceeding Ser. (2019). https://doi.org/10.1145/33304823330491
136. Badjatiya, P., Gupta, M., Varma, V.: Stereotypical bias removal for hate speech detection task using knowledge-based generalizations. Web Conf. 2019 - Proc World Wide Web Conf. WWW **10**(1145/3308558), 3313504 (2019)
137. G. Nascimento, F. Carvalho, A. M. Da Cunha, C. R. Viana, and G. P. Guedes, 2019 "Hate speech detection using Brazilian imageboards," *Proc. 25th Brazillian Symp. Multimed. Web, WebMedia.* https://doi.org/10.1145/3323503.3360619.
138. A. S. Saksesi, M. Nasrun, and C. Setianingsih, "Analysis Text of Hate Speech Detection Using Recurrent Neural Network," *Proc. - 2018 Int. Conf. Control. Electron. Renew. Energy Commun. ICCEREC 2018*, pp. 242–248, 2018, doi: https://doi.org/10.1109/ICCEREC.2018.8712104.
139. Mozafari, M., Farahbakhsh, R., Crespi, N.: A BERT-Based transfer learning approach for hate speech detection in online social media. Conf. Comp. Net, Their Appl Int (2020). https://doi.org/10.1007/978-3-030-36687-2_77
140. V. Basile *et al.*, "SemEval-2019 task 5: Multilingual detection of hate speech against immigrants and women in Twitter," *NAACL HLT 2019 - Int. Work. Semant. Eval. SemEval 2019, Proc. 13th Work.*, pp. 54–63, 2019, doi: https://doi.org/10.18653/v1/s19-2007.
141. N. Mehrabi, F. Morstatter, N. Saxena, and L. G. Jan, "A Survey on Bias and Fairness in Machine Learning," arXiv:1908.09635v3, 2022.
142. Ahmed, Z., Vidgen, B., Hale, S.A.: Tackling racial bias in automated online hate detection : towards fair and accurate detection of hateful users with geometric deep learning. EPJ Data Sci. (2022). https://doi.org/10.1140/epjds/s13688-022-00319-9
143. Watanabe, H., Bouazizi, M., Ohtsuki, T.: Hate speech on twitter: a pragmatic approach to collect hateful and offensive expressions and perform hate speech detection. IEEE Access **6**, 13825–13835 (2018). https://doi.org/10.1109/ACCESS.2018.2806394
144. Mollas, I., Chrysopoulou, Z., Karlos, S., Tsoumakas, G.: ETHOS: a multi-label hate speech detection dataset. Complex Intell. Syst. (2022). https://doi.org/10.1007/s40747-021-00608-2
145. A. Velankar, H. Patil, A. Gore, S. Salunke, and R. Joshi, "L3Cube-MahaHate: A Tweet-based Marathi Hate Speech Detection Dataset and BERT models," arXiv:2203.13778v2, pp. 1–12, 2022, [Online]. Available: http://arxiv.org/abs/2203.13778.
146. Mathew, B., Saha, P., Yimam, S.M., Biemann, C., Goyal, P., Mukherjee, A.: "HateXplain: a benchmark dataset for explainable hate speech detection",. 35th aaai conf Artif. Intell. AAAI **17A**, 14867–14875 (2021)
147. K. Yang, W. Jang, and W. I. Cho, "APEACH: Attacking Pejorative Expressions with Analysis on Crowd-Generated Hate Speech Evaluation Datasets," 2022, [Online]. Available: http://arxiv.org/abs/2202.12459.
148. J. A. Leite, D. F. Silva, K. Bontcheva, and C. Scarton, "Toxic Language Detection in Social Media for Brazilian Portuguese: New Dataset and Multilingual Analysis," arXiv:2010.04543, 2020, [Online]. Available: http://arxiv.org/abs/2010.04543.
149. C. S. de Alcântara, D. Feijó, and V. P. Moreira, "Offensive video detection: Dataset and baseline results," *Lr. 2020 - 12th Int. Conf. Lang. Resour. Eval. Conf. Proc.*, no. May, pp. 4309–4319, 2020.
150. T. Hartvigsen, S. Gabriel, H. Palangi, M. Sap, D. Ray, and E. Kamar, "ToxiGen: A Large-Scale Machine-Generated Dataset for Adversarial and Implicit Hate Speech Detection," 2022, [Online]. Available: http://arxiv.org/abs/2203.09509.
151. Evkoski, B., Pelicon, A., Mozetič, I., Ljubešić, N., Novak, P.K.: Retweet communities reveal the main sources of hate speech. PLoS ONE (2022). https://doi.org/10.1371/journal.pone.0265602
152. H. R. Kirk, B. Vidgen, P. Röttger, T. Thrush, and S. A. Hale, "Hatemoji: A Test Suite and Adversarially-Generated Dataset for Benchmarking and Detecting Emoji-based Hate," 2021, [Online]. Available: http://arxiv.org/abs/2108.05921.
153. N. Romim, M. Ahmed, M. S. Islam, A. Sen Sharma, H. Talukder, and M. R. Amin, "HS-BAN: A Benchmark Dataset of Social Media Comments for Hate Speech Detection in Bangla," arXiv:2112.01902v1, pp. 1–8, 2021, [Online]. Available: http://arxiv.org/abs/2112.01902.
154. M. R. Karim, B. R. Chakravarthi, J. P. McCrae, and M. Cochez,2020 "Classification Benchmarks for Under-resourced Bengali Language based on Multichannel Convolutional-LSTM Network. *Proc. - 2020 IEEE 7th Int. Conf. Data Sci. Adv. Anal. DSAA*. https://doi.org/10.1109/DSAA49011.2020.00053.
155. Wu, C.S., Bhandary, U.: Detection of hate speech in videos using machine learning. Int. Conf. Comput. Sci. Comput. Intell. CSCI Proc (2020). https://doi.org/10.1109/CSCI51800.2020.00104

156. M. Zampieri *et al.*, "SemEval-2020 Task 12: Multilingual Offensive Language Identification in Social Media (OffensEval 2020)," *Proc. Int. Work. Semant. Eval.*, no. OffensEval, 2020.
157. Zampieri, M., Malmasi, S., Nakov, P., Rosenthal, S., Farra, N., Kumar, R.: Predicting the type and target of offensive posts in social media. Proc. NAACL-HLT **2019**, 1415–1420 (2019)
158. Haddad, H., Mulki, H., Oueslati, A.: T-HSAB: a tunisian hate speech and abusive dataset. Commun. Comput. Inf. Sci. (2019). https://doi.org/10.1007/978-3-030-32959-4_18
159. H. Mulki, H. Haddad, C. Bechikh Ali, and H. Alshabani, "L-HSAB: A Levantine Twitter Dataset for Hate Speech and Abusive Language," pp. 111–118, 2019, doi: https://doi.org/10.18653/v1/w19-3512.
160. Elsherief, M., Nilizadeh, S., Nguyen, D., Vigna, G., Belding, E.: Peer to peer hate: hate speech instigators and their targets. AAAI Conf. Web Soc. Media (2018). https://doi.org/10.1609/icwsm.v12i1.15038
161. A. M. Founta *et al.*, "Large scale crowdsourcing and characterization of twitter abusive behavior," 12th *Int. AAAI Conf. Web Soc. Media, ICWSM 2018*, no. Icwsm, pp. 491–500, 2018
162. J. Moon, W. I. Cho, and J. Lee, "BEEP ! Korean Corpus of Online News Comments for Toxic Speech Detection," pp. 25–31, 2017.
163. H. Mubarak, K. Darwish, and W. Magdy, "Abusive Language Detection on Arabic Social Media," *Proc. First Work. Abus. Lang. Online*, pp. 52–56, 2017, doi: https://doi.org/10.18653/v1/w17-3008.
164. Toutenburg, H.: Mathematical statistics with applications. Computational Statistics & Data Anal (1992). https://doi.org/10.1016/0167-9473(92)90162-9
165. C. A. Goodfellow I, Bengio Y, *Deep Learning*. MIT Press, Cambridge, 2016.
166. T. Mikolov, A. Deoras, S. Kombrink, L. Burget, and J. H. Černocký, "Empirical evaluation and combination of advanced language modeling techniques," *Proc. Annu. Conf. Int. Speech Commun. Assoc. INTERSPEECH*, no. August, pp. 605–608, 2011.
167. De Souza, G.A., Da Costa-Abreu, M.: Automatic offensive language detection from Twitter data using machine learning and feature selection of metadata. Proc. Int. Jt. Conf. Neural Networks (2020). https://doi.org/10.1109/IJCNN48605.2020.9207652
168. M. Polignano *et al.*, "A L BERT O : Italian BERT Language Understanding Model for NLP Challenging Tasks Based on Tweets," *CEUR Workshop Proc.*, 2019.
169. Webb, G.I.: Decision tree grafting from the all-tests-but-one partition. IJCAI Int. Jt. Conf. Artif. Intell. **2**, 702–707 (1999)
170. S. Tulkens, L. Hilte, E. Lodewyckx, B. Verhoeven, and W. Daelemans, "A Dictionary-based Approach to Racism Detection in Dutch Social Media," 2016, [Online]. Available: http://arxiv.org/abs/1608.08738.
171. Burnap, P., Williams, M.L.: Cyber hate speech on twitter: an application of machine classification and statistical modeling for policy and decision making. Policy Internet **7**(2), 223–242 (2015). https://doi.org/10.1002/poi3.85

Publisher's Note Springer Nature remains neutral with regard to jurisdictional claims in published maps and institutional affiliations.

Springer Nature or its licensor (e.g. a society or other partner) holds exclusive rights to this article under a publishing agreement with the author(s) or other rightsholder(s); author self-archiving of the accepted manuscript version of this article is solely governed by the terms of such publishing agreement and applicable law.

This article has been accepted for publication in IEEE Transactions on Instrumentation and Measurement. This is the author's version which has not been fully edited and content may change prior to final publication. Citation information: DOI 10.1109/TIM.2023.3238021

A novel dual-slope resistance to digital converter with lead resistance compensation

Gopal Singh[1], *Graduate Student Member, IEEE*, Shiraz Sohail[1]*, *Senior Member, IEEE,* Umapathy Mangalanathan[1], *Member, IEEE*, Uma Gandhi[1], *Member, IEEE*, and Tarikul Islam[2], *Senior Member, IEEE*

***Abstract*—A novel dual-slope resistance to digital converter (RDC) for compensating lead resistance is presented. The RDC uses a dual-slope ADC structure along with three switches and a diode. It completes measurement in one charging-discharging cycle only, hence provides an improvement to existing RDCs based on direct microcontroller interfaces (DMI) where 2 or 3 charging-discharging cycles are required. Moreover, it incorporate the feature of lead resistance compensation in dual-slope RDCs. The scheme works by connecting the resistive sensor to the input terminal of the integrator of the dual-slope ADC. In the charging path (or mode), sensor resistance is present along with lead resistance; and in discharging path, sensor resistance is bypassed, and only lead resistance is there. The difference between the RC time constant during these two modes is used to find the sensor resistance. The diode is used to turn on a switch for bypassing the resistive sensor. The diode voltage drop is not there in the charging and discharging path, which is another novelty. A detailed error analysis is also carried to evaluate the performance of the scheme considering switch resistance, diode voltage drop, voltage mismatch and opamp noises. The scheme works with low-value resistive sensors (≈ 100 Ω), a feature not found in existing dual-slope RDCs. The hardware prototype of the proposed scheme on the breadboard shows a measurement time of 2.09 ms with an average error of ±0.04 % at 100 Ω when lead resistance varied from 20 Ω to 100 Ω. The scheme takes 23.44 % less time for measurement.**

***Index Terms*—Resistive sensor, lead resistance compensation, resistance to digital converter (RDC), resistance to time converter, dual-slope ADC.**

I. Introduction

Resistive sensors make an important class in instrumentation and measurement for a wide range of parameters such as temperature, displacement, strain, force, light, humidity, etc. The most popularly used resistive sensors are the following–resistance temperature detector (RTD), thermistor, potentiometer, strain gauge, load cell, light-dependent resistor (LDR), hygrometer, gas sensor, etc. In industry, mostly the resistive sensors are installed at remote locations, far from the control room (such as 100 m), where measurement units are placed. The measuring units display the measurement parameters and its output signals are feedback in closed-loop systems. Therefore, a pair of long lead wires are used for connecting the resistive sensors to the measuring units. A two-wire connection for a sensor placed 100 m apart using 30 standard wire gauge (SWG) copper wire results in a lead-wire resistance of 44.2 Ω at 20 °C [1]. This lead resistance is added to the sensor resistance, and thus the meter unit shows a measurement error and feedback also gives a faulty result. If the lead-wire resistance is known accurately, it can be subtracted from the measured resistance for the correct meter reading. But the lead wire resistance is not constant and varies with temperature and other environmental conditions. For example, copper lead wire resistance changes with a temperature coefficient of 0.00385Ω/ (Ω °C) which is of a similar order to the sensitivity of Pt100 RTD (0.00385Ω/°C). So, the approach to subtract lead resistance for accurate measurement will still give an error. Therefore, there is a need to develop an alternate method for interfacing remote location resistive sensors to compensate lead resistance and get an accurate measurement. Traditionally, three-wire or four-wire compensation techniques are used to nullify the effect of lead resistance [2]. But the accuracy of these techniques depends on the assumption that lead wires (forward and return) have equal resistance. Moreover, these techniques are costlier due to additional wires. In literature, compensation schemes for three-wire [3] and four-wire RTDs [4] are present using opamp, but it requires a large number of components and the output is affected by the static and dynamic noises of the opamp. In [5], a scheme is presented for the two-wire sensor in floating mode using a diode pair, current sources, and sample-hold circuits. The diode pair exclude the effect of change in lead resistance using a current source. In [6], an improvement is provided for the grounded sensor using current sources and a diode pair. The accuracy of schemes reported in [5] and [6] depends on the reliable working of the current source, diode pair, and sample-hold circuits. In [7], the current source is replaced by a voltage source, which is an improvement over [5-6] for stable output for interfacing a grounded sensor. However, in these methods [4-7], the measured outputs are analog signals. Nowadays, resistance-to-frequency (R-to-F) [8] and resistance-to-time (R-to-T) [9] converters are very popular for sensor interfacing. In the former, change in resistance is measured in terms of change in frequency of the signal, and in the latter, measurement is carried out using change in the time period. Both R-to-F and R-to-T possess a high order of noise immunity, resolution, and linearity and the output can be easily converted to a digital signal for interfacing with digital controllers. However, these methods do not provide lead resistance compensation. Recently, in literature, it is found that the basic structure of dual-slope ADC is altered to make an interface for the resistive sensor which gives digital output [10-13]. These resistance to digital converters (RDCs) provide good accuracy but lead resistance compensation is not present. Direct microcontroller interfaces (DMI) for the resistive sensor are also found in the literature, but they are sensitive to lead resistance and also to the internal

© 2023 IEEE. Personal use is permitted, but republication/redistribution requires IEEE permission. See https://www.ieee.org/publications/rights/index.html for more information.
Authorized licensed use limited to: DELHI TECHNICAL UNIV. Downloaded on January 31,2023 at 05:26:51 UTC from IEEE Xplore. Restrictions apply.

This article has been accepted for publication in IEEE Transactions on Instrumentation and Measurement. This is the author's version which has not been fully edited and content may change prior to final publication. Citation information: DOI 10.1109/TIM.2023.3238021

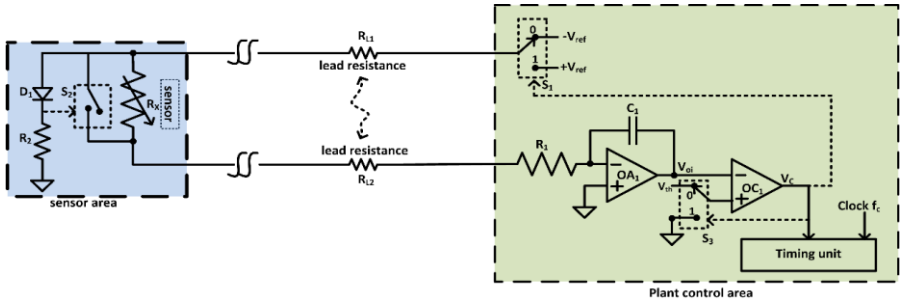

Fig. 1. Improved RDC.

resistance of the port pin (≈ 25 Ω) of the microcontroller [14-15]. Recently, a few DMI to compensate for the lead resistance is found in the literature [16-18]. In these techniques, measuring the charging/discharging time of an RC circuit through a resistive sensor is used for measurement. The time constant of the RC circuit affects the speed of the measurement, and hence should be chosen optimally. In [16], a DMI with four charging-discharging cycles is available in the literature which uses two single pole double throw (SPDT) switches and four diodes. An improvement is presented in [17] with three charging-discharging cycles having three SPDT, and two diodes. Another improvement is presented in [18] with two charging-discharging cycles having two SPDT, two diodes, and a NE555 timer. But, time delay and pin resistance of IC 555 timer are not discussed in the context of measurement time and error.

In this work, a novel dual-slope resistance to digital converter (RDC) for compensating lead resistance is presented which requires only one charging-discharging cycle for measurement. We reported a preliminary study on this technique [19], and this work is an extension for detailed analytical analysis and hardware results. This is an improvement over existing RDCs [10-13], and DMIs [14-18], and. The scheme works on the dual-slope ADC and uses three switches (2 SPDT and 1 SPST) and a diode. The resistive sensor is connected to the input terminal of the integrator of the dual-slope ADC. In the charging path (or mode), sensor resistance (R_X) is present along with lead resistance (R_L); and in discharging path, R_X is bypassed and only R_L is there. The difference between the RC time constant during these two modes is used to find the R_X. An SPST switch is connected across the R_X which is bypassed during the discharge mode. The diode is used to turn on the SPST. The diode voltage drop is not there in the charging and discharging path, which is another novelty of the proposed scheme. Moreover, the proposed scheme works with low-value resistive sensors (i.e. less than 1k) by adding a fixed resistance in charging and discharging path which is not found in earlier work [11] Thus, the proposed interface is faster, independent of diode drop, and workable with a low resistance value sensor. A detailed error analysis is also carried to evaluate the performance of the proposed scheme.

II. Dual Slope RDC with Lead Resistance Compensation

The proposed RDC consists of one opamp (OA_1), one comparator (OC_1), one fixed capacitor (C_1), one diode (D_1), two fixed resistors (R_1 and R_2), one sensor resistance (R_X), a timing unit (TU), and a couple of switches as shown in Fig. 1.

The circuit works similarly to a dual-slope ADC which consists of an integrator, a comparator, and a few switches. The input resistance of the integrator in a conventional dual-slope ADC is replaced with the resistive sensor (R_X) which includes lead wire resistance (R_L). In addition to this, a fixed resistance (R_1) is also connected in series with the sensor. This makes the improved RDC capable of working with low-value resistive sensors, which is an improvement over earlier lead wire compensation techniques in the literature [11]. S_1 and S_3 are single pole double throw (SPDT) switches used to change input voltage reference ($-V_{ref}$ and $+V_{ref}$) and comparator reference (V_{th} and V_{gnd}) respectively. S_2 is a single pole single throw (SPST) switch connected across sensor R_X to bypass it during discharge mode. Switches S_1 and S_3 are controlled by comparator output (V_C). S_2 is connected to the diode (D_1) and the resistor R_2 so that it can be operated by switch S_1 without a third lead wire. This makes the measurement scheme two-wire type. The timing unit (TU) measures the integrator charging and discharging time. The integrator feedback capacitance is C_1.

Fig. 2 shows the flowchart of the working principle of the improved RDC.

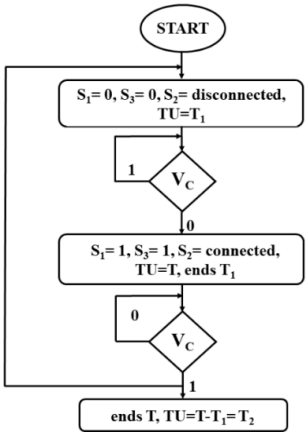

Fig. 2. Flowchart describing the complete measurement scheme.

The circuit works in two modes–one is charging (T_1 interval) and another is discharging (T_2 interval) which constitutes one complete cycle. During charging mode (T_1 interval), V_C is high because of which the switches S_1 and S_3 are in position 0, and S_2 is open-circuited due to reverse biasing of the diode (D_1). So, $-V_{ref}$ is connected to R_1; and OC_1 reference is connected to V_{th}. During this interval, current (i_c) starts flowing from integrator output (V_{oi} node), and passes through R_L (R_L=R_{L1}+R_{L2}), R_X, and R_1, and sinks to $-V_{ref}$. The expression of i_c is following

© 2023 IEEE. Personal use is permitted, but republication/redistribution requires IEEE permission. See https://www.ieee.org/publications/rights/index.html for more information.
Authorized licensed use limited to: DELHI TECHNICAL UNIV. Downloaded on January 31,2023 at 05:26:51 UTC from IEEE Xplore. Restrictions apply.

This article has been accepted for publication in IEEE Transactions on Instrumentation and Measurement. This is the author's version which has not been fully edited and content may change prior to final publication. Citation information: DOI 10.1109/TIM.2023.3238021

$$i_c = \frac{V_{ref}}{(R_1 + R_X + R_L)} \tag{1}$$

This leads to a gradual rise in the potential of the right plate of C_1. Hence, V_{oi} ramps linearly, the slope of which depends on the time constant $(\tau_C = [R_1 + R_X + R_L]C_1)$ of the current flowing path. The expression for V_{oi} is following

$$V_{oi} = \frac{V_{ref}}{(R_1 + R_X + R_L)sC_1} \tag{2}$$

Here we observe that the time constant for V_{oi} ramping up is dependent on both sensor as well as lead wire resistances. The V_{oi} node is connected to the inverting terminal of the comparator (OC_1) and the non-inverting terminal has V_{th} as the reference voltage. So, till the time V_{oi} is lower than V_{th}, the comparator output (V_C) remains high as shown in Fig. 3.

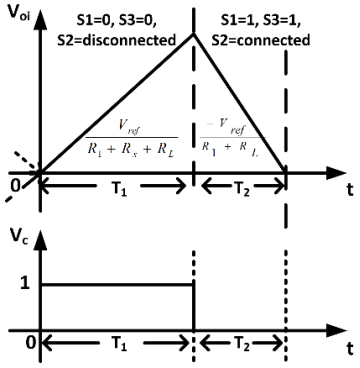

Fig. 3. Waveform of integrator and comparator.

Once V_{oi} is equal to V_{th}, the V_C goes low which marks the end of the T_1 interval. The voltage change in V_{oi} during the T_1 interval is following.

$$\Delta V_{oi} = \frac{V_{ref}}{(R_1 + R_X + R_L)C_1} T_1 = V_{th} \tag{3}$$

Since V_C is low, all switches change their position, and the circuit enters into the discharge mode (T_2 interval). S_1 and S_3 goes to position 1, and S_2 is close circuited due to the forward biasing of the diode (D_1). This leads to connecting R_1 with $+V_{ref}$ and the comparator reference is grounded. Closing of S_2 bypasses the sensor resistance (R_X) during the T_2 interval. Now, current (i_d) starts flowing from $+V_{ref}$, passes through R_1 and R_L ($R_L = R_{L1}+R_{L2}$), and sinks to the V_{oi} node. The expression of i_d is following.

$$i_d = \frac{V_{ref}}{R_1 + R_L} \tag{4}$$

Now, in this case, the potential of the right plate of C_1 gradually decreases, the slope of which depends on the time constant $(\tau_d = [R_1 + R_L]C_1)$ of the current flowing path. The expression for V_{oi} during discharge is following

$$V_{oi} = \frac{-V_{ref}}{(R_1 + R_L)sC_1} \tag{5}$$

So, here we see that time constant for V_{oi} $(\tau_d < \tau_c)$ decreases because it depends only on lead wire resistance (R_L), not on the R_X. Again, till the time V_{oi} is higher than ground potential, V_C remains low as shown in Fig. 3. Once V_{oi} is equal to ground potential, the V_C goes high and this marks the end of the T_2 interval. At this moment again, the circuit enters into the charging mode (T_1 interval) for the next cycle, and all switches changes to their earlier position; i.e., S_1 and S_3 go to position 0 and S_2 is open-circuited. The voltage change in V_{oi} during the T_2 interval of discharge mode is following

$$\Delta V_{oi} = \frac{-V_{ref}}{(R_1 + R_L)C_1} T_2 = V_{th} \tag{6}$$

The net charge in the C_1 capacitor will be zero at the end of the T_2 interval, and equations (3) and (6) can be equated as following

$$\frac{V_{ref}}{(R_1 + R_X + R_L)C_1} T_1 = \frac{V_{ref}}{(R_1 + R_L)C_1} T_2 \tag{7}$$

Finally, the sensor unknown resistance (R_X) can be obtained from equations (3), (6), and (7) as following

$$R_X = K(T_1 - T_2) \tag{8}$$

where $K = \left(\frac{V_{ref}}{V_{th}C_1}\right)$. Thus, R_X depends on T_1 and T_2 intervals only. and is independent of lead wire resistance (R_L). Since the proposed scheme requires only one cycle for sensor resistance measurement, its conversion time is faster compared to existing techniques in the literature [16-18].

III. Analysis of Proposed Scheme

The working of proposed method for interfacing resistive sensors with lead resistance compensation is based on ideal assumptions of circuit parameters (Fig. 1) which results in derivation of equation (8). Deviation of parameters from ideal values may lead to measurement error which is discussed in the following sub-sections. Table I outlines the typical parameter values used for analytical, simulation and experimental analysis of the proposed method.

TABLE I. Typical values of parameters

Parameters	Values
Input offset voltage (V_{OS})	30 µV for OP07
Input offset current (I_{OS})	0.5 nA for OP07
Comparator Input offset voltage (V_{IO})	2 mV for LM311
Threshold voltage (V_{th})	6 V
Lead resistance ($R_{L1} = R_{L2}$)	10 Ω
Switch ON resistance ($r_1 = r_2$)	1.25 Ω for MAX 4690
Inverter IC	SN 7404
Fixed resistance (R_1)	650 Ω
Feedback capacitor (C_1)	1 µF
Diode voltage drop (V_{D1})	0.7 V for IN4007
Resistance (R_2)	33 kΩ to 47 kΩ
Input voltage ($\pm V_{ref}$)	±5 V
Power Supply (V_{CC} and V_{EE})	±15 V

A. *Effect of 'ON' resistance of the SPST switches*

The 'ON' resistances (r_1, r_2) of the switches were considered zero for deriving equation (7) for the measurement of unknown sensor resistance (R_X). But in reality, the practical switch has some finite 'ON' resistance. The switch resistance adds in series with the existing resistance of the charging and

© 2023 IEEE. Personal use is permitted, but republication/redistribution requires IEEE permission. See https://www.ieee.org/publications/rights/index.html for more information.
Authorized licensed use limited to: DELHI TECHNICAL UNIV. Downloaded on January 31,2023 at 05:26:51 UTC from IEEE Xplore. Restrictions apply.

This article has been accepted for publication in IEEE Transactions on Instrumentation and Measurement. This is the author's version which has not been fully edited and content may change prior to final publication. Citation information: DOI 10.1109/TIM.2023.3238021

discharging patch of the integrator circuit. Hence, for the practical case equation (7) is modified as

$$\frac{V_{ref}}{(R_1+R_x+R_L+r_1)C_1}T_1=\frac{V_{ref}}{(R_1+R_L+r_1+r_2)C_1}T_2=V_{th}$$
$$T_1=\frac{V_{th}C_1\left(R_1+R_x+R_L+r_1\right)}{V_{ref}} \quad (9)$$
$$T_2=\frac{V_{th}C_1\left(R_1+R_L+r_1+r_2\right)}{V_{ref}}$$

Here r_1 and r_2 are the ON resistances of the switch S_1 and S_2 respectively. On solving equation (9) assuming $r_1=r_2=r$ we get

$$R_X=K(T_1-T_2)+r \quad (10)$$

On comparing equations (8) and (10), the ON resistance of the switches introduces an offset error of order r. This error can be removed by offset nulling incorporated inside the microcontroller programming during calibration. The error is quantified in Sections IV and V for simulation and experimental results. Equation (10) shows that the ON resistance of switches does not introduce gain error in the measurement.

B. *Effect of deviation of the fixed resistance (R_1) and capacitance (C_1)*

The fixed resistance (R_1) is used in Fig. 1 so that even a low resistance (≈ order of 100 Ω) sensor can be measured. The value of R_1 may change to R_1' due to aging or environmental condition. The following analysis is carried out to assess the effect of minute changes in R_1' on the measurement. Let us consider $\alpha=(R_1/R_1')$, so that equation (7) can be re-written as

$$\frac{V_{ref}}{(\alpha R_1^{'}+R_X+R_L)C_1}T_1=\frac{V_{ref}}{(\alpha R_1^{'}+R_L)C_1}T_2 \quad (11)$$

On further solving we get

$$R_X=K(T_1-T_2) \quad (12)$$

Equation (12) shows that the accuracy of sensor resistance measurement does not change with R_1.

Similarly, when the feedback capacitance C_1 is changed to C_1' due aging or environmental condition, the following analysis discusses the effect on the measurement. Let us consider $\beta=C_1/C_1'$, so equation (7) can be re-written as

$$\frac{V_{ref}}{(R_1+R_X+R_L)\beta C_1^{'}}T_1=\frac{V_{ref}}{(R_1+R_L)\beta C_1^{'}}T_2 \quad (13)$$

On further solving we get

$$R_X=K^{'}(T_1-T_2) \quad (14)$$

Here the gain is modified to $K^{'}=\left(\frac{V_{ref}}{V_{th}\beta C_1^{'}}\right)$. Thus to keep the gain constant, the feedback capacitor C_1 should be a class 1 ceramic capacitor that has a negligible aging effect [20]. The C_1 should also have low leakage and low dielectric absorption, so polystyrene, polypropylene, and Teflon type should be used [21]. It is important to note that if both R_1 and C_1 changes together, only the change in C_1 is accounted in the output as a gain error.

C. *Effect of reference voltage mismatch*

Simplified equation (7) for measurement of sensor resistance assumes bipolar reference voltages ($+V_{ref}$ and $-V_{ref}$) are equal in magnitude, but in practical cases, there could be a slight variation. In typical realization of a dual-slope integrator, $-V_{ref}$ is obtained from an inverting amplifier because of which mismatch is possible. The following analysis is carried out to assess the effect of the minute mismatch between bipolar power supplies. Again, let us consider $\left(\left|-V_{ref}\right|/\left|+V_{ref}\right|\right)=\beta$, so equation (7) can be re-written as

$$\frac{\beta V_{ref}}{(R_1+R_x+R_L)C_1}T_1=\frac{V_{ref}}{(R_1+R_L)C_1}T_2 \quad (15)$$

On, further solving equation (15), we get

$$R_X=K(\beta T_1-T_2) \quad (16)$$

A comparison between equations (16) and (8), implies that a gain error is introduced due to a mismatch in bipolar power supply. Thus, care should be taken by connecting low inductance decoupling capacitors (0.1 µF ceramic capacitors) at the supply pin of IC to bypass the noise to the ground [21-22]. Moreover, other advanced gain compensation techniques can also be used to minimize errors.

D. *Effect of OPAMP and comparator offset noise*

Opamp of integrator has input offset voltage (V_{OS}) and input offset current (I_{OS}), which produces an output offset error (E_O). Fig. 4 shows the equivalent circuit of the proposed scheme without input voltage for estimating error due to I_{OS} and V_{IO}. Opamp and comparator are only connected to supply voltage (V_{CC} and V_{EE}).

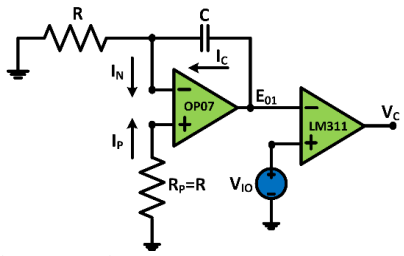

Fig. 4. Error due to I_{OS} and V_{IO}.

Error in integrator output due to I_{OS} at the end of T_1

$$E_{O1}(t)=\frac{1}{RC}\int_0^t\left[(R-R_P)I_B-(R+R_P)I_{OS}/2\right]dt \quad (17)$$

Substituting $R_P=R$ in equation (17)

$$E_{O1}(t)=\frac{1}{RC}\int_0^t -RI_{OS}\,dt=\frac{-I_{OS}}{C}t \quad (18)$$

Here, I_P and I_N are input base transistor currents of the opamp at non-inverting and inverting terminals respectively, $I_{OS}=I_P-I_N$, and I_B is the input bias current, $I_B=(I_P+I_N)/2$. Fig.

© 2023 IEEE. Personal use is permitted, but republication/redistribution requires IEEE permission. See https://www.ieee.org/publications/rights/index.html for more information.
Authorized licensed use limited to: DELHI TECHNICAL UNIV. Downloaded on January 31,2023 at 05:26:51 UTC from IEEE Xplore. Restrictions apply.

This article has been accepted for publication in IEEE Transactions on Instrumentation and Measurement. This is the author's version which has not been fully edited and content may change prior to final publication. Citation information: DOI 10.1109/TIM.2023.3238021

5 shows the equivalent circuit of the proposed scheme without input voltage for estimating error due to V_{OS} and V_{IO}.

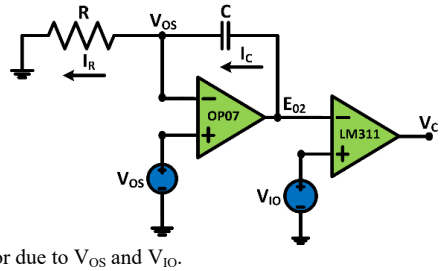

Fig. 5. Error due to V_{OS} and V_{IO}.

Error in integrator output due to V_{OS} at the end of T_1

$$E_{O2}(t)=\frac{1}{RC}\int_0^t V_{OS}\,dt=\frac{V_{OS}}{RC}t \tag{19}$$

Thus total error in integrator output

$$|E_O(t)|=|E_{O1}(t)|+|E_{O2}(t)|=\left(\frac{I_{OS}}{C}+\frac{V_{OS}}{RC}\right)t \tag{20}$$

Substituting t=T_1 will give integrator output at the end of T_1

$$|E_O(T_1)|=\left(I_{OS}+\frac{V_{OS}}{R_1+R_X+R_L+r}\right)\frac{T_1}{C_1} \tag{21}$$

Here, *R* is substituted with summation of all resistances of charging path of the integrator (refer equation 9)

Now, we are analyzing the effect of comparator's input offset voltage (V_{IO}) on the measurement (Fig. 4 and Fig. 5). The threshold voltage (V_{th}) of the comparator is shifted by V_{IO} and comparator output (V_C) swings from $+V_{sat}$ to $-V_{sat}$ when integrator output (including offset voltage) rises to $V_{th}+V_{IO}$. Thus, the voltage balance equation for finding T_1 is

$$\begin{aligned}&V_{th}+V_{IO}=V_{oi}(T_1)+E_O(T_1)\\&V_{oi}(T_1)=V_{th}+V_{IO}-\left[I_{OS}+\frac{V_{OS}}{R_1+R_X+R_L+r}\right]\frac{T_1}{C_1}\end{aligned} \tag{22}$$

For finding the expression of T_1, V_{oi} is substituted from equation (9)

$$\begin{aligned}&\frac{V_{ref}\times T_1}{(R_1+R_x+R_L+r)C_1}=V_{TH}+V_{IO}-\left[I_{OS}+\frac{V_{OS}}{R_1+R_X+R_L+r}\right]\frac{T_1}{C_1}\\&T_1=\frac{(V_{TH}+V_{IO})(R_1+R_X+R_L+r)C_1}{V_{ref}+V_{OS}+I_{OS}(R_1+R_X+R_L+r)}\end{aligned} \tag{23}$$

During discharge mode (T_2), integrator output decreases from (V_{TH} + V_{IO}) to V_{IO}, and V_C swings from $-V_{sat}$ to $+V_{sat}$. It is important to note that integrator output decreases due to input voltage ($+V_{ref}$). But at the same time, V_{oi} increases slowly due to input offset voltage and current of OA_1. However, the net effect decreases the V_{oi}. Thus, the voltage balance equation during T_2 is

$$\begin{aligned}&V_{oi}(T_2)-E_O(T_2)=V_{TH}\\&\frac{V_{ref}\times T_2}{(R_1+R_L+2r)C_1}-\left(I_{OS}+\frac{V_{OS}}{R_1+R_L+2r}\right)\frac{T_2}{C_1}=V_{TH}\\&T_2=\frac{V_{TH}(R_1+R_L+2r)C_1}{V_{ref}-V_{OS}-I_{OS}(R_1+R_L+2r)}\end{aligned} \tag{24}$$

From equation (23) and (24), we get

$$\begin{aligned}&\Delta T=T_1-T_2=\left(\frac{C_1R_X[P]+C_1[R]}{[Q]}\right)\\&R_X=\frac{\Delta T[Q]}{C_1[P]}-\frac{[R]}{[P]}\\&[P]=[(V_{ref}-V_{OS}-I_{OS}R_3-I_{OS}r)(V_{th}+V_{IO})\\&\quad -I_{OS}R_3V_{th}-I_{OS}rV_{th}]\\&[Q]=[V_{ref}^2-V_{OS}^2-V_{OS}I_{OS}(2R_3+R_X+r)+V_{ref}I_{OS}(R_X-r)\\&\quad -I_{OS}^2(R_3+r)(R_3+R_X)]\\&[R]=[V_{IO}(V_{ref}R_3-V_{OS}R_3-I_{OS}R_3^2-I_{OS}R_3r)\\&\quad -V_{th}(V_{ref}r-V_{OS}r-2V_{OS}R_3-2I_{OS}R_3^2-2I_{OS}R_3r)]\\&\frac{[R]}{[P]}=\frac{V_{IO}R_3V_{ref}}{V_{ref}V_{th}}-\frac{V_{IO}V_{OS}R_3}{V_{ref}V_{th}}-\frac{V_{th}V_{ref}r}{V_{ref}V_{th}}\\&\quad +\frac{V_{th}V_{OS}r}{V_{ref}V_{th}}+\frac{2V_{th}V_{OS}R_3}{V_{ref}V_{th}}\end{aligned} \tag{25}$$

Assuming $V_{th}+V_{IO}\cong V_{th}, V_{ref}-V_{OS}\cong V_{ref}$ and neglecting negligible terms (I_{OS}, V_{OS}^2), the equation (25) is simplified as

$$R_X=K(T_1-T_2)+r-(V_{IO}R_3/V_{th})-\left(2R_3V_{OS}/V_{ref}\right) \tag{26}$$

On comparing equation (8) and (26), it is found that V_{OS}, I_{OS}, V_{IO}, and r introduces an offset error that can be removed by offset nulling incorporated inside the microcontroller programming during calibration. The error is quantified for simulation and experimental results in Sections IV and V.

E. Effect of propagation delays and slew rate

The propagation delay of OC_1 and switch IC are introduced during both charging (T_1) and discharging (T_2) mode of the integrator. Hence, the difference (T_1-T_2) will be unaffected which is used for measurement. Moreover, the propagation delay introduced by OC_1 and MAX 4690 are 115 ns and 130 ns which is negligible compared to T_1 and T_2 (ms order). Therefore, the measurement accuracy will not be influenced by the propagation delays.

For analyzing the slew rate of OA_1, the fastest change in output of the integrator is required during T_2 mode because of the small time constant (τ_d). Hence a minimum slew rate of (V_{th}/τ_d) 0.0074 V/µs is required in OA_1 from the analytical analysis. For OP07, the slew rate is 0.3 V/µs which is much greater than the required and accounts for negligible error.

F. Errors due to diode voltage drop

In the proposed scheme, diode D_1 is used for ON/OFF operation of switch S_2 which makes the scheme a two-wire connection. During charging mode, D_1 is reverse bias and a reverse current of 81 pA order flows through the diode compared to mA order of charging current i_c. Hence the error caused is very negligible and can be ignored. However, during discharging mode, D_1 is forward bias and a forward current (i_{D1}) depending on R_2 flows. Because of this, the discharging current

© 2023 IEEE. Personal use is permitted, but republication/redistribution requires IEEE permission. See https://www.ieee.org/publications/rights/index.html for more information.
Authorized licensed use limited to: DELHI TECHNICAL UNIV. Downloaded on January 31,2023 at 05:26:51 UTC from IEEE Xplore. Restrictions apply.

This article has been accepted for publication in IEEE Transactions on Instrumentation and Measurement. This is the author's version which has not been fully edited and content may change prior to final publication. Citation information: DOI 10.1109/TIM.2023.3238021

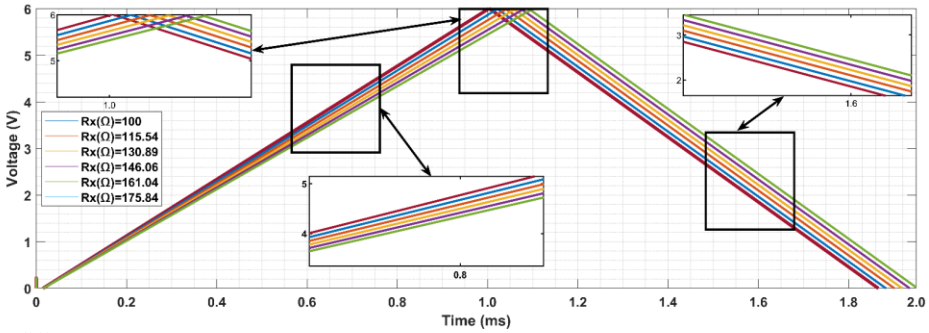

Fig. 6. Response of V_{oi} for different R_x.

(i_d') deviates from equation (4) (including switch resistance) which may result in measurement error. Therefore, an analysis is required to analyze the error which is presented following.

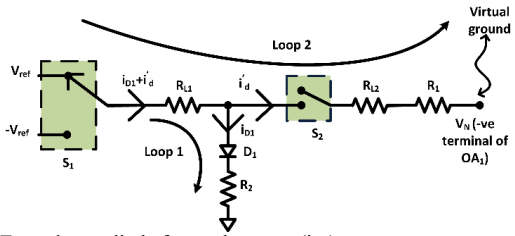

Fig. 7. Error due to diode forward current (i_{D1}).

From Fig. 7, KVL equation in loop 1

$$V_{ref} - V_D = i_{D1}(r_1 + R_{L1} + R_2) + i_d'(r_1 + R_{L1}) \quad (27)$$

From Fig. 7, KVL equation in loop 2

$$V_{ref} = i_{D1}(r_1 + R_{L1}) + i_d'(r_1 + r_2 + R_{L1} + R_{L2} + R_1) \quad (28)$$

Thereafter, equations (27) and (28) are solved to find the value of i_d' with parameter values referred in Table 1, and R_2 is varied from 1 kΩ to 50 kΩ in the step of 1 kΩ. Fig. 8 shows the plot of error (%) calculated between i_d' and i_d (calculated from equation 4 including switch resistance) with R_2 varying. It is found that the error is 0.0297 % and 0.0202 % when R_2 is 33 kΩ and 47 kΩ respectively. Thus, the error introduced due to D_1 is negligible.

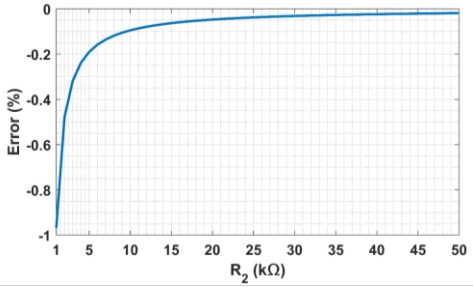

Fig. 8. Plot between R_2 and error.

It is important to note that conventional techniques and practices [21] are used and recommended for OA_1, OC_1, S_1, S_2, $\pm V_{ref}$, V_{CC}, and V_{EE} during an experiment to minimize the measurement error. Moreover, analytical computation and precise calibration inside the controller programming can be used for compensating other sources of error such as integrator non-linearity, circuit noise, and clock jitter [23].

IV. Simulation Study

The dual-slope RDC with lead wire compensation (Fig. 6) is simulated in LTSpice and Proteus software. In the simulation, OP07 and LM311 are used for opamp OA_1, and comparator OC_1 respectively. Macro model of SPST CMOS MAX 4690 and Inverter SN 7404 ICs are imported to realize S_1, S_2, and S_3 switches. The other components values are mentioned in Table I. The sensor resistance (R_x) and lead resistance ($R_{L1} = R_{L2}$) are considered as **100 Ω and 10 Ω respectively unless otherwise stated specifically.** These are typical values of Pt100 sensor at 0 °C and 33 m of 30 SWG copper wire respectively. The timing unit (TU) is realized using an Arduino Uno board with an ATMEGA328P microcontroller. A suitable C program is written in arduino sketch and burnt into the microcontroller for two timers which measure time T_1 and T_2. Timer T_1 is defined as the time taken by the integrator output (V_{oi}) to gradually rise to 6 V while timer T_2 is defined as the time taken by the integrator to decrease to 0 V. The values of T_1 and T_2 are used in equations (8), (10), and (26) to find unknown R_x. In the dual-slope RDC, Pt100 is used as the resistive sensor which is typically used for temperature measurement. The sensor has a resistance of 100 Ω at 0 °C, and a temperature coefficient (α) of 0.003851 Ω/ (Ω °C). The R_X changes with temperature following equation (29).

$$R_t = R_0(1 + \alpha(T - T_0)) \quad (29)$$

where R_0 is the resistance at $t = T_0$ °C, R_t is the resistance at $t = T$°C, T_0 is the initial temperature, and T is the final temperature.

First, in simulation sensor resistance (R_X) is varied from 100 Ω to 175.84 Ω which correspond to Pt100 resistance at 0 °C to 200 °C respectively [23]. Resistance change for 10 °C temperature change is considered as step size which corresponds to approximately ≈ 3.9 Ω.

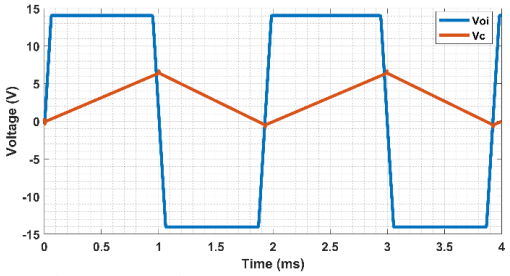

Fig. 9. V_{oi} and V_C response for Pt100.

© 2023 IEEE. Personal use is permitted, but republication/redistribution requires IEEE permission. See https://www.ieee.org/publications/rights/index.html for more information.
Authorized licensed use limited to: DELHI TECHNICAL UNIV. Downloaded on January 31,2023 at 05:26:51 UTC from IEEE Xplore. Restrictions apply.

This article has been accepted for publication in IEEE Transactions on Instrumentation and Measurement. This is the author's version which has not been fully edited and content may change prior to final publication. Citation information: DOI 10.1109/TIM.2023.3238021

Fig. 9 shows the plot of integrator output (V_{oi}) and comparator output (V_C) for R_X =100 Ω. V_C is a quasi-square wave whose duty cycle depends on the V_{oi} and V_{th}. Since V_{th} is fixed to 6 V, it primarily depends on the V_{oi}, which is a triangular waveform.

The rising slope of V_{oi} depends on R_X but the falling slope is independent of R_X as shown in fig. 6 and also in Table II. For example, the rising slope changes from 6.4847 V/ms to 5.8984 V/ms when R_X is varied from 100 Ω to 175.84 Ω. Due to different rising slopes for different R_X, each curve in fig. 6, reaches the V_{th} of 6 V at the different instants of time.

TABLE II. SLOPE FOR DIFFERENT R_X DURING FALLING

Value of R_X (Ω)	Temperature (°C)	Rising Slope (V/ms)	Falling Slope (V/ms)
100	0	6.4847	7.5675
115.54	40	6.3353	7.5357
130.89	80	6.2477	7.4285
146.06	120	6.0928	7.4793
161.04	160	6.0248	7.4355
175.84	200	5.8984	7.5405

Since they reach the V_{th} at different instants of time, the falling curves are separated from each other by a distance (≈ 4.49 µs for 10 °C change) which is found when they reached the V_{th} value. This separation is maintained throughout during falling but the slope of each curve is the same (avg. falling slope ≈ 7.4978 V/ms, Table II).

Fig. 10 shows the plot of charging mode (T_1 interval) with R_X. The T_1 interval increases linearly (R^2 ≈ 0.99) with a sensitivity of 1.190 µs/Ω with the increase in R_X in the range of 100 Ω to 175.84 Ω.

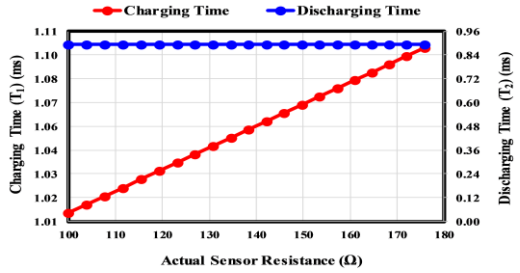

Fig. 10. Plot of T_1 and T_2 for different R_X.

Also, Fig. 10 shows the plot of discharging mode (T_2 interval) with R_X. The curve is flat and there is almost no change in the T_2 interval because R_X is bypassed.

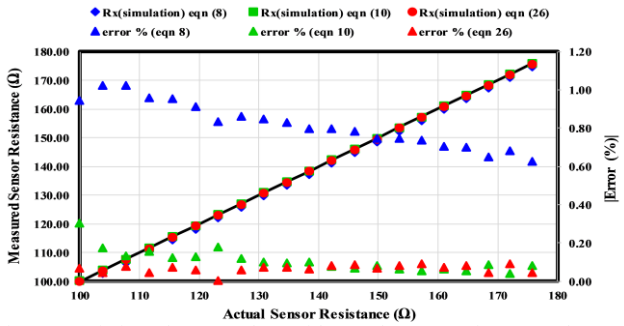

Fig. 11. Variation of measured R_X with actual sensor resistance and corresponding error from equations (8), (10) and (26) (simulation).

Fig. 11 shows the plot of measured sensor resistance from equations (8), (10), and (26) with the true value of R_X which is following a straight line. It is found that the measured resistances from equation (26) are closer to true values. For example, measured resistances from equation (26) are 100.07 Ω, 138.41 Ω, and 175.75 Ω for given R_X = 100 Ω, 138.5 Ω, 175.84 Ω which corresponds to 0 °C, 100 °C, 200 °C respectively. The slope of the curve is ≈ 1 (approx.).

Also, Fig. 11 shows the error plot in the measurement of R_X. It is found that the average errors are 0.82 %, 0.11%, and 0.07 % from equation (8), (10), and (26) respectively, and the maximum errors are ≈ 1.02 %, 0.30 %, 0.09 %. Here also, the minimum error plot is found for equation (26). Moreover, it is observed that the error decreases with an increase in R_X. So, for a resistive sensor having high resistance, the scheme would give more accurate results.

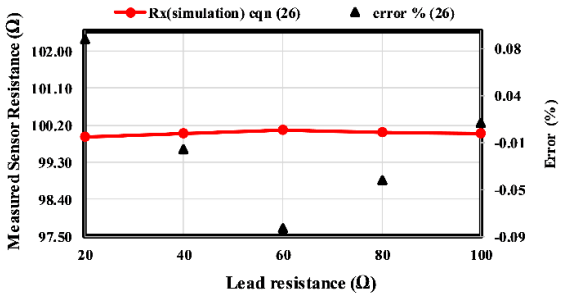

Fig. 12. Variation of measured sensor resistance with lead resistance along with its error.

Fig. 12 shows the plot of measured sensor resistance (equation 26) when R_X is fixed to 100 Ω and R_L (=R_{L1}+R_{L2}) is varied from 20 Ω to 100 Ω. The measured resistance is approximately 100.01 Ω irrespective of R_L variation. The maximum error introduced due to lead wire is ±0.08 % and the average error is 0.04 %.

V. EXPERIMENTAL SETUP AND RESULTS

A. Experimental Setup

The hardware prototype of the proposed dual-slope RDC is realized on the breadboard for testing. Fig. 13 shows the experimental setup.

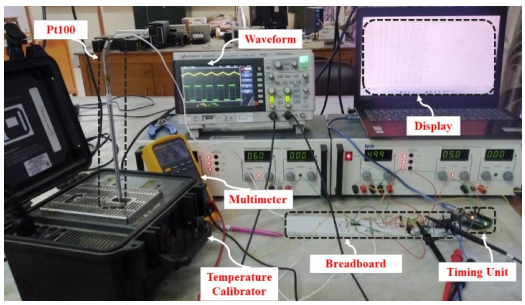

Fig. 13. Experimental setup.

The opamp (OA_1) and comparator (OC_1) are implemented using OP07 and LM311 ICs respectively. The switches S_1, S_2, and S_3 are realized using SPST CMOS MAX 4690 and Inverter SN 7404 ICs. The controlling signal V_C is inverted using IC SN7404 so that the switches S_1 and S_3 can change their positions between 0 and 1. IN4007 diode is used for generating the control signal for S_2 switch, which makes the proposed scheme a two-wire type. The feedback capacitor (C_1) is 1 µF. The resistance R_1 and R_2 are 650 Ω and 47 kΩ respectively, and the lead wire resistances R_{L1} and R_{L2} are 10 Ω each. The circuit is powered from DC regulated power supply (LQ6324T, Aplab). The positive reference voltage (+V_R) is obtained from IC 7805 and the negative reference voltage (-V_R) is obtained from IC 7905.

© 2023 IEEE. Personal use is permitted, but republication/redistribution requires IEEE permission. See https://www.ieee.org/publications/rights/index.html for more information.
Authorized licensed use limited to: DELHI TECHNICAL UNIV. Downloaded on January 31,2023 at 05:26:51 UTC from IEEE Xplore. Restrictions apply.

This article has been accepted for publication in IEEE Transactions on Instrumentation and Measurement. This is the author's version which has not been fully edited and content may change prior to final publication. Citation information: DOI 10.1109/TIM.2023.3238021

Standard decoupling capacitors are used for OP07, IC 7805 and IC 7905 to minimize ac noises. $+V_R$ and $-V_R$ is continuously monitored using two 4.5 digit multimeters (87V, Fluke) matched to ±10 µV. The Arduino Uno board with ATmega328 microcontroller is used for the timing unit, and PulseIn() function is used to measure T_{ON} and T_{OFF} of the V_C signal. Pt100 (Thermo Electric Company, Inc.) is taken as an RTD sensor (R_X) and tested using Fluke Calibration 9009 Dual-Well Dry-Well in the range of 0 °C - 200 °C in steps of 10 °C. The resistance of the Pt100 sensor is measured at different temperatures using a handheld LCR meter (U1733C, Keysight). The lead wire resistance is realized using two standard decade resistance boxes with a resolution of 1 Ω and an accuracy of ±0.01 %. The lead resistances (R_{L1} and R_{L2}) are fixed at 10 Ω each.

B. Experimental Results

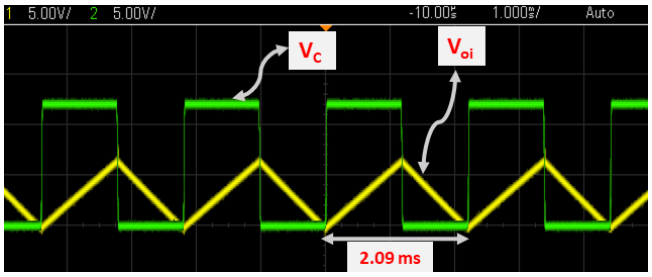

Fig. 14. V_{oi} and V_C waveforms experimental.

Fig. 14 shows the integrator and comparator outputs (V_{oi} and V_C), which are triangular and quasi-square waveforms similar to the simulation result (Fig. 9). The T_{ON} and T_{OFF} time at 0 °C (R_X = 100 Ω) is found to be 1.10 ms and 0.99 ms respectively. So, the total measurement time is $T_{ON} + T_{OFF}$ = 2.09 ms which is slightly more than simulation (1.90 ms). This may be due to stray capacitance and contact resistance of the bread board, and also due to opamp noises. In the proposed scheme, both charging and discharging times are used for measurement, but in three-cycle [17] and two-cycle [18] methods, only discharge time is used. The measurement time is 4.30 ms (simulated data) for [17] and 2.58 ms (simulated data) for [18] is shown in simulation only as claimed. Experimental measurement time is not shown. Thus, the earlier works in [17] and [18] take 105.74 % and 23.44 % time more compared to the present work, demonstrated experimentally.

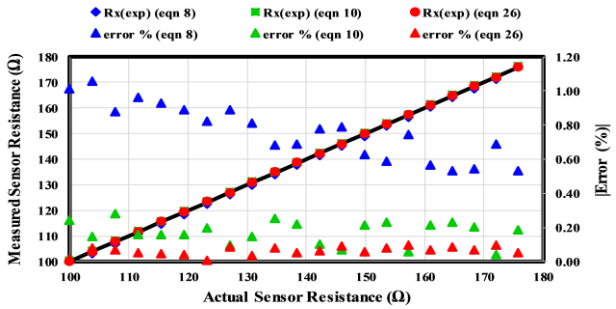

Fig. 15. Variation of measured R_X with actual sensor resistance and corresponding error from equations (8), (10) and (26) (experimental).

Fig. 15 shows the error plot for the measurement of R_X. The sensor resistance is calculated from equations (8), (10), and (26). The average errors are 0.75 %, 0.18%, and 0.05 % from equation (8), (10), and (26) respectively, and the maximum errors are ≈ 1.06 %, 0.28 %, 0.08 %. Here, the minimum error plot is found for equation (26) as also predicted in the simulation result (Fig. 11).

For the scheme to work with low R_X (≈ 100 Ω), R_1 is included in the circuit which decreases the measurement error. This is an improvement over existing RDCs that work with high R_X (≈10 kΩ) [11] only. But, the inclusion of R_1 increases the RC time constant, hence the measurement time increases, which is not a desirable characteristic. Further, it decreases the sensitivity of the scheme. It is to be noted that for high R_X, the R_1 resistance can be omitted from the circuit.

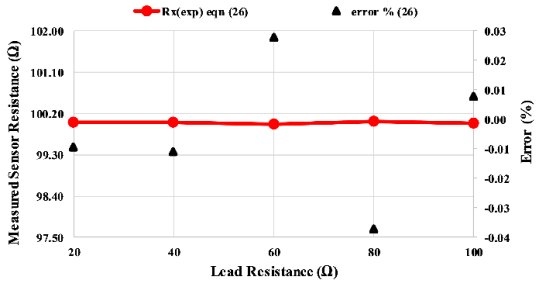

Fig. 16. Variation of measured sensor resistance with lead resistance along with its error (experimental).

Fig. 16 shows the plot of measured sensor resistance (from equation 26) when R_X is fixed to 100 Ω and R_L (=R_{L1}+R_{L2}) is varied from 20 Ω to 100 Ω. The measured resistance is approximately 100.01 Ω even if R_L is varying. The maximum error due to lead wire is ±0.04 % and the average error is 0.02 %. The plot in Fig. 16 is flat and is similar to the simulation results obtained in Fig. 12.

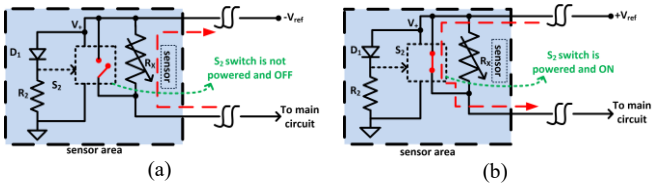

Fig. 17. Switch S_2 power supply. (a) During charging mode. (b) During discharging mode.

In our proposed scheme, the SPST switch (S_2) is required to operate during T_2 only, and it is not needed during T_1. As shown in Fig. 17(a), during T_1, the S_2 is not powered and is in OFF state because $-V_{ref}$ is connected to V_{CC} of S_2. So, the current passes through R_X and R_L. Similarly, during T_2, the V_{CC} of S_2 is connected to $+V_{ref}$. The S_2 is powered properly, and due to forward biasing of diode D_1, control signal is also fed to S_2. So, the S_2 is in ON state and current bypasses R_X as shown in Fig. 17(b). Thus, for S_2, additional power supply and connecting wires are not needed. It is to be noted that in our work, to realize S_2, MAX 4690 IC is used with single power supply (+ 5 V). Moreover, any drift or change in R_{L1}, R_{L2}, R_1, and C_1 due to aging or change in environmental condition will not affect the measurement because the same changed values of these elements are considered in both charging and discharging mode. They will cancel each other during measurement. Also, the lead wire inductance would be negligible because the circuit has a DC supply. Thus, the proposed scheme provides compensation of lead resistances.

VI. Conclusion

A dual-slope resistance to digital converter (RDC) for a low-value resistive sensor with lead resistance compensation is presented, analyzed, simulated, and experimentally verified. The proposed scheme requires one integrator, one comparator, three switches, a diode, resistors, and capacitors. The simulation and

© 2023 IEEE. Personal use is permitted, but republication/redistribution requires IEEE permission. See https://www.ieee.org/publications/rights/index.html for more information.
Authorized licensed use limited to: DELHI TECHNICAL UNIV. Downloaded on January 31,2023 at 05:26:51 UTC from IEEE Xplore. Restrictions apply.

This article has been accepted for publication in IEEE Transactions on Instrumentation and Measurement. This is the author's version which has not been fully edited and content may change prior to final publication. Citation information: DOI 10.1109/TIM.2023.3238021

experiment results show that the dual-slope RDC completes measurement in one charging-discharging cycle only, hence it provides improvement to existing RDCs, where lead compensation is not available. Moreover, it is faster compared to existing direct microcontroller interfaces (DMI) where 2 or 3 charging-discharging cycles are required. The diode voltage drop is not there in the charging and discharging path, and the error due to which is negligible. The scheme works with low-value resistive sensors (≈ 100 Ω), a feature not found in existing RDCs.

ACKNOWLEDGMENT

The authors are thankful to the Advanced Instrumentation and Measurement (AIM) Laboratory of the Instrumentation and Control Engineering dept. of NIT Tiruchirappalli for carrying out the research work.

REFERENCES

[1] *Wire Gauge Size and Resistance Calculator* [online]. Available: https://www.inchcalculator.com/wire-gauge-size-and-resistance-calculator/.

[2] R. Pallas-Areny and J. G. Webster, *Sensors and Signal Conditioning*, 2nd ed. New York: Wiley, 2000.

[3] S. Pradhan and S. Sen, "An improved lead compensation technique for three-wire resistance temperature detectors," *IEEE Trans. Instrum. Meas.,* vol. 48, no. 5, pp. 903–905, Oct. 1999.

[4] S. K. Sen, T. K. Pan, and P. Ghosal, "An improved lead wire compensation technique for conventional four wire resistance temperature detectors (RTDs)," *Measurement*, vol. 44, no. 5, pp. 842–846, 2011.

[5] T. K. Maiti, "A novel lead-wire-resistance compensation technique using two—Wire resistance temperature detector," *IEEE Sensors J.*,vol. 6, no. 6, pp. 1454–1458, Dec. 2006.

[6] W. Petchmaneelumka, P. Julsereewong, A. Julsereewong, and J. Tongpakpanang. "Simple interface circuit with lead-wire-resistance compensation for single resistive sensors," In 2012 12th *International Conference on Control, Automation and Systems*, 2012, pp. 1076-1079.

[7] T. K. Maiti and A. Kar, "Novel remote measurement technique using resistive sensor as grounded load in an opamp based V-to-I converter," *IEEE Sensors J.*, vol. 9, no. 3, pp. 244–245, Mar. 2009.

[8] T. Islam, L. Kumar, Z. Uddin, and A. Gangopadhyay, "Relaxation oscillator-based active bridge circuit for linearly converting resistance to frequency of resistive sensor," *IEEE Sensors J*., vol. 13, no. 5, pp. 1507–1513, May 2013.

[9] S. Kaliyugavaradan, "A linear resistance-to-time converter with high resolution," *IEEE Trans. Instrum. Meas*., vol. 49, no. 1, pp. 151–153, Feb. 2000.

[10] N. M. Mohan, B. George and V. J. Kumar, "Analysis of a Sigma–Delta Resistance-to-Digital Converter for Differential Resistive Sensors," *IEEE Trans. Instrum. Meas.*, vol. 58, no. 5, pp. 1617-1622, May 2009.

[11] N. M. Mohan, B. George and V. J. Kumar, "A Novel Dual-Slope Resistance-to-Digital Converter," *IEEE Trans. Instrum. Meas.*, vol. 59, no. 5, pp. 1013-1018, May 2010

[12] P. Ramanathan Nagarajan, B. George and V. J. Kumar, "An Improved Direct Digital Converter for Bridge-Connected Resistive Sensors," *IEEE Sensors J.*, vol. 16, no. 10, pp. 3679-3688, May 2016.

[13] V. Sreenath, K. Semeerali and B. George, "A Resistive Sensor Readout Circuit With Intrinsic Insensitivity to Circuit Parameters and Its Evaluation," *IEEE Trans. Instrum. Meas.*, vol. 66, no. 7, pp. 1719-1727, July 2017

[14] F. Reverter and R. Pallàs-Areny, "Direct Sensor-to-Microcontroller Interface Circuits: Design and Characterisation," Barcelona, Spain: Marcombo, 2005.

[15] F. Reverter, J. Jordana, M. Gasulla, and R. Pallàs-Areny, "Accuracy and resolution of direct resistive sensor-to-microcontroller interfaces," *Sens. Actuators A*, Phys., vol. 121, no. 1, 2005, pp. 78–87.

[16] R. N. Ponnalagu, B. George, and V. J. Kumar. "A microcontroller sensor interface suitable for resistive sensors with large lead resistance," *in Proc ICST*, Liverpool, UK, 2014, pp. 2-4.

[17] R. N. Ponnalagu, B. George, and V. J. Kumar. "Improved single-element resistive sensor-to-microcontroller interface," *IEEE Trans. Instrum. Meas.*, vol. 66, no. 10, pp. 2736-2744, June 2017.

[18] R. Anandanatarajan, U. Mangalanathan, and U. Gandhi. "Enhanced microcontroller interface of resistive sensors through resistance-to-time converter," *IEEE Trans. Instrum. Meas*., vol. 69, no. 6, pp. 2698-2706, Jul. 2019.

[19] G. Singh, U. Mangalanathan, U. Gandhi and S. Sohail, "Improved resistance to digital converter for low-value resistive sensor with lead wire compensation," *2022 IEEE Region 10 Symposium (TENSYMP)*, 2022, pp. 1-6, doi: 10.1109/TENSYMP54529.2022.9864569.

[20] Syter Technology limited, Norwich, Norfolk, UK. *Capacitance ageing of ceramic capacitors*. [online]. Available: https://www.knowlescapacitors.com/getmedia/0d900fa3-87c5-4b78-aae5-ff6a837f1a3a/an0006.pdf

[21] Sergio Franco, *Design with Operational Amplifiers and Analog Integrated Circuits*, 4th ed. New York: McGraw-Hill, 1990.

[22] Muhammad R. Rashid, *Microelectronic Circuits: Analysis and Design,* 2nd ed. Cengage Learning India, 2007.

[23] E. R. Hnatek, *A User's Handbook of D/A and A/D Converters*. Melbourne, FL: Krieger, 1988.

[24] https://www.sterlingsensors.co.uk/rtds

Gopal Singh (GSM'22) received the Bachelor's degree in Instrumentation and Control Engineering from the Institute of Engineering and Rural Technology (IERT) Allahabad (now Prayagraj), India, in 2017 and the Master's degree in Control and Instrumentation from the Delhi Technological University (DTU), New Delhi, India, in 2020. He is currently a research scholar with the Department of Instrumentation and Control Engineering, National Institute of Technology (NIT) Tiruchirappalli, India. His research areas include sensors and their signal conditioning for industrial applications.

Shiraz Sohail (GSM'15-M'17-SM'21) received the M.Tech. and the Ph.D. degree in Electrical Engineering from the Indian Institue of Technology (IIT) Kharagpur, India, in 2010 and 2016 respectively. He joined the Department of Instrumentation and Control Engineering, National Institute of Technology (NIT) Tiruchirappalli, India, in 2020 where he is currently working as an Assistant Professor. His research areas include measurements, sensors and electronic instrumentation. He is serving as one of the Associate Editor for the IEEE TRANSACTIONS ON INSTRUMENTATION AND MEASUREMENT (TIM) and the IET SCIENCE, MEASUREMENT AND TECHNOLOGY. He is selected as 2021 IEEE TIM Outstanding Reviewer, and also served one of the Associate TPC for I2MTC 2021 conference, Ottawa, Canada.

Umapathy Mangalanathan (M'19) received the Bachelor's degree in Instrumentation and Control Engineering from the Government College of Technology Coimbatore, India, in 1988, the Master's degree in Precision Engineering and Instrumentation from Indian Institue of Technology (IIT) Madras, India, in 1990 and the Ph.D. Degree in System and Control Engineering from Indian Institue of Technology (IIT) Bombay, India, in 2001. He joined the Department of Instrumentation and Control Engineering, National Institute of Technology Tiruchirappalli, India, in 1996 where he is currently working as a Professor HAG. His research areas include smart structure modelling and control, smart materials, MEMS and interval analysis.

Uma Gandhi (M'19) received her Bachelor's degree in Instrumentation and Control Engineering from the Government College of Technology Coimbatore, India, in 1989, the Master's degree in Instrumentation Engineering from the Madras Institute of Technology, Anna University, in 1992 and the Ph.D. Degree in Instrumentation and Control from the National Institute of Technology (NIT) Tiruchirappalli, India, in 2009. She joined the Department of Instrumentation and Control Engineering, National Institute of Technology Tiruchirappalli, India, in 1999 where she is currently working as a Professor. Her research areas include design and development of instrumentation systems, MEMS and process control.

Tarikul Islam (SM'17) received the M.Sc. Engg. degree in Instrumentation and Control System from Aligarh Muslim University (AMU), Aligarh, India, in 1997 and the Ph.D. (Engg.) degree from Jadavpur University, Kolkata, India, in 2007. He joined the Electrical Engineering Department, Jamia Millia Islamia (A Central University), New Delhi, India, in 1997 where he is currently working as a Professor. His research areas include sensors & sensing technologies, and electronic instrumentation. He is serving as one of the Topical Editor of IEEE SENSOR JOURNAL, Associate Editor of the IEEE TRANSACTIONS ON INSTRUMENTATION AND MEASUREMENT (TIM) and INTERNATIONAL JOURNAL ON SMART SENSING AND INTELLIGENT SYSTEMS. He is a Life Member of the IETE (India) and the ISTE (India).

© 2023 IEEE. Personal use is permitted, but republication/redistribution requires IEEE permission. See https://www.ieee.org/publications/rights/index.html for more information.
Authorized licensed use limited to: DELHI TECHNICAL UNIV. Downloaded on January 31,2023 at 05:26:51 UTC from IEEE Xplore. Restrictions apply.

Applied Biochemistry and Biotechnology
https://doi.org/10.1007/s12010-023-04350-y

ORIGINAL ARTICLE

A Novel Electrochemical Biosensor Based on Polyaniline-Embedded Copper Oxide Nanoparticles for High-Sensitive Paraoxon-Ethyl (PE) Detection

Saroj Paneru[1] · **Devendra Kumar**[1]

Accepted: 10 January 2023
© The Author(s), under exclusive licence to Springer Science+Business Media, LLC, part of Springer Nature 2023

Abstract
This paper proposes a fabrication of a hyper-sensitive amperometric biosensor for paraoxon-ethyl (PE) detection. In this developed biosensor, polyaniline (PANI) and copper oxide (CuO)–based nanocomposite is used as a sensing platform. The homogeneous distribution of CuO onto the PANI matrix enhances the surface area and conductivity of the nanocomposite. Additionally, the PANI produces a compatible environment for enzyme immobilization, which further enhances the rate of electron transfer. For biosensor fabrication, the nanocomposite is deposited electrophoretically onto the ITO glass substrate and immobilization of acetylcholinesterase (AChE) enzyme is conducted onto the fabricated electrode surface. The results validate good reproducibility, good stability, and high selectivity of the fabricated biosensor (AChE/PANI@CuO/ITO). The inhibition rate of paraoxon-ethyl (PE) is recorded in the concentration range of 1–200 nM with a low limit of detection of 0.096 nM or 96 pM. The sensitivity of the developed biosensor is found to be 49.86 $\mu A(nM)^{-1}$. The developed biosensor is further successfully accomplished for the detection of PE in real samples like rice and pulse.

Keywords Polyaniline (PANI) · Copper oxide (CuO) · Electrochemical biosensor · Organophosphate pesticides (OPs) · Acetyl cholinesterase (AChE)

Introduction

To increase productivity in the agricultural field and reduce insecticides, organophosphate pesticides (OPs) have been widely used in recent years. Although these pesticides have enormous uses in crop production, their residues in soil, water, fruits, and vegetables cause several health issues for mankind [1, 2]. The excess amount of OPs in the human body inhibits the activity of the acetylcholinesterase (AChE) enzyme, which further prevents the

✉ Devendra Kumar
dkumar@dce.ac.in

Saroj Paneru
saroj4843@gmail.com

[1] Department of Applied Chemistry, Delhi Technological University, Delhi 110042, India

Published online: 26 January 2023

hydrolysis of acetyl thiocholine chloride (ATCl). The accumulation of ATCl causes dysfunction of the brain and SLUDGE syndrome [3, 4]. Therefore, it is required to develop more advanced techniques for obtaining the optimal amount of OPs to achieve maximum crop productivity along with minimal health risks. In the literature, several analytical methods are available for determining the concentration of pesticides, among which liquid chromatography–associated mass spectrometry [5], high-pressure liquid chromatography [6], and gas chromatography coupled with mass spectroscopy [7] are the most popular. Although these methods are reliable, their complicated off-site procedure makes them more expensive and rigid in terms of implementation. Therefore, it is required to develop more robust methods which provide an authentic, cheap, and simple framework along with a low detection limit.

Electrochemical biosensors are an attractive alternative to these conventional techniques for OP detection due to their simple fabrication, easy miniaturization, the requirement of minimal concentration of analyte, and low detection limit [8–12]. Out of all electrochemical biosensors, AChE inhibition–based electrochemical biosensors are recently gaining more attention due to their high selectivity, easy fabrication, and prompt response. Their functionalities are based on the inhibition of AChE under the presence of OPs [13]. However, AChE-based biosensor suffers a low sensitivity problem due to the leakage of enzyme from the transducer surface [14]. The efficient immobilization of the AChE enzyme is highly recommended to enhance the charge transfer between enzyme and electrode surface for better sensitivity. In this regard, various transducers are developed using multiple nanocomposites [15–20].

In recent years, polyaniline (PANI) has been widely used as a supporting material for fabricating effective transducers. PANI exhibits outstanding properties like high conductivity, easy preparation, high film formation ability, and high stability. It acts significantly well as an effective mediator between enzyme and electrode surface by gaining or losing electrons (redox property) [21, 22]. Moreover, due to the presence of large amino groups, PANI shows high bio-affinity toward the AChE enzyme, which makes it more applicable in AChE-based biosensors [23]. In literature, PANI-based transducers are widely explored in biosensors [24], catalysis [25], supercapacitors [26], and glucose detection [21, 27–30]. However, very few studies of PANI-based AChE biosensors have been proposed to detect OPs [23, 31, 32].

The sensitivity and selectivity of PANI-based AChE biosensor are further improved by integrating some metal oxide. The incorporation of metal oxide provides a high surface area and enhances the catalytic activity, which further accelerates the rate of transfer of analyte molecules into the electrode surface [33]. Among all metal oxides, copper oxide (CuO) is harmless, inexpensive, highly stable, and capable of increasing the density of nanocomposite due to its incorporation with Cu and O orbitals [34, 35]. Its high catalytic and electrical properties make it more usable for supercapacitors [36] and gas sensors [37]. Additionally, its great compatibility with sulfur-containing compounds makes it the most suitable candidate for AChE-based biosensors [38].

By considering these characteristics of PANI and CuO in the biosensor fabrication, the contribution of this paper can be summarized in terms of the following novelties:

(1) This paper proposes a novel method for PE detection in which CuO and PANI contribute their unique characteristics to form an effective sensing platform. This platform enhances the sensitivity and efficiency of the proposed method due to (a) the incorporation of CuO in the PANI matrix that increases the surface area and

density of nanocomposite, which is responsible for the fast-spreading of analyte molecules; (b) PANI@CuO nanocomposite produces a compatible environment for AChE immobilization due to the presence of large amino groups in PANI, which prevents the leaching of the enzyme from the electrode surface; and (c) the integration of CuO with PANI enhances electrical conductivity and catalytic power of nanocomposite. Additionally, CuO accelerates the hydrolysis of ATCl due to its high affinity toward sulfur which further enhances the sensitivity of the proposed biosensor.

(2) To evaluate the performance of the proposed method, real sample analysis is also conducted for two samples.

(3) The literature review reveals that there is no study conducted so far regarding the fabrication of PANI@CuO nanocomposite–based transducer for electrochemical detection of PE, which further ensures the novelty of the present work.

Experimental Section

Materials and Reagents

Aniline (99%, purchased from Rankem) is used after distillation. Acetyl cholinesterase (C3389-2KU), acetyl thiocholine chloride (ATCl), paraoxon-ethyl, $CuSO_4.5H_2O$ (98.5%), sodium lauryl sulfate (85%), sodium hydroxide (NaOH) (97%), ammonium persulfate (APS) (98%), dibasic potassium phosphate (K_2HPO_4), monobasic potassium phosphate (KH_2PO_4), $K_4[Fe(CN)_6]0.3H_2O$ (98%), $K_3[Fe(CN)_6]0.3H_2O$ (99%), and sodium chloride (NaCl) are all procured from Sigma-Aldrich. All the solvents including acetone, ethanol, and hydrochloric acid are purchased from Sigma-Aldrich while the real samples (pulse and rice) are collected from the local market. Milli-Q water (18.2MΩ cm) is used for preparing all the solutions.

Synthesis of CuO Nanoparticles

CuO was synthesized by using the co-precipitation method. In this method, 1.5 g of $CuSO_4.5H_2O$ is dissolved in 50 mL of DI water under constant stirring for 30 min. Furthermore, 0.12 g of sodium lauryl sulfate was added at 90 °C with constant stirring. Subsequently, 0.4 M NaOH was added drop-wise and the resultant solution was stirred continuously for 3 h. The black precipitate of CuO was centrifuged and washed several times using ethanol and DI water. The resulting precipitate was collected and dried at 50 °C overnight. Finally, the black powder was calcined in a muffle furnace at 800 °C for 4 h.

Synthesis of PANI@CuO Nanocomposite

For preparing PANI@CuO nanocomposite, 0.114 g of as-prepared CuO nanoparticles was dispersed in 20 mL of DI water, followed by ultra-sonication until a homogeneous dispersion was obtained (solution I). Separately, 0.36 mL of distilled aniline was dispersed in 50 mL of 1 M HCl and stirred for 10 min at room temperature (solution II). The solution (I) was mixed with solution (II) and the resultant solution was stirred for 1 h. Furthermore, ammonium persulfate (APS) (1 M in DI water) was added drop-wise,

and finally, the solution was stirred for 4 h. The obtained solution was centrifuged and washed 3 to 4 times using DI water, followed by ethanol. Finally, the black precipitate was dried at 80 °C (Fig. 1A, step 1).

Electrophoretic Deposition (EPD) of PANI@CuO Nanocomposite and Then Fabrication of Biosensor

EPD of PANI@CuO nanohybrid was carried out using indium tin oxide (ITO)–coated glass substrate as a working electrode and platinum (Pt) wire as a counter electrode. In order to prepare a suspension of PANI and PANI@CuO, 10 mg of both materials was dispersed consecutively in a mixture of water and ethanol in the ratio of 5:1 through ultrasonication. Furthermore, 12 V of DC voltage was applied for 13 s to deposit PANI. Similarly, 12 V of DC voltage was applied for 14 s to deposit PANI@CuO nanohybrid. Finally, the deposited electrode was washed properly with DI water and dried at room temperature (Fig. 1A, step 2).

For biosensor fabrication, a solution of AChE enzyme was prepared by dissolving it into Tris buffer (7.5 pH) in the ratio of 1 mg/mL. The prepared solution was conserved at − 20 °C to prevent the denaturation of the enzyme. Furthermore, a stock solution was prepared by dissolving the enzyme solution in phosphate buffer 7.4 pH (0.1 mL in 1 mL PBS). For the immobilization of enzyme, 20 µL of stock solution was drop casted onto the electrode surface (Fig. 1A, step 3).

The fabricated biosensor (AChE/PANI@CuO/ITO) was kept in the refrigerator at 4 °C for overnight to achieve optimal immobilization. Before all the electrochemical

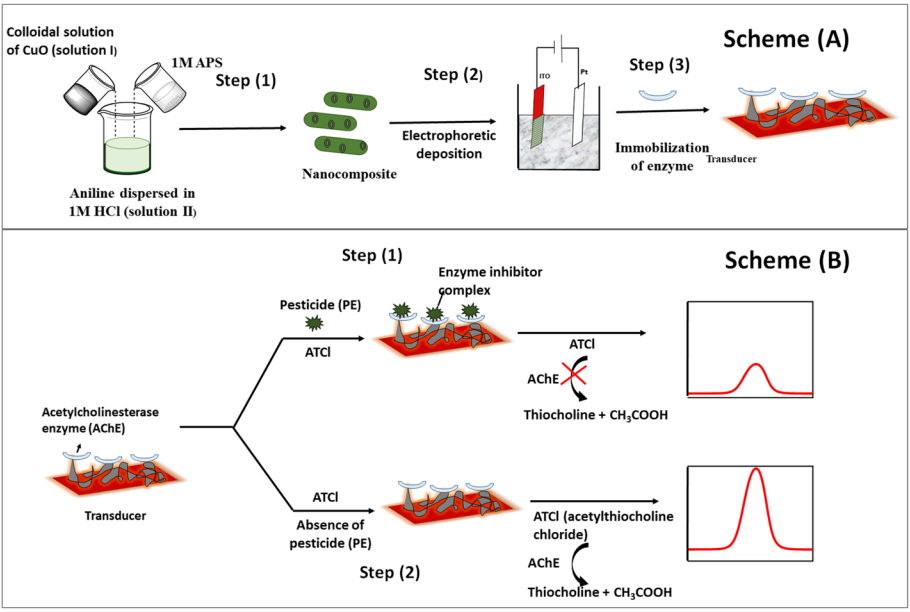

Fig. 1 **A** Schematic diagram for nanocomposite synthesis, electrophoretic deposition, and transducer fabrication. **B** Mechanism of AChE/PANI@CuO/ITO-based biosensor for PE detection

analysis, the finally prepared sensor electrode was washed with 100 µL PBS for the removal of unbounded enzyme. The concentration of AChE was also optimized by using previous studies [23, 39].

Results and Discussion

Fabrication of Sensor

In this proposed biosensor, a nanocomposite was chemically synthesized by reinforcing the CuO nanoparticles onto the PANI matrix (Fig. 1, scheme A, step 1). The incorporation of CuO helps to fill the voids of the PANI matrix, which provides a dense and smooth surface for the fast-spreading of analytes. For biosensor fabrication, the nanocomposite was electrophoretically deposited onto ITO-coated glass surface (Fig. 1, scheme A, step 2) and the enzyme was immobilized onto the fabricated electrode surface (Fig. 1, scheme A, step 3). The developed biosensor was further used to detect toxic paraoxon-ethyl (PE). In the absence of PE, thiocholine and acetic acid are formed by an electrocatalytic reaction between ATCl and AChE (Fig. 1, scheme B, step 2). Subsequently, thiocholine oxidizes into dithio-bis-choline while molecules of acetic acid spread over the surface of the electrode. The diffusion of acetic acid results in the protonation of PANI, which increases the peak current (Fig. 1, scheme B, step 2). On the other hand, the presence of PE inhibits the activity of AChE irreversibly by forming an enzyme-inhibitor complex. This inhibition restricts the hydrolysis of ATCl and reduces the peak current (Fig. 1, scheme B, step 1).

Figure 2 precisely describes the CuO-assisted mechanism involved in the electrocatalytic reaction of AChE and ATCl. In this figure, CuO catalyzes the substitution of

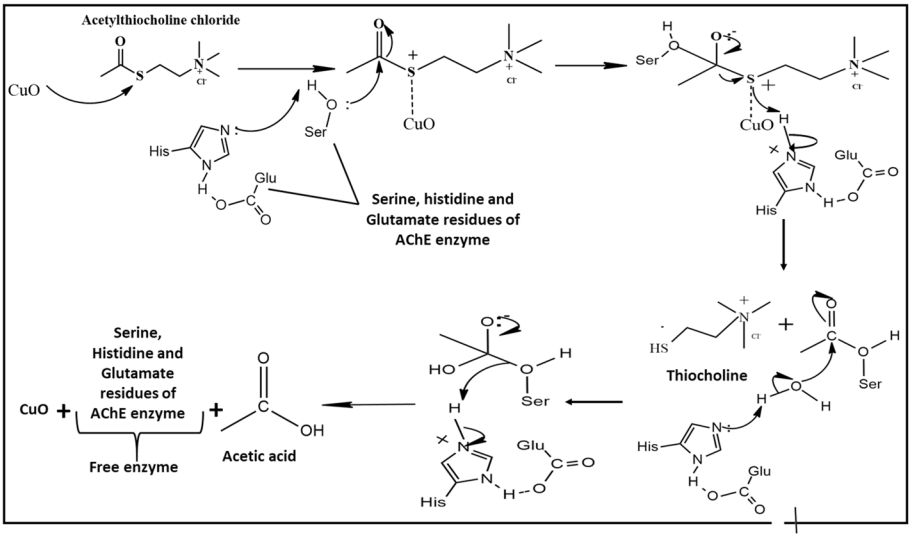

Fig. 2 CuO-assisted mechanism for the electrocatalytic reaction of AChE and ATCl

thiocholine due to its variable oxidation states (+1 and +2), which further improves the rate of electrocatalytic reaction and enhances the sensitivity of the proposed biosensor.

Studies on Chemical Structure and Components of PANI@CuO Nanocomposite

All the prepared sample materials were characterized by XRD, UV–visible, and FTIR spectroscopy. Figure 3A represents the XRD pattern of CuO, PANI@CuO, and PANI through its subgraphs (a), (b), and (c), respectively. In subgraph (a), the peaks positioned at angle 2θ = 32.6°, 35.5°, 38.8°, 45.5°, 48.4°, 53.60°, 58.3°, 61.7°, 65.8°, and 68.1° are characteristic peaks of monoclinic phase of CuO (JCPDS 48–1548) [40] [41]. In subgraph (c), a broad peak positioned at 2θ = 25° belongs to the pure PANI [42], while in subgraph (b), all defined peaks of PANI and CuO at 10°, 20°, 25°, 32.60°, 35.5°, 38.8°, 45.5°, 48.4°, 53.60°, 58.3°, 61.7°, 65.8°, and 68.1° indicate the successful incorporation of CuO onto PANI matrix [43].

The average crystallite sizes for CuO nanoparticles and PANI@CuO nanocomposite are calculated by using the following Debye–Scherrer equation:

$$D = K\lambda/\beta\cos\theta \tag{1}$$

In this equation, D represents the crystallite size, K is a constant called shape factor ($K = 0.68$–2.04, for spherical crystallite size $K = 0.94$), λ is the X-ray wavelength

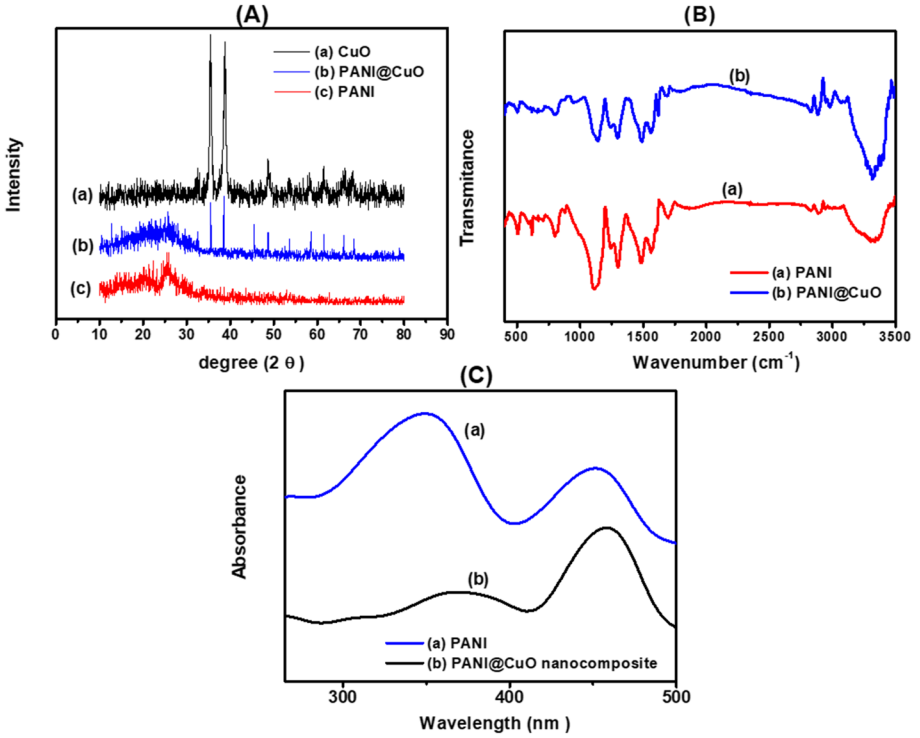

Fig. 3 **A** XRD pattern of CuO (a), PANI@CuO nanocomposite (b), and PANI (c). **B** FTIR of PANI (a) and PANI@CuO nanocomposite (b). **C** UV–visible spectra of PANI (a) and PANI@CuO nanocomposite (b)

(1.5406 Å), β is the line broadening at full-width half maxima in radian, and θ is the Bragg angle in degree. In this proposed work, the average crystallite size for CuO and PANI@CuO nanocomposite is empirically set to 30.7 and 58.8 nm, respectively.

The FTIR spectra of PANI and PANI@CuO nanocomposite are depicted in Fig. 3B through its subgraphs (a) and (b), respectively. In subgraph (a), the band obtained at 3330 cm^{-1} corresponds to –N–H stretching vibrations of aromatic amines, while the bands found at 1562 cm^{-1} and 1485 cm^{-1} correspond to C=C stretching vibrations in quinoid (Q) and benzenoid rings of PANI, respectively. The peaks located at 1245 cm^{-1} and 1294 cm^{-1} are based on C-N stretching vibrations of aromatic amine. A strong band that appears at 1120 cm^{-1} is the characteristic peak of PANI which is based on N-Q-N stretching vibrations. All the above-mentioned peaks confirm the successful synthesis of PANI. On the other hand, in subgraph (b), all the peaks of PANI@CuO nanocomposite show a slight increment in wave number (red shift) along with less intensity as compared to all defined peaks of PANI (subgraph (a), Fig. 3B). In subgraph (b), the bands of PANI (subgraph (a), Fig. 3B) at 1562 cm^{-1}, 1485 cm^{-1}, 1294 cm^{-1}, and 1120 cm^{-1} are shifted to 1568 cm^{-1}, 1490 cm^{-1}, 1304 cm^{-1}, and 1139 cm^{-1}, respectively. All the changes mentioned above in subgraph (b) are due to the presence of CuO, which causes disturbance in molecular order along with little loss of conjugation in PANI [37]. The FTIR of CuO is illustrated in Fig. S1(A), in which the bands at 443 cm^{-1} and 965 cm^{-1} correspond to the metal oxygen vibration of the Cu–O bond [40].

In Fig. 3C, subgraphs (a) and (b) show the UV–visible spectra of PANI and PANI@CuO nanocomposite, respectively. In subgraph (a), two bands are found at 347 and 451 nm. The first band appears due to the presence of π-π^* transition in the benzenoid ring. The second band appears due to the transition of polaron in the quinoid ring (polaron-π^* transition. These bands confirm the formation of PANI. In subgraph (b) (Fig. 3C), the bands of subgraph (a) (Fig. 3C) are shifted from 347 to 368 nm and 451 to 457 nm, respectively. This red shifting of the bands is due to the incorporation of CuO in the PANI matrix. In Fig. S1(B), the strong absorption band that appears at 224 nm is due to CuO [44].

Morphological Characterization of PANI, CuO, and PANI@CuO Nanocomposite

The surface morphology of all prepared materials is characterized by field emission scanning electron microscope (FE-SEM) and transmission electron microscope (TEM) images, as shown in Fig. 4. The porous network-like structure in Fig. 4A represents the FE-SEM image of PANI. Figure 4B and C represent the SEM and TEM images of spherical-shaped CuO nanoparticles. Figure 4C shows the SEM image of PANI@CuO nanohybrid. In this figure, CuO nanoparticles systematically fill the gap between the PANI matrixes. The interconnection of PANI and CuO provides a smooth surface which further increases the effective surface area and the composite's density. The empirical study confirms that the approximate average particle size of CuO is 29.96 nm (Fig. S1C).

The formation of PANI@CuO-based composite is confirmed by energy-dispersive X-ray (EDX) analysis (Fig. S2). In this figure, all peaks associated with C, N, O, and Cu are present, which confirms composite (PANI@CuO) is successfully synthesized.

Electrochemical Characterization of Fabricated Biosensor

Electrochemical studies of all the different modified electrodes are carried out by both cyclic voltammetry (CV) and electrochemical impedance spectroscopy (EIS) in 7.4 pH phosphate

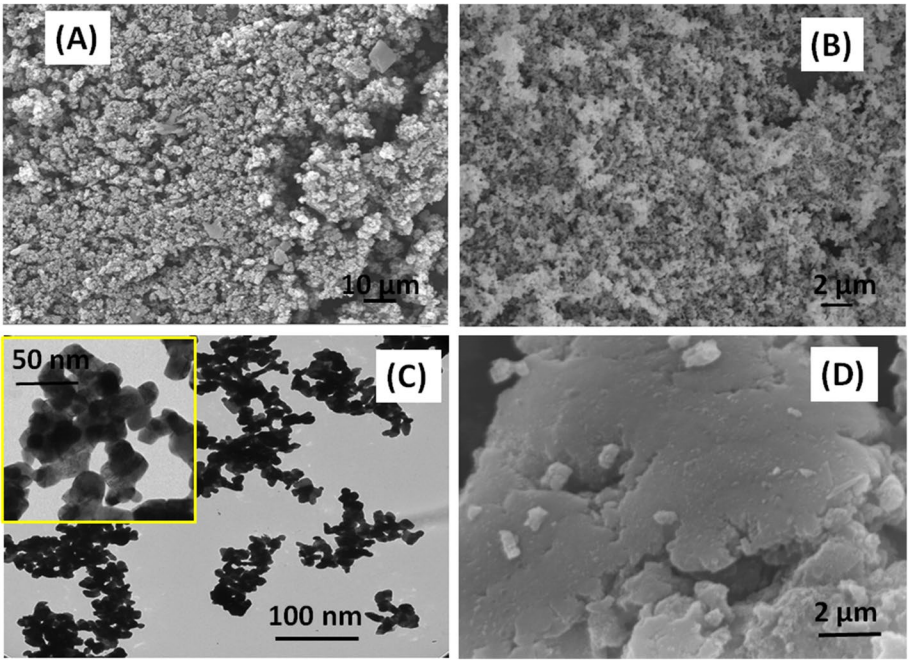

Fig. 4 **A** SEM image of PANI, **B** SEM image of CuO nanoparticles, **C** TEM image of CuO nanoparticles, **D** SEM image of PANI@CuO composite

buffer saline (PBS) containing 5 mM $[Fe(CN)_6]^{3-/4-}$ and 0.8% NaCl solutions at the scan rate of 30 mV/s. Figure 5A represents peak currents of PANI@CuO/ITO, PANI/ITO, ITO, and AChE/PANI@CuO/ITO through curves (a), (b), (c), and (d), respectively. In this figure, PANI@CuO modified ITO surface exhibits maximum peak current compared to PANI modified ITO surface along with plane ITO. The difference in peak currents occurs due to the high conductive nature and high electron transfer ability of the PANI@CuO nanocomposite, while the AChE immobilized PANI@CuO/ITO electrode shows the lowest peak current owing to the non-conducting nature of the enzyme.

Figure S3 (A) and S3 (B) illustrate CV studies of PANI and PANI@CuO nanocomposite at different scan rates (10–300 mV/s), respectively. As the scan rate increases from 10 to 300 mV/s, the anodic peak current (I_{pa}) moves toward a more positive value while the cathodic peak current (I_{pc}) tends to more negative value simultaneously. This behavior confirms the linear relation (Fig. 5B) between peak potentials (E_{pa} and E_{pc}) of PANI and PANI@CuO under logarithmic scan rate (log (υ), mV/s), which can be represented by the following equations:

$$E_{pa}\left[\text{PANI@CuO/ITO}\right] = 0.08519\text{V}\log(\upsilon) + 0.1537\text{V};R^2 = 0.9927 \quad (2)$$

$$E_{pc}\left[\text{PANI@CuO/ITO}\right] = -0.06594\text{V}\log(\upsilon) + 0.12156\text{V};R^2 = 0.9915 \quad (3)$$

$$E_{pa}\left[\text{PANI/ITO}\right] = -0.0828\text{V}\log(\upsilon) + 0.1299\text{V};R^2 = 0.9990 \quad (4)$$

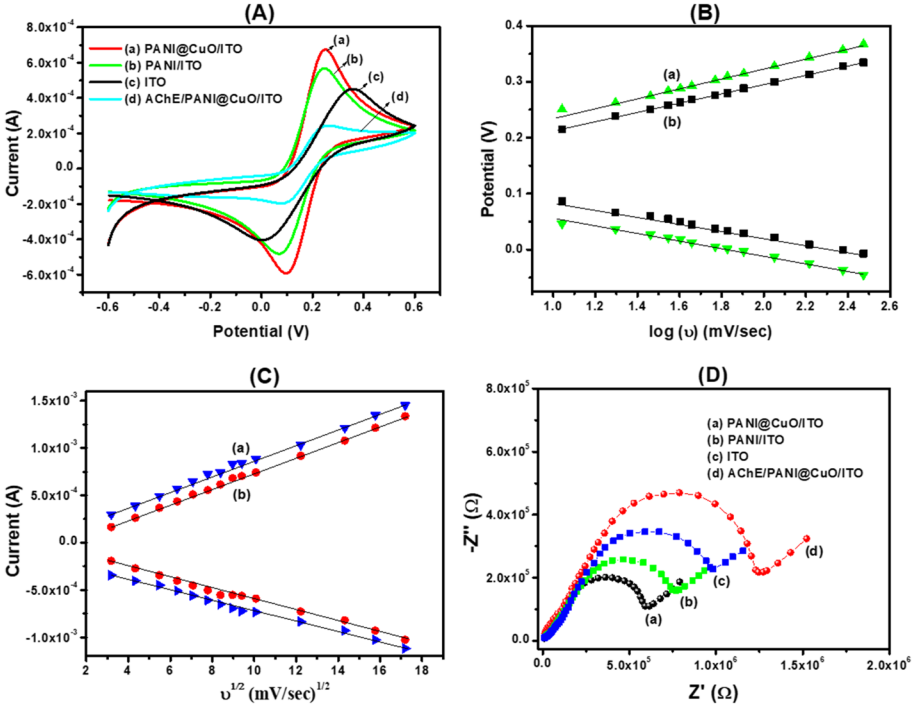

Fig. 5 **A** CV of PANI@CuO nanocomposite (a), PANI (b), ITO (c), and AChE/PANI@CuO/ITO (d) in PBS containing 5 mM $[Fe(CN)6]^{3/4-}$ and 0.8% NaCl at a scan rate of 30 mV/s. **B** Plots of potential vs. log (scan rate) for PANI@CuO nanocomposite (a) and PANI (b). **C** Plots of current vs. square root of scan rate for PANI@CuO nanocomposite (a) and PANI (b). **D** Electrochemical impedance spectroscopy (EIS) plot for PANI@CuO nanocomposite (a), PANI (b), ITO (c), and AChE/PANI@CuO/ITO (d)

$$E_{pc}\left[\text{PANI/ITO}\right] = -0.0648\text{V}\log(\upsilon) + 0.1533\text{V};R^2 = 0.9968 \tag{5}$$

The slopes of these equations are used to calculate the electron transfer coefficient (α). The calculated values of α for PANI and PANI@CuO nanocomposite are 0.899 and 0.901, respectively. Using these values of α, the charge transfer rate constant (K_s) of PANI and PANI@CuO nanocomposite is found to be 2.33×10^{-2} and 67×10^{-2}, respectively.

Figure 5C represents a relationship between peak currents (I_{pa} and I_{pc}) and square root of scan rates ($\upsilon^{1/2}$) of PANI and PANI@CuO nanocomposite modified ITO electrodes. It is clearly seen from the figure that this relationship is linear in nature and can be defined by the following equations:

$$I_{pa}\left[\text{PANI@CuO/ITO}\right] = 84.36\mu\text{A/mV/s}\times\upsilon^{1/2} + 104.36\mu\text{A};R^2 = 0.9970 \tag{6}$$

$$I_{pc}\left[\text{PANI@CuO/ITO}\right] = 54.53\mu\text{A/mV/s}\times\upsilon^{1/2} - 176.21\mu\text{A};R^2 = 0.9940 \tag{7}$$

$$I_{pa}\left[\text{PANI/ITO}\right] = 83.42\mu\text{A/mV/s}\times\upsilon^{1/2} + 21.25\mu\text{A};R^2 = 0.9984 \tag{8}$$

$$I_{pc}\left[\text{PANI/ITO}\right] = 58.56\mu\text{A/mV/s} \times \upsilon^{1/2} - 91.87\mu\text{A}; R^2 = 0.9904 \quad (9)$$

The notations in these equations have their usual meanings. Now, to calculate the effective surface area of the modified electrodes, the well-known Randles–Sevcik equation is used, which is expressed as follows:

$$I_p/\upsilon^{1/2} = 2.69 \times 10^5 n^{3/2} AD^{1/2} C \quad (10)$$

Here, I_p denotes peak currents corresponding to the anode (I_{pa}) and cathode (I_{pc}), and n is the number of electrons transferred during a redox reaction. A and υ denote an effective surface area and the scan rate of modified electrodes, respectively, while C is the concentration of $[Fe(CN)_6]^{3-/4-}$ in mol/cm^3 and D is the diffusion coefficient for $[Fe(CN)_6]^{3-/4-}$. The left-hand side of Eq. (10) represents the slope of lines formed by the linear relationship between I_p and $\upsilon^{1/2}$. Equations (6), (7), (8), and (9) help to find out the slopes for Eq. (10) to obtain the effective surface area of modified electrodes. The effective surface areas of PANI ($D = 34.81 \times 10^{-12}$ cm^2 s^{-1}) and PANI@CuO modified ITO electrodes ($D = 37.44 \times 10^{-12}$ cm^2 s^{-1}) are empirically calculated as 0.28×10^{-2} cm^2 and 1.6×10^{-2} cm^2, respectively.

Like CV, EIS is also used to investigate the electrochemical properties of the modified electrodes. EIS is based on a Nyquist plot embedded by a semicircle and a line. In this plot, the semicircle exists under the high-frequency range while the line lies in the low-frequency range. The diameter measurement of the semicircle evaluates the electron transfer resistance (R_{ct}) [45]. Figure 5D illustrates the EIS curves of the modified electrodes. In this figure, the lowest R_{ct} value of PANI@CuO nanocomposite modified ITO electrode (583.092 KΩ) (Fig. 5D, curve a) reveals that it bears a high conducting nature along with high charge transfer ability than PANI (760.100 ± 1.1 KΩ) (Fig. 5D, curve b) and ITO (981.994 ± 1.4 KΩ) (Fig. 5D, curve c), while AChE immobilized PANI@CuO/ITO electrode (1255.97 ± 1.2 KΩ) (Fig. 5D, curve d) shows the highest R_{ct} value due to the presence of non-conducting AChE which further prevents the transfer of electrons. This incremented R_{ct} value validates the successful immobilization of enzyme onto the surface of PANI@CuO modified electrode. R_{ct} is further used to calculate the exchange of current per geometric unit surface area (i_o) and an apparent electron transfer rate constant (K_{app}) by using the following equations:

$$i_o = nRT/R_{ct}F \quad (11)$$

$$K_{app} = RT/n^2F^2AR_{ct}C \quad (12)$$

Here, n, R, T, F, A, and C represent the number of transferred electrons, gas constant, temperature (K), Faraday constant, area of electrode, and concentration of $[Fe(CN)_6]^{3-/4-}$, respectively. The values of i_o and K_{app} for PANI/ITO electrode are found to be 6.08×10^{-8} A cm^{-2} and $1.28 \times 10^{--7}$ cm s^{-1}, respectively, while for PANI@CuO/ITO electrode, these values are found to be 8.21×10^{-8} A cm^{-2} and 1.73×10^{-7} cm s^{-1}, respectively.

Electrochemical Response of ATCl at Developed AChE/PANI@CuO/ITO Electrode

The electrochemical response of ATCl against AChE/PANI@CuO modified ITO electrode is examined by CV in 7.4 pH PBS at a scan rate of 50 mV/s. Figure S4 (A) represents the response of CV with 3 mM ATCl (graph a) and without ATCl (graph b). The peak

observed at 0.1 V in graph (a) indicates the presence of ATCl, while graph (b) does not contain any oxidation peak, which indicates the absence of ATCl.

On the other hand, Fig. S4 (B) represents the CV of the fabricated electrode (AChE/PANI@CuO/ITO) in the presence of ATCl having different concentrations (3 mM (curve a), 2 mM (curve b), 1 mM (curve c), and 0.5 mM (curve d). It is clear from this figure that the maximum oxidation peak current occurs at 0.1 V for the concentration value of 3 mM ATCl (Fig. S4 (B), curve a). Therefore, this concentration value is the optimal value for an excellent electrochemical performance of the fabricated electrode.

Optimization of Biosensing Parameters

To improve the efficiency of the developed biosensor for PE detection, it is required to optimize the pH value and incubation time. All optimizations were performed using the differential pulse voltammetry (DPV) technique. Figure S5 (A) shows the effect of different pH (6, 6.4, 7, 7.4, and 8) values of electrolytic solutions on sensor performance. This figure validates that the 7.4 pH value is optimal for all the electrochemical studies. Moreover, the incubation time of PE onto the AChE/PANI@CuO/ITO electrode surface plays an important role in the performance of the developed biosensor. It is clear from Fig. S5 (B) that the current decreases as the incubation time increases to the threshold limit of 10 min. After this threshold limit, the current gets a saturation stage which indicates that the hybridization is done under the threshold limit.

Determination of Pesticide

DPV is further used to estimate the concentration of PE also. The voltammetry study is carried out in 0.1 M PBS buffer (pH 7.4) containing 5 mM of $[Fe(CN)_6]^{3-/4-}$ and 3 mM ATCl using a potential window between − 0.6 and + 0.6 V at a scan rate of 50 mV/s. Figure 6A reveals the DPV studies of the AChE/PANI@CuO/ITO electrode after incubating different concentrations of PE. It is observed that the peak current decreases continuously as the concentration of PE increases from 1 to 200 nM. This decreasing trend occurs due to the inhibition of AChE under the presence of different concentrations of PE. PE covalently makes the bond with serine hydroxyl groups of AChE which further prevents the hydrolysis of ATCl and retards the production of the electron simultaneously. Figure 6B represents the calibration plot of inhibition (ΔI) vs. concentration of PE under a logarithmic scale (log C_{PE}). It is clear from this figure that the calibration plot follows linearity and can be defined as follows:

$$\Delta I = 49.86\mu A/(nM)^{-1} \times \log C_{PE} + 33.14\mu A; R^2 = 0.9984 \quad (13)$$

This is a regression equation through which the sensitivity (*S*) and limit of detection (LOD) of the developed biosensor are calculated. The sensitivity of fabricated biosensor is 49.86 μA $(nM)^{-1}$ (obtained from slope of Eq. 13) or 0.31 μA $(nM)^{-1}$ (cm^{-2}) (obtained from slope of Eq. 13/effective surface area). Furthermore, the limit of detection (LOD) of developed biosensor is calculated using following equation:

$$LOD = 3\sigma/S \quad (14)$$

Here, σ is the standard deviation and *S* is the sensitivity [45, 46]. The calculated value of LOD for developed biosensor is 0.096 nM or 96 pM. For the comparison of the

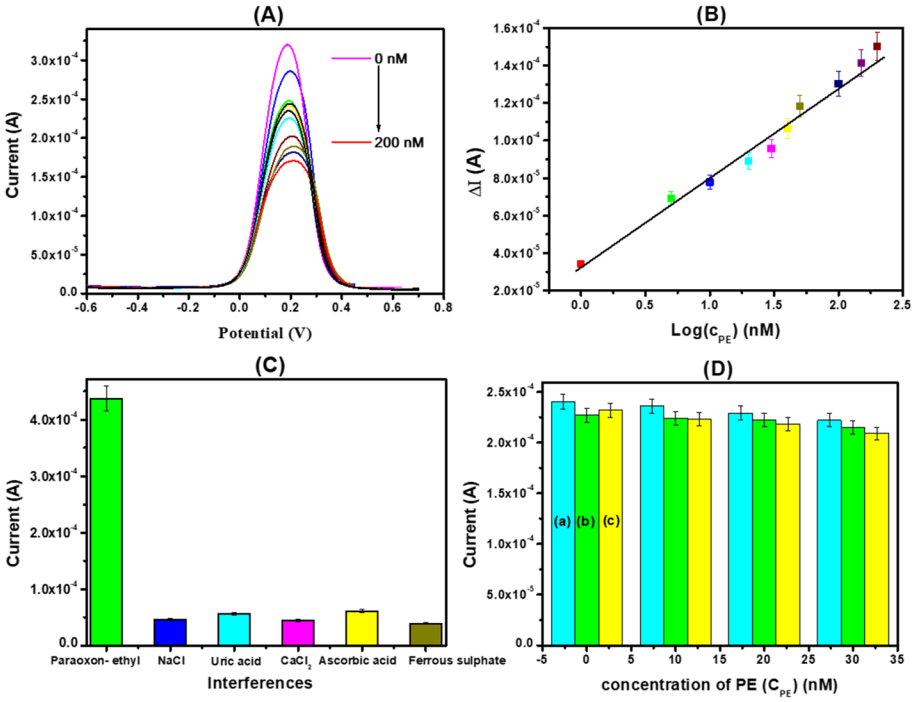

Fig. 6 **A** DPV response of AChE/PANI@CuO/ITO electrode after incubation of different concentrations of PE (1, 5, 10, 20, 30, 40, 50, 100, 150, 200 nM). **B** Calibration plot between log of PE concentration and change in current. **C** Specificity test of AChE/PANI@CuO/ITO-based biosensor in the presence of 1 μM paraoxon-ethyl, NaCl, uric acid, $CaCl_2$, ascorbic acid, and ferrous sulfate ($n=3$). **D** Electrochemical response (DPV) of biosensor in (a) PBS buffer, (b) spiked rice sample, and (c) spiked pulse sample

performance of developed biosensor, various well-known recently developed biosensors are taken under consideration for PE detection. Table 1 represents the experimental results of the considered biosensors in terms of three metrics: linear range, LOD, and sensitivity. The results validate the supremacy of the proposed biosensor over other considered biosensors in terms of all three metrics. This outstanding performance authenticates the high conductivity, high electron transfer ability, and high electrochemical properties of the proposed fabricated sensing platform. The presence of CuO nanoparticles in the PANI matrix provides a smooth and highly dense surface that helps to accelerate the electrochemical and electrical properties of the fabricated electrode. Furthermore, the presence of PANI prevents the leaching of enzymes from the electrode surface.

Studies of the Selectivity, Reproducibility, and Stability of Fabricated Biosensor

The selectivity of the developed biosensor (AChE/PANI@CuO/ITO) is studied using DPV in the presence of PE, NaCl, $CaCl_2$, uric acid, ascorbic acid, and ferrous sulfate (1 mM in 7.4 pH buffer). Their respective currents are shown in the bar diagram (Fig. 6C). Among all the considered interferents, the proposed biosensor achieves maximum peak current for PE only. It confirms that the developed biosensor is highly selective for PE.

Table 1 Comparison of the proposed biosensor with recently developed biosensors over PE detection

S. S.S. NoS. no	Fabricated electrodes	Linear range	Detection limit	Sensitivity	Sensor type	References
1	AChE/Au-MoS_2-rGO/PI	5–150 µM	1.4 µM	0.004 µA(µM)$^{-1}$	Enzymatic	[47]
2	Zn–Ni–P–S/GO/GCE	1–200 µM	35 nM	0.06369 µA(µM)$^{-1}$	Nonenzyme	[48]
3	AChE/MWCNTs-CS/AuNPs/SPCE	0.01–100 µM	0.03 µM	-	Enzymatic	[49]
4	AChE/Au-Pt-PDA	0.5–1000 nM	0.85 nM	-	Enzymatic	[50]
5	SPE/PHA/mPEG	1–10 µM	0.36 µM	0.05 µA(µM)$^{-1}$	Nonenzyme	[51]
6	GCE/YbM/f-CNFs	0.01–12 µM	0.002 µM	2.87 µA(µM)$^{-1}$ cm^{-2}	Nonenzyme	[52]
7	PdNPs/PNIPAM-CT microgel/GCE	0.01 µM to 1.3 mM	0.7 nM	1.60 µA(µM)$^{-1}$ cm^{-2}	Nonenzyme	[53]
8	AChE/PANI@CuO/ITO	1–200 nM	0.096 nM or 96 pM	49.86 µA(nM)$^{-1}$	Enzymatic	Present Work

On the other hand, reproducibility is checked by measuring DPV response toward five different electrodes (AChE/PANI@CuO/ITO) under the presence of 5 nM PE and 3 mM ATCl as shown in Fig. S6 A. It is clear from this figure that there is no significant difference among the peak currents corresponding to the five considered electrodes. The small value, which is 2.16% of their relative standard deviation (RSD), confirms the good reproducibility of the developed biosensor in the present work.

Furthermore, the stability of fabricated biosensor is also checked by analyzing the DPV response of the developed electrode (AChE/PANI@CuO/ITO) under the presence of the analyte (10 nM PE). This analysis is conducted four times within a period of 10 days. Figure S6 (B) represents the analysis in terms of a bar diagram. It is clear from this figure that there is no prominent change among the peak currents corresponding to 10, 20, and 30 days of storage time. It means that the fabricated electrode shows high stability for up to 30 days (RSD is 1.37%) of storage, while the sudden decrement of the peak current corresponding to 40 days of storage (RSD is 47.14%) confirms that it has good stability for up to 30 days storage only.

Real Sample Analysis

To check the applicability and efficiency of the developed biosensor, different concentrations of PE were measured from real samples (rise and pulse). The considered samples were pre-treated and further used for electrochemical studies. For the pre-treatment of these samples, firstly, both samples were washed with DI water, dried, and crushed. Then, 10 g of each sample was taken and mixed with 7.4 pH PBS buffer. Subsequently, the resultant sample was centrifuged at 2800 rpm for 10 min and then the supernatant liquid was separated. The separated liquids were spiked with known concentrations of PE (5 nM, 10 nM, 20 nM, 30 nM) and further used for DPV analysis [23]. Figure S7 (A) and S7 (B) represent the DPV curves of the PE spiked rice and pulse samples, respectively. It is clear from these figures that the current decreases continuously as the concentration of PE increases. On the other hand, Fig. S7 (C) and S7 (D) represent calibration plots of current vs. concentration of rice and pulse samples, respectively. The bar diagram (Fig. 6D) represents the DPV analysis through which peak currents are obtained under the presence of PE in PBS buffer ("a" in bar diagram 6D), spiked rice sample ("b" in bar diagram 6D), and spiked pulse sample ("c" in bar diagram 6D). The results presented in Table 2 validate that the biosensor shows good recovery in the range

Table 2 Detection of PE in real samples by using AChE/PANI@CuO/ITO electrode

Sample	Added amount (nM)	Found amount (nM)	Recovery (%)	RSD (%)
Pulse	5	5.4	108	5.97
	10	10.8	108	5.46
	20	21.4	107	5.22
	30	32.4	108	5.98
Rice	5	5.3	106	4.43
	10	10.4	104	5.1
	20	21.8	109	6.5
	30	33.3	111	6.6

of 104–111% along with RSD < 10% with spiked real samples. These results confirm good accuracy of the developed biosensor, which can be reliable for the detection of PE.

Conclusion

In this paper, a highly sensitive and novel electrochemical biosensor is developed for PE detection using CuO-embedded PANI nanocomposite. To achieve the optimal performance of the developed biosensor, it is further tuned in terms of different parameters like pH of PBS, amount of ATCl, and incubation time. The prepared nanocomposite possesses high conductivity, electrochemical properties, and high catalytic power through which the proposed biosensor gets its optimal performance. A comparative analysis with seven well-known and recently developed biosensors validates the outstanding performance of the proposed biosensor over PE detection in terms of sensitivity (49.86 μA $(nM)^{-1}$), linear range (1 to 200 nM), and LOD (0.096 nM or 96 pM). Additionally, the real-world applicability of the proposed biosensor is validated successfully over the PE detection for spiked rice and pulse samples.

Supplementary Information The online version contains supplementary material available at https://doi.org/10.1007/s12010-023-04350-y.

Acknowledgements The first author acknowledges to the University Grants Commission (UGC), Government of India, New Delhi, for their financial support (grant no. 351/CSIR-UGC NET DEC.2016).

Author Contribution Saroj Paneru: conceptualization, methodology, validation, and writing original draft. Devendra Kumar: supervision, writing—review and editing.

Data Availability Not applicable.

Declarations

Ethics Approval Not applicable.

Consent to Participate Not applicable.

Consent for Publication Not applicable.

Competing Interests The authors declare no competing interests.

References

1. Wei, M., & Feng, S. (2017). Amperometric determination of organophosphate pesticides using a acetylcholinesterase based biosensor made from nitrogen-doped porous carbon deposited on a boron-doped diamond electrode. *Microchimica Acta, 184*(9), 3461–3468.
2. Rajaji, U., Chinnapaiyan, S., Chen, S. M., Govindasamy, M., Oliveira Filho, J. I. D., Khushaim, W., & Mani, V. (2021). Design and fabrication of yttrium ferrite garnet-embedded graphitic carbon nitride: A sensitive electrocatalyst for smartphone-enabled point-of-care pesticide (mesotrione) analysis in food samples. *ACS Applied Materials & Interfaces, 13*(21), 24865–24876.
3. Ma, L., He, Y., Wang, Y., Wang, Y., Li, R., Huang, Z., ..., & Gao, J. (2019). Nanocomposites of Pt nanoparticles anchored on UiO66-NH2 as carriers to construct acetylcholinesterase biosensors for organophosphorus pesticide detection. *Electrochimica Acta*, *318*, 525–533.

4. Zhang, Y., Liu, H., Yang, Z., Ji, S., Wang, J., Pang, P., ..., & Yang, W. (2015). An acetylcholinesterase inhibition biosensor based on a reduced graphene oxide/silver nanocluster/chitosan nanocomposite for detection of organophosphorus pesticides. *Analytical methods*, *7*(15), 6213–6219.
5. Shin, Y., Lee, J., Lee, J., Lee, J., Kim, E., Liu, K. H., ..., & Kim, J. H. (2018). Validation of a multiresidue analysis method for 379 pesticides in human serum using liquid chromatography–tandem mass spectrometry. *Journal of agricultural and food chemistry*, *66*(13), 3550–3560.
6. He, L., Luo, X., Xie, H., Wang, C., Jiang, X., & Lu, K. (2009). Ionic liquid-based dispersive liquid–liquid microextraction followed high-performance liquid chromatography for the determination of organophosphorus pesticides in water sample. *Analytica chimica acta, 655*(1–2), 52–59.
7. Santos, C., Oppolzer, D., Gonçalves, A., Barroso, M., & Gallardo, E. (2018). Determination of organophosphorous pesticides in blood using microextraction in packed sorbent and gas chromatography–tandem mass spectrometry. *Journal of analytical toxicology, 42*(5), 321–329.
8. Rajaji, U., Murugan, K., Chen, S. M., Govindasamy, M., Chen, T. W., & Lin, P. H. (2019). Graphene oxide encapsulated 3D porous chalcopyrite (CuFeS2) nanocomposite as an emerging electrocatalyst for agro-hazardous (methyl paraoxon) detection in vegetables. *Composites Part B: Engineering, 160*, 268–276.
9. Govindasamy, M., Mani, V., Chen, S. M., Chen, T. W., & Sundramoorthy, A. K. (2017). Methyl parathion detection in vegetables and fruits using silver@ graphene nanoribbons nanocomposite modified screen printed electrode. *Scientific reports, 7*(1), 1–11.
10. Govindasamy, M., Umamaheswari, R., Chen, S. M., Mani, V., & Su, C. (2017). Graphene oxide nanoribbons film modified screen-printed carbon electrode for real-time detection of methyl parathion in food samples. *Journal of The Electrochemical Society, 164*(9), B403.
11. Govindasamy, M., Rajaji, U., Chen, S. M., Kumaravel, S., Chen, T. W., Al-Hemaid, F. M., ..., & Elshikh, M. S. (2018). Detection of pesticide residues (Fenitrothion) in fruit samples based on niobium carbide@ molybdenum nanocomposite: An electrocatalytic approach. *Analytica Chimica Acta*, *1030*, 52–60.
12. Govindasamy, M., Chen, S. M., Mani, V., Akilarasan, M., Kogularasu, S., & Subramani, B. (2017). Nanocomposites composed of layered molybdenum disulfide and graphene for highly sensitive amperometric determination of methyl parathion. *Microchimica Acta, 184*(3), 725–733.
13. Wei, M., & Wang, J. (2015). A novel acetylcholinesterase biosensor based on ionic liquids-AuNPs-porous carbon composite matrix for detection of organophosphate pesticides. *Sensors and Actuators B: Chemical, 211*, 290–296.
14. Amine, A., Mohammadi, H., Bourais, I., & Palleschi, G. (2006). Enzyme inhibition-based biosensors for food safety and environmental monitoring. *Biosensors and Bioelectronics, 21*(8), 1405–1423.
15. Joshi, K. A., Tang, J., Haddon, R., Wang, J., Chen, W., & Mulchandani, A. (2005). A disposable biosensor for organophosphorus nerve agents based on carbon nanotubes modified thick film strip electrode. *Electroanalysis: An International Journal Devoted to Fundamental and Practical Aspects of Electroanalysis, 17*(1), 54–58.
16. Kesik, M., Kanik, F. E., Turan, J., Kolb, M., Timur, S., Bahadir, M., & Toppare, L. (2014). An acetylcholinesterase biosensor based on a conducting polymer using multiwalled carbon nanotubes for amperometric detection of organophosphorous pesticides. *Sensors and Actuators B: Chemical, 205*, 39–49.
17. Dutta, R. R., & Puzari, P. (2014). Amperometric biosensing of organophosphate and organocarbamate pesticides utilizing polypyrrole entrapped acetylcholinesterase electrode. *Biosensors and Bioelectronics, 52*, 166–172.
18. Zhang, P., Sun, T., Rong, S., Zeng, D., Yu, H., Zhang, Z., ..., & Pan, H. (2019). A sensitive amperometric AChE-biosensor for organophosphate pesticides detection based on conjugated polymer and Ag-rGO-NH2 nanocomposite. *Bioelectrochemistry*, *127*, 163–170.
19. Turan, J., Kesik, M., Soylemez, S., Goker, S., Coskun, S., Unalan, H. E., & Toppare, L. (2016). An effective surface design based on a conjugated polymer and silver nanowires for the detection of paraoxon in tap water and milk. *Sensors and Actuators B: Chemical, 228*, 278–286.
20. Kaur, N., Thakur, H., & Prabhakar, N. (2016). Conducting polymer and multi-walled carbon nanotubes nanocomposites based amperometric biosensor for detection of organophosphate. *Journal of Electroanalytical Chemistry, 775*, 121–128.
21. Fang, L., Liang, B., Yang, G., Hu, Y., Zhu, Q., & Ye, X. (2014). Study of glucose biosensor lifetime improvement in 37 C serum based on PANI enzyme immobilization and PLGA biodegradable membrane. *Biosensors and Bioelectronics, 56*, 91–96.
22. Lai, J., Yi, Y., Zhu, P., Shen, J., Wu, K., Zhang, L., & Liu, J. (2016). Polyaniline-based glucose biosensor: A review. *Journal of Electroanalytical Chemistry, 782*, 138–153.

23. He, L., Cui, B., Liu, J., Song, Y., Wang, M., Peng, D., & Zhang, Z. (2018). Novel electrochemical biosensor based on core-shell nanostructured composite of hollow carbon spheres and polyaniline for sensitively detecting malathion. *Sensors and Actuators B: Chemical, 258*, 813–821.
24. Al-Sagur, H., Komathi, S., Khan, M. A., Gurek, A. G., & Hassan, A. (2017). A novel glucose sensor using lutetium phthalocyanine as redox mediator in reduced graphene oxide conducting polymer multifunctional hydrogel. *Biosensors and Bioelectronics, 92*, 638–645.
25. Bai, L., Chen, Y., Bai, Y., Chen, Y., Zhou, J., & Huang, A. (2017). Fullerene-doped polyaniline as new redox nanoprobe and catalyst in electrochemical aptasensor for ultrasensitive detection of Mycobacterium tuberculosis MPT64 antigen in human serum. *Biomaterials, 133*, 11–19.
26. Zhao, Y., Tan, R., Yang, J., Wang, K., Gao, R., Liu, D., ..., & Pan, F. (2017). 3D-hybrid material design with electron/lithium-ion dual-conductivity for high-performance Li-sulfur batteries. *Journal of Power Sources*, *340*, 160–166.
27. Kausaite-Minkstimiene, A., Mazeiko, V., Ramanaviciene, A., & Ramanavicius, A. (2010). Enzymatically synthesized polyaniline layer for extension of linear detection region of amperometric glucose biosensor. *Biosensors and Bioelectronics, 26*(2), 790–797.
28. Kim, R. E., Hong, S. G., Ha, S., & Kim, J. (2014). Enzyme adsorption, precipitation and crosslinking of glucose oxidase and laccase on polyaniline nanofibers for highly stable enzymatic biofuel cells. *Enzyme and microbial technology, 66*, 35–41.
29. Xu, Q., Gu, S. X., Jin, L., Zhou, Y. E., Yang, Z., Wang, W., & Hu, X. (2014). Graphene/polyaniline/gold nanoparticles nanocomposite for the direct electron transfer of glucose oxidase and glucose biosensing. *Sensors and Actuators B: Chemical, 190*, 562–569.
30. Cai, Q., Xu, B., Ye, L., Di, Z., Zhang, J., Jin, Q., ..., & Chen, X. (2014). Immobilization of biomolecules on cysteamine-modified polyaniline film for highly sensitive biosensing. *Talanta*, *120*, 462–469.
31. Nagabooshanam, S., John, A. T., Wadhwa, S., Mathur, A., Krishnamurthy, S., & Bharadwaj, L. M. (2020). Electro-deposited nano-webbed structures based on polyaniline/multi walled carbon nanotubes for enzymatic detection of organophosphates. *Food chemistry, 323*, 126784.
32. Kaur, B., & Srivastava, R. (2015). A polyaniline–zeolite nanocomposite material based acetylcholinesterase biosensor for the sensitive detection of acetylcholine and organophosphates. *New Journal of Chemistry, 39*(9), 6899–6906.
33. Thakur, D., Pandey, C. M., & Kumar, D. (2022). Highly sensitive enzymatic biosensor based on polyaniline-wrapped titanium dioxide nanohybrid for fish freshness detection. *Applied Biochemistry and Biotechnology*, *194*, 3765–3778.
34. Zhang, D., Jiang, C., Liu, J., & Cao, Y. (2017). Carbon monoxide gas sensing at room temperature using copper oxide-decorated graphene hybrid nanocomposite prepared by layer-by-layer self-assembly. *Sensors and Actuators B: Chemical, 247*, 875–882.
35. Jindal, K., Tomar, M., & Gupta, V. (2012). CuO thin film based uric acid biosensor with enhanced response characteristics. *Biosensors and Bioelectronics, 38*(1), 11–18.
36. Wang, K., Dong, X., Zhao, C., Qian, X., & Xu, Y. (2015). Facile synthesis of Cu2O/CuO/RGO nanocomposite and its superior cyclability in supercapacitor. *Electrochimica Acta, 152*, 433–442.
37. He, M., Xie, L., Zhao, X., Hu, X., Li, S., & Zhu, Z. G. (2019). Highly sensitive and selective H2S gas sensors based on flower-like WO3/CuO composites operating at low/room temperature. *Journal of Alloys and Compounds, 788*, 36–43.
38. Bao, J., Huang, T., Wang, Z., Yang, H., Geng, X., Xu, G., ..., & Hou, C. (2019). 3D graphene/copper oxide nano-flowers based acetylcholinesterase biosensor for sensitive detection of organophosphate pesticides. *Sensors and Actuators B: Chemical*, *279*, 95–101.
39. Loguercio, L. F., Thesing, A., Demingos, P., de Albuquerque, C. D., Rodrigues, R. S., Brolo, A. G., & Santos, J. F. (2021). Efficient acetylcholinesterase immobilization for improved electrochemical performance in polypyrrole nanocomposite-based biosensors for carbaryl pesticide. *Sensors and Actuators B: Chemical, 339*, 129875.
40. Iqbal, S., Javed, M., Bahadur, A., Qamar, M. A., Ahmad, M., Shoaib, M., ..., & Li, H. (2020). Controlled synthesis of Ag-doped CuO nanoparticles as a core with poly (acrylic acid) microgel shell for efficient removal of methylene blue under visible light. *Journal of Materials Science: Materials in Electronics*, *31*(11), 8423–8435.
41. Nagaraja, M., Prashanth, S., Pattar, J., Mahesh, H. M., & Rajanna, K. (2022). Polyaniline-CuO nanocomposite: Electrical, structural and sensor properties. *Materials Today: Proceedings, 1*(49), 1989–1992.
42. Ferreira, A. A., & Sanches, E. A. (2017). Multimorphologies of hydrochloride polyaniline synthesized by conventional and interfacial polymerization. *Journal of Molecular Structure, 1143*, 294–305.

43. de Souza, V. S., da Frota, H. O., & Sanches, E. A. (2018). Polyaniline-CuO hybrid nanocomposite with enhanced electrical conductivity. *Journal of Molecular Structure, 1153*, 20–27.
44. Mehto, A., Mehto, V. R., Chauhan, J., Singh, I., & Pandey, R. (2017). Preparation and characterization of polyaniline/ZnO composite sensor. *J. Nanomed. Res, 5*, 00104.
45. Jalil, O., Pandey, C. M., & Kumar, D. (2020). Electrochemical biosensor for the epithelial cancer biomarker EpCAM based on reduced graphene oxide modified with nanostructured titanium dioxide. *Microchimica Acta, 187*(5), 1–9.
46. Verma, S., Pandey, C. M., & Kumar, D. (2022). A highly efficient rGO grafted MoS 2 nanocomposite for dye adsorption and electrochemical detection of hydroquinone in wastewater. *New Journal of Chemistry*, *46*(44), 21190–21200.
47. Jia, L., Zhou, Y., Wu, K., Feng, Q., Wang, C., & He, P. (2020). Acetylcholinesterase modified AuNPs-MoS2-rGO/PI flexible film biosensor: Towards efficient fabrication and application in paraoxon detection. *Bioelectrochemistry, 131*, 107392.
48. Xiao, B. (2022). Electrochemical sensor based on Bimetallic phosphosulfide Zn–Ni–P–S Nanocomposite-reduced graphene oxide for determination of paraoxon ethyl in agriculture wastewater. *International Journal of Electrochemical Science, 17*(220672), 2.
49. Hua, Q. T., Ruecha, N., Hiruta, Y., & Citterio, D. (2019). Disposable electrochemical biosensor based on surface-modified screen-printed electrodes for organophosphorus pesticide analysis. *Analytical Methods, 11*(27), 3439–3445.
50. Wu, Y., Jiao, L., Xu, W., Gu, W., Zhu, C., Du, D., & Lin, Y. (2019). Polydopamine-capped bimetallic AuPt hydrogels enable robust biosensor for organophosphorus pesticide detection. *Small, 15*(17), 1900632.
51. Sgobbi, L. F., & Machado, S. A. (2018). Functionalized polyacrylamide as an acetylcholinesterase-inspired biomimetic device for electrochemical sensing of organophosphorus pesticides. *Biosensors and Bioelectronics, 100*, 290–297.
52. Karthik, R., Kumar, J. V., Chen, S. M., Kokulnathan, T., Yang, H. Y., & Muthuraj, V. (2018). Design of novel ytterbium molybdate nanoflakes anchored carbon nanofibers: Challenging sustainable catalyst for the detection and degradation of assassination weapon (Paraoxon-Ethyl). *ACS Sustainable Chemistry & Engineering, 6*(7), 8615–8630.
53. Mutharani, B., Ranganathan, P., Chen, S. M., & Karuppiah, C. (2019). Enzyme-free electrochemical detection of nanomolar levels of the organophosphorus pesticide paraoxon-ethyl by using a poly (N-isopropyl acrylamide)-chitosan microgel decorated with palladium nanoparticles. *Microchimica Acta, 186*(3), 1–11.

Publisher's Note Springer Nature remains neutral with regard to jurisdictional claims in published maps and institutional affiliations.

Springer Nature or its licensor (e.g. a society or other partner) holds exclusive rights to this article under a publishing agreement with the author(s) or other rightsholder(s); author self-archiving of the accepted manuscript version of this article is solely governed by the terms of such publishing agreement and applicable law.

Analog Integrated Circuits and Signal Processing
https://doi.org/10.1007/s10470-022-02121-z

A novel read decoupled 8T1M nvSRAM cell with improved read/write margin

Damyanti Singh[1] · Neeta Pandey[1] · Kirti Gupta[2]

Received: 11 February 2022 / Revised: 25 October 2022 / Accepted: 13 December 2022
© The Author(s), under exclusive licence to Springer Science+Business Media, LLC, part of Springer Nature 2022

Abstract
In this paper, a new memristor based read decoupled (RD) 8T1M non-volatile SRAM (nvSRAM) cell is introduced. It uses source switch transistor to improve the write performance of the proposed cell. This strategy effectively deals with the write '1' problem of single bitline cells. The isolated read port improves the read performance by avoiding the memristor connection with internal node. The non-volatile operation is performed using one transistor and one memristor (1T1M) structure and avoids the complexity during store/restore operations. The mathematical modelling for write delay, read delay and power consumption are put forward. The performance of the proposed cell is compared with the existing RD nvSRAM cells through simulation at 32 nm technology node. Compared with the existing RD nvSRAM cells, the proposed cell shows an improvement of 27.45%, 37.03%, 45.98% in write margin, read margin and read delay respectively. The proposed cell shows significant reductions upto 96.52% and 56.75% in write power and leakage power consumption in comparison to existing RD counterparts. The 1T1M structure avoids the discharging the read bitline RBL during store operation and reduces the store energy consumption by 28.92%.

Keyword nvSRAM · Memristor · HRS · LRS · Non-volatile · Volatile

1 Introduction

Static Random Access Memory (SRAM) cells occupy significant area on chip and are powered up constantly to maintain the stored data [1, 2]. The very nature of SRAM cells operation put restrictions on their use in portable devices due to limited battery life. Two macro scheme provides an alternative wherein a non-volatile memory (NVM) device is connected in parallel with SRAM [3]. The availability of power down mode allows to transfer the SRAM data to NVM device and in the event of power up the data is restored back from NVM device to SRAM cell. The scheme, despite being attractive, requires large area as SRAM and NVM devices are fabricated separately. Also, it requires longer time period to perform the store and restore operation.

The technological advancements have made fabrication of the NVM device on the CMOS chip possible which has led researchers to use single macro scheme [4]. Memristor is the best candidate among the existing NVM devices as it stores the data in the form of resistance and uses metal vias for fabrication leading to smaller footprints. The existing nvSRAM cells use the single macro scheme wherein memristor is used to perform the non-volatile operation [5–14]. In 8T3R cell [15], 1T1M structure in connected at both internal nodes of the cell to perform non-volatile operation and one memristor is connected between pull-down transistors and GND to improve read/write performance of the cell. The 8T1R cell [16] uses a feedback transistor which helps in reducing write power consumption. The 1T1M structure is used to perform non-volatile operation. In 6T2R2S cell [17], two phase transition materials (PTM) with two memristors are used to perform non-volatile operation. The 7T2M cell [18] uses self-controllable voltage level (SVL) technique to reduce power consumption and memristor is connected between power supply Vdd and PMOS transistor on both sides to perform non-volatile operation. Despite of having advantages, the available nvSRAM cell suffers from read/write conflict issue as they use same port for performing

✉ Kirti Gupta
kirtigupta22@gmail.com

[1] Department of Electronics and Communication Engineering, Delhi Technological University, Delhi 110042, India

[2] Department of Electronics and Communication Engineering, Bharati Vidyapeeth's College of Engineering, Delhi 110063, India

Published online: 28 December 2022

read and write operation. This issue is addressed in RD 8T1R [19] cell, MS 7T1R cell [20] and RD 8T1M cell [21] by introducing isolated read port in nvSRAM cells.

The existing RD 8T1R [19] cell and MS 7T1R cell [20] are shown in Fig. 1(a) and (b) respectively. Both the cells employ a back-to-back connected CMOS inverter pair Mn1-Mp1 and Mn2-Mp2 to store the single bit of data. The write operation is differential in [19] while [20] supports single ended write operation. Further, both of them has same read port, comprising of transistors T1 and T2 with T1 connected to signal RWL to control read operation in the cell. The memristor M1 is connected between the internal node Q and T1 of the read port. During read operation, two paths are formed: one from T1 and T2 and another through the T1 and M1 which affects the cell stability [19, 20]. Two paths exist during write operation in both the cells [19, 20], which affect the write margin. The store operation requires two phases namely SET and RESET wherein the use of voltage (V_{SET}) higher than Vdd, discharging of RBL to GND to set M1 in HRS results in high store energy consumption. Further, the restore operation has self-recovery to zero (SR0) and memristor data recovery (MDR) phases along with the requirement of additional inverters as the recovered data is opposite to the data restored in the cell. Thus, the two existing RD 8T1R [19] cell and MS 7T1R cell [20] has large restore delay and high energy consumption. The direct connection of M1 to the internal node Q affect the stability and also, it is a cause of leakage in the cells. In RD 8T1M cell [21], the feedback connection is formed between PMOS transistor Mp1 and inverter (Mn2-Mp2). The pull-down transistor Mn1 is turned OFF by connecting its gate terminal to GND. This topology supports write operation in single bitline cell. A two transistor (T1, T2) isolated read port is used to perform read operation. It improves the read performance as internal nodes are isolated from read path. The 1T1M structure controlled by control signals CTL1 and CTL2 exhibits the non-volatile operation. Although, RD 8T1M cell [21] has improved read, write performances and avoids the complex non-volatile operation, but the increased leakages due to removal of pull-down path is critical. To overcome the issues discussed above, a novel read decoupled (RD) 8T1M nvSRAM cell is proposed which has following features:

1) A column shared source switch transistor is employed to improve write margin.
2) The use of single write bitline is presented for lowering write power consumption.
3) The isolated read port along with elimination of memristor path improves the read margin of the proposed nvSRAM cell.
4) Reduce number of leakage current paths to lower the leakage power consumption in comparison to existing RD nvSRAM cells.

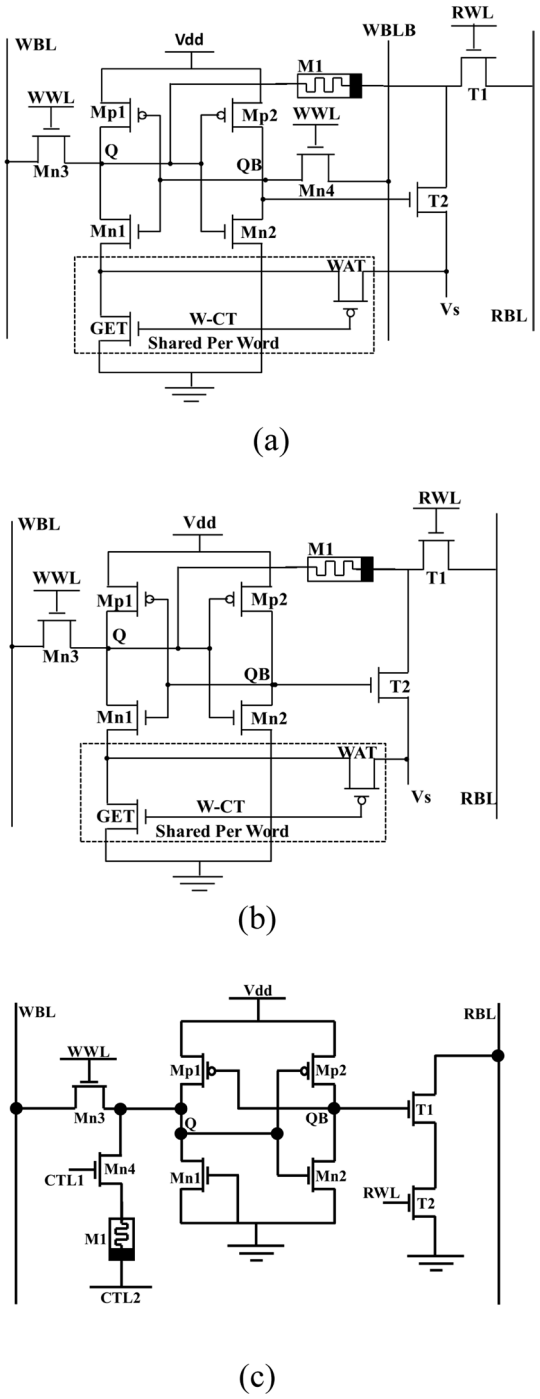

Fig. 1 Existing read decoupled nvSRAM Cells **a** RD 8T1R Cell [19] **b** MS 7T1R Cell [20] and **c** RD 8T1M Cell [21]

5) Avoiding the complete discharge of read bitline RBL during STORE operation for low store energy consumption in comparison to RD nvSRAM counterparts.

The rest of the paper is organized as follows: Sect. 2 presents the new RD 8T1M nvSRAM cell and discusses its operation. The analytical modelling of write and read

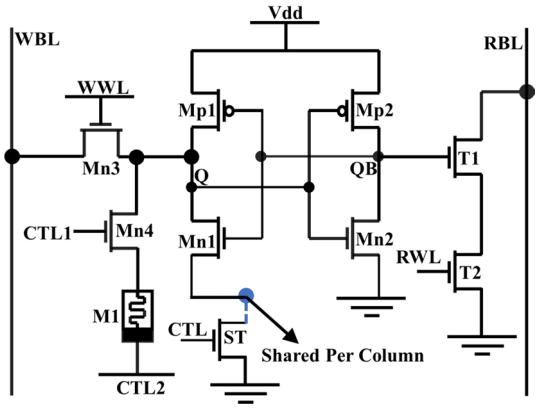

Fig. 2 Proposed RD 8T1M nvSRAM Cell

delay is put forward in Sect. 3. The functional verification of the proposed cell is done in Sect. 4 and its performance comparison with the existing nvSRAM cells is provided in Sect. 5. The effect of voltage scaling is also discussed. In the last, Sect. 6 concludes the paper.

2 Proposed RD 8T1M nvSRAM cell

The schematic of the proposed RD 8T1M nvSRAM cell is shown in Fig. 2. It consists of two back-to-back inverters formed by transistors Mn1-Mp1 and Mn2-Mp2. The pass transistor Mn3 is used to perform the write operation at the node Q and it is controlled by write wordline WWL. The transistors T1 and T2 form the read port and are controlled by node QB and the read wordline RWL. The bitlines WBL and RBL are used to perform the write and read operation, respectively. The transistor ST, controlled by the control signal CTL is a shared per column. During write operation, the signal CTL is set to LOW, turning OFF the ST transistor. It is done to improve the write ability of the proposed nvSRAM cell. While during read operation, the signal CTL is set to HIGH, turning ON the ST transistor so that there is a connection between pull-down transistors and ground. The nonvolatile operation is performed by the transistor Mn4 and memristor M1. The transistor Mn4 is controlled by the control signal CTL1 while the operation of memristor M1 is controlled by control signal CTL2. The data is stored in the memristor M1 in the form of resistance (LRS or HRS) during store operation and it is remained unaffected during power down state. This stored data can be restored to the proposed nvSRAM cell when the power is ON again.

Prior to the write operation, the bitline WBL is precharged to Vdd and after that the connection between power supply and bitline WBL is disconnected. In Fig. 3(a), the write '1' operation of the cell is depicted. During write '1' operation, the write bitline WBL is charged to Vdd while

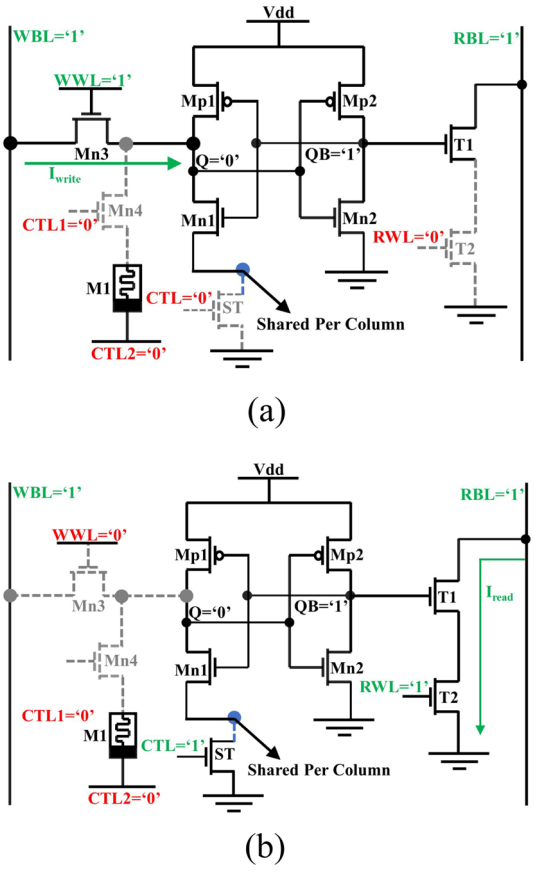

Fig. 3 Proposed RD 8T1M Cell during **a** Write '1' operation **b** Read '0' Operation

write wordline WWL and read wordline RWL are asserted HIGH and LOW respectively. The potential of internal node Q is increased to Vdd due to a current (I_{write}) flow from WBL to Q through transistor Mn3. Further the back-to-back connection of the inverters makes node QB at GND. Similarly, during write '0' operation, WBL is discharged to GND and node Q is discharge to GND through Mn3. The node QB then raises to logic '1' accordingly. Similarly, during write '0' operation, the bitline WBL is discharged to GND. The node Q is changed to logic '0' through transistor Mn3.When node Q is discharged to GND, the transistor Mp2 is turned ON and transistor Mn2 is turned OFF. It raises the potential of node QB to logic '1'. As memristor does not affect the potential of node Q during write operation therefore the write margin of the proposed RD 8T1M cell is enhanced in comparison to the existing RD nvSRAM cells.

Prior to the read operation, the bitline RBL is precharged to Vdd. In Fig. 3(b), the read '0' operation is performed. The write wordline WWL is asserted LOW, the read wordline RWL is asserted HIGH and the read bitline RBL is charged to Vdd. As the internal nodes Q and QB are at logic '0' and logic '1', respectively, the transistor T1 is turned ON. With

the assertion of signal RWL, a current (I_{read}) discharge path is formed through transistor T1 to transistor T2 to GND. It discharges the bitline RBL performing read '0' operation. For read '1' operation, node Q is at logic '1', the node QB will be at logic '0'. The transistor T1 turns OFF and the bitline RBL remains at Vdd. Since, the charging/discharging of bitline RBL does not affect the storage node Q and QB which occurs in the existing read decoupled nvSRAM cells, the stability of the proposed RD 8T1M nvSRAM cell is improved.

The non-volatile operation is performed in the proposed cell through the control signals CTL1 and CTL2. It is performed in four phases: initial-store-power down-restore. In initial phase, the proposed nvSRAM cell performs the read/write operations. During this phase, the control signals CTL1 and CTL2 remain LOW while the signals RWL, WWL and CTL are set to HIGH or LOW according to the requirement of read and write operation. The memristor M1 remains in its initial state which is HRS state. In store phase, the signal CTL1 is set to HIGH while CTL2 remains LOW. As shown in Fig. 4, node Q stores logic '1', the memristor M1 changes its state from HRS to LRS as there is a negative potential across the memristor M1. In power down phase, the power supply Vdd is turned OFF and all the control signals are set to LOW. It this phase, the node Q and QB are at logic '0' while the memristor M1 maintains its state. In restore phase, the power supply Vdd is turned ON again. The control signal CTL1 and CTL2 are set to HIGH while other control signals remain LOW. As memristor M1 is in LRS state, there is a large flow of current through transistor Mn4 and the node Q is restored to logic '1'. Similarly, the non-volatile operation for logic '0' is shown in Fig. 5. If the node Q stores logic '0', the memristor M1 does not change its state and remain in HRS state. After, the store phase, power down occurs and cell data is lost. After power down, the restore operation is carried out. As memristor is in HRS state, the node Q does not be able to rise from logic '0' and the logic '0' is restored in the cell. After restoring the data to the proposed nvSRAM cell, the memristor M1 change

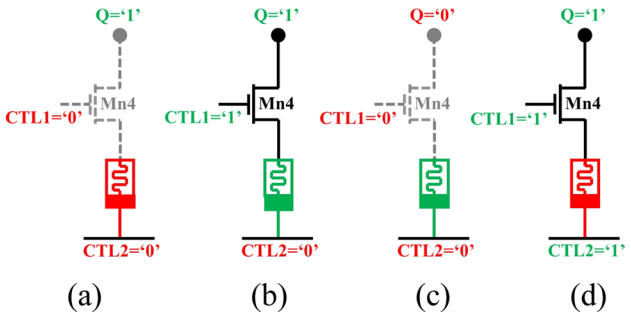

Fig. 4 Non-volatile phase **a** Initial **b** Store **c** Power Down **d** Restore for logic '1'

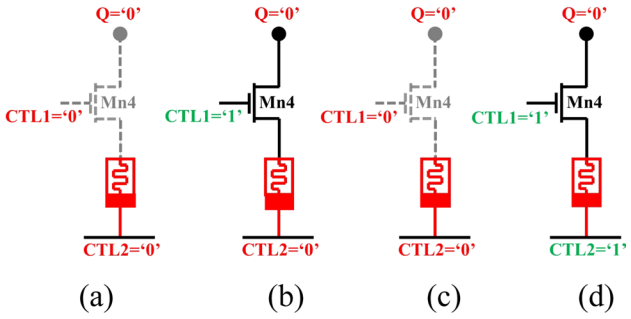

Fig. 5 Non-volatile phase **a** Initial **b** Store **c** Power Down **d** Restore for logic '0'

its state to the HRS which is its initial state also. Hence, the additional reset phase is not required in the proposed nvSRAM cell which is required in [5–9, 11, 12].

3 Analytical modelling for write and read delay

Considering the effects of short channel (like channel length modulation (λ), drain induced barrier lowering (DIBL) etc.,), the expression for drain current of a transistor is given as [22]:

$$I_{DS} = I_0 e^{K_1\left(\frac{V_{GS}-V_{th}}{\eta V_T}\right)+K_2\left(\frac{V_{GS}-V_{th}}{\eta V_T}\right)^2} e^{\frac{\lambda V_{DS}}{\eta V_T}} \left(1 - e^{-K_1\frac{V_{DS}}{V_T}}\right) \quad (1)$$

And

$$I_0 = \mu \frac{W}{L} V_T^2 K_0 \quad (2)$$

where K_0, K_1 and K_2 are fitting constants, λ is channel length modulation effect, μ is the carrier mobility, Ƞ is subthreshold swing parameter and V_T is thermal voltage.

3.1 Modelling for write delay of the proposed cell

The schematic of the proposed cell during write '1' operation is shown in Fig. 3(a). The minimum write time for write operation is given as:

$$T_{write} = C_Q \int_0^{V_{dd}/2} \frac{dV_Q}{I_{Mn3} + I_{Mp1}} \quad (3)$$

where, C_Q is the internal node Q capacitance and (Vdd/2) is the 50% charging point of internal node Q, I_{Mn3} and I_{Mp1} are the drain current of transistor Mn3 and Mp1, respectively. From the drain current expression of Eq. (1), the I_{Mn3} and I_{Mp1} are given as:

$$I_{Mn3} = I_{0n} e^{K_1\left(\frac{V_{WWL}-V_Q-V_{th}}{\eta V_T}\right)+K_2\left(\frac{V_{WWL}-V_Q-V_{th}}{\eta V_T}\right)^2} e^{\frac{\lambda\left(V_{WBL}-V_Q\right)}{\eta V_T}} \left(1 - e^{-K_1 \frac{V_{WBL}-V_Q}{V_T}}\right) \tag{4}$$

and

$$I_{Mp1} = I_{0p} e^{K_1\left(\frac{V_{QB}-V_{dd}-V_{th}}{\eta V_T}\right)+K_2\left(\frac{V_{QB}-V_{dd}-V_{th}}{\eta V_T}\right)^2} e^{\frac{\lambda\left(V_Q-V_{dd}\right)}{\eta V_T}} \left(1 - e^{-K_1 \frac{V_Q-V_{dd}}{V_T}}\right) \tag{5}$$

Here, V_{WWL} is the gate voltage, V_Q is the source voltage and V_{WBL} is the drain voltage of transistor Mn3. Similarly, V_{QB} is the gate voltage, Vdd is the source voltage and V_Q is the drain voltage of transistor Mp1. Now, let us assume that $K_1\left(\frac{V_{WL}-V_Q-V_{th}}{\eta V_T}\right) + K_2\left(\frac{V_{WL}-V_Q-V_{th}}{\eta V_T}\right)^2 = P\left(V_{WL}-V_Q, V_{thn}\right)$ and the last factor $\left(1 - e^{-K_1 \frac{V_{BL}-V_Q}{V_T}}\right) \approx 1$. On the other side, $K_1\left(\frac{V_{QB}-V_{dd}-V_{th}}{\eta V_T}\right) + K_2\left(\frac{V_{QB}-V_{dd}-V_{th}}{\eta V_T}\right)^2 = P\left(V_{QB}-V_{dd}, V_{thn}\right)$ and factor $\left(1 - e^{-K_1 \frac{V_Q-V_{dd}}{V_T}}\right) \approx 1$ □

By considering the above assumption in Eqs. (4) and (5) and putting the expressions of I_{Mn3} and I_{Mp1} is Eq. (3), the modified write delay is observed as:

$$T_{write} = C_Q \int_0^{V_{dd}/2} \frac{dV_Q}{I_{0n} e^{P(V_{WL}-V_Q,V_{thn})} e^{\frac{\lambda\left(V_{BL}-V_Q\right)}{\eta V_T}} + I_{0p} e^{P(V_{QB}-V_{dd},V_{thn})} e^{\frac{\lambda\left(V_Q-V_{dd}\right)}{\eta V_T}}} \tag{6}$$

The write power is calculated using following expression [23]:

$$P_{write} = \propto C_Q V_{dd}^2 f \tag{7}$$

where, $\propto$ is the activity factor, C_Q is the internal node Q capacitance and f is the frequency of write operation.

3.2 Modelling for read delay of the proposed cell

The schematic of the proposed cell during read '0' operation is shown in Fig. 3(b). The discharging current of read bitline (RBL) is given as:

$$-C_{RBL}\frac{dV_{RBL}}{dt} = I_{T1}\left(V_{GS} = V_{QB} - V_x, V_{DS} = V_{RBL} - V_X, V_{BS} = -V_X\right) \tag{8}$$

where C_{RBL} is the read bitline capacitance, I_{T1} is the current through transistor T_1, V_{QB}, V_x and V_{RBL} are the gate voltage, source voltage and drain voltages of transistor T_1 whose body is connected to GND terminal. The drain current of transistor T_1 can be expressed using Eq. (1) and the Eq. (8) can be rewritten as:

$$-C_{RBL}\frac{dV_{RBL}}{dt} = I_0 e^{K_1\left(\frac{V_{QB}-V_X-V_{th}}{\eta V_T}\right)+K_2\left(\frac{V_{QB}-V_X-V_{th}}{\eta V_T}\right)^2} e^{\frac{\lambda\left(V_{RBL}-V_X\right)}{\eta V_T}} \left(1 - e^{-K_1 \frac{V_{RBL}-V_X}{V_T}}\right) \tag{9}$$

Let us assume, $K_1\left(\frac{V_{QB}-V_X-V_{th}}{\eta V_T}\right) + K_2\left(\frac{V_{QB}-V_X-V_{th}}{\eta V_T}\right)^2 = P\left(V_{QB}, V_{th}\right)$, both the transistors T1 and T2 are of same size, hence, $V_x = Vdd/2$ and last factor $\left(1 - e^{-K_1 \frac{V_{RBL}-V_X}{V_T}}\right)$ is very close to 1. The above Eq. (9) can be rewritten as:

$$-C_{RBL}\frac{dV_{RBL}}{dt} = I_0 e^{P(V_{QB},V_{th})} e^{\frac{\lambda(V_{RBL}-V_X)}{\eta V_T}} \tag{10}$$

On integrating both side of Eq. (10):

$$-C_{RBL}\int_0^{\Delta V} e^{\frac{\lambda(V_X-V_{RBL})}{\eta V_T}} dV_{RBL} = I_0 e^{P(V_{QB},V_{th})} \int_0^{T_{read}} dt \tag{11}$$

where, ΔV is the change in read bitline voltage (V_{RBL}). The read delay after integrating Eq. (11) is observed as:

$$T_{read} = \frac{-C_{RBL}\int_0^{\Delta V} e^{\frac{\lambda(V_X-V_{RBL})}{\eta V_T}} dV_{RBL}}{I_0 e^{P(V_{QB},V_{th})}} \tag{12}$$

The read power is calculated using the following expression [24]:

$$P_{read} = \propto \times C_{RBL} \times V_{dd} \times \Delta V \times f \tag{13}$$

where, $\propto$ is the activity factor, C_{RBL} is the read bitline capacitance, ΔV is the change in read bitline voltage and f is the frequency of read operation.

4 Functional verification

The SPICE simulation for functional verification of the proposed RD 8T1M nvSRAM cell is performed at 32 nm PTM model. The memristor model used in this work is suggested in [25] and the following parameter values are used for simulation: $R_{OFF} = 16$ KΩ, $R_{ON} = 100$ Ω, mobility $\mu v = 10^{-14} m^2 V^{-1} S^{-1}$ and D = 10 nm. The simulations are done at Vdd = 1.0 V. Figure 6(a) and (b) shows the timing diagram of the proposed nvSRAM cell executing all the four phases: initial, store, power down and restore. The time period of each phase is taken as 2 ns which is more than two times of the time required to change the state of

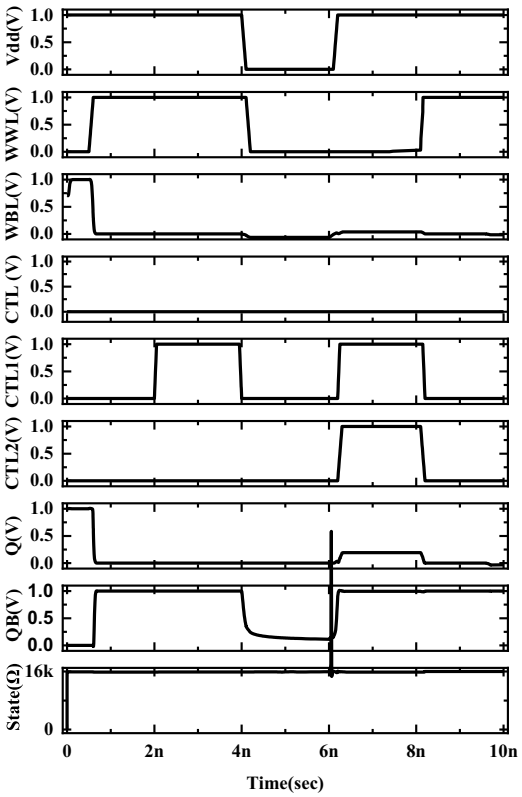

(a)

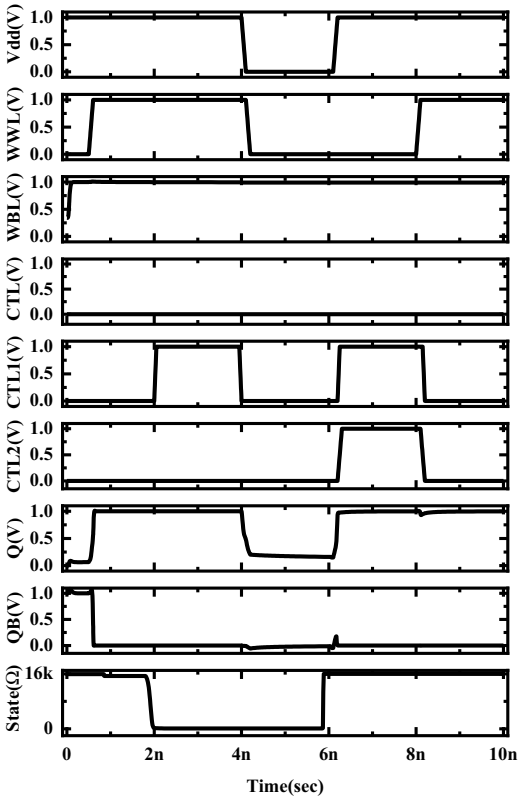

(b)

Fig. 6 Non-volatile operation of the proposed RD 8T1M nvSRAM cell for **a** Logic '0' **b** Logic '1'

the memristor [11]. The following observations are made through the Fig. 6(a).

1) The initial phase is carried from 0 to 2 ns. In this phase write '0' operation is performed. The bitline is precharged to Vdd prior to the write operation. The control signal WWL is set to HIGH while the signals CTL, CTL1 and CTL2 are set to LOW. The bitline WBL is discharge to GND and the data at node Q is changed to logic '0' through the pass transistor Mn3.
2) The store operation is performed from 2 to 4 ns. In this phase, the control signals WWL and CTL1 are set to HIGH while the signal CTL and CTL2 is set LOW. As the data at node Q is logic '0', there will be no potential difference across the memristor M1. The memristor M1 will remain in HRS state which is its initial state also.
3) In power down phase from 4 to 6 ns, the power supply and all the control signals will be LOW. The data at node Q and QB will be changed to logic '0' due to power down while memristor M1 will maintain its state which is HRS.
4) After power down, the restore operation will be performed from 6 to 8 ns. In restore phase, the power supply and the control signals CTL1 and CTL2 are set HIGH while other signals remain LOW. Due to the HRS state of the memristor M1, the node Q will not be able to rise quickly from logic '0' and the logic '0' is restored in the proposed nvSRAM cell. After restore operation, the normal operation is carried out.

Similarly, Fig. 6(b) shows the non-volatile operation for logic '1'. In the initial phase, write '1' operation is performed. As the bitline WBL is already precharged to Vdd, the node Q changes its data to logic '1'. In store phase, the memristor M1 changes its state from HRS to LRS. As the node Q is at logic '1', there will be a negative potential difference across the memristor M1 which results in change in the state of memristor M1. In power down phase, the memristor remains in LRS state while other controlling signals and power supply are set LOW. In restore phase, the power supply in ON again, there will be large flow of the current through transistor Mn4 which raises the potential of the node Q quickly and logic '1' is restored in the nvSRAM cell. After restoring the data at the node Q, the memristor M1 changes its state to HRS which is its initial state also and hence, an additional RESET phase is not required in the proposed nvSRAM cell.

Table 1 Dimension of Transistors of various nvSRAM Cells

Transistors	W/L (nm) of nvSRAM Cells			
	RD 8T1M [19]	MS 7T1R [20]	RD 8T1M [21]	Proposed RD 8T1M
Mn1	72/36	72/36	72/36	72/36
Mp1	72/36	72/36	72/36	72/36
Mn2	72/36	72/36	72/36	72/36
Mp2	72/36	72/36	72/36	72/36
Mn3	72/36	72/36	72/36	72/36
Mn4	72/36	-	72/36	72/36
T1	72/36	72/36	72/36	72/36
T2	72/36	72/36	72/36	72/36

5 Performance analysis

In this section, the proposed RD 8T1M nvSRAM cell is compared the existing RD 8T1R cell [19], MS 7T1R cell [20] and RD 8T1M [21] and their transistors dimension are given in Table 1. The read/write and store/restore performance of the proposed and existing nvSRAM cells is carried out at different Vdd.

5.1 Read performance

The read performance of RD 8T1R cell [19], MS 7T1R cell [20], RD 8T1M cell [21] and proposed RD 8T1M cell is carried out in terms of read delay, read margin and read power consumption.

5.1.1 Read delay

The read delay is defined as the time interval between the 50% point of RWL signal when there is low to high transition and the voltage of the RBL bitline until it is dropped by 200 mV, when logic '0' is stored at node Q [26]. The read delay of RD 8T1R cell [19], MS 7T1R cell [20], MS 8T1M cell [21] and proposed RD 8T1M nvSRAM cell is shown in Fig. 7(a) and improvement of 25.28% is observed in the read delay of proposed RD 8T1M cell in comparison to RD 8T1R cell [19] and MS 7T1R cell [20], at Vdd = 1.0 V. The read port in proposed cell is connected to GND which increases the potential of read port and hence the read current is increased. It results in fast read operation of the proposed nvSRAM cell. However, in existing nvSRAM cells, the read port is floating which reduces the potential across the read port and hence the read current is reduced. It decreases the read delay of the existing nvSRAM cells. The RD 8T1M cell [21] shows the read delay same as proposed cell. From Fig. 7(a), the decreasing trend in read delay is also observed with increase in power supply.

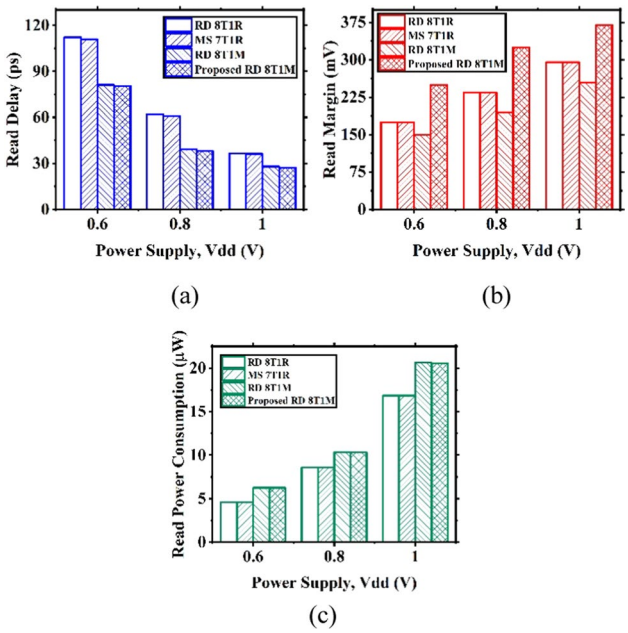

Fig. 7 **a** Read Delay **b** Read Margin **c** Read Power Consumption of RD 8T1R Cell [19], MS 7T1R Cell [20], RD 8T1M cell [21] and Proposed RD 8T1M Cell.

5.1.2 Read margin

It is defined as the maximum amount of DC noise voltage that can be tolerated by the cross coupled inverter pair such that the SRAM cell can retain its data. The length of the largest square that can be fitted inside the butterfly curve gives the value of the read margin [27]. The read margin of RD 8T1R cell [19], MS 7T1R cell [20] and proposed RD 8T1M cell is shown in Fig. 7(b). It is observed that the read margin of the proposed RD 8T1M cell is 25.42% better than existing nvSRAM cells at Vdd = 1.0 V. In existing nvSRAM cells, the direct connection of memristor to the storage node of the cell affects the node potential which reduces the stability of the cell. However, in proposed nvSRAM cell, the transistor Mn4 avoids the directs connection of memristor to the storage node of the cell and read margin is improved. While, in RD 8T1M cell [21], the grounded transistor Mn1 reduces the read margin of the cell. Also, the increasing trend in read margin is observed with increase in the power supply as shown in Fig. 7(b).

The nvSRAM cells show the worst case read margin during FS (Fast NMOS and Slow PMOS) corner [28]. During FS corner, the nvSRAM cells gives worst read margin. In this, NMOS become stronger than PMOS transistor. It increases the pull-down to access transistor ratio due to increased current driving capability of NMOS transistor. It

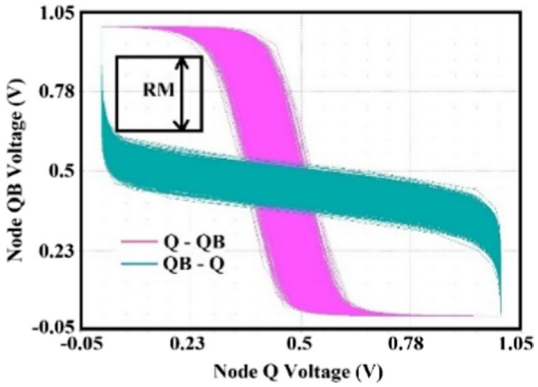

Fig. 8 Read margin of proposed RD 8T1M nvSRAM cell under 6σ global process and 1σ local mismatch variations @5000 runs

can easily flip the cell data during read mode and degrades the cell stability. In proposed cell, the series connection of NMOS transistors Mn1 and ST reduces the driving capability of pull-down path and improves the read margin of the cell. The Monte Carlo simulations are also carried out at 6σ global process and 1σ local mismatch variations for 5000 runs to analyze the performance of the proposed cell @ Vdd = 1.0 V. Figure 8 shows the read margin of 295 mV under process variations.

5.1.3 Read power consumption

The read power consumption of RD 8T1M cell [19], MS 7T1R cell [20] and proposed RD 8T1M nvSRAM cell is shown in Fig. 7(c). It is observed that the read power consumption of proposed cell is increased by 22.01% in comparison to RD 8T1R cell [19] and MS 7T1R cell [20]. In both the existing nvSRAM cells, the floating read port reduces the read current which reduces the read power consumption. In proposed nvSRAM cell, the read port is connected to GND due to which the read current is increased. It causes the more read power consumption of the proposed cell in comparison to existing RD 8T1M [19] and MS 7T1R [20] nvSRAM cells. The RD 8T1M cell [21] shows the read power consumption same as the proposed cell as both have similar read port. From Fig. 7(c), it is also observed that the increase in the power supply leads to more read power consumption.

5.2 Write performance

The write performance of RD 8T1R cell [19], MS 7T1R cell [20], RD 8T1M cell [21] and proposed RD 8T1M cell is carried out in terms of write delay, write margin and write power consumption.

5.2.1 Write delay

The write delay is measured as the time interval between the 50% point of signal which activates the write driver and the time when the node Q reach the 50% of full swing [26]. The write delay of the proposed RD 8T1M cell and existing nvSRAM cells is shown in Fig. 9(a). It is observed that the write delay of proposed RD 8T1M cell is increased by 44.78% in comparison to RD 8T1R cell [19] and decreased by 13.73% and 7.47% in comparison to MS 7T1R cell [20] and RD 8T1M cell [21], respectively, at Vdd = 1.0 V. In RD 8T1M cell [19], the write operation is differential i.e., bitlines WBL and WBLB are used to perform the write operation, which increases the write speed of the cell in comparison to the single ended write operation which is performed in MS 7T1R cell [20], RD 8T1M cell [21] and proposed RD 8T1M cell. Also, the proposed nvSRAM cell need more current through transistor Mn1 during write operation, which reduces the delay of the cell in comparison to MS 7T1R cell [20] and RD 8T1M cell [21]. It is also observed from Fig. 8(a) that increases in the power supply reduces the write delay of the nvSRAM cells.

5.2.2 Write margin

The write margin is defined by the write trip voltage, which is evaluated as the maximum amount of DC voltage required on the bitline to flip the cell data [27]. As the write operation

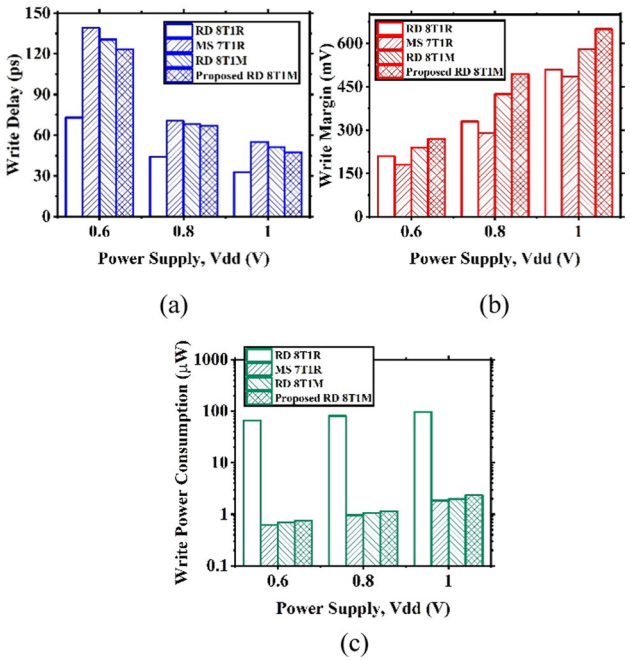

Fig. 9 **a** Write Delay **b** Write Margin **c** Write Power Consumption of RD 8T1R Cell [19], MS 7T1R Cell [20], RD 8T1M Cell [21] and Proposed RD 8T1M Cell

depends on single bitline WBL only, the word line sweep method, which is improvement over bitline sweep method, is used to calculate the write margin [29]. The write margin of proposed RD 8T1M cell and existing RD nvSRAM cells is shown in Fig. 9(b). It is observed that the write margin of proposed RD 8T1M cell is increased by 27.45%, 34.02% and 25.38% in comparison to RD 8T1R cell [19], MS 7T1R cell [20] and RD 8T1M cell [21], respectively, at Vdd = 1.0 V. In existing RD 8T1M [19] and MS 7T1R [20] nvSRAM cells, there are two paths to perform the write operation: one path is through pass transistor Mn3 and another path is through memristor. The current of the write path through memristor directly affect the node Q potential which reduces the stability of the cell. Form Fig. 8(b), it is also observed that at higher supply voltage, the write margin of the nvSRAM cells is increased.

The nvSRAM cells show the worst case write margin during SF (Slow NMOS and Fast PMOS) corner [28]. During SF corner, PMOS become stronger than NMOS transistor. It increases the current driving capability of PMOS transistor which results in reduced access to pull-up ratio. It degrades the write performance of the cell. In proposed cell, the isolation between NMOS transistor Mn1 and GND during write operation improves the write margin. The write '1' operation is crucial in single bitline nvSRAM cells as NMOS access transistor gives weak '1'. The absence of pull-down path in proposed cell improves the write '1' performance. The Monte Carlo simulations are also carried out at 6σ global process and 1σ local mismatch variations for 5000 runs to analyse the write margin of the proposed cell under process variations. Figure 10 shows the write margin of 480 mV @ Vdd = 1.0 V.

5.2.3 Write power consumption

The write power consumption of proposed RD 8T1M cell and existing nvSRAM cells is shown in Fig. 8(c). It is observed that the write power consumption of proposed RD 8T1M cell is decreased by 98.08% and increased by

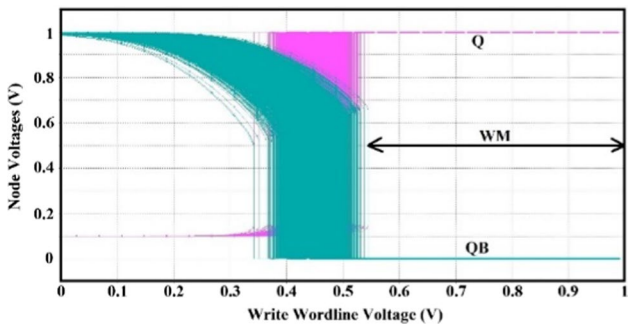

Fig. 10 Write margin of proposed RD 8T1M nvSRAM cell under 6σ global process and 1σ local mismatch variations @5000 runs

21.28% and 15.74% in comparison to RD 8T1R cell [19], MS 7T1R cell [20] and RD 8T1M cell [21], respectively at Vdd = 1.0 V. In proposed cell, the write operation is performed through single bitline WBL. This bitline WBL is discharged during write '0' operation and remain unaffected i.e., at Vdd during write '1' operation. However, in RD 8T1M cell, the bitlines WBL and WBLB are charged/discharged during both write '0' and write '1' operation which consumes most of the cell power. The increasing trend in write power consumption is observed with increase in power supply as shown in Fig. 9(c).

5.3 Leakage power

The leakage paths in proposed and existing RD nvSRAM cells in hold mode are shown in Fig. 11. In RD 8T1M cell [21], one of the pull-down transistors Mn1 remains OFF as shown in Fig. 11(a), which is a cause of increased leakage in the cell. Alternatively, in RD 8T1R [19] and MS 7T1R [20] cell, the direct connection of memristor to the internal node Q introduces a leakage path through memristor to transistor T2 to Vs (for Q = '0' and QB = '1'), shown in Fig. 11(b) and (c), respectively, and it increases leakage in the cell. This path is not present in the proposed nvSRAM cell as shown in Fig. 11(d). Figure 12 shows the variation in leakage power consumption in different RD nvSRAM cells with supply voltage. It is observed that the proposed cell shows minimum leakage power consumption and it is reduced by 44.41%, 20.18% and 56.75% in comparison to RD 8T1R, MS 7T1R and RD 8T1M cells, respectively, at Vdd = 1.0 V. Also, it is observed that the increase in power supply increases the leakage power consumption.

5.4 Store/restore performance

The store/restore performance of the proposed RD 8T1M cell and existing nvSRAM cells is evaluated in terms of delay and energy consumption. The store delay is the time required to change the state of memristor i.e. from HRS to LRS or LRS to HRS, according to the data stored at the storage node Q of the nvSRAM cell. While, the restore delay is the time required to restore the data from memristor to storage node Q of the cell after power down operation. In existing RD 8T1R cell [19] and MS 7T1R cell [20], the store operation requires two operations, namely SET and RESET, while, the restore operation requires SR0 and MDR operations. If logic '0' is present at the node Q, memristor needs to be in LRS state, the SET operation is performed and if memristor is connected to logic '1' node, memristor should be in HRS state, RESET operation is performed. To perform the restore operation, first, the storage node Q is initialized to logic '0' then the data is recovered from the memristor to the

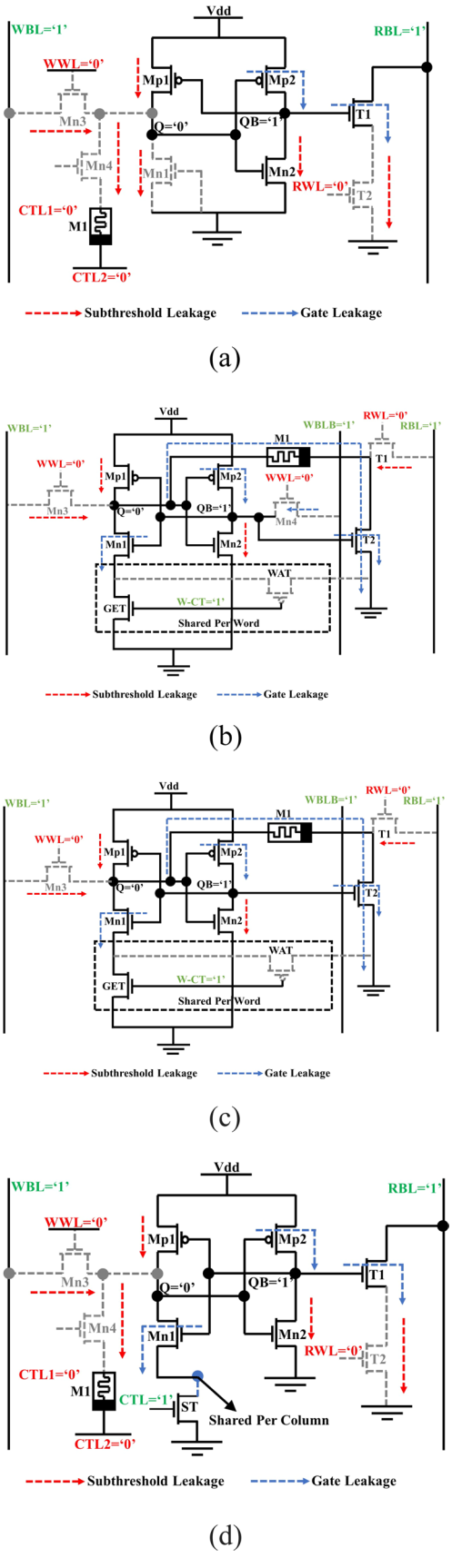

Fig. 11 Leakage current path in **a** RD 8T1M **b** RD 8T1R **c** MS 7T1R ▶ and **d** proposed RD 8T1M nvSRAM cell

storage node of the cell. The RD 8T1M cell [21] performs the store/restore operation same as proposed RD 8T1M cell and hence it shows similar store/restore delay and energy consumption.

The proposed RD 8T1M nvSRAM cell does not require such complex operation to perform the store/restore operation. The store/restore operation are controlled by control signals CTL1 and CTL2 as discussed in section II. The store/restore delay of the proposed RD 8T1M cell with variation in power supply is shown in Fig. 13. It is observed that with increase in power supply, the delay is decreasing. At Vdd = 1.0 V, the store delay is observed as 25.33 ps and restore delay is observed as 20.63 ps. Figure 14 shows the store/restore energy consumption of proposed RD 8T1M nvSRAM cell at different power supply. The increasing trend in energy consumption is observed with the power supply. At Vdd = 1.0 V, the store energy consumption is observed as 445 fJ and restore energy consumption is observed as 565 fJ.

5.5 Area comparison

The lithographically symmetrical layout of proposed and existing RD nvSRAM cells are shown in Fig. 15. The area occupied by MS 7T1R, RD 8T1R, RD 8T1M and proposed RD 8T1M nvSRAM cell is 0.33 μm^2, 0.42 μm^2, 0.46 μm^2 and 0.45 μm^2, respectively. The MS 7T1R nvSRAM cell consumes minimum area while the area occupied by RD 8T1R, RD 8T1M and proposed RD 8T1M nvSRAM cell is nearly same.

The performance comparison of the proposed and existing RD nvSRAM cells is summarized in Table 2 at Vdd = 1.0 V. From Table 2, it is clear that the proposed cell offers improved read delay, read margin, write margin, store/restore delay and energy consumption.

6 Conclusion

In this paper, a RD 8T1M nvSRAM cell is introduced which uses the column shared technique. The shared ST transistor is connected to the source terminal of pull-down transistor. It weakens the pull-down effect of inverter and supports the write '1' operation. It also improves the write margin of the cell. In addition to the 1T1M cell, it improves the restore yield of the cell also. The isolated read port is provided to perform the read operation and it improves the read margin of the cell. In case of power consumption, the uses of single

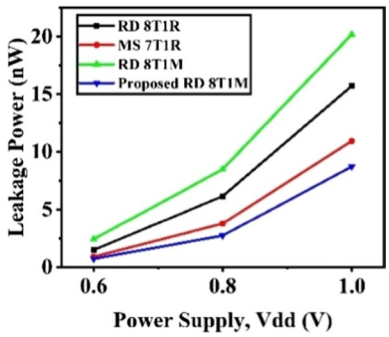

Fig. 12 Leakage power consumption of proposed RD 8T1M and existing RD nvSRAM cells

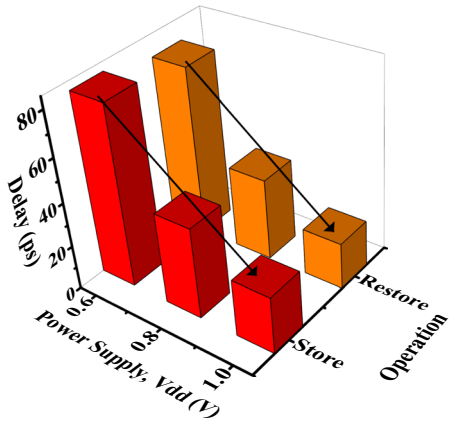

Fig. 13 Store and restore delay of proposed RD 8T1M nvSRAM cell

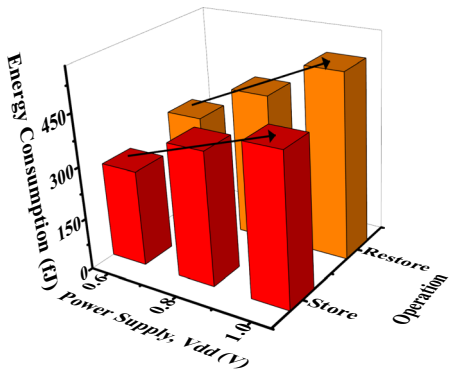

Fig. 14 Store and restore energy consumption of proposed RD 8T1M nvSRAM cell

bitline during write operation helps in consuming most of the cell power. The proposed RD 8T1M nvSRAM cell shows the improvement of 37.03% and 34.02% in read and write margin respectively, while, the read delay is improved by 45.98% in comparison to the existing read decoupled nvSRAM cells. In addition to this, the proposed cell provides the better store/restore performance in comparison to the existing counterparts.

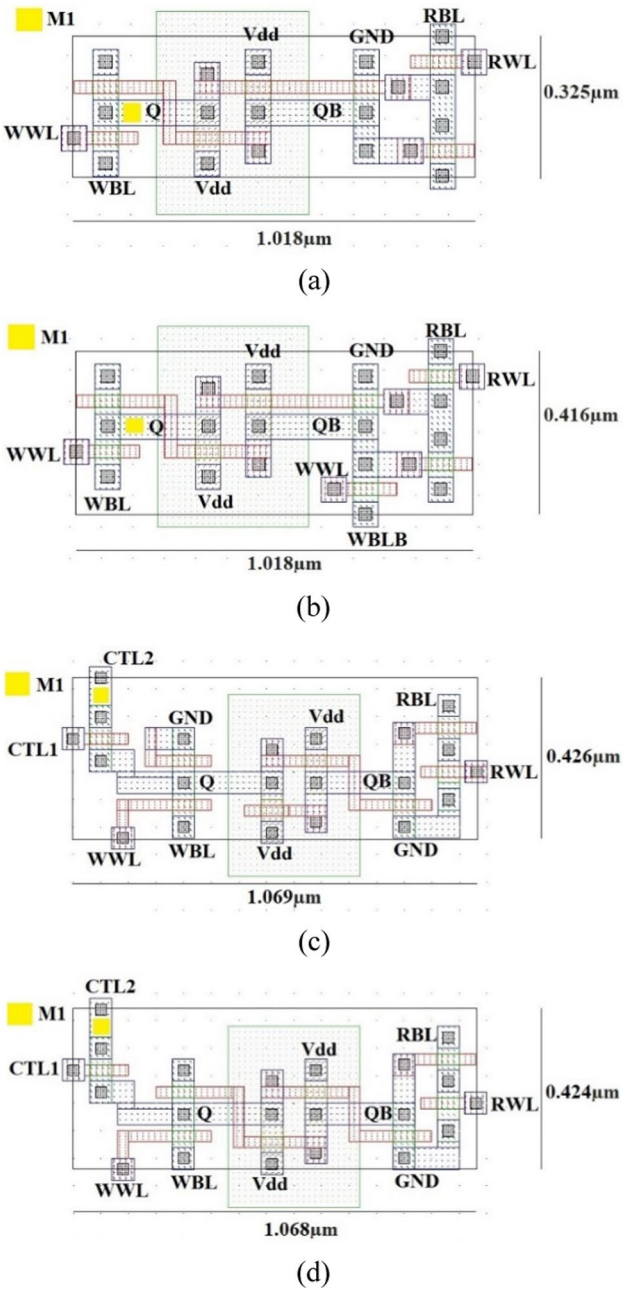

Fig. 15 Layout of **a** MS 7T1R **b** RD 8T1R **c** RD 8T1M and **d** proposed RD 8T1M nvSRAM cell

Table 2 Comparison of different performance parameters for different nvSRAM cells at Vdd = 1.0 V

Parameters	nvSRAM Cells			
	RD 8T1R	MS 7T1R	RD 8T1M	Proposed RD 8T1M
Read Delay (ps)	36.52	36.11	27.95	27.29
Read Margin (mV)	295	295	255	370
Read Power Consumption (μW)	16.85	16.85	20.62	20.56
Write Delay (ps)	32.76	54.98	51.26	47.43
Write Margin (mV)	510	485	580	650
Write Power Consumption (μW)	96.52	1.85	1.98	2.35
Leakage Power (nW)	15.71	10.94	20.18	8.73
Store Delay (ps)	30.56	30.56	25.33	25.33
Store Energy Consumption (fJ)	556	556	430	430
Restore Delay (ps)	26.15	26.15	20.63	20.63
Restore Energy Consumption (fJ)	615	615	526	526
Area Consumption (μm^2)	0.42	0.33	0.46	0.45

Data availability Data sharing not applicable to this article as no datasets were generated or analyzed during the current study.

References

1. Kursun, V., Tawfik, S. A., & Liu, Z. (2007). Leakage-aware design of nanometer SoC. In *2007 IEEE International Symposium on Circuits and Systems* (pp. 3231–3234).
2. Sery, G., Borkar, S., & De, V. (2002). Life is CMOS: Why chase the life after?. In *Proceedings of the 39th Annual Design Automation Conference* (pp. 78–83).
3. Sakimura, N., Sugibayashi, T., Nebashi, R., & Kasai, N. (2009). Nonvolatile magnetic flip-flop for standby-power-free SoCs. *IEEE Journal of Solid-State Circuits, 44*(8), 2244–2250.
4. Yamamoto, S., Shuto, Y., & Sugahara, S. (2009). Nonvolatile SRAM (NV-SRAM) using functional MOSFET merged with resistive switching devices. In *2009 IEEE Custom Integrated Circuits Conference* (pp. 531–534).
5. Wang, W., Gibby, A., Wang, Z., Chen, T. W., Fujita, S., Griffin, P., Wong, S. (2006). Nonvolatile SRAM cell. technical digest - international electron devices meeting, IEDM, (pp. 1–4).
6. Bazzi, H., Harb, A., Aziza, H., Moreau, M., & Kassem, A. (2021). RRAM-based non-volatile SRAM cell architectures for ultra-low-power applications. *Analog Integrated Circuits and Signal Processing, 106*(2), 351–361.
7. Sheu, S. S., Kuo, C. C., Chang, M. F., Tseng, P. L. (2013). A ReRAM integrated 7T2R non-volatile SRAM for normally-off computing application. In *Proceedings of the 2013 IEEE Asian Solid-State Circuits Conference, A-SSCC 2013* (pp. 245–248).
8. Turkyilmaz, O., Onkaraiah, S., Reyboz, M., Clermidy, F., & Bocquet, M. (2012). RRAM-based FPGA for "Normally Off, Instantly On" applications, In *2012 IEEE/ACM International Symposium on Nanoscale Architectures (NANOARCH), (pp.* 101–108).
9. Chiu, P.-F., Chang, M.-F., Wu, C.-W., Chuang, C.-H., Sheu, S.-S., Chen, Y.-S., & Tsai, M.-J. (2012). Low store energy, low VDD_{min}, 8T2R nonvolatile latch and SRAM with vertical-stacked resistive memory (Memristor) devices for low power mobile applications. *IEEE Journal of Solid-State Circuits, 47*(6), 1483–1496.
10. Singh, J., & Raj, B. (2019). Design and investigation of 7T2M-NVSRAM with enhanced stability and temperature impact on store/restore energy. *IEEE Transactions on Very Large Scale Integration (VLSI) Systems, 27*(6), 1322–1328.
11. Wei, W., Member, S., Namba, K., & Han, J. (2014). Design of a nonvolatile 7T1R SRAM cell for instant-on operation. *IEEE Transactions on Nanotechnology, 13*(5), 905–916.
12. Tosson, A. M. S. (n.d.). 8T1R : A novel low-power high-speed RRAM-based non-volatile SRAM design. In *2016 International Great Lakes Symposium on VLSI (GLSVLSI)*, (pp. 239–244).
13. Lee, A., Chang, M., Lin, C. (2015). JFS2-4 RRAM-based 7T1R nonvolatile SRAM with 2x reduction in store energy and 94x reduction in restore energy for frequent-off instant-on applications C77. In *2015 Symposium on VLSI Circuits (VLSI Circuits)*, (pp. C76–C77).
14. Peng, C., Xiao, S., Lu, W., Zhang, J., Wu, X., Chen, J., & Lin, Z. (2017). Average 7T1R nonvolatile SRAM with R/W margin enhanced for low-power application. *IEEE Transactions on Very Large Scale Integration (VLSI) Systems, 26*(3), 584–588.
15. Janniekode, U. M., Somineni, R. P., Khalaf, O. I., Itani, M. M., Chinna Babu, J., & Abdulsahib, G. M. (2022). A symmetric novel 8T3R non-volatile SRAM cell for embedded applications. *Symmetry, 14*(4), 768. https://doi.org/10.3390/SYM14040768
16. Singh, D., Gupta, K., & Pandey, N. (2022). A novel low-power nonvolatile 8T1M SRAM cell. *Arabian Journal for Science and Engineering, 47*(3), 3163–3179. https://doi.org/10.1007/s13369-021-06035-2
17. Sundara Raman, S. R., Nibhanupudi, S. S. T., & Kulkarni, J. P. (2022). Enabling In-memory computations in non-volatile SRAM designs. *IEEE Journal on Emerging and Selected Topics in Circuits and Systems, 12*(2), 557–568. https://doi.org/10.1109/JETCAS.2022.3174148
18. Kumar, C. S. H., & Kariyappa, B. S. (2022). Node voltage and KCL model-based low leakage volatile and non-volatile 7T SRAM cells. *IETE Journal of Research*. https://doi.org/10.1080/03772063.2022.2027279
19. Lin, Z., Wang, Y., Peng, C., Lu, W., Li, X., Wu, X., & Chen, J. (2019). Read-decoupled 8T1R non-volatile SRAM with dual-mode option and high restore yield. *Electronics Letters, 55*(9), 519–521.
20. Lin, Z., Wang, Y., Peng, C., Wu, X., Li, X., & Chen, J. (2020). Multiple sharing 7T1R nonvolatile SRAM with an improved read/write margin and reliable restore yield. *IEEE Transactions on Very Large Scale Integration (VLSI) Systems, 28*(3), 607–619.

21. Singh, D., Gupta, K., & Pandey, N. (2022). A novel read decoupled 8T1M nvSRAM cell for near threshold operation. *Microelectronics Journal, 126*(May), 105496. https://doi.org/10.1016/j.mejo.2022.105496
22. Shen, S., Cao, P., Ling, M., & Shi, L. (2022). A timing yield model for SRAM cells in sub/near-threshold voltages based on a compact drain current model. *IEEE Transactions on Computer-Aided Design of Integrated Circuits and Systems*. https://doi.org/10.1109/tcad.2022.3194812
23. Aly, R. E., & Bayoumi, M. A. (2007). Low-power cache design using 7T SRAM cell. *IEEE Transactions on Circuits and Systems II: Express Briefs, 54*(4), 318–322. https://doi.org/10.1109/TCSII.2006.877276
24. Maroof, N., & Kong, B. (2016). 10T SRAM using half-VDD precharge and row-wise dynamically powered read port for low switching power and ultralow RBL leakage. *IEEE Transactions on Very Large Scale Integration (VLSI) Systems, 25*(4), 1193–1203.
25. Biolek, D., Di Ventra, M., & Pershin, Y. V. (2013). Reliable SPICE simulations of memristors, memcapacitors and meminductors. *Radioengineering, 22*(4), 945–968.
26. Tawfik, S. A., & Kursun, V. (2008). Low power and robust 7T dual-Vt SRAM circuit. In *Proceedings - IEEE International Symposium on Circuits and Systems*, (pp. 1452–1455).
27. Singh, J., Mohanty, S. P., & Pradhan, D. K. (2012). *Robust SRAM designs and analysis*. Springer.
28. Gupta, S., Member, S., Gupta, K., Pandey, N., & Member, S. (2018). Pentavariate V min analysis of a subthreshold 10T SRAM bit cell with variation tolerant. *IEEE Transactions on Circuits and Systems I: Regular Papers, 65*(10), 3326–3337.
29. Gierczynski, N., Borot, B., Planes, N., & Brut, H. (2007). A new combined methodology for write-margin extraction of advanced SRAM. In *2007 IEEE international conference on microelectronic test structures* (pp. 97–100).

Publisher's Note Springer Nature remains neutral with regard to jurisdictional claims in published maps and institutional affiliations.

Springer Nature or its licensor (e.g. a society or other partner) holds exclusive rights to this article under a publishing agreement with the author(s) or other rightsholder(s); author self-archiving of the accepted manuscript version of this article is solely governed by the terms of such publishing agreement and applicable law.

Damyanti Singh was born in 1994 and is currently persuing Ph.D in VLSI from Delhi Technological University, New Delh. She has received B.Tech degree in Electronics and Communication Engineering from Uttar Pradesh Technical University, Lucknow, U.P., in 2014, M.Tech in VLSI from Delhi Technological University, New Delhi, in 2018. Her research interest includes design of non-volatile SRAM and DRAM memory.

Neeta Pandey received the M.E. degree in microelectronics from Birla Institute of Technology and Sciences, Pilani, India and the Ph.D. degree from Guru Gobind Singh Indraprastha University, New Delhi, India. She has served in Central Electronics Engineering Research Institute, Pilani; Indian Institute of Technology, New Delhi; Priyadarshini College of Computer Science, Noida; and Bharati Vidyapeeth's College of Engineering, New Delhi in various capacities. She is currently a Professor with the Electronics and Communication Engineering Department, Delhi Technological University, New Delhi. She has authored more than 180 technical papers in reputed national and international conferences and journals. Her current research interests include analog and digital VLSI design. Dr. Pandey is a Member of WIE Affinity Group, a Life Member of ISTE and a Senior Member of IEEE.

Kirti Gupta received the B.Tech. degree in electronics and communication engineering from Indira Gandhi Institute of Technology, New Delhi, India in 2002, the M.Tech. degree in information technology from the School of Information Technology, New Delhi, in 2006 and the Ph.D. degree in electronics and communication engineering from Delhi Technological University, New Delhi, India, in 2016. From 2002 to 2007, she served as an Assistant Professor and from 2008 to 2016, she served as an Associate Professor in the Bharati Vidyapeeth's College of Engineering, New Delhi, where she is currently a Professor. She has authored more than 70 technical papers in various international conferences and journals. Her current research interests include digital integrated circuit design. Dr. Gupta is a Life Member of ISTE and a Senior Member of IEEE.

Metabolomics (2023) 19:5
https://doi.org/10.1007/s11306-022-01970-z

ORIGINAL ARTICLE

Acute metabolic alterations in the hippocampus are associated with decreased acetylation after blast induced TBI

Megha Kumari[1,2] · Palkin Arora[1,3] · Priyanka Sharma[1] · Yasha Hasija[2] · Poonam Rana[1] · Maria M. D'souza[1] · Namas Chandra[4] · Richa Trivedi[1]

Received: 9 June 2022 / Accepted: 21 December 2022
© The Author(s), under exclusive licence to Springer Science+Business Media, LLC, part of Springer Nature 2023

Abstract

Introduction Blast induced Traumatic brain injury (BI-TBI) is common among military personnels as well as war affected civilians. In the war zone, people can also encounter repeated exposure of blast wave, which may affect their cognition and metabolic alterations.

Objective In this study we assess the metabolic and histological changes in the hippocampus of rats at 24 h post injury.

Method Rats were divided into four groups: (i) Sham; (ii) Mild TBI (mi); (iii) Moderate TBI (mo); and (iv) Repetitive mild TBI (rm TBI) and then subjected to different intensities of blast exposure. Hippocampal tissues were collected after 24 h of injury for proton nuclear magnetic resonance spectroscopy (1H NMR spectroscopy) and immunohistochemical (IHC) analysis.

Results The metabolic alterations were found in the hippocampal tissue samples and these alterations showed significant change in glutamate, N-Acetylaspartic acid (NAA), acetate, creatine, phosphoethanolamine (PE), ethanolamine and PC/choline concentrations in rmTBI rats only. IHC studies revealed that AH3 (Acetyl histone) positive cells were decreased in rm TBI tissue samples in comparison to other TBI groups and sham rats. This might reflect an epigenetic alteration due to repeated blast exposure at 24 h post injury. Additionally, astrogliosis was observed in miTBI and moTBI hippocampal tissue while no change was observed in rmTBI tissues.

Conclusion The present study reports altered acetylation in the presence of altered metabolism in hippocampal tissue of blast induced rmTBI at 24 h post injury. Mechanistic understanding of these intertwined processes may help in the development of better therapeutic pathways and agents for blast induced TBI in near future.

Keywords Acetylation · Acute injury · Blast induced TBI · Hippocampus · Metabolomics

Abbreviations

AH3	Acetyl histone
BAA	Branched-chain amino acids
CCI	Controlled cortical impact
Cho	Choline
GFAP	Glial fibrillary acidic protein
IHC	Immunohistochemistry
NAA	N-Acetylaspartic acid
PI	Post injury
PTSD	Post traumatic stress disorder
PBS	Phosphate buffer saline
PC	Phospho choline
PFA	Paraformaldehyde
PE	Phosphoethanolamine
rm TBI	Repetitive mild TBI
ROI	Region of interest

✉ Richa Trivedi
triricha@gmail.com

Priyanka Sharma
priyanka.inmas@gov.in

[1] Radiological, Nuclear and Imaging Sciences (RNAIS), Institute of Nuclear Medicine and Allied Science (INMAS), DRDO, Delhi, India

[2] Department of Biotechnology, Delhi Technological University, Delhi 110042, India

[3] Department of Biochemistry, Panjab University, Chandigarh 160014, India

[4] Center for Injury Biomechanics, New Jersey Institute of Technology, 323 Dr Martin Luther King Jr Blvd, Newark, NJ 07102, USA

Published online: 12 January 2023

TCA cycle Tricarboxylic cycle
TBI Traumatic brain injury

1 Introduction

Blast explosion and consequent blast related concussion is linked to destructive alteration in the brain leading to behavioral and cognitive impairments in the affected individuals (Clark et al., 2018) Importantly, soldiers deployed in Iraq war diagnosed with blast concussion showed symptoms of post traumatic stress disorder (PTSD) and depression (Hoge et al., 2015).

Detonation of explosives leads to concussive blast waves which are associated with cerebro-vascular damage along with disruption in the blood brain barrier. Low level blast exposure induces structural and functional changes in the brain vasculature including alterations in the arterial smooth muscle layer (Gama Sosa et al., 2019). Changes in the cerebral blood flow and damage associated with blast wave results in oxidative stress and dysfunctional cerebral metabolism in the exposed rats (Rana et al., 2020). Mild blast concussion may have serious outcomes if exposed repetitively, as a single insult increases cerebral vulnerability such that rats re-exposed to blast waves show increased oxidative stress, vascular pathologies and inflammation (Kamnaksh et al., 2014). Whereas, transient and mild symptoms of blast TBI results in re-deployment of military personnel to their services where re-exposure to blast waves may lead to repeated mild injuries.

A repeated mild injury further posses the individual at a risk of severe ongoing secondary injury mechanisms in the central nervous system (CNS) along with long term outcomes like neurodegenerative changes and chronic traumatic encephalopathy (Stern et al., 2011). At the molecular level it has been found that blast induced repetitive mild TBI is accompanied by a complex pathology involving changes in the cerebral metabolism with increased vascular and oxidative damage (Kamnaksh et al., 2014). Cerebro-cerebellar hypometabolism is found as a major contributing factor leading to chronic post concussive symptom in Iraq combat veterans with repetitive blast-trauma (Peskind et al., 2011). Similarly, Prins et al. (2013) reported a decrease in cerebral glucose metabolism in both parietal cortex and hippocampus in a subpopulation of children and young adults who experienced repetitive mild TBI (rm TBI).

Importantly cerebral metabolic alterations can influence the gene expression of the cell through mechanism of epigenetic modifications. Cellular metabolites are used by the histone modifying enzymes to alter histone modifications leading to reprogramming of gene expression (Katada et al., 2012). It has been observed that glucose concentration in the cell can influence histone acetyltransferase (HATs) activity via regulating the levels of acetyl CoA through tricarboxylic cycle (TCA cycle). Similarly, levels of SAM (S-adenosylmethionine) and SAH (S-adenosylhomocysteine) along with the concentration of co-factor FAD/FADH2 in the cell impact methylation pattern of the cell (Weinhold, 2006). Additionally, a decrease in histone methylation along with H3 acetylation specifically in the hippocampal region is observed after moderate controlled cortical impact (CCI) (Gao et al., 2006).

A huge percentage of preclinical studies on TBI have only used males for test subjects. Increase in the number of sex-balanced studies would result in more reliable human clinical trials or better understanding for diseases. This study was planned to understand metabolic changes in consideration of female health. Therefore, the present study was designed to understand how repetitive blast concussion reprograms the metabolism of the exposed female rats. Further the study involves understanding the interplay between metabolism and epigenetic alterations after repetitive blast injury.

2 Material and method

2.1 Chemicals

Acetonitrile (Sigma Aldrich, Germany), deuterium oxide (D_2O) (Sigma Aldrich, Germany), formalin, ketamine (Psychotropics India Limited, India), mylar membrane, potassium chloride (KCl), potassium dihydrogen phosphate (KH_2PO4), sodium chloride (NaCl), sodium hydrogen phosphate (Na_2HPO4) (Merck, Germany), trimethylsilylpropanoic acid (TSP) (Eurisotop, France) and xylazine (Indian immunologicals Limited, India).

2.2 Study design

All experiments of this study compiled with the ethical guidelines of the Institutional Animal Ethical Committee (INM/IAEC/2019/09/Ext1). To study the difference between concentration of neurometabolites in sham and blast exposed group we assumed that there is no difference between these parameters ($Ho = 0$). Alternatively, if a difference is observed ($Ha = 0.0$) at $\alpha = 0.05$ and 80% power of the test, the null hypothesis will be rejected. Under these assumptions for a two-tail test, the minimum number of subjects required was 5 per arm. Twenty ($n = 20$) Sprague Dawley female rats of 10–12 weeks of age, 5 rats per group with an average weight of 250–280 g each, were obtained from Experimental Animal Facility of Institute. They were provided with free access to food and water regularly in a

well-ventilated room whose conditions were controlled at a temperature of 22 ± 2ºC and relative humidity of 50 ± 10% under a 12 h day-night cycle.

2.3 Blast exposure

A compression-driven gas shock tube was used to generate the shock wave in this experiment following previous investigations by Mishra et al. (2016). Rats were divided into four groups at random: sham, mild TBI, moderate TBI, and rm TBI, with each group containing five animals. Rats were anesthetized using the 3.5% Isoflurane and zero air (contains around 19.9- 21.9% O_2) and placed horizontally on the platform inside the shockwave tube (Mishra et al., 2016). The mild and moderate groups received a single dose of shock wave of 100Kpa and 190Kpa respectively. The rm TBI group received three doses of shock wave of 100 Kpa, at 0 min, 30 min, and 24 h. Sham animals also received the same treatment except for injury. After 24 h of injury, the rats were perfused firstly with PBS (phosphate buffer saline) than PFA (paraformaldehyde) before dissection to prevent blood contamination during tissue extraction. After the animals were euthanized, the hippocampus was removed from one hemisphere of the brain and snapfrozen in liquid nitrogen and stored in -80^0C until use, while the other hemisphere was kept in 4% formalin for histological analysis.

2.4 Immunohistochemistry (IHC) Analysis

Fixed brains were processed and embedded in paraffin wax. Wax blocks were sliced in a microtome and 5 µm coronal sections were mounted on silane coated slides. Tissue sections were deparaffinized in xylene and rehydrated in different concentrations of ethanol to water gradient. Tissue sections were rinsed with PBS and incubated in heated sodium citrate at 85 °C for 1 h for antigen retrieval. Following this, tissue sections were treated with H_2O_2 for 15 min to suppress the endogenous peroxidase activity using Mouse and Rabbit Specific HRP/DAB (ABC) Detection IHC kit (ab64264). Sections were rinsed with PBS and treated with protein blocking buffer for 10 min and then incubated in primary antibody overnight at 4 °C in a humid chamber. Specific antibodies for GFAP (MA5-12,023, Thermo) and AH3 (MBS9126034, H3K9 My biosource) were used for quantification of astrocytic activation and acetylation respectively. Tissue sections were washed with PBS before 10 min incubation with secondary antibody. Then, the tissue sections were treated with streptavidin peroxidase for 10 min. Before DAB (3,3′-diaminobenzidine) incubation for 10 min, slides were washed with PBS and counterstained with hematoxylin for 30 s, then airdried, and coverslipped. Slides were examined using microscope (LMI BM-Prime, London, England) and images were captured at 20× magnification. GFAP positive and anti-AH3 positive cells were counted manually in the dentate gyrus of each image from mild, moderate and repetitive injury group.

Counting of the immunopositive cells was performed manually using an image analysis software (Image J, Bethesda, USA). Dentate gyrus (DG) of hippocampus were selected based on the study by Gao et al, 2006. ROIs (region of interest) were selected in each DG region of hippocampus tissue and the positive cells were counted and normalized per mm^2.

2.5 Sample Preparation and NMR spectra acquisition

The metabolites from the tissue samples were extracted using the acetonitrile extraction method. A handheld homogenizer (IKA T-10, Germany) was used to homogenize the tissue in (1:1, v/v) acetonitrile/water mixture 5 ml per 1gm of frozen tissue. The homogenized mixture was centrifuged at 12,000 rpm at 4 °C for 20 min. The supernatant was separated and stored at −80ºC until lyophilized. After the lyophilization the powdered sample was stored at −20 °C till further analysis. 1H NMR spectra were acquired on 600.33 MHz NMR spectrometer (Bruker, Biospin, Switzerland). For NMR spectral acquisition, the lyophilized sample were re-suspended into 600 µl D_2O + 0.5 mM TSP mixture and then centrifuged at speed of 12,000 rpm temp 4 °C for 10-15 min. After centrifuge 580 µl supernatant was pipetted in 5 mm NMR tubes. The water saturation NOESYPR1d pulse program, with pulse sequence (RD-90 -t- 90 -tm-90 -acq) was used with a total number of 64 scans, dummy scans 4, spectral width of 9009 Hz, an acquisition time of 3.63 s, and a relaxation delay of 4 s at 298 K.

Raw NMR spectra were processed using TOPSPIN3.5 (Bruker), the baseline and phase of each spectrum were corrected and then peaks were integrated manually (Fig. 1). Peaks were identified using Human Metabolome Database (HMDB) and previously published literature, TSP was used as a reference for integration. The integrated data were normalized to the total sum of integrals for each spectrum.

2.6 Concentration of metabolites

Concentration of metabolites in tissues were calculated using the following formula [Eq. 1 (Tyagi et al, 2011)]:

$$C(x) = C(TSP) \times \frac{N(TSP) \times I(X) \times V(s)}{N(x) \times I(TSP) \times W(s)} \quad (1)$$

where, C(x)- concentration of metabolite, C(TSP)- Concentration of TSP, I(X) – Intensity of metabolite, N(x) - Number of protons in integrated signal, N(TSP) -Number

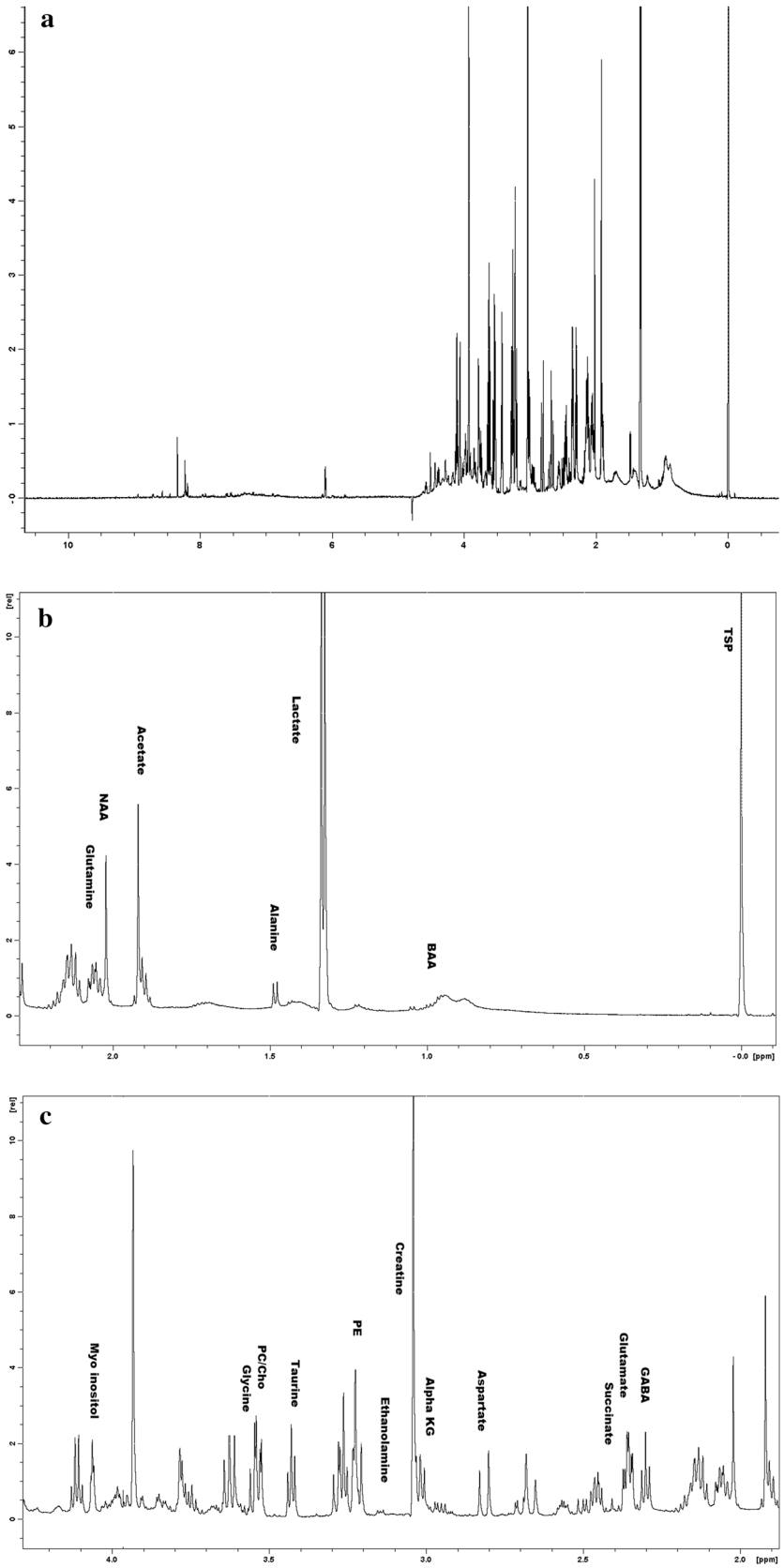

Fig. 1 Representative ^{1}H NMR spectra of hippocampal tissue sample with identified metabolites. **a** Complete NMR spectra ranging from 0 to 10 ppm, **b** NMR spectra ranging from 0 to 2.0 ppm, **c** NMR spectra ranging from 2.0 to 4.0 ppm, **d** NMR spectra ranging from 4.0 to 6.0 ppm, **e** NMR spectra ranging from 6.0 to 7.5 ppm

Fig. 1 (continued)

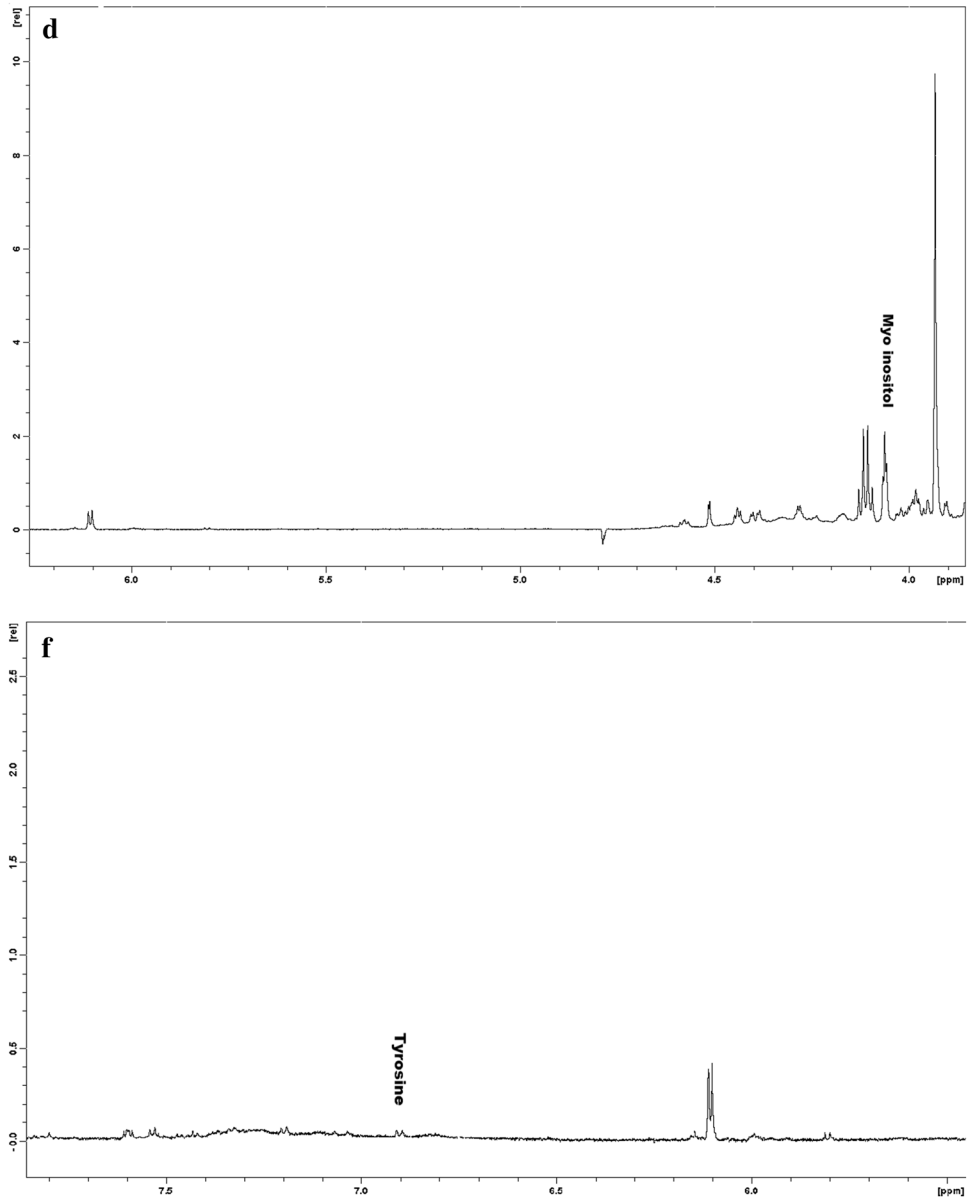

of protons in TSP, W(s) - Weight of wet tissues in grams, V(s) - Volume of sample in NMR tube.

The concentration of all metabolites (except for BAA) are summarized in supplementary table 2. Quantification of BAA concentration was not done due to the overlapping peaks of valine, leucine and iso-leucine. The relative intensity of BAAs are reported in supplementary table 2.

2.7 Statistical analysis

Metabolic alteration and immunohistochemical changes between groups were analysed using one-way analysis of variance (ANOVA) for comparison. Tukey's HSD test was selected for posthoc analysis. $p < 0.05$ was considered statistically significant. (SPSS version 20).

To understand the relation between metabolites of each injury group, Pearson's correlation coefficient was calculated for 19 identified metabolite in all samples using metaboanalyst software.

3 Results

The metabolic profiles of hippocampal tissue were evaluated to assess the blast-induced alteration in the hippocampus after 24 h of injury. Nineteen metabolites involved in a variety of metabolic processes like energy metabolism (lactate, succinate, creatine, α-ketoglutarate), ketone body metabolism (acetate), osmolytes (myo-inositol, taurine), neurotransmitter amino acids (glutamine, glutamate,

aspartate, GABA), amino acids; branched chain amino acids (valine, leucine and isoleucine) and alanine, glycine, tyrosine, N Acetyl aspartate (NAA), and membrane metabolites (phosphocholine/ choline, phosphoethanolamine (PE),ethanol amine) were identified.

3.1 Neurometabolic alteration among the groups

N-Acetylaspartic acid (NAA), glutamate, acetate, phosphocholine/choline (PC/choline), phosphoethanolamine (PE), ethanolamine and creatine exhibited significant change in repetitive TBI group only compared to sham 24 h PI. There was a significant upregulation in acetate whereas NAA, glutamate, PC/choline, PE, ethanolamine and creatine were downregulated significantly in repetitive TBI group, compared to sham rats. Lactate, alanine, and branched-chain amino acids (BAA) showed significant change in all three TBI groups in comparison to sham after 24 h of injury. Lactate showed upregulation whereas BAA and alanine levels were downregulated in all injury groups compared to sham control. (Fig. 2).

3.2 Correlation among the neurometabolites

To understand the relationship between metabolites altered after injury, a correlation heatmap was quantified using metaboanalyst. It was found that NAA had a positive correlation with glutamate, creatine, ethanolamine, PE and PC/Choline and negative correlation with acetate and lactate concentration after injury (Fig. 3).

3.3 Histological changes among the groups

The astrocytic activation following TBI was observed using GFAP immunostaining. At 24 h post injury, increased number of astrocytes were observed in the hippocampus of the mild and moderate injury groups compared to the sham group (Fig. 4). In comparison to the sham, the rmTBI group also showed substantial astrocyte proliferation in the hippocampus but was not significant.

To exhibit TBI induced epigenetic changes, AH3 positive cells were examined. One way ANOVA results showed a significant decrease in AH3 positive cells in rmTBI in comparion to sham as well as mTBI group (Fig. 5). We did not find any significant change in other groups.

4 Discussion

The growing attention to mTBI in clinical and pre-clinical research has yielded a wealth of data on post-injury brain metabolic alterations (Banoei et al., 2018). Mild blast TBI is fairly prevalent among active army soldiers who are exposed to many explosions during training, field trials, or war. (Hoge et al., 2015). It is already known that a mild blast can alter cognitive, metabolic, and behavioral functions (Arciniegas et al., 2002; Rana et al., 2020; Subramaniam et al., 2015). However, the time it takes for the brain to recover after an injury is controversial, and the assessment standards for these recoveries are currently being worked out. Therefore, the present study involved a comparative assessment of injury severity including; mild, moderate and repeated blast exposure post 24 h of injury. The study showed metabolic alteration in hippocampal tissue with significant changes in

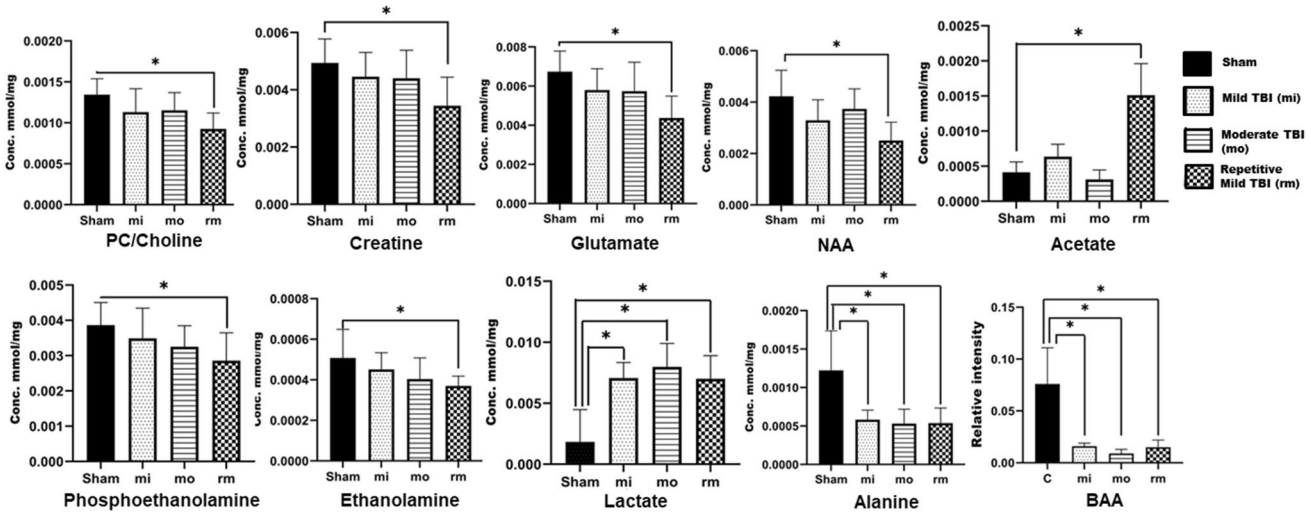

Fig. 2 Bar graphs of significantly changed metabolites in hippocampal tissue extracts at 24 h following TBI in different injury groups. *p-value < 0.05 considered significant

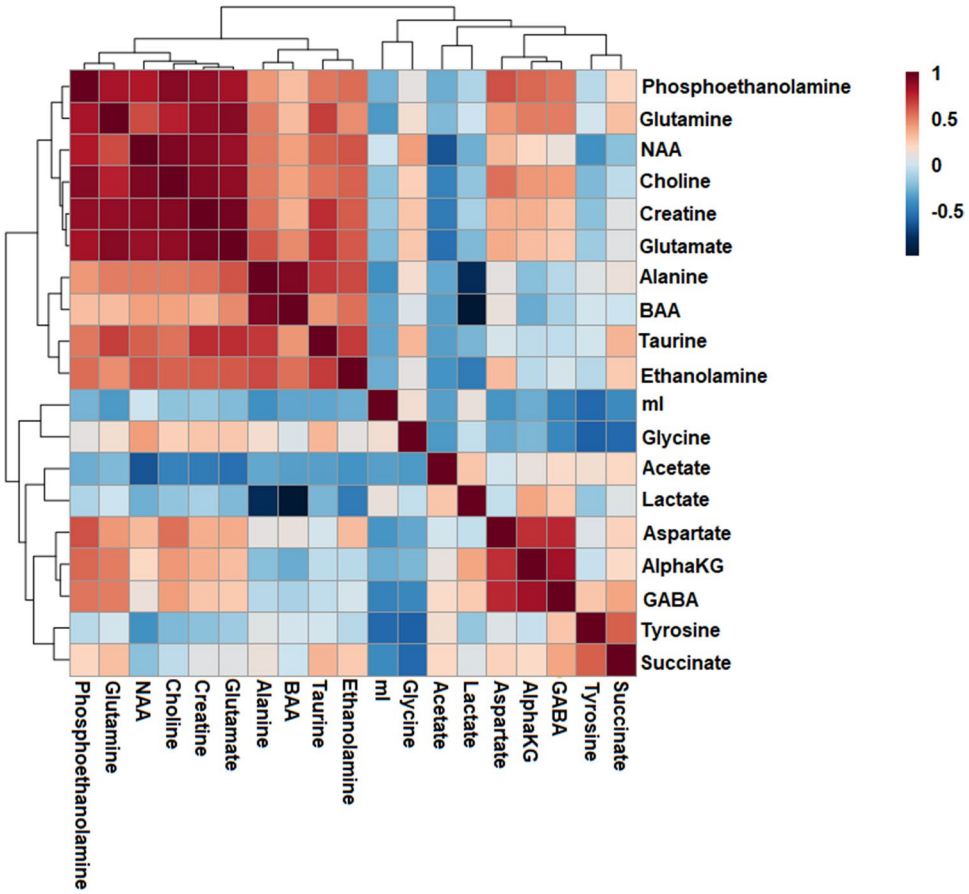

Fig. 3 Correlation heatmap of all metabolites

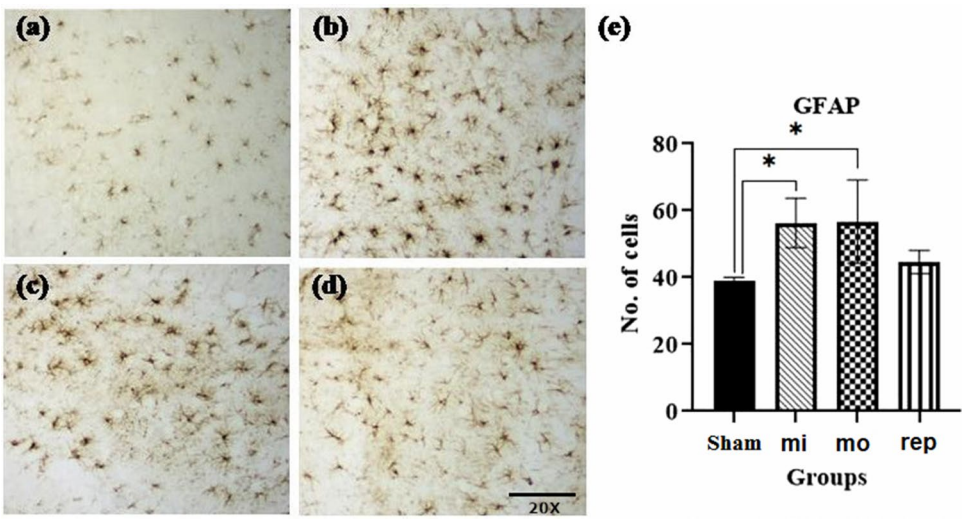

Fig. 4 Photomicrographs of GFAP positive cells in the dentate gyrus region of hippocampus of sham (**a**) and injury groups [(**b**) mild TBI, (**c**) moTBI, (**d**) rm TBI] at 24 h PI. (**e**) Bar graph represents GFAP positive cells in sham and injury groups. *p-value < 0.05 considered significant

the concentrations of NAA, acetate, PC/choline, PE, ethanolamine, glutamate, and creatine in only rmTBI rats compared with sham. The altered metabolism after blast exposure could result in the change in biochemical process and further amend the metabolic dependent processes, including epigenome. The present study provides an insight into hippocampal metabolite concentration with acetylation levels to help understand the interplay between metabolism and epigenetic mechanism. Histologically, decreased acetylated cells in the hippocampal tissue of rmTBI rats compared with sham were found post injury 24 h.

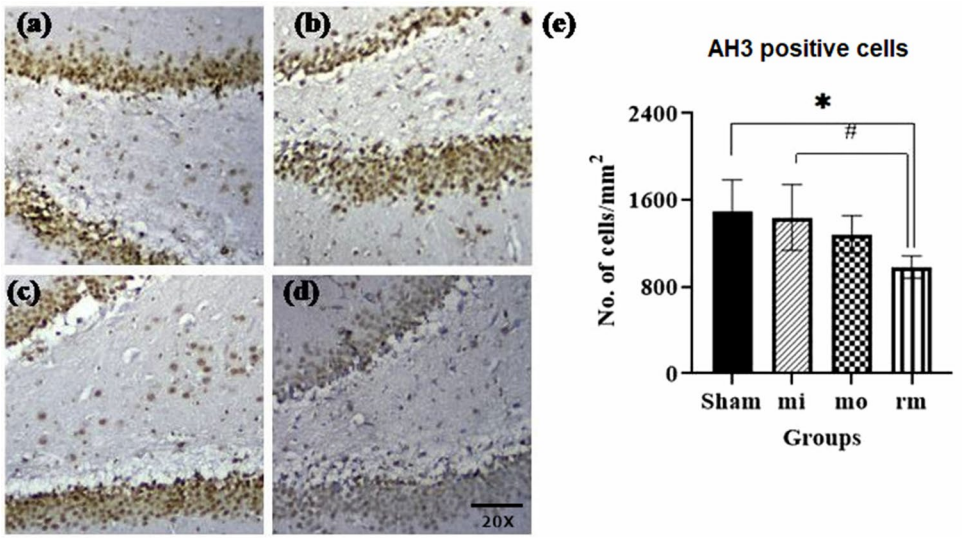

Fig. 5 Photomicrographs of AH3 positive cells in the dentate gyrus region of hippocampus of sham (**a**) and injury groups [(**b**) mild TBI, (**c**) moTBI, (**d**) rm TBI] at 24 h PI. (**e**) Bar graph represents AH3 positive cells in hippocampal region of sham and injury groups. Note: #shows significant difference between mild and rmTBI groups. *p-value < 0.05 considered significant

Histone acetylation is an epigenetic mechanism, AceCS1 plays an important role in this mechanism. Studies showed that cancer cells use acetate as energy source in hypoxic condition (Vazquez et al., 2016). Gao et al. found that acetate may induce epigenetic change in hypoxic condition in cancer cells. In a different study on CCI model induced moTBI they found decreased acetylation in CA3 region of hippocampus at 6 h and 24 h post injury (Gao et al., 2006). Similarly, our study has observed a decrease in AH3 positive cells/acetylation while acetate concentration were increased after rmTBI, indicating that injury results in flux of acetate for other biochemical processes including energy production after rmTBI in comparison to histone acetylation.

The increased acetate flux reported can be due to upregulated de-acetylation of NAA, as NAA concentrationwere decreased after rmTBI. It has been known that NAA is transported from the neuron to the oligodendrocyte, which contains ASPA (aminoacylaseII) and is responsible for the deacetylation of NAA as well as generation of free acetate (Reichelt & Kvamme, 1967; Truckenmiller et al., 1985; D'Adamo et al., 1972). This free acetate is then transformed to acetyl CoA by the action of enzyme AceCS1. AceCS1 is a nuclear cytoplasmic enzyme which participates in protein and histone acetylation reaction with Acetyl CoA (Takahashi et al., 2006; Wellen et al., 2009). Acetate can also be transported to astrocytes for energy production by the action of mitochondrial AceCS2 enzyme. Supporting this, an increased expression of AceCS1 in the rat brain nucleus has been reported after TBI in rats (Ariyannur et al., 2010).

On the other hand, transformation of NAA to glutamate has been observed (Clark et al., 2006). In addition, ^{13}C MRS studies demonstrate that glutamate turnover decreases in Alzheimer's disease in proportion to the loss of NAA concentration (Lin et al., 2003) and both glutamate and NAA concentrations reduced in the frontal lobes of Alzheimer's mice (Dedeoglu et al., 2004).The present study also observed a decrease in concentration of glutamate as well as NAA in rmTBI rats only, indicating impaired neurotransmission and a possible relation between NAA and glutamate. Supporting, studies on blunt rmTBI, Xiaoyun Xu and colleagues also observed decreased levels of glutamate post 48 h of the injury (Xu et al., 2021). Along with this, correlation analysis also showed a positive relation between NAA and glutamate. While NAA showed negative correlation with acetate and lactate. This possibly suggests NAA as an energy reservoir which can shuttle into TCA cycle or energy production with acetate and lactate as energy substrates after rmTBI. NAA also positively correlated with creatine, ethanolamine and phosphoethanolamine; suggesting their role in energy metabolism which need to be further studied.

In astrocytes, glutamate/glutamine cycle allows transamination of alanine to glutamate allowing ammonia to return to glial cells from neurons (Calvetti & Somersalo, 2013; Rae et al., 2003). Importantly, our study reported decreasing concentration of both alanine and glutamate after rmTBI but no change was observed in the glutamate concentration after mild and moderate TBI. A possible reason for this decrease in alanine and glutamate concentration after rmTBI suggests impaired glutamate-glutamine cycle. On contrary, it was observed that GFAP positive cells significantly increased after both mild and moderate injury with modest increase in the rmTBI group, highlighting severely altered cellular and metabolic response after rmTBI. Additionally, the increased astrogliosis after mild and moderate injury could have depleted the alanine pool of hippocampus to compensate for various biochemical processes for energy production. A study on mild blast-induced post-traumatic stress disorder (PTSD) rats have also reported that β-alanine supplementation for 30 days after the injury improved rat recovery and indicated that supplemented rats were less prone to engage

in PTSD behavior (Hoffman et al., 2017). Therefore, presence of altered alanine and glutamate concentration after injury could lead to impaired neurotransmission.

Additionally, a decrease in PC/choline was also observed in the rmTBI rats. Choline is a cell membrane-bound phospholipid which is essential for the synthesis of phosphatidylcholine and sphingomyelin. Along with this, acetylation of choline results in acetylcholine synthesis, important for cholinergic neurotransmission. Loss of choline in the CNS can reduce acetylcholine release leading to, spatial, cognition and memory deficits in the hippocampus (Zeisel, 1992; Zeisel et al., 2003). Decrease in the concentration of PC/choline after rmTBI in our study suggests changes in the neuronal membrane integrity and could further lead to altered cholinergic neurotransmission after injury.

Injury induced cellular cytotoxicity, oxidative stress and inflammation are the major confounding factors resulting in impaired neurotransmission, ATP production and cellular processes. Along with an imbalance in the concentration of neurotransmitters, a metabolic shift was also observed in energy metabolism including, glucose, lactate, creatine and BAA. Glucose is the primary energy substrate for the brain in normal conditions. After TBI, there is a sudden increase in the energy demand of the cells to maintain basic cellular functions. Metabolic imbalance and energy dysfunction of the cell can induce a change in the overall metabolic processes (Carpenter et al., 2015), and increase the production of lactate for energy production (Patet et al., 2015; Van Hall et al., 2009). TBI also results in increased astrocytic glycolysis, blood glucose uptake and glutamate release in neuronal synapse to maintain trauma induced energy requirements (Attwell et al., 2010). The present study found elevated lactate concentration in all injury groups compared to the sham. The increased lactate concentration acutely after injury signifies their primary role in the ATP production and lactate shuttle to increase the flux of oxidative and gluconeogeneic substrates after injury. (Dienel, 2014).

Creatine (N-[aminoiminomethyl]-N-methyl glycine) is synthesized in the liver, kidney, pancreas, and brain from the essential amino acids methionine, glycine, and arginine. Creatine and phosphocreatine system plays a crucial role as reserved sources of energy in tissues with high energy requirements like, the brain and muscles. Since, creatine is an important source for ATP release it serves as a critical energy metabolite. While after rmTBI, we reported decreased concentrationof creatine in rmTBI rats compared to sham (Andres et al., 2008; Brosnan & Brosnan, 2007). Andres et al. also reported that in case of CNS diseases creatine metabolism and the creatine kinase/phosphocreatine system is being compromised as the brain needs a comparatively high amount of ATP to maintain membrane potentials and signaling capacity (Andres et al., 2008). In addition, the concentration of phosphoethanolamine (PE) and ethanolamine were also down regulated after rmTBI which could also suggest the role of these molecules in energy production as it has been earlier observed that molecules like ethanolamine, phosphoethanolamine, or phosphatidylethanolamine can increase the rate of respiration (Karagezyan and Ovsepyan, 1975).

The BAAs are essential amino acids for energy metabolism, gluconeogenesis and regulation of protein synthesis. BAAs are also important for neurotransmitter synthesis. They are the leading nitrogen donors for glutamate synthesis (Shimomura & Kitaura, 2018). Our study observed a reduction of BAAs concentration in the hippocampal tissue samples after 24 h of injury in mild, moderate and repeat mild TBI rats compared to sham rats. Similary, it has been found that BAA levels deplete after TBI and their supplementation have emerged as a promising treatment. (Caplan et al., 2018).

Importantly, the present study has observed metabolic alterations specifically in rmTBI group in comparison to mild and moderate injured groups, possibly due to concomitant insults to the brain that promote secondary injury mechanisms. Changes in these energy metabolic markers also reflects impaired mitochondrial function after rmTBI which could lead to oxidative stress (Rana et al., 2020). As reported earlier, a single concussion impairs the neurometabolic, oxidative and inflammatory processes in the brain while a subsequent exposure makes the brain vulnerable to these secondary injury mechanisms (Roberto et al., 2008). Therefore, suggesting that rmTBI is more suspectible to secondary injury damage in earlier time periods than mild and moderate injury.

These global changes in metabolic flux of the cell can further promote variation in the levels of the co factors responsible for histone remodeling (Katada et al., 2012). In support of this, AH3 positive cells were found to be decreased in the rmTBI group, indicating adaptability of epigenetic modifications in response to the cellular metabolism. Epigenetic modulation is a key phenomenon that involves alteration in the cellular function and subsequent response towards the pathological state. During TBI, this dynamic relationship between the epigenetic mechanism and metabolism is least explored and remains an important area for translational value.

5 Conclusion

This study demonstrates that metabolic alterations post blast induced TBI at acute timepoint results in alteration in concentration of glutamate, NAA, acetate, creatine, PC/choline, PE, and ethanolamine mainly in rmTBI group. These metabolite specific changes post rmTBI is

associated with a significant decrease in acetylation in the hippocampus. Therefore, rmTBI results in altered metabolite concentration to favour energy production. Finally, the study also reported an increase in number of astrocytes in mild and mod TBI, while modest increase was observed in rmTBI. Conclusively the study suggests metabolic and epigenetic alterations after repeated exposure to mild blast. Further,evaluation will be required to understand the epigenetic mechanism.

Supplementary Information The online version contains supplementary material available at https://doi.org/10.1007/s11306-022-01970-z.

Author contributions MK: Draft Manuscript, Biological Data Collection, Data Acquisition, Data analysis. PA: Interpretation of results, Data Acquisition, Data Analysis. PS: Shock Wave Data Acquisition, Review, Editing. RT: Study Conception And Design, Interpretation of results, Draft Manuscript, Review And Editing. YH: Interpretation Of Results, Review And Editing. PR: Data Analysis and Interpretation of results, Review, Editing. MMMD: Review, Editing. Namas Chandra: Review, Editing. All authors reviewed the results and approved the final version of the manuscript.

Funding The work was supported by DRDO, New Delhi, India. Megha Kumari was supported by (UGC) University grants commission, (Fellowship Number: 344728). Palkin Arora was supported by DRDO (Fellowship Number–EST/3009/JRF2020). University Grants Commission, 344728, Defence Research and Development Organisation, EST/3009/JRF2020

Data availability The data provided in the study is available upon request.

Declarations

Competing interests The authors declare no competing interests.

Ethical approval The Institutional Experimental Animal Facility approved all protocols used in this study.

References

Andres, R. H., Ducray, A. D., Schlattner, U., Wallimann, T., & Widmer, H. R. (2008). Functions and effects of creatine in the central nervous system. *Brain Research Bulletin, 76*(4), 329–343. https://doi.org/10.1016/j.brainresbull.2008.02.035

Arciniegas, D. B., Held, K., & Wagner, P. (2002). Cognitive impairment following TBI. *Current Treatment Options in Neurology, 4*(1), 43–57.

Ariyannur, P. S., Moffett, J. R., Madhavarao, C. N., Arun, P., Vishnu, N., Jacobowitz, D. M., Hallows, W. C., Denu, J. M., & Namboodiri, A. M. (2010). Nuclear-cytoplasmic localization of acetyl coenzyme a synthetase-1 in the rat brain. *Journal of Comparative Neurology, 518*(15), 2952–2977. https://doi.org/10.1002/cne.22373.Nuclear-cytoplasmic

Attwell, D., Buchan, A. M., Charpak, S., Lauritzen, M., MacVicar, B. A., & Newman, E. A. (2010). Glial and neuronal control of brain blood flow. *Nature, 468*(7321), 232–243. https://doi.org/10.1038/nature09613

Banoei, M. M., Casault, C., Metwaly, S. M., & Winston, B. W. (2018). Metabolomics and biomarker discovery in traumatic brain injury. *Journal of Neurotrauma, 35*(16), 1831–1848. https://doi.org/10.1089/neu.2017.5326

Brosnan, J. T., & Brosnan, M. E. (2007). Creatine: Endogenous metabolite, dietary, and therapeutic supplement. *Annual Review of Nutrition, 27*(1), 241–261. https://doi.org/10.1146/annurev.nutr.27.061406.093621

Calvetti, D., & Somersalo, E. (2013). Quantitative in silico analysis of neurotransmitter pathways under steady state conditions. *Frontiers in Endocrinology, 4*, 1–14. https://doi.org/10.3389/fendo.2013.00137

Caplan, B., Bogner, J., Brenner, L., Malec, J., Sharma, B., Lawrence, D. W., & Hutchison, M. G. (2018). Branched chain amino acids (BCAAs) and traumatic brain injury: A systematic review. *Journal of Head Trauma Rehabilitation, 33*(1), 33–45.

Carpenter, K. L. H., Jalloh, I., & Hutchinson, P. J. (2015). Glycolysis and the significance of lactate in traumatic brain injury. *Frontiers in Neuroscience, 9*, 1–15. https://doi.org/10.3389/fnins.2015.00112

Clark, A. L., Merritt, V. C., Bigler, E. D., Bangen, K. J., Werhane, M., Sorg, S. F., Bondi, M. W., Schiehser, D. M., & Delano-Wood, L. (2018). Blast-exposed veterans with mild traumatic brain injury show greater frontal cortical thinning and poorer executive functioning. *Frontiers in Neurology, 9*(1), 11. https://doi.org/10.3389/fneur.2018.00873

Clark, J. F., Doepke, A., Filosa, J. A., Wardle, R. L., Lu, A., Meeker, T. J., & Pyne-Geithman, G. J. (2006). N-Acetylaspartate as a reservoir for glutamate. *Medical Hypotheses, 67*(3), 506–512. https://doi.org/10.1016/j.mehy.2006.02.047

D'Adamo, A. F., Jr., Smith, J. C., & Woiler, C. (1972). The occurrence of N-acetylaspartate amidohydrolase (Aminoacylase n) in the developing rat. *Journal of Neurochemistry, 20*(4), 1275–1278. https://doi.org/10.1016/0032-5910(72)80020-2

Dedeoglu, A., Choi, J.-K., Cormier, K., Kowall, N. W., & Jenkins, B. G. (2004). Magnetic resonance spectroscopic analysis of Alzheimer's disease mouse brain that express mutant human APP shows altered neurochemical profile. *Brain Research, 1012*(1–2), 60–65. https://doi.org/10.1016/j.brainres.2004.02.079

Dienel, G. A. (2014). Lactate shuttling and lactate use as fuel after traumatic brain injury: Metabolic considerations. *Journal of Cerebral Blood Flow & Metabolism, 34*(11), 1736–1748.

Gama Sosa, M. A., De Gasperi, R., Perez Garcia, G. S., Perez, G. M., Searcy, C., Vargas, D., Spencer, A., Janssen, P. L., Tschiffely, A. E., McCarron, R. M., & Ache, B. (2019). Low-level blast exposure disrupts gliovascular and neurovascular connections and induces a chronic vascular pathology in rat brain. *Acta Neuropathologica Communications, 7*(1), 6. https://doi.org/10.1186/s40478-018-0647-5

Gao, W.-M., Chadha, M. S., Kline, A. E., Clark, R. S. B., Kochanek, P. M., Dixon, C. E., & Jenkins, L. W. (2006). Immunohistochemical analysis of histone H3 acetylation and methylation—Evidence for altered epigenetic signaling following traumatic brain injury in immature rats. *Brain Research, 1070*(1), 31–34. https://doi.org/10.1016/j.brainres.2005.11.038

Hoffman, J. R., Zuckerman, A., Ram, O., Sadot, O., Stout, J. R., Ostfeld, I., & Cohen, H. (2017). Behavioral and inflammatory response in animals exposed to a low-pressure blast wave and supplemented with β-alanine. *Amino Acids, 49*(5), 871–886. https://doi.org/10.1007/s00726-017-2383-8

Hoge, C. W., McGurk, D., Thomas, J. L., Cox, A. L., Engel, C. C., & Castro, C. A. (2015). Mild traumatic brain injury in U.S. Soldiers returning from Iraq Charles. *New England Journal of Medicine, 358*(5), 453–463.

Kamnaksh, A., Ahmed, F., Kovesdi, E., Barry, E. S., Grunberg, N. E., Long, J. B., & Agoston, D. V. (2014). Molecular mechanisms of

increased cerebral vulnerability after repeated mild blast-induced traumatic brain injury. *Translational Proteomics, 3*, 22–37. https://doi.org/10.1016/j.trprot.2013.11.001

Karagezyan, K. G., & Ovsepyan, L. M. (1975). Role of ethanolamine, phosphoethanolamine, and phosphatidylethanolamine in oxidative phosphorylation of albino rat brain mitochondria. *Bulletin of Experimental Biology and Medicine, 80*, 1195–1196. https://doi.org/10.1007/BF00833158

Katada, S., Imhof, A., & Sassone-Corsi, P. (2012). Connecting threads: Epigenetics and metabolism. *Cell, 148*(1–2), 24–28. https://doi.org/10.1016/j.cell.2012.01.001

Lin, A. P., Shic, F., Enriquez, C., & Ross, B. D. (2003). Reduced glutamate neurotransmission in patients with Alzheimer's disease?An in vivo 13C magnetic resonance spectroscopy study. *MAGMA Magnetic Resonance Materials in Physics, Biology and Medicine, 16*(1), 29–42. https://doi.org/10.1007/s10334-003-0004-x

Mishra, V., Skotak, M., Schuetz, H., Heller, A., Haorah, J., & Chandra, N. (2016). Primary blast causes mild, moderate, severe and lethal TBI with increasing blast overpressures: Experimental rat injury model. *Scientific Reports, 6*(1), 26992. https://doi.org/10.1038/srep26992

Patet, C., Quintard, H., Suys, T., Pellerin, L., Magistretti, P., & Oddo, M. (2015). Neuroenergetic response to prolonged cerebral glucose depletion after severe brain injury and the role of lactate. *Critical Care, 19*(1), 1–27.

Peskind, E. R., Petrie, E. C., Cross, D. J., Pagulayan, K., McCraw, K., Hoff, D., Hart, K., Yu, C. E., Raskind, M. A., Cook, D. G., & Minoshima, S. (2011). Cerebrocerebellar hypometabolism associated with repetitive blast exposure mild traumatic brain injury in 12 Iraq war Veterans with persistent post-concussive symptoms. *NeuroImage, 54*(SUPPL. 1), S76–S82. https://doi.org/10.1016/j.neuroimage.2010.04.008

Prins, M., Alexander, D., Giza, C. C., & Hovda, D. A. (2013). Repeated mild traumatic brain injury: Mechanisms of cerebral vulnerability. *The Journal of Neurotrauma, 30*(1), 30–38. https://doi.org/10.1089/neu.2012.2399

Rae, C., Hare, N., Bubb, W. A., McEwan, S. R., Bröer, A., McQuillan, J. A., Balcar, V. J., Conigrave, A. D., & Bröer, S. (2003). Inhibition of glutamine transport depletes glutamate and GABA neurotransmitter pools: Further evidence for metabolic compartmentation. *Journal of Neurochemistry, 85*(2), 503–514. https://doi.org/10.1046/j.1471-4159.2003.01713.x

Rana, P., Rama Rao, K. V., Ravula, A., Trivedi, R., D'Souza, M., Singh, A. K., Gupta, R. K., & Chandra, N. (2020). Oxidative stress contributes to cerebral metabolomic profile changes in animal model of blast-induced traumatic brain injury. *Metabolomics, 16*(3), 1–12. https://doi.org/10.1007/s11306-020-1649-4

Reichelt, K. L., & Kvamme, E. (1967). Acetylated and peptide bound glutamate and aspartate in brain. *Journal of Neurochemistry, 14*(10), 987–996. https://doi.org/10.1111/j.1471-4159.1967.tb09510.x

Roberto, V., Signoretti, S., Tavazzi, B., Floris, R., Ludovici, A., Marziali, S., & Tarascio, G. (2008). Temporal window of metabolic brain vulnerability to concussion: A pilot 1H-magnetic resonance spectroscopic study in concussed athletes - Part III: Commentary. *Neurosurgery, 62*(6), 1286–1296. https://doi.org/10.1227/01.NEU.0000316421.58568.AD

Shimomura, Y., & Kitaura, Y. (2018). Physiological and pathological roles of branched-chain amino acids in the regulation of protein and energy metabolism and neurological functions. *Pharmacological Research, 133*(May), 215–217. https://doi.org/10.1016/j.phrs.2018.05.014

Stern, R. A., Riley, D. O., Daneshvar, D. H., Nowinski, C. J., Cantu, R. C., & McKee, A. C. (2011). Long-term consequences of repetitive brain trauma: Chronic traumatic encephalopathy. *PM&R, 3*(10 SUPPL. 2), S460–S467. https://doi.org/10.1016/j.pmrj.2011.08.008

Subramaniam, A., Agarwal, S. M., Kalmady, S., Shivakumar, V., Chhabra, H., Bose, A., Damodharan, D., Narayanaswamy, J. C., Hutton, S. B., & Venkatasubramanian, G. (2015). Effect of transcranial direct current stimulation on prefrontal inhibition in schizophrenia patients with persistent auditory hallucinations: A study on antisaccade task performance. *Indian Journal of Psychological Medicine, 37*(4), 419–422. https://doi.org/10.4103/0253-7176.168584

Takahashi, H., McCaffery, J. M., Irizarry, R. A., & Boeke, J. D. (2006). Nucleocytosolic acetyl-coenzyme a synthetase is required for Histone acetylation and global transcription. *Molecular Cell, 23*(2), 207–217. https://doi.org/10.1016/j.molcel.2006.05.040

Truckenmiller, M. E., Namboodiri, M. A. A., Brownstein, M. J., & Neale, J. H. (1985). N-acetylation of L-aspartate in the nervous system: Differential distribution of a specific enzyme. *Journal of Neurochemistry, 45*(5), 1658–1662. https://doi.org/10.1111/j.1471-4159.1985.tb07240.x

Tyagi, R., Rana, P., Khan, A. R., Deepak Bhatnagar, M., Devi, M., Chaturvedi, S., Tripathi, R. P., & Khushu, S. (2011). Study of acute biochemical effects of thallium toxicity in mouse urine by NMR spectroscopy. *Journal of Applied Toxicology, 31*(7), 663–670.

Van Hall, G., Støstad, M., Rasmussen, P., Jans, Ø., Zaar, M., Gam, C., Quistorff, B., Secher, N. H., & Nielsen, H. B. (2009). Blood lactate is an important energy source for the human brain. *Journal of Cerebral Blood Flow and Metabolism, 29*(6), 1121–1129. https://doi.org/10.1038/jcbfm.2009.35

Vazquez, A., Kamphorst, J. J., Markert, E. K., Schug, Z. T., Tardito, S., & Gottlieb, E. (2016). Cancer metabolism at a glance. *Journal of Cell Science, 129*(18), 3367–3373. https://doi.org/10.1242/jcs.181016

Weinhold, B. (2006). Epigenetic S. *Environmental Health, 114*(3), 160–167.

Wellen, K. E., Hatzivassiliou, G., Sachdeva, U. M., Bui, T. V., Cross, J. R., & Thompson, C. B. (2009). ATP-citrate lyase links cellular metabolism to histone acetylation. *Science, 324*(5930), 1076–1080. https://doi.org/10.1126/science.1164097

Xu, X., Cowan, M., Beraldo, F., Schranz, A., McCunn, P., Geremia, N., Brown, Z., Patel, M., Nygard, K. L., Khazaee, R., & Lu, L. (2021). Repetitive mild traumatic brain injury in mice triggers a slowly developing cascade of long-term and persistent behavioral deficits and pathological changes. *Acta Neuropathologica Communications, 9*(1), 1–27. https://doi.org/10.1186/s40478-021-01161-2

Zeisel, S. H. (1992). Choline: An important nutrient in brain development, liver function and carcinogenesis. *Journal of the American College of Nutrition, 11*(5), 473–481. https://doi.org/10.1080/07315724.1992.10718251

Zeisel, S. H., Mar, M.-H., Howe, J. C., & Holden, J. M. (2003). Concentrations of choline-containing compounds and betaine in common foods. *The Journal of Nutrition, 133*(5), 1302–1307. https://doi.org/10.1093/jn/133.5.1302

Publisher's Note Springer Nature remains neutral with regard to jurisdictional claims in published maps and institutional affiliations.

Springer Nature or its licensor (e.g. a society or other partner) holds exclusive rights to this article under a publishing agreement with the author(s) or other rightsholder(s); author self-archiving of the accepted manuscript version of this article is solely governed by the terms of such publishing agreement and applicable law.

arXiv:2301.05220v1 [cs.CL] 12 Jan 2023

ADVERSARIAL ADAPTATION FOR FRENCH NAMED ENTITY RECOGNITION

A PREPRINT

Arjun Choudhry*
Biometric Research Laboratory
Delhi Technological University, New Delhi, India
and
Université du Québec à Montréal
Montréal, QC, Canada
choudhry.arjun@gmail.com
*These authors contributed equally.

Inder Khatri*
Biometric Research Laboratory
Delhi Technological University, New Delhi, India
inderkhatri999@gmail.com
*These authors contributed equally.

Pankaj Gupta
Biometric Research Laboratory
Delhi Technological University, New Delhi, India
pankajgupta.dtu

Aaryan Gupta
Biometric Research Laboratory
Delhi Technological University, New Delhi, India
aryan227227@gmail.com

Maxime Nicol
Université du Québec à Montréal
Montréal, QC, Canada
nicol.maxime@courrier.uqam.ca

Marie-Jean Meurs
Université du Québec à Montréal
Montreal, QC, Canada
meurs.marie-jean@uqam.ca

Dinesh Kumar Vishwakarma
Biometric Research Laboratory
Delhi Technological University
New Delhi, India
dinesh@dtu.ac.in

ABSTRACT

Named Entity Recognition (NER) is the task of identifying and classifying named entities in large-scale texts into predefined classes. NER in French and other relatively limited-resource languages cannot always benefit from approaches proposed for languages like English due to a dearth of large, robust datasets. In this paper, we present our work that aims to mitigate the effects of this dearth of large, labeled datasets. We propose a Transformer-based NER approach for French, using adversarial adaptation to similar domain or general corpora to improve feature extraction and enable better generalization. Our approach allows learning better features using large-scale unlabeled corpora from the same domain or mixed domains to introduce more variations during training and reduce overfitting. Experimental results on three labeled datasets show that our adaptation framework outperforms the corresponding non-adaptive models for various combinations of Transformer models, source datasets, and target corpora. We also show that adversarial adaptation to large-scale unlabeled corpora can help mitigate the performance dip incurred on using Transformer models pre-trained on smaller corpora.

Keywords Named Entity Recognition · Adversarial Adaptation · Transformer · Limited Resource Languages · Large-scale corpora

1 Introduction

Named Entity Recognition (NER) is the task of identifying and extracting specific entities from unstructured text, and labeling them into predefined classes. Over the years, NER models for high-resource languages, like English, have seen noticeable improvements in task performance owing to model architecture advancements and the availability of large, labeled datasets. In sharp contrast, languages like French still lack openly available, large-scale, labeled, robust datasets free from biases, and have few general-domain language models, and barely any domain-specific ones. Creating large, robust NER datasets requires manual annotation and is prohibitively expensive, calling for less labeled data-reliant approaches, particularly for limited and low-resource languages.

Over the years, a variety of deep learning-based NER approaches have been proposed [22]. Some of the older approaches made use of external texts, or gazetteers, for the disambiguation of input words [21]. Several works have used combinations of Recurrent Neural Networks like LSTMs and GRUs with Conditional Random Fields to improve model performance for a variety of NER tasks [7, 8, 9].

Recent works have also incorporated the use of pre-trained contextualized language models for improved NER performance. Copara *et al.* [2] proposed an ensemble-based NER framework for Biomedical NER in French, using various combinations of French language models. Liu *et al.* [12] pre-trained a NER-BERT model on a large NER corpus to counter the underlying discrepancies between the language model and the NER dataset. They observed significantly better performance than the standard BERT [3] Transformer model across nine domains.

Researchers have also started incorporating various domain adaptation approaches for adapting NER models from high-resource domains to low-resource domains [25, 13]. Peng *et al.* [19] further proposed an entity-aware domain-adaptive framework using an attention layer to enable the improved transfer of features for models trained on one domain to another domain using adversarial learning. They observed noticeably better performance in cross-domain settings than without domain adaptation. However, due to the lack of robust and labeled datasets across multiple domains in limited-resource languages, these domain adaptive approaches are mostly restricted to high-resource languages. Wang *et al.* [26] further introduced an adversarial perturbation approach for reduced overfitting, while also proposing the use of Gated-CNN to fuse the spatial information between adjacent words. However, they tested their approach on English datasets and noticed marginal gains over baseline approaches.

In this work, which follows our preliminary exploration [1], we incorporate the use of adversarial adaptation to improve the performance of NER models in in-domain settings for French. We propose a Transformer-based NER approach, which uses adversarial adaptation to counter the lack of large-scale labeled NER datasets in French. This helps us evaluate the use of adversarial adaptation in enabling a model to learn improved, generalized features by adapting them to large-scale unlabeled corpora that are readily available and easy to generate for even low-resource languages. We further train Transformer-based NER models on labeled source datasets and use larger corpora from similar or mixed domains as target sets for improved feature learning by the model. Our proposed approach helps outsource wider domain and general feature knowledge from easily available large unlabeled corpora. We limit the purview of our evaluation to the French language in this paper. However, our approach could further be applied to other limited and low-resource languages for improved NER performance, as well as for other downstream tasks. This paper is organized as follows: the proposed methodology is introduced in Section 2. Section 3 presents our experiments and discusses the obtained results while Section 4 concludes our findings.

2 Proposed Methodology

2.1 Datasets and Preprocessing

In this work, we use the WikiNER French [18], WikiNeural French [24], and Europeana French [17] datasets as the labeled source datasets used for the supervised training branch in our model. The Europeana dataset contains text extracted from historic European newspapers using Optical Character Recognition (OCR). However, the dataset contains some OCR errors, thus making it noisy. This can lead to lower performance by models trained on Europeana.

For the unlabeled target corpora, we use WikiNER and WikiNeural datasets, and the Leipzig Mixed French corpus[1]. We remove the labels for the former two datasets for use as large, unlabeled target corpora. These corpora enable us to evaluate the impact of adapting the models to similar-domain data, as well as more generalized corpora.

During preprocessing, we convert all NER tags to Inside-Outside-Beginning (IOB) [20] format and store the datasets in the CoNLL 2002 [23] NER format for easier data input during training.

[1] `https://wortschatz.uni-leipzig.de/en/download/French`

2.2 Adversarial Adaptation to Similar Domain Corpus

Adversarial adaptation aids in selecting domain-invariant features which are transferable between source and target datasets [5]. Compared to other approaches to domain adaptation, adversarial adaptation incorporates a domain discriminator into the classification framework. A domain discriminator acts as a domain classifier and is trained on the features retrieved by the feature extractor layer in the framework. It is tasked with distinguishing between the features obtained from the source and target sets. With the help of a Gradient Reversal Layer (GRL) [4], the gradient flow of the domain discriminator is utilized to penalize the feature extractor for learning the domain-specific features, thus causing the feature extractor to learn domain-invariant features. GRL reverses the gradient direction and thus helps train different components of the neural network *adversarially*. This enables the feature extractor to yield features free from domain biases present in the source domain but not the target domain.

We propose the use of adversarial adaptation of NER models to large-scale, unlabeled corpora from similar or mixed domains. This helps us enable the model to extract relatively more generalizable features from the same domain as the source dataset, without altering the feature extractor significantly to learn overly generalized features that reduce in-domain performance. Adversarial adaptation to similar domain corpora thus helps reduces the risk of overfitting on the source intricate training set-specific features, as it aids the feature extractor in extracting more generalizable features, indistinguishable from the features from the large-scale target corpora. This helps counter the dearth of large and robust training datasets in languages like French, which are readily available in English.

We evaluate our approach for three scenarios: source and target datasets are from the same domain; source and target datasets are from relatively different domains; and the source belongs to a certain domain while the target dataset is a mixed-domain, large-scale, general corpus. The latter scenario helps generalize the model further, reducing the domain-specific feature extraction in favor of features common to both the source dataset and the target corpora. Figure 1 graphically illustrates our proposed framework.

Our Transformer model is trained using two losses: the NER classifier loss L_{NER}, defined in Equation 1, and the adversarial loss L_{adv}, defined in Equation 2. The total loss is defined in Equation 3. L_{NER} is the standard loss that penalizes the Transformer model's token classification error, encouraging it to make more accurate entity predictions. It is further responsible for optimizing the NER Classifier's weights. L_{adv} is used adversarially, where the Transformer model is optimized in a way to maximize L_{adv}, while the domain classifier is optimized to minimize L_{adv}. To achieve this, we use a Gradient Reversal Layer between the Transformer model and the domain classifier. The Gradient Reversal Layer acts as an identity function during forward propagation, but during back-propagation, it multiplies its input by -1. This causes the back-propagated gradient to perform gradient ascent on the Transformer model with respect to the domain classifier's classification loss, rather than gradient descent. We specifically use the adversarial domain classifier as a discriminator in our framework.

$$L_{NER} = \min_{\theta_f, \theta_n} \sum_{i=1}^{n_s} L_n^i \tag{1}$$

$$L_{adv} = \min_{\theta_d}(\max_{\theta_f}(\sum_{i=1}^{n_s} L_{ds}^i + \sum_{j=1}^{n_t} L_{dt}^j)) \tag{2}$$

$$L_{Total} = L_{NER} + \alpha(L_{adv}) \tag{3}$$

Here, n_s and n_t represent the number of samples in source and target sets respectively, θ_d, θ_n, and θ_f are the number of parameters for domain classifier, NER classifier, and Transformer model respectively, and L_{ds} and L_{dt} represent the Negative log-likelihood loss (NLLL) for the source and target respectively. We introduce another parameter α, which is the ratio between L_{NER} and L_{adv} in the total loss. This helps us with correctly penalizing the NER classifier and the domain classifier. We found the optimum value of α to be equal to 2, as this led to the best experimental results.

2.3 Language Models for NER

Recent NER research has incorporated large language models due to their contextual knowledge learned during pretraining [27, 6, 15]. We evaluate the efficacy of our proposed approach on three French language models: CamemBERT-base [16], CamemBERT-Wikipedia-4GB (a variant of CamemBERT pre-trained on only 4GB of Wikipedia French corpus), and FlauBERT-base [10]. FlauBERT is based on the BERT [3] architecture, while CamemBERT is based on the RoBERTa [11] architecture. FlauBERT is trained on nearly half the amount of training data (71GB) as CamemBERT (138GB). All three language models provide 768-dimensional word embeddings. Comparing CamemBERT-base and CamemBERT-Wiki-4GB helps us analyze if we can replace language models pre-trained on large corpora with models pre-trained on smaller corpora adapted to unlabeled corpora during fine-tuning on a downstream task.

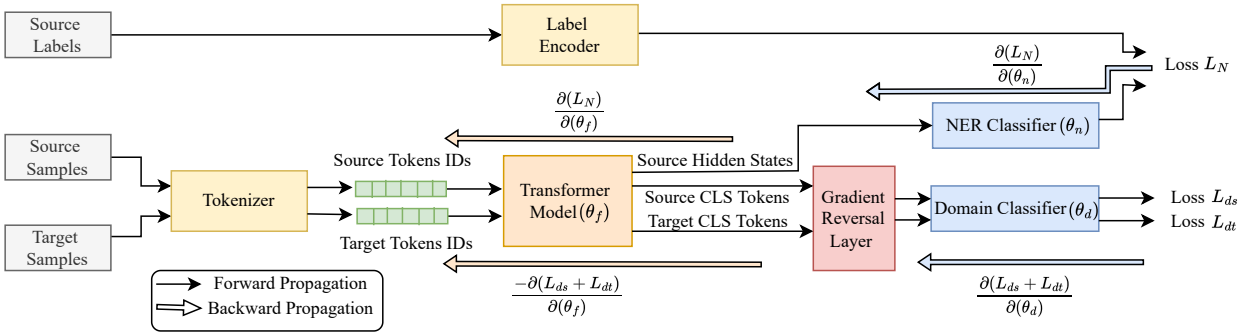

Figure 1: Graphical representation of our adversarial adaptation framework for training NER models on source and target sets.

3 Experiments and Results

We evaluated the performance of our approach for various combinations of language models, source datasets, and target datasets. Each model was evaluated on the test subset (20% of the total data) of the source dataset. All domain-adaptive and baseline models were trained for up to 16 epochs. The training was stopped when peak validation accuracy for the in-domain validation set was achieved. We used a batch size of 16 for each experiment. We used the AdamW optimizer [14], an optimized version of Adam with weight decay with a learning rate of 0.00002 and a learning rate scheduler while training. We used a Transformer encoder-based layer with 512 units for feature extraction. Both the NER and domain classifier branches consisted of two dense layers each. We used a gradient reversal layer for the adversarial domain classification branch, using the last two hidden embeddings as input. These experiments are fully reproducible, and the systems are made available as open-source[2] under GNU GPL v3.0. Table 1 illustrates our results. Some prominent findings observed are:

Models trained using our adversarial adaptation framework consistently outperformed their non-adaptive counterparts across all metrics. We observed that the adversarial adaptation models showed significant performance improvements across Precision, Recall, and F1-score over their non-adaptive counterparts across almost all combinations of source datasets, target datasets, and language models. This is beneficial for low and limited-resource languages, where adversarial adaptation to unlabelled corpora can mitigate the need for creating robust labeled datasets for training NER models.

Adversarial adaptation can help alleviate some of the performance loss incurred on using smaller models. On fine-tuning the CamemBERT-Wiki-4GB model using our adversarial approach, we observed performance similar to or close to the non-adapted CamemBERT-base model for select settings. In fact, CamemBERT-Wiki-4GB model, when trained on the WikiNER dataset and adapted to WikiNeural corpus, outperformed the unadapted CamemBERT-base model. Nearly every language model reported improved results with adversarial adaptation. Thus, the use of adversarial adaptation during fine-tuning can act as a substitute for using larger language models for downstream tasks, thus leading to reduced computational costs for pre-training as well as fine-tuning.

Adapting NER models to the same domain target corpus as the source dataset generally leads to slightly better performance than adapting to a mixed domain corpora. We observed that models adapted to a corpus from the same domain as the source dataset (like when WikiNER and WikiNeural are used as source and target datasets, or vice versa) showed similar to slightly better performance than the same models were adapted to general domain corpora. However, both of these cases were almost always better than the corresponding unadapted models.

Adapting NER models to a mixed-domain target corpus generally leads to better performance than adapting the models to a corpus from a different domain corpus. We observed that models, when adapted to a mixed-domain corpus (like in the case of Europeana to Mixed-Fr), showed noticeably better performance than the corresponding models adapted to a corpus from a slightly different domain (as in the case of Europeana to WikiNER). However, in most scenarios, both of these settings led to better performance than the unadapted setting.

[2] `https://github.com/Arjun7m/AA_NER_Fr`

Model	Source	Target	Precision	Recall	F1-Score
CamemBERT-Wiki-4GB	**WikiNER**	**-**	0.911	0.925	0.918
		WikiNeural	**0.966**	**0.963**	**0.969**
		Mixed-Fr	0.956	0.962	0.959
	WikiNeural	**-**	0.859	0.872	0.866
		WikiNER	**0.872**	**0.891**	**0.881**
		Mixed-Fr	0.870	0.879	0.875
	Europeana	**-**	0.728	0.642	0.682
		WikiNER	0.738	**0.691**	**0.714**
		Mixed-Fr	**0.774**	0.640	0.701
CamemBERT-base	**WikiNER**	**-**	0.960	0.968	0.964
		WikiNeural	**0.973**	0.976	**0.975**
		Mixed-Fr	0.972	**0.978**	0.974
	WikiNeural	**-**	0.943	0.950	0.946
		WikiNER	0.943	**0.953**	**0.948**
		Mixed-Fr	**0.946**	0.950	**0.948**
	Europeana	**-**	0.927	0.933	0.930
		WikiNER	0.911	0.927	0.920
		Mixed-Fr	**0.942**	**0.943**	**0.943**
FlauBERT-base	**WikiNER**	**-**	0.963	0.964	0.963
		WikiNeural	0.964	0.968	0.966
		Mixed-Fr	**0.974**	**0.972**	**0.973**
	WikiNeural	**-**	0.934	0.946	0.940
		WikiNER	0.935	**0.950**	**0.942**
		Mixed-Fr	**0.941**	0.943	**0.942**
	Europeana	**-**	0.835	0.863	0.849
		WikiNER	0.855	**0.865**	0.860
		Mixed-Fr	**0.882**	0.854	**0.867**

Table 1: Performance evaluation of our proposed adversarial adaptation approach to large-scale corpora for various combinations of models, source and target sets. We observe noticeably improved performance for the adversarial adaptation models as compared to their corresponding non-adaptive models across almost all settings.

4 Conclusion and Future Work

In this work, we proposed a Transformer-based Named Entity Recognition framework using adversarial adaptation to large-scale similar domain or mixed domain corpora for improved feature learning in French. We adapted our models using our framework to corpora from the same domain as the source dataset as well as mixed-domain corpora. We evaluated our approach on three French language models, three target datasets, and three large-scale corpora. We observed noticeably improved performance using our proposed approach, as compared to models trained without our approach, across almost all Transformers and datasets. We further observed that adapting a model to a large-scale corpus for a downstream task can help alleviate some of the performance loss incurred by using smaller language models pre-trained on less robust corpora. Our proposed framework can further be applied to other low and limited-resource languages for a variety of downstream tasks.

In the future, we intend to evaluate the efficacy of our approach for multi-lingual and cross-lingual NER, particularly for out-of-domain settings using a multi-lingual corpus as the target dataset for adaptation and multi-lingual transformer embeddings. This can help reduce the dependence on labeled datasets for each language for NER. We further aim to evaluate the impact of the underlying language script used as the target data, and how performance is affected upon using a target corpora composed of texts from languages from different scripts for improved generalization over the language-independent features.

Acknowledgments This research was enabled by support provided by Calcul Québec, The Digital Research Alliance of Canada and MITACS.

References

[1] Choudhry, A., Gupta, P., Khatri, I., Gupta, A., Nicol, M., Meurs, M.J., Vishwakarma, D.K.: Transformer-Based Named Entity Recognition for French Using Adversarial Adaptation to Similar Domain Corpora (2022). doi:10.48550/ARXIV.2212.03692, accessed 11 January 2023

[2] Copara, J., Knafou, J., Naderi, N., Moro, C., Ruch, P., Teodoro, D.: Contextualized French Language Models for Biomedical Named Entity Recognition. In: Actes de la 6e conférence conjointe Journées d'Études sur la Parole (JEP, 33e édition), Traitement Automatique des Langues Naturelles (TALN, 27e édition), Rencontre des Étudiants Chercheurs en Informatique pour le Traitement Automatique des Langues (RÉCITAL, 22e édition). Atelier DÉfi Fouille de Textes. pp. 36–48. ATALA et AFCP, Nancy, France (2020), https://aclanthology.org/2020.jeptalnrecital-deft.4, accessed 11 January 2023

[3] Devlin, J., Chang, M.W., Lee, K., Toutanova, K.: BERT: Pre-training of Deep Bidirectional Transformers for Language Understanding. In: Proceedings of the 2019 Conference of the North American Chapter of the Association for Computational Linguistics: Human Language Technologies, Volume 1 (Long and Short Papers). pp. 4171–4186. Association for Computational Linguistics, Minneapolis, Minnesota (2019). doi:10.18653/v1/N19-1423, accessed 11 January 2023

[4] Ganin, Y., Lempitsky, V.: Unsupervised Domain Adaptation by Backpropagation (2014). doi:10.48550/ARXIV.1409.7495, accessed 11 January 2023

[5] Ganin, Y., Ustinova, E., Ajakan, H., Germain, P., Larochelle, H., Laviolette, F., Marchand, M., Lempitsky, V.: Domain-Adversarial Training of Neural Networks. J. Mach. Learn. Res. **17**(1), 2096–2030 (2016), http://jmlr.org/papers/v17/15-239.html, accessed 11 January 2023

[6] Gong, C., Tang, J., Zhou, S., Hao, Z., Wang, J.: Chinese Named Entity Recognition with Bert. DEStech Transactions on Computer Science and Engineering (2019). doi:10.12783/dtcse/cisnrc2019/33299, accessed 11 January 2023

[7] Gridach, M., Haddad, H.: Arabic Named Entity Recognition: A Bidirectional GRU-CRF Approach. In: Computational Linguistics and Intelligent Text Processing, CICLing 2017. Lecture Notes in Computer Science, vol. 10761, pp. 264–275. Springer, Budapest, Hungary (2017). doi:10.1007/978-3-319-77113-7_21, accessed 11 January 2023

[8] Habibi, M., Weber, L., Neves, M., Wiegandt, D.L., Leser, U.: Deep Learning with Word Embeddings Improves Biomedical Named Entity Recognition. Bioinformatics **33**(14), 37–48 (2017). doi:10.1093/bioinformatics/btx228, accessed 11 January 2023

[9] Lample, G., Ballesteros, M., Subramanian, S., Kawakami, K., Dyer, C.: Neural Architectures for Named Entity Recognition. In: Proceedings of the 2016 Conference of the North American Chapter of the Association for Computational Linguistics: Human Language Technologies. pp. 260–270. Association for Computational Linguistics, San Diego, California (2016). doi:10.18653/v1/N16-1030, accessed 11 January 2023

[10] Le, H., Vial, L., Frej, J., Segonne, V., Coavoux, M., Lecouteux, B., Allauzen, A., Crabbé, B., Besacier, L., Schwab, D.: FlauBERT: Unsupervised Language Model Pre-training for French. In: Proceedings of The 12th Language Resources and Evaluation Conference. pp. 2479–2490. European Language Resources Association, Marseille, France (2020), https://www.aclweb.org/anthology/2020.lrec-1.302, accessed 11 January 2023

[11] Liu, Y., Ott, M., Goyal, N., Du, J., Joshi, M., Chen, D., Levy, O., Lewis, M., Zettlemoyer, L., Stoyanov, V.: RoBERTa: A Robustly Optimized BERT Pretraining Approach (2019). doi:10.48550/ARXIV.1907.11692, accessed 11 January 2023

[12] Liu, Z., Jiang, F., Hu, Y., Shi, C., Fung, P.: NER-BERT: A Pre-trained Model for Low-Resource Entity Tagging (2021). doi:10.48550/ARXIV.2112.00405, accessed 11 January 2023

[13] Liu, Z., Xu, Y., Yu, T., Dai, W., Ji, Z., Cahyawijaya, S., Madotto, A., Fung, P.: CrossNER: Evaluating Cross-Domain Named Entity Recognition. Proceedings of the AAAI Conference on Artificial Intelligence **35**(15), 13452–13460 (2021). doi:10.1609/aaai.v35i15.17587, accessed 11 January 2023

[14] Loshchilov, I., Hutter, F.: Decoupled Weight Decay Regularization (2017). doi:10.48550/ARXIV.1711.05101, accessed 11 January 2023

[15] Lothritz, C., Allix, K., Veiber, L., Bissyandé, T.F., Klein, J.: Evaluating Pretrained Transformer-based Models on the Task of Fine-Grained Named Entity Recognition. In: Proceedings of the 28th International Conference on Computational Linguistics. pp. 3750–3760. International Committee on Computational Linguistics, Barcelona, Spain (Online) (2020). doi:10.18653/v1/2020.coling-main.334, accessed 11 January 2023

[16] Martin, L., Muller, B., Ortiz Suárez, P.J., Dupont, Y., Romary, L., de la Clergerie, É., Seddah, D., Sagot, B.: CamemBERT: a Tasty French Language Model. In: Proceedings of the 58th Annual Meeting of the Association for Computational Linguistics. pp. 7203–7219. Association for Computational Linguistics, Online (2020). doi:10.18653/v1/2020.acl-main.645, accessed 11 January 2023

[17] Neudecker, C.: An Open Corpus for Named Entity Recognition in Historic Newspapers. In: Proceedings of the Tenth International Conference on Language Resources and Evaluation (LREC'16). pp. 4348–4352. European Language Resources Association (ELRA), Portorož, Slovenia (2016), https://aclanthology.org/L16-1689, accessed 11 January 2023

[18] Nothman, J., Ringland, N., Radford, W., Murphy, T., Curran, J.R.: Learning Multilingual Named Entity Recognition from Wikipedia. Artificial Intelligence **194**, 151–175 (2013). doi:10.1016/j.artint.2012.03.006, accessed 11 January 2023

[19] Peng, Q., Zheng, C., Cai, Y., Wang, T., Xie, H., Li, Q.: An Entity-Aware Adversarial Domain Adaptation Network for Cross-Domain Named Entity Recognition (Student Abstract). Proceedings of the AAAI Conference on Artificial Intelligence **35**(18), 15865–15866 (2021). doi:10.1609/aaai.v35i18.17929, accessed 11 January 2023

[20] Ramshaw, L.A., Marcus, M.P.: Text Chunking using Transformation-Based Learning (1995). doi:10.48550/ARXIV.CMP-LG/9505040, accessed 11 January 2023

[21] Ratinov, L., Roth, D.: Design Challenges and Misconceptions in Named Entity Recognition. In: Proceedings of the Thirteenth Conference on Computational Natural Language Learning (CoNLL-2009). pp. 147–155. Association for Computational Linguistics, Boulder, Colorado (2009), https://aclanthology.org/W09-1119, accessed 11 January 2023

[22] Roy, A.: Recent Trends in Named Entity Recognition (NER) (2021). doi:10.48550/ARXIV.2101.11420, accessed 11 January 2023

[23] Sang, E.F.T.K.: Introduction to the CoNLL-2002 Shared Task: Language-Independent Named Entity Recognition (2002). doi:10.48550/ARXIV.CS/0209010, accessed 11 January 2023

[24] Tedeschi, S., Maiorca, V., Campolungo, N., Cecconi, F., Navigli, R.: WikiNEuRal: Combined Neural and Knowledge-based Silver Data Creation for Multilingual NER. In: Findings of the Association for Computational Linguistics: EMNLP 2021. pp. 2521–2533. Association for Computational Linguistics, Punta Cana, Dominican Republic (2021). doi:10.18653/v1/2021.findings-emnlp.215, accessed 11 January 2023

[25] Wang, J., Kulkarni, M., Preotiuc-Pietro, D.: Multi-Domain Named Entity Recognition with Genre-Aware and Agnostic Inference. In: Proceedings of the 58th Annual Meeting of the Association for Computational Linguistics. pp. 8476–8488. Association for Computational Linguistics, Online (2020). doi:10.18653/v1/2020.acl-main.750, accessed 11 January 2023

[26] Wang, J., Xu, W., Fu, X., Xu, G., Wu, Y.: ASTRAL: Adversarial Trained LSTM-CNN for Named Entity Recognition. Knowledge-Based Systems **197**, 105842 (2020). doi:10.1016/j.knosys.2020.105842, accessed 11 January 2023

[27] Yan, R., Jiang, X., Dang, D.: Named Entity Recognition by Using XLNet-BiLSTM-CRF. Neural Process. Lett. **53**(5), 3339–3356 (2021). doi:10.1007/s11063-021-10547-1, accessed 11 January 2023

Journal Pre-proof

Ag-doped-CuO nanoparticles supported polyaniline (PANI) based novel electrochemical sensor for sensitive detection of paraoxon-ethyl in three real samples

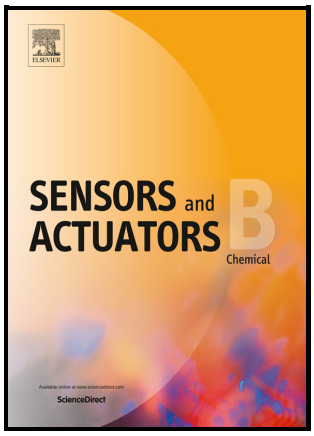

Saroj Paneru, Devendra Kumar

PII: S0925-4005(22)01913-X

DOI: https://doi.org/10.1016/j.snb.2022.133270

Reference: SNB133270

To appear in: *Sensors and Actuators: B. Chemical*

Please cite this article as: Saroj Paneru and Devendra Kumar, Ag-doped-CuO nanoparticles supported polyaniline (PANI) based novel electrochemical sensor for sensitive detection of paraoxon-ethyl in three real samples, *Sensors and Actuators: B. Chemical,* () doi:https://doi.org/10.1016/j.snb.2022.133270

This is a PDF file of an article that has undergone enhancements after acceptance, such as the addition of a cover page and metadata, and formatting for readability, but it is not yet the definitive version of record. This version will undergo additional copyediting, typesetting and review before it is published in its final form, but we are providing this version to give early visibility of the article. Please note that, during the production process, errors may be discovered which could affect the content, and all legal disclaimers that apply to the journal pertain.

© Published by Elsevier.

Journal Pre-proof

Ag-doped-CuO nanoparticles supported polyaniline (PANI) based novel electrochemical sensor for sensitive detection of paraoxon-ethyl in three real samples

Saroj Paneru, Devendra Kumar*

Department of Applied Chemistry, Delhi Technological University, Delhi 110042, India

*Corresponding author

Email: dkumar@dce.ac.in

ORCID No. orcid.org/0000-0001-9118-2070

Journal Pre-proof

Abstract

In this paper, a novel nanocomposite is chemically synthesized by reinforcing Ag-doped CuO (Ag@CuO) nanoparticles into the matrix of polyaniline (PANI). This nanocomposite is used as a sensing platform for paraoxon-ethyl (PE) detection. The homogeneous distribution of Ag@CuO nanoparticles onto the PANI matrix provides a smooth and dense surface area, further accelerating the transmission of electrons. The synergistic effect of Ag@CuO and PANI matrix is responsible for the outstanding conductivity, biocompatibility, and catalytic power of the proposed biosensor. For the biosensor fabrication, the nanocomposite is electrophoretically deposited onto the surface of the ITO glass substrate and then the acetylcholinesterase (AChE) enzyme is immobilized onto the fabricated electrode surface by using glutaraldehyde as a crosslinking agent. Under all optimized detection conditions, the proposed biosensor (AChE/Ag@CuO/PANI/ITO) shows a broad linear range from 5 to 100 pM with a low detection limit (LOD) of 11.35 pM. All the electrochemical results confirm the high sensitivity (0.5536 μA $(pM)^{-1}$ cm^{-2}), high selectivity, good reproducibility, and acceptable stability of the proposed biosensor.

Moreover, the proposed biosensor is successfully applied for paraoxon-ethyl (PE) detection in three real samples.

Keywords: Ag@CuO, polyaniline, electrochemical biosensor, OPs detection, acetylcholinesterase.

1: **Introduction**

The high insecticidal properties and potency of organophosphate pesticides (OPs) make them popular for agricultural productivity and pest control. Although OPs have enormous benefits in the farming industries but their excessive and careless uses cause serious health issues worldwide [1, 2]. Moreover, their inhibition activity towards the acetylcholinesterase (AChE) enzyme produces neurotoxicity in animals and humans, which further causes different severe diseases like Alzheimer's, Parkinson's, cognitive disorders, etc. [3,4]. Thus, it opens an opportunity to develop efficient techniques for optimal detection of OPs which enhance agricultural productivity and reduce the associated health risk simultaneously.

Reviews of existing literature reveal that there are few chromatography techniques, such as gas chromatography [5], gas chromatography associated with mass spectroscopy [6], and liquid chromatography-tandem mass spectrometry [7] which perform significantly well. However, their complex off-site procedures, overpriced instrumentation, and the requirement of skillful handling make them more vulnerable in terms of practical uses. To overcome these issues, biosensors came into existence as they are cheap, fast, and having simple on-site operating procedures. Recently, AChE inhibition-based biosensors have been widely explored for the detection of OPs owing to their high selectivity and quick response

[8]. Their mechanism is based on the enzyme's inhibition rate in the presence of OPs [9, 10]. The sensitivity of AChE enzyme-based biosensors heavily relies on two factors: (i) How to prevent the leakage of the enzyme from the electrode surface? (ii) How to enhance the electron transfer rate between enzyme and electrode surface? To consider these two important factors, various transducers have been explored by researchers so far [11-14].

In recent years, metal oxides have been gaining a lot of popularity in the fabrication of effective transducers due to their outstanding properties like high stability, non-toxic nature and high catalytic power. Among all metal oxides, copper oxide (CuO) shows a high affinity with sulfur-containing compounds and accelerates the hydrolysis of acetyl thiocholine chloride (ATCl), further improving the AChE-based biosensor's sensitivity [15]. It also shows high compatibility with substrate owing to its high absorption capacity and bonding ability [16]. Doping of CuO improves its conductivity by reducing the bandgap between the valence band and conduction band [17]. Therefore, several studies have been conducted in which CuO is doped by many metal nanoparticles [18, 19].

Among all metal nanoparticles, Ag has the highest conducting property along with high catalytic power. One of the most significant features of Ag is that it can effectively enhance the transportation of electrons. This transportation can be done either between the active matrix and its associated electrode or between the active matrix and analyte molecule present in the aqueous solution [20].

Polyaniline (PANI) has also gained tremendous popularity as a supporting material due to its outstanding conductivity, high surface area, easy synthesis procedure high and redox behaviour. It shows high bio affinity with the AChE enzyme due to its amino groups [21]. These remarkable properties of PANI make it a more application-oriented material for several research domains, such as glucose detection [22], supercapacitor [23], and catalysis [24].

This paper deals with all the mentioned characteristics of Ag, CuO, and PANI to develop a sensing device for PE detection having the following novelties: (1) In the present work, a novel nanocomposite is synthesized by reinforcing Ag@CuO nanoparticles into the PANI matrix. The prepared nanocomposite is further used as a sensing platform to construct an efficient electrochemical biosensor (AChE/Ag@CuO/PANI/ITO) for sensitive detection of PE. This proposed biosensor shows high sensitivity due to the following reasons: (a) The uniform distribution of Ag@CuO nanoparticles onto the PANI matrix enhances the surface area and density of the nanocomposite and generates a smooth path for transmission of the analytes. (b) To prevent the leaching of the enzyme from the electrode surface, a cross-linking agent is used in this study. This setup provides high enzyme loading, further enhancing the associated biosensor's efficiency. (c) The incorporation of Ag and CuO in the PANI matrix enhances the nanocomposite's conductivity and catalytic power. (2) The literature review reveals that there is no study conducted so far regarding the fabrication of Ag@CuO/PANI nanocomposite-based transducer for electrochemical detection of PE. (3) To check the real-world applicability and accuracy of the proposed method, three real samples are considered in this study.

2. Experimental section

2.1 Materials and reagents

Aniline (used after distillation), ammonium persulfate (APS) (98%), copper sulfate pentahydrate ($CuSO_4$. $5H_2O$) (98.5%), sodium lauryl sulfate (SDS) (85%), sodium hydroxide (NaOH) (97%), silver nitrate ($AgNO_3$) (99%), acetylcholinesterase (AChE) (C3389-2KU), acetyl thiocholine chloride (ATCl), paraoxon-ethyl (PE), and solvents (acetone, ethanol, and HCl) are purchased from Sigma-Aldrich, India. Dibasic potassium phosphate (K_2HPO_4), monobasic potassium phosphate (KH_2PO_4), potassium ferrocyanide (98%), potassium ferricyanide (99%), and potassium chloride (KCl) are purchased from

Fisher-Scientific, India. Real samples are purchased from the market. All solutions are prepared in Mill-Q water (18.2MΩ cm).

2.2 Synthesis of CuO and Ag@CuO

To prepare CuO, 0.7 g of $CuSO_4.5H_2O$ is dissolved in 25 mL of DI water followed by stirring for 15 min at 80^oC. Then, 0.07 g of SDS is added and stirred for 30 min at the same temperature. Subsequently, 1 M NaOH is added dropwise till the solution's pH reaches 14. The resultant solution is stirred for 6 h and further centrifuged at 3000 rpm for 10 min till the pH reaches 7. The obtained black precipitate of CuO is dried at 60^oC for 8 h and calcined in a muffle furnace at 800^oC for 5 h.

On the other hand, the Ag@CuO nanoparticle is prepared by dissolving 35 mg of $AgNO_3$ and 0.7 g of $CuSO_4.5H_2O$ into 25 mL of DI water followed by stirring at 80^oC for 1 h. After this step, the rest steps are the same as discussed above for the synthesis of CuO nanoparticles.

2.3 Synthesis of Ag@CuO/PANI based nanocomposite

To prepare the nanocomposite**,** 0.37 g of Ag@CuO is dispersed in DI water and then this dispersed solution is transferred to 0.2 M aniline hydrochloride solution (50 mL, 1M HCl) and stirred for 1 h. Subsequently, 1M APS (10 mL in 1 M HCl) is introduced dropwise, and the resultant solution is stirred for 8 h at room temperature. Later, the prepared solution is centrifuged at 2400 rpm for 15 min and washed 3 to 4 times with DI water and ethanol. The obtained black precipitate is finally dried in the oven at 60^oC.

2.4 Electrophoretic deposition of Ag@CuO/PANI nanocomposite and biosensor fabrication

For the electrophoretic deposition, the colloidal suspensions of Ag@CuO and Ag@CuO/PANI are prepared in a mixture of ethanol and water (0.1 mg in 1:5 ethanol:

water). For smooth deposition of Ag@CuO and Ag@CuO/PANI, 20 V of DC voltage is applied for 16 sec by taking ITO as a working electrode.

For biosensor fabrication, the prepared electrode is incubated (2h) at 25^{o}C with 0.2% glutaraldehyde (10 μL). Subsequently, 20 μL of the prepared AChE solution (0.1 mg/ml or 23.3 U/ml) is drop cast into the fabricated electrode. The developed biosensor is further stored in the refrigerator at 4^{o}C for 12 h. Before the electrochemical analysis, the prepared biosensor is washed with 100 μL PBS to remove the unbounded enzyme. Fig. 1(A) represents the schematic approach to biosensor fabrication.

2.5 Characterization

The X-ray studies of all prepared materials were performed in Bruker D-8 Advance X-ray diffractometer with monochromatic (Cu Kα) radiation (λ=1.5406 A°) at 2 θ = 10-80^{o} with speed of 2^{o}/min. The FTIR studies were performed in Perkin Elmer Spectrum 2 (Attenuated total reflection (ATR) mode) at the frequency range of 400-4000 cm^{-1}. All morphological analysis of all prepared materials were carried out by FESEM (EVO-18, ZEISS). The electrochemical studies were performed using Autolab potentiostat/galvanostat (Eco-Chemie) having three electrodes (working (AChE/Ag@CuO/PANI/ITO), reference (Ag/AgCl) and counter (Pt electrode). All electrochemical analyses were carried out in 0.2 mM phosphate buffer saline (PBS, 6.5 pH) containing 5 mM [Fe(CN)6]$^{3/4-}$.

3: Results and discussion

3.1 Design of proposed biosensor

This proposed work prepares a novel nanocomposite by reinforcing the Ag@CuO nanoparticle onto the matrix of PANI (Fig. 1, scheme A, step 1). The uniform distribution of Ag@CuO over the surface of PANI increases the surface area, which further enhances the diffusion of analyte and electron kinetics. The prepared nanocomposite is deposited onto the

ITO surface by using the electrophoretic technique (Fig. 1, scheme A, step 2). Subsequently, the AChE enzyme is immobilized onto the fabricated electrode using a cross-linking agent, glutaraldehyde (Fig. 1, scheme A, step 3). Glutaraldehyde chemically connects the –N groups of PANI and AChE enzyme, further providing high enzyme loading onto the fabricated electrode surface. Finally, the developed biosensor is used to determine the concentration of PE. In the absence of PE, the AChE enzyme catalyzes the hydrolysis of ATCl, which results the formation of electroactive thiocholine and acetic acid. Subsequently, thiocholine oxidizes into dithio-bis-choline and at the same time acetic acid diffuses into the surface of the electrode, which further causes the protonation of the PANI matrix. The protonation of PANI causes the conduction of electrons, which further generates signals (Fig. 1, scheme B, step 4) [21]. On the other hand, the presence of pesticides blocks the active sites of AChE, which prevents the hydrolysis of ATCl and decreases the signal intensity (Fig. 1, scheme B, step 5).

Fig. 2 represents the mechanism involved in the electrocatalytic reaction of AChE and ATCl in the presence of CuO. It is clearly shown in this figure that the incorporation of CuO enhances the rate of hydrolysis reaction due to its variable oxidation state (+1 and +2) and high affinity with sulfur [15, 25].

3.2 Chemical structure and component of Ag@CuO/PANI nanocomposite

Fig. (3A) represents the XRD spectra of CuO (curve a), Ag@CuO (curve b), Ag@CuO/PANI (curve c), and PANI (curve d). In curve (a), the peaks located at angle 2Θ = 32.5^{o}, 35.5^{o}, 38.9^{o}, 49^{o}, 53.7^{o}, 58.3^{o}, 61.7^{o}, 66.2^{o}, 68.3^{o}, 72.5^{o} 75.3^{o} are characteristic peaks of CuO. It is clear from the figure that the peaks located at $2\Theta = 35.5^{o}$ and 38.9^{o} are sharp and very intense among all peaks, which validates the high crystalline nature of CuO. The curve (b) illustrates all the characteristic peaks of CuO along with additional peaks of Ag at $2\Theta = 38.1^{o}$, 44.3^{o}, 64.4^{o}, and 77.6^{o}. This behavior confirms the presence of Ag and CuO in

the prepared nanoparticle [26]. In curve (d), the broad peak at $2\Theta = 25^{o}$ is the characteristic peak of PANI [27]. Finally, the diffraction peaks of CuO, Ag, and PANI in curve (c) confirm the successful incorporation of Ag@CuO into the PANI matrix. Now, the average crystallite size of prepared materials is calculated by the well-known Debye-Scherrer equation defined as:

$$\mathbf{D = K\lambda / \beta \cos\Theta} \quad \ldots\ldots (1)$$

Here, D is crystallite size, and K is the shape factor. λ is X-ray wavelength (1.5406 Å), β is line broadening at full-width half maxima in radian, and Θ is Braggs angle in degree. The average crystallite size for CuO, Ag@CuO, and Ag@CuO/PANI is set to be 78.39, 60.14, and 69.78 nm, respectively.

Fig. (3B) illustrates the FTIR spectra of CuO (curve a), Ag@CuO (curve b), and Ag@CuO/PANI (curve c). In curves (a) and (b), the bands that appeared at 419, 494, and 619 cm^{-1} are due to the metal-oxygen vibration of CuO. While in curve (b), the bands at 540 and 1136 cm^{-1} are characteristic bands of Ag [26, 28]. In curve (c), all bands having a frequency less than 1000 cm^{-1} represent the presence of CuO, while the band at 1136 cm^{-1} validates the existence of Ag. In addition, the band appears at 1120 cm^{-1} is due to N-Quinoid-N stretching vibration in PANI. The bands at 1245 and 1295 cm^{-1} are due to C-N stretching vibrations of aromatic amine. The peaks in 1483 and 1571cm^{-1} are due to C=C stretching vibrations of PANI's quinoid and benzenoid rings, respectively [27]. All these bands in curve (c) confirm the successful formation of Ag@CuO/PANI nanocomposite.

Fig. (S1) represents the UV-Visible spectra of CuO (curve a), Ag@CuO (curve b), and Ag@CuO/PANI (curve c). In curve (a), a broad absorption peak at 222 nm represents the successful formation of CuO. This absorption peak of CuO shifts itself from 222 to 231 nm (red shift) due to the presence of Ag (curve b). On the other hand, curve (c) represents two

absorption peaks at 270 and 330 nm due to CuO and $\pi \rightarrow \pi^*$ transition of the benzenoid ring in PANI, respectively. In this curve, a shifting appears in the absorption peak of CuO due to the incorporation of PANI [26].

3.3 Morphological characterization

Fig. (4) represents the field emission scanning electron microscope (FE-SEM) images of all prepared materials. The SEM image of PANI illustrates its large surface area having a porous structure (Fig. 4 A). The tiny spherical-shaped particles in Fig. 4 (B) illustrate the morphology of CuO nanoparticles. Fig. 4 (C) represents the morphology of tiny Ag@CuO nanoparticles. Finally, the smooth surface in Fig. 4 (D) illustrates the SEM image of Ag@CuO/PANI nanocomposite. In this figure, it can be easily observed that Ag@CuO nanoparticles uniformly cover the porous region of PANI, which develops the smooth path and forms a dense surface area. This phenomenon helps to accelerate the electron transmission which further enhances the sensitivity of the proposed biosensor. Further, the SEM image of Ag@CuO/PANI/ITO electrode is illustrated in Fig. 4(E), which confirms the successful deposition of nanocomposite into ITO glass substrate. Moreover, it can be clearly seen in Fig. 4D and Fig. 4E that the morphology of Ag@CuO/PANI and Ag@CuO/PANI deposited on the ITO electrode are same.

Fig. S2 illustrates the average particle size of CuO nanoparticle (S2 A), Ag@CuO nanoparticle (S2 B), and Ag@CuO/PANI nanocomposite (S2 C) are 86.88, 61.23, and 68.95 nm, respectively.

The SEM-Energy-dispersive X-ray (EDX) spectra of CuO, Ag@CuO and Ag@CuO/PANI are illustrated in Fig. 5(A), 5(B) and 5(C), respectively. In Fig. 5(A), the peaks of Cu, O and Au are observed, which confirm successful synthesis of CuO. In Fig. 5(B), the peaks of Ag, Cu, O and Au are observed, which confirm successful synthesis of Ag@CuO. Moreover, In Fig, 5(C), all peaks associated with Ag, Cu, O, C, N, H and Au are

observed, which confirm successful synthesis of Ag@CuO/PANI nanocomposite. The additional peak of Au in all EDX spectra are due to the gold coating of samples for SEM-EDX.

3.4 Electrochemical studies of fabricated electrodes

All fabricated electrodes (CuO/ITO, Ag@CuO/ITO, Ag@CuO/PANI/ITO, ITO, and AChE/Ag@CuO/PANI) are electrochemically examined through cyclic voltammetry (CV) and electrochemical impedance spectroscopy (EIS). Fig. 6(A) represents the CV curves of all modified electrodes at the scan rate of 50 mV/sec. It can be clearly seen in this figure that the Ag@CuO/PANI/ITO (curve a) electrode possesses highest current. The highest current signal confirms its high conductivity among all modified electrodes. The presence of the enzyme (AChE) reduces the conductivity and movement of electrons on the electrode surface due to its non-conducting behaviour (curve d) [29].

The graph between peak current and the square root of scan rate of different modified electrodes is represented in Fig. 6 (B). In this figure, all curves (a, b, and c) illustrate that the peak current follows the linear dependency with the square root of the scan rate. The linear relationship indicates that the transfer of electrons through Ag@CuO/PANI/ITO, Ag@CuO/ITO, and CuO/ITO electrodes is a surface-controlled process that satisfies the following equations:

I_{pa} [Ag@CuO/PANI/ ITO] = 91.69 μA / mV/ sec × $\upsilon^{1/2}$ mV/ sec + 326.35 μA; R^2 = 0.9956 ……..(2)

I_{pc} [Ag@CuO/PANI/ITO] = -55.84 μA / mV/ sec × $\upsilon^{1/2}$ mV/ sec – 470.21 μA; R^2 = 0.9946 ……..(3)

I_{pa} [Ag@CuO/ITO] = 75.53 μA / mV/ sec × $\upsilon^{1/2}$ mV/ sec + 174.41 μA; R^2 = 0.9651 …….(4)

I_{pc} [Ag@CuO/ITO] = -50.63 μA / mV/ sec × $\upsilon^{1/2}$ mV/ sec – 260.30 μA; R^2 = 0.9882 …….(5)

I_{pa} [CuO/ITO] = 59.31 μA / mV/ sec × $\upsilon^{1/2}$ mV/ sec + 3.08 μA; R^2 = 0.9968 …….(6)

I_{pc} [CuO/ITO] = -32.11 μA / mV/ sec × $\upsilon^{1/2}$ mV/ sec – 152.24 μA; R^2 = 0.9842 …….(7)

Fig. S3 (A), S3 (B), and S3 (C) represent CV curves of Ag@CuO/PANI/ITO, Ag@CuO/ITO, and CuO/ITO at different scan rates varying from 10 to 300 mV/sec. It is clear from these figures that the value of oxidation and reduction peak currents move towards more positive and negative values as the scan rate (10 to 300) increases. This is the reason behind the straight lines obtained after plotting the graph between voltage vs. log (scan rate) metrics (Fig. 6C) having 2.303 RT/(1-α)nF anodic and 2.303RT/αnF cathodic slopes. The value of the slope is further obtained by the following equations:

E_{pa} [Ag@CuO/PANI/ITO] = 0.0755 V log (υ mV/sec) + 0.1777 V; R^2 = 0.9946 ……(8)

E_{pc} [Ag@CuO/PANI/ITO] = -0.0754 V log (υ mV/sec) + 0.1657 V; R^2 = 0.9814 ……(9)

E_{pa} [Ag@CuO/ITO] = 0.07317 V log (υ mV/sec) + 0.16628 V; R^2 = 0.9930 ……(10)

E_{pc} [Ag@CuO/ITO] = -0.06936 V log (υ mV/sec) + 0.17638 V; R^2 = 0.9908 ……..(11)

E_{pa} [CuO/ITO] = 0.06782 V log (υ mV/sec) + 0.15566 V; R^2 = 0.9844 …….(12)

Journal Pre-proof

E_{pc} [CuO/ITO] = -0.06189 V log (υ mV/sec) + 0.18846 V; R^2 = 0.9920 ……..(13)

The obtained slopes from the above equations are further used to calculate the electron transfer coefficient (α) for all modified electrodes. The calculated value of α for all modified electrodes are summarized in Table 1.

Furthermore, the value of diffusion coefficient (D) and effective surface area (A) (Table 1) of all modified electrodes are calculated by using the slope of the above-mentioned equations from (1) to (6) along with the following Randles-Sevcik equation:

$I_p = 0.4463\ nFAC\ (nF\upsilon D / RT)^{1/2}$ or $I_p = 2.69\times10^5 n^{3/2} A D^{1/2} C \upsilon^{1/2}$ …….(14)

In these equations, I_p is peak current, n is the number of electrons transferred during a redox reaction, F is Faraday constant in C/mol, C is the concentration of $[Fe(CN)_6]^{3-/4-}$ in mol/cm^3, D is diffusion coefficient in cm^2/sec, R is gas constant in C K^{-1} mol^{-1} and υ is scan rate in V/ sec. Table 1 illustrates that the values of D and A is maximum for Ag@CuO/PANI/ITO electrode, which is due to precise diffusion of the redox ions through the electrode interface and the largest active detection area [30].

Fig. 6(D) represents the EIS of all modified electrodes, which further used for studying the interfacial charge transfer properties in each step of electrode modification. It is clear from the figure that the value of charge transfer resistance (R_{ct}) for ITO (curve a), AChE/Ag@CuO/PANI/ITO (curve b), CuO/ITO (curve c), Ag@CuO/ITO (curve d) and Ag@CuO/PANI/ITO (curve e) are 829±1.5, 498±1.3, 358±1.7, 220±1.2 and 130±1.5 Ω, respectively. The lowest R_{ct} value of Ag@CuO/PANI modified electrode shows its maximum conductivity among all modified electrodes. When the enzyme is immobilized on the surface of this electrode, the value of R_{ct} is increased (R_{ct} = 498 Ω, curve b) due to the non-conducting nature of the enzyme, which impedes charge transfer throughout the

electrode interface [29]. The increased value of R_{ct} confirms that the enzyme is successfully immobilized onto the surface of electrode.

The R_{ct} values of all modified electrodes are further used to investigate the electron transfer kinetics at the surface of electrode. The exchange of current per geometric unit surface area (i_o) and apparent electron transfer rate constant (K_{app}) are calculated using following equations:

$$i_0 = n R T / R_{ct} F \quad \text{..... (15)}$$

$$K_{app} = R T / n^2 F^2 A R_{ct} C \quad \text{..... (16)}$$

In these equations n is the number of transferred electrons, R is the gas constant, T is the temperature (K), F is the Faraday constant, A is the area of the electrode and C is the concentration of $[Fe(CN)_6]^{3-/4-}$, respectively. The value of i_o and Kapp for all modified electrodes are summarized in Table 1. The maximum i_o and Kapp value for Ag@CuO/PANI/ITO electrode confirm the highest electron transfer of redox ions throughout the electrode interface [31].

The response of the proposed biosensor is examined with cross-linker (glutaraldehyde) and without a cross-linker in 6.5 pH PBS buffer containing 2mM ATCl. It is clearly shown in Fig S3(D), the presence of crosslinking agent enhances the intensity of the oxidation current. Therefore in this study glutaraldehyde is further used to immobilize AChE for better sensitivity.

3.5 Optimization of experimental parameters

The performance of the developed biosensor highly depends upon its hyper-parameters like pH, incubation time of PE, and concentration of AChE enzyme. Therefore it is required to optimize these parameters to achieve the more robust performance of the developed biosensor. For optimizing each hyper-parameters, other hyper-parameters are operated under

their optimal conditions. The concentration of ATCl (2mM) was taken from the previous study, for optimizing other hyperparameters [21].

The pH of the electrolytic solution affects the enzyme activity and degradation of ATCl [13]. Therefore, in this work, pH of the electrolytic solution (6–8 pH) is optimized by DPV response of the fabricated electrode in the presence of 2 mM ATCl. It is clearly shown in Fig. S4 (A) that the highest current is obtained at pH 6.5, which is the optimal pH value for all subsequent biosensing studies.

The incubation time of PE is another factor that plays an important role in the performance of the developed biosensor. It is optimized by DPV in the presence of 2mM ATCl and 5 pM PE. Fig. S4 (B) illustrates the relationship between the peak current and the incubation time of PE. It is clear from this figure that the value of peak current decreases as the incubation time of PE increases up to 6 min. After 6 min, the current achieves a stable value which indicates that the complete reaction of enzyme and PE is done.

Finally, the amount of AChE enzyme immobilized onto the fabricated electrode surface is optimized by analyzing the DPV response of the fabricated electrode in the presence of 2mM ATCl and 5 pM PE. It can be easily seen in Fig. S4 (C) that as per the increment of the AChE concentration from 0.025 mg/mL to 0.125 mg/mL, the current response increases up to, the value of 0.1 mg/mL. After this value the current decreases due to high mass transfer resistance, which confirms that 0.1 mg/mL of AChE is the optimal amount for catalyzing the hydrolysis of ATCl.

3.6 Amperometric response of fabricated biosensor toward ATCl

The electrochemical performance of the developed biosensor towards ATCl (10-90 μM) is studied by chronoamperometry in a 6.5 pH PBS buffer. It is clear from Figure S5 (A) that the value of peak current increases gradually as the amount of ATCl increases from 10 μM to 90 μM. This increment of the peak current occurs due to the electrons produced by

the electrocatalytic reaction of enzyme and ATCl. Fig. S5 (B) represents the graph between current vs. concentration of ATCl (C_{ATCl}). The correlation between these two entities satisfies the following equation:

$$I = 17.72\ \mu A - 0.984\ \mu A / \mu M \times C_{ATCl}\ ;\ R^2 = 0.9869 \quad \ldots\ldots\ (17)$$

Now, the sensitivity of the developed biosensor for ATCl detection is calculated by using Eq (17). The developed biosensor exhibits good sensitivity of 1.22 μA $(\mu M)^{-1}$ towards ATCl detection, which is higher than 0.02 μA $(\mu M)^{-1}$ [15], 1.15 μA $(mM)^{-1}$ [32], 0.016 μA $(\mu M)^{-1}$ [33], 14.5 μA $(mM)^{-1}$ [34] previously reported biosensors.

3.7 Electrochemical Sensing study for PE detection

The electrochemical performance of the developed biosensor for the PE detection is examined by differential pulse voltammetry (DPV). Fig. 7 (A) represents the DPV response of fabricated electrode after incubation of different concentrations of PE in 0.2 M PBS (pH 6.5) containing 5 mM $[Fe(CN)_6]^{3-/4-}$ and 2 mM ATCl . It is clearly shown in the figure that the current continuously decreases as per the increment of PE concentration from 5-100 pM. The reduction in peak current occurs due to the inhibitory effect of PE on the AChE enzyme. Fig. 7 (B) represents the relationship between peak current and PE concentration which obeys the following regression equation:

$$I = 125.09\ \mu A - 0.227\ \mu A / pM \times C_{PE};\ R^2 = 0.9894 \quad \ldots\ldots\ (18)$$

Now, the sensitivity (slope / effective surface area) for developed biosensor was empirically set to 0.5536 μA $(pM)^{-1}$ cm^{-2}. The LOD was found to be 11.35 pM using the following equation:

$$LOD = 3\sigma/S \quad \ldots\ldots\ (19)$$

Here σ is the standard deviation of bioelectrode and S is the sensitivity obtained by the slope of Eq.(18) [31]. The performance of the proposed biosensor is further compared

with recently developed different biosensors for PE detection. Table 2 reports the results of the proposed and considered biosensors in terms of the three metrics, namely, sensitivity, the limit of detection, and linear range. Table 2 shows that the proposed biosensor outperforms the other considered biosensors in all the comparison metrics.

3.8 Selectivity, reproducibility and stability of AChE/Ag@CuO/PANI/ITO biosensor

The interference study of the developed biosensor is achieved by using DPV in 6.5 pH PBS containing 5 mM $[Fe(CN)_6]^{3-/4-}$ and 2 mM ATCl (Fig. 7 C). The interfering species such as Na^+, K^+, SO_4^{2-} ions, ascorbic acid, dopamine, and uric acid (1μM) are added with the coexistence of 5 pM PE. The bar diagram (Fig. 7 D) clearly illustrates that the current response does not show significant changes while adding the excess amount of the interfering species. The slight difference in current validates good selectivity of the developed biosensor for PE detection. The selectivity coefficient for the interfering species is calculated by using the following equation:

$$\mathbf{K_{selectivity} = I_{interferent} / I_{PE}} \quad \text{..... (20)}$$

The value of $\mathbf{K_{selectivity}}$ for all interfering species is found to be < 1, which indicates minimal effect of considered interferents on the performance of proposed biosensor [35].

Now, the reproducibility is checked by examining the DPV response of five different electrodes. It is clearly illustrated in Fig. S6 (A) that there is no significant difference among all the considered electrodes. The relative standard deviation (RSD) is found to be 1.74% which confirms good reproducibility of the proposed biosensor.

Finally, the stability is monitored every five days over a period of 20 days (Fig. S6 B). This analysis is conducted by analyzing the DPV response of the developed biosensor. After 20 days of storage, the current response remains 71.3 % of its initial current which further confirms the acceptable stability of the proposed biosensor.

3.9 Real sample analysis

The applicability and accuracy of the biosensor are examined by measuring different concentrations of PE from three real samples like banana, tomato, and soil. Firstly, all considered real samples were washed with DI water. Subsequently, the ground pulps of all samples were mixed with 6.5 pH PBS buffer, and the prepared sample was centrifuged. The supernatant liquid of all samples is separated and spiked with known concentrations (5, 10, 20 and 30 pM) of PE. Finally, the prepared sample is stored at 4^0C and used for DPV analysis using the proposed biosensor [21]. The DPV curves of PE spiked banana, tomato and soil samples are illustrated in Fig. S7 (A), S7 (B) and S7 (C), respectively. It is clearly shown in these figures that the peak current decreases continuously as PE concentration increases. All results presented in Table 3 confirms the good recovery (92- 111 %) and better accuracy (RSD < 10%) of the proposed biosensor for all the real samples used.

4. Conclusion

In this paper, a novel approach for PE detection is proposed by synthesizing a nanocomposite by chemical method. The prepared nanocomposite efficiently enhances the sensitivity and selectivity of AChE based biosensor. Furthermore, the three hyperparameters of this biosensor are optimized for better efficiency. A comparative analysis was conducted by considering eleven recently developed biosensors over three performance metrics like sensitivity, LOD, and linear range. Our results confirm the supremacy of the proposed biosensor over the other considered biosensors in all the metrics. Additionally, the accuracy and applicability of this biosensor for real-world scenarios are also checked in three real samples. The results confirm that this study offers an effective, high sensitive, high selective, and simple on-site procedure for PE detection.

Journal Pre-proof

Authorship contribution statement

Saroj Paneru: Conceptualization, methodology, validation, and writing the original draft

D. Kumar: Supervision, writing- review, and editing

Declaration of Competing Interest

The authors declare that they have no conflict of interest.

Acknowledgments

The first author acknowledges to the University Grants Commission (UGC), Government of India, New Delhi for their financial support (Grant No. 351/CSIR-UGC NET DEC.2016).

Journal Pre-proof

References:

[1] Pundir CS, Chauhan N. Acetylcholinesterase inhibition-based biosensors for pesticide determination: A review. Analytical Biochemistry. 2012 Oct 1;429(1):19-31.

[2] Rahmani T, Bagheri H, Behbahani M, Hajian A, Afkhami A. Modified 3D graphene-Au as a novel sensing layer for direct and sensitive electrochemical determination of carbaryl pesticide in fruit, vegetable, and water samples. Food Analytical Methods. 2018 Nov;11(11):3005-14.

[3] Iqubal A, Ahmed M, Ahmad S, Sahoo CR, Iqubal MK, Haque SE. Environmental neurotoxic pollutants. Environmental Science and Pollution Research. 2020 Aug 20:1-24.

[4] Alavinia SJ, Mirvaghefi A, Farahmand H, Rafiee G, Alavinia SJ, Shiry N, Moodi S. DNA damage, acetylcholinesterase activity, and hematological responses in rainbow trout exposed to the organophosphate malathion. Ecotoxicology and environmental safety. 2019 Oct 30;182:109311.

[5] de Pinho GP, Neves AA, de Queiroz ME, Silvério FO. Pesticide determination in tomatoes by solid–liquid extraction with purification at low temperature and gas chromatography. Food chemistry. 2010 Jul 1;121(1):251-6.

[6] Santos C, Oppolzer D, Gonçalves A, Barroso M, Gallardo E. Determination of organophosphorous pesticides in blood using microextraction in packed sorbent and gas

Journal Pre-proof

chromatography–tandem mass spectrometry. Journal of analytical toxicology. 2018 Jun 1;42(5):321-9.

[7] Shin Y, Lee J, Lee J, Lee J, Kim E, Liu KH, Lee HS, Kim JH. Validation of a multiresidue analysis method for 379 pesticides in human serum using liquid chromatography–tandem mass spectrometry. Journal of agricultural and food chemistry. 2018 Mar 14;66(13):3550-60.

[8] Alex AV, Mukherjee A. Review of recent developments (2018–2020) on acetylcholinesterase inhibition based biosensors for organophosphorus pesticides detection. Microchemical Journal. 2021 Feb 1;161:105779.

[9] Wei M, Wang J. A novel acetylcholinesterase biosensor based on ionic liquids-AuNPs-porous carbon composite matrix for detection of organophosphate pesticides. Sensors and Actuators B: Chemical. 2015 May 1;211:290-6.

[10] Li Y, Zhang Y, Han G, Xiao Y, Li M, Zhou W. An acetylcholinesterase biosensor based on graphene/polyaniline composite film for detection of pesticides. Chinese Journal of Chemistry. 2016 Jan;34(1):82-8.

[11] Xie X, Zhou B, Zhang Y, Zhao G, Zhao B. A multi-residue electrochemical biosensor based on graphene/chitosan/parathion for sensitive organophosphorus pesticides detection. Chemical Physics Letters. 2021 Mar 16;767:138355.

[12] Itsoponpan T, Thanachayanont C, Hasin P. Sponge-like CuInS2 microspheres on reduced graphene oxide as an electrocatalyst to construct an immobilized acetylcholinesterase electrochemical biosensor for chlorpyrifos detection in vegetables. Sensors and Actuators B: Chemical. 2021 Jun 15;337:129775.

[13] Zhang P, Sun T, Rong S, Zeng D, Yu H, Zhang Z, Chang D, Pan H. A sensitive amperometric AChE-biosensor for organophosphate pesticides detection based on

conjugated polymer and Ag-rGO-NH2 nanocomposite. Bioelectrochemistry. 2019 Jun 1;127:163-70.

[14]] Turan J, Kesik M, Soylemez S, Goker S, Coskun S, Unalan HE, Toppare L. An effective surface design based on a conjugated polymer and silver nanowires for the detection of paraoxon in tap water and milk. Sensors and Actuators B: Chemical. 2016 Jun 2;228:278-86.

[15] Bao J, Huang T, Wang Z, Yang H, Geng X, Xu G, Samalo M, Sakinati M, Huo D, Hou C. 3D graphene/copper oxide nano-flowers based acetylcholinesterase biosensor for sensitive detection of organophosphate pesticides. Sensors and Actuators B: Chemical. 2019 Jan 15;279:95-101.

[16] Zhang D, Jiang C, Liu J, Cao Y. Carbon monoxide gas sensing at room temperature using copper oxide-decorated graphene hybrid nanocomposite prepared by layer-by-layer self-assembly. Sensors and Actuators B: Chemical. 2017 Aug 1;247:875-82.

[17] Hu X, Zhu Z, Chen C, Wen T, Zhao X, Xie L. Highly sensitive H_2S gas sensors based on Pd-doped CuO nanoflowers with low operating temperature. Sensors and Actuators B: Chemical. 2017 Dec 1;253:809-17.

[18] Molavi R, Sheikhi MH. Facile wet chemical synthesis of Al doped CuO nanoleaves for carbon monoxide gas sensor applications. Materials Science in Semiconductor Processing. 2020 Feb 1;106:104767.

[19] Menazea AA, Mostafa AM. Ag doped CuO thin film prepared via pulsed laser deposition for 4-nitrophenol degradation. Journal of Environmental Chemical Engineering. 2020 Oct 1;8(5):104104.

Journal Pre-proof

[20] Li YY, Kang P, Wang SQ, Liu ZG, Li YX, Guo Z. Ag nanoparticles anchored onto porous CuO nanobelts for the ultrasensitive electrochemical detection of dopamine in human serum. Sensors and Actuators B: Chemical. 2021 Jan;327:128878.

[21] He L, Cui B, Liu J, Song Y, Wang M, Peng D, Zhang Z. Novel electrochemical biosensor based on core-shell nanostructured composite of hollow carbon spheres and polyaniline for sensitively detecting malathion. Sensors and Actuators B: Chemical. 2018 Apr 1;258:813-21.

[22] Lakhdari D, Guittoum A, Benbrahim N, Belgherbi O, Berkani M, Vasseghian Y, Lakhdari N. A novel non-enzymatic glucose sensor based on NiFe (NPs)–polyaniline hybrid materials. Food and Chemical Toxicology. 2021 May 1;151:112099.

[23] Zhao Y, Tan R, Yang J, Wang K, Gao R, Liu D, Liu Y, Yang J, Pan F. 3D-hybrid material design with electron/lithium-ion dual-conductivity for high-performance Li-sulfur batteries. Journal of Power Sources. 2017 Feb 1;340:160-6.

[24] Bai L, Chen Y, Bai Y, Chen Y, Zhou J, Huang A. Fullerene-doped polyaniline as new redox nanoprobe and catalyst in electrochemical aptasensor for ultrasensitive detection of Mycobacterium tuberculosis MPT64 antigen in human serum. Biomaterials. 2017 Jul 1;133:11-9.

[25] Nagase K, Zheng Y, Kodama Y, Kakuta J. Dynamic study of the oxidation state of copper in the course of carbon monoxide oxidation over powdered CuO and Cu2O. Journal of Catalysis. 1999 Oct 1;187(1):123-30.

[26] Iqbal S, Javed M, Bahadur A, Qamar MA, Ahmad M, Shoaib M, Raheel M, Ahmad N, Akbar MB, Li H. Controlled synthesis of Ag-doped CuO nanoparticles as a core with poly (acrylic acid) microgel shell for efficient removal of methylene blue under visible light. Journal of Materials Science: Materials in Electronics. 2020 Jun;31(11):8423-35.

Journal Pre-proof

[27] de Souza VS, da Frota HO, Sanches EA. Polyaniline-CuO hybrid nanocomposite with enhanced electrical conductivity. Journal of Molecular Structure. 2018 Feb 5;1153:20-7.

[28] Devagi P, Suresh TC, Sandhiya RV, Sairandhry M, Bharathi S, Velmurugan P, Radhakrishnan M, Sathiamoorthi T, Suresh G. Actinobacterial-mediated fabrication of silver nanoparticles and their broad spectrum antibacterial activity against clinical pathogens. Journal of Nanoscience and Nanotechnology. 2020 May 1;20(5):2902-10.

[29] Nagabooshanam S, John AT, Wadhwa S, Mathur A, Krishnamurthy S, Bharadwaj LM. Electro-deposited nano-webbed structures based on polyaniline/multi walled carbon nanotubes for enzymatic detection of organophosphates. Food chemistry. 2020 Sep 1;323:126784.

[30] Jalil O, Pandey CM, Kumar D. Highly sensitive electrochemical detection of cancer biomarker based on anti-EpCAM conjugated molybdenum disulfide grafted reduced graphene oxide nanohybrid. Bioelectrochemistry. 2021 Apr 1;138:107733.

[31] Thakur D, Pandey CM, Kumar D. Highly Sensitive Enzymatic Biosensor Based on Polyaniline-Wrapped Titanium Dioxide Nanohybrid for Fish Freshness Detection. Applied Biochemistry and Biotechnology. 2022 May 6:1-4.

[32] Song D, Jiang X, Li Y, Lu X, Luan S, Wang Y, Li Y, Gao F. Metal− organic frameworks-derived MnO2/Mn3O4 microcuboids with hierarchically ordered nanosheets and Ti3C2 MXene/Au NPs composites for electrochemical pesticide detection. Journal of hazardous materials. 2019 Jul 5;373:367-76.

[33] Liu T, Su H, Qu X, Ju P, Cui L, Ai S. Acetylcholinesterase biosensor based on 3-carboxyphenylboronic acid/reduced graphene oxide–gold nanocomposites modified electrode for amperometric detection of organophosphorus and carbamate pesticides. Sensors and actuators B: Chemical. 2011 Dec 15;160(1):1255-61.

Journal Pre-proof

[34] Zhao H, Ji X, Wang B, Wang N, Li X, Ni R, Ren J. An ultra-sensitive acetylcholinesterase biosensor based on reduced graphene oxide-Au nanoparticles-β-cyclodextrin/Prussian blue-chitosan nanocomposites for organophosphorus pesticides detection. Biosensors and bioelectronics. 2015 Mar 15;65:23-30.

[35] Verma S, Arya P, Singh A, Kaswan J, Shukla A, Kushwaha HR, Gupta S, Singh SP. ZnO-rGO nanocomposite based bioelectrode for sensitive and ultrafast detection of dopamine in human serum. Biosensors and Bioelectronics. 2020 Oct 1;165:112347.

[36] Yang G, He Y, Zhao J, Chen S, Yuan R. Ratiometric electrochemiluminescence biosensor based on Ir nanorods and CdS quantum dots for the detection of organophosphorus pesticides. Sensors and Actuators B: Chemical. 2021 Aug 15;341:130008.

[37] Xiao B. Electrochemical sensor based on Bimetallic phosphosulfide Zn–Ni–P–S Nanocomposite-reduced graphene oxide for determination of Paraoxon Ethyl in agriculture wastewater. Int. J. Electrochem. Sci. 2022;17(220672):2.

[38] Gopi PK, Ngo DB, Chen SM, Ravikumar CH, Surareungchai W. High-performance electrochemical sensing of hazardous pesticide Paraoxon using BiVO4 nano dendrites equipped catalytic strips. Chemosphere. 2022 Feb 1;288:132511.

[39] Rajkumar C, Kim H. Hybrid nanostructures of Pd–WO3 grown on graphitic carbon nitride for trace level electrochemical detection of paraoxon-ethyl. Microchimica Acta. 2021 Jul;188(7):1-1.

[40] Jia L, Zhou Y, Wu K, Feng Q, Wang C, He P. Acetylcholinesterase modified AuNPs-MoS_2-rGO/PI flexible film biosensor: Towards efficient fabrication and application in paraoxon detection. Bioelectrochemistry. 2020 Feb 1;131:107392.

[41] Aghaie A, Khanmohammadi A, Hajian A, Schmid U, Bagheri H. Nonenzymatic electrochemical determination of paraoxon ethyl in water and fruits by graphene-based NiFe

bimetallic phosphosulfide nanocomposite as a superior sensing layer. Food Analytical Methods. 2019 Jul;12(7):1545-55.

[42] Hua QT, Ruecha N, Hiruta Y, Citterio D. Disposable electrochemical biosensor based on surface-modified screen-printed electrodes for organophosphorus pesticide analysis. Analytical Methods. 2019;11(27):3439-45.

[43] Wu Y, Jiao L, Xu W, Gu W, Zhu C, Du D, Lin Y. Polydopamine-capped bimetallic AuPt hydrogels enable robust biosensor for organophosphorus pesticide detection. Small. 2019 Apr;15(17):1900632.

[44] Sgobbi LF, Machado SA. Functionalized polyacrylamide as an acetylcholinesterase-inspired biomimetic device for electrochemical sensing of organophosphorus pesticides. Biosensors and Bioelectronics. 2018 Feb 15;100:290-7.

[45] Karthik R, Kumar JV, Chen SM, Kokulnathan T, Yang HY, Muthuraj V. Design of novel ytterbium molybdate nanoflakes anchored carbon nanofibers: challenging sustainable catalyst for the detection and degradation of assassination weapon (Paraoxon-Ethyl). ACS Sustainable Chemistry & Engineering. 2018 May 29;6(7):8615-30.

[46] Mutharani B, Ranganathan P, Chen SM, Karuppiah C. Enzyme-free electrochemical detection of nanomolar levels of the organophosphorus pesticide paraoxon-ethyl by using a poly (N-isopropyl acrylamide)-chitosan microgel decorated with palladium nanoparticles. Microchimica Acta. 2019 Mar;186(3):1-1.

Journal Pre-proof

Biographies

Prof. Dr. D.Kumar

Dr. Kumar is working as Professor in the Department of Applied Chemistry, Delhi Technological University, Delhi for last twelve years. He had worked as **Head of the Department of Biotechnology, and Department of Applied Chemistry at Delhi Technological University, Delhi**. He has received several fellowships and awards including UGC Research Award. He has been awarded national/international projects including the International Project, viz, India–Japan Collaborative Research Project twice under DST-JSPS bilateral programme. He has guided 14 Ph.Ds, 85 M.E./M.Tech projects, published 04 chapters/books and over 110 papers in the journals of international repute including ***Biomaterials, Microchimica Acta, Bioelectrochemistry, Sensors and Actuators, Synthetic Metals, Canadian Journal of Chemistry, European Polymer Journal, Biosensors*** etc. in the areas like conducting polymers, sensors, conductive adhesives, smart hydrogels, helical materials and nanomaterials.

Ms. Saroj Paneru
Department of Applied Chemistry

Saroj Paneru received her MSc degree from Kumaun University Nainital, Uttarakhand, India. She is working on her doctoral degree under the guidance of Prof. D Kumar at Department of Applied Chemistry, Delhi Technological University, Delhi, India. Her main research interest includes development of biosensors based on conducting polymers and nanomaterials.

Journal Pre-proof

Table 1: The Kinetic parameters of all modified electrodes:

Modified electrodes	**Diffusion coefficient (D) (cm^2 sec^{-1})**	**Effective surface area (A) (cm^2)**	**Electron transfer coefficient (α)**	**i_o (A cm^{-2})**	**Kapp (cm sec^{-1})**
CuO/ITO	8.41×10^{-2}	3.8×10^{-1}	0.14	6.67×10^{-5}	3.35×10^{-4}
Ag@CuO/ITO	9.29×10^{-2}	4.1×10^{-1}	0.19	1.08×10^{-4}	5.45×10^{-4}
Ag@CuO/PANI/ITO	12.11×10^{-2}	4.2×10^{-1}	0.22	1.84×10^{-4}	9.23×10^{-4}

Table 2: Comparison of the proposed biosensor with recently developed biosensors for PE detection

S. No.	**Fabricated electrodes**	**Linear range**	**Detection Limit**	**Sensitivity**	**Sensor type**	**References**
1.	AChE-ChOx/Ir NRs@CdS QDs/GCE	5.0 pM-50 nM	1.67 pM	-	Enzymatic	[36]
2.	Zn–Ni–P–S/GO/GCE	1-200 µM	35 nM	0.06369 µA/µM	Nonenzyme	[37]
3.	$BiVO_4$/flexible SPCE		0.03 µM	0.345 µA$(\mu M)^{-1}$c m^{-2}	Nonenzyme	[38]

Journal Pre-proof

4.	Pd–WO_3/g-C_3N_4/SPCE	0.01–60 µM	0.03 nM	3.70 µA(µM)$^{-1}$ cm^{-2}	Nonenzyme	[39]
5.	AChE/Au-MoS_2-rGO/PI	0.005 - 0.150 µg/ml	0.0014 µg/mL	4.44 µA(µg/mL)$^{-1}$	Enzymatic	[40]
6.	Gr@NiFeSP	0.012 -10 µM	3.7 nM	10.24 µA(µM)$^{-1}$	Nonenzyme	[41]
7.	AChE/MWCNTs-CS/AuNPs/SPCE	0.01-100 µM	0.03 µM	46.20 µA(µM)$^{-1}$	Enzymatic	[42]
8.	AChE/Au-Pt-PDA	0.5-1000 nM	0.85 nM	-	Enzymatic	[43]
9.	SPE/PHA/mPEG	1-10 µM	0.36 µM	0.05 µA(µM)$^{-1}$	Nonenzyme	[44]
10.	GCE/YbM/f-CNFs	0.01-12 µM	0.002 µM	2.87 µA(µM)$^{-1}$ cm^{-2}	Nonenzyme	[45]
11.	PdNPs/PNIPAM-CT microgel/ GCE	0.01 µM to 1.3 mM	0.7 nM	1.60 µA(µM)$^{-1}$ cm^{-2}	Nonenzyme	[46]
12.	**AChE/Ag@CuO/PANI /ITO**	**5-100 pM**	**11.35 pM**	**0.55 µA (pM)$^{-1}$ cm^{-2}**	**Enzymatic**	**Present Work**

Table 3: Detection of PE in real samples (n=3)

Sample	Added amount (pM)	Found amount (pM) (SD<5%)	Recovery (%) (SD<4%)	RSD (%)

Soil	5	4.7	94	4.2
	10	9.4	93	5.1
	20	18.6	93	5.5
	30	28.2	94	5.06
Banana	5	5.25	105	3.48
	10	10.9	109	2.94
	20	20.40	102	2.04
	30	30.90	103	2.60
Tomato	5	5.45	109	6.5
	10	7.72	111	7.72
	20	6.56	109	6.56
	30	6.02	109	6.02

Journal Pre-proof

Figure Captions

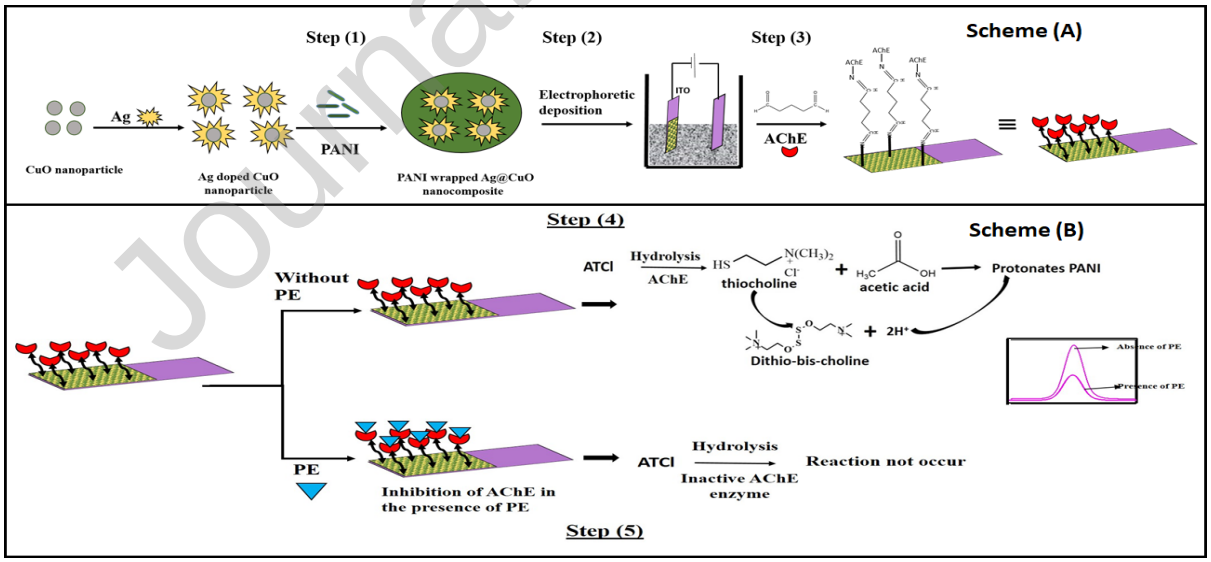

Fig. 1: (A) Schematic diagram for synthesis of nanocomposite, electrophoretic deposition and transducer fabrication. **(B)** Mechanism of AChE/Ag@CuO/PANI/ITO biosensor for PE detection.

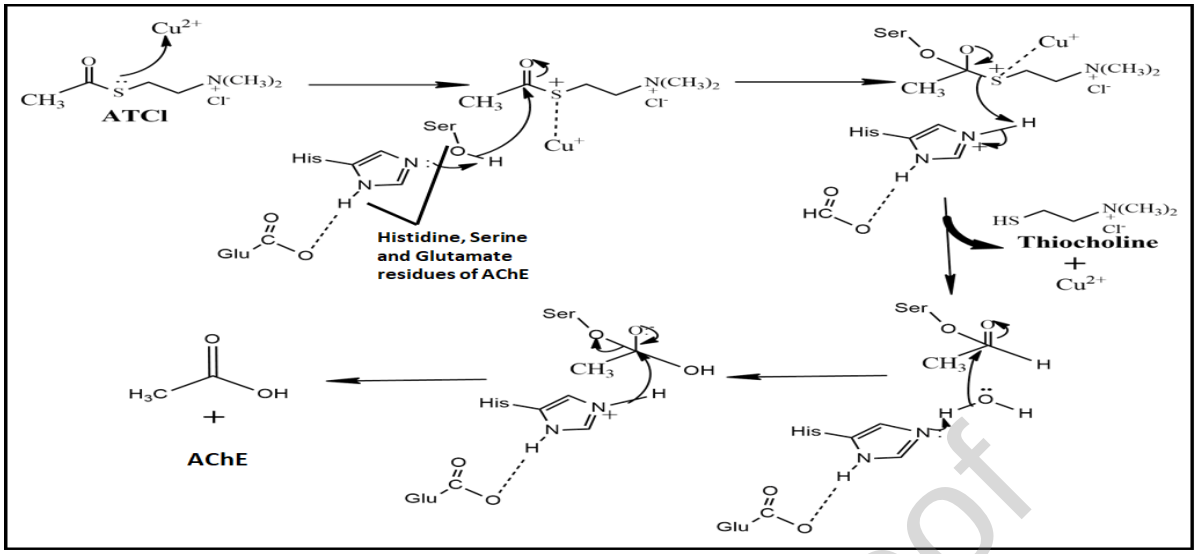

Fig. 2: CuO incorporated mechanism for electrocatalytic reaction of AChE and ATCl.

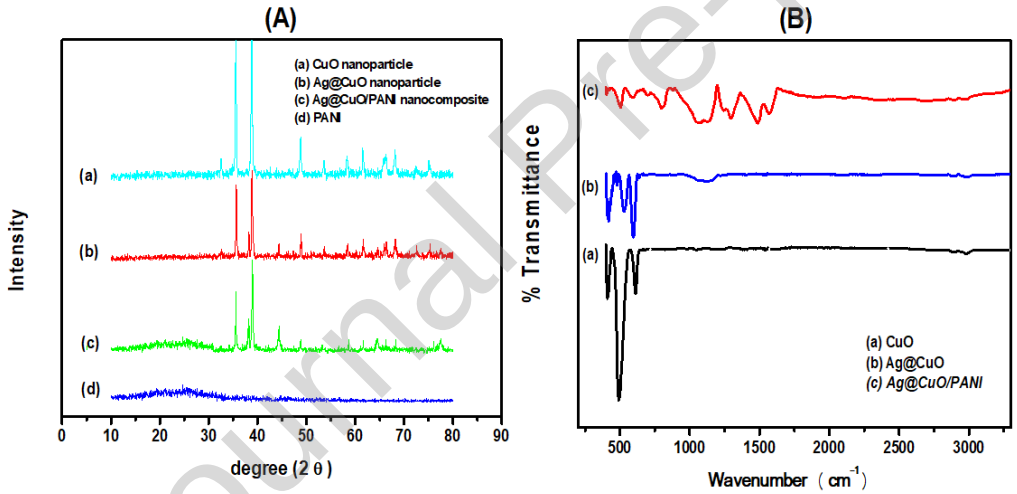

Fig. 3: (A) XRD pattern of CuO (a), Ag@CuO (b), Ag@CuO/PANI (c) and PANI (d). **(B)** FTIR of CuO (a), Ag@CuO (b) and Ag@CuO/PANI (c).

Journal Pre-proof

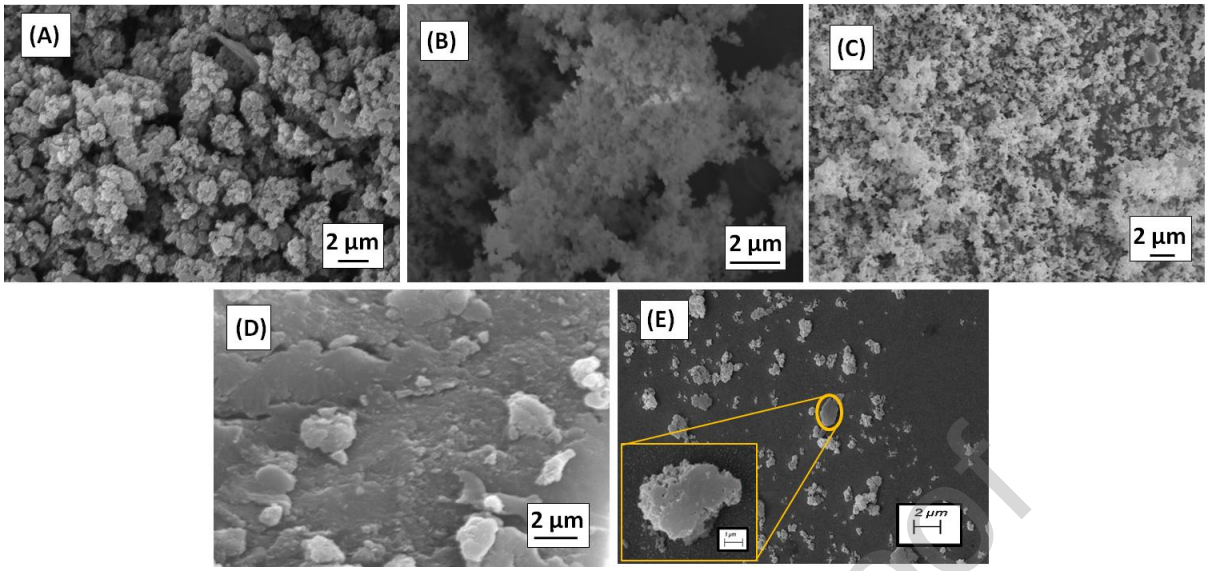

Fig. 4: SEM images of **(A)** PANI (Mag = 5.08 KX), **(B)** CuO nanoparticles (Mag = 10.00 KX), **(C)** Ag@CuO nanoparticles (Mag = 10KX), **(D)** Ag@CuO/PANI nanocomposite (Mag = 10 KX), and **(E)** Ag@CuO/PANI/ITO (Mag = 5KX)

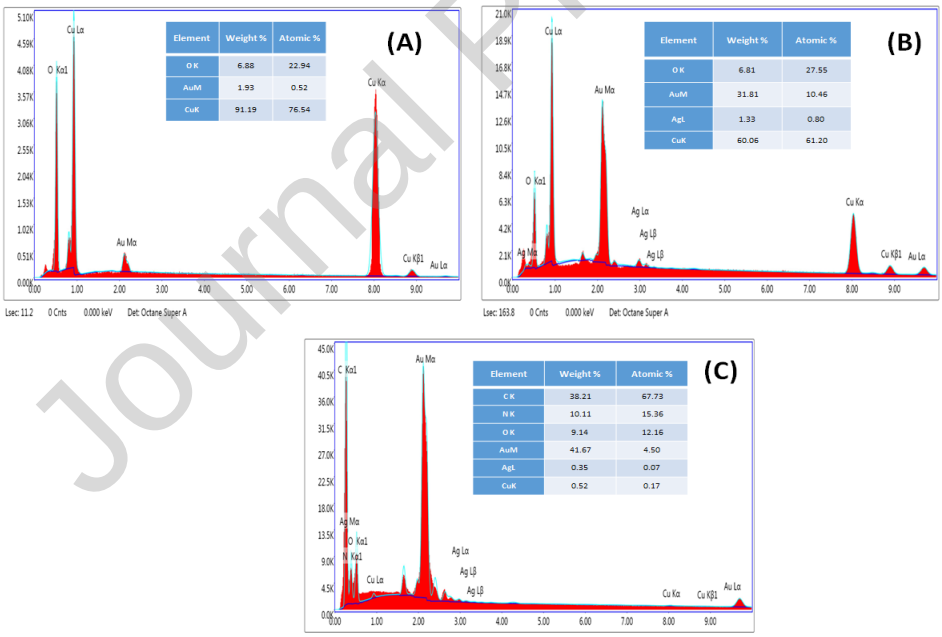

Fig. 5: SEM-EDX analysis of **(A)** CuO, **(B)** Ag@CuO, and **(C)** Ag@CuO/PANI.

Journal Pre-proof

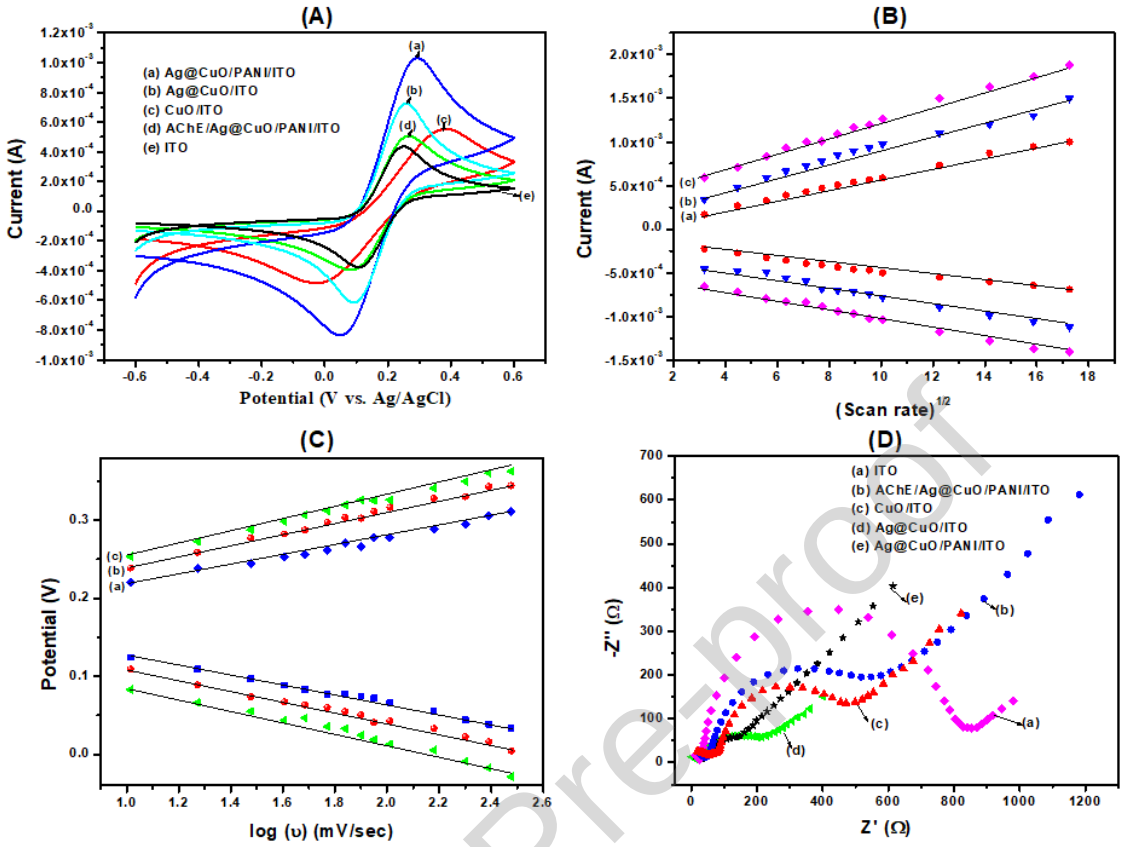

Fig. 6: (A) CV of Ag@CuO/PANI/ITO (a), Ag@CuO/ITO (b), CuO/ITO (c), AChE/Ag@CuO/PANI/ITO (d) and ITO (e) in 0.2M PBS containing 5mM $[Fe(CN)_6]^{3-/4-}$ and 0.8% NaCl at scan rate 50 mV/sec. **(B)** Plots of current vs. square root of scan rate for CuO (a), Ag@CuO (b), and Ag@CuO/PANI nanocomposite (c). **(C)** Plots of potential vs. log (scan rate) for CuO (a), Ag@CuO (b) and Ag@CuO/PANI nanocomposite (c), **(D)** Electrochemical impedance spectroscopy (EIS) plot for ITO (a), AChE/Ag@CuO/PANI/ITO (b) CuO/ITO (c), Ag@CuO/ITO (d) and Ag@CuO/PANI/ITO (e).

Journal Pre-proof

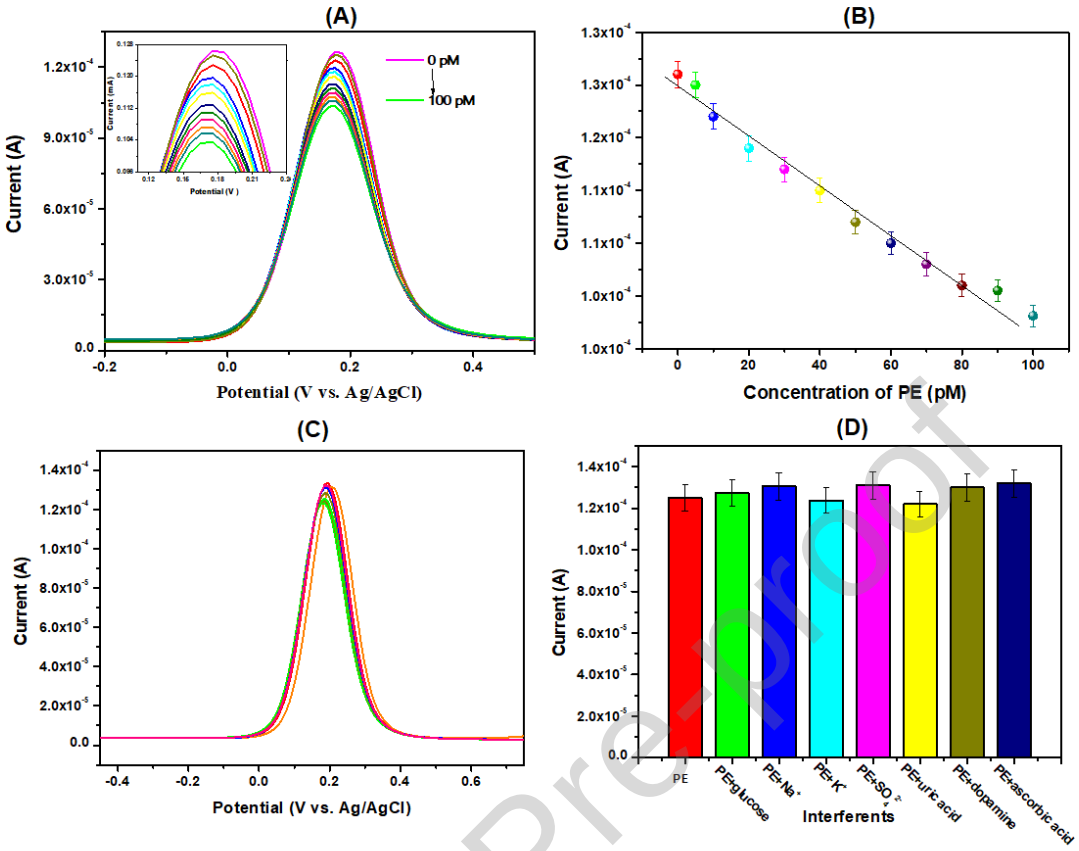

Fig. 7: (A) DPV response of AChE/Ag@CuO/PANI/ITO electrode after incubation of different concentrations of PE (0, 5, 10, 20, 30, 40, 50, 60, 70, 80, 90, and 100 pM). **(B)** Calibration plot between current vs. PE concentration. **(C)** Interference study in the presence of 1 μM Na^+, K^+, SO_4^{2-} ions, malathion, and uric acid with the coexistence of 5 pM PE (n=3) **(D)** Calibration plot of current vs. interferents.

CRediT authorship contribution statement

Saroj Paneru: Conceptualization, methodology, validation, and writing the original draft

D. Kumar: Supervision, writing- review, and editing

Declaration of Competing Interest

The authors declare that they have no known competing financial interests or personal relationships that could have appeared to influence the work reported in this paper.

The authors declare the following financial interests/personal relationships which may be

considered as potential competing interests:

Saroj Paneru reports financial support was provided by University Grants Commission.

Highlights

- A novel nanocomposite Ag@CuO/PANI is synthesized and further used as a sensing platform for sensitive detection of paraoxon-ethyl.
- Incorporation of Ag-doped- copper oxide into polyaniline matrix enhances the surface area, catalytic power and conductivity of nanocomposite, which is responsible for excellent sensitivity of the developed biosensor. In this study, cross-linking agent is used to improve the efficiency of enzyme immobilization
- The electrophoretic deposition of Ag@CuO/PANI nanocomposite onto ITO glass substrate enhances electrochemical performance
- The developed AChE/Ag@CuO/PANI/ITO electrode is utilized for the electrochemical detection of paraoxon - ethyl (5–100 pM) and shows high sensitivity (0.5536 μA $(pM)^{-1}$ cm^{-2}) with a low limit of detection (11.35 pM)
- Validation with real samples (banana, tomato and soil) shows its good accuracy and applicability for pesticide detection

Journal Pre-proof

All-Optical N-Bit Reversible Complex Multiplier

Diksha Ruhela
Department of Computer Science & Engineering
Delhi Technological University
Delhi, India
diksharuhela_phd2k19@dtu.ac.in

Rajni Jindal
Department of Computer Science & Engineering
Delhi Technological University
Delhi, India
rajnijindal@dce.ac.in

2022 8th International Conference on Signal Processing and Communication (ICSC) | 978-1-6654-5430-8/22/$31.00 ©2022 IEEE | DOI: 10.1109/ICSC56524.2022.10009114

***Abstract*- In this paper we have explored the implementation of n-bit complex multiplier design using MZI-SOA and RSOA-TAND switch, employing the ancient Vedic mathematic principle Urdhva–Tiryakbhyam. In this work we have studied two methods of multiplication, we named it as Design CM1 and Design CM2 and in each method, we have proposed four models design using different proposed unified adder-subtractor circuit. Parameter in terms of optical cost and optical delay have been studied and comparative analysis of all the n-bit optical complex multiplier circuits have been observed in terms of optical cost and optical delay.**

Keywords- Adder, Subtractor, Complex Multiplier, All-optical reversible logic gates, RSOA-TAND.

I INTRODUCTION

As per the study, the amount of computational power needed to carry out high performance computing tasks has grown massively- doubling every year since last few years. Thus, the growing need of computing power by the electronic devices and the fastest decay in the natural resources of energy enthral researchers to quest an alternative technique that curtail the power consumption globally. The various emerging technologies like quantum computing, reversible computing, quantum photonics, optical computing etc. have been used in designing the circuit to minimize the heat dissipation problem [1][2]. Todays, out of these listed technologies, optical computing is one that holds out hope for a new technological leap. In this work we are focusing on designing the reversible all-optical circuit using RSOA and MZI-SOA switch. Remarkable efforts have been shown by the researchers in designing various important basic building blocks of processing unit like adder, subtractor, multiplexer, de-multiplexer, multiplier and ALU etc. using reversible all-optical MZI-SOA switch [3][4][5].

Complex multiplier is one of the essential building blocks of DSP system. Its speed and complexity directly affect the performance parameter of the system. To perform the complex multiplication operation, speed and complexity of adder and subtractor are also play as important role. In order to boost the overall performance attributes of processing system it is essential to design the energy efficient, high speed with minimum complexity circuitry of adder, subtractor and multiplier.

In this paper, in section 2 we first revise the basics of reversible logic gates, introduce new NTG gate and its mapping with MZI-SOA and RSOA-TAND switch. In section 3, we demonstrate the proposed adder-subtractor circuit design using all-optical reversible RSOA-TAND and MZI-SOA switch-based logic gates. In section 4, we have discussed the realization of n-bit complex multiplier architecture using all-optical reversible logic gates and calculate the optimization parameters of the circuit and in last section 5 and 6, we have studied the performance evaluation and conclude the result, respectively.

II BASIC DEFINITIONS

Definition 1: Reversible Circuit and Reversible Logic Gate

Reversible logic gates are used to implement reversible circuits. A k x k logic gate is reversible, if it generates unique one-to-one mapping between the k input vectors and the k output vectors. Some design constraints like restriction of fan-out and feedback in realization of reversible logic circuits makes them more cumbersome in comparison with irreversible circuits. In order to competently integrate the reversible circuits, certain paradigm need to be optimized such as the number of gate count (GC), number of ancilla/constant inputs (CI), optical cost (OC), optical delay (OD) and the number of garbage/unused outputs (GO). Some commonly used reversible logic gates available in literature are FG gate, TG gate, FRG gate etc [6].

Definition 2: MZI-SOA Switch

The Mach Zehnder interferometer semiconductor optical amplifier is an all-optical component work as a 2 x 2 switch depicted in Fig.1. It is realized using two semiconductor optical amplifiers (SOA-1, SOA-2) and two couplers (C-1, C-2) It has two input ports, port A (p1): input incoming signal of wavelength (λ2) and port B (p2): input control signal of wavelength (λ1) and two output ports namely bar port (p3) and cross port (p4) respectively. In the presence of incoming signal at port A, i.e., A=1, control signal at port B decide the availability of light at bar port and cross port, i.e., if B=1, then light is present at bar port (p3), otherwise in the absence of control signal, i.e., B=0, light appears at cross port (p4).

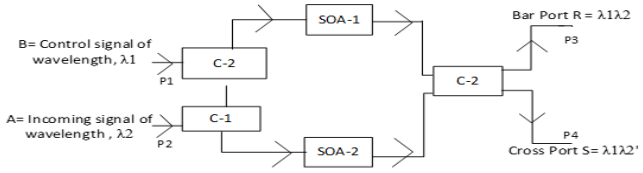

Figure 1: Block diagram of MZI-SOA switch [6]

Definition 3: RSOA-TAND Switch

Reflective semiconductor optical amplifier work as a 2x2 switch. Fig. 2 depict the block diagram of RSOA based TAND all-optical switch [7]. The basic mechanism behind the working of RSOA is cross modulation. In the presence of control signal(A) and input prob signal(B), gain of the amplifier get compressed, result in low output (P = 1, Q = 0). Where as in the absent of control signal, input prob signal passes through uncompressed gain result in high output (P= 0, Q = 1). The Boolean expression for RSOA-TAND gate can be written as:

P = A

Q= $\overline{A}$ B

Authorized licensed use limited to: DELHI TECHNICAL UNIV. Downloaded on January 17,2023 at 05:03:54 UTC from IEEE Xplore. Restrictions apply.

We have used RSOA based TAND gate [7] for realizing the basic reversible logic gates.

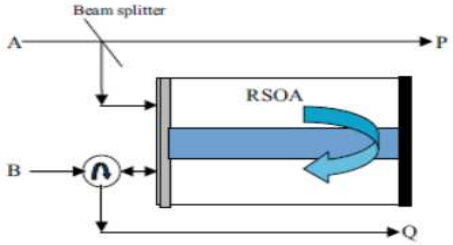

Figure 2: Block diagram of RSOA-TAND switch [7]

III ADDER-SUBTRACTOR

Adder and subtractor are one of the fundamental modules in designing the complex multiplier circuit. In this section, we have shown the mapping of reversible logic gates with RSOA-TAND switch and also discussed the new designs of unified adder-subtractor circuits implemented using RSOA-TAND and MZI-SOA based reversible logic gates.

Reversible logic gates:

Not gate:

The Not gate is a 2x2 reversible logic gate. The Boolean expression between the input vectors (A, B) and output vectors (P, Q) can be written as:

$P = A$

$Q = \overline{A}$

Not gate can be implement using RSOA-TAND switch by keeping input signal B at high state. Fig. 3 shows the block diagram of RSOA-TAND based reversible NOT gate. Both the optical cost and optical delay of NOT gate is 1.

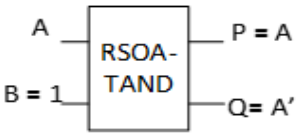

Figure 3: Optical mapping of NOT gate with RSOA-TAND switch [7]

FG gate:

The Feynman(gate) is a 2x2 reversible logic gate. The Boolean expression between the input vectors (A, B) and output vectors (P, Q) can be written as:

$P = A$

$Q = A \otimes B$

Fig. 4 shows the block diagram and the optical mapping of FG gate with RSOA based TAND switch. The all-optical implementation of FG consists of 2 RSOA-TANDs, 2 beam splitters (BS) and 1 beam combiner (BC). The optical delay of FG gate is 1 and the optical cost is 2.

NTG gate:

The NTG gate is a 3x3 reversible logic gate. The Boolean expression between the input vectors (A, B, C) and output vectors (P, Q, R) can be written as:

$P = A$

$Q = AB \otimes C$

$R = (A + B) \otimes C$

Fig. 5 shows the block diagram and the optical mapping of NTG gate with MZI-SOA and RSOA-TAND switch. The all-optical implementation of NTG gate consist of 1 MZI, 4 RSOA-TANDs, 7 beam splitters (BS) and 3 beam combiner (BC) The optical cost of NTG is 5 and the optical delay is 2. This proposed circuit alone work as NOR, NAND, AND, OR, EXOR and NOT gate. Application of this gate will be discussed in future work.

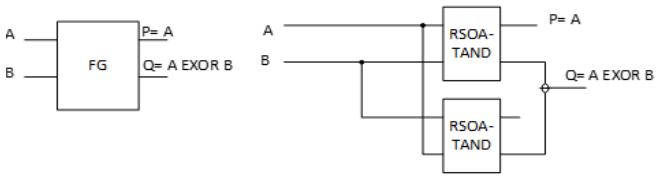

(a) (b)

● Beam splitter, ⇔ Beam combiner.

Figure 4: (a) Block diagram of NFR, (b) optical mapping of FG with RSOA-TAND switch.

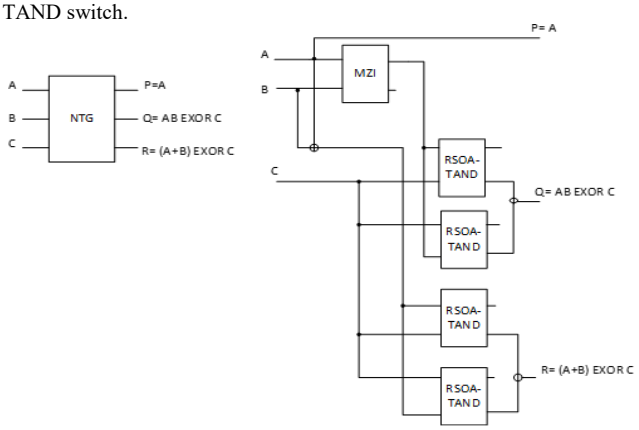

(a) (b)

● Beam splitter, ⇔ Beam combiner

Figure 5: (a) Block diagram of NTG, (b) optical mapping of NTG with MZI-SOA switch and RSOA-TAND switch.

Proposed Adder-Subtractor Circuit:

In this paper, we have proposed different designs of adder-subtractor circuit. We have used two different methods to perform subtraction operation. The following subsection discuss the implementation of proposed designs in detail using two different methods:

Method 1:

In this method we have studied, the implementation of n bit all-optical reversible subtractor circuit, based on the property $a - b = \overline{\bar{a} + b}$. In this approach control signal (ctrl) is used to performed the subtraction operation in three stages. Using this method, we have proposed two different styles of n-bit subtractor circuits discuss below in detail:

Let us consider a_n and b_n be the two binary number of n-bit each {where: $n \geq 4$ }.

Design 1a:

At first stage, we have used n numbers of two inputs all-optical reversible RSOA-TAND based FG gates shown in Fig. 4, keeping inputs $A_{n-1} = a_{n-1}$ and, $B_{n-1}=1$ (ctrl signal), to generate complement signal at output $Q_{n-1}=\bar{a}_{n-1}$. At second stage, summation $S_{n-1}=(\bar{a}_{n-1} + b_{n-1})$ is done using a stair case structure of n-bit CLA [8] depicted in Fig. 9 with inputs $a_{n-1} = \bar{a}_{n-1}$ and, $b_n = b_{n-1}$ and at last stage all-optical reversible RSOA-TAND based FG gate is used with inputs $A_{n-1} = S_{n-1}$ and, $B_{n-1} = 1$ (ctrl signal) to get $Q_{n-1} = \overline{\bar{a}_{n-1} + b_{n-1}}$. When the value of ctrl signal B is set to 0 the proposed circuit is work as an adder. Hence the value of ctrl signal plays an important role in the arithmetic operation of

Authorized licensed use limited to: DELHI TECHNICAL UNIV. Downloaded on January 17,2023 at 05:03:54 UTC from IEEE Xplore. Restrictions apply.

the circuit. The optical cost and optical delay of the circuit are calculated as 8n-2 and (n+2) Δ, respectively.

Design 1b:

At first stage, we have used n numbers of two inputs all-optical reversible RSOA-TAND based NOT gates shown in Fig. 3, keeping inputs $A_{n-1} = a_{n-1}$ and, $B_{n-1}=1$ (ctrl signal), to generate complement signal at output $Q_{n-1}=\bar{a}_{n-1}$. At second stage, summation $S_{n-1}=(\bar{a}_{n-1} + b_{n-1})$ is done using a stair case structure of n-bit CLA [8] depicted in Fig. 9 with inputs $a_{n-1} = \bar{a}_{n-1}$ and, $b_n = b_{n-1}$ and at last stage all-optical reversible RSOA-TAND based NOT gate is used with inputs $A_{n-1} = S_{n-1}$ and, $B_{n-1} = 1$ (ctrl signal) to get $Q_{n-1} = \overline{\bar{a}_{n-1} + b_{n-1}}$. The optical cost and optical delay of the circuit are calculated as 6n-2 and (n+2) Δ, respectively.

Method 2:

In this we have studied, the implementation of n bit all-optical reversible subtractor circuit, based on the property $a - b = a + \bar{b} + 1$. In this approach control signal (ctrl) is used to performed the subtraction operation in two stages.
Using this method, we have proposed two different styles of subtractor circuits discuss below in detail:

Design 2a:

At first stage, we have used n numbers of two inputs all-optical reversible RSOA-TAND based NOT gates shown in Fig. 3, keeping inputs $A_{n-1} = b_{n-1}$ and, $B_{n-1}=1$ (ctrl signal), to generate complement signal at output $Q_{n-1}=\bar{b}_{n-1}$. At second stage, summation $(a_{n-1} + \bar{b}_{n-1} + 1)$ is done using a n-bit hierarchical design structure of CLA [8] depicted in Fig. 10 with inputs $a_n = a_{n-1}$, $b_{n-1} = \bar{b}_{n-1}$ and $c_0 = 1$(ctrl signal) to get the final subtraction output. The optical cost of the circuit is given as $\{(82x + n + 3),\ where\ n \in 4^j, j \geq 2, n = 4^{x+1}\}$; $\{(38x + n + 3)\ , where\ n \in 2^j, j \geq 2, n = 2 * 4^x\}$ and the optical delay is calculated as (n+2) Δ.

Design 2b:

At first stage, we have used n number of 2 inputs all-optical reversible RSOA-TAND based FG gates shown in Fig. 4, keeping inputs $A_{n-1} = b_{n-1}$ and, $B_{n-1}=1$ (ctrl signal), to generate complement signal at output $Q_{n-1}=\bar{b}_{n-1}$. At second stage, summation $(a_{n-1} + \bar{b}_{n-1} + 1)$ is done using a n-bit hierarchical design structure of CLA [8] depicted in Fig. 10 with inputs $a_n = a_{n-1}$, $b_{n-1} = \bar{b}_{n-1}$ and $c_0 = 1$ (ctrl signal) to get the final subtraction output. When the value of ctrl signal B is set to 0 the proposed circuit is work as an adder. Hence the value of ctrl signal plays an important role in the arithmetic operation of the circuit. The optical cost is given as $(82x + 2n + 3)\{ where\ n \in 4^j, j \geq 2, n = 4^{x+1}\}$; $(38x + 2n + 3)\ \{where\ n \in 2^j, j \geq 2, n = 2 * 4^x\}$ and the optical delay is calculated as (n+2) Δ.

IV N-BIT COMPLEX MULTIPLIER ARCHITECTURE

Complex multiplication is the essential and most important part of any digital signal processing system to perform operations such as DFT, FFT etc. Complex number give solution to every polynomial equation where real number have no solution. Researcher's have been investigating to find out the most efficient solution to carry out this operation with more parallelism[10]. In this section two designs of vedic complex multiplication architecture is discussed.

Let us consider two complex numbers **C,** $Z_1 = a_{re} + i\ a_{img}$ and $Z_2 = b_{re} + i\ b_{img}$, with $\{a_{re}, b_{re}\}$ as a real part and $\{a_{img}, b_{img}\}$ as an imaginary part. Product of two complex numbers gives:

$Z_{re}=(a_{re}b_{re} - a_{img}b_{img})$ and $Z_{img}=(a_{re}b_{img}+ a_{img}b_{re})$ (1)

To implement the circuit for the multiplication of two complex numbers from equation (1), we required four multiplier, one adder and one subtractor, we represented it as design CM1 depicted in Fig. 6.

If we further simplify the equation (1) can be written as

$Z_{re} = a_{re}\ (\ b_{re} + b_{img}) - b_{img}\ (\ a_{re} + a_{img})$ (2)

$Z_{img} = a_{re}\ (\ b_{re} + b_{img}) + b_{re}\ (\ a_{img} - a_{re})$ (3)

As per the equation (2) and (3) for desiging the circuit for the multiplication of two complex numbers we reqired three multipliers, three adders and two subtractors represented it as design CM2 depicted in Fig. 7.

Proposed n-bit Complex Multiplier

In this section, we have discussed the different models of n-bit complex multiplier and calculated the optical design parameters of all the models in terms of optical cost and optical delay. To perform the multiplication, we have used Urdhva–Tiryakbhyam sutra of Vedic mathematics that we had already discussed in our previous work in detail [11][12]. In this work to perform the multiplication of n -bit binary number we have used n-bit VM Design 2 all optical MZI-SOA based Vedic multiplier [12] having $OC = 2^{2\log_2 n+1} + 3\sum_{i=2}^{N} 4^{N-i}(5.5 * 2^i - 5)$ and $OD = 3 + 3\sum_{i=2}^{N}(0.5 * 2^i + 2)\ \Delta$ and, to perform the addition operation we have used n-bit CSA [11] with OC = 5.5n-5 and OD =(.5n+2)Δ.

Design CM1:

In Design CM1 as shown in Fig. 6, multiplication of two n-bit complex numbers is carry out in two stages: At first stage (α_1), generation of the product terms are carried out and in second stage (α_2), the addition and subtraction of the product terms that are generated at the first stage is done, simultaneously.

In the implementation of Design CM1 n-bit complex multiplier total four multipliers, one adder and one subtractor are used. Based on the different designs of subtractors which we have discussed above, four models of Design CM1 n-bit complex multipliers are studied. In each model, to perform the multiplication and addition operation, we have used n-bit VM Design 2 all-optical MZI-SOA multiplier and n-bit CSA [11] shown in Fig. 8 and Fig. 11, respectively.

The analysis of optical design parameters of all the four models in terms of optical cost (*OC*) and optical delay (*OD*) are studied as follow. The total optical cost and optical delay of the circuit can be written as $OC(\alpha_{total}) = OC(\alpha_1) + OC(\alpha_2)$ and $OD(\beta_{total}) = OD(\beta_1) + OD(\beta_2)$. In this work, the optical cost of MZI-SOA and RSOA-TAND switch acknowledge as one and

Authorized licensed use limited to: DELHI TECHNICAL UNIV. Downloaded on January 17,2023 at 05:03:54 UTC from IEEE Xplore. Restrictions apply.

the optical cost of beam splitter and beam combiner are taken as zero. The optical delay is defined as the product of Δ unit with the numbers of MZIs or RSOA-TANDs used per stage in the critical path of realization. The performance parameters are calculated for the 4-bit and above.

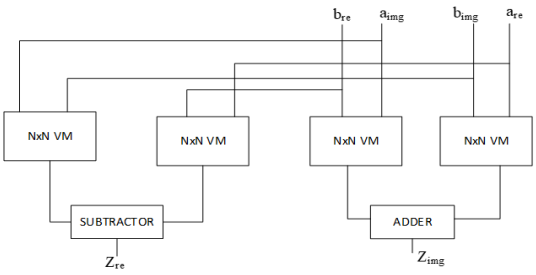

Figure 6: Design CM1 Complex multiplier design using four n-bit Vedic multiplier

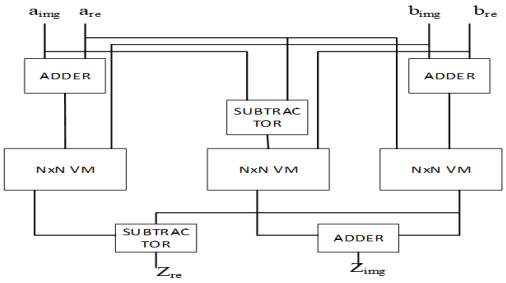

Figure 7: Design CM2 Complex multiplier design using three n-bit Vedic multiplier.

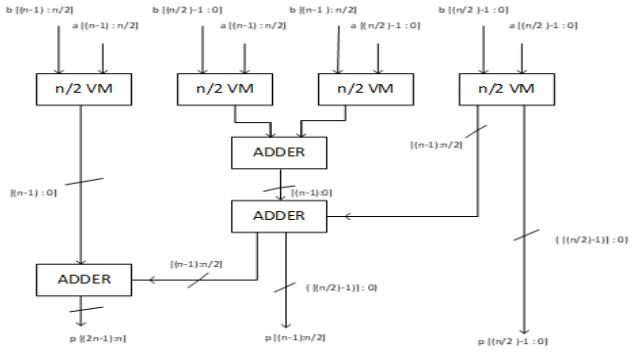

Figure 8: n-bit Vedic Multiplier

Let us consider a_n and b_n be the two binary number of n-bit each {where: $n \geq 4$ }. In the first stage four n-bit VM Design 2 all optical Vedic multipliers are used having the $OC(\alpha_1) = 4[2^{2\log_2 n+1} + 3\sum_{i=2}^{N} 4^{N-i}(5.5 * 2^i - 5)]$ and $OD(\beta_1) = 3 + 3\sum_{i=2}^{N}(0.5 * 2^i + 2)\Delta, where\ \mathrm{N} = \log_2 n$ to generate the partial product terms (common in all the four model).

Model 1:

In second stage, we have used one n-bit CSA [11] and one proposed Design 1a subtractor having $OC(\alpha_2)$ = 5.5n-5 + 8n-2 = 13.5n -7 and $OD(\beta_2)$ = (n+2) Δ to perform the addition and subtraction operation on the generated partial product term of the first stage simultaneously. The total optical cost $OC(\alpha_{total})$ and the total optical delay $OD(\beta_{total})$ of the n-bit complex multiplier can be written as:

$$OC(\alpha_{total}) = OC(\alpha_1) + OC(\alpha_2) = 4[2^{2\log_2 n+1} + 3\sum_{i=2}^{N} 4^{N-i}(5.5 * 2^i - 5)] + 13.5 * 2^N - 7$$
$$OD(\beta_{total}) = OD(\beta_1) + OD(\beta_2) = [5 + 3\sum_{i=2}^{N}(0.5 * 2^i + 2) + 2^N]\Delta$$

Model 2:

In second stage, we have used one n-bit CSA [11] and one proposed Design 1b subtractor having $OC(\alpha_2)$ = 5.5n-5 + 6n-2 = 11.5n -7 and $OD(\beta_2)$ = (n+2) Δ to perform the addition and subtraction operation on the generated partial product term of the first stage simultaneously. The total optical cost $OC(\alpha_{total})$ and the total optical delay $OD(\beta_{total})$ of the n-bit complex multiplier can be written as:

$$OC(\alpha_{total}) = OC(\alpha_1) + OC(\alpha_2) = 4[2^{2\log_2 n+1} + 3\sum_{i=2}^{N} 4^{N-i}(5.5 * 2^i - 5)] + 11.5 * 2^N - 7$$
$$OD(\beta_{total}) = OD(\beta_1) + OD(\beta_2) = [5 + 3\sum_{i=2}^{N}(0.5 * 2^i + 2) + 2^N]\Delta$$

Model 3:

In second stage, we have used one n-bit CSA[11] and one proposed Design 2a subtractor having $OC(\alpha_2) = \{(82x + 6.5n - 2),\ where\ n \in 4^j, j \geq 2, n = 4^{x+1}\}$; $\{(38x + 6.5n - 2), where\ n \in 2^j, j \geq 2, n = 2 * 4^x\}$ and $OD(\beta_2)$ = (n+2) Δ to perform the addition and subtraction operation on the generated partial product term of the first stage simultaneously. The total optical cost $OC(\alpha_{total})$ and the total optical delay $OD(\beta_{total})$ of the n-bit complex multiplier can be written as:

$$OC(\alpha_{total}) = OC(\alpha_1) + OC(\alpha_2) = 4[2^{2\log_2 n+1} + 3\sum_{i=2}^{N} 4^{N-i}(5.5 * 2^i - 5)] + (82x + 6.5n - 2), \{ where\ n \in 4^j, j \geq 2, n = 4^{x+1}\}$$
$$= 4[2^{2\log_2 n+1} + 3\sum_{i=2}^{N} 4^{N-i}(5.5 * 2^i - 5)] + (38x + 6.5n - 2), \{ where\ n \in 2^j, j \geq 2, n = 2 * 4^x\}$$
$$OD(\beta_{total}) = OD(\beta_1) + OD(\beta_2) = [5 + 3\sum_{i=2}^{N}(0.5 * 2^i + 2) + 2^N]\Delta$$

Model 4:

In second stage, we have used one n-bit CSA[11] and one proposed Design 2b subtractor having $OC(\alpha_2) = (82x + 7.5n - 2)\ \{where\ n \in 4^j, j \geq 2, n = 4^{x+1}\}$; $OC(\alpha_2) = (38x + 7.5n - 2)\{where\ n \in 2^j, j \geq 2, n = 2 * 4^x\}$ and $OD(\beta_2)$ = (n+2) Δ to perform the addition and subtraction operation on the generated partial product term of the first stage simultaneously. The total optical cost $OC(\alpha_{total})$ and the total optical delay $OD(\beta_{total})$ of the n-bit complex multiplier can be written as:

$$OC(\alpha_{total}) = OC(\alpha_1) + OC(\alpha_2) = 4[2^{2\log_2 n+1} + 3\sum_{i=2}^{N} 4^{N-i}(5.5 * 2^i - 5)] + (82x + 7.5n - 2), \{ where\ n \in 4^j, j \geq 2, n = 4^{x+1}\}$$
$$= 4[2^{2\log_2 n+1} + 3\sum_{i=2}^{N} 4^{N-i}(5.5 * 2^i - 5)] + (38x + 7.5n - 2), \{ where\ n \in 2^j, j \geq 2, n = 2 * 4^x\}$$
$$OD(\beta_{total}) = OD(\beta_1) + OD(\beta_2) = [5 + 3\sum_{i=2}^{N}(0.5 * 2^i + 2) + 2^N]\Delta$$

Design CM2:

In Design CM2 as shown in Fig. 7, multiplication of two n-bit complex numbers is carried out in three stages: first stage (x_1), second stage (x_2) and third stage (x_3) {x = α or β}. Where, x_1: defines the addition and subtraction of the initial terms and x_2: defines the product of terms that are generated at the first stage and x_3: defines the addition and subtraction operation of the partial product terms generated at the second stage, simultaneously. In the implementation of Design CM2 n-bit

Authorized licensed use limited to: DELHI TECHNICAL UNIV. Downloaded on January 17,2023 at 05:03:54 UTC from IEEE Xplore. Restrictions apply.

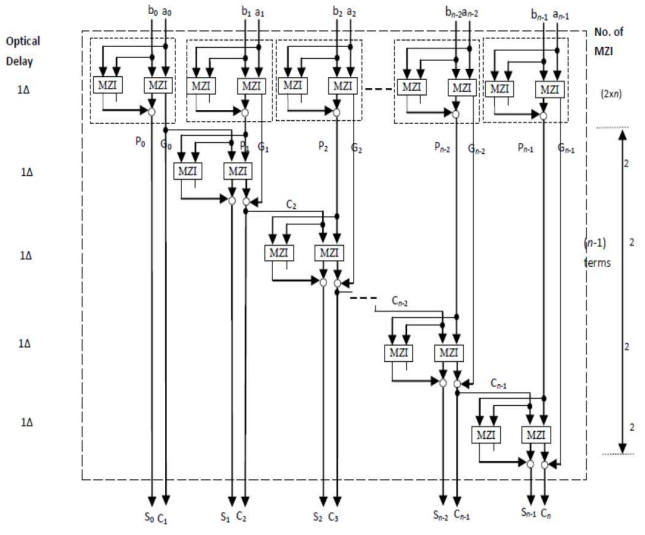

Figure 9: n-bit CLA [8]

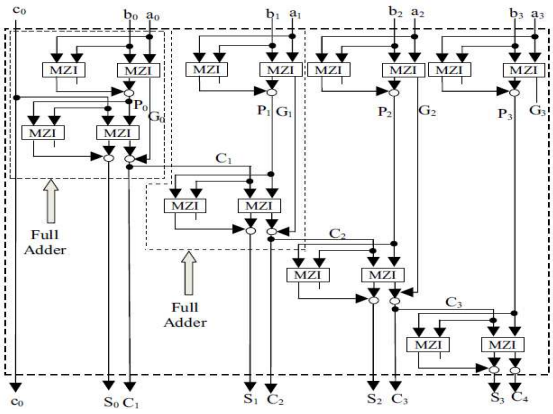

Figure 10: Hierarchical design of CLA [8]

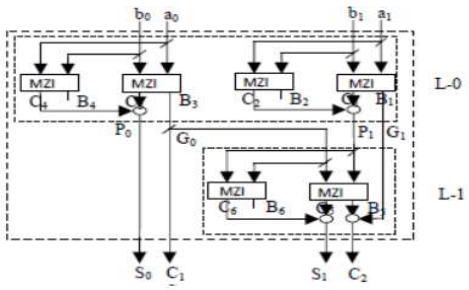

Figure 11: Basic block to design n-bit CSA [9]

complex multiplier total three multipliers, three adders and two subtractors are used. Based on the different designs of subtractor's which we have discussed above four models of Design CM2 n-bit complex multiplier are studied. In each model, to perform the multiplication and addition operation, we have used n-bit VM Design 2 all-optical MZI-SOA multiplier and n-bit CSA [11], respectively.

The analysis of optical design parameters of all the four models in terms of optical cost (*OC*) and optical delay (OD) are discussed as below. The *OC* and *OD* of the complete design can be written as $OC(\alpha_{total}) = OC(\alpha_1) + OC(\alpha_2) + OC(\alpha_3)$ and $OD(\beta_{total}) = OD(\beta_1) + OD(\beta_2) + OD(\beta_3)$.

Let takes a_n and b_n be the two binary number of n-bit each {where: $n \geq 4$ }. In the second stage three n-bit all optical Vedic multipliers are used having the $OC(\alpha_2) = 3[2^{2\log_2 n+1} + 3\sum_{i=2}^{N} 4^{N-i}(5.5 * 2^i - 5)]$ and $OD(\beta_2) = 3 + 3\sum_{i=2}^{N}(0.5 * 2^i + 2)\Delta$ to generate the partial product terms (common in all the four models).

Model 1:

In the first stage, we have used two n-bit CSA [11] adders and one proposed Design 1a subtractor having $OC(\alpha_1) = 2(5.5n-5) + 8n-2 = 19n -12$ and $OD(\beta_1) = (n+2)\,\Delta$ to perform the addition and subtraction operation on the initial inputs, simultaneously. In the last stage, we have used one n-bit CSA adder and one Design 1a subtractor to perform the addition and subtraction operation on the generated partial product terms having $OC(\alpha_3) = 5.5n-5 + 8n-2 = 13.5n -7$ and $OD(\beta_3) = (n+2)\,\Delta$. The final expression of total optical cost $OC(\alpha_{total})$ and optical delay $OD(\beta_{total})$ of the n-bit complex multiplier can be written as:

$$OC(\alpha_{total}) = OC(\alpha_1) + OC(\alpha_2) + OC(\alpha_3)$$
$$= 3[2^{2\log_2 n+1} + 3\sum_{i=2}^{N} 4^{N-i}(5.5 * 2^i - 5)] + 32.5 * 2^N - 19$$
$$OD(\beta_{total}) = OD(\beta_1) + OD(\beta_2) + OD(\beta_3)$$
$$= [7 + 3\sum_{i=2}^{N}(0.5 * 2^i + 2) + 2^{N+1}]\Delta$$

Model 2:

In the first stage, we have used two n-bit CSA [11] adders and one proposed Design 1b subtractor having $OC(\alpha_1) = 2(5.5n-5) + 6n-2 = 17n -12$ and $OD(\beta_1) = (n+2)\,\Delta$ to perform the addition and subtraction operation on the initial inputs, simultaneously. In the last stage, we have used one n-bit CSA adder and one Design 1b subtractor to perform the addition and subtraction operation on the generated partial product terms having $OC(\alpha_3) = 5.5n-5 + 6n-2 = 11.5n -7$ and $OD(\beta_3) = (n+2)\,\Delta$. The final expression of total optical cost $OC(\alpha_{total})$ and optical delay $OD(\beta_{total})$ of the n-bit complex Vedic multiplier can be written as:

$$OC(\alpha_{total}) = OC(\alpha_1) + OC(\alpha_2) + OC(\alpha_3)$$
$$= 3[2^{2\log_2 n+1} + 3\sum_{i=2}^{N} 4^{N-i}(5.5 * 2^i - 5)] + 28.5 * 2^N - 19$$
$$OD(\beta_{total}) = OD(\beta_1) + OD(\beta_2) + OD(\beta_3)$$
$$= [7 + 3\sum_{i=2}^{N}(0.5 * 2^i + 2) + 2^{N+1}]\Delta$$

Model 3:

In the first stage, we have used two n-bit CSA [11] adders and one proposed Design 2a subtractor having $OC(\alpha_1) = (82x + 12n - 7)\{\text{where } n \in 4^j, j \geq 2, n = 4^{x+1}\}$; $OC(\alpha_1) = (38x + 12n - 7)\{\text{ where } n \in 2^j, j \geq 2, n = 2 * 4^x\}$ and $OD(\beta_1) = (n+2)\,\Delta$ to perform the addition and subtraction operation on the initial inputs, simultaneously. In the last stage, we have used one n-bit CSA adder and one Design 2a subtractor to perform the addition and subtraction operation on the generated partial product terms having $OC(\alpha_3) = (82x + 6.5n - 2), \{ where\ n \in 4^j, j \geq 2, n = 4^{x+1}\}$; $OC(\alpha_3) = (38x + 6.5n - 2), \{ where\ n \in 2^j, j \geq 2, n = 2 * 4^x\}$ and $OD(\beta_3) = (n+2)\,\Delta$. The final expression of total optical cost $OC(\alpha_{total})$ and optical delay $OD(\beta_{total})$ of the n-bit complex multiplier can be written as:

$$OC(\alpha_{total}) = OC(\alpha_1) + OC(\alpha_2) + OC(\alpha_3)$$
$$= 3[2^{2\log_2 n+1} + 3\sum_{i=2}^{N} 4^{N-i}(5.5 * 2^i - 5)] + (164x + 18.5n - 9), \{ where\ n \in 4^j, j \geq 2, n = 4^{x+1}\}$$
$$= 3[2^{2\log_2 n+1} + 3\sum_{i=2}^{N} 4^{N-i}(5.5 * 2^i - 5)] + (76x + 18.5n - 9), \{ where\ n \in 2^j, j \geq 2, n = 2 * 4^x\}$$
$$OD(\beta_{total}) = OD(\beta_1) + OD(\beta_2) + OD(\beta_3)$$
$$= [7 + 3\sum_{i=2}^{N}(0.5 * 2^i + 2) + 2^{N+1}]\Delta$$

Authorized licensed use limited to: DELHI TECHNICAL UNIV. Downloaded on January 17,2023 at 05:03:54 UTC from IEEE Xplore. Restrictions apply.

Table 1: Comparison of proposed Design CM1 and Design CM2 models in terms of OC(α_{total}) and OD(β_{total}), where $N = \log_2 n$

	Parameter	OC	OD
Design CM1	**MODEL1**	$4[2^{2\log_2 n+1} + 3\sum_{i=2}^{N} 4^{N-i}(5.5 * 2^i - 5)] + 13.5 * 2^N - 7$	$[5 + 3\sum_{i=2}^{N}(0.5 * 2^i + 2) + 2^N]\Delta$
	MODEL2	$4[2^{2\log_2 n+1} + 3\sum_{i=2}^{N} 4^{N-i}(5.5 * 2^i - 5)] + 11.5 * 2^N - 7$	$[5 + 3\sum_{i=2}^{N}(0.5 * 2^i + 2) + 2^N]\Delta$
	MODEL3	$4[2^{2\log_2 n+1} + 3\sum_{i=2}^{N} 4^{N-i}(5.5 * 2^i - 5)] + (82x + 6.5n - 2), \{ where\ n \in 4^j, j \geq 2, n = 4^{x+1} \}$ $4[2^{2\log_2 n+1} + 3\sum_{i=2}^{N} 4^{N-i}(5.5 * 2^i - 5)] + (38x + 6.5n - 2), \{ where\ n \in 2^j, j \geq 2, n = 2 * 4^x \}$	$[5 + 3\sum_{i=2}^{N}(0.5 * 2^i + 2) + 2^N]\Delta$
	MODEL4	$4[2^{2\log_2 n+1} + 3\sum_{i=2}^{N} 4^{N-i}(5.5 * 2^i - 5)] + (82x + 7.5n - 2), \{ where\ n \in 4^j, j \geq 2, n = 4^{x+1} \}$ $4[2^{2\log_2 n+1} + 3\sum_{i=2}^{N} 4^{N-i}(5.5 * 2^i - 5)] + (38x + 7.5n - 2), \{ where\ n \in 2^j, j \geq 2, n = 2 * 4^x \}$	$[5 + 3\sum_{i=2}^{N}(0.5 * 2^i + 2) + 2^N]\Delta$
Design CM2	**MODEL 1**	$3[2^{2\log_2 n+1} + 3\sum_{i=2}^{N} 4^{N-i}(5.5 * 2^i - 5)] + 32.5 * 2^N - 19$	$[7 + 3\sum_{i=2}^{N}(0.5 * 2^i + 2) + 2^{N+1}]\Delta$
	MODEL2	$3[2^{2\log_2 n+1} + 3\sum_{i=2}^{N} 4^{N-i}(5.5 * 2^i - 5)] + 28.5 * 2^N - 19$	$[7 + 3\sum_{i=2}^{N}(0.5 * 2^i + 2) + 2^{N+1}]\Delta$
	MODEL3	$3[2^{2\log_2 n+1} + 3\sum_{i=2}^{N} 4^{N-i}(5.5 * 2^i - 5)] + (164x + 18.5n - 9), \{ where\ n \in 4^j, j \geq 2, n = 4^{x+1} \}$ $3[2^{2\log_2 n+1} + 3\sum_{i=2}^{N} 4^{N-i}(5.5 * 2^i - 5)] + (76x + 18.5n - 9), \{ where\ n \in 2^j, j \geq 2, n = 2 * 4^x \}$	$[7 + 3\sum_{i=2}^{N}(0.5 * 2^i + 2) + 2^{N+1}]\Delta$
	MODEL4	$3[2^{2\log_2 n+1} + 3\sum_{i=2}^{N} 4^{N-i}(5.5 * 2^i - 5)] + (164x + 20.5n - 9), \{ where\ n \in 4^j, j \geq 2, n = 4^{x+1} \}$ $3[2^{2\log_2 n+1} + 3\sum_{i=2}^{N} 4^{N-i}(5.5 * 2^i - 5)] + (76x + 20.5n - 9), \{ where\ n \in 2^j, j \geq 2, n = 2 * 4^x \}$	$[7 + 3\sum_{i=2}^{N}(0.5 * 2^i + 2) + 2^{N+1}]\Delta$

Model 4:

In the first stage, we have used two n-bit CSA[11] adders and one proposed Design 2b subtractor having $OC(\alpha_1) = (82x + 13n - 7)\{where\ n \in 4^j, j \geq 2, n = 4^{x+1}\}$; $OC(\alpha_1) = (38x + 13n - 7)\{ where\ n \in 2^j, j \geq 2, n = 2 * 4^x \}$ and $OD(\beta_1) = (n+2)\ \Delta$ to perform the addition and subtraction operation on the initial inputs, simultaneously. In the last stage, we have used one n-bit CSA adder and one Design 2b to perform the addition and subtraction operation on the generated partial product terms having $OC(\alpha_3) = (82x + 7.5n - 2), \{ where\ n \in 4^j, j \geq 2, n = 4^{x+1} \}$; $OC(\alpha_3) = (38x + 7.5n - 2), \{ where\ n \in 2^j, j \geq 2, n = 2 * 4^x \}$and $OD(\beta_3) = (n+2)\ \Delta$. The final expression of total optical cost $OC(\alpha_{total})$ and optical delay $OD(\beta_{total})$ of the n-bit complex multiplier can be written as:

$$OC(\alpha_{total}) = OC(\alpha_1) + OC(\alpha_2) + OC(\alpha_3)$$
$$= 3[2^{2\log_2 n+1} + 3\sum_{i=2}^{N} 4^{N-i}(5.5 * 2^i - 5)] + (164x + 20.5n - 9), \{ where\ n \in 4^j, j \geq 2, n + 4^{x+1} \}$$
$$= 3[2^{2\log_2 n+1} + 3\sum_{i=2}^{N} 4^{N-i}(5.5 * 2^i - 5)] + (76x + 20.5n - 9), \{ where\ n \in 2^j, j \geq 2, n = 2 * 4^x \}$$
$$OD(\beta_{total}) = OD(\beta_1) + OD(\beta_2) + OD(\beta_3)$$
$$= [7 + 3\sum_{i=2}^{N}(0.5 * 2^i + 2) + 2^{N+1}]\Delta$$

V Performance Evaluation

Table 1 shows the comparison of the total optical cost and the total optical delay of all the four models presented under Design CM1 and Design CM2. Experimental analysis depicts that there is trade -off between optical cost and optical delay between Design CM1 and Design CM2. Lets take for 32-bit, Design CM2 found approx 22% more efficient in terms of optical cost with an increase of approx 3% in optical delay in all the models. For 128-bit , in comparion among all the models in Design CM1 and Design CM2, Model3 of Design CM2 shows overall improvement of 32.7% in optical cost with an increase of ~2% in optical delay.

VI Conclusion

In this paper we have proposed the various models of n-bit complex multiplier mapped with RSOA-TAND and MZI-SOA switches. We have also discussed the mapping of reversible logic gates with RSOA-TAND switch. As per our knowledge no work towards the implementation of n-bit complex multiplier design using both MZI-SOA and RSOA-TAND switches is done. The significant adavntages of the proposed designs is that complex multiplication of n-bits number can be performed at ultra-high speed with all-optical in nature.

References

[1] M. Smit et al., "Moore's law in photonics," *Wiley J Laser Phot.*, Rev.vol. 6, no. 1, pp. 1–13, 2012.

[2] R. Wille et al., "Advanced Logic Synthesis," *Springer, Berlin*, 2018.

[3] R. Landauer, "Irreversibility and heat generation in the computing process," *IBM Journal of Research and Development*, vol. 5, no. 3, pp. 183–191, 1961.

[4] M. A. Nielsen et al, "Quantum Computation and Quantum Information," New York: Cambridge Univ. Press, 2000.

[5] M. A. Karim et al, "Optical computing: An introduction," New York: Wiley, chap. 7 and 9, 1992.

[6] C. Taraphdara, et al, "Mach-Zehnder interferometer-based all-optical reversible logic gate," *Optics and Laser Technology*, vol. 42, no. 2, pp. 249–259, 2010.

[7] Maji, K., et al, "Simulative Performance Analysis of All Optical Universal Logic TAND Gate Using Reflective Semiconductor Optical Amplifier (RSOA)." *Proceedings of International Conference on Frontiers in Computing and Systems. Advances in Intelligent Systems and Computing*, vol 1255. Springer, Singapore. 2021

[8] P. Dutta et al., "Mach-Zehnder interferometer based all optical reversible carry-lookahead adder", *ISVLSI*, pp. 412–417, 2014.

[9] R. Das et al., "All-optical reversible design of Mach-Zehnder interferometer-based carry-skip adder", *DISCOVER*, pp. 73–78, 2016.

[10] Rao KD et al., "FPGA implementation of complex multiplier using minimum delay Vedic real multiplier architecture," *IEEE UPCON,* 2016.

[11] B. Jagadguru Swami Sri Bharath *et al*., "Vedic mathematics or sixteen simple sutras from the Vedas", Motilal Banarsi Das, Varanasi, India, 1986.

[12] R. Jindal et al., "All-optical n-bit multiplier design using Mach Zehnder interferometer," *IEEE INCET,* 2021.

Authorized licensed use limited to: DELHI TECHNICAL UNIV. Downloaded on January 17,2023 at 05:03:54 UTC from IEEE Xplore. Restrictions apply.

Alzheimer's Disease Detection using Particle Swarm Optimization

Neha Garg
Department of Electronics and Communication,
Delhi Technological University,
Delhi, India
ngcoolneha@gmail.com

Mahipal Singh Choudhry
Department of Electronics and Communication,
Delhi Technological University,
Delhi, India
msc_1976@yahoo.com

Rajesh Mungasaji Bodade
Faculty of Communication Engineering,
Military College of Telecommunication Engineering,
Mhow, Indore, India
rajeshbodade@gmail.com

2022 8th International Conference on Signal Processing and Communication (ICSC) | 978-1-6654-5430-8/22/$31.00 ©2022 IEEE | DOI: 10.1109/ICSC56524.2022.10009510

***Abstract*—Alzheimer's disease is a chronic, progressive, and presently incurable neurologic disorder that leads to the demise of a patient. Alzheimer's Disease should be detected at an early stage so that an effective treatment may be provided to the patient in time. In the proposed method Dual tree complex wavelet transform is used for feature extraction. The Principal Component Analysis is used to transform the raw features into new low-dimensional feature space. Principal Component Analysis elects the features based on their eigen values. All high eigenvalue features may not provide assurance for high classification accuracy and sensitivity. The best solution to this problem is the feature optimization approach. Thus, Particle swarm optimization is used for the selection of optimum subset of transformed features. These selected features are given to four different classifiers for performance evaluation. The proposed method is also executed with Discrete Wavelet Transform to evaluate its performance and is compared with three models viz. Dual Tree Complex Wavelet Transform, Dual Tree Complex Wavelet Transform +Principal Component Analysis and Dual Tree Complex Wavelet Transform +Particle swarm optimization. The proposed technique yielded 95.5% accuracy, 97.6% sensitivity, and 93.4% specificity on the Open Access Series of Imaging Studies dataset with k-Nearest Neighbour classifier. The obtained results outperform the other existing methods for AD prediction.**

Keywords—Alzheimer's disease; Dual Tree Complex wavelet transform; Principal Component Analysis; Particle Swarm Optimization, Classification

I. INTRODUCTION

Alzheimer's disease (AD) is a serious health problem in elderly people worldwide. The number of diseased people is expected to increase further in the next 20 years with the increase in the elderly population. AD is not curable at present and there is no way to reverse its progression also [1]. This demands an early detection of AD which helps in controlling and slowing down its impact. AD is caused due to the formation of unwanted proteins in the brain which breaks the neuronal connections [2]. Loss of neurons in the AD brain leads to some structural changes which can be assessed by neuroimaging techniques viz. Positron emission tomography (PET), Magnetic Resonance Imaging (MRI), and functional MRI (fMRI). MRI is a medical imaging test which is non-invasive in nature. It gives high-quality structured images with good brain tissue contrast [3]. Extraction of relevant and optimum features from these images helps in the early detection of AD. Some researchers extracted features in terms of structural variation in brain during different stages of AD. These variations include reduction in hippocampal volume, thinning of the cortical surface, ventricular enlargement, and reduction in grey matter density [4]. These techniques are called Region of interest (ROI) based methods. The ROI-based method requires the segmentation of atrophied regions which needs prior information and expertise. This paper presents an approach based on the "whole-brain analysis" method for diagnosing AD. The whole-brain approach takes the entire brain as a single ROI, thus there is no need for segmentation in this method [5].

Chaplot et al. [6] employed Discrete Wavelet Transform (DWT) to decompose image into coefficients and obtained 94% accuracy for AD/NC (Normal Control) classification. Some researchers employed Dual Tree Complex Wavelet Transform (DTCWT) for image decomposition. Jha et al. [7] used high frequency coefficients at fifth level DTCWT decomposition as features and applied Principal Component Analysis (PCA) for dimensionality reduction. This study yielded 90.06 % accuracy with Feed forward Neural Network (FNN) classifier. Alam et al. [8] modified this work by adding Linear Discriminant Analysis (LDA) with PCA and using Twin support vector machine classifier (TSVM) as classifier. This study yielded an accuracy of 96.68 %. Jha et al. [9] used Extreme Learning Machine (ELM) in place of TSVM and obtained an accuracy of 95.72%.

In this paper, wavelet transform is used for image decomposition and detail wavelet coefficients at the fifth level are used as features. PCA is used in the proposed technique to reduce the high dimensionality of features. The optimum and relevant features are selected by using the feature selection algorithm viz. Particle Swarm Optimization (PSO). The proposed method is evaluated with two different wavelet transforms viz. DWT and DTCWT. The contribution of the paper lies in the following facts:

- DTCWT and Particle swarm optimization are used for feature extraction and selection respectively.
- Most of the state-of-the-art methods employed whole-brain analysis on only a single slice obtained from 3-D MRI of AD diseased brain. The single slice may not

978-1-6654-5430-8/22/$31.00 ©2022 IEEE

Authorized licensed use limited to: DELHI TECHNICAL UNIV. Downloaded on January 17,2023 at 05:01:02 UTC from IEEE Xplore. Restrictions apply.

.

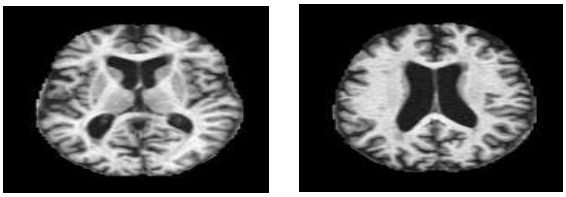

(i) (ii)

Fig. 1. Sample of 2-D MR image (i) AD and (ii) NC

contain the root of the disease. The proposed method considers the multiple slices obtained from 3-D MRI for each patient, so that obtained information is more precise, valid, and consistent.

- Proposed work comprises DTCWT for image decomposition, Particle Swarm Optimization (PSO) for feature selection, k-Nearest Neighbour (k-NN) for classification and shows higher accuracy when compared with the existing methods.
- In addition to the above contribution, the proposed method yields a computer assisted diagnosis (CAD) system. This system is helpful for clinicians as it can be used as an assisting tool in early AD diagnosis.

The proposed method is compared with three states of the art methods to verify its effectiveness. Comparison is based on the performance metrics including accuracy, sensitivity, and specificity. The paper is arranged as: Section II gives the details of dataset and background knowledge required for the work. Section III elucidates the experimental analysis. Finally, Section IV concludes the study with future directions

II. Method And Background Material

A. Dataset

The proposed work is executed by using Open Access Series of Imaging Studies (OASIS) dataset. OASIS stores 3D MR images of AD and NC classes. The OASIS dataset includes 416 subjects under the age span of 18 to 96 years [10]. In proposed work, 126 subjects including 63 ADs and 63 NCs are used for implementation. All images are skull stripped and intensity modulated. The XMedCon software is used for slice extraction from 3-D MR images. The 32 centre slices are extracted from each 3-D MR image and used for feature extraction. The centre slices which carry maximum information are extracted manually in PNG format. All 2-D slices have the dimension of 176 × 208 which is resized into 256 × 256 for further processing. A sample of 2-D MR image associated with AD and NC classes is illustrated in Fig. 1.

B. Methodology

The proposed method includes the first stage as DTCWT image decomposition. The detail coefficients are obtained at the fifth level of decomposition and are used as features. The fifth level provides the maximum accuracy when checked through the Grid search method [11]. The total number of 768 coefficients are obtained from a single 2-D MRI slice at fifth level. The proposed work used 32 2-D centre slices from each 3-D MRI, so each 3-D MRI provides 32 X 768 coefficients which is equivalent to 24576 coefficients. Now, matrix 32 X 768 is converted into row vector of 1 × 24,576. This row vector represents the 24576 number of coefficients for a single 3-D MRI. Now a matrix of dimensions 126 X 24576 is formed where 126 represents the total number of AD and NC subjects while 24576 represents the number of coefficients in single 3-D MRI. The dimension of the matrix is too high, so PCA is used for dimensionality reduction at second stage. PCA provides score matrix of size 126 X 125 where 126 represents total number of subjects and 125 represents principal components. At third stage, feature selection algorithm viz. PSO is introduced to improve the classification results. All 125 features are given to PSO. The total number of optimum and relevant features selected by PSO are 54 which are further given to classifier for testing. Fig. 2 shows the different stages in proposed methodology.

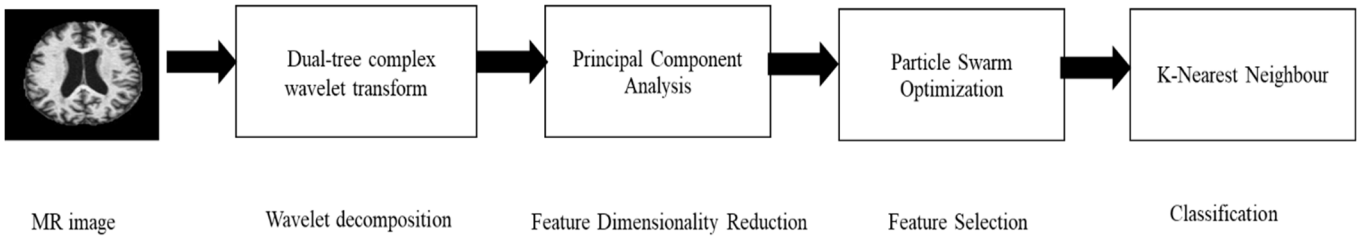

Fig. 2. Different stages in Proposed Methodology

Authorized licensed use limited to: DELHI TECHNICAL UNIV. Downloaded on January 17,2023 at 05:01:02 UTC from IEEE Xplore. Restrictions apply.

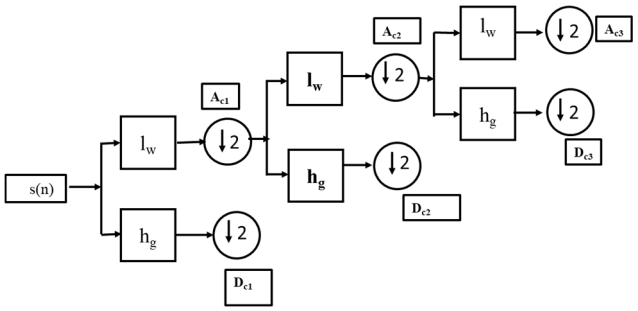

Fig. 3. Implementation of 1-D Discrete Wavelet Transform

C. Discrete Wavelet Transform

The structure of Discrete wavelet transform includes two filter banks, first one for Signal decomposition and second one for reconstruction. The analysis filter banks are used for decomposition and synthesis filter banks are used for the reconstruction purpose. Both filter banks consist of low pass filter and high pass filters [12]. The signal is decomposed into low-frequency components (approximation components) and high-frequency components (details components) through an analysis filter bank. Two sub-band signals, A_{c1} and D_{c1} are formed by down sampling the output of analysis filter bank with a multiple of 2. For a further level of decomposition, the approximation components are again decomposed into details and the approximation components, and so on. Fig. 3 shows the structure of 1-D DWT. The lowpass and high pass filters are denoted by l_w and h_g respectively.

D. Dual Tree Complex Wavelet Transform

In 1998, Kingsbury introduced the Dual Tree Complex Wavelet Transform [13]. It is not phase-sensitive and shows high directional sensitivity. 1-D DTCWT has two parallel real DWTs, for real components and imaginary components respectively. Fig. 4 shows the structure of 1-D DTCWT. Tree 1 and Tree 2 illustrate the real and imaginary part respectively. Tree 2 and Tree 1 wavelets form the Hilbert transform pair. In addition, both trees consist of analysis and synthesis filter banks. Analysis filters are used to decompose the signal and synthesis filters are used to reconstruct the signal. The analysis filter at first level is kept different from other levels to meet the condition of perfect reconstruction. The R_{low} & I_{low} represent the low pass filters and R_{high} & I_{high} correspond to the high pass filters.

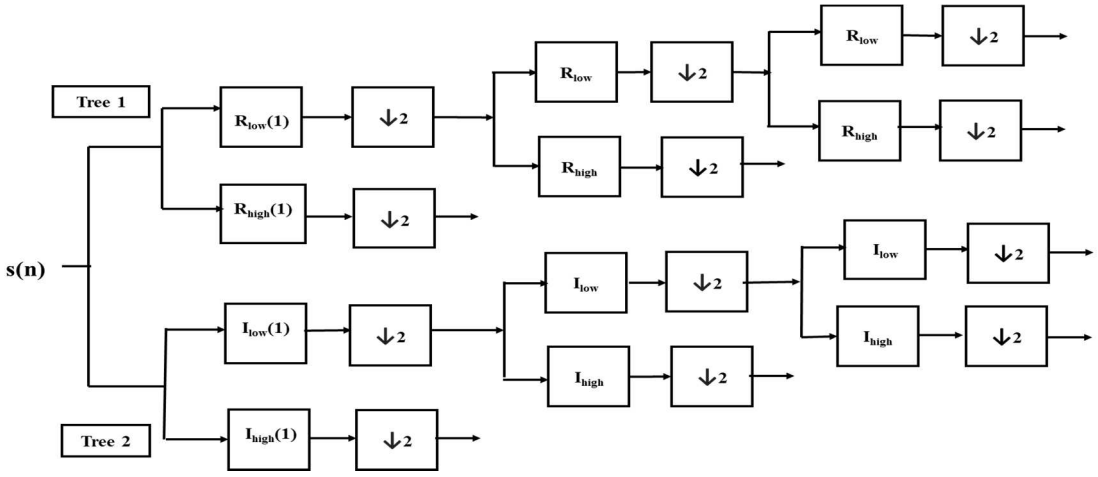

Fig. 4. Implementation of 1-D Dual Tree Complex Wavelet Transform

E. Principal Component Analysis(PCA)

Principal Component Analysis (PCA) is applied for reducing the dimension of features [14-15]. The aim of PCA is to reduce the number of features in a data set, while saving maximum information. It uses orthogonal transformation to recast the input data to a lower-dimensional space while keeping variance. PCA reduces overfitting and improves visualization. The PCA is completed in following steps:

(i) Let *I* is the input data matrix of M x L dimensions. Calculate the mean of each column of input matrix and standardize the input data by deducting mean from each column. Put the result in a form of matrix M_n having dimensions M x L.

Authorized licensed use limited to: DELHI TECHNICAL UNIV. Downloaded on January 17,2023 at 05:01:02 UTC from IEEE Xplore. Restrictions apply.

(ii) Calculate the covariance C_o of the matrix M_n.

$C_o = \frac{1}{M} M_n^T . M_n$

(iii) Calculate the eigenvalue and the eigenvector of covariance matrix $V^{-1} C_o V = D_g$, where V represents eigen vector matrix and D_g represents the diagonal matrix of eigen values of C_o.

(iv) Form the transformation matrix P of dimension M x S with eigen vectors arranged in columns as principal components. Eigen vectors are arranged in columns in decreasing order of their eigen values.

(v) Low dimensional matrix is obtained from initial data matrix with the help of principal components $F = P^T I$, where F represents final matrix of reduced dimensions (M x S).

F. Particle Swarm Optimization (PSO)

The Particle Swarm Optimization (PSO) was first introduced by Kennedy and Eberhart in 1995. PSO is an intelligent algorithm based on the social behaviour of swarms [16-17]. PSO has low computation efforts, high convergence rate and is better than other feature selection algorithm as it executes local and global research all together [18]. It is a computational approach that is used to find an optimum solution to the problem. It requires an objective function and very less hyperparameters. The algorithm is based on the swarm intelligence that can be observed at the time of their searching food. The swarms can reach the target location only due to their mutual co-operation, communication, and learning. In PSO, particles are just like swarms. The candid solution is the particle moving with definite velocity in a search space of optimization problem. Search space includes all possible solutions. The solution dealing with the global minimum is to be searched out. Particles are not aware of the location of the global minimum but all of them have fitness values (current position) which can be evaluated by the measurement of quality (fitness function) to be optimized. The position or coordinates of the particle p at j^{th} iteration in search space is given by

$$Pos_p^j = \left[pos_{0,p}^j, pos_{1,p}^j, pos_{2,p}^j, pos_{3,p}^j \dots\dots, pos_{N,p}^j\right] \quad (1)$$

In equation (1), N represents the problem dimension and different directions for particle movement. Each particle is in motion to find the optimum solution in terms of the global minimum. The velocity of particle p at j^{th} iteration is given as

$$Vc_p^j = \left[vc_{0,p}^j, vc_{1,p}^j, vc_{2,p}^j, vc_{3,p}^j \dots\dots, vc_{N,p}^j\right] \quad (2)$$

The best position searched by the p^{th} particle is denoted by personal best position (pbest) and best position searched by the entire group of particles is denoted by its best global position (gbest). The location of the p^{th} particle in $(j+1)^{th}$ iteration is given by

$$Pos_p^{j+1} = Pos_p^j + Vc_p^{j+1} \quad (3)$$

And the updated velocity at $(j+1)^{th}$ iteration is given by

$$Vc_p^{j+1} = wVc_p^j + c_1 r_1\left(pbest_p^j - Pos_p^j\right) + c_2 r_2\left(gbest_p^j - Pos_p^j\right) \quad (4)$$

In equation (4), *w* is the weight inertia constant that shows the ability of the particle to update its direction. The c1 and c2 are the acceleration coefficients and r_1 and r_2 are the random numbers. In proposed work, values of c1 and c2 is taken as 2. The w is taken as 0.9, N is 30 and number of iterations is 100. Fig. 5 indicates the convergence plot of PSO in proposed work.

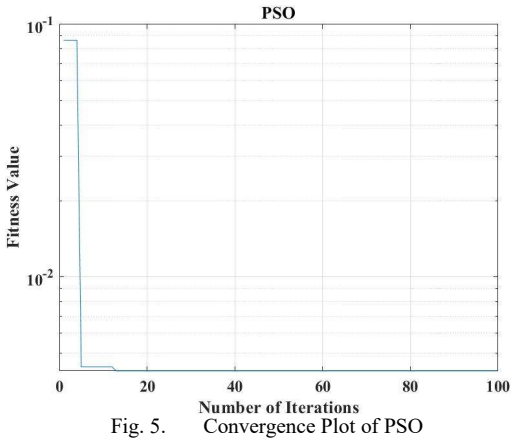

Fig. 5. Convergence Plot of PSO

III. Simulation Results And Discussion

A. Performance Measures

In proposed work Accuracy, Sensitivity and Specificity are used as parameters to evaluate the performance. Accuracy [19-21] represents the outcome in terms of true positive (Tu_p) and true negative $(Tu_n)$with respect to total subjects. True positive represents the number of AD subjects correctly classified as AD and True negative represents the number of normal persons correctly identified as normal. Total subjects include all the subjects to be identified as AD or NC. It is formulated as

$$\text{Accuracy} = \left(Tu_p + Tu_n\right)/\left(Tu_n + Tu_p + Fal_n + Fal_p\right) \quad (5)$$

Sensitivity [20-21] represents the outcome of the classifier in terms of true positive. It is formulated as

$$\text{Sensitivity} = \left(Tu_p\right)/\left(Tu_p + Fal_n\right) \quad (6)$$

Specificity represents the outcome of classifier in terms of true negative. It is formulated as

$$\text{Specificity} = \left(Tu_n\right)/\left(Tu_n + Fal_p\right) \quad (7)$$

where Fal_n represents the false negative and Fal_p represents the false positive. False negative refers to those AD subjects who are misclassified as normal while False positive refers to those normal persons who are misclassified as AD.

B. Performance Evaluation

Proposed method is compared with different models viz. DTCWT, DTCWT+PCA, DTCWT+PSO, DWT+PCA+PSO and tested with four different independent classifiers viz. Naive Bayes (NB), Decision Tree (DT),SVM, and k-NN for performance evaluation. The model DWT+PCA+PSO gives maximum result with k-NN classifier as 89.2% accuracy,91.1% sensitivity and 87.1% specificity. The performance of models DWT and DWT+PCA is also evaluated. These models reported very low accuracy. On applying DTCWT results get improved as DTCWT extracts features in six different directions. DTCWT also provides

Authorized licensed use limited to: DELHI TECHNICAL UNIV. Downloaded on January 17,2023 at 05:01:02 UTC from IEEE Xplore. Restrictions apply.

real and imaginary coefficients which provide average and structural information of image respectively. The model DTCWT with k-NN classifier gives 72.4% accuracy which is quite low. This model suffers from high dimensionality as number of features is 24576 which is quite high for classification. As a solution to this problem, PCA is used to reduce the feature dimensions. On applying PCA with DTCWT, results become better. The drawback of PCA is that it causes spatial loss of information. The model DTCWT+PCA provides 90.8 % accuracy. It is observed that the addition of feature selection stage viz. PSO in model DTCWT+PCA further improves the results. The proposed model DTCWT+PCA+PSO yields 95.5% accuracy, 97.6% sensitivity and 93.4% specificity. The performance of model DTCWT+PSO is also evaluated. This model provides an accuracy of 92.9%. This model needs high computation time subjecting to the low convergence speed of PSO due to high dimensional dataset [22]. Table I indicates the performance of different models on OASIS dataset.

TABLE I: PERFORMANCE COMPARISON OF DIFFERENT MODELS WITH PROPOSED METHOD

Method	Classifier	Acc	Sen	Spec
DWT+ PCA+ PSO	NB	83.1	88.4	77.7
	DT	83.2	80.6	85.9
	SVM	87.4	88.5	86.4
	KNN	89.2	91.1	87.1
DTCWT +PCA+ PSO	NB	87.8	86.4	89.2
	DT	87.4	90.3	84.5
	SVM	87.9	90.1	85.8
	KNN	95.5	97.6	93.4

Method	Classifier	Acc	Sen	Spec
DTCWT	KNN	72.4	82.9	62.2
DTCWT+PCA	KNN	90.8	92.5	89.03
DTCWT+PSO	KNN	92.9	95.1	90.9
DTCWT+PCA+PSO (Proposed)	KNN	95.5	97.6	93.4

TABLE II: COMPARATIVE ANALYSIS FOR PROPOSED AND EXISTING ALGORITHMS

Algorithms	Features	Dataset	Accuracy (%) [19]	Sensitivity (%) [19][20][21]	Specificity (%) [19] [20]
DTCWT+PCA+PSO+KNN [Proposed]	5th level detail coefficients	OASIS	95.5	97.6	93.4
Shearlet + KNN [23]	Entropy	OASIS	94.1	95.3	93.4
DTCWT+TSVM [24]	Entropy, Variance	OASIS	92	93	94
DTCWT+RCWF+FNN [25]	Energy, standard deviation, entropy	OASIS	90.7	91.2	92.4

The comparison between the proposed method and three existing methods [23-25] has been listed in Table II. The existing methods are implemented on MATLAB 2019 with the same dataset used for proposed work. The result of proposed method outperforms the existing algorithms. Acharya et al. [23] used shearlet transform to obtain Entropy features from different parts of the brain. On implementation, this method yielded 94.1% accuracy, 95.3% sensitivity and 93.4% specificity. Wang et al. [24] applied DTCWT for extracting features based on Entropy and Variance. On implementation, this method yielded 92% accuracy, 93% sensitivity, and 94% specificity with OASIS dataset. Recent study [25] extracted Energy and Entropy features by using DTCWT and Rotated Complex Wavelet Filter (RCWF). On implementation, this study yielded 90.7% accuracy,91.2% sensitivity and 92.4% specificity. Finally, the proposed method provided 95.5% classification accuracy, 97.6% sensitivity and 93.4% specificity with k-NN classifier. The proposed method provides high accuracy with promising performance measures of sensitivity and specificity. This shows the efficacy of proposed method over other existing algorithms. The Receiver Operating Characteristic (ROC) curve of proposed and existing algorithms is shown in Fig. 6.

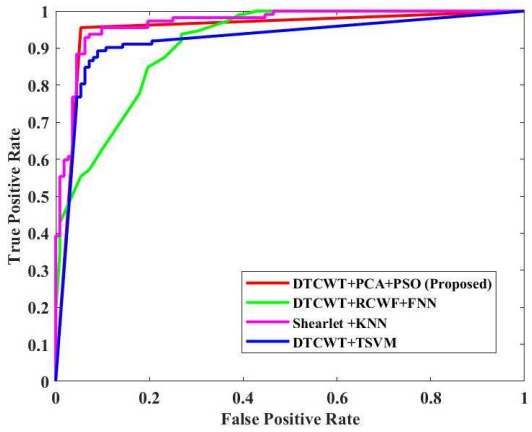

Fig. 6. ROC curve for proposed and existing algorithms

Authorized licensed use limited to: DELHI TECHNICAL UNIV. Downloaded on January 17,2023 at 05:01:02 UTC from IEEE Xplore. Restrictions apply.

IV. Conclusion

This paper introduces an accurate technique for AD/NC classification. Experiments performed indicate that the combination of DTCWT with PCA and PSO gives more auspicious results in comparison to the existing methods. The proposed method provides 95.5% accuracy,97.6% sensitivity, and 93.4% specificity. The future research will be focused on (i)implementation with other variants of wavelets viz.3-D DTCWT and fractional calculus (ii) using other modalities viz. Positron Emission Tomography (iii) implementation with other dimensionality reduction methods viz. probabilistic PCA, Independent Component Analysis (iv) enhancement of the image pre-processing step by applying image enhancement, image denoising, and image segmentation to improve the classification performance.

Acknowledgement

I express my sincere gratitude to my supervisors and Electronics and Communication Engineering Department, Delhi Technological University, Delhi for their valuable support.

References

[1] Tatulian, Suren A. "Challenges and hopes for Alzheimer's disease." *Drug discovery today* vol. 27,4 (2022): 1027-1043. doi: 10.1016/j.drudis.2022.01.016.

[2] Ossenkoppele R, van der Kant R, and Hansson O "Tau biomarkers in Alzheimer's disease: towards implementation in clinical practice and trials." *The Lancet. Neurology* vol. 21,8 (2022): 726-734. doi:10.1016/S1474-4422(22)00168-5

[3] Knudsen LV, Gazerani P, Duan Y, Michel TM, and Vafaee MS "The role of multimodal MRI in mild cognitive impairment and Alzheimer's disease." *Journal of neuroimaging: official journal of the American Society of Neuroimaging* vol. 32,1 (2022): 148-157. doi:10.1111/jon.12940

[4] Ávila-Villanueva M, Marcos Dolado A, Gómez-Ramírez J, and Fernández-Blázquez M "Brain Structural and Functional Changes in Cognitive Impairment Due to Alzheimer's Disease." *Frontiers in psychology* vol. 13 886619. 21 Jun. 2022, doi:10.3389/fpsyg.2022.886619

[5] J. Liu, M. Li, W. Lan, F. Wu, Y. Pan and J. Wang, "Classification of Alzheimer's Disease Using Whole Brain Hierarchical Network," in *IEEE/ACM Transactions on Computational Biology and Bioinformatics*, vol. 15, no. 2, pp. 624-632, 1 March-April 2018, doi: 10.1109/TCBB.2016.2635144.

[6] S. Chaplot, L. M. Patnaik, and N. R. Jagannathan, "Classification of magnetic resonance brain images using wavelets as input to support vector machine and neural network," Biomedical Signal Processing and Control, vol. 1, no. 1, pp. 86–92, 2006.

[7] Jha, J.-I. Kim, and G.-R. Kwon, "Diagnosis of alzheimers disease using dual-tree complex wavelet transform, pca, and feed-forward neural network," Journal of Healthcare Engineering, vol. 2017, (2017) https://doi.org/10.1155/2017/9060124.

[8] Alam S, Kwon GR, Kim JI, and Park CS "Twin SVM-Based Classification of Alzheimer's Disease Using Complex Dual-Tree Wavelet Principal Coefficients and LDA." Journal of healthcare engineering vol. 2017 (2017): 8750506. doi:10.1155/2017/8750506

[9] Jha, Debesh et al. "Alzheimer's Disease Detection Using Extreme Learning Machine, Complex Dual Tree Wavelet Principal Coefficients and Linear Discriminant Analysis." *Journal of Medical Imaging and Health Informatics* 8 (2018): 881-890.

[10] Ardekani BA, Figarsky K, Sidtis JJ (2013) Sexual dimorphism in the human corpus callosum: An MRI study 747 using the OASIS brain database. Cereb Cortex 23, 2514-2520.

[11] Ng, E.Y.K.; Jamil, M. Parametric sensitivity analysis of radiofrequency ablation with efficient experimental design. Int. J. Thermal Sci. 2014, 80, 41–47.

[12] Shensa, Mark J. "The discrete wavelet transform: wedding the a trous and Mallat algorithms." *IEEE Transactions on signal processing* 40.10 (1992): 2464-2482.

[13] I.W. Selesnick, R.G. Baraniuk, N.C. Kingsbury, The dual-tree complex wavelet transform, IEEE Signal Process. Mag. 22 (6) (2005) 123–151.

[14] Abdi, Hervé, and Lynne J. Williams. "Principal component analysis." *Wiley interdisciplinary reviews: computational statistics* 2.4 (2010): 433-459.

[15] Kamani, M. M., Haddadpour, F., Forsati, R., and Mahdavi, M. (2022). "Efficient fair principal component analysis." *Machine Learning*, 1-32.

[16] Poli, Riccardo, James Kennedy, and Tim Blackwell. "Particle swarm optimization." *Swarm intelligence* 1.1 (2007): 33-57.

[17] Piotrowski, Adam P., Jaroslaw J. Napiorkowski, and Agnieszka E. Piotrowska. "Population size in particle swarm optimization." *Swarm and Evolutionary Computation* 58 (2020): 100718.

[18] Gu, Qinghua, et al. "An improved competitive particle swarm optimization for many-objective optimization problems." *Expert Systems with Applications* 189 (2022): 116118.

[19] Trevethan R. Sensitivity, Specificity, and Predictive Values: Foundations, Pliabilities, and Pitfalls in Research and Practice. Front Public Health. 2017 Nov 20;5:307. doi: 10.3389/fpubh.2017.00307.

[20] Abdul Ghaaliq Lalkhen, MB ChB FRCA, Anthony McCluskey, BSc MB ChB FRCA, Clinical tests: sensitivity and specificity, Continuing Education in Anaesthesia Critical Care & Pain, Volume 8, Issue 6, December 2008, Pages 221–223, https://doi.org/10.1093/bjaceaccp/mkn041

[21] Parikh R,Mathai A,Parikh S,Chandra Sekhar G,Thomas R, Understanding and using sensitivity, specificity and predictive values. Indian journal of ophthalmology. 2008 Jan-Fe

[22] Gad, A.G. Particle Swarm Optimization Algorithm and Its Applications: A Systematic Review. Arch Computat Methods Eng 29, 2531–2561 (2022). https://doi.org/10.1007/s11831-021-09694-4

[23] Acharya, U Rajendra et al. "Automated Detection of Alzheimer's Disease Using Brain MRI Images- A Study with Various Feature Extraction Techniques." *Journal of medical systems* vol. 43,9 302. 9 Aug. 2019, doi:10.1007/s10916-019-1428-9

[24] Wang, Shuihua, et al. "Dual-tree complex wavelet transform and twin support vector machine for pathological brain detection." *Applied Sciences* 6.6 (2016): 169.

[25] Topannavar, Preeti S. "Rotational Wavelet Filters for Analysis of Brain MRI in Detection of Alzheimer's Disease" Vol. 12 No. 6 (2021), https://doi.org/10.17762/turcomat.v12i6.5789

Authorized licensed use limited to: DELHI TECHNICAL UNIV. Downloaded on January 17,2023 at 05:01:02 UTC from IEEE Xplore. Restrictions apply.

Proc. of the International Conference on Electrical, Computer, Communications and Mechatronics Engineering (ICECCME)
16-18 November 2022, Maldives

2022 International Conference on Electrical, Computer, Communications and Mechatronics Engineering (ICECCME) | 978-1-6654-7095-7/22/$31.00 ©2022 IEEE | DOI: 10.1109/ICECCME55909.2022.9987808

An Interpretable Network to Thermal Images for Breast Cancer Detection

Kamakshi Rautela
Department of Electronics and Communication Engineering
Delhi Technological University
Delhi, India
Kamakshi_2k19phdec06@dtu.ac.in

Dinesh Kumar
Department of Electronics and Communication Engineering
Delhi Technological University
Delhi, India
dineshkumar@dtu.ac.in

Vijay Kumar
Department of Computer Science Engineering
National Institute of Technology
Hamirpur, India
vijaykumarchahar@nith.ac.in

***Abstract*—Medical images have substantially greater resolutions and narrower areas of interest than natural images. Neural network designs that perform well for natural images may not be relevant to medical image processing due to these differences. A new approach for detecting breast cancer based on thermal imaging is adopted in this work. To select the most informative areas, our model first applies a memory-efficient network to the entire image. It then uses a relatively deep CNN to collect information from certain locations from thermal image dataset. We used transfer learning for training, 80% of the data from both the datasets are used to train the model and rest 20% is used to test. With a learning rate of 0.01 and a batch size of 50, the network was trained over 100 epochs. Presently, the model has a 92.52% accuracy rate.**

Keywords—Breast cancer detection, CNN, Medical Images, ResNet, Thermography

I. INTRODUCTION

Breast cancer is one of the most often reported cancers across the world. According to the World Health Organization, the number of novel breast cancer cases has reached 2 million. (representing approximately 24.5% of all new cancer cases) [1]. It has been recorded in both males and females, although its prevalence in females is considerably greater. So, the development of a breast cancer imaging tool is essential for early diagnosis and treatment of breast cancer. According to National Centre for Disease Informatics and Research (NCDIR) National cancer registry program, the estimated breast cancer cases and mortality in females in India [2]. Fig 1 shows the cancer data statistic 2020 for India. According to data given by NCDIR, breast cancer is among top 5 cancer cases.

It's difficult to develop a screening approach that uses a medical imaging modality that is non-invasive and does not require physical contact. Following detection by imaging exams such as clinical-breast examination (CBE) and breast self-examination (BSE), early therapy may be advantageous. CBE is a routine medical examination undertaken by healthcare experts to detect breast lesions, whereas BSE is a self-conducted physical examination of the breasts to examine physical changes and appearance. The practice of BSE encourages women to take charge of their own health. As a result, the World Health Organization recommends using BSE

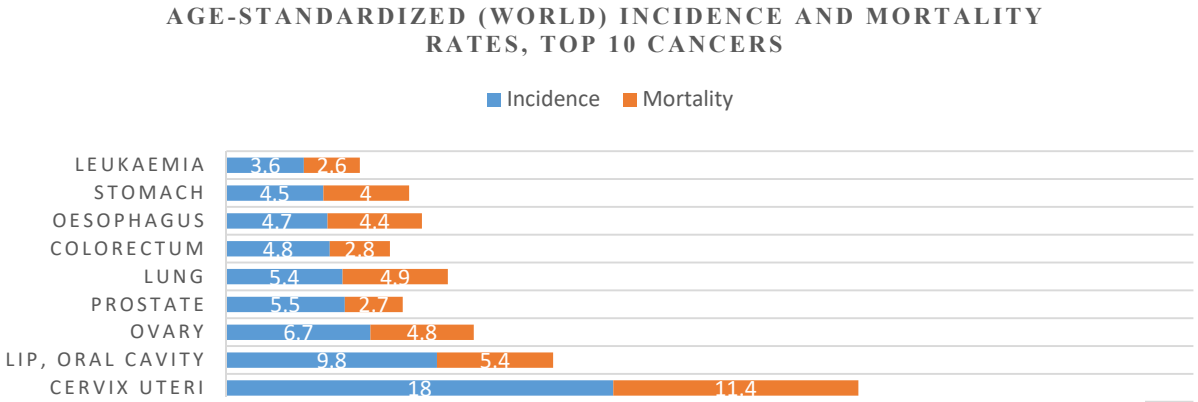

Fig. 1. Top 10 cancer cases found in India during 2020

978-1-6654-7095-7/22/$31.00 ©2022 IEEE

Authorized licensed use limited to: DELHI TECHNICAL UNIV. Downloaded on January 05,2023 at 06:28:43 UTC from IEEE Xplore. Restrictions apply.

to raise awareness among at-risk women [3]. Fig. 2 shows detection of breast cancer in asymptotic women. Awareness of breast cancer provides essential information that can assist people in making better healthcare decisions.

Breast medical images are produced via screening procedures. Human specialists, such as radiologists and physicians, are usually in charge of interpreting these pictures. Only a few research has used the deep neural network (DNN) method to provide noninvasive thermal imaging of breasts [4]. The study on this topic is still in its early phases, given the existing restricted resources. As a result, substantial work is necessary to create reliable non-invasive computer-assisted technologies for early breast cancer diagnosis. The low diagnostic accuracy of thermograms has been linked to a lack of technical competence and knowledge in analyzing such pictures, according to research. As a result, a network that can automatically classify thermograms into normal and abnormal categories is required. In light of this need, research into computer-based methods for classifying medical pictures has been steadily increasing.

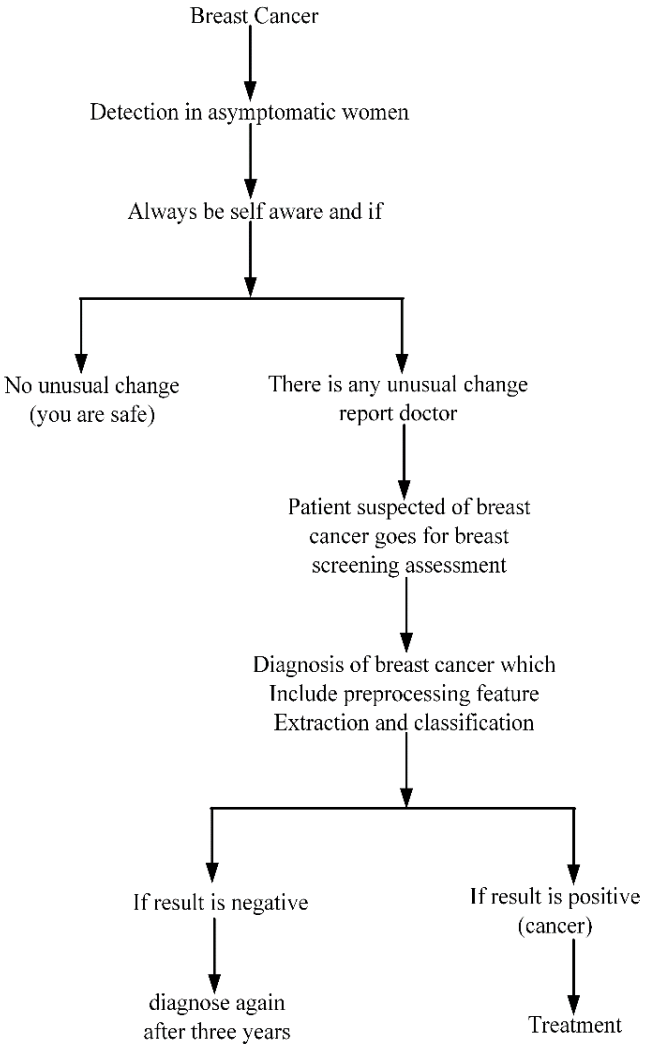

Fig. 2. Detection of breast cancer in asymptotic females

Diagnostic systems that use an infrared camera and deep convolutional neural networks help to enhance diagnostic accuracy and consistency [5]. The capability of a Convolutional Neural Network (CNN) may be utilized to extract attributes and help in the classification of benign and malignant lesions in medical images.

While looking at the research in the literature, it's clear that different classification and feature extraction methods are utilized for diagnosis of breast cancer. In a 2015 study, Aura Conci et al. [6] used the KNN (K-Nearest Neighbors) algorithm as a classifier. the diagnosis of breast cancer using thermography was accomplished utilizing statical representations as features. To enhance the dependability of performance, future research should evaluate other categorization methods, such as NN and SVM had similar findings. Madhavi et al [7] used URLBP and KPCA methods to extract features from thermal breast images for the diagnosis of breast cancer. These feature vectors were used to train the SVM.

Shahari et al. [8] investigated a successful image segmentation method based on color properties of pictures utilizing the K-means clustering methodology. They also advised using the Fuzzy C-Means and Level Set methods to improve the proposed strategy and get better outcomes.

Obtaining a database that can be investigated is one of the most essential aspects of the research. The majority of the investigations in the literature used thermal imaging obtained from local hospitals [9]. The Database for Mastology Research dataset commonly known as DMR produced by researcher at University of Federal Fluminense was found to provide the required parameters for this study as a result of the research [10] [11].

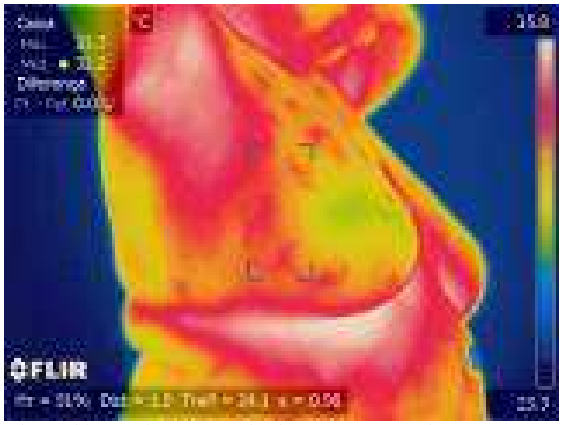

Fig. 3. Thermal image from DMR database as an example

Detection of breast cancer was carried out in this study using a gabor filter and a Convolutional Neural Network (CNN). The process in this paper are detailed in the methodology section.

II. METHODOLOGY

The major goal of this implementation is to identify breast cancer using thermal pictures. To do so, we created a deep

Authorized licensed use limited to: DELHI TECHNICAL UNIV. Downloaded on January 05,2023 at 06:28:43 UTC from IEEE Xplore. Restrictions apply.

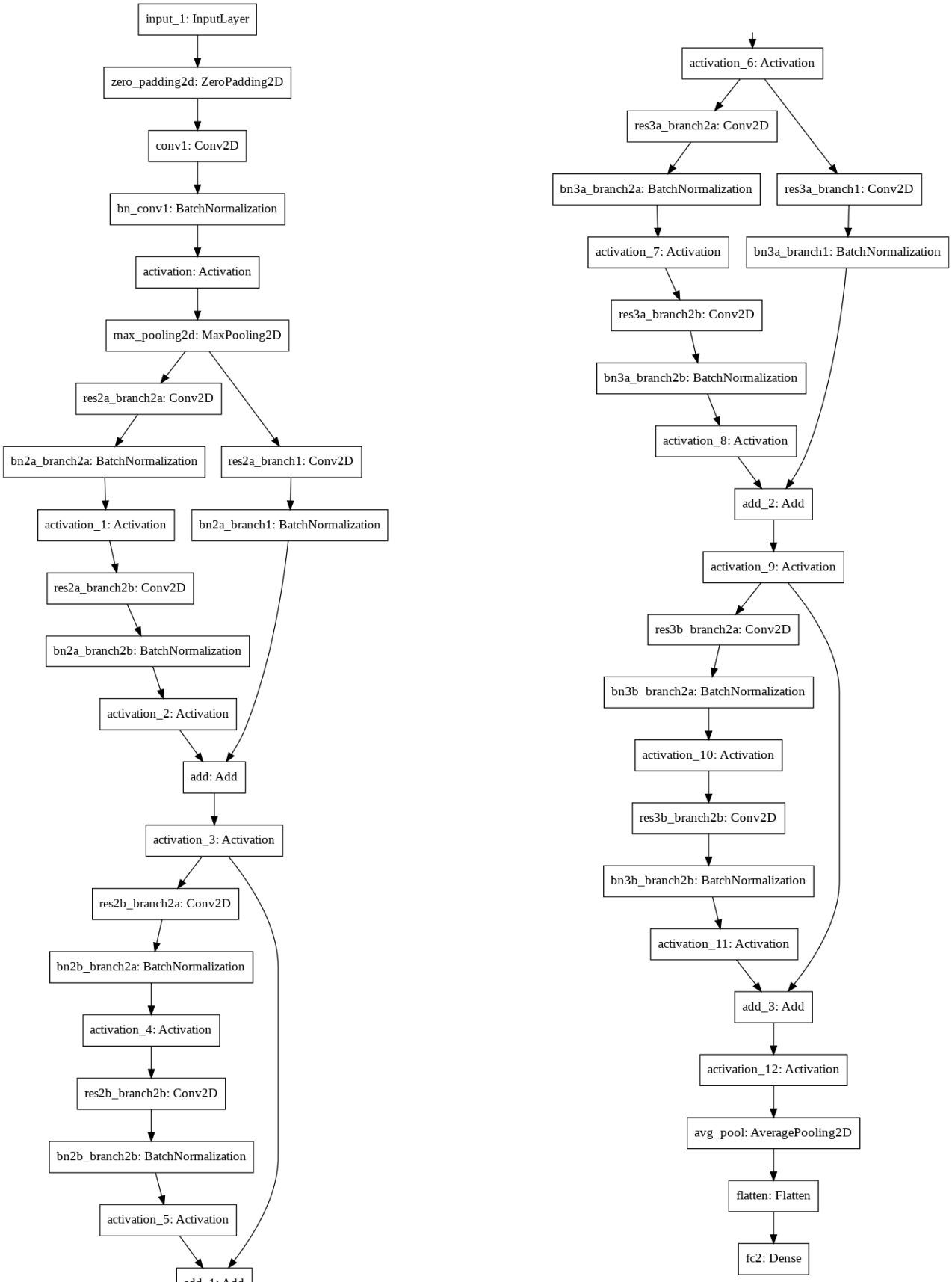

Fig. 4. Network architectures for Resnet18

Authorized licensed use limited to: DELHI TECHNICAL UNIV. Downloaded on January 05,2023 at 06:28:43 UTC from IEEE Xplore. Restrictions apply.

learning model that can extract characteristics from a given dataset, moreover can also provide on the go prediction. To achieve optimal output, images from the dataset are pre-processed. To process the raw thermal images, we used contrasting, resizing, equalization, and cutting. To enhance training data, we rotated and reversed the thermal images in the augmentation. When a large quantity of data needed to be taught with a Graphical Processing Unit, Deep Learning was used. It was utilized in feature extraction because it allowed for a greater number of epochs and iterations during the training of deep CNN like ResNet 18.

Fig. 4. shows the network architecture for ResNet 18 created for the proposed work. In ResNet 18, a parameter layer contains 4 sub layers. The Convolutional Neural Network (CNN) is the first layer, and it is in charge of identifying the form and size of the impacted region. Batch normalization is the second layer (BN). BN is in charge of normalizing picture quality in order to obtain the most optimal weights. Max pool is the third tier. Rectified Linear Unit is the final layer, it serves as an activation function as well as an update function for bias and weights.

The result will be sent to the following parameter layer with the starting inputs after each parameter layer computation, and the cycle will continue until the last parameter layer.

III. Description of Datasets

DMR- The work is carried out with a FLIR SC-620 IR sensor, having dimensions of 640 x 480 pixels, from the Database for Mastology Research (DMR). DMR includes the thermogram as well as mammogram images in jpeg format from frontal images [15]. It consists of images of 287 patients ageing between 29 to 85.

IV. Results

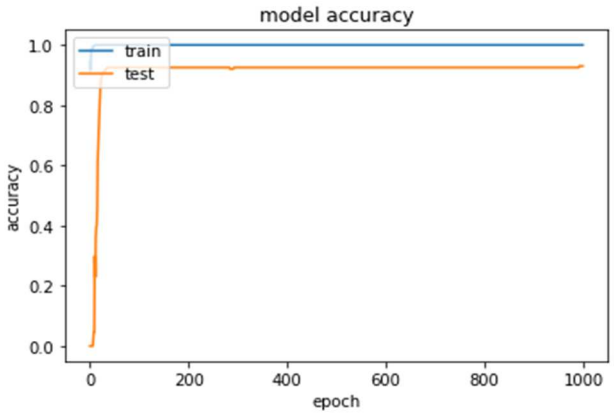

Fig. 5. Model accuracy with proposed ResNet 18.

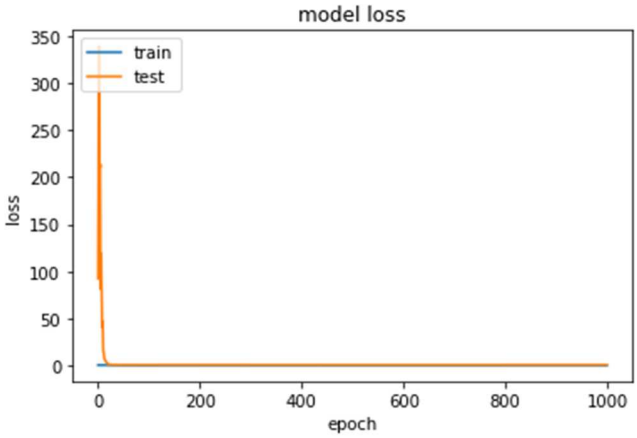

Fig. 6. Model loss for ResNet 18

Trials were performed using the DMR-IR dataset of breast thermography. In addition, the dataset was configured to 80% training and 20% testing. Fig. 5 displays the output accuracy of the model with ResNet 18.

Fig. 6. displays the output loss of the model with ResNet 18. From the graphs above we can clearly see that the loss at last epoch is minimum and test accuracy using proposed model is 92.52%. Table 1 compares the best results achieved from experimental investigations using various Deep Neural Networks for Breast Cancer Detection using Thermography. Proposed ResNet18 is the most effective network in fixing this issue, according to Table 1.

TABLE I.
EXAMINATION OF THE ACCURACY OF 4 DISTINCT DEEP NEURAL NETWORKS FOR DETECTION OF BREAST CANCER FROM THERMAL IMAGING.

Experimental Results			
Ref.	***No. of Images***	***Feature Extraction***	***Test Acc***
[7]	16	URLBP,KPCA	86%
[12]	22	pixel avg.	90.9%
[9]	144	CNN	88.89%
Proposed	**144**	**CNN**	**92.52%**

V. Conclusion

A deep neural network was used to identify breast cancer using thermographic images in this work. A highest accuracy of 92.52% is obtained from the tests. The network discovered a cancer feature that allowed it to detect breast cancer in real - time basis. The model was created with a light-weight design, allowing the entire architecture to be saved on a mobile device. This made such a solution more accessible to the general population.

In future research, it will be attempted to improve the overall system performance by increasing the amount of pictures utilized in the network's training and by experimenting with alternative segmentation techniques.

References

Authorized licensed use limited to: DELHI TECHNICAL UNIV. Downloaded on January 05,2023 at 06:28:43 UTC from IEEE Xplore. Restrictions apply.

1. Union for International Cancer Control's - International Agency for Research on Cancer WHO. https://www.uicc.org/news/globocan2020-new-global-cancer-data. [Online; accessed 1-March-2020].
2. National Cancer Registry Programme, "Report of population based cancer registries 2020 national cancer registry programme.," National Centre for Disease Informatics and Research. and Indian Council of Medical Research. https://www.ncdirindia.org/Reports.aspx.
3. W. H. Organization, "Breast cancer: prevention and control," 2019.
4. Roslidar, R., Rahman, A., Muharar, R., Syahputra, M.R., Arnia, F., Syukri, M., Pradhan, B. and Munadi, K., 2020. A review on recent progress in thermal imaging and deep learning approaches for breast cancer detection. IEEE Access, 8, pp.116176-116194.
5. M. Alkhaleefah and C. C. Wu, "A Hybrid CNN and RBF-Based SVM Approach for Breast Cancer Classification in Mammograms," in Proceedings - 2018 IEEE International Conference on Systems, Man, and Cybernetics, SMC 2018, Jan. 2019, pp. 894–899, doi: 10.1109/SMC.2018.00159.
6. Tatiana M. Mejía, Maria G. Pérez, Víctor H. Andaluz, Aura Conci, "Automatic Segmentation and Analysis of Thermograms Using Texture Descriptors for Breast Cancer Detection", 2015 Asia-Pacific Conference on Computer Aided System Engineering, pp. 24 - 29, 2015.
7. Vijaya Madhavi, Christy Bobby, "Assessment of Dynamic Infrared Images for Breast Cancer Screening using BEMD and URLBP", International Journal of Pure and Applied Mathematics, Volume:114, No.10, pp. 261 - 269, 2017.
8. Sheetal Shahari, Asmita Wakankar, "Color anaysis of thermograms for breast cancer detection", 2015 International Conference on Industrial Instrumentation and Control (ICIC), pp. 1577 - 1581, 2015
9. Kiymet, S., Aslankaya, M.Y., Taskiran, M. and Bolat, B., 2019. Breast Cancer Detection From Thermography Based on Deep Neural Networks. In 2019 Innovations in Intelligent Systems and Applications Conference (ASYU) (pp. 1-5). IEEE.
10. "Banco de Imagens mastológicas - Visual Lab." [Online]. Available: http://visual.ic.uff.br/dmi/. [Accessed: 07-Jul-2019].
11. L. F. Silva, D. C. M. Saade, G. O. Sequeiros, A. C. Silva, A. C. Paiva, R. S. Bravo, A. Conci, "A New Database for Breast Research with Infrared Image", Journal of Medical Imaging and Health Informatics, Volume 4(1), pp. 92-100(9), March 2014.
12. L. F. Silva, G. O. Sequeiros, M.L.O Santos, C.A. Fontes, D. C. Muchaluat-Saade, A. Conci,"Thermal Signal Analysis for Breast Cancer Risk Verification", In MedInfo, pp. 746-750, 2015.

Authorized licensed use limited to: DELHI TECHNICAL UNIV. Downloaded on January 05,2023 at 06:28:43 UTC from IEEE Xplore. Restrictions apply.

EasyChair Preprint

№ 9628

Analysis of Personalized Tourism Recommender Systems

Dipit Sharma, Eklavya Banwala, Imane Elouaghzani and Rahul Katarya

EasyChair preprints are intended for rapid dissemination of research results and are integrated with the rest of EasyChair.

January 27, 2023

Analysis of Personalized tourism recommender systems

Dipit Sharma
Department of Computer Science and Engineering
ds.techin@gmail.com
Delhi Technological University
Delhi, India

Eklavya
Department Of Computer Science and Engineering
eklavyab3@gmail.com
Delhi Technological University
Delhi, India

Imane Elouaghzani
Department of Computer Science and Engineering
imanecodeblack@gmail.com
Delhi Technological University
Delhi, India

Rahul Katarya
Department of Computer Science and Engineering
rahuldtu@gmail.com
Delhi Technological University
Delhi, India

***Abstract*— Traveling is one of the most important leisure pursuits in life. While on vacation from one's regular routine, one experiences a new culture, new food, and new sights. As a result, recommending tourist destinations based on the user's interests may enable an individual to have incredible new experiences. Currently, different types of recommendation systems are used in the industry. Our primary goal is to compare all of the methods and determine which one is the best recommendation system for tourism. In this paper, we investigated various recommendation system methods used in tourist recommendation systems. The goal of this research is to identify all of the recommendation systems used in the industry. We tested which method would be the best for tourism recommendation by implementing them on a common dataset. Since content-based is item-based and collaborative filtering is user-based, these two alone are insufficient to produce an accurate result; therefore, a deep learning model is required in addition to these two. According to the parameters and factors considered for tourism, we discovered that the hybrid is the best option. Additionally, no recommendation system considered personality as a factor, so we are currently developing a recommendation system that does.**

***Index Terms*— Collaborative Filtering, Content Filtering, Cosine Similarity, Hybrid Method, TF-IDF Equation**

I. INTRODUCTION

In 2021-22, the total number of domestic visitors recorded a 98% year-on-year growth [1]. In order to find the best method to recommend tourist destinations for a user, we must find out about the likes and dislikes of the user. In Section 2 we will discuss what methods and mathematical formulae are used for creating recommendation systems - mainly TF-IDF and Cosine Similarity methods. Then in Section 3, we jump into discussing 3 main types of filtering methods. We have mentioned their work with dataset examples, advantages, and disadvantages. Fig. 1 represents the basic functioning of any production-level recommendation system. In Section 4, we finally talk about the conclusion and future work, we talk about how we plan to remove the current inefficiencies and try to implement a completely new method of recommendation system. But first, let's highlight the factors that each visitor should consider while arranging a trip. There are different types of people with different resources and personal characteristics. So we discuss the important aspects, such as budget, destination economy, weather, religious or cultural importance, tourist personality, number of people traveling, etc [2]. These influencing factors are collected from a variety of research publications, studies, and surveys. There are all varieties of personalities represented: upper-class, middle-class, disabled, and so on [3].

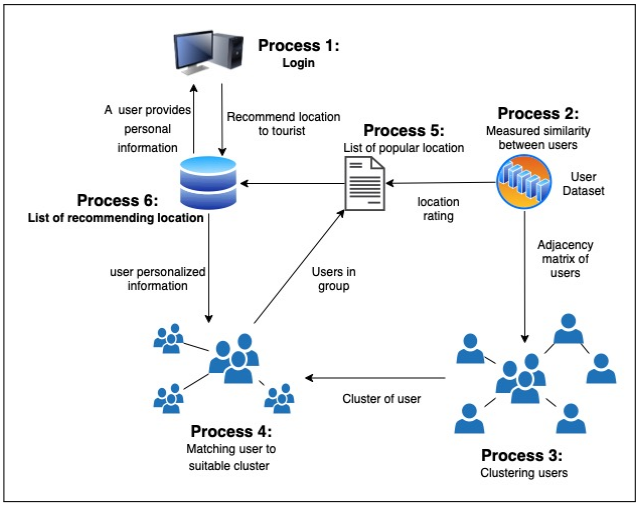

Fig. 1. Working flow of a tourist recommender system

A. Types Of Tourism

These are the following types of tourism, as briefed in Fig. 1.

1) Domestic Tourism: In this sort of tourism, travelers visit different parts of the same country. It is inexpensive

and knowing more about his or her country. For example, many Delhi residents vacation in Manali.

2) Health and Wellness Tourism: This type of tourism aids in the recovery of travelers from psychological and physical stress. It is an essential type of tourism. This usually entails places that are tranquil and near nature. India is an excellent demonstration of medical tourism since the physicians are well-qualified and speak English, and the treatment is also less costly.

3) Dark Tourism: Some areas of the country have passed through dark and tough periods. Travelers visit to learn about the incidents and their historical importance. For example, Jallian Wallan Bagh is well-known for the genocide committed during colonial rule.

4) Countryside Tourism: People would like to travel to remote regions to witness traditional and old-fashioned lifestyles. Solo tourists are the most likely to do this. Chokhi Dhani in Jaipur, for example, provides a taste of real Indian Rajasthani culture.

5) Business tourism: This is mostly a business trip. for example, import/export, employment, and inspection reasons, among others.

6) Educational tourism: This sort of tourism entails traveling with the intention of learning and studying new things. This is mostly for students and researchers.

B. Factors Depending On Tourist

These are the factors that change from traveler to traveler[5], as briefed in fig. 2.

1) Physical Accessibility: This refers to the physical amenities that are available at a location. This is only for travelers with disabilities. This facility most likely provides more than you realize. These amenities can help older persons become more self-sufficient.

2) Convenience: It refers to overcrowded food courts and a lack of basic essentials, which can make users feel disadvantaged. However, customers who do not require luxury but low-budget services might make advantage of these establishments. As a result, it is dependent on the user's preferences.

3) Security: Females and families traveling with infants may be more apprehensive about male users.

4) Peer Knowledge: Peers' or coworkers' recommendations may influence one's decision to visit a certain location. In general, individuals prefer to visit sites that have previously been visited by their peers and have gotten positive feedback.

5) Service: It includes the services offered during the journey. Hotel, transportation, tour guides, and other services may be provided.

C. Factors Depending On Location

These are the factors that change from location to location [6], as briefed in fig. 2.

1) Natural attractions: Climates, natural landscapes, beaches, and so forth. These criteria can be utilized to match the user's travel preferences.

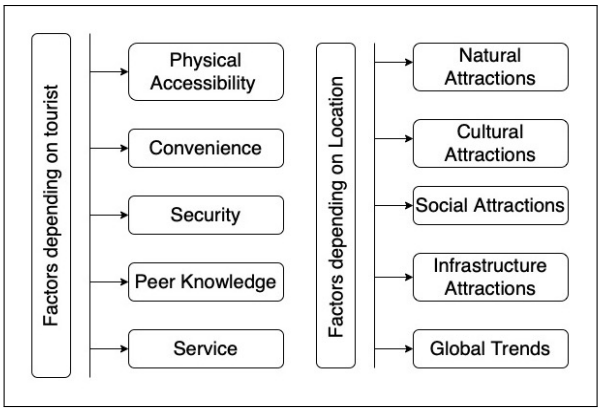

Fig. 2. Different parameters depending on tourists and locations

2) Cultural attractions: This represents the destination's culture. includes food, rituals, clothing, and so forth.

3) Social attractions: This consists of a location's hospitality as well as a welcoming population.

4) Infrastructure attractions: It focuses on luxury hotels, city lights, and breathtaking views. Essentially, the city's contemporary attractions and social life

5) Global Trends: Economic (low pricing), political (safe destination), environmental (environmental protection measures), demographic (health and leisure amenities), and technical aspects are all considered (internet connectivity).

II. RELATED WORKS

For related works, please refer to Table 1. In the table, we have discussed different papers that describe several recommendation methods for tourism. We have listed the inefficiency or scope of improvement in the respective techniques used. The main disadvantage was the methods were not personalized for a person. They are pretty general, for example, luxury, and high/low budgets are relative terms. They cannot be the same for every user. We need to take the status of the user in the account. The "status" means financial, health, emotional, etc.

The disadvantages can be summarised as follows:

- **limited dataset** - in the papers we considered the dataset used is not sufficient for consistent results, the data is neither generalized nor elaborate
- **subjective criteria for calculation** - the criteria used for the calculation of data in the dataset present is subjective to an individual user and not valid for a variety of people
- **factors** - the dataset also has a lack of factors taken into account that can influence a tourist
- **sentimental analysis** - none of the papers considered the personality of the users, which has a major contribution to the decision-making of any human

TABLE I

A SYSTEMATIC REPRESENTATION OF CURRENT WORKS AND THEIR SHORTCOMINGS

Author	Methods/Approaches Used	Limitations
Jinglei et al.[7] 2022	Based on Personalized Recommendation Algorithms (hybrid method based on social reviews)	Due to the limitations of research methods and research conditions, The variables selected in this study have not been fully considered, and the source of the questionnaire samples is relatively limited
Luis et al.[8] 2022	Based on User based Content Filtering and demographic information approach	the user's rating to tourist site does not exist.
Joseph et al.[9] 2021	context-based filtering	Images are classified into only two categories happy and sad while there can be meant emotions.
Praditya et al.[10] 2021	hybrid method	The sub-criteria used for data calculation is subjective as 50,000 Rp may be cheap for some but expensive for others.
Garipelly et al.[11] 2021	collaborative filtering	Fewer data and less accurate
Chiwong et. al.[12] 2020	Personalized travel planning system (PTPS)	Provides only recommendations based on other users and there is no cost or time estimates.
Z. Duan et. al.[13] 2020	The hybrid method used with deep learning	not pay attention to the efficiency of the OP orientation problem
Alnogaithan et. al.[14] 2019	input-output information recommendation technique, sentiment analysis, and rating review	Proposed tourism recommendation system for hotels based on user reviews, ratings, and sentiment. Limited to the local area and previous dataset
Ye J et. al.[15] 2019	Completely based on deep learning using social media data (LSTM)	The model includes only complement data and negative news which may affect the user influence.
Saputra et. al.[16] 2019	collecting tourist contextual data and making a database to support the recommendation system	Showed a correlation between user and tour data results and how condition change can affect decision-making for users.

III. TECHNIQUES USED IN TOURISM RECOMMENDATION SYSTEM

A. *TF-IDF Equation*

Similarities are calculated based on an overview of the place and location category. Vectors are constructed in order to create a similarity matrix, refer to Fig. 3 for example, it has few sentences with certain similarities. The cosine similarity of all vectors is then calculated[17]. So we considered a dataset that had 1000 destinations with their names, categories, and an overview of the location. So now, we've created a vector array using the TF-IDF Vectorizer. Here is a brief description of how the TF-IDF library works:

$$TD-IF = TF(t,d) * IDF(t) \tag{1}$$

In eq.(1), t is the number of times the term t appears in document d.

$$TF(t,d) = \sum_{x \in d} FR(x,t) \tag{2}$$

$$FR(x,t) = \begin{cases} 1 & \text{if } x = t \\ 0 & \text{if } otherwise \end{cases} \tag{3}$$

Here the TF(t,d) returns how many times the term t present in document d.

$$IDF(t) = \log \frac{|D|}{1 + |d : t \in d|} \tag{4}$$

In eq.(4)

$$|d : t \in d|$$

is the number of documents where the t term appears when the term frequency satisfies

$$TF(t,d) \neq 0$$

we are only adding 1 to the formula to avoid zero division.

In order to create the vector array we need to pass our data into the function (pseudo code): TF-IDF(dataset, name of the column). Here, the function takes in two arguments, the dataset is the main dataset that we have, and the name of the column is the name of the column in the dataset that we want the vector array to be based on.

B. *Cosine Similarity*

The cosine similarity method determines how similar two vectors are to one another. If the angle between them is less then vectors are similar and vice-versa. The equation for the cosine similarity between vector A and vector B is as follows:

$$S(A,B) = cos(\theta) = \frac{A.B}{|A|.|B|} \tag{5}$$

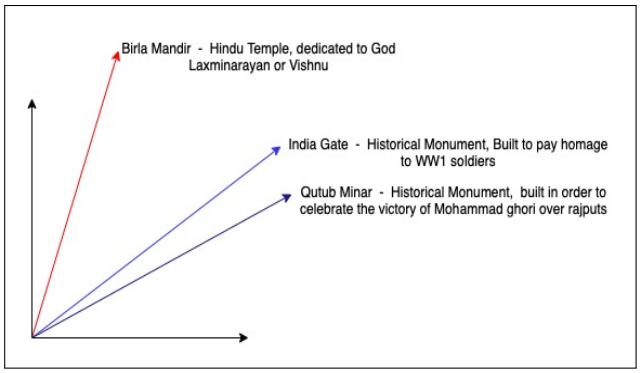

Fig. 3. Different sentences represented in the form of vectors

IV. DIFFERENT TYPE OF FILTERING METHODS

A. *Content-based recommendation system*

It is advised in content-based filtering to take into account the data provided about the item or the item's past history. The entire concept is built on the type of thing that the user loves or may enjoy. As a result, item-based matching. [18] . Consider a list of places and their respective classifications. To implement a content-based recommendation system, a vector matrix is built using TF-IDF formulas. Using vector points and cosine similarity methods, a similarity matrix is created as shown in Fig.4. In Fig.4, the blue regions among orange regions represent similar locations.

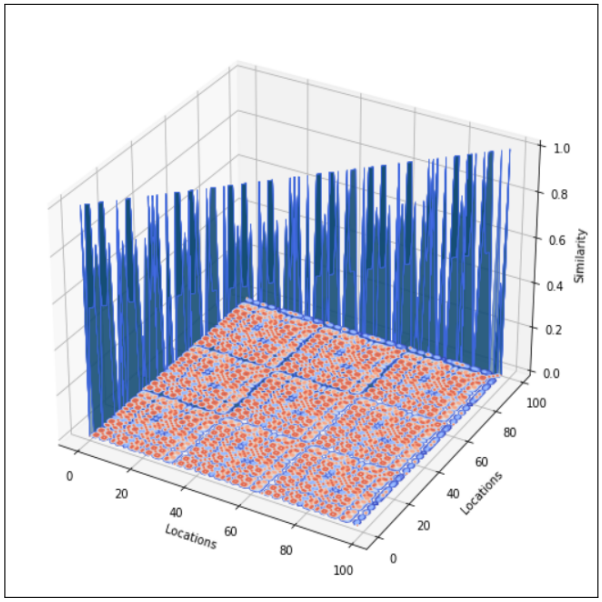

Fig. 4. Graph representing the similarity matrix among different locations

Advantages

- All the data is personalized to the user; they only get what they want. So anything that may not be of interest to them is not recommended.
- There is no need for any other user's data.

Disadvantages

TABLE II
LOCATIONS AND THEIR CATEGORY - A SAMPLE DATASET

Locations	Categories
Jaipur Zoo	Wildlife
K.V. Garden	Park
Anokhi Museum	Museum
Akshardham Temple	Pilgrimage
Albert Hall Museum	Museum
Hawa Mahal	Heritage
Birla Mandir	Pilgrimage
Nahargarh Fort	Heritage

- It is based on the actual interests of the users, and if those interests change or increase, it may expand accordingly.
- It will not be able to provide new items.

B. *Collaborative recommendation system*

This method of filter uses another similar user to recommend the content. Briefly, using the likes and dislikes of one user to filter content for another user is not restricted to one similar user; it can contain several users, perspectives, and data sources .

It has two types of inputs:

- **Implicit**: the system automatically recognizes the likes and dislikes of the user
- **Explicit**: The system needs input, whether the user likes the content or not.

So let's consider some data (table 2). Now, in collaborative filtering, we can process it in two ways:

- **1-D**: Creating a single line that indicates users' interest in the type of tourist location according to their age. Now if we get where user-4 (the new user) lies on this line, we can easily provide him with some relevant recommendations as shown in Fig. 5.

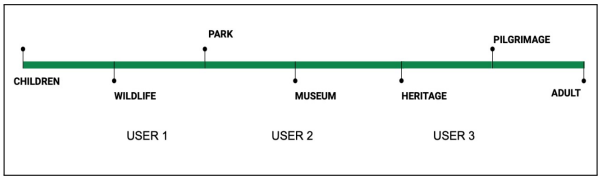

Fig. 5. 1-D Method of Of Categorizing Locations

- **2-D**: When one aspect of a location is insufficient for a recommendation, we integrate extra features, broadening the scope of our method. For example, we may include the range of the budget of the user for travel and tourism. We can map users as indicated in Fig. 6. We can determine a new user's area of interest and hence present him with better suggestions.

In its implementation, a user similarity matrix is created as depicted in Fig. 7, which is why this approach is known

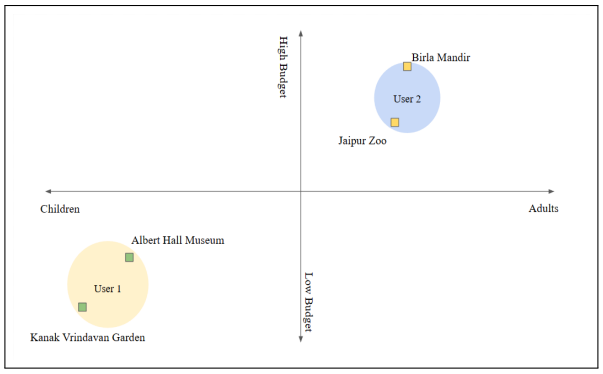

Fig. 6. 2-D Method of Of Categorizing Locations

as user-based filtering. The resemblance might be due to the user's employment, age, or other factors. [19].

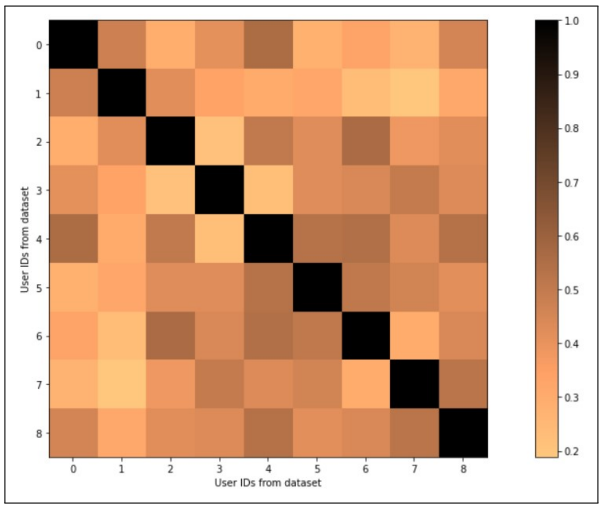

Fig. 7. Image of the similarity matrix among different users

Advantages

- It can recognize the likes and dislikes of users without requiring feedback.
- This model can present users with content that they may like and allow them to explore new content.
- It can be used by newly created systems with no existing data.

Disadvantages

- The prediction of the model for every given user-item combination is the dot product of the corresponding embedding. If an item isn't there during training, the system won't be able to generate a score for it. This is also known as the "cold start difficulty".
- Any characteristics that exist in addition to the query or item ID are referred to as side features. Country or age may be optional options for movie choices. Including usable features boosts the model's quality.

C. *Hybrid recommendation system*

Because one type of approach may not always yield correct results, we combine the two above methods to develop a new method known as the hybrid method. Deep learning is frequently used to improve the dynamic and accuracy of suggestions. [20].

If we understand it in the context of a tourist recommendation system, we will have factors like:

- Target Variable — Ratings can be explicit (i.e., the user leaves feedback) or implicit (i.e., assuming positive feedback if the user visits a location); either way, they are necessary.
- Product features —tags and descriptions of the items (i.e., location category), mostly used in the content-based methods.
- User Profile — Users' descriptive information can be demographic (such as gender and age) or behavioral (such as preferences, average time on screen, and most frequent time of usage).

We need a dataset for training and several data sets for testing because we are utilizing deep learning. Our dataset was separated into two parts: training and testing.

For the deep learning part, there are basically three primary layers: an input layer, a neural network layer, and an output layer. In Fig. 8 a sample layer model is depicted.

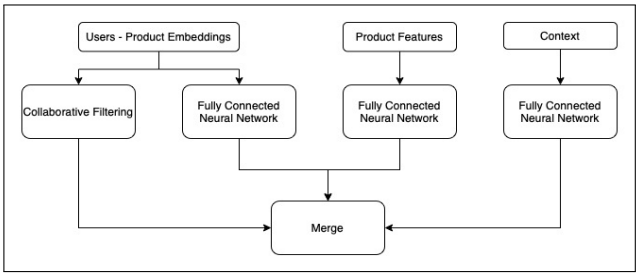

Fig. 8. A sample model for hybrid recommendation system

Advantages

- It covers all the limitations of content filtering and collaborative filtering

Disadvantages

- It has only the disadvantage that it is more difficult to implement than the other two methods.

V. Discussion

We analyzed multiple types of tourism and factors which take part in making recommendations. Moreover, we looked into various similarity detection techniques namely - the TF-IDF technique, which is based on finding creating vectors of the given sentences, and Cosine Similarity, which is basically used for creating a similarity matrix using dot products of the matrix. Then we listed various recommendation methods.

After studying different methods we tested all of them against a common dataset, and we deduced that content-based and collaborative filtering are good but do not fulfill personalized recommendation parameters. The content-based method involves item-item similarity and collaborative filtering involves user-user similarity, so

TABLE III

COMPARISON OF DIFFERENT METHODS ON THE BASIS OF PARAMETERS CONSIDERED

Method	Self Learning	No Dataset Required	User Based		
			Data Specific	Behaviour Specific	Personality Specific
Context-Based			✔		
Collaborative Filter	✔	✔		✔	
Hybrid Filter	✔	✔	✔	✔	

they each miss some parameters. The most appropriate is the hybrid method used with deep learning[21].

VI. CONCLUSION FUTURE WORK

In this paper, the techniques discussed have one or more drawbacks as depicted in Table 3. In order to overcome these drawbacks and integrate the best elements of both approaches, we need to create a hybrid recommendation system with a deep learning model which includes personal data. The fundamental goal of such hybridization is to increase rate prediction accuracy by overcoming the disadvantages of specific approaches when used independently.

In the future, we will introduce semantic analysis for each user along with existing data. Taking into account the preferences of multiple users with different personalities to create an evolved recommendation system.

REFERENCES

[1] A. Thananchana, K. Noinan and S. Wicha, "The Designing of Cultural-Based Tourism Recommendation System with Community Collaboration," 2022 Joint International Conference on Digital Arts, Media, and Technology with ECTI Northern Section Conference on Electrical, Electronics, Computer and Telecommunications Engineering (ECTI DAMT NCON), Chiang Rai, Thailand, 2022, pp. 510-513

[2] L. Febre, P. Valdiviezo-Diaz and R. Reátegui, "Collaborative Filtering Enhanced by Demographic Information for Tourist Sites Recommendations," 2022 17th Iberian Conference on Information Systems and Technologies (CISTI), Madrid, Spain, 2022, pp. 1-6

[3] L. Gang, "Personalized Recommendation of Tourist Attractions Based on Collaborative Filtering," 2020 13th International Conference on Intelligent Computation Technology and Automation (ICICTA), Xi'an, China, 2020, pp. 144-147

[4] M. L. Bai, R. Pamula and P. K. Jain, "Tourist Recommender System using Hybrid Filtering," 2019 4th International Conference on Information Systems and Computer Networks (ISCON), Mathura, India, 2019, pp. 746-749

[5] M. Li and J. Sasaki, "Recommendation Method for Attractive Destinations for Individual Tourists Using Profile Data," 2021 IEEE International Conference on Progress in Informatics and Computing (PIC), Shanghai, China, 2021, pp. 248-252

[6] M. Kamal and I. Chatzigiannakis, "Influential Factors for Tourist Profiling for Personalized Tourism Recommendation Systems– A Compact Survey," 2021 International Conference on Innovative Computing (ICIC), Lahore, Pakistan, 2021, pp. 1-6

[7] N. Chiwong and P. Rojanavasu, "Schedule Travel Planning System for Phayao Information Recommendation," 2020 Joint International Conference on Digital Arts, Media and Technology with ECTI Northern Section Conference on Electrical, Electronics, Computer and Telecommunications Engineering (ECTI DAMT NCON), Pattaya, Thailand, 2020, pp. 118-122

[8] N. Wayan Priscila Yuni Praditya, A. Erna Permanasari and I. Hidayah, "Designing a tourism recommendation system using a hybrid method (Collaborative Filtering and Content-Based Filtering)," 2021 IEEE International Conference on Communication, Networks and Satellite (COMNETSAT), Purwokerto, Indonesia, 2021, pp. 298-305

[9] O. Alnogaithan, S. Algazlan, A. Aljuraiban and A. A. Shargabi, "Tourism Recommendation System Based on User Reviews," 2019 International Conference on Innovation and Intelligence for Informatics, Computing, and Technologies (3ICT), Sakhier, Bahrain, 2019, pp. 1-5

[10] P. Padia, K. H. Lim, J. Cha and A. Harwood, "Sentiment-Aware and Personalized Tour Recommendation," 2019 IEEE International Conference on Big Data (Big Data), Los Angeles, CA, USA, 2019, pp. 900-909

[11] Q. Qi, J. Cao, Y. Tan and Q. Xiao, "Cross-Domain Recommendation Method in Tourism," 2018 IEEE International Conference on Progress in Informatics and Computing (PIC), Suzhou, China, 2018, pp. 106-112

[12] R. A. Wahurwagh and P. M. Chouragade, "Personalized POI Travel Recommendation With Multiple Tourist Information," 2019 IEEE International Conference on Electrical, Computer and Communication Technologies (ICECCT), Coimbatore, India, 2019, pp. 1-3

[13] S. Y. Shu, W. Hussain Wan Ishak and F. M. Yamin, "A Web-based Application for Interesting Place Recommendation," 2022 International Conference on Decision Aid Sciences and Applications (DASA), Chiangrai, Thailand, 2022, pp. 215-220

[14] T. Wenan, D. Shrestha, D. Shrestha, B. Gaudel and S. R. Jeong, "Analysis and Design of Tourism Recommender System for Religious Destinations of Nepal," 2020 IEEE International Conference on Sustainable Engineering and Creative Computing (ICSECC), Indonesia, 2020, pp. 214-220

[15] V. Garipelly, P. T. Adusumalli and P. Singh, "Travel Recommendation System Using Content and Collaborative Filtering - A Hybrid Approach," 2021 12th International Conference on Computing Communication and Networking Technologies (ICCCNT), Kharagpur, India, 2021, pp. 1-4

[16] X. Chen, Q. Liu and X. Qiao, "Approaching Another, Tourism Recommender," 2020 IEEE 20th International Conference on Software Quality, Reliability and Security Companion (QRS-C), Macau, China, 2020, pp. 556-562

[17] Y. A. Kusumawati and D. G. Renanda, "Architecture Design of Travel Guide Application for Tourism Recovery Post-Pandemic Covid-19," 2021 3rd International Conference on Cybernetics and Intelligent System (ICORIS), Makasar, Indonesia, 2021, pp . 1-7

[18] Y. Cui, C. Huang and Y. Wang, "Research on Personalized Tourist Attraction Recommendation based on Tag and Collaborative Filtering," 2019 Chinese Control And Decision Conference (CCDC), Nanchang, China, 2019, pp. 4362-4366

[19] Y. Xu, "Research on Travel Personalized Recommendation Information Retrieval Based on Big Data Improvement Algorithm," 2021 5th Annual International Conference on Data Science and Business Analytics (ICDSBA), Changsha, China, 2021, pp. 111-114

[20] Z. Duan, Y. Gao, J. Feng, X. Zhang and J. Wang, "Personalized tourism route recommendation based on user's active interests," 2020 21st IEEE International Conference on Mobile Data Management (MDM), Versailles, France, 2020, pp. 729-734

[21] Z. Jia, Y. Yang, W. Gao and X. Chen, "User-Based Collaborative Filtering for Tourist Attraction Recommendations," 2015 IEEE International Conference on Computational Intelligence Communication Technology, Ghaziabad, India, 2015, pp. 22-25

ResearchGate

See discussions, stats, and author profiles for this publication at: https://www.researchgate.net/publication/366518184

Analysis of QD-Si Solar Cell with Efficiency Enhancing Methods using Nano materials

Research · December 2022

DOI: 10.35629/5252-0412562571

CITATIONS
0

READS
21

1 author:

Ankush Rana
Delhi Technological University
3 PUBLICATIONS **0** CITATIONS

SEE PROFILE

Some of the authors of this publication are also working on these related projects:

Analysis of Si-QD Solar Cell with Efficiency Enhancing Methods View project

All content following this page was uploaded by Ankush Rana on 22 December 2022.

The user has requested enhancement of the downloaded file.

International Journal of Advances in Engineering and Management (IJAEM)
Volume 4, Issue 12 Dec. 2022, pp: 562-571 www.ijaem.net ISSN: 2395-5252

Analysis of QD-Si Solar Cell with Efficiency Enhancing Methods using Nano materials

Ankush, Anubhav Singh, Yogendra Kr. Meena, Manish Jain
[1,2,3]*Department of Applied Physics, Delhi Technological University, Bawana Road, Delhi 110042, India*
[4] *Department of Applied Chemistry, Delhi Technological University, Bawana Road, Delhi 110042, India*

Submitted: 10-12-2022 Accepted: 23-12-2022

ABSTRACT
Due to its ideal optoelectronic qualities for photovoltaic response, quantum dot solar cells are termed as solar cells of the third generation. Opportunities for dimensions and adaptability formation make QDs suitable suction devices to match the broad spectrum of the sun effectively. The potential for generations of multiple electron-hole pairs by a single photon number, i.e., generation of multiple charge carriers, demonstrates the ability to get beyond the theoretical limitations of a single conversion capability. Quantum solar dots show a dynamic efficiency of up till Twelve percent energy, remarkably similar to their solar dye-sensitive counterparts. Although, the efficiency of the Quantum Dot Solar Cells lags behind the standard solar single-junction photovoltaic. We'll talk about the first emergence of quantum solar dots in minimalist terms in this review. The study will also look at how critical building blocks are being developed and features like the several interoperability areas in the Quantum Dot Solar Cell, movement of charge transporter, and re-integration into all different visual connections, which affect the efficiency of power conversion. Additionally, carrier multiplication's fundamental notions and numerous exciton production are discussed in terms of their influence on the efficient quantum dot solar cells conversion.

Keywords: Quantum Dot, Semiconductor, Solar Cell, Junction, Bandgap, Electrode, Generation

I. INTRODUCTION

Consistent attempts from researchers and scientists to produce efficient and cost-effective green energy alternatives are required to meet ever-increasing world energy requirements and dwindling fossil resources, as well as global warming, which is reason for earth temperature rise. Earth receives 3 YJ/Year of energy from the Sun on a continual basis, with just 1/10,000th of this energy being adequate to fulfill earth energy requirements. The notion of fourth generation solar cells was recently brought to the photovoltaic world, taking into account the numerous technologies involved. There are four generations of solar cells. Solar cells of the first generation were produced from monocrystalline and polycrystalline silicon wafers. Structures of these photovoltaic cells are given in Fig. 1.

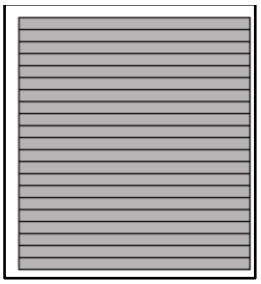

Fig: 1(a)
Monocrystalline Si Solar cell

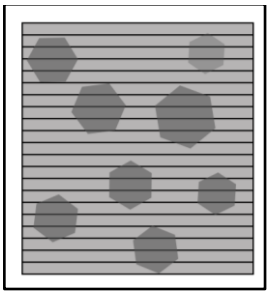

Fig: 1(b)
Polycrystalline Si Solar cell

International Journal of Advances in Engineering and Management (IJAEM)
Volume 4, Issue 12 Dec. 2022, pp: 562-571 www.ijaem.net ISSN: 2395-5252

Absorber with thin films are used to construct second generation solar panels , which aim to decrease the initial costs of first-generation photovoltaic cells. This includes photovoltaic technologies such as Cadmium telluride photovoltaic cell, amorphous Si-based cell cells, heterojunction and intrinsic thin layer (HIT). Fig. 2 shows some second generation solar cells.

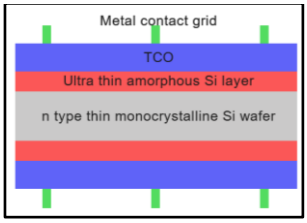

Fig. 2(a)
Heterojunction Intrinsic Thin layer solar cell

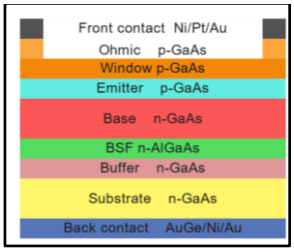

Fig. 2(b)
GaAs solar cell

Third generation photovoltaic cells intended to decrease both costs and achieve high efficiency. Third-generation photovoltaic cells use highly advanced concepts such as the integration of different bandgaps, which means solar cells are based on multi junctions and multi bands. Examples of third generation photovoltaic cells are Perovskite solar cells and Multijunction solar cells. Their structure is given in Fig. 3.

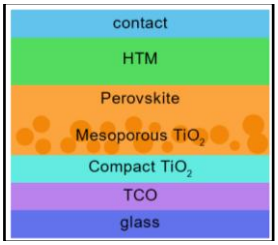

Fig. 3(a)
Perovskite solar cell

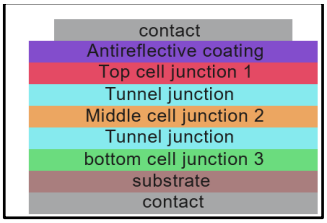

Fig. 3(b)
Multijunction solar cell

Table I summarizes the finest solar cells from various generations. The table also contains their various parameters like voltage with open circuit, current density in short circuit, fill factor and efficiency.

Photovoltaic cells can also be classified on their working principle, i.e., which includes the generation of carriers and the separation of electrons and holes. P-N junction photovoltaic cells are one form of photovoltaic cell, which use the absorber layer to generate a carrier, and the other one can be classified as solar cells with excitonics. Excitonic absorbers are used in this type of solar cell.

The development of an exciton (electron-hole pair) rather than a free electron-hole pair occurs in excitonic solar cells when sunlight is absorbed. These excitonic solar cells have the same process for generating current. However, their geometric structures are vastly different. In place of a free hole electron pair, as seen in standard Silicon or another P-N-based semiconductor cells, excitonic absorbers create excitons once solar energy is absorbed. In addition to the excitonic absorber, electrons and holes transporters are also the essential components of an excitonic solar cell. Errors, connections, alignment of power levels and charge carriers lifespan in material which transport holes and electrons may affect device functionality. As a result, proper material selection and preparation are essential for increased photovoltaic performance. Quantum Dot Sensitized Solar Cells

International Journal of Advances in Engineering and Management (IJAEM)
Volume 4, Issue 12 Dec. 2022, pp: 562-571 www.ijaem.net ISSN: 2395-5252

were developed as a consequence of efforts to replace molecular absorber dyes in dye sensitized photovoltaic cells with semiconductor nano absorbers. These solar cells are exactly the same in geometric construction and the difference is that semiconductor Quantum Dot is used as an excitonic absorber in Quantum Dot Solar Cell, unlike cell dye as the excitonic absorber used in Dye Sensitized Solar Cells. Titanium dioxide is widely investigated and other broad bandgap semiconductors, such as SnO_2 (Tin Oxide) and ZnO (Zinc Oxide) are used to transport electrons and examined as electron carrier transport material in both Dye Sensitized Solar Cells and Quantum Dot photovolatic Cells. The excitonic absorber absorbs the event from the sun's rays, resulting in the production of excitons in the absorber. The exciton produced by the image is separated from the electron transport material. From the excitonic absorber, the electron is sent to the electron transport material, while the hole is transmitted to the hole transport material, which will be compared later.

Table I Solar cells of several generations and their characteristics

Generation of solar cells	Solar cell architecture	Photovoltaic Performance			
		Open Circuit Voltage	Short Circuit Current Density	Fill Factor	Efficiency (%)
1st	Monocrystalline Si	0.738	42.65	84.9	26.7 ± 0.5
	Polycrystalline Si	0.6726	40.76	79.7	21.9 ± 0.4
2nd	Amorphous Si	0.896	16.36	69.8	10.2 ± 0.3
	Microcrystalline Si	0.55	28.72	75.0	11.9 ± 0.3
	CIGS	0.718	40.7	74.3	21.7 ± 0.5
	CdTe	0.88	30.25	79.4	21.0 ± 0.4
	CZTS	0.71	21.77	65.1	10.0 ± 0.2
	GaAs	1.12	29.68	86.5	28.8 ± 0.9
	HIT	0.75	39.5	83.2	24.7
3rd	Multi Junction	4.77	9.56	85.2	38.8 ± 1.2
	Dye sensitized	0.74	22.47	71.2	11.9 ± 0.4
	Perovskite	1.104	24.67	72.3	19.7 ± 0.6
	Organic	0.78	19.30	74.2	11.2 ± 0.3
	Quantum Dot sensitized	0.742	25.18	62.4	11.66 ± 0.17

Quantum dots are also integrated into the configuration of various geometrical solar photovolatic cells in addition to the sun-tested quantum dots. These structures include the Schottky quantum dot solar cells. The voltage in the open circuit of a cell is defined by Schottky's quantum dot photovoltaic cell in combination with acceptable power levels. The bending of bands at the metal and p-type semiconductor are used in Schottky quantum dot photovoltaic cells. A semiconductor layer of QDs is placed in the middle an electron acceptor material like Titanium dioxide and metal contact in a depletion heterojunction solar cell. Due to an appropriate band offset between Titanium dioxide and QDs, photogenerated electrons are effectively captured by Titanium dioxide, and holes are retrieved at a high work function metal like Gold contacts. Incoming photons are collected by quantum dots, excitons are received by an electron conductor such as Titanium dioxide, and holes are received by a material made from organic polymer in this form of solar cell. In the thin-walled solar absorber cells (ETA), a Quantum Dot inner layer with a high coefficient of dissipation is inserted in the middle of two electron-reflecting elements of the upper

International Journal of Advances in Engineering and Management (IJAEM)
Volume 4, Issue 12 Dec. 2022, pp: 562-571 www.ijaem.net ISSN: 2395-5252

band gap electron and the hole material.

Quantum Dots as excitonic collectors make Quantum dots-sensitized solar cells particularly fascinating, not just in terms of next-generation solar cells for harvesting of sun power, but also in terms of understanding fundamental principles like multi exciton creation at the expense of absorption of single photons. Quantum dots are extremely tiny geometrically. Quantum Dots are confined in 3D due to their size as compared to exciton radius and even after absorbing one photon, indicate the generation of multiple functional excitons. When compared to traditional solid solar cells, this can help Quantum Dot Sensitized Solar Cells perform better.

After addressing the chance of multi exciton production in these type devices, detailed balance studies recently showed that Quantum dots-sensitized solar cells can exceed the detailed balance restriction of traditional photovoltaic cells with one junction. Photovoltaic response. With heated carriers, the thermodynamic limit can be as high as 66%. To achieve such great photoelectric efficiencies, heated carriers in Quantum dots-sensitized solar cells can be used for multiple electron production, although the offset for multiple electron production may restrict the maximum thermodynamic efficiency. The Quantum Dot Photovoltaic Cell has a number of reviews. This review of Quantum Dot Photovoltaic Cells will be in line with the reports available for processing these features in depth. We shall go through the early advances as well as the understanding of the microscopic operating processes in this review. The review will also include building blocks for each Quantum Dot sensitized Photovoltaic Cell and its development over time to more effective Quantum Dot Sensitized Photovoltaic Cells. We'll also pay attention to exciton generation research related to colloidal Quantum Dots and their Photoelectric Conversion Efficiency.

II. EFFICIENCY ENHANCING METHODS

Several types and Quantum Dots based on various materials have been created and used in Quantum Dot Photovoltaic Cells over the years. From the photo-electrode side to the opposing side of the electrode, we summarized some of the Quantum Dots sensors and the arrangement of the rental solar cells. .super nanoporous electrode sensitivity refers to Quantum Dot adherence to a broad bandgap semiconductor. This can be done in a variety of ways, which are further divided into two categories as explained below.

(a) Sedentary sensitization:

Quantum Dots are amplified directly within the super nanoporous bandgap semiconductor electrode in this technique. This awareness can be achieved through a variety of means. The following are the most widely utilized methods:

(i) Adsorption and Reaction in Consecutive Ionic Layer:

This method allows you to quickly and easily insert Quantum Dots on the eyes-porous electrode.This method involves layer-by-layer adsorption of ionic species, which leads to the creation of Quantum Dots.The cationic and anionic precursors are dissolved separately in the suitable solvents in this procedure. Ionic forms are marketed over the super nanoporous electrode, which is submerged in a single precursor solution.

(ii) Chemical Bath Dumping:

To produce the chemical bath of ionic species, both the cationic and anionic precursors are dissolved separately in a suitable solvent and combined together.Chemical washing causes the ionic precursor to react somewhat, and it is then enforced to the terminal surface.

(b) Post-Reconciliation sensitization:

Early Quantum Dots are constructed independently to get the appropriate optoelectronic characteristics, and then deposited over a large super nanoporous semiconductor gap utilizing a number of ways in these sorts of procedure. The size and structure of Quantum Dots are typically not impacted during the placement procedure when using these techniques. Pre-assembled Quantum Dots' optoelectronic structures are therefore retained..

(i) Straight adsorption

For direct adsorption, the super nanoporous electrodes are simply submerged in the dissolved Quantum Dots solution.Due to their tiny size, quantum dots may readily pass the super nanoporous electrode pores and are put within the super nanoporous electrode.To thoroughly insert the super nanoporous electrode, the immersion period for Quantum Dot dispersion, dispersed Quantum Dot size, type Quantum Dots ligand, and Quantum Dot concentration in the solution are all adjusted.

International Journal of Advances in Engineering and Management (IJAEM)
Volume 4, Issue 12 Dec. 2022, pp: 562-571 www.ijaem.net ISSN: 2395-5252

(ii) Linker facilitate Straight adsorption:

Direct link-assisted advertising is identical to direct advertising with the exception that the super nanoporous electrode is first treated with special linking molecules to aid in Quantum Dot absorption across the super nanoporous electrodeOne active group is normally bonded to the Quantum Dots surface and the second active group is attached to the semiconductor handling region in connecting atoms.

(iii) Electrophoretic Dumping:

A heavy electric field (around 1500 V/cm) is used to create quantum dots.Quantum Dots are charged to the super nanoporous electrode and placed into the pores of the super nanoporous electrodes under the impact of an electric field.Quantum Dots are first inserted into the ultra nanoporous electrode pores, but the additional holes are plugged subsequently, and the Quantum Dots are only packed at the top.The implanted Quantum Dots' spintronic properties are preserved in cataphoretic implants, however uniform distribution and high localisation remain a challenge.

(iv) Pipetting:

Direct adsorption is quite similar to this method. The disintegration of Quantum Dots with an appropriate ligand is piped over the super nanoporous electrode, and the piped terminals are afterwards cleaned with a cleanser in this procedure.

As a result, the super nanoporous electrode region is not adequately covered.

Table II Quantum Dot absorber performance with efficiencies

Quantum Dots absorber	Cell Configuration	Open Circuit Voltage	Short Circuit Current Density	Fill Factor	Efficiency (%)
CdS	FTO/TiO_2/ZnS/CdS/S^{2-}-S_n^{2-}/FGO-Cu_2S/FTO	0.496	7.2	0.46	1.63
CdS-Mn		0.583	8.9	0.49	2.52
CdSe		0.561	16.96	0.566	5.42
CdS/CdSe	FTO/CdS-Mn/TiO_2/ZnS/S^{2-}-S_n^{2-}/FGO-Cu_2S/FTO	0.489	18.23	0.54	4.81
CdTe/CdSe		0.606	19.59	0.569	6.76
CdSeTe		0.700	20.69	0.622	9.01
ZnTe/CdSe		0.646	19.35	0.551	6.89
Zn-Cu-In-Se	TiO_2/CdSe-MPA/ZnS/S^{2-}-S_n^{2-}/Cu_2S/Brass	0.742	25.18	0.624	11.66
	TiO_2/CdS/CdSe/ZnS/S^{2-}-S_n^{2-}/Pt/FTO				
	TiO_2/CdTe/CdSe/ZnS/S^{2-}-S_n^{2-}/Cu_2S/Brass				
	TiO_2/CsSeTe/$TiCl_4$/ZnS/S^{2-}-S_n^{2-}/$Cu_{2-x}S$/Brass				
	TiO_2/CdSe/ZnTe/$Cu_{2-x}S$/ZnS/S^{2-}-S_n^{2-}/Brass				
	TiO_2/ZnS/Zn-Cu-In-Se/S^{2-}-S_n^{2-}/MC/Ti				

Electron Carrier material:

Electron transporters play an essential role in the performance of Quantum Dot Photovoltaic Cells.Image-generated electrons are received by ETM from a Quantum Dots emitter and transported to a TCO contact. An appropriate offset belt in the middle of the electron carrier material and the Quantum Dots absorber is necessary to

International Journal of Advances in Engineering and Management (IJAEM)
Volume 4, Issue 12 Dec. 2022, pp: 562-571 www.ijaem.net ISSN: 2395-5252

successfully absorb electrons from the Quantum Dots scanner. Several of the most well-known electron transmitters used by Quantum Dot Photovoltaic Cells are mentioned here:

(a) Titanium oxide (TiO_2):

Electron transporters for excitonic solar cells including dye-sensitized photovoltaic cells and quantum dots photovoltaic cells, among others.TiO2's appealing features, such as its low cost, bulkiness, and lack of toxicity, make it a good electron transport agent. Nano-particles of different sizes of TiO2 are used in a horizontal manner, which are tiny particles (~30 nm) of transparent layers and large particles (~250 nm) of layers with large distribution centers rather than transparent, to provide enough porosity of Quantum Dot advertising and dissipating material to illuminate the active light in the Quantum Dot Solar Cell.

(b) Zinc oxide (ZnO):

Zinc oxide is one of the most extensively used photoanode material alternatives for TiO2. Zinc oxide is a semiconductor band that spans the II through VI group families. It have a black mineral ZNS type crystal structure.Many electrical applications, including as imaging and LED performance improvement, employ Zinc Oxide.

(c) Tin oxide (SnO_2):

Quantum Dot Solar Cells also employ tin oxide as a photoelectrode material.This is related to the binary oxides Zinc oxide and Titanium oxide, and it has two benefits over Titanium Oxide:

(i) more ability to move

(ii) high negative conductivity in comparison to Titanium Oxide.

(d) Zinc stannate (Zn_2SnO_4):

Zinc stannate is a tetra oxide substance that has been used in Quantum Dot Solar Cells as a photoanode.. A cross-sectional structure with a larger band gap compared to 3.6 eV.The photovoltaic performance of Quantum Dot Solar Cells using zinc stannate has been found to be promising, although it still falls short of the typical Titanium Oxide photoanode.

(e) Zinc titanate:

Zinc titanate is an oxide that has three distinct spectroscopic phases.Zinc titanate's six-fold octahedral bond is remarkably close to the Ti arrangement in anatase TiO2.According to some findings, zinc titanate outperforms Titanium Oxide as a photoanode.

(f) Strontium titanate ($SrTiO_3$):

Similar to zinc titanate, strontium titanate is a tetraoxide molecule.It has a bandgap that is nearly comparable to titanium oxide, but it has a larger flat band strength, resulting in more open-circuit electricity.

Hole carrier material:

The hole from the oxidized Quantum Dots is received by the transport material.If the Quantum Dot's output rate is slow or the port driver has broken down the hole, the reconnection to the Quantum Dot Photovoltaic Cell will rise, lowering the photovoltaic effect. Redox electrolytes, quasi-solid terminals, and solid hole conductors like spiro-MeOTAD can all be employed as hole carriers.. The Quantum Dot Solar Cell tests a variety of perforated transit containers, and a few of these are mentioned below under the liquid, solid, and durable condenser part.

(a) Liquid Hole conductor:

In Dye Sensitized Solar Cells, liquid hole conductor was historically utilized in the form of redox electrolyte, followed by Quantum Dot Solar Cells. The following electrolytes were used in the Quantum Dot Solar Cell:

(i) Iodide electrolyte

(ii) Polysulfide electrolyte

(iii) Ferrocene electrolyte

(iv) Cobalt-based electrolyte

(b) Solid hole carrier material:

Solid hole transporters are also being investigated for Quantum Dot Solar Cells to prevent liquid redox electrolyte leaks.With a solid drilled transport material, getting the hole conductor into the alerting super nanoporous electrode is difficult.

(c) Gel electrolyte:

To turn liquid polysulfide electrolytes into gels, a particular gelatin agent is employed.In comparison to the new liquid polysulfide electrolyte, these gel-type electrolytes improve Quantum Dot Solar Cell stability while delivering a bit less output.

III. DIFFERENT EXCITON GENERATION IN QUANTUM DOT SOLAR CELL

Excessive production of exciton in solar cells is made up of quantum dot.The generation of more than one electron and a pair of perforations by the absorption rate of a single photon is called the production of multi exciton. Multi exciton

International Journal of Advances in Engineering and Management (IJAEM)
Volume 4, Issue 12 Dec. 2022, pp: 562-571 www.ijaem.net ISSN: 2395-5252

production predicted and demonstrated by Quantum dot tests using spectroscopic techniques. Harm-carrying companies are produced after absorbing photons with very high energy and these thermal carriers can create more than one electron and perforator pairs at the cost of absorbing one photon and thus , can display more than one 100% quantum efficiency.
The effect of heat charge carriers on Quantum Dots is define down.

Hot charge carrier in Quantum Dots:

When photons are consumed beyond the conductor's energy gap, electron pairs and holes (heat carriers) with high temperatures (E =hv-Eg) are produced, which are out of balance. In their active masses, excess energy is distributed among the electron and hole. The upper bouts featured two cutaways, for easier access to the higher frets. These thermal companies with high temperatures will return to balance through network distribution, phonon emissions, radiation combinations, and non-reheating. Changes in the dynamics of happy network companies are critical to the Quantum Dot Solar Cell application and are extensively investigated to call their agreement for distinct application.If the photon energy is greater than the bandgaps, more power is generated in the same way that the electron and hole are K.E dependent on their active mass. Boltzmann's distribution of charge carriers value is formed when vehicle carriers such as electrons and holes interact separately. The thermal conductivity process, which occurs on a time scale of 100 fs, is the first break.

The optical longitudinal (LO) pneumonia pens are used in this technique. Network carrier cooling by carrier-phonon interaction is the name for this method.

Heat carriers can be employed in two ways: they can be collected before resting, and then used for another creation of electron and hole pairs utilising impact ionisation in the second scenario. The second procedure is known as (MEG).

Multiple exciton generation in quantum dot-based solar cells:

Quantum arrangements like quantum springs & super-lattices, every slow cooling of the hotline charge carriers occurs with a bottle of hot pins, however the density of the manufactured charge carriers required is an order of 1018 / cm3. Such network congestion is not possible in the sun's rays, yet it can be produced by the radiance of powerful laser beams.

In the case of quantum dots, however, the slow-moving cooling of the charge carriers is possible with low light using a phonon bottle-neck, which aids in the heating process. This can easily be achieved with Quantum Dot solar panels.

Multiple exciton generation in colloidal quantum dot:

Quantum Dot Solar Cells use mix Quantum Dots, therefore, this is necessary to review multi-exciton studies for mix Quantum Dots. THz spectroscopy is used while in some current time measurements to investigate the production of large amounts of exciton is inspected.

Spectroscopy research involves the inspected of multi-excitons flux, in which multi-excitons are separated by a single exciton based on the time scale of various variables. In cases like this , 2 kind of variables are recognized:
(i) rapid variability is caused by Auger reconnect, whatever exceeds the exciton bottle & therefore, specify bi-exciton or MEG.
(ii) slow variability calculated. in one phonon and hole trapping kinetics for capping agents. This spectroscopy studies usually include its production of exciton operating a pulsed laser.

The dynamics of the charge carriers are measured by the various forces of pulsed laser to produce excitons in mix Quantum Dots. The most productive bi-exciton creation is seen in earlier times with the Auger rapid rearrangement on a ps measure although the exciton rearrangement time slower, around near the 2nd smaller scale. With pump power above 3Eg, bi-exciton motion is detected. This bi-exciton parts can exist subdivided toward a single-exciton exist and applied into descriptive decay. Here, even one charge carriers with the same size as Eg was enough to drive a power-saving approach to MEG. In addition, Schalleretal too wind up that multi-exciton production not at all fast-paced by cause of building time of the people involved, as well as your competition and intraband relaxations identical to that of amount content.

Another way to look at multi-exciton generation in-inclusion is to test the current dynamic current.. Here, the effectiveness of MEG is determined by computer-assisted quantum dot films.

The power of electron dynamics is investigated in Quantum Dot composite films at device level. Quantum Dots installed in fast electro-optical switches & powered by multicarrier image processing capabilities with 40 ps fixes to

International Journal of Advances in Engineering and Management (IJAEM)
Volume 4, Issue 12 Dec. 2022, pp: 562-571 www.ijaem.net ISSN: 2395-5252

solve Auger decay in many corporate regions.

This is considered to be the non-monic quadratic dependency about heart rate over average number of excitons per Quantum Dot. In addition, Gandmanetal also described every visualization of a multi-exciton creation style, based-upon eventful fulfillment about a few quantum electronic state intrapulse reciprocated by two photon transformations.

Multi-Exciton Production- a theoretical view:

Typically, In these texts,The two models for MEG acquisition are investigated.The photoionization limit is studied in two approaches: one is based on straightforward impact ionisation, 37, & the other is based-upon on quantum mechanical behaviour towards of coefficient photoionization. Kanye hlangene 3G ionisation Thermal carriers are formed following photon absorption by force beyond the Quantum Dot band gap, depending on whether the model is unchanged or the classic effect is ionised. Carriers continue to receive more electricity based on their operational volume. To create more, one charge carrier must have more power than the band gap.

Pairs of electrons and holes The MEG limit is roughly 3Eg when the electrons and active mass hole are the same, but it can be reduced to 2Eg if one of the network carriers has a low operational weight. Impact ionisation begins to compete with the remainder of the intra-band in this situation.

The Multi-Exciton generation model uses a combination of ME superposition and SE conditions. This model uses a time-based density matrix technique to allow for a consensus evaluation of energy interactions between SE and ME areas, as well as other falling values in those regions and NCs' short cardiac stimulation.

Multi-Exciton generation (MEG) at device level

Here, an atomically flat anatase Titanium dioxide plate was put together , & affected with MPA capped sulfanylidenelead Quantum Dots. The sensitised photocurrents are determined using photocurrent spectroscopy as a function of incoming incident radiation. Adsorption efficiency of photons to current is more than Hundred percent. This was ascribed to multiple exciton collection rather than multi exciton production.

Quantum Dot Solar Cells from MEG perspective

Multi exciton production in QDSSCs using heated electrons may be accomplished in two ways. For use with interfacial carrier transfer, hot carriers must be cooled for more than 10 ps, in first case.In the 2nd situation, if heated charge transporters cool down is slow enough & multiple excitons could be created prior to electron insertion over the interface, a single photon can easily insert multiple electrons into the carrier material. In this instance, hot charge carriers can affect Quantum Dot Sensitized Photovoltaic Cell's performance significantly.

IV. QUANTUM DOT SENSITIZED PHOTOVOLTAIC CELL: RECENT ADVANCES AND FUTURE PERSPECTIVE IN SOLAR CELL

Over the years, the photoelectric ability of infected quantum photovoltaic cells has improved from less than 2% to more than 13%.. Effective redox conductor such as poly sulfide electrolyte and magnificent countertop electrodes such as Cu_2S and carefully crafted quantum shell dots have resulted in a highly efficient Quantum Dot Solar Cell, showing up to 12 photovoltaic efficiency %. The production of multiple excitons is indicated by mix quantum dots and ideal frame, which explains the laboratory discovery.Because of the potential MEG potential, mix Quantum Dots could appear to have 100 percent inner quantum efficiency.Mix quantum dots and the ideal frame, which describe the laboratory finding, imply the synthesis of numerous excitons...

If proper electron transporters, Quantum Dots conductors, redox hole conductors, and electrode counters are designed, this increase can be more than 5%. Any significant excess that exceeds the Shockley-Queisser performance limit on Quantum Dot Solar Cells looks to be problematic without the appropriate ones instead of the typically Titanium dioxide, polysulfide lytes.

V. CONCLUSION

Quantum dot solar cells cause significant departures from photovoltaic efficiency, with a maximum of roughly 13% photoelectric efficiency estimated. Although, positive development band gap absorbers, electron transporters, and holes, as well as a stable electrolyte, are required for increased efficiency by better matching their energy levels.Furthermore, the MEG idea appears to be quite promising, and it may be able to help overcome the Shockley-Queisser restrictions of the next generation of Quantum Dot Solar Cells.

However, obtaining MEG tests at

Quantum Dot Solar Cell remains a difficulty, and will necessitate the design and development of new Quantum Dots with adequate band gap values, dynamic carrier dynamics, and life endurance.As a result, Quantum Dot Photovoltaic Cells appear to be very promising; however, overcoming the problems and challenges associated with the development of active Quantum Dot Photovoltaic Cells will necessitate both experiment and theory understanding of object properties and their integration into a device configuration.

REFERENCES

[1] Adegoke, O., Park, E.Y., 2016. Size-confined fixed-composition and composition-dependent engineered band gap alloying induces different internal structures in L-cysteinecapped alloyed quatetra CdZnTeS quantum dots. Sci Rep. 6, 27288. https://doi. org/10.1038/srep27288.

[2] Adler, F., Geiger, M., Bauknecht, A., Haase, D., Ernst, P., Dörnen, A., Scholz, F., Schweizer, H., 1998. Self-assembled InAs/GaAs quantum dots under resonant excitation. J. Appl. Phys. 83, 1631–1636. https://doi.org/10.1063/1.366876.

[3] Chiu, P.T., Law, D.C., Woo, R.L., Singer, S.B., Bhusari, D., Hong, W.D., Zakaria, A., Boisvert, J., Mesropian, S., King, R.R., Karam, N.H., 2014. 35.8% space and 38.8% terrestrial 5J direct bonded cells. 2014 IEEE 40th Photovolt. Spec. Conf. PVSC 2014, pp. 11–13. doi: 10.1109/PVSC.2014.6924957.

[4] Dibbell, R.S., Watson, D.F., 2009. Distance-Dependent Electron Transfer in Tethered Assemblies of CdS Quantum Dots and TiO2 Nanoparticles. J. Phys. Chem. C. 113, 13511–13519. https://doi.org/10.1021/la702127t.

[5] Ellingson, R.J., Beard, M.C., Johnson, J.C., Yu, P., Micic, O.I., Nozik, A.J., Shabaev, A., Efros, A.L., 2005. Highly efficient multiple exciton generation in colloidal PbSe and PbS quantum dots. Nano Lett. 5, 865–871. https://doi.org/10.1021/nl0502672.

[6] Ernst, K., Belaidi, A., Nenkamp, R.K., 2003. Solar cell with extremely thin absorber on highly structured substrate. Semicond. Sci. Technol. 18, 475–479. https://doi.org/ 10.1088/0268-1242/18/6/314

[7] Fang, J., Wu, J., Lu, X., Shen, Y., Lu, Z., 1997. Sensitization of nanocrystalline TiO2 electrode with quantum sized CdSe and ZnTCPc molecules. Chem. Phys. Lett. 270, 145–151. https://doi.org/10.1016/S0009-2614(97)00333-3.

[8] Gao, J., Fidler, A.F., Klimov, V.I., 2015. Carrier multiplication detected through transient photocurrent in device-grade films of lead selenide quantum dots. Nat. Commun. 6. https://doi.org/10.1038/ncomms9185.

[9] González-Pedro, V., Xu, X., Mora-Seró, I., Bisquert, J., 2010. Modeling high-efficiency quantum dot sensitized solar cells. ACS Nano 4, 5783–5790. https://doi.org/10. 1021/nn101534y.

[10] Gopi, C.V.V.M., Venkata-Haritha, M., Kim, S.-K., Kim, H.-J., 2015. Improved photovoltaic performance and stability of quantum dot sensitized solar cells using Mn–ZnSe shell structure with enhanced light absorption and recombination control. Nanoscale. 7, 12552–12563. https://doi.org/10.1039/C5NR03291A

[11] Gregg, B., Fox, M., Bard, A., 1990. Photovoltaic effect in symmetrical cells of a liquid crystal porphyrin. J. Phys. Chem. 94, 1586–1598. https://doi.org/10.1021/ j100367a068.

[12] Guijarro, N., Campiña, J.M., Shen, Q., Toyoda, T., Lana-Villarreal, T., Gómez, R., 2011. Uncovering the role of the ZnS treatment in the performance of quantum dot sensitized solar cells. Phys. Chem. Chem. Phys. 13, 12024–12032. https://doi.org/10. 1039/c1cp20290a.

[13] Hagfeldt, A., Grätzel, M., 2000. Molecular photovoltaics. Acc. Chem. Res. 33, 269–277. https://doi.org/10.1021/ar980112j.

[14] Halder, G., Bhattacharyya, S., 2015. Plight of Mn doping in colloidal CdS quantum dots to boost the efficiency of solar cells. J. Phys. Chem. C. 119, 13404–13412. https://doi. org/10.1021/acs.jpcc.5b01932.

[15] Heitz, R., Veit, M., Kalburge, A., Xie, Q., Grundmann, M., Chen, P., Ledentsov, N.N.N., Hoffmann, A., Madhukar, A., Bimberg, D., Ustinov, V.M.M., Kop'ev, P.S.S., Alferov, Z.I., 1998. Hot carrier relaxation in InAs/GaAs quantum dots. Phys. E LowDimensional Syst. Nanostructures. 2, 578–582. https://doi.org/10.1016/S1386-9477(98)00118-0

[16] Hod, I., Zaban, A., 2014. Materials and interfaces in quantum dot sensitized solar cells: Challenges, advances and prospects.

Langmuir 30, 7264–7273. https://doi.org/10.1021/la403768j.

[17] Hodes, G., Gorer, S., 1994. Quantum size effects in the study of chemical solution deposition mechanisms of semiconductor films. J. Phys. Chem. 98, 5338–5346. https://doi.org/10.1021/j100071a026.

[18] Huo, Z., Tao, L., Wang, S., Wei, J., Zhu, J., Dong, W., Liu, F., Chen, S., Zhang, B., Dai, S., 2015. A novel polysulfide hydrogel electrolyte based on low molecular mass organogelator for quasi-solid-state quantum dot-sensitized solar cells. J. Power Sources. 284, 582–587. https://doi.org/10.1016/j.jpowsour.2015.03.049.

[19] Inoshita, T., Sakaki, H., 1992. Electron relaxation in a quantum dot: Significance of multiphonon processes. Phys. Rev. B. 46, 7260–7263. https://doi.org/10.1103/PhysRevB.46.7260.

[20] Jiao, S., Shen, Q., Mora-Seró, I., Wang, J., Pan, Z., Zhao, K., Kuga, Y., Zhong, X., Bisquert, J., 2015. Band engineering in core/shell ZnTe/cdse for photovoltage and efficiency enhancement in exciplex quantum dot sensitized solar cells. ACS Nano 9, 908–915. https://doi.org/10.1021/nn506638n.

[21] Jovanovski, V., González-Pedro, V., Giménez, S., Azaceta, E., Cabañero, G., Grande, H., Tena-Zaera, R., Mora-Seró, I., Bisquert, J., 2011. A sulfide/polysulfide-based ionic liquid electrolyte for quantum dot-sensitized solar cells. J. Am. Chem. Soc. 133, 20156–20159. https://doi.org/10.1021/ja2096865.

[22] Klimov, V.I., 2000. Optical Nonlinearities and Ultrafast Carrier Dynamics in Semiconductor Nanocrystals. J. Phys. Chem. B. 104, 6112–6123. https://doi.org/10.1021/jp9944132.

[23] Klimov, V.I., 2006. Detailed-balance power conversion limits of nanocrystal-quantum-dot solar cells in the presence of carrier multiplication. Appl. Phys. Lett. 89, 123118. https://doi.org/10.1063/1.2356314

[24] Klimov, V., McBranch, D., 1998. Femtosecond 1P-to- 1S Electron Relaxation in Strongly Confined Semiconductor Nanocrystals. Phys. Rev. Lett. 80, 4028–4031. https://doi.org/10.1103/PhysRevLett.80.4028.

[25] Klimov, V.I., Mikhailovsky, A.A., McBranch, D.W., Leatherdale, C.A., Bawendi, M.G., 2000. Mechanisms for intraband energy relaxation in semiconductor quantum dots: The role of electron-hole interactions. Phys. Rev. B. 61, R13349–R13352. https://doi.org/10.1103/PhysRevB.61.R13349

[26] Luo, J., Wei, H., Huang, Q., Hu, X., Zhao, H., Yu, R., Li, D., Luo, Y., Meng, Q., 2013. Highly efficient core-shell CuInS2-Mn doped CdS quantum dot sensitized solar cells. Chem. Commun. (Camb) 49, 3881–3883. https://doi.org/10.1039/c3cc40715b.

[27] Milliron, D.J., 2014. Quantum dot solar cells: The surface plays a core role. Nat. Mater. 13, 772–773. https://doi.org/10.1038/nmat4032.

[28] Mora-Seró, I., Giménez, S., Moehl, T., Fabregat-Santiago, F., Lana-Villareal, T., Gómez, R., Bisquert, J., 2008. Factors determining the photovoltaic performance of a CdSe quantum dot sensitized solar cell: the role of the linker molecule and of the counter electrode. Nanotechnology. 19, 424007. https://doi.org/10.1088/0957-4484/19/ 42/424007.

[29] Ning, Z., Dong, H., Zhang, Q., Voznyy, O., Sargent, E.H., 2014. Solar cells based on inks of n-type colloidal quantum dots. ACS Nano 8, 10321–10327. https://doi.org/10.1021/ nn503569p.

[30] Nozik, A.J., 2008. Multiple exciton generation in semiconductor quantum dots. Chem. Phys. Lett. 457, 3–11. https://doi.org/10.1016/j.cplett.2008.03.094.

View publication stats

2022 IEEE 9th Uttar Pradesh Section International Conference on Electrical, Electronics and Computer Engineering (UPCON) | 979-8-3503-3250-6/22/$31.00 ©2022 IEEE | DOI: 10.1109/UPCON56432.2022.9986408

Applications of Human Activity Recognition in Different Fields: A Review

Yash Daga
Department of Software Engineering
Delhi Technological University
Delhi, India
yashdaga_2k21swe25@dtu.ac.in

Shweta Meena
Department of Software Engineering
Delhi Technological University
Delhi, India
shwetameena@dtu.ac.in

***Abstract*— Human activity recognition is a field where not enough work has been done yet, but its applications can be helpful in numerous domains. In this paper, we have discussed different methods by which implementation of human activity recognition can be carried away and compared those methods in terms of advantages, performance, accuracy, techniques, datasets, and limitations. We have also discussed numerous domains where this can be helpful such as healthcare, security, and augmented reality, along with the challenges and the type of method used.**

Keywords*— *Human Activity Recognition, Convolution Neural Network, Techniques, Dataset

I. INTRODUCTION

Nowadays, artificial intelligence and machine learning algorithms or techniques have helped in the advancement of numerous different fields. Thus, we have witnessed an increase in various areas such as healthcare, agriculture, management, and security. Computer vision is one such concept from which human activity recognition is active in research [1]. It is a highly dynamic and challenging area to research in which the algorithm understands the activities performed by a person or a set of persons through a source which can be a video or can also be obtained from different sensors, images irrespective of the environment in the group of persons are in [6].

The agriculture industry is responsible for providing a living for an enormous number of the World's population. Many farmers still want to continue the old-fashioned way of farming, even though this practice results in low revenue. Machine Learning techniques will help remove the middleman, mostly the person who purchases the raw materials from farmers at low cost and sell them to the consumers at a comparatively higher price from dealing with natural materials. The most common challenges of agriculture in machine learning are decision making, selecting which crops would grow better in the future, and supporting systems to ensure crop output is beneficial. Machine learning algorithms will help farmers profit from their production by analyzing which crops would give better results in the future based on the geographical location of the crops, climatic conditions of the crops being grown, and the current season where crops are being grown [5].

The goal of the human activity recognition system is to help monitor places where manual work can be reduced. For example, in terms of security, an automated video processing system to identify human activity can detect any malicious activity performed by an individual and instantaneously alert the concerned authorities. These systems can be installed in public places like metro or railway stations, airports, bus stands, shopping malls, tourist places, etc., to help prevent explosive attacks. Any person(s) leaving their luggage in a public place can be detected, thus reducing casualties. Identifying abnormal activities in real time might help victims, but this is highly time consuming and requires more resources as lengthy surveillance videos must be processed. As an escape, video files can be compressed using adaptive video compression technology. Adaptive video compression is a technique that compresses only the most minor required parts of the video, retaining the objects of interest [20]. Other security measures that can be helpful are theft detection, traffic rule breaking such as illegal parking or U-turn, and violence detection like punching, fighting, or shooting can also be detected [4][11].

Another application of the human activity recognition system is in healthcare. In the covid-19 pandemic, it was observed that there was a shortage of workforce in numerous hospitals, increasing the number of casualties across the globe. But now, with the help of such a system, we can monitor patients 24*7 without any interruptions. Nurses can take care of patients where more assistance is required rather than patients where less aid is needed. In an Intensive Care Unit (ICU), per patient, one nurse is assigned to monitor the patient's behavior, but now, the system can take over, and nurses can work for more critical patients. Furthermore, it will reduce the disease by regularly monitoring any individual’s physical activities, such as diabetes and obesity [12].

Identification of human activities is crucial in augmented reality concepts. Nowadays, the gaming industry is one of the most profitable businesses in the World. With technological advancements such as human activity recognition, a player can be present in the game instead of just pressing a few buttons. This will give the player an incredible and never-before-seen

Authorized licensed use limited to: DELHI TECHNICAL UNIV. Downloaded on January 17,2023 at 05:03:13 UTC from IEEE Xplore. Restrictions apply.

experience, totally different from conventional gaming. As the user experience improves, profit will increase by selling more products.

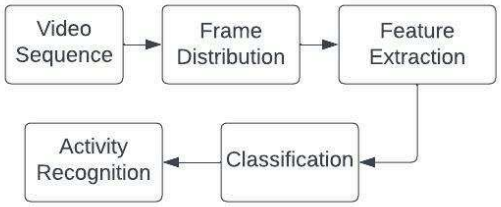

Fig 1: Human Activity Recognition Architecture

The process is divided into following steps such as frames extraction, usage of features extractor, and finally, we classify every frame based on the results obtained from extracted features. In HAR systems, the issue comprises that a single frame can have qualities of multiple features. For example, a frame of a person dancing can look like jumping or doing yoga as well, hence, to overcome such issue we select some frames and try to find plausible solutions. Output of these independent CNN is feeded to Recurrent Neural Network (RNN) and that network will use this extracted information temporarily.

II. RELATED WORK

In [7], human activity recognition is divided into two main categories: (i) unimodal and (ii) multimodal activity recognition methods. This characterization is done based on how sensor data they employ [7]. Identification of human activities from data based on a single mode (or modal) can be composed as Unimodal. Uni is for singles. The source of this can be photographed. Unimodal is divided into four categories, space-time, where activity recognition is done as a set of space-time features. Stochastic is another characterization of unimodal, where statistical methods like hidden Markov models do identification. The third characterization is a rule-based method, where identification is made based on a few available rules. The shape-based method is Unimodal's fourth and last characterization, where each motion of the human body part is processed, and later activity identification is performed [7].

Identification of human activities from numerous different sources is termed multimodal. Various activities' features are combined and later processed with data from multiple sources. Multimodal methods are divided into affective, behavioral, and social networking [7]. The effective category is based on a person's emotional communication. The behavioral approach is based on communications that do not take place verbally. These are dependent on the expressions of a person or gestures or body language of a person. At last, the social networking model works on data collected from a social gathering where human beings interact with other human beings. The author worked on gestures, verbal communication between the two, and body language or body motion [7].

In [19], human activity recognition based on smartphones has gained tremendous popularity in recent years due to its accessibility and wide range of features. They proposed a Neighbourhood Component Analysis (NCA) based feature selection method to select the required features from the pool of available hand-crafted features. The procedure is divided into two parts, the first being selecting the components needed and the second being the dense neural network for classification [19].

From all the available features, a few of the required features are selected according to the problem statement. There are numerous methods for feature selection; among those, NCA is chosen because it maximizes the elimination of one classification accuracy. Upon selection of all the required features by the NCA feature selection methods, we divide the features selected into different categories. For classification, we use Dense Neural Network (DNN) classification method. This is known to have good accuracy for a set of required features. A dense neural network is divided into several different layers. The output of one layer is treated as an input to the next layer. Each of these layers is for feed-forward networks and consists of pre-set units, neurons in this case [19].

In [17], the authors have worked on a computer vision model which uses deep learning algorithms to recognize the activities performed by an individual or a set of individuals. The CAD-60 dataset is used to study the activities. These are collected from the sensors of Microsoft Kinect. Using CNN for feature extraction and to classify multilayer perceptron, they achieved an accuracy of 81.8%. However, because the before mentioned process requires a lot of training time, we may enhance it by determining whether the input is compatible with the RNN algorithm and using it in place of the CNN to achieve better results.

In [14], the source of activity recognition is done using graphical models using skeleton data. The authors here propose a new strategy using probabilistic graphical models to identify the tasks performed by any individual. The model is tested using different datasets such as CAD-60, Florence 3-D, and UT-Kinect. The results were optimistic as the activity recognition model could predict both simple and complex tasks from each dataset. In [1], the authors reviewed a few sensing technologies papers. These sensing technologies include the camera as a source device, wearable devices such as smart glasses or watches, and depth sensors. The advantages and limitations of each source are discussed, showing that the cameras as a source are less reliable compared to depth and wearable sensors.

In [4], the authors have discussed suspicious human activity recognition through video sources. Sensitive public places such as shopping malls, schools, railway stations, and airports can be monitored to prevent explosive attacks. Any unattended luggage or malicious behavior of a person can be identified. Other factors such as theft, accidents, or even identification of a vehicle parked illegally can be identified. When working with live analysis of video frames, conventional training techniques may take longer time. As a result, we might try adding a few trackers like MIL, KCF, CSRT, Boosting trackers, to solve this problem and get better outcomes.

Authorized licensed use limited to: DELHI TECHNICAL UNIV. Downloaded on January 17,2023 at 05:03:13 UTC from IEEE Xplore. Restrictions apply.

III. RESULT ANALYSIS

TABLE I. COMPARISION OF DIFFERENT TECHNIQUES FOR HUMAN ACTIVITY RECOGNITION

S. No.	Title	Year	Dataset	Technique	Performance Measure	Limitations	Results
1	A Hybrid Approach for Human Activity Recognition with Support Vector Machine and 1D Convolutional Neural Network	2020	UCI-HAR dataset	1D Convolutional neural network (1D CNN), Random Forest, Support Vector Machine	170 seconds was the total training time for 100 epochs	For identification in real time, deploying this to low-power integrated circuits for wearable sensors.	The accuracy percentage was 97.71%. [18]
2	Smartphone-Based Human Activity Recognition with Feature Selection and Dense Neural Network	2020	UCI HAR data set	Dense Neural Network Model, Support Vector Machine	The proposed model outperformed many other deep learning methods.	Exploring other feature selection methods might also be helpful	The accuracy percentage was 95.79%. [19]
3	Implementation of an Anomalous Human Activity Recognition System	2020	UCF101 crime dataset	Adaptive Video Compression, CNN, Anomaly Detection.	The proposed system has more accurate favorable rates than the other existing systems.	In reality, the chances of occurrences of abnormal activity are meager, so the performance is measured in standard videos without anomalies, as having a low false alarm rate is challenging.	This approach outperforms previous approaches regarding accuracy and timeliness [20].
4	Activity recognition in manufacturing: The roles of motion capture and sEMG+inertial wearables in detecting fine vs. gross motion	2019	UCSD-MIT Human Motion Dataset	Linear Discriminant Analysis, k-Nearest Neighbors	For gross motion detection, motion capture was more accurate. But for fine-grained motion, wearable sensors were more accurate.	Only the arm motion of the candidates was stored.	Classification of fine-grained motion was more complex compared to gross activity.
5	Human Activity Recognition for Healthcare using Smartphones	2018	UCI repository	Artificial Neural Networks, Multi-Layer Perceptron	Performance accuracy of the accelerometer was 92%, gyroscope was 80%, combining them using accgyro we get 95%	At the lowest, 80% of accuracy was achieved from Gyroscope.	Accuracy can be increased using accelerometer and gyroscope data, but it consumes much of the

Authorized licensed use limited to: DELHI TECHNICAL UNIV. Downloaded on January 17,2023 at 05:03:13 UTC from IEEE Xplore. Restrictions apply.

							phone's battery. [12]
6	Human Physical Activity Recognition Based on Computer Vision with Deep Learning Model	2016	CAD-60	Convolutional neural network, Multi-layer Perceptron	total training time was 21:30 secs.	Results are promising, but there's room for improvement as only the skeleton model was used as input	The accuracy percentage was 81.8%. [17]
7	Deep Learning for Human Activity Recognition: A Resource Efficient Implementation of Low-Power Devices	2016	Active Miles, WISDM, Skoda, Daphnet	Deep Learning, CNN, Linear Classifier, Neural Network	The classification stage was implemented on low-power wearable devices with efficient resources.	There is a slight difference between computation time and spectrogram generation time while used on devices like Intel Edison, LG Nexus 5, and Samsung Galaxy S5.	The accuracies of ActiveMiles, WISDM, Skoda, Daphnet are 95.1, 98.2, 95.9 and 91.5 (Sensitivity) & 97.7 (Specificity) respectively [21].

The problem is identifying the activities performed by a human or a set of people from a source file. To work on this problem, we have worked on a secondary dataset. The secondary dataset is the dataset collected by someone else. This dataset is acquired from WISDM: Wireless Sensor Data Mining website [9]. We have used accelerometer data to train the model and, further, to predict the activities performed by the individual(s). An accelerometer is an instrument for detecting and measuring vibrations. It can be used to measure acceleration [2]. The WISDM data is a total of 1,098,207 examples collected through controlled laboratory conditions, and it comprises six classes: Jogging, Standing, Walking, Upstairs, Downstairs, and Sitting [3].

Convolution Neural Network (CNN) is widely used for image classification, image and face recognition, object detection, etc. It takes input as an image, does some pre-processing, and then processes it to classify them into various categories available. For the algorithm, the image is basically an array of pixels. It is completely dependent on image resolution. Hence, the algorithm will work better if the resolution is good. The image is *height(h)*width(w)*dimension(d)* matrix on RGB values. The CNN is divided into various layers, starting from the Convolution layer, which extracts the features from an input image. The second one is Strides, which corresponds to the number of pixel shifts from the original input matrix. Later, we perform a little padding wherever required, which is the third layer. Later comes the pooling layer. If the image is too large, we need to reduce some parameters performed by the pooling layer. Now, we are ready to work on a fully connected layer. Here, we club together all the required features to create a model [10]. Here, we have used the CNN algorithm, which is the most efficient and widely used everywhere [17].

Activity recognition is majorly done based on sensors. It is of various kinds, like only one user's activity recognition, multiple users' activity recognition, and group activity recognition. In single-user activity recognition, activities performed by a single user are identified and recorded. In multi-user activity recognition, actions performed by multiple users are identified and recorded. Group activity recognition differs from the above two, as here, the entire group is taken as a single entity, and the activities performed by that group are identified and recorded [8].

There are two significant kinds of surveillance systems, semi-autonomous and fully autonomous. Semi-autonomous is the one where the source is recorded at first and then later sent for review by experts. Such a system requires constant observation from a concerned authority which is difficult as there are chances of human errors. It is also expensive as the person continuously monitors the source to extract useful information. The second one is a fully autonomous system where no expert review is required. After installation is cheaper, less complicated, and does not require constant observations from concerned authorities.

The target is to understand human activity recognition's importance in various fields. From the above study, it is clear that one of the most suitable ways to implement a human activity recognition program is by using the CNN approach. TensorFlow is one of the most famous deep learning libraries by Google.

Human activity recognition can be unimodal and multimodal based on the source of datasets. Unimodal can be

Authorized licensed use limited to: DELHI TECHNICAL UNIV. Downloaded on January 17,2023 at 05:03:13 UTC from IEEE Xplore. Restrictions apply.

divided into space-time, stochastic, rule-based, and shape-based methods. Furthermore, multimodal can be divided into affective, behavioral, and social networking methods. Identification of human activity can be helpful in numerous fields, such as healthcare, augmented reality, security, and video surveillance.

IV. CHALLENGES

When it comes to Human Activity Recognition, there are numerous issues faced in developing an intelligent system that can identify the tasks performed by an individual(s). A few of these challenges include the changes in light at the time of day & night, also the changes when weather conditions change. This change makes identifying tasks challenging to understand through sensors or videos. Also, if the recorded image is noisy, the results might be affected as the input wasn't proper. It is easier to analyze the activity if the person is alone in the video. But, in real-time, we might have to consider that a group of people could perform different actions. The shadow of a person also changes the working of the algorithm as it changes the shape making the working of the algorithm more complex. Also, our program is written to detect moving objects, so identifying stationary objects becomes more difficult [4]. Some of the above challenges can be overcomed by using the popular RNN. RNN is easy to implement and resolves major complexities when input is obtained after output of independent CNN.

V. CONCLUSION

Human activity recognition is a complex topic. A few significant applications of the field include healthcare, augmented reality, and security. These applications can be expanded to various other areas as well. We also understand that CNN is currently one of the most efficient algorithms for feature selection, and then classification into activity takes place. Some other fields can be used for activity recognition, such as wildlife preservation. The application can be trained to understand whether an assault on any animal is being practiced or not. If any assault is being practiced on an animal by a human being, the system would immediately alert the concerned authorities, which would help conserve the environment. Also, this could be useful in case of illegal cutting of trees. The above method might need a multimodal approach following a social networking method. The dataset can be characterized into different classes, such as hitting, stone pelting, shooting, etc. Later, such practices can be identified and controlled whenever necessary. Another application of such a system could be in Sports, where the postures of a player need to be accurate. Instead of always having a coach to look after, one can automate it, which would be cheaper and less prone to errors. In the future, we will conduct a systematic literature review with more studies concerning machine learning and deep learning techniques.

REFERENCES

[1] O. C. Ann and L. B. Theng, "Human activity recognition: A review," 2014 IEEE International Conference on Control System, Computing and Engineering (ICCSCE 2014), pp. 389-393, 2014, DOI: 10.1109/ICCSCE.2014.7072750.

[2] Merriam-Webster, "accelerometer," merriam-webster.com, "https://www.merriam-webster.com/dictionary/accelerometer," (accessed 17 April 2022).

[3] Chintan Patel, "Human Activity Recognition," "medium.com," "https://patelchintan66.medium.com/human-activity-recognition-4d2b139c281d", (accessed 11 April 2022).

[4] Tripathi, R.K., Jalal, A.S. & Agrawal, S.C. Suspicious human activity recognition: a review. *Artif Intell Rev* **50**, 283–339 (2018). https://doi.org/10.1007/s10462-017-9545-7

[5] First, India & Pallathadka, Harikumar & Mustafa, Malik & Sanchez, Domenic & Sajja, Guna & Gour, Sanjeev & Naved, Mohd & Jawarneh, Malik. (2021). IMPACT OF MACHINE learning ON management, healthcare, AND AGRICULTURE. Materials Today: Proceedings. 10.1016/j.matpr.2021.07.042.

[6] Ranasinghe S, Al Machot F, Mayr HC. A review on applications of activity recognition systems with regard to performance and evaluation. *International Journal of Distributed Sensor Networks*. August 2016. doi:10.1177/1550147716665520

[7] Vrigkas, Michalis & Nikou, Christophoros & Kakadiaris, Ioannis. (2015). A Review of Human Activity Recognition Methods. Frontiers in Robotics and Artificial Intelligence. 2. 10.3389/frobt.2015.00028.

[8] Wikipedia, "Activity Recognition," wikipedia.org, "https://en.wikipedia.org/wiki/Activity_recognition," (accessed 21 April 2022).

[9] Fordham, "WISDM: Wireless Sensor Data Mining," "fordham.edu," "https://www.cis.fordham.edu/wisdm/dataset.php," (accessed on 2 April, 2022).

[10] Prabhu, "Understanding of Convolution Neural Network (CNN) -- Deep Learning," medium.com, "https://medium.com/@RaghavPrabhu/understanding-of-convolutional-neural-network-cnn-deep-learning-99760835f148", (accessed 11 April 2022).

[11] Ke, S.-R.; Thuc, H.L.U.; Lee, Y.-J.; Hwang, J.-N.; Yoo, J.-H.; Choi, K.-H. A Review on Video-Based Human Activity Recognition. Computers 2013, 2, 88-131. https://doi.org/10.3390/computers2020088

[12] G. Ogbuabor and R. La. 2018. Human Activity Recognition for Healthcare using Smartphones. In *Proceedings of the 2018 10th International Conference on Machine Learning and Computing* (*ICMLC 2018*). Association for Computing Machinery, New York, NY, USA, 41–46. https://doi.org/10.1145/3195106.3195157

[13] Kubota, Alyssa & Iqbal, Tariq & Shah, Julie & Riek, Laurel. (2019). Activity recognition in manufacturing: The roles of motion capture and sEMG+inertial

Authorized licensed use limited to: DELHI TECHNICAL UNIV. Downloaded on January 17,2023 at 05:03:13 UTC from IEEE Xplore. Restrictions apply.

wearables in detecting fine vs. gross motion. 6533-6539. 10.1109/ICRA.2019.8793954.

[14] M. M. Arzani, M. Fathy, A. A. Azirani and E. Adeli, "Switching Structured Prediction for Simple and Complex Human Activity Recognition," in IEEE Transactions on Cybernetics, vol. 51, no. 12, pp. 5859-5870, Dec. 2021, DOI: 10.1109/TCYB.2019.2960481.

[15] Anagnostis, A.; Benos, L.; Tsaopoulos, D.; Tagarakis, A.; Tsolakis, N.; Bochtis, D. Human Activity Recognition through Recurrent Neural Networks for Human-Robot Interaction in Agriculture. *Appl. Sci.*, vol 11, pp. 2188, 2021, https://doi.org/10.3390/app11052188.

[16] L. Fan, Z. Wang, and H. Wang, "Human Activity Recognition Model Based on Decision Tree," 2013 International Conference on Advanced Cloud and Big Data, 2013, pp. 64-68, DOI: 10.1109/CBD.2013.19.

[17] L. Mo, F. Li, Y. Zhu, and A. Huang, "Human physical activity recognition based on computer vision with deep learning model," 2016 IEEE International Instrumentation and Measurement Technology Conference Proceedings, 2016, pp. 1-6, DOI: 10.1109/I2MTC.2016.7520541.

[18] M. M. Hossain Shuvo, N. Ahmed, K. Nouduri and K. Palaniappan, "A Hybrid Approach for Human Activity Recognition with Support Vector Machine and 1D Convolutional Neural Network," 2020 IEEE Applied Imagery Pattern Recognition Workshop (AIPR), 2020, pp. 1-5, DOI: 10.1109/AIPR50011.2020.9425332.

[19] S. K. Bashar, A. Al Fahim and K. H. Chon, "Smartphone Based Human Activity Recognition with Feature Selection and Dense Neural Network," 2020 42nd Annual International Conference of the IEEE Engineering in Medicine & Biology Society (EMBC), 2020, pp. 5888-5891, DOI: 10.1109/EMBC44109.2020.9176239.

[20] Shreyas, D. & Raksha, S. & Prasad, B.. (2020). Implementation of an Anomalous Human Activity Recognition System. SN Computer Science. 1. 10.1007/s42979-020-00169-0.

[21] D. Ravi, C. Wong, B. Lo and G. -Z. Yang, "Deep learning for human activity recognition: A resource efficient implementation on low-power devices," 2016 IEEE 13th International Conference on Wearable and Implantable Body Sensor Networks (BSN), 2016, pp. 71-76, DOI: 10.1109/BSN.2016.7516235.

Authorized licensed use limited to: DELHI TECHNICAL UNIV. Downloaded on January 17,2023 at 05:03:13 UTC from IEEE Xplore. Restrictions apply.

Environment, Development and Sustainability
https://doi.org/10.1007/s10668-022-02876-5

Assessment of seasonal groundwater quality variation employing GIS and statistical approaches in Kabul basin, Afghanistan

Ali Reza Noori[1,2] · **S. K. Singh**[1]

Received: 22 June 2022 / Accepted: 21 December 2022
© The Author(s), under exclusive licence to Springer Nature B.V. 2023

Abstract
Increased demand for groundwater resources, restricted accessibility, and declining quality needs long-term groundwater conservation, particularly in metropolitan areas. The present study aimed to develop the regional spatial distribution of several groundwater quality parameters and assess their seasonal statistical significance in the Kabul basin of Afghanistan. Groundwater quality data of 54 monitoring wells were collected from the National Water Affairs Regulation Authority of Afghanistan, including the dry and wet seasons data. Some particular water quality measures, such as electrical conductivity, total dissolved solids, hardness, nitrate, chloride, fluoride, sulfate, sodium, and some heavy metals, were chosen for the analysis. These parameters' spatial distribution maps and temporal variations were developed to interpret spatial trends in groundwater quality and seasonal variations. Seasonal fluctuations in each quality metric were also tested to see if they were statistically significant. Based on the statistical findings, seasonal changes in the concentrations of magnesium, sodium, chloride, fluoride, iron, and manganese varied significantly. Out of the 20 assessments of water quality, 14 during the dry and 15 during the wet seasons revealed concentrations higher than the World Health Organization recommends. Variations in water quality metrics are correlated to the amount of recharge volume, hydraulic conductivity, and the geological formation of the region. The level of qualitative parameters has increased in the wet season, mainly in the wells located close to river routes or in agricultural areas. Results provide further insights into groundwater quality. Local authorities can utilize the outputs to develop sustainable water resource management.

Keywords Groundwater quality and seasonal variations · Paired *t*-test · Wilcoxon signed rank test · GIS

✉ S. K. Singh
sksinghdce@gmail.com

Ali Reza Noori
a.noori@kpu.edu.af

[1] Department of Environmental Engineering, Delhi Technological University, Delhi, India

[2] Department of Water Supply and Environmental Engineering, Faculty of Water Resources and Environmental Engineering, Kabul Polytechnic University, Kabul, Afghanistan

Published online: 06 January 2023

1 Introduction

Groundwater is one of the critical components of the hydrological cycle that is utilized as a safe, stable, and reliable source for drinking purposes in most regions of the globe. This source is the primary drinking water supply in most areas of the World, especially in arid and semi-arid environments. It is frequently utilized without treatment since it is a trustworthy source in terms of quality. On the other hand, over-extraction, climatic and environmental fluctuations, human influences, and other variables produce crises and stress over this vital resource. Groundwater is more vulnerable to over-exploitation, notably in arid and semi-arid areas with scarce and contaminated surface water resources (Goyal et al., 2021). In addition to natural causes of groundwater pollution, human activities release several pollutants into the subsurface aquifer system, depleting groundwater (Sarma & Singh, 2021). Therefore, researchers and managers of water resources are interested in the evaluation and assessment of groundwater quality and quantity (Aenab & Singh, 2015a, 2015b; Haritash et al., 2017; Jhamnani & Singh, 2015), and numerous research, particularly on the spatial evaluation of groundwater quality, has been released (Azimi et al., 2018; Najafi Saleh et al., 2020; Perera et al., 2022; Soujanya Kamble et al., 2020). GIS is essential for groundwater evaluation because it allows researchers to identify and statistically evaluate distinct spatial characteristics in groundwater quality data.

The temporal measurements of groundwater quality and its trend analysis are more complicated and frequently necessitate statistical evaluations of long-term groundwater quality data (Elçi & Polat, 2011). For instance, He et al., (2020) analyzed groundwater quality for ten years (2005–2015) in Xi'an Northwest China. Long-term groundwater quality data from 1996 to 2015 have been collected for the study. A study by Su et al., (2020) also analyzed the temporal variation of groundwater quality using long-term groundwater quality records. The properties and evolution of the depression cone and its influence on the quality of confined aquifers, groundwater level, and quality data for 29 years (1990–2019) and 27 years (1991–2018) were gathered and evaluated. With long-term data, modeling and forecasting water quality is also possible. This study has used the Grey Markov model to predict the concentration of total dissolved solids. Although studying groundwater quality trends and its temporal variation analysis gives more insights, it necessitates long-term monitoring.

Kabul has about five million inhabitants, is the country's capital, and is the nation's most populated city. Groundwater is the city's only potential source of water supply (Brati et al., 2019; Houben et al., 2009; Noori & Singh, 2021a, 2021b; Zaryab et al., 2017, 2021, 2022a). Based on trend analysis by (Noori & Singh, 2021b), water levels significantly declined in 82 percent of the observational wells. According to the Standardized Groundwater Level Index (SGI) statistics, most of the wells in the study area experienced progressively severe and chronic drought between 2014 and 2020. Several factors influence the reduction in groundwater levels in Kabul. For instance, climate change, overexploitation, population growth, and the loss of recharge zones have all been identified as significant critical contributors in several studies (Bohannon, 2010; Frischmann, 2012; Thomas et al., 2017; WHO, 2017; Jawid & Khadjavi, 2019; Dan & Jesse, 2020). The quality of groundwater in the Kabul plain has been addressed by some researchers (Brati et al., 2019; Hamdard et al., 2020; Hayat & Baba, 2017; Jawadi et al., 2020; JICA, 2011; Mack et al., 2009; Zahid et al., 2019; Zaryab et al., 2017, 2021, 2022a, 2022b). Nitrate, hardness, bacteriological contaminations, sulfate, fluoride,

heavy metals, arsenic, selenium, uranium, and lead are significant groundwater quality issues in the Kabul Basin.

The population of Kabul city increased significantly after 2001. Most Afghan refugees returned to their homeland after the new government took office in the nation (in 2001–2002), and many settled in the capital. Most people also relocated from the provinces to the capital for employment and educational opportunities. Furthermore, with the increase in population, urban development proceeded unplanned, and the lack of implementation of the urban master plan resulted in severe social and environmental challenges. Even though the Kabul Aquifer is the city's primary drinking water source, Kabul still lacks a coordinated infrastructure for collecting, disposing, and treating wastewater (Paiman & Noori, 2019). According to (Noori & Singh, 2021c) only 1% of the metropolitan population has access to a partially operational municipal sewage infrastructure. According to (Zaryab et al., 2022b), the groundwater in Kabul is susceptible to anthropogenic contamination, and sewage is the primary contributor to NO_3 in the Kabul Basin. Therefore, it can be said that in addition to natural and seasonal factors, anthropogenic factors also have a crucial impact on groundwater pollution in Kabul.

Since Kabul has a semi-arid climate and seasonal rainfall, it may cause changes in groundwater quality. The main focus of this research is to determine whether significant seasonal changes in groundwater quality parameters exist. Water quality data will be statistically analyzed to meet this objective. In addition, the research will investigate and assess groundwater quality on the Kabul plain and compare it to drinking water quality standards. Spatial evaluation will be carried out with the aid of ArcGIS to present and comprehend the spatial magnitude of qualitative indicators more effectively. Since most groundwater quality assessments studied in the research area are only in snapshots, examining seasonal water quality and evaluating its changes provides more insight into sustainable groundwater management. Furthermore, the outputs of this study can facilitate the provision of goal 6 (clean water and sanitation) of the sustainable development goals.

2 Materials and methods

2.1 Physical properties of the study area

The Kabul Basin (JICA, 2011) is the current research region, and it encompasses the bulk of Kabul, Afghanistan's capital. The geographical location of the research area is in the central-east of the country, between 34° 36′ 30″ N and 34° 24′ 40″ N latitude and 69° 01′ 25″ E and 69° 22′ 30″ E longitude (Fig. 1). The research area possesses a total area of 496 km^2. The climate condition in the basin is arid to semi-arid. Kabul's precipitation is seasonal, with most snowfall and rainfall occurring in the winter (December, January, and February) and early spring (March and April). The average yearly precipitation in the study area was around 330 mm (Noori & Singh, 2021a). The basin's maximum and minimum average air temperature ranges were recorded as 32 °C in July and − 7 °C in January (Zaryab et al., 2017). Built-up land is the study area's most frequent land use category (Noori & Singh, 2021b). It is the country's central business hub, and after 2001, many refugees returned to their homeland, settling mainly in Kabul. Many citizens from other regions also flocked to Kabul in search of work. Low but steep mountain ranges surround the basin. The basin's height ranges from 1763 to 2823 m (Fig. 1). The mountains on the southwest and southeast borders often have a more significant elevation than the others.

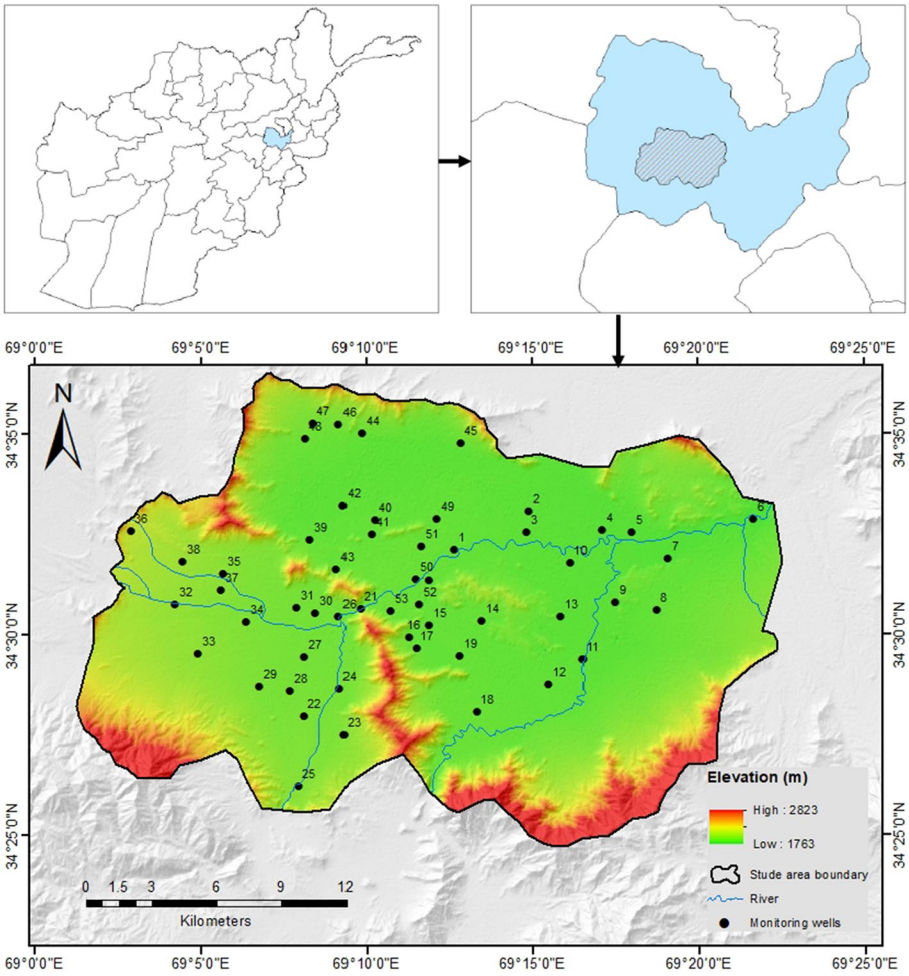

Fig. 1 The research area location map

2.1.1 Drainage system

Three waterways enter the basin from different directions and exit toward the northeast of the city. The Paghman Stream flows from east to west. The Maidan river, known as the Kabul River, enters the study region from the south side and runs for 21 km until merging with the Paghman River. One of the most significant branches of the Kabul River is the Logar River. It runs from south to north and enters the Kabul River roughly 17 km downstream of the Paghman streams mouth (Fig. 1). Due to snow melting in the late winter and early spring, as well as occasional seasonal rainfall, the Kabul and Paghman rivers have only had a slight discharge in the last two decades. In Kabul aquifers, the watercourse appears to be a key source of groundwater replenishment (Noori & Singh, 2021a). Due to various factors such as little precipitation, high evaporation, built-up regions covering recharge zones, and clay layers, the amount of infiltration recharge of aquifers by rainfall accounts for just a tiny part of overall recharge (Tünnermeier and Houben, 2005).

2.1.2 Geology

The study area is a part of the flat Kabul Basin. Most of the mountain range surrounding and underlying the study region comprises metamorphic rocks. The basin's structure was formed by tectonic movement during the Late Paleocene age. Plate movements affected the Kabul Basin's structure during the early Tertiary (Late Paleocene) period. The Kabul block is the result of the intersection of the main Bamyan-Panjshir-Herat faults (west and northwest faults) and the Soroubi fault (easterly), and the Chaman fault system (southeast fault). Conglomerate and sandstone, loess, metamorphic rocks, limestone, fan alluvium and colluvium, gneiss, limestone, dolomite, sandstone and siltstone, ultramafic intrusions, and river channel alluvium are the most prevalent surficial geological formations found in the Kabul Basin. The basin is largely uncemented and semi-consolidated lacustrine, fluvial, and aeolian sedimentary rocks such as sand, gravel, and silt from the Quaternary and Neogene eras (Mack et al., 2009; Tünnermeier and Houben, 2005; Zaryab et al., 2017).

2.1.3 Hydrogeology

Based on (JICA, 2011), there are three main aquifer clusters in the study region: The shallow aquifer is located within the alluvial deposits and a deeper aquifer in Neogene layers ("the upper Neogene aquifer"), and a deep aquifer ("the lower Neogene Aquifer"). The lower Neogene aquifer is categorized as "Fossil Water" because it is segregated from the usual hydrologic cycle. Deep aquifers are thought to be thousands of years old, but shallow aquifers with a depth of less than 100 m are usually (20–30) years old Mack et. al (2010).

The bulk of the public water supply wells is located next to riversides because riverbeds provide most groundwater recharge. According to some known literature, the city encompasses four major interconnected aquifers (Pell Frischmann, 2012; Uhl & Tahiri, 2003; Zaryab et al., 2017). Meanwhile, shallow aquifers, also known as "Alluvial Aquifers" or "Quaternary Aquifers," may be found across the city at different depths, albeit the deposits that store such groundwater are denser and have a larger groundwater potential near river systems. The Logar aquifer (in the southeast part of the basin) is 30–40 m thick, with a peak of 70 m. The surface of the water table follows the land's topography in the bulk of the basin, and the groundwater flow direction is comparable to surface water runoff (Broshears et al., 2005). A trend analysis of groundwater levels by (Noori & Singh, 2021b) indicates that the groundwater level has considerably decreased in the study area. From 2014 to 2020, the majority of wells in the city region endured intense and chronic droughts, according to the Standardized Groundwater Level Index (SGI). Variations in land use and land cover, overuse of groundwater, and decreased annual precipitation contribute to the fast decline in groundwater levels.

2.2 The process of data acquisition and selection

The required groundwater quality data from the General Directorate of Water Resources of Afghanistan's National Water Affairs Regulation Authority (NWARA) has been obtained. The NWARA has some monitoring wells that cover most parts of Kabul city. The hydrogeological authority of Kabul city has executed the monitoring of groundwater. They collected water samples and analyzed them from 14 August to 27 September 2017 (dry season) and 27 March to 9 May 2018 (wet season). The obtained groundwater quality data

includes the seasonal water quality data for 54 monitoring wells. Out of 54 monitoring wells, only one well does not have data in the dry season. This well was excluded from the study, and all 53 other wells were included in the current analysis. Groundwater quality figures obtained from the NWARA include the following data: static water level (SWL), Temperature (T), Electrical Conductivity (EC), pH, Dissolved Oxygen (DO), Total Dissolved Solids (TDS), Salinity, Color, Turbidity, Total Hardness (TH), Calcium (Ca), Magnesium (Mg), Sodium (Na), Total Alkalinity, Phenolphthalein Alkalinity, Carbonate (CO_3), Bicarbonate (HCO_3), Chloride (Cl), Fluoride (F), Sulfate (SO_4), Phosphate (PO_4), Potassium (K), Nitrite (NO_2), Nitrate (NO_3), Ammonia (NH_3), Iron (Fe), Manganins (Mn), Copper (Cu), Aluminum (Al), Arsenic (As) and Cyanide (CN). The following data from the collected dataset have been selected for the current analysis: EC, pH, TDS, TH, Mg, Na, HCO_3, Cl, F, SO_4, PO_4, K, Fe, Mn, Cu, Al, and CN. The analyzed parameters have been selected from the presented figures based on the following three fundamental factors. The parameters that have exceeded the permissible limits of World Health Organization (WHO) and Afghanistan National Standard Authority (ANSA). The parameters that show the most seasonal variations in visual observation. Quality parameters are essential in drinking water quality.

2.3 Development of geospatial distribution maps of groundwater quality data

Data on the quality of groundwater collected from the NWARA were aggregated and reviewed for irregularities and inconsistencies. To visualize and investigate the geospatial distribution of EC, TDS, TH, Ca, Mg, K, Mn, Na, Cl, F, Fe, and NO_3, the dataset was entered into a database created within an ArcGIS 10.7.1 environment. The principal method for deriving regional distributions of groundwater quality metrics in the following research was interpolation using the Inverse Distance Weighting (IDW) methodology. Interpolation was utilized to convert point data, such as concentration levels at each observational point, into a total averaged number. For this investigation, an IDW with a power coefficient of 2 was used, assuming that contents at any sample point should be closer to the recorded quantity at the measurement point.

Geospatial distribution maps depicting changes for each selected criterion were also created to measure seasonal changes in groundwater quality. The positive values indicate an increase in concentration, and the negative values show a decrease. The following equation was used to compute the change in concentration:

$$\text{Seasonal variation of concentration (mg/l)} = C_{\text{wet period}} - C_{\text{dry period}} \quad (1)$$

As a result, the regional distribution of variation in concentration of each groundwater quality indicator from fall (dry season data) to spring (wet season data) was depicted by these geospatial maps.

2.4 Statistical evaluations

The "one-sample Kolmogorov–Smirnov (K–S)" test was used to assess the normalcy of seasonal changes in the quality of groundwater samples (Elçi & Polat, 2011) before the testing to see if the seasonal variation in its quality was significant. In the normal distribution of seasonal variations, "the paired sample *t*-test" was employed. With the help of this parametric statistical test from a statistical standpoint, it will be established if the means of

two populations differ from one another. Only when the distribution of accessible data sets meets normal distribution criteria can the "*t*-test" be used (Elçi & Polat, 2011). Another prerequisite for carrying out this statistical test is that each group's sample size should be more than 30. When employing paired sample "*t*-tests," the computed *p*-value of two-tailed significance was compared to α (the significance level), set at 0.05 in this study. The hypotheses have been proposed as follows:

$\mathbf{H_0}$ The water quality data will not have any seasonal difference from the dry to wet period.

$\mathbf{H_s}$ The water quality data will have seasonal differences from the dry to wet period.

Suppose the *p*-value is estimated at less than α. In that case, the null hypothesis will be rejected, which indicates no seasonal changes in groundwater quality. The alternative hypothesis is accepted, suggesting the seasonal water quality difference. An alternative statistical test must be employed in case of unnormal distribution of seasonal variation. The alternate options for parametric statistical tests are nonparametric tests that do not have to follow any specific assumptions for data distribution.

Furthermore, the data ranks, a crucial feature of these techniques, are used rather than the data values. The alternative to the "*t*-test" is the "Wilcoxon signed-rank test" (Elçi & Polat, 2011), which is employed in this investigation to find out whether there is any significant variation in the concentrations of groundwater quality with differences of unnormal distribution. The *"one-sample Kolmogorov–Smirnov test,"* the *"paired-samples t-test,"* and the *"Wilcoxon signed-rank test"* were all performed using the statistical program SPSS statistics v25 to make statistical studies easier.

3 Results

The findings of the groundwater quality data subsequent processing and assessment are illustrated here. In the first stage, groundwater quality in the study region was evaluated using descriptive statistics and compared with drinking water quality regulations. Additionally, statistical studies such as the "paired-samples *t*-test" and "Wilcoxon signed-rank test" are available to evaluate the significance of seasonal variations in groundwater quality in the research region. Lastly, geospatial maps illustrating the regional distribution of groundwater quality characteristics with concentrations more than WHO/ANSA drinking water guidelines exhibit statistically significant seasonal changes. One parameter has no concentration more than WHO/ANSA guidelines and does not exhibit substantial changes are provided. Furthermore, change maps demonstrating seasonal changes in groundwater quality metrics are shown in a geographically dispersed format.

3.1 Generic evaluation of the quality of groundwater

A summarized output of statistical evaluation added a comparison of water quality with drinking water quality regulations represented in Tables 1 and 2. According to the findings, the Kabul basin's groundwater temperature (T) varied from 12.2 to 23.1 °C in August and September and from 12 to 27 °C in March and May. The pH ranges for all samples were 6.96–8.21 in the dry period and 7.08–8.57 in the wet period, indicating neutral to mild alkaline waters within permitted drinking water standards. The high EC values for

Table 1 Results of sample investigations statistically summarized and compared to drinking water quality requirements for Aug and Sep 2017 (Dry season)

Water quality parameters	Unit	Regulations for drinking water quality		Wells ($n=53$)				Samples exceeding WHO or ANSA limits	
		WHO	ANSA	Min.	Mean	Max.	Standard deviation	No. of sample	% of sample
T	C	12–25	12–25	12.20	17.24	23.10	2.09	Nil	Nil
pH	–	6.5–8.5	6.5–8.5	6.96	7.54	8.21	0.27	Nil	Nil
EC	µS/cm	1500	1500	364.00	1888.11	9600.00	1940.49	22.00	41.51
TDS	mg/l	1000	1500	241.76	1240.04	6353.64	1316.31	22.00	41.51
TH	mg/l	500	500	50.00	771.74	3580.00	744.57	27.00	50.94
Ca	mg/l	75	75	16.00	117.56	505.00	99.77	31.00	58.49
Mg	mg/l	30	30	13.10	285.64	1977.90	360.72	48.00	90.57
Na	mg/l	200	200	0.00	123.62	1400.00	247.63	7.00	13.21
HCO_3	mg/l	600	600	150.00	388.68	1600.00	217.29	4.00	7.55
F	mg/l	1.5	1.5	0.00	0.49	1.21	0.40	0.00	0.00
Cl	mg/l	NA	250	0.000	0.011	0.050	0.014	0.000	0.00
NO_3	mg/l	50	50	0.00	2.42	7.50	1.86	0.00	0.00
SO_4	mg/l	250	250	5.00	105.51	1000.00	134.16	2.00	3.77
PO_4	mg/l	NA	6	0.00	0.25	2.12	0.32	0.00	0.00
K	mg/l	10	10	0.90	17.73	146.20	29.20	16.00	30.19
Al	mg/l	0.2	0.2	0.000	0.035	0.214	0.062	6.000	11.11
Mn	mg/l	NA	0.3	0.000	0.724	11.500	1.554	30.000	55.56
Fe	mg/l	0.3	0.3	0.000	0.057	0.610	0.112	3.000	5.56
CN	mg/l	NA	0.05	0.000	0.012	0.270	0.039	3.000	5.56
Cu	mg/l	2	2	0.000	0.311	6.710	0.990	1.000	1.85

most samples and the comparatively significant standard deviations are evident. According to WHO and ANSA, the maximum permissible concentration of EC in drinking water is 1500 µS/cm (ANSA, 2013; WHO, 2011). More than 40% of sampling points have EC higher than regulations limits in both seasons.

TDS and TH values were statistically similar to EC. The TDS in sampling points ranged between 241 and 6354 mg/l in the dry period and 353–5807 mg/l in the wet period. The mean content of TDS is 1240 and 1205 mg/l for dry and wet seasons, respectively. More than 20% of the samples in both seasons exceeded the required limits (1500 mg/l suggested by ANSA) of TDS in drinking water. Total hardness in Apr-May varies from 28 to 2700 mg/l with a mean of 847 and a standard deviation of 567 mg/l. From Aug to Sep, it varies from 50 to 3580 with a mean value of 772 and a standard deviation of 745 mg/l. The maximum overall allowed total hardness suggested by WHO and ANSA is 500 mg/l. More than 50% of samples in the dry season and more than 70% in the wet season exceed the guidelines values.

The calcium concentration in the wet season varies from 8 to 721 mg/l, with 73% of samples greater than WHO and ANSA limitations (> 75 mg/l). The mean concentration of Ca in the wet season is 193, and its standard deviation is 170 mg/l. It ranges from 16 to 505 mg/l in the dry season, with 58% of samples greater than the guidelines value. In the

Table 2 Results of sample investigations statistically summarized and compared to drinking water quality requirements for Mar–May 2018 (Wet season)

Water quality parameters	Unit	Regulations for drinking water quality		Wells ($n=53$)				Samples exceeding WHO or ANSA limits	
		WHO	National	Min.	Mean	Max.	Standard deviation	No. of sample	% of sample
T	C	12–25	12–25	12.00	17.68	27.00	2.55	Nil	Nil
pH	–	6.5–8.5	6.5–8.5	7.08	7.58	8.57	0.30	Nil	Nil
EC	µS/cm	1500	1500	380.00	1817.40	8710.00	1552.47	25.00	47.17
TDS	mg/l	1000	1500	253.08	1205.67	5807.52	1042.71	11.00	20.75
TH	mg/l	500	500	28.80	847.34	2700.00	566.93	38.00	71.70
Ca	mg/l	75	75	8.02	192.82	721.40	170.62	39.00	73.58
Mg	mg/l	30	30	4.80	118.02	584.70	116.59	37.00	69.81
Na	mg/l	200	200	25.00	173.87	1800.00	272.14	9.00	16.98
HCO_3	mg/l	600	600	125.00	368.40	775.00	134.02	2.00	3.77
F	mg/l	1.5	1.5	0.020	0.751	4.010	0.727	3.00	5.66
Cl	mg/l	NA	250	−0.020	20.674	331.000	51.530	1.000	1.89
NO_3	mg/l	50	50	−2.60	2.69	8.70	2.22	0.00	0.00
SO_4	mg/l	250	250	7.00	165.64	1900.00	339.02	3.00	5.66
PO_4	mg/l	NA	6	0.05	0.32	4.05	0.56	0.00	0.00
K	mg/l	10	10	0.30	17.43	142.80	26.42	17.00	32.08
Al	mg/l	0.2	0.2	−0.020	0.026	0.152	0.045	0.000	0.00
Mn	mg/l	NA	0.3	−0.500	6.618	266.000	36.581	40.000	75.47
Fe	mg/l	0.3	0.3	0.000	0.114	1.160	0.221	5.000	9.43
CN	mg/l	NA	0.05	0.000	0.008	0.130	0.018	1.000	1.89
Cu	mg/l	2	2	0.00	0.31	4.26	0.79	3.000	5.66

autumn mean value of Ca is 118 mg/l, and the standard deviation of 100 mg/l. In the wet season, magnesium concentrations range from 4.8 to 589 mg/l, with a mean of 118.2 and a standard deviation of 117 mg/l. About 70% of samples exceed the guidelines for drinking water in the wet season. The minimum Mg concentration in the dry season is 13, and the maximum is 1977 mg/l, with a mean of 286 and a standard deviation of 360 mg/l. About 90% of samples exceeded WHO and ANSA standards for drinking water (> 30 mg/l). In the wet season, sodium concentrations vary from 25 to 1800 mg/l, with a mean of 173 mg/l. While in the dry season, it ranges from 0 to 1400 mg/l, with a mean of 123 mg/l. About 16% of samples in the spring and around 13% in the autumn exceed the drinking water guidelines requirements.

Manganese is the other ion concertation with a high concentration in both seasons. Roughly 75% of samples during the wet season and about 55% during the dry season surpass the recommended level. Potassium concentration in both seasons has exceeded the guideline with more than 30% sampling points. Fluoride, chloride, nitrate, and phosphate are the parameters with concertation less than the maximum limits of WHO and ANSA in the autumn. In the spring, fluoride and chloride concentrations exceed the guidelines in some low percentages. Bicarbonate, sulfate, aluminum, iron, cyanide, and copper are the parameters in which less than 10% of samples have a concentration higher than drinking water quality standards.

Eventually, the groundwater in the Kabul basin is of poor quality compared to existing guidelines. Most qualitative indicators, such as EC, TDS, TH, Ca, Mg, Na, Mn, and K, are the parameters that exceed the suggested ranges of guidelines for drinking water. On the other hand, from descriptive statistics, the concentration of most qualitative parameters in the spring is higher than in the autumn. This evaluation is discussed later in this article.

3.2 Seasonal variations in the groundwater quality

At the inception stage, the "K–S test" was employed to investigate the statistical distribution of variances. For each quality metric across data sets, the difference in values between spring and fall was stated as follows:

$$d_i = x_{1i} - x_{2i} \tag{2}$$

where i indicates the groundwater quality indicator,

x_{1i} shows metrics from the dry period (measurements of Aug–Sep 2017).

x_{2i} illustrates metrics of the wet period (measurements of Mar–May 2018).

The null (H_0) and alternative (Hs) hypotheses are developed as follows to figure out if the changes are normally distributed:

H_0 The observed data set has a normal distribution.

Hs The observed data set has no normal distribution.

The calculated p-values have been compared with the selected significance level ($\alpha = 0.05$), and the outputs statistical test is concluded in Table 3. Since all groundwater quality variables except calcium and nitrate have unnormal distribution (95% confidence interval) substantially, the nonparametric *"Wilcoxon rank test"* has been utilized to examine the significance of groundwater quality variation. For the Ca and NO_3 (differences of Ca and NO_3), the p values were larger than the α values ($p = 0.072 > 0.05$ and $p = 0.2 > 0.05$

Table 3 Result of the "Kolmogorov–Smirnov test" for normal distribution of seasonal changes ($n=53$)

Differences of parameters	Mean	SD	K–S statistic	p value	Hypothesis
EC	70.717	831.694	0.311	0.000	Hs
pH	−0.039	0.232	0.152	0.004	Hs
TDS	34.368	543.813	0.320	0.000	Hs
TH	−75.600	741.260	0.160	0.002	Hs
Ca	−75.260	187.179	0.116	0.072	H_0
Mg	167.619	341.657	0.189	0.000	Hs
Na	−46.962	193.054	0.177	0.000	Hs
HCO3	20.283	156.216	0.292	0.000	Hs
Cl	−20.663	51.532	0.344	0.000	Hs
F	−0.260	0.853	0.200	0.000	Hs
SO4	−60.136	349.471	0.420	0.000	Hs
PO4	−0.069	0.606	0.258	0.000	Hs
K	0.299	18.065	0.294	0.000	Hs
NO_3	−0.271	2.187	0.093	0.200	H_0
Fe	−0.057	0.218	0.287	0.000	Hs
Mn	−5.894	36.602	0.480	0.000	Hs
Cu	0.001	1.097	0.332	0.000	Hs
Al	0.009	0.085	0.229	0.000	Hs
CN	0.004	0.043	0.361	0.000	Hs

for Ca and NO_3 respectively); consequently, the alternative hypothesis has been rejected, and the data of Ca and NO_3 might be regarded to have a normal distribution with a 95% confidence interval.

To statistically examine seasonal groundwater quality changes, the following null (H_0) and alternative (Hs) hypotheses were proposed:

H_0 The change in seasonal concentration values between dry and wet seasons is insignificant.

Hs The change in seasonal concentration values between dry and wet seasons is significant.

The *"t*-test*"* can only be used for Ca and NO_3 variables based on the results of the statistical normality test because their seasonal fluctuation has a normal distribution. Ca's seasonal variation is statistically significant, as shown by the paired samples "*t*-test" analysis (Table 4). The alternative hypothesis was accepted because the *p*-value is smaller than the α value ($p=0.005$ less than 0.05). It was established with a 95% confidence interval that calcium concentrations have a significant variation from the dry to wet period. Although the mean Ca content increased from 117.56 to 192.82 mg/l over time (all sample sites), the statistical test findings significantly increased.

Furthermore, the "*t*-test" result for NO_3 shows that the seasonal change in its concentration is not statistically significant. The calculation results show that the value of p is larger than the α value ($p=0.372>0.05$); eventually, the null hypothesis was accepted, and the

Table 4 summary of paired sample "*t*-test" for Ca and NO_3

Parameters	Mean	SD	95% Confidence interval of the differences		*t*	*p*	Hypothesis
			Lower	Upper			
Ca	−75.260	187.179	−126.853	−23.667	−2.927	0.005	Ha
NO_3	−0.271	2.187	−0.874	0.332	−0.901	0.372	H_0

alternative hypothesis was rejected with a 95% confidence interval. It was concluded that there is no significant variation in NO_3 levels from the dry to rainy periods. In addition, the average NO_3 level increased from 2.42 to 2.69 mg/l over time. The increase was not significant according to the statistical test results.

The "Wilcoxon signed-rank test" was used to determine if seasonal variations in quantities of several groundwater quality measures, including EC, pH, TDS, TH, Mg, Na, HCO_3, Cl, F, SO_4, PO_4, K, Fe, Mn, Cu, Al, and CN, were statistically significant.

The test results are shown in (Table 5) and revealed that most seasonal variations were statistically insignificant. The changes in Mg, Na, Cl, F, Fe, and Mn contents, on the other hand, appeared significant. The table provided positive rankings to data pairs with the increasing condition in their values from dry to wet season. Negative ranks have been employed in the opposite instance. The alternative hypothesis has been accepted for the data pairs of Mg, Na, Cl, F, Fe, and Mn since $p < \alpha$. From a statistical standpoint, the seasonal variation in concentrations constituted significant. It can be summarized that except for Mg, which decreased its concentration from the dry to wet season, the concentration of all other parameters, i.e., Na, Cl, F, Fe, and Mn, increased in the spring. The null hypothesis has been clearly accepted since $p > \alpha$ for the rest of the water quality parameters.

Numerous factors, such as mineral dissolution, anthropogenic and urban influences, and evaporitic lacustrine deposits, are potential indicators that could have an impact on groundwater quality. The critical determining element of groundwater quality in the Kabul basin, according to Zaryab et al. (2021), is evaporitic lacustrine deposits. The interaction of water with particular rocks and minerals, such as gypsum and limestone, is the cause of the presence of calcium and magnesium in groundwater. The presence of sodium and chloride in groundwater can be attributed to several sources, “including the weathering of minerals in the soil, salt-bearing geological formations, deposition of salt spray, the use of salt for road de-icing, and in coastal areas, intrusion of salty ocean water into fresh groundwater sources.” Fluoride is found in groundwater due to weathering and leaching of fluoride-bearing minerals from sediments and rocks. The most frequent sources of iron and manganese in groundwater occur naturally, such as weathering rocks and minerals containing iron and manganese. Sewage, landfill leachate, industrial effluent, and acid-mine drainage can all add iron and manganese to the surrounding groundwater.

According to the aforementioned, the weathering of minerals and rocks is significant in determining the majority of quality criteria in groundwater. Seasonal precipitations may infiltrate the soil beds along rivers and nearby lands, sometimes agricultural fields and hillsides. During the infiltration process, they come into contact with rocks and minerals containing magnesium, sodium, Calcium, fluoride, and chloride. This can be the main reason for the increase of these parameters in the wet season in groundwater. The phenomenon of infiltration and weathering of minerals in the soil is also a case of iron and manganese. But another reason that may increase iron and manganese in groundwater is the infiltration of

Table 5 Summary of Wilcoxon signed-rank test

Parameters	Negative ranks			Positive ranks			Test statistics			Hypothesis
	n	Mean rank	sum of ranks	*n*	Mean rank	sum of ranks	Ties	*Z*	*p*	
EC	25	25.92	648	28	27.96	783	0	−0.598[b]	0.55	H_0
pH	23	24.57	565	29	28.03	813	1	−1.129[b]	0.259	H_0
TDS	24	24.52	588.5	28	28.2	789.5	1	−0.915[b]	0.36	H_0
TH	22	24.25	533.5	30	28.15	844.5	1	−1.416[b]	0.157	H_0
Mg	41	28.46	1167	12	22	264	0	−0.997[a]	0.000	Ha
Na	16	23.44	375	33	25.76	850	3	−2.363[b]	0.018	Ha
HCO_3	28	21.46	601	18	26.67	480	7	−0.666[a]	0.505	H_0
Cl	7	8.93	62.5	41	27.16	1113.5	5	−5.393[b]	0.000	Ha
F	19	25.24	479.5	34	27.99	951.5	0	−2.089[b]	0.037	Ha
SO4	25	23.32	558	26	29.54	768	2	−0.985[b]	0.325	H_0
PO4	21	24.4	512.5	29	26.29	762.5	3	−1.207[b]	0.227	H_0
K	20	29.28	585.5	33	25.62	845	0	−1.151[b]	0.25	H_0
Fe	11	28.55	314	37	23.3	862	5	−2.814[b]	0.005	Ha
Mn	20	23.15	463	33	29.33	968	0	−2.236[b]	0.025	Ha
Cu	22	28.59	629	30	24.97	749	1	−0.547[b]	0.584	H_0
Al	22	28.82	634	29	23.86	692	2	−0.272[b]	0.786	H_0
CN	18	22.08	397.5	26	22.79	592.5	9	−1.14[b]	0.254	H_0

[a]according to negative rank, [b]according to positive rank

surface water contaminated with sewage through the river beds and municipality channels because the city of Kabul does not have a sewage collection and disposal system.

3.3 Spatio-seasonal evaluation of groundwater quality criteria

In order to spatially depict the quality of groundwater in the Kabul basin, spatial distribution maps of some qualitative indicators of groundwater were prepared for both dry and wet seasons. Qualitative variables like EC, TDS, TH, Ca, Mg, K, and Mn were chosen for geographic distribution maps since their values exceed WHO and ANSA drinking water recommendations. Parameters like Ca, Mg, Na, Cl, F, Fe, and Mn were considered for spatial distribution maps because they have significantly changed. One parameter (NO_3) was chosen for the geographical distribution map from the other qualitative indicators that are not above WHO and ANSA criteria and have not been modified considerably. Furthermore, the spatial distribution maps of changes illustrating the degree of differences in measurement results were created to highlight how the regional distribution of several groundwater quality indicators altered as the seasons switched from dry to wet.

The spatial pattern of EC contents and Ca values for each measurement interval is presented in Fig. 2a, b. The concentration of electrical conductivity in the west and north parts of the basin is less than 3000 µS/cm. Only a few wells in the central-eastern part of the basin have an electrical conductivity higher than 3000 µS/cm for both seasons. As well as, the concentration of Ca is lower in the marginal areas added in the western and northern parts of the basin but increases in the central and southeastern parts of the basin and reaches more than 300 mg/l. Figure 2c, d illustrates the change in EC and Ca in the study area from the dry to wet season. The concentration of EC has grown throughout the study's peripheral regions, particularly in the south, north, and west. The EC value decreased in other parts of the area by changing the season from dry to wet. The minus marks in the figure's legends illustrate the decrease in concentration, while the plus marks indicate increased concentrations. Ca concentrations in the study region declined in the north, west, and some eastern sections up to −240 mg/l but climbed to 630 mg/l in the middle and south parts.

Figure 2e, f illustrates the spatial distribution maps of TDS and Mg concentrations. TDS values in most observation wells are less than 1000 mg/l in both seasons. Only three wells in the middle and central-eastern regions of the basin have values larger than 1500 mg/l during the dry season, whereas eleven wells have values greater than 1500 mg/l during the wet season. Mg concentration exceeds 400 mg/l in most parts of the basin during the dry period. In comparison, it has decreased in most parts of the basin in the wet period.

Based on Fig. 2g, the TDS concentration has increased in the western area of the basin up to +880 mg/l from dry to wet season. In contrast, the eastern part of the basin shows a negative trend, especially in the central-east, up to −3500 mg/l. As well as, the concentration of Mg (Fig. 2h) has similar distribution in the basin. It has increased up to +270 mg/l and decreased to −1800 mg/l in the same locations as TDS.

The spatial distribution map of TH and K is depicted in Fig. 3a and b. The concentration of TH has great values in the central parts of the study area. Eleven observational points have TH > 1000 mg/l in the autumn, increasing to 16 wells in the spring. The K content in the west part of the study area has fewer values (i.e., less than 10 mg/l) in both seasons. In autumn and spring, concertation rises in the middle area of the study and continues to the southeast.

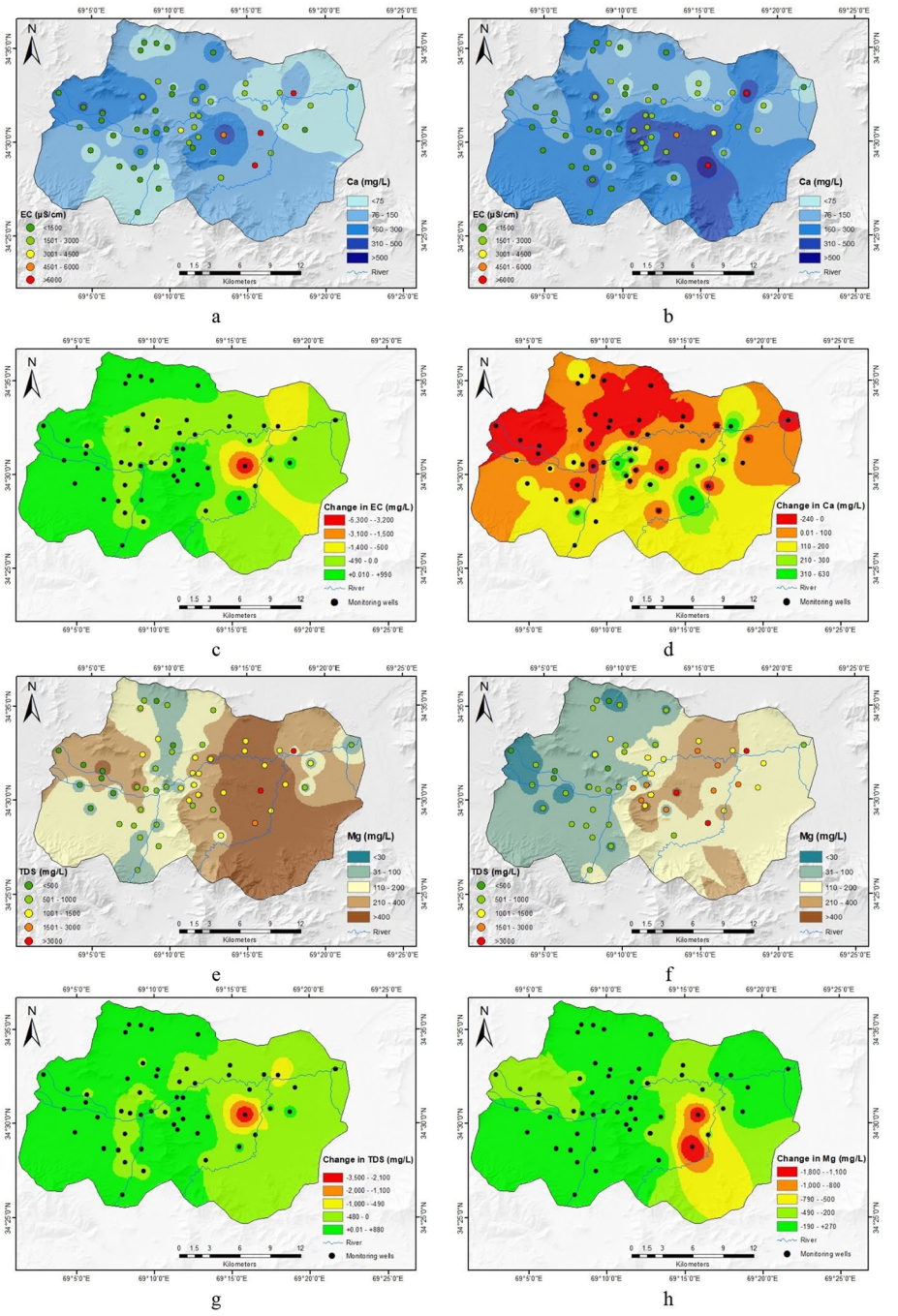

Fig. 2 Spatial distribution maps **a** Ca and EC dry season, **b** Ca and EC wet season, **c** change in EC, **d** Change in Ca, **e** TDS and Mg dry season, **f** TDS and Mg wet season, **g** Change in TDS, **h** Change in Mg

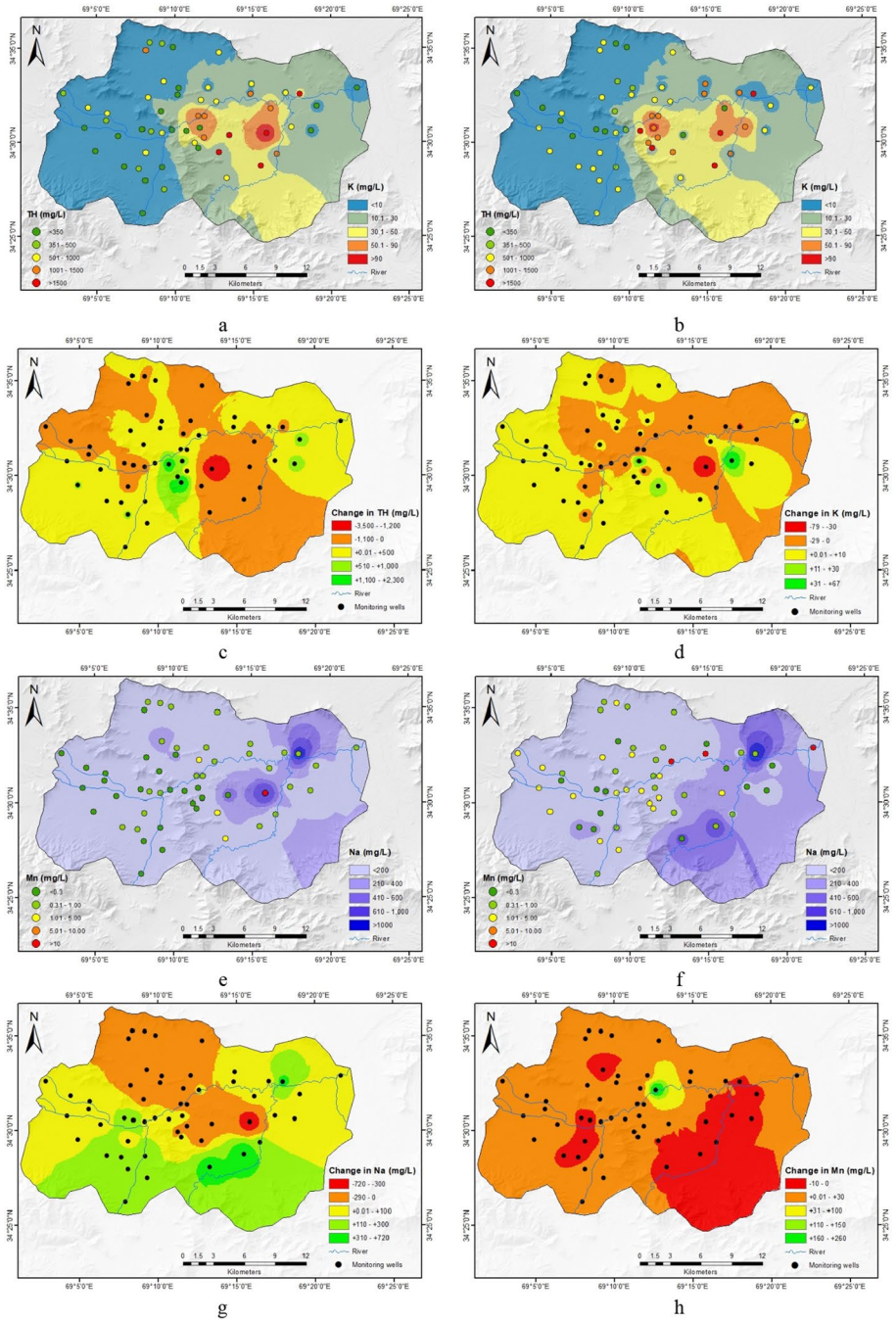

Fig. 3 Spatial distribution maps **a** TH and K dry season, **b** TH and K wet season, **c** change in TH, **d** Change in K, **e** Na and Mn dry season, **f** Na and Mn wet season, **g** Change in Na, **h** Change in Mn

In the west section of the research region and north to southeast, there is a reduction in TH concentration. The decreasing value in TH is up to − 3600 mg/l (Fig. 3c). Other parts of the study area have a light increase in TH concentration. A few wells in the central and east parts of the basin increased in concentrations up to 2200 mg/l. The concentration in K has almost similar conditions by means of spatial distribution. It dropped to − 79 mg/l and rose up to + 67 mg/l in some particular wells in the basin's center and east (Fig. 3d).

The spatial distribution map of Mn and Na has depicted in Fig. 3e and f. During the dry season, the concentration of Mn in three wells in the middle section of the study region reaches high levels. However, its concentration has increased in most wells across the entire study area during the wet season. The Na content is smooth in most parts of the basin during the dry season, while it has increased in the eastern region.

In the research area's middle to the northwest region, there is a reduction in Na concentration. It decreases to − 720 mg/l from the dry to wet season (Fig. 3g). Other parts of the basin have increased up to + 720 mg/l. The situation for Mn content is different in the basin. Smaller areas in the north and south of the basin and certain southeasterly regions have decreasing levels of up to − 10 mg/l (Fig. 3h). Other parts of the basin have a smooth increase, but only one well in the northern region has dramatically increased up to + 260 mg/l.

As illustrated in Fig. 4a and b, the spatial distribution of F and Fe is delineated for dry and wet climate conditions. The concentration of F is less than 0.5 mg/l in most of the study areas during the dry season. Some parts in the central western section, north to south, and a small part in the central-eastern portion of the basin has a concentration of greater than 0.5 mg/l. However, during the wet season, the concentration of F has increased in most of the research regions. Based on Fig. 4b, most of the basin has a concentration greater than 0.5 mg/l in the spring. Fe concentration in three sampling points has a value greater than 0.3 mg/l. Most other monitoring wells in the study area have concentrations less than 0.09 mg/l. The concentration of Fe during the wet period has increased in some wells, and the wells with a value greater than 0.3 mg/l are five wells. Some of the monitoring wells with low concentrations during the dry period have increased Fe concentrations during the wet period.

Spatially seasonal change in Fe concentration is illustrated in (Fig. 4c). The mainly northern part of the basin has decreased values up to − 0.55 mg/l. As well as, some wells around the central part of the basin have reduced values. But the majority of the study area has increased change in Fe concentration up to + 1 mg/l. The shift in F concentration looks similar to Fe in spatial distribution (Fig. 4d). It has mainly decreased in the north and south of the basin up to − 0.94 mg/l. While other parts of the basin have an increasing change in F concentration up to + 4 mg/l.

Figure 4e and f delineates the spatial distribution of NO_3 and Cl for both climate conditions. The content of NO_3 is less than 3 mg/l in most of the observational points during the dry season. Only five wells in the central section of the basin have a concentration greater than 5 mg/l in the dry period. But the concentration of NO_3 during the wet period has increased in some wells. The number of wells with rising NO_3 concentrations has risen, particularly in the basin's center region. The chloride concentration is very low during the dry period in the whole season. But it has increased dramatically in all parts of the basin. The spatial distribution of chloride concentration is uniform in all parts of the basin in the wet season except for one well in the east of the basin with a high concentration.

Spatially seasonal change in NO_3 concentration is illustrated in (Fig. 4g). Based on the change in NO_3 concentration, the basin is divided into two blocks, west, and east. The west part has decreased in NO_3 concentration while the east part of the basin has

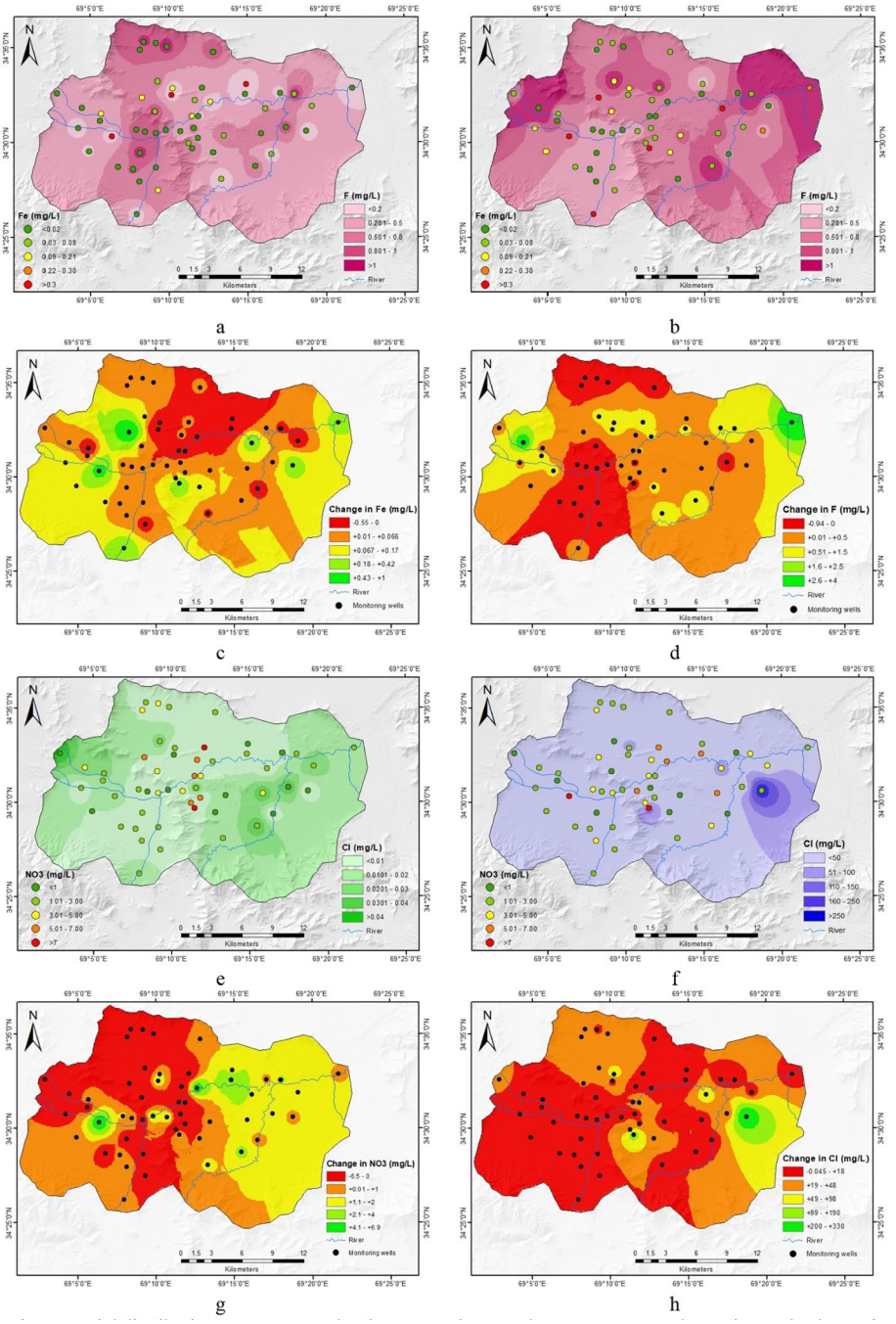

Fig. 4 Spatial distribution maps **a** Fe and F dry season, **b** Fe and F wet season, **c** change in Fe, **d** Change in F, **e** NO_3 and Cl dry season, **f** NO_3 and Cl wet season, **g** Change in NO_3, **h** Change in Cl

increased values. The decrease rate of NO_3 is about −6.5 mg/l, and the increasing rate is about + 5.9 mg/l. Cl concentration (Fig. 4h) has increased in almost all of the basin, but the eastern section of the basin has increased concentration values up to 330 mg/l.

With the increase in urbanization, the recharge area of groundwater has decreased significantly. On the other hand, the study area's groundwater level has decreased drastically during the last two decades (Noori & Singh, 2021b). Groundwater in Kabul city mainly recharges through river beds. Public water supply wells are also located next to river beds. Other recharge areas, such as hillsides and some open areas, can also have some role in groundwater recharge. Increasing and decreasing changes in water quality parameters are correlated to recharge volume, hydraulic conductivity, and the geological formation of the region. More groundwater recharge causes more contact and weathering of minerals and rocks, thus increasing the level of qualitative parameters in groundwater. This is the case for the wells that are located near the riverbeds. The level of qualitative parameters, such as calcium, sodium, iron, manganese, chloride, and fluoride, has increased in the wet season, mainly in the wells which are located close to river beds or in agricultural areas. In some wells located next to riverbeds or agricultural fields, and the quality parameters have not increased, the feeding path will probably have different geological formations.

On the other hand, the concentration of most parameters has decreased in the northern and western parts of the study area. The north and western parts of the study area have witnessed more urban development in the last two decades, and groundwater level has decreased significantly in these areas. These locations receive minimal recharge, and since the groundwater level is so much lower, the recharge water is probably unable to reach the groundwater in a single season due to its tiny volume and weak hydraulic conductivity. As a result, there is less of a concentration of quality factors in the groundwater in these areas.

4 Summary and conclusion

The main objective of this investigation was to determine if seasonal variations in groundwater quality variables are significant. In an urban setting, statistical testing was utilized to look at groundwater quality data from the Kabul basin aquifer during the dry and wet seasons. The statistical analysis indicates that most of the water quality parameters in the study area were not statistically significant; however, the concentrations of calcium, sodium, iron, manganese, chloride, and fluoride increased significantly from the dry to the wet period of the observation. Other parameters such as electrical conductivity, pH, total hardness, total dissolved solids, bicarbonate, sulfate, phosphate, potassium, copper, aluminum, cyanide, and nitrate are the parameters that are not significantly changed from the dry to the wet period of the study time, according to the statistical test.

According to the results of the descriptive statistics and the comparison with drinking water guidelines of WHO and ANSA, the following water quality parameters have exceeded the guideline in the dry season with different percentages: Mg (91%), Ca (58%), Mn (56%), TH (51%), EC (41%), TDS (41%), K (30%), Na (13%), Al (11%), HCO_3 (8%), Fe (6%), CN (6%), SO_4 (4%) Cu (2%). As well as the following parameters have exceeded the guidelines in the wet season with different percentages: Mn (75%), Ca (74%), TH (72%), Mg (69%), EC (47%), K (32%), TDS (21%), Na (17%), Fe (9%), F (6%), SO_4 (6%), Cu (6%), HCO_3 (4%), Cl (2%), CN (2%). As can be seen, most of the groundwater quality parameters in the Kabul aquifer in both studied periods are more polluted than drinking water; however, a few of these parameters exhibit significant seasonal variations.

Spatial distribution maps of some groundwater quality criteria were prepared for autumn and spring. Based on the outputs of spatially distributed maps and rank characteristics (positive and negative ranks),the type of variation and their spatial distribution as maximum and minimum will be interpreted. The levels of EC, TDS, Mg, TH, and Mn contents, mainly in the western part of the study area, have increased levels and, in the eastern part of the basin, exhibit decreasing conditions from dry to wet period. Calcium concentration decreased from the center of the basin to the north and increased to the south. Potassium is predominantly reduced in the central and eastern regions of the basin, while it is increased in the remainder. Sodium concentration decreases from the basin's center to the northeast and increases in the remaining parts. Manganese reduces in the southeastern parts and some central parts, increasing in the rest. Iron is decreased chiefly in the north and raised in the rest of the basin. Fluoride has a downward trend from the center to the south and in a part of the north of the basin and has an upward trend in the rest of the parts. Nitrate and chloride mostly divide the basin into eastern and western blocks. It has a downward trend on the west side and an upward trend on the east side.

Variations in water quality parameters are correlated to recharge volume, hydraulic conductivity, and the geological formation of the region. The level of qualitative parameters, such as calcium, sodium, iron, manganese, chloride, and fluoride, has increased in the wet season, mainly in the wells close to river paths or in agricultural areas. The groundwater level in the study area's north and west has decreased in the last two decades. Also, groundwater recharge in these areas is much less due to changes in land use/land cover pattern. The recharge water is probably unable to reach the groundwater in a single season due to its tiny volume and weak hydraulic conductivity. As a result, there is less of a concentration of quality factors in the groundwater in these areas.

Acknowledgements The authors are grateful to the General Directorate of Water Resources of the National Water Affairs Regulation Authority of Afghanistan for providing seasonal groundwater quality data for the study.

Funding This research did not receive any specific grant from funding agencies in the public, commercial, or not-for-profit sectors.

Data availability The datasets generated and/or analyzed during the current study are available from the corresponding author upon reasonable request.

Declarations

Conflict of interest The authors have no relevant financial or non-financial interests to disclose.

References

Aenab, A. M., & Singh, S. K. (2015). Al-Masab Al-Aam river (Third River) and surface water pollution within Baghdad division. *International Journal of Advanced Research, 3*(1), 396–404.

Aenab, A. M., & Singh, S. K. (2015b). Critical assessment of river water quality and wastewater treatment plant (WWTP). *International Journal of Advanced Research*. https://doi.org/10.9790/2402-08244448

ANSA (2013). National drinking water quality standard. ANSA, Kabul, Afghanistan.

Azimi, S., Azhdary Moghaddam, M., & Hashemi Monfared, S. A. (2018). Spatial assessment of the potential of groundwater quality using fuzzy AHP in GIS. *Arabian Journal of Geosciences, 11*, 1–22. https://doi.org/10.1007/s12517-018-3484-8

Bohannon, R. (2010). Geologic and topographic maps of the Kabul South 30' × 60' quadrangle, Afghanistan: U.S. geological survey scientific investigations map 3137, U.S. Geological Survey Scientific Investigations Map.

Brati, M. Q., Ishihara, M. I., & Higashi, O. (2019). Groundwater level reduction and pollution in relation to household water management in Kabul, Afghanistan. *Sustainable Water Resources Management, 5*, 1315–1325. https://doi.org/10.1007/s40899-019-00312-7

Broshears, R.E., Akbari, M.A., Chornack, M.P., Mueller, D.K., Ruddy, B.C., (2005). Inventory of groundwater resources in the Kabul basin, Afghanistan. USGS.

Dan, I., Jesse, D. (2020). Using terrain extractor (Trex) [WWW Document]. Bentely comunities. https://communities.bentley.com/products/hydraulics___hydrology/w/hydraulics_and_hydrology__wiki/8281/using-terrain-extractor-trex. Accessed 22 Jan 2021.

Elçi, A., & Polat, R. (2011). Assessment of the statistical significance of seasonal groundwater quality change in a karstic aquifer system near Izmir-Turkey. *Environmental Monitoring and Assessment, 172*, 445–462. https://doi.org/10.1007/s10661-010-1346-2

Goyal, D., Haritash, A. K., & Singh, S. K. (2021). A comprehensive review of groundwater vulnerability assessment using index-based, modelling and coupling methods. *Journal of Environmental Management*. https://doi.org/10.1016/j.jenvman.2021.113161

Hamdard, M. H., Soliev, I., Xiong, L., & Kløve, B. (2020). Drinking water quality assessment and governance in Kabul: A case study from a district with high migration and underdeveloped infrastructure. *Central Asian Journal of Water Research, 6*, 66–81. https://doi.org/10.29258/cajwr/2020-r1.v6-1/66-81.eng

Haritash, A. K., Mathur, K., Singh, P., & Singh, S. K. (2017). Hydrochemical characterization and suitability assessment of groundwater in Baga-Calangute stretch of Goa, India. *Environment and Earth Science, 76*, 1–10. https://doi.org/10.1007/s12665-017-6679-5

Hayat, E., & Baba, A. (2017). Quality of groundwater resources in Afghanistan. *Environmental Monitoring Assessment, 189*, 1–16. https://doi.org/10.1007/s10661-017-6032-1

He, S., Li, P., Wu, J., Elumalai, V., & Adimalla, N. (2020). Groundwater quality under land use/land cover changes: A temporal study from 2005 to 2015 in Xi'an, Northwest China. *Human and Ecological Risk Assessment, 26*, 2771–2797. https://doi.org/10.1080/10807039.2019.1684186

Houben, G., Niard, N., Tünnermeier, T., & Himmelsbach, T. (2009). Hydrogeology of the Kabul Basin (Afghanistan), part I: Aquifers and hydrology. *Hydrogeology Journal, 17*, 665–677. https://doi.org/10.1007/s10040-008-0377-z

Jawadi, H. A., Sagin, J., & Snow, D. D. (2020). A detailed assessment of groundwater quality in future development. *Water, 12*, 2890. https://doi.org/10.3390/w12102890

Jawid, A., & Khadjavi, M. (2019). Adaptation to climate change in Afghanistan: Evidence on the impact of external interventions. *Economic Analysis and Policy, 64*, 64–82. https://doi.org/10.1016/j.eap.2019.07.010

Jhamnani, B., & Singh, S. K. (2015). Groundwater contamination due to Bhalaswa Landfill site in New Delhi. *International Journal of Civil and Environmental Engineering., 3*, 181–185.

JICA (2011). The study on groundwater resources potential in Kabul basin in the Islamic republic of Afghanistan final report. JICA.

Mack, T.J., Akbari, M.A., Ashoor, M.H., Chornack, M.P., Coplen, T.B., Emerson, D.G., Hubbard, B.E., Litke, D.W., Michel, R.L., Plummer, L.N., Rezai, M.T., Senay, G.B., Verdin, J.P., & Verstraeten, I.M., (2009). *Conceptual model of water resources in the kabul basin, Afghanistan*, USGS. USGS.

Mack, T. J., Chornack, M. P., Coplen, T. B., Plummer, L. N., Rezai, M. T., & Verstraeten, I. M. (2010). Availability of water in the kabul basin, Afghanistan (Issue May). *US Geological Survey*. http://pubs.usgs.gov/sir/2009/5262

Najafi Saleh, H., Valipoor, S., Zarei, A., Yousefi, M., Baghal Asghari, F., Mohammadi, A. A., Amiri, F., Ghalehaskar, S., & Mousavi Khaneghah, A. (2020). Assessment of groundwater quality around municipal solid waste landfill by using Water Quality Index for groundwater resources and multivariate statistical technique: A case study of the landfill site, Qaem Shahr City, Iran. *Environmental Geochemistry and Health, 42*, 1305–1319. https://doi.org/10.1007/s10653-019-00417-0

Noori, A. R., & Singh, S. K. (2021a). Status of groundwater resource potential and its quality at Kabul, Afghanistan : A review. *Environment and Earth Science, 80*, 1–13. https://doi.org/10.1007/s12665-021-09954-3

Noori, A. R., & Singh, S. K. (2021). Spatial and temporal trend analysis of groundwater levels and regional groundwater drought assessment of Kabul Afghanistan. *Environmental Earth Sciences, 80*(20), 1–16. https://doi.org/10.1007/s12665-021-10005-0

Noori, A. R., & Singh, S. K. (2021). Assessment and modeling of sewer network development utilizing Arc GIS and SewerGEMS in Kabul city of Afghanistan. *Journal of Engineering Research*. https://doi.org/10.36909/jer.ICARI.15287

Paiman, Z., & Noori, A. R. (2019). Evaluation of wastewater collection and disposal in Kabul city and its environmental impacts. *Modern Environmental Science and Engineering, 5*, 451–458. https://doi.org/10.15341/mese(2333-2581)/05.05.2019/012

Pell Frischmann (2012). Afghanistan resource corridor development: Water strategy final Kabul river basin report version 4.0.

Perera, T. A. N. T., Herath, H. M. M. S. D., Piyadasa, R. U. K., Jianhui, L., & Bing, L. (2022). Spatial and physicochemical assessment of groundwater quality in the urban coastal region of Sri Lanka. *Environmental Science and Pollution Research, 29*, 16250–16264. https://doi.org/10.1007/s11356-021-16911-x

Sarma, R., & Singh, S. K. (2021). Simulating contaminant transport in unsaturated and saturated groundwater zones. *Water Environment Research, 93*, 1496–1509. https://doi.org/10.1002/wer.1555

Soujanya Kamble, B., Saxena, P. R., Kurakalva, R. M., & Shankar, K. (2020). Evaluation of seasonal and temporal variations of groundwater quality around Jawaharnagar municipal solid waste dumpsite of Hyderabad city, India. *SN Applied Sciences, 2*, 1–22. https://doi.org/10.1007/s42452-020-2199-0

Su, Z., Wu, J., He, X., & Elumalai, V. (2020). Temporal changes of groundwater quality within the groundwater depression cone and prediction of confined groundwater salinity using grey Markov model in Yinchuan area of Northwest China. *Expo Health, 12*, 447–468. https://doi.org/10.1007/s12403-020-00355-8

Thomas, B. F., Famiglietti, J. S., Landerer, F. W., Wiese, D. N., Molotch, N. P., & Argus, D. F. (2017). GRACE groundwater drought index: Evaluation of California central valley groundwater drought. *Remote Sensing of Environment, 198*, 384–392. https://doi.org/10.1016/j.rse.2017.06.026

Tünnermeier, T., Houben, G. (2005). Hydrogeology of the Kabul basin part I: Geology, aquifer characteristics, climate and hydrography. BGR.

Uhl, W. V., & Tahiri, M. Q. (2003). *An overview of groundwater resources and challenges*. Rana Associates.

WHO (2011). Guidelines for drinking-water quality, 4th edn.

WHO (2017). Guidelines for drinking water quality fourth edition incorporating the first addendum. Geneva.

Zahid, S., Asmawi, M. Z., & Abdullah, M. F. (2019). Assessment of the groundwater quality and pollution in Kabul city, Afghanistan. *Advanced Journal of Technical and Vocational Education, 3*, 20–26.

Zaryab, A., Nassery, H. R., & Alijani, F. (2021). Identifying sources of groundwater salinity and major hydrogeochemical processes in the Lower Kabul Basin aquifer, Afghanistan. *Environmental Science: Processes and Impacts, 23*, 1589–1599. https://doi.org/10.1039/d1em00262g

Zaryab, A., Nassery, H. R., & Alijani, F. (2022). The effects of urbanization on the groundwater system of the Kabul shallow aquifers, Afghanistan. *Hydrogeology Journal, 30*(2), 429–443. https://doi.org/10.1007/s10040-021-02445-6

Zaryab, A., Nassery, H. R., Knoeller, K., Alijani, F., & Minet, E. (2022). Determining nitrate pollution sources in the Kabul Plain aquifer (Afghanistan) using stable isotopes and Bayesian stable isotope mixing model. *Science of the Total Environment, 823*, 153749. https://doi.org/10.1016/j.scitotenv.2022b.153749

Zaryab, A., Noori, A. R., Wegerich, K., & Kløve, B. (2017). Assessment of water quality and quantity trends in Kabul aquifers with an outline for future drinking water supplies. *Central Asian Journal of Water Research, 3*, 3–11.

Publisher's Note Springer Nature remains neutral with regard to jurisdictional claims in published maps and institutional affiliations.

Springer Nature or its licensor (e.g. a society or other partner) holds exclusive rights to this article under a publishing agreement with the author(s) or other rightsholder(s); author self-archiving of the accepted manuscript version of this article is solely governed by the terms of such publishing agreement and applicable law.

Assessment of Water Quality of the River Gomti, India by Water Quality Index

Amit Krishan
Department of Environmental Engineering
Delhi Technological University
Delhi, India
krishan001amit@gmail.com

Rajeev Kumar Mishra
Department of Environmental Engineering
Delhi Technological University
Delhi, India
rajeevkumarmishra@dtu.ac.in

Anwar Khursheed
Department of Civil Engineering
King Saud University
Riyadh, Saudi Arabia
aahmad4@ksu.edu.sa

***Abstract*—Globally the various sources of pollution are continuously affecting the water quality of most of the rivers. Due to the heavy discharge of partially or untreated wastewater in the urban stretches, water pollution has now become one of the most significant problems concerning water bodies. Considering the heavy pollution load due to natural and anthropogenic activities, the Gomti River has been chosen to conduct this study. Total eight parameters, namely pH, electrical conductivity, TDS, TH, chloride, DO, BOD and alkalinity, have been selected to develop the water quality index. These parameters were measured at seven sampling stations (S1 to S7) along the Gomti River for the years 2013 – 2017 in the urban stretch of Lucknow city. The weighted arithmetic water quality index (WAWQI) was used to calculate the water quality index. The results of the study revealed that all of the water samples fall under different categories of poor (50 to 75), very poor (75 to 100), and unsuitable (>100). As the Gomti river entered the Lucknow city, its water quality was under fair index category, while the index worsens to marginal as it advanced within the city premises. During 2017, the recorded values of WQI was found in the range of 71.11 (minimum at S1) to 165.33 (maximum at S7), whereas in 2013, these were in the range of 67.90 (minimum at S1) to 143.63 (maximum at S7). To augment the water quality, effective wastewater treatment measures are urgently required to support any plan for sustainable river restoration.**

Keywords—Gomti River, Lucknow, WQI, Water quality, Water pollution

I. INTRODUCTION

The rivers play a vital role in the development of our nation, but during the process rivers are polluted due to an increasing number of industries, urbanization, and many other developmental activities [1]. These freshwater sources provide water for domestic, industrial, agricultural, and recreational purposes and have great importance in our lives being primary water resources. On one side, the water resources have been stressed due to increasing demand as a result of population growth, climate change, drought, but on the other side, the wastewater generated from industrial and agricultural activities deteriorates the quality of these water resources [2]. Inadequate wastewater treatment facilities with increasing sewage generation compound the problem of wastewater disposal to the rivers. This huge quantity of raw or partially treated wastewater is mostly discharged into nearby water bodies, mainly in the rivers. Therefore, it is imperative to monitor the quality of water resources within acceptable limits for sustainable use.

The ecological sustainability of water resources, underlying economic reasons, and human health requirements demand immediate control on water pollution and restoration of natural resources. The suitability of the water for human consumption can be quantified in terms of the water quality and is being used in multiple scientific publications that relate the necessities of sustainable water management [3]. Monitoring of river water quality is required to control the outbreak of diseases and to check the deterioration of its water quality, as it also provides a scope for pollution prevention and control [4].

About 70% of the river water in India is contaminated due to the presence of pollutants, thereby making them unfit for various designated municipal and industrial uses as per the data reported by the WHO (World Health Organization), CPCB (Central Pollution Control Board), BIS (Bureau of Indian Standards) and, ICMR (Indian Council of Medical Research) [5]. River water quality assessment using various parameters and techniques has been reported by Santosh et al. (2008) [6]; Yisa and Jimoh (2010) [7] and Shah et al. (2015) [8]. The water quality index is an efficient approach for determining river water quality in a consolidated form for its use, suitability, and application and to be utilised by the concerned agencies for policy making. The water quality index uses various mathematical equations to determine the water quality indices by incorporating the different physical, chemical, and biological parameters.

Horton (1965) [9], for the first time and later, Brown et al. (1970) [10] proposed the use of a Water Quality Index. Afterward, different methods are proposed by various researchers to calculate water quality indexes. Presently, the various Water Quality Indexes are being used worldwide e.g. US National Sanitation Water Quality Index (NSFWQI), British Columbia Water Quality Index (BCWQI), Canadian Council of Ministers of the Environment Water Quality Index (CCMEWQI), Weighted Arithmetic Water Quality Index (WAWQI) Oregon Water Quality Index (OWQI) [11]. Many countries like India [12], United Kingdom [13], Egypt [14], United States [15], Canada [16], Spain [17], Brazil [18], Iran [19], Argentina [20], and Malawi [21] are using these WQI to evaluate the quality of river waters.

Various physical, chemical, and biological parameters are the basis for the evaluation of WQI. The biggest challenge is to develop cost-effective pollution control strategies in developing countries. Therefore, for such circumstances, just a few critical parameters must be utilized to assess WQI. The water quality of numerous Indian rivers has been thoroughly contemplated, examined, and answered by their reasonableness for their different beneficial uses [22].

In the present study, a long-term evaluation of the water quality is done for interpreting the Province of Gomti River in the stretch of Lucknow city by creating a WQI to break down

and translate a gigantic dataset into significant information for propriety of the stream water in the study locations for human usage.

II. STUDY METHODOLOGY

A. Description of the study area

Gomti is one of the major groundwater-fed rivers that start from Gomathtal (earlier known as Fulhar Jheel) in Pilibhit district, and after traveling 940 kms, it drains into the River Ganges (Ganga river) close to Saidpur in Ghazipur district of U.P. From the origin to its confluence, 23 major and minor tributaries, contribute to the River Gomti. Gaichi (Gaihaaee) is the first tributary of Gomti, which originates after traveling 20 km from the origin. River Gomti continues being narrow stream till Mohammadi Kheri (Lakhimpur Kheri district), which is 100 km from origin and river is well defined here as many tributaries join it downstream, many tributaries as River Kathana and River Sarayan join the River Gomti at Mailani and Lakhimpur, respectively. River Sai joins River Gomti in Jaunpur district nearby Rajepur.

Throughout the year (except monsoon season), the flow of River Gomti is characterized as slow-moving whereas, during monsoon, heavy rainfall causes a manifold increase in its runoff. Thus, the monsoon season is the time when River Gomti gets maximum water budget. The river receives an annual discharge of about 7390 x 106 m^3 [23]. The flow velocity and river level both increase during the monsoon season, resulting in flood conditions in the low-lying areas. Generally, the rise and fall of 3 m in the water level is seen every year.

This river enters in Lucknow after traveling around a distance of 240 km. Lucknow, known as the city of Nawab's is the capital of U.P. (India), is located at 26° 52′N latitude and 80° 56′E longitude. The city has a humid subtropical climate, with a hot summer for April to June and a winter season from December to February. The temperature varies from 48.9^{0}C to 1.67^{0}C during the year. In July to September, the city gets annual precipitation of around 900 mm from the southwest monsoon. The city's elevation varies from 100 to 130 m above mean sea level at different locations and inclines towards the east. Lucknow is one of the fastest-growing cities in India, with an expected population of 4.7 million by 2031 from 2.8 million in the year 2011. Water is lifted from the River Gomti at Gaughat pumping station to supply water to Lucknow city. There are 28 significant drains, out of which 14 drains are available in the Cis-Gomti area, and the other 14 are in the Trans-Gomti area, in the city. Few drains are as big as to carry 78 MLD of sludge discharge, but others carry only 0.5 MLD discharge and increases the pollution level in it..

The primary drinking water source for the city is River Gomti, which is polluted due to the daily discharge of excessive untreated domestic wastes. Besides Lucknow, 14 other towns benefit from its drinking water supplies located at its bank. The discharge in the River Gomti during a lean period is around 500 MLD. It reaches approximately 55,000 MLD during the Monsoon season. Most of the time, the average discharge is about 1500 MLD/year [24]. There is a low water discharge in the post-monsoon season, which results in the depositional phase of the river.

B. Data collection

The important parameters that are considered to assess the surface water quality and indexing include pH, Electrical Conductivity, TDS, Total Hardness, Chloride, DO, BOD, and Alkalinity. The monthly data collection of all the above mentioned water quality parameters was done at seven sampling stations i.e., (S1) Station-1 Manjhi Ghat (S2) Station-2 Up Stream water intake (S3) Station-3 Kuriyaghat (S4) Station-4 Downstream Mohan Meakins (S5) Station-5 Nishat Ganj Bridge (S6) Station-6 Upstream Barrage and (S7) Station-7 Downstream after meeting STP Nala Bharwara of Gomti river by Uttar Pradesh Pollution Control Board, Lucknow (UPPCB, Lucknow) for the years 2013 – 2017. The details of sampling stations are presented in Fig. 1.

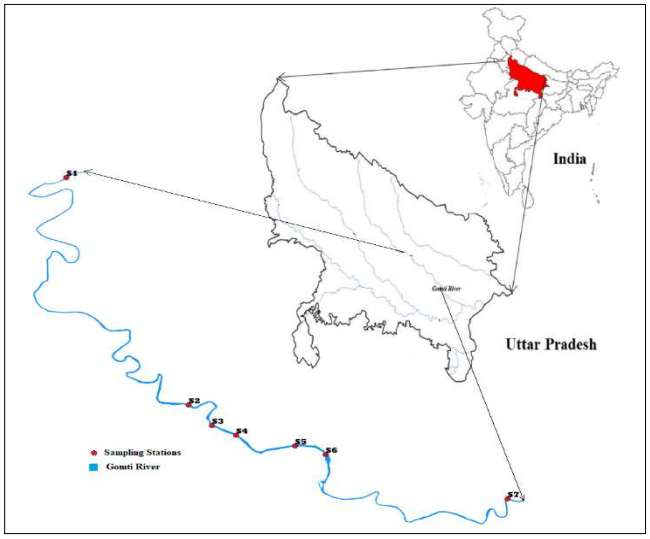

Fig. 1. Map showing sampling stations in Lucknow city of the Gomti River.

C. Calculation of Water Quality Index (WQI)

In this study, Weighted Arithmetic Index method Brown et al. 1970) [10] has been adopted to calculate the Water Quality Index (WQI) using the above mentioned selected parameters i.e. pH (units), Electrical Conductivity (µS/cm), Total Dissolved Solids (mg/l), Total Hardness (mg/l, $CaCO_3$), Chloride (mg/l), Dissolved Oxygen (mg/l), Biochemical Oxygen Demand (mg/l) and Alkalinity (mg/l, $CaCO_3$).

In this method, water quality parameters are multiplied by a weighting factor and then combined by simple arithmetic mean. At first, the quality rating scale (Qi) is calculated for each parameter to assess water quality, using the following equation:

$$Qi = \frac{(V_{observed} - V_{ideal})}{(V_{standard} - V_{ideal})} X\ 100 \quad \text{..... (1)}$$

Where,

Qi = Quality rating of the ith parameter for n numbers of water quality parameters.

$V_{observed}$ = Observed value of the water quality parameter (laboratory analysis).

V_{ideal} = "The Ideal value of the water quality parameter".

V_{ideal} for pH = 7, V_{ideal} for DO= 14.6 mg/l and V_{ideal} for other parameters = 0.

$V_{standard}$ = Standard of the water quality parameter (BIS and ICMR).

Relative (unit) weight (Wi) is inversely proportional to the recommended standards (Si) for the corresponding parameter and was calculated using equation 2:

$$Wi = \frac{K}{X_i} \quad \text{..... (2)}$$

Where,

Wi = Relative (unit) weight for nth parameter

Xi = Standard permissible value for n^{th} parameter

K = Proportionality constant

Finally, the overall WQI was calculated by using the following equation:

$$WQI = \frac{\sum Q_i W_i}{\sum W_i} \quad \text{..... (3)}$$

Where,

Qi = Quality rating

Wi = Relative weight

Calculation of WQI involves both standards of drinking water and relative weights assigned to each parameter, as given in Table 1. By considering WQI for humans uses the maximum permissible WQI was 100 scores for drinking purposes. The range of WQI, category, status, and water usage are presented in Table 2.

TABLE 1 RELATIVE WEIGHT (W_n) OF THE PARAMETERS USED FOR WQI DETERMINATION

Parameter	Unit	ICMR/BIS standard (V_s)	Unit weight (W_n)
pH	-	6.5-8.5	0.218412144
Electrical conductivity	µS/cm	300	0.006188344
TDS	mg/l	500	0.003713006
Total hardness	mg/l	300	0.006188344
Chloride	mg/l	250	0.007426013
DO	mg/l	5	0.371300644
BOD	mg/l	5	0.371300644
Total alkalinity	mg/l	120	0.01547086

III. RESULTS AND DISCUSSIONS

A. Water quality of River Gomti

The statistical summary for the years 2013-2017, of the selected water quality parameters at sampling stations (S1 – S7) of the River Gomti is presented in Annexure - I. Variation in pH was observed at the sampling stations (S1 – S7), is due to low annual variations in free CO_2. The pH value can explain water quality deterioration [6]. The pH changed its nature from alkaline to acidic as it moves from S1 to S7 (Fig. 2) and also through pre and post-monsoon to monsoon period at the sampling station. From Annexure - I, it can be deduced that the range of pH lies between 6.89 (August 2013, 2014) to 8.89 (June 2017), which exceeds the ICMR standard of 6.5 to 8.5 at some of the sampling stations. Overall, the pH value was within the alkaline range, due to its direct reception of domestic waste discharge and leached from the accumulation of organic waste along the banks of the river. Santosh et al. (2008) [6] and Shah et al. (2015) [8] reported similar results in the pH range 5.9 – 8.0 and 6.5 for River Netravathi and River Sabarmati, respectively.

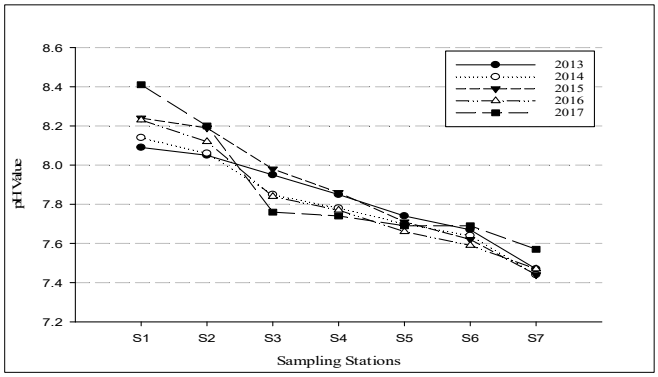

Fig. 2. Mean values of pH variations at the sampling stations of the Gomti River

In this study, EC values observed for the water samples of the River Gomti for stations S1 – S7 ranged between 172.0 – 560.2 µS/cm, 180.8 – 582.4 µS/cm, 201.0 – 772.5 µS/cm, 212.0 – 795.6 µS/cm, 224.6 – 558.5 µS/cm, 221.6 – 882.6 µS/cm and 240.6 – 984.2 µS/cm respectively for years 2013 – 2017 which exceeds the ICMR standard of 300 µS/cm at most of the sampling stations. The recorded data indicates that EC concentrations ranged from 172.0 µS/cm as the minimum value for station "S1" in July 2015, while regarding 984.2 µS/cm as the maximum value for station "S7" in May 2017. All Stations (S1 - S7) showed higher EC values, mainly during April, May, and June. It is noticed that EC had been gradually increased from S1 to S7, and from 2013 to 2017, as shown in Fig. 3. Sewage discharge and anthropogenic activities may have contributed to the increased level EC values [5]. Station S1 and S2 have lower EC values. As stated by Avvanavar and Shrihari (2008) [25], Land cover pattern, i.e., semi-green area and forest area, which resulted in less soil erosion of the topsoil, may have contributed to lower EC values at station S1 and S2.

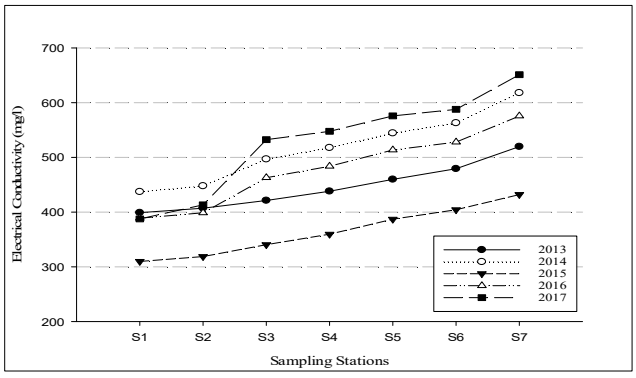

Fig. 3. Mean values of Electrical Conductivity variations at the sampling stations of Gomti River

TABLE 2 WQI RANGE, CATEGORY, STATUS AND POSSIBLE USAGE OF THE WATER SAMPLE

Value of WQI	Category of Water	Water Quality Status (WQS)	Possible Usage
0 – 25	A	Excellent	Drinking, irrigation and industrial
26 – 50	B	Good	Drinking, irrigation and industrial
51 – 75	C	Poor	Irrigation and industrial
76 – 100	D	Very poor	Irrigation
Above 100	E	Unsuitable for drinking and fish culture	Proper treatment required before use

High TDS in water indicates more ionic concentration, which is not suitable for human consumption and induces an adverse physicochemical reaction in the human body [26]. The river water recorded the TDS value ranged between 112 mg/l to 616 mg/l. In the case of the "S1" station, the TDS value recorded 112 mg/l as a minimum in July 2015, while maximum value was recorded 616 mg/l for station "S7" in June 2017, which was mostly in the desirable limit of 500 mg/l with few exceptions. Downstream region stations have higher TDS values than the Upstream stations [27]. Ascending trends in TDS were observed at each sampling station from S1 (upstream) to S7 (downstream) and with every consecutive year from 2013 to 2017 (Fig. 4). This may be due to the strong presence of dissociated electrolytes and dissolved organic matter, entering into the river water through several points and non-point sources. Jindal and Sharma (2010) [5] reported similar results for Potrero de los Funes River, had a TDS in the range of 156-582 mg/l, which may be due to the sewage discharges and anthropogenic activities along the bank of the river.

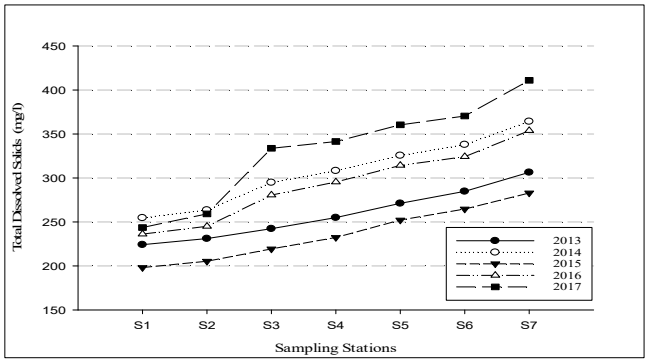

Fig. 4. Mean values of TDS variations at the sampling stations of Gomti River

Hardness values of water samples observed at stations S1, S2, S3, S4, S5, S6, and S7 ranged between 120 – 236 mg/l, 128 – 244 mg/l, 134 – 256 mg/l, 140 – 262 mg/l, 148 – 274 mg/l, 156 – 282 mg/l and 170 – 294 mg/l respectively for the years 2013 – 2017 (Fig. 5) which was in the desirable limit of 300 mg/l. The recorded data indicates that the total hardness concentrations ranged from 120 mg/l as the minimum value for station "S1" in August 2013 as well as August 2014, while regarding 294 mg/l as maximum value at station “S7” in July 2017. Based on the data collection, River Gomti water can be categorized as moderately hard to hard water. Bora and Goswami (2017) [28] was found similar results and reported the hardness in the range of 52 - 296 mg/l for River Kolong, Assam, India.

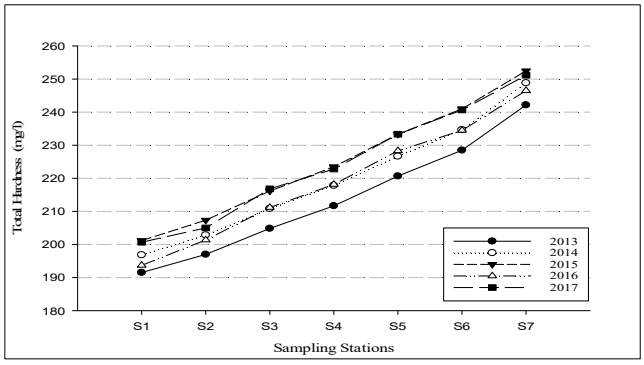

Fig. 5. Mean values of Total Hardness variations at the sampling stations of Gomti River

The chloride concentration in the water samples studied from 2013 to 2017 at Stations S1, S2, S3, S4, S5, S6, and S7 ranged between 8 – 17 mg/l, 11 – 19 mg/l, 12 – 22 mg/l, 13 – 24 mg/l, 14 – 27 mg/l, 15 – 29 mg/l and 18 – 33 mg/l respectively (Fig. 6), which was found within the BIS desirable limit, i.e., 250 mg/l. However, in September 2017, the chloride was very low (8 mg/l) at Station S1, while a high value (33 mg/l) was found at the Station S7 in October 2016 due to surface run-off from inorganic fertilizers dependent agricultural fields, irrigation discharge, animal feeds, etc [28]. This result is supported by the findings of Bora and Goswami (2017) [28], where they reported the chloride range of 19.88–94.56 mg/l for River Kolong, Assam, India.

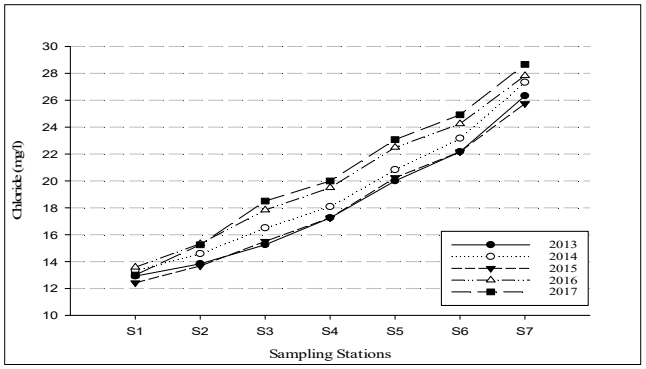

Fig. 6. Mean values of Chloride variations at the sampling stations of Gomti River

In this study, a large variation in DO which is a principle pollution indicator has been noticed. The DO for the studied water samples during 2013 – 2017, for stations S1, S2, S3, S4, S5, S6 and S7 ranged between 4.7 – 11.4 mg/l, 2.9 – 11.9 mg/l, 0.7 – 9.5 mg/l, 1.3 – 8.4 mg/l, 1.1 – 6.0 mg/l, 0.6 – 5.1 mg/l and 0.3 – 3.8 mg/l respectively. The annual average concentration of DO is depicted in Fig. 7. This gradual decrease in DO at stations S1 to S7 advances within the city premises at S3, S4, S5, S6, and worsen to marginal at S7. Discharge of industrial and domestic wastewater adds organic matter into the river, which increases microbial activity for their degradation process and results in a low concentration of dissolved Oxygen [7]. At stations S1, DO levels for most of the months were sufficient for aquatic life's survival. The minimum DO observe for S1 was 4.7 mg/l in August 2013 and August 2014. In summer, with the rise in temperature of the stream, the oxygen solubility decreases. Metabolism, growth, and reproduction of bacteria responsible for the biodegradation of the organic matter is directly affected by the temperature. As the temperature increases, the rate of biodegradation and biological activity increases, increasing the demand for oxygen in the water. At station S7, the minimum DO level was observed (0.30 mg/l), mainly due to the high level of organic pollutants, low flow during summer, and an increase in the water temperature. A DO value of 6.5 – 15 mg/l was reported by Sharma et al. (2008) [29], which was found under the prescribed limit as per WHO. Yisa and Jimoh (2010) [7] also reported similar DO values ranged between 3.1 – 5.2 mg/l for River Landzu.

BOD values over 5 mg/l were undesirable. The present study showed that water samples at stations S1, S2, S3, S4, S5, S6, and S7 ranged between 2.3 – 3.3 mg/l, 3.1 – 4.2 mg/l, 3.6 – 9.0 mg/l, 4.5 – 10.0 mg/l, 6.0– 11.5 mg/l, 6.5 – 12.5 mg/l and 8.5 – 18.6 mg/l respectively during 2013 – 2017 (Fig. 8) with values exceeding the desirable limit. It was observed that

the maximum value of BOD (18.6 mg/l) was found at sampling station S7 in September 2017 and minimum (2.3 mg/l) at sampling station S1 in September 2017. Less water current and higher decomposition of organic matter at high temperatures resulted in a high value of BOD [30]. At any site when DO increases, BOD decreases. BOD and DO are inversely proportional to each other with respect to temperature [31]. Similar results were also presented by Shah and Joshi (2017) [8], where DO values range between 3.0 to 19.0 mg/l for the River Sabarmati in Gujarat, India.

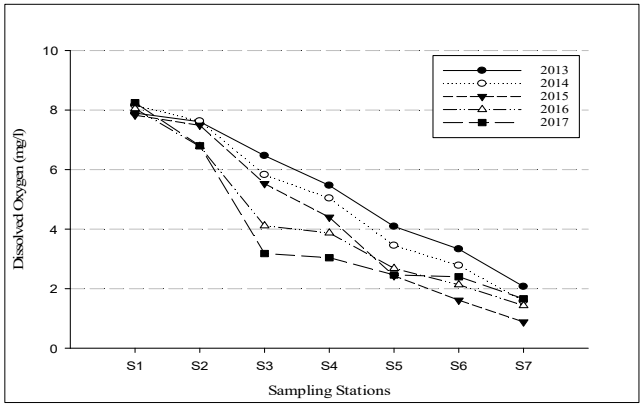

Fig. 7. Mean values of DO variations at the sampling stations of Gomti River

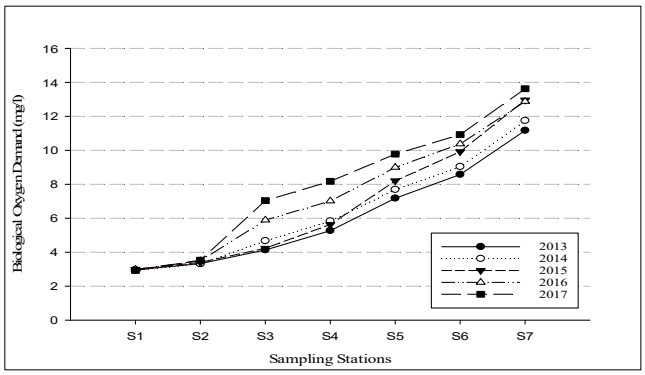

Fig. 8. Mean values of BOD variations at the sampling stations of Gomti River

Alkalinity is the capability of an aqueous solution to neutralize acids. It is due to the presence of carbonate, bicarbonate, and hydroxide ions. The average alkalinity concentration (as $CaCO_3$) for the monitored water samples during 2013 – 2017, for stations S1, S2, S3, S4, S5, S6, and S7 ranged between 142 – 252 mg/l, 148 – 264 mg/l, 156 – 272 mg/l, 162 – 278 mg/l, 168 – 286 mg/l, 172 – 298 mg/l and 146 – 316 mg/l respectively (Fig. 9) which exceeded the BIS prescribed limit of 120 mg/l. It was observed that the maximum value of alkalinity was found at sampling station S7 during July 2014, and a minimum was observed at sampling station S1 during August 2013 and 2014. Bora and Goswami (2017) [28] reported the similar kind of results in River Kolong, Assam, India.

B. Water quality index of Gomti River

The summary of the WQI values of the water samples from all the seven sampling stations (S1 – S7) for each year (2013 – 2017) is presented in Table 3. The results revealed that all of the water samples fall under poor (between 50 to 75), very poor (between 75 and 100), and unsuitable (>100) categories. These stations recorded the highest WQI values during 2017, ranging from 71.11 at Station S1 to 165.33 at Station S7.

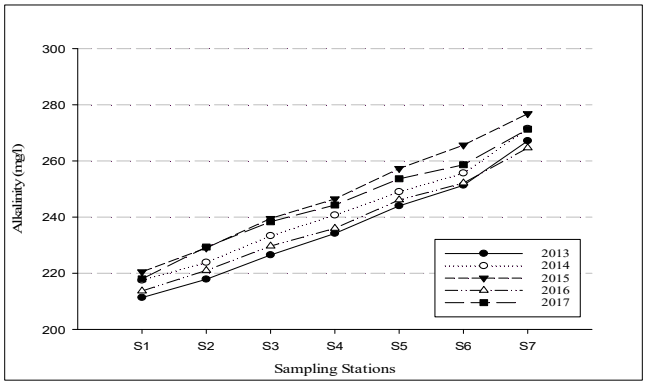

Fig. 9. Mean values of Alkalinity variations at the sampling stations of River Gomti

The WQI of the water samples collected at stations S1 and S2, was found better than other sampling stations. The WQI values ranged between 67.90– 71.11 for S1 and 71.35 – 78.39 for S2 for all the consecutive years 2013 - 2017. Samples collected at stations S1 and S2 have better water quality conditions, as these stations are present in the out skirts of the Lucknow city and have less urban agglomeration. Similar results were also observed by Iqbal et al. (2019) [33] for the River Gomti. The WQS at sampling station S3 and S4 was observed poor for 2013 – 2015 and was unsuitable in 2016 and 2017 because of the contamination contributed by the close-by urban settlements.

The WQI analysis unveiled the fact that sampling stations S5, S6, and S7 has the highest level of pollutants along the entire reach of the Gomti River. The sample's WQI values from stations S5, S6, and S7 during the sampling year were in the unsuitable water category (WQI>100), hence making the water unfit for any use, including irrigation, fish culture, and drinking. Not only high sewage disposal and eutrophication, but the lack of sufficient flow leads to the stagnancy of river water, which results in a high pollution level of sampling stations, which in turn reduces the self-purification capacity of the River Gomti River. In 2011, Rehana and Majumdar [33] reported similar impacts of altered river flow in River Tunga Bhadra. In addition to the above reasons, a continuous increase in the population, which resulted in riverbed encroachment and exploitation of river water for various chores, contributed to the deterioration of the water quality of the River Gomti.

IV. CONCLUSION

In the current study WAWQI has been found effective to determine the water quality status of River Gomti in Lucknow at seven sampling stations (S1 to S7), by considering eight water quality parameters. Out of the eight parameters, DO and BOD was found to have the highest influence on the WQI scores. The study concludes that water samples fall under either poor and very poor or unsuitable category. The current water quality index of the Gomti River indicates the threatened quality of the water, which is attributable to the recurrent release of waste effluents by numerous discharges pouring down directly into the river by anthropogenic sources. The water quality index of river Gomti shows variation at its entry in the city and when it leaves the city as index worsen to

TABLE 3 SUMMARY OF WQI OF THE RIVER GOMTI

Sampling Station	2013		2014		2015		2016		2017	
	WQI	***WQS***	***WQI***	***WQS***	***WQI***	***WQS***	***WQI***	***WQS***	***WQI***	***WQS***
S1	67.9	Poor	67.64	Poor	70.52	Poor	69.6	Poor	71.11	Poor
S2	71.35	Poor	71.45	Poor	74.27	Poor	76.72	Very Poor	78.39	Very Poor
S3	80.36	Very Poor	85.73	Very Poor	85.21	Very Poor	101.14	Unsuitable	112.44	Unsuitable
S4	91.39	Very Poor	96.55	Very Poor	98.35	Very Poor	109.61	Unsuitable	121.28	Unsuitable
S5	109.63	Unsuitable	115.53	Unsuitable	123.28	Unsuitable	127.52	Unsuitable	134.88	Unsuitable
S6	122.11	Unsuitable	127.46	Unsuitable	137.86	Unsuitable	139.06	Unsuitable	143.72	Unsuitable
S7	143.63	Unsuitable	149.74	Unsuitable	161	Unsuitable	158.79	Unsuitable	165.33	Unsuitable

marginal value as it travels through the city premises. The study shows the value of WQI increases from year 2011 to 2017 and from sampling station S1 (entry) to sampling station S7 (exit) by passing years, which gives the impression that pollution is ascribed to various sources. It has been summarized that, to augment the water quality, effective wastewater treatment measures of the polluting sources are urgently required to support any plan for sustainable river restoration.

ACKNOWLEDGMENT

Authors are incredibly grateful to UPPCB (Uttar Pradesh Pollution Control Board), Lucknow, India to providing data to conduct this research.

REFERENCES

[1] Mandal, H. S., A. Das, and A. K. Nanda. 2012. "Study of Some Physicochemical Water Quality Parameters of Karola River, West Bengal – An Attempt to Estimate Pollution Status." *International Journal of Environmental Protection* 2 (8): 16-22.

[2] Koop, S. H. A., and C. J. van Leeuwen. 2017. "The challenges of water, waste and climate change in cities." *Environment, Development and Sustainability* 19: 385–418.

[3] Parparov, A., K. D. Harbright, L. Hakanson, and A. Ostapenia. 2006. "Water Quality Quantification: Basics and Implementation." *Hydrobiologia* 560 (1): 1227-237.

[4] Sudevi, B., and K. S. Lokesh. 2012. "Evaluation of Cauvery River water quality at Srirangapatna in Karnataka using Principal Component Analysis." *International Journal of Engineering and Science* 1 (4): 6-12.

[5] Jindal, R., and C. Sharma. 2010. "Studies on water quality of Sutlej River around Ludhiana with reference to physicochemical parameters." *Environmental Monitoring and Assessment* 174: 417–425.

[6] Santosh, M., Avvannavar, and S. Shrihari. 2008. "Evaluation of water quality index for drinking purposes for river Netravathi, Mangalore, South India." *Environmental Monitoring and Assessment* 143:279–290.

[7] Yisa, J., and T. Jimoh. 2010. "Analytical Studies on water quality Index of River Landzu." *American Journal of Applied Sciences* 7 (4), 453–458.

[8] Kosha, A. S., and S. J. Geeta. 2017. "Evaluation of water quality index for River Sabarmati, Gujarat, India." *Applied Water Science* 7: 1349-1358.

[9] Horton, R. K. 1965. "An index number system for rating water quality." *Journal of Water Pollution Control Federation* 37 (3): 300–306.

[10] Brown, R. M., N. I. Mcclelland, R. A. Deininder, and R. G. Tozer. 1970. "A water quality index: do we dare?" *Water Sewage Works* 117 (10): 339–343.

[11] Abbasi, S. A. 2002. *Water Quality Indices, State of the Art Report.* Scientific Contribution No. INCOH/SAR-25/2002. INCOH, National Institute of Hydrology, Roorkee.

[12] Tiwari, T. N., and M. A. Mishra. 1985 "Preliminary assignment of water quality index of major Indian Rivers." *Indian Journal of Environmental Protection* 5 (4): 276–279.

[13] House, M. A. 1989. "A water quality index for river management." *Water and Environment Journal* 3 (4): 336–344.

[14] Amman. 1995. "UNEP development of water quality indices for sustainable development: a case study." *In: Proceeding of the Expert Group Meeting on the Implication of Agenda Region* 2–5 October 1995.

[15] Canter, L. W. 1996. *Environmental Impact Assessment, 2nd ed.* McGraw-Hill International Edition, New York, USA.

[16] CCMC (Canadian Council of Ministers of the Environment). 2001. *CCME Water Quality Index 1.0 Technical Report and User's Manual.* Canadian Environmental Quality Guidelines. Technical Subcommittee, Gatineau.

[17] Sanchez, E., M. F. Colmenero, J. Vicente, A. Rubio, M. G. Garcia, L, Travieso, and R. Borja. 2007. "Use of the water quality index and dissolved oxygen deficit as simple indicators of watersheds pollution." *Ecological Indicators* 7 (2): 315–328.

[18] Coletti, C., R. Testezlaf, T. A. P. Ribeiro, R. T. G. De Souza, and D. A. Peraira. 2010. "Water quality index using multivariate factorial analysis." *Revista Brasileira de Engenharia Agricola e Ambiental* 14 (5): 517–522.

[19] Nikoo, R., R. Kerachian, E. S. Malakpour, S. N. Bashi-Azghadi, and G. M. M. Azimi. 2011. "A probabilistic water quality index for River water quality assessment: a case study." *Environmental Monitoring and Assessment* 181 (1–4): 465–478.

[20] Almeida, C., S. O. Gonzalez, M. Mallea, and P. Gonzalez. 2012. "A recreational water quality index using chemical, physical and micro biological parameters." *Environmental science and pollution research International* 19 (8): 3400–3411.

[21] Wanda, E. M. M., L. C. Gulula, and G. Phiri. 2012. "Determination of characteristics and drinking water quality index in Mzuzu City, Northern Malawi." *Physics and Chemistry of the Earth, Parts A/B/C* 50–52: 92–97.

[22] Upadhyay, R., N. Dasgupta, A. Hasan, and S. K. Upadhyay. 2010 "Managing water quality of River Yamuna in NCR Delhi". *Physics and Chemistry of the Earth, Parts A/B/C* 36 (9–11): 372–378.

[23] Tangri, A. K., D. Kumar, D. S. Singh, and C. A. Dubey. 2018. "The Gomati River: Lifeline of Central Ganga Plain, D.S. Singh (ed.), *The Indian Rivers, Springer Hydrogeology* 135-150.

[24] Dutta, V., R. K. Srivastava, M. Yunus, S. Ahmed, V. V. Pathak, A. Rai, and N. Prasad. 2011. "Restoration Plan of Gomti River with Designated Best Use Classification of Surface Water Quality based on River Expedition, Monitoring and Quality Assessment." *Earth Science India* 4 (III): 80-104.

[25] Avvanavar, S. M., and S. Shrihari. 2008. "Evaluation of water quality index for drinking purposes for river Netravathi." *Environmental Monitoring and Assessment* 143: 279–290.

[26] Singh, A. N., R. Shivastava, D. Mohan, P. Kumar. 2018 Assessment of Spatial and Temporal Variations in Water Quality Dynamics of River Ganga in Varanasi. *Pollution* 4 (2): 239-250.

[27] Kumari, M., L. K. Mudgal, and A. K. Singh. 2013. "Comparative studies of physico-chemical parameters of two reservoirs of Narmada River, MP, India." *Current World Environment* 8 (3): 473–478.

[28] Bora, M., and D. C. Goswami. 2017. "Water quality assessment in terms of water quality index (WQI): case study of the Kolong River, Assam, India." *Applied Water Science* 7: 3125–3135.

[29] Sharma, S., S. Dixit, and P. Jain. 2008. "Statistical evaluation of hydrobiological parameters of Narmada River water at Hoshangabad City, India." *Environmental Monitoring and Assessment* 143:195–202.

[30] Sanap, R. R., A. K. Mohite, S. D. Pingle, and V. R. Gunale. 2006. "Evaluation of water qualities of Godawari River with reference to physicochemical parameters, district Nasik (M.S.), India." *Pollution Research* 25 (4): 775–778.

[31] Diamantini, E., S. R. Lutz, S. Mallucci, B. Majone, R. Merz, and A. Bellin. 2018 "Driver detection of water quality trends in three large European river basins." *Science of the Total Environment* 612: 49–62.

[32] Iqbal, K., S. Ahmad, and V. Dutta. 2019. "Pollution mapping in the urban segment of a tropical river: is water quality index (WQI) enough for a nutrient-polluted river?" *Applied Water Science* 9:197.

[33] Rehana, S., and P. P. Mujumdar. 2011. "River water quality response under hypothetical climate change scenarios in Tunga-Bhadra River, India." *Hydrological Processes* 25 (22): 3373-3386.

ANNEXURE I: LOCATION WISE STATISTICS OF WATER QUALITY PARAMETERS

	pH	Conductivity	T.D.S.	TH	Chloride	DO	BOD	Alkalinity	WAWQI
S1									
Mean	8.05	366.10	222.00	178.00	12.50	8.05	2.80	197.00	67.31
Average	8.22	384.47	231.37	196.77	13.05	8.04	2.96	216.20	69.35
Standard error	0.05	12.01	6.04	3.86	0.22	0.24	0.02	3.85	0.96
Median	8.29	388.40	233.00	206.00	13.00	7.60	2.95	228.00	69.57
Mode	8.29	336.00	184.00	228.00	13.00	6.80	2.90	228.00	77.94
Standard deviation	0.36	93.80	47.21	30.16	1.73	1.89	0.15	30.07	7.53
Minimum	7.20	172.00	112.00	120.00	8.00	4.70	2.30	142.00	52.66
Maximum	8.89	560.20	332.00	236.00	17.00	11.40	3.30	252.00	81.97
S2									
Mean	7.88	381.60	232.00	186.00	15.00	6.90	3.65	206.00	76.09
Average	8.12	397.10	240.83	202.70	14.53	7.26	3.41	224.20	74.44
Standard error	0.04	12.66	6.38	4.06	0.24	0.27	0.03	3.76	1.17
Median	8.21	413.80	240.00	212.00	14.00	6.70	3.30	236.00	74.79
Mode	8.54	348.00	192.00	232.00	14.00	6.50	3.30	236.00	83.38
Standard deviation	0.32	98.92	49.84	31.70	1.86	2.13	0.24	29.34	9.10
Minimum	7.17	180.80	118.00	128.00	11.00	2.90	3.10	148.00	56.31
Maximum	8.58	582.40	346.00	244.00	19.00	10.90	4.20	264.00	95.87
S3									
Mean	7.75	486.75	305.00	195.00	17.00	5.10	6.30	214.00	98.97
Average	7.87	450.83	274.23	211.97	16.72	5.02	5.19	233.47	92.98
Standard error	0.04	18.94	10.86	4.08	0.31	0.31	0.19	3.91	2.33
Median	7.83	440.40	255.00	220.00	16.00	5.05	4.60	244.00	90.70
Mode	7.82	364.00	270.00	236.00	15.00	3.50	4.00	258.00	94.80
Standard deviation	0.29	147.98	84.81	31.90	2.39	2.41	1.49	30.57	18.17
Minimum	7.11	201.00	128.00	134.00	12.00	0.70	3.60	156.00	63.89
Maximum	8.38	772.50	482.00	256.00	22.00	9.50	9.00	272.00	134.05
S4									
Mean	7.65	503.80	316.00	201.00	18.50	4.85	7.25	220.00	109.41
Average	7.80	469.44	286.53	218.80	18.42	4.36	6.39	240.33	103.43
Standard error	0.03	19.04	10.98	4.11	0.33	0.22	0.19	3.94	2.09
Median	7.77	454.45	266.00	228.00	18.00	4.20	6.00	252.00	103.34
Mode	7.71	388.00	232.00	244.00	20.00	4.20	6.00	252.00	106.77
Standard deviation	0.25	148.77	85.77	32.14	2.59	1.74	1.48	30.75	16.34
Minimum	7.04	212.00	136.00	140.00	13.00	1.30	4.50	162.00	79.68
Maximum	8.26	795.60	496.00	262.00	24.00	8.40	10.00	278.00	139.15
S5									
Mean	7.58	541.55	345.00	211.00	20.50	3.55	8.75	227.00	121.82
Average	7.70	496.19	304.77	228.47	21.33	3.02	8.37	250.03	122.17
Standard error	0.03	19.95	11.36	4.13	0.37	0.15	0.19	3.95	1.94
Median	7.70	474.60	282.00	238.00	21.00	2.80	8.50	260.00	122.82
Mode	7.69	426.00	274.00	254.00	24.00	3.20	8.50	268.00	131.84
Standard deviation	0.22	155.84	88.70	32.25	2.93	1.19	1.49	30.88	15.14
Minimum	7.00	224.60	152.00	148.00	14.00	1.10	6.00	168.00	91.92
Maximum	8.15	858.50	538.00	274.00	27.00	6.00	11.50	286.00	151.73
S6									
Mean	7.52	552.10	357.00	219.00	22.00	2.85	9.50	235.00	126.94
Average	7.64	512.50	316.47	235.87	23.33	2.45	9.77	256.70	134.04
Standard error	0.03	20.12	11.35	4.10	0.41	0.14	0.19	4.03	1.95
Median	7.64	489.10	293.00	244.00	23.00	2.10	10.00	266.00	134.93
Mode	7.62	456.00	290.00	258.00	25.00	3.00	10.00	282.00	149.50
Standard deviation	0.22	158.38	89.24	32.24	3.23	1.12	1.53	31.59	15.30
Minimum	6.95	221.60	160.00	156.00	15.00	0.60	6.50	172.00	96.16
Maximum	8.09	882.60	554.00	282.00	29.00	5.10	12.50	298.00	157.72
S7									
Mean	7.36	612.40	394.00	232.00	25.50	2.05	13.55	251.00	157.22
Average	7.48	559.40	343.73	248.23	27.18	1.52	12.48	270.30	155.70

	pH	Conductivity	T.D.S.	TH	Chloride	DO	BOD	Alkalinity	WAWQI
Standard error	0.02	22.94	12.75	4.22	0.44	0.11	0.22	4.12	2.03
Median	7.50	513.50	314.00	258.00	28.00	1.20	13.00	278.00	159.89
Mode	7.43	489.00	342.00	258.00	29.00	1.00	13.00	296.00	170.87
Standard deviation	0.19	179.19	99.63	32.94	3.44	0.86	1.69	32.15	15.89
Minimum	6.89	240.60	172.00	170.00	18.00	0.30	8.50	186.00	113.53
Maximum	7.82	984.20	616.00	294.00	33.00	3.80	18.60	316.00	200.91

Proceedings of the International Conference on Augmented Intelligence and Sustainable Systems (ICAISS-2022)
IEEE Xplore Part Number: CFP22CB2-ART; ISBN: 978-1-6654-8962-1

Automated Major Depressive Disorder (AMDD) Detection using Audio-Visual Feature Discriptor and CNN

Nikhil Singh
Research Scholar: Department of Electronics and Communication Engineering, Delhi Technological University, New Delhi, India.
nikhil_2k19phdec04@dtu.ac.in

Rajiv Kapoor
Professor: Department of Electronics and Communication Engineering, Delhi Technological University, New Delhi, India.
rajivkapoor@dce.ac.in

Ruchirangad Kapoor
Project Intern: Delhi Tech University,Delhi,India
ruchirangadk@gmail.com

Siddharth Arora
Project Intern: Delhi Tech University,Delhi,India
siddharth.arora7621@gmail.com

2022 International Conference on Augmented Intelligence and Sustainable Systems (ICAISS) | 978-1-6654-8962-1/22/$31.00 ©2022 IEEE | DOI: 10.1109/ICAISS55157.2022.10010907

Abstract—**The severe forms of depression, a widespread mental health issue, can result in self-harm or suicide. Clinical diagnosis and early intervention of depression are greatly aided by an automatic depression detection system. In this study, we suggest a novel automated major depressive disorder (AMDD) detection technique that makes use of audio-visual parameters from patients. PCA is used as dimension reduction for feature selection. After these two types of signals' effective characteristics were extracted and selected, we trained classifiers on each modality. SVM is taken into account for classification. According to our research, fusing features from different data modalities performs better than using just one, and combining audio-visual data modalities' features results in the highest classification accuracy. Comparing the accuracy of the feature selection approach to other methods, PCA significantly increased the accuracy. Also, SVM gives the best in class accuracy of 99.15% on DAIC-WOZ dataset.**

Keywords- Audoi-visual modality, Depression detection, Feature fusion, Psychological disorder.

I. INTRODUCTION

As long as mood fluctuations are not severe, frequent, or disruptive to that person's every day and social functions, mood fluctuations are a common component of most people's emotional lives [1]. A leading cause of disability worldwide, major depressive disorder is a psychological illness. It affects more than 300 million people each year, irrespective of age, and is a significant contributor to the worldwide burden of disease [2], [3]. MDD patients frequently find difficulty in socializing. They also suffer from low self-esteem, which negatively affects their day to day work or performance. Consequently, if undiagnosed and untreated, MDD may push sufferers to commit suicide [4]. When compared to the general population, depressive people have a more than 30-fold increased risk of suicide [5]. MDD can range in severity, linger for weeks, months, or even years, and be accompanied by distress and impairment that make it difficult for a person to carry out daily tasks.

Additionally, it has been reported that due to inaccurate diagnoses, a shortage of medical personnel, subpar facilities, and social stigma, only few of the patients worldwide receive adequate care [6]. In particular, MDD can be diagnosed based on standards outlined in the Diagnostic and Statistical Manual of Mental Disorders, Fifth Edition (DSM5). These requirements include having a poor mood for at least 2 weeks along with at least two or more other symptoms, such as [7]:

- thoughts of harming oneself
- fluctuating weight and hunger
- loss of focus, delayed thought processing
- feelings of worthlessness.

The outline of this manuscript is in the form, Section II contains the related works which have been done by various researchers in the past and motivation for this manuscript. Section III describes the methodology used to perform efficient MDD detection. Section IV shows visual and mathematical results and its comparison with state-of-art schemes. Section V ends the manuscript with the major findings of this study.

II. RELATED WORK

There was little interest in AMDD before to 2009. A rising number of people are now using important behavioural signs and physiological indicators to diagnose depression. In addition to increasing the precision of psychological diagnosis and treatment of many mental problems, the study of objective biological, physiological, and behavioural indicators also lessens the social and financial burdens brought on by these diseases [9]. This AMDD addresses the problem of misdiagnosing depression, which is regarded as one of the major obstacles to treating depression. These researches examined a number of indicators of depression, such as facial expression, head and body posture, speech patterns etc [10]. Rich visual signals of psychological states can be found in audio-visual cues. Patients with depression typically display distinct facial expressions and irregular head motions as compared to non-depressed people [11]. o extract such visual

Authorized licensed use limited to: DELHI TECHNICAL UNIV. Downloaded on January 19,2023 at 05:03:49 UTC from IEEE Xplore. Restrictions apply.

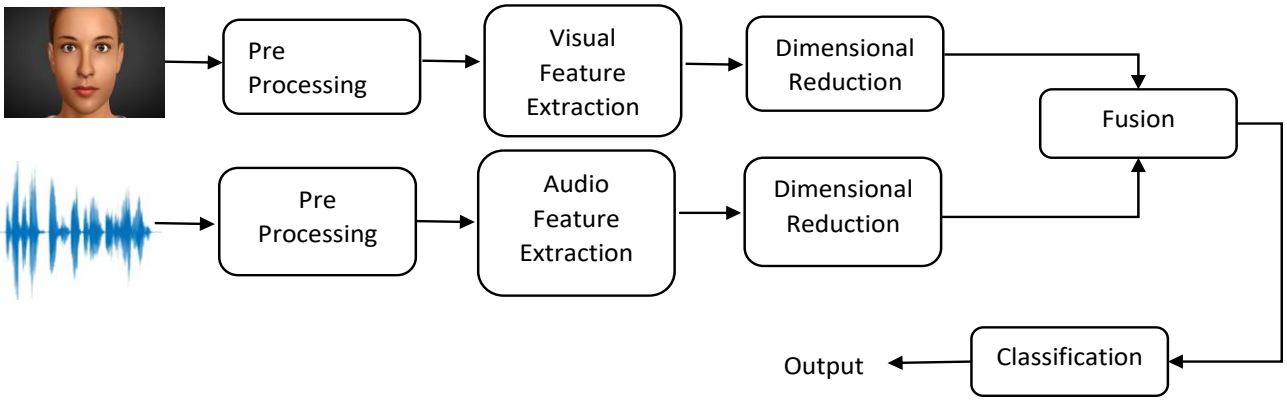

Fig 1. Block diagram of proposed AMDD

features schemes such as FACS (Facial action coding system), AAM (Active appearance model) are widely used on eye movement, head pose and body movement [8]. Also there present various schemes for early and efficient detection of depression such as: DCNN, DNN, LSTM and Bi-LSTM based.

In general, techniques for automatically detecting depression begin by extracting several sorts of features from patient interview audio or video in which they are questioned about a variety of carefully chosen subjects. Then, using the collected information, models are trained to either predict the presence of depression in patients or determine the severity of their depression. For an efficient detection of such medical conditions efficient database is needed. Few of such database are MINI [12], DAIC-WOZ [13], AVEC2017, AVEC2018 [14] etc. In our study we used DAIC-WOZ database details of which is mentioned in reference [13].

The current approaches do, however, have some drawbacks. We developed an AMDD detector based on audio-visual signals to more accurately predict the severity of depression. The basic block diagram of proposed scheme can be seen in figure 1. Here, the output is either depressed or not depressed.

III. METHODOLOGY

The four components of our method's general structure are preprocessing, feature extraction, feature selection, feature fusion, and data classification. To be more precise, we first group samples into sequences of specified shape.

A. Preprocessing

For efficient detection of depression preprocessing is an important step. The audio-visual data is divided into sequences in initial phase. Video as an input is processed in the following manner such as detection of face, alignment, illumination settings. For audio signal segmentation is to be carried out as preprocessing step. Viola and Jones have proposed the most well-liked algorithm for face detection. There also present toolkits such as Opensmile and Openface for performing preprocessing task

B. Feature Extraction

Feature extraction is a crucial phase in the processing workflow because it is completely dependent upon later processes. These extraction schemes can be categorized as *i)* appearance based and *ii)* geometry based. The classification of facial features includes features from the complete face, action units, facial landmarks, eyes and lips. Statistical measures are considered to compare depressed subjects with healthy subjects.

As per the literature study it is found that depressed people avoid direct eye contact. Hence eyes play and important role in detecting MDD. Eye activity can be tracked using subject specific AAM. Similarly we made subject specific AAM for facial muscle movement. These face movement traces motion of lips, cheek torso and eye blink ratio. VAD is used to extract voice features.

C. Feature Selection

After successful extraction dimensionality reduction is applied to remove the less important variables which reduce the noise as well as complexity from the model. Some example of dimension reduction algorithms are- Correlation, LDA, RFE, CCA, CFA, NPE, GDA, PCA etc. Here we took PCA for selecting features. Selection of principal components can be seen from figure 2.

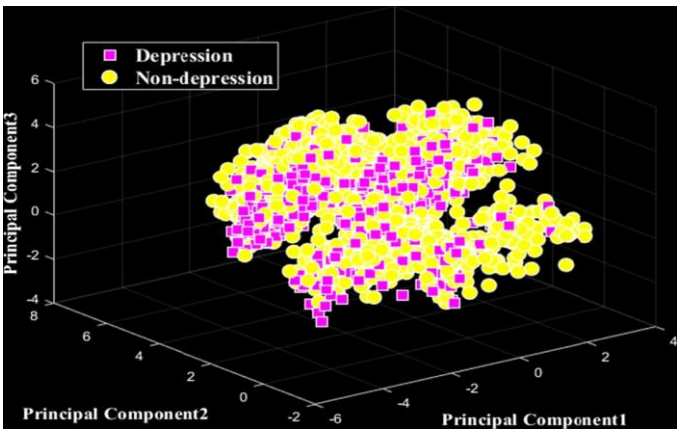

Fig 2. Feature selection using PCA

Authorized licensed use limited to: DELHI TECHNICAL UNIV. Downloaded on January 19,2023 at 05:03:49 UTC from IEEE Xplore. Restrictions apply.

D. Feature Fusion

Numerous methods incorporate a number of features derived from various modalities, as well as from that modality itself. Multiple feature sets are typically combined using fusion methods. The extracted feature vectors from the various modalities are concatenated during fusion, which occurs more frequently just after feature extraction. Dimensionality reduction may occur either before or after this concatenation. The concatenation of two types of embedding is defined as:

$$a=X_{embed}$$
$$b=X_{spec}$$
$$x_{fuse}= (a_1, a_2,\ldots,b_1,b_2,\ldots)$$

E. Classification

The technique that is most frequently used for categorical assessment of depression is Support Vector Machines (SVM). It can be explained through the statistic that SVMs are effective for high-dimensional binary problems, such as differentiating between high symptom severity/present depression and low symptom severity/absent depression. SVMs can also be used with non-linear combinations of kernel functions.

IV. Result and Discussion

Using the DAIC-WoZ training set, a classification model for predicting the presence of depression was developed. This is due to the reason that labels for the test set weren't mentioned, the trained model was assessed on the validation set rather than the test set. 20% of the whole dataset is designated as the test set. To divide the training dataset and the validation set for the remaining data, the leave one out approach is used. Accuracy, precision, recall, and F1 score are the measures used to assess the performance of various models. It is assumed that the sample has two categories in the binary classification problem: positive and negative. Performance evaluation is done w.r.t accuracy, precision, recall and f1-score.

$$Accuracy = \frac{TP + TN}{TP + TN + FP + FN}$$

$$\text{Re } call = \frac{TP}{TP + FN}$$

$$\text{Pr } ecision = \frac{TP}{TP + FP}$$

$$F1 - score = 2 \times \frac{\text{Pr } ecision \times \text{Re } call}{\text{Pr } ecision + \text{Re } call}$$

TABLE I. COMPARISON ON DIAC-WOZ DATA

Ref.	Accuracy	Precision	Recall	F1-score
[3]	-	-	-	0.70
[4]	-	0.714	0.833	0.769
[8]	-	0.56	0.71	0.63
[13]	-	**0.818**	0.75	0.783
Ours	**0.9915**	0.80	**0.88**	**0.82**

Comparison with other existing schemes can be seen in table 1. Confusion matrix defines the performance of classification measure used in matrix form where row and column represent the number of samples taken into account. Figure 3 shows the confusion matric of the proposed scheme between depressed and non-depressed subjects.

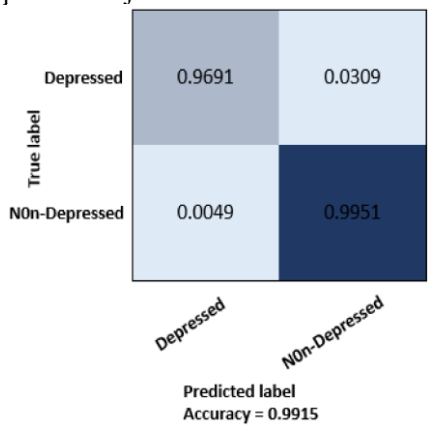

Fig 3. Confusion matric for proposed scheme

V. Conclusion

Clinical psychology and psychiatry are active and divisive fields when it comes to discussing depression diagnosis. The development of automated, objective assessment techniques may be beneficial for both clinical practice and research given the aforementioned unresolved concerns. In this manuscript we conduct an experiment on AMDD detection using audio-visual modality. To thoroughly investigate the sequence's differentiating data PCA is applied to select the important parameters after extraction and to serve the classification SVM is utilized. The DAIC-WOZ dataset serves as our method's validation. Extensive experimental findings demonstrate both the usefulness of the proposed method's components and its state-of-the-art performance in comparison to other relevant AMDD approaches. The proposed scheme achieves accuracy of 99.15%. In future other modalities such as physiological signal (EEG) and text will also be incorporated for efficient detection of depression.

References

[1] Alghowinem, S., Goecke, R., Wagner, M., Epps, J., Hyett, M., Parker, G., & Breakspear, M. (2016). Multimodal depression detection: fusion analysis of paralinguistic, head pose and eye gaze behaviors. IEEE Transactions on Affective Computing, 9(4), 478-490.J. Clerk Maxwell, A Treatise on Electricity and Magnetism, 3rd ed., vol. 2. Oxford: Clarendon, 1892, pp.68–73.

[2] Gray, J. P., Müller, V. I., Eickhoff, S. B., & Fox, P. T. (2020). Multimodal abnormalities of brain structure and function in major depressive disorder: a meta-analysis of neuroimaging studies. American Journal of Psychiatry, 177(5), 422-434.

[3] Khan, D. M., Masroor, K., Jailani, M. F. M., Yahya, N., Yusoff, M. Z., & Khan, S. M. (2022). Development of wavelet coherence EEG as a biomarker for diagnosis of major depressive disorder. IEEE Sensors Journal, 22(5), 4315-4325.

[4] Mahato, S., & Paul, S. (2019). Electroencephalogram (EEG) signal analysis for diagnosis of major depressive disorder (MDD): a review. Nanoelectronics, Circuits and Communication Systems, 323-335.

[5] Guze, S. B., & Robins, E. L. I. (1970). Suicide and primary affective disorders. The British Journal of Psychiatry, 117(539), 437-438.

[6] Frankish, H., Boyce, N., & Horton, R. (2018). Mental health for all: a global goal. Lancet (London, England), 392(10157), 1493-1494.

Authorized licensed use limited to: DELHI TECHNICAL UNIV. Downloaded on January 19,2023 at 05:03:49 UTC from IEEE Xplore. Restrictions apply.

[7] JH Balsters, M., J Krahmer, E., GJ Swerts, M., & JJM Vingerhoets, A. (2012). Verbal and nonverbal correlates for depression: a review. Current Psychiatry Reviews, 8(3), 227-234.

[8] Alghowinem, S. M., Gedeon, T., Goecke, R., Cohn, J., & Parker, G. (2020). Interpretation of depression detection models via feature selection methods. IEEE Transactions on Affective Computing.

[9] Parker, G., Hadzi-Pavlovic, D., Brodaty, H., Boyce, P., Mitchell, P., Wilhelm, K., ... & Eyers, K. (1993). Psychomotor disturbance in depression: defining the constructs. Journal of Affective Disorders, 27(4), 255-265.

[10] Gratch, J., Artstein, R., Lucas, G., Stratou, G., Scherer, S., Nazarian, A., ... & Morency, L. P. (2014). The distress analysis interview corpus of human and computer interviews. UNIVERSITY OF SOUTHERN CALIFORNIA LOS ANGELES.

[11] Nehru, M., & Padmavathi, S. (2017, January). Illumination invariant face detection using viola jones algorithm. In 2017 4th International Conference on Advanced Computing and Communication Systems (ICACCS) (pp. 1-4). IEEE.

[12] Baltrušaitis, T., Robinson, P., & Morency, L. P. (2016, March). Openface: an open source facial behavior analysis toolkit. In 2016 IEEE Winter Conference on Applications of Computer Vision (WACV) (pp. 1-10). IEEE.

[13] Eyben, F., Wöllmer, M., & Schuller, B. (2010, October). Opensmile: the munich versatile and fast open-source audio feature extractor. In Proceedings of the 18th ACM international conference on Multimedia (pp. 1459-1462).

Authorized licensed use limited to: DELHI TECHNICAL UNIV. Downloaded on January 19,2023 at 05:03:49 UTC from IEEE Xplore. Restrictions apply.

Journal of Applied Electrochemistry
https://doi.org/10.1007/s10800-023-01848-5

RESEARCH ARTICLE

Biosynthesized rGO@ZnO-based ultrasensitive electrochemical immunosensor for bovine serum albumin detection

Palak Garg[1] · Deeksha Thakur[1] · Sakshi Verma[1] · Owais Jalil[1] · Chandra Mouli Pandey[2] · Devendra Kumar[1]

Received: 4 November 2022 / Accepted: 2 January 2023
© The Author(s), under exclusive licence to Springer Nature B.V. 2023

Abstract

Bovine serum albumin (BSA) is a globular protein that plays a vital role in delivering fatty acids/amino acids and the reduction may leads to various diseases in cattle. Herein, we report a highly sensitive biosensor based on reduced graphene oxide-zinc oxide (rGO@ZnO) nanocomposite for the detection of BSA. Biosynthetic approach has been adopted for synthesizing rGO@ZnO nanocomposite by using *Aloe vera* leaf extract as a reducing agent. The characterization of the nanocomposite has been conducted using UV–visible spectroscopy, FT-IR, Zeta Potential, and TGA techniques. Further, the rGO@ZnO nanocomposite was deposited electrophoretically on an indium tin oxide (ITO)-coated glass substrate, followed by the immobilization of anti-BSA. The fabricated rGO@ZnO-based biosensor exhibits a wide linear range (0.001 to 30 ng mL^{-1}), and offers low detection limit (1 pg/mL) with acceptable selectivity and stability for BSA detection in urine sample. The remarkable electronic and electrochemical characteristics of rGO and its integration with a direct band gap semiconductor (ZnO) offer excellent charge transfer capacity, large surface area, and exceptional electrochemical properties.

Palak Garg and Deeksha Thakur have contributed equally to this study.

✉ Chandra Mouli Pandey
cmp.npl@gmail.com

✉ Devendra Kumar
dkumar@dce.ac.in

[1] Department of Applied Chemistry, Delhi Technological University, New Delhi, Delhi 110042, India

[2] Department of Chemistry, Faculty of Science, SGT University, Gurugram, Haryana 122505, India

Published online: 17 January 2023

Graphical abstract

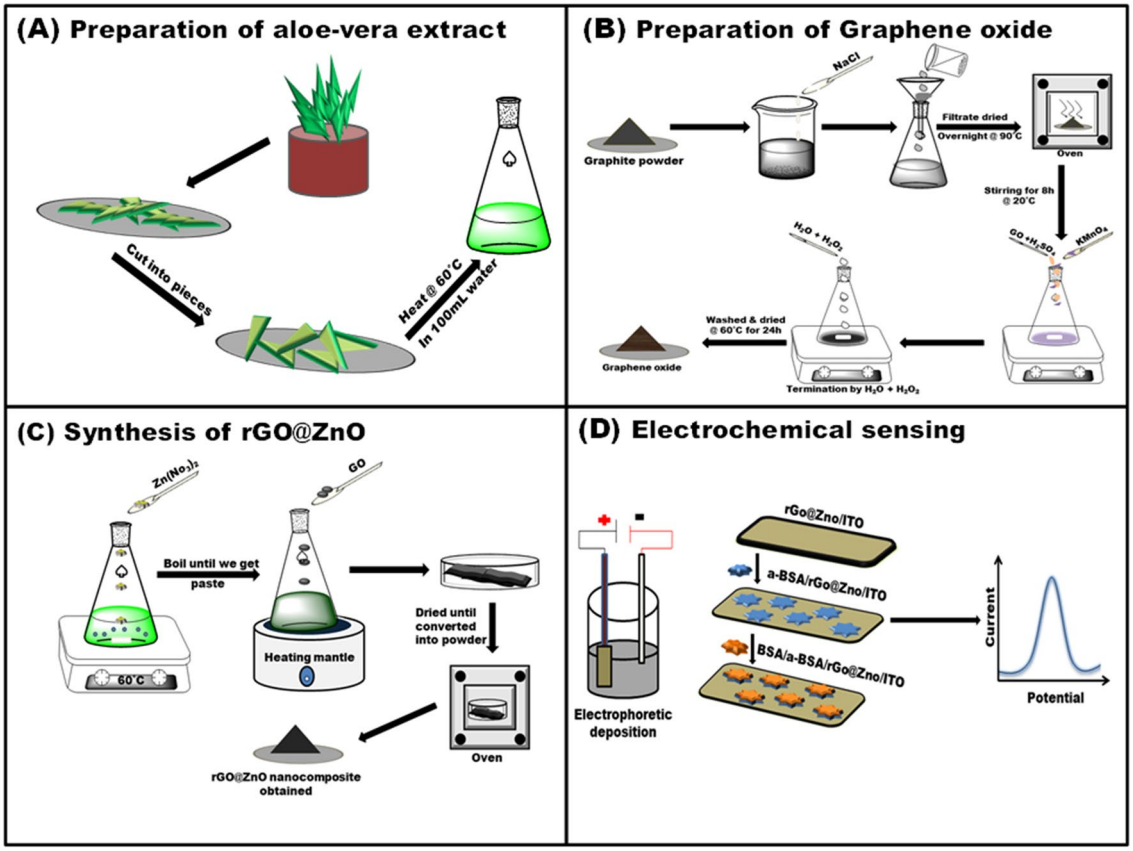

Keywords BSA · Graphene oxide · ZnO nanoparticle · *Aloe vera* · Biosensor

1 Introduction

Bovine Serum Albumin (BSA) is a cow protein that plays a vital role in the circulation of many endogenous and exogenous compounds into vertebrate blood to maintain the osmotic pressure of plasma [1]. BSA is composed of 17 cross-linked cysteine residues, 1 free cysteine, and 582 amino acid residues [2]. The traditional methods used for BSA detection are resonance light scattering [3, 4], voltammetry assays [5], surface-enhanced plasma resonance [6], surface-enhanced Raman spectroscopy [7], near-infrared reflection spectroscopy [8], fluorimetric determination [9], circular dichroic [10], spectrophotometry methods etc. These methods take a long time, use large volumes of reagents, and sometimes show a lack of sensitivity. Therefore, there is an urgent need to develop a simple, sensitive, cost-effective, and easy-to-use device to detect BSA. In this context, biosensors can play a pivotal role in detecting target analytes with greater sensitivity and selectivity [11]. Biosensors allow the detection of biomolecules with high affectability, and selectivity, with a low response time [12].

For biosensor fabrication, selecting effective matrix that help in the binding of the recognition molecule and provide faster access to the analyte is essential. Nowadays, graphene has attracted much interest in the development of biosensors. Graphene is a 2-D sheet of sp^2 hybridized carbon and is a reasonable material for robust electrodes because of its striking features like large interfacial surface area, electrical conductivity, quick electron mobilities, simplicity of functionalization, and large-scale manufacturing [13]. Graphene provides a suitable microenvironment for protein binding and provides a rapid electron movement of the biomolecules at the terminal surface [14]. Nanostructured metal oxides (NMO), due to their unique physical, chemical, and catalytic properties, have aroused interest as immobilization platforms in biosensors applications [15]. NMO of titanium, iron, tin, cerium, zirconium, zinc, and magnesium has fascinating functional biocompatibility, nano-morphological,

and electrochemical properties [16]. NMO shows improved electron efficiency and high adsorption abilities and provides suitable microenvironments for the immobilization of biomolecules [17]. Further, the integration of graphene with different metal oxide (MO) nanoparticles enhances the electrochemical catalytic activity compared to bare graphene [18]. The graphene-MO nanocomposite gives a more significant electrochemical dynamic surface, which brings about the assimilation of more biomolecules and expands the electron transfer between the electrode surface and the redox mediator [19]. GO@MO nanocomposite have excellent capabilities to stimulate direct electron transfer of the entrapped bio-molecules with sustained bioactivity [20]. Among the reported NMO, nanostructured ZnO has a vast surface area, quick electron mobilities, solid protein retention, great chemical stability, and ideal biocompatibility [21].

The chemical reduction of GO to rGO tends to form an irreversible aggregate composite with ZnO and due to strong *Vander waals* forces of attraction between graphene planes, the functionalization ability at the surface of 2D sheets increases [22]. Moreover, the chemical reduction is highly toxic due to the chemical reducing agents like hydrazine, dimethylhydrazine, and hydroquinone [23–25]. Recently, reducing GO using plant extract has attracted significant attention among researchers. This method is more eco-friendly, cost-effective, and sustainable than any other chemical reducing agent [26]. The phytochemicals present in plant extracts contain biomolecules, including amino acids, vitamins, pectin, alcoholic compounds, proteins, and enzymes that act as reducing agents [27]. In this work, we have prepared an electrochemical immunosensor for BSA detection using rGO@ZnO, which was biosynthesized using plant extract, i.e., *Aloe vera* leaves extract acting as a reducing agent. The biosynthesized composite was electrophoretically deposited onto ITO-coated glass substrate. The electrochemical detection of BSA in a urine sample taken from a healthy individual was performed, and the results indicate that the developed biosensors have good sensitivity with a lower detection limit [28].

2 Materials and methods

2.1 Materials required

Sodium chloride (99.5%; NaCl, Rankem), hydrogen peroxide (30% w/v H_2O_2, CDH), sulphuric acid (98%; H_2SO_4, Qualigens), hydrogen chloride (35–38%; HCl, Fisher-Scientific), graphite powder (< 20 µm, synthetic), zinc nitrate (98%; $Zn(NO_3)_2$), potassium permanganate (≥ 99%; $KMnO_4$), Polyethylene Glycol 1000 (PEG), N-(3-Dimethylaminopropyl)-N′-ethylcarbodiimide hydrochloride (≥ 98%, crystalline; EDC) and N-Hydroxysuccinimide (98%; NHS), bovine serum albumin (lyophilized powder, ≥ 96%;BSA) and anti-BSA were purchased from Sigma Aldrich. Deionized (DI) water (Mill-Q, Millipore, 18.2 MΩ cm) has been used for the preparation of reagents and the solution. All the glass ware were autoclaved prior to use.

2.2 Preparation of *Aloe Vera* extract

The *Aloe Vera* leaves were collected from the DTU campus, Delhi, India. The fresh plant leaves were washed under running water and then cut into small pieces. 25 g of *aloe vera* leaves pieces were heated at 50–60 °C in 100 mL of distilled water with continuous stirring for 2 h. The prepared extract was filtered using Whatman filter paper (Graphical abstract (A)).

2.3 Synthesis of graphene oxide (GO)

GO was synthesized by modified Hummer's method [29] with slight modification. Graphite powder was grounded with NaCl in a mortar and dissolved in distilled H_2O. The grounded graphite powder was filtered and dried for 6 h at 90 °C. The powder was broken down in sulfuric acid under a magnetic stirrer for 8 h and potassium permanganate was gradually included while the solution was kept at 20 °C. The solution's temperature was maintained at 40 °C for 30 min and afterward to 70° for 45 min. The reaction was ended by gradually adding 200 mL distilled water and 10 mL hydrogen peroxide. The final solution was washed with distilled water and dried at 60 °C for 24 h resulting in the formation of black powder of GO ((Graphical abstract (B)).

2.4 Biosynthesis of rGO@ZnO composite

For the biosynthesis of rGO@ZnO, 5 mL of *Aloe Vera e*xtract has been added to 0.5 g zinc nitrate at 50–60 °C. Then, prepared GO suspension was added to the original solution and the solution was continuously stirred for 2 h and heated at 60 °C until a paste was obtained. The paste was carefully transferred to the crucible and further heated at 100 °C until powder material was obtained (Graphical abstract (C)).

2.5 Electrode fabrication

Electrode preparation was done using a two-electrode system where platinum was taken as a counter electrode. The synthesized rGO@ZnO (2 mg) was dispersed in 25 mL of distilled water containing 5 mL ethanol, which was further sonicated for 1 h. Then, this solution was added to Milli-Q water in a 1:10 ratio (V/V) and again sonicated for 15 min.

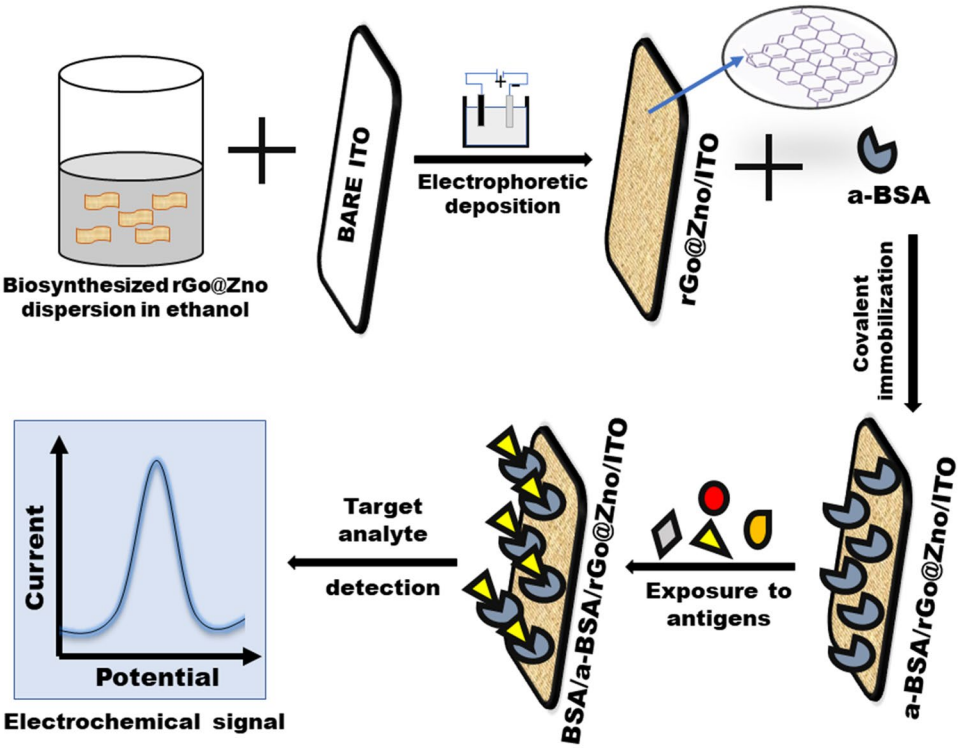

Fig. 1 Scheme showing the fabrication of rGO@ZnO-based biosensor

After that, electrophoretic deposition (EPD) was done on an ITO-coated glass substrate at 10 V for 10 s.

2.6 Fabrication of the biosensors

The rGO@ZnO/ITO electrodes were modified with EDC (10 µL, 5 mM) and NHS (10 µL, 5 mM) and placed in a humidity chamber at room temperature. After an hour, the electrodes were functionalized with (0.1%) PEG and then washed with PBS buffer (pH 7.2) to prevent the non-specific sites from other protein molecules [30]. Further, the electrodes were immobilized with 10 µg/mL anti-BSA and kept for 6 h in a humid chamber at 4 °C (Fig. 1).

2.7 Instrumentation techniques

FT-IR spectroscopy has been carried out using the Nicolet™ iS10 FTIR spectrometer at 25 °C in the frequency region of 400–4000 cm^{-1}. To record the X-ray diffraction (XRD) pattern in the 2θ range (5°–80°) at a scan speed of 2°/min, Bruker D-8 Advance X-ray Diffractometer with monochromatic (Cu Kα), radiation ($\lambda = 1.5406$ Å), was used. Thermal studies were carried out to analyze the thermal degradation of samples in the range 25 to 900°C with a heating rate of 10°C/min in nitrogen conditions using thermogravimetric analysis (TGA 4000, PerkinElmer). A UV–Vis absorption study was done using a UV–Vis spectrophotometer (Perkin-Elmer model UV-260). Electrochemical studies of the electrode were carried out by galvanostat/potentiostat (Autolab, Netherland) using the conventional three-electrode cell where platinum was used as the auxiliary electrode, Ag/AgCl as reference electrode and ITO as WE, in phosphate buffer saline (PBS, 100 mM, pH 7.2) containing 5 mM $[Fe(CN)_6]^{3-/4-}$.

3 Results and discussion

3.1 X-Ray Diffraction

The XRD pattern of the bio-synthesized rGO@ZnO composite recorded at diffraction angle in the range 10 to 80° has been shown in Fig. 2a. The broad peak around $2\theta = 20°–27°$ is assigned to rGO. The characteristic peaks at $2\theta = 31.75°$, 34.46°, 36.22°, 47.71°, 56.67°, 62.88°, 66.34°, 67.84°, 69.06° corresponds to (100), (002), (101), (102), (110), (103), (200), (112), and (201) crystalline planes which coincide with hexagonal wurtzite structure of ZnO [31]. The rGO@ZnO shows similar diffraction peaks as of ZnO and rGO, which indicates that ZnO does not lose its identity being incorporated into rGO. The characteristic sharp peak of GO (Fig S1) with excellent intensity can be clearly observed at around 10 degree, while this peak has been found to be absent in other XRD

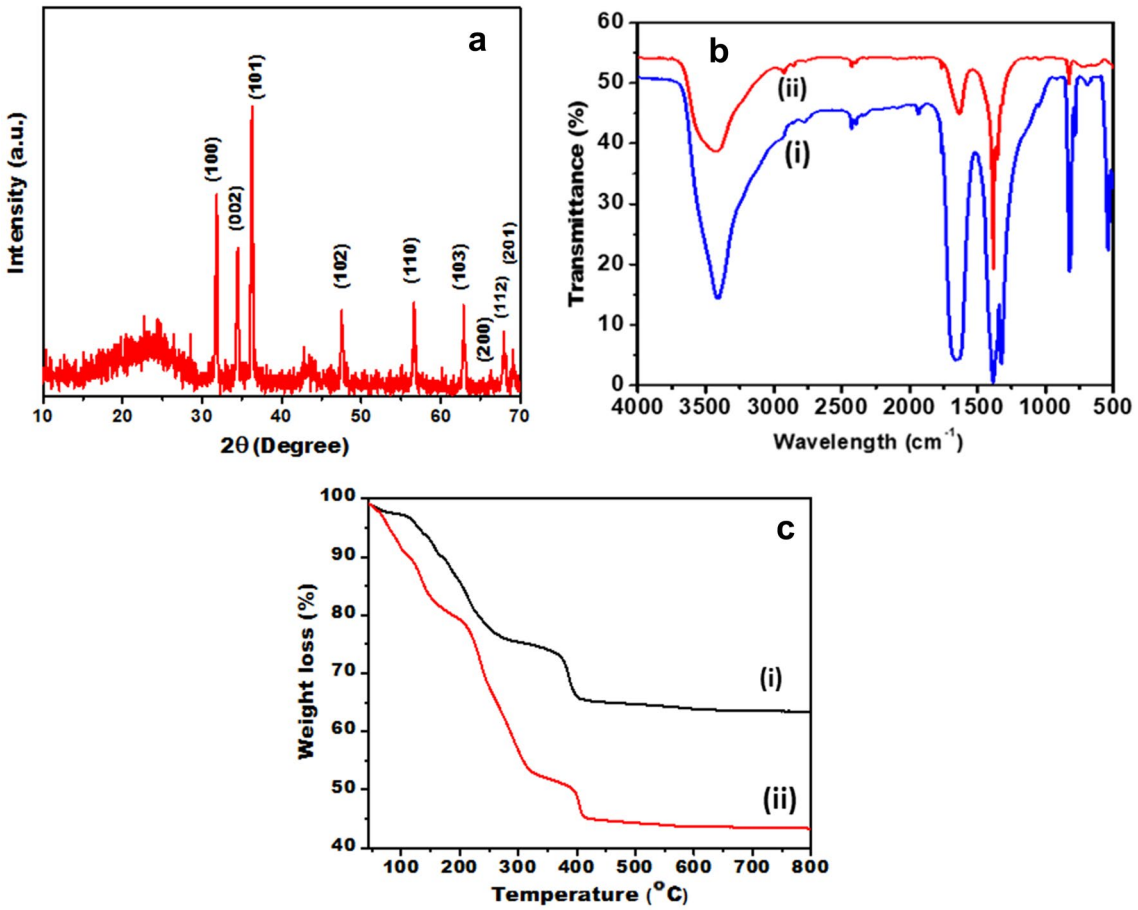

Fig. 2 **a** XRD of rGO@ZnO; **b** FT-IR spectra of (i) ZnO and (ii) rGO@ZnO; **c** TGA plot for (i) ZnO and (ii) rGO@ZnO in the range 25° to 900 °C (10 °C /min), in a nitrogen environment

patterns which indicated smooth reduction of GO to rGO [32].

3.2 Spectroscopic analysis

The biosynthesized rGO@ZnO was investigated by FT–IR spectroscopy (Fig. 2b). The spectrum shows a broad peak at 3428 cm^{-1} arising from O–H group stretching vibrations, and 1385 cm^{-1} peak shows C–O groups. The peaks at 2859 cm^{-1} and 2923 cm^{-1} are due to C–H group's symmetric and asymmetric vibrations, respectively. The peak observed at 1634 cm^{-1} is due to C=O stretching of the carboxylic/carbonyl moiety functional group. Peak at 1046 cm^{-1} shows C–OH stretching and 833 cm^{-1} shows C–O stretching. Also, a band has been observed at 500 cm^{-1} range which is due to the vibrations of Zn–O bonds [33]. Figure S2 shows the UV–Vis spectra of rGO, rGO@ZnO, and GO. The rGO spectra show a redshift from 293 to 305 nm because of the removal of oxygen-functional groups from GO and the re-establishment of the conjugated structure of rGO. Spectra of rGO@ZnO show a gentle slopping absorption peak at 353 nm due to the presence of ZnO [34].

3.3 Thermogravimetric analysis

TGA curves (Fig. 2c) of ZnO and rGO@ZnO show weight reduction at 100°C because of the removal of the water molecules. A significant weight reduction has been observed at 210–400 °C because of the expulsion of oxygen-rich functional groups, for example, CO_2 and CO. Till 420 °C, weight loss is due to the removal of remaining oxygen moieties.

3.4 Zeta potential and SEM analysis

The zeta potential results of GO, rGO@ZnO composite was found to be − 7.64 mV and − 29.4 mV, respectively. The high zeta potential of GO was due to the presence of negatively charged –OH and –COOH groups. The value of zeta in rGO@ZnO decreases due to reduction in oxygen functional groups and its better dispersion (Fig S3).

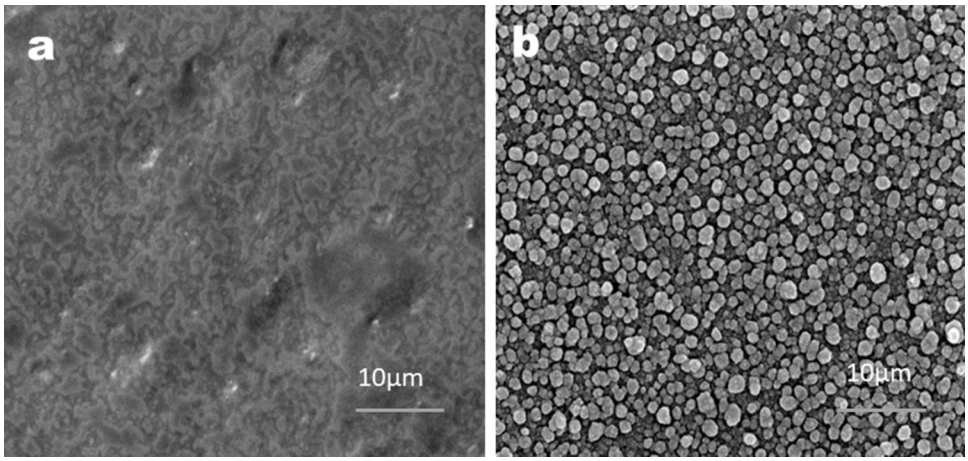

Fig. 3 SEM images of **a** rGO@ZnO/ITO electrode and **b** anti-BSA/rGO@ZnO/ITO electrode

The SEM image of rGO@ZnO/ITO electrode (Fig. 3a) shows uniformly distributed ZnO@rGO/ITO electrode. After, the immobilization of anti-BSA on the rGO@ZnO/ITO electrode, there was a change in the morphology, confirming that the enzyme has been successfully immobilized onto the rGO@ZnO/ITO surface (Fig. 3b).

4 Electrochemical studies

Electrochemical studies of the rGO@ZnO/ITO electrode, a-BSA/rGO@ZnO/ITO and BSA/a-BSA/rGO@ZnO/ITO bioelectrode have been performed in phosphate buffer saline (100 mM; pH 7.2; 0.9% NaCl) containing 5 mM of

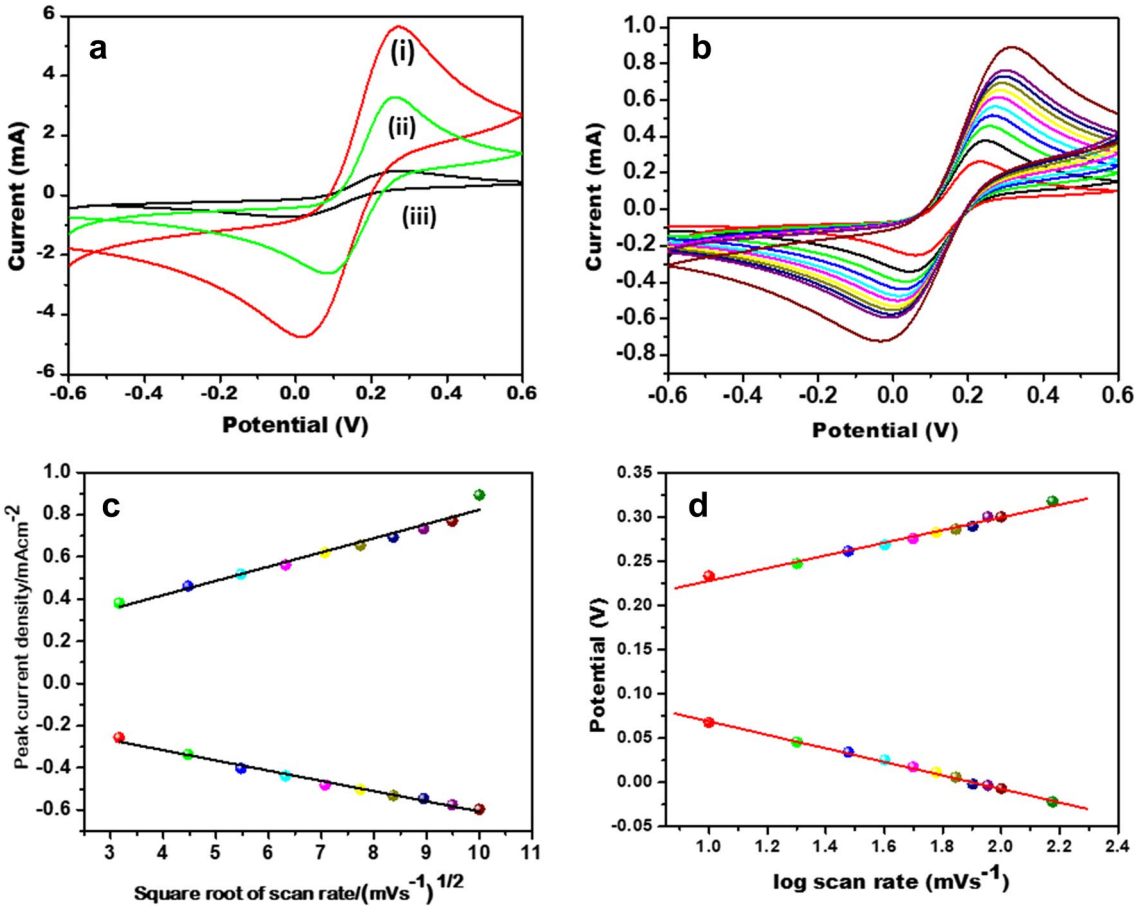

Fig. 4 CV studies of **a** (i) rGO/ITO, (ii) rGO@ZnO/ITO, and (iii) anti-BSA/rGO@ZnO/ITO; **b** rGO@ZnO/ITO electrode with varying scan rate (10-100 mV). The plots of **c** I_{pa}, I_{pc} vs. square root of scan rate and **d** potential with log of scan rate for rGO@ZnO/ITO electrode

$[Fe(CN_6)]^{3-/4-}$ using cyclic voltammetry (CV) technique [35]. Since BSA is negatively charged and rGO@ZnO forms a positive charge; thus, the main interaction between these two is electrostatic interaction, which leads to the changes in the electrochemical response [36].

Figure 4a shows the CV behavior of rGO/ITO electrode, rGO@ZnO/ITO electrode, and anti-BSA immobilized rGO@ZnO/ITO electrode at 50 mV/s. Potential peaks were observed at 0.27 V (oxidation) and 0.017 V (reduction) for rGO@ZnO/ITO and for anti-BSA/rGO@ZnO/ITO electrode, oxidation and reduction peak potential were obtained at 0.26 V and − 0.034 V, respectively. The peaks are due to the oxidation of Fe^{3+} to Fe^{4+} and the reduction of Fe^{4+} to Fe^{3+} on the electrode surface. The redox peak current of the rGO@ZnO/ITO electrode (curve (i); 5.62 mA) is higher than the redox peak current of the rGO/ITO electrode (curve (ii); 3.30 mA). This showed that due to synergetic interaction between rGO and ZnO nanoparticles, which provide large surface area, considerably superior conductivity, indicating improved electron mobility when compared to rGO/ITO as an electrode. The shift in peak potential values and decrease in peak current values of the anti-BSA/rGO@ZnO/ITO electrode is attributed to the immobilization of a less conductive layer of anti-BSA onto the rGO@ZnO/ITO electrode [5].

The effect of changing the scan rate on rGO@ZnO/ITO has been shown in Fig. 4b. As the scan rate increased from 10 to 100 mV/s, a linear increase in oxidation peak current and a positive shift in oxidation peak potential has been observed. Both anodic (I_{pa}) and cathodic (I_{pc}) peak current increases linearly with increasing scan rate (Fig. 4c). This peak current variation with scan rate behavior follows the Eqs. (1) and (2), showing surface adsorption-controlled kinetics [37].

$$I_{pa} = 1.22 \times 10^{-4} - 4.8 \times 10^{-5}\sqrt{v}; \quad R = 0.9877 \tag{1}$$

$$I_{pc} = 1.5 \times 10^{-4} + 6.7 \times 10^{-5}\sqrt{v}; \quad R = 0.9635 \tag{2}$$

Similarly, from Fig. 4d, a linear correlation was observed for anodic and cathodic peak potentials (E_{pa} and E_{pc}) with respect to the increasing natural logarithm scan rate; a linear regression equation depicting the same have been given as Eqs. (3) and (4), respectively.

$$E_{pa} = -0.0764 \ln(v) + 0.1459; \quad R = 0.99629 \tag{3}$$

$$E_{pc} = 0.0718 \ln(v) + 0.1561; \quad R = 0.98016 \tag{4}$$

At 50 mV/s, electron transfer rate constant (K_s) and charge transfer coefficient (α) of rGO@ZnO/ITO electrodes have been calculated to be 0.0253 s^{-1} and 0.925 s^{-1}, respectively (Eq. 5).

$$\ln(K_s) = \alpha \ln(1-\alpha) + (1-\alpha)\ln(\alpha) - \ln\left(\frac{RT}{nFv}\right) - \alpha(1-\alpha)\frac{nF\Delta E_p}{RT} \tag{5}$$

where α is the charge transfer coefficient, R is the gas constant, T is the room temperature, ΔE_p is the difference in the peak potential, n is the number of electrons transferred ($n=1$) [29].

Using linearity curves and Randles–Sevick equation Eq. (6), the diffusion coefficient (D) for the rGO@ZnO/ITO electrode is 5×10^{-11} cm^2 s^{-1}.

$$I_{pa} = \left(2.99 \times 10^5\right) \alpha^{1/2} n^{3/2} A\, C\, D^{1/2} v^{1/2} \tag{6}$$

where C is the molar concentration of $[Fe(CN)_6]^{3-/4-}$, and A is the electrode area. The different kinetic parameters calculated for the rGO/ITO and rGO@ZnO/ITO electrodes have been summarized in Table 1. The observed improved electrochemical performance of the Biosensor could be due to the high surface-to-volume ratio of rGO@ZnO. The density of functionalized antibodies increases, leading to the binding of many target analytes (BSA) compared to bare rGO [38].

4.1 Biosensing application of anti-BSA/rGO@ZnO/ITO electrode

The electrochemical response of anti-BSA/rGO@ZnO/ITO electrode was studied as a function of increasing concentration of BSA solution (0.001–30 ng mL^{-1}) in PBS (pH 7.2, 0.9% NaCl) containing 5 mM $[Fe(CN)_6]^{-3/-4}$ solution using differential pulse voltammogram (DPV). Figure 5a shows the DPV curve of BSA concentrations in the linear range from 0.001 to 30 ng mL^{-1}. It has been observed that, a decreasing trend is obtained with increasing BSA concentration as BSA forms an iron-binding complex in redox couple solution which results in the formation of iron chelates which hinders the migration of antigen to the electrode's surface [39, 40]. The calibration plot between current and

Table 1 Kinetic parameters of rGO/ITO and rGO@ZnO/ITO

S. no	Name of the electrode	Electron transfer coefficient, α	Charge transfer rate constant, K_s (s^{-1})	Effective surface area, A_{eff} (cm^2)	Average surface coverage, τ (mol cm^{-1})	Diffusion coefficient, D (cm^2 s^{-1})
1	rGO/ITO	0.90	0.1267	0.252	2.763×10^{-8}	1.67×10^{-11}
2	rGO@ZnO/ITO	0.92	0.0253	0.255	4.791×10^{-8}	5.0×10^{-11}

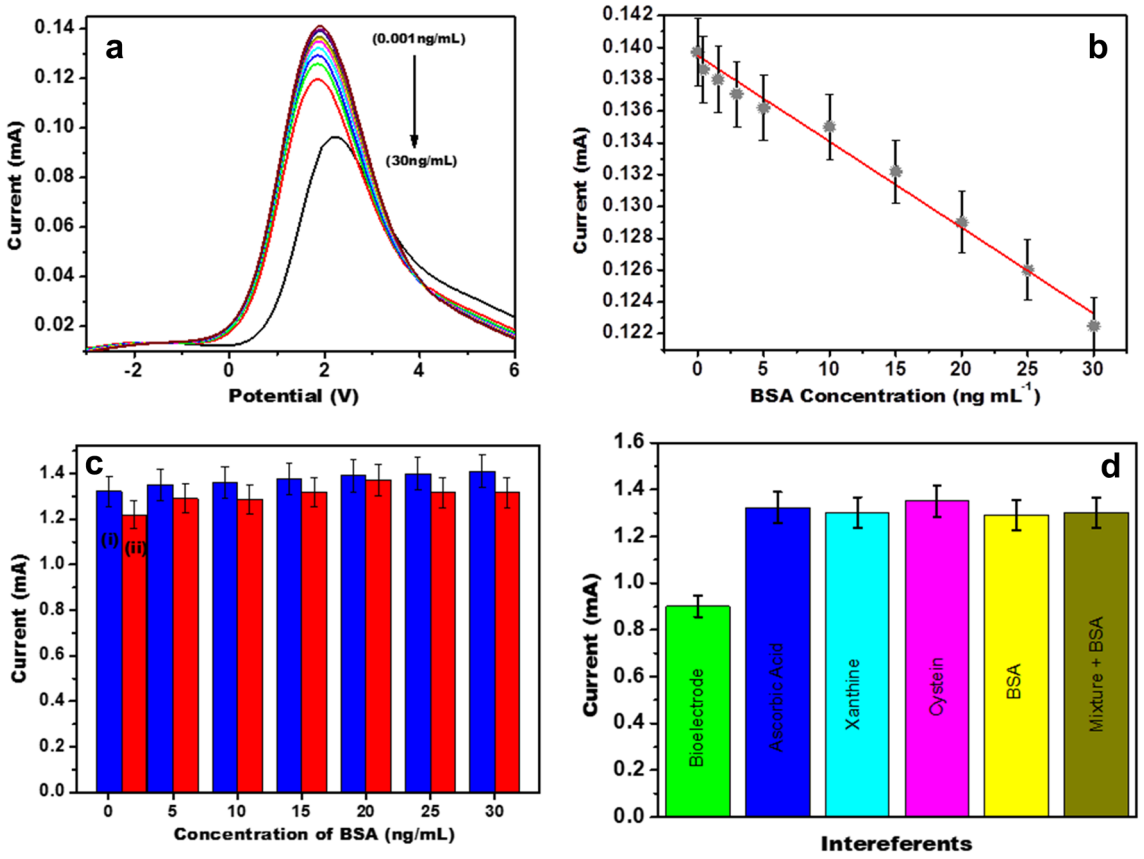

Fig. 5 **a** DPV response of anti-BSA/rGO@ZnO/ITO as a function of BSA concentration (0.001–30 ng mL^{-1}); **b** Calibration plot between the magnitudes of current recorded and log of BSA concentration (0.001–30 ng mL^{-1}); **c** Real sample analysis of biosensor with (i) buffer sample and (ii) real human urine sample and **d** Interference studies of the anti-BSA/rGO@ZnO/ITO electrode with other analytes

BSA concentration (0.001–30 ng mL^{-1}) has been shown in Fig. 5b. The sensitivity of the immunosensor was calculated using the regression equation, i.e., $y = 540.7\,x + 0.139$ (y = peak current and x = concentration of BSA) and has been found to be 2120.39 mA ng mL^{-1} cm^{-2}. The bioelectrode possesses a low detection limit of 1 pg mL^{-1} of BSA, calculated using the equation $3\sigma/S$, where σ is the standard deviation and S is the sensitivity obtained from the slope of the calibration curve.

4.2 Validation of the fabricated anti-BSA/rGO@ZnO/ITO with real urine sample

The developed rGO@ZnO nanocomposite-based sensor has been also tested for BSA in the human urine sample. Healthy volunteer's urine samples were taken with their consent, and spiked with BSA solutions (0.001–30 ng mL^{-1}) and used for the electrochemical quantification of BSA. The DPV results shows that the peak current steadily decreases as the concentration of BSA increases in urine sample from 0.001 to 30 ng mL^{-1} and results were identical to those of the BSA samples. Various biosensing characteristics of the synthesized rGO@ZnO-based biosensor were compared with other reported biosensors for BSA detection (Table 2). In our studies, the rGO@ZnO-based Biosensor shows the lowest LOD 1 pg mL^{-1}, which proves its superficial efficiency for BSA detection than any other methods reported in the literature.

4.3 Regeneration of immunosensor

The regeneration of the immunosensor was carried out by incubating 1 ng mL^{-1} BSA onto anti-BSA/rGO@ZnO/ITO electrode for 10 s in the glycine–HCl buffer (0.1 M, pH 3) and washing with PBS solution to prevent interfering with the antigen–antibody acting agent immune complex. A decline in the peak current was observed after every regeneration cycle (Fig S4). This is due to the shelling and denaturation of BSA or the structure of rGO@ZnO during the recovery process with glycine–HCl buffer and washing with the expansion of recovery times. This shows that the

Table 2 Comparison of anti-BSA/rGO@ZnO/ITO electrode performance with other biosensors reported for BSA detection

S. no	Matrix	Method	LOD	Refs.
1	Chitosan with MWCNT	DPV	0.028 ng mL^{-1}	[41]
2	Graphene oxide	AIE	0.4 µM	[42]
3	Aminopolycarboxyl-modified Ag_2S nanoparticles	RLS	112.6 ng mL^{-1}	[43]
4	Triangular silver nanoplates	LSPR	0.5 ng mL^{-1}	[2]
5	Amine-functionalized ZnO microwires	Micro-electronic chip	15 nM mL^{-1}	[44]
6	InGaP quantum dots	Fluorescence	10^5 ng mL^{-1}	[45]
7	MoS_2 nanosheets	CV	6 pg mL^{-1}	[46]
8	Biosynthesized rGO@ZnO	CV	1 pg mL^{-1}	Present work

MWCNT multiwalled carbon nanotubes, *Ag_2S* silver sulfide, *ZnO* zinc oxide, *InGaP* indium gallium phosphide, *MoS_2* molybdenum disulfide, *DPV* differential pulse voltammetry, *AIE* aggregation-induced emission, *RLS* resonance light scattering, *LSPR* localized surface plasmon resonance, *CV* Cyclic voltammetry

immunosensor can be reused and recovered at least 3 times with a relative standard deviation of 4.08%, which expresses a decent accuracy and high reproducibility.

4.4 Interference and stability

The specificity toward the target analyte is an essential feature of a suitable biosensor. To study the selectivity of the fabricated Biosensor, the electrochemical analysis was done with other interferants like ascorbic acid (1 ng/mL), xanthine (1 ng/mL), and cysteine (1 ng/mL). The measured response of the sensing probes expressed a distinct current response for BSA (0.001 ng/mL) (Fig. 5d). The performance of the developed Biosensor indicates that the proposed platform has been found to be more sensitive toward the detection of BSA. The specificity test was also conducted, and it has been observed that BSA retained its specificity, even in the mixture of interfering analytes.

Furthermore, stability studies were carried out for 30 days at 5 days interval, and the rGO@ZnO/ITO electrode maintained its activity for up to 30 days, with just 4% current loss on the 30th day, indicating that the fabricated electrode is very stable for up to 30 days at 4 °C (Fig. S5).

5 Conclusion

In this study, a highly sensitive and effective electrochemical immunosensor has been fabricated for BSA detection. For this purpose, rGO@ZnO composite has been successfully bio-synthesized via an eco-friendly and cost-effective method, using *aloe vera* leaves extract as a reducing agent. The biosynthesized rGO@ZnO was further utilized to fabricate a biosensing electrode for BSA detection in human urine sample. Electrochemical response was recorded under wide linear range of BSA concentration (0.001–30 ng mL^{-1}) with a low detection limit (1 pg mL^{-1}) and high sensitivity of 2120.39 mA ng mL^{-1} cm^{-2}. The fabricated bioelectrode offers excellent regenerability and stability measured upto 30 days. The response obtained using the fabricated immunosensor proved that it could be converted into a portable device for smart detection of other protein biomarkers.

Supplementary Information The online version contains supplementary material available at https://doi.org/10.1007/s10800-023-01848-5.

Acknowledgements Palak Garg acknowledges DTU and JMI for providing characterization facilities. Deeksha Thakur and Sakshi Verma thank DST-INSPIRE and UGC, respectively for the award of Senior Research Fellowship. C.M. Pandey acknowledges DST, New Delhi, India, for the DST-INSPIRE Faculty award (Grant No. DST/INSPIRE/04/2015/000932). For SEM analysis, the authors thank the Central facility, Jamia Millia Islamia, Central University, Delhi India.

Author contributions PG and DT: Conceptualization, Methodology, Data curation, Formal analysis, Writing—original draft. SV and OJ: Validation and visualization. CMP: Supervision, Investigation, Validation, review and editing, Project administration, Funding acquisition. DK: Supervision, Validation, review and editing.

Declarations

Competing interests The authors have no competing interests to declare that are relevant to the content of this article.

References

1. Sahu DP, Jammalamadaka SN (2019) Detection of bovine serum albumin using hybrid TiO2 + graphene oxide based Bio-resistive random access memory device. Sci Rep 9(1):1–10. https://doi.org/10.1038/s41598-019-52522-w
2. Zhang LL, Ma FF, Kuang YF, Cheng S, Long YF, Xiao QG (2016) Highly sensitive detection of bovine serum albumin based on the aggregation of triangular silver nanoplates. Spectrochim Acta A 154:98–102. https://doi.org/10.1016/j.saa.2015.10.019
3. Liu S, Yang Z, Liu Z, Kong L (2006) Resonance Rayleigh-scattering method for the determination of proteins with gold

nanoparticle probe. Anal Biochem 353(1):108–116. https://doi.org/10.1016/j.ab.2006.03.012
4. Guo ZX, Shen HX (1999) Highly sensitive assay for protein using resonance light-scattering technique with dibromohydroxyphenylfluorone-molybdenum(VI) complex. Spectrochim Acta A 55(14):2919–2925. https://doi.org/10.1016/S1386-1425(99)00168-7
5. Bhavani Devi L, Berchmans S, Mandal AB (2012) Highly sensitive detection of proteins using voltammetric assay in the presence of silver nanostructures. J Electroanal Chem 665:20–25. https://doi.org/10.1016/j.jelechem.2011.11.013
6. Nguyen HH, Park J, Kang S, Kim M (2015) Surface plasmon resonance: a versatile technique for biosensor applications. Sensors (Switzerland) 15(5):10481–10510. https://doi.org/10.3390/s150510481
7. Lin J, Lin J, Huang Z et al (2014) Raman spectroscopy of human hemoglobin for diabetes detection. J Innov Opt Health Sci. https://doi.org/10.1142/S179354581350051X
8. Sato T, Morishita T, Hara T, Suda I, Tetsuka T (2001) Near-infrared reflectance spectroscopic analysis of moisture, fat, protein, and physiological activity in buckwheat flour for breeding selection. Plant Prod Sci 4(4):270–277. https://doi.org/10.1626/pps.4.270
9. Wiśniewski JR, Gaugaz FZ (2015) Fast and sensitive total protein and peptide assays for proteomic analysis. Anal Chem 87(8):4110–4116. https://doi.org/10.1021/ac504689z
10. Varkovitzky RL (2012) Assimilation, accommodation, and overaccommodation: an examination of information processing styles in female victims of adolescent and adult sexual assault. ProQuest Diss Theses 1(6):218. https://doi.org/10.1038/nprot.2006.202.Using
11. Dzyadevych SV, Arkhypova VN, Soldatkin AP, El'skaya AV, Martelet C, Jaffrezic-Renault N (2008) Amperometric enzyme biosensors: past, present and future. IRBM 29(2–3):171–180. https://doi.org/10.1016/j.rbmret.2007.11.007
12. Chaubey A, Malhotra BD (2002) Review mediated biosensors. Biosens Bioelectron 7:441–456
13. Jalil O, Pandey CM, Kumar D (2020) Electrochemical biosensor for the epithelial cancer biomarker EpCAM based on reduced graphene oxide modified with nanostructured titanium dioxide. Microchim Acta 187(5):275. https://doi.org/10.1007/s00604-020-04233-7
14. Krishnan SK, Singh E, Singh P, Meyyappan M, Nalwa HS (2019) A review on graphene-based nanocomposites for electrochemical and fluorescent biosensors. RSC Adv 9(16):8778–8781. https://doi.org/10.1039/c8ra09577a
15. Solanki PR, Kaushik AK, Agrawal VV, Malhotra BD (2011) Nanostructured metal oxide-based biosensors. Npg Asia Mater 3:17–24
16. Kumar S, Panwar S, Kumar S, Augustine S, Malhotra BD (2019) Biofunctionalized nanostructured Yttria modified non-invasive impedometric biosensor for efficient detection of oral cancer. Nanomaterials. https://doi.org/10.3390/nano9091190
17. Malhotra BD, Pandey CM (2017) Biosensors: fundamentals and applications. De Gruyter, Berlin
18. Kumar S, Kumar S, Srivastava S et al (2015) Reduced graphene oxide modified smart conducting paper for cancer biosensor. Biosens Bioelectron 73:114–122. https://doi.org/10.1016/j.bios.2015.05.040
19. Khalil I, Rahmati S, Muhd Julkapli N, Yehye WA (2018) Graphene metal nanocomposites—recent progress in electrochemical biosensing applications. J Ind Eng Chem 59:425–439. https://doi.org/10.1016/j.jiec.2017.11.001
20. Parnianchi F, Nazari M, Maleki J, Mohebi M (2018) Combination of graphene and graphene oxide with metal and metal oxide nanoparticles in fabrication of electrochemical enzymatic biosensors. Int Nano Lett 8(4):229–239. https://doi.org/10.1007/s40089-018-0253-3
21. Zhao Z, Lei W, Zhang X, Wang B, Jiang H (2010) ZnO-based amperometric enzyme biosensors. Sensors 10(2):1216–1231. https://doi.org/10.3390/s100201216
22. Verma S, Pandey C, Kumar D (2022) A highly efficient rGO grafted MoS_2 nanocomposite for dye adsorption and electrochemical detection of hydroquinone in wastewater. New J Chem 46:21190. https://doi.org/10.1039/D2NJ04285A
23. Malik P, Shankar R, Malik V, Sharma N, Mukherjee TK (2014) Green chemistry based benign routes for nanoparticle synthesis. J Nanoparticles 2014:1–14. https://doi.org/10.1155/2014/302429
24. Shah M, Fawcett D, Sharma S, Tripathy SK, Poinern GEJ (2015) Green synthesis of metallic nanoparticles via biological entities. Materials 8:7278. https://doi.org/10.3390/ma8115377
25. Zhu Y, Murali S, Cai W et al (2010) Graphene and graphene oxide: synthesis, properties, and applications. Adv Mater 22(35):3906–3924. https://doi.org/10.1002/adma.201001068
26. Singh P, Singh KRB, Singh J, Prasad P, Singh RP (2021) Bioinspired triangular ZnO nanoclusters synthesized by *Argyreia nervosa* nascent leaf extract for the efficient electrochemical determination of vitamin C. RSC Adv 11(41):25752–25763. https://doi.org/10.1039/D1RA04704C
27. Moghaddasi S, Verma SK, Publications B (2011) Aloe vera their chemicals composition and applications: a review. Int J Biol Med Res 2(1):466–471
28. Ksenofontov AA, Bocharov PS, Ksenofontova KV, Antina EV (2022) Water-soluble BODIPY-based fluorescent probe for BSA and HSA detection. J Mol Liq 345:117031. https://doi.org/10.1016/j.molliq.2021.117031
29. Jalil O, Pandey CM, Kumar D (2020) Highly sensitive electrochemical detection of cancer biomarker based on anti-EpCAM conjugated molybdenum disulfide grafted reduced graphene oxide nanohybrid. Bioelectrochemistry 138:107733
30. Liu B, Huang P-JJ, Zhang X et al (2013) Parts-per-million of polyethylene glycol as a non-interfering blocking agent for homogeneous biosensor development. Anal Chem 85(21):10045–10050. https://doi.org/10.1021/ac4024654
31. Jaleh B, Jabbari A (2014) Evaluation of reduced graphene oxide/ZnO effect on properties of PVDF nanocomposite films. Appl Surf Sci 320:339–347. https://doi.org/10.1016/j.apsusc.2014.09.030
32. Abdolhosseinzadeh S, Asgharzadeh H, Sadighikia S, Khataee A (2016) UV-assisted synthesis of reduced graphene oxide–ZnO nanorod composites immobilized on Zn foil with enhanced photocatalytic performance. Res Chem Intermed. https://doi.org/10.1007/s11164-015-2291-z
33. Hosseini SA, Babaei S (2017) Graphene oxide/zinc oxide (GO/ZnO) nanocomposite as a superior photocatalyst for degradation of methylene blue (MB)-process modeling by response surface methodology (RSM). J Braz Chem Soc 28(2):299–307. https://doi.org/10.5935/0103-5053.20160176
34. Rattan S, Kumar S, Goswamy J (2020) In-situ one pot synthesis of graphene-ZnO nanohybrid and its application to UV light detection. Mater Res Express 7:15058. https://doi.org/10.1088/2053-1591/ab689a
35. Ertürk G, Berillo D, Hedström M, Mattiasson B (2014) Microcontact-BSA imprinted capacitive biosensor for real-time, sensitive and selective detection of BSA. Biotechnol Rep 3:65–72. https://doi.org/10.1016/j.btre.2014.06.006
36. Qi M, Zhao K, Bao Q et al (2019) Adsorption and electrochemical detection of bovine serum albumin imprinted calcium alginate hydrogel membrane. Polymers (Basel). https://doi.org/10.3390/polym11040622
37. Thakur D, Pandey C, Kumar D (2022) Highly sensitive enzymatic biosensor based on polyaniline-wrapped titanium dioxide

nanohybrid for fish freshness detection. Appl Biochem Biotechnol. https://doi.org/10.1007/s12010-022-03931-7
38. Kaushik S, Tiwari UK, Deep A, Sinha RK (2019) Two-dimensional transition metal dichalcogenides assisted biofunctionalized optical fiber SPR biosensor for efficient and rapid detection of bovine serum albumin. Sci Rep 9(1):6987. https://doi.org/10.1038/s41598-019-43531-w
39. Ferreira N, Moreira A, Sá M, Sales MG (2017) New electrochemically-derived plastic antibody on a simple conductive paper support for protein detection: application to BSA. Sens Actuators B 243:1127. https://doi.org/10.1016/j.snb.2016.12.074
40. Kuralay F, Bolat G, Torun H, Abaci S. Electrochemical detection of bovine serum albumin via conducting polymer deposited electrode. Chem Sens
41. Chen HJ, Zhang ZH, Luo LJ, Yao SZ (2012) Surface-imprinted chitosan-coated magnetic nanoparticles modified multi-walled carbon nanotubes biosensor for detection of bovine serum albumin. Sens Actuators B 163(1):76–83. https://doi.org/10.1016/j.snb.2012.01.010
42. Xu X, Huang J, Li J, Yan J, Qin J, Li Z (2011) A graphene oxide-based AIE biosensor with high selectivity toward bovine serum albumin. Chem Commun 47(45):12385–12387. https://doi.org/10.1039/c1cc15735c
43. Pan H, Tao X, Mao C, Zhu JJ, Liang F (2007) Aminopolycarboxyl-modified Ag2S nanoparticles: synthesis, characterization and resonance light scattering sensing for bovine serum albumin. Talanta 71(1):276–281. https://doi.org/10.1016/j.talanta.2006.03.057
44. Sanginario A, Cauda V, Bonanno A, Bejtka K, Sapienza S, Demarchi D (2016) An electronic platform for real-time detection of bovine serum albumin by means of amine-functionalized zinc oxide microwires. RSC Adv 6(2):891–897. https://doi.org/10.1039/c5ra15787k
45. Kumar P, Deep A, Sharma SC, Bharadwaj LM (2012) Bioconjugation of InGaP quantum dots for molecular sensing. Anal Biochem 421(1):285–290. https://doi.org/10.1016/j.ab.2011.10.037
46. Kukkar M, Sharma A, Kumar P, Kim KH, Deep A (2016) Application of MoS2 modified screen-printed electrodes for highly sensitive detection of bovine serum albumin. Anal Chim Acta 939:101–107. https://doi.org/10.1016/j.aca.2016.08.010

Publisher's Note Springer Nature remains neutral with regard to jurisdictional claims in published maps and institutional affiliations.

Springer Nature or its licensor (e.g. a society or other partner) holds exclusive rights to this article under a publishing agreement with the author(s) or other rightsholder(s); author self-archiving of the accepted manuscript version of this article is solely governed by the terms of such publishing agreement and applicable law.

Environmental Management
https://doi.org/10.1007/s00267-022-01776-8

Cadmium Uptake From Soil by Ornamental Metallophytes: A Meta-analytical Approach

Deepika[1] · Anil Kumar Haritash[1]

Received: 26 August 2022 / Accepted: 20 December 2022
© The Author(s), under exclusive licence to Springer Science+Business Media, LLC, part of Springer Nature 2022

Abstract

Soil pollution by cadmium (Cd) is a serious issue worldwide affecting environmental and human health. Conventional chemical and physical methods of treating contaminated soil are costly, time-consuming, and less effective. Phytoremediation using ornamental plants is a safe and effective method for the treatment of heavy metal-polluted soil due to their rapid growth and accumulation of biomass, high heavy metal tolerance, and non-edible nature. The present study is the first attempt for the meta-analysis of existing literature on Cd accumulation and translocation by ornamental plants. The uptake and transfer capacity of ornamental plants was measured using the bio-concentration factor (BCF) and translocation factor (TF). The results indicate that ornamental plants have varying Cd-absorption capacities. Among the 49 plant species identified from 31 articles, *Helianthus annuus* (BCF = 5.785), *Impatiens glandulifera* (BCF = 4.722), and *Crassocephalum crepidioides* (BCF = 3.623) represented higher accumulation capacity, whereas *Rorippa globosa* (TF = 1.653) and *Sedum spectabile Boreau* (TF = 1.579) represented significantly higher translocation capacity for Cd. The contribution of various environmental factors in influencing BCF was obtained through multiple linear regression analysis. Results showed that soil pH was the major factor influencing the BCF. To further explain the influence of four main factors that are soil pH, soil organic matter (SOM), cation exchange capacity (CEC), and soil Cd concentration on the accumulation efficiency of ornamental plants, a subgroup meta-analysis was performed. Results of the subgroup meta-analysis revealed that the BCF is negatively correlated with the soil pH and SOM, while the estimated limit of soil Cd concentration for growing ornamental plants was up to 50 mg/kg. Results of this study indicate that choosing a native hyperaccumulator is not the sole key to the success of a phytoremediation design, rather the conditions of the pedosphere will determine the regulating factor for efficient removal. In order to overcome the issue of recirculation and gradual release in the rhizosphere, it is important to match the type of hyperaccumulators to the soil environment (pH, CEC, SOM, etc.) to achieve maximum translocation and desired removal. This study will help researchers to pair the right plant with environmental conditions and customize more efficient phytoremediation systems.

Keywords Phytoremediation · Ornamental plants · Meta-analysis · Heavy metal · Cadmium · Bio-concentration factor · Translocation factor

Introduction

Soil contamination by heavy metals is the one among various global environmental issues, which is worthy of attention. Unsustainable industrial (Chauhan and Mathur, 2020), agricultural (Nagajyoti et al., 2010) and mining (Olivares et al., 2013) activities have increased the input of heavy metals in soil. Rise in concentration of heavy metals above the permissible limits threatens the health of exposed organisms in an ecosystem (Shi and Ma, 2017). Among all heavy metals, Cd is reported highly hazardous not only for plants, but also for humans due to its accumulation in the human body through ingestion of food crops grown in Cd polluted soil (Huang et al., 2020a). The Environmental Protection Agency (EPA) has established a reference dose of 5×10^{-4} mg/kg/day in water and 1×10^{-3} mg/kg/day in food (USEPA's Integrated Risk Information System USEPA IRIS, 2012). International Agency for Research on

✉ Deepika
deepika_2k20phden502@dtu.ac.in

[1] Environmental Microbiology and Bioremediation Laboratory, Department of Environmental Engineering, Delhi Technological University, Bawana Road, Shahbad Daulatpur, Delhi 110042, India

Published online: 27 December 2022

Cancer (IARC) has categorised Cd compounds as group 1 carcinogens in 1993 as these induce cytotoxicity and carcinogenicity upon long term environmental exposure. Thus, it is important to control the potential health risk of Cd exposure.

Phytoremediation has always been considered as an efficient, economical, eco-friendly, sustainable, and socially acceptable approach compared to conventional physical and chemical remediation procedures (Zeng et al., 2019; Farooq et al., 2020). This technique uses remarkable ability of plants to remove heavy metal contamination from soil (Raj et al., 2020). Many plant species have been reported for phytoremediation but only a few of them are termed as hyperaccumulators as less number of plants showed strong tolerance to pollutants and ability to efficiently translocate heavy metals from roots to shoots (Liu et al., 2010). Hyperaccumulators have 100-fold greater capacity to accumulate heavy metals than typically occurring plants. In addition, these plants should have TF greater than 1 (Rezapour et al., 2019). However, applicability of hyperaccumulators is limited in practice due to their long growth period and low biomass causing difficulty in mechanical harvesting (Farooq et al., 2020). Therefore, ornamental plants offer alternative proposition for treatment of heavy metal polluted soil due to their rapid growth and accumulation of biomass, high heavy metal tolerance and non-edible nature (Sehrawat et al., 2021; Zeng et al., 2018). Additionally, these plants may provide economic benefits and improve aesthetic values of contaminated site (Mahmood-ul-Hassan et al., 2020). Reports show that many ornamental plants can be utilized for phytostabilisation or phytoextraction of Cd polluted soil. For example, ornamental plants such as *Osmanthus fragrans, Ligustrum vicaryi, Cinnamomum camphora, Loropetalum chinense* and *Euonymus japonicas* were suggested as promising candidates for phytostabilisation of Cd-contaminated soil (Zeng et al., 2018). Biswal et al. (2021) revealed that *Tagetes erecta* can efficiently extract heavy metals from contaminated soil.

So far, the efficiency of ornamental plants for heavy metal removal from soil has been documented by few traditional narrative reviews. Many studies (Liu et al., 2018b; Khan et al., 2021) have summarized the results in qualitative manner, but to the best of our knowledge, no study on phytoremediation by ornamental plants used a systematic or statistical method to synthesize and assess the data collected. In this regard, meta-analysis is an approach that uses statistical process to combine findings from various studies (Li et al., 2015). Meta-analysis tends to provide a systematic solution to the problem of varying outcomes with the approach of combining, comparing, evaluating and synthesizing the accumulated results into a representative value (Jemna, 2017). The methodology has found wide applicability in medical and psychological fields, and now researchers in the field of environmental science also are gradually using it (Huang et al., 2020b; Song et al., 2022). For example, Huang et al. (2020) screened out 19 species of leafy vegetables from 67 articles through meta-analysis to understand their potential for Cd uptake from soil and transport from roots to aboveground biomass. Results showed that *Brassica juncea* (BCF = 5.10) and *Brassica pekinensis* (BCF = 1.90) considerably had greater Cd absorption capacity in soil among the 19 studied species, whereas *Brassica pekinensis* (TF = 2.52) and *Coriandrum sativum* (TF = 2.18) showed higher Cd transport capacity. Similarly, Song et al. (2022) performed meta-analysis to compare the accumulation characteristics of heavy metals in two *Sedum* species (*Sedum alfredii* and *Sedum plumbizincicola*) and analyse the effects of soil organic matter (SOM) and soil pH on heavy metal accumulation by *Sedum* sp. Tőzsér et al. (2017) also evaluated the capability of accumulating and translocating heavy metals in different parts of willow species through meta-analysis.

The objective of this study was to: (1) evaluate and quantify the Cd accumulation and translocation capacity of ornamental plants in soil (2) analyse the influence of various factors such as soil pH, SOM, CEC, and Cd content on heavy metal accumulation capacity of ornamental plants through meta-analysis, and (3) review, all published scientific data on the absorption of Cd by ornamental plants through meta-analytical approach, to contribute reliable reference for future researchers.

Materials and Methods

Literature Search and Selection Criteria

To conduct an extensive and in-depth literature review, research articles from all possible sources such as Google Scholar, SCOPUS, Science Direct, Web of Science and Research Gate were retrieved using the keywords "phytoremediation", "heavy metals", "cadmium", and "ornamental plants". In addition, reference sections of the articles included in this study were scanned to find out publications of our interest. The articles in this analysis were selected if (1) the study reported the uptake of Cd in roots and shoots of ornamental plants from contaminated soil; (2) the experiment is carried out without adding any amendments that can influence Cd uptake; and (3) the information of soil composition, especially soil pH and organic matter is given.

The above selection criteria helped in the inclusion of only relevant papers and rejection of irrelevant papers. These criteria are seriously met before selecting a paper, otherwise the meta-analysis result will become meaningless. This is indicated in a process diagram also known as

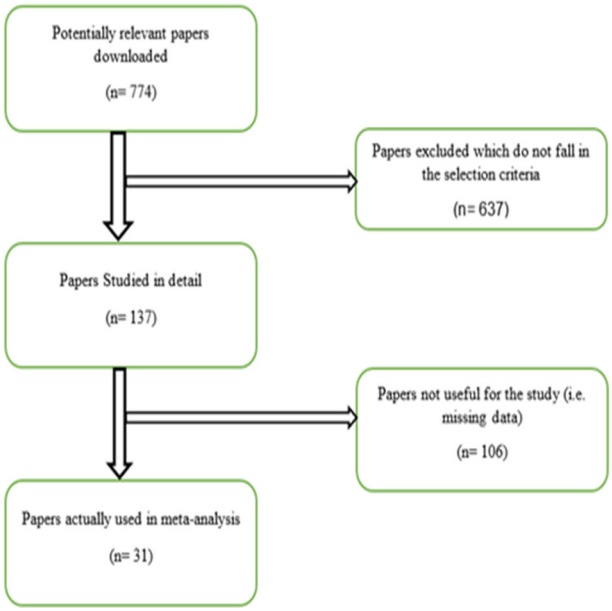

Fig. 1 The PRISMA diagram

PRISMA (Preferred Reporting Items of Systematic Reviews and Meta-Analysis) chart (Fig. 1). The appropriate information was selected from the included articles: first author's name, published year, species name, Cd concentration in soil and plant, and primary physico-chemical properties of soil (pH, SOM, CEC, and soil texture).

Statistical Analysis

Calculation of effect size (ES) and variance

To integrate various studies performed in different conditions, we assumed that each research study included in this analysis was independent. To reduce variations brought on by growing conditions, soil heavy metal concentration, species, etc., the ES has been calculated as response ratio (RR). Both, the ES/response ratio and its variance (V) were calculated for every observation.

$$RR = log_e\left(\frac{\overline{Xe}}{\overline{Xc}}\right) \quad (1)$$

$$V = \frac{Se^2}{ne\overline{Xe}^2} + \frac{Sc^2}{nc\overline{Xc}^2} \quad (2)$$

where, $\overline{Xe}$ and $\overline{Xc}$ represent the mean values of experimental and control groups, respectively, n_e and n_c are the sample size of the experimental and control groups, and Se^2 and Sc^2 are their standard deviations.

In the present analysis, RR has been used as a metric of ES and holds its practical significance. Through this we can arrive at different conclusions by using different interpretations of RR. For example, when the control and experimental groups represent Cd concentration in soil and the corresponding plant, RR is the logarithmic value of BCF. Similarly, when the control and experimental groups denote the Cd concentration in roots and shoots of the plant, RR denotes the logarithmic value of TF, which shows the plant ability to translocate heavy metals from roots to shoots (Huang et al., 2020a).

Data Analysis

The primary step in the data analysis is to choose the summary effect model. Of the two models used for calculating summary effect i.e., fixed and random, we used random effect model to calculate overall mean effect values or weighted mean and generated 95% confidence interval. Random effect model is used in this analysis, because it is very difficult to expect a common ES due to variable environmental conditions and methods used in each study (Tőzsér et al., 2017). Whereas, a fixed effect model assumes that the studies will have more or less same ES, and variations between results in different studies is due to random error (Ahn and Kang, 2018). Heterogeneity which measures the variance between studies was determined by Cochran's Q statistic and I^2 index. Ranging from 0 to 100%, the value of $I^2 \leq 25\%$ shows homogeneity between studies (use of fixed effect model is preferred in this case) while the value of $I^2 \geq 75\%$ indicates high heterogeneity (use of random effect model is preferred in this case) (Srivastava et al., 2021).

The multiple linear regression analysis was performed to evaluate various environmental factors and BCF, and the contribution of each factor to BCF was obtained. To arrive at more significant and convincing results and explain heterogeneities, we performed subgroup analysis. In this article, OpenMEE, an open-source software for meta-analysis in ecology and evolutionary biology, was used to calculate ES and its variance and to fit the data into forest plots. In addition to the meta-analysis process, Jamovi version 2.3.12.0 software was used to perform subgroup and multiple linear regression analysis.

Publication Bias

Meta-analysis is often subjected to publication bias as study with statistically significant results is more likely to be accepted by journals than other similar articles with non-significant results (Fragkos et al., 2014). Rosenthal (1979) termed this issue as *file drawer problem* because null or nonsignificant outcomes are closed in file drawers without ever being published. To eliminate such influence, the publication bias was assessed through

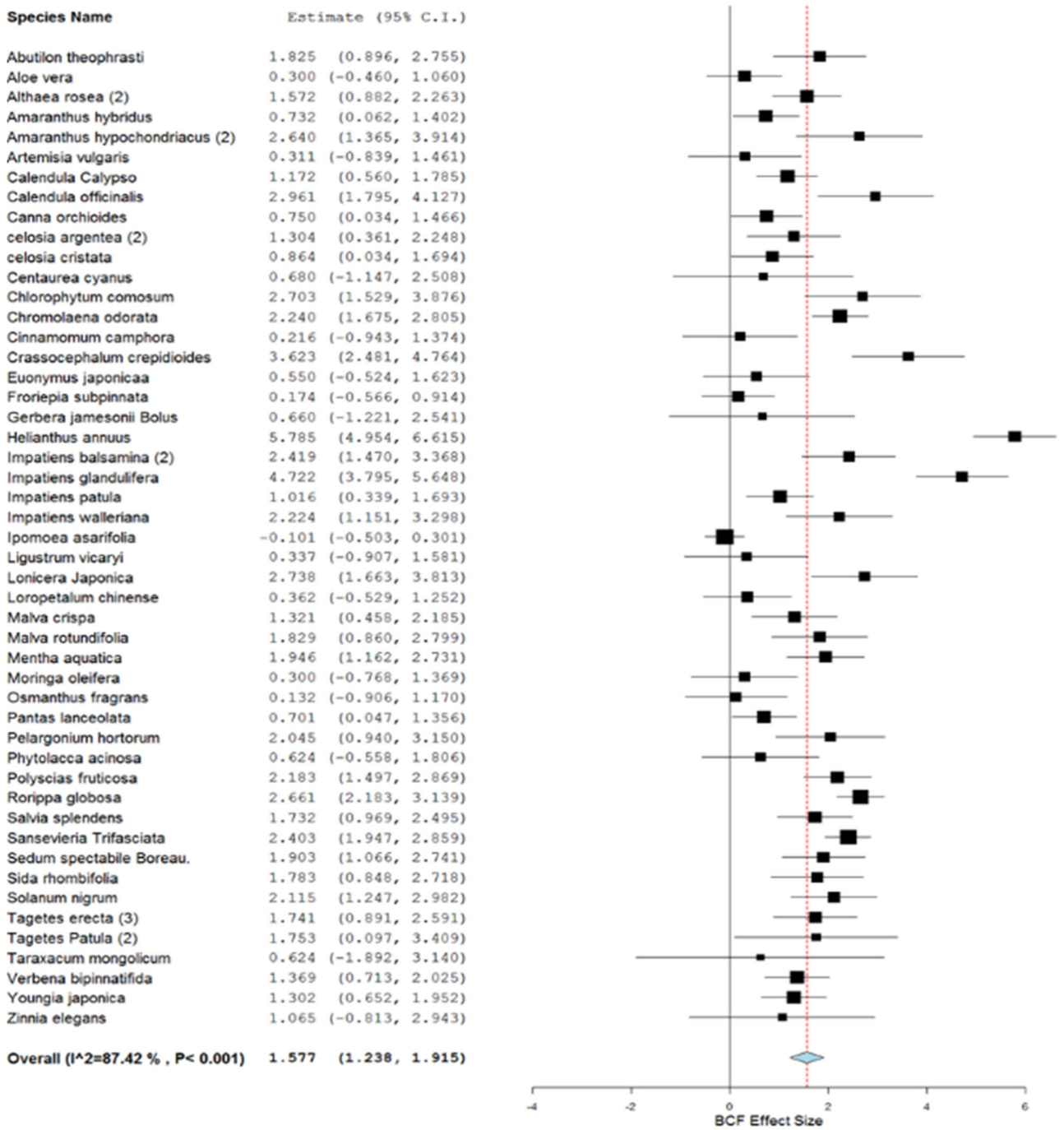

Fig. 2 The BCF of ornamental plants represented as mean ES and 95% CI in a forest plot. Numerals in brackets indicate the number of studies from which the mean ES was calculated. 'Overall' indicated the common ES of all species

Rosenberg's Fail-safe N method (Rosenberg et al., 2000). The Fail-safe number suggests the number of non-significant or unpublished research studies that would require to be added to meta-analysis to convert observed statistically significant results into non-significant. If this number is big compared to observed studies, we can conclude that there is minimal publication bias (Rosenberg, 2005).

Results and Discussion

BCF of Different Species

In this analysis, 49 ornamental plant species were identified from 31 articles obtained after screening. The ES ($\log_n$ BCF) of each plant species is represented in the form of forest plot (Fig. 2). The ES of same ornamental plant from different

studies were combined to calculate means and 95% confidence intervals. Significant heterogeneity was observed in this meta-analysis ($I^2 = 84.42\%$, $P < 0.001$). The overall ES of all species was greater than 1 (mean = 1.577, CI: 1.238 to 1.915). The ES of *Helianthus annuus* was highest among the 49 species (mean = 5.785, CI: 4.954 to 6.615) followed by *Impatiens glandulifera* (mean = 4.722, CI: 3.795 to 5.648), and *Crassocephalum crepidioides* (mean = 3.623, CI: 2.481 to 4.764). These results are in accordance with various previous studies. Benavides et al. (2021) compared the Cd accumulation potential of *Helianthus annuus, Brassica napus* and *Chyrsopogon zizanioides* and concluded that accumulation capacity of the three species investigated was highest for *Helianthus annuus*. Alaboudi et al. (2018) also confirmed the potential of *H. annuus* for remediation of Cd contaminated soil through pot experiment. Similarly, potential of *I. glandulifera* and *C. creoidioides* as Cd accumulators was also confirmed through pot experiments (both, pot and hydroponic experiment in case of *C. creoidioides*) (Coakley et al., 2019; Yamato et al., 2008). Besides, *Calendula officinalis, Amaranthus hypochondriacus, Chlorophytum comosum, Lonicera japonica, Chromolaena odorata, Impatiens balsamina, Impatiens walleriana, Pelargonium hortorum, Polyscias fruticose, Rorippa globosa, Sansevieria trifasciata*, and *Solanum nigrum* also showed higher ES (ranging from 2 to 3). In comparison to the ornamental plants mentioned above, the ES of *Abutilon theophrasti, Althaea rosea, Calendula calypso, Celosia argentea, Impatiens patula, Malva crispa, Malva rotundifolia, Mentha aquatica, Salvia splendens, Sedum spectabile Boreau., Sida rhombifolia, Tagetes erecta, Tagetes Patula, Verbena bipinnatifida, Youngia japonica*, and *Zinnia elegans* were moderate (ranging from 1–2). The ES of *Aloe vera, Amaranthus hybridus, Artemisia vulgaris, Canna orchiodes, Centaurea cyanus, Celosia cristata, Cinnamomum camphora, Euonymus japonica, Froriepia subpinnata, Gerbera jamesonii Bolus, Ligustrum vicaryi, Loropetalum chinense, Moringa oleifera, Osmanthus fragrans, Pantas lanceolate, Phytolacca acinosa*, and *Taraxacum mongolicum* were significantly lower for their 95% confidence interval overlapping or very close to 0. The only species which showed the negative ES was *Ipomoea asarifolia* (mean = −0.101, CI: −0.503 to 0.301). In this analysis, BCF of ornamental plants varied with the species. Plant species are more important contributors in the aspect of affecting the uptake of Cd compared to soil pH, Cd concentration and other environmental factors (Huang et al., (2020a)). Wu et al. (2018) conducted an experiment to screen 7 ornamental plants to find possible Cd accumulators or hyperaccumulators. Results revealed that *Malva rotundifolia* exhibited high Cd tolerance and *Malva crispa, Sida rhombifolia, Celosia argentea* and *Celosia cristata* were moderate, whereas *Althaea rosea* and *Abutilon theophrasti* were sensitive towards Cd stress. Thus, each plant responded differently to Cd stress even when grown in same environmental conditions. The Fail-safe N (11174) was significantly greater than 5k + 10 (k-represents the number of observations i.e., 56), which showed that there was no publication bias.

Factors Influencing BCF

The environment of soil is highly dynamic and is affected by various physical, chemical and biological factors such as climate, precipitation, soil pH, SOM, CEC, bulk density and microbial diversity etc. All these factors play a significant role in influencing the phytoremediation ability of ornamental plants. However, most of the studies consider one or two factors (pH, SOM, CEC) and the role of climate, precipitation etc. is seldom reported. So, the studies reporting soil Cd concentration, soil pH, SOM, and CEC are included in the present study.

Rank of factors influencing BCF

Multiple linear regression analysis was performed to find the contribution of factors that affect the ability of ornamental plants to accumulate Cd. Factors such as soil pH, SOM, soil CEC, and soil Cd were defined as independent variables/covariates influencing BCF (dependent variable). Therefore, the estimated equation of regression analysis was as follows: $\log_n$ BCF = Intercept + soil pH + soil Cd + SOM + CEC. Results of regression analysis suggested that soil pH was the significant factor affecting the heavy metal absorbing ability of plant whereas CEC, soil Cd, and SOM were the minor factors (in descending order) (Table 1).

High adjusted R^2 value indicated that the model explained well the mechanism of Cd uptake in ornamental plants and reason of heterogeneity in results. However, more number of observations could have enhanced the reliability of results. Additionally, *p*-value was not significant in case of SOM and soil CEC which indicates risk of no association between covariate and BCF. Though, these outputs fulfilled the main purpose of our use of this model that was to conclude which factors were the major and minor contributors in affecting BCF.

Table 1 Results of multiple linear regression analysis ($n = 17$)

Covariates	Estimate	SE	t-value	*p*-value
Intercept	27.87578	4.52790	6.156	<0.001
Soil pH	−3.33444	0.54583	−6.109	<0.001
Soil Cd	−0.03867	0.00996	−3.882	0.002
SOM	0.00790	0.01211	0.653	0.526
Soil CEC	−0.05478	0.05486	−0.999	0.338

Adjusted $R^2 = 0.759$

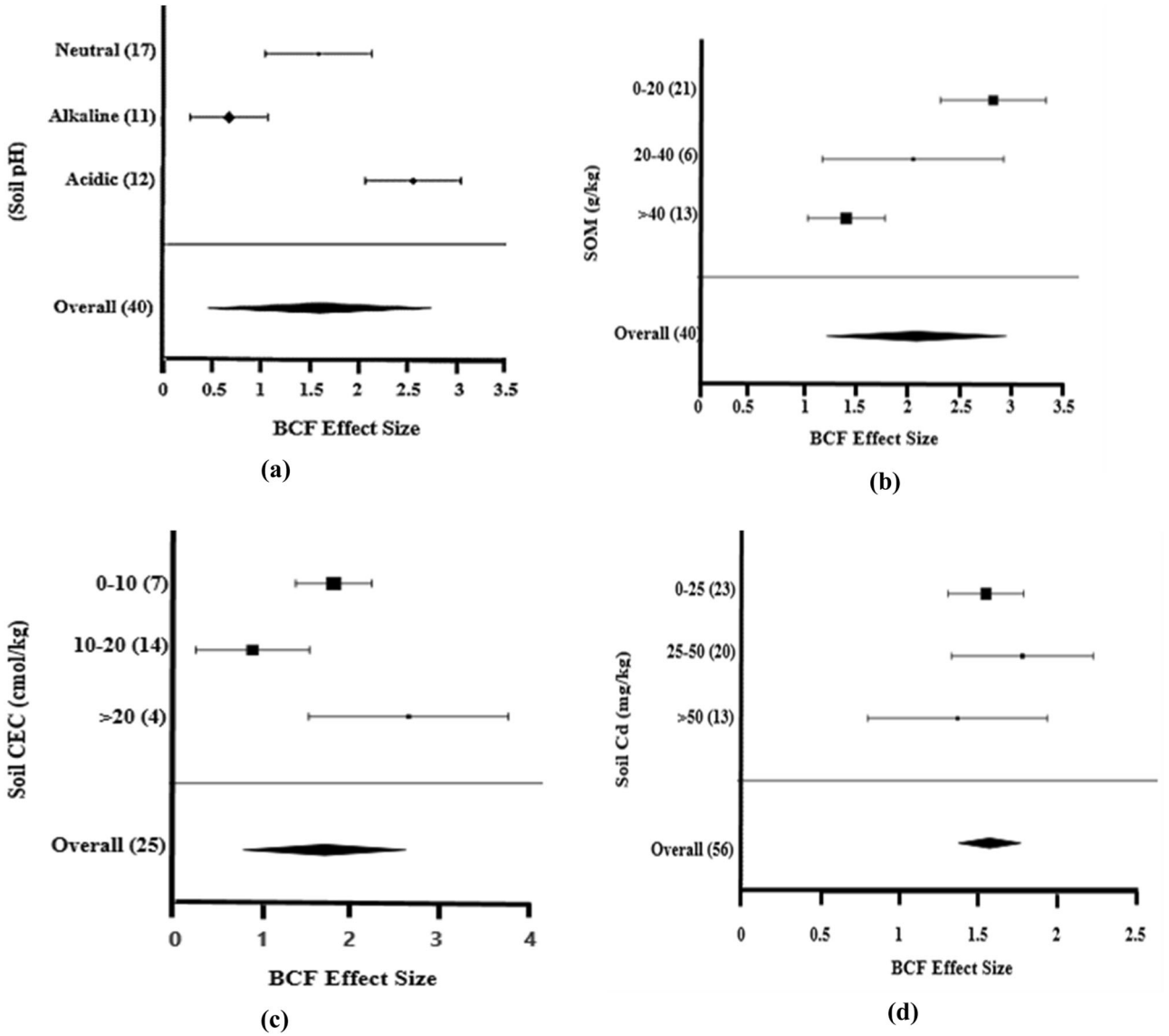

Fig. 3 The BCF of ornamental plants as affected by soil pH (**a**), SOM (**b**), CEC (**c**), and soil Cd (**d**) (mean ES and 95% CI; Values in brackets refer to the number of observations)

Effect of soil pH

Based on the pH values of soil, 40 observations were divided into 3 groups: neutral (6.5–7.5), alkaline (>7.5) and acidic (<6.5). Then the data was analysed through subgroup meta-analysis. Figure. 3a represents the BCF of ornamental plants as affected by soil pH. It could be inferred from the analysis that BCF of ornamental plants grown in acidic group soil was highest (mean = 2.56, CI: 2.07 to 3.04) followed by neutral (mean = 1.59, CI: 1.05 to 2.13) and alkaline group (mean = 0.68, CI: 0.29 to 1.08). These outcomes are in accordance with the multiple linear regression results which indicated that soil pH was negatively correlated with the BCF. The Fail-safe N (7194) was significantly higher than $5k + 10$ (k-refers to the number of observations i.e., 40) which means that no publication bias was suggested by Rosenberg's method.

It was inferred from the analysis that the heavy metal accumulation was more under acidic conditions than in neutral and alkaline soils. Soil pH is an important parameter which directly affects the bioavailability of heavy metals, as acidic soil is known to increase the heavy metal solubility and mobility (Elekes, 2014). The availability of cations or metal ions normally increases at lower pH due to the exchange of cations by H^+ ions (Hooda, 2007). This concept of inverse relation between soil pH and Cd bioavailability has been confirmed by many previous studies (Du Laing et al., 2007; Zeng et al., 2011; Huang et al., 2020a). For example, Huang et al., (2020a) conducted an

experiment with five ornamental plants in two types of soil (acidic and alkaline soil) contaminated with Cd and revealed that four out of five plants grew well in the acidic soil, with 19.59–39.63% higher biomass compared to alkaline soil. Moreover, *Thlaspi caerulescens* plants were reported to accumulate higher Cd and Zn under acidic soil conditions than alkaline. Similarly, McBride (2003) concluded that alkaline pH decreases bioavailability of metals. In contrast, a few studies have reported that alkaline pH may increase the bioavailability of Cd in soil (Shuman, 1985; Kacálková et al., 2014).

Effect of SOM

To perform subgroup meta-analysis on SOM, 40 observations were divided into three groups based on the amount of SOM (0–20, 20–40, and >40 g/kg). As shown in simplified forest plot (Fig. 3b), BCF was highest when SOM was in the range of 0–20 g/kg (mean = 2.82, CI: 2.32 to 3.33). Although, the BCF was high while SOM was between 20–40 g/kg (mean = 2.05, CI: 1.18 to 2.92) but its CI was comparatively wide indicating heterogeneity among observations. The BCF was lowest among three when SOM was >40 (mean = 1.40, CI: 1.03 to 1.78). Overall ES was greater than 2 with high heterogeneity (mean = 2.08, CI: 1.22 to 2.95). The Fail-safe N (7962) was significantly higher than 5k + 10 (k-refers to the number of observations i.e., 40) which means that publication bias was not suggested by Rosenberg's method.

Apart from soil pH, SOM is also an important property that affects the bioavailability of heavy metals in soil (Zeng et al., 2011). The correlation between SOM and ES ($\log_n$ BCF) indicated that BCF significantly decreased when SOM content was >40 g/kg whereas it was highest in the SOM range of 0–20 g/kg. SOM consists of different functional groups (hydroxyl, carboxyl, phenolic, and amino groups) which might affect the fate of heavy metals in the soil through a series of reactions like adsorption, complexation, and chelation (Masoom et al. 2016). There are various contradicting reports on the effect of organic matter amendments in the soil. One view is that heavy metal bioavailability is positively related to the SOM content as it delivers organic chemicals to the soil that can act as chelates and enhance heavy metal-availability to the plants (Antoniadis et al. 2008; McCauley et al., 2009). For example, addition of organic matter content in paddy increased the availability of heavy metals and their uptake. (Zeng et al., 2011). Likewise, increased mobility of Cd in soil and its uptake by rye grass was reported by addition of organic matter (Almås, Singh, 2001). Other view is that addition of organic matter content led to reduce the bioavailability of heavy metals (Pinto et al., 2004; Shahid et al., 2014; Kwiatkowska-Malina, 2017), which is in accordance with our study. Skłodowski et al. (2006) reported that addition of brown coal based organic amendment reduced the content of bioavailable heavy metal ions due to complexation. Another study demonstrated that humic substances derived from brown coal had immobilization effect on heavy metal ions (Kwiatkowska-Malina, 2017). Thus, it can be concluded that the availability of heavy metal ions is regulated by chemical nature of organic substance than by its organic nature alone.

Effect of soil CEC

The amount of organic matter in soil has a positive influence on the cation exchange capacity resulting in metal-organic complexation and helps in the minimization of heavy metal absorption by plants (Gupta & Sinha, 2007; Yobouet et al., 2010). Therefore, subgroup meta-analysis was performed on CEC. A simplified forest plot representation for change in BCF against soil CEC is given in Fig. 3c. Less number of observations (25) were analysed in this case as many studies did not report CEC. The total mean ES was 1.71 whose 95% CI was between 0.79 and 2.62. The BCF ES was 1.81 with 95% CI ranging from 1.38 to 2.23 while soil CEC was in the range of 0–10 cmol/kg. The ES value dropped sharply when CEC was between 10–20 cmol/kg (mean = 0.90, CI: 0.26 to 1.54). However, it increased again while soil CEC was >40 cmol/kg (mean = 2.65, CI: 1.53 to 3.77). Because of significant heterogeneity (wide 95% confidence interval) in the subgroup with CEC > 40 cmol/kg, the trend of this two way change was not very credible. In addition, this subgroup had very less number of observations (4) that is why increase in ES was not very obvious. Previous studies have also confirmed that Cd uptake is negatively correlated with CEC (Yousaf et al., 2016; Huang et al., 2018; Huang et al., 2020a) as indicated by the results of multiple linear regression analysis. Cui et al. (2021) showed that *Amaranthus hypochondriacus* grown in low CEC soils had higher BCF values for Cd. This inverse relation is probably due to that soil with higher CEC is more able of reducing the mobility of Cd ions (Abdel-Sabour and Rabie, 2003). In addition, wide 95% CI indicated that there was large heterogeneity among results and the effect of CEC on ornamental plants might be influenced by soil texture and clay minerals composition as well. The Fail-safe N (4145) was significantly higher than 5k + 10 (k-refers to the number of observations i.e., 25) which means that publication bias was not suggested by Rosenberg's method.

Effect of Cd concentration in soil

One more environmental factor which was considered in this analysis is soil Cd concentration. Total of 56 observations were included in the analysis and a simplified forest plot was drawn (Fig. 3d). Results revealed that the ES was lowest when soil Cd was >50 mg/kg (mean = 1.37, CI: 0.80 to 1.94). Compared with ES when soil Cd was between 0–25 mg/kg (mean = 1.55, CI: 1.31 to 1.79), the ES was more while soil

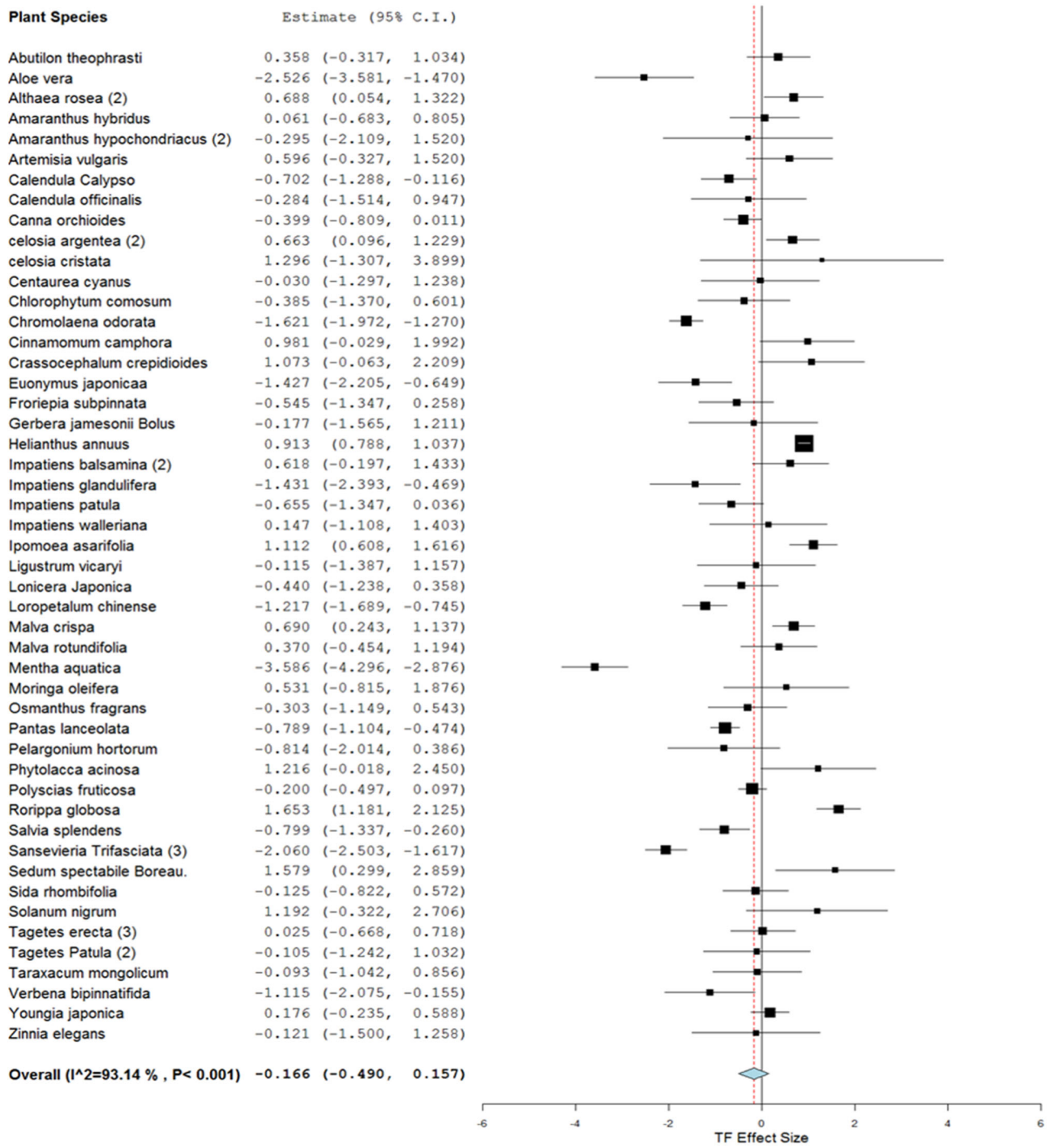

Fig. 4 The TF of ornamental plants represented as mean ES and 95% CI in a forest plot. Numerals in brackets indicate the number of studies from which the mean ES was calculated. 'Overall' indicated the common ES of all species

Cd was ranging from 25–50 mg/kg (mean = 1.78, CI: 1.33 to 2.23). Overall mean ES was 1.57, and 95% confidence interval was between 1.38 and 1.77. The Fail-safe N (11174) was significantly greater than (5k + 10) (k- represents the number of observations i.e., 56), which showed that there was no publication bias.

From subgroup meta-analyis, it was easy to infer that high concentration of Cd does not essentially mean that all of it is in available form, but low concentration of Cd led to low concentration of available Cd since initial Cd concentration determines the upper limit of available Cd. In addition, high concentration of Cd may change the nutrient absorption and

accumulation characteristics of plant due to toxic effects of heavy metal. For example, when *Chromolaena odorata* and *Impatiens patula* were grown in Cd spiked soil (20, 40, 60, and 80 mg Cd/kg of soil), the BCF value was observed to be highest under 20 mg/kg Cd stress and lower under high Cd stress for both the plants (Jampasri et al., 2021). While high Cd concentration in soil provided enough amount for plants to accumulate, it also produced toxicity in plants causing hindrance in plant growth and metabolism, which would ultimately affect the plant ability to absorb Cd (Das et al., 1997; Sun et al., 2013). Thus, it can be concluded from the analysis that Cd concentration had positive correlation with the BCF but up to a certain range.

TF of Different Species

TF is the ratio of heavy metal ions in the aboveground biomass to that in the roots. Generally, there are two pathways for heavy metal ions to enter into plant roots: symplastic (intercellular) and apoplastic (extracellular) (Sarwar et al., 2016). Hyperaccumulators use symplastic pathway to translocate heavy metal ions into the shoot through the xylem and entry of heavy metal ions into the xylem stream occurs through root symplasm (Tester and Leigh, 2001). However, some reports suggested phloem as one of the transport pathways for Cd (Grandy et al., 2009). There are various strategies through which plants inhibit the translocation of Cd ions from roots to shoots such as chelation of Cd ions (Huang et al., 2017) and most imprtant is the diversity in the physiological structure of ornamental plants and the ability of each plant to translocate Cd ions from roots to shoots varies broadly (Wu et al., 2018).

In the present study, the ES ($\log_n$ TF) of the same ornamental plant species were combined to calculate means and 95% CI. Total of 49 species were included in this analysis and TF of each species is shown in forest plot (Fig. 4). Large heterogeneity ($I^2 = 93.14\%$, $p < 0.001$) was observed in the analysis. The overall ES was less than 0 (mean = −0.166, CI: −0.490 to 0.157). The Cd translocation from roots to shoots was maximum in *Rorippa globosa* (mean = 1.653, CI: 1.18 to 2.12) and *Sedum spectabile Boreau* (mean = 1.579, CI: 0.299 to 2.85) and this result was confirmed by various previous studies (Sun et al., 2007; Wei et al., 2015; Guo et al., 2017). The accumulation of Cd in the shoots of *Celosia cristata, Crassocephalum crepidioides, Ipomoea asarifolia, Phytolacca acinosa*, and *Solanum nigrum* was significantly higher (>1) than their roots. Further, Cd accumulation in the shoots of *Aloe vera, Chromolaena odorata, Euonymus japonica, Impatiens glandulifera, Loropetalum chinense, Mentha aquatica, Sansevieria Trifasciata*, and *Verbena bipinnatifida* were significantly lower (<−1) than in their roots, which is consistent with the previous results (Amadi and Tanee, 2016; Jampasri et al., 2021; Hasanpour et al., 2019). Other species did not show any significant difference in Cd accumulation between shoots and roots. Overall, among the 49 ornamental plant species studied, *Rorippa globose, Sedum spectabile, Celosia cristata, Crassocephalum crepidioides, Ipomoea asarifolia, Phytolacca acinosa*, and *Solanum nigrum* had translocation factor more than 1 and can be classified as potential Cd hyperaccumulators. The Fail-safe N (82000) was significantly greater than (5k + 10) (k represents the number of observations i.e., 56), which showed that there was no publication bias.

Conclusion

Total of 31 articles met the selection criteria of this study and 49 ornamental plants were identified. The multiple linear regression results demonstrated that the major environmental factor affecting the Cd accumulation capacity of ornamental plants was soil pH. Therefore, soil pH is the important factor to be considered in the process of phytoremediation. Based on the results of subgroup meta-analysis, we found that Cd accumulation by ornamental plants was negatively correlated with the soil pH, SOM, and soil CEC. Additionally, the optimum concentration of Cd in soil to grow ornamental plants was suggested up to the limit of 50 mg/kg. Among all the studied plant species, *Helianthus annuus* (BCF = 5.785), *Impatiens glandulifera* (BCF = 4.722), and *Crassocephalum crepidioides* (BCF = 3.623) were found to have more Cd accumulation capacity than other species, whereas *Rorippa globosa* (TF = 1.653) and *Sedum spectabile Boreau* (TF = 1.579) had significantly higher Cd translocation capacity. The total BCF and TF values for ornamental plant species were 1.577 and −0.166, respectively. The results of the present study would help the future researchers to have an idea about the potential accumulators and hyperaccumulators and important environmental factors that should be taken care of for successful phytoremediation of Cd-contaminated soil.

Author Contributions All authors contributed to the study conception, design, data collection, and analysis.

Compliance with Ethical Standards

Conflict of Interest The authors declare no competing interests.

References

Abdel-Sabour MF, Rabie FH (2003) Accumulation of heavy metals in vegetable plants grown in mostorod area. Egypt J Soil Sci 43:63–76

Ahn E, Kang H (2018) Introduction to systematic review and meta-analysis. Korean J Anesthesiol 71(2):103–112. https://doi.org/10.4097/kjae.2018.71.2.103

Alaboudi K, Ahmed B, Brodie G (2018) Phytoremediation of Pb and Cd contaminated soils by using sunflower (*Helianthus annuus*) plant. Anal Agric Sci 63:123–127. https://doi.org/10.1016/j.aoas.2018.05.007

Almås ÅR, Singh BR (2001) Plant uptake of cadmium-109 and zinc-65 at different temperature and organic matter levels. J Environ Qual 30(3):869–877. https://doi.org/10.2134/jeq2001.303869x

Amadi N, Tanee FBG (2016) Comparative study of three ornamental plant species for their phytoextraction potentials of cadmium polluted soil. J Adv Biol Biotechnol 9(1):1–8. https://doi.org/10.9734/JABB/2016/27744

Antoniadis V, Robinson JS, Alloway BJ (2008) Effects of short-term pH fluctuations on cadmium, nickel, lead, and zinc availability to ryegrass in a sewage sludge-amended field. Chemosphere 71(4):759–764. https://doi.org/10.1016/j.chemosphere.2007.10.015

Benavides BJ, Drohan PJ, Spargo JT, Maximova SN, Guiltinan MJ, Miller DA (2021) Cadmium phytoextraction by Helianthus annuus (sunflower), Brassica napus cv Wichita (rapeseed), and Chyrsopogon zizanioides (vetiver). Chemosphere 265:129086. https://doi.org/10.1016/j.chemosphere.2020.129086

Biswal B, Singh S, Patra A, Mohapatra K (2021) Evaluation of phytoremediation capability of French marigold (*Tagetes patula*) and African Marigold (*Tagetes erecta*) under heavy metals contaminated soils. *International Journal of Phytoremediation*. https://doi.org/10.1080/15226514.2021.1985960

Chauhan P, Mathur J (2020) Phytoremediation efficiency of *Helianthus annuus* L. for reclamation of heavy metals contaminated industrial soil. Environ Sci Pollut Res 27:29954–29966. https://doi.org/10.1007/s11356-020-09233-x

Coakley S, Cahill G, Enright AM, O'Rourke B, Petti C (2019) Cadmium hyperaccumulation and translocation in Impatiens glandulifera: from foe to friend. Sustainability 11(18):5018. https://doi.org/10.3390/su11185018

Cui X, Mao P, Sun S, Huang R, Fan Y, Li Y, Li Y, Zhuang P, Li Z (2021) Phytoremediation of cadmium contaminated soils by Amaranthus Hypochondriacus L.: The effects of soil properties highlighting cation exchange capacity. Chemosphere 283:131067. https://doi.org/10.1016/j.chemosphere.2021.131067

Das P, Samantaray S, Rout GR (1997) Studies on cadmium toxicity in plants: a review. Environ Pollut 98(1):29–36. https://doi.org/10.1016/S0269-7491(97)00110-3

Elekes C (2014) Eco-technological solutions for the remediation of polluted soil and heavy metal recovery. *In: Hernández-Soriano, MC, Ed., Environmental Risk Assessment of Soil Contamination, InTech, Rijeka*, 309–335. https://doi.org/10.5772/57314

Farooq A, Nadeem M, Abbas G, Shabbir A, Khalid M, Javeed HM, Akhtar G (2020) Cadmium partitioning, physiological and oxidative stress responses in marigold (*Calendula calypso*) grown on contaminated soil: implications on phytoremediation. Bull Environ Contamination Toxicol 105:270–276

Fragkos KC, Tsagris M, Frangos CC (2014) Publication bias in meta-analysis: confidence intervals for Rosenthal's fail-safe number. *International scholarly research notices*, *2014*. https://doi.org/10.1155/2014/825383

Grandy AS, Strickland MS, Lauber CL, Bradford MA, Fierer N (2009) The influence of microbial communities, management, and soil texture on soil organic matter chemistry. Geoderma 150(3-4):278–286. https://doi.org/10.1016/j.geoderma.2009.02.007

Guo JM, Lei M, Yang JX, Yang J, Wan XM, Chen TB, Guo GH (2017) Effect of fertilizers on the Cd uptake of two sedum species (Sedum spectabile Boreau and Sedum aizoon L.) as potential Cd accumulators. Ecol Eng 106:409–414

Gupta A, Sinha S (2007) Phytoextraction capacity of the plants growing on tannery sludge dumping sites. Bioresour Technol 98:1788–1794. https://doi.org/10.1016/j.biortech.2006.06.028

Hasanpour R, Zaefarian F, Rezvani M, Jalili B (2019) Potential of Mentha aquatica L., Eryngium caucasicum Trautv. and Froriepia subpinnata Ledeb. for phytoremediation of Cd-contaminated soil. Braz J Bot 42(3):399–406. https://doi.org/10.1007/s40415-019-00550-1

Hooda V (2007) Phytoremediation of toxic metals from soil and waste water. J Environ Biol 28(2):367–376

Huang L, Wang Q, Zhou Q, Ma L, Wu Y, Liu Q, Feng Y (2020a) Cadmium uptake from soil and transport by leafy vegetables: A meta-analysis. Environ Pollut 264:114677. https://doi.org/10.1016/j.envpol.2020.114677

Huang Q, Yu Y, Wan Y, Wang Q, Luo Z, Qiao Y, Li H (2018) Effects of continuous fertilization on bioavailability and fractionation of cadmium in soil and its uptake by rice (Oryza sativa L.). J Environ Manag 215:13–21. https://doi.org/10.1016/j.jenvman.2018.03.036

Huang Y, He C, Shen C, Guo J, Mubeen S, Yuan J, Yang Z (2017) Toxicity of cadmium and its health risks from leafy vegetable consumption. Food Funct 8(4):1373–1401. https://doi.org/10.1039/C6FO01580H

Huang R, Dong M, Mao P, Zhuang P, Paz-Ferreiro J, Li Y, Li Z (2020b) Evaluation of phytoremediation potential of five Cd (hyperaccumulators) in two Cd contaminated soils. *Science of the Total Environment*, *721*. https://doi.org/10.1016/j.scitotenv.2020.137581

Jampasri K, Saeng-Ngam S, Larpkern P, Jantasorn A, Kruatrachue M (2021) Phytoremediation potential of Chromolaena odorata, Impatiens patula, and Gynura pseudochina grown in cadmium-polluted soils. Int J Phytoremediation 23(10):1061–1066. https://doi.org/10.1080/15226514.2021.1876626

Jemna LM (2017) Using quantitative and mixed research methods in marketing: A meta-analytic approach. Acta Universitatis Danubius Œconomica 13(4):227–249

Kacálková L, Tlustoš P, Száková J (2014) Chromium, nickel, cadmium, and lead accumulation in maize, sunflower, willow, and poplar. Pol J Environ Stud 23(3):753–761

Khan A, Kiyani A, Mirza C, Butt T, Barros R, Ali B, Yousaf S (2021) Ornamental plants for the phytoremediation of heavy metals: Present knowledge and future perspectives. *Environ Res*, *195*. https://doi.org/10.1016/j.envres.2021.110780

Kwiatkowska-Malina J, Applied Soil Ecology (2017), https://doi.org/10.1016/j.apsoil.2017.06.021

Du Laing G, Vanthuyne DRJ, Vandecasteele B, Tack FMG, Verloo MG (2007) Influence of hydrological regime on pore water metal concentrations in a contaminated sediment-derived soil. Environ Pollut 147(3):615–625. https://doi.org/10.1016/j.envpol.2006.10.004

Li J, Yu H, Luan Y (2015) Meta-analysis of the copper, zinc, and cadmium absorption capacities of aquatic plants in heavy metal-polluted water. Int J Environ Res public health 12(12):14958–14973. https://doi.org/10.3390/ijerph121214959

Liu J, Xin X, Zhou Q (2018b) Phytoremediation of contaminated soils using ornamental plants. Environ Rev 26(1):43–54. https://doi.org/10.1139/er-2017-0022

Liu J, Zhou Q, Wang S (2010) Evaluation of chemical enhancement on phytoremediation effect of Cd- contaminated soils with *Calendula officinalis L. Int J Phytoremediation*, 503–515. https://doi.org/10.1080/15226510903353112

Mahmood-ul-Hassan M, Yousra M, Saman L, Ahmad R (2020) Floriculture: alternate non-edible plants for phyto-remediation of heavy metal contaminated soils. Int J Phytoremediation 22(7):725–732. https://doi.org/10.1080/15226514.2019.1707772

Masoom H, Courtier-Murias D, Farooq H, Soong R, Kelleher BP, Zhang C, Simpson AJ (2016) Soil organic matter in its native state:

unravelling the most complex biomaterial on earth. Environ Sci Technol 50(4):1670–1680. https://doi.org/10.1021/acs.est.5b03410
McBride MB (2003) Toxic metals in sewage sludge-amended soils: has promotion of beneficial use discounted the risks? Adv Environ Res 8(1):5–19
McCauley A, Jones C, Jacobsen J (2009) Soil pH and organic matter. Nutrient Manag Modul 8(2):1–12
Nagajyoti PC, Lee KD, Sreekanth TV (2010) "Heavy metals, occurrence and toxicity for plants: a review. Environ Chem Lett 8(3):199. https://doi.org/10.1007/s10311-010-0297-8
Olivares AR, Carrillo-González R, González-Chávez MDCA, Hernández RMS (2013) Potential of castor bean (Ricinus communis L.) for phytoremediation of mine tailings and oil production. J Environ Manag 114:316–323. https://doi.org/10.1016/j.jenvman.2012.10.023
Pinto AP, Mota AD, De Varennes A, Pinto FC (2004) Influence of organic matter on the uptake of cadmium, zinc, copper and iron by sorghum plants. Sci total Environ 326(1-3):239–247. https://doi.org/10.1016/j.scitotenv.2004.01.004
Raj D, Kumar A, Maiti SK (2020) Brassica juncea (L.) Czern (Indian mustard): a putative plant species to facilitate the phytoremediation of mercury contaminated soils. Int J Phytoremediation 22(7):733–744. https://doi.org/10.1080/15226514.2019.1708861
Rezapour S, Atashpaz B, Moghaddam SS, Kalavrouziotis IK, Damalas CA (2019) Cadmium accumulation, translocation factor, and health risk potential in a wastewater-irrigated soil-wheat (Triticum aestivum L.) system. Chemosphere 231:579–587. https://doi.org/10.1016/j.chemosphere.2019.05.095
Rosenberg MS (2005) The file-drawer problem revisited: a general weighted method for calculating fail-safe numbers in meta-analysis. Evolution 59(2):464–468. https://doi.org/10.1111/j.0014-3820.2005.tb01004.x
Rosenberg MS, Adams DC, Gurevitch J (2000) Meta-win: Statistical software for meta-analysis. Sinauer Associates, Sunderland (Massachusetts. Version 2.1)
Rosenthal R (1979) The file drawer problem and tolerance for null results. *Psychol Bull*, *86*(3). https://psycnet.apa.org/doi/10.1037/0033-2909.86.3.638
Sarwar N, Muhammad I, Shaheen M, Ishaq W, Kamran A, Matloob A, Hussain S (2016) Phytoremediation stratgies for soils contaminated with heavy metals: modifications and future perspectives. *Chemosphere*. https://doi.org/10.1016/j.chemosphere.2016.12.116
Sehrawat G, Singh R, Kaushik A (2021) Tolerance of three ornamental plant species to chromium contamination in soil and their potential for phytoextraction and phytostabilization of the toxic metal. Curr World Environ 16(2):386. https://doi.org/10.12944/CWE.16.2.06
Shahid M, Sabir M, Arif Ali M, Ghafoor A (2014) Effect of organic amendments on phytoavailability of nickel and growth of berseem (Trifolium alexandrinum) under nickel contaminated soil conditions. Chem Speciat Bioavailab 26(1):37–42. https://doi.org/10.3184/095422914X13886890590610
Shi W, Ma X (2017) Effects of heavy metal Cd pollution on microbial activities in soil. Ann Agric Environ Med 24(4):722–725
Shuman LM (1985) Fractionation method for soil microelements. Soil Sci 140(1):11–22
Skłodowski P, Maciejewska A, Kwiatkowska J (2006) The effect of organic matter from brown coal on bioavailability of heavy metals in contaminated soils. Soil and Water Pollution Monitoring, Protection and Remediation. NATO Science Series, vol. 69. Springer, Dordrecht. https://doi.org/10.1007/978-1-4020-4728-2_19
Song W, Wang J, Zhai L, Ge L, Hao S, Shi L, Chen Y (2022) A meta-analysis about the accumulation of heavy metals uptake by Sedum alfredii and Sedum plumbizincicola in contaminated soil. Int J Phytoremediation 24(7):744–752. https://doi.org/10.1080/15226514.2021.1970103
Srivastava M K, Gupta G (2021) Synthesis and Analysis of Factors affecting Environmentalism: A Meta-Analysis Approach, *New Horizons*, A, ISSN-2277-5218, Vol. XVIII, August 2021, pp. 42-56
Sun Y, Sun G, Xu Y, Wang L, Liang X, Lin D, Hu F (2013) Assessment of natural sepiolite on cadmium stabilization, microbial communities, and enzyme activities in acidic soil. Environ Sci Pollut Res 20(5):3290–3299. https://doi.org/10.1007/s11356-012-1261-x
Sun YB, Zhou QX, Ren LP (2007) Growth responses of Rorippa globosa and its accumulation characteristics of Cd and As under the Cd-As combined pollution. *Huan Jing ke Xue=*. Huanjing Kexue 28(6):1355–1360
Tester M, Leigh RA (2001) Partitioning of nutrient transport processes in roots. J Exp Bot 52(suppl 1):445–457
Tőzsér D, Magura T, Simon E (2017) Heavy metal uptake by plant parts of willow species: a meta-analysis. J Hazard Mater 336:101–109. https://doi.org/10.1016/j.jhazmat.2017.03.068
USEPA's Integrated Risk Information System (USEPA IRIS), 2012. Human Health Risk Assessment; Risk-Based Screening
Wei S, Ji D, Twardowska I, Li Y, Zhu J (2015) Effect of different nitrogenous nutrients on the cadmium hyperaccumulation efficiency of Rorippa globosa (Turcz.) Thell. Environ Sci Pollut Res 22(3):1999–2007. https://doi.org/10.1007/s11356-014-3448-9
Wu M, Luo Q, Liu S, Zhao Y, long Y, Pan Y (2018) Screening ornamental plants to identify potential Cd hyperaccumulators for bioremediation. Ecotoxicol Environ Saf 162:35–41. https://doi.org/10.1016/j.ecoenv.2018.06.049
Yamato M, Yoshida S, Iwase K (2008) Cadmium accumulation in Crassocephalum crepidioides (Benth.) S. Moore (Compositae) in heavy-metal polluted soils and Cd-added conditions in hydroponic and pot cultures. Soil Sci Plant Nutr 54(5):738–743. https://doi.org/10.1111/j.1747-0765.2008.00295.x
Yobouet Y, Adouby K, Trokourey A, Yao B (2010) Cadmium, copper, lead and zinc speciation in contaminated soils. Int J Eng Sci Technol 2:802–812
Yousaf B, Liu G, Wang R, Zia-ur-Rehman M, Rizwan MS, Imtiaz M, Shakoor A (2016) Investigating the potential influence of biochar and traditional organic amendments on the bioavailability and transfer of Cd in the soil–plant system. Environ Earth Sci 75(5):1–10. https://doi.org/10.1007/s12665-016-5285-2
Zeng F, Ali S, Zhang H, Ouyang Y, Qiu B, Wu F, Zhang G (2011) The influence of pH and organic matter content in paddy soil on heavy metal availability and their uptake by rice plants. Environ Pollut 159(1):84–91. https://doi.org/10.1016/j.envpol.2010.09.019
Zeng P, Guo Z, Cao X, Xiao X, Liu Y, Shi L (2018) Phytostabilisation potential of ornamental plants grown in soil contaminated with cadmium. Int J Phytoremediation 20(4):311–320. https://doi.org/10.1080/15226514.2017.1381939
Zeng P, Guo Z, Xiao X, Peng C, Feng W, Xin L, Xu Z (2019) Phytoextraction potential of Pteris vittata L. co-planted with woody species for As, Cd, Pb and Zn in contaminated soil. Sci Total Environ 650:594–603. https://doi.org/10.1016/j.scitotenv.2018.09.055

Publisher's note Springer Nature remains neutral with regard to jurisdictional claims in published maps and institutional affiliations.

Springer Nature or its licensor (e.g. a society or other partner) holds exclusive rights to this article under a publishing agreement with the author(s) or other rightsholder(s); author self-archiving of the accepted manuscript version of this article is solely governed by the terms of such publishing agreement and applicable law.

Cavity-Backed Slot Loaded Substrate Integrated Waveguide Self-Diplexing Antenna for C Band Applications

Sudarshan Kumar
Department of Electronics and Communication Engineering
Delhi Technological University
New Delhi, India
sudarshanmanav@gmail.com

Asok De
Department of Electronics and Communication Engineering
Delhi Technological University
New Delhi, India
asok.de@gmail.com

2022 IEEE 6th Conference on Information and Communication Technology (CICT) | 978-1-6654-7312-5/22/$31.00 ©2022 IEEE | DOI: 10.1109/CICT56698.2022.9997872

***Abstract*—This paper proposed a cavity-backed slot loaded substrate integrated waveguide (SIW) self-diplexing antenna. The proposed antenna consists of a rectangular slot backed by a SIW cavity. The proposed antenna resonates at two distinct frequencies and is fed by two separate offset inset microstrip lines. The various parameters like return loss, gain, radiation efficiency, and the E-plane and the H-plane radiation patterns, etc. are investigated for the antenna. The antenna resonates at two distinct frequencies of 6.5 GHz and 7 GHz with a total gain of 4.8 dBi and 6.4 dBi in the broadside direction, respectively. More than 30 dB of isolation is obtained between the two input feed ports, which is desirable for achieving diplexing property.**

Keywords—Cavity-backed antenna, self-diplexing antenna, SIW

I. INTRODUCTION

Wireless communication systems at present are rapidly evolving, which has increased the demand for low-profile, low-cost, high-performance planar dual-band antennas. Dual-band antennas with good isolation are required for wireless portable devices, wireless antenna integrated receiver systems, and radar transceiver systems with separate uplink and downlink channels. The design of self-diplexing antennas has attracted more attention recently since it eliminates the requirement for higher order diplexers and lowers the cost and complexity of the RF front-end system by lowering the number of components [1, 2]. In addition to this it has a unidirectional pattern, low cost, decreased insertion losses, and ease of excitation of the necessary modes. The microstrip patch antenna with the self-diplexing property has also been reported in the literature [2-7].In [2] an orthogonal polarized printed antenna with high isolation is designed. Both feeding ports are designed to keep the up-link and down-link frequency bands isolated from each other. The patch is circular in shape and made of a material with a high dielectric constant. In [3] and [4], a multilayered microstrip patch antenna is designed and uses additional filtering operations to improve the isolation. SIW has emerged as an effective choice for antenna design. In [5] and [6] the antenna with self diplexing operation is done on non-planar structure. In [8] the microstrip patch is loaded with the T shaped stubs.

The SIW is a planar form of a dielectric-filled conventional rectangular waveguide, and the top and bottom walls are formed by metal cladding on the substrate's upper and lower sides, respectively. The rows of the conductive vias on each side act as the SIW vertical side walls. All wireless systems can be constructed utilizing SIW technology since active components, passive structures, and other devices can all be integrated onto a single substrate [9, 10].

Several cavity-backed slotted SIW antennas with unidirectional patterns had already reported [11, 12], and SIW-based cavity-backed slotted dual-band antennas with high gain are described [13–15]. Along with these antennas, diplexing circuits are mainly used in the transmitter and receiver sections of the RF front-end transceiver systems.

In this article, a novel cavity-backed, slot-loaded SIW antenna is presented. Inset microstrip line feeding techniques are used to feed the proposed antenna. The isolation achieved between the feed lines is high. In order to establish a high level of isolation between both the two ports, the off-set feed lines are used. In the SIW cavities, these two feed line ports produce the two resonant modes. The cavity made in SIW is useful in the generation of high gain in the antenna while the planarity of the structure remains the same. The proposed antenna can be used for a wide range of C-band wireless communication systems, such as sub-6 GHz, 5G wireless communication, and the sub-7 GHz spectrum for satellite communication uplink and downlink frequencies, etc.

II. ANTENNA CONFIGURATIONS

The proposed SIW antenna is made on a dielectric substrate RT duroid 5880 with a permittivity of 2.2 and a loss tangent of 0.004. The thickness of the dielectric substrate is 0.787 mm. Fig.1 shows the geometrical configurations of the proposed antenna. Here, F_1 and F_2 are two feed lines ports. The feed lines are orthogonal and off set to each other.

978-1-6654-7312-5/22/$31.00 ©2022 IEEE

Authorized licensed use limited to: DELHI TECHNICAL UNIV. Downloaded on January 17,2023 at 05:04:22 UTC from IEEE Xplore. Restrictions apply.

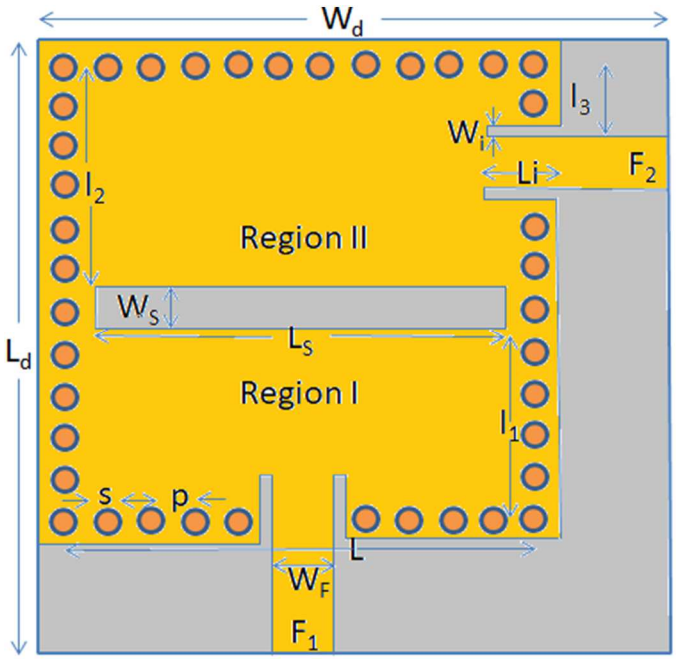

Fig.1. Configuration of proposed antenna (L_d =29, W_d =29, L = 22, Li = 3, l_1 = 9, l_2 = 11, l_3=3.3. Ls = 20, Ws = 2, W_F = 2.33, S = 1, p = 2 mm and W_i = 0.5, all in mm)

The cavity resonator in the shape of a square is designed by the four conductive rows of the vias that act as the metallic walls of the SIW; two off-set inset feed microstrip lines of 50 Ω impedance, each and a rectangular slot in the upper ground plane. The rectangular slot bifurcates the upper ground plane into two unequal radiating apertures to radiate at two different resonating frequencies. The parameters l_1 and l_2 show the length of region 1 and region 2 respectively. The resonating frequencies are decided by l_1 and l_2 and it is also a function of slot length L_S. The two radiating apertures are termed region I and region II. The pitch (p) and the diameter(s) of the conductive vias are chosen such that $\frac{S}{\lambda} \leq \frac{1}{10}$ and $\frac{P}{S} < 2$, so that there is minimal energy leakage between the vias [16], where λ is the operating wavelength. The dimensions of a SIW cavity resonator are 0.52 λ_g *X* 0.52 λ_g, where λ_g is the guided wavelength.

III. Results and Discussions

The proposed SIW antenna is designed and simulated using the electromagnetic solver high frequency structure simulator (HFSS). HFSS uses the finite element method for analyzing the electromagnetic structures. Due to the difference in the dimensions of the radiating regions I and II, differing resonating modes gets excited in the cavity with different perturbed fields. Region I has the shorter length, so it resonates at a higher frequency (7 GHz) when feed line F_1 is excited and feed line F_2 is matched with 50 Ω. Region II has the longer length, so it resonates at a lower frequency (6.5 GHz) when feed line F_2 is excited and F_1 is matched with 50 Ω lines plane giving a more detailed explanation of the radiation mechanism. Fig. 2 (a) shows the surface current distribution at 7 GHz. When the feed line F_1 is excited, the surface current becomes dominant in the region I and is maximum at the lower edge of the slot and negligible in the region II. Fig. 2 (b) shows the surface current distribution at 6.5 GHz. When the feed line F_2 is excited, the surface current becomes dominant in the region II and is maximum at the upper edge of the slot and negligible in the region I.

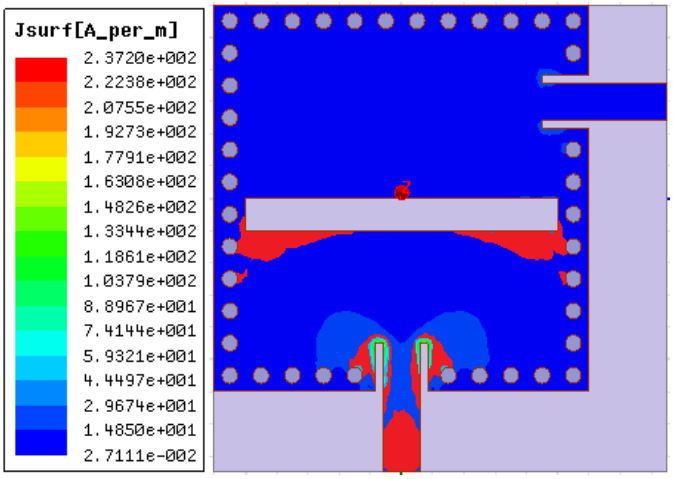

(a)

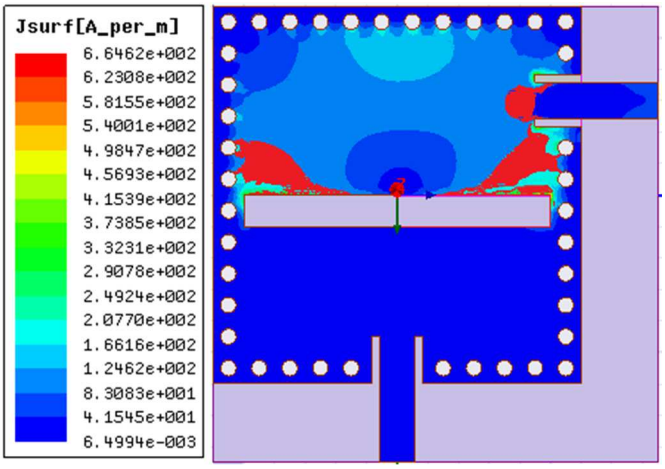

(b)

Fig. 2. (a) Surface current distribution on upper ground plane at 7 GHz (Feed F_1 is excited) (b) Surface current distribution at 6.5 GHz (Feed F_2 is excited).

The S-parameters vs. frequency curve of the proposed antenna is shown in Fig. 3. At the lower resonating frequency of 6.5 GHz, the reflection coefficient $|S_{22}|$ is 14 dB, and at the upper resonating frequency of 7 GHz, the reflection coefficient $|S_{11}|$ is 13 dB. Isolation of more than 30 dB is achieved between the two feed line ports.Such a high value of isolation is achieved by off setting the feed lines as they are weakly coupled to each others. The metalized vias that make up the SIW cavity are used mainly to stop the edge-diffraction effects of surface waves that travel over the whole substrate and keep the energy under the radiating patch.

Authorized licensed use limited to: DELHI TECHNICAL UNIV. Downloaded on January 17,2023 at 05:04:22 UTC from IEEE Xplore. Restrictions apply.

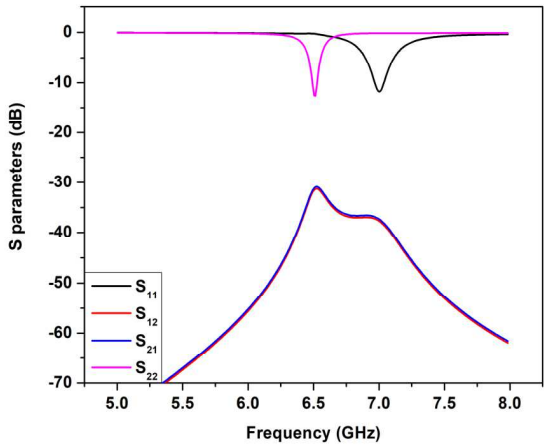

Fig. 3. S parameters of the proposed antenna (l_1 = 9 mm)

The resonating frequency of the proposed antenna varies according to the slot position. The S-parameters comparison curve for the different values of the slot is shown in Fig. 4. If the parameter l_1 is reduced, the lower resonating frequency is decreased and the upper resonating frequency is increased. For l_1=8.5 mm, the lower resonating frequency shifts to 6.3 GHz and the upper resonating frequency shifts to 7.3 GHz. For l_1=8 mm, the lower resonating frequency shifts to 6.1 GHz and the upper resonating frequency shifts to 7.6 GHz. The isolation between the two feed line ports is greater than 30 dB shifts according to resonating frequency.

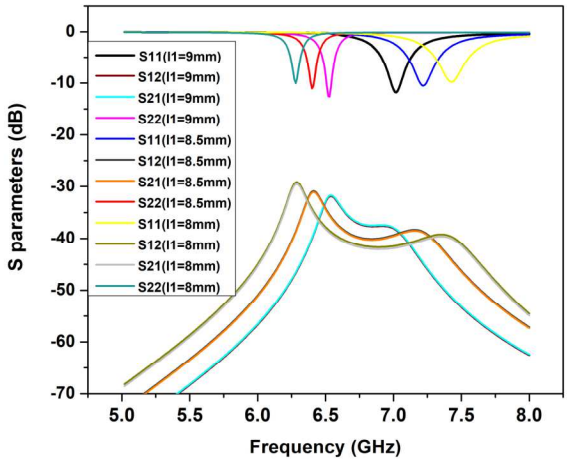

Fig. 4. S-parameters comparison curve for different slot positions (l_1=9 mm, 8.5 mm and 8 mm)

In a planar dielectric substrate, a self-diplexing operation is accomplished with keeping fundamental feeding topologies, since the majority of the fed energy is radiated from the respective region to marginal transmission to the other port. Fig. 5(a, b) shows the proposed antenna E-plane and H-plane radiation patterns (l_1 = 9 mm) at 6.5 and 7 GHz, respectively.

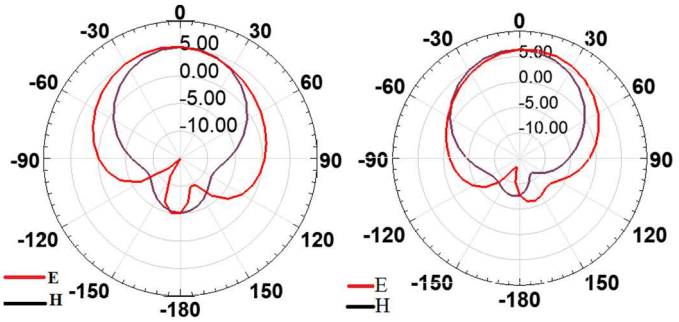

Fig. 5. E-and H-plane radiation patterns at (a) 6.5 GHz (b) 7 GHz

The antenna's total gain is 4.8 dBi at the lower resonating frequency of 6.5 GHz and 6.4 dBi at the upper resonating frequency of 7 GHz, respectively. The E-plane and H-plane radiation patterns have low differences due to the absence of side lobes. The proposed antenna has unidirectional broadside radiation at both of the resonant frequencies. The radiation pattern of this antenna makes it suitable for C-band transceiver systems. Fig. 6 shows the proposed antenna's radiation efficiency curve.

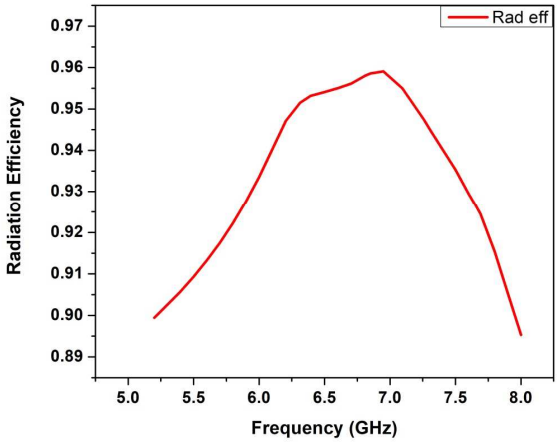

Fig. 6. Radiation efficiency vs. frequency curve

The radiation efficiency of the proposed antenna at a lower resonating frequency of 6 GHz is 92.7% and at a higher resonating frequency of 7 GHz is 95.5%.The efficiency of the proposed antenna is high as compared to dipole and microstrip patch antennas. The radiation efficiency of the proposed antenna is high as compared to wire, aperture and printed planar antennas. The radiation efficiency is greater than 90 % at different values of resonating frequencies, which is achieved by changing the region lengths l_1 and l_2. Table I compares the proposed antenna's performance to that of several other antennas described in the literature. The proposed antenna shows the greater total gain with the unidirectional radiation pattern. The antenna along these parameters shows that the proposed antenna is an efficient

Authorized licensed use limited to: DELHI TECHNICAL UNIV. Downloaded on January 17,2023 at 05:04:22 UTC from IEEE Xplore. Restrictions apply.

way of achieving a self-diplexing mechanism within a trans-receiver system.

Table I. Comparison of the proposed antenna's performance

Ref. No.	Resonating Freq.(GHz)	Gain (dB)	Radaition Pattern	$\lvert S_{21}\rvert$(dB) $\lvert S_{12}\rvert$(dB)
1.	8.26/10.46	3.56/5.24	Unidirectional	27.9
7.	2.45/5.5	1.9/4.4	Bidirectional	25
8.	9/11.2	4.3/4.2	Unidirectional	25
Proposed Work	6.5/7	4.8/6.4	Unidirectional	30

IV. CONCLUSIONS

In this article, a cavity-backed SIW self-diplexing antenna is designed. A rectangular slot has been made in the upper ground plane, which divides it into two regions. Two offset orthogonal inset microstrip feed lines have been used. The designed antenna resonates at two different resonating frequencies. More than 30 dB isolation has been obtained in between two feed lines. A parametric analysis has been done on the position of the slots. The designed antenna has proved suitable for C-band wireless applications.

REFERENCES

[1] S. Nandi and A. Mohan, "An SIW Cavity-Backed Self-Diplexing Antenna," in IEEE Antennas and Wireless Propagation Letters, vol. 16, pp. 2708-2711, 2017. doi: 10.1109/LAWP.2017.2743017

[2] Dong-Kook Park, R. Waterhouse, Yongxi Qian and T. Itoh, "Self-diplexed integrated antenna transceiver for wireless applications," IEEE Antennas and Propagation Society International Symposium. 2001 Digest. Held in conjunction with: USNC/URSI National Radio Science Meeting (Cat. No.01CH37229), 2001, pp. 444-447 vol.3, doi: 10.1109/APS.2001.960130.

[3] J. M. de. Paz, E. U. Munoz, F. J. H. Martinez, V. G. Posadas, L. E. G. Munozand and D. S. Vargas, "Multifrequency Self-Diplexed Single Patch Antennas Loaded with Split Ring Resonators," Progress In Electromagnetics Research, Vol. 113, 47-66, 2011.doi:10.2528/PIER10121703

[4] F. J. Herraiz-Martinez, E. Ugarte-Munoz, V. Gonzalez-Posadas, L. E. Garcia-Munoz and D. Segovia-Vargas, "Self-Diplexed Patch Antennas Based on Metamaterials for Active RFID Systems," in IEEE Transactions on Microwave Theory and Techniques, vol. 57, no. 5, pp. 1330-1340, May 2009, doi: 10.1109/TMTT.2009.2017301.

[5] K. R. Boyle, M. Udink, A. de Graauw and L. P. Ligthart, "A Dual-Fed, Self-Diplexing PIFA and RF Front-End," in IEEE Transactions on Antennas and Propagation, vol. 55, no. 2, pp. 373-382, Feb. 2007, doi: 10.1109/TAP.2006.889852.

[6] C. -Y. -D. Sim, C. -C. Chang and J. -S. Row, "Dual-Feed Dual-Polarized Patch Antenna With Low Cross Polarization and High Isolation," in IEEE Transactions on Antennas and Propagation, vol. 57, no. 10, pp. 3321-3324, Oct. 2009, doi: 10.1109/TAP.2009.2028702.

[7] Y. -C. Lu and Y. -C. Lin, "A Mode-Based Design Method for Dual-Band and Self-Diplexing Antennas Using Double T-Stubs Loaded Aperture," in IEEE Transactions on Antennas and Propagation, vol. 60, no. 12, pp. 5596-5603, Dec. 2012, doi: 10.1109/TAP.2012.2211852.

[8] S. Mukherjee and A. Biswas, "Design of Self-Diplexing Substrate Integrated Waveguide Cavity-Backed Slot Antenna," in IEEE Antennas and Wireless Propagation Letters, vol. 15, pp. 1775-1778, 2016, doi: 10.1109/LAWP.2016.2535169.

[9] S. Kumar and A. De, "Design and analysis of sinusoidally modulated substrate integrated waveguide and filter" Int J RF Microw Comput Aided Eng.; 32(1):e22912, 2022. doi:10.1002/mmce.22912

[10] M. Bozzi, L. Perregrini and C. Tomassoni, "A Review of Compact Substrate Integrated Waveguide (SIW) Interconnects and Components," 2019 IEEE 23rd Workshop on Signal and Power Integrity (SPI), 2019, pp. 1-4, doi: 10.1109/SaPIW.2019.8781646.

[11] G. Q. Luo, Z. F. Hu, L. X. Dong and L. L. Sun, "Planar Slot Antenna Backed by Substrate Integrated Waveguide Cavity," in IEEE Antennas and Wireless Propagation Letters, vol. 7, pp. 236-239, 2008, doi: 10.1109/LAWP.2008.923023.

[12] S. Mukherjee, A. Biswas and K. V. Srivastava, "Bandwidth enhancement of substrate integrated waveguide cavity backed slot antenna by offset feeding technique," 2013 IEEE Applied Electromagnetics Conference (AEMC), 2013, pp. 1-2, doi: 10.1109/AEMC.2013.7045029.

[13] G. Q. Luo, Z. F. Hu, W. J. Li, X. H. Zhang, L. L. Sun and J. F. Zheng, "Bandwidth-Enhanced Low-Profile Cavity-Backed Slot Antenna by Using Hybrid SIW Cavity Modes," in IEEE Transactions on Antennas and Propagation, vol. 60, no. 4, pp. 1698-1704, April 2012, doi: 10.1109/TAP.2012.2186226.

[14] S. Mukherjee, A. Biswas and K. V. Srivastava, "Broadband Substrate Integrated Waveguide Cavity-Backed Bow-Tie Slot Antenna," in IEEE Antennas and Wireless Propagation Letters, vol. 13, pp. 1152-1155, 2014, doi: 10.1109/LAWP.2014.2330743.

[15] T. Zhang, W. Hong, Y. Zhang and K. Wu, "Design and Analysis of SIW Cavity Backed Dual-Band Antennas With a Dual-Mode Triangular-Ring Slot," in IEEE Transactions on Antennas and Propagation, vol. 62, no. 10, pp. 5007-5016, Oct. 2014, doi: 10.1109/TAP.2014.2345581.

[16] Ramesh Garg, Inder Bahl and Maurizio Bozi, "Microstrip lines and slot linrs" Artech House, Third edition. Artech House. pp. 513, 2013.

Authorized licensed use limited to: DELHI TECHNICAL UNIV. Downloaded on January 17,2023 at 05:04:22 UTC from IEEE Xplore. Restrictions apply.

Classification and Analysis of Textual data using Naive Bayes with TF-IDF

1st Chingmuankim
dept. of Computer Science Engineering
Delhi Technological University
New Delhi, India
Chingmuankim@ieee.org

2nd Prof. Rajni Jindal
dept. of Computer Science Engineering
Delhi Technological University
New Delhi, India
rajnijindal@dce.ac.in

2022 4th International Conference on Electrical, Control and Instrumentation Engineering (ICECIE) | 978-1-6654-8076-5/22/$31.00 ©2022 IEEE | DOI: 10.1109/ICECIE55199.2022.10000309

***Abstract*—Text classification has become an emerging topic in this modern era as it allow us to extract meaningful information from the data and improve the performance of business and organization. Often termed as Text Tagging or Categorization, these textual data can be Structured, Semi-Structured and Unstructured. This work has utilized unstructured data with the help of twitter API. These unstructured data are then structured using NLP cloud API as the process of manual sorting is time consuming and tedious. The structured textual data comprises of a set of categorical data that is labelled on the basis of the content of the comments. Text Classification has various use cases such as Sentiment analysis, Polarity Checking, Natural Language Inference and accessing grammatical correctness. Earlier experimental work has been carried out using Naive Bayes with a Bag of Words (BOW) feature extraction technique by previous researchers. The objective of this work is to analyze the transformed structured imbalanced data and study the impact it has on the accuracy of Naive Bayes model using Term Frequency-Inverse Document Frequency (TF-IDF) technique. Naive Bayes is a linear, probabilistic and supervised machine learning classifier based on Bayesian theorem. On training and testing the data using the proposed model, it is found that there is an improvement in the overall accuracy with 2-3%.**

***Index Terms*—Text Classification, Naive Bayes, TF-IDF, Polarity Checking**

I. Introduction

Text Classification may be defined as the technique of transforming the unorganized set of data into a more organized data by annotating the unlabeled data and assigning different classes to the text based on the contents of the comments. In the earlier times, prior to the eminence of Machine Learning, the process of text categorization was a tedious process as there were no tools to automate the task. As time goes by, the amount of data keeps rising, thereby causing it to consume more time and man power which makes it challenging to manage these big data manually. However, with the advancement in technology, there are lot of toolkits and cloud API available to us that can aid the process of text classification automation. These text classifiers can automatically analyze the sequence of data and then assign labels to it based on its content. It is important to classify these textual datas as it is used by humans as a medium of communication, expression of idea and documentation of meeting records which can help us learn about the emotions, intentions and mental state of an individual and provide assistance or take action based on the seriousness of the post. Ever since the emergence of internet, social media platforms such as websites, twitter, facebook, LinkedIn etc. become a place to share one's thoughts by writing, expressing and documenting an event. These textual data is divided into Structured, Semi-Structured and Unstructured. Structured data are represented in a tabular form which are in a pre-defined format. As these datas are in a pre-defined format, they are easy to be explored and analyzed. They are Quantitative and have a file extension of csv and xml. Semi-Structured datas are usually in the form of json, csv and xml file types. Unstructured data are those data which are found in social networking platforms such as websites, chat messengers and email. As these data are not in a pre-defined structure, they require more task to be process and understand. Unstructured data is in variety of formats such as pdf, jpg and mp3. Different approaches of Text Classification on these unstructured text data are Rule Based and Machine Learning algorithms. Rule based has a collection of words that decide the sentiment of the text. It is useful only for small datasets. Therefore, it is not cost effective for analyzing large sets of data. Machine Learning algorithms like Naive Bayes, Logistic Regression, Artificial Neural Network, Decision Tree and SVM can be used for Text Classification. In this paper, the data is analyzed using a linear classifier called Naive Bayes with a TF-IDF model. Naive Bayes classifier is of three types namely the Gaussian model, Bernoulli model and Multinomial model. The Gaussian model is suitable for a continuous data. While the Bernoulli model is suitable for Boolean and discrete data. Similarly, the multinomial model is preferred for discrete data. Naive Bayes algorithm is used in Real-time predictions of diagnosis of diseases and decision making about the treatment process etc. Performance of the Naive Bayes models depend on the techniques applied and the appropriate selection of good features. [1]. Naive Bayes has few limitations due to its Naive assumption and the problem of Zero Conditional probability. Adding more dependency among the attributes can overcome the problem of the conditional independence and applying the technique of Laplace smoothing can solve the zero conditional probability problem [2]. In addition to what has been referred in the previous context, there are several other factors that

978-1-6654-8076-5/22/31.002022$IEEE$

Authorized licensed use limited to: DELHI TECHNICAL UNIV. Downloaded on January 12,2023 at 07:05:20 UTC from IEEE Xplore. Restrictions apply.

can improve the performance of the Naive Bayes model such as Distribution entropy, completely independent features and functionally dependent features [3]. The following sections will discuss in detail about the Related work, Methodology, Algorithm, Performance Evaluation, outcome of the experiment, Problem Formulation, Conclusion and Future Scope.

II. Related Work

This section will highlight the experimental work and findings of earlier research on Naive Bayes Classifier. TABLE I summarizes the experimental study carried out on the different types of Naive Bayes model.

TABLE I
SUMMARY TABLE

Classifier	Experimental work		
	Model	***Vocabulary size***	***Result***
Linear	Multinomial, Bernoulli	Large	Multinomial outperforms Bernoulli [1]
	Multinomial with Map Reduce	Large	Obtained good impact on model performance, good scalability and extensibility, better accuracy[5]
	Gaussian with Information Entropy measure	Small	On adding more data, the accuracy of the model is significantly improved. Information entropy ensures the performance classifier [7]
	Multinomial with Dirichlet hyper-parameters	Large	There is no change in the result on Combining the Multinomial Naive Bayes Classifier with suitable Dirichlet hyper-parameters. [8]
	Multinomial with TF-IDF	Large	Observed improved in accuracy of 89%.[9]
	Multinomial, Bernoulli	Medium	Accuracy of 73.404% is obtained. Multinomial model shows better predictor [10]

A. Literature Review

A study conducted by Irina Rish (2014) concludes that a good result can be obtained with a low entropy feature distribution, features that are fully and functionally dependent. She also concluded that there is no direct correlation between the classifier and the volume of feature dependency. The number of knowledge lost about the class could be a better predictor of the classifier due to the conditional assumption of the classifier. [3]. W. Zhang and F. Gao (2011) applied a traditional method to choose the auxiliary features. The datasets were obtained from CCERT, that contains two different classes, out of which the junk mails comprises of 45396 and the rest 18314 are normal. 30000 junk mails and 10000 normal mails are used for experimentation. They tried to enhance the performance of the Naive Bayes Classifier by adjusting the corresponding probability of the selected auxiliary feature. The experiment was conducted with three test cases on which they have observed the auxiliary features and feature representation. The experiment was carried out five times, with 10 fold cross validation using Naïve Bayes algorithm [6]. M. Baygin (2019) conducted an experiment by using the features of n-gram on a document in Turkish. The categorical data comprises of five different classes. Performance metrics such as Accuracy, Precision, Recall and F-measure were evaluated. The analysis achieved 92% success rate11. F. Peng and D. Schuurmans (2003) combined n-gram language model with the traditional model to overcome the challenges of the Naïve Bayes Classifier. The result of this newly proposed model outperformed the Tree augmented model. This was done by restricting the attribute dependency to form a chain like structure. They have also applied Smoothing technique to solve the zero probability issue which is a finer technique than the Laplace Smoothing [12]. J. Shah (2019) performed text classification on n-gram based word level data using a combination of multinomial model with hierarchical classifier. He also addressed the challenges that occurs at the top level and provides his suggestion to reduce the execution time in calculating the probability. [13]. S. George K and S. Joseph (2014) experimented the Unigram based model and proposed a new model to overcome the limitations of this model by incorporating the sequential features to the BOW. Their proposed model appears to be a good classifier. [14]. N. V M and D. A. Kumar R, (2019) carried out experiment on a categorical data such as anger, boredom etc which are based on emotions. This was done with the BOW model and a high score was achieved for the Neutral Sentiment, followed by happiness and anger. [15]. D. Yan, K. Li et al. (2020) collected words with high semantic value and a high level structure to enhance the existing Bag of Word model. This newly proposed model outperforms the existing model with high efficiency [16]. H. Zhou (2021) perform text classification using TF-IDF algorithm. Words are represented using word2vec and its weight is calculated by multiplying the word vector and its weight. He also addressed that the traditional text classifier ignores the value of the context-based semantics. His experimental results shows TF-IDF outperforms the traditional model. [17]. B. Das and S. Chakraborty (2018) applied a TF-IDF technique with Next Word Negation on three different datasets of a movie and product review by IMDB, Amazon and Spam detection dataset. The experiment was performed with a 10-fold cross validation and the results achieve a good score of accuracy for each datasets [18].

Authorized licensed use limited to: DELHI TECHNICAL UNIV. Downloaded on January 12,2023 at 07:05:20 UTC from IEEE Xplore. Restrictions apply.

B. Summary of Previous Related Research

As it can be seen on TABLE I, a literature review was carried out only for the linear classifiers of Naive Bayes model. With the help of the information provided in the table, it can be observed and concluded that multinomial and Bernoulli model works well with large datasets while the Gaussian model is used with smaller datasets. Multinomial model performs better than Bernoulli in more than one of the results obtained. A combination of Multinomial with MapReduce technique, Multinomial with Dirichlet hyper-parameters, Multi-nomial with TF-IDF, and Gaussian with Information Entropy measure has shown an improvement in the accuracy of the model. Therefore, it is our motivation to compare and analyze the performance of the three types of Naive Bayes model by employing the technique of TF-IDF using the knowledge of previous work done as listed in TABLE I.

III. Methodology

Fig. 1. Proposed Workflow

The purpose of this work is to analyze the classified tweets which are already in the structured format, predict the outcome of the unlabeled text using a predictive classifier called Naive Bayes and improve the existing state of the model in terms of accuracy. Due to time constraint and to avoid the tedious process of manual creation, the tweet classification was done automatically using an NLP cloud API which gives the polarity score of the input text, based on which the tweets annotation was done. After taking the approval of permission from Twitter Developers, the twitter data for experimentation was extracted with the help of an API using the keys and tokens generated on the author(s) account. The research was conducted using a Scientific method by applying alternative hypothesis to improve the accuracy of the model. The assumption was that application of TF-IDF technique by adding n-gram can enhance the accuracy of the existing model. To prove the hypothesis, a white box testing was carried out on unlabeled datasets using Gaussian, Bernoulli and Multinomial Naive Bayes combined with two feature extraction technique called Bag of Words and Term Frequency-Inverse Document Frequency. The experiment was carried out on Google Collab. On evaluating the performance of the model, it is found that Naive Bayes combined with TF-IDF augmented with n-gram outperforms the other model by 2-3%. This section will discuss in detail about the various stages involved in performing the proposed work. Fig 1 shows each stages of the work.

A. Data Collection and Data Tagging

The initial step for every NLP tasks is to gather unlabeled data from various sources, accompanied by importing the libraries necessary for performing the experimental work. The Data for this task is obtained through Twitter API. Since the data obtained is in unstructured format, we use NLP cloud API to categorize the data and transform it into a structured data.

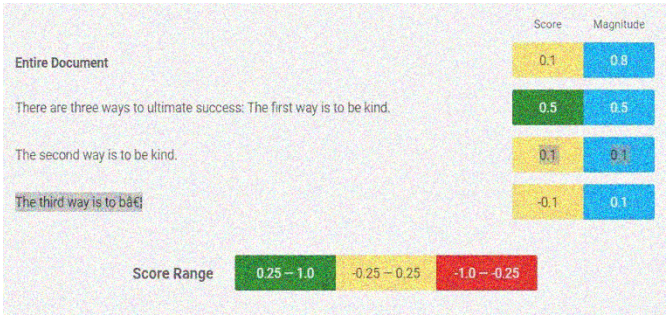

Fig. 2. Automatic Text Tagging

Fig 2 generates the polarity score of the given text. Counting is done by summing up the score of the entire document displayed in the figure and it comes out to be positive which is nearly 1. Therefore the statement is labelled as positive.

B. Import the Libraries and Python functions

The following list of libraries and functions in TABLE II are used for carrying out our experimental work.

C. Load the dataset

The raw dataset are loaded to the program for further processing. The dataset comprises of about 33086 tweet comments and 3 columns where the positive tweet comments are labelled as 0 and vice versa.

D. Data Exploration and Visualization

The training data can be visualised and explored using python library. All tweet comments in the dataset are first concatenated into one string before using the wordcloud library. By exploring and visualizing the data, we can find

Authorized licensed use limited to: DELHI TECHNICAL UNIV. Downloaded on January 12,2023 at 07:05:20 UTC from IEEE Xplore. Restrictions apply.

out the frequently occurring words in different classes. Let us dive deeper into these two terms.

TABLE II
IMPORTED PACKAGES AND LIBRARIES

S.no	*Library*	*Function*
1	Numpy	used to perform mathematical operations such as linear algebra, fourier transform, and matrices.
2	Pandas	used for the analysis of data
3	Seaborn	used for exploring and understanding the data
4	Matplotlib	used for data visualization and data plotting
5	Wordcloud	shows the frequency of importance of each word in the document
6	Nltk	a package for working with NLP task such as importing pre-defined stopwords etc
7	String	used to handle textual data
8	Stopwords	a corpus that contains the English words that doesn't add much value to meaning.
9	Scikit-learn	used when working with Machine Learning and statistical models
10	Countvectorizer	transforms a given text to vector and count the data
11	Tfidfvectorizer	Tokenize, count and normalizes the data
12	Confusionmatrix	Evaluates the model's accuracy

1) Data Exploration:

a) Count of Character and Word: These two terms are used to count the individual alphabets and chunk of the tokens without taking into account the white spaces.

b) Length of the Comment: The length of the comment can be explored such as the comment that has the highest, lowest and average word and character count.

c) Unique Word Count: This unique word count displays the number of the times this unique word occurs in the dataset in a tabular form. The dataset used in this work comprises of about 46684 unique word count.

2) Data Visualization: By visualizing the data, we can see the characteristics and details of the data. As it can be seen on Fig 3 the positive comments with label 0 comprises of around 29720 comments and 3366 Negative comments with label 1. Fig 3 shows the frequency distribution of the sequence of words in the dataset.

E. Pre-Processing the Data

Data needs to be pre-processed for smooth functioning and processing of the data. This stage involved several techniques such as:

1) Data Cleaning: It is crucial to remove trivial data for smooth and better processing of the data. Insignificant features from the raw dataset are first filtered out before actually feeding them to the model. In this work, we have performed the following:

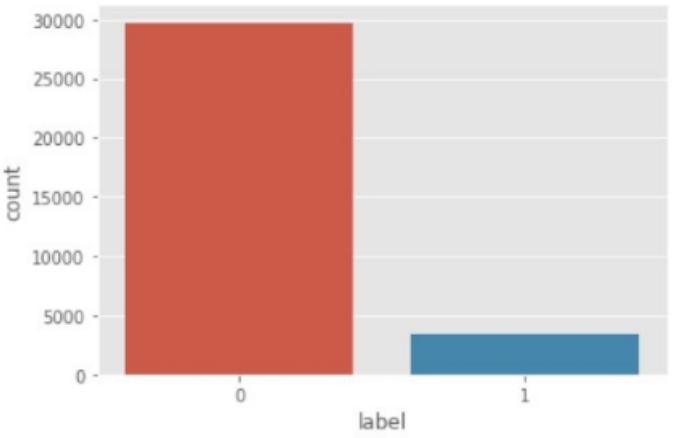

Fig. 3. Frequency distribution of classes

a) Removing of handle such as the symbol '@' in email.
b) Removing of punctuation such as '!', '.', ',' etc.
c) Removing of stopwords such as 'a', 'an', 'the' etc
d) Converting all uppercase data to lowercase.
e) Tokenizing the data.

2) Feature Extraction: This technique is applied to reduce the dimension of the data without losing any relevant data. It can help to yield better performance. The following describes the two techniques of feature extraction:

a) BagofWords: A vector representation of the textual data by creating a vocabulary set for the non-redundant words with its count. This model has two different counts which are Binary and Absolute count. The Binary count utilizes a one-hot encoding feature representation of the words which is either 1 or 0. While Absolute count is the count of the number of times the word occur in the dataset. Previous researchers prefer this technique [4].

b) TF-IDF: This technique is used as a feature representation of words in the dataset by a feature vector whose value is the frequency of that word in the comment. This technique is introduced to overcome the drawback observed in Bag of Words. TF-IDF considers the semantics of text and is preferred for text classification task. As mentioned in the previous context, it prioritize the semantics and contexts of words and evaluates the score of its relevance in the comment. Mathematically, it can be computed as:

$$TF = \frac{No.ofwordsrepeatedinadocument}{Totalno.ofwordinacomment}$$

$$IDF = \frac{logTotalno.ofcommentsinthedataset}{No.ofcommentscontainingthecorrespondingword}$$

$$\text{TF-IDF} = TF \times IDF$$

On performing computation with TF-IDF, it generates related Quantitative data which is determined by the closeness of the score of the corresponding words. The relevance of data is determined by its score. Every token have varying score in

Authorized licensed use limited to: DELHI TECHNICAL UNIV. Downloaded on January 12,2023 at 07:05:20 UTC from IEEE Xplore. Restrictions apply.

each comment based on the context. We have utilized this technique and combine it with n-gram to enhance our model's accuracy.

F. Model Building

The pre-processed data are then trained and tested on the three variants of Naive Bayes classifier. These classification models are:

1) Gaussian Naive Bayes: Gaussian model is a Naive Bayesian model that works with a continuous data. It follows a Normal distribution. Before training a large dataset on Gaussian Naive Bayes, the sparse data is required to be converted to dense data to generate a matrix representation. Thereafter, it is passed onto the classifier. The likelihood Gaussian is calculated as:

$$P\left(\frac{Wt}{Cn}\right) = \frac{1}{\sqrt{2\pi\sigma 2Cn}} e - \frac{(x-\mu Cn)^2}{2\sigma^2 Cn}$$

2) Bernoulli Naive Bayes: Bernoulli, also referred as Multivariate Bernoulli Naive Bayes is a probabilistic technique that works with discrete data. It utilizes binary count for feature representation. Boolean value is generated as its output. The likelihood and prior probability can be mathematically represented as: where n(Wt) is the occurrence of the word

$$P(\frac{Wt}{Cn}) = \frac{\Pi n(Wt)}{Ndn}$$

$$P(Cn) = log\left(\frac{N}{Nn}\right)$$

$$TF\text{-}IDF = P\left(\frac{Wt}{Cn}\right) * P(Cn)$$

count in a tweet comment, Ndn represents total number of words in a document of class 'n', Nn denotes count of comment that contains the corresponding word of class 'n' and N is the amount of comments in a dataset.

3) Multinomial Naive Bayes: Multinomial model is a probabilistic model that predicts the class of the unknown dataset by making use of the frequency of a specified word in the text document. This model is suitable for discrete data and utilizes the absolute count is used for feature representation. Unlike Bernoulli, the non occurrence of word in the dataset have no effect on the probability. The likelihood and its prior probability will be calculated as: where n(Wt) is the count of the occurrence of word in a tweet comment and n(Ws) is the total word count in a comment of class 'n', Nn represents the count of tweet comment that contains the corresponding word of class 'n' and N is the total number of training dataset. V represents the dimension of vocabulary.

$$P\left(\frac{Wt}{Cn}\right) = \frac{\Pi n(Wt)}{\sum_1^v \in \Pi n(Ws)}$$

$$P(Cn) = log\left(\frac{N}{Nn}\right)$$

$$TF\text{-}IDF = P\left(\frac{Wt}{Cn}\right) * P(Cn)$$

G. Training and Testing

A pre-defined library called train_test_split is used for training and testing our data and fit our data to it.

H. Performance Evaluation

Confusion matrix is used for evaluating the number of times the prediction model accurately and inaccurately generate the output and its type by feeding unlabeled datasets. There are four possible outcomes with this metrics.

1) True Postitive(TP): contains the correctly predicted unseen data as positive.

2) False Postitive(FP): contains the incorrectly classified value as positive.

3) False Negative(FN): contains the incorrectly classified values as negative.

4) True Negative(TN): contains the correctly predicted as an actual negative.

Let us look in detail the Performance metrics used.

5) Accuracy: measures the degree of closeness between the predicted value and true value.

$$Accuracy = \frac{TP + TN}{TP + TN + FP + FN}$$

6) Precision: measures the degree of closeness between the results.

$$Precision = \frac{TP}{TP + FP}$$

7) Recall: measures the number of the Actual Positives model captures

$$Recall = \frac{TP}{TP + FN}$$

8) F1-Score: measures the balance between Recall and Precision

$$F1 - Score = 2 * \frac{Precision * Recall}{Precision + Recall}$$

The value of precision and recall determines the number of relevant result. Therefore, we can conclude that higher the value of precision and recall, better is the result.

IV. Algorithm

Naive Bayes algorithm is a supervised machine learning algorithm and a linear probabilistic classifier derived from the Bayesian Network with an independent assumption among the features. Let us see the pseudo code for this Naive Bayes algorithm.

Authorized licensed use limited to: DELHI TECHNICAL UNIV. Downloaded on January 12,2023 at 07:05:20 UTC from IEEE Xplore. Restrictions apply.

A. Pseudo Code

a) Generate $|V|$ that contains the unique word.
b) Sum up the following variable count from the training dataset.
   Number of tweets, denoted by N
   Number of tweets annotated with class n for n=1,2.....n
   Number of tweets in class n, containing word wt for class n=1...n and t=1...$|v|$
c) Evaluate the likelihood probability P(Wt/Cn) for the three models.
d) Evaluate the prior probability P(Cn) for Bernoulli and Multinomial model.
e) For the Gaussian model, the class of new data is predicted by substituting the parameters with new values in the likelihood probability, whereas in the case of Bernoulli and Multinomial model, using BOW or TF-IDF technique, the class of the unseen data is decided by the higher posterior probability score.

V. Problem Formulation

(USE CASES OF DERIVED FORMULA)

1) Bernoulli Naive Bayes: Consider a dataset with a class tag of love (L) and hate (H). Given a training set of 11 comments, estimate the Naive Bayes Classifier using Bernoulli Document Model to predict the class of the new data.

Given: Class= love (L), hate (H)
Count of tweets in the dataset=11
Assuming a vocabulary set of 8 words:
$|V|$= {w1, w2, w3, w4, w5, w6, w7, w8}

TABLE III
VOCABULARY

|V|	Unique words
w1	adore
w2	pretty
w3	worthy
w4	punch
w5	elevate
w6	praise
w7	wonderful
w8	lovely

Out of the 11 tweets in the dataset, 6 of them belongs to the class love and 5 of them belongs to hate.

a) Matrix representation of the dataset for each class using Bag of Words model: Let the two classes be denoted as T^{love} and T^{hate}.

$$T^{love} = \begin{bmatrix} 1 & 0 & 0 & 0 & 1 & 1 & 1 & 1 \\ 0 & 0 & 1 & 0 & 1 & 1 & 0 & 0 \\ 0 & 1 & 0 & 1 & 0 & 1 & 1 & 0 \\ 1 & 0 & 0 & 1 & 0 & 1 & 0 & 1 \\ 1 & 0 & 0 & 0 & 1 & 0 & 1 & 1 \\ 0 & 0 & 1 & 0 & 0 & 0 & 1 & 1 \end{bmatrix}$$

$$T^{hate} = \begin{bmatrix} 0 & 1 & 1 & 0 & 0 & 0 & 1 & 0 \\ 1 & 1 & 0 & 1 & 0 & 0 & 1 & 1 \\ 0 & 1 & 1 & 0 & 0 & 1 & 0 & 0 \\ 0 & 0 & 0 & 0 & 0 & 0 & 0 & 0 \\ 0 & 0 & 1 & 0 & 1 & 0 & 1 & 0 \end{bmatrix}$$

b) Classify the new data (b1,b2) into two classes love, hate using Naive Bayes Classifier.: Given data, we have:
Total number of comments, N =11
Number of comments belonging to class set love, NL= 6
Number of comments belonging to class set hate NH=5
Estimating the prior probability of the two classes:

$$P(L) = \frac{6}{11}$$

$$P(H) = \frac{5}{11}$$

TABLE IV
LIKELIHOOD ESTIMATION

|V|	ηL(Wt)	$P\left(\frac{Wt}{L}\right)$	ηH(Wt)	$P\left(\frac{Wt}{H}\right)$
w1	3	0.5	1	0.2
w2	1	0.2	3	0.6
w3	2	0.3	3	0.6
w4	3	0.5	1	0.2
w5	3	0.5	1	0.2
w6	4	0.7	1	0.4
w7	4	0.7	3	0.6
w8	4	0.7	1	0.2

$$P\left(\frac{Wt}{Cn}\right) = \frac{\eta n(Wt)}{Ndn} \quad \textit{Equation 1}$$

$$P\left(\frac{Ck}{bn}\right) = P(K) * \prod_{t=1}^{|v|}\left[bn.t.P\left(\frac{Wt}{K}\right) + (1 - bnt)(1 - P\left(\frac{Wt}{K}\right))\right]$$

Equation 2

As we can refer from Table IV, the above equation 1 represents the ratio of the word count of comments and the total number of comments in each of the two classes.
In order to predict the class of the new dataset (b1, b2), we

Authorized licensed use limited to: DELHI TECHNICAL UNIV. Downloaded on January 12,2023 at 07:05:20 UTC from IEEE Xplore. Restrictions apply.

have the decision probability given by Equation 2, where n=1,2 and K=love, hate. The higher probability score among the two classes is the class of the new dataset.

c) Mathematical representation of Naive Bayes using TF-IDF: Mathematical representation of Naive Bayes with TF-IDF is given by equation 3 and 4.

$$P(Cn) = log\left(\frac{N}{Nn}\right) \qquad Equation\ 3$$

$$TF\text{-}IDF = P\left(\frac{Wt}{Cn}\right) * P(Cn) \quad Equation\ 4$$

2) Multinomial Naive Bayes: Similarly for Multinomial Naive Bayes, we can predict the class of the new dataset. The only difference is the matrix representation of the training data. In case of Bernoulli, we use one hot encoding to represent the comment. In the case of Multinomial, we took the frequency of the unique word count to represent the comments.

For example: Given a vocabulary of 8 word set, we have $|V|$ = {w1, w2, w3, w4, w5, w6, w7, w8}

$$T^{love} = \begin{bmatrix} 2 & 0 & 0 & 0 & 1 & 2 & 3 & 1 \\ 0 & 0 & 1 & 0 & 2 & 1 & 0 & 0 \\ 0 & 1 & 0 & 1 & 0 & 2 & 1 & 0 \\ 1 & 0 & 0 & 2 & 0 & 1 & 0 & 1 \\ 2 & 0 & 0 & 0 & 1 & 0 & 1 & 3 \\ 0 & 0 & 1 & 2 & 0 & 0 & 2 & 1 \end{bmatrix}$$

$$T^{hate} = \begin{bmatrix} 0 & 1 & 1 & 0 & 0 & 0 & 1 & 0 \\ 1 & 2 & 0 & 1 & 0 & 0 & 1 & 1 \\ 0 & 1 & 1 & 0 & 0 & 2 & 0 & 0 \\ 0 & 0 & 0 & 0 & 0 & 0 & 0 & 0 \\ 0 & 0 & 1 & 0 & 1 & 0 & 1 & 0 \end{bmatrix}$$

On calculating the likelihood probability for each word in both the classes using Equation 5, we create a frequency table that contains the maximum score of the class.

TABLE V
FREQUENCY TABLE

V	T_1	T_2	T_3	T_4	T_5	T_6
W_1	$0.4_{(L)}$	$0.2_{(H)}$	0	$0.3_{(L)}$	$0.5_{(L)}$	0
W_2	$0.3_{(H)}$	$0.4_{(H)}$	$0.3_{(H)}$	0	0	0
W_3	$0.3_{(H)}$	$0.3_{(L)}$	$0.3_{(H)}$	0	$0.3_{(H)}$	$0.3_{(L)}$
W_4	0	$0.2_{(H)}$	$0.5_{(L)}$	$0.5_{(L)}$	0	$0.5_{(L)}$
W_5	$0.2_{(L)}$	$0.6_{(L)}$	0	0	$0.3_{(H)}$	0
W_6	$0.4_{(L)}$	$0.3_{(L)}$	$0.6_{(H)}$	$0.3_{(L)}$	0	0
W_7	$0.6_{(L)}$	$0.2_{(H)}$	$0.3_{(L)}$	0	$0.3_{(H)}$	$0.5_{(L)}$
W_8	$0.2_{(L)}$	$0.2_{(H)}$	0	$0.3_{(L)}$	$0.8_{(L)}$	$0.3_{(L)}$

$$P\left(\frac{Wt}{Cn}\right) = \frac{\Pi n(Wt)}{\sum_{1}^{V} \in \Pi n(Ws)} \quad Equation\ 5$$

$$P(Cn) = log\left(\frac{N}{Nn}\right) \quad Equation\ 6$$

Using Equation 6, we calculate the IDF value for both the classes and noted down the maximum score along with its label of the class. Let us look at the following TABLE VI that gives us the Stack of words after normalization.

TABLE VI
STACK OF WORDS

V	IDF	T_1	T_2	T_3	T_4	T_5	T_6
W_1	$0.69_{(L)}$	$0.4_{(L)}$	$0.2_{(H)}$	0	$0.3_{(L)}$	$0.5_{(L)}$	0
W_2	$1.79_{(L)}$	$0.3_{(H)}$	$0.4_{(H)}$	$0.3_{(H)}$	0	0	0
W_3	$1.10_{(L)}$	$0.3_{(H)}$	$0.3_{(L)}$	$0.3_{(H)}$	0	$0.3_{(H)}$	$0.3_{(L)}$
W_4	$0.69_{(L)}$	0	$0.2_{(H)}$	$0.5_{(L)}$	$0.5_{(L)}$	0	$0.5_{(L)}$
W_5	$0.69_{(L)}$	$0.2_{(L)}$	$0.6_{(L)}$	0	0	$0.3_{(H)}$	0
W_6	$1.61_{(H)}$	$0.4_{(L)}$	$0.3_{(L)}$	$0.6_{(H)}$	$0.3_{(L)}$	0	0
W_7	$0.51_{(H)}$	$0.6_{(L)}$	$0.3_{(L)}$	$0.3_{(L)}$	0	$0.3_{(H)}$	$0.5_{(L)}$
W_8	$1.61_{(H)}$	$0.2_{(L)}$	$0.2_{(H)}$	0	$0.3_{(L)}$	$0.8_{(L)}$	$0.3_{(L)}$

TABLE VII
TF-IDF

Tweets	W1	W2	W3	W4	W5	W6	W7	W8
T_1	0.3	0.5	0.3	0	0.1	0.6	0.3	0.3
T_2	0.1	0.7	0.3	0.1	0.4	0.2	0.2	0.3
T_3	0	0.5	0.3	0.3	0	0.1	0.2	0
T_4	0.1	0	0	0.3	0	0.5	0	0.5
T_5	0.3	0	0.3	0	0.2	0	0.2	1.3
T_6	0	0	0.3	0.3	0	0	0.3	0.5

The above Table VII displays the result of TF-IDF which is obtained from the product of TF and IDF. On analysis, all the example tweets fall into the category of *'L'*. As it can be seen from the table, it not only gives detail about the sentiment, it also gives information about the importance of the word in the tweet that helps us to find out the intent of the text.

Authorized licensed use limited to: DELHI TECHNICAL UNIV. Downloaded on January 12,2023 at 07:05:20 UTC from IEEE Xplore. Restrictions apply.

Fig. 4. Confusion Matrix

VI. Experimental Result

Fig 4 displays the generated result of the Naive Bayes model evaluation using Confusion matrix. On experimenting with large dataset of about 33086, the test case failed for the Gaussian model. Nevertheless, this model can work with smaller data. On evaluating the model with smaller data of around 1166 tweet comments, this model gives a really low accuracy below 50

TABLE VIII
RESULT

Feature Extraction	Model	Performance Metrics				
		Accuracy	Precision	Recall	F1-Score	Support
Bag of Words	*Gaussian*	✗	✗	✗	✗	✗
	Bernoulli	89.9%	95%	100%	90%	5950
	Multinomial	90.2%	95%	100%	90%	5950
TF-IDF with n-gram	*Gaussian*	✗	✗	✗	✗	✗
	Bernoulli	92%	96%	100%	93%	5943
	Multinomial	93%	97%	100%	93%	5943

TABLE VIII displays the best scores obtained after 6 iterations. The data from the table shows that the new model with TD-IDF and n-gram performs better than the existing model. As per the observation from the table, our proposed model can predict 92% and 93% of the positive comments for each classifiers accurately, but performs badly in predicting the negative comments. Our experiment is carried out on an imbalanced dataset which consist of maximum number of positive class label dataset. Therefore, the model is able to accurately predict more number of the positive comments. The table also has a record for different performance metrics such as precision, recall and F1 scores. From the classification report similar results are obtained. The result generated by F1- score shows that the classifier can accurately classify the positive comments, but score is quiet low for classifying the negative comments. This issue can be rectified by upsampling the amount of negative comments in the data or also by using a different classifier.

VII. Evaluation of Model

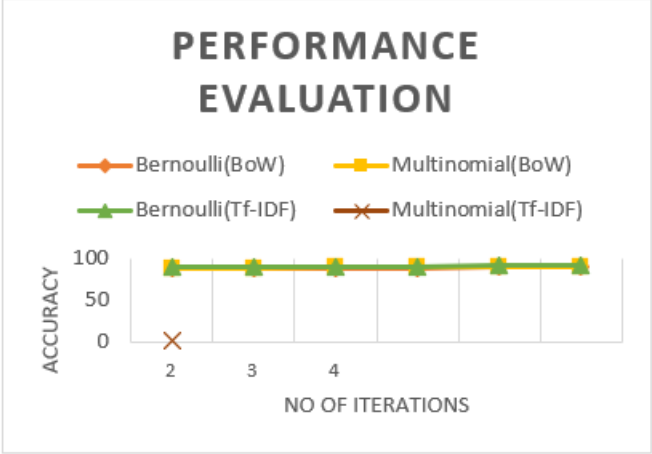

Fig. 5. Performance Evaluation

As we can see it from the above Fig 5, that after 6 number of iterations, the accuracy of Multinomial and Binomial with TF-IDF model dominates the other two.

VIII. Conclusion and Future Work

This paper performs a scientific research on predicting the class of unannotated tweets using Naive Bayes Classifier and the purpose of the study is to improve the accuracy of the model by testing our hypothesis. Initially, we extract the unstructured data from twitter using an API, which is then structured with the help of NLP cloud API to avoid the tedious process of manual text classification. Text Classification is important to improve the performance of an individual, business and organisation. The experiment was performed on Google Collab with 33086 tweets that contains both positive and negative classes annotated as 0 and 1 respectively. The existing technique make use of Bag of Words feature extraction which takes into account only the unique words that occurred in the training data. On analysis, it is observed that the significance of semantics is completely ignored due to its independent

Authorized licensed use limited to: DELHI TECHNICAL UNIV. Downloaded on January 12,2023 at 07:05:20 UTC from IEEE Xplore. Restrictions apply.

assumption of the features. This limitation is eradicated by employing TF-IDF technique with n-gram that takes into account the sequence of words. On doing so, the model now have the ability to understand the semantics of words. TF-IDF also provides information about the degree of the importance of words (refer Table VII) that helps in determining the intent of the textual data. Moreover, on evaluating the accuracy of the model, it is found that the improved model performs better than the existing model by 2-3 %. As provided in Table VIII, the test was conducted on different types of Naive Bayes model using two different feature extraction technique where the test case failed for Gaussian model as it cannot work with large dataset, while Bernoulli and Multinomial model shows an improvement in its accuracy with the new technique. It can also be inferred from the same table that Multinomial model outperforms Bernoulli by 1%. Finally, with all these evidence and justification, we can conclude that the performance of Naive Bayes can be enhanced by combining TF-IDF with n-gram model. Furthermore, it is expected that incrementing the volume of data and exploring more characteristics may contribute towards achieving a better accuracy. Future work is to examine the performance of the model with more Machine Learning algorithms, balanced dataset, identify Non Linear classifiers and compare it with Linear Classifiers.

ACKNOWLEDGMENT

This paper would not have been possible without the permission of twitter developers. Therefore, we would like to acknowledge our thanks to twitter for allowing us to extract the data required for performing this research.

DISCLOSURE AND CONFLICTS OF INTEREST

The author(s) declare(s) that there is no conflict of interest.

REFERENCES

[1] S. Raschka, "Naive Bayes and Text Classification I - Introduction and Theory," pp. 1–20, 2014.

[2] P. Kaviani and S. Dhotre, "International Journal of Advance Engineering and Research Short Survey on Naive Bayes Algorithm," Int. J. Adv. Eng. Res. Dev., vol. 4, no. 11, pp. 607–611, 2017.

[3] I. Rish, "An Empirical Study of the Naïve Bayes Classifier An empirical study of the naive Bayes classifier," Cc.Gatech.Edu, no. January 2001, pp. 41–46, 2014.

[4] G. Sanguinetti, "Text Classification using Naive Bayes = Learning only =," no. February, 2012.

[5] H. Chen and D. Fu, "An Improved Naive Bayes Classifier for Large Scale Text," vol.146, no. Icaita, pp. 33–36, 2018, doi: 10.2991/icaita-18.2018.9.

[6] W. Zhang and F. Gao, "An improvement to naive bayes for text classification," Procedia Eng., vol. 15, pp. 2160–2164, 2011, doi: 10.1016/j.proeng.2011.08.404.

[7] Z. Bi, Y. Han, C. Huang, and M. Wang, "Gaussian Naive Bayesian Data Classification Model Based on Clustering Algorithm," vol. 168, no. Masta, pp. 396–400, 2019, doi: 10.2991/masta-19.2019.67.

[8] S. Xu, Y. Li, and Z. Wang, "Bayesian multinomial naïve bayes classifier to text classification," Lect. Notes Electr. Eng., vol. 448, no. May, pp. 347–352, 2017, doi: 10.1007/978-981-10-5041-1-57.

[9] M. Abbas, K. Ali, A. Jamali, K. Ali Memon, and A. Aleem Jamali, "Multinomial Naive Bayes Classification Model for Sentiment Analysis," IJCSNS Int. J. Comput. Sci. Netw. Secur., vol. 19, no. 3, p. 62, 2019, doi: 10.13140/RG.2.2.30021.40169.

[10] G. Singh, B. Kumar, L. Gaur, and A. Tyagi, "Comparison between Multinomial and Bernoulli Naïve Bayes for Text Classification," 2019 Int. Conf. Autom. Comput. Technol. Manag. ICACTM 2019, no. May 2020, pp. 593–596, 2019, doi: 10.1109/ICACTM.2019.8776800.

[11] M. Baygin, "Classification of Text Documents based on Naive Bayes using N-Gram Features," 2018 Int. Conf. Artif. Intell. Data Process. IDAP 2018, no. 1, p. 940, 2019, doi: 10.1109/IDAP.2018.8620853.

[12] F. Peng and D. Schuurmans, "Combining naive Bayes and n-gram language models for text classification," Lect. Notes Comput. Sci. (including Subser. Lect. Notes Artif. Intell. Lect. Notes Bioinformatics), vol. 2633, pp. 335–350, 2003, doi: 10.1007/3-540-36618-0-24.

[13] J. Shah, "Performance evaluation of applying n-gram based naïve bayes classifier for hierarchical classification," Proc. 3rd Int. Conf. Comput. Methodol. Commun. ICCMC 2019, no. Iccmc, pp. 92–98, 2019, doi: 10.1109/ICCMC.2019.8819751.

[14] S. George K and S. Joseph, "Text Classification by Augmenting Bag of Words (BOW) Representation with Co-occurrence Feature," IOSR J. Comput. Eng., vol. 16, no. 1, pp. 34–38, 2014, doi: 10.9790/0661-16153438.

[15] N. V M and D. A. Kumar R, "Implementation on Text Classification Using Bag of Words Model," SSRN Electron. J., no. May, pp. 241–248, 2019, doi: 10.2139/ssrn.3507923.

[16] D. Yan, K. Li, S. Gu, and L. Yang, "Network-Based Bag-of-Words Model for Text Classification," IEEE Access, vol. 8, pp. 82641–82652, 2020, doi: 10.1109/ACCESS.2020.2991074.

[17] H. Zhou, "Research of Text Classification Based on TF-IDF and CNN-LSTM," J. Phys. Conf. Ser., vol. 2171, no. 1, pp. 218–222, 2022, doi: 10.1088/1742-6596/2171/1/012021

[18] B.Das and S.Chakraborty, "An Improved Text Sentiment Classification Model using TF-IDF and Next Word Negation," 2018.

Authorized licensed use limited to: DELHI TECHNICAL UNIV. Downloaded on January 12,2023 at 07:05:20 UTC from IEEE Xplore. Restrictions apply.

CERN IdeaSquare Journal of Experimental Innovation, 2022; X(X): X-X
DOI: https://doi.org/10.23726/cij.2022.1387

ARTICLE IN PRESS

Comparing differences of trust, collaboration and communication between human-human vs human-bot teams: an experimental study

Ruchika Jain[1], Naval Garg[1], Shikha N. Khera[1]

[1]Delhi Technological University, Bawana Rd, Delhi Technological University, Shahbad Daulatpur Village, Rohini, New Delhi, Delhi 110042
Corresponding author: ruchika2083@gmail.com

ABSTRACT

As machines enter the workplace, organizations work toward building their collaboration with humans. There is a limited understanding in litearture of how human-machine collaboration differs from human-human collaboration. Using an experimental design the study aimed at studying differences in trust, collaboration and communication between the two teams: humans and bot and humans-only teams. Due to limited availability of bots that express collaboration this set up was chosen. The findings highlight the differences in communication and collaboration between humans and bots as teammates. There were no differences in trust experienced by humans. The originality of the research is that it focuses on collaboration as a process and outcome rather than the team's performance.

*Keywords**:** Human-bot; trust; collaboration; communication.*

Received: September 2022; Accepted: November 2022

INTRODUCTION

Today, machines loaded with intelligence (artificial intelligence, machine learning, etc.) emulate the ability to think, reason, learn, and perform tasks like humans (Russell & Norvig, 1995; Grosz & Stone, 2018). Various fields rely on the guidance of these machines to make crucial decisions, like selecting job applicants for job postings (Von Krogh, 2018), health care (Yu et al., 2018), and judicial and law (Nissan, 2017) to name a few examples. Machine's inputs collaborate with human inputs to make decisions that exceed either capabilities (Wang et al., 2016; Kamar, 2016). This collaborative structure enables curated intelligence for higher efficiency (Malone, 2018; Wilson & Daugherty, 2018).

Today, machines significantly contribute in managing organizations (Daugherty et al., 2019; De Cremer, 2020), thus forcing management to relook at their design and explore forms of collaboration with humans (George et al., 2020).The most commonly used form of machine with intelligence is a bot. They can be found in many organizations and personal setups.

When humans and machines collaborate, several team-like structures emerge where machines function as independent members (Appenzeller, 2017; Shrestha et al., 2019; Lee et al., 2012; Demir et al., 2015). The machine contributes to group tasks by producing actions and coordinating activities through communication, developing trust, and commitment (Harbers et al., 2014).

This collaboration between humans and machines can lead to new emerging behaviours with mixed-initiative (Bansal et al., 2019; Puranam, 2021). Even with the growing interest in human-machine collaboration, there is still much to learn about them as teammates (Seeber et al., 2020). Previously, the human-machine team was primarily studied for the overall performance of the team, where humans would typically have a supervisory role and technology would have a low-level capacity (Guzman & Lewis, 2020). The presence of a machine as a teammate could influence the dynamics, thereby impacting the performance of the team (Guzman & Lewis, 2020; Demir et al., 2020; Fiore & Wiltshire, 2016).

Understanding the influence on trust, and communication of human and machines while collaborating can be helpful in designing future human-machine teams. The previous work was primarily in computer science, with only minor contributions from management and social science (Glikson & Wolley, 2020). There is a need for an interdisciplinary, human-centric approach that considers the needs of human perception and behavioural response to social and relational aspects of this team (Shank et al., 2019).

The present study aims at exploring differences in human-team behaviour to human-bot teams. It intends to explore if the human-human team interaction is similar to that of the human-bot team. An experimental design was used to understand the influence of teammates being

2413-9505 / © The author/s, 2022
Published by CERN under the Creative Common Attribution 4.0 Licence (CC BY 4.0)

a bot or human on trust, collaboration, and communication. This research will aid in understanding the role of communication and trust in collaboration teams, which will aid in the design of future human-machine teams (Seeber, 2020; Walliser et al., 2019).

THEORETICAL BACKGROUND

As we move away from the human vs machines debate, this synergy has "Intelligence augmented", where the intelligences of both are put together for effective decisions (Malone, 2018; Jarrahi, 2018; De Cremer, 2020). Studies suggest that several factors can influence human-machine collaboration, and it cannot be categorized as all or none (Brandstetter et al., 2014; Shiomi & Hagista, 2013). Researchers in the field of computer science within the laboratory setup have drawn comparisons between human and human-machine teams to better understand this collaboration and highlighted the differences in collaboration and coordination (Demir et al., 2018; Walliser et al., 2019; Hertz et al., 2019). Spence et al. (2014) have shared that the knowledge of interaction with a bot influences the perception of humans. Even before interacting with the bot, they discovered a decreased liking and increased uncertainty. This influence is not limited to interaction but also impacts team behaviour and outcome, where both collaborate as teammates (Demir et al., 2018). Humans demonstrated to experience challenges in planning their activities and anticipating their teammates' needs when partnering with machines (Demir et al., 2018). The perceived expertise of the machine influences the usage of the machine and thus impacts collaboration (Zhang et al., 2021).

For collaboration to succeed, trust also plays a critical role in human-technology adoption (Przegalinska et al., 2019; Glikson & Wolley, 2020). Using the machine's inputs is evidence of trust in them (Madhavan & Wiegmann, 2007; Lee et al., 2013). In many lab-based studies, humans highly trust machines that provide decisions (Demier et al., 2020; Dietvorst et al., 2015). It is critical to emphasize that there is a greater tendency in many situations to over-rely on machines and become complacent in their advice, a phenomenon known as automation bias (Goddard et al., 2012; Parasuraman & Manzey, 2010). Recent works show that with increased exposure to new forms of technology, anthropomorphic differences bring no changes in trust and in how humans treat machines as social actors (Alarcon et al., 2021). Xie et al. (2019) highlighted that trust in machines could not be calibrated alone, as human needs (and use) are multi-faceted across different contexts. As a result, there is a significant need to understand human-machine interactions in terms of how people trust, use, and interpret their advice (Prahl & Swol, 2017).

Studies in human-computer interaction and human-robot interaction share evidence of decreased interaction (Lee & Liang, 2015). Researchers have highlighted these differences due to the interactive strategies adopted with partnering with machines (Amalberti et al., 1993; Shechtman & Horowitz, 2003; Demir et al., 2019; Walliser et al., 2019). This reduced interaction could be due to lower perceived attractiveness toward the machine (Spence et al., 2014). In addition, there is an impact on humans' social behaviour when interacting with other humans (Spence et al., 2019). Humans tend to focus more on building social relationships with human teammates (Shechtman & Horowitz, 2003). When teammates are machines, there is less focus on sharing information, with a lowered expectation of contribution from the teammate (Demir et al., 2018). Rich interaction between team members is critical for outcomes that lead to collaboration (Chen & Barnes, 2014). Mou and Xu (2017) highlighted that when interacting with machines, humans are less open, more agreeable, and experience greater anxiety (Mou & Xu, 2017).

Research question 1: *How is level of trust experienced in human-human collaboration in comparison to human-machine collaboration?*

Research question 2: *How does human-human collaboration differ from human-machine collaboration?*

Research question 3: *How does communication in human-human collaboration differ from human-machine collaboration?*

METHODS AND DATA

Study participants

The sample comprised students registered with the Delhi Technological University, New Delhi, India. There were 120 participants in the experiment who were randomly assigned to the two experimental teams. The participants included 58 females (48.3%) and 62 males (51.6%). The participants' age ranged from 18 to 30 years, with a mean of 21.1 (SD=2.46). Participants received attendance credit for taking part in the study. There were 56 (46.6%) students from undergraduate programs, 48 (40%) from postgraduate programs, and 16 (13.3%) from PhD programs.

Procedure

Study Design

An experimental design was used in the study, where two teams were created namely condition 1 and condition 2. After the participants consented, they were randomly assigned to condition 1 or 2. In each condition, there were two members. The two members were not aware of who the other participant was. In condition 1,

both team members were informed that they were collaborating with another human. In condition 2, they were informed that they collaborated with a machine (bot). In either of the conditions, they were interacting with a human. In condition 2, the participants were also told that the bot used in the study was not designed to respond to irrelevant questions and could only accept input concerning an ongoing task. The particular setup was chosen due to the limited availability of bots that can demonstrate collaboration skills. Also, the presence of another human would make the interaction more human-like than scripted. Also the study was a pilot setup for further exploration of humans and machines.

To interact with team members, the online collaborative platform Slack (https://slack.com/intl/en-in/) was used. The pair was studied as a team, as they shared a goal and would work towards achieving it. A channel was created in which different identities of User 1 (team member 1), User 2 (team member 2), and the experimenter were created. There were other terminals for Users 1, 2, and the experimenter, and they operated from separate rooms. The task required the team to collaborate and label the images after reaching a consensus. Three images (Appendix B), psychological illusions, were selected. The images selected were chosen as they created ambiguity, and there would be more than one response to each image. The task also did not require any pre-set skills, so neither humans nor a perceived machine could be considered experts in performing the task.

As the participants were at the terminal, the experimenter shared the individual instructions in each condition. After viewing each image, a conversation ensued in the chat, where the goal was to reach a consensus based on the discussion. Once they finalized the label, the experimenter shared the following image. After labeling the three images, the participants were asked to complete a post-task questionnaire. The post-task questionnaire included two sections –demographics and measures of team behaviour. The post-task questionnaire was collected on google docs. Post the experiment, the participants were informed that they were interacting with another human than a bot.

Tools and Data Analysis

Trust

An adapted version of Merritt's trust scale (Merritt, 2011) was used to measure trust between team members. There were 6 items on the trust scale (e.g., "*I have faith in what my teammate is telling me*") at a 5-point Likert scale (1 = strongly disagree and 5 = strongly agree). The Cronbach's alpha for the trust scale was 0.723. None of the teams were reverse-scored. The higher trust refered to higher trust with the machines.

Collaboration

The interaction between human-human and the human-bot was studied using the process and the decision made by the teams. The interaction between the members was studied. If the final response chosen included the participation of both teammates and was different from their initial proposition, the outcome was considered a collaborative outcome. Collaborative outcomes were coded as 2. When either of the partners agreed to the proposition of the other without discussion or deliberation, it was a non-collaborative outcome. Such conditions were coded as 1. To reduce subjectivity, three different coders were used to code each outcome. The majority of code for a given image was the accepted code.

Communication

All the messages shared during the task were recorded. The communication between team members was studied using the duration of the interaction and the number of words used in the interaction (Hill et al., 2015; Lortie & Guitton, 2011). Further, the content of the messages was reviewed, and all the pre-task and irrelevant messages were filtered out. The task-related discussion in the team was categorized into three groups: rapport building (acknowledgement, greeting, and understanding of the problem), task-based discussion (idea generation and discussion for building on ideas and suggestions), and clarification seeking (opposition and asking for rational ideas). The coding and categorization of the message were done with three different coders. The message that received the maximum vote was included in that category.

Control Variables

To ensure the effectiveness of the manipulation, some variables were controlled.

Past experience with technology

The participants checked if they had experienced or used chatbots in the past. The variable was assessed using a single item, "*Have you in the past used a chatbot?*" The response to the item was recorded in a yes or no response.

Satisfaction

The participants' satisfaction with being part of the team was assessed. An adapted version of Bushe and Coetzer's (1995) scale for satisfaction with membership was used. There are 3 items on the scale (being a team member was a positive experience). The Cronbach alpha for the scale was 0.83.

Interacting with a bot

To assess if the participants believed that they interacted with the bot in the experimental group, participants were asked a single item ("*Did you believe that you were interacting with a bot?*"). The response to the item was recorded as yes or no.

RESULTS AND DATA ANALYSIS

Using SPSS, independent sample t-tests were conducted to evaluate the difference in collaboration between the participants in the experimental (human-bot team) and the control group (human-only team).

Research question 1 assessed the differences in the level of trust experienced by the teams. There was no significant difference in the two dimensions of the two groups. The t-test was not statistically significant for trust (t= 1.012, p=.315, d=.21).

Research question 2 assessed the differences in the level of collaboration experienced by the teams. There was a significant difference between the two teams. The t-test was statistically significant for collaboration (t= 1.72, p=.044, d=.36), as presented in Table 1 (see Appendix A).

Research question 3 measured the differences in communication between the two teams. The t-test was statistically significant for the duration of the interaction (t=2.20, p=.031, d=.49) (Table 2, see Appendix A) and words exchanged (t=2.413, p=.018, d=.53) (Table 2, see Appendix A) between the members. Further, the messages were analyzed, and we found a statistical difference in rapport building (t=2.35, p=.021, d=.52) and clarification seeking (t=2.52. p=.045, d=.35). There were statistically more messages exchanged in the human-human team than in the human-machine team. The members focused more on rapport-building and clarification-seeking in the human teams as they completed the collaborative task. There were no statistical differences in the number of messages exchanged between the two teams regarding task-related discussion (t= .942, p=.231, d=.18). The results are presented in Table 2 (Appendix A). Some examples of rapport-building tasks included ("*Let's get this done*!"; '*so we have to label together. the pics*') and clarification seeking ("*I don't see an old man in the pic, where do you see it?*"; "*I don't think there is any young couple in the pic*").

DISCUSSION

The study seeks to understand team differences between humans and bots. The results found greater collaboration exhibited in human teams with increased communication and usage of words and greater duration of interaction with the team member. The communication emphasized rapport building and clarification seeking in the human team. There was no significant difference in team behaviour with respect to trust. The findings are in agreement with past studies highlighting the difference between human-machine teams and human-human teams (Demir et al., 2019; Spence et al., 2019).

The first research question assessed the difference in trust experienced by humans in different teams. The result found no differences in the level of trust experience. The findings are supported by media equation studies (Nass & Moon, 2000; Reeves & Nass, 1996), which propose machines are seen as social actors and humans share the same level of social responsiveness to them in team setups (Groom and Nass, 2008). Furthermore, Edwards et al. (2016) and Spence et al. (2019) have shared similar results with bots where there were no perceived differences in the credibility of the machine. Thus humans do consider machines a credible source to partner with in decision making tasks.

The second research question looked at the differences in the collaborative outcomes of the two teams. Collaboration was considered when there was participation by both team members, and over time they mutually agreed on a decision different from their initial proposed decision. The result found more collaboration with human partners than with bots. In tasks of high uncertainty, where humans cannot claim expertise, decision moves in the direction of the machine, as they are presumed to have the expertise (Elson et al., 2018), as seen in the human-bot team. Shaikh and Cruz (2019) highlighted how machines reduce collaboration and interaction in teams, especially when there is a time restriction.

The third research question compared the differences in communication between the two teams. The communication pattern was assessed with the duration of interaction and the number of words used. The result found a significant difference in the usage of words and duration of interaction between the two teams. There was less interaction in the human-machine team than in the human team. The subcategories of communication were analyzed on rapport building, task-related discussion, and clarification seeking. There was a significant difference in communication for rapport building and clarification seeking. Studies on human-computer interaction or human-robot interaction also share evidence of decreased interaction (Lee & Liang, 2015). There is evidence of greater identification with the human partner than with a machine (Pena et al., 2017; Shechtman & Horowitz, 2003). Research in linguistics has shown shorter messages and differences in content and vocabulary when interacting with machines (Hill et al., 2015).

For human and machine collaboration, there is a need for a scientific understanding of the most effective way humans and machines can come together as teammates (Sebeer, 2020). In fact, there are differences in collaboration and applying the principles of human-human interaction to human-bot can not be effective. The results show that humans consider machines credible information sources and readily collaborate with them to complete the task. However, it is critical to note that this collaboration can impact on the team's communication and performance. Therefore, the communication and

interactive interfaces between humans and machines should be cautiously designed.

LIMITATIONS AND FUTURE DIRECTIONS

There are some limitations in the present study. The study was carried out in a laboratory setting with a small sample and thus has limited generalizability. To propose a machine and human collaboration it would be great if the IdeaSquare lab at CERN could run such experiments on large samples with significant variability in the sample with respect to age, education, and gender to help understand how collaboration can work with larger masses.

It would be interesting to see how this collaboration plays out in terms of the actual development of a bot capable of assisting with decision-making tasks. Also, studies involving higher stakes regarding rewards or penalties for performance on the task should be carried out, as high stakes can influence the pattern of interaction and the dynamics of collaboration. Studies exploring a focused, goal-directed task that demands collaboration between humans and machines independent of their capability would help understand the social cues segregating the human-machine team from the human-human team.

CONCLUSIONS

This study aimed to compare the human-bot teams to the human-human teams as they collaborate. The findings highlighted the acceptance of bots as teammates but cautioned about some differences in this collaboration. The perception of collaborating with a bot influences human behavior. There are differences in communication and collaboration in human-bot teams as they engage in a task, with reduced interaction between members, leading to greater conformity to the machine's suggestion. The present study is a small step in understanding human-bot collaboration as we adopt machines in different decision-making setups

REFERENCES

Amalberti, R., Carbonell, N., & Falzon, P., 1993, User representations of computer systems in human-computer speech interaction. International Journal of Man-Machine Studies, 38(4): 547–566. https://doi.org/10.1006/imms.1993.1026

Alarcon, G. M., Gibson, A. M., Jessup, S. A., & Capiola, A., 2021, Exploring the differential effects of trust violations in human-human and human-robot interactions. Applied Ergonomics, 93, 103350. https://doi.org/10.1016/j.apergo.2020.103350

Appenzeller, T., 2017, The AI revolution in science. Science. Retrieved November 29, 2021. https://www.science.org/content/article/ai-revolution-science

Bansal, G., Nushi, B., Kamar, E., Weld, D. S., Lasecki, W. S., & Horvitz, E., 2019, Updates in human-AI teams: Understanding and addressing the performance/compatibility tradeoff, Proceedings of the AAAI Conference on Artificial Intelligence. Proceedings of the AAAI Conference on Artificial Intelligence, 33: 2429–2437. https://doi.org/10.1609/aaai.v33i01.33012429

Brandstetter, J., Racz, P., Beckner, C., Sandoval, E. B., Hay, J., & Bartneck, C., 2014, A peer pressure experiment: Recreation of the asch conformity experiment with Robots, IEEE Publications. https://doi.org/10.1109/IROS.2014.6942730

Bushe, G. R., & Coetzer, G., 1995, Appreciative inquiry as a team-development intervention: A controlled experiment, Journal of Applied Behavioral Science, 31(1): 13–30. https://doi.org/10.1177/0021886395311004

Castelo, N., Bos, M. W., & Lehmann, D. R., 2019, Task-dependent machines aversion, Journal of Marketing Research, 56(5): 809–825. https://doi.org/10.1177/0022243719851788

Chen, J. Y. C., & Barnes, M. J., 2014, Human-agent teaming for Multirobot Control: A review of human factors issues, IEEE Transactions on Human-Machine Systems, 44(1): 13–29. https://doi.org/10.1109/THMS.2013.2293535

Cremer, D. D., 2020, Leadership by machines: Who leads and who follows in the Ai era? Harriman House.

Demir, M., Cooke, N. J., & Amazeen, P. G., 2018, A conceptual model of team dynamical behaviors and performance in human-autonomy teaming, Cognitive Systems Research, 52: 497–507. https://doi.org/10.1016/j.cogsys.2018.07.029

Demir, M., McNeese, N. J., She, M., & Cooke, N. J., 2019, Team coordination of team situation awareness in human-autonomy teaming. In: Proceedings of the Human Factors and Ergonomics Society Annual Meeting, Vol. 63, No. 1, pp. 146-147, SAGE Publications, Los Angeles, CA, USA.

Demir, M., McNeese, N. J., & Cooke, N. J., 2020, Understanding human–robot teams in light of all-human teams: Aspects of team interaction and shared cognition, International Journal of Human-Computer Studies, 140, 102436. https://doi.org/10.1016/j.ijhcs.2020.102436

Demir, M., McNeese, N. J., Cooke, N. J., Ball, J. T., Myers, C., & Frieman, M., 2015, Synthetic teammate communication and coordination with humans. In: Proceedings of the Human Factors and Ergonomics Society Annual Meeting, Vol. 59, No. 1, pp. 951-955. SAGE Publications, Los Angeles, CA, USA. https://doi.org/10.1177/1541931215591275

Dietvorst, B. J., Simmons, J. P., & Massey, C., 2015, Machines aversion: People erroneously avoid machines after seeing them err, Journal of Experimental Psychology. General, 144(1): 114–126. https://doi.org/10.1037/xge0000033

Edwards, C., Edwards, A., Spence, P. R., & Westerman, D., 2016, Initial interaction expectations with robots: Testing the human-to-human interaction script, Communication Studies, 67(2): 227–238. https://doi.org/10.1080/10510974.2015.1121899

Elson, J. S., Derrick, D., & Ligon, G., 2018, Examining trust and reliance in collaborations between humans and

Automated Agents. Proceedings of the Annual Hawaii International Conference on System Sciences. Proceedings of the 51st Hawaii International Conference on System Sciences. https://doi.org/10.24251/HICSS.2018.056

Fiore, S. M., & Wiltshire, T. J., 2016, Technology as teammate: Examining the role of external cognition in support of team cognitive processes, Frontiers in Psychology, 7: 1531. https://doi.org/10.3389/fpsyg.2016.01531

Glikson, E., & Woolley, A. W., 2020, Human trust in artificial intelligence: Review of empirical research, Academy of Management Annals, 14(2): 627–660. https://doi.org/10.5465/annals.2018.0057

Goddard, K., Roudsari, A., & Wyatt, J. C., 2012, Automation bias: A systematic review of frequency, effect mediators, and mitigators, Journal of the American Medical Informatics Association, 19(1): 121–127. https://doi.org/10.1136/amiajnl-2011-000089

Groom, V., & Nass, C., 2007, Can robots be teammates? Interaction Studies, Social Behaviour and Communication in Biological and Artificial Systems, 8(3): 483–500. https://doi.org/10.1075/is.8.3.10gro

Grosz, B. J., & Stone, P., 2018, A century-long commitment to assessing artificial intelligence and its impact on society, Communications of the ACM, 61(12): 68–73. https://doi.org/10.1145/3198470

Gunkel, D. J., 2012, The Machine question. MIT Press. https://doi.org/10.7551/mitpress/8975.001.0001

Guzman, A. L., & Lewis, S. C., 2020, Artificial Intelligence and Communication: A human–machine communication research agenda, New Media and Society, 22(1): 70–86. https://doi.org/10.1177/1461444819858691

Hancock, P. A., Billings, D. R., Schaefer, K. E., Chen, J. Y., de Visser, E. J., & Parasuraman, R., 2011, A meta-analysis of factors affecting trust in human–robot interaction: The Journal of the Human Factors and Ergonomics Society, Human Factors, 53(5): 517–527. https://doi.org/10.1177/0018720811417254

Harbers, M., Catholijn, M., Jonker, C. M., Birna, M., & Riemsdijk, M. B. V., 2014, Context-sensitive sharedness criteria for teamwork, Proceedings of the 2014 international conference on Autonomous agents and multi-agent systems, pp. 1507-1508. https://dl.acm.org/doi/abs/10.5555/2615731.2616035

Hertz, N., & Wiese, E., 2019, Good advice is beyond all price, but what if it comes from a Machine? Journal of Experimental Psychology Applied, 25(3): 386–395. https://doi.org/10.1037/xap0000205

Hill, J., Randolph Ford, W., & Farreras, I. G., 2015, Real conversations with artificial intelligence: A comparison between human-human online conversations and human–chatbot conversations, Computers in Human Behavior, 49: 245–250. https://doi.org/10.1016/j.chb.2015.02.026

Jarrahi, M. H., 2018, Artificial Intelligence and the future of work: Human-AI symbiosis in organizational decision making, Business Horizons, 61(4): 577–586. https://doi.org/10.1016/j.bushor.2018.03.007

Kamar, E., 2016, Directions in hybrid intelligence: Complementing AI systems with human intelligence, Proceedings of the Twenty-Fifth International Joint Conference on Artificial Intelligence, pp. 4070-4073. https://dl.acm.org/doi/10.5555/3061053.3061219

Lee, J. J., Knox, W. B., Wormwood, J. B., Breazeal, C., & DeSteno, D., 2013, Computationally modeling interpersonal trust, Frontiers in Psychology, 4: 893. https://doi.org/10.3389/fpsyg.2013.00893

Lee, M. K., Kiesler, S., Forlizzi, J., & Rybski, P., 2012, Ripple effects of an embedded social agent, In: Proceedings of the SIGCHI Conference on Human Factors in Computing Systems, 695–704. https://doi.org/10.1145/2207676.2207776

Lee, S. A., & Liang, Y. J., 2015, Reciprocity in computer-human interaction: Source-based, norm-based, and affect-based explanations, Cyberpsychology, Behavior and Social Networking, 18(4): 234–240. https://doi.org/10.1089/cyber.2014.0458

Lewis, K., 2003, Measuring transactive memory systems in the field: Scale Development and validation, Journal of Applied Psychology, 88(4), 587–604. https://doi.org/10.1037/0021-9010.88.4.587

Lortie, C. L., & Guitton, M. J., 2011, Judgment of the humanness of an interlocutor is in the eye of the beholder, PLOS ONE, 6(9), e25085. https://doi.org/10.1371/journal.pone.0025085

Madhavan, P., & Wiegmann, D. A., 2007, Similarities and differences between human-human and human-automation trust: An integrative review, Theoretical Issues in Ergonomics Science, 8(4): 277–301. https://doi.org/10.1080/14639220500337708

Malone, T. W., 2018, How human-computer 'Superminds' are redefining the future of work, MIT Sloan Management Review. Retrieved November 30, 2021. https://sloanreview.mit.edu/article/how-human-computer-superminds-are-redefining-the-future-of-work/

Merritt, S. M., & Ilgen, D. R., 2008, Not all trust is created equal: Dispositional and history-based trust in human-automation interactions: The Journal of the Human Factors and Ergonomics Society, Human Factors, 50(2): 194–210. https://doi.org/10.1518/001872008X288574

Merritt, S. M., 2011, Affective processes in human–automation interactions, Human Factors, 53(4), 356-370. https://doi.org/10.1177/0018720811411912

Mou, Y., & Xu, K., 2017, The media inequality: Comparing the initial human-human and human-ai social interactions. Computers in Human Behavior, 72: 432–440. https://doi.org/10.1016/j.chb.2017.02.067

Nass, C., & Moon, Y., 2000, Machines and mindlessness: Social responses to computers, Journal of Social Issues, 56(1): 81–103. https://doi.org/10.1111/0022-4537.00153

Nissan, E., 2018, Computer tools and techniques for lawyers and the judiciary, Cybernetics and Systems, 49(4): 201-233. https://doi.org/10.1080/01969722.2018.1447766

Parasuraman, R., & Manzey, D. H., 2010, Complacency and bias in human use of automation: An attentional integration: The Journal of the Human Factors and Ergonomics Society, Human Factors, 52(3): 381–410. https://doi.org/10.1177/0018720810376055

Peña-López, I., 2017, OECD digital economy outlook 2017. https://doi.org/10.1787/9789264276284-en

Prahl, A., & Van Swol, L., 2017, Understanding machines aversion: When is advice from automation discounted? Journal of Forecasting, 36(6), 691–702. https://doi.org/10.1002/for.2464

Przegalinska, A., Ciechanowski, L., Stroz, A., Gloor, P., & Mazurek, G., 2019, In bot we trust: A new methodology of chatbot performance measures, Business Horizons, 62(6): 785–797. https://doi.org/10.1016/j.bushor.2019.08.005

Puranam, P., 2021, Human–AI collaborative decision-making as an organization design problem, Journal of Organization Design, 10(2): 75–80. https://doi.org/10.1007/s41469-021-00095-2

Reeves, B., & Nass, C. I., 1996, The media equation: How people treat computers, television, and new media like real people and places. CSLI Publishing.

Russell, S., & Norvig, P., 1995, A modern, agent-oriented approach to introductory artificial intelligence, ACM SIGART Bulletin, 6(2): 24–26. https://doi.org/10.1145/201977.201989

Seeber, I., Bittner, E., Briggs, R. O., de Vreede, T., de Vreede, G.-J., Elkins, A., Maier, R., Merz, A. B., Oeste-Reiß, S., Randrup, N., Schwabe, G., & Söllner, M., 2020, Machines as teammates: A research agenda on AI in team collaboration, Information and Management, 57(2), 103174. https://doi.org/10.1016/j.im.2019.103174

Shaikh, S. J., & Cruz, I., 2019, Alexa, do you know anything? the impact of an intelligent assistant on team interactions and creative performance under time scarcity. Retrieved November 30, 2021. https://arxiv.org/abs/1912.12914

Shank, D. B., Graves, C., Gott, A., Gamez, P., & Rodriguez, S., 2019, Feeling our way to Machine minds: People's emotions when perceiving mind in Artificial Intelligence, Computers in Human Behavior, 98: 256–266. https://doi.org/10.1016/j.chb.2019.04.001

Shechtman, N., & Horowitz, L. M., 2003, Media inequality in conversation. Proceedings of the Conference on Human Factors in Computing Systems—CHI, 2003. https://doi.org/10.1145/642611.642661

Shiomi, M., & Hagita, N., 2016, Do synchronized multiple robots exert peer pressure? In Proceedings of the Fourth International Conference on Human-Agent Interaction, 27–33. https://doi.org/10.1145/2974804.2974808

Shrestha, Y. R., Ben-Menahem, S. M., & von Krogh, G., 2019, Organizational decision-making structures in the age of Artificial Intelligence, California Management Review, 61(4): 66–83. https://doi.org/10.1177/0008125619862257

Spence, P. R., Edwards, A., Edwards, C., & Jin, X., 2019, 'the bot predicted rain, grab an umbrella': Few perceived differences in communication quality of a weather Twitterbot versus professional and amateur meteorologists, Behaviour and Information Technology, 38(1): 101–109. https://doi.org/10.1080/0144929X.2018.1514425

Spence, P. R., Westerman, D., Edwards, C., & Edwards, A., 2014, Welcoming our robot overlords: Initial expectations about interaction with a robot, Communication Research Reports, 31(3): 272–280. https://doi.org/10.1080/08824096.2014.924337

Strohkorb Sebo, S., Traeger, M., Jung, M., & Scassellati, B., 2018, The ripple effects of vulnerability. In Proceedings of the 2018 ACM/IEEE International Conference on Human-Robot Interaction, 178–186. https://doi.org/10.1145/3171221.3171275

Von Krogh, G., 2018, Artificial intelligence in organizations: New opportunities for phenomenon-based theorizing, Academy of Management Discoveries, 4(4): 404-409. https://doi.org/10.5465/amd.2018.0084

Walliser, J. C., de Visser, E. J., Wiese, E., & Shaw, T. H., 2019, Team structure and team-building improve human–machine teaming with Autonomous Agents, Journal of Cognitive Engineering and Decision Making, 13(4): 258–278. https://doi.org/10.1177/1555343419867563

Wang, N., Pynadath, D. V., & Hill, S. G., 2016, Trust calibration within a human–robot team: Comparing automatically generated explanations 11th ACM/IEEE International Conference on Human-Robot Interaction (HRI). https://doi.org/10.1109/HRI.2016.7451741

Wilson, H., & Daugherty, P., 2018, Collaborative intelligence: Humans and AI are joining forces. Harvard Business Review. Retrieved December 1, 2021. https://hbr.org/2018/07/collaborative-intelligence-humans-and-ai-are-joining-forces

Xie, Y., Bodala, I. P., Ong, D. C., Hsu, D., & Soh, H., 2019, Robot capability and intention in trust-based decisions across tasks. In 14th ACM/IEEE International Conference on Human-Robot Interaction (HRI), pp. 39–47, IEEE Publications. https://doi.org/10.1109/HRI.2019.8673084

Yu, K. H., Beam, A. L., & Kohane, I. S., 2018, Artificial intelligence in healthcare, Nature Biomedical Engineering, 2(10): 719-731. https://doi.org/10.1038/s41551-018-0305-z

Zhang, R., McNeese, N. J., Freeman, G., & Musick, G., 2021, 'An Ideal Human' expectations of AI teammates in human-AI teaming, Proceedings of the ACM on Human-Computer Interaction, 4, 1–2.

Appendix A

Table 1. Independent sample t-test analysis of the measures.

Dependent Variable	Experimental Conditions: Human-Human (60) Mean (Sd)	Experimental Conditions: Human-Machine (60) Mean (Sd)	t-value	df	Sig.(2-Tailed)	Cohen's d
Collaboration	17.80 (3.53)	15.25 (3.19)	2.32	118	0.044	.36
Trust	19.25 (2.96)	18.62 (2.53)	1.01	118	0.315	.21

Source: Primary Data, *Sig. at 0.05

Table 2. Independent sample t-test analysis of communication measures.

Dependent Variable	Experimental Conditions: Human-Human (60) Mean (Sd)	Experimental Conditions: Human-Machine (60) Mean (Sd)	t-value	df	Sig.(2-Tailed)	Cohen's d
Words	206.97 (145.86)	138.87 (102.86)	2.41	110.09	0.018*	.53
Duration	25.75 (20)	17.55 (12.39)	2.20	105.09	0.030*	.49
Rapport Building	25.32 (13.77)	19.07 (9.56)	2.35	109.50	0.021*	.52
Task-related discussion	27.43 (15.42)	25.57 (15.73)	0.942	111.40	0.231	.18
Clarification seeking	22.84 (14.44)	13.06 (6.85)	2.52	107.70	0.034*	.35

Source: Primary Data, *Sig. at 0.05

Appendix B

Image 1 (Source: Hill, W. E. (1915). My wife and my mother-in-law. Puck, 16, 11)

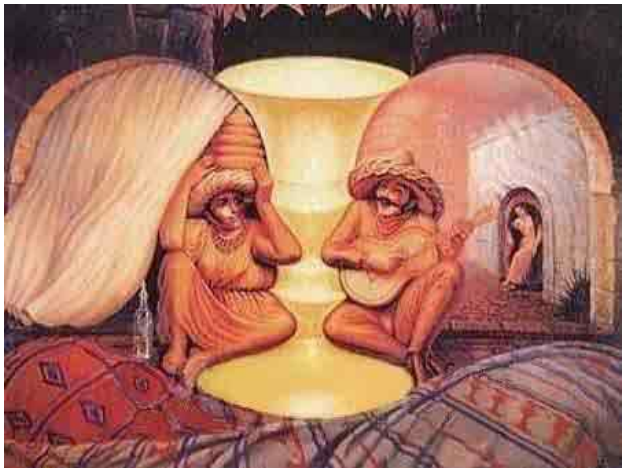

Image 2 (Painting of Octavio Ocampo. Always Forever)

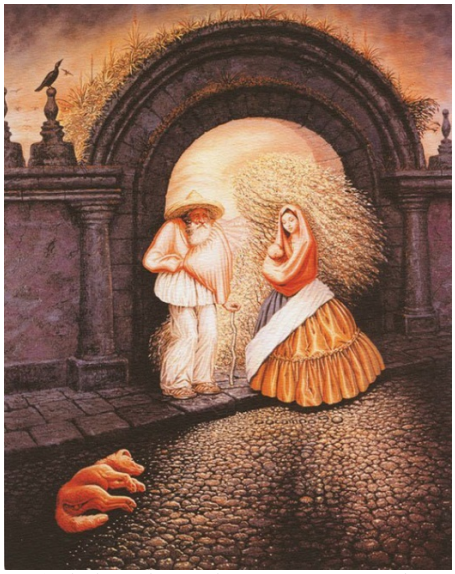

Image 3 (Painting of Octavio Ocampo. General's Family)

ResearchGate

See discussions, stats, and author profiles for this publication at: https://www.researchgate.net/publication/366947365

Convertible Uni-Bike Based on Inverted Pendulum Model and Prototype Using Additive Manufacturing

Article · January 2022

CITATIONS
0

Some of the authors of this publication are also working on these related projects:

Control Engineering View project

All content following this page was uploaded by Sareta Kiji on 07 January 2023.

The user has requested enhancement of the downloaded file.

Advanced Production and Industrial Engineering
R.M. Singari and P.K. Kankar (Eds.)

© 2022 The authors and IOS Press.
This article is published online with Open Access by IOS Press and distributed under the terms of the Creative Commons Attribution Non-Commercial License 4.0 (CC BY-NC 4.0).
doi:10.3233/ATDE220786

Convertible Uni-Bike Based on Inverted Pendulum Model and Prototype Using Additive Manufacturing

Rohit Kumar MISHRA [a,1], Rishabh RATHORE [a], Ritesh Kumar JANGID [a], SAMRAT [a]
[a] *Department of Mechanical Engineering, Delhi Technological University, Delhi, India*

Abstract. This paper explores the methodology used to develop the miniature working concept (prototype) of a Uni-wheel Electric bike (E-bike) convertible to an E-bike where the Uni-wheel works on an inverse pendulum mechanism and the prototype model is manufactured using Poly Lactic Acid (PLA) filament-based additive manufacturing using a Fused Deposition Modelling based 3D printer. Uni-bike, which can be converted into a normal bike as per the convenience of the rider. Because of the growing awareness of pollution and the energy scarcity situation, vehicles and motorbikes are no longer the ideal modes of mobility. As the cost of petroleum products rises, a more cost-effective and efficient form of transportation is required. This miniature prototype might be utilized to create a human-ridable model in the future.

Keywords. Uni-wheel, Inverse pendulum mechanism, Additive manufacturing, Cost-effective.

1. Introduction

A unicycle is a one-wheeled vehicle that is driven by the rider's pedaling or by motors that rotate the wheels. A unicycle works on the same principles as an inverted pendulum. In a unicycle problem, the rider's pedaling, or wheel torque, helps to stabilize the unicycle in the wheel's plane. In an inverted pendulum model, the movement of a movable platform, which is a linear translational motion, impacts the pendulum's stability.

A standard pendulum is in an equilibrium position; since there is no external force or torque acting on the pendulum, it will remain stationary, and if there is any displacement, it will come under the effect of a restoring torque that will bring it back to the initial position. An unstable equilibrium point is reached when a pendulum's bob is inverted and maintained exactly above the pivot with the help of a solid rod. Since the bob is exactly 180 degrees from its stable position, there is no torque acting on the pendulum at this point, but even a small displacement will generate a gravitational torque, accelerating it away from its prior position and causing it to lose balance.

A feedback control system has been implemented to balance the pendulum in the inverted position. It inputs the pendulum's angle at regular intervals and varies the position of the pivot when the pendulum starts to displace from equilibrium to keep it in a stable position, i.e., 180 degrees from the standard pendulum equilibrium position

[1] Corresponding Author: Rohit Kumar Mishra, Department of Mechanical Engineering, Delhi Technological University, 110042 Delhi, India; E-mail: rohitkumarmishra_2k18me178@dtu.ac.in.

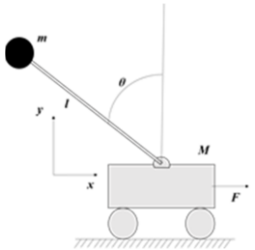

Figure 1. Inverted pendulum mounted on a cart.

Equations of motion correspond to the given problem statement using Lagrange's equations.

$$(M+m)\ddot{x} - ml\ddot{\theta}cos\theta + ml\dot{\theta}^2 sin\theta = F \quad (1)$$

$$l\ddot{\theta} - gsin\theta = \ddot{x}cos\theta \quad (2)$$

These equations are used as equations of motion for unicycle and are imported as an input for the control algorithm, which works as the basis of the Arduino code uploaded to the micro-controller for the self-balancing of the given prototype.

2. Literature Review

[1] A. Kadis, D. Caldecott et al. (2010) The kinematics of the unicycle were derived and described in this study. This deduction was verified using numerical simulations. This data was then utilized to create a computer simulation of a PD controller, whose performance was compared to that of the practical Micycle system. The creation of a model-based non-linear controller and a backstepping controller is among the projects planned for the future. The best control technique will be integrated into the Micycle design when it has been compared and benchmarked. To reduce the high tendency to saturate, a greater capacity motor controller should be added to the system. The introduction of active stabilization in the roll direction is another planned enhancement. This actuator will enable the Micycle to be a totally self-electric unicycle by using either a response wheel or a control moment gyroscope.

[2] Manjunatha G et al. (2020) The completion of this project results in a sleek design and self-balancing structure, which is helpful for customers to handle and drive easily. The air pollution and parking /spacing problems can be solved by the foldable and electric features of our "Monowheel Electric Vehicle." Due to its compact and foldable design, it can be carried easily on the subways, metro, trains, etc. And it produces very low noise, which reduces sound pollution.

[3] D. Hazry M. Sofian A. Zul Azfar et al. (2009) performed an investigation into the inertial measurement unit (IMU). The author has conducted a thorough investigation into the different kinds of IMU sensors on the market and offers useful advice on how to combine IMU sensors with GPS tracking in order to use additional functions in machines like unmanned vehicles and aircraft.

[4] N. K. Nasir, M. A. Ahmad, R. M. T. Raja Ismail et al. (2010) used MATLAB software to compare the input tracking and disturbance rejection capabilities of various stability regulating strategies such as LQR and PID for most non-linear vehicles. In

comparison, both the LQR and PID control systems have been demonstrated to be effective in regulating non-linear vehicles in both linear and angular modes.

[5] Yohanes Daud, Abdullah Al Mamun, Jian Xin Xu et al. (2013) discussed the many issues that arise when balancing a lateral pendulum unicycle. Three linear control strategies for developing the controller in terms of their longitudinal and lateral form have been proposed for these balancing challenges. The author analyzed several initial postures that pose a threat to balancing and came to the conclusion that it shows very little balancing, i.e., just for initial conditions.

[6] Sreevaraham Kumar, Bangaru Akash, and T. Delsy et al. (2014) designed and built a monowheel by deploying a self-balancing algorithm. The MPU6050 sensors were utilized, which have both an accelerometer and a gyroscope built into one chip. While employing similar strategies as others in their project, such as a microcontroller that aids in the execution of the program and provides the output to power the drive. The MPU6050, in conjunction with a 16 MHz external resonator tiny Arduino ATmega 328. This monowheel has a top speed of 20 kilometers per hour.

[7] Desna Nugroho, Raden Sanggar Dewanto, Dadet Pramadihanto et al. (2016) discussed the PENS wheel, which is a mono-wheel and self-balances, assuring rider's safety in either direction. The author suggests using a few key components in the design of PENS wheels, such as a BLDC motor and an IMU sensor. The PID controlling technique is used by the PENS wheel to automatically maintain its equilibrium. After completing all of these steps in the experimental model, the author concluded that the PID controller was effective within a ±10° tilt angle.

[8] Mukesh Sahu, Naved Shaikh, Saurabh Jadhao, Yash Yadav et al. (2017) recommended an investigation of RYNO motors which is based in Portland, Oregon, to see where the genesis of the RYNO motor comes into play. In RYNO, the driving source of energy is primarily a gyroscope and accelerometer unit, controller, DC motor drive, and battery. The authors have also mentioned a number of benefits and drawbacks, such as the ease with which the remaining battery charge can be checked and the ease with which the remaining battery charge can be checked. A 12V DC battery can be used to charge a personal tablet or phone. It can be parked anywhere, but there are a few issues because only one device controls both speeds.

[9] P. Sarala, S. F. Kodad, and B. Sarvesh et al. (2017) did a study that compares a variety of converters for BLDC motors, including simple Buck converters, Bridgeless Buck converters, and Hybrid Buck converters, as input supply needs to be rectified for varied applications to correct the power factor. Simulink models developed in MATLAB/SIMULINK software are used to compare the results. The power factor angle was always given in comparison, and hybrid buck converters were shown to be considerably superior to basic buck and bridgeless buck converters.

[10] Prof. Yogesh Risodkar, Mr.Ganesh Shirsath, Ms.Monali Holkar, Mr.Mayur Amle, et al. (2015) have discussed the necessity for alternate modes of transportation, as well as a basic overview for constructing the prototype, such as the monowheel based on inverted pendulum model, which will be used for modeling. It has also been suggested that gyroscopic sensors will be required for an intelligent car to detect the rider's angle and steer or brake the vehicle properly.

3. Methodology

The following objectives were set for the project.

1. To design and manufacture a chassis using additive manufacturing with PLA as the raw material and optimizing the same through varying the different printing variables.
2. Convertible Uni to bike through trailing arm mechanism.
3. To carry out the balancing of the uni-bike prototype on the pitch axis using the principle of inverted pendulum model, stepper motor, Inertial Measurement Unit (IMU), and Proportional, Integral, Derivative (PID) control.
4. To carry out the balancing of the uni-bike prototype on the roll axis through wheel geometry.

The following components were selected for materializing the prototype, followed by the factors considered.

1. Lithium-Polymer Battery (LiPo) – High energy density along with availability.
2. Microprocessor Unit (MPU) 6050 – Micro Electro Mechanical System technology-based single chip with both the accelerometer and the gyroscope embedded.
3. Arduino Nano – Small-sized Atmega328-based microcontroller.
4. HC-05 module – Bluetooth Serial Port Protocol with master and slave mode, connection with the smartphone using a terminal application.
5. A4988 stepper motor driver – micro-stepping motor driver designed to operate bipolar stepper motors up to $1/16^{th}$ step modes.
6. NEMA 17 – Hybrid stepping motor with 200 steps per revolution, precise position control with holding torque of 3.2 kg-cm.
7. PLA spool – Polylactic acid is a cheap thermoplastic filament extracted from renewable resources with a low melting point, making it easy to work with.
8. Wheels

3.1. PITCH CONTROL ALGORITHM

To explain the general algorithm of the pitch controller of our unicycle, we first have to define a few key terms that are often used while referring to PID control.

- Proportional Gain (K_p) A given level of error is maintained while increasing the control signal proportionally to the increase in K_p. Maintaining the level of error causes the closed-loop to act quickly but also overshoot the target.
- Derivation Term (K_d) The error increasing causes the control signal to increase, allowing the controller to dampen, thereby controlling the overshoot caused by K_p. Steady-state error is not affected.
- Integral Term (K_i) A steady error causes Ki to decrease the error by increasing the control signal persistently. Processing time causes the system to act sluggishly as time gets added persistently along with the control signal.

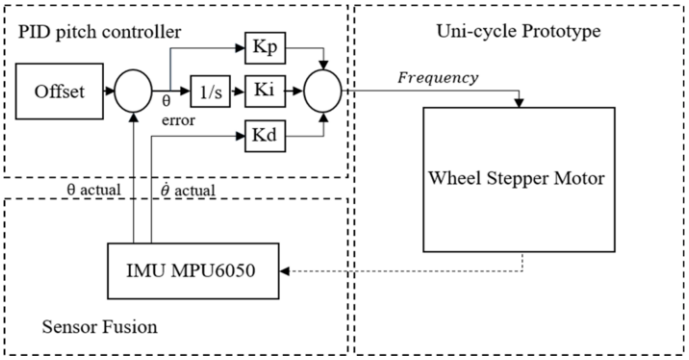

Figure 2. Pitch Control Algorithm of the Self-balancing Unicycle.

4-step calibration using the heuristic method for getting appropriate PID parameters:

1. Increase K_p until the prototype is ready to balance and starts oscillating.
2. Increase K_d to reduce the prototype's oscillation.
3. Increase K_i to stabilize the prototype.
4. Kp and Ki are reduced if a large oscillation is observed while disturbing the prototype.

By this method of trial and error, we calibrated our prototype's balance.

3.2. Design and Modeling

The CAD model was created on Solid Works 2020 software. These points were derived after a literature review after considering various CAD Models discussed. The following specifications were taken into consideration while modeling:

- The lightweight frame of the prototype.
- Only four parts (i.e., left and right frame platform and trailing arm) to make Assembly fast without any complication.
- The simple design of the parts so that they can be 3D printed easily and in less time
- Calculation according to the weight of stepper motor and battery pack because these two components are the heaviest of all other components.
- Designing the Frame symmetrical to minimize CG movement and keep it in the center Frame.

3.3. CAD Methodology

According to the stepper motor dimensions, the left and right frames were modeled. A pair of wheels with a 100 mm diameter was taken to prevent the chassis from touching the ground while leaning forward and backward. With the dimensions and size of other electronic components like the stepper motor driver, Arduino, battery pack, and Bluetooth module, the track width of the model was taken 136 mm, and the height is 160 mm to keep CG above the ground for better stability and control. The platform was designed to keep all electronic components which had a dimension of 92 mm X 140 mm and 3mm thickness, and was mounted between the left and right Frame at the height of 130 mm from the ground. To prevent the use of extra nuts and bolts, we have designed

a horizontal platform with a straight slot that is inserted into the side frames slot holes to make Assembly fast and easy and to reduce the weight.

After modeling all the frame parts, these parts are assembled in Solid Works 2020 assembly with all other components and the stepper motor. The interference detection tool was used to check interference detection between the components. Minor changes were made to reduce the weight of the Frame, which brings us to the specific design shapes represented in the diagrams below.

Fig 3. Left and right Frame CAD

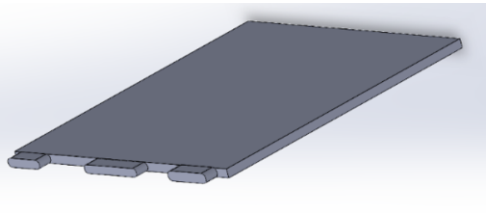

Fig 4. The horizontal platform that links to Frame represented in Fig 3

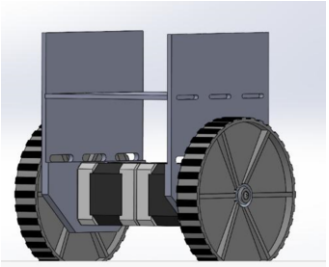

Fig 5. Front View of the Uni-bike

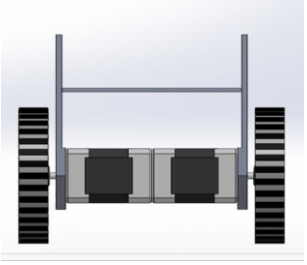

Fig 6. Final Uni-bike cad

Design and modeling of the trailing arm are done in Solid works 2020 software. The idea of the design is to slightly lean the main chassis from the vertical to increase stability by moving the center of gravity (COG) from the center of the chassis towards the rear wheel while in normal bike mode. Rear-wheel with a diameter of 73mm and a trailing arm with a total length of 170mm is designed. After modeling, all the components are assembled to check the interference detection.

The trailing arm is manually operated, i.e., when the bike is working in Uni wheel mode, the trailing is moved above the chassis as shown in fig. below, and when it is converted to a normal bike by moving the trailing arm.

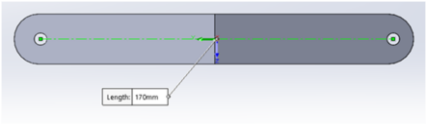

Fig 7. Trailing Arm

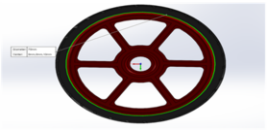

Fig 8. Rear Wheel Diameter 70mm CAD

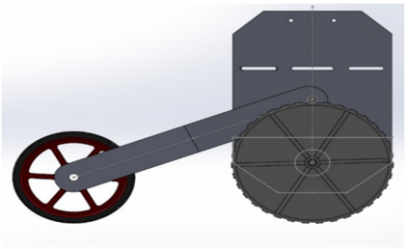

Fig 9. Complete Assembly of convertible Uni wheel e-bike prototype

Slicing the model in Ultimaker CURA to be printed on Ender 3 pro

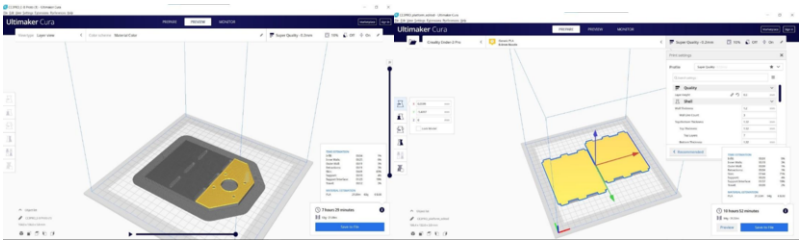

Fig 10 & 11. Side panels and linking panels are used for the main chassis assembly.

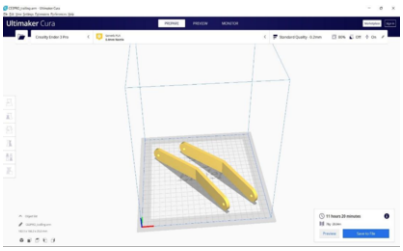

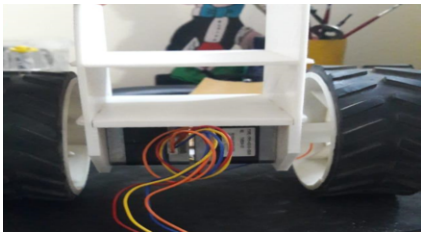

Fig 12 & 13. Trailing arm and the main chassis assembly with stepper motors.

Fig 14. The final chassis and trailing arm assembly with a total printing time of 26 hours with a 20% infill of the PLA+ filament with a 0.4 mm nozzle.

4. Results and Discussion

Balancing of the prototype was successfully achieved by installing the mentioned system. Using additive manufacturing over conventional methods gave us the opportunity to in-house manufacture this prototype in no time. Comparing the process with other conventional methods like liquid molding, etc., the time taken to fabricate the chassis was significantly reduced for the molding process, a significantly accurate mold needs to be fabricated, then the plastics or polymer along with other agents is melted, and mixed and transferred into barrels and then injected into the mold. After that, the mixture needs to be cooled down and cured. In additive manufacturing or 3D printing, we just printed the CAD model of the chassis, and after an overnight run, all the parts were ready to be combined and form a compound body without the use of any adhesive.

5. Conclusions

Comparing the overall cost of prototype production through fused deposition modeling-based additive manufacturing with conventional manufacturing methods, additive comes out superior as the filament used in the entire project was cheaper and no extra operation were performed to produce or assemble the model. For conventional, different operations needs to be performed like sheet metal cutting, drilling, welding etc. in order to achieve the final model. The entire project was completed on a single 3D Printing machine (Ender 3 Pro) that was readily available. Whereas in the case of conventional manufacturing, the number of manufacturing operations drives up the cost significantly as compared to the manufacturing method discussed.

References

[1] Kadis, A.L., Caldecott, D., Edwards, A., Jerbic, M., Madigan, R.J., Haynes, M.W., Cazzolato, B.S., & Prime, Z. (2010). Modeling, simulation, and control of an electric unicycle.
[2] Manjunatha, G., Naheen, P.C., Muzammil, A.K., Sainath., Dharmendara, M. (2020). Mono Wheel Electric Vehicle.
[3] Hazry, D., Sofian, M., Azfar, A.Z. (2009). Study of Inertial Measurement Unit Sensor.
[4] Ahmad, M. A., Ismail, R. M. T. R., Ramli, M. S., Nasir, A. N. K., & Hambali, N. (2009). Feed-forward Techniques for Sway Suppression in a Double-Pendulum-Type Overhead Crane. 2009 International Conference on Computer Technology and Development.
[5] Daud, Y., Mamun, A.A., and Xu, J.X. (2013). Properties of lateral-pendulum-controlled unicycle robot in states of balance and motion, 6th IEEE Conference on Robotics, Automation and Mechatronics (RAM), 2013, pp. 162-167.
[6] Kumar, S.R.N. & Akash, B. & Kennedy, Delsy. (2016). Designing the monowheel by using the Self-balancing technique.
[7] Riattama, D., Binugroho, E.H., Dewanto, R.S., & Pramadihanto, D. (2016). PENS-wheel (one-wheeled self-balancing vehicle) balancing control using PID controller.
[8] Sahu, M., Shaikh, N., Jadhao, S., Yadav, Yash. (2017). A Review of One Wheel Motorbike.
[9] Sarala, P., Kodad, S.F., & Sarvesh, B. (2016). Analysis of closed-loop current-controlled BLDC motor drive. *2016 International Conference on Electrical, Electronics, and Optimization Techniques (ICEEOT)*, 1464-1468.
[10] Risodkar, Y., Shirsath, G., Holkar, M., Amle, M. (2015). Designing the Self–Balancing Platform (Segway).

ORIGINAL ARTICLE

Eastern Journal of Medicine

East J Med 23(1): 87-93, 2023
DOI: 10.5505/ejm.2023.82474

Correlation Between COVID 19 and Selected Risk Factors: An Ecological Study

Deepak Dhamnetiya[1], Shalini Shalini[2], Abhishek Mehra[3], Ravi Prakash Jha[1*]

[1]Department of Community Medicine, Dr Baba Saheb Ambedkar Medical College and Hospital, Delhi, India
[2]Lady Hardinge Medical College, New Delhi, India
[3]Department of Mathematics and Computing, Delhi Technological University, Delhi, India

ABSTRACT

The World Health Organization (WHO), on March 11, 2020, has declared the novel coronavirus (COVID-19) outbreak a global pandemic. COVID-19 originated from Wuhan; China spread to 218 Countries and Territories around the world. We planned this study to assess the correlation between COVID 19 and selected risk factors.

An ecological study was conducted in December 2020. Data regarding the COVID-19 confirmed cases and deaths per million populations were retrieved using Our World in Data until 28th November 2020. Data regarding socio-demographic related factors of countries and health-related factors were also extracted from the same database. We categorized countries into a) seven Global Burden of Disease (GBD) super regions and World Bank income levels. We have applied Spearman's rank correlation coefficient to assess the correlation between COVID-19 cases and deaths with various socio-demographic related and health-related factors. Statistical analysis has been performed using Statistical Package for Social Sciences (SPSS) 27.0 (Trial Version). A p-value of <0.05 is considered significant.

In this study, highest number of COVID-19 confirmed cases and deaths were reported in World Bank high-income groups. Globally, we found significant positive correlations between COVID-19 deaths per million with various socio-demographic related and health related factors like median age ($r=0.543, p<0.001$), percentage of population aged ≥65 years ($r=0.546, p<0.001$), GDP per capita ($r=0.531, p<0.001$), HDI ($r=0.567, p<0.001$), female smoking ($r=0.509, p<0.001$), availability of hand-washing facilities ($r=0.608, p<0.001$), diabetes ($r=0.166, p<0.05$) and hospital beds per 1000 population ($r=0.383, p<0.001$), whereas extreme poverty is negatively correlated ($r= -0.490, p<0.001$).

Extra emphasis on high-income countries is required to reduce the burden of COVID 19 cases and deaths. A multi-centric study should be planned to know the reasons for the high burden of cases and deaths in high-income countries.

Keywords: COVID-19, Diabetes, Smoking, Hand-washing, HDI, Poverty

Introduction

The World Health Organization (WHO), on March 11, 2020, has declared the novel coronavirus (COVID-19) outbreak a global pandemic (WHO 2020a). COVID-19 originated from Wuhan; China spread to 218 Countries and Territories around the world. A total of 61.8 million reported cases of coronavirus and 1.4 million deaths globally since the start of the pandemic, as of 29 November 2020 (WHO 2020b). This data is increasing day by day throughout the Globe, which is a matter of serious concern. The virus has raised world concern because of its high transmission capability as well as high mobility and mortality (Chen 2020; Phelan 2020; Li 2020).

This ongoing pandemic of COVID-19 is a global challenge which resulted in significant morbidity and mortality worldwide. Since the beginning of the pandemic, researchers trying to assess the potential risk factors of COVID 19, which either increases the risk of getting an infection or worsen the outcome of the COVID 19 disease. Researchers found that diabetes is associated with increased incidence and severity of COVID-19 (Singh 2020), whereas active smoking is significantly linked with the risk of more severity of COVID-19 (Tsigaris 2020). To prevent virus transmission, the Center for Disease Control (CDC) recommends frequent hand washing with soap and water for 20 seconds (CDC 2020), so the unavailability of a handwashing facility might increase the risk of COVID 19 infection. Though a high human development index (HDI) means longer life expectations, better education, and better living standards, it is surprising that it associates with a higher infection rate and

***Corresponding Author:** Ravi Prakash Jha, Statistician cum Tutor, Department of Community Medicine, Dr Baba Saheb Ambedkar Medical College and Hospital, Sector-6, Rohini, Delhi, India -110085.
E-mail: ravijha0292@gmail.com, Phone: +918004417689
ORCID ID: Deepak Dhamnetiya: 0000-0002-5634-3315, **Shalini Shalini:** 0000-0003-2954-811X, **Abhishek Mehra:** 0000-0001-8138-4648, **Ravi Prakash Jha:** 0000-0001-5230-1436
Received: 30.10.2021, **Accepted:** 12.10.2022

mortality rate for COVID 19 (Liua 2020).To the best of our knowledge, there is no research study published that depicts the correlation of these factors with COVID 19 at the Global level, so we planned this study to assess the correlation between COVID 19 and selected risk factors.

Material and Methods

An ecological study was conducted in December 2020 to assess the correlation between COVID 19 and selected risk factors. Data regarding the COVID-19 confirmed cases and deaths per million populations was retrieved using Our World in Data (Roser 2020) up to 28th November 2020. Socio-demographic related factors of countries like median age, percentage of population aged ≥65 years, GDP per capita, percentage of extreme poverty, population density and HDI and data regarding health-related factors like the prevalence of male and female smoking, diabetes, handwashing facilities and availability of hospital beds per 1000 population were also extracted from the same database. We categorized countries into a) seven Global Burden of Disease (GBD) (GBD 2020) super regions, including 1. South Asia, 2. Southeast Asia, East Asia & Oceania, 3. Central Europe, Eastern Europe & Central Asia, 4. North Africa &Middle East, 5. Sub-Saharan Africa, 6. Latin America & Caribbean, and7. High-income; b) World Bank income levels (World Bank 2020), including (1. Low-income countries, 2. Lower middle-income countries, 3. Upper middle-income countries, and 4. High-income countries).

Data has been extracted and recorded in an MS-Excel spreadsheet. We have calculated COVID-19 confirmed cases and deaths per million populations with their 95% confidence intervals (CIs) by each region classified according to GBD and World Bank. We have applied Spearman's rank correlation coefficient to assess the correlation between COVID-19 cases and deaths with various socio-demographic related and health-related factors. A Scatter plot matrix has been prepared for Socio-demographic related factors and health-related factors with COVID-19 cases and deaths separately. Statistical analysis has been performed using Statistical Package for Social Sciences (SPSS) 27.0 (Trial Version). A p-value of <0.05 is considered significant.

Results

As of November 28, 2020, the highest number of COVID-19 confirmed cases and deaths per million were reported in high-income regions (24477.67) and Latin America and the Caribbean region (670.30), respectively. The lowest COVID-19 confirmed cases (570.42) and deaths (14.82) per million were reported in Southeast Asia, East Asia, and Oceania region of GBD study super regions (Table 1A).

According to World Bank Classification, the highest number of COVID-19 confirmed cases (23552.65) and deaths (512.73) per million were reported in high-income groups. In contrast, the lowest number of COVID-19 confirmed cases (498.46) and deaths (12.46) were reported in low-income groups (Table 1B).

The median age and percentage of the population aged ≥65 years were highest in the high-income region and high-income countries, whereas it was lowest in Sub-Saharan Africa and low-income countries. We have provided the values of countries having minimum and maximum population density, GDP per capita, percentage of the population in extreme poverty, HDI, female smoking, male smoking, diabetes, hand washing facilities and hospital beds per 1000 population for each GBD Super region and World Bank income groups (Table 1, Table 2).

Globally, we found significant moderate positive correlations between COVID-19 cases per million with various socio-demographic related factors like median age ($r=0.609, p<0.001$), percentage of population aged ≥65 years($r=0.532, p<0.001$), GDP per capita($r=0.632, p<0.001$) and HDI($r=0.652, p<0.001$) whereas extreme poverty is negatively correlated ($r=-0.548, p<0.001$) and no significant correlation was found for population density ($r=-0.116$, $p=0.118$)(Fig. 1A).. A significant positive correlations was found between COVID-19 cases per million with various health related factors like female smoking($r=0.502, p<0.001$), availability of hand-washing facilities($r=0.525, p<0.001$) and hospital beds per 1000 population($r=0.419, p<0.001$); however, there is no significant correlation for male Smoking ($r=-0.078$, $p=0.361$) and diabetes ($r=-0.124$, $p=0.095$)(Fig.1B).

Globally, we found significant positive correlations between COVID-19 deaths per million with various socio-demographic related factors like median age ($r=0.543, p<0.001$), percentage of population aged ≥65 years

Table 1. Global Burden and Mortality of COVID-19, Various Socio-Demographic Related Factors: Results Classified According To The A) Global Burden of Disease Super Region Classification and B) World Bank Income Level Based Classification

A. Global Burden of Disease Study super regions								
	Covid-19			Socio-Demographic related Factors				
Super Regions	Cases per Million (95% CI)	Deaths per Million (95% CI)	Age, Median (IQR)	Population aged ≥ 65 years (%)	Population Density/1000 pop (min,max)	GDP per Capita (min,max)	Extreme Poverty % (min,max)	HDI (min,max)
Central Europe, Eastern Europe, and Central Asia Region	16866.33 (16613.94-17118.72)	287.84 (254.59-321.09)	40.75 (36.65 - 43.15)	13.49	(1.98, 137.18)	(2896.91, 32605.91)	(0.1, 5.7)	(0.65, 0.90)
High-income Region	24477.67 (24174.80-24780.54)	562.46 (515.99-608.93)	41.60 (37.9 - 43.3)	18.31	(3.20, 19347.50)	(18933.91, 94277.97)	(0.1,2.0)	(0.80, 0.95)
North Africa and Middle East region	7188.25 (7022.67-7353.82)	186.36 (159.60-213.11)	30.7 (23.2 -32.4)	5.38	(3.62, 1935.91)	(1479.15, 116935.60)	(0.1,18.8)	(0.45, 0.86)
South Asia region	5810.05 (5661.09-5959.01)	84.72 (66.68-102.76)	26.25 (23.5 - 28.2)	5.65	(21.19, 1265.04)	(2442.80, 8708.60)	(1.5,21.2)	(0.56, 0.64)
Latin America and Caribbean region	18662.06 (18396.82-18927.31)	670.30 (619.57-721.03)	29.35 (26.9 - 32.85)	7.61	(3.61, 664.46)	(1653.17, 28763.07)	(1.3, 23.5)	(0.50, 0.81)
Sub-Saharan Africa	1250.44 (1181.18-1319.71)	28.46 (18.00-38.92)	19.25 (17.9 - 21.75)	3.11	(3.08, 494.87)	(661.24, 22604.87)	(3.4, 77.6)	(0.35, 0.72)
Southeast Asia, East Asia, and Oceania region	570.42 (523.62-617.21)	14.82 (7.27-22.36)	29.3 (25.2 -34.1)	9.21	(18.22, 1454.43)	(2205.92, 26808.16)	(0.1, 30.3)	(0.54, 0.80)
B. World Bank classifications								
	Covid-19			Socio-Demographic related Factors				
Income Levels	Cases per Million (95% CI)	Deaths per Million (95% CI)	Age, Median (IQR)	Population aged ≥ 65 years (%)	Population Density/1000 pop (min, max)	GDP per Capita (min, max)	Extreme Poverty % (min, max)	HDI (min, max)
High Income	23552.65 (23255.42-23849.89)	512.73 (468.36-557.10)	41.1 (36.2 -43.2)	17.73	(3.20, 19347.50)	(16978.07, 116935.60)	(0.1, 5.7)	(0.78, 0.95)
Upper Middle Income	6578.98 (6420.53-6737.44)	203.22 (175.29-231.16)	31.25 (28.8 - 38.35)	9.77	(3.08, 1454.43)	(3819.20, 26808.16)	(0.1, 18.9)	(0.59, 0.83)
Lower Middle Income	4472.26 (4341.47-4603.04)	72.83 (56.11-89.56)	25.05 (20.35 - 28.4)	5.38	(1.98, 1265.04)	(1413.89, 13913.84)	(0.1, 59.6)	(0.48, 0.77)
low Income	498.46 (454.71-542.21)	12.46 (5.53-19.36)	18.75 (17.5 - 19.4)	3.1	(7.48, 494.87)	(661.24, 4466.51)	(4.8, 77.6)	(0.35, 0.65)

Table 2: Global Burden and Mortality of COVID-19, Various Health-Related Factors: Results Classified According to the A) Global Burden of Disease Super Region Classification and B) World Bank Income Level Based Classification

A. Global Burden of Disease Study super regions							
	Covid-19		Health related factors				
Super Regions	Cases per Million (95% CI)	Deaths per Million (95% CI)	Smoking % (Female) (min, max)	Smoking % (Male) (min, max)	Diabetes % (min, max)	Hand-washing Facilities% (min, max)	Hospital Beds/1000 Pop (min, max)
Central Europe, Eastern Europe, and Central Asia Region	16866.33 (16613.94-17118.72)	287.84 (254.59-321.09)	(0.3, 44.0)	(24.7, 58.3)	(3.67, 10.08)	(71.18,99.00)	(2.60, 11.00)
High-income Region	24477.67 (24174.80-24780.54)	562.46 (515.99-608.93)	(2.0, 35.3)	(15.2, 52.7)	(3.28,12.79)	-	(2.11, 13.80)
North Africa and Middle East region	7188.25 (7022.67-7353.82)	186.36 (159.60-213.11)	(0.2, 26.9)	(15.6, 65.8)	(5.35, 17.72)	(37.75, 97.40)	(0.5, 3.70)
South Asia region	5810.05 (5661.09-5959.01)	84.72 (66.68-102.76)	(1.0, 9.5)	(20.6, 44.7)	(7.26, 10.39)	(34.81, 79.81)	(0.30, 1.70)
Latin America and Caribbean region	18662.06 (18396.82-18927.31)	670.30 (619.57-721.03)	(1.9, 17.1)	(9.9, 53.3)	(5.55, 17.11)	(22.86, 90.65)	(0.60, 5.80)
Sub-Saharan Africa	1250.44 (1181.18-1319.71)	28.46 (18.00-38.92)	(0.1, 9.7)	(7.7, 53.9)	(0.99, 15.67)	(1.19, 52.23)	(0.10, 6.30)
Southeast Asia, East Asia, and Oceania region	570.42 (523.62-617.21)	14.82 (7.27-22.36)	(0.3, 23.5)	(27.0, 78.1)	(4.00,30.53)	(25.21,95.80)	(0.80, 5.90)
B. World Bank classifications							
	Covid-19		Health related factors				
Income Levels	Cases per Million (95% CI)	Deaths per Million (95% CI)	Smoking % (Female) (min, max)	Smoking % (Male) (min, max)	Diabetes % (min, max)	Hand-washing Facilities % (min, max)	Hospital Beds/1000 Pop (min, max)
High Income	23552.65 (23255.42-23849.89)	512.73 (468.36-557.10)	(0.5,35.3)	(9.9, 52.7)	(3.28, 22.02)	(88.47, 97.40)	(1.20, 13.80)
Upper Middle Income	6578.98 (6420.53-6737.44)	203.22 (175.29-231.16)	(0.3, 44.0)	(12.3, 76.1)	(3.94, 30.53)	(24.64, 99.00)	(0.60, 11.00)
Lower Middle Income	4472.26 (4341.47-4603.04)	72.83 (56.11-89.56)	(0.2, 23.5)	(7.7, 78.1)	(0.99, 18.68)	(2.12, 90.65)	(0.30, 8.80)
low Income	498.46 (454.71-542.21)	12.46 (5.53-19.36)	(0.1, 8.8)	(8.5, 41.3)	(1.91, 15.67)	(1.19, 72.70)	(0.10, 4.80)

(r=0.546,p<0.001), GDP per capita (r=0.531,p<0.001) and HDI (r=0.567,p<0.001) whereas extreme poverty is negatively correlated (r= -0.490,p<0.001) and no significant correlation was found for population density (r= -0.008, p=0.922) (Fig.2A). A significant positive correlations was found between COVID-19 deaths per million with various health related factors like female smoking (r=0.509,p<0.001), availability of hand-washing facilities (r=0.608,p<0.001), diabetes (r=0.166,p<0.05) and hospital beds per 1000 population (r=0.383,p<0.001); however, there is no significant correlation for male Smoking (r=-0.075, p=0.390) (Fig.2B).

Discussion

In this study, we found that the highest number of COVID-19 confirmed cases were reported in World Bank high-income group which include countries like USA, Japan, South Korea and Hongkong, Australia, New Zealand, Western European countries etc. large population from China travel to these countries for various reasons like trade, tourism, education and employment. The first four countries are China's top most

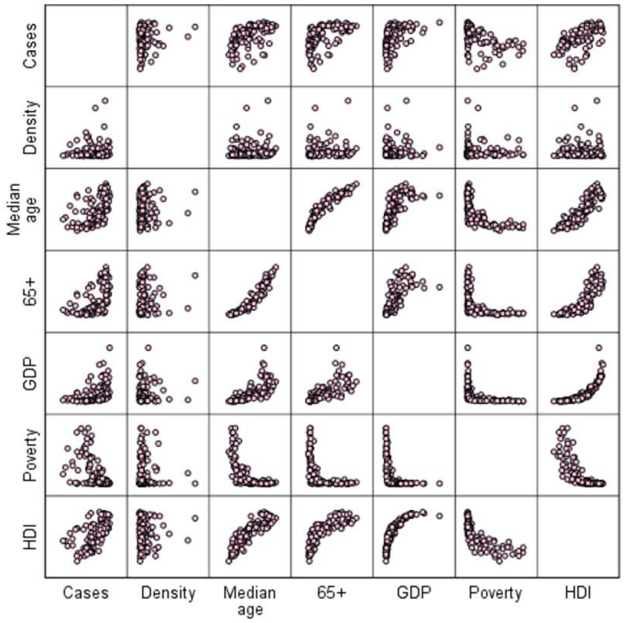

Fig. 1A. Correlation Between COVID 19 Cases With Socio-Demographic Related Factors

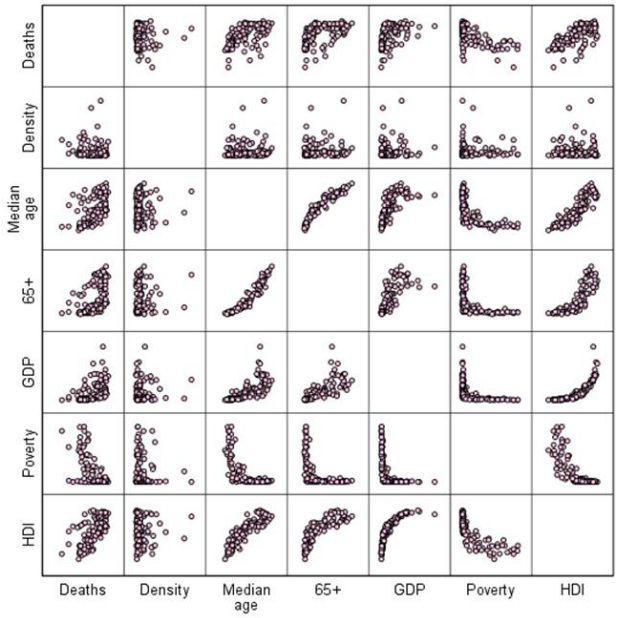

Fig. 2A. Correlation Between COVID 19 Deaths With Socio-Demographic Related Factors

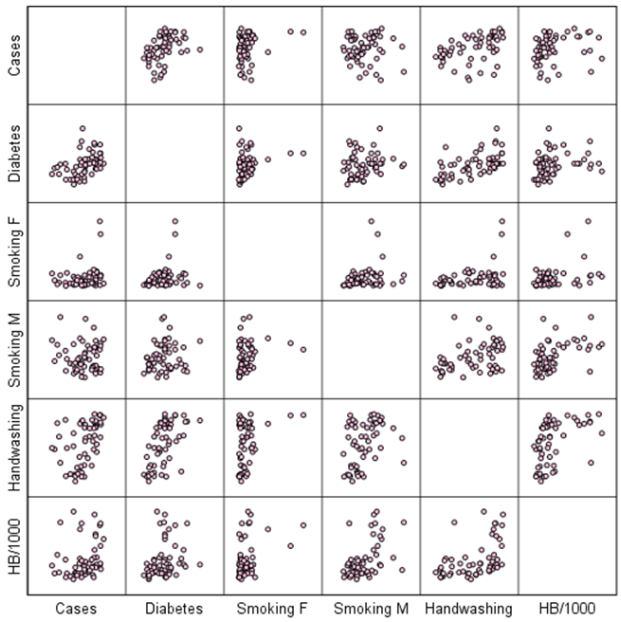

Fig. 1B. Correlation Between COVID 19 Cases With Health-Related Factors

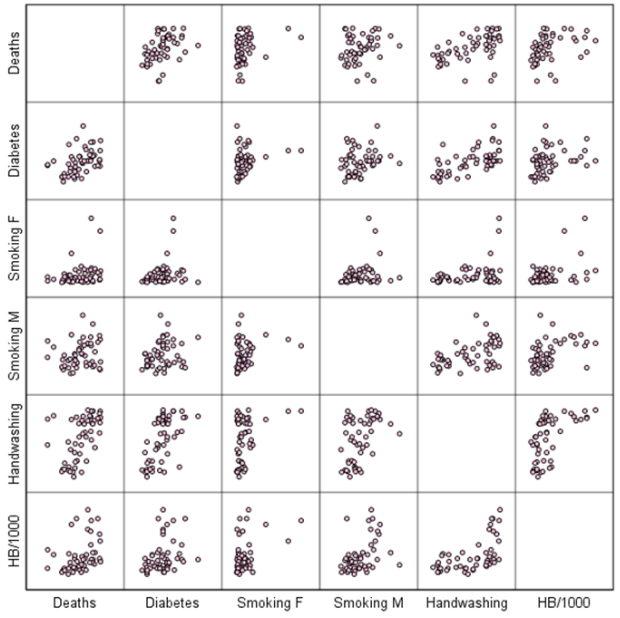

Fig. 2B. Correlation Between COVID 19 Deaths With Health-Related Factors

export and import partners (41.65% partner share) (WITS 2018). These might be the reasons for reporting of the highest number of cases from high-income groups. The high-income group also reported the highest number of COVID 19 deaths, whereas the low-income group reported the lowest number of COVID 19 deaths; this might be because of the population composition of these groups, the high-income group had 17.73% of the population aged above 65 years, and the low-income group had 3.1% of population aged above 65 years. We have also found a significant positive correlation between population aged above 65 years and COVID 19 deaths; this is corroborated with the studies conducted by Nikolich-Zugich et al. (2020), Onder et al. (2020), Wu et al. 2020 and Zhu et al. (2020). This may be because immune responses in older adults are slower, less coordinated, and less efficient, making older adults more susceptible to emerging infections (Chen et al., 2021). This may also be due to negative effect of previous diagnosed diseases (Liu et al., 2020 and Onden et al., 2020). Additionally, elderly persons who live alone or in

poor circumstances may find it difficult to obtain food, medicine, and other supplies while under quarantine (Armitage et al., 2020; Lloyd-Sherlock et al., 2020a and Lloyd-Sherlock et al., 2020b).

We found a significant positive correlation between median age and COVID 19 cases & deaths; the same results were seen in a study conducted by other researchers (Sun 2020). HDI, which indicates longer life expectancy, better education and a decent standard of living, is positively correlated with COVID 19 cases & deaths; this is corroborated with the study conducted by Liua K et al. (2020).

In our study, extreme poverty is significantly negatively correlated with COVID 19 cases & deaths; this is a surprising finding as one link between poverty and disease that is readily observable to most physicians is the increased vulnerability of the poor to communicable diseases and the lack of medical care once infected (Alsan 2011).

In this study, a significant positive correlation has been found between female smoking and COVID 19 cases & deaths. In contrast, the study conducted by Tsigaris et al. (2020) found a negative correlation between smoking and COVID 19 cases at a population level. Zhou et al. (2020) and Yang et al. (2020) found that smoking is not a risk factor for COVID 19 mortality.

We have found a significant positive correlation between handwashing facilities and COVID 19 cases & deaths; this is again very unlike finding as hand washing reduces communicable disease transmission rate; this may be because of several confounding factors like better handwashing facilities are available in high-income countries.

Whether people with diabetes have a higher susceptibility to COVID-19 is currently unknown. Still, there is a perception that the risk of infection and severe disease is higher in people with diabetes. In this ecological study, we have found no correlation between diabetes and COVID 19 cases, but a significant positive correlation exists with COVID 19 mortality. It implies that diabetes increases the severity of COVID 19 disease. In studies conducted to know the prevalence of diabetes among survivor and non-survivor COVID 19 patients, it has been found that the prevalence of diabetes is more than twice among non-survivor patients vis-à-vis survivor patients (Zhou 2020; Yang 2020).

Strength of the present study. First, To the best of our knowledge this is first study which assess the correlation between COVID 19 cases and death with socio-demographic and health related factors together at global level. Second, this study utilised large data from GBD study and Our World in Data.

This study has few limitations. First, We have correlated selected risk factors with COVID 19 cases and deaths at various GBD Super regions and World bank groups; it may not accurately reflect the true association between individuals within those regions. Second, being an ecological study, we could not establish a cause-and-effect relationship.

In this study, the highest number of COVID-19 confirmed cases and deaths were reported in World Bank high-income groups. We found a significant positive correlation between median age, percentage of population aged ≥65 years, GDP per capita, HDI, female smoking, availability of handwashing facilities, hospital beds per 1000 population and COVID-19 cases & deaths per million. In contrast, extreme poverty is significantly negatively correlated with COVID-19 cases& deaths per million. Diabetes had a significant positive correlation with COVID 19 deaths, but no correlation was found with COVID-19 cases. This study shows no significant correlation between population density and male smoking with COVID 19 cases & deaths.

Extra emphasis on high-income countries is required to reduce the burden of COVID 19 cases and deaths. A multi-centric study should be planned to know the reasons for a high burden of cases and deaths in high-income countries.

References

1. Alsan MM, Westerhaus M, Herce M, Nakashima K, Farmer PE (2011). Poverty, global health, and infectious disease: lessons from Haiti and Rwanda. Infect Dis Clin North Am; 25: 611-ix.
2. Armitage R, Nellums LB (2020). COVID-19 and the consequences of isolating the elderly. The Lancet Public Health 5(5):e256.
3. Centers for Disease Control and Prevention (2020). Show me the science-how to wash your hands. Available at: https://www.cdc.gov/handwashing/show-me-the-science-handwashing.html. Accessed on Dec 8, 2020.
4. Chen N, Zhou M, Dong X, Qu J, Gong F, Han Y et al. (2020) Epidemiological and clinical characteristics of 99 cases of 2019 novel coronavirus pneumonia in Wuhan, China: a descriptive study. Lancet ;395:507–13

5. Chen Y, Klein SL, Garibaldi BT, Li H, Wu C, Osevala NM, Li T, Margolick JB, Pawelec G, Leng SX (2021). Aging in COVID-19: Vulnerability, immunity and intervention. Ageing research reviews 65:101205.
6. Global burden of disease super-regions classification (2020) .Available at http://www.healthdata.org/sites/default/files/files/Projects/GBD/GBDRegions_countries.pdf last assessed on 08 December 2020.
7. Li Q, Guan X, Wu P, Wang X, Zhou L, Tong Y et al. (2020) Early Transmission Dynamics in Wuhan, China, of Novel Coronavirus-Infected Pneumonia. N Engl J Med. ;382(13):1199-1207
8. Liu K, Chen Y, Lin R, Han K (2020). Clinical features of COVID-19 in elderly patients: A comparison with young and middle-aged patients. Journal of Infection 80(6):e14-8.
9. Liua K, Heb M, Zhuangc Z, Hec D, Lid H (2020). Unexpected positive correlation between human development index and risk of infections and deaths of COVID-19 in Italy. One Health;10: 100174
10. Lloyd-Sherlock P, Ebrahim S, Geffen L, McKee M (2020a). Bearing the brunt of covid-19: Older people in low and middle income countries, A global expert group on older people might be useful. BMJ 368, 1052.
11. Lloyd-Sherlock P, Kalache A, McKee M, Derbyshire J, Geffen L, Casas GL, Gutierrez LM (2020b). Covid-19: Open letter to who and member states, who must prioritise the needs of older people in its response to the covid-19 pandemic. BMJ 368, 1164.
12. Nikolich-Zugich J, Knox KS, Rios CT, Natt B, Bhattacharya D, Fain MJ (2020). SARSCoV-2 and COVID-19 in older adults: what we may expect regarding pathogenesis, immune responses, and outcomes, Geroscience 42:505–514.
13. Onder G, Rezza G, Brusaferro S (2020). Case-fatality rate and characteristics of patients dying in relation to COVID-19 in Italy. JAMA. 323, 1775–1776.
14. Phelan AL, Katz R, Gostin LO (2020). The Novel Coronavirus Originating in Wuhan, China: Challenges for Global Health Governance. JAMA ;323:709-10
15. Roser M, Ritchie H, Ortiz-Ospina E and Hasell J (2020) "Coronavirus Pandemic (COVID-19)". Published online at OurWorldInData.org. 2020. Available at https://ourworldindata.org/coronaviruslast assessed on 30 November 2020.
16. Singh AK, Gupta R, Ghosh A, Misra A. (2020). Diabetes in COVID-19: prevalence, pathophysiology, prognosis and practical considerations. Diabetes MetabSyndr; 14: 303-310.
17. Sun Y, Koh V, Marimuthu K, Ng OT, Young B, Vasoo S (2020). National Centre for Infectious Diseases COVID-19 Outbreak Research Team. Epidemiological and Clinical Predictors of COVID -19. Clin Infect Dis 2020; 71: 786-792.
18. The World Bank (2020), World Bank Country and Lending Groups, World Bank Data Help Desk(2020),Available at https://datahelpdesk.worldbank.org/knowledgebase/articles/906519-worldbank-country-and-lending-groups ,last accessed on 08 December 2020.
19. Tsigaris P, Teixeira da Silva JA (2020). Smoking Prevalence and COVID-19 in Europe. Nicotine Tob Res. 2020;22(9):1646-1649. doi:10.1093/ntr/ntaa121
20. World integrated Trade Solutions (2018). Available at https://wits.worldbank.org/countrysnapshot/en/chn last accessed on 08 December 2020.
21. WHO (2020a) Director-General's opening remarks at the media briefing on COVID19 - March 2020
22. WHO (2020b) COVID-19 Weekly Epidemiological Update. Available on https://www.who.int/publications/m/item/weekly-epidemiological-update---1-december-2020 last accessed on 5th Dec 2020.
23. Wu C, Chen X, Cai Y, Zhou X, Xu S, Huang H, Zhang L, Zhou X, Du C, Zhang Y, Song J (2020). Risk factors associated with acute respiratory distress syndrome and death in patients with coronavirus disease 2019 pneumonia in Wuhan, China. JAMA internal medicine. 180(7):934-43.
24. Yang X, Yu Y, Xu J (2020). Clinical course and outcomes of critically ill patients with SARS-CoV-2 pneumonia in Wuhan, China: a single-centered, retrospective, observational study. Lancet Respir Med. 2020; 20: S2213 – S2600. DOI: 10.1016 / S2213-2600 (20) 30079-5.
25. Zhou F, Yu T, Du R (2020). Clinical course and risk factors for mortality of adult inpatients with COVID-19 in Wuhan, China: a retrospective cohort study. Lancet; 395: 1054–1062.
26. Zhu N, Zhang D, Wang W, Li X, Yang B, Song J, Zhao X, Huang B, Shi W, Lu R, Niu P (2020). A novel coronavirus from patients with pneumonia in China, 2019. N. Engl. J. Med. 382, 727–733.

arXiv:2301.10278v1 [gr-qc] 24 Jan 2023

Cosmological tests of the osculating Barthel-Kropina dark energy model

Amine Bouali,[1,*] Himanshu Chaudhary,[2,†] Rattanasak Hama,[3,‡]
Tiberiu Harko,[4,5,6,§] Sorin V. Sabau,[7,8,¶] and Marco San Martín[9,**]

[1] *Laboratory of Physics of Matter and Radiation, Mohammed I University, BP 717, Oujda, Morocco,*
[2] *Department of Applied Mathematics, Delhi Technological University, Delhi-110042, India,*
[3] *Faculty of Science and Industrial Technology, Prince of Songkla University, Surat Thani Campus, Surat Thani, 84000, Thailand,*
[4] *Department of Physics, Babes-Bolyai University, Kogalniceanu Street, Cluj-Napoca, 400084, Romania,*
[5] *Department of Theoretical Physics, National Institute of Physics and Nuclear Engineering (IFIN-HH), Bucharest, 077125 Romania,*
[6] *Astronomical Observatory, 19 Ciresilor Street, Cluj-Napoca 400487, Romania,*
[7] *School of Biological Sciences, Department of Biology, Tokai University, Sapporo 005-8600, Japan*
[8] *Graduate School of Science and Technology, Physical and Mathematical Sciences, Tokai University, Sapporo 005-8600, Japan,*
[9] *Faculty of Engineering, Pontifical Catholic University of Valparaiso, Chile*

(Dated: January 26, 2023)

We further investigate the dark energy model based on the Finsler geometry inspired osculating Barthel-Kropina cosmology. The Barthel-Kropina cosmological approach is based on the introduction of a Barthel connection in an osculating Finsler geometry, with the connection having the property that it is the Levi-Civita connection of a Riemannian metric. From the generalized Friedmann equations of the Barthel-Kropina model, obtained by assuming that the background Riemannian metric is of the Friedmann-Lemaitre-Robertson-Walker type, an effective geometric dark energy component can be generated, with the effective, geometric type pressure, satisfying a linear barotropic type equation of state. The cosmological tests, and comparisons with observational data of this dark energy model are considered in detail. To constrain the Barthel-Kropina model parameters, and the parameter of the equation of state, we use 57 Hubble data points, and the Pantheon Supernovae Type Ia data sample. The st statistical analysis is performed by using Markov Chain Monte Carlo (MCMC) simulations. A detailed comparison with the standard ΛCDM model is also performed, with the Akaike information criterion (AIC), and the Bayesian information criterion (BIC) used as the two model selection tools. The statefinder diagnostics consisting of jerk and snap parameters, and the $Om(z)$ diagnostics are also considered for the comparative study of the Barthel-Kropina and ΛCDM cosmologies. Our results indicate that the Barthel-Kropina dark energy model gives a good description of the observational data, and thus it can be considered a viable alternative of the ΛCDM model.

PACS numbers: 03.75.Kk, 11.27.+d, 98.80.Cq, 04.20.-q, 04.25.D-, 95.35.+d

CONTENTS

I. Introduction 2

II. Quick introduction to Finsler geometry, (α, β) metrics, and the Barthel connection 4
A. Finsler geometry, and particular Finsler spaces 5
1. Particular Fisnler geometries - Randers, Kropina and general (α, β) metrics 5
B. From the Barthel connection to the Y-osculating Riemann spaces 6
1. The Barthel connection 6
2. The Y-osculating Riemann geometry 6
C. The generalized curvature tensor 7

III. Review of the Barthel-Kropina cosmological model 7
A. Metric and thermodynamic quantities 7
B. The generalized Friedmann equations for the background cosmological evolution 8

IV. The Barthel-Kropina dark energy model 9
A. Alternative representation of the generalized Friedmann equation 9
B. Dark energy, and its equation of state 9
C. Cosmological evolution in the redshift space 10

V. Cosmological tests of the Barthel-Kropina dark energy model 10
A. Methodology 11
B. Data description 12

* a1.bouali@ump.ac.ma
† himanshuch1729@gmail.com
‡ rattanasak.h@psu.ac.th
§ tiberiu.harko@aira.astro.ro
¶ sorin@tokai.ac.jp
** mlsanmartin@uc.cl

1. $H(z)$ Dataset 12
2. Pantheon Dataset 12
C. Results 13
1. Constraining the Barthel-Kropina dark energy model parameters 13
2. Comparison with the ΛCDM model 14
3. Observational, and theoretical comparisons of the Hubble functions 14
D. Cosmographic analysis 14
1. Cosmological quantities 15

VI. Discussions and final remarks 19

Acknowledgments 20

References 20

I. INTRODUCTION

Finsler geometry [1] is an interesting and important extension of Riemannian geometry [2]. The relationship between the two geometries was best described by Chern, who described it as "Finsler Geometry is just Riemannian geometry without the quadratic restriction" [3]. Indeed, in his Habilitationsvortrag [2] Riemann has already introduced a metric structure in a general space based on the invariant distance element $ds = F\left(x^1, x^2, ..., x^n; dx^1, dx^2, ..., dx^n\right) = F(x, y)$, where for $y \neq 0$, F is a positive definite function defined on the tangent bundle TM. Moreover, F is assumed to be homogeneous of degree one in y. Riemannian geometry is a special case of the general metric, with $F^2 = g_{ij}(x)dx^i dx^j$. Hence, in a proper sense, Finsler geometry is not a generalization of the Riemannian geometry, but it is the Riemannian geometry without the quadratic restriction [3]. However, it is customary in both mathematical and physical literature to make a clear distinction between Riemann and Finsler geometries, and in the present work we will adopt the standard terminology. In a physically more intuitive way we may consider Finsler geometry as a geometry in which the metric tensor is a function of both coordinates defined on the base manifold, and of the tangent vectors, $g_{ij} = g_{ij}(x, y)$, or, as a geometry in which the metric tensor is a function of both coordinates and velocities. For in depth presentations and discussions of Finsler geometry see [4–8].

Despite its systematic and rigorous nature, and its many attractive features, the physical applications of the Finsler geometry were shadowed by the immense successes of the theory of general relativity, which is essentially based on Riemannian geometry [9–11]. The advent of general relativity also led to important developments in mathematics, like Weyl geometry [12], geometries with torsion [13, 14], or geometries with absolute parallelism [15]. All these geometries have found important applications in physics, and opened new perspectives in the understanding of the gravitational interaction. On the other hand, the applications of the Finsler geometry to physics did appear relatively late. One important step in this direction was taken in the work by Randers [16], initially still formulated in a higher dimensional Riemannian context, with the goal of obtaining a unified theory of gravity and electromagnetism. However, Randers geometry is a typical example of a Finsler geometry, with $F(x, y) = \left(a_{ij}(x)dx^i dx^j\right)^{1/2} + A_k(x)y^k$, where $A_k(x)$ is an arbitrary vector field. Recently, Randers geometry was extensively applied in the study of various gravitational phenomena in [17–24]. Finsler geometry has also important applications in the geometric description of quantum mechanics [25–28]. General relativistic kinetic gas theory was investigated by using methods from Finsler geometry in [29].

The first attempts at formulating a Finslerian theory of gravitation belonged to Horváth [30], and Horváth and Moór [31]. Early Finslerian type gravitational theories were also formulated in [32] and [33], respectively. The set of the Finslerian type gravitational field equations proposed in these works are given by

$$R_{\mu\nu} - \frac{1}{2}g_{\mu\nu}R + \lambda g_{\mu\nu} = \chi T_{\mu\nu}, \tag{1}$$

$$K_{\mu\nu} - \frac{1}{2}g_{\mu\nu}K + \lambda g_{\mu\nu} = \chi T_{\mu\nu}, \tag{2}$$

and

$$S_{\mu\nu} - \frac{1}{2}g_{\mu\nu}S - \lambda^{(i)}g_{\mu\nu} = -\chi^{(i)}T^i_{\mu\nu}, \tag{3}$$

respectively, where χ is the gravitational constant, λ is the cosmological constant, while $\lambda^{(i)}$ and $\chi^{(i)}$ denote the internal cosmological and gravitational constants, respectively. The geometrical quantities $R_{\mu\nu}$, R, $K_{\mu\nu}$, K are the contracted third curvatures, while $S_{\mu\nu}$ and S are the v-Ricci curvature tensors, and the v-scalar curvature, respectively. Moreover, $T_{\mu\nu}$ denotes the ordinary matter energy-momentum tensor, while $T^i_{\mu\nu}$ is the internal energy-momentum tensor.

An interesting Finslerian approach to gravity was introduced in [34], with the main focus on the Finslerian interpretation of the particle motion in a gravitational field. For detailed presentations of the Finslerian type extensions of general relativity see [35]. The Schwarzschild type Finslerian metrics were considered in [36, 37].

The vector bundle point of view was adopted to propose a system of Einstein type gravitational field equations in [38]. The basic idea of this approach is to consider the field y as a fibre at the point x of the base x manifold. For this vector bundle the total space is constructed as a unification of the x and y fields [39]. The adapted frame is defined for these unified fields as

$$X_A = \left(\frac{\delta}{\delta x^\lambda} = \frac{\partial}{\partial x^\lambda} - N^i_\lambda \frac{\partial}{\partial y^i}, \frac{\partial}{\partial y^i}\right),$$
$$X^A = \left(dx^\kappa, \delta y^i = dy^i + N^i_\lambda dx^\lambda\right), \tag{4}$$

where X_A is the adapted basis of the tangent space T_xM, while X^A is the adapted cobasis in the cotangent space T_x^*M. In Eq. (4) the indices A, B take the values $A, B = (\kappa, i) \in \{0, 1, 2, 3, ..., 7\}$, while $\lambda, \kappa = 0, 1, 2, 3$. Moreover, N_λ^i denotes the nonlinear connection. The frame (4) is adapted to the metric $G = (G_{AB})$, given by $G = g_{\lambda\kappa}(x, y)dx^\kappa dx^\lambda + g_{ij}(x, y)\delta y^i \delta y^j$. On the total space the gravitational field equations are postulated to have the standard form, $\mathcal{R}_{AB} - (1/2)\mathcal{R}G_{AB} = \tau_{AB}$, where τ_{AB} is the matter energy-momentum tensor, and they can be decomposed to take the form [38]

$$R_{\lambda\nu} - \frac{1}{2}(R + S)g_{\lambda\nu} = \tau_{\lambda\nu}, \overset{1}{P}_{i\lambda} = \tau_{i\lambda}, \overset{2}{P}_{\lambda i} = -\tau_{\lambda i}, \quad (5)$$

$$S_{ij} - \frac{1}{2}(R + S)g_{ij} = \tau_{ij}. \quad (6)$$

An alternative approach to the Finslerian geometric type gravity was proposed in [40], by assuming that the Einstein vacuum equations are given by $H = H_i^i = 0$, with H_k^i constructed from the first and second derivatives of the quantity $G^l = \gamma_{jk}^l \dot{x}^j \dot{x}^k/2$. For a Riemannian metric, the gravitational field equation reduce to the general relativistic Einstein gravitational field equations. Finslerian type solutions of the field equations can also be obtained.

An interesting and important class of Finsler space are the Berwald-Finsler spaces. In these geometries a particular set of gravitational field equations was introduced and discussed in [41]. To obtain the gravitational field equations in the Berwald-Finsler space the Bianchi identities satisfied by the Chern curvature have been used. The geometric part of the gravitational field equation is nonsymmetric in general, indicating that the principle of the local Lorentz invariance is not satisfied.

Finsler type gravitational field equations have been obtained from a Finsler-Lagrange function L in [42], with the use of a variational principle, The field equations are given by

$$2R - \frac{L}{3}g^{Lij}R_{\cdot i\cdot j} + \frac{2L}{3}g^{Lij}\left[(\nabla P_i)_{\cdot j} + P_{i|j} - P_i P_j\right] = 0, \quad (7)$$

where $g_{ij}^L = \frac{1}{2}\frac{\partial^2 L}{\partial \dot{x}^i \partial \dot{x}^j} = \frac{1}{2}L_{\cdot i\cdot j}$, $R_{\cdot i\cdot j}$ is the geodesic deviation operator, R is its trace, and P is the Landsberg tensor. The action from which the above field equations can be derived is given by $S[L] = \int_{\Sigma \subset TM} \mathrm{vol}(\Sigma)R_{|\Sigma}$, where $\Sigma = \{(x, \dot{x}) \in TM | F(x, \dot{x}) = 1\}$ is the unit tangent bundle, and $\mathrm{vol}(\Sigma)$ is the volume form on Σ, constructed with the use of the Finsler metric.

In its Riemannian formulation the theory of General Relativity was extremely successful in explaining the gravitational phenomenology at the level of the Solar System, where it passes all high precision observational tests, including the light deflection, the perihelion advance of Mercury, the Shapiro time delay, the Nordtvedt effect in lunar motion, and frame-dragging, respectively [43]. An important confirmation of the predictions of general relativity is represented by the experimental detection of the gravitational waves [44], which opened a deep view on the Universe, also leading, for example, to a new perspective on the mass distribution of the neutron stars [45]. However, when extended to gravitational systems far bigger than the Solar System, namely, at the galactic and cosmological scales, General Relativity is facing a number of very serious difficulties, whose solutions may require a fundamental change in our view of the gravitational interaction.

The precise measurements of the temperature fluctuations of the Cosmic Microwave Background Radiation (CMBR) by the Planck satellite [46, 47], together with the astrophysical observations of the distant supernovae, extending up to a redshift of $z \approx 2$ [48–55] have firmly indicated that the present-day Universe is in a phase of accelerating expansion. Moreover, the amazing result that its matter content consists of only 5% baryonic matter has also been confirmed. Hence, these observations strongly point out that 95% of the matter-energy content of the Universe consists of two main (and mysterious) components, dark energy and dark matter, respectively.

An explanation of these cosmological observations can be obtained if one reintroduces in the Einstein gravitational field equations of the cosmological constant Λ, first introduced by Einstein in 1917 [56]. For discussions about the history of the cosmological constant, and its possible interpretations see [57–59]. The corresponding cosmological model, obtained by also adding a cold dark matter component in the Einstein field equations is called the ΛCDM model, and it has become one of the main theoretical tool for the understanding of the cosmic dynamics.

The ΛCDM paradigm can give excellent fits to the observational data. However, due to the lack of a convincing theoretical basis, and of the many problems raised by the cosmological constant itself, the physical basis of the ΛCDM model is (at least) uncertain. Therefore, to obtain a mathematically, physically and observationally consistent description of the Universe, three major, and distinct, theoretical approaches have been proposed, called the dark components model, the dark gravity model, and the geometry-matter coupling model, respectively [60]. The dark components model [61–65] postulates that the basic constituents of Universe are dark energy, and dark matter, respectively, of (yet) unknown physical origin. There are many proposals for the nature of these dark constituents. A simple dark energy model can be obtained in the framework of the quintessence models [66–70], in which the dynamics of the Universe is determined by a single self-interacting scalar field ϕ, in the presence of a potential $V(\phi)$. For the quintessence models the gravitational action is given by

$$S = \int \left[\frac{M_p^2}{2}R - \partial_\mu \phi \partial^\mu - V(\phi)\right]\sqrt{-g}d^4x, \quad (8)$$

where R is the Ricci scalar, and M_p denotes the Planck

mass.

In the dark gravity approach it is proposed that to explain the gravitational interaction that changes on astrophysical (galactic) and cosmological scales, one must go beyond the Riemannian geometry of general relativity, and that more general geometries must be used for a theoretical description of gravity. In this direction theories in the presence of torsion [71–74], of nonmetricity [75–80], or in the Weitzenböck geometry [81, 82] have been intensively investigated. The third theoretical approach to the gravitational phenomenology assumes that ordinary matter may play a dominant role in the cosmological dynamics due to its coupling with geometry, via a curvature - matter coupling that could explain the observed gravitational phenomenology [83–87]. For reviews of modified gravity models see [88–92]. For a detailed analysis of theories with geometry-matter coupling see [93].

In the dark gravity approach, which goes beyond the mathematical formalism of the Riemann spaces, Finsler type cosmological models represent an interesting alternative to the standard ΛCDM model, as geometric explanations, or replacements, of dark energy, and perhaps even of dark matter. Many studies have been devoted to the applications of the Finsler geometry in cosmology, with the goal of understanding from a new point of view the dynamical evolution of the cosmic structures [94–121].

In particular, in [121], the cosmological implications of the Kropina geometry have been investigated in detail, by using the mathematical formalism of the osculating Finsler spaces, in which the internal variable is a function of the base manifold coordinates only. Moreover, in order to describe gravitational phenomena, the Barthel connection was adopted, which has the remarkable property that it is the Levi-Civita connection of a Riemannian metric. To describe the gravitational phenomena it was assumed that in the Barthel-Kropina geometry the Ricci type curvatures are related to the matter energy-momentum tensor by the standard Einstein equations. The generalized Friedmann equations in the Barthel-Kropina geometry have been derived by considering that the background Riemannian metric is of Friedmann-Lemaitre-Robertson-Walker (FLRW) type. The model admits a de Sitter type solution, and an effective fluid type dark energy component, described by an effective energy density and thermodynamic pressure, related by a linear equation of state, can also be obtained. A preliminary comparison of the dark energy model with the observational data and with the standard ΛCDM model was also performed, and it was found that the Barthel-Kropina-FLRW type models give a satisfactory description of the observations.

It is the goal of the present paper to perform a detailed comparison between the theoretical predictions of the Barthel-Kropina dark energy model, and the cosmological observations. The Barthel-Kropina dark energy model contains three free parameters, the coefficient of the equation of state ω, and the present day values of the coefficient of the one form β, and of its derivative, respectively. To find the values, and the constraints, on these parameters, we used the statistical MCMC approach, with the Bayesian technique. Moreover, we fit the theoretical predictions with two different observational samples, containing Hubble data, and the Pantheon data. Hence, we can obtain in this way the best fit values of the model parameters. With the fitted values of the parameters we perform a cosmographic (statefinder) analysis of the model, by investigating the behaviors of the deceleration parameter, and of the jerk and snap parameters, respectively. The $Om(z)$ diagnostic is also considered. In all cases, by using the fitted values of the model parameters, we compare the Barthel-Kropina model with the standard ΛCDM model.

The present paper is organized as follows. In Section II we briefly review the basic Finsler geometric concepts used in the construction of the gravitational model, including the definitions of the Barthel connection, and of the osculating Finsler geometry. The basic principles of the Barthel-Kropina cosmology are introduced in Section III, where the generalized Friedmann equations are also written down. We present the Barthel-Kropina dark energy model, and discuss its properties in Section IV. A detailed comparison of the theoretical predictions of the model and the observational data is performed in Section V. We discuss and conclude our results in Section VI.

II. QUICK INTRODUCTION TO FINSLER GEOMETRY, (α, β) METRICS, AND THE BARTHEL CONNECTION

In the present Section we will briefly review the basic concepts of the Finsler geometry to be used in the cosmological applications. Specifically, we focus on the concept of Finsler and (α, β)-metrics. In our approach the Kropina metric plays a central role, and therefore we will consider it in some detail. Our investigations are essentially based on the concept of osculating Finsler spaces, and of the Barthel connection, respectively, which makes necessary a brief presentation of the basics of the Barthel-Kropina geometry. For in depth presentations of the Finsler geometry, and of some of its applications, see [4–8].

Finsler geometry has many applications in classical Newtonian physics, especially in the description of the dissipative effects. In classical mechanics the equations of motion of a system of particles in the presence of external forces F_i, $i = 1, 2, ..., n$, which cannot be derived from a potential, can be obtained from a regular Lagrangian L, defined on an n-dimensional differentiable manifold M, by using the Euler-Lagrange equations, given by

$$\frac{d}{dt}\frac{\partial L}{\partial y^i} - \frac{\partial L}{\partial x^i} = F_i, i \in \{1, 2, ..., I\}, \tag{9}$$

The Euler-Lagrange equations (9) are equivalent to a system of second-order differential equations,

$$\frac{d^2x^i}{dt^2}+2G^i\left(x,y,t\right)=0,i\in\left\{1,2,...,n\right\}. \tag{10}$$

From a mathematical point of view, Eqs. (10) describe geodesic motion in a Finsler space.

A. Finsler geometry, and particular Finsler spaces

In the present day approach to the basic laws describing natural phenomena a basic assumption is that time and space form together a single structure, called the space-time. Mathematically, the space-time is described as a four dimensional differentiable manifold M, on which a pseudo-Riemannian metric tensor g_{IJ}, $I,J,K...=0,1,2,3$, can be defined. According to the chronological hypothesis, the space-time distance (interval) between two events x^I and x^I+dx^I is obtained according to the prescription $ds=\left(g_{IJ}dx^Idx^J\right)^{1/2}$ [122, 123]. In Riemannian geometry, the metric tensor g_{IJ} is a function of the coordinates x^I of the space-time manifold only, so that $g_{IJ}=g_{IJ}(x)$. But more general geometries than the Riemannian one can also be constructed. One of the important metrical generalizations of the Riemann geometry is the Finsler geometry [1, 4–8].

Finsler spaces are a class of metric spaces, in which the distance ds between two neighbouring points $x=(x^I)$ and $x+dx=(x^I+dx^I)$ is obtained according to the relation,

$$d\hat{s}=F\left(x,dx\right). \tag{11}$$

The Finsler metric function F, introduced in the above definition, is a positively homogeneous of degree one function in dx, with the basic property

$$F\left(x,\lambda dx\right)=\lambda F\left(x,dx\right),\text{for}\lambda>0. \tag{12}$$

The Finsler metric function F is usually expressed by using the canonical coordinates $(x,y)=(x^I,y^I)$ of the tangent bundle TM, where $y=y^I\frac{\partial}{\partial x^I}$, is a tangent vector at x. By using the canonical coordinates, the Finsler metric tensor $\hat{g}_{IJ}$ is defined according to

$$\hat{g}_{IJ}\left(x,y\right)=\frac{1}{2}\frac{\partial^2F^2\left(x,y\right)}{\partial y^I\partial y^J}, \tag{13}$$

on the tangent bundle TM=TM\0. Hence, we can write Eq. (11) as $d\hat{s}^2=\hat{g}_{IJ}\left(x,y\right)y^Iy^J$. Riemann spaces can be considered as particular cases of Finsler spaces, obtained when $\hat{g}_{IJ}\left(x,y\right)=g_{IJ}\left(x\right)$, $y^I=dx^I$, leading to $ds^2=g_{IJ}(x)dx^Idx^J$, respectively. For a discussion on the relation between Riemann and Finsler geometries see [3, 7].

One can also introduce an important additional geometric quantity, the Cartan tensor $\hat{C}(x,y)$, which is defined as

$$\hat{C}_{IJK}=\frac{1}{2}\frac{\partial\hat{g}_{IJ}\left(x,y\right)}{\partial y^K}. \tag{14}$$

The Cartan tensor gives an estimation of the deviation of a Finsler geometry from a Riemannian one.

1. *Particular Fisnler geometries - Randers, Kropina and general (α,β) metrics*

There are a large number of special Finsler geometries, obtained by specifying the functional form of the metric tensor $\hat{g}_{IJ}\left(x,y\right)$. One of the first considered Finsler geometries, which has many applications in physics, are the Randers spaces [16], representing a special type of Finsler structures, with the Finsler metric function defined as

$$F=\left[g_{IJ}(x)dx^Idx^J\right]^{1/2}+A_I(x)dx^I=\alpha+\beta, \tag{15}$$

where $g_{IJ}(x)$ is the metric tensor of a *Riemann space*, and $A_I(x)dx^I$ is a linear 1-form, defined on the tangent bundle TM.

Another important class of Finsler geometries are the Kropina spaces [124, 125], which are special Finsler spaces with metrics given by

$$F\left(x,y\right)=\frac{g_{IJ}(x)y^Iy^J}{A_I(x)y^I}. \tag{16}$$

A generalization of the above geometries was done by Matsumoto [126, 127], by introducing *the concept of the (α,β) metrics*. An (α,β) metric is obtained when the Finsler metric function F *is a positively homogeneous function $F(\alpha,\beta)$ of first degree in two variables* $\alpha\left(x,y\right)=\left[g_{IJ}(x)dx^Idx^J\right]^{1/2}$ and $\beta\left(x,y\right)=A_I(x)y^I$, respectively.

As for α, we assume that it is a non-degenerate (regular), and positive-definite*Riemannian metric*. Both the Randers and the Kropina metrics belong to the class of the (α,β) metrics. In the case of the Randers metric $F=\alpha+\beta$, while $F=\frac{\alpha^2}{\beta}$ for the Kropina metric. One can also define general (α,β) metrics, with the Finsler metric function given by $F(\alpha,\beta)=\alpha\phi\left(\beta/\alpha\right)=\alpha\phi\left(s\right)$, where $s=\beta/\alpha$, and $\phi=\phi(s)$ is a C^∞ positive function, defined on an open interval $(-b_o,b_o)$ [121].

For the fundamental metric tensor of the (α,β) metric we obtain the expression

$$\begin{aligned}\hat{g}_{IJ}(x,y)=&\frac{L_\alpha}{\alpha}h_{IJ}+\frac{L_{\alpha\alpha}}{\alpha^2}y_Iy_J+\frac{L_{\alpha\beta}}{\alpha}\left(y_IA_J+y_JA_I\right)\\&+L_{\beta\beta}A_IA_J,\end{aligned} \tag{17}$$

where we have denoted $L=F^2/2$, and

$$h_{IJ}=\alpha\frac{\partial^2\alpha(x,y)}{\partial y^I\partial y^J}=g_{IJ}-\frac{y_Iy_J}{\alpha^2}. \tag{18}$$

As usual, the indices α, β of L denote partial differentiation with respect to α and β, respectively.

B. From the Barthel connection to the Y-osculating Riemann spaces

We now briefly present the two basic mathematical concepts on which the cosmological applications of the Kropina metrics, considered in the present study, are based, namely, the Barthel connection, and the osculating Finsler spaces.

1. The Barthel connection

Let's consider now that (M^n, F) is a Finsler space, defined on a base manifold M^n. On M^n a vector field $Y(x) \neq 0$ is also defined. We can define now a particular mathematical structure $(M^n, F(x,y), Y(x))$, representing a Finsler space $(M^n, F(x,y))$ *which has a tangent vector field* $Y(x)$. *For a vector* Y *that does not vanish in any point on* M, *the Finslerian metric* $\hat{g}(x,y)$ *generates the* Y*-Riemann metric* $\hat{g}_Y(x) = \hat{g}(x, Y)$.

Point Finsler spaces represent an important class of Finsler spaces. *A point Finsler space is an* n*-dimensional space, which is locally Minkowskian, and, in general, not locally Euclidean* [128, 129]. A general Finsler geometry is *inhomogeneous and anisotropic*, while a Minkowski space is *flat, homogeneous, but still anisotropic. The Finsler* n*-space can be called a Barthel-Finsler space*, or a *point Finsler space.*

Let's assume that a point vector field $Y^I(x)$ and a Finsler metric tensor $\hat{g}(x,y)$ are given. Then, we define the absolute differential of the vector Y as [130]

$$DY^I = dY^I + Y^K b^I_{KH}(x, Y) dx^H, \tag{19}$$

where $b^I_{KH}(x, Y)$ denotes *the coefficients of the Barthel connection.* The coefficients $b^I_{KH}(x, Y)$ are obtained with the help of the generalized Christoffel symbols $\hat{\gamma}_{JIH}$, defined, as in Riemann geometry, according to the relation

$$\hat{\gamma}_{IJH} := \frac{1}{2}\left(\frac{\partial \hat{g}_{JI}}{\partial x^H} + \frac{\partial \hat{g}_{IH}}{\partial x^J} - \frac{\partial \hat{g}_{HJ}}{\partial x^I}\right). \tag{20}$$

To obtain the explicit expression of the Barthel connection $b^I_{KH}(x, Y)$ we write the expressions in the second term of Eq. (19) as

$$Y^K b^I_{KH} = Y^K \left(\hat{\gamma}^I_{KH} - \hat{\gamma}^R_{KS} Y^S \hat{C}^I_{RH}\right), \tag{21}$$

which allows us to obtain the Barthel connection as [130]

$$b^I_{KH} = \hat{\gamma}^I_{KH} - \hat{\gamma}^R_{KS} Y^S \hat{C}^I_{RH}. \tag{22}$$

The Barthel connection has several interesting properties. First of all, *it depends on the vector field on which it acts*, a property that does not appear in Riemann geometry. Hence, the Barthel connection is very different, as compared to the connections in Riemann geometry. Generally, for anisotropic metrics, all geometric properties do depend on the direction. However, *for the Barthel connection, the dependence is only on the direction of the vector field, and not on its magnitude.* Moreover, the Barthel connection *is the simplest connection that keeps the metric function unchanged by the parallel transport.* In the case of Finsler vector fields, which are functions of both x and y, the Barthel connection permits a natural transition to the Cartan geometry of the Finsler spaces. Hence, in the following, we consider *the connection of a point Finsler space as the Barthel connection.*

The Barthel connections, unlike the usual Levi-Civita connection of a Riemannian metric, or, more general affine connections, do not live on the base manifold M, but on the total space of the tangent bundle [7, 8]. This important characteristic may lead to major differences between the geometrical theories of Finsler and Riemann manifolds.

2. The Y-osculating Riemann geometry

The concept of osculating Riemann spaces of Finsler geometries was developed by Nazim [131], and it was later studied in great detail in [132]. The osculating approach associates to a complex geometric structure, like, for example, a Finsler geometry, and a Finsler connection, a simpler mathematical format, like a Riemann metric, or an affine or a linear connection. In doing this one assumes that the simpler, osculating structure, approximates, in some sense, the most complicated one. Hence, by using the osculation approach, one can obtain mathematical results that allow the understanding of the properties of the mathematically more complicated geometries.

Let's consider now a local section Y of $\pi_M : TM \to M$. It is a basic mathematical result that geometric objects defined on TM can be pulled back to M. By taking into account that $\hat{g}_{IJ} \circ Y$ is a function defined on U, we can introduce a new metric, defined as

$$\hat{g}_{IJ}(x) := \hat{g}_{IJ}(x, y)|_{y=Y(x)}, \quad x \in U. \tag{23}$$

The pair $(U, \hat{g}_{IJ})$ *correspond to a Riemannian manifold*, while $\hat{g}_{IJ}(x)$ represents the Y*-osculating Riemannian metric* corresponding to (M, F).

The Christoffel symbols of the first kind are defined for the osculating Riemannian metric (23) as,

$$\hat{\gamma}_{IJK}(x) := \frac{1}{2}\left\{\frac{\partial}{\partial x^J}\left[\hat{g}_{IK}(x, Y(x))\right] + \frac{\partial}{\partial x^K}\left[\hat{g}_{IJ}(x, Y(x))\right] - \frac{\partial}{\partial x^I}\left[\hat{g}_{JK}(x, Y(x))\right]\right\}. \tag{24}$$

Explicitly, after using the law of the derivative of the

composed functions, we find

$$\hat{\gamma}_{IJK}(x) = \hat{\gamma}_{IJK}(x,y)|_{y=Y(x)} + 2\left(\hat{C}_{IJL}\frac{\partial Y^L}{\partial x^K} + \hat{C}_{IKL}\frac{\partial Y^L}{\partial x^J} - \hat{C}_{JKL}\frac{\partial Y^L}{\partial x^I}\right)\Big|_{y=Y(x)}, \quad (25)$$

where $\hat{C}_{IJL}$ is the Cartan tensor. Therefore, if a non-vanishing global section Y of TM does exist, with the property $Y(x) \neq 0$, $\forall x \in M$, the osculating Riemannian manifold $(M, \hat{g}_{ij})$ can always be defined.

Let's now consider the case of an (α, β) metric. For this geometry we choose the vector field $Y = A$, with $A^I = g^{IJ}A_J$. By taking into account that the vector field A is non-vanishing globally on M, it follows that β has no zero points. Therefore, for (α, β) metrics we can define *the A-osculating Riemannian manifold* $(M, \hat{g}_{IJ})$, where the Riemann metric is given by $\hat{g}_{IJ}(x) := \hat{g}_{IJ}(x, A)$.

For the length $\tilde{a}$ of A with respect to α we immediately obtain $\tilde{a}^2 = A_I A^I = \alpha^2(x, A)$ and $Y_I(x, A) = A_I$, respectively.

Explicitly, the A-osculating Riemannian metric can be written as

$$\hat{g}_{IJ}(x) = \frac{L_\alpha}{\tilde{a}}\Big|_{y=A(x)} g_{IJ} + \left(\frac{L_{\alpha\alpha}}{\tilde{a}^2} + 2\frac{L_{\alpha\beta}}{\tilde{a}} + L_{\beta\beta} - \frac{L_\alpha}{\tilde{a}^3}\right)\Big|_{y=A(x)} A_I A_J. \quad (26)$$

Furthermore, we have the relations $\beta(x, A) = \tilde{a}^2$, and $p_I(x, A) = 0$, Therefore, from the definition of the Cartan tensor, and its expression for an (α, β) metric, we obtain the basic result that $\hat{C}_{IJK}(x, A) = 0$. On the other hand, for $Y = A$, we obtain

$$\hat{\gamma}_{IJK}(x) = \hat{\gamma}_{IJK}(x,y)|_{y=A(x)}. \quad (27)$$

Hence, we obtain the fundamental result that for *an (α, β)-metric, the Barthel connection - the linear A-connection with $A^I = \left(g^{IJ}A_J\right)$, is nothing but the Levi-Civita connection of the A-Riemannian metric.* After evaluating the fundamental tensor $g_{ij}(x, y)$ of (M, F) at $(x, Y(x))$, one obtains a Riemannian metric g_Y on M, having its own Levi-Civita connection.

C. The generalized curvature tensor

As we have already seen, the Barthel connection, having local coefficients $\left(b^A_{BC}(x)\right)$, *is an affine connection.* The curvature tensor of an affine connection, with local coefficients $\left(\Gamma^A_{BC}(x)\right)$, is generally given by

$$R^A_{BCD} = \frac{\partial \Gamma^A_{BD}}{\partial x^C} - \frac{\partial \Gamma^A_{BC}}{\partial x^D} + \Gamma^E_{BD}\Gamma^A_{EC} - \Gamma^E_{BC}\Gamma^A_{ED}. \quad (28)$$

Hence, the curvature of the Barthel connection can be obtained from the above equation by taking $\left(\Gamma^A_{BC}(x)\right) = \left(b^A_{BC}(x)\right)$. In the case of the Kropina metric $F = \alpha^2/\beta$, on which we will focus in the following, the Barthel connection is identical with the Levi-Civita connection of the osculating metric $\hat{g}_{AB}(x) = g_{AB}(x, A(x))$, where $A_I(x)$ are the components of the one-form β, and g_{AB} is the fundamental tensor of F. Therefore, by taking into account that $b^A_{BC} = \hat{\gamma}^A_{BC}$, where $\hat{\gamma}^A_{BC}$ are the Levi-Civita connection coefficients, we obtain for the curvature tensors of the Kropina metric the expressions

$$\hat{R}^A_{BCD} = \frac{\partial \hat{\gamma}^A_{BD}}{\partial x^C} - \frac{\partial \hat{\gamma}^A_{BC}}{\partial x^D} + \hat{\gamma}^E_{BD}\hat{\gamma}^A_{EC} - \hat{\gamma}^E_{BC}\hat{\gamma}^A_{ED}, \quad (29)$$

and

$$\hat{R}_{BD} = \sum_A \left[\frac{\partial \hat{\gamma}^A_{BD}}{\partial x^A} - \frac{\partial \hat{\gamma}^A_{BA}}{\partial x^D} + \sum_E \left(\hat{\gamma}^E_{BD}\hat{\gamma}^A_{EA} - \hat{\gamma}^E_{BA}\hat{\gamma}^A_{ED}\right)\right], \quad (30)$$

respectively, where the indices A, B, C, D, E takes values in the set $\{0, 1, 2, 3\}$, $\hat{R}_{BD} = \hat{R}^A_{BAD}$, and $\hat{R}^B_D = \hat{g}^{BC}\hat{R}_{CD}$, respectively [120]. Finally, the generalized Ricci scalar is defined as $\hat{R} = \hat{R}^B_B$.

III. REVIEW OF THE BARTHEL-KROPINA COSMOLOGICAL MODEL

In the present Section we will review the basics and the background evolution of the Barthel-Kropina cosmological model, as introduced in [121]. The generalized Barthel-Kropina-Friedmann equations will represent the theoretical basis for the detailed comparison of this cosmological model with the observations. Moreover, they offer a deeper insight into the mathematical and physical structure of the model, and into the possible relevance of the Finsler geometric structure for the understanding and description of the cosmological dynamics.

A. Metric and thermodynamic quantities

The Barthel-Kropina cosmological model is based on a Finsler type (α, β) geometry, in which the fundamental metric function of the geometry is defined as $F = \alpha^2/\beta$, with α a positive non-degenerate Riemann metric, and β an one form. In the following we adopt a coordinate system with $\left(x^0 = ct, x^1 = x, x^2 = y, x^3 = z\right)$.

To build-up consistently a cosmological model based on the Kropina metric function, we need to supplement the Finsler framework with several mathematical and physical assumptions [121], which we list below:

a. The Riemann metric $g_{IJ}(x)$ is Friedmann-Lemaitre-Robertson-Walker. We postulate that the metric in α is given by the Friedmann-Lemaitre-Robertson-Walker (FLRW) metric,

$$ds^2 = \left(dx^0\right)^2 - a^2\left(x^0\right)\left[\left(dx^1\right)^2 + \left(dx^2\right)^2 + \left(dx^3\right)^2\right], \quad (31)$$

where $a\left(x^0\right)$ is the scale factor. Hence, as assume that the Universe is homogeneous and isotropic, with a uniform flow of the cosmological time t.

b. Validity of the Cosmological Principle. We assume the validity of the Cosmological Principle throughout the large scale Universe, by requiring that all geometrical and physical quantities depend on the cosmological time only. Thus, in the one-form β, the components of the vector A depend on the cosmological time only, $A_I = A_I\left(x^0\right)$.

c. The vector A has only one time-like independent component, $A_0\left(x^0\right)$. We assume that the space-like components of A vanish, so that $A_1 = A_2 = A_3 = 0$. The non-satisfaction of this condition leads to the violation of the Cosmological Principle, and to the existence of a preferred direction in the Universe. But this would contradict the observationally well confirmed large scale spatial isotropy of the Universe. Therefore, in the following we consider that the 1-form field β has the form

$$(A_I) = \left(a\left(x^0\right)\eta\left(x^0\right), 0, 0, 0\right) = (A^I), \tag{32}$$

where by $\eta\left(x^0\right)$ we have denoted an arbitrary function of the cosmological time.

d. Matter comoves with the cosmological expansion. We assume that in the Barthel-Kropina geometry *a comoving frame*, in which all observers move together with the Hubble flow in the Riemannian geometry described by the metric $g_{IJ}(x)$.

e. Matter and thermodynamics. We assume that the matter content of the Universe can be described as a perfect fluid, characterized by two thermodynamic quantities only, the energy density ρc^2, and the thermodynamic pressure p, respectively. Since the matter is comoving with the cosmological expansion, and the Universe is homogeneous and isotropic, the only non-vanishing components of the matter energy-momentum tensor $\hat{T}_{AB}$ are

$$\hat{T}_0^0 = \rho c^2, \hat{T}_{00} = \hat{g}_{00}\hat{T}_0^0, \hat{T}_k^k = -p, \hat{T}_{ii} = -\hat{g}_{ik}\hat{T}_i^k. \tag{33}$$

f. Gravity from geometry. We postulate that the Einstein gravitational field equations are given in the Barthel-Kropina geometry by

$$\hat{R}_{BD} - \frac{1}{2}\hat{g}_{BD}\hat{R} = \kappa^2\hat{T}_{BD}, \tag{34}$$

where G and c are the Newtonian gravitational constant, and the speed of light, respectively, and $\kappa^2 = 8\pi G/c^4$ is the gravitational coupling constant. $\hat{T}_{BD}$ denotes the matter energy-momentum tensor, obtained in the usual way from the standard thermodynamic quantities, with the help of the Finslerian metric tensor $\hat{g}_{BD}$.

Therefore, from the previous assumptions, we can summarize the mathematical structure of the Barthel-Kropina-FLRW cosmological model as follows [121],

(i) $(A_I) = \left(a\left(x^0\right)\eta\left(x^0\right), 0, 0, 0\right) = \left(A^I\right)$;

(ii) $(g_{IJ}) = \begin{pmatrix} 1 & 0 & 0 & 0 \\ 0 & -a^2(x^0) & 0 & 0 \\ 0 & 0 & -a^2(x^0) & 0 \\ 0 & 0 & 0 & -a^2(x^0) \end{pmatrix}$;

(iii) $\alpha|_{y=A(x)} = a(x^0)\eta(x^0)$;

(iv) $\beta|_{y=A(x)} = [a(x^0)\eta(x^0)]^2$.

B. The generalized Friedmann equations for the background cosmological evolution

The Einstein gravitational field equations in the Barthel-Kropina-FLRW geometry,

$$\hat{G}_{00} = \frac{8\pi G}{c^4}\hat{g}_{00}\rho, \hat{G}_{ii} = -\frac{8\pi G}{c^4}\hat{g}_{ii}p, \tag{35}$$

gives the generalized Friedmann equations for the background cosmological evolution, which take the form [121],

$$\frac{3(\eta')^2}{\eta^2} = \frac{8\pi G}{c^2}\frac{1}{a^2\eta^2}\rho, \tag{36}$$

and

$$2\frac{\eta''}{\eta} + 2\mathcal{H}\frac{\eta'}{\eta} - 3\frac{(\eta')^2}{\eta^2} = \frac{8\pi G}{c^4}\frac{p}{a^2\eta^2}, \tag{37}$$

respectively, where we have denoted $\mathcal{H} = \left(1/a\left(x^0\right)\right)\left(da\left(x^0\right)/dx^0\right)$. By eliminating the term $-3\left(\eta'\right)^2$ by using Eq. (36), Eq. (37) takes the simple form

$$a\eta\frac{d}{dx^0}\left(\eta' a\right) = \frac{4\pi G}{c^4}\left(\rho c^2 + p\right). \tag{38}$$

The set of the generalized Friedmann equations in the Barthel-Kropina geometry consists of two equations with four unknowns (a, η, ρ, p). Even after imposing an equation of state for the ordinary matter, $p = p(\rho)$, the system of generalized Friedmann equations is still underdetermined. Hence, to close it, we need to impose an independent relation between two of the model parameters.

a. Conservation of matter and energy. In standard Friedmann cosmology the matter energy-density is conserved. This is not the case in the Barthel-Kropina-FLRW model. The matter energy-momentum balance equation can be obtained easily by multiplying Eq. (36) with a^3, and taking the derivative of the result with respect to x^0. By combining this relation with the second generalized Friedmann equation, we find the energy balance equation in the Barthel-Kropina-FLRW cosmology as given by [121],

$$\frac{8\pi G}{c^4}\left[\frac{d}{dx^0}\left(\rho c^2 a^3\right) + p\frac{d}{dx^0}a^3\right] = 6a^5\Big[\mathcal{H}\left(\eta'\right)^2 + \left(\eta' + \mathcal{H}\eta\right)\eta'' + \mathcal{H}^2\eta\eta'\Big]. \tag{39}$$

We can also rewrite the energy balance equation in a form that is closer to the standard general relativistic result as

$$\frac{4\pi G}{c^4}\left[\frac{d}{dx^0}\left(\rho c^2 a^3\right)+p\frac{d}{dx^0}a^3\right] = 3a^5\left[\frac{8\pi G}{2c^4}\left(\frac{5}{3}\rho c^2+p\right)\frac{\mathcal{H}}{a^2}+\eta'\eta''\right]. \quad (40)$$

b. Recovering standard General Relativistic cosmology. An important characteristics of the cosmological equations of the Barthel-Kropina-FLRW model, Eqs. (36) and (37), respectively, is that they reduce to the standard Friedmann equations of general relativity *in the limit* $\eta \to \pm 1/a$, $\beta = (1,0,0,0)$,

$$\frac{3(a')^2}{a^2}=\frac{8\pi G}{c^2}\rho,\ \ 2\frac{a''}{a}+\frac{(a')^2}{a^2}=-\frac{8\pi G}{c^4}p. \quad (41)$$

The Friedmann equations of standard general relativistic cosmology lead to the conservation of the energy density ρ, which takes the form, $\dot{\rho}+3H\left(\rho+p/c^2\right)=0$, where by a dot we have denoted the derivative with respect to the cosmological time t, and we have introduced the standard Hubble function defined as $H=c\mathcal{H}$.

IV. THE BARTHEL-KROPINA DARK ENERGY MODEL

In the present Section we will introduce the Barthel-Kropina dark energy model, which is based on an appropriate splitting of the generalized Friedmann equations (36) and (37). More exactly, after introducing an appropriate representation for the coefficient η of the one-form β, which brings the cosmological field equations to a form similar to the standard Friedmann equations, we will interpret the extra terms in these equations as describing a dynamical cosmological dark energy, whose effective energy density and pressure can be related by a linear equation of state.

A. Alternative representation of the generalized Friedmann equation

In order to bring the Barthel-Kropina-FLRW cosmological equations to a form as close as possible to the Friedmann equations of general relativity, we represent the function η in a general form as

$$\eta\left(x^0\right)=\frac{1}{a\left(x^0\right)}\left[1+\psi\left(x^0\right)\right], \quad (42)$$

where $\psi\left(x^0\right)$ is a time dependent arbitrary function, which must be determined from the field equations. For this form of η, the generalized Friedmann equations of the Barthel-Kropina-FLRW model take the form [121],

$$3\frac{(a')^2}{a^2}=\frac{8\pi G}{c^2}\rho+6(1+\psi)\psi'\mathcal{H}-3\left(\psi'\right)^2-3(2+\psi)\psi\mathcal{H}^2 = \frac{8\pi G}{c^2}\rho+\rho_{DE}, \quad (43)$$

and

$$\frac{2a''}{a}+\frac{(a')^2}{a^2}=-\frac{8\pi G}{c^4}\frac{p}{(1+\psi)^2}+4\frac{\psi'}{1+\psi}\mathcal{H}-3\frac{\left(\psi'\right)^2}{(1+\psi)^2} +2\frac{\psi''}{1+\psi}=-\frac{8\pi G}{c^4}\frac{p}{(1+\psi)^2}+p_{DE}, \quad (44)$$

respectively, where we have denoted

$$\rho_{DE}=6(1+\psi)\psi'\mathcal{H}-3\left(\psi'\right)^2-3(2+\psi)\psi\mathcal{H}^2, \quad (45)$$

and

$$p_{DE}=4\frac{\psi'}{1+\psi}\mathcal{H}-3\frac{\left(\psi'\right)^2}{(1+\psi)^2}+2\frac{\psi''}{1+\psi}, \quad (46)$$

respectively. For $\psi \to 0$, and $\eta \to 1/a$, we reobtain the Friedmann equations of standard cosmology. The generalized Friedmann equations describe the evolution of the Universe with the standard general relativistic evolution modified by the presence of extra terms generated by the Finsler geometric effects in the cosmological space-time.

B. Dark energy, and its equation of state

We interpret the extra terms in Eqs. (43) and (44) as describing *an effective, dynamical geometrical fluid type dark energy*, with energy density ρ_{DE}, and pressure p_{DE}, respectively. To obtain an effective dark energy term, we impose on the geometric fluid the equation of state

$$p_{DE}=\omega\rho_{DE}, \omega=\text{constant}, \quad (47)$$

which gives for the function ψ the following differential equation,

$$\frac{2\psi''}{1+\psi}+2\mathcal{H}\left[-3\omega(1+\psi)+\frac{2}{1+\psi}\right]\psi' +3\left[\omega-\frac{1}{(1+\psi)^2}\right]\left(\psi'\right)^2+3\omega\psi(2+\psi)\mathcal{H}^2=0. \quad (48)$$

The energy density and the pressure of the dynamical cosmological dark energy are dependent on the scale factor, and on the properties of coefficient η of the one form β.

In the limit of small values of $\psi\left(x^0\right)$, $\psi\left(x^0\right) << 1$, corresponding to small deviations from standard general relativity, and in the de Sitter limit, with $\mathcal{H}=\mathcal{H}_0=$ constant, Eq. (48) can be written as

$$\psi''+\mathcal{H}_0(2-3\omega)\psi'+3\mathcal{H}_0\omega\psi=0, \quad (49)$$

where we have also neglected the small term containing $(psi')^2$. Eq. (49) has the general solution

$$\psi\left(x^0\right)=e^{(3\omega-2)\mathcal{H}_0x^0}\left(C_1e^{\sqrt{\delta}\mathcal{H}_0x^0}+C_2e^{-\sqrt{\delta}\mathcal{H}_0x^0}\right), \tag{50}$$

where C_1 and C_2 are arbitrary constants of integration, and $\delta=9\omega^2-24\omega+4$. *delta* is negative for ω in the range $\omega\in(0.1,2.5)$, and hence for these values of the equation of state parameter, and in the de Sitter regime, *psi* has an oscillatory behavior. For small values of ω, so that $\omega<<2/3$, ψ becomes a constant, $\psi=C_1$.

We will consider in the following only the late time cosmological evolution of the Universe, and hence we will assume that the ordinary matter pressure vanishes, $p=0$.

C. Cosmological evolution in the redshift space

In order to simplify the mathematical formalism, and to bring it closer to the observational data, we introduce the dimensionless time parameter τ, defined as $\tau=\mathcal{H}_0x^0$, as well as the normalized Hubble function h, defined as $\mathcal{H}=\mathcal{H}_0h$, with $\mathcal{H}_0=H_0/c$, and H_0 denoting the present day value of the Hubble function. Furthermore, we denote $\sigma(\tau)=d\psi(\tau)/d\tau$.

Hence, the basic equations describing the time dynamics of the generalized Friedmann equations of the Barthel-Kropina-FLRW cosmological model take the form

$$\frac{d\psi}{d\tau}=\sigma, \tag{51}$$

$$2\frac{dh}{d\tau}+3h^2=4h\frac{\sigma}{1+\psi}-3\frac{\sigma^2}{(1+\psi)^2}+\frac{2}{1+\psi}\frac{d\sigma}{d\tau}, \tag{52}$$

$$\frac{2}{1+\psi}\frac{d\sigma}{d\tau}+2h\left[\frac{2}{1+\psi}-3\omega(1+\psi)\right]\sigma +3\left[\omega-\frac{1}{(1+\psi)^2}\right]\sigma^2+3\omega\psi(2+\psi)h^2=0. \tag{53}$$

We also introduce the critical matter density $\rho_c=3H_0^2/8\pi G$, as well as the matter density parameter defined according to $\Omega_m=\rho/\rho_c$. Then, from the first generalized Friedmann equation we obtain the matter density parameter in the form

$$\Omega_m=h^2+\sigma^2+(2+\psi)\psi h^2-2(1+\psi)h\sigma. \tag{54}$$

To allow a direct confrontation of the theoretical model with the observations, we will reformulate the cosmological Barthel-Kropina-FLRW evolution equations in terms of the redshift variable z, defined as $1+z=1/a$. Hence, in the redshift space the system of equations (51)-(53) take the form

$$-(1+z)h\frac{d\psi}{dz}=\sigma, \tag{55}$$

$$-2(1+z)h\frac{dh}{dz}+3h^2=4h\frac{\sigma}{1+\psi}-3\frac{\sigma^2}{(1+\psi)^2} -2(1+z)\frac{h}{1+\psi}\frac{d\sigma}{dz}, \tag{56}$$

$$-2(1+z)\frac{h}{1+\psi}\frac{d\sigma}{dz}+2h\left[\frac{2}{1+\psi}-3\omega(1+\psi)\right]\sigma +3\left[\omega-\frac{1}{(1+\psi)^2}\right]\sigma^2+3\omega\psi(2+\psi)h^2=0. \tag{57}$$

The matter density parameter is obtained in the redshift space as

$$\Omega_m=h^2\left[1+(1+z)^2\left(\frac{d\psi}{dz}\right)^2+(2+\psi)\psi+2(1+z)(1+\psi)\frac{d\psi}{dz}\right]. \tag{58}$$

The general properties of a cosmological model can be extracted from the study of a number of specific observational quantities. The first such quantity we will consider is the deceleration parameter, defined as

$$q=\frac{d}{d\tau}\frac{1}{H}-1=-\frac{1}{a}\frac{d^2a}{d\tau^2}\left[\frac{1}{a}\frac{da}{d\tau}\right]^{-2}. \tag{59}$$

The deceleration parameter of the Barthel-Kropina-FLRW cosmological model can be obtained explicitly in the form

$$q=\frac{1}{2}+\frac{3}{2}\frac{\frac{8\pi G}{c^4}\frac{p}{(1+\psi)^2}-p_{DE}}{\frac{8\pi G}{c^2}\rho+\rho_{DE}}. \tag{60}$$

We will also investigate the behavior of the jerk and snap parameters j and s, defined according to

$$j=\frac{1}{a}\frac{d^3a}{d\tau^3}\left[\frac{1}{a}\frac{da}{d\tau}\right]^{-3}=q(2q+1)+(1+z)\frac{dq}{dz}, \tag{61}$$

and

$$s=\frac{1}{a}\frac{d^4a}{d\tau^4}\left[\frac{1}{a}\frac{da}{d\tau}\right]^{-4}=\frac{j-1}{3\left(q-\frac{1}{2}\right)}, \tag{62}$$

respectively.

V. COSMOLOGICAL TESTS OF THE BARTHEL-KROPINA DARK ENERGY MODEL

In the present Section we will perform a detailed comparison between the predictions of the Barthel-Kropina-FLRW dark energy model, and we will also investigate the observational constraints on the model. In our analysis we are going to use two observational datasets, the $H(z)$ data, and the Pantheon data set, which contain 57, and 1048 points, respectively. From the comparison with the cosmological data we find the best fit ranges of the four free parameters of the Barthel-Kropina dark

energy model, $(\omega, \sigma_0, \psi_0)$, which must be considered together with the present day value of the Hubble function h. To constrain the cosmological model parameters, we use the standard Bayesian technique, and likelihood function approach, along with the Markov Chain Monte Carlo (MCMC) method. Once the best fit values of the model parameters are known, we will investigate the model from a cosmographic point of view, by analysing the evolution of the deceleration, jerk, and snap parameters. In all cases we compare the model predictions with the standard ΛCDM cosmological model.

A. Methodology

Presently, a large amount of observational data, obtained from different cosmological observations, such as Supernovae type Ia, Baryon Acoustic oscillations (BAO), Cosmic Microwave Background (CMB), and Hubble rate measurements, respectively, can be used to test cosmological theories. This comparison between observation and theory allows to clearly discriminate between observationally supported models, and the unsupported ones. Due to the presence of a large amount of data, statistical analysis and methods are necessary to confront theoretical models and observational data. The estimation of the cosmological parameters is performed in the framework of the Bayesian inference [134, 135]. In this approach the model parameters are considered as random variables, described by probability distributions. In the Bayesians interpretation probabilities are considered as a degree of belief in a hypothesis. Mathematically, this is expressed by Bayes' theorem,

$$\mathcal{P}(H|D) = \frac{\mathcal{L}(D|H)\mathcal{P}(H)}{\mathcal{P}(D)}, \tag{63}$$

where D denotes the observational/experimental data, while H denotes the hypothesis to be tested, which usually can be considered as the parameters of the model, or the model itself. Moreover, $\mathcal{P}(H|D)$, $\mathcal{P}(H)$, and $\mathcal{P}(D)$, respectively, denote the posterior distribution, the prior distribution, and the evidence. The later is a normalization factor, often omitted, since it is model independent. On the other hand, $\mathcal{P}(H)$ is taken mainly from previous experiments, and acquired information about the parameters. For a flat prior, i.e., for $\mathcal{P}(H) = 1$, Bayes' theorem takes the form,

$$\mathcal{P}(H|D) \propto \mathcal{L}(D|H). \tag{64}$$

Although Bayes' theorem seems very simple, it relates the posterior distribution $\mathcal{P}(H|D)$ to the easily computable quantity, $\mathcal{L}(D|H)$, which expresses the probability of the hypothesis being true. In the case where the errors follow a Gaussian distribution, the likelihood function takes the form,

$$\chi^2(\theta) = -2\ln\mathcal{L}(\theta). \tag{65}$$

To estimate the model parameters, we look for the parameters vector maximizing the posterior distribution, i.e., $\hat{\theta}_{\rm b.f}$ [1]. From Eq. (65), one can see that maximizing the posterior distribution is practically the same as minimizing the chi-squared function. The above results indicate the theoretical framework of the parameters inference.

In order to infer the best fit values of the cosmological parameters we use the Markov Chains Monte Carlo (MCMC) method [136]. In what follows, we give a short description to the basic concepts of the MCMC approach, taking as an example the Metropolis-Hasting algorithm [137]. We summarize the MCMC algorithm used in the present study in five steps:

a) Choose a starting point, which could be just a guess, or it could be based on a previous estimates, or theoretical inferences.

b) Generate a new point from a proposed initial distribution, which is in general a multivariate normal distribution.

c) Compare the posterior height of the new proposal to the posterior height of the current points. If the new proposal has a higher posterior value than the most current state, then accept the new proposal. If not, choose to accept, or reject randomly, the new proposal.

d) Attribute the new proposal to the next sample, if it is accepted, otherwise copy the most recent sample to the next sample.

e) Repeat the above steps, except initialization, until running all the iterations.

To graphically present the errors in two dimensions, as well as the correlations between the estimated model parameters, it is convenient to plot the iso-probability contours,

$$\chi^2 = \chi^2_{min} + \Delta\chi^2(\nu, n\sigma), \tag{66}$$

where $\chi^2_{min} = \chi^2(\hat{\theta}_{\rm b.f})$ is the minimal chi-square value, and $\Delta\chi^2$ is the desired confidence level, calculated as follows,

$$\Delta\chi^2(\nu, n\sigma) = 2\mathcal{G}\left(\frac{\nu}{2}, 1 - \mathrm{erf}\left(\frac{n\sigma}{\sqrt{2}}\right)\right), \tag{67}$$

where μ and $n\sigma$ denote the number of free parameters, and the confidence interval, respectively, while $\mathcal{G}$ is the inverse of the regularized $\Gamma(x)$ function. Moreover, $\mathrm{erf}(x)$ is the error function, given by,

$$\mathrm{erf}(x) = \frac{2}{\sqrt{\pi}}\int_0^x e^{-t^2}dt. \tag{68}$$

[1] We denote the best fit parameters, or the best fit vector, by $b.f$

To figure out which model gives the best description of the observational data we use the corrected Akaike's Information Criterion (AIC_c), given by [138],

$$AIC_c = \chi^2_{min} + 2\mathcal{N}_{\rm f} + \frac{2\mathcal{N}_{\rm f}(\mathcal{N}_{\rm f}+1)}{\mathcal{N}_{\rm Tot}-\mathcal{N}_{\rm f}-1}, \qquad (69)$$

where $\mathcal{N}_{\rm f}$ and $\mathcal{N}_{\rm Tot}$ denote the number of free parameters, and the total data points used in the observational confrontation, respectively.

The AIC_c is a very powerful tool when it comes to classify a set of models according to their statistical significance. By definition, the model with the minimal AIC_c is the most supported, and taken to be a reference. In practice, we are interested in the quantity

$$\Delta AIC_c = AIC_{c,model} - AIC_{c,reference}, \qquad (70)$$

which reveals how much each model is statistically close to the reference model. If $0 < \Delta{\rm AIC}_c < 2$, the model is substantially supported, and if $4 < \Delta{\rm AIC}_c < 7$, the model has less observational support. Models with $\Delta{\rm AIC}_c > 10$ are not supported with respect to the reference model.

B. Data description

In the present Section we briefly present the observational datasets used for the tests of the Barthel-Kropina cosmological model.

1. $H(z)$ Dataset

In order to obtain strong constraints on the cosmological model parameters one must confront it with several observational datasets. In our analysis of the Barthel-Kropina dark energy model, to constrain the model parameters, we make use of the $H(z)$ measurements, together with the Pantheon sample. In general, Hubble data can be derived by measuring the BAO in the radial direction of galaxy clustering [139], or by the differential age approach, in which the redshift dependence of the Hubble function is given by,

$$H(z) = -\frac{1}{1+z}\frac{dz}{dt},$$

where $dz/\ dt$ is inferred from two passively evolving galaxies. In our analysis, 57 data points for $H(z)$, distributed in the redshift range $0.07 \leqslant z \leqslant 2.42$.

To estimate the model parameters ω, σ_0, ψ_0 and h, we compare the theoretical expectations of the Barthel-Kropina model with the uncorrelated Hubble measurements, using the chi-square function, defined as

$$\chi^2_H(\omega,\sigma_0,\psi_0,h) = \sum_{i=1}^{57} \frac{\left[H_{th}(z_i,\omega,\sigma_0,\psi_0,h) - H_{obs}(z_i)\right]^2}{\sigma^2_{H(z_i)}}, \qquad (71)$$

Observational Hubble parameter data

z	$H(z)$	σ_H	Ref.	z	$H(z)$	σ_H	Ref.
0.070	69	19.6	[146]	0.51	90.4	1.9	[152]
0.120	68.6	26.2	[146]	0.52	94.35	2.64	[149]
0.170	83	8	[147]	0.56	93.34	2.3	[149]
0.1791	75	5	[150]	0.57	87.6	7.8	[155]
0.1993	75	5	[150]	0.57	96.8	3.4	[156]
0.200	72.9	29.6	[154]	0.59	98.48	3.18	[149]
0.240	79.69	2.99	[139]	0.593	104	13	[150]
0.270	77	14	[147]	0.60	87.9	6.1	[153]
0.280	88.8	26.6	[154]	0.61	97.3	2.1	[152]
0.300	81.7	6.22	[148]	0.64	98.82	2.98	[149]
0.310	78.18	4.74	[149]	0.6797	92	8	[150]
0.340	83.8	3.66	[139]	0.73	97.3	7	[153]
0.350	82.7	9.1	[151]	0.7812	105	12	[150]
0.3519	83	4	[150]	0.8754	125	17	[150]
0.360	79.94	3.38	[149]	0.880	90	40	[146]
0.380	81.5	1.9	[152]	0.900	69	12	[147]
0.3802	83	13.5	[157]	0.900	117	23	[147]
0.400	95	17	[147]	1.037	154	20	[150]
0.400	82.04	2.03	[149]	1.300	168	17	[147]
0.4004	77	10.2	[157]	1.363	160	33.6	[156]
0.4247	87.1	11	[157]	1.430	177	18	[147]
0.43	86.45	3.97	[139]	1.530	140	14	[147]
0.44	82.6	7.8	[153]	1.750	202	40	[147]
0.44	84.81	1.83	[149]	1.965	186.5	50.4	[156]
0.4497	92.8	12.9	[157]	2.30	224	8.6	[159]
0.470	89	34	[162]	2.33	224	8	[160]
0.4783	80	99	[157]	2.34	222	8.5	[159]
0.480	87.79	2.30	[149]	2.36	226	9.3	[161]
0.480	97	62	[146]				

TABLE I. The 57 data points of the Hubble parameter considered in the present paper.

where $H_{\rm th}$, H_{obs} and $\sigma_{H(z_i)}$ represent the model prediction, the observed value of Hubble rate, and the standard error at the redshift z_i, respectively. The numerical values of the Hubble function at the corresponding redshifts are presented in Table I.

2. Pantheon Dataset

The observation of type Ia supernova (SN Ia) had played a key role in the discovery of the comic accelerating expansion. Thus far, SN Ia are one of the most effective tools for investigating the nature of the dark energy. During the recent years, various supernova data compilations have been released. We cite for instance Union [140] , Union2 [141] and Union2.1 [142] from the

Model	Parameter	Prior	Best fit	Mean
ΛCDM	$\Omega_{\rm m}$	$[0.001, 1]$	$0.27859^{+0.0139588}_{-0.0139588}$	$0.279249^{+0.0139493}_{-0.0139493}$
	h	$[0.4, 1]$	$0.691892^{+0.008881}_{-0.0088881}$	$0.691857^{+0.0088838}_{-0.00888348}$
Barthel-Kropina	ω	$[0, 6]$	$2.02382^{+0.819655}_{-0.819655}$	$2.53314^{+0.817497}_{-0.817497}$
	σ_0	$[-3, 3]$	$0.619373^{+0.0939505}_{-0.0939505}$	$0.652573^{+0.0936745}_{-0.0936745}$
	ψ_0	$[-3, 3]$	$0.40882^{+0.141627}_{-0.141627}$	$0.458615^{+0.141176}_{-0.141176}$
	h	$[0.4, 1]$	$0.684579^{+0.0108078}_{-0.0108078}$	$0.683052^{+0.0108017}_{-0.0108017}$

TABLE II. Summary of the best fit and of the mean values of the free cosmological parameters of the Barthel-Kropina dark energy model.

Supernova Cosmology Project, Joint Light-cure Analysis (JLA) [143] and the Pantheon data [2] [144]. The later, contains 1048 spectroscopically confirmed SN Ia covering the redshift range $0 < z < 2.3$. Besides, SN Ia are astrophysical objects, considered as standard candles, which measure relative distances. Therefore, SN Ia sample are used via the distance modulus $\mu = m - M$, where m denotes the apparent magnitude of a given SN Ia.

The chi-square of the SN Ia dataset is given by

$$\chi^2_{SN} = \Delta\mu^T \,.\, \mathbf{C}^{-1}_{SN} \,.\, \Delta\mu. \tag{72}$$

Here $\mathbf{C}_{SN}$ is the covariance matrix, and $\Delta\mu = \mu_{obs} - \mu_{th}$, where μ_{obs} denotes the observed distance modulus of a given SN Ia, while μ_{th} is the theoretical distance modulus, given by

$$\mu_{th}(z) = 5\log_{10}\frac{D_L(z)}{(H_0/c)Mpc} + 25, \tag{73}$$

where H_0 is the Hubble rate at the present time, and c is the speed of light. For the flat, homogeneous and isotropic Friedmann-Lemaître-Robertson-Walker (FLRW) Universe, the luminosity distance, D_L, is expressed as follows,

$$D_L(z) = (1+z)H_0\int_0^z \frac{dz'}{H\,(z')}. \tag{74}$$

Since we also constrain the free parameters of the model, i.e., $\omega, \sigma_0, \psi_0, h$ by using the Pantheon sample, and therefore,

$$\chi^2_{SN}(\omega,\sigma_0,\psi_0,h) = \Delta\mu^T(\omega,\sigma_0,\psi_0,h)\times\mathbf{C}^{-1}_{Pantheon} \times\Delta\mu(\omega,\sigma_0,\psi_0,h). \tag{75}$$

The total chi-square of the Barthel-Kropina dark energy model is therefore given by,

$$\chi^2_{tot}(\omega,\sigma_0,\psi_0,h) = \chi^2_H + \chi^2_{SN}. \tag{76}$$

C. Results

To figure out if the Barthel-Kropina dark energy model is observationally supported, and to determine the level of this support, we confront the model with the cosmological observations by minimizing the χ^2 function. Since from the model we do not have an explicit form of the Hubble parameter, $H(z)$, the system of differential equations defining the Barthel-Kropina dark energy model, Eqs. ((51)-(53)), is solved numerically. In practice, to solve a given differential equation one must define a set of initial conditions. For the Barthel-Kropina dark energy model, the initial conditions themselves are free parameters, to be obtained from observations.

[2] An update of the Pantheon sample was recently released [145].

Therefore, the system of differential equations must be solved for each MCMC iteration, thus obtaining a numerical solution for $H(z)$ for each MCMC state. Once we have the numerical solution, we compute the total chi-square $\chi^2_{tot}(\omega,\sigma_0,\psi_0,h)$.

1. *Constraining the Barthel-Kropina dark energy model parameters*

In Table II, we present the best fit, and the mean values of the Barthel-Kropina dark energy model parameters, with their corresponding errors. The prior used in this analysis is also shown.

2. Comparison with the ΛCDM model

To test statistically the Barthel-Kropina dark energy model, we compare it with the standard ΛCDM cosmological model. For that purpose, we use the AIC_c criterion, which takes into account the number of free parameters, and the total number of data points. To obtain a reliable result, we constrain the ΛCDM and the Barthel-Kropina dark energy model with the same data type, i.e., $H(z)$+Pantheon. The analysis shows that even that the Barthel-Kropina dark energy model is not the most favoured ($AIC_c^{\Lambda\mathrm{CDM}} < AIC_c^{Barthel-Kropina}$), it is still very well supported by observations ($\Delta AIC_c = 0.48$) with respect to the most accepted ΛCDM model, making the Barthel-Kropina dark energy model extremely competitive to the standard model of cosmology. The statistical details of the comparison of the ΛCDM model and of the Barthel-Kropina dark energy model are presented in Table III.

a. Confidence levels. In Fig. 1, the 1D and 2D posterior distributions at 68.3% (1σ) and 95.4% (2σ) confidence levels are shown, obtained after constraining the Barthel-Kropina dark energy model with the Pantheon+$H(z)$ observational data. Besides, the MCMC contour plots show a positive correlation between (ω, σ_0), (ω, ψ_0) and (σ_0, ψ_0), while they shows a negative correlation between (h, ω) and (h, ψ_0), respectively.

3. Observational, and theoretical comparisons of the Hubble functions

Now, once the free parameters of the Barthel-Kropina dark energy model are obtained, we can proceed to compare the model predictions with the observational data, and with the ΛCDM model, respectively.

a. Comparison with the Hubble data points. First, we consider the comparison of the Barthel-Kropina dark energy model with the Hubble 57 data points, and with the ΛCDM model. The results of the comparison are presented in Fig. 2. We observe from the Figure that the Barthel-Kropina dark energy model describes very well the Hubble data.

b. Comparison with the Pantheon data. We proceed now to compare the $\mu(z)$ distance modulus function of the Barthel-Kropina dark energy model with the Pantheon data. From Fig. 3, one can see that Barthel-Kropina model fits the Pantheon distance modulus, based on 1048 observation points, very well.

c. Relative difference between Barthel-Kropina and ΛCDM. Finally, in Fig 4, we plot the relative difference between the Barthel-Kropina dark energy model, and ΛCDM standard paradigm. The Figure shows that for $z < 1.4$, the Barthel-Kropina dark energy model and the standard ΛCDM model behave almost similarly. However, some differences between the two models do appear for $z > 1.4$, and these differences do increase with the redshift. Hence, in order to make the Barthel-Kropina model consistent with the observations, high redshift corrections may be necessary, which would involve, for example, a redshift dependent parameter of the equation of state of the dark energy. The consideration of the matter pressure, and of the radiation component, may also alleviate the differences between the two models at high redshifts. On the other hand, the precise determination of the Hubble function at high redshifts may provide a powerful test for discriminating between these two cosmological models.

D. Cosmographic analysis

Cosmographic analysis provides an universal and effective way to compare the solutions of the theoretical models with the cosmological observations. From the observational data we obtain a set of cosmological parameters, which must be compared with the predicted values of the same parameters, obtained from a given model. The result of the comparison allows us to conclude on the acceptability of the considered model. Thus, for a complete comparison of the Barthel-Kropina dark energy model with the observations, and the ΛCDM model, we will consider an extended set of parameters, constructed from the higher order time derivatives of the scale factor. More exactly, we will concentrate on the comparative behavior of the deceleration, jerk and snap parameters in the Barthel-Kropina and ΛCDM models.

a. The deceleration parameter. The redshift dependence of the deceleration parameter q is represented comparatively for the Barthel-Kropina and for the ΛCDM models, in Fig. 5. The behavior of this parameter in the two models is almost identical in the redshift range $z \in (0, 10)$, including the numerical value of the transition redshift z_{tr} from the decelerating to the accelerating phase. However, the large time behavior of the two models is very different: while in the ΛCDM model the Universe ends in a de Sitter phase, with $q = -1$, in the Barthel-Kropina cosmology a super-accelerated evolution does occur, with $q(-1) \approx -2.7$.

b. The jerk parameter, The redshift evolution of the jerk parameter $j(z)$ is represented in Fig. 6. At high redshifts $z > 6$ the predictions of the two models basically coincide. However, important differences do exist at lower redshifts, with a very significant difference appearing at $z = 1$, where the Barthel-Kropina model predicts a value twice as high as the ΛCDM value. The observational determination of the present day value of j may thus provide an important test of the Barthel-Kropina cosmological model.

c. The snap parameter. The variation with redshift of the snap parameter $s(z)$ is represented in Fig. 7. In this case there is a systematic difference between the numerical values of s in the Barthel-Kropina and the ΛCDM models, extending from low to high redshifts. Similarly to the ΛCDM model, s is a constant in the Barthel-Kropina cosmology for $z > 2$, but becomes a slightly

Model	$\chi^{2\ min}_{\rm tot}$	$\chi^2_{\rm red}$	AIC_c	ΔAIC_c
ΛCDM	1081.5479	0.978776	1085.56	0
Barthel-Kropina	1078.0028	0.975568	1086.04	0.48

TABLE III. Summary of the $\chi^{2\ min}_{\rm tot}$, $\chi^2_{\rm red}$, AIC_c and ΔAIC_c.

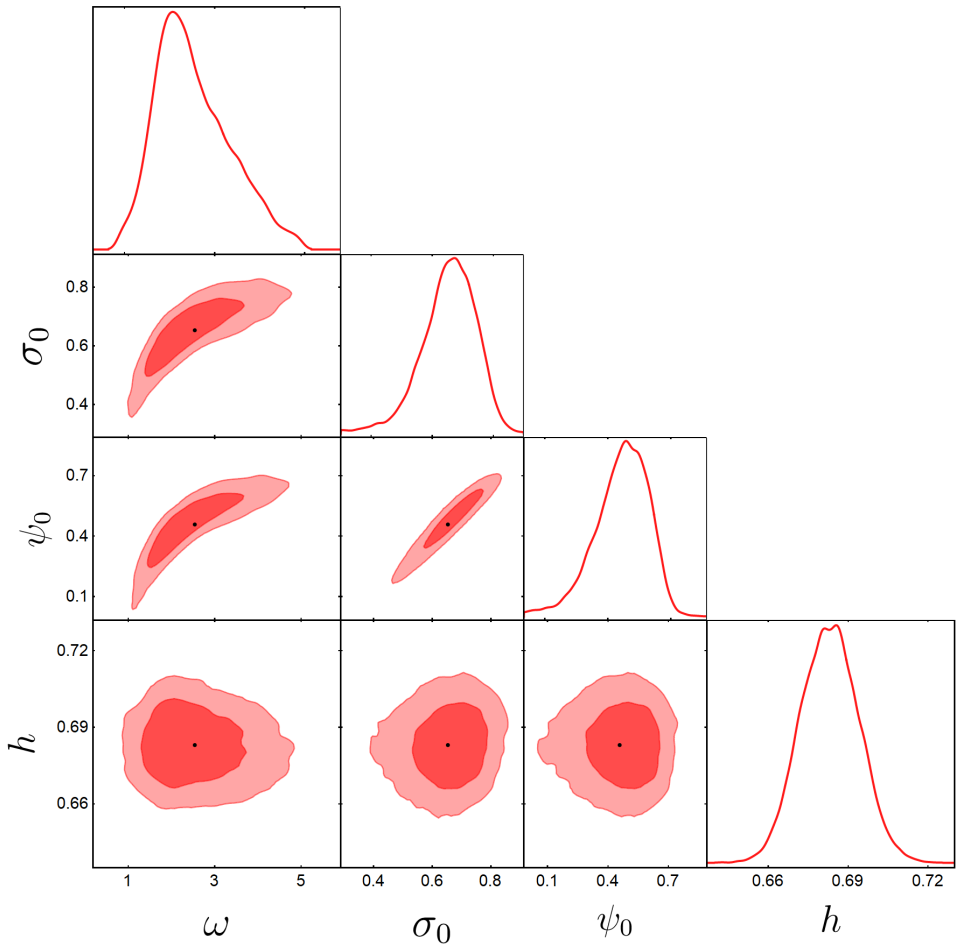

FIG. 1. MCMC confidence contours at 1σ and 2σ, obtained after constraining the Barthel-Kropina dark energy model with SNIa+H(z) data.

increasing function for z in the range $z \in (0, 2)$, with the value of $s(0)$ having some differences in the two models.

However, the differences between the predictions of the two models are highlighted more strongly when considering the parametric dependence of the snap parameter on the jerk parameter, and of the jerk parameter on the deceleration parameter, respectively. The functions $s = s(j)$ and $j = j(q)$ are represented in Figs. 8 and 9, respectively, indicating a significant difference between the Barthel-Kropina and ΛCDM models. Thus, the observational determination of these cosmographic relations could offer a strong test of the validity of Finsler geometrical cosmological models.

1. *Cosmological quantities*

a. Matter densities. We consider now the comparative behavior of the relevant physical parameters of the Barthel-Kropina and ΛCDM models. The evolution

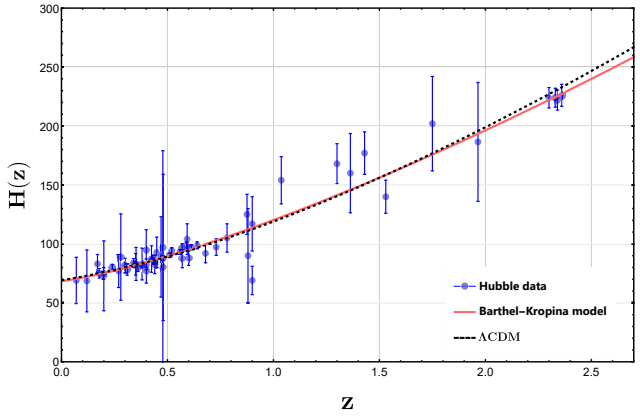

FIG. 2. The evolution of the Hubble parameter H(z) of the Barthel-Kropina and ΛCDM models as a function of the redshift z against the Hubble measurements.

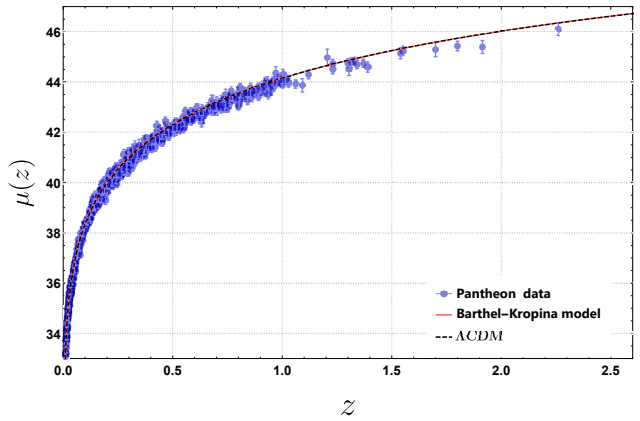

FIG. 3. The evolution of the distance modulus $\mu(z)$ of the Barthel-Kropina dark energy model, and of the ΛCDM model in terms of the redshift z against the Pantheon data.

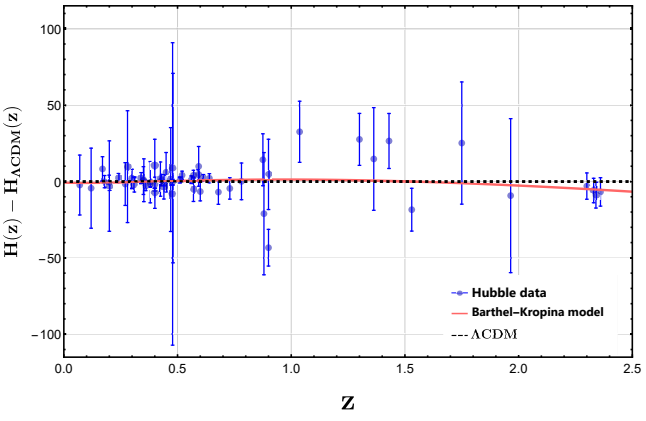

FIG. 4. The variation of the difference between the Barthel-Kropina dark energy model, and the ΛCDM model as a function of the redshift z against the Hubble measurements.

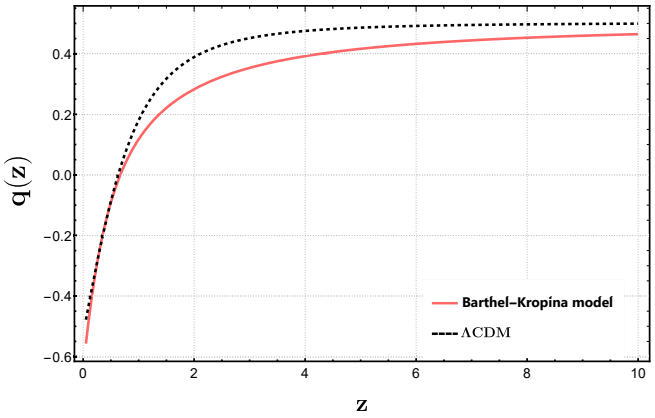

FIG. 5. Evolution of the deceleration parameter as a function of the redshift z for the Barthel-Kropina and ΛCDM cosmologies.

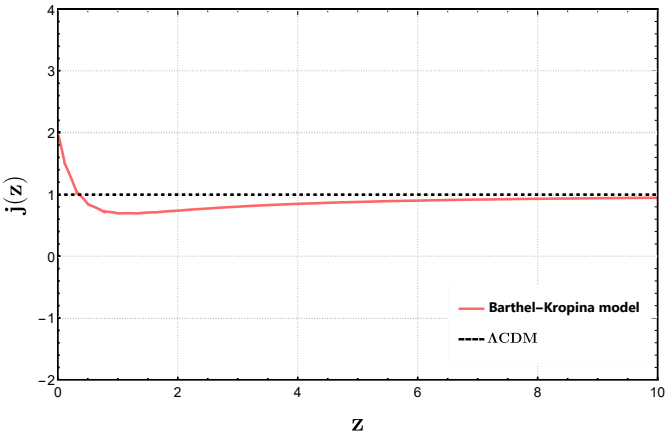

FIG. 6. Evolution of the jerk parameter as a function of the redshift z for the Barthel-Kropina and ΛCDM cosmological models.

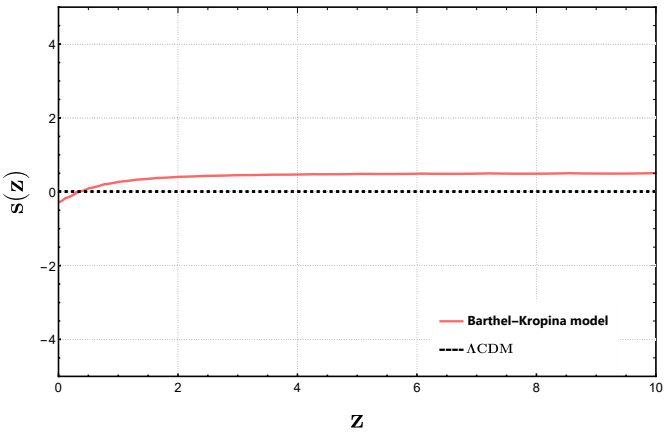

FIG. 7. The evolution of the snap parameter s as a function of the redshift z in the Barthel-Kropina and ΛCDM models.

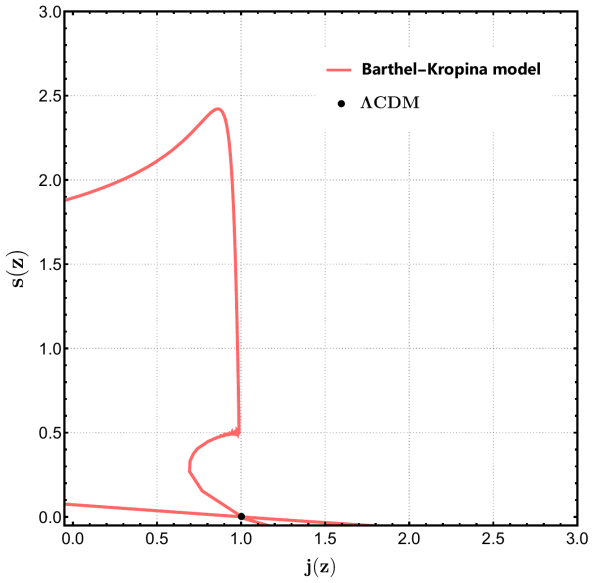

FIG. 8. The evolution of the snap parameter s as a function of the jerk parameter j in the Barthel-Kropina and ΛCDM models.

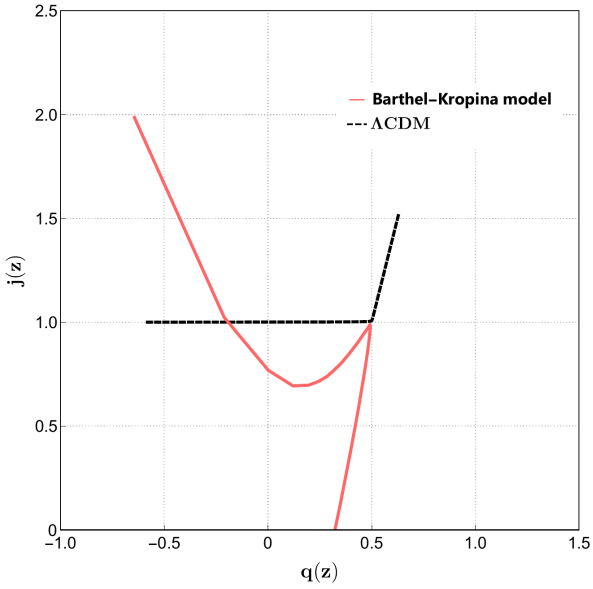

FIG. 9. The evolution of the jerk parameter j as a function of the deceleration parameter q in the Barthel-Kropina and ΛCDM models.

of the matter density parameters Ω_m are presented in Fig. 10. Up to redshift of around $z \approx 2$ the matter densities in the two models almost coincide. However, at higher redshifts, significant differences begin to appear in the baryonic matter distributions, with the Barthel-Kropina model predicting a higher value of the matter density parameter. The comparisons of the reduced matter and dark energy density parameters in the two models are presented in Fig. 11. There is a good concordance between the theoretical predictions of both models for redshifts $z > 2$. However, at low redshifts, significant differences in the behaviors of the reduced matter and dark energy density parameters can be seen, leading, at least in principle, to another possibility of observationally testing the Bearthel-Kropina dark energy model.

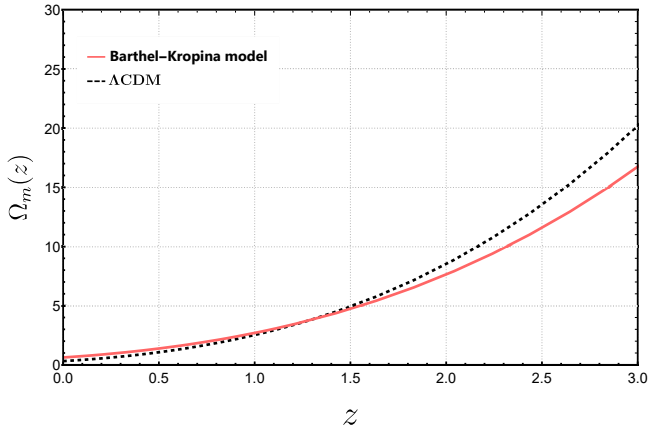

FIG. 10. The evolution of the matter density parameter as a function of the redshift z.

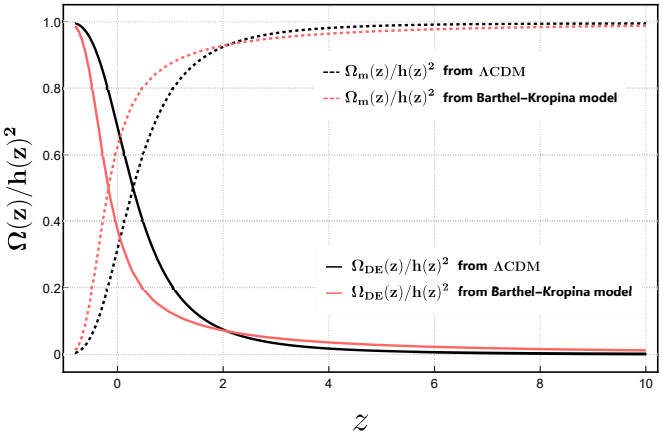

FIG. 11. The reduced matter density parameters as a function of the redshift z in the Barthel-Kropina and ΛCDM cosmological models.

b. Dark energy properties. When introducing the Barthel-Kropina dark energy model we have defined formally a geometric energy density, and a geometric pressure, related by a linear barotropic equation of state. However, in order to interpret physically these quantities, we need to take into account the energy conditions, that requires that the energy density must be positive. Hence, ion order to obtain from the geometric quantities physical quantities, we redefine them, in order to obtain a positive physical dark energy density, so that $\rho_{DEphy} = -\rho_{DE}$, and $p_{DEphy} = -p_{DE}$, respectively.

The variation of the physical dark energy density is represented in Fig. 12. The physical Finsler type dark

energy density is positive for all redshift values, and increases almost linearly for large redshift values. On the other hand, the effective physical pressure p_{DEphy}, depicted in Fig. 13, is negative, and it is a monotonically decreasing function of the redshift. This situation is similar to most of the dark energy models, in which the energy density is positive, and the accelerating evolution of the Universe is triggered by a negative pressure. The properties of the physical dark energy density and pressure may have important implications for the further observational testing of the Finsler geometry based cosmological models.

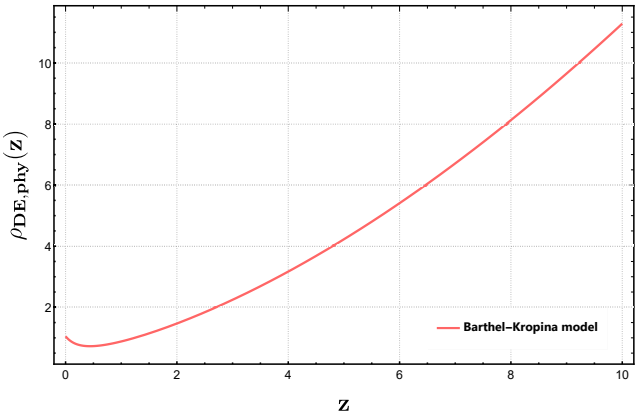

FIG. 12. The evolution of the physical energy density ρ_{DEphy} in the Barthel-Kropina dark energy model, as a function of the redshift z.

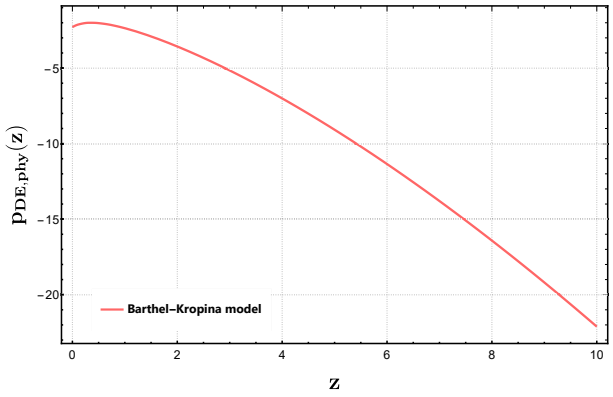

FIG. 13. The evolution of the physical pressure p_{DEphy} in the Barthel-Kropina dark energy model as a function of the redshift z.

The comparison between the dark energy equation of state parameters in the ΛCDM and the Barthel-Kropina models is represented in Fig. 14. While in the ΛCDM model $\omega = -1$, in the Barthel-Kropina model $\omega = -2$, double the value of the standard cosmological model.

c. The coefficient of the one form β. The variation of the coefficient β of the Kropina cosmological metric is depicted in Fig. 16. η is a linearly monotonically increasing function of z, which takes a finite value at the present time.

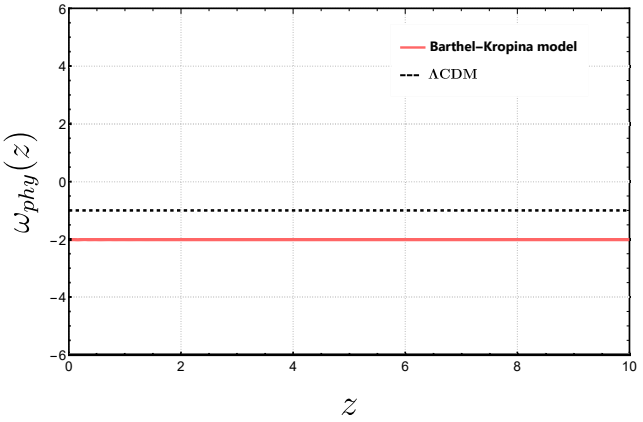

FIG. 14. The evolution of the equation of state parameter ω_{phys} as a function of the redshift z.

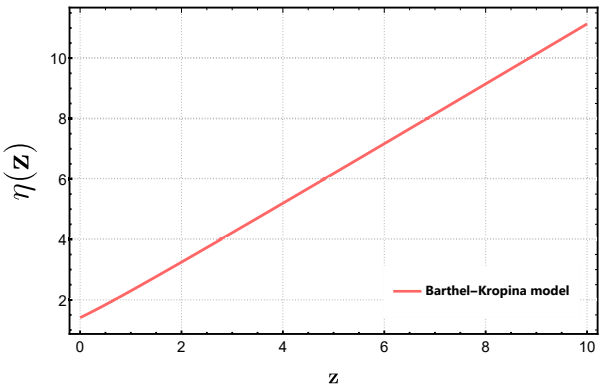

FIG. 15. The evolution of the coefficient $\eta(z) = (1+z)(1+\psi(z))$ of the one form β of the Kropina metric.

d. $Om(z)$ diagnostic The $Om(z)$ diagnostic [163] is a powerful tool used to distinguish alternative cosmological models from the ΛCDM model. The $Om(z)$ function is defined as

$$Om(z) = \frac{(H(z)/H_0)^2 - 1}{(1+z)^3 - 1}. \tag{77}$$

For the ΛCDM model, the function $Om(z)$ is always constant and equal to the present matter density Ω_{m0}. Moreover, for models having a constant EoS, i.e. $\omega =$ constant, a positive slope of $Om(z)$ indicate a phantom behaviour, while a negative slope corresponds to a quintessence like behaviour. In the case of the standard general relativistic cosmology, and in the presence of a dark energy term obeying a linear barotropic equation of state, with the equation of state parameter denoted by ω, the first Friedmann equation can be written as

$$\left(\frac{H(z)}{H0}\right)^2 = \Omega_{m0}(1+z)^3 + (1-\Omega_{m0}) \times \mathrm{Exp}\left[3\int_0^z \frac{1+\omega(z')}{1+z'}dz'\right]. \tag{78}$$

For a constant ω, we obtain

$$\left(\frac{H(z)}{H0}\right)^2 = \Omega_{m0}(1+z)^3+(1-\Omega_{m0})\,(1+z)^{3(1+\omega)}. \quad (79)$$

Hence, it follows that,

$$Om(z) = \frac{\Omega_{m0}(1+z)^3 + (1-\Omega_{m0})\,(1+z)^{3(1+\omega)} - 1}{(1+z)^3 - 1}. \quad (80)$$

For the ΛCDM model we have $\omega = -1$, and thus,

$$Om(z) = \Omega_{m0}. \quad (81)$$

By assuming that the Hubble function of the Barthel-Kropina model differs little from the ΛCDM one, so that $H^{BK}(z) = H^{\Lambda\text{CDM}}(z) + \Delta H(z)$, with $\Delta H(z)/H^{\Lambda\text{CDM}}(z) << 1$, from Eq. (77) we obtain, by neglecting the second order terms in ΔH, the approximate expression

$$\begin{aligned} Om^{BK}(z) &\approx Om^{\Lambda\text{CDM}}(z) \\ &+\frac{2}{(1+z)^3-1}\frac{H^{\Lambda\text{CDM}}(z)}{H_0^2}\Delta H(z) \\ &= Om^{\Lambda\text{CDM}}(z) + \Delta Om^{BK}(z). \end{aligned} \quad (82)$$

The variations with respect of the redshift of the $Om(z)$ functions on both Barthel-Kropina and ΛCDM cosmological models are represented in Fig. 16.

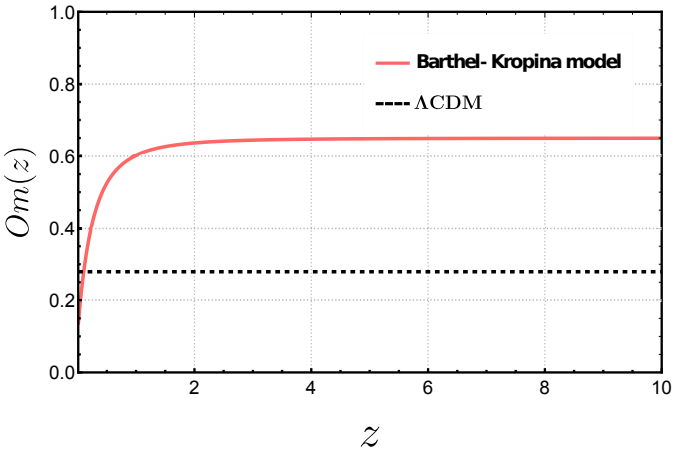

FIG. 16. The evolution of the $Om(z)$ function in the Barthel-Kropina and ΛCDM models.

The $Om(z)$ functions are rather different for the two considered cosmological models. While for ΛCDM $Om(z)$ is an absolute constant, for redshifts in the range $z < 2$, $Om(z)$ for the Barthel-Kropina model is an increasing function, reaching a constant value for $z > 2$. In the constant region range, the numerical value of $Om(z)$ for the Barthel-Kropina cosmology is around two times higher than the corresponding ΛCDM value.

VI. DISCUSSIONS AND FINAL REMARKS

In the present paper we have considered a detailed comparison of the theoretical predictions of a Finsler geometric type cosmological model, and the observations. More exactly, we have adopted as the basic metric function of our model the Kropina metric, which is a particular form of the general (α, β) metrics. Kropina spaces have many applications in physics, like, for example, quantum mechanics [27], dissipative classical mechanics [164], liquid crystal under the influence of an external electromagnetic field [165], nonequilibrium thermodynamic systems [166], and in the study of nonlinear path of fluids flow through inhomogeneous media [167]. However, the first investigations of the possible relevance of the Kropina geometry for the description of the gravitational phenomena were initiated in [121], where the generalized Friedmann equations, describing the cosmological evolution, were obtained. In this Finslerian type approach it is assumed that the gravitational field is described by a Riemannian metric $g(x)$, which satisfies the Einstein gravitational field equations. However, the standard Einstein theory can be extended by nonlocalizing (anisotropizing) the background Riemann geometry, by attaching to each point $x = x^I$, $I = 0, 1, 2, 3$, an internal variable $y = y^J$, $J = 0, 1, 2, 3$. By further assuming that the internal variable y is a vector, the nonlocalized Riemann geometry becomes a Finsler type geometry, leading to a Finsler type description of the gravitational interaction. Alternatively, one can describe the geometric properties of the Fisnlerian gravity by using the geometry of a general vector bundle.

In the nonlocal standard Finsler geometry the metric tensor $\hat{g}$ is a function of both local coordinates x and of the internal vector y, so that $\hat{g} = \hat{g}(x, y)$. But in many realistic physical situations one can assume that the internal variable y depends explicitly on the position, so that $y = Y(x)$. Therefore, the Finslerian metric becomes $\hat{g} = \hat{g}(x, Y(x)))$. Thus, in this type of geometric and physical models, the Finsler metric tensor $\hat{g}$ becomes a function of x only. The corresponding geometric structure is called the osculating Finsler manifold. In this particular osculating Finsler space one can introduce a specific connection, which is called the Barthel connection, which has the remarkable property that in the case of the Kropina geometry, and in all (α, β) type geometries) it is the Levi-Civita connection of the Riemannian metric $\hat{g}(x) = \hat{g}\,(x, Y(x)))$.

By adopting for the background Riemann metric the Friedmann-Lemaitre-Robertson-Walker (FLRW) form, one can obtain the generalized Friedmann equations of Barthel-Kropina cosmological model. These equations are mathematically simple, and, after an appropriate choice of the coefficient of the one-form β, they closely resemble the Friedmann equations of standard general relativity, but also contain extra terms generated by the Finsler geometric effects. In the present approach, for simplicity, we interpret these geometric terms as describ-

ing dark energy only, even that the possibility they describe both dark matter and dark energy could be also considered. In order to close the system of cosmological equations we have imposed a linear relation between the geometric dark energy and dark pressure terms. Hence, with this choice the system of generalized field equations can be closed, and it can be formulated as a dynamical system in the redshift space. However, the solution of the system can be obtained only numerically, and it depends on three model parameters: the present day values of one form component η and of its derivative, and of the parameter of the geometric equation of state ω.

In the present work we have performed a systematic and rigorous analysis of the cosmological implications of the Barthel-Kropina dark energy model, by comparing it with the cosmological observations for 57 Hubble function values, and for the Pantheon dataset. To obtain the best fit values of the model parameters we have used the MCMC method, from which one can infer the optimal fits for the model parameters. The parameter of the geometric dark energy equation of state turns out to be of the order $\omega \approx 2.5$, while the present day values of η are obtained as $\eta(0) \approx 1.45$, and $\eta'(0) \approx 1.65$, respectively. Hence, our results indicate the presence of significant Finsler geometric effects in the $z = 0$ Universe. By using the optimal fits values, the fittings of the Hubble function data give very good results, for both the Hubble and the Pantheon data. Moreover, there is a very close relationship between the Barthel-Kropina and the ΛCDM cosmologies, with both overlapping for small ($z < 1.5$) redshift values. The comparison of the two models has also been performed in a more quantitative way by studying the Akaike Information Criterion, which indicates that the Barthel-Kropina cosmology is rather closed to the standard general relativistic description in the presence of a cosmological constant.

In order to obtain a better estimate of the strengths and weaknesses of the Barthel-Kropina cosmology we have also performed a detailed comparison of the cosmographic parameters, and of other relevant cosmological quantities. If the behavior of the deceleration parameter agrees well with that of the standard ΛCDM, significant differences do appear between models when one considers the jerk and snap parameters. Hence, the cosmographic approach can offer the possibility of discriminating between Riemann and Finsler geometry based cosmological models. The variations of the matter and density parameters of the two models are also relatively similar, and even coincide on some redshift ranges.

There are several possibilities for explaining the recent cosmological observational data, which can be described as the dark components approach, the dark geometry approach, and the dark couplings approach, respectively [60]. The present investigation of the evolution and dynamics of the Universe, including the study of the accelerating expansion, has been done in the framework of the dark geometry approach, by assuming that the true geometry of the Universe goes far beyond the Riemann geometry of general relativity, and that the extra geometric terms coming from the post-Riemannian mathematical structures may be responsible for the presence of dark matter and dark energy in the Universe. In the present work we have investigated in detail, from the point of view of the consistency with observations, an example of a dark geometric model, the osculating Barthel-Kropina-FLRW geometry, which has its roots in the Finsler geometry. In this model, an effective fluid type dark energy can be generated from the geometric structures underlying the dark Barthel-Kropina geometry. An interesting property of this model is the close relation between the general relativistic Friedmann cosmological evolution equations, and the Barthel-Kropina ones, with this relation allowing to introduce in a natural way a fluid type geometric dark energy term for the description of the gravitational dynamics. The model also gives a very good description of the observational data in terms of only three free parameters, the present day values of the coefficients of the one form β, and the parameter of the equation of state. It also almost exactly reproduces the ΛCDM model predictions, but significant differences still exist for high redshifts, and in the values of some cosmographic parameters. Therefore, the Barthel-Kropina-FLRW cosmological model could become an appealing geometric alternative to the standard ΛCDM model in terms of the explanations of the observational data. It could also provide some new insights, and a better understanding of the complex interaction between abstract mathematical structures, and the physical reality.

ACKNOWLEDGMENTS

We would like to thank the anonymous Referee for comments and suggestions that helped us to improve our work. The work of TH is supported by a grant of the Romanian Ministry of Education and Research, CNCS-UEFISCDI, project number PN-III-P4-ID-PCE-2020-2255 (PNCDI III).

[1] P. Finsler, Über Kurven und Flächen in allgemeinen Räumen, Dissertation, Göttingen, JFM 46.1131.02 (1918); Reprinted by Birkhäuser (1951).
[2] B. Riemann, Habilitationsschrift, 1854, Abhandlungen der Königlichen Gesellschaft der Wissens??chaften zu Göttingen **13**, 1 (1867).
[3] S. S. Chern, Notices of the American Mathematical Society **43**, 959 (1996).
[4] H. Rund, The Differential Geometry of Finsler Spaces, Springer-Verlag, 1959

[5] G. S. Asanov, Finsler Geometry, Relativity and Gauge Theories, D. Reidel Publishing Company, Dordrecht, Boston, Lancaster, Tokyo, 1985
[6] A. Bejancu, Finsler Geometry and Applications, Ellis Horwood, New York, NY, USA, 1990
[7] D. Bao, S.-S. Chern, and Z. Shen, An introduction to Riemann-Finsler geometry, Springer-Verlag New York, Berlin, Heidelberg, 2000
[8] Y.-B. Shen and Z. Shen, Introduction to modern Finsler geometry, World Scientific, Singapore, 2016
[9] A. Einstein, Sitzungsberichte der Preussischen Akademie der Wissenschaften zu Berlin, 844 (1915).
[10] A. Einstein, Annalen der Physik **49**, 769 (1916).
[11] D. Hilbert, Nachrichten von der Gesellschaft der Wissenschaften zu Göttingen - Mathematisch - Physikalische Klasse **3**, 395 (1915).
[12] H. Weyl, Sitzungsberichte der Königlich Preussischen Akademie der Wissenschaften zu Berlin **1918**, 465 (1918).
[13] É. Cartan, Annales École Normale **41**, 1 (1924).
[14] É. Cartan, Annales École Normale **42**, 17 (1925).
[15] R. Weitzenböck, Invariantentheorie, Noordhoff, Groningen, 1923
[16] G. Randers, Phys. Rev. **59**, 195 (1941).
[17] S. Basilakos and P. Stavrinos, Phys. Rev. **D 87**, 043506 (2013).
[18] Q. Exirifard, JCAP **11**, 026 (2015).
[19] J. E. G. Silva, R. V. Maluf, and C. A. S. Almeida, Phys. Lett. **B 766**, 263 (2017).
[20] G. Papagiannopoulos, S. Basilakos, A. Paliathanasis, S. Savvidou, and P. C. Stavrinos, Classical and Quantum Gravity **34**, 225008 (2017).
[21] R. Raushan and S. Chaubey, The European Physical Journal Plus **135**, 228 (2020).
[22] G. Papagiannopoulos, S. Basilakos, A. Paliathanasis, Supriya Pan, and P. Stavrinos, Eur. Phys. J. **C 80**, 816 (2020).
[23] A. Triantafyllopoulos, S. Basilakos, E. Kapsabelis, and P. C. Stavrinos, Eur. Phys. J. **C 80**, 1200 (2020).
[24] E. Kapsabelis, A. Triantafyllopoulos, S. Basilakos, and P. C. Stavrinos, Eur. Phys. J. **C 81**, 990 (2021).
[25] I. Tavernelli, Annals of Physics **371**, 239 (2016).
[26] I. Tavernelli, Annals of Physics **393**, 447 (2018).
[27] S.-D. Liang, S. V. Sabau, and T. Harko, Phys. Rev. **D 100**, 105012 (2019).
[28] I. Tavernelli, Foundations of Physics **51**, 46 (2021).
[29] M. Hohmann, C. Pfeifer, and N. Voicu, Eur. Phys. J. **C 80**, 809 (2020).
[30] J. I. Horváth, Phys. Rev. 80, 901 (1950).
[31] J. I. Horváth and A. Moór, Zeits. Phys. 131, 548 (1952).
[32] Y. Takano, Lettere al Nuovo Cimento 10, 747 (1974).
[33] Y. Takano, Lettere al Nuovo Cimento 11, 486 (1974).
[34] G. S. Asanov, Foundations of Physics **11**, 137 (1981).
[35] G. S. Asanov, Finder Geometry, Relativity and Gauge Theories, D. Reidel, Dordrecht, 1985
[36] G. S. Asanov, Fortschr. Phys. **39**, 185 (1991).
[37] G. S. Asanov, Fortschr. Phys. **40**, 667 (1992).
[38] R. Miron and M. Anastasiei, Vector bundles, Lagrangre spaces, and Applications to the theory of relativity (in Romanian), Editura Academiei R. S. Romania, Bucharest, 1987
[39] S. Ikeda, Advanced Studies in Applied Geometry, Seizansha, Sagamihara, 1995
[40] S. F. Rutz, General Relativity and Gravitation **25**, 1139 (1993).
[41] X. Li and Z. Chang, Chinese Phys. **C 34**, 28 (2010).
[42] M. Hohmann, C. Pfeifer, and N. Voicu, Phys. Rev. **D 100**, 064035 (2019).
[43] C. Will, Living Reviews in Relativity **17**, 4 (2014).
[44] B. P. Abbott, et al. (LIGO Scientific Collaboration and Virgo Collaboration), Phys. Rev. Lett. **116**, 061102 (2016).
[45] R. Abbott et al., Astrophys. J. Lett. **896**, L44 (2020).
[46] Y. Akrami et al., Planck 2018 results. I. Overview and the cosmological legacy of Planck, Astron. Astrophys. **641**, A1 (2020).
[47] N. Aghanim et al., Planck 2018 results. VI. Cosmological parameters, Astron. Astrophys. **641**, A6 (2020).
[48] A. G. Riess et al., Astron. J. **116**, 1009 (1998).
[49] S. Perlmutter et al., Astrophys. J. **517**, 565 (1999).
[50] P. de Bernardis et al., Nature **404**, 955 (2000).
[51] S. Hanany et al., Astrophys. J. **545**, L5 (2000).
[52] R. A. Knop et al., Astrophys. J. **598**, 102 (2003).
[53] M. Hicken, W. M. Wood-Vasey, S. Blondin, P. Challis, S. Jha, P. L. Kelly, A. Rest, and R. P. Kirshner, Astrophys. J. **700**, 1097 (2009).
[54] R. Amanullah et al., Astrophys. J. **716**, 712 (2010).
[55] D. H. Weinberg, M. J. Mortonson, D. J. Eisenstein, C. Hirata, A. G. Riess, and E. Rozo, Physics Reports **530**, 87 (2013).
[56] A. Einstein, Sitzungsberichte der Königlich Preussischen Akademie der Wissenschaften, Berlin, part 1: 142 (1917).
[57] S. Weinberg, Reviews of Modern Physics **61**, 1 (1989).
[58] H. Martel, P. R. Shapiro, and S. Weinberg, Astrophys. J. **492**, 29 (1998).
[59] S. Weinberg, The Cosmological Constant Problems, in Sources and Detection of Dark Matter and Dark Energy in the Universe. Fourth International Symposium, February 23-25, 2000, at Marina del Rey, California, USA, David B. Cline, Editor, Springer-Verlag, Berlin, New York, p.18, 2001; arXiv:astro-ph/0005265v1.
[60] F. S. N. Lobo and T. Harko, Int. J. Mod. Phys. D **31**, 2240010 (2022).
[61] A. Joyce, B. Jain, J. Khoury, and M. Trodden, Phys. Rept. **568**, 1 (2015).
[62] A. Joyce, L. Lombriser, and F. Schmidt, Annu. Rev. Nucl. Part. Sci. **66**, 95 (2016).
[63] A. N. Tawfik and E. A. El Dahab, Gravitation and Cosmology **25**, 103 (2019).
[64] N. Frusciante and L. Perenon, Phys. Rept. **857**, 1 (2020).
[65] A. Arbey and F. Mahmoudi, Progress in Particle and Nuclear Physics **119**, 103865 (2021).
[66] B. Ratra and P. J. E. Peebles, Phys. Rev **D 37**, 3406 (1988).
[67] P. J. E. Peebles and B. Ratra, Astrophys. J. Lett. **325**, L17 (1988)
[68] R. R. Caldwell, R. Dave, and P. J. Steinhardt, Phys. Rev. Lett. **80**, 1582 (1998).
[69] Y. Fujii and K. Maeda, The Scalar-Tensor Theory of Gravitation, Cambridge, Cambridge University Press, 2003
[70] V. Faraoni, Cosmology in scalar-tensor gravity, Dordrecht, Boston, Kluwer Academic Publishers, 2004
[71] F. W. Hehl, Gen. Rel. Grav. **4**, 333 (1973)

[72] F. W. Hehl, P. von der Heyde, D. G. Kerlick, and J. M. Nester, Reviews of Modern Physics **48**, 393 (1976).
[73] C. G. Boehmer, P. Burikham, T. Harko, and M. J. Lake, Eur. Phys. J. **C 78**, 253 (2018).
[74] T. M. Guimarães, R. de C. Lima, and S. H. Pereira, Eur. Phys. J. **C 81**, 271 (2021).
[75] J. M. Nester and H.-J. Yo, Chinese Journal of Physics **37**, 113 (1999).
[76] J. Beltran Jimenez and T. S. Koivisto, Phys. Lett. **B 756**, 400 (2016).
[77] J. Beltran Jimenez, L. Heisenberg, and T. Koivisto, Phys. Rev. **D 98**, 044048 (2018).
[78] D. M. Ghilencea, Phys. Rev. **D 101**, 045010 (2020).
[79] D. M. Ghilencea, Eur. Phys. J. **C 81**, 510 (2021).
[80] D. M. Ghilencea, Eur. Phys. J. **C 82**, 23 (2022).
[81] Z. Haghani, T. Harko, H. R. Sepangi, and S. Shahidi, JCAP **10**, 061 (2012).
[82] Z. Haghani, T. Harko, H. R. Sepangi, and S. Shahidi, Phys. Rev. **D 88**, 044024 (2013).
[83] O. Bertolami, C. G. Boehmer, T. Harko and F. S. N. Lobo, Phys. Rev. **D 75**, (2007).
[84] T. Harko, F. S. N. Lobo, S. Nojiri and S. D. Odintsov, Phys. Rev. **D 84** (2011).
[85] T. Harko and F. S. N. Lobo, Eur. Phys. J. **C 70**, 373 (2010).
[86] Y. Xu, G. Li, T. Harko, and S.-D. Liang, Eur. Phys. J. **C 79**, 708 (2019).
[87] T. Harko and S. Shahidi, Eur. Phys. J. **C 82**, 219 (2022).
[88] T. P. Sotiriou and V. Faraoni, Rev. Mod. Phys. **82**, 451 (2010).
[89] A. De Felice and S. Tsujikawa, Living Rev. Rel. **13**, 3 (2010).
[90] Y. F. Cai, S. Capozziello, M. De Laurentis and E. N. Saridakis, Rept. Prog. Phys. **79**, 106901 (2016).
[91] S. Nojiri, S. D. Odintsov, and V. K. Oikonomou, Physics Reports **692**, 1 (2017).
[92] D. Langlois, Int. J. Mod. Phys. **D 28**, 1942006-3287 (2019).
[93] T. Harko and F. S. N. Lobo, Extensions of f(R) Gravity: Curvature-Matter Couplings and Hybrid Metric Palatini Theory, Cambridge University Press, Cambridge, UK, 2018
[94] D. Boccaletti, M. di Bari, P. Cipriani, and G. Pucacco, Nuovo Cimento B **112B**, 213 (1997).
[95] G. A. Asanov, Reports on Mathematical Physics **59**, 111 (2007).
[96] Z. Chang and X. Li, Phys. Lett. **B 668**, 453 (2008).
[97] P. C. Stavrinos, · A. P. Kouretsis, and M. Stathakopoulos, Gen. Relativ. Gravit. **40**, 1403 (2008).
[98] A. P. Kouretsis, M. Stathakopoulos, and P. C. Stavrinos, Phys. Rev. **D 79**, 104011 (2009).
[99] Z. Chang and X. Li, Chinese Physics **C 33**, 626 (2009).
[100] P. Stavrinos, Nonlinear Analysis **71**, e1380 (2009).
[101] S. I. Vacaru, Phys. Lett. **B 690**, 224 (2010).
[102] A. P. Kouretsis, M. Stathakopoulos, and P. C. Stavrinos, Phys. Rev. **D 82**, 064035 (2010).
[103] N. E. Mavromatos, V. A. Mitsou, S. Sarkar, and A. Vergou, Eur. Phys. J. **C 72**, 1956 (2012).
[104] S. I. Vacaru, Int. J. Mod. Phys. **D 21**, 1250072 (2012).
[105] Z. Chang, M. Li, and X. Li, Chinese Phys. **C 36**, 710 (2012).
[106] S. Basilakos and P. Stavrinos, Phys. Rev. **D 87**, 043506 (2013).
[107] S. Basilakos, A. P. Kouretsis, E. N. Saridakis, and P. Stavrinos, Phys. Rev. **D 88**, 123510 (2013).
[108] X. Li and Z. Chang, Phys. Rev. **D 90**, 064049 (2014).
[109] M. Hohmann, Int. J. Mod. Phys. **A 31**, 1641012 (2016).
[110] M. Hohmann and C. Pfeifer, Phys. Rev. **D 95**, 104021 (2017).
[111] G. Papagiannopoulos, S. Basilakos, A. Paliathanasis, S. Savvidou, and P. C. Stavrinos, Classical and Quantum Gravity **34**, 225008 (2017).
[112] D. Wang and X.-H. Meng, Physics of the Dark Universe **21**, 55 (2018).
[113] S. Ikeda, E. N. Saridakis, P. C. Stavrinos, and A. Triantafyllopoulos, Phys. Rev. **D 100**, 124035 (2019).
[114] R. Raushan and R. Chaubey, The European Physical Journal Plus **135**, 228 (2020).
[115] C. C. Perelman, Annals of Physics **416**, 168143 (2020).
[116] M. Hohmann, C. Pfeifer, and N. Voicu, Universe **6**, 65 (2020).
[117] G. Papagiannopoulos, S. Basilakos, A. Paliathanasis, S. Pan, and P. Stavrinos, Eur. Phys. J. **C 80**, 816 (2020).
[118] P. Stavrinos and S. I. Vacaru, Universe **7**, 89 (2021).
[119] S. Konitopoulos, E. N. Saridakis, P. C. Stavrinos, and A. Triantafyllopoulos, arXiv:2104.08024
[120] R. Hama, T. Harko, S. V. Sabau, and S. Shahidi, Eur. Phys. J. **C 81**, 742 (2021).
[121] R. Hama, T. Harko, and S. V. Sabau, Eur. Phys. J. **C 82**, 385 (2021)
[122] R. K. Tavakol and N. Van den Bergh, Phys. Lett. **A 112**, 23 (1985).
[123] R. K. Tavakol, International Journal of Modern Physics **A 24**, 1678 (2009).
[124] V. K. Kropina, Nauchn. Dokl. Vyssh. Shkoly, Fiz.-Mat. Nauki **2**, 38 (1959).
[125] V. K. Kropina, Uch. Zap. Arkhang. Gas. Ped. Inst. **4**, 111 (1959).
[126] M. Matsumoto, Tensor, NS. **24**, 29 (1972).
[127] M. Matsumoto, Reports on Mathematical Physics **31**, 43 (1992).
[128] W. Barthel, Math. Z. **58**, 358 (1953).
[129] W. Barthel, Arch. Math. **4**, 346 (1953).
[130] R. S. Ingarden and L. Tamássy, Mathl. Comput. Modelling **20**, 93 (1994).
[131] A. Nazim, Über Finslersche Räume, Diss., München (1936).
[132] O. Varga, Monatshefte für Math. und Phys. **50**, 165 (1941).
[133] S. Bacsó, X. Cheng and Z. Shen, ASPM **48**, 73 (2007).
[134] R. Trotta, Contemp. Phys. **49**, 71 (2008) .
[135] A. R. Liddle, Ann. Rev. Nucl. Part. Sci. **59**, 95 (2009) .
[136] S. Nesseris, G. Pantazis and L. Perivolaropoulos, Phys. Rev. D **96**, no.2, 023542 (2017) .
[137] A. FM. Smith and G. O. Roberts, Journal of the Royal Statistical Society: Series B, **55**, 3 (1993) .
[138] H. Akaike, [https://ieeexplore.ieee.org/document/1100705].
[139] E. Gaztanaga, A. Cabre and L. Hui, Mon. Not. Roy. Astron. Soc. **399**, 1663 (2009).
[140] M. Kowalski *et al.* [Supernova Cosmology Project], Astrophys. J. **686**, 749 (2008) .
[141] R. Amanullah, C. Lidman, D. Rubin, G. Aldering, P. Astier, K. Barbary, M. S. Burns, A. Conley, K. S. Dawson and S. E. Deustua, *et al.* Astrophys. J. **716**, 712 (2010) .

[142] N. Suzuki *et al.* [Supernova Cosmology Project], Astrophys. J. **746**, 85 (2012) .
[143] M. Betoule *et al.* [SDSS], Astron. Astrophys. **568**, A22 (2014) .
[144] D. M. Scolnic *et al.* [Pan-STARRS1], Astrophys. J. **859**, 101 (2018).
[145] D. Scolnic, D. Brout, A. Carr, A. G. Riess, T. M. Davis, A. Dwomoh, D. O. Jones, N. Ali, P. Charvu and R. Chen, *et al.*, arXiv:2112.03863 (2021).
[146] D. Stern, R. Jimenez, L. Verde, M. Kamionkowski and S. A. Stanford, JCAP **02**, 008 (2010).
[147] J. Simon, L. Verde and R. Jimenez, Phys. Rev. **D 71**, 123001 (2005).
[148] A. Oka, S. Saito, T. Nishimichi, A. Taruya and K. Yamamoto, Mon. Not. Roy. Astron. Soc. **439**, 2515 (2014) .
[149] Y. Wang *et al.* [BOSS], Mon. Not. Roy. Astron. Soc. **469**, 3762 (2017) .
[150] M. Moresco, A. Cimatti, R. Jimenez, L. Pozzetti, G. Zamorani, M. Bolzonella, J. Dunlop, F. Lamareille, M. Mignoli and H. Pearce, *et al.* JCAP **08**, 006 (2012) .
[151] C. H. Chuang and Y. Wang, Mon. Not. Roy. Astron. Soc. **435**, 255 (2013) .
[152] S. Alam *et al.* [BOSS], Mon. Not. Roy. Astron. Soc. **470**, 2617 (2017) .
[153] C. Blake, S. Brough, M. Colless, C. Contreras, W. Couch, S. Croom, D. Croton, T. Davis, M. J. Drinkwater and K. Forster, *et al.* Mon. Not. Roy. Astron. Soc. **425**, 405 (2012) .
[154] C. Zhang, H. Zhang, S. Yuan, T. J. Zhang and Y. C. Sun, Res. Astron. Astrophys. **14**, no.10, 1221-1233 (2014) .
[155] C. H. Chuang, F. Prada, A. J. Cuesta, D. J. Eisenstein, E. Kazin, N. Padmanabhan, A. G. Sanchez, X. Xu, F. Beutler and M. Manera, *et al.* Mon. Not. Roy. Astron. Soc. **433**, 3559 (2013) .
[156] M. Moresco, Mon. Not. Roy. Astron. Soc. **450**, L16 (2015) .
[157] M. Moresco, L. Pozzetti, A. Cimatti, R. Jimenez, C. Maraston, L. Verde, D. Thomas, A. Citro, R. Tojeiro and D. Wilkinson, JCAP **05**, 014 (2016) .
[158] L. Anderson *et al.* [BOSS], Mon. Not. Roy. Astron. Soc. **441**, 24 (2014) .
[159] T. Delubac *et al.* [BOSS], Astron. Astrophys. **574**, A59 (2015) .
[160] J. E. Bautista, N. G. Busca, J. Guy, J. Rich, M. Blomqvist, H. d. Bourboux, M. M. Pieri, A. Font-Ribera, S. Bailey and T. Delubac, *et al.* Astron. Astrophys. **603**, A12 (2017) .
[161] A. Font-Ribera *et al.* [BOSS], JCAP **05**, 027 (2014) .
[162] A. L. Ratsimbazafy, S. I. Loubser, S. M. Crawford, C. M. Cress, B. A. Bassett, R. C. Nichol and P. Väisänen, Mon. Not. Roy. Astron. Soc. **467**, 3239 (2017) .
[163] V. Sahni, A. Shafieloo and A. A. Starobinsky, Phys. Rev. D **78**, 103502 (2008) .
[164] P. L. Antonelli, R. S. Ingarden, and M. Matsumoto, The Theory of Sprays and Finsler Spaces with Applications in Physics and Biology, Kluwer Academic Publishers, Dordrecht, 1993
[165] R. S. Ingarden, Contemp. Math. **196**, 213 (1996).
[166] R. Mrugala, Open Syst. Inf. Dyn. **1**, 379 (1992).
[167] T. Yajima and H. Nagahama, Nonlinear Analysis: Real World Applications **25**, 1 (2015).

Research Square

Preprints are preliminary reports that have not undergone peer review.
They should not be considered conclusive, used to inform clinical practice,
or referenced by the media as validated information.

DEA based fuzzy portfolio evaluation models integrated with TOPSIS techniques to rank the efficient Portfolios under different risk indicators

Abha Aggarwal
Guru Gobind Singh Indraprastha University
Anjana Gupta
DTU: Delhi Technological University
Rajkumar Verma
University of Chile: Universidad de Chile
Reenu Kumari (reenu_kumari@msit.in)
Maharaja Surajmal Institute of Technology

Research Article

Keywords: Fuzzy Set, Data Envelopment Analysis, Decision Making Units, TOPSIS method

Posted Date: January 3rd, 2023

DOI: https://doi.org/10.21203/rs.3.rs-2424889/v1

License: This work is licensed under a Creative Commons Attribution 4.0 International License.
Read Full License

DEA based fuzzy portfolio evaluation models integrated with TOPSIS techniques to rank the efficient Portfolios under different risk indicators

Abha Aggarwal[1], Anjana Gupta[2†], Rajkumar Verma[3†] and Reenu Kumari[2,4*†]

[1]University School of Basic and Applied Sciences, Guru Gobind Singh Indraprastha University Sector 16, Dwarka, 110078, Delhi, India.

[2]Department of Applied Mathematics, Delhi Technological University, Bawana Road, Rohini, 110042, Delhi, India.

[3]Department of Management Control and Information Systems, University of Chile , Av. Diagonal Paraguay 257, 8330015, Santigo, Chile.

[4]Department of Applied Sciences, Maharaja Surajmal Institute of Technology, C4, Janakpuri, 110058, Delhi, India.

*Corresponding author(s). E-mail(s): reenu_kumari@msit.in;
Contributing authors: abhaaggarwal27@gmail.com; anjanagupta@dce.ac.in; rkver83@gmail.com, rverma@fen.uchile.cl;
†These authors contributed equally to this work.

Abstract

Data Envelopment Analysis models estimates the relative efficiency of a group of identical Decision-Making Units (DMUs) with multiple inputs and outputs. Since the rank of all efficient DMUs in DEA is one, thus there is no other method to distinguish their performance. Now, as all the efficient DMUs may be considered an alternative, the ranking of all efficient units is required. Here, we made an attempt to assess the

portfolios from two perspectives: efficiency and performance. Accordingly, the portfolios have been ranked through a two-stage process using DEA-based fuzzy portfolio estimation models in stage 1 and the Technique for Order of Preference by Similarity to Ideal Solution (TOPSIS) method in stage 2. To evaluate the portfolio efficiency in a fuzzy environment, two types of portfolios are considered, having possibilistic mean return as output and possibilistic variance and possibilistic semi-variance as input criteria, respectively. As an output variable can take positive as well as negative values, the Range Directional Measure (RDM) model of DEA has been extended to fuzzy environment and used to rank all the portfolios as per their efficiency score. By utilizing the properties and advantages of both methods, this paper proposed a hybrid approach (DEA-TOPSIS method) which provides the complete ranking of all efficient fuzzy portfolios. Detailed numerical illustrations are presented here to authenticate the proposed approach, and the obtained results are compared with other existing DEA methods that validate the accuracy and feasibility of the proposed technique.

Keywords: Fuzzy Set, Data Envelopment Analysis , Decision Making Units, TOPSIS method

1 Introduction

In financial terminology, a portfolio is simply a collection of financial assets such as stocks, bonds, cash, currency, derivatives, etc. Portfolio optimization is a technique to construct an optimal basket of assets, where an optimal is to be understood in the context of investor objectives and desires. The major revolution in portfolio selection theory came in 1952 with the path-breaking work of Markowitz (1968). His insight resulted in an optimization model, now famous as the Mean-Variance model, where the portfolio's return and risk are quantified using the statistical measures of expected return and variance of the portfolio return distribution, respectively. Thus, an efficient portfolio has the minimum risk level for a given return or the maximum return for a given level of risk. The distance between the portfolio under evaluation and its projection on the efficient frontier can be used to calculate the efficiency of the portfolio by the M-V model [Zhou et al. (2018)]. This strategy is also known as the frontier-based strategy. Efficient frontiers are, nevertheless, challenging to obtain, particularly for large-scale evaluation problems, due to the many limitations associated with actual investment circumstances [Xiao et al. (2020)]. To deal with this issue, the traditional DEA methodologies are widely used to approximate the portfolio efficiency. DEA is one of the most prevalent approaches for evaluating the relative efficiency of concern portfolios based on multiple inputs and outputs. The first DEA model was initiated in 1978 by Charnes et al. (1978) to calculate the efficiency of an educational centre and then further developed by Banker et al. (1984) in 1984. In

1997,Murthi et al. (1997) first applied this approach to portfolio performance estimation with various transaction costs. Since then, many researchers have applied DEA models to obtain portfolio efficiency. Using simulation findings to show how the DEA frontier approximates the portfolio frontier with a larger sample size, Ding et al. (2014) presented a portfolio performance evaluation problem considering margin limitations. Liu et al. (2015) applied a DEA frontier improvement technique to suggest a re-balancing strategy for portfolios inside the MV framework. Zhou et al. (2018) presents a segmented DEA method that depends on data segment points to handle the problem of cardinality constraints in portfolio selection problems.

The studies mentioned above are modeled in the probabilistic environment that was created under the assumption that future asset values are determined ex-ante. However, a perfect forecast of the security returns from the existing historical data is impossible due to the financial sector's inherent complexity and volatility. There are many non-probabilistic aspects, such as policies, economics, regulations, laws, human psychology, etc., particularly in the fundamental financial markets. As a result of the complexity and cyclical nature of the financial markets, it is challenging to ensure the assumption mentioned above in practice. In general, fuzzy techniques might better suit investors' ambiguous objectives than probabilistic approaches. In order to better understand the uncertainty in financial markets, fuzzy theory should be used. The fuzzy theory put forward by Zadeh (1965) can be used to address portfolios with fuzzy returns in this situation. Numerous ideas have been put forth to preach the problem of fuzzy portfolio selection, including possibility theory, credibility theory, random fuzzy theory, and others. The possibility theory, coined by Zadeh (1978), is an uncertainty theory devoted to handling incomplete and imprecise information. The concept of possibility theory used in fuzzy-set approaches is generally more applicable when examining an early stage of a decision process and when little information is available. This is in contrast with the probabilistic theory, h requires probability density functions and other data for decision-making. As real-valued functions can be extended to functions of fuzzy numbers in this context, possibility theory provides the essential framework for fuzzy-set approaches. Carlsson and Fullér (2001) proposed the definition of lower and upper possibilistic mean values of a fuzzy number and considered them as possibility distributions. Besides, Zhang and Nie (2003) defined the lower and upper possibilistic variances and covariances of fuzzy numbers. Carlsson et al. (2002) developed a possibilistic approach to portfolio selection with the highest utility score by assuming the returns of assets as trapezoidal fuzzy numbers. Liu and Zhang (2013) formulated two possibilistic mean semi-variance models for portfolio selection, in which market risk and liquidity risk are measured by lower possibilistic semivariance. Mashayekhi and Omrani (2016) proposed a fuzzy multi-objective Markowitz-DEA cross-efficiency method in a possibilistic framework. Chen et al. (2018) introduced DEA-based fuzzy portfolio estimation models to find the fuzzy portfolio efficiency. They construct three types of DEA-based

fuzzy portfolio models assuming different risk indicators, i.e., possibilistic variance, possibilistic semi-variance, and possibilistic semi-absolute deviation. Later, possibility theory and credibility theory-based fuzzy portfolio optimization models were proposed by Chen (2015), Vercher and Bermúdez (2015), Mehlawat et al. (2020), Gupta et al. (2020). Additionally, it should be noted that DEA models implicitly presuppose that the input and output values are non-negative; however, in a variety of circumstances, negative inputs or outputs can be encountered, such as the loss experienced relative to net profit, negative net income when expenses exceed revenues, return rates for investments, etc. Portela et al. (2004) introduced the range directional model (RDM) in 2004, which is applicable in such circumstances. Some other DEA-based models for dealing with negative inputs and outputs are the modified slacks-based measure model (MSBM) by Sharp et al. (2007), the semi-oriented radial measure (SORM) model by Emrouznejad et al. (2010), the Variant of the radial measure (VRM) model by Cheng et al. (2013), BP-SBM model by Tone et al. (2020) etc.

It should be observed that while the research mentioned above focused on portfolio selection and performance assessment, to the best of our knowledge, no study in the literature deals with the comprehensive ranking of efficient fuzzy portfolios. Hence, we integrate the DEA-based fuzzy portfolio selection models introduced in Chen et al. (2018) with an MCDM method TOPSIS to obtain the full ranking of the efficient portfolio. The Multi-Criteria Decision-making (MCDM) method makes decisions when multiple alternatives are available for contradictory criteria. Its principal goal is to maintain control over the decision-making process in case of various alternative and criterion diversity. The models that are qualitative and rank the countable number of alternatives through multiple measures, to name a few, Technique for Order of Preference by Similarity to Ideal Solution (TOPSIS) by Hwang and Yoon (1981), Analytic Hierarchy Process (AHP) by Saaty (1986), Analytic Network Process (ANP) by Sayyadi and Awasthi (2018) and many more. TOPSIS is a powerful approach developed by Hwang and Yoon (1981) to evaluate the performance of different alternatives based on the similarity degree with the ideal solution. According to this technique, the best option should have the shortest distance from the ideal solution and the farthest distance from the negative ideal. Following the work presented in [Chen et al. (2018)], we offer the hybrid DEA-TOPSIS technique that considers efficient fuzzy portfolios as the available alternative and different inputs and outputs of efficient portfolios as the evaluation attributes. Similar to the work Chen et al. (2018), randomly generated fuzzy portfolios are considered in this study, where the return from the asset is a trapezoidal fuzzy number. Two types of risk measures, possibilistic variance and possibilistic semi-variance, are considered here with numerical examples which effectively verify the proposed approach.

The remainder of the paper is organized in the following manner. Section 2 presents a brief literature review on the DEA ranking models. Section 3

presents some basic definitions and preliminaries regarding the fuzzy numbers and their possibilistic mean, variance and semi-variance for portfolio selection. Section 4 offers the DEA-based fuzzy portfolio estimation models for positive as well as negative returns in a possibilistic framework. Section 5 presents the various steps of the TOPSIS method to rank the efficient portfolios. Section 6 offers other DEA models, such as Super efficiency models in the fuzzy environment, for comparison purposes. In Section 7, numerical examples are presented to justify the proposed approach. Finally, Section 8 present the conclusions with some future directions.

2 Literature Review

In DEA, each DMU is self-evaluated with the most favourable weights for input and output to obtain the relative efficiency. Consequently, DEA might assess too many DMUs as the best and cannot distinguish them further. To cope with this issue, Andersen and Petersen Andersen and Petersen (1993) introduced a VRS-based super efficiency (SE) DEA model in which the efficient DMU under SE evaluation is excluded and compared with a linear combination of the remaining DMUs in the production possibility set. An efficient DMU is called super-efficient if it can achieve the efficient frontier formed by the remaining DMUs either by increasing its inputs or decreasing its outputs. Despite being feasible in some cases, Super-efficiency models are widely applied and extended in literature. Tran et al. (2019) Integrate the super efficiency model with the SBM model. Pan et al. (2020) applied the SE model to the water use efficiency Shandong Province cities. Although the DEA-super efficiency models provide a unique raking to the efficient DMUs, researchers still argued for developing more methods for ranking efficient DMUs due to the problem of the infeasibility of DEA-SE models in many problems. Another famous technique for finding unique ranking is Cross-efficiency, initiated by Sexton et al. (1986). Traditional cross-efficiency has some limitations, such as non-uniqueness of weights and nonpareto solutions. For a more detailed study of cross-efficiency models, see ¿itewu2021methods.

In DEA, there are several ranking techinques have been used by various academicians to rank the DMUs in recent years, as discussed above. It is worth mentioning that each method follows a certain theory and framework to rank the considered DMUs so that they may give different ranking orders to a DMU. In practice, choosing a ranking method, the results of which the Decision Maker (DM) would be able to trust, is an important issue. This problem of ranking the efficient DMUs can be corrected using MCDM techniques, although the techniques work differently than DEA models. To rank efficient DMUs, Sinuany-Stern (2000) developed a two-phase AHP-DEA method by integrating a well-known analytic hierarchy process (AHP) with DEA. In the first phase, the pairwise comparison matrix is evaluated. In the second phase, the criteria weights obtained from the pairwise evaluation matrix are

utilized to rank and scale the units via the Analytical Hierarchical Process (AHP). They conclude that there is a complete match of ranking by DEA and AHP/DEA. Further, Alrezaee et al. Alirezaee and Sani (2011) proposed a modified two-stage AHP-DEA methodology for ranking DMUs that removes all the shortcomings of the method introduced by Sinuany-Stern (2000) method. Wang et al. (2021) used DEA and AHP methods to select the optimal wind power plant. The AHP/DEA approach provides the same results as DEA in the case of a single input-output scenario. The other MCDM technique integrated with DEA is TOPSIS. Some studies combined TOPSIS and DEA under a single framework to establish a unique DMU ranking of the DMUs, as briefly described in the introduction. They select one of these techniques as the primary technique and the other as a secondary, supplemental technique. Decision-makers should be able to accomplish the goals of a corporate sourcing strategy using both DEA and TOPSIS as potential evaluation tools. Lotfi et al. (2011) considered efficient DMUs from different DEA models and ranked them using the TOPSIS method. Recently Banihashemi and Khalilzadeh (2020) proposed a new method for ranking efficient units and compared it with the other methods presented in the literature, such as the super-efficiency model in DEA, the concept of Shapley value in game theory, and the TOPSIS method in multi-criteria decision making. Rakhshan (2017) utilized a hybrid approach based on TOPSIS and DEA methods to obtain a rational ranking of efficient DMUs. Jablonsky (2012) presented two models for ranking efficient units. Both are based on MCDM methods; the first uses the goal programming technique for deriving a super-efficiency measure, and the second combines AHP and DEA principles. Omrani et al. (2022) used a three-step DEA model to obtain four types of efficiency (technical efficiency, social efficiency, environmental efficiency scores and sustainable efficiency) for Iranian airlines. They integrate DEA models with the TOPSIS method to aggregate the final efficiency score. A detailed review of DEA ranking models has been presented in Aldamak and Zolfaghari (2017). They categorized the ranking methods into ten groups. They conclude that which DEA ranking method is used fully depends upon the application being considered. From the detailed analysis of the literature, we conclude that using DEA and TOPSIS is a good idea to handle the problem of robust ranking of DMUs. Also, we can not find any study that provides a complete ranking for the efficient portfolio that can take positive and negative input-out t in a fuzzy environment. So we made an effort to find the ranking of efficient fuzzy portfolios the DEA-TOPSIS method

2.1 Contributions and Purpose

In this study, we have made an effort to add one more aspect to the DEA application, i.e. ranking of efficient fuzzy portfolios with various risk metrics. The following are the key highlights of the current study.

1. In this paper, inspired by the work of Chen et al. (2018), we discuss the

performance of fuzzy portfolios in different risk metrics. Further, DEA fuzzy portfolio estimation models are integrated with MCDM to find the unique ranking of the portfolios in this study.

2.According to the discussion based on earlier findings, academics from various fields generally agree that using DEA and TOPSIS is a good idea. Furthermore, previous studies have not effectively analyzed the portfolio's performance. More research is required to create a baseline for decision-makers by examining portfolio performance in a dynamic environment.

3. Implementing the DEA-based fuzzy portfolio estimation models with TOPSIS for ranking the efficient portfolios is a new application in the field of DEA.

4. Additionally, we consider the portfolios having negative returns also. To the best of our knowledge, this is the first time the RDM model has been extended in the possibilistic framework to deal with the fuzzy variables and has been integrated with the TOPSIS method for getting a unique ranking. In the literature, significantly fewer studies discuss the full ranking of the DMUs with the negative input-output variable. We integrate the results of the RDM fuzzy portfolio model with TOPSIS and take advantage of both methods.

5. Comparing the results of the hybrid DEA-TOPSIS method with other ranking methods in the literature, like Cross-efficiency (DEA game cross-efficiency), is not possible in our case as we have considered a single input/output application.

6.The benefit over other existing methods of integrating the TOPSIS method with DEA lies in the fact that the computational complexity of the TOPSIS is much better than any other MCDM technique. It can save computational time for large-scale practical applications.

7. We demonstrate the applicability and effectiveness of our methodology using actual data from the Stock Exchange in portfolio construction challenges.

In the existing studies on portfolio performance evaluation, no studies deal with the full ranking of portfolios under the possibilistic environment with different risk measures. Through this study, we advance to the literature on portfolio performance analysis and ranking by integrating DEA fuzzy models with TOPSIS.

3 Preliminaries

For various notations, terminologies, and the basics of fuzzy sets, fuzzy numbers, and possibility theory, we shall refer to Zadeh (1978) and Zimmermann (2011) respectively. Further, the mathematical models of Carlsson et al. (2002), for computing the possibilistic mean, possibilistic variance, and possibilistic semi-variance of a fuzzy number are presented here.

Definition 1 Let X be a universal set. A fuzzy set $\tilde{A}$ in X is denoted by

$$\tilde{A} = \left\{ \langle x, \mu_{\tilde{A}}(x) \rangle \mid x \in X \right\},$$

where $\mu_{\tilde{A}} : X \to [0,1]$ describes the degree of belongings of an element $x \in X$ to the set $\tilde{A}$.

Definition 2 (γ-cut) Let $\tilde{A}$ be a fuzzy set in X and $\gamma \in (0,1]$. The γ-cut of the fuzzy set $\tilde{A}$ is the crisp set A_γ given by

$$A_\gamma = \{x \in X : \mu_{\tilde{A}}(x) \geq \gamma\}.$$

Definition 3 A fuzzy set $\tilde{A}$ in $\mathbb{R}$ is called a fuzzy number if it satisfies the following conditions

1. $\tilde{A}$ is normal.
2. $\tilde{A}_\gamma$ is a closed interval for every $\gamma \in (0,1]$.
3. The support of $\tilde{A}$ is bounded.

Definition 4 (Trapezoidal fuzzy number (TrFN)) A fuzzy number $\tilde{A}$ represented by the quadruplet $\tilde{A} = [a, b, \alpha, \beta]$, where $[a, b]$ is the tolerance interval; α and β denote the left and right width of the TrFN- $\tilde{A}$, respectively, is called a trapezoidal fuzzy number if its membership function is given by

$$\mu_{\tilde{A}}(x) = \begin{cases} 0, & x \leq a - \alpha, x \geq b + \beta, \\ \dfrac{x - a + \alpha}{\alpha}, & a - \alpha \leq x \leq a, \\ 1, & a \leq x \leq b, \\ \dfrac{b + \beta - x}{\beta}, & b \leq x \leq b + \beta, \end{cases}$$

Further, the γ-cut of the TrFN $\widetilde{A} = (a, b, \alpha, \beta)$ is the closed interval and given by

$$A^\gamma = [a_1^\gamma, a_2^\gamma] = [(a - (1-\gamma)\alpha,\ b + (1-\gamma)\beta], \quad \gamma \in (0,1].$$

Definition 5 Let $\tilde{A}$ be a fuzzy number with $A^\gamma = [a_1^\gamma, a_2^\gamma], \quad \gamma \in (0,1]$. The (crisp) possibilistic mean (or expected value) and possibilistic variance of a fuzzy number $\tilde{A}$, denoted by $E(\tilde{A})$ and $Var(\tilde{A})$, is defined as

$$E(\tilde{A}) = \int_0^1 \gamma \left(a_1^\gamma + a_2^\gamma\right) d\gamma,$$

and

$$Var(\tilde{A}) = \frac{1}{2} \int_0^1 \gamma \left(a_2^\gamma - a_1^\gamma\right)^2 d\gamma.$$

respectively.

It is easy to see that for a TrFN $\tilde{A} = [a, b, \alpha, \beta]$

$$E(\tilde{A}) = \int_0^1 \gamma[a - (1-\gamma)\alpha + b + (1-\gamma)\beta]d\gamma = \frac{(a+b)}{2} + \frac{(\beta-\alpha)}{6},$$

and

$$Var(\tilde{A}) = \left[\frac{(b-a)}{2} + \frac{(\alpha+\beta)}{6}\right]^2 + \frac{(\alpha+\beta)^2}{72}.$$

Further, Saeidifar and Pasha (2009) defined the lower possibilistic semi-variance of a fuzzy number $\tilde{A}$ denoted by $Var^-(\tilde{A})$, as

$$Var^-(\tilde{A}) = \int_0^1 2\gamma\left(E(\tilde{A}) - a_1^\gamma\right)^2 d\gamma.$$

Thus for a TrFN $\tilde{A} = [a, b, \alpha, \beta]$, the lower possibilistic semi-variance is as follows

$$Var^-(\tilde{A}) = \left[\frac{(b-a)}{2} + \frac{(\alpha+\beta)}{6}\right]^2 + \frac{(\alpha)^2}{18}.$$

Assume there are n risky assets whose returns are TrFNs represented by $\tilde{r}_i = (a_i, b_i, \alpha_i, \beta_i),\ i = 1, 2, \ldots, n$ with investment proportion $w_i,\ i = 1, 2, \ldots, n$, such that $w_i \geq 0;\ \sum_{i=1}^{n} w_i = 1$. Also, there is a fixed linear transaction cost k_i associated with each asset. As a result, the portfolio's probabilistic expected net return, variance, and lower semi-variance, denoted by R, σ^2 and $(\sigma^2)^-$ are given by as follows

$$R = E\left(\sum_{i=1}^{n} \tilde{r}_i w_i - \sum_{i=1}^{n} k_i w_i\right) = \sum_{i=1}^{n}\left[\left\{\frac{1}{2}\left(a_i + b_i + \frac{1}{3}(\beta_i - \alpha_i)\right)w_i\right\} - k_i w_i\right],$$

$$\sigma^2 = Var\left(\sum_{i=1}^{n} \tilde{r}_i w_i\right) = \left[\left(\frac{(b_i - a_i)}{2} + \frac{(\alpha_i + \beta_i)}{6}\right)w_i\right]^2 + \frac{1}{72}\left[\sum_{i=1}^{n}(\alpha_i + \beta_i)w_i\right]^2,$$

and

$$(\sigma^2)^- = Var^-\left(\sum_{i=1}^{n} \tilde{r}_i w_i\right) = \left[\left(\frac{(b-a)}{2} + \frac{(\alpha+\beta)}{6}\right)w_i\right]^2 + \frac{1}{18}\left[\sum_{i=1}^{n}(\alpha_i w_i)\right]^2,$$

respectively.

In the following section, we present the DEA-based fuzzy portfolio estimation models introduced in Chen et al. (2018) and the extension of RDM model in the fuzzy framework.

4 DEA-based fuzzy portfolio evaluation models in the framework of possibilistic theory

The convex hull of the existing DMUs spans the production frontiers of the BCC model, in contrast to the CCR model, and it also results in variable returns to scale characterizations. Because of this, we will build DEA-based fuzzy portfolio estimate models in this study using the BCC model.

Assume that there are P portfolios to be evaluated. To evaluate a portfolio performance, we consider the risk associated with the portfolio as the input indicator, and the corresponding return as the output indicator. In this study, we assume n risky assets with fuzzy return as $\tilde{r}_i = (a_i, b_i, \alpha_i, \beta_i)$, $i = 1, 2, ..., n$ with investment proportions w_{ij}, $i = 1, 2, ..., n$; $j = 1, 2, \ldots, P$, such that $\sum_{i=1}^{n} w_{ij} = 1$, are considered for constructing j^{th} portfolio which is considered to be a DMU. Suppose k_i is the unit transaction cost of a unit for the i^{th} risky asset. Then the expected net return, variance and semi-variance of the j^{th} portfolio denoted by $\overline{R}_j$, σ_j^2 and $(\sigma^2)_j^-$ respectively for $(j = 1, 2, \ldots, P)$ are given respectively. To employ the DEA models for the efficiency evaluation of all portfolios, in our study we consider one input and one output criteria as risk and return respectively. The mathematical models will be presented in the following subsection to obtain risk-oriented portfolio efficiency.

4.1 Risk-oriented DEA fuzzy portfolio model in possibilistic mean-variance framework

The Risk oriented DEA fuzzy portfolio model to estimate the efficiency of a portfolio which is being under evaluation is as follows:

$$\textbf{(Model I)} \qquad \min \theta = \theta_0$$

$$s.t. \sum_{j=1}^{P} \lambda_j \left(\left\{ \sum_{i=1}^{n} \frac{1}{2} \left[(b_i - a_i) + \frac{\alpha_i + \beta_i}{3} \right] w_{ij} \right\}^2 + \frac{1}{72} \left[\sum_{i=1}^{n} (\alpha_i + \beta_i) w_{ij} \right]^2 \right)$$

$$\leq \theta_0 \left(\left\{ \sum_{i=1}^{n} \frac{1}{2} \left[(b_i - a_i) + \frac{\alpha_i + \beta_i}{3} \right] w_{i0} \right\}^2 + \frac{1}{72} \left[\sum_{i=1}^{n} (\alpha_i + \beta_i) w_{i0} \right]^2 \right)$$

$$\sum_{j=1}^{P} \lambda_j \left(\sum_{i=1}^{n} \frac{1}{2} \left[(b_i + a_i) + \frac{\beta_i - \alpha_i}{3} \right] w_{ij} - \sum_{i=1}^{n} k_i w_{ij} \right)$$

$$\geq \sum_{i=1}^{n} \frac{1}{2} \left[(b_i + a_i) + \frac{\beta_i - \alpha_i}{3} \right] w_{i0} - \sum_{i=1}^{n} k_i w_{i0},$$

$$\sum_{j=1}^{P} \lambda_j = 1, \ \lambda_j \geq 0, j = 1, 2...P.$$

Similarly, we can construct the DEA-based fuzzy portfolio evaluation model in the possibilistic mean semi-variance scenario.

4.2 RDM fuzzy portfolio evaluation model in the framework of possibilistic Theory

Here it is to be noted that the conventional DEA models evolved with the presumption that all inputs and outputs are non-negative, whereas, this assumption is very limited and is not always exist in the real world. Portela et al. (2004) introduced a model namely the Range Directional Measure (RDM) method, in which the input and the output variables can take both positive and negative values. In this section, we present RDM fuzzy portfolio estimation model to handle the unpredictability of the variables. The mathematical form of RDM fuzzy portfolio model with possibilistic variance and semi-variance as input (risk) and possibilistic return as output is given as follows:

$$\textbf{(Model II)} \qquad \max \phi \ = \ \phi_0$$

$$s.t. \sum_{j=1}^{P} \lambda_j \left(\left\{ \sum_{i=1}^{n} \frac{1}{2} \left[(b_i - a_i) + \frac{\alpha_i + \beta_i}{3} \right] w_{ij} \right\}^2 + \frac{1}{72} \left[\sum_{i=1}^{n} (\alpha_i + \beta_i) w_{ij} \right]^2 \right)$$

$$\leq \left(\left\{ \sum_{i=1}^{n} \frac{1}{2} \left[(b_i - a_i) + \frac{\alpha_i + \beta_i}{3} \right] w_{i0} \right\}^2 + \frac{1}{72} \left[\sum_{i=1}^{n} (\alpha_i + \beta_i) w_{i0} \right]^2 \right) - \phi d1_o$$

$$\sum_{j=1}^{N} \lambda_j \left(\sum_{i=1}^{n} \frac{1}{2}[(b_i + a_i) + \frac{\beta_i - \alpha_i}{3}]w_{ij} - \sum_{i=1}^{n} k_i w_{ij} \right)$$

$$\geq \left(\sum_{i=1}^{n} \frac{1}{2}[(b_i + a_i) + \frac{\beta_i - \alpha_i}{3}]w_{i0} - \sum_{i=1}^{n} k_i w_{i0} \right) + \phi d2_o$$

$$\sum_{j=1}^{P} \lambda_j = 1 \quad \lambda_j \geq 0, j = 1, 2...P.$$

Where, ($d1_0$, and $d2_0$ represent the range of feasible improvements for the portfolio that is being evaluated, given by as

$$d1_0 = \left(\sum_{i=1}^{n} (\frac{1}{2}[(b_i - a_i) + \frac{\alpha_i + \beta_i}{3}]w_{i0})^2 + \frac{1}{72}[\sum_{i=1}^{n} (\alpha_i + \beta_i)w_{i0}]^2 \right) - \min_{j=1,2,...,P} \left(\sum_{i=1}^{n} (\frac{1}{2}[(b_i - a_i) + \frac{\alpha_i + \beta_i}{3}]w_{i} \right.$$

$$d2_0 = \max_{j=1,2,...,P} \left(\sum_{i=1}^{n} \frac{1}{2}[(b_i + a_i) + \frac{\beta_i - \alpha_i}{3}]w_{ij} - \sum_{i=1}^{n} k_i w_{ij} \right) - \left(\sum_{i=1}^{n} \frac{1}{2}[(b_i + a_i) + \frac{\beta_i - \alpha_i}{3}]w_{i0} - \sum_{i=1}^{n} k_i w_{i0} \right)$$

Let $(\phi^*, \lambda_1^*, \lambda_2^* \ldots, \lambda_N^*)$ be an optimal solution of (Model II). Here, the optimal objective value ϕ^* of the RDM fuzzy model (Model II) shows the maximum inefficiency of under evaluation $portfolio_0$ and it lies between 0 and 1. The maximum efficiency of under evaluation portfolio, is $1 - \phi^*$.

In the similar manner, we use the possibilistic lower semi-variance of the return associated with the portfolio as risk (input parameter), and mean return as return (output parameter) in the RDM model presented in Portela et al. (2004). Thus, RDM fuzzy portfolio model is as follows:

(**Model III**) $\max \phi = \phi_0$

$$s.t. \sum_{j=1}^{N} \lambda_j \left(\left\{ \sum_{i=1}^{n} \frac{1}{2}\left[(b_i - a_i) + \frac{\alpha_i + \beta_i}{3}\right]w_{ij} \right\}^2 + \frac{1}{18} \sum_{i=1}^{n} \left[\alpha_i w_{ij}\right]^2 \right)$$

$$\leq \left(\left\{ \sum_{i=1}^{n} \frac{1}{2}\left[(b_i - a_i) + \frac{\alpha_i + \beta_i}{3}\right]w_{i0} \right\}^2 + \frac{1}{18} \sum_{i=1}^{n} \left[\alpha_i w_{i0}\right]^2 \right) - \phi d3_o$$

$$\sum_{j=1}^{N} \lambda_j \left(\sum_{i=1}^{n} \frac{1}{2}[(b_i + a_i) + \frac{\beta_i - \alpha_i}{3}]w_{ij} - \sum_{i=1}^{n} k_i w_{ij} \right)$$

$$\geq \left(\sum_{i=1}^{n} \frac{1}{2}[(b_i + a_i) + \frac{\beta_i - \alpha_i}{3}]w_{i0} - \sum_{i=1}^{n} k_i w_{i0} \right) + \phi d2_0$$

$$\sum_{j=1}^{P} \lambda_j = 1 \quad \lambda_j \geq 0, j = 1, 2...P.$$

Where

$$d3_0 = \left(\left\{ \sum_{i=1}^{n} \frac{1}{2}\left[(b_i - a_i) + \frac{\alpha_i + \beta_i}{3}\right]w_{i0} \right\}^2 + \frac{1}{18} \sum_{i=1}^{n} \left[\alpha_i w_{i0}\right]^2 \right) - \min_{j=1,2,\ldots,N} \left(\left\{ \sum_{i=1}^{n} \frac{1}{2}\left[(b_i - a_i) + \frac{\alpha_i + \beta_i}{3}\right]w_{ij} \right\}^2 -$$

and $d2_0$ is same as described in Model II.

It's worth noting that if multiple portfolios are efficient, we won't be able to find a complete and unique ranking of the portfolios. As a result, we use the TOPSIS to rank all efficient portfolios to generate a unique rating. The TOPSIS method was introduced by Hwang and Yoon (1981). It is a practical method for organizing the available options based on numerous criteria. It outperforms other MCDM methods for solving a wide range of decision-making problems in real-world, due to its simple computational approach and systematic procedure. Some researchers have recently extended the TOPSIS method to work in various information environments and applications.

5 TOPSIS method to rank the efficient portfolio

TOPSIS is founded on the notion of selecting the best alternative (here DMU) that is as close to the positive ideal solution at the same time being as far away from the negative ideal solution as possible. The best performance values for each portfolio demonstrated by each criterion (here criterion as risk and return) in the decision matrix make up the perfect solution. As a result, we used a negative feature criterion for risk and a positive feature criterion for return.

Let L be the number of efficient portfolios. Suppose we have m inputs and s outputs for each portfolio, let D_1 and D_2 denotes respectively the input and

output matrix corresponding to L efficient portfolios. Therefore

$$D_1 = \begin{bmatrix} x_{11} & x_{12} & \dots & x_{1L} \\ x_{21} & x_{22} & \dots & x_{2L} \\ \vdots & \vdots & \vdots & \vdots \\ x_{m1} & x_{m2} & \dots & x_{mL} \end{bmatrix} \qquad D_2 = \begin{bmatrix} y_{11} & y_{12} & \dots & y_{1L} \\ y_{21} & y_{22} & \dots & y_{2L} \\ \vdots & \vdots & \vdots & \vdots \\ y_{s1} & y_{s2} & \dots & y_{sL} \end{bmatrix}$$

Now we have to follow the following steps:

Step 1. Normalization

Calculate the normalized decision matrix corresponding to the cost criterion (m inputs) and benefit criteria (s outputs). Let p_{il} and q_{rl} ($i = 1, 2, \dots, m;\ \ r = 1, 2, \dots, s$) denotes the normalized value of i^{th} input and r^{th} outpt of l^{th} DMU respectively. Now we have as follows

$$p_{il} = \frac{x_{il}}{\sqrt{\sum_{k=1}^{L} x_{ik}^2}}, \quad \forall i = 1, 2, \dots, m,\ l = 1, 2, \dots, L$$

and

$$q_{rl} = \frac{y_{rl}}{\sqrt{\sum_{k=1}^{L} y_{rk}^2}}, \quad \forall r = 1, 2, \dots, s,\ \ l = 1, 2, \dots, L.$$

Step 2. Determine the positive ideal and negative-ideal points: Let p_{iw} and q_{rw} denotes respectively be the i^{th} input and r^{th} output of the worst DMU (D_w). Similarly let p_{ib} and q_{rb} denotes respectively be the i^{th} input and r^{th} output of the best DMU (D_b). Then

$$p_{iw} = \max_{1 \le l \le L} p_{il}, \quad i = 1, 2, \dots, m,$$

and

$$q_{rw} = \min_{1 \le l \le L} q_{rl}, \quad r = 1, 2, \dots, s.$$

Similarly

$$p_{ib} = \min_{1 \le l \le L} p_{il}, \quad i = 1, 2, \dots, m,$$

and

$$q_{rb} = \max_{1 \le l \le L} q_{rl}, \quad r = 1, 2, \dots, s.$$

Step 3. Measuring the distance from the ideal and negative ideal points: Let d_{lw} be the distance between the target DMU l and the worst DMU D_w (best DMU D_b), so

$$d_{lw} = \sqrt{\sum_{i=1}^{m} (p_{il} - p_{iw})^2 + \sum_{r=1}^{s} (q_{rl} - q_{rw})^2}, \quad l = 1, 2, \dots, L,$$

and

$$d_{lb} = \sqrt{\sum_{i=1}^{m}(p_{il} - p_{ib})^2 + \sum_{r=1}^{s}(q_{rl} - q_{rb})^2}, \quad l = 1, 2, \ldots, L.$$

Step 4. Calculate the similarity to the worst condition:
Let s_{lw} be the relative closeness of the target DMU l to the worst DMU D_w.

$$s_{lw} = \frac{d_{lw}}{d_{lw} + d_{lb}}, \quad l = 1, 2, \ldots, L.$$

Here, $0 \leq s_{lw} \leq 1$, and

$$s_{lw} = \begin{cases} 1, & \text{if and only if the alternative solution has the best condition} \\ 0, & \text{if and only if the alternative solution has the worst condition.} \end{cases}$$

Step 5. Ranking criterion:
Rank the alternatives or portfolios in the descending order of s_{lw}, the alternative with maximum value of s_{lw} is the best performing alternative.
The working procedure of the proposed approach has been described in the algorithm 1.

Algorithm 1 Computation Procedure of the proposed method

Input: The Fuzzy returns of Stocks with the different proportion invested in the stocks.
Output: The full ranking of efficient portfolios.
Step 1. Calculate the Efficiency of portfolios by using DEA fuzzy portfolio models.
Step 2. Rank the portfolios according to the efficiency score.
Step 3. If the no. of efficient portfolio ≥ 1, then apply TOPSIS method.
Step 4. Identification of attributes (Return, Risk) for all the alternatives (efficient portfolios).
Step 5. Form a weighted normalized decision matrix.
Step 6. Calculate the positive and negative ideal points.
Step 7. Evaluate the similarity to the worst condition as the measure of relative closeness s_{lw}.
Step 8. Rank the efficient portfolio in the decreasing order of s_{lw}.

We present the Super efficiency models in a fuzzy environment with possibility theory for the comparison purpose in the following section.

6 Super Efficiency DEA fuzzy estimation models

The efficient DMU in DEA has an efficiency score of one. This efficiency score is often shared by multiple DMUs. Many models have been reported in the literature under the heading of super-efficiency for the complete ranking of the DMUs. We can refer to Hadi-Vencheh and Esmaeilzadeh (2013), Tone (2001) and Andersen and Petersen (1993) method to name a few. The very first supper efficiency DEA method was introduced by Andersen and Petersen (1993) for positive input and output only. We present the super-efficiency DEA model in possibilistic mean variance framework for whole ranking of efficient fuzzy portfolios as follows:

$$\textbf{(Model IV)} \quad \min \ \eta = \eta_0$$

$$\text{s. t.} \sum_{\substack{j=1 \\ j\neq 0}}^{P} \lambda_j \left(\left\{ \sum_{i=1}^{n} \frac{1}{2} \left[(b_i - a_i) + \frac{\alpha_i + \beta_i}{3} \right] w_{ij} \right\}^2 + \frac{1}{72} \left[\sum_{i=1}^{n} (\alpha_i + \beta_i) w_{ij} \right]^2 \right)$$

$$\leq \eta_0 \left(\left\{ \sum_{i=1}^{n} \frac{1}{2} \left[(b_i - a_i) + \frac{\alpha_i + \beta_i}{3} \right] w_{i0} \right\}^2 + \frac{1}{72} \left[\sum_{i=1}^{n} (\alpha_i + \beta_i) w_{i0} \right]^2 \right)$$

$$\sum_{\substack{j=1 \\ j\neq 0}}^{P} \lambda_j \left(\sum_{i=1}^{n} \frac{1}{2} \left[(b_i + a_i) + \frac{\beta_i - \alpha_i}{3} \right] w_{ij} - \sum_{i=1}^{n} k_i w_{ij} \right)$$

$$\geq \sum_{i=1}^{n} \frac{1}{2} \left[(b_i + a_i) + \frac{\beta_i - \alpha_i}{3} \right] w_{i0} - \sum_{i=1}^{n} k_i w_{i0},$$

$$\sum_{\substack{j=1 \\ j\neq 0}}^{P} \lambda_j = 1 \ \lambda_j \geq 0, j = 1, 2 \ldots P.$$

Let $(\eta_0^*, \lambda_1^*, \lambda_2^* \ldots, \lambda_P^*)$ be an optimal solution of (Model IV). It should noted that if a portfolio, is efficient, its super-efficiency value η_0^* will be larger than one, whereas an inefficient one will have a super-efficiency value equal to the efficiency value of the inefficient one.

6.1 Modified slacks-based fuzzy portfolio method

To handle the problem of negative data and to provide a full ranking of all DMUs, Wei et al. (2019) suggested a novel MSBM (modified slacks-based model). We extend the model presented in Wei et al. (2019) in the possibilistic framework as follows:

$$\textbf{(Model V)} \qquad \min \ \rho = \frac{1-\frac{s_{1o}^{-}}{R_1^{-}}}{1+\frac{s_{2o}^{+}}{R_2^{+}}}$$

$$\text{s. t.} \ \sum_{j=1}^{P}\lambda_j\left(\left\{\sum_{i=1}^{n}\frac{1}{2}\Big[(b_i-a_i)+\frac{\alpha_i+\beta_i}{3}\Big]w_{ij}\right\}^2+\frac{1}{72}\Big[\sum_{i=1}^{n}(\alpha_i+\beta_i)w_{ij}\Big]^2\right)+s_{10}^{-}$$

$$\leq\left(\left\{\sum_{i=1}^{n}\frac{1}{2}\Big[(b_i-a_i)+\frac{\alpha_i+\beta_i}{3}\Big]w_{i0}\right\}^2+\frac{1}{72}\Big[\sum_{i=1}^{n}(\alpha_i+\beta_i)w_{i0}\Big]^2\right)$$

$$\sum_{j=1}^{P}\lambda_j\left(\sum_{i=1}^{n}\frac{1}{2}\Big[(b_i+a_i)+\frac{\beta_i-\alpha_i}{3}\Big]w_{ij}-\sum_{i=1}^{n}k_iw_{ij}\right)-s_{20}^{-}$$

$$\geq\sum_{i=1}^{n}\frac{1}{2}\Big[(b_i+a_i)+\frac{\beta_i-\alpha_i}{3}\Big]w_{i0}-\sum_{i=1}^{n}k_iw_{i0},$$

$$\sum_{j=1}^{P}\lambda_j=1 \ \ \lambda_j\geq 0, j=1,2...P.\ , s_{1o}^{-},\ s_{2o}^{+}\geq 0, \quad j=1,2,\ldots,P$$

Here, (R_1^{-} and R_2^{+}) are the feasible directions to move, and are defined as follows:

$$R_1^{-}=\max_{j=1,2,\ldots,P}\left(\sum_{i=1}^{n}(\frac{1}{2}[(b_i-a_i)+\frac{\alpha_i+\beta_i}{3}]w_{ij})^2+\frac{1}{72}[\sum_{i=1}^{n}(\alpha_i+\beta_i)w_{ij}]^2\right)-\min_{j=1,2,\ldots,P}\left(\sum_{i=1}^{n}(\frac{1}{2}[(b_i-a_i)+\frac{\alpha_i+}{3}\right.$$

$$R_2^{+}=\max_{j=1,2,\ldots,P}\left(\sum_{i=1}^{n}\frac{1}{2}[(b_i+a_i)+\frac{\beta_i-\alpha_i}{3}]w_{ij}-\sum_{i=1}^{n}k_iw_{ij}\right)-\min_{j=1,2,\ldots,P}\left(\sum_{i=1}^{n}\frac{1}{2}[(b_i+a_i)+\frac{\beta_i-\alpha_i}{3}]w_{ij}-\sum_{i=1}^{n}k_i\right.$$

Let $(\rho^*, \lambda_1^*, \lambda_2^* \ldots, \lambda_N^*)$ be an optimum solution of (Model V). Further, ρ_0^* indicates the optimal efficiency score of the portfolio under evaluation (0^{th}) Here, s_{1o}^- and s_{2o}^+, respectively denote the excess of input (risk) and shortfall of output(return) of 0th portfolio, and they are identified as slacks. The λ_j ($j = 1, 2, \ldots, P$) denote the weight of j^{th} portfolio, Let $J_e = \{p : \rho_p^* = 1\}$ and $J_{ine} = \{k : \rho_k^* < 1\}$, where $J_e \cup J_{ine} = \{1, 2, \ldots, P\}$ respectively, denotes the set of efficient and inefficient portfolios.

To rank the efficient DMUs when few inputs and outputs take negative values, by using (Model V) Wei et al. (2019) presented the steps to find full ranking. We have written the all models of Wei et al. (2019) in the possibilistic mean-variance scenario as follows:

Step 1 Let $k \in J_e$ and $p \in J_{ine}$. Evaluate the optimum value $\rho_{p,k}^*$ of $portfolio_p$ under the condition that $portfolio_k$ is excluded from the set of references.

$$\rho_{p,k}^{\star} = \min \ \rho_{p,k} = \frac{1 - \frac{s_{1p}^-}{R_1^-}}{1 + \frac{s_{2p}^+}{R_2^+}}$$

$$\text{subject to} \sum_{\substack{j=1 \\ j \neq k}}^{P} \lambda_j \left(\left\{ \sum_{i=1}^{n} \frac{1}{2} \left[(b_i - a_i) + \frac{\alpha_i + \beta_i}{3} \right] w_{ij} \right\}^2 + \frac{1}{72} \left[\sum_{i=1}^{n} (\alpha_i + \beta_i) w_{ij} \right]^2 \right) + s_{1p}^-$$

$$\leq \left(\left\{ \sum_{i=1}^{n} \frac{1}{2} \left[(b_i - a_i) + \frac{\alpha_i + \beta_i}{3} \right] w_{ip} \right\}^2 + \frac{1}{72} \left[\sum_{i=1}^{n} (\alpha_i + \beta_i) w_{ip} \right]^2 \right)$$

$$\sum_{\substack{j=1 \\ j \neq k}}^{P} \lambda_j \left(\sum_{i=1}^{n} \frac{1}{2} \left[(b_i + a_i) + \frac{\beta_i - \alpha_i}{3} \right] w_{ij} - \sum_{i=1}^{n} k_i w_{ij} \right) - s_{2p}^-$$

$$\geq \sum_{i=1}^{n} \frac{1}{2} \left[(b_i + a_i) + \frac{\beta_i - \alpha_i}{3} \right] w_{ip} - \sum_{i=1}^{n} k_i w_{ip},$$

$$\sum_{\substack{j=1 \\ j \neq k}}^{P} \lambda_j = 1 \quad \lambda_j \geq 0, j = 1, 2 \ldots P. \quad s_{1p}^-, s_{2p}^+ \geq 0$$

StepII

Let Ω_k be the influence of efficient $portfolio_k$ on all inefficient portfolio and is

given by as

$$\Omega_k = \sum_{p \in J_{ine}} \mid \rho^*_{p,k} - \rho^* \mid, \quad k \in J_e.$$

Step III

Let $k, d \in J_e$. Calculate the optimum value $\rho^*_{p,kd}$ of $portfolio_p$ with the assumption that $portfolio_k$ and $portfolio_d$ both are eliminated from the reference set.

$$\rho^{\star}_{p,kd} = \min \ \rho_{p,kd} = \frac{1 - \frac{s^-_{1p}}{R^-_1}}{1 + \frac{s^+_{2p}}{R^+_2}}$$

$$\text{subject to} \sum_{\substack{j=1 \\ j \neq k,d}}^{P} \lambda_j \left(\left\{ \sum_{i=1}^{n} \frac{1}{2} \left[(b_i - a_i) + \frac{\alpha_i + \beta_i}{3} \right] w_{ij} \right\}^2 + \frac{1}{72} \left[\sum_{i=1}^{n} (\alpha_i + \beta_i) w_{ij} \right]^2 \right) + s^-_{1p}$$

$$\leq \left(\left\{ \sum_{i=1}^{n} \frac{1}{2} \left[(b_i - a_i) + \frac{\alpha_i + \beta_i}{3} \right] w_{ip} \right\}^2 + \frac{1}{72} \left[\sum_{i=1}^{n} (\alpha_i + \beta_i) w_{ip} \right]^2 \right)$$

$$\sum_{\substack{j=1 \\ j \neq k,d}}^{P} \lambda_j \left(\sum_{i=1}^{n} \frac{1}{2} \left[(b_i + a_i) + \frac{\beta_i - \alpha_i}{3} \right] w_{ij} - \sum_{i=1}^{n} k_i w_{ij} \right) - s^-_{2p}$$

$$\geq \sum_{i=1}^{n} \frac{1}{2} \left[(b_i + a_i) + \frac{\beta_i - \alpha_i}{3} \right] w_{ip} - \sum_{i=1}^{n} k_i w_{ip},$$

$$\sum_{\substack{j=1 \\ j \neq k,d}}^{P} \lambda_j = 1 \ \ \lambda_j \geq 0, j = 1, 2 ... P. s^-_{1p}, s^+_{2p} \geq 0, \quad j = 1, 2, \ldots, P$$

Let $\Omega_{k,d}$ denotes the influence of $portfolio_d$, on all inefficient portfolios after the removal of $portfolio_d$ and $portfolio_k$ from the reference set and is calculated by

$$\Omega_{d,k} = \sum_{p \in J_{ine}} \mid \rho^*_{p,kd} - \rho^*_{p,k} \mid, \quad k, d \in J_e.$$

StepIV

Let $\mid \Omega_{d,k} - \Omega_d \mid$ denotes the impact of efficient $portfolio_k$ on another efficient

$port folio_d$ then ψ_k indicates the influence of efficient $port folio_k$ on all the other efficient portfolios.

$$\psi_k = \sum_{d \in J_e} \mid \Omega_{d,k} - \Omega_d \mid, \quad k \in J_e.$$

StepV

Let ϕ_k be defined as the impact of efficient $port folio_k$ on all efficient and inefficient ones, excluding itself by $\phi_k = \Omega_k + \psi_k$ for all $k \in J_e$.

Similarly we can write the model IV and V in the possibilistic mean semi-variance scenario to show the the portfolio assessment and ranking with different risk measure.

7 Numerical Illustration

To demonstrate the applicability and validity of the proposed work, three numerical examples are considered here. In first example, we consider only those assets in which the inputs and outputs both are positive, whereas in the second and third example negative inputs and/or outputs are considered by using possibilistic variance and possibilistic semi-variance as outputs. All simulations have been implemented in MATLAB software.

Example 1

Here we consider the same stocks as taken by Chen et al. (2018) in their study. This real-time data has been taken from the Shanghai Stock Exchange. The five stocks' historical data, which spans the period of January 2003 to December 2006, has been used in this illustration. The possibility distributions of the return as well as the cost of transaction on all the 5 assets given there are now enlisted in Table 1. To generate the 30 different portfolios samples randomly, the weight of each stock invested, are tabulated in Table 2.

Table 1 The possibilistic distributions of the return of 5 stocks

Stocks	a_i	b_i	α_i	β_i	k_i
$\mathbb{A}_1$	0.022	0.026	0.020	0.030	0.003
$\mathbb{A}_2$	0.053	0.060	0.050	0.054	0.003
$\mathbb{A}_3$	0.078	0.085	0.072	0.094	0.004
$\mathbb{A}_4$	0.120	0.164	0.008	0.176	0.005
$\mathbb{A}_5$	0.006	0.086	0.072	0.090	0.005

In Table 3, fourth & fifth column depict the efficiency score and corresponding ranking score of these sample portfolios obtained from input focused DEA fuzzy portfolio evaluation model, (Model I) in the possibilistic mean variance scenario. As the efficiency score to the portfolios 4, 5, 11, 18 is one, so these portfolios are to be stated as efficient and the remaining 26 portfolios are to be inefficient. This result can also be verified by Super efficiency (Model IV) model and modified slack-based model (Model V) and corresponding efficiency score from these models are presented in sixth and eighth column respectively. On following the various steps given in Section 5, we

Table 2 The weight of each stocks in different randomly generated portfolios

w_p	1	2	3	4	5	6	7	8	9	10
w_1	0.1875	0.2660	0.2616	0.1956	0.2608	0.1677	0.0637	0.0948	0.3678	0.0891
w_2	0.1566	0.1102	0.2422	0.0962	0.3080	0.2472	0.2610	0.2547	0.2150	0.0561
w_3	0.3301	0.2483	0.1600	0.2975	0.2684	0.2437	0.1899	0.2408	0.0389	0.3180
w_4	0.1585	0.0805	0.2621	0.3064	0.1287	0.1964	0.2413	0.0050	0.2217	0.2013
w_5	0.1673	0.2905	0.0741	0.1043	0.0340	0.1450	0.2442	0.4048	0.1567	0.3355
w_p	11	12	13	14	15	16	17	18	19	20
w_1	0.0099	0.2206	0.3053	0.2608	0.1184	0.1714	0.0244	0.3602	0.0844	0.3571
w_2	0.2762	0.3457	0.2831	0.1016	0.3696	0.0105	0.2256	0.1147	0.0871	0.0746
w_3	0.2373	0.1664	0.0314	0.1039	0.0955	0.1306	0.2335	0.1934	0.2467	0.3654
w_4	0.2792	0.0005	0.1601	0.1654	0.2866	0.3579	0.1711	0.2879	0.2542	0.0149
w_5	0.1974	0.2669	0.2201	0.3684	0.1299	0.3296	0.1253	0.0438	0.3276	0.1879
w_p	21	22	23	24	25	26	27	28	29	30
w_1	0.2904	0.1345	0.0715	0.1815	0.1990	0.0479	0.2311	0.0904	0.2334	0.2311
w_2	01905.	0.0337	0.2241	0.1996	0.2874	0.2777	0.2503	0.0134	0.0418	0.1278
w_3	0.2333	0.3373	0.2388	0.4058	0.0994	0.2683	0.1133	0.2684	0.4218	0.0272
w_4	0.0792	0.2580	0.1773	0.0647	0.1409	0.2410	0.0752	0.2950	0.1474	0.3668
w_5	0.2066	0.2366	0.2884	0.1484	0.2734	0.1651	0.3301	0.3328	0.1556	0.2452

can further rank all the supper efficient portfolios as shown in column 7 and column 9 respectively. In order to obtain the full ranking we apply the TOPSIS method as described above. Table 4, shows the ranking of efficient portfolios by existing super efficiency models and our proposed DEA-TOPSIS method. Figure 1 depicts the rankings of efficient portfolios secured by super-efficiency methods and the proposed approach.

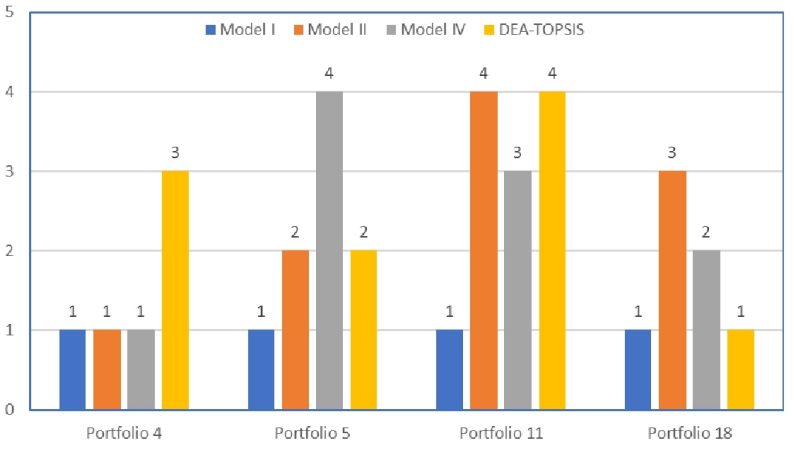

Fig. 1 Rankings of efficient portfolios in possibilistic mean-variance framework

Remark 1 DEA and MCDM both have two different goals. In DEA the objective is to analyze the productive efficiency of a system by comparing how well the system transforms inputs into outputs, while MCDM models are to determine a set of alternatives according to their conflicting criteria. As both the models work on two

Table 3 The efficiency score and the ranking of portfolios in possibilistic mean-variance framework

portfolio	Return	Risk	θ_0^*	ranking from Model I	η_0^*	ranking from Model IV	ρ_0^*	ranking from Model V
1	0.0730	0.0015	0.68	18	0.68	18	0.68	12
2	0.0590	0.0016	0.57	23	0.57	23	0.49	22
3	0.0785	0.0012	0.91	5	0.91	5	0.93	5
4	0.0889	0.0016	1.00	1	1.23	1	1.00	1
5	0.0671	0.0009	1.00	1	1.22	2	1.00	4
6	0.0758	0.0014	0.73	11	0.73	11	0.74	9
7	0.0816	0.0020	0.62	21	0.62	21	0.56	19
8	0.0541	0.0020	0.46	30	0.46	30	0.28	29
9	0.0666	0.0012	0.76	10	0.76	10	0.73	10
10	0.0788	0.0024	0.47	28	0.47	28	0.26	30
11	0.0892	0.0020	1.00	1	1.03	4	1.00	3
12	0.0491	0.0013	0.72	13	0.72	13	0.52	20
13	0.0609	0.0013	0.70	16	0.70	16	0.62	15
14	0.0633	0.0020	0.46	29	0.46	29	0.36	27
15	0.0835	0.0015	0.87	6	0.87	6	0.88	6
16	0.0886	0.0025	0.63	20	0.63	20	0.45	23
17	0.0705	0.0012	0.77	9	0.77	9	0.79	7
18	0.0795	0.0011	1.00	1	1.18	3	1.00	2
19	0.0830	0.0024	0.54	26	0.54	26	0.34	28
20	0.0525	0.0011	0.82	7	0.82	7	0.61	16
21	0.0580	0.0012	0.72	12	0.72	12	0.604	18
22	0.0852	0.0021	0.68	18	0.68	18	0.60	17
23	0.0751	0.0020	0.52	27	0.52	27	0.43	25
24	0.0651	0.0013	0.71	15	0.71	15	0.67	14
25	0.0634	0.0016	0.57	23	0.57	23	0.52	21
26	0.0849	0.0018	0.79	8	0.79	8	0.78	8
27	0.0549	0.0016	0.56	25	0.56	25	0.45	24
28	0.0879	0.0026	0.60	22	0.60	22	0.39	26
29	0.0730	0.0015	0.69	17	0.69	17	0.69	11
30	0.0857	0.0020	0.72	13	0.72	13	0.67	13

Table 4 Ranking of efficient portfolios by different methods possibilistic mean-variance framework

Portfolio	Return	Risk	ranking by Model I	ranking by Model IV	ranking by Model V	ranking by DEA-TOPSIS method
4	0.0889	0.0016	1	1	1	3
5	0.0671	0.0009	1	2	4	2
11	0.0892	0.0020	1	4	3	4
18	0.0795	0.0011	1	3	2	1

different theories so we rank the efficient portfolios in two steps. From Table 3, it's worth noting that Model IV and Model V are both supper-efficiency models, but they rank differently to all portfolios in particular for efficient portfolios also. As a result, a decision-maker is always faced with the difficulty of which approach to trust.

Now, Table 4 depicts the ranking of efficient unit from DEA-TOPSIS method.The suggested method's most significant advantage is its feasibility when compared to super-efficiency methods, which are in some situations infeasible.

Further, it can be noted that the cross-efficiency techniques which give a solution to the ranking of efficient units can not provide a unique ranking in our case as we have taken only one input-output (return-risk) variable. Hence the comparison of our method with cross-efficiency is not possible.

Example 2

In this example, the returns from risky assets/stocks are provided in Table 5 as trapezoidal fuzzy numbers and are the same as taken by Mehlawat et al. (2020) in their study. In this experimental analysis, the historical data of 20 assets during the period of April 2009 to March 2015, in terms of the weekly closing prices are used to simulate the future returns given in Mehlawat et al. (2020) Furthermore, we create the random sample portfolios using the same weights as shown in Table 2. It's worth noting that the mean return of the randomly generated portfolios is also negative. For convenience, we select only those 5 stocks whose returns are negative. We employ the RDM model (Model II) to calculate the efficiency score for by taking risk measure possibilistic variance.

Table 5 The possibility distribution of the return rates and their respective transaction cost of 5 stocks

Stocks	a_i	b_i	α_i	β_i	k_i
S_1	-0.1071	−0.0703	0.0105	0.0541	0.003
S_2	0.0883	0.1057	0.057	0.0772	0.003
S_3	0.0874	0.0948	0.0132	0.0928	0.003
S_4	-0.0907	-0.082	0.0055	0.0336	0.003
S_5	-0.0954	-0.0816	0.0093	0.013	0.003

Remark 2 Table 6 shows that the efficiency score of the portfolios 16, 17, 24, 28 is the same, and we cannot distinguish between efficient portfolios further. The DEA-TOPSIS approach, as stated above, is used to determine the whole ranking. The fourth, fifth and sixth column of the Table 7 depicts the ranking of efficient portfolios by RDM model (Model II), supper efficiency model (Model IV) and the DEA-TOPSIS method respectively. Figure 2 shows the ranking of efficient portfolios graphically. It should be highlighted that the supper efficiency model (Model IV) of Wei et al. (2019) provides us with the whole ranking of all randomly produced portfolios. However, the Super efficiency model of Hadi-Vencheh and Esmaeilzadeh (2013) poses an in-feasibility concern. In this instance, too, the decision maker is unable to locate a model on that he or she can trust on. The ranking by the proposed method for portfolio 16 and portfolio 28 is the same as obtained by the model (IV). As compared to the method given by Wei et al. (2019), the proposed approach is less calculative and very easy to handle. To

Table 6 The efficiency score and the ranking of portfolios by different methods in possibilistic mean-variance framework

portfolio	Return	Risk	$1-\phi_0^*$	ranking by Model II	ρ_0^*	ranking by Model V
1	0.0043	0.00052	0.3346	13	0.4714	16
2	-0.0198	0.00048	0.1962	26	0.4396	18
3	-0.0112	0.00057	0.2110	24	0.3138	25
4	-0.0124	0.00045	0.2312	22	0.5188	13
5	0.0212	0.00072	0.5352	6	0.3558	23
6	0.0048	0.00055	0.3310	14	0.4168	19
7	-0.0033	0.00045	0.2821	19	0.5696	11
8	0.0040	0.00049	0.3436	11	0.5376	12
9	-0.0392	0.00056	0.1409	30	0.272	29
10	-0.0174	0.00034	0.5023	8	0.672	5
11	0.0085	0.00045	0.4278	9	0.6361	7
12	0.0076	0.00065	0.3288	15	0.2256	30
13	-0.0286	0.00058	0.1536	29	0.2756	28
14	-0.0488	0.00039	0.2845	18	0.4689	17
15	-0.0004	0.00055	0.2809	20	0.3918	20
16	-0.0605	0.00027	1.0000	1	1.0000	4
17	0.0177	0.00031	1.0000	1	1.0000	2
18	-0.0280	0.00055	0.1572	28	0.3207	2
19	-0.0249	0.00033	0.5347	7	0.6474	6
20	-0.0042	0.00060	0.2453	22	0.3018	27
21	-0.0078	0.00059	0.2267	23	0.3122	26
22	-0.0172	0.00036	0.3979	10	0.6346	8
23	-0.0012	0.00044	0.3018	17	0.5908	9
24	0.0263	0.00061	1.0000	1	1.0000	1
25	-0.0155	0.00053	0.1987	25	0.3816	21
26	0.0148	0.00050	0.5418	5	0.5745	10
27	-0.0200	0.00052	0.182	27	0.3782	22
28	-0.0343	0.00028	1.0000	1	1.0000	3
29	0.0005	0.00049	0.3041	16	0.5065	14
30	-0.0577	0.00036	0.3362	12	0.4788	15

the best of our knowledge a small number of studies on the full ranking of the DMUs which can take positive as well as negative input-output.

It's worth noting that if asset return distributions aren't symmetric, using variance as a risk indicator isn't recommended because it initiate to portfolio's projections drastically different from what would be expected in real-life

Table 7 Ranking of efficient portfolios by different methods in possibilistic mean variance framework

DMU	Return	Risk	ranking by Model II	ranking from Model IV	ranking by DEA-TOPSIS method
16	-0.0605	0.00027	1	4	4
17	0.0177	0.00031	1	2	1
24	0.0263	0.00061	1	1	2
28	-0.0343	0.00028	1	3	3

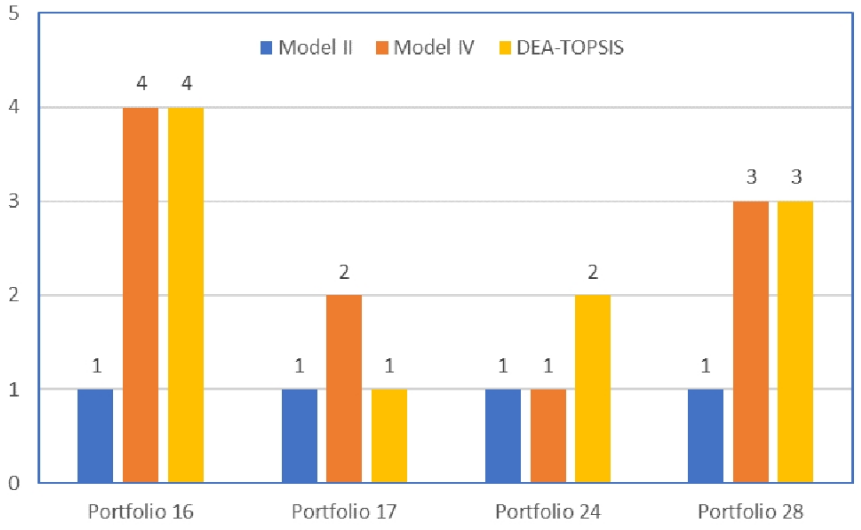

Fig. 2 Rankings of efficient portfolios in possibilistic mean-variance framework

situations. Excessively high and low returns are both regarded undesirable by variance, which is one of the key disadvantages. Many academics have utilised a variety of techniques to deal with such problems. Risk can be classified using semi-variance as an alternative risk measure. Therefore, instead of possibilistic variance, a downside risk metric called possibilistic semi-variance is utilised here as an input parameter. By taking possibilistic semi-variance and possibilistic mean as the input and output variable the DEA efficiency and supper efficiency of the portfolios which are generated randomly are presented in Table 8 while the Table 9 depicts the full ranking of such efficient portfolios by DEA-TOPSIS method.

Table 8 The efficiency score and the ranking of portfolios in possibilistic mean semi-variance framework

Portfolio	Return	Risk	$1-\phi_0^*$	ranking by Model III	ρ^*	ranking by MSBM in possibilistic semi-variance
1	0.0043	0.00045	0.3260	12	0.4694	15
2	-0.0198	0.00043	0.1809	26	0.4175	18
3	-0.0112	0.00051	0.2029	24	0.2866	25
4	-0.0124	0.00039	0.2171	22	0.5195	12
5	0.0212	0.00064	0.5128	6	0.3272	23
6	0.0048	0.00049	0.3201	13	0.4014	19
7	-0.0033	0.00040	0.2728	17	0.5524	11
8	0.0040	0.00044	0.3301	11	0.5082	14
9	-0.0392	0.00052	0.1268	30	0.2289	28
10	-0.0174	0.00029	0.4371	8	0.6719	5
11	0.0085	0.00039	0.4176	9	0.6316	8
12	0.0076	0.00060	0.3109	14	0.167	30
13	-0.0286	0.00053	0.1467	29	0.2242	29
14	-0.0488	0.00036	0.2031	23	0.4413	17
15	-0.0004	0.00050	0.2686	18	0.353	20
16	-0.0605	0.00025	1.00	1	1.00	3
17	0.0177	0.00027	1.0000	1	1.00	1
18	-0.0280	0.00049	0.1516	28	0.2996	24
19	-0.0249	0.00029	0.4493	7	0.6418	6
20	-0.0042	0.00053	0.2369	20	0.2853	26
21	-0.0078	0.00052	0.2178	21	0.2826	27
22	-0.0172	0.00031	0.3424	10	0.638	7
23	-0.0012	0.00039	0.2925	16	0.5777	9
24	0.0263	0.00053	1.0000	1	1.00	2
25	-0.0155	0.00048	0.1901	25	0.3387	21
26	0.0148	0.00043	0.5305	5	0.5724	10
27	-0.0200	0.00047	0.1748	27	0.335	22
28	-0.0343	0.00025	1.0000	1	1.00	4
29	0.0005	0.00042	0.2977	15	0.5146	13
30	-0.0577	0.00033	0.2413	19	0.4547	16

Table 9 Ranking of efficient portfolios by in possibilistic mean semi-varinace framework

DMU	Return	Risk	ranking by Model II	ranking by Model IV	ranking by TOPSIS method
16	-0.0605	0.00025	1	3	4
17	0.0177	0.00027	1	1	1
24	0.0263	0.00053	1	2	2
28	-0.0343	0.00025	1	4	3

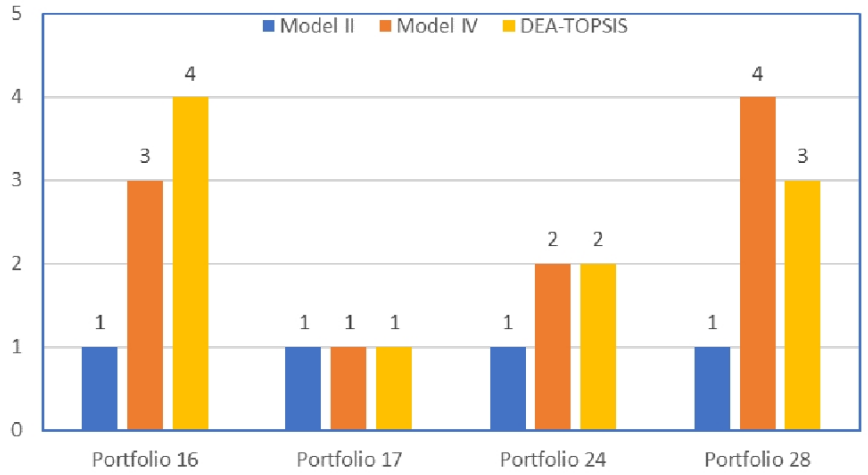

Fig. 3 Rankings of efficient portfolios obtained by different methods

For each of the scenarios given above, we calculate the correlation coefficient. The results produced by various methodologies and the suggested DEA-TOPSIS method are substantially correlated. Furthermore, the procedure has been confirmed for each example using a statistical t-test.

7.1 Computation Complexity

In this study, we compute the computational complexity by taking into account all logical-mathematical operations, such as addition, subtraction, multiplication, division,exponentiation and square root as described in Rashidi and Cullinane (2019). The mathematical operations used for creating the return risk are the same for each strategies used in this study. As a result, they weren't taken into account while determining computational complexity. Suppose we have n efficient portfolio (to be considered as alternative) and m criteria (return and risk) in the study,then it will take 3nm operations to reached at the weighted normalized matrix, 2(6nm) calculations required to determine the distance between efficient portfolio and the ideal and negative ideal points. nm-n calculations are required for calculating the positive ideal and negative-ideal points. Lastly, 2n computations are used to calculate each portfolio's "closeness coefficient." As a result, the TOPSIS's computational complexity to determine the full ranking of efficient fuzzy portfolio in the second stage is determined as follows:

$$T_{n,m} = 3nm + 12nm + nm - n + 2n$$

.

The hybrid DEA- TOPSIS requires 132 simple operations for the empirical

analysis included in this analysis, whereas other DEA models need to solve the mathematical models repeatedly to get the whole ranking for efficient portfolios. Hence, Our method is substantially less intricate than the existing methods, so finding the most effective portfolio will take less time. In contrast to our approach, which uses basic operations to find the best portfolio in the second phase, the super efficiency and modified MSBM models often solve at least three models for each portfolio to determine the best portfolio.

8 Conclusion and Future Research Directions

The ranking problem of all efficient fuzzy portfolios with positive and negative input-output variables is investigated in this work. We know that if a sufficiently large number of portfolios are designated efficient, the DEA's discrimination ability decreases. By combining the DEA fuzzy portfolio model with the TOPSIS method, the work has established a hybrid strategy for ranking efficient alternative portfolios in a fuzzy environment. We considered the returns from the risky assets in terms of trapezoidal fuzzy numbers to handle the unpredictability of the financial market. The developed approach provides a novel method to enhance the discrimination power of DEA analysis and assigns a unique ranking order to all efficient portfolios. We proposed the procedures for the problems that include positive as well as positive and negative returns that suits the fluctuating nature of the financial market. The results are compared with Super-efficiency DEA models.

In future work, this approach will be explored to investigate the classification of fuzzy portfolios having input as possibilistic semi-absolute deviation (SAD), possibilistic VaR and CvaR. Furthermore, the method can be used to study the performance of those fuzzy portfolios that have returned as the normal fuzzy variable. The uncertainty of the returns is described using possibility theory in this study. However, there could potentially be statistical errors in this assumption. We may take into account several issues related to evaluating the performance of a portfolio, such as returns in probabilistic framework with uncertain predicted returns treated as random fuzzy variables. In this research, only 1st and 2nd order moments (mean, variance and semi-variance) have been used as output and input. The higher-order moments can be utilized as the input-output values for future work. In future work, we will apply the projected approach to problems with undesirable input-output scenarios.

Conflict of interest

The authors declare that they have no conflict of interest.

Ethical statement

This article does not contain any studies with human participants or animals performed by the author.

Funding

The authors declare that this research received no specific grant from any funding agency.

Data availability statement

All data generated or analyzed during this study are included in this published article https://doi.org/10.1007/s10479-017-2411-9.

References

Aldamak, A. and S. Zolfaghari. 2017. Review of efficiency ranking methods in data envelopment analysis. *Measurement* 106: 161–172 .

Alirezaee, M.R. and M.R.R. Sani. 2011. New analytical hierarchical process/data envelopment analysis methodology for ranking decision-making units. *International Transactions in Operational Research 18*(5): 533–544 .

Andersen, P. and N.C. Petersen. 1993. A procedure for ranking efficient units in data envelopment analysis. *Management science 39*(10): 1261–1264 .

Banihashemi, S.A. and M. Khalilzadeh. 2020. A new approach for ranking efficient DMUs with data envelopment analysis. *World Journal of Engineering 17*(4): 573–583 .

Banker, R.D., A. Charnes, and W.W. Cooper. 1984. Some models for estimating technical and scale inefficiencies in data envelopment analysis. *Management science 30*(9): 1078–1092 .

Carlsson, C. and R. Fullér. 2001. On possibilistic mean value and variance of fuzzy numbers. *Fuzzy Sets and Systems 122*(2): 315–326 .

Carlsson, C., R. Fullér, and P. Majlender. 2002. A possibilistic approach to selecting portfolios with highest utility score. *Fuzzy sets and systems 131*(1): 13–21 .

Charnes, A., W.W. Cooper, and E. Rhodes. 1978. Measuring the efficiency of decision making units. *European journal of operational research 2*(6): 429–444 .

Chen, W. 2015. Artificial bee colony algorithm for constrained possibilistic portfolio optimization problem. *Physica A: Statistical Mechanics and its Applications* 429: 125–139 .

Chen, W., Y. Gai, and P. Gupta. 2018. Efficiency evaluation of fuzzy portfolio in different risk measures via DEA. *Annals of Operations Research 269*(1): 103–127 .

Cheng, G., P. Zervopoulos, and Z. Qian. 2013. A variant of radial measure capable of dealing with negative inputs and outputs in data envelopment analysis. *European Journal of Operational Research 225*(1): 100–105 .

Ding, H., Z. Zhou, H. Xiao, C. Ma, and W. Liu. 2014. Performance evaluation of portfolios with margin requirements. *Mathematical Problems in Engineering* 2014 .

Emrouznejad, A., A.L. Anouze, and E. Thanassoulis. 2010. A semi-oriented radial measure for measuring the efficiency of decision making units with negative data, using dea. *European Journal of Operational Research 200*(1): 297–304 .

Gupta, P., M.K. Mehlawat, A. Kumar, S. Yadav, and A. Aggarwal. 2020. A credibilistic fuzzy dea approach for portfolio efficiency evaluation and rebalancing toward benchmark portfolios using positive and negative returns. *International Journal of Fuzzy Systems 22*(3): 824–843 .

Hadi-Vencheh, A. and A. Esmaeilzadeh. 2013. A new super-efficiency model in the presence of negative data. *Journal of the Operational Research Society 64*(3): 396–401 .

Hwang, C.L. and K. Yoon. 1981. Methods for multiple attribute decision making, *Multiple attribute decision making*, 58–191. Springer.

Jablonsky, J. 2012. Multicriteria approaches for ranking of efficient units in DEA models. *Central European Journal of Operations Research 20*(3): 435–449 .

Liu, W., Z. Zhou, D. Liu, and H. Xiao. 2015. Estimation of portfolio efficiency via dea. *Omega* 52: 107–118 .

Liu, Y.J. and W.G. Zhang. 2013. Fuzzy portfolio optimization model under real constraints. *Insurance: Mathematics and Economics 53*(3): 704–711 .

Lotfi, F.H., R. Fallahnejad, and N. Navidi. 2011. Ranking efficient units in DEA by using TOPSIS method. *Applied Mathematical Sciences 5*(17): 805–815 .

Markowitz, H.M. 1968. *Portfolio selection*. Yale university press.

Mashayekhi, Z. and H. Omrani. 2016. An integrated multi-objective markowitz-DEA cross-efficiency model with fuzzy returns for portfolio selection problem. *Applied Soft Computing* 38: 1–9 .

Mehlawat, M.K., P. Gupta, A. Kumar, S. Yadav, and A. Aggarwal. 2020. Multiobjective fuzzy portfolio performance evaluation using data envelopment analysis under credibilistic framework. *IEEE Transactions on Fuzzy Systems 28*(11): 2726–2737 .

Murthi, B., Y.K. Choi, and P. Desai. 1997. Efficiency of mutual funds and portfolio performance measurement: A non-parametric approach. *European Journal of Operational Research 98*(2): 408–418 .

Omrani, H., M. Shamsi, and A. Emrouznejad. 2022. Evaluating sustainable efficiency of decision-making units considering undesirable outputs: an application to airline using integrated multi-objective dea-topsis. *Environment, Development and Sustainability*: 1–32 .

Pan, Z., Y. Wang, Y. Zhou, and Y. Wang. 2020. Analysis of the water use efficiency using super-efficiency data envelopment analysis. *Applied Water Science 10*(6): 1–11 .

Portela, M.C., E. Thanassoulis, and G. Simpson 2004. Negative data in dea: A directional distance approach applied to bank branches. In *Journal of the Operational Research Society*, Volume 55, pp. 1111–1121.

Rakhshan, S.A. 2017. Efficiency ranking of decision making units in data envelopment analysis by using TOPSIS-DEA method. *Journal of the Operational Research Society 68*(8): 906–918 .

Rashidi, K. and K. Cullinane. 2019. A comparison of fuzzy dea and fuzzy topsis in sustainable supplier selection: Implications for sourcing strategy. *Expert Systems with Applications* 121: 266–281 .

Saaty, T.L. 1986. Axiomatic foundation of the analytic hierarchy process. *Management science 32*(7): 841–855 .

Saeidifar, A. and E. Pasha. 2009. The possibilistic moments of fuzzy numbers and their applications. *Journal of computational and applied mathematics 223*(2): 1028–1042 .

Sayyadi, R. and A. Awasthi. 2018. A simulation-based optimisation approach for identifying key determinants for sustainable transportation planning. *International Journal of Systems Science: Operations & Logistics 5*(2): 161–174 .

Sexton, T.R., R.H. Silkman, and A.J. Hogan. 1986. Data envelopment analysis: Critique and extensions. *New Directions for Program Evaluation 1986*(32): 73–105 .

Sharp, J.A., W. Meng, and W. Liu. 2007. A modified slacks-based measure model for data envelopment analysis with 'natural' negative outputs and inputs. *Journal of the Operational Research Society 58*(12): 1672–1677 .

Sinuany-Stern, Z. 2000. An AHP/DEA methodology for ranking decision making units. *International Transactions in Operational Research* 7: 109–124 .

Tone, K. 2001. A slacks-based measure of efficiency in data envelopment analysis. *European journal of operational research 130*(3): 498–509 .

Tone, K., T.S. Chang, and C.H. Wu. 2020. Handling negative data in slacks-based measure data envelopment analysis models. *European Journal of Operational Research 282*(3): 926–935 .

Tran, T.H., Y. Mao, P. Nathanail, P.O. Siebers, and D. Robinson. 2019. Integrating slacks-based measure of efficiency and super-efficiency in data envelopment analysis. *Omega* 85: 156–165 .

Vercher, E. and J.D. Bermúdez. 2015. Portfolio optimization using a credibility mean-absolute semi-deviation model. *Expert Systems with Applications 42*(20): 7121–7131 .

Wang, C.N., H.P. Nguyen, and J.W. Wang. 2021. A two-stage approach of dea and ahp in selecting optimal wind power plants. *IEEE Transactions on Engineering Management* .

Wei, F., J. Song, C. Jiao, and F. Yang. 2019. A modified slacks-based ranking method handling negative data in data envelopment analysis. *Expert Systems 36*(1): e12329 .

Xiao, H., T. Ren, and T. Ren. 2020. Estimation of fuzzy portfolio efficiency via an improved dea approach. *INFOR: Information Systems and Operational Research 58*(3): 478–510 .

Zadeh, L.A. 1965. Fuzzy set theory and its applications. *University of California, California* 8: 338 .

Zadeh, L.A. 1978. Fuzzy sets as a basis for a theory of possibility. *Fuzzy sets and systems 1*(1): 3–28 .

Zhang, W.G. and Z.K. Nie 2003. On possibilistic variance of fuzzy numbers. In *International Workshop on Rough Sets, Fuzzy Sets, Data Mining, and Granular-Soft Computing*, pp. 398–402. Springer.

Zhou, Z., Q. Jin, H. Xiao, Q. Wu, and W. Liu. 2018. Estimation of cardinality constrained portfolio efficiency via segmented dea. *Omega* 76: 28–37 .

Zimmermann, H.J. 2011. *Fuzzy set theory—and its applications*. Springer Science & Business Media.

Decoding the role of MDM2 as a potential ubiquitin E3 ligase and identifying the therapeutic efficiency of alkaloids against MDM2 in combating Glioblastoma

Sudhanshu Sharma[1], Pravir Kumar[1*]

[1]Molecular Neuroscience and Functional Genomics Laboratory, Delhi Technological University, Shahabad Daulatpur, Bawana Road, Delhi 110042

*Author to whom correspondence should be addressed:
Pravir Kumar, PhD
Dean, International Affairs
Professor and Head, Department of Biotechnology
Molecular Neuroscience and Functional Genomics Laboratory
*Former Dean***,** Delhi Technological University (Formerly Delhi College of Engineering)
Former Faculty, Tufts University School of Medicine, Boston, MA, USA
Room# FW4TF3, Mechanical Engineering Building
Shahbad Daulatpur, Bawana Road, Delhi 110042; Phone: +91- 9818898622
Email: pravirkumar@dtu.ac.in; kpravir@gmail.com
https://www.ncbi.nlm.nih.gov/myncbi/1DW465XG9bp5p/bibliography/public/
https://scholar.google.co.in/citations?user=WVLI4i4AAAAJ&hl=en
ORCID ID: 0000-0001-7444-2344; **Scopus ID:** 14831447800; **ISI Research ID:** B-2164-2015

Supporting information Table 1: Representation of various ubiquitin E3 ligases present in datasets GSE4290, GSE50161, and GSE 104291

	GSE4290 (89)	GSE 50161 (50)	GSE 104291 (42)
Ubiquitin E3 Ligases	UHRF1, DTL, MDM2, TRIM5, FBXO4, CDCA3, NEDD4 , UBE3C, TRIM22, SOCS3, TRIM38, BRCA1, MAP3K1, ITCH, TRAF4, SMURF2, CBL, DYRK2, RBCK1, SIAH1, BARD1, ARID1B, CCNB1P1, TANK, RNF216, HUWE1, RBBP6, RNF115, CNOT4, CHFR, RNF40, MKRN1, RLIM, VHL, RAD18, TRIM13, DDB2, KLHL20, MIB2, SKP2, CBLB, TRIM25, WWP2, TNFAIP3, SH3RF1, TRAF2, TRIM21, RAG1, MIB1, RNF138, TRAF6, XIAP, F2R1, TRIM65, DCAF1, RNF4, SMURF1, KCTD10, FBXO45, FBXO21, RBX1, WWP1, RNF2, RCHY1, TRIM32, PJA2, RNF43 FBXO3, MYLIP, RNF14, TRIM62, TRAF3, STUB1, RNF8, CDC34, RFFL, FBXW11, UBE4B, TRIM17, CRBN, RNF220, TRIM37, TRIM9, TRIM24, KLHL2, RNF41, LNX1, FBXO2, FBXW7, UBE3A, NEDD4L	RNF220, TRIM25, TANK, RBCK1, MDM2, SKP2, STUB1, TRIM21 RNF41, ITCH, FBXD4 RFWD3, RAD18 BRCA1, BARD1, TRIM24, TRIM5, TRIM37, DTL, CDCA3, CDC20, NEDD4, TNFAIP3 RNF8, CRBN RNF13, UBE3A TRAF3, PELI1 TRIM17, SMURF1 MYLIP, UBE4B, CHFR, RHOBTB1 RNF43, BIRC2 TRIM38, CBLB TRIM22, WWP1 RLIM, DDB2, PJA2 FBXO28, CBL, HUWE1, BIRC3, NEDD4L	TRIM21, TANK, TRIM37, BRCA1, TRIM38, DTL, RAD18, FBXO4, TRIM5, UBE3C, RBCK1, MIB1, RNF138, TNFAIP3, CDC20, BIRC2, MDM2, TRIM22, RNF41, MYLIP, MAP3K1, TRIM25, DDB2, FBXO28, SIAH1, TRAF6, ARID1B, CNOT4, TRIM62, TRIM9, NEDD4, TRIM2, BRAP, CISH, SMURF2, FBXO31, CCNB1IP1 , ASB2, SKP2, FBXO32, TRIM24, UBE3A

Supporting information Table 2: Tabular representation of common interacting ubiquitin E3 ligases filtered using Venn analysis

Names	Total	Elements
GSE 104291; GSE 4290; GSE 50161	21	RNF138, BRCA1, TNFAIP3, SKP2, DTL, TRIM5, TRIM21, MYLIP, MDM2, DDB2, NEDD4, TRIM37, RAD18, RBCK1, RNF41 TRIM24, TRIM22, TRIM38, TRIM25, TANK

		, UBE3A, CDCA3, STUB1, UBE4B, BARD1, CBLB, WWP1, RNF43, CHFR, PJA2, RNF220, NEDD4L, TRAF3, CBL, RNF8, CRBN, TRIM17, SMURF1, HUWE1, RLIM, ITCH
GSE 4290; **GSE 50161**	20	STUB1, UBE4B, BARD1, CBLB, WWP1, RNF43, CHFR, PJA2, RNF220, NEDD4L, TRAF3, CBL, RNF8, CRBN, TRIM17, SMURF1, HUWE1, RLIM, ITCH
GSE 104291; GSE 4290	11	UBE3C, MIB1, FBXO4, TRIM9, TRIM62, CNOT4, SMURF2, TRAF6, SIAH1, ARID1B, MAP3K1
GSE 104291; GSE 50161	3	CDC20, FBXO28, BIRC2

S2

Supporting information Table 3: Tabular representation of various alkaloids with their BBB scores and ADMET profiling

Final List of alkaloids crosses BBB												
PubChem Id	**Alkaloid**	**Canonical SMILES**	**SVM_MACCSFPBBB Score**	**BBB predictor**	**BBBScore**	**BBB_SWISS ADME**	**MOLECULAR MASS (<500Da)**	**H-BOND DONOR (<5)**	**H-BOND ACCEPTOR (<10)**	**OCTAL WATER PARTITION COEFFICIENT (log<5)**	**MOLAR REFRACTIVITY (40-130)**	**LIPINSKI RULE**
10723258	3,5'-dihydroxythalifaboramine	CN1CCC2=C3C1CC4=C(C(=C(C=C4C3=C(C(=C2O)OC)OC)OC)O)OC5=CC=C(C=C5)CC6C7=CC(=C(C(=C7CCN6C)O)OC)OC	0.044	yes	1.22	no	684.77 g/mol	3	11	4.72	197.55	No; 2 violations
10170	Berbamine	CN1CCC2=CC(=C3C=C2C1CC4=CC=C(C=C4)OC5=C(C=CC(=C5)CC6C7=C(O3)C(=C(C=C7CCN6C)OC)OC)O)OC	0.036	YES	2.94	no	608.72 g/mol	1	8	5.15	181.6	Yes; 1 violation
442021	Brucine	COC1=C(C=C2C(=C1)C34CCN5C3CC6C7C4N2C(=O)CC7OCC=C6C5)OC	0.064	YES	4.74	yes	394.46 g/mol	0	5	1.84	114.04	Yes; 0 violation
161215	Brucine N-oxide	COC1=C(C=C2C(=C1)C34CC[N+]5(C3CC6C7C4N2C(=O)CC7OCC=C6C5)[O-])OC	0.082	YES	4.06	no	410.46 g/mol	0	5	0.49	117.41	Yes; 0 violation

2703	Cheleryt hrine	C[N+]1=C2C(=C3C=CC(=C(C3=C1)OC)OC)C=CC4=CC5=C(C=C42)OCO5	0.058	YES	4.12	yes	348.37 g/mol	0	4	3.02	101.6	Yes; 0 violation
82143	Cryptole pine	CN1C2=CC=CC=C2C=C3C1=C4C=CC=CC4=N3	0.115	YES	3.98	yes	232.28 g/mol	0	1	3.29	76.01	Yes; 0 violation

S3

73481	Fangchi noline	CN1CCC2=CC(=C3C=C2C1CC4=CC=C(C=C4)OC5=C(C=CC(=C5)CC6C7=C(O3)C(=C(C=C7CCN6C)OC)O)OC)OC	0.036	YES	2.96	no	608.72 g/mol	1	8	5.16	181.6	Yes; 1 violation
3565	Harmalo l	CC1=NCCC2=C1NC3=C2C=CC(=C3)O	0.046	YES	5.16	yes	200.24 g/mol	2	2	1.99	64.76	Yes; 0 violation
5281404	Harman e	CC1=NC=CC2=C1NC3=CC=CC=C23	0.105	YES	5.14	yes	182.22 g/mol	1	1	2.7	58.57	Yes; 0 violation
5280953	Harmine	CC1=NC=CC2=C1NC3=C2C=CC(=C3)OC	0.058	YES	5.21	yes	212.25 g/mol	1	1	2.78	65.06	Yes; 0 violation
68094	Harmol	CC1=C2C(=C3C=CC(=O)C=C3N2)C=CN1	0.037	YES	4.57	yes	198.22 g/mol	2	0	1.86	61.39	Yes; 0 violation
197835	Hydrasti ne	CN1CCC2=CC3=C(C=C2C1C4C5=C(C(=C(C=C5)OC)OC)C(=O)O4)OCO3	0.061	YES	4.11	yes	383.39 g/mol	0	7	2.55	103.38	Yes; 0 violation
11024113	Isostryc hnine	C1CN2CC(=CCO)C3CC2C14C5C3=CCC(=O)N5C6=CC=CC=C46	0.183	YES	5.11	yes	334.41 g/mol	1	3	1.85	102.77	Yes; 0 violation
4072580	Mahani mbicine	CC1=CC2=C(C=C1)NC3=C2C=CC4=C3C=CC(O4)(C)CCC=C(C)C	0.094	YES	4.55	no	331.45 g/mol	1	1	5.63	108.45	Yes; 1 violation
167963	Mahani mbine	CC1=CC2=C(C3=C1OC(C=C3)(C)CCC=C(C)C)NC4=CC=CC=C42	0.094	YES	4.56	no	331.45 g/mol	1	1	5.62	108.45	Yes; 1 violation

36689305	Mahanine	CC1=CC2=C(C3=C1OC(C=C3)(C)CCC=C(C)C)NC4=C2C=CC(=C4)O	0.022	YES	4.61	no	347.45 g/mol	2	2	5.2	110.48	Yes; 0 violation
10105653	Marcanine A	CC1=CC(=O)NC2=C1C(=O)C3=CC=CC=C3C2=O	0.106	YES	3.09	yes	239.23 g/mol	1	3	1.72	65.34	Yes; 0 violation

S4

91466	Matrine	C1CC2C3CCCN4C3C(CCC4)CN2C(=O)C1	0.121	YES	5.02	yes	248.36 g/mol	0	2	1.79	79.59	Yes; 0 violation
124256	N-(4-hydroxyundecanoyl)anabasine	CCCCCCCC(CCC(=O)N1CCCCC1C2=CN=CC=C2)O	0.098	YES	4.53	yes	346.51 g/mol	1	3	3.78	107.37	Yes; 0 violation
390526	Neocryptolepine	CN1C2=CC=CC=C2C=C3C1=NC4=CC=CC=C43	0.158	YES	3.82	yes	232.28 g/mol	0	1	3.47	76.01	Yes; 0 violation
162334	N-n-octanoylnornicotine	CCCCCCCC(=O)N1CCCC1C2=CN=CC=C2	0.122	YES	4.94	yes	274.40 g/mol	0	2	3.35	86.98	Yes; 0 violation
275196	Noscapine	CN1CCC2=CC3=C(C(=C2C1C4C5=C(C(=C(C=C5)OC)OC)C(=O)O4)OC)OCO3	0.042	YES	3.7	no	413.42 g/mol	0	8	2.55	109.88	Yes; 0 violation
4680	Papaverine	COC1=C(C=C(C=C1)CC2=NC=CC3=CC(=C(C=C32)OC)OC)OC	0.092	YES	4.76	yes	339.39 g/mol	0	5	3.32	97.16	Yes; 0 violation
5983	Physostigmine	CC12CCN(C1N(C3=C2C=C(C=C3)OC(=O)NC)C)C	0.14	YES	5.03	yes	275.35 g/mol	1	3	1.68	84.93	Yes; 0 violation
5281408	Rhynchophylline	CCC1CN2CCC3(C2CC1C(=COC)C(=O)OC)C4=CC=CC=C4NC3=O	0.06	YES	3.9	yes	384.47 g/mol	1	5	2.46	113.39	Yes; 0 violation
13422573	Rohitukine	CC1=CC(=O)C2=C(O1)C(=C(C=C2O)O)C3CCN(CC3O)C	0.068	YES	3.27	no	332.33 g/mol	0	4	2.88	94.68	Yes; 0 violation

5154	Sanguinarine	C[N+]1=C2C(=C3C=CC4=C(C3=C1)OCO4)C=CC5=CC6=C(C=C52)OCO6	0.115	YES	4.13	yes	334.41 g/mol	0	3	2.09	101.05	Yes; 0 violation
441071	Strychnine	C1CN2CC3=CCOC4CC(=O)N5C6C4C3CC2C61C7=CC=CC=C75	0.128	YES	5.25	yes	622.75 g/mol	0	8	5.41	186.07	Yes; 1 violation

S5

73078	Tetrandrine	CN1CCC2=CC(=C3C=C2C1CC4=CC=C(C=C4)OC5=C(C=CC(=C5)CC6C7=C(O3)C(=C(C=C7CCN6C)OC)OC)OC)OC	0.056	YES	3.15	no	413.64 g/mol	2	3	4.67	127.23	Yes; 1 violation
12442871	Tomatidenol	CC1CCC2(C(C3C(O2)CC4C3(CCC5C4CC=C6C5(CCC(C6)O)C)C)C)NC1	0.13	YES	4.5	yes	415.65 g/mol	2	3	4.9	127.7	Yes; 1 violation
65576	Tomatidine	CC1CCC2(C(C3C(O2)CC4C3(CCC5C4CCC6C5(CCC(C6)O)C)C)C)NC1	0.105	YES	4.51	yes	354.44 g/mol	1	4	2.61	103.74	Yes; 0 violation
15376	Vincamine	CCC12CCCN3C1C4=C(CC3)C5=CC=CC=C5N4C(C2)(C(=O)OC)O	0.047	YES	4.88	yes	265.31 g/mol	1	3	2.88	80.13	Yes; 0 violation
160597	(-)-anonaine	C1CNC2CC3=CC=CC=C3C4=C2C1=CC5=C4OCO5	0.11	YES	5.43	yes	365.42 g/mol	2	5	2.96	109.37	Yes; 0 violation
161749	(+)-tylophorinidine	COC1=CC2=C(C=C1)C3=C(CN4CCCC4C3O)C5=CC(=C(C=C52)O)OC	0.049	YES	4.23	yes	363.45 g/mol	0	4	4.07	112.67	Yes; 0 violation
639288	(R)-antofine	COC1=CC2=C(C=C1)C3=C(CC4CCCN4C3)C5=CC(=C(C=C52)OC)OC	0.098	YES	5.18	yes	377.48 g/mol	0	4	4.35	117.48	Yes; 0 violation
92765	(R)-cryptopleurine	COC1=CC2=C(C=C1)C3=C(CC4CCCCN4C3)C5=CC(=C(C=C52)OC)OC	0.076	YES	5.14	yes	393.48 g/mol	0	5	4.04	119.16	Yes; 0 violation

92114	(R)-tylophorine	COC1=C(C=C2C(=C1)C3=C(CN4CCCC4C3)C5=CC(=C(C=C52)OC)OC)OC	0.08	YES	4.94	yes	409.47 g/mol	1	5	3.47	120.75	Yes; 0 violation
373661	(S)-tyloindicine I	COC1=C(C=C(C=C1)C2=CN3CCCC3C=C2C4=CC(=C(C(=C4)OC)OC)O)OC	0.024	YES	4.23	yes	250.25 g/mol	0	3	2.38	74.15	Yes; 0 violation
9881423	9-methoxycanthin-6-one	COC1=CC2=C(C=C1)C3=C4N2C(=O)C=CC4=NC=C3	0.116	YES	4.67	yes	266.25 g/mol	0	3	1.72	77.52	Yes; 0 violation

S6

44593495	9-methoxycanthin-6-one 3N-oxide	COC1=CC2=C(C=C1)C3=C4N2C(=O)C=CC4=[N+](C=C3)[O-]	0.121	YES	4.35	yes	240.26 g/mol	2	3	2.15	69.95	Yes; 0 violation
5375436	beta-carboline-1-propionic acid	C1=CC=C2C(=C1)C3=C(N2)C(=NC=C3)CCC(=O)O	0.049	YES	4.18	yes	220.23 g/mol	0	2	2.39	67.66	Yes; 0 violation
97176	canthin-6-one	C1=CC=C2C(=C1)C3=C4N2C(=O)C=CC4=NC=C3	0.137	YES	4.82	yes	305.41 g/mol	2	3	3.43	90.52	Yes; 0 violation
1548943	Capsaicin	CC(C)C=CCCCCC(=O)NCC1=CC(=C(C=C1)O)OC	0.064	YES	4.16	yes	331.36 g/mol	1	5	0.53	91.35	Yes; 0 violation
637173	Cephalotaxine alpha-N-oxide	COC1=CC23CCC[N+]2(CCC4=CC5=C(C=C4C3C1O)OCO5)[O-]	0.068	YES		no	331.36 g/mol	1	5	0.53	91.35	Yes; 0 violation
10404434	Cephalotaxine beta-N-oxide	COC1=CC23CCC[N+]2(CCC4=CC5=C(C=C4C3C1O)OCO5)[O-]	0.068	YES		no	606.71 g/mol	0	8	5.36	179.15	Yes; 1 violation
10206	Cepharanthine	CN1CCC2=CC3=C(C4=C2C1CC5=CC=C(C=C5)OC6=C(C=CC(=C6)CC7C8=CC(=C(C=C8CCN7C)OC)O4)OC)OCO3	0.076	YES		no	369.45g/mol	0	5	3.33	108.8	Yes; 0 violation
101301	Corydaline	CC1C2C3=CC(=C(C=C3CCN2CC4=C1C=CC(=C4OC)OC)OC)OC	0.021	YES		yes	622.75 g/mol	0	8	5.47	186.07	Yes; 1 violation

121313	Cycleanine	CN1CCC2=CC(=C(C3=C2C1CC4=CC=C(C=C4)OC5=C6C(CC7=CC=C(O3)C=C7)N(CCC6=CC(=C5OC)OC)C)OC)OC	0.056	YES		no	246.31 g/mol	1	1	3.92	81.04	Yes; 0 violation
3213	Ellipticine	CC1=C2C=CN=CC2=C(C3=C1NC4=CC=CC=C43)C	0.118	YES		yes	303.36 g/mol	1	1	2.7	97.67	Yes; 0 violation

S7

151289	Evodiamine	CN1C2C3=C(CCN2C(=O)C4=CC=CC=C41)C5=CC=CC=C5N3	0.139	YES		yes	315.49 g/mol	1	2	3.88	96.52	Yes; 0 violation
12310548	Holamine	CC(=O)C1CCC2C1(CCC3C2CC=C4C3(CCC(C4)N)C)C	0.069	YES	4.66	yes	315.36 g/mol	1	5	1.98	88.77	Yes; 0 violation
10245167	Isocephalotaxine	COC1=C2C3=CC4=C(C=C3CCN5C2(CCC5)CC1O)OCO4	0.025	YES		yes	622.75 g/mol	0	8	5.41	186.07	Yes; 1 violation
5351212	Isotetrandrine	CN1CCC2=CC(=C3C=C2C1CC4=CC=C(C=C4)OC5=C(C=CC(=C5)CC6C7=C(O3)C(=C(C=C7CCN6C)OC)OC)OC)OC	0.056	YES		no	275.26 g/mol	0	4	2.88	76.67	Yes; 0 violation
10144	liriodenine	C1OC2=C(O1)C3=C4C(=C2)C=CN=C4C(=O)C5=CC=CC=C53	0.157	YES		yes	478.62 g/mol	0	6	4.43	147.34	Yes; 0 violation
15560508	Psychotrine	CCC1CN2CCC3=CC(=C(C=C3C2CC1CC4=NCCC5=CC(=C(C=C54)OC)OC)OC)OC	0.021	YES	4.81	yes	393.48 g/mol	0	5	4.08	119.16	Yes; 0 violation

637044	Secoantofine	COC1=CC=C(C=C1)C2=C(CC3CCCN3C2)C4=CC(=C(C=C4)OC)OC	0.091	YES	5.45	yes	381.46 g/mol	1	5	3.32	113.12	Yes; 0 violation
246845	tylocrebrine	COC1=C(C2=C(C=C1)C3=C(CC4CCCN4C3)C5=CC(=C(C=C52)OC)OC)OC	0.08	YES	4.95	yes	393.48 g/mol	0	5	4.08	119.16	Yes; 0 violation
373658	tyloindicine F	COC1=CC=C(C=C1)C2=CC3(CCCN3CC2C4=CC(=C(C=C4)OC)OC)O	0.074	YES	4.96	yes	381.46 g/mol	1	5	3.32	113.12	Yes; 0 violation
373659	tyloindicine G	COC1=C(C=C2C(=C1)C3CN4CCCC4(C=C3C5=CC(=C(C=C25)OC)OC)O)OC	0.082	YES	4.57	yes	409.47 g/mol	1	6	3.24	118.61	Yes; 0 violation
44443382	tylophoridicine C	COC1=CC2=C(C=C1)C3=C(C[N+]4(CCCC4C3O)[O-])C5=CC(=C(C=C52)O)OC	0.085	YES		no	381.42 g/mol	2	5	0.78	112.73	Yes; 0 violation
44443383	tylophoridicine F	COC1=CC2=C(C=C1)C3=C(C[N+]4(CCCC4C3O)[O-])C5=CC(=C(C=C52)OC)OC	0.102	YES		yes	395.45 g/mol	1	5	1.11	117.2	Yes; 0 violation

249332	Vincristine sulfate	CCC1(CC2CC(C3=C(CCN(C2)C1)C4=CC=CC=C4N3)(C5=C(C=C6C(=C5)C78CCN9C7C(C=CC9)(C(C(C8N6C=O)(C(=O)OC)O)OC(=O)C)CC)OC)C(=O)OC)O.OS(=O)(=O)O	0.047	YES		no	923.04 g/mol	5	16	2.26	247.33	No; 2 violations
92114	(S)-tylophorine	COC1=C(C=C2C(=C1)C3=C(CN4CCCC4C3)C5=CC(=C(C=C52)OC)OC)OC	0.08	YES		yes	393.48 g/mol	0	5	4.04	119.16	Yes; 0 violation

S9

9975115	6-O-desmethylantofine	COC1=C(C=C2C(=C1)C3=C(CN4CCCC4C3)C5=C2C=C(C=C5)O)OC	0.096	YES		yes	349.42 g/mol	1	4	3.67	108.2	Yes; 0 violation

11741391	13(R)-14(R)-hydroxyantofine-N-oxide	COC1=CC2=C(C=C1)C3=C(CC4CCC[N+]4(C3)[O-])O)C5=CC(=C(C=C52)OC)OC	0.096	YES		yes	395.45 g/mol	1	5	1.74	117.2	Yes; 0 violation
51041425	Saprosmine B	CCOC1(C2=CC=CC=C2C(=O)C3=C1C(=CC(=O)N3)C)OC	0.026	YES		yes	299.32 g/mol	1	4	2.24	81.39	Yes; 0 violation

10263500	9-hydroxycanthin-6-one	C1=CC2=C3C=CNC4=C3N(C2=CC1=O)C(=O)C=C4	0.051	YES		yes	236.23 g/mol	1	2	1.55	70.49	Yes; 0 violation
10408269	Isotylocrebrine	COC1=C(C2=C(C=C1)C3=C(CN4CCCC4C3)C5=CC(=C(C=C52)OC)OC)OC	0.080	YES	4.94	yes	393.48 g/mol	0	5	4.04	119.16	Yes; 0 violation

S10

Supporting information Figure 1: Representation of expression of various ubiquitin E3 ligases in GBM.

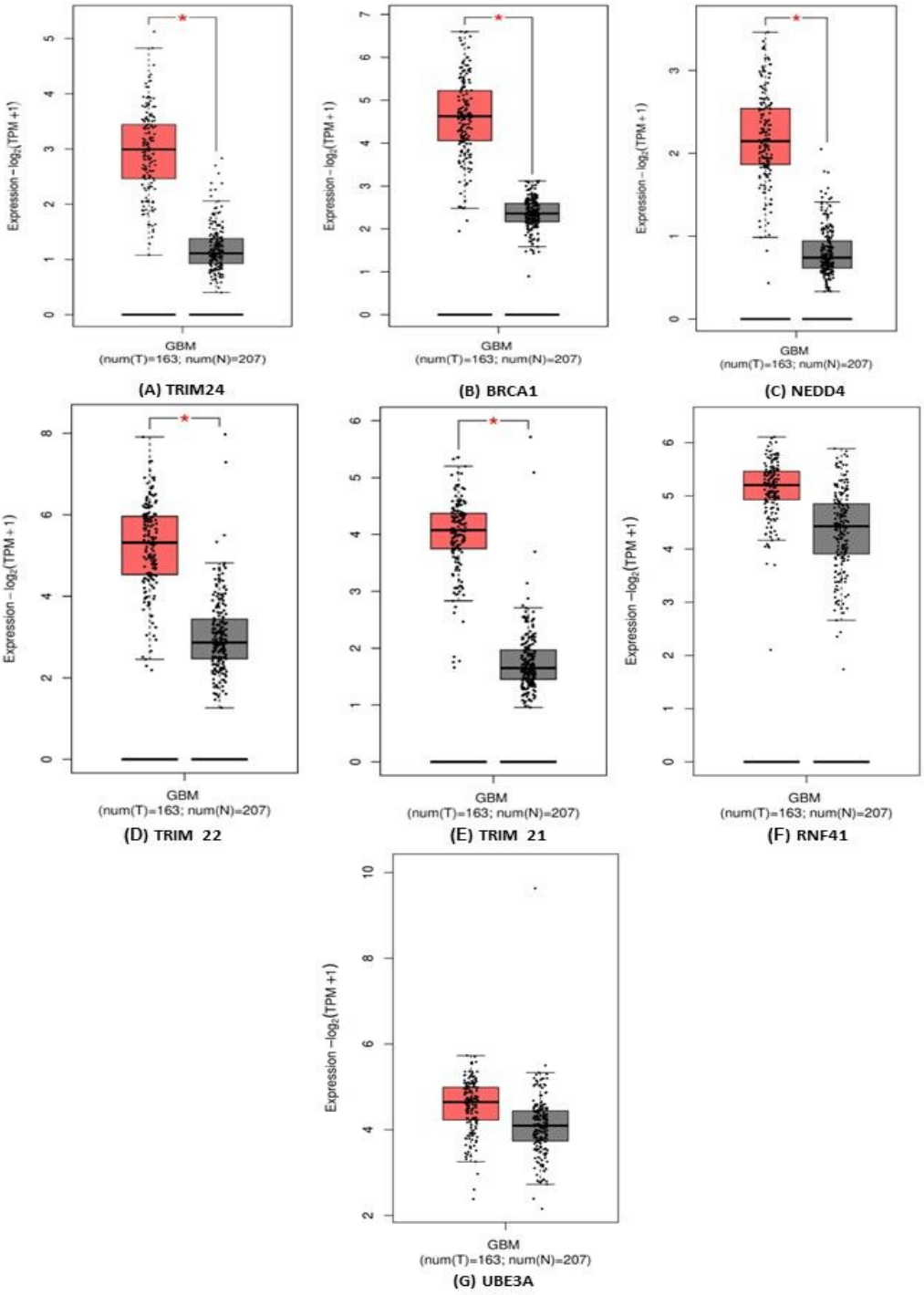
Expression – log2(TPM +1)
GBM
(num(T)=163; num(N)=207)
(A) TRIM24
(B) BRCA1
(C) NEDD4
(D) TRIM 22
(E) TRIM 21
(F) RNF41
(G) UBE3A

Research Square

Preprints are preliminary reports that have not undergone peer review.
They should not be considered conclusive, used to inform clinical practice,
or referenced by the media as validated information.

Design and Analysis of Fabric Antenna for Medical and Wireless Applications

SHRUTI AWASTHI
Delhi Technological University
Priyanka Jain (priyankajain@dtu.ac.in)
Delhi Technological University

Research Article

Keywords: Wearable antenna, SAR, medical applications, WiMAX

Posted Date: January 10th, 2023

DOI: https://doi.org/10.21203/rs.3.rs-2447613/v1

License: This work is licensed under a Creative Commons Attribution 4.0 International License. Read Full License

Abstract

This paper aimed towards wearability of antenna by inspecting the probability of designing and fabrication of wearable microstrip antenna operating from 2–6 GHz, centered at 2.5 GHz and 5.3 GHz. The antenna is fabricated on jeans material with dielectric constant, ε_r = 1.7and thickness as 1mm. The proposed design is simulated on High frequency simulation software (HFSS) version 2015, followed by fabrication using 50 µm copper film on jeans substrate. The fabricated design is then tested by Anritsu MS2038C VNA Master. Also, specific absorption rate (SAR) values are computed for medical applications to account for the tumor detection in Human Breast tissue.

1. Introduction

Wearable antennas are getting more attention now a days because of comfortability and their ease to integrate into daily wears. Related to biological applications, these wearable sensors- antennas are capable of interconnecting with nearby devices wirelessly, referred as body-centric networks [1-3]. 2-6GHz band is an interesting band to implement as it doesn't require line of sight communication and can be useful for end to end communication wirelessly and making wearable devices to work in this band can be an addition of feather in the cap.

However, the performance of these wearable antennas suffers from certain losses in terms of gain, efficiency and impedance matching when they are subjected to human body depending upon antenna design complexity or the characteristic of the wearable materials. These challenges provide hindrance in the reliability and development of wearable devices for body-centric communications [4-5].

Despite such obstacles, wearable antennas have become the area of research and in this regard, many research papers have been published as reported in [6-8].

The work presented in this paper contributes to the designing and fabrication of wearable antenna designed for medical and WiMAX applications using jeans as the substrate having dielectric constant as 1.7 with the thickness of 1mm simulated on HFSS. Also, this work explores the manufacturing of the inexpensive conductive tape based Wearable antenna instead of the conducting thread used in the embroidery based fabrication method [9, 10]. The Fabricated antenna is measured using Anritsu MS2038C VNA Master.

The paper is organized as follows: Section 2 presents the wearable antenna design. Section 3 represents the fabrication process with the measurement results followed by section 4 with the SAR measurements and concluding with section 5.

2. Designing Of Wearable Antenna Using Jeans As The Substrate

The modeled wearable antenna printed on very thin 1mm thick jean fabric of size L x W = 50mm x 35 mm respectively as shown in figure 1(a) and figure 1(b), designed to operate around 2.45GHz and 5.3 GHz , considering as a suitable frequency for healthcare and wireless applications. The area of the conductive patch is 611.365295784mm^2. In the full-wave simulations, the patch was fed by microstrip feed using an ideal lumped port. The design starts with rectangular patch having hexagonal patch in the center of the rectangular patch and partial ground plane with dimensions as 20 x35 mm (Lp x Wp) as shown in figure 1(a), refereed as Antenna A. The Antenna A gives the perfect matching at 2.4 GHz with the S11 as -25.8 dB and -12 dB at 5.3 GHz. To provide the entire band from 2-6 GHz for Wireless Communication, Circular ring and rectangular slot has been subtracted from outside the patch and inside the hexagonal slot as shown in figure 1(b), referred as Antenna B. Both the Antennas are designed and simulated in HFSS v.15.0 based on finite element method (FEM).

The dimensions of modelled Antenna (Antenna B) are shown in figure 2(a) with the simulation result as shown in figure 2(b), proving the band from 2.28-3GHz, centered at 2.5 Ghz and 4.5-6 GHz, cornered at 5.3 GHz. The Comparison of Simulated results for Antenna A and Antenna B is illustrated in figure 3, depicting the 2-6 GHz band for Antenna B. To further verify the

design, the Antenna B has been simulated in CST also which can be seen from figure 4. Figure 3 and figure 4 simulation results are compatibile and thus verified.

2.1 Surface Current Distribution

The surface current distribution of the modelled antenna (Antenna B) for two resonant frequencies (2.5 and 5.3 GHz) is shown in figure 5(a) and figure 5(b). The surface current distribution at 2.5 GHz is shown in figure 5(a) which is found to be 26.3 A/m^2. The major current distribution is around the lower corner of the patch and uniform current distribution is observed throughout the whole patch of the antenna. Therefore, adjusting the lower corners of the patch may adjust the lower frequency band. In figure 5(b), the surface current distribution of 59.6 A/m^2 at 5.3 GHz is displayed. The large amount of surface current gets distributed at upper part of the patch and inside the inner circle of the radiating patch. This indicates the upper horizontal slot is responsible for the upper frequency range.

2.2 Radiation Pattern and Gain

The spreading of radiated power density by antenna is represented through the radiation pattern of the antenna. It is the depiction of the electromagnetic waves' radiation in the far field zone [11]. The simulated radiation Pattern for E and H-plane at 2.5 and 5.3 GHz is shown in figure 6 and figure 7. More energy is radiated in E-plane at 2.5 GHz whereas the reverse is observed at 5.3 GHz, where there is more radiation of energy in H-plane as compared to E-plane. Also, at 5.3 GHz, the back-lobe in E-plane is more evident.

The gain of the antenna illustrates power transmission in the direction of maximum radiation at 2.5 and 5.3 GHz as observed in figure 8(a, b) respectively.

The Gain at 2.5 GHz is obtained as 8.2 dB and 15.4 dB at 5.3 GHz. To further validate the results, co-polarization and cross-polarization in both E and H-plane are observed at 2.5 and 5.3 GHz. As seen from the 2-D polar plot (figure (9, 10)), the radiated energy is somewhat elliptically polarized. Although the level of cross-polarization in H-plane is slightly higher at 5.3 GHz because of high gain value at 5.3GHz. The high gain values expands the plot while lower gain values make all the patterns shrink towards the center.

3. Fabrication Of The Wearable Antenna

There are various methods to design the conductive parts of the fabric based antennas, using conductive inks [12-14] and conductive threads using embroidery machine [15].We have adopted low-cost copper sheet for the designing the conducting part of the antenna. The design was manually attached on the jeans fabric through high heat and pressure which was further etched using formaldehyde solution.

The fabrication of the antenna on Jeans is explained with the help of flowchart, followed by the steps in detail, as given in the figure 11.

1. Conversion of HFSS File into DXF file. After conversion, the DXF file was hatched using AutoCAD 2021 software for printing the design on the high quality Kodak paper.
2. The printed design was then placed on the copper sheet using ethanol solution pressed under high heat and pressure.
3. After applying high heat and pressure onto the copper containing the design, the design was immersed into water to remove the excess paper around the design as shown in figure 12.
4. After removing the excess paper, the desired patch and ground structure on the design was covered through adhesive tapes and immersed into the formaldehyde solution for the etching process.
5. After 20mins, the etching process was done and the patch and the ground part was glued to the fabric through hot glue gun and again pressed onto the fabric.

6. When the patch and the ground part get pasted properly on the fabric, the 50 Ω connector was soldered to the patch's feeding point for the testing.

The fabricated wearable antenna was measured through Anritsu MS2038C VNA Master as shown in figure 13.

The VNA was first calibrated using open, short and load calibration process and after that the designed antenna is connected to VNA through 50- Ω connector. The Comparison of simulated and measurement results is shown in figure 14.There is slight variation in the Reflection Coefficient values (2.5 GHz to approximately 2.4 GHz, an advantage from healthcare application point of view) during the measurement process which might be due to the rough edges of the fabric or the burning of the jean material during the soldering process. Also, the Copper sheet might have breaks or dirt which can be responsible for the deviation of measurement results from the simulated results.

4. Sar Computation

The placement of antenna closer to the Human surface suffers from mismatching and part of the signal gets reflected/absorbed by the Human tissues which leads to high Specific Absorption Rate (SAR) [16]. Specific Absorption Rate accounts for the measurement of wave absorption or penetration inside the Human tissues. Mathematically, SAR is defined in terms of Electric field as equation (1).

$$\mathrm{SAR} = \frac{E^2\sigma}{\rho}\ \mathrm{W/Kg} \qquad (1)$$

Where E is the Electric field, is density and is the conductivity of the tissue.

Also, It can be expressed as the energy dissipated (dW) per unit mass (dm) in a volume (dV) of a given density ( ) as given by equation (2) and (3).

$$\mathrm{SAR} = \frac{d}{dt}\left(\frac{(dW)}{(dm)}\right) \qquad (2)$$

$$\mathrm{SAR} = \frac{d}{dt}\left(\frac{(dW)}{(\rho(dV)}\right) \quad = \frac{1}{\rho}\left(\frac{dW}{dt}\right) \qquad (3)$$

The SAR values at 2.5GHz for 1W power in Human Breast skin was observed as 0.2 W/kg when the wearable antenna is placed at a distance of 8mm from the Breast tissue as shown in figure 15. The healthy standards for SAR limit set by United Sates are 1.6W/kg per 1g tissue and it is 2W/kg per 10g of tissue according to European Union [17]. The designed wearable antenna is clearly meeting the standard limits of SAR for the detection of tumor in the Human Breast tissue at 2.5 GHz. The dielectric properties of Breast tissue considered for SAR measurement are tabulated in table 1.

For Tumor detection, a spherical structure with radius as 15mm is considered which increases the SAR to 1.9 W/kg at 2.5 GHz which is greater than healthy standards as shown in figure 16. Higher Specific absorption rate indicates the presence of tumor at 2.5 GHz.

Table 1: Dielectric properties of Human Breast tissue [17]

Breast Layers (Radius)	Permittivity(F/m)	Conductivity (S/m)
Fatty Layer (38mm)	4.8393	0.26229
Skin (40 mm)	36.587	2.3404
Tumor (15mm)	67	49

Table 2: Comparison of SAR values

Tissue	At 2.5GHz frequency
Without Tumor	0.004 W/kg
With Tumor	0.015 W/kg

Increased value of SAR in unhealthy tissue (tumor) in comparison to healthy tissue (no tumor) shows the detection of tumor with the designed antenna as given in table2. The comparison of proposed work with previous works has been tabulated in table 3.

Table 3: Comparison with previous works

S. No.	References	Substrate	Dimension (mm)	Frequency Range	Applications	SAR computation	Impedance Bandwidth (%)	Gain
1	[18]	FR4	30 x 21	6.80–7.30 GHz 9.7-11.7 GHz	C and X band	-	7.09 5.35dB	5.54dB
2	[19]	Cotton (1.68)	29 x24	2.25-2.75GHz 4.3-6.8 GHz	Wireless and WiMAX	-	19.60 45.50	0.64dB 2.39dB
3	[20]	Felt Fabric	26 x 47	2.16-2.63 GHz 4.45-5.90 GHz	WLAN	-	19 28	3.2dB
4	[21]	Felt	80 x92	2/5.8GHz	-	-	9.48	8.26/9.86dB
5	[22]	Felt	70 x70	2.45/5.3	WLAN	-	5.3/3.14	6dB
6	Proposed	Jeans (1.7)	50 x 35	2-6 GHz (2.15-6.3 GHz)	WiMAX, WLAN, ISM Band	YES	138.33	8.2dB at 2.5GHz and 15.2dB at 5.3 GHz.

Conclusion

The following paper represents the design and fabrication of low cost Wearable microstrip patch antenna on Jeans material operable at 2.5GHz and 5.3 GHz with a band of 2–6 GHz with an aim to achieve the wearable antenna in reality. The Jean material has the dielectric property of 1.7 with the thickness of 1mm simulated using HFSS. The surface current density, gain and the radiation pattern was observed at 2.5 GHz and 5.3 GHz. Further, SAR value is also computed for the Human Breast tissue for the cancer detection purpose for 1W power source. Higher Values of SAR in Breast tissues containing tumor in comparison to healthy Breast tissues (without Tumor) indicates the presence of Tumor. The wearable antenna was fabricated manually using low cost copper sheet and tested using Anritsu MS2038C VNA Master. The measured results matched somewhat closely to the simulated results. The future works of this study involves the experimental analysis of this wearable antenna on Tumor containing Breast tissues (homogeneous and heterogeneous).

Declarations

Conflicts of Interest: The authors declare that they have no conflicts of interest.

References

1. Matzeu, Giusy et al. (2015). Advances in wearable chemical sensor design for monitoring biological fluids. *Sensors and Actuators B-chemical*, Vol. 211, pp. 403-418.
2. Wu, Jianfeng et al. (2018).Human Limb Motion Detection with Novel Flexible Capacitive Angle Sensor Based on Conductive Textile. *Electronics*.
3. G. Tartare, X. Zeng and L. Koehl. (2018).Development of a wearable system for monitoring the firefighter's physiological state.*2018 IEEE Industrial Cyber-Physical Systems (ICPS)*, pp. 561-566.
4. P. S. Hall and Y. Hao. (2017). Antennas and propagation for body centric communications.*2006 First European Conference on Antennas and Propagation*, pp. 1-7.
5. Y. Hao, A. Alomainy, P. S. Hall, Y. I. Nechayev. (2015).C. G. Parini and C. C. Constantinou.Antennas and propagation for body centric wireless communications. *IEEE/ACES International Conference on Wireless Communications and Applied Computational Electromagnetics*, pp. 586-589.
6. Langenhove, L. V. (2007). *Smart Textiles for Medicine and Healthcare*, CRC Press, Cambridge, England.
7. S. Park and S. Jayaraman. (2007). Wearable Biomedical Systems: Research to Reality. *2007 IEEE International Conference on Portable Information Devices*, pp. 1-7.
8. Sankaralingam, S. and B. Gupta. (2010). Development of textile antennas for body wearable applications and investigations on their performance under bent conditions. *Progress In Electromagnetics Research B*, Vol. 22, 53–71.
9. Castano, Lina and Alison B. Flatau. (2014). Smart fabric sensors and e-textile technologies: a review." *Smart Materials and Structures,* vol. 23.
10. T. Maleszka and P. Kabacik. (2010). Bandwidth properties of embroidered loop antenna for wearable applications. *The 3rd European Wireless Technology Conference*, pp. 89-92.
11. IEEE Standard Definitions of Terms for Radio Wave Propagation. (2019). in *IEEE Std 211-2018 (Revision of IEEE Std 211-1997)*, vol., no., pp.1-57.
12. J. -S. Roh, Y. -S. Chi, J. -H. Lee, Y. Tak, S. Nam and T. J. Kang. (2010). Embroidered Wearable Multiresonant Folded Dipole Antenna for FM Reception. in *IEEE Antennas and Wireless Propagation Letters*, vol. 9, pp. 803-806.
13. Mai A. R. Osman Mohamad Kamal Abd Rahim Noor Asmawati Samsuri Hashim Ali M. Salim Mohammed F. Ali. (2011).Embroidered Fully Textile Wearable Antenna for Medical Monitoring Applications. *Progress In Electromagnetics Research*, Vol. 117, 321-337.
14. Y. Kim, H. Kim and H. -J. Yoo. (2010). Electrical Characterization of Screen-Printed Circuits on the Fabric. in *IEEE Transactions on Advanced Packaging*, vol. 33, no. 1, pp. 196-205.
15. Tsolis, Aris, William G. Whittow, Antonis A. Alexandridis, and J. C. Vardaxoglou. (2014).Embroidery and Related Manufacturing Techniques for Wearable Antennas: Challenges and Opportunities. *Electronics* 3, no. 2, pp.314-338.
16. U. Ali *et al.* (2017).Design and SAR Analysis of Wearable Antenna on Various Parts of Human Body, Using Conventional and Artificial Ground Planes. *Journal of Electrical Engineering and Technology*, vol. 12, pp. 317–328.
17. G. Kaur and A. Kaur. (2020). Breast tissue tumor detection using 'S' parameter analysis with an UWB stacked aperture coupled microstrip patch antenna having a ' ' shaped defected ground structure. *International Journal of Microwave and Wireless Technologies*, vol. 12, no. 7, pp. 635–651.
18. Mourad Meloui Mohammad Essaaidi. (2014). A Dual Ultra Wide Band Slotted Antenna for C and X Bands Application. *Progress In Electromagnetics Research Letters*, Vol. 47, 91-96.
19. A. Mersani and L. Osman. (2016).Design of dual-band textile antenna for 2.45/5.8-GHz wireless applications.*2016 5th International Conference on Multimedia Computing and Systems (ICMCS)*, pp. 397-399.

20. W. Chaihongsa and C. Phongcharoenpanich. (2015).Performance of textile antenna using two layers of strip line and round-off circular patch. *2015 IEEE Conference on Antenna Measurements & Applications (CAMA)*, pp. 1-3.
21. F. Khajeh-Khalili, A. Shahriari, and F. Haghshenas. (2021).A simple method to simultaneously increase the gain and bandwidth of wearable antennas for application in medical/communications systems. *International Journal of Microwave and Wireless Technologies*, vol. 13, no. 4, pp. 374–380.
22. H. A. Mashaghba *et al*. (2020).Bending Assessment of Dual-band Split Ring-shaped and Bar Slotted All-Textile Antenna for Off-body WBAN/WLAN and 5G Applications. *2020 2nd International Conference on Broadband Communications, Wireless Sensors and Powering (BCWSP)*, pp. 1-5.

Figures

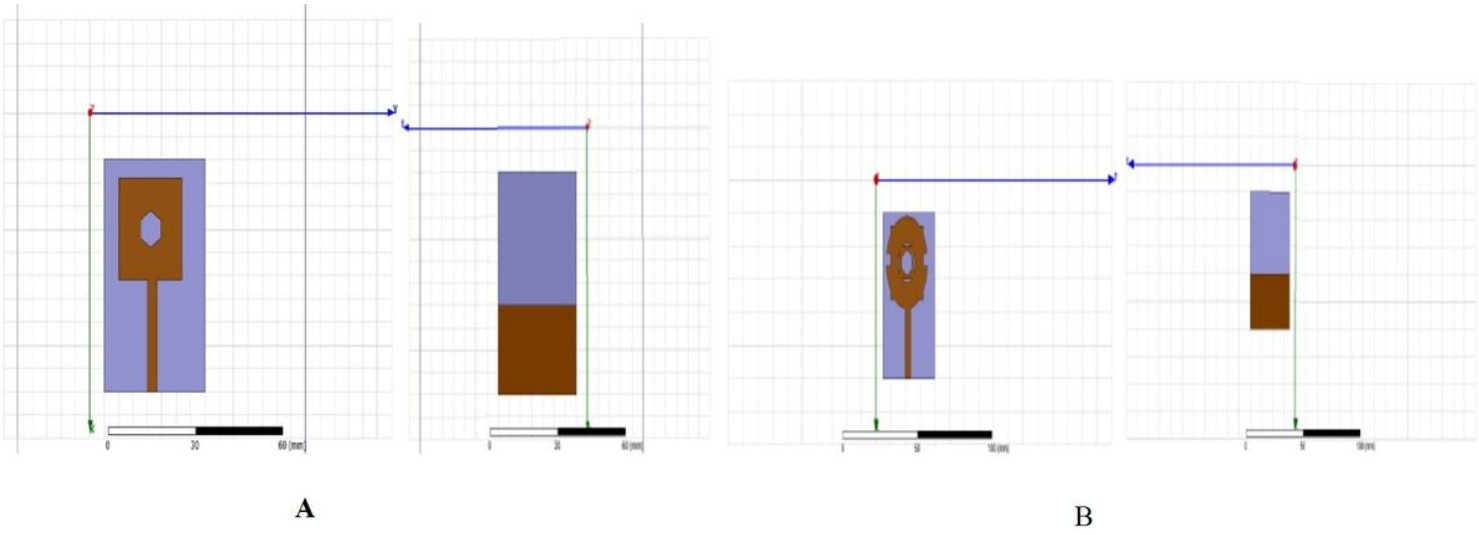

Figure 1

(a): A Antenna (b): B antenna

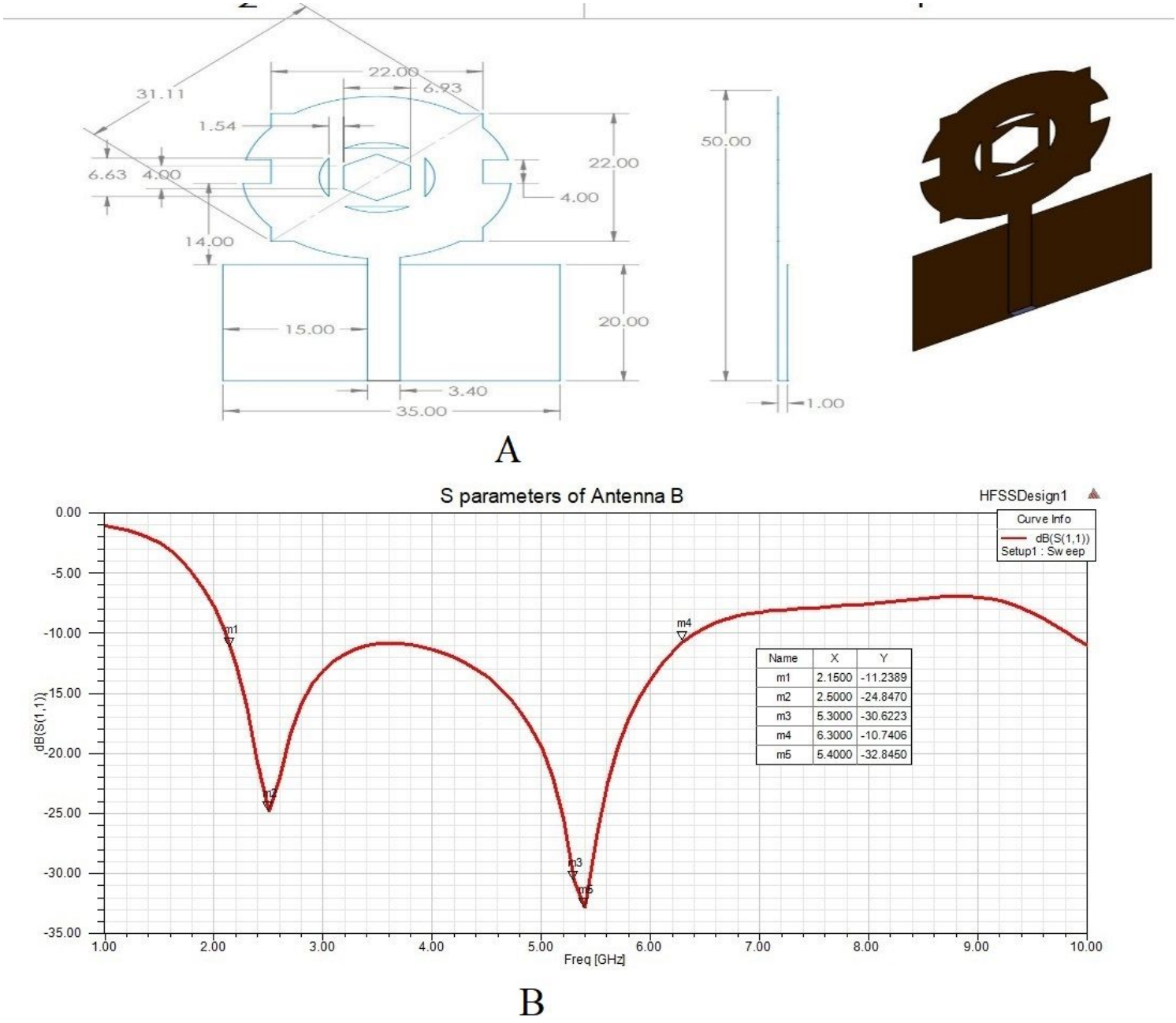

Figure 2

(a) : Physical Dimensions of Antenna B (b) : Reflection Coefficient Values of Antenna B

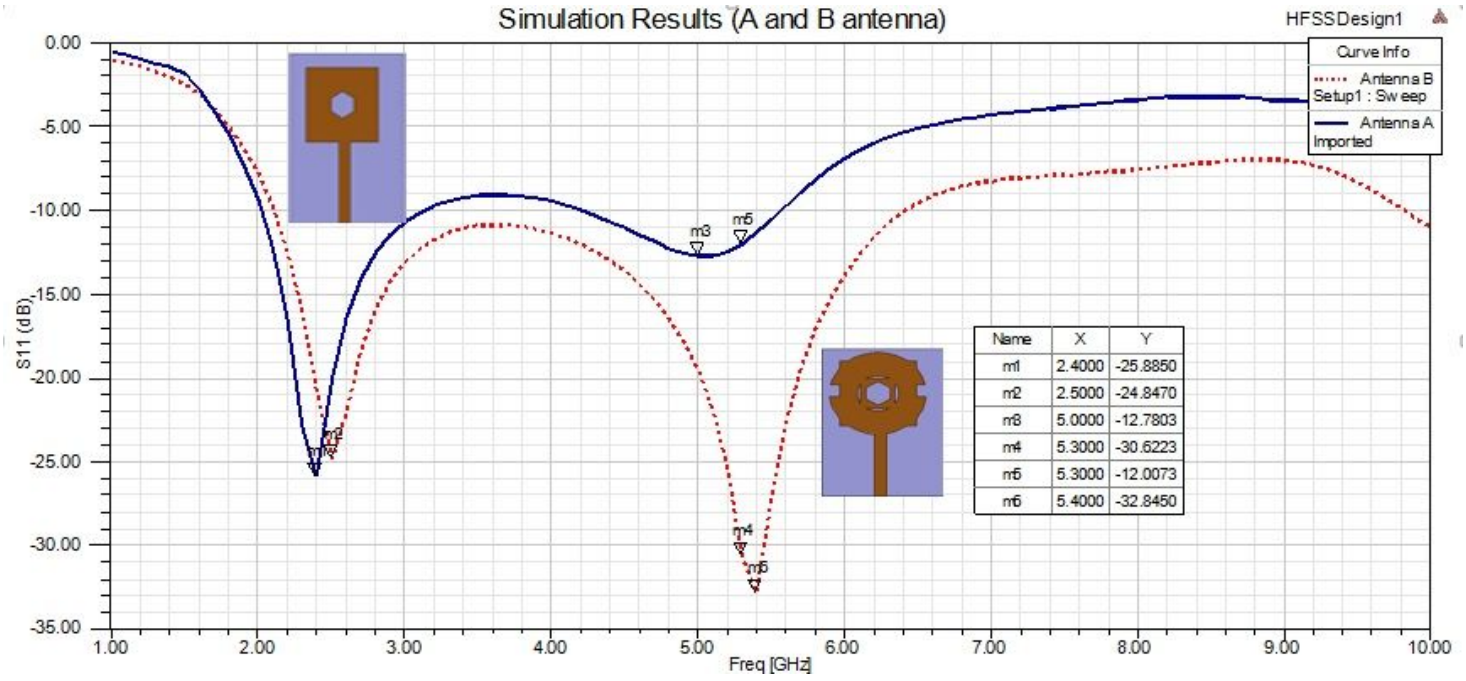

Figure 3

Simulation Results for Antenna A and Antenna B

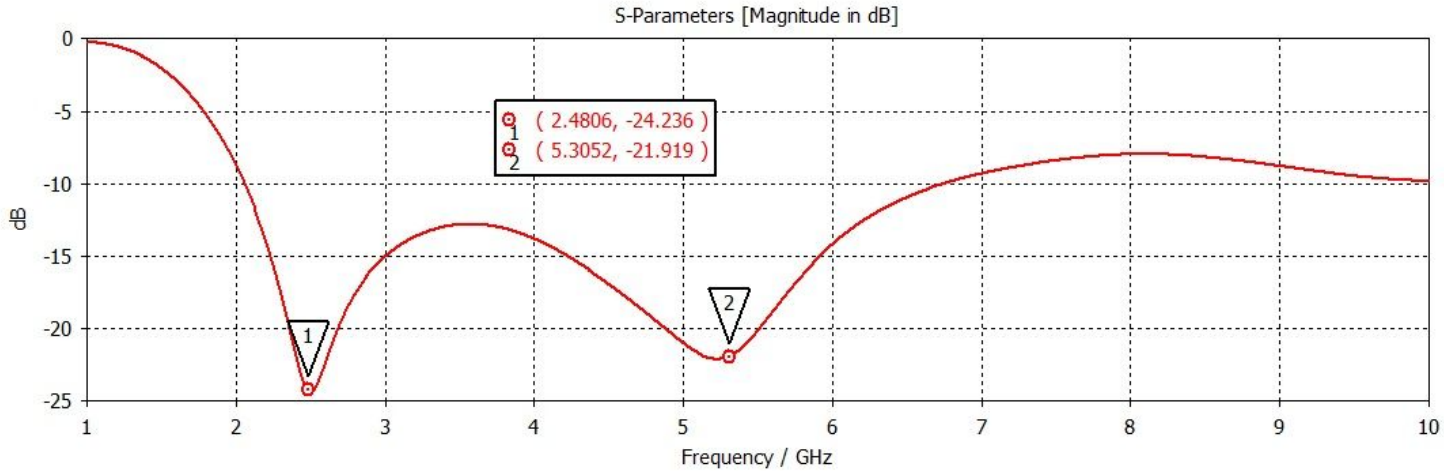

Figure 4

Simulated Reflection Coefficient Results of wearable Antenna on Jeans in CST

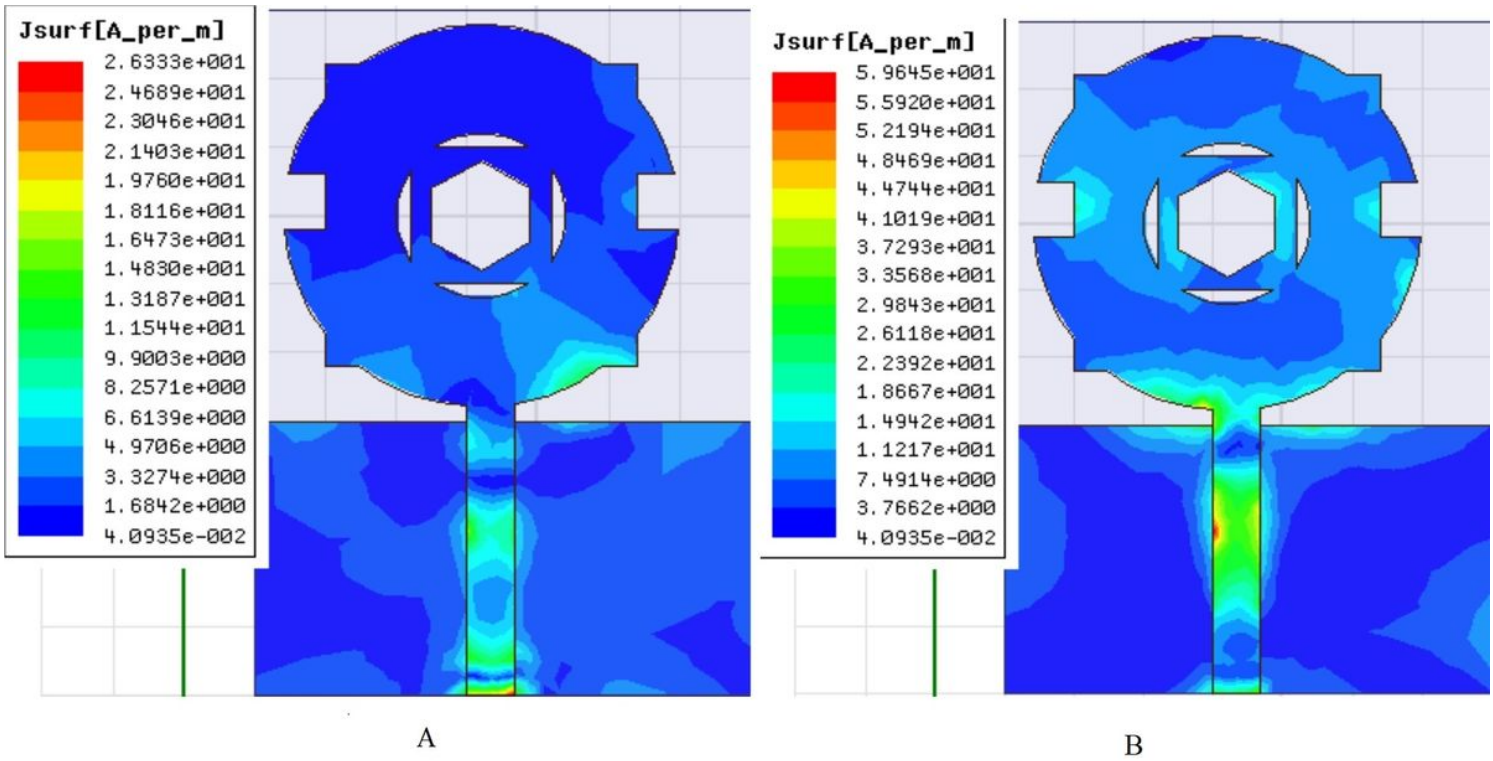

Figure 5

Surface Current Distribution at a) 2.5 GHz b) 5.3 GHz

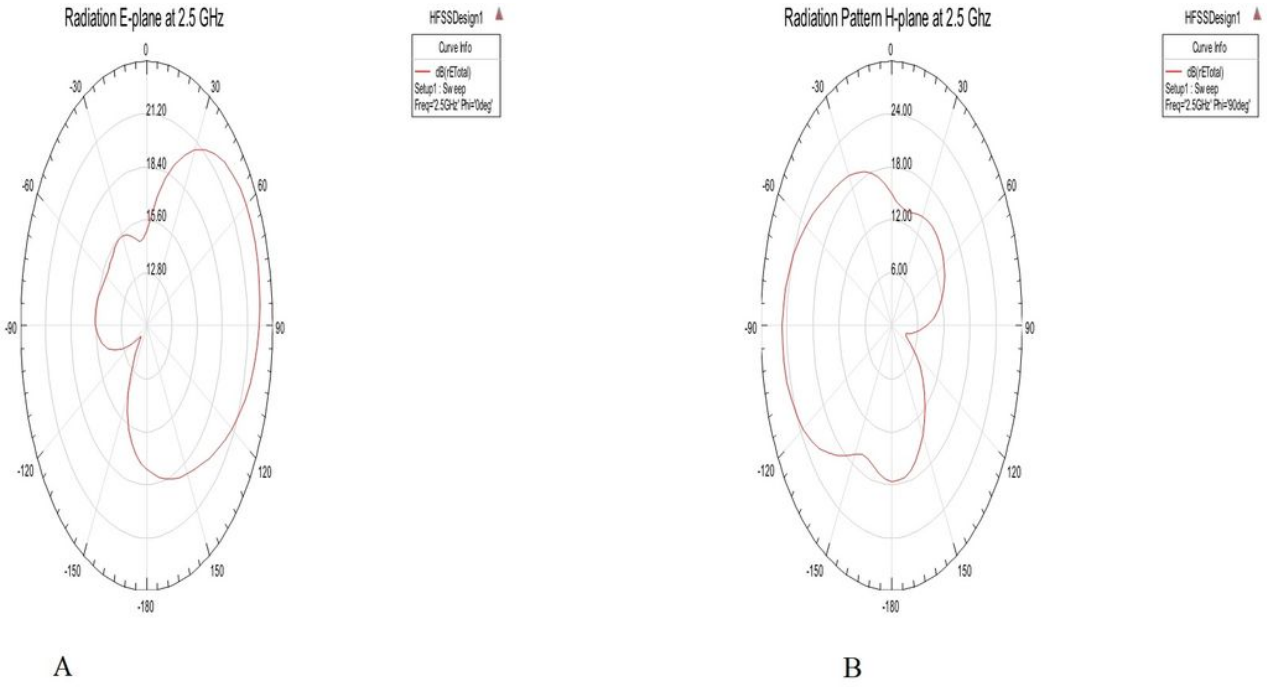

Figure 6

Radiation pattern a) E-plane at 2.5 GHz b) H-plane at 2.5 GHz

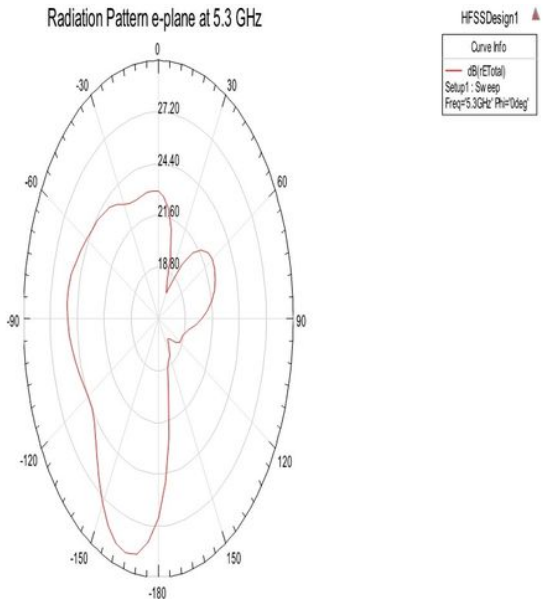

A

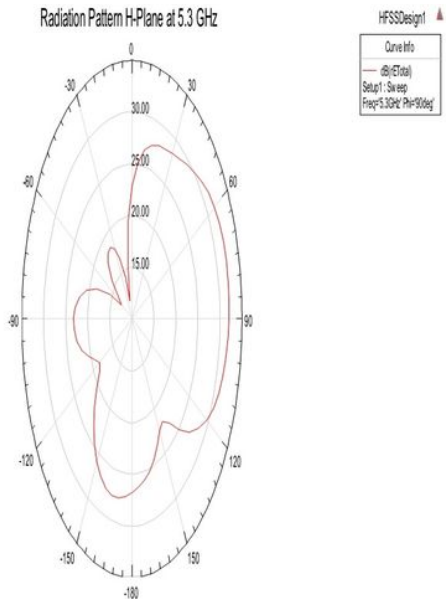

B

Figu

Figure 7

Radiation Pattern a) E-plane at 5.3 GHz b) H-plane at 5.3 GHz

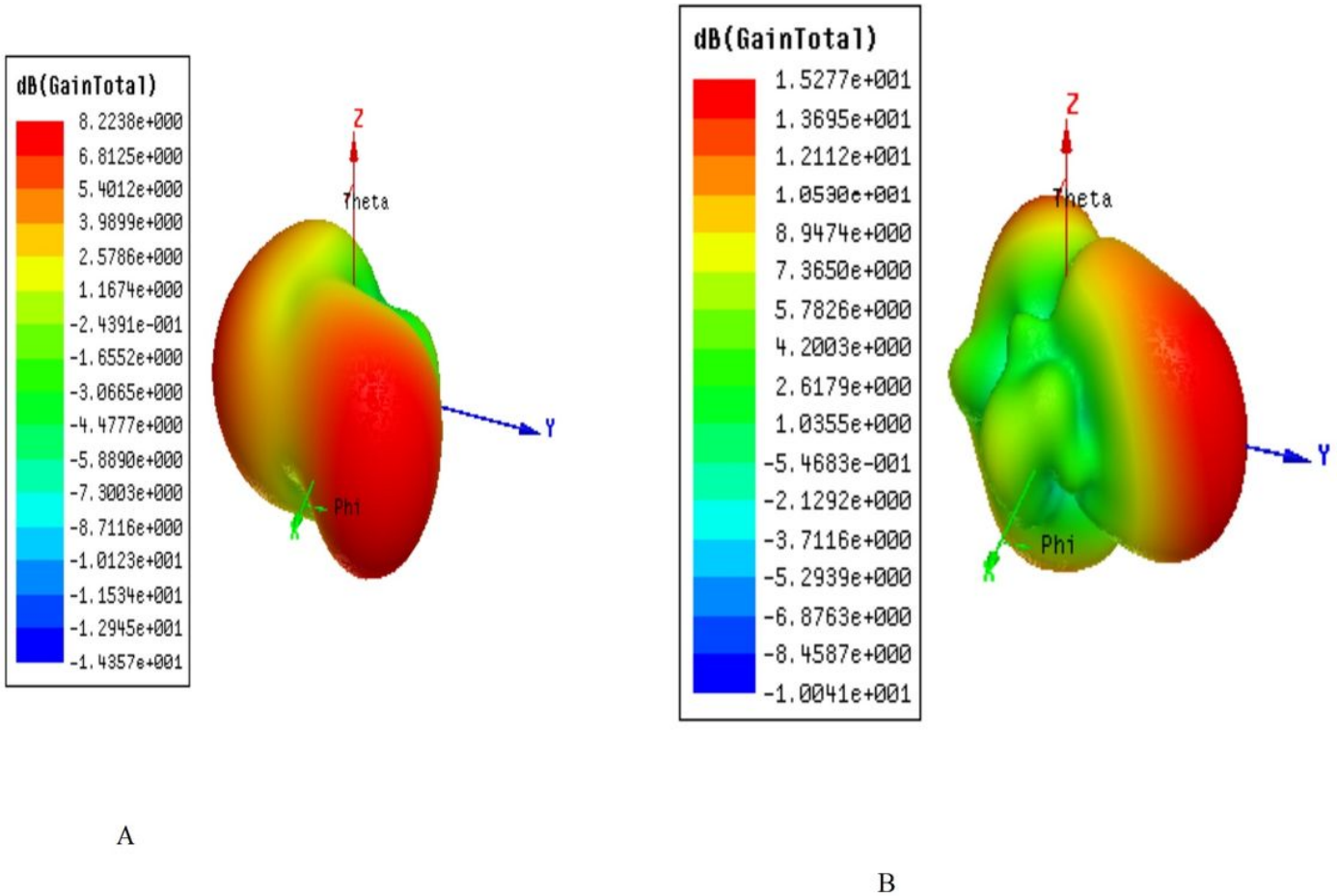

A

B

Figure 8

Gain a) 2.5GHz b) 5.3 GHz

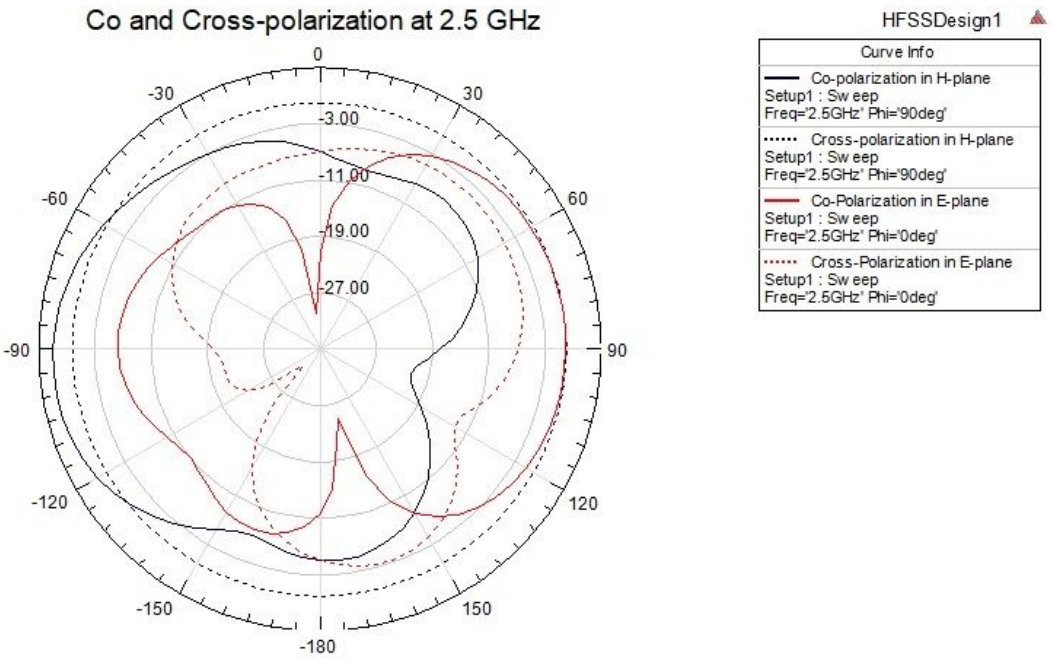

Figure 9

Co- and Cross- polarization at 2.5 GHz

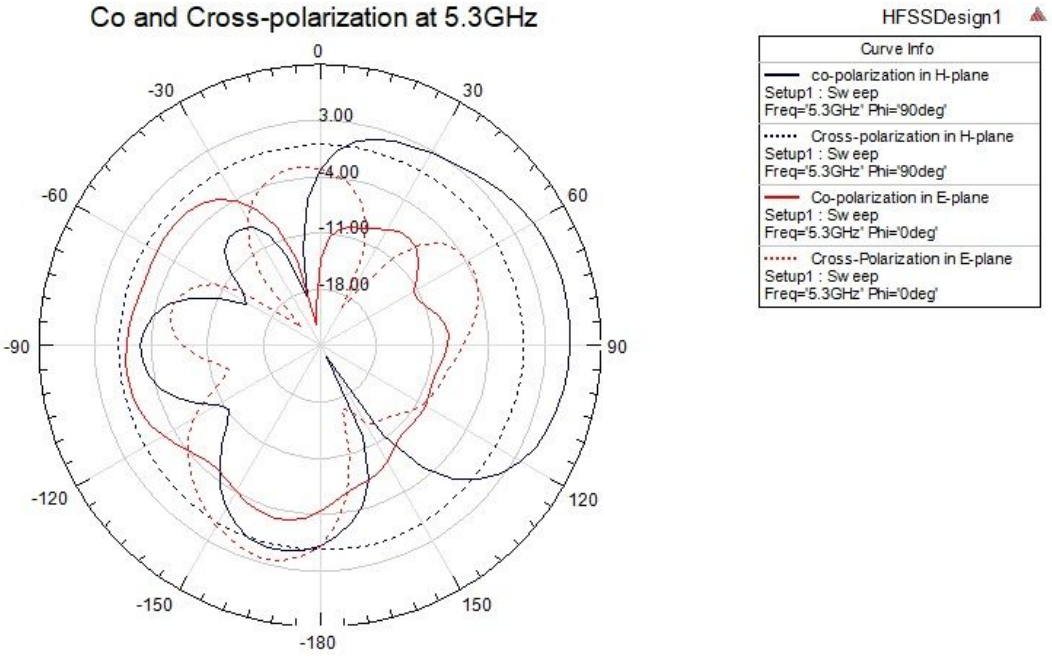

Figure 10

Co- and Cross- polarization at 5.3 GHz

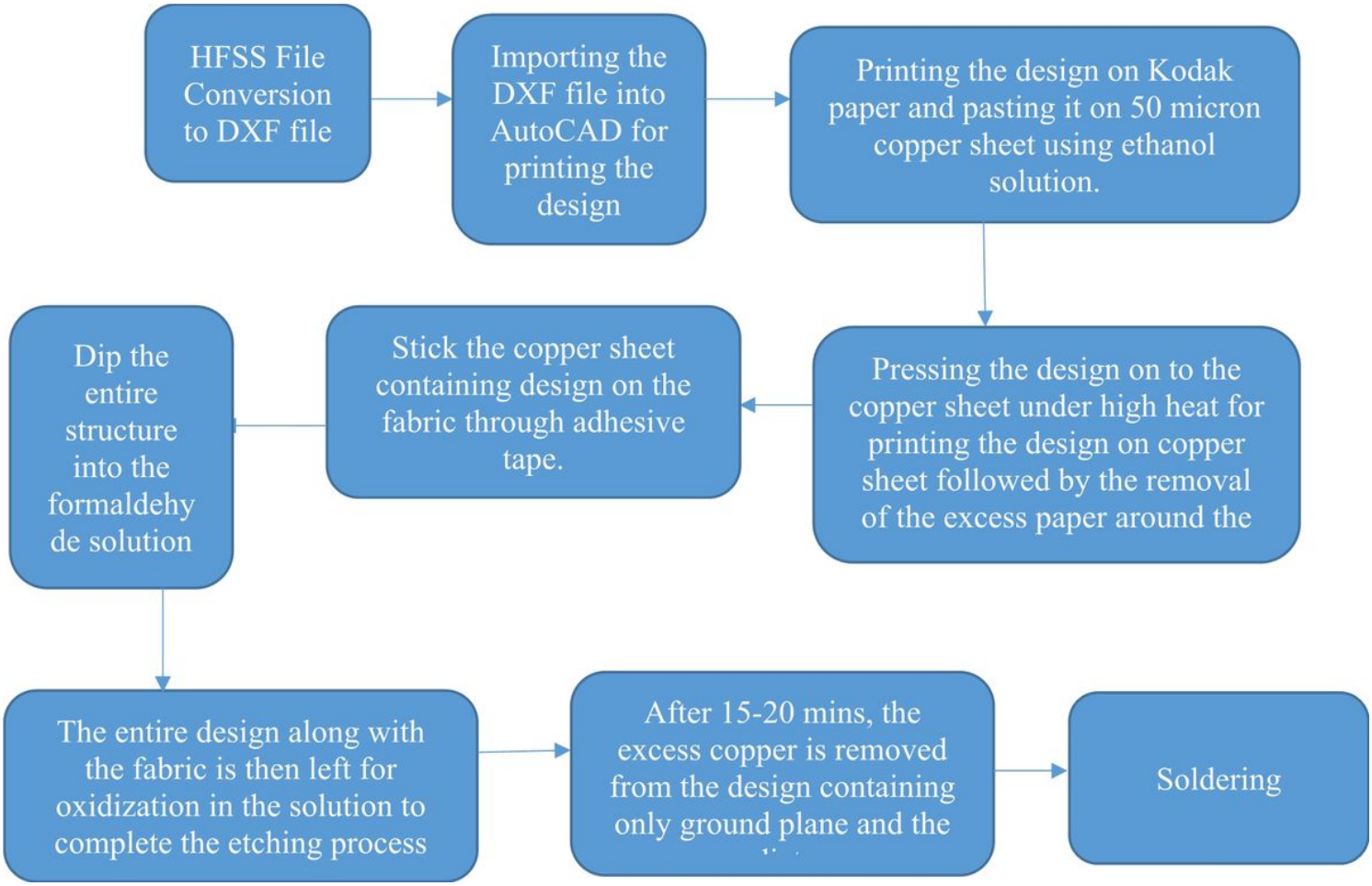

Figure 11

Flowchart of the entire fabrication process of the Wearable Antenna

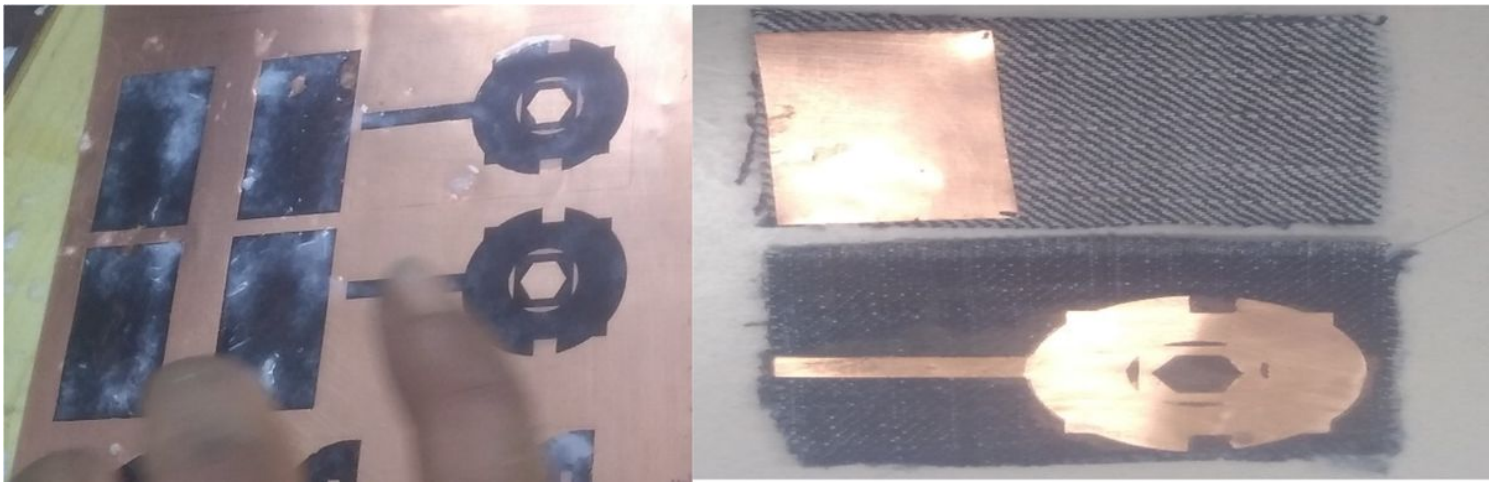

Figure 12

Removal of Excess paper from the design using Water solution and the fabricated antenna on Jeans after etching process

Figure 13

The Measurement Set up

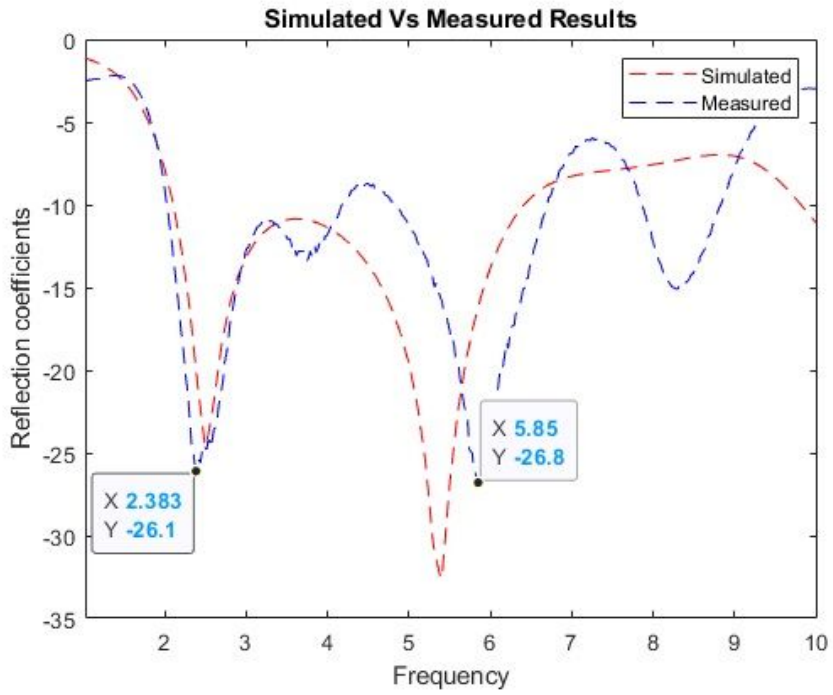

Figure 14

Simulation vs. Measurement Results of Wearable Antenna (Jeans)

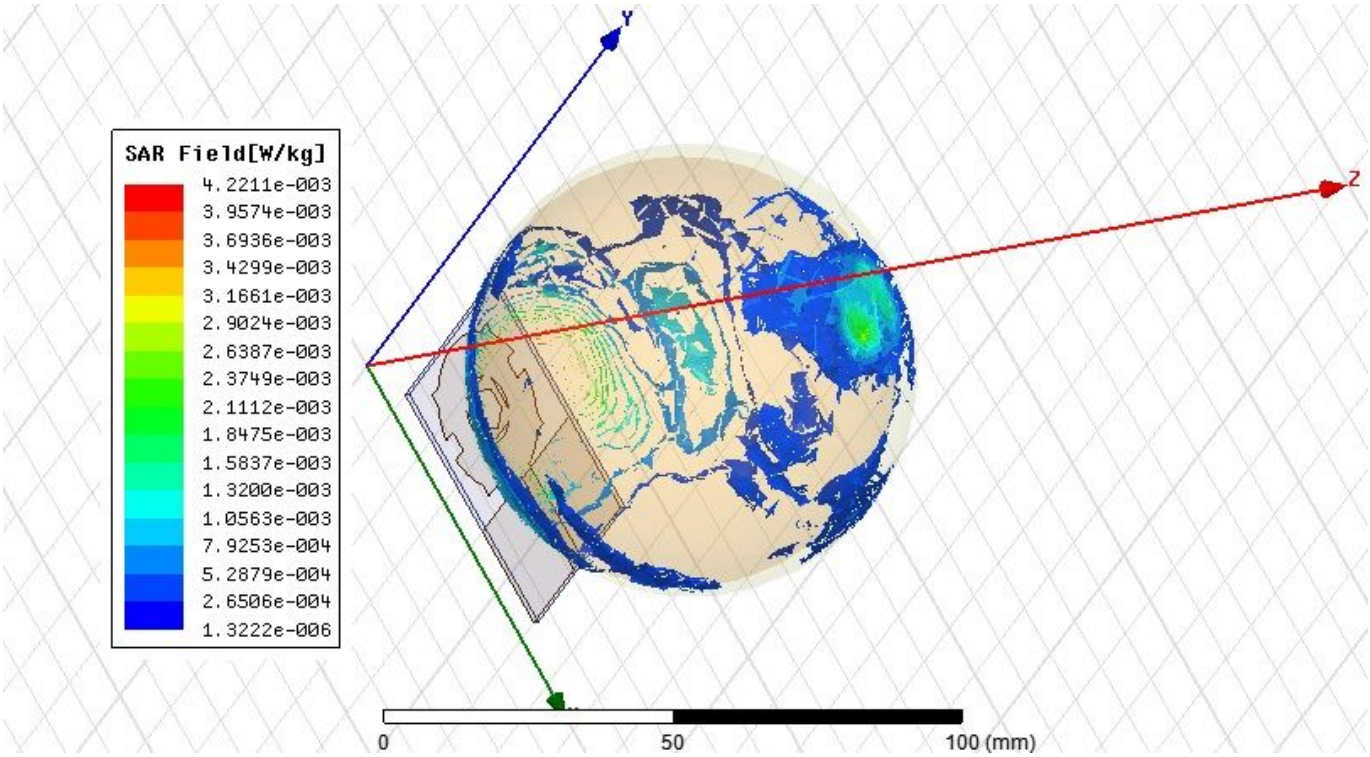

Figure 15

SAR value at 2.5GHz for 1W Power Source in healthy Breast tissue

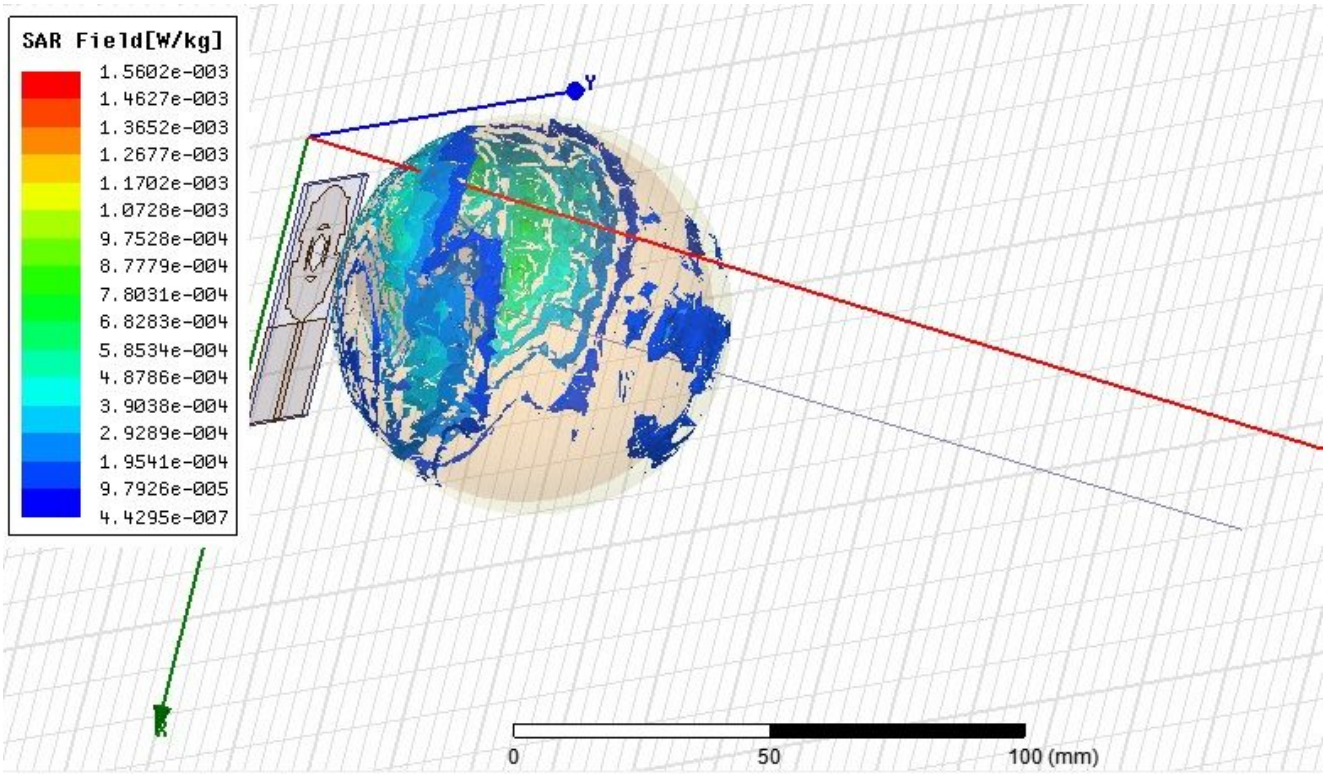

Figure 16

SAR value at 2.5 GHz for 1 mW Power Source containing Tumor

Results in Optics 10 (2023) 100366

Contents lists available at ScienceDirect

Results in Optics

journal homepage: www.sciencedirect.com/journal/results-in-optics

Design and analysis of wavelength tunable metamaterial reflector

Ankit [a], Kamal Kishor [a], Ravindra Kumar Sinha [a,b,*]

[a] TIFAC-Center of Relevance and Excellence in Fiber Optics and Optical Communication, Department of Applied Physics, Delhi Technological University, Bawana Road, Delhi 110042, India

[b] Gautam Buddha University, Greater Noida, Gautam Budh Nagar, Uttar Pradesh 201312, India

ARTICLE INFO

Keywords:
Metamaterial (MTM)
μ-negative (MNG) metamaterial
Effective permittivity ($\varepsilon_{eff.}$)
Effective permeability ($\mu_{eff.}$)
Effective refractive index ($\eta_{eff.}$)
Effective medium ratio (EMR)

ABSTRACT

This paper reports the design and performance characteristics of perfect reflector tunable metamaterial (MTM). The reported MTM parameters are optimized to achieve nearly 100 % reflection at resonance wavelength (λ_r) 1550 nm. The propagation characteristic of the proposed MTM structure was obtained by the finite element method (FEM). The electromagnetic parameters such as effective permittivity ($\varepsilon_{eff.}$), effective permeability ($\mu_{eff.}$), and effective refractive index ($\eta_{eff.}$) are calculated using Nicolson-Ross-Weir (NRW) method and analysed for the 1400–1700 nm wavelength range. It has been observed that the proposed MTM structure exhibits μ-negative (MNG) metamaterial characteristics as well as a negative effective refractive index at λ_r. Further, it has also been shown that by varying the number of arrays of unit cells and using a mirror image of the unit cell, the operating wavelength can be easily tuned as required for different applications. The overall perfect reflectance and the tunable performance of the proposed MTM has a potential applications in the design and development of compact photonic devices such as optical resonators and antennas.

1. Introduction

Metamaterial (MTM) is an area of tremendous scientific and technological importance with optical properties that are very different from ordinary materials (Islam et al., 2021; Liu and Zhang, 2011). These properties include negative refractive index (Smith et al., 2004), improved optical reflection, transmission (Fan et al., 2005), and absorption (Landy et al., 2008), etc. The materials can be classified as single negative, double negative, and double positive based on their effective permittivity (ε_{eff}) and effective permeability (μ_{eff}) parameters. The single negative (SNG) metamaterial can be further classified into two types, i.e., ε-negative (ENG) and μ-negative (MNG) metamaterial, in which either the effective permittivity or effective permeability is negative. Recently, many metamaterial unit cell structures, such as H-shaped, modified H-shaped, I-shaped, oval-shaped, dumbbell-shaped etc, have been proposed (Askari et al., 2018; Hossain et al., 2018; Kishor et al., 2015; Idrus et al., 2022; Hossain et al., 2021). For instance, tunable negative refractive index metamaterial (Kishor et al., 2014), biosensing (Alizadeh et al., 2022), terahertz absorber (Nourbakhsh et al., 2020), antenna (Bai et al., 2020), refractive index and temperature sensor (Agarwal et al., 2022) and invisibility cloaking (Paul et al., 2012) are the applications of these MTM structures.

Over the last two decades, metamaterials have realized various fascinating electromagnetic properties, covering a vast operating frequency from GHz (Vendik and Vendik, 2013) and THz (Xu et al., 2017) to infrared and visible regions. The core of the early research at GHz and THz used the electric-dipole resonance in metallic wires and the magnetic-dipole resonance in the split-ring resonator (SRR) to achieve negative permittivity and negative permeability, respectively (Smith et al., 2000). Due to the loss associated with resonant metallic structures, it has often been difficult to apply these metamaterial design concepts to geometry with submicron or nanoscale in the infrared and optical frequency ranges (Xiao et al., 2010). Another approach to produce electric or magnetic resonances with less loss is based on the interaction of electromagnetic waves with dielectric particles with a wide range of potential photonic devices such as perfect reflectors (O'Brien and Pendry, 2002; Zhao et al., 2009). Instead of using metallic mirrors, Bragg reflectors can also achieve high reflectivity. The main drawback of Bragg reflectors is that they require large number of layers to obtain the necessary reflectivity; therefore, the deposition of various dielectric materials is a time-consuming procedure that raises the cost of the product (Slovick et al., 2013). The benefit of MTM over metallic mirrors

* Corresponding author at: TIFAC-Center of Relevance and Excellence in Fiber Optics and Optical Communication, Department of Applied Physics, Delhi Technological University, Bawana Road, Delhi 110042, India.
E-mail address: dr_rk_sinha@yahoo.com (R.K. Sinha).

https://doi.org/10.1016/j.rio.2023.100366
Received 15 November 2022; Received in revised form 20 December 2022; Accepted 18 January 2023
Available online 21 January 2023
2666-9501/© 2023 The Authors. Published by Elsevier B.V. This is an open access article under the CC BY-NC-ND license (http://creativecommons.org/licenses/by-nc-nd/4.0/).

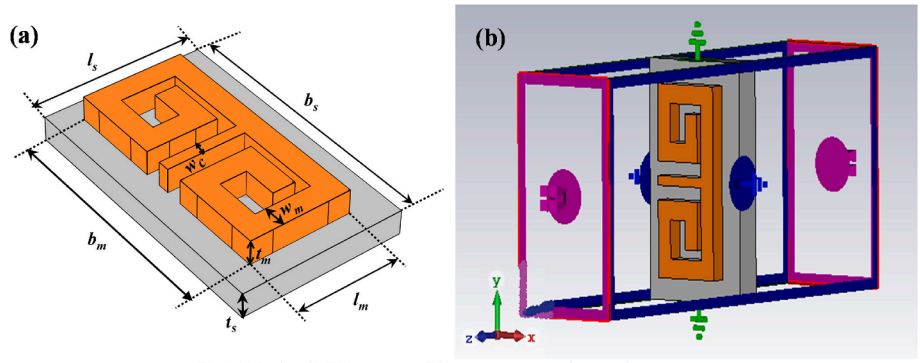

Fig. 1. (a) Designed MTM structure and (b) setup arrangement for scattering parameters.

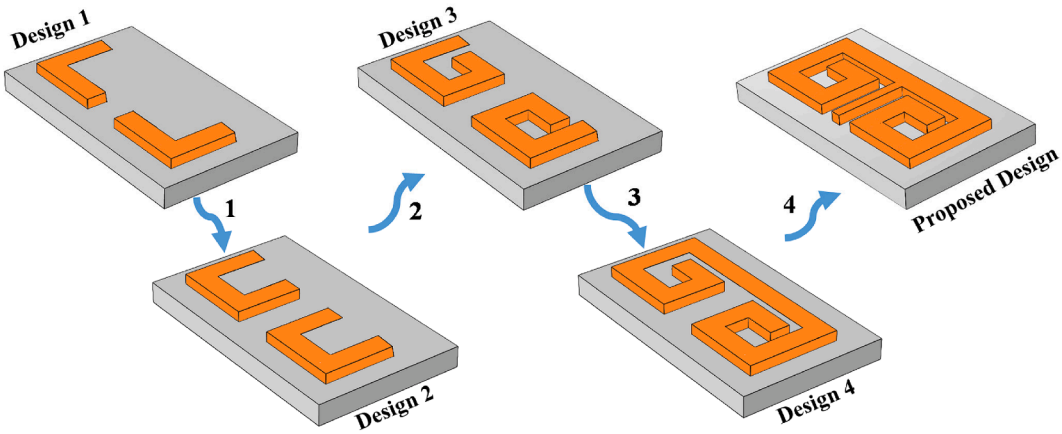

Fig. 2. MTM unit cell design methodology.

is their suitability for large-area applications due to the absence of periodicity requirement for truly homogeneous media (Smith et al., 2005).

Our primary focus in the present research work is to design an MTM unit cell with nearly 100 % reflection for operating wavelength at 1550 nm in the C-band of the optical communication window. The operating wavelength can also easily be tuned by varying the number of arrays and using the mirror image arrangement, resulting in a significant shift in resonance wavelength from the C-band to the S-band of optical communication. The proposed MTM structure exhibit μ-negative (MNG) metamaterial characteristic and negative effective refractive index at λ_r. The effective medium ratio (EMR) is calculated and achieved to a value of 2.23, proving its significance in designing and developing compact tunable photonic devices such as perfect reflectors, antennas and filters, etc.

2. Metamaterial design and simulation geometry

The proposed MTM unit cell consists of 90 nm thick silicon (permittivity (ε) of 11.7 (Shur, 1990) over an 1180 nm × 690 nm silica ((n_s) = 1.45Malitson, 1965) substrate. The schematic scenario of the MTM unit cell is represented in Fig. 1, wherein Fig. 1(a) exhibits the perspective view of the MTM unit cell, and Fig. 1(b) shows the setup with input and output ports for the measurement of scattering

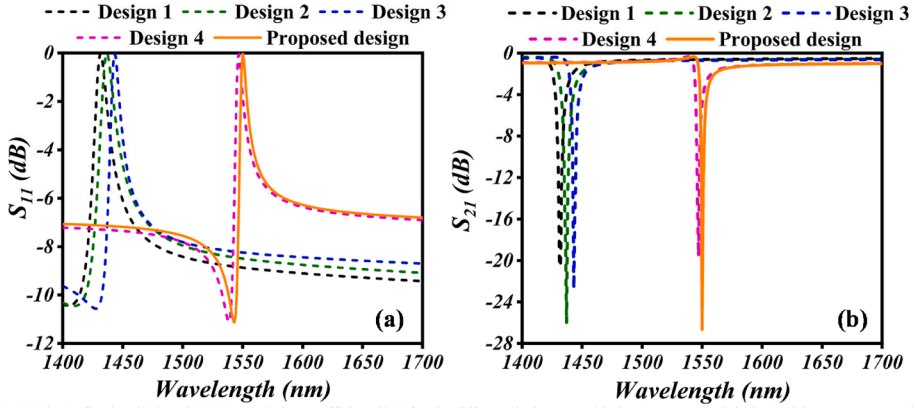

Fig. 3. (a) The Reflection (S_{11}) and (b) Transmission coefficient (S_{21}) for the different designs step (design 1 to proposed design) with respect to wavelength from 1400 nm to 1700 nm.

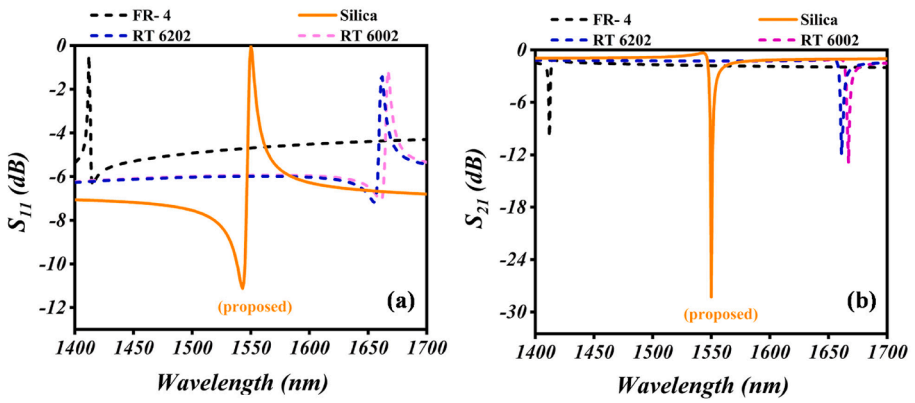

Fig. 4. Variation of (a) reflection coefficient (S_{11}) and (b) transmission coefficient (S_{21}) with the incident wave with the change in the different dielectric substrates.

Table 1
Various properties and S_{21} parameters results from different substrate materials.

Sr. No.	Substrate	Relative permittivity	Resonance wavelength of S_{21} (nm)	Optical wavelength band	Magnitude (dB)
1.	FR-4	4.5	1412	E (Extended band)	−10
2.	**Silica (proposed)**	**3.75**	**1550**	**C (Conventional band)**	**−28.2**
3.	Roger's RT 6202	2.9	1661	U (Ultra long wavelength)	−11.9
4.	Roger's RT 6002	2.94	1667	U (Ultra long wavelength)	−12.9

parameters of MTM.

The perfect magnetic conductor (PMC) and perfect electric conductor (PEC) boundary conditions are used along the *x*- and *y*-axis, respectively. At MTM unit cell, the electromagnetic wave is incident normally along the *z*-axis with a linearly polarized electric field along the y-axis. Two waveguide ports are kept at the specified positive and negative z-directions to analyse the MTM behaviour along the operating wavelength between 1400 nm to 1700 nm. The modelling and simulation analysis has been performed using the finite element method (FEM) and verified using two commercial simulation tools: COMSOL MULTIPHYSICS and CST MICROWAVE STUDIO.

3. Optimization of MTM unit cell

3.1. Design methodology

In Fig. 2, the design methodology of the proposed MTM structure has been shown, including five design steps.

Design 1 is obtained by combining two L-shaped mirror strips on the substrate. The strips create resonance when propagating electromagnetic wave incidences on their surface along the z-axis. With Design 1, we achieved nearly 100 % reflection coefficient at 1432 nm resonance wavelength, as shown in Fig. 3(a). For design 2, two more horizontal strips are added in Design 1, and the resonance wavelength is observed at 1437 nm. In Design 3, two more vertical strips are added at the ends of Design 2 and acquire a resonance wavelength of 1443 nm.

Further, a vertical strip is inserted to connect the two mirror shapes resulting in Design 4 with a 1547 nm resonance wavelength. Finally, one horizontal strip is added between the two similar shapes to obtain the proposed design to achieve a nearly 100 % reflection coefficient at λ_r as shown in Fig. 3(a). Corresponding transmission coefficient (S_{21}) for all designs are also calculated and plotted in Fig. 3(b).

3.2. Parametric investigation on proposed MTM unit cell

In this section, we have performed a detailed computational analysis to examine the impact of various parameters including substrate material, geometrical parameters of resonator and substrate on the resonance wavelength.

3.2.1. Effect of different substrate materials

The various dielectric materials such as FR-4, Roger's versions (RT

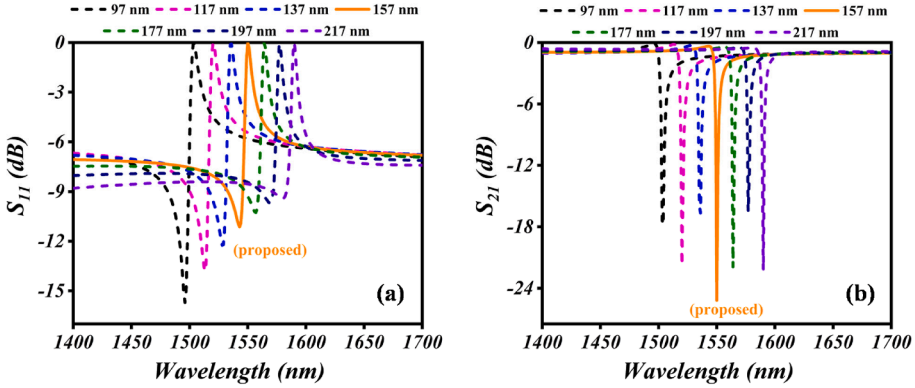

Fig. 5. Variation of different substrate thicknesses (t_s) of the designed MTM with the incident wave resulting in its impact on (a) reflection coefficient (S_{11}) and (b) transmission coefficient (S_{21}).

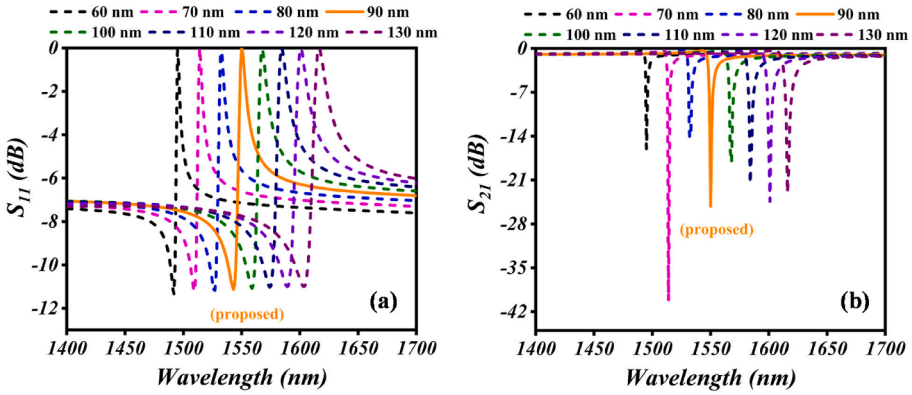

Fig. 6. Variation of silicon dielectric resonator thickness (t_m) of the designed MTM with the incident wave resulting in its impact on (a) reflection coefficient (S_{11}) and (b) transmission coefficient (S_{21}).

6002 and RT 6202) and Silica have been considered as substrate. The obtained reflection and transmission coefficient are plotted in Fig. 4.

From Fig. 4, we observed that MTM is resonating at 1412 nm, 1661 nm, 1667 nm, and 1550 nm for FR-4, RT 6202, RT 6002, and Silica, respectively, as substrate materials. All the above findings are summarized in Table 1. The resonance shifted towards the lower wavelength when we used FR-4 and Silica substrate instead of Roger's versions, which indicates that the MTM performance depends on the substrate selection, as shown in Fig. 4. The impact of silica substrate on the resonance wavelength is highly noticeable and it is showing nearly 100 % reflection. Using Silica as a substrate in the proposed MTM structure, the transmission coefficient (S_{21}) value is near to −30 dB shown in Fig. 4 (b). Correspondingly, the maximum reflectance (0 dB) is shown in the reflection coefficient (S_{11}) (Fig. 4(a)) at 1550 nm resonance wavelength. However, the remaining substrate materials do not give nearly 100 % reflectance and resonates at other wavelengths than that of 1550 nm. Therefore, we kept Silica as a substrate material for the proposed MTM unit cell.

3.2.2. *Effect of silica substrate thickness (t_s)*

The substrate acts as a dielectric medium, creating capacitance between the two waveguide ports. Now, as the thickness of the substrate (t_s) increases, the parallel capacitance increases, increasing the resonance wavelength (Bellal Hossain et al., 2022). We have analysed the variation of thickness of substrate material "silica" from 97 nm to 217 nm, and the obtained result is plotted in Fig. 5. In the proposed MTM unit cell, the resonance wavelength of S_{11} & S_{21} parameters shifted towards the higher wavelength side with an increase in t_s.

From Fig. 5, it is observed that the proposed MTM unit cell gets the required resonance wavelength in C-band at λ_r with a substrate thickness of 157 nm.

3.2.3. *Effect of resonator material (silicon) thickness (t_m)*

We varied the resonator material thickness from 60 nm to 130 nm and observed the corresponding variation in the resonance wavelength. The following equation represents the relation between wavelength and inductance:

$$\lambda = \frac{c}{f} = c\sqrt{LC} \tag{1}$$

where c is speed of light, L is inductance and C is capacitance.

In our proposed MTM structure, the inductance plays a significant role. In Fig. 6, when the thickness of silicon material (t_m) increases, inductance also increases resulting in increase in resonance wavelength (Eq. (1)), called red-shift.

From Fig. 6, it is reported that the proposed MTM unit cell with silicon resonator acquires the required resonance wavelength in C-band at λ_r with a thickness of 90 nm. The geometrical parameters of the optimized MTM unit cell are presented in Table 2.

Table 2
Unit Cell Dimension.

Parameters	Values (nm)	Description
b_s	1180	breadth of substrate in y
l_s	692	length of substrate in x
l_m	425	material length in x
b_m	949	material length in y
t_s	157	substrate thickness
w_c	47	width of central line
t_m	90	thickness of material
w_m	94	width of MTM strip

4. Results and discussion

In this section, the effective electromagnetic parameters have been calculated and analysed. The tunability characteristic of the designed MTM is also investigated and discussed using the structure's array analysis and mirror image.

4.1. *Scattering parameters of optimized MTM unit cell*

The Drude-Lorentz variables were applied to evaluate the scattering parameters using FEM-based COMSOL Multiphysics and CST Microwave studio simulation tools.

According to Fig. 7(a and b), the study of S_{11} & S_{21} from two different simulation platforms showed great similarity. In Fig. 7(c) the reflectance spectra of the proposed structure is plotted. It is observed that due to the magnetic dipole resonance, the designed MTM structure exhibits nearly 100 % reflectance at λ_r. The primary condition for perfect reflectance is achieved by the nature of permeability (μ) and permittivity (ε). When the value of μ>0 and ε < 0, it corresponds to the electric dipole resonance, whereas when μ < 0 and ε > 0, it corresponds to the magnetic dipole resonance (Slovick et al., 2013; Moitra et al., 2015). It is clearly seen in Fig. 8(a) that the μ is negative and ε is positive at the operating resonance wavelength i.e., 1550 nm where nearly 100 % reflection is achieved. The reflectance of different metamaterial structures has been summarized in Table 3. It can be observed that the reflectance of the proposed structure is higher at 1550 nm resonance wavelength compared to other structures presented in Table 3 below (Slovick et al., 2013; Moitra et al., 2015; Moitra et al., 2014; Chen et al., 2020).

4.2. *Effective electromagnetic parameters*

To explore the extraordinary electromagnetic behaviour of the MTM structure, we require to evaluate its effective electromagnetic parame-

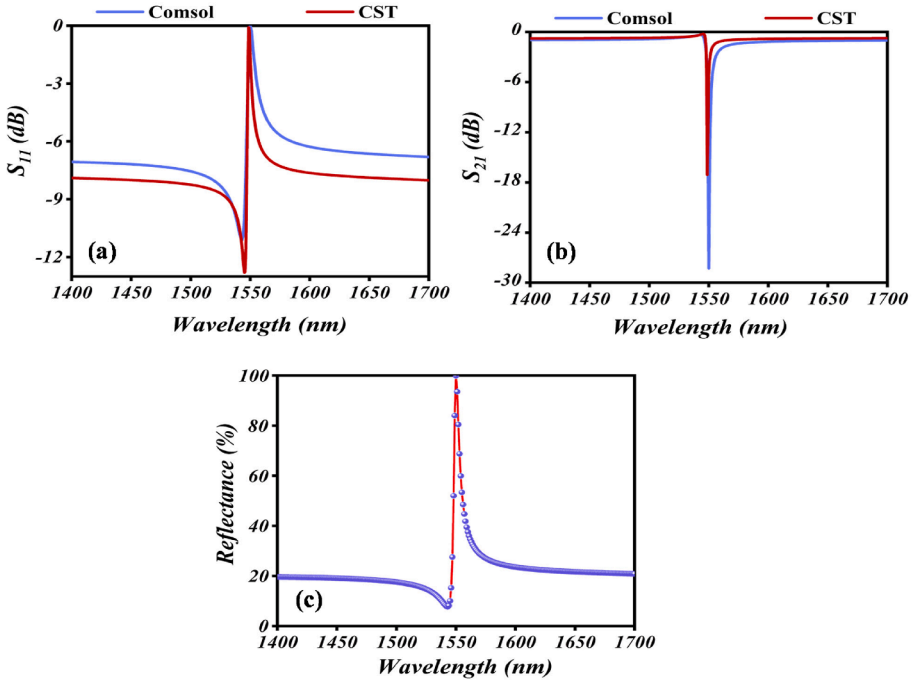

Fig. 7. (a) Reflection (S_{11}) and (b) Transmission (S_{21}) coefficient have been calculated from both COMSOL and CST software (c) calculated reflectance spectra of the proposed metamaterial from COMSOL.

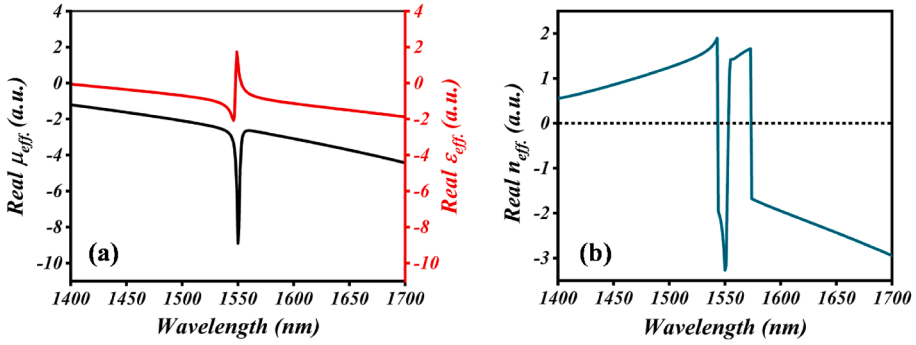

Fig. 8. (a) The real parts of $\mu_{eff.}$ (effective permeability) and $\varepsilon_{eff.}$ (effective permittivity), (b) $n_{eff.}$ (effective refractive index) curves of the proposed MTM structure.

Table 3
Comparison of % reflectance of the designed MTM structure with previous literature data.

Ref.	Period (nm)	Shape	Resonance wavelength	Reflectance (%)
(Slovick et al., 2013)	820×820	Silicon cubes	1500 nm	99.9
(Moitra et al., 2014)	660×660	Silicon cylinder	1450 nm	99.9
(Moitra et al., 2015)	820×820	Silicon cylinder	1530 nm	99.7
(Chen et al., 2020)	720×720	• Si disk array Diamond disc array	• 1050–1110 nm 1040–1100 nm	>97
Our work	692×1180	Silicon structure	1550 nm	99.8

ters, such as permittivity, permeability, and refractive index. Ziolkowski et al. present a mathematical form to extract effective permittivity and permeability based on the most widely used Nicolson-Ross Wier (NRW) method. NRW method extracts the $\varepsilon_{eff.}$, $\mu_{eff.}$ and $n_{eff.}$ using the transmission coefficient (S_{21}) and reflection coefficient (S_{11}). The following simplified equations are being used (Rothwell et al., 2016; Islam et al., 2015; Ziolkowski and Heyman, 2001; Chen et al., 2004):

$$\varepsilon_{eff.} = \frac{2}{jk_0 d} \times \frac{(1-V_1)}{(1+V_1)} = \frac{c}{j\pi\nu d} \frac{(1-S_{21}-S_{11})}{(1+S_{21}+S_{11})} = \frac{\lambda}{j\pi d} \frac{(1-S_{21}-S_{11})}{(1+S_{21}+S_{11})} \quad (2)$$

$$\mu_{eff.} = \frac{2}{jk_0 d} \times \frac{(1-V_2)}{(1+V_2)} = \frac{c}{j\pi\nu d} \frac{(1-S_{21}+S_{11})}{(1+S_{21}-S_{11})} = \frac{\lambda}{j\pi d} \frac{(1-S_{21}+S_{11})}{(1+S_{21}-S_{11})} \quad (3)$$

$$n_{eff.} = \sqrt{\varepsilon_r \mu_r} = \frac{c}{j\pi\nu d} \sqrt{\left\{ \frac{(S_{21}-1)^2 - (S_{11})^2}{(S_{21}+1)^2 - (S_{11})^2} \right\}} = \frac{\lambda}{j\pi d} \sqrt{\left\{ \frac{(S_{21}-1)^2 - (S_{11})^2}{(S_{21}+1)^2 - (S_{11})^2} \right\}} \quad (4)$$

where $V_1 = |S_{21}| + |S_{11}|$, $V_2 = |S_{21}| - |S_{11}|$, $k_0 = \frac{2\pi\nu}{c}$, c is the velocity of light, d is the metamaterial slab thickness, and λ is the operating wavelength.

Using the above Eqs. (2)-(4) the effective permittivity ($\varepsilon_{eff.}$), effective

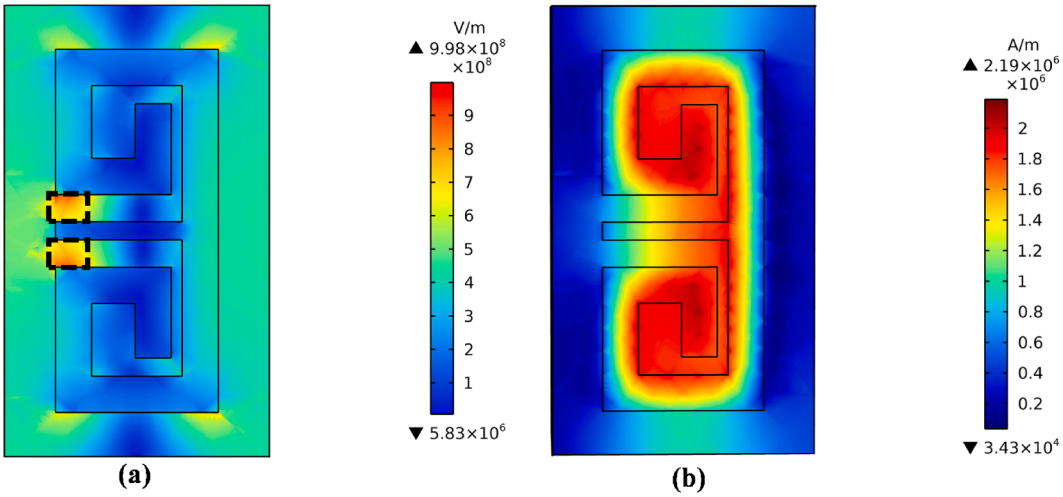

Fig. 9. A plot of normalized (a) Electric Field and (b) Magnetic Field Distribution of the MTM structure atλ_r

permeability ($\mu_{eff.}$) and effective refractive index ($n_{eff.}$) is calculated with respect to the operating wavelength and plotted in Fig. 8.

From Fig. 8(a), it can be seen that at λ_r, 1550 nm, $\varepsilon_{eff.}$ has a positive value whereas $\mu_{eff.}$ has a negative value. Also, the $\mu_{eff.}$ exhibits entirely negative behaviour beyond 1560 nm however, effective permeability is utterly negative in 1400–1700 nm confirming the MNG characteristic of the proposed MTM. Also, achieving negative permeability at the resonance wavelength could be beneficial in long-distance communication. Further, from Fig. 8(b) it is observed that n_{eff} is having a negative value at λ_r.

Furthermore, the EMR, one of the significant aspects for the design and development of metamaterial which provides the compactness of the metamaterial structure, is also calculated using the following formula (Almutairi et al., 2019):

$$EMR = \frac{Operating\ \ Wavelength\ \ for\ \ the\ \ unit\ \ cell}{length\ \ of\ \ the\ \ unit\ \ cell} \tag{5}$$

The EMR of the reported MTM unit cell is achieved to 2.23 at the operating resonance wavelength, 1550 nm. The relatively high value of EMR ensures the compactness of the devices assembled using the reported MTM.

4.3. Analysis of normalized electric and magnetic field distribution

MTM unit cell is projected with a normal electromagnetic wave along z-axis with a linearly polarized electric field along the y-axis. The split gap of the proposed MTM builds the capacitance and generates electric resonance, whereas the resonator strip creates the inductance, resulting in magnetic resonance (Islam et al., 2014). The electric field and magnetic field distribution of the MTM structure have been evaluated for the λ_r and demonstrated in Fig. 9(a and b).

From Fig. 9(a), it is observed that the maximum accumulation of electric field distribution is of the order of 10^8 V/m. Further, it is along the gap between the edge of the central line (w_c) and the edge of the MTM resonator strip shown by the yellowish region enclosed by a black

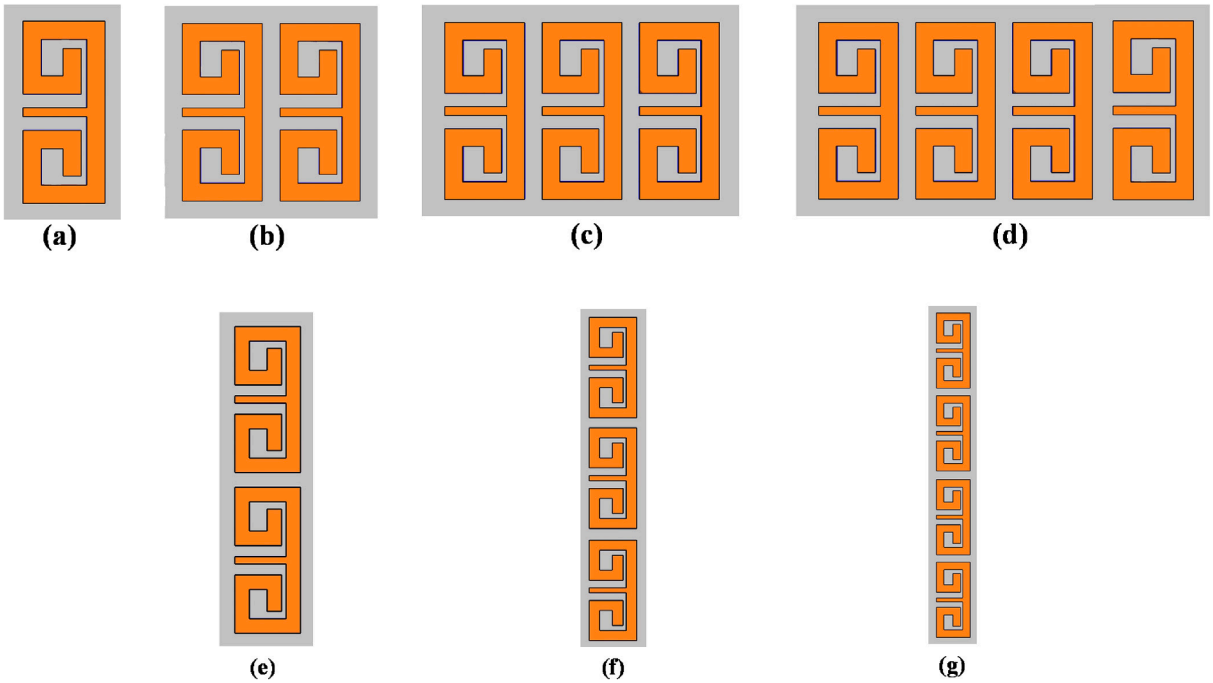

Fig. 10. Top view of the arrays of the metamaterial (a) (1×1), (b) (1×2), (c) (1×3), (d) (1×4), (e) (2×1), (f) (3×1) and (g) (4×1) of the proposed MTM structure.

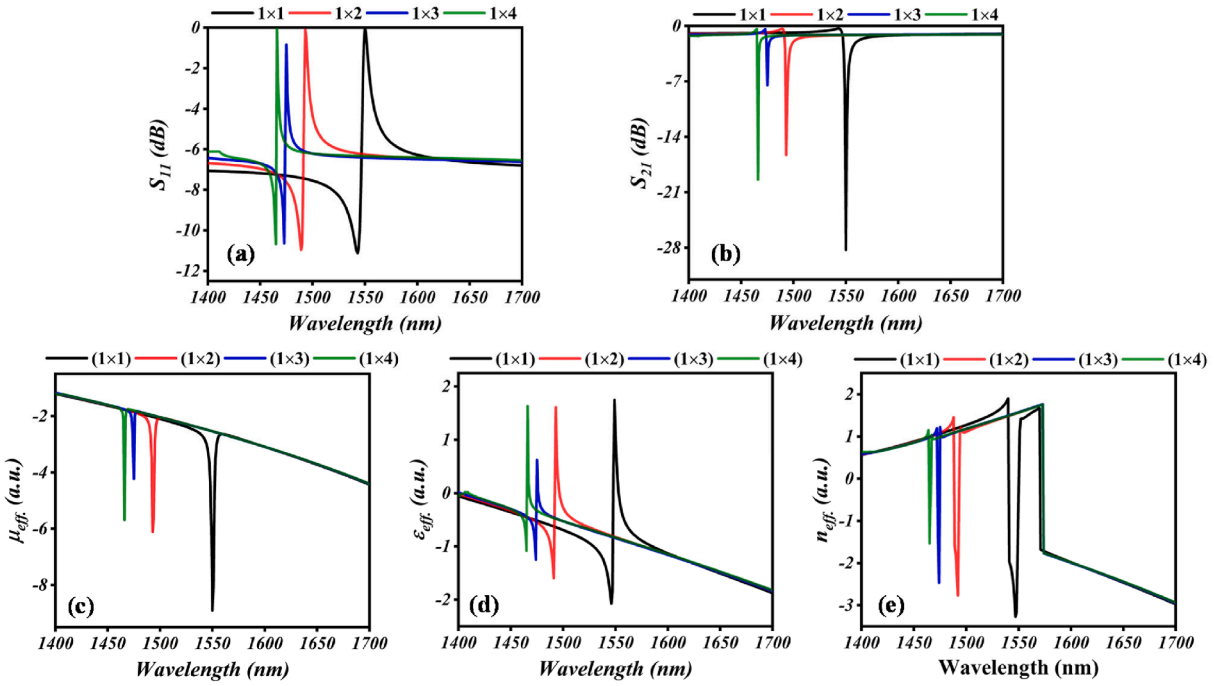

Fig. 11. Variation of (a) S_{11} (reflection coefficient), (b) S_{21} (transmission coefficient), (c) $\mu_{eff.}$ (effective permeability), (d) $\varepsilon_{eff.}$ (effective permittivity) and (e) $n_{eff.}$ (effective refractive index) with wavelength for the proposed MTM structure's (1×1), (1×2), (1×3) and (1×4) arrays.

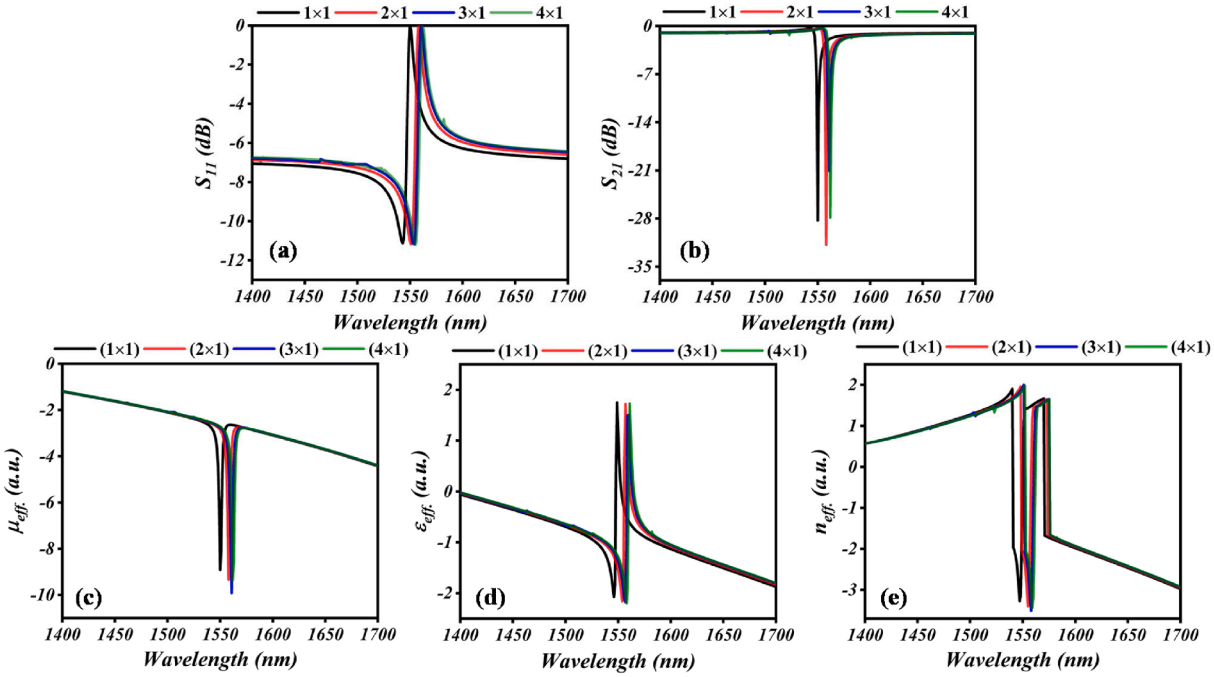

Fig. 12. Variation of (a) S_{11} (reflection coefficient), (b) S_{21} (transmission coefficient), (c) $\mu_{eff.}$ (effective permeability), (d) $\varepsilon_{eff.}$ (effective permittivity) and (e) $n_{eff.}$ (effective refractive index) with wavelength for the proposed structure's (1×1), (2×1), (3×1) and (4×1) arrays.

dotted rectangle. However, the accumulation of magnetic field distribution is maximum in the middle of the structure, of the order of 10^6 A/m, shown in Fig. 9(b).

4.4. Tunability characteristic of MTM unit cell

The arranging a number of MTM unit cells in a regular fashion is investigated to analyse the tunability of the reported MTM structure. This investigation will help in design and development of tunable MTM for different applications.

4.4.1. Design and analysis of (1×1), (1×2), (1×3), (1×4) and (2×1), (3×1), (4×1) of the unit cell structure

We have studied (1×1), (1×2), (1×3), (1×4) and (2×1), (3×1), (4×1) arrays structure of MTM unit cell shown below in Fig. 10. The physical dimension of each unit structure of every assembly has similar

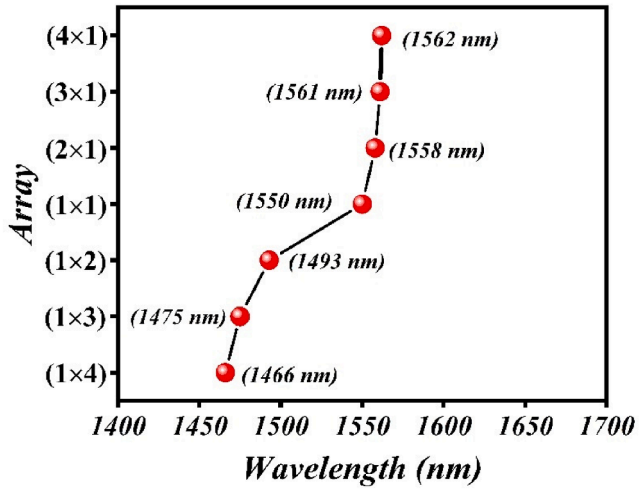

Fig. 13. Variation of resonance wavelength with different arrays of the MTM structure.

physical dimensions as shown in Table 1. The boundary conditions, wavelength range, and the direction of an incident plane wave on an MTM unit cell are used same as already mentioned above to study the influence of different array structures.

Firstly, the variation of scattering parameters, effective permeability, effective permittivity, and effective refractive index with the wavelength of an incident wave for (1×1), (1×2), (1×3) and (1×4) MTM array structures have been calculated and plotted in Fig. 11. In Fig. 11, when we form arrays of (1×1), (1×2), (1×3) and (1×4), the inductor of one unit cell is in parallel to the other. Therefore, the equivalent inductance decreases consequently resonance wavelength decreases, called blue-shift (using Eq. (1)).

Secondly, the variation of scattering parameters, effective permeability, effective permittivity, and effective refractive index with the wavelength of an incident wave for (2×1), (3×1) and (4×1) MTM array structures have also been calculated and plotted in Fig. 12.

In Fig. 12, when we form arrays of (1×1), (2×1), (3×1) and (4×1), the inductor of one unit cell is in series to the other. Therefore, the equivalent inductance increases consequently resonance wavelength increases, called red-shift (using Eq. (1)). It is also reported that when we move in the column-wise increment in the array structure, i.e., (2×1), (3×1) and (4×1) keeping the one row fixed, then the shifting in the resonance wavelength is negligible. It indicates that making the array in this form less affects the resonance wavelength. The variation of resonance wavelength with the array of the MTM unit cell is plotted and shown in Fig. 13.

It is seen from Fig. 13 that the variation of resonance wavelength in the view of the increase of column (i.e., (1×1), (1×2), (1×3) and (1×4)) is significant i.e., the resonance wavelength decreases from 1550 nm to 1466 nm however, with the row variation ((2×1), (3×1) and (4×1)) is insignificant in the form of an array of the MTM structure.

4.4.2. *Mirror image of the proposed MTM unit cell structure*

Further, we have analysed the effect on resonance wavelength by adding the mirror image of the design in the MTM unit cell, as shown in the inset of Fig. 14(a). The reflection and transmission characteristics, along with variation in electromagnetic parameters (μ_{eff}, ε_{eff}, n_{eff}) are calculated and plotted in Fig. 14.

From Fig. 14, it is observed that adding the mirror image of structure in the MTM unit cell shows the same behaviour but with a shift in resonance wavelength from 1550 nm (C-band) to 1504 nm (S-band). This way, the reported work will provide a potentially more straight forward method to tune the resonance wavelength for our desired application. Hence, this study will help in the design and development of tunable MTM.

5. Conclusion

In brief, a nearly 100 % perfect reflector tunable MTM structure is designed and analysed for optical communication with operating resonance wavelength 1550 nm. The optimization of the structure in terms of design methodology and parametric investigation on MTM unit cell, i.e., effect of different substrate materials, the effect of silica substrate thickness (t_s) and the effect of silicon resonator thickness (t_m), results in

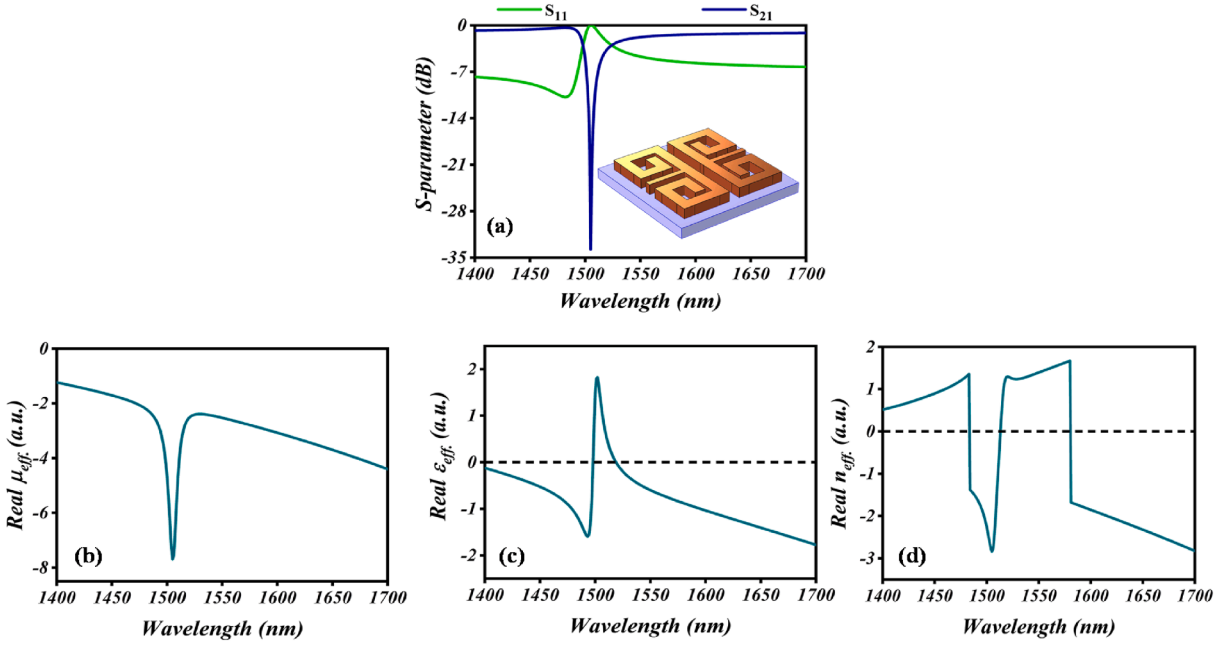

Fig. 14. Variation of (a) scattering parameter i.e., S_{11} (reflection coefficient) and S_{21} (transmission coefficient), (inset shows the designed mirror image of the metamaterial unit cell) (b) $\mu_{eff.}$ (effective permeability), (c) $\varepsilon_{eff.}$ (effective permittivity) and (d) $n_{eff.}$ (effective refractive index) of the mirror image of MTM structure with wavelength.

the $\lambda_r = 1550$ nm. The effective propagation characteristic of the proposed MTM was investigated over 1400–1700 nm wavelength range, and the effective medium parameters were obtained. Analysis of the proposed MTM exhibits an effective negative refractive index and MNG characteristics at λ_r. At resonance wavelength, the structure behaves as a perfect reflector with nearly 100 % reflectance. The normalized electric and magnetic field distribution has been plotted at the resonance wavelength. The evaluated EMR of the designed metamaterial structure is 2.23, which shows the structure's compactness. It is also evaluated that the arrays of the designed MTM structure, i.e., (1×2), (1×3), (1×4) and (2×1), (3×1), (4×1) confirm the tunability of the proposed MTM. Furthermore, the mirror image of the proposed MTM structure resonates at 1505 nm wavelength, which lies in S-band used for Passive optical network systems. The perfect reflectance and tunable performance of the reported MTM unit cell make it a suitable candidate for the devices and components operated for long-distance transmission systems.

Declaration of Competing Interest

The authors declare that they have no known competing financial interests or personal relationships that could have appeared to influence the work reported in this paper.

Data availability

Data will be made available on request.

Acknowledgments

Authors gratefully acknowledge the initiatives and support from the TIFAC-Centre of Relevance and Excellence in Fiber Optics and Optical Communication at Delhi College of Engineering, now DTU, Delhi, under the Mission REACH program of Technology Vision-2020, Government of India. One of the authors, Mr. Ankit, would like to acknowledge (i) Delhi Technological University, Delhi, for financial support in the Research Fellowship, (ii) Dr. Yogita Kalra, DTU Delhi, and (iii) Dr. Monu Nath Baitha of Yonsei University for critical and useful discussions on this research work.

References

Agarwal, P., Kishor, K., Sinha, R.K., 2022. Ultrasensitive dual-band terahertz metasurface sensor based on all InSb resonator. Opt. Commun. 522, 128667 https://doi.org/10.1016/J.OPTCOM.2022.128667.

Alizadeh, S., Zareian-Jahromi, E., Mashayekhi, V., 2022. A tunable graphene-based refractive index sensor for THz bio-sensing applications. Opt. Quantum Electron. 54, 1–13. https://doi.org/10.1007/s11082-021-03434-5.

Almutairi, A.F., Islam, M.S., Samsuzzaman, M., Islam, M.T., Misran, N., Islam, M.T., 2019. A complementary split ring resonator based metamaterial with effective medium ratio for C-band microwave applications. Results Phys. 15, 102675 https://doi.org/10.1016/j.rinp.2019.102675.

Askari, M., Zakery, A., Jahromi, A.S., 2018. A low loss semi H-shaped negative refractive index metamaterial at 4.725 THz. Photonics Nanostructures - Fundam. Appl. 30, 78–83. https://doi.org/10.1016/j.photonics.2018.03.001.

C.X. Bai, Y.J. Cheng, Y.R. Ding, J.F. Zhang, A Metamaterial-Based S/X -Band Shared-Aperture Phased-Array Antenna With Wide Beam, 68 (2020) 4283–4292.

Bellal Hossain, M.d., Rashed Iqbal Faruque, M., Alshammari, A.S., Tariqul Islam, M., 2022. Tariqul Islam, Wide bandwidth enriched symmetric hexagonal split ring resonator based triple band negative permittivity metamaterial for satellite and Wi-Fi applications. Results Phys. 37 https://doi.org/10.1016/j.rinp.2022.105511.

Chen, X., Grzegorczyk, T.M., Wu, B.I., Pacheco, J., Kong, J.A., 2004. Robust method to retrieve the constitutive effective parameters of metamaterials. Phys. Rev. E - Stat. Physics, Plasmas, Fluids, Relat. Interdiscip. Top. 70, 7. https://doi.org/10.1103/PhysRevE.70.016608.

Chen, C., Wang, Z., Zheng, Z., Liu, Y., Huang, W., Chen, L., 2020. Large-area, low-cost near-infrared meta-surface reflector based on a pixelated two-dimensional silicon disk array. Opt. Express. 28, 38355. https://doi.org/10.1364/oe.412521.

Fan, W., Zhang, S., Minhas, B., Malloy, K.J., Brueck, S.R.J., 2005. Enhanced Infrared Transmission through Subwavelength Coaxial Metallic Arrays. Phys. Rev. Lett. 94, 033902 https://doi.org/10.1103/PhysRevLett.94.033902.

Hossain, M.B., Faruque, M.R.I., Islam, S.S., Islam, M.T., 2021. Modified double dumbbell-shaped split-ring resonator-based negative permittivity metamaterial for satellite communications with high effective medium ratio. Sci. Rep. 11, 19331. https://doi.org/10.1038/s41598-021-98703-4.

Hossain, T.M., Jamlos, M.F., Jamlos, M.A., Soh, P.J., Islam, M.I., Khan, R., 2018. Modified H-shaped DNG metamaterial for multiband microwave application. Appl. Phys. A Mater. Sci. Process. 124, 1–7. https://doi.org/10.1007/s00339-018-1593-6.

Idrus, I.N., Faruque, M.R.I., Abdullah, S., Khandaker, M.U., Tamam, N., Sulieman, A., 2022. An Oval-Square Shaped Split Ring Resonator Based Left-Handed Metamaterial for Satellite Communications and Radar Applications. Micromachines. 13 (4), 578.

Islam, S.S., Faruque, M.R.I., Islam, M.T., 2014. A new double negative metamaterial for multi-band microwave applications. Appl. Phys. A. 116, 723–733. https://doi.org/10.1007/s00339-014-8549-2.

Islam, S.S., Faruque, M.R.I., Islam, M.T., 2015. A new direct retrieval method of refractive index for the metamaterial. Curr. Sci. 109, 337–342. https://doi.org/10.18520/cs/v109/i2/337-342.

Islam, M.R., Islam, M.T., Moniruzzaman, M., Samsuzzaman, M., Arshad, H., 2021. Penta band single negative meta-atom absorber designed on square enclosed star-shaped modified split ring resonator for S-, C-, X- and Ku- bands microwave applications. Sci. Rep. 11, 8784. https://doi.org/10.1038/s41598-021-87958-6.

Kishor, K., Baitha, M.N., Sinha, R.K., Lahiri, B., 2014. Tunable negative refractive index metamaterial from V-shaped SRR structure: fabrication and characterization. J. Opt. Soc. Am. B. 31, 1410. https://doi.org/10.1364/josab.31.001410.

Kishor, K., Baitha, M.N., Sinha, R.K., 2015. Design and simulation of "i" shaped split ring resonator metamaterial at optical communication window around 1.55 μm. Optik (Stuttg) 126, 4708–4711. https://doi.org/10.1016/j.ijleo.2015.08.086.

Landy, N.I., Sajuyigbe, S., Mock, J.J., Smith, D.R., Padilla, W.J., 2008. Perfect Metamaterial Absorber. Phys. Rev. Lett. 100, 207402 https://doi.org/10.1103/PhysRevLett.100.207402.

Liu, Y., Zhang, X., 2011. Metamaterials: a new frontier of science and technology. Chem. Soc. Rev. 40, 2494. https://doi.org/10.1039/c0cs00184h.

Malitson, I.H., 1965. Interspecimen Comparison of the Refractive Index of Fused Silica*,†. J. Opt. Soc. Am. 55, 1205. https://doi.org/10.1364/JOSA.55.001205.

Moitra, P., Slovick, B.A., Gang Yu, Z., Krishnamurthy, S., Valentine, J., 2014. Experimental demonstration of a broadband all-dielectric metamaterial perfect reflector. Appl. Phys. Lett. 104 (17), 171102.

Moitra, P., Slovick, B.A., Li, W., Kravchencko, I.I., Briggs, D.P., Krishnamurthy, S., Valentine, J., 2015. Large-Scale All-Dielectric Metamaterial Perfect Reflectors. ACS Photonics. 2, 692–698. https://doi.org/10.1021/acsphotonics.5b00148.

Nourbakhsh, M., Zareian-Jahromi, E., Basiri, R., Mashayekhi, V., 2020. An Ultra-Wideband Terahertz Metamaterial Absorber Utilizing Sinusoidal-Patterned Dielectric Loaded Graphene. Plasmonics. 15, 1835–1843. https://doi.org/10.1007/s11468-020-01203-w.

O'Brien, S., Pendry, J.B., 2002. Photonic band-gap effects and magnetic activity in dielectric composites. J. Phys. Condens. Matter. 14, 4035–4044. https://doi.org/10.1088/0953-8984/14/15/317.

Paul, O., Urzhumov, Y., Elsen, C., Smith, D., Rahm, M., 2012. Construction of invisibility cloaks of arbitrary shape and size using planar layers of metamaterials. J. Appl. Phys. 111 (12) https://doi.org/10.1063/1.4729012.

Rothwell, E.J., Frasch, J.L., Ellison, S.M., Chahal, P., Ouedraogo, R.O., 2016. Analysis of the Nicolson-Ross-Weir method for characterizing the electromagnetic properties of engineered materials. Prog. Electromagn. Res. 157, 31–47. https://doi.org/10.2528/PIER16071706.

Shur, M., 1990. Physics of semiconductor devices. Prentice Hall, Englewood Cliffs, NJ.

Slovick, B., Yu, Z.G., Berding, M., Krishnamurthy, S., 2013. Perfect dielectric-metamaterial reflector. Phys. Rev. B. 88, 165116 https://doi.org/10.1103/PhysRevB.88.165116.

Smith, D.R., Padilla, W.J., Vier, D.C., Nemat-Nasser, S.C., Schultz, S., 2000. Composite Medium with Simultaneously Negative Permeability and Permittivity. Phys. Rev. Lett. 84, 4184–4187. https://doi.org/10.1103/PhysRevLett.84.4184.

Smith, D.R., Pendry, J.B., Wiltshire, M.C.K., 2004. Metamaterials and Negative Refractive Index, Science (80-.) 305, 788–792. https://doi.org/10.1126/science.1096796.

Smith, D.R., Vier, D.C., Koschny, T., Soukoulis, C.M., 2005. Electromagnetic parameter retrieval from inhomogeneous metamaterials. Phys. Rev. E. 71, 036617 https://doi.org/10.1103/PhysRevE.71.036617.

Vendik, I.B., Vendik, O.G., 2013. Metamaterials and their application in microwaves: A review. Tech. Phys. 58, 1–24. https://doi.org/10.1134/S1063784213010234.

Xiao, S., Drachev, V.P., Kildishev, A.V., Ni, X., Chettiar, U.K., Yuan, H.-K., Shalaev, V.M., 2010. Loss-free and active optical negative-index metamaterials. Nature. 466, 735–738. https://doi.org/10.1038/nature09278.

Xu, W., Xie, L., Ying, Y., 2017. Mechanisms and applications of terahertz metamaterial sensing: A review. Nanoscale. 9, 13864–13878. https://doi.org/10.1039/c7nr03824k.

Zhao, Q., Zhou, J., Zhang, F., Lippens, D., 2009. Mie resonance-based dielectric metamaterials. Mater. Today. 12, 60–69. https://doi.org/10.1016/S1369-7021(09)70318-9.

Ziolkowski, R.W., Heyman, E., 2001. Wave propagation in media having negative permittivity and permeability. Phys. Rev. E - Stat. Physics, Plasmas, Fluids, Relat. Interdiscip. Top. 64, 15. https://doi.org/10.1103/PhysRevE.64.056625.

2022 International Conference on Electrical, Computer, Communications and Mechatronics Engineering (ICECCME) | 978-1-6654-7095-7/22/$31.00 ©2022 IEEE | DOI: 10.1109/ICECCME55909.2022.9988588

Design and Implementation of Different Machine Learning Algorithms for Credit Card Fraud Detection

Aditi Singh
Dept. of Information Technology
Delhi Technological University
New Delhi, India
aditi.23082000@gmail.com

Anoushka Singh
Dept. of Information Technology
Delhi Technological University
New Delhi, India
anoushkajaipur23@gmail.com

Anshul Aggarwal
Dept. of Information Technology
Delhi Technological University
New Delhi, India
aggarwalanshul01@gmail.com

Anamika Chauhan
Dept. of Information Technology
Delhi Technological University
New Delhi, India
anamika@dtu.ac.in

***Abstract*—It is essential that credit card companies are able to detect fraudulent transactions so that customers are not charged for items they did not purchase. Data can be used to solve these issues. Science and its importance, as well as machine and soft learning, could not be more critical. When someone defrauds you of your money or otherwise harms your financial well-being through deception or other illegal means, this is referred to as financial fraud. Billions of dollars worth of financial fraud is committed every year.According to the Federal Trade Commission(FTC), the number of theft reports has more than doubled in the last two years. One of the major types of financial fraud is credit card fraud. As the number of online transactions is growing, so is the number of credit card frauds. An effective solution is necessary to reduce loss due to fraudulent transactions at the initial stage. An effective way to do so would be to use machine learning algorithms to detect credit card fraud.This paper examines latest advances and application in the field of machine learning-based credit card fraud detection. In this paper four machine learning algorithms have been analyzed and compared on the basis of their accuracies. It is found out that Catboost algorithm works best to detect credit card fraud with an accuracy of 99.87 percentage. The dataset for credit card fraud detection was taken from kaggle.**

***Index Terms*—Credit card, Fraud detection, Machine Learning, Supervised Learning, Logistic Regression, Decision Tree, Random Forest, CatBoost**

I. Introduction

Fraud is defined as the unauthorized and unwanted use of a record by a person who isn't the account's owner[7]. Credit and debit card frauds are the most common types of fraud in the banking world, and the odds of credit card fraud are particularly high.The reason for this is that with credit cards, the fraudster can steal money that is not owned by the victim, i.e. the credit card's whole limit, however with debit cards[8], the fraudster can only steal money that is in the victim's bank account and nothing more. The number of credit card frauds have risen in the past few years as seen in Fig.1.

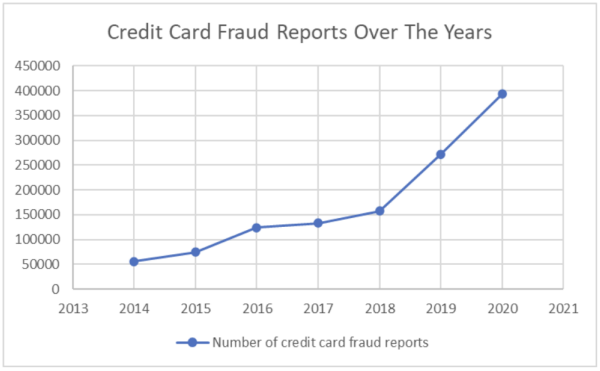

Fig. 1. Number of Credit Card Frauds vs Year

As technology has evolved and new e-service payment options, for example, e-commerce and mobile payments, have arisen, credit card transactions have grown in popularity[9]. Fraudsters are more prone to commit fraud as a result of the widespread adoption of cashless transactions[10]. Fraudsters continuously alter their tactics in order to avoid being caught. Because every bank system has certain flaws and is imperfect[11], securing a system for authentication and preventing client fraud becomes a difficult task.

These fraudulent operations can be examined and detected in order to reduce and prevent credit card theft in the future[12]. Fraud detection employing effective machine learning algorithms is the most efficient strategy to prevent these losses. In our paper, we looked at a few of these machine learning methods and compared their accuracy and

978-1-6654-7095-7/22/$31.00 ©2022

Authorized licensed use limited to: DELHI TECHNICAL UNIV. Downloaded on January 04,2023 at 09:14:29 UTC from IEEE Xplore. Restrictions apply.

TABLE I. TYPES OF CREDIT CARD FRAUD

S.No.	Type of Fraud	Description
1.	Card-not-present (CNP) fraud	Happens when the fraudster has the card details. Transactions can be made online using these details without the physical card.
2.	Counterfeit and skimming fraud	Happens when data is fraudulently obtained to create a fake credit card.
3.	Fraudulent use of a lost or stolen card	Happens on cards that get misplaced or stolen until they are canceled.
4.	Card that do not arrive fraud	Happens when the card is either seized or stolen before it is delivered in the mail or reaches you.
5.	Fake application fraud	Happens when the account is made using some other person's identity or details.

effectiveness in detecting fraud transactions.

II. Literature Review

A study was done by Lakshmi and Selvani Deepthi Kavila in 2018 [1]. For the dataset, three strategies were used, and the work was done in R. The effectiveness of the approaches was assessed for various variables based on sensitivity, specificity, accuracy and error percent. The results suggest that the Random forest outperforms logistic regression and decision tree approaches after comparing the algorithms.

Aadhya Kaul, Mihika Chahabra and others researched the CCFD model by using multiple ML and DL techniques in 2020 [2]. On the credit card dataset, they used logistic regression, Naive Bayes,support vector machines (SVM),K-nearest neighbour, decision tree, k-means,random forest classification, and keras. The techniques were evaluated based on accuracy and f1-score, demonstrating that random forest classification (RFC) outperforms all other methods used.

Another research was done by Varun Kumar K S, Vijaya Kumar V G and others in 2020 [3] by comparing machine learning techniques. They mostly use classification machine learning techniques, statistics, and calculus to predict with the help of features such as transaction timing and amount. The experiment shows that ANN has the highest accuracy than all other algorithms.

In another research work done by Sanobar Khan, Suneel Kumar and others in 2021 [4] in which they used Random Forest for classifying. They also used Local Outlier Algorithm which calculates difference of trial data with the adjacent ones. The part examined is 10 percent of the total dataset. They try to inscribe a quantity of false positives and the experiment shows that the model is accurate in detecting Credit card fraud.

Another research was done by Ibtissam Benchaji, Samira Douzi and two others in 2021 [5]. They proposed a new credit card fraud detection system based on LSTM networks and an attention mechanism, which is essentially a form of artificial recurrent neural network (RNN). It selects and extracts features based on 3 models i.e PCA, t-SNE, UMAP. The conclusion indicated that SVM, KNN do not give good precision and recall. The proposed algorithm was considered best and exhibited more promising performance.

In 2021, Kartik Madkaikar, Manthan Nagvekar, and others used preprocessing approaches and classification algorithms such as SVM, KNN, Logistic Regression, Nave Bayes, Random Forest, EBPA, and Gradient Boosting to compare accuracy [6]. Through this they showed that different algorithms give different results in different types of environments. The experiment demonstrates that the Gradient Boosting algorithm outperforms the others.

III. METHODOLOGY

This paper proposes a credit card fraud detection system that will track the user's credit card spending pattern and determine whether a transaction is fraudulent or not. Machine learning techniques are used to analyse previous historical transactions by the system. The following steps have been followed as shown in Fig.2.

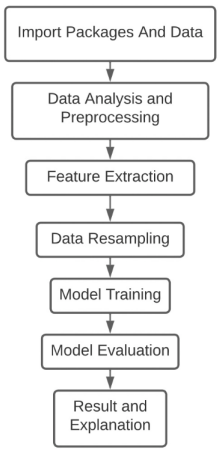

Fig. 2. Architecture Diagram

A. Data Preprocessing

Data from the real world may have noise, missing values, or be in an unsuitable format that machine learning models

Authorized licensed use limited to: DELHI TECHNICAL UNIV. Downloaded on January 04,2023 at 09:14:29 UTC from IEEE Xplore. Restrictions apply.

TABLE II. RESULT OF SOME PREVIOUS WORK

Reference	Author Name	Model Used	Accuracy (in percentage)
[1]	Sanobar khan, Sanovar, Suneel Kumar, Mr Hitesh Kumar	Random Forest	99.68
[2]	Ibtissam Benchaji, Samira Douzi, Bouabid El Ouahidi, Jaafar Jaafari	SVM Long Short Term Memory	93.49 97.48
[3]	Kartik Madkaikar, Manthan Nagvekar, Preity Parab, Riya Raikar, Supriya Patil	SVM K-Nearest Neighbor Logistic Regression Naïve Bayes Random Forest EBPA Gradient Boosting	94.7 87 90 94 94.9 93.73 95.9
[4]	Lakshmi, Selvani Deepthi Kavila	Logistic regression Decision tree Random Forest	90.0 94.3 95.5
[5]	Aadhya Kaul, Mihika Chahabra, Prachi Sachdeva, Rachna Jain, Preeti Nagrath	Logistic Regression Decision Tree Random Forest Classifier Naive Bayes (Gaussian) Naive Bayes (Bernoulli) K-Neighbors Classifier ANN DL	78.83 72.66 80.16 61.5 75.83 72.5 77.63
[6]	Varun Kumar K S, Vijaya Kumar V G, Vijay Shankar A, Pratibha K	Logistic Regression Naive Bayes Decision Tree ANN model	94.84 91.62 92.88 98.69

cannot use directly. To take care of this, we employ data preprocessing, which is a required step in cleaning data and preparing it for usage in a machine learning model. It aids in the accuracy and efficiency of the model. In our data, we took care of missing values. The categorical data variables such as transaction category and transaction day were converted into numeric values using One Hot Encoding to improve the predictions and accuracy of our machine learning models.

B. Dataset

The dataset for credit card fraud detection was taken from Kaggle.Brandon Harris' Sparkov Data Generation Tool was used to generate the transactions, which span the months of January 1st, 2019 through December 31st, 2020. The transactions were across 14 distinct purchasing categories and involved about 1000 clients and 800 vendors. Plots for our dataset are displayed in Fig.3.

C. Data Resampling

Credit Card transaction data is a very unbalanced dataset. There are only 0.5 percent fraudulent transactions in the dataset,so there are 200:1 occurrences in the majority class compared to the minority class. The presence of a highly imbalanced dataset poses a significant challenge when using Machine Learning to detect fraud. This is an issue since the machine learning models can be biased more towards majority class examples,causing some to ignore the minority class entirely. We can solve this problem using resampling. Resampling is the process of repeatedly pulling samples from training data and refitting our model on each sample to get more information about the fitted model. Before resampling, we separated our data into training and testing sets. The two main methods of resampling are-

- Undersampling : It involves picking samples from the majority class at random and removing them from the training set, until a more balanced distribution is achieved.
- Oversampling : It involves copying minority class instances at random and adding them to the training data.

D. Implementation

The code has been written in Python. 80 percent of the dataset is used in training and 20 percent of the dataset is used in testing. The most important features of the models are: amount spent, average amount spent by the user in the last 24 hours and transaction hour.

- Average amount spent by the user in the last 24 hours: The user's average spending over the past 24 hours has a big impact since consecutive high-value transactions can be fraudulent, especially if the user usually follows a low-transaction spending pattern.
- Amount Spent: The likelihood of fraud increases as transaction amounts increase. Because frauds frequently involve large sums of money.
- Transaction hour: The chances of frauds in the early morning or in the late night hours is high. Hence, the chance of transaction being predicted fraud is higher.

Authorized licensed use limited to: DELHI TECHNICAL UNIV. Downloaded on January 04,2023 at 09:14:29 UTC from IEEE Xplore. Restrictions apply.

Hence the models were built giving these features more importance while making the predictions. In this paper we have analyzed 4 different algorithms-

1) **Logistic regression**- Logistic Regression is a linear model. It's a supervised learning-based classification technique that predicts the likelihood of a target variable.The target variable has a dichotomous character, which means there are only two classes.

$$y = \frac{e^{(\beta o+\beta 1x)}}{1+e^{(\beta o+\beta 1x)}}$$

Here, y is Predicted result
βo = Bias/intercept term
$\beta 1$ = Coefficient for single input value x

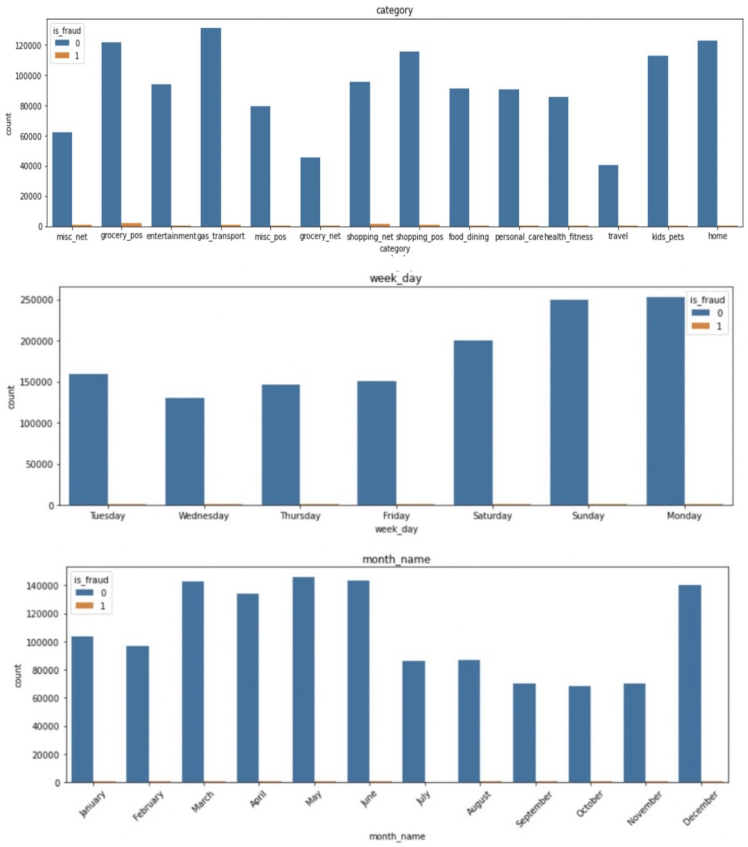

Fig. 3. Plots for Dataset

2) **Decision tree**- It is a supervised learning technique, mostly used for solving classification problems. It is a recursive algorithm. In this the data is continuously split using some parameter. The tree consists of decision nodes and leaves. The leaves signify the final outcomes, where further splitting is not possible and the nodes are where the data is split. It is used to represent decisions and decision making. The performance of this algorithm can be improved by pruning. Pruning removes the branches which use features of low importance. It prevents overfitting. To determine when to stop splitting, "Entropy" is used. It's a metric that determines how much uncertainty there is in a dataset. The aim is to decrease uncertainty.
The formula for entropy is-

$$E(s) = -p_{(+)}logp_{(+)} - p_{(-)}logp_{(-)}$$

Here, p_+ is the likelihood of positive class and p- is the likelihood of negative class. A subset of the training dataset is taken as S.
To make a decision tree, entropy is measured at each node to calculate impurity. We make it into a leaf node when the purity is 100
Although this algorithm is simple and easy to visualize, small changes in the data might cause decision trees to become unstable, resulting in an entirely different tree being created. This is termed as variance. It can be reduced using methods like bagging and boosting. We have tried to achieve this using random forest and catboost algorithms.

3) **Random forest**- Random forest algorithm is a supervised machine learning approach which is often used to solve regression and classification problems. It tackles the problem of high variance and overfitting in decision trees, which helps to improve accuracy. It basically combines the output of multiple decision trees to get to a single output. This approach generates a random collection of features, guaranteeing that decision trees have low correlation. This is in contrast to the decision tree algorithm where all possible feature splits are considered.
To select features to split further,we need to know the impurity of the split. We'll take that feature as the root node which gives the lowest impurity or in other words, has the lowest "Gini index".
Gini Index can be written as-

$$Gini\ Index = 1 - \sum_{i=1}^{n} (P_i)^2$$
$$= 1 - [(P_+)^2 + (P_-)^2]$$

P_+ is the likelihood of positive class and P- is the likelihood of negative class. Random forest tries to find the Gini Index for all possible splits and chooses the feature for the root node which gives the lowest Gini Index.

4) **Catboost**- CatBoost or Categorical Boosting is a machine learning technique for gradient boosting on decision trees. Gradient decision trees are used in this

Authorized licensed use limited to: DELHI TECHNICAL UNIV. Downloaded on January 04,2023 at 09:14:29 UTC from IEEE Xplore. Restrictions apply.

approach. A series of decision trees is built sequential while training this model. Each consecutive tree is bu with a lower loss than the prior tree as training advance Gradient boosting fits the decision trees in a sequenti manner, allowing the fitted trees to learn from tl mistakes of previous trees, reducing errors. To calcula the residuals for each data point, CatBoost trains l (number of data points) models. It simply considers pri data points when calculating, hence it takes less time predict. Another advantage is that without considerab hyper-parameter adjustment, CatBoost produces goo results. However, certain important parameters in Ca Boost can be tweaked to improve the outcome. Fig.4 a Fig.5 show the false postive rate and recall calculated f our CatBoost model.

Model characteristics-

a) Splits- MVS (Minimum Variance Sampling) is applied. This is a variation of Stochastic Gradient Boosting that uses weighted sampling. In this technique, weighted sampling takes place at the tree level rather than at the split level. Split score accuracy is maximized by sampling the observations of each boosting tree.
b) Leaf Growth- A balanced tree is grown by Catboost. In each level of such a tree, the feature-split pair that results in the least loss (as determined by a penalty function) is chosen and applied to all nodes in that level.

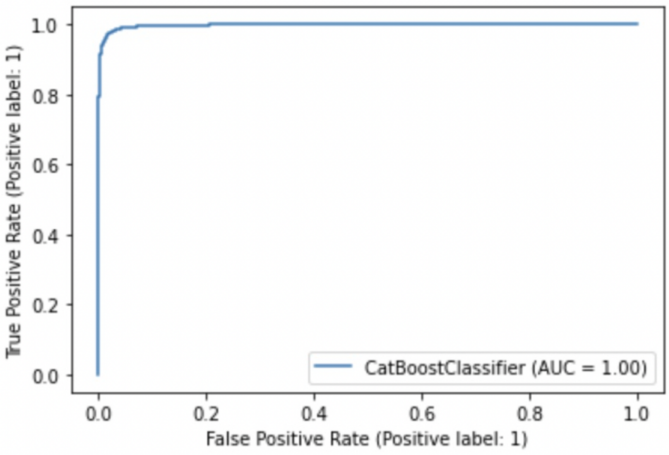

Fig. 4. False Positive rate

c) Feature importance-
   i) PredictionValuesChange- PredictionValuesChange displays how much the prediction changes on average when the feature value changes for each feature. When a change in the feature value causes a large change in the predicted value, the feature becomes more important.
   ii) LossFunctionChange- The value for each feature represents the difference between the model's loss value with and without that feature. Because retraining the model without one of the features is computationally expensive, this model is based on the original model with this feature deleted from all of the trees in the ensemble.

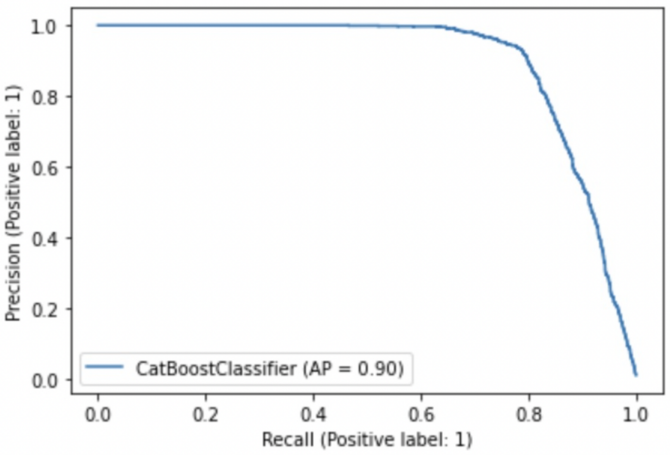

Fig. 5. Recall

IV. Model Evaluation and Result

- Accuracy-It's calculated by dividing the total correct predictions by the number of sample inputs.

$$Accuracy = \frac{(TP + TN)}{(TP + FN + FN + TN)}$$

Where,
TP= True Positive
TN= True Negative
FP= False Positive
FN= False Negative

- Confusion Matrix- It refers to a matrix that illustrates how well a classification model (or "classifier") performs on a testing dataset with known true values. Confusion matrix displayed in Fig.6.

As can be seen from Table III we have performed Four machine learning techniques for detecting fraud in credit card systems in this study. We have used 80 percent of the dataset for training and 20 percent for testing to evaluate the algorithms. We used accuracy as our evaluation criteria. We can clearly see that Catboost has the best accuracy among all the algorithms we analyzed.

V. Conclusion and Discussion

The aim of this paper was to develop a more accurate fraud detection system for credit card transactions. We looked into four distinct machine learning techniques: logistic regression, random forest,decision trees, and catboost. The algorithms were assessed using data from 80 percent of the training dataset and 20 percent of the testing data. The proposed

Authorized licensed use limited to: DELHI TECHNICAL UNIV. Downloaded on January 04,2023 at 09:14:29 UTC from IEEE Xplore. Restrictions apply.

TABLE III. RESULT COMPARISON OF DIFFERENT MODELS

	Model	Accuracy(in percentage)
Linear Model	Logistic Regression	93.70
Piecewise Linear Model	Decision Tree	99.40
Series Ensembling	Random Forest	99.60
Parallel Ensembling	Catboost	99.87

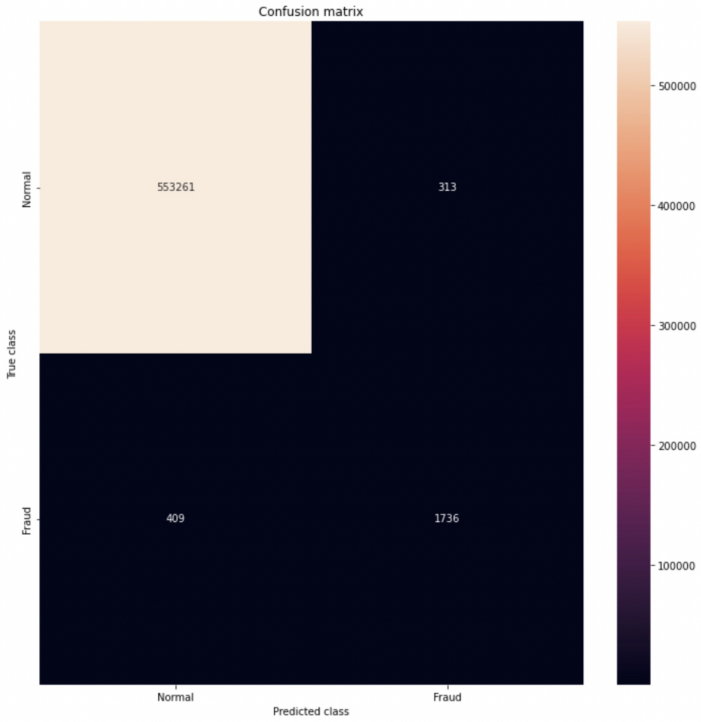

Fig. 6. Confusion Matrix of CatBoost Model

systems' performance was assessed using accuracy. The accuracy for logistic regression, Decision tree ,random forest and Catboost classifier are 93.70, 99.40, and 99.60 and 99.87 percent respectively. By comparing all the methods ,we found that Catboost has better accuracy than the other algorithms.

REFERENCES

[1] Lakshmi S. V. S. S., and S. D. Kavilla, "Machine learning for credit card fraud detection system," International Journal of Applied Engineering Research 13, no. 24, 2018, pp. 16819-16824.

[2] A. Kaul, M. Chhabra, P. Sachdeva, R. Jain, and P. Nagrath, "Credit Card Fraud Detection Using Different ML and DL Techniques," Proceedings of the International Conference on Innovative Computing & Communication (ICICC) 2021, December 2020, Available at SSRN: https://ssrn.com/abstract=3747486 or http://dx.doi.org/10.2139/ssrn.3747486

[3] V. Kumar, V. Kumar, A. Vijayshankar , P. Kumar, 2020, "Credit Card Fraud Detection using Machine Learning Algorithms," INTERNATIONAL JOURNAL OF ENGINEERING RESEARCH & TECHNOLOGY (IJERT) Volume 09, Issue 07, July 2020.

[4] S. khan, Sanovar, S. Kumar, and H. Kumar, "Credit Card Fraud Detection Using Machine Learning," International Journal of Scientific and Research Publications (IJSRP), 11(6), pp. 2250-3153, DOI: http://dx.doi.org/10.29322/IJSRP.11.06.2021.p11410

[5] I. Benchaji, S. Douzi, B. E. Ouahidi1, and J. Jaafari, "Enhanced credit card fraud detection based on attention mechanism and LSTM deep model," J Big Data 8, 151, 2021, https://doi.org/10.1186/s40537-021-00541-8

[6] K. Madkaikar, M. Nagvekar, P Parab, R Raikar, and S. Patil, "Credit Card Fraud Detection System," International Journal of Recent Technology and Engineering (IJRTE), 10, pp. 158-162, 10.35940/ijrte.B6258.0710221.

[7] Breiman, Leo, "Bagging predictors," Machine learning 24, no. 2, 1996, pp. 123-140.

[8] J. T. Wei, S. Y. Lin, and H. H. Wu, "A review of the application of RFM model," African Journal of Business Management 4, no. 19 (2010): 4199-4206, December 2010.

[9] S. Kotsiantis, D. Kanellopoulos, and P. Pintelas, "Handling imbalanced datasets: A review," GESTS international transactions on computer science and engineering 30, no. 1, 2006, pp. 25-36.

[10] C. Meng, L. Zhou, and B. Liu, " A case study in credit fraud detection with SMOTE and XGBoost," In Journal of Physics: Conference Series, vol. 1601, no. 5, p. 052016. IOP Publishing, 2020.

[11] W. Krämer, "Wojtek J. Krzanowski and David J. Hand: ROC curves for continuous data," 2011, p. 979.

[12] G. Menardi, and N. Torelli, "Training and assessing classification rules with imbalanced data," Data mining and knowledge discovery 28, no. 1, 2014, pp. 92-122.

[13] J. A. Swets, "Signal detection theory and ROC analysis in psychology and diagnostics: Collected papers," Psychology Press, 2014.

[14] A. C. Bahnsen, A. Stojanovic, D. Aouada, and B. Ottersten, "Cost sensitive credit card fraud detection using Bayes minimum risk," In 2013 12th international conference on machine learning and applications, vol. 1, pp. 333-338. IEEE, 2013.

[15] J. O. Awoyemi, A. O. Adetunmbi, and S. A. Oluwadare, "Credit card fraud detection using machine learning techniques: A comparative analysis," In 2017 international conference on computing networking and informatics (ICCNI), pp. 1-9. IEEE, 2017.

Authorized licensed use limited to: DELHI TECHNICAL UNIV. Downloaded on January 04,2023 at 09:14:29 UTC from IEEE Xplore. Restrictions apply.

Design of an Autonomous UAV for Racing Applications

Nimish Bahl
Department of Electronics and Communication Engineering
Delhi Technological University
Delhi, India
nimishbahl_2k19ec116@dtu.ac.in

Pranav Sharma
Department of Electronics and Communication Engineering
*Delhi Technological Universi*ty
Delhi, India
pranavsharma_2k19ec126@dtu.ac.in

Arshpreet Singh
Shiv Nadar School
Noida, U.P. India
arshpreetsingh2006@gmail.com

Pooja Sahu
Department of Electronics and Communication Engineering
Delhi Technological University
Delhi, India
poojasahu_2k19ec124@dtu.ac.in

Pranshu Gautam
Department of Electronics and Communication Engineering
Delhi Technological University
Delhi, India
pranshugautam_2k19ec127@dtu.ac.in

Akanksha Srivastava
Department of Electronics and Communication Engineering
Delhi Technological University
Delhi, India
akankshasrivastava30@gmail.com

2022 8th International Conference on Signal Processing and Communication (ICSC) | 978-1-6654-5430-8/22/$31.00 ©2022 IEEE | DOI: 10.1109/ICSC56524.2022.10009254

***Abstract*— A drone is an Unmanned Aerial Vehicle (UAV) that can be controlled manually by humans as well as by other algorithms not involving any human interaction. In this paper, we have described the way through which we have developed a robust and responsive racing drone alongside the simulation that includes the use of the ROS Mavlink as one of the ways to control the drone using a base station as well as path planning for autonomous flight travel. The drone will be controlled; by using a Pixhawk autopilot having a high processing capability, and easy interaction with other peripheral devices. With this, we were successfully able to design a low-weight racing drone, with each motor producing an upward thrust of 350g. Along with this, we have used a single ppm output receiver channel which reduces the number of wires and ultimately reduces the complexity of the drone, and that too at a very reasonable cost.**

Keywords—Racing Drone, Pixhawk, UAV, jMAVsim, PPM Output, Path Planning.

I. INTRODUCTION

In today's world, the concept of flying is being used in such an expansive way that from basic travel through flight airplanes we have developed unmanned aerial vehicles capable of autopilot from distant ranges. From rockets, shuttles, orbiters, satellites, and airbus to multirotor drones, fixed wings, and hybrid structures. And one similarity among all these aerial vehicles is that all of them involve the concept of thrust in various ways depending upon the positioning of the BLDC motors. As per our interest, we have built a robust and highly responsive racing drone. Through the means of this research paper, we will be presenting the research done and all that was implemented in order to develop. It would include the 4 basic rotor mechanics, the simulation done through ROS MAV link using jMAVsim as the simulator through Pixhawk packages, and thecircuitry as well as all components involved.

There are various methods to build a racing drone, several authors are there who worked on it. In [1], they built a quadcopter that is quite heavy in weight and less a flight time of 16.4 minutes. In this paper, we have designed a quadcopter that is 742 grams in weight and flight time of more than 18 minutes. In [2], the authors designed a drone using a less capable flight controller i.e., APM. We have used Pixhawk which has high processing power in comparison to APM. This feature is important for multirotor drones, after starting data logging, APM will not be able to respondquickly whereas in the case of Pixhawk we did not find any difficulty. Another downside of their model is that they have used a single PWM for every six channels of receiver signal which ultimately increases the complexity of their design. But here we have used thesingle-wire PPM output for all six signals of the receiver channel. In [3], the authors created a drone using inertial sensors, SONAR, and computer vision techniques. We have used the Mission Planner application, Qgroundcontrol, and telemetry for our drone. In the paper [4] they mainly focused on the causes of crashes during the racing competition but they did not provide any solution for it whereas in our model we have added a failsafe feature in which it auto lands the drone whenever its communication goes out of the range and the battery is low. This way the drone is more cost-efficient and compact. We are also able to trace the trajectory and path of our drone in real-time with less complexity. Figure 1 shows the drone implementation.

Figure 1: Drone Implemented

There is a need to design a drone with high efficiency, flight time, and less weight, and with this research paper, we weresuccessfully able to fabricate a drone that has a high processing capability and easy interactions with the other peripheral devices.

978-1-6654-5430-8/22/$31.00 ©2022 IEEE

Authorized licensed use limited to: DELHI TECHNICAL UNIV. Downloaded on January 17,2023 at 05:02:46 UTC from IEEE Xplore. Restrictions apply.

We also managed to triumphantly design and execute an efficient light weight racing drone where each motor is producing a thrust equal to 350 g. And finally, we were able to reduce the complexity of the drone by minimizing the number of wires used since we used a single ppm output receiver and that too at a comparatively low budget.

- The System Model used in this paper is based on the pixhawk flight controller, RC transmitter-receiver, Electronic Speed Controller, BLDC Motors, Power Distribution Board, power module, compass & GPS, IMU, and Mission Planner for calibration purposes.
- Novelty - The system model of the drone is based on a unique combination of hardware and software which through various flight tests has shown the most optimum performance as shown in the literature survey.
- Robust - This drone can effectively be used for high-speed racing applications due to the compact size of the frame, rotors, and sturdiness that it offers. There are several other aspects such as the thrust which is offered by the motors which make this drone perfect for high-speed short-distance racing applications. The 4500mah lipo battery used offers us an excellent flight time of 16.4 minutes which is very impressive for a racing drone
- Novelty - The drone which we built is quite affordable compared to the other alternatives available in the market. Our total cost came around to $220 as compared to the usual cost of making a drone which comes at around $1000 and above.
- Racing Applications - This drone can be used for security purposes and various military applications due to its small size and high speed. We have incorporated object tracking in our drone with the use of an on-system embedded camera. The use case of which can be effectively used for better surveillance and tracking
- Miscellaneous Applications - The quadcopter can also be used in the agriculture industry to spray pesticides and chemicals instantly and additionally can also be used to provide the farmers with the necessary information about the growth of the crop and the condition of the soil.
- Responsive - Our drone is highly responsive because of the fact that the operating bandwidth of our transmitter is set at 2.4 GHz which helps tremendously in establishing good communication with the drone at longer ranges over other commonly used bandwidths for quadcopter communication. The PPM enabled interaction between the RC and Pixhawk helps in simplifying the circuit.
- Novelty - The amalgamation of these makes our drone highly versatile and useful over a large range of applications

II. Flight Controller Simulation using JMAVSIM

MAV defined as the Micro Air Vehicle link is used for setting up communication with unmanned vehicles. It sets up communication from the base station to the processing unit of the rotor which can be used as an application in ROS (Robot Operating System). MAVros is an extensible node for communication for robot operating systems aka ROS for ground control or base station.

jMAVsim is a practical simulator for rotor/fixed wing operation which gives a brief about the working of the rotor along with flight modes as well as arms disarms it along with GPS check accordingly whether it is ready to fly or not. It is used for testing the rotor whether it can fly or not with the parameters we have acquitted our drone with. The flight controller used in the simulation was Pixhawk autopilot.

III. Application of QGroundControl as a Base Station and Autonomous Mission Planning

In the following simulation, the application of Qground control which is a similar software as Mission Planner is shown. The QGC is used for calibrating and programming the hardware and also for autonomous flight mission planning by mapping the coordinates or feeding the route to the GPS accordingly. We have shown the autonomous flight stack and path planning by simulating it with a jMAVsim simulator as can be seen from [5]. The path is provided through a satellite map present on the screen because of the feed from GPS.

Through simulation, a person gets the idea of what are the parameters which must be taken care of before flying the quadcopter in real life. Various arming checks are done to ensure that the vehicle is in the proper orientation, battery health is checked, IMU and compass check is done, and GPS fix is also checked whether it has got fixed with satellites or not. After checking the above parameter, the vehicle is armed i.e., it is ready to fly. From the satellite imagery shown one can directthe drone to that particular location, orbit around that location, or make that particular area a reference point for flight missions.

IV. Calibration and Coding

We have used the software known as mission planner for our calibration, it is a ground station for copters, planes, and rovers. We will be using a mission planner for copters in this case. Mission planner gives basic information like 3D fix GPS connectivity, armed-disarming of the drone, ground speed, altitude, yaw, and vertical speed, it can change the actions of different modes and do preflightchecks. Its application can be further seen in [6]. Figure 2 indicates the interface of the mission planner.

Figure 2: Interface of Mission Planner [6]

The ardupilot was used to compile the code for the drone and upload it into the Pixhawk microcontroller. There are three types of modes that we have included in our UAV They are

1. Stabilize mode: Stabilize mode is the basic functioning mode which can be considered as manual mode.
2. Loitering mode: Flying a copter in loiter mode will make it hold the position in the current state or can say maintain its location, heading and altitude and
3. Land mode: Operating the copter in land mode will make the vehicle land in whatever position it was in.

V. Design

The design of our Unmanned aerial vehicle is basically divided into four subsystems mainly- (a) Drive system, (b) Communication system, (c) Power system, (d) Embedded System which will be described briefly along with the function of the various components used in the present section. Figure 3 presents a flowchart of drone system distribution.

Authorized licensed use limited to: DELHI TECHNICAL UNIV. Downloaded on January 17,2023 at 05:02:46 UTC from IEEE Xplore. Restrictions apply.

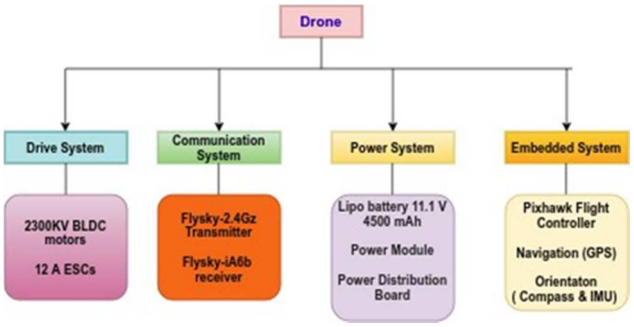

Figure 3: Drone system distribution flowchart

The frame size we used for building the 4-rotor copter is 250 mm i.e., distance between the diagonal rotors of the frame. The 250 mm sized frame provided us with a faster, more responsive, and robust mechanism for the vehicle. The frame type we used was an HX frame. It is an inclusion of both H and X-type frames as H provides us with more component carrying space and X provides high stability to the drone. The selection process of drone frame is studied from [7]. Figure 4 shows a 250 mm-sized frame.

Figure 4: 250mm Sized Frame [7]

We will now briefly describe the various components and their functions utilized in the various subsystems, respectively

A. Drive System-

The drive system of our drone includes the use of four 12 ampere Electronic Speed Controllers along with four 2300 KV BLDC motors for vertical, turning, forward, and sideways rotation of the vehicle depending upon the signal generated along with the algorithm used in accordance with the conservation of the angular momentum and Newton's third law of motion as well.

The ESCs are powered by the 11.1 V source and the signal input ofthe speed controllers is connected to the Pixhawk I/O pwm out motor ports (max up to 8) which provides pulse width modulated signal output depending upon the message from the transmitter's 6 channels. The electronic speed controllers provide a three-phase signal output to the BLDC motors involving a three-wire connection to each motor. The ESCs have an individually programmable processor which stores the throttle (Used for generating thrust), and the maximum and minimum values depending upon the calibration technique used. The ESCs can be calibrated individually or we can apply the all-in-one calibration technique as well which leads to the storage of the signal output in all the ESCs.

The 2300 KV BLDC motors provide us with the optimum thrust required for the vertical takeoff of a drone of a particular size type. Each motor generates a maximum thrust of 350g having a total upthrust of 1500 g which is ideal for a drone of the weight of 742 g.

B. Communication System-

The communication system of our drone involves the use of the Flysky-i6 transmitter operating on a bandwidth of 2.4GHz consisting of 2 joysticks that consist of 4 channel motions. We have also associated the other channels on the transmitter for switching between the various flight modes. We used the Flysky-iA6b as the receiver of our communication system and a link was set up between the transmitter and receiver by binding them. The transmitter was bound initially through the use of a cable acting as a key.

A single-wire communication connection was made between the Pixhawk and the receiver by enabling the PPM output instead of using a PWM for separate individual channels which reduced a lot of space and wired connections. The receiver was powered up by the Pixhawk and in turn, input the PPM output signal from it. The four primary controls of the transmitter for the motion of the drone are mentioned below which can be read in detail from [8]-

- Roll- used for right and left motions
- Pitch - used for forward and backward motion
- Yaw- for clockwise and counterclockwise rotation
- Throttle- For upward lifting and landing.

The rest of the 2 channels of the 6-channel receiver were utilized for switching between the flight modes which will be discussed in the upcoming sections.

C. Power System-

In the power system of our unmanned vehicle, we have used the orange 3S 11.1V 4500mAh lipo battery as the main source for powering up the vehicle. The 4500mAh battery provides the drone a flight time of more than 18 mins which is very optimal as well as the high discharge provides a high stability to our drone when in motion. The flowchart-based on power distribution is shown in Figure 5.

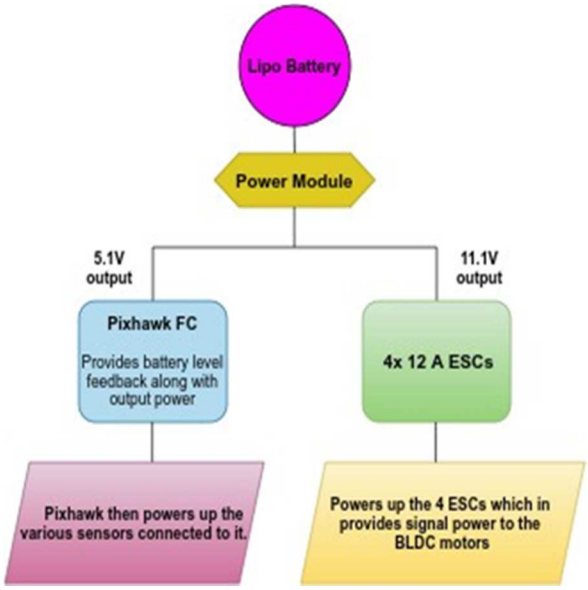

Figure 5: Power Distribution Flowchart

We have used a power module that consists of input power wires which are connected to the lipo battery and two outputs, one consisting of an output voltage of 11.1V connected to the Power Distribution board and the other output cable of voltage 5.1 V consisting of a JST connector which is routed to the Pixhawk flight controller for powering it up.

Authorized licensed use limited to: DELHI TECHNICAL UNIV. Downloaded on January 17,2023 at 05:02:46 UTC from IEEE Xplore. Restrictions apply.

The power distribution board parallelly divided the battery voltage among the four electronic speed controllers for powering them up which in turn resulted in the motor movement.

D. Embedded System-

In the embedded system, we utilized the Pixhawk controller as the main processing unit of our drone. The Pixhawk provides high processing capability when comparing it with other flight controllers along with stable connections with other devices serving different applications. It controls and monitors various actions including the Inertial measurement unit data collection, GPS coordinate mapping, PWM output as well as can be used for nav cams gimbals and for various communication protocols including PPM, S-BUS, PWM along with ports for I2C, UART, ADC, CAN. The further specs are listed in [7]. We have also programmed our controller in such a way that whenever there is a low battery and if communication range is lost then the drone would automatically land without any extra effort or a backup device. Figure 6 indicates Pixhawk flight controller.

It is a multi-functioning device controlling all the activities including- BLDC signal supply, Autonomous navigation, and Receiver communication, and includes internal IMU as well as a safety alert system through the use of a piezo buzzer. It is also embedded with analtitude barometer which helps in determining the altitude of the vehicle when in operation by providing feedback to the base station (here, the base station is the mission planner). The connection ofthe Pixhawk to GPS is described in [9].
It consists of an STM32F427 microcontroller having a clock frequency of 180Mhz along with a backup CPU consisting of an STM bluepill board.

Figure 6: Pixhawk Flight Controller [7]

(i). Navigation

For navigation, a GPS module along with a compass was used for providing the coordinates as well as direction to the drone of the particular location and also for autonomous path planning through the use of telemetry along with base station software.

(ii). Orientation and Altitude

The embedded IMU consisting of an accelerometer, gyroscope, and magnetometer provides the proper orientation of the drone when in operation along with the pre-flight check of whether the flight controller is in the proper position or not. The altitude of the drone was monitored through the use of a barometer which was already calibrated and programmed with the pressure of the various vertical points according to the earth's atmosphere. Figure 7 indicates the integration of various components with Pixhawk.

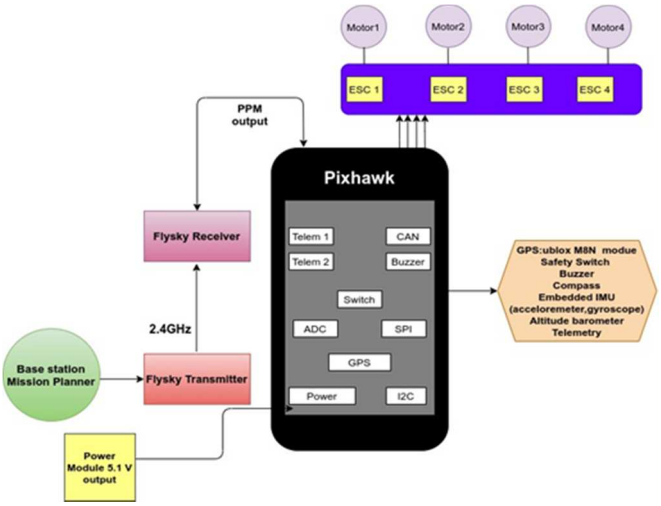

Figure 7: Circuitry of various components integrated with Pixhawk [7]

VI. IMPLEMENTATION

Above, in the simulation part using jMAVsimulator through PX4 packages along with Qgroundcontrol as the base station we showed the pre-flight checks and various parameters which are required in order for arming a drone and flight to take place. The autonomous flight traversal was also shown where the path planning could be done through the use of a base station. The implementation begins with the installation of mission planner software and the construction of various parts that were used in building the drone. The components used in the construction of this 250 mm-sized UAV had been designed to maximize efficiency while keeping the power consumption as low as possible and not compromising the capabilities of the system. These components provide a robust and fast responsive mechanism to the aerial vehicle. The ardupilot was used to compile the code (firmware) for the drone and upload it into the Pixhawk microcontroller. The microcontroller is then programmed and calibrated according to the requirements of the system and the hardware is carefully assembled to make the drone as compact as possible. The IMU direction mapping along with ESC signal calibration is done. The radio communication link is verified. The power distribution board is drilled onto the frame after frame building using glass fiber. Figure 8 indicates the integration of the power distribution board.

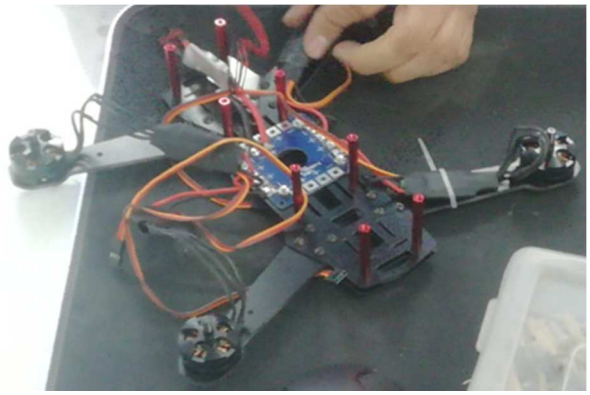

Figure 8: Power Distribution Board mounted

Authorized licensed use limited to: DELHI TECHNICAL UNIV. Downloaded on January 17,2023 at 05:02:46 UTC from IEEE Xplore. Restrictions apply.

After the proper assembly and programming, the drone is taken out for flight testing where we fly it and collect the data obtained. The data is then analyzed to check the safety aspects of the drone and whether there are any faults or errors with the algorithms and calibration of the drone. The drone proved to be highly efficient.

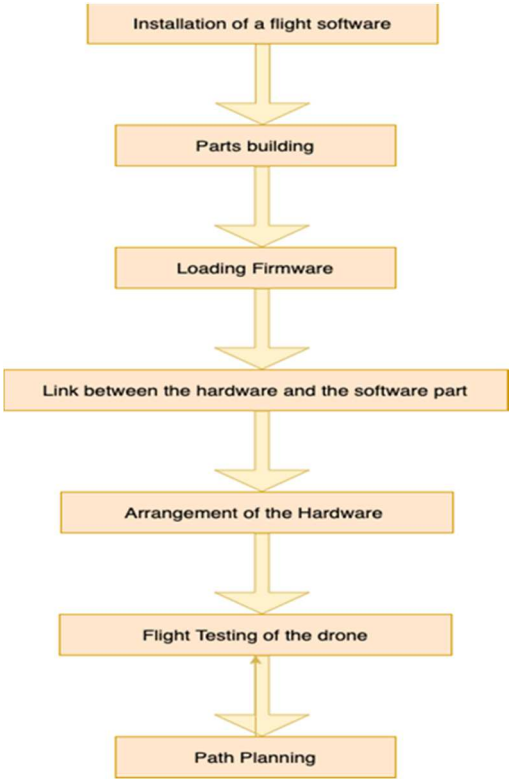

Figure 9: Flowchart of the implemented steps

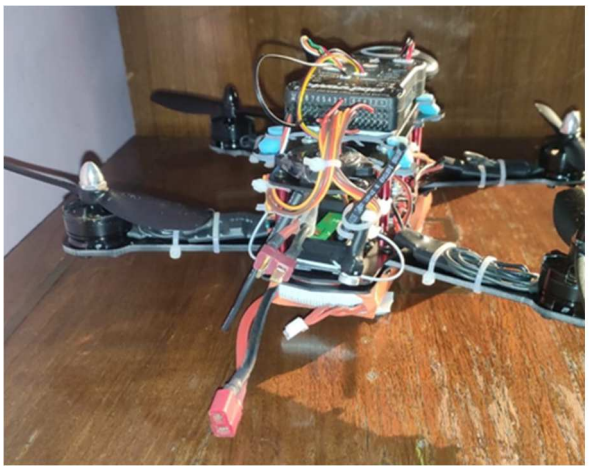

Figure 10: Assembled Drone

Path planning is done at this stage to provide a specific trajectory and path to the drone. The path of the drone consists of source coordinates and the coordinates of the destination along with the altitude. This helps in the autonomous movement of the vehicle without any manual control through the use of a global positioning system. The drone can be provided with multiple commands through telemetry and the real-time feed would be obtained at our base station. Figures 9 and 10 show flowcharts of the implemented steps and assembled drone respectively.

Figure 11: Drone Flight

The Pixhawk was programmed with flight modes depending upon the flight conditions. Stabilize, loiter and land were the three flight modes chosen as described in the previous sections for a smooth flight. Figure 11 indicates drone flight.

Figure 12: AutoLand Flight Mode

The above implementation of the racing UAV has a lot of scope in the times ahead. With the development in technology, the following drone could be utilized in various fields including agriculture, soil topology determination, smart security monitoring system, and also in the health care system supplying medical aid at the time of need as the researchers have mentioned in [10], [11]. The autonomous and robust mechanism of the drone makes it capable of efficient flight without any human intervention which is an attractive application in the upcoming times. Figure 12 shows AutoLand flight mode.

VII. Conclusion

In the following paper, we have described the hardware implementation of a 250 mm-sized racing drone that has speed, agility, and durability. The approach we have used to build the quadcopter is using a Pixhawk flight controller. We have shown the Mavlink simulation of the communication of the flight controller stack using jmav simulator. The path planning of the drone through the use of GPS was also simulated using QGC as the base station and jmav simulator as the virtual world drone simulator. The calibration process is done using the software Mission Planner. The drone system is described in the paper and we have successfully built a racing drone with lightweight. And with the help of some futuristic additions, we can also use this racing UAV for various other purposes like security monitoring, helping farmers improve the use of their inputs, and dropping crucial medical supplies.

References

[1] E. T. Efaz, M. M. Mowlee, J. Jabin, I. Khan, and M. R. Islam, "Modeling of a high-speed and cost-effective FPV quadcopter for surveillance," 2020 23rd International Conference on Computer and Information Technology (ICCIT), pp. 1-6, 2020.

[2] M.F.A. Rahman, A.I.C. Ani, S.Z. Yahaya, Z. Hussain, R. Boudville, A. Ahmad. "Implementation of quadcopter as a teaching tool to enhance engineering courses.", IEEE 8th International Conference on engineering education (ICEED), pp-32-37, 2016.

Authorized licensed use limited to: DELHI TECHNICAL UNIV. Downloaded on January 17,2023 at 05:02:46 UTC from IEEE Xplore. Restrictions apply.

[3] A. Srivastava, M. S. Gupta, G. Kaur, “Impact of Artificial Intelligence on Future Green Communication”, Artificial Intelligence to Solve Pervasive Internet of Things Issues, Elsevier, 2021.

[4] S. Swarnkar, H. Parwana, M. Kothar, and A. Abhishek, “Development of flight dynamics model and control of biplane-quadrotor UAV, 2018.

[5] A. Srivastava, M. S. Gupta, G. Kaur, “Energy efficient transmission trends towards future green cognitive radio networks (5G): Progress, taxonomy and open challenges”, Journal of Network and Computer Applications, Elsevier, vol. 168, pp. 102760, 2020.

[6] R. Luppicini and A. So, “A technological review of commercial drone use in the context of governance, ethics, and privacy,” 2016.

[7] Y. Bazi and F. Melgani, "Convolutional SVM Networks for Object Detection in UAV Imagery," IEEE Transactions on Geoscience and Remote Sensing, vol. 56, no. 6, pp. 3107-3118, 2018.

[8] W. Khawaja, I. Guvenc, D. Matolak, U.-C. Fiebig, and N. Schneckenberger, "A survey of air-to-ground propagation channel modeling for unmanned aerial vehicles," 2018.

[9] Y. Parasher, P. Singh, G. Kaur, “Green Smart Security System”, Green and Smart Technologies for Smart Cities. CRC Press, pp. 165-184, 2019.

[10] A. Srivastava, M. S. Gupta, G. Kaur, “A Game Theory Based Approach for Opportunistic Channel Access in Green Cognitive Radio Networks”, IEEE International Conference on Advanced Networks and Telecommunications Systems (ANTS), IEEE, pp. 1--6, 2019.

[11] M. S. Gupta, K. Kumar, “AFSOS: An auction framework and Stackelberg game oriented optimal network’s resource selection technique in cognitive radio networks,” IEEE Transactions on Network and Service Management, 2021.

Authorized licensed use limited to: DELHI TECHNICAL UNIV. Downloaded on January 17,2023 at 05:02:46 UTC from IEEE Xplore. Restrictions apply.

Proc. of the International Conference on Electrical, Computer, Communications and Mechatronics Engineering (ICECCME)
16-18 November 2022, Maldives

2022 International Conference on Electrical, Computer, Communications and Mechatronics Engineering (ICECCME) | 978-1-6654-7095-7/22/$31.00 ©2022 IEEE | DOI: 10.1109/ICECCME55909.2022.9988585

Development and deployment of a Hybrid Controller for a Dual-Axis Solar Tracker System

Yatharth Ahuja
Dept. of Electrical Engineering
Delhi Technological University
Delhi, India
yatharth.rd@gmail.com

Ghanvir Singh
Dept. of Mechanical Engineering
Delhi Technological University
Delhi, India
sghanvir@gmail.com

Sushrut M. Singh
Dept. of Electrical Engineering
Delhi Technological University
Delhi, India
sushrutsingh1707@gmail.com

Suraj Bhat
Dept. of Mechanical Engineering Indian
Institute of Technology Delhi
Delhi, India
suraj576@gmail.com

Subir Kumar Saha
Dept. of Mechanical Engineering Indian
Institute of Technology Delhi
Delhi, India
saha@mech.iitd.ac.in

***Abstract*—This paper presents the development and control of a photovoltaic Dual-Axis Solar Tracker system. The system constructed in this study caters to the application of renewable energy harvesting techniques to a mobile street vending cart solution. The strategy of control deployed is that of a Hybrid Controller, which is a novel combination of Astronomical equations based on open-loop control and Differential Flatness based control over the tracking movement of the photovoltaic panel used. The development takes into account the with mechanical and embedded designs with focus on manufacturing aspects. Finalised prototype was tested in overcast and sunny conditions to evaluate performance against a static solar energy photovoltaic harvesting system. The developed tracker photovoltaic increased the energy acquisition by more than 25%.**

***Index Terms*—Hybrid Controller, Flat Controller, Solar Tracker, Astronomical Equations, Renewable Energy**

I. Introduction

The problem of energy harvesting has profound applications and the Dual-Axis Tracker is a well established method of Solar Energy Acquisition with proven contribution and improvements over traditional methods. However, with the advent of mobile technology and electronics deployment, a versatile version with robust control strategy is a desirable version of the famous technology. Dual Axis trackers work by following the Sun's trajectory to achieve optimal orientation for best possible energy acquisition at any given instant.

A solar photovoltaic (PV) module is a type of solar energy harvester that collects and converts solar energy radiation into electrical energy [1]. Solar photovoltaic system are classified into two categories depending on their capacity to move: stationary and tracker modules [2]. Solar tracking systems are systems that can trace the sun's passage across the sky and maintain the solar photovoltaics at optimal angles to generate greater power output, therefore increasing the quantity of energy gathered [3]. When compared to fixed solar photovoltaics, solar trackers can enhance direct exposure to sunshine. Solar tracking systems are classified into two categories based on the number of axes used to follow the sun: single-axis solar trackers and dual-axis solar trackers. A single-axis solar tracker is a one-way device that may move horizontally or vertically at any moment [4], while dual axis solar trackers are those trackers which can track the sun by moving about two axis, i.e, transverse axis and longitudinal axis. Improving the performance of solar tracking devices is a prominent research topic right now [5]. There have been numerous studies [6] [7] [8] and experimentation in the field of Solar Tracker systems, mainly focused towards improving the tracking accuracy so as to render the process feasible and relevant. Tracking strategies can be classified into two types on the basis of degrees of freedom controlled: Single-Axis and Dual-Axis trackers.

Further classification of existing Dual-Axis trackers can be done on the basis of the control loop they deploy: Open-Loop(i.e, no sensory feedback), Closed-Loop(i.e, with sensory feedback), and Hybrid-Loop(i,e comprising both coarse open-loop and finer adjustments from closed loop) [9]. Deployment of feedback loops is of interest as it enhances the control quality and in turn offers an effective way to enhance the performance of Autonomous Solar Tracking Systems [1]. In the study [3], closed loop operation of dual-axis trackers were explored with PID and Fuzzy Logic controllers. PV sensors were deployed and experimentation results depicted slower response of PID with respect to Fuzzy Logic. This can be attributed to rather imprecision and variances in the systems model.

First stage of the solar tracker development comprises search mode deploying predefined motion to search for a

978-1-6654-7095-7/22/$31.00 ©2022 IEEE

Authorized licensed use limited to: DELHI TECHNICAL UNIV. Downloaded on January 04,2023 at 09:25:58 UTC from IEEE Xplore. Restrictions apply.

general direction based on irradiation intensity threshold. Then the control is transferred to a PI controller for finer adjustments. This ensures efficient power acquisition, as shown in [4], providing consistent radiation capture. Considering the factors such as weather, wind, solar axes, radiation in different seasons, the tracker model can be considered as a nonlinear system. Since neural networks consisting of perceptrons in multilayered structure are able to depict non-linearities very well [5], they can be used very efficiently to model tracker systems as done in [6]. Another study in [7] depicts Adaptive Neuro-Fuzzy Inference System (ANFIS) in a hybrid loop with astronomical equations for coarse adjustments. Similar hybrid strategy with a sensor and astronomical equations based controller has been deployed in [8]. In the study [10], a hybrid loop model was designed with the initial adjustments based on LDR (Light Dependent Resistor) operation. The panel is aligned with respect to the coarse errors provided by LDR sensors and finer adjustments in the range of 0.15° were achieved by similar geometrical alignment by camera input. An interesting use of polynomial regression was done in [11] to predict the expected signal values from LDR sensors in the tracking system.

The developed system reported in this paper works on the principle of Hybrid control by combining strengths of the astronomical tracking method and robustness of flatness based controllers. These controllers are chosen due to their lack of exploration in the concerned application as well as their robust performance [12]. Such a combination of astronomical and differential flatness based control has not been explored and developed before with respect to renewable energy application, as per the best of our knowledge.

II. Experimental Setup

In the proposed system, LDR sensors convert the light intensity into the equivalent resistance. This output is supplied to the microcontroller, which identifies the highest intensity light direction based on the programme fed to it. The microcontroller will then use the customised algorithm to manage the system of variable stroke length linear actuators to spin the 125W solar panel around two mutually perpendicular axes in order to maximise solar energy production.

A. Mechanical Setup

A robust frame design is required to execute actuation commands and support the panels in their motion. As we are aiming for the 9am-3pm time period during which we usually achieve maximum amount of sun intensity, maximum and minimum angles needed are 65°to 112°about the transverse axis of the solar panel, and 75°to 115°about longitudinal axis of the solar panel. This linear actuator positioning iteration was assumed to have the bottom pivot passing through the center line of the pin between the panel and the frame support at point *B* and at point *O* (Fig. 1). The horizontal and vertical dimensions to position the linear actuator are defined as *x* and *y* respectively.

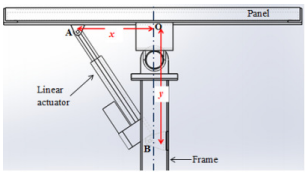

Fig. 1. Geometric characteristics of the actuator setup. Linear actuators attached along the lines *AB* and *OB* control rotation of the panel in the longitudinal and transverse direction respectively. Thus, their notation.

$$xy = \frac{L_1^2 - L_2^2}{2cos\theta} \tag{1}$$

Where, L_1, L_2 : Length of actuators along longitudinal and transverse axes of panel, respectively.
Θ : Angle between panel and base pole during operation
After analysing the equation for different values of *x* and *y* we came to a conclusion that we need 203.2 mm, along the longitudinal axis, and 152.4 mm stroke length, along the transverse axis, for our actuators as per our tracking requirements. The solar tracker was fabricated using aluminium and the total weight of setup was around 16 kg.

B. System Modelling

The Embedded Design of the tracker system deals with the implementation and perception support for the control algorithm as well as driving the external load as per application. To devise proper control strategies, the system was modelled in complex and time domain. Referring to Figs.2 and 3:

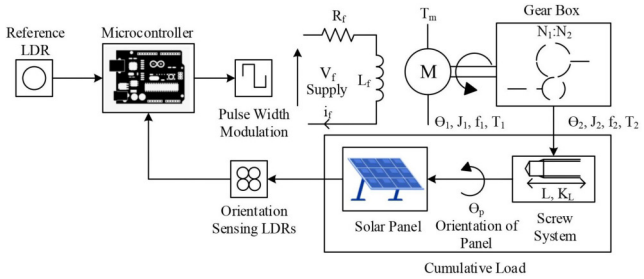

Fig. 2. Schematic diagram

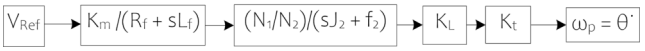

Fig. 3. Open Loop Block diagram

Where, $E_f = V_i$: Field Voltage or Input Voltage; R_f : Field Resistance; L_f : Field Inductance; T_m: Torque generated by the motor of electromagnetic actuator; ϑ_1 J_1, f_1 : Respective parameters of Rotation; theta, Load Moment of Inertia, Viscous Friction; p : Rotation experienced by the panel respective to an actuator; N_1, N_2 : Gear ratios; l : Length moved by the actuator; K_m : Motor torque constant; K_l : Actuator 2 to l

Authorized licensed use limited to: DELHI TECHNICAL UNIV. Downloaded on January 04,2023 at 09:25:58 UTC from IEEE Xplore. Restrictions apply.

constant
Now, considering the dynamics of the system, we know:

$$E_f = V_i = i_f \times R_f + L_f \times \frac{di_f}{dt} \quad (2)$$

$$T_m = J_1 \frac{d^2\theta_1}{dt^2} + \frac{f_1 d\theta_1}{dt} = \frac{N_1}{N_2}\left(\frac{J_2 d^2\theta_2}{dt^2} + \frac{f_2 d\theta_2}{dt}\right) \quad (3)$$

$$T_m = K_m \times i_f \quad (4)$$

Using Laplace Transform, one gets an equivalent set of equations for Eq. 2 and 4 as:

$$E_f(s) = V_i(s) = I_f(s)[R_f + sLf] \quad (5)$$

$$T_m(s) = K_m I_f(s) = \frac{N_1}{N_2}\frac{s^2 J_2 \theta_2(s)}{s f_2 \theta_2(s)} \quad (6)$$

From Eq. 5 and 6, one obtains the following:

$$\frac{s\theta_2(s)}{V_i(s)} = \frac{\omega_2(s)}{V_i(s)}\frac{K_m}{[R_s + sL_f][sJ_2 + f_2]} \quad (7)$$

Eq. 7 provides us a transfer function related to the angular velocity provided by the gear box inside electro-mechanical actuator (EMA) and voltage input to the EMA. However, we are interested in linear velocity provided by the EMA. Hence, as known for an EMA, length moved by the actuator is directly proportional to the angle moved by gear box shaft attached to screw i,e $\ell = K_l\vartheta_2$. Therefore, 7 is modified as Eq. 8.

$$\frac{s_l(s)}{V_i(s)} = \frac{V(s)}{V_i(s)} = \frac{N_1}{N_2}\frac{K_m K_l}{[R_f + sL_f][sJ_2 + f_2]} \quad (8)$$

Eq. 8 is the open-loop transfer function of the system at hand. Further, we intend to determine the tilt achieved by the panel with respect to the voltage input. This has been achieved by running linear regression on the experimental data obtained between length of the actuator achieved and corresponding tilt in the panel(p). Following graphs in Fig. 4 depict the relation in experimental data recorded for both actuators:

For longitudinal actuator: ϑ_p = 0.2021ℓ +66.903 and ω_p = 0.2021 v
For transverse actuator: ϑ_p = 0.2971 ℓ +74.173 and ω_p = 0.2971 v

Hence, it can be generalised that for actuators under consideration, $p = K_t\ v$, where K_t represents a constant for tilt relation. To develop a transfer function between voltage input and panel tilt angular velocity, the Eq. 8 can be modified by incorporating the feedback effect of LDR error input as:

$$\frac{\omega_p(s)}{V_i(s)} = \frac{\frac{N_1}{N_2}K_m K_l K_t}{\frac{N_1}{N_2}K_m K_l K_t + [R_f + sL_f][sJ_2 + f_2]} \quad (9)$$

Upon testing the system for input voltage and corresponding tilt angular velocity for the actuators, plots shown in Fig. 5 were obtained.

The resultant transfer functions using parameter values obtained either factually or experimentally for each actuator

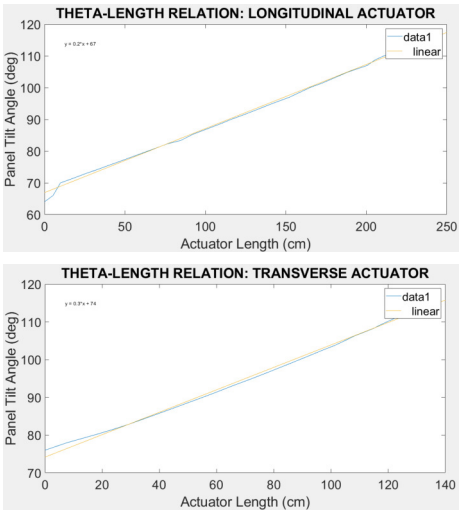

Fig. 4. Panel tilt v/s Actuator length: (a) longitudinal and (b) transverse actuators

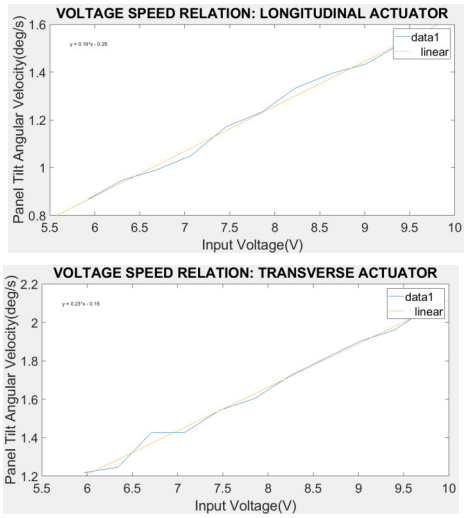

Fig. 5. Angular velocity v/s Input voltage plot for tilt: (a) longitudinal and (b) transverse actuators

are:
For longitudinal actuator:

$$\frac{\omega_p(s)}{V_i(s)} = \frac{1}{[2.91 \times 10^{-5}s^2 + 6.18s + 1]} \quad (10)$$

For transverse actuator:

$$\frac{\omega_p(s)}{V_i(s)} = \frac{1}{[3.24 \times 10^{-5}s^2 + 22.59s + 1]} \quad (11)$$

III. Tracking System

Optimisation requirements for the speed and accuracy of tracker orientation with respect to solar axes demands for a precise control methodology. This problem of precise tracking has been approached with a hybrid model of controller i.e., Astronomical Method and Sensor based feedback method.

Authorized licensed use limited to: DELHI TECHNICAL UNIV. Downloaded on January 04,2023 at 09:25:58 UTC from IEEE Xplore. Restrictions apply.

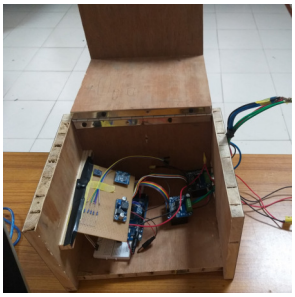

Fig. 6. The developed solar tracker prototype (a) Embedded box (microcontroller and sensors), (b) Tracker system mounted on a vending cart for testing

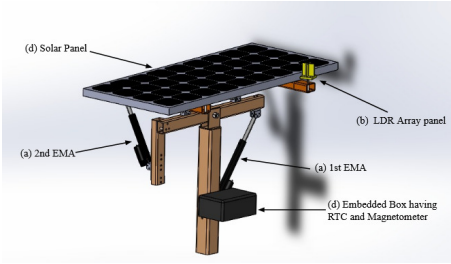

Fig. 7. System showing (a) EMA placement, (b) LDR Array, (c) RTC and Magnetometer and (d) Solar Panels

The system, as shown in Fig. 7, operates using two Electromagnetic Actuators (EMA) fixed in complementary fashion offering 2 degrees of freedom. The input data is from: i) Magnetometer and RTC for approximate astronomical alignment; and ii) LDR sensor array for real-time finer adjustment of the solar panel. The overall data sensing and algorithms deployed for the tracker can be represented in Fig. 8.

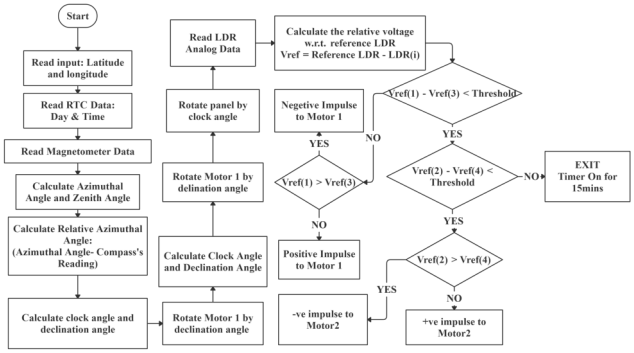

Fig. 8. Flowchart for the Dual-Axis solar Tracker

For experimentation, these data streams were combined to find out an astronomical positioning of the Sun. LDR Panel adjustment methods are allotted a total duration of 3 minutes followed by a 12 minute duration of rest. This helps in maintaining balance of energy consumption and acquisition thus contributing to sustainability of the system.

A. Astronomical Method of Tracker Alignment

Achieving coarse panel orientation of the solar panel with respect to solar axes is done using the method of declination-clock manipulation [8], which is based on the principle of pseudo-azimuthal system [13]. The two angles obtained from this procedure, declination and clock angles, are executed on longitudinal and transverse actuators. They are shown in Fig. 9.

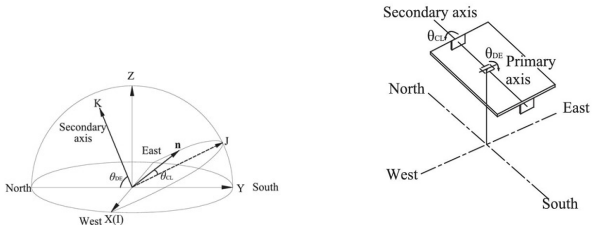

Fig. 9. Solar angle representations (a) Schematics of the solar orientation vector, n, in declination-clock mounting system [8], (b) Tracking schematics of declination-clock mounting [8]

B. Flat controller design

A differential flat system is the one in which an output, flat output h, can be devised as a function of the system's state X, and input's u's, and their derivatives [14]. A flatness based generalisation of any system is established by exploiting the equivalence of initial and (fictitious) final systems [15]. This results in characterisation of the system in terms of flat outputs as non-deferentially algebraic over the flat output's differential field [16]:

$$y = f(X, u', u'', ..., u_r) \tag{12}$$

where, y is the flat output; X is the system state vector; u is the input vector; r $\in$ Z such that $0 \leq r \leq \infty$,

For a linear systems, such as the one under consideration, they can be considered as a flat system only when they are controllable [15]. Considering the linear system as:

$$x' = Ax + Bu \tag{13}$$

The flatness based approach enables us to devise the state, x, and inputs, u, of the system in terms of flat output and its derivatives.

1) Flat Output: A linear systems input and state variables can further be expressed as [17]:

$$X = P(S)y(s), U = Q(s)y(s) \tag{14}$$

Where *P(s)* and *Q(s)* are polynomials which follow the matrix output characterisation treatment [17] and help in expressing the system variables in terms of the flat output. Following the treatment further we arrive at the Eq. 15-18.

$$C_t \times B = 0 \tag{15}$$

$$C_t \times A_1 P = 0 \tag{16}$$

$$\text{As for some } A_1\text{: } A_1 x = Bu \geq A_1 = sI - A \tag{17}$$

$$Q = (B^T B)^{-1} B^T A_1(s) P(s) \tag{18}$$

Authorized licensed use limited to: DELHI TECHNICAL UNIV. Downloaded on January 04,2023 at 09:25:58 UTC from IEEE Xplore. Restrictions apply.

where matrix C is of rank n-m and is orthogonal to B. Once A_1 and B are known, evaluating C, P, Q can be done using the Eqns. 15-18. This enables further proceeding in flatness based controller design. For the dual axis solar tracker system in this study, we have the flat output based system model for the transverse and longitudinal actuator subsystems as depicted in the Eqn. 19-22.

$$X_{longitudinal} = [(1 + s3..09 \times 10^{-5})(1.43 \times 10^{-6} + s^2(4.42 \times 10^{-11}))]y \quad (19)$$

$$U_{longitudinal} = (0.84 + 0.72 \times 10^{10}s - 4.46s^2)y \quad (20)$$

$$X_{transverse} = [(1 + s2.47 \times 10^{-5}), (4.8 \times 10^{-6} + s^2(1.6210^{-11}))]y \quad (21)$$

$$U_{transverse} = (0.96 + 2.16 \times 10^{10}s - 12.7s^2)y \quad (22)$$

Where $X = [\ w, w'\ ]$ is the state variable vector and U is the input variable to the system. Where w represents panels angular speed about the axis controlled by the respective actuator.

2) Trajectory Determination and Execution: Trajectory based motion control has its advantages in better motion tracking and lesser power demand [14]. For the transverse system, obtained flatness output based system can be expressed as:

$$\begin{aligned} y_1 &= y_2 y_2' \\ &= (U_{transverse}/0.96) - (2.16 \times 10^{10}s - 12.7s^2)y \end{aligned} \quad (23)$$

For longitudinal system,

$$y_1 = (U_{longitudinal}/0.84) - (0.72 \times 10^{10}s - 4.46s^2)y \quad (24)$$

As per the trajectory derivation procedure [16], the trajectory associated to a second order system is provided as:

$$y_1 \times (\tau) = y_{10} + \tau_2(a_2 + \tau a_3)\Delta y_{01} \quad (25)$$

Where,

$$\Delta y_{10} = y_{1\infty} - y_{10} \quad (26)$$

$$y_1 \times (\tau) = y_{10} + \tau(2a_2 + 3\tau a_3)\Delta y_{01} \quad (27)$$

Also,

$$\begin{bmatrix} a_0 & a_1 \end{bmatrix} = \begin{bmatrix} 1 & 1 \\ 2 & 3 \\ 1 \times 2 & 2 \times 3 \end{bmatrix}^{-1} \begin{bmatrix} 1 & 0 \end{bmatrix} \quad (28)$$

and similarly for y_2. This particular derivation follows from Newton's Interpolation applied to the system's outputs at initial time and final time, providing a robust trajectory reference over the period of operation. Taking the y_1, y_2 as reference trajectories/outputs, a the system's control can be thus implemented using the following equations [18], where the gains are calculated using the dominant pole method to form closed-loop pole dynamics [19]:

$$U_{longitudinal}* = (0.84(y - y*) + 0.72 \times 10^{10}(y' - y'*) - 4.46(y'' - y''*)) \quad (29)$$

$$U_{transverse} = U_{transverse}* + (0.55(y - y*) + 0.54 \times 10^{10}(y' - y'*) - 8.14(y'' - y''*)) \quad (30)$$

Which yields the implementable reference input equations.

IV. Experimental Results

To evaluate the performance of the Dual Axis Solar Tracking system shown in Fig. 6 we have compared the power generated by the solar panel when attached to the tracking system with a static solar panel. The power was measured by observing the open circuit voltage and short circuit current of the panel during a certain time interval. The measurements are done with the help of a multi-meter.

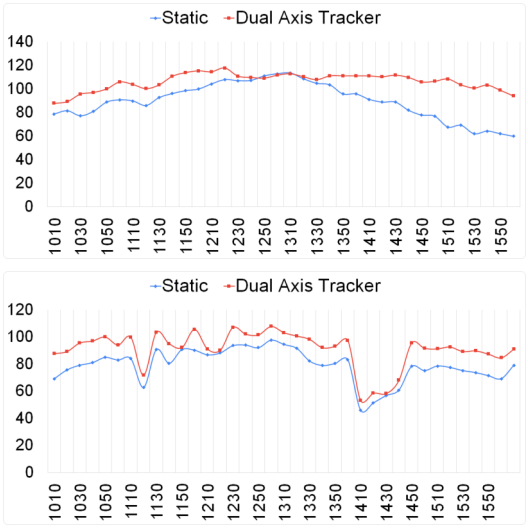

Fig. 10. Performance of the tracker with Flat controller in (a) Sunny, (b) Overcast conditions

The results of the experimentation are shown below in Figs. IV-IV. Fig. IV shows the performance of the system when a PID controller is used to process the error generated from the data received from the LDRs and Magnetometer. Fig. IV shows the performance of a flat controller based algorithm. The performance of the system is also tracked in overcast conditions. The tracker system is able to increase the power generated by a factor of around 20%. We have compared the results for multiple weather conditions as seen in Fig. 10. The proposed tracker system works well for both sunny and overcast conditions. The average increase in performance is shown in table I.

TABLE I.
Energy Output Increase

Controller	Increase in Power Generated
Flat (Overcast)	21.57%
Flat (Sunny)	25.09%

Authorized licensed use limited to: DELHI TECHNICAL UNIV. Downloaded on January 04,2023 at 09:25:58 UTC from IEEE Xplore. Restrictions apply.

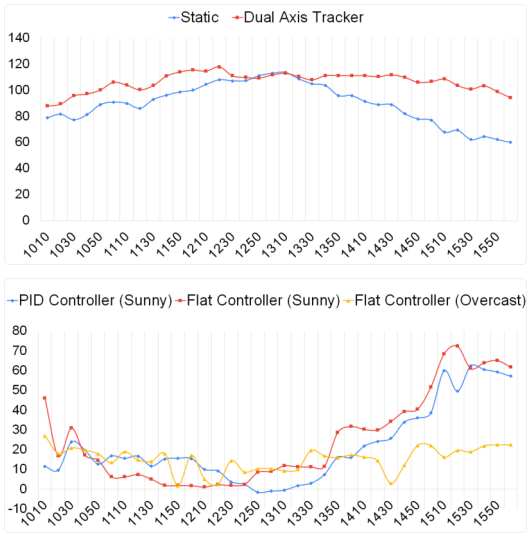

Fig. 11. Comparison of different controllers (a) Performance of the tracker with PID control (Sunny), (b) Percentage increase in the power generated by the panel for each control algorithm

V. Conclusions

The developed Dual-Axis Solar Tracker system in this study operates in tandem with requirements. The strategy of control deployed is that of a Hybrid Controller, combining Astronomical equations based open-loop control and Differential Flatness Based control over the tracking movement of the photovoltaic panel. The fast acting control mechanism acts in accordance to the requirements in a mobile setting. The LDR sensor array panel was able to detect finer variations in solar intensity. Hence it is able to direct the controller according to the updates of solar orientations. Manufactured frame designs and embedded circuits were suitable for proper and smooth functioning in various weather conditions. The prototype was tested in sunny and overcast conditions to evaluate performance against a static solar energy photovoltaic harvesting system. The developed tracker photovoltaic increased energy acquisition by more than 25%. This is in tune to with the higher expectations from a dual axis tracker using a polycrystalline photovoltaic panel [20]. Thus, a novel Differential Flatness and Astronomical equations based control method has been presented and executed in this study.

VI. Acknowledgements

We would like thank the Department of Science and Technology, Govt. of India, for providing the necessary funds to undertake this study under the ”Improved Smart Vending Cart for Fresh Fruits and Vegetable” project at IIT Delhi. We would also like to thank Mr. Yashwant Prasad, RuTAG IIT Delhi, for his genuine guidance; and Ms. Apurba Paul, NIT Patna, for her important contributions in developing the Solar Tracker.

References

[1] R. Garrido, & A. Díaz (2016). Cascade closed-loop control of solar trackers applied to HCPV systems. Renewable Energy, 97, 689-696.

[2] L. Salgado-Conrado (2018). A review on sun position sensors used in solar applications. Renewable and Sustainable Energy Reviews, 82, 2128-2146.

[3] A. Yazidi, F. Betin, G. Notton, & G. A. Capolino (2006, July). Low cost two-axis solar tracker with high precision positioning. In 2006 first international symposium on environment identities and Mediterranean area (pp. 211-216). IEEE.

[4] F. R. Rubio, M. G. Ortega, F. Gordillo & M. Lopez-Martinez (2007). Application of new control strategy for sun tracking. Energy Conversion and Management, 48(7), 2174-2184.

[5] S. N. Kumpati, & P. Kannan (1990). Identification and control of dynamical systems using neural networks. IEEE Transactions on neural networks, 1(1), 4-27.

[6] E. Li, B. Li, & H. Li (2021). Designing and Implementing a Novel Solar Panel Tracker Leveraging Reinforcement Learning Technique. Journal of Student Research, 10(4).

[7] A. A. Aldair, A. A. Obed, & A. F. Halihal (2018). Design and implementation of ANFIS-reference model controller based MPPT using FPGA for photovoltaic system. Renewable and Sustainable Energy Reviews, 82, 2202-2217.

[8] Y. Yao, Y. Hu, S. Gao, G. Yang, & J. Du (2014). A multipurpose dual-axis solar tracker with two tracking strategies. Renewable Energy, 72, 88-98.

[9] R. F. Fuentes-Morales, A. Diaz-Ponce, M. I. Peña-Cruz, P. M. Rodrigo, L. M. Valentín-Coronado, F. Martell-Chavez, & C. A. Pineda-Arellano (2020). Control algorithms applied to active solar tracking systems: A review. Solar Energy, 212, 203-219.

[10] K. Azizi, & A. Ghaffari (2013). Design and manufacturing of a high-precision sun tracking system based on image processing. International journal of photoenergy, 2013.

[11] G. E. Mustafa, B. A. Sidahmed, & M. O. Nawari (2019, October). The Improvement of LDR Based Solar Tracker's Action using Machine Learning. In 2019 IEEE Conference on Energy Conversion (CENCON) (pp. 230-235). IEEE.

[12] P. Thounthong, S. Sikkabut, P. Mungporn, L. Piegari, B. Nahid-Mobarakeh, S. Pierfederici, & B. Davat (2015). DC bus stabilization of li-ion battery based energy storage for a hydrogen/solar power plant for autonomous network applications. IEEE transactions on industry applications, 51(4), 2717-2725.

[13] M. Alata, M. A. Al-Nimr, & Y. Qaroush (2005). Developing a multipurpose sun tracking system using fuzzy control. Energy Conversion and Management, 46(7-8), 1229-1245.

[14] J. T. Agee, & A. A. Jimoh (2012). Flat controller design for hardware-cost reduction in polar-axis photovoltaic systems. Solar energy, 86(1), 452-462.

[15] L. Bitauld, M. Fliess, & J. Lévine (1997, July). A flatness based control synthesis of linear systems and application to windshield wipers. In 1997 European Control Conference (ECC) (pp. 2460-2465). IEEE.

[16] P. Martin, R. M. Murray, & P. Rouchon (2003). Flat systems, equivalence and trajectory generation.

[17] J. Lévine, & D. V. Nguyen (2003). Flat output characterization for linear systems using polynomial matrices. Systems & control letters, 48(1), 69-75.

[18] M. Fliess, J. Lévine, P. Martin, & P. Rouchon (1995). Flatness and defect of non-linear systems: introductory theory and examples. International journal of control, 61(6), 1327-1361.

[19] J. T. Agee, & A. A. Jimoh (2010). Control of a 3kW polar-axis solar power platform with nonlinear measurements. Solar Energy, 432, 43-67.

[20] O. A. Hassan, H. Hashim, A. A. A. Ma'Radzi, M. S. B. AHMAD, T. N. T. Ibrahim, & S. A. B. ZULKIFLI (2020). Iot Based Dual Axis Solar Tracker Implementation For Polycrystalline Photovoltaic With Energy Storage. Advances in Computing and Intelligent System, 2(2).

Authorized licensed use limited to: DELHI TECHNICAL UNIV. Downloaded on January 04,2023 at 09:25:58 UTC from IEEE Xplore. Restrictions apply.

Semiconductor Science and Technology

ACCEPTED MANUSCRIPT

DuAl gate AlGaN/GaN MOS-HEMT Biosensor for electrical detection of biomolecules-analytical model

To cite this article before publication: Ruby Mann *et al* 2023 *Semicond. Sci. Technol.* in press https://doi.org/10.1088/1361-6641/acb0f3

Manuscript version: Accepted Manuscript

Accepted Manuscript is "the version of the article accepted for publication including all changes made as a result of the peer review process, and which may also include the addition to the article by IOP Publishing of a header, an article ID, a cover sheet and/or an 'Accepted Manuscript' watermark, but excluding any other editing, typesetting or other changes made by IOP Publishing and/or its licensors"

This Accepted Manuscript is **© 2023 IOP Publishing Ltd**.

During the embargo period (the 12 month period from the publication of the Version of Record of this article), the Accepted Manuscript is fully protected by copyright and cannot be reused or reposted elsewhere.
As the Version of Record of this article is going to be / has been published on a subscription basis, this Accepted Manuscript is available for reuse under a CC BY-NC-ND 3.0 licence after the 12 month embargo period.

After the embargo period, everyone is permitted to use copy and redistribute this article for non-commercial purposes only, provided that they adhere to all the terms of the licence https://creativecommons.org/licences/by-nc-nd/3.0

Although reasonable endeavours have been taken to obtain all necessary permissions from third parties to include their copyrighted content within this article, their full citation and copyright line may not be present in this Accepted Manuscript version. Before using any content from this article, please refer to the Version of Record on IOPscience once published for full citation and copyright details, as permissions will likely be required. All third party content is fully copyright protected, unless specifically stated otherwise in the figure caption in the Version of Record.

View the article online for updates and enhancements.

This content was downloaded from IP address 14.139.251.98 on 11/01/2023 at 04:59

DUAL GATE AlGaN/GaN MOS-HEMT BIOSENSOR FOR ELECTRICAL DETECTION OF BIOMOLECULES-ANALYTICAL MODEL

Ruby Mann, Sonam Rewari, Shobha Sharma, R.S. Gupta

Abstract—This paper proposes an analytical model for a Dual gate AlGaN/GaN MOS-HEMT biosensor for electrical detection of neutral species such as Biotin, Keratin, ChOx, and Zein. When only one subband is occupied and the AlGaN layer is assumed to have been fully ionized, the Fermi-Dirac statistic and 2D state density are used to produce a self-consistent calculation of the carrier density in the quantum well at the interface. It is done by analyzing the impact of biomolecule concentration by inserting a biomolecule of appropriate dielectric permittivity in the cavity area beneath the gate region. The impact of cavity length has been analyzed on the sensor's performance. The proposed device significantly changes the channel potential, transconductance, drain current, and threshold voltage. Dual gate structures offer superior resistance to short channel effects. Due to enhanced transport characteristics, high carrier mobility, drain current, and a variety of other factors, double gate MOS HEMT outperforms single-gate MOS HEMT. The maximal transconductance, drain on sensitivity, and the maximal drain current that has been attained in this work is 0.017S, 0.22 and 0.129mA, respectively, for biomolecule concentration, $N_b=3\times10^{12}$.Among all the biomolecules used in this study, Keratin has achieved the maximum shift in threshold voltage and transconductance of 0.4V and 0.016S. The increase in current for Keratin, Biotin, Zein, and ChOx is 0.67%, 78%, 17%, and 42%, respectively, from single to Dual gate AlGaN/GaN MOS-HEMT. SiO_2, Al_2O_3, and HfO_2oxides have been compared by filling them in the left side of the cavity. Dual gate AlGaN/GaN MOS-HEMT biosensor presents an opportunity to develop robust, low-cost, specific detection and analysis of neutral biomolecule. The analytical model provides good results for drain current according to the comparison of simulation and analytical model findings.

Index Terms— ***MOS-HEMT, AlGaN barrier, Threshold Voltage Dosimeter, Sensor.***

I. INTRODUCTION

In the last decade, GaN has been regarded as the superior substance for high-frequency and high-power applications over Silicon due to its better electron saturation velocity, wider bandgap, and high breakdown voltage[1]. Due to the theoretical limits of Si material, such as the low operating temperature range (junction temperature limit-150°C) in most devices, silicon devices are not viable in harsh conditions like high temperatures [2].

R.Mann and S.Sharma are with the Department of Electronics and Communication Engineering, Indira Gandhi Delhi Technical University for Women, New Delhi-110006, India (email: rubymann28360@gmail.com, shobhaa_sharma16@yahoo.co.in)

S. Rewari is with the Department of Electronics and Communication Engineering, Delhi Technological University, New Delhi-110042, India (email:rewarisonam@gmail.com)

R. S. Gupta is with the Department of Electronics and Communication Engineering, Maharaja Agrasen Institute of Technology, New Delhi 110086, India (email: rsgupta1943@gmail.com).

In a high-frequency field effect transistor such as a MOSFET or MESFET, it is desirable to have a thin, highly conductive layer in close proximity to the gate electrode. This increases the modulation of the gate on the channel, the transconductance, and in turn, increases the cutoff frequency of the transistor. Also desirable is to have high mobility of electrons in this conducting channel. However, high mobility implies low doping which seems to be at odds with a high electron concentration. In a MOSFET, these two beneficial properties, high mobility and high concentration come for free. Electrons come from heavily doped regions to either side of the gate while the channel under the gate is low doped but provides a potential well for the electrons to flow into. In MESFETs, which are usually made of III-V semiconductor materials, getting both high concentration and low doping is not as easy. That's where the HEMT comes in. A high electron mobility transistor, HEMT, uses a heterojunction between a heavily doped, high bandgap material such as AlGaAs, and a low doped, lower bandgap material such as GaAs. This structure produces a quantum well for the electrons in the GaAs. The electrons come from the AlGaAs. The slide below is of the conduction band of the AlGaAs/GaAs heterojunction. One of the allowed energy levels in the quantum well is below the Fermi level and thus has a very high concentration of electrons.

In MESFETs, both low doping and high concentration are not easy; therefore, HEMT structure has become the most interesting subject for intense research in which heterojunction between low-doped and heavily doped material is formed, and electrons are confined on the low-doped side but in a very high-concentration and a potential well is formed. Therefore, the electron density is easily controlled as they are confined in one space dimension. HEMTs are an excellent choice due to their outstanding properties like high cut-off frequency, low turn-on resistance, and low parasitic capacitance[3]–[5].More recently, HEMT structures have revealed their extraordinary ability to accomplish as micro-sensors, strain sensors, chemical detectors and combustion gas sensors for detecting anions, metal ions and biomolecules due to their excellent properties[6]–[9].

In most cases, the piezoelectric-induced carrier density in the channel changes as the surface conditions change, thereby changing the drain-source or gate current. It is currently the most promising device for electronic biosensors. Ambacher and colleagues demonstrated that AlGaN/GaN heterostructures are highly sensitive to ions, polar liquids, hydrogen gas, and even biological materials[10]–[14].MRI in the medical field, adulterant detection, environmental monitoring, pathogenic food bacteria detection, agriculture, and other biosensing applications have recently used laboratory-based conventional methods. Although these traditional methods are more accurate, We created two-gate HEMT-based biosensors for simplicity, low cost, and quick results. [15]–[17].

Accepted Manuscript

An analytical model for the dual gate AlGaN/GaN MOS-HEMT structure is proposed in this work to examine the biomolecule's detection. This device is used to detect biomolecules electrically like ChOx (used in various samples for cholesterol level detection; k=3.30), Zein (widely used for films, coatings, and promising potential in the biodegradable plastic industries; k=5), and Biotin (a protein used to keep hair, nails, and skin healthy; k=2.63), Keratin (a protein used in maintaining a healthy pregnancy; k=8), APTES(used as an amino-silane which is mainly used as a dispersant; k=3.57), Streptavidin (protein that is utilized as a biolink on bead coatings; k=2.1)[18]–[21]. The following is how this paper is structured. Device fabrication and simulation are done in the section "Device Fabrication and Simulation. Analytical model work has been done in the section “Analytical drain current model” Analysis of the proposal is presented in the section titled "Results and discussion." The conclusions are made in the section "conclusions."

II. DEVICE FABRICATION AND SIMULATION

Figure 1 depicts a full schematic outlook of a two-gate AlGaN/GaN MOS-HEMT with a 20 nm AIN nucleation layer to lessen the lattice incongruity between the GaN buffer and the sapphire substrate. GaN buffer layer of 2µm has been considered between the nucleation layer and the 25nm Al0.3Ga0.7N layer. Aluminium is used for the drain and source ohmic contacts, and Ni/Au metal is utilized to form the Schottky gate contact. The distance from the source to gate 1(L_{sg1}) and gate2 to drain(L_{g2d}) is2µm. The spacing between two gates(L_{g12}) is 2µm. The length of both gates is 1µm. Region A and A’ is the cavity under gate1 and gate2, respectively. Concentration Dependent Mobility (CONMOB), Polarization model, field-dependent mobility model (FLDMOB), albrct.n, and Shockley Read Hall are some of the models used in this simulation (SRH). Below both, the gates cavity has been formed, and the cavity has been divided into two parts. The right side of the cavity is filled with various biomolecules, while the left is filled with various oxides (SiO_2, Al_2O_3, HfO_2).

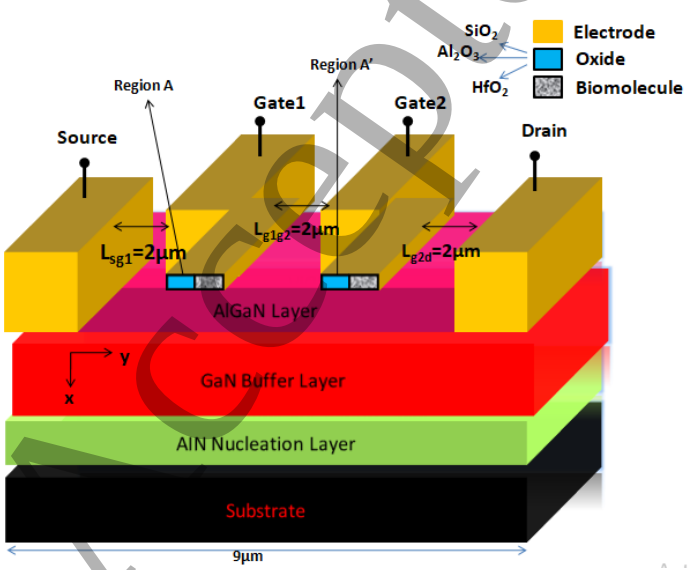

Figure 1. 2-D structure of AlGaN/GaN MOS-HEMT Biosensor

Fig1(b) shows the flowchart of fabrication. In a metal-organic chemical vapour deposition (MOCVD) mechanism, the AlGaN/GaN heterostructure was placed on a sapphire substrate. A 20-nm AlN nucleation layer, a 2-µm GaN buffer layer, and a 25-nm AlGaN barrier layer comprised the epitaxial layers. Hall effect measurements showed that the sheet carrier density and 2DEG mobilities were 1.01×10^{12} cm^{-2} and 1915 $cm^2/V\bullet s$, respectively. The source and drain electrodes were created by evaporating Ti/Al/Ni/Au and then annealing for 30 seconds in an N_2 ambient at 830 °C. The mesa was then isolated using Cl-based reactive ion etching (RIE). After that, a Schottky gate was created by evaporating Ni/Au. Fig.2 shows the I_{ds}-V_{ds} characteristics of the device with the experimental work done by Hu et al.[22]. The proposed device's simulated result agrees well with the exploratory findings of Hu et al. [22].

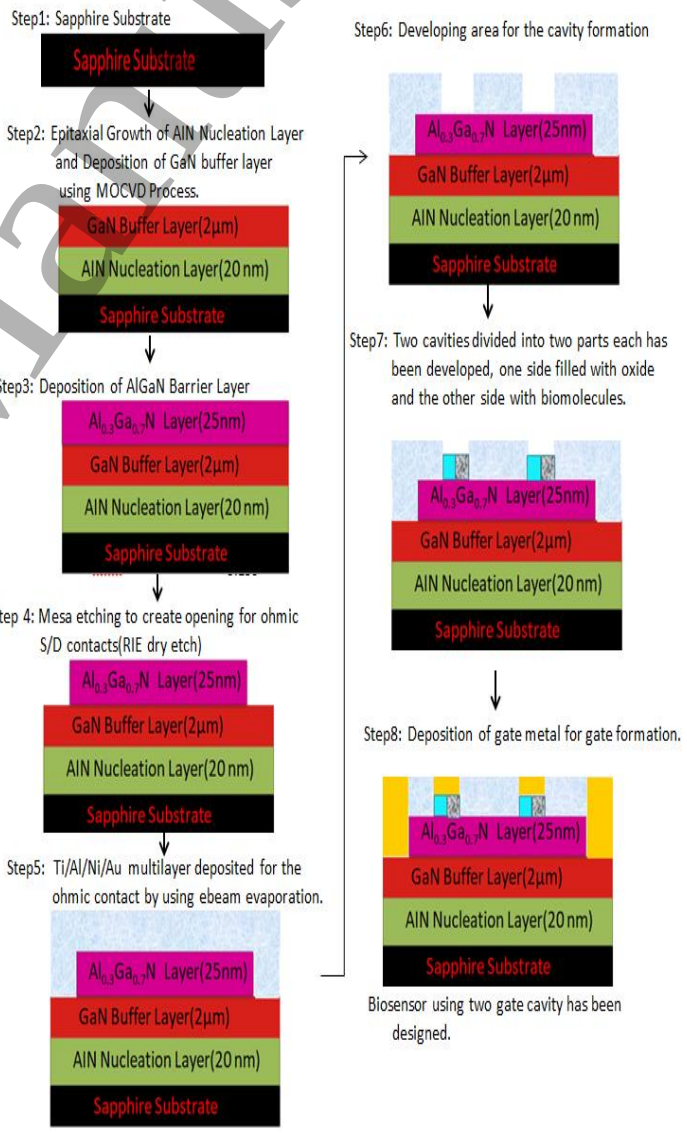

Figure 1(b). Flowchart of Fabrication

Accepted Manuscript

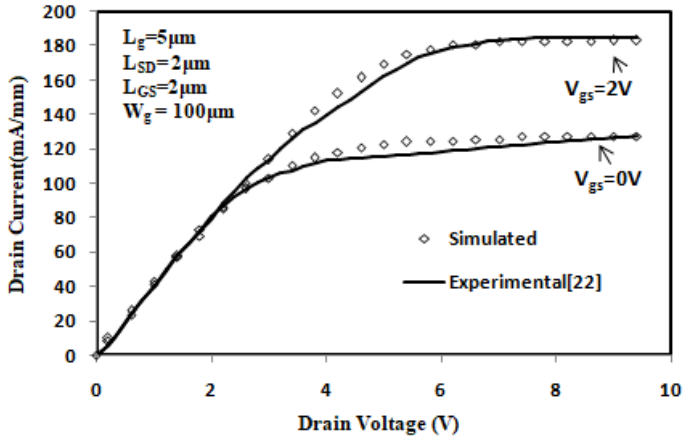

Figure 2. I_{ds}-V_{ds} characteristics of the MOS-HEMT device

III. ANALYTICAL DRAIN CURRENT MODEL

As shown in Figure 1, one region has been filled with biomolecules under gate1 and gate 2 and the other is filled with an oxide layer. Therefore, various important parameters such as capacitance of oxide and biomolecule to determine the behaviour of the device are given by Eqs. (1) and (2)[23]:

$$C_{ox} = \frac{\varepsilon_{ox}}{t_{ox}} \quad (1)$$

$$C_{Bio} = \frac{\varepsilon_{Bio}}{t_{Bio}} \quad (2)$$

Where $t_{ox}, \varepsilon_{ox}, t_{Bio}, \varepsilon_{Bio}$ are thicknesses and permittivities of the oxide layer and the biomolecules, respectively. Eq. (3) gives the total effective capacitance of both regions under both gates[23].

$$C_{eff} = C_{ox} + C_{Bio} \quad (3)$$

The total capacitance of the MOS-HEMT device is given by Eq. (4).

$$C_{moshemt} = \frac{\varepsilon_{AlGaN}\varepsilon_{ox}}{\varepsilon_{AlGaN} t_{AlGaN} + \varepsilon_{ox} t_{ox}} \quad (4)$$

By Considering only two sub-bands, the n_d carrier density in quantum well at the interface can be calculated using the Fermi-Dirac statistic[24]–[26],

$$n_d = \frac{qm^*}{\pi\hbar^2}\int_{E^0}^{E^1}\frac{dE}{1+e^{\left(\frac{q(E-E_f)}{kT}\right)}} + \int_{E^1}^{\infty}\frac{dE}{1+e^{\left(\frac{q(E-E_f)}{kT}\right)}} \quad (5)$$

Where $D_s = qm^*/\pi\hbar^2$ is the density of states for two-dimensional states representing the Fermi-Dirac probability function. Evaluating equation (5) yields:

$$n_d = D_s\frac{kT}{q}\left(\ln\left(\exp\left(\frac{E_f - E_o}{kT/q}\right)+1\right) + \ln\left(\exp\left(\frac{E_f - E_1}{kT/q}\right)+1\right)\right) \quad (6)$$

Where $E_f, E_0 = \gamma_0 n_d^{2/3}, E_1 = \gamma_1 n_d^{2/3}$ is the position of Fermi level, first sub-band and second sub-band, respectively. $\gamma_0 = 2.5\times10^{-12}, \gamma_1 = 3.2\times10^{-12}$ are constants experimentally calculated from cyclotron resonance experiment[27]–[29].

n_d in equation (6) is related to the gate and the channel voltages, and by assuming the AlGaN layer has been completely ionized, we get,

$$n_d = \frac{\varepsilon_{AlGaN}}{q\times t_{AlGaN}}((V_{Gi} - V_o) - E_f - V_x) \quad (7)$$

Where V_{Gi} represent applied gate voltage for i=1,2 for gate 1 and gate 2, respectively V_o, V_x is the cut-off and channel voltage. Using the expression E_f, E_0 in equation(6) and considering only one subband is occupied. Here, considering the first band is occupied, the correlation between n_d and $(V_{Gi} - V_o)$ can be established and is given by Eq(8).

$$\left((V_{Gi} - V_o) - V\right) = \frac{qt_{AlGaN} n_d}{\varepsilon} + \gamma_0 n_d^{2/3} + \frac{k.T}{q}\ln\left(\frac{n_d q}{D_s k.T}\right) \quad (8)$$

Where V is quasi-Fermi potential and Drain current along the channel can be given by

$$I_D = \frac{W_g}{L_g}\int_{V_{source}}^{V_{drain}} qn_d \mu dV \quad (9)$$

Where L_g and W_g are the gate length and width of the device. μ is the low-field mobility of the device. Substituting the value of dV from equation (8) after differentiating with respect to charge density in (9) and integrating the equation(9) from source to drain results in the simplified equation of the drain current, which can be given as

$$I_D = -q\mu\frac{W_g}{L_g}\left(\frac{2}{5}\gamma_o\left(n_{drain}^{\frac{5}{3}} - n_{source}^{\frac{5}{3}}\right) + \frac{kT}{q}\left(n_{drain} - n_{source}\right) + \frac{qt_{AlGaN}}{2\varepsilon_{AlGaN}}\left(n_{drain}^2 - n_{source}^2\right)\right) \quad (10)$$

Accepted Manuscript

Where n_{drain} and n_{source} are the charge carrier concentrations at the drain and the source sides and is given by Eq.(11)

$$n_{source} = \left(\left(\frac{\varepsilon_{AlGaN}}{qt_{AlGaN}} (V_{Gi} - V_o) \right) \left(\frac{(V_{Gi} - V_o) + \frac{k.T}{q}\left[(1 - \ln(\beta V_{goin})\right] - \frac{\gamma_0}{3}\left(\frac{\varepsilon_{AlGaN}}{qt_{AlGaN}}\right)^{2/3}}{(V_{Gi} - V_o)\left(1 + \frac{k.T}{q.V_{goid}}\right) + \frac{2}{3}\gamma_0 \left(\frac{\varepsilon_{AlGaN}}{qt_{AlGaN}}(V_{Gi} - V_o)\right)^{2/3}} \right) \right) \quad (11)$$

Here V_{goid} V_{goin} are functions of V_{goi} where i=1,2for gate1 and gate2, respectively and are given by Eq.(12)

$$V_{goix} = \frac{V_{goi} Y_x}{V_{goi}^{\ 2} + Y_x^{\ 2}} \quad (12)$$

Where $Y_n = e/\beta$ and $Y_d = 1/\beta$ are constants and β are given asEq(13)

$$\beta = \frac{\varepsilon_{AlGaN}}{D_s kTt_{AlGaN}} \quad (13)$$

IV. RESULTS AND DISCUSSION

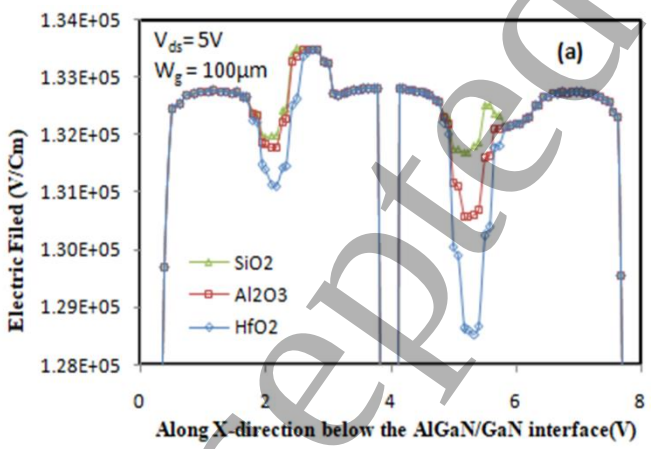

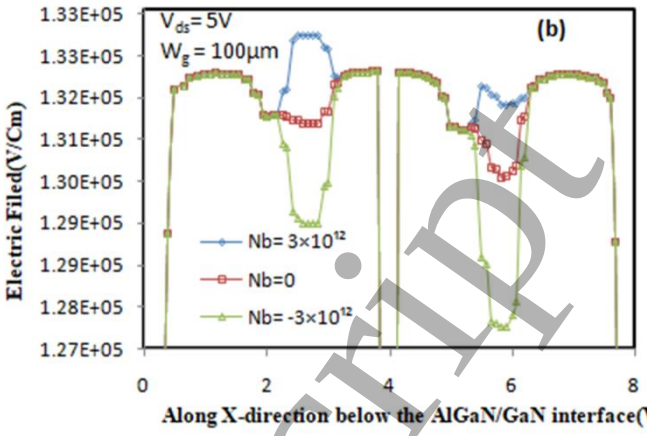

Figure 3. Electric field plot along the X-direction of MOS-HEMT. **(a).**For different oxides **(b).**For different biomolecule concentrations.

Figure 3 depicts the plot of the electric field along the x-axis for different oxides used in this paper(Fig 3(a)) and for different concentrations of biomolecule induced(Fig 3(b)).

In figure3(a), biomolecule concentration(N_b= 3×10^{12}) is considered for all three different oxides. Although HfO_2 has a high dielectric constant,HfO_2 suffers from severe transparency to oxygen that would degrade the interface quality due to Ga-O bond introduction in GaN devices. Bare HfO_2 has low interface state density than SiO_2 and Al_2O_3; therefore, drain current reduces and hence electric field [30][31]. As we can observe from Fig 3(a) Higher the dielectric constant lower the electric field.

Influence on the electric field by changing the biomolecule concentration (positive/negative) can be seen in Figure 3(b). The high biomolecule concentration increases the carrier concentration in the channel region, which results in high polarization, and high surface potential and improves the flux density and hence electric field. With an increase in the biomolecule concentration (either positive or negative), the higher will be the electric field can be inferred from Figure 3(b) reason being inducing the interface charges changes the carrier concentration in 2DEG, which results in a change in the electric field at the interface. Given the negative charge entrapment of the AlGaN layer, the electric field at the interface will be reduced, allowing for a lower electronic density. However, if the accumulated charge at the interface is positive, the carrier density and electric field will increase. This 2DEG variation leads to channel potential modulation below the gate.

Figures 4(a) and 4(b) show that the plot of drain current (I_{ds}) versus gate voltage (V_{gs}) at a drain bias of 5V for all the biomolecules which are filled in the cavity region ($W_{cavity1}$=20nm, $L_{cavity1}$=1µm, $W_{cavity2}$=20nm, $L_{cavity2}$=1µm) and variation in I_{ds} for biomolecules with respect to the air-filled cavity. The maximum deviation of drain current observed for Keratin in relation to the air-filled cavity is 0.037A, with a minimum variation of 0.005A observed for Streptavidin in relation to the air-filled cavity.

Accepted Manuscript

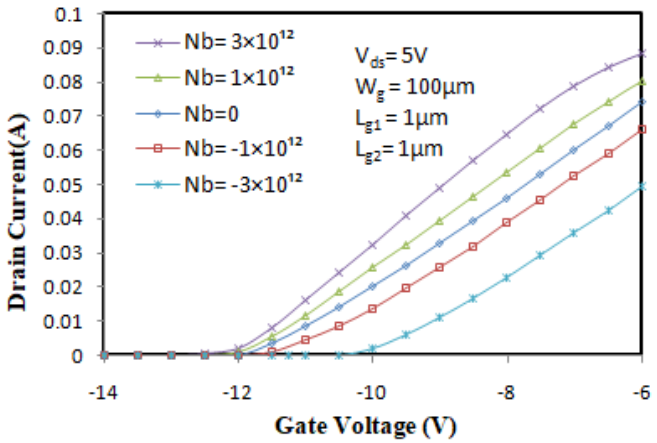

Figure 4(a). Ids-Vgs plot for different biomolecule concentration

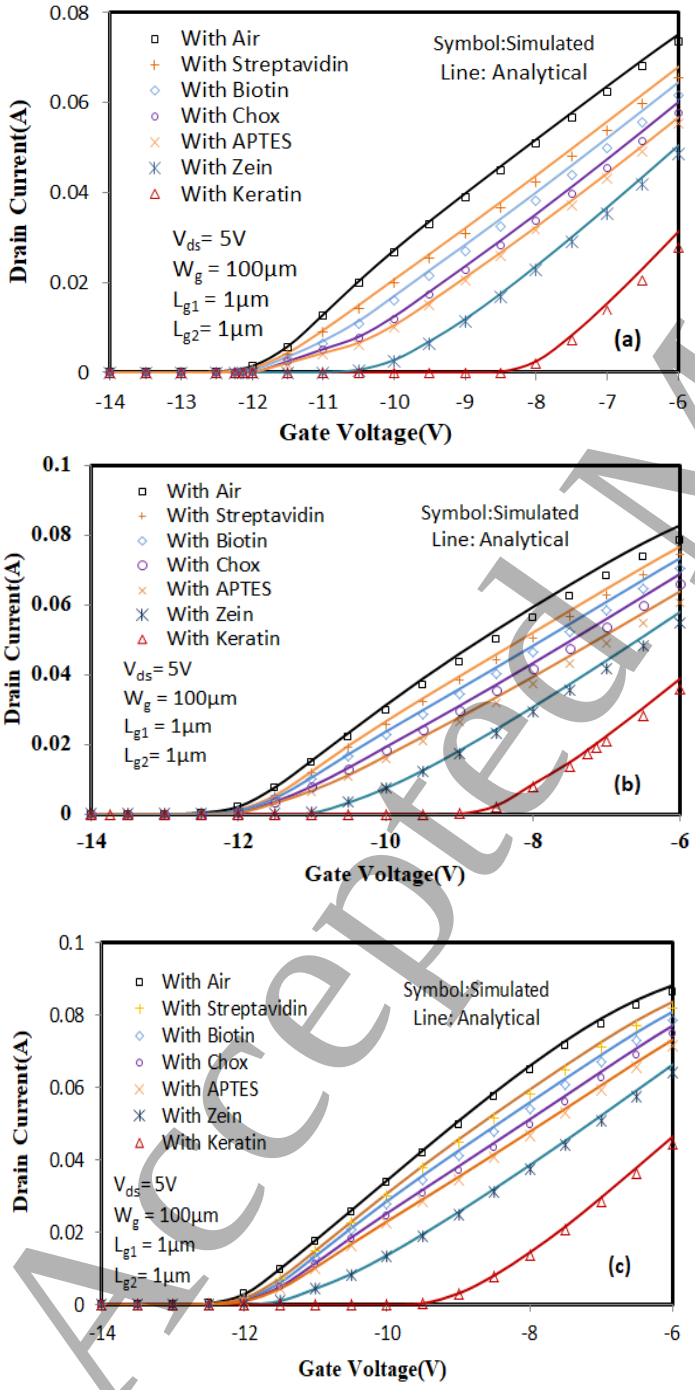

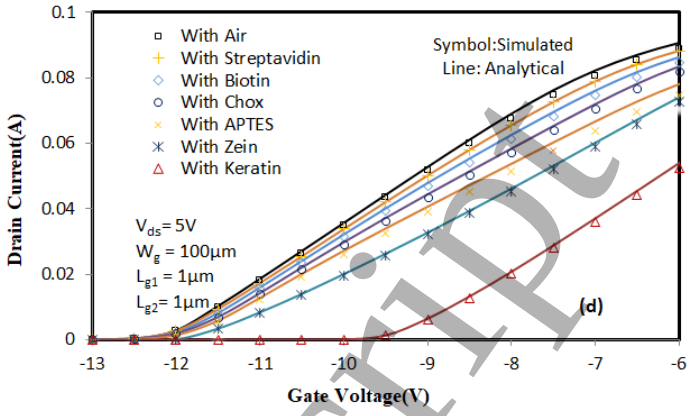

Figure 4(b). Ids-Vgs plot for different biomolecules **(a)** For Single gate Single Cavity **(b)**For Single gate Double Cavity **(c)** For Double gate Single Cavity **(d)** For Double gate Double Cavity.

Figure 4(b) depicts the Ids-Vgs plot for different biomolecules (a) For Single gate Single Cavity (b) For Single gate Double Cavity (c) For Double gate Single Cavity (d) For Double gate Double Cavity. As we can see from the figures 4(b) that the Double gate Double cavity MOS-HEMT device has shown the better result over the other three devices. By changing the dielectric the effective oxide capacitance gets altered and hence performance of double cavity structure improves. In Single gate MOS-HEMT device, although scaling the device improves performance, it also increases the device's short-channel effects. To counteract this effect, a double-gate technology is proposed that eliminates the buffer from the single-gate structure HEMT.

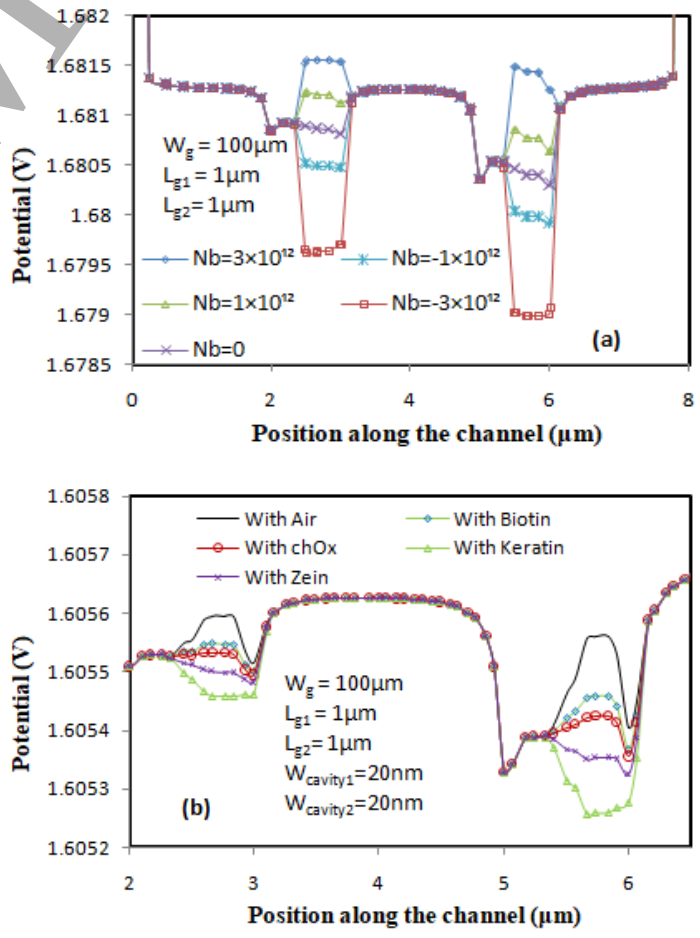

Figure 5. Channel potential along the x-axis below AlGaN/GaN interface of MOS-HEMT.**(a).**For different biomolecule concentrations.**(b).**For different biomolecules.

Accepted Manuscript

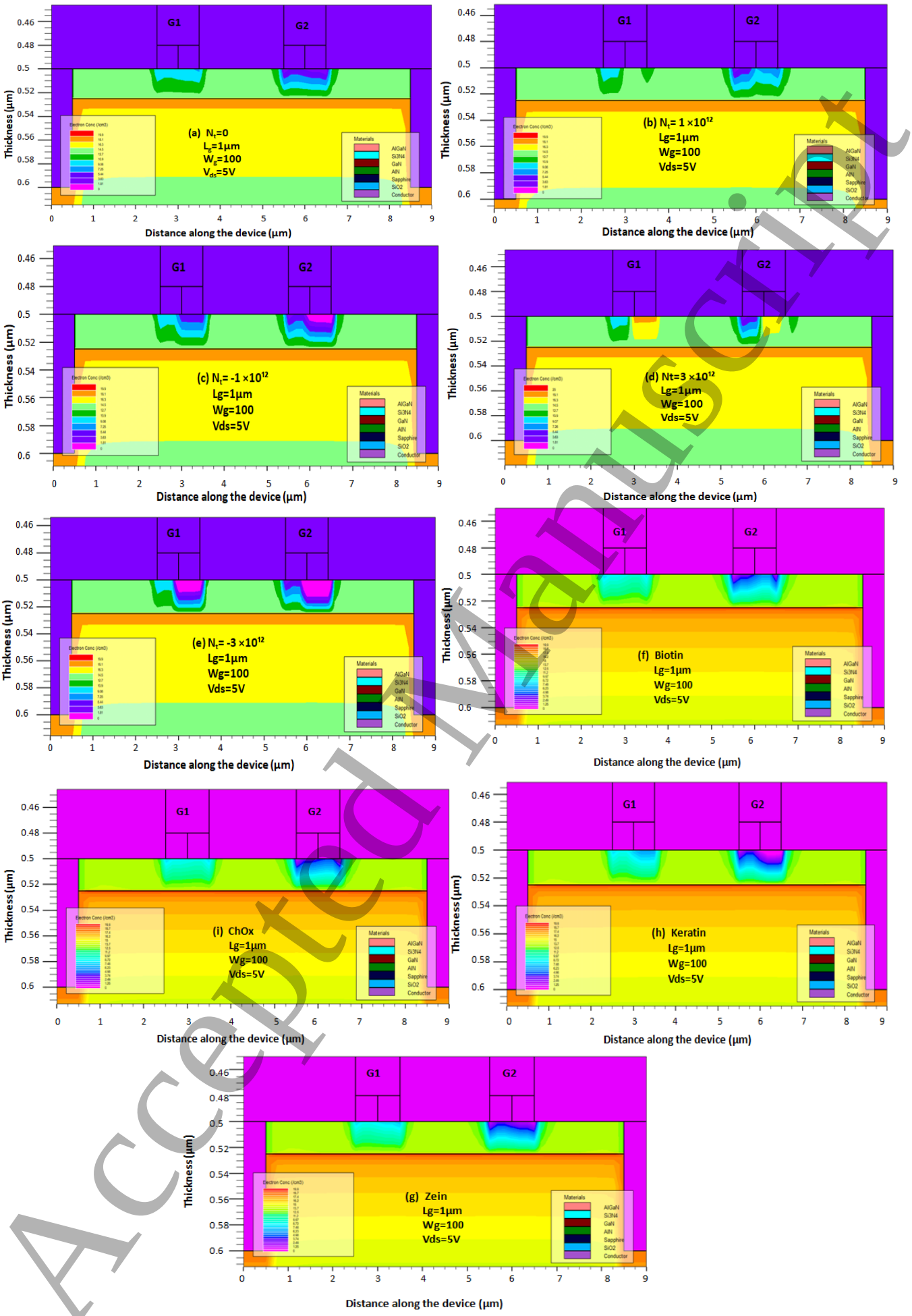

Figure 6. Electron concentration contour plot of MOS-HEMT **(a).** N_b=0×10^{12}cm^{-2} **(b).**1×10^{12}cm^{-2}**(c).**-1×10^{12}cm^{-2} **(d)** .3×10^{12}cm^{-2} **(e).** -3×10^{12}cm^{-2} **(f).** Biotin **(g).**ChOx **(h).**Keratin **(i).** Zein

Accepted Manuscript

This double-gate (DG) structure has better channel control than conventional single-gate HEMTs (SG-HEMT). This DG-HEMT architecture has a high current driving capability as well as a high carrier concentration in the two-dimensional electron gas (2DEG) [32]. So it can be summarised that the lower the biomolecule's dielectric constant, the lower the variation in drain current in the air-filled cavity. The maximum drain current of 0.086A and a minimum of 0.05A at a gate voltage of -6V have been observed for Streptavidin and Keratin. As a result, we can conclude that as the dielectric constant of biomolecules decreases, resistance decreases and on-state current increases. As the dielectric constant increases, oxide capacitance increases, and the depletion capacitance decreases as the width of the depletion layer decreases; therefore, the drain current increases[33].

Figure 5 depicts the deviation in channel potential caused by the injection of biomolecules into the cavity. It shows that when biomolecules are injected into the cavity, the change in channel potential is significant.Figure5 shows double humps in the curve due to dual-gate presence. In figure 5(a), a variation of channel potential with biomolecule concentration can be seen.
Figure 5(a) shows that as the concentration of biomolecules increases, so does the channel potential. Figure 5(b) depicts the surface potential as a function of position along the channel for various biomolecules introduced into the cavity.
It can be observed that Biotin has the highest change in potential out of all the biomolecules considered due to its lowest dielectric constant. This is due to the fact that as the dielectric constant of biomolecules decreases, the On-state current increases[34].Figure 6 shows that biomolecules injected in the cavity under the gate near the source region have a higher potential for all biomolecules than those injected in the cavity below the gate near the drain region[23][35].

Figure 6(a-e) shows the contour plot of electron concentrations for induced different biomolecule concentrations, and Figure 6(f-i) shows the contour plot for induced different biomolecules (N_b). Fig 6(a) indicates that when biomolecule concentration (N_b) equals N_b= 0, then no effect can be seen for electron concentration that no change has been noticed, but as we insert the biomolecule depending upon the concentration value (positive or negative), carrier concentration changes. The high concentration induced shows a significant impact on the carrier concentrations.

$$\Delta V_{th} = V_{th\,(Biomolecule)} - V_{th(Air)} \big| at\ I_{on} = const. \quad (14)$$

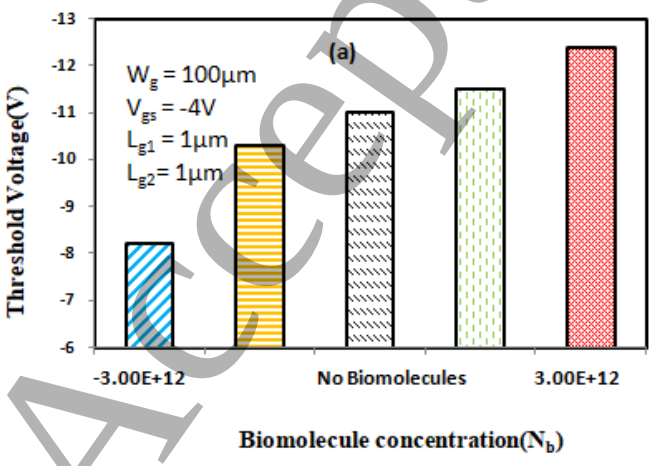

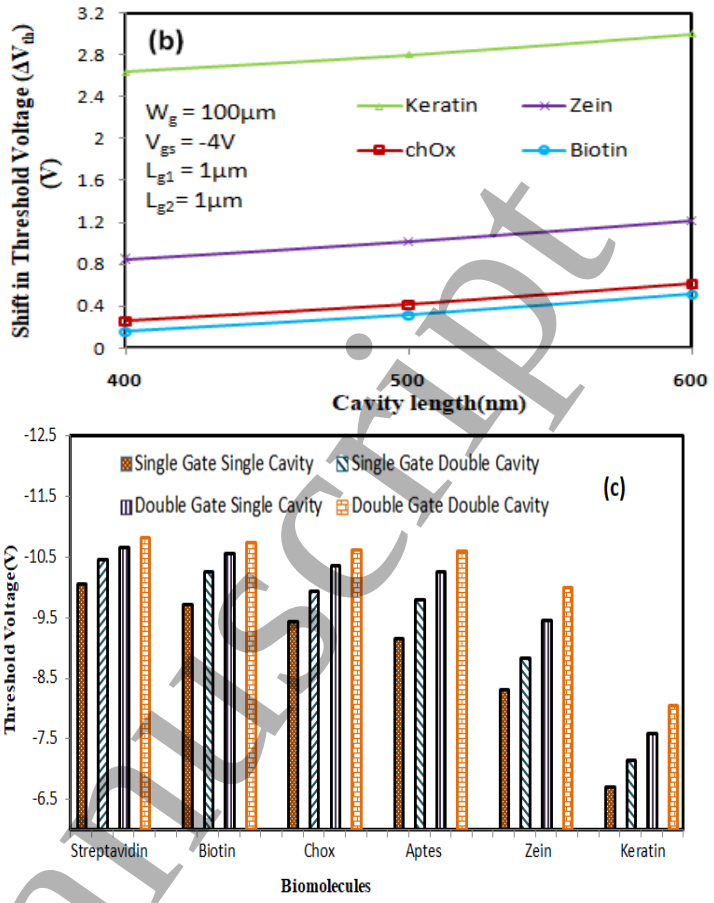

Figure7(a).Threshold voltage plots for biomolecule concentration(b).Shift in threshold voltage plots for all the biomolecules with varying lengths of the cavity (nm).(c).For different biomolecules w.r.t Single gate Single Cavity , Single gate Double Cavity, Double gate Single Cavity , Double gate Double Cavity.

Figure 7(a) depicts the plot of threshold voltage for various biomolecule concentrations, that is, negatively charged biomolecule, uncharged (neutral) and positively charged biomolecule. The proposed sensor shows the maximum threshold voltage of -12.4V for the positively charged biomolecule because the concentration of the charge carriers in 2DEG is lower for the negatively charged biomolecule and vice versa, and increasing charge carrier concentration results in a decrease in the threshold voltage since the threshold voltage is directly proportional to the carrier concentration of 2DEG. Figure 7(b) shows how the threshold voltage changes as the cavity length change from 400 nm to 600 nm. When the cavity length has surged from 400 nm to 600 nm, the threshold voltage for Keratin shifts by about 0.4 Volt. Equation 14 shows the shift in threshold voltage. The alteration in threshold voltage increases as cavity length increases. This is due to the fact that as the cavity length increases, a larger area becomes available for more biomolecules to interact with the AlGaN layer.
This modification demonstrates that the transference in threshold voltage can be used as a sensing parameter for identifying and optimizing biomolecule species. Figure 7(c) shows the threshold voltage plot for different biomolecules w.r.t Single gate Single Cavity, Single gate Double Cavity, Double gate Single Cavity, Double gate Double Cavity. We can see from the figure7(c) that that the Double gate Double cavity MOS-HEMT device has shown the better threshold voltage over the other three devices.

Accepted Manuscript

Table I. Difference in Change in current and Threshold voltage for Single and Dual gate MOS-HEMT.

Biomolecules	Change in current(mA/mm)		Change in threshold Voltage(ΔV_{th})	
	Single Gate MOS-HEMT Biosensor-[36], [37]	Dual Gate MOS-HEMT Biosensor	Single Gate MOS-HEMT Biosensor	Dual Gate MOS-HEMT Biosensor
Keratin	442	445	2.924	3.1
Biotin	52	93	0.467	0.51
Zein	209	245	1.685	1.70
ChOx	79	138	0.312	0.812
Streptavidin	50.9	86	0.092	0.114
APTES	112	120.4	0.849	0.879

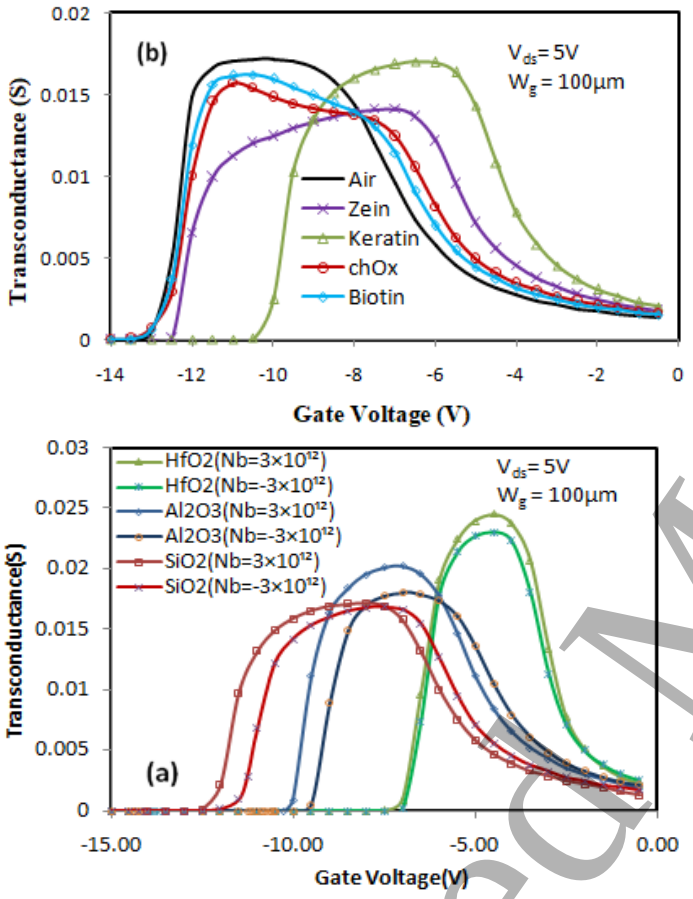

Figure 8. Transconductance plots at a drain voltage of 5V. **(a).** For oxides and biomolecule concentration **(b).** For different biomolecules.

Figure 8(a, b) shows gm v/s Vgs plotted for the proposed sensor. Figure 8(a) illustrates the transconductance variation for different concentrations of induced biomolecules and various oxides filled in Region A and A' (shown in figure1) under the gate at Vds=5V. It can be seen from figure8(a) that HfO_2 has the highest transconductance of 2.42E-02S with N_b= 3×10^{12} because of the higher dielectric constant of HfO_2 among all the oxides considered.

The device's sensitivity parameter can be calculated as follows[38]:

$$S_D = \frac{I_{(With\ biomolecules)} - I_{(With\ Air)}}{Ion(air)} \Big| at\ V_D = const. \quad (15)$$

Where $I_{(WithAir)}$ is the drain current when the cavity is infused with Air, and $I_{(With\ biomolecules)}$ is the drain current when the cavity is infused with biomolecules.

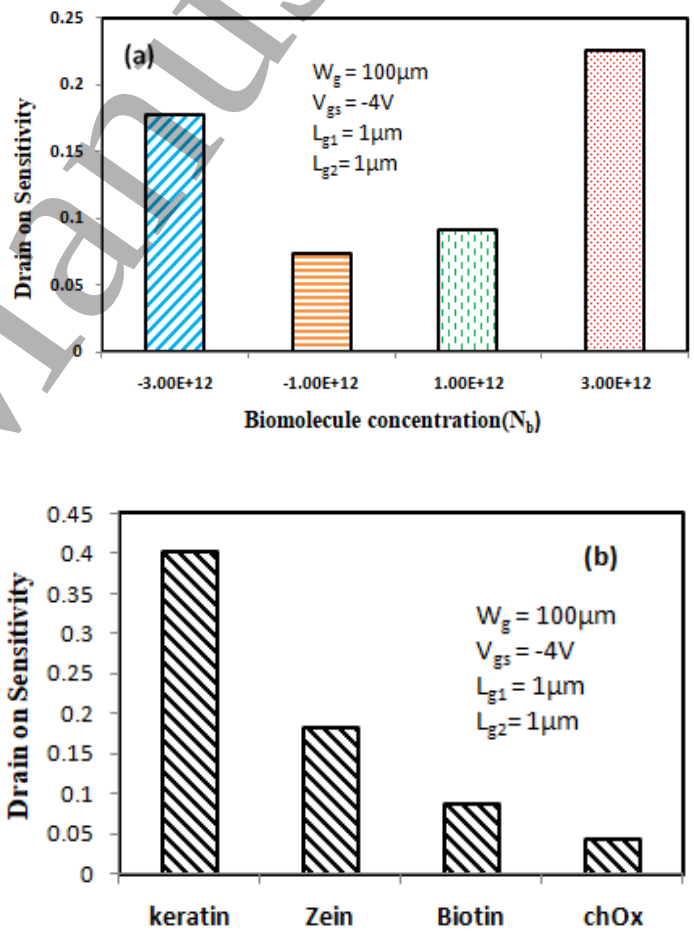

Figure 9. Drain on sensitivity plot **(a).** For different biomolecule Concentrations **(b).** For different biomolecules.

Table II. Parameters for dual gate MOS-HEMT.

PARAMETERS	Biomolecule concentration(N_b)			Biomolecules			
	-3×10^{12}	0	$+3\times10^{12}$	Keratin	Biotin	Zein	ChOx
Sensitivity	0.17	0.18	0.22	0.40	0.08	0.18	0.04
Transconductance(S) at V_{gs}=-8V	1.66E-02	1.69E-02	1.72E-02	1.69E-02	6.96E-03	1.22E-02	8.14E-03
Drain current(A)	8.15E-02	1.09E-01	1.29E-01	9.07E-9	1.25E-01	1.09E-01	1.21E-01

Accepted Manuscript

Figure9(a) shows a sensitivity plot for different biomolecule concentrations. The higher the concentration of the biomolecule, the higher the sensitivity, so the biomolecule will be detected more easily. Figure 9(b) shows plotted various biomolecule's Drain on sensitivity. As the molecule with higher dielectric is introduced into the cavity, the device's sensitivity also increases. Keratin biomolecule has shown the most heightened sensitivity in all the plotted biomolecules, i.e. 0.4. Amassing of biomolecules in the cavity will increase the capacitance that is accountable for improving the drain current.

As a result, a surge in the dielectric constant raises the threshold voltage and, thus, the device's sensitivity[39].

Table I compares the change in current and threshold voltage of single and dual-gate MOS-HEMT Biosensors. Table II compares the device's positive and negative biomolecule concentrations based on the overall performance of various characteristics.

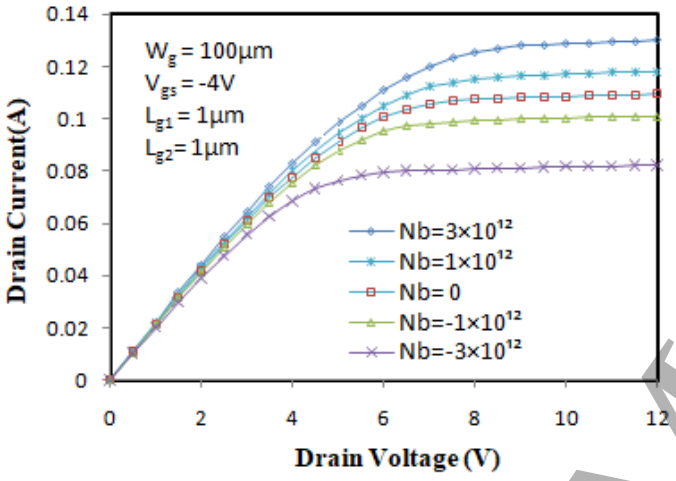

Figure 10(a). I_{ds}-V_{ds} plot for different biomolecules concentration

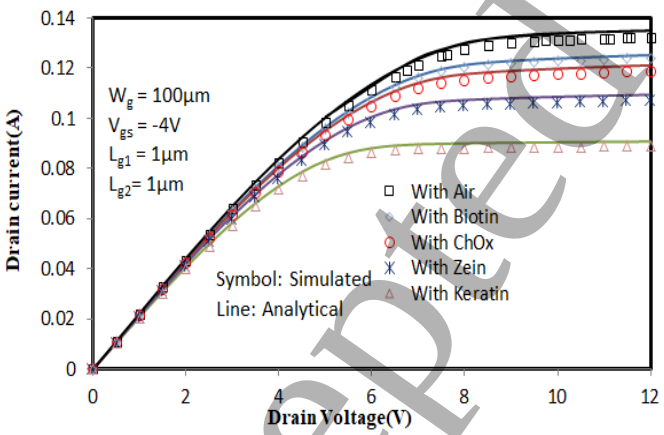

Figure 10(b). I_{ds}-V_{ds}plot for different biomolecules

In figure 10, the plot of drain current (I_{ds}) versus drain voltage (V_{ds}) has been shown at V_{gs}=-4V for all the biomolecules and at different biomolecule concentrations. The drift in I_{ds} with V_{gs} for various biomolecules with respect to the air-filled cavity is also shown in figure 10(b).Insertion of the interface charges leads to a change in the concentration of the carriers present in the 2DEG layer to maintain the charge neutrality condition, so when the negative charge is accumulated at the interface, it will decrease the carrier density hence electric field and therefore drain current[40], [41] therefore by analyzing figure10(a), we can deduce that the higher the positive biomolecule concentration(N_b), the higher is the drain current. The higher shift in drain current is observed for negative biomolecule concentration(N_b=-3×10¹²)). The maximum and minimum drain currents of 0.129A and 0.0815A can be seen for N_b= 3×10¹² and -3×10¹², respectively. From figure 10(b), it can be seen that at V_{ds}=12V, the Biotin shows the minimum change of 0.009A in drain current. In contrast, the maximum difference in the drain current is indicated by Keratin of 0.04A due to its higher dielectric constant of Keratin(K=8).Figure3 (a) shows that a maximum change of 0.02A can be noticed for N_b= 3×10¹² to detect biomolecules.

V. CONCLUSION

A double gate AlGaN/GaN HEMT-based biosensor has been critically examined to study the behaviour and presence of biomolecules in the double gate AlGaN/GaN HEMT device. It has a high sensitivity to biomolecules. It is done by analyzing analytically the behaviour of AlGaN MOS-HEMT for different biomolecules like Biotin, Keratin, Zein, ChoX and for different biomolecule concentrations. The shift in threshold voltage increases with cavity length, and drain current, sensitivity, channel potential, and transconductance increase with biomolecule permittivity. The increase in current for Keratin, Biotin, Zein, and ChOx is 0.67%, 78%, 17%, and 42%, respectively, from single to dual gate AlGaN/GaN MOS-HEMT. It is also investigated how variations in biomolecule concentration affect the electron charge density. As ours is a non-experimental work, we have neglected the effect of unwanted binding sites in the simulation as well as in the analytical model.

ACKNOWLEDGEMENT

The authors would like to thank the Director, Maharaja Agrasen Institute of Technology, Delhi, for carrying out this research work. This work has been done at the Device Research Lab, Maharaja Agrasen Institute of Technology, New Delhi, India.

REFERENCES

[1] A.-C. Liu *et al.*, "The Evolution of Manufacturing Technology for GaN Electronic Devices," *Micromachines*, vol. 12, no. 7, p. 737, 2021.

[2] S. Lu, R. Burgos, and G.-Q. Lu, "Packaging and high-temperature characterization of a 650 V, 150 A eGaN HEMT," *Semicond. Sci. Technol.*, vol. 36, no. 3, p. 34006, 2021.

[3] M. A. K. Khan, M. A. Alim, and C. Gaquiere, "2DEG transport properties over temperature for AlGaN/GaN HEMT and AlGaN/InGaN/GaN pHEMT," *Microelectron. Eng.*, vol. 238, p. 111508, 2021.

[4] S. K. Dubey, M. Mishra, and A. Islam, "Characterization of AlGaN/GaN based HEMT for low noise and high frequency application," *Int. J. Numer. Model. Electron. Networks, Devices Fields*, p. e2932, 2021.

[5] A. Soltani *et al.*, "Power performance of AlGaN/GaN high-electron-mobility transistors on (110) silicon substrate at 40 GHz," *IEEE electron device Lett.*, vol. 34, no. 4, pp. 490–492, 2013.

[6] F. Ren and S. J. Pearton, *Semiconductor-Based Sensors*. World Scientific, 2016.

[7] P. R. Coulet and L. J. Blum, *Biosensor principles and applications*. CRC Press, 2019.

[8] A. M. Bhat and C. Periasamy, "Investigation of AlGaN/GaN HEMT for pH sensing applications and sensitivity optimization," *Superlattices Microstruct.*, p.

Accepted Manuscript

107067, 2021.
[9] M. A. H. Khan, M. V Rao, and Q. Li, "Recent advances in electrochemical sensors for detecting toxic gases: NO2, SO2 and H2S," *Sensors*, vol. 19, no. 4, p. 905, 2019.
[10] J. Schalwig, G. Müller, M. Eickhoff, O. Ambacher, and M. Stutzmann, "Gas sensitive GaN/AlGaN-heterostructures," *Sensors Actuators B Chem.*, vol. 87, no. 3, pp. 425–430, 2002.
[11] R. Mehandru *et al.*, "AlGaN/GaN HEMT based liquid sensors," *Solid. State. Electron.*, vol. 48, no. 2, pp. 351–353, 2004.
[12] P. Kachhawa *et al.*, "Antigen-Antibody Interaction-Based GaN HEMT Biosensor for C3G Detection," *IEEE Sens. J.*, vol. 22, no. 7, pp. 6256–6262, 2022.
[13] S. Mishra, P. Kachhawa, P. Mondal, S. Ghosh, C. Tripura, and N. Chaturvedi, "AlGaN/GaN HEMT Based Biosensor for Detection of the HER2 Antigen Spiked in Human Serum," *IEEE Trans. Electron Devices*, vol. 69, no. 8, pp. 4527–4533, 2022.
[14] N. Chaturvedi *et al.*, "AlGaN/GaN HEMT based sensor and system for polar liquid detection," *Sensors Actuators A Phys.*, vol. 302, p. 111799, 2020.
[15] S. Gupta and G. P. Mishra, "Design and Performance Analysis of Z-Shaped Charge Plasma TFET-based label-free Biosensor," in *2021 Devices for Integrated Circuit (DevIC)*, 2021, pp. 449–466.
[16] S. Hou, A. Zhang, and M. Su, "Nanomaterials for biosensing applications." Multidisciplinary Digital Publishing Institute, 2016.
[17] A. Turner, I. Karube, and G. S. Wilson, *Biosensors: fundamentals and applications*. Oxford university press, 1987.
[18] W. Shi and M.-J. Dumont, "bio-based films from zein, keratin, pea, and rapeseed protein feedstocks," *J. Mater. Sci.*, vol. 49, no. 5, pp. 1915–1930, 2014.
[19] A. Dattola *et al.*, "Role of vitamins in skin health: A systematic review," *Curr. Nutr. Rep.*, vol. 9, no. 3, pp. 226–235, 2020.
[20] D. E. Ziskin and G. J. Nesse, "Pregnancy gingivitis: history, classification, etiology," *Am. J. Orthod. Oral Surg.*, vol. 32, no. 6, pp. A390–A432, 1946.
[21] N. Ruecha, W. Siangproh, and O. Chailapakul, "A fast and highly sensitive detection of cholesterol using polymer microfluidic devices and amperometric system," *Talanta*, vol. 84, no. 5, pp. 1323–1328, 2011.
[22] W. D. Hu *et al.*, "Simulation and optimization of GaN-based metal-oxide-semiconductor high-electron-mobility-transistor using field-dependent drift velocity model," *J. Appl. Phys.*, vol. 102, no. 3, p. 34502, 2007.
[23] S. M. Kang and Y. Leblebici, *CMOS digital integrated circuits*. MacGraw-Hill, 2003.
[24] D. Delagebeaudeuf and N. T. Linh, "Metal-(n) AlGaAs-GaAs two-dimensional electron gas FET," *IEEE Trans. Electron Devices*, vol. 29, no. 6, pp. 955–960, 1982.
[25] B. Vinter, "Subbands and charge control in a two-dimensional electron gas field-effect transistor," *Appl. Phys. Lett.*, vol. 44, no. 3, pp. 307–309, 1984.
[26] S. Khandelwal, Y. S. Chauhan, and T. A. Fjeldly, "Analytical modeling of surface-potential and intrinsic charges in AlGaN/GaN HEMT devices," *IEEE Trans. Electron Devices*, vol. 59, no. 10, pp. 2856–2860, 2012.
[27] H. L. Störmer, R. Dingle, A. C. Gossard, W. Wiegmann, and M. D. Sturge, "Two-dimensional electron gas at a semiconductor-semiconductor interface," *Solid State Commun.*, vol. 29, no. 10, pp. 705–709, 1979.
[28] G. Abstreiter, "Electronic properties of the two-dimensional system at GaAs/AlxGa1− xAs interfaces," *Surf. Sci.*, vol. 98, no. 1–3, pp. 117–125, 1980.
[29] D. C. Tsui and R. A. Logan, "Observation of two-dimensional electrons in LPE-grown GaAs-Al x Ga1− x As heterojunctions," *Appl. Phys. Lett.*, vol. 35, no. 2, pp. 99–101, 1979.
[30] J. Madan, R. Pandey, H. Arora, and R. Chaujar, "Analysis of varied dielectrics as surface passivation on AlGaN/GaN HEMT for analog applications," in *2018 6th Edition of International Conference on Wireless Networks & Embedded Systems (WECON)*, 2018, pp. 15–18.
[31] A. Dubey, A. Singh, R. Narang, M. Saxena, and M. Gupta, "Modeling and simulation of junctionless double gate radiation sensitive FET (RADFET) dosimeter," *IEEE Trans. Nanotechnol.*, vol. 17, no. 1, pp. 49–55, 2017.
[32] N. Mohankumar, *Advanced Indium Arsenide-Based HEMT Architectures for Terahertz Applications*. CRC Press, 2021.
[33] C. Chong, H. Liu, S. Wang, S. Chen, and H. Xie, "Sensitivity Analysis of Biosensors Based on a Dielectric-Modulated L-Shaped Gate Field-Effect Transistor," *Micromachines*, vol. 12, no. 1, p. 19, 2021.
[34] T. Radsar, H. Khalesi, and V. Ghods, "Improving the performance of graphene nanoribbon field-effect transistors by using lanthanum aluminate as the gate dielectric," *J. Comput. Electron.*, vol. 19, no. 4, pp. 1507–1515, 2020.
[35] P. Pal, Y. Pratap, M. Gupta, and S. Kabra, "Open gate AlGaN/GaN HEMT biosensor: Sensitivity analysis and optimization," *Superlattices Microstruct.*, p. 106968, 2021.
[36] P. Pal, Y. Pratap, M. Gupta, S. Kabra, and H. D. Sehgal, "Performance analysis of ScAlN/GaN high electron mobility transistor (HEMT) for biosensing application," in *2020 5th International Conference on Devices, Circuits and Systems (ICDCS)*, 2020, pp. 203–206.
[37] A. M. Bhat, A. Varghese, N. Shafi, and C. Periasamy, "A Dielectrically Modulated GaN/AlN/AlGaN MOSHEMT with a Nanogap Embedded Cavity for Biosensing Applications," *IETE J. Res.*, pp. 1–10, 2021.
[38] R. Mann, S. Rewari, P. Pal, S. Sharma, and R. S. Gupta, "Radiation-Sensitive AlGaN/GaN MOS-HEMT-Based Dosimeter," *J. Electron. Mater.*, pp. 1–8, 2022.
[39] S. I. Amin, L. Gajal, and S. Anand, "Analysis of dielectrically modulated doping-less transistor for biomolecule detection using the charge plasma technique," *Appl. Phys. A*, vol. 124, no. 9, pp. 1–8, 2018.
[40] A. C. V. Bôas *et al.*, "Ionizing radiation hardness tests of GaN HEMTs for harsh environments," *Microelectron. Reliab.*, vol. 116, p. 114000, 2021.
[41] B. Ho, X. Sun, C. Shin, and T.-J. K. Liu, "Design optimization of multigate bulk MOSFETs," *IEEE Trans. Electron Devices*, vol. 60, no. 1, pp. 28–33, 2012.

Accepted Manuscript

ECG Signal Feature Extraction and Waveform Representation

Atul Kumar
Dept. Of Biomedical Engineering
Deenbandhu Chhotu Ram University of Science and Technology, Murthal Sonipat, India
atulkumar98244@gmail.com

Dinesh Kumar Atal
Dept. Of Biomedical Engineering
Deenbandhu Chhotu Ram University of Science and Technology, Murthal Sonipat, India
dinesh20atal@gmail.com

2022 IEEE 6th Conference on Information and Communication Technology (CICT) | 978-1-6654-7312-5/22/$31.00 ©2022 IEEE | DOI: 10.1109/CICT56698.2022.9997920

***Abstract*- Electrocardiogram (ECG) data processing has become a fascinating study. The essential elements covered in data processing are signal analysis, feature extraction, and classification to detect abnormalities in a patient's ECG signal. Many researchers have described the automated ECG classification system with different ECG characteristics and feature extraction to represent normal ECG & arrhythmia signals. Feature extraction from an electrocardiogram is a necessary procedure for detecting cardiovascular disorders. Furthermore, identifying a group of essential elements that can obtain high accuracy is the main stage in ECG classification. Due to the difficulty in interpreting ECG signals, researchers decided to investigate the automatic detection of cardiac arrhythmia problems. Using data processing techniques and specific computer software, researchers quickly understood complex ECG patterns and predicted the presence or absence of cardiac arrhythmia. Furthermore, finding a group of essential features that can achieve the highest accuracy is the primary stage in ECG classification. This paper analyzes the PTB ECG diagnostic database and ECG parameters analysis extracted & classifications.**

Keywords: ECG Signal, PQRST Wave, MIT BIH Database.

I. INTRODUCTION

An ECG is a diagnostic visual signal used to examine the electrical movements of the cardiac muscles. It is recorded using 12 separate electrodes placed on some body areas. Medical professionals frequently utilize the ECG signal to check the heart's rhythm and function. Arrhythmias are heart irregularities in which the heart beats faster or slower than usual. Atrial depolarization is indicated by a P wave. Q is the first hazardous diversion after P. The first positive diversion is the R wave, The ventricular repolarization wave is the T wave, and the S wave is the next harmful diversion after the R wave [1-2]. Arrhythmia is described as any disorder that disrupts the heart's regular rhythm. Some arrhythmias, such as ventricular fibrillation, are deadly and can result in the patient's death. Arrhythmia detection is critical in clinical situations since it can lead to life-saving treatments. Many techniques like linear discriminant analysis, SVM, convolutional neural networks, etc. have been used to categorize regular and irregular heartbeats using ECG signals. The P-QRS-T wave is commonly considered for extracting useful features from the ECG signal, and further, it is used to compare and extract the features like amplitude, intervals, heart rate variability, etc. Signals are picked up by placing an electrode array over the subject's body surface to trace these waves from the patient. It helps in providing the information that would be appropriate for the treatment of cardiac patients. It has been widely used in detecting abnormalities as a clinically significant input in diagnostic systems.

Characteristic features define the amplitudes and intervals of ECG. The heartbeat interval and statistics like mean, median, autocorrelation, and morphological features like P, QRS, and T wave. ECG comprises of Wave, complexes, segments, and intervals. P wave, QRS complex (comprising Q, R, and S waves), T wave, PR interval, QT interval, and ST-segment are used to describe them. **Electrocardiogram** (ECG) is a **simple, non-invasive** test detecting cardiac problems. The standard wave amplitude and intervals are mentioned in table 1, which are taken as standard and help compare the abnormal signals with the normal ones.

ECG Parameter	Amplitude(mv)& Interval /Wave Duration	ECG Parameter	Amplitude(mv)& Interval /Wave Duration
P -Wave	0.25 mV	Q-T Interval	0.35 - 0.44 s

978-1-6654-7312-5/22/$31.00 ©2022 IEEE

Authorized licensed use limited to: DELHI TECHNICAL UNIV. Downloaded on January 17,2023 at 05:30:29 UTC from IEEE Xplore. Restrictions apply.

R -Wave	1.60 mV	S-T Segment	0.05 - 0.15 s
Q- Wave	0.025 mV	QRS Interval	0.08 - 0.12 s
T -Wave	0.1 - 0.5 mV	R-R Interval	0.6 - 1.20 s
P-R Interval	0.12 - 0.20 s	Heart Rate	60-100 bpm

Table 1: Intervals and Amplitudes of Standard ECG waves

II. METHODOLOGY

This section describes the methodology used in this paper, depicted in figure 1. In the first step, the ECG signal from PTB ECG diagnostic has been imported from the physionet database and further pre-processed in the second step. Useful features are extracted, waveforms are represented in the 3rd and 4th step and finally classified into normal and abnormal signals.

The ECG signal's range and the breadth of QRS intervals are graphical depictions of critical focus points.

The Proposed methodology system comprises the following step:

1. PTB ECG Data Base Importation
2. Pre-Processing
3. Feature Extraction
4. Wave Form Representation
5. Classification

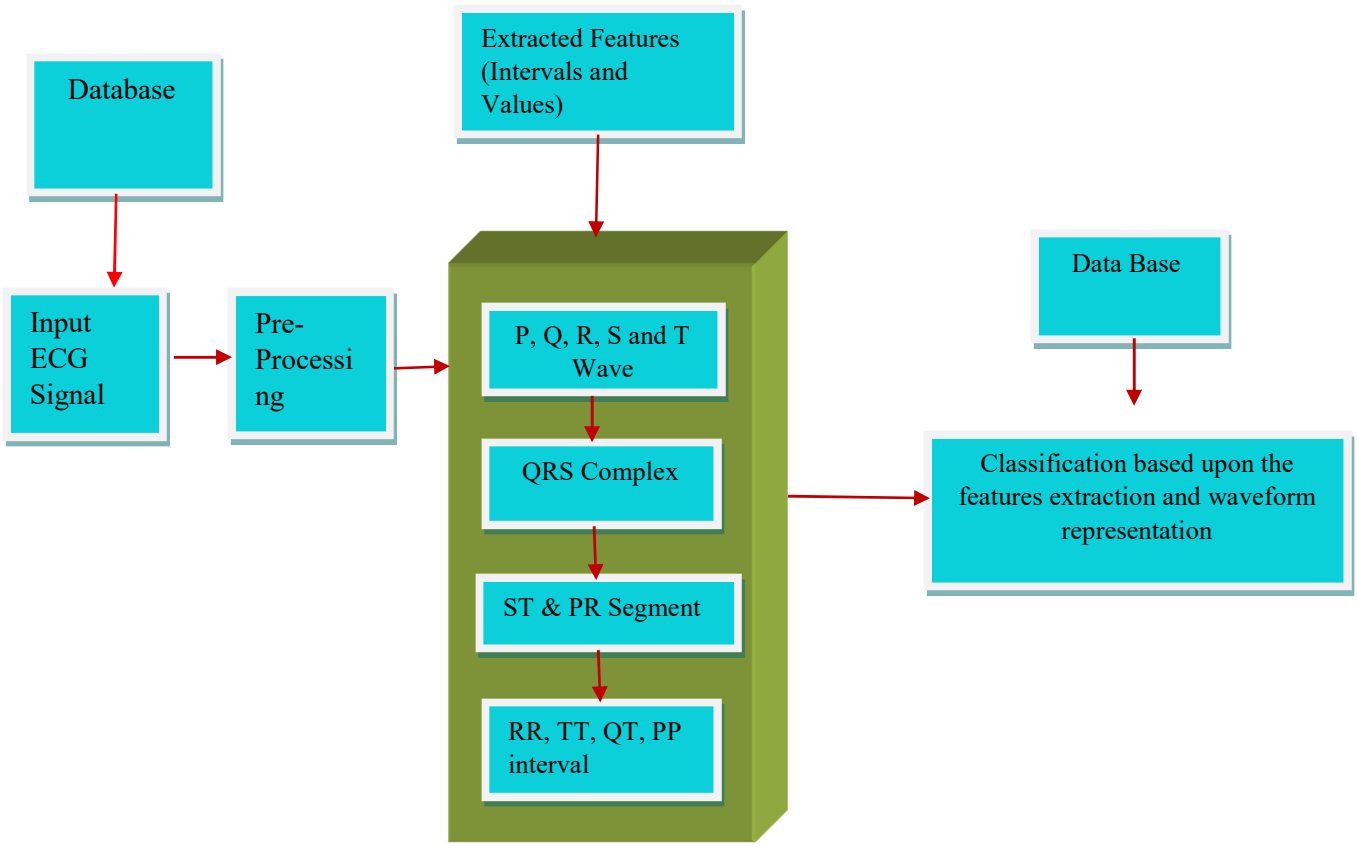

Fig. 1 Flowchart of the Proposed System

978-1-6654-7312-5/22/$31.00 ©2022 IEEE

Authorized licensed use limited to: DELHI TECHNICAL UNIV. Downloaded on January 17,2023 at 05:30:29 UTC from IEEE Xplore. Restrictions apply.

III. FEATURE EXTRACTION, ECG PATTERNS, AND CLASSIFICATION

Generating the feature vector that represents the original ECG segment is essential for recognizing cardiac rhythms. A decent recognition system should be based on the features that reflect the ECG signals so that the difference between the ECG waveforms is highlighted for waveforms that correspond to various heartbeats but muted for waveforms of the same type. The primary objective of obtaining the ECG signal's properties is to determine the parameters used to characterize the signal [4-6]. The spectral function is used to investigate the energy content of many frequency bands from 0.5 - 9 Hz. To make a proper categorization, peak values for P, Q, R, S, and T waves are also evaluated. Amplitudes and intervals are extracted to benefit each input signal of ECG in PTB Diagnostic for the proposed work. The PTB Diagnostic ECG database [3,10] has been implemented for this present study, mentioned in table 2. A total of 81 records from the database were evaluated for the current investigation. Here, two records from each diagnostic class from both databases have been chosen for simplification to highlight the various ECG characteristics.

Diagnostic Classes	**Number of Subjects**	**Number of Records Used** for **Present Work**
Bundle Branch Block	15	17
Cardiomyopathy/ Heart failure	18	19
Dysrhythmia	14	16
Healthy Controls	52	29

TABLE 2: Diagnostic Classes of Cardiac Diseases [10]

ECG Databases ⇨ / Parameters of ECG Amplitude(mv) & Interval(s)) ⇩	B_s0448_re.dat (B: Bundle Branch Block)	B_s0431_re.dat (B: Bundle Branch Block)
Amplitude of P-Wave	0.9529	0.9961
Amplitude of Q-Wave	0.0549	0.0
Amplitude of R-Wave	0.3059	0.9961
Amplitude of S- Wave	0.0078	0.3098
Amplitude of T-Wave	0.9373	0.9961
QRS complex	0.2000	0.3000

TABLE 3: ECG characteristics extracted for bundle branch block

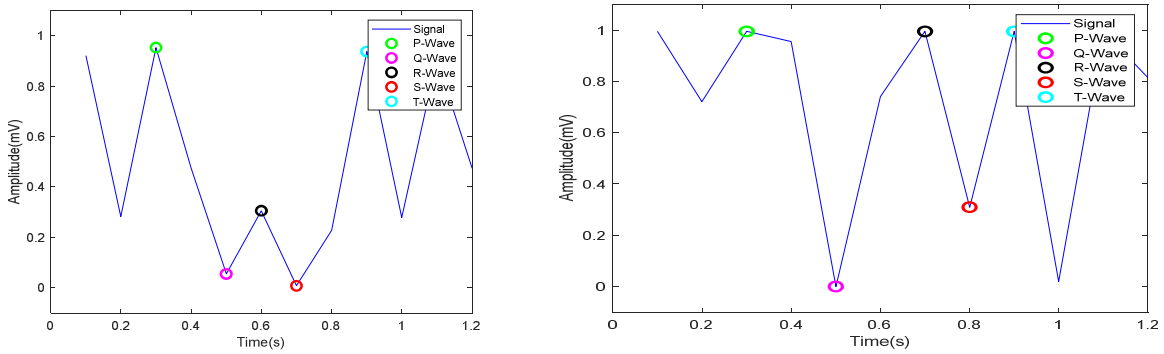

(B_s0448_re.dat B: Bundle Branch Block) (B_s0431_re.da t B: Bundle Branch Block)

Fig. 2 ECG of extracted feature using Bundle branch block

978-1-6654-7312-5/22/$31.00 ©2022 IEEE

Authorized licensed use limited to: DELHI TECHNICAL UNIV. Downloaded on January 17,2023 at 05:30:29 UTC from IEEE Xplore. Restrictions apply.

ECG Databases ⇨ / Parameters of ECG Amplitude(mv) & Interval(s)) ⇩	C_s0489_re.dat (C: Cardiomyopathy/Heart Failure	C_s0550_re.dat (C: Cardiomyopathy/Heart Failure
Amplitude of P-Wave	0.7412	0.5647
Amplitude of Q-Wave	0.0431	0.0
Amplitude of R-Wave	0.9882	0.9961
Amplitude of S- Wave	0.0980	0.0
Amplitude of T-Wave	0.9765	0.9961
QRS complex	0.3000	0.4000

TABLE 4: ECG characteristics extracted for Cardiomyopathy/ Heart Failure

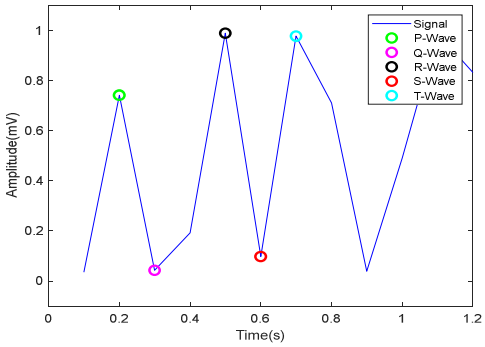

(C_s0489_re.dat C: Cardiomyopathy/ Heart Failure)

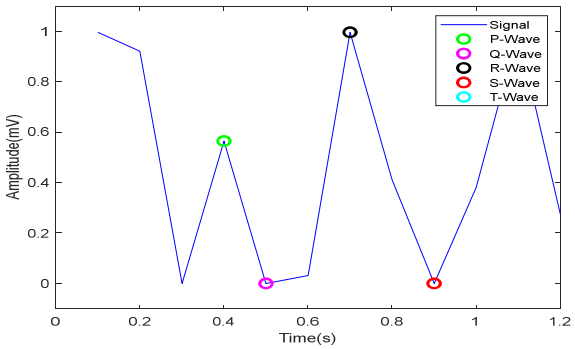

(C_s0550_re.d at C:Cardiomyopathy/Heart Failure)

Fig. 3 ECG of extracted feature using Cardiomyopathy/ Heart Failure

ECG Databases ⇨ / Parameters of ECG Amplitude(mv) & Interval(s)) ⇩	D_s0169_re.dat (D: Dysrhythmia)	Ds0366Ire.dat (D: Dysrhythmia)
Amplitude of P-Wave	0.3216	0.7412
Amplitude of Q-Wave	0.0039	0.0078
Amplitude of R-Wave	0.1451	0.9961
Amplitude of S- Wave	0.0	0.7059
Amplitude of T-Wave	0.9961	0.9961
QRS complex	0.2000	0.3000

TABLE 5: ECG characteristics extracted for Dysrhythmia

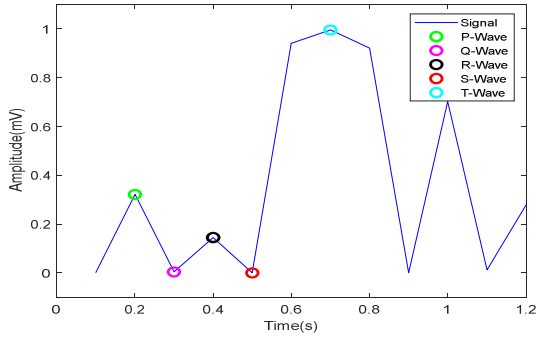

Ds0169_re. dat. D: Dysrhythmia)

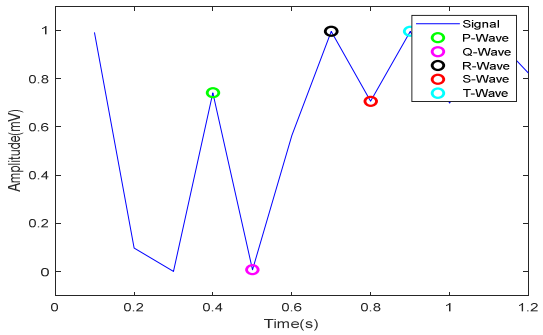

(Ds0366Ire .dat. D: Dysrhythmia)

Fig. 4 ECG of extracted feature using Dysrhythmia

978-1-6654-7312-5/22/$31.00 ©2022 IEEE

Authorized licensed use limited to: DELHI TECHNICAL UNIV. Downloaded on January 17,2023 at 05:30:29 UTC from IEEE Xplore. Restrictions apply.

ECG Databases ⇨ / Parameters of ECG Amplitude(mv) & Interval(s)) ⇩	Hes0311 lre.dat (He: Healthy Controls)	Hes0328 lre.dat (He: Healthy Controls)
Amplitude of P-Wave	0.0745	0.3882
Amplitude of Q-Wave	0.0039	0.0
Amplitude of R-Wave	0.9961	0.9961
Amplitude of S- Wave	0.6706	0.0
Amplitude of T-Wave	0.9961	0.9569
QRS complex	0.3000	0.4000

TABLE 6: ECG characteristics extracted for Healthy Controls

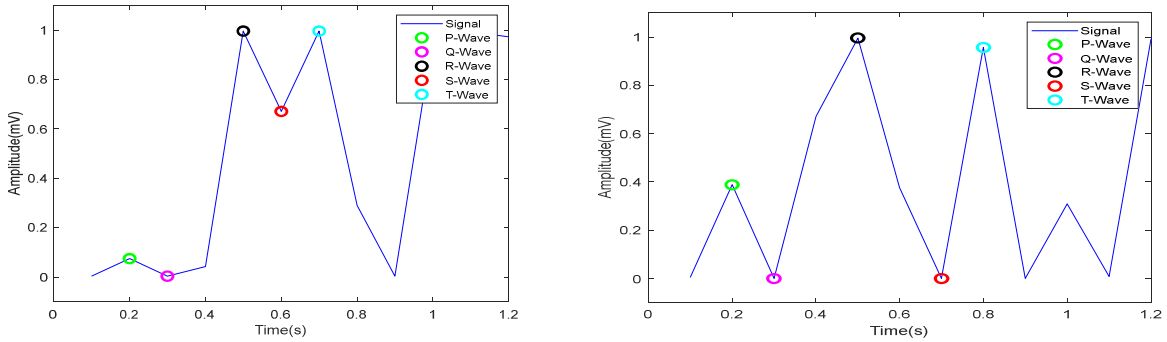

(Hes0311Ire.dat (He: Healthy Controls) (Hes0328Ire.dat (He: Healthy Controls)

Fig. 5. ECG of extracted feature using Healthy Controls

After feature extraction tables 3 to 6, signals are graphically represented in figures 2 to 5, representing Myocardial Hypertrophy, Bundle Branch Block, Healthy Controls, Cardiomyopathy/Heart Failure, Dysrhythmia, Valvular Heart Disease, Myocardial Infarction [7-9]. The QRS complex represents the depolarization of the ventricles, T wave represents the ventricular repolarization, and the P-wave reflects atrial depolarization (activation). Since an electrical vector is generated in the heart is made up of a QRS complex waveform. QRS complex time duration <12s is an abnormal condition. PR Interval is the distance between the beginning of the QRS complex and the P-wave [11-15]. When the heart is healthy, the QRS complex lasts between 80 - 120 milliseconds. The abnormality of the Q-wave indicates the existence of an infraction.

In clinical diagnostics, the QRS complex is significant. Heart conditions such as cardiac arrhythmias, ventricular hypertrophy, myocardial infarction, and aberrant conduction can all be diagnosed using the amplitude, length, and shape of the QRS complex [16-18].

(i) Abnormality in the Q wave is indicated by infarction.

(ii) A high amplitude of R shows cardiac hypertrophy.

Statistical strategies to classify normal and abnormal signals were also available. However, the computing complexity, security, and standardization of ECG characteristics are reduced. It was discovered that there were no optimal classification rules for ECG classification. As a result, the categorization must be educated in this manner.

IV. CONCLUSION

This research presented an ECG feature extraction and waveform representation system directly adaptable to other abnormal signals with comparable waveforms. The ECG analyzing system significantly depends on the precise and reliable detection of the QRS complex and the T and P waves. The essential purpose of research should be to use the chosen feature extraction and classification algorithms to improve accuracy and extend the types of heart disease that can be classified. An ECG analysis system that is quick and easy can be developed and predict differentiation in normal and abnormal ECG signals. The PTB Diagnostic ECG database has been utilized to assess this system. Furthermore, the results of these strategies are

978-1-6654-7312-5/22/$31.00 ©2022 IEEE

Authorized licensed use limited to: DELHI TECHNICAL UNIV. Downloaded on January 17,2023 at 05:30:29 UTC from IEEE Xplore. Restrictions apply.

evaluated using the MATLAB simulation program to characterize it further into different abnormal and normal signals graphically.

DECLARATIONS

Conflict of interest: The authors declare that there is no conflict of interest.

Funding: The authors declare that this study did not receive any funds from any agency.

REFERENCES

1. Dayong Gao, Michael Madden, Des Chambers, and Gerard Lyons, "Bayesian ANN Classifier for ECG Arrhythmia Diagnostic System: A Comparison Study", IJCNN '05. Proceedings, IEEE International Joint Conference on Neural Networks, 4: 2383-2388, 2005.

2. Al Rahhal MM, Bazi Y, AlHichri H, Alajlan N, Melani F, Yager RR (2016) Deep learning approach for active classification of electrocardiogram signals. Inf Sci 345:340–354.

3. Ardan A, Ma'arif M, Aisyah Z, Olivia M, Titin S (2019) Myocardial infarction detection system from PTB diagnostic ECG database using Fuzzy inference system for ST waves. J Phys Conf Ser:012071

4. Feng N, Xu S, Liang Y, Liu K (2019) A probabilistic process neural network and its application in ECG classification. IEEE Access 7:50431–50439.

5. Jovanovic BD, Litovski VB, Pavlović M (2015) "QRS complex detection-based ECG signal artifact discrimination," Facta Universitatis. Series: Electronics and Energetics 28:571–584

6. Li H, Liang H, Miao C, Cao L, Feng X, Tang C, et al (2016) Novel ECG signal classification based on KICA nonlinear feature extraction. Circuits, Systems, and Signal Processing 35:1187–1197

7. Reddy KG, Vijaya P, Suhasini S (2017) ECG Signal Characterization and Correlation to Heart Abnormalities. International Research Journal of Engineering and Technology (IRJET) 4:1212–1216.

8. Plageras AP, Psannis KE, Stergiou C, Wang H, Gupta BB (2018) Efficient IoT-based sensor BIG data collection–processing and analysis in smart buildings. Futur Gener Comput Syst 82:349–357

9. Psannis KE, Ishibashi Y (2006) Impact of video coding on delay and jitter in 3G wireless video multicast services. EURASIP J Wirel Commun Netw 2006:024616

10.(2017). The PTB Diagnostic ECG Database. Available: https://www.physionet. org/physiobank/database/ptbdb/

11, Wu F, Jing X-Y, Yue D (2017) Multi-view discriminant dictionary learning via learning view-specific and shared structured dictionaries for image classification. Neural Process Lett 45:649–666

12. Okada, M. 1979. A digital filter for the QRS complex detection, IEEE Trans. Biomed. Eng., Vol. BME-26, pp. 702-703

13. Dinh, HAN., Kumar, DK., Pah, ND and Burton, P. 2001.Wavelets for QRS detection, in Proc. 23rd IEEE EMBS Int. Conf, pp. 1883– 1887.

14. Laguna, P., Jane, R and Caminal, P. 1994. Automatic detection of wave boundaries in multi-lead ECG signals: Validation with the CSE database, Comput. Biomed. Res., vol. 27, no. 1, pp. 45–60.

15.Chouhan, V.S and Mehta, S.S. 2008. Threshold-based detection of P and T-wave in ECG using new feature signal, Int. J. Comp. Science Net. Security, vol. 8, no. 2, pp. 144–152.

16. Cuiwei Li., Chongxun Zheng and Changfeng Tai. 1995. Detection of ECG Characteristic points using Wavelet Transforms, IEEE Trans. Biomed. Eng, Vol. 42, No. 1.

17. Saxena, SC., Kumar, V and Hande, ST. 2002. QRS Detection using New Wavelets, Journal of Medical Engineering & Technology, Volume 26, November 1, pages 7-15.

18.Chouhan, V.S., Mehta, SS and Ligayat, N.S. 2008. Delineation QRS Complex, P and T wave in 12 Lead ECG" IJCSNS Vol. 8 No.4.

AUTHOR(S) BIBLIOGRAPHY

Atul Kumar is presently a final semester M.Tech student in the Department of Biomedical Engineering at Deenbandhu Chhotu Ram University of Science and Technology (DCRUST), Sonipat (Haryana) India. Atul received B.Tech. Degree in Biomedical Engineering in 2019 from Deenbandhu Chhotu Ram University of Science and Technology (DCRUST), Sonipat (Haryana) India. He has working experience in Hospital. Atul is a graduate student member of IEEE (Membership no. 98517021).

Dinesh Kumar Atal is presently working as an Associate Professor in the Department of Biomedical Engineering at Deenbandhu Chhotu Ram University of Science and Technology (DCRUST), Sonipat (Haryana), India. Dr. Dinesh received B.Tech. Degree in Biomedical Engineering in 2005 from Guru Jambheshwar University of Science & Technology, Hisar (Haryana) India, M.Tech. in Instrumentation & Control Engineering under Electrical Engineering Department from Deenbandhu Chhotu Ram University of Science & Technology, Sonipat (Haryana) India in 2011 and completed Ph.D. in Electrical Engineering from Delhi Technological University, Delhi in 2021. Dinesh's research interests include machine learning, data compression, filtering, classification algorithms, biometric analysis, biomedical signals, and image processing of human physiological signals. He has published several journals and conference papers on ECG and EEG signals analysis and processing in SCI Elsevier and Springer journals.
He has Biomedical Industrial experience where he has learned the hardware and software designing of ECG, EEG, and EMG machines with their quality control procedures. Dinesh is a graduate student member of IEEE (membership no. 93344398) and has a membership in the IEEE Engineering in Medicine and Biology Society.

978-1-6654-7312-5/22/$31.00 ©2022 IEEE

Authorized licensed use limited to: DELHI TECHNICAL UNIV. Downloaded on January 17,2023 at 05:30:29 UTC from IEEE Xplore. Restrictions apply.

Journal of Luminescence 257 (2023) 119687

Contents lists available at ScienceDirect

Journal of Luminescence

journal homepage: www.elsevier.com/locate/jlumin

Full Length Article

Effect of Ce^{4+}→Ce^{3+} conversion on the structural and luminescence properties of Ce^{4+} doped $Gd_2Ti_2O_7$ pyrochlore oxide

Umang Berwal, Vinod Singh *, Rinku Sharma

Department of Applied Physics, Delhi Technological University, New Delhi, 110042, India

ARTICLE INFO

Keywords:
Pyrochlore Oxides
Optical properties
Reduction of Ce
Raman Spectroscopy
X-ray photoelectron spectroscopy

ABSTRACT

Ternary oxides with cerium oxide as dopant are now useful as blue chip for the production of WLED's. In this present work, pyrochlore oxides $Gd_2Ti_{2-x}Ce_xO_7$ with doping concentration x = 0, 0.04, 0.08, 0.12, and 0.16, were prepared through standard solid-state reaction route. A pyrochlore structured phase is formed in the synthesized series as confirmed by conventional techniques; *i.e.,* X-ray diffraction and Raman spectroscopy. Both techniques were revealed a systematic unit cell expansion as a function of doping concentration. The SEM micrograph confirms the formation of spherically agglomerated micron sized grains. In the later section of the manuscript, Ce^{4+}→Ce^{3+} conversion effect on structural and luminescent properties were investigated. A relatively larger amount of cell expansion and accumulation of the strain is observed in the pyrochlore structured reduced samples. X-ray photoelectron spectroscopic (XPS) was used to investigate the oxidation state of the Gd, and Ti cations and oxygen anion. PL excitation spectra showed two broad bands centered around 255 nm and 360 nm due to the 4f→5 d transition of Ce^{3+} ions at λ_{em} = 425 nm. Moreover, PL emission spectrum shows a broad peak around 425 nm at λ_{ex} = 360 nm due to the 5 d to $^2F_{7/2}$ and $^2F_{5/2}$ transitions. We observed that for the Ce^{4+}→Ce^{3+} conversion both the PL emission and excitation spectra give far better results as compared to unreduced samples. Concentration quenching effect was observed for the doping concentration of 4% of cerium dopant. For 4% doping of cerium ion, CIE chromaticity results showed that the reduced as well as unreduced samples produce a bright blue colored emission line. The present study provides an insight about the potential use of Ce^{4+}→Ce^{3+}: $Gd_2Ti_2O_7$ to synthesize blue LED chips for the fabrication of WLED's.

1. Introduction

Light emitting diodes (LED's) are the successful contender for lighting due to their quickly enhancing durability, reliability, efficiency, flexibility in size, and ecofriendly components [1]. Due to environmental issues, researchers are now more focused on the alternatives to the fossil fuels as energy sources emitting on carbon dioxide gas. White LED's (WLED's) are one of the most efficient and best candidates as WLED's notably reduces global power requirements and the harnessing of fossil fuels. A numerous investigation have been done on WLED's due to their large number of advantages over other LED's such as small size, low energy consumption, long lifetimes, high brightness and reliability, high efficiency etc. [2,3]. WLED's can be produced by two methods; (a) Multi chip-LED method includes the mixing of red, green, and blue LED's light which produces white light. (b) Phosphor conversion method, Phosphor material are deposited on the top layer of LED chip [4]. The mixing of light from the phosphor and the LED chip generates white light. The second approach is currently giving higher efficiency and superior light distribution characteristic compared to the multi color LED chip method [5]. Blue LED usage in the WLED's formation, avoids the formation of ultraviolet (UV) light by a fluorescent lamp. Yum et al. synthesized $Y_3Al_5O_{13}$: Ce^{3+} yellow phosphors and used it as blue chip for the fabrication of WLED's with near UV chips with a highly efficient solid-state light [3]. Hence, near ultraviolet phosphor used in WLED's have great interest in the area of solid-state lighting. Thus, it is necessary to develop a new blue phosphor that can be efficiently excited in the ultraviolet range (~ nearly 400 nm) for the luminescence intensity enhancement.

Luminescent materials need two main things for its fabrication: crystalline host and dopant for their production. Pyrochlore ternary oxides, with chemical formula $A_2B_2O_7$ belongs to Fd-3m space group and having face centered cubic structure, were more explored and investigated structure due to their large variety of physical, chemical, and magnetic properties that depends on the cations substituted at A and

* Corresponding author.
E-mail address: vinodsingh@dtu.ac.in (V. Singh).

https://doi.org/10.1016/j.jlumin.2023.119687
Received 28 July 2022; Received in revised form 6 January 2023; Accepted 8 January 2023
Available online 10 January 2023
0022-2313/© 2023 Published by Elsevier B.V.

B sites with different valency [6]. The larger cation A is generally a trivalent rare earth ion with an inert pair of electrons and cation B is a smaller transition metal with higher valency. Larger cation at A site is eight-fold coordinated with oxygen and situated on the 16c site at position (0.5, 0.5, 0.5) within an elongated cubic polyhedron. B site with smaller sized cation is six-fold coordinated to oxygen (loss of oxygen causes reduction in the coordination of B-site cation from eight to six-fold) on the 16 d site at position (0,0,0) and located within a distorted octahedron [7]. Some of the pyrochlore oxides are excellent refractory materials display interesting phosphorescent and fluorescent properties and therefore, used as host matrix in phosphor materials. Hence pyrochlore oxides were explored world-wide as multifunctional materials due to their various use in dielectrics and fast ion conduction [8], electrocatalysts [9], high temperature catalysts [10], magnetic devices [11], in thermal barrier coatings [12], nuclear waste encapsulation [13,14], and in luminescent materials as host matrix [15–19]. The stability of an ordered pyrochlore structure is basically determined by the cationic radii ratio r_A/r_B which must be within 1.46–1.78 [18]. Present work focused on the titanate based pyrochlore oxides as they were easily formed at ambient temperatures and are promising candidate for ceramic pigments, fulfilling the basic requirement of high melting temperature (greater than 1600 °C), high refractive index, and have the potential to accommodate first row transition metal ions in the crystal lattice at the place of octahedrally coordinated site [20]. Rare earth based pyrochlore ternary oxide, $Gd_2Ti_2O_7$ selected as host lattice in luminescent material for the enhancement of luminescence intensity as $Gd_2Ti_2O_7$ produces high-quality doped material free from defect and would be ideal for practical applications [21,22]. In the present work, the rare earth ion cerium is used as the dopant (impurity) due to its existence in two stable valence states *i.e.,* Ce^{3+}/Ce^{4+} [23].

The most probable electric transition 5 d → 4f with tens of nanoseconds decay lifetime in Ce^{3+} ions are responsible for the intense radiative emission. Moreover, there is a large energy gap between 4f and 5 d level making it one of the most effective emission centers as this large energy gap reduces the multi-phonon relaxation rate. The cerium in Ce^{3+} valence state is characterized by broad absorption and emission bands due to the high sensitivity of 5 d orbitals to the host phosphor matrix [24]. Cerium in the valence state Ce^{4+} has strong UV absorption due to the charge transfer transition from oxygen emission to Ce^{3+} ions and therefore has very less luminescence. Here, CeO_2 is used as the blue light emitting luminescent dopant at the B-site of pyrochlore $Gd_2Ti_2O_7$ host in valence state Ce^{4+}. The cationic radii of Ti^{4+} and Ce^{4+} are 0.605 Å and 0.87 Å, respectively. Therefore, the cationic radii ratio r_{Gd}/r_{Ti} and r_{Gd}/r_{Ce} are obtained as 1.7405 and 1.6816, respectively which means the maximum doping of Ce^{4+} (for 8%) at the place of titanium (B-site) does not affect the basic pyrochlore structure. The first part of the paper presents the structural and optical properties of $Gd_2Ti_2O_7$ doped with Ce^{4+} and the later section focuses on the effect of reduction on optical properties in Ce^{4+} doped $Gd_2Ti_2O_7$. These samples with prior and post reduction were studied by means of XRD, Raman spectroscopy, CIE chromaticity coordinates and photoluminescence (PL) spectroscopy. The oxidation state of various cations is confirmed through X-ray photoelectron spectroscopy.

2. Experimental details

2.1. Sample preparation

2.1.1. Ce^{4+} doped $Gd_2Ti_2O_7$

Series of pure phasic $Gd_2Ti_2O_7$ pyrochlore matrix doped Ce^{4+} samples have been prepared by mixing and grinding of high purity raw powders Gd_2O_3 (CAS No.: 12,064-62-9, 99.99% purity, Sigma Aldrich), CeO_2 (CAS No.:1306-38-3, 99.95% purity, Sigma Aldrich), and TiO_2 (CAS No.12188-41-9, 99.99%), *via* conventional multi-step solid-state reaction method. The systematic process was done during solid-state rection method for the production of powdered samples as shown in Fig. 1. Since lanthanide-based oxides are highly reactive towards water and carbon dioxide, therefore, these oxides easily form hydroxides, carbonates, and oxycarbonates when exposed to the atmospheric environment. That being the case, in the very first step oxide powders Gd_2O_3, CeO_2, and TiO_2 were essentially preheated at a temperature of 850 °C for 4 h for the removal of excess moisture and volatile impurities. Later preheating step, stoichiometric amounts of all the reagents Gd_2O_3, CeO_2, and TiO_2, were accurately weighted using weighing machine as reported in Table 1. Using agate mortar pestle a single collection of 3 g (g) of all precursors Gd_2O_3, CeO_2, and TiO_2 were mixed well and ground properly for 7.5 h to construct homogeneity and uniformity in the final experimental product. These finely mixed and grounded powdered products were converted into pellets of ~10 mm diameter and 1.5 nm thickness by applying a pressure of 4.5 torr on the hydraulic press machine using a stainless-steel die set. These pellets were sintered in the alumina boat at a temperature 1200 °C for 24 h of duration in the air atmosphere by using the high temperature muffle furnace (Nabertherm).

In order to form high density products, the pellets were re-grounded for 3 h in mortar pestle and pelletized again and were annealed at a final temperature 1300 °C with a heating rate of 5 °C/min and for 48 h and cooling rate 2 °C/min. A series of powdered samples of $Gd_2Ti_{2-x}Ce_xO_7$ (x = 0.0.04, 0.08, 0.12, and 0.16) were prepared using solid state route from the starting precursors Gd_2O_3, CeO_2, and TiO_2 following the below

Table 1
Precursor's Gd_2O_3, CeO_2, and TiO_2 weight used for the synthesis of 3 g batch of $Gd_2Ti_{2-x}Ce_xO_7$ series.

Doping (%)	$Gd_2Ti_{2-x}Ce_xO_7$	Gd_2O_3 (g)	TiO_2 (g)	CeO_2 (g)
0	$Gd_2Ti_2O_7$	2.0824	0.9176	0
2%	$Gd_2Ce_{0.04}Ti_{1.96}O_7$	2.0678	0.8929	0.0393
4%	$Gd_2Ce_{0.08}Ti_{1.92}O_7$	2.0534	0.8686	0.0780
6%	$Gd_2Ce_{0.12}Ti_{1.88}O_7$	2.0392	0.8446	0.1162
8%	$Gd_2Ce_{0.16}Ti_{1.84}O_7$	2.0252	0.8210	0.1538

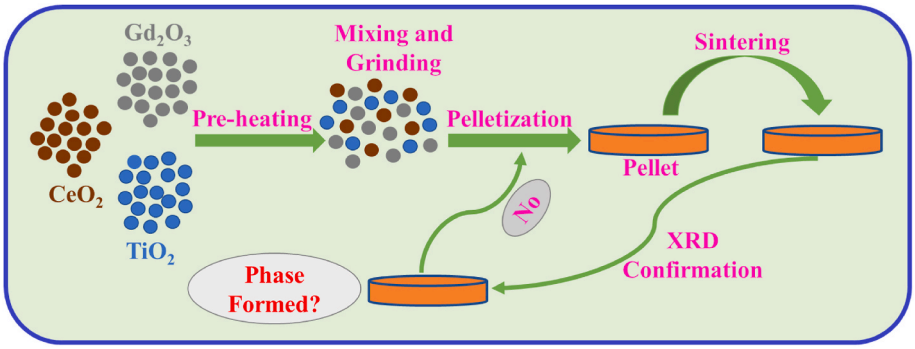

Fig. 1. Systematic flow chart for the preparation of Ce^{4+} doped $Gd_2Ti_2O_7$ pyrochlore oxide through solid state method.

reaction (1);

$$Gd_2O_3 + xCeO_2 + (2-x)TiO_2 \xrightarrow{1200^\circ C,24\ h+1300\ ^\circ C,48\ h} Gd_2Ti_{2-x}Ce_xO_7 \quad (x = 0, 0.04, 0.08, 0.12, 0.16) \quad (1)$$

2.1.2. Reduction of $Ce^{4+} \rightarrow Ce^{3+}$

All the finally sintered pellets of Ce^{4+} doped $Gd_2Ti_2O_7$ pyrochlore host samples were finely grounded and each composition was placed in different cylindrical alumina crucibles with marking. After that all the cylindrical crucibles containing Ce^{4+} doped $Gd_2Ti_2O_7$ powders were placed in quartz tube of length of 1 m and heated at a temperature of 1000 °C for the duration of 24 h in the environment of H_2 and Ar gas at a flow rate of 10%/sccm (standard cubic centimeter) and 90%/sccm, respectively in the round vacuum sealed tube furnace. Schematic diagram of the setup for cerium reduction was shown in Fig. 2. The Ce^{4+} get reduced to Ce^{3+} through the following equation:

$$Ce^{4+} \xrightarrow[1200^\circ C\ for\ 24\ hours]{H_2(10\%) + Ar(90\%)} Ce^{3+} \quad (2)$$

2.2. Characterization

For the structural examination, all unreduced and reduced pellets were evaluated using X ray diffraction characterization. XRD results for both the set of pellets were recorded in the 2θ angle range from 10°-70° using 0.02° step size and scanning rate 0.5° min^{-1} through Bruker company X-ray diffraction machine (Model Number-D8-Advance) using CuK_α radiation source of wavelength λ = 1.5406 Å at Delhi technological university (DTU), New Delhi. The measurements were carried out for microstructural investigations using field emission scanning electron microscopy (FESEM-MIRA-II, TESCAN) at Inter-University Accelerator Centre (IUAC), New Delhi. Raman patterns for both the set of pellets (unreduced + reduced pellets) were noted by applying laser light of 532 nm using the WITec Alpha 300RA Raman microscopy equipped with a 50 × objective lens at Jawaharlal Nehru University (JNU), New Delhi. X-ray photoemission spectrum for all the elements present in the reduced sample of 6% doping were noted using a monochromatic Al-Kα source with ESCA + Omicron Nano Technology at Materials Research Centre (MRC) in Malaviya National Institute of Technology (MNIT) Jaipur. PL excitation and emission spectrum for all the samples were recorded using a Jasco-8300 fluorescence spectrometer at room temperature using Xenon lamp, at DTU, New Delhi.

3. Results and discussion

3.1. Microstructural analysis

SEM photographs of undoped $Gd_2Ti_2O_7$ sample sintered at a temperature of 1300 °C for 48 h was depicted in Fig. 3. The grain size of the undoped host $Gd_2Ti_2O_7$ estimated under the high magnification order of 20,000 times. The captured SEM micrograph contains nearly spherical agglomerated particles and submicron sized pores which were clearly seen at the very compact morphological surface. The diameter of spherical grains was calculated with the help of Image J software program, and the grain size come out to be 1.2 ± 0.006 μm for pristine $Gd_2Ti_2O_7$ host. Average grain size was estimated from the Gaussian fitting size distribution histogram method as shown in Fig. 3(b). The elemental mapping through energy dispersive x-ray analysis of pristine host samples shows the uniform distribution of Gd, Ti and O ions throughout the composition shown by Fig. 3(c–e).

3.2. Structural analysis using XRD

3.2.1. Ce^{4+} doped $Gd_2Ti_2O_7$

XRD patterns for unreduced Ce^{4+} doped series of $Gd_2Ti_2O_7$ were recorded within 2θ range 10°-70° represented in Fig. 4(a) to examine the crystalline nature and phase formation of samples. Two types of diffraction peaks were observed. The first type of high intensity peaks has even order miller indices (222), (400), (440), (622), and (444) belongs to the fluorite basic framework and were found at 2θ values 30.50°, 35.35°, 50.80°, 60.38°, and 63.31°, respectively. Second type of low intensity diffraction peaks with odd miller indices (111), (311), (331), (511), and (531) belongs to ordered pyrochlore superstructure, and were observed at 2θ values 15.15°, 29.17°, 38.63°, 46.4°, and 53.29° respectively (represented by star '*' mark). All the XRD spectra are similar and indicating that the final product has an ordered pyrochlore cubic crystal structure which are in good agreement with the previous studies of $Gd_2Ti_2O_7$ [25,26]. Hence, from the XRD results we found that with the introduction of Ce^{4+} over Ti^{4+} into $Gd_2Ti_2O_7$ does not distort the basic crystal structure of pyrochlore oxide and concluded that the rare earth Ce^{4+} ion have been completely dissolved at B site within the host $Gd_2Ti_2O_7$ lattice.

A series of Ce^{4+} doped $Gd_2Ti_2O_7$ pyrochlore structure can be produced through solid state reaction method and their structural stability can be decided by the cationic radii ratio r_A/r_B, which can be estimated by using the following relation (3),

$$\left[\frac{r_{Gd}}{r_{Ce,Ti}}\right] = \left[\frac{r_{Gd}}{r_{Ti} \times atomic\ \% + r_{Ce} \times atomic\ \%}\right] \quad (3)$$

Where r_{Gd} = 1.0530 Å, r_{Ti} = 0.6050 Å and r_{Ce} = 0.8700 Å, are the ionic radius for the trivalent and tetravalent cations of pyrochlore oxide $Gd_2Ti_2O_7$. The cationic radii ratio for the different doping concentrations of Ce^{4+} were calculated and tabulated into Table 2, which decreases from 1.7405 to 1.6816 with increasing Ce^{4+} content. The r_A/r_B ratio for all compositions lies with pyrochlore stability range and XRD results supports these estimations.

The magnified view of the high intensity diffraction peak (222) is plotted from 29.5° to 31.5° as shown in Fig. 4(b). Here it is clearly observable that this (222) peak is monotonically shifted on lower angle side from 2θ = 30.53° to 30.47° on successive doping of Ce^{4+} which is

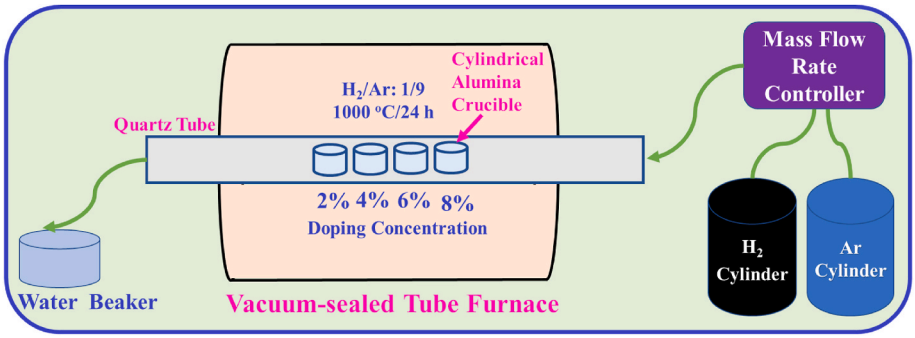

Fig. 2. Setup for the reduction of Ce^{4+} into Ce^{3+} through round vacuum sealed tube furnace setup.

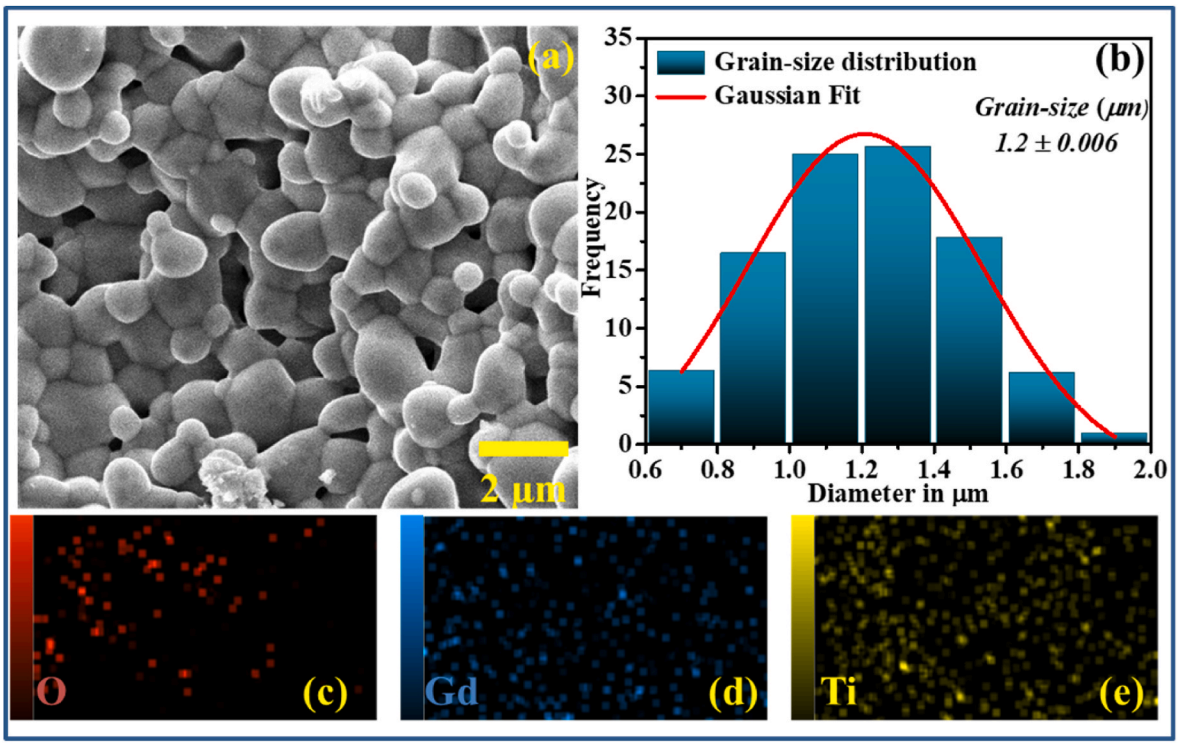

Fig. 3. **(a)** Systematic SEM micrograph of pristine host $Gd_2Ti_2O_7$, **(b)** Gaussian fitting size distribution histogram, and **(c–e)** elemental mapping of undoped host.

represented by the short dash dotted line in Fig. 4(b). As Ce^{4+} doping doesn't affect the peak intensity for all samples indicating, the stability of crystalline texture has prevailed. However, shifting of (222) indexed peak toward lower angle side for all the samples indicates an increase in lattice parameter from 10.1143 Å to 10.1332 Å on increasing doping content of Ce^{4+} due to the expansion of crystalline host lattice, which is attributed due to the substitution of large sized Ce^{4+} (0.87 Å) at relatively smaller sized Ti^{4+}(0.605 Å). A maximum doping of Ce^{3+} into $Gd_2Ti_2O_7$ structure induces a 0.18% increment in unit cell parameter.

Using Williamson-Hall (W–H) plot [27], the crystallite size for the complete series were calculated and described by the following equation (4),

$$\frac{\beta_{h,k,l}\cos\theta}{\lambda} = \frac{K}{D} + \frac{4\varepsilon\sin\theta}{\lambda} \tag{4}$$

Here, $\beta_{h,k,l}$ is the width of diffraction maxima (FWHM) for different 2θ values, the parameter 'ε' represents the lattice strain, and 'λ' is the wavelength of X-ray source (1.5046 Å) used in XRD. Here 'K' is the structure factor used for spherical particles having cubic structure and 'D' is the crystallite size. The estimated values of $\beta_{hkl}.\cos\theta$ were plotted as a function of $\sin\theta$ values and fitted with a straight line to calculate the strain and crystallite size, as shown in Fig. 4(c) for the complete series. The slope of straight line and y-intercept were further used to calculate strain 'ε' and crystallite size 'D', respectively [28]. These calculated structural parameters from XRD patterns of Ce^{4+} doped samples were represented in Table 2.

Fig. 4(d) shows a variation in crystallite size and strain as a function of Ce^{4+} doping concentration. A gradual decrement is found in crystallite size from 331.4 ± 1.8 Å to 275.83 ± 9.4 Å with successive doping concentration, respectively. Moreover, it is found that the strain increases from 0.000197 to 0.000835 on replacing Ce^{4+} over Ti^{4+}. It may be noted that the almost ~3.2 times strain is induced into the host lattice by the 8% doping of a relatively larger cation at the B-site. This decreasing trend in crystallite size with the substitution of relatively larger cation at Ti-site is in accordance with the reported results for $Gd_2Ti_{2-y}Zr_yO_7$ pyrochlore series [25].

3.2.2. *Reduced $Ce^{4+}\rightarrow Ce^{3+}$ doped $Gd_2Ti_2O_7$*

To carry out the structural investigation of complete reduced series of cerium doped $Gd_2Ti_2O_7$, the XRD has been executed and were also shown in Fig. 5(a). All the reduced samples show perfectly single pyrochlore phase similar to XRD patterns of unreduced samples. There were no additional impurity peaks on the complete reduced series of $Ce^{4+}\rightarrow Ce^{3+}$ doped $Gd_2Ti_2O_7$, indicating that the reduction $Ce^{4+}\rightarrow Ce^{3+}$ has not affected the dissolution of cerium into pyrochlore unit cell. Moreover, it was found that the XRD diffraction peaks of $Ce^{4+}\rightarrow Ce^{3+}$ doped $Gd_2Ti_2O_7$ shifts towards lower 2θ angle side with increasing cerium doping, in comparison to standard data of pristine host $Gd_2Ti_2O_7$. The most intense XRD peak centered around ~30.53° (with miller indices (222)), is separately plotted for all the compositions and shown in Fig. 5(b), to depict peak shifting towards lower 2θ angle side. Since the cationic size of Ce^{3+} (1.01 Å) is larger than the B-site cation *i.e.,* Ti^{4+} (0.605 Å), therefore, unit cell parameter increases as indicated by shifting of diffraction pattern on lower 2θ value. It is noteworthy that the unit cell parameter calculated through (222) diffraction peak increases from 10.1143 Å to 10.1527 Å as reported in Table 3. A maximum doping of Ce^{4+} into $Gd_2Ti_2O_7$ structure under reduced environment causes a 0.40% increment in unit cell parameter. W–H plots deduced from XRD patterns of reduced samples were depicted in Fig. 5(c). The crystallite size and strain estimated through W–H plots are reported in Table 3 and plotted as a function of $Ce^{4+}\rightarrow Ce^{3+}$ concentration in Fig. 5 (d). A variation in strain with respect to increasing doping concentration clearly shows that the strain increases on increasing cerium content. The host lattice with maximum doping concentration of reduced cerium is examined as ~4.3 times of that persist in pristine $Gd_2Ti_2O_7$ lattice.

The reduction of cerium cation causes a lattice distortion which is shown by increased strain. The crystallite size does not show any significant variation as on increasing doping concentration. A gradual decrement in crystallite size as on increasing Ce^{4+} content is harnessed by reduction of Ce^{4+} to a larger sized Ce^{3+} ion and structural distortion caused unit cell expansion.

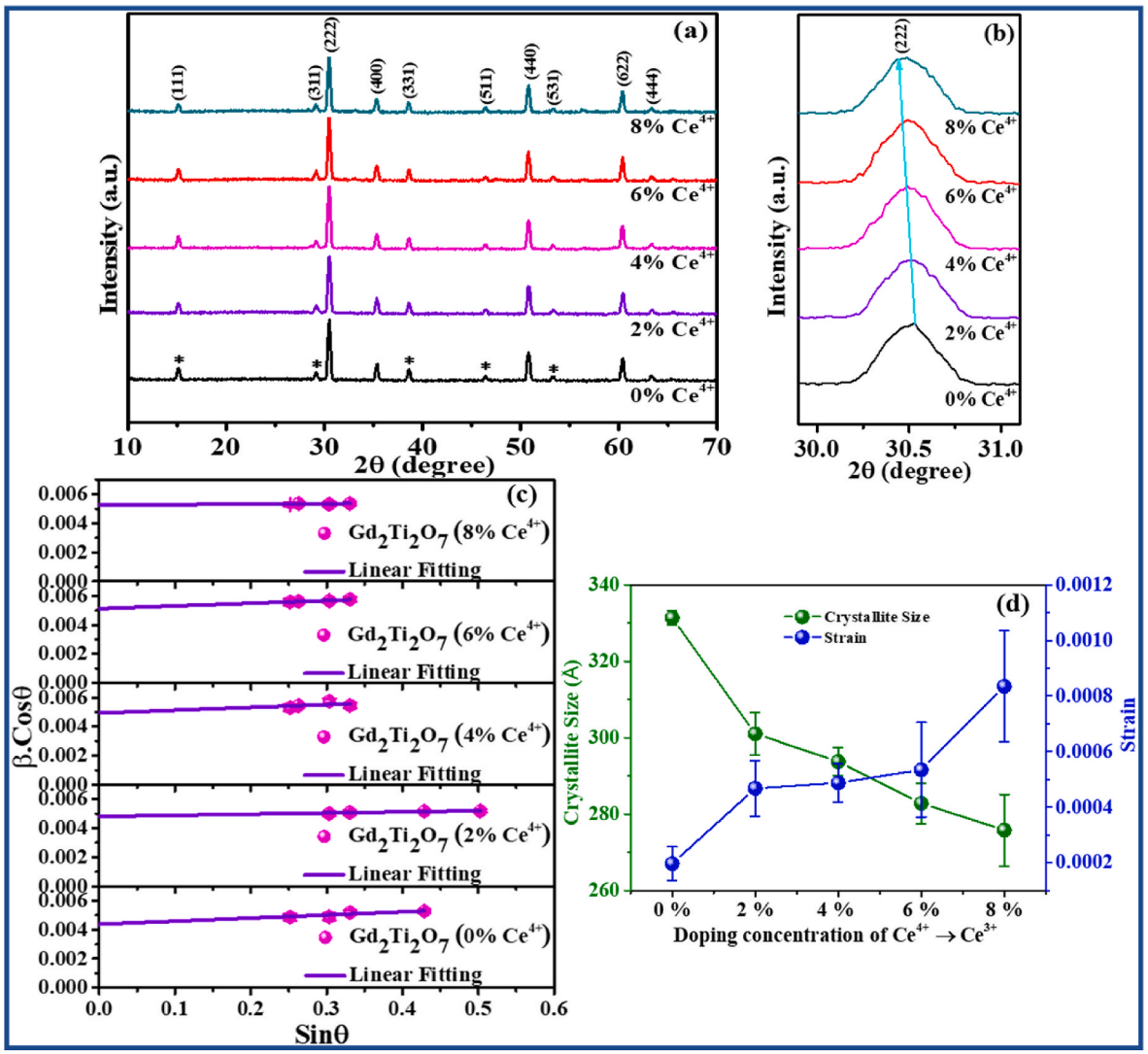

Fig. 4. **(a)** XRD patterns for complete series of Ce^{4+} doped $Gd_2Ti_2O_7$, **(b)** peak shifting of (222) peak, **(c)** W–H plot for all the compositions, and **(d)** crystallite size and strain distribution with cerium doping.

Table 2
Structural variables calculated for pristine and Ce^{4+} doped samples of $Gd_2Ti_2O_7$ from XRD results.

Doping (%)	$Gd_2Ce_xTi_{2-x}O_7$	r_A/r_B	Crystallite Size (D) in Å	Strain	Lattice Constant (Å)
0%	$Gd_2Ti_2O_7$	1.7405	331.38 ± 1.8	0.000197 ± 0.00006	10.1143 ±0.0002
2%	$Gd_2Ce_{0.04}Ti_{1.96}O_7$	1.7254	301.07 ± 5.6	0.000468 ± 0.0001	10.1177 ±0.0001
4%	$Gd_2Ce_{0.08}Ti_{1.92}O_7$	1.7105	293.74 ± 3.7	0.000488 ± 0.00007	10.1208 ±0.0005
6%	$Gd_2Ce_{0.12}Ti_{1.88}O_7$	1.6959	282.84 ± 5.3	0.000535 ± 0.00017	10.1247 ±0.0003
8%	$Gd_2Ce_{0.16}Ti_{1.84}O_7$	1.6816	275.83 ± 9.4	0.000835 ± 0.0002	10.1332 ±0.0001

3.2.3. *Effect of Ce^{4+}→Ce^{3+} conversion*

It was clearly observed from XRD analysis that in case of reduced samples the shifting of diffraction pattern towards lower angle side is more as compared to unreduced samples. This is due to the reason that the size of Ce^{3+} (1.01 Å) is more as compared to Ce^{4+} (0.87 Å). Hence as Ce^{4+} converted to Ce^{3+}, then due to the bigger size of Ce^{3+} as compared to Ti^{4+} (0.605 Å), the host lattice expands more. Ce^{4+}→Ce^{3+} reduction generates more strain in the pyrochlore single phasic cell. It is concluded from the reduction caused variation in crystallite size that the Ce^{4+}→Ce^{3+} reduction causes an increment in crystallite size which is encountered by a reduction in crystallite size driven by doping. Although, structural investigation through XRD is not produced any structural transformation or significant structural distortion.

3.3. *Structural analysis using Raman spectroscopy*

3.3.1. *Ce^{4+} doped $Gd_2Ti_2O_7$*

Principal factor investigation of $A_2B_2O_7$ pyrochlore oxides with Fd-3m space group indicates the presence of six Raman active modes: A_{1g}, E_g, and four T_{2g}. Only oxygen atoms (O_{8b} and O_{48f}) are displaced from their respective position for all these vibrational modes. Out of all the modes, only single T_{2g} mode is appeared due to the O_{8b} oxygen vibrations and other three T_{2g} are present due to the O_{48f} oxygen vibrations [29,30]. Raman spectra for complete set of Ce^{4+} doped $Gd_2Ti_2O_7$ host oxides were shown in Fig. 6(a) and de-convoluted Raman spectra were also represented by Fig. 6(b–f) for each composition, at room temperature. For the pristine host $Gd_2Ti_2O_7$ sample, the Raman spectra were recorded within 140–800 cm^{-1} wavenumber range, are in good agreement with the previous reports [18,31,32]. Raman spectrum

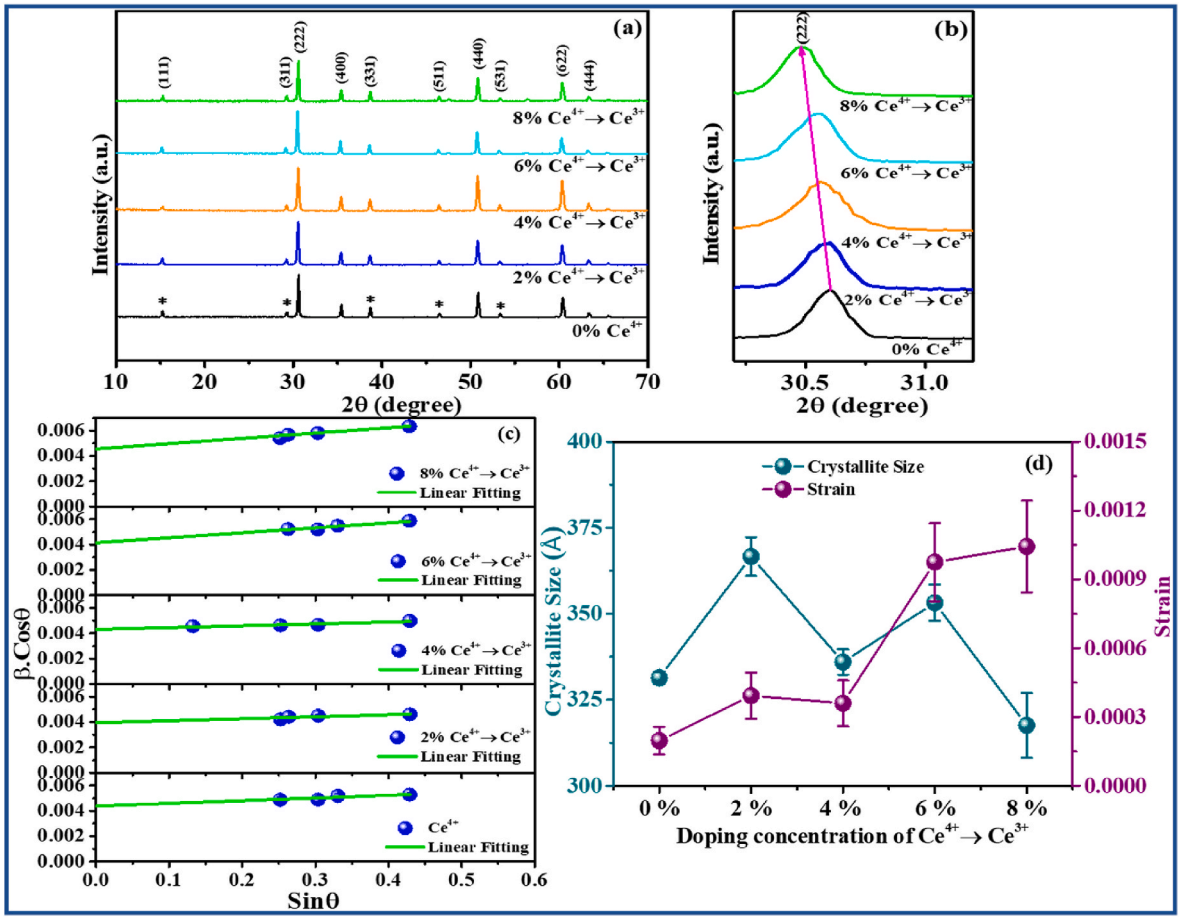

Fig. 5. **(a)** XRD patterns for complete series of Ce^{4+}→Ce^{3+} doped $Gd_2Ti_2O_7$, **(b)** peak shifting of (222), **(c)** W–H plot for all the compositions, and **(d)** Crystallite size and strain distribution with cerium doping.

Table 3
Structural variables calculated for pristine and Ce^{4+}→Ce^{3+} doped samples of $Gd_2Ti_2O_7$ through XRD results.

Doping (%)	$Gd_2Ce_xTi_{2-x}O_7$	Crystallite Size (D) in Å	Strain	Lattice Constant (Å)
0%	$Gd_2Ti_2O_7$	331.38 ± 1.80	0.000197 ± 0.00006	10.1143 ±0.0002
2%	$Gd_2Ce_{0.04}Ti_{1.96}O_7$	366.61 ± 16.2	0.000393 ± 0.00015	10.1413 ±0.0001
4%	$Gd_2Ce_{0.08}Ti_{1.92}O_7$	335.99 ± 7.60	0.000360 ± 0.00009	10.1433 ±0.0003
6%	$Gd_2Ce_{0.12}Ti_{1.88}O_7$	353.20 ± 27.2	0.000975 ± 0.000033	10.1477 ±0.0006
8%	$Gd_2Ce_{0.16}Ti_{1.84}O_7$	317.57 ± 12.0	0.001043 ± 0.000174	10.1527 ±0.0012

contains two most intense bands; one is due to the combination of E_g and T_{2g} with very close wave number centered around ~310 cm^{-1} is attributed due to the *O*-Gd-O bending mode; and the second most intense band is centered around ~516 cm^{-1} ascribed as A_{1g} band is assigned due to the presence of internal stretching of Gd–O. The other four bands have weaker intensity. Out of these remaining four weak bands, three bands were presented at ~212 cm^{-1}, ~545 cm^{-1} and ~680 cm^{-1}. The remaining T_{2g} bands appears due to Ti–O stretching. The Raman spectrum for Ce^{4+} doped $Gd_2Ti_2O_7$ samples shows the same pattern as that of pristine host, therefore, we can say that Ce^{4+} ions well dissolved in the pristine host $Gd_2Ti_2O_7$ without introducing much structural distortion. But with the doping of Ce^{4+}, it is found that an extra small intensity peak centered around ~457 cm^{-1} is appeared due to the trace amounts of TiO_2 [29]. From XRD results, it is found that with Ce^{4+} ion doping in $Gd_2Ti_2O_7$ host matrix, the radii ratio of cation A (Gd) and cation B(Ti/Ce) decreases from 1.7405 to 1.6816 and the pyrochlore unit cell experiences lattice expansion from 10.1143 Å to 10.1332 Å. It causes a small decrement in force constant among various Raman active bands. The doping of larger cation allows an increment in bond length due to loosen Raman modes and is evidenced by a shifting of all Raman peaks towards lower wavenumber side as on increasing Ce^{4+} content. Thus, Raman spectroscopic results are in accordance with XRD results.

3.3.2. *Reduced Ce^{4+}→Ce^{3+} doped $Gd_2Ti_2O_7$*

Since Raman spectroscopy is useful to probe the vibrations of cations as well as anions, Raman results would show the effect of reduction in cerium ions more prominently than XRD. Raman spectra were recorded for the series of Ce^{4+} doped $Gd_2Ti_2O_7$ annealed at a temperature of 1000 °C under the reducing environment. Fig. 7(a) represents a series of vibrations recorded for all reduced samples *i.e.,* $Gd_2Ti_2O_7$: Ce^{4+}→Ce^{3+} as on increasing doping concentration from bottom to top. Raman data for each sample is deconvoluted into six Raman modes and represented in Fig. 7(b–e) for the doping concentrations of 2%, 4%, 6%, and 8% respectively. A similar Raman spectrum is obtained for the reduced samples except a small red shift in all vibrations. The reduction of doped cerium does not allow any significant structural distortion as evidenced by XRD results. Like Raman results of unreduced samples, larger size of Ce^{3+} (1.01 Å) ion than Ti^{4+} (0.605 Å) is responsible for the red shift in doped sample $Gd_2Ti_2O_7$: Ce^{4+}→Ce^{3+}.

3.3.3. *Effect of Ce^{4+}→Ce^{3+} conversion*

The effect of reduction of cerium dopants from Ce^{4+} to Ce^{3+} is

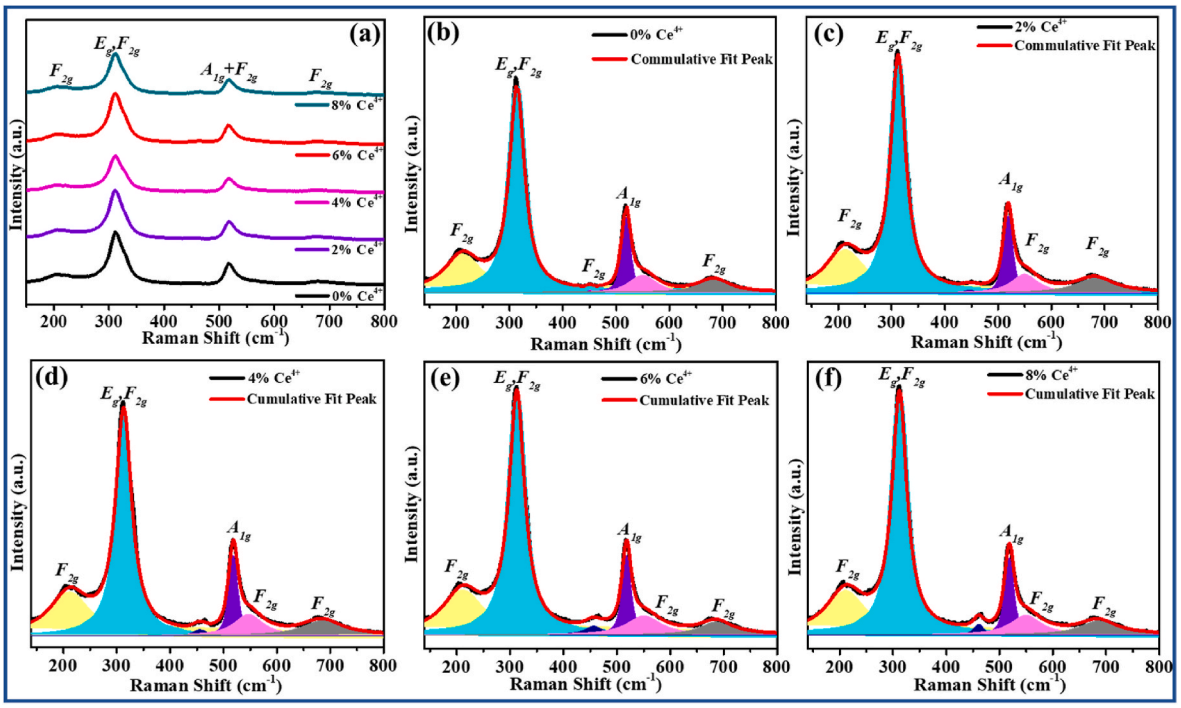

Fig. 6. **(a)** Raman spectra for all the Ce^{4+} doped $Gd_2Ti_2O_7$ host samples and **(b–f)** Raman de-convolution for each composition of Ce^{4+} doped $Gd_2Ti_2O_7$.

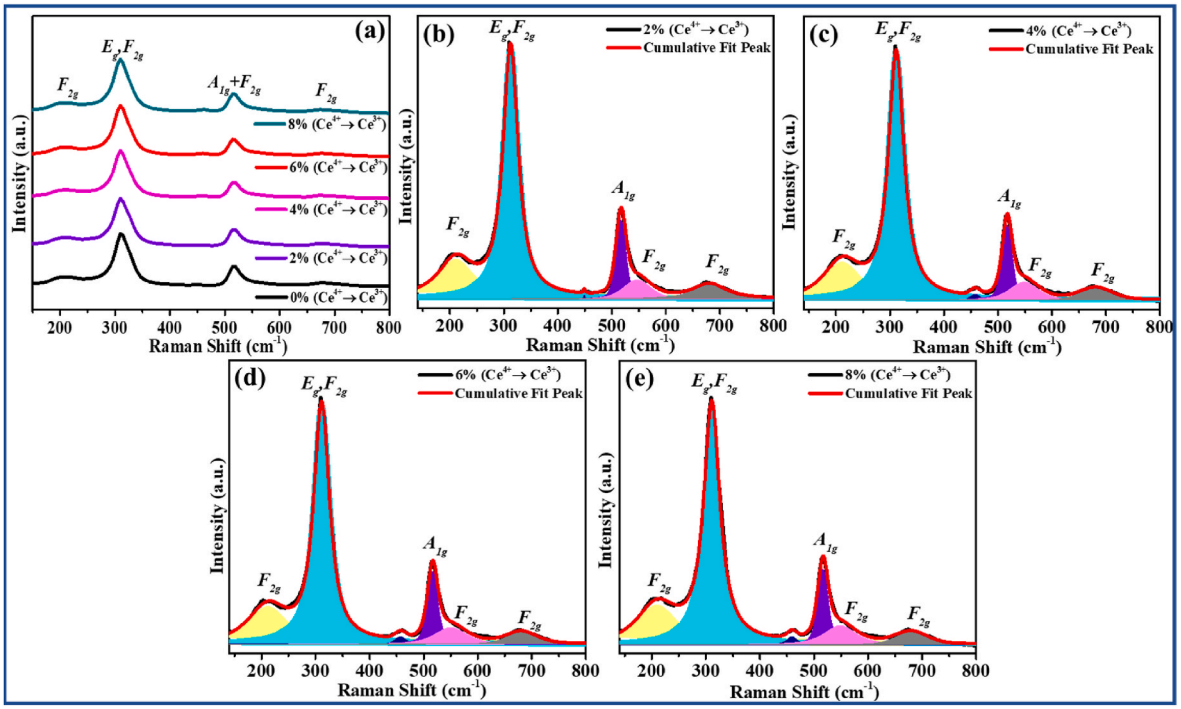

Fig. 7. **(a)** Raman spectrum for all the reduced samples $Gd_2Ti_2O_7$: Ce^{4+}→Ce^{3+} with various doping concentration and **(b–e)** Raman de-convolution for each composition of Ce^{4+} doped $Gd_2Ti_2O_7$.

characterized by a larger red shift in respective composition. This is due to the reason that the size of Ce^{3+} cation (1.01 Å) is bigger as compared to the size of Ce^{4+} cation which is 0.870 Å. So, in the case of Ce^{3+} the lattice expansion is more as well explained by the XRD results also. Therefore, force constant decreases more and bond length increases more. Hence, shifting of 2nd, and 4th most intense Raman vibrational bands are more for the reduced Ce^{4+}→Ce^{3+} samples as compared to Ce^{4+} doped $Gd_2Ti_2O_7$. This shifting in Raman active vibrations were estimated for unreduced and reduced set of samples and tabulated in Table 4 and respective red and blue shift are well represented in Fig. 8 ((a) and (b) by subscript R and B. The high intensity Raman band shows the maximum peak shifting *i.e.,* 1.6 cm^{-1} for unreduced sample, but in the case of reduced sample, the maximum shifting for the same Raman band is 2.9 cm^{-1}. The value of the peak shifting in 2nd most intense Raman band is 0.6 cm^{-1} for the Ce^{4+} doped $Gd_2Ti_2O_7$, but for the reduced $Gd_2Ti_2O_7$: Ce^{4+}→Ce^{3+} sample, the respective peak shifting is

Table 4
Peak shifting in raman modes as a function of doping concentration for both Ce^{4+} doped $Gd_2Ti_2O_7$ and reduced $Gd_2Ti_2O_7$: Ce^{4+}→Ce^{3+} samples.

Doping	Ce^{4+} (Peak Shifting Δω cm^{-1})						Ce^{4+}→Ce^{3+} (Peak Shifting Δω cm^{-1})					
	1st Peak	2nd Peak	3rd Peak	4th Peak	5th Peak	6th Peak	1st Peak	2nd Peak	3rd Peak	4th Peak	5th Peak	6th Peak
0%	0.0	0.0	0.0	0.0	0.0	0.0	0.0	0.0	0.0	0.0	0.0	0.0
2%	0.6 $_B$	1.0 $_R$	3.2 $_R$	0.3 $_R$	2.2 $_B$	3.2 $_R$	2.0 $_R$	2.0 $_R$	6.2 $_R$	1.2 $_R$	4.0 $_B$	8.4 $_R$
4%	0.6 $_B$	1.2 $_R$	1.9 $_R$	0.3 $_R$	0.1 $_R$	1.0 $_R$	0.8 $_R$	2.4 $_R$	2.9 $_B$	1.4 $_R$	1.1 $_B$	7.3 $_R$
6%	0.4 $_B$	1.6 $_R$	6.2 $_B$	0.3 $_R$	0.1 $_R$	0.9 $_B$	0.7 $_R$	2.5 $_R$	2.5 $_B$	1.8 $_R$	3.0 $_B$	7.5 $_R$
8%	1.3 $_B$	1.2 $_R$	3.7 $_B$	0.6 $_R$	0.5 $_R$	2.8 $_B$	3.0 $_R$	2.9 $_R$	4.5 $_B$	1.8 $_R$	1.2 $_B$	8.8 $_R$

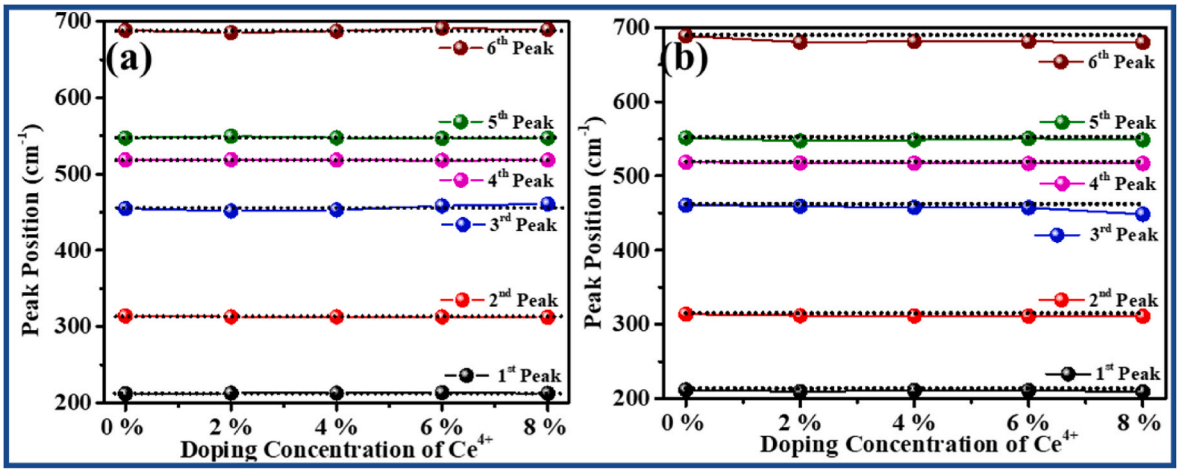

Fig. 8. **(a)** Shifting of all the raman peaks for Ce^{4+} doped $Gd_2Ti_2O_7$ and **(b)** the reduced samples $Gd_2Ti_2O_7$: Ce^{4+}→Ce^{3+} with various doping concentration.

1.8 cm^{-1}. The maximum shifting of 3.2 cm^{-1} in the peak position was observed for the last vibrational band centered around ~680 cm^{-1} for without reduction, but the same band shows maximum peak shifting of 8.8 cm^{-1} for reduced samples. Thus, reduction of cerium dopant has introduced a small amount of disordering in the lattice of oxygen ions examined by Raman spectroscopy which is not much significant that would allow a phase transformation.

3.4. X-ray photoemission spectroscopic analysis

X-ray photoelectron spectroscopy (XPS) is used to confirm the presence and oxidation states of Gd, Ti and oxygen ions present in the finally sintered samples. The XPS spectrum of Ce^{4+} doped $Gd_2Ti_2O_7$ pyrochlore oxide for 6% cerium doped sample after reduction were analyzed in order to find the charge state of different ions. Fig. 9(a–e) show the survey and core level spectra of different elements present in

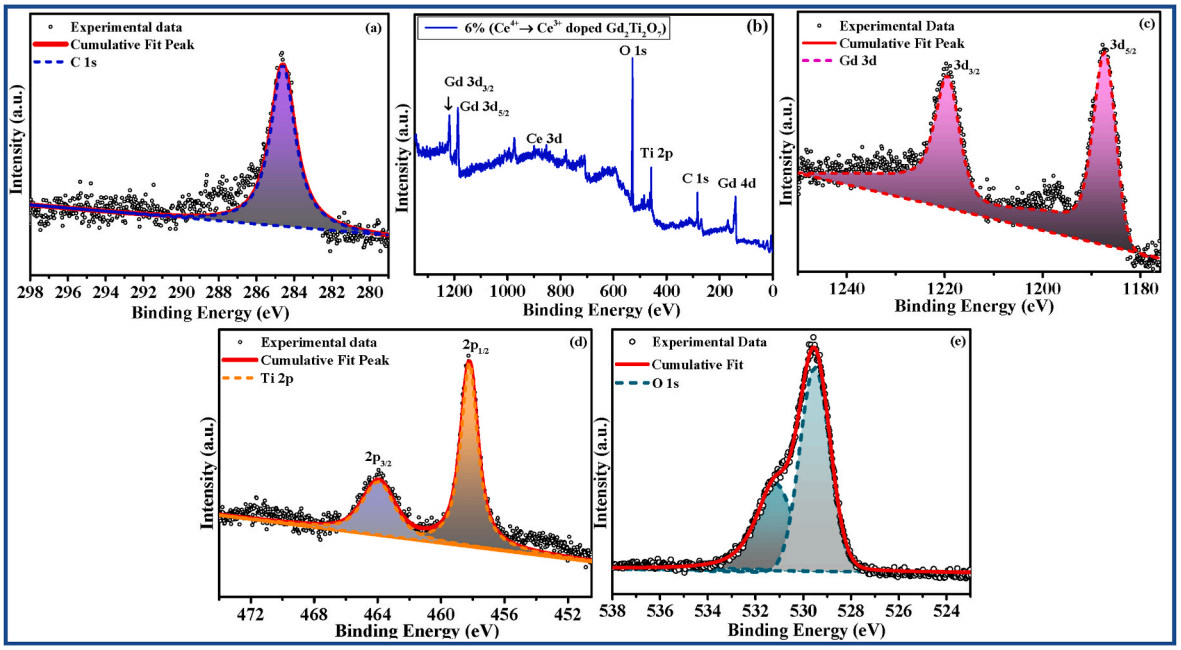

Fig. 9. XPS spectrum of 6% Ce^{4+} doped $Gd_2Ti_2O_7$ thermally heated in reduced environment for **(a)** C 1s, **(b)** survey spectrum, **(c)** Gd 4f, **(d)** Ti 2p, **(e)** O 1s, and here black circles are the measured XPS spectra and red line represents cumulative fit.

the sample. Each core level spectra were fitted using the Pseudo Voigt peak shape after subtracting the Shirley or linear background. In order to account for the instrumental offset, each spectrum was calibrated using the C 1*s* peak, as shown in Fig. 9(a). A reference value of 284.6 eV was used for the C 1*s* binding energy and the corrected difference was then used for each element [33,34]. The charge neutralizer was used during the measurement due to the insulating nature of the sample. Fig. 9(b) shows the XPS survey spectra of the 6% Ce^{4+} doped reduced $Gd_2Ti_2O_7$ pyrochlore oxide. All the prominent peaks have been assigned to the respective energy levels of the different elements present in the sample, which discard the possibility of any elemental impurity in the synthesized sample.

Fig. 9(c) show the Gd 3*d* core level spectra, where the two-spin orbit split components $3d_{5/2}$ and $3d_{3/2}$ are present at 1187.48 eV and 1219.49 eV and the binding energy difference for these two peaks are 32.01 eV and the area ratio for both the peaks are 2:3, which indicate the 3+ oxidation state of Gd in the compound [35]. Further, the Ti 2p core level spectra for the 6% cerium doped $Gd_2Ti_2O_7$ reduced sample is shown in Fig. 9(d), where the two peaks centered around 463.82 eV and 458.25 eV are assigned to the $2p_{1/2}$ and $2p_{3/2}$ components with energy gap 5.57 eV and area ratio of both the peaks are 1:2 indicating the peak positions and the energy separation of the two components indicate the 4+ valence state of TiO_2 in the sample [33,36]. The absence of any distortion/splitting in the components discard the possibility of the deviation of the Ti atoms from the tetravalent state.

Fig. 9(f) represents the deconvoluted O 1s XPS spectrum of 6% cerium doped $Gd_2Ti_2O_7$, after thermal treatment in reduced environment. The O 1s XPS spectra show the main peak at 529.5 eV, found to be due to the oxygen bounded in lattice (O^{2-}) and the second weak intense component at 531.2 eV corresponds to the surface contamination, i.e., OH-group present on the outermost surface layer of the sample [34]. Also, these two peaks may arise from the two different types of oxygen coordination geometries in the pyrochlore $Gd_2Ti_2O_7$ host. Note that in the pyrochlore structures, two different oxygen environments and cationic disordering between Gd–O and Ti–O site give rise to change of oxygen anion chemical environment. The cation Gd is less electronegative than the Ti cation and hence the Ti–O bond's ionic character is weaker than Gd–O bond. Therefore, the O 1*s* peak with the higher binding energy (531.25 eV) is attributed to the oxygen anions bounded to site cations. On the other hand, O 1s the peak with at the lower binding energy (529.52 eV) may result from the oxygen atoms bounded to Ti–O bond [37].

3.5. Photoluminescence (PL) results

The Ce^{3+} involves 4f to 5 d electric dipole transition which strongly depends on the provincially surrounding of the Ce^{3+} sites present in the host $Gd_2Ti_2O_7$ pyrochlore oxide. This is why trivalent Ce^{3+} ions producing not only strong excitation and emission but also produces slight shifting in both the excitation and emission spectrum over a broad range of wavelength. Up to now, a clear difference between Ce^{3+} and Ce^{4+} emission and excitation bands have not been observed. Reducing conditions are applied to enable a clear difference between the Ce^{3+} and Ce^{4+} emission and excitation bands.

3.5.1. Ce^{4+} doped $Gd_2Ti_2O_7$ and effect of reduction

We report a comparative experimentally observed PL excitation and emission spectrum results of Ce^{4+} doped $Gd_2Ti_2O_7$ pyrochlore samples and for the same samples series annealed at a temperature of 1000 °C for time 24 h in reducing environment under the flow of gas mixture hydrogen and argon, were well represented in Fig. 10(a) and Fig. 10(b), at room temperature. The excitation spectrum in Fig. 10(a) shows two broad bands centered around wavelength of 255 nm and 360 nm similar to earlier report [38]. The excitation broad band from 320 nm to 400 nm with peak at nearly 360 nm is ascribed due to the band-to-band absorption of the undoped $Gd_2Ti_2O_7$ host lattice which give rise to excitation of luminescent centers [21]. Tetravalent cation Ce^{4+} does not perform 4 d → 5f transition emission and excitation, therefore in Fig. 10 (a) all the unreduced samples of Ce^{4+} doped $Gd_2Ti_2O_7$, shows that with increasing Ce^{4+} ion doping in host $Gd_2Ti_2O_7$, reduces the excitation intensity of host material $Gd_2Ti_2O_7$ which is also represented by inset enlarged view for the unreduced samples. But for the reduced samples, these bands at 255 nm and 360 nm were appeared due to the 4f → 5 d transition of the cerium trivalent (Ce^{3+}) ion presence as Ce^{4+} ions reduced to Ce^{3+} and at the 360 nm excitation peak of host $Gd_2Ti_2O_7$ also appeared and the peak intensity increases with the reduction and doping. The emission spectrum for fixing excitation wavelength λ_{ex} = 255 nm were recorded and represented in Fig. 10(b) shows that the emission band nearly around ~ 400 nm wavelength were observed due to the 5 d to 4f transition of Ce^{3+} ions. But as the excitation wavelength spectrum has high intensity band at 360 nm as compared to 255 nm, so we have taken into consideration the emission spectrum at λ_{ex} = 360 nm [39].

The emission spectrum at fixed excitation wavelength λ_{ex} = 360 nm, for the complete series with or without reduction were presented in Fig. 10(c). For the host, emission spectrum was recorded at excitation wavelength of 360 nm, it was observed that an emission peak around 425 nm is attributed due to host $Gd_2Ti_2O_7$ containing gadolinium ion [18]. As tetravalent cation Ce^{4+} does not perform 4 d → 5f transition emission, therefore it is charge transfer (CT) emission in case of reduced samples. The band in case of reduced samples exhibits a broad band centered around 425 nm can be attributed due to the transition from lowest 5 d state to $^2F_{5/2}$ and $^2F_{7/2}$ components of the ground state as shown in Fig. 10(b). Thus, we can say that CT emission might occur in the same place as 4 d → 5f in case of Ce^{3+} emission. In the excitation spectra, the reduced samples have tail from the lower energy side suggesting few constituents. According to crystal field splitting of d^1 orbital of Ce^{3+} ions in a cubic symmetry ($Gd_2Ti_2O_7$), the T_{2g} energy level always

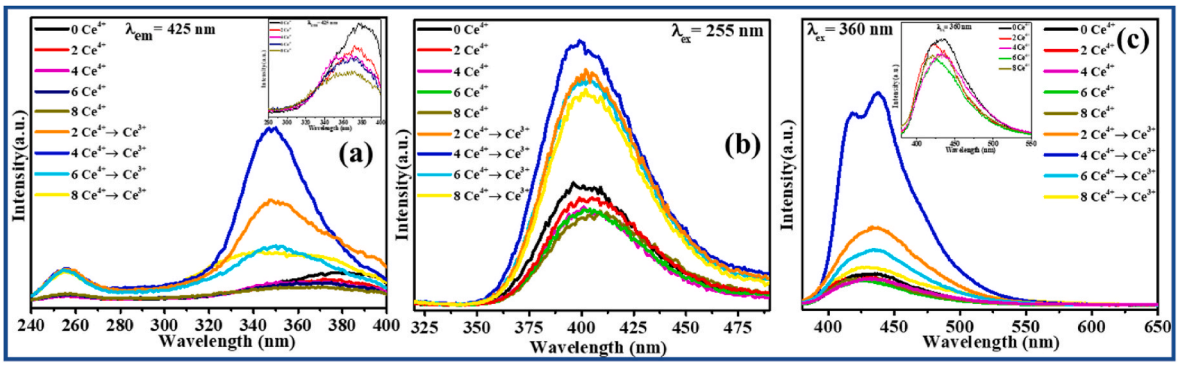

Fig. 10. Comparative **(a)** excitation, **(b)** emission spectrum (for λ_{ex} = 255), and **(c)** emission spectrum (for λ_{ex} = 360) for Ce^{4+} doped $Gd_2Ti_2O_7$ pyrochlore host and reduced Ce^{4+} → Ce^{3+} samples.

lying below the E_g. As we know Ce^{3+} has $4f^1$ ground state having only one electron and this electron is excited to 5 d level and it produces excitation peak at 360 nm. This excitation peak is due to the radiative transition from 5 d (T_{2g}) level to the $^2F_{5/2}$ and $^3F_{7/2}$ levels of the ground state causing emission peak doublet around 425 nm. We observed that the PL spectrum shows blue shifting of Ce^{3+} emission peaks in cubic crystal structure of $Gd_2Ti_2O_7$ host. When cerium entering in the cubic host lattice $Gd_2Ti_2O_7$, the electron shell of cerium expands and therefore, decreases electrostatic interaction between the electrons due to which the excited state energy reduces from their free ion values. This blue shift in the emission spectrum is interpreted in terms of chemical bonding properties of ligands like oxygen, which affects the absorption band position [40]. Moreover, it was clearly observed from the emission results of all the cerium doped samples with or without reduction show bright blue emission and the emission intensity depends on the concentration of cerium ion.

Overall, it is found for the series of Ce^{4+} doped samples that the emission intensity decreases with increasing doping of Ce^{4+} ion in the host as Ce^{4+} does not show emission due to 4f → 5 d transition. But for the reduced samples firstly the intensity goes on maximum up to doping concentration of 4% after that it again decreases due to the effect of concentration quenching [41]. Therefore, the emission intensity increases under reducing environment as a result of reduction of Ce^{4+} ions to Ce^{3+}, for the complete series of samples at room temperature. This is because in comparison to the closed shell of Ce^{4+}, the trivalent Ce^{3+} is having single optically active electron which is associated with the $^2F_{7/2}$ → $^2F_{5/2}$ electronic transition within the $4f^1$ orbital in the ground state configuration of Ce^{3+} [42].

3.5.2. CIE chromaticity coordinates

The exact information about the emission color and the color purity of the prepared samples can be measured using chromaticity diagram and CIE coordinates [43]. Customary Commission International de I'Eclairage (CIE) 1931 diagram is used to estimate the emission color and color coordinates (x, y) of $Gd_2Ti_2O_7$ doped Ce^{4+} and simultaneously for the same set of samples sintered at high temperature in reduced environment under the excitation wavelength of 360 nm. In Fig. 11, the CIE coordinates (x = 0.1544, y = 0.0590) and (x = 0.1562, y = 0.0079) represented by the green- and yellow-colored spherical balls for both the unreduced ($Gd_2Ti_2O_7$: Ce^{4+}) and reduced ($Gd_2Ti_2O_7$: Ce^{4+}→Ce^{3+}) samples respectively, for the optimized concentration (*i.e.,* 4% doping of cerium). The calculated CIE coordinates for both the samples are found to present in the pure blue region of the CIE color plot suggesting that the prepared samples may be used as blue emitting phosphors for the further production of WLED's.

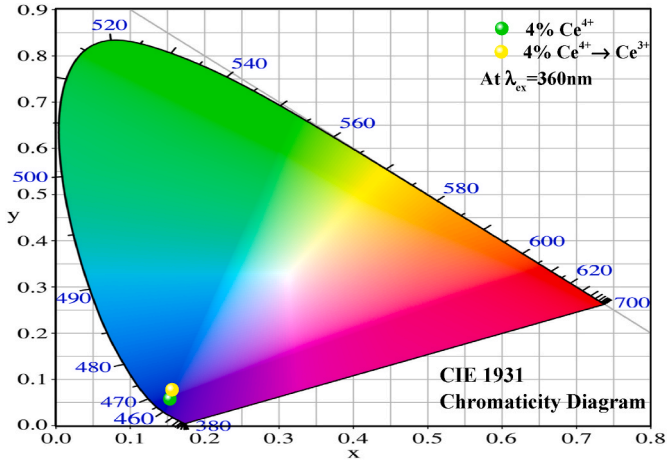

Fig. 11. Schematic CIE 1931 diagram for the cerium doped $Gd_2Ti_2O_7$ reduced and unreduced samples.

The quality of the color emission has been calculated through Corelated Color Temperature (CCT) using CIE coordinates. And the CCT has been measured using McCamy empirical formula which is given by the following equation [41];

$$CCT = -449u^3 + 3525u^2 - 6823.3u + 5520.33 \quad (5)$$

Here, $= \frac{x-x_e}{y-y_e}$; is the inverse slope line. And the $x_e = 0.3320, y_e = 0.1858$ are the epicenter coordinates. The values of CCT calculated from equation (4) were found to be 1779 K and 2021 K for the $Gd_2Ti_2O_7$: Ce^{4+} and reduced ($Gd_2Ti_2O_7$: Ce^{4+}→Ce^{3+}) samples respectively, for the optimum doping concentration of 4% of cerium, which could be useful for the production of WLEDs.

4. Conclusion

A series of Ce^{4+} doped $Gd_2Ti_2O_7$ pyrochlore oxides with a doping concentration; namely 2%, 4%, 6%, and 8% were successfully formed *via* high temperature solid state reaction route. The crystal structure and disordering driven luminescence properties were investigated for all the samples. XRD analysis along with Raman vibrational spectroscopy confirms the formation of single phasic pyrochlore oxide structure. SEM micrographs confirms the formation of nearly spherical agglomerated particles having average grain size ~1.2 ± 0.006 μm in the synthesized highly dense materials. The doping of bigger sized Ce^{4+} ion over Ti^{4+} at the B-site results in lattice expansion and introduction of lattice strain. All the Raman vibrational bands show a red-shifts caused by increasing bond-length or decreasing force constant on the compositional substitution of Ce^{4+} atoms at the place of Ti^{4+} with mismatched ionic radii causing disordering in the crystal structure. The Ce^{4+} cationic oxidation state was converted to Ce^{3+} oxidation state by heating in reduced environment of H_2 (10%) and argon (90%) flow at a temperature of 1000 °C for 24 h duration. XPS results for the 6% cerium doped pyrochlore sample showed an oxidation state of 3+ and 4+ for gadolinium and titanium cations respectively. The effect of Ce^{4+}→Ce^{3+} conversion is effectively studied *via* XRD, Raman, and Photoluminescence results. Diffraction patterns of reduced samples show a relatively larger shifting towards lower 2θ value as compared to unreduced samples due to the conversion of Ce^{4+} (0.87 Å) into Ce^{3+} (1.01 Å). The reduction has also induced more strain in the pyrochlore lattice structure. Like XRD results, Raman spectra of all the reduced samples also show relatively more vibrational band shifting (red shift) on compositional substitution of cerium cation as comparison to the unreduced samples. The PL excitation (at λ = 425 nm) contains two broad bands at 255 nm (4f to 5 d transition of the cerium trivalent ion) and 360 nm (due to band-to-band absorption of host $Gd_2Ti_2O_7$ and due to the 4f to 5 d transition of the cerium trivalent ion). PL intensity goes on increasing up to a doping of 4% of cerium after that again decreases due to the concentration quenching effect. PL emission (at λ = 360 nm) exhibits a broad band centered around 425 nm can be attributed due to the transition from lowest 5 d state to $^2F_{5/2}$ and $^2F_{7/2}$ components of the ground state. This radiative transition from 5 d (T_{2g}) level to the $^2F_{5/2}$ and $^3F_{7/2}$ levels of the ground state causing emission peak at doublet around 425 nm. The Photoluminescence results for both the reduced and unreduced series shows that on reduction of Ce^{4+} into Ce^{3+} state, reduced samples show blue shifting of Ce^{3+} emission peaks in cubic crystal structure of $Gd_2Ti_2O_7$ host, due to the expansion of crystal size of cerium in Ce^{3+} state. It was clearly observed from the emission results of all the ceria doped samples with or without reduction that bright blue emission and the emission intensity depends on the concentration of cerium ion. Hence, reduced samples of Ce^{4+}: $Gd_2Ti_2O_7$ would have a potential application in the mass production of blue LED chips for the further, fabrication of WLED's.

Authors statement

Umang Berwal: Conceptualization, Methodology, Formal analysis, Investigation, Writing - Original Draft, Visualization, Data Curation. **Vinod Singh:** Resources, Writing - Review & Editing, Supervision, and Funding acquisition. **Rinku Sharma:** Resources, Writing - Review & Editing, and Supervision.

Declaration of competing interest

The authors declare that they have no known competing financial interests or personal relationships that could have appeared to influence the work reported in this paper.

Data availability

Data will be made available on request.

Acknowledgement

One of the authors (Umang Berwal) is thankful to Delhi Technological University for providing DTU fellowship with file number 2K19/Ph. D/AP/119/08/3062, to conduct the research work. Authors would also like to thankful Dr. Rajender Singh Dhaka, Department of Physics Indian Institute of Technology New Delhi, for providing high temperature furnace during sample preparation. IUAC and AIRF, JNU are acknowledged for FESEM measurements and Raman measurements, respectively.

References

[1] C.C. Lin, R. Liu, Advances in Phosphors for Light-Emitting Diodes, 2011, pp. 1268–1277, https://doi.org/10.1021/jz2002452.
[2] S. Dalmasso, B. Damilano, C. Pernot, A. Dussaigne, D. Byrne, N. Grandjean, M. Leroux, J. Massies, Injection dependence of the electroluminescence spectra of phosphor free GaN-based white light emitting diodes, Phys. Status Solidi Appl. Res. 192 (2002) 139–143, https://doi.org/10.1002/1521–396X(200207)192:1<139::AID-PSSA139>3.0.CO;2-G.
[3] J. Yum, S.-Y. Seo, S. Lee, Y.-E. Sung, $Y_3Al_5O_{12}$:$Ce_{0.05}$ phosphor coatings on gallium nitride for white light emitting diodes, J. Electrochem. Soc. 150 (2003) H47, https://doi.org/10.1149/1.1535207.
[4] R.-J. Xie, Y.Q. Li, N. Hirosaki, H. Yamamoto, Nitride Phosphors and Solid-State Lighting, 2016, https://doi.org/10.1201/b10939.
[5] C. Feldmann, T. Jüstel, C.R. Ronda, P.J. Schmidt, Inorganic luminescent materials: 100 Years of research and application, Adv. Funct. Mater. 13 (2003) 511–516, https://doi.org/10.1002/adfm.200301005.
[6] S.K. Sharma, V. Grover, R. Shukla, A. Hussain, A. Mishra, R.C. Meena, P.K. Kulriya, Evidence of improved tolerance to electronic excitation in nanostructured $Nd_2Zr_2O_7$, J. Appl. Phys. 129 (2021), https://doi.org/10.1063/5.0039390.
[7] Y.T.H. O, S.A. Annamma, J. Jijimon, K.T. Sam, S. Solomon, Structural and optical characterization of $Y_2Ti_2O_7$ and $Y_2Ti_{1.5}Hf_{0.5}O_7$nanomaterials, J. Mater. Sci. Mater. Electron 28 (2017) 18497–18507, https://doi.org/10.1007/s10854-017-7797-2.
[8] S.K. Sharma, H.S. Mohanty, D.K. Pradhan, A. Kumar, V.K. Shukla, F. Singh, P. K. Kulriya, Structural, dielectric and electrical properties of pyrochlore-type $Gd_2Zr_2O_7$ ceramic, J. Mater. Sci. Mater. Electron. 31 (2020) 21959–21970, https://doi.org/10.1007/s10854-020-04699-4.
[9] J.B. Goodenough, R.N. Castellano, Defect pyrochlores as catalyst supports, J. Solid State Chem. 112 (1982) 108–112, https://doi.org/10.1016/0022-4596(82)90406-6.
[10] Y. Ma, X. Wang, X. You, J. Liu, J. Tian, X. Xu, Nickel-Supported on $La_2Sn_2O_7$ and $La_2Zr_2O_7$ Pyrochlores for Methane Steam Reforming : Insight into the Difference between Tin and Zirconium in the B Site of the Compound, 2014, pp. 3366–3376, https://doi.org/10.1002/cctc.201402551, 330013.
[11] $Bi_{2-x}Ca_xIr_2O_{6+y}$ Pyrochlore Phases Structure and Properties with Varied Ir Oxidation State from 3.9+ to 4.3+, https://doi.org/10.1021/acs.inorgchem.7b00345.
[12] H. Zhang, K. Haule, D. Vanderbilt, Metal-Insulator Transition and Topological Properties of Pyrochlore Iridates, 2017, pp. 1–6, https://doi.org/10.1103/PhysRevLett.118.026404, 026404.
[13] A. Panghal, Y. Kumar, P.K. Kulriya, P.M. Shirage, N.L. Singh, Structural assessment and irradiation response of $La_2Zr_2O_7$ pyrochlore_Impact of irradiation temperature and ion fluence, J. Alloys Compd. 862 (2021), 158556, https://doi.org/10.1016/j.jallcom.2020.158556.
[14] R.C. Ewing, W.J. Weber, J. Lian, W.J. Weber, Nuclear Waste Disposal — Pyrochlore (A2B2O7): Nuclear Waste Form for the Immobilization of Plutonium and " Minor " Actinides APPLIED PHYSICS REVIEWS $A_2B_2O_7$: Nuclear Waste Form for the Immobi, 2010, p. 5949, https://doi.org/10.1063/1.1707213.
[15] M. Marinovic, Synthesis and luminescent properties of rare earth (Sm^{3+} and Eu^{3+}) Doped $Gd_2Ti_2O_7$ pyrochlore nanopowders eljka, Antic 37 (2014) 598–606, https://doi.org/10.1016/j.optmat.2014.08.001.
[16] V. Lojpur, Ć. Sanja, M.D. Drami, Ratiometric Luminescence Thermometry with Different Combinations of Emissions from Eu^{3+} Doped $Gd_2Ti_2O_7$ Nanoparticles, vol. 169, 2016, pp. 534–538, https://doi.org/10.1016/j.jlumin.2015.01.027.
[17] A. Kumar, Structural and optical properties of highly thermally active $Gd_2Zr_2O_7$: Dy^{3+} phosphors for lighting applications, 0, J. Mater. Sci. Mater. Electron. (2019), https://doi.org/10.1007/s10854-018-0509-8, 0.
[18] U. Berwal, V. Singh, R. Sharma, Key role of Tb^{3+} doping on structural and photoluminescence properties of $Gd_2Ti_2O_7$ pyrochlore oxide, Ceram. Int. (2022), https://doi.org/10.1016/j.ceramint.2022.04.231.
[19] U. Berwal, V. Singh, R. Sharma, Structural and optical studies on Dy^{3+} doped $Gd_2Ti_2O_7$ pyrochlore as white light emission, Ceram. Int. (2022), https://doi.org/10.1016/j.ceramint.2022.11.045.
[20] F. Matteucci, G. Cruciani, M. Dondi, G. Baldi, A. Barzanti, Crystal structural and optical properties of Cr-doped $Y_2Ti_2O_7$ and $Y_2Sn_2O_7$ pyrochlores, Acta Mater. 55 (2007) 2229–2238, https://doi.org/10.1016/j.actamat.2006.11.008.
[21] Y. Z, D. Linghong, P. Xinling, Z. Weifeng, Influence of annealing temperature on luminescent properties of Eu^{3+}/V^{5+} co-doped nanocrystalline $Gd_2Ti_2O_7$ powders, J. Rare Earths 27 (2009) 900–904, https://doi.org/10.1016/S1002-0721(08)60359-2.
[22] M. Saif, Luminescence based on energy transfer in silica doped with lanthanide titania ($Gd_2Ti_2O_7$:Ln^{3+}) [Ln^{3+} = Eu^{3+} or Dy^{3+}], J. Photochem. Photobiol. Chem. 205 (2009) 145–150, https://doi.org/10.1016/j.jphotochem.2009.04.020.
[23] H.E. Liying, S.U. Yumin, J. Lanhong, S.H.I. Shikao, Recent advances of cerium oxide nanoparticles in synthesis , luminescence and biomedical studies : a review, J. Rare Earths 33 (2015) 791–799, https://doi.org/10.1016/S1002-0721(14)60486-5.
[24] Cerium Doped Glasses Containing Reducing Agent for Enhanced Luminescence, vol. 222 (2020) 15–17. https://doi.org/10.1016/j.jlumin.2020.117175.
[25] A. Kumar, P.K. Kulriya, S.K. Sharma, V. Grover, A.K. Tyagi, V.K. Shukla, Structural and compositional effects on the electronic excitation induced phase transformations in $Gd_2Ti_{2-y}Zr_yO_7$ pyrochlore, J. Nucl. Mater. 539 (2020), 152278, https://doi.org/10.1016/j.jnucmat.2020.152278.
[26] X. Wang, Y. Wang, Synthesis , Structure , and Photoluminescence Properties of Ce 3 + - Doped $Ca_{2-y}Zr_2Al_3O_{12}$:A Novel Garnet Phosphor for White LEDs, 2015, https://doi.org/10.1021/acs.jpcc.5b01552.
[27] S.K. Sharma, V. Grover, A.K. Tyagi, D.K. Avasthi, U.B. Singh, P.K. Kulriya, Probing the temperature effects in the radiation stability of $Nd_2Zr_2O_7$ pyrochlore under swift ion irradiation, Materialia 6 (2019), 100317.
[28] G.M. Mustafa, S. Atiq, S.K. Abbas, S. Riaz, S. Naseem, Tunable structural and electrical impedance properties of pyrochlores based Nd doped lanthanum zirconate nanoparticles for capacitive applications, Ceram. Int. 44 (2018) 2170–2177, https://doi.org/10.1016/j.ceramint.2017.10.172.
[29] G. Sattonnay, S. Moll, L. Thoḿ, C. Decorse, C. Legros, P. Simon, J. Jagielski, I. Jozwik, I. Monnet, Phase transformations induced by high electronic excitation in ion-irradiated $Gd_2(Zr_xTi_{1-x})_2O_7$ pyrochlores, J. Appl. Phys. 108 (2010), https://doi.org/10.1063/1.3503452.
[30] A. Kumar, S.K. Sharma, V. Grover, Y. Singh, V. Kumar, V.K. Shukla, P.K. Kulriya, Probing the Short-Range Ordering of Ion Irradiated Gd2Ti2-yZryO7 ($0.0 \leq y \leq 2.0$) Pyrochlore under Electronic Stopping Regime, J. Nucl. Mater. 564 (2022), 153682, https://doi.org/10.1016/j.jnucmat.2022.153682.
[31] N.J. Hess, B.D. Begg, S.D. Conradson, D.E. McCready, P.L. Gassman, W.J. Weber, Spectroscopic investigations of the structural phase transition in $Gd_2(Ti_{1-y}Zr_y)_2O_7$ pyrochlores, J. Phys. Chem. B 106 (2002) 4663–4677, https://doi.org/10.1021/jp014285t.
[32] P.K. Kulriya, T. Yao, S.M. Scott, S. Nanda, J. Lian, In fl uence of grain growth on the structural properties of the nanocrystalline $Gd_2Ti_2O_7$, J. Nucl. Mater. 487 (2017) 373–379, https://doi.org/10.1016/j.jnucmat.2017.02.032.
[33] G. Greczynski, L. Hultman, X-ray photoelectron spectroscopy: towards reliable binding energy referencing, Prog. Mater. Sci. (2019), 100591, https://doi.org/10.1016/j.pmatsci.2019.100591.
[34] N. Cioatera, E.A. Voinea, E. Panaintescu, A. Rolle, S. Somacescu, C.I. Spinu, R. N. Vannier, Changes in structure and electrical conductivity of rare-earth titanate pyrochlores under highly reducing atmosphere, Ceram. Int. 42 (2016) 1492–1500, https://doi.org/10.1016/j.ceramint.2015.09.095.
[35] D. Raiser, J.P. Deville, Study of XPS Photoemission of Some Gadolinium Compounds, vol. 57, 1991, pp. 91–97, https://doi.org/10.1016/0368-2048(91)85016-M.
[36] X. Photoelectron, O , peaks, These Measurements Have Shown that the Number of Satellites Is Higher than Found from Previous to the Main Peak Were Deconvofuted with a Gaussian (B) A moIecu ~ Ar-Orbital caIculation on Metal Octahe- draBy Coordinated with Oxygen Developed, vol. 61, 1979, pp. 453–456.
[37] Z. Fang, L. Gao, H. Chen, K. Liang, Z. Liu, Z. Guan, J. Zhang, XPS study of probing evidence for displacive disorder in Ni-doped bismuth magnesium niobate pyrochlore, Mater. Sci. Eng. B Solid-State Mater. Adv. Technol. 259 (2020), 114601, https://doi.org/10.1016/j.mseb.2020.114601.
[38] Y.M. Sgibnev, N. V Nikonorov, A.I. Ignatiev, Luminescence of silver clusters in ion-exchanged cerium-doped photo-thermo-refractive glasses, J. Lumin. 176 (2016) 292–297, https://doi.org/10.1016/j.jlumin.2016.04.001.
[39] R. Yu, J. Wang, M. Zhang, J. Zhang, H. Yuan, Q. Su, A New Blue-Emitting Phosphor of Ce^{3+} -activated $CaLaGa_3S_6O$ for White-Light-Emitting Diodes, vol. 453, 2008, pp. 197–201, https://doi.org/10.1016/j.cplett.2008.01.039.
[40] A. Bahadur, Y. Dwivedi, S.B. Rai, Spectrochimica acta Part A : molecular and biomolecular spectroscopy optical properties of cerium doped oxyfluoroborate

glass, Spectrochim. Acta Part A Mol. Biomol. Spectrosc. 110 (2013) 400–403, https://doi.org/10.1016/j.saa.2013.03.066.
[41] H. Kaur, M. Jayasimhadri, M.K. Sahu, P.K. Rao, N.S. Reddy, Synthesis of orange emitting Sm^{3+} doped sodium calcium silicate phosphor by sol-gel method for photonic device applications, Ceram. Int. (2020), https://doi.org/10.1016/j.ceramint.2020.04.224.
[42] V.M. Orera, R.I. Merino, F. Peña, Ce^{3+}↔Ce^{4+} conversion in ceria-doped zirconia single crystals induced by oxido-reduction treatments, Solid State Ionics 72 (1994) 224–231, https://doi.org/10.1016/0167-2738(94)90151-1.
[43] Amit K. Vishwakarma, Kaushal Jha, M. Jayasimhadri, Emerging cool white light emission from Dy^{3+} doped single phase alkaline earth niobate phosphors for indoor lighting applications, https://doi.org/10.1039/C5DT02436F.

This article has been accepted for inclusion in a future issue of this journal. Content is final as presented, with the exception of pagination.

Effective Governance Through Crowdsourcing: A Strategic Framework for Empowered Participation

Divya Mishra and Nidhi Maheshwari

***Abstract*—Crowdsourcing in governance has gained widespread popularity and has become a powerful tool to leverage the collective intelligence of citizens for the nation's social welfare. Despite the growing importance of transforming government–citizen relationships, the design aspect is highly unstructured and fragmented. Thus, an in-depth understanding of the notion is essential, given its expanding importance in practice. This article aims to identify and describe elements and design principles phase-wise to improve the government's potential to derive value from crowdsourcing initiatives for civic participation and collaborative governance. Synthesizing all elements and principles in a strategic crowdsourcing framework is a novel conceptual configuration that contributes to the overall understanding of designing crowdsourcing initiatives in the government sector. The article adopts a systematic literature review and a morphological analysis technique to identify and synthesize all the elements and principles of designing crowdsourcing initiatives. Three crowdsourcing initiatives of the government sector were investigated to evaluate the framework in a practical setting and comprehend its efficacy. Government agencies can ensure enhanced interactivity and bidirectionality by emphasizing the nuances of elements and design principles for executing crowdsourcing initiatives that create epistemic and economic value.**

***Index Terms*—Crowdsourcing designing, design principles, strategic crowdsourcing framework, systematic literature review.**

I. Introduction

WEB 2.0 emergence has led to a revolution in information and hyper-connectivity, resulting in transparency, empowered participation of citizens in policy decisions, and changing the relationship between citizens and government [1]. Second-generation Web tools like social media and networking sites [2], [3] provide a participatory and social virtual platform to collaborate and network with stakeholders [4]. Therefore, public agencies have started incorporating novel technologies to encourage citizen participation in collaborative governance. Challenge.gov platform of the USA [5] and MyGov India's portal [6] included disenfranchised citizens in solving complex problems of society and policy designing, which has opened a vista of the digital transition of government from thin democracies to strong democracies [7]. The involvement of citizens in government policy-making and improvement leads to a participatory governance scenario in a country, reducing the chances of policy failure [8] and achieving the three pillars of open government: transparency, participation, and collaboration [9].

The "crowd" (i.e., citizens) is the heart of any governance system. Therefore, every government machinery needs active and empowered citizens to execute the policies successfully. There was a surge of interest to leverage the crowd's collective intelligence to enrich public participation in governance and get work done with an amateur crowd. This phenomenon of using the collective intelligence of citizens to produce something together [10], [11], [12], [13] is known as crowdsourcing. Crowdsourcing practices used by the government to tap the collective intelligence of citizens are also known as citizensourcing [17], [71]. Crowdsourcing or citizensourcing mainly refers to a participative online activity where the government engages in a top-down management process to obtain bottom-up creative input from citizens in a virtual community. The government uses citizensourcing to get citizens' diverse ideas, opinions, and suggestions, thereby establishing a continuous contact loop. It was seen as an enabler of increased and improved governance via enriched engagement (e-participation) [14], involvement of democratic communities (inclusive e-governance and e-inclusion) [15], increased accountability, transparency in delivery, and standard of government services and through democracy (e-democracy) [16]. This phenomenon of citizen sourcing has changed the perspective of the government on the public from "users and choosers" to "makers and shapers" of government policies and decisions [17]. The widespread adoption of new phenomena resulted in the addition of democratic principles from by the people, for the people, and of the people to with the people, and from the people [18].

Although crowdsourcing can change the reality of governance in many developing countries, the outcomes are not very satisfactory [19], [20]. The literature shows that crowdsourcing in the public sector is still in its infancy since e-government success stories are limited [21], [22], [23], [24], [25], [26], [27], [28], [29], [30]. The failure rate of e-government initiatives, specifically in developing nations, is alarming, as Furuholt and Wahid [31] reported that more than 60% of projects have not achieved the desired outcome. Of these failures, 35% were categorized as total failures, and 50% were classified as partial failures due to nonattainment of goals or detrimental outcomes. These failures lead to unbearable losses in the form of valuable resources, loss of status, financial crisis, and many political impediments [18]. This implies that crowdsourcing can be a double-edged sword as it has enormous potential to improve citizen–government relationships, reduce administrative costs [32], [33], and improve the efficiency and effectiveness of government services [34], [35]. In contrast, it may also lead to adverse effects if unmanaged well.

Manuscript received 22 December 2021; revised 7 March 2022, 8 May 2022, 20 July 2022, and 1 September 2022; accepted 20 October 2022. Review of this manuscript was arranged by Department Editor E. Viardot. *(Corresponding author: Divya Mishra.)*

The authors are with the University School of Management and Entrepreneurship, Delhi Technological University, New Delhi 110042, India (e-mail: divyamishra919@gmail.com; nidhimaheshwari@dtu.ac.in).

Color versions of one or more figures in this article are available at https://doi.org/10.1109/TEM.2022.3218188.

Digital Object Identifier 10.1109/TEM.2022.3218188

0018-9391 © 2023 IEEE. Personal use is permitted, but republication/redistribution requires IEEE permission.
See https://www.ieee.org/publications/rights/index.html for more information.

Authorized licensed use limited to: DELHI TECHNICAL UNIV. Downloaded on January 19,2023 at 05:07:01 UTC from IEEE Xplore. Restrictions apply.

This article has been accepted for inclusion in a future issue of this journal. Content is final as presented, with the exception of pagination.

Crowdsourcing research in the government sector has mainly focused on single aspects of designing crowdsourcing, such as citizen rewards, motivation, task design [36], [37], [38], feedback, and validation [39], [40]. This fragmented approach to crowdsourcing literature poses threats to the effective implementation of crowdsourcing initiatives. Successful adoption of crowdsourcing requires a conceptual understanding of all the design elements and principles that focus on citizen, technology, and channel orientation [41] in every crowdsourcing phase. Although government agencies have started to experiment with crowdsourcing for empowered citizenship, they have not yet mapped the crowdsourcing implementation framework that leads to the satisfaction of citizens' requirements, building relationships with the coordinating agencies, and using technology innovatively with respect to governance. Failures in implementing crowdsourcing initiatives for the empowered participation of citizens suggest the lack of an integrated approach to understanding all the design elements and principles of crowdsourcing adoption. Certain elements and design principles may impact the successful implementation of crowdsourcing initiatives. Therefore, this study aims to fill the knowledge gap and guide government agencies to improve the crowdsourcing initiatives in progress.

The research study that focuses on standardized processes for the phase-wise designing of crowdsourcing initiatives and the crowdsourcing strategic framework that represents the different elements and design principles for government agencies is not yet established [42]. No such guidelines exist in crowdsourcing literature that properly guides practitioners in initiating and managing crowdsourcing initiatives [43]. From a practical viewpoint, it is essential to have a standardized and comprehensive blueprint that addresses the government challenges when setting up crowdsourcing initiatives. This gap leaves room for writing this research article. In particular, the important research question investigated in this study is "What elements and design principles should be considered by government agencies while making a blueprint of crowdsourcing initiatives?" The elements and principles will provide direction on what decisions government agencies must make while designing crowdsourcing initiatives to motivate the citizens to engage in governance decision-making, ensure that solutions are implemented well, and provide value to government agencies. Paik et al. [44] suggested to remain cautious while planning and designing crowdsourcing initiatives because crowdsourcing is costly. Therefore, the proposed strategic framework can help public administrators and government agencies identify common pitfalls and issues in design, such as having postimplementation government strategies early in the designing phase of crowdsourcing initiatives that may lead to the attainment of desirable outcomes from crowdsourcing.

The current study is the leading study that conceptualizes the designing of crowdsourcing initiatives in three phases, with the overall goal of developing a crowdsourcing framework. The study further adds to the call for future research related to the rigorous need for "comprehensive guidelines" and "lack of standardization" to manage and understand crowdsourcing initiatives well [42], [43], [45]. A strategic crowdsourcing framework will facilitate and support effectively designing crowdsourcing initiatives for civic participation and collaborative governance. Effective design can help the government leverage the benefits of collaborative governance at four levels, namely, attractor effects [46], learning [47], leverage, and synergy [33]. In the emerging Indian market, despite the growing importance of the use of crowdsourcing, it is underexplored. Therefore, from a practical viewpoint, the framework will help government agencies save their precious time and resources on crowdsourcing initiatives rather than wasting time on legalities. The contribution of this article is twofold. First, identifying and describing elements and design principles phase-wise contribute to the overall understanding of designing crowdsourcing initiatives in the government sector. This refined understanding provides scope to conduct future research positioning on the proposed strategic crowdsourcing framework, leading to a more logical study design. Second, with a focus on the Indian context, this study proposes a framework that disentangles the efforts of the government to engage citizens in the crowdsourcing initiatives effectively and to further identify the strengths and weaknesses of those efforts taken by the government. Public administrators can use the proposed strategic framework to gain more insights into designing crowdsourcing initiatives.

This article is structured as follows. To identify the designing principles that government agencies should consider, a comprehensive systematic literature review of published literature was adopted to attain a comprehensive view of the current state of crowdsourcing research. As a result, a strategic crowdsourcing framework was developed and discussed. Three crowdsourcing government initiatives were elaborated on and discussed to check the applicability of the proposed framework. The findings were then presented to open the arena for future research.

II. Background

A. Crowdsourcing in the Government Sector

Brabham [34] proposed that crowdsourcing is a government–citizen relationship where the government executes a top-down process and seeks to obtain bottom-up, open, and creative citizens' input from an online citizen community, making it productive and full of potential to achieve social welfare. Crowdsourcing is not a panacea but a crucial part of the new governance system [33] that has become popular after the emergence of Web 2.0 to enhance citizen engagement and ultimately increase trust in the democratic process. There has been a rapid growth in the use of crowdsourcing for e-governance, policy recommendations, increased public participation [48], sourcing ideas and solutions from citizens for increased satisfaction and empowerment [49], and e-democracy [23].

Crowdsourcing in governance works well with long-standing concepts of deliberate democracy, public participation, and e-democracy. Information flows from citizens to the government. In return, the public helps the government be more responsive and effective. Thus, citizens are empowered to strengthen political legitimacy [5], [23], [27], [34]. Many researchers called this new phenomenon citizen sourcing, where sourcing refers to how government agencies acquire collective intelligence of citizens for the accomplishment of their mission. Hence, citizen sourcing done in crowdsourcing enhances citizens' knowledge. Moreover, competence enriches confidence and trust in citizen–government relationships and increases the chances of successful policy execution [43]. Crowdsourcing can be used as a strategic tool for realizing the ideals of participatory democracy, resulting in effective government [50]. Crowdsourcing made the constitution reform process efficient by gathering a diverse range

Authorized licensed use limited to: DELHI TECHNICAL UNIV. Downloaded on January 19,2023 at 05:07:01 UTC from IEEE Xplore. Restrictions apply.

This article has been accepted for inclusion in a future issue of this journal. Content is final as presented, with the exception of pagination.

of knowledge from the citizens of Iceland, as evident from the Constitution Reform of Iceland. Similarly, budget preparation in Chicago and Calgary used crowdsourcing to gather ideas and perspectives of citizens regarding the budget, leading to transparency in governance. Thus, crowdsourcing is a technological enabler that supports the government in solving governance issues [51], informing [50], communicating [35], strengthening public participation [52], [53], and empowering citizens [27] to solve the day-to-day problems [54], [55].

B. Related Work

Since the emergence of crowdsourcing, numerous studies have focused on fragmented aspects of crowdsourcing initiatives, such as task meaningfulness, well-framed tasks, worker participation, the quantity of output and quality outcomes [56], fundamental pillars (i.e., the crowdsourced task, the crowd, the crowdsourcer, and the platform) [57], crowd identification and evaluation of crowds [58], crowdsourcing stages (e.g., task designing, workflow design, and quality control) [59], [60], [61], task clarity and type, crowd motivation, offering extrinsic and intrinsic motivation, incentives, or rewards for the public [62].

Most studies were tilted toward the private sector, as crowdsourcing was initially applied to leverage collective intelligence for designing and creative industries. The government sector started to experiment with crowdsourcing in the much later stages "to collect citizens' opinions," information, expertise, and knowledge to solve the complex issues of society [63], [64], [65]. However, the design and implementation principles used in the corporates may present valuable insights and hints for crowdsourcing implementation in the government sector. Crowdsourcing initiatives in governance are mainly undertaken for social innovation, whereas the private sector focuses on business innovation [66]. Therefore, elements of the private crowdsourcing process may not be directly applicable in government agencies because the nature of objectives, duties, and challenges are different. Additionally, the private sector undervalues, overvalued, or ignores the important design aspects [67]. Therefore, there is a requirement to conduct a holistic study on the identification of design elements of the planning, implementation, and postimplementation phases of crowdsourcing initiatives, with special context to the government sector [30], [18], [34], [39], [66], [68], [69].

III. Research Methodology

Different qualitative techniques were primarily used to fulfill the aim of the study. A comprehensive systematic literature review was conducted to extract and analyze all the elements and principles of the three phases of designing crowdsourcing. The theoretical background has the power to integrate and evaluate all previous findings of crowdsourcing elements, which cannot be possible if a single study is assessed in isolation. Thus, a literature review is an appropriate research method to systematically extract and synthesize past research, acting as a basis for the further expansion of knowledge and theory development [70].

A. Systematic Literature Review

The systematic literature review used a five-step procedure, i.e., definition of a central topic and research goals, sources and types of data for review, data extraction, data evaluation, and data analysis and synthesis, as proposed by Tranfield et al. [71] and Hallinger [72].

1) Definition of Central Topic of Interest and Research Goals: The first step of a systematic literature review is to state the research problem that needs to be addressed. Later, a search strategy is decided, such as search terms, databases, data extraction, evaluation criteria, analysis, and synthesis of searched data. As mentioned earlier, the study aims to identify and comprehend the elements and design principles that government agencies should consider while making a blueprint for crowdsourcing initiatives. Therefore, this study focuses on studying all individual elements that need to become accustomed to different phases of crowdsourcing initiatives.

2) Definition of Sources and Type of Data for Review: The data sources need to be defined to select the appropriate literature for the study. The search for articles was performed extensively on three databases, Web of Science, Emerald, and ScienceDirect, which have the highest number of publications in our research area. The three databases were selected because of their multidisciplinary research articles published in 30 000 peer-reviewed journals. The choice of database is consistent with past studies conducted [73], [85]. A broad keyword was used to obtain a complete picture of the previous research conducted in this area. For convenience, the keywords used were separated by *AND and OR*. The search incorporates academic papers written in English and within the time frame of a 15-year period, i.e., from 2006 (when the crowdsourcing term was coined) to 2021. As Snyder [76] proposed narrowing the search results by a predefined criterion, four-level criteria were used to conduct the final analysis. Articles that emphasize crowdsourcing in business, management, and governmental contexts were referred to at the initial stage, and the articles that focus on crowdsourcing initiatives were then selected. Later articles based on the crowdsourcing framework and conceptual models were extracted. Finally, articles related to crowdsourcing and design elements were selected.

3) Data Extraction: The search was performed using the keywords in all mentioned databases. Four criteria were applied to limit our articles. First, the search includes academic papers written in English and within the time frame of 15-year period, i.e., from 2006 to 2021. Using this criterion, metadata of *13 670* articles were created. This offered a broader view of studies conducted in the area researched. Now the data results were narrowed down as per the focus of the study. Therefore, in the second-level criteria, only those papers that include crowdsourcing studies conducted in business, management, and public administration were searched. Now the search results declined to *4 417* research papers. This decline in articles showcases that there are fewer studies conducted in business, public administration, and management contexts. A third criterion was established to include those articles that focused on crowdsourcing initiatives in business, public administration, and management. In doing this, the articles declined to *458*. As a final criterion, articles that mentioned crowdsourcing framework or crowdsourcing designing elements were considered. This was done to ensure that only those articles relevant to attain the research objectives were to be taken into our corpus of review. The above criteria were met by reading the title, abstract, keywords, introduction, and conclusion. If this was not sufficient for the decision, the paper was read thoroughly. Therefore, this final step resulted in a total of *347* articles that were relevant to this study's research purpose, as presented in Table I. Data evaluation was performed to remove the duplicate papers, resulting in a total of *131* articles.

Authorized licensed use limited to: DELHI TECHNICAL UNIV. Downloaded on January 19,2023 at 05:07:01 UTC from IEEE Xplore. Restrictions apply.

This article has been accepted for inclusion in a future issue of this journal. Content is final as presented, with the exception of pagination.

TABLE I
SYSTEMATIC REVIEW PROCESS RESULTS

Databases	First criteria	Second criteria	Third criteria	Fourth criteria
Web of Science	4885	462	165	50
Emerald	1681	1435	151	65
Science Direct	7104	2520	142	232
Total	13670	4417	458	347

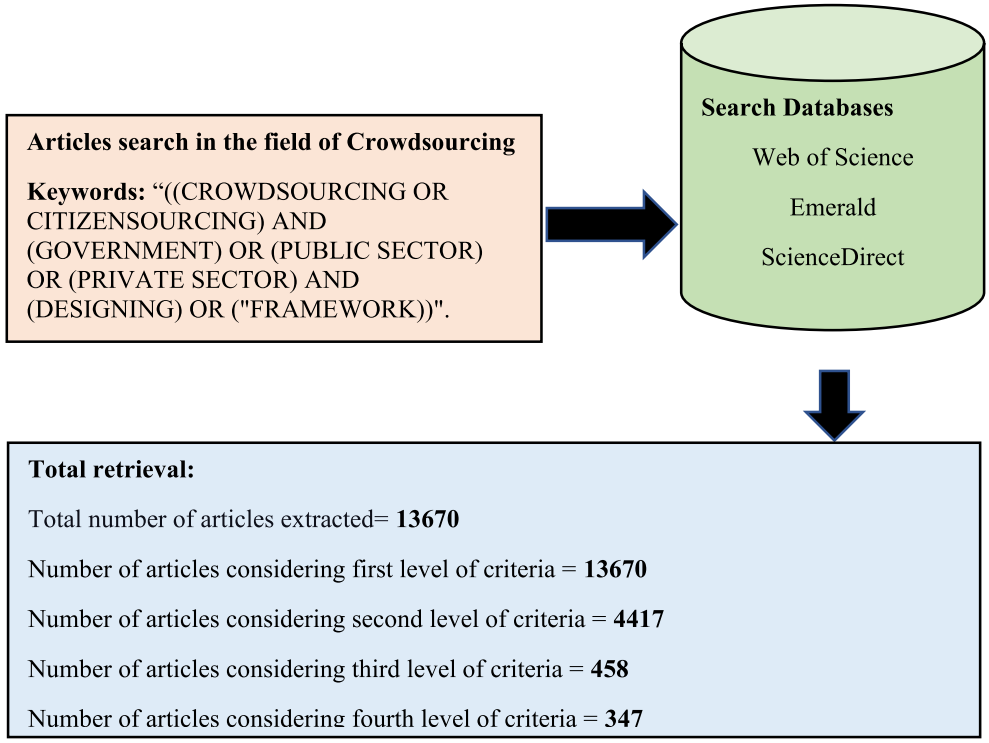

Fig. 1. Systematic review process results.

Fig. 1 illustrates the selection and evaluation process of articles incorporated under study.

4) Data Evaluation: All the extracted papers that mentioned individual elements of crowdsourcing initiatives were studied in detail. Designing elements and principles were divided into three phases per their need and relevance, i.e., preparation, execution, and postexecution. All papers were thoroughly analyzed to determine the designing elements phase-wise. There were a total of 131 articles after the data extraction and evaluation process. After having a closer look, researchers noticed that the number of studies conducted that focused on designing elements for crowdsourcing in the government sector was less than that in the business and management sector. The findings of the prior research show that many researchers considered monetary rewards to be the most important reward, whereas in the government sector, there was community-oriented motivation, building professional networks, and intrinsic motivation to solve complex societal issues in general. The monetary incentive did not lead to citizens' increased participation rate [22], [36], [66], [77]. "To attract the citizen's attention," there was a need to frame, define, and delineate the purpose of using crowdsourcing. There must be rubrics for how the solution evaluation will be performed and implemented after the final selection because this only creates enthusiasm in citizens to contribute and make a difference in the government sector.

5) Data Analysis and Synthesis: The results of the systematic literature were meticulously analyzed to identify all the design elements and principles from the individual papers extracted.

Authorized licensed use limited to: DELHI TECHNICAL UNIV. Downloaded on January 19,2023 at 05:07:01 UTC from IEEE Xplore. Restrictions apply.

This article has been accepted for inclusion in a future issue of this journal. Content is final as presented, with the exception of pagination.

TABLE II
CROWDSOURCING: DESIGNING ELEMENTS AND PRINCIPLES

Phases	Elements	Principles	Sources
Preparation	Plan and design	Goals specification	Lim et al. [78]; Sharma [79]; Ahuah and Tucci [80]; Lykourentzou et al. [81]; Bassi et al. [82]; Malone et al. [83]; Rosen [84]
		Task description	Schafer et al. [85]; Nguyen et al. [86]; Moussawi and Koufaris [87]; Tokarchuk et al. [88]; Leimeister et al. [89]; Muhdi et al. [90]
		Task duration	Ayaburi et al. [91]; Chen et al. [92]; Boudreau et al. [93]; Massa and Testa [94]; Kulkarni et al. [95]; Nakatsu et al. [96]
		Task decomposition	Natalicchio et al. [97]; Pee et al. [98]; Blohm et al. [99]; Kittur et al. [100]; Hetmank [101]
		Citizen qualification	Geiger and Schader [102]; Christensen and Karlsson [103]; Bücheler and Sieg [104]
		Coordinating agencies	Heeks and Nicholson [105]
		Infrastructure	Surowiecki [106]; Potter et al. [107]; Wexler [108]
		Level of commitment	Ozcan et al. [32]; Hansson et al. [109]
Execution	Promote and act	Launch promotional plans	Choi and Lee [110]; Naparat and Finnegan [111]; Doan et al. [112]; Kaufmann et al. [113]
		Incentives	Chandler and Kepelner [56]; Sun et al. [114]; Zhou and Zhu [115]; Zou et al. [116]; Allahbakhsh et al. [117]; Stewart et al. [118]
		Crowd management	Piezunka and Dahlander [119]; Khazankin et al. [120]; Sauerwein et al. [121]; De Beer et al. [122]
		Regulatory guidelines	Hirth et al. [123]; Downs et al. [124]
		Technical assistance	Srivastava and Mostafavi [40]; Zogaj et al. [25]
		Quality control	Kim et al. [125]; Lampe [126]; Dellarocas [127]
Postexecution	Evaluate and feedback	Evaluation	Saxton et al. [128]; Baruch et al. [129]; Wooten and Ulrich [130]
		Acknowledgment and recognition	Brabham [49]; Srivastava and Mostafavi [40]; Baruch et al. [129]
		Feedback	Nguyen et al. [86]; Sauerwein et al. [121]; Jian et al. [131]; Chen et al. [92]; Kiran and Sharma [132]

All the design elements were classified under three phases according to their importance. Table II presents the six elements and 17 design principles highlighted in the literature that guide public administrators to create a roadmap for crowdsourcing implementation.

B. Strategic Framework of Crowdsourcing: Morphological Analysis

Morphological analysis was applied to develop a strategic crowdsourcing framework that considers different phases, elements, and principles of designing crowdsourcing in the government sector. Morphological analysis is a qualitative analytical technique to identify, investigate, structure, and accommodate different multidimensional elements from the literature into a holistic conceptual system [133]. Hence, this analysis works well in consolidating the findings of the systematic literature review into a theoretical framework.

Morphological analysis is used to present a comprehensive and holistic view of the relevant findings from the literature. Once the dimensions of crowdsourcing initiatives are identified, a concept-specific method is used to comprehend them cohesively. All the phases, elements, and design principles of crowdsourcing were organized in a morphological box matrix. This

Authorized licensed use limited to: DELHI TECHNICAL UNIV. Downloaded on January 19,2023 at 05:07:01 UTC from IEEE Xplore. Restrictions apply.

This article has been accepted for inclusion in a future issue of this journal. Content is final as presented, with the exception of pagination.

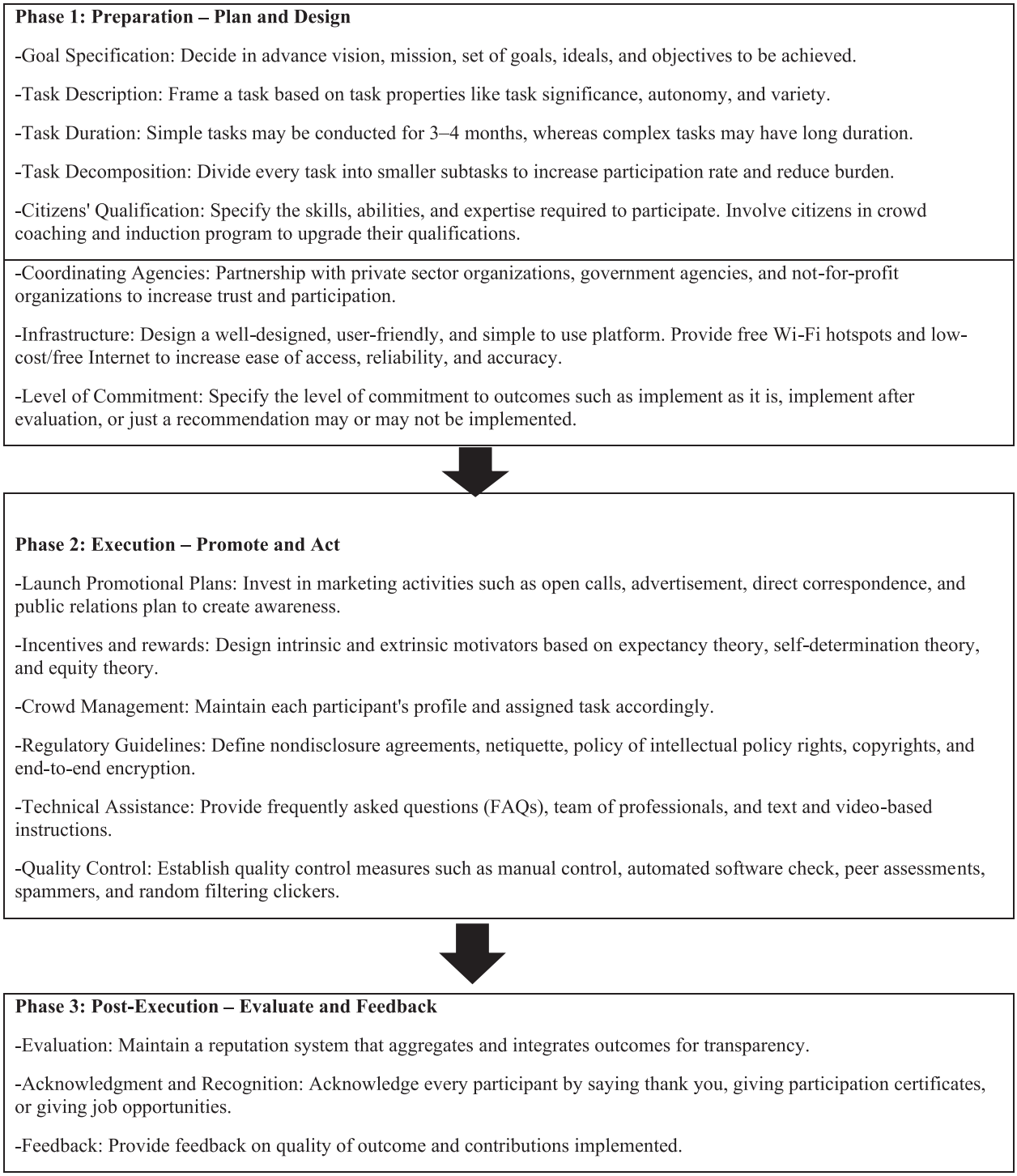

Fig. 2. Strategic framework of designing crowdsourcing initiatives.

morphological box will work as a strategic framework to guide public administrators in designing crowdsourcing initiatives. The strategic framework has three phases for designing crowdsourcing, namely, preparation, execution, and postexecution. Fig. 2 shows the developed strategic crowdsourcing framework for designing crowdsourcing initiatives in the government sector. A strategic theoretical framework gives public administrators an overall view for designing crowdsourcing initiatives.

IV. Examples of Crowdsourcing Initiatives of Government

This section suggests a wider applicability of the framework for government and public administration. While locating how the proposed framework fits within governance, researchers discussed three examples of governmental crowdsourcing initiatives. These instances allow the researchers to generate theoretical propositions and develop theories based on empirical

Authorized licensed use limited to: DELHI TECHNICAL UNIV. Downloaded on January 19,2023 at 05:07:01 UTC from IEEE Xplore. Restrictions apply.

This article has been accepted for inclusion in a future issue of this journal. Content is final as presented, with the exception of pagination.

evidence in a real-life setting. It provides a detailed explanation of every component and structure of phenomena to gain an in-depth understanding from different angles. Along these lines, this methodology justifies that the proposed framework is an asset for designing crowdsourcing initiatives in the government sector. The three illustrations discussed give an overview of the crowdsourcing practices of the Indian government. Since India is an emerging market, the framework relevance can be checked appropriately. The initiatives were chosen not randomly but instead because they support testing the proposed strategic framework for government crowdsourcing. Many more crowdsourcing instances might have been included in the article, but the decision was made to stick with only three for the sake of parsimony. Real-life illustrations help understand the crowdsourcing design framework applicability and present an overall picture of the context, situation, relationship, and social setting in which the research event is situated. Considering the differing population volumes and the digital literacy rate, the researcher discussed the examples from both the central and state levels. The three crowdsourcing initiatives of India have ingenious concepts of idea generation and microtasking that helped the government to achieve effective governance.

In the first example, a state-level initiative is discussed where the government used citizens' contributions (citizensourcing) to combat pollution issues and rectify them on time. The second and third example is a crowdsourcing initiative of the central government where citizens' participation led to the improvement and development of applications in India. The examples were chosen based on their diverse crowdsourcing goals and context-idea generation and microtasking for solving pollution problems, upgradation, and developing applications. Practitioners interested in adopting crowdsourcing in their organizations can learn from the three successful crowdsourcing initiatives.

A. *Green Delhi*

Green Delhi is an interactive e-governance mobile application that empowers and engages citizens to complain about antipollution norms, which are forwarded to the concerned department for timely rectification. This app was launched on October 30, 2020, as a part of the antipollution measure "Yuddh, Pradushan Ke Viruddh" campaign. The objectives behind this initiative were to beat air and noise pollution by the government and citizens' combined efforts in the capital. The app is a free mobile phone application available to android phone users. Therefore, the enabling infrastructure is already present with the ubiquity of mobile phones in India[1]. Hence, the effort required for involvement in the initiatives was minimal. No specific crowd qualification was needed as the government motive was the maximum participation. The government stated that citizens should report the activities causing any pollution to the concerned authorities in the Green Delhi app. For the ease of citizens, the tasks were divided into three parts: directly attaching photos, videos, or voice notes to a complaint registered through the app. The demographic details of citizens were collected at sign-up for crowd management. The location was detected using phone GPS, and the complaint was communicated to the government authorities for a quick resolution. Monitoring was performed 24/7 in a "Green War Room" for quality evaluation of the received complaints. The government was committed to solving complaints after ground verification. The only motivation for citizens' participation was quick resolution and an intrinsic motive to solve the practical issues of their society. The initiative was criticized for technical failures and lack of assistance, creating a hurdle in participation (see Fig. 3). To keep a check on false reporting, 12 coordinators evaluated every complaint and overlooked resolution. For monitoring, 21 departments have been attached. These linkages with coordinating agencies added a trust factor to the campaigns, which increased participation from citizens. The initiative has been a hit in just three days of the launch due to high media visibility. Over 250 complaints were lodged every day, which made this initiative successful in three days. The total complaint received within one month was 11 946[2]. Therefore, involving citizens to solve ground-level issues will lead to transparency, empowered participation, and collaboration as citizens' awareness will increase.

B. *Aatmanirbhar Bharat App Innovation*

Aatmanirbhar Bharat App Innovation is a crowdsourcing initiative launched by the Prime Minister of India, Narendra Modi, on July 4, 2020, the day after the government banned 59 Chinese apps. This challenge was a hunt to recognize the best Indian app that can become world-class.

The campaign aims to recognize and honor the efforts of the unsung digital warriors that have the potential to empower Brand India and showcase India as the leading app-developing country in the world. The government gave specific tasks to entrepreneurs, companies, and Indian Tech developers to accomplish this mission. The task was to create an app that can be used worldwide and identify existing apps that can be scaled to become world-class. The task decomposition was done in two parts. First, citizens should submit their proposals. In the second phase, a practical demonstration was then performed by citizens for further app development. As per the objective of the initiative, the government permitted only citizens with technical expertise to participate. In an attempt to manage the voluminous crowd, a profile was maintained using login and registration details filled on "MyGov portal"[3], a citizen engagement platform of the government concerning India. The coordinating agencies that actively supported and collaborated with this crowdsourcing initiative were NITI Aayog, the Atal Innovation Mission Ministry of Electronics and Information Technology (MeitY) Startup Hub, and the National e-governance Division under the Digital India Program of the MeitY. External support provided by these reputable organizations increased the trust factor, resulting in maximum citizen participation. The government promoted this initiative on social media handles such as Twitter, LinkedIn, and newspaper advertisements to make citizens aware of the campaign. The challenge fits in well with the fundamental ambitions of the crowd. Therefore, a total of 6940 entries (see Fig. 4) were received until July 26, 2020[4]. The challenge witnessed massive participation from across the country, ranging from large cities to small towns.

Once the entries were received, they were screened and evaluated by jury members with expertise in the technical field. The

[1][Online]. Available: https://www.aninews.in/news/national/general-news

[2][Online]. Available: https://www.hindustantimes.com/India-news

[3][Online]. Available: www.my.gov.in

[4][Online]. Available: https://pib.gov.in/

Authorized licensed use limited to: DELHI TECHNICAL UNIV. Downloaded on January 19,2023 at 05:07:01 UTC from IEEE Xplore. Restrictions apply.

This article has been accepted for inclusion in a future issue of this journal. Content is final as presented, with the exception of pagination.

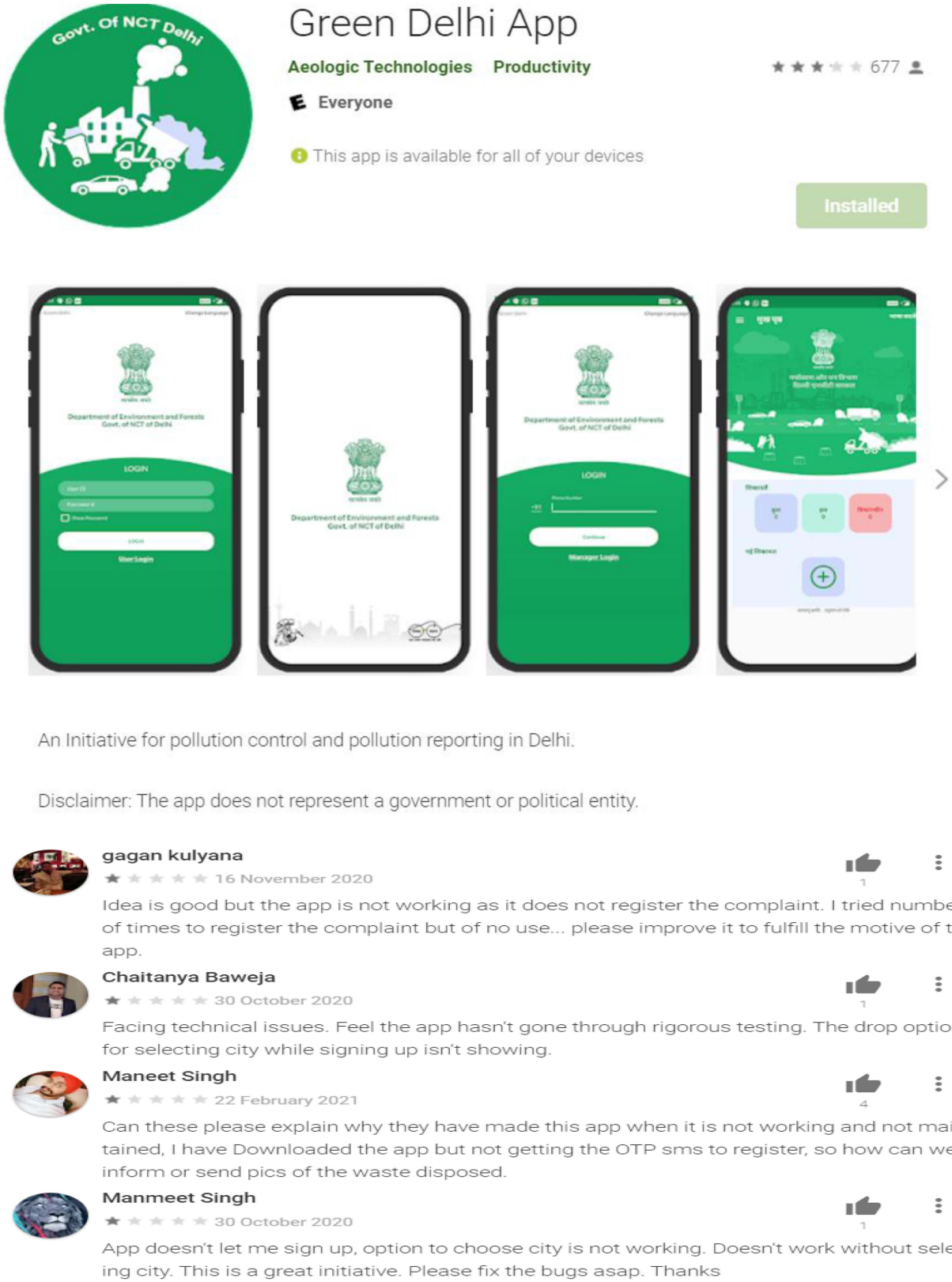

Fig. 3. Green Delhi application overview and citizens' reviews. *Source:* https://play.google.com/store/apps/details?id=com.aeologic.green_delhi&hl=en, accessed on October 16, 2021.

Authorized licensed use limited to: DELHI TECHNICAL UNIV. Downloaded on January 19,2023 at 05:07:01 UTC from IEEE Xplore. Restrictions apply.

This article has been accepted for inclusion in a future issue of this journal. Content is final as presented, with the exception of pagination.

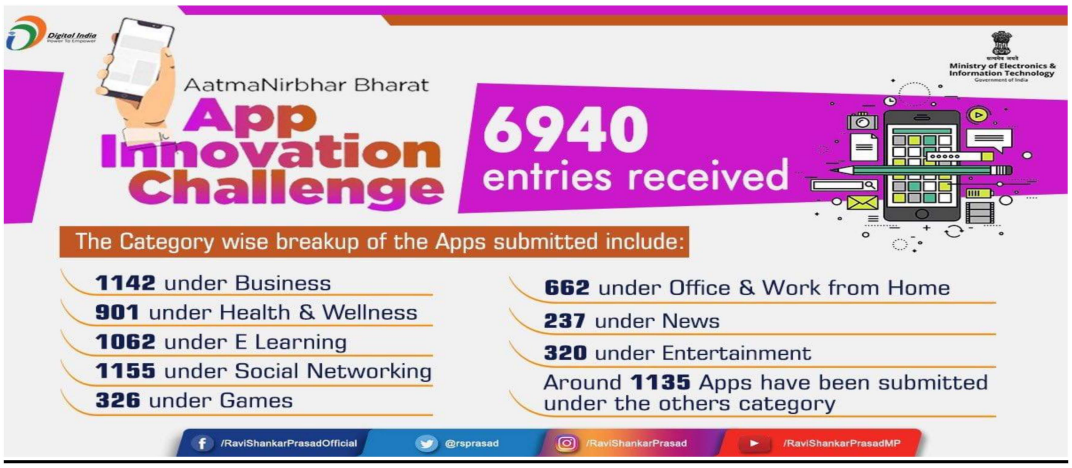

Fig. 4. Snapshot of Aatmanirbhar App Innovation crowdsourcing initiative results. *Source:* https://telecomtalk.info/aatma-nirbhar-bharat-app-entries, accessed on September 4, 2021.

MeitY made the final decision in all stages. In advance, the government stated that the prize money of Rs. 20 lakhs, Rs. 15 lakhs, and Rs. 10 lakhs as monetary incentives will be given to all 24 winners for the first, second, and third positions. The guidelines were laid down on the platform to protect citizens' personal information and the intellectual property rights of contributions (MyGov portal[5]. Technical assistance was also provided at every step by various coordinating agencies for the ease of citizens. The unprecedented success of the crowdsourcing initiative led to transparency, responsiveness, equity, accountability, inclusiveness, and empowerment of citizens in governance-related activities.

C. Innovative Ideas for PMO's Mobile App

India's government citizens engagement platform (MyGov) [134] launched a nationwide contest on March 4, 2015, to design and develop a mobile application for the Prime Minister's Office (PMO). The competition occurred in different colleges and universities around the country. With an increase in smartphones and Internet users, this seems to be a significant step toward allowing people to use their phones as a window to look into the PMO. Additionally, this initiative has boosted the idea of democratization of governance through "Jan Bhagidari" and Digital India's motive of maximum digital awareness.

This initiative aims to seek suggestions from citizens regarding the structure and content of the application. The tasks to be performed were divided into three parts. Phase 1 was the idea submission phase, phase 2 was the wireframe development phase, and phase 3 was the app development and mentorship phase[6]. Every Indian citizen aged 18 years or above with technical skills was qualified to participate in the idea submission phase by registering or logging in on MyGov[7]. In contrast, citizens with thorough knowledge and experience in app designing and development were eligible to contribute to the other two phases. The government used social media handles, such as Twitter, LinkedIn, and newspaper advertisements to promote this campaign. This initiative was launched with the partnership of Internet giant Google and MyGov. All types of technical issues citizens had were resolved with FAQs and video tutorials that were present on the platform. Google provided guidance and mentoring, which resulted in maximum participation. During the ideation phase, which was held between March 4 and March 23, 2015, more than 9273 entries were received (see Fig. 5). The top 20 contributions[8] with specific features of the PM India and MyGov websites were included in the blueprint. A panel of jury members evaluated all 110 mock-ups submitted and selected the top five teams to design and develop the apps. The rewards provided to winning teams were an android device from Google, an appreciation certificate from MyGov, six weeks of Google mentorship for app development, and a sponsored trip to the USA to meet Google developers. The result of the crowdsourcing initiative was declared on the MyGov portal, and the winning PMO mobile app was launched in India. The regulatory guidelines of these initiatives were agreed on from the initiation stage, whether they related to the government having copyrights of entries submitted or participants not disclosing any information to the third party. This initiative achieved tremendous success with the continuous collaboration of government, jury members, organizations, and citizens.

V. Results

Crowdsourcing is a novel approach to strengthening civic participation and collaborative governance [46]. Most promisingly, it creates a trustworthy and transparent relationship between citizens and government, provided the initiatives are managed well. Therefore, there was a pressing need to know the design aspect of crowdsourcing that guides public administrators. The study developed a strategic framework to provide a comprehensive view of elements and designing principles of a successful crowdsourcing initiative that government agencies must consider. A crowdsourcing initiative's design process may differ based on its objective and purpose. When running crowdsourcing initiatives, three general phases can be distinguished: preparation, execution, and postexecution. Following each phase is of utmost importance to public administrators.

[5][Online]. Available: www.my.gov.in
[6][Online]. Available: https://www.mygov.in/search?title=PMO&type=All
[7][Online]. Available: http://mygov.in
[8][Online]. Available: https://blog.mygov.in/unveiling-the-winning-ideas-ofpmo-mobile-app-contest-phase-i/

Authorized licensed use limited to: DELHI TECHNICAL UNIV. Downloaded on January 19,2023 at 05:07:01 UTC from IEEE Xplore. Restrictions apply.

This article has been accepted for inclusion in a future issue of this journal. Content is final as presented, with the exception of pagination.

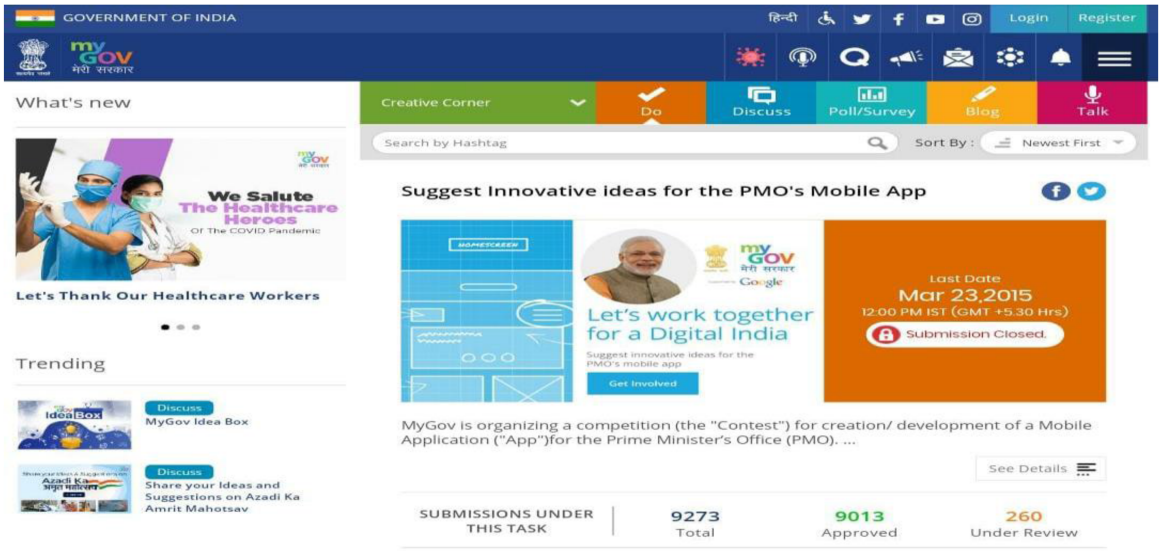

Fig. 5. Snapshot of the PMO mobile app crowdsourcing initiative on MyGov. *Source:* https://www.mygov.in/task/suggest-innovative-ideas-pmos-mobile-app/, accessed on September 5, 2021.

A. *Preparation Phase: Plan and Design*

The first phase is the preparation phase, which provides a roadmap for planning and designing a crowdsourcing initiative. This is the most critical phase because the attainment of objectives is impossible and ultimately fails without proper planning. Hence, the need arises to follow specific elements and principles for the successful preparation of crowdsourcing initiatives in the government sector.

Goals Specification: Every crowdsourcing initiative must have a predefined set of goals, ideals, and objectives, which gives a direction to achieving the end results. The clarity in vision is an essential design principle for crowdsourcing to be successful [78], [79], [80], [81], [82], [83], [84]. When government organizations specify well-defined goals in advance, citizens perceive the initiative as well intentioned and valuable.

Task Description: Well-framed tasks or activities must be specified before initiating any crowdsourcing campaign. A successful crowdsourcing solution is the outcome of the clarity of tasks or activities to citizens [85], [86], [87], [88], [89]. For task description, task properties, such as significance, autonomy, and variety, must be considered [90].

Task Duration: To attract more participation, the time frame for each task must be specified in advance [91], [92], [93]. It may range from three to four months [94], [95]. The complex challenges may run for a longer duration [96].

Task Decomposition: Every task of crowdsourcing initiative should be divided into smaller subtasks. This resulted in increased participation of crowds [97], [98], [99], [100], [101]. The chunking of tasks reduces the burden on anyone, particularly citizens who contribute to the project.

Citizen Qualification: Clearly specify the skills, abilities, and expertise required from citizens for participation. This is the most important determinant of meaningful participation [102], [103], [104]. To upgrade the qualifications of citizens, crowd coaching should be used, where experienced participants may assist new participants. Meanwhile, an induction program must be conducted to make participating citizens practice sample tasks and become accustomed to performing the task properly.

Coordinating Agencies' Specification: Coordinating authorities and agencies in crowdsourcing initiatives must be clearly specified, namely, private sector organizations, government agencies, not-for-profit organizations, or software/app development companies [105]. These linkages add substantial trust factors to crowdsourcing initiatives.

Infrastructure Specification: A well-designed, user-friendly, and simple-to-use platform catalyzes the growth of crowdsourcing. Heeks and Nicholson [105] claimed that crowd participation requires the ease of access, reliability, and accuracy of information and communication technology such as telecom and the Internet. The government sector may provide free Wi-Fi and low-cost or free Internet services in public places with the help of a public–private partnership. The citizen's motivation to participate increases due to the accessibility of infrastructure facilities [106], [107], [108].

Specify the Level of Commitment: Every organization, whether public or private, must state clearly in beginning their commitment to the participant's contributions. Whether the outcome of the crowd will be implemented as it is or the government commits to the outcome after evaluation of experts or the contributions is a recommendation that the government may or may not implement. This can act as a confidence booster for crowd participation [32], [109]. Otherwise, participants will remain skeptical and discourage future governance activities.

B. *Execution Phase: Promote and Act*

The second phase includes elements that guide public administrators in promotion and action activities. The government should spend their time promoting the crowdsourcing campaign, motivating participants to contribute, managing the excessive crowds involved in the process, preventing the misappropriate behavior of citizens, providing all types of technical assistance demanded by the group, and finally becoming involved in quality control mechanisms for keeping track of crowdsourcing initiatives.

Authorized licensed use limited to: DELHI TECHNICAL UNIV. Downloaded on January 19,2023 at 05:07:01 UTC from IEEE Xplore. Restrictions apply.

This article has been accepted for inclusion in a future issue of this journal. Content is final as presented, with the exception of pagination.

Launch Promotional Plans: Crowd participation is an important element of a successful crowdsourcing initiative. Therefore, there should be an investment in marketing activities to grow and sustain the community. Tools used to position crowdsourcing initiatives in citizens' minds are open calls and advertisements [110], [111], [112] and direct correspondence with the selected crowd [113]. An aggressive public relations plan and marketing activities should be done on the launch of crowdsourcing initiatives.

Incentive and Rewards Specification: Incentives act as a driving force for the engagement and attraction of citizens for participation**.** A literature review clearly indicates that crowdsourcing systems use incentives as a motivation, namely, intrinsic motivations, such as meaningful tasks [56], fun [114], and love for the community [115]. Moreover, extrinsic motivations such as monetary prizes and rewards can create a willingness to participate. Fundamental theories such as expectancy theory [116], self-determination theory [117], and equity theory [118] can be used to understand extrinsic and monetary incentives.

Crowd Management: In the implementation phase of crowdsourcing initiatives, a need arises to properly manage citizens participating in accomplishing the defined task. It mainly has two components: the profiling of crowds and the assignment of tasks. The required number of participants for performing the task needs to be identified to maintain the profiles of contributing participants [119]. This will restrict unwanted crowds from landing on crowdsourcing platforms [120], [121]. Based on maintained participants' profiles, the task can be assigned properly to attain the desired outcome [122].

Regulatory Guidelines: Clear policies must be framed that consider the legal needs of the government sector and online community. A nondisclosure agreement and netiquette should be established to avoid the exploitation of crowdsourcing solutions outside and to handle the misbehavior of participants [123], [124]. A policy of protecting the intellectual property rights and copyrights of crowdsourcing contributions must be specified well on the platform. To ensure participant privacy protection, guidelines need to be framed, such as end-to-end encryption to be applied to the data collected through crowdsourcing, reducing citizens' resistance to participation. This encryption is similar to what WhatsApp uses for the protection of user calls and messages.

Technical Assistance: A technical assistance team must be available on the crowdsourcing website to address citizens and coordinate agency problems. FAQs must be present on the crowdsourcing platform, giving instructions for the use and participation steps. A team of software professionals is hired to solve issues such as hacking, system crashes, and failures, including bug reports [40]. Text and video-based instructions for smoothly solving crowdsourcing tasks must be present on crowdsourcing websites [25], [40].

Quality Control: Crowdsourcing tasks or activities are performed by participants with different skills, expertise, and backgrounds, which can result in low-quality contributions [125]. Hence, quality control becomes a critical part of a positive outcome. Measures to control quality can be manual control where solutions are manually checked. Another one can be automated software that can countercheck the solutions. Peer assessments can also be used, where citizens evaluate each other's solutions. Outcomes need to be vetted by the administration to remove off-topics and irrelevant content, which can drift too much if ignored. Spammers and random filtering clickers may be used to check the quality of outcomes [126], [127].

C. Postexecution Phase: Evaluate and Feedback

In the final phase of postexecution, crowdsourcing initiatives come to an end by accepting all contributions from citizens. The government should now adopt elements such as evaluation and feedback to discuss what went wrong and how to improve crowdsourcing initiatives in the future. This phase is one of the most rewarding stages of crowdsourcing because it gives an opportunity for the government to recognize and acknowledge valuable citizens and celebrate their success for continuous engagement in future crowdsourcing initiatives.

Evaluation: After obtaining a plethora of contributions from citizens, it becomes indispensable to have a reputation system for evaluating the outcomes received. A well-designed reputation mechanism that connects activities with participant contributions while maintaining transparency is needed [128], [129], [130]. This system can display aggregated reviews after integrating outputs, such as scores, votes, and ratings editing from peer reviews. Researchers have advocated that the effectiveness of such an evaluation system can filter the crowdsourcing outputs, citizens' preferences can be disclosed, and it can enhance the transparency of reward systems.

Acknowledgment and Recognition of Contribution: Once the crowdsourcing task or activities are completed by citizens properly, giving acknowledgment is necessary [40], [49] for keeping citizens connected and for encouraging them to participate in future governance-related activities. Acknowledgment can take the form of saying "thank you" to the mass participants for their cooperation and valuable contributions. Sometimes, individual participants demand recognition for their contributions [129], which can be fulfilled by giving out participation certificates for extraordinary performance. These certificates can be used for advancing career opportunities.

Feedback: Citizens spend a lot of time and effort completing crowdsourcing activities, so they remain keen to receiving feedback on their performance. This can take the form of conveying to citizens the quality of work they have contributed [86], [121], and contributions being implemented or considered must be clearly mentioned [92], [131], [132]. These types of feedback can act as facilitators for making citizens aware that their contributions are taken seriously and getting to know about feasible solutions.

VI. Discussion and Implications

The three pillars of governance, transparency, participation, and collaboration, can be achieved as more data becomes freely accessible to the public through crowdsourcing. Citizens will be better able to comprehend and participate in their government in novel, possibly even exciting ways. James Surowiecki [135] asserts that there is true wisdom in crowds, but it will be challenging to harness the power of a highly skilled workforce in a meaningful way. As government agencies become more accustomed to crowdsourcing, the need arises to efficiently design the process and elements of crowdsourcing initiatives. This study intends to answer the design-related factors the government must consider in the fundamental phase of developing crowdsourcing initiatives. Table III serves as a roadmap for the conclusions and explanation of how the practitioners can devise a design strategy for crowdsourcing initiatives by understanding the intricacies of all the design elements.

Based on the investigation of three crowdsourcing initiatives in the government sector, six elements and 17 design principles were identified and integrated into a strategic crowdsourcing

Authorized licensed use limited to: DELHI TECHNICAL UNIV. Downloaded on January 19,2023 at 05:07:01 UTC from IEEE Xplore. Restrictions apply.

This article has been accepted for inclusion in a future issue of this journal. Content is final as presented, with the exception of pagination.

TABLE III
APPLICATION OF STRATEGIC CROWDSOURCING FRAMEWORK IN GOVERNMENT CROWDSOURCING INITIATIVES

Designing elements	Designing principles	Green Delhi	Aatmanirbhar Bharat App Innovation	Innovative ideas for PMO's mobile app
Preparation				
Plan and design	**Goal specification**	The empowerment and engagement of citizens for reporting violations of antipollution norms, locating, viewing, and discussing and getting it resolved by government officials.	To allow and empower citizens to participate in the app-making challenge and make India a leading app-developing country globally.	To seek suggestions from citizens on the structure and content of PMO's mobile app leading to a democratization of governance.
	Task description	Complaints to be registered under nine heads of different departments using the Green Delhi app.	Development of world class 'Made in India' apps, identification of best existing apps of India that can scale up to the world-class app.	Creation and development of an app for PMO office
	Task decomposition	Photos, videos, and voice notes to be attached to the app in every complaint registered by users.	The first task includes submitting proposals on leader boards, and in the second task, citizens present a demo for evaluation.	Task divided and assigned into three phases idea submission, wireframe development, and app development.
	Crowd qualification	No specific skill and minimum age limit were prescribed for citizens participation.	Indian entrepreneurs and start-ups having technical expertise were qualified to participate.	Indian citizens aged 18 or above were qualified for idea submission, whereas prior technical experience and expertise were required for wireframe and app development. For the development of app-making skills in citizens, mentorship activities were conducted.
	Coordinating agencies' specification	They were started by the Delhi Government, supported by 70 green marshals for ground verification of complaints, 830 enforcement field personnel to resolve complaints, 12 coordinators to check and overlook complaints, and 21 departments to monitor protests.	My Startup Hub, National e-governance Division under Digital India Program of Meity, Atal Innovation Mission, and NITI Aayog	The initiative is launched with the partnership of Google and MyGov.

Authorized licensed use limited to: DELHI TECHNICAL UNIV. Downloaded on January 19,2023 at 05:07:01 UTC from IEEE Xplore. Restrictions apply.

This article has been accepted for inclusion in a future issue of this journal. Content is final as presented, with the exception of pagination.

TABLE III
(CONTINUED)

Execution phase **Promote and act**	**Infrastructure specification**	Available for android phone users	Registration and submission of proposals on MyGov portal: (www.my.gov.in)	Citizens can register and submit their proposals through the MyGov portal: (www.my.gov.in).
	Specify level of commitment	Complaint resolution has been made after ground verification.	The decision of the MeitY will be final and binding	The decision of jury members will be final and obligatory to be followed in all stages of shortlisting.
	Launch promotional plans	Promotion of initiatives done on Twitter and newspaper advertisement	The promotion was posted on Twitter, LinkedIn, and newspaper advertisement	Promotional activities on LinkedIn, Twitter, and newspaper advertisements.
	Incentive specification	Rewards were not identified	The shortlisted app will be awarded Rs. 20, Rs. 15, and Rs. 10 lakhs. The government accepted suitable apps and guide them to reach a more comprehensive level.	Financial incentives lacking. Rewards include android devices, certificate of appreciation, sponsored trip to the USA and mentorship.
	Crowd management	Demographic details were collected through registration on apps	Task assignment done to Indian entrepreneurs and start-ups; a profile of participants was maintained with registration and login details.	The task was assigned to Indian citizens aged 18 years and above; the profile of participants was maintained with registration and login details.
	Regulatory guidelines	Privacy and protection of information was not available	Intellectual property rights of innovation shall remain with participants. For privacy protection, citizens agreed that MeitY would share information with panel experts and reviewers. Rejection of proposals to be done if participants provide incorrect information.	The government of India has copyrights of all submitted ideas. All guidelines were specified on the MyGov portal.
	Technical assistance	Technical help service to resolve citizens' issues was lacking.	Various coordinating agencies assisted, but FAQs and video-based training displaying sample tasks were not	Frequently asked questions (FAQs) as well as video-based tutorials are present

Authorized licensed use limited to: DELHI TECHNICAL UNIV. Downloaded on January 19,2023 at 05:07:01 UTC from IEEE Xplore. Restrictions apply.

This article has been accepted for inclusion in a future issue of this journal. Content is final as presented, with the exception of pagination.

TABLE III
(CONTINUED)

	Quality control	Green marshals deployed for quality control	present to understand the task. Screening of entries done by a panel of experts, and top two entries are shortlisted in each category.	on the website for technical assistance. To ensure best-quality outcomes, filtration and shortlisting are done by jury members.
Post-execution phase				
Evaluate and feedback	**Evaluation**	12 coordinators deployed to check on complaints received, and false reporting was prohibited	Evaluation of contributions is done based on "ease of use, robustness, security features, scalability" by jury members who were experts from the private sector and academia with actual demo.	Evaluation of contributions done by jury members who are experts on different parameters
	Acknowledgment and recognition of contribution	No public recognition and appreciation.	Shortlisted apps of participants to be awarded and displayed on leader boards for recognition.	Selected participants received certificates of appreciation from MyGov and Google for advancement in career opportunities.
	Feedback	Department uploaded a picture after the resolution of complaints. If citizens were unsatisfied, complaints reopen.	Regular feedback to participants is given through emails provided by participants. After campaign success, the government adopts a suitable app to ideate, incubate, build, nurture, and sustain it.	Regular feedback and results were displayed on the MyGov platform of India.

framework. A comparison of three crowdsourcing government initiatives reveals the following three key findings.

1) The preparation phase (Phase 1): All three cases have clear and precise goals and task descriptions in terms of involving citizens' collaboration and maximum participation in solving governance-related issues. Therefore, the first design principle the government must consider in the preparation phase is to decide the initiative's goals in advance [78], [79], [80], [81], [82], [83], [84]. The problem statement that is easy to understand [85], [86], [87], [88], [89], [90] results in improved work performance. It was also observed that for the convenience of citizens, the task was divided and split into smaller tasks [97], [98], [99], [100], [101], making complex problem-solving easy. Furthermore, as a diverse pool of citizens participates, the government decides the citizens' qualifications [102], [103], [104] to participate in advance. This principle restrains the unwanted traffic of citizens from landing on crowdsourcing initiatives, which, if not controlled, results in a waste of time and resources of the government. The age limit of citizens, specific skills, and expertise required to participate should be prescribed in advance because the quality of inputs may vary according to citizens' qualifications and expertise. The strong information management system and infrastructure capabilities [106], [107], [108] helped the government efficiently manage the process and obtain optimum results in a shorter period.
2) The execution phase (Phase 2): was characterized by interactivity and bidirectionality among government officials and citizens. The government should use a series of marketing activities to reach citizens and increase awareness of crowdsourcing campaigns. In the example, it was observed that monetary incentives trigger citizens to participate. Alternatively, intrinsic motivation such as solving environmental issues, the satisfaction of doing

Authorized licensed use limited to: DELHI TECHNICAL UNIV. Downloaded on January 19,2023 at 05:07:01 UTC from IEEE Xplore. Restrictions apply.

This article has been accepted for inclusion in a future issue of this journal. Content is final as presented, with the exception of pagination.

morally good deeds, and a greater sense of accomplishment with the community are also important motivators. The initiative's success depends on appropriate crowd management, so the design rules of demographic profiling of citizens must be considered for managing a diverse citizen group. Accordingly, the task should be assigned to citizens. The anonymous and voluntary contributions of citizens were put into quality check with jammers, a jury of experts, and citizens doing peer reviewing. Thus, the design principles of quality control [125], [126], [127] were considered to obtain the desired outcome. The study revealed that citizens gave their maximum contribution and high-quality inputs when they understood the task and purpose well. Therefore, there exists a relationship between clear goals, task specifications, motivation, and quality outcomes.

3) The postexecution phase (Phase 3): The government sector must provide immediate feedback when citizens offer their time and efforts to contribute to crowdsourcing initiatives. The citizens were informed of how the selected contribution would be further developed with their collaboration and implemented for massive use. This principle indicated that citizens' participation was not a hollow exercise and that their contributions were valuable. Delayed feedback gave better results in the simple task, whereas solving complex tasks in-between and delayed feedback worked better. These results show that feedback plays a pivotal role in motivating, guiding, and enhancing citizens' participation in future crowdsourcing opportunities [86], [92], [121], [131], [132]. Therefore, comparing the three crowdsourcing initiatives with the developed crowdsourcing framework showcases the theory-based framework's relevance and practicality for successful crowdsourcing initiatives. The progressive crowdsourcing design guides implementers to accelerate crowdsourcing initiatives from growth to maturity.

The following implications can be deduced from a theoretical standpoint. First, the limited empirical research on crowdsourcing in governance could be expanded. Second, the phase-wise process and design elements of the crowdsourcing initiative combined into a single integrated strategic framework provide a one-stop point for practitioners. From a practical perspective, the proposed strategic framework can guide public administrators and government agencies to identify common pitfalls and issues, such as having postimplementation government strategies early in the designing phase of crowdsourcing initiatives that lead to the attainment of desirable outcomes from crowdsourcing. Government agencies can better understand the intricacies of all elements and principles and devise a design strategy for crowdsourcing implementation. The public administrators in government agencies can gain insights from the results to increase their level of knowledge and expertise in designing crowdsourcing initiatives. Therefore, the lessons learned from designing principles or rules will create epistemic value for government agencies. The interactivity and bidirectionality among government officials and citizens can be promoted in the execution phase of crowdsourcing. This aspect helps in creating economic value for government administrators. Finally, the crowdsourcing strategic framework might be utilized as a guide and decision step when envisioning and conducting crowdsourcing initiatives.

VII. Conclusion

Though the article gives the first idea for government implementers to design crowdsourcing initiatives using a strategic crowdsourcing designing framework, it is not free from limitations. The morphological approach gives a systematic overview of various design elements but does not capture potential linkages or interdependencies. Due to the morphological methodology, we believe these interdependencies are outside the scope of this article. As developing a crowdsourcing initiative involves several interrelated decisions, future studies should explore the interrelationships among the design elements, as certain decisions may limit the decision opportunities for others. Further research should examine whether there is a hierarchy between design choices, such that early decisions influence others and limit the decision space of other design aspects.

The article focused mostly on crowdsourcing initiatives for idea generation and microtasking; however, the outcomes may vary in various crowdsourcing contexts, such as knowledge pooling or open collaboration. Although we presented a beginning point, further research can be conducted with alternative sorts of crowdsourcing using the developed strategic framework of designing crowdsourcing and modifying it as necessary.

Lastly, the exploratory study outlines crowdsourcing design elements in Indian-based crowdsourcing initiatives. Although the geographic focus may seem limited, the selected examples are valid in a specific judicial and political framework. Transferring crowdsourcing practices to other countries needs an in-depth review of the legal situation, such as territorializing government levels and responsibilities, evaluating local property rights, and determining if monetary incentives are allowed in government. Therefore, from a methodological standpoint, future research could check the crowdsourcing design framework in a more extensive empirical study with different countries and initiatives. This will provide further insights to implementers of the government sector.

Acknowledgment

The authors would like to acknowledge the constant support of Prof. T. U. Daim, Editor in Chief IEEE Transactions on Engineering Management for constant support throughout the review process. The authors would also like to thank the three anonymous reviewers for their constructive feedback and suggestions, which helped them improve this research article.

References

[1] U. Sivarajah, Z. Irani, and V. Weerakkody, "Evaluating the use and impact of Web 2.0 technologies in local government," *Government Inf. Quart.*, vol. 32, no. 4, pp. 473–487, 2015.

[2] A. V. Anttiroiko, "Innovation in democratic e-governance: Benefitting from Web 2.0 applications in the public sector," *Int. J. Electron. Government Res.*, vol. 6, no. 2, pp. 18–36, 2010.

[3] S. G. Grimmelikhuijsen and A. J. Meijer, "Does Twitter increase perceived police legitimacy?," *Public Admin. Rev.*, vol. 75, no. 4, pp. 598–607, 2015.

[4] T. O'reilly, "What is Web 2.0: Design patterns and business models for the next generation of software," *Commun. Strategies*, vol. 65, no. 1, pp. 17–37, 2007.

[5] I. Mergel and K. C. Desouza, "Implementing open innovation in the public sector: The case of Challenge.gov," *Public Admin. Rev.*, vol. 73, no. 6, pp. 882–890, 2013.

Authorized licensed use limited to: DELHI TECHNICAL UNIV. Downloaded on January 19,2023 at 05:07:01 UTC from IEEE Xplore. Restrictions apply.

This article has been accepted for inclusion in a future issue of this journal. Content is final as presented, with the exception of pagination.

[6] V. Gandhi, "Citizens need to participate more in making policy decisions related to their own surroundings," The Economic Times, 2016. Accessed: Oct. 10, 2021. [Online]. Available: https://economictimes.indiatimes.com/blogs/et-commentary/citizens-need-to-participate-more-in-making-policydecisions-related-to-their-own-surroundings/

[7] R. Vragov and N. Kumar, "The impact of information and communication technologies on the costs of democracy," *Electron. Commerce Res. Appl.*, vol. 12, no. 6, pp. 440–448, 2013.

[8] E. Murotua, G. E. Iyawa, M. Ujakpa, J. O. Osakwe, C. O. Oduor, and N. Suresh, "Open innovation in government services: An empirical view of citizens' participation," in *Proc. IST-Afr. Conf.*, 2020, pp. 1–10.

[9] P. McDermott, "Building open government," *Government Inf. Quart.*, vol. 27, no. 4, pp. 401–413, 2010.

[10] J. Howe, "The rise of crowdsourcing," *Wired Mag.*, vol. 14, no. 6, pp. 1–4, 2006.

[11] J. Howe, *Crowdsourcing: How the Power of the Crowd is Driving the Future of Business*. New York, NY, USA: Random House, 2008.

[12] H. O. Ikediego, M. Ilkan, A. M. Abubakar, and F. V. Bekun, "Crowdsourcing (who, why and what)," *Int. J. Crowd Sci.*, vol. 2, no. 1, pp. 27–41, 2018.

[13] L. A. Toledo and F. H. A. D. Leon, "Crowdsourcing as production model that uses collective intelligence, the collaborative culture and the formation of communities," *Innov. Manage. Rev.*, vol. 16, no. 4, pp. 344–356, 2019.

[14] Z. Khan, D. Ludlow, W. Loibl, and K. Soomro, "ICT enabled participatory urban planning and policy development: The UrbanAPI project," *Transforming Government, People, Process Policy*, vol. 8, no. 2, pp. 205–229, 2014.

[15] D. V. Bala, "Governance to good governance through e-governance-a critical review of concept, model, initiatives & challenges in India," *Int. J. Manage., I.T. Eng.*, vol. 8, no. 10, pp. 224–269, 2018.

[16] Digital Government in the Decade of Action for Sustainable Development, "E-Government Survey," Department of Economic and Social Affairs, United Nations, 2020.

[17] C. J. Lukensmeyer and L. H. Torres, "Citizensourcing: Citizen participation in a networked nation," in *Civic Engagement in a Network Society*. Charlotte, NC, USA: Inf. Age Publ., 2008, pp. 207–233.

[18] T. Nam, "Suggesting frameworks of citizen-sourcing via Government 2.0," *Government Inf. Quart.*, vol. 29, no. 1, pp. 12–20, 2012.

[19] F. Belanger and L. Carter, "Digitizing government interactions with constituents: An historical review of e-government research in information systems," *J. Assoc. Inf. Syst.*, vol. 13, no. 5, pp. 363–394, 2012.

[20] B. W. Wirtz and P. Daiser, "A meta-analysis of empirical e-government research and its future research implications," *Int. Rev. Administ. Sci.*, vol. 84, no. 1, pp. 144–163, 2018.

[21] H. Elkadi, "Success and failure factors for e-government projects: A case from Egypt," *Egyptian Inform. J.*, vol. 14, no. 2, pp. 165–173, 2013.

[22] E. Loukis and Y. Charalabidis, "Active and passive crowdsourcing in government," in *Policy Practice and Digital Science*. Cham, Switzerland: Springer, 2015, pp. 261–289.

[23] M. Lastovka, "Crowdsourcing as new instrument in policy-making: Making the democratic process more engaging," *Eur. View*, vol. 14, no. 1, pp. 93–99, 2015, doi: 10.1007/s12290-015-0345-7.

[24] V. Lehdonvirta and J. Bright, "Crowdsourcing for public policy and government," *Policy Internet*, vol. 7, no. 3, pp. 263–267, 2015.

[25] S. Zogaj, N. Leicht, I. Blohm, U. Bretschneider, and J. M. Leimeister, "Towards successful crowdsourcing projects: Evaluating the implementation of governance mechanisms," 2015. [Online]. Available: https://ssrn.com/abstract=3140601

[26] V. Chandrasekaran, S. V. Rajan, R. K. Vasani, A. Menon, P. B. Sivakumar, and C. S. Velayutham, "A crowdsourcing-based platform for better governance," in *Proc. Int. Conf. Soft Comput. Syst.*, 2016, pp. 519–527.

[27] H. K. Liu, "Crowdsourcing design: A synthesis of literatures," in *Proc. 50th Hawaii Int. Conf. Syst. Sci.*, 2017, pp. 2751–2760.

[28] A. Taeihagh, "Crowdsourcing: A new tool for policy-making?," *Policy Sci.*, vol. 50, no. 4, pp. 629–647, 2017.

[29] K. Venturini and C. Verbano, "Open innovation in the public sector: Resources and performance of research-based spin-offs," *Bus. Process Manage. J.*, vol. 23, no. 6, pp. 1337–1358, 2017.

[30] B. Y. Clark, N. Zingale, J. Logan, and J. Brudney, "A framework for using crowdsourcing in government," in *Crowdsourcing: Concepts, Methodologies, Tools, and Applications*. Hershey, PA, USA: IGI Global, 2019, pp. 194–214.

[31] B. Furuholt and F. Wahid, "E-government challenges and the role of political leadership in Indonesia: The case of Sragen," in *Proc. 41st Annu. Hawaii Int. Conf. Syst. Sci.*, 2008, p. 411.

[32] S. Ozcan, D. Boye, J. Arsenyan, and P. Trott, "A scientometric exploration of crowdsourcing: Research clusters and applications," *IEEE Trans. Eng. Manage.*, vol. 69, no. 6, pp. 3023–3037, Dec. 2022.

[33] P. Dutil, "Crowdsourcing as a new instrument in the government's arsenal: Explorations and considerations," *Can. Public Admin.*, vol. 58, no. 3, pp. 363–383, 2015.

[34] D. C. Brabham, *Crowdsourcing in the Public Sector*. Washington, DC, USA: Georgetown Univ. Press, 2015.

[35] M. Bott and G. Young, "The role of crowdsourcing for better governance in international development," *Praxis, Fletcher J. Hum. Secur.*, vol. 27, no. 1, pp. 47–70, 2012.

[36] A. Bozzon, M. Brambilla, S. Ceri, A. Mauri, and R. Volonterio, "Designing complex crowdsourcing applications covering multiple platforms and tasks," *J. Web Eng.*, vol. 14, pp. 443–473, 2015.

[37] S. Royo and A. Yetano, "Crowdsourcing as a tool for e-participation: Two experiences regarding CO_2 emissions at municipal level," *Electron. Commerce Res.*, vol. 15, no. 3, pp. 323–348, 2015.

[38] K. Cupido and J. Ophoff, "A conceptual model of critical success factors for an e-government crowdsourcing solution," in *Proc. 14th Eur. Conf. e-Government*, Jun. 2014, pp. 77–84.

[39] I. Mergel, "Opening government: Designing open innovation processes to collaborate with external problem solvers," *Social Sci. Comput. Rev.*, vol. 33, no. 5, pp. 599–612, 2015.

[40] P. Srivastava and A. Mostafavi, "Challenges and opportunities of crowdsourcing and participatory planning in developing infrastructure systems of smart cities," *Infrastructures*, vol. 3, no. 4, 2018, Art. no. 51.

[41] S. Malodia, A. Dhir, M. Mishra, and Z. A. Bhatti, "Future of e-government: An integrated conceptual framework," *Technological Forecasting Social Change*, vol. 173, 2021, Art. no. 121102.

[42] F. R. A. Neto and C. A. Santos, "Understanding crowdsourcing projects: A systematic review of tendencies, workflow, and quality management," *Inf. Process. Manage.*, vol. 54, no. 4, pp. 490–506, 2018.

[43] A. Amrollahi, "A process model for crowdsourcing: Insights from the literature on implementation," in *Proc. 26th Australas. Conf. Inf. Syst.*, 2015, pp. 1–12.

[44] J. H. Paik, M. Scholl, R. Sergeev, S. Randazzo, and K. R. Lakhani, "Innovation contests for high-tech procurement," *Res.-Technol. Manage.*, vol. 63, no. 2, pp. 36–45, 2020.

[45] H. Zheng, D. Li, and W. Hou, "Task design, motivation, and participation in crowdsourcing contests," *Int. J. Electron. Commerce*, vol. 15, no. 4, pp. 57–88, 2011.

[46] D. C. Brabham, "Using crowdsourcing in government," IBM Center for the Business of Government, 2013, pp. 1–42.

[47] C. Ansell and A. Gash, "Collaborative platforms as a governance strategy," *J. Public Admin. Res. Theory*, vol. 28, no. 1, pp. 16–32, 2018.

[48] C. Shirky, *Here Comes Everybody: The Power of Organizing Without Organizations*. Baltimore, MD, USA: Penguin, 2008.

[49] D. C. Brabham, "Crowdsourcing the public participation process for planning projects," *Plan. Theory*, vol. 8, no. 3, pp. 242–262, 2009.

[50] T. Aitamurto, *Crowdsourcing for Democracy: A New Era in Policy-Making*, vol. 1. Helsinki, Finland: Committee Future, Parliament Finland , 2012.

[51] D. C. Brabham, "Crowdsourcing the public participation process for planning projects," *Plan. Theory*, vol. 8, no. 3, pp. 242–262, 2019.

[52] J. Prpić, A. Taeihagh, and J. Melton, "The fundamentals of policy crowdsourcing," *Policy Internet*, vol. 7, no. 3, pp. 340–361, 2015.

[53] C. Certoma, F. Corsini, and F. Rizzi, "Crowdsourcing urban sustainability. Data, people and technologies in participatory governance," *Futures*, vol. 74, pp. 93–106, 2015.

[54] C. Certomà and F. Rizzi, "Crowdsourcing processes for citizen-driven governance," in *Citizen Empowerment and Innovation in the Data-Rich City*. Cham, Switzerland: Springer, 2017, pp. 57–77.

[55] K. S. Al-Omoush, M. Orero-Blat, and D. Ribeiro-Soriano, "The role of sense of community in harnessing the wisdom of crowds and creating collaborative knowledge during the COVID-19 pandemic," *J. Bus. Res.*, vol. 132, pp. 765–774, 2021.

[56] D. Chandler and A. Kapelner, "Breaking monotony with meaning: Motivation in crowdsourcing markets," *J. Econ. Behav. Org.*, vol. 90, pp. 123–133, 2013.

[57] M. Hosseini, K. Phalp, J. Taylor, and R. Ali, "The four pillars of crowdsourcing: A reference model," in *Proc. IEEE 8th Int. Conf. Res. Challenges Inf. Sci.*, 2014, pp. 1–12.

Authorized licensed use limited to: DELHI TECHNICAL UNIV. Downloaded on January 19,2023 at 05:07:01 UTC from IEEE Xplore. Restrictions apply.

This article has been accepted for inclusion in a future issue of this journal. Content is final as presented, with the exception of pagination.

[58] E. Cullina, K. Conboy, and L. Morgan, "Choosing the right crowd: An iterative process for crowd specification in crowdsourcing initiatives," in *Proc. 49th Hawaii Int. Conf. Syst. Sci.*, 2016, pp. 4355–4364.

[59] S. Rocheska, M. Angeleski, D. Nikoloski, and G. Mancheski, "Harnessing innovation potential of crowdsourcing," in *Proc. 8th Int. Conf. Challenges Knowl. Soc.*, 2014, pp. 541–548.

[60] N. H. Thuan, P. Antunes, and D. Johnstone, "A process model for establishing business process crowdsourcing," *Australas. J. Inf. Syst.*, vol. 21, pp. 1–21, 2017, doi: 10.3127/ajis.v21i0.1392.

[61] I. Mergel, "Open innovation in the public sector: Drivers and barriers for the adoption of Challenge.gov," *Public Manage. Rev.*, vol. 20, no. 5, pp. 726–745, 2018.

[62] L. Dahlander and H. Piezunka, "Open to suggestions: How organizations elicit suggestions through proactive and reactive attention," *Res. Policy*, vol. 43, no. 5, pp. 812–827, 2014.

[63] K. Randhawa, R. Wilden, and J. West, "Crowdsourcing without profit: The role of the seeker in open social innovation," *R&D Manage.*, vol. 49, no. 3, pp. 298–317, 2019.

[64] D. Hilgers and C. Ihl, "Citizensourcing: Applying the concept of open innovation to the public sector," *Int. J. Public Participation*, vol. 4, no. 1, pp. 67–88, 2010.

[65] K. C. Desouza, "Challenge.gov: Using competitions and awards to spur innovation," IBM Center for the Business of Government, Oct. 2012. [Online]. Available: https://www.businessofgovernment.org

[66] D. Linders, "From e-government to we-government: Defining a typology for citizen coproduction in the age of social media," *Government Inf. Quart.*, vol. 29, no. 4, pp. 446–454, 2012.

[67] T. Kohler and H. Chesbrough, "From collaborative community to competitive market: The quest to build a crowdsourcing platform for social innovation," *R&D Manage.*, vol. 49, no. 3, pp. 356–368, 2019.

[68] E. Seltzer and D. Mahmoudi, "Citizen participation, open innovation, and crowdsourcing: Challenges and opportunities for planning," *J. Plan. Literature*, vol. 28, no. 1, pp. 3–18, 2013.

[69] G. Koch, J. Füller, and S. Brunswicker, "Online crowdsourcing in the public sector: How to design open government platforms," in *Proc. Int. Conf. Online Communities Social Comput.*, Jul. 2011, pp. 203–212.

[70] J. Paul and A. R. Criado, "The art of writing literature review: What do we know and what do we need to know?," *Int. Bus. Rev.*, vol. 29, no. 4, 2020, Art. no. 101717.

[71] D. Tranfield, D. Denyer, and P. Smart, "Towards a methodology for developing evidence-informed management knowledge by means of systematic review," *Brit. J. Manage.*, vol. 14, no. 3, pp. 207–222, 2003.

[72] P. Hallinger, "A conceptual framework for systematic reviews of research in educational leadership and management," *J. Educ. Admin.*, vol. 51, no. 2, pp. 126–149, 2013.

[73] A. Sarı, A. Tosun, and G. I. Alptekin, "A systematic literature review on crowdsourcing in software engineering," *J. Syst. Softw.*, vol. 153, pp. 200–219, 2019.

[74] F. R. P. M. Vianna, A. R. Graeml, and J. Peinado, "The role of crowdsourcing in Industry 4.0: A systematic literature review," *Int. J. Comput. Integr. Manuf.*, vol. 33, no. 4, pp. 411–427, 2020.

[75] Y. Zhen, A. Khan, S. Nazir, Z. Huiqi, A. Alharbi, and S. Khan, "Crowdsourcing usage, task assignment methods, and crowdsourcing platforms: A systematic literature review," *J. Softw., Evol. Process*, vol. 33, no. 8, 2021, Art. no. e2368.

[76] H. Snyder, "Literature review as a research methodology: An overview and guidelines," *J. Bus. Res.*, vol. 104, pp. 333–339, 2019.

[77] A. J. Meijer, "New media and the coproduction of safety: An empirical analysis of Dutch practices," *Amer. Rev. Public Admin.*, vol. 44, no. 1, pp. 17–34, 2014.

[78] J. E. Lim, J. Lee, and D. Kim, "The effects of feedback and goal on the quality of crowdsourcing tasks," *Int. J. Hum.–Comput. Interact.*, vol. 37, no. 13, pp. 1207–1219, 2021.

[79] A. Sharma, "Crowdsourcing critical success factor model: Strategies to harness the collective intelligence of the crowd," London School of Economics, London, U.K., pp. 1–22, 2010.

[80] A. Afuah and C. L. Tucci, "Crowdsourcing as a solution to distant search," *Acad. Manage. Rev.*, vol. 37, no. 3, pp. 355–375, 2012, doi: 10.5465/amr.2010.0146.

[81] I. Lykourentzou, D. J. Vergados, K. Papadaki, and Y. Naudet, "Guided crowdsourcing for collective work coordination in corporate environments," in *Proc. Int. Conf. Comput. Collective Intell.*, Sep. 2013, pp. 90–99.

[82] H. Bassi, C. J. Lee, L. Misener, and A. M. Johnson, "Exploring the characteristics of crowdsourcing: An online observational study," *J. Inf. Sci.*, vol. 46, no. 3, pp. 291–312, 2020.

[83] T. W. Malone, R. Laubacher, and C. Dellarocas, "The collective intelligence genome," *MIT Sloan Manage. Rev.*, vol. 51, no. 3, pp. 21–31, 2010.

[84] P. A. Rosen, "Crowdsourcing lessons for organizations," *J. Decis. Syst.*, vol. 20, no. 3, pp. 309–324, 2011.

[85] S. Schäfer, D. Antons, D. Lüttgens, F. Piller, and T. O. Salge, "Talk to your crowd: Principles for effective communication in crowdsourcing a few key principles for communicating with solvers can help contest sponsors maintain and grow their base of participants," *Res.-Technol. Manage.*, vol. 60, no. 4, pp. 33–42, 2017.

[86] C. Nguyen, O. Oh, D. Kocsis, and G. J. Vreede, "Crowdsourcing as Lego: Unpacking the building blocks of crowdsourcing collaboration processes," in *Proc. Int. Conf. Inf. Syst.*, 2013, pp. 1–9.

[87] S. Moussawi and M. Koufaris, "The crowd on the assembly line: Designing tasks for a better crowdsourcing experience," in *Proc. Int. Conf. Inf. Syst.*, 2013, pp. 1–17.

[88] O. Tokarchuk, R. Cuel, and M. Zamarian, "Analyzing crowd labor and designing incentives for humans in the loop," *IEEE Internet Comput.*, vol. 16, no. 5, pp. 45–51, Sep./Oct. 2012.

[89] J. M. Leimeister, M. Huber, U. Bretschneider, and H. Krcmar, "Leveraging crowdsourcing: Activation-supporting components for IT-based ideas competition," *J. Manage. Inf. Syst.*, vol. 26, no. 1, pp. 197–224, 2009.

[90] L. Muhdi, M. Daiber, S. Friesike, and R. Boutellier, "The crowdsourcing process: An intermediary mediated idea generation approach in the early phase of innovation," *Int. J. Entrepreneurship Innov. Manage.*, vol. 14, no. 4, pp. 315–332, 2011.

[91] E. W. Ayaburi, J. Lee, and M. Maasberg, "Understanding crowdsourcing contest fitness strategic decision factors and performance: An expectation-confirmation theory perspective," *Inf. Syst. Front.*, vol. 22, no. 5, pp. 1227–1240, 2020.

[92] L. Chen, P. Xu, and D. Liu, "Effect of crowd voting on participation in crowdsourcing contests," *J. Manage. Inf. Syst.*, vol. 37, no. 2, pp. 510–535, 2020.

[93] K. J. Boudreau, N. Lacetera, and K. R. Lakhani, "Incentives and problem uncertainty in innovation contests: An empirical analysis," *Manage. Sci.*, vol. 57, no. 5, pp. 843–863, 2011.

[94] S. Massa and S. Testa, "Opening up innovation processes through contests in the food sector," *Bus. Process Manage. J.*, vol. 23, no. 6, pp. 1290–1310, 2017.

[95] A. Kulkarni, M. Can, and B. Hartmann, "Collaboratively crowdsourcing workflows with turkomatic," in *Proc. ACM Conf. Comput. Supported Cooperative Work*, Feb. 2012, pp. 1003–1012.

[96] R. T. Nakatsu, E. B. Grossman, and C. L. Iacovou, "A taxonomy of crowdsourcing based on task complexity," *J. Inf. Sci.*, vol. 40, no. 6, pp. 823–834, 2014.

[97] A. Natalicchio, A. M. Petruzzelli, and A. C. Garavelli, "Innovation problems and search for solutions in crowdsourcing platforms—A simulation approach," *Technovation*, vol. 64, pp. 28–42, 2017.

[98] L. G. Pee, E. Koh, and M. Goh, "Trait motivations of crowdsourcing and task choice: A distal-proximal perspective," *Int. J. Inf. Manage.*, vol. 40, pp. 28–41, 2018.

[99] I. Blohm, S. Zogaj, U. Bretschneider, and J. M. Leimeister, "How to manage crowdsourcing platforms effectively?," *California Manage. Rev.*, vol. 60, no. 2, pp. 122–149, 2018.

[100] A. Kittur et al., "The future of crowd work," in *Proc. Conf. Comput. Supported Cooperative Work*, Feb. 2013, pp. 1301–1318.

[101] L. Hetmank, "Components and functions of crowdsourcing systems—A systematic literature review," in *Proc. Int. Conf. Wirtschaftsinformatik*, 2013, vol. 4, pp. 55–69.

[102] D. Geiger and M. Schader, "Personalized task recommendation in crowdsourcing information systems—Current state of the art," *Decis. Support Syst.*, vol. 65, pp. 3–16, 2014.

[103] I. Christensen and C. Karlsson, "Open innovation and the effects of crowdsourcing in a pharma ecosystem," *J. Innov. Knowl.*, vol. 4, no. 4, pp. 240–247, 2019.

[104] T. Bücheler and J. H. Sieg, "Understanding science 2.0: Crowdsourcing and open innovation in the scientific method," *Proc. Comput. Sci.*, vol. 7, pp. 327–329, 2011, doi: 10.1016/j.procs.2011.09.014.

[105] R. Heeks and B. Nicholson, "Software export success factors and strategies in 'follower' nations," *Competition Change*, vol. 8, no. 3, pp. 267–303, 2004.

Authorized licensed use limited to: DELHI TECHNICAL UNIV. Downloaded on January 19,2023 at 05:07:01 UTC from IEEE Xplore. Restrictions apply.

This article has been accepted for inclusion in a future issue of this journal. Content is final as presented, with the exception of pagination.

[106] J. Surowiecki, *The Wisdom of Crowds: Why the Many Are Smarter Than the Few and How Collective Wisdom Shapes Business, Economies, Societies and Nations*. New York, NY, USA: Doubleday, 2004.
[107] A. Potter, M. McClure, and K. Sellers, "Mass collaboration problem solving: A new approach to wicked problems," in *Proc. Int. Symp. Collaborative Technol. Syst.*, 2010, pp. 398–407.
[108] M. N. Wexler, "Reconfiguring the sociology of the crowd: Exploring crowdsourcing," *Int. J. Sociol. Social Policy*, vol. 31, no. 1/2, pp. 6–20, 2011.
[109] K. Hansson, T. Aitamurto, T. Ludwig, M. Muller, and I. K. Hansson, "Editorial for the workshop 'toward a typology of participation in crowdwork'," in *Proc. ACM Conf. Comput.-Supported Cooperative Work Social Comput. Workshop, Toward Typol. Participation Crowdwork*, 2016, pp. 5–11.
[110] J. H. Choi and J. S. Lee, "Online social networks for crowdsourced multimedia-involved behavioral testing: An empirical study," *Front. Psychol.*, vol. 6, 2016, Art. no. 1991.
[111] D. Naparat and P. Finnegan, "Crowdsourcing software requirements and development: A mechanism-based exploration of 'opensourcing'," in *Proc. Americas Conf. Inf. Syst.*, 2013, pp. 1–7.
[112] A. Doan, R. Ramakrishnan, and A. Y. Halevy, "Crowdsourcing systems on the worldwide web," *Commun. ACM*, vol. 54, no. 4, pp. 86–96, 2011.
[113] N. Kaufmann, T. Schulze, and D. Veit, "More than fun and money. Worker motivation in crowdsourcing—A study on mechanical turk," in *Proc. Americas Conf. Inf. Syst.*, Aug. 2011, vol. 11, pp. 1–11.
[114] Y. Sun, Y. Fang, and K. H. Lim, "Understanding sustained participation in transactional virtual communities," *Decis. Support Syst.*, vol. 53, no. 1, pp. 12–22, 2012.
[115] Y. Zhao and Q. Zhu, "Evaluation on crowdsourcing research: Current status and future direction," *Inf. Syst. Front.*, vol. 16, no. 3, pp. 417–434, 2014.
[116] L. Zou, J. Zhang, and W. Liu, "Perceived justice and creativity in crowdsourcing communities: Empirical evidence from China," *Social Sci. Inf.*, vol. 54, no. 3, pp. 253–279, 2015.
[117] M. Allahbakhsh, A. Ignjatovic, B. Benatallah, S.-M.-R. Beheshti, E. Bertino, and N. Foo, "Reputation management in crowdsourcing systems," in *Proc. 8th Int. Conf. Collaborative Comput., Netw., Appl. Worksharing*, Oct. 2012, pp. 664–671.
[118] O. Stewart, D. Lubensky, and J. M. Huerta, "Crowdsourcing participation inequality: A SCOUT model for the enterprise domain," in *Proc. ACM SIGKDD Workshop Hum. Comput.*, Jul. 2010, pp. 30–33.
[119] H. Piezunka and L. Dahlander, "Distant search, narrow attention: How crowding alters organizations' filtering of suggestions in crowdsourcing," *Acad. Manage. J.*, vol. 58, no. 3, pp. 856–880, 2015.
[120] R. Khazankin, D. Schall, and S. Dustdar, "Predicting QoS in scheduled crowdsourcing," in *Proc. Int. Conf. Adv. Inf. Syst. Eng.*, Jun. 2012, pp. 460–472.
[121] C. Sauerwein, M. Gander, M. Felderer, and R. Breu, "A systematic literature review of crowdsourcing-based research in information security," in *Proc. IEEE Symp. Serv.-Oriented Syst. Eng.*, 2016, pp. 364–371.
[122] J. De Beer, I. P. McCarthy, A. Soliman, and E. Treen, "Click here to agree: Managing intellectual property when crowdsourcing solutions," *Bus. Horiz.*, vol. 60, no. 2, pp. 207–217, 2017.
[123] M. Hirth, T. Hoßfeld, and P. Tran-Gia, "Analyzing costs and accuracy of validation mechanisms for crowdsourcing platforms," *Math. Comput. Model.*, vol. 57, no. 11/12, pp. 2918–2932, 2013.
[124] J. S. Downs, M. B. Holbrook, S. Sheng, and L. F. Cranor, "Are your participants gaming the system? Screening mechanical turk workers," in *Proc. SIGCHI Conf. Hum. Factors Comput. Syst.*, Apr. 2010, pp. 2399–2402.
[125] S. H. Kim, H. Yun, and J. S. Yi, "How to filter out random clickers in a crowdsourcing-based study?," in *Proc. BELIV Workshop, Beyond Time Errors-Novel Eval. Methods Vis.*, Oct. 2012, pp. 1–7.
[126] C. A. Lampe, "Ratings use in an online discussion system: The Slashdot case," Ph.D. dissertation, Univ. Michigan, School Inf., Ann Arbor, MI, USA, 2006.
[127] C. Dellarocas, "Online reputation systems: How to design one that does what you need," *MIT Sloan Manage. Rev.*, vol. 51, no. 3, pp. 33–38, 2010.
[128] G. D. Saxton, O. Oh, and R. Kishore, "Rules of crowdsourcing: Models, issues, and systems of control," *Inf. Syst. Manage.*, vol. 30, no. 1, pp. 2–20, 2013.
[129] A. Baruch, A. May, and D. Yu, "The motivations, enablers and barriers for voluntary participation in an online crowdsourcing platform," *Comput. Hum. Behav.*, vol. 64, pp. 923–931, 2016.
[130] J. O. Wooten and K. T. Ulrich, "Idea generation and the role of feedback: Evidence from field experiments with innovation tournaments," *Prod. Oper. Manage.*, vol. 26, no. 1, pp. 80–99, 2017.
[131] L. Jian, S. Yang, S. Ba, L. Lu, and C. Jiang, "Managing the crowds: The effect of prize guarantees and in-process feedback on participation in crowdsourcing contests," Univ. Connecticut School Bus., Storrs, CT, USA, Res. Paper 18–11, 2018.
[132] B. S. Kiran and R. Sharma, "Designing and driving crowdsourcing contests in large public service organizations: Using the proposed six-stage framework for crowdsourcing contests, public service organizations can leverage internal and external knowledge to cocreate effective solutions," *Res.-Technol. Manage.*, vol. 64, no. 3, pp. 48–57, 2021.
[133] T. Ritchey, "General morphological analysis," in *Wicked Problems–Social Messes*. Berlin, Germany: Springer, 2011, pp. 7–18.
[134] A. Singh and A. Kaushik, "Platform for citizen engagement for good governance in India: A case study of MyGov," in *Civic Engagement Frameworks and Strategic Leadership Practices for Organization Development*. Hershey, PA, USA: IGI Global, 2020, pp. 48–66.
[135] N. Springer, *James Surowiecki's the Wisdom of Crowds: Why the Many Are Smarter Than the Few and How Collective Wisdom Shapes Business, Economics, Societies, and Nations*. London, U.K.: Macat Library, 2018.

Divya Mishra received the bachelors's and master's degrees in commerce from the University of Allahabad, Prayagraj, India, specializing in human resource management and marketing, in 2016 and 2018, respectively.

She is currently a Ph.D. Research Scholar with the Department of University School of Management and Entrepreneurship, Delhi Technological University, New Delhi, India. Her research interests include human resource management, organizational behavior, technology, and innovation management.

Ms. Mishra was the recipient of Gold Medals for outstanding performance in the academic field.

Nidhi Maheshwari received the MBA degree from Banasthali Vidyapith, Tonk, India, in 2000, and the LL.B. and Ph.D. degrees from Mohanlal Sukhadia University, Udaipur, India, in 2003 and 2009, respectively.

She is currently an Associate Professor with Delhi Technological University, New Delhi, India. She is an experienced Associate Professor with a demonstrated history of working in the higher education industry. She is a strong education professional, skilled in market research, management, organizational development, and training. She has been in the research and teaching profession for over a decade. During her doctoral studies in the area of emotional and spiritual quotient area, she had widely published papers in refereed international and national journals. Her research interests include technoinnovation and HR analytics.

Authorized licensed use limited to: DELHI TECHNICAL UNIV. Downloaded on January 19,2023 at 05:07:01 UTC from IEEE Xplore. Restrictions apply.

Evaluating the Robustness of Biomedical Concept Normalization

Sinchani Chakraborty
IIT Kharagpur
sinchanichakraborty@gmail.com

Harsh Raj
Delhi Technological University
harsh777111raj@gmail.com

Srishti Gureja
University of Delhi
srishtigureja1110@gmail.com

Tanmay Jain
Delhi Technological University
tanmayj2020@gmail.com

Atif Hassan
IIT Kharagpur
atif.hit.hassan@gmail.com

Sayantan Basu
IIT Guwahati
sayantan18@iitg.ac.in

Abstract

Biomedical concept normalization involves linking entity mentions in text to standard concepts in knowledge bases. It aids in resolving challenges to standardising ambiguous, variable terms in text or handling missing links. Therefore, it is one of the essential tasks of text mining that helps in effective information access and finds its utility in biomedical decision-making. Pre-trained language models (e.g., BERT) achieve impressive performance on this task. It has been observed that such models are insensitive to word order permutations and vulnerable to adversarial attacks on tasks like Text Classification, Natural Language Inference. However, the effect of such attacks is unknown for the task of Normalization, especially in the biomedical domain. In this paper, we propose heuristic-based Input Transformations (word level modifications and word order variations) and Adversarial attacks to study the robustness of BERT-based normalization models across various datasets consisting of different biomedical entity types. We conduct experiments across three datasets: NCBI disease, BC5CDR Disease, and BC5CDR Chemical. We observe that for Input Transformations, pre-trained models often fail to detect invalid input. On the other hand, our proposed Adversarial attacks that add imperceptible perturbations result in affecting the ranking of a concept list for a given mention (or vice versa). We also generate natural adversarial examples that lead to performance degradation of $\sim$30% in the F1-score. Additionally, we explore existing mitigation strategies to help a model recognize invalid inputs.

1 Introduction

Biomedical concept normalization aims to map an entity mention occurring in free-form text to a unique concept in a knowledge base or an ontology [Xu and Bethard, 2021;Ji et al., 2020;D'Souza and Ng, 2015]. In the biomedical domain, concepts exhibit different surface forms, that include various morphological and orthographic variations [Zhou et al., 2004]. A concept can be linked to different mentions, e.g., the following entity mentions {*breast cancer, breast tumor, breast carcinoma*} are linked to the same concept *breast neoplasm* with a unique ID "D001943" in the MeSH ontology [Zieman and Bleich, 1997]. This makes it crucial to link mentions with their standard canonical forms present in an ontology or a knowledge base, rich with semantic structure.

Workshop on Transfer Learning for Natural Language Processing, 2022, New Orleans.

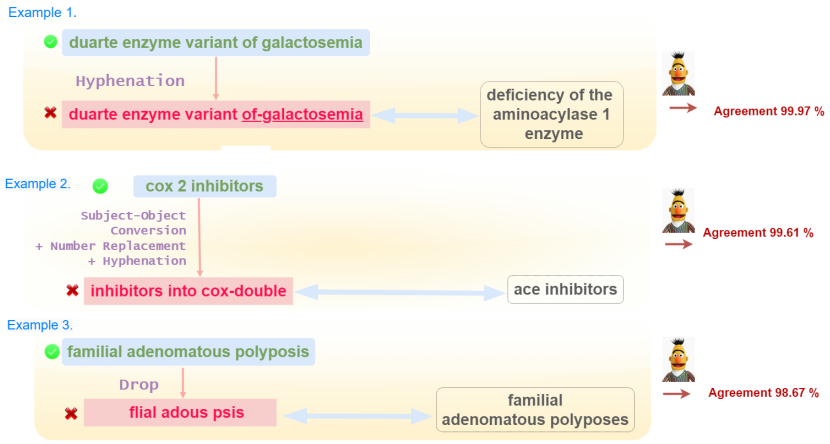

Figure 1: A Fine-tuned Clinical BERT model assigns high probability to invalid mention names that does not have correspondence to the candidate in an Ontology. Green : Original Concept/Mention; Red : Transformed Concept/Mention; Grey: Mention in a text/Concept in an Ontology.

Normalization is one of the fundamental tasks of data mining, that is utilized in automated medical decision making which is directly responsible for the well-being of patients [Matheson, 2019]. The robustness of such models is therefore crucial to maintain. Biomedical normalization models [Xu and Bethard, 2021;Ji et al., 2020;Li et al., 2019] achieve impressive results using pre-trained contextualized models like BERT [Devlin et al., 2018]. However, recent studies reveal BERT being vulnerable to adversarial attacks [Szegedy et al., 2013; Goodfellow et al., 2014] and insensitive to certain textual transformations that permute the word order [Gupta et al., 2021; Hessel and Schofield, 2021]. Figure 1 shows a BERT-based normalization model that retains the same predictions, for three different examples consisting of invalid transformed inputs as for a valid term, with extremely high agreement scores. This can lead to the linking of wrong invalid inputs to a concept in an ontology. In the biomedical domain, [Araujo et al., 2020] proposes adversarial attacks that introduces natural spelling errors and typos made by humans to analyze the robustness for Named Entity Recognition and Semantic Textual Similarity tasks. [Mondal, 2021] utilizes BERT to generate adversaries that constitute domain specific synonym replacement, spelling variations and number replacement for the task of biomedical Text Classification. To the best of our knowledge we are the first to study the effect of input transformations and adversarial attacks for the task of biomedical concept normalization.

In this paper, we study the responses of BERT-based normalization models to Input Transformations (word-level modifications and word-order variations). The word-level modifications are inspired from hand-crafted rules that were used to compose a multi-pass sieve in order to find a match between a candidate and mention [D'Souza and Ng, 2015]. While these kinds of transformations lead to changes detectable by a human, modifications that are adversarial in nature lead to imperceptible changes [Michel et al., 2019]. Adversarial attacks confuse the models and lead to performance degradation. In our work, we also focus on generating natural-looking adversarial examples to study the response of normalization models. Moreover, it has been observed for the task of image classification, adversarial ranking attacks can alter the ranks of a candidate by adding perturbation to a candidate list [Zhou et al., 2020]. We adopt this approach to study the effect of candidate ranking, on adding imperceptible perturbations, of existing normalization approaches that consist of a two-step framework: a candidate generator (produces potential candidates from an ontology) and a supervised candidate ranker (ranks potential candidates) [Xu and Bethard, 2021;Ji et al., 2020]. Finally, we also explore mitigation strategies with the aim of helping the model in identifying invalid inputs that result in the application Input transformations.

To demonstrate the efficacy of the proposed input transformations and adversarial attacks, we select ranking-based normalization models [Ji et al., 2020]. Based on this model we perform experiments on 4 types of BERT models : BERT [Devlin et al., 2018], BioBERT [Lee et al., 2019], ClinicalBERT [Alsentzer et al., 2019], PubMed BERT [Gu et al., 2021]. Additionally we consider a separate model that performs a triplet-search based ranking for normalization and trains the candidate generator space unlike the previous model [Xu and Bethard, 2021]. The evaluation of the task was performed on three

datasets: NCBI [Doğan et al., 2014], BC5CDR-Disease [Li et al., 2016], and BC5CDR-Chemical [Li et al., 2016].

Our experiments and observations reveal that most of the individual input transformations that involve word-level modifications and word-order variations, go undetected by a model. However, when transformations are chained or certain important words are affected we find the model starts detecting invalid input. For adversarial attacks, our experiments reveal that the best-performing models are brittle on imperceptible perturbations and natural-looking adversaries. Summarily, we make the following contributions in this paper[1].

1. We systematically study the effect of input transformations to understand the sensitivity of the model to word-level modifications and word order variations for biomedical concept normalization. We apply thirteen individual transformations for effective analysis.
2. We propose Adversarial Attacks that lead to a significant drop in model performance (86.0 to 58.05 in F1-score) on NCBI [Doğan et al., 2014] dataset, revealing the brittle nature of top-performing Normalization models.
3. Finally, we explore existing mitigation strategies to make models sensitive to invalid input transformations for the task of Normalization.

2 Task Formulation

Given a corpus H and an Ontology O, the aim of concept normalization is to find a mapping function f, that maps a mention m in a free-form text corpus H to a concept c which is a unique identifier in Ontology O, i.e., $c = f(m)$. A concept c is part of a set C consisting of all concepts in an Ontology.

In the following section 3 and 4 we describe each *Input transformations* and *Adversarial Attacks* in details, that we apply to analyze the robustness of biomedical concept normalization.

3 Input Transformations

For the given task consisting of an input $x \epsilon X$ and a function f that maps inputs to $y \epsilon Y$ which corresponds to a label space. An input transformation is a function $\sigma : X \rightarrow X$ that acts on input x to produce $x^{'}$ such that f($x^{'}$) is not defined. For each of the transformations defined below there is a high probability that one can map to the original candidate. In that case we remove it from the list. While this is a single instance of such a case to appear, the remaining combinations can serve as invalid mention entities that are formed through the following transformations.

Hyphenation A mention term undergoes hyphenation if it does not consist of hyphens whereas it undergoes dehyphenation if it consists of hyphens in the original term by considering consecutive pairs at a time. E.g., a mention "hereditary breast and ovarian cancer" will form the following variations: {"hereditary-breast and ovarian cancer", "hereditary breast-and ovarian cancer", "hereditary breast and-ovarian cancer", "hereditary breast and ovarian-cancer"}. This is performed only with multiword mentions.

Number Replacement We perform this transformation only on those mentions that consist of a pre-existing numeral while the other mentions devoid of any numeral retain their original form. The numbers are replaced as their equivalent form of the roman, cardinal, or multiplicative numeral. E.g., "c9 deficiency" has the following forms {"cnine deficiency", "cix deficiency"}.

Disorder Synonym/Mention Term Concatenation Given an entity mention *m* we generate samples of the form $(m + q)$ where q is a disorder synonym or a frequently appearing modifier for chemicals (depends on the domain usage). We collected a list of roughly fifteen disorder synonyms from [D'Souza and Ng, 2015] and concatenated this at the end of every mentions where these terms are absent. So for each mention there are fifteen different variants. Similarly, for chemicals we manually enlist fourteen terms and concatenate those at the end of every mention.

[1]Our code is available at https://github.com/deepwizai/robust-normalization

Table 1: Agreement scores on Transformations for three datasets on finetuned-BioBERT model

Transformations	NCBI disease	BC5CDR disease	BC5CDR chemical
Unperturbed	0.93	0.92	0.94
Hyphenation (H)	0.89	0.88	0.92
Subject Object Conversion (SOC)	0.90	0.89	0.93
Number Replacement (Num-R)	0.88	0.89	0.91
Disorder Synonym/Mention Term Concatenation (C)	0.90	0.89	0.91
Stemming (S)	0.87	0.87	0.92
H + SOC	0.89	0.90	0.94
H + SOC + Num-R	0.87	0.89	0.93
H + SOC + Num-R + C + S	0.86	0.87	0.92
Copy-Sort	0.91	0.90	0.14
Sort	0.90	0.89	0.92
Reverse	0.91	0.89	0.92
Shuffle	0.91	0.89	0.92
Drop	0.85	0.85	0.88
Repeat	0.84	0.84	0.88
Replace	0.83	0.82	0.89
Copyone	0.76	0.77	0.87

Stemming Using Porter Stemmer [Porter, 1980] from the NLTK library [Bird, 2006], the words of the mentions are stemmed and are then replaced with the corresponding occurrence. E.g., the mention of the term "chromosomal fragmentation during meiosis" changes to "chromosom fragment during meiosi". The stems are hard to interpret since they do not form actual words, thus altering the meaning of the mention terms.

Subject Object Conversion We generate examples for Subject-Object conversion using the steps detailed in [D'Souza and Ng, 2015]. There are four ways to generate samples for Subject-Object conversion. Given a mention m that contains a preposition: 1) Replacing with other prepositions; 2) Deleting the preposition and swapping surrounding token; 3) Shifting last token to the front and then inserting a preposition while shifting the other remaining tokens; 4.) Shifting first token to the end and adding a preposition as the second last token followed by shifting remaining tokens to the rest.

In the above transformations, the first four are word-level transformations that make changes in the word level or append additional terms to the neighboring words. The transformation- Subject Object Conversion- leads to change in word order. Following [Gupta et al., 2021] we perform two classes of additional transformations which are: 1.) Lexical-overlap based transformations retains the bag of word collection but it changes the word order in four different ways which are as follows: *Sort* - sorting input tokens; *Reverse* - reversing the token sequence; *Shuffle* - shuffling tokens randomly; *Copy Sort* - transforming a candidate c as a copy of the mention m with the words sorted alphabetically. The transformations Reverse and Copy Sort are part of Lexical overlap based transformations which exhibit random word order. 2.) Gradient level transformations consider change in the loss for i'th input token in a given mention m to measure the token importance. Based on this calculation four operations are defined: *Drop* - this drops the least important token in a mention; *Repeat* - least important token is repeated ; *Replace* - Least important token is replaced by random tokens; *Copy One* - The most important token is copied from the mention m and put as the only token in the candidate c . These transformations target to destroy the semantic meaning entirely conveyed in the phrase. In Figure1, we see Example 3 as the transformation Drop is being applied, where a pre-trained model is unable to catch the transformation and treating it as correct input.

Each of these transformations are performed individually as well as we perform chained evaluations. The second example in Figure 1 is based on chaining three transformations: *Subject-Object Conversion* followed by *Number Replacement* and finally *Hyphenation*. Since the task of normalization involves pair of texts as input constituting the mention level text and candidate concepts, performing transformations on any one of these should suffice in order to carry out robustness analysis.

4 Adversarial Attacks

We perform two types of Ranking Attacks for the task of normalization. Both of these attacks are adversarial in nature thus involving imperceptible changes to form an adversary.

Adversarial Ranking Attack (Adv-Rank) For a set of chosen candidate $X = \{c_1, c_2, ..., c_n\}$ with respect to a specific mention from the set M = $\{m_1, m_2, ..., m_n\}$ we perform two types of Adversarial Ranking Attacks: 1) Mention Attack (MA): Attack targeted to mention m and 2) Candidate Attack (CA) : Attack targeted to candidate c. We define MA+ and MA- as variants of Mention Attacks to raise or lower the rank of a candidate set C by perturbing a single mention m. Similarly, we define CA+ and CA- as variants of Candidate Attacks to raise or lower the rank of a single candidate c with respect to the mention set M. The ranks are altered by adding universal perturbation r. The final ranking order for a Deep Neural Network is defined by the sample positions in a common embedding space so adding an adversarial perturbation to it can lead to potential alteration in ranking. This is performed using a surrogate loss in the form of Triplet loss. For CA+ it is defined as:

$$L_{CA^+}(c, M; X) = \sum_{q \epsilon M} \sum_{x \epsilon X} [d(q, c) - d(q, x)]_+ \tag{1}$$

where X denotes set of all candidates; M denotes set of all mentions; c is the candidate whose rank is raised w.r.t mention q ϵ M. In the same way the Triplet loss is defined for CA-, MA+ and MA-. We refer the reader to consult the original work for a detailed overview on Adversarial Ranking [Zhou et al., 2020]. In our work we can utilize any one of the shifts (CA+ or CA-; MA+ or MA-) to make imperceptible changes to the ranking order.

Table 2: Adversarial Ranking Attack on BERT based ranking model. The "+" in MA indicates that the rank of the chosen candidate is raised. The changes in average rank using Cosine Distance Triplet Loss is reported with (%) omitted. Emb Shift: Embedding Shift.

Dataset	Emb Shift	Attack	Clinical BERT	Bio BERT
NCBI	1.3	MA+	$\sim$50 $\rightarrow$ 51.8	$\sim$50 $\rightarrow$ **44.2**
BC5CDR Chemical	1.3	MA+	$\sim$50 $\rightarrow$ **42.6**	$\sim$50 $\rightarrow$ 50.9

Least Similar Entity Concatenation (LSEC) We present Least Similar Entity Concatenation (LSEC) that modifies the candidate set by concatenating the most dissimilar entity belonging to a parent class same as the original candidate, corresponding to an ontology or a knowledge base. In the following steps we lay down the approach taken by LSEC attack. Given a mention m and a candidate c :

Step 1: Find the concept identifier of c that links it to an ontology.

Step 2: Access the immediate root which corresponds to the parent concept and find the set of existing siblings.

Step 3: Find pair-wise cosine similarity between the concept and the existing set of candidates.

Step 4: Select the most dissimilar entity and append it with the candidate c to form c'.

For example, given a mention-candidate pair - ("meningitis", "encephalomeningitis") - the identifier for the candidate c, "encephalomeningitis" is MESH:D008590 corresponding to MEDIC Ontology [Davis et al., 2012]. The immediate parent is tracked and the most dissimilar sibling based on cosine similarity, corresponding to the candidate under the same parent ID is determined, in this case, it is "Pseudorabies". Finally, the modified candidate c' is formed by appending both the terms as a composite mention: "encephalomeningitis and pseudorabies". The attacks consisting of entities belonging to the same class corresponding to an Ontology or a Knowledge Base are considered to be adversarial in nature [Lin et al., 2021]. Since both c and c' belong to the same parent class, hence we tag instances generated from LSEC attack as natural adversarial examples. Furthermore, the

adversarial examples obtained are natural since it consists of real and valid entities, devoid of any grammatical disfluency.

5 Experimental Setup

Datasets: We evaluate transformation on three different biomedical normalization datasets : 1) NCBI [Doğan et al., 2014] 2) BC5CDR-Disease [Li et al., 2016] and 3) BC5CDR-Chemical [Li et al., 2016].

Models: For evaluating transformations we perform experiments on BERT-based Ranking [Ji et al., 2020] . We use the following BERT models for reporting the results on BERT-based Ranking : BioBERT [Lee et al., 2019], Clinical-BERT [Alsentzer et al., 2019], PubMed BERT [Gu et al., 2021] and BERT [Devlin et al., 2018]. We perform fine-tuning on the training data using Adam Optimizer [Kingma and Ba, 2014]. For evaluating Ranking Attacks we only use BERT-base-uncased models. We set a threshold α of 0.75 for cosine similarity for LSEC attack. We provide more details in the Appendix.

6 Metrics

6.1 Input Transformations

We use Agreement and Confidence scores following [Gupta et al., 2021] for all the Transformations defined over the input.

Agreement: It is defined as the percentage of examples that retains the same prediction after applying transformations.

Confidence: The average probability scores of the predicted level gives the Confidence score.This depends on the number of classes N (in our case N=2).

A low confidence score and an agreement score close to random suggests that a model is reliable that is successfully able to detect invalid input.

6.2 Adversarial attacks

We perform two types of Adversarial attacks: 1) Adversarial Ranking (Adv-Rank) 2) Least Similar Entity Concatenation (LSEC). Below are the metrics that are used to evaluate these attacks.

Adversarial Ranking Attack (Adv-Rank) The effectiveness of the attack is calculated by the magnitude of change in normalized rank. Given a candidate c the normalized rank is given as follows:

$$R(m, c) = \frac{Rank_X(m, c)}{|X|} \times 100\% \tag{2}$$

where c ϵ X; $|X|$ is the length of full ranking list and $R(q, c)$ ϵ [0,1]

Least Similar Entity Concatenation (LSEC) We report the F1-score on the original test set and the F1-score after the attack . In addition, we also report the average confidence with which the predictions are performed.

7 Results and Analysis

This section discuss the results for Input Transformations and Adversarial Attacks. We also investigate through various analyses: 1) How do the model performance change for a varying percentage of invalid inputs? 2) Does invalid examples go undetected for a different approach? 3) Using existing strategies to make a model performing the normalization task, sensitive to invalid input transformations.

7.1 Main results

Input Transformations We apply various morphological, lexical and gradient-based transformations to the input belonging to three different datasets. Table 1 shows that the model exhibits high agreement scores. This is indicative of the fact that the model maintains its original predictions. *CopySort* and *CopyOne* are the transformations for which the model can identify invalid output, since those consists of a repetition of a single selected word lacking of other terms in a mention/candidate. The agreement scores are comparatively lower for *Gradient-based perturbations* where the important tokens are altered. A similar drop in scores is observed for *Chained Transformations*. On the contrary, for each individual transformation (except for stemming which leads to a meaning change in the input) the agreement scores are much higher. The model might pick up spurious correlations related to the common representation of biomedical entity names or phrases during training. Also, high agreement scores on lexical transformations confirm that the model is insensitive to word order.

Adversarial Ranking Attack (Adv-Rank) As shown in Table 2 for a designated embedding shift there is a considerable shift in the average rank for Mention Attack (MA+). The default value without the attack is 50%. The target of this attack is to make random changes in the ranked candidates after the model generates it. This is a black-box attack and significant shifts lead to 4% to 5% dip in model performance for BERT based ranking attacks.

Least Similar Entity Concatenation (LSEC) Table 3 shows the performance of the attack performed for Least Similar Entity Concatenation (LSEC). Compared to Adv-Rank this is a better attack that confuses the model and its performance is degraded.

Table 3: F1 scores before and after LSEC attack for two variants of BERT based ranking models on NCBI. Confidence : The average confidence with which the predictions are made after an attack is reported

Models	Before Attack	After Attack	Confidence
PubMed BERT	0.853	0.580	0.986
Bio BERT	0.859	0.582	0.990

7.2 Varying transformation of input (%)

Table 4 shows the results when 20%, 60% and 80% of the test data undergo transformations. We report the scores for transformations that include individual *Input transformations*, chained *Input transformations* and destructive transformations including *Lexical-overlap* and *Gradient-based perturbations*. The highlighted values of the accuracy scores denote instances where the model learns to detect the invalid inputs successfully, due to which there is a dip in the score. We observe a considerable change in the reported accuracy for every *Chained Transformations* and *Gradient-based transformations* this suggests that when there is a considerable transformation, like in the case of *Chained Transformations* (where the modifications leading to invalid changes in the input become more detectable), and for Gradient level transformations (where the most important token is affected), the model does a better job in classifying the invalid inputs.

Table 4: Accuracy Scores (%) for the BioBERT model undergoing transformations with different data coverage. **H:** Hyphenation; **SOC:** Subject Object Conversion; **NR:** Number Replacement; **C:** Disorder Synonym /Mention Term Concatenation; **S:** Stemming

Input (%)	Transformations											
	H	SOC	NR	C	S	H+ SOC	H + SOC+ NR	H + SOC+ NR+ C+S	Copy Sort	Shuffle	Drop	Copy One
20%	0.87	0.88	0.88	0.87	0.88	0.88	0.87	0.87	0.87	0.79	0.88	0.87
60%	0.88	0.88	0.87	0.88	0.87	0.88	0.85	0.84	0.87	0.81	0.87	0.80
80%	0.89	0.89	**0.87**	0.89	0.88	**0.84**	**0.82**	**0.81**	0.87	**0.77**	**0.86**	**0.77**

7.3 Are the transformations undetectable across different approaches?

To better understand the effect of the transformations, we conduct the experiments on a different model that performs the task of normalization which is Triplet-search ConNorm [Xu and Bethard, 2021]. Table 5 shows the results on the Input Transformations. Compared to the BERT-based ranking model in Table1 we find that this model shows a considerable accuracy drop for NCBI dataset on individual transformations apart from the lexical based transformation. For BC5CDR-Disease and BC5CDR Chemical the model performance is almost similar to BERT based ranking model. For detecting Gradient level perturbation, Triplet Search based Concept Normalization model does a better job.

Table 5: Accuracy Scores (%) of Triplet Search based Concept Normalization model across three datasets NCBI, BC5CDR disease, BC5CDR chemical. The "None" value is on untransformed training set. **H:** Hyphenation; **SOC:** Subject Object Conversion; **NR:** Number Replacement; **C:** Disorder Synonym /Mention Term Concatenation; **S:** Stemming; **Rev:** Reverse

	Transformations											
Dataset	None	H	SOC	NR	C	S	Sort	Rev	Shuffle	Drop	Repeat	Replace
NCBI	0.95	0.64	0.63	0.87	0.66	0.55	0.94	0.87	0.87	0.87	0.79	0.88
BC5CDR disease	0.94	0.92	0.94	0.94	0.94	0.79	0.93	0.93	0.92	0.48	0.46	0.46
BC5CDR chemical	0.99	0.97	0.97	0.93	0.75	0.95	0.97	0.98	0.98	0.24	0.25	0.21

7.4 Analysis of mitigation strategies for Input Transformations

We explore two strategies to enhance the ability of the model to recognize invalid input transformations.

Augmented Training : We follow a straightforward approach wherein we randomly select 50% of training data which then undergoes all possible transformations mentioned in Section 4. This set of invalid examples is augmented with the original training data, and the final version of the training set is obtained.

Entropic Regularization : This approach helps in training the model to be less certain on invalid inputs [Feng et al., 2018]. Given an original dataset D and the dataset constituting invalid examples D'. This method adds a loss term for the invalid examples weighted by the additions of a new hyperparameter.

Table 6 shows a comparative analysis between Augmented Training (Aug-Data) and Entropic Regularization (Ent Reg). The experiment is conducted for the NCBI dataset for the BERT-based Ranking model consisting of PubMed BERT and Bio-BERT. We observe that the Data Augmentation (Aug-Data) reports a marginally better performance when compared to Entropic Regularization.

Table 6: Comparative Analysis of Mitigation Strategies reported on NCBI for BERT-based ranking model. **Aug-Data**: Agreement on Augmented Training; **Ent Reg**: Agreement after Entropic Regularization

Model	Aug-Data	Ent Reg
PubMed-BERT	**0.828**	0.826
Bio-BERT	**0.769**	0.759

8 Conclusions and Future Work

In this paper, we study the effect of Input Transformations and Adversarial Attacks on the task of biomedical concept normalization. The Input transformations include word level modifications

and word order variations. A part of our proposed input transformations is motivated by surface form variations in the biomedical domain. Our work shows surprising results on invalid Input transformation, wherein BERT-based normalization models find it hard to identify such samples. The models are seen to be invariant to random word order permutations. In addition, we propose two types of Adversarial attacks, one of which form natural looking adversaries while the other affect the ranking of candidate/mention sets on adding imperceptible perturbations. These attacks lead to model performance degradation. We conduct this empirical study considering different BERT-based normalization models that operates on a ranking-based approach. We explore mitigation strategies and techniques to increase model sensitivity to input transformations. For future work, we plan to incorporate better mitigation strategies to increase sensitivity to invalid samples and defence mechanisms to reduce the brittleness of the model to adversarial attacks.

Acknowledgments

We thank the anonymous reviewers for their helpful insights and feedback. We would also like to thank past members of NLP group at IIT Kharagpur for providing us with valuable suggestions.

References

Emily Alsentzer, John R Murphy, Willie Boag, Wei-Hung Weng, Di Jin, Tristan Naumann, and Matthew McDermott. Publicly available clinical bert embeddings. *arXiv preprint arXiv:1904.03323*, 2019.

Vladimir Araujo, Andres Carvallo, Carlos Aspillaga, and Denis Parra. On adversarial examples for biomedical nlp tasks. *arXiv preprint arXiv:2004.11157*, 2020.

Steven Bird. Nltk: the natural language toolkit. In *Proceedings of the COLING/ACL 2006 Interactive Presentation Sessions*, pages 69–72, 2006.

Allan Peter Davis, Thomas C Wiegers, Michael C Rosenstein, and Carolyn J Mattingly. Medic: a practical disease vocabulary used at the comparative toxicogenomics database. *Database*, 2012, 2012.

Jacob Devlin, Ming-Wei Chang, Kenton Lee, and Kristina Toutanova. Bert: Pre-training of deep bidirectional transformers for language understanding. *arXiv preprint arXiv:1810.04805*, 2018.

Rezarta Islamaj Doğan, Robert Leaman, and Zhiyong Lu. Ncbi disease corpus: a resource for disease name recognition and concept normalization. *Journal of biomedical informatics*, 47:1–10, 2014.

Jennifer D'Souza and Vincent Ng. Sieve-based entity linking for the biomedical domain. In *Proceedings of the 53rd Annual Meeting of the Association for Computational Linguistics and the 7th International Joint Conference on Natural Language Processing (Volume 2: Short Papers)*, pages 297–302, 2015.

Shi Feng, Eric Wallace, Alvin Grissom II, Mohit Iyyer, Pedro Rodriguez, and Jordan Boyd-Graber. Pathologies of neural models make interpretations difficult. *arXiv preprint arXiv:1804.07781*, 2018.

Ian J Goodfellow, Jonathon Shlens, and Christian Szegedy. Explaining and harnessing adversarial examples. *arXiv preprint arXiv:1412.6572*, 2014.

Yu Gu, Robert Tinn, Hao Cheng, Michael Lucas, Naoto Usuyama, Xiaodong Liu, Tristan Naumann, Jianfeng Gao, and Hoifung Poon. Domain-specific language model pretraining for biomedical natural language processing. *ACM Transactions on Computing for Healthcare (HEALTH)*, 3(1): 1–23, 2021.

Ashim Gupta, Giorgi Kvernadze, and Vivek Srikumar. Bert & family eat word salad: Experiments with text understanding. In *Proceedings of the AAAI Conference on Artificial Intelligence*, volume 35, pages 12946–12954, 2021.

Jack Hessel and Alexandra Schofield. How effective is bert without word ordering? implications for language understanding and data privacy. In *Proceedings of the 59th Annual Meeting of the Association for Computational Linguistics and the 11th International Joint Conference on Natural Language Processing (Volume 2: Short Papers)*, pages 204–211, 2021.

Zongcheng Ji, Qiang Wei, and Hua Xu. Bert-based ranking for biomedical entity normalization. *AMIA Summits on Translational Science Proceedings*, 2020:269, 2020.

Diederik P Kingma and Jimmy Ba. Adam: A method for stochastic optimization. *arXiv preprint arXiv:1412.6980*, 2014.

Jinhyuk Lee, Wonjin Yoon, Sungdong Kim, Donghyeon Kim, Sunkyu Kim, Chan Ho So, and Jaewoo Kang. Biobert: A pre-trained biomedical language representation model for biomedical text mining. bioinformatics, btz682, 2019.

Fei Li, Yonghao Jin, Weisong Liu, Bhanu Pratap Singh Rawat, Pengshan Cai, Hong Yu, et al. Fine-tuning bidirectional encoder representations from transformers (bert)–based models on large-scale electronic health record notes: an empirical study. *JMIR medical informatics*, 7(3):e14830, 2019.

Jiao Li, Yueping Sun, Robin J Johnson, Daniela Sciaky, Chih-Hsuan Wei, Robert Leaman, Allan Peter Davis, Carolyn J Mattingly, Thomas C Wiegers, and Zhiyong Lu. Biocreative v cdr task corpus: a resource for chemical disease relation extraction. *Database*, 2016, 2016.

Bill Yuchen Lin, Wenyang Gao, Jun Yan, Ryan Moreno, and Xiang Ren. Rockner: A simple method to create adversarial examples for evaluating the robustness of named entity recognition models. *arXiv preprint arXiv:2109.05620*, 2021.

Rob Matheson. Automating artificial intelligence for medical decision-making, 2019.

Paul Michel, Xian Li, Graham Neubig, and Juan Miguel Pino. On evaluation of adversarial perturbations for sequence-to-sequence models. *arXiv preprint arXiv:1903.06620*, 2019.

Ishani Mondal. Bbaeg: Towards bert-based biomedical adversarial example generation for text classification. *arXiv preprint arXiv:2104.01782*, 2021.

Martin F Porter. An algorithm for suffix stripping. *Program*, 1980.

Christian Szegedy, Wojciech Zaremba, Ilya Sutskever, Joan Bruna, Dumitru Erhan, Ian Goodfellow, and Rob Fergus. Intriguing properties of neural networks. *arXiv preprint arXiv:1312.6199*, 2013.

Thomas Wolf, Lysandre Debut, Victor Sanh, Julien Chaumond, Clement Delangue, Anthony Moi, Pierric Cistac, Tim Rault, Rémi Louf, Morgan Funtowicz, et al. Transformers: State-of-the-art natural language processing. In *Proceedings of the 2020 conference on empirical methods in natural language processing: system demonstrations*, pages 38–45, 2020.

Dongfang Xu and Steven Bethard. Triplet-trained vector space and sieve-based search improve biomedical concept normalization. Association for Computational Linguistics (ACL), 2021.

Guodong Zhou, Jie Zhang, Jian Su, Dan Shen, and ChewLim Tan. Recognizing names in biomedical texts: a machine learning approach. *Bioinformatics*, 20(7):1178–1190, 2004.

Mo Zhou, Zhenxing Niu, Le Wang, Qilin Zhang, and Gang Hua. Adversarial ranking attack and defense. In *European Conference on Computer Vision*, pages 781–799. Springer, 2020.

Yuri L Zieman and Howard L Bleich. Conceptual mapping of user's queries to medical subject headings. In *Proceedings of the AMIA Annual Fall Symposium*, page 519. American Medical Informatics Association, 1997.

A Appendix

A.1 Reproducibility

Model Used. We performed the attacks on two types of entity normalization methods, a ranking based normalization [Ji et al., 2020] and Triplet Search ConNorm [Xu and Bethard, 2021] which is trained via a triplet objective. For both methodologies we took a set of pretrained BERT models, namely - "bio-clinical-bert", "pubmed-bert" and "bio-bert-cased" to base our experiments. These are BERT like models but are trained on biomedical specific dataset. For such pretrained models, we used Huggingface's transformers repository [Wolf et al., 2020].

Dataset. We used 3 benchmark datasets in the biomedical domain for biomedical normalization, namely, NCBI [Doğan et al., 2014], BC5CDR-Disease [Li et al., 2016], BC5CDR-Chemical [Li et al., 2016]. The hyperparameters were kept the same irrespective of the data used.

The NCBI disease corpus contains 17324 manually annotated disorder mentions from 792 PubMed abstracts. The disorder mentions are mapped to 750 MEDIC lexicon [Davis et al., 2012]) concepts. We split the released training set in 5134 training mentions and 787 development mentions, and keep the 960 mentions from the original test set as evaluation. We use the 2012 version of MEDIC ontology which contains 11915 concepts and 71923 synonyms.

BC5CDR-Disease and BC5CDR-Chemical corpora were used in the BioCreative V chemical-induced disease (CID) relation extraction challenge [2]. BC5CDR-Disease and BC5CDR-Chemical contain 12850 disease mentions and 15935 chemical mentions, respectively. The annotated disease mentions are mapped to 1075 unique concepts out of 11915 concepts in the 2012 version of MEDIC ontology [Davis et al., 2012]. The chemical mentions are mapped to 1164 unique concepts out of 171203 concepts from the 2019 version of Comparative Toxicogenomics Database (CTD) chemical ontology [3]. We use similar train-dev-test splits as outlined in the BioCreative V challenge.

Hyperparameters

BERT-based Ranking for Entity Normalization: For the text encoder we used 3 pretrained models, namely, BioBERT [Lee et al., 2019], Clinical-BERT [Alsentzer et al., 2019], PubMed BERT [Gu et al., 2021] and BERT [Devlin et al., 2018]. For fine-tuning the sentence-pair classifier, same model hyperparameters were used as those saved in the pre-trained model, with the exception of the batch size, learning rate, and number of training epochs. In this study, we fixed the learning rate at $1e^{-5}$, weight decay to $1e^{-2}$, tuned the batch size to 16 and 32, tuned the number of training epochs from 1 to 10, and saved the model with the best performance.

Triplet Search ConNorm: For the text encoder we used 3 pretrained models, namely, BioBERT [Lee et al., 2019], Clinical-BERT [Alsentzer et al., 2019], PubMed BERT [Gu et al., 2021] and BERT [Devlin et al., 2018]. We used the Pytorch implementation of sentence-transformers [4] to train the Triplet Network for concept normalization [Xu and Bethard, 2021]. We used the following hyper-parameters during training of the triplet network: `max_sequence_length` $= 16$, `train_batch_size` $= 1024$, `epoch_size` $= 3$, `optimizer` $=$ Adam, `learning_rate` $= 3e^{-5}$, `warmup_steps` $= 0$.

Regularization Parameter in Entropic Regularization. The parameter λ in Entropic regularization provides a trade-off between the amount of regularization and original cross-entropy loss (refer to sub-section Entropic Regularization in section 7.4). It was found via multiple experiments with different values that large values of λ tend to decrease accuracy on the original validation set. We thus fix $\lambda = 0.1$ for all our experiments. Set of values tried: $\{0.01, 0.1, 0.2, 0.3, 0.5, 0.7, 1.0, 5.0\}$.

Compute Infrastructure Most of our experiments (except most Input Transformations other than gradient-based transformations) required access to GPU accelerators. We primarily ran our experiments on 2 machines: NVIDIA Quadro P5000 (16GB VRAM) and NVIDIA Quadro RTX4000 (8GB VRAM). We used Paperspace [5] and Google Colab [6] platforms to run our experiments.

[2] https://biocreative.bioinformatics.udel.edu/tasks/biocreative-v/

[3] URL: http://ctdbase.org/

[4] https://www.sbert.net/

[5] https://www.paperspace.com/

[6] https://colab.research.google.com/

EXPLORING BEHAVIORAL BIASES IN STOCK MARKET: EVIDENCE FROM INDIA

Deepali Malhotra[1]

Abstract

Due to the positive association between investments and the development of the economy, the rise of investment will progressively influence the economy's overall growth and vice versa. Thus, investors' decisions play a significant role in describing the market trend, which in turn affects the economy. Individuals invest with unique planning or no planning at all based on their available funds, time span, and financial goal. Ultimately, the majority of them want high returns that will make them wealthy overnight Regardless of how strong the company fundamentals are, strong negative emotions can wreck down a robust bullish market trend. The investor behavior is guided by many factors, such as investment horizons, other investors' actions, risk capacity, personality, and level of volatility in equity markets. Past studies have highlighted that individuals commit various behavioral anomalies due to incomplete information, shortage of technical skills, and belief in their competencies to invest while investing. This study has empirically tried to determine the presence of the predominant behavioral anomalies; the herding bias, overconfidence bias, disposition effect, and noise trading in the Indian stock market. Herding has been tested using the cross-sectional absolute deviation methodology as described by Chang et al. (2000). The other biases have been tested using a time-series regression model, such as VAR and Granger causality. Our sample consists of Nifty 50 companies for 21 years (January, 2000-December, 2020). The research shows that Indian stock markets are efficient as we fail to validate the herding bias for the overall market. However, herd mentality exists in crisis and extreme market conditions. The results also validate the existence of anomalies, such as the disposition effect, overconfidence, and noise trading in the Indian stock market.

KEYWORDS- Inclusive Leadership, Thriving At Work, Innovative Work Behavior, Hospitality Employees

JEL Classification- G1,G4,G5

[1] Assistant Professor, Delhi School of Management, Delhi Technological University

1. INTRODUCTION

Mackay(1841) highlighted the incident of Dutch Tulip bubble to demonstrate the erratic behavior of crowd. During the Dutch Golden era, a flower named as *"Tulip"* was pioneered in the Netherlands which grabbed the attention of large number of investors. The Netherlands population got excited about this tulip flower and began investing in it. In a short span of time, investing in this exotic flower became a fad which escalated its value tremendously. According to past studies, during the peak time, price of one bulb was higher than ten multiples of the annual pay of a worker. The bubble eventually burst when investors realized that they have devoted a large amount on a flower bulb and they began to sell them. As a result, the price plunged, leading to huge losses. Occurrences such as the tulip mania compels us to raise a simple query that 'are investors actually rational?' Since 1980s, a large number of researches have fostered some problems leading to over or under reaction of the investors, which has led to the rejection of the traditional EMH hypothesis. Behavioral finance is a new domain in the area of financial markets that has emerged in retort to hurdles faced by traditional paradigm. As per Sewell (2007), *"Behavioral finance is the study of the influence of psychology on the behaviour of financial practitioners and the subsequent effect on markets."* Day to day investment related choices depend on amalgamation of various facets, such as, sentiments, logic, fondness, pattern and social interaction. The field of behavioral finance tries to elucidate why people make mistakes which further leads to market anomalies. Prior researches in this domain have examined the influence of behavioral anomalies particularly in the developed economies. However, the evidence from the Indian market is scant. This study is an effort to examine the existence of predominant biases in Indian stock market. These are herding, overconfidence bias, disposition effect, and the noise trading. The research is distinctive in the sense that it offers practical validation for the above-mentioned irrationalities at market level rather than generally analyzed conceptually at individual investor level.

2. Review of literature

The traditional finance theory has been challenged by researchers claiming that investors possess psychological and emotional anomalies and tend to act in an irrational manner. Behavioral finance is a recent finance domain that attempts to comprehend the role of emotions and cognitive mistakes in impacting investors' judgements. All the available relevant literature is cited here factor-wise to develop further the hypotheses examined under this study.

A. Herding

One of the most evident features of human being which is visible in social affairs is imitation which leads to herding. In other words, people learn basics in their lives by imitating others. Primarily, it is logical and wise to imitate others when people are short of sufficient time, energy and resources to take a decision. Individual investors display herd behavior as they are more willing to follow the decisions of popular analysts, large group, or noise traders. One of the reasons could be that a human being is a social animal and tend to seek acceptance from a group instead of being alone in a crowd. A large amount of research has investigated the presence of herding behavior in developed as well as emerging economies. The results are contradictory from country to country. Chiang & Zheng (2010) studied herding behavior in 18 countries worldwide for the time-period 1988-2009. Their research validated that crowding behavior exists in developed economies except for the United States. Khan et al. (2011) focused on herd behavior in European nations comprised of France, the UK, Germany, and Italy. It was concluded that the UK market shows less herding behavior than other countries. Also, during the market stress, herding can be seen more evidently than in other periods. Lindhe (2012) investigated the presence of herding in four Nordic states: Denmark, Finland, Norway, and Sweden and exhibited no market-wide herding behavior in Demark, Norway, and Sweden. However, significant evidence of herding was found in Finland. Chiang et al. (2013) tested herding behavior among investors for ten Pacific-Basin markets and established its presence. Kanojia et al. (2020) analyzed the market-wide herding in the Indian stock market and found no impact of herding on the stock returns in the Indian stock market during the normal market conditions. Prosad et al. (2012) demonstrated that herding behavior exists only in the period of stress. Lakshman et al. (2013) validated the herding bias's presence, specifically among the mutual fund investor. On the contrary, Jose et al. (2018) obtained no evidence of crowding in the Indian stock market as a whole. Dhall & Singh (2020) examined the herding behavior in the Indian stock market and established the non-existence of herding behavior at the industry level. However, the study validated herding behaviour during the covid-19 period.

B. Overconfidence Bias

According to Tapia & Yermo, 2007, "Overconfidence is the tendency for people to overestimate their knowledge, abilities and the precision of their information, for that reason investment decisions become based on conjecture rather than fundamental value". Prior surveys in this domain have enlightened the influence of the overconfidence on rational decision-making. They argue that the investors who overrate their investment trading skills are

likely to engage more in trading due to high observed market returns (Daniel et al., 1998). Gervais & Odean (2001) revealed that overconfident investors trade more and increase their volatility, which in turn negatively influence their trading results and they suffer losses. Chuang & Lee (2006) have established a positive and significant link between current trading volume and lagged market returns that is in accordance with overconfidence bias. Statman et al. (2006) conducted study on USA stock market to investigate the presence of overconfidence bias and validated a positive association between market volume and past market returns, thereby, indicating the presence of overconfidence. Furthermore, Odean (1999) comprehended that investors become overconfident and engage in excess trading and suffer losses as they do not gain much to cover their transaction costs. Similarly, Barber & Odean (2000) found that excessive trading realized less returns. Zaiane (2013) examined the overconfidence bias in the Tunisian and Chinese markets and in both the markets, they demonstrated overconfidence bias. Tariq & Ulla (2013) investigated overconfidence bias in Pakistan stock exchange and found that lagged returns have positive impact on current turnover, which implies that Pakistani investors are overconfident. Prosad et al., (2013) exhibit overconfidence bias in Indian equity market.

C. Disposition effect

Shefrin & Statman (1985) introduced the disposition effect theory as a predominant bias in the domain of Behavioral finance. It states that investors are prone to sell the winning shares (whose price has increased) and tend to keep loss-making assets (whose price has dropped) as they are unwilling to realize losses but are more willing to realize gains prematurely. This occurs due to the belief that when investors sell a losing stock, the loss gets registered and is expected to give pain to the investors. To avoid such pain, investors prefer not to sell the losing stocks. Shefrin & Statman (1985) empirically proved that investors sell the winning stock and hold on to the loss-making asset. However, past studies have commented that during year-end, people are more eager to dispose of their loss-making investments, majorly due to tax motivation. Odean (1999) investigated the trading activity of household investors from the time period of 1987 to 1993. The study revealed that investors have a greater propensity to sell stocks that has risen in their value in comparison to the one whose value has decreased. Shumway & Wu (2006) find evidence of disposition effect by conducting a study on 13,460 Chinese investors. Moreover, many empirical studies (Bailey et al., 2011; Frazzini, 2006; Grinblatt & Keloharju, 2001; Weber & Camerer, 1998; Barberis & Xiong, 2009) have proved

this bias. The literature reveals that this bias can have a detrimental effect on investing performance as the investors are not aware of when to quit and when to continue.

D. Noise trading

Noise trading refers to the concept wherein investors trade based on 'noise' in the market rather than information. Such traders ignore the fundamental knowledge and trade on the basis of gossip or rumor in the market. According to De Long et al. (1990), the presence of noise traders in stock markets creates a risk in the stock prices and causes prices to diverge significantly from their fundamental values even if all other investors are rational. Prior studies have determined the presence of noise trading in the stock markets by analyzing the causality between prices and trading volume. Noise traders momentarily manipulate the security price in the short run or take their investment decisions based on historical price changes. Therefore, a positively significant causality between trading volume and security prices is in accordance with the premise that price changes are the consequence of noise traders' actions. Shrestha (2017) observed unidirectional Granger causality from stock prices to trading volume in Nepalese stock market along with Heimstra & Jones (1994) in DJIA index, Jain & Joh (1988) in S&P 500 stocks, Chen et al. (2001) in nine developed stock markets, and Mahajan & Singh (2009) in Indian stock market, that is indicative of noise trading in the respective markets. Studies like Ghazali et al. (2011) and Al-Samman & Al-Jafari (2015) observed unidirectional Granger causality from trading volume to stock returns but not vice versa in the case of the DAX 30 index and Muscat securities market, respectively. On the contrary, Gunduz & Hatemi (2005) found no causality in the Chez Republic stock market and bidirectional relationship in the case of countries like Poland and Hungary. Also, Abdullahi et al. (2014) failed to show the presence of noise trading in West Texas Intermediates and Brent crude oil futures.

3.Research objectives

The study focuses on achieving the following specific objectives:

A. To determine the existence of herding in Indian stock market in the following situations:
   - Market as a whole,
   - Bullish and bearish phases of the stock market, and
   - Extreme market conditions.

B. To determine the existence of overconfidence bias and disposition effect in the Indian stock market in the following situations:
   - Market as a whole, and

- on individual securities.

C. To determine the existence of noise trading in Indian stock market.

4. Hypotheses

In order to achieve the above objectives, the following hypotheses have been developed:

***Hypothesis H_a1**: Herding bias has a significant impact on the Indian stock market*

***Hypothesis H_a2**: Overconfidence bias has a significant impact on the Indian stock market*

***Hypothesis H_a3**: Disposition effect has a significant impact on the Indian stock market*

***Hypothesis H_a4**: Noise trading has a significant impact on the Indian stock market*

5. Data collection

The paper has employed secondary data to validate the existence of behavioral factors or biases in Indian stock market. The data comprises of various market indicators (daily basis) of Nifty 50 stocks from January 1, 2000 to December 31, 2020, such as:

- Prices (closing, opening, high, low) of the index and individual stocks
- Transaction volume of the index and individual stocks.

The data has been obtained from the official NSE website.

6. Research methodology

The existence of the above-mentioned biases in stock market have been analyzed with the help of methodology as specified in the prior studies. Some of these techniques are specific to the particular biases. These techniques are shown in Figure 1.

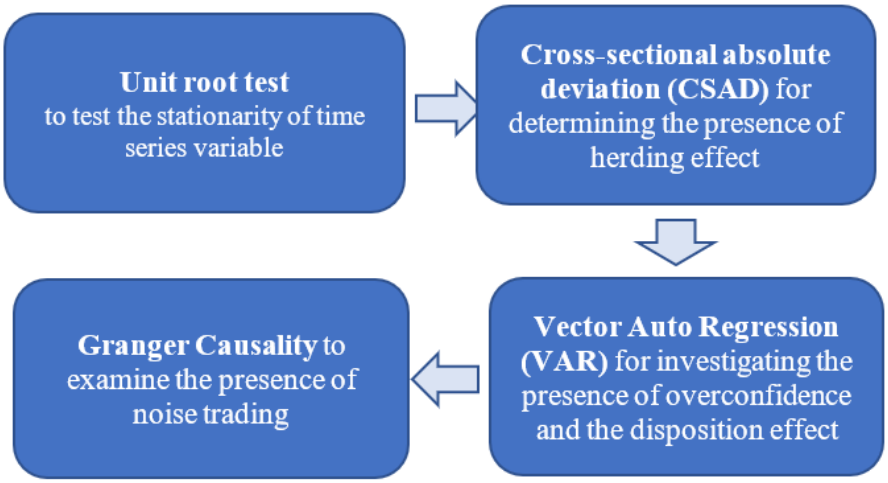

Source: Author's contribution

Figure 1: Statistical Techniques used for Data Analysis

In line with pioneering studies, cross-sectional absolute deviation (CSAD) has been employed to investigate the presence of market-wide herding during normal market conditions and

extreme market conditions in Indian stock market. Chang et al. (2000) proposed that individual stock return deviation would reduce when herd behavior follows. The author suggested that this relationship should be negative and non-linear in presence of herding (Chang et al., 2000). The nonlinear relationship is represented by following equation:

$$CSAD_t = \alpha + \beta_1|R_{mt}| + \beta_2 R^2_{mt} + e_t \quad \text{Eq. 1}$$

$$CSADt = \frac{1}{N}\sum_{s=1}^{n}|Rst - Rmt| \quad \text{Eq. 2}$$

where R_{st} represents stock return and R_{mt} is the market return. Here, the presence of a negative and significant β_2 represents herding.

Since the study has been carried out for an extensive time duration to capture the impact of behavioral biases in Indian stock market, it has been divided into four phases: - pre-crisis (2000-2007), during crisis (2008-2009), after crisis (2010-2019), and during covid crisis (Jan 2020-Dec 2020). This study has tried to investigate the presence of herding in different market conditions i.e., bull market, bear market, extreme up market, and extreme down market.

A. Testing herding on the overall market as a whole

In line with the methodology suggested by Chang et al., (2000), a non-linear (quadratic) regression model is run to determine the effect of market return on CSAD.

B. Testing herding in bullish and bearish market

Taking into consideration that the stock movements may be distorted during bull and bear phase of markets, the generalized relationship can be divided into following;

$CSAD_t^{UP} = \alpha + \beta 1^{UP}|R_{mt}^{UP}| + \beta 2^{UP}(R^2_{mt}{}^{UP}) + \varepsilon_t \quad R_{mt} > 0 \quad$ Eq. 3

$CSAD_t^{DOWN} = \alpha + \beta 1^{DOWN}|R_{mt}^{DOWN}| + \beta 2^{DOWN}(R^2_{mt}{}^{DOWN}) + \varepsilon_t \quad R_{mt} < 0 \quad$ Eq. 4

According to this method, statistically significant negative value of $\beta 2^{UP}$ and $\beta 2^{DOWN}$ captures herding.

C. Testing herding in Extreme up market and extreme down market

To test herding in the extreme market phases, regression model as suggested by "CCK (2000) model" run separately for extreme up (bullish) and extreme down (bearish) market using the daily data across all the two criteria 95% and 99%. The equations are:

$CSAD_t^{UP} = \alpha + \beta 1^{UP}|R_{mt}^{UP}||*D_t^{UP} + \beta 2^{UP}(R^2_{mt}{}^{UP}) * D_t^{UP} + \varepsilon_t \quad R_{mt} > 0 \quad$ Eq. 5

$CSAD_t^{DOWN} = \alpha + \beta 1^{DOWN}|R_{mt}^{DOWN}| * D_t^{DOWN} + \beta 2^{DOWN}(R^2_{mt}{}^{DOWN}) * D_t^{DOWN} + \varepsilon_t \quad R_{mt} < 0$

Eq. 6

In this case also, negative and significant $\beta 2^{UP}$ and $\beta 2^{DOWN}$ captures herding behavior.

Vector Auto Regression (VAR) is a type of time-series forecasting and is used to examine the existence of market anomalies, such as, overconfidence and the disposition effect. In this model, the overconfidence bias will be analyzed by running VAR model on market-wide trading volume and market returns. Also, disposition effect will be analyzed with the help of VAR on security-wide transaction volume and security returns, as proposed by Statman et al. (2006).

A. Market-wide VAR to determine overconfidence bias

In line with Statman et al., (2006) we have used a VAR model in order to analyze the association between daily market returns and transaction volume.

Here the endogenous variables are market transaction volume and daily market return, and the exogenous variable is the daily index volatility. The exogenous variable volatility has been included in this research to control for alternative explanations for trading activity.

$$Volume_t = \alpha + \sum_{J=1}^{k} \beta_i \, Volume_{t-j} + \sum_{J=1}^{k} \gamma_i \, MRT_{t-j} + \sum_{J=1}^{l} v_i Volatility_{t-j} + \varepsilon_\tau \qquad \text{Eq. 7}$$

$$MRT_t = \alpha' + \sum_{J=1}^{k} \beta' \, Volume_{t-j} + \sum_{J=1}^{k} \gamma'_j \, MRT_{t-j} + \sum_{J=1}^{l} v_i Volatility_{t-j} + \varepsilon_{2\tau} \qquad \text{Eq. 8}$$

Where:

$Volume_t$ = daily transaction volume;

MRTt = daily stock returns;

Volatility = daily volatility of index computed by taking difference of using daily high and low prices.

Here, k is the number of lags for endogenous variables and l is number of lags for exogenous variable, decided on the basis of Akaike Information Criteria.

Here the positive value of γj captures the presence of overconfidence bias.

B. Security-wide VAR to determine disposition effect and overconfidence

The existing literature suggests that the transaction volume of individual stocks is positively related to past returns of that particular stock which captures the disposition effect, and past return of the overall market that captures the overconfidence.

$$Volume_t = \alpha + \sum_{J=1}^{k} \beta_i \, Volume_{t-j} + \sum_{J=1}^{k} \gamma_i \, SRT_{t-j} + + \sum_{J=1}^{k} \lambda_i \, MRT_{t-j} + \varepsilon_{1\tau} \qquad \text{Eq. 9}$$

$$SRT_t = \alpha' + \sum_{J=1}^{k} \beta' \; Volumet\text{-}j + \sum_{J=1}^{k} \gamma'_{\;i} \; SRT_{t-j} + + \sum_{J=1}^{k} \lambda'_{\;i} \; MRT_{t-j} + \varepsilon_{2\tau} \qquad \text{Eq. 10}$$

$$MRT_t = \alpha'' + \sum_{J=1}^{k} \beta'' \; Volumet\text{-}j + \sum_{J=1}^{k} \gamma''_{\;j} \; SRT_{t-j} + + \sum_{J=1}^{k} \lambda''_{\;j} \; MRT_{t-j} + \varepsilon_{3\tau} \qquad \text{Eq. 11}$$

Where:

$Volume_t$= daily transaction volume;

MRTt = daily market returns;

SRT_t = daily stock returns;

and k = number of lag and has been decided based on Akaike Information Criteria.

According to the literature, the statistically significant positive value of γj indicates the existence of the disposition effect and positive value of λj indicates overconfidence.

Lastly, the **Granger causality test** the test has been used to examine the presence of noise trading in the stock exchange by determining the contemporaneous relation between market return and market transaction volume. Here, the null hypothesis (Ho) is that X-series do not explain the variation in Y, i.e., X(t) doesn't Granger-cause Y(t). If the p-value is less than 0.05, we do not accept the null hypothesis. In other words, X is Granger reason of variable Y.

7. Analysis and Discussion

The results for investigating the presence of herding, over-confidence, disposition effect, and noise trading in the Indian stock market have been presented and analyzed in following section:

A. Herding

The regression model results for determining the existence of herding on the aggregate market for the whole time period (2000-2020) and different phases of the market, i.e., pre-crisis (2000-2007), during the crisis (2008-2009), post-crisis (2010-2019), and during covid crisis (Jan 2020- Dec 2020), have been shown in table 1. Panel 1 of table 1 demonstrates the result for aggregate market as a whole. The results indicate the nonexistence of herd formation over the entire time period in the Indian stock market as the value of b2-coefficient [b2=0.102] is positive and significant. These results are in accordance with prior studies (Kanojia et al., 2020; Prosad et al., 2012; Jose et al., 2018, Ganesh et al., 2016), showing no sign of herding in the Indian stock market during a long period of time. Also, validating that the Indian investors does not mimic crowd behavior. Further, the coefficient value b2 is positive and significant (0.061, 0.076, and 0.148) in the different periods, i.e., before the crisis (2000-2007), during the crisis (2008-2009), and after the crisis (2010-2019), indicating the absence of herding behavior in all the time phases. The nonexistence of herding in the Indian stock market might be due to large

institutional investors' impact as it is perceived that they have access to better information sources, more competent traders, and hence, are less likely to imitate. Moreover, due to extremely low participation of individual investment in Indian stock market, impact of herding is not evident. However, the results indicate the presence of herding behavior during the covid crisis period (Jan-Dec 2020) as the value of b2-coefficient [b2=-0.010] is negative and significant in the Indian stock market. Indian retail investors are scattered and have very little participation in the entire volume of trade. During different time periods spanning from 2000 to 2019, there have been many ups and downs in the stock market, but covid crisis period (March 2020-Dec 2020), was unprecedented, hence, longest ever retail participation exhibit herding during 2020. These results follow previous studies such as, Prosad et al. (2012) and Dhall & Singh (2020) validating the existence of herding behavior during crisis or stress time in the Indian stock market.

Panel B and C of Table 1 reveals the bull and bear market results, which suggest the nonexistence of herding in the bullish phase of the Indian stock market (as $b2^{BL}$-coefficient is positive and significant). Further, it may be deduced that there is no indication of herding in the bearish phase of the market for the overall time period (2000-2020), before crisis, during crisis, and after crisis period (positive and significant $b2^{BR}$). The excessively positive and significant b2 coefficient validates dispersion of stock returns from overall market returns, indicating the absence of a crowding mentality. On the contrary, the results indicate the presence of herding behavior during the covid crisis period as the value of b2-coefficient [b2=-0.006] is negative and significant. This indicates that mutual imitation is more evident in crisis situation as investors depend more on masses information instead of their own in times of heightened uncertainty. Moreover, due to panic and fear of loss during crisis, individuals sell their securities by imitating or following others particularly when the market is in its bearish phase.

In the literature, it was suggested that investors follow the group consensus to seek conviction and conformity in the extreme market stress phase. They do not follow their own judgment or belief to avoid the fretfulness of making erroneous decisions during market stress uncertainty and thereby leading to herding. This study intends to capture the existence of herding in the extreme up and extreme down market. Panel D -G show results of regression results for extreme market conditions. Here, 5% and 1% criteria have been used as cut-off points to decide extreme up and down-market conditions. Panel D shows that the value of coefficient b2 is negative and significant for the whole period (2000-2020) [b2=-0.025] and after the crisis period (2010-

2019) [b2=-0.003], thereby, affirming the presence of crowding behavior in Indian stock market in an extremely down market. Panel E shows a negative and significant value of b2 [b2=-0.048] during the crisis period (2008-09) in the extreme upmarket, indicating the presence of more severe herding behavior during the crisis period in the Indian stock market. Similarly, panel F shows a significantly negative value of b2 for the whole period [b2=-0.101] and before the crisis period [b2=-0.028] validates the presence of herd mentality in the extremely down market. Also, panel G shows a significantly negative value of b2 for the after the crisis period [b2=-0.140] affirming the presence of crowding.

Table 1: Regression outcome for CSAD and market return for overall market level and different time phases

Panel	Variable	Whole Period (2000-2020)	Before crisis (2000-2007)	During crisis (2008-09)	After the crisis (2010-2019)	Covid crisis (Jan-Dec 2020)
A. Aggregate Makret	α	1.476*	1.484*	2.089*	1.396*	1.118*
	b1	0.218*	0.358*	0.236*	-0.048*	0.374*
	b2	0.102*	0.061*	0.076*	0.148*	**-0.010****
B. Bull Market	α	1.436*	1.570*	2.006*	1.363*	1.116*
	b1	0.186*	0.024*	0.315*	-0.032	0.375*
	b2	0.167*	0.222*	0.097*	0.179*	0.003
C. Bear Market	α	1.471*	1.536*	2.178*	1.334	1.158*
	b1	0.378*	0.399*	0.111*	0.242	0.298*
	b2	0.007*	0.004*	0.082*	0.012	**-0.006***
D. Extreme down market (5%)	α	0.985*	1.422*	2.73*	1.337*	3.563**
	b1	0.666*	0.439**	-0.233**	0.256*	-0.385
	b2	**-0.025***	0.001*	0.129**	**-0.003***	0.034
E. Extreme upmarket (5%)	α	0.481	1.684*	0.191**	-0.135	1.096*
	b1	0.754*	-0.083*	1.458	0.851*	1.463**
	b2	0.109*	0.239*	**-0.048****	0.103*	-0.101
F. Extreme down market (1%)	α	-1.139*	0.54*	4.93	1.998	NA
	b1	1.533**	0.781**	-1.217	-0.008	NA
	b2	**-0.101****	**-0.028***	0.237	0.019	NA
G. Extreme upmarket (1%)	α	-1.765*	-0.108*	-0.809	-8.094*	NA
	b1	1.609*	0.778*	1.707	4.031*	NA
	b2	0.042*	0.144*	-0.06	**-0.14***	NA

NA-Data not sufficient

**Significant at 1% **Significant at 5%*

Source: Research Output

Thus, herding is exhibited during extreme market conditions and might be caused by the irrational exuberance of individual investors who can easily be manipulated or influenced by

media or blinded by greediness. Indian investors develop fear of missing out (FOMO) or lagging behind when their friends, colleagues, and relatives seems like making money, which drives them to follow the crowd. Also, Indian investors exhibit herding during crisis period, especially when market crisis is the most talked information covered in news, internet, by experts, non-experts, entertainment magazines, tea-time conversations, etc. During such phase, anchoring bias, representativeness bias, loss aversion bias, mental accounting bias, all indicate towards one action which is taken by majority of retail investors, thereby leading to herding. On the basis of above findings, we may reject null hypothesis (H_o1), which states that herding bias does not exist in the Indian stock market. The findings of this research are consistent with preceding studies, such as Lao & Singh (2011), Prosad et al. (2012), etc.

B. Overconfidence bias- Result for market-wide VAR

As the preceding section provides empirical evidences for herding captured in Indian stock markets, this section details the evidences for overconfidence bias. In line with Statman et al. (2006) and Prosad et al. (2013), overconfidence bias has been analyzed by running the VAR model on market-wide trading volume and market returns. This study has tried to investigate the presence of overconfidence bias for the overall time period of 21 years and separately for pre-crisis (2000-2007), during crisis (2008-2009), after crisis (2010-2019), and during covid crisis (Jan 2020-Dec 2020) periods.

For choosing the optimal lag length, prior literature offers various alternatives such as Akaike information criterion (AIC), Hannah-Quinn (HQ), Schwarz information criteria (SIC), and final prediction error (FPE). There is no hard and fast rule with respect to selecting the best criterion for determining the optimal lag length. In line with prior studies (Phan et al., 2020 and Zia et al., 2017), an optimal lag selection has been based on Akaike (AIC), as shown in table 2. "Akaike information criteria are most popular in identifying the lag of endogenous variables." (Zia et al., 2017).

Table 2: Optimal lag selection

Whole Period (2000-2020)				Before crisis (2000-2007)				During crisis (2008-09)				After the crisis (2010-2019)				Covid crisis (Jan-Dec 2020)			
AIC(n)	HQ(n)	SC(n)	FPE(n)	AIC(n)	HQ(n)	SC(n)	FPE(n)	AIC(n)	HQ(n)	SC(n)	FPE(n)	AIC(n)	HQ(n)	SC(n)	FPE(n)	AIC(n)	HQ(n)	SC(n)	FPE(n)
10	10	8	10	10	10	5	10	6	6	5	10	10	9	8	10	10	6	1	10

Source: Research Output

After determining the optimal lag length, we estimated VAR to analyze the association between daily market returns and transaction volume. Table 3 provide the results of equation VAR. For each variable, we have reported the coefficient value, t statistic and p-value. Consistent with our supposition from the overconfidence hypothesis, the results reveal that many of the lagged MRT coefficients (market return) in the volume regression are positive and statistically significant (refer table 3). To be specific, the daily trading volume of the Nifty 50 index is positively and significantly related to the first, second, and sixth lag of market return. This result validates the existence of overconfidence bias in the Indian stock market for the whole time period (2000-2020). On the basis of above findings, we may reject second null hypothesis (H_o2), which states that overconfidence bias does not exist in the Indian stock market. The findings of this research are consistent with prior studies of overconfidence such as, Prosad et al. (2013) and Kanojia et al. (2020). The findings also support studies like Statman et al. (2006), Chuang & Lee (2006), Zaiane (2015), though the results depict scenario from USA and China. Further, table 3 shows the results to determine the overconfidence bias in the different periods, i.e., before the crisis, during the crisis, after the crisis, and during covid crisis. The overconfidence hypothesis is verified for the first lag (MRT_{-1}) (as the coefficient value (γ_p) is positive and significant at a 5% level) for before crisis and during crisis period. However, none of the coefficients on lagged MRT (market return) in the volume regression is positive and statistically significant for after crisis and during covid crisis periods. In other words, our findings do not validate the existence of overconfidence bias in the Indian stock market after 2008-09 crisis. It might be due to the fact that after crisis, institutional investors have started using long-term holding as a strategic option against short term trading. Investors have started following Warren Buffett's 'buy and hold' strategy which implies that investments should be made in businesses that will endure to offer a competitive advantage decade down the line. He mentioned in his letter to shareholders, "if you aren't willing to own a stock for ten years, don't even think about owning it for ten minutes" (Buffett & Clark, 2008). Individual investors also participate indirectly in the stock market through pension funds, mutual funds, and ulip plans which require blocking of funds for a longer period of time. Though the overall participation in stock market has increased after crisis along with the increasing market return, still its impact is not much reflected on transaction volume as investors focus has shifted to investments with long-term horizons instead of short-term trading. Moreover, Indian investors have recently opened 14.2 million new demat accounts in financial year 2021, an all time high in its history (Livemint, April 2021). This is an increase of approximately three times the new accounts

opened in the previous financial year. This indicates a significant increase in retail investors participation in overall stock market, however, its impact on transaction volume will be visible in future only when they will start transacting more. Subsequent to that we will be able to validate the existence of overconfidence bias in the Indian stock market in post crisis period.

Table 3: Market VAR estimation (Indian stock market)

Whole Period (2000-2020)				Before crisis (2000-2007)				During crisis (2008-09)				After the crisis (2010-2019)				Covid crisis (Jan – Dec 2020)			
	Estimate	t value	P value		Estimate	t value	P value		Estimate	t value	P value		Estimate	t value	P value		Estimate	Std. Error	t value Pr(>|t|)
const	9.04766	1.97909	4.95e-06 ***	const	5.43490	4.477	8.01e-06 ***	const	17.55208	2.167	0.030726 *	const	17.71716	3.563	0.000373 ***	const	1.590e+02	2.379	0.01826 *
MRT.l1	**1.16577**	**1.965**	**0.04945 ***	**MRT.l1**	**0.87322**	**3.133**	**0.001754 ****	**MRT.l1**	**3.46829**	**3.499**	**0.000512 *****	MRT.l1	0.97264	0.712	0.476392	MRT.l1	-1.781e+00	-0.295	0.76792
MRT.l2	**1.04013**	**1.066**	**0.04724***	MRT.l2	0.32700	1.128	0.259629	MRT.l2	1.73885	1.700	0.089807 .	MRT.l2	-1.31224	-0.953	0.340500	MRT.l2	-5.151e+00	-0.803	0.42308
MRT.l3	0.54070	0.889	0.37418	MRT.l3	0.34826	1.196	0.231834	MRT.l3	0.61767	0.599	0.549495	MRT.l3	-0.86592	-0.626	0.531625	MRT.l3	3.400e+00	0.545	0.58642
MRT.l4	0.04020	0.066	0.94739	MRT.l4	0.13751	0.471	0.637412	MRT.l4	0.92212	0.902	0.367702	MRT.l4	1.41274	1.016	0.309539	MRT.l4	-1.073e+01	-1.686	0.09324 .
MRT.l5	0.45397	0.746	0.45591	MRT.l5	-0.04051	-0.139	0.889798	MRT.l5	0.69327	0.677	0.498718	MRT.l5	-0.57191	-0.411	0.680757	MRT.l5	1.611e+00	0.253	0.80041
MRT.l6	**1.07066**	**1.762**	**0.04805***	MRT.l6	-0.28338	-0.971	0.331646	MRT.l6	0.82084	0.819	0.412979	MRT.l6	-0.01964	-0.014	0.988717	MRT.l6	-1.033e+01	-1.759	0.08000 .
MRT.l7	-0.43096	-0.710	0.47780	MRT.l7	-0.18833	-0.648	0.517163	volatility.l1	1227.98499	8.144	3.57e-15 ***	MRT.l7	1.49935	0.531	0.344204	MRT.l7	1.197e+00	0.207	0.83585
MRT.l8	-0.93509	-1.547	0.12191	MRT.l8	-0.08381	-0.290	0.771832	volatility.l2	-349.95755	-2.075	0.038563 *	MRT.l8	-1.51408	-1.095	0.273549	MRT.l8	-1.017e+01	-1.761	0.07973 .
MRT.l9	0.58405	0.971	0.33153	MRT.l9	0.01120	0.039	0.968900	volatility.l3	-259.16389	-1.545	0.123079	MRT.l9	0.86854	0.630	0.528874	MRT.l9	-4.504e-01	-0.079	0.93744
MRT.l10	0.28717	0.488	0.62558	MRT.l10	-0.04497	-0.166	0.868442	volatility.l4	-343.93476	-2.061	0.039885 *	MRT.l10	1.32311	0.963	0.335846	MRT.l10	-5.457e+00	-0.965	0.33558
volatility.l1	315.54348	3.563	0.00037 ***	volatility.l1	162.06734	3.824	0.000135 ***	volatility.l5	-229.59180	-1.359	0.174703	volatility.l1	248.14453	1.213	0.225170	volatility.l1	-2.005e+03	-2.099	0.03701 *
volatility.l2	-150.51064	-1.63	0.10297	volatility.l2	-54.45727	-1.227	0.219957	volatility.l6	145.59225	0.915	0.360697	volatility.l2	255.35336	1.253	0.210397	volatility.l2	-7.367e+02	-0.762	0.44698
volatility.l3	56.36476	0.608	0.54306	volatility.l3	-40.68144	-0.908	0.363767	VOLUME.l1	0.45510	9.759	< 2e-16 ***	volatility.l3	223.62344	1.095	0.273513	volatility.l3	1.793e+03	1.914	0.05695 .
volatility.l4	-174.91964	-1.884	0.05964 .	volatility.l4	18.38827	0.411	0.680785	VOLUME.l2	0.16450	3.234	0.001308 **	volatility.l4	272.26581	1.335	0.182124	volatility.l4	-1.087e+03	-1.135	0.25765
volatility.l5	-190.57907	-2.046	0.04078 *	volatility.l5	-169.95863	-3.787	0.000157 ***	VOLUME.l3	0.04181	0.817	0.414141	volatility.l5	-436.43030	-2.128	0.033429 *	volatility.l5	1.207e+03	1.296	0.19636
volatility.l6	-99.65564	-1.070	0.28451	volatility.l6	-10.59234	-0.235	0.814154	VOLUME.l4	0.06781	1.317	0.188454	volatility.l6	-257.81838	-1.257	0.208768	volatility.l6	-1.649e+03	-1.757	0.08037 .
volatility.l7	-183.89493	-1.983	0.04739 *	volatility.l7	-5.10589	-0.114	0.909283	VOLUME.l5	0.07050	1.377	0.169149	volatility.l7	-881.70396	-4.324	1.59e-05 ***	volatility.l7	-4.032e+02	-0.418	0.67646
volatility.l8	-49.11122	-0.531	0.59537	volatility.l8	6.43738	0.143	0.886039	VOLUME.l6	0.09587	2.208	0.027715 *	volatility.l8	-584.64472	-2.863	0.004238 **	volatility.l8	4.992e+02	0.523	0.60171
volatility.l9	262.95597	2.860	0.00425 **	volatility.l9	16.16478	0.364	0.715752					volatility.l9	449.69993	2.211	0.027148 *	volatility.l9	1.293e+03	1.306	0.19298
volatility.l10	-45.89929	-0.529	0.59690	volatility.l10	-15.04078	-0.370	0.711678					volatility.l10	-45.34606	-0.223	0.823411	volatility.l10	4.127e+02	0.425	0.67123
VOLUME.l1	0.41144	29.247	< 2e-16 ***	VOLUME.l1	0.46802	19.957	< 2e-16 ***					VOLUME.l1	0.28247	13.691	< 2e-16 ***	VOLUME.l1	6.739e-01	9.592	< 2e-16 ***
VOLUME.l2	0.08435	5.556	2.89e-08 ***	VOLUME.l2	0.02951	1.145	0.252166					VOLUME.l2	0.08617	4.026	5.85e-05 ***	VOLUME.l2	-9.893e-02	-1.194	0.23374
VOLUME.l3	0.13045	8.572	< 2e-16 ***	VOLUME.l3	0.15982	6.177	7.92e-10 ***					VOLUME.l3	0.11333	5.329	1.08e-07 ***	VOLUME.l3	1.358e-01	1.682	0.09401 .
VOLUME.l4	0.06114	4.008	6.22e-05 ***	VOLUME.l4	0.02721	1.040	0.298341					VOLUME.l4	0.03000	1.413	0.157804	VOLUME.l4	1.472e-01	1.824	0.06953 .
VOLUME.l5	0.07690	5.037	4.89e-07 ***	VOLUME.l5	0.21284	8.141	6.88e-16 ***					VOLUME.l5	0.10046	4.727	2.40e-06 ***	VOLUME.l5	-1.009e-01	-1.263	0.20799
VOLUME.l6	0.03042	1.992	0.04643 *	VOLUME.l6	-0.03605	-1.378	0.168284					VOLUME.l6	0.00559	0.263	0.792542	VOLUME.l6	1.780e-01	2.235	0.02650 *
VOLUME.l7	0.10520	6.885	6.48e-12 ***	VOLUME.l7	-0.01340	-0.512	0.608851					VOLUME.l7	0.11541	5.410	6.93e-08 ***	VOLUME.l7	8.592e-02	1.069	0.28649
VOLUME.l8	0.02882	1.889	0.05890 .	VOLUME.l8	0.02446	0.943	0.345557					VOLUME.l8	0.14513	6.807	1.25e-11 ***	VOLUME.l8	-2.130e-01	-2.646	0.00876 **
VOLUME.l9	0.02918	1.919	0.05500 .	VOLUME.l9	-0.00308	-0.119	0.905284					VOLUME.l9	0.02653	1.237	0.216377	VOLUME.l9	1.624e-01	1.998	0.04695 *
VOLUME.l10	0.01869	1.329	0.18385	VOLUME.l10	0.08418	3.608	0.000316 ***					VOLUME.l10	0.05667	2.739	0.006205 **	VOLUME.l1	-1.863e-01	-2.531	0.01209 *

*Significant codes: '***' 0.001 '**' 0.01 '*' 0.05* Volume= daily transaction volume of index; MRT = daily stock returns of N number of stocks, which has been calculated by difference of successive day's closing price divided by previous day closing price of the index, Volatility = daily volatility of index computed by taking the difference of using daily high and low prices

Source: Research Output

C. Overconfidence bias and disposition effect- Result for security-wide VAR

The existing literature suggests that individual stocks' transaction volume is positively related to past market return that captures the overconfidence bias. However, disposition effect occurs when individual stocks' transaction volume is positively related to its own past returns because investors enjoy realizing gain on individual securities. Therefore, investors are prone to sell the winning shares (whose price has increased) and tend to keep loss-making assets (whose price has dropped) as they are unwilling to realize losses but are more willing to realize gains prematurely, thereby leading to disposition effect (Statman et al., 2006; Prosad, 2013; Zaine, 2013). VAR model has been used to test the hypothesis H_O3, i.e., existence of disposition bias in the Indian stock market. Disposition effect has been analyzed by running the VAR model on security-wide transaction volume and security returns. The statistically significant positive value of γp (in equation 3) indicates the disposition effect's existence, and the positive value of λp indicates overconfidence. Our findings demonstrate that out of total 50 securities, the disposition effect and overconfidence bias has been identified in 9 and 14 companies respectively as shown in table 4. This demonstrates that overconfidence bias is predominant amongst the two. Out of these companies, 7 are common which have been affected by both biases. Table 4 infers that overconfidence bias and disposition effect are more visible in stocks having high PE ratio or have high market capitalization, such as, Bajaj Finserv Ltd., Eicher Motors Ltd., ICICI Bank Ltd., Kotak Mahindra Bank Ltd., Maruti Suzuki India Ltd., Reliance Industries Ltd. Tata Motors Ltd., and others. These are the stocks which investors keep on buying even at a premium price. Looking at the effect of investors' behavior on transaction volume instigate us to question the validity of conventional financial theories. High transaction volume might impact the stock prices in a biased manner that may not be validated by their price/earnings (P/E) ratio. This might lead to overvaluation or undervaluation of stocks. Thus, we may reject null hypothesis (H_o3), i.e., Disposition effect does not exist in the Indian stock market.

Table 4: List of Nifty 50 affected by Over-confidence Bias and Disposition Effect

Company Name	Overconfidence Bias	Disposition Effect
Adani Ports and SEZ Ltd.	Yes (Lag 1,2)	No
Asian Paints Ltd.	Yes (Lag 1,2,5)	No
Axis Bank Ltd.	Yes (lag 2, 5)	Inconclusive (Lag 2)
Bajaj Finserv Ltd.	Yes (Lag 2,3)	Yes (Lag 1,2)
Eicher Motors Ltd.	Yes (Lag 6)	Yes (Lag 1,2,3)

Grasim Industries Ltd.	Yes (Lag 1,2)	No
ICICI Bank Ltd.	Yes (Lag 1)	Inconclusive (Lag 1,4,5,7,9)
Kotak Mahindra Bank Ltd.	Yes (Lag 1,2,5)	Yes (Lag 1,2)
Maruti Suzuki India Ltd.	Yes (Lag 1)	Yes (Lag 1,2)
Oil & Natural Gas Corporation Ltd.	No	Yes (Lag 1)
Reliance Industries Ltd.	Yes (lag 1,5)	No
State Bank of India	Yes (Lag 1)	No
Tata Motors Ltd.	Yes (Lag 1,4)	Yes (Lag 1,4,7,8)
Tech Mahindra Ltd.	Yes (Lag 1,4)	Yes (Lag 1,2)
UPL Ltd.	No	Yes (Lag 1)
Zee Entertainment Enterprises Ltd.	Yes (Lag 1,2)	Yes (Lag 1,3,5)

Source: Research Output

D. Results for Granger Causality

According to De Long et al. (1990), the presence of noise traders in stock markets creates a risk in the stock prices and causes prices to diverge significantly from their fundamental values even if all other investors are rational. Table 5 documents the result for granger causality test which has been used to investigate the contemporaneous relation between market return and market transaction volume in the Indian stock market. On the basis of findings shown in table 5, it could be claimed that market return granger cause market transaction volume. However, the market volume is not found to granger cause or forecast market return as P-value > 0.05. Therefore, we can say that there is unidirectional causality from the market return to market transaction volume that proves noise trading in the Indian Stock market. Thus, we may reject the null hypothesis (H_o4). In other words, there exists a significant presence of noise trading in the Indian stock market. Our findings provide support to prior studies, such as Mahajan & Singh (2009) in Indian stock market, Heimstra & Jones (1994) in DJIA index, Jain & Joh (1988) in S&P 500 stocks, Chen et al. (2001) in nine developed stock markets, and Shrestha (2017) in Nepalese stock market.

Table 5: Granger Causality for Market Transaction Volume versus Market Return

Null Hypothesis	**F-statistic**	**p-value**
VOLUME does not Granger Cause RETURN	1.4233	0.2329
RETURN does not Granger Cause VOLUME	6.7851	0.009219**

Signif. code: '**' 0.01

8. Conclusion

This study has tried to determine the existence of the predominant behavioral anomalies; the herding bias, disposition effect, overconfidence bias, and noise trading in Indian stock market. The result of the research shows that Indian stock markets are efficient as we fail to validate the

existence of herding for the overall market as well as during the pre-crisis period, crisis period and post- crisis period. The results are in accordance with prior studies like Lakshman et al. (2011); Prosad et al. (2012); Jose et al. (2018), showing no sign of herding in Indian stock market as a whole. Also, validating that the Indian investors are well apprised and rational in investment decisions, they don't mimic the behavior of crowd. It might be because of the influence of large institutional investors as it is perceived that they have access to better information sources, more competent traders, and hence, are less probable to imitate. However, the results indicate the presence of herding behavior during the covid crisis period for the overall market and bearish market. Moreover, herding is found to be evident in extreme market conditions (5% and 1%). It may be because investors pursue the market crowd due to the irrational exuberance of individual investors who can easily be manipulated or influenced by the media or blinded by greediness. Indian investors develop fear of missing out (FOMO) or lagging behind when their friends, colleagues, and relatives seems like making money, which drives them to follow the crowd. Also, Indian investors exhibit herding during crisis period, especially when market crisis is the most talked information covered in news, internet, by experts, non-experts, entertainment magazines, tea-time conversations, etc. During such phase, anchoring bias, representativeness bias, mental accounting bias, all indicate towards one action which is taken by majority of retail investors, thereby leading to herding. These results follow previous studies such as, Prosad et al. (2012) and Dhall & Singh (2020) validating the existence of herding behavior during crisis or stress time in the Indian stock market.

The results also validate the existence of anomalies such as overconfidence, disposition effect, and noise trading in Indian stock market. Findings of this research are consistent with prior studies, such as Statman et al. (2006), Chuang & Lee (2006), Zaiane (2013), Prosad et al. (2013), etc. in the manner that the transaction volume at overall market level escalates when people become overconfident whereas it rises at individual security level to demonstrate disposition effect. This study provides conclusive evidence for presence of the behavioral biases in the Indian stock market. These biases impact the performance of investors' individual portfolios, consequently impacting the overall wealth generated by them. Moreover, investors are more susceptible to behavioral anomalies during market crashes and react irrationally due to the fear and panic caused by the uncertainty. Indian stock markets have encountered many roller coaster rides in their history wherein acute crashes and sharp corrections have led to severe stock market crashes. Such turbulence in the markets has made it

challenging for ordinary investors to behave rationally and to thrive and generate consistent returns through such an arduous phase. Thus, it is imperative to eliminate these biases to help investors survive market crashes. Although investors cannot circumvent all behavioural errors, but they can try to reduce their effects. The best way to avoid these biases requires a proper understanding of one's behavioural mistakes, resisting the propensity to engage in such behaviours, and formulating and implementing rational and objective investment strategies. Investors are also required to devote their resources for the longer horizon, assess their risk appetite, establish an apt asset allocation strategy, and rebalance their portfolios periodically. Always remember, the secret to float during turbulence is to remain unemotional and examine the scenario in a calm and logical manner. This will definitely lead to judicious investment decisions.As every study is constrained by time and resources, so do the present study is subject to few limitations. The study has included only selected Indian companies. Future research can be conducted on enlarged sample size to check the consistency of the results. Future research can focus on other countries as well to determine whether worldwide investors encounter same behavioural biases or are there any differences. Moreover, this study has taken into consideration only a few behavioral anomalies, while many other biases, such as, anchoring, loss aversion, representativeness, mental accounting, etc. have not been taken into consideration and these can be incorporated for further researches in future.

References

Abdullahi, S. A., Kouhy, R., & Muhammad, Z. (2014). Trading volume and return relationship in the crude oil futures markets. *Studies in Economics and Finance*. https://doi.org/10.1108/SEF-08-2012-0092

Al-Samman, H., & Al-Jafari, M. K. (2015). Trading volume and stock returns volatility. Evidence from industrial firms of Oman. Asian Social Science, 11, 139–146. https://doi.org/10.5539/ass.v11n24p139

Barber, B.M., & Odean,T. (2000). Trading Is Hazardous to Your Wealth: The Common Stock Investment Performance of Individual Investors. *Journal of Finance, LV,* 773–806. https://doi.org/10.1111/0022-1082.00226

Barberis, N., & Xiong, W. (2009). What Drives the Disposition Effect? An Analysis of a Long-Standing Preference-Based Explanation. *The Journal of Finance*, *64*(2), 751-784. https://doi.org/10.1111/j.1540-6261.2009.01448.x

Bailey, W., Kumar, A., & Ng, D. (2011). Behavioral biases of mutual fund investors. *Journal of Financial Economics*, *102*(1), 1-27. https://doi.org/10.1016/j.jfineco.2011.05.002

Buffett, M. & Clark, D. (2008). Warren Buffett and the Interpretation of Financial Statements: The Search for the Company with a Durable Competitive Advantage. *Scribner, NY.*

Chang, E. C., Cheng, J. W., & Khorana, A. (2000). An examination of herd behavior in equity markets: An international perspective. *Journal of Banking & Finance*, *24*(10), 1651-1679. https://doi.org/10.1016/S0378-4266(99)00096-5

Chen, J., Hong, H., & Stein, J. C. (2001). Forecasting crashes: Trading volume, past returns, and conditional skewness in stock prices. *Journal of financial Economics*, *61*(3), 345-381. https://doi.org/10.1016/S0304-405X(01)00066-6

Chiang, T. C., & Zheng, D. (2010). An empirical analysis of herd behavior in global stock markets. *Journal of Banking & Finance*, *34*(8), 1911-1921. https://doi.org/10.1016/j.jbankfin.2009.12.014

Chiang, T. C., Li, J., & Tan, L. (2010). Empirical investigation of herding behavior in Chinese stock markets: Evidence from quantile regression analysis. *Global Finance Journal*, *21*(1), 111-124. https://doi.org/10.1016/j.gfj.2010.03.005

Chuang, W. I., & Lee, B. S. (2006). An empirical evaluation of the overconfidence hypothesis. *Journal of Banking & Finance*, *30*(9), 2489-2515. https://doi.org/10.1016/j.jbankfin.2005.08.007

Daniel, K., Hirshleifer, D., & Subrahmanyam, A. (1998). Investor Psychology and Security Market Under- and Overreactions. *Journal of Finance, LIII*, 1839–1885. https://doi.org/10.1111/0022-1082.00077

De Long, J. B., Shleifer, A., Summers, L. H., & Waldmann, R. J. (1990). Noise trader risk in financial markets. *Journal of political Economy*, *98*(4), 703-738. http://dx.doi.org/10.1086/261703

Dhall, R., & Singh, B. (2020). The COVID-19 pandemic and herding behaviour: Evidence from India's stock market. *Millennial Asia*, *11*(3), 366-390. https://doi.org/10.1177/0976399620964635

Frazzini, A. (2006). The disposition effect and underreaction to news. *The Journal of Finance*, *61*(4), 2017-2046. https://doi.org/10.1111/j.1540-6261.2006.00896.x

Ganesh, R., Naresh, G., & Thiyagarajan, S. (2016). Industry herding behaviour in Indian stock market. *American Journal of Finance and Accounting*, *4*(3-4), 284-308. https://doi.org/10.1504/AJFA.2016.10001602

Gervais, S., & Odean, T. (2001). Learning to be overconfident. *Review of Financial studies*, 14(1), 1-27. https://doi.org/10.1093/rfs/14.1.1

Ghazali, R., Hussain, A. J., & Liatsis, P. (2011). Dynamic Ridge Polynomial Neural Network: Forecasting the univariate non-stationary and stationary trading signals. *Expert Systems with Applications*, *38*(4), 3765-3776. https://doi.org/10.1016/j.eswa.2010.09.037

Grinblatt, M., & Keloharju, M. (2001). What makes investors trade?. *The Journal of Finance*, *56*(2), 589-616. https://doi.org/10.1111/0022-1082.00338

Gunduz, L., & Hatemi-J, A. (2005). Stock price and volume relation in emerging markets. *Emerging Markets Finance and Trade*, *41*(1), 29-44. https://doi.org/10.1080/1540496X.2005.11052599

Hiemstra, C., & Jones, J. D. (1994). Testing for linear and nonlinear Granger causality in the stock price-volume relation. *The Journal of Finance*, *49*(5), 1639-1664. https://doi.org/10.1111/j.1540-6261.1994.tb04776.x

Jain, P. C., & Joh, G. H. (1988). The dependence between hourly prices and trading volume. *Journal of Financial and Quantitative Analysis*, 269-283. https://doi.org/10.2307/2331067

Jose, B., Varghese, J., & Surendran, A. (2018). Investors' Herding In Indian Stock Market; An Empirical Analysis. *IOSR Journal of Business and Management*, *20*(1), 76-86. https://doi.org/10.9790/487X-2001047686

Kanojia, S., Singh, D., and Goswami, A. (2020), "Impact of herding on the returns in the Indian stock market: an empirical study", Review of Behavioral Finance, Vol. 14 No. 1, pp. 115-129. https://doi.org/10.1108/RBF-01-2020-0017

Khan, H., Hassairi, S. A., & Viviani, J. L. (2011). Herd behavior and market stress: The case of four European countries. *International Business Research, 4*(3), 53. https://doi.org/10.5539/ibr.v4n3p53

Lakshman, M.V., Basu, S., & Vaidyanathan, R. (2011). Market wide herding and the impact of institutional investors in the Indian capital market. Working Paper 327, Indian Institute of Management, Banglore. https://doi.org/10.1177/0972652713494046

Lao, P., & Singh, H. (2011). Herding behaviour in the Chinese and Indian stock markets. *Journal of Asian Economics, 22*(6), 495-506. https://doi.org/10.1016/j.asieco.2011.08.001

Lindhe, E. (2012). Herd behavior in stock markets: A Nordic study. Retrieved from http://lup.lub.lu.se/student-papers/record/3046944

Mackay, C. (1841). *Memoirs of Extraordinary Popular Delusions and the Madness of Crowds*. (1 ed.). London: Richard Bentley.

Mahajan, S., & Singh, B. (2009). The empirical investigation of relationship between return, volume and volatility dynamics in Indian stock market. *Eurasian Journal of Business and Economics, 2*(4), 113-137. Retrieved from https://ejbe.org/index.php/EJBE/article/view/27

Odean, T. (1999). Do Investors Trade Too Much?. *American Economic Review*, 1279–1298. https://doi.org/10.1257/aer.89.5.1279

Prosad, J. M., Kapoor, S., & Sengupta, J. (2012). An examination of herd behavior: An empirical evidence from Indian equity market. *International Journal of Trade, Economics and Finance, 3*(2), 154. https://doi.org/10.7763/IJTEF.2012.V3.190

Prosad, J. M., Kapoor, S., & Sengupta, J. (2013). Impact of overconfidence and the disposition effect on trading volume: An empirical investigation of Indian Equity Market. *International Journal of Research in Management and Technology*, *3*(4), 109-116. https://doi.org/10.1177/0972150917726660

Sewell, M. (2007). *Behavioral Finance*. Retrieved from http://www.behaviouralfinance.net/behavioural-finance.pdf.

Shefrin, H., & Statman, M. (1985). The disposition to sell winners too early and ride losers too long: Theory and evidence. *The Journal of finance*, *40*(3), 777-790. https://doi.org/10.1111/j.1540-6261.1985.tb05002.x

Shrestha, S. (2017). Contemporaneous Relationship between Trading Volume and Stock Returns Volatility: Evidence from Nepalese Stock Market. *PYC Nepal Journal of Management, 10*(1), 40-63. https://doi.org/10.3126/pycnjm.v10i1.36067

Shumway, T., & Wu, G. (2006). Does Disposition Drive Momentum? University of Michigan working paper.

Sonavane, R.N. (2021, September 16). Indian stock market overtakes France; becomes sixth biggest. *Livemint.com*. Retrieved from https://www.livemint.com/market/stock-market-news/indian-stock-market-overtakes-france-becomes-sixth-biggest-11631730375607.html

Statman, M., Thorley, S., & Vorkink, K. (2006). Investor overconfidence and trading volume. *Review of Financial Studies*, *19*(4), 1531-1565. https://doi.org/10.1093/rfs/hhj032

Tapia, W., & Yermo, J. (2007). Implications of Behavioural Economics for Mandatory Individual Account Pension Systems. https://doi.org/10.1787/19936397

Tariq, B., & Ullah, N. (2013). Investor overconfidence and stock returns: Evidence from pakistan. *IOSR Journal of Business and Management*, *8*(1), 77-84. https://doi.org/10.9790/487X-0817784

Weber, M., & Camerer, C. F. (1998). The disposition effect in securities trading: An experimental analysis. *Journal of Economic Behavior & Organization*, *33*(2), 167-184. https://doi.org/10.1016/S0167-2681(97)00089-9

Zaiane, S. (2013). Overconfidence, trading volume and the disposition effect: Evidence from the Shenzhen Stock Market of China. *Journal Issues ISSN*, *2350*, 157X. Available online at http://www.journalissues.org/IBME/

Zia, L., Ilyas Sindhu, M., & Haider Hashmi, S. (2017). Testing overconfidence bias in Pakistani stock market. *Cogent Economics & Finance*, *5*(1), 1289656. https://doi.org/10.1080/23322039.2017.1289656

The current issue and full text archive of this journal is available on Emerald Insight at:
https://www.emerald.com/insight/0951-354X.htm

Exploring the psychometric properties of the Cyberbullying Attitude Scale (CBAS) and its relation with teasing and gratitude in Indian collegiates

Received 23 May 2022
Revised 4 October 2022
13 November 2022
Accepted 14 November 2022

Suhans Bansal and Naval Garg
Delhi Technological University, New Delhi, India, and
Jagvinder Singh
University of Delhi, New Delhi, India

Abstract

Purpose – This study aims to examine the psychometric properties of the Cyberbullying Attitude Scale (CBAS) in Indian college students with the help of two independent studies.

Design/methodology/approach – The first study investigated the factorial validity of the scale using exploratory factor analysis (EFA) and confirmatory factor analysis (CFA), resulting in a seven-item, two-component model of CBAS. Two statements were excluded owing to inadequate factor loading. The second study evaluated the reliability and criterion validity of the model extracted after CFA using the Weight-Based Teasing Scale (WBTS), PhQ9 as convergent indices and Gratitude Questionnaire 6 (GQ6) as divergent indices.

Findings – It was observed that the Indian version of the scale differs from the original version in two ways. First, the Indian CBAS comprised seven items, while the original CBAS consisted of nine items. Second, in the original CBAS, two factors of cyberbullying, i.e. hostile cyberbullying attitudes (HCA) and general cyberbullying characteristics (GCC), contained five and four statements, respectively. However, the Indian CBAS comprised five and two statements, respectively. Further, the Indian CBAS showed convergence with WBTS and PhQ9 and divergence with GQ6.

Originality/value – This study is one of the first to explore the psychometric properties of Indian CBAS and its relations with teasing and gratitude.

Keywords Cyberbullying attitude scale, Psychometric, India, Bullying, Mental health

Paper type Research paper

1. Introduction

The advancement of Internet technologies has been hailed as a double-edged sword. It benefits humanity with comfort, speed, connectivity, etc. But simultaneously, it poses severe challenges of hacking and cyberbullying. Cyberbullying has emerged as a significant problem for Internet users, especially among schools and college students (Olweus, 2013). Researchers have used various terminologies to describe bullying in cyberspace, like the Internet, online and electronic bullying. However, the word cyberbullying is widely used among researchers and practitioners (Chan *et al.*, 2019, 2021). It has been defined as repeated, conscious, intentional and hostile acts of individuals/groups in the online world to inflict harm and discomfort on the targets (Chan *et al.*, 2019). It involves using a digital platform to harass, threaten, embarrass and target another person (Sharma *et al.*, 2017). Cyberbullying behavior has been identified over time, including threats, flaming, rumors, sexual remarks, cyber-stalking and exclusion (Slonje *et al.*, 2013). The basis of cyberbullying may be skin color, caste, creed, religion, gender, sexual orientation, nationality, etc. It can happen through social media, messaging and gaming platforms, emails, etc (Barragán Martín *et al.*, 2021; Verma *et al.*, 2022).

International Journal of Educational Management
© Emerald Publishing Limited
0951-354X
DOI 10.1108/IJEM-05-2022-0198

Unlike traditional bullying, cyberbullying can be particularly scary for victims for three significant reasons. First, this form of bullying leaves a perennial digital footprint. Memories of bullying may fade away with time, but cyberbullying has a long-lasting or relatively permanent presence (Hashemi, 2021). Second, it has a larger audience. The instance of cyberbullying may be shared with an infinite number of users by a simple click or likening comment (Smith, 2016). And lastly, cyberbullying is not a face-to-face experience. It gives the bullies a certain degree of anonymity, making them insensitive and ignorant of the consequences of their actions (Slonje and Smith, 2008). These differences make cyberbullying more potent, which leads to disastrous consequences (Gonultas, 2022). Bullied people show higher anxiety, depression, stress, loneliness, powerlessness and anger (Zhu *et al.*, 2021). It also leads to poor self-esteem, resilience, confidence and optimism (Larrañaga *et al.*, 2018; Waasdorp and Bradshaw, 2015). Although cyberbullying severely impacts people of all ages, students are more prone to online victimization (Zhu *et al.*, 2021). Impulsiveness, lack of guidance and experience, sensation and thrill-seeking attitude, the heat of passion and peer pressure make young students easy targets of cyberbullying (Zhu *et al.*, 2021; Reyna and Farley, 2006; Verma and Garg, 2022).

Bernardo *et al.* (2020) reported that cyberbullying among students leads to higher absenteeism rates and school dropouts. It also results in loneliness, lower empathy, self-doubt and lower self-esteem among students (Bevilacqua *et al.*, 2017). The situation is more critical for young students from developing countries like India, which are at a crucial juncture of technological advancement. With India progressively moving toward the digital era, there are ever-increasing chances of an exponential rise in cases of cyberbullying. Nowadays, access to the Internet through a computer, tablet, or mobile phone has grown exponentially (Sayeed *et al.*, 2021). The COVID-19 pandemic and the subsequent shift to online studies have accelerated the Internet penetration rate among Indian students (Madhukalya, 2020; Garg *et al.*, 2022). Since most of these students are first-generation Internet users, they fail to get parental guidance in dealing with cyberbullying (Chen *et al.*, 2020). Also, India is a peculiar country with a considerable power distance. It leads to limited communication and discussion between parents and children (Shah and Nakhat, 2018). Also, the rigid Indian hierarchical family structure often restricts the free flow of communication, ideas and feelings (Chadda and Deb, 2013).

Further, digital transformation is in the initial phase in India; cyberbullying is a relatively new phenomenon for Indians. In a survey conducted by Newall (2018), 37% of the Indian respondents failed to recognize cyberbullying because of little understanding of the intricacies of cyberbullying. Victims of cyberbullying do not recognize that they are being bullied as it is normalized within the digital space, and thereby they lose their opportunity to report and seek redressal. Besides, people are unaware of the legal options to deal with cyberbullying crimes, which leads to underreporting of online harassment and bullying incidents (Maheshwari, 2020). Also, policies in both the workplace and educational institutions align with the laws in India and give impetus to them as an intervention against physical bullying (Sandhu and Kaur, 2022). The government also gives the organizations a free hand to frame anti-bullying policies according to their needs. For instance, students at the college level are mandated to provide an anti-bullying affidavit stating that they will never indulge in bullying and ragging others, failing which the individual will face repercussions from being debarred to being sued in court (Gautam, 2020; University Grants Commission: Ragging Related Circulars, 2009). The Medical Council of India also supports eradicating bullying and ragging from medical colleges in India (Medical Council of India, 2018). However, the policies and rules regulating physical and verbal bullying in educational institutions and workplaces in India do not meet international standards and are limited to meeting specific criteria only (Jain, 2018). For instance, foreign schools regularly evaluate the effectiveness of anti-bullying policies and amend them as per

the need (Pearce *et al.*, 2011). The administration of the school tries to create a conducive environment that supports the school's culture against bullying and encourages students to come forward and talk freely about their bullying experiences during school (Farrington, 1993, 2011). Also, as a part of their policies, many schools educate parents regarding cyberbullying and other forms of bullying and their dire consequences, appoint peer monitors to keep a vigil on victims and educate students on cyberbullying (Hutson *et al.*, 2017).

Regretfully, India lacks any specific laws and policies to regulate cyberbullying. Although a few sections of the Information Technology Act 2000 and the Indian Penal Code (IPC) lay down provisions for penalizing the act of cyberbullying, they fail to address cyberbullying as a crime as these provisions are just guiding in nature. Consequently, not having adequate policies and laws and limiting them to physical and verbal bullying has aggravated the problem of cyberbullying in India. For instance, cases of cyberbullying and cyberstalking of women or children increased by 36% in 2018 compared to 2017 (Maheshwari, 2020). A study conducted by Ipsos in 28 countries reported that the menace of cyberbullying is particularly problematic for India, with the highest rate of parents (37%) confirming instances of cyberbullying and regular occurrence of the same (Newall, 2018; McCarthy, 2018). With impending digital transformation, researchers and practitioners expect an increase in the rate of cyberbullying (Jain *et al.*, 2020). Thus, policymakers and academicians encourage scientific and empirical exploration of cyberbullying in the Indian context.

Researchers argue that the first and foremost requirement for any scientific study is the availability of a reliable and valid scale to measure the phenomenon. Unfortunately, it has been observed that almost no studies are available on developing new scales or validating existing scales to measure attitudes toward cyberbullying in Indian students. The present study examines the psychometric properties of Cyberbullying Attitude Scale (CBAS) among Indian college students. Attitude is typically understood as a learned tendency to evaluate things in a certain way. It has a potent influence on human behavior (Hill, 1990). Attitudes significantly and substantially predict future behavior, especially with affective-cognitive solid consistency (Glasman and Albarracín, 2006; Cavalcanti *et al.*, 2019; Kraus, 1995). For instance, researchers have reported that aggressive attitudes aggravate violent behavior (Blinkhorn *et al.*, 2016). In the context of cyberbullying, Huang and Chou (2010) found that an attitude of indifference and apathy toward cyberbullying has deepened the problem. Substantial research has proven that maintaining a positive attitude toward cyberbullying plays a significant role in its proliferation. For instance, it was noted that cyberbullying is a function of positive attitudes toward cyberbullying, and positive attitudes increase the frequency of acts of cyberbullying (Barlett, 2015; Barlett and Gentile, 2012). Also, it was found that a favorable attitude mediated the relationship between aggressor-perceived anonymity and cyberbullying behavior (Barlett *et al.*, 2016a, b). Doane *et al.* (2014) conducted a study among college students and demonstrated that lower empathy led to positive attitudes toward cyberbullying, which intensified the intentions to cyberbully. Since attitude influences behavior, researchers have suggested an investigation of attitude to understand current behavior and develop interventions to change the attitude toward cyberbullying (Garg *et al.*, 2021).

Previous researchers have developed and tested specific scales to measure the attitude toward cyberbullying (Barlett *et al.*, 2014; Barlett and Gentile, 2012; Boulton *et al.*, 2012; Doane *et al.*, 2016; Heirman and Walrave, 2012). Barlett and Gentile (2012) developed a nine-item scale to measure cyberbullying attitude. But the scale was later criticized for low internal consistency and outdated items. Heirman and Walrave (2012) proposed a four-item scale, but it was also criticized for the lack of construct validity indices (Cavalcanti *et al.*, 2019). Later, Doane *et al.*'s (2014) scale was also discouraged for the low internal consistency of items. After a deliberate review of the existing measures, Barlett *et al.* (2016a, b) developed a new scale that

addresses the fallibilities of previous scales. The scale was referred to as CBAS (Barlett *et al.*, 2016a, b). It has good internal reliability and concurrent and predictive validity. This nine-item self-reported CBAS scale has been developed taking into view the changing landscape of the virtual world, resulting in an updated, brief measure with good scale properties (Barlett *et al.*, 2016a, b). The scale measure two facets of cyberbullying: harmful cyberbullying attitudes (HCA; five items) and general cyberbullying characteristics (GCC; four items).

Barlett *et al.* (2016a, b) urged researchers to test the CBAS in culturally diverse settings for cross-cultural evidence. Consequently, Cavalcanti *et al.*, (2019) determined the psychometric properties of the CBAS in the Brazilian context and concluded it to be a valid and reliable measure. Thus, in a similar vein, the present study explored the reliability and validity of the CBAS among Indian college students with the help of two independent studies.

2. Study 1

2.1 Methodology

Study 1 examined the factorial validity of the CBAS among Indian college students. It evaluated the construct validity of CBAS using exploratory factor analysis (EFA) and confirmatory factor analysis (CFA) applied on two independent samples of college students.

2.1.1 Participants. An online survey using convenience sampling was undertaken to collect the data from a sample of 435 college students of Delhi Technological University (DTU) by sharing the questionnaire on their official email addresses. Table 1 shows the demographic information of the respondents. Male students were 225 (51.7%), and females were210 (48.2%). The age of students ranged between 17 and 31 years. Also, students registered in undergraduate, postgraduate and doctoral courses were 194 (44.6%), 187 (43%) and 54 (12.4%). Of the surveyed students, 187 (43.0) were enrolled in science courses, 154 (35.4%) in commerce (including management) courses and 94 (21.6%) in humanities courses.

2.1.2 Instruments. A structured questionnaire was used to collect the data. The first section assessed demographic information like gender, courses (science, commerce, or humanities) and education qualification (undergraduate, postgraduate, or doctoral). The second part of the questionnaire captured participants' bullying attitudes in cyberspace using CBAS developed by Barlett *et al.* (2016a, b). It is a positively coded nine-item scale that rates statements using a five-point rating scale, ranging from 1 (strongly disagree) to 5 (strongly agree). A few items on the scale are "It is fun to tease or make fun of others with offensive messages online" and "Harming others using electronic means is acceptable". Indian education system promotes English as one of the languages essential for students' academic and professional success in this globalized world. English is taught from the very beginning of the student's academic life. Thus, Indian students develop a good understanding of the language till they reach college to pursue their graduation and

Table 1. Demographic structure

Variables	Category	Study 1 Subsample 1	Study 1 Subsample 2	Study 2
Gender	Female	112	99	153
	Male	106	118	247
Course	Under-graduate	101	93	143
	Postgraduate	77	110	237
	PhD	40	14	20
Stream	Science	67	120	259
	Commerce (including Management)	103	51	72
	Humanities	48	46	69

Source(s): Primary Data

higher degrees (Garg and Mehak, 2021). Hence, the original English version of CBAS was used in this study.

2.1.3 Procedure. A short description of the study was provided to the participants, and their informed consent was taken. The anonymity of the participants was promised. Also, respondents were assured of strict academic use of data. They were also ensured that collected data would not be shared with any third party.

2.2 Data analysis

The sample of 435 was split into two subsamples using IBM SPSS split sample. Even responses were included in the first subsample ($n_1 = 218$), and odd responses were added in the second subsample ($n_2 = 217$). EFA was applied on the first subsample, and the second sample was used to check the model fit (using CFA) of the factorial structure derived from EFA. Before EFA, the Kaiser-Meyer-Olkin (KMO) test of sampling adequacy and Bartlett's test of sphericity were conducted to check the suitability of the first subsample for factor analysis. These tests, along with EFA, were performed using SPSS 21. The KMO test of sampling adequacy value was 0.832, which was greater than the threshold value of 0.70. Also, Bartlett's test of sphericity was significant at a 0.05 significance level. These results indicated the suitability of data for applying EFA. Subsequently, nine statements of CBAS were subjected to EFA using Principal Axis Factoring with Promax (Oblique) Rotation and Kaiser Normalization in IBM SPSS v21. EFA resulted in a two-component solution that explained 56.38% of the total variance. The results also reported that the factor loading of item 4 (I have no reservations about using technology to hurt others when they deserve it) was 0.461, and that of item 6 (school/colleges rules are inefficient for stopping cyberbullying) was 0.456, which were less than the minimum acceptable value of 0.50 (Hair *et al.*, 2003; Chao *et al.*, 2013; Maskey *et al.*, 2018). Thus, items 4 and 6 were discarded. The first factor comprised five statements and was referred to as a "hostile cyberbullying attitude (HCA)". The second factor consisted of two statements and was labeled as "general cyberbullying characteristics (GCC)". Table 2 presents factor loadings, commonalities (h^2), and the total variance explained by seven items of the CBAS scale in the Indian context.

No.	Statements	Loadings	h^2	Eigenvalues
Hostile cyberbullying attitudes (HCA)				
1	I feel good about attacking others online when they deserve it	0.564*	0.318	2.064
2	Harming others using electronic means is acceptable	0.643*	0.413	
3	Sending malicious electronic messages to others is less harmful than face-to-face communication	0.757*	0.573	
4	Attacking others online may be justified	0.501*	0.251	
5	Because I am not face-to-face with the other person when I'm online, I feel I can say what I want, even if it is evil and offensive	0.713*	0.508	
General cyberbullying characteristics (GCC)				
1	It is fun to tease or make fun of others with offensive messages online	0.893*	0.797	1.711
2	It is okay to send messages to or make offensive online posts about others	0.956*	0.914	
	Number of items		7	
	Eigenvalues		3.775	
	Explained Variance		56.38%	

Source(s): Primary Data, *Satisfactory Factor Loadings (i.e. greater than |0.5|.), h^2: Communalities

Table 2. Factorial structure of Indian CBAS

CFA was applied on the second subsample of 217 students to verify the two-component factor structure enumerated through EFA. According to Şimşek (2007), acceptable values of model fit indices are RMSEA < 0.08, SRMR ≤ 0.05, GFI ≥ 0.95 and CFI ≥ 0.97, and Xia and Yang (2018) and Bentler and Bonett (1980) have further recommended TLI as another model fit indices with an acceptable value of TLI > 0.90. The two-factored CBAS indicated satisfactory values with RMSEA = 0.058, SRMR = 0.0310, GFI = 0.972, CFI = 0.983 and TLI = 0.973. Also, the $\chi^2 = 23.546$, df = 13 and value of p of the model is less than 0.05 ($p = 0.036$). Figure 1 shows the results of the CFA model of CBAS in the Indian context. The results of EFA and CFA recommended adequate factorial validity of two-factored seven-item CBAS among Indian students, which is in accordance with the recommendations of previous studies conducted by Barlett *et al.* (2016a, b) and Cavalcanti *et al.* (2019). Subject to further reliability and validity study, this two-factored scale may be referred to as Indian CBAS.

3. Study 2

3.1 Methodology

Study 2 explored the reliability of Indian CBAS using Cronbach's (Cronbach and Shavelson, 2004) alpha and composite reliability (CR) values. It also examined the convergent, discriminant and construct validity of the two-factored seven-item CBAS in the Indian context.

3.1.1 Participants. An online survey based on convenience sampling was conducted to collect the data from 400 college students of DTU. There were 225 (56.3%) male students and 175 (43.7%) female students, of which 143 belonged to undergraduate, 237 were from postgraduate and 20 were from doctoral courses. Also, out of these 400 students, 259 belonged to science, 72 were from commerce (including management) and 69 were from

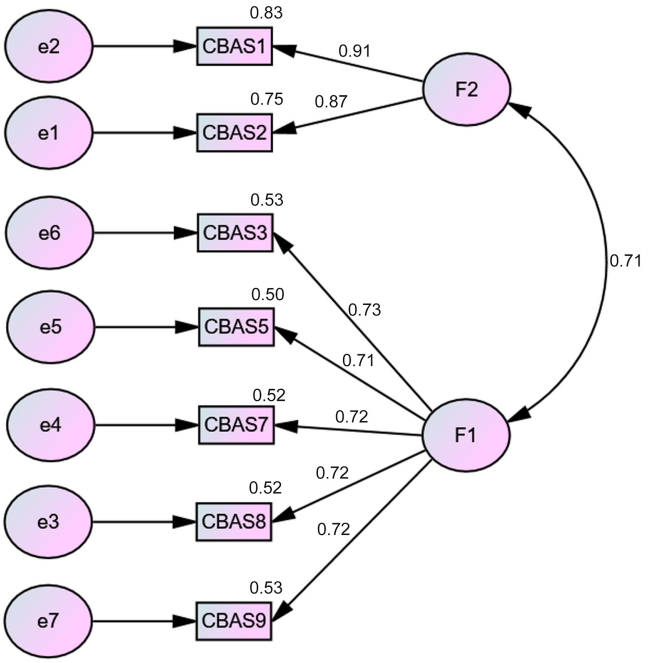

Source(s): Primary Data

Figure 1.
Factorial structure of Indian CBAS

humanities courses. Table 1 also summarizes the demographic information of this sample.

3.1.2 Instruments. The data were collected using a structured questionnaire comprising five sections. The first section contained the participants' demographic details (gender, course and education level). The second section consisted of the Indian CBAS scale derived from study 1. It is comprised of seven items rated on a five-point rating scale.

3.1.3 Scales used for comparison. 3.1.3.1 Weight-based teasing scale. In the third section, Eisenberg *et al.*'s (2003) Weight-Based Teasing Scale (WBTS) was used to measure the teasing-based victim feeling among the participants. It is a five-item scale that captures one's feelings on a five-point rating scale ranging from 0 (never) to 4 (at least once a week). A few statements of the scale are "you are treated with less respect than other people" and "you are called names or insulted".

3.1.3.2 Gratitude Questionnaire 6. The fourth section captured respondents' experience of gratitude using McCullough *et al.*'s (2002) Gratitude Questionnaire 6 (GQ-6) scale. It is a six-item scale that rates gratitude on a seven-point rating scale ranging from 1 (strongly disagree) to 7 (strongly agree). It consists of statements like "I have so much in life to be thankful for" and "I am grateful to a wide variety of people".

3.1.3.3 PhQ-9. Lastly, the PhQ-9 questionnaire was used to access the depression symptoms among the participants. The scale was developed by Kroenke *et al.* (2001). It is a nine-item scale that assesses one's proneness to develop depression on a four-point rating scale ranging from 0 (not at all) to 3 (nearly every day). A few scale statements are "Little interest or pleasure in doing things" and "Poor appetite or overeating". Though initially developed for patients, the validity and reliability of the scale on college and school students were tested, proved and recommended by Tsai *et al.* (2014).

We used WBTS as a good convergent indicator because the study conducted on cyberbullying by Cavalcanti *et al.* (2019) suggests a positive correlation between various forms of bullying and cyberbullying in Brazil, but they did not test the correlation between weight-based teasing and cyberbullying. Furthermore, the study conducted by Jolliffe *et al.* (2019) also suggests psychological disorders, especially depressive symptoms, as the outcome of the crime. Moreover, the jail records and studies conducted on the inmates of Tihar Jail, New Delhi, second the recommendations of Jolliffe *et al.* (2019), as these records and studies have shown depressive symptoms as the result of offending in the inmates of Tihar Jail, New Delhi (Jolliffe *et al.*, 2019; Vipassana Research Institute, 2000).

3.1.4 Procedure. As a standard practice, the respondents were informed about the study's purpose and were assured anonymity and strict academic use of data. Informed consent was also taken from the participants. The reliability of the seven-item Indian CBAS was verified with the help of Cronbach's alpha (Cronbach and Shavelson, 2004) (CA) and CR values. The average variance extracted (AVE) values were used to assess the convergent validity of the Indian version of CBAS. The acceptable value of CA (Cronbach and Shavelson, 2004) and CR is 0.70 (George and Mallery, 2003), and that of AVE is 0.50 (Fornell and Larcker, 1981). The Fornell and Larcker (1981) testing system was used to judge the discriminant validity. Also, the criterion validity of the Indian CBAS was explored by examining the correlation coefficients between the Indian CBAS, WBTS, GQ-6 and PhQ-9 scores. The values and correlation coefficients of the CA (Cronbach and Shavelson, 2004) were determined using SPSS 21. The CR and AVE values were calculated with the help of the below-mentioned formulas.

$$\mathrm{CR} = \frac{\sum \boldsymbol{\lambda i^2}}{\sum \boldsymbol{\lambda i^2} + \sum \left(\mathbf{1} - \boldsymbol{\lambda i^2}\right)} \tag{1}$$

$$\text{AVE} = \frac{\sum \lambda i^2}{N} \quad (2)$$

where λ represents standardized factor loadings for items and N represents the number of items in a factor.

3.2 Data analysis

The results suggested that CA (Cronbach and Shavelson, 2004) values of the Indian CBAS, HCA, and GCC were 0.889, 0.871 and 0.858, respectively. The CR values for Indian CBAS, HCA and GCC were 0.91, 0.84 and 0.88, respectively. These values concluded the reliability of the seven-item CBAS in the Indian context. The AVE values for Indian CBAS, HCA and GCC were 0.60, 0.52 and 0.79, respectively. These scores confirmed the convergent validity of the scale. According to Fornell and Larcker's (1981) testing system, the squared correlation of the factors should be less than their AVE values to establish discriminate scale validity. Table 3 reported that AVE values were greater than squared correlations of factors, which confirmed the discriminant validity of two-factored Indian CBAS. The correlation coefficients between the scores of CBAS in the Indian context, WBTS, GQ-6 and PhQ-9 were calculated. Respondents with high cyberbullying attitudes are more likely to positively correlate with teasing and depression attitudes. Respondents with high cyberbullying attitudes are also likely to have lower gratitude levels. The results of the study revealed that WBTS scores were positively correlated with Indian CBAS ($r = 0.362$, $p < 0.01$), HCA ($r = 0.331$, $p < 0.01$) and GCC ($r = 0.304$, $p < 0.01$). Similarly, scores of PhQ-9 were also positively correlated with Indian CBAS scores ($r = 0.411$, $p < 0.01$), HCA ($r = 0.334$, $p < 0.01$) and GCC ($r = 0.301$, $p < 0.01$). In addition, GQ-6 negatively correlated with Indian CBAS scores ($r = -0.136$, $p < 0.01$) and HCA ($r = -0.172$, $p < 0.01$) and GCC ($r = -0.142$, $p < 0.01$). Table 4 reports the correlation matrix of various variables of the study. These values recommended the convergent validity of Indian CBAS.

4. Discussion

There is an exponential rise in the proliferation of technology and technology-enabled devices among Indians. They often use information and communication technologies (ICT) for

Table 3. Fornell and Larcker testing system (FLTS)

Variables	Factor 1	Factor 2
HCA	1 *(0.52)*	
GCC	0.24	1 *(0.79)*

Source(s): Primary Data, AVE values in italic

Table 4. Correlation matrix

Scales	CBAS	HCA	GCC	WBTS	GQ-6	PhQ-9
CBAS	1					
HCA	0.978	1				
GCC	0.843	0.714	1			
WBTS	0.362	0.331	0.304	1		
GQ-6	−0.136	−0.172	−0.142	−0.152	1	
PhQ-9	0.411	0.334	0.301	0.398	−0.172	1

Source(s): Primary Data, CBAS = Cyberbullying Attitude Scale, WBT = Weight-Based Teasing Scale

academic, entertainment, social and employment purposes (Bhat *et al.*, 2017). The ongoing COVID-19 pandemic has further accelerated the rate of technology adoption by professionals, employees, homemakers, retired personnel and students. Researchers have also listed various other factors that resulted in the digital penetration of Indian villages and hamlets. These reasons include a spike in social media and OTT platforms, dwindling costs of technology and devices, online courses and employment opportunities, etc. With the large-scale technology adoption by Indians, the challenge of cyberbullying has also spiked in recent times. The majority of Indians are first-generation users of ICT devices. Thus, they find themselves ill-equipped while confronting cyberbullying. Since it is a recent phenomenon, they hardly get any support from their previous generations. Also, a lack of orientation regarding cyberbullying during student and employment life makes it difficult for Indians to react to cyberbullying appropriately. It also leads to the unintentional indulgence of an individual in bullying others in online modes.

In addition, victims of cyberbullying generally face social stigma in societies like India. Victims become a laughing stock, so they avoid disclosing such events. The situation further aggravates owing to inadequate and poorly published legal provisions. Indian IT laws are heavily criticized for being incompetent and too complex to comprehend by a commoner. Also, local law enforcement agencies do not have adequate IT infrastructure and skills to arrest the culprit. These pathetic situations encourage us to understand cyberbullying in the Indian context comprehensively. The first and foremost step in the holistic understanding of a social phenomenon is the availability of a reliable and valid scale to measure it.

Accordingly, this study is aimed to explore and document the psychometric properties of CBAS in the Indian milieu. Therefore, two separate studies were carried out with independent samples of college students. The results evinced a two-factor structure similar to Barlett *et al.*'s (2016a, b) study. For study 1, the sample was bifurcated into two subsamples. EFA was carried out for the first subsample. Before applying EFA, we explored the KMO test of sampling adequacy and Bartlett's test of sphericity. The data were appropriate for using EFA because the values of the KMO (0.832) and Bartlett's test of sphericity at 0.05 significance level indicated the stability of the data. EFA revealed a seven-item, two-component model of CBAS. Items number 4 and 6 were excluded owing to inadequate factor loading. Our beliefs and values are based on the principle of "सर्वजन हिताय, सर्वजन सुखाय" (meaning – welfare to all, happiness to all) stops us from being deliberately indulged in criminal activities like cyberbullying. Hence, this may be one of the possibilities behind this result. Since the sample consisted of college students, this result could be due to students' incredulity regarding the effectiveness of rules and regulations laid down by educational institutions in preventing and tackling cyberbullying. Further, cyberbullying is not restricted to educational institutions; thus, any rules drafted by colleges are bound to be ineffective in eliminating cyberbullying among students. It was also observed that one statement (attacking others online may be justified) was part of the GCC factor in the original CBAS; however, this statement moved to the HCA factor in the Indian version of CBAS. It looked justified as the stated statement is more about a hostile attitude, wherein respondents consider attacking others as justified. This seven-item scale was subjected to CFA to confirm the factorial validity of the revised scale. Adequate model fit indices concluded the factorial validity of the seven-item CBAS scale, referred to as Indian CBAS, in the Indian context.

The second study evaluated the reliability, convergent, discriminant and criterion validity of the Indian CBAS. Adequate values (greater than 0.70) of CA (Cronbach and Shavelson, 2004) and CR suggested the internal consistency reliability of the Indian CBAS. In addition, all AVEs values were more significant than 0.05, which confirmed the convergent validity. The criterion validity was adjudged using correlation coefficients of the Indian CBAS with WBTS, GQ-6 and PhQ-9 scales. As expected theoretically, positive linkages were established in the Indian CBAS and WBTS and PhQ-9. The results also concluded a statistically significant negative correlation between Indian CBAs and GQ-6. These results recommended acceptable criterion validity of a

two-factor, seven-item CBAS scale among Indian students. The overall findings of the present study provide significant insights into the psychometric properties of CBAS in the Indian context and are in line with the original study and subsequent validation of the Brazilian sample (Barlett *et al.*, 2016a, b; Cavalcanti *et al.*, 2019). Psychometric properties present crucial information on the meaningfulness, appropriateness and usefulness in a particular context. From this standpoint, the current study has validated the CBAS, which befits the country's context.

5. Implementations

As there exists a void for a reliable and valid scale to measure the cyberbullying attitude among Indian college students, validating CBAS in the Indian context is one step toward filling this gap. Further, the scale will help the researchers correlate cyberbullying attitudes with variables like substance abuse, revenge and moral disengagement. Finally, the insights from the study will add to the available literature, as little literature exists on cyberbullying in the Indian context. The adoption of this scale will open a dimension of opportunities for the stakeholders like psychologists and teachers to assess the bullying attitude of students, which would help develop and deploy effective countermeasures against cyberbullying. For instance, the scale can be used during admissions in schools or colleges or by recruiters while recruiting employees. This scale will help the admission officer or recruiter determine the candidate's cyberbullying attitude. Hence, a vigil can be set on a person with a cyberbullying attitude if admitted/recruited. Also, counseling or a seminar can be arranged to sensitize the candidate to cyberbullying intentions regarding the negative consequences to the victim and the dire repercussions to the bully. The seminar or workshops can further help modify the beliefs supporting aggression, especially cyberbullying (Ang, 2015). These policy interventions can further detail the correct procedure(s) to report cyberbullying and the person to be contacted if any individual requires help quitting cyberbullying. Educational institutions may expand their policies to start anti-cyberbullying programs and educate students. In India, volunteers of the National Service Scheme (NSS) or policymakers may collaborate with educational institutions to spread awareness regarding cyberbullying and its consequences for both victims and bullies.

6. Limitations

Although the present study offers exciting findings, it has certain limitations too. First, the current study is based on a sample of students. Since previous studies have suggested significant generation-based variations in techno-ethical orientation, the findings of the present study must be validated among respondents of different generations. Also, future researchers can focus on validating the scale on other target groups based on occupation, age, or socio-economic factors. Second, only internal consistency reliability has been assessed in this study. Future scholars may explore inter-rater or test-retest reliability. Further, it would also be interesting to examine cyberbullying attitudes in association with other variables such as psychological well-being, distress, aggressive behaviors, etc.

7. Summary

In summary, the current study has validated the CBAS in Indian college students. The Indian version of the scale differs from the original version in two ways. First, the Indian CBAS comprised seven statements, while the original CBAS consisted of nine items. Second, in the original CBAS, HCA and GCC contained five and four statements, respectively. However, in Indian CBAS, they comprised five and two statements, respectively. In a nutshell, seven-item CBAS proves to be a valid and reliable instrument in the Indian context and should be used without any trepidation.

References

Ang, R.P. (2015), "Adolescent cyberbullying: a review of characteristics, prevention and intervention strategies", *Aggression and Violent Behavior*, Vol. 25, pp. 35-42, doi: 10.1016/j.avb.2015.07.011.

Barlett, C.P. (2015), "Predicting adolescent's cyberbullying behavior: a longitudinal risk analysis", *Journal of Adolescence*, Academic Press, Vol. 41, pp. 86-95.

Barlett, C.P. and Gentile, D.A. (2012), "Attacking others online: the formation of cyberbullying in late adolescence", *Psychology of Popular Media Culture*, American Psychological Association (APA), Vol. 1 No. 2, pp. 123-135.

Barlett, C.P., Gentile, D.A., Anderson, C.A., Suzuki, K., Sakamoto, A., Yamaoka, A. and Katsura, R. (2014), "Cross-cultural differences in cyberbullying behavior: a short-term longitudinal study", *Journal of Cross-Cultural Psychology*, Vol. 45 No. 2, pp. 300-313.

Barlett, C.P., Gentile, D.A. and Chew, C. (2016a), "Predicting cyberbullying from anonymity", *Psychology of Popular Media Culture*, American Psychological Association (APA), Vol. 5 No. 2, pp. 171-180.

Barlett, C.P., Helmstetter, K. and Gentile, D.A. (2016b), "The development of a new cyberbullying attitude measure", *Computers in Human Behavior*, Pergamon, Vol. 64, pp. 906-913.

Barragán Martín, A.B., Molero Jurado, M.D.M., Pérez-Fuentes, M.D.C., Simón Márquez, M.D.M., Martos Martínez, F., Sisto, M. and Gázquez Linares, J.J. (2021), "Study of cyberbullying among adolescents in recent years: a bibliometric analysis", *International Journal of Environmental Research and Public Health*, Vol. 18 No. 6, p. 3016, doi: 10.3390/ijerph18063016.

Bentler, P.M. and Bonett, D.G. (1980), "Significance tests and goodness of fit in the analysis of covariance structures", *Psychological Bulletin*, Vol. 88 No. 3, pp. 588-606, doi: 10.1037/0033-2909.88.3.588.

Bernardo, A.B.I., Mendoza, N.B., Simon, P.D., Cunanan, A.L.P., Dizon, J.I.W.T., Tarroja, M.C.H., Balajadia-Alcala, M.A. and Saplala, J.E.G. (2020), "Coronavirus pandemic anxiety scale (CPAS-11): development and initial validation", *Current Psychology*, Vol. 41 No. 8, pp. 5703-5711, doi: 10.1007/s12144-020-01193-2.

Bevilacqua, L., Shackleton, N., Hale, D., Allen, E., Bond, L., Christie, D., Elbourne, D., Fitzgerald-Yau, N., Fletcher, A., Jones, R., Miners, A., Scott, S., Wiggins, M., Bonell, C. and Viner, R.M. (2017), "The role of family and school-level factors in bullying and cyberbullying: a cross-sectional study", *BMC Pediatrics*, Vol. 17 No. 1, doi: 10.1186/s12887-017-0907-8.

Bhat, S.K., Pande, N. and Ahuja, V. (2017), "Virtual team effectiveness: an empirical study using SEM", *Procedia Computer Science*, Vol. 122, pp. 33-41, doi: 10.1016/j.procs.2017.11.338.

Blinkhorn, V., Lyons, M. and Almond, L. (2016), "Drop the bad attitude! Narcissism predicts acceptance of violent behaviour", *Personality and Individual Differences*, Pergamon, Vol. 98, pp. 157-161.

Boulton, M., Lloyd, J., Down, J. and Marx, H. (2012), "Predicting undergraduates' self-reported engagement in traditional and cyberbullying from attitudes", *Cyberpsychology, Behavior, and Social Networking*, Vol. 15 No. 3, pp. 141-147.

Cavalcanti, J.G., de Lima Pinto, A.V., Pimentel, C.E. and de Melo, L.M.F. (2019), "Psychometric parameters of the cyberbullying attitude scale in Brazil", *Current Psychology*, Springer, Vol. 40 No. 8, pp. 3897-3907.

Chadda, R.K. and Deb, K. (2013), "Indian family systems, collectivistic society and psychotherapy", *Indian Journal of Psychiatry*, Vol. 55 No. 6, p. 299, doi: 10.4103/0019-5545.105555.

Chan, T.K.H., Cheung, C.M.K. and Wong, R.Y.M. (2019), "Cyberbullying on social networking sites: the crime opportunity and affordance perspectives", *Journal of Management Information System*, Vol. 36 No. 2, pp. 574-609.

Chan, T.K.H., Cheung, C.M.K. and Lee, Z.Y.H. (2021), "Cyberbullying on social networking sites: a literature review and future research directions", *Information and Management*, Vol. 58 No. 2, pp. 1-16.

Chao, C.C., Lirn, T.C. and Shang, K.C. (2013), "Market segmentation of airline cargo transport", *The Service Industries Journal*, Vol. 33 Nos 15-16, pp. 1672-1685, doi: 10.1080/02642069.2011.638920.

Chen, L., Wang, Y., Yang, H. and Sun, X. (2020), "Emotional warmth and cyberbullying perpetration attitudes in college students: mediation of trait gratitude and empathy", *PLoS One*, Vol. 15 No. 7, e0235477, doi: 10.1371/journal.pone.0235477.

Doane, A.N., Pearson, M.R. and Kelley, M.L. (2014), "Predictors of cyberbullying perpetration among college students: an application of the Theory of Reasoned Action", *Computers in Human Behavior*, Pergamon, Vol. 36, pp. 154-162.

Cronbach, L.J. and Shavelson, R.J. (2004), "My current thoughts on coefficient alpha and successor procedures", *Educational and Psychological Measurement*, Vol. 64 No. 3, pp. 391-418.

Doane, A.N., Kelley, M.L., Chiang, E.S. and Padilla, M.A. (2016), "Development of the cyberbullying experiences survey", *Emerging Adulthood*, SAGE Publications, Vol. 1 No. 3, pp. 207-218.

Eisenberg, M.E., Neumark-Sztainer, D. and Story, M. (2003), "Associations of weight-based teasing and emotional well-being among adolescents", *Archives of Pediatrics and Adolescent Medicine*, Vol. 157 No. 8, p. 733, doi: 10.1001/archpedi.157.8.733.

Farrington, D.P. (1993), "Understanding and preventing bullying", *Crime and Justice*, University of Chicago Press, Vol. 17, pp. 381-458.

Farrington, D.P. (2011), "Effectiveness of school-based programs to reduce bullying: a systematic and meta-analytic review", *Journal of Experimental Criminology*, Vol. 7 No. 1, pp. 27-56, doi: 10.1007/s11292-010-9109-1.

Fornell, C. and Larcker, D.F. (1981), "Evaluating structural equation models with unobservable variables and measurement error", *Journal of Marketing Research*, Vol. 18 No. 1, pp. 39-50, doi: 10.1177/002224378101800104.

Garg, N., Katiyar, N. and Mehak (2021), "Gratitude questionnaire (GQ-6)—exploring psychometric properties in India", *Journal of Religion and Health*, Vol. 60 No. 5, pp. 3716-3731, doi: 10.1007/s10943-021-01419-y.

Garg, N. and Mehak (2021), "Gratitude resentment and appreciation scale (GRAT-16): analyzing psychometrics properties in the Indian context", *Current Psychology*. doi: 10.1007/s12144-021-02169-6.

Garg, N., Verma, S. and Palframan, J.T. (2022), "Positive reframing as a mediator between gratitude and technostress amongst Indian students during the COVID-19 pandemic", *Kybernetes*, doi: 10.1108/k-12-2021-1250 (In press).

Gautam, K. (2020), "Threats of ragging in higher educational institutions in India", *Parishodh Journal*, Vol. 9 No. 1, pp. 437-448.

George, D. and Mallery, P. (2003), *Reliability and Validity Assessment*, Sage, Thousand Oaks, CA.

Glasman, L.R. and Albarracín, D. (2006), "Forming attitudes that predict future behavior: a meta-analysis of the attitude-behavior relation", *Psychological Bulletin*, Vol. 132 No. 5, pp. 778-822.

Gönültaş, M. (2022), "Cyber bullying and victimization among university students", *International Journal of Psychology and Educational Studies*, Vol. 9 No. 2, pp. 297-307, doi: 10.52380/ijpes.2022.9.2.441.

Hair, J., Money, A., Samouel, P. and Babin, B. (2003), *Essentials of Business Research Methods*, 1st ed., Wiley, New Jersey.

Hashemi, A. (2021), "Effects of COVID-19 on the academic performance of Afghan students' and their level of satisfaction with online teaching", *Cogent Arts and Humanities*, Vol. 8 No. 1, doi: 10.1080/23311983.2021.1933684.

Heirman, W. and Walrave, M. (2012), "Predicting adolescent perpetration in cyberbullying: an application of the theory of planned behavior", *Psicothem*, Vol. 24 No. 4, pp. 614-620.

Hill, R.J. (1990), "Attitudes and behavior", in Rosenberg, M. and Turner, R.H. (Eds), *Social Psychology: Sociological Perspectives*, Routledge, Vol. 1, doi: 10.4324/9781315129723.

Huang, Y.Y. and Chou, C. (2010), "An analysis of multiple factors of cyberbullying among junior high school students in Taiwan", *Computers in Human Behavior*, Pergamon, Vol. 26 No. 6, pp. 1581-1590.

Hutson, E., Kelly, S. and Militello, L.K. (2017), "Systematic review of cyberbullying interventions for youth and parents with implications for evidence-based practice", *Worldviews on Evidence-Based Nursing*, Vol. 15 No. 1, pp. 72-79, doi: 10.1111/wvn.12257.

Jain, A. (2018), "Workplace bullying in India: the current policy context, implications and future directions", *Indian Perspectives on Workplace Bullying*, pp. 237-263, doi: 10.1007/978-981-13-1017-1_9.

Jain, O., Gupta, M., Satam, S. and Panda, S. (2020), "Has the COVID-19 pandemic affected the susceptibility to cyberbullying in India?", *Computers in Human Behavior Reports*, Elsevier, Vol. 2, 100029.

Jolliffe, D., Farrington, D.P., Brunton-Smith, I., Loeber, R., Ahonen, L. and Palacios, A.P. (2019), "Depression, anxiety and delinquency: results from the pittsburgh youth study", *Journal of Criminal Justice*, Vol. 62, pp. 42-49, doi: 10.1016/j.jcrimjus.2018.08.004.

Kraus, S.J. (1995), "Attitudes and the prediction of behavior: a meta-analysis of the empirical literature", *Personality and Social Psychology Bulletin*, Sage Publications: Thousand Oaks, CA, Vol. 21 No. 1, pp. 58-75.

Kroenke, K., Spitzer, R.L. and Williams, J.B.W. (2001), "The PHQ-9", *Journal of General Internal Medicine*, Vol. 16 No. 9, pp. 606-613, doi: 10.1046/j.1525-1497.2001.016009606.x.

Larrañaga, E., Yubero, S. and Navarro, R. (2018), "Parents' responses to coping with bullying: variations by adolescents' self-reported victimization and parents' awareness of bullying involvement", *Social Sciences*, Vol. 7 No. 8, p. 121, doi: 10.3390/socsci7080121.

Madhukalya, A. (2020), "India's internet consumption up during Covid-19 lockdown, shows data", Hindustan Times, available at: https://www.hindustantimes.com/india-news/india-s-internet-consumption-up-during-covid-19-lockdown-shows-data/story-ALcov1bP8uWYO9N2TbpPlK.html (accessed 16 January 2022).

Maheshwari, R. (2020), "Cyberbullying of Indian teenagers and women rose by 36% while conviction rates fell in 2017-'18", Scroll, available at: https://scroll.in/article/956085/in-one-year-alone-cyberbullying-of-indian-women-and-teenagers-rose-by-36 (accessed 15 January 2022).

Maskey, R., Fei, J. and Nguyen, H.O. (2018), "Use of exploratory factor analysis in maritime research", *The Asian Journal of Shipping and Logistics*, Vol. 34 No. 2, pp. 91-111, doi: 10.1016/j.ajsl.2018.06.006.

McCarthy, N. (2018), "New report: cyberbullying is most prevalent in India", Forbes, available at: https://www.forbes.com/sites/niallmccarthy/2018/10/29/new-report-cyberbullying-is-most-prevalent-in-india-infographic/?sh=6c5e91547537 (accessed 15 January 2022).

McCullough, M.E., Emmons, R.A. and Tsang, J.A. (2002), "The grateful disposition: a conceptual and empirical topography", *Journal of Personality and Social Psychology*, Vol. 82 No. 1, pp. 112-127, doi: 10.1037/0022-3514.82.1.112.

Medical Council of India (2018), "Medical Council of India (prevention and prohibition of ragging in medical colleges/institutions) regulations, 2009", Nmc (MCI-34(1)/2009-Med./25453), NMC, available at: https://www.nmc.org.in/wp-content/uploads/2017/10/Anti-Ragging-Regulation-1.pdf (accessed 28 September 2022).

Newall, M. (2018), "Cyberbullying: a global advisor survey", in *IPSOS*, IPSOS, available at: https://www.ipsos.com/sites/default/files/ct/news/documents/2018-06/cyberbullying_june2018.pdf

Olweus, D. (2013), "School bullying: development and some important challenges", *Annual Review of Clinical Psychology*, Vol. 9 No. 1, pp. 751-780, doi: 10.1146/annurev-clinpsy-050212-185516.

Pearce, N., Cross, D., Monks, H., Waters, S. and Falconer, S. (2011), "Current evidence of best practice in whole-school bullying intervention and its potential to inform cyberbullying interventions", *Australian Journal of Guidance and Counselling*, Vol. 21 No. 1, pp. 1-21, doi: 10.1375/ajgc.21.1.1.

Reyna, V.F. and Farley, F. (2006), "Risk and rationality in adolescent decision making", *Psychological Science in the Public Interest*, Vol. 7 No. 1, pp. 1-44, doi: 10.1111/j.1529-1006.2006.00026.x.

Sandhu, D. and Kaur, K. (2022), "Cyberbullying and online negative experiences of school and college students in India", in *Understanding Psychology in the Context of Relationship, Community, Workplace and Culture*, pp. 121-140, doi: 10.1007/978-981-19-2693-8_8.

Sayeed, A., Rahman, M.H., Hassan, M.N., Christopher, E., Kundu, S., Banna, M.H.A., Hasan, A.R., Mallick, T., Meem, A.E. and Hasan, M.T. (2021), "Problematic internet use associated with depression, health, and internet-use behaviors among university students of Bangladesh: a cross-sectional study", *Children and Youth Services Review*, Vol. 120, 105771, doi: 10.1016/j.childyouth.2020.105771.

Shah, S. and Nakhat, P. (2018), "Parent child relationship of Indian students and suggestive techniques", *International Journal of Indian Psychology*, Vol. 6 No. 2, pp. 12-20, DIP:18.01.102/20180602, doi: 10.25215/0602.102.

Sharma, D., Kishore, J., Sharma, N. and Duggal, M. (2017), "Aggression in schools: cyberbullying and gender issues", *Asian Journal of Psychiatry*, Elsevier Science B.V., Vol. 29, pp. 142-145.

Şimşek, Ö.F. (2007), *Introduction to Structural Equation Modeling*, Ekinoks Publishing, Ankara.

Slonje, R. and Smith, P.K. (2008), "Cyberbullying: another main type of bullying?", *Scandinavian Journal of Psychology*, John Wiley & Sons, Vol. 49 No. 2, pp. 147-154.

Slonje, R., Smith, P.K. and Frisén, A. (2013), "The nature of cyberbullying, and strategies for prevention", *Computers in Human Behavior*, Pergamon, Vol. 29 No. 1, pp. 26-32.

Smith, P.K. (2016), "Bullying: definition, types, causes, consequences and intervention", *Social and Personality Psychology Compass*, John Wiley & Sons, Vol. 10 No. 9, pp. 519-532.

Tsai, F.J., Huang, Y.H., Liu, H.C., Huang, K.Y., Huang, Y.H. and Liu, S.I. (2014), "Patient health questionnaire for school-based depression screening among Chinese adolescents", *Pediatrics*, Vol. 133 No. 2, pp. e402-e409, doi: 10.1542/peds.2013-0204.

University Grants Commission::Ragging Related Circulars (2009), available at: https://www.ugc.ac.in/page/ragging-related-circulars.aspx (accessed 28 September 2022).

Verma, S. and Garg, N. (2022), "Exploring intergenerational differences in technology-oriented ethical behavior", *Kybernetes*, Vol. ahead-of-print No. ahead-of-print, doi: 10.1108/K-09-2021-0897.

Verma, S., Garg, N. and Arumugam, T. (2022), "Being ethically resilient during COVID-19: a cross-sectional study of Indian supply chain companies", *The International Journal of Logistics Management*, Vol. ahead-of-print No. ahead-of-print, doi: 10.1108/ijlm-05-2022-0203.

Vipassana Research Institute (2000), "Research paper on inmates of tihar jail, Delhi | Vipassana research institute. vridhamma.org", available at: https://www.vridhamma.org/research/Research-Paper-on-Inmates-of-Tihar-Jail-Delhi (accessed 9 May 2022).

Waasdorp, T.E. and Bradshaw, C.P. (2015), "The overlap between cyberbullying and traditional bullying", *Journal of Adolescent Health*, Elsevier, Vol. 56 No. 5, pp. 483-488.

Xia, Y. and Yang, Y. (2018), "RMSEA, CFI, and TLI in structural equation modeling with ordered categorical data: the story they tell depends on the estimation methods", *Behavior Research Methods*, Vol. 51 No. 1, pp. 409-428, doi: 10.3758/s13428-018-1055-2.

Zhu, C., Huang, S., Evans, R. and Zhang, W. (2021), "Cyberbullying among adolescents and children: a comprehensive review of the global situation, risk factors, and preventive measures", *Frontier in Public Health*, Vol. 9, 634909, doi: 10.3389/fpubh.2021.634909.

Further reading

Bartlett, J.E. and Bartlett, M.E. (2011), "Workplace bullying: an integrative literature review", *Advances in Developing Human Resources*, SAGE PublicationsSage CA: Los Angeles, CA, Vol. 13 No. 1, pp. 69-84.

Weston, R. and Gore, P.A. (2016), "A brief guide to structural equation modeling", *The Counseling Psychologist*, Sage PublicationsSage CA: Thousand Oaks, CA, Vol. 34 No. 5, pp. 719-751.

Corresponding author
Naval Garg can be contacted at: naval.garg@dtu.ac.in

For instructions on how to order reprints of this article, please visit our website:
www.emeraldgrouppublishing.com/licensing/reprints.htm
Or contact us for further details: **permissions@emeraldinsight.com**

Fake News Detection via Graph-Based Markov Chains

Shashank Parmar
Department of Software Engineering
Delhi Technological University
New Delhi, India
parmarshashank11@gmail.com

Shashank Taneja
Department of Software Engineering
Delhi Technological University
New Delhi, India
shashanktaneja72@gmail.com

Rahul
Department of Software Engineering
Delhi Technological University
New Delhi, India
Rahul@dtu.ac.in

Abstract

Social media platforms have seen a major boom in the past decade. Apart from entertainment and establishing social connections, the use of social media to read news articles has become prevalent. News has not only become less costly but also fast and accessible. However, accessing news via social media has its own demerits. It is next to impossible for the end users to establish the validity of the news articles. Manual review of each and every article on the internet is neither quick nor economically feasible, considering the vast amount of news articles that are published on day-to-day basis. Hence, there arises a need for quick and highly accurate machine learning models to detect the fake news articles. In this paper, we propose a method to detect fake news via Graph based Markov chains. We initiate the classification process by first segregating the fake news articles from the real ones, then training two separate Markov Chains for both the classes, and finally calculating the probability that a news article was generated by a given Markov Chain. Our approach of establishing similarity between a text sequence and a Markov chain relies on probabilistic and statistical calculations, attained by performing random walks on the Markov chains. Such an approach has proven to provide a high accuracy on multiple datasets.

Keywords: Markov Chains, Fake news detection Online social media, Supervised Learning, Hidden Markov Model

1. Introduction

Fake news is often a result of clever wordplay. Fake news detection algor[1]ithms often recognise each word as a feature. Such techniques fail to recognise clever wordplays as they do not give any weightage to the structure of the sentence [1], [2], [3], [4], [5], [6].

E.g.: let us consider a real news, S_1, "The government increased the taxation on petrol even though global prices have decreased by a huge margin". Now consider a fake news, S_2, "The government decreased the taxation on petrol even though global prices have increased by a huge margin". The Bag of Words and the TF-IDF representation of the sentences S_1 and S_2 would be identical [1], [2], [3], [4], [5], [6]. Hence, a machine learning algorithm that makes use of such representations would fail to distinguish between these two sentences. Such cases promote the need of a machine learning model that not only has high accuracy but also gives weightage to the sentence structure.

Markov chains [7], [8], [9], [10], [11], [12], [13] give immense weightage to sentence structures. A hidden Markov model [12],[13] works on the assumption that a future state depends only on the current state and not any state before that. Each node in a Markov chain leads to a set of words that occurred after it in the training dataset. Such a construction makes wordplay detection easier.

Traditionally Hidden Markov Model (HMM) [12] based classification schemes function by training a

[1] Corresponding Author: Shashank Parmar, parmarshashank11@gmail.com, address: C-3/181, Yamuna Vihar, Delhi – 110053, India

single Hidden Markov Model for each class [14]. Then these HMMs are used to calculate class-conditional densities via the Bayes Classification paradigm. Then the sequence is classified upon which class-based Markov model would have most likely generated that sequence. Such a rule is known as maximum-likelihood (ML) classification rule [14].

The issue with such a Markov model-based classification is that it works upon the Bayes Classification paradigm [14]. This limits the model's ability to take into consideration only the word frequencies and not the actual order of words. In this paper, we have proposed a new methodology of determining the likelihood that a sequence would have been generated by a given Markov model. This scheme takes into consideration the sentence structure, instead of just the word frequencies.

We have performed our experimentational work on the "Fake News" dataset from Kaggle [15] and the ISOT fake news dataset [16], [17]. We have then verified the results of our experiments on the WellFake dataset [18]. We have also compared our results with other previously published results [19], [20], [21].

2. Literature Survey

The literature regarding similarity-based classification is scarce. However, in the recent years Markov model and graph-based classification techniques have been quite popular. One of the first research works in this field was carried out by Martin Szummer and Tommi Jaakkola, who applied Markov models to perform classification. They made use of K-nearest neighbour (KNN) to define edges of an object with its neighbours. They then performed random walk on the data to classify the unlabelled data points [22]. Their research was further improved by Zhu et al. who introduced Gaussian Fields and Harmonic Functions to classify the unlabelled data [23]. Based on the research work by Zhu et al. Zhou at al. proposed a global and local consistency method based on the intuition of spreading activation networks [24]. Fei Wang and Changshui Zhang made further improvements by introducing a novel graph based semi supervised learning approach. They made use of neighbourhood information of objects. Their approach works on the assumption that a point can be reconstructed by a linear combination of its neighbours [25].

All the approaches quoted till now made use of some metric to calculate the similarity or dissimilarity between two objects. S. Hassan, R. Mihalcea and C. Banea made notable contributions in determining the edge weights between two objects. Traditional models, which generally relied on Bag of Words and TF-IDF data representations, made use of word frequencies and gave equal weightage to all the words. They employed Graph based Ranking algorithms and random walks on such graphs to find a more representative weight for a word [26]. Md. Rafiqul Islam and Md. Rakibul Islam made further contributions to the work by Hasan et al. by performing optimizations of the term weighing methods [27].

Bhagat et al. provided a survey of graph based-classification techniques such as the iterative classification method, random walk-based methods such as label propagation, graph regularization, adsorption, etc. The label propagation method, works on the underlying assumption that the probability of labelling a node, N, with a label, L, is the total probability that a random walk starting at node N will end at a node labelled L [28].

Ping He and Xiaohua Xu attempted to perform multiclass classification via Markov Chains. They marked all the labelled objects as absorbing states and all the unlabelled objects as transitive states. They verified their method on Text classification and Face recognition datasets [29].

Sam Blasiak and Huzefa Rangwala made use of Hidden Markov model variant for sequence classification. They performed classification by first converting sequences into fixed length vectors. They established that classification of these fixed length vectors is easier and more accurate as compared to performing classification on the sequences themselves [30].

Bicegoa et al. proposed a novel similarity-based classification of sequences via the Hidden Markov Model. He made use of the Hidden Markov Model to represent objects by a vector of similarities with respect to other objects [14].

Nguyen et al. proposed the method of fake news detection using Deep Markov Random fields, which aims to first establish correlation between news articles before applying Deep Learning models for classification. They established these correlations via the Markov Random Fields [31].

Mor et al. performed a survey of Hidden Markov models and their applications. He performed his study on nine different variants of the hidden Markov model namely:

1. First-order Hidden Markov Model
2. Higher order Hidden Markov Model
3. Hidden-semi–Markov Model
4. Factorial Hidden Markov Model
5. Second-order Hidden Markov Model
6. Layered Hidden Markov Model
7. Auto-regressive Hidden Markov Model
8. Non-stationary Hidden Markov Model
9. Hierarchical Hidden Markov Model

He summarised their usages domains as speech recognition, musicology, gesture recognition, tool wearing, part-of-speech tagging, bioinformatics, data pre-processing, network analysis, human activity recognition, label sequencing, earthquake prediction, etc. However, their paper lacked the domain of sequence classification [12]. The aim of this paper is to perform text sequence classification, w.r.t Fake News, via Graph based Markov Chains.

3. Methodology and Experiments

3.1. Markov Chains – a brief introduction

Consider a set of amino acid sequences (proteins).

Sequence,

S_1 = {A, T, G, C}
S_2 = {G, T, A, C}
S_3 = {A, T, C, A}
S_4 = {T, T, G, C}

Markov chains are built upon the Markov property, which states that a future state is dependent solely on the current state and not any state that occurred before it [9], [10], [11].

Amino acid "A" is followed by "T", "C" and "T" in sequences S_1, S_2 and S_3 respectively.

Based on the given amino acids, we can create a probability emission matrix, based on the Markov property, as follows [10]:

➔ Probability of "A" being followed by "T": 2/3
➔ Probability of "A" being followed by "C": 1/3
➔ Probability of "A being followed by "G": 0/3

Similarly, probabilities can be calculated for all pairs of amino acids.

	A	T	G	C
A	0	0.67	0	0.34
T	0.20	0.20	0.20	0.40
G	0	0.34	0	0.67
C	1.00	0	0	0

Table 1: Emission probability Matrix for amino acids

The emission probability matrix in table 1 has been visually represented in the form of Markov chain in figure 1.

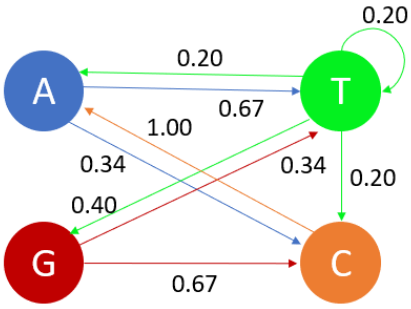

Figure 1: Markov Chain representation for amino acid sequences.

3.2. Probability of sequence generation from a given Markov chain

We now aim to determine the probability or likelihood that a particular sequence was generated by a given Markov model. Traditional approaches such make use of Bayesian Classification paradigm for such calculation [14]. However, as stated earlier, such a method relies solely on word count/frequencies and completely ignores the order of the words or the sentence structure. We aim to devise a method for probability calculation such that importance is paid to the word order as well.
Given a Markov Chain and its corresponding emission matrix, E, and s sequence, S = {o_1, o_2, o_3, …, o_n}, the probability that S belong to, or is generated from, M can be calculated as:

$$P_{generation_{S,M}} = E[o_1][o_2] * E[o_2][o_3] * \ldots * E[o_{n-1}][o_n] \quad \text{eq. 1}$$

For e.g.: consider the emission matrix, E, shown in Table 1 and an amino acid sequence, S = {T, A, C}.

$$P_{generation_{S,M}} = E[T][A] * E[A][C]$$
$$= 0.20 * 0.34$$
$$= 0.068$$

3.2.1 Dealing with Infinitesimal results

$P_{generation_{S,M}}$ defined in eq.1 is quite trivial to compute. However, multiplication of probabilities can lead to precision errors as the final product may end up becoming infinitesimal.

Hence, we have made use of log-based probabilities to deal with infinitesimal probability results. Eq. 1 is modified as:

$$\log_{10}(P_{generation_{S,M}}) = \log_{10}(E[o_1][o_2] * E[o_2][o_3] * \ldots * E[o_{n-1}][o_n]) \quad \text{eq.2}$$

$$\Rightarrow \log_{10}(P_{generation_{S,M}}) = \log_{10}(E[o_1][o_2]) + \log_{10}(E[o_2][o_3]) + \ldots + \log_{10}(E[o_{n-1}][o_n]) \quad \text{eq.3}$$

This simple alteration eliminates the chances of dealing with infinitesimal values and prevent any sort of precision errors.

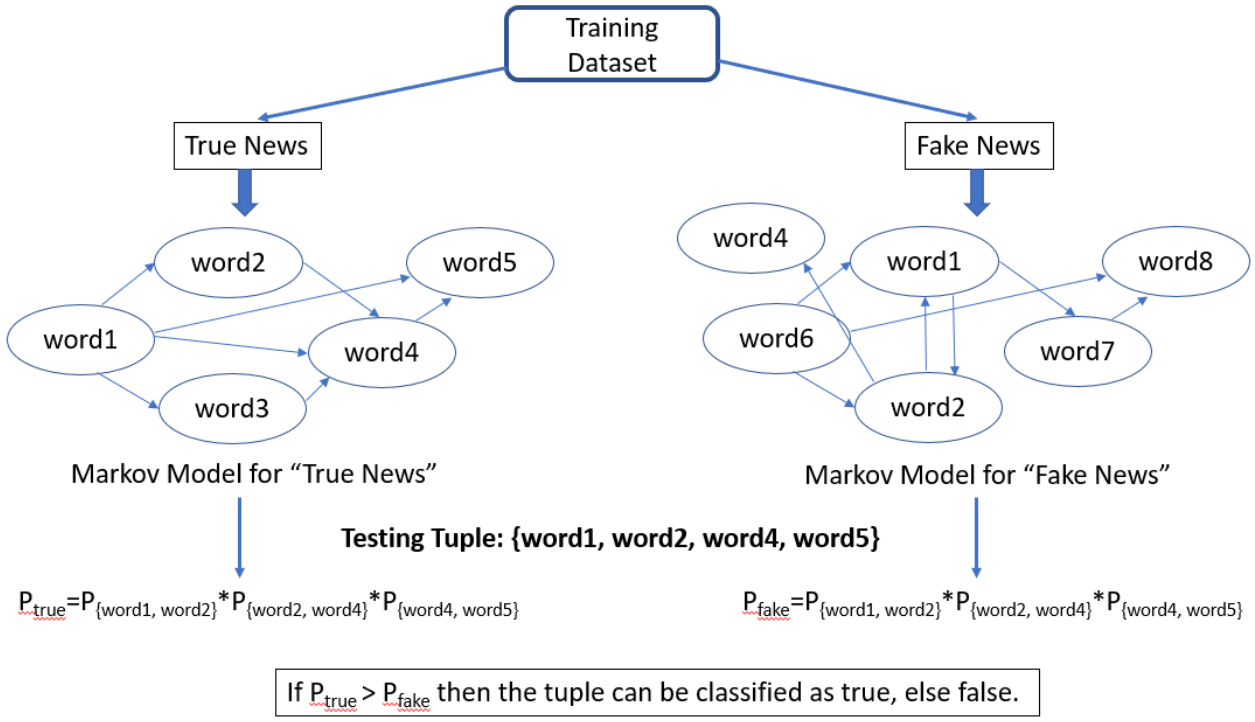

Figure 2: Classification methodology

3.3. Classification Methodology

In order to classify the tuples via Markov models, we begin by first splitting the training dataset. In the case of Fake News Detection, we split the training dataset based on whether the news is real or fake [14].

We then consider each of the split datasets and generate a Markov model or Markov chain for each. These Markov chains will allow us to find the probability that a testing tuple was generated by either of them.

This approach has been summarised in figure 2.

Let the probability that the testing tuple was generated by the Markov chain representing true news be equal to P_1, and the probability that the testing tuple was generated by the Markov chain representing fake news be equal to P_2.

If $P_1 > P_2$, then the tuple is classified as "Real News" else it is classified as "Fake News".

3.4. Challenges in the classification methodology

Our classification methodology, though robust, but assumes a training model with all the possible words in the English language with all possible connections between them. However, it is impossible to come up with such a training dataset.

In English language, the average sentence length is 15-20 words [32]. Total words in the English language are estimated to be around 171,476 [33]. Hence, the total possible sentence-permutations come out to be $(171476)^{15}$. It is impossible to gather a dataset with such a large number of articles.

To better understand this let us consider the following example:
Fake News Training Dataset:

1. "Shashank eats apples."
2. "Shashank plays football."
3. "Apples grow on trees."

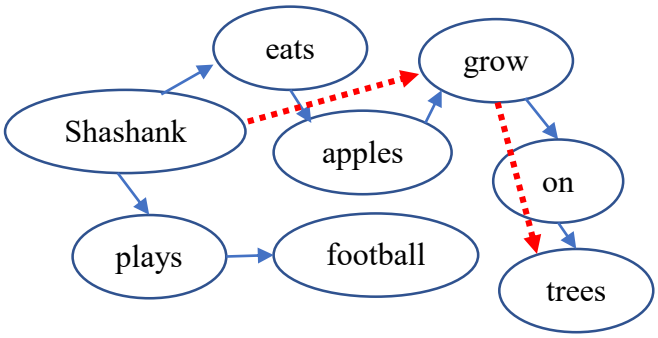

Figure 3: Markov chain to represent the training data.

In figure 3, solid arrows represent connections from the training dataset, whereas dotted edges represent edges which cannot be found in the training dataset but are required to classify the testing tuple, T = "Shashank grows a tree." Such cases occur frequently when the classification methodology discussed in section 3 is employed to classify fake news data.

3.5. Solutions for the missing edge problem

In order to solve the missing edge problem discussed in Section 4, we have conducted numerous experiments. The datasets used to perform these experiments are Fake news dataset from kaggle.com [15] and the ISOT Fake news dataset [16], [17]. We have used 80% of the dataset for training and the remaining 20% for testing.

Both the datasets make use of '1' to represent fake news and '0' to represent true news.

Metrics used:

a) Accuracy
b) Precision
c) Recall Score
d) F1-Score

3.5.1 *Approach 1: Ignoring the missing edges altogether*

In this approach we ignored the problem of missing edges altogether. While performing random walks for classification, whenever we encountered a missing edge, we simply stopped the process and assumed the $\log_{10}(P_{generations_{S,M}})$ to be negative infinity (-10^{15}).

In this approach, we encountered a plethora of tuples which could not be classified as neither the fake news Markov chain nor the true news Markov chain could accommodate them. These entries were marked by '2'. The results are summarised in Table 2, Figure 4, and Figure 5.

	Accuracy	Precision	Recall	F1-score
Kaggle Dataset [15]	0.021	0.021	0.021	0.021
ISOT [16], [17]	0.211	0.211	0.211	0.211

Table 2: Result metrics for 3.5.1

```
confusion_matrix(Y_test, pred, labels=[0, 1, 2])

array([[   0,    0, 2029],
       [   1,   91, 2030],
       [   0,    0,    0]], dtype=int64)
```

Figure 4: Confusion Matrix for kaggle dataset [15], for 3.5.1

```
confusion_matrix(Y_test, pred, labels=[0, 1, 2])

array([[ 169,    0, 4091],
       [   0, 1733, 2987],
       [   0,    0,    0]], dtype=int64)
```

Figure 5: Confusion Matrix for ISOT fake news dataset [16], [17], for 3.5.1

From the results (Table 2, Figure 4 and Figure 5) we can conclude that not only the model has poor accuracy, recall, precision and f1-score but also is unable to classify majority of the tuples.

3.5.2 *Approach 2: Probability smoothing via constant value*

What does the weight of an edge in a Markov chain represent? It simply represents the probability that a given word will be followed by another word. These edges weights give us an idea regarding how strongly the two words are connected.

In this approach we assume the missing edges to have a probability of the order of 10^{-8}. Why such a miniscule value? Such a value has been chosen arbitrarily and its magnitude has been kept exceedingly small in comparison to the other edge weights in order to represent that the two words are very loosely connected/interrelated. The results are summarised in Table 3, Figure 6, and Figure 7.

	Accuracy	Precision	Recall	F1-score
Kaggle Dataset [15]	0.895	0.993	0.800	0.886
ISOT [16], [17]	0.975	0.973	0.979	0.976

Table 3: Result metrics for 3.5.2

```
confusion_matrix(Y_test, pred, labels=[0, 1])

array([[2018,   11],
       [ 424, 1698]], dtype=int64)
```

Figure 6: Confusion Matrix for Kaggle dataset [15], for 3.5.2

```
confusion_matrix(Y_test, pred, labels=[0, 1])

array([[4222,  122],
       [  94, 4542]], dtype=int64)
```

Figure 7: Confusion Matrix for ISOT dataset [16], [17], 3.5.2

3.5.3 *Defining a few terms:*

Before we discuss other approaches for probability smoothing, let us first define a few terms.

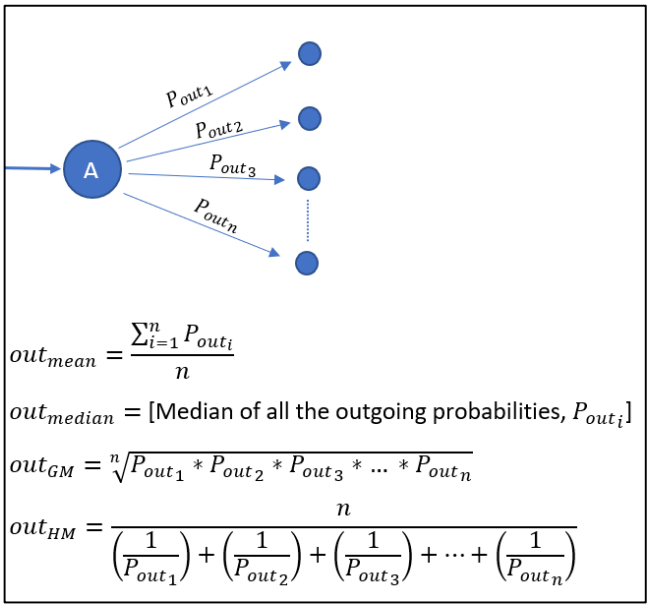

Figure 8: Defining outward probabilities

Consider a node, let us name it as A, as in Figure 8. Let this node be connected to n different nodes. The probability of reaching these n nodes be P_{out_1}, P_{out_2}, P_{out_3}, P_{out_4}, …, P_{out_n}. Using these probabilities, we define terms such as out_{mean}, out_{median}, out_{GM} and out_{HM}, where out_{mean} is the mean of all the outgoing probabilities, out_{median} if the median of the outgoing probabilities, out_{GM} is the geometric mean of the outgoing probabilities and out_{HM} is the harmonic mean of the outgoing probabilities.

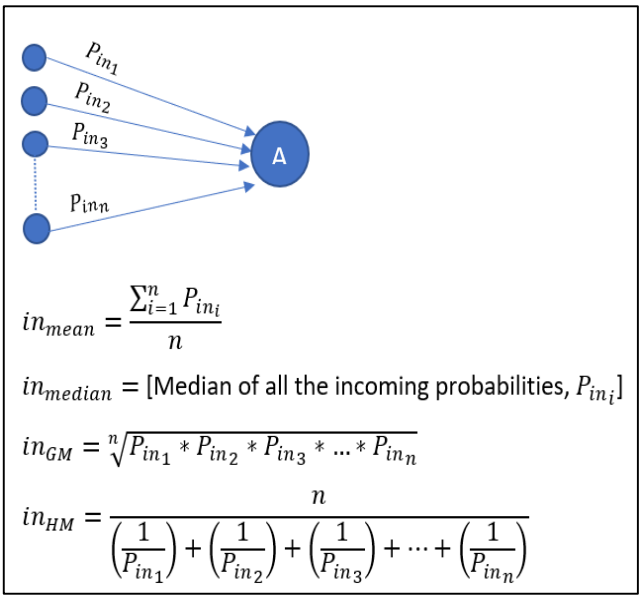

Figure 9: Defining inward probabilities

Like outward probabilities (Figure 8), we can also define inward probabilities. Consider a node, A, let this node be directly reachable from n different nodes. Let the probabilities than these n nodes reach node 'A' be equal to P_{in_1}, P_{in_1}, P_{in_1}, …., P_{in_1}. Using these probabilities, we define terms such as in_{mean}, in_{median}, in_{GM} and $in_{HM,}$ where in_{mean} is the mean of all the incoming probabilities, in_{median} if the median of the incoming probabilities, in_{GM} is the geometric mean of the incoming probabilities and in_{HM} is the harmonic mean of the incoming probabilities.

3.5.4 *Approach 3: Imaginary Edge insertion*

In this approach we insert a single imaginary edge between the two disconnected nodes. We then try applying different measures discussed in figure 8 and 9 as the edge weights.

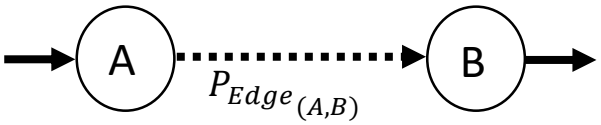

Figure 10: Single imaginary edge insertion between two disconnected nodes

a) Probability smoothing via $(out_{mean})_A$:

$$P_{Edge_{(A,B)}} = (out_{mean})_A$$

Note: in case the node 'A' does not exist in the Markov chain, the probability is assumed to be 10^{-8}, as discussed in *Approach 2*.

The results for this experiment are summarised in Table 4.

	Accuracy	Precision	Recall	F1-score
Kaggle Dataset [15]	0.694	0.635	0.941	0.758
ISOT [16], [17]	0.814	0.914	0.707	0.798

Table 4: Result metrics for 3.5.4 (a)

b) Probability smoothing via $(in_{mean})_B$:

$$P_{Edge_{(A,B)}} = (in_{mean})_B$$

Note: in case the node 'B' does not exist in the Markov chain, the probability is assumed to be 10^{-8}, as discussed in *Approach 2*.

The results of this experiment are summarised in Table 5.

	Accuracy	Precision	Recall	F1-score
Kaggle Dataset [15]	0.553	0.540	0.839	0.657
ISOT [16], [17]	0.400	0.413	0.373	0.392

Table 5: Result metrics for 3.5.4 (b)

c) Probability smoothing via the mean of $(in_{mean})_B$ and $(out_{mean})_A$:

$$P_{Edge_{(A,B)}} = \frac{(in_{mean})_B + (out_{mean})_A}{2}$$

Note: in case either node 'B' or node 'A' do not exist in the Markov chain, the probability is assumed to be 10^{-8}, as discussed in *Approach 2*.

The results of this experiment are summarised in Table 6.

	Accuracy	Precision	Recall	F1-score
Kaggle Dataset [15]	0.668	0.629	0.852	0.724
ISOT [16], [17]	0.719	0.730	0.731	0.731

Table 6: Result metrics for 3.5.4 (c)

d) Probability smoothing via the geometric mean of $(in_{mean})_B$ and $(out_{mean})_A$:

$$P_{Edge_{(A,B)}} = \sqrt{((out_{mean})_A * (in_{mean})_B)}$$

Note: in case the node 'B' does not exist in the Markov chain, the probability is assumed to be 10^{-8}, as discussed in *Approach 2*.

The results of this experiment are summarised in Table 7.

	Accuracy	Precision	Recall	F1-score
Kaggle Dataset [15]	0.703	0.652	0.901	0.756
ISOT [16], [17]	0.800	0.824	0.786	0.804

Table 7: Result metrics for 3.5.4 (d)

e) *Probability smoothing via the harmonic mean of* $(in_{mean})_B$ *and* $(out_{mean})_A$*:*

$$P_{Edge_{(A,B)}} = \frac{2 * (in_{mean})_B * (out_{mean})_A}{(in_{mean})_B + (out_{mean})_A}$$

Note: in case either node 'B' or node 'A' do not exist in the Markov chain, the probability is assumed to be 10^{-8}, as discussed in *Approach 2*.

The results of this experiment are summarised in Table 8.

	Accuracy	Precision	Recall	F1-score
Kaggle Dataset [15]	0.761	0.702	0.925	0.798
ISOT [16], [17]	0.884	0.914	0.859	0.886

Table 8: Result metrics for 3.5.4 (e)

3.5.5 *Approach 4: Imaginary State Insertion*

Methods discussed in Approach 3 were considerably better than the original model (discussed in *Approach 1*). However, we hit a plateau at 0.761(experiment 3e) and 0.884(experiment 3e) accuracy for the Kaggle [15] and ISOT [16], [17] datasets, respectively.

Hence, we modified our approach. In this approach instead of inserting an imaginary edge we inserted an imaginary state 'i'.

Note: For all experiments in approach 4 if either node 'B' or node 'A' do not exist in the Markov chain, the probability is assumed to be 10^{-8}, as discussed in *Approach 2*.

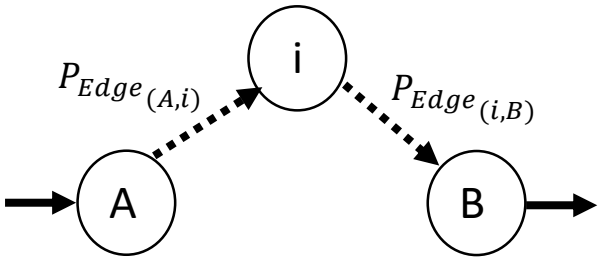

Figure 11: Imaginary state insertion between two disconnected nodes

Now, Probability of reaching B from A can be simply calculated as:

$$P_{Edge_{(A,i)}} = P_{Edge_{A,i}} * P_{Edge_{i,B}}$$

But how to calculate $P_{Edge_{A,i}}$ *and* $P_{Edge_{i,B}}$?

a) Probability smoothing via $(out_{mean})_A$ *and* $(in_{mean})_B$

$$P_{Edge_{(A,i)}} = (out_{mean})_A * (in_{mean})_B$$

We found a substantial improvement in the results when we assigned the value of $(out_{mean})_A$ and $(in_{mean})_B$ to $P_{Edge_{A,i}}$ *and* $P_{Edge_{i,B}}$ respectively.

The results for this experiment have been summarised in Table 9.

	Accuracy	Precision	Recall	F1-score
Kaggle Dataset [15]	0.910	0.884	0.948	0.915
ISOT [16], [17]	0.977	0.973	0.983	0.978

Table 9: Results for 3.5.5 (a)

3.5.6 *Introducing Penalizing Factors*

The results we achieved in 3.5.5 (a) were considerably better that *Approach 1(3.5.1)*, *2(3.5.2)*, and *3(3.5.4)*. In 3.5.5 (a) we gave equal weightage to both the edges. In the next set of experiments, we gave different weightage to both the edges.

We can express this mathematically as (from figure 11),

$$P_{Edge_{A,B}} = \left(P_{Edge_{A,i}}\right)^{P_1} * \left(P_{Edge_{i,B}}\right)^{P_2}$$

where, P_1 and P_2 are the penalizing factors for $Edge_{(A,i)}$ and $Edge_{(i,B)}$ respectively (as in figure 11).

We now tried to study the effect of these penalizing factors on the accuracy.

a) *Probability smoothing via $(out_{mean})_A$ and $(in_{mean})_B$ and range P_1 and P_2 from 1 to 5*

X-axis denotes P_1 and Y-axis denotes P_2 in Table 10 and 11. Table 10 and 11 summarise the accuracy findings for the Kaggle and ISOT dataset. Figure 12 and 13 shows how the accuracy increases with the change in the penalizing factors for the Kaggle and ISOT datasets respectively.

	1	2	3	4	5
1	0.911	0.932	0.933	0.930	0.923
2	0.931	0.932	0.928	0.924	0.919
3	0.926	0.923	0.921	0.917	0.912
4	0.916	0.914	0.912	0.909	0.908
5	0.908	0.909	0.906	0.906	0.903

Table 10: Effect of penalizing factors on *$(out_{mean})_A$ and $(in_{mean})_B$; X-axis: P_1, Y-axis: P_2; Dataset: Kaggle, (3.5.6 a)*

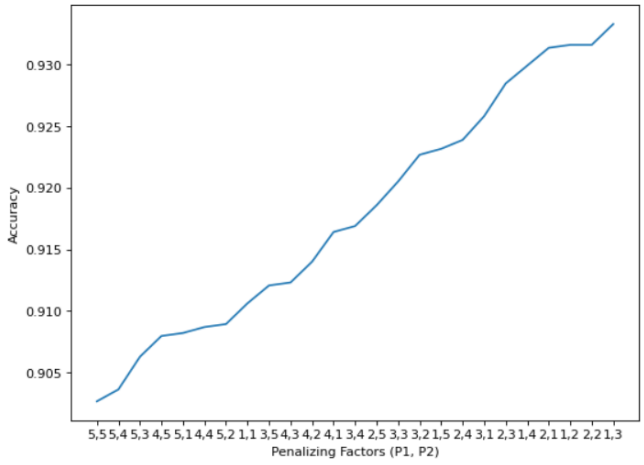

Figure 12: Effect of penalizing factors on *$(out_{mean})_A$ and $(in_{mean})_B$; X-axis: (P_1, P_2), Y-axis: accuracy; Dataset: Kaggle, (3.5.6 a)*

	1	2	3	4	5
1	0.975	0.976	0.976	0.974	0.973
2	0.976	0.975	0.974	0.974	0.972
3	0.973	0.973	0.974	0.973	0.971
4	0.972	0.972	0.971	0.970	0.969
5	0.970	0.971	0.970	0.969	0.968

Table 11: Effect of penalizing factors on *$(out_{mean})_A$ and $(in_{mean})_B$; X-axis: P_1, Y-axis: P_2; Dataset: ISOT Fake News Dataset, (3.5.6 a)*

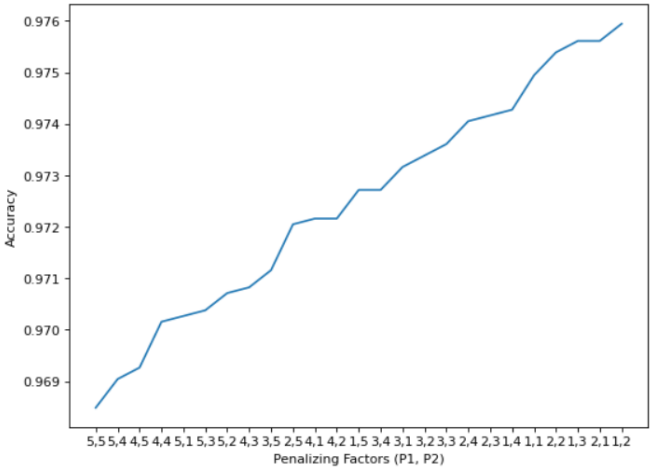

Figure 13: Effect of penalizing factors on *$(out_{mean})_A$ and $(in_{mean})_B$; X-axis: (P_1, P_2), Y-axis: accuracy; Dataset: ISOT Fake News Dataset, (3.5.6 a)*

b) *Probability smoothing via $(out_{GM})_A$ and $(in_{GM})_B$ and range P_1 and P_2 from 1 to 5*

X-axis denotes P_1 and Y-axis denotes P_2 in Table 12 and 13. Table 12 and 13 summarise the accuracy findings for the Kaggle and ISOT dataset. Figure 14 and 15 shows how the accuracy increases with the change in the penalizing factors for the Kaggle and ISOT datasets respectively.

	1	2	3	4	5
1	0.935	0.936	0.932	0.925	0.920
2	0.930	0.927	0.922	0.917	0.912
3	0.921	0.915	0.913	0.909	0.907
4	0.912	0.909	0.907	0.906	0.903
5	0.906	0.905	0.902	0.902	0.901

Table 12: Effect of penalizing factors on *$(out_{GM})_A$ and $(in_{GM})_B$; X-axis: P_1, Y-axis: P_2; Dataset: Kaggle, (3.5.6 b)*

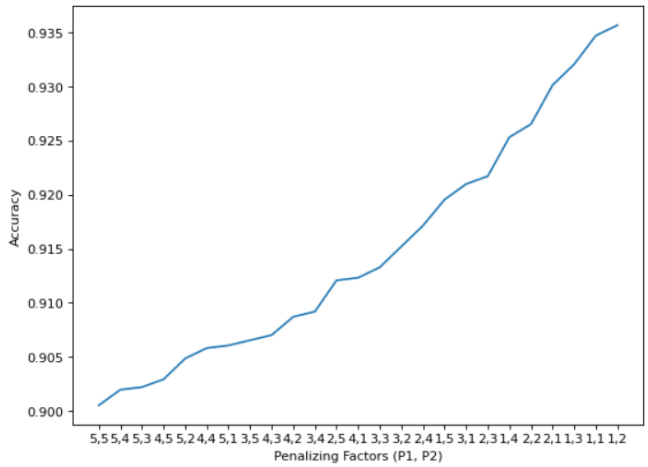

Figure 14: Effect of penalizing factors on $(out_{GM})_A$ *and* $(in_{GM})_B$*; X-axis:* (P_1, P_2)*, Y-axis: accuracy; Dataset: Kaggle, (3.5.6 b)*

	1	2	3	4	5
1	0.936	0.974	0.973	0.972	0.971
2	0.973	0.972	0.972	0.970	0.969
3	0.971	0.971	0.970	0.969	0.968
4	0.968	0.968	0.969	0.968	0.967
5	0.966	0.966	0.967	0.966	0.966

Table 13: Effect of penalizing factors on $(out_{GM})_A$ *and* $(in_{GM})_B$*; X-axis:* P_1*, Y-axis:* P_2*; Dataset: ISOT Fake News Dataset, (3.5.6 b)*

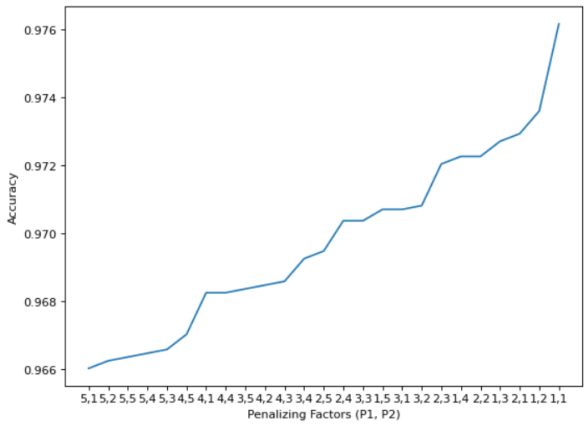

Figure 15: Effect of penalizing factors on $(out_{GM})_A$ *and* $(in_{GM})_B$*; X-axis:* (P_1, P_2)*, Y-axis: accuracy; Dataset: ISOT Fake News Dataset, (3.5.6 b)*

c) *Probability smoothing via* $(out_{HM})_A$ *and* $(in_{HM})_B$ *and range* P_1 *and* P_2 *from 1 to 5*

X-axis denotes P_1 and Y-axis denotes P_2 in Table 14 and 15. Table 14 and 15 summarise the accuracy findings for the Kaggle and ISOT dataset. Figure 16 and 17 shows how the accuracy increases with the change in the penalizing factors for the Kaggle and ISOT datasets respectively.

	1	2	3	4	5
1	0.935	0.929	0.920	0.911	0.906
2	0.925	0.917	0.911	0.905	0.899
3	0.915	0.909	0.905	0.901	0.896
4	0.907	0.903	0.900	0.896	0.893
5	0.902	0.898	0.896	0.893	0.887

Table 14: Effect of penalizing factors on $(out_{HM})_A$ *and* $(in_{HM})_B$*; X-axis:* P_1*, Y-axis:* P_2*; Dataset: Kaggle, (3.5.6 c)*

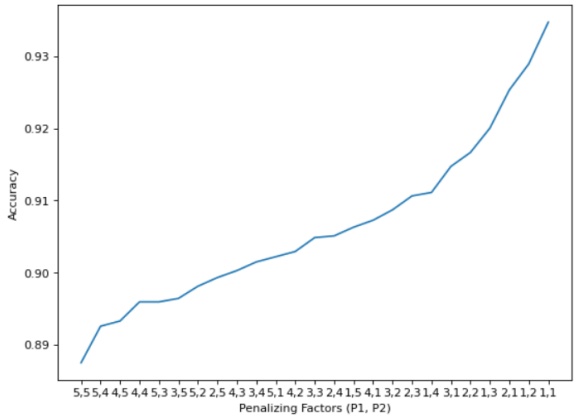

Figure 16: Effect of penalizing factors on $(out_{HM})_A$ *and* $(in_{HM})_B$*; X-axis:* (P_1, P_2)*, Y-axis: accuracy; Dataset: Kaggle, (3.5.6 c)*

	1	2	3	4	5
1	0.979	0.977	0.974	0.973	0.971
2	0.976	0.974	0.973	0.972	0.970
3	0.973	0.973	0.971	0.970	0.969
4	0.971	0.970	0.969	0.968	0.967
5	0.969	0.968	0.968	0.967	0.966

Table 15: Effect of penalizing factors on $(out_{HM})_A$ *and* $(in_{HM})_B$*; X-axis:* P_1*, Y-axis:* P_2*; Dataset: ISOT Fake News Dataset, (3.5.6 c)*

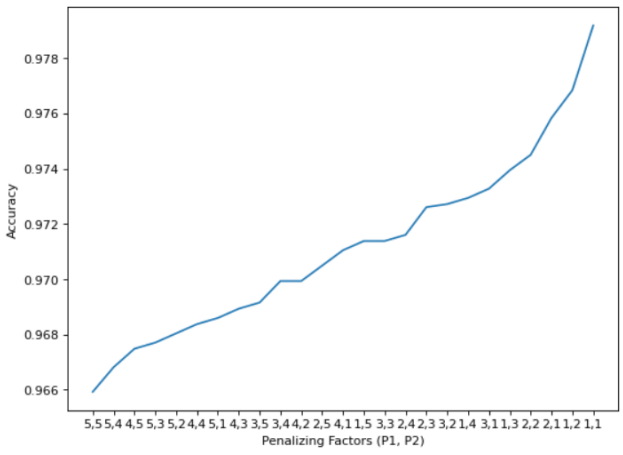

Figure 17: Effect of penalizing factors on $(out_{HM})_A$ *and* $(in_{HM})_B$*; X-axis:* (P_1, P_2)*, Y-axis: accuracy; Dataset: ISOT Fake News Dataset, (3.5.6 c)*

d) *Probability smoothing via $(out_{median})_A$ and $(in_{median})_B$ and range P_1 and P_2 from 1 to 5*

X-axis denotes P_1 and Y-axis denotes P_2 in Table 16 and 17. Table 16 and 17 summarise the accuracy findings for the Kaggle and ISOT dataset. Figure 18 and 19 shows how the accuracy increases with the change in the penalizing factors for the Kaggle and ISOT datasets respectively.

	1	2	3	4	5
1	0.934	0.932	0.926	0.918	0.912
2	0.922	0.917	0.914	0.909	0.906
3	0.911	0.911	0.905	0.904	0.901
4	0.904	0.902	0.901	0.898	0.897
5	0.898	0.897	0.896	0.896	0.894

Table 16: Effect of penalizing factors on *$(out_{median})_A$ and $(in_{median})_B$; X-axis: P_1, Y-axis: P_2; Dataset: Kaggle, (3.5.6 d)*

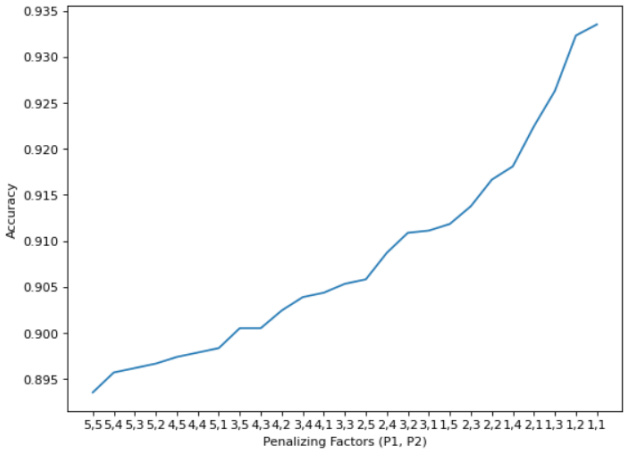

Figure 18: Effect of penalizing factors on *$(out_{median})_A$ and $(in_{median})_B$; X-axis: (P_1, P_2), Y-axis: accuracy; Dataset: Kaggle, (3.5.6 d)*

	1	2	3	4	5
1	0.978	0.978	0.976	0.973	0.971
2	0.977	0.976	0.973	0.971	0.971
3	0.974	0.972	0.970	0.970	0.969
4	0.971	0.970	0.969	0.968	0.967
5	0.968	0.968	0.967	0.966	0.966

Table 17: Effect of penalizing factors on *$(out_{median})_A$ and $(in_{median})_B$; X-axis: P_1, Y-axis: P_2; Dataset: ISOT Fake News Dataset, (3.5.6 d)*

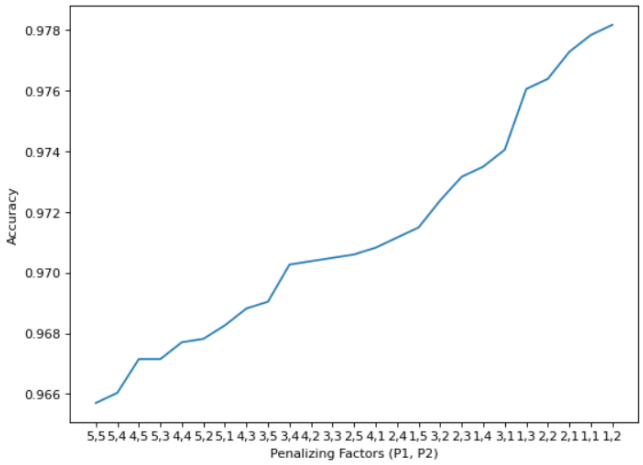

Figure 19: Effect of penalizing factors on *$(out_{median})_A$ and $(in_{median})_B$; X-axis: (P_1, P_2), Y-axis: accuracy; Dataset: ISOT Fake News Dataset, (3.5.6 d)*

4. Analysing and comparing the results

4.1 *Concluding with a formula and summarising results*

We have achieved considerable accuracy on both the Kaggle [15] and ISOT [16], [17] fake news datasets, via our experimentation, especially from the experiments caried out in the section 3.5.6.

Based on the experimentation performed, we have concluded with the following formula:

$$P_{A-B} = [(out_{M.C.T})_A]^{P_1} * [(in_{M.C.T})_B]^{P_2}$$

where,

- $P_{(A-B)}$ is the probability of reaching node B from node A. (A and B are disconnected nodes in the Markov chain).
- M.C.T is the measure of central tendency. For e.g.: mean, geometric mean, harmonic mean, and median.
- P_1 and P_2 are the penalizing factors.
- $(out_{M.C.T})_A$ is the measure of central tendency of outgoing probabilities for the initial edge 'A'.
- $(in_{M.C.T})_B$ is the measure of central tendency of incoming probabilities for the final edge 'B'.

From the figure 12 to 19, we can observe that the maximum accuracy is obtained when (P_1, P_2) range from [1, 3].

The results of our work have been summarised on three different datasets (table 18). The results have been calculated by keeping/standardising:

- $(out_{M.C.T})_A : (out_{mean})_A$
- $(in_{M.C.T})_B : (in_{mean})_B$
- (P1, P2): (2, 2)

	Accuracy	Precision	Recall	F1-score
Kaggle [15]	0.931	0.946	0.918	0.932
ISOT [16], [17]	0.975	0.972	0.980	0.976
WELFake [18]	0.931	0.939	0.925	0.932

Table 18: Summary of results obtained on different datasets.

4.2 *Comparing results*

We have compared our results (table18) with the works by Feyza Altunbey Ozbay and Bilal Alatas [19] (table 19, table 20), Reham Jehad and Suhad A. Yousif [20] (table 21) and Hadeer Ahmed, Issa Traore1, and Sherif Saad [21] (table 22).

	Accuracy	Precision	Recall	F-measure
BayesNet	0,586	0,587	0,586	0,586
JRip	0,607	0,611	0,588	0,599
OneR	0,559	0,567	0,560	0,547
Decision Stump	0,564	0,574	0,564	0,549
ZeroR	0,501	0,501	**1,000**	0,667
SGD	0,589	0,590	0,583	0,586
CVPS	0,501	0,501	**1,000**	0,667
RFC	0,526	0,525	0,534	0,530
LMT	0,607	0,604	0,616	0,610
LWL	0,570	0,573	0,570	0,566
CvC	0,553	0,556	0,526	0,541
WIHW	0,501	0,501	**1,000**	0,667
Ridor	0,557	0,563	0,558	0,549
MLP	0,565	0,565	0,571	0,568
OLM	0,516	0,540	0,516	0,430
SimpleCart	0,604	0,607	0,586	0,597
ASC	0,588	0,598	0,534	0,564
J48	0,558	0,558	0,563	0,560
SMO	0,534	0,536	0,489	0,512
Bagging	0,598	0,603	0,576	0,589
Decision Tree	**0,968**	**0,963**	0,973	**0,968**
IBk	0,551	0,551	0,551	0,550
KLR	0,606	0,605	0,614	0,609

Table 19: The performance of different supervised artificial intelligence algorithms for the ISOT Fake News data set. Results compiled by *Feyza Altunbey Ozbay and Bilal Alatas.*[19]

4.2.1 *Comparing our results (table 18: ISOT) with the work by Feyza Altunbey Ozbay and Bilal Alatas [19] (table 19)*

	Accuracy	Precision	Recall	F1-score
Our results (table 18: ISOT)	**0.975**	**0.972**	0.980	**0.976**
Feyza Altunbey Ozbay and Bilal Alatas [19] (table 19)	0.968 (Decision Tree)	0.963 (Decision Tree)	**1.000** (Zero-R, CVPS, WIHW)	0.968 (Decison Tree)

Table 20: Comparing our results (table 18: ISOT) with the works by Feyza Altunbey Ozbay and Bilal Alatas [19] (table 19)

From table 20, we can conclude that our model has the highest accuracy, precision and F1-score as compared to the works compiled Feyza Altunbey Ozbay and Bilal Alatas [19] (table19).

4.2.2 *Comparing our results (table 18: Kaggle) with the work by Reham Jehad and Suhad A. Yousif [20] (table 21)*

	Accuracy	Precision	Recall	F1-score
Our results (table 18: Kaggle)	**0.931**	**0.946**	**0.918**	0.932
Reham Jehad and Suhad A. Yousif [20]	0.8911 (Decision Trees)	0.921 (Random Forest)	0.8839 (Decision Trees)	N/A

Table 21: Comparing our results (table 18: Kaggle) with the works by Reham Jehad and Suhad A. Yousif [20]

From table 21, we can conclude that our model has the highest accuracy, recall and precision as compared to the works compiled by Reham Jehad and Suhad A. Yousif [20]

4.2.3 *Comparing our results (table 18: ISOT) with the work by Hadeer Ahmed, Issa Traore1, and Sherif Saad [21] (table 22)*

	Accuracy	Precision	Recall	F1-score
Our results (table 18: ISOT)	**0.975**	0.972	0.980	0.976
Hadeer Ahmed, Issa Traore1, and Sherif Saad [21]	0.920	N/A	N/A	N/A

Table 22: Comparing our results (table 18: ISOT) with the works by Hadeer Ahmed, Issa Traore1, and Sherif Saad [21]

From table 22, we can conclude that our model has the highest accuracy as compared to the works compiled by Hadeer Ahmed, Issa Traore1, and Sherif Saad [21].

5. Conclusion and Future Work

Social media platforms have seen a major boom in the past decade. The use of social media to read news articles has become prevalent. However, it is next to impossible for the end users to establish the validity of the news articles. Hence, there arises a need for quick and highly accurate machine learning models to detect the fake news articles. In this study we have proposed a new fake news classification model. We have performed a series of experiments to verify our model. In our experiments we have monitored parameters such as accuracy, precision, recall and F1-score. We have verified our results on 3 well known datasets namely, ISOT Fake News dataset, WELFake Dataset and a fake news dataset from kaggle. We have also compared our results on the ISOT Fake

News Dataset and Kaggle dataset with the results published by numerous authors [19], [20], [21] and have found that our model works considerably better than the previously proposed solutions.

In terms of future work, we aim to further improve the accuracy of our model and apply it on diverse kinds of sequence-based datasets.

References

[1] D. Rohera *et al*., A Taxonomy of Fake News Classification Techniques: Survey and Implementation Aspects, in *IEEE Access*, vol. 10 (2022) pp. 30367-30394, doi: 10.1109/ACCESS.2022.3159651.

[2] K. Poddar, G. B. Amali D. and K. S. Umadevi, Comparison of Various Machine Learning Models for Accurate Detection of Fake News, 2019 Innovations in Power and Advanced Computing Technologies (i-PACT), (2019) pp. 1-5, doi: 10.1109/i-PACT44901.2019.8960044.

[3] S. Lyu and D. C. -T. Lo, Fake News Detection by Decision Tree, 2020 SoutheastCon, (2020) pp. 1-2, doi: 10.1109/SoutheastCon44009.2020.9249688.

[4] M. Granik and V. Mesyura, Fake news detection using naive Bayes classifier, 2017 IEEE First Ukraine Conference on Electrical and Computer Engineering (UKRCON), (2017) pp. 900-903, doi: 10.1109/UKRCON.2017.8100379.

[5] A. Jain and A. Kasbe, Fake News Detection, 2018 IEEE International Students' Conference on Electrical, Electronics and Computer Science (SCEECS), (2018) pp. 1-5, doi: 10.1109/SCEECS.2018.8546944.

[6] P. Jain, S. Sharma, Monica and P. K. Aggarwal, Classifying Fake News Detection Using SVM, Naive Bayes and LSTM, 2022 12th International Conference on Cloud Computing, Data Science & Engineering (Confluence), (2022) pp. 460-464, doi: 10.1109/Confluence52989.2022.9734129.

[7] Ching, WK., Huang, X., Ng, M.K., Siu, TK, Introduction, in: Markov Chains, International Series in Operations Research & Management Science, vol 189, Springer, Boston, MA, (2013), https://doi.org/10.1007/978-1-4614-6312-2_1

[8] Ching, WK., Huang, X., Ng, M.K., Siu, TK, Hidden Markov Chains, in: Markov Chains, International Series in Operations Research & Management Science, vol 189, Springer, Boston, MA, (2013), https://doi.org/10.1007/978-1-4614-6312-2_8

[9] Chung, K.L, Fundamental definitions, in: Markov Chains with Stationary Transition Probabilities, Die Grundlehren der Mathematischen Wissenschaften, vol 104, Springer, Berlin, Heidelberg, (1960), https://doi.org/10.1007/978-3-642-49686-8_1

[10] Chung, K.L, Transition probabilities, in: Markov Chains with Stationary Transition Probabilities, Die Grundlehren der Mathematischen Wissenschaften, vol 104, Springer, Berlin, Heidelberg, (1960), https://doi.org/10.1007/978-3-642-49686-8_2

[11] Chung, K.L, A random walk example, in: Markov Chains with Stationary Transition Probabilities, Die Grundlehren der Mathematischen Wissenschaften, vol 104, Springer, Berlin, Heidelberg, (1960), https://doi.org/10.1007/978-3-642-49686-8_12

[12] B. Mor, S. Garhwal and A. Kumar, A Systematic Review of Hidden Markov Models and Their Applications, Arch Computational Methods Eng, 28 (2021) 1429–1448, https://doi.org/10.1007/s11831-020-09422-4

[13] Pietrzykowski, Marcin & Sałabun, Applications of Hidden Markov Model: state-of-the-art, International Journal of Computer Technology and Applications, Vol 5(4) (2014) 1384-1391.

[14] M. Bicego, V. Murino, and M. A. T. Figueiredo. Similarity-based classification of sequences using hidden markov models. Pattern Recognition, 37(12):2281–2291, 2004.

[dataset] [15] WilliamLifferth, (2018), Fake News, Kaggle, https://kaggle.com/competitions/fake-news

[dataset] [16] Ahmed H, Traore I, Saad S. “Detecting opinion spams and fake news using text classification”, Journal of Security and Privacy, Volume 1, Issue 1, Wiley, January/February 2018.

[dataset] [17] Ahmed H, Traore I, Saad S. (2017) "Detection of Online Fake News Using N-Gram Analysis and Machine Learning Techniques. In: Traore I., Woungang I., Awad A. (eds) Intelligent, Secure, and Dependable Systems in Distributed and Cloud Environments. ISDDC 2017. Lecture Notes in Computer Science, vol 10618. Springer, Cham (pp. 127- 138).

[dataset] [18] Pawan Kumar Verma, Prateek Agrawal, & Radu Prodan. (2021). WELFake dataset for fake news detection in text data [Data set]. In IEEE Transactions on Computational Social Systems (0.1, Numbers doi: 10.1109/TCSS.2021.3068519, pp. 1–13), Zenodo, https://doi.org/10.5281/zenodo.4561253

[19] F. A. Ozbay and B. Alatas, Fake news detection within online social media using supervised artificial intelligence algorithms, Physica A, 540 (2020) 123174, doi: https://doi.org/10.1016/j.physa.2019.123174

[20] R. Jehad and S. A. Yousif, Fake News Classification Using Random Forest and Decision Tree (J48), ANJS, Vol.23(4) (2020) pp. 49-55, doi: 10.22401/ANJS.23.4.09

[21] H. Ahmed, I. Traore, S. Saad, Detection of Online Fake News Using N-Gram Analysis and Machine Learning Techniques, in: Traore, I., Woungang, I., Awad, A. (eds) Intelligent, Secure, and Dependable Systems in Distributed and Cloud Environments, ISDDC 2017, Lecture Notes in Computer Science (), vol 10618, Springer, Cham (2017), doi: https://doi.org/10.1007/978-3-319-69155-8_9

[22] M. Szummer and T. Jaakkola, Partially labeled classification with Markov random walks, Proc. 14th Int. Conf. Neural Inf. Process. Syst. Natural Synthetic, (2001) pp. 945-952, doi: https://dl.acm.org/doi/10.5555/2980539.2980661

[23] X. Zhu, Z. Ghahramani, and J. Lafferty, Semi-supervised learning using gaussian fields and harmonic functions, Proceedings of the 20th International Conference on Machine Learning, (2003) pp. 912-919, doi: https://dl.acm.org/doi/10.5555/3041838.3041953

[24] D. Zhou, O. Bousquet, T. N. Lal, J. Weston, and B. Schölkopf, Learning with local and global consistency, Advances in Neural Information Processing Systems, (2004) pp. 321–328, doi: https://dl.acm.org/doi/10.5555/2981345.2981386

[25] F. Wang and C. Zhang, Label Propagation through Linear Neighborhoods, IEEE Transactions on Knowledge and Data Engineering, vol. 20 (2008) pp. 55-67, doi: https://doi.org/10.1109/TKDE.2007.190672

[26] S. Hassan, R. Mihalcea and C. Banea, Random-Walk Term Weighting for Improved Text Classification, International Conference on Semantic Computing (ICSC 2007), (2007) pp. 242-249, doi: 10.1109/ICSC.2007.56.

[27] M. R. Islam and M. R. Islam, An effective term weighting method using random walk model for text classification, 2008 11th International Conference on Computer and Information Technology, (2008) pp. 411-414, doi: 10.1109/ICCITECHN.2008.4803000.

[28] S. Bhagat, G. Cormode, S. Muthukrishnan, Node Classification in Social Networks, in: Aggarwal, C. (eds) Social Network Data Analytics. Springer, Boston, MA, (2011), doi: https://doi.org/10.1007/978-1-4419-8462-3_5

[29] P. He and X. Xu, Classification with Graph-Based Markov Chain, in: Gelbukh, A., Espinoza, F.C., Galicia-Haro, S.N. (eds) Nature-Inspired Computation and Machine Learning. MICAI 2014. Lecture Notes in Computer Science(), vol 8857. Springer, Cham, (2014), doi: https://doi.org/10.1007/978-3-319-13650-9_28

[30] S. Blasiak and H. Rangwala, A hidden markov model variant for sequence classification, Proceedings of the International Joint Conferences on Artificial Intelligence (IJCAI), (2011) pp. 1192–1197, doi: https://dl.acm.org/doi/10.5555/2283516.2283596

[31] D. M. Nguyen, T. H. Do, R. Calderbank, and N. Deligiannis. Fake News Detection using Deep Markov Random Fields, Proceedings of the 2019 Conference of the North American Chapter of the Association for Computational Linguistics: Human

Language Technologies, Volume 1 (Long and Short Papers), (2019) pp. 1391–1400, doi: http://dx.doi.org/10.18653/v1/N19-1141

[32] Technical Communicators Association, How many words make a sentence?, https://techcomm.nz/Story?Action=View&Story_id=106, 2016, (accessed 23rd December, 2022)

[33] BBC, How many words do you need to speak a language?, https://www.bbc.com/news/world-44569277, 2018, (accessed 23rd December, 2022)

Genetic Landscape of Major Depressive Disorder: Assessment of Potential Diagnostic and Antidepressant Response Markers

Priyanka Singh, M.Sc[1,2], Ankit Srivastava, Ph.D[1,3], Debleena Guin, M.Sc[1,4], Sarita Thakran, M.Sc[1,2], Jyoti Yadav, Ph.D[1], Puneet Chandna, Ph.D[5], Mamta Sood, M.D.[6], Rakesh Kumar Chadda, M.D. [6], Ritushree Kukreti, Ph.D*[1, 2]

[1]Genomics and Molecular Medicine Unit, Council of Scientific and Industrial Research (CSIR) - Institute of Genomics and Integrative Biology (IGIB), New Delhi-110007, India

[2]Academy of Scientific and Innovative Research (AcSIR), Ghaziabad- 201002, India

[3]Department of Pharmacology, School of Pharmaceutical Education and Research, Jamia Hamdard, New Delhi 110062, India

[4]Department of Biotechnology, Delhi Technological University, Shahbad Daulatpur, Main Bawana Road, Delhi 110042, India

[5]Indian Society of Colposcopy and Cervical Pathology (ISCCP), Safdarjung Hospital, New Delhi, 110029, India

[6]Department of Psychiatry, All India Institute of Medical Sciences, Ansari Nagar, New Delhi 110029, India

***Correspondence:**

Ritushree Kukreti

Genomics and Molecular Medicine Unit, Institute of Genomics and Integrative Biology (Council of Scientific and Industrial Research), Mall Road, Delhi 110 007, India

Phone: 91-11-27662202; Fax: 91-11-27667471; Email: ritus@igib.res.in,

ritushreekukreti@gmail.com

© The Author(s) 2023. Published by Oxford University Press on behalf of CINP.
This is an Open Access article distributed under the terms of the Creative Commons Attribution License (https://creativecommons.org/licenses/by/4.0/), which permits unrestricted reuse, distribution, and reproduction in any medium, provided the original work is properly cited.

Accepted Manuscript

Downloaded from https://academic.oup.com/ijnp/advance-article/doi/10.1093/ijnp/pyad001/6992242 by Delhi Technological University user on 31 January 2023

Significance Statement

Our work provides a holistic landscape of all genetic association studies related to Major depressive disorder (MDD) risk and antidepressant response. In consideration of the well-established fact that several genetic association investigations have identified variants underlying disease susceptibility and antidepressant response outcome, no biomarker is available to date for clinical application. Therefore, our prime objective was to evaluate the accumulating genetic findings to unearth the clinically important genetic markers. Hence, we curated all the existing literature of genetic association studies related to MDD susceptibility and antidepressant response. Additionally, we examined functional relevance and diagnostic predictability of the replicated variants. Altogether, our work proposed some potential candidate variants from literature, that are likely to be utilized for clinical translation in MDD following an appropriate validation.

Accepted Manuscript

Downloaded from https://academic.oup.com/ijnp/advance-article/doi/10.1093/ijnp/pyad001/6992242 by Delhi Technological University user on 31 January 2023

Abstract

Background: The clinical heterogeneity in major depressive disorder (MDD), variable treatment response and conflicting findings limit the ability of genomics towards the discovery of evidence-based diagnosis and treatment regimen. This study attempts to curate all genetic association findings to evaluate potential variants for clinical translation.

Methods: We systematically reviewed all candidate and genome-wide association studies for both MDD susceptibility and antidepressant response, independently, using MEDLINE, particularly to identify replicated findings. These variants were evaluated for functional consequences using different *in silico* tools and further estimated their diagnostic predictability by calculating positive predictive values (PPV).

Results: A total of 217 significantly associated studies comprising 1200 variants across 545 genes and 128 studies including 921 variants across 412 genes were included with MDD susceptibility and antidepressant response, respectively. Although, majority of associations were confirmed by single study, we identified 31 and 18 replicated variants (in atleast 2 studies) for MDD and antidepressant response. Functional annotation of these 31 variants predicted 20% coding variants as deleterious/damaging and 80.6% variants with regulatory effect. Similarly, for the response-related 18 variants revealed 25% coding variant as damaging and 88.2% with substantial regulatory potential. Finally, we could calculate the diagnostic predictability of 19 and 5 variants whose PPV ranges between 0.49 to 0.66 for MDD and 0.36 to 0.66 for response.

Conclusions: The replicated variants presented in our data are promising for disease diagnosis and improve response outcomes. Though, these quantitative assessment measures are solely directive of available observational evidence, robust homogenous validation studies are required to strengthen these variants for molecular diagnostic application.

Keywords: major depressive disorder, antidepressants response, genetic association studies, diagnostic predictability, pharmacogenetics

Accepted Manuscript

Downloaded from https://academic.oup.com/ijnp/advance-article/doi/10.1093/ijnp/pyad001/6992242 by Delhi Technological University user on 31 January 2023

Introduction

Major depressive disorder (MDD) is a common, complex and debilitating neuropsychiatric disorder which contributes a significant burden on both the individual and society (Norkeviciene et al., 2022). It is primarily characterized by symptoms that include low mood, anhedonia, fatigue, alteration in sleep and appetite, lack of concentration, feeling of guilt, helplessness and in worst case suicidal ideations (Malhi and Mann, 2018). According to WHO, nearly 4.4% of the world population are affected by depression with a significant rate of suicidal deaths, approximately one million per year (World Health Organization, 2017).

To date, the diagnosis of MDD revolves around the symptom-based approach, which often becomes difficult due to the lack of defined natural boundaries and overlapping symptoms between affective disorders (Feczko et al., 2019; García-Gutiérrez et al., 2020). Furthermore, the treatment of depression involves a trial-and-error approach, wherein, initially monotherapy is favoured followed by multi-drug therapy in case patients fails to respond to initial therapy. Nevertheless, one third of the patients do not respond adequately to the existing pharmacotherapy regimen. This variability could be a consequence of intrinsic biological (inter-individual genetic variations) and environmental heterogeneity among MDD patients (Fabbri et al., 2019; Srivastava et al., 2019). Therefore, it is imperative to identify certain bio signatures (such as SNPs) which are associated with the MDD susceptibility and antidepressant response, enabling the appropriate diagnosis and to promote personalized medication/therapy.

The etiology of MDD is multifactorial, which involves a complex interaction of both genetic and environmental factors. The genetic contribution to pathophysiology has been demonstrated by plethora of genetic association studies in addition to twin studies that reported the heritability of MDD to be approximately 40% (Sullivan et al., 2000; Shadrina et al., 2018; Schwabe et al., 2019). The existing literature regarding the genetics of MDD and

Accepted Manuscript

Downloaded from https://academic.oup.com/ijnp/advance-article/doi/10.1093/ijnp/pyad001/6992242 by Delhi Technological University user on 31 January 2023

treatment response is enormous and complex. Wherein, the two complementary approaches which primarily exploited in genetic studies are the Genome Wide Association Studies (GWAS) and candidate gene studies. Until recently, majority of candidate studies primarily focused on genes related to widely accepted hypothesis based on serotonergic, HPA Axis, neural plasticity, glutamatergic system considering their role in MDD pathophysiology and the fact that they might be the targets of antidepressant drugs (Basu et al., 2015, 2019). Most of them have reported the positive association with the disease susceptibility and treatment response, in spite of that low power of the study and contradictory findings, limits their clinical applicability. Moreover, a recent study by Border R et al. (2019) on a large sample pool examined the association of 18 highly studied candidate gene polymorphisms with depression and found no substantial contribution of any of the polymorphism to depression liability. On the other hand, earlier GWAS studies have failed to detect SNPs of genome wide significance level (Lewis et al., 2010; Muglia et al., 2010; Rietschel et al., 2010; Shi et al., 2011) but recent GWAS and meta-analysis have revealed 15 (Hyde et al., 2016), 16 (Howard et al., 2021), 44 (Wray et al., 2018), 102 (Howard et al., 2019) genetic loci to be significantly associated with MDD susceptibility. However, these results across studies were not consistently reproducible. These inconsistencies may likely be explained by methodological differences such as the definition of depression and sampling strategies employed. We speculate positive association in single study can be argued as false positive thus, reproducible associations holds promise and would have tremendous importance in prognosis, diagnosis, and therapeutics.

Therefore, in the present study we systematically collated the available genetic association data and identified the replicated genetic variants and performed their functional annotation and diagnostic predictability analysis in MDD susceptibility and antidepressant response, independently, via PubMed based search strategy. Our work is an attempt to find if any

Accepted Manuscript

Downloaded from https://academic.oup.com/ijnp/advance-article/doi/10.1093/ijnp/pyad001/6992242 by Delhi Technological University user on 31 January 2023

genetic variant holds the potential for clinical translation based on the available observational evidence.

1. Method

A systematic search was performed using MEDLINE database. Wherein, we independently retrieved the literature for all genetic association studies related to MDD susceptibility and antidepressant response.

1.1 Search strategy and study selection

Acquisition of MDD risk associated studies

A comprehensive PubMed search (https://pubmed.ncbi.nlm.nih.gov/) was conducted using a combination of the following Medical Subject heading (MeSH) terms "major depressive disorder", "major depression", "depressive disorder", "genetics", "gene", "SNP", "polymorphism", "variants" with AND/OR Boolean operators to retrieve relevant publications till June 2021. Articles were manually screened for titles, abstracts, and full-texts by two authors (PS and AS) independently. Any discrepancies were resolved on consensus agreement with a third author (RK). Two authors (DG and ST) crosschecked the data to ensure consistency. Additionally, the bibliography of included articles were subsequently screened for additional references. The inclusion criteria were as follows: (i) the patients primarily diagnosed as MDD; (ii) a case-control study-design; (iii) the study must examine the association between a variant/s and MDD; and (iv) study published in English. Exclusion criteria: (i) non-genetic studies; (ii) other than case-control study design; (iii) studies focusing on the antidepressant response; (iv) *in vitro* and animal studies; (v) enrolled patients who had depressive episodes due to other psychiatric disorder or studies evaluating other phenotypes

Accepted Manuscript

Downloaded from https://academic.oup.com/ijnp/advance-article/doi/10.1093/ijnp/pyad001/6992242 by Delhi Technological University user on 31 January 2023

in depressive patients (suicide etc.) (vi) articles with only abstract and no full text available; (vii) review articles, meta-analysis, case studies, commentary, editorial.

Acquisition of antidepressant response associated studies

To retrieve genetic association studies related to antidepressant response, the search string using "antidepressants", "SSRIs", "MAOIs", "SNRIs", "TCAs", "Atypical antidepressants" AND "pharmacogenetics", "pharmacogenomics", genetics", "gene", "SNP", "polymorphism", "variants" with AND/OR was conducted. Articles were extracted till June 2021. Manual screening of the titles and abstracts and further full-text evaluation was performed. Furthermore, bibliographic cross-reference was also included for additional studies. Articles were included if (i) the patients had a primary diagnosis of major depressive disorder; (ii) the study examined the association between the candidate or genome-wide variants and antidepressant response; (iii) the study should have dichotomous groups (like between responder and non-responder or remitter and non-remitter); (iv) response/ remission assessed by using relevant severity scales like Hamilton Rating Scale for Depression (HAMD), Montgomery and Asberg Depression Rating Scale (MADRS) etc and (v) the study published in the English language. Articles were excluded from our study in case of (i) non-genetic studies; (ii) studies other than antidepressant response; (iii) studies focusing on disease-associated variants or studies with pharmacokinetic outcomes without gene/variant association (iv) enrolled patients who had depressive episodes due to other psychiatric condition; (v) *in vitro* and animal studies; (vi) articles with only abstract and no full text available; (vii) review articles, meta-analysis, case studies.

Accepted Manuscript

Downloaded from https://academic.oup.com/ijnp/advance-article/doi/10.1093/ijnp/pyad001/6992242 by Delhi Technological University user on 31 January 2023

1.2 Data extraction

Data from selected full-text articles were extracted by PS and AS and checked by RK and ST. Full-text articles were further segregated into candidate and genome-wide genetic studies. The following data were extracted from eligible articles: (1) study details (author, publication year, PubMed ID); (2) population characteristics (gender, age, ethnicity/country/race); (3) clinical characteristics (phenotype definition, diagnostic criteria, overall sample size); (4) genetic variant details (gene, genetic polymorphism, risk allele, odds ratio (OR), confidence interval, unadjusted p-value, study MAF, genotyping method). Studies in which variant(s) showed statistically significant ($p<0.05$) association were considered as a positive association. The characteristics of included studies are summarized in Supplementary Table S1-S4. We preferred reporting allelic association over genotypic if both significant. In case, only genotypic association reported in the study then we calculated the allelic p-value using raw data (like allele frequency or minor allele frequency) and checked for significance and if found significant then reported the allelic p-value.

Next, we checked for reproducible genetic variants and genes which showed significant association in at least two studies. The detailed data of reproducible genetic variants and genes in candidate association studies, GWAS studies and in both (candidate and GWAS) are represented in Table 1- 4.

2.3 Functional annotation

The SNPs were mapped to genes using NCBI dbSNP following the GRCh38.p13 genome assembly. To predict the functional consequences of the included genetic variants, we used different *in-silico* prediction tools to assess the deleterious effect of the amino acid change in case of a missense variant and the regulatory potential of intronic SNPs (Kaur et al., 2014). The different tools used for function prediction were SIFT (Ng and Henikoff, 2001),

Accepted Manuscript

Downloaded from https://academic.oup.com/jnp/advance-article/doi/10.1093/jnp/pyad001/6992242 by Delhi Technological University user on 31 January 2023

PolyPhen2 (Adzhubei et al., 2010), RegulomeDB 2.0.3 (Boyle et al., 2012), and SNP info (Xu and Taylor, 2009). Additionally, we checked the genes of these replicated variants (i) for which behaviour/neurological phenotype was observed in knockout mice and the phenotype data was extracted from the Mouse Genome Informatics database (http://www.informatics.jax.org/) (ii) assessed whether the gene is a known target of an antidepressant drug as detailed in the drug-gene interaction database (www.DGidb.com) (iii) whether gene is preferentially expressed in the brain means the average expression in all brain tissues was higher than the average expression in non-brain tissues. This was assessed by using gene-expression data from all 53 tissues of the Gene-Tissue expression (GTEx) Consortium. Data obtained from each tool has been described in Supplementary Table S5 and S6.

2.4 Assessment of diagnostic predictability of genetic variants

The diagnostic predictability of genetic variants indicates its ability to precisely predict the occurrence of a disease phenotype in patients carrying the risk allele. We attempted to evaluate the diagnostic predictability for genetic variants with more than one publication of disease-variant association as well as response-variant association. True positives (TP) and false negatives (FN) are values representing the risk allele and wild type allele carrier, respectively, in cases. Conversely, true negatives (TN) and false positives (FP) are defined as wild type and risk allele carriers, respectively, in controls. The true positive rate or sensitivity are calculated as $\Sigma TP/(\Sigma TP+\Sigma FN)$ and specificity is $\Sigma TN/(\Sigma TN+\Sigma FP)$. Furthermore, the positive predictive values are calculated as $\Sigma TP/(\Sigma TP+\Sigma FP)$.

Accepted Manuscript

Downloaded from https://academic.oup.com/ijnp/advance-article/doi/10.1093/ijnp/pyad001/6992242 by Delhi Technological University user on 31 January 2023

3 Results

3.1. Literature search

Acquisition of MDD risk associated studies

Systematic search strategy for identifying MDD associated genes extracted 10,631 genetic association studies, which were further reduced to 280 articles of relevance after the title and abstract screening. Among these excluded articles, 2382 non-human/other language, 6081 other disorder/phenotype/comorbidity, 201 association study of MDD with other phenotype, 120 no association, and 1567 other articles including non-genetic studies, review articles, editorials, meta, comments and letters were also removed. Remaining 280 articles were then searched for their full text and 63 articles were again excluded from the study, as they did not meet the inclusion criteria, leading to a final of 217 articles for data extraction and processing. Of which 12 were GWAS studies and 205 were candidate association studies (Figure 1).

Acquisition of antidepressant response associated studies

Similarly, systematic search strategy for identifying antidepressant response associated genes extracted 7892 genetic association studies, which further reduced to 345 articles of relevance after the title and abstract screening. Among these excluded articles, 3109 non-human, 160 other language, 1768 not an antidepressant response study, 533 other disorders, 39 methylation/miRNA, protein related studies, 82 no association studies and 1856 other articles including non-genetic studies, review articles, genome-wide studies, editorials, and letters were also removed. The remaining articles were then searched for their full text and 222 articles were again excluded from the study, as they did not meet the inclusion criteria, leading to a final of 128 articles (including 5 articles that are additionally added through

Accepted Manuscript

Downloaded from https://academic.oup.com/jnp/advance-article/doi/10.1093/jnp/pyad001/6992242 by Delhi Technological University user on 31 January 2023

cross-references) for data extraction and processing. Of these 11 were GWAS response studies and 117 were candidate response association studies (Figure 2).

3.2 Study characteristics

Candidate genetic association studies related to MDD risk

We have summarized the main characteristics of the identified studies in Supplementary Table S1**.** Only significant p-values and odds ratios (OR) are presented. The 205 articles reported nominal significant associations ($p<0.05$). These 205 articles reported significant results for 378 polymorphisms in 156 unique genes. A total of 196339 individuals (n= 80891 cases and n= 115448 controls) were included in all the studies. The 27 genetic variants were confirmed by at least two studies. The number of patients ranged from 11 to 1738, and their age varied from 14 to 102 years. Ratio of male to female was 1.30 and 1.35 in cases and controls respectively. Of all the candidate association studies, 90 studies were performed in East Asia, 87 in Europe, 11 in America, 7 in Caucasian population, 4 in Middle Eastern countries, 3 in South Asia, 2 of Mixed population and 1 in Africa, white and white non-Hispanics. The most used MDD diagnostic criterion was based on diagnostic and statistical manual (DSM) (n = 164), followed by The International Classification of Diseases (ICD) (n = 21), studies used both DSM and ICD criteria (n = 7), and others (n = 11).

GWAS studies related to MDD risk

A total of 12 GWAS determine the association of genetic variants in MDD. These 12 articles reported significant results for 819 polymorphisms in 387 genes. In total 268481 patients of MDD and 841656 controls were included. Mean age of the included subjects were 45.55 years for MDD cases and 49.71 years for controls. The overall ratio of male to female was

Accepted Manuscript

Downloaded from https://academic.oup.com/ijnp/advance-article/doi/10.1093/ijnp/pyad001/6992242 by Delhi Technological University user on 31 January 2023

1.12. Most of the studies were performed in European population (n = 9), Han Chinese (n = 1) and mixed population (n = 2). The MDD patients were diagnosed based on Structured Clinical Interview fulfilling DSM/ ICD criteria (n =11). Although in one of the study self-reported MDD patients were also recruited. The majority of studies included patients with MDD/unipolar depression/recurrent depression (n=10), Except in two studies, where in one recurrent early-onset MDD patients and in another broad depression and probable MDD patients were recruited in the study. All studies employed array-based genotyping method. The characteristics of the included studies and genotypic/allelic distributions of the polymorphisms are shown in Supplementary Table S2.

Candidate genetic association studies related to antidepressant response

Total 116 articles reported nominal significant associations ($p<0.05$). The characteristics of the included studies and genotypic/allelic distributions of the polymorphisms are shown in Supplementary Table S3. The table include only those studies which were either in the form of responder vs non-responder (n = 64) or remitter vs non-remitter (n = 34). Thirteen studies have examined both response as well as remission status. Additionally, six studies checked the association in treatment-resistant patients. A total of 21753 (12577 responders and 9029 non-responders) and 11299 (4546 remitters and 4906 non-remitters) patients were included in the studies. The recruited cohort were of East Asian (55.17%), European (27.58%), American (7.75%), and others (9.48 %) origin. All the studies have recruited their patients based on either DSM (n=112) or ICD-10 (n=4) diagnostic criteria. Remission was defined as a final Hamilton Rating Scale for Depression (HAM-D) or Montgomery and Asberg Depression Rating Scale (MADRS) total score of 7 or less and response was defined as at least 50% decrease in HAM-D or MADRS total score. Maximum studies have employed HAM-D scale

Accepted Manuscript

Downloaded from https://academic.oup.com/ijnp/advance-article/doi/10.1093/ijnp/pyad001/6992242 by Delhi Technological University user on 31 January 2023

(n=69), followed by Quick Inventory of Depressive Symptomatology (QIDS) (n=5), MADRS (n=2), and Beck's Depression Inventory (n=1) for accessing the response in the patients. Similarly, for remission assessment HAMD/ MADRS scale (n= 39) and QIDS (n=5) were employed on the patients. Furthermore, we observed the majority of studies were based on Selective serotonin reuptake inhibitors (SSRIs) (n=69) followed by mixed therapy (n=33), Serotonin and norepinephrine reuptake inhibitors (SNRIs) (n=9), Atypical (n=3) and Tricyclic antidepressants (TCA) (n=2). Of these 60 studies were on monotherapy. There were some studies (n=6) that determined the response association with multi-drug therapy and further also examined the association based on monotherapy. The follow-up period in all the studies ranges from 2 weeks to 18 weeks. In total, 97 unique genes and 217 variants were found to be significantly associated with antidepressant response.

GWAS studies related to antidepressant response

A total of 11 studies have examined association between SNPs and antidepressant response (Supplementary Table S4). There were three response studies, three remission studies and five of those association with both response and remission status. Total 39533 patients (23141 responder and 11322 non-responders; 2392 remitter and 1413 non-remitter) were included in either discovery or replication cohort of all the studies. Included studies were performed in different ethnic population from Korean (n=3), European (n=2), Japanese (n=1), Mexican American (n=1), White non-Hispanic (n=1), Caucasian (n=1) and Mixed (n=3). The male to female ratio in response studies was 1.32 and in remission studies 0.79. We could not determine the mean age of all the studies due to the heterogeneity in data reporting as well as the unavailability of raw data in some of the studies. All studies employed the DSM/ICD-10 diagnostic criteria to determine the MDD phenotype except one study which utilized a questionnaire designed by 23andMe to recruit self-reported patients. These 11 studies

Accepted Manuscript

Downloaded from https://academic.oup.com/ijnp/advance-article/doi/10.1093/ijnp/pyad001/6992242 by Delhi Technological University user on 31 January 2023

reported significant results for 704 polymorphisms in 315 genes. Only rs1908557 SNP have shown genome-wide significance with p value of 2.6×10^{-8}.

3.3 Reproducibility of findings

To narrow the focus of the results presented above, we chose to concentrate our analysis on the replicated genetic variants and genes that were reported two or more time across studies. Of all the positive associations, we found a total of 34 replicated variants with MDD susceptibility. However, 3 variants (rs120074175/TPH2, rs6195/NR3C1 and rs6189+rs6190/NR3C1) had minor allele frequency (MAF) <0.05, hence removed from further analysis. The remaining, 31 replicated variants from candidate studies (N=24), GWAS (N=3) and both candidate and GWAS studies (N=4) are shown in Table 1 and Figure 3a. Additionally, information related to the number of studies reported no association between these variants and MDD susceptibility provided in Supplementary Table S7a. Further, The 5-HTTLPR/*SLC6A4* was the genetic factor that was most frequently investigated (n = 10), followed by rs6265/*BDNF* (n = 8), rs4680/*COMT* (n = 6), rs1801133/*MTHFR* (n = 4) and others. Interestingly, Out of all 31 replicated variants, we observed 13 variants (3 from GWAS, 7 from candidate and 3 from both) i.e. C allele of rs2273289/*PLOD1* in 2 studies , C allele of rs2715148/*PCLO* in 2 studies, C allele of rs2423618/*LINC00687* in 2 studies, T allele of rs1801133/*MTHFR* in 4 studies, T allele of rs5443/*GNB3* in 4 studies, G allele of rs242939/*CRHR1* in 3 studies, G allele of rs6295/*HTR1A* in 3 studies, A allele of rs1006737/*CACNA1C* in 2 studies, T allele of rs4880/*SOD2* in 2 studies, C allele of rs1801131/*MTHFR* in 2 studies, A allele of rs2715147/*PCLO*, G allele of rs9416742/*BICC1* and A allele of rs999845/*BICC1* showed the consistency in reporting the risk allele whereas 18 variants had inconsistent risk allele across studies. Moreover, we have also checked the reproducibility of genes where 27 genes in candidate studies, 8 genes in GWAS and 7 genes

Accepted Manuscript

Downloaded from https://academic.oup.com/ijnp/advance-article/doi/10.1093/ijnp/pyad001/6992242 by Delhi Technological University user on 31 January 2023

in both candidate and GWAS studies replicated which is represented in Table 2 and Figure 3b.

On the other hand, we found 15 genetic variants in candidate, 2 in GWAS and 1 common in candidate and GWAS studies for drug response, as shown in Table 3 and Figure 4a. Whereas, information related to the number of studies reported no association with the antidepressant response provided in Supplementary Table S7b. SNPs located in *SLC6A4*, *BDNF*, *HTR2A*, *HTR1A*, *GNB3*, *CYP1A2*, *NR3C1*, *TPH2*, *COMT*, *GRIK4*, *FKBP5*, *CFAP61* and *UBE3C* were positively replicated in independent populations. Moreover, the only variant that showed a positive association in both GWAS and candidate studies was rs6127921 of *BMP7* gene. Besides, 18 genes in candidate studies, 11 in GWAS and 4 genes in both candidate and GWAS studies were found to be replicated in response studies, represented in Table 4 and Figure 4b.

3.4 Functional annotation of reproducible findings

This study further sought to explore the molecular consequences of these reproducible genetic variants (missense and non-coding) from MDD susceptibility and antidepressant response studies, by using different computational methods. The different functionality prediction servers such as SIFT, PolyPhen-2, RegulomeDB and SNP info were utilized. SIFT and PolyPhen-2 sieved the deleterious non-synonymous SNPs, followed by RegulomeDB which provides information about regulatory SNPs. The prediction analysis of the effect of SNPs on specific functions including splicing regulations, miRNA binding site, regulatory potential and conserveness was performed using the FuncPred tool of SNPinfo. Consequently, we checked a total of 31 replicated variants (7 missense, 14 intronic, 6 UTR/upstream, 1 downstream and 3 synonymous) resulting from MDD susceptible studies

Accepted Manuscript

Downloaded from https://academic.oup.com/ijnp/advance-article/doi/10.1093/ijnp/pyad001/6992242 by Delhi Technological University user on 31 January 2023

shown in Supplementary Table S5. Here, out of 7 missense SNPs, SIFT predicted 1 SNP (14.2%) as deleterious and the rest 7 (85.7%) as tolerated. PolyPhen-2 predicted 2 SNPs (28.5%) as damaging and 5 SNPs (71.4 %) as neutral or benign. Importantly, only nonsynonymous/ missense variant rs1801133/*MTHFR* was predicted to be deleterious and probably damaging by SIFT and PolyPhen-2 respectively. In addition, rs6265/*BDNF* was also predicted as possibly damaging by PolyPhen-2 though tolerated by SIFT. These findings were further strengthened by ClinVar database as rs1801133 was reported to be pathogenic and rs6265 as a risk factor for other psychiatric disorders like schizophrenia and bipolar respectively. Out of all 31 variants, SNPinfo predicted, one variant i.e. rs2715148/*PCLO* affects the miRNA binding site activity and 7 variants (rs4680, rs4880, rs1801131, rs2522833, rs1045642, rs4343, rs2522833) were found to affect the splicing activity. Moreover, 26.6% of SNPs had more than 80% conservation and 16.6% of SNPs had more than 40% regulatory potential. Further, among the 31 variants evaluated with RegulomeDB, 25 variants were predicted to have a regulatory effect ranging from 1d to 5. Out of these 25 variants, two variants i.e. rs1800629/*TNF* (score = 1d) and rs1801131/*MTHFR* (score = 1f) got the lowest scores and thus most likely to be involved in eQTL functions. Similarly, 4 variants i.e. rs4343/*ACE*, rs2242446/*SLC6A2*, rs41423247/NR3C1, rs2273289/*PLOD1* was assigned a rank of 2b which indicate TF binding + any motif + DNase Footprint +DNase peak.

We also observed, of 31 replicated variants, 26 (83.8%) and 16 (51.6%) genes were found to have behavioral/neurological knockout mouse model and are known targets of antidepressant drugs, respectively. Further, 12 (38.7 %) genes have shown to preferentially expressed in the brain (Supplementary table S5).

Likewise, we checked the functional relevance of 18 variants (7 intronic, 5 UTR/upstream, 3 synonymous, 1 missense and 2 unknown) resulted from antidepressant response studies

Accepted Manuscript

Downloaded from https://academic.oup.com/ijnp/advance-article/doi/10.1093/ijnp/pyad001/6992242 by Delhi Technological University user on 31 January 2023

shown in Supplementary Table S6. One missense variant rs6265/*BDNF* was predicted to be possibly damaging by PolyPhen-2. Of all genetic variants, SNPInfo predicted none of the SNPs to affect splicing and miRNA binding activity. However, 3 SNPs had more than 80% conservation and 3 SNPs had more than 40% regulatory potential. Further, RegulomeDB analysis identified 15 SNPs with regulatory effect ranging from 1f to 5. Three variants, rs2470890/*CYP1A2* (score = 1f), rs41423247/*NR3C1* (score = 2b) and rs6313/*HTR2A* (score = 3a) was found most likely to affect the transcription factor binding activity with a score <3. Besides, 15 (83.3%) and 13 (72.2%) genes of replicated variants were found to have behavioral/neurological knockout mouse phenotype and known targets of antidepressant drugs, respectively. Also, 13 (72.2 %) genes have shown to preferentially expressed in the brain (Supplementary table S6).

3.5 Diagnostic predictability

The allele frequency of reproducible variants were utilized for sensitivity and specificity analysis (Table 1). The majority of replicated findings were inconsistent in their reported risk allele such as the 5-HTTLPR, which appeared in ten studies, the short (S) form was reported in 7 studies and long (L) form in 3 studies. Therefore, studies reported the same type of risk allele were pooled together for sensitivity and specificity analysis. G allele of rs6265/*BDNF* had the highest sensitivity (0.78) whereas G allele of rs242939/*CRHR1* had the highest specificity (0.93). Moreover, the positive predictive values for 19 genetic variants range from 0.49 to 0.66. Most of them had moderate PPV. However, we could not perform the diagnostic predictability for a few variants (n = 6) due to unavailable raw data. Additionally, if a replication of variant is because of two studies that reported the two different risk alleles (n = 6) then assessment of sensitivity and specificity could not be calculated.

Accepted Manuscript

Downloaded from https://academic.oup.com/ijnp/advance-article/doi/10.1093/ijnp/pyad001/6992242 by Delhi Technological University user on 31 January 2023

In response studies, out of 18 variants, we could only assess the diagnostic predictability of 5 variants (PPV between 0.36 to 0.66) as the majority of replicated findings were inconsistent in their response status, drug class, associated phenotype, population and reported risk allele, therefore cannot be cumulated/pooled (Table 3).

4. Discussion

This study comprehensively evaluated the original articles on genetic association studies of MDD susceptibility and antidepressant treatment response, independently. A total of 217 studies of MDD susceptibility and 128 studies of drug response met our *apriori* inclusion criteria and were described in the present study. The results of this article have shown that the majority of the positive associations were confirmed by only one study thereby cannot exclude the possibility of having been obtained by chance, and thus are not sufficient to establish a link with MDD susceptibility or antidepressant treatment response. Therefore, the rest of the discussion is limited to reproducible findings at the SNP or gene level generated in more than one independent study. In total, we found 31 and 18 replicated variants in MDD susceptibility and antidepressant drug response, respectively. Further, taking all these findings into account, it appears most studies used the candidate gene approach, as a result, a large number of SNPs and genes were found to be replicated in candidate studies as compared to GWAS studies which demonstrate the surprisingly small overlap of genetic variants across studies. Also, none of the variants from candidate studies appeared among the top hits in any of the identified GWAS. Nevertheless, we identified an important overlap of positive association of 4 (rs2522833/*PCLO*, rs2715147/*PCLO*, rs9416742/ *BICC1*, and rs999845/ *BICC1*) and 1 (rs6127921/*BMP7*) variant between candidate and GWAS studies in MDD susceptibility and antidepressant response, respectively. Replication of variants between candidate and unbiased GWAS studies greatly increases the acceptability of genotype and phenotype association. Besides replication, several evidence regarding the

Accepted Manuscript

Downloaded from https://academic.oup.com/ijnp/advance-article/doi/10.1093/ijnp/pyad001/6992242 by Delhi Technological University user on 31 January 2023

biological relevance of *PCLO*, *BICC1* and *BMP7* have also been reported in the literature. A meta-analysis by Hek et al. (2010) provided additional evidence of significant association ($p = 2.16 \times 10^{-3}$) between SNP rs2522833/PCLO and depressive disorders in a population-based study. In addition, rs2522833 variant causes change in amino acid from serine to alanine in a piccolo C2A calcium binding domain (Verbeek et al., 2012), whose overexpression causes depression like behavior in mice (Furukawa-Hibi et al., 2010). Similarly, expression of *BICC1* was reported to be upregulated in the post-mortem brains of individuals with MDD and expression levels of the same observed to be reduced after antidepressant treatment in rat models of chronic stress (Ota et al., 2015). Furthermore, a significant reduction in the expression of *BMP7* gene in locus coeruleus region of post-mortem brains of individuals with MDD has also been evidenced in the literature (Ordway et al., 2012). Thus, these variants would most likely be of considerable interest in future studies.

Further, the functional annotation of reproducible variants of MDD susceptibility revealed two non-synonymous/missense variants (rs1801133/*MTHFR* and rs6265/*BDNF*) as deleterious/damaging and 6 variants (rs1800629/*TNF*, rs1801131/*MTHFR*, rs4343/*ACE*, rs2242446/*SLC6A2*, rs2273289/*PLOD1*, and rs41423247/*NR3C1*) with a score of <3 had high regulatory effect in disease condition. On the other hand, functional annotation of variants from antidepressant treatment response predicted one non-synonymous/missense variant (rs6265/*BDNF*) as damaging and three non-coding variants (rs2470890/*CYP1A2*, rs6313/*HTR2A*, and rs41423247/*NR3C1*) with high regulatory effect. Moreover, diagnostic predictability of reproducible variants revealed moderate PPV ranges between 0.49 to 0.66 in MDD susceptibility and 0.36 to 0.66 in antidepressant drug response. This quantitative measure offers a substantial hint towards a direction of predictability and also corroborates to increasing the significance of replicated findings.

Accepted Manuscript

Downloaded from https://academic.oup.com/ijnp/advance-article/doi/10.1093/ijnp/pyad001/6992242 by Delhi Technological University user on 31 January 2023

Of all the positive association studies, 5-HTT gene-linked polymorphic region (5-HTTLPR) polymorphism has achieved a particular attention for being the most replicated variant in both disease (N=10) and drug response studies (N=22). The two allelic variants, S and L, are due to deletion and insertion of 44 bp in promoter region, respectively. S allele is demonstrated to have lower transcriptional activity than L allele, resulting in the reduction of serotonin transporter in the cell membrane. Consequently, the reduction of 5-HTT causes the imbalance of serotonin concentration and function (Fratelli et al., 2020). However, we observed a significant inconsistency in the reported risk allele across studies. For example, in disease, 5HTTLPR, appeared in ten studies, wherein the S form was reported as risk allele in 7 studies and L form in 3 studies. The heterogeneity in reported risk allele even within same geographical population weakens our confidence in proposing them as a probable genetic diagnostic marker. In a similar line, there were 17 (rs6265, rs4680, rs2242446, rs1045642, rs9340799, rs2234693, rs4291, rs6311, rs1360780, rs4713916, rs1800532, rs1800629, rs4295, rs6195, rs2522833, rs4343 and rs41423247) and 9 (5HTTLPR, rs6265, rs7997012, rs6295, rs5443, rs2470890, rs6313, rs2171363, rs1954787) replicated variants associated with MDD susceptibility and drug response, respectively, where authors have found discrepancy in reported risk allele, suggesting a more robust future study design for such candidate gene studies.

Therefore, reproducible variants reported single risk allele across studies are of prime importance and could be taken forward for diagnostic and therapeutic application. In total 14 variants in MDD susceptibility and 6 in antidepressant response reported the consistent findings in terms of risk allele. However, due to the unavailability of raw data we could assess the diagnostic predictability of only 7 and 2 variants in disease and drug response, respectively. Interestingly, we observed variants of *FKBP5* and *HTR2A* genes are being commercially utilized for diagnostic application in MDD gene panels (Rubinstein et al.,

Accepted Manuscript

Downloaded from https://academic.oup.com/ijnp/advance-article/doi/10.1093/ijnp/pyad001/6992242 by Delhi Technological University user on 31 January 2023

2013) and the replication of variants in these gene, rs1360780/*FKBP5* (PPV=0.53), rs4713916/*FKBP5* (PPV=0.53) and rs6311/*HTR2A* (PPV=0.54) are demonstrated in our analysis. Though, the diagnostic predictability of these variants were found to be moderate. This observation inclined our interest to all the other reproducible variants with moderate diagnostic predictability and suggested the importance of other potential variants for diagnostic purposes. And since there is no specific guidelines to date regarding selection of diagnostic or predictive marker, we are proposing few probable candidates (shown in Table 5) for diagnostic/predictive genetic panel for MDD susceptibility and to predict antidepressant response.

In addition to reproducibility with single risk allele, these variants have clinical relevance as well. Like, out of seven, there were missense (rs1801133/*MTHFR*, rs1801131/*MTHFR*, rs4880/*SOD2*) variants including one SNP (rs1801133/*MTHFR*) annotated as having deleterious/damaging effect. Two of the SNPs (rs4880/*SOD2*; and rs1801131/*MTHFR*) were identified to be present at splice site. In addition, of all the variants were predicted to have a regulatory role in transcription factor binding site activity, importantly, rs1801133/*MTHFR* (score = 1F) that involved eQTL function as well. Majority of genes have shown to be preferentially expressed in brain and are known targets of antidepressant drugs. Moreover, all the 7 variants from disease and two variants from drug response, consistently been found to be associated with moderate positive predictive value. Hence, this work holds promise highlighting biologically important markers for MDD susceptibility and antidepressant response assessment.

Even though, this study is an attempt to provide a wide landscape of genetic literature, we must acknowledge the limitations as well. First and foremost, our search is limited to only MEDLINE, and studies in English, there is possibility of non-inclusion of relevant data outside these criteria. Secondly, in antidepressant response search data was excluded where

Accepted Manuscript

Downloaded from https://academic.oup.com/ijnp/advance-article/doi/10.1093/ijnp/pyad001/6992242 by Delhi Technological University user on 31 January 2023

response is assessed based on percentage improvement, and where data was not compared between responder and non-responder or remitter and non-remitter groups. However, the exclusion was according to the protocol, as we have aimed to focus specifically on studies considered dichotomous groups. Moreover, heterogeneity in antidepressant class, response status, inconsistent risk allele and unavailability of raw data limits us to calculate the predictability of most of the replicated polymorphisms. Nevertheless, we maintained the consensus across studies by calculating the unadjusted p value and odds ratio for risk allele, wherever raw data (allele frequency) was provided. We found most findings were inconsistent in reporting the risk allele even in same population across studies which unqualified us to draw any robust conclusion by nullifying the assumption of population specific risk allele. The reason for these inconsistencies could be addressed by small sample size and large publication bias in addition to other technical or methodological differences among studies. Further, GWAS published to date have largely not replicated the candidate gene polymorphisms that have been conducted over the past many years, which may be attributed to the polygenic nature of the disease. Lastly, the use of sensitivity and specificity as quantitative assessment to estimate diagnostic predictability was solely based on available evidence. With the publication of more new studies, such measures may vary. Hence, our study only suggests a direction of predictability and should be used judiciously for clinical interpretations.

5. Conclusion and future directions

This study attempted to provide a holistic landscape of all genetic association studies related to MDD risk and antidepressant response. Despite of substantial heterogeneity in genetic association across studies, study design, and drugs administered, we identified 31 and 18

Accepted Manuscript

Downloaded from https://academic.oup.com/ijnp/advance-article/doi/10.1093/ijnp/pyad001/6992242 by Delhi Technological University user on 31 January 2023

genomic regions which showed independent replication in MDD susceptibility and antidepressant response studies, respectively. Importantly, 4 variants (rs2522833/PCLO, rs2715147/PCLO, rs9416742/ BICC1, and rs999845/ BICC1) in MDD and 1 (rs6127921/BMP7) variant with antidepressant response are of high potential as they are significantly associated in both candidate and GWAS studies. Further, the variants that are significantly replicated in the candidate as well as GWAS studies, with consistent risk allele and moderate positive predictive values i.e., 7 (rs1801133, rs5443, rs242939, rs1006737, rs4880, rs6295, rs1801131) with MDD, and 2 (STin2, rs41423247) with antidepressant drug response are of high interest for diagnostic and therapeutic applications after appropriate validation. Besides, this article would serve as the basis for selecting the candidate variants and researchers can directly take up these replicated variants (31 in MDD disease and 18 in drug response) for performing future meta-analysis and functional validation. Moreover, it is also important to emphasize on remaining significant associations found in single study. Hence, replication of these genetic associations are crucial in order to ascertain the significance, whether random or causal.

Accepted Manuscript

Downloaded from https://academic.oup.com/ijnp/advance-article/doi/10.1093/ijnp/pyad001/6992242 by Delhi Technological University user on 31 January 2023

Funding

This work was supported by Indian Council of Medical Research (ICMR) funded project (GAP0136) and Council of Scientific and Industrial Research (CSIR) funded project (OLP1120).

Acknowledgements

The authors would like to acknowledge Dr. Anurag Agarwal, Director, CSIR-IGIB, for his unconditional support in resource management and scientific vision. PS acknowledges UGC, Govt. of India, AS and ST acknowledge CSIR, Govt. of India, and DG acknowledges ICMR for providing their respective fellowships.

Statement of interest

The authors declare no potential conflict of interest.

Authors' contributions

RK conceived the concept of this study and structured the study design. RK and PS designed the pipeline of this article. RK reviewed the manuscript and supervised the overall study. PS, AS prepared the tables and supplementary material. PS, AS and RK interpreted and managed the data. They also visualized, designed and generated the figures. DG, ST and RK scrutinized the data/ manuscript and provided valuable insights to improve the manuscript. All authors reviewed successive drafts and approved the final version of the article.

Accepted Manuscript

Downloaded from https://academic.oup.com/jnp/advance-article/doi/10.1093/jnp/pyad001/6992242 by Delhi Technological University user on 31 January 2023

References

Aberg E, Fandino-Losada A, Sjoholm LK, Forsell Y, Lavebratt C (2011) The functional Val158Met polymorphism in catechol-O-methyltransferase (COMT) is associated with depression and motivation in men from a Swedish population-based study. *J Affect Disord* 129:158-166.

Adzhubei IA, Schmidt S, Peshkin L, Ramensky VE, Gerasimova A, Bork P, Kondrashov AS, Sunyaev SR (2010) A method and server for predicting damaging missense mutations. *Nat Methods* 7:248-249.

Aldoghachi AF, Tor YS, Redzun SZ, Lokman KAB, Razaq NAA, Shahbudin AF, Badamasi IM, Cheah PS, Stanslas J, Veerakumarasivam A, Rosli R, Ibrahim N, Lye MS, Ling KH (2019) Screening of brain-derived neurotrophic factor (BDNF) single nucleotide polymorphisms and plasma BDNF levels among Malaysian major depressive disorder patients. *PLoS One* 14:e0211241.

Alexopoulos GS, Murphy CF, Gunning-Dixon FM, Glatt CE, Latoussakis V, Kelly RE, Jr., Kanellopoulos D, Klimstra S, Lim KO, Young RC, Hoptman MJ (2009) Serotonin transporter polymorphisms, microstructural white matter abnormalities and remission of geriatric depression. *J Affect Disord* 119:132-141.

Ancelin ML, Carriere I, Scali J, Ritchie K, Chaudieu I, Ryan J (2013) Angiotensin-converting enzyme gene variants are associated with both cortisol secretion and late-life depression. *Transl Psychiatry* 3:e322.

Angunsri R, Sritharathikhun T, Suttirat S, Tencomnao T (2009) Association of angiotensin-converting enzyme gene promoter single nucleotide polymorphisms and haplotype with major depression in a northeastern Thai population. *J Renin Angiotensin Aldosterone Syst* 10:179-184.

Accepted Manuscript

Downloaded from https://academic.oup.com/ijnp/advance-article/doi/10.1093/ijnp/pyad001/6992242 by Delhi Technological University user on 31 January 2023

Arias B, Catalan R, Gasto C, Gutierrez B, Fananas L (2003) 5-HTTLPR polymorphism of the serotonin transporter gene predicts non-remission in major depression patients treated with citalopram in a 12-weeks follow up study. *J Clin Psychopharmacol* 23:563-567.

Arinami T, Yamada N, Yamakawa-Kobayashi K, Hamaguchi H, Toru M (1997) Methylenetetrahydrofolate reductase variant and schizophrenia/depression. *Am J Med Genet* 74:526-528.

Baghai TC et al. (2006) Polymorphisms in the angiotensin-converting enzyme gene are associated with unipolar depression, ACE activity and hypercortisolism. *Mol Psychiatry* 11:1003-1015.

Basu A, Chadda RK, Sood M, Kaur H, Kukreti R (2015) Association of serotonin transporter (SLC6A4) and receptor (5HTR1A, 5HTR2A) polymorphisms with response to treatment with escitalopram in patients with major depressive disorder: A preliminary study. *Indian J Med Res* 142:40-45.

Basu A, Chadda RK, Sood M, Kaur H, Kukreti R (2019) A preliminary association study between serotonin transporter (5-HTTLPR), receptor polymorphisms (5-HTR1A, 5-HTR2A) and depression symptom-clusters in a north Indian population suffering from Major Depressive Disorder (MDD). *Asian J Psychiatr* 43:184-188.

Biernacka JM et al. (2015) The International SSRI Pharmacogenomics Consortium (ISPC): a genome-wide association study of antidepressant treatment response. *Transl Psychiatry* 5:e553.

Binder EB et al. (2004) Polymorphisms in FKBP5 are associated with increased recurrence of depressive episodes and rapid response to antidepressant treatment. Nat Genet 36:1319-1325.

Border R, Johnson EC, Evans LM, Smolen A, Berley N, Sullivan PF, Keller MC (2019) No Support for Historical Candidate Gene or Candidate Gene-by-Interaction Hypotheses for Major Depression Across Multiple Large Samples. *Am J Psychiatry* 176:376-387.

Accepted Manuscript

Downloaded from https://academic.oup.com/ijnp/advance-article/doi/10.1093/ijnp/pyad001/6992242 by Delhi Technological University user on 31 January 2023

Boyle AP, Hong EL, Hariharan M, Cheng Y, Schaub MA, Kasowski M, Karczewski KJ, Park J, Hitz BC, Weng S, Cherry JM, Snyder M (2012) Annotation of functional variation in personal genomes using RegulomeDB. *Genome Res* 22:1790-1797.

Bozina N, Peles AM, Sagud M, Bilusic H, Jakovljevic M (2008) Association study of paroxetine therapeutic response with SERT gene polymorphisms in patients with major depressive disorder. *World J Biol Psychiatry* 9(3):190-7.

Calabro M, Fabbri C, Crisafulli C, Albani D, Forloni G, Kasper S, Sidoti A, Velardi E, Zohar J, Juven-Wetzler A, Souery D, Montgomery S, Mendlewicz J, Serretti A (2018) The serotonin transporter and the activity regulated cytoskeleton-associated protein genes in antidepressant response and resistance: 5-HTTLPR and other variants. *Hum Psychopharmacol* 33:e2682.

Camarena B, Alvarez-Icaza D, Hernandez S, Aguilar A, Munch L, Martinez C, Becerra-Palars C (2019) Association Study Between Serotonin Transporter Gene and Fluoxetine Response in Mexican Patients With Major Depressive Disorder. *Clin Neuropharmacol* 42:9-13.

Cao MQ, Hu SY, Zhang CH, Xia DS (2007) Study on the interrelationship between 5-HTTLPR/G-protein beta3 subunit (C825T) polymorphisms and depressive disorder. *Psychiatr Genet* 17:233-238.

Cao S, Li H, Lou L, Xie Z, Zhao X, Pang J, Sui J, Xie G (2015) Association study between 5-HT2A and NET gene polymorphisms and recurrent major depression disorder in Chinese Han population. *Pak J Pharm Sci* 28:1101-1108.

Cerri AP, Arosio B, Viazzoli C, Confalonieri R, Teruzzi F, Annoni G (2009) -308(G/A) TNF-alpha gene polymorphism and risk of depression late in the life. *Arch Gerontol Geriatr* 49 Suppl 1:29-34.

Accepted Manuscript

Downloaded from https://academic.oup.com/ijnp/advance-article/doi/10.1093/ijnp/pyad001/6992242 by Delhi Technological University user on 31 January 2023

Chang HS, Lee HY, Cha JH, Won ES, Ham BJ, Kim B, Lee MS (2014) Interaction of 5-HTT and HTR1A gene polymorphisms in treatment responses to mirtazapine in patients with major depressive disorder. *J Clin Psychopharmacol* 34:446-454.

Chen J, Wang M, Waheed Khan RA, He K, Wang Q, Li Z, Shen J, Song Z, Li W, Wen Z, Jiang Y, Xu Y, Shi Y, Ji W (2015) The GSK3B gene confers risk for both major depressive disorder and schizophrenia in the Han Chinese population. *J Affect Disord* 185:149-155.

Chi MH, Chang HH, Lee SY, Lee IH, Gean PW, Yang YK, Lu RB, Chen PS (2010) Brain derived neurotrophic factor gene polymorphism (Val66Met) and short-term antidepressant response in major depressive disorder. *J Affect Disord* 126:430-435.

Choi MJ, Kang RH, Ham BJ, Jeong HY, Lee MS (2005) Serotonin receptor 2A gene polymorphism (-1438A/G) and short-term treatment response to citalopram. *Neuropsychobiology* 52:155-162.

Choi MJ, Kang RH, Lim SW, Oh KS, Lee MS (2006) Brain-derived neurotrophic factor gene polymorphism (Val66Met) and citalopram response in major depressive disorder. *Brain Res* 1118:176-182.

Choi MJ, Lee HJ, Lee HJ, Ham BJ, Cha JH, Ryu SH, Lee MS (2004) Association between major depressive disorder and the -1438A/G polymorphism of the serotonin 2A receptor gene. *Neuropsychobiology* 49:38-41.

Cocchi E, Fabbri C, Han C, Lee SJ, Patkar AA, Masand PS, Pae CU, Serretti A (2016) Genome-wide association study of antidepressant response: involvement of the inorganic cation transmembrane transporter activity pathway. *BMC Psychiatry* 16:106.

Congiu C, Minelli A, Bonvicini C, Bortolomasi M, Sartori R, Maj C, Scassellati C, Maina G, Trabucchi L, Segala M, Gennarelli M (2015) The role of the potassium channel gene KCNK2 in major depressive disorder. *Psychiatry Res* 225:489-492.

Accepted Manuscript

Downloaded from https://academic.oup.com/ijnp/advance-article/doi/10.1093/ijnp/pyad001/6992242 by Delhi Technological University user on 31 January 2023

consortium C (2015) Sparse whole-genome sequencing identifies two loci for major depressive disorder. *Nature* 523:588-591.

Dong C, Wong ML, Licinio J (2009) Sequence variations of ABCB1, SLC6A2, SLC6A3, SLC6A4, CREB1, CRHR1 and NTRK2: association with major depression and antidepressant response in Mexican-Americans. *Mol Psychiatry* 14:1105-1118.

Dorado P, Penas-Lledo EM, Gonzalez AP, Caceres MC, Cobaleda J, Llerena A (2007) Increased risk for major depression associated with the short allele of the serotonin transporter promoter region (5-HTTLPR-S) and the CYP2C9*3 allele. *Fundam Clin Pharmacol* 21:451-453.

El-Hage W, Vourc'h P, Gaillard P, Leger J, Belzung C, Ibarguen-Vargas Y, Andres CR, Camus V (2015) The BDNF Val(66)Met polymorphism is associated with escitalopram response in depressed patients. *Psychopharmacology* (Berl) 232:575-581.

Esaki K, Kondo K, Hatano M, Saito T, Kishi T, Umene-Nakano W, Yoshimura R, Nakamura J, Ozaki N, Ikeda M, Iwata N (2013) Further evidence of an association between a genetic variant in BMP7 and treatment response to SSRIs in major depressive disorder. *J Hum Genet* 58:568-569.

Evinova A, Babusikova E, Straka S, Ondrejka I, Lehotsky J (2012) Analysis of genetic polymorphisms of brain-derived neurotrophic factor and methylenetetrahydrofolate reductase in depressed patients in a Slovak (Caucasian) population. *Gen Physiol Biophys* 31:415-422.

Fabbri C, Drago A, Serretti A (2013) Early antidepressant efficacy modulation by glutamatergic gene variants in the STAR*D. *Eur Neuropsychopharmacol* 23:612-621.

Fabbri C, Corponi F, Souery D, Kasper S, Montgomery S, Zohar J, Rujescu D, Mendlewicz J, Serretti A (2019) The Genetics of Treatment-Resistant Depression: A Critical Review and Future Perspectives. *Int J Neuropsychopharmacol* 22:93-104.

Accepted Manuscript

Downloaded from https://academic.oup.com/ijnp/advance-article/doi/10.1093/ijnp/pyad001/6992242 by Delhi Technological University user on 31 January 2023

Feczko E, Miranda-Dominguez O, Marr M, Graham AM, Nigg JT, Fair DA (2019) The Heterogeneity Problem: Approaches to Identify Psychiatric Subtypes. *Trends Cogn Sci* 23:584-601.

Firouzabadi D, Firouzabadi N, Kalani K, Zomorrodian K, Tehrani ES (2019) Response to sertraline is influenced by GNbeta3 gene G-350A variant in patients with major depressive disorder. *Eur J Clin Pharmacol* 75:189-194.

Firouzabadi N, Shafiei M, Bahramali E, Ebrahimi SA, Bakhshandeh H, Tajik N (2012) Association of angiotensin-converting enzyme (ACE) gene polymorphism with elevated serum ACE activity and major depression in an Iranian population. *Psychiatry Res* 200:336-342.

Fratelli C, Siqueira J, Silva C, Ferreira E, Silva I (2020) 5HTTLPR Genetic Variant and Major Depressive Disorder: A Review. *Genes* (Basel) 11.

Fujii T, Ota M, Hori H, Sasayama D, Hattori K, Teraishi T, Yamamoto N, Hashikura M, Tatsumi M, Higuchi T, Kunugi H (2012) Association between the functional polymorphism (C3435T) of the gene encoding P-glycoprotein (ABCB1) and major depressive disorder in the Japanese population. *J Psychiatr Res* 46:555-559.

Fukui N, Suzuki Y, Sugai T, Watanabe J, Ono S, Tsuneyama N, Someya T (2014) Promoter variation in the catechol-O-methyltransferase gene is associated with remission of symptoms during fluvoxamine treatment for major depression. *Psychiatry Res* 218:353-355.

Furukawa-Hibi Y, Nitta A, Fukumitsu H, Somiya H, Furukawa S, Nabeshima T, Yamada K (2010) Overexpression of piccolo C2A domain induces depression-like behavior in mice. *Neuroreport* 21:1177-1181.

Gabriela Nielsen M, Congiu C, Bortolomasi M, Bonvicini C, Bignotti S, Abate M, Milanesi E, Conca A, Cattane N, Tessari E, Gennarelli M, Minelli A (2015) MTHFR: Genetic variants,

Accepted Manuscript

Downloaded from https://academic.oup.com/ijnp/advance-article/doi/10.1093/ijnp/pyad001/6992242 by Delhi Technological University user on 31 January 2023

expression analysis and COMT interaction in major depressive disorder. *J Affect Disord* 183:179-186.

Galecka E, Szemraj J, Bienkiewicz M, Majsterek I, Przybylowska-Sygut K, Galecki P, Lewinski A (2013) Single nucleotide polymorphisms of NR3C1 gene and recurrent depressive disorder in population of Poland. *Mol Biol Rep* 40:1693-1699.

Galecki P, Smigielski J, Florkowski A, Bobinska K, Pietras T, Szemraj J (2010) Analysis of two polymorphisms of the manganese superoxide dismutase gene (Ile-58Thr and Ala-9Val) in patients with recurrent depressive disorder. *Psychiatry Res* 179:43-46.

García-Gutiérrez MS, Navarrete F, Sala F, Gasparyan A, Austrich-Olivares A, Manzanares J (2020) Biomarkers in Psychiatry: Concept, Definition, Types and Relevance to the Clinical Reality. *Front Psychiatry* 11:432.

Garriock HA, Kraft JB, Shyn SI, Peters EJ, Yokoyama JS, Jenkins GD, Reinalda MS, Slager SL, McGrath PJ, Hamilton SP (2010) A genomewide association study of citalopram response in major depressive disorder. *Biol Psychiatry* 67:133-138.

Gasso P, Blazquez A, Rodriguez N, Boloc D, Torres T, Mas S, Lafuente A, Lazaro L (2018) Further Support for the Involvement of Genetic Variants Related to the Serotonergic Pathway in the Antidepressant Response in Children and Adolescents After a 12-Month Follow-Up: Impact of the HTR2A rs7997012 Polymorphism. *J Child Adolesc Psychopharmacol* 28:711-718.

Geng LY, Ye DQ, Shi YY, Xu Z, Pu MJ, Li ZY, Li XL, Li Y, Zhang ZJ (2014) Influence of genetic polymorphisms involved in the hypothalamic-pituitary-adrenal axis and their interactions with environmental factors on antidepressant response. *CNS Neurosci Ther* 20:237-243.

Geng YG, Su QR, Su LY, Chen Q, Ren GY, Shen SQ, Yu AY, Xia GY (2007) Comparison of the polymorphisms of androgen receptor gene and estrogen alpha and beta gene between

Accepted Manuscript

Downloaded from https://academic.oup.com/ijnp/advance-article/doi/10.1093/ijnp/pyad001/6992242 by Delhi Technological University user on 31 January 2023

adolescent females with first-onset major depressive disorder and controls. *Int J Neurosci* 117:539-547.

Gratacos M, Soria V, Urretavizcaya M, Gonzalez JR, Crespo JM, Bayes M, de Cid R, Menchon JM, Vallejo J, Estivill X (2008) A brain-derived neurotrophic factor (BDNF) haplotype is associated with antidepressant treatment outcome in mood disorders. *Pharmacogenomics J* 8:101-112.

Green EK, Grozeva D, Jones I, Jones L, Kirov G, Caesar S, Gordon-Smith K, Fraser C, Forty L, Russell E, Hamshere ML, Moskvina V, Nikolov I, Farmer A, McGuffin P, Wellcome Trust Case Control C, Holmans PA, Owen MJ, O'Donovan MC, Craddock N (2010) The bipolar disorder risk allele at CACNA1C also confers risk of recurrent major depression and of schizophrenia. *Mol Psychiatry* 15:1016-1022.

Grünblatt E, Löffler C, Zehetmayer S, Jungwirth S, Tragl KH, Riederer P, Fischer P (2006) Association study of the 5-HTTLPR polymorphism and depression in 75-Year-Old nondemented subjects from the Vienna Transdanube Aging (VITA) study. *J Clin Psychiatry* 67:1373-1378.

Gutiérrez B, Pintor L, Gastó C, Rosa A, Bertranpetit J, Vieta E, Fañanás L (1998) Variability in the serotonin transporter gene and increased risk for major depression with melancholia. *Hum Genet* 103:319-322.

Haenisch B, Linsel K, Bruss M, Gilsbach R, Propping P, Nothen MM, Rietschel M, Fimmers R, Maier W, Zobel A, Hofels S, Guttenthaler V, Gothert M, Bonisch H (2009) Association of major depression with rare functional variants in norepinephrine transporter and serotonin1A receptor genes. *Am J Med Genet B Neuropsychiatr Genet* 150B:1013-1016.

Ham BJ, Lee BC, Paik JW, Kang RH, Choi MJ, Choi IG, Lee MS (2007) Association between the tryptophan hydroxylase-1 gene A218C polymorphism and citalopram

Accepted Manuscript

Downloaded from https://academic.oup.com/ijnp/advance-article/doi/10.1093/ijnp/pyad001/6992242 by Delhi Technological University user on 31 January 2023

antidepressant response in a Korean population. *Prog Neuropsychopharmacol Biol Psychiatry* 31:104-107.

He K, An Z, Wang Q, Li T, Li Z, Chen J, Li W, Wang T, Ji J, Feng G, Lin H, Yi Q, Shi Y (2014) CACNA1C, schizophrenia and major depressive disorder in the Han Chinese population. *Br J Psychiatry* 204:36-39.

Hek K, Mulder CL, Luijendijk HJ, van Duijn CM, Hofman A, Uitterlinden AG, Tiemeier H (2010) The PCLO gene and depressive disorders: replication in a population-based study. *Hum Mol Genet* 19:731-734.

Hoefgen B, Schulze TG, Ohlraun S, von Widdern O, Hofels S, Gross M, Heidmann V, Kovalenko S, Eckermann A, Kolsch H, Metten M, Zobel A, Becker T, Nothen MM, Propping P, Heun R, Maier W, Rietschel M (2005) The power of sample size and homogenous sampling: association between the 5-HTTLPR serotonin transporter polymorphism and major depressive disorder. *Biol Psychiatry* 57:247-251.

Hong CJ, Chen TJ, Yu YW, Tsai SJ (2006) Response to fluoxetine and serotonin 1A receptor (C-1019G) polymorphism in Taiwan Chinese major depressive disorder. *Pharmacogenomics J* 6:27-33.

Howard DM et al. (2021) Author Correction: Genome-wide association study of depression phenotypes in UK Biobank identifies variants in excitatory synaptic pathways. *Nat Commun* 12:2012.

Howard DM et al. (2019) Genome-wide meta-analysis of depression identifies 102 independent variants and highlights the importance of the prefrontal brain regions. *Nat Neurosci* 22:343-352.

Hua P, Liu W, Chen D, Zhao Y, Chen L, Zhang N, Wang C, Guo S, Wang L, Xiao H, Kuo SH (2014) Cry1 and Tef gene polymorphisms are associated with major depressive disorder in the Chinese population. *J Affect Disord* 157:100-103.

Accepted Manuscript

Downloaded from https://academic.oup.com/ijnp/advance-article/doi/10.1093/ijnp/pyad001/6992242 by Delhi Technological University user on 31 January 2023

Huang X, Yu T, Li X, Cao Y, Li X, Liu B, Yang F, Li W, Zhao X, Feng G, Zhang X, Dong Z, He L, Sun X, He G (2013) ABCB6, ABCB1 and ABCG1 genetic polymorphisms and antidepressant response of SSRIs in Chinese depressive patients. *Pharmacogenomics* 14:1723-1730.

Hwang JP, Tsai SJ, Hong CJ, Yang CH, Lirng JF, Yang YM (2006) The Val66Met polymorphism of the brain-derived neurotrophic-factor gene is associated with geriatric depression. *Neurobiol Aging* 27:1834-1837.

Hyde CL, Nagle MW, Tian C, Chen X, Paciga SA, Wendland JR, Tung JY, Hinds DA, Perlis RH, Winslow AR (2016) Identification of 15 genetic loci associated with risk of major depression in individuals of European descent. *Nat Genet* 48:1031-1036.

Illi A, Poutanen O, Setala-Soikkeli E, Kampman O, Viikki M, Huhtala H, Mononen N, Haraldsson S, Koivisto PA, Leinonen E, Lehtimaki T (2011) Is 5-HTTLPR linked to the response of selective serotonin reuptake inhibitors in MDD? *Eur Arch Psychiatry Clin Neurosci* 261:95-102.

Inoue K, Itoh K, Yoshida K, Shimizu T, Suzuki T (2004) Positive association between T-182C polymorphism in the norepinephrine transporter gene and susceptibility to major depressive disorder in a japanese population. *Neuropsychobiology* 50:301-304.

Ishitobi Y, Nakayama S, Yamaguchi K, Kanehisa M, Higuma H, Maruyama Y, Ninomiya T, Okamoto S, Tanaka Y, Tsuru J, Hanada H, Isogawa K, Akiyoshi J (2012) Association of CRHR1 and CRHR2 with major depressive disorder and panic disorder in a Japanese population. *Am J Med Genet B Neuropsychiatr Genet* 159B:429-436.

Jansson M, Gatz M, Berg S, Johansson B, Malmberg B, McClearn GE, Schalling M, Pedersen NL (2003) Association between depressed mood in the elderly and a 5-HTR2A gene variant. *Am J Med Genet B Neuropsychiatr Genet* 120B:79-84.

Accepted Manuscript

Downloaded from https://academic.oup.com/ijnp/advance-article/doi/10.1093/ijnp/pyad001/6992242 by Delhi Technological University user on 31 January 2023

Jelen AM, Salagacka A, Zebrowska MK, Mirowski M, Talarowska M, Galecki P, Balcerczak EI (2015) The Influence of C3435T Polymorphism of the ABCB1 Gene on Genetic Susceptibility to Depression and Treatment Response in Polish Population - Preliminary Report. *Int J Med Sci* 12:974-979.

Ji W, Li T, Pan Y, Tao H, Ju K, Wen Z, Fu Y, An Z, Zhao Q, Wang T, He L, Feng G, Yi Q, Shi Y (2013) CNTNAP2 is significantly associated with schizophrenia and major depression in the Han Chinese population. *Psychiatry Res* 207:225-228.

Ji Y, Biernacka J, Snyder K, Drews M, Pelleymounter LL, Colby C, Wang L, Mrazek DA, Weinshilboum RM (2012) Catechol O-methyltransferase pharmacogenomics and selective serotonin reuptake inhibitor response. *Pharmacogenomics J* 12:78-85.

Jun TY, Pae CU, Hoon H, Chae JH, Bahk WM, Kim KS, Serretti A (2003) Possible association between -G308A tumour necrosis factor-alpha gene polymorphism and major depressive disorder in the Korean population. *Psychiatr Genet* 13:179-181.

Kang HJ, Kim KT, Yoo KH, Park Y, Kim JW, Kim SW, Shin IS, Kim JH, Kim JM (2020) Genetic Markers for Later Remission in Response to Early Improvement of Antidepressants. *Int J Mol Sci* 21.

Kang RH, Wong ML, Choi MJ, Paik JW, Lee MS (2007) Association study of the serotonin transporter promoter polymorphism and mirtazapine antidepressant response in major depressive disorder. *Prog Neuropsychopharmacol Biol Psychiatry* 31:1317-1321.

Kato M, Fukuda T, Wakeno M, Fukuda K, Okugawa G, Ikenaga Y, Yamashita M, Takekita Y, Nobuhara K, Azuma J, Kinoshita T (2006) Effects of the serotonin type 2A, 3A and 3B receptor and the serotonin transporter genes on paroxetine and fluvoxamine efficacy and adverse drug reactions in depressed Japanese patients. *Neuropsychobiology* 53:186-195.

Kato M, Fukuda T, Wakeno M, Okugawa G, Takekita Y, Watanabe S, Yamashita M, Hosoi Y, Azuma J, Kinoshita T, Serretti A (2009) Effect of 5-HT1A gene polymorphisms on

Accepted Manuscript

Downloaded from https://academic.oup.com/ijnp/advance-article/doi/10.1093/ijnp/pyad001/6992242 by Delhi Technological University user on 31 January 2023

antidepressant response in major depressive disorder. *Am J Med Genet B Neuropsychiatr Genet* 150B:115-123.

Kaur H, Jajodia A, Grover S, Agarwal N, Baghel R, Kukreti R (2014) Pharmacogenomics of neuropsychiatric disorders: analysis of genetic variability in 162 identified neuroreceptors using 1000 Genomes Project data. *Pharmacogenomics* 15:1575-1587.

Kelly CB, McDonnell AP, Johnston TG, Mulholland C, Cooper SJ, McMaster D, Evans A, Whitehead AS (2004) The MTHFR C677T polymorphism is associated with depressive episodes in patients from Northern Ireland. *J Psychopharmacol* 18:567-571.

Kim DK, Lim SW, Lee S, Sohn SE, Kim S, Hahn CG, Carroll BJ (2000) Serotonin transporter gene polymorphism and antidepressant response. *Neuroreport* 11:215-219.

Kim H, Lim SW, Kim S, Kim JW, Chang YH, Carroll BJ, Kim DK (2006) Monoamine transporter gene polymorphisms and antidepressant response in koreans with late-life depression. *Jama* 296:1609-1618.

Kishi T, Kitajima T, Ikeda M, Yamanouchi Y, Kinoshita Y, Kawashima K, Okochi T, Okumura T, Tsunoka T, Ozaki N, Iwata N (2009a) CLOCK may predict the response to fluvoxamine treatment in Japanese major depressive disorder patients. *Neuromolecular Med* 11:53-57.

Kishi T, Tsunoka T, Ikeda M, Kawashima K, Okochi T, Kitajima T, Kinoshita Y, Okumura T, Yamanouchi Y, Inada T, Ozaki N, Iwata N (2009b) Serotonin 1A receptor gene and major depressive disorder: an association study and meta-analysis. *J Hum Genet* 54:629-633.

Kishi T, Yoshimura R, Kitajima T, Okochi T, Okumura T, Tsunoka T, Yamanouchi Y, Kinoshita Y, Kawashima K, Naitoh H, Nakamura J, Ozaki N, Iwata N (2010) HTR2A is associated with SSRI response in major depressive disorder in a Japanese cohort. *Neuromolecular Med* 12:237-242.

Accepted Manuscript

Downloaded from https://academic.oup.com/ijnp/advance-article/doi/10.1093/ijnp/pyad001/6992242 by Delhi Technological University user on 31 January 2023

Kloiber S, Czamara D, Karbalai N, Muller-Myhsok B, Hennings J, Holsboer F, Lucae S (2012) ANK3 and CACNA1C--missing genetic link for bipolar disorder and major depressive disorder in two German case-control samples. *J Psychiatr Res* 46:973-979.

Kocabas NA, Faghel C, Barreto M, Kasper S, Linotte S, Mendlewicz J, Noro M, Oswald P, Souery D, Zohar J, Massat I (2010) The impact of catechol-O-methyltransferase SNPs and haplotypes on treatment response phenotypes in major depressive disorder: a case-control association study. *Int Clin Psychopharmacol* 25:218-227.

Kocabas NA, Antonijevic I, Faghel C, Forray C, Kasper S, Lecrubier Y, Linotte S, Massat I, Mendlewicz J, Noro M, Montgomery S, Oswald P, Snyder L, Zohar J, Souery D (2011) Brain-derived neurotrophic factor gene polymorphisms: influence on treatment response phenotypes of major depressive disorder. *Int Clin Psychopharmacol* 26:1-10.

Koks S, Nikopensius T, Koido K, Maron E, Altmae S, Heinaste E, Vabrit K, Tammekivi V, Hallast P, Kurg A, Shlik J, Vasar V, Metspalu A, Vasar E (2006) Analysis of SNP profiles in patients with major depressive disorder. *Int J Neuropsychopharmacol* 9:167-174.

Kovanen L, Donner K, Kaunisto M, Partonen T (2017) PRKCDBP (CAVIN3) and CRY2 associate with major depressive disorder. *J Affect Disord* 207:136-140.

Kraft JB, Slager SL, McGrath PJ, Hamilton SP (2005) Sequence analysis of the serotonin transporter and associations with antidepressant response. *Biol Psychiatry* 58:374-381.

Lee HJ, Cha JH, Ham BJ, Han CS, Kim YK, Lee SH, Ryu SH, Kang RH, Choi MJ, Lee MS (2004) Association between a G-protein beta 3 subunit gene polymorphism and the symptomatology and treatment responses of major depressive disorders. *Pharmacogenomics J* 4:29-33.

Lee SH, Choi TK, Lee E, Seok JH, Lee SH, Lee HS, Kim SJ (2010) Serotonin transporter gene polymorphism associated with short-term treatment response to venlafaxine. *Neuropsychobiology* 62:198-206.

Accepted Manuscript

Downloaded from https://academic.oup.com/ijnp/advance-article/doi/10.1093/ijnp/pyad001/6992242 by Delhi Technological University user on 31 January 2023

Lekman M, Laje G, Charney D, Rush AJ, Wilson AF, Sorant AJ, Lipsky R, Wisniewski SR, Manji H, McMahon FJ, Paddock S (2008) The FKBP5-gene in depression and treatment response--an association study in the Sequenced Treatment Alternatives to Relieve Depression (STAR*D) Cohort. *Biol Psychiatry* 63:1103-1110.

Lemonde S, Turecki G, Bakish D, Du L, Hrdina PD, Bown CD, Sequeira A, Kushwaha N, Morris SJ, Basak A, Ou XM, Albert PR (2003) Impaired repression at a 5-hydroxytryptamine 1A receptor gene polymorphism associated with major depression and suicide. *J Neurosci* 23:8788-8799.

Lewis CM et al. (2010) Genome-wide association study of major recurrent depression in the U.K. population. *Am J Psychiatry* 167:949-957.

Li QS, Wajs E, Ochs-Ross R, Singh J, Drevets WC (2020) Genome-wide association study and polygenic risk score analysis of esketamine treatment response. *Sci Rep* 10:12649.

Licinio J, Dong C, Wong ML (2009) Novel sequence variations in the brain-derived neurotrophic factor gene and association with major depression and antidepressant treatment response. *Arch Gen Psychiatry* 66:488-497.

Lim SW, Won HH, Kim H, Myung W, Kim S, Kim KK, Carroll BJ, Kim JW, Kim DK (2014) Genetic prediction of antidepressant drug response and nonresponse in Korean patients. *PLoS One* 9:e107098.

Lin E, Chen PS, Chang HH, Gean PW, Tsai HC, Yang YK, Lu RB (2009a) Interaction of serotonin-related genes affects short-term antidepressant response in major depressive disorder. *Prog Neuropsychopharmacol Biol Psychiatry* 33:1167-1172.

Lin KM, Tsou HH, Tsai IJ, Hsiao MC, Hsiao CF, Liu CY, Shen WW, Tang HS, Fang CK, Wu CS, Lu SC, Kuo HW, Liu SC, Chan HW, Hsu YT, Tian JN, Liu YL (2010) CYP1A2 genetic polymorphisms are associated with treatment response to the antidepressant paroxetine. *Pharmacogenomics* 11:1535-1543.

Accepted Manuscript

Downloaded from https://academic.oup.com/ijnp/advance-article/doi/10.1093/ijnp/pyad001/6992242 by Delhi Technological University user on 31 January 2023

Lin KM, Chiu YF, Tsai IJ, Chen CH, Shen WW, Liu SC, Lu SC, Liu CY, Hsiao MC, Tang HS, Liu SI, Chang LH, Wu CS, Tsou HH, Tsai MH, Chen CY, Wang SM, Kuo HW, Hsu YT, Liu YL (2011) ABCB1 gene polymorphisms are associated with the severity of major depressive disorder and its response to escitalopram treatment. *Pharmacogenet Genomics* 21:163-170.

Lin YM, Ko HC, Chang FM, Yeh TL, Sun HS (2009b) Population-specific functional variant of the TPH2 gene 2755C>A polymorphism contributes risk association to major depression and anxiety in Chinese peripartum women. *Arch Womens Ment Health* 12:401-408.

Liou YJ, Chen TJ, Tsai SJ, Yu YW, Cheng CY, Hong CJ (2009) Support for the involvement of the KCNK2 gene in major depressive disorder and response to antidepressant treatment. *Pharmacogenet Genomics* 19:735-741.

Liu W, Gu N, Feng G, Li S, Bai S, Zhang J, Shen T, Xue H, Breen G, St Clair D, He L (1999) Tentative association of the serotonin transporter with schizophrenia and unipolar depression but not with bipolar disorder in Han Chinese. *Pharmacogenetics* 9:491-495.

Liu Z, Zhu F, Yao L, Yang C, Xiao L, Zhu J, Wang H, Wang G, Liu W, Xiao Z (2013a) PDLIM5 gene polymorphisms and short term antidepressant response in Chinese major depressive disorders. *Int J Clin Exp Med* 6:677-682.

Liu Z, Zhu F, Wang G, Xiao Z, Wang H, Tang J, Wang X, Qiu D, Liu W, Cao Z, Li W (2006) Association of corticotropin-releasing hormone receptor1 gene SNP and haplotype with major depression. *Neurosci Lett* 404:358-362.

Liu Z, Liu W, Yao L, Yang C, Xiao L, Wan Q, Gao K, Wang H, Zhu F, Wang G, Xiao Z (2013b) Negative life events and corticotropin-releasing-hormone receptor1 gene in recurrent major depressive disorder. *Sci Rep* 3:1548.

Accepted Manuscript

Downloaded from https://academic.oup.com/ijnp/advance-article/doi/10.1093/ijnp/pyad001/6992242 by Delhi Technological University user on 31 January 2023

Lucae S, Ising M, Horstmann S, Baune BT, Arolt V, Muller-Myhsok B, Holsboer F, Domschke K (2010) HTR2A gene variation is involved in antidepressant treatment response. *Eur Neuropsychopharmacol* 20:65-68.

Ma HY, Liu ZF, Xu YF, Hu XD, Sun N, Li XR, Zhang KR (2019) The association study of CLOCK gene polymorphisms with antidepressant effect in Chinese with major depressive disorder. *Per Med* 16:115-122.

Ma J, Xiao H, Yang Y, Cao D, Wang L, Yang X, Qiu X, Qiao Z, Song J, Liu Y, Wang P, Zhou J, Zhu X (2015) Interaction of tryptophan hydroxylase 2 gene and life events in susceptibility to major depression in a Chinese Han population. *J Affect Disord* 188:304-309.

Ma J, Wang L, Yang Y, Qiao Z, Fang D, Qiu X, Yang X, Zhu X, He J, Pan H, Ban B, Zhao Y, Sui H (2017) GNB3 and CREB1 gene polymorphisms combined with negative life events increase susceptibility to major depression in a Chinese Han population. *PLoS One* 12:e0170994.

Malhi GS, Mann JJ (2018) Depression. *Lancet* 392:2299-2312.

Mandal T, Bairy LK, Sharma P (2020) Association between functional polymorphisms in serotonin transporter gene (SLC6A4) and escitalopram treatment response in depressive patients in a South Indian population. *Eur J Clin Pharmacol* 76:807-814.

Mann JJ, Huang YY, Underwood MD, Kassir SA, Oppenheim S, Kelly TM, Dwork AJ, Arango V (2000) A serotonin transporter gene promoter polymorphism (5-HTTLPR) and prefrontal cortical binding in major depression and suicide. *Arch Gen Psychiatry* 57:729-738.

Manoharan A, Shewade DG, Rajkumar RP, Adithan S (2016) Serotonin transporter gene (SLC6A4) polymorphisms are associated with response to fluoxetine in south Indian major depressive disorder patients. *Eur J Clin Pharmacol* 72:1215-1220.

Massat I, Souery D, Del-Favero J, Nothen M, Blackwood D, Muir W, Kaneva R, Serretti A, Lorenzi C, Rietschel M, Milanova V, Papadimitriou GN, Dikeos D, Van Broekhoven C,

Accepted Manuscript

Downloaded from https://academic.oup.com/ijnp/advance-article/doi/10.1093/ijnp/pyad001/6992242 by Delhi Technological University user on 31 January 2023

Mendlewicz J (2005) Association between COMT (Val158Met) functional polymorphism and early onset in patients with major depressive disorder in a European multicenter genetic association study. *Mol Psychiatry* 10:598-605.

Matsumoto Y, Fabbri C, Pellegrini S, Porcelli S, Politi P, Bellino S, Iofrida C, Mariotti V, Melissari E, Menchetti M, Martinelli V, Cappucciati M, Bozzatello P, Brignolo E, Brambilla P, Balestrieri M, Serretti A (2014) Serotonin transporter gene: a new polymorphism may affect response to antidepressant treatments in major depressive disorder. *Mol Diagn Ther* 18:567-577.

Mbarek H, Milaneschi Y, Hottenga JJ, Ligthart L, de Geus EJC, Ehli EA, Willemsen G, Davies GE, Smit JH, Boomsma DI, Penninx B (2017) Genome-Wide Significance for PCLO as a Gene for Major Depressive Disorder. *Twin Res Hum Genet* 20:267-270.

Min W, Li T, Ma X, Li Z, Yu T, Gao D, Zhang B, Yun Y, Sun X (2009) Monoamine transporter gene polymorphisms affect susceptibility to depression and predict antidepressant response. *Psychopharmacology* (Berl) 205:409-417.

Minelli A, Scassellati C, Cloninger CR, Tessari E, Bortolomasi M, Bonvicini C, Giacopuzzi M, Frisoni GB, Gennarelli M (2012) PCLO gene: its role in vulnerability to major depressive disorder. *J Affect Disord* 139:250-255.

Mitjans M, Serretti A, Fabbri C, Gasto C, Catalan R, Fananas L, Arias B (2013) Screening genetic variability at the CNR1 gene in both major depression etiology and clinical response to citalopram treatment. *Psychopharmacology* (Berl) 227:509-519.

Monteleone P, Bifulco M, Maina G, Tortorella A, Gazzerro P, Proto MC, Di Filippo C, Monteleone F, Canestrelli B, Buonerba G, Bogetto F, Maj M (2010) Investigation of CNR1 and FAAH endocannabinoid gene polymorphisms in bipolar disorder and major depression. *Pharmacol Res* 61:400-404.

Accepted Manuscript

Downloaded from https://academic.oup.com/ijnp/advance-article/doi/10.1093/ijnp/pyad001/6992242 by Delhi Technological University user on 31 January 2023

Muglia P, Tozzi F, Galwey NW, Francks C, Upmanyu R, Kong XQ, Antoniades A, Domenici E, Perry J, Rothen S, Vandeleur CL, Mooser V, Waeber G, Vollenweider P, Preisig M, Lucae S, Muller-Myhsok B, Holsboer F, Middleton LT, Roses AD (2010) Genome-wide association study of recurrent major depressive disorder in two European case-control cohorts. *Mol Psychiatry* 15:589-601.

Myung W, Lim SW, Kim S, Kim H, Chung JW, Seo MY, Kim JW, Carroll BJ, Kim DK (2013) Serotonin transporter genotype and function in relation to antidepressant response in Koreans. *Psychopharmacology* (Berl) 225:283-290.

Myung W, Kim J, Lim SW, Shim S, Won HH, Kim S, Kim S, Lee MS, Chang HS, Kim JW, Carroll BJ, Kim DK (2015) A genome-wide association study of antidepressant response in Koreans. *Transl Psychiatry* 5:e633.

Ng PC, Henikoff S (2001) Predicting deleterious amino acid substitutions. *Genome Res* 11:863-874.

Norkeviciene A, Gocentiene R, Sestokaite A, Sabaliauskaite R, Dabkeviciene D, Jarmalaite S, Bulotiene G (2022) A Systematic Review of Candidate Genes for Major Depression. *Medicina* (Kaunas) 58.

Noro M, Antonijevic I, Forray C, Kasper S, Kocabas NA, Lecrubier Y, Linotte S, Mendlewicz J, Montgomery S, Snyder L, Souery D, Verbanck P, Zohar J, Massat I (2010) 5HT1A and 5HT2A receptor genes in treatment response phenotypes in major depressive disorder. *Int Clin Psychopharmacol* 25:228-231.

Nouraei H, Firouzabadi N, Mandegary A, Zomorrodian K, Bahramali E, Shayesteh MRH, Ansari S (2018) Glucocorticoid Receptor Genetic Variants and Response to Fluoxetine in Major Depressive Disorder. *J Neuropsychiatry Clin Neurosci* 30:45-50.

Accepted Manuscript

Downloaded from https://academic.oup.com/ijnp/advance-article/doi/10.1093/ijnp/pyad001/6992242 by Delhi Technological University user on 31 January 2023

Ogilvie AD, Battersby S, Bubb VJ, Fink G, Harmar AJ, Goodwim GM, Smith CA (1996) Polymorphism in serotonin transporter gene associated with susceptibility to major depression. *Lancet* 347:731-733.

Ohara K, Nagai M, Suzuki Y, Ohara K (1998) Low activity allele of catechol-o-methyltransferase gene and Japanese unipolar depression. *Neuroreport* 9:1305-1308.

Ordway GA, Szebeni A, Chandley MJ, Stockmeier CA, Xiang L, Newton SS, Turecki G, Duffourc MM, Zhu MY, Zhu H, Szebeni K (2012) Low gene expression of bone morphogenetic protein 7 in brainstem astrocytes in major depression. *Int J Neuropsychopharmacol* 15:855-868.

Organization WH (2017) Depression and Other Common Mental Disorders. *Global Health Estimates. In*.

Ota KT, Andres W, Lewis DA, Stockmeier CA, Duman RS (2015) BICC1 expression is elevated in depressed subjects and contributes to depressive behavior in rodents. *Neuropsychopharmacology* 40:711-718.

Ozbey G, Yucel B, Taycan SE, Kan D, Bodur NE, Arslan T, Percin F, Yuksel N, Guzey C, Uluoglu C (2014) ABCB1 C3435T polymorphism is associated with susceptibility to major depression, but not with a clinical response to citalopram in a Turkish population. *Pharmacol Rep* 66:235-238.

Ozsoy F, Nursal AF, Karakus N, Demir MO, Yigit S (2021) Estrogen Receptor 1 Gene rs22346939 and rs9340799 Variants are Associated with Major Depressive Disorder and its Clinical Features. *Curr Neurovasc Res*. 18(1):12-19

Paddock S, Laje G, Charney D, Rush AJ, Wilson AF, Sorant AJ, Lipsky R, Wisniewski SR, Manji H, McMahon FJ (2007) Association of GRIK4 with outcome of antidepressant treatment in the STAR*D cohort. *Am J Psychiatry* 164:1181-1188.

Accepted Manuscript

Downloaded from https://academic.oup.com/ijnp/advance-article/doi/10.1093/ijnp/pyad001/6992242 by Delhi Technological University user on 31 January 2023

Papiol S, Arias B, Gasto C, Gutierrez B, Catalan R, Fananas L (2007) Genetic variability at HPA axis in major depression and clinical response to antidepressant treatment. *J Affect Disord* 104:83-90.

Perez-Olmos I, Bustamante D, Ibanez-Pinilla M (2016) Serotonin transporter gene (5-HTT) polymorphism and major depressive disorder in patients in Bogota, Colombia. *Biomedica* 36:285-294.

Peters EJ, Slager SL, McGrath PJ, Knowles JA, Hamilton SP (2004) Investigation of serotonin-related genes in antidepressant response. *Mol Psychiatry* 9:879-889.

Pu M, Zhang Z, Xu Z, Shi Y, Geng L, Yuan Y, Zhang X, Reynolds GP (2013) Influence of genetic polymorphisms in the glutamatergic and GABAergic systems and their interactions with environmental stressors on antidepressant response. *Pharmacogenomics* 14:277-288.

Ramoz N, Hoertel N, Nobile B, Voegeli G, Nasr A, Le Strat Y, Courtet P, Gorwood P (2020) Corticotropin releasing hormone receptor CRHR1 gene is associated with tianeptine antidepressant response in a large sample of outpatients from real-life settings. *Transl Psychiatry* 10:378.

Ran L, Ai M, Wang W, Chen J, Wu T, Liu W, Jin J, Wang S, Kuang L (2020) Rare variants in SLC6A4 cause susceptibility to major depressive disorder with suicidal ideation in Han Chinese adolescents and young adults. *Gene* 726:144147.

Rietschel M et al. (2010) Genome-wide association-, replication-, and neuroimaging study implicates HOMER1 in the etiology of major depression. *Biol Psychiatry* 68:578-585.

Rozycka A, Slopien R, Slopien A, Dorszewska J, Seremak-Mrozikiewicz A, Lianeri M, Maciukiewicz M, Warenik-Szymankiewicz A, Grzelak T, Kurzawinska G, Drews K, Klejewski A, Jagodzinski PP (2016) The MAOA, COMT, MTHFR and ESR1 gene polymorphisms are associated with the risk of depression in menopausal women. *Maturitas* 84:42-54.

Accepted Manuscript

Downloaded from https://academic.oup.com/ijnp/advance-article/doi/10.1093/ijnp/pyad001/6992242 by Delhi Technological University user on 31 January 2023

Rubinstein WS et al. (2013) The NIH genetic testing registry: a new, centralized database of genetic tests to enable access to comprehensive information and improve transparency. *Nucleic Acids Res* 41:D925-935.

Ryan J, Artero S, Carriere I, Maller JJ, Meslin C, Ritchie K, Ancelin ML (2016) GWAS-identified risk variants for major depressive disorder: Preliminary support for an association with late-life depressive symptoms and brain structural alterations. *Eur Neuropsychopharmacol* 26:113-125.

Ryan J, Scali J, Carriere I, Peres K, Rouaud O, Scarabin PY, Ritchie K, Ancelin ML (2011) Oestrogen receptor polymorphisms and late-life depression. *Br J Psychiatry* 199:126-131.

Ryu SH, Lee SH, Lee HJ, Cha JH, Ham BJ, Han CS, Choi MJ, Lee MS (2004) Association between norepinephrine transporter gene polymorphism and major depression. *Neuropsychobiology* 49:174-177.

Sahraian S, Babashams M, Reza-Soltani P, Najmabadi H, Kahrizi K, Gorgani SH (2013) Serotonin Transporter Polymorphism (5-HTTLPR) and Citalopram Effectiveness in Iranian Patients with Major Depressive Disorder. *Iran J Psychiatry* 8:86-91.

Santos M, Carvalho S, Lima L, Nogueira A, Assis J, Mota-Pereira J, Pimentel P, Maia D, Correia D, Gomes S, Cruz A, Medeiros R (2014) Common genetic polymorphisms in the ABCB1 gene are associated with risk of major depressive disorder in male Portuguese individuals. *Genet Test Mol Biomarkers* 18:12-19.

Sarubin N, Hilbert S, Naumann F, Zill P, Wimmer AM, Nothdurfter C, Rupprecht R, Baghai TC, Buhner M, Schule C (2017) The sex-dependent role of the glucocorticoid receptor in depression: variations in the NR3C1 gene are associated with major depressive disorder in women but not in men. *Eur Arch Psychiatry Clin Neurosci* 267:123-133.

Sasayama D, Hiraishi A, Tatsumi M, Kamijima K, Ikeda M, Umene-Nakano W, Yoshimura R, Nakamura J, Iwata N, Kunugi H (2013) Possible association of CUX1 gene

Accepted Manuscript

Downloaded from https://academic.oup.com/ijnp/advance-article/doi/10.1093/ijnp/pyad001/6992242 by Delhi Technological University user on 31 January 2023

polymorphisms with antidepressant response in major depressive disorder. *Pharmacogenomics J* 13:354-358.

Schosser A et al. (2013) Genome-wide association study of co-occurring anxiety in major depression. *World J Biol Psychiatry* 14:611-621.

Schulze TG, Müller DJ, Krauss H, Scherk H, Ohlraun S, Syagailo YV, Windemuth C, Neidt H, Grässle M, Papassotiropoulos A, Heun R, Nöthen MM, Maier W, Lesch KP, Rietschel M (2000) Association between a functional polymorphism in the monoamine oxidase A gene promoter and major depressive disorder. *Am J Med Genet* 96:801-803.

Schumacher J, Jamra RA, Becker T, Ohlraun S, Klopp N, Binder EB, Schulze TG, Deschner M, Schmal C, Hofels S, Zobel A, Illig T, Propping P, Holsboer F, Rietschel M, Nothen MM, Cichon S (2005) Evidence for a relationship between genetic variants at the brain-derived neurotrophic factor (BDNF) locus and major depression. *Biol Psychiatry* 58:307-314.

Schwabe I, Milaneschi Y, Gerring Z, Sullivan PF, Schulte E, Suppli NP, Thorp JG, Derks EM, Middeldorp CM (2019) Unraveling the genetic architecture of major depressive disorder: merits and pitfalls of the approaches used in genome-wide association studies. *Psychol Med* 49:2646-2656.

Seripa D, Pilotto A, Paroni G, Fontana A, D'Onofrio G, Gravina C, Urbano M, Cascavilla L, Paris F, Panza F, Padovani A, Pilotto A (2015) Role of the serotonin transporter gene locus in the response to SSRI treatment of major depressive disorder in late life. *J Psychopharmacol* 29:623-633.

Serretti A, Zanardi R, Cusin C, Rossini D, Lorenzi C, Smeraldi E (2001) Tryptophan hydroxylase gene associated with paroxetine antidepressant activity. *Eur Neuropsychopharmacol* 11:375-380.

Shadrina M, Bondarenko EA, Slominsky PA (2018) Genetics Factors in Major Depression Disease. *Front Psychiatry* 9:334.

Accepted Manuscript

Downloaded from https://academic.oup.com/ijnp/advance-article/doi/10.1093/ijnp/pyad001/6992242 by Delhi Technological University user on 31 January 2023

Shen X, Wu Y, Guan T, Wang X, Qian M, Lin M, Shen Z, Sun J, Zhong H, Yang J, Li L, Yuan Y (2014) Association analysis of COMT/MTHFR polymorphisms and major depressive disorder in Chinese Han population. *J Affect Disord* 161:73-78.

Shen X, Wu Y, Qian M, Wang X, Hou Z, Liu Y, Sun J, Zhong H, Yang J, Lin M, Li L, Guan T, Shen Z, Yuan Y (2011) Tryptophan hydroxylase 2 gene is associated with major depressive disorder in a female Chinese population. *J Affect Disord* 133:619-624.

Shi J et al. (2011) Genome-wide association study of recurrent early-onset major depressive disorder. *Mol Psychiatry* 16:193-201.

Srivastava A, Singh P, Gupta H, Kaur H, Kanojia N, Guin D, Sood M, Chadda RK, Yadav J, Vohora D, Saso L, Kukreti R (2019) Systems Approach to Identify Common Genes and Pathways Associated with Response to Selective Serotonin Reuptake Inhibitors and Major Depression Risk. *Int J Mol Sci* 20.

Steffens DC, Svenson I, Marchuk DA, Levy RM, Hays JC, Flint EP, Krishnan KR, Siegler IC (2002) Allelic differences in the serotonin transporter-linked polymorphic region in geriatric depression. *Am J Geriatr Psychiatry* 10:185-191.

Su YA, Li JT, Dai WJ, Liao XM, Dong LC, Lu TL, Bousman C, Si TM (2016) Genetic variation in the tryptophan hydroxylase 2 gene moderates depressive symptom trajectories and remission over 8 weeks of escitalopram treatment. *Int Clin Psychopharmacol* 31:127-133.

Suchanek R, Owczarek A, Kowalczyk M, Kucia K, Kowalski J (2011) Association between C-281A and val66met functional polymorphisms of BDNF gene and risk of recurrent major depressive disorder in Polish population. *J Mol Neurosci* 43:524-530.

Sullivan PF, Neale MC, Kendler KS (2000) Genetic epidemiology of major depression: review and meta-analysis. *Am J Psychiatry* 157:1552-1562.

Accepted Manuscript

Downloaded from https://academic.oup.com/ijnp/advance-article/doi/10.1093/ijnp/pyad001/6992242 by Delhi Technological University user on 31 January 2023

Sullivan PF et al. (2009) Genome-wide association for major depressive disorder: a possible role for the presynaptic protein piccolo. *Mol Psychiatry* 14:359-375.

Sun HS, Tsai HW, Ko HC, Chang FM, Yeh TL (2004) Association of tryptophan hydroxylase gene polymorphism with depression, anxiety and comorbid depression and anxiety in a population-based sample of postpartum Taiwanese women. *Genes Brain Behav* 3:328-336.

Sun N, Yang CX, Liu ZF, Li XR, Xu Y, Zhang KR (2016) Effects of polymorphisms of serotonin transporter promoter (5-HTTLPR) and brain derived neurotrophic factor gene (G196A rs6265) on the risk of major depressive disorder in the Chinese Han population. *Eur Rev Med Pharmacol Sci* 20:1852-1859.

Sun N, Xu Y, Wang Y, Duan H, Wang S, Ren Y, Peng J, Du Q, Shen Y, Xu Q, Zhang K (2008) The combined effect of norepinephrine transporter gene and negative life events in major depression of Chinese Han population. *J Neural Transm* (Vienna) 115:1681-1686.

Sun Q, Yuan F, Yuan R, Ren D, Zhu Y, Bi Y, Hu J, Guo Z, Xu F, Niu W, Ma G, Wu X, Yang F, Wang L, Li X, Yu T, He L, He G (2019) GRIK4 and GRM7 gene may be potential indicator of venlafaxine treatment reponses in Chinese of Han ethnicity. *Medicine* (Baltimore) 98:e15456.

Sun RF, Zhu YS, Kuang WJ, Liu Y, Li SB (2011) The G-712A polymorphism of brain-derived neurotrophic factor is associated with major depression but not schizophrenia. *Neurosci Lett* 489:34-37.

Sunada N, Takekita Y, Nonen S, Wakeno M, Koshikawa Y, Ogata H, Kinoshita T, Kato M (2019) Brain Volume-Related Polymorphisms of the Glycogen Synthase Kinase-3beta Gene and Their Effect on Antidepressant Treatment in Major Depressive Disorder. *Neuropsychobiology* 78:136-144.

Accepted Manuscript

Downloaded from https://academic.oup.com/ijnp/advance-article/doi/10.1093/ijnp/pyad001/6992242 by Delhi Technological University user on 31 January 2023

Suzuki Y, Sawamura K, Someya T (2004) The effects of a 5-hydroxytryptamine 1A receptor gene polymorphism on the clinical response to fluvoxamine in depressed patients. *Pharmacogenomics* J 4:283-286.

Szczepankiewicz A, Leszczynska-Rodziewicz A, Pawlak J, Rajewska-Rager A, Dmitrzak-Weglarz M, Wilkosc M, Skibinska M, Hauser J (2011) Glucocorticoid receptor polymorphism is associated with major depression and predominance of depression in the course of bipolar disorder. *J Affect Disord* 134:138-144.

Szczepankiewicz A, Leszczynska-Rodziewicz A, Pawlak J, Narozna B, Rajewska-Rager A, Wilkosc M, Zaremba D, Maciukiewicz M, Twarowska-Hauser J (2014) FKBP5 polymorphism is associated with major depression but not with bipolar disorder. *J Affect Disord* 164:33-37.

Takahashi H, Yoshida K, Higuchi H, Kamata M, Inoue K, Suzuki T, Ishigooka J (2014) Bcl1 polymorphism of the glucocorticoid receptor gene and treatment response to milnacipran and fluvoxamine in Japanese patients with depression. *Neuropsychobiology* 70:173-180.

Taylor WD, Züchner S, McQuoid DR, Steffens DC, Speer MC, Krishnan KR (2007) Allelic differences in the brain-derived neurotrophic factor Val66Met polymorphism in late-life depression. *Am J Geriatr Psychiatry* 15:850-857.

Tsai SJ, Wang YC, Hong CJ, Chiu HJ (2003) Association study of oestrogen receptor alpha gene polymorphism and suicidal behaviours in major depressive disorder. *Psychiatr Genet* 13:19-22.

Tsai SJ, Gau YT, Hong CJ, Liou YJ, Yu YW, Chen TJ (2009a) Sexually dimorphic effect of catechol-O-methyltransferase val158met polymorphism on clinical response to fluoxetine in major depressive patients. *J Affect Disord* 113:183-187.

Accepted Manuscript

Downloaded from https://academic.oup.com/ijnp/advance-article/doi/10.1093/ijnp/pyad001/6992242 by Delhi Technological University user on 31 January 2023

Tsai SJ, Hong CJ, Liou YJ, Yu YW, Chen TJ, Hou SJ, Yen FC (2009b) Tryptophan hydroxylase 2 gene is associated with major depression and antidepressant treatment response. *Prog Neuropsychopharmacol Biol Psychiatry* 33:637-641.

Tzvetkov MV, Brockmöller J, Roots I, Kirchheiner J (2008) Common genetic variations in human brain-specific tryptophan hydroxylase-2 and response to antidepressant treatment. *Pharmacogenet Genomics* 18:495-506.

Umene-Nakano W, Yoshimura R, Ueda N, Suzuki A, Ikenouchi-Sugita A, Hori H, Otani K, Nakamura J (2010) Predictive factors for responding to sertraline treatment: views from plasma catecholamine metabolites and serotonin transporter polymorphism. *J Psychopharmacol* 24:1764-1771.

van Rossum EF, Binder EB, Majer M, Koper JW, Ising M, Modell S, Salyakina D, Lamberts SW, Holsboer F (2006) Polymorphisms of the glucocorticoid receptor gene and major depression. *Biol Psychiatry* 59(8):681-8

Van West D, Van Den Eede F, Del-Favero J, Souery D, Norrback KF, Van Duijn C, Sluijs S, Adolfsson R, Mendlewicz J, Deboutte D, Van Broeckhoven C, Claes S (2006) Glucocorticoid receptor gene-based SNP analysis in patients with recurrent major depression. *Neuropsychopharmacology* 31:620-627.

Vancova Z, Cizmarikova M, Dragasek J, Zofcakova S, Kolarcik P, Mojzis J (2018) Does G2677T Polymorphism of the MDR1 Gene Make a Difference in the Therapeutic Response to Paroxetine in Depressed Patients in a Slovakian Population? *Med Sci Monit* 24:3136-3145.

Ventura-Junca R, Symon A, Lopez P, Fiedler JL, Rojas G, Heskia C, Lara P, Marin F, Guajardo V, Araya AV, Sasso J, Herrera L (2014) Relationship of cortisol levels and genetic polymorphisms to antidepressant response to placebo and fluoxetine in patients with major depressive disorder: a prospective study. *BMC Psychiatry* 14:220.

Accepted Manuscript

Downloaded from https://academic.oup.com/ijnp/advance-article/doi/10.1093/ijnp/pyad001/6992242 by Delhi Technological University user on 31 January 2023

Verbeek EC, Bevova MR, Bochdanovits Z, Rizzu P, Bakker IM, Uithuisje T, De Geus EJ, Smit JH, Penninx BW, Boomsma DI, Hoogendijk WJ, Heutink P (2013) Resequencing three candidate genes for major depressive disorder in a Dutch cohort. *PLoS One* 8:e79921.

Verbeek EC, Bakker IM, Bevova MR, Bochdanovits Z, Rizzu P, Sondervan D, Willemsen G, de Geus EJ, Smit JH, Penninx BW, Boomsma DI, Hoogendijk WJ, Heutink P (2012) A fine-mapping study of 7 top scoring genes from a GWAS for major depressive disorder. *PLoS One* 7:e37384.

Viikki M, Kampman O, Illi A, Setala-Soikkeli E, Anttila S, Huuhka M, Nuolivirta T, Poutanen O, Mononen N, Lehtimaki T, Leinonen E (2010) TPH1 218A/C polymorphism is associated with major depressive disorder and its treatment response. *Neurosci Lett* 468:80-84.

Wang HC, Yeh TL, Chang HH, Gean PW, Chi MH, Yang YK, Lu RB, Chen PS (2011) TPH1 is associated with major depressive disorder but not with SSRI/SNRI response in Taiwanese patients. *Psychopharmacology* (Berl) 213:773-779.

Wang L, Shi C, Zhang K, Xu Q (2014a) The gender-specific association of EHD3 polymorphisms with major depressive disorder. Neurosci Lett 567:11-14.

Wang XC, Xu DJ, Chen GH, Xia Q, Liu LN (2014b) Association of 2 neurotrophic factor polymorphisms with efficacy of paroxetine in patients with major depressive disorder in a Chinese population. *Ther Drug Monit* 36:612-617.

Wang Y, Liu X, Yu Y, Han Y, Wei J, Collier D, Li T, Ma X (2012) The role of single nucleotide polymorphism of D2 dopamine receptor gene on major depressive disorder and response to antidepressant treatment. *Psychiatry Res* 200:1047-1050.

Wigner P, Czarny P, Synowiec E, Bijak M, Bialek K, Talarowska M, Galecki P, Szemraj J, Sliwinski T (2018a) Variation of genes involved in oxidative and nitrosative stresses in depression. *Eur Psychiatry* 48:38-48.

Accepted Manuscript

Downloaded from https://academic.oup.com/ijnp/advance-article/doi/10.1093/ijnp/pyad001/6992242 by Delhi Technological University user on 31 January 2023

Wigner P, Czarny P, Synowiec E, Bijak M, Bialek K, Talarowska M, Galecki P, Szemraj J, Sliwinski T (2018b) Association between single nucleotide polymorphisms of TPH1 and TPH2 genes, and depressive disorders. *J Cell Mol Med* 22:1778-1791.

Wilkie MJ, Smith D, Reid IC, Day RK, Matthews K, Wolf CR, Blackwood D, Smith G (2007) A splice site polymorphism in the G-protein beta subunit influences antidepressant efficacy in depression. *Pharmacogenet Genomics* 17:207-215.

Wilkie MJ, Smith G, Day RK, Matthews K, Smith D, Blackwood D, Reid IC, Wolf CR (2009) Polymorphisms in the SLC6A4 and HTR2A genes influence treatment outcome following antidepressant therapy. *Pharmacogenomics J* 9:61-70.

Won ES, Chang HS, Lee HY, Ham BJ, Lee MS (2012) Association between serotonin transporter-linked polymorphic region and escitalopram antidepressant treatment response in Korean patients with major depressive disorder. *Neuropsychobiology* 66:221-229.

Wong ML, Dong C, Maestre-Mesa J, Licinio J (2008) Polymorphisms in inflammation-related genes are associated with susceptibility to major depression and antidepressant response. *Mol Psychiatry* 13:800-812.

Wong ML, Arcos-Burgos M, Liu S, Velez JI, Yu C, Baune BT, Jawahar MC, Arolt V, Dannlowski U, Chuah A, Huttley GA, Fogarty R, Lewis MD, Bornstein SR, Licinio J (2017) The PHF21B gene is associated with major depression and modulates the stress response. *Mol Psychiatry* 22:1015-1025.

Wray NR, James MR, Gordon SD, Dumenil T, Ryan L, Coventry WL, Statham DJ, Pergadia ML, Madden PA, Heath AC, Montgomery GW, Martin NG (2009) Accurate, Large-Scale Genotyping of 5HTTLPR and Flanking Single Nucleotide Polymorphisms in an Association Study of Depression, Anxiety, and Personality Measures. *Biol Psychiatry* 66:468-476.

Wray NR et al. (2018) Genome-wide association analyses identify 44 risk variants and refine the genetic architecture of major depression. *Nat Genet* 50:668-681.

Accepted Manuscript

Downloaded from https://academic.oup.com/ijnp/advance-article/doi/10.1093/ijnp/pyad001/6992242 by Delhi Technological University user on 31 January 2023

Wu Y, Xu Y, Sun Y, Wang YF, Li X, Lang XE, Wang WP, Zhang KR (2008) Association between the serotonin 1A receptor C(-1019)G polymorphism and major depressive disorder in the northern Han ethnic group in China. *Chin Med J* (Engl) 121:874-876.

Xiao Z, Liu W, Gao K, Wan Q, Yang C, Wang H, Wang X, Wang G, Liu Z (2011) Interaction between CRHR1 and BDNF genes increases the risk of recurrent major depressive disorder in Chinese population. *PLoS One* 6:e28733.

Xu Z, Taylor JA (2009) SNPinfo: integrating GWAS and candidate gene information into functional SNP selection for genetic association studies. *Nucleic Acids Res* 37:W600-605.

Xu Z, Reynolds GP, Yuan Y, Shi Y, Pu M, Zhang Z (2016) TPH-2 Polymorphisms Interact with Early Life Stress to Influence Response to Treatment with Antidepressant Drugs. *Int J Neuropsychopharmacol* 19.

Xu Z, Zhang Z, Shi Y, Pu M, Yuan Y, Zhang X, Li L, Reynolds GP (2012) Influence and interaction of genetic polymorphisms in the serotonin system and life stress on antidepressant drug response. *J Psychopharmacol* 26:349-359.

Yang Z, Ma X, Wang Y, Wang J, Xiang B, Wu J, Deng W, Li M, Wang Q, Li T (2012) Association of APC and REEP5 gene polymorphisms with major depression disorder and treatment response to antidepressants in a Han Chinese population. *Gen Hosp Psychiatry* 34:571-577.

Yeh YW, Chen CJ, Jang FL, Kuo SC, Chen CY, Liang CS, Ho PS, Yen CH, Shyu JF, Wan FJ, Lu RB, Huang SY (2015) SLC6A2 variants may predict remission from major depression after venlafaxine treatment in Han Chinese population. *J Psychiatr Res* 61:33-39.

Yoshida K, Takahashi H, Higuchi H, Kamata M, Ito K, Sato K, Naito S, Shimizu T, Itoh K, Inoue K, Suzuki T, Nemeroff CB (2004) Prediction of antidepressant response to milnacipran by norepinephrine transporter gene polymorphisms. *Am J Psychiatry* 161:1575-1580.

Accepted Manuscript

Downloaded from https://academic.oup.com/ijnp/advance-article/doi/10.1093/ijnp/pyad001/6992242 by Delhi Technological University user on 31 January 2023

Yoshida K, Ito K, Sato K, Takahashi H, Kamata M, Higuchi H, Shimizu T, Itoh K, Inoue K, Tezuka T, Suzuki T, Ohkubo T, Sugawara K, Otani K (2002) Influence of the serotonin transporter gene-linked polymorphic region on the antidepressant response to fluvoxamine in Japanese depressed patients. Prog Neuropsychopharmacol *Biol Psychiatry* 26:383-386.

Youssef MM, Underwood MD, Huang YY, Hsiung SC, Liu Y, Simpson NR, Bakalian MJ, Rosoklija GB, Dwork AJ, Arango V, Mann JJ (2018) Association of BDNF Val66Met Polymorphism and Brain BDNF Levels with Major Depression and Suicide. *Int J Neuropsychopharmacol* 21:528-538.

Yu YW, Tsai SJ, Chen TJ, Lin CH, Hong CJ (2002) Association study of the serotonin transporter promoter polymorphism and symptomatology and antidepressant response in major depressive disorders. *Mol Psychiatry* 7:1115-1119.

Yu YW, Tsai SJ, Liou YJ, Hong CJ, Chen TJ (2006) Association study of two serotonin 1A receptor gene polymorphisms and fluoxetine treatment response in Chinese major depressive disorders. *Eur Neuropsychopharmacol* 16:498-503.

Yu YW, Tsai SJ, Hong CJ, Chen TJ, Chen MC, Yang CW (2005) Association study of a monoamine oxidase a gene promoter polymorphism with major depressive disorder and antidepressant response. *Neuropsychopharmacology* 30:1719-1723.

Yuan F, Yuan R, Ren D, Bi Y, Niu W, Guo Z, Wu X, Xu F, Sun Q, Ma G, Yang F, Zhu Y, Yu T, Li X, He L, Shi L, He G (2020) A novel NR3C2 polymorphism and the increased thyroid-stimulating hormone concentration are associated with venlafaxine treatment outcome in Chinese Han MDD patients. *Psychiatry Res* 284:112690.

Zeman M, Jáchymová M, Jirák R, Vecka M, Tvrzická E, Stanková B, Zák A (2010) Polymorphisms of genes for brain-derived neurotrophic factor, methylenetetrahydrofolate reductase, tyrosine hydroxylase, and endothelial nitric oxide synthase in depression and metabolic syndrome. *Folia Biol* (Praha) 56:19-26.

Accepted Manuscript

Downloaded from https://academic.oup.com/ijnp/advance-article/doi/10.1093/ijnp/pyad001/6992242 by Delhi Technological University user on 31 January 2023

Zhang K, Yang C, Xu Y, Sun N, Yang H, Liu J, Xu Q, Shen Y (2010) Genetic association of the interaction between the BDNF and GSK3B genes and major depressive disorder in a Chinese population. *J Neural Transm* (Vienna) 117:393-401.

Zhang K, Xu Q, Xu Y, Yang H, Luo J, Sun Y, Sun N, Wang S, Shen Y (2009) The combined effects of the 5-HTTLPR and 5-HTR1A genes modulates the relationship between negative life events and major depressive disorder in a Chinese population. *J Affect Disord* 114:224-231.

Zhang X, Gainetdinov RR, Beaulieu JM, Sotnikova TD, Burch LH, Williams RB, Schwartz DA, Krishnan KR, Caron MG (2005) Loss-of-function mutation in tryptophan hydroxylase-2 identified in unipolar major depression. *Neuron* 45:11-16.

Zhu Y et al. (2019) CYP1A2 Genetic Polymorphism Is Associated With Treatment Remission to Antidepressant Venlafaxine in Han Chinese Population. *Clin Neuropharmacol* 42:32-36.

Zill P, Baghai TC, Zwanzger P, Schule C, Eser D, Rupprecht R, Moller HJ, Bondy B, Ackenheil M (2004) SNP and haplotype analysis of a novel tryptophan hydroxylase isoform (TPH2) gene provide evidence for association with major depression. *Mol Psychiatry* 9:1030-1036.

Zobel A, Schuhmacher A, Jessen F, Hofels S, von Widdern O, Metten M, Pfeiffer U, Hanses C, Becker T, Rietschel M, Scheef L, Block W, Schild HH, Maier W, Schwab SG (2010) DNA sequence variants of the FKBP5 gene are associated with unipolar depression. *Int J Neuropsychopharmacol* 13:649-660.

Accepted Manuscript

Downloaded from https://academic.oup.com/ijnp/advance-article/doi/10.1093/ijnp/pyad001/6992242 by Delhi Technological University user on 31 January 2023

Figures and Tables

Figure 1: Identification and selection process of relevant genetic association studies of MDD.

Figure 2: Identification and selection process of relevant genetic association studies of antidepressant response.

Figure 3a: Significantly associated reproducible* genetic variants: 24 in candidate studies, 3 in Genome-wide Studies and 4 variants that are common in both i.e. candidate and GWAS studies. Colour represent the studies; Gradient represents the no. of studies/evidence. Label order: Gene, SNPs, No. of studies/evidence. *minimum in 2 studies

Figure 3b: Reproducible Genes from Genome-wide and candidate association studies: 27 in candidate studies, 8 in Genome-wide Studies and 7 variants that are common in both i.e. candidate and GWAS studies

Figure 4a: Significantly associated reproducible* genetic variants: 15 in candidate studies, 2 in Genome-wide Studies and one variant that is common in both i.e. candidate and GWAS studies. Colour represent the studies; Gradient represents the no. of studies/evidence. Label order: Gene, SNPs, No. of studies/evidence. *minimum in 2 studies

Figure 4b: Reproducible Genes from Genome-wide and candidate drug response association studies: 18 in candidate studies, 11 in Genome-wide Studies and 4 variants that are common in both i.e. candidate and GWAS studies.

Accepted Manuscript

Downloaded from https://academic.oup.com/ijnp/advance-article/doi/10.1093/ijnp/pyad001/6992242 by Delhi Technological University user on 31 January 2023

Table1: List of all reproducible genetic variants with their sensitivity, specificity and PPV in candidate studies, GWAS studies and in both related to MDD susceptibility.

S. No.	Variant [No. of studies]	Gene	Location/ Position	Variant type	Polymorphism (Reference/ alternate)	Global Minor Allele Frequency (MAF)	Phenotype	Sample size (case/control)	Population /Country	Reported Risk allele/genotype	OR [CI]	P value	References	Calculated Risk Allele *	Sensitivity	Specificity	PPV (positive predictive value)
Candidate Variants																	
1	rs7746 76466; 5HTTL PR [10]	*SLC6A4/5 HTT/SERT*	17:302 37299	44bp deletion: Upstream gene variant	L/S	0.19 (ALF A)	MDD	35/33	Colombian	S	2.75 [0.876-8.637]	0.038	(Perez-Olmos et al., 2016)	S	0.53	0.57	0.55
							MDD	70/142	Spanish	S	2.03	< 0.05	(Dorado et al., 2007)				
							Depression	184/158	Han Chinese	S	1.817 [1.260–2.619]	0.01	(M. Q. Cao et al., 2007)				
							Depression	184/360	German	S	1.4013 [1.086-1.808] #	0.009	(Grünblatt et al., 2006)				
							MDD	466/836	German	S	1.26 [1.07-1.48]	0.0068	(Hoefgen et al., 2005)				
							Major depression	53/107	Racially mixed	LL vs LS vs SS	NA	0.008	(Mann et al., 2000)				
							Depression	57/38	Racially mixed	SS [SS vs LS+LL]	5.31 [1.13–25.11]	0.02	(Steffens et al., 2002)	S	-	-	-
							MDD	459/412	Han Chinese	LS vs. LL+ SS	1.42 [1.05-1.91]	0.02	(N. Sun et al., 2016)	L	0.36	0.69	0.54
							Depression	366/327	Australia/European	S	0.75 [0.603-0.930] #	0.0088	(Wray et al., 2009)				
							MDD	401/391	Han Chinese	L	1.446 [1.143–1.830]	0.002	(K. Zhang et al., 2009)				
2	rs6265 [8]	*BDNF*	11:276 58369	SNV: Missense Variant	G/A	0.20 (1000 Geno	MDD	300/300	Malaysian	AA [AA vs GG+GA	2.05 [1.48–3.65]	0.015	(Aldoghachi et al., 2019)	A	0.40	0.65	0.53

Accepted Manuscript

Downloaded from https://academic.oup.com/ijnp/advance-article/doi/10.1093/ijnp/pyad001/6992242 by Delhi Technological University user on 31 January 2023

						me)				]						
							MDD	45/45	NA	A	NA	0..01 1	(Youssef et al., 2018)				
							Depressive Disorder	42/41	Czech population	AA [GG vs GA vs AA]	NA	0.011 3[#]	(Zeman et al., 2010)				
							Unipolar MD	245/94	White	A [GG vs GA+AA]	1.92 [1.09-3.38]	0.024	(Taylor et al., 2007)				
							MDD	110/171	Chinese	A	1.807[1.283-2.546][#]	0.001	(Hwang et al., 2006)				
							Recurrent MDD	116/218	Polish	C	1.72 [1.06–2.79]	0.027 [#]	(Suchanek et al., 2011)	G	0.78	0.31	0.53
							Major Depression	202/346	Chinese	C	1.296 [1.014–1.658]	0.039	(R. F. Sun et al., 2011)				
							MDD	272/264	Mexican-American	G	1.66 [1.14-0 .41]	0.009	(Licinio et al., 2009)				
3	rs4680 [6]	*COMT*	22:19963748	SNV: Missense Variant	G/A	0.36 (1000 Genome)	Depression (Postmenopausal women)	332/219	Polish	A [GG vs. GA + AA]	2.171 [1.203–3.920]	0.009	(Rozycka et al., 2016)	A	0.50	0.49	0.49
							MDD	613/463	Italian	GA vs GG+AA	NA	0.03	(Gabriela Nielsen et al., 2015)				
							MDD	368/219	Han Chinese	AG	1.52 [1.04–2.21]	0.02	(Shen et al., 2014)				
							Depression	405/2151	Swedish	A [AA+AG vs GG]	1.49 [1.11–2.00]	0.009	(Aberg et al., 2011)				
							Depressive disorder	75/135	Japanese	GG vs AG vs AA	2.19 [1.19–4.03]	0.0161	(Ohara et al., 1998)				
							EO-MDD	120/628	European	G	1.48[1.09-1.91]	0.009	(Massat et al., 2005)	G	-	-	-
4	rs1801133 [4]	*MTHFR*	1:11796321	SNV: Missense Variant	C/T	0.24 (1000 Genome)	Depression (Perimenopausal	54/102	Polish	T	1.969 [1.202–3.226]	0.007	(Rozycka et al., 2016)	T	0.42	0.68	0.56

Accepted Manuscript

Downloaded from https://academic.oup.com/ijnp/advance-article/doi/10.1093/ijnp/pyad001/6992242 by Delhi Technological University user on 31 January 2023

							women)											
							Depression (Postmenopausal women)	113/219		T	1.812 [1.294–2.538]	0.0005					
							MDD	368/219	Han Chinese	T	1.81 [1.40–2.34]	<0.001	(Shen et al., 2014)				
							Depressive episode	100/89	Northern Irish	T [TT+TC vs CC]	1.90 [1.00–3.62]	0.03	(Kelly et al., 2004)				
							Major depression	32/419	Japanese	TT	2.8 [1.3–6.4]	0.005	(Arinami et al., 1997)				
5	rs2242446 [4]	*SLC6A2*	16:55656513	SNV: 5'UTR Variant	C/T	0.24 (1000 Genome)	MDD	579/437	Han Chinese	T	1.250 [1.031-1.517]	0.023	(Min et al., 2009)	T	0.72	0.34	0.52
							MDD	145/164	Japanese	CC vs TC vs TT	NA	0.02	(Inoue et al., 2004)				
							Major Depression	388/388	Han Chinese	C	1.33 [1.07–1.65]	0.011	(N. Sun et al., 2008)	C	0.40	0.62	0.51
							Major depression	112/136	Korean	C[TT vs. TC + CC]	1.86 [1.11–3.12]	0.019	(Ryu et al., 2004)				
6	rs5443 [4]	*GNB3*	12:6845711	SNV: Synonymous variant	C/T	0.49 (1000 Genome)	Major Depression	512/513	Han Chinese	C	0.77 [0.65-0.92]	0	(J. Ma et al., 2017)	T	0.55	0.55	0.55
							Depression	184/158	Han Chinese	T	2.214 [1.619–3.029]	0.001	(M. Q. Cao et al., 2007)				
							MDD	106/133	Korean	T	1.46 [1.02–2.10]	0.041	(H. J. Lee et al., 2004)				
							Major depression	78/111	German	T	1.7952[1.164-2.7689][#]	0.008[#]	(Zill et al., 2004)				
7	rs1045642 [4]	*ABCB1*	7:87509329	SNV: Synonymous variant	T/C	0.39 (1000 Genome)	rDD	90/96	Polish	T	1.661 [1.101 - 2.505][#]	0.015[#]	(Jelen et al., 2015)	T	0.43	0.59	0.51
							MDD	631/1100	Japanese	T	1.16 [1.01-	0.034	(Fujii et al., 2012)				

Accepted Manuscript

Downloaded from https://academic.oup.com/jjnp/advance-article/doi/10.1093/jjnp/pyad001/6992242 by Delhi Technological University user on 31 January 2023

											1.34]						
							MDD	54/70	Turkish	C	1.82 [1.095-3.024]#	0.02	(Ozbey et al., 2014)	C	0.62	0.53	0.57
							MDD	21/42	Portuguese	T	0.36 [0.140–0.920]	0.018	(Santos et al., 2014)				
8	rs9340799 [4]	*ESR1*	6:151842246	SNV: Intron variant	A/G	0.28 (1000 Genome)	Depression (Postmenopausal women)	113/217	Polish	G	0.703 [0.503–0.981]	0.037	(Rozycka et al., 2016)	A	0.62	0.38	0.51
							Severe late life current MDD	454/3071	French Caucasian	G [AA vs GG]	0.60 [0.41–0.88]	0.009	(Ryan et al., 2011)				
							MDD	89/126	Han Chinese	A	1.6703 [1.0769-2.5908]	0.02	(Tsai SJ et al 2003)				
							MDD	101/95	Turkish	G [GG vs AA+AG]	2.71 [1.10 - 7.29]	0.028	(Ozsoy et al, 2021)	G	-	-	-
9	rs6295[3]	*5HTR1A*	5:63962738	SNV: Upstream transcript variant	C/G	0.45 (1000 Genome)	MDD	401/391	Han Chinese	C	0.763 [0.609–0.956]	0.018	(K. Zhang et al., 2009)	G	0.33	0.75	0.56
							MDD	400/400	Han Chinese	G	1.4417 [1.153-1.802]#	0.001	(Wu et al., 2008)				
							MDD	129/134	Ontario (Majority Caucasians)	G	#1.8439 [1.3022-2.6109]	0.0006	(Lemonde et al., 2003)				
10	rs2234693 [3]	*ESR1*	6:151842200	SNV: Intron variant	T/C	0.44 (1000 Genome)	Severe late life current MDD	454/3071	French Caucasian	**C** [TT vs CC]	0.61 [0.44–0.84]	0.003	(Ryan et al., 2011)	T	0.58	0.46	0.52
							MDD	89/126	Han Chinese	T	1.7642 [1.1911-2.6131]#	0.004	(Tsai SJ et al 2003)				
							MDD	101/95	Turkish	CC vs TT+TC	2.05 [1.00-4.34]	0.049	(Ozsoy et al, 2021)	C	-	-	-
11	rs4291 [3]	*ACE*	17:63476833	SNV: Upstream transcript variant	T/A	0.34 (1000 Geno	MDD	187/207	Northeastern Thai	A	0.702 [0.508–0.971]	0.04	(Angunsri et al., 2009)	T	0.38	0.68	0.54

Accepted Manuscript

Downloaded from https://academic.oup.com/jjnp/advance-article/doi/10.1093/jjnp/pyad001/6992242 by Delhi Technological University user on 31 January 2023

						me)	Unipolar depression	642/608	German	TT (TT vs TA vs AA]	NA	0.00076	(Baghai et al., 2006)					
								201/245	German Caucasian	TT (TT vs TA vs AA]	NA	0.0043						
							Depression	255/750	French	TT	0.44 [0.27–0.71]	0.001	(Ancelin et al., 2013)	A	-	-	-
12	rs242939 [3]	*CRHR1*	17:45818213	SNV: Intron variant	C/G	0.11 (1000 Genome)	Recurrent MDD	256/272	Han Chinese	A	0.5271 [0.3491–0.7958]	0.0069*	(Z. Liu et al., 2013b)	G	0.13	0.93	0.66	
							Recurrent MDD	181/186	Han Chinese	G	2.201 [1.291 - 3.75][#]	0.018*	(Xiao et al., 2011)					
							Major depression	206/195	Han Chinese	G	NA	0.0008	(Z. Liu et al., 2006)					
13	rs6311 [3]	*5-HTR2A*	13:46897343	SNV: Upstream transcript variant	G/A	0.44 (1000 Genome)	MDD	300/300	Han Chinese	T	0.722 [0.574-0.910][#]	0.006	(S. Cao et al., 2015)	G	0.46	0.61	0.54	
							MDD	189/148	Korean population	G	1.52 [1.12–2.06]	0.007	(Choi et al., 2004)					
							Depressed Mood	377/1215	Swedish	AA [AA vs GG]	1.5 [1.05–2.15]	0.028	(Jansson et al., 2003)	A	-	-	-	
14	rs1360780 [3]	*FKBP5*	6:35639794	SNV: Intron variant	T/C	0.32 (1000 Genome)	MDD	218/742	Polish	TT vs TC vs CC	NA	0.011	(Szczepankiewicz et al., 2014)	T	0.32	0.72	0.53	
							MDD	1256/634	White Non-Hispanic	TT vsTC vs CC	TT vs TC: 0.72 [0.51–1.01]; TT vs TC: 1.01 [0.74–1.40]; TC vs CC:1.394 [1.137-1.709]	0.0038	(Lekman et al., 2008)					
							Recurrent unipolar depression	268/284	German	C	1.31 [1.01–1.70]	0.0356	(Zobel et al., 2010)	C	-	-	-	

Accepted Manuscript

Downloaded from https://academic.oup.com/ijnp/advance-article/doi/10.1093/ijnp/pyad001/6992242 by Delhi Technological University user on 31 January 2023

15	rs4713916 [3]	*FKBP5*	6:35702206	SNV: Genic upstream transcript variant	A/G	0.22 (1000 Genome)	MDD	218/742	Polish	AA vs AG vs GG	NA	0.038	(Szczepankiewicz et al., 2014)	A	0.31	0.73	0.53
							MDD	1256/634	White Non-Hispanic	AA vs AG vs GG	AA vs AG: 0.84 [0.59–1.19]; AA vs GG: 1.08 [0.77–1.52]; AG vs GG:1.29 [1.05–1.58]	0.046	(Lekman et al., 2008)				
							Recurrent unipolar depression	268/284	German	G	1.38 [1.07–1.79]	0.0135	(Zobel et al., 2010)	G	-	-	-
16	rs1800532 [3]	*TPH1*	11:18026269	SNV: Intron variant	C/A	0.32 (1000 Genome)	Depressive disorder	280/230	Polish	AA	2.416 [1.180–4.947]	0.016	(Wigner et al., 2018b)	A	0.41	0.65	0.53
							MDD	115/105	Taiwanese	A	1.9703 [1.3285-2.9222][#]	0.000692[#]	(H. C. Wang et al., 2011)				
							MDD	217/395	Finnish /Caucasian	C	1.437 [1.132-1.824][#]	0.003	(Viikki et al., 2010)	C	-	-	-
17	rs1006737 [2]	*CACNA1C*	12:2236129	SNV: Intron variant	G/A	0.30 (1000 Genome)	MDD	1045/1235	Han Chinese	A	1.425 [1.160-1.752]	0.0007	(He et al., 2014)	A	0.31	0.78	0.59
							Recurrent Major Depression	1196/11373	British Isles (European)	A	1.17 (1.07–1.27)	0.000711[#]	(Green et al., 2010)				
18	rs4880 [2]	*SOD2*	6:15969 2840	SNV: Missense Variant	T/C	0.41 (1000 Genome)	Depressive disorder	281/229	Polish	TT	2.524 [1.308–6.096]	0.008	(Wigner et al., 2018a)	T	0.46	0.61	0.54
							rDD	91/83	Polish	T	1.8 [1.18–2.77]	0.006[#]	(Galecki et al., 2010)				
19	rs1801131 [2]	*MTHFR*	1:11794419	SNV: Missense Variant	A/C	0.24 (1000 Geno	MDD	414/257	Italian	CC vs AA+AC	1.97[1.03–3.61]	0.01	(Gabriela Nielsen et al., 2015)	C	0.33	0.71	0.53

Accepted Manuscript

Downloaded from https://academic.oup.com/ijnp/advance-article/doi/10.1093/ijnp/pyad001/6992242 by Delhi Technological University user on 31 January 2023

						me)	MDD	134/143	Slovak	C	1.52 [1.07 – 2.17]	0.019	(Evinova et al., 2012)					
20	rs2522833 [2]	*PCLO*	7:82824392	SNV: Missense Variant	A/C	0.40 (1000 Genome)	MDD	522/375	Italian	C [CC vs AA+AC]	1.22 [1.07–1.38]	0.005	(Minelli et al., 2012)	C	-	-	-	
							MDD	238/691	French	C [AA vs CA+CC	0.65 [0.47 0.88]	0.0058	(Ryan et al., 2016)	A				
21	rs1800629 [2]	*TNF-α*	6:31575254	SNV: Upstream transcript variant	G/A	0.09 (1000 Genome)	Major depression	50/240	Italian	GG [GG vs Ga vs AA]	2.433 [1.09-5.43]	0.007	(Cerri et al., 2009)	G	-	-	-	
							MDD	108/125	Korean	A	2.242 [1.219–4.121]	0.0125	(Jun et al., 2003)	A				
22	rs4295 [2]	*ACE*	17:63478937	SNV: Genic upstream transcript variant	C/G	0.36 (1000 Genome)	Depression	255/750	French	GG	0.45 [0.28–0.72]	0.001	(Ancelin et al., 2013)	C	-	-	-	
							Unipolar depression	642/608	German	GG [GG vs GC vs CC]	NA	0.0011	(Baghai et al., 2006)	G				
23	rs4343 [2]	*ACE*	17:63488670	SNV: Synonymous variant	G/A	0.35 (1000 Genome)	MDD	191/104	Iranian	G	1.52 [1.07–2.18]	0.015	(N. Firouzabadi et al., 2012)	G	-	-	-	
							Depression	255/750	French	GG	0.54 [0.35–0.84]	0.006	(Ancelin et al., 2013)	A				
24	rs41423247	*NR3C1*	5:143399010	SNV: intron variant	G/C	0.25 (1000 Genome)	rDD	181/149	Polish	C	2.11 [1.53–2.92]	<0.00001	(Gałecka et al., 2013)	C	-	-	-	
							rDD	419/496	German	GG vs GC +CC	1.8[1.04.–3.2]	0.03	(Van Rossum et al., 2006)	G				
GWAS Variants																		
1	rs2273289 [2]	*PLOD1*	1:119588233	SNV: Intron variant	T/C	0.25 (1000 Genome)	MDD	1522/1588	European	C	1.414	3.19 E-05	(Schosser et al., 2013)	C	-	-	-	
							Recurrent Depression	1766/1745	European	C	1.377	8.16 E-06	(Lewis et al., 2010)					
2	rs2715148 [2]	*PCLO*	7:82820719	SNV: Intron variant	A/C	0.34 (1000 Genome)	MDD	1942/4565	European	A	0.79 [0.73-0.86]	3.89 E-08	(Mbarek et al., 2017)	C	-	-	-	
							MDD	1738/1802	European	A	0.79 [0.72-	1.00 E-06	(Sullivan et al., 2009)					

Accepted Manuscript

Downloaded from https://academic.oup.com/ijnp/advance-article/doi/10.1093/ijnp/pyad001/6992242 by Delhi Technological University user on 31 January 2023

											0.87]							
3	rs2423618 [2]	*LINC00687*	20:11828794	SNV: Intron variant	T/C	0.31 (1000 Genome)	MDD	1522/1588	European	C	1.312	2.21 E-05	(Schosser et al., 2013)	C	-	-	-
							Recurrent Depression	1766/1745	European	C	1.262	2.12 E-05	(Lewis et al., 2010)				
GWAS & Candidate variants																		
1	rs2522833 [3]	*PCLO*	7:82824392	SNV: Missense Variant	A/C	0.40 (1000 Genome)	MDD	1738/1802	European	C	1.26 [1.15-1.39]	2.00 E-06	(Sullivan et al., 2009)	C	-	-	-
							MDD	522/375	Italian	C [CC vs AA+AC]	1.22 [1.07–1.38]	0.005	(Minelli et al., 2012)				
							MDD	238/691	French	C [AA vs CA+CC	0.65 [0.47 0.88]	0.0058	(Ryan et al., 2016)	A			
2	rs2715147 [2]	*PCLO*	7:82819089	SNV: Intron variant	C/A	0.35 (1000 Genome)	MDD	1738/1802	Western European	C	0.79	1.50 E-06	(Verbeek et al., 2013)	A	-	-	-
							MDD	1942/4565	European	C	0.79 [0.73-0.86]	3.89 E-08	(Mbarek et al., 2017)				
3	rs9416742 [2]	*BICC1*	10:58782934	SNV: Intron variant	G/A	0.07 (1000 Genome)	Recurrent Depression	1766/1745	European	A	0.719	1.30 E-07	(Lewis et al., 2010)	G	-	-	-
							MDD	62/306	French	A [GG vs GA+AA]	0.48 [0.24 0.96]	0.038	(Ryan et al., 2016)				
4	rs999845 [2]	*BICC1*	10:58776160	SNV: Intron variant	T/C	0.17 (1000 Genome)	Recurrent Depression	1766/1745	European	A	0.7273	3.12 E-07	(Lewis et al., 2010)	C	-	-	-
							MDD	62/306	French	A [GG vs GA+AA]	0.49 [0.25 0.94]	0.033	(Ryan et al., 2016)				

[#] Self Calculated values

Accepted Manuscript

Downloaded from https://academic.oup.com/ijnp/advance-article/doi/10.1093/ijnp/pyad001/6992242 by Delhi Technological University user on 31 January 2023

Table2: List of all reproducible genes in GWAS studies, candidate studies and in both related to MDD susceptibility.

S. No.	Gene	Name	Location	Phenotype	Sample size (case/control)	Population/Country	References	Function
Candidate Genes								
1	*SLC6A4/5HTT/SERT*	Solute carrier family 6 member 4	17q11.2	MDD	74/150	Han Chinese	(Ran et al., 2020)	Monoamine Transport
				MDD	35/33	Colombian	(Perez-Olmos et al., 2016)	
				MDD	459/412	Han Chinese	(N. Sun et al., 2016)	
				Depression	366/327	Australia/European	(Wray et al., 2009)	
				MDD	401/391	Han Chinese	(K. Zhang et al., 2009)	
				MDD	272/264	Mexican Americans	(Dong et al., 2009)	
				MDD	70/142	Spanish	(Dorado et al., 2007)	
				Depression	184/158	Han Chinese	(M. Q. Cao et al., 2007)	
				Depression	184/360	German	(Grünblatt et al., 2006)	
				MDD	466/836	German	(Hoefgen et al., 2005)	
				Depression	57/38	Racially mixed	(Steffens et al., 2002)	
				Major depression	53/107	Racially mixed	(Mann et al., 2000)	
				Unipolar depression	33/362	Han Chinese	(W. Liu et al., 1999)	
				Major depression with melancholia	74/84	Spanish	(Gutiérrez et al., 1998)	
				Unipolar depressive disorder	39/193	Edinburgh (UK)	(Ogilvie et al., 1996)	
2	*BDNF*	Brain derived neurotrophic factor	11p14.1	MDD	300/300	Malaysian	(Aldoghachi et al., 2019)	Promotes neuronal survival in the adult brain
				MDD	45/45	NA	(Youssef et al., 2018)	
				Recurrent MDD	116/218	Polish	(Suchanek et al., 2011)	
				Major Depression	202/346	Chinese	(R. F. Sun et al., 2011)	
				MDD	272/264	Mexican-American	(Licinio et al., 2009)	
				Depressive Disorder	42/41	Czech	(Zeman et al., 2010)	
				Unipolar MD	245/94	White	(Taylor et al., 2007)	
				MDD	110/171	Chinese	(Hwang et al., 2006)	
				MDD	456/1097	German	(Schumacher et al., 2005)	
3	*TPH2*	Tryptophan hydroxylase 2	12q21.1	Depressive Disorder	280/230	Polish	(Wigner et al., 2018b)	Biosynthesis of serotonin
				Major depression	289/289	Han Chinese	(J. Ma et al., 2015)	
				MDD	90/182	Han Chinese	(Shen et al., 2011)	
				Major depression	117/83	Chinese	(Y. M. Lin et al., 2009b)	
				MDD	508/463	Han Chinese	(Tsai et al., 2009b)	
				Unipolar major depression	87/219	Majority Caucasians	(X. Zhang et al., 2005)	

Accepted Manuscript

Downloaded from https://academic.oup.com/ijnp/advance-article/doi/10.1093/ijnp/pyad001/6992242 by Delhi Technological University user on 31 January 2023

				Major Depression	300/265	German	(Zill et al., 2004)	
4	*ABCB1*	ATP binding cassette subfamily B member 1	7q21.12	rDD	90/96	Polish	(Jelen et al., 2015)	Transportation of various molecules across extra- and intra-cellular membranes; involved in multidrug resistance
				MDD	54/70	Turkish	(Ozbey et al., 2014)	
				MDD	21/42	Portuguese	(Santos et al., 2014)	
				MDD	631/1100	Japanese	(Fujii et al., 2012)	
				MDD	272/264	Mexican Americans	(Dong et al., 2009)	
				Depression	284/331	Maxican Americans	(Wong et al., 2008)	
5	*MTHFR*	Methylenetetrahydrofolate reductase	1p36.22	Depression (Perimenopausal women)	54/102	Polish Caucasian	(Rozycka et al., 2016)	A co-substrate for homocysteine remethylation to methionine; Neural Tube Defects, Folate-Sensitive.
				Depression (Postmenopausal women)	113/219			
				MDD	414/257	Italian	(Gabriela Nielsen et al., 2015)	
				MDD	368/219	Han Chinese	(Shen et al., 2014)	
				MDD	134/143	Slovak	(Evinova et al., 2012)	
				Depressive episode	100/89	Northern Irish	(Kelly et al., 2004)	
				Major depression	32/419	Japanese	(Arinami et al., 1997)	
6	*COMT*	Catechol-O-methyltransferase	22q11.21	Depression (Postmenopausal women)	332/219	Polish Caucasian	(Rozycka et al., 2016)	Catalyzes the transfer of a methyl group from S-adenosylmethionine to catecholamines (dopamine, epinephrine, and norepinephrine)
				MDD	613/463	Italian (Caucasian)	(Gabriela Nielsen et al., 2015)	
				MDD	368/219	Han Chinese	(Shen et al., 2014)	
				Depression	405/2151	Swedish	(Aberg et al., 2011)	
				Depressive disorder	75/135	Japanese	(Ohara et al., 1998)	
				EO-MDD	120/628	European	(Massat et al., 2005)	
7	*ACE*	Angiotensin I converting enzyme	17q23.3	Depression	255/750	French	(Ancelin et al., 2013)	Blood pressure regulation and electrolyte balance
				MDD	191/104	Iranian	(N. Firouzabadi et al., 2012)	
				MDD	187/207	Northeastern Thai	(Angunsri et al., 2009)	
				Unipolar depression	642/608	German (Majority) Caucasian	(Baghai et al., 2006)	
8	*CRHR1*	Corticotropin releasing hormone receptor 1	17q21.31	Recurrent MDD	256/272	Han Chinese	(Z. Liu et al., 2013b)	G protein-coupled receptor activity; major regulator of the hypothalamic-pituitary-adrenal pathway
				MDD	173/285	Japanese	(Ishitobi et al., 2012)	
				Recurrent MDD	181/186	Han Chinese	(Xiao et al., 2011)	
				Major depression	206/195	Han Chinese	(Z. Liu et al., 2006)	
9	*GNB3*	G protein subunit beta 3	12p13.31	Major Depression	512/513	Han Chinese	(J. Ma et al., 2017)	Integrate signals between receptors and effector
				Depression	184/158	Han Chinese	(M. Q. Cao et al., 2007)	
				MDD	106/133	Korean	(H. J. Lee et al., 2004)	

Accepted Manuscript

Downloaded from https://academic.oup.com/ijnp/advance-article/doi/10.1093/ijnp/pyad001/6992242 by Delhi Technological University user on 31 January 2023

				Major depression	78/111	German	(Zill et al., 2004)	proteins
10	*SLC6A2/NET*	Solute carrier family 6 member 2	16q12.2	MDD	579/437	Han Chinese	(Min et al., 2009)	Regulates norepinephrine homeostasis
				Unipolar MD	426/643	German	(Haenisch et al., 2009)	
				Major Depression	388/388	Han Chinese	(N. Sun et al., 2008)	
				Major depression	112/136	Korean	(Ryu et al., 2004)	
				MDD	145/164	Japanese	(Inoue et al., 2004)	
11	*NR3C1*	Nuclear receptor subfamily 3 group C member 1	5q31.3	MDD	251/307	German Caucasian	(Sarubin et al., 2017)	(Wong et al., 2008)Involved in inflammatory responses, cellular proliferation, and differentiation in target tissues
				rDD	181/149	Polish	(Galecka et al., 2013)	
				MDD	193/732	Polish	(Szczepankiewicz et al., 2011)	
				Depression	284/331	Maxican Americans	(Wong et al., 2008)	
				MDD	180/173	Belgian	(van West et al., 2006)	
12	*TPH1*	Tryptophan hydroxylase 1	11p15.1	Depressive disorder	280/230	Polish	(Wigner et al., 2018b)	Biosynthesis of serotonin
				MDD	115/105	Taiwanese	(H. C. Wang et al., 2011)	
				MDD	217/395	Finnish /Caucasian	(Viikki et al., 2010)	
				Depression	30/86	Taiwanese	(H. S. Sun et al., 2004)	
13	*CACNA1C*	Calcium voltage-gated channel subunit alpha1 C	12p13.33	MDD	1045/1235	Han Chinese	(He et al., 2014)	Calcium channels; mediate the influx of calcium ions upon membrane polarization.
				MDD	640/542	German	(Kloiber et al., 2012)	
				Recurrent Major Depression	1196/11373	British Isles (European)	(Green et al., 2010)	
14	*FKBP5*	FKBP prolyl isomerase 5	6p21.31	MDD	218/742	Polish	(Szczepankiewicz et al., 2014)	role in immunoregulation; involving protein folding and trafficking
				MDD	1256/634	White Non-Hispanic	(Lekman et al., 2008)	
				Recurrent unipolar depression	268/284	German (Caucasian)	(Zobel et al., 2010)	
15	*PCLO*	Piccolo presynaptic cytomatrix protein	7q21.11	MDD	238/691	French	(Ryan et al., 2016)	Synaptic vesicle trafficking
				MDD	1738/1802	Western European	(Verbeek et al., 2013)	
				MDD	522/375	Italian	(Minelli et al., 2012)	
16	*5-HTR2A*	5-hydroxytryptamine receptor 2A	13q14.2	MDD	300/300	Han Chinese	(S. Cao et al., 2015)	Serotonergic neurotransmission
				MDD	189/148	Korean (Caucasian)	(Choi et al., 2004)	
				Depressed Mood	377/1215	Swedish (Caucasians)	(Jansson et al., 2003)	
17	*CNR1*	Cannabinoid receptor 1	6q15	Major depression (Melancholic)	151/150	Spanish	(Mitjans et al., 2013)	G protein-coupled receptor activity and cannabinoid receptor activity
				Recurrent MD	83/117	Italian (Caucasian)	(Monteleone et al., 2010)	
18	*CRY1*	Cryptochrome circadian regulator 1	12q23.3	MDD	383/4154	Finnish	(Kovanen et al., 2017)	Regulates the circadian clock
				Dysthymia	166/4154			
				Depressive disorder	479/4154			

Accepted Manuscript

Downloaded from https://academic.oup.com/ijnp/advance-article/doi/10.1093/ijnp/pyad001/6992242 by Delhi Technological University user on 31 January 2023

				MDD	105/485	Chinese	(Hua et al., 2014)	
19	*DRD2*	Dopamine receptor D2	11q23.2	MDD	403/475	Han Chinese	(Y. Wang et al., 2012)	Dopamine receptor; include G protein-coupled receptor activity
				MDD	177/160	Estonian	(Koks et al., 2006)	
20	*GSK3B*	Glycogen synthase kinase 3 beta	3q13.33	MDD	1045/1235	HanChinese	(Chen et al., 2015)	A negative regulator of glucose homeostasis; involved in energy metabolism, inflammation, ER-stress, mitochondrial dysfunction, and apoptotic pathways
				MDD	447/432	Han Chinese	(K. Zhang et al., 2010)	
21	*HTR1A*	5-hydroxytryptamine receptor 1A	5q12.3	MDD	331/804	Japanese	(Kishi et al., 2009b)	Serotonergic neurotransmission; G protein-coupled serotonin receptor activity
				Unipolar MD	426/643	German	(Haenisch et al., 2009)	
				MDD	401/391	Han Chinese	(K. Zhang et al., 2009)	
				MDD	400/400	Northern Han Chinese	(Wu et al., 2008)	
				MDD	129/134	Ontario (Majority Caucasians)	(Lemonde et al., 2003)	
22	*KCNK2*	Potassium two pore domain channel subfamily K member 2	1q41	MDD	590/441	Italian (Caucasian)	(Congiu et al., 2015)	Potassium channel activity
				MDD	449/421	Han Chinese	(Liou et al., 2009)	
23	*TNF-α*	Tumor necrosis factor	6p21.33	Major depression	50/240	Italian (Caucasian)	(Cerri et al., 2009)	multifunctional proinflammatory cytokine; involved in cell proliferation, differentiation, apoptosis, lipid metabolism, and coagulation
				MDD	108/125	Korean	(Jun et al., 2003)	
24	*ESR1/ER-α*	Estrogen receptor 1	6q25.1-q25.2	MDD	125/120	Turkish	(Ozsoy et al, 2021)	DNA-binding transcription factor activity and enzyme binding
				Depression (Postmenopausal women)	113/219	Polish Caucasian	(Rozycka et al., 2016)	
				Severe late life current MDD	454/3071	French	(Ryan et al., 2011)	
				MDD	89/126	Han Chinese	(Tsai et al., 2003)	
25	*ESR2/ ER-β*	Estrogen receptor 2	14q23.2-q23.3	Severe late life current MDD	454/3071	French	(Ryan et al., 2011)	DNA-binding transcription factor activity and enzyme binding
				MDD	102/150	Han Chinese	(Y. G. Geng et al., 2007)	
26	*sod2*	Superoxide dismutase 2	6q25.3	Depressive disorder	281/229	Polish	(Wigner et al., 2018a)	A mitochondrial

Accepted Manuscript

Downloaded from https://academic.oup.com/ijnp/advance-article/doi/10.1093/ijnp/pyad001/6992242 by Delhi Technological University user on 31 January 2023

				rDD	91/83	Polish	(Galecki et al., 2010)	protein binds to the superoxide byproducts and converts them to hydrogen peroxide and diatomic oxygen
27	*MAOA*	Monoamine oxidase A	Xp11.3	Depression (Perimenopausal women)	54/102	Polish Caucasian	(Rozycka et al., 2016)	Monoamine transport; oxidoreductase activity
				Depression (Postmenopausal women)	113/219			
				MDD	228/213	Chinese	(Yu et al., 2005)	
				Recurrent MDD	73/68	German	(Schulze et al., 2000)	
GWAS Genes								
1	*ARHGAP8*	Rho GTPase activating protein 8	22q13.31	MDD	203/196	Mexican-American & European	(Wong et al., 2017)	Regulates cell processes
				Recurrent MDD	926/866	European	(Muglia et al., 2010)	
2	*CSMD1*	CUB and Sushi multiple domains 1	8p23.2	Major depression	604/1364	German	(Rietschel et al., 2010)	-
				Recurrent early-onset MDD	724/720	European	(Shi et al., 2011)	
3	*FHIT*	Fragile histidine triad diadenosine triphosphatase	3p14.2	Recurrent early-onset MDD	296/916	European	(Shi et al., 2011)	Involved in purine metabolism
				Recurrent MDD	926/866	European	(Muglia et al., 2010)	
4	*LHPP*	Phospholysine phosphohistidine inorganic pyrophosphate phosphatase	10q26.13	Recurrent MDD	5303/5337	Han Chinese	(consortium, 2015)	Metabolism of nucleotides
				Recurrent MDD	926/866	European	(Muglia et al., 2010)	
5	*PCLO*	Piccolo presynaptic cytomatrix protein	7q21.11	MDD	1942/4565	European	(Mbarek et al., 2017)	Synaptic vesicle trafficking
				MDD	1738/1802	European	(Sullivan et al., 2009)	
6	*PLOD1*	Procollagen-lysine,2-oxoglutarate 5-dioxygenase 1	1p36.22	MDD	1522/1588	European	(Schosser et al., 2013)	Protein homodimerization activity and iron ion binding
				Recurrent Depression	1766/1745	European	(Lewis et al., 2010)	
7	*LINC00687*	Long intergenic non-protein coding RNA 687	20p12.2	MDD	1522/1588	European	(Schosser et al., 2013)	-
				Recurrent Depression	1766/1745	European	(Lewis et al., 2010)	
8	*LOC100996549*	Uncharacterized LOC100996549	2p25.1	MDD	1522/1588	European	(Schosser et al., 2013)	-
				Recurrent MDD	492/1052	European	(Muglia et al., 2010)	
Candidate and GWAS Genes								
1	*PCLO*	Piccolo presynaptic cytomatrix protein	7q21.11	MDD	1942/4565	European	(Mbarek et al., 2017)	Synaptic vesicle trafficking
				MDD	1738/1802	European	(Sullivan et al., 2009)	

Accepted Manuscript

Downloaded from https://academic.oup.com/ijnp/advance-article/doi/10.1093/ijnp/pyad001/6992242 by Delhi Technological University user on 31 January 2023

				MDD	238/691	French	(Ryan et al., 2016)	
				MDD	1738/1802	Western European	(Verbeek et al., 2013)	
				MDD	522/375	Italian	(Minelli et al., 2012)	
2	*ESR1*	Estrogen receptor 1	6q25.1-q25.2	Major depression	604/1364	German	(Rietschel et al., 2010)	DNA-binding transcription factor activity; role in growth, metabolism, sexual development
				MDD	125/120	Turkish	(Ozsoy et al, 2021)	
				Depression (Postmenopausal women)	113/219	Polish Caucasian	(Rozycka et al., 2016)	
				Severe late life current MDD	454/3071	French	(Ryan et al., 2011)	
				MDD	89/126	Han Chinese	(Tsai et al., 2003)	
3	*APC*	APC regulator of WNT signaling pathway	5q22.2	Recurrent MDD	926/866	European	(Muglia et al., 2010)	Antagonist of the Wnt signaling pathway; cell migration and adhesion, transcriptional activation, and apoptosis
				MDD	397/473	Han Chinese	(Yang et al., 2012)	
4	*GRM7*	Glutamate metabotropic receptor 7	3p26.1	Recurrent MDD	926/866	European	(Muglia et al., 2010)	Glutamatergic neurotransmission
				MDD	1738/1802	Western European	(Verbeek et al., 2013)	
5	*CNTNAP2*	Contactin associated protein 2	7q35-q36.1	Recurrent MDD	492/1052	European	(Muglia et al., 2010)	Cell adhesion molecules and receptors; mediates interactions between neurons and glia
				MDD	1135/1135	Han Chinese	(W. Ji et al., 2013)	
6	*EHD3*	EH domain containing 3	2p23.1	Recurrent MDD	1418/1918	European	(Muglia et al., 2010)	Role in endocytic transport,Golgi maintenance and morphology
				MDD	283/248	Han Chinese	(L. Wang et al., 2014a)	
7	*BICC1*	BicC family RNA binding protein 1	10q21.1	Recurrent Depression	1766/1745	European	(Lewis et al., 2010)	Regulating gene expression by modulating protein translation
				MDD	62/306	French	(Ryan et al., 2016)	

Accepted Manuscript

Downloaded from https://academic.oup.com/ijnp/advance-article/doi/10.1093/ijnp/pyad001/6992242 by Delhi Technological University user on 31 January 2023

Table 3: List of all reproducible genetic variants with their sensitivity, specificity and PPV in candidate studies, GWAS studies and in both related to antidepressant response.

S. No.	Variant [no. of studies]	Gene	Location:Position (GRCh38)	Variant type	Polymorphism (Reference/alternate)	Global Minor Allele Frequency (MAF)	Response Status	Drug class	Associated Phenotype	Sample size (responder/nonresponder)	Population	Reported Risk allele/genotype	OR [CI]	P value	References	Calculated Risk Allele*	Sensitivity	Specificity	PPV (positive predictive value)
Candidate Variants SNPs																			
1	rs7746776466; 5-HTTLPR [22]	*SLC6A4/5HTT/SERT*	17:30237299	Insertion/deletion (44bp)	L/S	0.19 (ALFA)	Response: ≥50% reduction in HAMD, MADRS, Beck score after treatment	SSRIs	Non-responder	148 (65/83)	South Indian	S	7.41 [3.87-14.20]#	<.0001#	(Mandal et al., 2020)	S	0.70	0.44	0.53
									Non-responder	102 (56/46)	South Indian	S carrier [LL vs LS + SS]	4 [1.45–11.03]	0.0066	(Manoharan et al., 2016)				
									Non-responder	104 (65/39)	Iranian	SS [SS vs LS+LL]	2.625 [1.127-6.1139]#	0.023#	(Sahraian et al., 2013)				
									Non-responder	362 (243/119)	Han Chinese	S carrier [LL vs LS + SS]	2.85[1.0687-7.6002]#	0.03	(Min et al., 2009)				
									Non-responder	130 (65/65)	Croatian	S	2.55 [1.53-4.25]#	0.0004	(Bozina et al., 2008)				
									Non-reponder	224 (81/143)	Han Chinese/ Taiwanese	S	2.0404 [1.3365 - 3.1151]#	0.0009#	(Hong et al., 2006)				
									Non-responder	121 (40/81)	Chinese	S	2.0271 [1.1181 -	0.019	(Yu et al., 2002)				

Accepted Manuscript

Downloaded from https://academic.oup.com/ijnp/advance-article/doi/10.1093/ijnp/pyad001/6992242 by Delhi Technological University user on 31 January 2023

| | | |

								TCA	Non-responder	89 (55/34)	Koreans	L	3.3462 [1.6911 - 6.6211] #	0.0004 #	(H. Kim et al., 2006)	L	-	-	-
								Atypical	Non-responder	101 (62/39)	Korean	L	2.8629 [1.2611 - 6.4993] #	0.009 #	(R. H. Kang et al., 2007)	L	-	-	-
								Mixed	TRD	128 (98/30)	Caucasian	L carrier [LL+LS vs SS]	5.0556 [1.1246 - 22.7263]#	0.023 #	(Wilkie et al., 2009)	L	-	-	-
								Remission: MADRS score ≤7 after treatment	SSRIs	Non-remitter	85 (29/56)	Finnish/Caucasian	S carrier [LL vs LS + SS]	3.2143 [1.2471 - 8.2844] #	0.01375#	(Illi et al., 2011)	S	0.36	0.81	0.57
										Non-remitter	131 (91/40)	Spanish	SS[SS vs LS+LL]	3.23 [1.24–8.5]	0.006	(Arias et al., 2003)				
										Non-remitter	27 (16/11)	Caucasians	S carrier [LL vs LS + SS]	10 [1.0256 - 97.5046]#	0.04	(Alexopoulos et al., 2009)	S	Raw data not available		
										Non-remitter	362 (156/206)	Han Chinese	LLvsLSvsSS	NA	0.007	(Min et al., 2009)	L	-	-	-
2	rs5709 8334; STin2-VNTR [5]	*SLC6A4*	17:3022 1568	Insertion /deletion	L/S	0.025 - 0.15*	Response: ≥50% reduction in HAMD score after treatment	SSRIs	Non-responder	119 (69/50)	Koreans	S	18.0759 [4.1284 - 79.1441]#	<.0001#	(H. Kim et al., 2006)	S	0.18	0.94	0.63
									Non-responder	362 (239/123)	Han Chinese	10	1.7314 [1.0525 - 2.8484]	0.029	(Min et al., 2009)				
									Non-responder	120 (87/33)	Korean	S	21.25 [6.9629 - 64.8527]#	<.0001#	(D. K. Kim et al., 2000)				

Accepted Manuscript

Downloaded from https://academic.oup.com/ijnp/advance-article/doi/10.1093/ijnp/pyad001/6992242 by Delhi Technological University user on 31 January 2023

									Non-responder	239 (154/85)	Korean	ll vs. sl+ss	3.86 (1.90–7.84)	0.0002	(Lim et al., 2014)	S	Raw data not available		
								Atypical	Non-responder	283 (100/183)	Korean	10 repeat [10.10+12.10 vs 12.12]	2.4375 [1.1595 - 5.1241] #	0.016 #	(Chang et al., 2014)	S	-	-	-
							Remission:HAMD score ≤8 after treatment	SSRIs	Non-remitter	362 (151/211)	Han Chinese	10 carrier [12/12 vs 12/10+10/10]	1.7756 [1.000-3.1535]	0.048	(Min et al., 2009)	S	-	-	-
3	rs6265 [5]	*BDNF*	11:27658369	SNV: Missense Variant	G/A	0.20 (1000 Genome)	Response: ≥50% reduction in HAMD score after treatment	SSRIs	Non-responder	298 (219/79)	Chinese	G	2.076 [1.43-3.008]	<.0001 #	(X. C. Wang et al., 2014b)	G	0.62	0.57	0.36
									Non-responder	83 (57/26)	Korean		2.5 [1.249–5.005]	0.009	(Choi et al., 2006)				
									Non-responder	187 (108/52)	Caucasian	GG [GG vs AA+GA]	2.377 [1.170-4.828]	0.015	(El-Hage et al., 2015)	G	Raw data not available		
								Mixed	Non-responder	188 (71/117)	European	G	2.0704 [1.22–3.506]	0.00629	(Kocabas et al., 2011)	G	-	-	-
								SNRI	Non-responders	117 (23/39)	Han Chinese (Taiwanese)	AA	NA	0.006	(Chi et al., 2010)	A	-	-	-
4	rs7997012 [4]	*HTR2A*	13:46837850	SNV: Intron Variant	A/G	0.27 (1000 Genome)	Response: ≥50% reduction in QIDS score after treatment	SSRI	Non-responder	935 (675/260)	Mixed (White, Black and other)	G	NA	1.3E-05	(Paddock et al., 2007)	G	-	-	-

Accepted Manuscript

Downloaded from https://academic.oup.com/ijnp/advance-article/doi/10.1093/ijnp/pyad001/6992242 by Delhi Technological University user on 31 January 2023

							Resistant: Failed to reach an HAMD-17 score < 17,after at least two adequate antidepressant treatments within the current episode	Mixed	Non-responder (resistant)	206 (58/74)	European	A	1.7402 [1.0309 - 2.9373] #	0.037	(Noro et al., 2010)	A	-	-	-
							Remission:HAMD score ≤8/ QIDS-C ≤5 after treatment	SSRI	Non remitter	46 (32/14)	Caucasian	A	5.4[2.0718-14.0746]#	0.000329#	(Gasso et al., 2018)	A	-	-	-
									Non-remitter	NA	Mixed (White, Black and other)	G	NA	9.5E-05	(Paddock et al., 2007)	G	-	-	-
								Mixed	Non-remitter	186 (61/125)	Caucasian/Northern Germany	A	1.7953[1.1521-2.7975]#	0.00938	(Lucae et al., 2010)	A	-	-	-
5	rs6295 [4]	*5HTR1A*	5:63962738	SNV: Upstream gene variant	C/G	0.45 (1000 Genome)	Response: ≥50% reduction in HAMD score after treatment	SSRIs	Non-responder	222 (83/139)	Han Chinese/ Taiwanese	G	2.0516 [1.2936 - 3.2536] #	0.002#	(Yu et al., 2006)	G	same cohort			
									Non responder	224 (81/143)	Han Chinese/ Taiwanese	G	2.0598 [1.2893 - 3.2908] #	0.002#	(Hong et al., 2006)	G				
								Mixed	Non-responders	137 (22/115)	Japanese	C carrier (CC+CG vs GG]	8.2963 [1.713-40.1795]#	0.0129#	(Kato et al., 2009)	C	-	-	-

Accepted Manuscript

Downloaded from https://academic.oup.com/ijnp/advance-article/doi/10.1093/ijnp/pyad001/6992242 by Delhi Technological University user on 31 January 2023

							Resistant: Failed to reach an HAMD-17 score < 17,after at least two adequate antidepressant treatments within the current episode	Mixed	Non-responder (resistant)	206 (58/75)	European	C	1.693[1.04–2.77]	0.035	(Noro et al., 2010)	C	-	-	-
							Remission: HAMD score ≤7 after 2 weeks of treatment	Mixed	Non-remitters	137 (15/122)	Japanese	G carrier [CC vs CG + GG]	7.375 [1.474-36.913] #	0.028 #	(Kato et al., 2009)	G	-	-	-
6	rs5443 [3]	*GNB3*	12:6845711	SNV: Synonymous Variant	C/T	0.49 (1000 Genome)	Response: ≥50% reduction in HAMD score after treatment	Mixed	Non-responder	163 (58/105)	Caucasian	CC vs CT vs TT	NA	0.04	(Wilkie et al., 2007)	C	0.71	0.14	0.66
									Non-responder	106 (67/39)	Korean	CC [CC vs TT+TC]	2.8973 [1.0492-8.0008] #	0.035	(H. J. Lee et al., 2004)				
									Non-responder	101 (35/66)	Han Chinese/ Taiwanese	TT (CC+CT vs TT)	2.8889 [1.0954-7.619]#	0.029	(E. Lin et al., 2009a)	T	-	-	-
							Remission: HAMD score ≤7 after treatment	Mixed	Non-remitter	110 (70/40)	Caucasian	CC vs CT vs TT	NA	0.02	(Wilkie et al., 2007)	T	-	-	-
7	rs334558 [2]	*GSK3B*	3:120094435	SNV:5 prime UTR Variant	T/C	0.40 (1000 Geno	Response: ≥50% reduction in HAM-	Mixed (SSRIs and SNRI)	Non-responder	143 (90/53)	Japanese	TT vs CC+CT	10.4 [1.332-81.186] #	0.007 #	(Sunada et al., 2019)	T	-	-	-

Accepted Manuscript

Downloaded from https://academic.oup.com/ijnp/advance-article/doi/10.1093/ijnp/pyad001/6992242 by Delhi Technological University user on 31 January 2023

						me)	D score after treatment	SSRIs	Non-responder	168 (75/93)	Han Chinese/ Taiwanese	T	1.6971 [1.0835 - 2.6583] [#]	0.02	(Tsai et al., 2009b)	T	-	-	-
							Remission: HAM-D score ≤ 7 points after treatment	Mixed	Non-remitter	143 (18/125)	Japanese	TT vs CC+CT	3.986 [1.1972 - 13.2713] [#]	0.032 [#]	(Sunada et al., 2019)	T	-	-	-
8	rs2470890 [2]	*CYP1A2*	15:74755085	SNV: Synonymous Variant	T/C	0.40 (ALFA)	Remission:HAMD score ≤ 7 points after treatment	SNRI	Non-remitter	175 (97/78)	Han Chinese	T	2.438 [1.234–4.815]	0.0087	(Zhu et al., 2019)	T	-	-	-
								SSRI	Non-remitter	171 (69/102)	Han Chinese	C	2.7623 [1.3662 - 5.585] [#]	0.0035 [#]	(K. M. Lin et al., 2010)	C	-	-	-
9	rs6313 [2]	*HTR2A*	13:46895805	SNV: Synonymous Variant	C/T	0.44 (1000 Genome)	Remission:Disease free state for atleast 2 weeks	SSRI	Non-remitter	46 (32/14)	Caucasian	T	NA	0.0225	(Gasso et al., 2018)	T	-	-	-
					G/C		Remission:MADRS remission (score ≤10)	SSRI	Non-remitter	166	Han Chinese	G	1.69 [1.00-2.84]	0.049	(Su et al., 2016)	G	-	-	-
10	rs2066713 [2]	*SLC6A4*	17:30224647	SNV: Intron Variant	C/T	0.25 (1000 Genome)	Response: ≥50% reduction in HAMD score after treatment	SSRI	Non-responder	239 (154/85)	Korean	T	4.0548 [1.9722 - 8.3366] [#]	0.0000802 [#]	(Lim et al., 2014)	T	-	-	-
							Remitter: Disease free state for alteast 2 weeks	SSRI	Non-remitter	46 (32/14)	Caucasian	T	NA	0.038	(Gasso et al., 2018)	T	Raw data not available		
11	rs4142 3247 [2]	*NR3C1*	5:143399010	SNV: Intron Variant	G/C	0.25 (1000 Genome)	Response :≥50% reduction in HAM-D score after treatment	SSRI	Non-responder	100 (70/30)	Caucasian (Iranian)	C	2.2[1.09–4.44]	0.032	(Nouraei et al., 2018)	C	0.55	0.34	0.42
										160 (104/56)	Japanese	C	5.11 [1.14-22.82] [#]	0.019	(Takahashi et al.,				

Accepted Manuscript

Downloaded from https://academic.oup.com/ijnp/advance-article/doi/10.1093/ijnp/pyad001/6992242 by Delhi Technological University user on 31 January 2023

															2014)				
12	rs2171363 [2]	*TPH2*	12:71966484	SNV: Intron Variant	A/G	0.40 (1000 Genome)	Response: ≥50% reduction in HDRS score after treatment	Mixed (SSRIs & SNRIs)	Non-responder	281 (205/76)	Han Chinese	A	1.544 [1.055–2.258]	0.02478	(Xu et al., 2016)	A	-	-	-
								SSRIs	Non-responder	187 (126/61)	Han Chinese/ Taiwanese	CC vs CT vs TT	NA	0.009	(Tsai et al., 2009b)	C	-	-	-
13	rs2075507 [2]	*COMT*	22:19940569	SNV: Upstream Variant	G/A	0.34 (1000 Genome)	Remission:HAMD score ≤ 8 points after treatment	SSRI	Non-remitters	123 (24/35)	Japanese	C	7.5 [2.11-26.63][#]	0.0006[#]	(Fukui et al., 2014)	G	-	-	-
							Resistant: Failed to reach an HAMD-17 score < 17,after at least two adequate antidepressant treatments within the current episode	Mixed	Non-responder (resistant)	166 (61/105)	Caucasian	GG vs GA vs AA	NA	0.005	(Kocabas et al., 2010)	G	-	-	-
14	rs1954787 [2]	*GRIK4*	11:120792654	SNV: Intron Variant	A/G	0.49 (IK Genome)	Response: ≥50% reduction in HDRS/QIDS score after treatment	Mixed (SSRI,SNRI)	Non-responder	281 (205/76)	Han Chinese	A	1.868 [1.173–2.975]	0.0078	(Pu et al., 2013)	A	-	-	-
					T/C			SSRI	Non-responder	935 (675/260)	Mixed (White, Black and other)	T	NA	0.00023	(Paddock et al., 2007)	T	-	-	-
							Remission:QIDS-C-16 score ≤5	SSRI	Non-remitter	NA	Mixed (White, Black and other)	T	NA	0.00034	(Paddock et al., 2007)	T	-	-	-

Accepted Manuscript

Downloaded from https://academic.oup.com/ijnp/advance-article/doi/10.1093/ijnp/pyad001/6992242 by Delhi Technological University user on 31 January 2023

15	rs1360780 [2]	*FKBP5*	6:35639794	SNV: Intron Variant	T/C	0.32 (IK Genome)	Early response: ≥25% reduction in HAMD score after treatment	Mixed	Non-responder	233 (147/86)	German/ Caucasian	C	1.6574 [1.072-2.5624] [#]	0.02[#]	(Binder et al., 2004)	C	-	-	-
										85 (43/42)			2.3974 [1.2181 - 4.7186] [#]	0.01[#]		C	-	-	-
							Remission:QIDS-C-16 score ≤5 after treatment	SSRIs	Non-remission	799 (516/283)	White non-Hispanic	CC [CC vs TT+CT]	1.43 [1.0685 - 1.9138] [#]	0.015 [#]	(Lekman et al., 2008)	C	-	-	-
GWAS Variants																			
1	rs6046805 [2]	*CFAP61*	20:20343697	SNV: Intron Variant	G/A, G/C	0.41 (1000 genome)	Remission	SSRI	Remitter	840/837	Mixed	NA	NA	0.01744	(Cocchi et al., 2016)	-	-	-	-
										743/608	Mixed	NA	NA	5.4E-05	(Garriock et al., 2010)	-	-	-	-
							Response	SSRI	Responder	883/608	Mixed	NA	NA	4.4E-05	(Garriock et al., 2010)	-		-	-
2	rs6966038 [2]	*UBE3C*	7:157087704	SNV	A/G	0.25 (1000 Genome)	Response	SSRI	Responder	840/837	Mixed	NA	0.7525	0.00056	(Cocchi et al., 2016)	-	-	-	-
										883/608	Mixed	NA	1.64 [1.35-1.99]	4.7E-07	(Garriock et al., 2010)	-	-	-	-
							Remission	SSRI	Remitter	575/1102	Mixed	NA	0.7083	3.4E-05	(Cocchi et al., 2016)	-	-	-	-
										743/608	Mixed	NA	1.68 [1.37-2.04]	3.6E-07	(Garriock et al., 2010)	-	-	-	-

Accepted Manuscript

Downloaded from https://academic.oup.com/ijnp/advance-article/doi/10.1093/ijnp/pyad001/6992242 by Delhi Technological University user on 31 January 2023

GWAS & Candidate Variants																		
1	rs6127921 [2]	*BMP7*	20:57063694	SNV	A/C	0.21 (1000 Genome)	Response: ≥50% reduction in HAMD score after treatment	SSRI	Responder	129/95	Japanese	A	0.59 [0.39-0.88]	0.0098	(Esaki et al., 2013)	-	-	-	-
							Response: QIDS	SSRI	NA	883/608	Mixed	NA	0.61 [0.49-0.75]	3.5E-06	(Garrock et al., 2010)	-	-	-	-
							Remitter: QIDS	SSRI	NA	743/608	Mixed	NA	0.57 [0.46-0.72]	1.1E-06		-	-	-	-

[#] Self Calculated values; *based on literature as not available on NCBI database

Accepted Manuscript

Downloaded from https://academic.oup.com/ijnp/advance-article/doi/10.1093/ijnp/pyad001/6992242 by Delhi Technological University user on 31 January 2023

Table4: List of all reproducible genes in GWAS studies, candidate studies and in both related to antidepressant response.

S. No.	Gene	Name	Location	Drug class	Phenotype	Sample size (responder/non-responder)	Population	References	Function
Candidate Genes									
1	*SLC6A4*	Solute carrier family 6 member 4	17q11.2	SSRI	Non-responder	65/83	South Indian	(Mandal et al., 2020)	Monoamine Transport
				SSRI	Non-responder	59/33 44/22	Maxican	(Camarena et al., 2019)	
				SSRI	Non-responder	80/93	Majority Caucasians	(Calabro et al., 2018)	
				SSRI	Non-remitter	32/14	Caucasian	(Gasso et al., 2018)	
				SSRI	Non-responder	56/46	South Indian	(Manoharan et al., 2016)	
				SSRI	Non-responder	164/70	Caucasians	(Seripa et al., 2015)	
				SSRI	Non-responder	154/85	Korean	(Lim et al., 2014)	
				Mixed	Non-responder	63/34	Italian	(Matsumoto et al., 2014)	
				Atypical	Non-responder	100/183	Korean	(Chang et al., 2014)	
				SSRIs	Non-responder	59/56	Korean	(Won et al., 2012)	
				SSRIs	Non-responder	46/42	Korean	(Myung et al., 2013)	
				SNRIs	Non-responder	54/27	Korean	(S. H. Lee et al., 2010)	
				SSRIs	Non-remitter	29/56	Finnish/Caucasian	(Illi et al., 2011)	
				SSRIs	Non-responder	37/22	Japanese	(Umene-Nakano et al., 2010)	
				SSRIs	Non-responder Non-remitter	243/119 156/206	Han Chinese	(Min et al., 2009)	
				SSRIs	Non-remitter	16/11	Caucasians	(Alexopoulos et al., 2009)	
				Mixed	TRD	98/30	Caucasian	(Wilkie et al., 2009)	
				Atypical	Non-responder	62/39	Korean	(R. H. Kang et al., 2007)	
				TCAs	Non-	55/34	Korean	(H. Kim et al., 2006)	

Accepted Manuscript

Downloaded from https://academic.oup.com/ijnp/advance-article/doi/10.1093/ijnp/pyad001/6992242 by Delhi Technological University user on 31 January 2023

					responder				
				SSRIs		69/50			
				SSRIs	Non-responder	68/12	Japanese	(Kato et al., 2006)	
				SSRIs	Non-responder	65/65	Croatian	(Bozina et al., 2008)	
				SSRIs	Non-responder	81/143	Han Chinese/ Taiwanese	(Hong et al., 2006)	
				SSRIs	Non-remitter	22/49	Korean	(Choi et al., 2005)	
				SSRIs	Non-responder	77/19	Mixed	(Kraft et al., 2005)	
				SSRIs	Non-remitter	91/40	Spanish	(Arias et al., 2003)	
				SSRIs	Non-responder	40/81	Chinese	(Yu et al., 2002)	
				SSRIs	Non-responder	35/19	Japanese	(Yoshida et al., 2002)	
				SSRIs	Non-responder	87/33	Korean	(D. K. Kim et al., 2000)	
				SSRIs	Non-responder	65/39	Iranian	(Sahraian et al., 2013)	
2	*HTR2A*	5-hydroxytryptamine receptor 2A	13q14.2	SSRIs	Non-remitter	32/14	Caucasian	(Gasso et al., 2018)	Serotonergic neurotransmission
				SSRIs	Non-remitter	NA	Han Chinese	(Su et al., 2016)	
				Mixed	TRD	58/74	European	(Noro et al., 2010)	
				SNRI and SSRIs	Non-responder	150/115	Japanese	(Kishi et al., 2010)	
					Non-remitter	103/162			
				Mixed	Non-remitter	61/125	Caucasian/Northern Germany	(Lucae et al., 2010)	
				SSRIs	Non-responder	30/46	Caucasian	(Wilkie et al., 2009)	
					Non-remitter	21/51			
				SSRIs	Non-responder	675/270	Mixed (White, Black and other)	(Paddock et al., 2007)	
					Non-remitter	NA			
				SSRIs	Non-remitter	22/49	Korean	(Choi et al., 2005)	
				SSRIs	Non-responder	57/39	Mixed	(Peters et al., 2004)	
3	*TPH2*	Tryptophan hydroxylase 2	12q21.1	SSRIs & SNRIs	Non responder	205/76	Han Chinese	(Xu et al., 2016)	Biosynthesis of serotonin
				SSRIs	Non remission		Han Chinese	(Su et al., 2016)	
				SSRIs	Non-responder	154/85	Korean	(Lim et al., 2014)	
				Mixed	Non-responder	224/84	Han Chinese	(Xu et al., 2012)	

Accepted Manuscript

Downloaded from https://academic.oup.com/ijnp/advance-article/doi/10.1093/ijnp/pyad001/6992242 by Delhi Technological University user on 31 January 2023

				SSRIs	Non-responder	126/61	Han Chinese/Taiwanese	(Tsai et al., 2009b)	
				Mixed	Non-responder	84/99	Majority Germans/Caucasians	(Tzvetkov et al., 2008)	
				SSRIs	Non-responder	57/39	Mixed	(Peters et al., 2004)	
4	*BDNF*	Brain derived neurotrophic factor	11p14.1	SSRIs	Non-responder	108/52	Caucasian	(El-Hage et al., 2015)	Promotes neuronal survival in the adult brain
				SSRIs	Non-responder	219/79	Chinese	(X. C. Wang et al., 2014b)	
				Mixed	Non-responder	71/117	European	(Kocabas et al., 2011)	
				SNRI	Non-responder	23/39	Han Chinese (Taiwanese)	(Chi et al., 2010)	
				SSRIs and SNRI	Non-remitter	82/191	Caucasoid/Spanish	(Gratacos et al., 2008)	
				SSRIs	Non-responder	57/26	Korean	(Choi et al., 2006)	
5	*HTR1A*	5-hydroxytryptamine receptor 1A	5q12.3	Mixed	Non-responder	224/84	Han Chinese	(Xu et al., 2012)	Serotonergic neurotransmission; G protein-coupled serotonin receptor activity
				Mixed	TRD	58/75	European	(Noro et al., 2010)	
				SSRI, SNRI	Non-responder	22/115	Japanese	(Kato et al., 2009)	
					Non-remitter	78/59			
				SSRI	Non-responder	83/139	Han Chinese/ Taiwanese	(Yu et al., 2006)	
				SSRI	Non-responder	81/143	Han Chinese/ Taiwanese	(Hong et al., 2006)	
				SSRI	Non-responder	35/17	Japanese	(Suzuki et al., 2004)	
6	*ABCB1*	ATP binding cassette subfamily B member 1	7q21.12	SSRI	Non-responder	27/34	Caucasian (Slovakian)	(Vancova et al., 2018)	Transportation of various molecules across extra- and intra-cellular membranes; involved in multidrug resistance
				SSRI	Non-responder	220/70	Han Chinese	(Huang et al., 2013)	
				SSRI	Non-remitter	48/26	Han Chinese	(K. M. Lin et al., 2011)	
				TCA and SSRI	Non-remitter	142	Mexican-Americans	(Dong et al., 2009)	
				SSRI & TCA	Non-responder	147	Mexican Americans	(Wong et al., 2008)	
7	*GRIK4*	Glutamate ionotropic receptor kainate type subunit 4	11q23.3	SNRI	Non-responder	146/29	Han Chinese	(Q. Sun et al., 2019)	Glutamate transmission viaactivation of ligand-gated ion channels and G protein-coupled
				SSRI	Non-responder	154/85	Korean	(Lim et al., 2014)	
				SSRI,SNRI	Non-responder	205/76	Han Chinese	(Pu et al., 2013)	

Accepted Manuscript

Downloaded from https://academic.oup.com/ijnp/advance-article/doi/10.1093/ijnp/pyad001/6992242 by Delhi Technological University user on 31 January 2023

				SSRI	Non-responder	260/525	White and African-American	(Fabbri et al., 2013)	membrane receptors
				SSRI	Non-responder	675/260	Mixed (White, Black and other)	(Paddock et al., 2007)	
					Non-remitter				
8	*SLC6A2*	Solute carrier family 6 member 2	16q12.2	SNRI	Non-remitter	76/86	Han Chinese	(Yeh et al., 2015)	Regulates norepinephrine homeostasis
				TCA	Non-remitter		Mexican-Americans	(Dong et al., 2009)	
				SSRI	Non-remitter				
				TCAs	Non-responder	55/34	Koreans	(H. Kim et al., 2006)	
				SNRI	Non-responder	50/30	Japanese	(Yoshida et al., 2004)	
9	*COMT*	Catechol-O-methyltransferase	22q11.21	SSRI	Non-remitters	24/35	Japanese	(Fukui et al., 2014)	Catalyzes the transfer of a methyl group from S-adenosylmethionine to catecholamines (dopamine, epinephrine, and norepinephrine)
				SSRIs	Non-remitters	691/541	White non-Hispanic	(Y. Ji et al., 2012)	
				Mixed	TRD	73/294	Caucasian	(Kocabas et al., 2010)	
						61/105			
				SSRI	Non-remitters	24/35	Japanese	(Fukui et al., 2014)	
				SSRI	Non responder	101/52	Han Chinese	(Tsai et al., 2009a)	
10	*GNB3*	G protein subunit beta 3	12p13.31	SSRI	Non-responder	33/67	Iranian	(D. Firouzabadi et al., 2019)	Integrate signals between receptors and effector proteins
				SSRIs and SNRI	Non-responder	35/66	Han Chinese/Taiwanese	(E. Lin et al., 2009a)	
				Mixed	Non-responder	58/105	Caucasian	(Wilkie et al., 2007)	
					Non-remitters	70/40			
				Mixed	Non-responder	67/39	Korean	(H. J. Lee et al., 2004)	
11	*CRHR1*	Corticotropin releasing hormone receptor 1	17q21.31	Atypical	Responder	1298/1734	French (Caucasian)	(Ramoz et al., 2020)	G protein-coupled receptor activity; major regulator of the hypothalamic-pituitary-adrenal pathway
					Remission				
				SSRI	Non-responder	37/108	Chilean	(Ventura-Junca et al., 2014)	
				SSRI, SNRI	Non-remitter	150/123	Han Chinese	(L. Y. Geng et al., 2014)	
12	*GRM7*	Glutamate metabotropic receptor 7	3p26.1	SNRI	Non-responder	146/29	Han Chinese	(Q. Sun et al., 2019)	Glutamatergic neurotransmission
				SSRI	Non-responder	260/525	White and African-American	(Fabbri et al., 2013)	
					Non-responder	189/352	White non-Hispanic		

Accepted Manuscript

Downloaded from https://academic.oup.com/ijnp/advance-article/doi/10.1093/ijnp/pyad001/6992242 by Delhi Technological University user on 31 January 2023

13	*CYP1A2*	Cytochrome P450 family 1 subfamily A member 2	15q24.1	SNRI	Non-responder	97/78	Han Chinese	(Zhu et al., 2019)	Involved in drug metabolism and synthesis of cholesterol, steroids and other lipids
				SSRI	Non-remitters	69/102	Han Chinese	(K. M. Lin et al., 2010)	
14	*CLOCK*	clock circadian regulator	4q12	SSRIs	Non-responder	284/47	Han Chinese	(H. Y. Ma et al., 2019)	Regulation of circadian rhythms
				SSRIs	Non-responder	60/61	Japanese	(Kishi et al., 2009a)	
					Non-remitter	45/76			
15	*NR3C1*	Nuclear receptor subfamily 3 group C member 1	5q31.3	SSRIs	Non-responder	70/30	Caucasian (Iranian)	(Nouraei et al., 2018)	Involved in inflammatory responses, cellular proliferation, and differentiation in target tissues
				SSRIs	Non-responder	104/56	Japanese	(Takahashi et al., 2014)	
16	*CRHR2*	Corticotropin releasing hormone receptor 2	7p14.3	TCA	Non-responder		Mexican Americans	(Wong et al., 2008)	G protein-coupled receptor activity; major regulator of the hypothalamic-pituitary-adrenal pathway
				SSRI	Non-responder	97/51	Spanish	(Papiol et al., 2007)	
17	*FKBP5*	FKBP prolyl isomerase 5	6p21.31	SSRIs	Non-responder	954/416	Mixed (White non-Hispanic, Black)	(Lekman et al., 2008)	Role in immunoregulation ; involving protein folding and trafficking
					Non-remitter	723/467	Mixed (White non-Hispanic, Black)		
				Mixed	Non-responder	147/86	German/Caucasian	(Binder et al., 2004)	
18	*TPH1*	Tryptophan hydroxylase 1	11p15.1	SSRIs	Non-remitter	61/44	Korean	(Ham et al., 2007)	Biosynthesis of serotonin
				SSRIs	Non-responder	35/42	Italian	(Serretti et al., 2001)	
GWAS Genes									

Accepted Manuscript

Downloaded from https://academic.oup.com/ijnp/advance-article/doi/10.1093/ijnp/pyad001/6992242 by Delhi Technological University user on 31 January 2023

1	*CNTN5*	Contactin 5	11q22.1	Mixed	Responder vs non-responder	61/31	Japanese	(Sasayama et al., 2013)	Role in the formation of axon connections in the developing nervous system
				Dissociative anesthetics (S-ketamine)	Remission vs non-remission	255/272	European	(Li et al., 2020)	
2	*LHFPL3*	LHFPL tetraspan subfamily member 3	7q22.2-q22.3	Dissociative anesthetics (S-ketamine)	Remission vs non-remission	255/272	European	(Li et al., 2020)	Sensory perception of sound
				Remission	SSRI	743/608	African-American and Caucasian	(Garriock et al., 2010)	
3	*AGBL1*	AGBL carboxypeptidase 1	15q25.3	Dissociative anesthetics (S-ketamine)	Remission vs non-remission	255/272	European	(Li et al., 2020)	Protein side chain deglutamylation
				SSRI	Remission	840/837	Mixed	(Cocchi et al., 2016)	
4	*CRADD*	CASP2 and RIPK1 domain containing adaptor with death domain	12q22	Dissociative anesthetics (S-ketamine)	Remission	255/272	European	(Li et al., 2020)	Acts in promoting apoptosis
				SSRI	Remission	42/67	Korean	(Cocchi et al., 2016)	
5	*LARGE1*	LARGE xylosyl- and glucuronyltransferase 1	22q12.3	Dissociative anesthetics (S-ketamine)	Response	255/272	European	(Li et al., 2020)	
				Remission	SSRI	743/608	African-American and Caucasian	(Garriock et al., 2010)	
6	*Y_RNA*	Ro60, Y RNA binding protein	1q31.2	Dissociative anesthetics (S-ketamine)	Remission	255/272	European	(Li et al., 2020)	Enables RNA binding activity
				SSRI	Remission	263/218	Korean	(Myung et al., 2015)	
7	*MYO5B*	Myosin VB	18q21.1	Dissociative anesthetics (S-ketamine)	Response	255/272	European	(Li et al., 2020)	Involved in vesicular trafficking via its association with the CART complex
				SSRI	Response	263/218	Korean	(Myung et al., 2015)	
8	*ARHGAP 8*	Rho GTPase activating protein 8	22q13.31	Dissociative anesthetics (S-ketamine)	Remission	255/272	European	(Li et al., 2020)	Regulate cell processes involved in cytoskeletal changes
				SSRI	Remission	42/67	Korean	(Cocchi et al., 2016)	
9	*CFAP61*	Cilia and flagella associated protein 61	20p11.23	SSRI	Remission	840/837	Mixed	(Cocchi et al., 2016)	involved in cilium movement and cilium organization
				SSRI	Responder vs non-responder	883/608	African-American and Caucasian	(Garriock et al., 2010)	

Accepted Manuscript

Downloaded from https://academic.oup.com/ijnp/advance-article/doi/10.1093/ijnp/pyad001/6992242 by Delhi Technological University user on 31 January 2023

					Remitter vs non-Reponders	743/608			
10	*MTCL1*	Microtubule crosslinking factor 1	18p11.22	SSRI	Response	416/449	Mixed	(Biernacka et al., 2015)	Enables microtubule binding activity
				SSRI	Response	263/218	Korean	(Myung et al., 2015)	
11	*AUTS2*	Activator of transcription and developmental regulator AUTS2	7q11.22	SSRI	Response	840/837	Mixed	(Cocchi et al., 2016)	Act as key regulator of the transcriptional network during brain development
				SSRI	Response	263/218	Korean	(Myung et al., 2015)	
				SSRI	Response	118/112			
				TCA	Response	116/43			
GWAS and Candidate Genes									
1	*COMT*	Catechol-O-methyltransferase	22q11.21	SSRI	Non-remitters	24/35	Japanese	(Fukui et al., 2014)	Catalyzes the transfer of a methyl group from S-adenosylmethionine to catecholamines (dopamine, epinephrine, and norepinephrine)
				SSRIs	Non-remitters	691/541	White non-Hispanic	(Y. Ji et al., 2012)	
				Mixed	TRD	73/294	Caucasian	(Kocabas et al., 2010)	
						61/105			
				SSRI	Non-remitters	24/35	Japanese	(Fukui et al., 2014)	
				SSRI	Non responder	101/52	Han Chinese	(Tsai et al., 2009a)	
				Mixed	Non-remitters	119/36	South Korea	(H. J. Kang et al., 2020)	
2	*PDLIM5*	PDZ and LIM domain 5	4q22.3	SSRI	Non-responder	98/87	Han Chinese	(Z. Liu et al., 2013a)	Function in cardiomyocyte expansion and in restraining postsynaptic growth of excitatory synapses
				Mixed	Response	61/31	Japanese	(Sasayama et al., 2013)	
3	*NR3C2*	Nuclear receptor subfamily 3 group C member 2	4q31.23	SSRI	Response	840/837	Mixed	(Cocchi et al., 2016)	Mineralcorticoid receptor; Inhibitory control of HPA axis; memory
				SNRI	Non-remission	94/75	Han Chinese	(Yuan et al., 2020)	
4	*HTR2A*	5-hydroxytryptamine receptor 2A	13q14.2	SSRI	Response	840/837	Mixed	(Cocchi et al., 2016)	Serotonergic neurotransmission
				SSRIs	Non-remitter	32/14	Caucasian	(Gasso et al., 2018)	
				SSRIs	Non-remitter	NA	Han Chinese	(Su et al., 2016)	
				Mixed	TRD	58/74	European	(Noro et al., 2010)	
				SNRI and	Non-	150/115	Japanese	(Kishi et al., 2010)	

Accepted Manuscript

Downloaded from https://academic.oup.com/ijnp/advance-article/doi/10.1093/ijnp/pyad001/6992242 by Delhi Technological University user on 31 January 2023

				SSRIs	responder				
					Non-remitter	103/162			
				Mixed	Non-remitter	61/125	Caucasian/Northern Germany	(Lucae et al., 2010)	
				SSRIs	Non-responder	30/46	Caucasian	(Wilkie et al., 2009)	
					Non-remitter	21/51			
				SSRIs	Non-responder	675/270	Mixed (White, Black and other)	(Paddock et al., 2007)	
					Non-remitter	NA			
				SSRIs	Non-remitter	22/49	Korean	(Choi et al., 2005)	
				SSRIs	Non-responder	57/39	Mixed	(Peters et al., 2004)	

Accepted Manuscript

Downloaded from https://academic.oup.com/ijnp/advance-article/doi/10.1093/ijnp/pyad001/6992242 by Delhi Technological University user on 31 January 2023

Table 5: List of replicated variants with single risk allele in MDD susceptibility and antidepressant response.

S. No.	Variant	Gene	Variant type	Polymorphism (Reference/alternate allele)	Calculated Risk Allele*	Sensitivity	Specificity	PPV (positive predictive value)	Regulome DB rank	Splice site	miRNA	SIFT/Polephen	Regulatory potential /conservartion	Knockout mouse	Drug target	Brain expression
MDD Susceptibility variants																
1	rs1801133	*MTHFR*	Missense	C/T	T	0.42	0.68	0.56	4	-	-	Deleterious/ Probably damaging	0.358/1.000	-	-	-
2	rs5443	*GNB3*	Synonymous	C/T	T	0.55	0.55	0.55	4	-	-	-	0.438/0.200	-	Y	Y
3	rs242939	*CRHR1*	Intron	C/G	G	0.13	0.93	0.66	5	-	-	-	0.238/0.000	Y	Y	Y
4	rs1006737	*CACNA1C*	Intron	G/A	A	0.31	0.78	0.59	5	-	-	-	0/0	Y	Y	Y
5	rs4880	*SOD2*	Missense	T/C	T	0.46	0.61	0.54	4	Y	-	Tolerated/benign	0.22/0	Y	-	-
6	rs6295	*5HTR1A*	Upstream	C/G	G	0.33	0.75	0.56	4	-	-	-	0/0	Y	Y	Y
7	rs1801131	*MTHFR*	Missense	A/C	C	0.33	0.71	0.53	1F	Y	-	Tolerated/benign	0.40/1.00	Y	-	-
Drug Response Variants																
1	STin2	*SLC6A4*	Copy number loss	L/S (12/10)	S (SSRI non response)	0.18	0.94	0.63	4	-	-	-	-	Y	Y	Y
2	rs41423247	*NR3C1*	Intron	G/C	C (SSRI non response)	0.55	0.34	0.42	2b	-	-	-	0/0	Y	Y	Y

Accepted Manuscript

Downloaded from https://academic.oup.com/ijnp/advance-article/doi/10.1093/ijnp/pyad001/6992242 by Delhi Technological University user on 31 January 2023

Figure 1

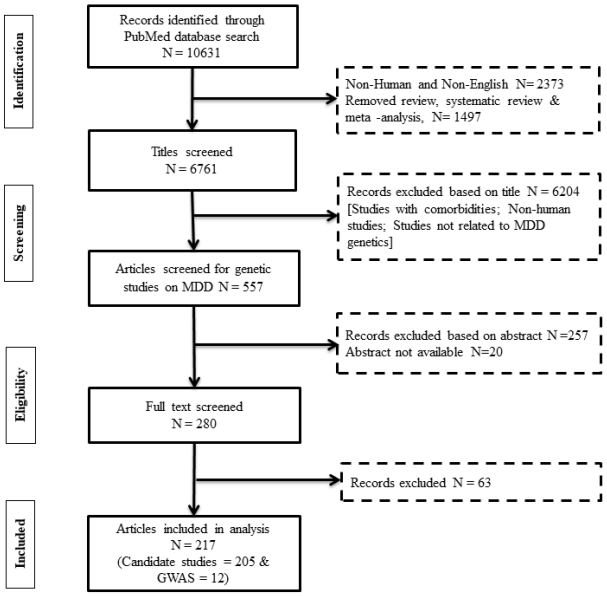

Accepted Manuscript

Downloaded from https://academic.oup.com/jnp/advance-article/doi/10.1093/jnp/pyad001/6992242 by Delhi Technological University user on 31 January 2023

Figure 2

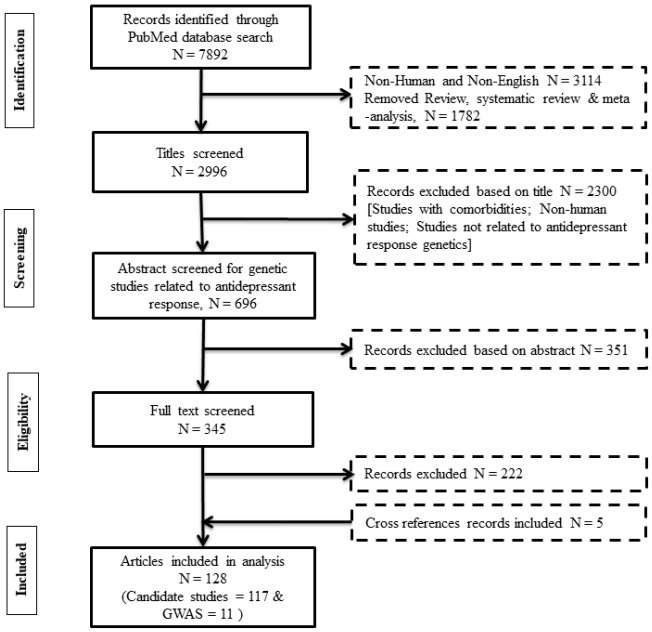

Accepted Manuscript

Downloaded from https://academic.oup.com/ijnp/advance-article/doi/10.1093/ijnp/pyad001/6992242 by Delhi Technological University user on 31 January 2023

Figure 3a

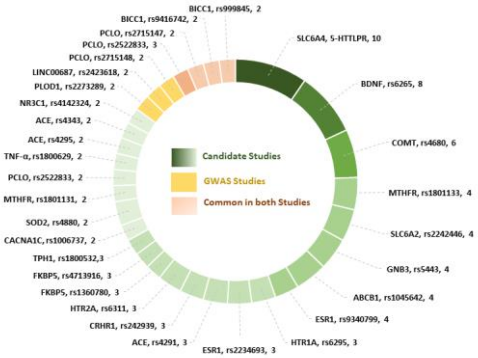

Accepted Manuscript

Downloaded from https://academic.oup.com/ijnp/advance-article/doi/10.1093/ijnp/pyad001/6992242 by Delhi Technological University user on 31 January 2023

Figure 3b

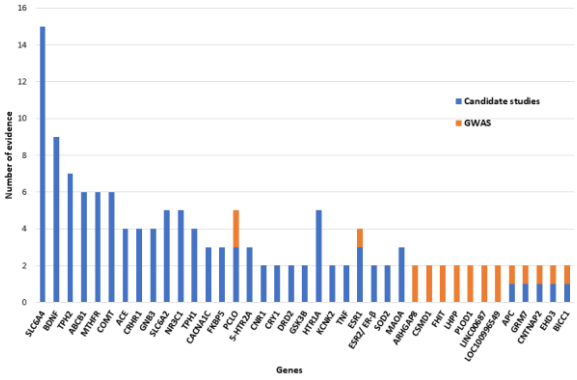

Accepted Manuscript

Downloaded from https://academic.oup.com/ijnp/advance-article/doi/10.1093/ijnp/pyad001/6992242 by Delhi Technological University user on 31 January 2023

Figure 4a

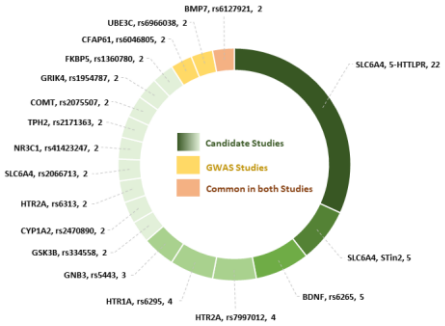

Accepted Manuscript

Downloaded from https://academic.oup.com/ijnp/advance-article/doi/10.1093/ijnp/pyad001/6992242 by Delhi Technological University user on 31 January 2023

Figure 4b

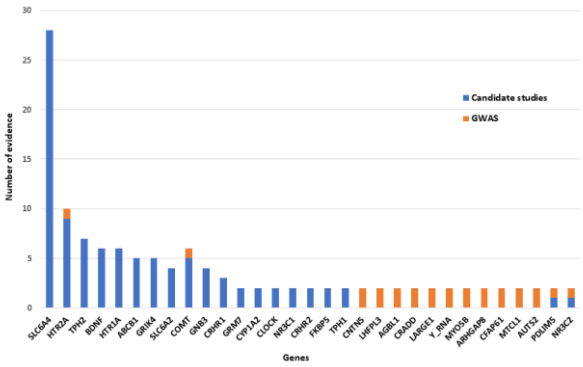

Accepted Manuscript

Downloaded from https://academic.oup.com/ijnp/advance-article/doi/10.1093/ijnp/pyad001/6992242 by Delhi Technological University user on 31 January 2023

ACS OMEGA

http://pubs.acs.org/journal/acsodf

Article

Graphitic Carbon Nitride-Wrapped Metal-free PoPD-Based Biosensor for Xanthine Detection

Deeksha Thakur, Chandra Mouli Pandey,* and Devendra Kumar*

Cite This: https://doi.org/10.1021/acsomega.2c06727

Read Online

ACCESS | Metrics & More | Article Recommendations | Supporting Information

Downloaded via ESS INFLIBNET PCA 4 on January 4, 2023 at 09:26:36 (UTC).
See https://pubs.acs.org/sharingguidelines for options on how to legitimately share published articles.

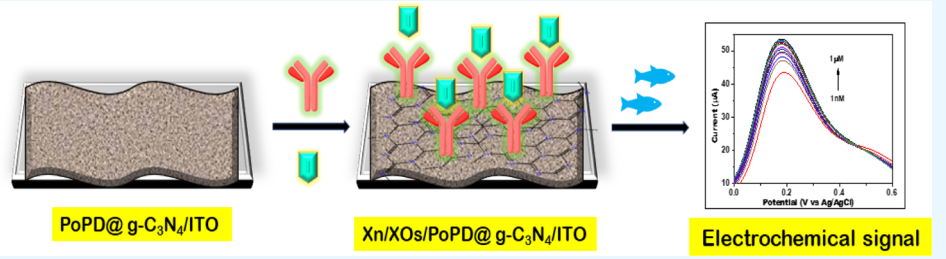

ABSTRACT: A metal-free, enzymatic biosensor was developed using graphitic carbon nitride (g-C_3N_4)-wrapped poly-*ortho*-phenylenediamine (PoPD) for the determination of xanthine (Xn). Field emission scanning electron microscopy, Fourier transform infrared spectroscopy, and X-ray diffraction confirmed the successful formation of the PoPD, g-C_3N_4 nanosheets and PoPD@g-C_3N_4 nanocomposite. Furthermore, the electrochemical behavior of the biosensor was characterized by cyclic voltammetry and electrochemical impedance spectroscopy. The prepared enzyme electrode exhibited maximum response at pH 7.5 with a response time of 5 s, and its sensitivity was 5.798 μAM^{-1}. The nanocomposite shows exceptional sensing capabilities for detecting Xn, having a wide linear range from 1 nM to 1 μM with a relatively low detection limit of 0.001 nM. The biosensor shows good stability (4 weeks) and reproducibility and can detect the presence of Xn from other interfering analytes. Validation of the biosensor with real samples obtained from Rohu (*Labeo rohita*) fish shows that the fabricated biosensor has the requisite potential to be used for Xn detection in meat samples.

1. INTRODUCTION

Graphitic carbon nitride is the most stable allotrope of carbon nitride under ambient conditions. It is a two-dimensional (2D) nanosheet material having a molecular thickness and many attracting physicochemical properties.[1] Among many 2D layered systems, graphitic carbon nitride (g-C_3N_4) is a prominent group of metal-free conjugated polymers with weak van der Waals interactions between layers and a peculiar electrical band structure.[2] Its chemistry of varied morphologies, structures, and applications has received significant interest among researchers. Its exceptional properties, such as its low cost, large surface area, easy preparation, fast electron transfer-conjugation structure, biocompatibility, and catalytic applications, make it an important choice of material for various applications.[3,4] Recently, g-C_3N_4 nanosheets have been used to fabricate biosensors because of their superior catalytic and biocompatibility properties.[5] However, the bare g-C_3N_4 nanosheet synthesized by the thermal condensation procedure has low electrocatalytic activity due to the fast recombination of electrogenerated carriers.[6] A lot of work has been devoted to enhancing the electroactive property of the g-C_3N_4 nanosheet, including nanoscaling, doping, surface modification, and coupling with other conducting polymers.[7] In this context, pairing g-C_3N_4 nanosheets with conducting polymers such as poly-*o*-phenylenediamine (PoPD) is a great way to increase the electrochemical activity of g-C_3N_4.[8]

PoPD is a derivative of polyaniline, having a quinoxaline or 2,3-diaminophenazine repeating unit, which has the advantages of variable conductivity, robust electroactivity, and good optical activity.[9] Its low cost, high stability, and environmental friendliness are crucial for potential applications.[10] PoPD as an interference-rejecting layer offers good selectivity and specificity to the various biomolecules present in biological fluids, which might affect the selectivity of the biosensor.[11] Thus, integrating PoPD with g-C_3N_4 has been considered as an ideal method for increasing electrochemical performance of g-C_3N_4 nanosheets.[8]

Recently, there has been an urgency for quality control in the food industry, increasing demand for fish as a wholesome foodstuff in both developed and developing countries.[12] According to the reported literature, seafood rotting is caused

Received: October 19, 2022
Accepted: December 23, 2022

© XXXX The Authors. Published by American Chemical Society

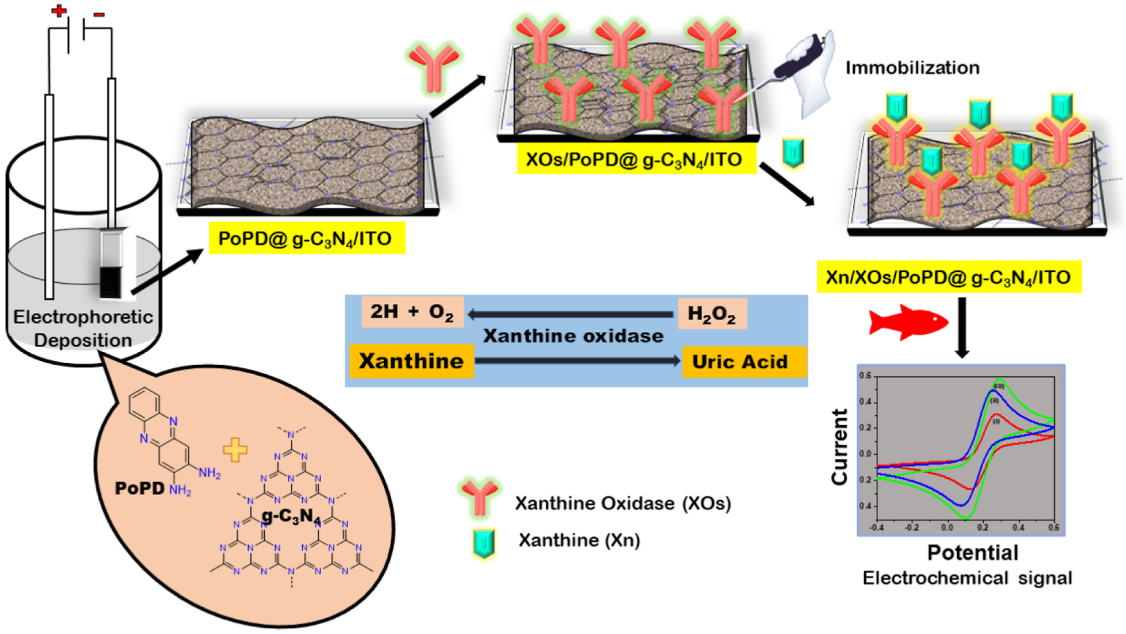

Figure 1. Scheme showing the fabrication of the PoPD@g-C_3N_4 nanohybrid-based biosensor.

by a high concentration of certain enzymes.[13] One of the several enzymes is xanthine (Xn), a key metabolite involved in the disintegration of ATP molecules in fish meat, whose concentration level increases continuously with storage.[14] Since the presence of Xn in fish meat signifies its freshness, the physiological conversion of Xn by xanthine oxidase (XOs) is of great interest.[15] Additionally, measuring the amount of Xn in serum/urine samples makes it possible to gather essential details about specific metabolic disorders such as hyperuricemia, xanthinuria, and renal failure.[16] Numerous analytical methods, such as high-performance liquid chromatography, enzymatic colorimetry, capillary electrophoresis, and so forth, have been used to detect Xn. However, these methods need a lot of effort, resources, and expertise.[17,18] Consequently, there is a critical need to develop a rapid and sensitive method to detect Xn.[19]

Nowadays, electrochemical techniques gained interest as being simple, sensitive, reliable, and affordable to use.[20,21] From the last decade, for hypoxanthine or xanthine detection, various conducting polymer-based nanocomposite biosensors are of interest such as polypyrrole-polyvinyl sulfonate (PPy-PTS) films,[22] polypyrrole-*para*-toluenesulfonate (PPy-pTS),[23] disposable amperometric biosensor with a screen-printed electrode, gold nanoparticles with single-walled carbon nanohorn (GNPs/SWCNH),[24] polymeric mediator/multiwalled carbon nanotube (MWCNT)[25] reduced graphene oxide/iron oxide bio-nanocomposite interface,[26] polymerized 10-[4 *H*-dithieno (3,2-*b*: 2′,3′-*d*) pyrrole-4-yl] decane-1-amine film,[27] and so forth. However, these biosensors show a higher limit of detection, and the linear range may be due to slow electron transfer, poor stability, reusability, fragility, and poor absorption ability, which created requirement for introducing a system with a highly desirable lower detection limit and fast electron transfer. Even, most of the electrochemical biosensors reported for Xn detection usually involve active metal catalysts to provide a higher surface functionality for immobilizing enzymes, increased electroactive surface, and improved charge transfer efficiency.[28]

Herein, efforts have been made to fabricate a metal-free biosensor based on PoPD@g-C_3N_4 nanocomposites, synthesized using a simple oxidative polymerization method. To the best of our knowledge, PoPD@g-C_3N_4 nanocomposite-based biosensors have never been used for Xn detection. With exceptional sensitivity values, it has been revealed that g-C_3N_4 nanosheets modified with P*o*PD for electrode modification can be an effective platform for immobilizing XOs. The synthesized nanocomposite efficiently acted as a metal-free and highly selective sensor to amplify the signal for Xn detection, thus emerging as an innovative electrochemical sensing technique for monitoring fish meat quality.

2. RESULTS AND DISCUSSION

X-ray diffraction (XRD) of P*o*PD (Figure 2A) revealed prominent peaks in the range 2θ = 10−30°, indicating the crystalline behavior of P*o*PD. The broad peak centered at 2θ = 26.5° reveals the polymer chain's local crystallinity.[4]

Furthermore, the crystalline peaks positioned at 2θ = 10.8, 16.5, 18.6, and 28.7° show the nature of the synthesized P*o*PD featuring well-aligned morphology.[29] The XRD diffraction pattern of g-C_3N_4 sheets revealed a weakly intense peak at 2θ = 27.7°, which is indexed to (002) planes.[30] The XRD of g-C_3N_4 and PoPD@g-C_3N_4 showed two similar diffraction peaks at 27.7°, which is attributed to the characteristic (002) plane for interlayer stacking that corresponds to the graphitic structure[31]. It is worth noting that no apparent diffraction peaks of P*o*PD were observed in the PoPD@g-C_3N_4 sample due to the weak crystallinity and small adding content of PoPD.[32]

The FT-IR (Figure 2B) of the g-C_3N_4 nanosheet shows a broad peak at 3164 cm^{-1} for terminal NH_2 or NH groups and C═N stretching peaks at 1575 and 1642 cm^{-1}, stretching peaks at 1245, 1324, and 1404 cm^{-1} were observed for aromatic C−N stretching, and a sharp peak at 808 cm^{-1} is due to the vibration of tri-*s*-triazine units.[4,33] The IR spectrum of the homopolymer PoPD showed the N−H stretching vibration peak at 3143 cm^{-1}, and peaks at 1626 and 1561 cm^{-1} are attributed to the C═C stretching vibrations of quinoid and

https://doi.org/10.1021/acsomega.2c06727
ACS Omega XXXX, XXX, XXX−XXX

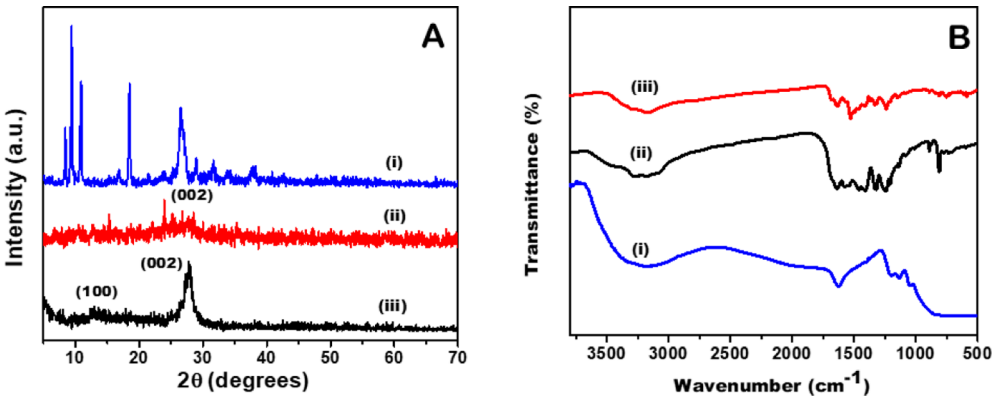

Figure 2. (A) XRD of (i) PoPD, (ii) PoPD@g-C_3N_4 nanohybrid and (iii) g-C_3N_4 nanosheets and (B) FT-IR spectra of (i) PoPD, (ii) g-C_3N_4 nanosheets, and (iii) PoPD@g-C_3N_4 nanohybrid.

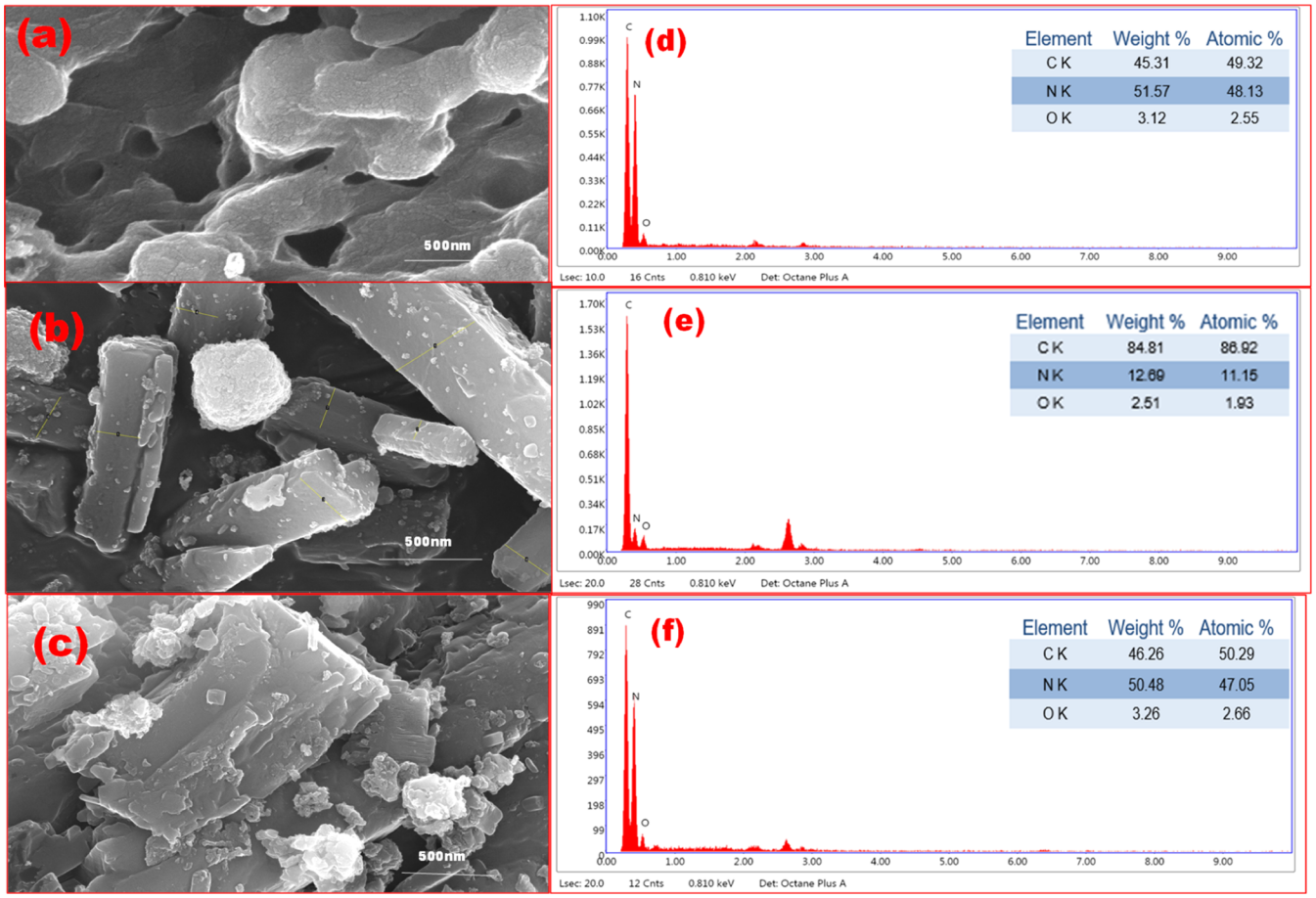

Figure 3. FESEM images (a–c) and EDX images (d–f) for (a) g-C_3N_4, (b) PoPD, and (c) PoPD@g-C_3N_4 nanohybrid obtained at an operating voltage of 15 kV.

benzenoid rings, respectively, while C–N stretching vibrations of quinoid and benzenoid rings appear at 1397 and 1206 cm^{-1}, respectively.[29,34] In the PoPD@g-C_3N_4 nanocomposite, Fourier transform infrared spectroscopy peaks are slightly shifted to higher or lower wavenumber when compared to PoPD. Several characteristic solid peaks in the range of 1700–1200 cm^{-1} are assigned to the stretching vibration of g-C_3N_4. Meanwhile, the characteristic peaks at 820 and 884 cm^{-1} are attributed to the triazine units.[35] Most of the characteristic vibrational peaks of pure g-C_3N_4 are observed in PoPD@g-C_3N_4, indicating the existence of the g-C_3N_4 nanosheet in the composite.

The field emission scanning electron microscopy (FESEM) image of g-C_3N_4 is compared to that of PoPD and PoPD@g-C_3N_4, and the results are shown in Figure 3. As indicated by the microscopic images of g-C_3N_4 (Figure 3a), the layered morphology of g-C_3N_4 and rod-like morphology of PoPD remained the same as in the PoPD@g-C_3N_4 nanocomposite. This confirms that the PoPD particles are randomly distributed on the g-C_3N_4 sheets, which is further evidence for the successful formation of the PoPD@g-C_3N_4 nanocomposite. The EDX spectra shown in Figure 3d–f) confirmed the loading of g-C_3N_4 in the PoPD@g-C_3N_4 framework. In the

https://doi.org/10.1021/acsomega.2c06727
ACS Omega XXXX, XXX, XXX–XXX

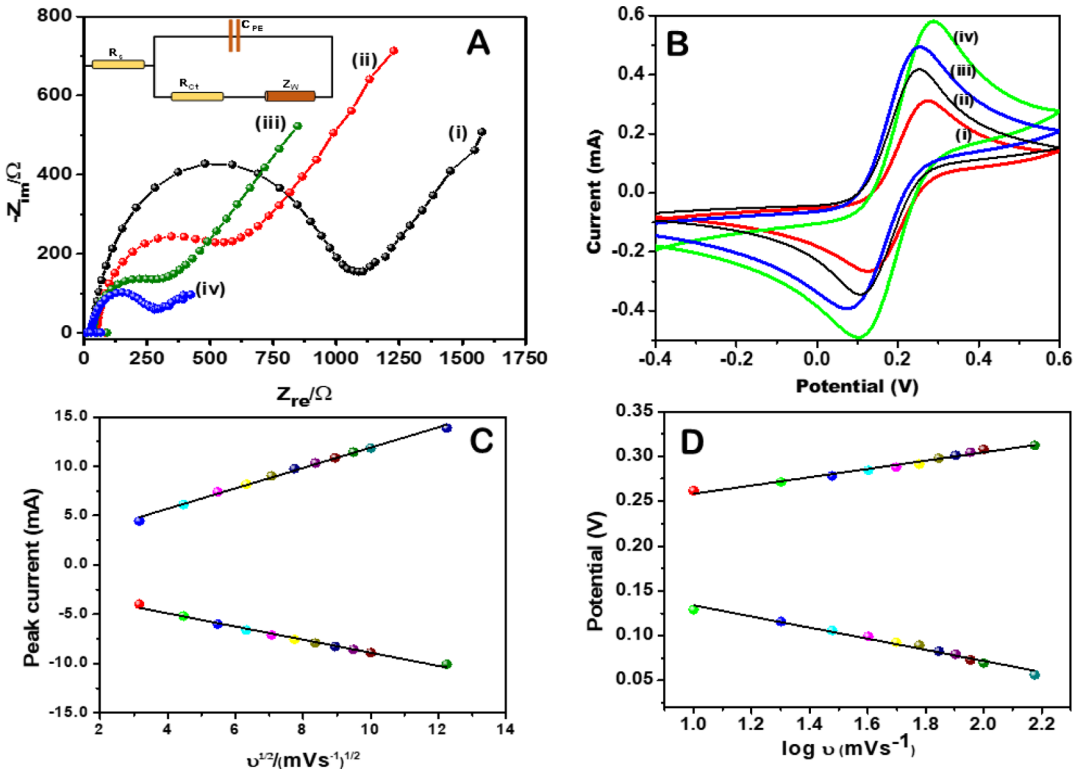

Figure 4. (A) Nyquist diagram for the Faradic impedance for (i) ITO, (ii) g-C_3N_4/ITO electrode, (iii) PoPD/ITO, and (iv) PoPD@g-C_3N_4/ITO electrode measured in PBS solution (pH 7.5) containing 5 mM $[Fe(CN)_6]^{3-/4-}$, in the frequency range from 10^5 to 10^{-2} Hz; (B) CV studies of (i) g-C_3N_4/ITO, (ii) PoPD/ITO, (iii) XOs/PoPD@g-C_3N_4/ITO, and (iv) PoPD@g-C_3N_4/ITO electrodes. The plots of (C) I_{pa}, I_{pc} vs square root of scan rate and (D) potential with the log of scan rate with varying scan rate (10−300 mV) for the PoPD@g-C_3N_4/ITO electrode.

case of PoPD@g-C_3N_4, the wt % of nitrogen content (50.58%) is higher than that of PoPD (12.69%), indicating the successful incorporation of g-C_3N_4 in PoPD. Moreover, the FESEM images, before and after immobilization of XOs on PoPD@g-C_3N_4/ITO with the real image of the fabricated electrode, also validate the morphology change (Figure S6).

2.1. Electrochemical Studies of the Fabricated Electrodes. Electrochemical studies have been carried out for bare ITO, g-C_3N_4/ITO, PoPD/ITO, and PoPD@g-C_3N_4/ITO electrodes using electrochemical impedance spectroscopy (EIS; PBS comprising 5 mM $[Fe(CN)_6]^{3-/4-}$). The Nyquist plot shows a linear region at lower frequencies for the diffusion-controlled electron transfer resistance process and a semicircle region for the electron transfer resistance limited process.[36,37] The solution resistance (R_s), electron transfer resistance (R_{ct}), Warburg impedance (Z_w), and constant phase element (CPE) constitute the equivalent circuit [Figure 4A (inset)]. The obtained Impedance curve has been fitted using FRA software to deduce the different circuit parameters.

The R_{ct} for the ITO electrode was measured to be 1081.5 Ω [curve (i)], whereas the R_{ct} for the g-C_3N_4/ITO, PoPD/ITO, and PoPD@g-C_3N_4/ITO electrodes was found to be 554.43 Ω [curve (ii)], 315.7 Ω [curve (iii)], and 285.08 Ω [curve (iv)], respectively. The significantly smaller diameter of the semicircular Nyquist plot shows a lower electron transfer resistance and a higher interfacial charge transfer characteristic of the PoPD@g-C_3N_4/ITO electrode. The result shows that the addition of PoPD has a favorable impact on the separation and transfer of photogenerated charge carriers, which is compatible with the PoPD@g-C_3N_4 system.[8]

Electrochemical electrode reactions have been studied using electron transfer kinetics based on obtained R_{ct} values. Equations 1 and 2 have been used to compute the apparent electron transfer rate constant (K_{app}) and exchange current per geometric unit area (i_o) for g-C_3N_4/ITO electrodes and PoPD@g-C_3N_4/ITO electrodes.

$$i_o = nRT/R_{ctF} \quad (1)$$

$$K_{app} = RT/n^2F^2AR_{ct}C \quad (2)$$

On comparing, it was found that the PoPD@g-C_3N_4/ITO electrode possesses a higher i_o value (9.007×10^{-5} A cm^{-2}) than g-C_3N_4/ITO (4.631×10^{-5} A cm^{-2}). Furthermore, the values of K_{app} for the g-C_3N_4/ITO and PoPD@g-C_3N_4/ITO electrodes were 0.381×10^{-6} and 0.669×10^{-6} cm s^{-1}, respectively. The increased values of i_o and K_{app} for the PoPD@g-C_3N_4/ITO electrode are due to the synergistic interaction between PoPD and g-C_3N_4 nanosheets, improving conductivity and better electron transfer.

Cyclic voltammetric (CV) studies for g-C_3N_4/ITO, PoPD/ITO, PoPD@g-C_3N_4/ITO, and XOs/PoPD@g-C_3N_4/ITO electrodes in PBS buffer have been shown in Figure 4B. Compared to other electrodes [g-C_3N_4/ITO, 0.31 mA; PoPD/ITO, 0.41 mA; and XOs/PoPD@g-C_3N_4/ITO, 0.49 mA)], the PoPD@g-C_3N_4/ITO electrode displayed a well-defined pair of redox peaks with a greater peak current [curve (iv); 0.58 mA]. The increased peak current of PoPD@g-C_3N_4/ITO suggests that the composite material generated more redox sites for the probe and enhanced electron transport, showing that PoPD and g-C_3N_4 have a positive synergy. After immobilization of the enzyme (XOs) on PoPD@g-C_3N_4/ITO, a well-defined

https://doi.org/10.1021/acsomega.2c06727
ACS Omega XXXX, XXX, XXX−XXX

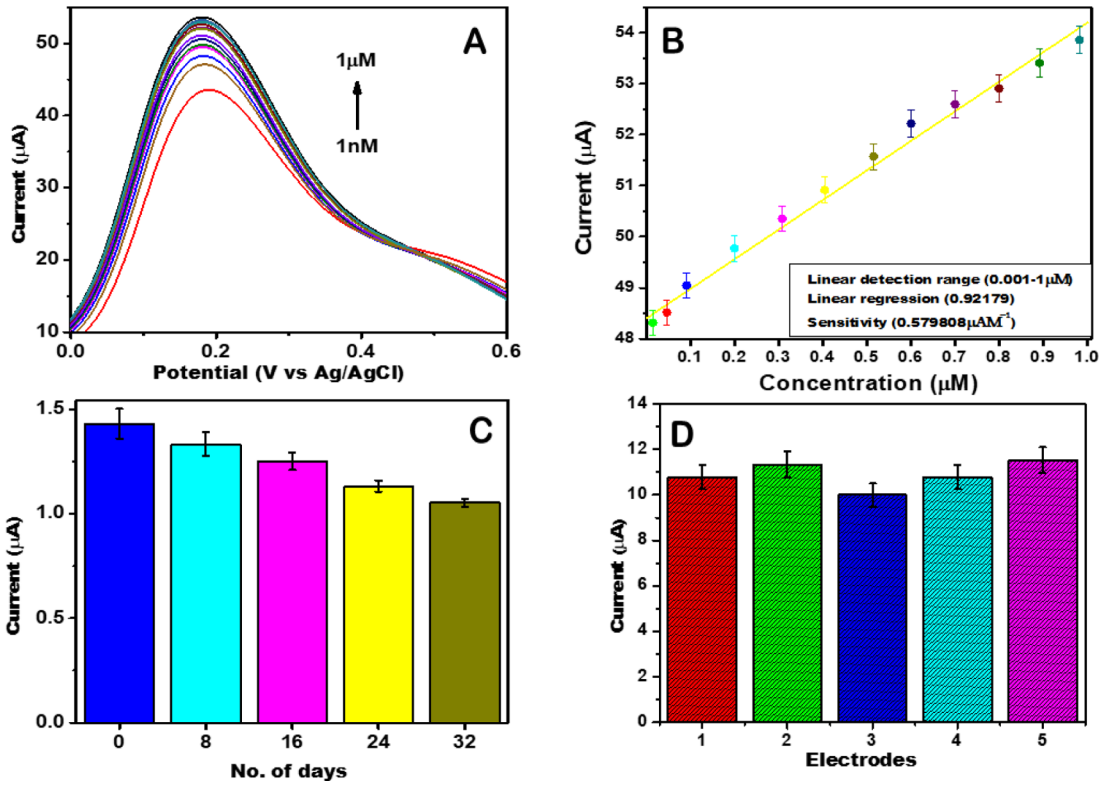

Figure 5. (A) DPV studies showing the response of the XOs/PoPD@g-C_3N_4/ITO electrode with increasing concentration of Xn (0.001−1 μM); (B) calibration plot showing a linear relationship between the magnitudes of current recorded and concentration of Xn; (C) shelf-life tests of the sensor up to 4 weeks, and (D) reproducibility study at five modified electrodes.

redox peak indicates that XOs was successfully immobilized on the surface of the PoPD@g-C_3N_4/ITO and has undergone an oxidation−reduction process at the electrode [curve (iii)].The electroactive surface areas of the electrodes were calculated using the Randles−Sevcik equation

$$I_p = (2.99 \times 10^5)\, \alpha^{1/2}\, n^{3/2} A\, C\, D^{1/2}\, v^{1/2} \quad (3)$$

where n is the number of electrons, v (mV/s) is the scan rate, A (cm^2) is the area of the electrode, C is the concentration in mol/L, D (cm^2/s) is the diffusion coefficient of $[Fe(CN)_6]^{3-/4-}$ in PBS at room temperature which has been reported to be 0.5253×10^{-10} cm^2/s, and I_p (A) is the peak current. The PoPD@g-C_3N_4/ITO exhibits the largest active surface area of 0.997 cm^2 compared to 0.930 and 0.988 cm^2 for g-C_3N_4/ITO and PoPD/ITO, respectively. A high electroactive surface area is expected to offer benefits for electroanalysis.

For the PoPD@g-C_3N_4/ITO (Figure 4C) and XOs/PoPD@g-C_3N_4/ITO (Figure S1) electrodes, the performance of the electrodes was investigated by varying the scan rate (10 to 150 mV/s). It has been observed that the oxidation peak current increases linearly with a positive shift in the peak potential. Both the anodic peak current (I_{pa}) and cathodic peak current (I_{pc}) increase linearly with increasing scan rate and following eqs 3−5, showing surface adsorption-controlled process kinetics for the PoPD@g-C_3N_4/ITO electrode.[38]

$$I_{pa}(\mu A) = 1.5 \times 10^{-3} + 1.0 \times 10^{-3}\sqrt{v}\ (\text{mV/s}) \qquad R = 0.9973 \quad (4)$$

$$I_{pc}(\mu A) = -2.25 \times 10^{-3} - 6.653 \times 10^{-4}\sqrt{v}\ (\text{mV/s}) \qquad R = 0.9941 \quad (5)$$

The anodic and cathodic peak potentials (E_{pa} and E_{pc}) also showed a linear relation with the natural logarithm of scan rate (ln v). The corresponding linear regression equations, eqs 6 and 7, have been given in Figure 4D.

$$E_{pa}(V) = 0.21209 \ln(v) + 0.0462;\ R = 0.9896 \quad (6)$$

$$E_{pc}(V) = 0.19583 \ln(v) - 0.0619;\ R = 0.9903 \quad (7)$$

Using Laviron's equation,[39] the charge transfer coefficient (α) and heterogeneous electron transfer coefficient (K_s) for the PoPD@g-C_3N_4/ITO electrode have been calculated, and they are found to be 0.9105 and 2.3859 s^{-1}, respectively, at a scan rate (v) of 50 mV/s.

The effect of the loading volume of XOs (5 to 30 μL) on the response current toward Xn (0.1 μL) has been shown in Figure S2. The peak current increased initially, up to 20 μL and then reduced with further increasing the loading volume of XOs. An excessive amount of XOs would slow down the passage of electrons, decreasing the sensor's sensitivity. Therefore, 20 μL of XOs solution was used for subsequent studies.

Figure S3 shows the performance of the Xn/XOs/PoPD@g-C_3N_4/ITO electrode in various pH electrolytic solutions ranging from 6.5 to 8.5. Notably, the maximum current response was recorded at a pH of 7.5 in PBS buffer containing 5 mM $Fe[CN_6]^{3-/4-}$. Therefore, pH 7.5 has been chosen as the ideal pH for the electrochemical detection of Xn.

https://doi.org/10.1021/acsomega.2c06727
ACS Omega XXXX, XXX, XXX−XXX

Table 1. Comparison of the Performance of PoPD@g-C_3N_4/ITO With Other CP-Based Biosensors for Xn Detection[a]

S. no.	immobilization matrix	detection technique	linear range (μM)	LOD	ref.
1.	Au-XOR/fMWCNT-PEDOT/GCE	DPV	0.1−10	5.45×10^{-2} μM	40
2.	XODNPs/Au	CV	0.01−1	0.01 μM	41
3.	XO/Poly(l-Asp)/MWCNT/GCE	DPV	0.001−0.004	3.5×10^{-4} μM	42
4.	XOD/ZnO/Ch/c-MWCNT/PANI/Pt	CV	0.1−100	0.1 μM	43
5.	Au-PPy	CV	0.4−100	0.4 μM	44
6.	XOD/c-MWCNT/PANI/Pt	CV	0.6−58	0.6 μM	14
7.	Ch/PPy/AuNPs/GCE	CV	1−200	0.25 μM	45
8.	PANI@TiO_2/ITO	DPV	1−100	0.1 μM	21
9.	poly-TTCA/Au	CV	5−0.001	1 μM	46
10.	PoPD@g-C_3N_4	DPV	0.001−1	0.001 nM	**present work**

[a]Abbreviations: Au: gold nanoparticles; XOR: xanthine oxidoreductase; fMWCNT: functionalized multiwalled carbon nanotube; PEDOT: poly(3,4-ethylenedioxythiophene); GCE: glassy carbon electrode; XODNPs: xanthine oxidase nanoparticle; [poly(l-asp):poly(l-aspartic acid)]; ZnO: zinc oxide; Ch: chitosan; PANI: polyaniline; Pt: platinum; PPy: polypyrrole; c-MWCNT: carboxylated multiwalled carbon nanotube; TiO_2: titanium dioxide; ITO: indium tin oxide; poly-TTCA: poly-5,2′:5′,2″-terthiophine-3-carboxylic acid; CV: cyclic voltammetry; and DPV: differential pulse voltammetry.

2.2. Electrochemical Biosensing Response of the XOs/PoPD@g-C_3N_4/ITO Electrode. The electrochemical biosensing response study for the XOs/PoPD@g-C_3N_4/ITO electrode has been carried out by varying Xn concentrations (0.001−1 μM) (Figure 5A). The peak current response increased linearly from 0.001 to 1 μM (Figure 5B), confirming the PoPD@g-C_3N_4 nanocomposite's efficiency and good electrocatalytic capabilities for Xn detection. The sensitivity of the biosensor was calculated to be 5.798 μAM^{-1}, using the regression equation $y = 48.403 \times 10^{-6}x + 5.798 \times 10^{-6}$ (y = peak current and x = concentration of Xn) having $R^2 = 0.9217$. Equation 3 σ/S was used to calculate the limit of detection, which was found to be 0.001 nM, where σ is the standard deviation of the bioelectrode and S is the sensitivity derived from the slope of the calibration curve.

2.3. Validation of the Biosensor with the Real Sample. The developed PoPD@g-C_3N_4 nanocomposite-based sensor has been tested for Xn in the fish meat samples using DPV. An easy method suggested by Watanabe et al. has been used to extract Xn from Rohu (*Labeo rohita*) fish and prepare the Xn solution.[21] The DPV study shows that the peak current steadily increases as the concentration of Xn increases from 0.001 to 1 μM. These results were identical to those of the synthetic Xn samples. Various biosensing characteristics of the synthesized XOs/PoPD@g-C_3N_4-based biosensor were compared with previously reported polymer-based biosensors for Xn detection (Table 1). It was observed that the developed biosensor could detect the presence of Xn in fish meat samples with the lowest LOD.

The suggested biosensor was also used to measure the current response for a time ranging from 0 to 5 days at room temperature to examine the level of xanthine in fish extract while preserved for a certain period of time. The findings also showed an increase in xanthine levels which by day 5 had increased 32 times from day one (Figure S4).

2.4. Shelf Life, Reproducibility, and Specificity. Figure 5C shows the shelf life of the PoPD@g-C_3N_4/ITO electrode, determined using the DPV technique. The DPV response of the five bioelectrodes against Xn with 1 μM was observed weekly to test the stability of the XOs/PoPD@g-C_3N_4/ITO electrode. Also, the result indicates that the biosensor is stable for at least 4 weeks when kept at 4 °C in a dry state, and it merely lost 0.4 μA current when compared to the current response of the initial electrode.

Additionally, five parallel electrodes were prepared to investigate the reproducibility of the developed electrochemical sensor. A relative standard deviation of 5.9% was obtained, indicating excellent reproducibility of the newly developed electrochemical sensor (Figure 5D).

The interference test of the biosensor has been conducted by incubating the XOs/PoPD@g-C_3N_4/ITO electrode with the interfering analytes (ascorbic acid, urea, uric acid, sodium benzoate, and glucose) of various concentrations (10-fold) higher than the concentration of Xn. It has been observed that there was a specific current response for every analyte, proving the selectivity of the biosensor for Xn detection (Figure S5). The specificity test was also conducted, and it has been observed that Xn retained its specificity, even in the mixture of interfering analytes. Additionally, we tested the performance of this biosensor at 10-fold excess concentration for all the analytes.

However, the response profiles to sodium benzoate, ascorbic acid, and glucose were relatively comparable, but the response to urea and uric acid was slightly higher than before. The result, expressed as the tolerance limit, shows a relative error of approximately ±5% in determination of the analyte (Table 2). Therefore, XOs/PoPD@g-C_3N_4/ITO can be a good biosensor for Xn recognition.

Table 2. Table of Tolerance Limit for Foreign Analytes

S. no.	analytes	(change in current response) tolerance limit (%)
1.	ascorbic acid	±0.5
2.	urea	±4.9
3.	uric acid	±4.5
4.	sodium benzoate	±1.3
5.	glucose	±1.9

3. CONCLUSIONS

In the present work, a stable binary PoPD@g-C_3N_4 nanocomposite has been synthesized via a simple oxidative polymerization technique. Various spectroscopic and morphological techniques have been used to validate the successful formation of PoPD@g-C_3N_4. An increase in electron transfer values for the PoPD@g-C_3N_4 electrode compared to bare PoPD and g-C_3N_4 makes it promising to be used for the immobilization of XOs. The fabricated XOs/PoPD@g-C_3N_4/

https://doi.org/10.1021/acsomega.2c06727
ACS Omega XXXX, XXX, XXX−XXX

ITO electrode successfully detected Xn in real fish samples with a detection limit of 0.001 nM (S/N = 3). In addition, the developed biosensing electrode offers suitable sensitivity, a very low detection limit, acceptable stability, reproducibility, and anti-interference characteristics. Consequently, the PoPD@g-C_3N_4 nanocomposite-based biosensor proves to be a viable platform for Xn monitoring.

4. MATERIALS AND METHODS

4.1. Chemicals. Melamine (97.5%) was purchased from Central Drug House, Pvt. Ltd. India, ferric chloride (Anhydrous, 96% $FeCl_3$) was procured from Rankem, India, and 1,2-phenylenediamine (o-PD, 99.5%), glutaraldehyde, xanthine oxidase (XOs, ≥7 units/mg protein), and xanthine (≥99.5%) were purchased from Sigma-Aldrich, USA. Double-distilled water (Milli-Q, Millipore, 18.2 MU) was used to prepare the solutions, and all the glassware was autoclaved before use.

4.2. Synthesis of g-C_3N_4. Melamine was thermally condensed to form graphitic carbon nitride (g-C_3N_4). Typically, 10 g of melamine was added to a crucible with a lid. The crucible was then placed in a muffle furnace and heated for 4 h at a rate of 5 °C min^{-1}, reaching a temperature of 550 °C. The product was collected, crushed into powder, and allowed to cool to room temperature.[47]

4.3. Synthesis of PoPD. The 1,2-phenylenediamine (*o*-PD) monomer (5 g) has been added to a 100 mL conical flask containing ethanol and water 1:1 v/v (25 mL). $FeCl_3$ (4 g) was added to the reaction mixture as an oxidant. The solution changed its color from transparent to brown, indicating rapid polymerization of the monomer. The flask was then subjected to sonication for 2 h, and the temperature was maintained at 30 °C. The synthesized PoPD was removed and repeatedly washed with distilled water/ethanol. To ensure that almost all water and contaminants were completely removed from the material, it was dried for 72 h at 70 °C in a vacuum oven.

4.4. One-Pot Synthesis of the PoPD@g-C_3N_4 Nanohybrid. To prepare the PoPD@g-C_3N_4 nanocomposite, 2.5 g of *o*-phenylenediamine (OPD) was ultrasonicated after being dispersed in 50 mL of DI water. Then, 1.5 g of g-C_3N_4 was added to the mixture, and the solution was ultrasonicated for 30 min. After that, 1.75 g of $FeCl_3$ was added to the mixture and heated at 60 °C for 24 h. The mixture was cooled before being washed with ethanol and DI water. The obtained filtrate was vacuum-dried and heated to 400 °C, forming a light brownish powder.

4.5. Electrophoretic Deposition of the PoPD@g-C_3N_4 Nanocomposite. The PoPD@g-C_3N_4 nanohybrid was deposited electrophoretically onto a hydrolyzed ITO electrode using a two-electrode setup. Both electrodes were positioned 0.5 cm apart. Before deposition, the PoPD@g-C_3N_4 nanohybrid was sonicated in DI water until a clear solution was obtained. For EPD, 10 mL of the solution was diluted with 5 mL of ethanol, and the film was deposited at 12 V for 15 s.

4.6. Fabrication of the PoPD@g-C_3N_4 Nanohybrid-Based Biosensor. For the immobilization of XOs, the PoPD@g-C_3N_4/ITO electrode was incubated with 0.1% glutaraldehyde and left at room temperature for 2 h to activate the functional group on the electrode surface. Afterward, the electrode was washed with phosphate buffer saline (PBS 100 mM, pH 7.4), followed by the covalent immobilization of XOs. The methodology for developing the electrode and synthesizing the PoPD@g-C_3N_4 nanohybrid is shown in Figure 1.

4.7. Instrumentation. The XRD pattern in the 2θ range (10−80°) was recorded using the Bruker D8 ADVANCE X-ray Diffractometer with monochromatic (Cu Kα) radiation (λ = 1.5406 Å), at a scan speed of 2°/min. To investigate the formation of PoPD@g-C_3N_4, FT-IR experiments were carried out using Nicolet TM iS10 in a frequency range of 400−4000 cm^{-1}. The surface morphology of g-C_3N_4/ITO and PoPD@ g-C_3N_4/ITO was studied using FESEM (FEI NOVA NANO-SEM 450). Electrochemical studies were carried out in phosphate buffer (PBS, 100 mM, pH 7.4, 0.9% NaCl) containing 5 mM $[Fe(CN)_6]^{3-/4-}$, using an Autolab potentiostat/galvanostat (Eco-Chemie, Netherlands) with ITO as a working electrode, platinum as an auxiliary electrode, and Ag/AgCl as a reference electrode.

■ ASSOCIATED CONTENT

Supporting Information

The Supporting Information is available free of charge at https://pubs.acs.org/doi/10.1021/acsomega.2c06727.

Fabrication of the PoPD@g-C_3N_4 nanohybrid-based biosensor (PDF)
XRD and FT-IR spectra (PDF)
FESEM images (PDF)
Nyquist diagram and CV studies (PDF)
DPV studies, calibration plot, shelf-life tests, and reproducibility study (PDF)
Scan rate study of the XOs/PoPD@g-C_3N_4/ITO electrode, loading volume optimization of XOs, pH optimization, increase in Xn concentration as a function of days, interference studies, and FESEM images of PoPD@g-C_3N_4/ITO and XOs/PoPD@g-C_3N_4/ITO electrodes (PDF)

■ AUTHOR INFORMATION

Corresponding Authors

Chandra Mouli Pandey − *Department of Chemistry, Faculty of Science, SGT University, Gurugram 122505 Haryana, India;* orcid.org/0000-0003-0079-0586; Email: cmp.npl@gmail.com

Devendra Kumar − *Department of Applied Chemistry, Delhi Technological University, Delhi 110042, India;* orcid.org/0000-0001-9118-2070; Email: dkumar@dce.ac.in

Author

Deeksha Thakur − *Department of Applied Chemistry, Delhi Technological University, Delhi 110042, India;* orcid.org/0000-0003-4205-7139

Complete contact information is available at: https://pubs.acs.org/10.1021/acsomega.2c06727

Notes

The authors declare no competing financial interest.

■ ACKNOWLEDGMENTS

Deeksha acknowledges DST-INSPIRE for the SRF Award. C.M.P. acknowledges the Department of Science and Technology, New Delhi, India, for the DST-INSPIRE Faculty award.

■ REFERENCES

(1) Zhao, Z.; Sun, Y.; Dong, F. Graphitic carbon nitride based nanocomposites: a review. *Nanoscale* **2015**, *7*, 15−37.

(2) Goettmann, F.; Fischer, A.; Antonietti, M.; Thomas, A. Metal-free catalysis of sustainable Friedel−Crafts reactions: direct activation of benzene by carbon nitrides to avoid the use of metal chlorides and halogenated compounds. *J.C.C.* **2006**, *43*, 4530−4532.
(3) Xing, W.; Li, C.; Chen, G.; Han, Z.; Zhou, Y.; Hu, Y.; Meng, Q. Incorporating a novel metal-free interlayer into g-C3N4 framework for efficiency enhanced photocatalytic H2 evolution activity. *Appl. Catal., B* **2017**, *203*, 65−71.
(4) Fahimirad, B.; Asghari, A.; Rajabi, M. Magnetic graphitic carbon nitride nanoparticles covalently modified with an ethylenediamine for dispersive solid-phase extraction of lead(II) and cadmium(II) prior to their quantitation by FAAS. *Microchim. Acta* **2017**, *184*, 3027−3035.
(5) Idris, A.; Oseghe, E.; Msagati, T. A. M.; Kuvarega, A.; Feleni, U.; Mamba, B. Graphitic Carbon Nitride: A Highly Electroactive Nanomaterial for Environmental and Clinical Sensing. *Sensors* **2020**, *20*, 5743.
(6) Zhu, J.; Xiao, P.; Li, H.; Carabineiro, S. A. C. Graphitic Carbon Nitride: Synthesis, Properties, and Applications in Catalysis. *ACS Appl. Mater. Interfaces* **2014**, *6*, 16449−16465.
(7) Xing, W.; Chen, G.; Li, C.; Sun, J.; Han, Z.; Zhou, Y.; Hu, Y.; Meng, Q. Construction of Large-Scale Ultrathin Graphitic Carbon Nitride Nanosheets by a Hydrogen-Bond-Assisted Strategy for Improved Photocatalytic Hydrogen Production and Ciprofloxacin Degradation Activity. *ChemCatChem* **2016**, *8*, 2838−2845.
(8) Chen, X.; Liu, L.; Zhao, Y.; Zhang, J.; Li, D.; Hu, B.; Hai, X. A Novel Metal-Free Polymer-Based POPD/g-C3N4 Photocatalyst with Enhanced Charge Carrier Separation for the Degradation of Tetracycline Hydrochloride. *ChemistrySelect* **2017**, *2*, 9256−9260.
(9) Huo, P.; Lu, Z.; Liu, X.; Wu, D.; Liu, X.; Pan, J.; Gao, X.; Guo, W.; Li, H.; Yan, Y. Preparation photocatalyst of selected photo-degradation antibiotics by molecular imprinting technology onto TiO2/fly-ash cenospheres. *Chem. Eng. J.* **2012**, *189−190*, 75−83.
(10) Huo, P.; Lu, Z.; Liu, X.; Liu, X.; Gao, X.; Pan, J.; Wu, D.; Ying, J.; Li, H.; Yan, Y. Preparation molecular/ions imprinted photo-catalysts of La3+@POPD/TiO2/fly-ash cenospheres: Preferential photodegradation of TCs antibiotics. *Chem. Eng. J.* **2012**, *198−199*, 73−80.
(11) Kirwan, S. M.; Rocchitta, G.; McMahon, C. P.; Craig, J. D.; Killoran, S. J.; O'Brien, K. B.; Serra, P. A.; Lowry, J. P.; O'Neill, R. D. Modifications of Poly(o-phenylenediamine) Permselective Layer on Pt-Ir for Biosensor Application in Neurochemical Monitoring. *Sensors* **2007**, *7*, 420−437.
(12) Kamil Reza, K.; Singh, M. K.; Yadav, S. K.; Singh, J.; Agrawal, V. V.; Malhotra, B. D. Quantum dots based platform for application to fish freshness biosensor. *Sens. Actuators, B* **2013**, *177*, 627−633.
(13) Sahyar, B. Y.; Kaplan, M.; Ozsoz, M.; Celik, E.; Otles, S. Electrochemical xanthine detection by enzymatic method based on Ag doped ZnO nanoparticles by using polypyrrole. *Bioelectrochemistry* **2019**, *130*, 107327.
(14) Devi, R.; Yadav, S.; Pundir, C. S. Electrochemical detection of xanthine in fish meat by xanthine oxidase immobilized on carboxylated multiwalled carbon nanotubes/polyaniline composite film. *Biochem. Eng. J.* **2011**, *58−59*, 148−153.
(15) Albelda, J. A. V.; Uzunoglu, A.; Santos, G. N. C.; Stanciu, L. A. Graphene-titanium dioxide nanocomposite based hypoxanthine sensor for assessment of meat freshness. *Biosens. Bioelectron.* **2017**, *89*, 518−524.
(16) Lawal, A. T.; Adeloju, S. B. Progress and recent advances in fabrication and utilization of hypoxanthine biosensors for meat and fish quality assessment: a review. *Talanta* **2012**, *100*, 217−228.
(17) Jalil, O.; Pandey, C. M.; Kumar, D. Electrochemical biosensor for the epithelial cancer biomarker EpCAM based on reduced graphene oxide modified with nanostructured titanium dioxide. *Microchim. Acta* **2020**, *187*, 275.
(18) Yadav, S. K.; Singh, J.; Agrawal, V. V.; Malhotra, B. D. Nanostructured nickel oxide film for application to fish freshness biosensor. *Appl. Phys. Lett.* **2012**, *101*, 023703.
(19) Solanki, S.; Pandey, C. M.; Gupta, R. K.; Malhotra, B. D. Emerging Trends in Microfluidics Based Devices. *Biotechnol. J.* **2020**, *15*, No. e1900279.
(20) Dolmaci, N.; Çete, S.; Arslan, F.; Yaşar, A. An amperometric biosensor for fish freshness detection from xanthine oxidase immobilized in polypyrrole-polyvinylsulphonate film. *Artif. Cell Blood Substit. Biotechnol.* **2012**, *40*, 275−279.
(21) Thakur, D.; Pandey, C.; Kumar, D. Highly Sensitive Enzymatic Biosensor Based on Polyaniline-Wrapped Titanium Dioxide Nano-hybrid for Fish Freshness Detection. *Appl. Biochem. Biotechnol.* **2022**, *194*, 3765−3778.
(22) Görgülü, M.; Çete, S.; Arslan, H.; Yaşar, A. Preparing a new biosensor for hypoxanthine determination by immobilization of xanthine oxidase and uricase in polypyrrole-polyvinyl sulphonate film. *Artif. Cell Nanomed. Biotechnol.* **2013**, *41*, 327−331.
(23) Erol, E.; Yildirim, E.; Cete, S. Construction of biosensor for hypoxanthine determination by immobilization of xanthine oxidase and uricase in polypyrrole-paratoluenesulfonate film. *J. Solid State Electrochem.* **2020**, *24*, 1695−1707.
(24) Zhang, L.; Lei, J.; Zhang, J.; Ding, L.; Ju, H. Amperometric detection of hypoxanthine and xanthine by enzymatic amplification using a gold nanoparticles−carbon nanohorn hybrid as the carrier. *Analyst* **2012**, *137*, 3126−3131.
(25) Dervisevic, M.; Custiuc, E.; Çevik, E.; Şenel, M. Construction of novel xanthine biosensor by using polymeric mediator/MWCNT nanocomposite layer for fish freshness detection. *Food Chem.* **2015**, *181*, 277−283.
(26) Dervisevic, M.; Custiuc, E.; Çevik, E.; Durmus, Z.; Şenel, M.; Durmus, A. Electrochemical biosensor based on REGO/Fe3O4 bionanocomposite interface for xanthine detection in fish sample. *Food Control* **2015**, *57*, 402−410.
(27) Dervisevic, M.; Dervisevic, E.; Azak, H.; Çevik, E.; Şenel, M.; Yildiz, H. B. Novel amperometric xanthine biosensor based on xanthine oxidase immobilized on electrochemically polymerized 10-[4H-dithieno(3,2-b:2′,3′-d)pyrrole-4-yl]decane-1-amine film. *Sens. Actuators, B* **2016**, *225*, 181−187.
(28) Malhotra, D.; Tran, P. K. L.; Tran, D. T.; Kim, N. H.; Lee, J. H. Cobalt-doped cerium oxide nanocrystals shelled 1D SnO2 structures for highly sensitive and selective xanthine detection in biofluids. *J. Colloid Interface Sci.* **2021**, *600*, 299−309.
(29) Wang, Z.; Liao, F.; Yang, S.; Guo, T. A Novel Route Synthesis of Poly(ortho-phenylenediamine) Fluffy Microspheres Self-assembled from Nanospheres. *Fibers Polym.* **2011**, *12*, 997−1001.
(30) Rashidizadeh, A.; Ghafuri, H.; Esmaili Zand, H. R.; Goodarzi, N. Graphitic Carbon Nitride Nanosheets Covalently Functionalized with Biocompatible Vitamin B1: Synthesis, Characterization, and Its Superior Performance for Synthesis of Quinoxalines. *ACS Omega* **2019**, *4*, 12544−12554.
(31) Cao, J.-L.; Qin, Q.; Wang, Y.; Zhang, H.; Sun, G.; Zhang, Z. Solid-State Method Synthesis of SnO2-Decorated g-C3N4 Nano-composites with Enhanced Gas-Sensing Property to Ethanol. *Materials* **2017**, *10*, 604.
(32) Shcherban, N.; Mäki-Arvela, P.; Aho, A.; Sergiienko, S.; Yaremov, P.; Eränen, K.; Murzin, D. Melamine-derived graphitic carbon nitride as a new effective metal-free catalyst for Knoevenagel condensation of benzaldehyde with ethylcyanoacetate. *Catal. Sci. Technol.* **2018**, *8*, 2928−2937.
(33) Elshafie, M.; Younis, S. A.; Serp, P.; Gad, E. A. M. Preparation characterization and non-isothermal decomposition kinetics of different carbon nitride sheets. *Egypt. J. Pet.* **2020**, *29*, 21−29.
(34) Paulraj, P.; Manikandan, D.; Manikandan, M.; Pandian, P.; Moodley, M.; Roro, K.; Murugan, K. Solid-State Synthesis of POPD@AgNPs Nanocomposites for Electrochemical Sensors. *J. Nanosci. Nanotechnol.* **2018**, *18*, 3991−3999.
(35) Pareek, S.; Quamara, J. Dielectric and optical properties of graphitic carbon nitride−titanium dioxide nanocomposite with enhanced charge sepaeration. *J. Mater. Sci.* **2018**, *53*, 604−612.

https://doi.org/10.1021/acsomega.2c06727
ACS Omega XXXX, XXX, XXX−XXX

(36) Soni, A.; Pandey, C. M.; Pandey, M. K.; Sumana, G. Highly efficient Polyaniline-MoS_2 hybrid nanostructures based biosensor for cancer biomarker detection. *Anal. Chim. Acta* **2019**, *1055*, 26−35.
(37) Abaci, S.; Nessark, B.; Riahi, F. Preparation and characterization of polyaniline+TiO2 composite films. *Ionics* **2014**, *20*, 1693−1702.
(38) Elgrishi, N.; Rountree, K. J.; McCarthy, B. D.; Rountree, E. S.; Eisenhart, T. T.; Dempsey, J. L. A Practical Beginner's Guide to Cyclic Voltammetry. *J. Chem. Educ.* **2018**, *95*, 197−206.
(39) Laviron, E. General expression of the linear potential sweep voltammogram in the case of diffusionless electrochemical systems. *J. Electroanal. Chem. Interfacial Electrochem.* **1979**, *101*, 19−28.
(40) Sen, S.; Sarkar, P. An interference-free new xanthine biosensor based on immobilized enzyme-nanogold conjugate on carbon nanotube doped poly(3,4-Ethylenedioxythiophene) composite film. *Int. J. Biol. Macromol.* **2022**, *199*, 275−286.
(41) Joon, A.; Ahlawat, J.; Aggarwal, V.; Jaiwal, R.; Pundir, C. S. An improved amperometric determination of xanthine with xanthine oxidase nanoparticles for testing of fish meat freshness. *Sens. Bio-Sens. Res.* **2021**, *33*, 100437.
(42) Yazdanparast, S.; Benvidi, A.; Abbasi, S.; Rezaeinasab, M. Enzyme-based ultrasensitive electrochemical biosensor using poly(l-aspartic acid)/MWCNT bio-nanocomposite for xanthine detection: A meat freshness marker. *Microchem. J.* **2019**, *149*, 104000.
(43) Devi, R.; Yadav, S.; Pundir, C. S. Amperometric determination of xanthine in fish meat by zinc oxide nanoparticle/chitosan/multiwalled carbon nanotube/polyaniline composite film bound xanthine oxidase. *Analyst* **2012**, *137*, 754−759.
(44) Devi, R.; Yadav, S.; Pundir, C. S. Au-colloids−polypyrrole nanocomposite film based xanthine biosensor. *Colloids Surf., A* **2012**, *394*, 38−45.
(45) Dervisevic, M.; Dervisevic, E.; Çevik, E.; Şenel, M. Novel electrochemical xanthine biosensor based on chitosan−polypyrrole−gold nanoparticles hybrid bio-nanocomposite platform. *J. Food Drug Anal.* **2017**, *25*, 510−519.
(46) Rahman, M. A.; Won, M.-S.; Shim, Y.-B. Xanthine Sensors Based on Anodic and Cathodic Detection of Enzymatically Generated Hydrogen Peroxide. *Electroanalysis* **2007**, *19*, 631−637.
(47) Rajkumar, C.; Kim, H. Hybrid nanostructures of Pd−WO3 grown on graphitic carbon nitride for trace level electrochemical detection of paraoxon-ethyl. *Microchim. Acta* **2021**, *188*, 233.

https://doi.org/10.1021/acsomega.2c06727
ACS Omega XXXX, XXX, XXX−XXX

PLOS ONE

RESEARCH ARTICLE

Identifying oral microbiome alterations in adult betel quid chewing population of Delhi, India

Mayank Bahuguna[1], Sunila Hooda[1], Lalit Mohan[2], Rakesh Kumar Gupta[1], Prerna Diwan[1]*

1 Department of Microbiology, Ram Lal Anand College, University of Delhi, South Campus, New Delhi, India, **2** Department of Biotechnology, Delhi Technological University, Rohini, Delhi, India

* prernadiwan.mic@rla.du.ac.in

Check for updates

OPEN ACCESS

Citation: Bahuguna M, Hooda S, Mohan L, Gupta RK, Diwan P (2023) Identifying oral microbiome alterations in adult betel quid chewing population of Delhi, India. PLoS ONE 18(1): e0278221. https://doi.org/10.1371/journal.pone.0278221

Editor: David M. Ojcius, University of the Pacific, UNITED STATES

Received: July 11, 2022

Accepted: November 11, 2022

Published: January 4, 2023

Copyright: © 2023 Bahuguna et al. This is an open access article distributed under the terms of the Creative Commons Attribution License, which permits unrestricted use, distribution, and reproduction in any medium, provided the original author and source are credited.

Data Availability Statement: Data are available from NCBI SRA [Bio sample Accession number-PRJNA853176].

Funding: The authors (PD and RKG) received funding from Indian Council of Medical Research (ICMR/2019-3072; https://www.icmr.gov.in) India for this work.The funders had no role in study design, data collection and analysis, decision to publish, or preparation of the manuscript.

Competing interests: The authors have declared that no competing interests exist.

Abstract

The study targets to establish a factorial association of oral microbiome alterations (oral dysbiosis) with betel quid chewing habits through a comparison of the oral microbiome of Betel quid chewers and non-chewing individuals. Oral microbiome analysis of 22 adult individuals in the Delhi region of India through the 16S sequencing approach was carried out to observe the differences in taxonomic abundance and diversity. A significant difference in diversity and richness among Betel Quid Chewers (BQC) and Betel Quid Non-Chewers (BQNC) groups was observed. There were significant differences in alpha diversity among the BQC in comparison to BQNC. However, in the age group of 21–30 years old young BQC and BQNC there was no significant difference in alpha diversity. Similar result was obtained while comparing BQC and Smoker-alcoholic BQC. BQ smoker-chewers expressed significant variance in comparison to BQC, based on cluster pattern analysis. The OTU-based Venn Diagram Analysis revealed an altered microbiota, for BQ chewing group with 0–10 years exposure in comparison to those with 10 years and above. The change in the microbial niche in early chewers may be due to abrupt chemical component exposure affecting the oral cavity, and thereafter establishing a unique microenvironment in the long-term BQC. Linear discriminant analysis revealed, 55 significant features among BQC and Alcoholic-Smoker BQC; and 20 significant features among BQC and Smoker BQC respectively. The study shows the abundance of novel bacterial genera in the BQC oral cavity in addition to the commonly found ones. Since the oral microbiome plays a significant role in maintaining local homeostasis, investigating the link between its imbalance in such conditions that are known to have an association with oral diseases including cancers may lead to the identification of specific microbiome-based signatures for its early diagnosis.

1. Introduction

The oral microbiome is a highly personalized and diverse microbiota in the human body playing a pivotal role in the health maintenance of the host [1,2]. Studies have highlighted

microbial variation and its relation to various diseases, but there is a lack of knowledge on the onset of oral dysbiosis caused due to harmful masticatory products like Betel quid (BQ). The oral cavity is made up of diverse structures and tissues, including cheeks, gingiva, gingival sulcus, lips, teeth, tongue and palate, providing different habitats, nutrients, and growth conditions [3] for microbes. Changes in oral microbiota have been associated with different types of cancer [4], but whether those changes are the cause or the consequence of the pathological processes or are the external effects drawn from substance exposure such as BQ, leading to dysbiosis of primitive microbiome is still not clear [3].

Betel Quid (BQ), a preparation of betel leaf (*Piper betle*), areca nut (*Areca catechu*), and catechu (*Acacia catechu*) along with slaked lime, is consumed with or without tobacco [5]. The chemical components of these smokeless tobacco (SLT's) forms mainly comprise polyphenols and alkaloids such as arecoline, arecaidine, guvacoline, guvacine, and tannins. These components have multifaceted effects on the oral cavity of a betel quid chewer (BQC) when compared to betel quid non-chewers (BQNC) including the changes in local microbiome.

Areca nut (AN) in BQ preparation is chewed by around 10–20% of the world's population accounting for around 700 million individuals [6–8]. Areca nut is the most commonly used addictive substances in the world after tobacco, alcohol, and caffeine [9]. The prevalence of BQ chewing is high among the Indian population and this trend is also observed in other parts of South Asia and Melanesia [6]. BQ chewing has decreased in certain regions of Thailand but on the other hand, there has been a 72–80% rise in BQ usage in the west pacific region. In a previously reported Asian study, chewing rates among men were significantly higher in the neighbouring countries of India, such as Mainland China, Nepal, and Sri Lanka [9]. India being, one of the largest producers of BQ components worldwide is also one of its highest consumer [8]. Its use as a masticatory product is highly prevalent in the North East region of India as part of the cultural ethnicity, also accounting for a significant number of cancer cases associated with the use of SLTs as per recent data [10,11]. BQ is also popular as a home remedy across the Indian subcontinent due to its pain-relieving property, especially in toothaches, which has resulted in growing addiction among the lower class population in India [11]. It is also used in wide-ranging human diseases and disorders, including anemia, digestive disorders and infections, vitiligo or leucoderma, leprosy, dental infections, urinary infections as well as obesity. AN acts as a general stimulant [8]. Its component arecoline is a muscarinic acetylcholine receptor agonist, which initiates a cholinergic effect on the parasympathetic nervous system [12]. It also functions as a psychoactive agent inducing various responses, which acts as a stimulant for neurodegenerative responses, including an upsurge in sense of alertness, capacity to work for a longer time, diminished hunger, euphoria, palpitation, salivation, warmth, feeling of wellbeing, and easy digestion. Areca nut chewing, alcohol and smoking, together have been considered to be primary causes of oral cancer in the previously reported study by Zini et al. 2010 [13]. The alkaloid, arecoline is carcinogenic and reported to eventually transform the stem cells with carcinogenic properties [5,6,14,15]. It undergoes a nitrosation reaction giving rise to a diverse array of betel quid-specific nitrosamines (BSNAs) within the oral cavity, which could lead to a prevalent shift of acid-tolerant bacteria. Likewise, nitrosamine formation may also be facilitated by bacterial nitric oxide or other trace elements present in areca nut [16–18]. Other than nitrosation, arecoline also triggers other pro-carcinogenic alterations such as the production of reactive oxygen species, p53 inhibition, up-regulation of inflammatory cytokines, repression of DNA repair, and DNA damage [19,20]. Major polyphenols in areca nut including: arecoline, catechin, flavonoids, and leucoanthocyanidin (flavan 3:4-diols) have been reported to exhibit pathological alterations after epithelial inflammation [21]. Betel leaf, another component of BQ contains (hydroxychavicol), a phenolic component that could be detected in saliva at 4.6mM concentration after betel quid chewing [22]. Slaked lime in BQ,

may alter intracellular calcium homeostasis, and excess calcium may bring some changes in the oral microbiota [23]. Various investigations have been done to comprehend and explain the relationship between BQ chewing habits with associated substances and patterns in various locales through study of histological changes displayed a relation to cancer progression known as precancerous lesions [8,24–26]. Some studies also have reported alcohol abuse along with BQ chewing, affects the microbiome balance leading to oral dysbiosis, and developing the risk of oral cancer in habitual chewers [27,28]. Alcohol may cause damage to epithelial cells, increasing the permeability of the epithelial cell membrane, which facilitates the penetration of carcinogens into the epithelium [27–29]. In previously done investigations, it is reported that alcohol and smoking habits with betel quid chewing might alter oral microbial compositions [30,31]. BQ along with smoking also modulates cigarette carcinogen benzo[a]pyrene-mediated toxic effects through dihydrodiol dehydrogenase (DDH) and hypoxanthine phosphoribosyl-transferase (HPRT) induction [32].

BQ chewing potentially influences oral microbiota epidemiologically in the population [7,8,33,34]. Strong evidence is available for the role of *Porphyromonas gingivalis*, as a biomarker for oral cancer, and oral squamous cell carcinoma (OSCC) [35]. Oral bacteria can infect hard and soft tissues majorly observed in dental caries and periodontitis, additionally by the rupture of epithelial cells through BQ chewing. Its toxicity mainly depends on the chewing exposure and its duration [36,37]. Similar effects of BQ products leading to dysbiosis are also enhanced by various local cultural practices, lifestyle choices, and its abundant easy availability at a cheap cost. These initiations to such harmful oral diseases finally leading to oral cancer appear to be a major factor at the base level for the dysbiotic changes which in turn may slowly precede the change in the microbiota of an individual's oral microbiome. In previous studies [38] the high prevalence of BQ chewing has shown to lead to Oral submucosal fibrosis (OSF), which later develops into OSCC [39].

Oral microbiota compositional changes have recently been found linked to oral cancer, where a colonization shift in tumor and non-tumorous site are distinguishable. The oral metagenomic data can be analyzed [40] and compared to databases such as the Human Oral Microbiome Database (HOMD) and NCBI which provides more than 700 phylotypes of bacteria, residing in the human oral cavity. The 12 major phyla reported in the oral sites include *Firmicutes*, *Fusobacteria*, *Proteobacteria*, *Actinobacteria*, *Bacteroidetes*, *Chlamydiae*, *Chloroflexi*, *Spirochaetes*, *SR1*, *Synergistetes*, *Saccharibacteria* (TM7), and *Gracilibacteria* (GN02) [41]. A study by (Pushalkar et al.) displayed bacterial species of *Streptococcus sp. oral taxon 058*, *Peptostreptococcus stomatis*, *Streptococcus salivarius*, *Streptococcus gordonii*, *Gemella haemolysans*, *Gemella morbillorum*, *Johnsonella ignava*, and *Streptococcus parasanguinis* reported as highly associated with tumor site in terms of prevalence [42]. In a stage-specific study of OSCC patients, a relative abundance profile for Fusobacteria was observed in oral cancer progression with comparison to healthy controls (2.98%) to OSCC stage 1 (4.35%) through stage 4 (7.92%). As a checkpoint, a lower relative abundance was reported for the genera of Streptococcus, Haemophilus, Porphyromonas, and Actinomyces. *Fusobacterium periodonticum*, *Parvimonas micra*, *Streptococcus constellatus*, *Haemophilus influenza*, and *Filifactor alocis* were certain bacteria that were detected also in the cases of cancer-associated diseases like periodontitis and dental caries [30].

Studies have shown an association between BQ and carcinogenesis and recent reports are linking oral microbiome alterations with cancer [31]. However, dysbiotic changes involving BQ-induced carcinogenesis largely remain unexplored. Therefore, the present study aims to identify the taxonomic compositional changes in the oral microbiome through 16S rRNA sequencing and community structure variance in BQ chewers and non-chewers. This will facilitate the understanding of whether the chewing and associated substances will lead to

dysbiosis which may further be associated with progression of oral diseases including cancer [1,43,44]. This approach may also lead to identification of potential strategies for early detection of precancerous changes and apply this information in developing consortia of microbes, which can reverse the changes in the oral cavity of an individual through probiotic-based products.

2. Materials and methodology

2.1 Study population

The study was approved by Institutional Ethics Committee (IEC) and consent taken from participating sample population. The information was obtained through a questionnaire. A total of 32 individuals (28 males and 4 females) pursuing different occupations were identified. The study groups were divided into 3 categories: BQ chewers (BQC)—Habitual individuals for BQ chewing, non-chewers (BQNC)–Individuals with no history of BQ chewing, and Occasional/previous chewers (BQOC)–Having a frequency of BQ chewing either once in a couple of months or having a previous history of chewing as confirmed from the participant after confirmation of chewing habits.

2.2 Data and oral sample collection

A structured questionnaire was presented explaining the purpose of the study. The information was inquired for demography, BQ chewing with or without smoking and alcohol consumption, BQ chewing habit (duration and frequency of consumption), and antibiotic intake.

Samples from different sites of the oral cavity including tongue surface, hard and soft palate, subgingival region, cheeks, and buccal mucosa were collected under the supervision of a dental clinician and research staff and suspended in 1ml sterile saline solution (0.85% NaCl) provided in Himedia Transport Swab Kit (http://surl.li/aeapx). All samples were processed immediately. The cotton swab was swirled and cut down inside the tube followed by a short cycle of vortexing. The remaining material from the swab was procured by pressing against the walls of the microcentrifuge tube to extract the exfoliated cheek cells as well as other tissues into the saline solution. After getting the material of swabs dislodged into the saline, extracted volumes were pooled 6 times by collecting 6 different swabs from each individual. The pooled saline was centrifuged at 10,000g for 10 mins to pellet down the cells and other tissues. A final volume of 1ml was processed further, and the remaining supernatant was discarded. The DNA extraction was carried out following the processing protocol of QIAamp DNA Microbiome Kit (QIAGEN) www.qiagen.com/hb-1792 with minor modifications under a controlled condition. The modification included: Substitution of tissue lyser step with vortexing the reaction mix for 10 minutes at high speed. The samples were stored at -20˚C until sent to the 16S rDNA sequencing facility to obtain the raw sequence data.

2.3 16S rDNA sequencing

The total DNA concentration of the samples was checked by NanoDrop 2000 spectrophotometer for QC criteria fulfillment, and extracted DNA was pooled for performing PCR and further, sequencing. The assay targeted the V3-V4 region of the bacterial 16S ribosomal RNA gene, by utilizing barcoded universal primers V13F and V13R with a sequence of (5' AGAGTTTGATGMTGGCTCAG 3' for forward and 5' TTACCGCGGCMGCSGGCAC 3' for reverse primer) [45]. The amplicons generated were purified with ampure beads (removal of unused primers) and 8 cycles of PCR were performed additionally using Illumina barcoded adapters for preparation of sequencing libraries. Quantification was done through Qubit dsDNA High

Sensitivity assay kit (https://www.thermofisher.com/order/catalog/product/Q32851#/Q32851) followed by sequencing using Illumina Miseq with a 2x300PE v3 sequencing kit (http://surl.li/aeare) to generate 0.2 to 0.5 million paired-end reads (Biokart India).

2.4 Data processing and statistical analysis

The sequence data analysis was carried out against the NCBI and eHOMD databases. The bcl data was de-multiplexed into.fastq raw data format. The de-multiplexed data quality was checked using Fastqc (Version 0.11.9) and Multiqc (Version 1.10.1) tools followed by trimming of adapters and low-quality reads by TRIMGALORE (for workflow refer to, S17 Fig). The QC passed samples qualified for further analysis were processed by (Biokart Pipeline) for 16S metagenomics studies. After finishing the run, the raw OTU table was obtained followed by clustering utilizing reference based approach with 97% similarity threshold and further processed for visualization. The abundance feature tables and the top ten genera in each sample were constructed using Microsoft excel (2010). Further, Alpha diversity, Beta diversity, PCoA plot, LEfSe, etc were done using Microbiomeanalyst (online tool: https://www.microbiomeanalyst.ca/). The diversity measures were applied at the genus level to get the maximum out of the results obtained. The data was rarefied from the raw counts of the OTU table from the mentioned 16s metagenomic pipeline. In addition to other technical mentions, the community diversity profiling was primarily done by employing Vegan R packages in Microbiome Analyst [46]. Alpha diversity, the diversity present within a sample of a group was drawn based on the Shannon-diversity index (for the number of unique taxa and its richness) and the Shannon-evenness index (providing a relative abundance of unique taxa), which describes the actual diversity of a community. The outlier points from Shannon indices box plots were considered as samples presenting less diversity. The major concern of other statistical methods employed for the estimation of diversity depends on the analysis feasibility of our study. For ex- Chao1 statistical method, estimates the richness by including the number of rare organisms that may have been lost due to under-sampling. On the other hand, the observed genus explains the number of unique taxa present in a sample set.

Beta Diversity i.e., diversity differences (similarity or dissimilarity) between the two samples based on the dissimilarity matrix. This diversity analysis involved (a) How much similarity is present between samples using a non-phylogenetic Bray-Curtis index; (b) Dissimilarity matrix visualization in lower dimensions through Principal Coordinate Analysis (PCoA) in 2 D or 3-D plot format. Each point in the 3D plot represents the microbiome of a single sample within a microbial community. Each axis represents the variation percentage between samples, where the X-axis represents the highest dimension of variation and the Y-axis, the second-highest dimension of variation. Further, each point or sample displayed on PCoA plots is coloured based on the sample group of a specific feature. The statistical significance of the clustering pattern in ordination plots was evaluated using Permutational ANOVA (PERMANOVA). The criteria of PERMDISP explain a difference in dispersion (variance) between any of the groups, while ANOISM, explains the presence/absence or abundance of taxa present in a dataset, with a statistical significance.

Linear Discriminant Analysis (LDA) Effect Size (LEfSe) Plot which employs the Kruskal-Wallis rank-sum test was used for detection the features with significant differential abundance with regards to genus. The analysis evaluated the relevance or effect size of differential abundant features based on a p-value cut-off of 0.05 with the original filter and Log LDA score of 2.0. The test was used to analyse the abundant genera in a group compared to another group, for knowledge about the distribution of taxa/ organism among/ between the groups [47]. Unique OTU with differential comparison was done through an interactive online tool of

Venn Diagram depiction (https://bioinfogp.cnb.csic.es/tools/venny/index.html) for comparing lists. It shows the percentage of unique organisms present in each sample and the percentage of organisms common to the pair and all the samples.

3. Results

3.1 Characteristic of the study population

32 oral samples were collected from people living in different parts of Delhi, India along with their information about demography, BQ chewing exposure, associated substances (smoking-alcohol) consumption, and gender. The final sample set analysed constituted 20 males and 2 females, where 9 were Current chewers (BQC), 9 Non-chewers (BQNC), and 4 with either former history of chewing or Occasional chewers (BQOC). Furthermore, 4 BQC individuals additionally had the habit of Smoking and 2 BQC individuals had an association with alcohol along with smoking (Table 1). The sequencing analysis filtered out 10 low-quality reads, removed chimeras, and normalized all samples for comparative analysis.

3.2 Oral bacteriome taxonomic classification

The oral specimens of the 22 study subjects generated a total of 11,136,729 raw sequences and 11,058,370 quality-filtered sequences. Category-wise, BQC, BQNC, and BQOC yielded an average of 450538 (std. dev. 2,29,961), 549301 (std. dev. 1,99,667), and 514951 (std. dev.

Table 1. Characteristics of study individuals (n = 22).

Categories		Number of Participants
Category I	**Chewers versus Non-chewers and Occasional (Overall Population)**	
	Total individuals	18
	Betel quid chewers	9
	Betel quid non-chewers	9
Category II	**Age range group [21–30 years] Chewers Vs. Non-chewers**	
	Total individuals	8
	Betel quid chewers (21–30 years Age)	4
	Betel quid non-chewers (21–30 years Age)	4
Category III	**Sex difference group [Males] Chewers Vs. Non-chewers**	
	Total individuals	12
	Betel quid chewers (Males)	6
	Betel quid non-chewers (Males)	6
Category IV	**Associated Substances grouping Chewers Vs. Alcoholic-smoker Chewers**	
	Total individuals	8
	Betel quid chewers	4
	Betel quid chewers (Alcoholics-Smokers)	4
Category V	**Smoking associated grouping Chewers Vs. Smoker Chewers**	
	Total individuals	8
	Betel quid chewers	4
	Betel quid chewers (Smokers)	4
Category VI	**Chewing history grouping [In association with betel quid]**	
	0–10 years	5
	10 years and above	5

https://doi.org/10.1371/journal.pone.0278221.t001

1,30,212) quality-filtered sequences respectively, with a mean length of 528 bp. Three samples yielded $\leq$ 0.1 M sequences and were excluded for diversity and taxonomic comparisons. The complete sequencing dataset was submitted to the National Centre for Biotechnology Information (NCBI) [Bio sample Accession number- PRJNA853176]. A total of 3,129,170 reads with an average count of (1,42,235), were identified among 1233 OTUs in a sample set of 22 individuals after filtering with an approximate (0.03–0.5%) default threshold. Overall, 100% OTUs were classified at the phylum level, 77.21% at the genus level, and 58.10% were observed at the species level. With eHOMD database, for human Oral microbiome provided a total OTU count of 1286 post-filtration, with a default threshold of (0.75%). Taxonomic levels below phylum and above genus, e.g., class, order, and family, were not included in the criteria. Considering the whole sample population data based on NCBI; 14 bacterial phyla were identified among which, the most abundant ones, based on relative abundance with a threshold value of (1%<) were Firmicutes with the highest percentage (38.64%), followed by Proteobacteria (29.02%), Bacteroidetes (24.78%), Actinobacteria (4.16%), and Fusobacteria (2.58%). While, less abundant phyla included Acidobacteria (0.22%), Chloroflexi (0.17%), Planctomycetes (0.14%), Gemmatimonadetes (0.09%), Verrucomicrobia (0.04%), Ignavibacteriae (0.03%), Cyanobacteria, Candidatus Saccharibacteria, and Spirochaetes (0.02%) (S1 Fig). *Prevotella* (15%) was the most abundant among the 78 identified genera, followed by *Bacteroides* (12%), *Streptococcus* (11%), *Neisseria* (10%), *Haemophilus* (9%) and *Lactobacillus*, *Fusobacterium and Acetobacter* (3%) based on the threshold value of (1% <) for determining abundance factor. *Rothia*, *Bacillus* (2%), and *Geosporobacter* (1%) were low in abundance, among others (S2 Fig). An overall count of 75 species was recorded including *Prevotella denticola* (17%), *Streptococcus mutans* (11%), *Neisseria animalis* (10%), *Bacteroides dorei* (8%), *Haemophilus parainfluenzae* (6%) and *Fusobacterium nucleatum* (4%) (S3 Fig). 30 genera were identified with unclassified as well as classified species, among which *Bacteroides* (an average of 21%) was the most abundant, followed by *Streptococcus* (14%), *Acetobacter* (12%), *Prevotella* (10%), *Haemophilus* (8%), and *Neisseria* (6%). While the low abundant ones included *Rothia*, *Leuconostoc*, *Bacillus*, *Pediococcus*, *Arachidicoccus* (1%) respectively (S4 Fig). The two genera not classified at the species level were *Cycloclasticus* and *Lachnoclostridium* which could be a unique lead to unidentified bacteria up to species level in the oral samples collected.

With eHOMD 93% OTUs were identified at the phylum level, 78.79% at the genus level, and 39.82% observed at the species level. Considering the phylum level classification, 4 bacterial phyla were identified among which, Firmicutes was the most abundant, based on threshold value of (1%<) followed by Bacteroides (23%), Proteobacteria (21%), and Actinobacteria (6%). In case of BQ chewers, and BQNC a similar trend was observed. While BQOC, displayed Proteobacteria with (29%) as the 2nd relatively abundant phylum (S14 Fig).

Groupwise classifications based on NCBI database. A total of 16 phyla, 114 genera, and 108 species were identified in the BQC group. Out of the 16 phyla, Firmicutes was the predominant phylum comprising 41% OTU counts followed by Bacteroidetes (31%), Proteobacteria (20%), Actinobacteria (4%), and Fusobacteria (1%). *Prevotella* was the most abundant genus (based on percent relative abundance, among the OTU assigned) comprising 29% of taxa followed by *Bacteroides* (11%), *Lactobacillus*, *Neisseria*, *Streptococcus*, and *Haemophilus* (5%), and *Faecalibacterium* (4%), which were detected in all BQC (Fig 1A and 1B). At the species level, the most abundant ones included: *Prevotella denticola* (33%), *Bacteroides dorei* (7%), and *Fecalibacterium prausnitzii* (5%). Two *Prevotella* species were identified including *Prevotella denticola* and *Prevotella melaninogenica*. The abundance variation observed for *Prevotella* species ranged from 0.52% for *Prevotella melaninogenica* to 33% for *Prevotella denticola*.

Among BQNC, a total of 15 phyla, 102 genera, and 99 species were identified in the oral samples. Among the 15 phyla, Firmicutes predominantly comprised 38% of OTU counts

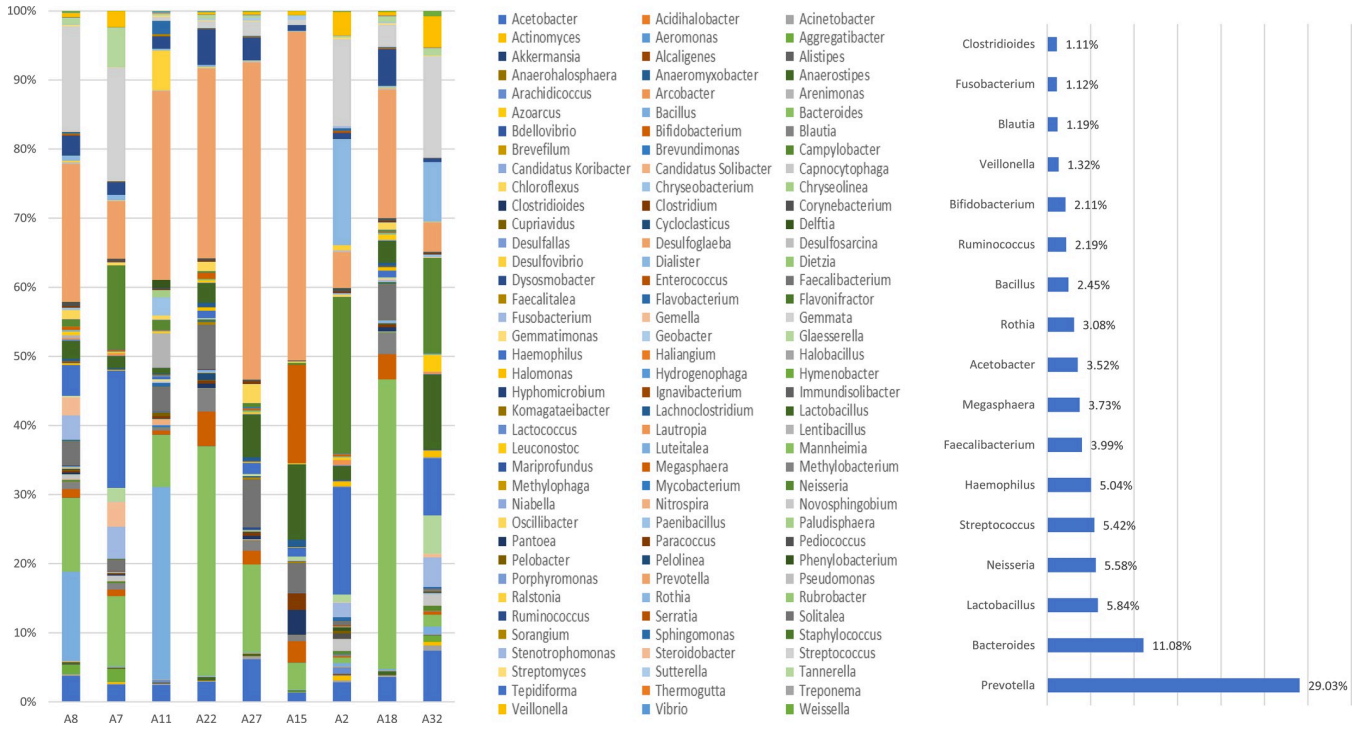

Fig 1. **a.** Genus-level oral microbiome composition of Betel quid Chewers: 114 genera including *Prevotella* (29%), *Bacteroides* (11%), *Lactobacillus*, *Neisseria*, *Streptococcus*, and *Haemophilus* (5%); **b.** Abundant genera detected in the Betel quid chewer individuals (excluding genera detected in lower than 1% of relative abundance among the samples).

https://doi.org/10.1371/journal.pone.0278221.g001

followed by Proteobacteria (31%), Bacteroidetes (22%), and Nitrospirae, Actinobacteria, and Fusobacteria (3.3%). *Bacteroides* was the most abundant genera (based on percent relative abundance, among the OTU) comprising 14.56% of taxa followed by *Streptococcus* (14%), *Neisseria* (13%), *Haemophilus* (10%), *Prevotella* (9%), *Fusobacterium* (3%), and *Veillonella*, *Lactobacillus*, *Acetobacter*, and *Tannerella* (2.5%) which were detected in all the individuals of Betel quid non-chewers (Fig 2A and 2B). At the species level, the highest abundant taxon comprised *Streptococcus mutans* and *Neisseria animalis* (13%), *Bacteroides dorei* (10%) followed by *Prevotella denticola* (9%). Six *Bacteroides* species were identified including *Bacteroides dorei*, *Bacteroides uniformis*, *Bacteroides fragilis*, *Bacteroides caccae*, *Bacteroides vulgatus*, and *Bacteroides salanitronis*. The abundance variation observed for *Bacteroides* species ranged from 0.0066% for *Bacteroides salanitronis* to 10% for *Bacteroides dorei*.

A comparative analysis was also done to compare the top 3 abundant phylum based on NCBI and eHOMD database among the BQC and BQNC. The groups displayed the differences in the Log transformed count graph, on the basis of median shift observation, for Proteobacteria and Firmicutes, but the p-value reporting for the intergroup comparison was non-significant (0.05<p-value) (S15 and S16 Figs).

A total of 16 phyla, 119 genera, and 128 species were reported in the BQOC group oral samples. In a total of 16 phyla, Proteobacteria was predominant comprising 38% of OTU counts followed by Firmicutes (34%), Bacteroidetes (16%), and Actinobacteria (4%). *Streptococcus* was the most abundant genus (based on percent relative abundance and OTU assigned) comprising 16% of taxa followed by *Haemophilus* (13%), *Neisseria* (12%), *Bacteroides* (8%), *Prevotella* (5%), and *Fusobacterium* (4%), *Rothia*, *Acetobacter*, and *Veillonella* (2%) and *Lactobacillus* (1%) all of which were detected in all the individuals of BQOC group (Fig 3A and 3B). At the species level,

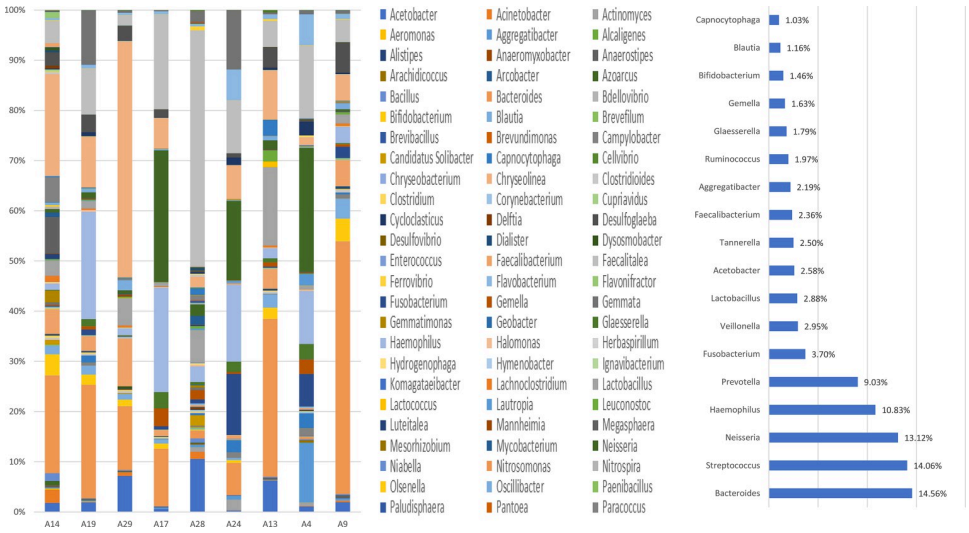

Fig 2. **a.** Genus-level oral microbiome composition of Betel quid Non-Chewers: 102 genera including *Bacteroides* (14.56%), *Streptococcus* (14%), *Neisseria* (13%), *Haemophilus* (10%), and *Prevotella* (9%); **b**. The abundant genera detected in the Betel quid non-chewer individuals (excluding genera with less than 1% of relative abundance).

https://doi.org/10.1371/journal.pone.0278221.g002

the highest abundant species observed were *Streptococcus mutans* (16%), *Neisseria animalis* (13%), *Haemophilus parainfluenzae* (11%), *Fusobacterium nucleatum*, and *Bacteroides dorei* (6%). Three *Streptococcus* species were identified including *Streptococcus mutans*, *Streptococcus pneumoniae*, and *Streptococcus salivarius*. The abundance variance pattern was observed for *Streptococcus* species ranging from 0.004% for *Streptococcus salivarius* to 16% for *Streptococcus mutans*.

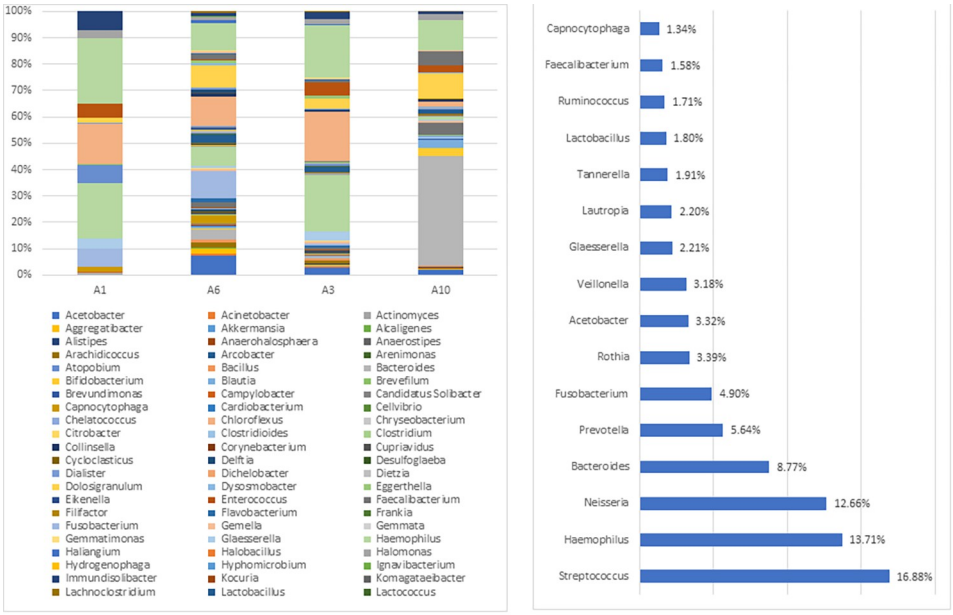

Fig 3. **a.** Genus-level oral microbiome composition of Occasional: 119 genera including *Streptococcus* (16%), *Haemophilus* (13%), *Neisseria* (12%), *Bacteroides* (8%), and *Prevotella* (5%); **b.** Abundant genera detected in the Betel quid Occasional chewer individuals (excluding genera with less than 1% of relative abundance).

https://doi.org/10.1371/journal.pone.0278221.g003

3.3 Alpha and beta diversity comparisons in betel quid chewers and non-chewers

Based on the total number of bacterial sequences, **a significant difference** was observed between BQC (mean 4,50,538; std. dev. 2,29,961); BQNC (mean 5,49,301; std. dev. 1,99,667) ($p = 0.041108$), displaying more diversity and richness.

Alpha diversity. Alpha diversity was estimated through the Shannon diversity index. The results showed a positive difference for genera among BQC and BQNC based on the T-test statistic that checks whether the two means (averages) are reliably different from each other/not, thus explaining variance within the group. Therefore, a higher t-value signifies the difference in the genera inside the group and vice-versa. The T-test stat (0.364679) and p-value (0.726118) depicted the presence of a positive difference in genera in the analysis of the group comparison of BQC and BQNC (Table 2).

Based on age group, young individuals 21–30 years displayed less difference among the genera in BQC and BQNC as signified with a negative T-test stat value of (-0.919483) and confirmed with a p-value (0.4549096), that there is more than 45% chance for this pattern occurrence in further analysis. However, a slight positive difference in diversity was found among Male BQC Vs. Male BQNC, with a T-test stat of (0.004298), and p-value (0.996776). In subjects consuming associated substances besides BQ, a T-test stat (-5.05042) and p-value of (0.037041) was observed for BQC and BQC [Smoking-Alcohol association], displaying a negative difference but with a pattern reoccurrence of 3%; whereas a t-test value of (2.374983) with p-value (0.140792) for BQC and Smoker BQC represent a high level of difference between these categories at the genus level.

In samples tested with respect to lengths of chewing time of BQ, a positive difference at the genus level with a p-value (0.181089) and a T-test stat (1.735327). Therefore, an overall significant difference was observed among the majority of the groups; except 21–30 years old young BQC and BQNC, and BQC and BQC (Alcohol-Smoking Associated) at the genus level with a less difference of genera based on the Shannon-index diversity measure.

Alpha diversity- differential diversity measures basis. Alpha diversity measured through the Shannon-evenness index indicated a higher relative abundance for unique genera in the entire study population, with a 95% filtered diversity value threshold. Among BQC in comparison to the BQNC group, a significantly higher presence of unique taxa was seen based on Observed Genus ($p = 0.05$). However, a lower or nearly no unique taxa presence was observed in BQC as compared to BQNC in the age group of 21–30 years old (young individuals), based on Shannon ($p = 0.45$), Chao1 ($p = 0.46$), Observed genus ($p = 0.49$) (Table 3).

Table 2. Alpha diversity (comparison chart).

Grouping	T-test stat	p-value
Betel quid Chewers/Non-chewers	0.36	0.72
Age range group [21–30 years] Chewers/Non-chewers	- 0.91	0.45
Sex difference group [Males] Chewers/Non chewers	0.004	0.99
Associated products grouping Chewers/Chewers [Alcohol and Smoking association]	-5.05	0.03
Smoking associated grouping Chewers/Chewers [Smoking association]	2.37	0.14
Chewing Time exposure group [Chewers in association to chewing substances]	1.73	0.18

https://doi.org/10.1371/journal.pone.0278221.t002

Table 3. Comparison of within-sample (alpha) diversity to bacterial microbiome based on the study population.

	Diversity Measures											
	Shannon				Chao1				Observed Genus			
Grouping	**Mean**	**Standard Deviation**	**t-stat**	**p-value**	**Mean**	**Standard Deviation**	**t-stat**	**p-value**	**Mean**	**Standard Deviation**	**t-stat**	**p-value**
Betel quid Chewers Vs. Non-chewers												
Chewers	2.47	0.33	0.36	0.72	145.95	8.69	0.50	0.62	129.77	16.55	2.30	0.05
Non-Chewers	2.48	0.20			140.27	10.04			122	22.05		
Age range group [21–30 years] Chewers Vs. Non-chewers												
Betel quid Chewers	2.48	0.21	-0.91	0.45	157.10	7.35	0.89	0.46	145	6.96	0.82	0.49
Betel quid Non-chewers	2.51	0.21			131.45	5.14			123.75	15.89		
Sex difference group [Males] Chewers Vs. Non-chewers												
Betel quid Chewers (Males)	2.47	0.33	0.004	0.99	138.14	8.60	-1.08	0.33	122.83	16.05	-0.07	0.94
Betel quid Non-chewers (Males)	2.48	0.20			136.61	7.93			122.5	20.14		
Associated products grouping: Chewers Vs. Chewers with alcohol and smoking association												
Betel quid Chewers	2.77	0.01	-5.05	0.03	165.56	6.18	-1.70	0.23	155.25	17.35	-0.12	0.91
Betel quid chewers with alcohol + smoking habit	2.30	0.009			154.78	5.60			145.75	1.29		
Smoking associated grouping: Chewers Vs. Chewers [Smoking association]												
Betel quid Chewers	2.76	0.02	2.37	0.14	161.69	10.57	-0.27	0.80	141.5	14.51	-0.93	0.44
Betel quid Chewers (Smokers)	2.44	0.37			141.80	9.68			124.75	20.75		
Chewing Time exposure group [Chewers in association to chewing substances]												
0–10 years	2.72	0.45	1.73	0.18	189.84	10.42	-2.65	0.07	167.40	24.33	3.14	0.05
10 years and above	2.61	0.23			184.77	13.41			154.60	12.40		

https://doi.org/10.1371/journal.pone.0278221.t003

When comparing male BQC and BQNC, alpha diversity was found to be significantly lower in BQC based on Shannon ($p = 0.99$), explaining a low or no unique taxa presence at the genus level. BQC group displayed a higher alpha-diversity in terms of unique taxa at the genus level, described by Shannon ($p = 0.03$) in comparison to BQC with smoking and alcohol association. A trend of lower unique taxa was explained based on Shannon ($p = 0.14$) concerning the alpha diversity between the BQC and smoker BQC. Individuals with a chewing exposure history of 0–10 years displayed a higher alpha diversity as compared to individuals with more than 10 years of chewing history, based on the Observed genus ($p = 0.05$).

Beta diversity. Beta diversity i.e. in between-group/samples diversity observed in the ordination plots was evaluated through Permutational ANOVA (PERMANOVA). The f-value is used to determine the variance between the samples. The null hypothesis is considered to be equal to diversity and the alternate hypothesis to be the difference in PCoA plot patterns. To confirm this hypothesis, the p-value helps to test the significance, whereas the R-squared value calculates the amount of variation.

Among BQC and BQNC, PCoA plots demonstrated a strong clustering pattern. The plot was constructed as per the Bray-Curtis index, inferring a non-significant 5% variance with a ($p < 0.41$) PERMANOVA, which differs from that of ANOISM ($p < 0.50$) displaying a 0.5% of diversity. A similar level of low variance was also observed in the case of Jaccard index, with only a 4% diversity ($p < 0.55$) for PERMANOVA (S5A Fig) (Table 4A). Young individuals of 21–30 years displayed a clustering pattern within the groups of BQC and BQNC. The values based on the Bray Curtis index showed more than 17% variance in the samples($p < 0.23$), while a difference of 4% variance is observed in ANOISM ($p < 0.43$). A differential variance was observed in the case of BQC evident through a single outlier point, while BQNC displayed none. With regards to the Jaccard index, a slight variation of 13% ($p < 0.37$) was observed in

Table 4. (a) Comparison of in between groups (beta) bacterial diversity based on the study population. (b) Comparison of in between groups (beta) bacterial diversity for the study population.

Grouping		Distance Methods	Statistical Methods					
			PERMANOVA		ANOISM		PERMDISP	
			F	p-value	R^c	p-value	F	p-value
Betel quid Chewers Vs. Non-chewers								
Chewers	Non-Chewers	Bray-Curtis Index	0.91	< 0.41	-0.024	<0.502	0.10	0.74
		Jaccard Index	0.80	< 0.55	-0.024	<0.499	0.16	0.68
Age range group [21–30 years] Chewers Vs. Non-chewers								
Betel quid Chewers	Betel quid Non-Chewers	Bray-Curtis Index	1.30	<0.23	0.02	<0.433	0.05	0.82
		Jaccard Index	0.97	< 0.37	0.02	<0.433	0.03	0.85
Sex difference group [Males] Chewers Vs. Non-chewers								
Betel quid Chewers (Males)	Betel quid Non-Chewers (Males)	Bray-Curtis Index	1.80	< 0.13	0.11	<0.153	1.64	0.22
		Jaccard Index	1.32	< 0.18	0.11	<0.153	1.54	0.24
Grouping		**Distance Methods**	PERMANOVA		ANOISM		PERMDISP	
			F	p-value	R^c	p-value	F	p-value
Associated products grouping Chewers Vs. Chewers with alcohol and smoking association								
Betel quid Chewers	Betel quid Chewers (Alcoholics)	Bray-Curtis Index	35.06	<0.041	1	<0.041	59	0.003
		Jaccard Index	19.63	<0.041	1	<0.042	77	0.001
Smoking associated grouping Chewers Vs. Chewers [Smoking association]								
Betel quid Chewers	Betel quid Chewers (Smokers)	Bray-Curtis Index	8.50	<0.034	0.77	<0.034	4.09	0.089
		Jaccard Index	5.41	<0.034	0.77	<0.034	6.37	0.044
Chewing Time exposure group[Chewers in association to chewing substances]								
0–10 years	10 years and above	Bray-Curtis Index	0.55	< 0.64	0.08	<0.594	0.0006	0.98
		Jaccard Index	0.60	< 0.75	0.08	<0.595	0.002	0.95

https://doi.org/10.1371/journal.pone.0278221.t004

the case of PERMANOVA, while ANOISM expressed a similar percentage of 4% ($p < 0.43$) (S5B Fig).

The male BQC group showed a variance of more than 15% in diversity ($p < 0.13$) (S6A Fig) and 1% of the variance in ANOISM ($p < 0.15$). A similarity matrix was evident with no outlier points observed; therefore, a strong correlation was inferred between the groups. While in the case of the Jaccard index, a slight variation of 11% ($p < 0.18$), was observed in the case of PERMANOVA, similar to ANOISM expressing 1% ($p < 0.15$). Bray Curtis Index displayed a variance of more than 85% diversity (p-value < 0.041) for BQ chewing associated with other habits, while ANOISM expressed a huge difference in a variance of 1% only with a ($p < 0.041$) (Table 4B) among BQC and Alcoholic-smoker BQC when considered. The PCoA plot displayed no correlation between the groups as indicated by a clearly separate zone verifying the variance value of 85% (S6B Fig). Individuals with smoking-associated habits, displayed a clustering pattern within the groups and expressed a variance of 58% diversity with (p-value < 0.03) as per the Bray-Curtis index, while ANOISM expressed a 59% of variance. With Jaccard Index, a 47% diversity difference was noted with a (p-value < 0.034). A higher variance was observed in the case of BQC with 2 outlier points, contributing to the group difference (Table 4B) (S7A Fig).

The BQ chewing history data provided an overall clustering pattern, and variation of only 6% in diversity for different chewing exposure, (p-value < 0.648) as per the Bray-Curtis index, while ANOISM drew only a 0.07% of the variation, ($p < 0.594$) (Table 4B). An average

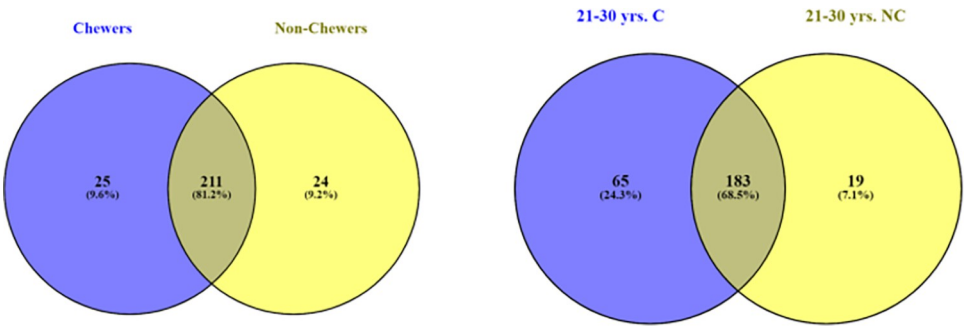

Fig 4. **a.** Genus-level oral microbiome Unique OTU elements composition of Betel quid chewers Vs. Non-Chewers; **b.** (Age Grouping) 21–30 years young individuals Betel quid Chewers Vs. Non-Chewers.

https://doi.org/10.1371/journal.pone.0278221.g004

variance was observed in the case of 10 years and above individuals with 1 outlier point, displaying a lower diversity and a good clustering pattern expressed among the groups (S7B Fig).

3.4 Unique operational taxonomic elements

Unique OTU refers to the sequence count identifying the classified taxa subjected to clustering and correlation algorithm through Marker data profiling. Venn's diagram was used to compare the list of genera for observing the unique taxon variance between BQC and BQNC. The data depicts (25) unique elements in BQC and (24) in BQNC (Fig 4A). Young individuals displayed a higher (65) unique count in BQC in comparison to BQNC (19) (Fig 4B). Among males, BQC displayed a slightly higher count of unique OTU (31) than BQNC (29) (Fig 5A). BQC showed a much higher unique OTU (71), as compared to Alcoholic-smoker chewers (35) (Fig 5B). BQ chewers displayed a higher count of unique OTUs (65) as compared to Smoker chewers (27) (Fig 6A). Chewing exposure history, also showed an altered microbiota, with a unique OTU count of (67) for a chewing exposure of 0–10 years and only (13) for 10 years and above chewing exposure (Fig 6B). This concludes a prominent change in microbiome of early chewers possibly due to the first exposure of components coming from BQ in the oral cavity, which stabilises with prolonged exposure, establishing a unique microenvironment build-up in long-term BQC.

3.5 Distinct taxon between the groups

The bacterial communities in different groups were analyzed at the genus level by lefse plots. The abundance of a specific bacterial genus was compared to BQ chewing status. Significant

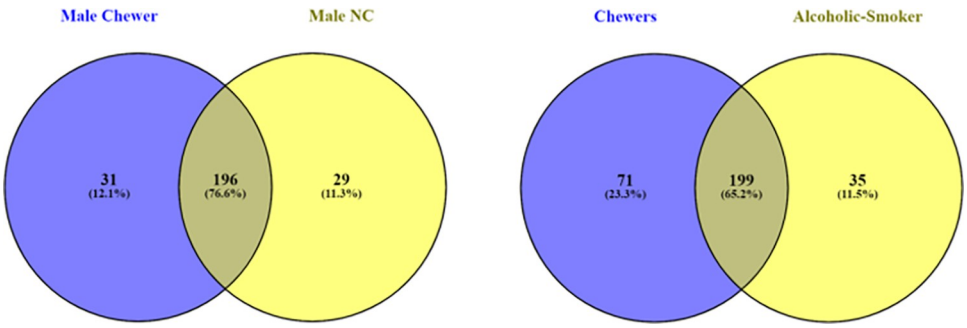

Fig 5. **a.** Genus-level oral microbiome Unique OTU elements composition of Betel quid Male chewers Vs. Non-Chewers; (Intra-Grouping); **b.** Betel quid Chewers Vs. Alcoholic-Smoker Chewer individuals.

https://doi.org/10.1371/journal.pone.0278221.g005

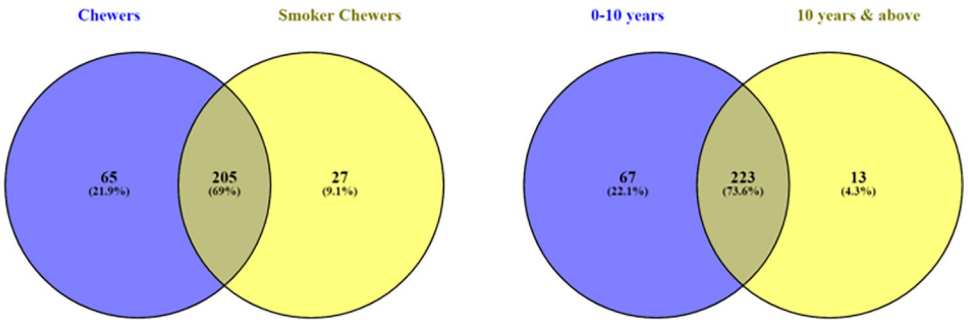

Fig 6. a. Genus-level oral microbiome Unique OTU elements composition of (Associated-Substance Grouping): Betel quid Chewers Vs. Smoker Chewers; **b.** Chewing History interval: 0–10 years, and 10 years-above chewing exposure time in years.

https://doi.org/10.1371/journal.pone.0278221.g006

different features were determined with a threshold value of (Original $p<0.05$) and a log LDA score of 2.0, for comparing the abundance of prevalent genera. The x-axis of the plot represents the effect size (LDA score) in the study population and colors represent in which group the genus was found to be more abundant compared to the other groups. The LDA score may be obtained as negative due to the order of numerator and denominator while calculating the effect size. The absolute values of the effect size interpret the scale difference between 2 groups for a certain taxon. In BQC Vs. BQNC, a total of (4) significant features were reported. The abundance was observed for *Arcobacter* genus detected in the oral cavity of BQC compared to that of BQNC, (p-value = 0.012) and LDA score of 3.06, expressing it to be significantly abundant (Figs 7A and S8A). In the case of 21–30 years age group, BQ chewing young individuals, an overall count of (11) significant features were observed among BQC and BQNC. A higher level of abundance was reported for *Pediococcus* detected in BQC, supported with (p-value = 0.043), LDA score of 3.69, in comparison to BQNC (Figs 7B and S8B).

When comparing male BQC with male BQNC 5 significant features were seen. The abundance was observed for *Campylobacter*, detected in BQNC with a p-value = 0.037 and LDA score of 4.47, verifying significant abundance (Figs 8A and S9A). While studying samples of associated substances with BQ chewing habit, 55 significant features among BQC and Alcoholic-Smoker BQC were recorded. The abundance was observed for *Bacteroides* detected in BQ alcoholic-smoker chewers (p-value = 0.020) and LDA score of 6.2, verifying significance with concern to BQC (Figs 8B and S9B). 20 significant features were observed among BQC and Smoker BQC with the highest abundance for *Neisseria* detected in BQC (p-value = 0.020

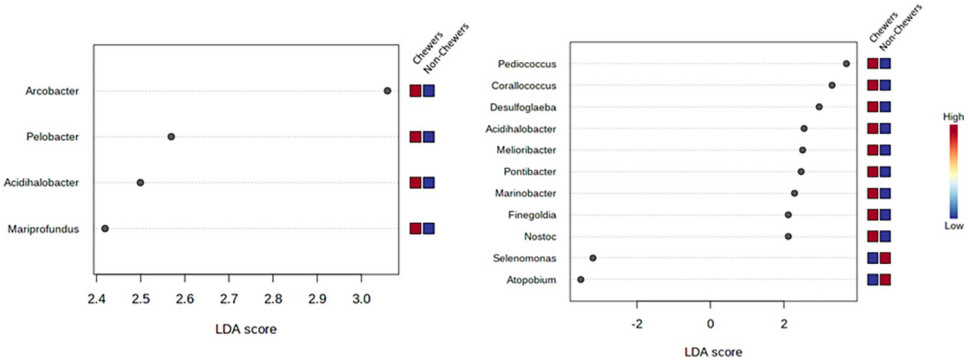

Fig 7. a. Lefse Plots: Genus-level oral microbiome significant features composition of Betel quid chewers Vs. Non-Chewers; **b.** (21–30 years old young individuals) Betel quid chewers Vs. Non-Chewers.

https://doi.org/10.1371/journal.pone.0278221.g007

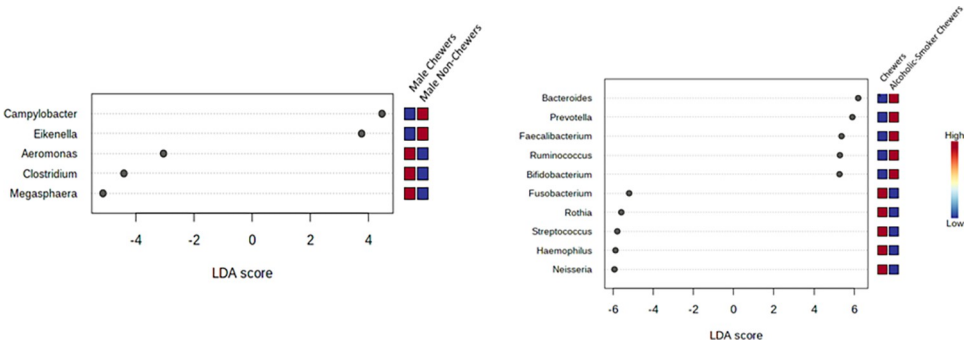

Fig 8. a. Lefse Plots: Genus-level oral microbiome significant features composition of Betel quid (Males) Chewers Vs. Non-Chewers; **b**. Betel quid Chewers Vs. Alcoholic-Smoker Chewers.

https://doi.org/10.1371/journal.pone.0278221.g008

and LDA score of 5.92), verifying significant abundance (Figs 9A and S10A). With regards to BQ chewing history, an overall count of 6 significant features was observed with the abundance of *Acinetobacter* in the oral cavity of BQC with a chewing history of 0–10 years, in comparison to 10 years and above, (p-value = 0.036 and LDA score of 4.11) (Figs 9B and S10B).

The prevalence of organisms at the genus level is provided through core microbiome plots, to detect the threshold, based on abundance. LDA plots are thus, self-explanatory to the extent that they give us a clear idea about taxon which is highly present in one group, while observed vice-versa in the other group. Thus, BQC Vs. Alcoholic-smoker chewers displayed the highest significant feature count.

Discussion

The present study was aimed at characterizing the diversity of oral microbiome in BQC and its comparison to BQNC and BQOC to identify specific microbial signatures. We found 14 bacterial phyla, 78 genera, and 75 species, of which 30 genera with unclassified species. Bacteroidetes, comprising *Prevotella* and *Bacteroides* genera make up a substantial part of the human oral microbiome. These exist in a complex mutualistic relationship degrading biopolymers (proteins and long-chain carbohydrates), facilitating the growth of other commensal and pathogenic microbial flora [48]. *Prevotella*, *Bacteroides*, and *Streptococcus* were the most abundant in all groups including chewers, non-chewers, and occasional chewers respectively (S11 Fig). The nutrient sources shapes the oral microbiome, exemplified by the rise in Betaproteobacteria and Fusobacteria with saturated fatty acid levels; sugars, and water-soluble vitamins with an

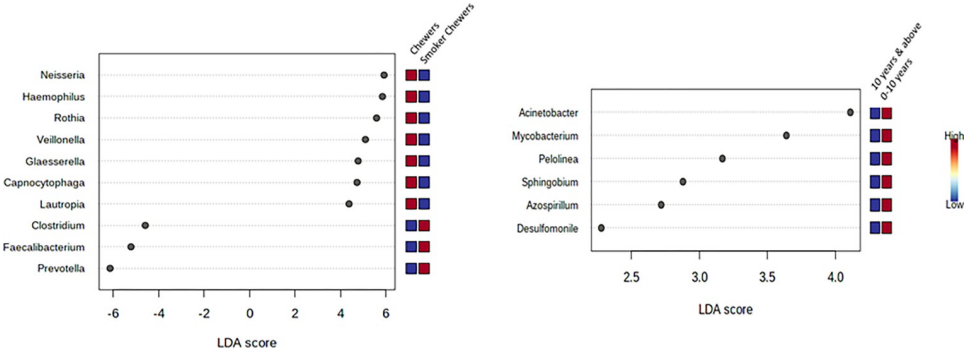

Fig 9. a. Lefse Plots: Genus-level oral microbiome significant features composition of Betel Quid chewer Vs. Smoker Chewers; **b**. Betel Quid Chewer (Chewing History).

https://doi.org/10.1371/journal.pone.0278221.g009

abundance of Lactobacillaceae and Fusobacteria respectively [49,50]. Enterobacteriaceae, Proteobacteria, and Streptococcus have been found to be abundant in the oral cavity of the Indian population [51]. Similar results were obtained in the present study with Firmicutes- *Streptococcus*, *Lactobacillus*; Proteobacteria- *Neisseria*, *Haemophilus*, *Acetobacter*; Bacteroidetes- *Bacteroides*, *Prevotella*, and Fusobacteria- *Fusobacterium*; constituting a majority of the oral microbiome.

Several saccharolytic and aciduric species hasten the progress of OSCC and oral cancer, due to endotoxin release in the oral cavity including *Fusobacterium*, *Streptococcus*, and *Prevotella* species: *P. melaninogenica*, *P. intermedia*, *P. nigrescens*, and *P. veroralis* [51–55]. *Streptococcus*, *Prevotella*, and *Tannerella* are also notable oral pathogens, leading to various dental diseases such as periodontitis and dental caries [52,56,57]. *Bacteroides* (*B. gingivalis*, *B. intermedius*, *B. endodontalis*) are associated with destructive periodontitis, gingivitis, endodontal infections, and abscesses and are reported in the oral cavity of periodontal patients contrary in healthy subjects [58–60]. BQC having a long chewing history may form an oral abscess in the cavity, also hosting periodontal infectious *Bacteroides* leading to pockets formation. S. *pneumoniae*, *S. salivarius*, *and S. mutans* were identified in the oral cavity of BQOC. *However*, a decrease in *Streptococcus* genus was observed among BQC, contrary to the earlier observation by Hernandez et. al, 2017 [31] showing a 4-fold increase. *S. infantis*, a commensal oral microorganism [61] was found to increase considerably in BQC. *Streptococcus salivarius* has been shown to be significant in the cancer samples as compared to control samples [42,62] which can serve as a diagnostic marker along with *Prevotella* species for BQ association with OSCC [31,44,52,56].

Tobacco-specific nitrosamines (TSNA) and alcohol, has been reported to cause oral dysbiosis over prolonged usage contributing to the progress of oral cancer [26,63] changing profile from Gram-negative to Gram-positive bacteria resulting in high salivary acetaldehyde concentration [64,65] that gets readily absorbed. Oral bacteria such as *Streptococcus gordonii*, *S. oralis*, *S. mitis*, *S. salivarius*, and *S. sanguinis*, possessing the enzyme alcohol dehydrogenase (ADH), convert alcohol to acetaldehyde, hence playing an essential role in alcohol-related carcinogenesis in humans [56].

The commensal oral microbiome composition responsible for maintaining a healthy state may get affected by the incessant habit of BQ chewing. In BQC with chewing history from 0–10 years, the relative abundance of *Prevotella* increased; whereas it considerably decreased for *Haemophilus*, *Streptococcus*, and *Rothia*, while *Lactobacillus* was observed to be relatively stable. *Prevotella* followed by *Bacteroides* were the most abundant genera in the BQC group. *Bacteroides*, *Streptococcus*, *Neisseria*, *Haemophilus*, *Prevotella*, *Fusobacterium*, *Veillonella*, and *Lactobacillus* were found to be a major part of the commensal oral microbiota of BQNC, consistent with studies reporting healthy microbiota [61,66–70]. An increased abundance for *Prevotella*, *Lactobacillus*, *Faecalibacterium*, *Ruminicoccus*, and *Bifidobacterium* genera observed among the microbial community of BQC was in sync with the recent study by Uehara et. al, 2021 [44]. While, a decreasing pattern for *Bacteroides*, *Streptococcus*, *Neisseria*, *Haemophilus*, *Fusobacterium*, and *Veillonella* in BQC was observed (S12 Fig). 4 unique elements seen in BQC were *Megasphaera*, *Bacillus*, *Rothia*, *Clostridioides*, and *Tannerella*, *Aggregatibacter*, *Glaesserella*, *Gemella*, *Capnocytophaga* in BQNC.

With regard to alpha diversity, more unique taxa and a higher level of relative abundance was found in BQC as compared to BQNC at the genus level, and high evenness in BQC as compared to BQNC based on Observed genus indices (S13 Fig). Also, a higher level of diversity significance was observed for the groups of BQC and Smoker-Alcoholic BQC and differential chewing exposures, while the other 3 groups of Male BQC and BQNC, 21–30 yrs. BQC and BQNC, and Smoker BQC and BQC, displayed the least evenness.

Dealing with beta diversity, we observed less differences between BQC and BQNC with a strong clustering pattern (S5A Fig) as in case of male BQC and BQNC (S6A Fig). A slight

difference in diversity is observed with outliers in the common zone of similarity, in 21–30 years young individuals and differential chewing exposure of BQ group. BQC vs. Smoker-alcoholic BQC and BQC with the smoking association in comparison to non-smoker BQC was observed with a noticeable differential matrix with a differential zone among the grouping samples (S6B and S7A Figs), validated with 85% and 58%) diversity respectively. Maximum unique OTUs were observed in the microbiome of 21–30 years BQC and BQNC, BQC Vs. smoker-alcoholic BQC, and among BQC Vs. smoker BQC individuals (Figs 4B, 5B and 6A). A nearly identical microbial community was observed in the oral cavity of BQC and BQNC in the overall population, male BQC and BQNC (Figs 4 and 5A). There was an abrupt rise in the unique oral community in early chewers, probably due to variations in pH and various other molecular and chemical changes which ensue, affecting the oral cavity (Fig 6b).

Lefse Plot encompasses distinction between the groups in terms of abundantly significant taxon [71]. Based on the LDA score and p-value, for the category BQC Vs. BQNC: significance was displayed by *Arcobacter* in BQC; for the category 21–30 years old BQC vs BQNC: 9 significant features out of 11 for BQC were observed with a trend above 2.0 LDA score. Some major phyla included *Pediococcus*, *Corallococcus*, *Desulfoglaeba*, etc. In case of Male BQC vs. BQNC, 5 significant features with ($<$ -2.0) LDA score was observed for BQC: *Aeromonas*, *Clostridium*, *Megasphaera*. BQC Vs. Alcoholic-smoker BQC showed, 55 significant features with the presence of *Bacteroides* at a significant level in Alcoholic-smoker BQC. In relation to associated smoking habits, *Clostridium* was the most significant feature obtained in BQC. *Acinetobacter* was observed to be the most significant among BQC having a chewing exposure of 0–10 years. In a previous study, the Actinobacteria phylum was reported to be the second most abundant oral bacterial phylum associated with betel nut chewing [31]. *Arcobacter* is a zoonotic food and water-borne pathogen, responsible for diarrhoea and known to harbor antibiotic and multi-drug resistance [72,73]. There could be an enhanced invasion in the oral cavity of BQC, due to an imbalance of beneficial microbes. *Aeromonas* and *Clostridium* have been reported to disturb the microbiome [74,75,79,80] *and* being associated with dental caries formation. Presence of *Clostridium* in the male smoker BQC corroborated with earlier studies claiming its involvement in oral carcinogenesis along with *Streptococcus*, *Prevotella*, and *Fusobacterium* [56,76,77]. Further focussed studies may discern the role of BQ chewing, smoking, and alcoholism-induced dysbiosis in oral cancer. Recent Studies are now exploring the role of probiotic organisms displaying anti-tumor and antimicrobial activities [78,79]. This approach of consumption of probiotics as an aid to reverse the effects of long-term BQ chewing effect exerted on the oral microbiome and to delay the deleterious effects of the BQ chewing habit needs to be explored.

In BQC, *Lachnoclostridium* and *Cycloclasticus* were not classified up to species level. Other than these, *Desulfosarcina*, *Herbaspirillum* in BQNC, *Chelatococcus*, *Optitus*, and *Xanthomonas* were reported among BQOC. *Desulfosarcina*, a sulfate-reducing anaerobic bacterium is a probable resident of subgingival sites [80] which plays a role in hydrocarbon degradation in marine trenches [81]. Thus, it can be prospected for its role in ethanol metabolism in drinkers and metabolism of hydrocarbons in the oral cavity of smoker BQC. *Lachnoclostridium* is a common human gut bacterium displaying homeostatic and anti-inflammatory behaviour [74,82]. *Cycloclasticus* is generally found in the marine habitat which degrades polycyclic aromatic hydrocarbon (PAH) compounds aerobically [83]. This bacterium may be involved in the degradation of the polycyclic hydrocarbons present in tobacco-associated products like BQ, where areca nut releases such harmful chemicals during the roasting/ preparation phase or mastication [84]. These chemicals include nitrites from the conjoined effects of salivary and BQ inflow to give rise to areca-derived nitrosamines N-nitrosoguvacoline, N-nitrosoguvacine, and 3-methylnitrosamino-propionitrile, a probable cause for DNA damage [85–87]. In BQ

preparations, polycyclic aromatic hydrocarbons get involved through the combination of areca nut, calcium hydroxide (responsible for alkalinity), nicotine (from tobacco), flavorants, and colouring agents influencing the oral bacteria which play an important role in nitrate-nitrite-nitric oxide homeostasis [88].

BQ chewing has been linked to cancers and is a prevalent habit in India and other Asian countries as part of cultural practices and due to other reasons. The role of microbiome is emerging in various diseases including cancers. The present study has highlighted differences in oral microbiome in betel quid chewers and non-chewers with reference to its role in progression of oral diseases including cancer. The study was limited to the identification of alterations in the relative abundances of different bacterial communities in the BQ chewing and non-chewing population (n = 22) in the Delhi region of India. Also, there may be a number of factors including diet, genetics which can affect the microbial composition at the time of sampling, Besides, there are limitations of the meta-omics technology including standard procedures and computational tools for accurately analyzing the data stating a drawback of the 16s metagenomic approach. Further analysis for pathways will enable the identification of mechanisms to understand ways to re-establish homeostasis and regain a healthy state [89,90] in BQ chewing population.

Supporting information

S1 Fig. a. Phylum-level oral microbiome composition of whole population sampling (n = 22): 14 phyla including Firmicutes (38%), Proteobacteria (29%), Bacteroidetes (25%); **b.** Relatively Abundant phyla detected in (n = 22) on the basis of OTU.
(TIF)

S2 Fig. a. Genus-level oral microbiome composition of whole population sampling (n = 22): 78 genera including *Prevotella* (15%), *Bacteroides* (12%), *Streptococcus* (11%), *Neisseria* (10%) and *Haemophilus* (9%); **b**. Relatively abundant genera detected in (n = 22) based on OTU assigned and (>1%) threshold.
(TIF)

S3 Fig. a. Genus-species level oral microbiome composition of whole population sampling (n = 22): 75 species including *Prevotella denticola* (17%), *Streptococcus mutans* (11%), *Neisseria animal*is (10%), Bacteroides dorei (8%), and *Haemophilus parainfluenzae* (6%); **b.** Relatively abundant genera detected in (n = 22) based on (>1%) threshold and OTU assigned.
(TIF)

S4 Fig. a. Genus-unclassified species-level taxonomy for the oral microbiome of whole population sampling (n = 22): 30 Genus-unclassified species including *Bacteroides* (21%), *Streptococcus* (14%), *Acetobacter* (12%), *Prevotella* (10%), *Haemophilus* (8%), and *Neisseria* (6%); **b.** Relatively abundant genera-unclassified species detected in (n = 22) on the basis of OTU assigned.
(TIF)

S5 Fig. PCoA plot: **a.** Chewers Vs. Non-Chewers; **b.** Age-group (21–30 years) Chewers Vs. Non-Chewers.
(TIF)

S6 Fig. PCoA plot: **a.** Males Chewers Vs. Non-Chewers; **b.** Associated substances: Chewers Vs. Alcohol and smoking chewers.
(TIF)

S7 Fig. PCoA plot: **a.** Associated substances: Chewers Vs. Smoker chewers; **b.** BQ Chewing history (0–10 years Vs. 10 years and above.
(TIF)

S8 Fig. Most Significant Features Comparison with lowest p-value of **a.** Betel quid chewers Vs. Non-Chewers; **b.** (21–30 years old young individuals) Betel quid chewers Vs. Non-Chewers.
(TIF)

S9 Fig. Most Significant Features Comparison with lowest p-value of **a**. Betel quid (Males) Chewers Vs. Non-Chewers; **b.** Betel quid Chewers Vs. Alcoholic-Smoker Chewers.
(TIF)

S10 Fig. Most Significant Features Comparison with lowest p-value of **a**. Betel Quid Vs. Smoker Chewers; **b.** Betel Quid Chewer (Chewing History).
(TIF)

S11 Fig. Relative abundance displayed for *Prevotella*- chewers, *Bacteroides*- non-chewers, and *Streptococcus*- Occasional chewers.
(TIFF)

S12 Fig. Unique elements in between chewers and Non-chewer abundant microbial community.
(TIF)

S13 Fig. Alpha Diversity pattern: **a.** Box and whisker plots of diversity and richness of microbiome Diversity analyzed through the Observed Genus diversity index. Dark horizontal lines represent the median, the box plots- the first (Q1) and third (Q3) quartiles, the outer fences- interquartile range, and the circles outside- outliers. **b.** Evenness index of Observed genus plots, explaining higher evenness among BQ chewer and non-chewer individuals.
(TIF)

S14 Fig. Comparative representation of most abundant phylum in reference to NCBI and eHOMD database.
(TIF)

S15 Fig. Whisker-Box plots representation for Phylum Proteobacteria, based on relative abundance expressed according to **a.** NCBI database, **b.** eHOMD database.
(TIF)

S16 Fig. Whisker-box plots representation for Phylum Firmicutes, based on relative abundance expressed according to **a.** NCBI database, **b.**) eHOMD database.
(TIF)

S17 Fig. Workflow for data filtration and processing.
(TIF)

S1 Graphical abstract.
(TIF)

Acknowledgments

I thank all the Lab staff and Lab mates who contributed in their way to the publication.

Author Contributions

Conceptualization: Rakesh Kumar Gupta, Prerna Diwan.

Data curation: Mayank Bahuguna, Lalit Mohan.

Formal analysis: Mayank Bahuguna.

Funding acquisition: Prerna Diwan.

Investigation: Mayank Bahuguna, Sunila Hooda, Prerna Diwan.

Methodology: Mayank Bahuguna, Sunila Hooda, Prerna Diwan.

Project administration: Prerna Diwan.

Supervision: Sunila Hooda, Rakesh Kumar Gupta, Prerna Diwan.

Validation: Prerna Diwan.

Visualization: Prerna Diwan.

Writing – original draft: Mayank Bahuguna, Lalit Mohan.

Writing – review & editing: Sunila Hooda, Rakesh Kumar Gupta, Prerna Diwan.

References

1. Zarco MF, Vess TJ, Ginsburg GS. The oral microbiome in health and disease and the potential impact on personalized dental medicine. Oral Dis. 2012; 18: 109–120. https://doi.org/10.1111/j.1601-0825.2011.01851.x PMID: 21902769
2. Gao L, Xu T, Huang G, Jiang S, Gu Y, Chen F. Oral microbiomes: more and more importance in oral cavity and whole body. Protein Cell 2018 95. 2018; 9: 488–500. https://doi.org/10.1007/s13238-018-0548-1 PMID: 29736705
3. Duran-Pinedo AE, Frias-Lopez J. Beyond microbial community composition: functional activities of the oral microbiome in health and disease. Microbes Infect. 2015; 17: 505–516. https://doi.org/10.1016/j.micinf.2015.03.014 PMID: 25862077
4. Whitmore SE, Lamont RJ. Oral Bacteria and Cancer. PLOS Pathog. 2014; 10: e1003933. https://doi.org/10.1371/journal.ppat.1003933 PMID: 24676390
5. WHO. Betel-quid and Areca-nut Chewing and Some Areca-nut-derived N-Nitrosamines. IARC Monogr Eval Carcinog Risks to Humans. 2004;85. Available: https://www.ncbi.nlm.nih.gov/books/NBK316570/.
6. Gupta PC, Warnakulasuriya S. Global epidemiology of areca nut usage. Addict Biol. 2002; 7: 77–83. https://doi.org/10.1080/13556210020091437 PMID: 11900626
7. Sharan RN, Choudhury Y. Betel nut and susceptibility to cancer. Environ Factors, Genes, Dev Hum Cancers. 2010; 401–428. https://doi.org/10.1007/978-1-4419-6752-7_15
8. Sharan RN, Mehrotra R, Choudhury Y, Asotra K. Association of Betel nut with carcinogenesis: Revisit with a clinical perspective. PLoS One. 2012;7. https://doi.org/10.1371/journal.pone.0042759 PMID: 22912735
9. Lee CH, Ko AMS, Warnakulasuriya S, Yin BL, Sunarjo, Zain RB, et al. Intercountry prevalences and practices of betel-quid use in south, southeast and eastern Asia regions and associated oral preneoplastic disorders: an international collaborative study by Asian betel-quid consortium of south and east Asia. Int J Cancer. 2011; 129: 1741–1751. https://doi.org/10.1002/ijc.25809 PMID: 21128235
10. Sung H, Ferlay J, Siegel RL, Laversanne M, Soerjomataram I, Jemal A, et al. Global Cancer Statistics 2020: GLOBOCAN Estimates of Incidence and Mortality Worldwide for 36 Cancers in 185 Countries. CA Cancer J Clin. 2021; 71: 209–249. https://doi.org/10.3322/caac.21660 PMID: 33538338
11. Mathur P, Sathishkumar K, Chaturvedi M, Das P, Sudarshan KL, Santhappan S, et al. Cancer Statistics, 2020: Report From National Cancer Registry Programme, India. JCO Glob Oncol. 2020; 1063–1075. https://doi.org/10.1200/GO.20.00122 PMID: 32673076
12. Papke R, Horenstein N, Stokes C. Nicotinic Activity of Arecoline, the Psychoactive Element of "Betel Nuts", Suggests a Basis for Habitual Use and Anti-Inflammatory Activity. PLoS One. 2015; 10: e0140907–e0140907. https://doi.org/10.1371/journal.pone.0140907 PMID: 26488401
13. Zini A, Czerninski R, Sgan-Cohen HD. Oral cancer over four decades: epidemiology, trends, histology, and survival by anatomical sites. J Oral Pathol Med. 2010; 39: 299–305. https://doi.org/10.1111/j.1600-0714.2009.00845.x PMID: 20040019
14. Huang JL, McLeish MJ. High-performance liquid chromatographic determination of the alkaloids in betel nut. J Chromatogr A. 1989; 475: 447–450. https://doi.org/10.1016/S0021-9673(01)89702-8

15. Li YC, Chang JT, Chiu C, Lu YC, Li YL, Chiang CH, et al. Areca nut contributes to oral malignancy through facilitating the conversion of cancer stem cells. Mol Carcinog. 2016; 55: 1012–1023. https://doi.org/10.1002/mc.22344 PMID: 26087469

16. D Hoffmann K Brunnemann D, Prokopczyk B and MVD. Tobacco-specific N-nitrosamines and Areca-derived «metajournal.com. In: American Health Foundation, Valhalla, New York 10595. J Toxicol Environ Health. 1994 Jan 1; 41 (1): [Internet]. 1994 [cited 29 Apr 2022] pp. 1–52. Available: https://www.metajournal.com/articles/1364399/tobacco-specific-n-nitrosamines-areca-derived-n-nitrosamines-chemistry.

17. Dave BJ, Trivedi AH, Adhvaryu SG. In vitro genotoxic effects of areca nut extract and arecoline. J Cancer Res Clin Oncol 1992 1184. 1992; 118: 283–288. https://doi.org/10.1007/BF01208617 PMID: 1577847

18. Calmels S, Ohshima H, Bartsch H. Nitrosamine formation by denitrifying and non-denitrifying bacteria: implication of nitrite reductase and nitrate reductase in nitrosation catalysis. J Gen Microbiol. 1988; 134: 221–226. https://doi.org/10.1099/00221287-134-1-221 PMID: 3141563

19. Hung SL, Lin YJ, Chien EJ, Liu WG, Chang HW, Liu TY, et al. Areca nut extracts-activated secretion of leukotriene B4, and phosphorylation of p38 mitogen-activated protein kinase and elevated intracellular calcium concentrations in human polymorphonuclear leukocytes. J Periodontal Res. 2007; 42: 393–401. https://doi.org/10.1111/j.1600-0765.2006.00958.x PMID: 17760816

20. Su S, Chang L, Huang H, Peng C, Chuang C, Chen Y, et al. Oral microbial dysbiosis and its performance in predicting oral cancer. 2021; 42: 127–135. https://doi.org/10.1093/carcin/bgaa062 PMID: 32621740

21. Trivedy CR, Craig G, Warnakulasuriya S. The oral health consequences of chewing areca nut. Addict Biol. 2002; 7: 115–125. https://doi.org/10.1080/13556210120091482 PMID: 11900631

22. Lee-Chen SF, Chen CL, Ho LY, Hsu PC, Chang JT, Sun CM, et al. Role of oxidative DNA damage in hydroxychavicol-induced genotoxicity. Mutagenesis. 1996; 11: 519–523. https://doi.org/10.1093/mutage/11.5.519 PMID: 8921515

23. Islam S, Muthumala M, Matsuoka H, Uehara O, Kuramitsu Y, Chiba I, et al. How Each Component of Betel Quid Is Involved in Oral Carcinogenesis: Mutual Interactions and Synergistic Effects with Other Carcinogens—a Review Article. Curr Oncol Rep. 2019; 21: 1–13. https://doi.org/10.1007/s11912-019-0800-8 PMID: 31028548

24. Srivastava S, Ghosh S, Kagan J, Mazurchuk R, Boja E, Chuaqui R, et al. The Making of a PreCancer Atlas: Promises, Challenges, and Opportunities. Trends in Cancer. 2019; 5: 263. https://doi.org/10.1016/j.trecan.2019.01.002

25. Tisserand R, Young R. Cancer and the immune system. Essent Oil Saf. 2014; 165–186. https://doi.org/10.1016/B978-0-443-06241-4.00012–6

26. Lee CH, Ko YC, Huang HL, Chao YY, Tsai CC, Shieh TY, et al. The precancer risk of betel quid chewing, tobacco use and alcohol consumption in oral leukoplakia and oral submucous fibrosis in southern Taiwan. Br J Cancer 2003 883. 2003; 88: 366–372. https://doi.org/10.1038/sj.bjc.6600727 PMID: 12569378

27. Chen M-NS and T H-. Impact of betel quid, tobacco and alcohol on three-stage disease natural history of oral leukoplakia and cancer: implication for prevention of oral cancer on JSTOR. In: European Journal of Cancer Prevention [Internet]. 2004 [cited 29 Apr 2022] pp. 39–45 (7 pages). Available: https://www.jstor.org/stable/45051315?seq=1.

28. Petti S, Masood M, Scully C. The magnitude of tobacco smoking-betel quid chewing-alcohol drinking interaction effect on oral cancer in South-East Asia. A meta-analysis of observational studies. PLoS One. 2013; 8: e78999. https://doi.org/10.1371/journal.pone.0078999 PMID: 24260143

29. Goldstein BY, Chang SC, Hashibe M, La Vecchia C, Zhang ZF. Alcohol consumption and cancers of the oral cavity and pharynx from 1988 to 2009: An update. Eur J Cancer Prev. 2010; 19: 431–465. https://doi.org/10.1097/CEJ.0b013e32833d936d PMID: 20679896

30. Yang CY, Yeh YM, Yu HY, Chin CY, Hsu CW, Liu H, et al. Oral Microbiota Community Dynamics Associated With Oral Squamous Cell Carcinoma Staging. Front Microbiol. 2018;9. https://doi.org/10.3389/FMICB.2018.00862 PMID: 29774014

31. Hernandez BY, Zhu X, Goodman MT, Gatewood R, Mendiola P, Quinata K, et al. Betel nut chewing, oral premalignant lesions, and the oral microbiome. PLoS One. 2017; 12: e0172196. https://doi.org/10.1371/journal.pone.0172196 PMID: 28225785

32. Tang DW, Chang KW, Chi CW, Liu TY. Hydroxychavicol modulates benzo[a]pyrene-induced genotoxicity through induction of dihydrodiol dehydrogenase. Toxicol Lett. 2004; 152: 235–243. https://doi.org/10.1016/j.toxlet.2004.05.005 PMID: 15331132

33. Winstock A. Areca nut-abuse liability, dependence and public health. Addict Biol. 2002; 7: 133–138. https://doi.org/10.1080/13556210120091509 PMID: 11900633

34. Gupta P, Pindborg J, Mehta F. Comparison of carcinogenicity of betel quid with and without tobacco: an epidemiological review. Ecol Dis. 1982; 1: 213–219. Available: https://europepmc.org/article/MED/6765307. PMID: 6765307

35. Atanasova KR, Yilmaz O. Looking in the Porphyromonas gingivalis cabinet of curiosities: the microbium, the host and cancer association. Mol Oral Microbiol. 2014; 29: 55–66. https://doi.org/10.1111/omi.12047 PMID: 24506890

36. Sankaranarayanan R, Duffy SW, Padmakumary G, Day NE, Nair MK. Risk factors for cancer of the buccal and labial mucosa in Kerala, southern India. J Epidemiol Community Heal. 1990; 44: 286–292. https://doi.org/10.1136/jech.44.4.286 PMID: 2277249

37. Radoï L, Luce D. A review of risk factors for oral cavity cancer: the importance of a standardized case definition. Community Dent Oral Epidemiol. 2013; 41: 97–109. https://doi.org/10.1111/j.1600-0528.2012.00710.x PMID: 22882534

38. Reichart PA, Zhang X. Misconceptions related to the areca nut chewing habits of Mainland China. Oral Oncol. 2007; 43: 958–959. https://doi.org/10.1016/j.oraloncology.2007.01.020 PMID: 17826301

39. Liu B, Shen M, Xiong J, Yuan Y, Wu X, Gao X, et al. Synergistic effects of betel quid chewing, tobacco use (in the form of cigarette smoking), and alcohol consumption on the risk of malignant transformation of oral submucous fibrosis (OSF): a case-control study in Hunan Province, China. Oral Surg Oral Med Oral Pathol Oral Radiol. 2015; 120: 337–345. https://doi.org/10.1016/j.oooo.2015.04.013 PMID: 26130067

40. Verma D, Garg PK, Dubey AK. Insights into the human oral microbiome. Arch Microbiol 2018 2004. 2018; 200: 525–540. https://doi.org/10.1007/s00203-018-1505-3 PMID: 29572583

41. Sultan AS, Kong EF, Rizk AM, Jabra-Rizk MA. The oral microbiome: A Lesson in coexistence. PLOS Pathog. 2018; 14: e1006719. https://doi.org/10.1371/journal.ppat.1006719 PMID: 29370304

42. Pushalkar S, Ji X, Li Y, Estilo C, Yegnanarayana R, Singh B, et al. Comparison of oral microbiota in tumor and non-tumor tissues of patients with oral squamous cell carcinoma. BMC Microbiol. 2012; 12: 1–15. https://doi.org/10.1186/1471-2180-12-144/TABLES/2

43. Kilian M, Chapple ILC, Hannig M, Marsh PD, Meuric V, Pedersen AML, et al. The oral microbiome–an update for oral healthcare professionals. Br Dent J 2016 22110. 2016; 221: 657–666. https://doi.org/10.1038/sj.bdj.2016.865 PMID: 27857087

44. Uehara O, Hiraki D, Kuramitsu Y, Matsuoka H, Takai R, Fujita M, et al. Alteration of oral flora in betel quid chewers in Sri Lanka. J Microbiol Immunol Infect. 2021; 54: 1159–1166. https://doi.org/10.1016/j.jmii.2020.06.009 PMID: 32611503

45. Klindworth A, Pruesse E, Schweer T, Peplies J, Quast C, Horn M, et al. Evaluation of general 16S ribosomal RNA gene PCR primers for classical and next-generation sequencing-based diversity studies. Nucleic Acids Res. 2013; 41: e1–e1. https://doi.org/10.1093/nar/gks808 PMID: 22933715

46. Dixon P. VEGAN, a package of R functions for community ecology. J Veg Sci. 2003; 14: 927–930. https://doi.org/10.1111/J.1654-1103.2003.TB02228.X

47. Dhariwal A, Chong J, Habib S, King IL, Agellon LB, Xia J. MicrobiomeAnalyst: a web-based tool for comprehensive statistical, visual and meta-analysis of microbiome data. Nucleic Acids Res. 2017; 45: W180–W188. https://doi.org/10.1093/nar/gkx295 PMID: 28449106

48. Thomas F, Hehemann JH, Rebuffet E, Czjzek M, Michel G. Environmental and gut Bacteroidetes: The food connection. Front Microbiol. 2011; 2: 93. https://doi.org/10.3389/fmicb.2011.00093 PMID: 21747801

49. Kato I, Vasquez A, Moyerbrailean G, Land S, Djuric Z, Sun J, et al. Nutritional Correlates of Human Oral Microbiome. 2016; 36: 88–98. https://doi.org/10.1080/07315724.2016.1185386 PMID: 27797671

50. Murtaza N, Burke LM, Vlahovich N, Charlesson B, O'neill HM, Ross ML, et al. Analysis of the Effects of Dietary Pattern on the Oral Microbiome of Elite Endurance Athletes. Nutr 2019, Vol 11, Page 614. 2019; 11: 614. https://doi.org/10.3390/nu11030614 PMID: 30871219

51. Chattopadhyay I, Verma M, Panda M. Role of Oral Microbiome Signatures in Diagnosis and Prognosis of Oral Cancer. Technol Cancer Res Treat. 2019;18. https://doi.org/10.1177/1533033819867354 PMID: 31370775

52. Mager DL, Haffajee AD, Delvin PM, Norris CM, Posner MR, Goodson JM. The salivary microbiota as a diagnostic indicator of oral cancer: A descriptive, non-randomized study of cancer-free and oral squamous cell carcinoma subjects. J Transl Med. 2005; 3: 1–8. https://doi.org/10.1186/1479-5876-3-27/FIGURES/3

53. Mok SF, Karuthan C, Cheah YK, Ngeow WC, Rosnah BZ, Yap SF, et al. The oral microbiome community variations associated with normal, potentially malignant disorders and malignant lesions of the oral cavity. Malays J Pathol. 2017; 39: 1–15. PMID: 28413200

54. Chen PH, Mahmood Q, Mariottini GL, Chiang TA, Lee KW. Adverse health effects of betel quid and the risk of oral and pharyngeal cancers. Biomed Res Int. 2017;2017. https://doi.org/10.1155/2017/3904098 PMID: 29376073

55. Hsiao JR, Chang CC, Lee WT, Huang CC, Ou CY, Tsai ST, et al. The interplay between oral microbiome, lifestyle factors and genetic polymorphisms in the risk of oral squamous cell carcinoma. Carcinogenesis. 2018; 39: 778–787. https://doi.org/10.1093/carcin/bgy053 PMID: 29668903

56. Karpiński TM. Role of Oral Microbiota in Cancer Development. Microorg 2019, Vol 7, Page 20. 2019; 7: 20. https://doi.org/10.3390/microorganisms7010020 PMID: 30642137

57. Shah HN, Collins DM. Prevotella, a new genus to include Bacteroides melaninogenicus and related species formerly classified in the genus Bacteroides. Int J Syst Bacteriol. 1990; 40: 205–208. https://doi.org/10.1099/00207713-40-2-205 PMID: 2223612

58. van Winkelhoff AJ, van Steenbergen TJM, de Graaff J. The role of black-pigmented Bacteroides in human oral infections. J Clin Periodontol. 1988; 15: 145–155. https://doi.org/10.1111/j.1600-051x.1988.tb01561.x PMID: 3280611

59. Tanner ACR, Listgarten MA, Ebersole JL, Strzempko MN. Bacteroides forsythus sp. nov., a slow-growing, fusiform Bacteroides sp. from the human oral cavity. Int J Syst Bacteriol. 1986; 36: 213–221. https://doi.org/10.1099/00207713-36-2-213/CITE/REFWORKS

60. SS S., HA D., CM A., C. S, L. KR. Microbial complexes in subgingival plaque. J Clin Periodontol. 1998; 25: 134–144. https://doi.org/10.1111/j.1600-051x.1998.tb02419.x PMID: 9495612

61. Bik EM, Long CD, Armitage GC, Loomer P, Emerson J, Mongodin EF, et al. Bacterial diversity in the oral cavity of 10 healthy individuals. ISME J 2010 48. 2010; 4: 962–974. https://doi.org/10.1038/ismej.2010.30 PMID: 20336157

62. Anjali K, Arun A, Bastian T, Parthiban R, Selvamani M, Adarsh H. Oral microbial profile in oral cancer patients before and after radiation therapy in a cancer care center–A prospective study. J Oral Maxillofac Pathol. 2020; 24: 117. https://doi.org/10.4103/jomfp.JOMFP_213_19 PMID: 32508459

63. Homann N, Tillonen J, Meurman JH, Rintamäki H, Lindqvist C, Rautio M, et al. Increased salivary acetaldehyde levels in heavy drinkers and smokers: a microbiological approach to oral cavity cancer. Carcinogenesis. 2000; 21: 663–668. https://doi.org/10.1093/carcin/21.4.663 PMID: 10753201

64. Liu Y, Chen H, Sun Z, Chen X. Molecular Mechanisms of Ethanol-associated Oro-esophageal Squamous Cell Carcinoma. Cancer Lett. 2015; 361: 164. https://doi.org/10.1016/j.canlet.2015.03.006 PMID: 25766659

65. Salaspuro MP, Mezey E. Acetaldehyde, microbes, and cancer of the digestive tract. Crit Rev Clin Lab Sci. 2003; 40: 183–208. https://doi.org/10.1080/713609333 PMID: 12755455

66. Zaura E, Keijser BJ, Huse SM, Crielaard W. Defining the healthy "core microbiome" of oral microbial communities. BMC Microbiol. 2009; 9: 1–12. https://doi.org/10.1186/1471-2180-9-259/FIGURES/7

67. Zaura E, Nicu EA, Krom BP, Keijser BJF. Acquiring and maintaining a normal oral microbiome: Current perspective. Front Cell Infect Microbiol. 2014; 4: 85. https://doi.org/10.3389/fcimb.2014.00085 PMID: 25019064

68. Burcham ZM, Garneau NL, Comstock SS, Tucker RM, Knight R, Metcalf JL, et al. Patterns of Oral Microbiota Diversity in Adults and Children: A Crowdsourced Population Study. Sci Reports 2020 101. 2020; 10: 1–15. https://doi.org/10.1038/s41598-020-59016-0 PMID: 32034250

69. Avila M, Ojcius DM, Yilmaz Ö. The oral microbiota: Living with a permanent guest. DNA Cell Biol. 2009; 28: 405–411. https://doi.org/10.1089/dna.2009.0874 PMID: 19485767

70. Jenkinson H, Lamont R. Oral microbial communities in sickness and in health. Trends Microbiol. 2005; 13: 589–595. https://doi.org/10.1016/j.tim.2005.09.006 PMID: 16214341

71. Segata N, Izard J, Waldron L, Gevers D, Miropolsky L, Garrett WS, et al. Metagenomic biomarker discovery and explanation. Genome Biol. 2011; 12: 1–18. https://doi.org/10.1186/gb-2011-12-6-r60 PMID: 21702898

72. Ho HTK, Lipman LJA, Gaastra W. Arcobacter, what is known and unknown about a potential foodborne zoonotic agent! Vet Microbiol. 2006; 115: 1–13. https://doi.org/10.1016/j.vetmic.2006.03.004 PMID: 16621345

73. Ferreira S, Queiroz JA, Oleastro M, Domingues FC. Insights in the pathogenesis and resistance of Arcobacter: A review. 2015; 42: 364–383. https://doi.org/10.3109/1040841X.2014.954523 PMID: 25806423

74. Barlow JT, Leite G, Romano AE, Sedighi R, Chang C, Celly S, et al. Quantitative sequencing clarifies the role of disruptor taxa, oral microbiota, and strict anaerobes in the human small-intestine microbiome. Microbiome. 2021; 9: 1–17. https://doi.org/10.1186/S40168-021-01162-2/FIGURES/5

75. Igbinosa IH, Igumbor EU, Aghdasi F, Tom M, Okoh AI. Emerging Aeromonas species infections and their significance in public health. Sci World J. 2012;2012. https://doi.org/10.1100/2012/625023 PMID: 22701365

76. Nagy KN, Sonkodi I, Szöke I, Nagy E, Newman HN. The microflora associated with human oral carcinomas. Oral Oncol. 1998; 34: 304–308. https://doi.org/10.1016/S1368-8375(98)80012-2 PMID: 9813727

77. Nakashima C, Yamamoto K, Kishi S, Sasaki T, Ohmori H, Fujiwara-Tani R, et al. Clostridium perfringens enterotoxin induces claudin-4 to activate YAP in oral squamous cell carcinomas. Oncotarget. 2020; 11: 309–321. https://doi.org/10.18632/oncotarget.27424 PMID: 32064037

78. Meurman JH. Probiotics: do they have a role in oral medicine and dentistry? Eur J Oral Sci. 2005; 113: 188–196. https://doi.org/10.1111/j.1600-0722.2005.00191.x PMID: 15953242

79. Jiang S, Cai L, Lv L, Li L. Pediococcus pentosaceus, a future additive or probiotic candidate. Microb Cell Factories 2021 201. 2021; 20: 1–14. https://doi.org/10.1186/s12934-021-01537-y PMID: 33593360

80. Heggendorn FL, Souza Gonçalves L, Dias EP, Silva Junior A, Galvão MMH, Lutterbach MTS. Detection of sulphate-reducing bacteria in human saliva. 2013; 71: 1458–1463. https://doi.org/10.3109/00016357.2013.770163 PMID: 23638810

81. Kleindienst S, Herbst FA, Stagars M, Von Netzer F, Von Bergen M, Seifert J, et al. Diverse sulfate-reducing bacteria of the Desulfosarcina/Desulfococcus clade are the key alkane degraders at marine seeps. ISME J 2014 810. 2014; 8: 2029–2044. https://doi.org/10.1038/ismej.2014.51 PMID: 24722631

82. Dandachi I, Anani H, Hadjadj L, Brahimi S, Lagier JC, Daoud Z, et al. Genome analysis of Lachnoclostridium phocaeense isolated from a patient after kidney transplantation in Marseille. New Microbes New Infect. 2021; 41: 100863. https://doi.org/10.1016/j.nmni.2021.100863 PMID: 33898042

83. Staley JT. Cycloclasticus: A Genus of Marine Polycyclic Aromatic Hydrocarbon Degrading Bacteria. Handb Hydrocarb Lipid Microbiol. 2010; 1781–1786. https://doi.org/10.1007/978-3-540-77587-4_128

84. Gupta PC, Ray CS, Papke RL, Stepanov I, Khariwala SS, Chaturvedi P, et al. Perspectives on areca nut with some global implications: Symposium report: 2018; 3: 2057178X1881406. https://doi.org/10.1177/2057178X18814068

85. Nair J, Ohshima H, Friesen M, Croisy A, Bhide S V., Bartsch H. Tobacco-specific and betel nut-specific N-nitroso compounds: occurrence in saliva and urine of betel quid chewers and formation in vitro by nitrosation of betel quid. Carcinogenesis. 1985; 6: 295–303. https://doi.org/10.1093/CARCIN/6.2.295 PMID: 3971493

86. Sundqvist K, Liu Y, Nair J, Bartsch H, Arvidson K, Grafström RC. Cytotoxic and Genotoxic Effects of Areca Nut-related Compounds in Cultured Human Buccal Epithelial Cells. Cancer Res. 1989;49. PMID: 2766297

87. Prokopczyk B, Rivenson A, Bertinato P, Brunnemann KD, Hoffmann D. 3-(Methylnitrosamino)propionitrile: Occurrence in Saliva of Betel Quid Chewers, Carcinogenicity, and DNA Methylation in F344 Rats. Cancer Res. 1987;47.

88. Hezel MP, Weitzberg E. The oral microbiome and nitric oxide homoeostasis. Oral Dis. 2015; 21: 7–16. https://doi.org/10.1111/odi.12157 PMID: 23837897

89. Allaker RP, Ian Douglas CW. Non-conventional therapeutics for oral infections. 2015; 6: 196–207. https://doi.org/10.4161/21505594.2014.983783 PMID: 25668296

90. Chugh P, Dutt R, Sharma A, Bhagat N, Dhar MS. A critical appraisal of the effects of probiotics on oral health. J Funct Foods. 2020; 70: 103985. https://doi.org/10.1016/J.JFF.2020.103985

JMEPEG
https://doi.org/10.1007/s11665-022-07780-7

©ASM International
1059-9495/$19.00

TECHNICAL ARTICLE

Investigation of Microstructure and Several Quality Characteristics of AA7075/Al_2O_3/Coconut Shell Ash Hybrid Nano Composite Prepared through Ultrasonic Assisted Stir-Casting

Ashish Kumar, R.C. Singh, and Rajiv Chaudhary

Submitted: 17 June 2022 / Revised: 29 November 2022 / Accepted: 4 December 2022

The present study focuses on the investigation of mechanical, thermal, and corrosion behaviors of cast hybrid nano-metal matrix composites of AA7075 with Al_2O_3 and coconut shell ash (CSA) nano- and micro-sized particulates, respectively, as reinforcements. Using an ultrasonic assisted stir-casting technique, the hybrid composites were fabricated using 2, 4, and 6% by weight of CSA and 0.5% by weight of Al_2O_3 in equal proportions. SEM, EDS, XRD, porosity, tensile, damping, dislocation density, coefficient of thermal expansion, and polarization tests were used to characterize four different combinations. The findings indicated that the nano- and micro-sized particulates were spread evenly in the matrix. The dislocation density, which is caused by a thermal mismatch between the matrix and the reinforced particles, as well as composite porosity, have been found to have a significant impact on the damping behaviors of hybrid composites. Also, the thermal expansion coefficient of HMMCs decreased with the addition of Al_2O_3 and CSA. The corrosion resistance was gradually increased by increasing the weight percentage of reinforcement in the AA7075 matrix.

Keywords corrosion, damping characteristics, dislocation density, hybrid composite, nano-reinforcement, thermal property

1. Introduction

Hybrid metal matrix composites (HMMCs) were developed to improve the performance of composites that were previously restricted to single reinforcement. In a hybrid metal matrix, two or more synthetic ceramics are added to a metal matrix. Carbides, oxides, and borides could be used as ceramic particles to reinforce the aluminum matrix (Ref 1-3). The most widely employed reinforcing materials are alumina (Ref 4), silicon carbide (Ref 5), boron carbide (Ref 6), and graphite (Ref 7), among others. Moreover, aluminum oxide and graphite particles made from these are more affordable. The desirable properties, like the flexible coefficient of thermal expansion and the solid lubricating characteristic, render these reinforcement particle forms suitable for producing components such as engine bearings, cylinder liners, pistons, and piston rings (Ref 8-12). The present scenario in the fabrication of hybrid composite is reinforcing agriculture waste (secondary reinforcement) with synthetic ceramic (primary reinforcement) (Ref 9). The broad applicability of such hybrid composites has attracted the attention of researchers who have designed and conducted experiments to develop superior and cost-efficient MMCs. Several good attempts have been made at producing MMCs from industrial wastes like graphite (Ref 7), fly ash (Ref 6), red mud (Ref 13), and the ashes of agricultural wastes like bagasse ash (Ref 14), coconut shell ash (Ref 15), corn cob (Ref 16), basalt fibers (Ref 17), coconut shell char (Ref 18), maize stalk (Ref 19), and rice husk ash (Ref 20). The advantages of including CSA are ease of access, low cost, low density, and lower pollution (Ref 21). According to the literature review, AMCs with CSA play a significant role in the progress of HMMCs due to their improved mechanical behaviors and widespread applications in a variety of fields. However, reinforcing natural ceramic is insufficient to improve the composite's quality characteristics. As a result, it's been combined with synthetic ceramic to increase mechanical, corrosion, and tribological properties.

In current scenario, nano-sized reinforcing particulates are being utilized in the metal matrix nanocomposite (MMnC). The use of nanoscale reinforced particulates at matrix interfaces provides a larger surface area, which results in improved composite properties like fatigue life, mechanical strength, and creep resistance at high temperatures without any loss of ductility (Ref 15, 22-25). The sizes, shapes, distribution of particulates, thermal stability, and hardening mechanism of nano-reinforcement materials have a significant impact on the final characteristics of MMnCs (Ref 23). The most difficult issue in the stir-casting method for processing MMnCs is achieving uniform reinforcement dispersion. The significant variability in densities between nanoparticles and molten

Ashish Kumar, Department of Mechanical Engineering, Delhi Technological University, New Delhi, Delhi 110042, India; and Galgotias College of Engineering and Technology, Greater Noida 201306, India; and **R.C. Singh** and **Rajiv Chaudhary**, Department of Mechanical Engineering, Delhi Technological University, New Delhi, Delhi 110042, India. Contact e-mail: ashuatcoer@gmail.com.

Published online: 27 December 2022

matrix, as well as the significantly higher specific surface area, results in lower wet-ability. Some authors improve the wetting properties of nano-reinforcements by combining stir casting and an ultrasonic effect during casting, which results in reinforcement agglomeration breaking (Ref 26). In MMnCs, micro-size ceramic particles are combined with nano-size reinforcements, and improved results in terms of quality attributes have been documented as compared to micro-size particles-reinforced MMCs (Ref 15, 27). Because of their superior characteristics over single-reinforced composites, hybrid nano-metal matrix composites (HnMMC) are being studied by researchers all over the world. To ensure the precise behavior of such materials, the damping capacity (Ref 28-30), thermal expansion (Ref 31), and corrosion resistance (Ref 32-34) must be monitored.

Numerous crucial alloys and metals have limited damping capacities, making them unsuitable for use in dynamic structures. Though, by adding reinforced particulates with better damping capacities to form MMCs, it is promising to get better damping capability from such materials (Ref 30). Although the aluminum alloys show low damping behavior, they are nevertheless used because of their higher strength-to-density ratio. By adding SiC to AlSi, Madeira et al. (Ref 29) increased its damping capacity. The reduction in thermal expansion coefficient indicates superior dimensional stability, which can be achieved by incorporating reinforced particulates into AMCs. Several efforts have been made to investigate the microstructure, mechanical, and wear behavior of various reinforced particulates included with AA7075 (Ref 6, 7, 9, 11, 15, 26). The coefficient of thermal expansion Al-Mg-AA535 composites reinforced with fly ash was found to reduce with an enhancement in the content of fly ash. Corrosion of materials is a serious issue in the aircraft and shipping industries, as it can occur in a variety of locations throughout the structure. Localized corrosions such as crevice, pitting, intergranular, and exfoliation can occur in various parts of AA7xxx series aircraft. Corrosion is a severe issue in older airplanes; intergranular (IGC), pitting, exfoliation, and crevice corrosion are examples of confined corrosion. They arise at various points in wing structures through AA7xxx (Ref 33).

The novelty of this study is that it looks at the mechanical, damping, dislocation density, coefficient of thermal expansion, and corrosion behaviors in depth; these qualities are critical for materials used in airplanes, automobiles, and ships. This type of investigation would be extremely beneficial in assisting in the efficient design of Al7075/Al_2O_3/CSA hybrid composites as well as the precise prediction of their mechanical and corrosion characteristics.

2. Materials and Methods

AA7075 is an imperative material for industrial purposes, hence its selection as the matrix material. Micro-sized (40-60 μm) CSA and nano-sized (40-90 nm) alumina particles were selected for the reinforcement. The chemical analysis of AA7075 reveals the weight percentage of major elements such as Zn (5.31), Cu (1.13), Mg (2.12), Si (0.41), Fe (0.52), Mn (0.29), Ti (0.22), Cr (0.18), and balance Al. The XRF oxide analysis of CSA particles reveal the weight percentages of main oxides such as SiO_2 (46.35), Fe_2O_3 (18.80), Al_2O_3 (20.85), MgO (13.15), Na_2O (0.85), CaO (0.62), ZnO (0.31), and others. The morphology and particle size of nanoscale Al_2O_3 powder were determined using a transmission electron microscope (TEM). Approximately 10 mg/L of alumina nanoparticles were immersed in an acetone solution, followed by 4-5 min of ultrasonic treatment. Figure 1(a), (b), (c), and (d) shows the TEM analysis of alumina particles and the SEM analysis of CSA particulates, respectively. Based upon previous research work, the range of reinforcement (alumina and CSA) was finalized. The preheated (up to 250 °C) CSA was ultrasonically assisted stir-cast into the base aluminum alloy 7075 matrix to achieve uniform wettability and homogeneous mixing, resulting in better bonding among the AA7075 matrix.

Figure 2 shows the experimental setup of the ultrasonic assisted stir-casting process. As per previous literature (Ref 26), a preheated mechanical stirrer having a graphite impeller was used to generate vortex motion in a molten melt to ensure uniform mixing. At the same time, the preheated (200 °C) nano-alumina particles were mixed well with pure aluminum powder and added at a constant feed rate. During the process of melting, about 10 g of Na_3AlF_6 was mixed into the molten melt to avoid slag formation and to enhance the casting efficiency. A synchronized motor was used to rotate the mechanical impeller between 500 and 700 rpm during the process of addition. It is evidence of the homogeneous dispersion of the reinforcement during the molten melt.

The melt temperature was kept at 800 °C for another 6 min after adequate stirring of the molten slurry. After dipping a titanium waveguide into the molten metal and ultrasonically treating it for 6 min to break up the bigger clusters, the sonication process was prolonged for another 6 min to remove any remaining agglomerations, degas, and improve the matrix grain size. Instantly after the achievement of the addition of the reinforced particles into the molten melt slurry, it was cast into the preheated (500 °C) mold of gray cast iron. Three dissimilar combinations of hybrid composites and AA7075 alloy without reinforcement were fabricated. Each combination of hybrid composite contains 0.5% Al_2O_3 by weight in an equal proportion. CSA0, CSA2, CSA4, and CSA6 are the codes for samples with 0, 2, 4, and 6 weight percentages of CSA, respectively. A wire electro-discharge machine (WEDM) was used for the fabrication of the test specimen.

2.1 Metallographic Studies

OM and SEM were used to examine the microstructure of the produced samples at the micron level. Polishing is performed on the prepared samples by global metallurgical processes. The next step is an etching, which is done with Keller's reagent on all of the samples. Optical metallographic and SEM images were analyzed to examine the finished surfaces. EDS and XRD analyses have been done for confirmation of the existence of constituent phases and elements in the developed composite.

2.2 Mechanical, Damping, Thermal and Corrosion Tests

Experimental density was determined by the Archimedes' principle. In this method of density measurement, the specimen is weighed in air and another fluid of known density. The rule of mixture (ROM) method was used to find the experimental and theoretical densities. The variation of theoretical density and experimental density gives the porosity in the fabricated composites. A universal testing machine (UTM) was employed to examine the tensile behaviors of the developed hybrid

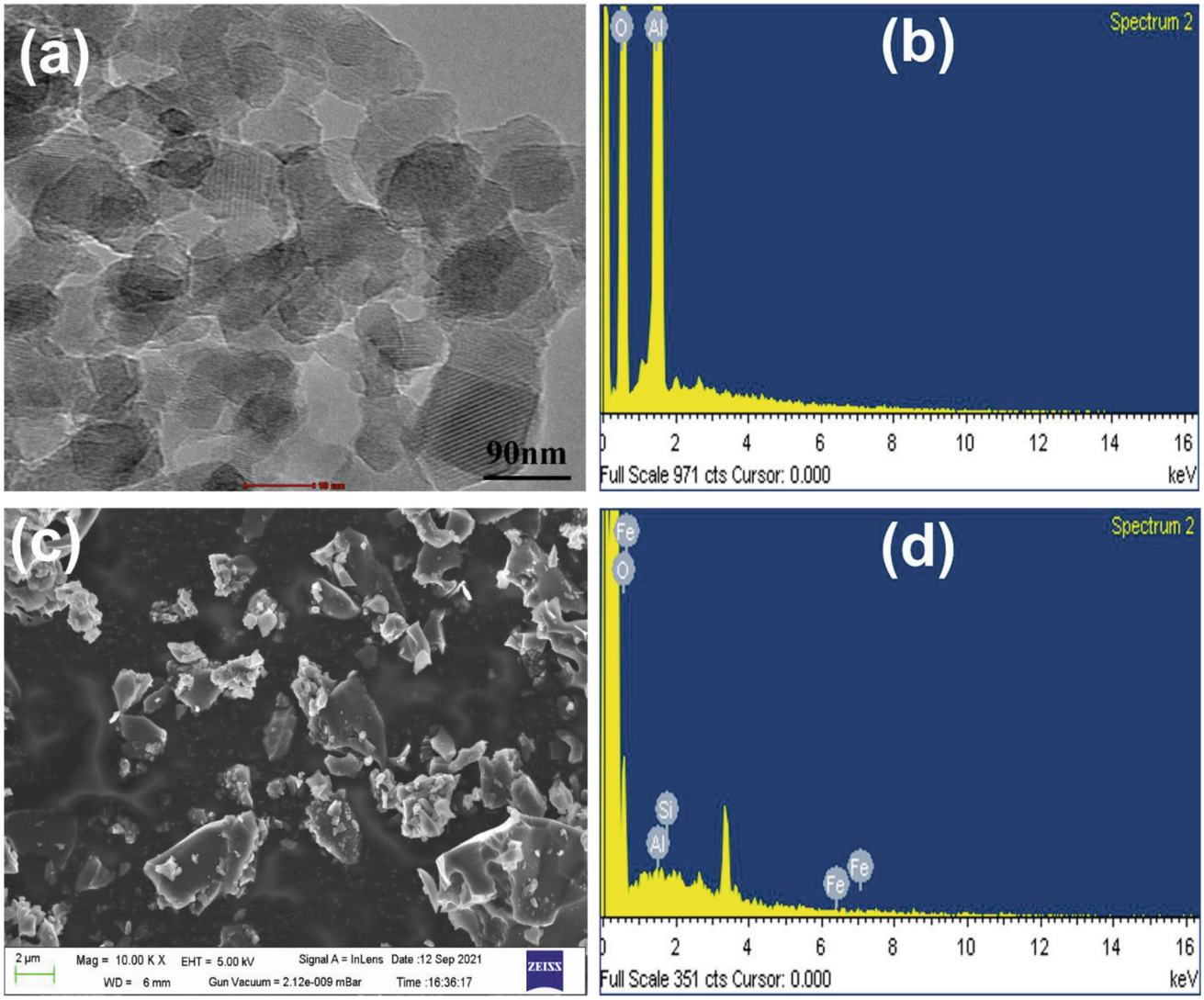

Fig. 1 (a), (b) TEM analysis of nano-alumina powder and (c), (d) SEM morphology of CSA particulates

composite for tensile response. The samples were prepared as per the ASTM-E8 standard, and the tensile test was done under room temperature at 100 kN. The elongation of specimens was tested in an additional test at a uniform strain rate of 0.25 mm/s. On each combination, four tests were done, and the average value of the ultimate tensile strength (UTS), elastic modulus (E), and ductility test findings was used in the computation. Using a 3-point bending machine, the damping behavior of as-cast composites was investigated (i) with varying loading frequencies (5-20 Hz) at constant strain (2.5-6 m) and (ii) with varying temperature in the range of 20 to 200 °C by using a constant heating rate and cooling rate of 5 and 8 °C/min, respectively. The damping behaviors were measured using a specimen with dimensions (60 mm × 10 mm × 2.5 mm). Each sample's damping capacity was calculated in terms of tan δ (Ref 30). The coefficient of thermal expansion (CTE) computed by the thermal–mechanical analyzer (TMA) of the fabricated hybrid composite specimens. A load of 0.05 N was applied to perform thermal expansion measurements in the temperature range of 25-275 °C under a nitrogen gas atmosphere. Corrosive solutions were made with 35 g of sodium chloride solution in 1 L of distilled water. The dimension of corrosion sample is (9 × 9 × 9) mm^3 in size, and it is metallographically polished to produce an electrode. In a 3.5% sodium chloride solution, the samples were evaluated for 5 h and 7 days. To find out the corrosion nature of the specimens, the linear potentiodynamic polarization (LPP) method was used (Ref 33). In the presence and absence of inhibitors, AA7075 and hybrid composite specimens were tested using anode and cathode polarization in sodium chloride solution. The corrosion potential, linear polarization resistance, and corrosion current were calculated.

3. Results and Discussion

3.1 Microstructural Study

Figure 3(a), (b), (c), and (d) depicts the microstructure of monolithic alloy AA7075 and Al_2O_3/CSA-based hybrid composite specimens. The homogeneous dispersion of reinforced particles in the matrix is depicted in Fig. 3(b), (c), and (d). The intermetallic phases like $MgZn_2$, Mg_2Si, $Al_{13}Fe_4$, and Al_2CuMg may be formed during the solidification of AA7075 (Ref

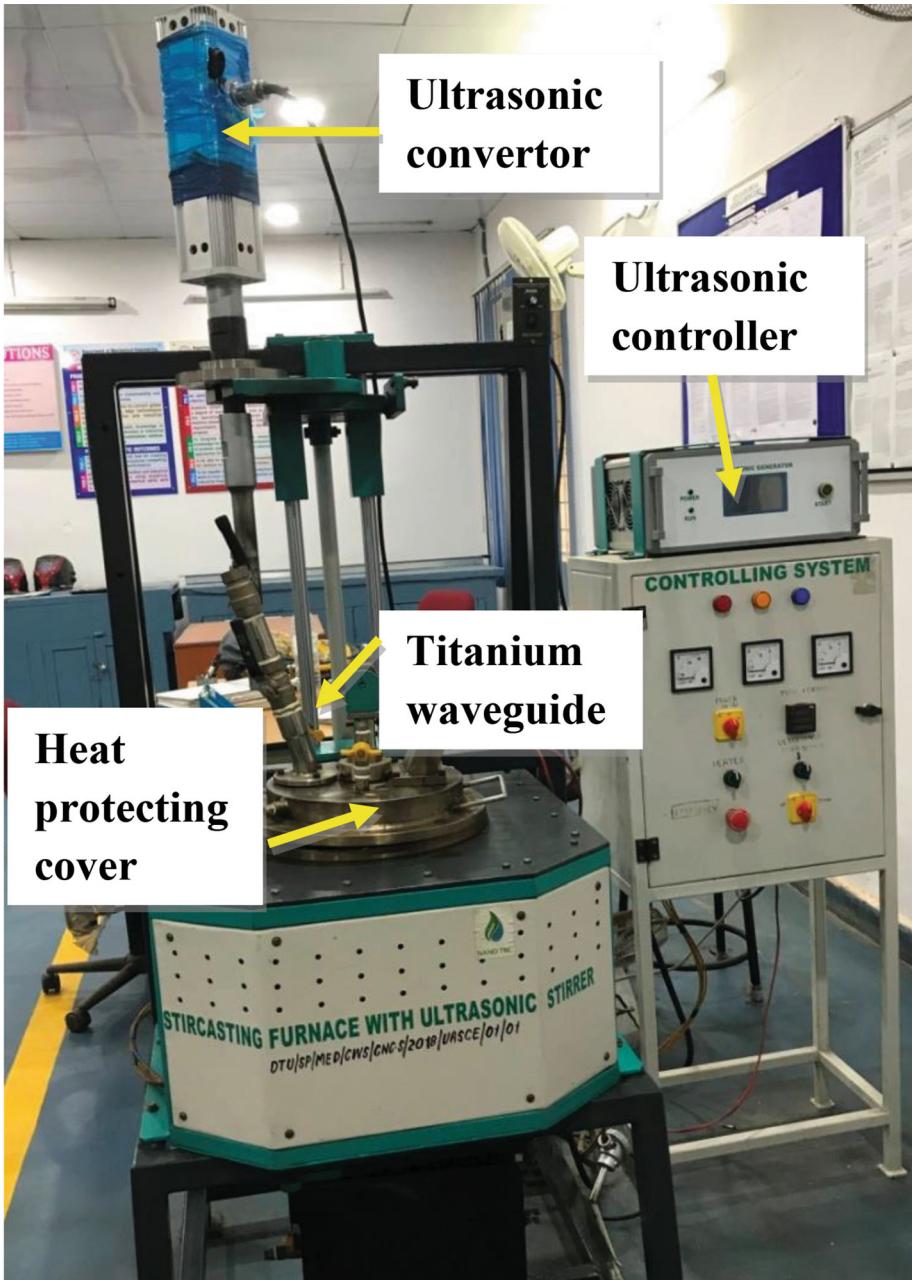

Fig. 2 Experimental setup of ultrasonic assisted stir-casting

9). Figure 3(a) depicts the homogeneous distributions of $MgZn_2$ phase with fine grain. The maximum level of porosity is clearly shown in Fig. 3(d). Grain refinements occur as the percentage of reinforcement increases, as shown in Fig. 3(c) and (d).

SEM imaging of AA7075 and developed composite specimens is shown in Fig. 4(a), (b), (c), and (d). The existence of nearly continuous intermetallic phases in the inter-dendritic zones is revealed by a SEM micrograph of the monolithic alloy (Fig. 4a). The critical analysis of the inter-dendritic region reveals the creation of at least two distinct types of intermetallic phases, one with bright contrast and high Zn content, and a different with shaded contrast and low Zn content but high Cu content. In the base alloy 7075, the formation of β-phase or secondary phase was discovered. However, this period was limited (Ref 35). As shown in Fig. 4(b), the AA7075 matrix had a homogeneous distribution of nano-sized Al_2O_3 and micro-sized CSA particles. Moreover, the fabricated composite has very few defects that recognize the interface of reinforced particulate and matrix. Furthermore, the SEM spectra in Fig. 4(c) and (d) confirmed that there is a slight indication of accumulation or clustering of Al_2O_3 and CSA particulates in the developed composite, which proved a sound casting process.

Figure 5(a), (b), (c), and (d) shows the EDS analysis of composites CSA2, CSA4, and CSA6, which confirm the presence of alloying elements and reinforcement (Al_2O_3 and CSA). The peaks of Al, Zn, Si, O_2, and Fe, etc., are detected in energy dispersive spectra, which are evidence of the presence

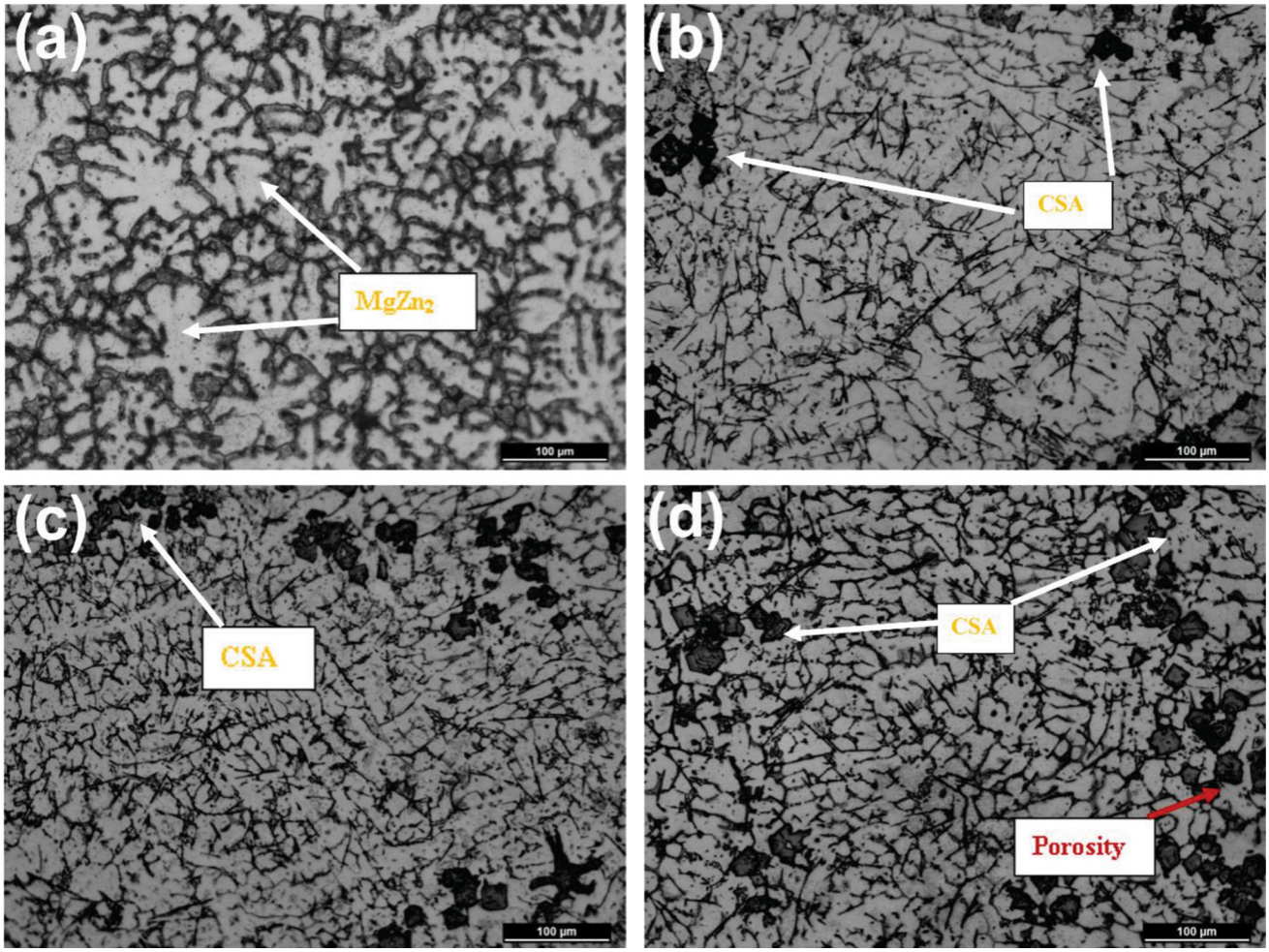

Fig. 3 Optical metallographic images of (a) AA7075, (b-d) composite specimen CSA2, CSA4 and CSA6, respectively

of Al_2O_3 and CSA. EDS spot analysis confirmed the absence of Al_4C_3 phases.

The nominal composition of the AA7075 matches the elemental analysis of the dendritic zone. Furthermore, the elemental mappings of the AA7075/Al_2O_3/CSA hybrid composites are shown in Fig. 6(a), (b), (c), (d), (e), (f), and (g), demonstrating the homogeneous dispersion of the reinforcing and alloying elements.

Figure 7 depicts the XRD patterns of both the monolithic alloy and the AA7075/Al_2O_3/CSA hybrid composite. $MgZn_2$, Al_2CuMg, and a slight fraction of Al_8Fe_2Si intermetallic phases are confirmed by XRD studies in the cast materials. During the casting of AA7075, $MgZn_2$, and Al_2CuMg intermetallic phases form naturally. For Al 7075 alloy, the Al_8Fe_2Si intermetallic phase is considered an inclusion, and precipitation of this phase in the base alloy has previously been reported (Ref 35). The existence of substantial amounts of SiO_2 and Al_2O_3 in the XRD profile is also evident in the occurrence of CSA and Al_2O_3 in the developed composite. There are no traces of secondary elements forming, indicating that the composites were successfully cast. It can only be achieved by carefully controlling the casting process parameters of reaction duration, reaction temperature, and melt stirring time.

3.2 Density and Porosity

The theoretical density was measured by the ROM, and the actual density was calculated by the Archimedes principle. The difference between theoretical density and actual density gives the porosity of the hybrid composites. The well-known densities of the AA7075 matrix, Al_2O_3, and CSA particles were 2.81, 3.97, and 1.65 g/cm^3, respectively. Figure 8 depicts the change in density with the weight percentage of reinforcements. The density of hybrid composites depends on the fractional arrangement of the number of atoms per unit volume. Moreover, the density-determining function is also how the atoms are arranged in the lattice (Ref 36). It is observed from the reading that the porosity level is between 2 and 4% for all hybrid composites. This is confirmation of the exposition of a lesser amount of porosity in the hybrid composites.

3.3 Tensile Response

When compared to the alloy, the UTS of the sample (CSA4) improved by 57.54%, but it was quite low for the composite (CSA6). The UTS improved from composite (CSA2) to composite (CSA6) before dropping to composite (CSA6). The summary of base alloy and hybrid composite of tensile test specimens is tabulated in Table 1. In composite (CSA2), the percentage elongation increases by 21.91%. The strength of the developed composite outperformed that of the AA7075 matrix

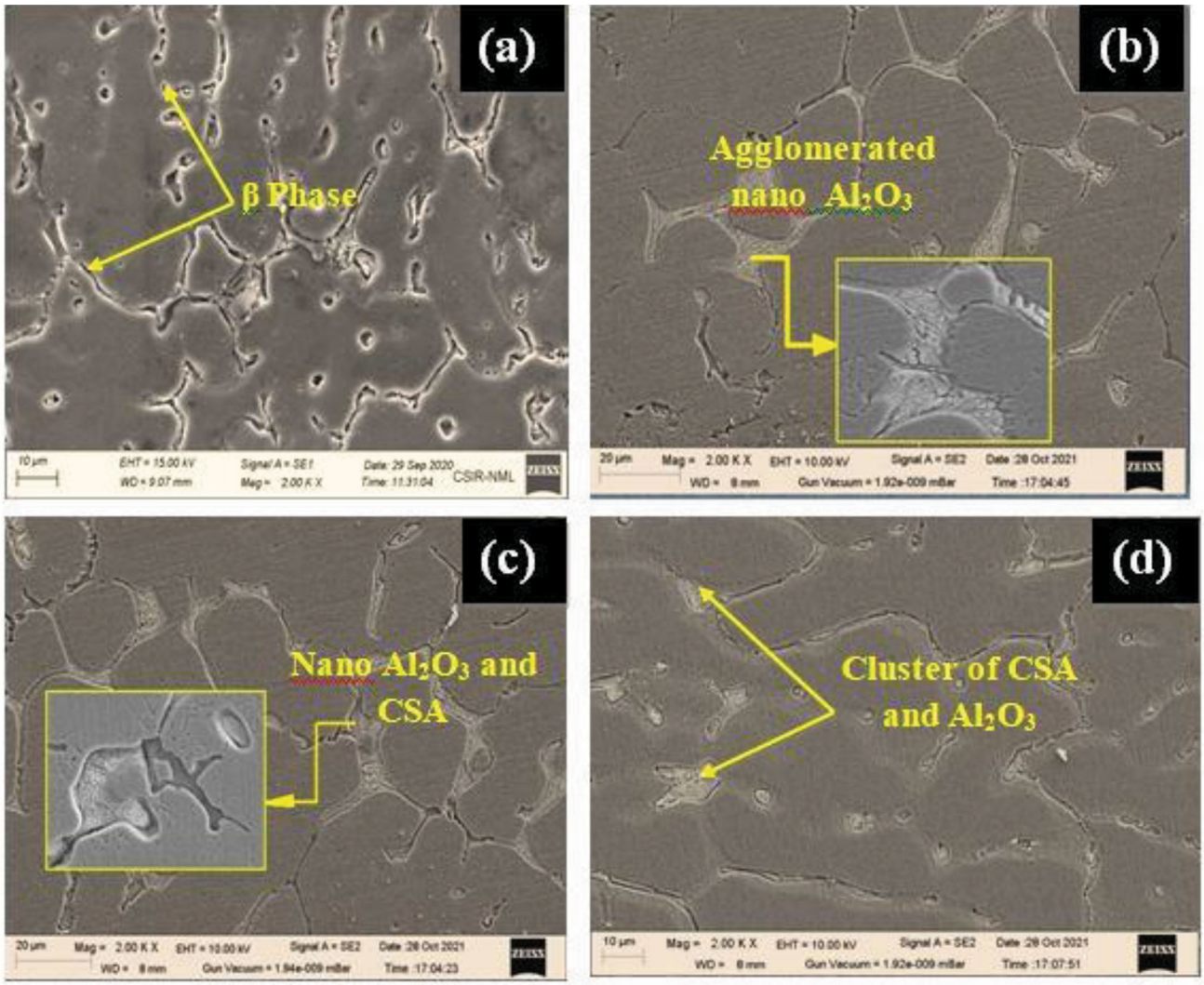

Fig. 4 SEM images of (a) AA7075, (b-d) hybrid composite specimen

due to the increased number of reinforcements. The engineering stress and strain behaviors of as-cast hybrid composites are shown in Fig. 9(a). The variation of UTS, E, and percentage elongation with a weight percentage of reinforcements is shown in Fig. 9(b). The formability, however, was hampered. Particulate agglomerations were detected in the sample (CSA6). This might explain why the tensile strength of that composite has decreased.

The elastic modulus (E) describes how stiff a material is inside the elastic limit, and the sample (CSA6) is stiffer inside the elastic region. And, because UTS indicates how much force a material can withstand before forming a neck, the composite specimen (CSA4) is the most load-bearing of the entire composite (Ref 37). The percentage elongation represents the ductility of a material; the hybrid composite (CSA2) is more ductile.

The elongations were seen to be reduced with a high content of reinforced particulate, reflecting that the ductility of hybrid composites is decreased. The homogeneously distributed reinforced particulates offer the resistance toward dislocation movement consequently the tensile strength of the hybrid composites was improved as reported by Orowan strengthening criteria (Ref 38). The higher grain fineness results in the additional ductility of the composite material. Due to the larger disarray of the lattice, grain refinement was used to resist dislocation movement, resulting in higher yield strength of the material (Ref 39). The higher the restriction, the more particles that can be present, and the particle size can be lowered to the nanoscale, as in this study. The UTS of the hybrid composite (CSA6) is improved up to 57.5% as compared to base AA7075. Kumar et al. reported similar results when combining CSA and ZrO_2 reinforcement particles to produce a hybrid composite by stir casting (Ref 40).

Figure 10 shows the fracture morphology of base alloys and hybrid composites at various $Al2O_3$ concentrations along with CSA particle concentrations. Numerous voids are equally dispersed across the fracture surface of the aluminum alloy AA7075, as shown in Fig. 10(a). The presence of deep voids suggests the fracture is ductile. The association of many voids inside the fracture surface specimens is reduced, as shown in Fig. 10(b), (c), and (d). In comparison with an unreinforced alloy, the voids are smaller. The grain refinement caused by the Al_2O_3 and CSA particles can be attributed to the smaller voids. The tensile fracture is caused by the crack initiation starting from voids and its consequent propagation, as indicated by the fracture morphology. As the crack propagates, it limits the

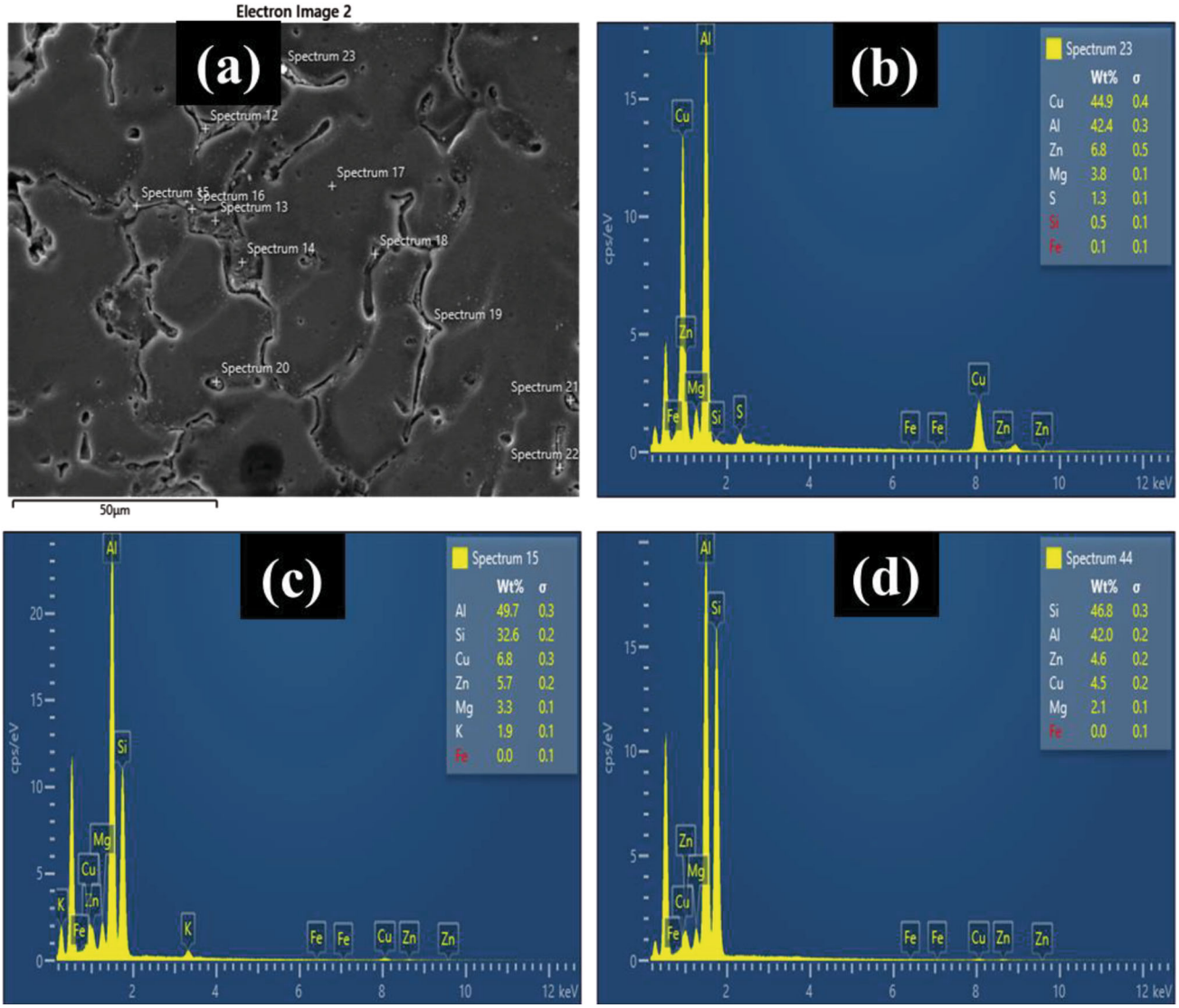

Fig. 5 (a-d) EDS analysis of AA7075/Al_2O_3/CSA hybrid composite

reinforcement by preventing the grain boundary from precipitating. The cleavage facets are formed as a result of the tensile force, which contributes to the specimens' failure (Ref 40-42). The presence of ductile shear bands on the fracture surface indicates that the composite retains ductility to a certain extent. On the fracture surface, a considerable number of fragmented CSA particles can also be seen, indicating excellent interfacial bonding.

3.4 Damping Behaviors

The damping capacity of the AA7075 was found to be 0.00539 at 1 Hz, indicating low damping. It was also seen that, as the frequency increased, the damping capability increased. Figure 11 depicts the fluctuation of damping capability with frequency for various weight percentages of reinforced particles. It can be seen from the graph that the damping capacity improves as the weight percentage of reinforcement increases. For every hybrid composite, a rising trend in damping capacity has been seen with rising frequency. Also, the damping capacity of the CSA2 sample shows similar tendencies to that of the base alloy, but with no substantial increase in damping capability. According to the literature, the damping capability of composites is higher than that of single-reinforced composites. A comparison of the damping capabilities of rice husk ash-reinforced Al composites (Ref 43) and hybrid composites was done to explain this trend. For each investigation of a different combination of reinforcement, hybrid composites have a higher damping capacity. A comparison of the damping capability of SiC reinforced aluminum composites (Ref 30) and AA7075/Al_2O_3/CSA hybrid composites was also done.

The ratio of the loss modulus to the storage modulus is called damping capacity. This relationship indicates that an increase in the value of the loss modulus or a reduction in the storage modulus will enhance the damping capacity. CSA addition reduces storage modulus, as shown in Fig. 11(b), especially for composites containing 4 and 6 weight percent of CSA. With increasing temperature, the storage modulus decreases as the bond strength decreases. The loss modulus increases with temperature as well as with Al_2O_3 and CSA additions. The temperature dependency of the elastic modulus explains the primary drop in storage modulus. The lower the

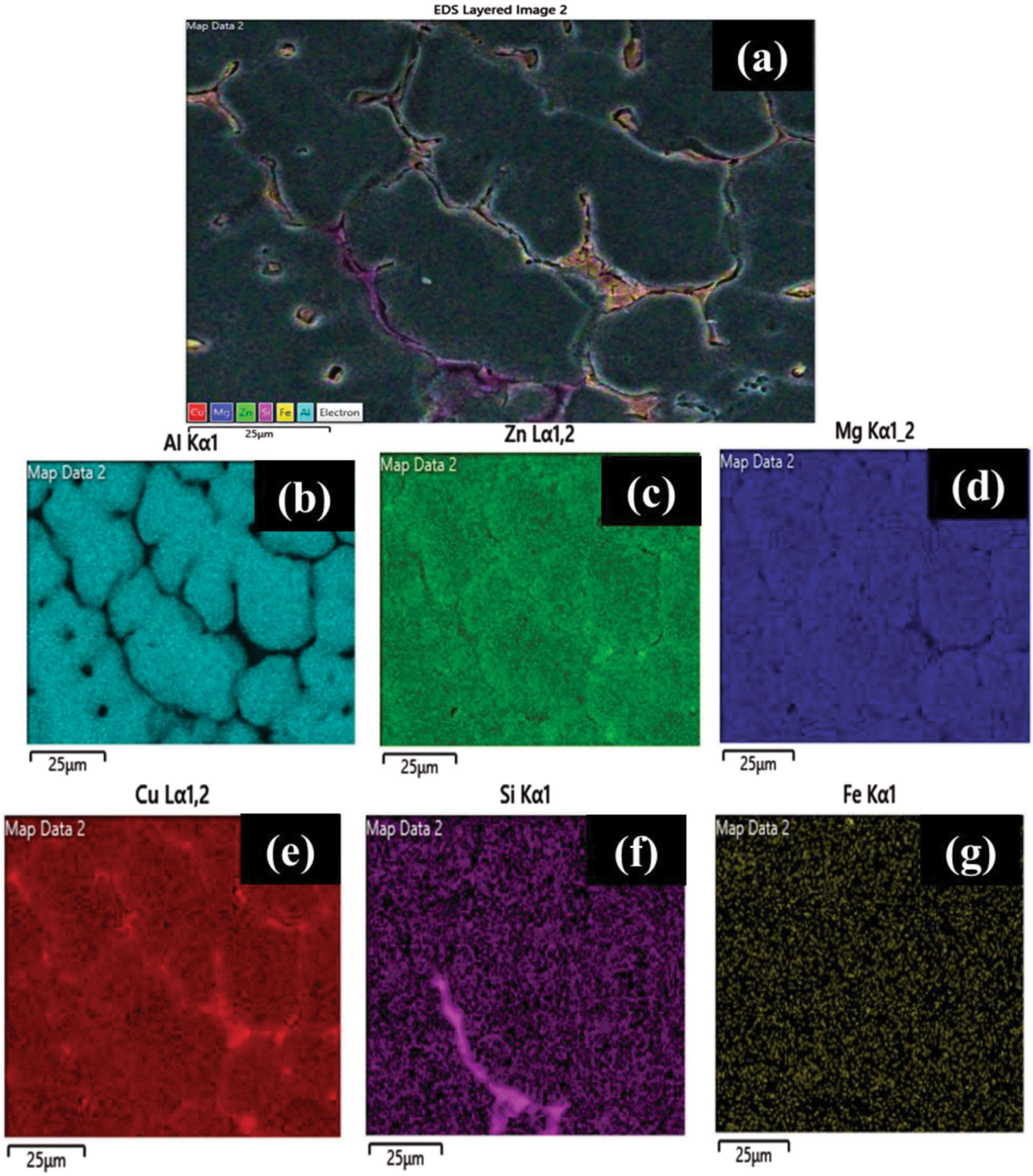

Fig. 6 (a-g) Elemental mapping of AA7075/Al_2O_3/CSA hybrid composite

frequency, the greater the reduction in storage modulus with temperature, as well as the transfer to elevated temperatures of the inflexion and confined utmost as frequency rises, indicating an Arrhenius-type relaxation rate behavior and indicating that the mechanical relaxation time decreases as temperature rises. At higher temperatures, the excitation frequency has a greater impact on the storage and loss moduli (Ref 44). Since the reinforcements are stiffer than the AA356 matrix and may promote precipitation hardening, the aluminum matrix composite is stiffer than the AA356 matrix. When compared to most of the materials investigated, the AMC's quick fall in storage modulus begins at a higher temperature, making it one of the most stable. Moreover, the precipitates and reinforcements pin the grain boundaries, and the normal relaxation peak in the matrix due to grain boundary segregation is censored in the AMC (Ref 45). Although adding 0.5 weight percent CNTs to AZ91D reduces its damping capacity at room temperature, adding 2 weight percent CNTs improves its performance.

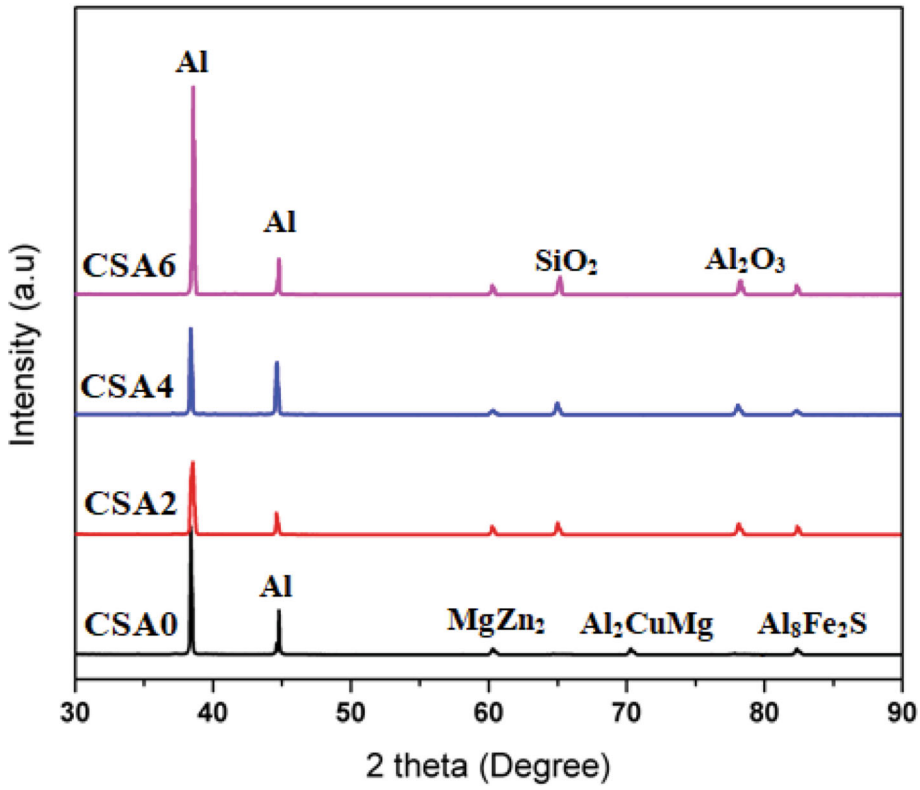

Fig. 7 XRD analysis of AA7075/Al_2O_3/CSA hybrid composite

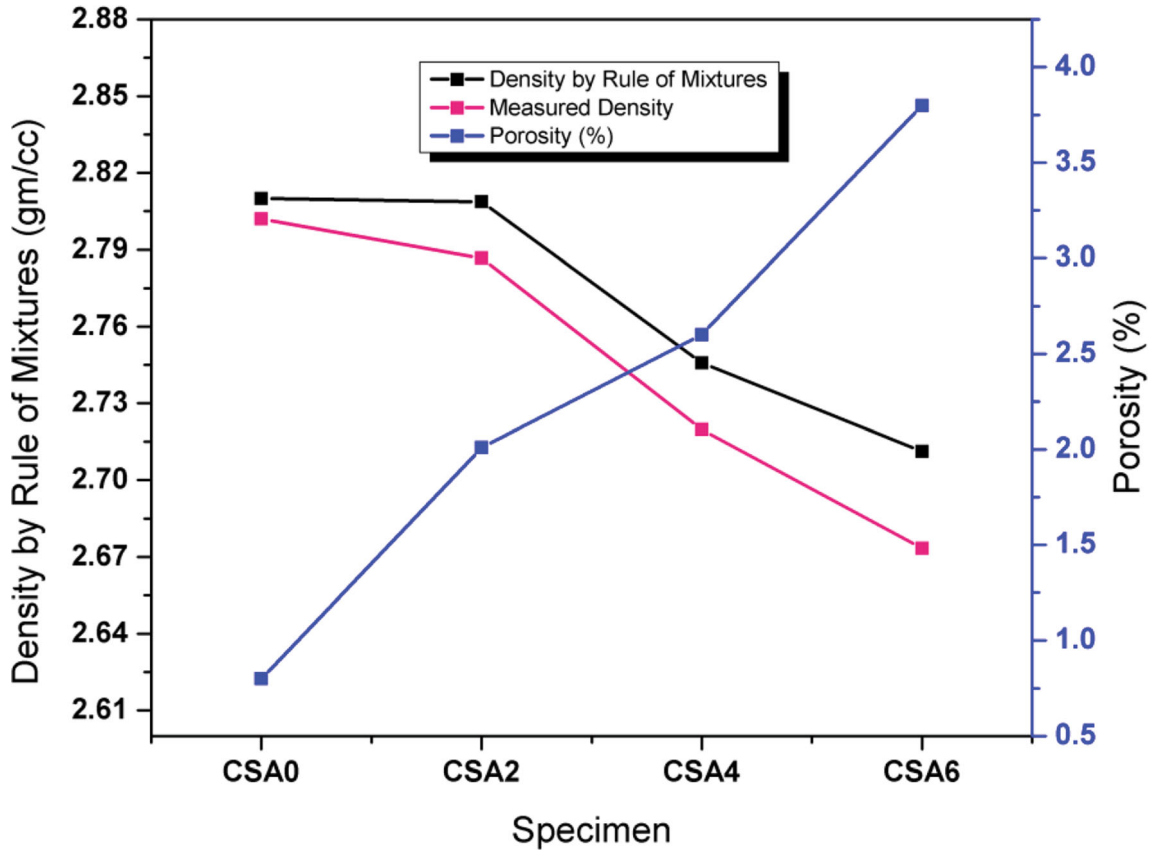

Fig. 8 Density variation of all specimens

Table 1 Summary of tensile response of base alloy and hybrid composite

Specimen	Elastic modulus, *E*, GPa	Ultimate tensile strength, UTS, MPa	Elongation, %
CSA0	56.42 ± 0.50	203 ± 6	21.67 ± 0.25
CSA2	67.06 ± 0.47	251 ± 8	26.42 ± 0.22
CSA4	75.85 ± 0.53	403 ± 9	30.31 ± 0.28
CSA6	72.31 ± 0.49	348 ± 5	23.21 ± 0.23

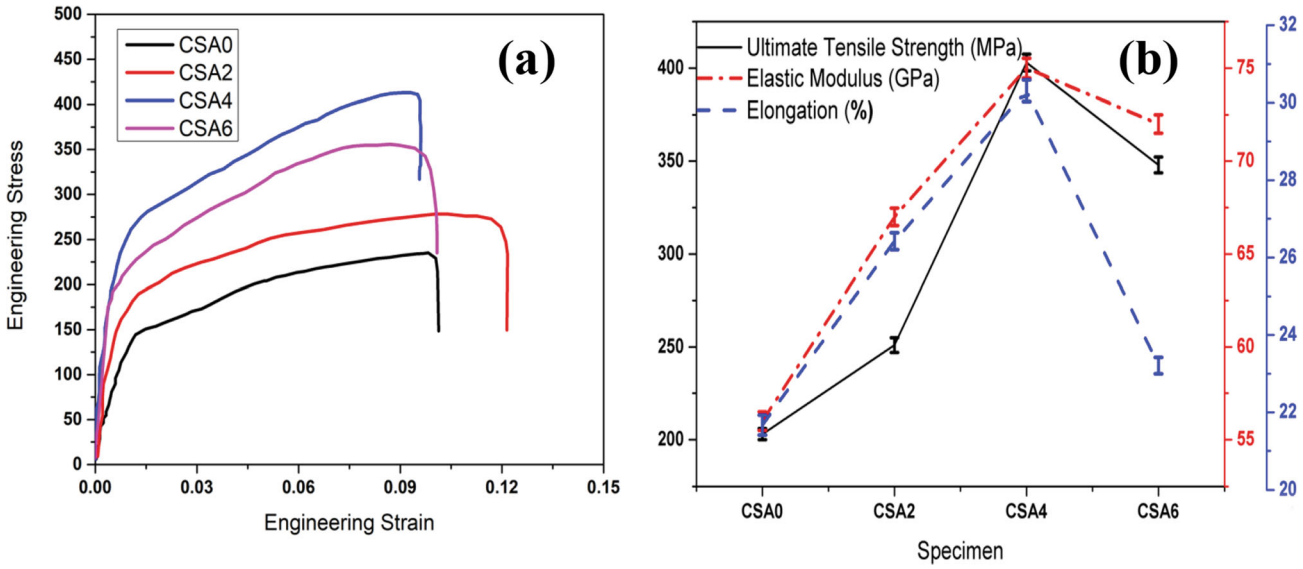

Fig. 9 (a) Engineering stress strain behaviors, (b) Variation of ultimate tensile strength, elastic modulus, percentage elongation of hybrid composites

Furthermore, regardless of the amount of CNT added, the high-temperature damping capacity improves when compared with the base aluminum alloy (Ref 46). Based on these results, it is possible to conclude that the addition of Al_2O_3 and CSA reduces the storage modulus while increasing the loss modulus. The combined action leads to damping enhancement.

3.5 Dislocation Density and Coefficient of Thermal Expansion

The strengthening of metal matrix composites has been explained by a variety of mechanisms and theories. Though the strength of a composite is not determined by a single mechanism, but by a combination of mechanisms. The strengthening mechanism in this study is mostly due to an improved dislocation density caused by a temperature difference between the reinforcement and matrix. MMCs are characterized by a huge difference in the CTE of the reinforcement and the matrix ($CTE_{AA7075} = 23.6 \times 10^{-6}$/°C, $CTE_{alumina} = 10.3 \times 10^{-6}$/°C and $CTE_{CSA} = 0.12.8 \times 10^{-6}$/°C). Thermal stresses are generated within the matrix as a result of even minor temperature changes. These stresses may be reduced in part by dislocation generation near the interfaces due to work hardening that causes dislocations to occur during the cooling of a composite, which are immobilized at the particle–matrix interface and have a high hardness that diminishes as distance from the interface increases. As a result, the generated dislocation density may be relatively significant at the interface.

The thermal expansion coefficient of composites is well known to be dependent on a number of material parameters, including composition, reinforced particulate volume fraction and distribution, matrix microstructure, in addition to residual stresses caused by CTE mismatch, volume fraction, interface strength, and porosity (Ref 47). Due to these parameters, the CTE of hybrid composites is difficult to estimate. Nevertheless, there are some analytical methods for predicting the CTE of hybrid composites, including simple mixture rules and thermo-elastic energy principles, for example the Turner and Kerner models (Ref 48).

According to the foregoing calculations, as the proportion of reinforced particles raises, the dislocation density increases from 14.2×10^{11} to 25.7×10^{11} m^3/Kg. The dislocation densities for the developed composites were computed using Burgers vector assumption of 0.32 nm for aluminum. Figure 12(a) and (b) depicts the variation of thermal expansion coefficient of each sample with a varying weight percentage of Al_2O_3 and CSA and in the ranges of temperature from 25 to 200 °C, respectively. The enhancement in CSA particle content along with an equal proportion of alumina tends to decrease the CTE of a developed composite.

The hybrid composites have a lower CTE value as compared to base AA7075. Al_2O_3 and CSA are ceramic materials with low values of CTE. When these reinforcements are incorporated into the base alloy matrix, it is expected that the values of CTE in hybrid composites will decrease. Aluminum alloys' high CTE value causes dimensional instability as temperature rises. This makes it unsuitable for end applications like

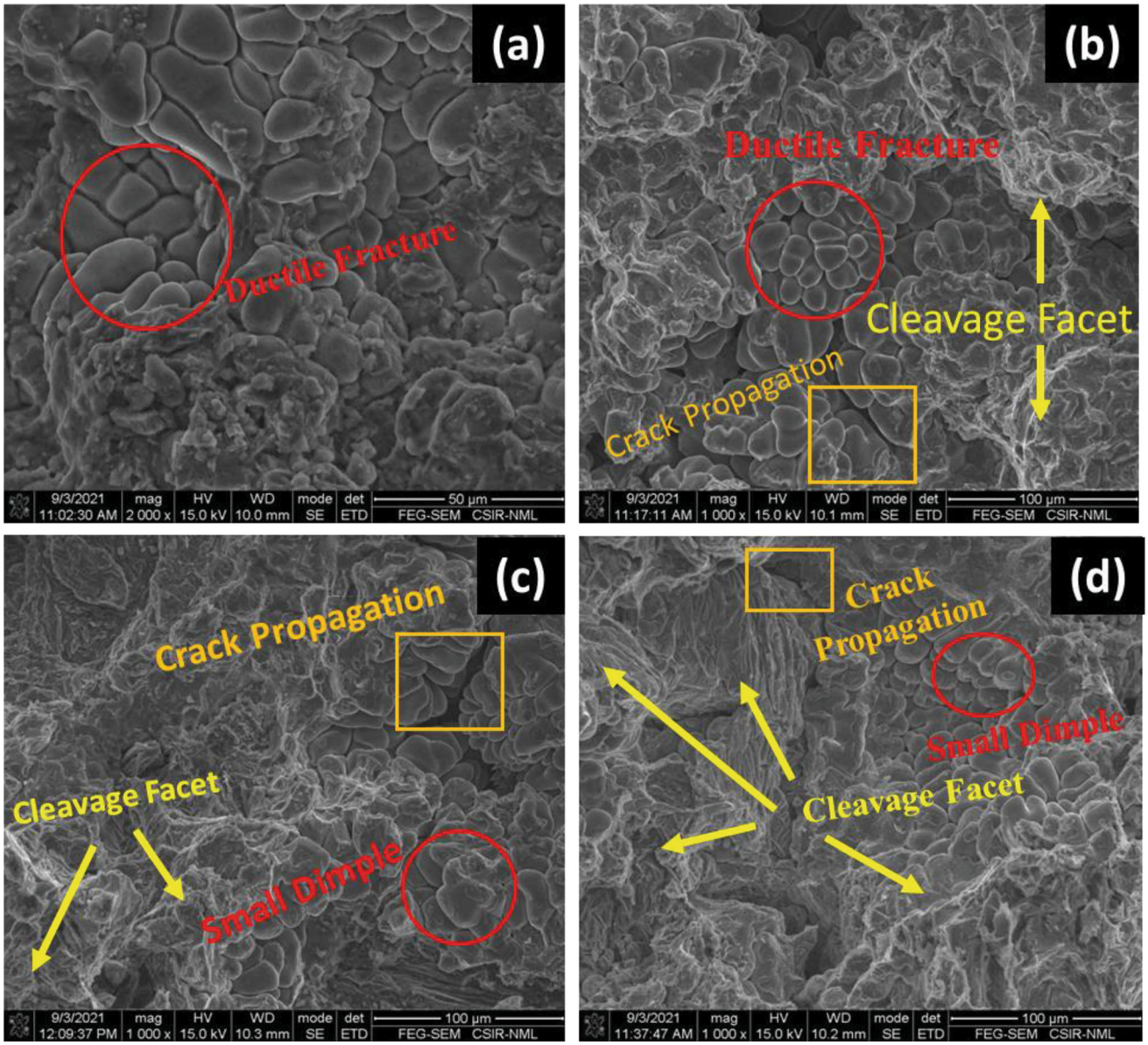

Fig. 10 Fracture morphology of AA7075/Al_2O_3/CSA hybrid composite: (a) CSA0 sample, (b) CSA2 sample, (c) CSA4 sample, and (d) CSA6 sample

electrical and electronic packaging. However, by combining reinforcements with AA7075, one can customize the CTE to meet the needs of various industry applications. Ten readings were undertaken for each sample. The result shows the efficacy of hybrid composites is higher and more dimensionally stable than base alloys in relation to changes in temperature (Ref 49). The coefficient of thermal expansion of hybrid composites is influenced by the particle size, the thermal expansion mismatch between matrix and reinforcement, and interfacial reactions.

3.6 Corrosion Behavior (Polarization Curves of Potentiodynamic Analysis)

Figure 13(a) shows the Tafels plots of the polarization curve for AA7075 monolithic alloy and hybrid composites. To investigate the corrosion dynamic layer on the projected surface, the specimens are immersed in a 3.5% sodium solution. With the inclusion of alumina and CSA particles, the potential became further negative, along with the current density dropping, as seen in Fig. 13(a). As a result, it was demonstrated that adding alumina and CSA particles to the AA7075 matrix increased corrosion resistance. The corrosion behavior was investigated by Kenneth and Olubambi (Ref 20) for an Al-Mg-Si matrix composite and it was found that rate of corrosion decreases with addition of rice husk ash and alumina in a 3.5% NaCl solution. The corrosion characteristics of the composites allegedly declined as the weight percentage of rice husk ash increased, owing to rice husk ash's lower density (0.3 g/cm^3). The potentiodynamic polarization curve depicts a decrease in current with an increase in potential in the negative direction. Loto and Babalola (Ref 50) reported similar results and well established with the explanation of reporting the corrosion behavior of Al1070 silicon carbide matrix composites.

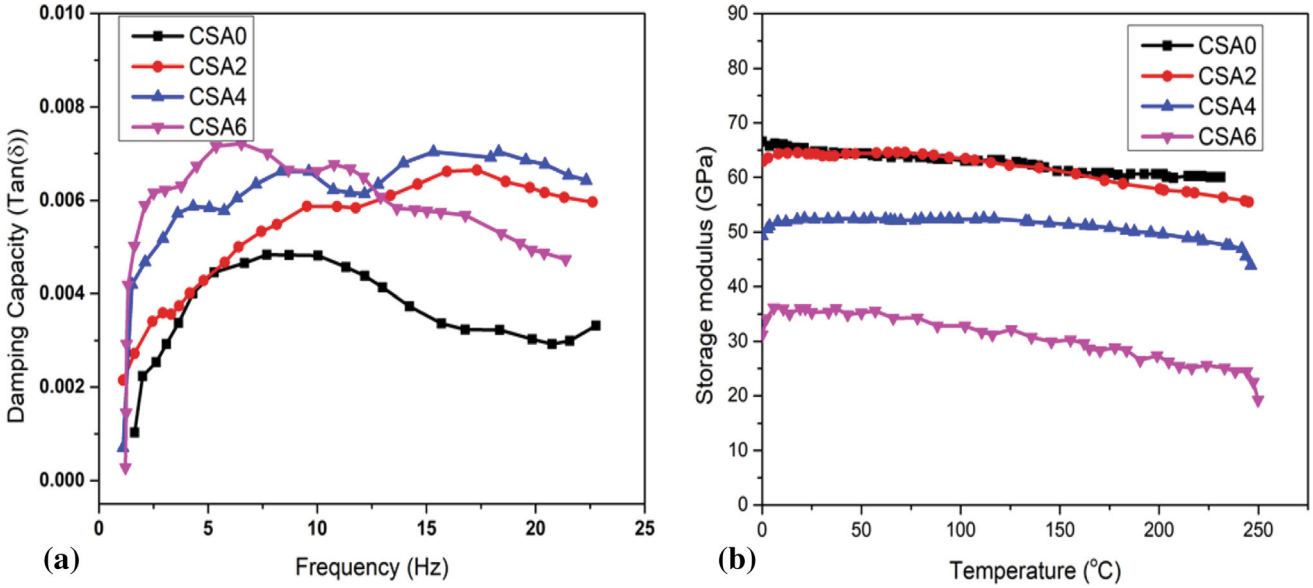

Fig. 11 (a) Variation of damping capacity with frequency at room temperature and (b) variation of storage modulus with temperature of each sample

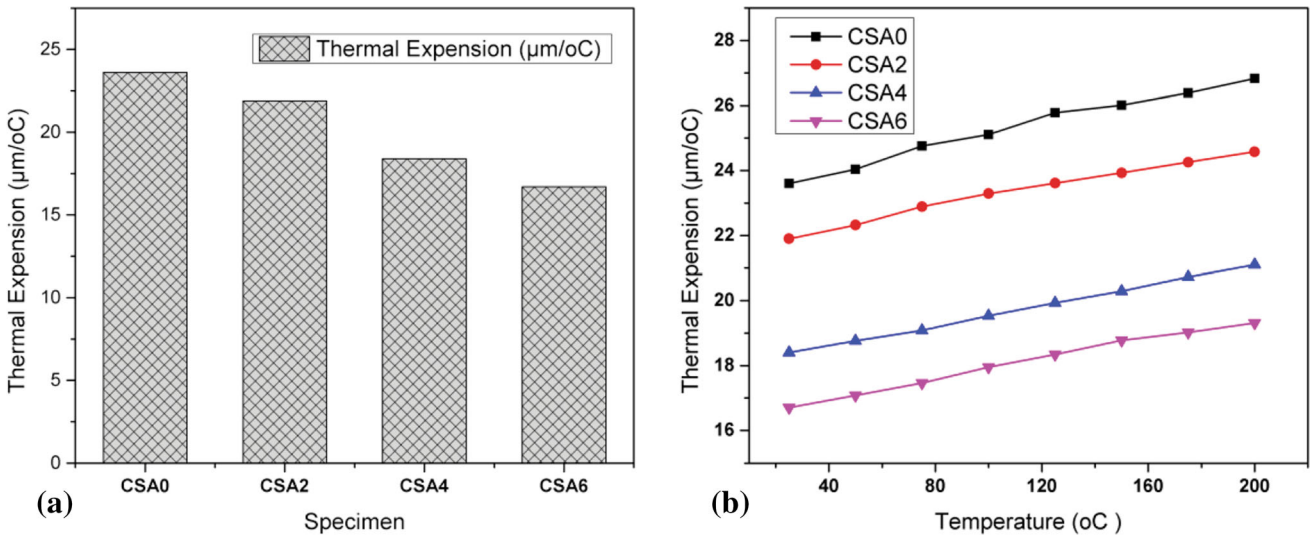

Fig. 12 (a) Variation of thermal Expansion coefficient of each sample at room temperature, (b) Thermal Expansion coefficient of each sample with varying temperature

The current density of corrosion dropped from 1.54 to 1.51 mA/cm^2 when Tafel polarization curves were plotted, confirming that adding 4 wt.% CSA along with 0.5 wt.% Al_2O_3 to AA7075 hybrid composite improves its corrosion resistance rate. There is a slight decrease in corrosion resistance for 6 wt.% CSA composites, which is seen in Fig. 13(a).

As shown in Fig. 13(b), inferior corrosion rates are related to the phase of intermetallic and the amorphous nature of reinforced composites. All cast samples have a semi-circular capacitive arc, as seen in Nyquist plots; however, there are variances in the diameter of the semi-circular arc between base alloys and hybrid composites with various and the same exposure times, respectively. The diameter of the semi-circular arc is known to reflect the corrosion resistance of the composites, with a bigger diameter suggesting stronger corrosion resistance, as reported by I. Oztürk et al. (Ref 51). The reinforced composite degradation rate reduces as the amount of CSA in the composite increases. Y. Ma et al. investigated whether the corrosion of the test alloys deteriorated first and then improved to some degree when the exposure period in the sodium chloride solution was increased. The production of $Al(OH)_3/Al_2O_3$ and corrosive layers on the specimen surfaces may be ascribed to the oxide layer lying on the specimen surfaces, the deterioration of the oxide layer for the duration of exposure in the sodium chloride solution, and the formation of Al $(OH)_3/Al_2O_3$ and corrosive layers (Ref 52). The rate of corrosion resistance of AA7075 alloy was considerably boosted by the accumulation of various weight percent (2, 4, and 6) of CSA along with 0.5 wt.% of Al_2O_3 particles, as shown by Tafels plots. The corrosion rates of the as-cast specimens after 30 days of immersion in the 3.5 weight percentage sodium chloride solution are shown in Fig. 13(c). Samuel et al. studied

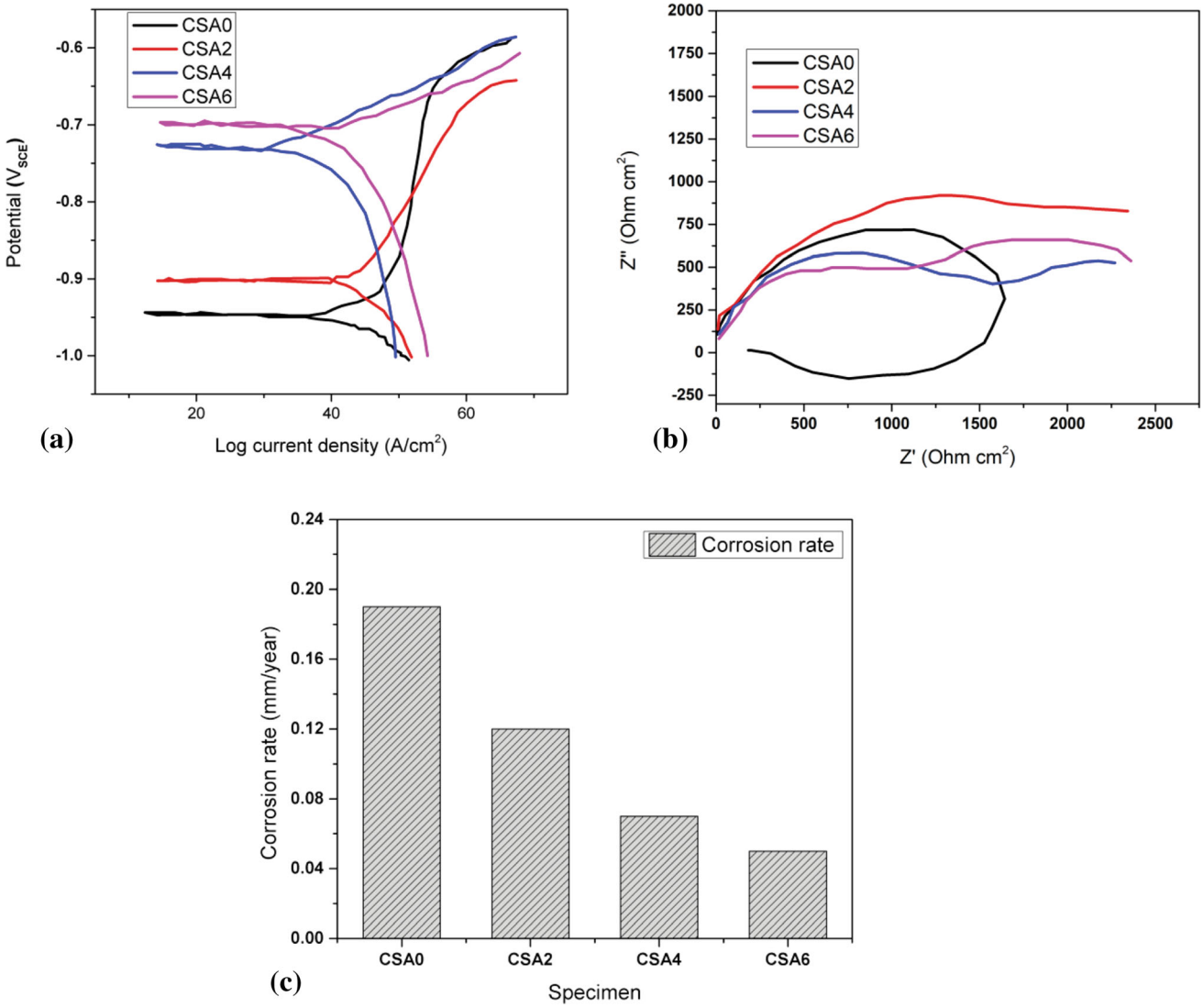

Fig. 13 (a) Potentiodynamic polarization curve, (b) Nyquist (Z′ vs. Z″) of electrochemical spectrographs and (c) Comparison of corrosion rate of as-cast specimens

corrosion behaviors of Al based composite and reported similar findings, recommending that corrosion studies of aluminum matrix composites in warm and cold conditions (except ambient temperature) be studied. This will expand their use as ship hauls, heat exchangers, and sacrificial anodes for underground pipeline protection in settings with varying ion concentrations (Ref 53). SEM and EDS analysis were used to analyze the surface morphology of AA7075 Al_2O_3/CSA hybrid composite MMC after corrosion studies. SEM micrographs and EDS analyses of corroded samples are shown in Fig. 14(a), (b), (c), and (d). The deterioration of aluminum alloys with (Al_2O_3 + CSA) is clearly caused by a regular attack in a 3.5 weight percentage of sodium chloride solution. After corrosion testing, the AA7075 sample shows pits, minor cracks, and deep precipitates, all of which indicate simultaneous metal loss on the sample surface. Because the AA7075 contains no reinforcing particles, the aluminum monolithic alloy becomes weaker, making it more susceptible to crack and pit formation. The particles of Al_2O_3 and CSA in MMCs stopped a 3.5% NaCl solution from attacking them. As shown in Fig. 14(b), (c), and (d), reinforcement in the presence of particulates improves corrosion resistance in composite specimens. The protective layer of corrosion is created on the AA7075/Al_2O_3/CSA hybrid composite surface, according to the SEM pictures.

4. Conclusions

The current study proposes the development of a hybrid MMC with nano-sized Al_2O_3 and micro-sized CSA as reinforcing particles. The ultrasonic assisted stir-casting process was used to fabricate the aforementioned composite. Based on the analysis of mechanical and thermal properties and the microstructural characterization of the cast hybrid MMC samples, the following conclusions have been made:

- Ultrasonic assisted casting played a key role in the uniform distribution of the nano-Al_2O_3, and the sample CSA4 had the maximum tensile strength, with a 59.5% as compared to AA7075 due to lesser amount of porosity. Whereas, the maximum porosity of around 3.8% was

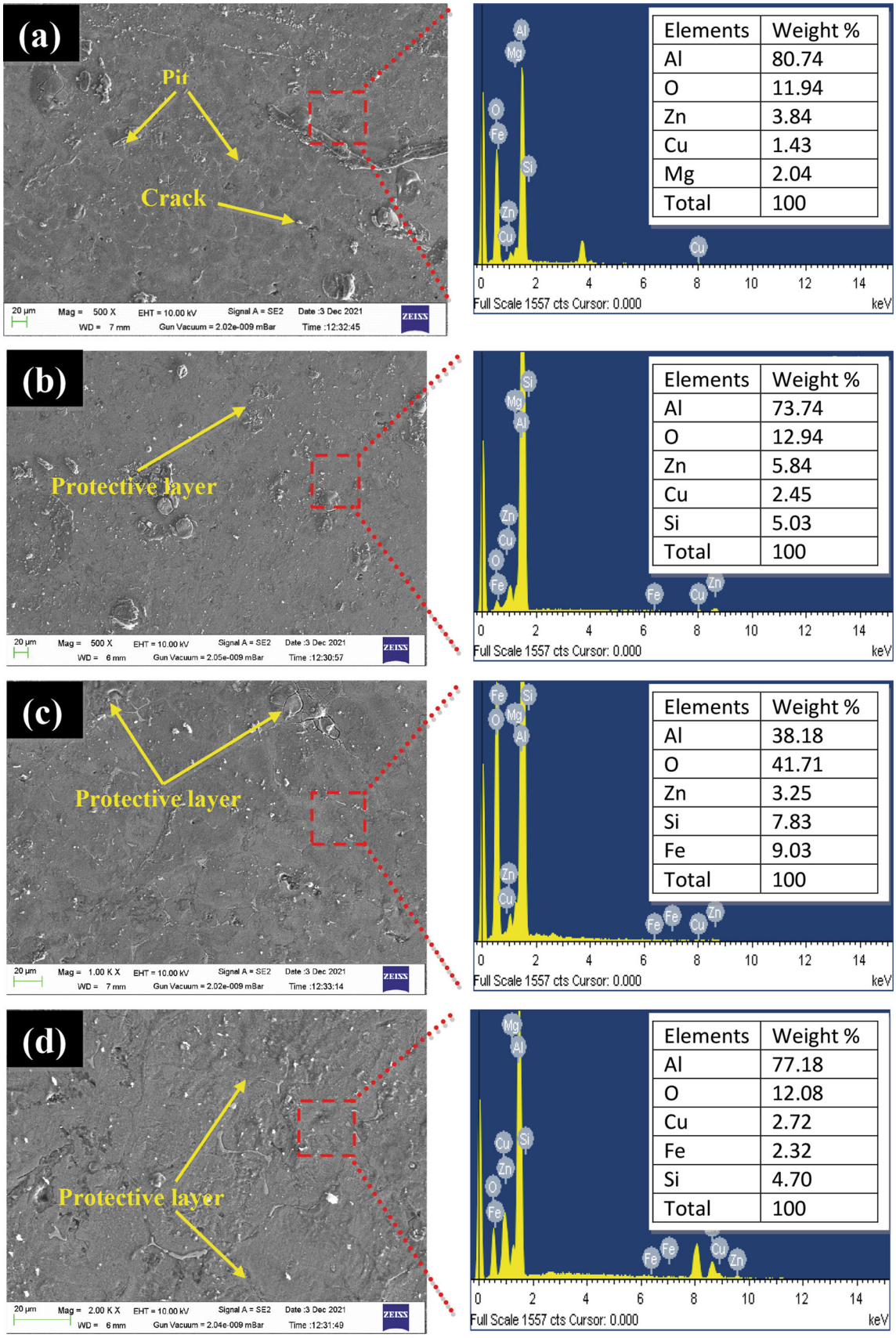

Fig. 14 SEM and corresponding EDS analysis of (a) AA7075, (b-d) hybrid composite specimen

found for the composite sample CSA6, which contained 6% by weight of CSA particles.

- The frequency-dependent damping capacity of stir-cast composites significantly increased with the variation of weight percentage of CSA. Sample CSA6 exhibited about 2 times better damping at 5 Hz, as compared to the base alloy. The significant improvement in damping behaviors is because of grain refinement along with homogenous dispersion of Al_2O_3 and CSA.
- The dislocation density increases as the reinforcing content increases, and it has an inverse relationship with CTE values.
- The inclusion of Al_2O_3 and CSA particles in AA7075 reduced the corrosion rate when exposed to potentiodynamic polarization. Hybrid composite CSA6 possesses better corrosion resistance. From Nyquist plot, it was also confirmed that the addition of Al_2O_3 and CSA particles increased the corrosion resistance of the hybrid composite.

Acknowledgments

The authors would like to appreciate the CSIR-National Metallurgical Laboratory, Jamshedpur, India for providing the facilities for material characterizations. The authors would also like to thank Delhi Technological University (DTU), Delhi, India for providing the testing facilities.

Conflict of interest

The authors declare that they have no conflict of interest.

Ethics Approval and Consent to Participate

Not applicable.

References

1. P. Samal, P.R. Vundavilli, A. Meher and M.M. Mahapatra, Recent Progress in Aluminum Metal Matrix Composites: A Review on Processing, Mechanical and Wear Properties, *J. Manuf. Process.*, 2020, **59**, p 131–152.
2. A.K. Singh, S. Soni and R.S. Rana, A Critical Review on Synthesis of Aluminum Metallic Composites through Stir Casting: Challenges and Opportunities, *Adv. Eng. Mater.*, 2020, **22**(10), p 2000322.
3. P.L. Kumar, A. Lombardi, G. Byczynski, S.V.S. NarayanaMurty, B.S. Murty and L. Bichler, Recent Advances in Aluminium Matrix Composites Reinforced with Graphene-Based Nanomaterial: A Critical Review, *Prog. Mater. Sci.*, 2022, **128**, p 100948.
4. S. Suresh, G. HarinathGowd and M.L.S. Kumar, Mechanical and Wear Behavior of Al 7075/Al_2O_3/SiC/mg Metal Matrix Nanocomposite by Liquid State Process, *Adv. Compos. Hybrid Mater.*, 2019, **2**(3), p 530–539.
5. X. Yu, H. Bakhtiari, J. Zhou, M.O. Bidgoli and K. Asemi, Investigating the Effect of Reinforcing Particles Size and Content on Tensile and Fatigue Properties of Heat-Treated Al7075-SiC Composites Fabricated by the Stir Casting Method, *JOM*, 2022, **74**(5), p 1859–1869.
6. T.P. Reddy, S. Jaya Kishore, P. CharanTheja and P. Punna Rao, Development and Wear Behavior Investigation on Aluminum-7075/B4C/Fly Ash Metal Matrix Composites, *Adv. Compos. Hybrid Mater.*, 2020, **3**(2), p 255–265.
7. A. Baradeswaran and A. ElayaPerumal, Study on Mechanical and Wear Properties of Al 7075/Al_2O_3/Graphite Hybrid Composites, *Compos. Part B Eng.*, 2014, **56**, p 464–471.
8. S.V. Prasad and R. Asthana, Aluminum Metal-Matrix Composites for Automotive Applications: Tribological Considerations, *Tribol. Lett.*, 2004, **17**(3), p 445–453.
9. R. Manikandan and T.V. Arjunan, Studies on Micro Structural Characteristics, Mechanical and Tribological Behaviours of Boron Carbide and Cow Dung Ash Reinforced Aluminium (Al 7075) Hybrid Metal Matrix Composite, *Compos. B Eng.*, 2020, **183**, p 107668.
10. P. Saini and P.K. Singh, Physical, Morphological, and Mechanical Characterization of Al-4032/GMP Composite Fabricated through Stir Casting, *JOM*, 2022, **74**(4), p 1340–1349.
11. C. Kannan and R. Ramanujam, Comparative Study on the Mechanical and Microstructural Characterisation of AA 7075 Nano and Hybrid Nanocomposites Produced by Stir and Squeeze Casting, *J. Adv. Res.*, 2017, **8**(4), p 309–319.
12. S. Liu, Y. Wang, T. Muthuramalingam and G. Anbuchezhiyan, Effect of B4C and MOS_2 Reinforcement on Micro Structure and Wear Properties of Aluminum Hybrid Composite for Automotive Applications, *Compos. Part B Eng.*, 2019, **176**, p 107329.
13. A. Ramanathan, P.K. Krishnan and R. Muraliraja, A Review on the Production of Metal Matrix Composites through Stir Casting–Furnace Design, Properties, Challenges, and Research Opportunities, *J. Manuf. Process.*, 2019, **42**, p 213–245.
14. V.S. Aigbodion, S.B. Hassan, E.T. Dauda and R.A. Mohammed, The Development of Mathematical Model for the Prediction of Ageing Behaviour for Al-Cu-Mg/Bagasse Ash Particulate Composites, *J. Miner. Mater. Charact. Eng.*, 2010, **9**(10), p 907–917.
15. A. Kumar, R.C. Singh and R. Chaudhary, Investigation of Nano-Al_2O_3 and Micro-coconut Shell Ash (CSA) Reinforced AA7075 Hybrid Metal–Matrix Composite using Two-Stage Stir Casting, *Arab. J. Sci. Eng.*, 2022, **47**, p 15559–15573.
16. O.B. Fatile, J.I. Akinruli and A.A. Amori, Microstructure and Mechanical Behaviour of Stir-Cast Al-Mg-Sl Alloy Matrix Hybrid Composite Reinforced with Corn Cob Ash and Silicon Carbide, *Int. J. Eng. Technol. Innov.*, 2014, **4**(4), p 251.
17. I.M.R. Najjar, A.M. Sadoun, M.A. Elaziz, A.W. Abdallah, A. Fathy and A.H. Elsheikh, Predicting Kerf Quality Characteristics in Laser Cutting of Basalt Fibers Reinforced Polymer Composites using Neural Network and Chimp Optimization, *Alex. Eng. J.*, 2022, **61**(12), p 11005–11018.
18. R.S.S. Raju, M.K. Panigrahi, R.I. Ganguly and G. Srinivasa Rao, Tribological Behaviour of Al-1100-Coconut Shell Ash (CSA) Composite at Elevated Temperature, *Tribol. Int.*, 2019, **129**, p 55–66.
19. J.E. Oghenevweta, V.S. Aigbodion, G.B. Nyior and F. Asuke, Mechanical Properties and Microstructural Analysis of Al-Si-Mg/Carbonized Maize Stalk Waste Particulate Composites, *J. King Saud Univ. Eng. Sci.*, 2016, **28**(2), p 222–229.
20. K.K. Alaneme and P.A. Olubambi, Corrosion and Wear Behaviour of Rice Husk Ash—Alumina Reinforced Al-Mg-Si Alloy Matrix Hybrid Composites, *J. Mater. Res. Technol.*, 2013, **2**(2), p 188–194.
21. R. Siva Sankara Raju, M.K. Panigrahi, R.I. Ganguly and G. Srinivasa Rao, Investigation of Tribological Behavior of a Novel Hybrid Composite Prepared with Al-Coconut Shell Ash Mixed with Graphite, *Metall. Mater. Trans. A*, 2017, **48**(8), p 3892–3903.
22. S.C. Tjong, Recent Progress in the Development and Properties of Novel Metal Matrix Nanocomposites Reinforced with Carbon Nanotubes and Graphenenanosheets, *Mater. Sci. Eng. R. Rep.*, 2013, **74**(10), p 281–350.
23. P. Madhukar, N. Selvaraj, C.S.P. Rao and G.B. Veeresh Kumar, Fabrication and Characterization Two Step Stir Casting with Ultrasonic Assisted Novel AA7150-hBN Nanocomposites, *J. Alloys Compd.*, 2020, **815**, p 152464.
24. A.M. Sadoun, I.M.R. Najjar, M.S. Abd-Elwahed and A. Meselhy, Experimental Study on Properties of Al–Al_2O_3 Nanocomposite Hybridized by Graphene Nanosheets, *J. Market. Res.*, 2020, **9**(6), p 14708–14717.
25. H. Su, W. Gao, Z. Feng and Z. Lu, Processing, Microstructure and Tensile Properties of Nano-sized Al_2O_3 Particle Reinforced Aluminum Matrix Composites, *Mater. Des. (1980–2015)*, 2012, **36**, p 590–596.
26. ThellaBabu Rao, Microstructural, Mechanical, and Wear Properties Characterization and Strengthening Mechanisms of Al7075/SiCnp Composites Processed through Ultrasonic Cavitation Assisted Stir-Casting, *Mater. Sci. Eng. A*, 2021, **805**, p 140553.
27. O.B. Bembalge and S.K. Panigrahi, Development and Strengthening Mechanisms of Bulk Ultrafine Grained AA6063/SiC Composite Sheets

with Varying Reinforcement Size Ranging from Nano to Micro Domain, *J. Alloys Compd.*, 2018, **766**, p 355–372.
28. X. Meng, D. Zhang, W. Zhang, C. Qiu and D. Chen, Achieving High Damping Capacity and Strength Simultaneously in a High-Zinc Aluminum Alloy via Melt Spinning and Hot Extrusion, *Mater. Sci. Eng. A*, 2022, **833**, p 142376.
29. S. Madeira, O. Carvalho, V.H. Carneiro, D. Soares, F.S. Silva and G. Miranda, Damping Capacity and Dynamic Modulus of Hot Pressed AlSi Composites Reinforced with Different SiC Particle Sized, *Compos. B Eng.*, 2016, **90**, p 399–405.
30. R. Bauri and M.K. Surappa, Damping Behavior of Al-Li-SiCp Composites Processed by Stir Casting Technique, *Metall. Mater. Trans. A*, 2005, **36**(3), p 667–673.
31. W.A. Uju and I.N.A. Oguocha, A Study of Thermal Expansion of Al-Mg Alloy Composites Containing Fly Ash, *Mater. Des.*, 2012, **33**, p 503–509.
32. M. Rahsepar and H. Jarahimoghadam, The Influence of Multipass Friction Stir Processing on the Corrosion Behavior and Mechanical Properties of Zircon-Reinforced Al Metal Matrix Composites, *Mater. Sci. Eng. A*, 2016, **671**, p 214–220.
33. R. Bertolini, E. Simonetto, L. Pezzato, A. Fabrizi, A. Ghiotti and S. Bruschi, Mechanical and Corrosion Resistance Properties of AA7075-T6 Sub-zero Formed Sheets, *Int. J. Adv. Manuf. Technol.*, 2021, **115**, p 1–24.
34. A. Bakkar and S. Ataya, Corrosion Behaviour of Stainless Steel Fibre-Reinforced Copper Metal Matrix Composite with Reference to Electrochemical Response of Its Constituents, *Corros. Sci.*, 2014, **85**, p 343–351.
35. S. Sardar, S.K. Karmakar and D. Das, High Stress Abrasive Wear Characteristics of Al 7075 Alloy and $7075/Al_2O_3$ Composite, *Measurement*, 2018, **127**, p 42–62.
36. K.P. Kumar, M. Gopi Krishna, J. Babu Rao and N.R.M.R. Bhargava, Fabrication and Characterization of Aluminium–High Entropy Alloy Composites, *J. Alloys Compd.*, 2015, **640**, p 421–427.
37. R. Escalera-Lozano, C.A. Gutiérrez, M.A. Pech-Canul and M.I. Pech-Canul, Degradation of Al/SiCp Composites Produced with Rice-Hull Ash and Aluminum Cans, *Waste Manag.*, 2008, **28**(2), p 389–395.
38. J. Zhu, W. Jiang, G. Li, F. Guan, Yu. Yang and Z. Fan, Microstructure and Mechanical Properties of SiCnp/Al6082 Aluminum Matrix Composites Prepared by Squeeze Casting Combined with Stir Casting, *J. Mater. Process. Technol.*, 2020, **283**, p 116699.
39. Z. Zhang and D.L. Chen, Contribution of Orowan Strengthening Effect in Particulate-Reinforced Metal Matrix Nanocomposites, *Mater. Sci. Eng., A*, 2008, **483**, p 148–152.
40. K.R. Kumar, T. Pridhar and V.S. SreeBalaji, Mechanical Properties and Characterization of zirconium oxide (ZrO_2) and Coconut Shell Ash (CSA) Reinforced Aluminium (Al 6082) Matrix Hybrid Composite, *J. Alloys Compd.*, 2018, **765**, p 171–179.
41. J.-Q. Han, J.-S. Wang, M.-S. Zhang and K.-M. Niu, Relationship Between Amounts of Low-Melting-Point Eutectics and Hot Tearing Susceptibility of Ternary Al-Cu-Mg Alloys during Solidification, *Trans. Nonferrous Met. Soc. China*, 2020, **30**(9), p 2311–2325.
42. W. Jiang, J. Zhu, G. Li, F. Guan, Yu. Yang and Z. Fan, Enhanced Mechanical Properties of 6082 Aluminum Alloy via SiC Addition Combined with Squeeze Casting, *J. Mater. Sci. Technol.*, 2021, **88**, p 119–131.
43. D.S. Prasad and A.R. Krishna, Effect of T6 Heat Treatment on Damping Characteristics of Al/RHA Composites, *Bull. Mater. Sci.*, 2012, **35**(6), p 989–995.
44. J.I. Rojas and D. Crespo, Modeling of the Effect of Temperature, Frequency, and Phase Transformations on the Viscoelastic Properties of AA 7075-T6 and AA 2024-T3 Aluminum Alloys, *Metall. and Mater. Trans. A.*, 2012, **43**(12), p 4633–4646.
45. J.I. Rojas, B.V. Siva, K. Lal Sahoo and D. Crespo, Viscoelastic Behavior of a Novel Aluminum Metal Matrix Composite and Comparison with Pure Aluminum, Aluminum Alloys, and a Composite made of Al-Mg-Si Alloy Reinforced with SiC Particles, *J. Alloys Compd.*, 2018, **744**, p 445–452.
46. M. Ebrahimi, Li. Zhang, Q. Wang, H. Zhou and W. Li, Damping Characterization and Its Underlying Mechanisms in CNTs/AZ91D Composite Processed by Cyclic Extrusion and Compression, *Mater. Sci. Eng. A*, 2021, **821**, p 141605.
47. H. Hatta, T. Takei and M. Taya, Effects of Dispersed Microvoids on Thermal Expansion Behavior of Composite Materials, *Mater. Sci. Eng., A*, 2000, **285**(1–2), p 99–110.
48. Ke. Chu, X.-H. Wang, Y.-B. Li, D.-J. Huang, Z.-R. Geng, X.-L. Zhao, H. Liu and Hu. Zhang, Thermal Properties of Graphene/Metal Composites with Aligned Graphene, *Mater. Des.*, 2018, **140**, p 85–94.
49. T. Wang, T. Fan, D. Zhang, G. Zhang and D. Xiong, Preparation and Thermal Properties of Metal Matrix Composites with Wood-Structure, *Mater. Des.*, 2008, **29**(6), p 1275–1279.
50. R.T. Loto and P. Babalola, Corrosion polarization behavior and microstructural analysis of AA1070 aluminium silicon carbide matrix composites in acid chloride concentrations, *Cogent Eng.*, 2017, **4**(1), p 1422229.
51. İ Öztürk, G.H. Ağaoğlu, E. Erzi, D. Dispinar and G. Orhan, Effects of Strontium Addition on the Microstructure and Corrosion Behavior of A356 Aluminum Alloy, *J. Alloys Compd.*, 2018, **763**, p 384–391.
52. Y. Ma, Y. Liu and M. Wang, Microstructures and Corrosion Resistances of Hypoeutectic Al-6.5Si-0.45Mg Casting Alloy with Addition of Sc and Zr, *Mater. Chem. Phys.*, 2022, **276**, p 125321.
53. S.O. Akinwamide, B.T. Abe, O.J. Akinribide, B.A. Obadele and P.A. Olubambi, Characterization of Microstructure, Mechanical Properties and Corrosion Response of Aluminium-Based Composites Fabricated via Casting—A Review, *Int. J. Adv. Manuf. Technol.*, 2020, **109**(3), p 975–991.

Publisher's Note Springer Nature remains neutral with regard to jurisdictional claims in published maps and institutional affiliations.

Springer Nature or its licensor (e.g. a society or other partner) holds exclusive rights to this article under a publishing agreement with the author(s) or other rightsholder(s); author self-archiving of the accepted manuscript version of this article is solely governed by the terms of such publishing agreement and applicable law.

Hindawi
Wireless Communications and Mobile Computing
Volume 2023, Article ID 2744706, 29 pages
https://doi.org/10.1155/2023/2744706

Research Article

Localization and Detection of Multiple Attacks in Wireless Sensor Networks Using Artificial Neural Network

Gebrekiros Gebreyesus Gebremariam,[1,2] **J. Panda**,[2] **and S. Indu**[2]

[1]*Department of Electronics and Communication Engineering, Raya University, Maychew, 7020 Tigray, Ethiopia*
[2]*Department of Electronics and Communication Engineering, Delhi Technological University, Shahbad Daulatpur, Main Bwana Road, Delhi 110042, India*

Correspondence should be addressed to Gebrekiros Gebreyesus Gebremariam; kiros2004comp@gmail.com

Received 11 June 2022; Revised 30 November 2022; Accepted 19 December 2022; Published 10 January 2023

Academic Editor: Javier Prieto

Copyright © 2023 Gebrekiros Gebreyesus Gebremariam et al. This is an open access article distributed under the Creative Commons Attribution License, which permits unrestricted use, distribution, and reproduction in any medium, provided the original work is properly cited.

Security enhancement in wireless sensor networks (WSNs) is significant in different applications. The advancement of routing attack localization is a crucial security research scenario. Various routing attacks degrade the network performance by injecting malicious nodes into wireless sensor networks. Sybil attacks are the most prominent ones generating false nodes similar to the station node. This paper proposed detection and localization against multiple attacks using security localization based on an optimized multilayer perceptron artificial neural network (MLPANN). The proposed scheme has two major part localization techniques and machine learning techniques for detection and localization WSN DoS attacks. The proposed system is implemented using MATLAB simulation and processed with the IBM SPSS toolbox and Python. The dataset is classified into training and testing using the multilayer perceptron artificial neural network to detect ten classes of attacks, including denial-of-service (DoS) attacks. Using the UNSW-NB, WSN-DS, NSL-KDD, and CICIDS2018 benchmark datasets, the results reveal that the suggested system improved with an average detection accuracy of 100%, 99.65%, 98.95%, and 99.83% for various DoS attacks. In terms of localization precision, recall, accuracy, and f-score, the suggested system outperforms state-of-the-art alternatives. Finally, simulations are done to assess how well the suggested method for detecting and localizing harmful nodes performs in terms of security. This method provides a close approximation of the unknown node position with low localization error. The simulation findings show that the proposed system is effective for the detection and secure localization of malicious attacks for scalable and hierarchically distributed wireless sensor networks. This achieved a maximum localization error of 0.49% and average localization accuracy of 99.51% using a secure and scalable design and planning approach.

1. Introduction

Hierarchically distributed microsensor nodes in the field are linked together with multihop wireless communication technologies to form a wireless sensor networks (WSNs) [1]. The sensor nodes have sensing and wireless communication modules, storage, and processing units. Wireless sensor networks (WSNs) monitor and collect network information, including network state and data transmission. They also monitor object positioning and tracking [2]. WSNs are vulnerable to multiple, including Sybil attacks, wormhole attacks and eavesdropping [3]. The Sybil attack is the most harmful routing attack that fabricates and depreciates multiple fake identities launching a malicious attack on the legitimate node to lower service quality [4, 5]. It is the key research challenge in wireless sensor networks like the other applications, including architecture, healthcare, disaster management, deployment quality of service, calibration [6], and synchronization. Wireless sensor nodes sense and record data from the environment and send the data to the cluster head for the aggregation process. An intelligent sensing and computing framework is essential for the security localization and detection of attacks using an artificial neural network (ANN). This scheme is gaining attention due to its low computational cost and faster convergence. In this paper we proposed an optimized multilayer perceptron artificial

neural network for detection and localization of routing attacks in WSNs.

Emerging applications of wireless sensor networks (WSNs) include traffic management and object tracking, both of which require localization of sensor nodes [7]. For efficient routing and location-aware services, it is crucial to have an accurate estimation of the sensor node location. Without knowing where the sensor is located, the data collected by WSN is often useless. As a result of their potential utility in a wide range of WSN applications, the localization techniques are garnering a rising amount of attention from researchers. Based on the information required, localization techniques can be divided into two broad categories: range-based techniques, which rely on the known distances or angles between nodes to make location estimates, and range-free techniques, which instead make location estimates based on the closeness of a number of reference nodes. Range-free approaches are replacing range-based methods in WSN localization due to their lower hardware and computational requirements. The clustering and localization algorithm is a well-known example of a range-free technique since it uses adjacent reference nodes' positions to estimate the node's own location. During the setup phase, the starting positions of the reference nodes are either hard-coded or computed.

1.1. MLPANN Applications in WSNs. Network traffic identification is becoming increasingly popular as a field of study in the field of network administration, drawing researchers from all over the world [8]. The growth in network capacity is closely proportional to this rise. New forms of network applications, such as peer-to-peer (P2P) file sharing, have rendered some of the more traditional methods of traffic identification, including port-based or deep packet inspection, ineffective. Selecting an appropriate feature selection method, which can select the best features according to the impact of the great traffic behaviour characteristics, is essential for achieving higher recognition efficiency and greater identification accuracy when performing traffic identification based on ML (Machine Learning). The MLP (Multilayer Perceptron) approach is superior to other identification algorithms in terms of identification accuracy. It has been shown that as the number of training samples grows, the identification rate also rises. But MLP is not without its own value and drawbacks that mean it needs to be enhanced.

There is now a great deal of academic focus on creating fingerprint localization algorithms that make use of artificial neural networks (ANNs). Despite noisy RSSI measurements, the ANN can still give accurate recognition of the node's position, which is a major advantage. Using ANNs eliminate the need for detailed knowledge of the indoor environment or the locations of reference nodes. In order to approximate a mapping between the multidimensional fingerprint space and the coordinates of nodes, ANN interpolates the acquired data in the fingerprint database. During the ANN's training process, the collected RSSI vectors are used to fine-tune the weights of connections between neurons. Although training may take a while, the localization process is far faster than any analytical estimates of the node's position.

Multilayer perceptron (MLP) is the most widely utilized ANN architecture in modern range-free wireless sensor node localization applications. In WSN, fingerprint-based localization was accomplished using the MLPANN. For this evaluation, we evaluated 43 distinct backpropagation training algorithms to determine the method's accuracy. Something very close to that was proposed as a tactic. The ANN training has been kept up-to-date at regular intervals so it can adjust to changing conditions on the wireless channel. Four MLPANNs, each with a different amount of inputs, formed an ensemble that was shown to the audience. This tactic specifies that, if the localization operation must be executed, an ANN with the same number of inputs as the currently connected reference nodes is selected and issued. Given the poor scalability of this approach, we settled on a cap of four connections between reference nodes. When compared to methods based on fuzzy learning systems or genetic algorithms, the localization results generated by the ANNs ensemble were shown to be more reliable. Here we propose a cooperatively optimized and secure multilayer perceptron artificial neural network (MLPANN) for scalable and broad area networks that combines range-based and range-free localization technique approaches from the realm of artificial intelligence (AI) to problems inherent to wireless sensor networks (WSNs) [9], such as data aggregation and fusion, routing, task scheduling, optimal deployment, and localization as shown in Figure 1. In this context, the term "computational intelligence" refers to a subfield of machine learning that combines techniques with roots in biology, such as neural networks, fuzzy systems, and evolutionary algorithms, to develop forecasting models. This algorithm for learning could be built using cascading decision chains for recognizing nonlinear and complex functions. However, the high-computational requirements for learning the network weights and the substantial administrative overhead mean that distributed neural networks are not yet widely used in WSNs. Neural networks, on the other hand, are well-suited for handling many network difficulties with a single model because of their ability to simultaneously learn multiple outputs and decision boundaries in centralized solutions.

1.2. WSN Routing Attacks. Attacks on the wireless sensor network's network layer can hinder performance by rendering a genuine node unreachable to the service. The following section will go through some of the more common types of attacks seen in WSNs. With these kinds of attacks, sensitive data is compromised before it even reaches the target node. The attacks in wireless sensor networks operate in all layers of the network exploiting resources and degrading the service quality of the network.

1.2.1. Wormhole Attack. The wormhole attack is created by two malicious nodes having a tunnel path in the two locations and misapprehension. Wormhole attack attracts and manipulates significant network data traffic launching various attacks. It advertises its packets using the intermediate nodes to sniff, modify, and drop from reaching the destination [10]. Figure 2 cluster A shows a wormhole attack scenario depicting when source node S sends the packet to the sink node. A

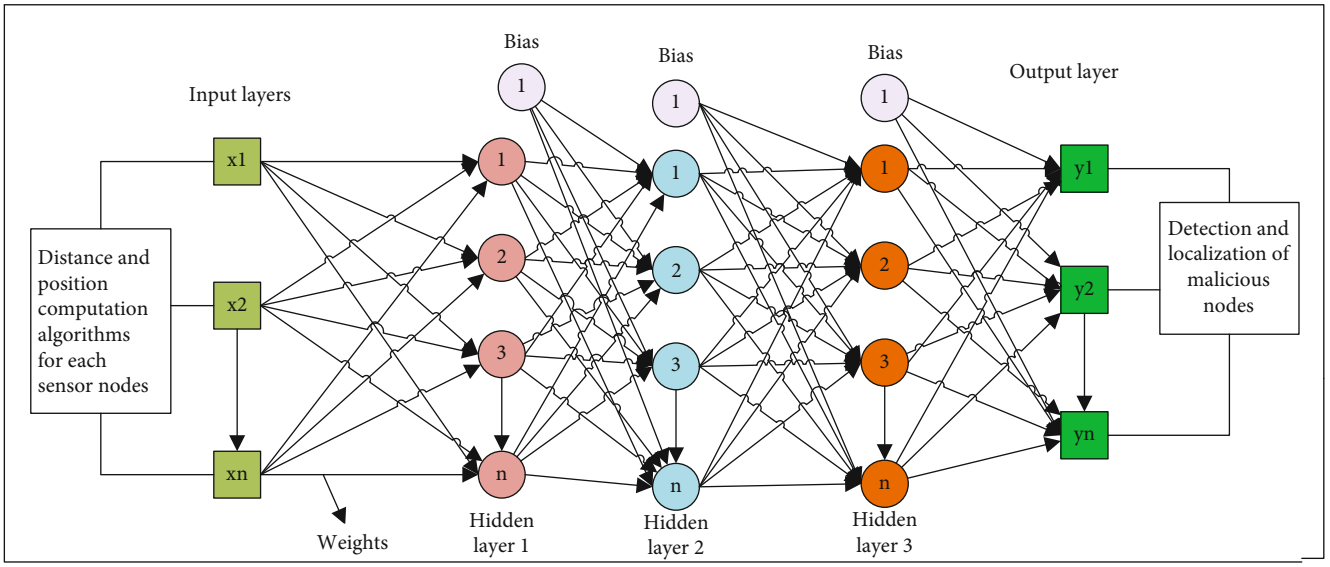

Figure 1: Illustration of MLPANN for detection and localization of WSN attacks based on localization algorithms.

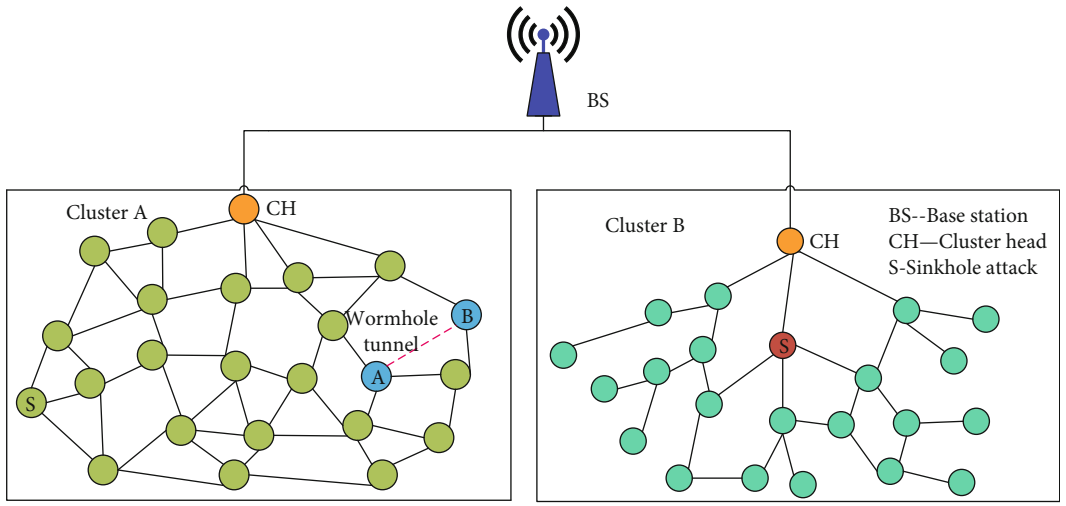

Figure 2: Illustration of wormhole and sinkhole attacks in WSNs in cluster A and B, respectively.

wormhole tunnel is created between malicious nodes A and B. The packet is dropped and modified by the tunnel before reaching the base station. At least the two hostile nodes employing a secure communication channel known as a tunnel can detect a wormhole assault [11]. It is at this point that the wormhole tunnel will begin to collect the data packets and forward them on. The malicious node on the other end of the tunnel receives a control packet. At the other end, it uses a private channel to relay the packet to another node that has caught its attention. For enhanced metrics, such as fewer hops or less time, the private channel is selected as the conduit for communication between the source and the destination. The attack usually consists of two phases. Multiple initial directions are of relevance to the wormhole nodes. The second stage is when the packets begin to make use of the malicious nodes. It is possible for these nodes to hinder the network's performance in a number of ways. Wormhole nodes can be used to steal information or communicate it to a third party if they delete, tamper with, or send it.

1.2.2. Sinkhole Attack. Sinkhole attack advertises routing paths to the base stations, making itself a normal node misguiding the neighbor nodes that cause threats to the network. The malicious nodes create a hole in the routing path that can damage the regular operations of the network. The sinkhole attack uses a compromised node with fewer hops to advertise the route to the destination. This misuse of routing information misguides the legitimate node and attracts the node closer. Figure 2 cluster B illustrates the scenario of a sinkhole attack for attracting and capturing packets from the neighbor nodes. The sinkhole attack utilizes a secret tunnel for attracting nodes and capturing packets. The malicious node then deceived and sent packets to the base station.

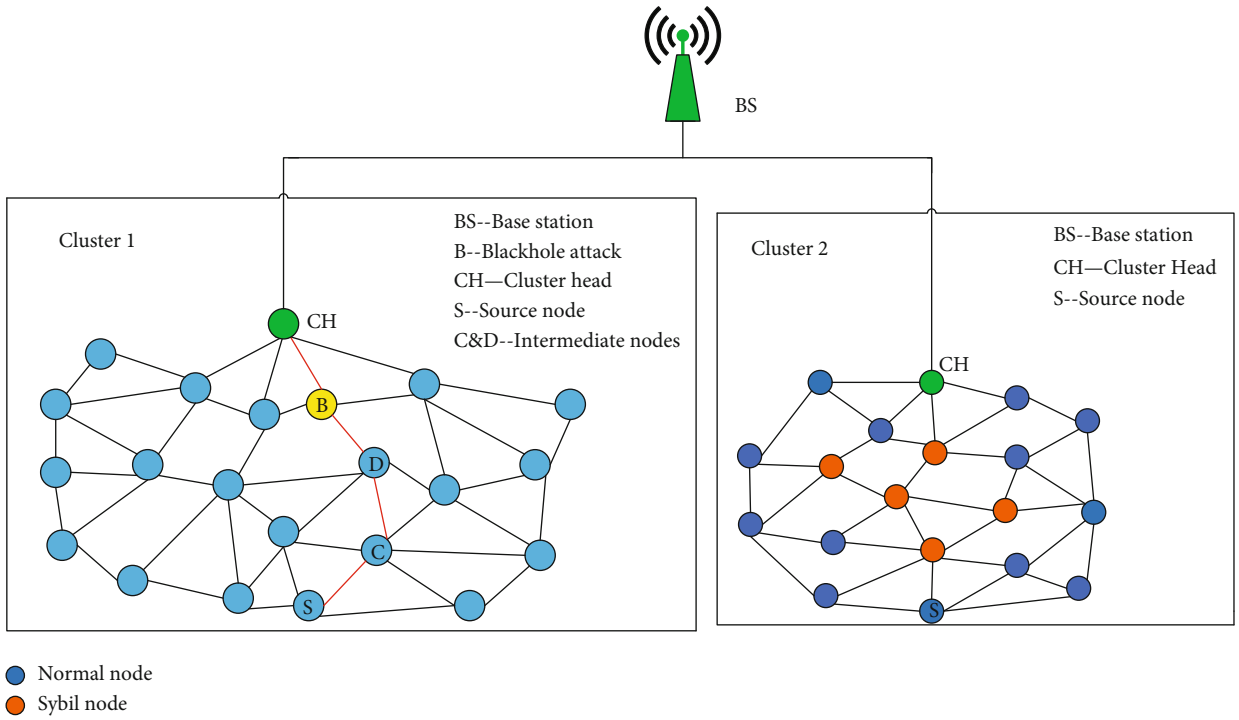

Figure 3: Illustration of blackhole and Sybil attack scenario in WSNs for cluster 1 and cluster 2, respectively.

1.2.3. Blackhole Attack. Blackhole attacks capture and reprogram sensor nodes to block packets instead of receiving and forward to the base station [10]. The blackhole attack compromises the information with the malicious node that enters the blackhole region. The blackhole attack undermines the network performance by using the network partitioning so the essential updates cannot reach the base station. It degrades the network performance metrics and consumes large network traffic. The source node S sends a packet to the base station using the intermediate C and D nodes, as shown in Figure 3 of cluster 1. The blackhole node consumes the entire traffic and is not forwarded to the destination node.

The blackhole attack performs suspicious activity using loopholes for discovering the routing [12]. The blackhole attack compromises the legitimate node with a malicious node so that the packets are dropped and unable to reach the destination nodes. The suspicious node cause packet is dropping for targeted nodes and customizing set of nodes for packet dropping. The information that comes to the blackhole is dropped and sent fake packets to the base station. The routing requests and routing response messages by the blackhole attacks have higher order number which is greater than the normal node request and response so that the normal node will not respond to the routing request with higher order number which causes deletion of routine from the networks [13].

1.2.4. Sybil Attack. Sybil attack forges and spoofs the identity of the legitimate node in wireless sensor networks [14]. Sybil attack interrupts the routing table and the trust value of the node of the legitimate node. Sybil attack duplicates multiple identities for confusing the neighbor nodes [15]. This attack uses geographic routing protocols for targeting authorized nodes. Sybil attack takes numerous identities to disguise the storage entities of the legitimate node [16], as shown in Figure 3 of cluster 2. The malicious node transmits data with imaginary events multiple times. This type of attack creates illusion that makes it difficult to detect the whole network.

1.3. Problem Formulation. Most of the existing literature review papers dealt with single attacks with low localization and detection accuracy in WSNs. Thus the deployment of wireless sensor nodes seeks optimal and intelligent localization methods for accurate node position and attack identification. To overcome this problem, it is essential to design and implement a new effective technique. This paper proposes a security localization and detection scheme employing optimized multilayer perceptron artificial neural network for various classes of attacks against wireless sensor networks, which are vulnerable to a wide variety of denial-of-service (DoS) attacks that exploit the network's resources. The proposed method is designed for multiple attack detection and classification, representing the input and output relationships using the ANN technique. The design and planning of distributed hierarchical clustered topology are also discussed that consists of sink node, cluster head, malicious and sensor nodes as shown in Figure 4. Also, we discuss the effectiveness of the proposed system using the benchmark datasets including CICIDS2018, UNSW-NB 15, WSN-DS and NSL-KDD with different evaluation metrics using training and testing samples as a benchmark for performance evaluation. The dataset is processed using batch mode.

1.4. Research Contribution. The proposed attack localization and detection scheme is based on an optimization multilayer

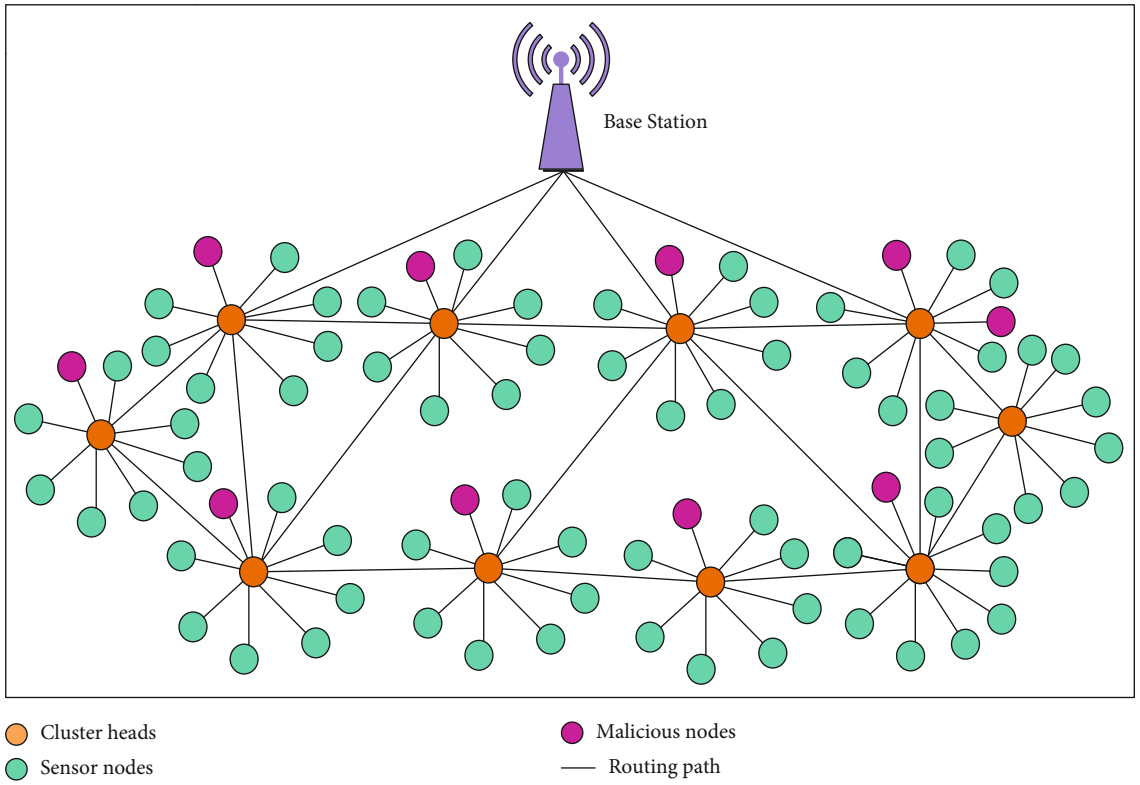

Figure 4: Clustering in hierarchically distributed wireless sensor network model.

perceptron neural network [17]. The proposed system possesses different phases with the proper network planning and node configuration. These include network data processing and feature extraction, training, and testing for attack detection and classification. Some of the novel contributions of this work are as follows:

(1) To design and simulate wireless sensor network topology with attack detection and localization features

(2) To explore the various routing attacks and techniques simulating these attacks using clustering and routing protocols

(3) Evaluate the network performance using a sample public dataset as a benchmark with attack detection localization metrics

(4) Explore machine learning techniques secure localization and detection of routing in wireless sensor networks in all layers of the network

(5) A multilayer perceptron neural network technique enables the detection and classification of malicious nodes using network traffic data and feature extraction. It maximizes the location and position accuracy of the suspicious node

(6) To detect and localize multiple attacks with greater classification accuracy for clustered and hierarchical network architecture

(7) Measure the security performance of the scheme using comparison performance for effective validation and confirmation with similar previous works

(8) Explore hybrid range-based and range-free localization techniques for unknown and malicious nodes that affect quality of service in WSN using collaborative approach

The rest contents of this paper are organized into different sections and structures. Section 2 encompasses the previous literature works. Section 3 describes the network and attack models depicting graphically in detail using clustering and routing protocols. The next part is Section 4, which discusses the proposed attack localization and detection technique in WSNs using MLPANN approach. The next Section 5 details the simulation and experimental analysis using a benchmark dataset for different classes of routing attacks. The last section is Conclusion and remarking for future works.

2. Related Works

Messous and Liouane [1] presented an online successive distance vector hop scheme for node localization accuracy in WSNs. They also discussed the variation of anchor nodes with optimized distance between nodes in the network. Dong et al. [2] examined the distance vector hop algorithm against Sybil attacks for effective node localization and

accuracy for improved security in WSN. The scheme also reduces the average error localization by 3%, setting the beacon nodes 50 in the simulation that is 78%. Chelouah et al. [18] addressed localization algorithm in mobile WSNs. They also presented the mobility of nodes for coverage optimization, connectivity, and analysis. Hadir et al. [19] presented a localization technique in WSNs using an effective distance vector hop scheme. They also discuss the average hop size and localization accuracy by exploiting the information. Almomani et al. [20] designed a low cost and efficient, intelligent DoS attack detection and prevention technique. They also discuss different DoS attack classifications using a specialized dataset for WSN. Patel and Mistry [21] presented Sybil node detection [22] using various schemes. They also discussed and analyzed the protocols used in WSNs. Yavuz et al. [23] proposed detecting IoT-routing attacks using a deep learning machine learning technique. The Cooja simulator generates high-fidelity attack data in the IoT network with 1000 sensors. Sujatha and Anita [24] examined the detection of Sybil attack detection using hybrid fuzzy and powerful extreme learning machines. They also discussed ARM as the main CPU with LEACH environment and ZigBee transceivers on real-time testbeds. Qi et al. [25] researched a localization algorithm to improve the node position accuracy and reducing localization error in WSNs using MA-MDS. They also use the Prussian analysis algorithm for accurate coordinate transformation. Li et al. [26] presented a localization trust valuation scheme to detect spoofing and Sybil attacks. This scheme is obtained by selecting localization performance, estimated distance, and transmission with the threshold property set in WSNs. Song et al. [27] proposed a chaotic hybrid mutation and chaotic inertial weight-updating technique with a glowworm swarm optimization approach. The scheme also avoids premature convergence with better convergence and higher accuracy. Saud Khan and Khan [28] presented Sybil attack detection using signed response authentication techniques for global mobile communication systems. They also discussed the probabilistic model to analyze Sybil attack detection performance.

Abbreviations, acronyms, and shorter variants of terms and phrases used as resources in this paper are included as shown in Table 1

3. Network Model

Sink, cluster head, sensor, and attacker nodes are all represented in the simulated network. The sensor nodes tend to group together throughout the system. When sending information to the beacon nodes and the base station, each cluster chooses its own cluster head node to act as the central hub for that cluster. The beacon nodes decide on the optimal routing path by employing an optimization strategy based on a fitness function. In this context, the terms beacon nodes and anchor nodes are synonymous. Sybil attacks and wormhole assaults are the types of attacks that can be used against this network paradigm. The positioning and placement of anchor nodes are dependent on their relationship to other nodes. Once an anchor node has been put in a network, it will remain in the same location permanently. The sensor nodes have claimed their territory. The localization scheme is used for providing accurate position and location of the sensor nodes by making clustering of the nodes having one cluster head for each group [29, 30]. Unknown nodes locate their positions using the anchor node assistance. Sensor nodes update their locations periodically by the system. Malicious nodes broadcast their positions by creating multiple fake identities and advertising themselves as the beacon nodes. The malicious node also creates tunnels for dropping packets before reaching the destination. The hierarchical clustering of the sensor deployments enables less energy consumption and enhances the network life time as shown in Figure 4.

The legitimate nodes are assumed to be homogenous in computational processing, storage capacity, communication level, and activation energy in the model [31]. Malicious nodes are considered more effective than the legitimate node for the activity in capturing the security key of the base station and clusters. The attacker disrupts the normal functioning of the network by cloning the authorized node.

3.1. Cluster Formation and Data Aggregation. Clustering is a method of organizing a set of sensors to increase the durability of the network and decrease its power consumption [32]. The network's sensor nodes are organized into groups of similar devices. Collectively, the sensor nodes that make up the cluster gather data and send it on to the cluster coordinator. The data is aggregated and filtered by the cluster head before being sent to the hub. The sensor's stable functioning and neighbor evaluation are aided by the clustering method. Cluster heads (CHs) are the most important nodes in the cluster since they serve as the hub for monitoring. The three selection criteria are used to determine which of the sensor nodes will become the cluster head.

(i) The number of nearby neighbor nodes

(ii) The quality of the received signal from the sensor node

(iii) The node's remaining energy before it is activated

(iv) The minimum distance to the base station as calculated by the distance vector protocol. The distance D between any two sensor nodes is computed using the distance vector technique as shown below

$$D = \sqrt{\left(u_i - u_j\right)^2 + \left(v_i - v_j\right)^2}. \quad (1)$$

The u and v coordinate for nodes i and j, respectively. Computing the distance between the base stations to any node with a small distance is likely the cluster head. The energy employed for the communication and activation of the network model is evaluated by setting the threshold parameters with the multipath model approach. The amount of energy E_{TX} for k-bits of data transmission over D distance and D_o threshold distance is given as in

Table 1: List of abbreviations and acronyms used in this paper.

Abbreviations	Descriptions
BS	Base station
WSNs	Wireless sensor networks
CH	Cluster head
D	Distance
E	Energy of the sensor node
RSSI	Received signal strength indicator
DV-H	Distance vector hop
IoT	Internet of Things
ANN-IDS	Artificial neural network-based intrusion detection system
FEMs	Fuzzy extreme machines
MK-ELM	Multikernel extreme learning machine
LEACH-ANN	Low-energy adaptive clustering hierarchy based on ANN
CNN-MCL	Convolutional neural network and mean convolutional layer
HTM-LSTM	Hierarchical temporal memory and long short-term memory
MLPANN	Multilayer perceptron artificial neural network
RL-IDS	Reinforcement learning-based IDS
GBFS-IDS	Gradient boosting feature selection for IDS
ML-ID	Machine learning-based intrusion detection
UWB	Ultrawide band
DI-ADS	Deep intelligent attack detection scheme
PO-CFNN-	Political optimizer based on cascade forward neural network
RNN	Recurrent neural network
ECGAL	Energy-efficient clustering and localization centered on genetic algorithm
LSTM-FFNN	Long short-term memory and feed-forward neural network
DNN-CSO	Deep neural networks with chicken swarm optimization

$$E_{TX} = \begin{cases} k \times E_e + k \times E_f \times D^2, & \text{if } D \le D_o, \\ k \times E_e + k \times E_m \times D^4, & \text{if } D > D_o, \end{cases} \quad (2)$$

where E_{TX} is the transmitted energy, E_f is the reception energy, and E_e is the power dissipated in the transmitter or receiver for single-bit data transmission. The dissipated energy depends on signal spreading, filtering, modulation, and channel-coding factors. The threshold transmission distance D_o with k-length of data transmission is given by

$$D_o = \sqrt{\frac{E_f}{E_m}}. \quad (3)$$

For k-bits of message reception, the energy consumed by the receiver node is

$$E_{\mathrm{RX}(k)} = k \times E_e. \quad (4)$$

3.2. Localization Techniques. Numerous wireless sensor network (WSN) applications rely on localization to locate a target by comparing the signal strengths of transmitters and receivers already set up in the region of interest [33, 34]. Some algorithms are essential for finding and assessing the location and position of the nodes and security enhancement for precise location of the target. The scheme is divided into range-based and range-free localization techniques. The latter one is cost-effective with special hardware requirements. The received signal strength indicator (RSSI) and distance vector hop localization algorithms evaluate wireless sensor node accurate position and location. The distance vector localization procedure is essential to compute the coordinates of the sensor nodes and cluster heads using the beacon nodes [1]. The scheme calculates and manipulates the position and distance of the unidentified nodes. The distance vector hop procedure helps to find the spaces among the beacon nodes in WSN. The calculated minimum distance is the average hop size using the distance vector approach. This algorithm was first identified by [2]. The distance vector localization scheme is a range-free strategy [19] with a series of steps in Table 2.

The average distance hop for the anchor node is computed and obtained relative to another beacon with the minimum hop count given by

$$\mathrm{HS}_i = \frac{\sum_{i \ne j} \sqrt{(ui - uj)^2 + (vi - vj)^2}}{\sum_{i \ne j} hij}. \quad (5)$$

The interpretation of the variables is shown in Table 3.

Table 2: Steps in distance vector technique for computing the position of unknown nodes.

Steps	Description of steps
Routing initialization	Beacon node broadcasts to all nodes and the hop count of its location information with 0 value initialized in the network [19].
Calculating distance	The average size of the hop and the unknown node distance is calculated with the assistance of the beacon node.
Position estimation	Unknown nodes estimate their position by the triangulation algorithm or maximum likelihood estimators or polygon method with the help of the anchor node.

Table 3: Equation (1) variable description and interpretation.

Variable	Description of the variable
i, j	True anchor nodes
(ui, vi), (uj, vj)	The known and true coordinates for i and j
Hij	Hop counts of the anchor nodes
HSi	Average hop distance

Anchor node transmits its information [2] followed by hop-size calculation. The distance between sensor node and anchor computed with hop-size details is given by

$$D_{pk} = HpSi_{i\times} hp_{pk}. \tag{6}$$

The polygon technique enables the estimation of the position (P) of each anonymous node. P is the spot of the unidentified node denoted as (u, v) and di, the space among anchor and indefinite nodes. The position of the strange node p assuming n beacon nodes involved is estimated by [2].

$$\begin{aligned}
(u-u_1)^2 + (v-v)^2 &= {D_1}^2,\\
(u-u)^2 + (v-v)^2 &= {D_2}^2,\\
&\vdots\\
(u-u_n)^2 + (v-v_n)^2 &= {D_n}^2.
\end{aligned} \tag{7}$$

We can get a set $(n-1)$ of expressions subtracting from the first equations to make the system linear, given as depicted in

$$\begin{aligned}
{u_1}^2 + v^2 - {u_n}^2 - {v_n}^2 - 2(u-v_n)u - 2(v_1-v_n)v &= {D_1}^2 - {D_n}^2,\\
{u_2}^2 + {v_2}^2 - {u_n}^2 - {v_n}^2 - 2(u_2-u_n)u - 2(v_2-v_n)v &= {D_2}^2 - {D_n}^2,\\
&\vdots\\
{u_{n-1}}^2 + {v_{n-1}}^2 - {u_n}^2 - {v_n}^2 - 2(u_{n-1}-u_n)u - 2(v_{n-1}-v_n)v &= {D_{n-1}}^2 - {D_n}^2.
\end{aligned} \tag{8}$$

Rearranging the previous equations into the formula of ui $= \mathrm{BA}^{-1}$, where A, ui, and B are expressed as in

$$A = \begin{cases} 2(u-u_n)2(v_1-v_n), \\ 2(u_2-u_n)2(v_2-v_n), \\ \vdots \\ 2(y_{n-1}-u_n)2(v_{n-1}-v_n), \end{cases} \tag{9}$$

$$B = \begin{cases} {u_1}^2 + v^2 - {u_n}^2 - v^2 + {D_n}^2 - {D_1}^2 \\ {u_2}^2 + v^2 - {u_n}^2 - {v_n}^2 + {D_n}^2 - {D_2}^2 \\ \vdots \\ {u_{n-1}}^2 + {v_{n-1}}^2 - {u_n}^2 - {v_n}^2 + {D_n}^2 - {D_{n-1}}^2 \end{cases}, \tag{10}$$

$$U_i = \left(\frac{u}{v}\right). \tag{11}$$

The location of the node is computed solving the least square method stated as in

$$U = \left(A'A\right)^{-1} A'B. \tag{12}$$

The clustering and distance vector-routing protocols are used in the proposed scheme for effective wireless sensor network deployment.

In contrast to its range-based equivalents, RSSI-based localization algorithms have gained a lot of traction in the academic community for a variety of compelling reasons [35]. Today's wireless sensor nodes typically include features like RSSI measurement and data transmission to higher stack layers. For RSSI-based localization, no time-synchronization between nodes, ultrawide band (UWB) radios for more precise time of arrival calculations, or antenna arrays are needed. In terms of both software and hardware, it is a straightforward and inexpensive approach to achieving node localization. However, the DV-hop algorithm completely skips measuring the real distances between the one-hop neighbor nodes and leveraging these distances for more precise localization in massive-scale wireless sensor networks.

To localize wireless nodes using the DV-hop technique, the hybrid approach takes two extra steps, as indicated above for improvement of the localization accuracy and malicious

node detection. Instead of relying on the average hop distance like the original DV-hop algorithm did, we first use the RSSI data to estimate the distances between the anchor nodes and their one-hop surrounding sensor nodes. Using the RSSI value does not necessitate any specialized hardware or additional expenditures because the MAC sublayer in most modern wireless sensor nodes computes RSSI value for every received packet and sends that value to higher layers. Second, after a sensor node N has been located, it is elevated to the role of anchor, which is utilized to localize other sensor nodes. With more (repurposed) anchor nodes to work with, the remaining sensor nodes can be localized with greater precision. That is especially useful in wireless networks when there are fewer anchor nodes. Third, differential evolution (DE) is a technique used in evolutionary computation to find the optimal solution to a problem by iteratively trying to enhance a candidate solution with respect to some quality metric. Metaheuristics are approaches that search enormous spaces of possible solutions while making few or no assumptions about the underlying problem. Unfortunately, metaheuristics like DE cannot promise you will get the best possible result every time.

Since DE does not rely on the gradient of the optimization problem, DE can be applied to optimization problems involving multidimensional real-valued functions even if the problem cannot be differentiated, as is the case with traditional optimization techniques like gradient descent and quasi-newton methods. For this reason, DE can be applied to optimization problems that are inherently noncontinuous, noisy, dynamic, etc. Using its basic equations, DE optimizes a problem by keeping a population of candidate solutions, generating new candidate solutions by merging old ones, and finally keeping the candidate solution with the highest score or fitness on the optimization task at hand. As a result, the gradient is unnecessary because the optimization issue is viewed as a black box that only delivers a measure of quality given a candidate solution.

The problem of the localization of techniques is transformed into multilayer perceptron artificial neural network by computing the distance and position of each type of nodes with unique identity for detection and localization of the malicious nodes as shown in Figure 5. The sensor nodes in our purpose are assumed to both homogenous and heterogeneous wireless sensor networks. The beacon nodes have high-computational data processing and have their own localization that helps for other nodes to estimate and compute their location and positon of the ordinary sensor nodes in the network. Adding machine learning to WSN localization helps increase the precision of range-free node positioning [36]. In particular, the use of artificial neural networks (ANNs) in range-free localization algorithms has significantly improved their accuracy and performance compared to more conventional methods. The MLPANN learning strategy is needed that starts with a labelled dataset in order to construct a model that can appropriately generalize to data that was not included in the training set before we can make any adjustments to the weights [37].

3.3. Attack Model. One hundred nodes are distributed randomly in 1000×1000 m square areas with sensor, cluster head, and malicious nodes. The proposed scheme aims to enhance the detection accuracy of security localization [2] to routing attack using the distance vector hop procedure and clustering protocols in WSN using an artificial neural network approach. Figure 6 is the Sybil attack model with three sets of wireless nodes. A Sybil attack is a type of network assault in which a malicious node purposely and illegally displays a large number of forging or false identities to other sensor nodes [38]. This is accomplished by either independently generating new identities or illegally assuming the identities of other sensor nodes. By creating an unpredictable number of fake node identities, a Sybil node might interfere with WSN operations like multipath routing, which uses a variety of routes to find the best one between a source and a destination. The attack model shows how malicious nodes launch fake behaviors creating multiple identities against the position and location of the legitimate node with various routing paths. This degrades the lifetime of the network by reducing the computational performance of the authorized nodes.

The other routing attacks including scheduling, blackhole, grayhole and flooding attacks are used in for simulating and implementation of the proposed scheme using the WSN-DS dataset as a benchmark for evaluating for localization and detection.

3.4. Benchmark Datasets. In this section, three benchmark datasets including UNSW-NB 15, WSN-DS, and NSL-KDD are utilized to measure the effectiveness attack detection and localization accuracy. The raw network packets of the UNSW-NB 15 dataset were generated by cyber LAB using the IXIA PerfectStorm tool for cyber security for generating attack behaviors [39]. The cyber security dataset [40] is structured into training and testing samples using the batch mode for updating the total error for each weight, as shown below in Table 4. The dataset contains ten classes of attacks with different statistical frequency distribution in the network.

There are various attack activities in the dataset for processing and classification of the proposed system. The attacks are classified as normal, shellcode, analysis, backdoor, backdoors, DoS, exploits, fuzzers, reconnaissance, generic, and worms [39, 42–46].

The frequency distribution of the four types of routing attacks found in the WSN-DS dataset is provided in Table 5 and is utilized as a benchmark against which the performance of the proposed can be measured. There are a total of 84556 data points and 23 features available to use in creating a predictive model, eighty percent are utilized for training, while twenty percent are used for testing.

The other benchmark dataset for evaluating the proposed technique is the NSL-KDD containing 100069 samples and with classes of attacks including denial-of-service (DoS), probes, user to root (U2R), root to local (R2L), and normal as shown in Table 5. The dataset has 41 features with 38 numerical and 3 categorical features.

4. Proposed System

The proposed system consists of a series of phases: design and planning, deployment and routing, data processing, training and testing, attack classification, attack detection,

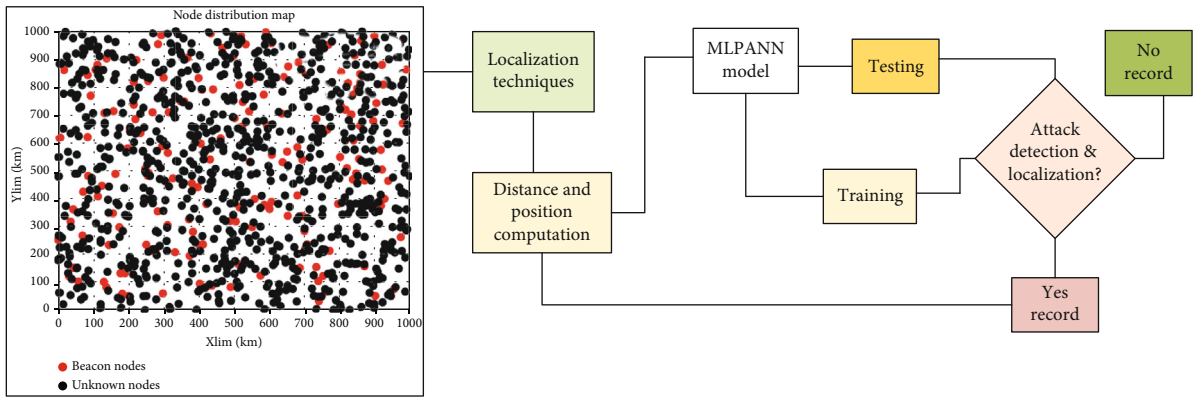

Figure 5: Secure localization techniques for detection and localization of malicious attacks using MLPANN in WSNs [36].

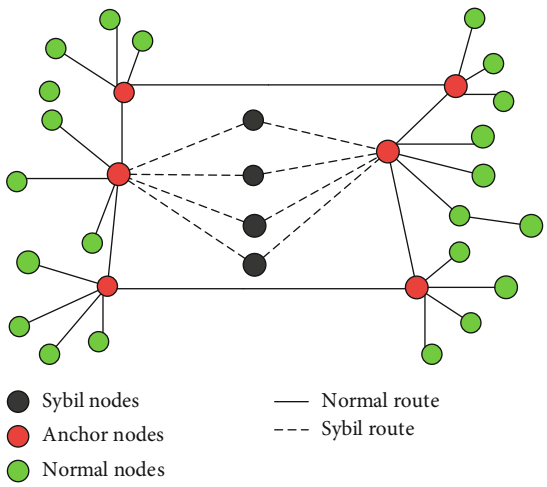

Figure 6: Illustration of routing Sybil attack in wireless sensor networks [2].

and localization. The data processing phase includes feature selection and normalization of the network traffic security dataset. The proposed system shown in Figure 7 is designed using optimized multilayer perceptron artificial neural network (MLPANN). The MLP is a feed-forward ANN with backpropagation to calculate the gradient used for weight calculation [48]. The ANN technique is a stochastic learning model for decision-making using interconnected information processing units [49]. ANN can estimate the nonlinear relationship between inputs and outputs and map the exchange of information among the nodes. The multilayer perceptron (MLP), as shown in Figure 8, configured with input layers, three hidden layers, and output layers. The proposed system used a gradient descent optimization for speeding and enhancing accuracy for detection and localization of attacks. This approach also uses a statically driven technique for training and testing using multilayer perceptron.

Several procedures are included in the proposed framework to identify malicious or unexpected routing. The method begins with a network data collection and preprocessing stage [50]. Next, it must find any missing values in the system and then fill in those blanks with appropriate values that were not present before processing began. We use the mean as our default. Subsequently, the dataset is cleaned up by removing any occurrences of duplicate values. After that, data encoding and normalization are carried out. In order to facilitate data handling, the encoded data undergoes a dimension's reduction procedure. To aid with anomaly detection, it is necessary to do feature optimization in order to extract the most useful characteristics from the data. In order to spot outliers in the dataset, optimal feature selection is crucial. For the same information, it aids in lowering the computational cost required to process it. Below is an equation that can be used to determine the entropy

$$E = -\sum_{i}^{L} P_i \log_2 P_i, \tag{13}$$

where p is the chance of finding a particular class label in the dataset. In this study, a hybrid machine learning approach is recommended for intrusion detection in a wireless sensor network after the optimal selection of features for anomaly detection.

4.1. Artificial Neural Networks. The multilayer perceptron artificial neural network (MLPANN) is a supervised machine learning approach using a human neuron model for data classification [47]. ANN processes and produces accurate information using a massive number of neurons and classify data-based neuron model that digests data and deliver correct output having layers and connecting nodes and active duty [51]. The layers of ANN are connected with nodes with the activation function. The configuration of typical ANN is depicted in Figure 9 with nodes and hidden layers varying from to three of the network using trainable parameters. ANN has wide applications in improving the efficiency of various schemes, including detection and localization of sensor nodes, routing and congestion control, and data aggregation in WSN. Artificial Neural Networks are data-driven tools for demonstrating nonlinear dynamic systems. They are efficient for the identification and modeling of nonlinear systems. They have standard approximation abilities and flexible structures to capture nonlinear

Table 4: Frequency distribution of DoS attacks for training and testing in the dataset [41].

Attack class	Frequency	Percent	Attack class	Frequency	Percent
Analysis	29	0.3	Generic	147	1.5
Normal	8632	86.0	Exploits	538	5.4
DoS	382	3.8	Reconnaissance	97	1.0
Backdoor	21	0.2	Shellcode	48	0.5
Fuzzers	122	1.2	Worms	17	0.2
Total	9186	91.5	Total	847	8.6

Table 5: Frequency distribution of DoS attack in WSN-DS and NSL-KDD dataset.

	WSN-DS dataset			NSL-KDD dataset	
Attack type	Frequency	Percent	Attack type	Frequency	Percent
Blackhole	2607	3.1	DoS	37403	33.7
Flooding	1019	1.2	Normal	61355	55.2
Grayhole	3287	3.9	Probes	10600	9.5
Normal	75300	89.1	R2L	913	.8
Scheduling	2343	2.8	U2R	839	.8
Total	84556	100.0	Total	111110	100.0

characteristics [52]. The input data $x1, x2, \cdots, xn$ denotes the input parameters of the dataset containing various protocols, services and the identity of the nodes, and $y1, y2, \cdots, yn$ represents the classified DoS attacks depending on the benchmark dataset. The ANN addresses the localization of sensor nodes and detection of the malicious nodes [18]. The proposed scheme has multiple trainable parameters for accurate attack localization and detection including the input nodes, hidden layers, bias and output nodes and also the connecting neurons. The ANN technique in WSNs improves the computational intelligence for scalable and adaptable features [30]. The ANN scheme was also used to obtain the accurate position of the sensor node using multilayer perceptron. It is also effective for prediction and clustering to get the location and position accuracy of nodes in WSNs.

The activation functions used for the artificial neural network multilayer perceptron are sigmoid and softmax, respectively. They are activation functions for the hidden layers and output layer, respectively. The sigmoid and softmax functions are stated below as in

$$Y = \frac{1}{1 + e^{-x}}, \tag{14}$$

$$z = \frac{e^{x}}{\sum_{k=1}^{n} e^{x}}, \tag{15}$$

where x is the vector of input to the output layer and y is the network's response with k index and n elements for the multilayer perceptron. The softmax function z is applied for activating for the classifier in the output layer. The number of hidden layers varies from one to three in our case for conducting the performance evaluation. The next step is to shrink the sampling dataset in order to better localize the feature that has to be extracted [53]. The pooling techniques are used to achieve this. In order to reduce the size of the image and the number of computations necessary, pooling is used. The max pooling approach was employed. Max pooling generates a new map after determining the feature maps' maximum value. A node's output in response to an input or combination of inputs is determined by the activation function of that node.

4.2. Optimization and Tuning Techniques. The goal of an ANN's optimization phase is to identify the optimal weighting scheme that leads to optimal performance. This is a tough optimization issue since it is categorized as a continuing nonlinear optimization problem. There are a lot of algorithms in books. Backpropagation is one of the most popular algorithms. This last one achieves excellent results, although it may run into a local minimum difficulty. To circumvent this issue and improve the likelihood of rapid convergence, we incorporate a local search method with a differential evolution algorithm. When training a neural network model, we utilize Adam optimizer to update the weights of the network based on the model's learned parameters with the greatest possible efficiency. Authors claim that Adam is a combination of the best features of two existing extensions of stochastic gradient descent: the Adaptive Gradient (AdaGrad) algorithm and the Root Mean Squared Propagation (RMSProp) algorithm. These two algorithms have a common characteristic: they both maintain a constant learning rate across all parameters. Adam sees the value in AdaGrad and RMSProp [53]. To fine-tune the weights of the neurons, we compute the gradient of the loss function and apply gradient descent optimization. The networks are trained via a gradient-based algorithm and the gradient descent nonlinear optimization method [29]. The gradient descent algorithm

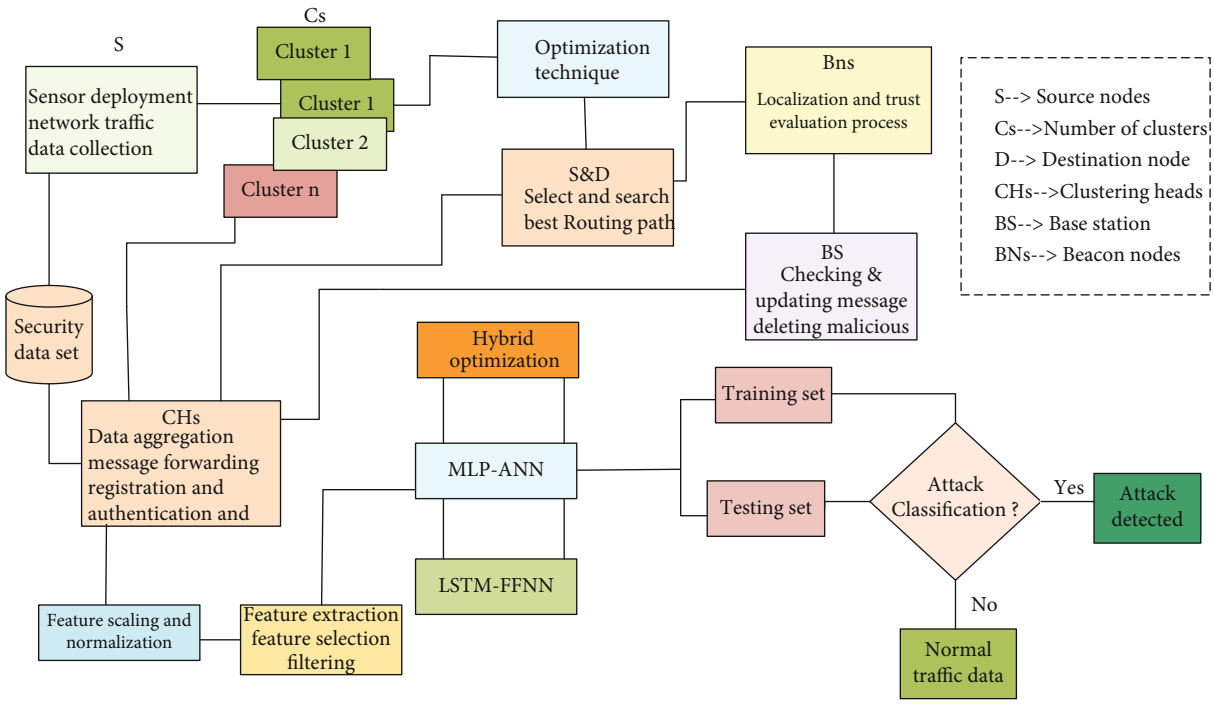

Figure 7: The proposed block diagram for attack localization and detection scheme in WSNs.

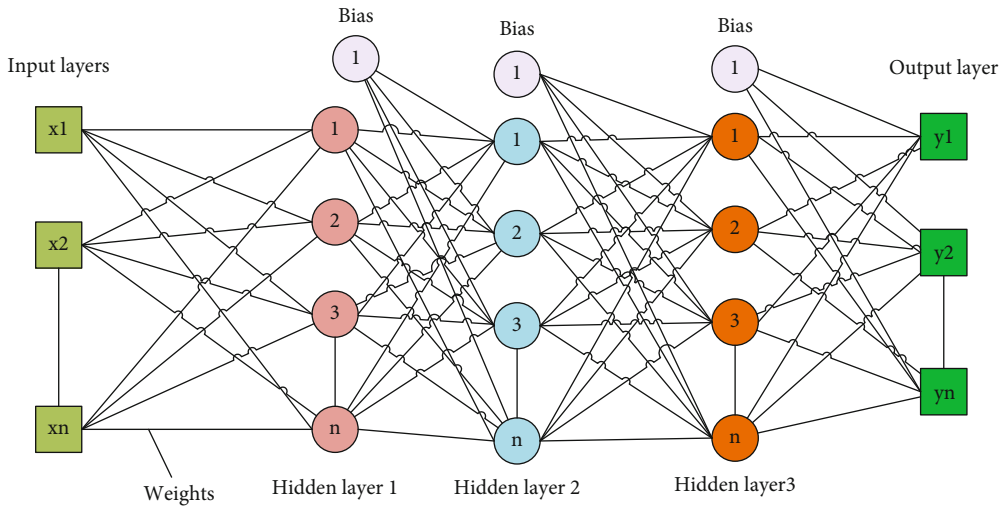

Figure 8: Structure of the proposed MLPANN architecture with three hidden layers [47].

speeds up the training phase on the artificial neural network multilayer perceptron. The algorithm also helps to converge the weight iterations of the network.

Optimal weights, the optimal number of hidden layers and hidden nodes, and the optimal set of relevant characteristics are all necessary for building a multilayer perceptron [54]. The layer-by-layer weighted output data are collected at a secret node. The value of a bias node's weight is also given to it. One uses a nonlinear activation function on the aggregate of the weighted input values. The only restrictions are that the nonlinear function be differentiable and that the function's output values lie inside some interval. Finding an optimal set of weights that approximates both actual and estimated outputs is the goal of the MLP optimization issue. Continuous optimization is used to model this issue, invoking the problem classification of optimization techniques.

4.3. LSTM-FFNN. Using long short-term memory and feed-forward neural networks (LSTM-FFNNs), the suggested optimized multilayer perceptron artificial neural network achieved better results. Within the realm of DL, the long short-term memory (LSTM) RNN is analogous to a recursive function that repeatedly calls itself. With a recurrent neural network, the same computation is performed repeatedly on each data point in a recursive fashion, giving rise to the term "recurrent." The RNN suffers from the gradient vanishing and explosion issues. In contrast to other DL

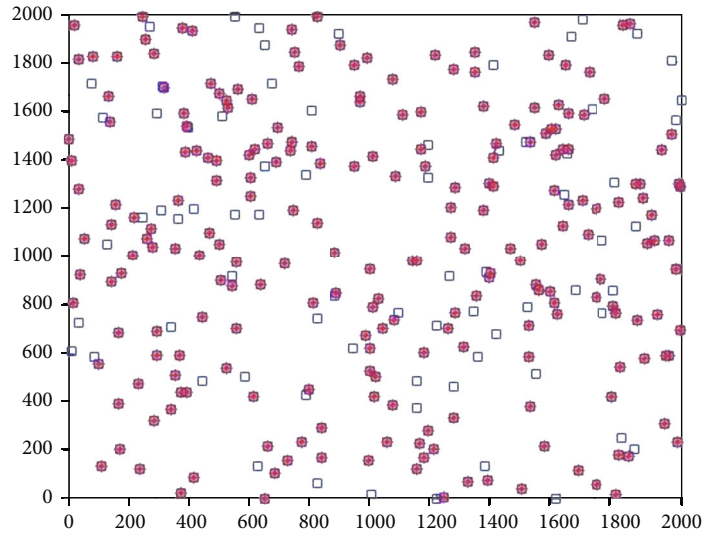

(a) Beacon node distribution phases

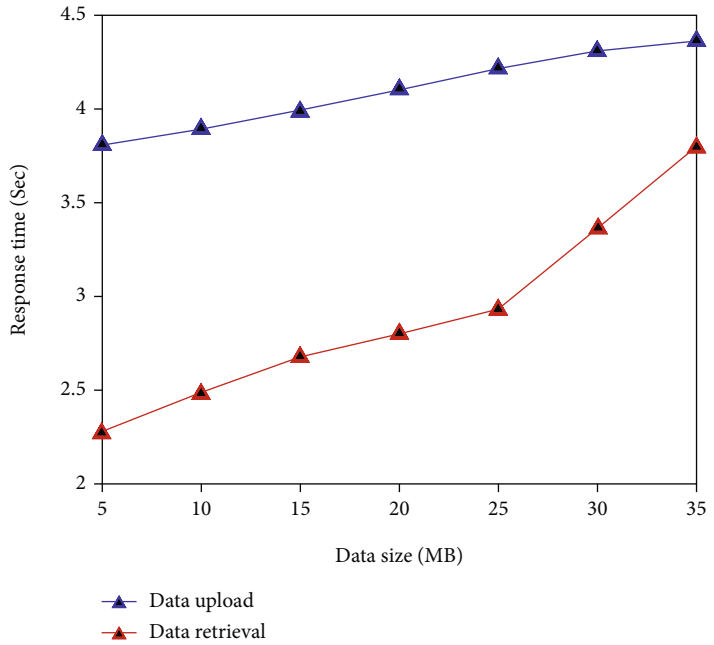

(b) Data uploading and retrieval phases

Figure 9: Continued.

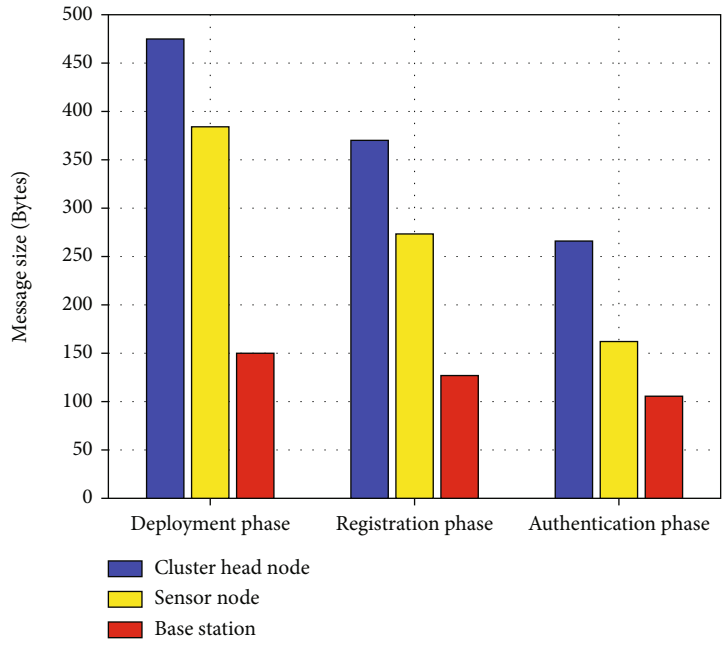

(c) Authentication and registration phases in SN, CH, and BS

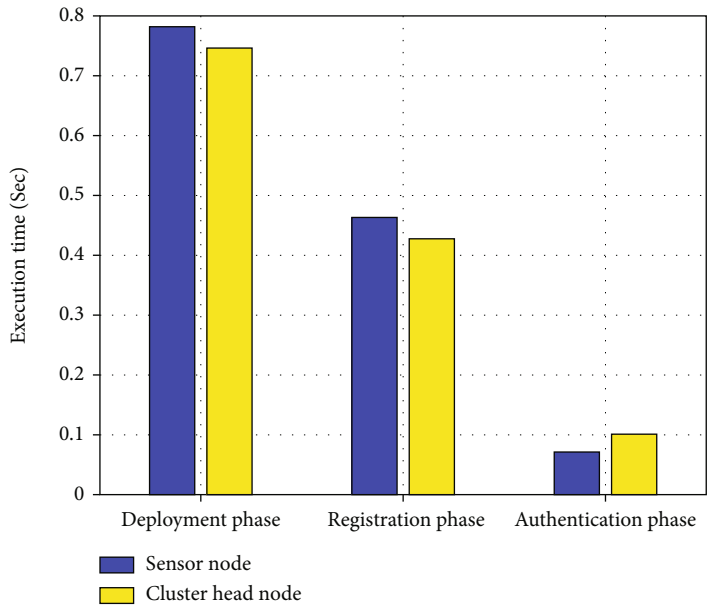

(d) Authentication and registration phases in SN and CH

Figure 9: The various phases of authentication and registration in the network model for secure data aggregation and transmission in WSNs.

techniques like deep NNs, the LSTM can recognize interdependencies in a time series and remember important data from earlier iterations to use in future predictions. We suppose that the model's inputs consist of the three preceding time steps. The data from the first unit flows into the second, as seen in the unfolded version [55, 56].

In contrast to the RNN-like LSTM, NNs like the fast forward neural network (FFNN) derive their predictions without looking back at prior time steps. They make their predictions based solely on data from the present lag. Inputs plus an n-node hidden layer make up the FFNN. Each node's output is a function of its inputs and the weights of the connections between them. Our model consists of five distinct layers: a vector input layer, three hidden layers, and a single-node output layer that returns a 1 or 0 depending on the type of classification being performed.

In this paper, we applied various activation functions considering the threshold value. The ReLU activation function is being used. It is an acronym for a nonlinear operation's rectified linear unit. Since the real world is typically highly nonlinear, the goal of adding nonlinearity to the network is achieved. It can be defined as mathematically as in

$$\text{Re Lu}(x) = \begin{cases} x & \text{if } x \geq 0, \\ 0 & \text{if } x < 0. \end{cases} \tag{16}$$

The sigmoid (or logistic) activation function (δ) was used to input the z value into the logistic function and generate values between 0 and 1 using a threshold of 0.5 as the reference value. This can be defined as mathematically

$$\delta(z) = \frac{1}{1 + e^{-x}}. \tag{17}$$

The choice of activation function is motivated by the presence of two classes of labels (outputs) for this method. Therefore, the method of binary classification technique should be used. Cross-entropy, a well-known loss function for ANNs, was the one we employed. Specifically, [47] defines cross-entropy (C) as

$$\begin{aligned} C &= -\frac{1}{n}\sum_{x}^{n}[\text{ylna} + (1-y)\ \ln\ (1-a)], \\ a &= \delta(z) = \delta\left(\sum_{j} w_j x_j + b\right), \end{aligned} \tag{18}$$

where Adam, the hybrid optimizer, will iteratively adjust the weights w and biases b. Adam is an improved version of the Stochastic Gradient Descent (SGD) algorithm. According to the scikit-learn documentation, Adam performs reasonably well on huge datasets. There are four variables you can adjust in Adam: the rate at which one is learning, the exponential decay rate for first-moment estimates, the rate at which one's second-moment estimates decay, and a very small amount to avoid a division by zero. Also, Adam is superior to SGD in noisy environments because it combines the advantages of two other popular optimizers (the adaptive gradient algorithm and root mean square propagation). We get things off with an early architecture for hyperparameter optimization that seeks optimal performance with as little computational complexity as possible.

5. Simulation and Result Discussion

The simulation setting configuration and evaluation metrics will be discussed in this section. Wireless sensors are distributed randomly forming clustering with cluster heads in the target field with an area of $1000 \times 1000\ \text{m}^2$. The routing protocols are used for making clustering and selection of the cluster head in each round of the simulation and localization of the unknown nodes with help of the beacon nodes and sink nodes. The cluster head achieves more computational data processing from the sensor nodes and communication with base station. The simulation parameter configuration is shown in Table 6. Intel (R) Xeon (R) Silver 4214 CPU @ 2.20GHz 2.19GHz (2 processors) with 128 GB (128 GB useable), x64-based processor, and 64-bit operating system running Windows using MATLAB R2021a is used for network planning and simulation.

Table 6: Simulation setup for the proposed network model.

Parameter	Values
Number of sensors	300-1000
Beacon nodes	60-120
Unknown nodes	240-840
Protocol type	Clustering and routing
Deployment area	$1000 \times 1000\ \text{m}^2$
Mobility	Random
Number of clusters	10
Sink position	500, 1000
Number of attacks	5-60
Data size	4000 kb
Attacks	Routing
Transmission radius	400 m

Our primary effort is devoted to determining how well various hybrid-based improvements to the original DV-hop algorithm perform in detecting and pinpointing hostile nodes that have hijacked the beacon node and are supplying false routing information [57]. All of our proposed algorithms have been implemented in the MATLAB simulator for thorough testing and analysis of their localization faults and precision. Numerous researchers rely on MATLAB, a simulation programed and numerical computing environment, to test out new ideas, conduct research, and build models. In our tests, we have examined the localization accuracy and the localization error per node by changing the percentage of anchor nodes, the total number of sensor nodes, and the nodes' communication range across four different topologies. One way to measure an algorithm's efficacy in localization is by looking at how it performs on average with regard to localization errors. We employ IBM SPSS, Python, and the WEKA Java toolboxes for data processing and analysis to gauge the effectiveness of the suggested strategy against the dataset [58]. The average error of localization to all the nodes is calculated using Equation (15). The clustering and routing protocols are used for clustering and selection of the cluster head selection and maximizing the network lifetime and improving the network performance. The routing attacks including the sinkhole attacks, blackhole attacks, and Sybil attacks are used in the simulation scenario for evaluating the localization and detection accuracy.

The simulation results depict that the data processed from the environment is authenticated and registered. Figure 9 shows data processing and aggregation by the cluster head sent to the base station (BS). Figures 9(a) and 9 show the dynamic clustering and data retrieval of the sensors by the beacon nodes. The cluster head (CH) aggregates huge message size as in Figures 9(c) and 2(d); the sensor nodes (SNs) consume greater time form data execution.

Registration phases are utilized to identify sensor nodes, aggregation nodes, and base stations using smart contact of the public blockchain [59]. The intelligent communications verify the existence of the aggregation node validated by its MAC address and its identity checked by the base station.

The public blockchain records of validated aggregated nodes and stored data of the aggregated node provide reliable authentication techniques in WSNs. The sensor nodes are allowed to join the blockchain after the completion of the registration process to reduce external attacks on WSNs. The sensor nodes have aggregation nodes after random deployment in the target field. The aggregation nodes authenticate the identities of the sensor nodes using a private for communicating with them, and the base station also authenticates the aggregation node for communicating with it using a public key. The aggregation nodes communicate with each other using mutual authentication process.

Figure 10 shows the distribution and the experimental simulation of the nodes. Moreover, this work introduces the average localization error and coverage, localization, and detection accuracy as evaluation metrics. The average localization error (ALE), average localization accuracy (ALA), accuracy, detection rate precision, and recall are used as evaluation metrics. The average error localization, shortened as ALE [2], is computed as follows in Equation (19). The ALE is the summation of the LE of all the unknown nodes to the total number of unknown nodes. The LE is the difference between estimated and actual position of unknown nodes.

$$\begin{aligned}
\text{Localization Error (LE)} &= \sqrt{\left(u_i' - u_i\right)^2 + (v_i' - v_i)^2}, \\
\text{Average Localization Error (ALE)} &= \sum_{i=1}^{n} \frac{\sqrt{\left(u_i' - u_i\right)^2 + (v_i' - v_i)^2}}{\text{nR}}, \\
\text{Average Localization Accuracy (ALA)} &= \left(1 - \left(\sum_{i=1}^{n} \frac{\sqrt{\left(u_i' - u_i\right)^2 + (v_i' - v_i)^2}}{\text{nR}}\right)\right) \times 100\%,
\end{aligned} \tag{19}$$

where (u_i' and v_i') are the real coordinates of the anonymous node i and (ui, vi) are the computed coordinates, n denotes unknown nodes, and R is radius of communication in the network. Wireless sensor nodes are deployed and simulated using localization process using the beacon nodes as in Figure 10(a). The error for the anonymous sensor nodes is displayed in Figure 10(b). The position and error for each node are computed using the localization scheme. The computation of the localization accuracy for each node enables for effective identification and localization of the malicious nodes with help of the beacon nodes and the base station.

The effectiveness of the distance vector hop algorithm is measured by malicious node detection, localization accuracy, and localization efficiency [60]. The practical localization estimation of the unknown and malicious nodes is determined by the number of the anchor nodes for its evaluation metrics, as shown in Figure 11. The relative error defines between the computed position of the node and the actual location of the node. Malicious nodes affect nodes' distribution and localization accuracy by creating the wrong position and location of the unknown sensor nodes in WSNs. Malicious nodes mislead the sensor nodes' routing path and information, making the network service and performance degrade.

The average localization accuracy and detection accuracy of the proposed system are 99.51% and 99.83% with 840 unknown nodes and 160 beacon nodes for accurate computation of malicious nodes, respectively, as shown in Figures 11(a) and 11(b).

According to the findings of the simulation, anchor nodes have a greater number of neighbors and a higher degree of connectedness than regular sensor nodes, as can be seen in Figure 12(a). If we use the regular model, we can determine that the average connectivity of the network is 404, and the average number of neighbor nodes that each anchor node has is 63. As can be seen in Figure 12(b), the overall network's average localization error was reduced to 0.0049 thanks to the simulation's efforts, and this was achieved across all nodes. This would imply that all sensor nodes are precisely located and have a unique identity thanks to the beacon nodes, which help in the identification and localization of malicious nodes.

The simulation results demonstrate that the suggested method utilizes hybrid localization techniques utilizing both range-free and range-based approaches to accurately determine the position and location of each unknown node while minimizing energy consumption. As twenty mobile anchor nodes are utilized in the proposed method, the price is kept low while the accuracy of pinpointing malicious nodes in WSNs is much enhanced. Figures 13(a) and 13(b) for the beacon nodes and the unknown nodes, respectively, illustrate how the hybrid strategy combining the DV-hop technique with other approaches such as RSSI and DE improves the average localization accuracy of the proposed scheme.

The experimental findings for calculating the location error against changing numbers of beacon nodes are displayed in Figures 14(a) and 14(b). In addition, the localization error for all the algorithms gradually decreases as the number of the activated sensor nodes grows [34]. The proposed hybrid method has the lowest localization error score of all the methods we have tested. With 200 beacon nodes, more reference points are detected, reducing the margin of error for localization. Figure 14 shows conclusive proof that the new method outperforms conventional location-based algorithms when it comes to pinpointing the origin of an error. In the same setup, nearly all of the methods that have been tried and tested have been effective. As a result of having more points of reference for the target nodes, the suggested method allows for a gradual decline. In contrast, the network is strengthened by an adequate number of anchor nodes, as the distance between the unknown nodes and the anchor nodes decreases.

As may be shown in Figures 14(a) and 14(b), the ALE of four different localization techniques decreases as the number of beacon nodes increases. Since there are more anchor nodes now, the average distance travelled in one hop can be calculated with more precision. The distances predicted by the anchor nodes from the unknown nodes are more accurate [61, 62]. This shows that the proposed approach is effective to estimate the placement of unknown nodes as the number of anchors grows because it has more

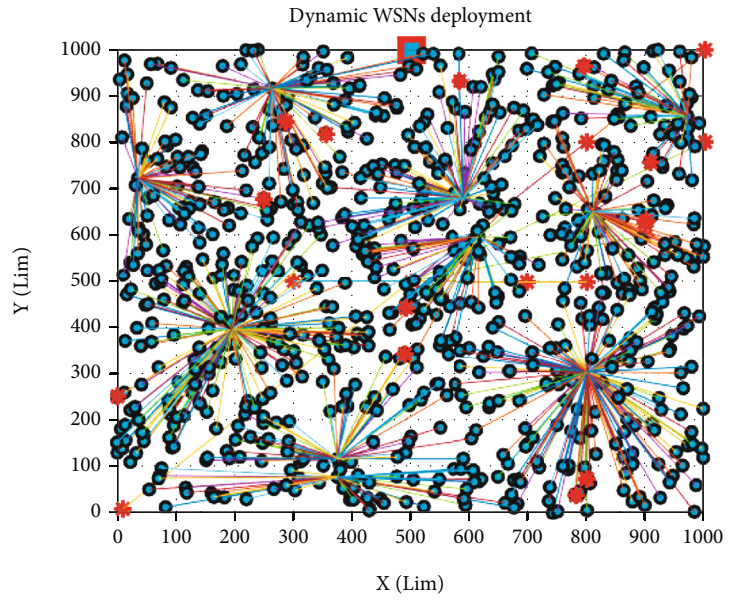

(a) Clustering and localization of WSNs

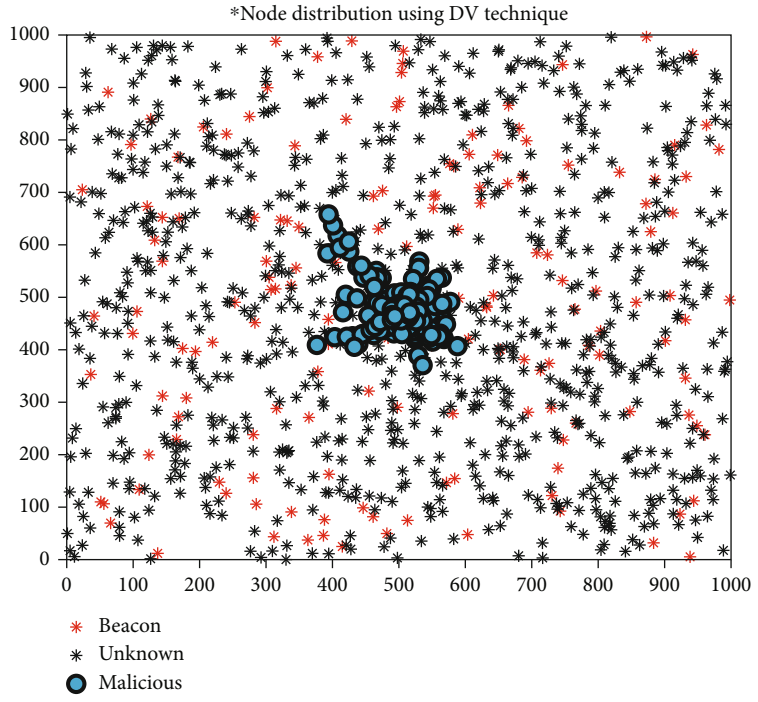

(b) Malicious node localization in WSNs

Figure 10: Sensor node deployment using distance vector protocol and triangulation process in WSNs.

circumstances to work with. Given that some fraction of the nodes can serve as anchor nodes for node localization, the suggested methodology exhibits lower error compared to the previous methods.

5.1. Performance Metrics. In this section, a cybersecurity dataset is applied with different types of attack categories. The benchmark datasets are utilized for analyzing and processing using the optimized artificial neural network technique to detect and localize multiple attacks to evaluate the proposed system about the Sybil attacks. The dataset is used as a benchmark for the security localization and detection of accuracy of various classes of routing attacks in the network. The Python programming language, SPSS, and WEKA toolboxes are used for data processing and classification to detect the different classes of attacks in WSNs [20]. There are different types of performance metrics for measuring the effectiveness of the proposed scheme. Table 7 shows the measurement entities of the system with mathematical equations.

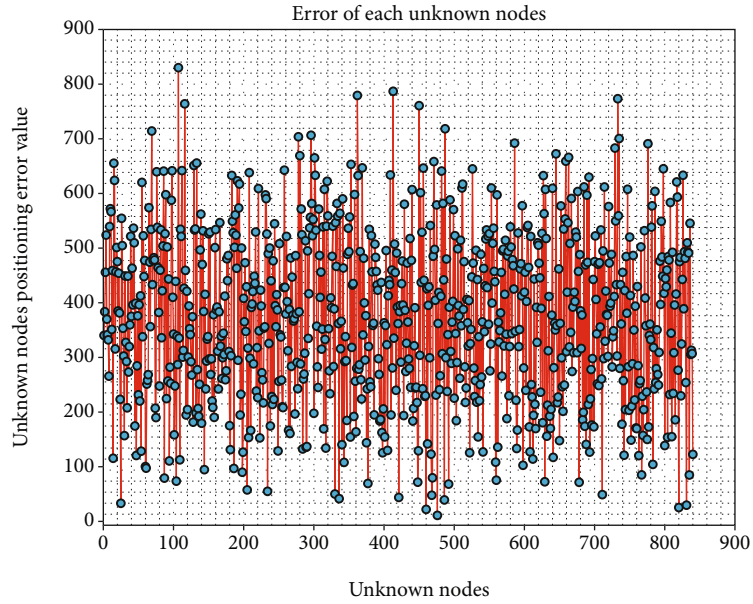

(a) Positioning error of unknown nodes

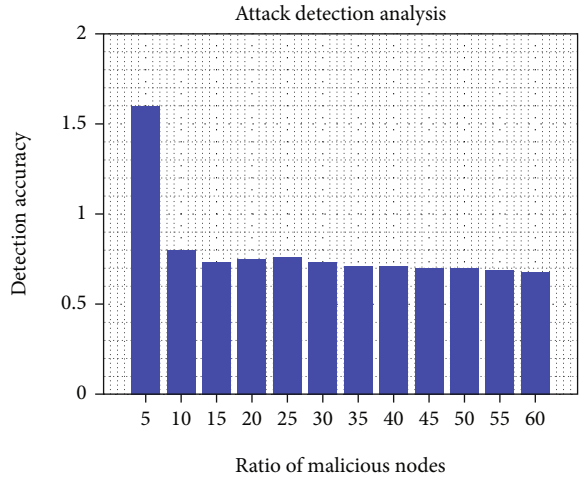

(b) Detection of accuracy of malicious nodes

Figure 11: Computing localization and position of unknown node errors and detection accuracy of malicious nodes using distance vector hop algorithm and trilateration process.

The parameters are false negatives = F_n [47], true positives = T_p, true negatives = T_n, and false positives = F_p [63]. Accuracy is the parameter for evaluating the performance of proposed classification model [64]. Informally, it is the section of predictions the model achieved successfully. Formally, it can be computed [20] as shown in Table 7. The F-measure [65] is a combination of recall and precision [63] computed as in Table 7. The Matthews correlation coefficient (MCC) is also the measure of the performance for scoring prediction of the model. The proposed system has training and testing phases using the cybersecurity dataset as benchmark with different classes of attacks. The system is based on the ANN approach achieves an accuracy of 99.84% and error of 0.16% using three hidden layers with 10-fold cross-validation using CICIDS2018 a benchmark dataset. The different attacks are correctly detected and localized, greater than 78% proposed by Dong et al. [2] using the distance vector hop scheme with an error of 22% malicious node localization.

Receiver operating characteristic analysis is useful to assess the model's accuracy using the ANN technique [66]. The total area under the ROC represents the statistical probability prediction of the classification of the proposed model for different types of attacks using a threshold cutting point $C\epsilon(0, 1)$ as shown in Table 7. This ROC analysis supports the inference area under the curve and Precision-recall curves. The ROC is a plot of the sensitivity versus 1-specificity, as shown above in Figure 15(a). Sensitivity is the number of attacks correctly identified in the network. 1-specificity is the attack classes wrongly rejected. The cumulative chart gain in Figure 15(b) shows the overall percentage of the total observations for the given class of attacks in the network. The target category is the percentage of the overall amount

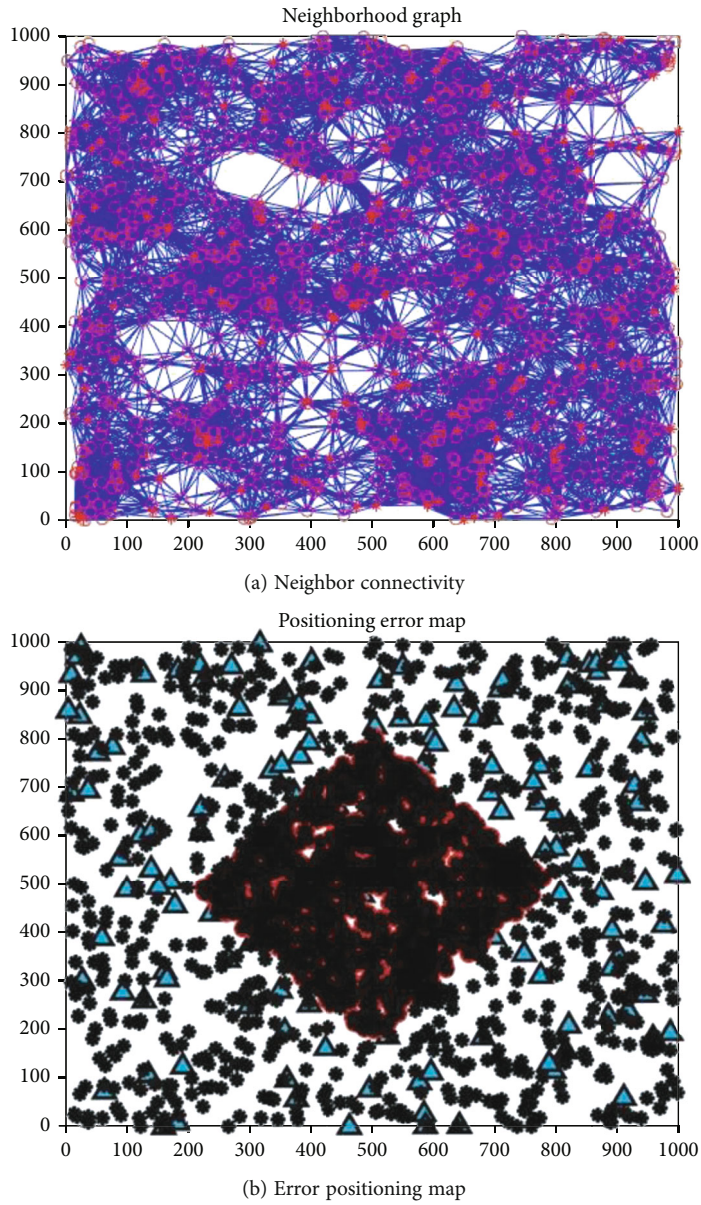

(a) Neighbor connectivity

(b) Error positioning map

Figure 12: Simulated results of sensor deployment (a) and neighbor relationship diagram (b).

of samples in the dataset. The diagonal line is the baseline for the classification of the target samples. The cumulative gain chart is a cutoff choosing the attack classification and mapping the appropriate cutoff values. Table 8 depicts the area under the curve detection rate performance for each type of attack.

The area under curve is visualized in Figure 16 for each attack category of the dataset. The area under the curve is more significant for the standard class in the proposed network traffic analysis. The ROC analysis shows that the MLPANN approach is practical for multiclass attack localization and detecting DoS attacks. The ROC shows that the proposed scheme is effective for DoS attack classification using a benchmark dataset.

The area under the curve is a statistical summary of the ROC curve, and the values represent each attack category. The area under the curve also indicates the probability of the classification model. The standard class of the attack has a greater extent, which is effectively detected. The pseudopredictive probability in Figure 17 describes each attack class's scaling by dividing their sum of classification accuracy. The effectiveness of the scheme can be proved using other attacks types and datasets as threshold measurements.

The average classification of the proposed system is 96% using the predictive probability model. Figure 17 shows the effectiveness of the various attack classification model. The classification model is trained 80% of the dataset, and 20% tested samples using the batch mode with the activation function using gradient descent algorithm with three hidden layers and trainable parameters.

5.2. Performance Comparison. The performance of the proposed methodology is validated and confirmed by comparing and testing with other previous works using various

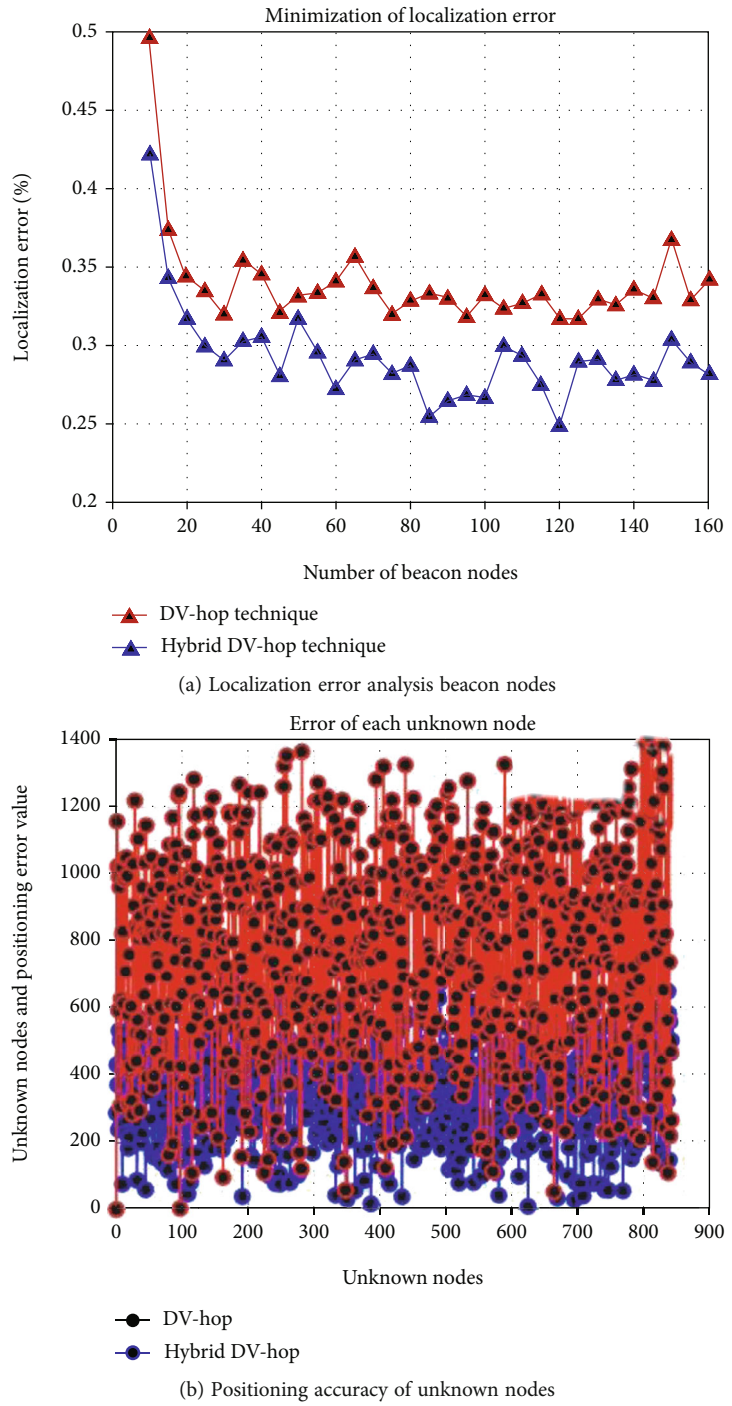

Figure 13: Improving the localization and position accuracy of wireless sensor nodes using hybrid scheme.

benchmark datasets. The comparison performance of recent works as shown in Table 9 suggests the optimized MLPANN technique is effective for detection and localization of attacks in WSNs.

Figures 18(a) and 18(b) show the performance comparison of the proposed system using four benchmark datasets and different attack detection models using the accuracy, precision, recall, and F1-measure. This suggests that the proposed scheme is effective for detecting and localization attacks in WSNs.

This suggests that the proposed system is more effective than the previous work by Almomani et al. [20] artificial neural network-based intrusion detection system (ANN-IDS) for routing attack detection and classification, as shown in Figure 18(b) with an average detection accuracy of 97.2% using sample WSN-dataset using ten-fold cross-validation with three hidden layers. Dong et al. [2] used the distance vector hop algorithm to detect Sybil attacks with a localization accuracy of 78%, which is less than the proposed scheme. The proposed work is also

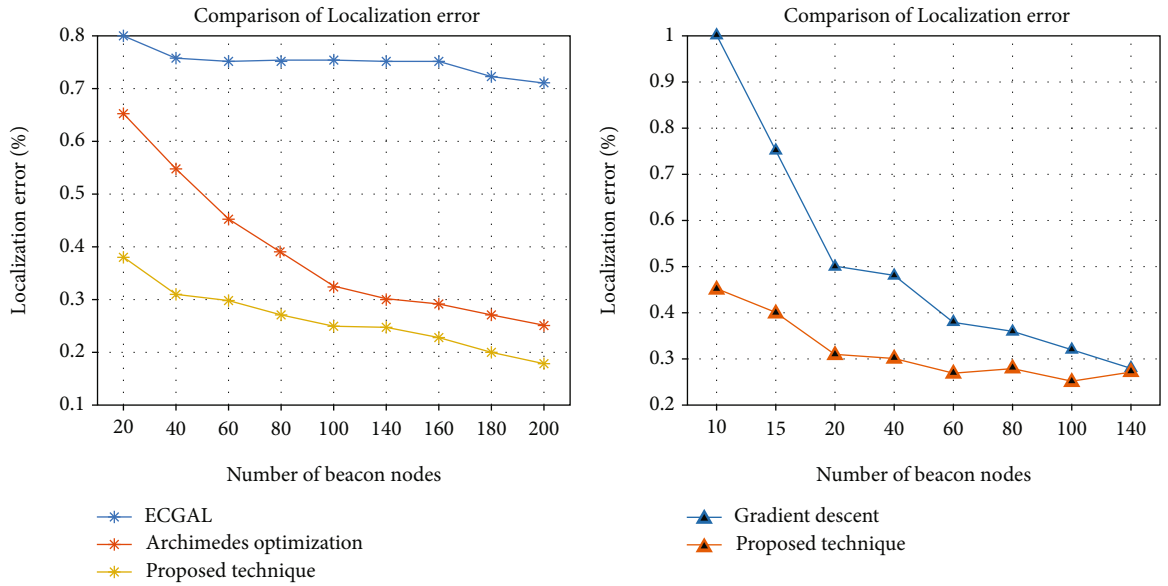

(a) Comparison of localization schemes

(b) Comparison with gradient descent

Figure 14: Comparison of the localization error of the proposed scheme with other modes by varying the number of nodes.

Table 7: Performances metrics of the proposed system with their technical and mathematical expressions.

Metrics	Technical description	Mathematical equations
Sensitivity	The positive prediction of the model	$\text{Sensitivity} = \frac{T_p}{T_p + F_n}$
Specificity	The negative prediction of the model	$\text{Specificity} = \frac{T_n}{F_n + T_p}$
Precision	Truly identified instances of samples	$\text{Precision}(p) = \frac{T_p}{F_p + T_p}$
ROC	Classifier performances of the model	$\text{ROC}(.) = \{\text{FPR}(C), \text{TPR}(C), C\epsilon(0,1)\}$
Recall	Equivalent to TP rate	$\text{Recall} = \frac{T_p}{T_p + F_n}$
F-measure	Combination of precision and recall	$\text{F} - \text{measure} = \frac{2 \times T_p}{2 \times T_p + F_p + F_n}$
Accuracy	Classification prediction of the model	$\text{Acc.} = \frac{T_n + T_p}{T_n + T_p + F_n + F_p}$
FP rate	Wrongly classified events	$\text{FPR} = \frac{F_p}{F_p + T_n}$
Energy	Energy consumption analysis	$E_c = E_t - E_l$
Lifetime	Over all alive nodes (N)	$\text{Aliv}(N) = \text{Total}(N) - \text{Dead}(N)$
MCC	Binary classification	$\text{Mcc} = \frac{T_p.T_n - F_p.F_n}{\sqrt{(T_p + F_p).(T_p + F_n).(T_n + F_p).(T_n + F_n)}}$
ALE	Average localization error	$\text{ALE} = \sum_{i=1}^{n} \frac{\sqrt{\left(u_i' - u_i\right)^2 + (v_i' - v_i)^2}}{nR}$

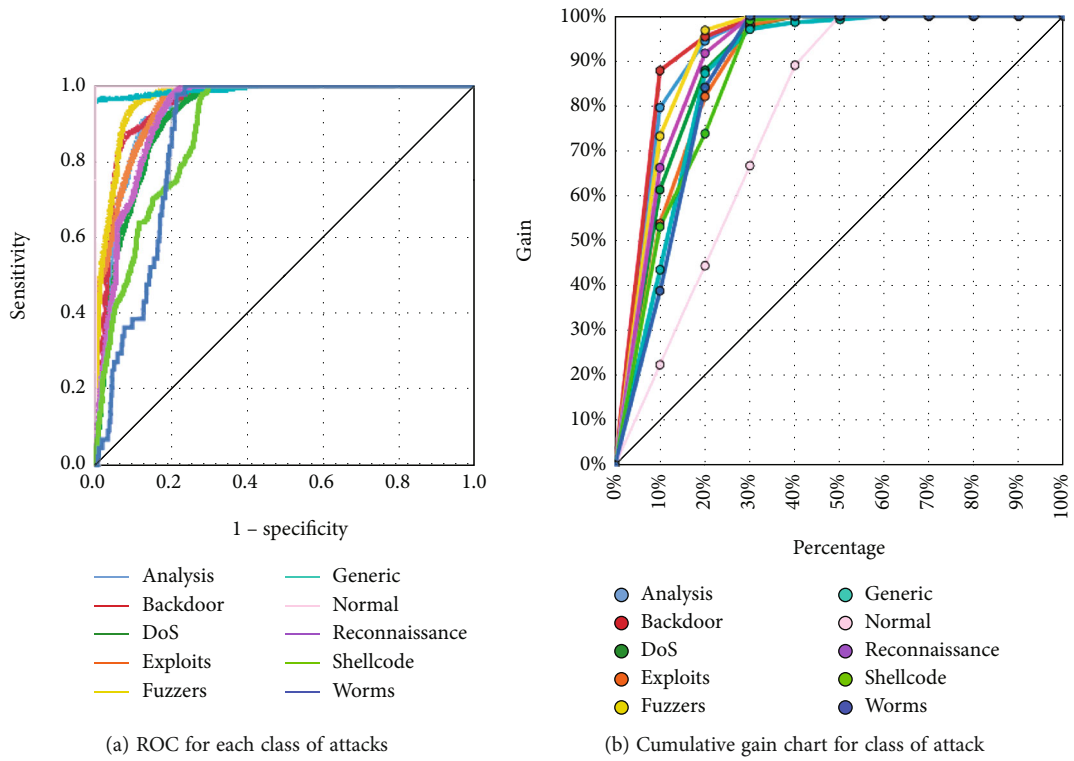

(a) ROC for each class of attacks

(b) Cumulative gain chart for class of attack

Figure 15: Receiver operating characteristics (ROCs) and cumulative chart of the proposed system.

Table 8: Area under the curve for each class of attack.

Class	Analysis	DoS	Backdoor	Exploits	Fuzzers	Generic	Normal	Reconnaissance	Shellcode	Worms
Area	99.8%	98.8%	97.2%	99.1%	99.9%	96.7%	100%	99.2%	97.8%	94.9%

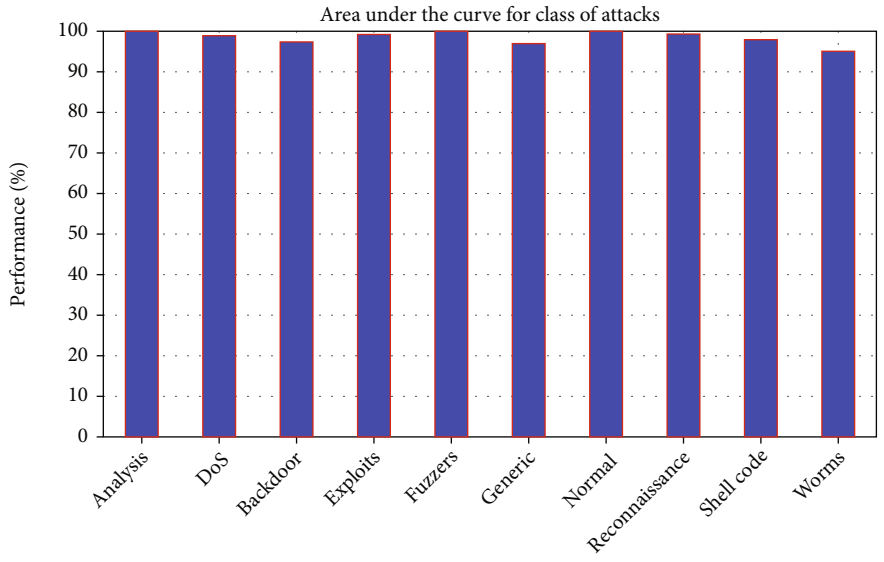

Figure 16: Area of under the curve for each class of attack using UNSW-NB 15 benchmark dataset.

practical compared to the MK-ELM model [67], which has an accuracy of 92.10% using UNSW-NB 15 dataset. Figure 18 shows the detection and localization for the proposed ANN approach compared with other works for Sybil attack detection. The comparison performance is using sample experimental dataset examined by Sujatha and Anita [24] with an average detection rate of 97% using fuzzy extreme machines (FEMs).

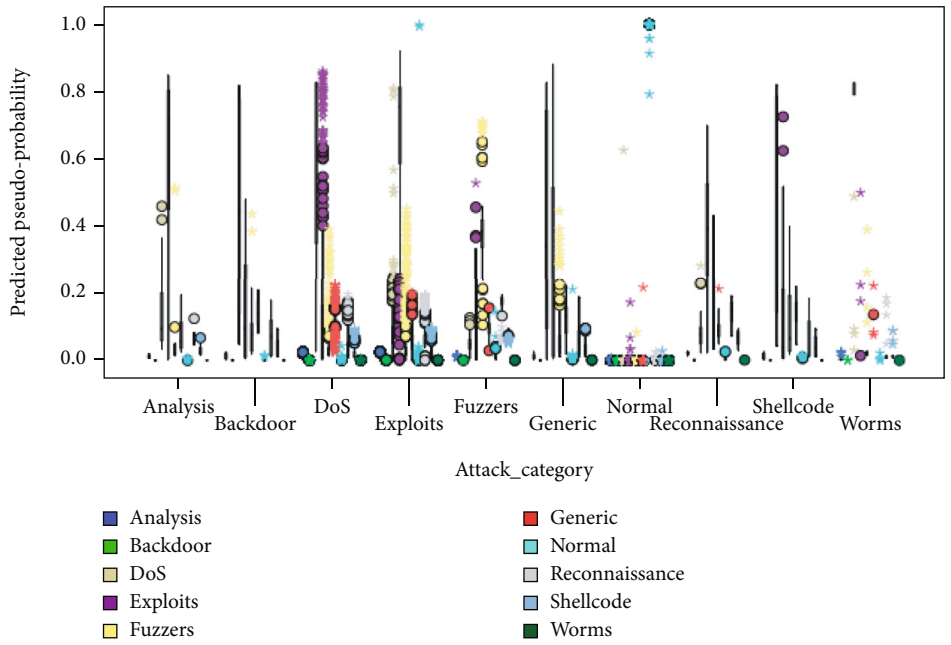

Figure 17: Attack classification prediction probability of the model.

Table 9: Comparative analysis of the proposed technique with recent attack detection models using CICIDS2018 dataset.

	Methods	Accuracy	Precision	Recall	F1-score
Zhou et al. [8]	MLP	97.56	99.12	98.79	98.23
Almomani et al. [20]	ANN-IDS	97.18	97.8	97.5	97.69
Sujatha and Anita [24]	FEM	99	98	98	98.98
Zhang et al. [67]	MK-ELM	98.34	98.03	97.63	97.64
Khan et al. [68]	LEACH++-ANN	97	96.8	96	96.4
Mohammadpour et al. [69]	CNN-MCL	99.46	99.76	99.15	99.46
Xinlong and Zhibin [70]	HTM-LSTM	97.74	97.20	97.92	97.72
Proposed system	MLPANN	99.83	99.71	100.00	99.85

The proposed attack detection and localization scheme achieve 100% using the same dataset. Hasan et al. [71] determined the detection accuracy of 91.66% of the malicious node using an optimized artificial neural network using the packet delivery and energy consumption evaluation metrics. The various comparison performances conclude our proposed scheme is effective for the detection localization of attacks in WSNs. Khan et al. [68] analyzed the detection of routing attacks using the LEACH++ protocol based on an artificial neural network (LEACH++-ANN) and achieved a detection accuracy of 98%. This proves the proposed scheme is more effective for detecting routing attacks, with an average detection accuracy of 99.62%. The proposed system also achieves average detection accuracy of 98.4% using the benchmark dataset NSL-KDD as shown in Figure 18(b) for each class of attack. The proposed approach is practical for detecting and localization DoS attacks in WSNs compared to the convolutional neural network and mean convolutional layer (CNN-MCL) model proposed by Mohammadpour et al. [69] with an average detection accuracy of 99.46%. Zhang et al. [67] proposed an hierarchical intrusion detection model (HIDM) for WSNs using a multikernel-based extreme learning machine (MK-ELM) classification technique using UNSW-NB and NSL-KDD benchmark datasets.

The proposed system's average localization and detection rate are validated by comparing previous works with different classes of attacks. Table 10 shows that when applied the UNSW-NB 15 dataset, which serves as a benchmark for identifying and classifying routing assaults, the proposed approach improves detection accuracy by class using 80% of training and 20% of testing of samples with five hidden layers. The demonstration further shows that the verification of the suggested performance parameters and metrics (accuracy, precision, F1-score, and recall) against those of recently published attack detection models.

The performance of the proposed system is effective for detection and localization of DoS attacks in WSNs using benchmark datasets in terms of the evaluation metrics such as accuracy, precision, recall and F1-score as shown in

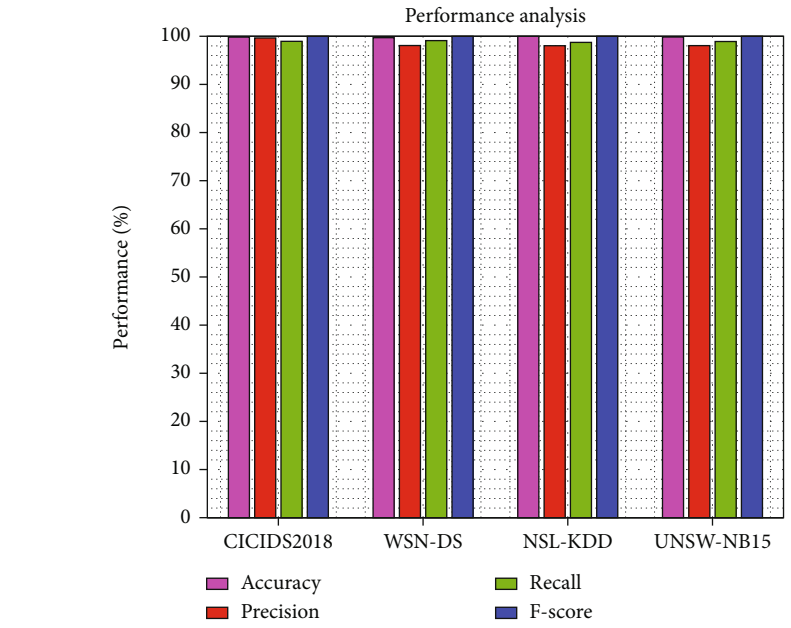

(a) Comparison using benchmark datasets

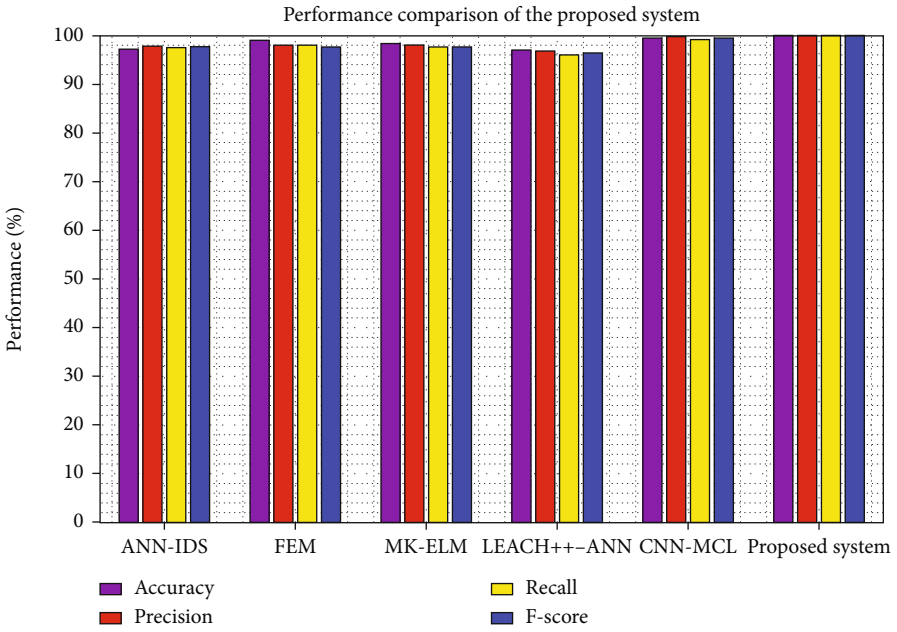

(b) Comparison of various attack detection models

Figure 18: Performance comparison of the proposed system using benchmark datasets for attack detection and classification.

Table 10: Comparative analysis of the proposed technique with recent attack detection models using UNSW-NB 15 dataset.

Author	Method	Accuracy	Precision	Recall	F1-score
Pasikhani,et al. [72]	RL-IDS	98.35	98.36	97.04	98.34
Upadhyay et al. [73]	GBFS-IDS	92.96	92.50	92.40	92.44
Abdan and H. Seno [11]	ML-ID	98.9	87.7	99.6	92.78
Gudla et al. [74]	DI-ADS	99.44	99.02	99.60	99.30
Alghamdi [75]	PO-CFNN	99.86	99.89	99.58	99.72
Khilar et al. [76]	DNN-CSO	99.46	99.75	99.62	99.76
Proposed system	MLPANN	100.00	100.00	100.00	100.00

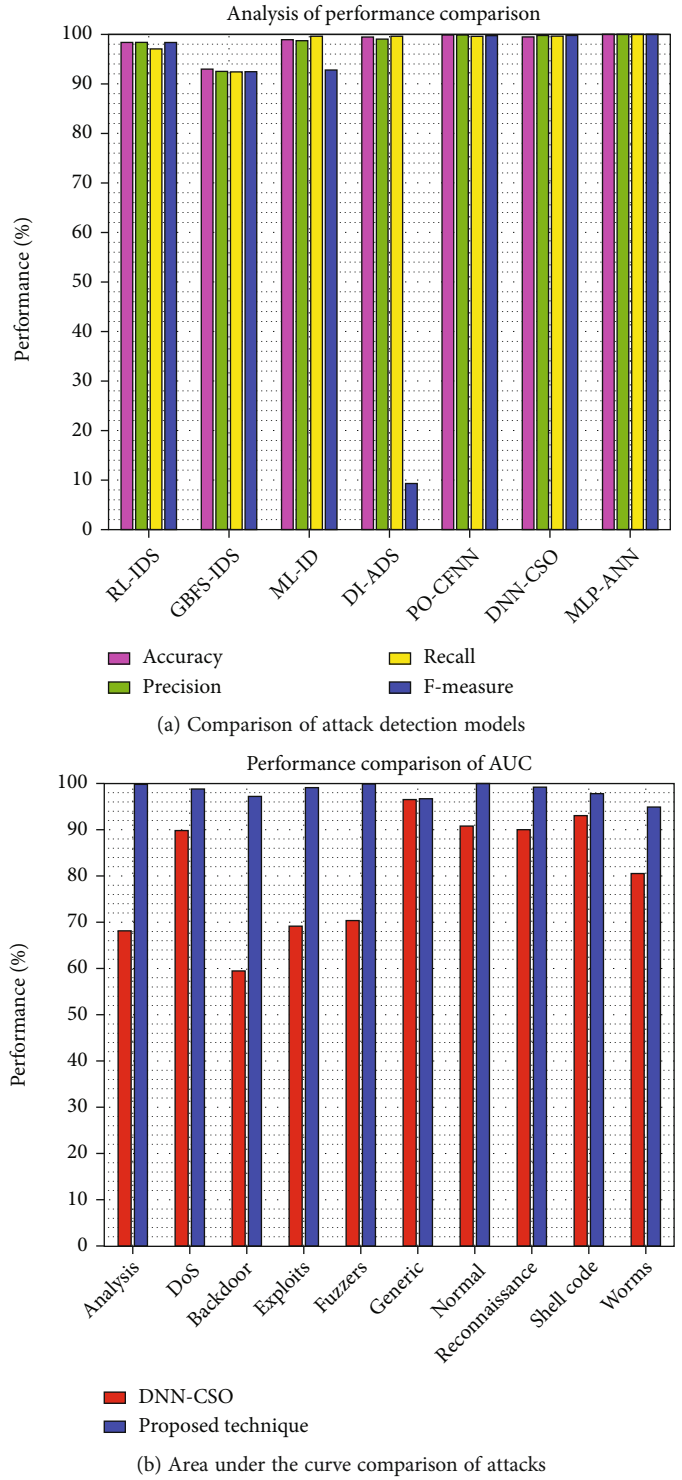

(a) Comparison of attack detection models

(b) Area under the curve comparison of attacks

Figure 19: Performance comparison of the proposed system with recent works using benchmark datasets.

Figure 19(a). The area under the curve (AUC) is also used for evaluating the performance of the system as show in Figure 19(b). This confirms that the optimized MLPANN approach is effective in attack detection and localization of WSNs attacks.

The proposed multilayer perception artificial neural network (MLPANN) technique is further compared with MK-ELM using the NSL-KDD benchmark dataset, taking a section of 14,000 sample records with three hidden layers, as shown below in Table 11. The average detection accuracy of the proposed technique is 98.4% using 111,110 samples which is more effective than MK-ELM with 14,000 samples with an average detection accuracy of 98.34%.

Table 11: Comparison of performance of the proposed MLPANN with MK-ELM using the section of the NSL-KDD dataset with hidden layers.

Class of attacks	TP rate (%)		FP rate (%)		FN rate (%)		TN rate (%)	
	MK-ELM	Proposed scheme	MK-ELM	Proposed scheme	MK-ELM	Proposed scheme	MK-ELM	Proposed scheme
DoS	98.04	99.00	0.49	0.001	1.96	1.00	99.51	99.90
Probes	95.67	97.20	0.47	0.001	4.33	2.80	99.53	99.90
R2L	76.12	96.80	0.11	0.015	23.88	3.20	99.89	99.98
U2R	50.00	90.04	0.00	0.003	50.00	9.96	100.00	99.99

Table 12: Comparison performance of machine learning models using the CICIDS2017 benchmark dataset.

Classifier	ML models results				Hybrid PTE-BO ML model results			
	Accuracy	Precision	Recall	F1-score	Accuracy	Precision	Recall	F1-score
XGBoost	99.82	99.82	99.82	99.80	99.82	99.86	99.82	99.83
Ensemble stacking	99.82	99.91	99.82	99.85	99.82	99.91	99.82	99.85
Random forest	99.77	99.77	99.77	99.75	99.82	99.82	99.82	99.80
Decision tree	99.77	99.77	99.77	99.75	99.82	99.91	99.82	99.85
Extra tree	99.82	99.82	99.82	99.80	99.82	99.80	99.82	99.80

The validation of the result can also be confirmed by comparing the previous works as stated theoretically and graphically. The multilayer perception artificial neural network (MLPANN) effectively detects and classifies multiple attacks using public datasets, including UNSW-NB, WSN-DS, and NSL-KDD, as a benchmark for performance evaluation. By combining a tree based on the Parzen estimation (PTE) with hyperparameter and Bayesian optimization (BO) techniques, we are able to better classify the machine learning models for the proposed scheme on the benchmark dataset as shown in Table 12. Every single machine learning task uses hyperparameters to fine-tune the aforementioned parameters and get optimal results. Hyperparameter optimization (HPO) accomplishes both of these goals with less manual labor and better results from machine learning [77].

The MLPANN technique also achieves better detection accuracy of 99.62% using the WSN-DS benchmark dataset. The proposed scheme is effective for the localization and detection of different classes of attacks, approving that the proposed system has optimal average detection for multiple suspicious nodes. The novelty of this work is that it is effective in the detection and localization of various attacks. The proposed scheme is innovative for its ability to scale in both security and performance for optimal area coverage in wireless sensor networks with a hierarchical architecture and both heterogeneous and homogeneous sensor nodes.

6. Conclusion and Remarks

In this work, we proposed a multilayer perceptron artificial neural network (MLPANN) for detecting and localizing multiple attacks in WSNs. The proposed scheme achieved an average detection accuracy of 100%, 99.65%, 98.95%, and 99.83% for the various malicious nodes using UNSW-NB, WSN-DS, NSL-KDD, and CICIDS2018 benchmark datasets, respectively. The optimized localization approach is more effective and performs more significantly by 20% than the distance vector hop technique, with average localization accuracy of 99.12% using 160 beacon nodes. The validation of the proposed method is confirmed with the previous studies using the ANN classification technique using Python, IBM SPSS, and WEKA toolboxes for data processing and MATLAB R2021a for network planning and simulation. The datasets are used to evaluate the proposed system for detecting and localization accuracy of different attacks. The effectiveness of the proposed scheme is assessed using detection rate, ROC, false-positive rate, a lifetime of the network, residual energy, and the area under the curve metrics. The beacon, sensor, and malicious nodes were used hierarchically to simulate the target field. It is recommended to enhance further the detection and localization of accuracy of malicious nodes using different approaches in WSNs. We will extend this work with various attack classes and methods. The results show that performance and security of the proposed scheme are applicable for scalable and large network coverage in wireless sensor networks with heterogeneous and homogenous sensors for ensuring quality of services and availably. The proposed scheme will be examined in the future using other network planning and tools with different public datasets as benchmarks for detecting and localization attacks in WSNs.

Data Availability

The underlying dataset used to generate the results presented in this article is available upon request to the corresponding author.

Conflicts of Interest

The authors declare that there is no competing interest in this work.

References

[1] S. Messous and H. Liouane, "Online sequential DV-hop localization algorithm for wireless sensor networks," *Mobile Information Systems*, vol. 2020, Article ID 8195309, 14 pages, 2020.

[2] S. Dong, X. G. Zhang, and W. G. Zhou, "A security localization algorithm based on DV-hop against Sybil attack in wireless sensor networks," *Journal of Electrical Engineering and Technology*, vol. 15, no. 2, pp. 919–926, 2020.

[3] G. Farjamnia, Y. Gasimov, and C. Kazimov, "An improved DV-hop for detecting wormhole attacks in wireless sensor networks," *Journal of Communication Engineering*, vol. 9, no. 1, pp. 1–24, 2020.

[4] S. T. Patel and N. H. Ministry, "A Review: Sybil Attack Detection Techniques in WSN," in *4th International Conference on Electronics and Communication Systems (ICECs)*, pp. 4–8.

[5] J. Jiang, G. Han, C. Zhu, Y. Dong, and N. Zhang, "Secure localization in wireless sensor networks: a survey (invited paper)," *The Journal of Communication*, vol. 6, no. 6, pp. 460–470, 2011.

[6] B. Madagouda and R. Sumathi, "Artificial neural network approach using mobile agent for localization in wireless sensor networks," *Advances in Science, Technology and Engineering Systems Journal*, vol. 6, no. 1, pp. 1137–1144, 2021.

[7] M. Bernas and B. Płaczek, "Fully connected neural networks ensemble with signal strength clustering for indoor localization in wireless sensor networks," *International Journal of Distributed Sensor Networks*, vol. 11, no. 12, Article ID 403242, 2015.

[8] D. Zhou, W. Liu, W. Zhou, and S. Dong, "Research on network traffic identification based on multi layer perceptron," *Telkomnika (Telecommunication Computing Electronics and Control)*, vol. 12, no. 1, pp. 201–208, 2014.

[9] M. A. Alsheikh, S. Lin, D. Niyato, and H. P. Tan, "Machine learning in wireless sensor networks: algorithms, strategies, and applications," *IEEE Communication Surveys and Tutorials*, vol. 16, no. 4, pp. 1996–2018, 2014.

[10] M. Wazid and A. K. Das, "An efficient hybrid anomaly detection scheme using K-means clustering for wireless sensor networks," *Wireless Personal Communications*, vol. 90, no. 4, pp. 1971–2000, 2016.

[11] M. Abdan and S. A. H. Seno, "Machine learning methods for intrusive detection of wormhole attack in mobile ad hoc network (MANET)," *Wireless Communications and Mobile Computing*, vol. 2022, Article ID 2375702, 12 pages, 2022.

[12] B. Ahmad, W. Jian, Z. A. Ali, S. Tanvir, and M. S. A. Khan, "Hybrid anomaly detection by using clustering for wireless sensor network," *Wireless Personal Communications*, vol. 106, no. 4, pp. 1841–1853, 2019.

[13] G. Farjamnia, Y. Gasimov, and C. Kazimov, "Review of the techniques against the wormhole attacks on wireless sensor networks," *Wireless Personal Communications*, vol. 105, no. 4, pp. 1561–1584, 2019.

[14] R. Singh, J. Singh, and R. Singh, "Fuzzy based advanced hybrid intrusion detection system to detect malicious nodes in wireless sensor networks," *Wireless Communications and Mobile Computing*, vol. 2017, Article ID 3548607, 14 pages, 2017.

[15] M. Mahajan, K. T. V. Reddy, and M. Rajput, "Design and simulation of a blacklisting technique for detection of hello flood attack on LEACH protocol," *Procedia Computer Science*, vol. 79, pp. 675–682, 2016.

[16] U. Jain and M. Hussain, "Securing wireless sensors in military applications through resilient authentication mechanism," *Procedia Computer Science*, vol. 171, no. 2019, pp. 719–728, 2020.

[17] S. Z. Wang, Y. Li, and W. Cheng, "Distributed classification of localization attacks in sensor networks using exchange-based feature extraction and classifier," *Journal of Sensors*, vol. 2016, Article ID 8672305, 18 pages, 2016.

[18] L. Chelouah, F. Semchedine, and L. Bouallouche-Medjkoune, "Localization protocols for mobile wireless sensor networks: a survey," *Computers and Electrical Engineering*, vol. 71, pp. 733–751, 2018.

[19] A. Hadir, K. Zine-Dine, M. Bakhouya, and J. El Kafi, "An improved DV-hop localization algorithm for wireless sensor networks," in *2018 13th IEEE conference on industrial electronics and applications (ICIEA)*, pp. 330–334, Wuhan, China, June 2014.

[20] I. Almomani, B. Al-Kasasbeh, and M. Al-Akhras, "WSN-DS: a dataset for intrusion detection systems in wireless sensor networks," *Journal of Sensors*, vol. 2016, Article ID 4731953, 16 pages, 2016.

[21] S. T. Patel and N. H. Mistry, "A review: Sybil attack detection techniques in WSN," in *2017 4th International conference on electronics and communication systems (ICECS)*, vol. 17, pp. 184–188, Coimbatore, India, February 2017.

[22] O. Cheikhrouhou and A. Koubaa, "BlockLoc: secure localization in the internet of things using blockchain," in *2019 15th International Wireless Communications & Mobile Computing Conference (IWCMC)*, pp. 629–634, Tangier, Morocco, June 2019.

[23] F. Y. Yavuz, D. Ünal, and E. Gül, "Deep learning for detection of routing attacks in the internet of things," *International Journal of Computational Intelligence Systems*, vol. 12, no. 1, pp. 39–58, 2018.

[24] V. Sujatha and E. A. M. Anita, "FEM-hybrid machine learning approach for the detection of sybil attacks in the wireless sensor networks," *International Journal of Innovative Technology and Exploring Engineering*, vol. 8, no. 7, pp. 1171–1179, 2019.

[25] X. Qi, X. Liu, and L. Liu, "A combined localization algorithm for wireless sensor networks," *Mathematical Problems in Engineering*, vol. 2018, Article ID 4648109, 10 pages, 2018.

[26] P. Li, X. Yu, H. Xu, J. Qian, L. Dong, and H. Nie, "Research on secure localization model based on trust valuation in wireless sensor networks," *Security and Communication Networks*, vol. 2017, Article ID 6102780, 12 pages, 2017.

[27] L. Song, L. Zhao, and J. Ye, "DV-hop node location algorithm based on GSO in wireless sensor networks," *Journal of Sensors*, vol. 2019, Article ID 2986954, 9 pages, 2019.

[28] M. Saud Khan and N. M. Khan, "Low complexity signed response based Sybil attack detection mechanism in wireless sensor networks," *Journal of Sensors*, vol. 2016, Article ID 9783072, 9 pages, 2016.

[29] A. Payal, C. S. Rai, and B. V. R. Reddy, "Artificial neural networks for developing localization framework in wireless sensor networks," in *2014 international conference on data mining and intelligent computing (ICDMIC)*, p. 5, Delhi, India, September 2014.

[30] R. Dela Cruz, "Artificial neural network-based localization in wireless sensor networks artificial neural network-based localization in wireless sensor networks," p. 14, 2019.

[31] J. Jiang, G. Han, H. Wang, and M. Guizani, "A survey on location privacy protection in wireless sensor networks," *Journal of*

Network and Computer Applications, vol. 125, pp. 93–114, 2019.

[32] R. Rastogi, S. Srivastava, M. S. Tarun, V. Manshahia, and N. Kumar, "A withdrawn: a hybrid optimization approach using PSO and ant colony in wireless sensor network," *Materials Today: Proceedings*, vol. 2021, 2021.

[33] Z. Han, L. Lin, Z. Wang et al., "CNN-based attack defense for device-free localization," *Mobile Information Systems*, vol. 2022, Article ID 2323293, 7 pages, 2022.

[34] J. Chen, S. H. Sackey, J. H. Anajemba, X. Zhang, and Y. He, "Energy-efficient clustering and localization technique using genetic algorithm in wireless sensor networks," *Complexity*, vol. 2021, Article ID 5541449, 12 pages, 2021.

[35] O. Cheikhrouhou, G. M. Bhatti, and R. Alroobaea, "A hybrid DV-hop algorithm using RSSI for localization in large-scale wireless sensor networks," *Sensors*, vol. 18, no. 5, pp. 1–14, 2018.

[36] W. He, F. Lu, J. Chen, Y. Ruan, T. Lu, and Y. Zhang, "A kernel-based node localization in anisotropic wireless sensor network," *Scientific Programming*, vol. 2021, Article ID 9944358, 8 pages, 2021.

[37] B. K. Madagouda and R. Sumathi, "Analysis of localization using ANN models in wireless sensor networks," in *2019 IEEE Pune Section International Conference (PuneCon)*, pp. 18–21, Pune, India, December 2019.

[38] R. Singh, J. Singh, and R. Singh, "Detection of Sybil Nodes in wireless sensor networks," *Journal of Advanced Computer Science & Technology*, vol. 10, no. 3, pp. 185–202, 2017.

[39] N. Moustafa, G. Creech, and J. Slay, "Anomaly detection system using beta mixture models and outlier detection," in *Progress in Computing, Analytics and Networking. Advances in Intelligent Systems and Computing*, P. Pattnaik, S. Rautaray, H. Das, and J. Nayak, Eds., vol. 710, Springer, Singapore, 2018.

[40] "Cybersecurity_attacks|Kaggle," 2021, https://www.kaggle.com/iamranjann/cybersecurity-attacks.

[41] Z. Zoghi, G. Serpen, and C. Science, "UNSW-NB15 computer security dataset: analysis through visualization".

[42] N. Moustafa, G. Creech, and J. Slay, "Flow aggregator module for analysing network traffic," in *Progress in Computing, Analytics and Networking. Advances in Intelligent Systems and Computing*, P. Pattnaik, S. Rautaray, H. Das, and J. Nayak, Eds., vol. 710, Springer, Singapore, 2018.

[43] "The UNSW-NB15 data set description," 2021, https://www.unsw.adfa.edu.au/unsw-canberra-cyber/cybersecurity/ADFA-NB15-Datasets/.

[44] N. Moustafa and J. Slay, "A network forensic scheme using correntropy-variation for attack detection," *IFIP Advances in Information and Communication Technology*, vol. 532, pp. 225–239, 2018.

[45] N. Moustafa, G. Creech, and J. Slay, "Big data analytics for intrusion detection system: statistical decision-making using finite Dirichlet mixture models," in *Data Analytics and Decision Support for Cybersecurity*, pp. 127–156, Springer, 2017.

[46] N. Moustafa and J. Slay, "The evaluation of network anomaly detection systems: statistical analysis of the UNSW-NB15 data set and the comparison with the KDD99 data set," *Information Security Journal: A Global Perspective*, vol. 25, no. 1–3, pp. 18–31, 2016.

[47] D. Praveen Kumar, T. Amgoth, and C. S. R. Annavarapu, "Machine learning algorithms for wireless sensor networks: a survey," *Information Fusion*, vol. 49, pp. 1–25, 2019.

[48] C. R. Panigrahi, "Advanced computing and intelligent engineering," *Proceedings of ICACIE*, vol. 1, 2018.

[49] M. N. A. Shaon and K. Ferens, "A computationally intelligent approach to the detection of wormhole attacks in wireless sensor networks," *Advances in Science, Technology and Engineering Systems*, vol. 2, no. 3, pp. 302–320, 2017.

[50] M. Mittal, R. P. de Prado, Y. Kawai, S. Nakajima, and J. E. Muñoz-Expósito, "Machine learning techniques for energy efficiency and anomaly detection in hybrid wireless sensor networks," *Energies*, vol. 14, no. 11, 2021.

[51] R. Ahmad, R. Wazirali, and T. Abu-Ain, "Machine learning for wireless sensor networks security: an overview of challenges and issues," *Sensors*, vol. 22, no. 13, p. 4730, 2022.

[52] "Artificial neural network - an overview | ScienceDirect Topics," 2021, https://www.sciencedirect.com/topics/engineering/artificial-neural-network.

[53] V. Hassija, S. Batra, V. Chamola et al., "A blockchain and deep neural networks-based secure framework for enhanced crop protection," *Ad Hoc Networks*, vol. 119, article 102537, 2021.

[54] K. Ncibi, T. Sadraoui, M. Faycel, and A. Djenina, "A multilayer perceptron artificial neural networks based a preprocessing and hybrid optimization task for data mining and classification," *International Journal of Economics, Finance and Management Sciences*, vol. 5, no. 1, pp. 12–21, 2017.

[55] M. Al-Imran and S. H. Ripon, "Network intrusion detection: an analytical assessment using deep learning and state-of-the-art machine learning models," *International Journal of Computational Intelligence Systems*, vol. 14, no. 1, pp. 1–20, 2021.

[56] D. Kothona, I. P. Panapakidis, and G. C. Christoforidis, "A novel hybrid ensemble LSTM-FFNN forecasting model for very short-term and short-term PV generation forecasting," *IET Renewable Power Generation*, vol. 16, no. 1, pp. 3–18, 2022.

[57] A. Hadir, Y. Regragui, and N. M. Garcia, "Accurate range-free localization algorithms based on PSO for wireless sensor networks," *IEEE Access*, vol. 9, pp. 149906–149924, 2021.

[58] H. Chen, W. Lou, Z. Wang, J. Wu, Z. Wang, and A. Xi, "Securing DV-Hop localization against wormhole attacks in wireless sensor networks," *Pervasive and Mobile Computing*, vol. 16, pp. 22–35, 2015.

[59] S. Awan, N. Javaid, S. Ullah, A. U. Khan, A. M. Qamar, and J. G. Choi, "Blockchain based secure routing and trust management in wireless sensor networks," *Sensors*, vol. 22, no. 2, pp. 1–24, 2022.

[60] G. Kumar, M. K. Rai, H. J. Kim, and R. Saha, "A secure localization approach using mutual authentication and insider node validation in wireless sensor networks," *Mobile Information Systems*, vol. 2017, Article ID 3243570, 12 pages, 2017.

[61] M. Cheng, T. Qin, and J. Yang, "Node localization algorithm based on modified Archimedes optimization algorithm in wireless sensor networks," *Journal of Sensors*, vol. 2022, Article ID 7026728, 18 pages, 2022.

[62] Z. Ansari, R. Ghazizadeh, and Z. Shokhmzan, "Gradient descent approach to secure localization for underwater wireless sensor networks," in *2016 24th Iranian Conference on Electrical Engineering (ICEE)*, pp. 103–107, Shiraz, Iran, May 2016.

[63] "Classification: accuracy|Machine Learning Crash Course," 2021, https://developers.google.com/machine-learning/crash-course/classification/accuracy.

[64] D. Parikh and V. Menon, "Machine learning applied to cervical cancer data," *International Journal of Mathematics and Computer Science*, vol. 5, no. 1, pp. 53–64, 2019.

[65] "What are TP rate, FP rate, precision, recall, F measure, MCC, ROC area and PRC areas in the Weka tool?- Quora," 2020, https://www.quora.com/What-are-TP-rate-FP-rate-precision-recall-F-measure-MCC-ROC-area-and-PRC-areas-in-the-Weka-tool.

[66] "ROC analysis," 2021, https://www.ibm.com/support/knowledgecenter/SSLVMB_sub/statistics_mainhelp_ddita/spss/base/idh_roc.html.

[67] W. Zhang, D. Han, K. C. Li, and F. I. Massetto, "Wireless sensor network intrusion detection system based on MK-ELM," *Soft Computing*, vol. 24, no. 16, pp. 12361–12374, 2020.

[68] F. A. Khan, A. H. Farooqi, and A. Derhab, "A comprehensive security analysis of LEACH++ clustering protocol for wireless sensor networks," *The Journal of Supercomputing*, vol. 75, no. 4, pp. 2221–2242, 2019.

[69] L. Mohammadpour, T. C. Ling, C. S. Liew, and A. Aryanfar, "A mean convolutional layer for intrusion detection system," *Security and Communication Networks*, vol. 2020, Article ID 8891185, 16 pages, 2020.

[70] L. Xinlong and C. Zhibin, "DDoS attack detection by hybrid deep learning methodologies," *Security and Communication Networks*, vol. 2022, Article ID 7866096, 7 pages, 2022.

[71] B. Hasan, S. Alani, and M. A. Saad, "Secured node detection technique based on artificial neural network for wireless sensor network," *International Journal of Electrical & Computer Engineering*, vol. 11, no. 1, pp. 536–544, 2021.

[72] A. M. Pasikhani, J. A. Clark, and P. Gope, "Reinforcement-learning-based IDS for 6LoWPAN," in *2021 IEEE 20th International Conference on Trust, Security and Privacy in Computing and Communications (TrustCom)*, pp. 1049–1060, Shenyang, China, 2022.

[73] D. Upadhyay, J. Manero, M. Zaman, and S. Sampalli, "Gradient boosting feature selection with machine learning classifiers for intrusion detection on power grids," *IEEE Transactions on Network and Service Management*, vol. 18, no. 1, pp. 1104–1116, 2021.

[74] S. P. K. Gudla, S. K. Bhoi, S. R. Nayak, and A. Verma, "DI-ADS: a deep intelligent distributed denial of service attack detection scheme for fog-based IoT applications," *Mathematical Problems in Engineering*, vol. 2022, Article ID 3747302, 17 pages, 2022.

[75] M. I. Alghamdi, "A hybrid model for intrusion detection in IoT applications," *Wireless Communications and Mobile Computing*, vol. 2022, Article ID 4553502, 9 pages, 2022.

[76] R. Khilar, K. Mariyappan, M. S. Christo et al., "Artificial intelligence-based security protocols to resist attacks in Internet of Things," *Wireless Communications and Mobile Computing*, vol. 2022, Article ID 1440538, 10 pages, 2022.

[77] M. Feurer and F. Hutter, "Hyperparameter optimization," in *Automated Machine Learning. The Springer Series on Challenges in Machine Learning*, F. Hutter, L. Kotthoff, and J. Vanschoren, Eds., Springer, Cham, Switzerland, 2019.

Low Voltage Schmitt Trigger Full Adders Design for High Noise Immunity

Bhawanand Jha
Electronics & Communication Engineering
Delhi Technological University & Bharati Vidyapeeth's College of Engineering
Delhi, India
bhawanandjha@gmail.com

Kirti Gupta
Electronics & Communication Engineering
Bharati Vidyapeeth's College of Engineering
Delhi, India
kirtigupta22@gmail.com

Rajeshwari Pandey
Electronics & Communication Engineering
Delhi Technological University
Delhi, India
rpandey@dce.ac.in

2022 8th International Conference on Signal Processing and Communication (ICSC) | 978-1-6654-5430-8/22/$31.00 ©2022 IEEE | DOI: 10.1109/ICSC56524.2022.10009098

***Abstract*— In this paper three full adders with high noise immunity, designed using three variants of Schmitt trigger (ST) are proposed. The three variants of ST adders are based on conventional ST, dynamic threshold MOS (DTMOS) ST and variable threshold CMOS (VTCMOS) ST. The performances of the proposed ST adders are measured in terms of the hysteresis width, delay, dynamic power and I_{ON}/I_{OFF} ratio in LT spice simulator using 45 nm PTM technology parameters. It is found that the SUM and CARRY of VTCMOS ST adder has the largest hysteresis width thus providing high noise immunity. It is also confirmed through corner analysis. The SUM and CARRY of DTMOS ST adder provides the highest I_{ON}/I_{OFF} ratio among all adders. It is also true for SUM of DTMOS ST for fast, typical and slow corner analysis. It is also observed that CMOS adder consumes the lowest dynamic power consumption with zero hysteresis width while VTCMOS ST adder lowers dynamic power dissipation then DTMOS ST adder. Hence the VTMOS ST adder is suitable for improved noised immunity and low voltage applications.**

Keywords*— Conventional ST, DTMOS ST, VTCMOS ST, full adder, noise immunity, low power, and corner analysis.

I. INTRODUCTION

The demand of energy constrained applications such as healthcare systems, environmental monitoring, IoT applications, surveillance systems, where energy required below the minimum energy per operation are on rise. The tight energy budget for such applications has motivated the researchers to explore the possibility of reducing power consumption of the circuit by decreasing V_{DD} beyond the minimum energy per operation point. It may work for systems where most blocks are in sleep mode but, some blocks cannot be switched off and minimum voltage is required to keep active blocks operational. This has drawn the attention of researchers to shift in subthreshold logic circuit design. There are several approaches to reduce supply voltages. Some of these approaches are optimized process with near zero threshold [1], gates sizing with optimized topologies [2] and body biasing [3]. However, the supply voltage reduction leads to degradation of I_{ON} to I_{OFF} ratio in digital circuits due to the fact that the threshold voltage is not scaled as aggressively as the supply voltage. This incurs degradation of static noise margin and the signal becomes more vulnerable to external noise and electromagnetic interference. The ratio of maximum current from active block and leakage current from complementary block reduces to a point where output voltage levels deviate from the levels representing the HIGH and LOW logic levels which leads to logic failure.

Many solutions[4-10] are available in literature for noise immunity enhancement. The Schmitt Trigger based logic style is yet another solution which can be appropriately used to enhance noise immunity of the circuit. Unlike comparator, the switching threshold of Schmitt trigger depends on direction of input signal and differs for increasing and decreasing signals. This phenomenon is called hysteresis. In presence of hysteresis, the switching threshold voltage for increasing (decreasing) input signal is slightly greater (lower) than the switching threshold voltage of comparator. If this switching threshold difference is greater than amplitude of input signal variations, output signal will not respond directly to input which makes ST circuit more noise immune to undesired electromagnetic noise[11-12].

In literature three variants of Schmitt trigger are available namely conventional Schmitt trigger (ST), dynamic threshold MOS (DTMOS) ST and variable threshold CMOS (VTCMOS) ST. These variants are used to implement basic ST gates with improved performance. In this paper the authors have proposed the designs of conventional ST adder, DTMOS ST adder and VTCMOS ST adder. The focus of this paper is to present full adder designs with improved I_{ON}/I_{OFF} ratio with reduced supply voltages. Their effect on the noise immunity, delay, power and I_{ON}/I_{OFF} are investigated and compared with CMOS counterparts.

Rest of the paper is presented as follows: In section II basics of conventional ST, DTMOS ST and VTCMOS ST are explained. Three full adder designs based on ST logic style are described in section III. Then simulation results and performance comparison are presented in section IV. Finally, the conclusions are drawn in section V.

II. EXISTING SCHMITT TRIGGER CIRCUITS

A conventional ST consists of a CMOS inverter (M2, M3) along with two more CMOS pairs (M1, M4) and (M5, M6) as shown in Fig. 1a. The two more pairs provide positive feedback which play crucial role in the noise immunity. When low input voltage is applied at the input then M3 and M4 of pull up network would conduct as a result output reaches to high logic value that would switch on M5. The gate source voltage of M2 becomes negative which

978-1-6654-5430-8/22/$31.00 ©2022 IEEE

Authorized licensed use limited to: DELHI TECHNICAL UNIV. Downloaded on January 17,2023 at 05:00:28 UTC from IEEE Xplore. Restrictions apply.

decreases leakage current and hence I_{ON}/I_{OFF} increases [12].

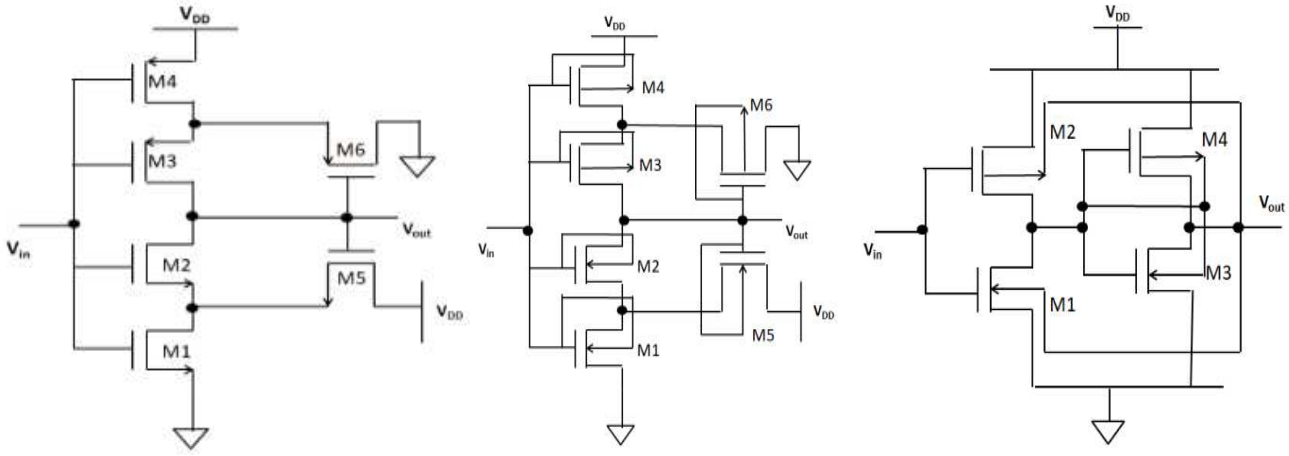

Fig.1(a)Conventional ST[11] (b)DTMOS ST[12] (C)VTCMOS ST[12]

In contrast, when logic high is applied then M1 and M2 would conduct and hence output will be grounded that switch on M6 transistor which will increase source voltage of M3 leading to improved I_{ON}/I_{OFF} ratio. The DTMOS ST is shown in Fig. 1b. In this structure, body and gate are tied together. When low voltage is applied it decreases the threshold voltage of PMOS and when high voltage is applied, it decreases the threshold voltage of NMOS due to body bias effect. The delay is directly proportional to threshold voltage. Hence it decreases delay of adder which is also confirmed through corner analysis.

The VTCMOS inverter is shown in Fig.1c. It is a two stage arrangement of CMOS pairs (M1, M2) and (M3, M4) in which M3 and M4 are used in DTMOS arrangement by connecting their body and gate terminals together. Next, the output of second stage is connected to body of first stage gate, due to this, threshold voltage of first stage is controlled by output of second stage which is called variable threshold voltage CMOS (VTCMOS) inverter. It increases threshold voltage for increasing signal and decreases threshold voltage for decreasing signal which increases hysteresis width and hence noise immunity increases. As far as dynamic power is concerned, there is a extra current injection due to current feedback transistors in DTMOS ST, which is not found in VTMOS ST due to voltage feedback. In addition, it increases threshold voltage than DTMOS ST due to substrate bias conditions in active state and hence it decreases the dynamic power consumptions of the circuits[12].

III. Proposed Full Adder

In this section, the design of Schmitt trigger (ST) full adders using three different variants, conventional ST, DTMOS ST and VTCMOS ST are proposed. The realization of full adder requires two XOR gates, two AND gate and one OR gate as shown in Fig. 2.

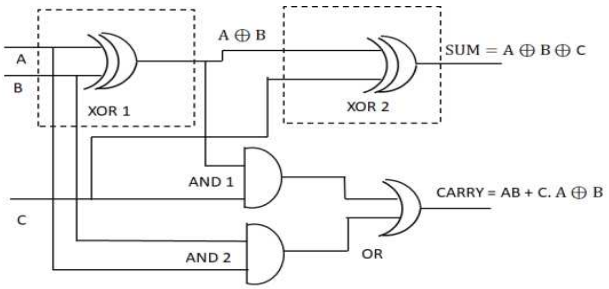

Fig. 2 Block diagram of Full Adder

In order to design the conventional ST adder, ST AND gate, ST OR gate and ST XOR gate are designed first using conventional ST. The transistors(M1-M4) as a pull down network(PDN) and transistors(M5-M8) as a pull up network(PUP) are employed to design ST NAND gate as shown in Fig.3a wherein inputs are connected in such a way which make both network dual of each other. The feedback transistors M9 and M10 are responsible for noise immunity of the circuit. The 2-input NOR gate using conventional ST is drawn as shown in Fig.3b. In this PDN is a parallel arrangement with respect to inputs A, B while the PUN connects the input transistors in such a manner that they produce a series combination of the inputs at the output of the gate. The above two circuit design techniques are used to form the conventional ST XNOR gate as shown in Fig. 3c since its functionality is represented as sum of products which requires both AND and OR gates. Both the true and complemented inputs A, B, $\overline{A}$, $\overline{B}$ are applied to ST XNOR gate. Subsequently, normal DTMOS inverter which is combination of M3 and M4 as shown in Fig.1c is connected at the output of ST NAND gate, ST NOR gate and ST XNOR gate to get ST AND, ST OR, and ST XOR gates [12]. Eventually, conventional ST full adder is designed using ST AND gate, ST OR gate and ST XOR gate. Further, DTMOS ST full adder is designed. The design is similar to conventional ST based gates with the bodies of MOS transistors connected to their respective gate terminals. The schematics are not drawn for the sake of brevity. Further, to design VTCMOS ST full adder first the VTCMOS ST based AND, OR and XOR gates are designed. The

Authorized licensed use limited to: DELHI TECHNICAL UNIV. Downloaded on January 17,2023 at 05:00:28 UTC from IEEE Xplore. Restrictions apply.

VTCMOS ST AND gate is depicted in Fig.4a, wherein M1 and M2 are the PDN network which is dual of PUN network which consists transistor M3 and M4 in the first stage. Similarly, in the second stage, M5 and M6 are the transistors of PDN and PUN network which are dual of each other. The output of second stage is connected to first stage through voltage feedback which play crucial role in noise immunity and power dissipation of the circuit. In Fig.4b, VTCMOS ST OR is designed wherein M1 and M2 are transistor of PDN network which are connected in such a way that make dual of PUP network which consist transistors M3 and M4 in the first stage. Similarly, M5 and M6 of the PDN and PUP network are connected in such a way that make dual of each other in second stage. The output of second stage is connected to body of first stage which make it VTCMOS ST OR gate. The above two design VTCMOS AND and OR gate techniques are used to make VTCMOS XOR gate because its functionality has sum of product which require both AND and OR gate as shown in Fig.4c. It is worth noting that VTCMOS ST based AND, OR and XOR gates use lesser number of transistor as compared to DTMOS ST based gates. This reduces the chip area and complexity of the design. It has also huge impact on the performance of the system [13].

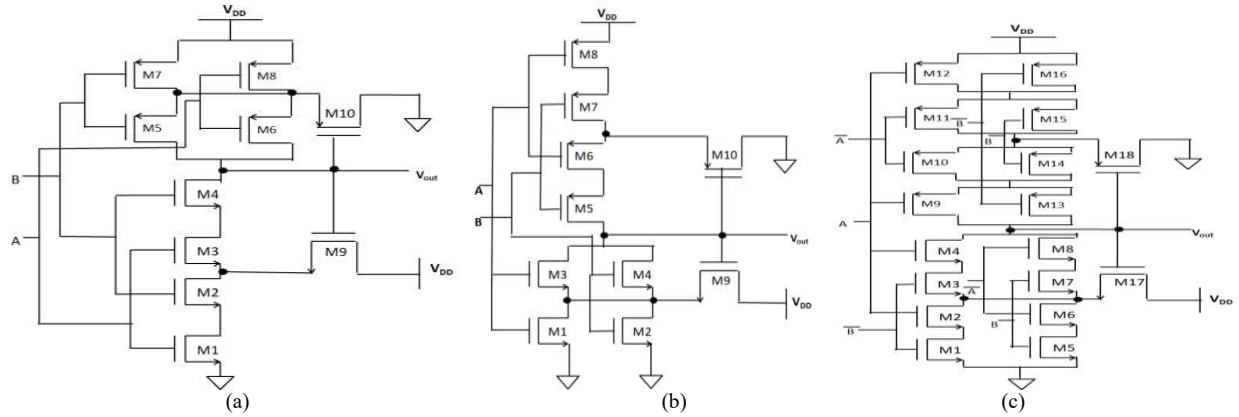

Fig. 3 Conventional ST2 inputs (a) NAND gate (b) NOR gate (c) Ex-NOR gate

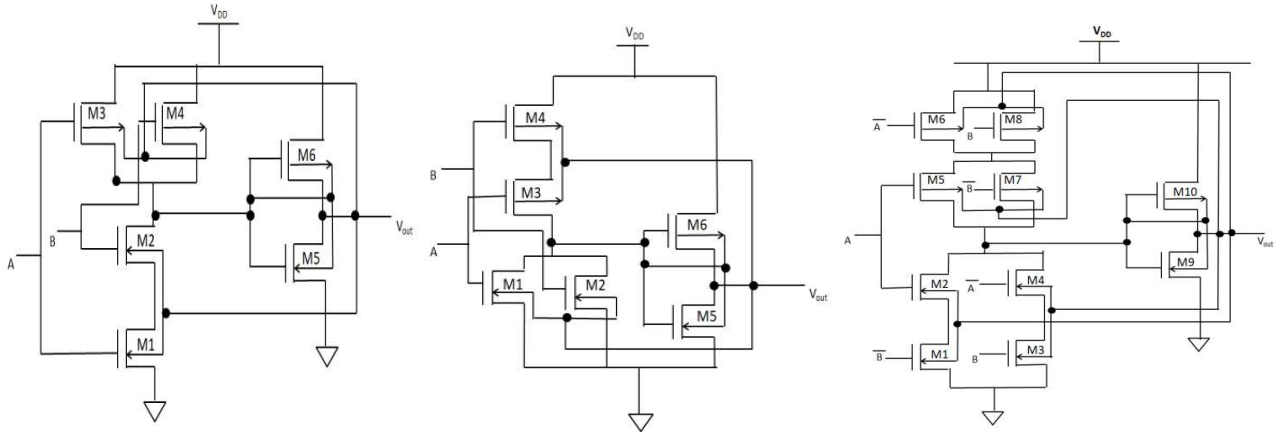

Fig. 4 VTCMOS ST2 inputs (a) AND gate (b) OR gate (c) Ex-OR gate

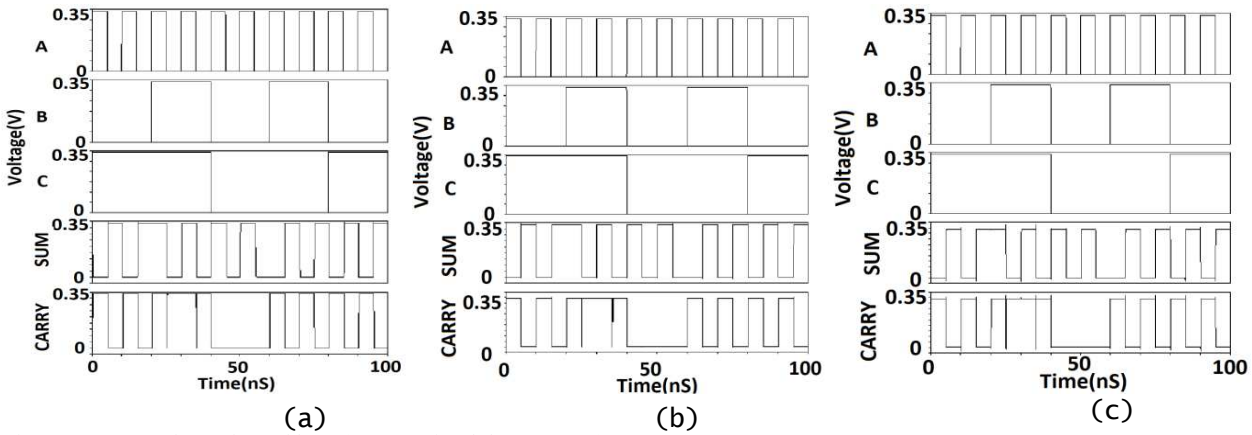

Fig. 5 Output waveform of ST adders (a) Conventional (b) DTMOS (c)VTCMOS

Authorized licensed use limited to: DELHI TECHNICAL UNIV. Downloaded on January 17,2023 at 05:00:28 UTC from IEEE Xplore. Restrictions apply.

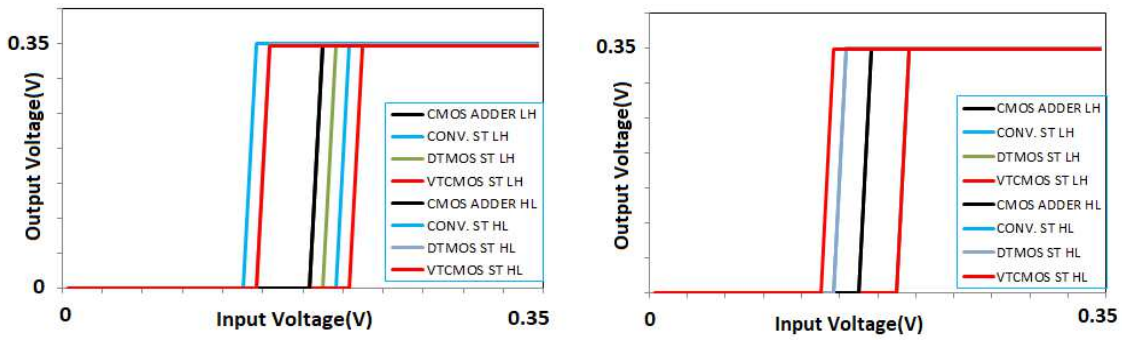

(a) (b)

Fig. 6 Hysteresis plot for (a) SUM (b) CARRY for low to high(LH) and high to low(HL) transition

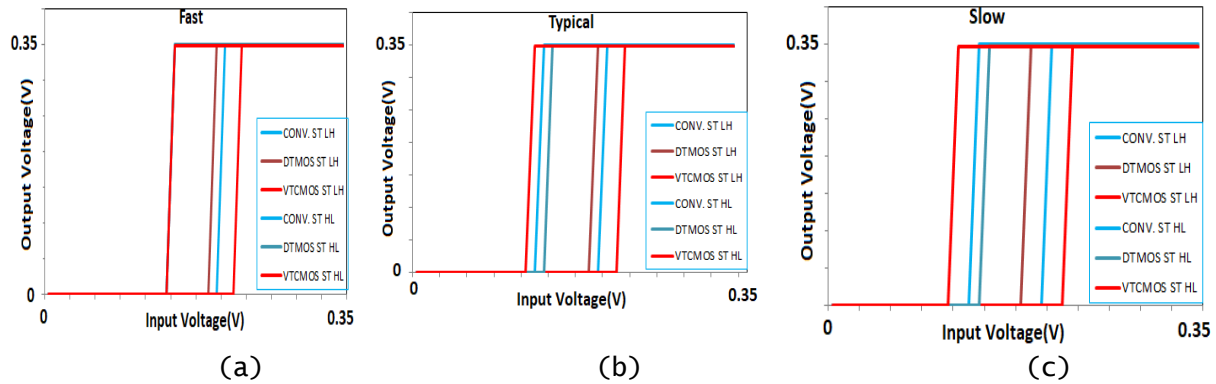

Fig. 7 Hysteresis plot of adder SUM using (a) Fast (b) Typical (c) Slow corner analysis

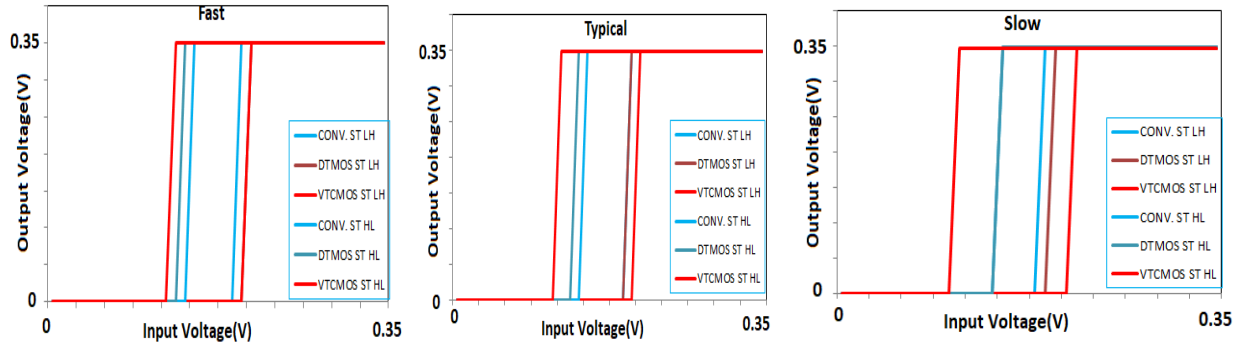

Fig. 8 Hysteresis plot of adder CARRY using (a) Fast (b) Typical (c) Slow corner analysis

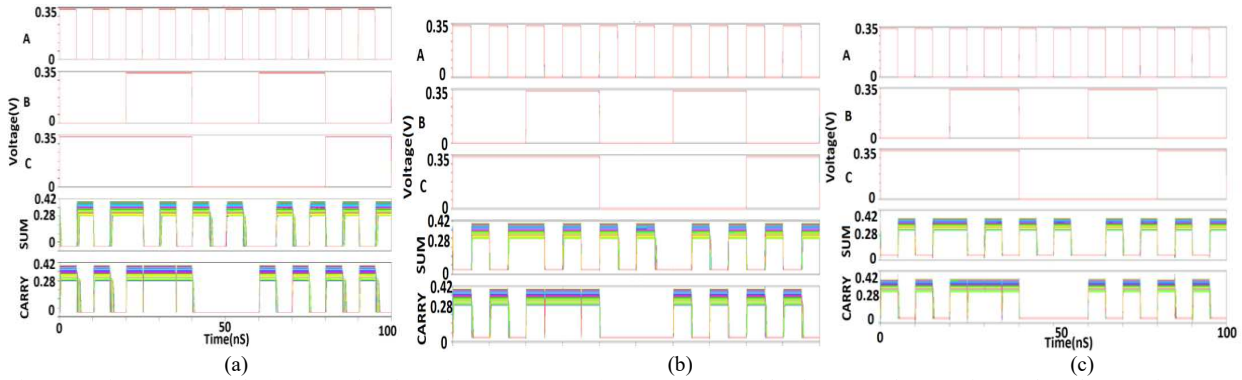

Fig.9 Transient response of (a) Conventional ST (b) DTMOS ST (c) VTCMOS ST adder for 20% tolerances in supply voltages using 100 runs of Monte Carlo Simulation.

IV. Result and Discussion

The conventional ST, DTMOS ST and VTCMOS ST full adders are implemented using 45 nm PTM technology parameters in LT spice simulation. The designed adders are simulated with a power supply of 0.35 V and their functionalities are verified. The waveforms of conventional ST, DTMOS ST and VTCMOS ST full adders are shown in Fig.5. It can be verified that all the circuits exhibit the

Authorized licensed use limited to: DELHI TECHNICAL UNIV. Downloaded on January 17,2023 at 05:00:28 UTC from IEEE Xplore. Restrictions apply.

functionality of a full adder. The simulation results of the proposed adder are listed in TABLE I and II. The performance of the designs is compared in terms of hysteresis width, delay, dynamic power and I_{ON}/I_{OFF} ratio. The results at different corners (Typical, Slow and Fast) are shown in TABLE III and IV. The hysteresis plot of conventional ST, DTMOS ST and VTCMOS ST adder for SUM and CARRY output along with corner analysis (Fast, typical and slow) are shown in Figs. 6, 7 and 8 respectively. The following are the obeservations:

- The VTCMOS ST adder attains the highest hysteresis width, thus providing highest noise immunity. The results are also confirmed through corner analysis. The ST VTCMOS SUM provides 42%, 57% and 32%, and 99%, 175% and 59% more hysteresis width than conventional ST and DTMOS ST adder for typical, slow and fast corner condition respectively. The ST VTCMOS CARRY of adder provides 81%, 174% and 59%, and 50%, 118% and 14% more hysteresis width than conventional ST and DTMOS ST adder for typical, slow and fast corner condition respectively.
- DTMOS ST adder is having highest I_{ON}/I_{OFF} ratio for both SUM and CARRY respectively. It is also confirmed through corner analysis of SUM of DTMOS ST adder as shown in TABLE III. In this structure body and gate are tied together. It decreases threshold voltage in active state due to substrate bias condition which increases on current. It increases threshold voltage in off state due to substrate condition which decreases off current. Hence it increase I_{on}/I_{OFF} ratio.
- With reference to delay, it is clear from the results as shown in TABLE I and II that CMOS adder SUM and VTCMOS adder CARRY ensure lowest delay while conventional ST adder is slowest which form limitation of the proposed design. It is also analyzed through corner analysis. The SUM and CARRY of CMOS adder is having lowest delay than other adder for fast corner analysis. Although, delay of SUM and CARRY of CMOS adder is comparable with DTMOS adder and VTCMOS adder for typical and slow corner analysis. Further, it is again verified that there exist a tradeoff between the delay and other performances.
- As far as dynamic power is concerned, CMOS is still best option. The DTMOS ST is having highest power. It occurs due to extra parasitic load capacitances and extra transistors which are connected as feedback. This feedback transistors take extra current path which resist the output signal variations due to injection of noises into input signal. Apart from this, source body voltage of transistor decreases in active state which decreases threshold voltage leads to more current flow. Hence, it consumes more power.

TABLE I. PERFORMANCES PARAMETERS OF DIFFERENT TOPOLOGIES FOR SUM

Performance parameters	CMOS Adder	Conventional ST Adder	DTMOS ST Adder	VTCMOS ST Adder
Hysteresis Width(mV)	-	71.9	51.3	72.4
Delay(nS)	3.8	13.4	4.4	4.5
Dynamic Power(nW)	33	85	1705	808
I_{ON}/I_{OFF}	13.03	28.12	39.25	15.4

TABLE II. PERFORMANCE PARAMETERS OF DIFFERENT TOPOLOGIES FOR CARRRY

Performance parameters	CMOS Adder	Conventional ST Adder	DTMOS ST Adder	VTCMOS ST Adder
Hysteresis Width(mV)	-	51.8	51.8	61.8
Delay(nS)	4.9	13.6	6.1	3.1
Dynamic Power(nW)	68	421	3050	1660
I_{ON}/I_{OFF}	22.53	27.70	152	118

The transient responses of 100 runs of Monte Carlo simulation for adders are done to know effect of process variations. The effect of 20% tolerances in supply voltage on upper and lower switching threshold of ST adders have been checked. The upper switching threshold and lower switching threshold for the majority of iterations of conventional ST, DTMOS ST and VTCMOS ST adder SUM fit in about 205mV ± 24%, 195mV ±15% and 216mV ± 18%, and 133mV ± 19%, 143mV ± 17% and 143mV± 21% respectively. The upper switching threshold and lower switching threshold for the majority of iterations of conventional ST, DTMOS ST and VTCMOS ST adder CARRY fit in about 195mV± 18%, 196mV ±18% and 196mV ± 18%, and 144mV ± 20%, 144mV ± 17% and 133mV ± 18% respectively.The transient plots of conventional ST, DTMOS ST and VTCMOS ST adder are shown in Fig.9. Apparently, it tells about approximate solution for allowed tolerances in any optimized parameters, so that performance of ST adders circuits can be analyzed.

TABLE III. PERFORMANCE PARAMETERS OF DIFFERENT TOPOLOGIES USING CORNER ANALYSIS(TT, SS AND FF) FOR SUM

Performance parameters	CMOS Adder			Conventional ST Adder			DTMOS ST Adder			VTCMOS ST Adder		
	TT	SS	FF	TT	SS	FF	TT	SS	FF	TT	SS	FF
Hysteresis Width(mV)	-	-	-	72.1	72.1	62.08	51.5	41.2	51.8	102.8	113.6	82.4
Delay(nS)	4.0	8.6	1.8	15.8	33.4	6.8	3.7	6.7	2.7	4.5	9.5	2.6

Authorized licensed use limited to: DELHI TECHNICAL UNIV. Downloaded on January 17,2023 at 05:00:28 UTC from IEEE Xplore. Restrictions apply.

Dynamic Power(nW)	27.5	12.7	89.2	72.9	35.4	228.6	1000.4	1271	2830	922	740	998.8
I_{ON}/I_{OFF}	19.6	16.3	20.0	26.5	37.0	28.9	51	65.4	96.7	10.2	14.4	12.0

TABLE IV. PERFORMANCE PARAMETERS OF DIFFERENT TOPOLOGIES USING CORNER ANALYSIS(TT,SS AND FF) FOR CARRY

Performance parameters	CMOS Adder			Conventional ST Adder			DTMOS ST Adder			VTCMOS ST Adder		
	TT	SS	FF	TT	SS	FF	TT	SS	FF	TT	SS	FF
Hysteresis Width(mV)	-	-	-	51.2	41.2	51.8	61.8	51.8	72.4	92.7	113.1	82.4
Delay(nS)	6.2	13.0	1.8	10.3	19.7	5.0	3.4	12.8	2.0	2.7	6.1	1.86
Dynamic Power(nW)	57.2	25.8	193	389.1	290	716.6	2000	2540	4360	1000	1540	1950
I_{ON}/I_{OFF}	87.3	45.6	18.8	45.2	28.5	110.0	95.1	76.5	52.8	135.0	97.9	132.12

V. CONCLUSION

In this paper, Schmitt trigger adders using three different implementation styles conventional ST, DTMOS ST and VTCMOS ST are proposed. Their performances have been compared with CMOS adder using 45 nm PTM technology parameters in LT spice simulator. The performances are measured in terms of hysteresis width, delay, dynamic power and I_{ON}/I_{OFF} ratio. The all proposed adders are showing hysteresis width that enhance electromagnetic noise immunity of the circuit. They also improve I_{ON}/I_{OFF} ratio, only slight issue with SUM of VTCMOS ST and CARRY of conventional ST adder for corner analysis at the cost of power dissipation and delay. Although, delay is also improving for DTMOS and VTCMOS adder for typical and slow corner analysis. It is found that the VTCMOS ST adder shows highest noise immunity and lowers power dissipation than DTMOS ST. The DTMOS ST adder provides highest I_{ON}/I_{OFF} ratio except one. The CARRY of VTCMOS ST adder also provides highest I_{ON}/I_{OFF} ratio for corner analysis. It can be preferred for low voltage and high noise immunity applications. As far as dynamic power is concerned, CMOS adder is the optimum solution.

REFERENCES

[1] J. Burr, "Cryogenic ultra low power CMOS," IEEE Symp. Low Power Electronics. 1995, pp. 82–83.

[2] A. Wang, A. Chandrakasan, "180-mV subthreshold FFT processor using a minimum energy design methodology," IEEE J. SolidState Circuits.

[3] M.-E. Hwang, K. Roy, "A 135 mV 0.13 uW process tolerant 6T subthreshold DTMOS SRAM in 90nm technology," In Proc IEEE Custom Integerated Circuits Conf.(CICC). 2008, pp. 419-422.

[4] V. Golumbeanu, P. Svasta, AND D. Leonescu, "The noise immunity for the low voltage logic circuits," Proc. of 9th Mediterranean Electrotechnical Conf. 1998, pp. 116–119.

[5] K. L. Shepard, "Design methodologies for noise in digital integrated circuits," Proc. of 35th Annu. Design Autom. Conf. 1998, pp. 94–99.

[6] B. L. Dokic, "CMOS NAND and NOR Schmitt circuits," Microelectron. J. 1996, vol. 27, no. 8, pp. 757–765.

[7] H. Soeleman, K. Roy, AND B. C. Paul, "Robust ultra-low power subthreshold DTMOS logic," Proc.of IEEE Int. Symp. Low-Power Electron. Des. 2000, pp. 25–30.

[8] A. Richelli, "Increasing EMI immunity in novel low-voltage CMOS opamps," IEEE Trans. Electromagn. Compat. 2012, vol. 54, no. 4, pp. 947– 950.

[9] A. Richelli, "EMI susceptibility of DTMOS opamps," Electron. Lett. 2013, vol. 49, no. 2, pp. 98–99.

[10] S. Sbaraini, A. Richelli, and Z. M. Kovacs-Vajna, "EMI susceptibility in bulk-driven Miller opamp," Electron. Lett. 2010, vol. 46, no. 16, pp. 1111–1113.

[11] N. Lotze, Y.Manoli, "CMOS standard cell design technique using schmitt trigger logic," IEEE Journal of solid state circuits. 2012, Vol.47, No.1.

[12] K. Kim, and S.Y.Kim, "Design of schmitt trigger logic using DTMOS for enhanced electromagnetic immunity," IEEE transaction on electromagnetic compatibility.2015.

[13] N. Lotze, and Y.Manoli, "Ultra –subthreshold operation of always-on digital circuits for IoT application by use of schmitt trigger gates," IEEE transaction on circuit and system-I. 2017, Vol.64, No.11.

[14] T. Mihai, W. Ibrahim, F. Kharabash, and V. Beiu, "Reliability and performance of optimised Schmitt trigger gates," IET Journals. 2018, Iss. 8, pp. 735-744.

[15] V. Beiu, W. Ibrahim, M.Tache,and F.Kharbash, "When one should consider schmitt trigger gates," Proceedings of the 15th IEEE international conference on nanotechnology. 2015.

Authorized licensed use limited to: DELHI TECHNICAL UNIV. Downloaded on January 17,2023 at 05:00:28 UTC from IEEE Xplore. Restrictions apply.

Mobile Application based Tracking using GPS and GSM

Mayank Kumar Jarwal
Department of Electronics and Communication
Delhi Technological University
New Delhi, Delhi, India
mayankkumarjarwal_2k18ec097@dtu.ac.in

Abhimanyu Barun
Department of Electronics and Communication
Delhi Technological University
New Delhi, Delhi, India
abhimanyubarun_2k18ec010@dtu.ac.in

Arshpreet Singh
Shiv Nadar School
Noida, U.P. India
arshpreetsingh2006@gmail.com

Akanksha Srivastava
Department of Electronics and Communication
Delhi Technological University
New Delhi, Delhi, India
akankshasrivastava30@gmail.com

2022 8th International Conference on Signal Processing and Communication (ICSC) | 978-1-6654-5430-8/22/$31.00 ©2022 IEEE | DOI: 10.1109/ICSC56524.2022.10009250

***Abstract*— Many Global Positioning System (GPS) and Global System for Mobile Communication (GSM) based trackers are available in the market. However, the current ones in the market are either costly, inaccurate, unreliable, or have poor User Interfaces mobile applications. This paper describes a practical model for tracking location, based on the GPS and GSM, which is inexpensive, versatile, secure, and reliable. The location can be known using a mobile application that fetches the location from a secure online database where the location gets stored after some interval of time. By incorporating an emergency protocol where a message goes to a specified mobile number containing the latest location with an alert in the mobile application, we have made the model better than most available in the market.**

Keywords — GPS, GSM, Mobile applications, Arduino Nano

I. INTRODUCTION

In this era of technology, people are becoming more engaged in work than the days earlier. Work is our necessity, but the rising number of crimes, rapes, thefts, and kidnappings are major hindrances that affect our mindset and our willingness to move out of our abodes. This fear is intelligible, and safety is our main concern. Other problems in this domain are faced by parents who consistently worry about their kids who need to go out alone for their classes and cannot carry smartphones due to the rules and regulations of schools and the fear of theft. Moreover, students who travel far from their homes for studies have a right to feel secure and let their parents know that they are safe. In addition to this, the rate of violence has also been perpetrated against women in recent years due to the increased exposure of women in all walks of life. In the past, women had been restricted to the four walls of the home, but now that globalization has occurred, they have the chance and the opportunity to compete in all sectors equally with their male counterparts. Many women now drive cabs. They work as a police officer, engineers, doctors, and the CEO of top companies. Women Account for at least 40% of the Total Workforce in many Countries [1].

While surveying and researching the market, we came across the following companies/products that were similar to our device like the Apple Watch Series [1], various products by Lync [2], Relyeon [3], Tile Inc [4] and Mini GPS Tracker [5]. We found that some of them were extremely expensive [6], some had very poor accuracy [7], some were fragile, some had very poor application interfaces and some were not reliable. Owing to all situations, there are devices that can help in emergency situations, but there is still a need to design a model that is inexpensive, accurate, reliable, versatile, secure, and has a better User Interface [8].

A. Novelty of the proposed work- This study describes an efficient, adaptable, safe, and trustworthy location monitoring methodology based on GPS and GSM. A mobile application that retrieves the location from a secure internet database where it is maintained for a while can be used to determine the location. The key novelty of the proposed framework is the incorporation of an emergency protocol with the most recent position, and an alarm goes to a certain mobile number. It is the most significant advantage of the proposed model compared to other existing models on the market.

B. Contribution- This research paper will design a new GPS and GSM-based tracking model - "Abhirakshak," a model that is a combination of both hardware and software solutions. It is inexpensive to manufacture, reliable, constantly uploading data to the server, has a Horizontal Position Accuracy of 2.5m, can be produced in various sizes, is secure, and has a better User Interface (UI) and User Experience (UX).

II. PROPOSED SYSTEM MODEL AND TECHNIQUE

Figure 1 shows the device, which is based on this model, will update the location of the person wearing it or a vehicle carrying it at regular intervals using GPS and GSM [9] technology which can be monitored by family, friends, or

978-1-6654-5430-8/22/$31.00 ©2022 IEEE

Authorized licensed use limited to: DELHI TECHNICAL UNIV. Downloaded on January 17,2023 at 04:59:48 UTC from IEEE Xplore. Restrictions apply.

any authorized person. It will also incorporate an emergency protocol that can raise an alarm to her family or friends.

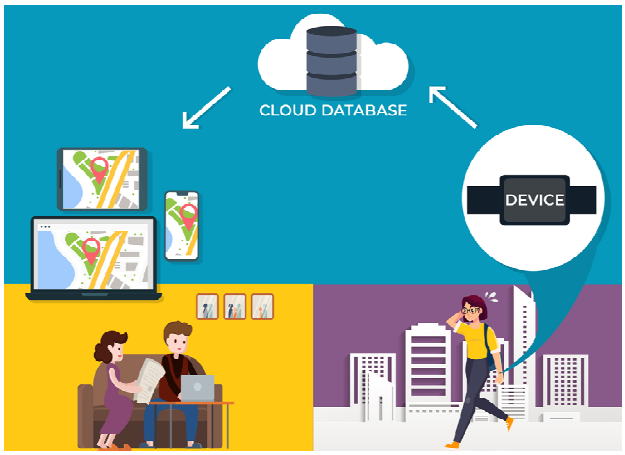

Figure 1: Device based on model [5]

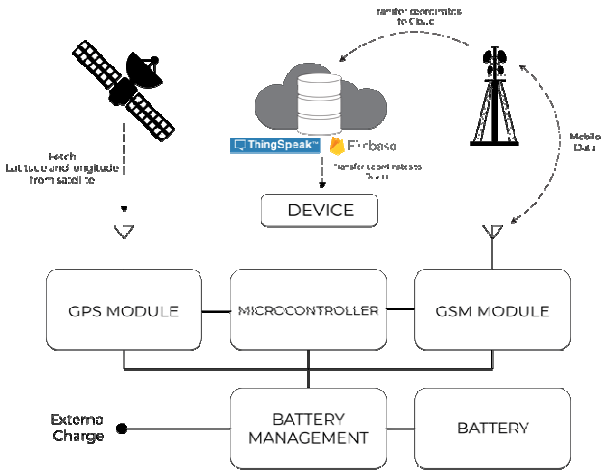

Figure 2: Proposed working Diagram of a device based on "Abhirakshak"

As shown in figure 2, the device will contain an **Arduino Nano** which will provide initialization and ongoing control to the **GPS** and **GSM** modules respectively via serial links. Logic functions are performed here like assembling data for the transmission of data. Arduino Nano will be programmed in order to send the data to the Firebase cloud database via ThingSpeak using the GSM module which will be using the internet services to transfer the data to the servers. The device will contain a **Lithium-Ion battery**. The battery will simultaneously power the Arduino Nano, GPS module, and GSM module. A Battery Management Module will ensure that the Li-Ion battery is appropriately charging and discharging whenever needed. It will include a charging port and will detect when the battery is fully charged. The **GPS** Module will be responsible for finding the accurate position or coordinates of the device. The **GSM** unit will establish communication with the Global GSM cellular network [8] as a SU (Subscriber Unit). The data can now be sent to the ThingSpeak server and in turn, can be stored in the Firebase database. The ideal goal is to make this model as small as possible. The family or authorized person can take an appropriate call to action, if needed, using their mobile devices.

A. Model Hardware Specifications

The **GPS** module (NEO-6M) will fetch the geographic coordinates from the **satellite** [10]. It then transfers the data to the **ATmega328 microcontroller present in Arduino Nano.** The microcontroller processes the data and transfers it to the **GSM** module (SIM900A) which sends it to the **ThingSpeak Server** and in turn, stores it in **Firebase Cloud Database** through **Internet services** [11], [12]. The microcontroller is also responsible for repeating the whole working cycle over certain time intervals.

The complete flow chart of the working model is given below in figure 3.

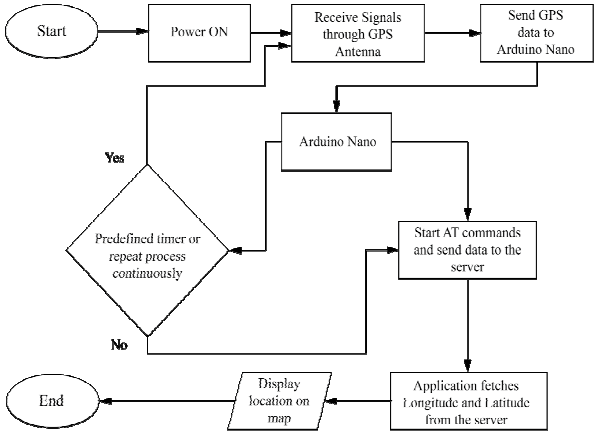

Figure 3: Flow Chart of Working

B. Mobile Application Specifications

For application development, we have used Flutter. Flutter is an open-source UI software framework kit developed by Google. It is utilized to build cross-platform apps for Windows, Linux, Android, Google Fuchsia, Mac, and iOS.

The significant advantage we experienced using Flutter is the Single codebase, which means writing the code for once and running it on almost any platform.

Another tool that played a meaningful role in the development of the application is Google Maps SDK. No doubt, Google maps is the most widely used map application globally, which is used for navigation to booking cabs online. We have incorporated the same in our project for the same reasons.

Figure 4: Name and Logo

As shown in figure 4, we named the application "Abhirakshak". Being a hindi word – Abhirakshak, means **Custodian** (one that guards and protects).

Authorized licensed use limited to: DELHI TECHNICAL UNIV. Downloaded on January 17,2023 at 04:59:48 UTC from IEEE Xplore. Restrictions apply.

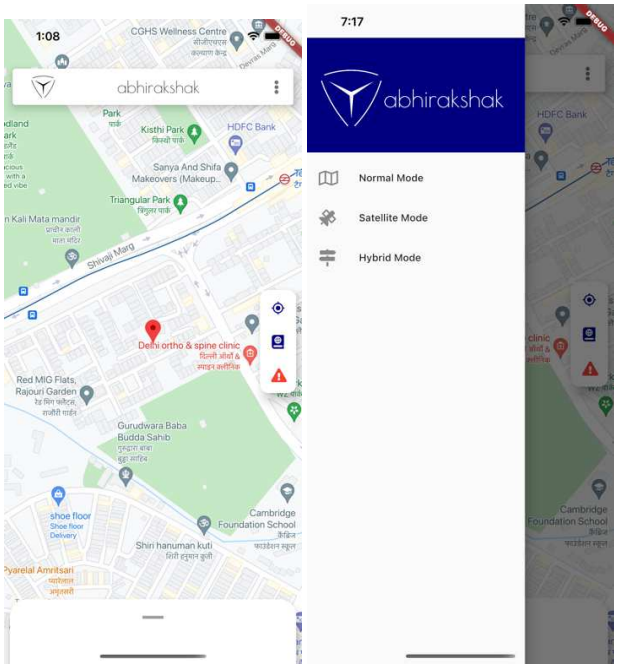

Figure 5: Application Screenshots -1

The home screen of the mobile application is shown in figure 5 (left). It displays the latest updated location of the registered device i.e., being carried by the person.

The application works in three different map modes namely, NORMAL MODE – Simple mode with detailed labeling, SATELLITE MODE – Satellite imaging mode, HYBRID MODE – Combination of Satellite and detailed labeling of normal mode (figure 6 (*right*)). The mode-changing panel can be opened from the navigation drawer (slide from the left corner to right).

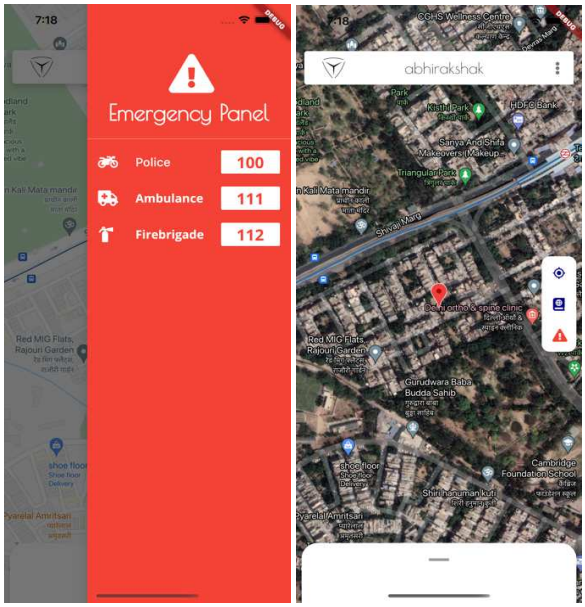

Figure 6: Application Screenshots-2

As shown in figure 6 (left), the application also consists of an EMERGENCY PANEL, which can be directly to call the emergency services.

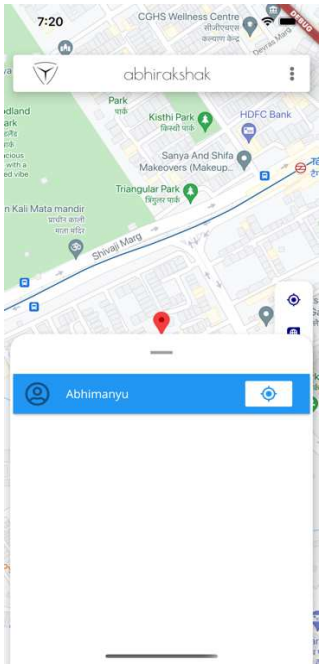

Figure 7: Application Screenshots-3

The application can support multiple devices which can be added simultaneously, and their locations can be revealed on the map with just a click of the location button (figure 7). Currently, the application is available for Android and IOS.

III. RESULTS

We are able to upload the data to the ThingSpeak server within 2 minutes. The mobile application was able to display the new data without any issues or restart. The model is working as expected. We were also able to implement an SOS button that will alert family, friends, or any other authorized person with an SMS containing their location. Figure 8 shows the model of the invention. After that figure 9 represents the current position identified by the mobile application. Next, the Monitoring live ThingSpeak is indicated by figure 10, and figure 11 shows the SMS on the registered device when pressing the SOS button

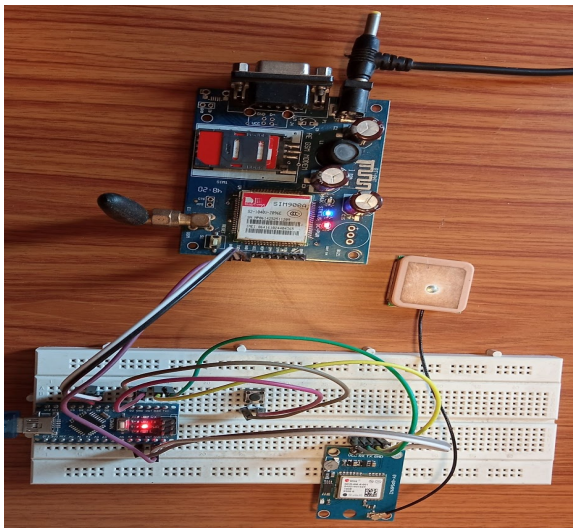

Figure 8: Proposed Model

Authorized licensed use limited to: DELHI TECHNICAL UNIV. Downloaded on January 17,2023 at 04:59:48 UTC from IEEE Xplore. Restrictions apply.

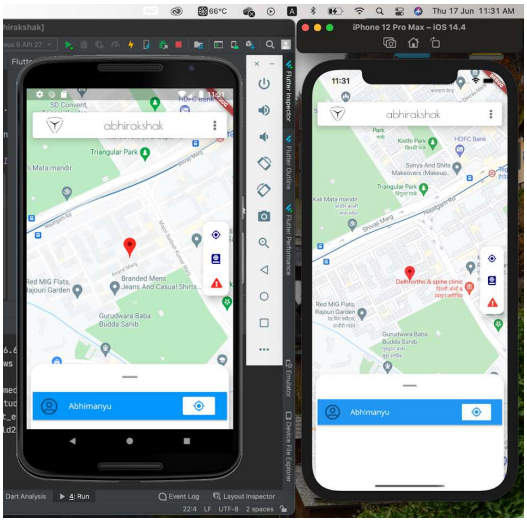

Figure 9: Mobile Application showing current Position

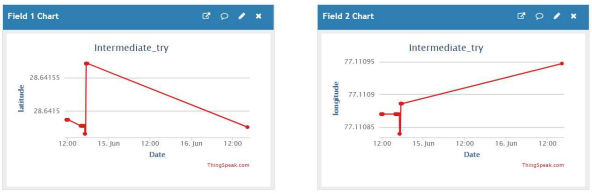

Figure 10: Monitoring live ThingSpeak

Figure 11: SMS on registered device when pressed the SOS button

IV. Future Scope

After incorporating some hardware parts and suitable software modifications, this system can also utilize to disable the engine of the vehicle if the vehicle is stolen. The system could be further upgraded by adding the concepts of artificial intelligence (AI) techniques.

V. Conclusion

In the present scenario, the security issue has become an important topic for research. Thus, this work focuses on the security issue and presents a practical model for location tracking. This tracking system is designed for broad geographical areas. This model has utilized GPS and GSM technologies simultaneously in addition to the mobile application for IOS and Android platforms. There are many devices in the market for location tracking, but they are either costly or they struggle with the quality parameter in software or hardware. This model is simplified, inexpensive to produce, accurate, reliable, versatile, secure, and has a better User Interface made with industry-grade tools.

VI. Acknowledgement

We are thankful to the Dean of Student Welfare, Delhi Technological University, Delhi for providing financial assistance for this work under File No. D.T.U/D.S. W/2020/F. No. 303/3317-3324.

References

[1] https://vaya.in/smart-tracker/lynks-sets
[2] https://www.relyeon.in/
[3] https://www.amazon.in/Tile-Pro-Replaceable-Battery-Pack/dp/B07GLXY253
[4] M. A. Al Rashed, O. A. Oumar, and D. Singh, “A Real Time GSM / GPS Based Tracking System Based on GSM Mobile Phone”, Second International Conference on Future Generation Communication Technologies (FGCT 2013), London, UK, IEEE,65– 68 (2013).
[5] M. S. Gupta, K. Kumar, “Application-Aware Networks’ Resource Selection Decision Making Technique using Group Mobility in Vehicular Cognitive Radio Networks”, Vehicular Communications, Elsevier, vol. 26, pp. 100263, 2020.
[6] A. Srivastava, M. S. Gupta, G. Kaur, “Impact of Artificial Intelligence on Future Green Communication”, Artificial Intelligence to Solve Pervasive Internet of Things Issues, Elsevier, 2021.
[7] N. Mangla, T. Mehta, “A Survey Paper on Big Data Analytics using Map Reduce and Hive on Hadoop Framework”, International Journal of Recent Advances in Engineering & Technology (IJRAET) 2016.
[8] A. Srivastava, M. S. Gupta, G. Kaur, “Energy efficient transmission trends towards future green cognitive radio networks (5G): Progress, taxonomy and open challenges”, Journal of Network and Computer Applications, Elsevier, vol. 168, pp. 102760, 2020.
[9] A. Srivastava, G. Kaur, “Resource management for traffic imbalance problem in green cognitive radio networks”, Physical Communication. Elsevier, vol. 48, pp. 101437, 2021.
[10] Y. Parasher, P. Singh, G. Kaur, “Green Smart Security System”, Green and Smart Technologies for Smart Cities. CRC Press, pp. 165-184, 2019.
[11] R. C. Jisha, A. Jyothindranath, and S. K. L, “IoT Based School Bus Tracking and Arrival Time Prediction”, International Conference on Advances in Computing, Communications and Informatics (ICACCI), Udupi, India, IEEE ,509–514(2017).
[12] A. Srivastava, M. S. Gupta, G. Kaur, “A Game Theory Based Approach for Opportunistic Channel Access in Green Cognitive Radio Networks”, IEEE International Conference on Advanced Networks and Telecommunications Systems (ANTS), IEEE, pp. 1--6, 2019.

Authorized licensed use limited to: DELHI TECHNICAL UNIV. Downloaded on January 17,2023 at 04:59:48 UTC from IEEE Xplore. Restrictions apply.

Journal of Ambient Intelligence and Humanized Computing
https://doi.org/10.1007/s12652-022-04499-0

ORIGINAL RESEARCH

Mul-FaD: attention based detection of multiLingual fake news

Nishtha Ahuja[1] · **Shailender Kumar**[1]

Received: 27 January 2021 / Accepted: 28 November 2022
© The Author(s), under exclusive licence to Springer-Verlag GmbH Germany, part of Springer Nature 2023

Abstract
The latest buzzword in today's world is fake news. The circulation of false information influences elections, public health, brand reputations, and violence. Hence, the severity of the threat of fake news is increasing. The danger for fake news exists everywhere globally and is not specific to one language or nation. The creators of fake news layer the facts in the news with misinformation to confuse the readers. Hence, a need arises for creating a model for detecting fake news in multiple languages. This paper proposes a unified attention-based model Mul-FaD to detect fake news in various languages. We have created our dataset with around 40000 articles in English, German, and French. This paper also shows an exploratory analysis of the dataset created. In this paper, we perform experiments from a multilingual perspective in which we use an altered hierarchical attention-based network to detect fake news. Our model is able to achieve an accuracy of 93.73 and an F1 score of 92.9 for the combined corpus of the three languages.

Keywords Fake news · Deep learning · Social media · Natural language processing

1 Introduction

Social media has changed the landscape of news consumption. People use social media for personal relationships, sharing their opinions on a public platform, sharing personal achievements, news, etc. Along with this, people's inclination has shifted towards social media for news consumption as well due to its convenience in terms of time and availability. Apart from entertainment and knowledge purposes, social media is also used to create large volumes of fake news, hoaxes, and rumors. These fake news circulates on social media and messaging platforms like wildfire. With the reducing costs of the internet and exponentially increasing users of social media, the reach of fake news is also expanding. Fake News shared by social media users is not just specific to political topics. Misinformation pertinent to businesses, technology, urban legends, and science is also enormously shared by users. Figure 1 shows some of the fake news circulated in the United States. Recent daunting surveys have reported that people obtain their daily dose of news more from social media websites than from our conventional sources of information[1]. A statistic survey by Statistica[2]ocial-media-users states that social media will connect a third of the global population by 2021 due to the increasing affordability and availability. The primary reason for such behavior can be that it is much more convenient and cheaper than traditional news sources. Newspapers and Televisions. Thus making it very important to curb misinformation circulating on such platforms.

The primary motives for initiating false information circulation can be altering other people's opinions or gaining monetary benefits. Misinformation has a profound impact, which makes it one of the modern threats to our society. With the advent of the Covid-19 pandemic, this circulation of fake news is surging. This swift spread of misinformation has led to the coining of the term "infodemic" by WHO (World Health Organization), which means the surge of misinformation circulating. This fact-checking is also getting encouraged by the governments of certain countries. The number of country-specific fact-checking websites is also increasing to curb this spread of misinformation. There are

✉ Shailender Kumar
shailender.kumar@dce.ac.in

Nishtha Ahuja
nishthaahuja25@gmail.com

[1] Department of Computer Science and Engineering, Delhi Technological University, Delhi, India

[1] https://www.forbes.com/sites/petersuciu/2019/10/11/more-americans-are-getting-their-news-from-social-media/?sh=7246217e3e17.

[2] https://www.statista.com/chart/15355/social-media-users.

Published online: 14 January 2023

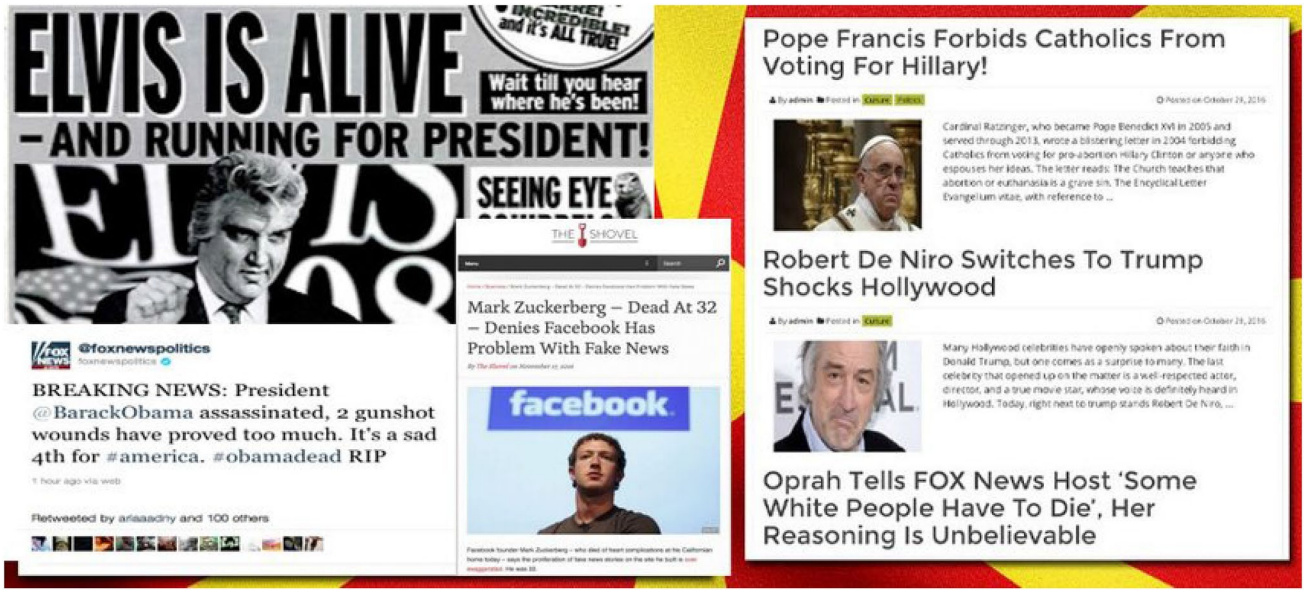

Fig. 1 Fake news examples [Source: www.google.com]

multiple fact-checking websites like Politifact,[3], Snopes[4], etc., whose sole purpose is to provide correct information on the currently trending fake news. Reporterslab[5] is a website that graphically presents the list of fact-checking websites specific to various geographical locations. Many websites like The Quint[6], Full Fact[7], etc., have created a separate fact-check portal for rumors and fake news related to Covid-19 as a measure to combat this infodemic. Various definitions exist for fake news in literature catering to different aspects of it. We provide a cohesive definition of fake news as:

Definition 1 "Any piece of text, image, or video that is published on the internet or disseminated on the messaging platforms and contains current, factually incorrect information or misleads the reader with or without malicious intent is termed *fake news*.."

This definition covers all aspects of fake news in terms of sharing platforms, timing, and intention. We have loosened up the intention criteria in our paper because we believe that some readers tend to share the fake news without any malicious intention as they genuinely believe it to be true. Shao et al. (2018) sheds light on human nature where humans naturally tend to believe the information provided to them without verifying. Since we can't verify the user's intention, our definition removes the existing criteria of intention as stated by other authors.

The prime contribution of this paper is to create a multilingual dataset and propose a unified attention-based model - MuLFaD (MultiLingual Fake-news Detection) to detect fake news in different languages. We have used a modified Hierarchical Attention Network for this task. The model was able to achieve an accuracy of 93.73 on our dataset. The rest of the paper is structured as follows:

- Section 2 discusses the related work in this area of fake news detection focusing on its multilingual aspect.
- Section 3 explains the dataset created for this paper. This section also shows the exploratory analysis of the data.
- Section 4 explains the proposed attention-based model used in this research.
- Finally, Section 5 illustrates the results obtained by the proposed model on this dataset.

2 Related work

The researchers have made several attempts to resolve the problem of automatic fake news detection. Researchers are continuing to develop novel methodologies that cater specifically to this issue. The task of Fake News Detection can be divided into two sub-categories: *Content-Based Detection* and *Social Context Based Detection*. Content-Based strategies can further be divided into *Knowledge-Based* and *Style-Based*. Knowledge-Based Systems utilize the public

[3] www.politifact.com.
[4] www.snopes.com.
[5] https://reporterslab.org/fact-checking/.
[6] https://www.thequint.com/topic/coronavirus-fact-check.
[7] https://fullfact.org/.

knowledge available and convert it into a structured format, while Style-Based methods exploit the given text's linguistic features and writing styles. Social Context Based strategies, on the other hand, makes use of the propagation patterns and diffusion of misleading content on social media. These models are more suitable for detecting deceptive content on social media as they work in a language-independent manner and utilize the network structure. But, they require additional meta-data about the propagation structures, which poses a disadvantage to this style. On the other hand, content-based models need just the textual content of the news for them to perform well. In this section, we will discuss various techniques that have been used to date in this area.

Most of the work done using Content-Based Techniques using linguistic features has been done in English, Chinese and Spanish. A lot of research uses deep learning techniques for predictions. For instance, Varshney and Vishwakarma (2020) have worked towards real-time credibility detection while Ahuja and Kumar (2020) have used the attention networks for the detection of fake news in the English language. None of these have used news in multiple languages as their data. There is a lack of research in this area of fake news detection on multilingual data. Furthermore, there is an absence of a gold standard dataset for this problem, leading to a scarcity of research in this area. However, some research has been performed in this area. For example, Guibon et al. (2019) have focused on satire detection along with detecting fake news in multilingual data. They have used a CNN-based model and have achieved the F1 score of 95.78 on trusted news, 93.33 on fake news, and 68.98 on satires. Vogel and Meghana (2020) on the other hand, have employed an approach to identify the spreaders of fake news on social media by evaluating the text-independent features. An accuracy of 78% was achieved on English and 87% on Spanish corpus. Abonizio et al. (2020) have also employed the same approach of using language-independent features to identify the misinformation on social media. They have worked upon English, Spanish, and Portuguese news content.

While there is a lack of a general multilingual fake news corpus, there are few corpora that focus on covid specific news in multiple languages like MM-COVID by Li et al. (2020), FakeCovid by Shahi and Nandini (2020) and GeoCov19 by Qazi et al. (2020). These datasets can be utilized for the detection of COVID-specific fake news in multiple languages. Table 1 compares the current research work on Multilingual Fake News Detection. As seen in the table, there is a gold standard dataset on Covid-19 specific news that can be used, but there is a lack of a proper dataset for general fake news spreading in multiple domains. Our work here aims to create our dataset in three languages of general news not pertaining to a single domain and create a multilingual model which works on it.

3 Data collection and analysis

There is an absence of a gold standard dataset for detecting fake news in multiple languages. So, we have created our dataset for this problem. This section will explain the whole process followed for the creation of the dataset. The exploratory analysis of the final dataset generated is also shown in this section. For our data, we have taken multiple datasets from Kaggle[8][9][10][11][12]. The news text and label was taken from all datasets and the duplicates were removed from them. The resulting dataset consisted of a total of 43488 articles in the English language. To convert it into a multilingual dataset, we divided 26000 articles from the dataset into two equal parts and then used google translate api to translate the articles into French and German. The rest of the dataset was kept in the English language itself. The distribution of the final dataset is shown in Table 2. We have carried out a manual verification on a random sample of 5000 articles from the French and German languages to certify the translations. The manual verification was performed by a group of 10 students who can speak or understand at least one of the two languages. A standard process was followed for this. The students picked the translated articles at random and matched them with their corresponding English text. The same article is cross-verified by some other student for cross-validation. This whole process took over a month. We then calculated the Cohen's Kappa score to measure the agreement between the verifiers. It is a statistical measure used to estimate the degree of reliability between different raters. The rating can only be done on quantifiable items. The Kappa score is calculated by using the formula given in Equation 1. Here, TN and TP stand for true negative and true positive, respectively, while FP and FN stand for false positive and false negative. The news is given the label TP/TN when both the verifiers give the same label as correctly translated/incorrectly translated respectively. The calculated Kappa score was 0.84, which infers a good level of agreement between the verifiers and when extrapolated for the whole dataset, suggests the correctness of the dataset. Further, an exploratory analysis was performed on the dataset for further inferences, which is discussed further.

$$\kappa = \frac{2 * (TN * TP - FP * FN)}{(TP + FP) * (FP + TN) + (TP + FN) * (FN + TN)} \quad (1)$$

[8] https://www.kaggle.com/jruvika/fake-news-detection.

[9] https://www.kaggle.com/mrisdal/fake-news.

[10] https://www.kaggle.com/hassanamin/textdb3.

[11] https://www.kaggle.com/ksaivenketpatro/fake-news-detection-dataset.

[12] https://www.kaggle.com/surekharamireddy/fake-news-detection.

Table 1 Comparison of research work done on multilingual fake news detection. [Abbreviations used- *EN* English, *PT* Portuguese, *ES* Spanish, *FR* French, *HI* Hindi, *BN* Bengali, *GR* German]

Paper	Dataset used/generated	Languages	Dataset size	News domain	Main contribution
(Schwarz et al. 2020)	Social Media Verification Challenge 2015 and 2016 (Twitter)	Not mentioned	18952 (Without data Augmentation)	General	Use multilingual encoder transformer to identify reliability of small messages.
(Abonizio et al. 2020)	For EN:Horne and Adali (2017) For PT:Monteiro et al. (2018) For ES:Posadas-Durán et al. (2019)	English, Portuguese and Spanish	9930	General	Use language independent features for identifying fake, trusted and satirical content.
(Vogel and Meghana 2020)	PAN 2020 author profiling corpus	English and Spanish	EN: 30000 ES: 30000	Random fake topics identified on Politifact and Snopes	Identify the fake news spreaders
(Li et al. 2020)	MM-COVID	English, Spanish, Portuguese, Hindi, French and Italian		Specific to COVID-19	Creation of Dataset
(Qazi et al. 2020)	GeoCov19	63 languages	More than 524 million	Specific to COVID-19	Creation of dataset
(Guibon et al. 2019)	Storyzy	English and French	EN: 5105 Fr: 941	Advertising	Sature detection
(Shahi and Nandini 2020)	Fake-Covid	English, Hindi and German	EN: 2116 HI: 141 GR: 47	Specific to COVID-19	Creation of dataset
(Koloski et al. 2020)	PAN 2020 author profiling corpus	English and Spanish	EN: 30000 ES: 30000	Random fake topics identified on Politifact and Snopes	Identify the spreaders of fake news
(Kar et al. 2020)	For English: Covid-19 Infodemic dataset For Hindi: Scraped from Twitter For Bengali: Dataset created by Avishek Garain	English, Hindi and Bengali	EN: 504 BN: 480 HI: 454	Specific to COVID-19	Use mBERT to identify fake COVID tweets

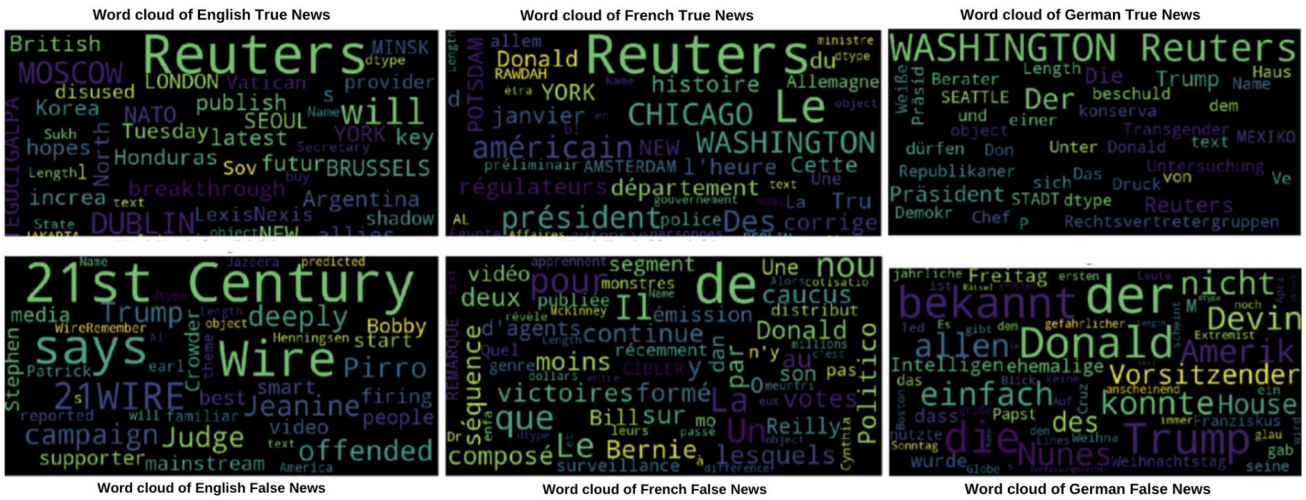

Fig. 2 Word cloud of true and fake news in English, French and German language

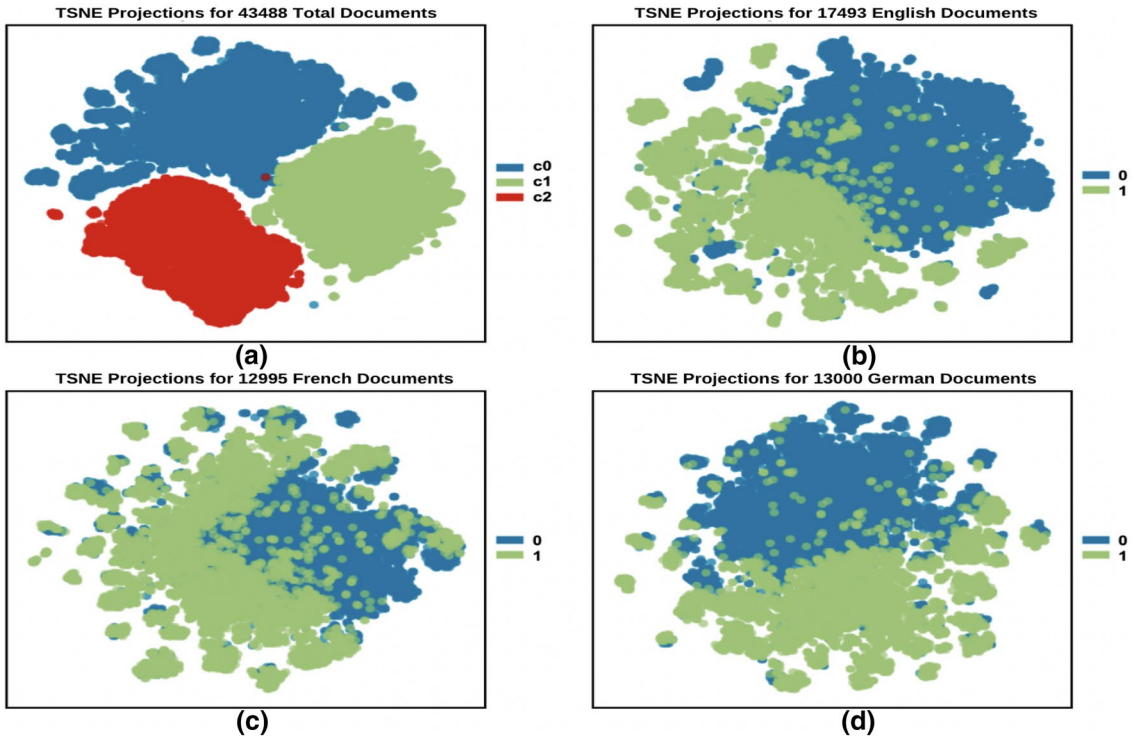

Fig. 3 **a** TSNE Projections of all news **b** TSNE Projections of English News **c** TSNE Projections of French News **d** TSNE Projections of German News [Labels Used - c0: English, c1: German, c2: French, 0: Fake News, 1: True News]

Fig. 4 Sentence length distribution of true news and fake news

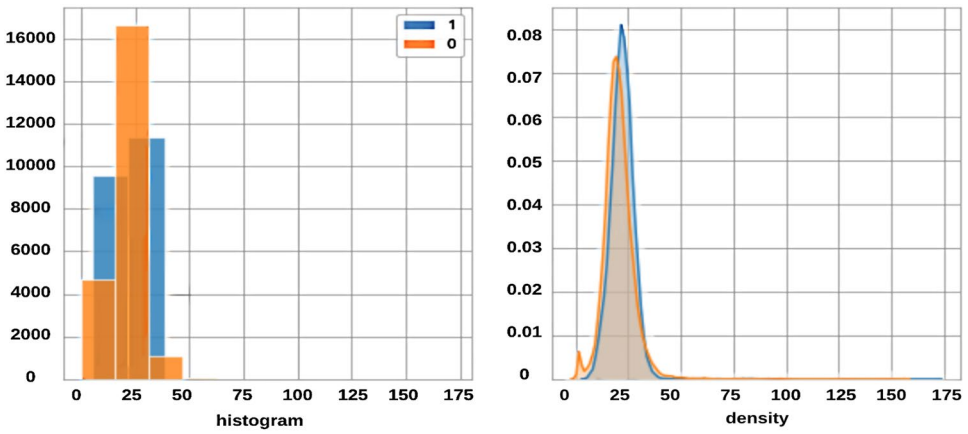

Figure 2 shows the word cloud of the top 30 of authentic and fake news of all three languages. The trustworthy news of all the three languages feature 'Reuters' as one of the most frequently used words. These word clouds show that true news cites authentic news sources. Also, it can be inferred from the word cloud that true news use more objective words than fake news. Figure 5 shows the polarity of fake news and true news. It can be inferred from the plots that the sentiment of true news is more clustered towards neutral. On the other hand, the sentiment of fake news is more diverse, but as the length of the news increases, the sentiment starts becoming neutral. Figure 4 on the other hand, shows the distribution of sentence length of true and fake news. The density plot shows that the distribution of sentence length of both the news is similar. On further analysis, it was inferred that both the news show similar characteristics in terms of their word count, sentence count, sentence length, and character count. Further, we also plotted the t-SNE projections of the news articles. These projections introduced by Van der Maaten and Hinton (2008) effectively represent the higher dimension data into two dimensions and thus enable the cluster

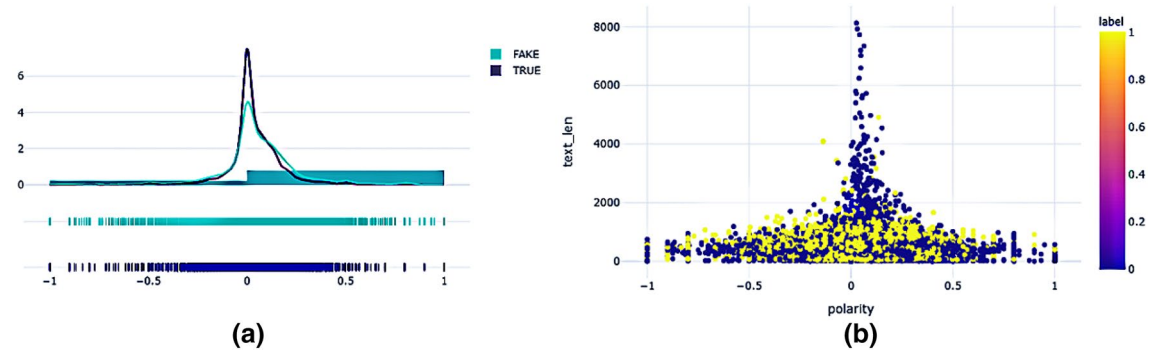

Fig. 5 Sentiment polarity of Fake News vs True News. Figure **a** represents the distribution of polarity with respect to the news label while **b** represents the distribution of polarity with respect to news label and text length

Table 2 Dataset distribution

	English	German	French	Total
Fake	9475	7000	5996	22471
Real	8018	6000	6999	21017
Total	17493	13000	12995	43488

representation of similar documents. Figure 3(a) depicts the t-SNE projections of all news while the (b), (c), and (d) show individual t-SNE projections of separate languages. In all the figures, 0 stands for fake news and 1 stands for true news. The figures clearly show the distinction between the news projections of every language. A demarcation also exists between the projections of fake and true news in an individual language.

4 Methodology

In this paper, we have proposed a unified attention-driven model for the purpose of multilingual fake news detection. As mentioned in the previous sections, our dataset consists of news in English, German, and French. We have used fasttext pretrained multilingual embeddings[13] for our text representations. The texts of different languages are represented using these pretrained fasttext embeddings, currently available for 157 languages. Those embeddings are then given as an input to the attention network, consisting of an encoder and an attention mechanism. It works hierarchically, first on the word level and then on a sentence level to extract deeper and important features from the text. These 'hierarchical attention networks' were initially proposed by Yang et al. (2016) for the purpose of document classification. The fundamental thought behind the hierarchy implementation was that "Words make sentences and sentences make documents". It was implied that a sentence vector could be created which consists of the important words in the sentence, and further, a document vector can be created using the important sentences. The working of the model is explained further in this section:

4.1 Word level

The input to the model is a set of structured tokens represented by t^{is} which represents the i^{th} word of s^{th} sentence. The embedding layer processes the structured tokens. An embedding algorithm assigns multidimensional vectors (T_a t_{it}) independently to all tokens. Hence, the numerical depiction of the words is given by:

$$w_{in} = T_a \cdot t_{in}, n \in [1, N] \tag{2}$$

Here, the total number of news sentences is represented by N and x_{in} represent the projection of the word in the semantic vector space. These projections are passed on to the word encoder layer. The context annotations of each individual word is returned. Bidirectional Gated Recurrent Units (GRU) is then used to summarize the information from both sides and returns word annotations (c_{in}). We have stacked text-CNN with GRU in order to achieve better results. For the input representations, abstraction of levels over time is added by the addition of stacked GRU layers.

$$\begin{aligned} p_{in} &= text - CNN(x_{in}) \\ \vec{c}_{in} &= \overrightarrow{GRU}(p_{in}), n \in [1, N] \\ \overleftarrow{c}_{in} &= \overleftarrow{GRU}(p_{in}), n \in [N, 1] \\ c_{in} &= [\vec{c}_{in}, \overleftarrow{c}_{in}] \end{aligned} \tag{3}$$

The computed context is then passed to the attention layer at word level. A vector of importance weights is computed for the same at this layer. The computed annotations (c_{in}) are then further passed through a one-layer Multilayer Perceptron. Here, the aim of using the perceptron is to perform

[13] https://fasttext.cc/.

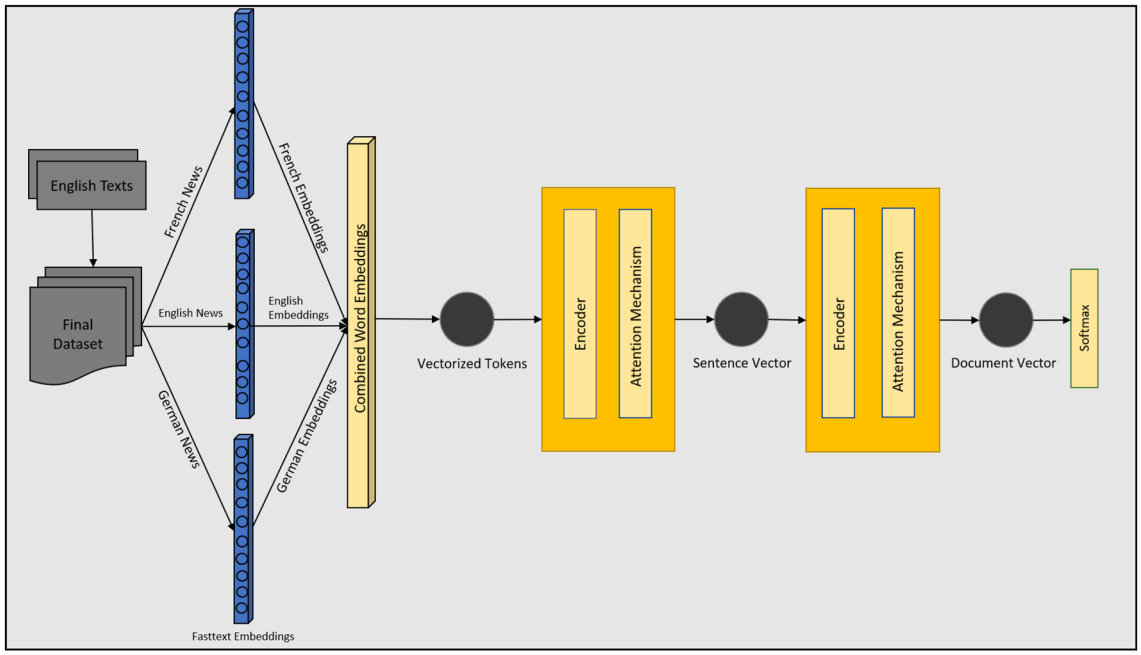

Fig. 6 System architecture of the proposed model

weight and bias learning through training and is represented by t_{in}.

$$t_{in} = tanh(W_w \cdot c_{in} + b_w) \tag{4}$$

The validity of range of values between -1 and 1 is ensured by tanh. The computed annotations are then multiplied by a trainable context vector t_v. The importance per weight is calculated after normalization. Softmax function is applied for this task. The importance weights are then iteratively added to the calculated context annotations to create a sentence vector(v_i).

$$\alpha_{is} = \exp\left(t_{is}^T \cdot t_v\right) / \sum_s exp\left(t_{is}^T \cdot t_v\right) v_i = \sum_s \alpha_{is} \cdot c_{is} \tag{5}$$

4.2 Sentence level

On the sentence level, the same process as that of word level is repeated. The pivot shifts to sentences in this phase. The sentence vector generated in the previous phase is now passed onto the sentence encoders of this layer. The Sentence Encoder in this phase performs in a similar manner like the word encoder. The main task of this encoding layer is to summarize the document using bidirectional GRU. Stacking of text-CNN with GRU is done as this layer as well for the same purpose of learning deeper meanings and give the importance weight to the sentences.

$$\begin{aligned} p_i &= text - CNN(v_i) \\ \vec{c}_i &= \overrightarrow{GRU}(p_i), s \in [1, D] \\ \overleftarrow{c}_i &= \overleftarrow{GRU}(p_i), s \in [D, 1] \\ c_i &= [\vec{c}_i, \overleftarrow{c}_i] \end{aligned} \tag{6}$$

The values are contained within the range of -1 to 1 with the use of tanh. Again, the computed annotations are then multiplied by a trainable context vector t_s. The importance per weight is again calculated after normalization for the document level. The importance weights are then iteratively added to the calculated context annotations to create a sentence vector(d_i). The final document vector d_i is calculated at the sentence attention layer. It is used as the feature for final document classification.

$$\begin{aligned} t_i &= \tanh(W_s \cdot w_i + b_s) \\ \alpha_i &= \exp\left(t_i^T \cdot t_s\right) / \sum_s \exp\left(t_i^T \cdot t_s\right) \\ d_i &= \sum_s \alpha_i \cdot c_i \end{aligned} \tag{7}$$

The overall architecture of our model is shown in Figure 6. The input to the model is the news dataset collected. The translation of the input dataset is performed using google translate api, as explained in the previous section. The data is then randomly shuffled. The training data consists of a roughly equal number of news from all three languages. The ratio of training data to testing data is 0.8 to 0.2. The news from all three languages are then converted into its vectorized form by using their separate fasttext embeddings.

Table 3 Performance evaluation of Mul-FaD [E+G+F : English + German +French]

	Tested on English	Tested on German	Tested on French	Tested on E+G+F
Trained on English	94.6	59.3	50.23	75.3
Trained on German	55.33	90.2	52.44	68.45
Trained on French	70.6	63.11	87.45	77.42
Trained on E+G+F	**96.57**	**93.22**	**93.14**	**93.73**

The vectorized tokens of training data are then passed on to the two layers of the model consecutively, one focusing on words and the other focusing on sentences. The final predictions are computed using the document vector generated through the softmax function.

5 Results and discussions

The proposed model Mul-FaD was evaluated on various parameters. Our attention-based model was applied to the dataset created. The dataset was split into training and test data with a ratio of 0.8 to 0.2. We have used a ten-fold cross-validation strategy in our experiments and the final results shown are reported after averaging the results across all folds. The model is implemented in Python using the Keras framework. The execution was performed on a free Tesla K80 GPU provided by Google Colab. The comparison of our model with the following baseline models is performed: TF-IDF, word2vec, text-CNN, HAN, Multilingual BERT, and Language-Independent Fake News Detection(LIFND):

- **TF-IDF**(Ramos 2003): The textual features were calculated using Term Frequency - Inverse Document Frequency and Multinomial Naive Bayes was applied as a classifier on top of it.
- **Word2Vec**(Mikolov et al. 2013): Word2Vec was applied on our dataset with Logistic Regression applied as the classifier.
- **Text-CNN**(He et al. 2016) : text-Convolutional Neural Network is applied as a baseline for the comparison. 128 filters were used with a kernel size of 3.
- **HAN**(Yang et al. 2016): This conventional Hierarchical Attention Network was applied on our dataset. It uses two LSTM layers along with the attention mechanism on the hierarchy of word and sentence level.
- **mBERT**(Kar et al. 2020): This model uses the pretrained Bidirectional Encoder Representation from Transforms combined with relevant features from Twitter. The code for this is available at GitHub[14]. The online tensorflow library was used in for the implementation.
- **Language Independent Fake News Detection (LIFND)**(Abonizio et al. 2020): This is a language independent model proposed for fake news detection. It aims at identifying the veracity of a piece of news using language independent textual features. This model was applied on our dataset using the features proposed in the paper.

The results for all models shown are calculated by averaging the results of ten-fold cross validation applied on the dataset. Based on our experiments, we will answer the following research questions in this section for detailed discussion :

- RQ1: How well does this model perform if it is trained on one language and tested on another?
- RQ2: Does the use of different embeddings affect the result?
- RQ3: Does multilingual model perform better than monolingual one?

5.1 RQ1: How well does this model perform if trained on one language and tested on another?

We have tested our model on various parameters. We first trained our model on a single language and tested it on news of other languages. We did this for all three languages. The results of the experiments are shown in Table 3. Evidently, the best results obtained were when the model was trained and tested on the same language. Altogether, the best results were obtained when the model was trained and tested on all three languages with an accuracy of 93.73. These results prove that our multilingual model - Mul-FaD performs better on our data of multiple languages.

[14] https://github.com/DebanjanaKar/Covid19_FakeNews_Detection.

Table 4 Performance comparison of Mul-FaD when applied on word embeddings vs fasttext embeddings

	Accuracy	F1
Word embedding	89.42	87.88
Multilingual BERT	91.7	90.9
Fasttext embeddings	**93.73**	**92.9**

to produce better results than it. The results produced by the model of Abonizio et al. (2020) had an accuracy comparable to ours. However, as seen in figure 7, their model achieved a peak and suddenly started declining rapidly while our model gave good accuracy consistently for few epochs before declining.

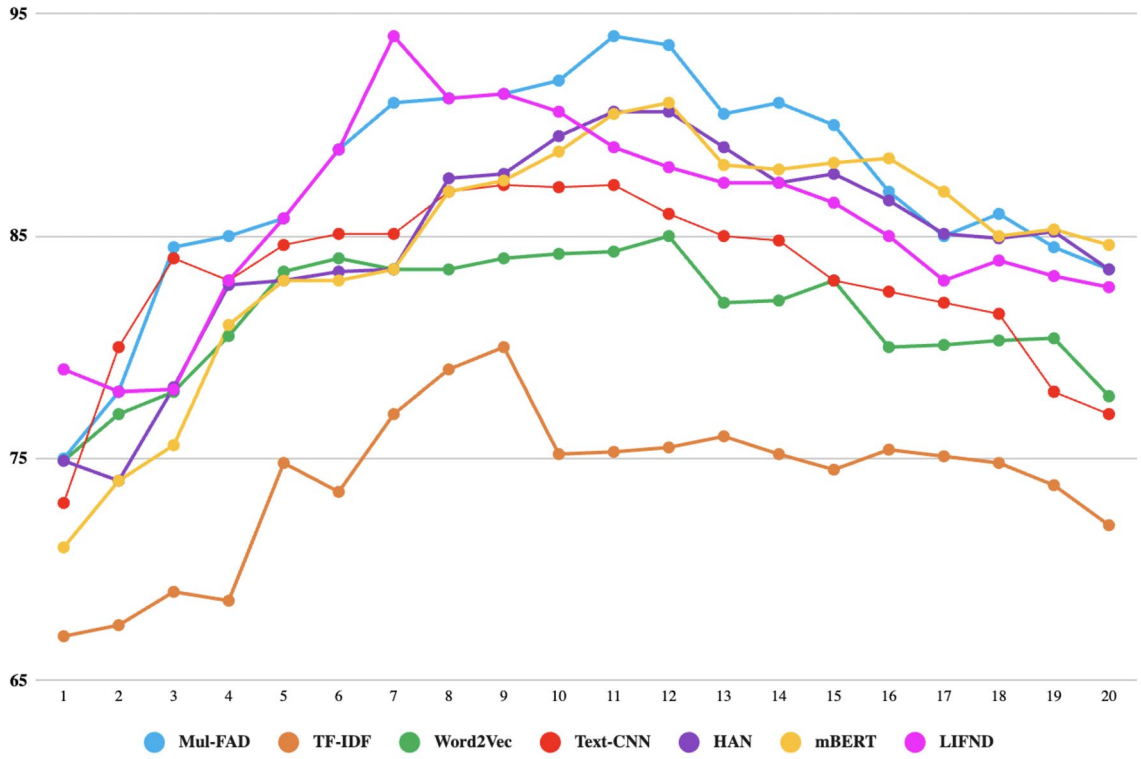

Fig. 7 Performance comparison of various models over a single iteration

5.2 RQ2: Does the use of different embeddings affect the result?

In our evaluation, we tested our model on two kinds of embeddings: word2vec embeddings for separate languages[15] and fasttext embeddings to identify the better suitable one for our model. The result of the evaluation is shown in Table 4. As seen in the result, Fasttext embeddings gave better results on our model as compared to the word embeddings by a significant margin. Also, it was noticed that fasttext embeddings were faster by a small margin. We have also tested our dataset on the pretrained multilingual BERT embeddings as proposed by Kar et al. (2020) and our model was able

5.3 RQ3: Does multilingual model perform better than monolingual one?

This research question was one of the prime intents of this paper that does a mulitlingual model perform better than one which works only on a single model. This question is partly answered by Table 3 and partly by Table 5. The former table compares our model when it works monolingually vs when it performs multilingually while the latter table compares our model with other models. The comparison of all models over a single iteration have been shown in figure 7 while figure 8 shows the performance comparison of all models in terms of accuracy and F1 score. It is clearly evident from the results in both tables that our multilingual model performs better than other models and can be successfully used in detection of fake news in multiple languages. The language independent model proposed by Abonizio et al. (2020) have

[15] http://vectors.nlpl.eu/repository/.

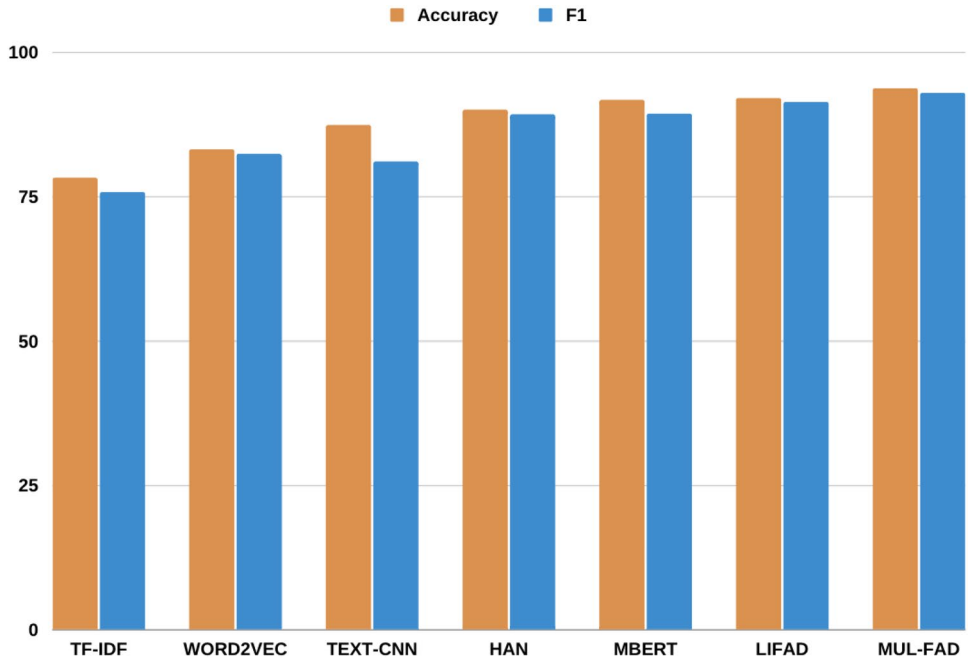

Fig. 8 Result comparison of various models

Table 5 Performance comparison of Mul-FaD with other models [SD - Standard Deviation for Accuracy]

Models	Accuracy	F1	SD
TF-IDF with MNB	78.2	75.7	1.12
Word2Vec with LR	83.11	82.34	0.96
Text-CNN	87.33	81.02	1.12
HAN	91.1	90.9	1.31
mBERT	91.7	89.3	1.53
LIFND	92	91.33	1.41
Mul-FaD	**93.73**	**92.9**	1.17

very similar results to us, ours being slightly better. This signifies that the extracted language independent features are not sufficient for the detection of fake news. Our attention based model based on stacking of text-CNN and GRU was able to extract better features for a better classification. Our modified attention model was even able to produce better results than the original HAN model.

6 Conclusion

Fake news has penetrated every sector of society. It is affecting brand images, increasing propaganda, and is even leading to violence. Since fake news poses an immediate and severe threat to society, there is a need for a tool that can automatically detect fake news. We have created our dataset by combining existing datasets of the English language and translating parts of it to French and German language, and then verifying it. The total summed up to around 40000 news articles. We have also proposed a model Mul-FaD that can address fake news detection in multiple languages scenarios. Texts in three languages - English, German and French were used in our model. For text representations, we used fasttext embeddings available for multiple languages. Our proposed model uses an altered hierarchical attention network, which adds a layer of attention and extracts better text representations and meanings. Also, it works on both word and sentence levels. Hence, better and even more critical representations can be extracted from the text. Our model gave notably better results than other baseline models, with an accuracy of 93.73 and an F1 score of 92.9. Our model outperforms other baseline models on this dataset. Our results concur that it is successfully possible to identify fake news in a multilingual framework. Due to the intense manual effort to verify google translations, we had to limit our work to only three languages. In the future, we would like to work on a more dynamic model which is not restricted to just three languages. We would also like to work on optimizing the model in terms of time taken in this task of mulitilingual fake news detection.

Data Availability Statement Data available on request from the authors.

Declarations

Conflict of interest The authors of this paper declare that they have no conflict of interest.

References

Abonizio HQ, de Morais JI, Tavares GM, Barbon Junior S (2020) Language-independent fake news detection: English, portuguese, and spanish mutual features. Future Internet 12(5):87

Ahuja N, Kumar S (2020) S-han: Hierarchical attention networks with stacked gated recurrent unit for fake news detection. 2020 8th International Conference on Reliability. Infocom Technologies and Optimization (Trends and Future Directions)(ICRITO), IEEE, pp 873–877

Guibon G, Ermakova L, Seffih H, Firsov A, Le Noé-Bienvenu G (2019) Multilingual fake news detection with satire. In: CICLing: International Conference on Computational Linguistics and Intelligent Text Processing

He T, Huang W, Qiao Y, Yao J (2016) Text-attentional convolutional neural network for scene text detection. IEEE trans image process 25(6):2529–2541

Horne B, Adali S (2017) This just in: Fake news packs a lot in title, uses simpler, repetitive content in text body, more similar to satire than real news. In: Proceedings of the International AAAI Conference on Web and Social Media, vol 11

Kar D, Bhardwaj M, Samanta S, Azad AP (2020) No rumours please! a multi-indic-lingual approach for covid fake-tweet detection. arXiv preprint arXiv:2010.06906

Koloski B, Pollak S, Skrlj B (2020) Multilingual detection of fake news spreaders via sparse matrix factorization. In: CLEF (Working Notes)

Li Y, Jiang B, Shu K, Liu H (2020) Toward a multilingual and multimodal data repository for covid-19 disinformation. In: 2020 IEEE International Conference on Big Data (Big Data), IEEE, pp 4325–4330

Mikolov T, Sutskever I, Chen K, Corrado GS, Dean J (2013) Distributed representations of words and phrases and their compositionality. Advances in neural information processing systems. MIT Press, Cambridge, pp 3111–3119

Monteiro RA, Santos RL, Pardo TA, De Almeida TA, Ruiz EE, Vale OA (2018) Contributions to the study of fake news in portuguese: New corpus and automatic detection results. International Conference on Computational Processing of the Portuguese Language. Springer, Berlin, pp 324–334

Posadas-Durán JP, Gómez-Adorno H, Sidorov G, Escobar JJM (2019) Detection of fake news in a new corpus for the spanish language. J Intell Fuzzy Syst 36(5):4869–4876

Qazi U, Imran M, Ofli F (2020) Geocov19: a dataset of hundreds of millions of multilingual covid-19 tweets with location information. SIGSPATIAL Special 12(1):6–15

Ramos J (2003) Using tf-idf to determine word relevance in document queries. Proceed first instr conf mach learn 242(1):29–48

Schwarz S, Theóphilo A, Rocha A (2020) Emet: Embeddings from multilingual-encoder transformer for fake news detection. ICASSP 2020–2020 IEEE International Conference on Acoustics. Speech and Signal Processing (ICASSP), IEEE, pp 2777–2781

Shahi GK, Nandini D (2020) Fakecovid–a multilingual cross-domain fact check news dataset for covid-19. arXiv preprint arXiv:2006.11343

Shao C, Ciampaglia GL, Varol O, Yang KC, Flammini A, Menczer F (2018) The spread of low-credibility content by social bots. Nat commun 9(1):1–9

Van der Maaten L, Hinton G (2008) Visualizing data using t-sne. Journal of machine learning research 9(11)

Varshney D, Vishwakarma DK (2020) Hoax news-inspector: a real-time prediction of fake news using content resemblance over web search results for authenticating the credibility of news articles. J Ambient Intell Humaniz Comput 896:1–14

Vogel I, Meghana M (2020) Detecting fake news spreaders on twitter from a multilingual perspective. In: 2020 IEEE 7th International Conference on Data Science and Advanced Analytics (DSAA), IEEE, pp 599–606

Yang Z, Yang D, Dyer C, He X, Smola A, Hovy E (2016) Hierarchical attention networks for document classification. In: Proceedings of the 2016 conference of the North American chapter of the association for computational linguistics: human language technologies, pp 1480–1489

Publisher's Note Springer Nature remains neutral with regard to jurisdictional claims in published maps and institutional affiliations.

Springer Nature or its licensor (e.g. a society or other partner) holds exclusive rights to this article under a publishing agreement with the author(s) or other rightsholder(s); author self-archiving of the accepted manuscript version of this article is solely governed by the terms of such publishing agreement and applicable law.

Proc. of the International Conference on Electrical, Computer, Communications and Mechatronics Engineering (ICECCME)
16-18 November 2022, Maldives

2022 International Conference on Electrical, Computer, Communications and Mechatronics Engineering (ICECCME) | 978-1-6654-7095-7/22/$31.00 ©2022 IEEE | DOI: 10.1109/ICECCME55909.2022.9987760

Negative Capacitance Multiplier Configuration Using Single CFOA Employing Grounded Capacitor

Meghana Shrivastava
Electrical Engineering Department
Delhi Technological University
Delhi, India
meghanashrivastava_2k21phdee15@dtu.ac.in

Pragati Kumar
Electrical Engineering Department
Delhi Technological University
Delhi, India
pragatikumar@dtu.ac.in

D. R. Bhaskar
Electrical Engineering Department
Delhi Technological University
Delhi, India
drbhaskar@dtu.ac.in

***Abstract*—A single Current Feedback Operational Amplifier (CFOA), three resistors and a grounded capacitor based new grounded negative capacitance multiplier (GNCM) is presented. The multiplication factor of the presented GNCM circuit can be controlled uniquely using a resistor. Performance of the presented circuit has been validated using macromodel of CFOA AD844. Various analyses such as frequency analysis, transient analysis and temperature analysis have been included to support the theoretical results. The proposed GNCM circuit can produce a multiplication factor upto 26.**

***Keywords*—** *capacitance multiplier, negative capacitance multiplier, cfoa, pspice*

I. Introduction

In low frequency applications, higher value of capacitance is required. For IC implementation of higher capacitance values large chip area is needed. Therefore, many researchers have proposed active capacitance multiplier circuits using various active building blocks (ABB), using which a lower value of physical capacitor can provide a higher capacitance value. In the open literature, a large number of positive capacitance multiplier circuits have been reported [1, 2, 3, 4, 5, 6, 7, 8, 9, 10, 11, 12, 13, 14, 15, 16]. Negative capacitance multiplier (NCM) circuits on the other hand, play an important role in analog signal processing where they can be employed to cancel parasitic capacitances present at different terminals of some ABBs. Therefore, researchers have also shown their interest in the realization of NCM employing different ABBs such as operational amplifier (Op-Amp) [17], operational transconductance amplifier (OTA) [18], current differencing transconductance amplifier (CDTA) [19], second generation voltage conveyor (VCII) [20, 21, 22] current follower transconductance amplifier (CFTA) [23], operational transresistance amplifier (OTRA) [24] etc. Since the paper deals with the realisation of a NCM circuit using grounded capacitor, in the following we present the important features of various negative capacitance multiplier circuits available in the open literature.

In [17], a negative capacitance multiplier (CM) has been presented using a negative impedance converter which has been designed using Op-Amp. This reported circuit can be used for low frequency applications. In [18], the proposed circuit consists of a translinear loop stage and OTA stage. This design has wide tunablitiy range and is also insensitive to temperature variations. The circuit was used for implementation of low frequency filters and oscillators and other biomedical applications. In [19], authors have proposed two grounded capacitance multipliers using one CDTA, one capacitor, pseudo-grounded via a low impedance CDTA input terminal, and one or two resistors. These multipliers can be modified into a floating capacitance multiplier by using difference voltage amplifier.

In [20], an electronically tunable second generation voltage conveyor (VCII) based CM has been presented alongwith a single floating capacitor. The reported circuit has been modified into a GNCM by simply replacing EVCII+ with EVCII-. An electronically tunable positive/negative floating CM has been reported in [21] employing two different active blocks (one VCII and one DVCC), a single grounded capacitor and does not employed any resistors. In [22], a new grounded positive/negative CM circuit has been reported using VCIIs. The proposed positive grounded capacitance multiplier (PGCM) circuit has been designed using one VCII+, one VCII-, one capacitor and two resistors. The presented PGCM circuit can also be converted into GNCM circuit just by replacing VCII- by a VCII+. In [23], two positive and two negative lossless grounded CM circuits have been reported using two CFTAs, one capacitor and two grounded resistors. The presented GCM configurations do not require any matching conditions. Recently, an OTRA-based positive/negative CM circuit has been presented in [24] wherein a voltage follower, one capacitor and three resistors have also been used. The negative and positive capacitance multiplication factors of the presented circuits are depending on the values of three resistors. In [25], four different configurations of negative CM circuits have been proposed wherein two of them employ two CFOAs and the other two use only one CFOA alongwith two resistors and one capacitor. In [26], a negative capacitance multiplier was realized using single non-inverting CFOA, one grounded capacitor, two grounded resistors and one resistor. In [27], a negative impedance multiplier has been realized using one CFOA, two OTAs and one grounded impedance and this multiplier functioned properly in the frequency range from 2Hz to 7MHz. In [28], an inverting CFOA, one grounded capacitor and two resistors based grounded CM configuration has been proposed. The multiplication factor of the reported circuit work satisfactorily within the frequency range from 1Hz to 30kHz.

From the above summary it may be noted that despite the availability of several realizations of the negative capacitance multiplier circuits using different active building blocks, and different features, the research work on new realizations of capacitance multiplier circuits is far from complete. In this paper, thus, we have presented a new negative capacitance multiplier circuit using only one active element, minimum number of passive element (03) including a grounded capacitor resulting into a simple configuration, thus minimizing the complexity of the circuit. Various analyses have been corroborated to validate the proposed circuit. The presented circuit is insensitive to temperature variations. Application example has also been added.

978-1-6654-7095-7/22/$31.00 © 2022 IEEE

Authorized licensed use limited to: DELHI TECHNICAL UNIV. Downloaded on January 05,2023 at 06:27:10 UTC from IEEE Xplore. Restrictions apply.

II. Proposed Negative Capacitance Multiplier Circuit

The proposed grounded negative capacitance multiplier using a single CFOA, three resistors and a grounded capacitor is shown in Fig 1.

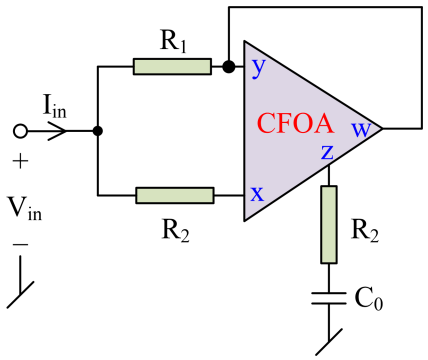

Fig. 1. Proposed GNCM configuration using CFOA

Assuming ideal CFOA characterized by: $I_y = 0$, $V_x = V_y$, $V_w = V_z$, $I_z = I_x$, the analysis of circuit shown in Fig. 1 yields the following input impedance:

$$\frac{V_{in}}{I_{in}} = Z_{in} = \frac{-1}{sC_0\left(1+\frac{R_2}{R_1}\right)} = \frac{-1}{sC_{eq}} \tag{1}$$

where

$$C_{eq} = -C_0\left(1+\frac{R_2}{R_1}\right) \tag{2}$$

From equation (1), it is seen that the proposed circuit shown in Fig.1 provides a negative capacitance with a multiplication factor of $\left(1+\frac{R_2}{R_1}\right)$ which is given in equation (2). From equation (2), it is observed that the value of capacitance can be controlled using the resistor R_1.

III. Simulation Results

The functionality of the proposed negative capacitance multiplier has been verified using macro-model of AD844 type CFOA in PSPICE simulations. The biasing voltages of CFOA used were ±10V. The passive component values R_1 = 1kΩ, R_2 = 25kΩ, C_0 = 100pF were used for obtaining the C_{eq} 2600pF.

The magnitude and phase of impedance were also varied by varying resistor R_1 through 1kΩ, 1.25kΩ, 1.75kΩ, 2.5kΩ, 4kΩ respectively and the corresponding results have been displayed in Fig. 2 and Fig. 3 respectively.

The simulated capacitance with their theoretical values have been shown in Fig. 4. By varying the values of resistors proposed circuit can produce multiplication factor upto 26 times of the value of capacitance. The simulated and theoretical values of capacitance for different multiplication factors have been shown in Table 1.

The magnitude-frequency and phase-frequency responses of impedance with temperature variation by selecting R_1 = 10kΩ, R_2 = 25kΩ and C_0 = 100pF and corresponding results have been displayed in Fig.5 and Fig. 6 respectively. Therefore, the proposed GNCM is insensitive to temperature variation.

The simulated transient responses of input voltage and current of the proposed GNCM are displayed in Fig. 7

TABLE I. Simulated and Theoretical capacitance values

R_1(kΩ)	*Ceq (Simulated)*	*Ceq (Theoretical)*	*MF*
1	***2789.5 pF***	***2600 pF***	***26***
1.25	***2252.9 pF***	***2100 pF***	***21***
1.75	***1639.8 pF***	***1528.5 pF***	***15.285***
2.5	***1179.9 pF***	***1100 pF***	***11***
4	***777.6 pF***	***725 pF***	***7.25***

* MF : Multiplication factor.

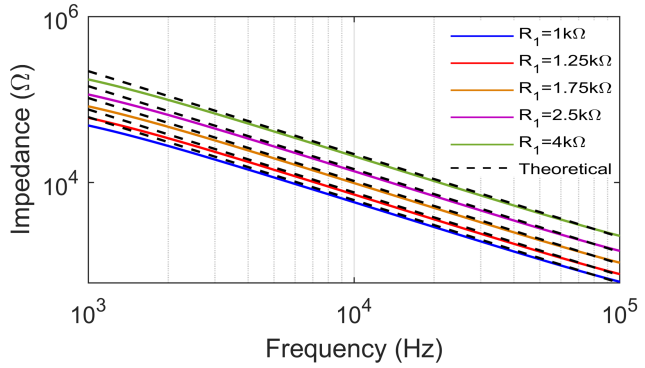

Fig. 2. Simulated magnitude responses of proposed GNCM

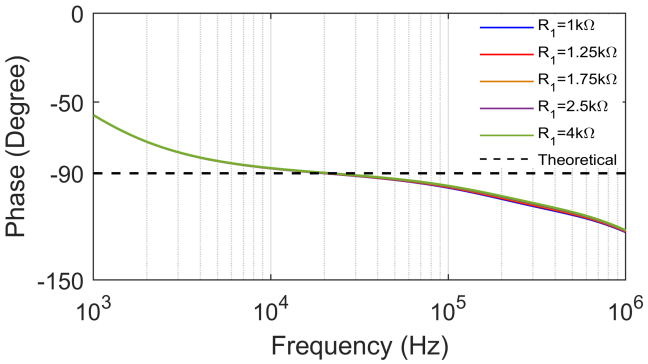

Fig. 3. Simulated phase responses of proposed GNCM

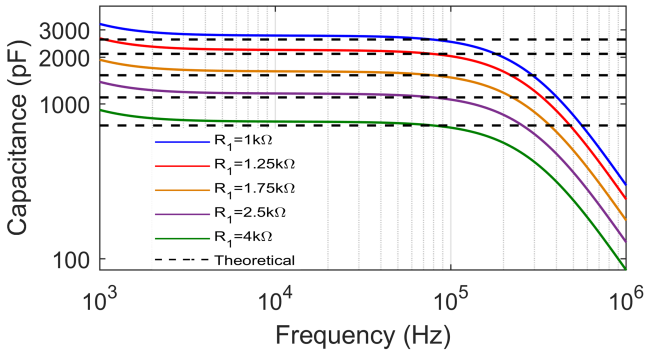

Fig. 4. Simulated magnitude response of capacitance of proposed GNCM

IV. Application Example

The proposed negative capacitance multiplier circuit has also been validated by designing a capacitive cancellation circuit as shown in Fig. 8. The relationship between input voltage (V_{in}) and input current (I_{in}) of the circuit of Fig. 8 can be written as:

$$\frac{V_{in}}{I_{in}} = R + \frac{R'}{1+sR'(C+C_{eq})} \tag{3}$$

Authorized licensed use limited to: DELHI TECHNICAL UNIV. Downloaded on January 05,2023 at 06:27:10 UTC from IEEE Xplore. Restrictions apply.

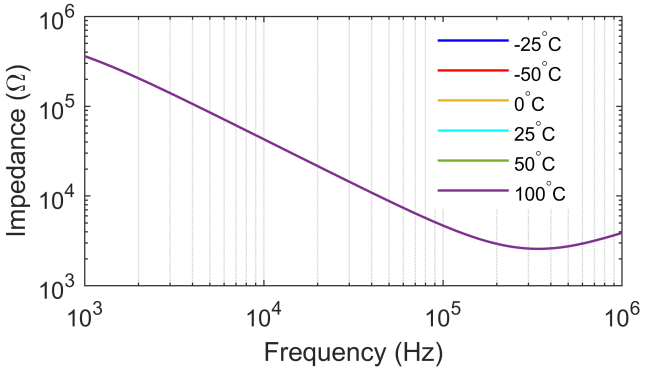

Fig. 5. Variation of temperature on impedance magnitude

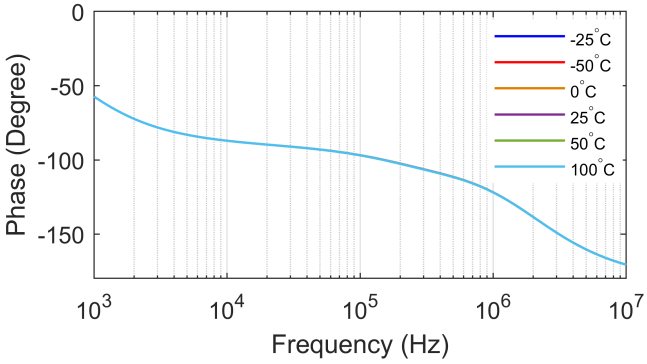

Fig. 6. Variation of temperature on impedance phase

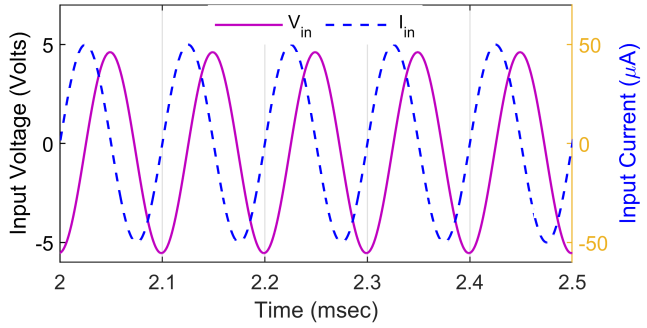

Fig. 7. Simulated waveforms of V_{in} and I_{in} for proposed GNCM

The capacitive cancellation circuit shown in Fig. 8 is verified by selecting R = 100Ω, R' = 200Ω, C = 2.6nF, C_0 = 100pF, R_1 = 1kΩ, R_2 = 25kΩ. The simulated transient responses of V_{in} and I_{in} of the capacitive cancellation circuit have been shown in Fig. 9 from where it can be seen that both V_{in} and I_{in} are in phase.

From Fig. 2- Fig. 9, it is, thus, concluded that these simulation results validate the workability of the proposed GNCM circuit.

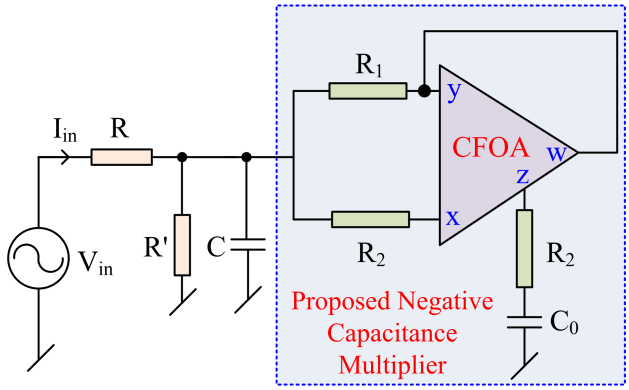

Fig. 8. Capacitance cancellation circuit using proposed GNCM

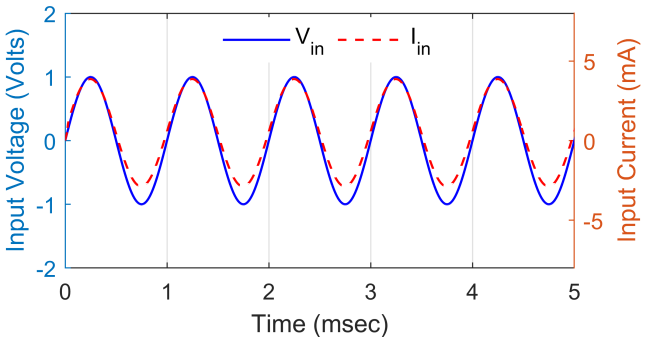

Fig. 9. Simulated waveforms of V_{in} and I_{in} of the capacitive cancellation circuit

V. Conclusions

A new grounded negative capacitance multiplier employing one CFOA, three resistors and one grounded capacitor has been proposed in this paper. It uses only one active element which reduces the circuit complexity. The simulations of the proposed circuit were done on PSPICE using macro-model of AD844 type CFOA to validate the theoretical results. The proposed circuit was also tested for different temperature to check the robustness and found that the circuit is insensitive to temperature variation. An exemplary application of proposed GNCM circuit as capacitance cancellation has also been provided. The presented circuit, thus, enlarges the existing repertoire of negative capacitance multiplier circuits.

References

[1] A. Yesil, E. Yuce, and S. Minaei, "Grounded capacitance multipliers based on active elements," *AEU-International Journal of Electronics and Communications*, vol. 79, pp. 243–249, 2017.

[2] P. Moonmuang and W. Tangsrirat, "Electronically tunable resistorless capacitance multiplier employing VDBAs," in *Proceedings of the 3rd International Conference on Communication and Information Processing*, 2017, pp. 512–515.

[3] P. Moonmuang, T. Pukkalanun, and W. Tangsrirat, "Voltage differencing buffered amplifier-based electronically tunable grounded capacitance multiplier," in *Proceedings of the 8th International Conference on Informatics, Environment, Energy and Applications*, 2019, pp. 208–211.

[4] R. Verma, N. Pandey, and R. Pandey, "Novel CFOA based capacitance multiplier and its application," *AEU-International*

Authorized licensed use limited to: DELHI TECHNICAL UNIV. Downloaded on January 05,2023 at 06:27:10 UTC from IEEE Xplore. Restrictions apply.

Journal of Electronics and Communications, vol. 107, pp. 192–198, 2019.

[5] M. Dogan and E. Yuce, "A new CFOA based grounded capacitance multiplier," *AEU-International Journal of Electronics and Communications*, vol. 115, p. 153034, 2020.

[6] E. Özer, M. E. Başak, and F. Kaçar, "Realizations of lossy and lossless capacitance multiplier using CFOAs," *AEU-International Journal of Electronics and Communications*, vol. 127, p. 153444, 2020.

[7] D. Singh, D. Nand, and A. Kumar, "Newly realized grounded capacitance multiplier using single CFDITA," in *2021 7th International Conference on Signal Processing and Communication (ICSC)*. IEEE, 2021, pp. 362–365.

[8] D. Özenli, E. Alaybeyoğlu, and H. Kuntman, "A grounded capacitance multiplier circuit employing VDTA," in *2021 13th International Conference on Electrical and Electronics Engineering (ELECO)*. IEEE, 2021, pp. 38–41.

[9] S. Singh, Jatin, N. Pandey, and R. Pandey, "Electronically tunable grounded capacitance multiplier," *IETE Journal of Research*, pp. 1–12, 2020.

[10] W. Tangsrirat and O. Channumsin, "Tunable floating capacitance multiplier using single fully balanced voltage differencing buffered amplifier," *Journal of Communications Technology and Electronics*, vol. 64, no. 8, pp. 797–803, 2019.

[11] J. Pimpol, "Electronically regulable capacitance multiplier circuit with a single voltage differencing gain amplifier (VDGA)," *Informacije MIDEM*, vol. 49, no. 4, pp. 211–218, 2019.

[12] J. Vavra, "A capacitance multiplier based on DBTA," in *2017 IEEE Nordic Circuits and Systems Conference (NORCAS): NORCHIP and International Symposium of System-on-Chip (SoC)*. IEEE, 2017, pp. 1–5.

[13] R. Arslanalp and T. Yücehan, "Capacitance multiplier design by using CFOA," in *2015 23nd Signal Processing and Communications Applications Conference (SIU)*. IEEE, 2015, pp. 1393–1396.

[14] W. Jaikla and M. Siripruchyanan, "An electronically controllable capacitance multiplier with temperature compensation," in *2006 International Symposium on Communications and Information Technologies*. IEEE, 2006, pp. 356–359.

[15] M. A. Al-Absi and A. A. Al-Khulaifi, "A new floating and tunable capacitance multiplier with large multiplication factor," *IEEE Access*, vol. 7, pp. 120 076–120 081, 2019.

[16] M. E. Başak and E. Özer, "Electronically tunable grounded inductance simulators and capacitor multipliers realization by using single current follower transconductance amplifier (cfta)," *Analog Integrated Circuits and Signal Processing*, pp. 1–15, 2022.

[17] A. De Marcellis, G. Ferri, and V. Stornelli, "Nic-based capacitance multipliers for low-frequency integrated active filter applications," in *2007 Ph. D Research in Microelectronics and Electronics Conference*. IEEE, 2007, pp. 225–228.

[18] M. A. Al-Absi and A. A. Al-Khulaifi, "A new high multiplication factor tunable grounded positive and negative capacitance simulator," in *2018 IEEE Asia pacific conference on circuits and systems (APCCAS)*. IEEE, 2018, pp. 564–567.

[19] D. Biolek, J. Vavra, and A. U. Keskin, "Cdta-based capacitance multipliers," *Circuits, Systems, and Signal Processing*, vol. 38, no. 4, pp. 1466–1481, 2019.

[20] V. Stornelli, L. Safari, G. Barile, and G. Ferri, "A new extremely low power temperature insensitive electronically tunable VCII-based grounded capacitance multiplier," *IEEE Transactions on Circuits and Systems II: Express Briefs*, vol. 68, no. 1, pp. 72–76, 2020.

[21] G. Ferri, L. Safari, G. Barile, M. Scarsella, and V. Stornelli, "New resistor-less electronically controllable±c simulator employing VCII, DVCC, and a grounded capacitor," *Electronics*, vol. 11, no. 2, p. 286, 2022.

[22] V. Stornelli, L. Safari, G. Barile, and G. Ferri, "A new VCII based grounded positive/negative capacitance multiplier," *AEU-International Journal of Electronics and Communications*, vol. 137, p. 153793, 2021.

[23] E. Ozer, "Electronically tunable CFTA based positive and negative grounded capacitance multipliers," *AEU-International Journal of Electronics and Communications*, vol. 134, p. 153685, 2021.

[24] D. Bhaskar, G. Mann, and P. Kumar, "OTRA-based positive/negative grounded capacitance multiplier," *Analog Integrated Circuits and Signal Processing*, vol. 111, no. 3, pp. 469–481, 2022.

[25] A. Lahiri and M. Gupta, "Realizations of grounded negative capacitance using CFOAs," *Circuits, Systems, and Signal Processing*, vol. 30, no. 1, pp. 143–155, 2011.

[26] M. Dogan and E. Yuce, "Supplementary single active device based grounded immittance function simulators," *AEU-International Journal of Electronics and Communications*, vol. 94, pp. 311–321, 2018.

[27] M. A. Al-Absi and M. T. Abuelma'atti, "A novel tunable grounded positive and negative impedance multiplier," *IEEE Transactions on Circuits and Systems II: Express Briefs*, vol. 66, no. 6, pp. 924–927, 2018.

[28] T. Yucehan and E. Yuce, "A new grounded capacitance multiplier using a single ICFOA and a grounded capacitor," *IEEE Transactions on Circuits and Systems II: Express Briefs*, 2021.

Authorized licensed use limited to: DELHI TECHNICAL UNIV. Downloaded on January 05,2023 at 06:27:10 UTC from IEEE Xplore. Restrictions apply.

Appendix A: Supporting information

Nickel complexes bearing ONS chelating ligands: A promising contender for i*n vitro* cytotoxicity effect on human pancreatic cancer MIA-PaCa-2 cells

Deepika Tanwar[a,b], Tashmeen Kaur[c], Robin Kumar[a], Deepali Ahluwalia[d], Deepika Sharma[c]*, Umesh Kumar[a]*

[a]*Catalysis and Bioinorganic Research Lab, Department of Chemistry, Deshbandhu College, University of Delhi, New Delhi-110019, India.*
[b]*Department of Chemistry, University of Delhi, New Delhi-110007, India.*
[c]*Institute of Nano Science and Technology, Knowledge City, Mohali, Punjab-140306, India*
[d]*Department of Applied Chemistry, Delhi Technological University, New Delhi-110042, India.*

Email: ukumar@db.du.ac.in

1. Materials and Methods

All chemicals were purchased from commercial vendors and used without further purification. The solvents were distilled using drying agents before use. The IR spectral data for samples were obtained using an IR Affinity–1 Shimadzu FTIR spectrometer from powdered samples by ATR method and on a Shimadzu IR435 spectrometer using KBr pellets and data are presented in the frequency range 400–4000 cm^{-1}. Elemental analyses were analyzed on an ElementarAnalysenSysteme GmbH VarioEL V3.00. The ^{1}H NMR and $^{13}C\{^{1}H\}$ NMR spectra were recorded on Bruker AV-400 MHz/Jeol ECX 400 MHz spectrometer operating at field strengths of 400 and 100.5 MHz, respectively and the chemical shifts are reported in ppm relative to TMS. The electrospray ionization mass spectra (ESI−MS) were recorded on a Waters Q-TOF Premier Micromass with CH_3OH as the carrier solvent.

1.1 X-ray Diffraction Studies

Single crystal XRD data for complex **1** was collected on Oxford Xcalibur S diffractometer (4-circle kappa goniometer, Sapphire-3 CCD detector, omega scans, graphite monochromator, and a single wavelength Enhance X-ray source with MoKα radiation) [1]. Pre-experiment, data collection, data reduction, and absorption corrections were performed with the CrysAlisPro software suite [2]. The structure was solved and refined using the*SIR* 2004 and SHELX-2017 program package, respectively (within the Olex2 program package) [3-5]. Non-hydrogen atoms were refined anisotropically. C−H hydrogen atoms were placed in geometrically calculated positions by using a riding

model. The molecular structure and non-covalent interactions were created using Diamond software [6]. Crystallographic data are given in Table S1.

1.2 Computational Methods

The computational calculation for geometry optimization was carried out using the Gaussian 09W program. The optimization is carried out in two steps. Initially, a lesser accurate Hartree-Fock method is employed along with a 3-21G basis set [7]. The output file of this was then utilized for a more accurate energy calculation method. The crystal structure was subjected to geometry optimization using the Becke- three parametric hybrid exchange functional (B3) combined with Lee-Yang-Parr correlation functional (LYP) in conjunction with LANL2DZ basis set, which is apt for the study of heavy elements [8-10]. The solvent effect was incorporated through polarization continuum model (PCM) with DMSO as solvent. The stability of this complex was also checked in vacuum phase. The calculations converged with no constraint in the geometry. The geometry optimization achieved at the same level of theory; thus, the structure is true to energy minimum as it lacked imaginary values in the wavenumber calculations. The frontier molecular orbitals and electrostatic potential surfaces were visualized using the GaussView5.0 program [11,12].

1.3 Hirshfeld Surface Analysis

The three-dimensional Hirshfeld surfaces (HS) along with its two-dimensional fingerprint plots reveal strong information about the type and regions of intermolecular interactions that a molecule undergoes in the unit cell [13,14]. The HS analysis for the present

molecule is done using Crystal Explorer software version 17.5 using the crystal in CIF format [15]. The visualization of the mapped surfaces is done in transparent mode, incorporating the element's label. The d_{norm}, shape index, and curvedness surfaces have been shown in a similar orientation for a better understanding. The two-dimensional fingerprint plots are shown in an expanded fashion for a better vision. The plot has been drawn between d_e, i.e., distance from the point to the nearest nucleus external to the surface, and d_i, i.e., the distance from the nucleus internal to the surface, for a quantitative study of the crystal structure. The intermolecular interactions are calculated using an equation based on d_e, d_i and Van der Waals radii (VDW) of the atom that gives normalized contact distance d_{norm} [16,17].

$$d_{norm} = \frac{d_i - r_i^{vdw}}{r_i^{vdw}} + \frac{d_e - r_e^{vdw}}{r_e^{vdw}}$$

References:

1. ENHANCE, Oxford Xcalibur Single Crystal Diffractometer, version 1.171.34.49, Oxford Diffraction Ltd: Oxford, U.K., (2006).
2. CrysAlisPro, version 1.171.34.49, Oxford Diffraction Ltd: Oxford, U.K., (2011).
3. Sheldrick, G. M. SHELXS-97 and SHELXL-97, program for crystal structure solution and refinement, University of Gottingen, Gottingen, Germany, (2017).
4. Altomare, A.; Cascarano, G.; Giacovazzo, C.; Guagliardi, A.; Burla, M.C.; Polidori, G.; Camalli, M. *SIRPOW*.92 – a program for automatic solution of crystal structures by direct methods optimized for powder data. *J. Appl. Crystallogr.* **1994**, *27,* 435-436.

5. Dolomanov, O. V.; Bourhis, L. J.; Gildea, R. J.; Howard, J. A. K.; Puschmann, H. *OLEX2*: a complete structure solution, refinement and analysis program. *J. Appl. Crystallogr.* **2009**, *42*, 339-341.
6. Putz, H.; GbR, K. B. Diamond-crystal and molecular structure visualization crystal impact, Kreuzherrenstr, 102, 53227 Bonn, Germany.
7. Hariharan, P. C.; Pople, J. A. The influence of polarization functions on molecular orbital hydrogenation energies. *Theor. Chim. Acta* **1973**, *28*, 213-222.
8. Hehre, W. J.; Ditchfield, R.; Pople, J. A. Self-consistent molecular orbital methods. XII. Further extensions of Gaussian-type basis sets for use in molecular orbital studies of organic molecules. *J. Chem. Phys.* **1972**, *56,* 2257-2261.
9. Hay, P. J.; Wadt, W. R. Ab Initio effective core potentials for molecular calculations. Potentials for the transition metal atoms Sc to Hg. *J. Chem. Phys.* **1985**, *82,* 270-283.
10. Chiodo, S.; Russo, N.; Sicilia, E. LANL2DZ basis sets recontracted in the framework of density functional theory. *J. Chem. Phys.* **2006**, *125,* 104107-104116.
11. Becke, A. D. Density-functional thermochemistry. III. the role of exact exchange. *J. Chem. Phys*. **1993**, *98*, 5648-5652.
12. Frisch, M. J.; Trucks, G. W.; Schlegel, H. B.; Scuseria, G. E.; Robb, M. A.; Cheeseman, J. R.; Scalmani, G.; Barone, V.; Mennucci, B.; Petersson, G. A.; Nakatsuji, H.; Caricato, M.; Li, X.; Hratchian, H. P.; Izmaylov, A. F.; Bloino, J.; Zheng, G.; Sonnenberg, J. L.; Hada, M.; Ehara, M.; Toyota, K.; Fukuda, R.; Hasegawa, J.; Ishida, M.; Nakajima, T.; Honda, Y.; Kitao, O.; Nakai, H.; Vreven,

T.; Montgomery Jr., J. A.; Peralta, J. E.; Ogliaro, F.; Bearpark, M.; Heyd, J. J.; Brothers, E.; Kudin, K. N.; Staroverov, V. N.; Keith, T.; Kobayashi, R.; Normand, J.; Raghavachari, K.; Rendell, A.; Burant, J. C.; Iyengar, S. S.; Tomasi, J.; Cossi, M.; Rega, N.; Millam, J. M.; Klene, M.; Knox, J. E.; Cross, J. B.; Bakken,V.; Adamo, C.; Jaramillo, J.; Gomperts, R.; Stratmann, R. E.; Yazyev, O.; Austin, A. J.; Cammi, R.; Pomelli, C.; Ochterski, J. W.; Martin, R. L.; Morokuma, K.; Zakrzewski, V. G.; Voth, G. A.; Salvador, P.; Dannenberg, J. J.; Dapprich, S.; Daniels, A. D.; Farkas, O.; Foresman, J. B.; Ortiz, J. V.; Cioslowski, J.; Fox, D. J. Gaussian, Inc., Wallingford CT, 2010. Gaussian 09, revision B.01.

13. Spackman, M. A.; Jayatilaka, D. Hirshfeld surface analysis. *CrystEngComm.* **2019**, *11,* 19-32.

14. (a) Spackman, M. A.; McKinnon, J. J.; Jayatilaka, D. Electrostatic potentials mapped on Hirshfeld surfaces provide direct insight into intermolecular interactions in crystals. *CrystEngComm.* **2018**, *10*, 377-388. (b) Spackman, M. A.; Byrom, P. G. A novel definition of a molecule in a crystal. *Chem. Phys. Lett.* **1997**, 267 215-220. (c) McKinnon, J. J.; Spackman, M. A.; Mitchell, A. S. Novel tools for visualizing and exploring intermolecular interactions in molecular crystals. *Acta Cryst.* **2004**, B60, 627-668. (d) Rohl, A. L.; Moret, M.; Kaminsky, W.; Claborn, K.; Mckinnon, J. J.; Kahr, B. Hirshfeld surfaces identify inadequacies in computations of intermolecular interactions in crystals: pentamorphic 1,8-dihydroxyanthraquinone. *Cryst. Growth Des.* **2008**, *8*, 4517-4525. (e) Parkin, A.; Barr, G.; Dong, W.; Gilmore, C. J.; Jayatilaka, D.; Mckinnon, J. J.; Spackman,

M. A.; Wilson, C. C. Comparing entire crystal structures: structural genetic fingerprinting. *CrystEngComm.* **2007**, *9*, 648-652. (f) Fabbiani, F. P. A.; Byrne, L. T.; Mckinnon, J. J.; Spackman, M. A. Solvent inclusion in the structural voids of form II carbamazepine: single-crystal X-ray diffraction, NMR spectroscopy and Hirshfeld surface analysis. *CrystEngComm.* **2007**, *9*, 728-731.

15. Wolff, S. K.; Grimwood, D. J.; McKinnon, J. J.; Turner, M. J.; Jayatilaka, D.; Spackman, M. A. *Crystal Explorer 17.5*, University of Western Australia, **2012**.
16. Seth, S. K. Tuning the formation of MOFs by pH influence: X-ray structural variations and Hirshfeld surface analyses of 2-amino-5-nitropyridine with cadmium chloride. *CrystEngComm.* **2013**, *15,* 1772-1781.
17. Seth, S. K. Structural elucidation and contribution of intermolecular interactions in *o*-hydroxy acyl aromatics: Insights from X-ray and Hirshfeld surface analysis. *J. Mol. Struct.* **2014**, *1064,* 72-75.

Table S1

Crystallographic data and structure refinement summary for complex **1**

	Complex **1**
Formula	$C_{27}H_{22}N_2NiO_3S_2$
Formula weight	545.29
T/K	293(2)
λ/Å	0.71073
Crystal system	monoclinic
Space group	$P2_1/c$
a/Å	13.9206(4)
b/Å	16.2632(4)
c/Å	11.7655(4)
α/deg	90.0
β /deg	113.257(3)
γ/deg	90.0
Vol/Å^3	2447.19(13)
Z	4
D_{calcd}/g cm^{-3}	1.480
F(000)	1128.0
*Θ*range/deg	6.27 to 58.988
Reflections measured	35405
Reflections used	6287 [R_{int} = 0.0376, R_{sigma} = 0.0324]
Parameters	6287/0/316
μ(Mo Kα) (cm^{-1})	9.96
R_1, wR_2[I> 2σ(I)][a]	R_1 = 0.0387, wR_2 = 0.0817
R_1, wR_2 (all data)[b]	R_1 = 0.0561, wR_2 = 0.0902
GooF[c]	1.021

[a] $R_1 = \Sigma||F_o| - |F_c||/\Sigma|F_o|$. [b] $wR_2 = \{\Sigma[w(F_o^2 - F_c^2)^2]/\Sigma[w(F_o^2)^2]\}^{1/2}$ [c] $S = \{\Sigma[w(F_o^2 - F_c^2)^2]/(n-p)^2]\}^{1/2}$

Table S2

Cartesian co-ordinates of complex **1** optimized in vacuum phase.

B3LYP/LANL2DZ energy= -1566.6480919 a.u.

Ni	0.411085000	-0.452544000	-0.797481000	H	-2.118722000	4.096388000	0.276760000
S	-1.087682000	-2.756266000	0.009130000	C	4.342370000	-1.809296000	-1.236151000
S	-1.033970000	-2.431219000	2.327525000	H	4.240882000	-2.187024000	-2.249553000
O	2.010721000	-1.322482000	-1.235500000	C	-0.002451000	1.599666000	2.480905000
O	1.226076000	1.564481000	-1.596876000	H	0.746558000	2.262654000	2.058017000
O	0.076722000	-1.015764000	-2.707897000	C	1.521108000	3.892243000	-1.140254000
H	0.989498000	-1.385464000	-2.810769000	H	2.528298000	3.816511000	-1.542157000
N	-1.349158000	0.359219000	-0.688194000	C	-0.320466000	5.182017000	-0.154096000
N	0.918890000	-0.195963000	1.073636000	H	-0.706856000	6.135500000	0.195015000
C	-2.515680000	-0.445333000	-0.869373000	C	-1.984366000	-0.109619000	3.488589000
C	3.175721000	-1.302433000	-0.591651000	H	-2.752544000	-0.778156000	3.866706000
C	-0.041819000	0.258228000	2.051346000	C	4.569970000	-0.833192000	1.395341000
C	-1.530211000	1.676346000	-0.488113000	H	4.644699000	-0.461639000	2.416655000
H	-2.541702000	1.971165000	-0.192900000	C	1.014566000	5.092217000	-0.673409000
C	-2.563287000	-1.835177000	-0.547136000	H	1.634009000	5.987262000	-0.704596000
C	2.161318000	-0.342191000	1.496909000	C	5.574025000	-1.810360000	-0.582441000
H	2.355690000	-0.106409000	2.547064000	H	6.451482000	-2.195369000	-1.098090000
C	0.737944000	2.669989000	-1.124456000	C	-0.934573000	2.083152000	3.415821000
C	-0.617313000	2.762687000	-0.568130000	H	-0.884921000	3.120745000	3.735074000
C	-3.682712000	0.123489000	-1.455235000	C	-0.271160000	-0.056741000	-3.767505000
H	-3.656674000	1.152174000	-1.801609000	H	-0.145770000	-0.540733000	-4.743469000
C	3.296978000	-0.809378000	0.751033000	H	-1.321573000	0.198284000	-3.619121000
C	-4.853383000	-0.623204000	-1.645588000	H	0.354088000	0.835929000	-3.673581000
H	-5.721348000	-0.147934000	-2.096667000	C	-1.936511000	1.230259000	3.913822000
C	-3.748200000	-2.576135000	-0.742786000	H	-2.673583000	1.598519000	4.622563000
H	-3.748593000	-3.627573000	-0.470792000	C	5.701532000	-1.317898000	0.745744000
C	-1.024111000	-0.614122000	2.583462000	H	6.666920000	-1.326258000	1.243119000
C	-4.899731000	-1.982376000	-1.281253000				
H	-5.801691000	-2.568971000	-1.430583000				
C	-1.102621000	4.041950000	-0.115398000				

Table S3

Cartesian coordinates of complex 1, optimized in DMSO solvent

B3LYP/LANL2DZ energy= - 1566.66931706 a.u.

Ni	0.415661000	-0.431495000	-0.825377000
S	-1.128570000	-2.759974000	-0.109101000
S	-1.012066000	-2.550228000	2.223410000
O	2.007523000	-1.313714000	-1.282158000
O	1.306116000	1.628601000	-1.503256000
O	0.066266000	-0.883339000	-2.752425000
H	0.965066000	-1.239906000	-2.949771000
N	-1.330712000	0.399389000	-0.684183000
N	0.915153000	-0.257199000	1.061218000
C	-2.516491000	-0.383147000	-0.880022000
C	3.176742000	-1.307295000	-0.634467000
C	-0.050019000	0.153297000	2.057712000
C	-1.493892000	1.709078000	-0.447385000
H	-2.503983000	2.012659000	-0.162785000
C	-2.588890000	-1.782065000	-0.602790000
C	2.156634000	-0.410547000	1.484029000
H	2.351153000	-0.209027000	2.539974000
C	0.795308000	2.724878000	-1.011609000
C	-0.567723000	2.794789000	-0.482268000
C	-3.676955000	0.225668000	-1.436620000
H	-3.638858000	1.262614000	-1.753686000
C	3.296239000	-0.848575000	0.720400000
C	-4.866678000	-0.490028000	-1.632376000
H	-5.728340000	0.017476000	-2.057637000
C	-3.793948000	-2.492996000	-0.800965000
H	-3.817709000	-3.552187000	-0.563022000
C	-1.024680000	-0.746352000	2.557358000
C	-4.939214000	-1.858139000	-1.304784000
H	-5.855701000	-2.419898000	-1.457135000
C	-1.069438000	4.057536000	-0.005351000
H	-2.092584000	4.096371000	0.367455000
C	4.344510000	-1.791658000	-1.293821000
H	4.247894000	-2.144380000	-2.316987000
C	-0.018462000	1.474748000	2.543862000
H	0.731894000	2.158413000	2.159033000
C	1.567606000	3.950998000	-0.984703000
H	2.584137000	3.901890000	-1.369146000
C	-0.295169000	5.207301000	0.000840000
H	-0.695586000	6.146608000	0.370718000
C	-1.988943000	-0.289935000	3.483827000
H	-2.750195000	-0.977239000	3.840966000
C	4.569375000	-0.883212000	1.364556000
H	4.642781000	-0.539482000	2.394835000
C	1.046238000	5.140136000	-0.495785000
H	1.661960000	6.037831000	-0.493948000
C	5.579293000	-1.804002000	-0.640415000
H	6.457572000	-2.170948000	-1.166733000
C	-0.954068000	1.911888000	3.498993000
H	-0.910132000	2.933658000	3.865144000
C	-0.381830000	0.100347000	-3.756977000
H	-0.255387000	-0.330157000	-4.755547000
H	-1.439035000	0.283977000	-3.564541000
H	0.191765000	1.024383000	-3.644980000
C	-1.950740000	1.032842000	3.962246000
H	-2.689129000	1.366833000	4.685352000
C	5.704249000	-1.345577000	0.699960000
H	6.669417000	-1.361962000	1.196857000

Table S4

Frontier molecular orbital and their energy values

FMOs	Energy (eV)
LUMO+1	-2.055
LUMO	-2.687
HOMO	-4.911
HOMO-1	-5.250

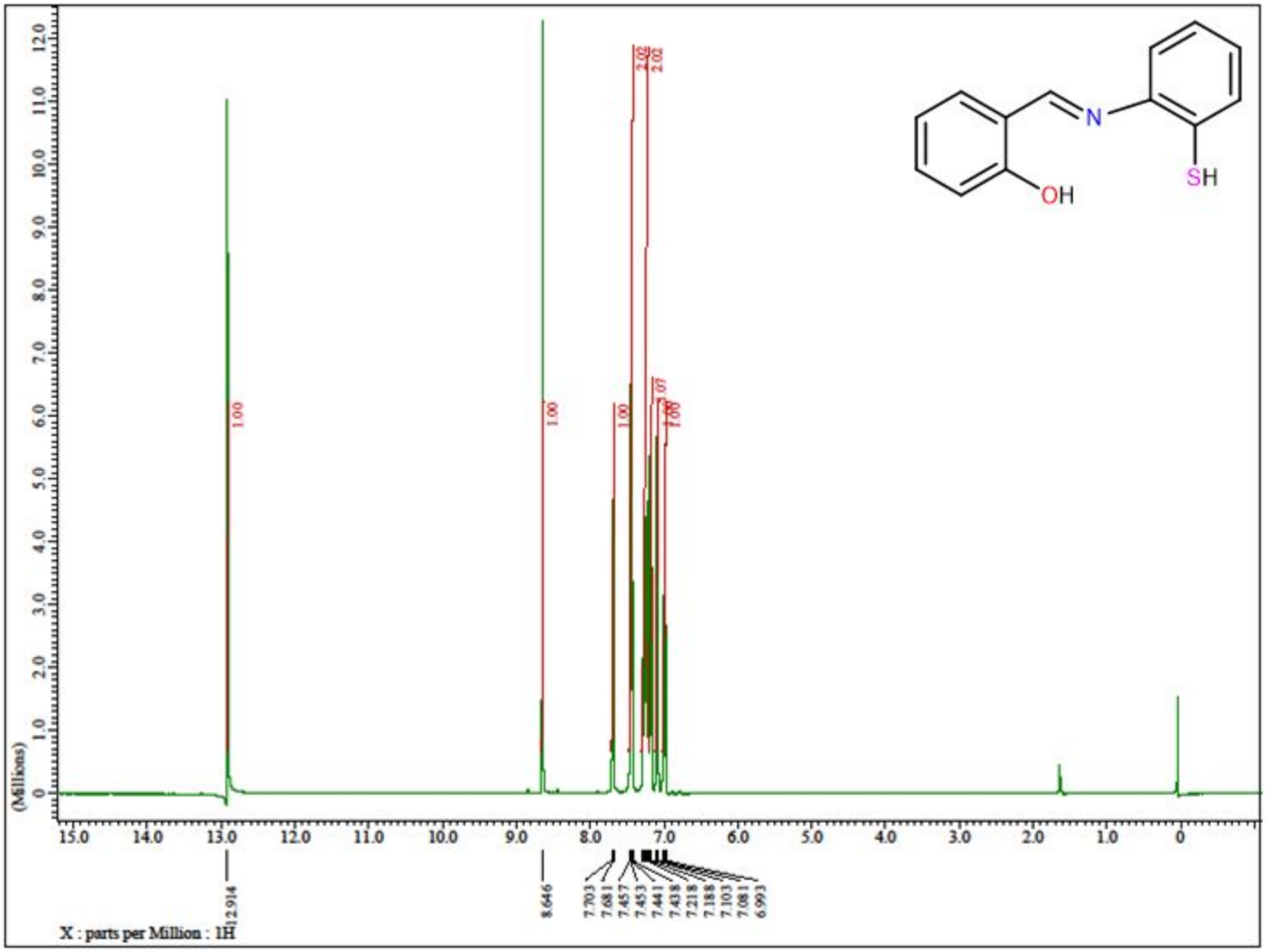

Fig. S1. ^{1}H NMR ($CDCl_3$, 400 MHz) spectrum of **L1**.

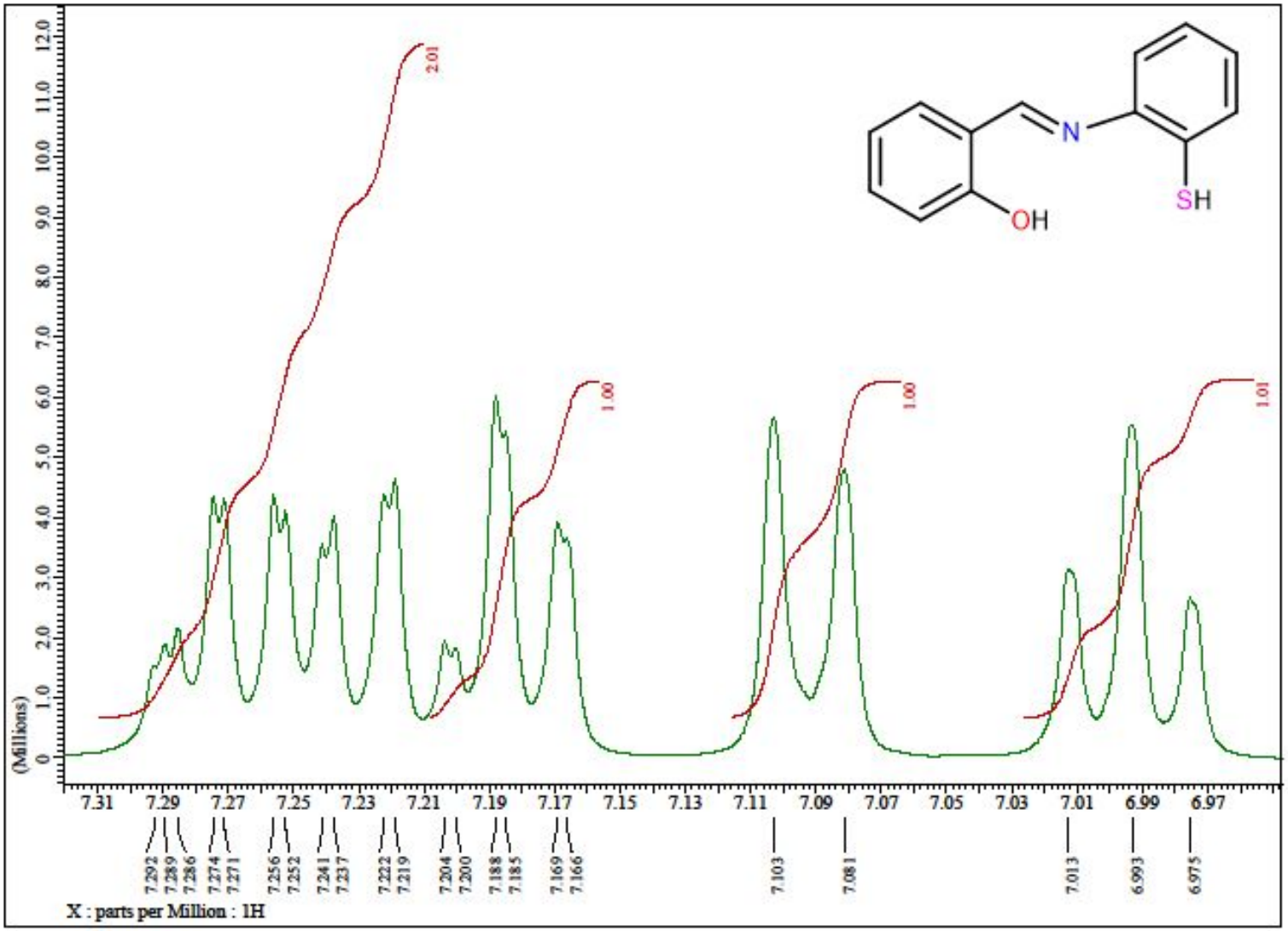

Fig. S2. ^{1}H NMR ($CDCl_3$, 400 MHz) spectrum of **L1** in aryl region.

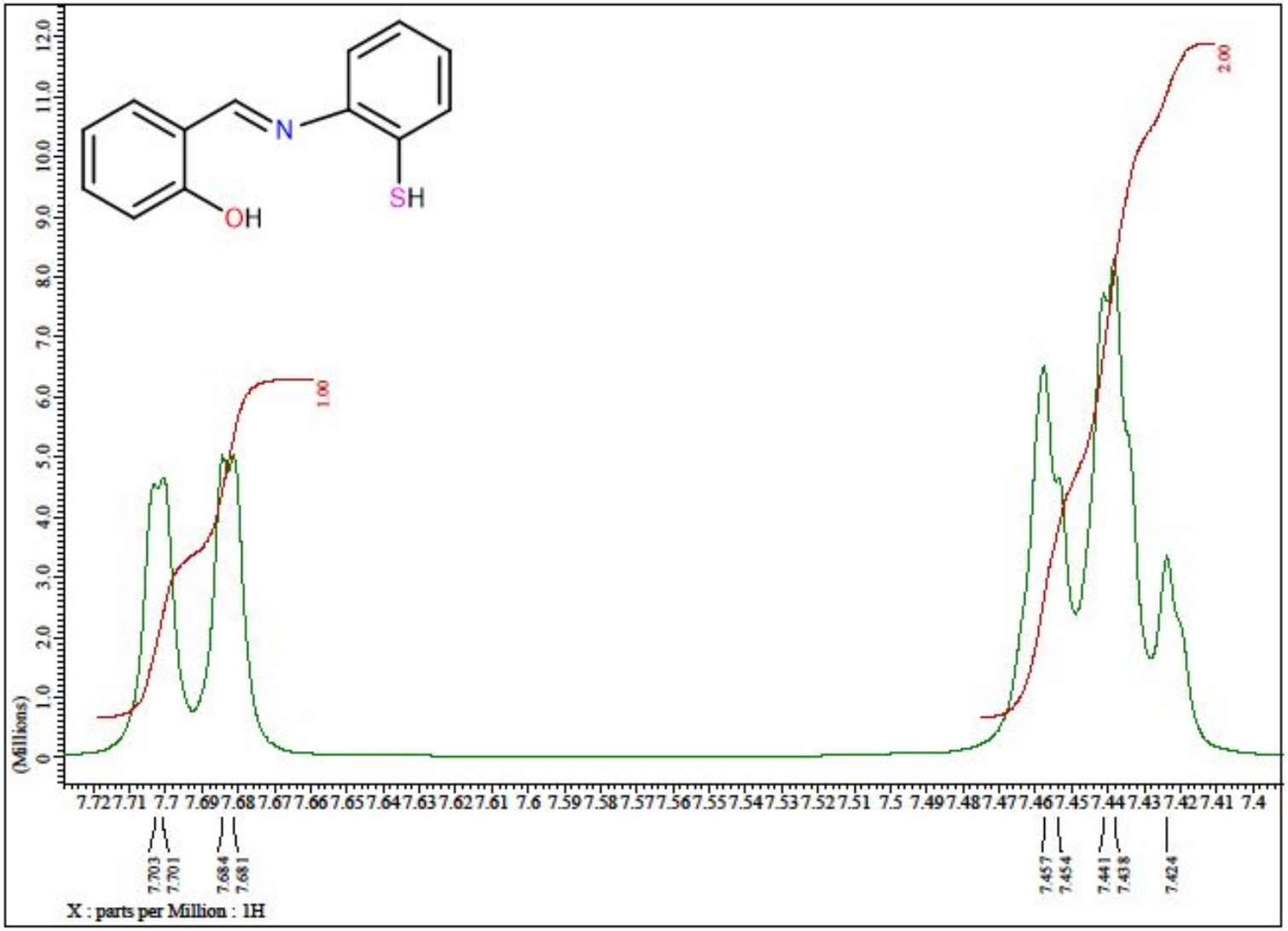

Fig. S3. ^{1}H NMR ($CDCl_3$, 400 MHz) spectrum of **L1** in aryl region.

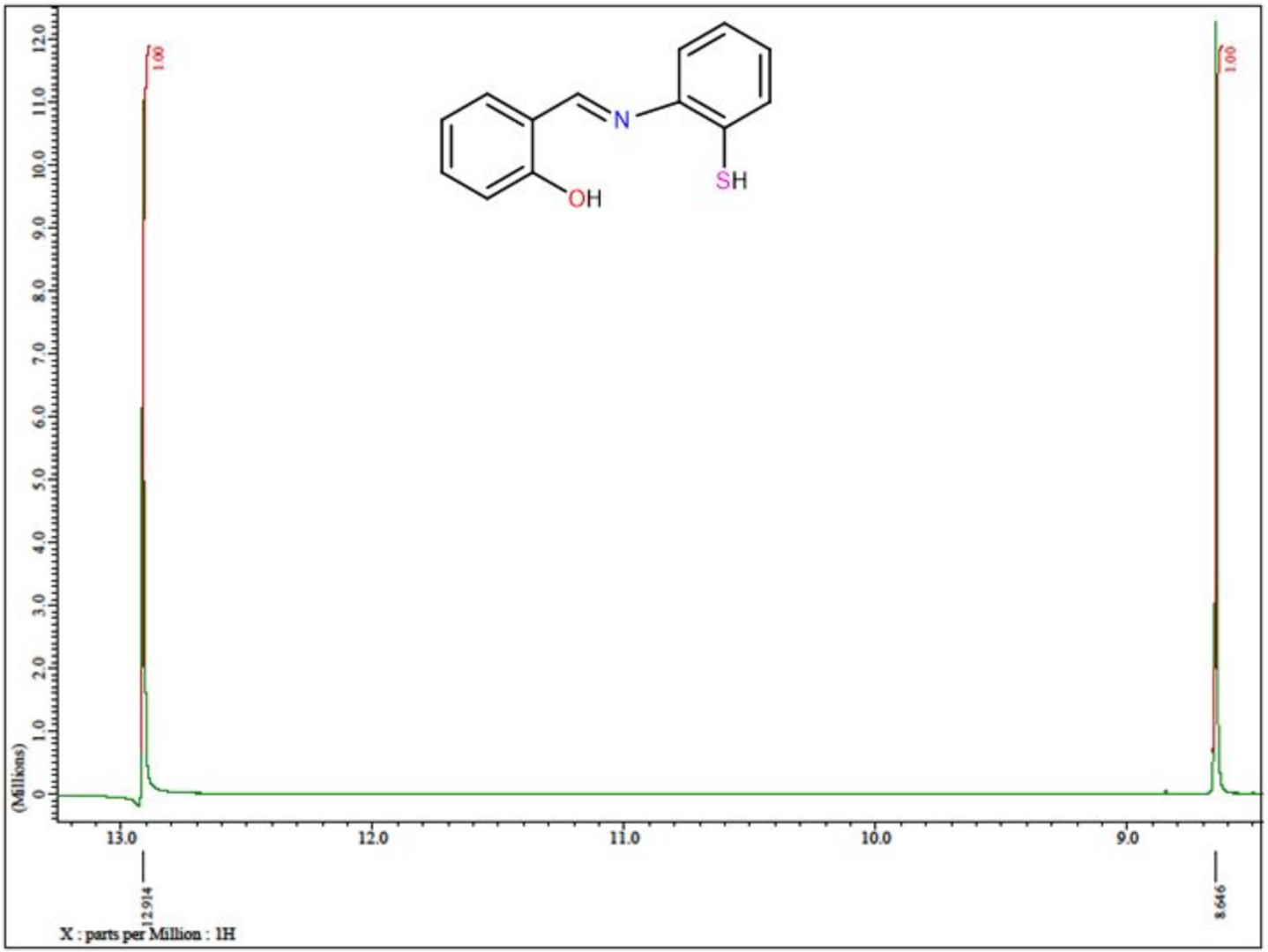

Fig. S4. ^{1}H NMR ($CDCl_3$, 400 MHz) spectrum of **L1** in aryl region.

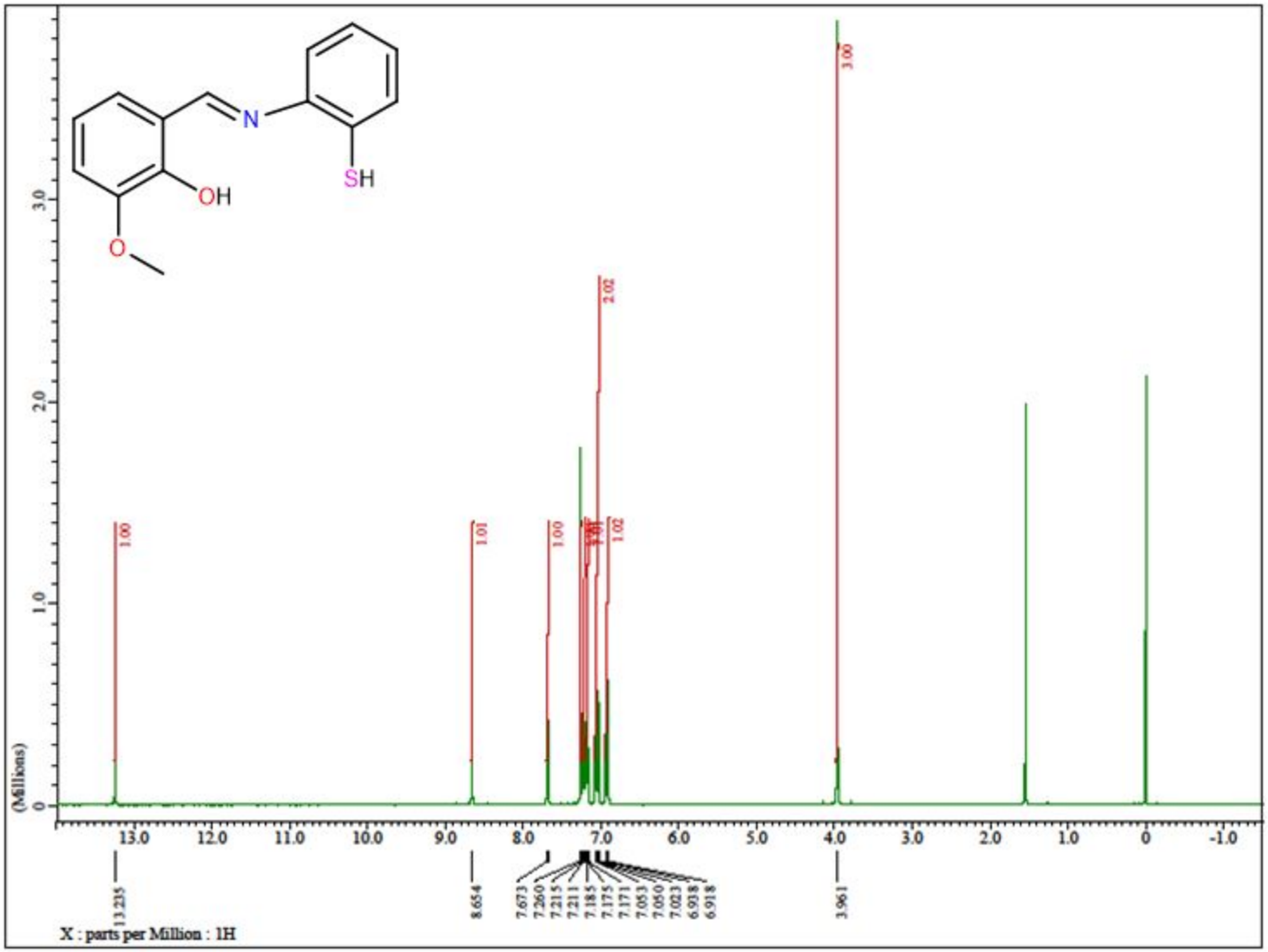

Fig. S5. ^{1}H NMR ($CDCl_3$, 400 MHz) spectrum of **L2.**

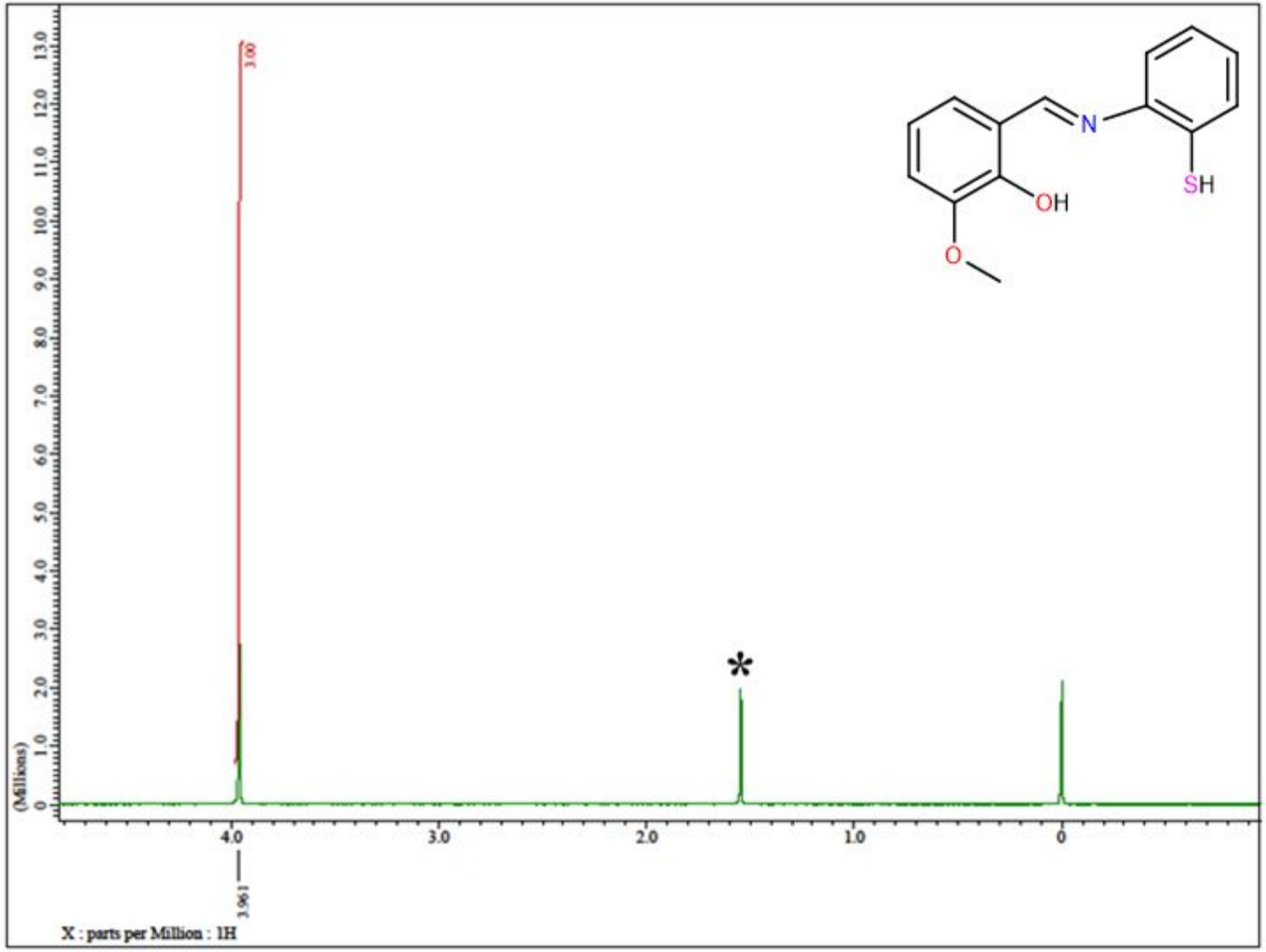

Fig. S6. ^{1}H NMR ($CDCl_3$, 400 MHz) spectrum of **L2** in alkyl region and asterisk (*) represents the adventitious water.

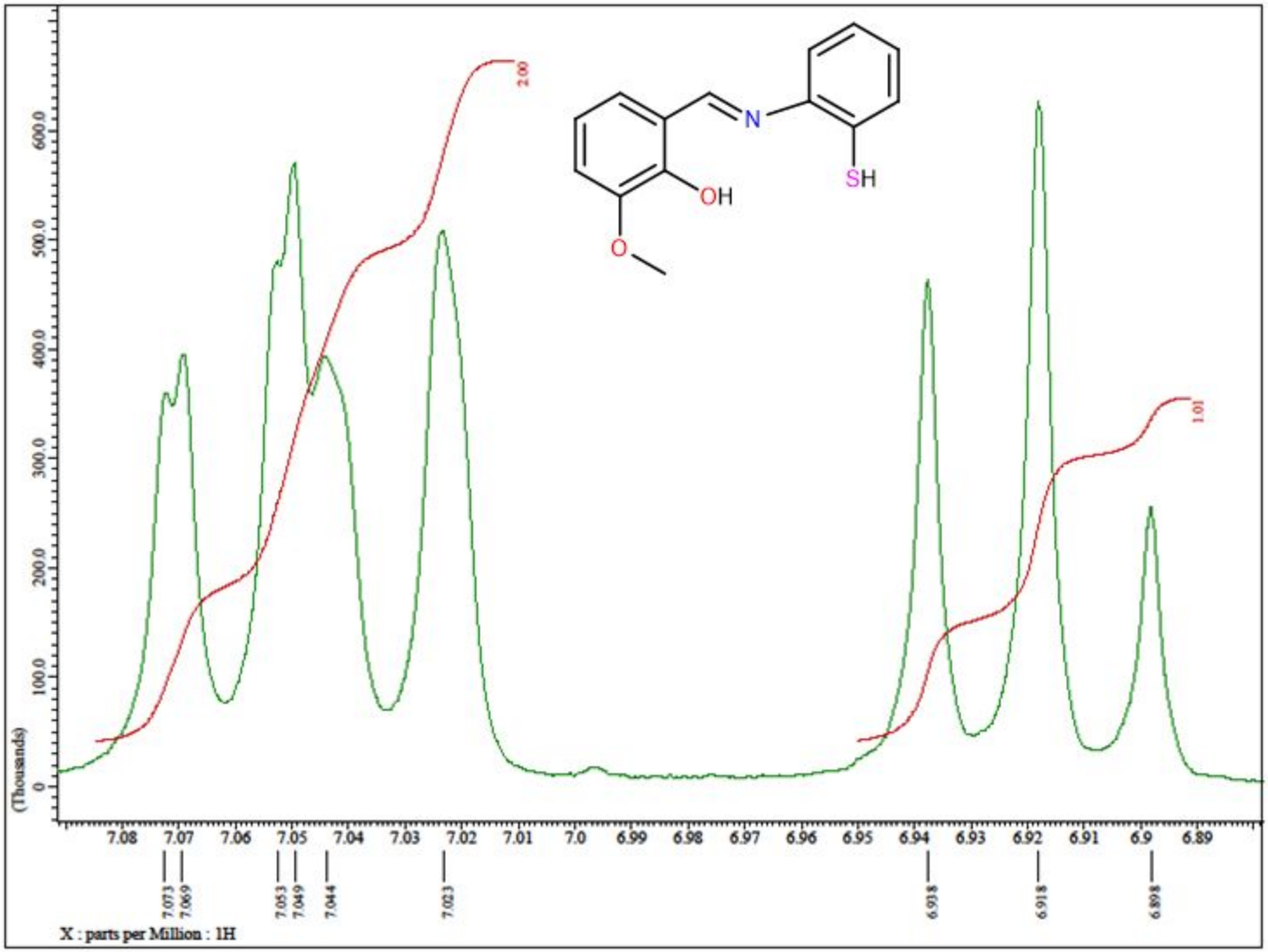

Fig. S7. ^{1}H NMR ($CDCl_3$, 400 MHz) spectrum of **L2** in aryl region.

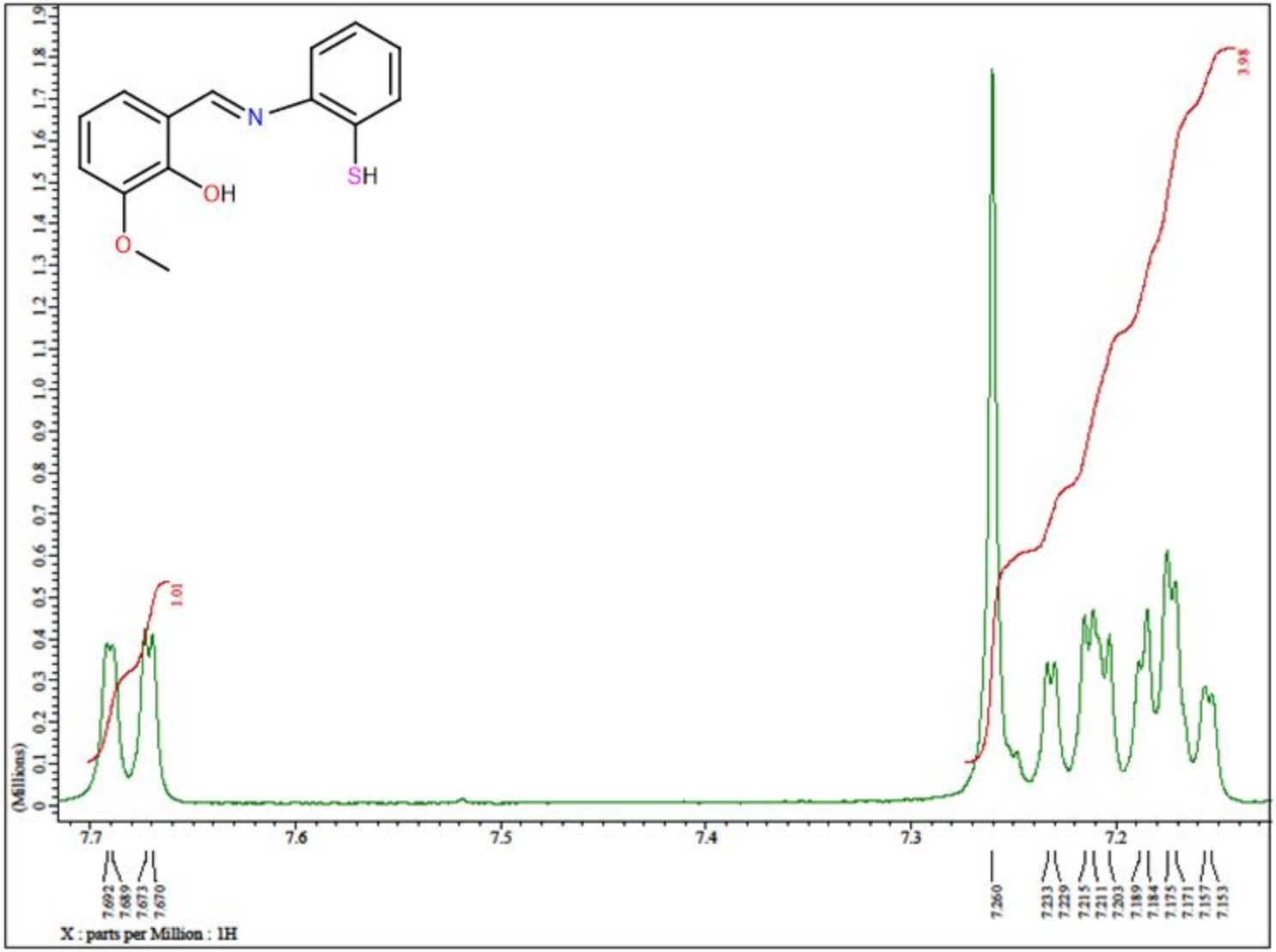

Fig. S8. ^{1}H NMR ($CDCl_3$, 400 MHz) spectrum of **L2** in aryl region.

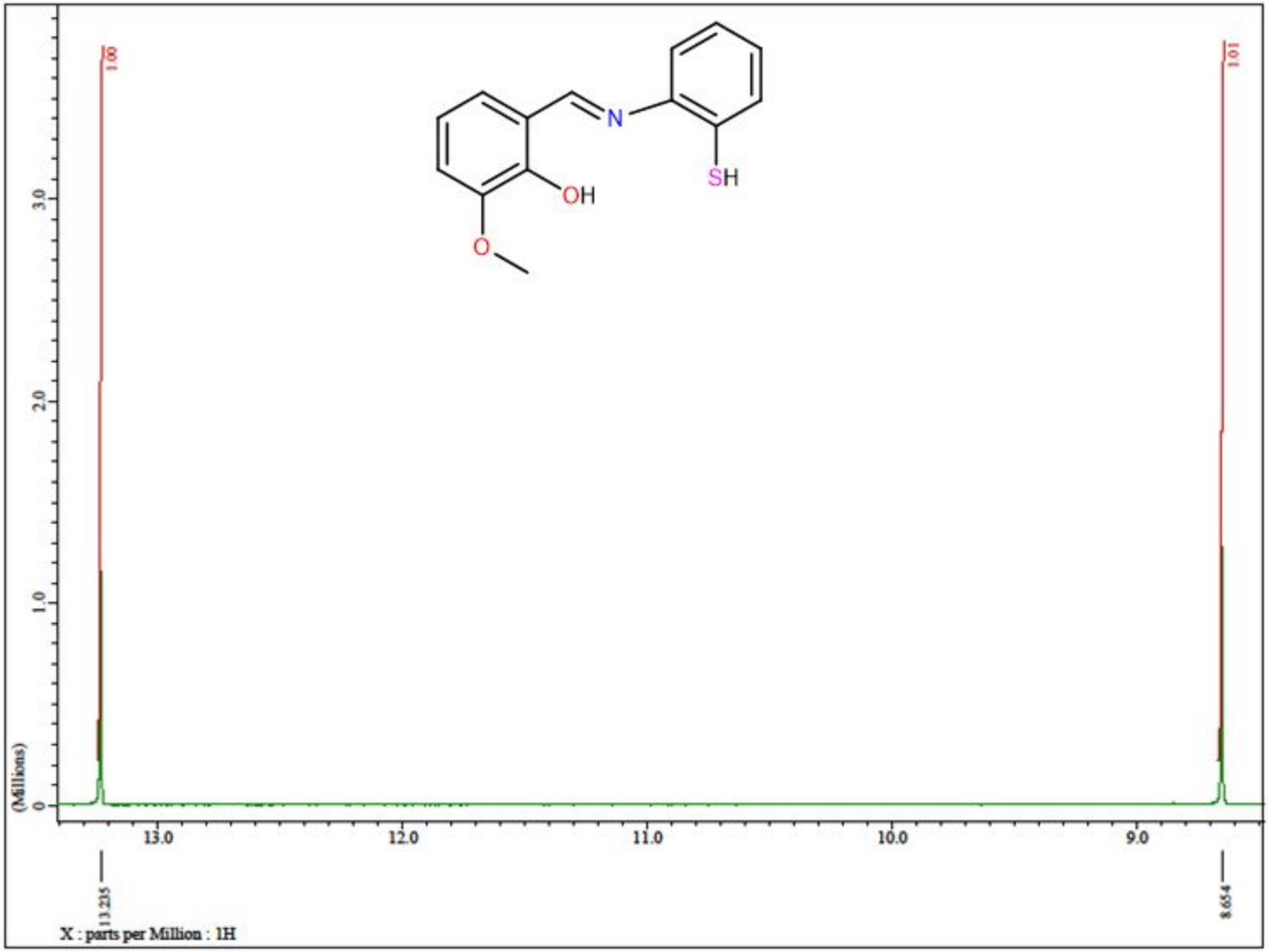

Fig. S9. ^{1}H NMR ($CDCl_3$, 400 MHz) spectrum of **L2** in aryl region.

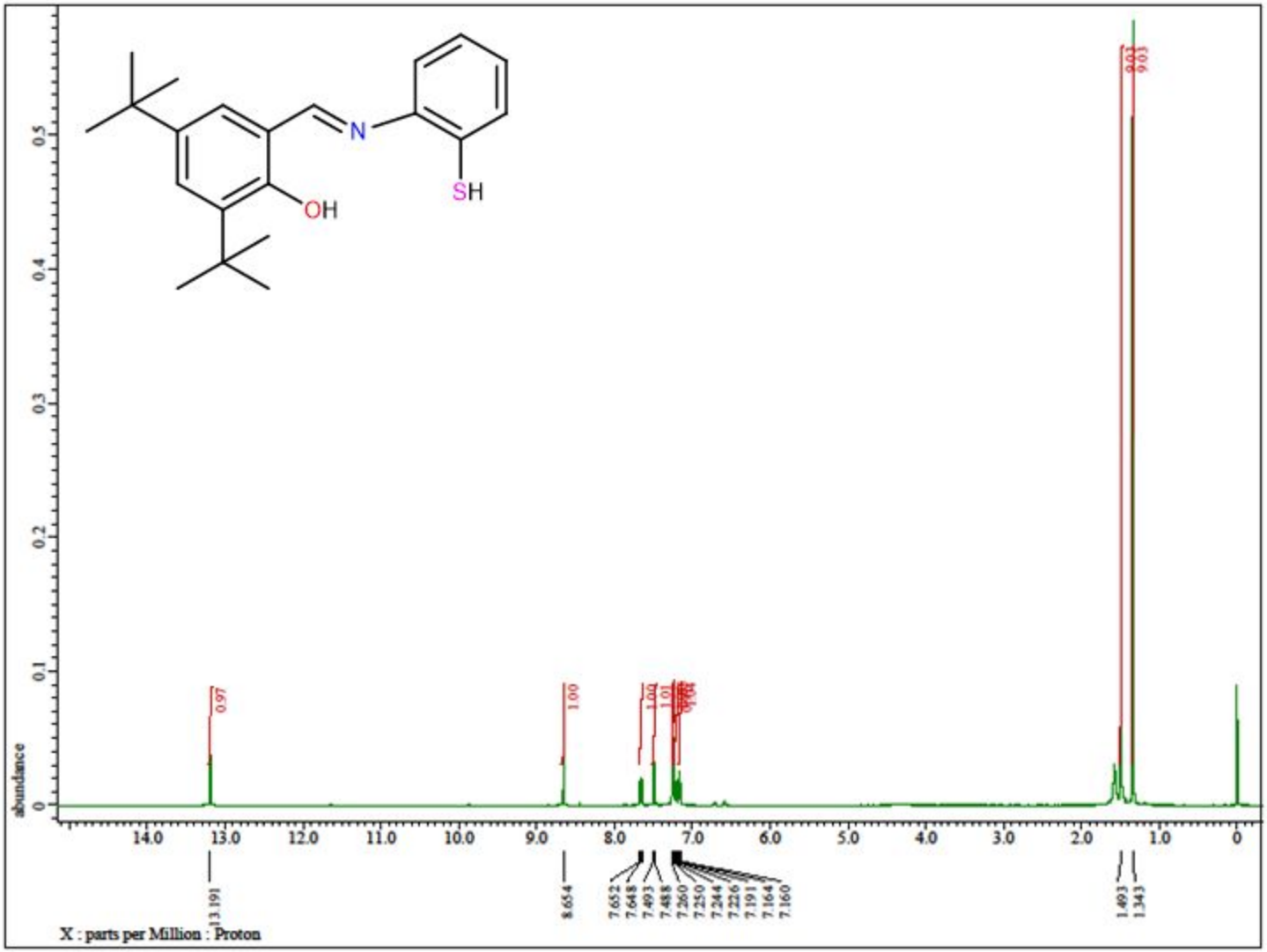

Fig. S10. ^{1}H NMR ($CDCl_3$, 400 MHz) spectrum of **L3**.

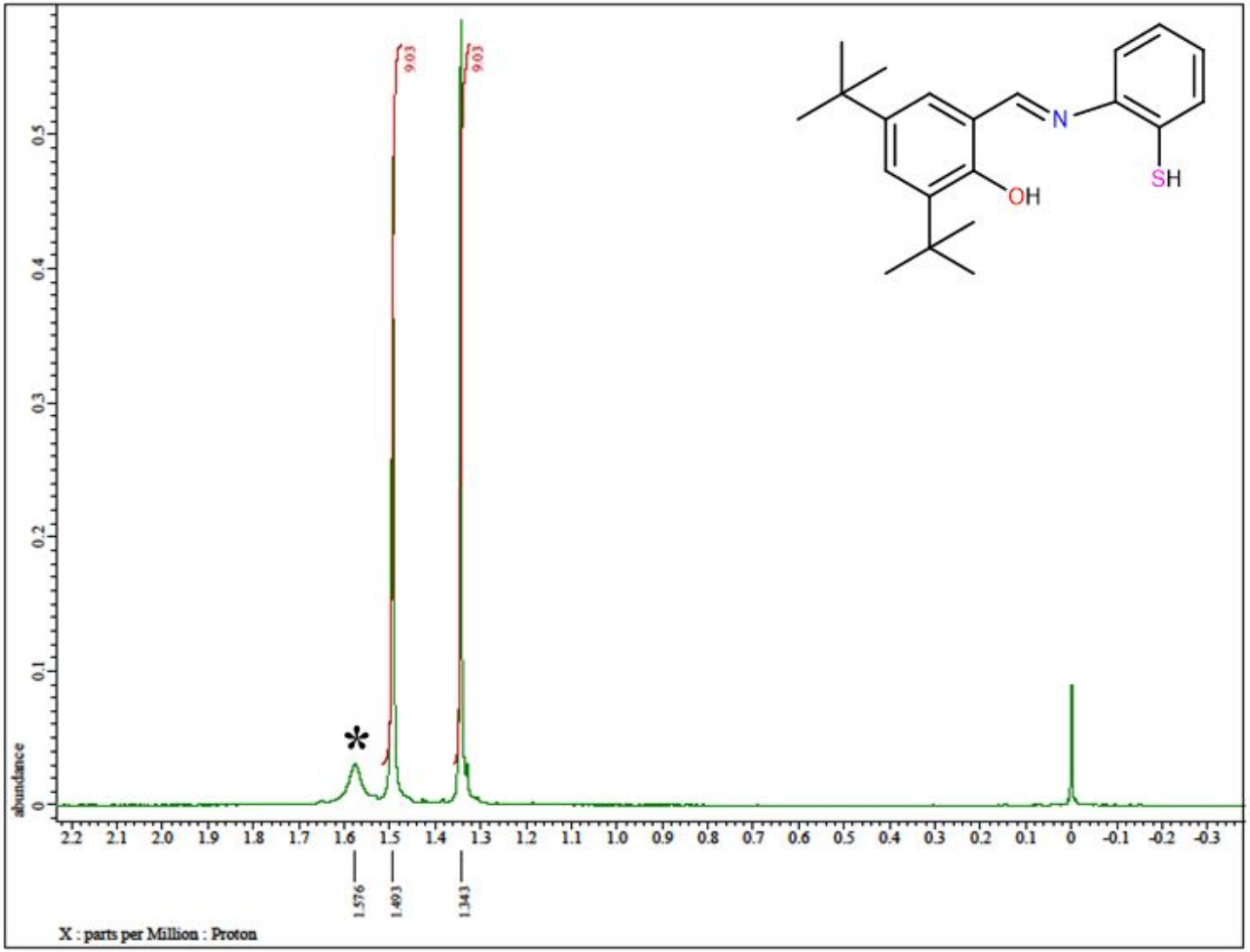

Fig. S11. ^{1}H NMR ($CDCl_3$, 400 MHz) spectrum of **L3** in alkyl region and asterisk (*) represents the adventitious water.

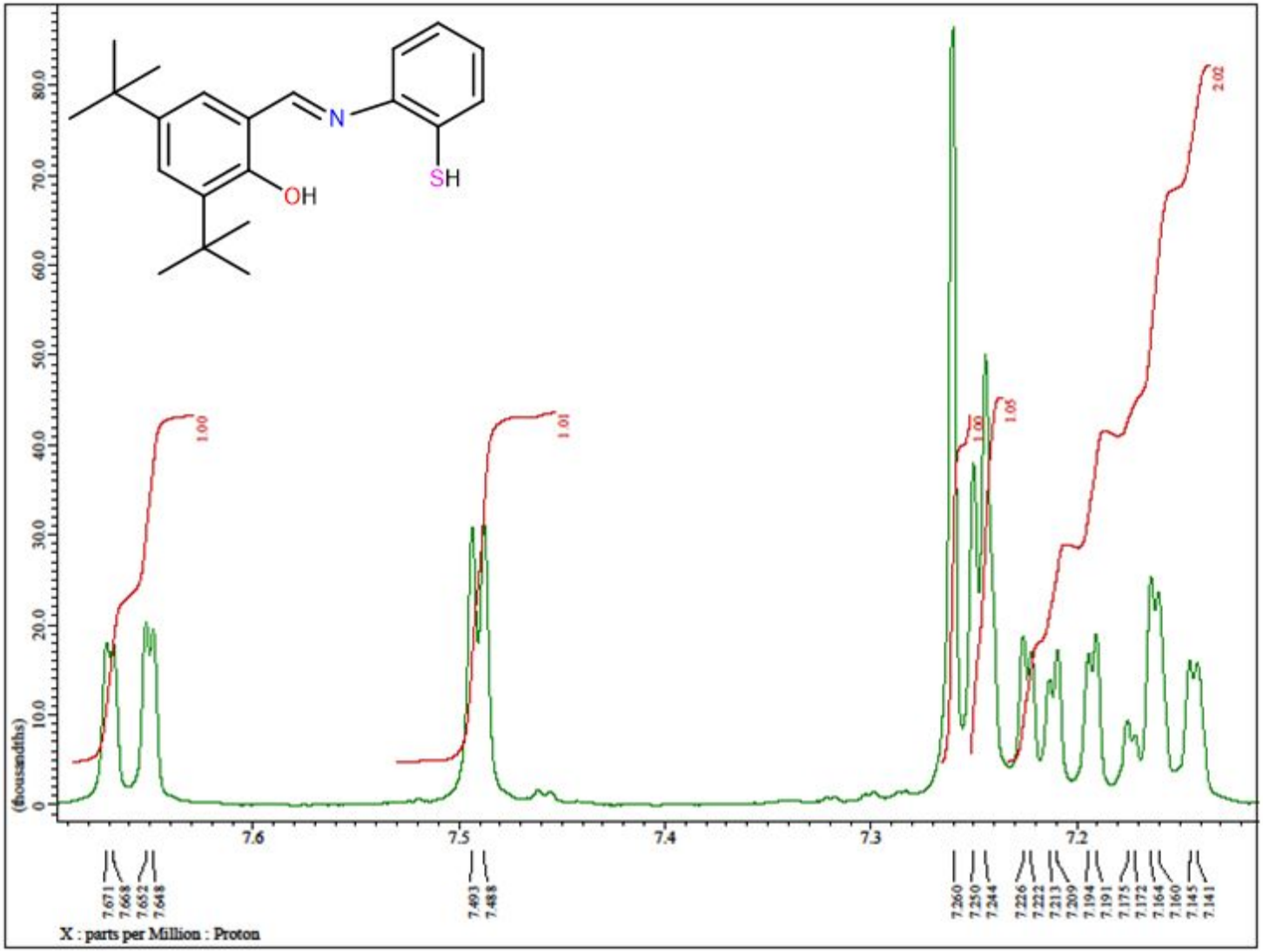

Fig. S12. ^{1}H NMR ($CDCl_3$, 400 MHz) spectrum of **L3** in aryl region.

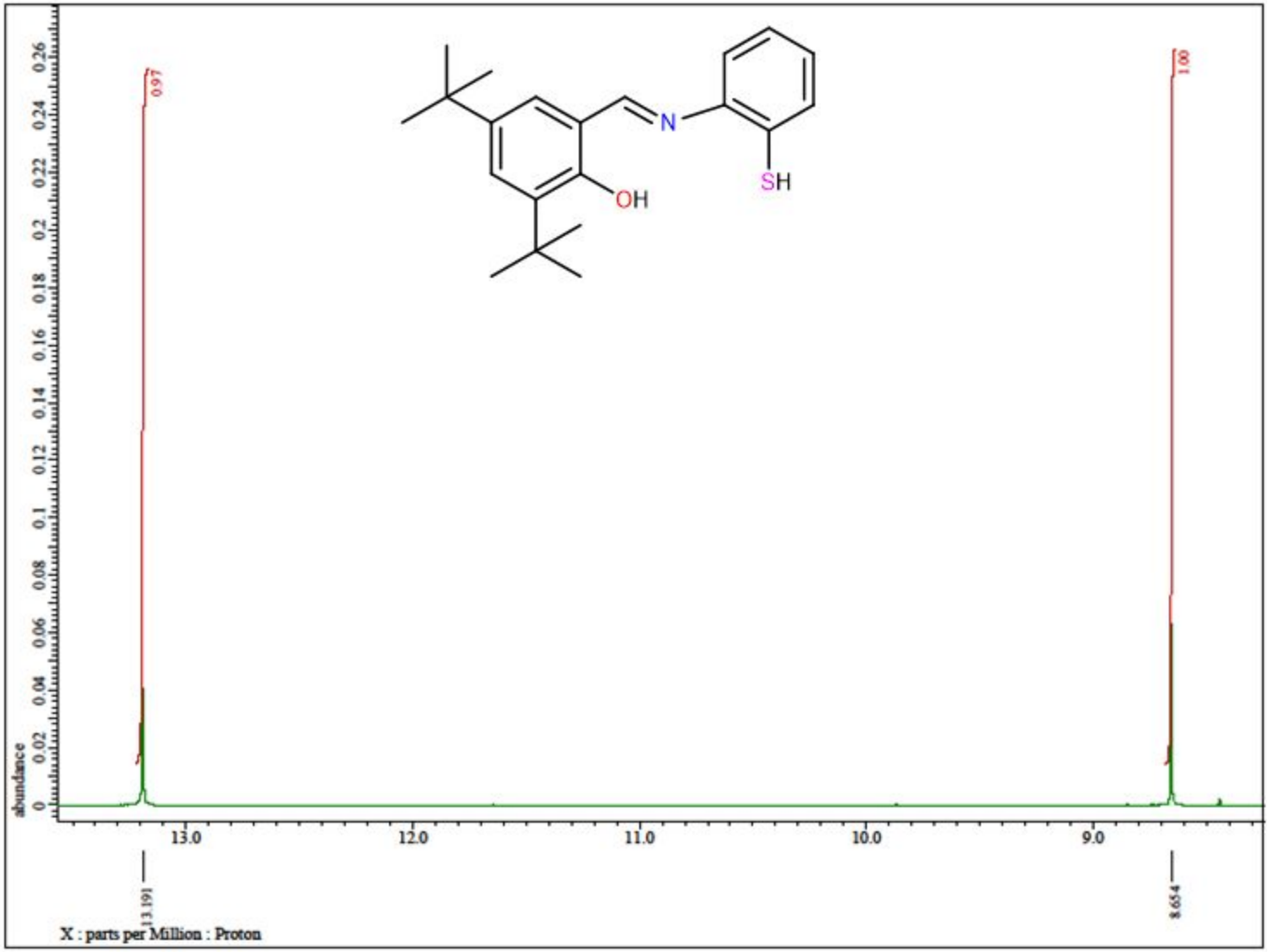

Fig. S13. ^{1}H NMR ($CDCl_3$, 400 MHz) spectrum of **L3** in aryl region.

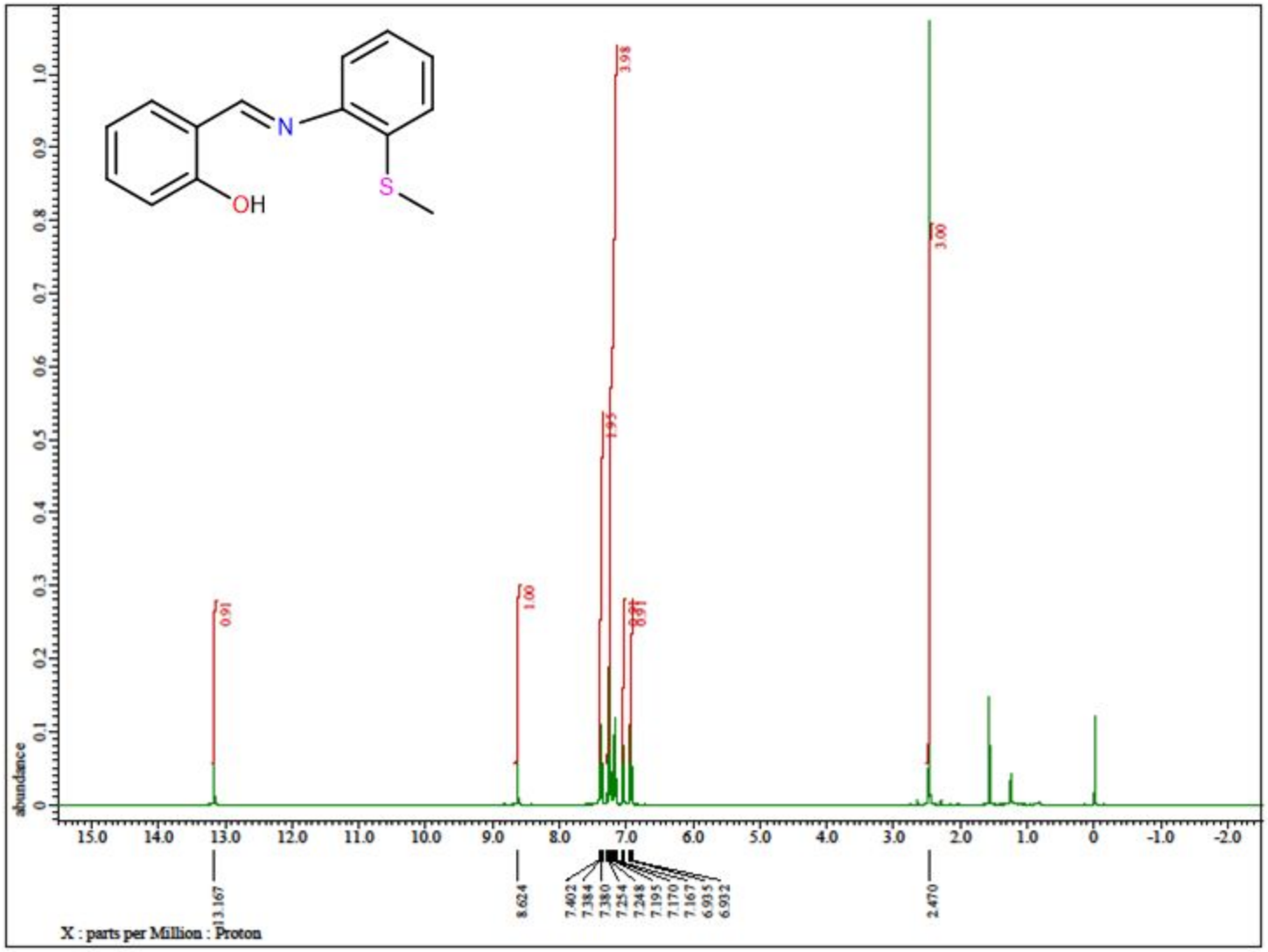

Fig. S14. ^{1}H NMR ($CDCl_3$, 400 MHz) spectrum of **L4**.

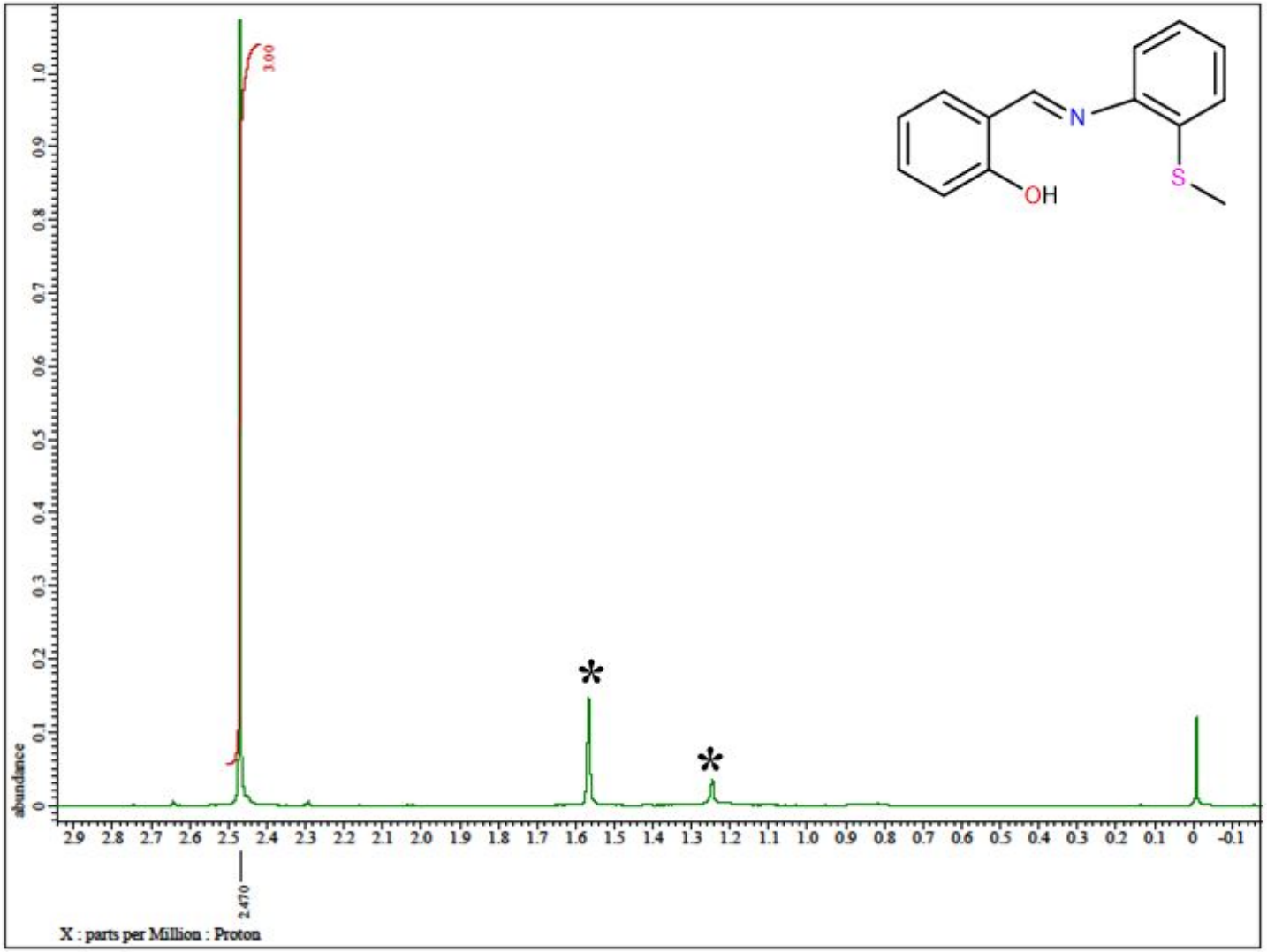

Fig. S15. ^{1}H NMR ($CDCl_3$, 400 MHz) spectrum of **L4** in alkyl region and asterisk (*) represents the residual solvent and adventitious water.

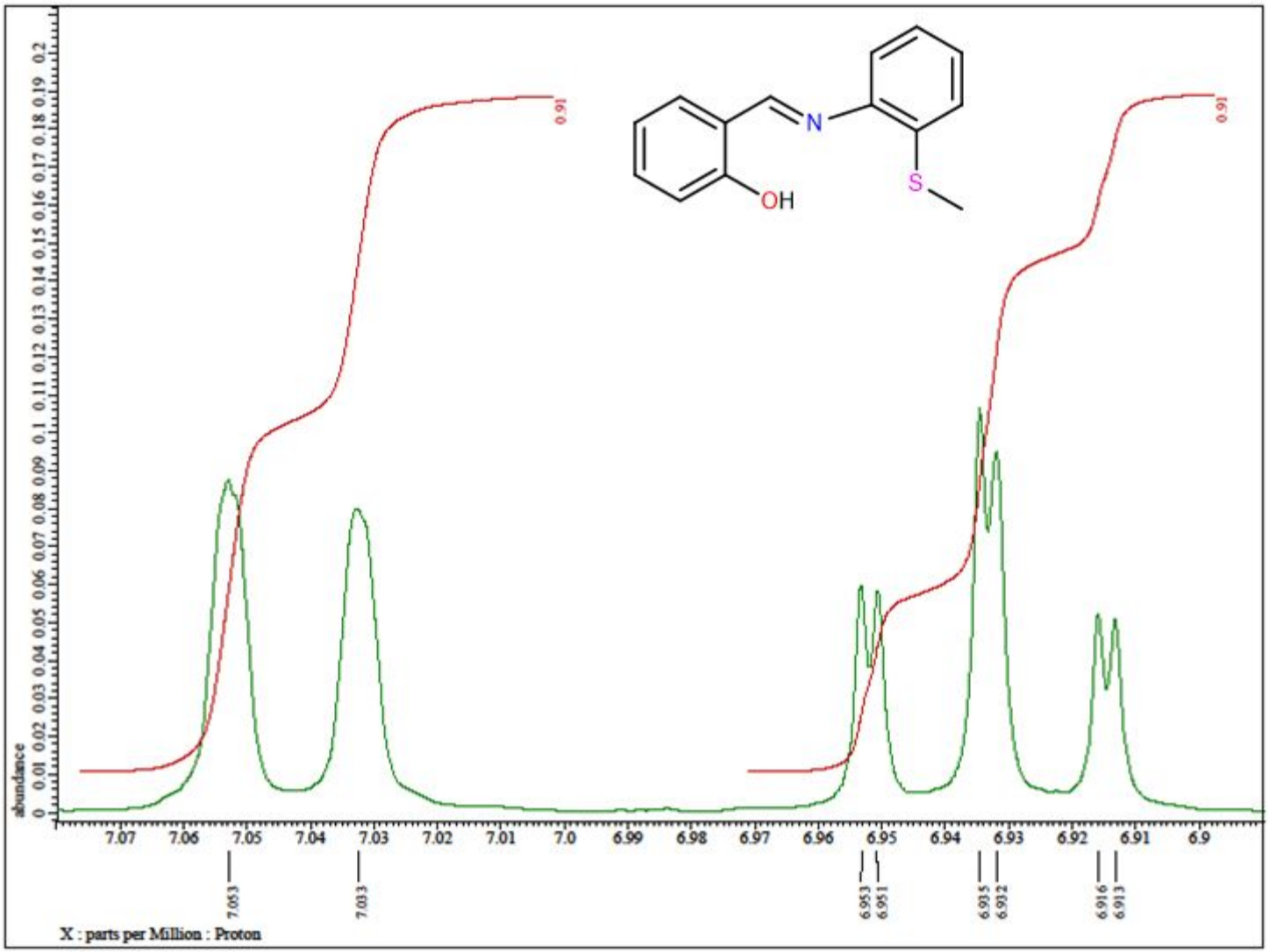

Fig. S16. ^{1}H NMR ($CDCl_3$, 400 MHz) spectrum of **L4** in aryl region.

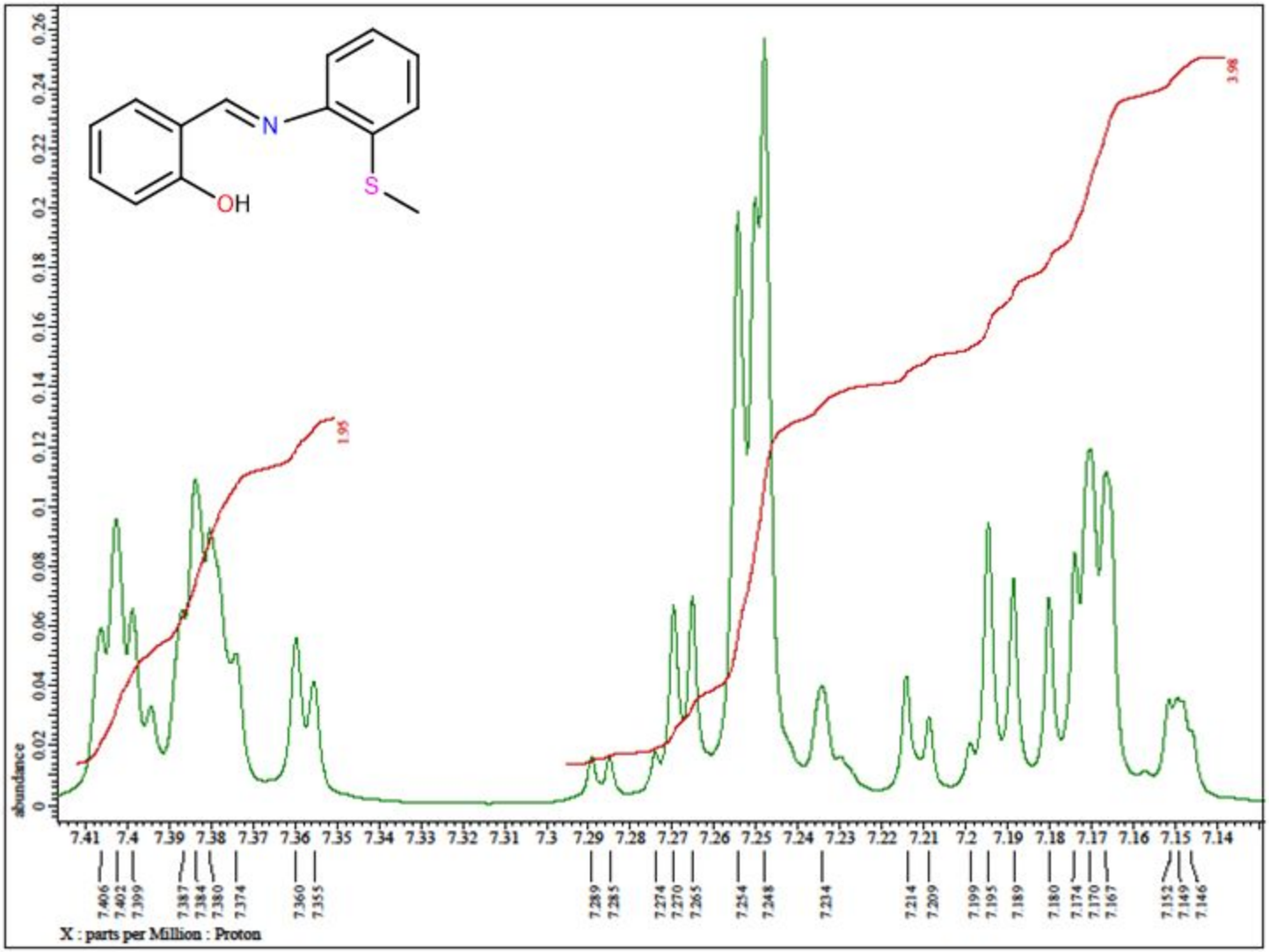

Fig. S17. ^{1}H NMR ($CDCl_3$, 400 MHz) spectrum of **L4** in aryl region.

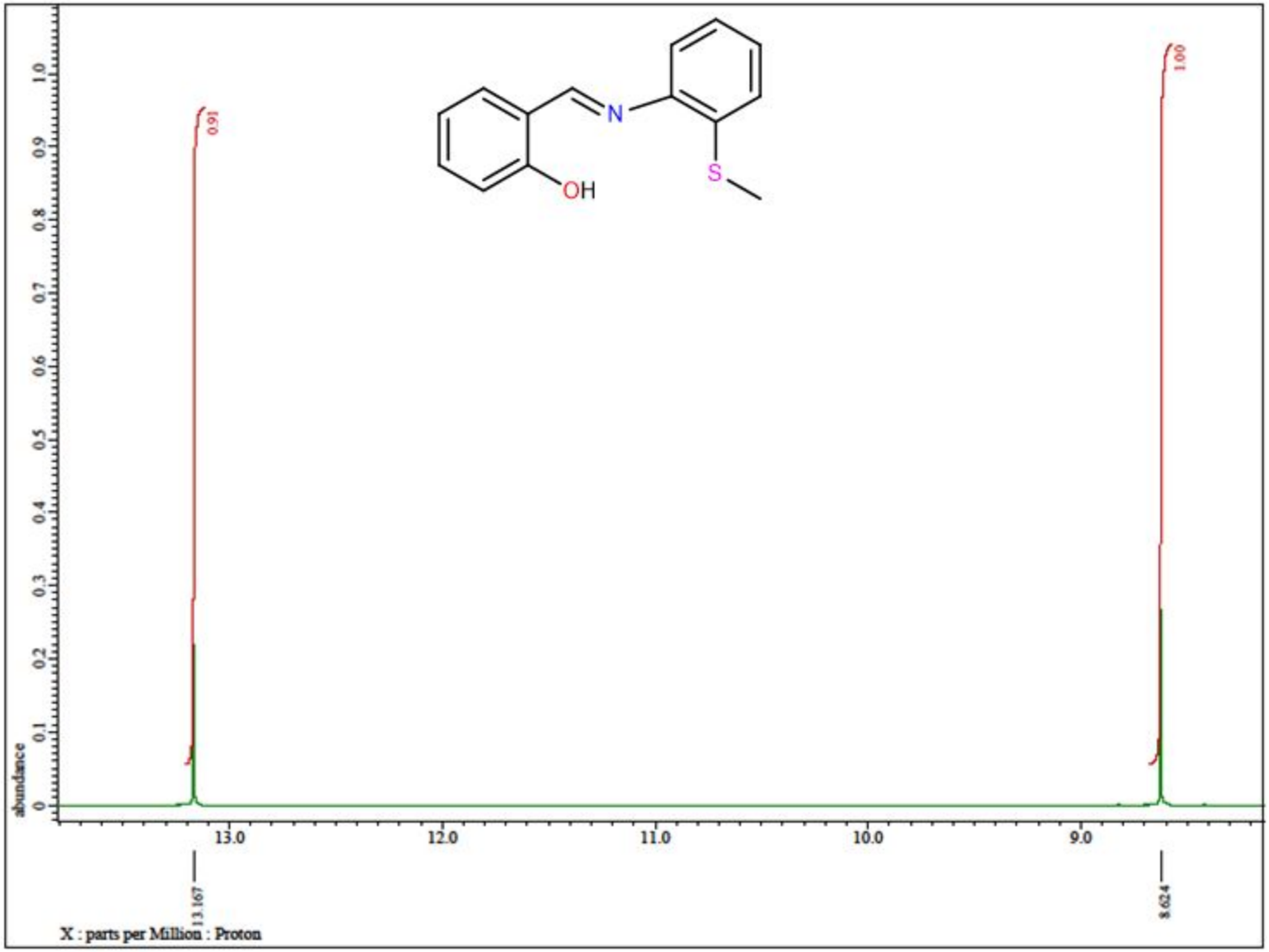

Fig. S18. ^{1}H NMR ($CDCl_3$, 400 MHz) spectrum of **L4** in aryl region.

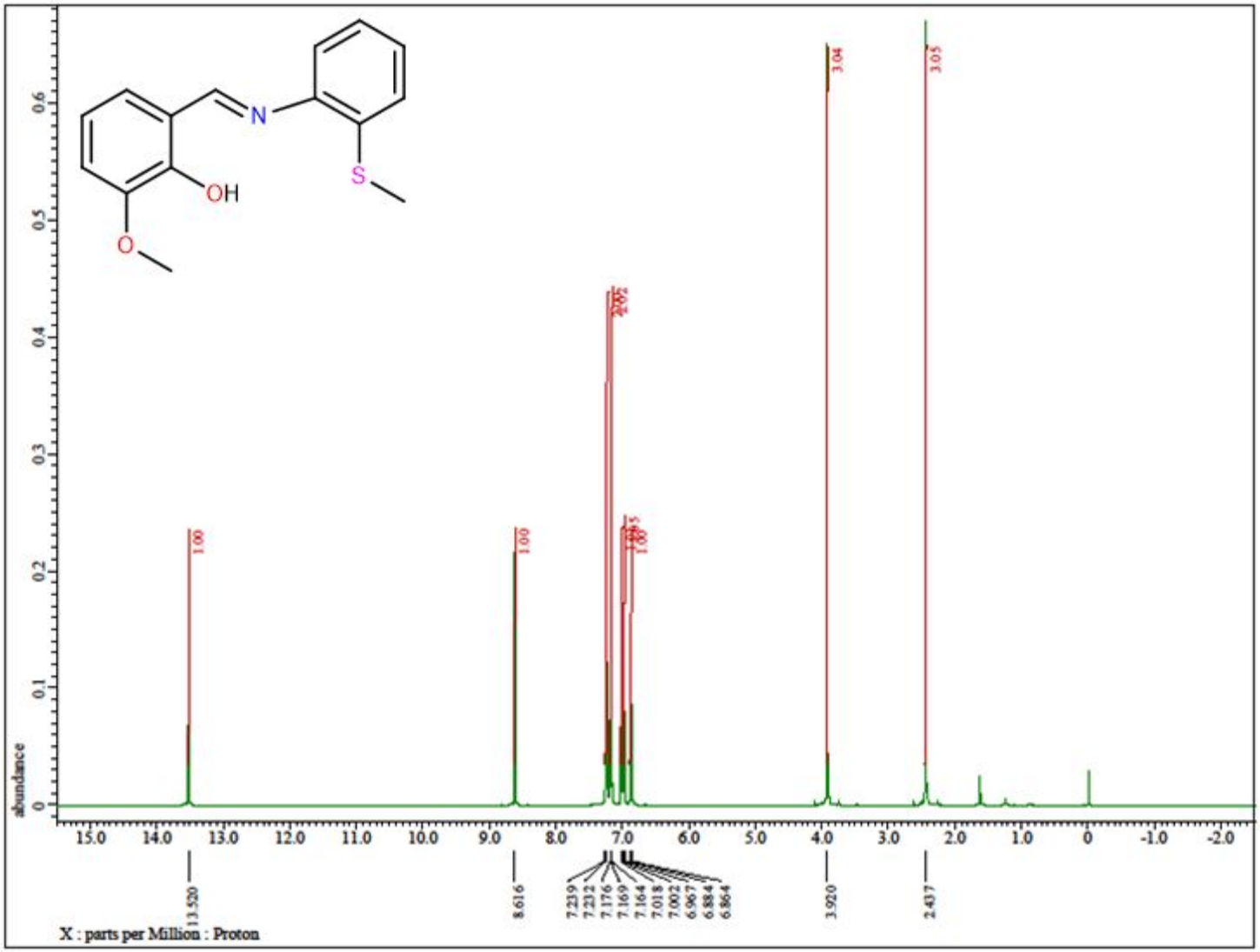

Fig. S19. ^{1}H NMR ($CDCl_3$, 400 MHz) spectrum of **L5**.

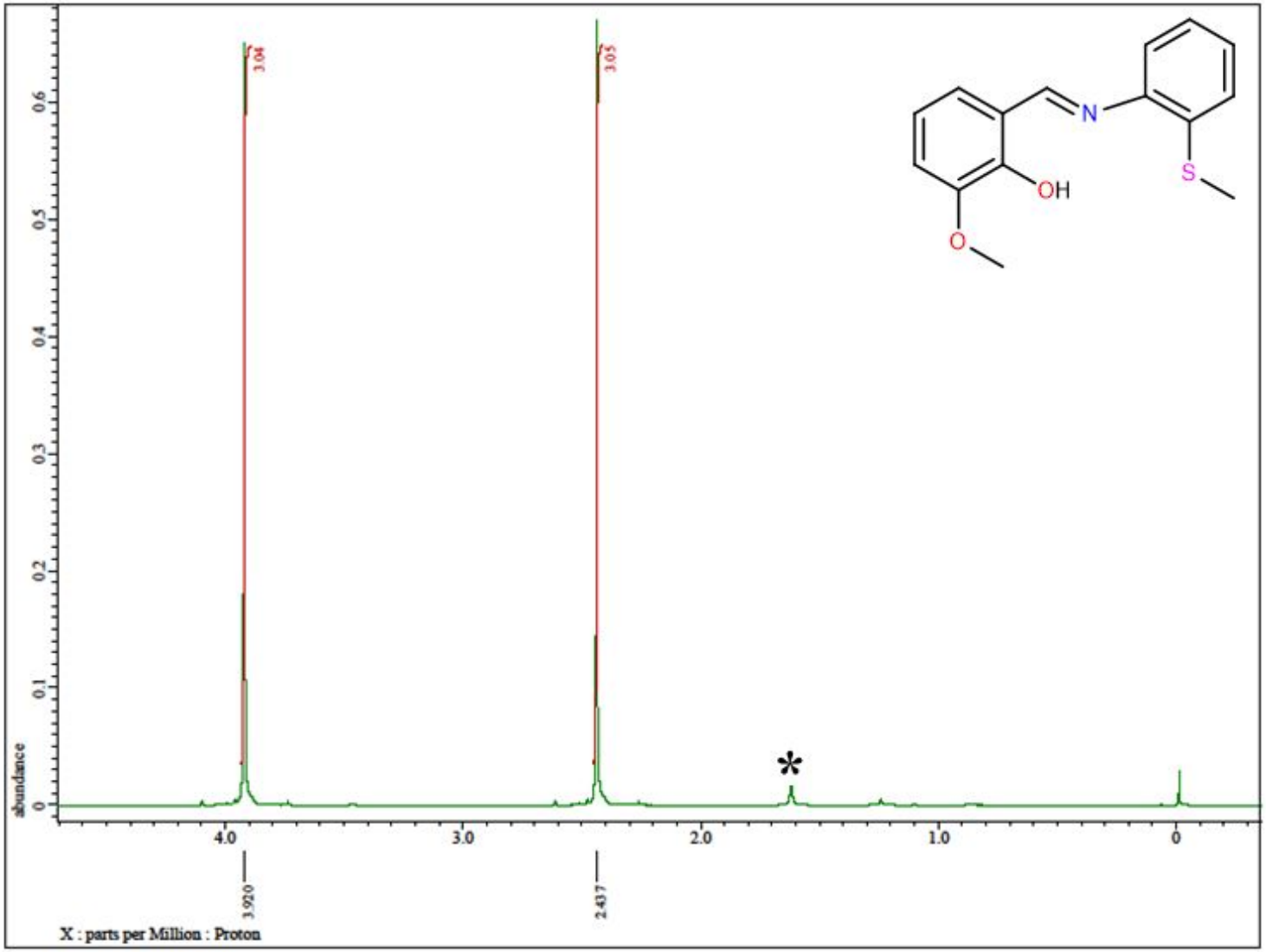

Fig. S20. ^{1}H NMR ($CDCl_3$, 400 MHz) spectrum of **L5** in alkyl region and asterisk (*) represents the residual solvent.

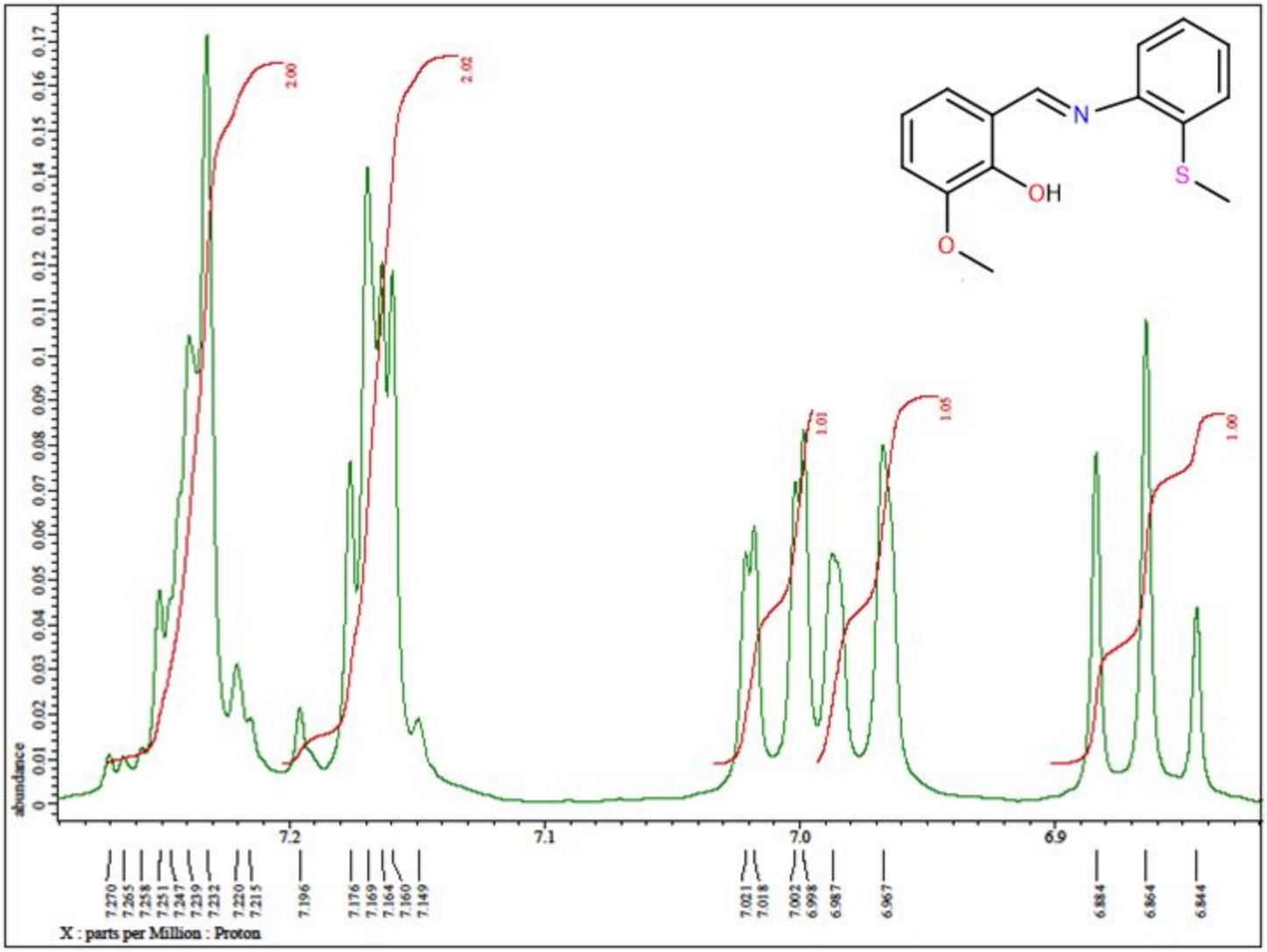

Fig. S21. ^{1}H NMR ($CDCl_3$, 400 MHz) spectrum of **L5** in aryl region.

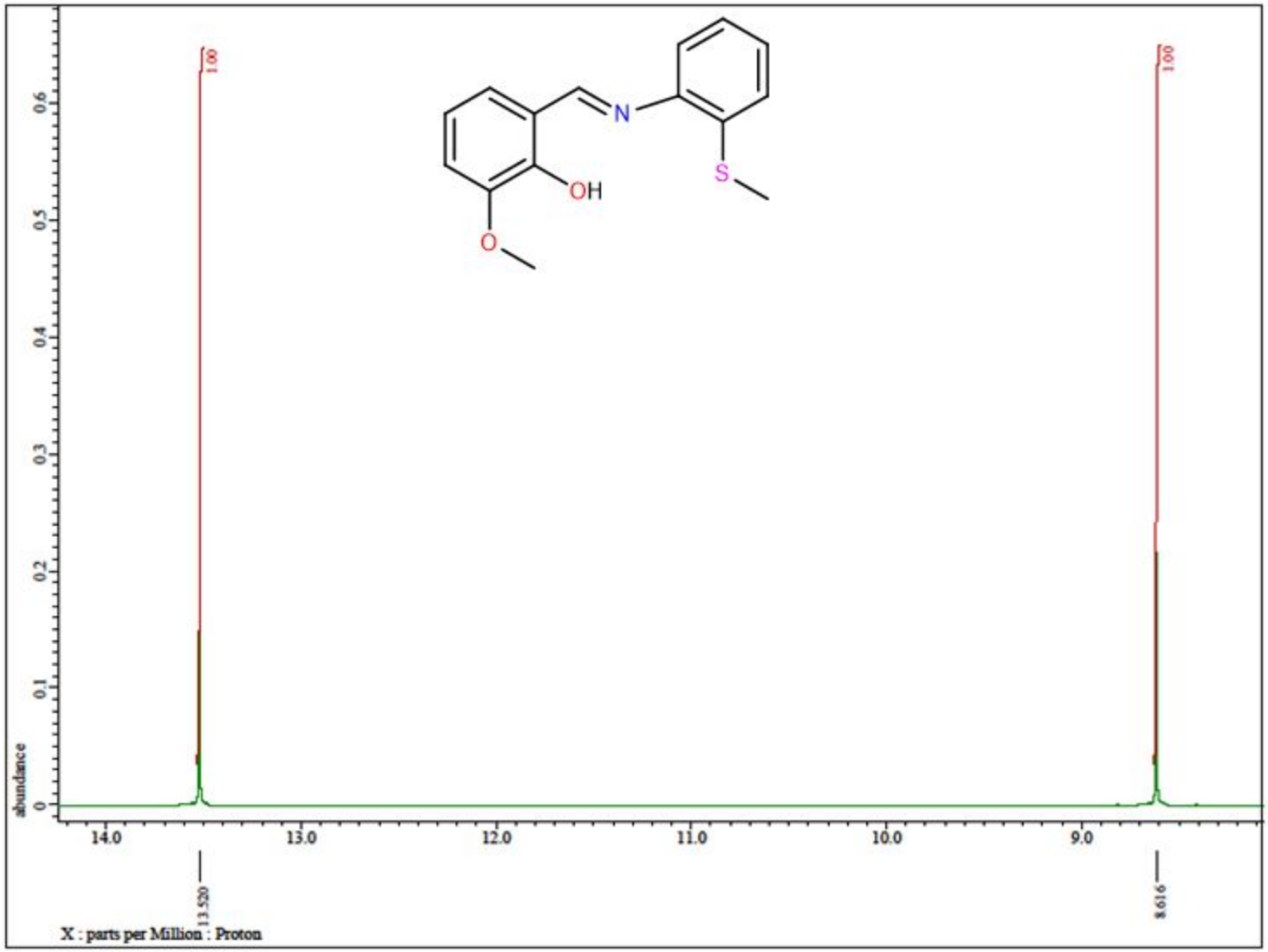

Fig. S22. ^{1}H NMR ($CDCl_3$, 400 MHz) spectrum of **L5** in aryl region.

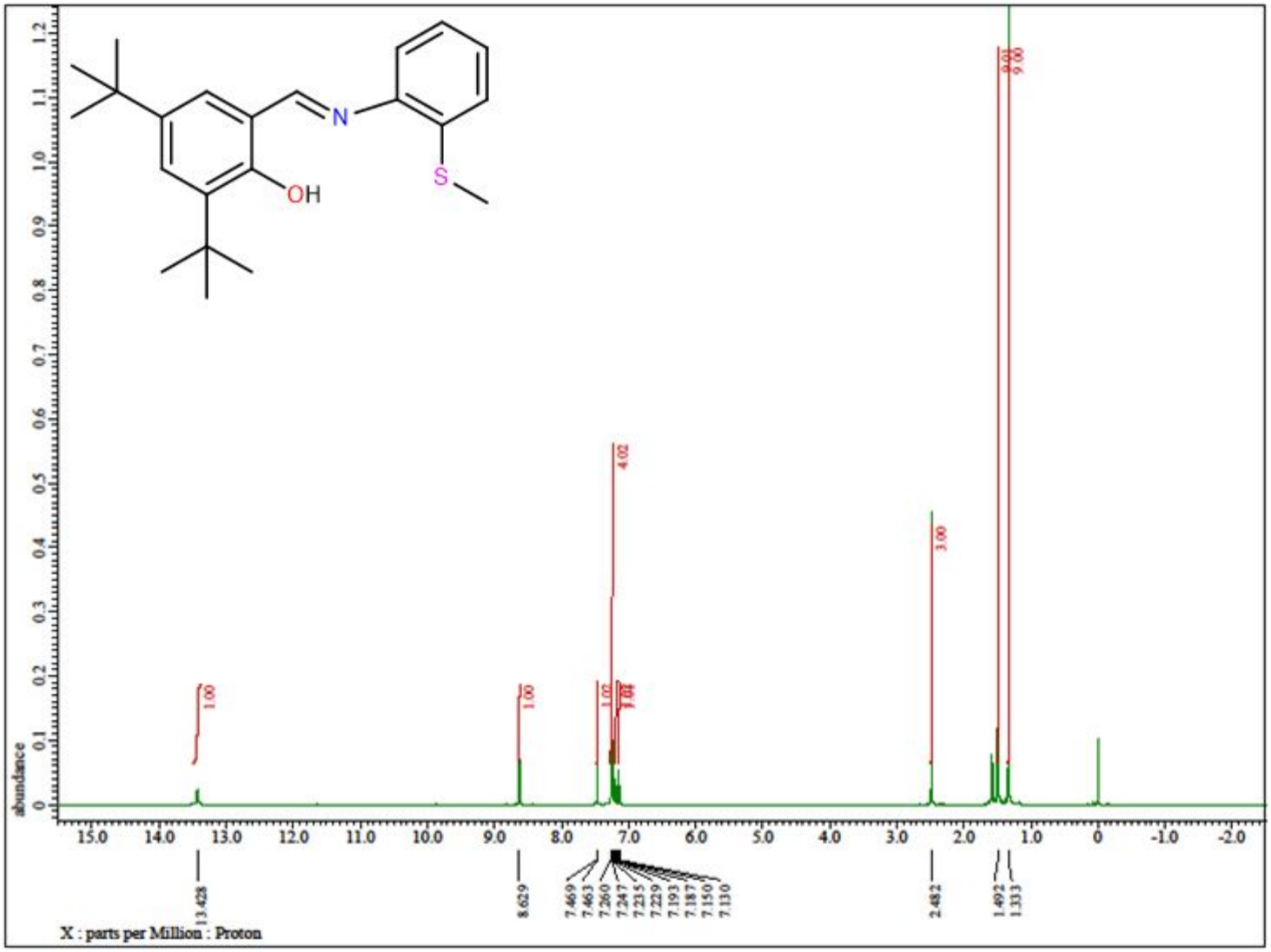

Fig. S23. ^{1}H NMR ($CDCl_3$, 400 MHz) spectrum of **L6**.

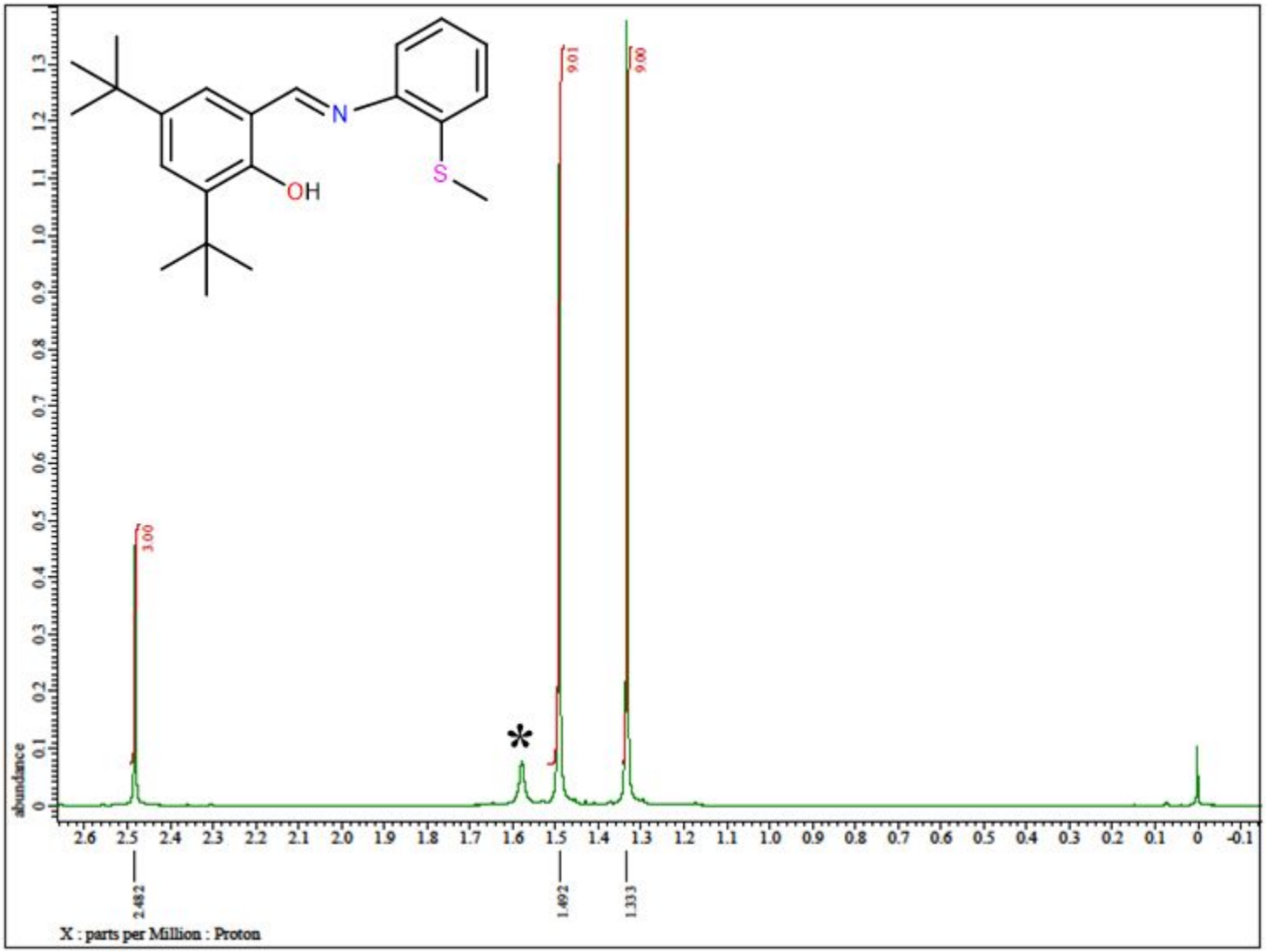

Fig. S24. ^{1}H NMR ($CDCl_3$, 400 MHz) spectrum of **L6** in alkyl region and asterisk (*) represents the adventitious water.

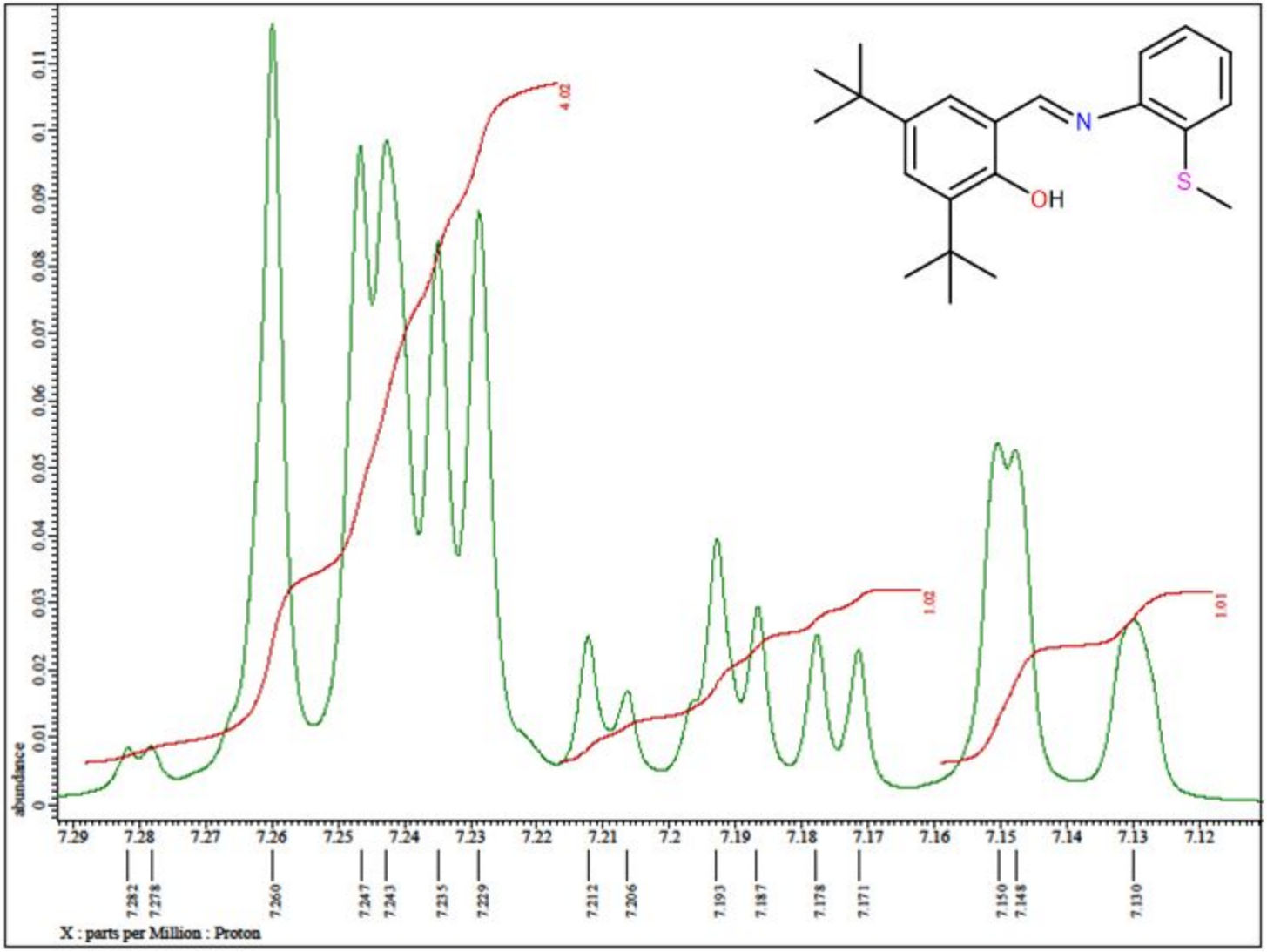

Fig. S25. ^{1}H NMR ($CDCl_3$, 400 MHz) spectrum of **L6** in aryl region.

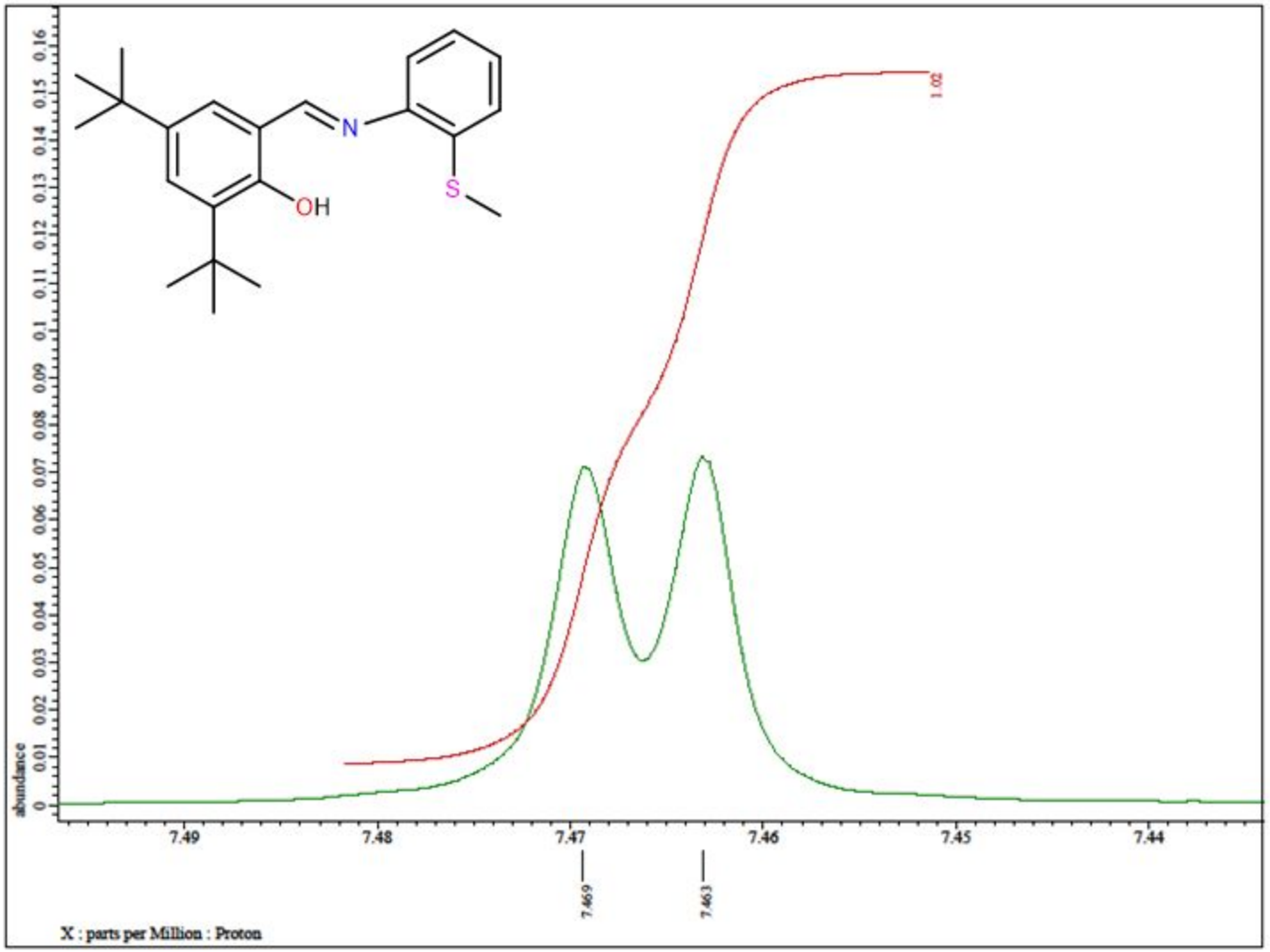

Fig. S26. ^{1}H NMR ($CDCl_3$, 400 MHz) spectrum of **L6** in aryl region.

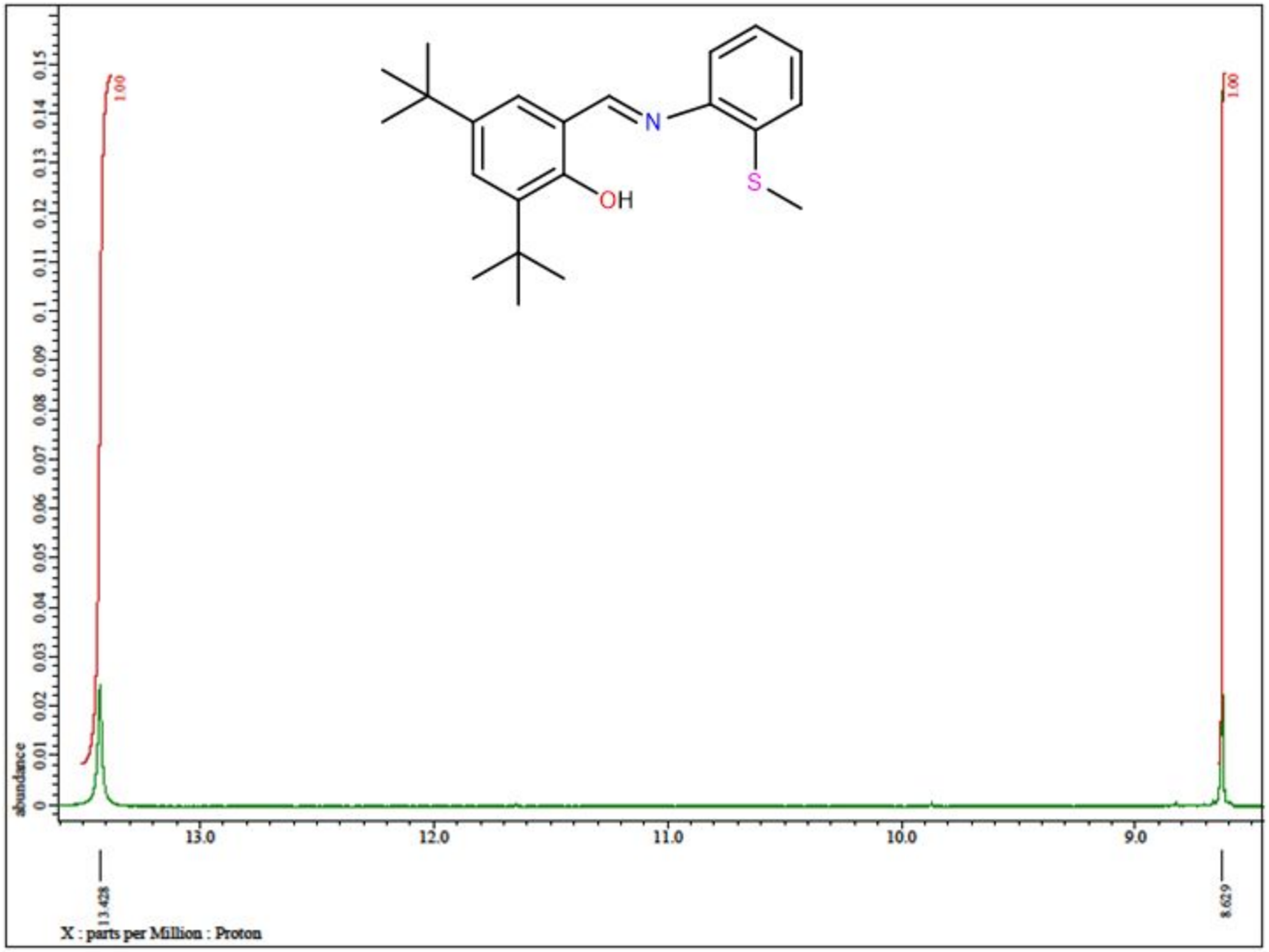

Fig. S27. ^{1}H NMR ($CDCl_3$, 400 MHz) spectrum of **L6** in aryl region.

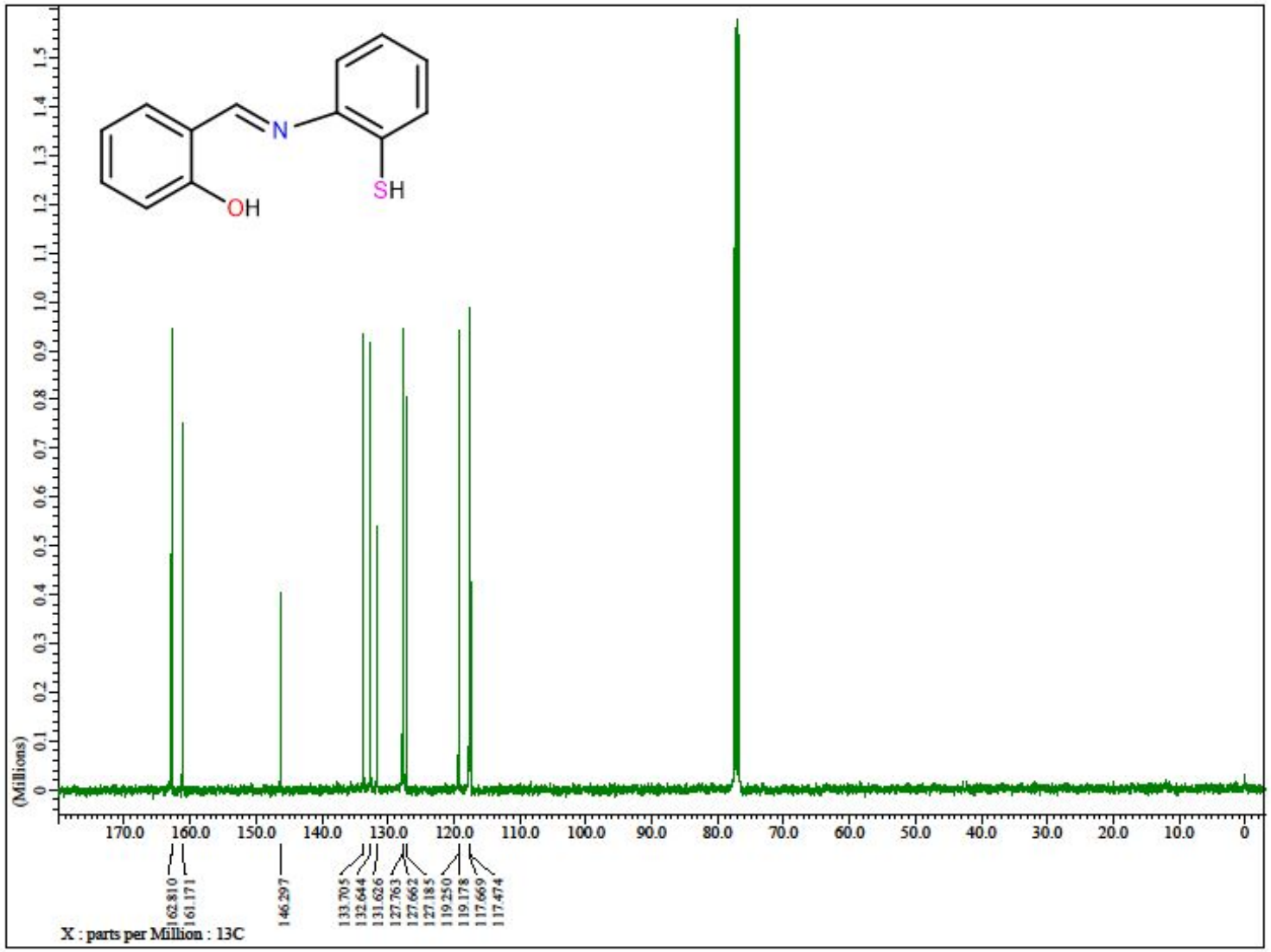

Fig. S28. $^{13}C\{^{1}H\}$ NMR ($CDCl_3$, 100.5 MHz) spectrum of **L1**.

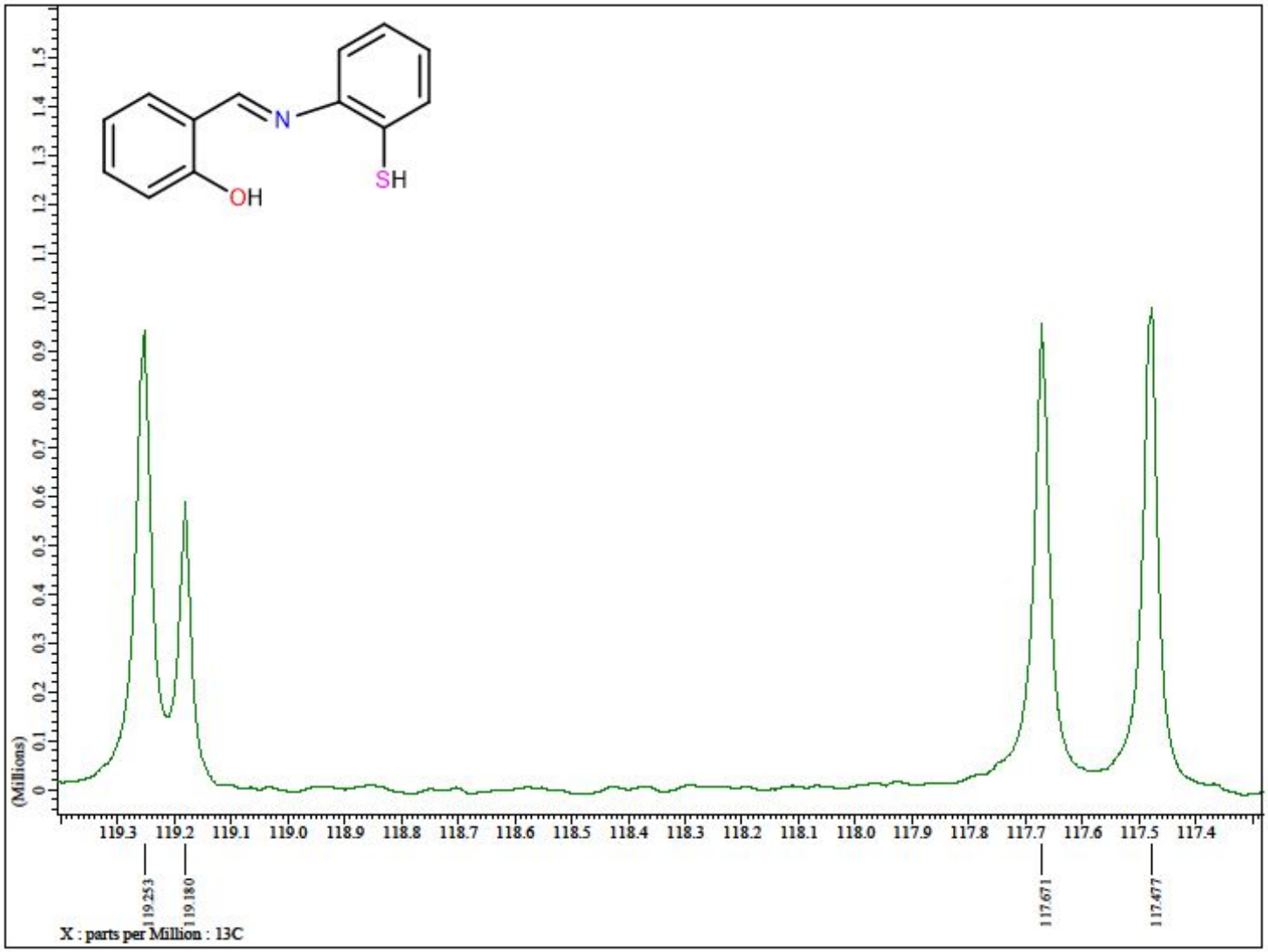

Fig. S29. $^{13}C\{^{1}H\}$ NMR ($CDCl_3$, 100.5 MHz) spectrum of **L1** in the aryl region.

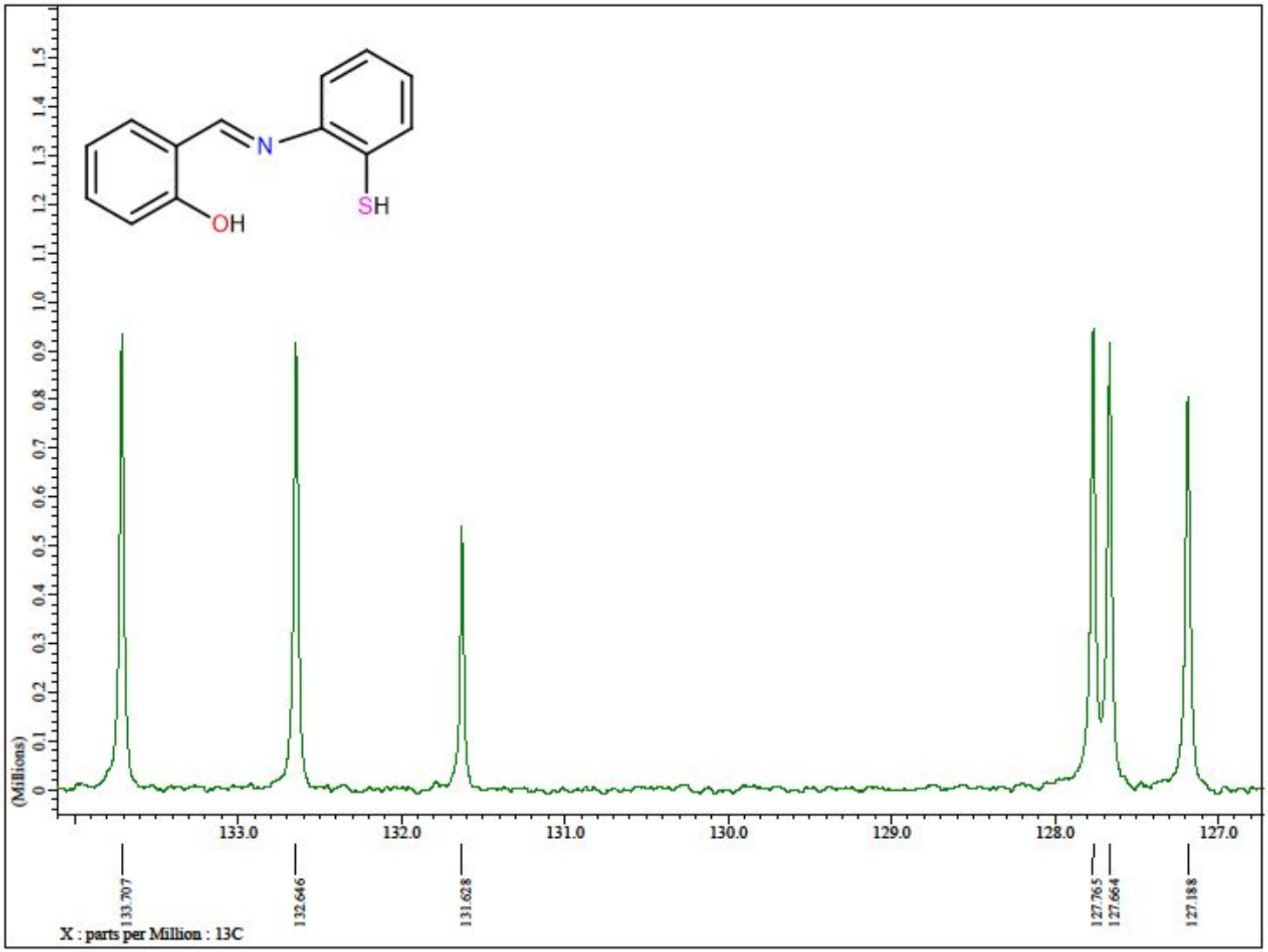

Fig. S30. $^{13}C\{^{1}H\}$ NMR ($CDCl_3$, 100.5 MHz) spectrum of **L1** in the aryl region.

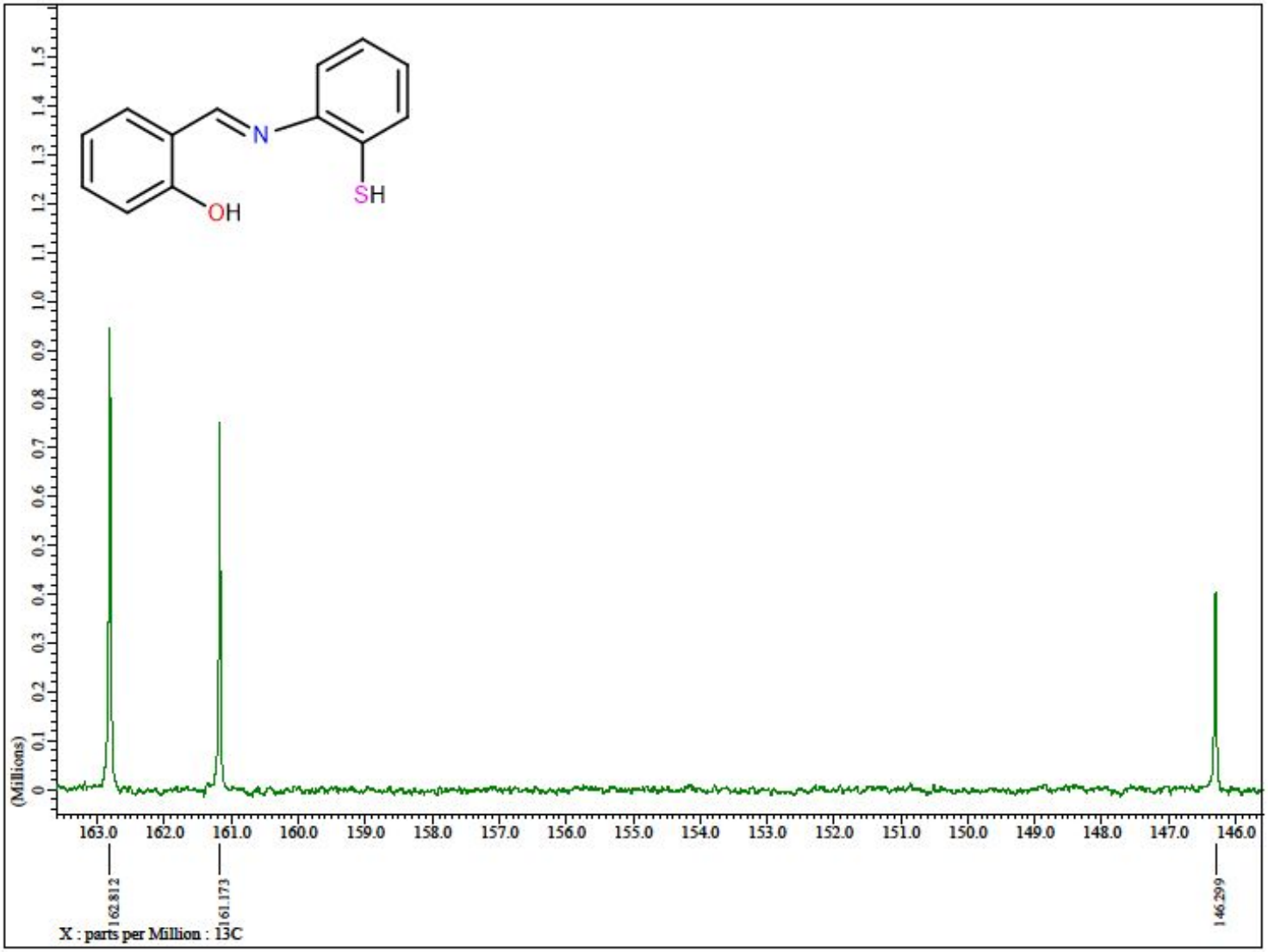

Fig. S31. $^{13}C\{^{1}H\}$ NMR ($CDCl_3$, 100.5 MHz) spectrum of **L1** in the aryl region.

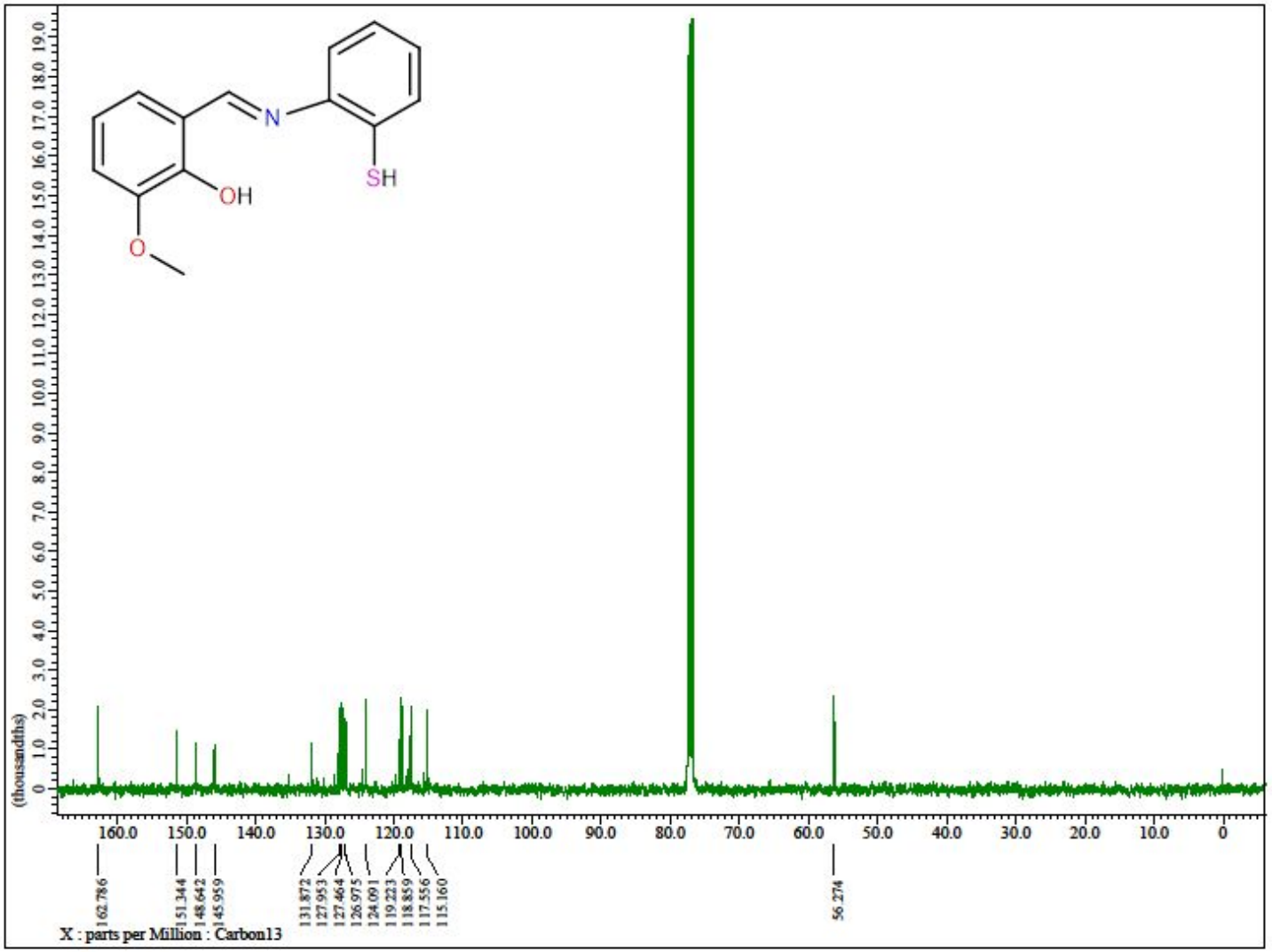

Fig. S32. $^{13}C\{^{1}H\}$ NMR ($CDCl_3$, 100.5 MHz) spectrum of **L2**.

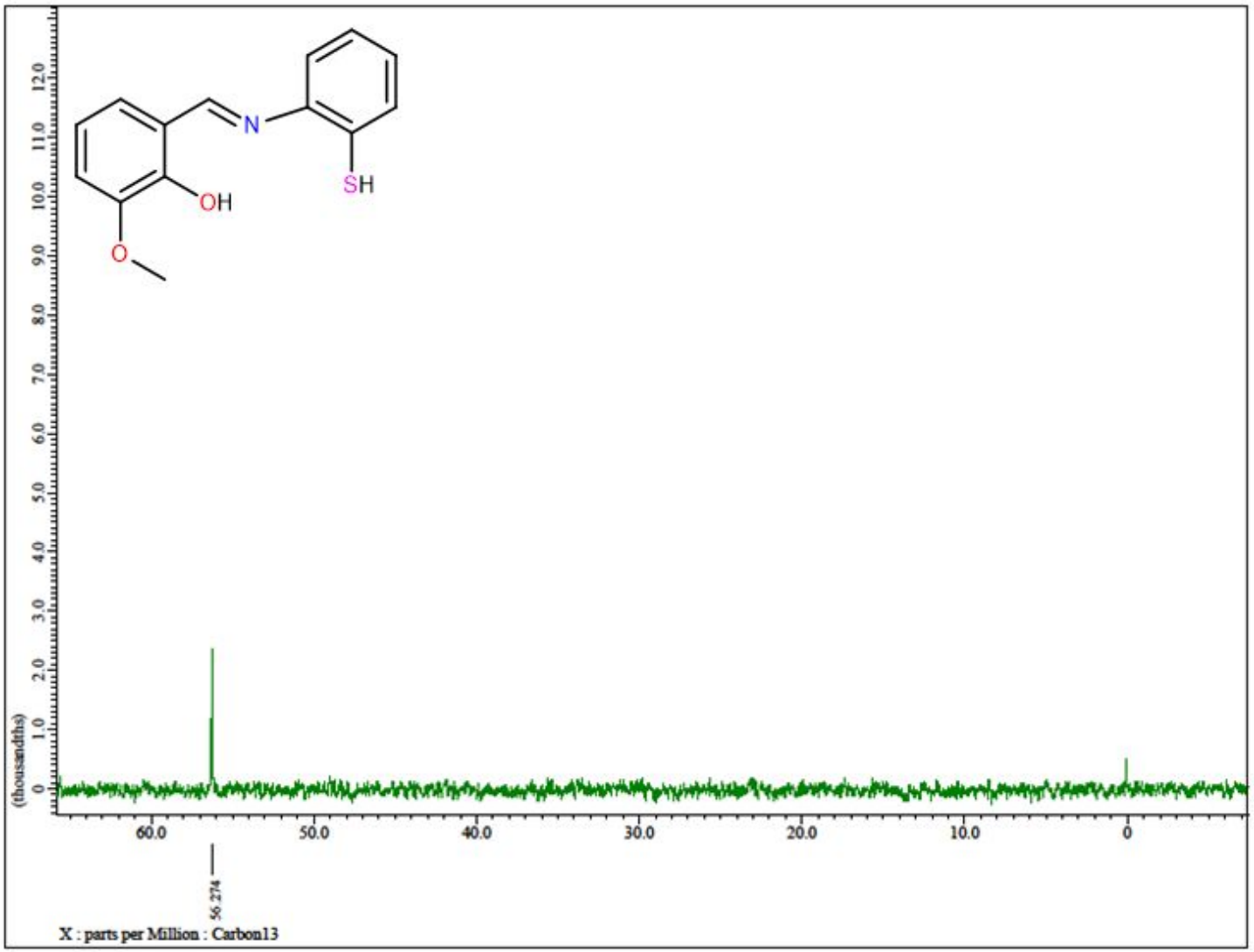

Fig. S33. $^{13}C\{^{1}H\}$ NMR ($CDCl_3$, 100.5 MHz) spectrum of **L2** in the alkyl region.

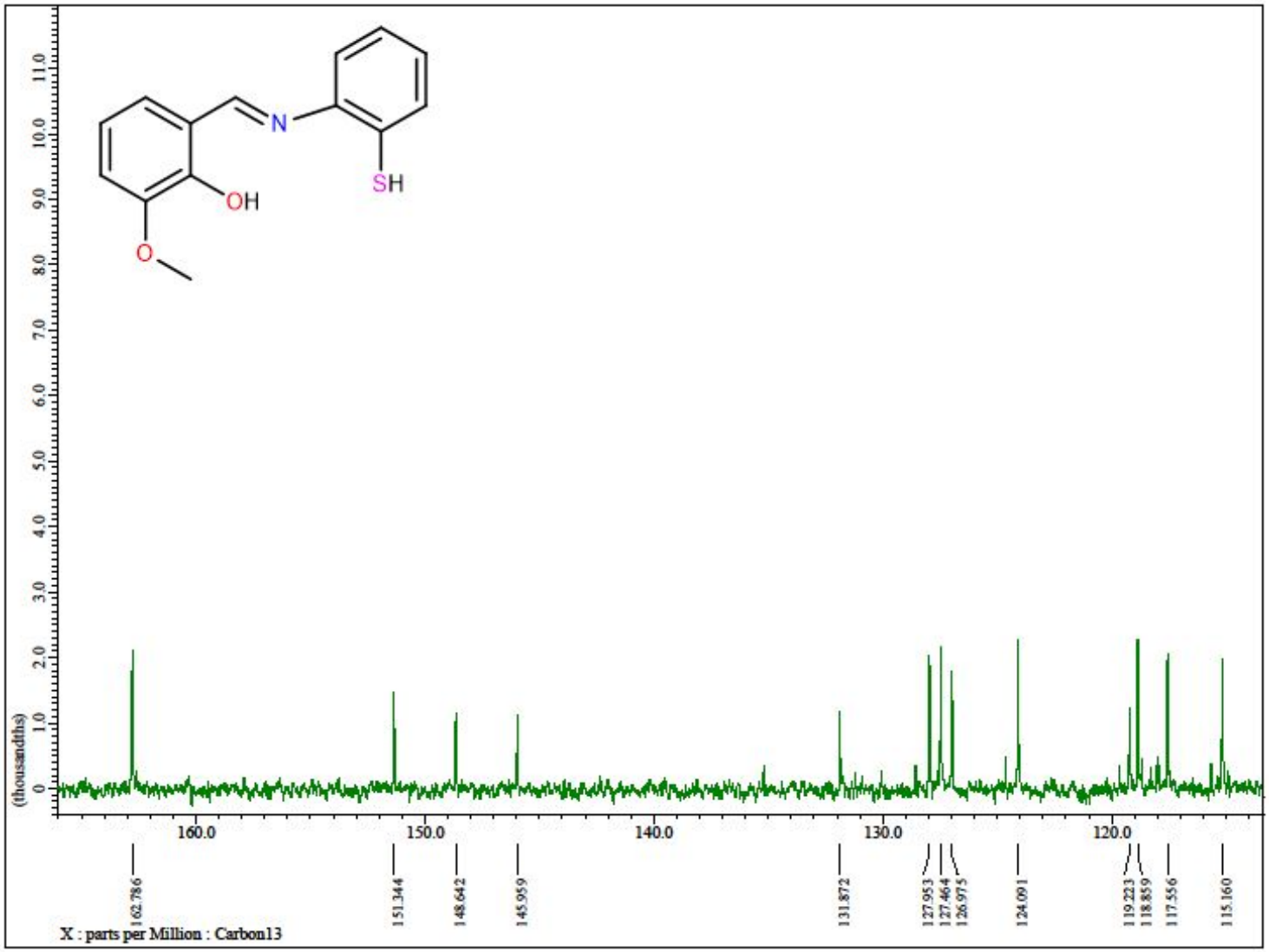

Fig. S34. $^{13}C\{^{1}H\}$ NMR ($CDCl_3$, 100.5 MHz) spectrum of **L2** in the aryl region.

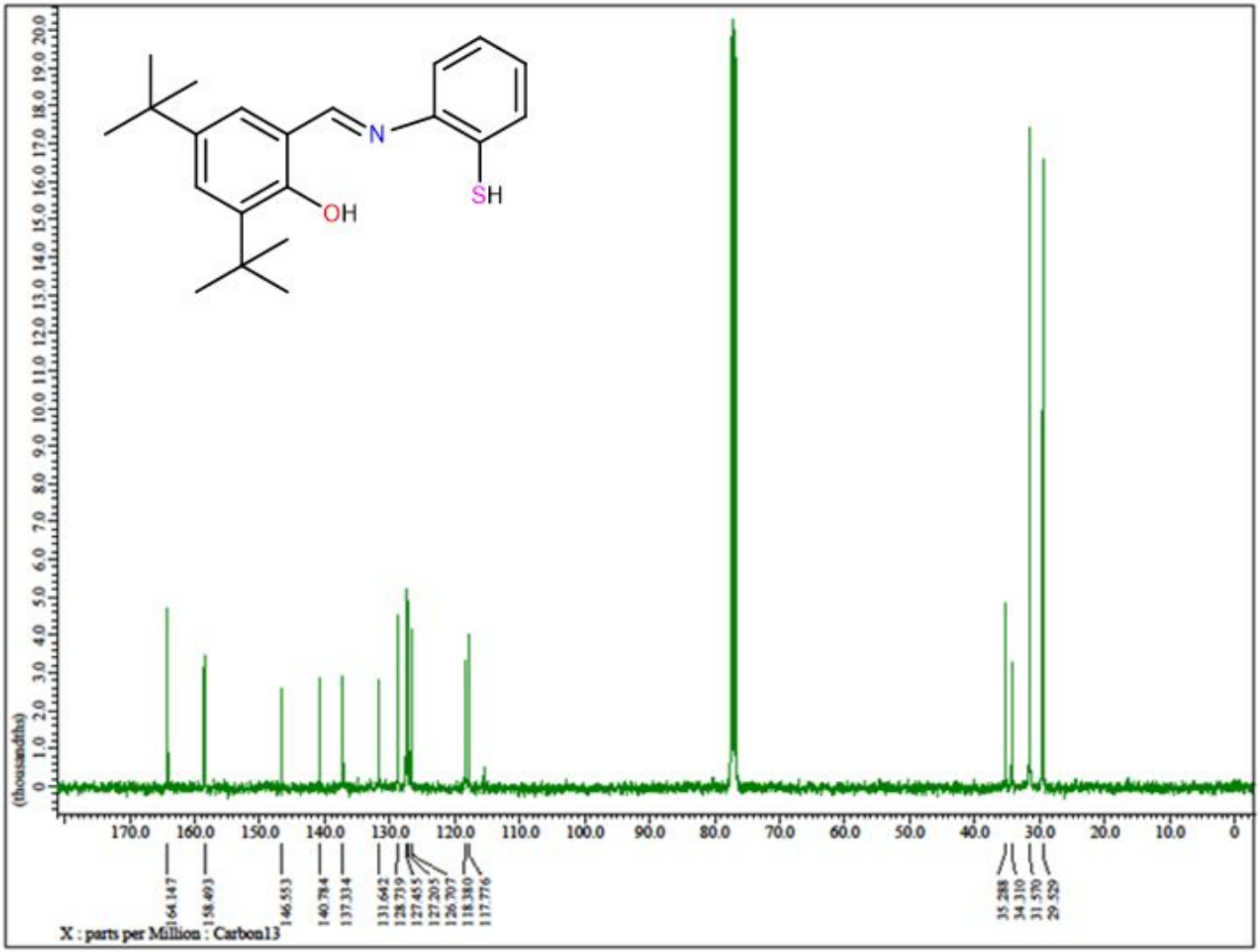

Fig. S35. $^{13}C\{^{1}H\}$ NMR ($CDCl_3$, 100.5 MHz) spectrum of **L3**.

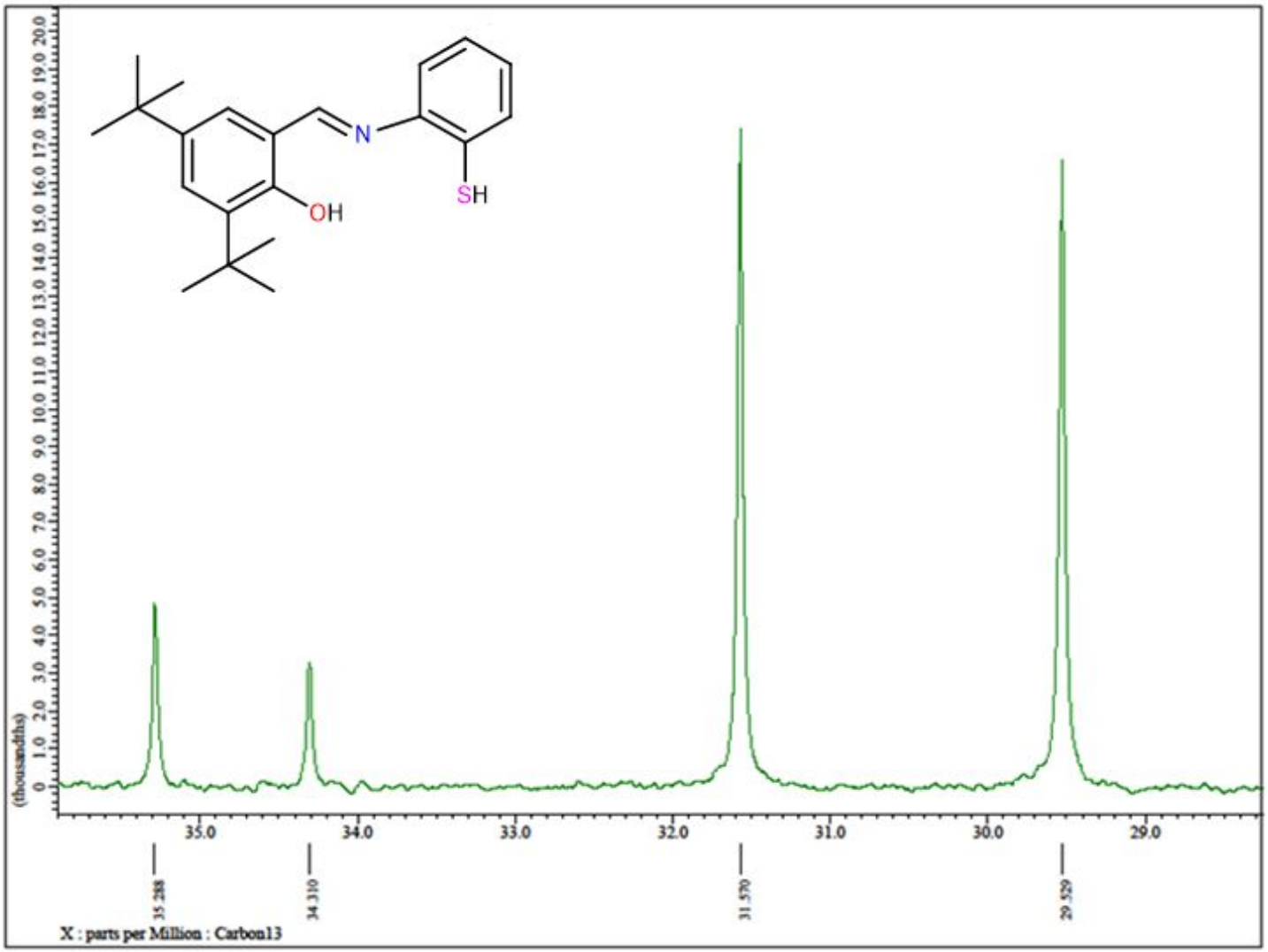

Fig. S36. $^{13}C\{^{1}H\}$ NMR ($CDCl_3$, 100.5 MHz) spectrum of **L3** in the alkyl region.

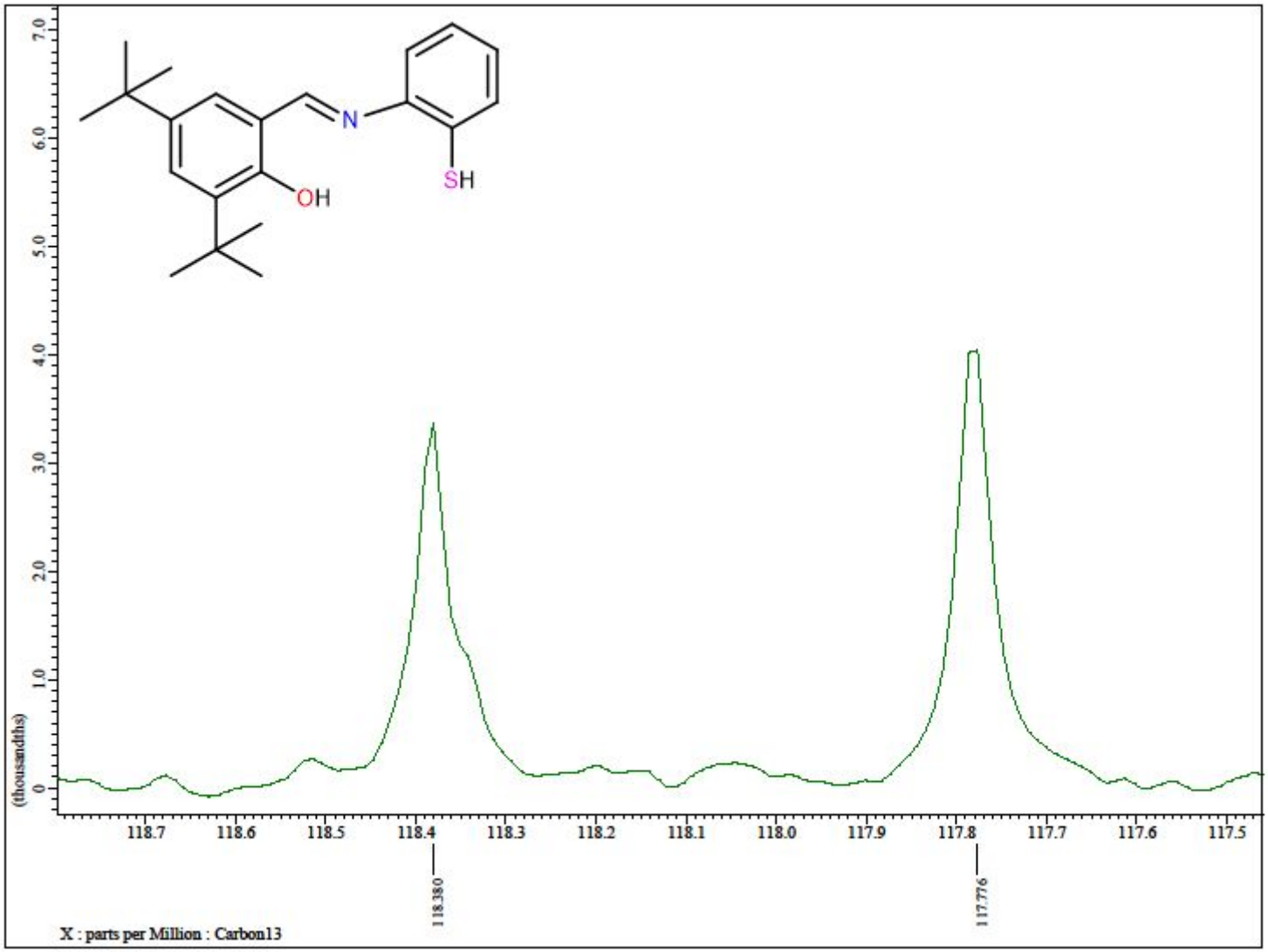

Fig. S37. $^{13}C\{^{1}H\}$ NMR ($CDCl_3$, 100.5 MHz) spectrum of **L3** in the aryl region.

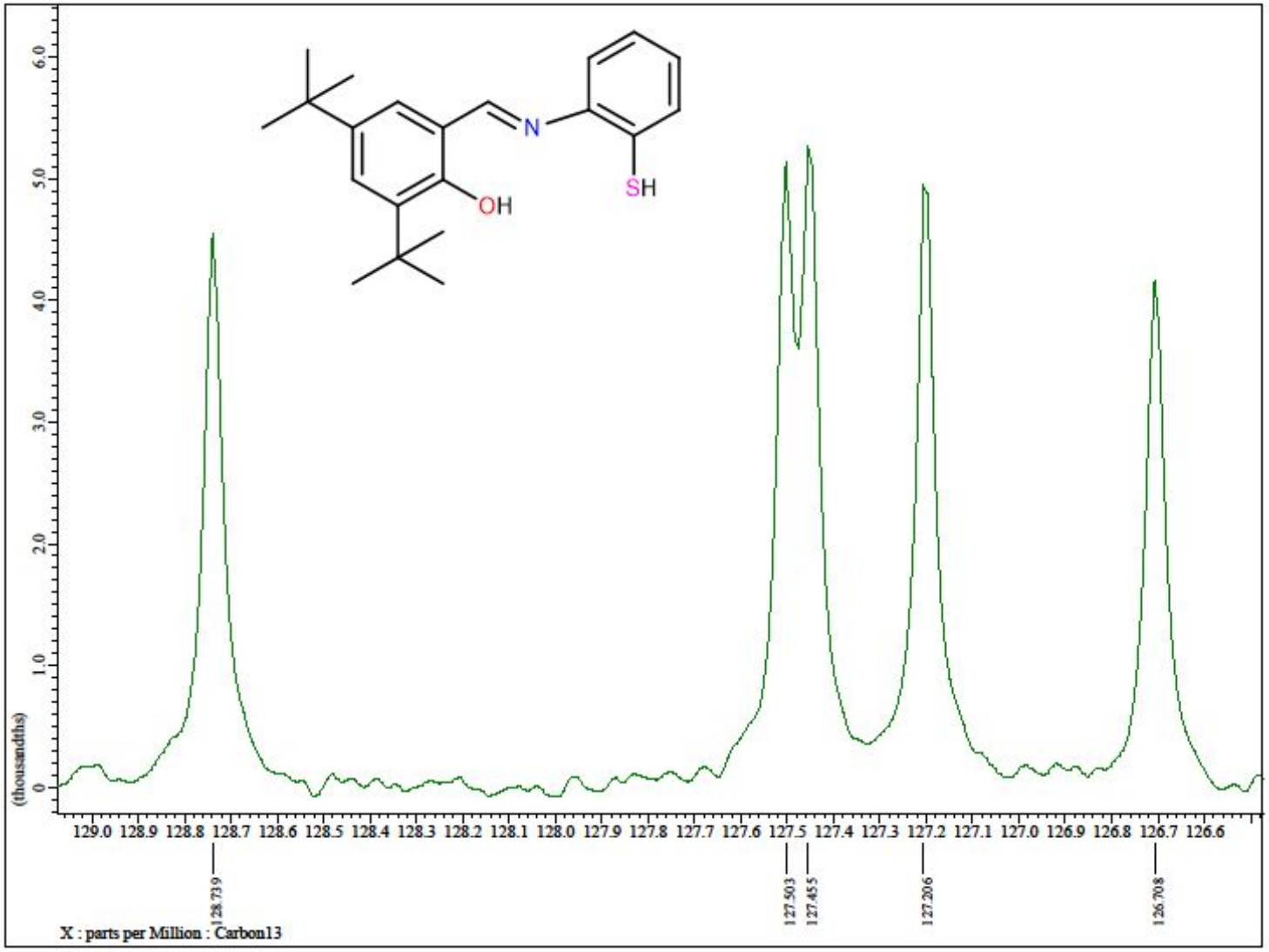

Fig. S38. $^{13}C\{^{1}H\}$ NMR ($CDCl_3$, 100.5 MHz) spectrum of **L3** in the aryl region.

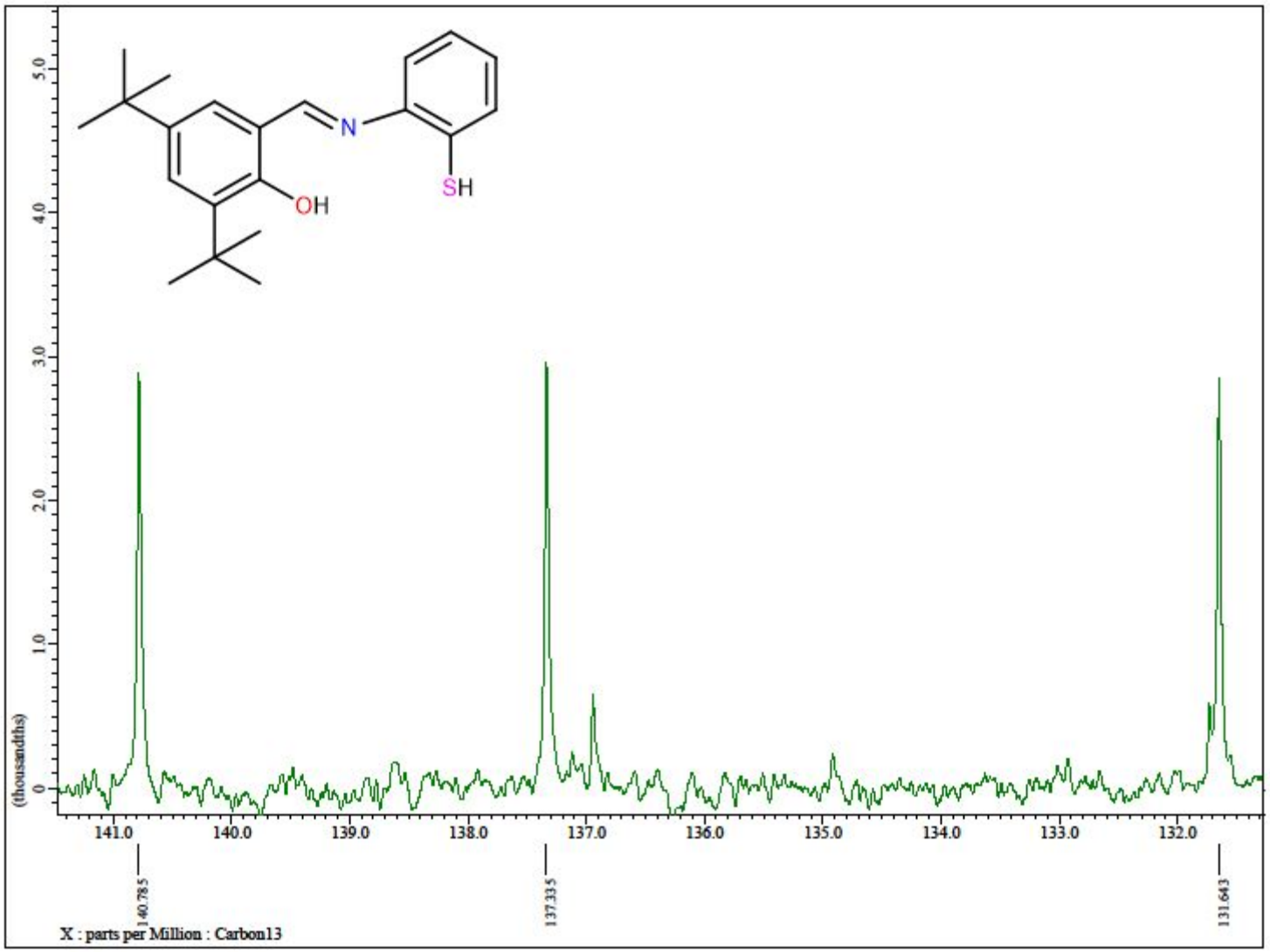

Fig. S39. $^{13}C\{^{1}H\}$ NMR ($CDCl_3$, 100.5 MHz) spectrum of **L3** in the aryl region.

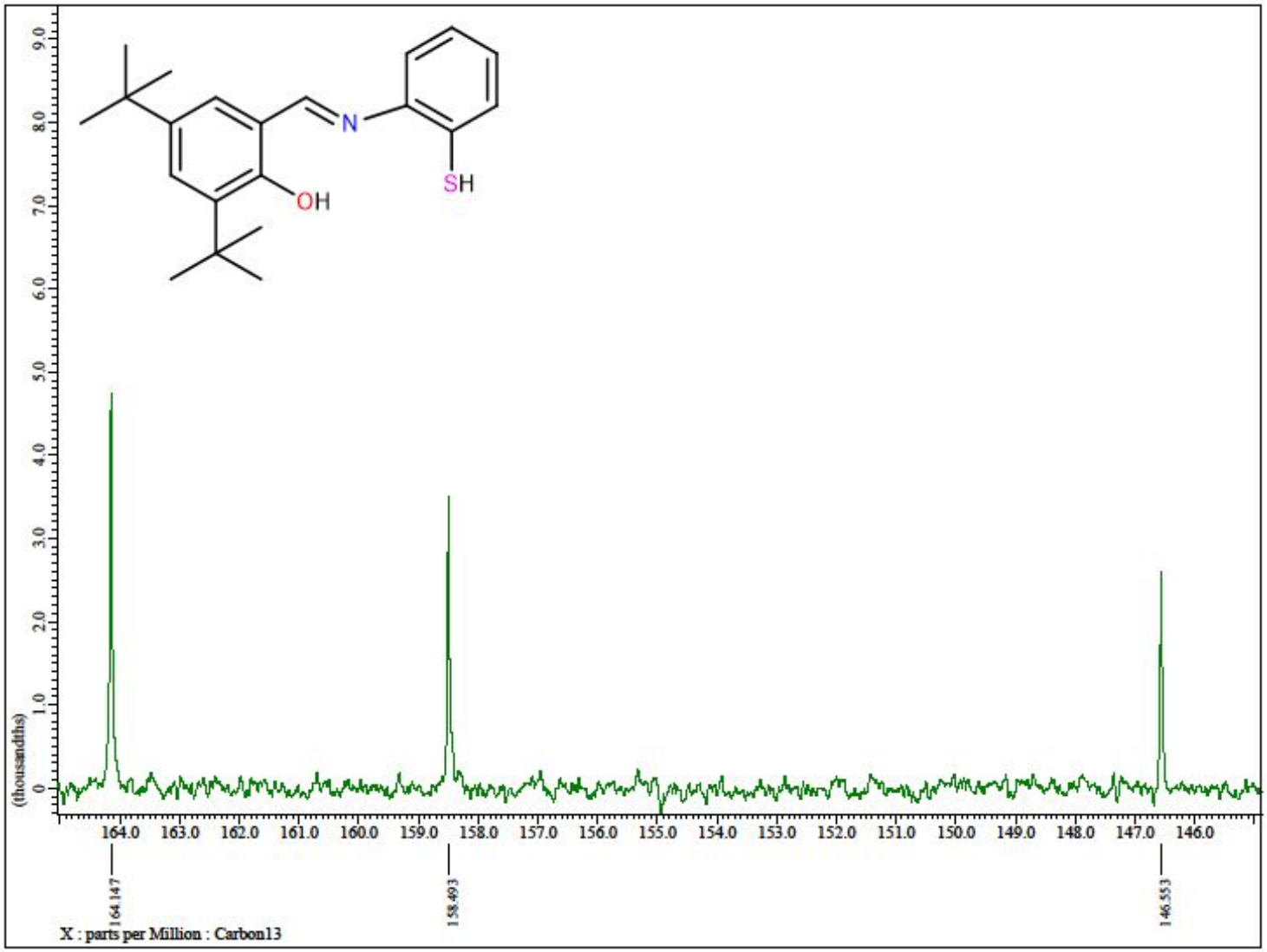

Fig. S40. $^{13}C\{^{1}H\}$ NMR ($CDCl_3$, 100.5 MHz) spectrum of **L3** in the aryl region.

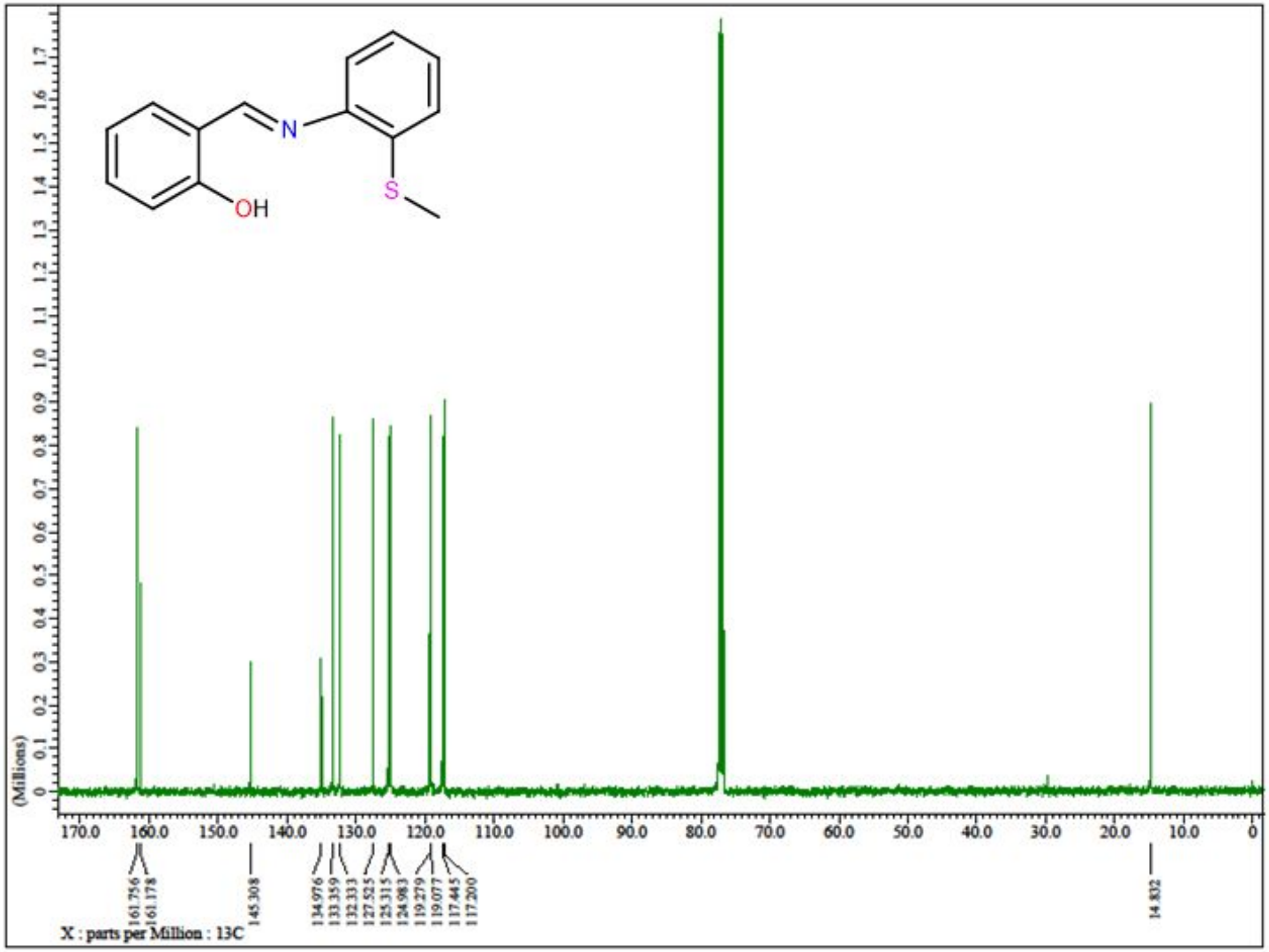

Fig. S41. $^{13}C\{^{1}H\}$ NMR ($CDCl_3$, 100.5 MHz) spectrum of **L4**.

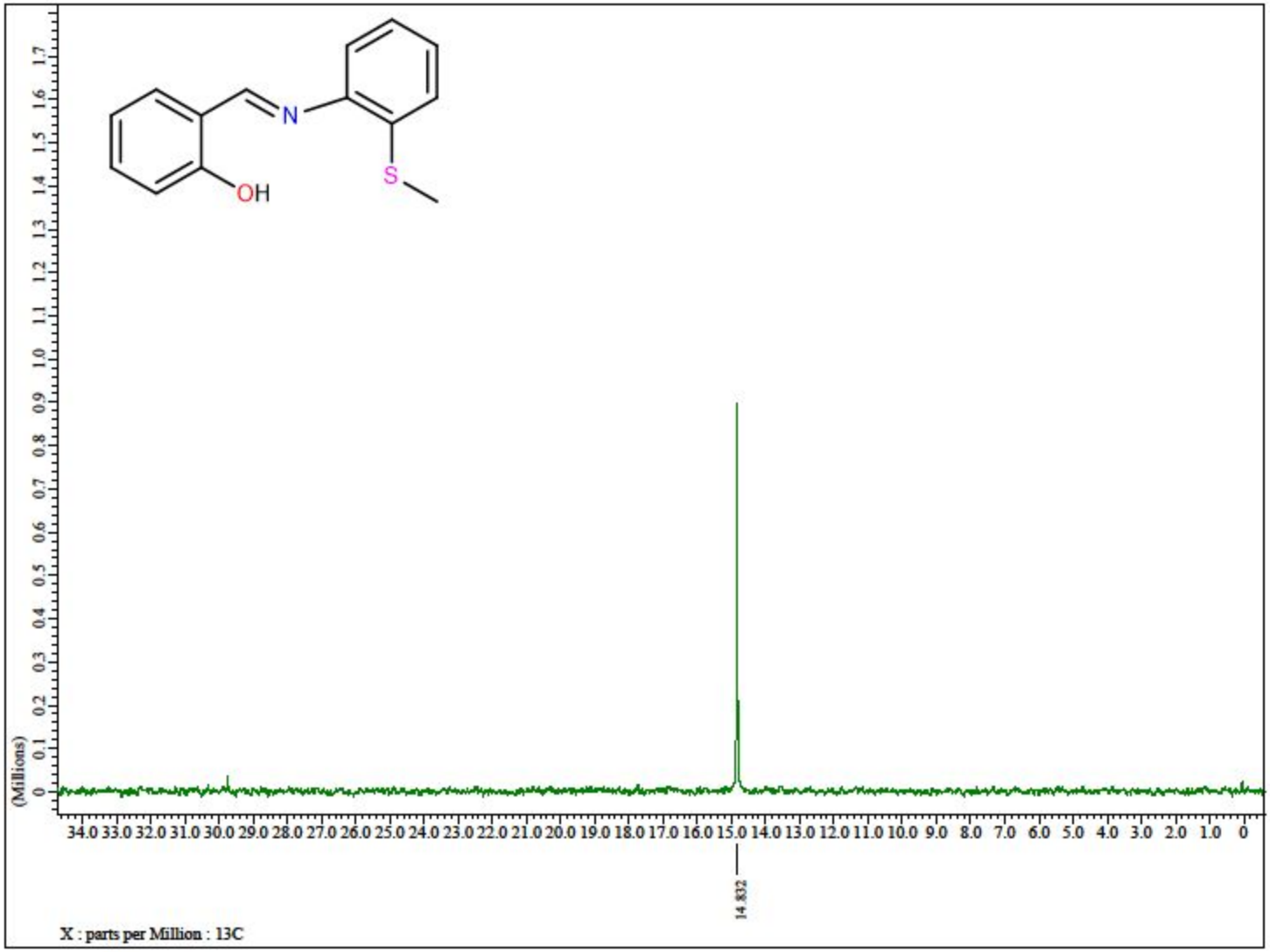

Fig. S42. $^{13}C\{^{1}H\}$ NMR ($CDCl_3$, 100.5 MHz) spectrum of **L4** in the alkyl region.

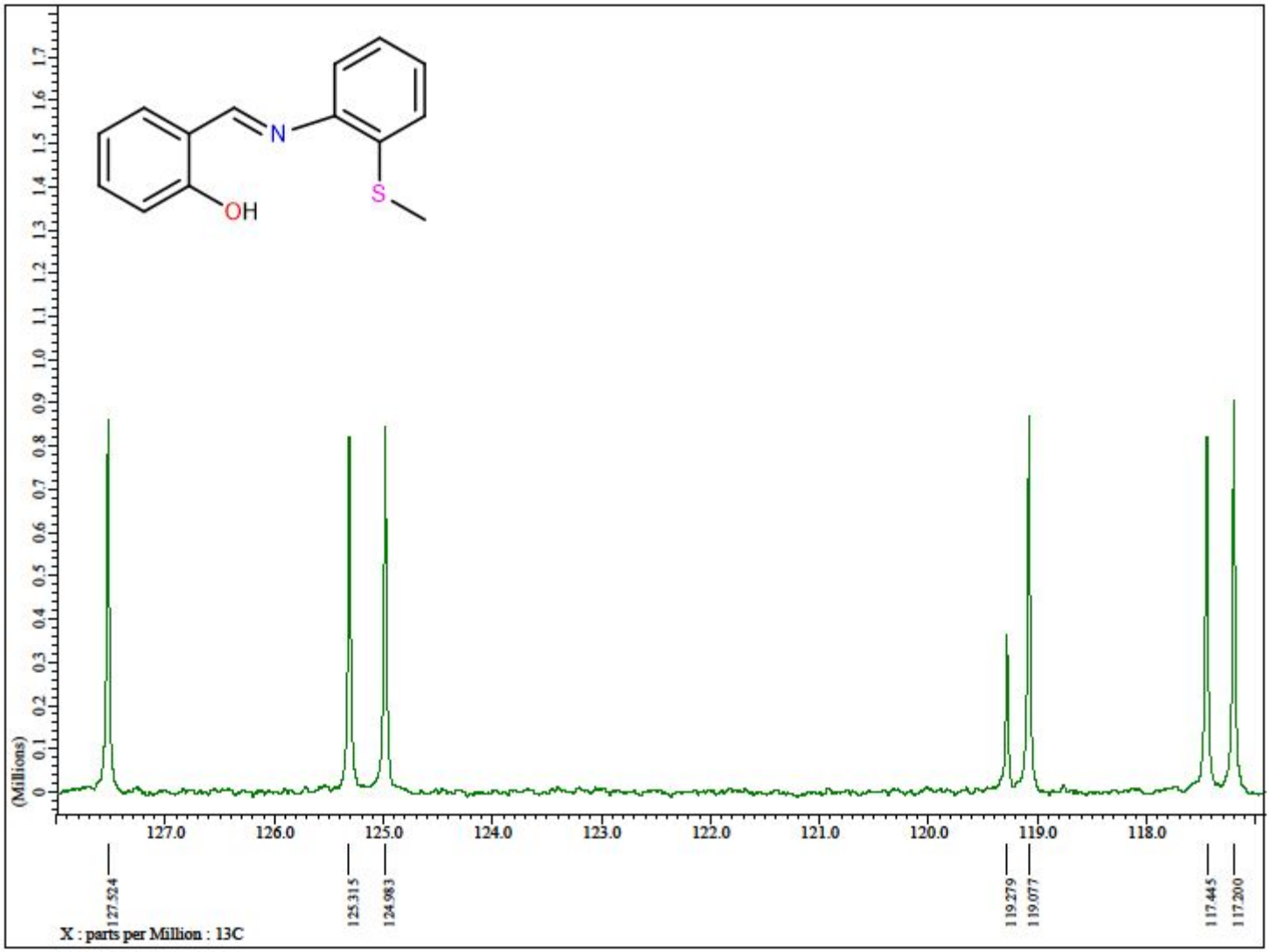

Fig. S43. $^{13}C\{^{1}H\}$ NMR ($CDCl_3$, 100.5 MHz) spectrum of **L4** in the aryl region.

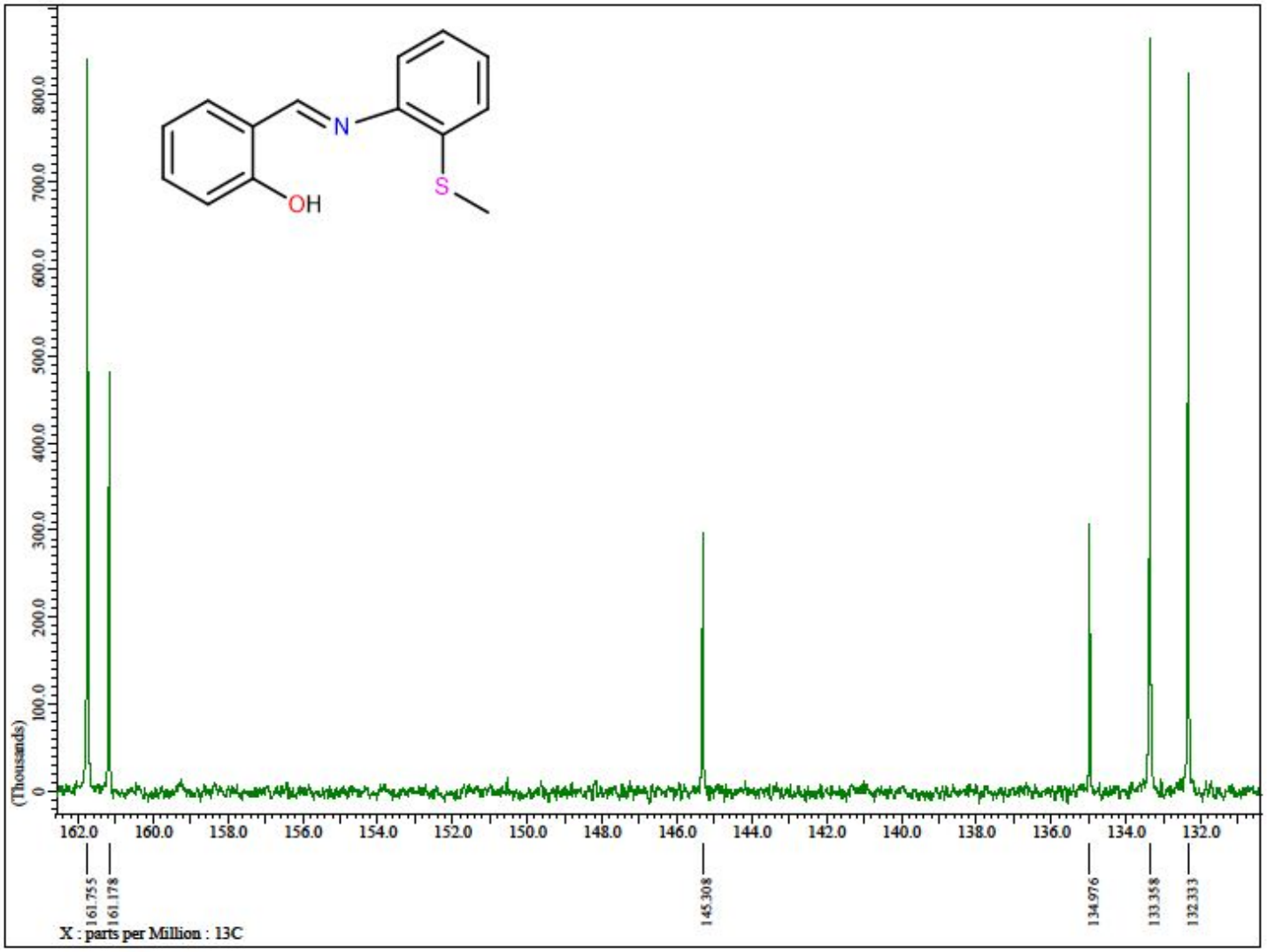

Fig. S44. $^{13}C\{^{1}H\}$ NMR ($CDCl_3$, 100.5 MHz) spectrum of **L4** in the aryl region.

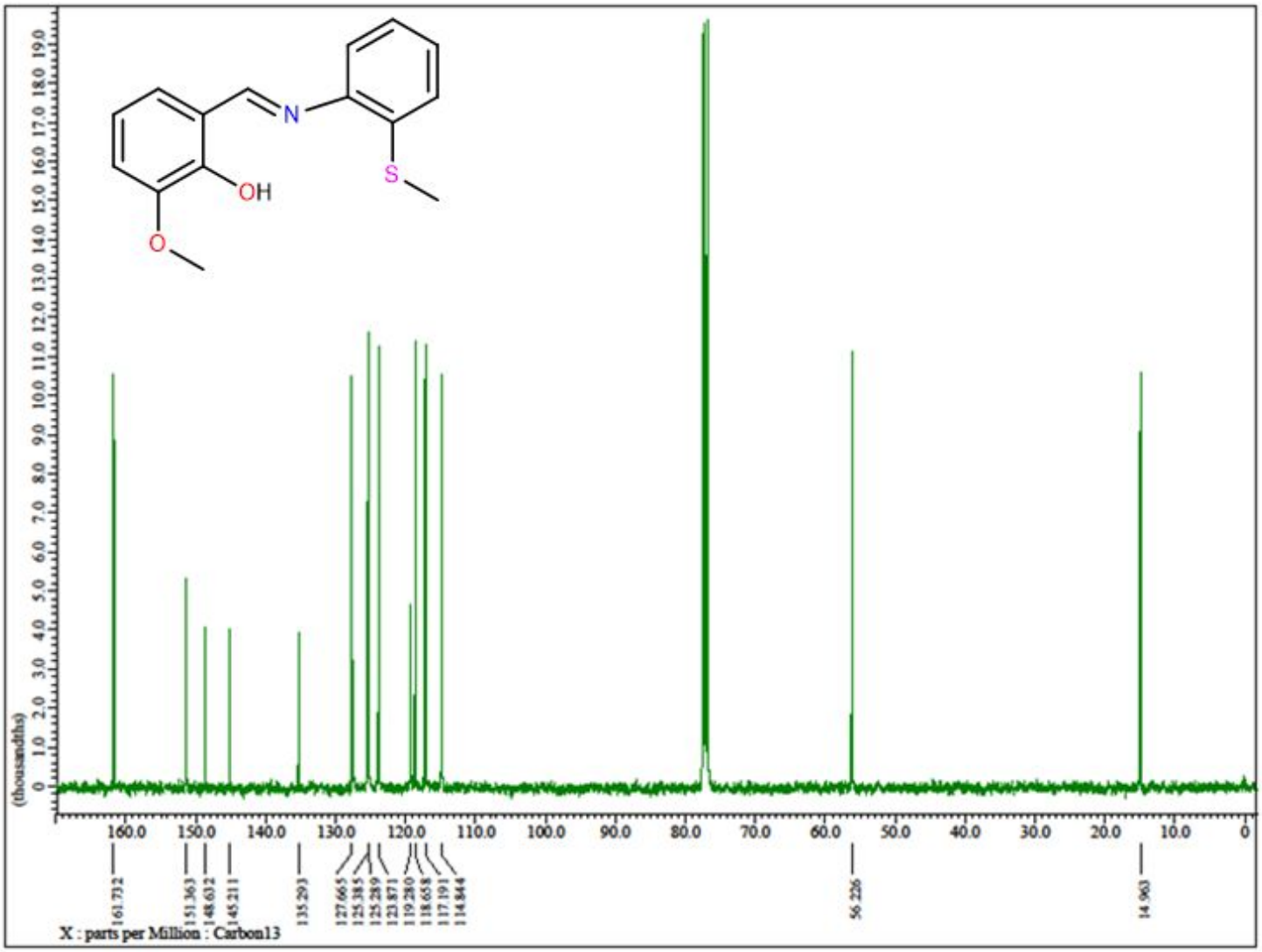

Fig. S45. $^{13}C\{^{1}H\}$ NMR ($CDCl_3$, 100.5 MHz) spectrum of **L5**.

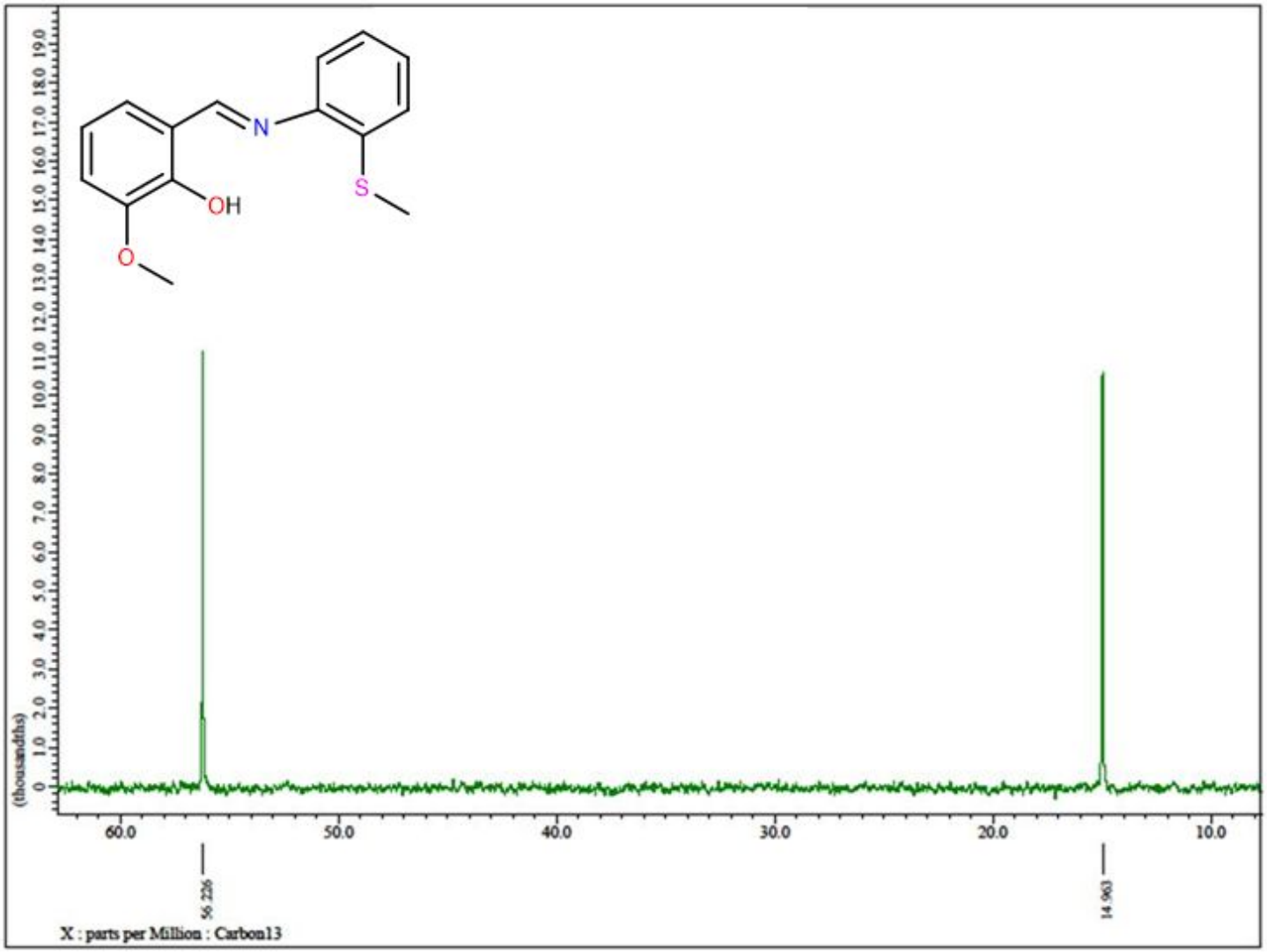

Fig. S46. $^{13}C\{^{1}H\}$ NMR ($CDCl_3$, 100.5 MHz) spectrum of **L5** in the alkyl region.

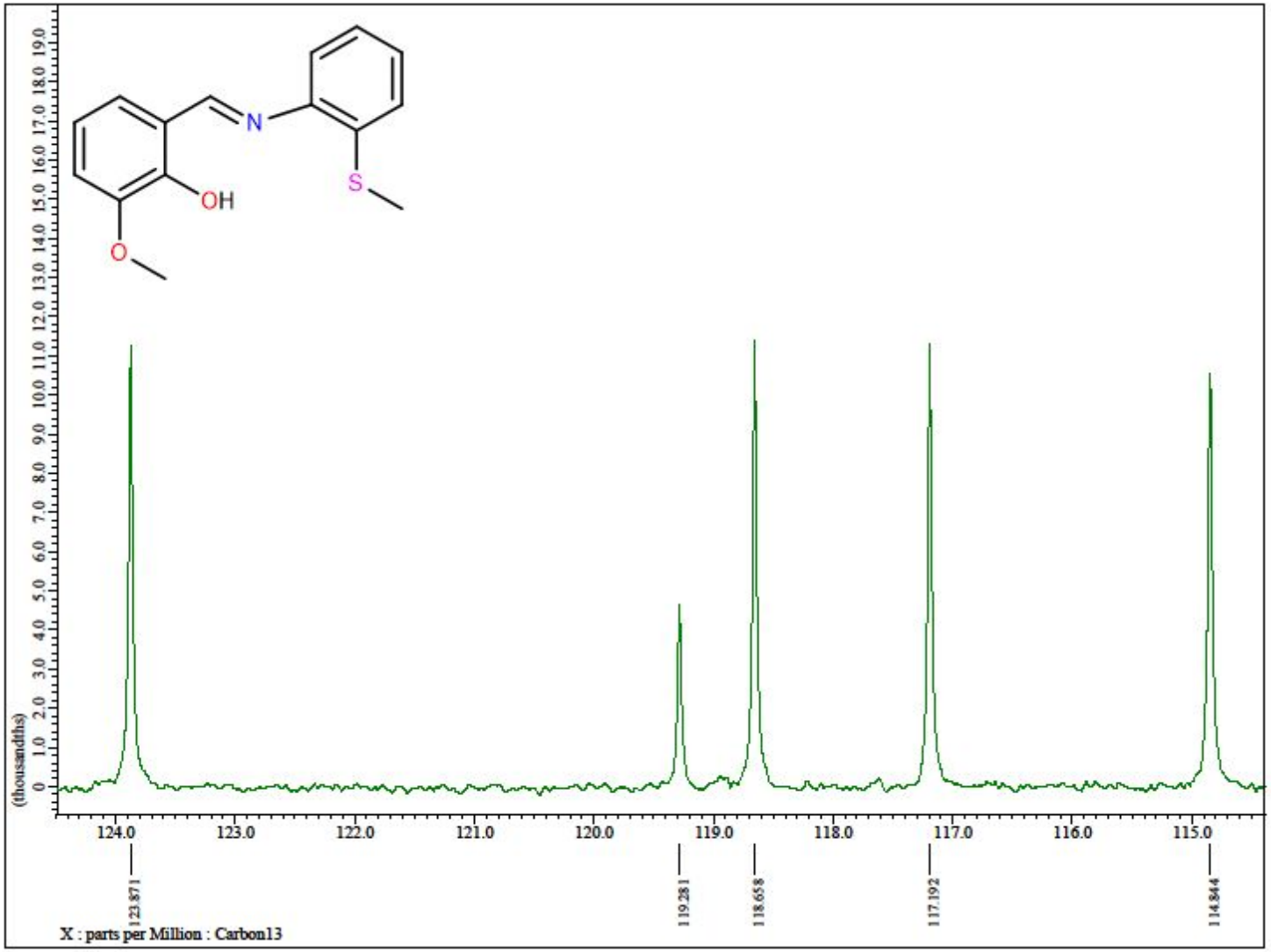

Fig. S47. $^{13}C\{^{1}H\}$ NMR ($CDCl_3$, 100.5 MHz) spectrum of **L5** in the aryl region.

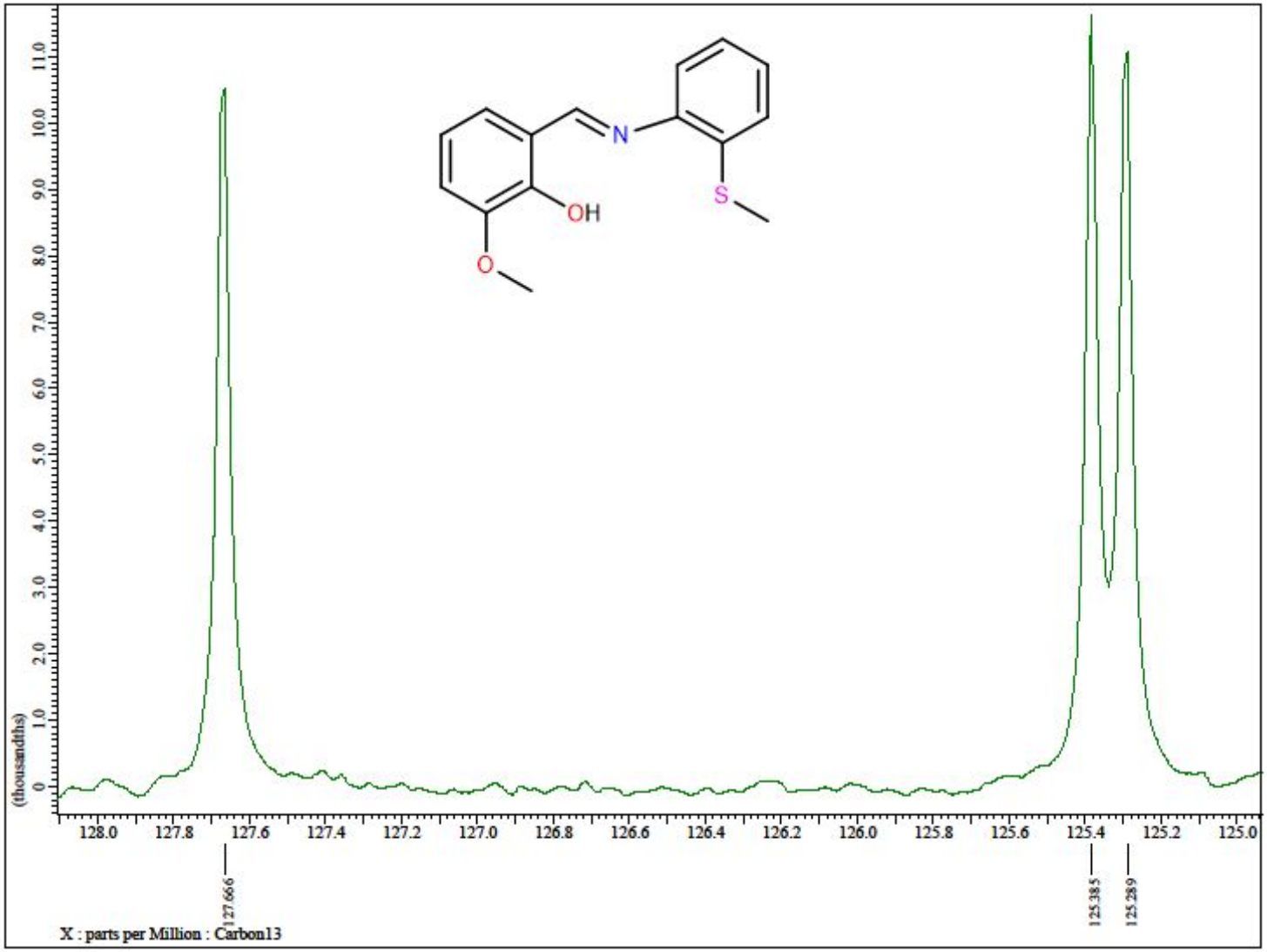

Fig. S48. $^{13}C\{^{1}H\}$ NMR ($CDCl_3$, 100.5 MHz) spectrum of **L5** in the aryl region.

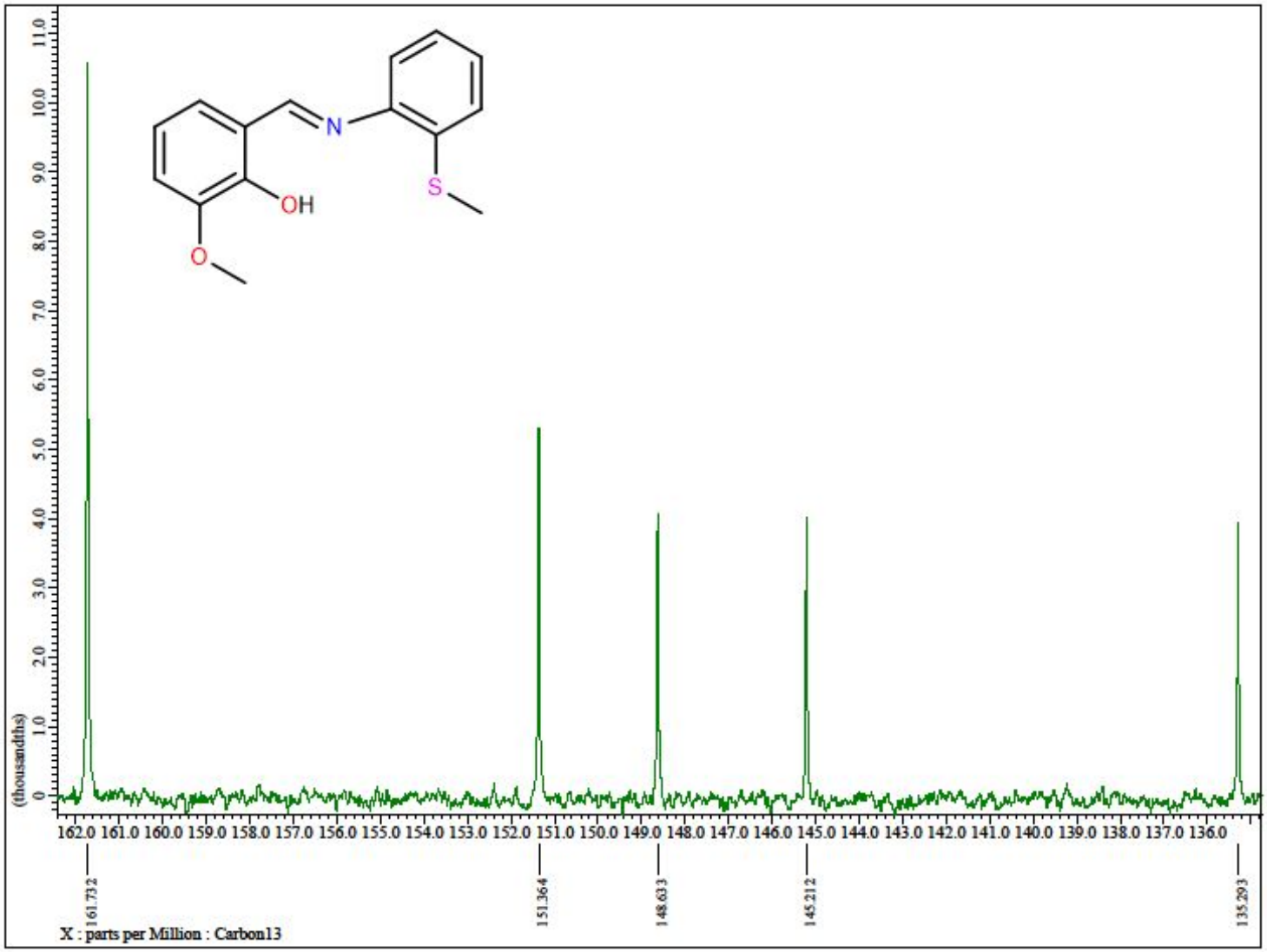

Fig. S49. $^{13}C\{^{1}H\}$ NMR ($CDCl_3$, 100.5 MHz) spectrum of **L5** in the aryl region.

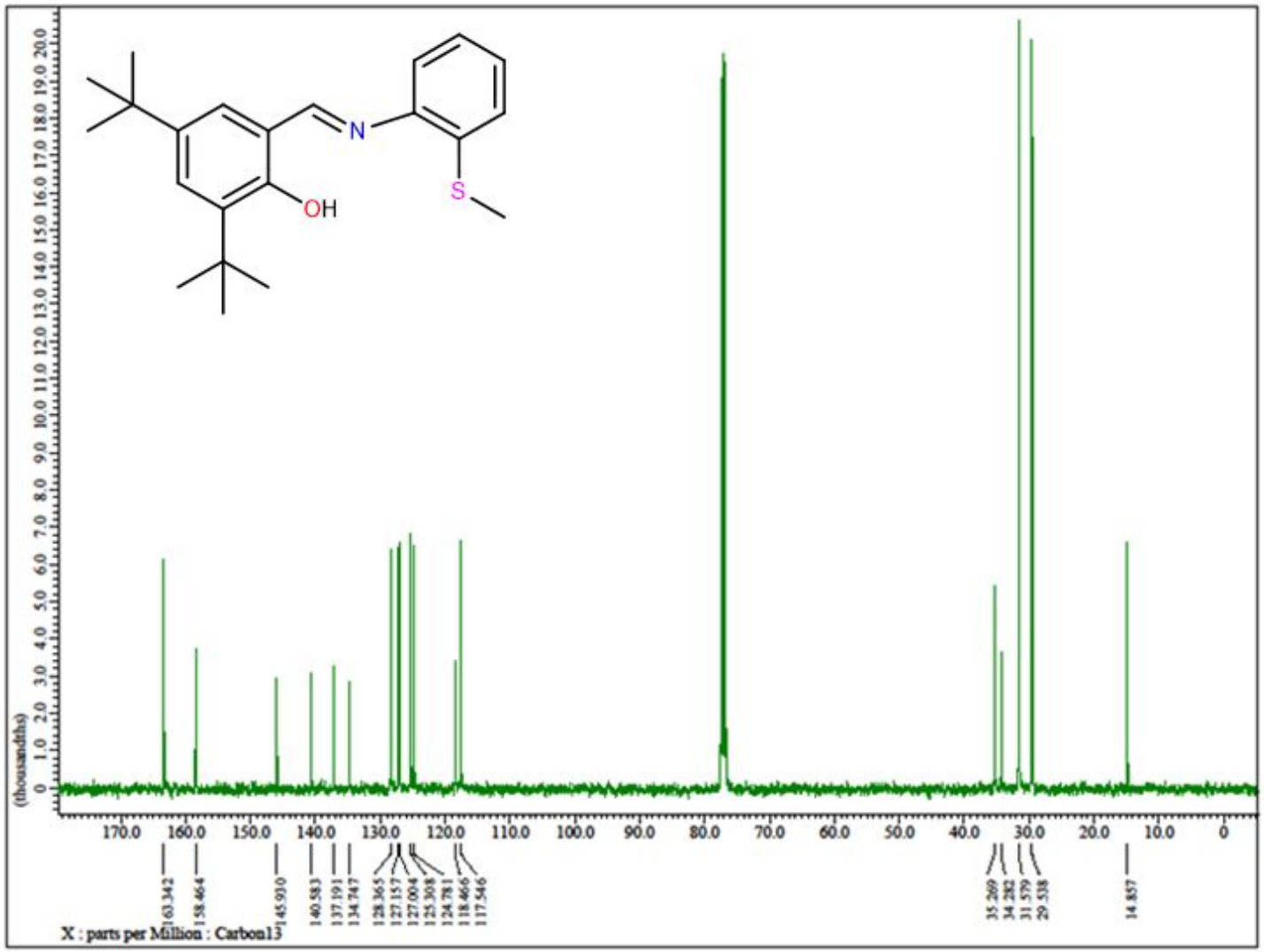

Fig. S50. $^{13}C\{^{1}H\}$ NMR ($CDCl_3$, 100.5 MHz) spectrum of **L6**.

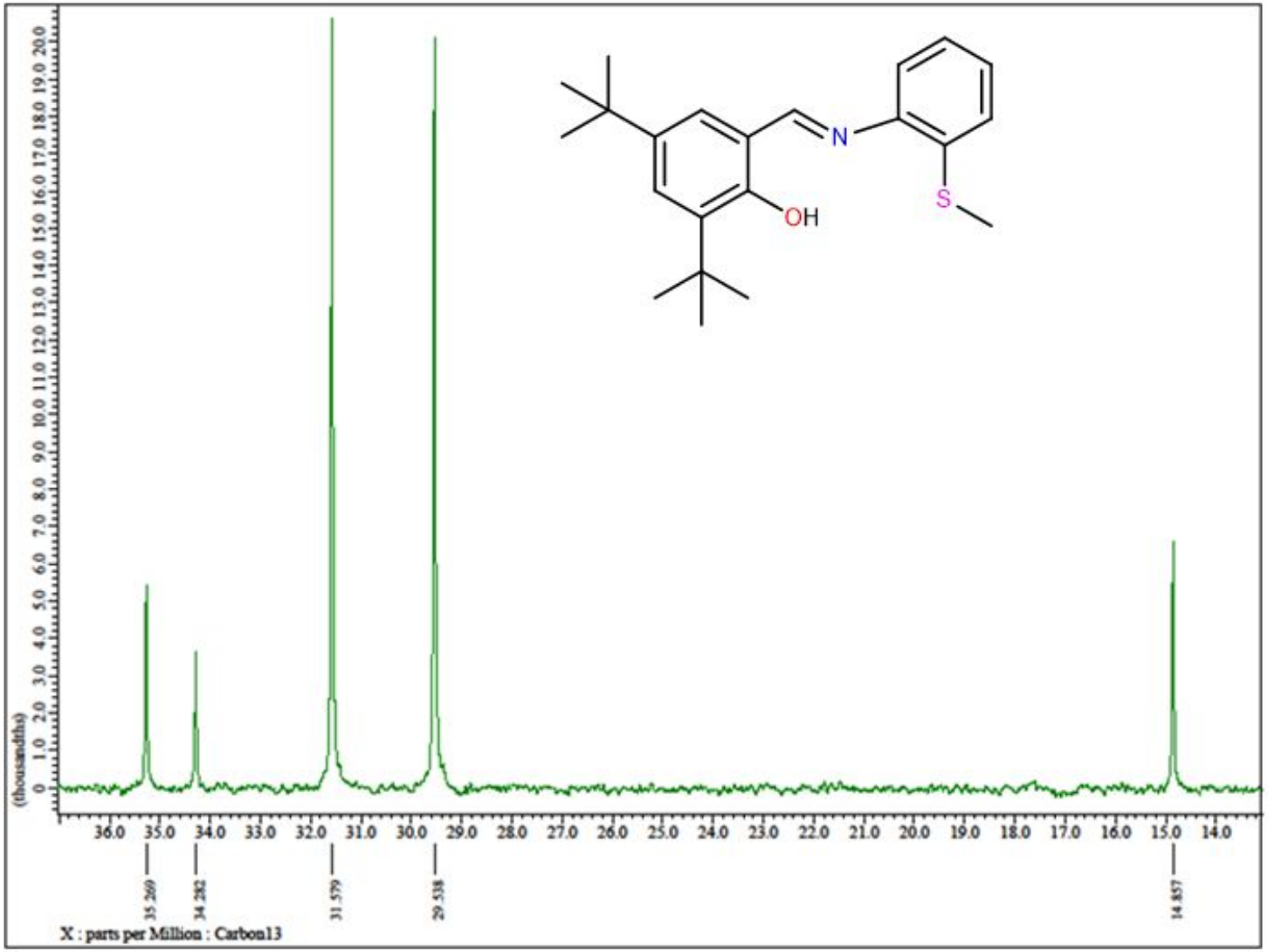

Fig. S51. $^{13}C\{^{1}H\}$ NMR ($CDCl_3$, 100.5 MHz) spectrum of **L6** in the alkyl region.

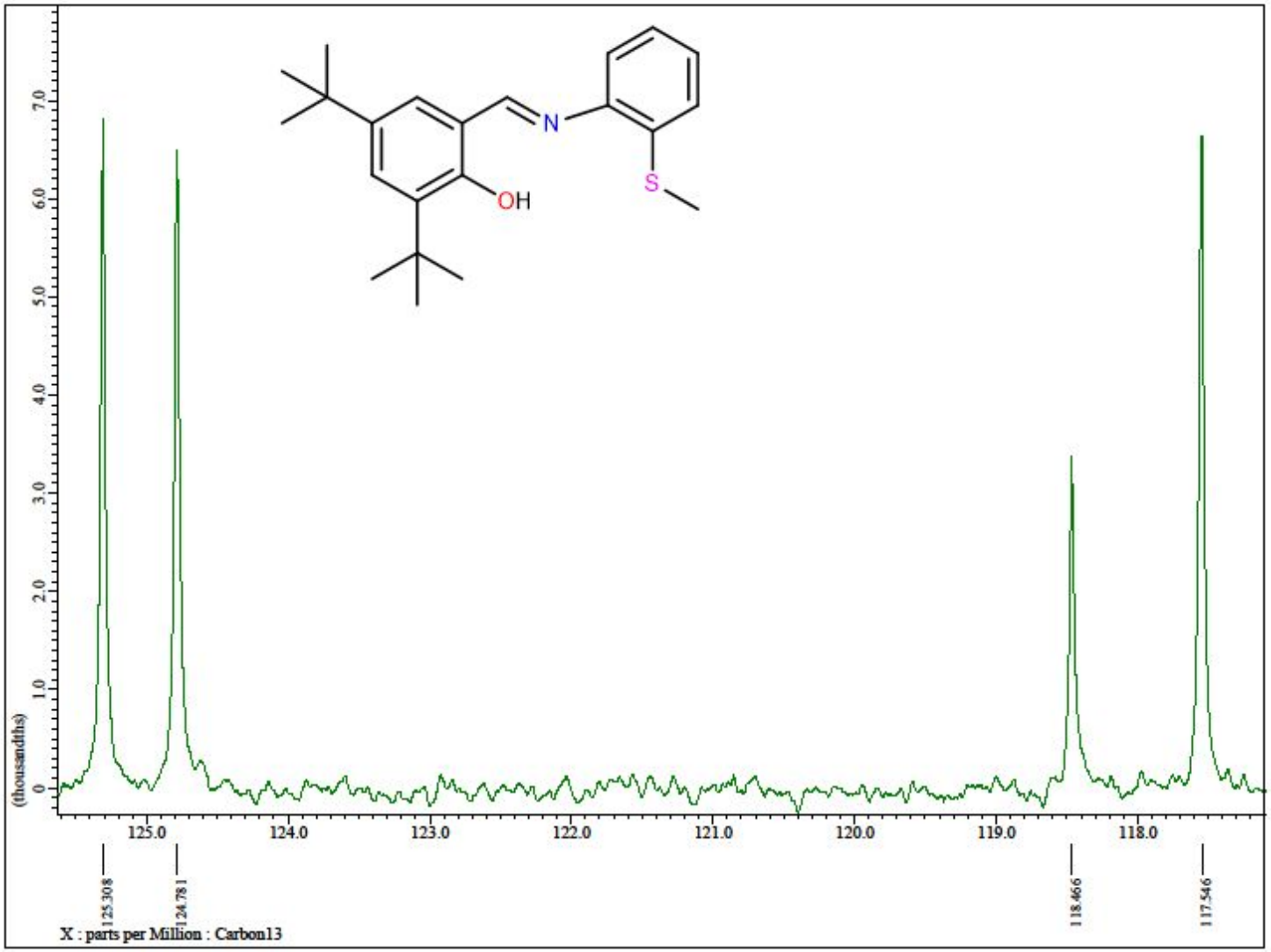

Fig. S52. $^{13}C\{^{1}H\}$ NMR ($CDCl_3$, 100.5 MHz) spectrum of **L6** in the aryl region.

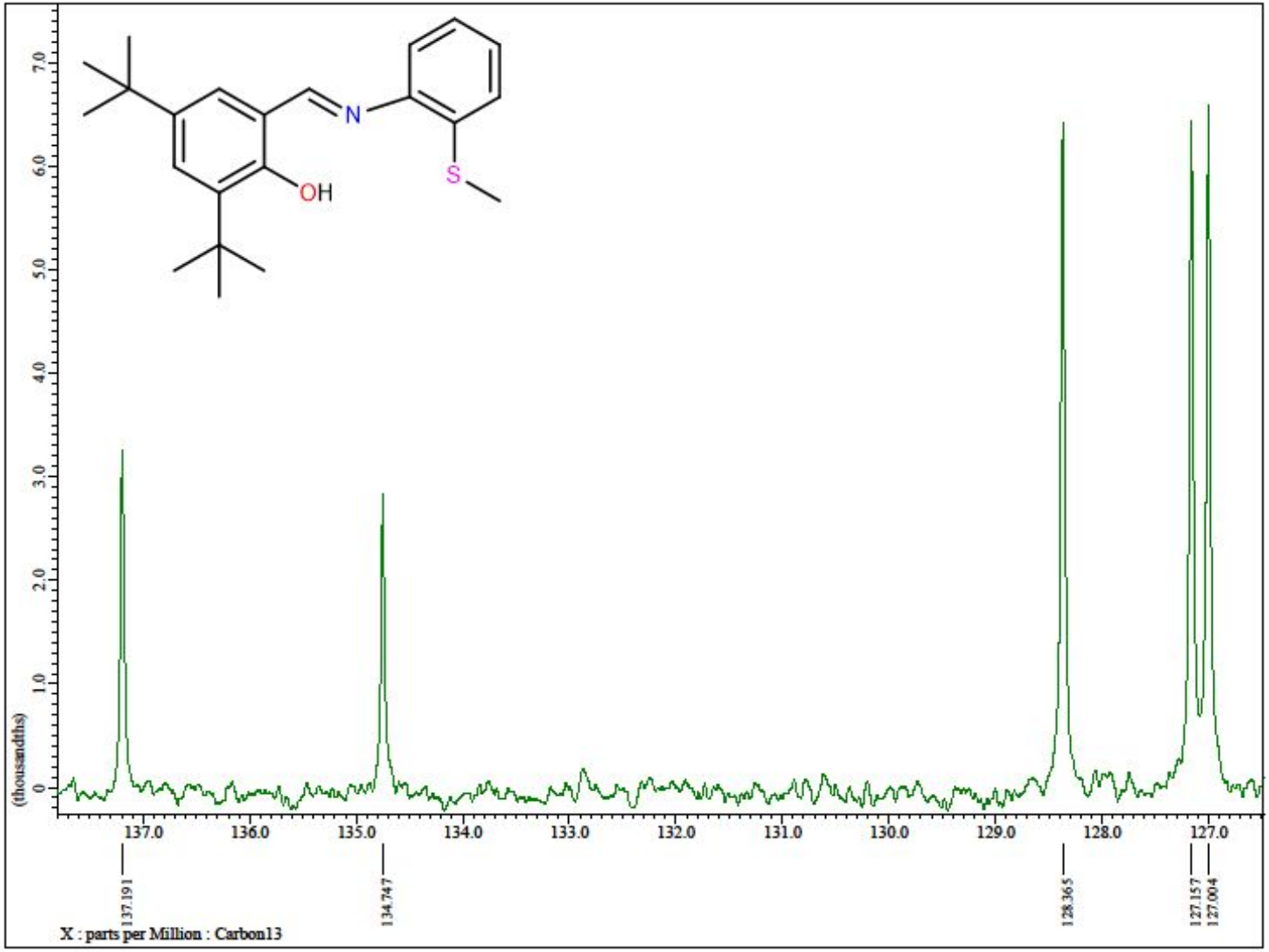

Fig. S53. $^{13}C\{^{1}H\}$ NMR ($CDCl_3$, 100.5 MHz) spectrum of **L6** in the aryl region.

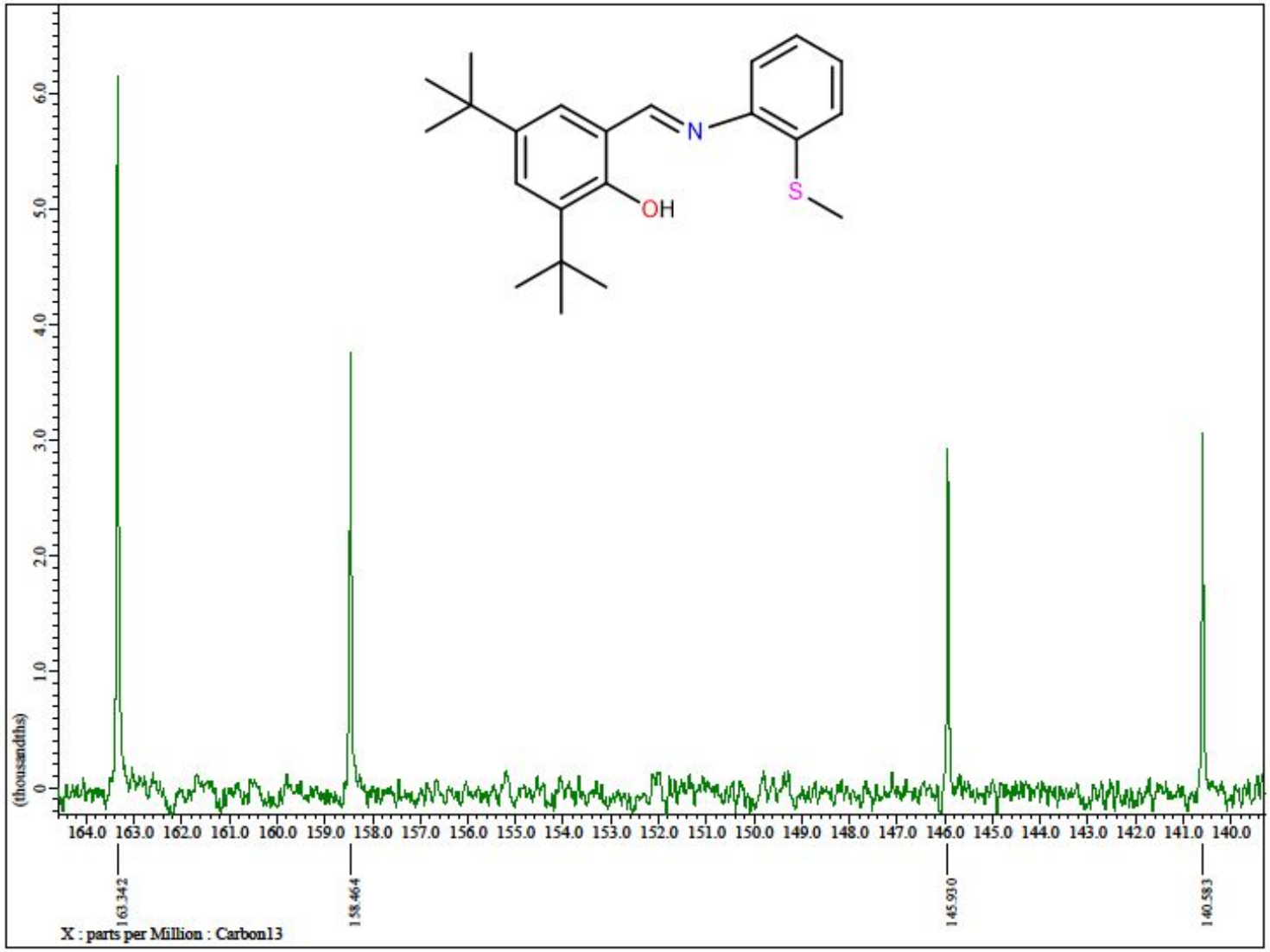

Fig. S54. $^{13}C\{^{1}H\}$ NMR ($CDCl_3$, 100.5 MHz) spectrum of **L6** in the aryl region.

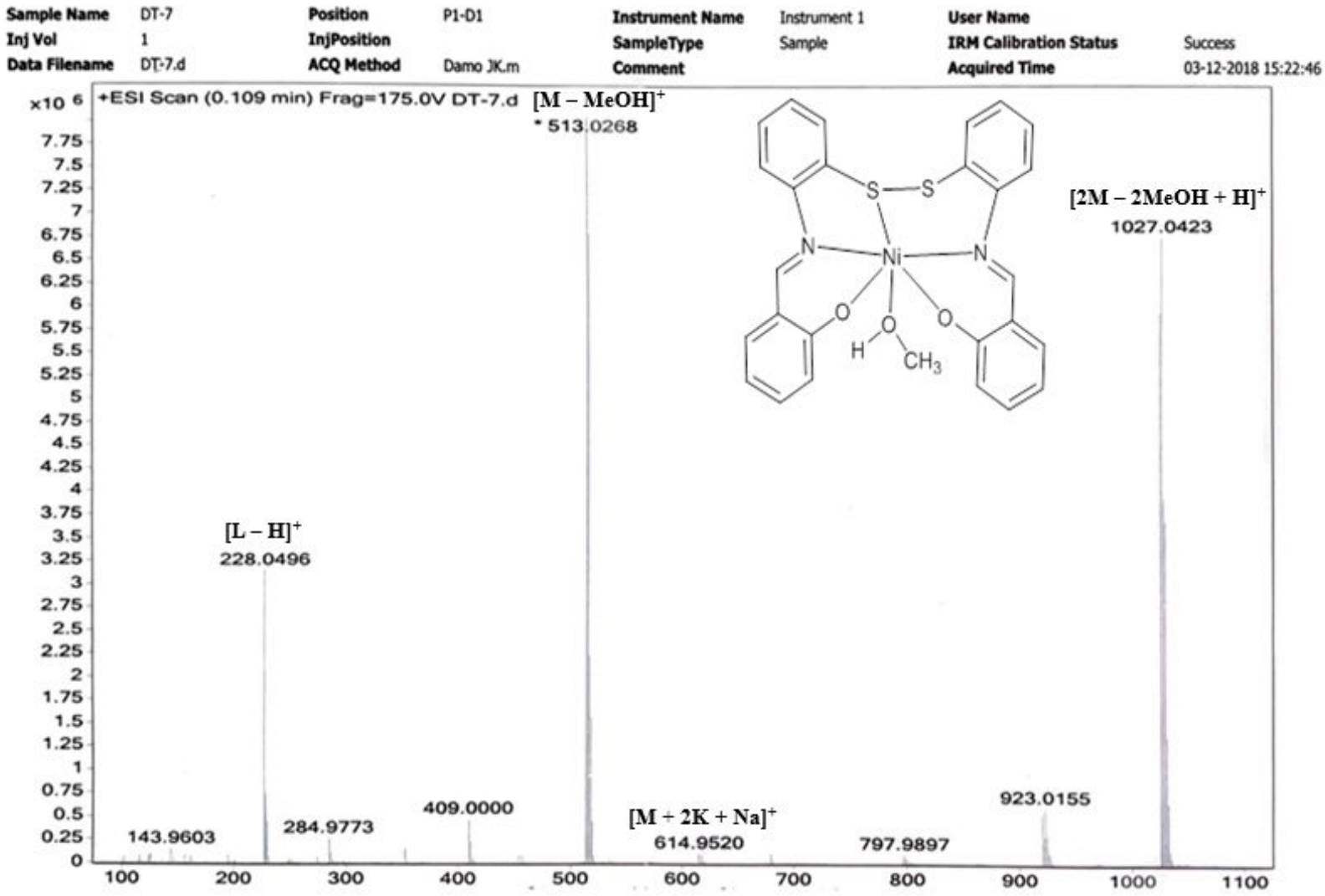

Fig. S55. ESI^{+}-MS spectrum of complex **1.**

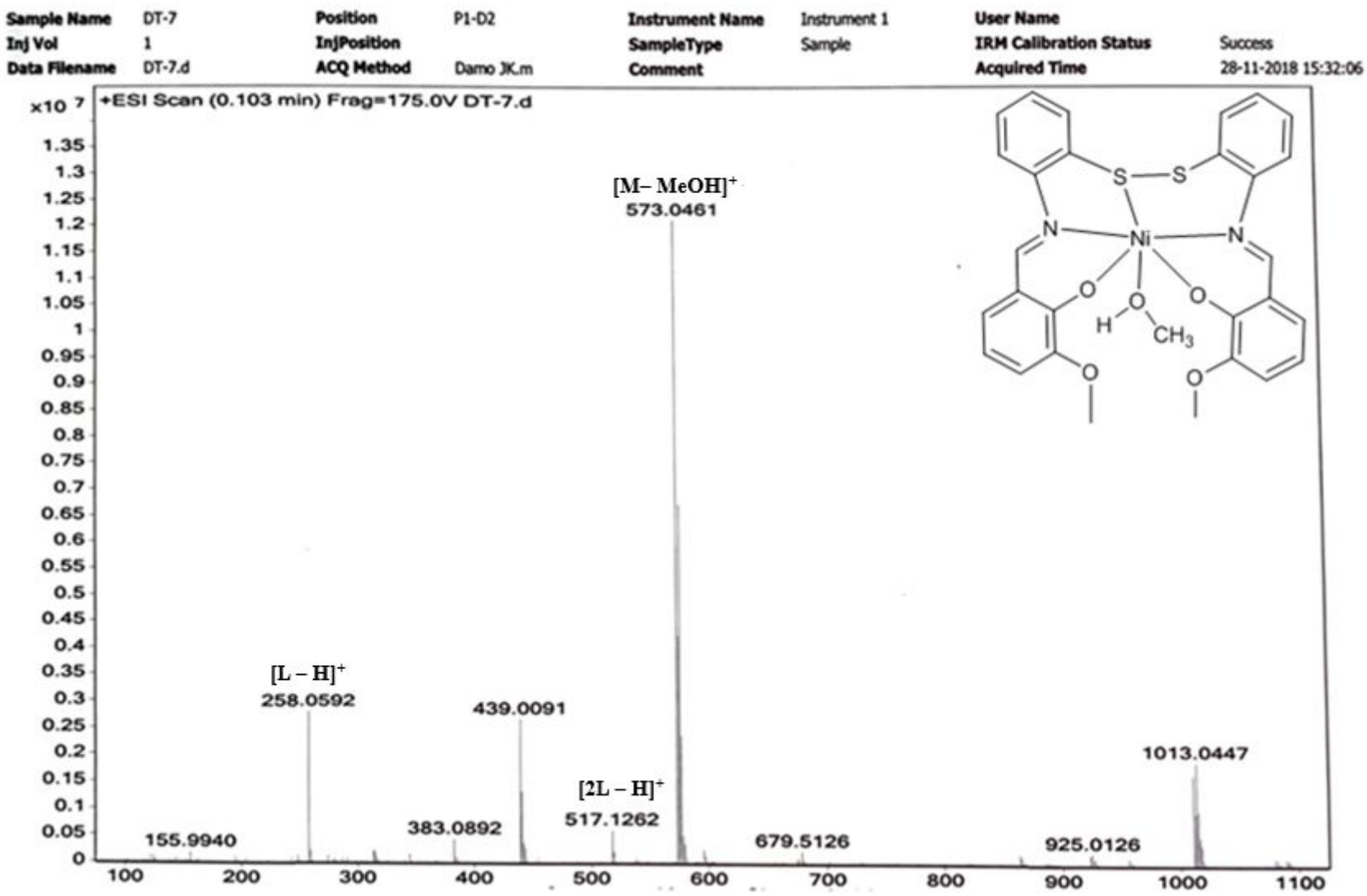

Fig. S56. ESI^{+}-MS spectrum of complex **2.**

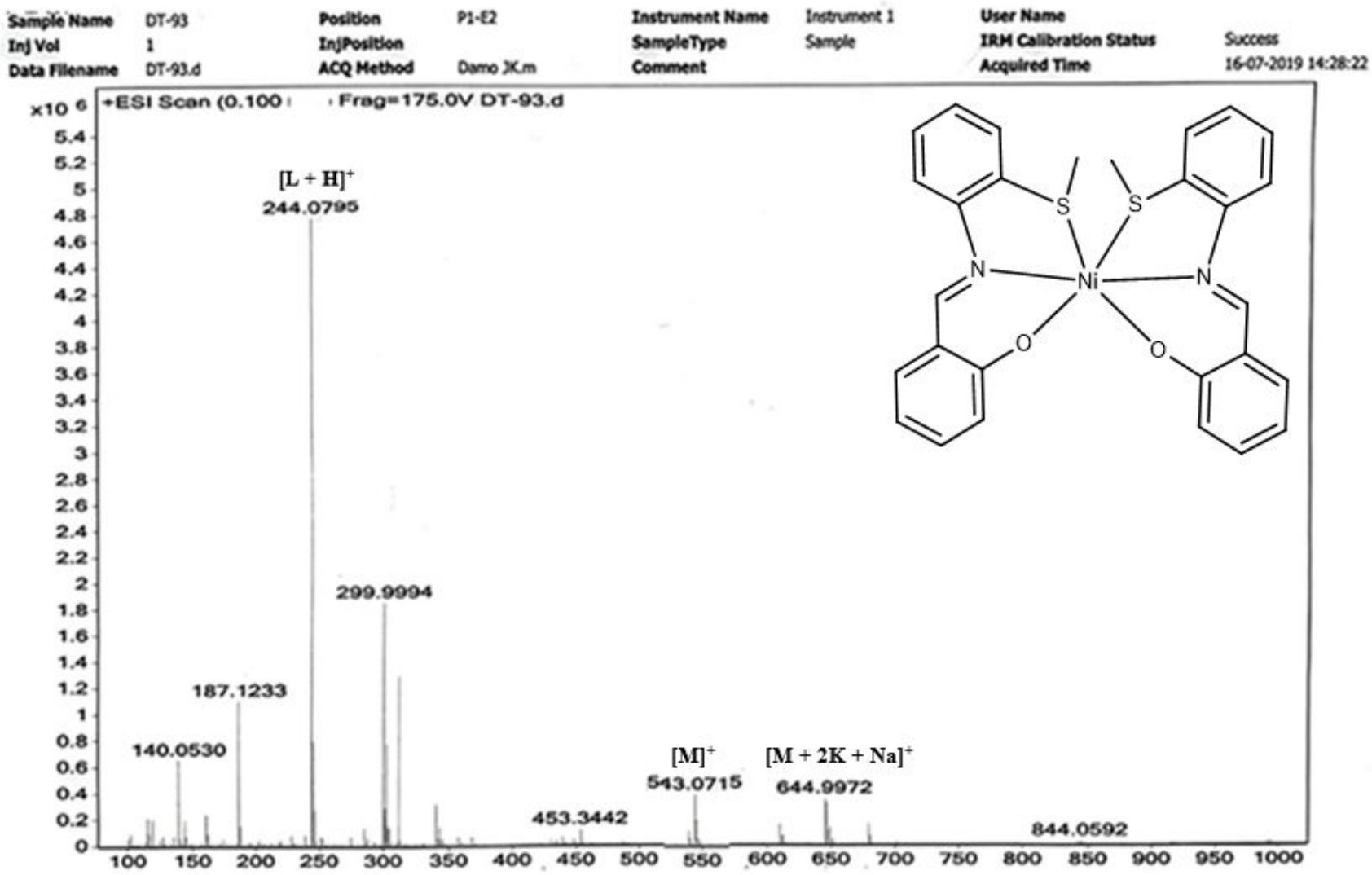

Fig. S57. ESI^{+}-MS spectrum of complex **4.**

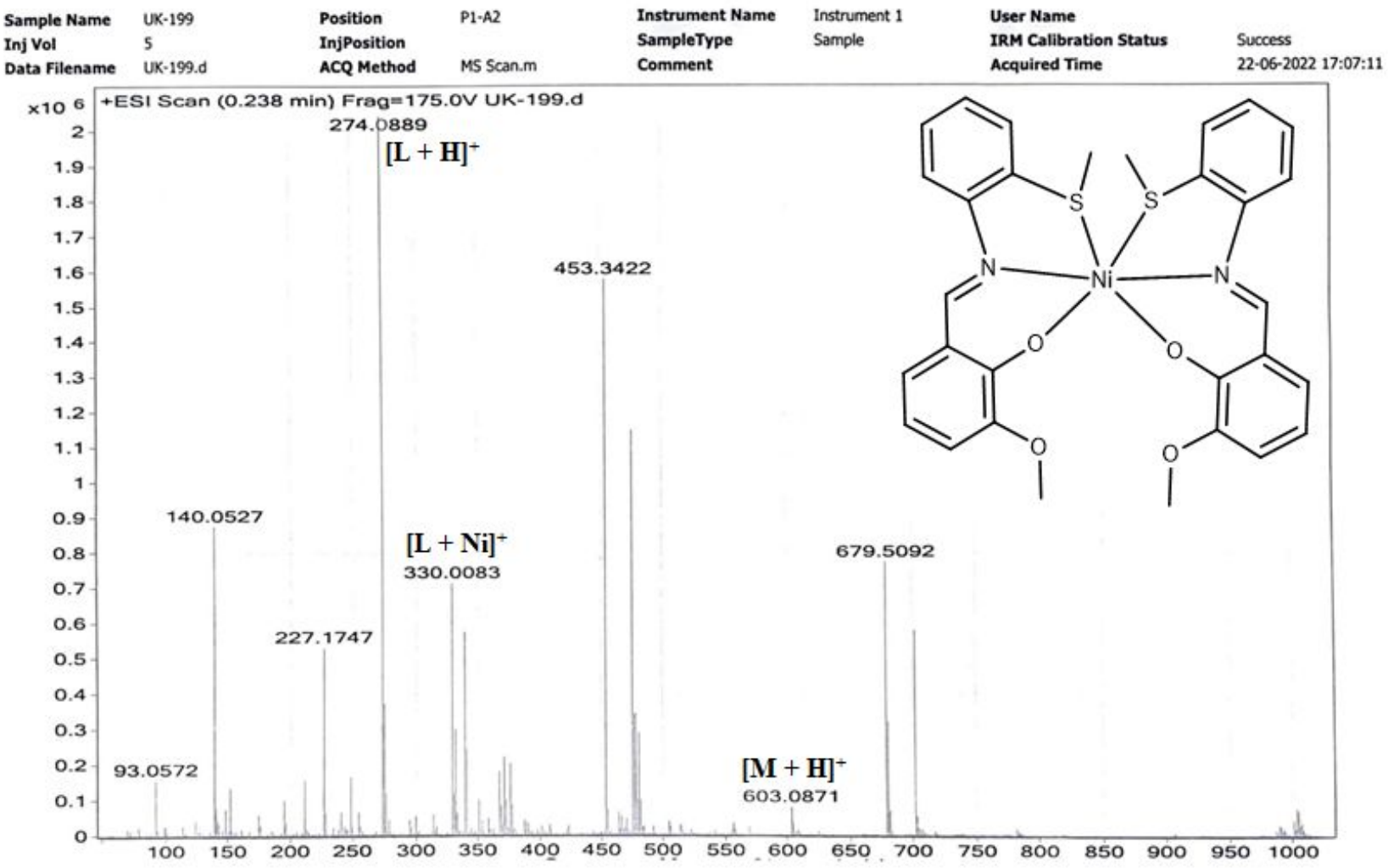

Fig. S58. ESI^{+}-MS spectrum of complex **5.**

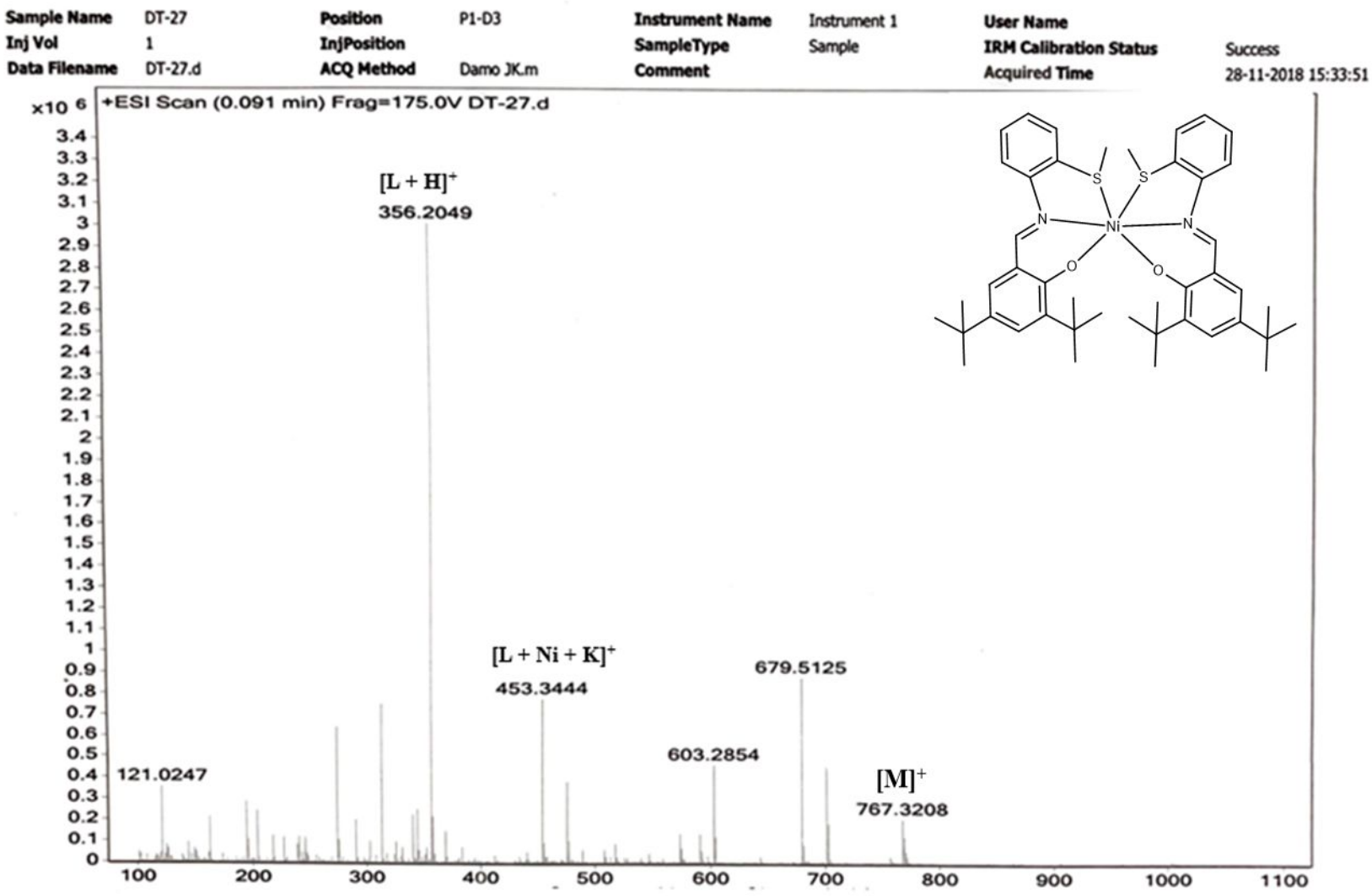

Fig. S59. ESI^{+}-MS spectrum of complex **6.**

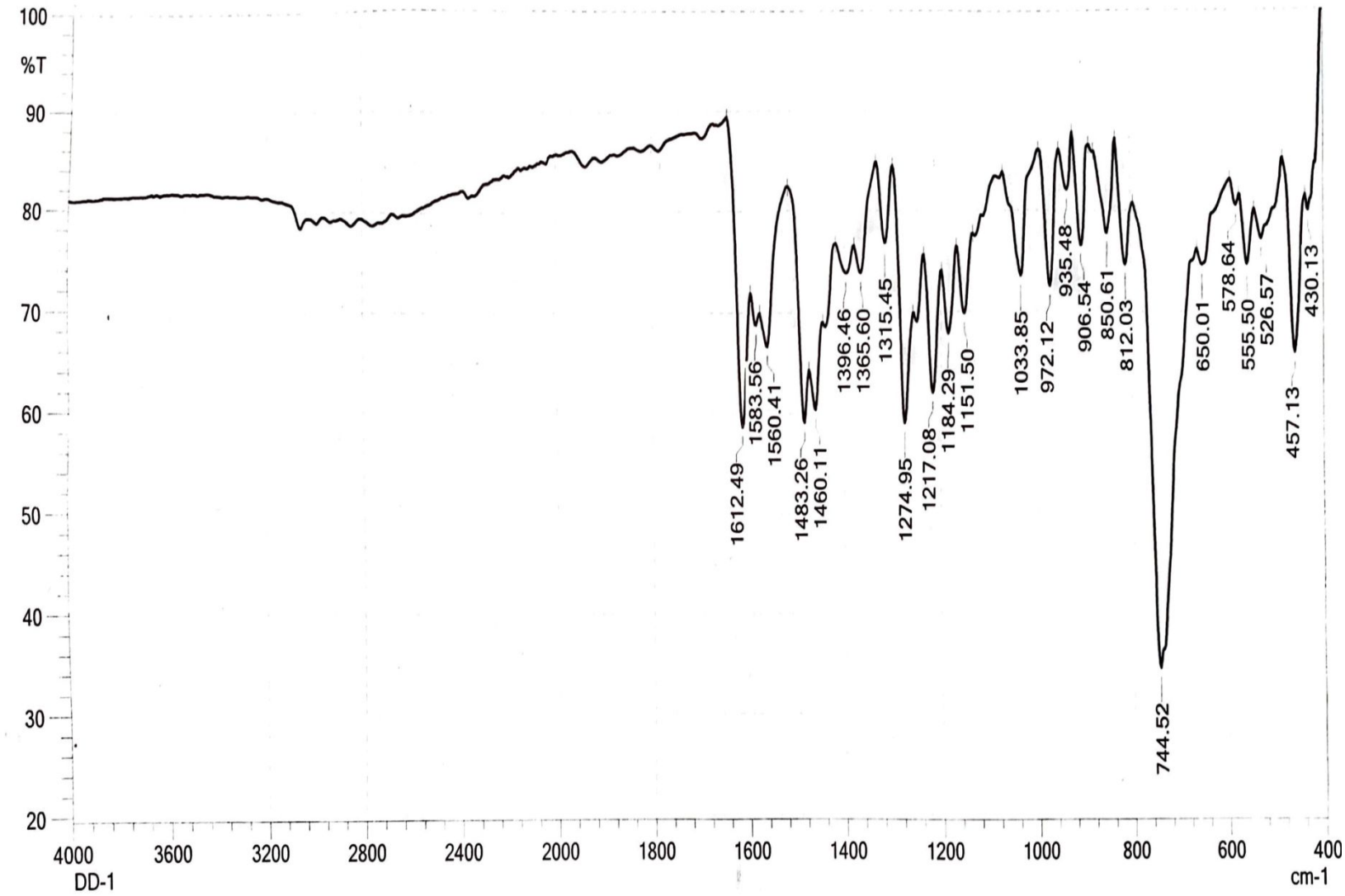

Fig. S60. FTIR spectra of **L1.**

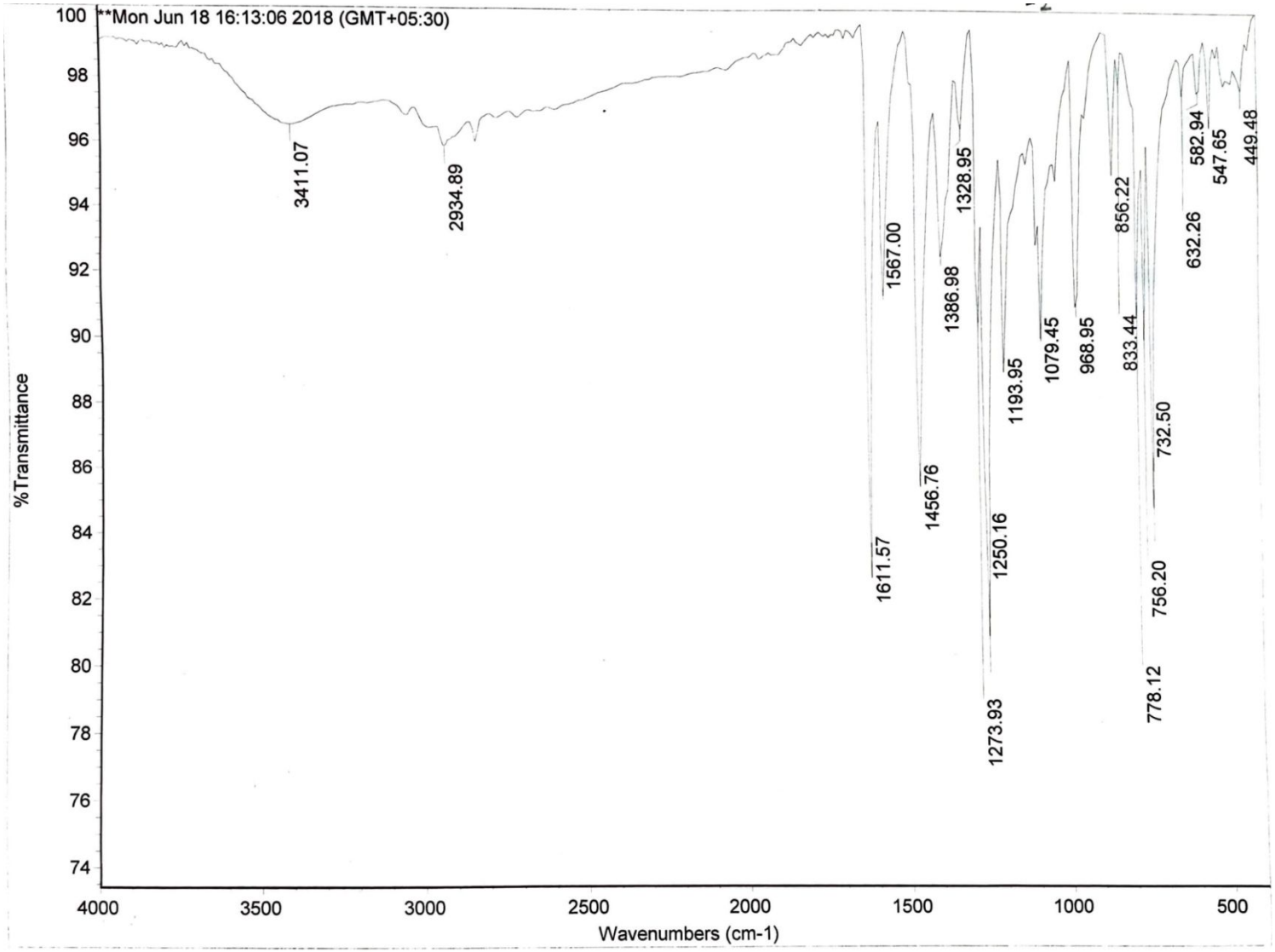

Fig. S61. FTIR spectra of **L2.**

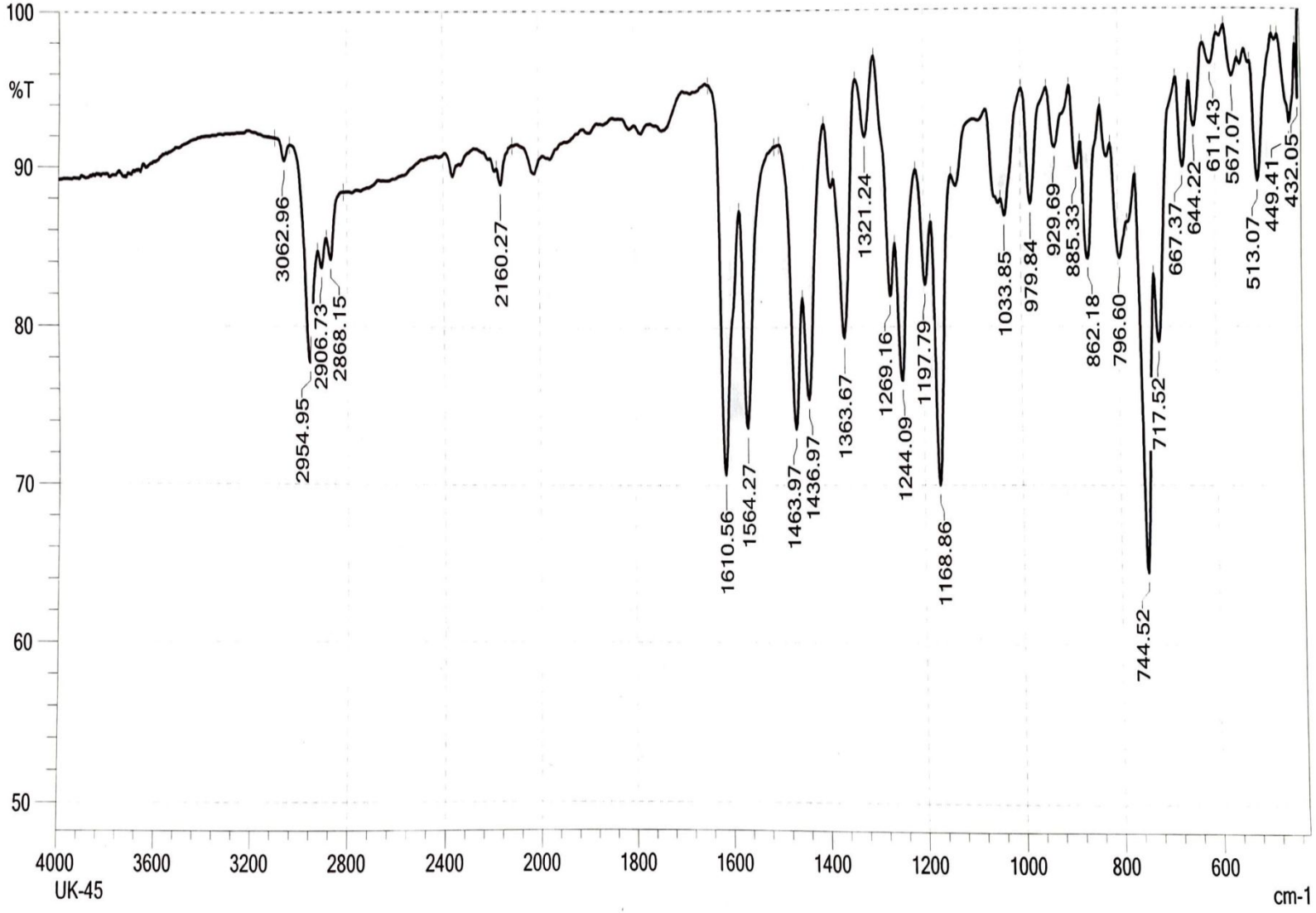

Fig. S62. FTIR spectra of **L3.**

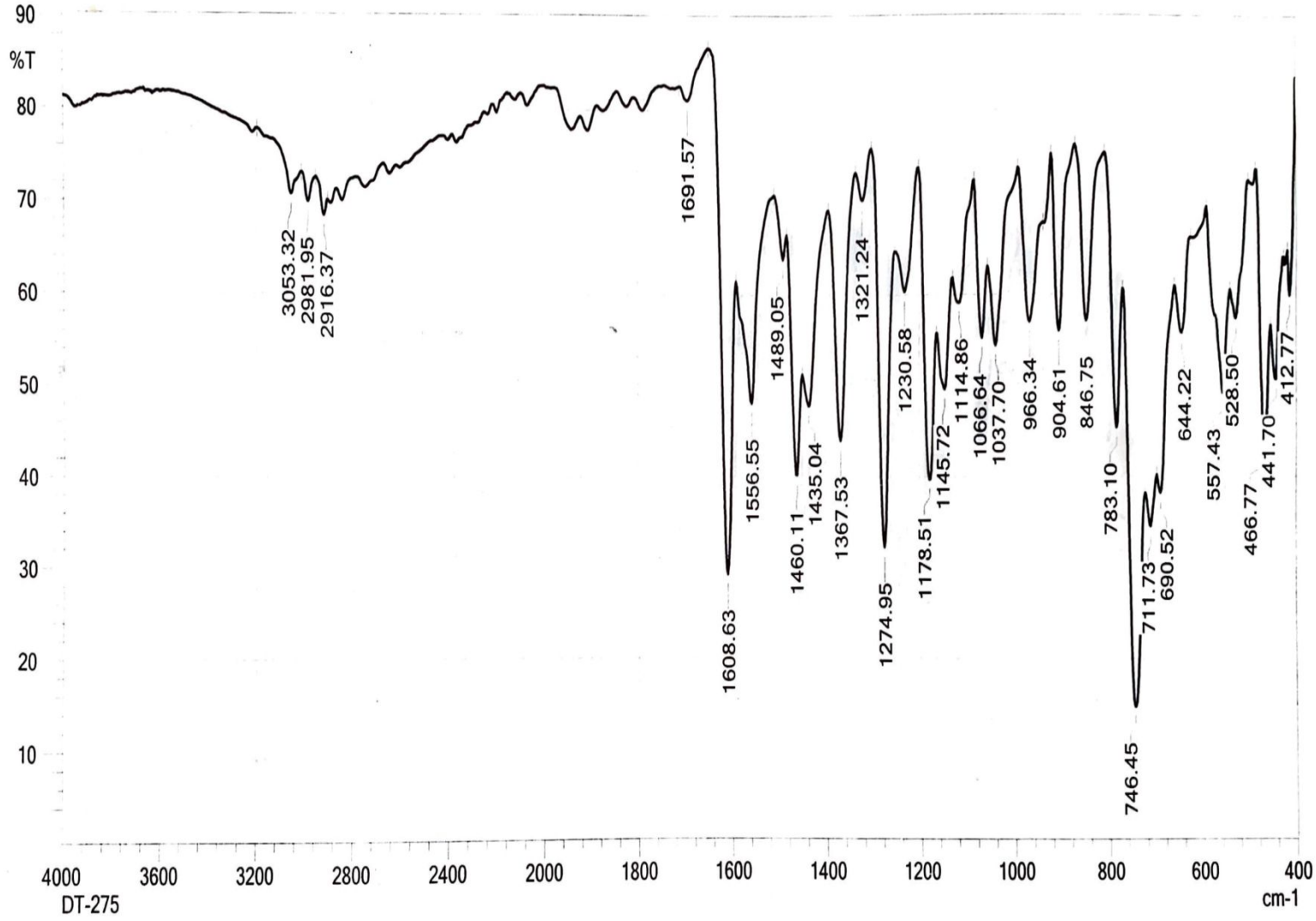

Fig. S63. FTIR spectra of **L4.**

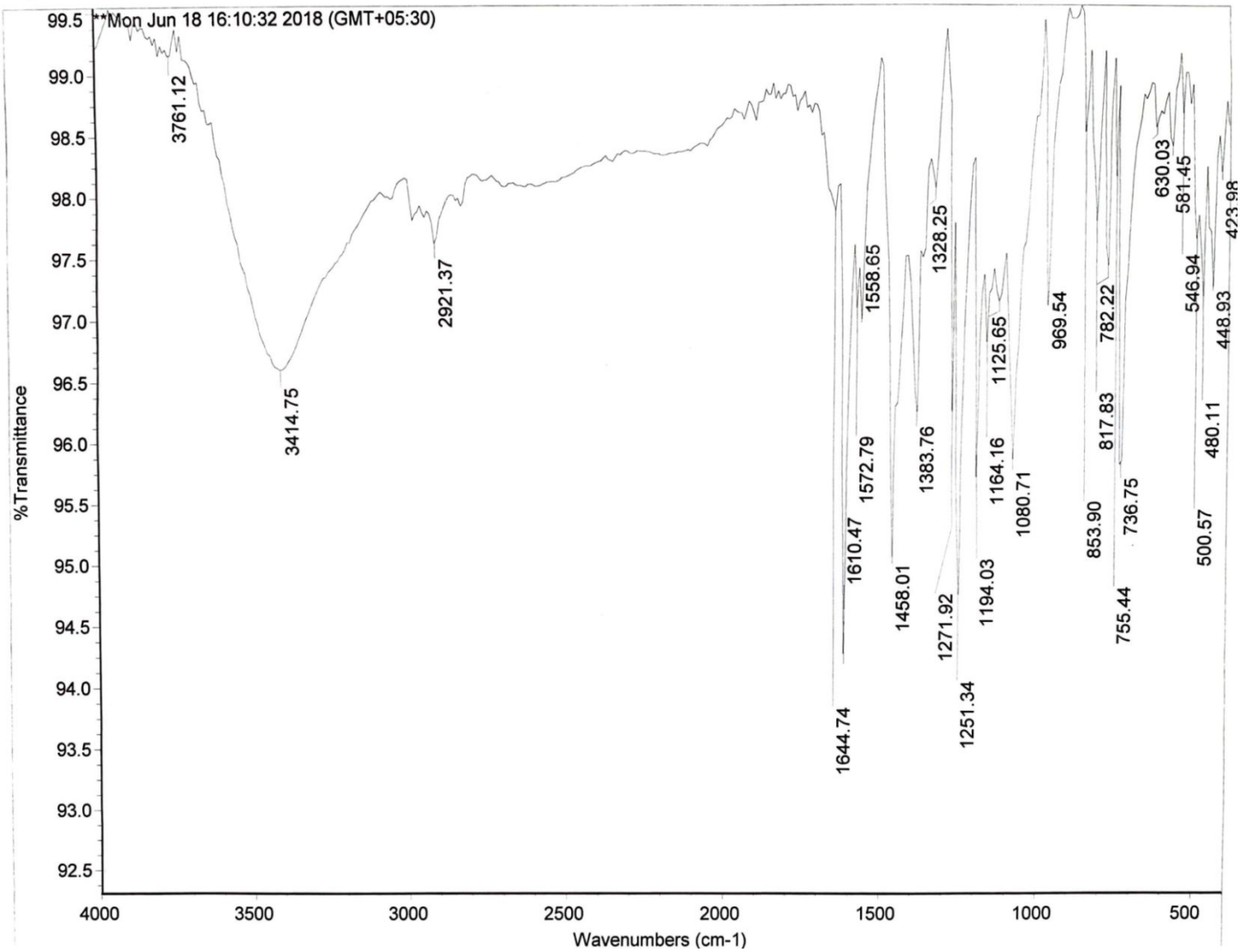

Fig. S64. FTIR spectra of **L5.**

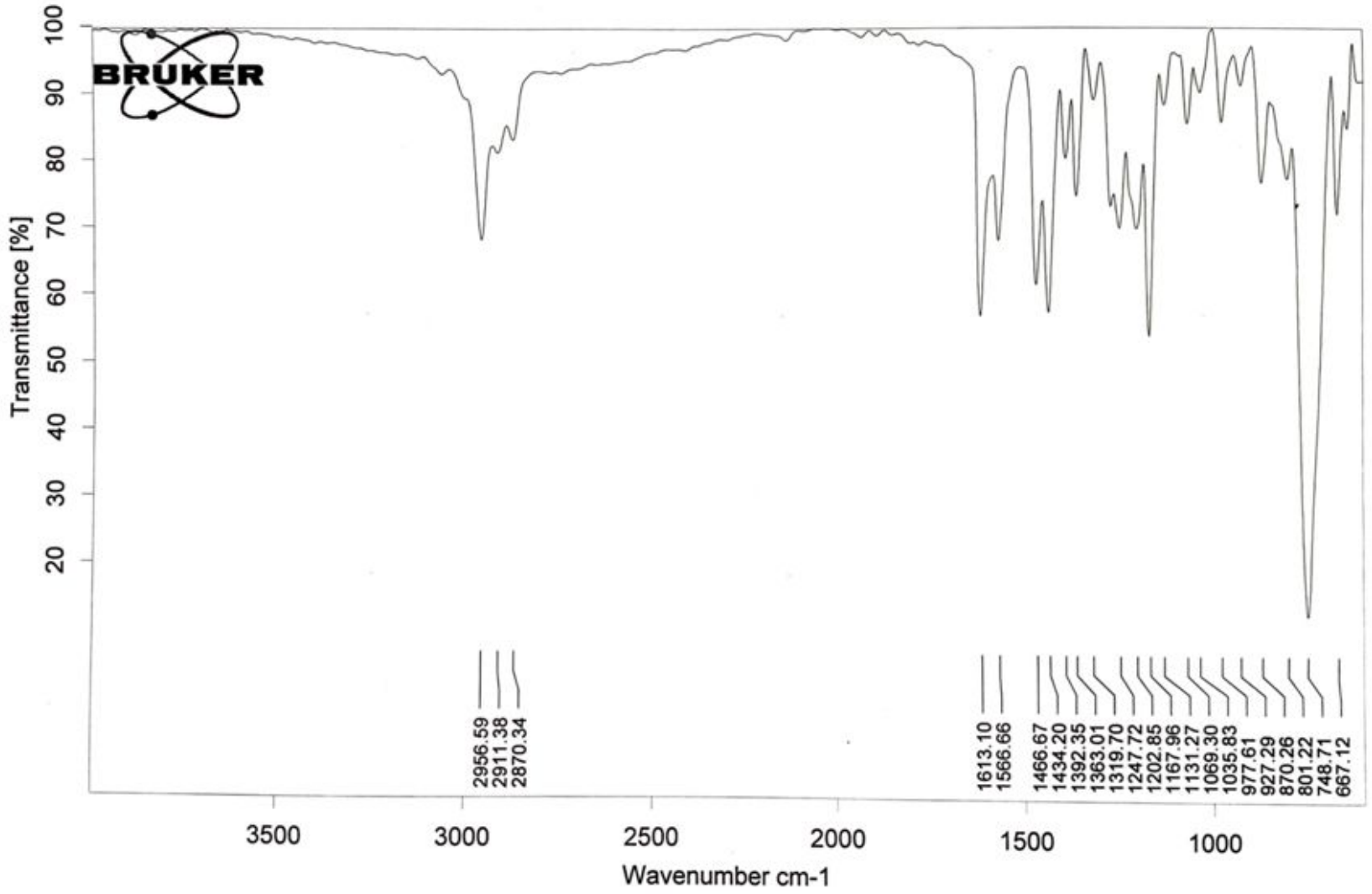

Fig. S65. FTIR spectra of **L6.**

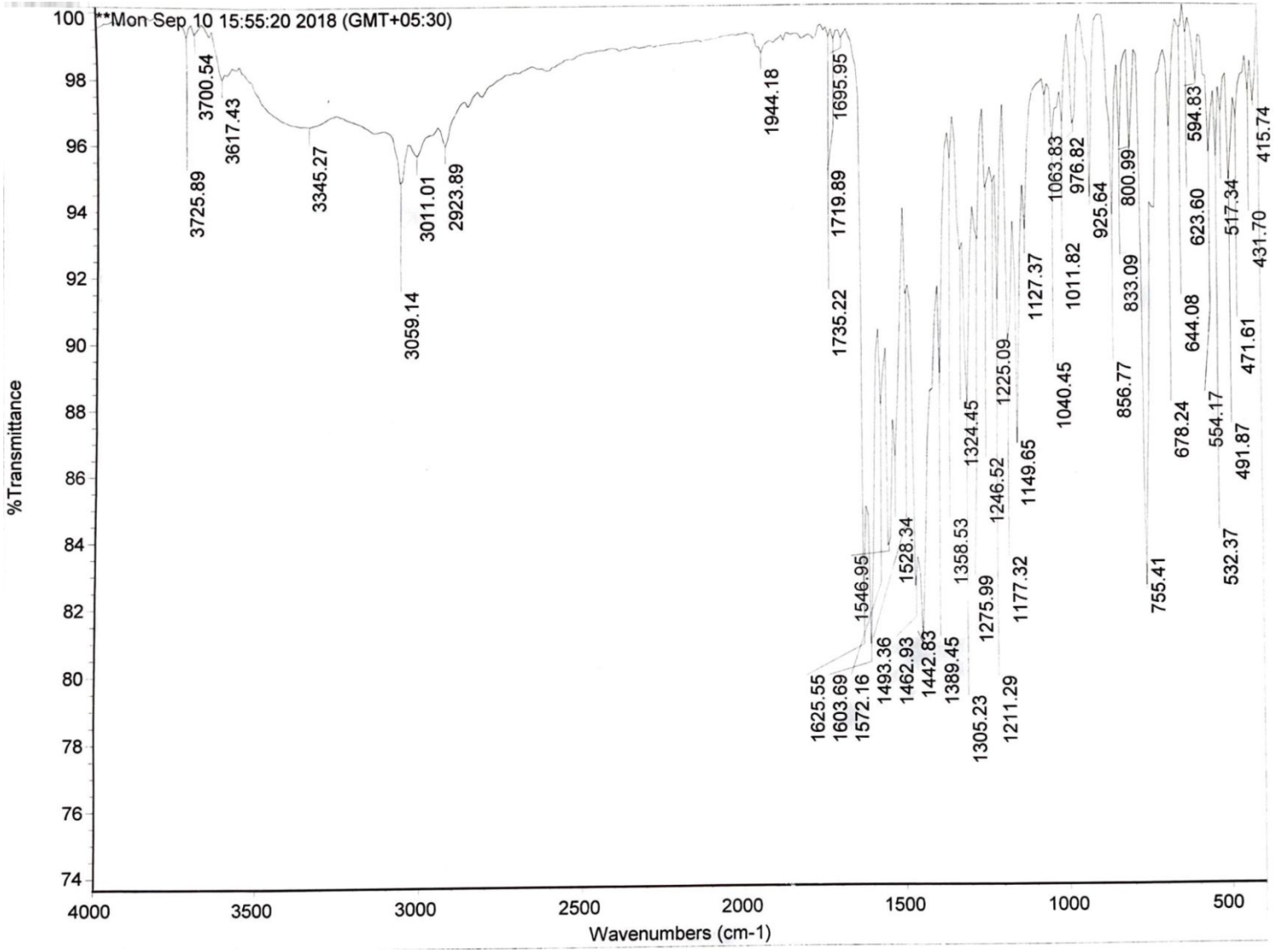

Fig. S66. FTIR spectra of complex **1.**

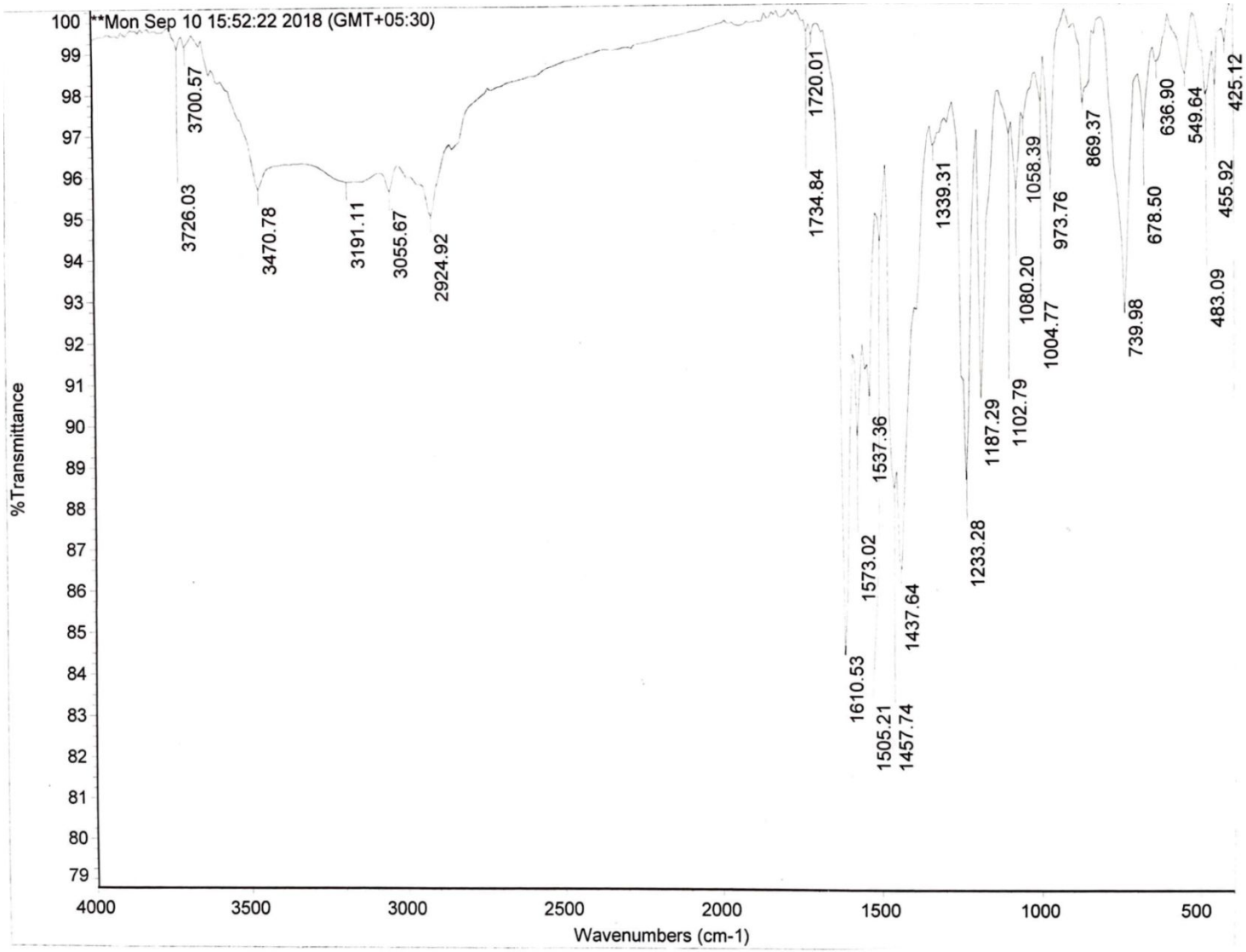

Fig. S67. FTIR spectra of complex **2.**

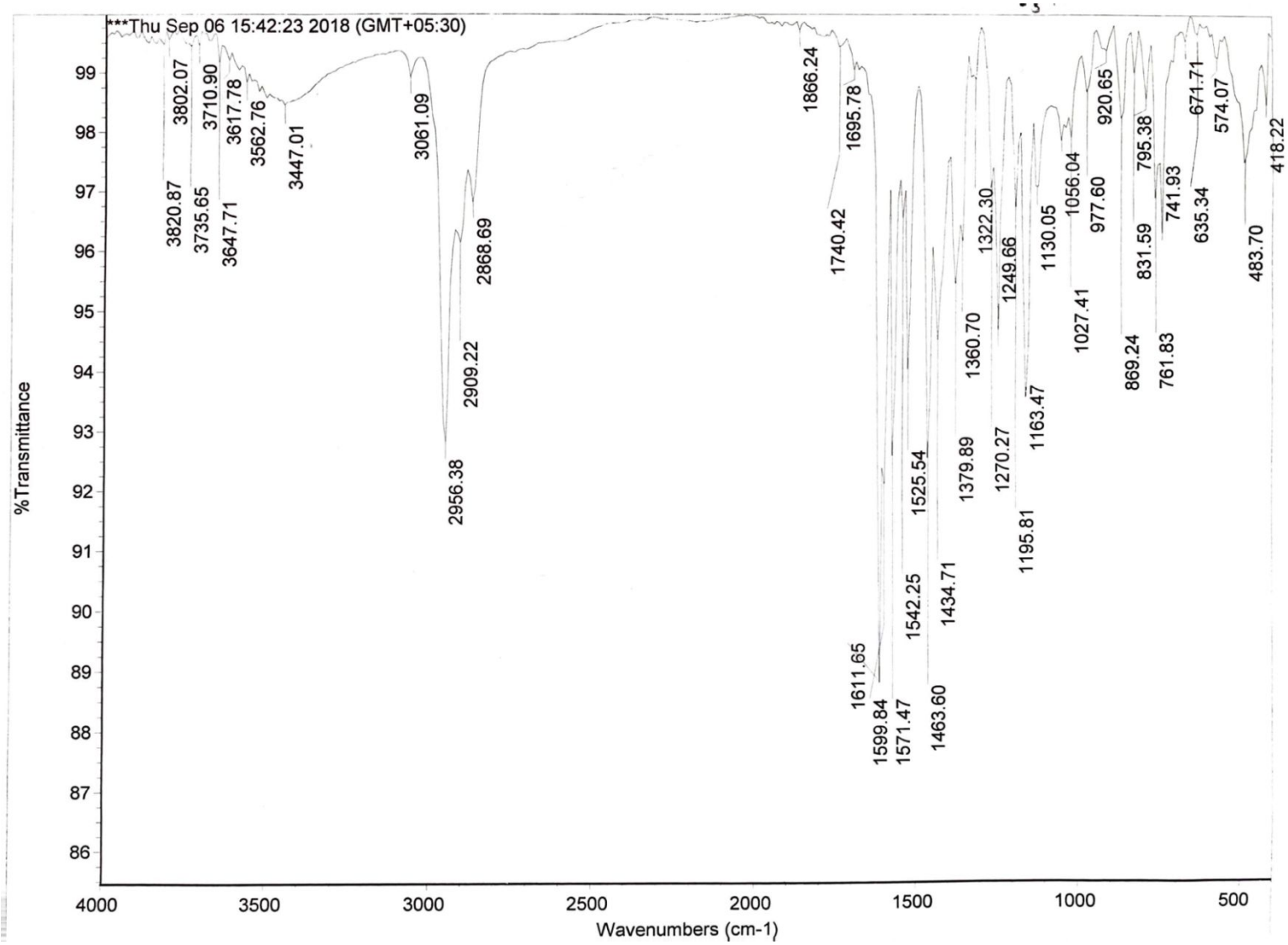

Fig. S68. FTIR spectra of complex **3.**

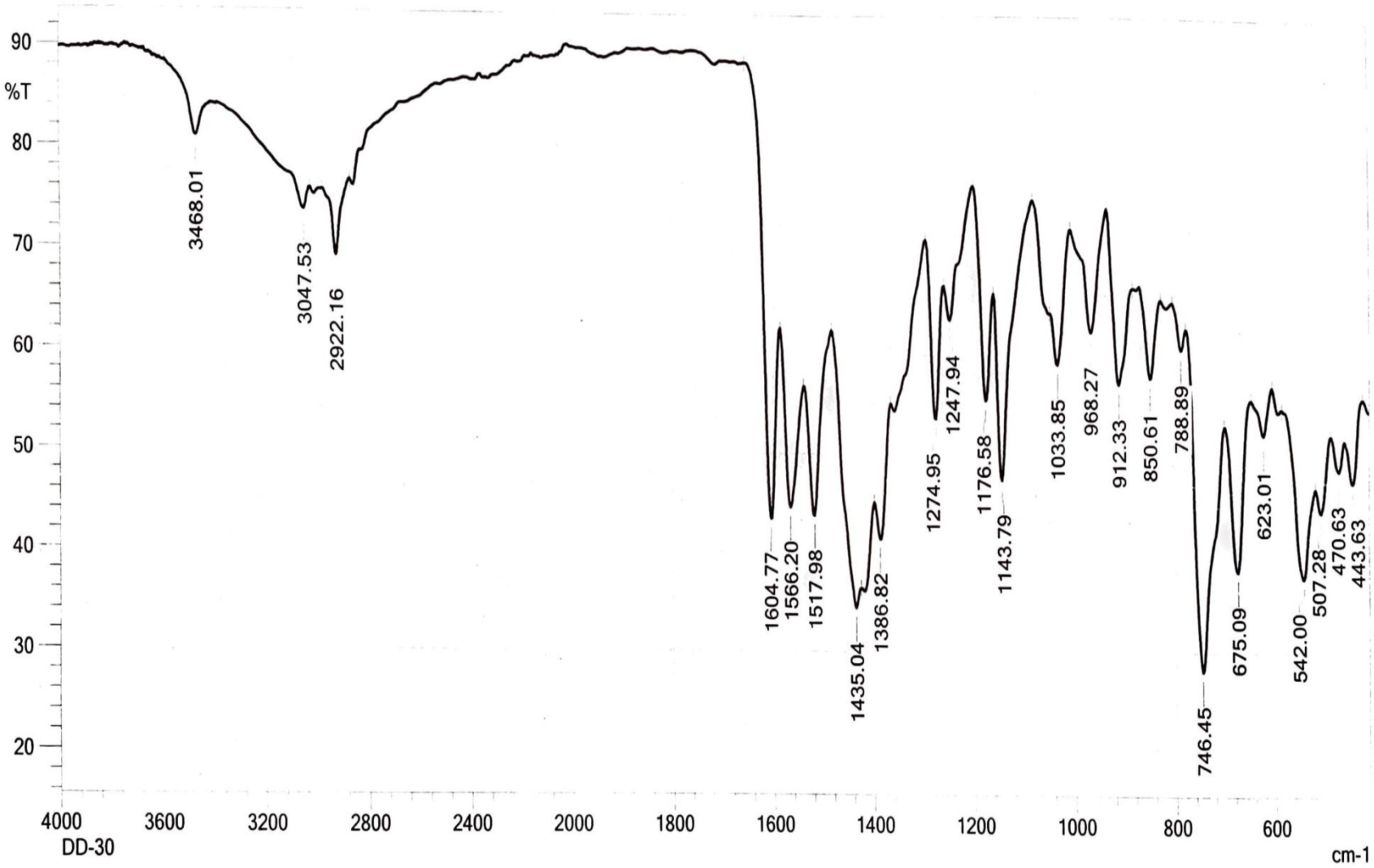

Fig. S69. FTIR spectra of complex **4.**

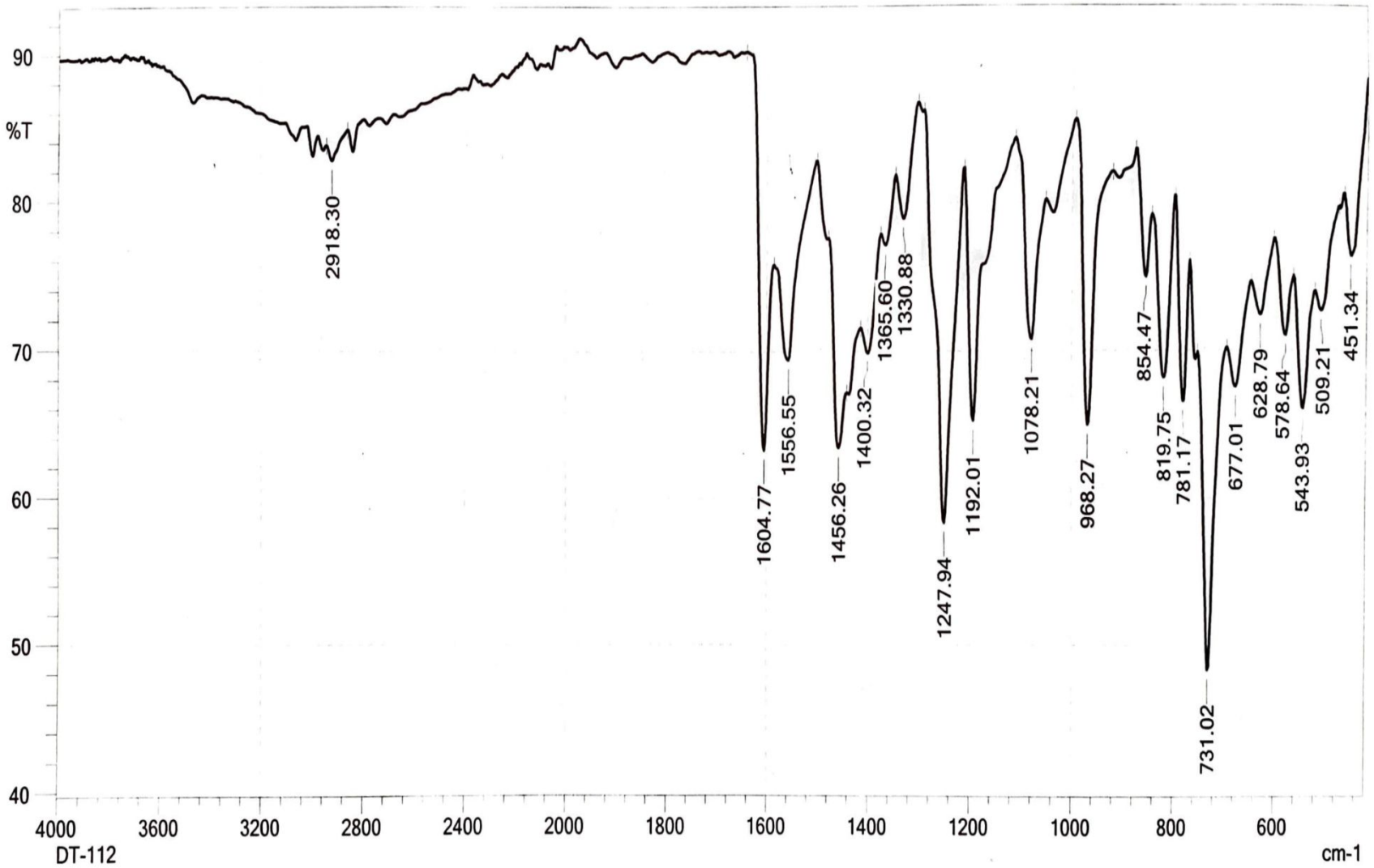

Fig. S70. FTIR spectra of complex **5.**

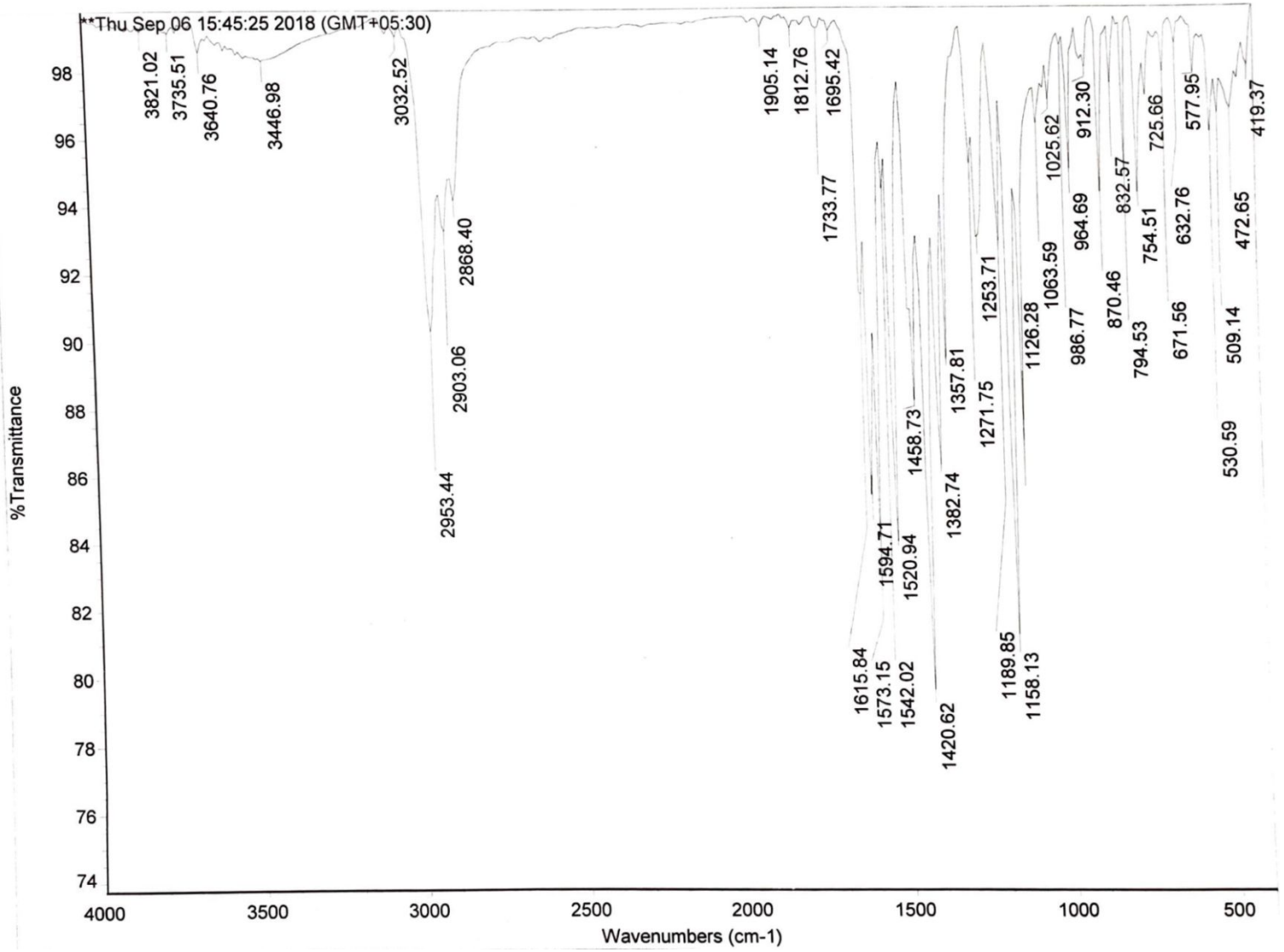

Fig. S71. FTIR spectra of complex **6.**

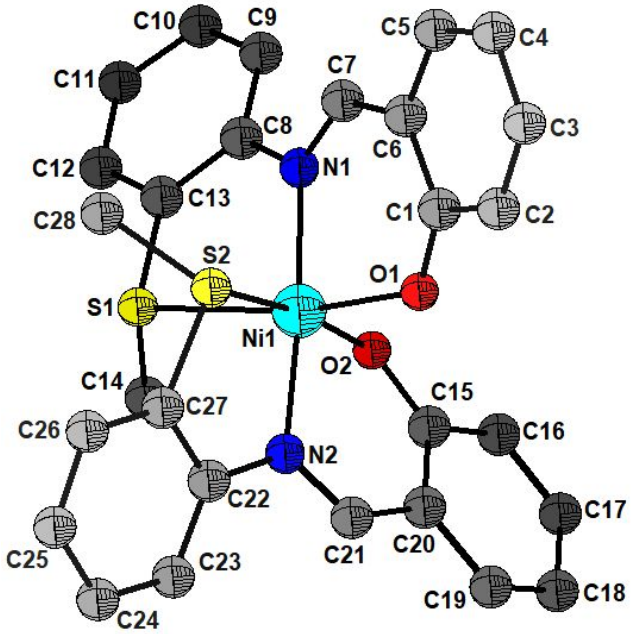

Fig. S72: Molecular structure of complex **4**.

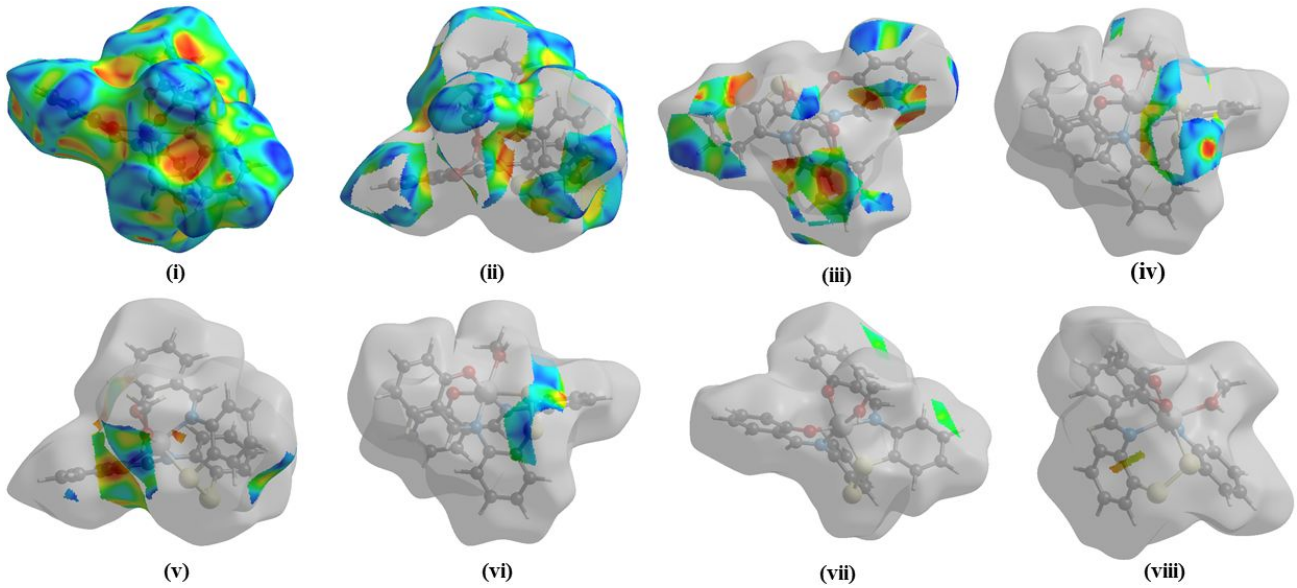

Fig. S73. Three-dimensional visualization of the colored regions depicts intermolecular interaction contribution in crystal packing of complex **1**, through (i) Complex **1**, (ii) H···H, (iii) C···H/H···C, (iv) S···H/H···S, (v) O···H/H···O, (vi) S···C/C···S, (vii) C···C, (viii) N···H/H···N.

Journal Pre-proof

On the Approximation of Dam-Break Problems Using a Fuzzified HR-TVD Scheme

Ruchika Lochab, Vivek Kumar

PII: S2215-0161(23)00008-0
DOI: https://doi.org/10.1016/j.mex.2023.102003
Reference: MEX 102003

To appear in: *MethodsX*

Please cite this article as: Ruchika Lochab, Vivek Kumar, On the Approximation of Dam-Break Problems Using a Fuzzified HR-TVD Scheme, *MethodsX* (2023), doi: https://doi.org/10.1016/j.mex.2023.102003

This is a PDF file of an article that has undergone enhancements after acceptance, such as the addition of a cover page and metadata, and formatting for readability, but it is not yet the definitive version of record. This version will undergo additional copyediting, typesetting and review before it is published in its final form, but we are providing this version to give early visibility of the article. Please note that, during the production process, errors may be discovered which could affect the content, and all legal disclaimers that apply to the journal pertain.

© 2023 Published by Elsevier B.V.
This is an open access article under the CC BY license (http://creativecommons.org/licenses/by/4.0/)

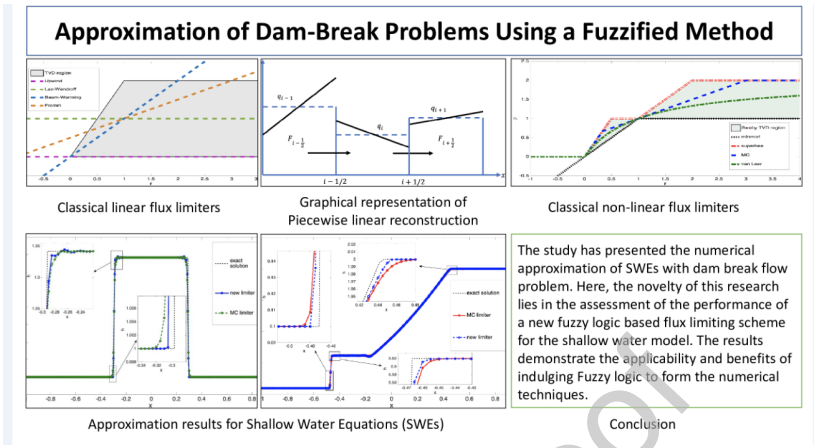

Journal Pre-proof

Journal Pre-proof

On the Approximation of Dam-Break Problems Using a Fuzzified HR-TVD Scheme[1]

Ruchika Lochab[1], Vivek Kumar*

Department of Applied Mathematics

Delhi Technological University, Shahbad Daulatpur, Main Bawana Road, Delhi-110042. India[1,]*

Abstract

The construction of the proposed second-order accurate scheme is based on the Monotonic Upstream Schemes for Conservation Laws (MUSCL) strategy. Using some strong notions from fuzzy logic, like fuzzy modifiers and fuzzy inference systems, the work offers a new avenue for optimizing the execution of classical flux-limiting algorithms. A numerical study has also been included to compare the new limiting scheme and the classical Monotonized Central (MC) scheme. The key themes of the research work are:

- Development of the background theory and augmented Riemann finite volume (FV) framework required to construct the new fuzzy logic-based limiter for the Shallow Water Equations (SWEs) over flat bottom topography.
- The proposed fuzzy flux limiting technique has been employed in a structured one-dimensional FV model to compute the SWEs.
- The idealized dam-break flows verify the new fuzzified High-Resolution (HR), Total Variation Diminishing (TVD) technique.

Keywords: shallow water equations, fuzzy modifiers, HR-TVD, Saint-Venant equations, dam-break, fuzzy logic.

*Vivek Kumar (Corresponding Author)

Email address: vivekkumar.ag@gmail.com (Delhi Technological University, Shahbad Daulatpur, Main Bawana Road, Delhi-110042. India)

[1]Research Fellow, Department of Applied Mathematics, Delhi Technological University.

Journal Pre-proof

Journal Pre-proof

1. Introduction

The SWEs are the partial differential equations (PDEs) exhibiting a hyperbolic nature. Such equations are frequently used in various applications such as earthquakes, ocean currents, floods, reservoirs flows, and many more [1, 2, 3, 4, 5, 6, 7]. The one-dimensional SWEs represent shallow water dam-break flows, a non-linear coupled system of hyperbolic PDEs [8, 9, 10]. The shallow water models have been used repeatedly in plenty of fields, and some frequently occurring examples are irrigation flows, drainage systems, floods, and tidal flows [11, 12]. In recent years significant efforts have been made to model one-dimensional open channel shallow water dam-break flow problems [8, 11, 13]. Quite a range of computational methods have been proposed and successfully applied to solve the SWEs [14, 15, 16]. The main idea is based upon the concept of solving a series of Riemann problems for the fluid at each time step to perform cell averaging. But, this becomes a tedious process, and it becomes impossible for some non-linear cases [9, 10, 17]. While LeVeque has certainly done great things for the numerical solution of hyperbolic PDEs, the idea of using Riemann solvers dates back to (Godunov, 1959) [18]. The Riemann solvers for solving the shallow water equations are indeed quite robust and mature [19, 20].

Dam-break events are related to major ecological problems triggered by the rapid release of reservoir-stored water. The actual wave structure observed experimentally varies in large parts of the wave profile, such as the negative and positive fronts. Three specific problems occur in the numerical simulation of the shallow water models for various wave propagation phenomena over real domains [21]. The first issue is the approximation of the fronts or abrupt waves of fluid that could be interpreted as a numerically propagating discontinuity [19, 22, 23]. The second issue stems from sudden alterations in bathymetry (the measurement of the depth of water in water bodies). Most simulation methods offer a practical approach to the flow as long as the bottom surface remains relatively smooth [3]. In addition, the third issue occurs when these systems are implemented to examine the propagation of the wavefront over a dry bed. Some challenges are to be tackled during the simulations of such a work, involving the dam-break problems; hence, the shallow water dam-break models are worth a vital

Journal Pre-proof

concern. In general, it is challenging to find solutions to these equations due to the hyperbolic behavior of the SWEs. These issues are robustly triggered by implementing some modern shock-capturing strategies to compute the shallow water dam-break flow systems.

The main interest in this work is to formulate the fuzzy logic-based numerical technique for the Shallow water system and its variants for flows over flat topography and cross-section using FV flux-limited methods [1, 24, 25]. The proposed fuzzy flux limiting technique has been employed in a structured one-dimensional FV model to compute the SWEs [24, 26, 27]. This work is leaned towards the computation of one dimensional SWEs using some robust concepts from the fuzzy logic theory. In the next sections, these objectives are systematically documented. The paper is now structured in the following manner.

- The mathematics of the flow model including the governing equations, discretization techniques, and the numerical approach has been mentioned in the Section 2.
- In the Section 3, the new FV based numerical technique with a brief discussion on fuzzy logic concepts has been discussed for a rectangular domain.
- After that, a numerical assessment is shown in the Section 4. For validation purpose, a comparison of the proposed limiter and the classic MC limiter has been presented here.
- The information about the notations used in this work is given in the Section 5.
- Furthermore, in the Section 7, the work has been concluded with several observations and the scope of future studies.

2. Numerical model

The Navier Stokes equations are employed to study the behavior of fluids. The behavior of a fluid in shallow areas is defined by these equations. Despite the strong assumptions used during approximations, the outcomes are comparable to reality, even

Journal Pre-proof

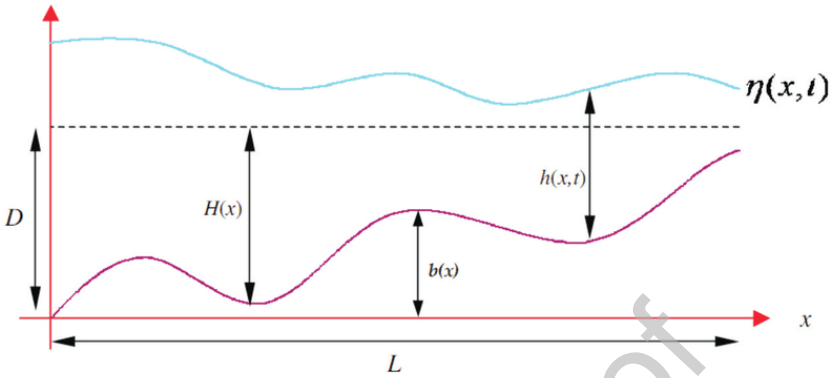

Figure 1: A graphical representation of shallow water model, here η is the manning's roughness coefficient [28].

in cases where many of these assumptions aren't really fulfilled. Among various solvable problems are sea currents, tidal flows, flow in channels, or propagation of shock waves. The one-dimensional version of these Navier-stokes equations leads to the SWEs under particular assumptions. But, despite considerable simplifications, the Navier Stokes equations have no analytical solution, even in one-dimensional SWEs. Thus, approximation methods are imposed to simulate such non-linear systems. The numerical model in this work is about the flow pattern formed due to the collapse of a dam, which can be expressed mathematically by the SWEs [13].

2.1. The Governing Equations

By assuming negligible vertical velocity, a constant horizontal velocity, and a constant density, the Navier-Stokes equations become the SWEs for an in-compressible fluid. The vertical velocity is thus ignored for the dam break situations. The horizontal velocity is considered constant across any vertical line between the base and the surface of the reservoir. (as shown in the Figure 1) By performing vertical integration to the Navier Stokes equations, the resultant are the SWEs. The velocity and gradients in the horizontal direction parallel to the dam also are overlooked in the dam break problems. Thus, in one space dimension, the SWEs [17] in the conservative form for

Journal Pre-proof

the rectangular domain of unit width, can be presented via the following equation:

$$q_t + f(q)_x = s, \tag{2.1}$$

where q, f, and s vectors are as follows:

$$q = \begin{pmatrix} h \\ hu \end{pmatrix}, f(q) = \begin{pmatrix} hu \\ hu^2 + 1/2gh^2\alpha \end{pmatrix}, s(q) = \begin{pmatrix} 0 \\ -ghb_x \end{pmatrix}.$$

Here, $h(x,t)$ represents the height of the water, $u(x,t)$ is the fluid velocity, g is the notation for gravitational constant and the function of bottom topography is represented by $b(x)$. As, this research is mainly concentrated towards hyperbolic conservation laws, hence the function $b(x)$ has been taken as zero. So, the Equation 2.1 becomes:

$$\partial_t \begin{pmatrix} h \\ hu \end{pmatrix} + \partial_x \begin{pmatrix} hu \\ hu^2 + \frac{1}{2}gh^2 \end{pmatrix} = \begin{pmatrix} 0 \\ 0 \end{pmatrix}. \tag{2.2}$$

The FV paradigm has been chosen in this study because it avoids any global alterations in the conserved components, ensuring that the entire scheme is conservative. As shown in the subsequent sections, both spatial and time discretizations are handled in a higher-order accurate manner.

2.2. Discretization technique

For the spatial discretization, the aforementioned three techniques, namely the FDMs, FEMs, and FVMs, could be used for the shallow water dam-break numerical simulations [29, 30]. The Finite-Difference Approach is the oldest, but, possibly because of its lack of versatility from the geometric point of view, its popularity has steadily declined. For this work, the FV formulation is employed since the development of numerical algorithms in the FV frameworks needs less computational work also these are suitable for complex geometries, both structured and unstructured [31, 32, 33].

2.3. Numerical approach based on the FV framework

A spatial reconstruction, called the MUSCL scheme, has been used for achieving high order accuracy in space. To formulate the FV framework, the key task is the discretization of the spatial domain into smaller nodes $[x_{i-1/2}, x_{i+1/2}]$, having a uniform

Journal Pre-proof

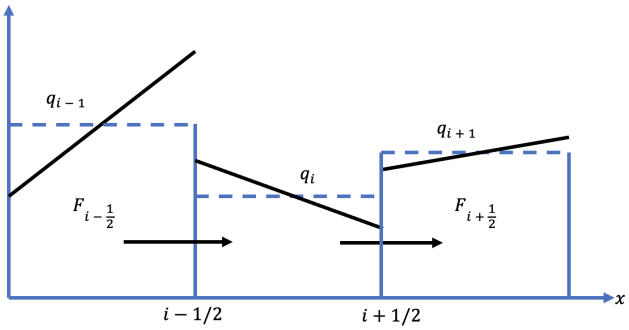

Figure 2: A sketch demonstrating the piecewise linear reconstruction while performing the FV approximation.

length Δx in space component, hence $x_i = \Delta x(i + 1/2)$. In same manner, the time interval is discretized into sub divisions $[t^n, t^{n+1}]$ with a same time step of length Δt. Thus, $t^n = (\Delta t)n$. $[x_{i-1/2}, x_{i+1/2}]$ represents the i^{th} computational volume, where $x_i = (i + 1/2)\Delta x$ is the midpoint of this cell. The initial fluid interface pattern and rate of the fluid flow should be defined and followed along-with the domain of the channel for the approximation of unsteady flow systems before the beginning of the computational process.

An approximation of the non-linear hyperbolic conservation laws, presented in the Subsection 2.1 requires a FV Godunov method of upwind-type. The FV solutions of the Equation 2.2 for capturing the shocks by implementing the Godunov's upwind technique, and some robust flux limiting schemes, lead to accurate simulation results of the considered shallow water dam break systems [3, 18, 34]. The integral form of the Equation 2.1 over a uniform mesh in the x-t plane is:

$$\int_t^{t+\Delta t} \int_{x_{i-1/2}}^{x_{i+1/2}} \frac{\partial \mathbf{q}}{\partial t} \, \mathrm{d}x \, \mathrm{d}t + \left(\int_t^{t+\Delta t} \mathbf{f} \mathrm{d}t \right)_{i+1/2} - \left(\int_t^{t+\Delta t} \mathbf{f} \mathrm{d}t \right)_{i-1/2} = \int_t^{t+\Delta t} \int_{x_{i-1/2}}^{x_{i+1/2}} \mathbf{s} \mathrm{d}x \, \mathrm{d}t \tag{2.3}$$

after removing the source term, for hyperbolic case it is:

$$\int_t^{t+\Delta t} \int_{x_{i-1/2}}^{x_{i+1/2}} \frac{\partial \mathbf{q}}{\partial t} \, \mathrm{d}x \, \mathrm{d}t + \left(\int_t^{t+\Delta t} \mathbf{f} \mathrm{d}t \right)_{i+1/2} - \left(\int_t^{t+\Delta t} \mathbf{f} \mathrm{d}t \right)_{i-1/2} = 0. \tag{2.4}$$

To solve the above equation, the FV approach is used, for a uniform mesh with rectangular grids in the cartesian plane, a conservative form used to update the vector q

Journal Pre-proof

corresponding to the Equation 2.2 is written as:

$$q_i^{n+1} = q_i^n - \frac{\Delta t}{\Delta x}\Big(F_{i+1/2} - F_{i-1/2}\Big), \tag{2.5}$$

where

$$q_i^n \approx \frac{1}{\Delta x}\int_{x_{i-1/2}}^{x_{i+1/2}} q(x, t^n)dx \tag{2.6}$$

is the cell average corresponding to the spatial components, and $F_{i\pm1/2}$ are the computational flux functions, expressed as the cell averages corresponding to the time component in the form written as:

$$F_{i+1/2} \approx \frac{1}{\Delta t}\int_{t^n}^{t^{n+1}} f(q(x_{i+1/2}, t))dt. \tag{2.7}$$

The treatment phase starts at time level T with the cell-averaged values of conserved variables, q_i^n. The important task in approximating such conservation laws is the proper selection of the numerical flux presented in the Equation 2.7. The numerical flux needs an evaluation with the help of the cell averages, i.e.,

$$F_{i+1/2} = F_{i+1/2}(q_i, q_{i+1}). \tag{2.8}$$

On a generalized note, the sort of the construction strategies discussed above demands the solutions of various Riemann problems at each cell interface. Therefore, a comparatively less complex approach is used such as the high resolution TVD approach.

2.3.1. Flux limiting High Resolution TVD schemes

A piece-wise linear reconstruction is performed inside each cell for second-order space accuracy (Figure 2). To avoid spurious oscillations near discontinuities, linear slopes originating from the reconstructed solution should be constrained. It is possible to boost spatial accuracy to second-order by applying the monotone upwind centered schemes for conservation laws (MUSCL) [32], which requires a linear extrapolation, now the numerical flux function is:

$$F_{i+1/2} = F_{i+1/2}(q^l_{i+1/2}, q^r_{i+1/2}), \tag{2.9}$$

where $q^l_{i+1/2}$ is a resultant of the linear extrapolation of q_i and q_{i-1} to the left-side of the computational cell $x_{i+1/2}$ (as shown in the Figure 2), while $q^r_{i+1/2}$ is formed by

Journal Pre-proof

linearly extrapolating q_{i+1} and q_{i+2} to the right-side of the computational cell $x_{i+1/2}$. But as the process of extrapolation leads to spurious profiles near a shock, because a TVD method is not yielded out of some simple extrapolation process. Hence, the slope-limiting methods are used with slopes denoted as $s^-(q_i)$ and $s^+(q_{i+1})$. The associated slope at an extremum is placed equal to zero, i.e. first-order. The following extrapolated values are used for the slope limited MUSCL methodology with the minimum-modulus limiter:

$$q^l_{i+1/2} = q_i + \frac{\Delta x}{2}\text{minmod}(s^-(q_i), s^+(q_i)), \tag{2.10}$$

$$q^r_{i+1/2} = q_{i+1} - \frac{\Delta x}{2}\text{minmod}(s^-(q_{i+1}), s^+(q_{i+1})), \tag{2.11}$$

where the minmod (short for minimum-modulus) operator is defined as:

$$\text{minmod}(\alpha, \beta) = \begin{cases} \alpha, & |\alpha| \leq |\beta| \text{ and } \alpha\beta > 0 \\ \beta, & |\beta| \leq |\alpha| \text{ and } \alpha\beta > 0 \\ 0, & \alpha\beta \leq 0. \end{cases} \tag{2.12}$$

The Lax-Friedrichs flux function for the slope limited MUSCL approach [32], is presented as:

$$F_{i+1/2} = \frac{1}{2}(F(q^l_{i+1/2} + F(q^r_{i+1/2})) - \frac{\Delta x}{2\Delta t}(q^r_{i+1/2} - q^l_{i+1/2}). \tag{2.13}$$

In a high resolution method, the numerical flux function is calculated by blending together the numerical fluxes of complementary orders. For $f(q) = aq$, with a positive speed *'a'*, the formulation for the Lax-Wendroff numerical method is:

$$q^{n+1}_i = q^n_i - \nu(q^n_i - q^n_{i-1}) - \frac{1}{2}\nu(1-\nu)(q^n_{i+1} - 2q^n_i + q^n_{i-1}), \tag{2.14}$$

where $a.\Delta t/\Delta x$ is known as the Courant number, which is represented by ν. This scheme is a first order upwind technique along with an anti-diffusive component of second order. The numerical method in the Equation 2.14 is second-order accurate, but it still does not follows the TVD property. Therefore, the Equation 2.14 is further modified by introducing a limiter function, say, ϕ in the following manner:

$$q^{n+1}_i = q^n_i - (q^n_i - q^n_{i-1})\left[\nu + \frac{1}{2}\nu(1-\nu)\left(\frac{\phi(r_{i+1/2})}{r_{i+1/2}} - \phi(r_{i-1/2})\right)\right], \tag{2.15}$$

Journal Pre-proof

where the function $r_{i+1/2}$ is defined as:

$$r_{i+1/2} = \frac{q_i^n - q_{i-1}^n}{q_{i+1}^n - q_i^n}. \tag{2.16}$$

A high resolution technique is developed whenever the limiting functional component given in the Equation 2.15 is positive [35]. To advance the solution in time, the numerical fluxes are computed as:

$$F(q_{i+1/2}) = f_{i+1/2}^l - \phi(r_i)\big(f_{i+1/2}^l - f_{i+1/2}^h\big), \tag{2.17}$$

in above equation, f^l is representing the low-resolution and f^h is showing the high-resolution [35] flux (numerical) functions. An enhancement to the approach framed on the total variation non increasing theory could be applied to remove or minimise the harmful unrealistic oscillations in the high resolution FVM techniques. The concept of TVD schemes was introduced by Harten [26]. For several systems, the TVD formulations constraint that the overall variation does not increase in time in general, that is for equation 2.1,

$$\sum_{i=1}^{N+1} |q_{i+1}^{n+1} - q_i^{n+1}| \leq \sum_{i=1}^{N+1} |q_{i+1}^n - q_i^n|. \tag{2.18}$$

The right hand side at the problem is computed by implementing the second-order Runge-Kutta technique at each stage to accommodate the proper boundary treatment. For the implementation of flux limiters [9] in the numerical scheme, the step of reconstructing must itself satisfy the TVD constraint given as:

$$\phi(r) = max\{0, min\{2r, 2\}\}. \tag{2.19}$$

Several frequently employed flux limiting TVD functions could be presented as follows:

- Minmod limiter: $max(0, min(r, 1))$, Roe (1986) [3].
- Superbee limiter: $max(0, min(2r, 1), min(r, 2))$, Roe (1986) [30].
- leer Albada limiter: $\frac{r(r+1)}{r^2+1}$, Leer Albada (1982) [8].
- MC limiter: $max(0, min(2r, (1 + r)/2, 2))$, Leer (1977) [36].

Journal Pre-proof

- leer Leer limiter: $\frac{r+|r|}{1+|r|}$; Leer (1974) [9].

Refer to the citations provided with each limiter for a more complete explanation. Further a pictorial depiction of the above mentioned limiters [37] is shown in the Figure 3. The work is focused on a core principle of modifying and optimising standard limiters in order to enhance the overall computational results.

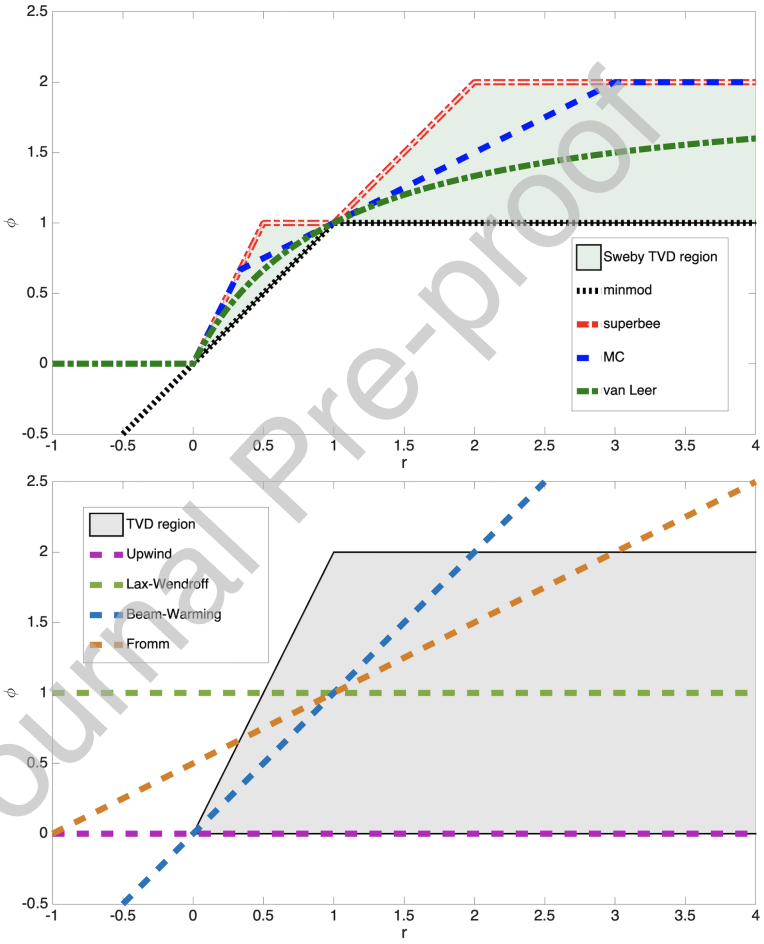

Figure 3: Graphical view of some classical non-linear flux limiters (top), and some linear flux limiters (bottom) inside the TVD regions.

Journal Pre-proof

Journal Pre-proof

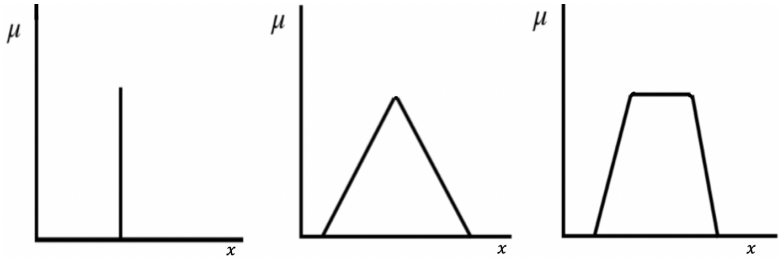

Figure 4: Examples of fuzzy sets: singleton set (left), triangular set (center), trapezoidal set (right).

3. The New Flux-Limiter scheme

The current work entails optimising a particular classical flux limiter in order to provide a superior hybrid option. Many flux limiters are available in the literature to prevent discontinuities [34]. Some key notions from the field of fuzzy mathematics are also crucial to optimize the classical techniques.

3.1. Preliminaries

Fuzzy sets:. Fundamentally, a fuzzy set is a crisp set (classical set) with a unique feature that permits every element of the universe of discourse to be associated with this classical set by an appropriate intensity level (called membership value). The frequency of membership relies on the scale of compatibility of a specific entity with the classical set. In fuzzy sets, the mostly employed set for membership values is $[0, 1]$. However, for a crisp set this set restricts to the discrete values $\{0, 1\}$. Mathematically, for a classical set T in the universe of discourse U, a fuzzy set A can be written as: $A = \{(x, \mu(x)) \mid x \in T\}$, where the membership function μ relates the elements of the classical set T to $[0, 1]$. (Refer to the Figure 4)

Fuzzy Linguistics:. The fuzzy logic variables which are made up of a set of words in the sense of Fuzzy mathematics, are known as fuzzy linguistics or simply linguistic terms. These variables assist in connecting the universal set's entities with a releleert membership value, which can then be used to build a relationship between that entity and the fuzzy set in concern [38]. Fuzzy values are significantly more adaptable to real-

Journal Pre-proof

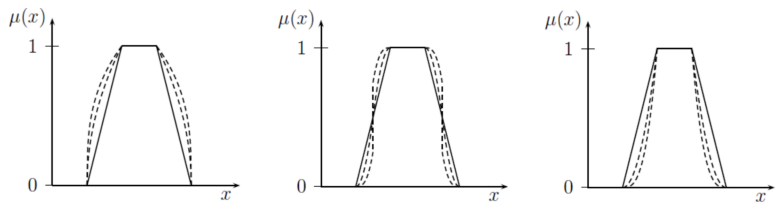

Figure 5: Examples of Fuzzy modifier functions: Dilation modifier (left), Contrast modifier (center), and Concentration modifier (right).

life models than crisp values because they capture measurement as a result of baseline data.

Fuzzy Hedges/Modifiers:. Fuzzy modifiers are a key feature of the new limiter's construction. By altering the membership level for the associated fuzzy sets, fuzzy hedges alter the perception of existing data. Corresponding to the fuzzy set A, as mentioned above, some of the frequently used hedges are: the Dilation hedge ($\{(y, \sqrt[p]{(\mu(y))}) \mid y \in U\}$), and the Concentration hedge ($\{(y, (\mu(y))^p)) \mid y \in U\}$) [30], here p is a real number. (Refer to the Figure 5)

By optimising the classical limiters, the next portion of this section comprises of establishing some new limiters. In this section, the whole framework is focused on appropriate tuning of different parameters in the flux limiting techniques leveraging suitable fuzzy modifier operators.

3.2. Formulation of the new hybrid flux limiter:

With the aid of fuzzy modifiers, this section emphasises parameter tuning. The applications of the standard dilation, contrast, and concentration operators are considered for optimising flux limited techniques. This work focuses only on the MC limiter and min-mod limiter, however if it serves the problem, such operators can be enforced on any flux limiter.

This paper focuses on an optimization of the classic MC limiter. In the piece-wise

Journal Pre-proof

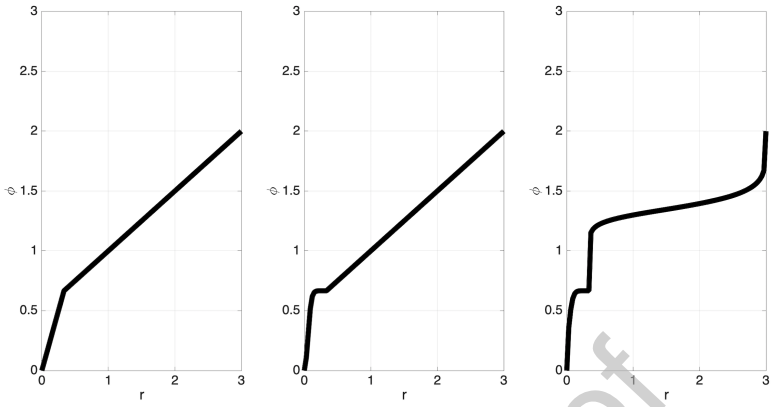

Figure 6: The graphical representation of the new fuzzified hybrid fuzzy flux limiters.

form, the MC limiter can be written as:

$$\phi(r) = \begin{cases} 0, & r \leq 0 \\ 2r, & 0 < r \leq 0.\bar{3} \\ 0.5(1+r), & 0.\bar{3} < r \leq 3 \\ 2, & \text{else.} \end{cases} \tag{3.1}$$

This is optimised by implementing the concentration modifying operator of intensity $p = 6$ and $p = 8$ to the smooth parts and extreme regions (regions having extrema) respectively, and remaining parts are same [32]. So, the new limiting scheme could be mathematically presented as follows:

$$\phi(r) = \max\left(0, \min\left(\frac{\frac{2}{3}(\frac{9-3r}{8})^6 + 2\frac{3r-1}{8}}{(\frac{9-3r}{8})^6 + \frac{3r-1}{8}}, 2, \frac{\frac{2}{3}(3r)^6}{(1-3r)+(3r)^6}\right)\right). \tag{3.2}$$

The new fuzzified limiter is presented in the Figure 6. In the framework of Fuzzy Mathematics, this technique brings up an incredible number of flux limiting function possibilities [2]. One more hybrid flux construction could be made by using the concentration modifier function of intensity $p = 6$ to the extreme points and the dilation modifier of intensity $p = 8$ to sharp areas, as shown in Figure 6. The Shallow water problem, expressed as the Equation 2.2, is computed in the next part to show the efficiency of the proposed fuzzy limiter described in the Equation 2.16.

Journal Pre-proof

4. Numerical Simulation and Results

To show the efficiency, robustness, and accuracy of the new scheme, computational results are compared with existing experimental data. It must be observed that, some test cases with analytical solutions are of literary interest only, but still they allow for conclusive assessment of the performance of the computational methods [39]. For the comparison of numerical computations some of the classical flux limiting functions namely the MC limiter, and the MM limiter are used in this section.

Throughout this section of numerical validation [27], the gravitational constant is taken as $g = 9.81$ (also known as the acceleration due to gravity) and the standard SI measuring units corresponding to the physical quantities [27, 40] (like m (meters), kg (kilograms), s (seconds), etc.) are ignored in the test cases. Uniform cartesian grids have been used for the space discretization.

To analyse the order of accuracy for the hybrid method proposed in this paper, assume $q(x_i, t^n)$ to be the exact solution, and q_i^n to be the computationally obtained solution corresponding to the i^{th} grid value at the n^{th} step in time, then the L_1 error norm (represented by $\|e_n\|_1$) is given as:

$$\|e_n\|_1 = \sum_{i=1}^{N} \left| q\left(x_i, t^n\right) - q_i^n \right| \Delta x. \tag{4.1}$$

and the L_∞ error ($\|e_n\|_\infty$) is given as:

$$\|e_n\|_\infty = \max_{1 \le i \le N} \left| q\left(x_i, t^n\right) - q_i^n \right|. \tag{4.2}$$

where N represents the computational points.

4.1. Numerical Wave computation using the idealized Dam Break Model

Dam break problems act as a crucial case study to analyse the capacity of a computational model to address upstream and downstream wave propagations involving changes and shocks in the SWEs. The proposed solution scheme has been assessed by using the dam break model in a rectangular channel with flat topography. The numerical domain is taken as $[-1, 1]$, and the step size of the discretized interval is $\Delta x = 0.005$. The results for the both the new scheme and the classical scheme have

Journal Pre-proof

N	L_1 error (classical)	L_1 error (new)	L_∞ error (classical)	L_∞ error (new)
100	4.96e-03	4.45e-03	1.42e-01	1.36e-01
150	3.18e-03	2.27e-03	1.16e-01	1.07e-01
200	2.63e-03	2.39e-03	1.55e-01	1.52e-01
250	2.04e-03	1.84e-03	1.48e-01	1.44e-01

Table 1: Error analysis for the TP 1 using L_1 and L_∞ error norms.

been plotted for $N = 400$ grid points. In this work, the initial data used by Tseng et al. in their research article has been used [39]. For computational purposes, MATLAB 2015b version has been used with macOS Mojave, RAM 8 GB and 2.3 GHz Intel Core i5.

4.2. Test Problems (TPs)

4.2.1. TP 1: Riemann profile in velocity

The form of the initial condition used in this TP for numerically computing the dam-break [27] problem is:

$$h(x,0) = 1, \tag{4.3}$$

$$u(x,0) = \begin{cases} u_l = 1 & x < 0 \\ u_r = -1 & x \geq 0. \end{cases} \tag{4.4}$$

For the error analysis related to this test case, refer to the Table 1. Also, the Figures 7 - 8 validate that the computational results obtained by using the classical limiting technique and the new limiting technique are comparable. The results are better and improved for the proposed new limiter, refer to the Table 1.

4.2.2. TP 2: Riemann profile in height

For computing the dam-break problem, the form of the initial condition used in this TP is:

$$u(x,0) = 0, \tag{4.5}$$

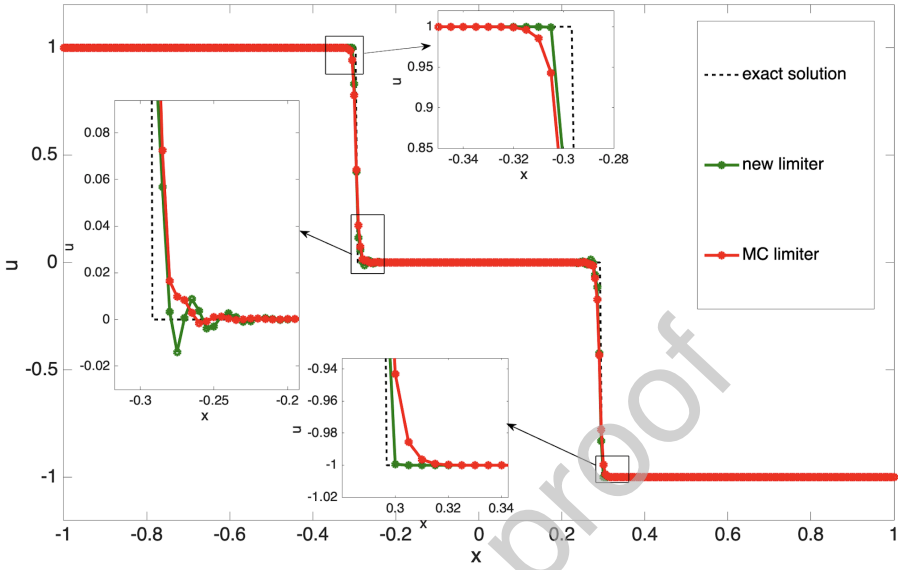

Figure 7: Approximation results corresponding to the velocity component for the TP 1 using the proposed scheme and the classic MC scheme for $\Delta t = 0.003$ and $N = 400$ at $t = 0.2$.

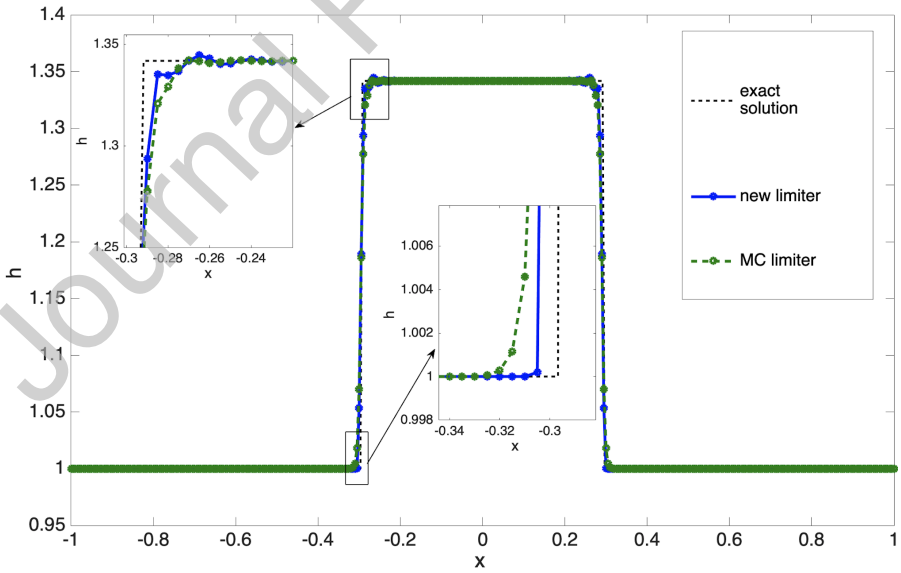

Figure 8: Computational solution profiles for the TP 1 using the proposed limiting scheme and the classical MC scheme for $\Delta t = 0.003$, and $N = 400$ at $t = 0.2$.

Journal Pre-proof

Journal Pre-proof

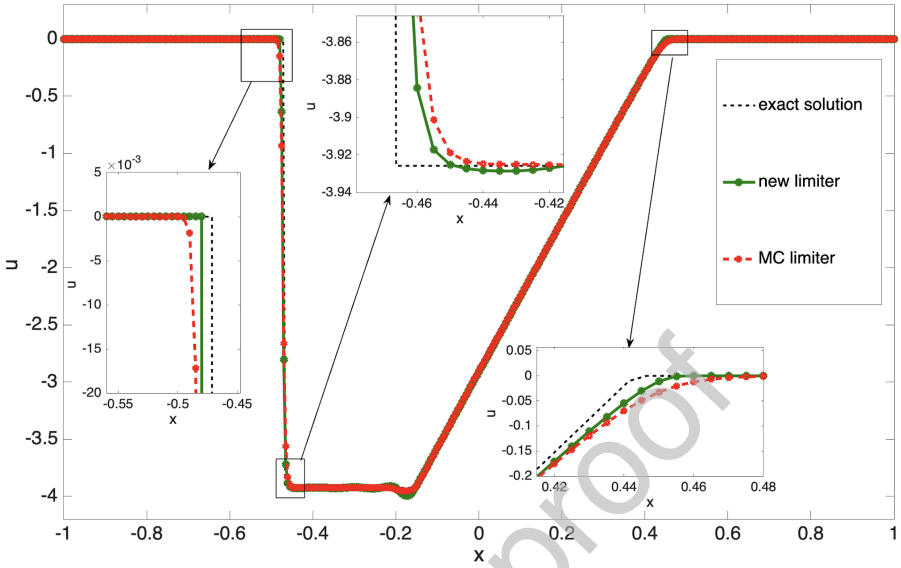

Figure 9: Approximation results corresponding to the velocity component for the TP 2 using the proposed limiting scheme and the classical MC scheme for $\Delta t = 0.003$ at $t = 0.2$ and $N = 400$.

$$h(x,0) = \begin{cases} h_l = 0.01 & x < 0 \\ h_r = 2 & x \geq 0. \end{cases} \tag{4.6}$$

Figures 9 - 10 show that the numerical outputs achieved by the MC limiter and the hybrid limiter are comparable. Although, in the Figure 10, the solution from the new limiter dips at about $x = -0.2$, while the original version seems to capture the solution better. This is the point of transcritical flow, where linearised Riemann solvers usually require an entropy fix. Still, the new method is capable of generating a nice comparable resolution, with smooth solutions. In the Table 2 the point-wise errors are presented. The improvised trait of the new method as compared to the classical method is validated by the numerical computations and the error magnitude comparison.

4.2.3. TP 3: Riemann profile in velocity

The form of the initial condition used in this TP for numerically computing the dam-break [27] problem is:

$$h(x,0) = 1, \tag{4.7}$$

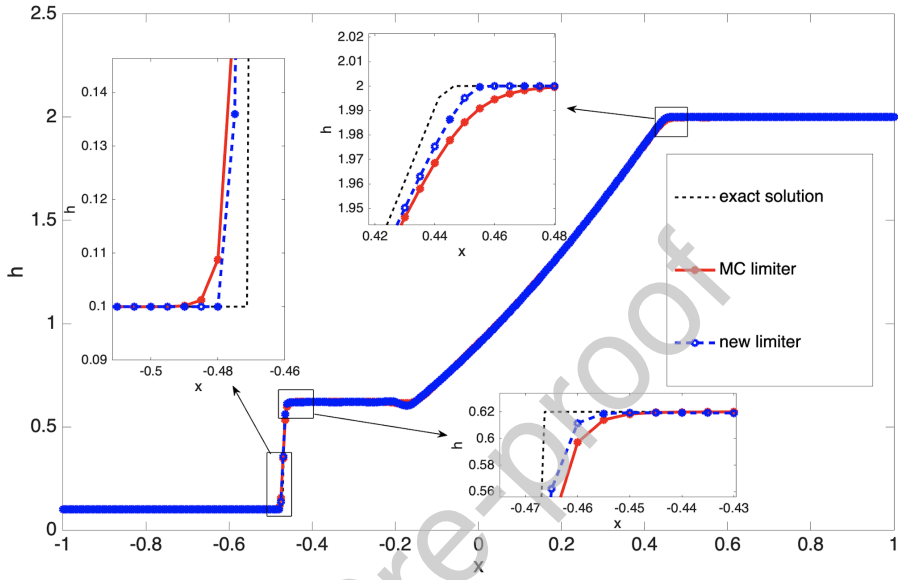

Figure 10: Approximation results corresponding to the height component for the TP 2 using the proposed limiting scheme and the classical MC scheme for $\Delta t = 0.003$ and $N = 400$ at $t = 0.2$.

N	L_1 error (classical)	L_1 error (new)	L_∞ error (classical)	L_∞ error (new)
100	5.64e-03	4.77e-03	2.04e-01	9.15e-02
150	2.62e-03	2.39e-03	1.32e-01	7.35e-02
200	2.16e-03	2.01e-03	1.66e-01	1.05e-01
250	1.96e-03	1.62e-03	1.97e-01	1.30e-01

Table 2: Error analysis for the TP 2 using L_1 and L_∞ error norms.

Journal Pre-proof

Journal Pre-proof

N	L_1 error (classical)	L_1 error (new)	L_∞ error (classical)	L_∞ error (new)
100	2.13e-03	1.97e-03	4.00e-02	3.86e-02
150	1.24e-03	1.12e-03	2.84e-02	2.66e-02
200	8.68e-04	7.75e-04	2.77e-02	2.51e-02
250	6.27e-04	5.50e-04	2.19e-02	1.97e-02

Table 3: Error analysis for the TP 3 using L_1 and L_∞ error norms.

$$u(x,0) = \begin{cases} u_l = -1 & x < 0 \\ u_r = 1 & x \geq 0. \end{cases} \tag{4.8}$$

Figure 11 validates that the approximated results are giving better convergence using the new optimised limiting scheme. A nice improvisation could be observed in the solution profiles. The outputs of both the depth and height solutions are comparable [1].

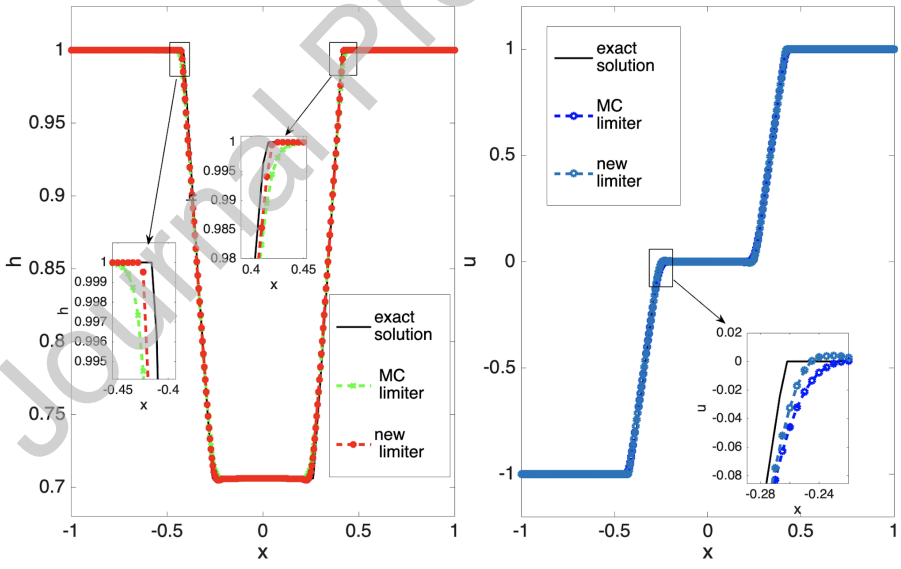

Figure 11: Approximation results corresponding to the TP 3 for $N = 400$, obtained by imposing the new and the classical scheme for $\Delta t = 0.003$ at the time $t = 0.2$. Here velocity profile (u) is on the right, and the height profile (h) is on the left.

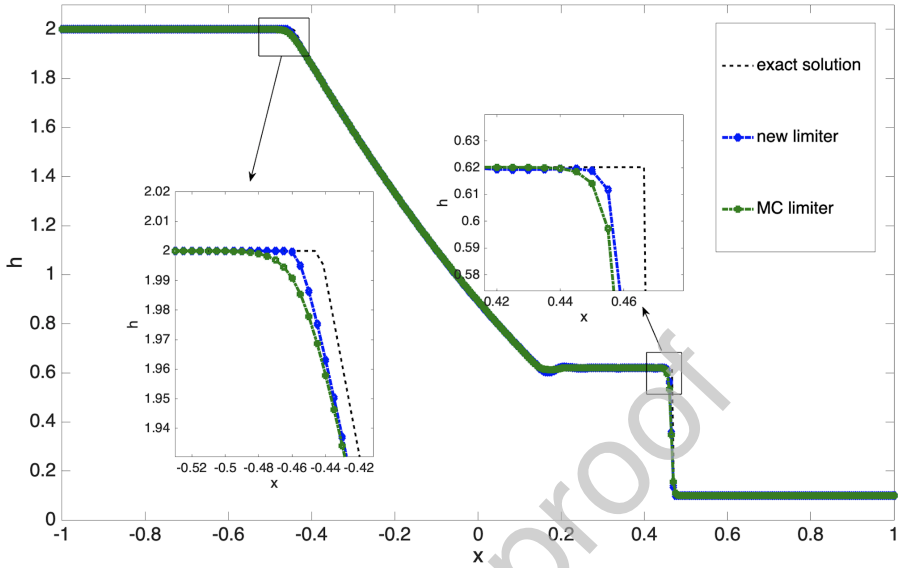

Figure 12: Approximation results for the height profile corresponding to the TP 4 using the proposed limiter and the MC limiter for $\Delta t = 0.003$ at $t = 0.2$ and $N = 400$.

4.2.4. TP 4: Riemann profile in height

The form of the initial condition used in this TP for numerically computing the dam-break [27] problem is:

$$u(x,0) = 0, \tag{4.9}$$

$$h(x,0) = \begin{cases} h_l = 2 & x < 0 \\ h_r = 0.01 & x \geq 0. \end{cases} \tag{4.10}$$

Table 4 shows the point-wise flaws caused by the classical technique and the new technique for the L_1 norm at $t = 0.2$ units, and the Figure 12 shows the approximate solution profile obtained by employing the classic MC limiting scheme and the new one. It is observable that the results are comparable. In fact, the computational output through the new limiter appears to be slightly improved, as shown in the Table 4, with the exception of slight dissipation at the corners. Table 4 gives the error analysis for the classical and the proposed scheme for the L_1 and the L_∞ norms. It is clear from the output data, that the MC limiter is capable of capturing the solution profile with a

Journal Pre-proof

N	L_1 error (classical)	L_1 error (new)	L_∞ error (classical)	L_∞ error (new)
100	4.98e-03	4.32e-03	3.16e-01	7.51e-02
150	3.07e-03	2.95e-03	1.56e-01	5.17e-02
200	2.54e-03	1.97e-03	1.43e-01	1.12e-01
250	1.63e-03	1.02e-03	1.27e-01	1.18e-01

Table 4: Error analysis for the TP 4 using the L_1 and $L\infty$ error norms.

slight oscillation profile near $x = 0.5$. However, the numerical outcome obtained from the new limiter looks more promising.

5. Notations

The following is the list of all the notations/symbols used in this work:

- x: space variable
- t: time variable
- q: vector of flow components
- u: flow velocity component
- h: height component
- g: gravitational constant
- N: number of computational points
- f: physical flux function
- s: source term
- η: manning constant
- α, β: some arbitrary values
- Z: topography function

Journal Pre-proof

Journal Pre-proof

- i: sub-script for spatial discretization
- n: super-script for temporal integration
- Δx: spatial step size
- Δt: temporal step
- F: flux function (numerical)
- q^l: linear extrapolation corresponding to the left side of cell interface
- q^r: linear extrapolation corresponding to the right side of cell interface
- s^-: slope function at left interface
- s^+: slope function at right interface
- ν: Courant number (CFL number)
- ϕ: limiter function
- f^l: low order numerical flux
- f^h: high order numerical flux
- μ: membership function
- T: classical/crisp set
- p: any real number
- U: Universal set
- y: an element from the universal set U
- e_n: error term at n^{th} time step
- s: seconds
- kg: kilograms
- m: meters

Journal Pre-proof

6. Declarations

6.1. Contributions

All authors contributed equally to the planning, execution, and analysis of this research paper.

6.2. Funding

This work was not supported by any organization.

6.3. Conflict of Interest

The authors declare that they have no competing interest.

7. Discussion and remarks

The study has presented the numerical approximation of one-dimensional SWEs with dam break flow problem. Here, the novelty of this research lies in the assessment of the performance of a new fuzzy logic based flux limiting scheme for the shallow water model.

- This concept offers a new way to compute the numerical results of shallow water flows with the aid of a completely different subject: Fuzzy Mathematics.
- The basic approach to tackle the problem is based as usual on the rules of conservation.
- The major difference between the classical and the new scheme lies in its important key feature namely the Fuzzy modifiers.
- On smooth solutions, the method has the second order of convergence, while on discontinuities, it has the first order of convergence, which corresponds to the accuracy of Godunov-type techniques.
- From the experiments it has revealed clearly that the optimized scheme is more accurate than the classical schemes because the error term in the new scheme are less than the MM and MC scheme, as seen in the Tables 1 - 4.

Journal Pre-proof

Journal Pre-proof

In this work, we have proposed the one dimensional shallow water model with the fuzzy FV method. Similar work may be extended to higher dimensions, and many real-life applications such as safety analysis in case of flood events etc.; we leave these ideas as our future work. The results demonstrate the applicability and benefits of indulging Fuzzy logic to form the numerical techniques.

Acknowledgements

The authors gratefully acknowledge the anonymous referees for their insightful feedback, which significantly improved this article.

References

[1] R. Lochab, V. Kumar, A new reconstruction of numerical fluxes for conservation laws using fuzzy operators, International Journal for Numerical Methods in Fluids 93 (6) (2021) 1690–1711. doi:https://doi.org/10.1002/fld.4948.

[2] H. H. O. Altaie, D. Pierre, Numerical solutions for 2d depth-averaged shallow water equations, International Mathematical Forum 13 (2018) 79–90. doi:10.12988/imf.2018.712102.

[3] V. Kumar, B. Srinivasan, An adaptive mesh strategy for singularly perturbed convection diffusion problems, Appl. Math. Model. 39 (7) (2015) 2081–2091. doi:10.1016/j.apm.2014.10.019.

[4] S. Tang, M. Li, Construction and application of several new symmetrical flux limiters for hyperbolic conservation law, Comput. & Fluids 213 (2020) 104741. doi:10.1016/j.compfluid.2020.104741.

[5] C. Biscarini, S. Di Francesco, P. Manciola, Cfd modelling approach for dam break flow studies, Hydrology and Earth System Sciences 14 (4) (2010) 705–718. doi:10.5194/hess-14-705-2010.

Journal Pre-proof

Journal Pre-proof

[6] S. K. Das, J. Bagheri, Modelling of shallow-water equations by using compact MacCormack-type schemes with application to dam-break problem, Int. J. Adv. Appl. Math. Mech. 2 (3) (2015) 60–71.

[7] V. Kumar, B. Srinivasan, A novel adaptive mesh strategy for singularly perturbed parabolic convection diffusion problems, Differ. Equ. Dyn. Syst. 27 (1-3) (2019) 203–220. doi:10.1007/s12591-017-0394-2.

[8] R. J. LeVeque, Numerical methods for conservation laws, 2nd Edition, Lectures in Mathematics ETH Zürich, Birkhäuser Verlag, Basel, 1992. doi:10.1007/978-3-0348-8629-1.

[9] E. F. Toro, Riemann solvers and numerical methods for fluid dynamics: a practical introduction, 3rd Edition, Springer-Verlag, Berlin, 2009. doi:10.1007/b79761.

[10] E. Tadmor, A review of numerical methods for nonlinear partial differential equations, Bull. Amer. Math. Soc. (N.S.) 49 (4) (2012) 507–554. doi:10.1090/S0273-0979-2012-01379-4.

[11] S. Aliabadi, M. Akbar, R. Patel, Hybrid finite element/volume method for shallow water equations, Internat. J. Numer. Methods Engrg. 83 (13) (2010) 1719–1738. doi:10.1002/nme.2886.

[12] M. ALIPARAST, Two-dimensional finite volume method for dam-break flow simulation, International Journal of Sediment Research 24 (1) (2009) 99 – 107. doi:https://doi.org/10.1016/S1001-6279(09)60019-6.

[13] M. Mehra, B. V. R. Kumar, Time accurate fast three-step wavelet-Galerkin method for partial differential equations, Int. J. Wavelets Multiresolut. Inf. Process. 4 (1) (2006) 65–79. doi:10.1142/S0219691306001099.

[14] M. M. Rahaman, A comparative study between finite difference method and finite volume method for shallow water-dam break flow problem, Global Journal of Science Frontier Research.

Journal Pre-proof

[15] D. Dutykh, D. Mitsotakis, On the relevance of the dam break problem in the context of nonlinear shallow water equations, Discrete Contin. Dyn. Syst. Ser. B 13 (4) (2010) 799–818. doi:10.3934/dcdsb.2010.13.799.

[16] V. Kumar, M. Mehra, Wavelet optimized finite difference method using interpolating wavelets for self-adjoint singularly perturbed problems, J. Comput. Appl. Math. 230 (2) (2009) 803–812. doi:10.1016/j.cam.2009.01.017.

[17] B. V. R. Kumar, M. Mehra, Time accurate fast wavelet-Taylor Galerkin method for partial differential equations, Numer. Methods Partial Differential Equations 22 (2) (2006) 274–295. doi:10.1002/num.20092.

[18] S. K. Godunov, A difference method for numerical calculation of discontinuous solutions of the equations of hydrodynamics, Mat. Sb. (N.S.) 47 (89) (1959) 271–306.

[19] J. S. Hesthaven, T. Warburton, Nodal discontinuous Galerkin methods, Vol. 54 of Texts in Applied Mathematics, Springer, New York, 2008, algorithms, analysis, and applications. doi:10.1007/978-0-387-72067-8.

[20] R. Lochab, V. Kumar, A comparative study of high-resolution methods for nonlinear hyperbolic problems, ZAMM - Journal of Applied Mathematics and Mechanics / Zeitschrift für Angewandte Mathematik und Mechanik 102 (7) (2022) e202100462. doi:https://doi.org/10.1002/zamm.202100462.

[21] H. Yu, Y.-P. Liu, A second-order accurate, component-wise TVD scheme for nonlinear, hyperbolic conservation laws, J. Comput. Phys. 173 (1) (2001) 1–16. doi:10.1006/jcph.2001.6834.

[22] R. Lochab, V. Kumar, Numerical simulation of hyperbolic conservation laws using high resolution schemes with the indulgence of fuzzy logic, Sergeyev Y., Kvasov D. (eds) Numerical Computations: Theory and Algorithms 11974 (2020) 139–153. doi:10.1007/978-3-030-40616-5.

Journal Pre-proof

[23] V. Kumar, G. Leugering, Singularly perturbed reaction-diffusion problems on a k-star graph, Mathematical Methods in the Applied Sciences 44 (2021) 14874–14891. doi:https://doi.org/10.1002/mma.7749.

[24] R. Lochab, V. Kumar, An improved flux limiter using fuzzy modifiers for hyperbolic conservation laws, Mathematics and Computers in Simulation 181 (2021) 16 – 37. doi:10.1016/j.matcom.2020.09.012.

[25] M. Mehra, V. Kumar, Fast wavelet-Taylor Galerkin method for linear and non-linear wave problems, Appl. Math. Comput. 189 (2) (2007) 1292–1299. doi:10.1016/j.amc.2006.12.013.

[26] A. Harten, High resolution schemes for hyperbolic conservation laws, J. Comput. Phys. 49 (3) (1983) 357–393. doi:10.1016/0021-9991(83)90136-5.

[27] R. Lochab, V. Kumar, High resolution tvd scheme based on fuzzy modifiers for shallow-water equations, Paszynski M., Kranzlmüller D., Krzhizhanovskaya V.V., Dongarra J.J., Sloot P.M.A. (eds) Computational Science – ICCS 12742 (2021) 480–492. doi:10.1007/978-3-030-77961-0-39.

[28] S.-H. Peng, 1d and 2d numerical modeling for solving dam-break flow problems using finite volume method, Journal of Applied Mathematics 2012, Special Issue. doi:10.1155/2012/489269.

[29] P. B. Bochev, M. D. Gunzburger, Least-squares finite element methods, Vol. 166 of Applied Mathematical Sciences, Springer, New York, 2009. doi:10.1007/b13382.

[30] P. R. M. Lyra, K. Morgan, A review and comparative study of upwind biased schemes for compressible flow computation. III. Multidimensional extension on unstructured grids, Arch. Comput. Methods Engrg. 9 (3) (2002) 207–256. doi:10.1007/BF02818932.

[31] B. Srinivasan, V. Kumar, The versatility of an entropy inequality for the robust computation of convection dominated problems, Procedia Computer Science 108 (2017) 887–896. doi:10.1016/j.procs.2017.05.099.

Journal Pre-proof

[32] B. van Leer, Towards the ultimate conservative difference scheme. v. a second-order sequel to godunov's method, Journal of Computational Physics 32 (1) (1979) 101–136. doi:https://doi.org/10.1016/0021-9991(79)90145-1.

[33] R. Liska, B. Wendroff, Comparison of several difference schemes on 1D and 2D test problems for the Euler equations, SIAM J. Sci. Comput. 25 (3) (2003) 995–1017. doi:10.1137/S1064827502402120.

[34] M. Breuss, D. Dietrich, On the optimization of flux limiter schemes for hyperbolic conservation laws, Numer. Methods Partial Differential Equations 29 (3) (2013) 884–896. doi:10.1002/num.21736.

[35] B. Srinivasan, A. Jameson, S. Krishnamoorthy, An upwinded state approximate Riemann solver, Internat. J. Numer. Methods Fluids 70 (5) (2012) 578–602. doi:10.1002/fld.2701.

[36] N. P. Waterson, H. Deconinck, Design principles for bounded higher-order convection schemes—a unified approach, J. Comput. Phys. 224 (1) (2007) 182–207. doi:10.1016/j.jcp.2007.01.021.

[37] P. K. Sweby, High resolution schemes using flux limiters for hyperbolic conservation laws, SIAM J. Numer. Anal. 21 (5) (1984) 995–1011. doi:10.1137/0721062.

[38] F. Kemm, A comparative study of TVD-limiters—well-known limiters and an introduction of new ones, Internat. J. Numer. Methods Fluids 67 (4) (2011) 404–440. doi:10.1002/fld.2357.

[39] M.-H. Tseng, C.-A. Hsu, C. Chu, Channel routing in open-channel flows with surges, Journal of Hydraulic Engineering-asce - J HYDRAUL ENG-ASCE 127 (2001) 115–122. doi:10.1061/(ASCE)0733-9429(2001)127:2(115).

[40] T.-J. Chang, H.-M. Kao, K.-H. Chang, M.-H. Hsu, Numerical simulation of shallow-water dam break flows in open channels using smoothed particle hydrodynamics, Journal of Hydrology 408 (2011) 78–90. doi:10.1016/j.jhydrol.2011.07.023.

Journal Pre-proof

Declaration of Competing Interest

The authors declare that they have no known competing financial interests or personal relationships that could have appeared to influence the work reported in this paper.

Journal Pre-proof

Opinion Leaders for Information Diffusion Using Graph Neural Network in Online Social Networks

OL for information diffusion using GNN in OSNs

LOKESH JAIN

Department of Computer Science, Delhi Technological University, New Delhi-India, nsitlokesh.jain@gmail.com

RAHUL KATARYA

Department of Computer Science, Delhi Technological University, New Delhi-India, rahuldtu@gmail.com

SHELLY SACHDEVA

Department of Computer Science, National Institute of Technology, New Delhi-India, shellysachdeva@nitdelhi.ac.in

Due to the diverse nature of the social network and researchers' insatiable, various opportunities come to depict different domains. An opinion leader is a human entity or cluster of people who can redirect human assessment strategy by intellectual skills in the social network. A more comprehensive range of approaches is developed to detect opinion leaders based on network-specific and heuristic parameters. For many years, deep learning-based models have solved various real-world multifaceted graph-based problems with high accuracy and efficiency. The Graph Neural Network (GNN) is a deep learning-based model that modernized neural networks' efficiency by analyzing and extracting the latent dependencies and confined embedding via message passing and neighborhood aggregation of data in the network. In this paper, we have proposed an exclusive GNN for Opinion Leader Identification (GOLI) model utilizing the power of GNN to categorize the opinion leaders and their impact on online social networks. In this model, we first measure the n-node neighbor's reputation of the node based on materialized trust and next perform centrality conciliation instead of the input data's conventional node embedding mechanism. We experiment with the proposed model on six different online social networks consisting of billions of users' data to validate the model's authenticity. Finally, after training, we found the top-N opinion leaders for each data set and analyzed how the opinion leaders are influential in information diffusion. The training-testing accuracy and error rate are also measured and compared with the other state-of-art standard Social Network Analysis (SNA) measures. We analyze that the GNN-based model produced high performance concerning accuracy and precision.

CCS CONCEPTS • Opinion Leader • Graph Neural Network • Reputation • Information diffusion• Online Social Network

1 INTRODUCTION

A social network plays a vital position in individuals living through innovative and dynamic features in the current digital era. Perhaps, the existence of human life is moving around social networking sites. Nowadays, an individual has an account(s) on multiple social networking sites, such as Facebook, Twitter, Instagram, etc., to share and receive information [26,54]. Some organizations use social networks to promote their products and materials [85]. Social networking sites are very significant in finding the target consumer for the industry directly [64]. The current scenario is highly competitive, volatile, and struggling to promote its material due to Covid-19 [38]. Due to this pandemic, most companies closed their workshops, centers, and offices. Besides, most IT industry appeals to their employees remotely or work from home. Hence, one of the industry's biggest challenges is determining whom consumers might want to purchase their products from and diverting their decision-making toward them [74]. One solution to the problem is recognizing an appropriate leader who can influence consumers' decision-making through intelligence and grit [19].

Permission to make digital or hard copies of all or part of this work for personal or classroom use is granted without fee provided that copies are not made or distributed for profit or commercial advantage and that copies bear this notice and the full citation on the first page. Copyrights for components of this work owned by others than the author(s) must be honored. Abstracting with credit is permitted. To copy otherwise, or republish, to post on servers or to redistribute to lists, requires prior specific permission and/or a fee. Request permissions from permissions@acm.org.
© 2023 Copyright held by the owner/author(s). Publication rights licensed to ACM.
1559-1131/2023/1-ART1 $15.00
https://doi.org/10.1145/3580516

Just Accepted

An opinion leader is a human being or group of competent people who diverts the human selection process through their practical skills [70,78]. The opinion leader characteristics include high social status, effective leadership, intense listening and oration, educated, technically sound, excessive product knowledge, great coverage in mass media, great prominence, higher risk preference, higher visual with dense analytical power, practical communication, gregarious, and dogmatism [40]. For the past many years, various researchers and analyses have discovered multiple approaches to finding the list of suitable opinion leaders. Yet, no typical method can identify the opinion leader with total efficiency. Many information and content posted by various users based on day-to-day activities impact other decision-making processes because of social media's extensive usage [51]. People assign different information on social media and share it with their friends, relatives, colleagues, and acquaintances, eventually becoming an extensive social network[30]. Most methods and algorithms have used the complex network structure and dynamics to measure the node probability of being a follower or a leader. Researchers have used features such as clustering coefficient, network density, average path length, network diameter, spanning tree, mean, median, mode, centralities, eigenvector, cohesive subgraph, and many others to find the opinion leaders in the network [10,67].

Opinion leader identification is a two-phase procedure in which, in the initial phase, the user receives information from society via various communication mediums. The followers follow the processed and refined knowledge in the next step [32]. Therefore, opinion leaders' responsibility is also significant for innovation diffusion in the current digital era [63]. Innovation can be any object, entity, content, material, product, sense, and idea that an individual thinks is unique and novel. In the current competitive scenario, various organizations opted for opinion leaders to promote their products in the real world [90].

Opinion leaders broadly can be classified into five classes; i) monomorphic and polymorphic opinion leaders based on operative and working areas. Monomorphic opinion leader works in a particular domain and has expertise in that field. Polymorphic opinion leader works in multiple disciplines with aggregative knowledge. Due to their versatile experience, they can influence more followers than others; ii) regional and universal opinion leaders are classified based on their expanse range. Regional opinion leaders affect the local community or group. The ubiquitous opinion leaders influence the massive amount of followers belonging to a large community. Regional opinion leaders are directly or via neighbors connected with the users, while universal opinion leaders are indirectly connected with users via their followers; iii) interim and eternal opinion leaders can be defined based on their active time. Interim opinion leaders work for a short time, i.e., actively achieving a short-term goal. On the other side, eternal opinion leaders do to accomplish long-term goals, i.e., they act for a long time, and their service time duration is enormous, up to 15-20 years; iv) warm and cold opinion leaders are classified based on their working techniques. Warm opinion leaders work with aggression, passion, dare, and courage, while cold opinion leaders are very calm, relaxed, gentle, and used in an untroubled manner; v) biased and unbiased opinion leaders are influenced by some environmental factors. Political, technological, commercial, financial, or social changes affect the biased opinion leader and pronounce the more dominant side. Unbiased opinion leaders are not much affected by the mentioned factors.

On the other side, over the last many years, the deep learning-based model has achieved more sensation and strengthened the research in the domain of image processing and restoration, natural language processing, computer vision, speech recognition, healthcare, finance, automobiles, bioinformatics, defense, grid computing, and many more [22,37,66]. Various machine learning tasks such as object identification, classification, regression, outlier detection, and many more have been modernized by different stem-to-

Just Accepted

stern deep learning archetypes such as Artificial neural network (ANN), Recurrent Neural Network, Convolution Neural Network(CNN), Autoencoders, Long-Short-Term-Memory(LSTM) and many more [3]. The advanced electronic circuit, i.e., GPU (Graphical processing unit), speedily updates memory using parallelization to step up the generation of image, text, and video in a frame buffer, also one of the prominent causes behind the exposure of deep learning models. Besides, handling and processing a large amount of training data, capturing the multi-scale confined latent features, and mapping them into Euclidian space strengthens the deep learning-based model's power. In general, the deep learning-based model has six main components: raw input, number of multiple hidden layers, shared weights, activation functions (Sigmoid, ReLU, etc.), loss function (Gradient Descent, etc.), and output (Binary Classification, Multi-class Classification, Regression, Clustering, etc.) [2].

Another impulse for GNN is Network Embedding to represent the high-dimension graph structure (Bipartite, Direct, indirect, static, dynamic, etc.)includes a relatively massive number of nodes, edges, and features, into low-dimension vectors as shown in Fig.1 [20,98]. So, network embedding's primary phenomenon is to analyze the encoding for the nodes and edges in the network. The similarity between the nodes and edges must be preserved in node and edge embedding space, respectively. Various embedding algorithms are developed for different graphs based on their weight, structure, domain, and degree. For example, network embedding can represent a molecular graph that is tiny and static. At the same time, the same can also be used for the social network, which is opaque, massive, and dynamic. So, it isn't easy to find the appropriate embedding method for a different graph with high accuracy. Network embedding applies in various applications such as social network analysis, recommendation systems, natural language processing, knowledge graph, community detection, graph clustering, and many others. Network embedding includes DeepWalk, LINE (Large-scale Information Network Embedding), Node2Vec, SDNE (Structural Deep Network Embedding), Struc2Vec, and many other variants based on these methods [53,84].

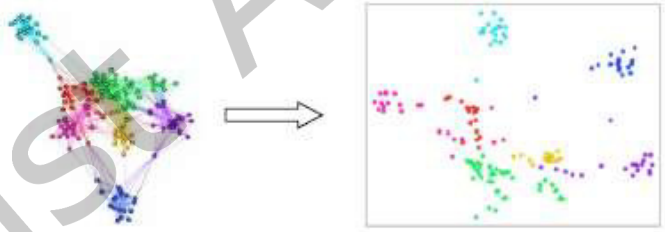

Fig.1. Network embedding illustration

Various researchers showed their profound concern in the graph due to its ubiquitous nature and applicability in different domains such as bioinformatics, molecule reaction, physics, social science, social network analysis, etc. Besides, graphs are used to model the complex structure, depicting real-world challenges like link prediction, community detection, node classification, image segmentation, etc. The leading factor behind the development of GNN is Network Embedding and synchronous message-passing mechanism. Although the traditional embedding methods efficiently represent the complex graph structure in low-dimension Euclidian space. They suffered from shallow learning techniques and were far behind in identifying the graph's additional hidden features. GNN achieved great attainment on many real-world applications due to their expressive capability to recognize in-depth latent aristocratic features on the grid-like pattern as image, text, etc., producing more accurate outcomes. Moreover, many methods have been developed for convolution operations on the graph or network [84].

Just Accepted

The social network architecture is also considered a graph where the user depicts a node while the links show the edges [94]. The formation of the relations between the users depends upon various features such as trust, common interest, homophily, structural hole, user's total number of followers, social status, common religion or community, same age group, gender, common sports/music/movie interest, and many other factors [47]. Nowadays, everyone has registered with more than one login account on multiple social networking sites. People post messages to learn about any product before purchasing and receive feedback from friends and acquaintances. Similarly, companies share their products and brands through digital marketing, blogs, hashtags, advertisements, and identifying the target audience. Although various strategies are available to promote the brand or product, it is crucial to alter human decision-making if it is rigid on a particular product, either positively or negatively [39]. One of the best promising solutions for this problem is finding opinion leaders who can influence and impact human decision-making through their proficiency and expertise. In the current scenario, where every organization wants to rapidly grow and secure their business, the opinion leader's liability is imperative and challenging.

Hence, how do we find opinion leaders in the social network by considering the latent feature? In this paper, we addressed the unique **G**NN for **O**pinion **L**eader **I**dentification (**GOLI**) model for opinion leaders identification in online social networks through the user reputation score and trust. Our primary target is to develop an approach that captures the hidden and latent information from the network, so we explored the power and features of GNN. Currently, GNN based model outperformed for node classification belonging to multiple fields. Usually, a node has features based on the graph's geographical and structural components, such as diameter, degree, number of neighbors, node clustering coefficient, centrality, dependencies, and many others.

In GNN, the node features are represented as feature vectors measured via any network embedding or encoding mechanism. All the nodes behave as a recurrent entity after encoding, and all the edges work as the feed-forward neural network. Next, each recurrent unit wrapped up embedding information in a message and propagated it to its neighbors through the neural network. Similarly, all the recurrent entity neighbors also wrapped up embedding information in a statement and repetitively propagated until equilibrium is achieved. Once a recurrent unit receives its neighbor's message, it must follow specific propagation rules, including aggregation and propagation. The updated embedding of the recurrent entity is transforming the current recurrent entity embedding and neighboring node embedding received through the feed-forward neural network. The neighborhood aggregation or message-passing phase can use aggregation methods for summarizing the messages. In contrast, a global transition function uses to characterize the input into n-dimensions space in the transformation step. The loss function is optimized by gradient descent until the fixed point elucidation is achieved [81,93].

This research considered the network parameters and user characteristics, social status, tweets, response time, and more features as input. Traditional approaches only considered the network dynamics or the user's features as input to the model. Therefore, we have addressed a unique, innovative mixed approach by utilizing the power of GNN with online social networks to find a suitable list of opinion leaders. In this research, we have initially determined the feature vectors of the node based on the user's features and derived a features vector matrix. Next, we anticipated a trusted network to divide the whole network into clusters to reduce the complexity and processing time; further, we deployed the proposed GNN model and calculated the node reputation score. Finally, top-n(=5) opinion leaders are identified based on the maximum reputation score. Moreover, there is no standard method till now to compare the

Just Accepted

results. So, we have used the classical centrality-based method to measure the proposed approach's performance.

Now, we discuss the article's constitution as follows: in the opening section, we discuss the literature and previously developed approaches to finding opinion leaders. We also illustrate the limitations and advantages of earlier methods concerning the proposed method. In the next section, we elaborate on the online social network's necessary details and GNN needed to comprehend the proposed model deeply. We discuss the various types of centralities, social network properties, and layered GNN structures. Further, in the next section, we elaborate on the proposed GOLI model and the merits of discovering opinion leaders. Next, to prove the proposed model's validity, we deploy the proposed model on six different datasets. We found the list of top-5 opinion leaders in each dataset. The subsequent section measures each dataset's training accuracy, testing accuracy, and error rate and compares the results with the other standard SNA measures. The final section discusses the future scope, limitations, and relevance of opinion leaders in different areas. Therefore the original contribution of this article is as follows:

- *The unique GOLI model proposes to find opinion leaders in online social networks.*
- *Trust and centrality-based functions apply to compute the reputation score.*
- *Accomplish experiments on six different datasets to validate the result.*
- *Attain enhanced results w.r.t. accuracy and precision over other SNA measures.*

2 RELATED WORK

In the current revolutionized world, social media changes users' roles from typical users to experts competent enough to divert human decision-making. According to the study, around 3.96 billion users use social media globally, i.e., 51% of the universal population engages with social media platforms. So, companies, communities, and users' responsibility is pivotal to providing authentic and productive information because the followers follow that information to some extent. Opinion leaders can assist industries in presenting a genuine offer. Identifying opinion leaders is pivotal to finding appropriate opinion leaders in the social network due to the online social network's dynamic nature. Many investigators utilized various methods, algorithms, and models to find opinion leaders. So, every investor has a different viewpoint on identifying opinion leaders with some limitations and advantages. Some researchers also used meta-heuristic nature-inspired algorithms, game theory approach, probabilistic mathematical model, text mining, machine learning, and deep learning-based model to classify the opinion leader. Table 1 briefly summarizes each process and its virtues and demerits.

Just Accepted

Table 1. Encapsulate view of literature survey

Subject	Experimental data	Explanation	Virtues	Demerits
[14]	Online forum	Based on text mining and social network analysis, positive and opposing views are gathered. Opinion leaders are selected based on higher complimentary views.	Simple; Beneficial to automatically set opinions; applicable for business simulation.	Only appropriate for bounded datasets; Limited parameters.
[15]	Reviews of Apple's iPhone	An innovative model suggested identifying the connections within the user's group and finding the user's social actions. Further, the text mining technique is also used to select the opinion leader based on these actions.	Uncomplicated; Easy to understand; Mainly used in the recommendation system.	No way to validate the database; Only appropriate for online groups and blogs.
[4]	Epinions dataset	Reliable users are determined based on an improved version of the Advogato trust metric. Further, identify the strong user relationship and repeatedly diffuse the scope of the intended user. Finally, a set of reliable users is found based on capacity-first maximum flow method.	Applicable for the recommended system; Helpful to avoid unreliable users.	Considering only the binary-link relation; The proposed metric is not suitable for global connection.
[19]	Synthesized dataset	Define an approach that selects opinion leaders based on the total number of followers and having a high diffusion speed. The authors also observed that users with maximum sociality are suitable for diffusion and that users with maximum centrality have managed many followers.	Applicable in business strategies and adoption process; Appropriate for secondary advocacy system.	Only bounded centrality measures are used for analysis; Other node characteristics are needed for the adoption process.
[52]	Educational blogs dataset, Parent-child forum dataset	Addressed an integrated approach included the user's relation with other's consumers, importance, attitude, and acknowledgment time. Four key features are also characterized in finding the opinion leaders.	Measured performance based on centrality and novelty; Siginicant for online forums and blogs.	Only topic-specific opinion leaders are discovered; Limited scope.
[60]	Amazon.com dataset	A ranking model suggested discovering opinion leaders in online communities and forums based on domain sensitivity. A customer expertise matrix is used for evaluation purposes.	Applicable for product diffusion; Helpful in resolving cold start problems.	Suitable only for online review forums; Customer authority and coverage required.
[89]	Facebook dataset, citation network dataset (Google scholar & DBLP)	An epidemic time blight-based formula designed to specify and scale the importance of opinion leaders. They made the sequences of brunt related to opinion leader action. Further, it created a universal series of actions by refining every probable user's activity.	Significant to discover influence way; Useful for ordering community leader	Limited parameters; Complex and difficult to understand; Restricted dataset.
[25]	Web-based Chinese stock Forum dataset	A new technique is suggested to capture the user's actions based on the wording posted on online forums and blogs. Clustering techniques are explored to discover opinion leaders. Next, opinion leaders' quality is measured in sentiment analysis as the stock market's movement provides a stable platform for company growth.	Significant for the stock market and suggested system; Uncomplicated.	Applicable only with online trading, forum, and blogs; Exclusively used PageRank centrality for comparison.
[6]	Synthesized dataset	Initially, the proposed approach discovered the area of interest in a particular field. Next, the capability and knowledge of the user are evaluated to become the opinion leader.	Simple and easy to implement; Provide high mean precision and accuracy.	Pre domain knowledge required; Considered only posted tweets.
[87]	Douban.com	A novel algorithm is suggested indicating how the node's importance impacts the whole network. A multi-relation matrix is designed to depict the multiple connections between the users. A user who has high importance score is elected as an opinion leader.	Produced better outcomes for the multi-relational social network; Fast convergence.	The limited feature used to create the matrix; Only considered page Rank for differentiation.

Just Accepted

[1]	Epinions dataset	A simple method addressed that identifies opinion leaders based on the total trust value. The total trust value is calculated based on in-degree and out-degree centralities.	Relatively simple hybrid approach; Easy to understand and implement.	Limited applicability; Used a lesser number of features.
[18]	Mobile01 Forum	An inventive method D_OLMiner is suggested that utilizes the network attributes to make a dynamic social network. Besides, a community identification procedure has also been developed to resolve the overlapping issue.	Perfect for the dynamic social network; Suitable for information dissemination in communities.	Restricted datasets; Limited metrics applied for comparison.
[17]	Mobile01 Forum	A K-means clustering algorithm addressed that found the total number of clusters in the network. A metric calculated the value of each cluster. A cluster has the highest score selected as a leading participant for opinion leader selection.	Easily understandable; Helpful to solve superimposed impact issues.	Restricted metrics are used to compare the outcomes; Used only for the static dataset.
[23]	turnbackhoax.id	Two approaches are suggested; the first one is edge weighting which identifies the importance of each relation by calculating the total number of responses. The second is centrality weighting which allocates some load to the centralities based on agreement. This weighting information is used for opinion leader detection.	Useful for rumor transmission network; focused on edge and centrality weightage.	Limited datasets; Finite centralities and connections used for comparing the consequences.
[57]	KOL dataset using Instagram API, Synthesized dataset	An innovative network embedding technique that represents social media information into a low dimension sub-space is addressed. The network's topological structure, different features, and consistency between the datasets have been analyzed to find the trivial subspace for diverse modalities. Next, the whole experiment is decomposed into a common eigen-decomposition problem to find the opinion leaders.	Unique linear training model; Perform well over other subspace learning techniques.	Complicated and extensive to understand; Not consider the non-linear relation among modalities.
[96]	Synthesized dataset	A closeness and betweenness centrality-based method is proposed to find the opinion leaders. Delay in the information diffusion and the position of non-adjacent nodes are considered for method evaluation. Further, the outcomes compared with the Independent Cascade model.	Generated superior effects over betweenness centrality; Simple and easily implementable; Presented enhanced independent cascade model.	Used small synthesized datasets; Limited metrics are used for comparing the outcomes.
[97]	Sina micro-blog dataset	The suggested method mainly focused on the opinion leaders who are subject-oriented and can help spread only subject-related information. A proposed propagation model selects the top-k users and the number of users influenced by users. The users take lesser time for information diffusion and are declared opinion leaders.	Effective for viral and product marketing; Implement a modified and updated IC model.	Network's topological knowledge is needed; Only suited for selected datasets.
[41]	Synthesized dataset	A fuzzy logic-based approach focused on fuzzy trust predicates. These predicates are applied and evaluated on online social networks to find the list of opinion leaders based on esteem scores.	Involved human reasoning; Trust evolves while producing the results.	Only the stable datasets are explored; Limited arguments are used for fuzzy trust predicates.
[55]	Chinese Sina BBS	A novel hybrid procedure addressed based on PageRank mainly focused on grouping users and measuring users' leadership on other users over time in the network. A comprehensive analysis is performed based on sensitivity and time to achieve the goal.	Straightforward; Provide better accuracy over PageRank.	Not suitable for large datasets; Examine only PageRank centrality.

Just Accepted

[16]	Facebook, Twitter, Google+	An exceptionally dynamic model presented found interconnected entities with the same opinion vector. The entire framework is classified into three phases, including opinion leaders, communities, and opinion matrix formulation.	Detect game communities based on the game model with high mean accuracy; Fairley dynamic and robust.	Difficult to understand; Applicable only for networks having non-overlapping clusters.
[77]	Twitter	A different parameter milestone centrality is offered specially dedicated to intended users and focused on their importance on some topic. A user selected as an opinion leader has the maximum milestone centrality.	A new centrality measure is offered; Simple and easy to perform.	Performed investigation on limited topics; Applicable only on limited datasets.
[49]	Local Motor community	Suggested a multi-features decision-making method that considered the close centralities, degree, median, and other statistical characteristics. The user gained the highest statistical score, thought the opinion leader. Other terms like value and benefits indicators are also explored to enhance the overall accuracy.	Decisive for the cooperative-directed weighted network; Easy to implement and understand;	Limited scope; Absence of promotional degree.
[42]	slashdot dataset	Universal and local opinion leaders identified based on the meta-heuristic firefly algorithm in global and regional clusters. The reputation of each user is recognized based on an objective function. An improved Louvain method is also developed to select clusters in social networks.	Innovation and easy to implement; High accuracy; Suitable for dense datasets.	Limited parameters; Applicable for static datasets
[95]	travel community dataset	Proposed a model that selected prominent users in the virtual travel community. A social network analysis-based approach is used that calculates the text, explication reputation, and operations to express the impact on human determination.	Suitable for virtual transit groups; effectively measured the control of opinion leader influence.	Significant only for the virtual travel community; A lesser number of features examine for recognition.
[43]	Wiki-vote and synthesized datasets	A unique and different whale optimization-based meta-heuristic algorithm suggested discovering users' reputations in online social networks. Initially, the optimization function was measured using their centralities, and the following various optimization functions were deployed on the proposed algorithm to identify regional and universal opinion leaders.	Operated better for large data sets; Improved whale optimization algorithm suggested with low complexity.	Applicable for static datasets; Only considered user centrality for optimization function.
[75]	Higgs Boson data from Twitter	A procedure is addressed based on the in-degree and out-degree nodes to discover the most prominent user in the network. Betweenness centrality measures are used to designate the user as an opinion leader. For community classification, the usual Louvain procedure is used.	Straightforward and uncomplicated; Easy to execute; Used simple statistical formulas.	Acceptable only for static datasets; limited centrality measured deliberated.
[44]	Wiki-vote and Bitcoin OTC trust-weighted network	Game theory-based unique procedure determined the opinion leader clusters based on the trust-trustee tree and provisional probability. Shapley value is used to calculate the individual payoff. Opinion leader clusters are recognized based on the most significant aggregated synergy.	Potential innovation of game theory; Represent the power of significant users by their synergy.	Applicable for static data set; Minor parameters used for measuring distance.

Just Accepted

Besides the mentioned approaches, various investigators proposed different moves toward finding opinion leaders in multiple domains using numerous enormous fields such as e-commerce, computer science, sociology, political science, healthcare, business, mathematics, and marketing [24,28,83,101,102]. They captured the critical features of the realm and knowledge about user behavior based on actions and activities. In [73], the researchers proposed an approach in which the representation power of GNN is combined with the logic of the Markov Logic Network to develop a unique ExpressGNN mode to encode the knowledge graph. Another approach designed a Graph-based neural model called GoRecfor opinion

leader identification in the recommendation system [92]based on opinion leader and items interaction. A translation-based embedding method is used to stimulate opinions, and the GNN model is deployed for the opinion diffusion process for better suggestions. Another approach is used to solve the social influence locality problem using GNN[72]. The user's latent features are discovered, and the social influence over their neighbor's action status is identified in online social networks. A GNN-based learning framework called Deepinf includes network embedding, graph convolution, and self-attention techniques. The proposed work performed well w.r.t. Precision, Recall, and F1-score. The limitation of the work is that it uses the random walk to gather the information without any consideration.

Thus, the entire proposed techniques, algorithms, models, frameworks, and approaches can belong to any one or more of the class(es) as; i) Geographical measures based on centralities, structural holes, homophily, and network structure, ii) Data mining methods based on clustering, text mining, sentiment analysis, and pattern mining techniques, iii) Definitive measures based on the survey, polling, interview, and interpretation, iv) Dispersal process-based methods depend on opinions, sentiments, influence, coalitions, and reputation, v) Statistical measures based on the clustering coefficient, complex parameters, non-parameters, and estimators, vi) Hybrid methods based on mixed frameworks, integrated centralities, and ontologies, vii) Theoretical methods are based on concepts, assumptions, phenomenon, and experiences.

Other factors that also affect the opinion leader detection mechanism and are used as a mediocre in any analysis involve the user's physical characteristics, the total number of tweets posted by the user, retweet response time, social media usage frequency, trust, community structure, kind of datasets, data collection, cleaning, transformation, domain knowledge, etc. Despite the various encroachments in opinion leader detection methodologies, we have identified the following shortcoming in the existing methods:

- **The exploitation of traditional approaches:** Generally, most of the stated techniques followed the classical courses, including centrality measure, network topology, network dynamics, etc., but as the technology changed, new methods and models, such as the deep learning-based model, came into the frame that significantly provides the better results. In this paper, we have also used the advanced GNN-based model that efficiently detects the opinion leader in the social network.
- **Highly multifaceted:** Most techniques apply complex mathematical formulas, statistical methods, and compound functions for analysis and evaluation. The time and space complexity to execute these procedures are also very high and take a large amount of storage memory. Our approach is based on the GNN model that took lots of space during execution but produced more optimized and improved results than other models.
- **Influence of data mining techniques:** For the last many years, data mining-based approaches such as classification, regression, clustering, text mining, association rule mining, etc., performed well for the majority of the real-world application. Although researchers also utilized some data mining techniques in social networks to discover opinion leaders, they have not achieved better outcomes due to the dynamic nature and excessive data.
- **Restricted datasets:** Normally, most methods are appropriate and perform well with static social network datasets. Some researchers also performed operations and evaluations on online review forums, blogs, citation networks, trust networks, etc. Although we also use static datasets to corroborate the proposed model, we investigate and experiment with different datasets to validate and authenticate the suggested model.
- **Insignificant accrual results:** It is observed that almost all the techniques produced the optimized outcome according to specific datasets. Once they are applied to some other dataset, their performance might be reduced or not produce the optimized results. We develop a model that works well with almost all datasets and gives

Just Accepted

nearly the same routine. We also compare the outcomes based on accuracy, precision, error rate, and execution time with other standard SNA measures.

- **Lack of feature vectors:** Most approaches used the node's attributes and social network properties to access opinion leaders. Adjacency or connection matrix is derived for depicting the predetermined graph in 2-D format. In contrast, GNN uses network embedding representing the node and edge features in low-dimension space while protecting the network knowledge and formation. The primary advantage of feature vectors is determining the hidden dependencies among the nodes and links in the network.
- **Ineffective to control network size:** Sometimes, handling a considerable amount of data and producing the consequence with the same accuracy as limited or low data is challenging. Only a few approaches can significantly control and manage the massive data and optimize outcomes. As we have mentioned, the deep learning-based model performed well for large datasets. Similarly, the GNN model is a deep learning-based model that can manage massive datasets via concurrent computation and high comprehensibility. GNN provides a framework that recursively gathers the node information through the neighborhood's aggregation and transformation.
- **Limited graph representation:** Mainly, all the discussed approaches do not consider the latent features of the graph; they use the network's characteristics, such as clustering coefficient, centralities, density, structural holes, and many more, as the necessary component for analysis purposes. Conversely, GNN models are highly potent, operative, and active on graph province data. Analyzing a graph is a highly complex task compared to other kinds of data, such as images, audio, text, etc. GNN models can represent the structural graph information due to the extensive influence of Graph embedding and CNN.

This study also analyzed that only a few researchers utilized the GNN model's supremacy to discover the opinion leaders in online social networks. The applicability of the proposed model is also meaningful for real-world applications such as recommendation systems, image processing, molecular engineering, knowledge graph, graph optimization, and other diverse fields due to the detailed illustration of graphical data.

3 BACKGROUND

This segment discusses the elementary features of online social networks and GNN. The primary purpose of this section is to understand and take the feel of SNA measures and GNN. First, we discussed the thorough knowledge of online social networks and SNA measures. Next, we discussed in-depth information about GNN.

3.1 Social Network

A social network deliberated as a directed or undirected graph consists of multiple nodes and edges. A node in a graph typically shows an end-user, an actor, a cluster, an organization, a workgroup, a political party, or an individual who performs some activity in the network. In contrast, the nodes' edges show the connections, associations, links, or ties among the nodes. The reference contains the entire list of multidimensional relationships, i.e., the relationship can be one-to-one, one-many, or vice versa, depending on the various mutual understanding and trust. There are multiple types of social networks depending upon the temperament of relationships and multiple users. The network considers a homogenous network if all the same type of users belong to the same community, workplace, region, religion, or country, otherwise regarded as heterogeneous. Other social network analysis factors include centralities, degree, density, clustering coefficient, homophily, triadic and dyadic closure, structural holes, strong-weak ties, and network size[35,61].

Just Accepted

3.2 SNA measures

The social network uses centrality to find the vital node using mathematical formulas and graph theory-based concepts. Now, we discuss the brief of various centrality measures as follows:

- **Degree Centrality (DC)**: The degree centrality of a node is the summation of all the direct links associated with the node.
- **Betweenness Centrality (BC)**: Betweenness centrality (BC) can be defined as the fraction between the total number of existing shortest paths passing through the node to the total number of the current shortest paths in the network.
- **Closeness Centrality (CC):** Closeness centrality assigns a value based on the sum of the length of the shortest paths between the node and all the other nodes in the network.
- **PageRank Centrality (PR):** PageRank centrality is used to uncover influential or important nodes whose influence extends beyond just their straight acquaintances.
- **EigenVector Centrality (EC):** EigenVector Centrality is used to identify the influence of a node in the network. A value is assigned to each node based on the concept that a highly connected node has a high score than a node with a low score.
- **LeaderRank Algorithm (LR)**: In the LeaderRank algorithm, a score is assigned to each node based on a random network walk using the adjacency matrix and out-degree of the node. A mathematical formula is used to iteratively compute the node's rank at a specific time [58].
- **K-shell Decomposition (KSD):** K-shell Decomposition identifies the key nodes on the network based on the maximal marginal influence degree. The nodes are arranged in different buckets based on their significant degree.
- **Cross Clique Centrality (CCC):** Cross Clique Centrality determines the node's degree of association with the clique in the network. A clique is a subgraph of a graph in which every node is directly connected. A higher Cross Clique Centrality node is connected with more cliques in the network[27].
- **Katz Centrality (KC)**: Katz centrality is used to compute a node's comparative degree of influence. For the computation purpose, direct neighbors of the node are considered, and the nodes connected with those neighbors thought any walk also focused[45].
- **Clustering Coefficient (CC)**: The clustering coefficient of a node refers to the node's affinity to make a coalition based on the total number of triplets in the social network. If the nodes are connected densely with each other, the clustering coefficient of the network would be higher. So, it is the average of the densities of the neighborhoods of all the nodes. It depicts the embeddedness of the nodes in the network. So the simple formula to calculate the clustering coefficient of a node *i* in an undirected graph is as follows:

$$CC_i = \frac{2 * N_i}{d_i(d_i - 1)}$$

Where N_v is the total number of edges that exists between the neighbors of node i while d_i is the degree of node *i.* The global clustering coefficient of graph G is the average of the clustering coefficient of all the nodes in the network.

$$CC(G) = \frac{\sum_{j \in V} CC_j}{V}$$

- **Diameter:** The graph's diameter is the maximal length between a couple of nodes. In other words, It is defined as the highest length between the pair of vertices. If a network has a long diameter than the average path length, the vertices are not distributed and connected similarly over the network.

3.3 Graph Neural Network

Just Accepted

The GNN is ubiquitous and pervasive in depicting deep neural networks on graph structure data. Naturally, the developed deep learning-based models are not so capable of managing and optimizing graph data. For example, CNN is a sound building for structured grid data, while the RNN sounds suitable for time series data and progression. The GNN-based model integrates both of these frameworks without any geographical constraints. Usually, the adjacency matrix or variations are used as input data in the previous build-up approach. The adjacency matrix's primary issue is the dependency on the arrangement of nodes. Considering the isomorphic graph and evaluating it, the different forms of adjacency matrix give the same network's other output. So, the first primary problem with the graph data is that it can not be represented in Euclidian space, i.e., it can not be depicted in any coordinate system [86].

The second problem with the graph is that they do not have a fixed organization because of isomorphism. So, one of the foremost benefits of GNN is to produce the same results for all possible permutations. The leading function of the GNN is to identify the node embedding of each node by considering the information received from its neighbors. In Fig.2, we observed that different nodes could be embedded in n-dimensional Euclidian space through respective feature vectors. A Euclidian space or vector space is the n-dimensional (usually 2-dimensional or 3-dimensional) space to store x-points of real numbers. Graph embedding techniques such as Locally Linear Embedding, HOPE, Word2vec, DeepWalk, Node2vec, Structural Deep Network Embedding, Autoencoder, and many more are used for capturing node's state information [33]. The state of the node is updated according to the neighbor's participation. A local transition function is distributed mutually among all the nodes, accountable for the state modification, while the local output function defines the produced outcomes.

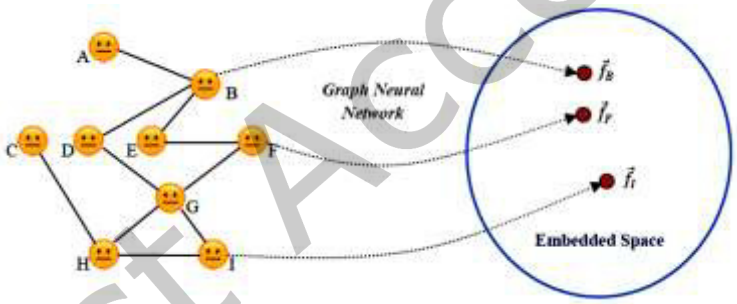

Fig.2. Graph implantation in embedding space using Graph neural network

During the message passing phase, the node's network embedding message transformed and updated the node's state according to the node's neighborhood, as shown in Fig.3. All the corresponding neighbors aggregated and updated the embedding information received from a node.

Just Accepted

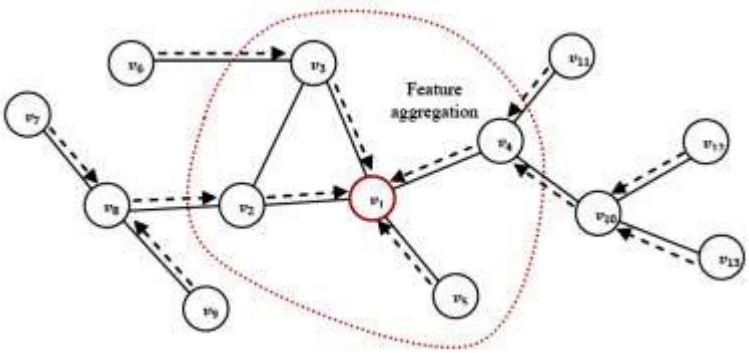

Fig.3. Feature aggregation by a node

Therefore, technically, in the conventional GNN, the feature vector of a node x at (l-1)-th layer is represented by $\vec{f}_x^{l-1}$, modified using the cumulative feature vectors collected from the neighborhood set И(x) of node x, and probably the weight $w_{x,y}^{l}$ received from neighbor y. The aggregation function is repeated up to the L layer, and the feature vector of the (l-1)-th layer becomes the input of the l-th layer. Hence, after the total L(1,2,3,...,l) number of repetitions, node x received the L-th order feature vector representation via their neighbors, as shown in Fig.4. The feature learning representation of node x at layer l is indicated in Eq.(1) and Eq.(2).

$$\vec{f}_{И(x)}^{l} \leftarrow \text{Transformationl (Aggregation (} [\vec{f}_x^{l-1}, w_{x,y}^{l}] \mid y \in И(x)])) \quad \ldots (1)$$

$$\vec{f}_x^{l} \leftarrow \text{Join } (\vec{f}_{И(x)}^{l} U \vec{f}_x^{l-1}) \quad \ldots (2)$$

The Aggregation function can be the min-max or average pooling function in the above equations. At the same time, the Transformation is a model-driven operation that performs some non-linear transformations based on input received from (l-1)-th layer and a few non-linear variables, i.e., σ(.). Join is a union operation used to combine the feature vector of a node x and collective neighborhood depiction.

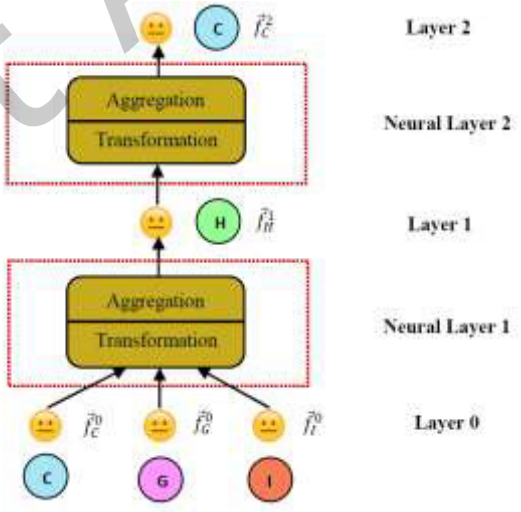

Fig.4. The layered architecture of graph neural network

Just Accepted

3.3 Problem statement

As mentioned, a social network represents a graph consisting of multiple nodes and links. It is noticeable that some nodes in the network have more control and influence over other nodes. So, it is essential to identify such kinds of nodes in the network. Moreover, due to the high recognition, versatility, and applicability in real-world applications, more attention has been shifted to the GNN model. Therefore, we propose a GOLI model that maps the non-negative reputation score with the node based on reputation aggregation and degree of trust in online social networks. This model is also effective for the network with a higher density as the network size increase gradually, the nodes receive more information from the neighbors.

4 PROPOSED MODEL

In this segment, we represent the proposed GNN for Opinion Leader Identification (GOLI) model in online social networks. Initially, we focused on the motivation and key factors behind the generation of the model. Next, we discuss the proposed model architecture that consists of trust calculation, centrality reconciliation, and reputation aggregation. We also discuss the training mechanism of the model in this section.

4.1 Motivation

We found the following aspects that stimulate the opinion leader identification process.

- **Centrality knowledge:** A node with high centrality is considered the most powerful node in the network with no other measure. However, this is not the right way for assortment, yet one of the essential factors for the opinion leader selection. Centrality defines the power, connectivity, and influence of a node in the network.
- **Neighborhood consciousness:** A node is connected with multiple nodes in the network directly or indirectly. The neighbors of a node directly communicate with the other nodes and share state features. Dyadic and triadic relations are formed due to the neighborhood's homophily properties, i.e., the node's affinity to connect with the nodes having analogous attributes.
- **Mutual trustworthiness:** Trust is one of the well-known factors for the construction and development of the network. Connections between the nodes break or become weak due to the lack of trust. So, it is vital to consider and measure the degree of trust among the nodes. A trust can be direct, indirect, or recommended, depending on mutual connection and experience.
- **Utilization of reputation:** Besides network structure, node reputation also needs and provides lots of information to find opinion leaders. The reputation of the node signifies its prominence, power, and strength of the node.
- **Agile adjustment:** In the real-world, different kind of social network exists because of their working style, structure, content delivery, and users. So, it is essential to make such a model that could be easily adaptable to most social networks and may utilize their characteristics effectively.
- **Social collaboration:** Building a strong community and network structure requires designing a system that works towards achieving the goal through social involvement and association. Social collaboration determines the best strategy, structure, and community that focuses on expanding and developing innovations in business management. Thus, for identifying opinion leaders, the role of social collaboration is substantial and unavoidable.
- **Interpretability:** Often, it is very demanding to understand human reasoning and represent that reasoning as an abstract concept. The main reason behind this lack is the complex structure of social networks and the inability to interpret classification results correctly. Interpretability is also required to identify the sub-structure in the network for decision-related jobs. Therefore, interpretability depicts the degree to which an analyst can comprehend the foundations of assessment.

Just Accepted

- **Graph embedding:** Graph embedding involves the representation of the network from high dimension vector to a low-dimension space by catching the essential feature by dropping dimensions. So, the primary significance of graph embedding is representing the network so that various vector-compatible statistical, mathematical, and machine learning-based operations can be performed on the graph. Therefore, a model is needed to support such embedding and represent the data in the vector of statistical values for comparison with other structures.
- **Non-Euclidean spatial data:** The social network structure is complex and huge, so it is impossible to represent those data in Euclidean space or a grid-like structure. If the social network is modeled in 3-D space, most critical information, like edge quality, edge direction, node value, etc., must be lost. Thus it is not a worthy approach to map those attributes into much higher space for embedding purposes.
- **Representation learning:** Generally, learning and understanding the theoretical and fundamental concepts makes things better for predicting and classification purposes. Thus, representation learning is required to determine and extract the latent features from the original network and transform the data into some new representation of interest required for prediction.

Therefore, the primary target of the proposed model is to accomplish all the mentioned requirements as much as possible. The general building block of the proposed methodology is shown in Fig.5. Initially, we estimated the feature vector matrix of the nodes. The feature vector matrix comprises the latent feature derived from the network topology and node neighbors' information. The value of the feature vector varies from network to network because of different working styles and topologies. Next, the anticipated trust network is formed based on the feature vectors and trust. Here, trust plays a critical function in developing a network. The leading cause behind the generation of trust networks is to informally predict the degree of confidence and trustworthiness among the nodes to sustain the decision-making process in the network.

In some cases, where trust is not a significant concern, the trusted network would be ignored. Next, we apply the proposed GOLI model to calculate the node's reputation. Finally, the top-n opinion leaders elect based on the uppermost reputation score.

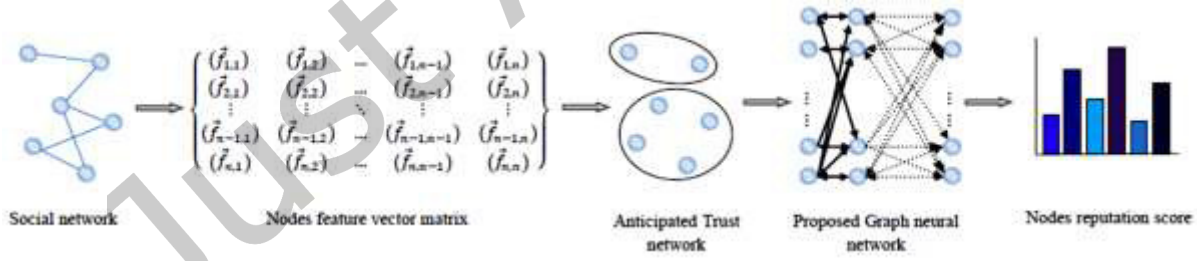

Fig.5. The building block of the proposed GOLI model

We use a few symbols during experimental analysis and model generation. The symbol, along with their description, is shown in Table 2.

Just Accepted

Table 2. Used symbols along with their description

$\mathcal{R}$	Set of nodes with a recognized reputation score
$\vec{f_x}$	The feature vector of node x
L	Total number of reputation aggregation layers
И(x)	Total numbers of first-order neighbors of node x
r_x^{η}	Reputation score of node x by Reputation Aggregator (RA) in η -th layer
L_{η}	η-th level of the reputation aggregation layer
r_x^*	Final reputation score of node x
d(x)	In-degree of node x
d'(x)	Preliminary centrality of node x
$T_{x,y}^{\eta}$	Node x trust on node y calculated by RA at η-th layer
$\vec{\delta}_{\eta}$	Attainable parameters used by RA at $\eta-$ th layer to measure $T_{x,y}^{\eta}$
β_{η}, γ_{η}	Learnable parameters used for tuning and normalization at η-th layer

4.2 Structural design of Model

The straightforward GOLI model architecture consists of a solo reputation aggregation layer(i.e., l-th layer) trailed by the centrality reconciliation module, as shown in Fig.6. Initially, the feature vector of nodes is computed based on the various attributes depending on the network's nature and services—the feature vectors ensemble the latent features, which grant more embedding knowledge of a node. Next, the information received from the feature vectors utilizes to measure the node's initial reputation by its neighbors at layer zero. As soon as all nodes receive the information about their neighbors' initial reputation, they anticipate a trusted network. Although the construction of the expected trust network is merely based on user experience, social persuade privacy and social interaction with other nodes.

Further, the single reputation aggregation layer cumulates the reputation score and the measured trust received from multiple neighbors. All the layers follow the exact instructions simultaneously for all the nodes. Hence the entire procedure supports parallel computation.

Now we explain the whole procedure along with operational notations empirically. Let L be the total number of aggregation layers and L_{η} be the η-th number of the reputation aggregation layer. We describer $r_x^{\eta-1}$ as the reputation score of node x by reputation aggregator in (η-1)-th layer that would be transmitted to cumulate the reputation score at η-th layer. At the initial layer, the reputation score r_x^0 of the node measured by applying the Artificial Neural network (ANN) on the input feature vector $\vec{f}_C^0$. The reputation score produced by the preceding layers (L>0) uses for calculating the mean of the reputation score in the succeeding layers. Therefore, each layer's reputation score's importance also strongly influences the aggregate reputation score estimation. The reputation aggregator also considers the trust $T_{x,y}^{\eta}$, obtained from its corresponding neighbors for the computation of reputation score.

Further, centrality reconciliation deploys by each reputation aggregator at each layer because of the enhanced node importance. Each aggregator uses the different parameters β_{η} and γ_{η} for tunning and optimization purposes. The final reputation score r_x^* at the ending L-th layer is computed by measuring the mean of the multiplication of extended and reassigned centrality and reputation score along with lateral constant for normalization.

Just Accepted

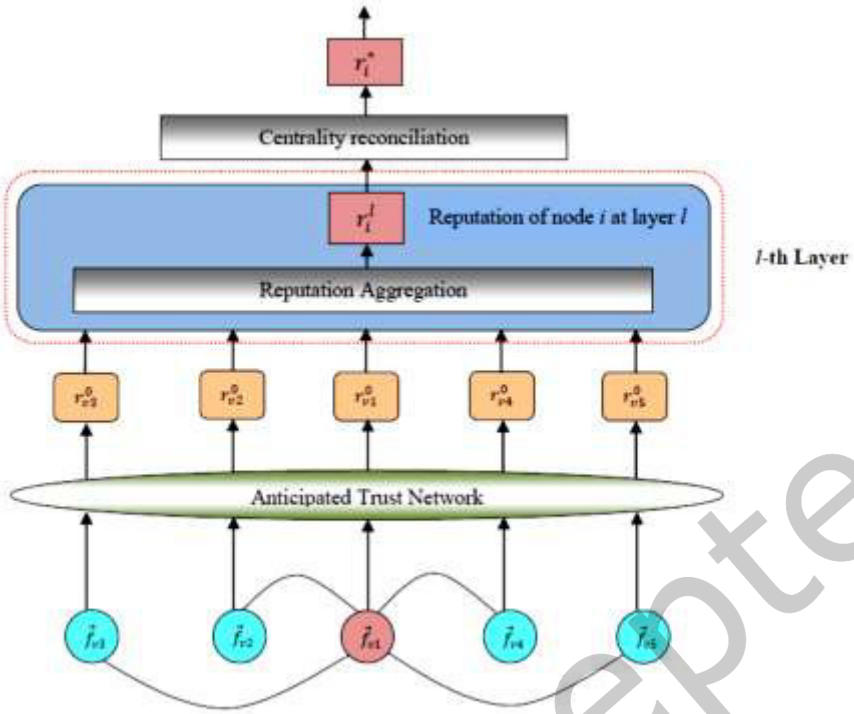

Fig.6. Layered architecture of the GOLI model

Now, we discuss every step in detail as follows.

4.2.1 Centrality Reconciliation

Centrality is a significant component affecting the node's attractiveness in the network. A node with higher centrality captures the center of attraction and impacts the influencing power of other nodes. Generally, multiple centralities measures, such as degree, betweenness, closeness, eigenvector, PageRank, etc., has high gratitude for a critical leader's recognition [29]. So, the preliminary centrality d'(x) of node x is described in Eq.(3).

$$d'(x)= \log(d(x) +\varepsilon) \quad \ldots (3)$$

Here, ε is a constant used for scaling and normalization. Further, the node in-degree centrality has an active impact on the opinion leader identification, so we updated and reassigned centrality $d^*_\eta(x)$ for the final reputation score calculation. The updated centrality of node x is measured by the score aggregator r^η_x at η-th layer is represented in Eq.(4).

$$d^*_\eta(x)= \beta_\eta * d'(x) + \gamma_\eta \quad \ldots (4)$$

Here, β_η and γ_η both are the learnable parameters used for tuning and optimization purposes. We have also utilized this centrality parameter to calculate the node reputation score.

4.2.2 Early Trust computation

Trust plays an active role in online social networks for inherent future behavior and actions. Trust is a noteworthy feature that supports forming a connection between the users [31][34]. In online social networks, the concept of trust can be broadly classified into two categories: social and system. Social trust is based on

Just Accepted

user attitude, behavior, social interaction, reputation, social status, and human psychology. Such trust is eventually subjective depending upon user expectations and trustworthiness without any upcoming activities. The system trust is raised from the various online platforms, i.e., online social networks where users communicate and interact and provide responses, feedback, and opinions based on past interactions and experiences. Generally, it has been observed that the feedback and response system is influenced by various other factors like knowledge, confidence, experience, cognizance, etc. Hence, identifying absolute trust is eventually complex in online social networks [91].

In this research, three types of trust: direct trust, indirect trust, and recommended trust, respectively, are defined to measure the early trust of each user and support in establishing a trusted network. In direct trust, the trust is derived from the connections that are the immediate neighbors of a node. In indirect trust, the trust is derived in a subsidiary manner. The nodes that are not directly connected with the specific node generate the information from other sources and, after processing, forward the outcomes to adjacent nodes. In Recommended trust, the trust is endorsed by other users either directly or indirectly influenced from a future perspective. Experts, decision-makers, and promoters generally influence such trust to improve their products' productivity in online social networks. Various attributes are used in the different social networks to define trust based on the network dynamics and characteristics. In this research, we have used Mutual friends (MF), Conjoint attributes (CA), Total number of direct followers (TDF), Total active duration (TAD), Total number of Posts (TNP), user's review (UR), user's tagging Information (UTF), Followers/Fellowes Quotient (FFQ) parameters are used to identify the user's early trust. The description of each attribute are as follows:

- **Mutual friends (MF):** Mutual friends refer to the number of familiar friends between the users. A notion of homophily plays a significant role in establishing communication between the users. A component u_{MF} is used to depict the mutual friends between users as follows:

$$(\mathrm{u_{MF}})_{\mathrm{i}} = \begin{cases} \dfrac{(\mathrm{t_{MF}})_{\mathrm{ij}}}{\mathrm{A_{MF}}} & (\mathrm{t_{MF}})_{\mathrm{ij}} < \mathrm{A_{MF}} \\ 1 & (\mathrm{t_{MF}})_{\mathrm{ij}} \geq \mathrm{A_{MF}} \end{cases}$$

Where, t_{MF} is the total number of mutual friends between users i and j while A_{AF} is the average of the number of mutual friends of each user in the network.

- **Conjoint attributes (CA):** Conjoint attributes refer to the total number of shared features between the users in the network. A component u_{CA} is used to represent the conjoint attributes between users as follows:

$$(\mathrm{u_{CA}})_{\mathrm{i}} = \begin{cases} \dfrac{(\mathrm{t_{CA}})_{\mathrm{ij}}}{\mathrm{A_{CA}}} & (\mathrm{t_{CA}})_{\mathrm{ij}} < \mathrm{A_{CA}} \\ 1 & (\mathrm{t_{CA}})_{\mathrm{ij}} \geq \mathrm{A_{CA}} \end{cases}$$

Where $(t_{CA})_{ij}$ is the total number of common attributes between user i and j while A_{CA} is the average of number of features shared by the user in the network.

- **Total number of direct followers (TDF):** It refers to the total number of followers who openly follow the specific user in the network. A component $(u_{TDF})_i$ is used to represent the total number of direct followers of user i as follows:

$$(\mathrm{u_{TDF}})_{\mathrm{i}} = \begin{cases} \dfrac{\mathrm{t_{TDF}}}{\mathrm{A_{TDF}}} & \mathrm{t_{TFD}} < \mathrm{A_{TDF}} \\ 1 & \mathrm{t_{TDF}} \geq \mathrm{A_{TDF}} \end{cases}$$

Where, t_{TDF} is the total number of direct followers of user i and A_{TDF} is the average number of direct followers of the entire users in the network.

Just Accepted

- **Total active duration (TAD):** It refers to the total busy time that a user spends on online social networks. An element $(u_{TAD})_i$ is used to represent the total active duration of user *i* as follows:

$$(\mathrm{u_{TAD}})_\mathrm{i} = \begin{cases} \frac{\mathrm{t_{TAD}}}{\mathrm{A_{TAD}}} & \mathrm{t_{TAD}} < \mathrm{A_{TAD}} \\ 1 & \mathrm{t_{TAD}} \geq \mathrm{A_{TAD}} \end{cases}$$

Where, t_{TAD} is the total active time of user *i* and A_{TDF} is the average total active time of the entire users in the network.

- **Total number of Posts (TNP):** It indicates the total number of posts posted by a user on the online social network. An element $(u_{TNP})_i$ is used to represent the total number of posts posted by the user *i* as follows:

$$(\mathrm{u_{TNP}})_\mathrm{i} = \begin{cases} \frac{\mathrm{t_{TNP}}}{\mathrm{A_{TNP}}} & \mathrm{t_{TNP}} < \mathrm{A_{TNP}} \\ 1 & \mathrm{t_{TNP}} \geq \mathrm{A_{TNP}} \end{cases}$$

Where, t_{TNP} is the total number of posts by user *i* and A_{TNP} is the average of the total number of posts posted by other users in the network.

- **User's review (UR) (RT):** It refers to the total number of reviews or comments posted by the user on the online social network. A factor $(u_{UR})_i$ is used to represent the total reviews of user *i* as follows:

$$(\mathrm{u_{UR}})_\mathrm{i} = \begin{cases} \frac{\mathrm{t_{UR}}}{\mathrm{A_{UR}}} & \mathrm{t_{UR}} < \mathrm{A_{UR}} \\ 1 & \mathrm{t_{UR}} \geq \mathrm{A_{UR}} \end{cases}$$

Where, t_{UR} is the total number of posts by user *i* and A_{TNP} is the average of the total number of posts posted by the entire users in the network.

- **User's tagging (UT) (IDT):** It refers to the number of times other users tag a particular user in their messages. A factor u_{UT} is used to represent the user *i* tagging by user *j* as follows:

$$(u_{UT})_i = \begin{cases} \frac{(t_{UT})_{ij}}{A_{UT}} & (t_{UT})_{ij} < A_{UT} \\ 1 & (t_{UT})_{ij} \geq A_{UT} \end{cases}$$

Where, $(t_{UT})_{ij}$ is the total number of times user *i* is tagged by user *j* and A_{UT} is the average number of times other users are tagged in the network.

- **Followers/Fellowees Quotient (FFQ) (IDT):** A component $(u_{FFQ})_i$ indicates the fraction between the total number of followers of a user and fellowees by the user in the network as follows:

$$(u_{FFQ})_i = \begin{cases} \frac{q_{FFQ}}{A_{FFQ}} & q_{FFQ} < A_{FFQ} \\ 1 & q_{FFQ} \geq A_{FFQ} \end{cases}$$

Where, q_{FFQ} is the value of followers/followees quotient of user *i* and A_{FFQ} is the average of followers/followees quotient of the other users in the network.

These elements imitate the user's cumulative credibility and reproduce the inclination to establish an alliance with other users. Thus, a new method is proposed to compute the early trust of each user in online social networks. The pseudo-code of the technique is shown in Algorithm 1 as follows.

Just Accepted

Algorithm 1: Early trust (ET) computation algorithm

Input: *n* number of users in the Social network.

Output: Early Trust (ET) of user *i.*

Steps:

1. $ET_i=\{0\}$;
2. **for** ∀ node i ϵ {V} do

   Measure Early Direct Trust (EDT) of the node *i*

   $EDT(v_i) = \sum_{j\epsilon N_{(i)}} w_1(u_{MF})_i + w_2(u_{TAD})_i + w_3(u_{TNP})_i + w_4(u_{CA})_i$

   Where $N_{(i)}$ is a set of neighbors of user i and w_n (n =1, 2, 3, 4) are the weightage assigned to each parameters.

3. **If** $(EDT(v_i) > p)$ then

   $ET_1 = EDT(v_i)$

   else

   $ET_1 = 0$

   end if;

4. **Measure Early In-Direct Trust (EIDT) of the node *i***

   $EIDT(v_i) = \sum_{j\epsilon W_{(i)}} \sum_{k\epsilon W_{(i)}} (u_{UT})_i \, C_k$

   Where $N_{(i)}$ the set of neighbors of a neighbor of user i and C_k is the local clustering coefficient of node i.

5. **if** $(EIDT(v_i) > q)$ then

   $ET_2 = EIDT(v_i)$

   else

   $ET_2 = 0$

   end if;

6. **Measure Early Recommendation Trust (ERT) of the node *i***

   Suppose a user received m number of recommendations from other

   $RT(v_i) = \beta + \alpha \sum_{j\epsilon W_{(i)}} \frac{A_i}{\acute{M}_j^{out}} (u_{UR})_i \, RT(v_i)$

   Here, β is the tunable balance parameters, A_i is the adjunct matrix of the graph *G* w.r.t. node *i* and $\acute{M}_j^{out}$ is the out-degree of node *j*.

7. **if** $(ERT(v_i) > r)$ then

   $ET_3 = ERT(v_i)$

   else

   $ET_3 = 0$

   end if;

   end loop;

8. $ET_i = \sum_{i\epsilon N}(ET_1 + ET_2 + ET_3)$
9. **end;**

The above algorithm defines the three constant threshold variables p, q, and r: (p, q, r) ϵ R, and all the variables vary in the range [0.5, 1), respectively. The threshold value of the entire three variables depends on social network construction, size, and dynamics.

4.2.3 Trust measurement

As we have discussed, trust is a significant concern about neighborhood consciousness. The proposed GOLI model mainly focuses on neighbor trustworthiness. Trust also plays a lead role in opinion leader identification in the social network [7,46]. Even in the real world, only a trusted person can gain the

Just Accepted

other's favor and support to disseminate a particular thing. Trust mainly depends on direct and indirect interactions. Sometimes, recommended trust is also significant for the decision-making process. GOLI follows the one-order trust calculation and utilizes the initial reputation value that a node gained from direct neighbors and their neighbors. The trust between the nodes is calculated at each layer by the Reputation Aggregator (RA). So, the node x trust $T_{x,y}^{\eta}$ on node y calculated by RA at η–th layer represented in Eq.(5).

$$T_{x,y}^{\eta} = \frac{\exp(\alpha_{\delta}(\sum \vec{\delta}_{\eta}{}^{T}(r_x^l \times |r_y^l)))}{\sum_{z \epsilon И(x) U \{x\}} \exp(\alpha_{\delta}(\sum \vec{\delta}_{\eta}{}^{T}(r_x^l \times |r_z^l)))} \quad \ldots (5)$$

Here, $\vec{\delta}_{\eta}$ is a power vector used by RA at η-th layer while α_{δ} is non-linearity. r_x^l, r_y^l, and r_z^l depicts reputation score of node x, node y, and node z respectively by reputation aggregator in η -th layer. $|\times|$ operator indicates the multiplication operation between two reputations aggregation scores.

4.2.4 Reputation aggregation

As we have discussed earlier, instead of a node embedding mechanism, we use the reputation aggregation score to find the importance of a node in the network. The proposed model used the mean weighted assemblage of the median values from the node and its neighbors. One of the benefits of score aggregation over node embedding is to trim down the overall number of total parameters. The initial reputation score r_x^0 of node x is measured using any neural network and feature vector $\vec{f}_x^0$ of the node. We have used the fully connected Artificial Neural Network (ANN) that returned the initial importance based on network characteristics and knowledge, as shown in Eq.(6).

$$r_x^0 = \mathrm{ANN}(\vec{f}_x^0) \quad \ldots (6)$$

Further, the reputation aggregation score of node x at layer η,i.e., $r_x^{\eta}$is calculated in Eq.(7).

$$r_x^{\eta} = \sum_{y \epsilon И(x) U(x)} r^{\eta-1}(y)\, T_{x,y}^{\eta} \quad \ldots (7)$$

Where $T_{x,y}^{\eta}$ represents node x trust on node y calculated by RA at η-th layer, $И(x)$ indicates the total number of first-order neighbors of node x, and $r^{\eta-1}(y)$ reputation aggregation score received from the neighbors in the preceding $(\eta - 1)$ layers.

Thus, in a nutshell, The reputation aggregation score of a node x is represented as in Eq.(8)

$$r_x^L = \begin{cases} \mathrm{ANN}(\vec{f}_C^0) & \text{if } L = 0 \\ \sum_{y \epsilon И(x) U(x)} r_x^{\eta-1}(y)\, T_{x,y}^{\eta} & \text{if } L > 0 \end{cases} \quad \ldots (8)$$

As we also mentioned, centrality reconciliation $d_{\eta}^{*}(x)$is applied at the last concluding layer to include the centrality weightage of node x. Thus the concluding reputation score r_x^* of node x is the mean of the multiplication centrality reconciliation and reputation aggregation score of node x using σ a lateral constant, as shown in Eq.(9).

$$r_x^* = \sigma(\mathrm{mean}\{d_{\eta}^{*}(x) * r_x^L\} | \eta = 1,2,3,\ldots,L) \quad \ldots (9)$$

4.2.5 Model training

Training the model for measuring the reputation score as accurately as possible is required to avoid overfitting and underfitting. Due to the dynamic nature of the social network, it is very challenging to find the ground truth about the network. Still, we train the GOLI model by calculating the mean squared error between the obtained reputation score and the known reputation score t(i) from the set $\mathcal{R} \subseteq$ V. Hence; the loss function S is represented using Eq.(10).

Just Accepted

$$S = \frac{1}{V}\sum_{i \in \mathcal{R}} (r_i^* - t(i))^2 \quad \ldots (10)$$

In this research, we have applied static datasets whose labels are defined with the instances. Without knowing the 'label' of each instance, it is impossible to recognize the reputation score t(i) that supports the computation of mean squared error. The 'label' in each dataset signifies the class containing three types of value: opinion leader, follower, and neutral user. Thus, the term 'label' only signifies the 'class name' for a specific user instance to which it belongs.

4.2.6 Parameter setting

This research uses various parameters for calculating reputation score, trust, centrality, and model learning purpose. The weighted optimized value of these parameters obtains during the model learning. The accurate parameter value enhances the predictive power and decreases the training time of the model. This research considers issues like overfitting, learning rate, batch size, and gradient descent for local minima calculation. Thus, we choose the following parameter values based on multiple tests, as shown in Table 3.

Table 3. Parameters value with the corresponding testing value range

Parameter	Optimal value	Testing value range
Learning rate(τ)	0.01	(0,0.5]
Batch size(B)	500	[100, 2000]
Total number of layers (L)	16	[2, 30]
Total number of epochs	400	[100, 1000]
$\vec{\delta}_\eta$	0.25	(0,1]
β_η, γ_η	Varies in each layer	(0,1]

4.3 Model's Merits

- **Sustain parallelism:** One of the main reasons behind choosing the GNN is that it maintains workflow parallelism, i.e., all the nodes perform the computation concurrently without any external inference. The calculation involves feature aggregation, reputation score aggregation, trust calculation, etc. The entire nodes receive and send the information parallelly to other neighbors during the model's training.
- **Capable of handling big data:** Often, most models and approaches can not control the enormous data size, but the GOLI model is GNN based model that quickly takes a large amount of data. The dataset's density is a significant factor in finding the number of strong-weak ties and triangles. GOLI analyzed the latent features of nodes efficiently because of the profoundly layered architecture. As soon as the network's volume gradually enhanced, all the nodes functioned efficiently and aggregated neighbor's information simultaneously.
- **Support various datasets:** One of the most significant issues with the previous models is supporting a limited number of datasets applicable only in a finite domain. The proposed model is very efficient in holding a wide range of datasets. For authorization, we use the six datasets of the diverse province as input in the model and successfully capture the top-n opinion leaders for each dataset. Thus, it is applicable in various real-world applications.
- **Control network isomorphism:** The proposed model can manage the isomorphic network dilemma by converting the network to graph isomorphic. In network isomorphism, the two networks' structure looks different but identical and shares the same features. Some models produced different results for the isomorphic network, but the proposed model has the same effect.
- **Highly enhanced results:** The proposed model achieved around 92% accuracy, 95.4% precision, 96% recall, and 95% F1-score for all the experimental over other standard SNA measures. Although other models also produced

Just Accepted

improved results, only in the specific field. Our model covers diverse datasets and lucratively achieves the desired target.

5 EXPERIMENTAL SETUP AND RESULTS

This research uses the six real datasets covering different types of online social networks. The main issue behind selecting these datasets is covering all kinds of activities and behavior on the social network. All the datasets have features and services supporting different types of information exchange. We explore the graph analyzing software Gephi 0.9.2 [11] to reveal and investigate. We use Intel Core i7-9700K 9th Generation 3.6 GHz processor and python 3.6 along with networkx, PyTorch, and Tensorflow (with GPU momentum) libraries [80] for instruction interpretation as well as execution. After completing the GOLI model, we found the top-n (n=5) opinion leaders list for entire datasets. Finally, we assess the results with the other standard SNA measures.

5.1 Datasets

5.1.1 Slashdot dataset

Slashdot datasets is an advanced technology-rich news broadcasting website in which website authors submit newsletters and reports related to advanced technologies and techniques. Further, the editors are to evaluate these reports that make their decision about acceptance or rejection. One of Slashdot dataset features is tagging done by one author to other authors as acquaintances or rivals. Therefore, an acquaintance or rival connection establish among the users. The dataset includes a total of 77360 users and 905468 edges among them. We utilized the user's tagging information for initial reputation computation [50].

5.1.2 Epinions dataset

Epinion dataset defines the 'who-trust-whom' network based on the customer comments on a particular product through the website 'epinion.com.' So, the user has to register on the website and then be able to submit their reviews on products. It merely depends on other consumers to follow other reviews or not. The user review then makes a web of trust and integrates the reviews rating to determine the recommendation of products to the customers. The dataset has 75879 users and 508837 connections based on the user's suggestions. This dataset uses the total number of trustors and no rating for reputation computation[76].

5.1.3 LiveJournal dataset

LiveJournal is a famous social networking website for promoting and creating a diary, journal, or blog. If one user is not present in another user's friend list and has no mutual friends, still, they can mutually become friends without any contraction. The dataset consists of 3,017,286 users and 87,037,567 directed links among them. We used friendship relationships and user-to-user citation links for reputation computation[9].

5.1.4 Last.fm dataset

Last.fm is one of the websites related to music and the user's recommendation. A user can seek a different kind of music according to their taste, choice, and advice. So, the website offers a flowless radio service and a variety of styles of music. The website also maintained a specific user profile that is the base for music suggestions. Last.fm network consists of a total of 136,420 users and 1,685,524 connections among them [12].

Just Accepted

5.1.5 Bitcoin alpha trust weighted signed network dataset

Bitcoin alpha trust weighted signed network represents the trusted network in which various customers trade Bitcoins using the Bitcoin Alpha portal. In this trading, it is required to maintain the user's details and separate transactions as all the users' statuses are unidentified, i.e., users have a masked identity. To prevent forgery and supervise trustworthiness, all the members graded in the range of -10 to +10. The user with high positive grading has more reliability and vice-versa. Overall, the network has 3783 nodes and 24186 edges [48].

5.1.6. Weibo-Net-Tweet dataset

Weibo-Net-Tweet network pursues the 'who follows whom' kind of structure. Initially, some random number of users picked up from the network and then collected the total number of followers. The exact process has recursively been carried out, and the collective number of large users formed a vast network. It is observed that, on average, every user has around 200 followers. The dataset includes approximately 1,776,950 users, and 308,489,739 edges exist based on user comments and retweets. We used the user's and followers' profile information for analysis [99].

The summarised description of each dataset is shown in Table 4.

Table 4. Summarized datasets description

Dataset	Nodes	Edges	Density	Avg. Clustering Coefficient	Diameter
Slashdot	77360	905468	0.00032	0.0603	11
Epinions	75879	508837	0.00017	0.0578	14
LiveJournal	3,017,286	87,037,567	1.91*10-5	0.0371	16
Last.fm	136,420	1,685,524	0.00018	0.0822	8
Bitcoin alpha	3783	24186	0.00338	0.0523	7
Weibo-Net-Tweet	1,776,950	308,489,739	0.00019	0.0783	22

5.2 Estimated outcomes analysis and visualization

As mentioned in the preceding section, this section publicized the outcomes of applying the GOLI to real data sets. We initially measure each node's feature vector based on multiple characteristics depending on network topology and neighbor's knowledge. In the social network realm, it is critical to measure trust due to unstable relations among the users. But, as a trust, we consigne a normalized value between 0 and 1 to each node based on network-specific attributes to achieve the experimental motive. Next, we compute each node's initial reputation score and pass the same information to the respective node's neighbors. We use various parameters during the model training and efficient execution. We conduct around 100 tests to find the best possible value of parameters. The model's learning rate is 0.01, and a single batch of 500 observations is put together. A total of 16 layers or channels are used for network configuration and reputation transmission, while the entire process requires around 400 epochs.

Further, the node's reputation score and trust are recursively forwarded to the next level layers, where RA computes each node's aggregated reputation score. Finally, the node with a higher reputation score declares as the opinion leader. This research applies the GOLI model to six datasets; Epinions, LiveJournal, Last.fm, Bitcoin alpha, and Weibo-Net-Tweet, respectively. As we discussed, no ordinary methods are introduced to find the key users in the social network. Still, graph theory's centrality-based standard SNA measures work as state-of-the-art techniques by researchers. In this research, to validate the authenticity

Just Accepted

of the proposed method, the obtained outcomes are compared with the other SNA centralities measures like DC, CC, BC, EC, PR, LR, KC, and CCC. Table 5, Table 6, Table 7, Table 8, Table 9, and Table 10 show the top-n(=5) opinion leaders in each SNA measure along with the used experimental dataset

.

Table 5. Top-5 opinion leaders for Slashdot dataset

User id	DC	User id	CC	User id	BC	User id	EC	User id	PR
23845	0.2344314	65402	0.1927551	26512	0.1447860	29087	0.1334562	40067	0.1145022
65213	0.2344312	28712	0.1927550	39821	0.1447860	11090	0.1334562	3267	0.1145022
40781	0.2344311	8956	0.1927549	6982	0.1447859	61890	0.1334562	18590	0.1145022
1278	0.2344311	44231	0.1927548	55782	0.1447859	39055	0.1334562	72334	0.1145021
55402	0.2344310	71092	0.1927547	1095	0.1447858	4902	0.1334561	50893	0.1145020

User id	LR	User id	KC	User id	CCC	User id	KSD	User id	GOLI Reputation
39056	0.1744398	2985	0.1297095	32801	0.0992714	53883	0.1483287	**39089**	**0.3022736**
2751	0.1744398	18937	0.1297095	7285	0.0992714	9427	0.1483286	**71092**	**0.3022735**
69205	0.1744397	49324	0.1297094	25278	0.0992713	63072	0.1483286	**67845**	**0.3022734**
1184	0.1744397	9849	0.1297094	19378	0.0992713	1278	0.1483285	**56119**	**0.3022734**
59309	0.1744397	29558	0.1297093	48392	0.0992713	18590	0.1483285	**26512**	**0.3022733**

Table 6. Top-5 opinion leaders for Epinions dataset

User id	DC	User id	CC	User id	BC	User id	EC	User id	PR
27852	0.3487869	47720	0.2842291	52358	0.3047477	21158	0.1640095	7364	0.1765642
19983	0.3487868	71958	0.2842290	39068	0.3047475	38694	0.1640093	43626	0.1765641
345	0.3487868	20085	0.2842288	63954	0.3047474	8634	0.1640092	27575	0.1765640
69434	0.3487867	639	0.2842287	28768	0.3047472	28468	0.1640090	58363	0.1765638
54764	0.3487866	11593	0.2842285	13869	0.3047471	67364	0.1640089	11675	0.1765636

User id	LR	User id	KC	User id	CCC	User id	KSD	User id	GOLI Reputation
66931	0.2108933	5839	0.1492218	8492	0.1963723	6895	0.2470412	**20085**	**0.3573947**
482	0.2108933	27493	0.1492218	14271	0.1963723	21482	0.2470412	**37756**	**0.3573945**
26119	0.2108933	70892	0.1492217	25347	0.1963723	4633	0.2470411	**58671**	**0.3573944**
53892	0.2108932	837	0.1492217	39301	0.1963723	34075	0.2470411	**19686**	**0.3573942**
8634	0.2108932	55229	0.1492216	5242	0.1963722	64837	0.2470411	**7665**	**0.3573941**

Just Accepted

Table 7. Top-5 opinion leaders for LiveJournal dataset

User id	DC	User id	CC	User id	BC	User id	EC	User id	PR
2085943	0.1045491	675749	0.0985694	583920	0.1300784	860509	0.0767853	1185760	0.0938963
29581	0.1045491	2960049	0.0985694	1956950	0.1300784	457302	0.0767852	748495	0.0938962
698043	0.1045490	57584	0.0985693	438596	0.1300784	2958690	0.0767852	2986090	0.0938962
584953	0.1045490	957482	0.0985693	857469	0.1300783	6859	0.0767851	48493	0.0938962
1773829	0.1045489	1859684	0.0985693	29586	0.1300783	986849	0.0767851	986893	0.0938961

User id	LR	User id	KC	User id	CCC	User id	KSD	User id	GOLI Reputation
459452	0.0548625	578431	0.0683772	964657	0.0538721	2715732	0.1005183	**759430**	**0.1389832**
2724492	0.0548625	1641545	0.0683772	174573	0.0538721	814432	0.1005183	**1946397**	**0.1389832**
815213	0.0548625	2984649	0.0683771	362430	0.0538720	2047865	0.1005183	**597940**	**0.1389832**
674232	0.0548624	34656	0.0683771	40246	0.0538720	377950	0.1005183	**28575**	**0.1389831**
357190	0.0548624	2845488	0.0683771	1313507	0.0538720	635973	0.1005182	**699301**	**0.1389831**

Table 8.Top-5 opinion leaders for Last.fm dataset

User id	DC	User id	CC	User id	BC	User id	EC	User id	PR
59293	0.2933422	82364	0.1743229	85023	0.1699493	57232	0.1833385	28644	0.1418205
107821	0.2933422	18432	0.1743227	64172	0.1699492	6693	0.1833384	65733	0.1418204
8632	0.2933421	84561	0.1743226	448	0.1699492	28319	0.1833384	38376	0.1418204
17901	0.2933420	117281	0.1743226	16482	0.1699491	118473	0.1833383	9251	0.1418203
14873	0.2933419	1167	0.1743225	59072	0.1699490	928	0.1833381	13932	0.1418202

User id	LR	User id	KC	User id	CCC	User id	KSD	User id	GOLI Reputation
52494	0.1743728	9243	0.1525398	31625	0.2417538	55287	0.1095832	**9034**	**0.2744035**
100538	0.1743728	59215	0.1525397	18320	0.2417537	4386	0.1095832	**29422**	**0.2744034**
1952	0.1743727	453	0.1525397	73513	0.2417537	73991	0.1095831	**14880**	**0.2744034**
74923	0.1743726	47340	0.1525397	2891	0.2417537	136329	0.1095831	**847**	**0.2744033**
55264	0.1743726	128533	0.1525396	129470	0.2417537	7382	0.1095830	**100982**	**0.2744032**

Table 9. Top-5 opinion leaders for Bitcoin alpha dataset

User id	DC	User id	CC	User id	BC	User id	EC	User id	PR
748	0.2178362	2083	0.1610389	839	0.1429575	920	0.1857445	476	0.192294
1063	0.2178361	185	0.1610388	43	0.1429574	582	0.1857414	805	0.1922930
93	0.2178360	449	0.1610387	2782	0.1429573	2558	0.1857412	2639	0.192291
384	0.2178359	63	0.1610387	736	0.1429571	1005	0.1857412	382	0.1922899
2559	0.2178358	1996	0.1610386	527	0.1429570	2026	0.1857411	1063	0.1922899

User id	LR	User id	KC	User id	CCC	User id	KSD	User id	GOLI Reputation
472	0.1372842	289	0.1847326	182	0.1593621	92	0.1859377	**2690**	**0.2289953**
826	0.1372842	1846	0.1847326	946	0.1593620	582	0.1859377	**698**	**0.2289952**
1837	0.1372842	72	0.1847325	1529	0.1593620	309	0.1859376	**1503**	**0.2289952**
2508	0.1372842	931	0.1847325	530	0.1593620	2863	0.1859375	**812**	**0.2289951**
76	0.1372842	2751	0.1847325	721	0.1593620	732	0.1859375	**448**	**0.2289950**

Just Accepted

Table 10. Top-5 opinion leaders for Weibo-Net-Tweet dataset

User id	DC	User id	CC	User id	BC	User id	EC	User id	PR
94534	0.1223454	984	0.1445641	58254	0.1840643	1159002	0.1334523	47093	0.1006747
1403515	0.1223454	1045342	0.1445641	160036	0.1840643	263389	0.1334522	262363	0.1006746
843514	0.1223453	564509	0.1445640	483284	0.1840642	724373	0.1334522	504993	0.1006746
201633	0.1223452	197846	0.1445640	35742	0.1840642	2903	0.1334521	925381	0.1006745
583862	0.1223452	1347568	0.1445639	765627	0.1840641	534490	0.1334520	1205994	0.1006745

User id	LR	User id	KC	User id	CCC	User id	KSD	User id	GOLI Reputation
85209	0.1793282	77490	0.1208376	219831	0.1516834	29854	0.2018438	**843514**	**0.2035639**
724373	0.1793282	28951	0.1208375	8423	0.1516834	1383211	0.2018437	**5380**	**0.2035639**
130314	0.1793282	9948	0.1208375	60034	0.1516833	83802	0.2018437	**1489402**	**0.2035638**
59001	0.1793282	120067	0.1208375	130893	0.1516833	7298	0.2018437	**77381**	**0.2035637**
197846	0.1793281	1119588	0.1208374	83992	0.1516833	183955	0.2018437	**1026185**	**0.2035637**

Further, in the social network, the user does not only portray as a recipient, and the activity and behaviors play a significant role in the evolution of network and information diffusion. Thus, one of the critical chores with the social network is how to measure the diffusion of information. However, various models are proposed to calculate the diffusion rate [75][56][69][13]. Information diffusion is generally defined as a process of the dissemination of information, innovation, and ideas from one user to another user through communication over the network. The basic theory behind information diffusion is who the user that influences others through their expertise is. In online social networks, two types of models, (i) explanatory and (ii) predictive models, are used for information diffusion. Explanatory models support the analysis of the path occupied by the chunk of the information, while predictive models support expecting the dissemination process in the network. Predictive models again are classified into two categories, (i) Graph-based models and (ii) non-graph-based models. Graph-based model is further categorized into two classes, Linear Threshold (LT) model and (ii) Independent Cascades (IC) models. The graph-based model works on a graph-structured network where each node can be divided into (i) active state and (ii) deactivated state. The user is already influenced in the active state, while in the deactivated state, the user is not influenced and is unaware of the information. In this research, we have used the classical Independent Cascades (IC) model to demonstrate the information diffusion process for each SNA measure and proposed approach. IC model is a stochastic information diffusion model in which information is spread among the users through cascades [79][5][65]. The main reason behind choosing this model is to depict the information diffusion process by each approach in a simpler manner. Initially, the opinion leaders, say seed nodes, receive the information, become active, and forward it to their neighbors. A propagation probability determines the possibility that an active node can influence the other deactivate node up to what extent. We have chosen the same probability for all the relations for experimental purposes. Initially, a small set of opinion leaders (=1000), are selected to begin the process for each approach. In the successive steps, each opinion leader attempt to activate its neighbors only if the propagation probability is higher than the threshold value.

In this research, we observe the outlook of the GOLI for information diffusion over time with other standard SNA measures. A probability distribution function p measures the number of users influenced over time. In Fig.7, we illustrate the information dissemination process where the x-axis represents the

JUST Accepted

time (in sec.) while the y-axis depicts the probability distribution function. For instance, if p =1, i.e., all the nodes get affected and spread information throughout the network. We find that GOLI needs less time for information dissemination than other standards SNA measures for all the datasets. Thus, we can explain that the proposed GOLI model also achieved success for information diffusion.

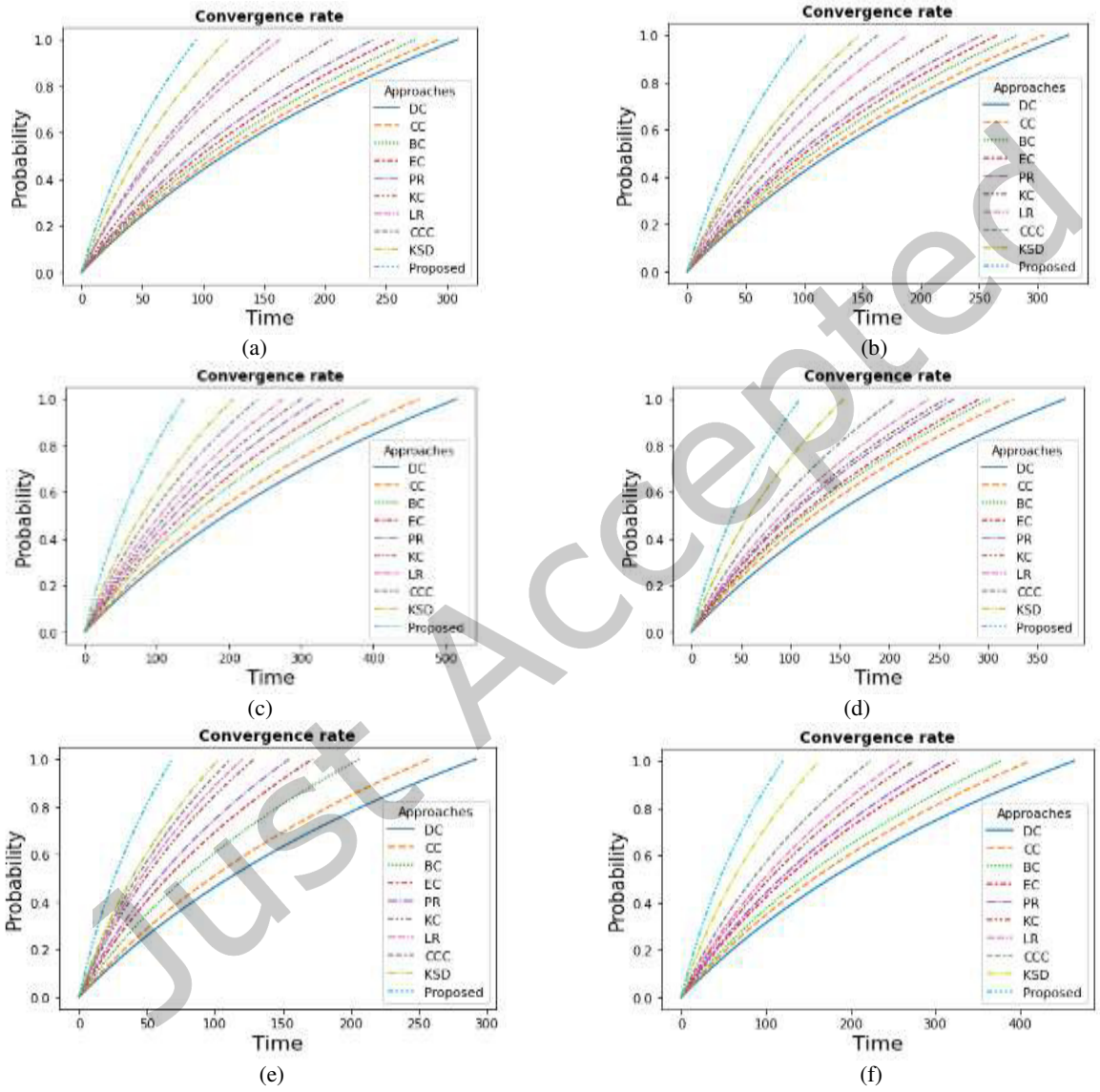

Fig.7. Visualization of Information diffusion over time for (a) Slashdot, (b) Epinions, (c) LiveJournal, (d) Last.fm, (e) Bitcoin alpha, and (f) Weibo-Net-Tweet dataset

5.3 Performance evaluation

Various parameters are used to boost and scrutinize the performance of GNN based model. We consider data splitting, training accuracy, testing accuracy, and error percentage to observe the model performance. The best parameter value often affects the model's performance by overcoming the overfitting or

Just Accepted

underfitting problem [36]. So, we use approximately 67% of training data and 33% for testing operations. In Fig. 8, we visualize the GOLI training and testing accuracy for all six datasets. We find that GOLI obtains around 91% training and 92% testing accuracy with an approximately 1% error rate. The discrete value of training accuracy, test accuracy, and error rate mentioned for all the experimental datasets is depicted in Table 11.

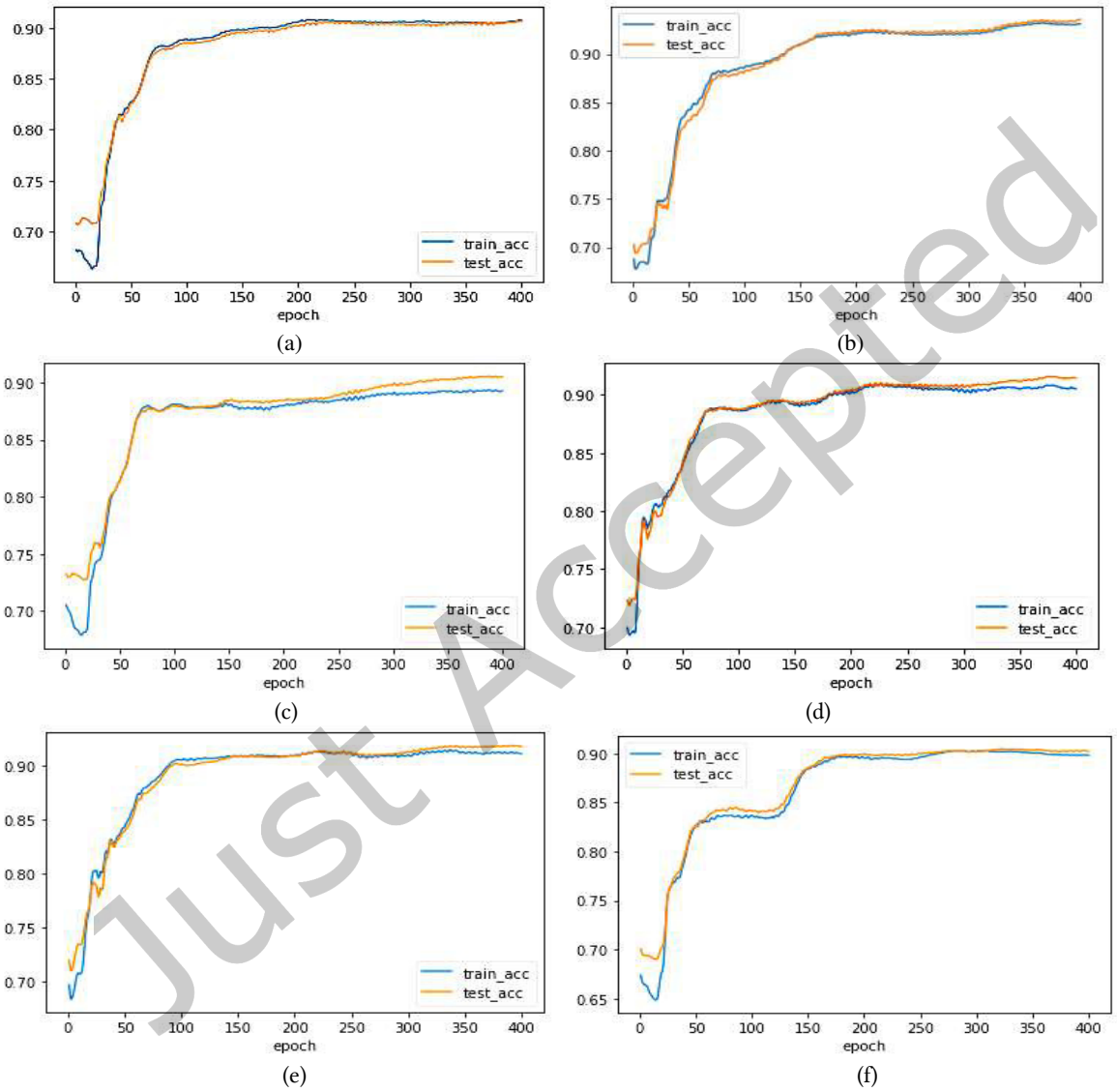

Fig.8. Training and Testing accuracy visualization for (a) Slashdot, (b) Epinions, (c) LiveJournal, (d) Last.fm, (e) Bitcoin alpha, and (f) Weibo-Net-Tweet dataset

Just Accepted

Table 11. Training accuracy, Test accuracy, and Error rate for all the datasets

Dataset	Training accuracy	Test accuracy	Error rate
Slashdot	0.91684 ± 0.00111	0.91881 ± 0.00152	± 0.0226%
Epinions	0.94738 ± 0.00019	0.94729 ± 0.00104	± 0.0027%
LiveJournal	0.90841 ± 0.00273	0.92267 ± 0.00084	± 2.0244%
Last.fm	0.91328 ± 0.00122	0.92027 ± 0.00042	± 1.0028%
Bitcoin alpha	0.91454 ± 0.00104	0.92829 ± 0.00128	± 1.0819%
Weibo-Net-Tweet	0.90492 ± 0.00016	0.91205 ± 0.00057	± 1.0025%

5.4 Performance metrics

Generally, opinion leader detection is assumed to be the binary classification problem in which we classify whether a particular user is an opinion leader or not. However, various metrics are used to check the quality, productivity, and efficiency of the model. The grounded and most straightforward method is to calculate the Accuracy, Precision, Recall, and F1-score of the model [71,88]. Four elementary components, true positive, true negative, false positive, and false negative, are calculated to measure the metrics. The meaning of true and false is to assess the designated class rightly and wrongly, respectively. Now, we defined these four elements in brief as follows:

- **True Positive (TP):** Describe the total number of positive observations correctly predicted by the model.
- **True Negative (TN):** Describe the total number of negative observations correctly predicted by the model.
- **False Positive (FP):** Describe the total number of positive observations incorrectly predicted by the model.
- **False Negative (TN):** Describe the total number of negative observations incorrectly predicted by the model.

Now, we illustrate Accuracy, Precision, Recall, and F1-score based on the above outcomes, as follows:

$$\text{Accuracy} = \frac{TP+TN}{TP+TN+FP+FN} \qquad \text{Precision} = \frac{TP}{TP+FP} \qquad \text{Recall} = \frac{TP}{TP+FN} \qquad \text{F1-score} = 2 * \frac{\text{Recall} * \text{Precision}}{\text{Recall}+\text{Precision}}$$

Next, we found the progressive comparative outcomes based on the network's pre-defined ground truth information, as shown in Fig.9. We can also observe that the GOLI model offered improved qualitative results over other SNA measures for all six datasets. The addressed GOLI model produces approximately 92% accuracy, 95.4% precision, 96% Recall, and 95% F1-score over other SNA measures.

Just Accepted

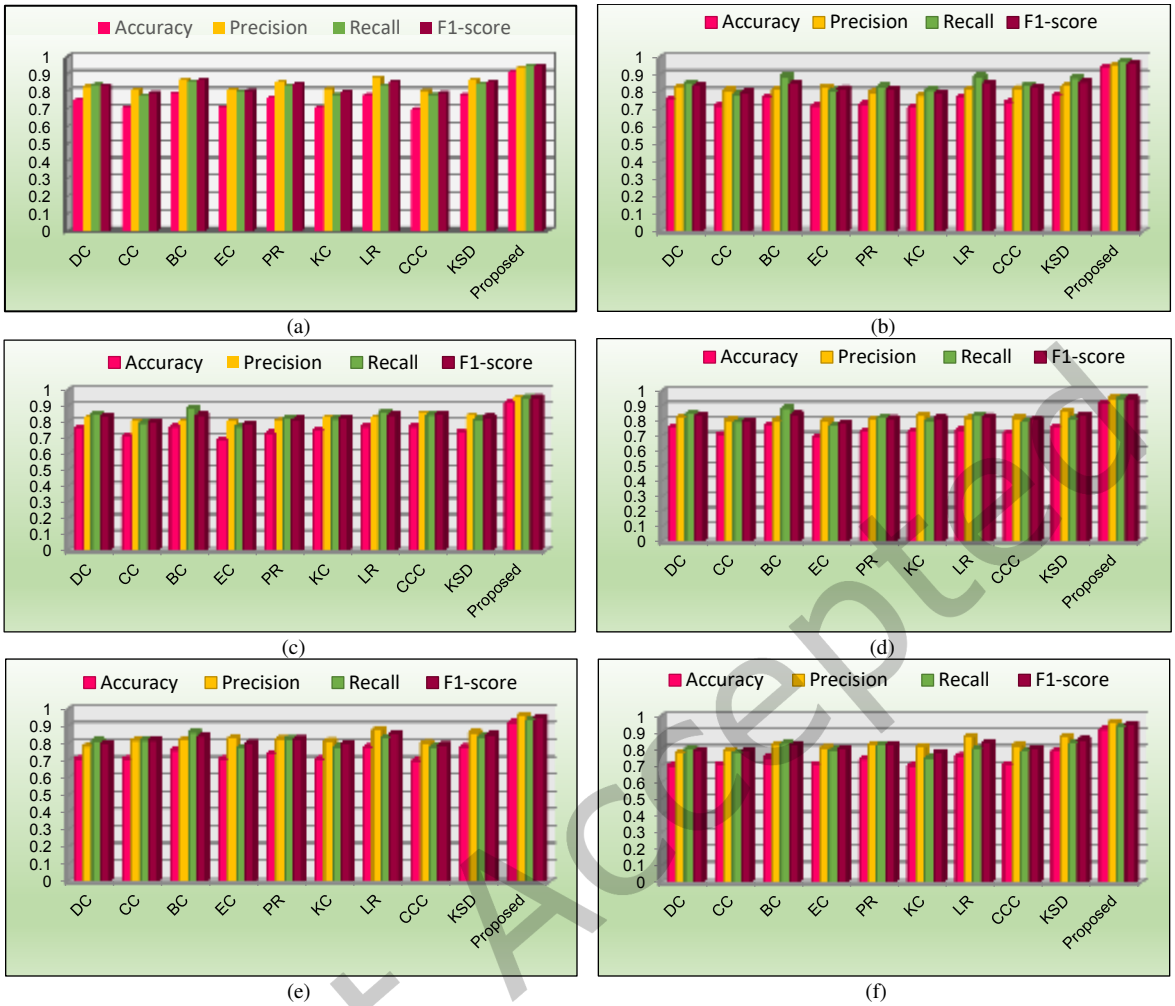

Fig.9. Performance metrics contrastive analysis between standard SNA measures and proposed approach for (a) Slashdot, (b) Epinions, (c) LiveJournal, (d) Last.fm, (e) Bitcoin alpha, and (f) Weibo-Net-Tweet dataset

Another issue that also impacts a model's performance and plays a vital role in the model's selection is time complexity. In practice, various factors such as activation function, transformation function, level of neighbor's reachability, batch size, learning rate, regularization, learnable and attainable parameters' value, etc., are intrinsically responsible for the model's time complexity. Because of this, the model's training required a certain amount of time to gain knowledge about the nature of the network. Thus, it is very complicated and complex to determine the time complexity of the model. Still, we put forward and measure the time complexity of the proposed model while considering the mentioned parameter setting. The entire computation time includes data preprocessing, data loading, model training, code execution, and result visualization. We calculated the total execution time for the standard SNA measures and demonstrated the compared outcomes in Fig.10. The x-axis shows the various approaches and the proposed methods, while the y-axis depicts the total computation time required to execute the corresponding model. For example, the execution time by using DC for Slashdot, Epinions, LiveJournal, Last.fm, Bitcoin alpha, and Weibo-Net-Tweet dataset are 539, 587, 1956, 742, 364, and 1493 sec. Again, the total computation time for the proposed approach is 254, 261, 1472, 403, 228, and 1025 sec., respectively, for all six datasets. Similarly, for every SNA measure and other approaches, the computational time is

Just Accepted

exclusively mentioned on each slab corresponding to the approach. Thus, the obtained outcomes prove that the proposed method took lesser computational time than other SNA measures and procedures.

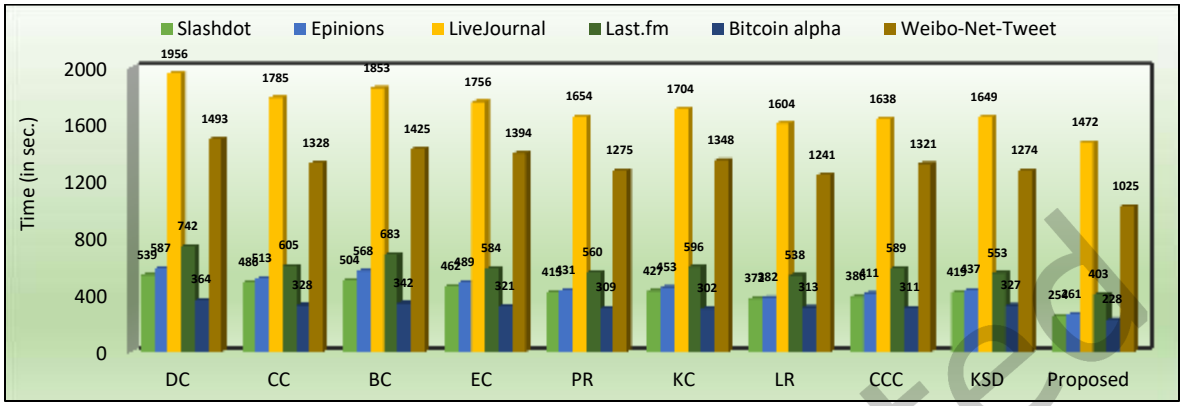

Fig.10. Time complexity comparison between standard SNA measures and proposed approach for (a) Slashdot, (b) Epinions, (c) LiveJournal, (d) Last.fm, (e) Bitcoin alpha, and (f) Weibo-Net-Tweet dataset

6 CONCLUSION AND FUTURE SCOPE

In the current situation, when the new companies are struggling to establish business, and most countries face negative GDP growth rates, the role and responsibility of the opinion leaders also become extensive and challenging. After analyzing graph-based research, we find that the GNN provides the most appropriate feature due to its broad applicability in the graph and complex network-related problems [21,59].

Therefore, the power of GNN is used in the GOLI model to measure the user's reputation in the network. Initially, the latent features of the nodes measure and construct the feature vector matrix. The feature vector matrix includes the vector of attributes about the node. Further, the neighbors transmit and aggregate the information to compute the node's reputation score. Based on the reputation score and trust, and anticipated trust network is formed to fetch the network's trustworthiness. Next, at every model layer, reputation score and trust aggregate as per the proposed method based on neighbor's information. Finally, to include the importance of in-degree centrality, a centrality settlement formulates to calculate the node's final reputation score. Based on the highest reputation score, a list of user prepared and top-n(n=5) users declared as opinion leaders. We compare the findings with the other standard SNA measures for six real-world datasets to evaluate the model's strength. We agree that the proposed model produced improved results w.r.t. evaluation metrics (accuracy, precision, recall, F1-score, error rate, execution time). So, to achieve the perfect opinion leaders, the GOLI carries out well over other standard SNA measures.

As discussed, no standard method has been proposed to recognize opinion leaders. Each model has some limitations and constraints specific to a particular domain and subject. Our model also has some limitations, and in the future, we would like to overcome these limitations by proposing more pioneering and precise methods. The first restraint with the model is that it works on the static dataset, so we would like to experiment on the proposed model with a dynamic dataset considering user activities over time [68,82]. As technology evolves, the new GNN-based model also comes into view for graph-based data.

Just Accepted

Therefore, the variant of GNN with online social networks would be further impactful and exciting for perfect opinion leader detection. Besides, we would also explore the more advanced deep-learning-based models associated with other users' multi-relational characteristics, such as user's response time, geographical location, the domain of interest, etc., as upcoming directives [8,62,100].

In a nutshell, we can declare that the GOLI model's applicability is too significant for identifying critical nodes in various realm graph-related problems. Traditionally, the scope of opinion leaders includes a broader range of domains such as online campaigns, advertising, marketing, healthcare, agriculture, pooling, recommendation system, finance, defense system, etc. Still, as soon as the era and technologies change, opinion leaders' role and accountability also significantly revolutionize. The pertinence of the GOLI model would also be appreciably helpful in other modern applications such as catalyst analysis in the chemical reaction, GIS, biological pattern, modern algebra, regression analysis, cloud computing, load balancing, distributed computing, and many more as an influencer, key leader, opinion booster, opinion miner, key miner, candidate user, change agent, and other deviated forms.

Just Accepted

REFERENCES

[1] Samad Mohammad Aghdam and Nima Jafari Navimipour. 2016. Opinion leaders selection in the social networks based on trust relationships propagation. *Karbala Int. J. Mod. Sci.* (2016). DOI:https://doi.org/10.1016/j.kijoms.2016.02.002

[2] Forest Agostinelli, Matthew Hoffman, Peter Sadowski, and Pierre Baldi. 2015. Learning activation functions to improve deep neural networks. In *3rd International Conference on Learning Representations, ICLR 2015 - Workshop Track Proceedings*.

[3] Jamil Ahmad, Haleem Farman, and Zahoor Jan. 2019. Deep Learning Methods and Applications. In *SpringerBriefs in Computer Science*. DOI:https://doi.org/10.1007/978-981-13-3459-7_3

[4] Samah Al-Oufi, Heung Nam Kim, and Abdulmotaleb El Saddik. 2012. A group trust metric for identifying people of trust in online social networks. *Expert Syst. Appl.* 39, 18 (2012), 13173–13181. DOI:https://doi.org/10.1016/j.eswa.2012.05.084

[5] M. K. Alasadi and H. N. Almamory. 2019. Diffusion model based on shared friends-aware independent cascade. In *Journal of Physics: Conference Series*. DOI:https://doi.org/10.1088/1742-6596/1294/4/042006

[6] Abolfazl Aleahmad, Payam Karisani, Maseud Rahgozar, and Farhad Oroumchian. 2016. OLFinder: Finding opinion leaders in online social networks. *J. Inf. Sci.* 42, 5 (2016), 656–674. DOI:https://doi.org/10.1177/0165551515605217

[7] Lora Aroyo, Pasquale De Meo, and Domenico Ursino. 2010. Trust and reputation in social internetworking systems. In *CEUR Workshop Proceedings*, 42.

[8] Davide Bacciu, Federico Errica, Alessio Micheli, and Marco Podda. 2020. A gentle introduction to deep learning for graphs. *Neural Networks 129*. DOI:https://doi.org/10.1016/j.neunet.2020.06.006

[9] Lars Backstrom, Dan Huttenlocher, Jon Kleinberg, and Xiangyang Lan. 2006. Group formation in large social networks: Membership, growth, and evolution. In *Proceedings of the ACM SIGKDD International Conference on Knowledge Discovery and Data Mining*.

[10] Seyed Mojtaba Hosseini Bamakan, Ildar Nurgaliev, and Qiang Qu. 2019. Opinion leader detection: A methodological review. *Expert Systems with Applications 115*, 200–222. DOI:https://doi.org/10.1016/j.eswa.2018.07.069

[11] Mathieu Bastian, Sebastien Heymann, and Mathieu Jacomy. 2009. Gephi: An Open Source Software for Exploring and Manipulating Networks. *Third Int. AAAI Conf. Weblogs Soc. Media* (2009). DOI:https://doi.org/10.1136/qshc.2004.010033

[12] Thierry Bertin-Mahieux, Daniel P.W. Ellis, Brian Whitman, and Paul Lamere. 2011. The million song dataset. In *Proceedings of the 12th International Society for Music Information Retrieval Conference, ISMIR 2011*.

[13] Sutapa Bhattacharya and Dhrubasish Sarkar. 2021. Study on Information Diffusion in Online Social Network. In *Advances in Intelligent Systems and Computing*, 279–288. DOI:https://doi.org/10.1007/978-981-15-7834-2_26

[14] Freimut Bodendorf and Carolin Kaiser. 2009. Detecting Opinion Leaders and Trends in Online Social Networks. *Proc. 2nd ACM Work. Soc. web search Min.* (2009). DOI:https://doi.org/10.1109/ICDS.2010.29

[15] Freimut Bodendorf and Carolin Kaiser. 2010. Detecting opinion leaders and trends in online communities. In *4th International Conference on Digital Society, ICDS 2010, Includes CYBERLAWS 2010: The 1st International Conference on Technical and Legal Aspects of the e-Society*. DOI:https://doi.org/10.1109/ICDS.2010.29

[16] Zhan Bu, Hui Jia Li, Chengcui Zhang, Jie Cao, Aihua Li, and Yong Shi. 2020. Graph K-means Based on Leader Identification, Dynamic Game, and Opinion Dynamics. *IEEE Trans. Knowl. Data Eng.* 32, 7 (2020), 1348–1361. DOI:https://doi.org/10.1109/TKDE.2019.2903712

[17] Yi Cheng Chen. 2019. A novel algorithm for mining opinion leaders in social networks. *World Wide Web* 22, 3 (2019), 1279–1295. DOI:https://doi.org/10.1007/s11280-018-0586-x

[18] Yi Cheng Chen, Lin Hui, Chun I. Wu, Hsin Yu Liu, and Sheng Chih Chen. 2017. Opinion leaders discovery in dynamic social network. In *Ubi-Media 2017 - Proceedings of the 10th International Conference on Ubi-Media Computing and Workshops with the 4th International Workshop on Advanced E-Learning and the 1st International Workshop on Multimedia and IoT: Networks, Systems and Applications*, 1–6. DOI:https://doi.org/10.1109/UMEDIA.2017.8074110

[19] Youngsang Cho, Junseok Wang, and Daeho Lee. 2012. Identification of effective opinion leaders in the diffusion of technological innovation: A

social network approach. *Technol. Forecast. Soc. Change* 79, 1 (2012), 97–106. DOI:https://doi.org/10.1016/j.techfore.2011.06.003

[20] Peng Cui, Xiao Wang, Jian Pei, and Wenwu Zhu. 2019. A Survey on Network Embedding. *IEEE Transactions on Knowledge and Data Engineering 31*. DOI:https://doi.org/10.1109/TKDE.2018.2849727

[21] Nima Dehmamy, Albert László Barabási, and Rose Yu. 2019. Understanding the representation power of graph neural networks in learning graph topology. In *Advances in Neural Information Processing Systems*.

[22] Li Deng and Dong Yu. 2013. Deep learning: Methods and applications. *Foundations and Trends in Signal Processing 7*. DOI:https://doi.org/10.1561/2000000039

[23] Fatia Kusuma Dewi, Satrio Baskoro Yudhoatmojo, and Indra Budi. 2018. Identification of opinion leader on rumor spreading in online social network Twitter using edge weighting and centrality measure weighting. In *2017 12th International Conference on Digital Information Management, ICDIM 2017*. DOI:https://doi.org/10.1109/ICDIM.2017.8244680

[24] Pedro Domingos and Matt Richardson. 2001. Mining the network value of customers. In *Proceedings of the seventh ACM SIGKDD international conference on Knowledge discovery and data mining - KDD '01*, 57–66. DOI:https://doi.org/10.1145/502512.502525

[25] Jiangjiao Duan, Jianping Zeng, and Banghui Luo. 2014. Identification of opinion leaders based on user clustering and sentiment analysis. In *Proceedings - 2014 IEEE/WIC/ACM International Joint Conference on Web Intelligence and Intelligent Agent Technology - Workshops, WI-IAT 2014*, 377–383. DOI:https://doi.org/10.1109/WI-IAT.2014.59

[26] Nicole B. Ellison, Charles Steinfield, and Cliff Lampe. 2007. The benefits of facebook "friends:" Social capital and college students' use of online social network sites. *J. Comput. Commun.* 12, 4 (2007), 1143–1168. DOI:https://doi.org/10.1111/j.1083-6101.2007.00367.x

[27] Mohammad Reza Faghani and Uyen Trang Nguyen. 2013. A study of xss worm propagation and detection mechanisms in online social networks. *IEEE Trans. Inf. Forensics Secur.* 8, 11 (2013), 1815–1826. DOI:https://doi.org/10.1109/TIFS.2013.2280884

[28] Linton C. Freeman. 1978. Centrality in social networks conceptual clarification. *Soc. Networks* 1, 3 (1978), 215–239. DOI:https://doi.org/10.1016/0378-8733(78)90021-7

[29] Linton C Freeman. 1978. Centrality in Social Networks. *Soc. Networks* 1, 3 (1978), 215–239. DOI:https://doi.org/10.1016/0378-8733(78)90021-7

[30] Laura Garton, Caroline Haythornthwaite, and Barry Wellman. 2006. Studying Online Social Networks. *J. Comput. Commun.* 3, 1 (2006). DOI:https://doi.org/10.1111/j.1083-6101.1997.tb00062.x

[31] Seyed Mohssen Ghafari, Amin Beheshti, Aditya Joshi, Cecile Paris, Adnan Mahmood, Shahpar Yakhchi, and Mehmet A. Orgun. 2020. A Survey on Trust Prediction in Online Social Networks. *IEEE Access* 8, (2020), 144292–144309. DOI:https://doi.org/10.1109/ACCESS.2020.3009445

[32] David Gold, Elihu Katz, Paul F. Lazarsfeld, and Elmo Roper. 1956. Personal Influence: The Part Played by People in the Flow of Mass Communications. *Am. Sociol. Rev.* 23, 4 (1956), 572–574. DOI:https://doi.org/10.2307/2088435

[33] Palash Goyal and Emilio Ferrara. 2018. Graph embedding techniques, applications, and performance: A survey. *Knowledge-Based Syst.* 151, (2018). DOI:https://doi.org/10.1016/j.knosys.2018.03.022

[34] Sonja Grabner-Kräuter and Sofie Bitter. 2014. Trust in online social networks: A multifaceted perspective. *Forum Soc. Econ.* 44, 1 (2014), 48–68. DOI:https://doi.org/10.1080/07360932.2013.781517

[35] Mark S. Granovetter. 1973. The Strength of Weak Ties. *Am. J. Sociol.* 78, 6 (1973), 1360–1380. DOI:https://doi.org/10.1086/225469

[36] Jiawei Han, Micheline Kamber, and Jian Pei. 2012. *Data Mining: Concepts and Techniques*. DOI:https://doi.org/10.1016/C2009-0-61819-5

[37] William Grant Hatcher and Wei Yu. 2018. A Survey of Deep Learning: Platforms, Applications and Emerging Research Trends. *IEEE Access* 6, (2018). DOI:https://doi.org/10.1109/ACCESS.2018.2830661

[38] Hongwei He and Lloyd Harris. 2020. The impact of Covid-19 pandemic on corporate social responsibility and marketing philosophy. *J. Bus. Res.* 116, (2020). DOI:https://doi.org/10.1016/j.jbusres.2020.05.030

[39] Lokesh Jain. 2022. An entropy-based method to control COVID-19 rumors in online social networks using opinion leaders. *Technol. Soc.* 70, (August 2022), 102048. DOI:https://doi.org/10.1016/j.techsoc.2022.102048

[40] Lokesh Jain and Rahul Katarya. 2018. A Systematic Survey of Opinion Leader in Online Social Network. In *ICSNS 2018 - Proceedings of IEEE International Conference on Soft-Computing and Network Security*, IEEE, 1–5. DOI:https://doi.org/10.1109/ICSNS.2018.8573639

[41] Lokesh Jain and Rahul Katarya. 2018. Identification of opinion leader in online social network using fuzzy trust system. In *2018 IEEE 8th International Advance Computing Conference (IACC)*, IEEE, 233–239. DOI:https://doi.org/10.1109/IADCC.2018.8692095

[42] Lokesh Jain and Rahul Katarya. 2019. Discover opinion leader in online social network using firefly algorithm. *Expert Syst. Appl.* 122, (May 2019), 1–15. DOI:https://doi.org/10.1016/j.eswa.2018.12.043

[43] Lokesh Jain, Rahul Katarya, and Shelly Sachdeva. 2020. Opinion leader detection using whale optimization algorithm in online social network. *Expert Syst. Appl.* 142, (March 2020), 113016. DOI:https://doi.org/10.1016/j.eswa.2019.113016

[44] Lokesh Jain, Rahul Katarya, and Shelly Sachdeva. 2020. Recognition of opinion leaders coalitions in online social network using game theory. *Knowledge-Based Syst.* 203, (September 2020), 106158. DOI:https://doi.org/10.1016/j.knosys.2020.106158

[45] Leo Katz. 1953. A new status index derived from sociometric analysis. *Psychometrika* 18, 1 (1953). DOI:https://doi.org/10.1007/BF02289026

[46] Cinu C. Kiliroor and C. Valliyammai. 2017. Trust analysis on social networks for identifying authenticated users. *2016 8th Int. Conf. Adv. Comput. ICoAC 2016* (2017), 37–41. DOI:https://doi.org/10.1109/ICoAC.2017.7951741

[47] Ravi Kumar, Jasmine Novak, and Andrew Tomkins. 2010. Structure and evolution of online social networks. In *Link Mining: Models, Algorithms, and Applications*. DOI:https://doi.org/10.1007/978-1-4419-6515-8-13

[48] Srijan Kumar, Francesca Spezzano, V. S. Subrahmanian, and Christos Faloutsos. 2017. Edge weight prediction in weighted signed networks. In *Proceedings - IEEE International Conference on Data Mining, ICDM*. DOI:https://doi.org/10.1109/ICDM.2016.175

[49] Shaojuan Lei, Xiaodong Zhang, and Yuning Yan. 2019. Research on opinion leaders recognition based on TOPSIS in open source design community. In *Proceedings of the 2019 IEEE 23rd International Conference on Computer Supported Cooperative Work in Design, CSCWD 2019*, 307–312. DOI:https://doi.org/10.1109/CSCWD.2019.8791850

[50] Jure Leskovec, Kevin J. Lang, Anirban Dasgupta, and Michael W. Mahoney. 2009. Community structure in large networks: Natural cluster sizes

Just Accepted

and the absence of large well-defined clusters. *Internet Math.* 6, 1 (2009). DOI:https://doi.org/10.1080/15427951.2009.10129177

[51] Kevin Lewis, Marco Gonzalez, and Jason Kaufman. 2012. Social selection and peer influence in an online social network. *Proc. Natl. Acad. Sci. U. S. A.* 109, 1 (2012). DOI:https://doi.org/10.1073/pnas.1109739109

[52] Yanyan Li, Shaoqian Ma, Yonghe Zhang, Ronghuai Huang, and Kinshuk. 2013. An improved mix framework for opinion leader identification in online learning communities. *Knowledge-Based Syst.* 43, (May 2013), 43–51. DOI:https://doi.org/10.1016/j.knosys.2013.01.005

[53] Lizi Liao, Xiangnan He, Hanwang Zhang, and Tat Seng Chua. 2018. Attributed Social Network Embedding. *IEEE Trans. Knowl. Data Eng.* 30, 12 (2018). DOI:https://doi.org/10.1109/TKDE.2018.2819980

[54] Nan Lin. 1999. Building a Network Theory of Social Capital. *Connections* 22, 1 (1999), 28–51. DOI:https://doi.org/10.1108/14691930410550381

[55] Qiu Liqing, Dai Jinlong, Liu Haiyan, and Wen Yan. 2018. Detecting opinion leaders in online social networks using HybridRank algorithm. *J. Intell. Fuzzy Syst.* 35, 1 (2018), 513–522. DOI:https://doi.org/10.3233/JIFS-169607

[56] Xiaoyang Liu and Chao Liu. 2018. Information diffusion and opinion leader mathematical modeling based on microblog. *IEEE Access* 6, (2018). DOI:https://doi.org/10.1109/ACCESS.2018.2849722

[57] Yang Liu, Zhonglei Gu, Tobey H. Ko, and Jiming Liu. 2018. Identifying Key Opinion Leaders in Social Media via Modality-Consistent Harmonized Discriminant Embedding. *IEEE Trans. Cybern.* (2018), 1–12. DOI:https://doi.org/10.1109/TCYB.2018.2871765

[58] Linyuan Lü, Yi Cheng Zhang, Chi Ho Yeung, and Tao Zhou. 2011. Leaders in social networks, the delicious case. *PLoS One* 6, 6 (2011). DOI:https://doi.org/10.1371/journal.pone.0021202

[59] Haggai Maron, Heli Ben-Hamu, Hadar Serviansky, and Yaron Lipman. 2019. Provably powerful graph networks. In *Advances in Neural Information Processing Systems*.

[60] Qingliang Miao, Shu Zhang, Yao Meng, and Hao Yu. 2013. Domain-sensitive opinion leader mining from online review communities. In *Proceedings of the 22nd International Conference on World Wide Web - WWW '13 Companion*, ACM Press, New York, New York, USA, 187–188. DOI:https://doi.org/10.1145/2487788.2487882

[61] Alan Mislove, Massimiliano Marcon, Krishna P. Gummadi, Peter Druschel, and Bobby Bhattacharjee. 2007. Measurement and analysis of online social networks. In *Proceedings of the ACM SIGCOMM Internet Measurement Conference, IMC*. DOI:https://doi.org/10.1145/1298306.1298311

[62] Conceptual Model, El Hihi, Anand Jayarajan, Jinliang Wei, Garth Gibson, Alexandra Fedorova, Gennady Pekhimenko, Adam Lerer, Ledell Wu, Jiajun Shen, Timothee Lacroix, Luca Wehrstedt, Abhijit Bose, Alex Peysakhovich, Multi-layer Neural Networks, Zhihao Jia, James Thomas, Todd Warszawski, Mingyu Gao, Matei Zaharia, Alex Aiken, L Arge Scale, I Mage C Lassification, Boris Ginsburg, Mikhail Belkin, Jungwook Choi, Swagath Venkataramani, Vijayalakshmi Srinivasan, Kailash Gopalakrishnan, Eric Breck, Neoklis Polyzotis, Sudip Roy, Steven Euijong Whang, Martin Zinkevich, Paulo Roberto, Simões Pellucci, Renato Ribeiro De Paula, Walter Borges De Oliveira, Ana Paula Ladeira, Sangkug Lym, Armand Behroozi, Wei Wen, Ge Li, Yongkee Kwon, Mattan Erez, Maximilian Golub, Guy Lemieux, Mieszko Lis, With Resnet, Dibakar Gope, Ganesh Dasika, and Matthew Mattina. 2019. Deep Graph Library Towards efficient and scalable deep learning on graphs. *Learning* 89, April (2019).

[63] Niyoosha Jafari Momtaz, Abdollah Aghaie, and Somayeh Alizadeh. 2011. Identifying Opinion Leaders for Marketing by Analyzing Online Social Networks. *Int. J. Virtual Communities Soc. Netw.* 3, 1 (2011), 43–59. DOI:https://doi.org/10.4018/978-1-4666-4022-1.ch010

[64] Reza Mousavi, Monica Johar, and Vijay S. Mookerjee. 2020. The Voice of the Customer: Managing Customer Care in Twitter. *Inf. Syst. Res.* (June 2020). DOI:https://doi.org/10.1287/isre.2019.0889

[65] Seth A. Myers, Chenguang Zhu, and Jure Leskovec. 2012. Information diffusion and external influence in networks. In *Proceedings of the ACM SIGKDD International Conference on Knowledge Discovery and Data Mining*, 33–41. DOI:https://doi.org/10.1145/2339530.2339540

[66] Maryam M. Najafabadi, Flavio Villanustre, Taghi M. Khoshgoftaar, Naeem Seliya, Randall Wald, and Edin Muharemagic. 2015. Deep learning applications and challenges in big data analytics. *J. Big Data* 2, 1 (2015). DOI:https://doi.org/10.1186/s40537-014-0007-7

[67] Social Network and Data Analytics. 2011. Social Network Data Analytics. *Media* (2011). DOI:https://doi.org/10.1007/978-1-4419-8462-3

[68] Nam P. Nguyen, Thang N. Dinh, Ying Xuan, and My T. Thai. 2011. Adaptive algorithms for detecting community structure in dynamic social networks. In *Proceedings - IEEE INFOCOM*. DOI:https://doi.org/10.1109/INFCOM.2011.5935045

[69] John K. Omoniyi, Folasade Adedeji, and Joshua J. Tom. 2021. A Prediction Model for Information Diffusion in Online Social Network. *Int. J. Comput. Appl.* 174, 27 (2021). DOI:https://doi.org/10.5120/ijca2021921158

[70] Tore Opsahl, Filip Agneessens, and John Skvoretz. 2010. Node centrality in weighted networks: Generalizing degree and shortest paths. *Soc. Networks* 32, 3 (2010), 245–251. DOI:https://doi.org/10.1016/j.socnet.2010.03.006

[71] D.M.W. POWERS. 1994. Denpasar Declaration on Population and Development. *Integration* 40 (1994), 27–29. DOI:https://doi.org/10.1234/2013/999990.

[72] Jiezhong Qiu, Jian Tang, Hao Ma, Yuxiao Dong, Kuansan Wang, and Jie Tang. 2018. DeepInf: Social influence prediction with deep learning. In *Proceedings of the ACM SIGKDD International Conference on Knowledge Discovery and Data Mining*. DOI:https://doi.org/10.1145/3219819.3220077

[73] Meng Qu and Jian Tang. 2019. Probabilistic logic neural networks for reasoning. In *Advances in Neural Information Processing Systems*.

[74] Arvind Rangaswamy and Gerrit H. Van Bruggen. 2005. Opportunities and challenges in multichannel marketing: An introduction to the special issue. *J. Interact. Mark.* 19, 2 (2005). DOI:https://doi.org/10.1002/dir.20037

[75] Ateeq Ur Rehman, Aimin Jiang, Abdul Rehman, Anand Paul, Sadia Din, and Muhammad Tariq Sadiq. 2020. Identification and role of opinion leaders in information diffusion for online discussion network. *J. Ambient Intell. Humaniz. Comput.* (January 2020). DOI:https://doi.org/10.1007/s12652-019-01623-5

[76] Matthew Richardson, Rakesh Agrawal, and Pedro Domingos. 2003. Trust management for the Semantic Web. *Lect. Notes Comput. Sci. (including Subser. Lect. Notes Artif. Intell. Lect. Notes Bioinformatics)* 2870, (2003), 351–368. DOI:https://doi.org/10.1007/978-3-540-39718-2_23

[77] Fabian Riquelme, Pablo Gonzalez-Cantergiani, David Hans, Rodolfo Villarroel, and Roberto Munoz. 2019. Identifying Opinion Leaders on Social Networks Through Milestones Definition. *IEEE Access* 7, (2019), 75670–75677. DOI:https://doi.org/10.1109/ACCESS.2019.2922155

[78] Everett M. Rogers. 2002. New Product Adoption and Diffusion. *J. Consum. Res.* (2002). DOI:https://doi.org/10.1086/208642

[79] Kazumi Saito, Ryohei Nakano, and Masahiro Kimura. 2008. Prediction of information diffusion probabilities for independent cascade model. In

Just Accepted

Lecture Notes in Computer Science (including subseries Lecture Notes in Artificial Intelligence and Lecture Notes in Bioinformatics), 67–75. DOI:https://doi.org/10.1007/978-3-540-85567-5_9

[80] M. F. Sanner. 1999. Python: A programming language for software integration and development. *Journal of Molecular Graphics and Modelling*.

[81] Franco Scarselli, Marco Gori, Ah Chung Tsoi, Markus Hagenbuchner, and Gabriele Monfardini. 2009. The graph neural network model. *IEEE Trans. Neural Networks* 20, 1 (2009). DOI:https://doi.org/10.1109/TNN.2008.2005605

[82] Vedran Sekara, Arkadiusz Stopczynski, and Sune Lehmann. 2016. Fundamental structures of dynamic social networks. *Proc. Natl. Acad. Sci. U. S. A.* 113, 36 (2016). DOI:https://doi.org/10.1073/pnas.1602803113

[83] H Sharara, L Getoor, and M Norton. 2011. Active Surveying: A Probabilistic Approach for Identifying Key Opinion Leaders. *Twenty-Second Int. Jt. Conf. Artif. Intell.* (2011).

[84] Xiao Shen and Fu Lai Chung. 2020. Deep Network Embedding for Graph Representation Learning in Signed Networks. *IEEE Trans. Cybern.* 50, 4 (2020). DOI:https://doi.org/10.1109/TCYB.2018.2871503

[85] Katharina Simbeck. 2013. Opinion Leaders and Lead Users in Marketing and Management Accounting and Impact on Small Business Performance. *Soc. Netw.* 02, 01 (2013). DOI:https://doi.org/10.4236/sn.2013.21002

[86] José Suárez-Varela, Sergi Carol-Bosch, Krzysztof Rusek, Paul Almasan, Marta Arias, Pere Barlet-Ros, and Albert Cabellos-Aparicio. 2019. Challenging the generalization capabilities of graph neural networks for network modeling. In *SIGCOMM 2019 - Proceedings of the 2019 ACM SIGCOMM Conference Posters and Demos, Part of SIGCOMM 2019*. DOI:https://doi.org/10.1145/3342280.3342327

[87] Gengxin Sun and Sheng Bin. 2018. A new opinion leaders detecting algorithm in multi-relationship online social networks. *Multimed. Tools Appl.* 77, 4 (2018), 4295–4307. DOI:https://doi.org/10.1007/s11042-017-4766-y

[88] Paul Thagard. 2008. Machine Learning. In *A Companion to Cognitive Science*. DOI:https://doi.org/10.1002/9781405164535.ch16

[89] Ming Feng Tsai, Chih Wei Tzeng, Zhe Li Lin, and Arbee L.P. Chen. 2014. Discovering leaders from social network by action cascade. *Soc. Netw. Anal. Min.* 4, 1 (2014), 1–10. DOI:https://doi.org/10.1007/s13278-014-0165-9

[90] P. W. Turnbull and A. Meenaghan. 1980. Diffusion of Innovation and Opinion Leadership. *Eur. J. Mark.* 14, 1 (1980). DOI:https://doi.org/10.1108/EUM0000000004893

[91] Feng Wang, Jinhua She, Yasuhiro Ohyama, Wenjun Jiang, Geyong Min, Guojun Wang, and Min Wu. 2021. Maximizing positive influence in competitive social networks: A trust-based solution. *Inf. Sci. (Ny).* 546, (2021), 559–572. DOI:https://doi.org/10.1016/j.ins.2020.09.002

[92] Jianling Wang, Kaize Ding, Ziwei Zhu, Yin Zhang, and James Caverlee. 2020. Key opinion leaders in recommendation systems: Opinion elicitation and diffusion. In *WSDM 2020 - Proceedings of the 13th International Conference on Web Search and Data Mining*. DOI:https://doi.org/10.1145/3336191.3371826

[93] Zonghan Wu, Shirui Pan, Fengwen Chen, Guodong Long, Chengqi Zhang, and Philip S. Yu. 2020. A Comprehensive Survey on Graph Neural Networks. *IEEE Trans. Neural Networks Learn. Syst.* (2020). DOI:https://doi.org/10.1109/tnnls.2020.2978386

[94] Ke Xu, Sai Zhang, Hao Chen, and Hai Tao Li. 2014. Measurement and analysis of online social networks. *Jisuanji Xuebao/Chinese J. Comput.* (2014). DOI:https://doi.org/10.3724/SP.J.1016.2014.00165

[95] Jinbi Yang, Yukang Zhang, and Libo Liu. 2019. Identifying Opinion Leaders in Virtual Travel Community Based on Social Network Analysis. In *Lecture Notes in Computer Science (including subseries Lecture Notes in Artificial Intelligence and Lecture Notes in Bioinformatics)*, 276–294. DOI:https://doi.org/10.1007/978-3-030-22338-0_23

[96] Li Yang, Yafeng Qiao, Zhihong Liu, Jianfeng Ma, and Xinghua Li. 2018. Identifying opinion leader nodes in online social networks with a new closeness evaluation algorithm. *Soft Comput.* 22, 2 (2018), 453–464. DOI:https://doi.org/10.1007/s00500-016-2335-3

[97] Li Yang, Yaping Tian, Jin Li, Jianfeng Ma, and Junwei Zhang. 2017. Identifying opinion leaders in social networks with topic limitation. *Cluster Comput.* 20, 3 (2017), 2403–2413. DOI:https://doi.org/10.1007/s10586-017-0732-8

[98] Daokun Zhang, Jie Yin, Xingquan Zhu, and Chengqi Zhang. 2019. Attributed network embedding via subspace discovery. *Data Min. Knowl. Discov.* 33, 6 (2019). DOI:https://doi.org/10.1007/s10618-019-00650-2

[99] Jing Zhang, Biao Liu, Jie Tang, Ting Chen, and Juanzi Li. 2013. Social influence locality for modeling retweeting behaviors. In *IJCAI International Joint Conference on Artificial Intelligence*.

[100] Ziwei Zhang, Peng Cui, and Wenwu Zhu. 2020. Deep Learning on Graphs: A Survey. *IEEE Trans. Knowl. Data Eng.* (2020). DOI:https://doi.org/10.1109/tkde.2020.2981333

[101] Yiyi Zhao, Gang Kou, Yi Peng, and Yang Chen. 2018. Understanding influence power of opinion leaders in e-commerce networks: An opinion dynamics theory perspective. *Inf. Sci. (Ny).* (2018). DOI:https://doi.org/10.1016/j.ins.2017.10.031

[102] Andrei Zinovyev, Nadya Morozova, Nora Nonne, Emmanuel Barillot, Annick Harel-Bellan, and Alexander N Gorban. 2010. Dynamical modeling of microRNA action on the protein translation process. *BMC Syst. Biol.* 4, 1 (December 2010), 13. DOI:https://doi.org/10.1186/1752-0509-4-13

Just Accepted

Outage probability analysis of RF/FSO System Over Nakagami-m Fading and Fisher-Snedecor Distribution with Pointing Error

Rekha Rani[1], Dr. Gurjit Kaur[2], and Dr. Lakshmanan. M.[3]
Sirhan Maheshwari[4] Vikash Kumar Pandey[6] Sneha Porwal[5] Asad[7]

[1,2]*Delhi Technological University, India*
[3,4,5,6,7] *Galgotias College of Engineering and Technology, India*
<rekhaaggarwalece@gmail.com><gurjitkaur@dtu.ac.in><hodece@galgotiacollege.edu >
<sirhanmaheshwari@gmail.com><vikashpandey6065@gmail.com><snehaporwal669@gmail.com><sadali3690@gmail.com>

2022 International Conference on Advances in Computing, Communication and Materials (ICACCM) | 978-1-6654-7439-9/22/$31.00 ©2022 IEEE | DOI: 10.1109/ICACCM56405.2022.10009180

Abstract— *FSO is a technology utilizing LOS methodlogy, used for both indoor and outdoor application. Utilizing unexploited optical spectrum, it can solve the bottleneck broadband connectivity problem. The restricted requirement of free uninterrupted line of sight for its propagation limits its usage to few meters to several kilometre Now a days, RF/FSO system gives the better result. Motive of our literature is to measure performance of a DH (dual hop) RF/FSO system with Nakagami-m fading channel and Fisher-snedecor distribution ($\mathcal{F}$ distribution) with PE (pointing error) is analysed, Novel closed form expression for outage probability(OP) is procured in terms of Meijer-G-function. Outage probability(OP) w.r.t SNR is analysed as a performance parameter.*

Keywords— **FSO Communication system, f-distribution, PE(pointing error), OP(Outage Probability). E2E(end to end)**

I. INTRODUCTION

Free Space optical(FSO) is technological evolution for all bandwidth-hungry services, it utilizes a wireless network operated at unregulated infrared spectrum. It can be an alternative due to the problems that occur in RF or microwave links [1]. Also, FSO systems can provide data rates from 1 Gbps, which can be extended to 10 Gbps which makes them perfect for terrestrial and satellite communications [2].

FSO communication system conveys variation w.r.t atmospheric turbulences like fog, mist, rain, etc [3]. Sometimes, the misalignment in the transmitter and receiver, due to the thermal expansion of the building, vibration in the transmitted beam due to earthquakes, wind, etc. causes the PE (pointing error) [4].

To overcome these challenges (turbulence and pointing error (PE)), many researchers are being carried out such as introducing a relay in between the FSO communication system, in which radio frequency signals are transmitted to the relay from source and from relay to destination optical signals are transmitted. This type of system is also known as dual-hop RF/FSO system [5].

It was found that $\mathcal{F}$ distribution gives a precise and accurate model for effects arousing from the combination of multipath and shadowing. Simple novel expressions of respective distribution are derived in [6]. PDF and CDF expression of $\mathcal{F}$ distribution along with PE have been derived [7].

With the utilization of OP, BER and Ergodic capacity(EC) are calculated considering the NZ (non-zero) boresight PE where RF-link used κ-μ distribution and FSO-link is followed by $\mathcal{F}$ distribution for AF-based RF/FSO system [8]. The use of fixed gain relay with multiuser diversity, η − μ fading at RF−link followed by Malaga distribution is proposed for RF/FSO system [9]. The performance of dual-hop RF/FSO system under various receiver detection techniques has been analyzed assuming RF /FSO link experienced by Mixed κ-μ Fading and M-Distribution [10].

The performance of fixed gain AF at relay for Nakagami-m/ GG with PE is considered is analyzed using the IM/DD and Heterodyne detection [11]. With the deployment of decode and forward(DF) at the relay, in RF/FSO framework Gamma-Gamma($\mathcal{GG}$) turbulence with PE is used at the FSO-link and Nakagami-m is at RF−link then ABER has been analyzed [12]. OP and ABER performance is accomplished for κ-μ fading/exponential Weibull distribution function for RF/FSO [13].

Performance matrices are calculated for the RF/FSO system where η − μ distribution at RF−link and $\mathcal{GG}$-distribution at FSO-link is applied [14]. RF/FSO-communication system-is examined. In RF−link Double generalized gamma is used and at FSO-link Nakagami $\mathcal{M}$ distribution under PE is used [15].

A hybrid RF/FSO system is proposed in which RF is used as a backup. The fading model used is generalized Malaga distribution along with the atmospheric turbulences at the FSO link and PE [16]. The performance of a DF-based RF/FSO system is examined. Rayleigh fading distribution is used at the RF channel and K-μ/IG distribution is used at the FSO channel. Many schemes such as BPSK, QPSK, etc. to calculate the BER and OP are used [17].

The performance metrics for RF/FSO-communication framework/model where fixed-gain AF at the relay-point with Nakagami-m/GG distribution are calculated with zero and NZ boresight PE [18]. OP, BER for an asymmetric AF with Nakagami-m/ $\mathcal{GG}$ distribution under the effect of PE are derived [19].

Authorized licensed use limited to: DELHI TECHNICAL UNIV. Downloaded on January 17,2023 at 05:05:32 UTC from IEEE Xplore. Restrictions apply.

Motivated by above literatures statements, we proposed a system using AF-relay in the RF/FSO system where the Nakagami-m distribution model is deployed at RF−link and $\mathcal{F}$-distribution is used at FSO link with PE for a IM/DD detection technique. Also, for estimation of performance of the proposed system, a novel expression for OP has been procured which is in closed form.

The structure of this paper is as followed:

The section-2 presents the system model of the dual-hop RF/FSO system. Section 3 gives the channel statistics comprising of CDF for E2E (End-to-End) SNR of the proposed system. In section 4 novel expression for OP in closed form has been procured. Section 5 presents results and discussion on OP and last section 6 summarizes and provides the conclusion of the proposed framework.

II. SYSTEM MODEL

In this section, RF/FSO system/framework is considered in which the Nakagami-m model is used in the RF channel whereas the FSO channel follows Fisher-Snedecor distribution under PE.

The propagation of signal completed in two hops. In the first hop, signal is send in the RF form source (S) to relay (R) where the fading channel consider is Nakagami fading channel the signal receives at the relay supposed as:

$$y_{SR} = h_{RF}x + n_{RF} \tag{1}$$

y_{SR} is the signal received at Relay through RF−link, after facing different fading, h_{RF} represent fading. The fading coefficients are represented as h_{RF} , the signal transmitted from the source is denoted by x and n_{RF} represents the zero mean AWGN with mean-variance $\sigma_{RF}^2 = N_{RF}$.

The received electrical signal is converted into an optical spectrum at AF based relay. The signal thus collected at the destination is,

$$y_{RD} = h_{FSO}G\eta h_{RF}x + h_{FSO}G\eta n_{RF} + n_{FSO} \tag{2}$$

where, z_{FSO}= zero means AWGN noise. η = electrical to Optical conversion coefficient. h_{FSO} = Channel fading coefficient. Channel. The Channel fading coefficient is given by, $h_{FSO} = h_a h_l h_p$where h_l represents the path loss, and *pointing* loss is represented by h_p and h_a represents atmospheric turbulence.

A. Channel model:

RF link:

The PDF of the Nakagami distribution is given by [2]

$$f(\gamma_{RF}) = \frac{m^m {\gamma_{RF}}^{m-1}}{\Gamma m\, {\bar{\gamma}_{RF}}^m}\, exp\left(\frac{-m\gamma_{RF}}{\bar{\gamma}_{RF}}\right) \tag{3}$$

CDF of Nakagami-m distribution [10] is depicted by:

$$F(\gamma_{RF}) = \frac{\gamma(m, \frac{m}{\bar{\gamma}_{RF}}\gamma_{RF})}{\Gamma \mathrm{m}} \tag{4}$$

where, $\gamma(-,-)$ represent lower incomplete function, m represents the Nakagami-m fading parameter which should be greater than ½. γ_{RF} is the SNR of the source to relay, $\bar{\gamma}_{RF}$ is the SNR of the send RF signal.

$$\gamma_{RF} = \frac{\mathbb{E}|h_{RF}|^2}{N_{RF}} \tag{5}$$

$$\bar{\gamma}_{RF} = \frac{1}{N_{RF}} \tag{6}$$

FSO link:

The PDF of the Fisher-Snedecor distribution with pointing error is given as [7]:

$$f(\gamma_{FSO}) = z^2 {\gamma_{FSO}}^{-1} \frac{G_{2,2}^{2,1}\left[\frac{az^2{\gamma_{FSO}}^{1/t}}{(b-1)(1+z^2){\bar{\gamma}_{FSO}}^{1/t}}\middle|\begin{matrix}1-b,\ 1+z^2\\ a,\ z^2\end{matrix}\right]}{t\,\Gamma(\mathrm{a})\Gamma(\mathrm{b})} \tag{7}$$

Where, z=w_{zeq}/σ_z, in which w_{zeq} represent equivalent beam width and z is the PE displacement, representing a degree of deviation. If z increases consequence of the pointing error decreases and if z decreases consequence of the pointing error increases and if $z \to \infty$ Pointing error is not considered γ_{FSO} is the instantaneous SNR of the FSO channel. $\bar{\gamma}_{FSO}$ represent the average SNR of the FSO side channel, a whereas b represent atmospheric turbulence parameters.

The instantaneous received SNR at the destination is represented as,

$$\gamma_{FSO} = \frac{|\eta h_{FSO}|^2}{N_{FSO}} \tag{8}$$

Where, N_1= Variance of AWGN, η represents the optical to electrical conversion factor, h_{FSO} represents the channel fading coefficient.

The average received signal-to-noise ratio at the FSO receiver is written as

$$\bar{\gamma}_{FSO} = \frac{\eta^2\mathbb{E}|h_{FSO}|^2}{N_{FSO}} \tag{9}$$

Fixed gain relaying model is applied at Relay, the received SNR at the destination point is represented by,

$$\gamma_{end-to-end} = \frac{h_{FSO}.G^2\,\eta_{FSO}^2 h_{RF}^2}{h_{RF}^2\ G^2\eta_{FSO}^2 N_{RF} + N_{FSO}} \tag{10}$$

III. CHANNEL CHARACTERISTICS

A. Cumulative distributive function

The E2E SNR of AF based relay for dual hop RF/FSO system is represented as given,

$$\gamma_{end-to-end} = \frac{\gamma_{FSO}\gamma_{RF}}{\gamma_{FSO}+C} \tag{11}$$

where, C is relay gain

The CDF of E2E (source to destination) SNR [15],

Authorized licensed use limited to: DELHI TECHNICAL UNIV. Downloaded on January 17,2023 at 05:05:32 UTC from IEEE Xplore. Restrictions apply.

$$F(\gamma_{end-to-end}) = P_r\left[\frac{\gamma_{FSO}\gamma_{RF}}{\gamma_{FSO}+C} \leq \gamma\right] \quad (12)$$

Which can be expressed as,

$$F(\gamma_{end-to-end}) = \int_0^{\infty} P_r\left[\frac{\gamma_{FSO}\gamma_{RF}}{\gamma_{FSO}+C} \leq \gamma\right] f(\gamma_{FSO}) d\gamma_{FSO}$$
$$F(\gamma_{end-to-end}) = \int_0^{\infty} P_r\left[\gamma_{RF} \leq \frac{\gamma(\gamma_{FSO}+C)}{\gamma_{FSO}}\right] \times f(\gamma_{FSO}) d\gamma_{FSO} \quad (13)$$

Using Eq. (3) and Eq. (7),

$$F(\gamma_{end-to-end})$$
$$= \int_0^{\infty} \frac{\gamma\left(m, \frac{m}{\bar{\gamma}_{RF}}\left(\frac{\gamma_{FSO}+C}{\gamma_{FSO}}\right)\gamma\right)}{\Gamma m} . z^2 \gamma_{FSO}^{-1} \frac{G_{2,2}^{2,1}\left[\frac{az^2\gamma_{FSO}^{1/2}}{(b-1)(1+z^2)\bar{\gamma}_{FSO}^{1/2}}\middle|\begin{matrix}1-b, & 1+z^2 \\ a, & z^2\end{matrix}\right]}{2\,\Gamma a \Gamma b} d\gamma_{FSO} \quad (14)$$

Thus, the CDF of E2E SNR resulted as,

$$F(\gamma_{end-to-end})$$
$$= \left[1 - \frac{(z)^2 2^{a+b-1}}{2\,\Gamma(a).\Gamma(b)\, 2\pi exp\left(m\frac{\gamma}{\bar{\gamma}_{RF}}\right)} \sum_{n=0}^{m-1} \frac{\left(\frac{m\gamma}{\bar{\gamma}_{RF}}\right)^n}{n!} \sum_{k=0}^{n}\binom{n}{k}\left(\frac{\bar{\gamma}_{RF}}{m\gamma}\right)^k G_{4,\ 5}^{5,\ 2}\left(\left(\frac{az^2}{(b-1)(1+z^2)\bar{\gamma}_{FSO}^{1/2}}\right)^2 m\frac{\gamma}{\bar{\gamma}_{RF}} C\middle|\begin{matrix}\frac{1-b}{2} & \frac{2-b}{2} & \frac{1+z^2}{2} & \frac{z^2+2}{2} & - \\ \frac{a}{2} & \frac{a+1}{2} & \frac{z^2}{2} & \frac{z^2+1}{2} & k\end{matrix}\right)\right] \quad (15)$$

IV. PERFORMANCE ANALYSIS

A. *Outage Probability*

Outage-Probability(OP) can be stated as the probability at which the E2E SNR γ falls beyond the predetermined threshold value γ_{th}.

$$P_{out} = \Pr(\gamma \leq \gamma_{th}) \quad (16)$$

The E2E OP of the proposed framework is given as,

$$F(\gamma_{TH}) = \left[1 - \frac{(z)^2 2^{a+b-1}}{2\Gamma a\Gamma b\, 2\pi exp\left(m\frac{\gamma_{TH}}{\bar{\gamma}_{RF}}\right)} \sum_{n=0}^{m-1} \frac{\left(\frac{m\gamma_{TH}}{\bar{\gamma}_{RF}}\right)^n}{n!} \sum_{k=0}^{n}\binom{n}{k}\left(\frac{\bar{\gamma}_{RF}}{m\gamma_{TH}}\right)^k G_{4,\ 5}^{5,\ 2}\left(\left(\frac{az^2}{(b-1)(1+z^2)(\bar{\gamma}_{FSO})^{1/2}}\right)^2 m\frac{\gamma_{TH}}{\bar{\gamma}_{RF}} C\middle|\begin{matrix}\frac{1-b}{2} & \frac{2-b}{2} & \frac{1+z^2}{2} & \frac{z^2+2}{2} & - \\ \frac{a}{2} & \frac{a+1}{2} & \frac{z^2}{2} & \frac{z^2+1}{2} & k\end{matrix}\right)\right] \quad (17)$$

V. NUMERICAL RESULTS

In the given section numerical results of the proposed system are carried out. This system is considered under various atmospheric fading turbulences like weak, moderate, and strong along with pointing error impairment. In this performed system IM/DD detection technique is used. Also, z=w_{zeq}/σ_z, in which w_{zeq} are the equivalent beam width and z is the PE i.e. displacement deviation. If z increases the effect of pointing error decreases and if z decreases the effect of PE increases and if $z \to \infty$ PE is not considered

Following the same approach in the literature review [5], [6], [7], parameters α and β values depicting atmospheric fading due to turbulence are given in table 1:

Turbulences	α	β
weak	4.5916	7.0941
moderate	2.3378	4.5323
strong	1.4321	β=3.4948

Table 1*: value of α,β for different atmospheric turbulences*

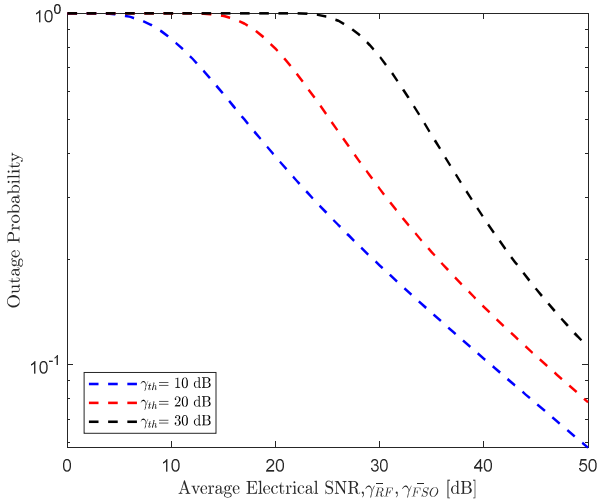

Fig 1: *OP of the given system w.r.t the $\bar{\gamma}$ weak atmospheric condition for different threshold values.*

The performance of OP depicted in fig. 1 for the performed system in weak turbulence while varying γ_{th} *i. e.*, 10 *dB*, 20 *dB and* 30 *dB*. The fading parameter is fixed to m=1. As expected, γ_{th} =10dB, the OP is lesser than at γ_{th} = 30 dB.

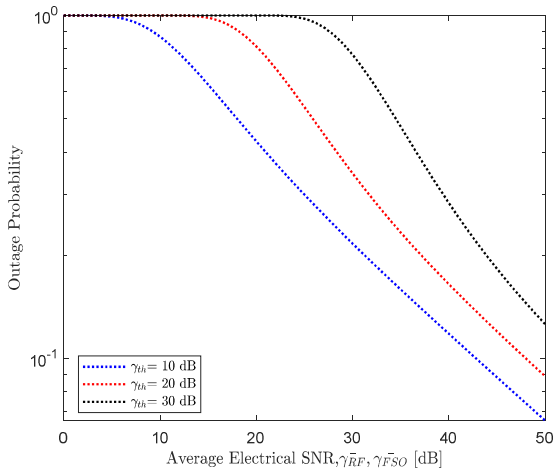

Fig.2: *OP of the given system w.r.t the $\bar{\gamma}$ for moderate atmospheric turbulence conditions for different threshold values.*

Similarly, Fig. 2 for the moderate and Fig. 3 are plotted for strong atmospheric turbulence respectively. To obtain an amalgamate result of all plots Fig.4 is plotted.

Authorized licensed use limited to: DELHI TECHNICAL UNIV. Downloaded on January 17,2023 at 05:05:32 UTC from IEEE Xplore. Restrictions apply.

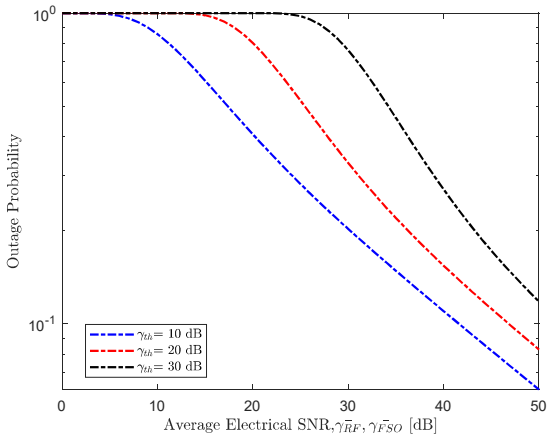

Fig.3: *OP of the given system w.r.t the $\bar{\gamma}$ under strong atmospheric turbulence conditions for different threshold values.*

From fig.1, fig.2 and fig.3, depicts, increasing↑ value of threshold γ_{th}, the OP increases↑ and thus decreasing↓ system performance.

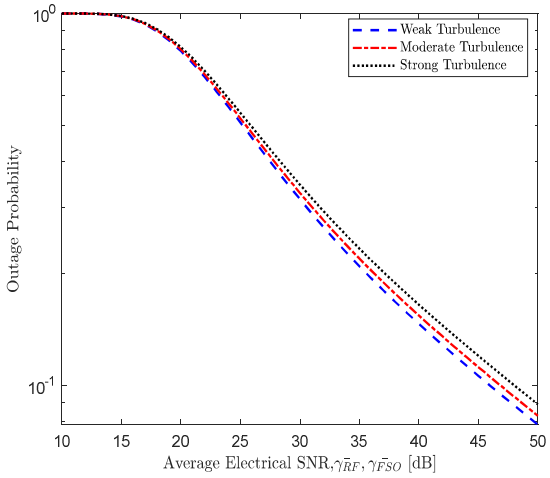

Fig.4: *comparison between OP of the given system/framework w.r.t the $\bar{\gamma}$ under various atmospheric turbulence condition(weak, moderate and strong).*

Fig. 4 depicts the comparison between the OP w.r.t their $\bar{\gamma}$ for all the atmospheric turbulences i.e., weak, moderate and strong. Also, values for effect of pointing error, Nakagami-m fading parameter, channel gain and threshold of average SNR are set to z=0.5, m=1, c=1 and γ_{th} =20dB.

.

VI. CONCLUSION

The performance of RF/FSO system over Nakagami-m/ $\mathcal{F}$ distribution with pointing error under different atmospheric turbulences have been analysed in term of OP under IM/DD detection scheme. As expected, the performance of the system degrades when PE as well as atmospheric turbulence becomes severe. All numerical results are simulated using MATLAB. The current work can be extended for analyzing the other parameters such as ABER and Ergodic capacity.

REFERENCES

[1] Arun K. Majumdar, "Advanced Free Space Optics (FSO): A Systems Approach", 10 September, 2014.

[2] Sanya Anees and Manav R. Bhatnagar, "Performance of an Amplify-and-Forward Dual-Hop Asymmetric RF–FSO Communication System", J. Opt. commun. netw./vol. 7, no. 2, february 2015.

[3] R. Rani and G. Kaur, "Design and Analysis of MIMO FSO System and WDM FSO System for Leh (Ladakh), India under Worst Weather Conditions," 2021 7th International Conference on Signal Processing and Communication (ICSC), 2021, pp. 31-36, doi: 10.1109/ICSC53193.2021.9673278.

[4] K. Borah and D. G. Voelz, "Pointing error effects on free space optical communication links in the presence of atmospheric turbulence," J. Lightwave Technol., vol. 27, no. 18, pp. 3965–3973, Sept. 2009.

[5] I. S. Ansari, F. Yilmaz, and M.-S. Alouini, "Impact of pointing errors on the performance of mixed RF/FSO dual-hop transmission systems," IEEE Wireless Commun. Lett., vol. 2, no. 3, pp. 351–354, Jun. 2013

[6] Seong Ki Yoo, Simon L. Cotton, Paschalis C, Sofotasios, Michail Matthaiou, Mikko Valkama and George K. Karagiannids, "The Fisher-Snedecor $\mathcal{F}$ distribution: A Simple and Accurate Composite Fading Model", IEEE Communications Letters Volume: 21, July 2017.

[7] Osamah S. Badarneh , Rawan Derbas, Fares S. Almehmadi, Faissal El Bouanani ,Sami Muhaidat, "Performance Analysis of FSO Communications Over F Turbulence Channels With Pointing Errors", IEEE communication letter, VOL. 25, NO. 3, MARCH 2021.

[8] Junrong Ding; Xiaolong Xie, Liying Tan, Jing Ma, and Dongpeng Kang, "Dual Hop RF/FSO System over κ-μ shadowed and Fisher-Snedecor $\mathcal{F}$ Fading Channels with NZBoresight Pointing Error", Journal of Lightwave Technology, vol, 40, issue 3, February 2022

[9] Liang Yang, Jinhai Yuan, Jun Zhang, Yi Feng, "Unified Performance Analysis of Mixed η-μ and $\mathcal{M}$-Distribution Dual-Hop RF/FSO Systems", IEEE conference 2017, beijing China.

[10] Guanjun Xu, Zhaohui Song, "Performance Analysis for Mixed κ-μ Fading and M-Distribution Dual-Hop Radio Frequency/Free Space Optical Communication Systems", IEEE Transaction on Wireless Communication VOL 20, no 3, 3 March, 2021.

[11] Hongjiang Lei, Zhijun Dai Imran Shafique Ansari, Ki-Hong Park, Member, Gaofeng Pan, Mohamed-Slim Alouini, "On Secrecy Performance of Mixed RF-FSO Systems", IEEE Photonics Journal, Vol. 9, No. 4, August 2017.

[12] Anees, S., Meerur, P., & Bhatnagar, M. R, "Performance analysis of a DF based dual hop mixed RF-FSO system with a direct RF link", IEEE Global Conference on Signal and Information Processing (GlobalSIP) (pp. 1332-1336)... (2015, December).

[13] Yamin wang,peng yue, xiang yi, cong shen, "Exact performance analysis for mixed k-u shadowed and exponentiated weibull distributed dual-hop RF/FSO system" IEER/CIC international conference on communication, china

[14] Parul garg, Ankur bansal, Nikhil sharma, "Decode-and-forward relaying in mixed η − μ and gamma–gamma dual hop-transmission system"., IET communication 10(14).

[15] Ehsan Soleimani-Nasab, Murat Uysal, "Generalized Performance Analysis of Mixed RF/FSO Cooperative Systems", (2016). IEEE Transactions on Wireless Communications, 2016

[16] Banbitra Bag, Akinchan Das , Chayanika Bose, Aniruddha Chandra, "Hybrid FSO/RF-FSO Systems over Generalized Malaga Distributed Channels with Pointing Errors" , 2019 IEEE European signal processing conference spain

[17] Juhi Gupta, Vivek K. Dwivedi and Vikram Karwal, "On the performance of RF-FSO system over rayleigh and kappa-mu/inverse gaussian fading environment" Journal of IEEE access Vol. 6, 23rd January 2018.

[18] Kehinde O. Odeyemi1, Pius A. Owolawi2, "Impact of transmission techniques in asymmetric RF/FSO system over Nakagami-m and

Authorized licensed use limited to: DELHI TECHNICAL UNIV. Downloaded on January 17,2023 at 05:05:32 UTC from IEEE Xplore. Restrictions apply.

gamma-gamma fading channels with pointing errors" November 2018
[19] Emma Zedini, Imran Shafique Ansari, Mohamed-salim Alouini, "Performance Analysis of Mixed Nakagami-m and Gamma-Gamma Dual-Hop FSO Transmission System", IEEE Photonics Journal Volume 7, Number 1, March 2015.
[20] Meijer G Wolfram Research, function.wolfram.com
[21] I.S. Gradshtein, I. M. Ryzhik, Y. V. Geronimus, and M. Y. Tseytlin, "Table of Integrals, Series, and Products", New York, NY, USA: Academic, 2007

Authorized licensed use limited to: DELHI TECHNICAL UNIV. Downloaded on January 17,2023 at 05:05:32 UTC from IEEE Xplore. Restrictions apply.

Performance Analysis of Cascaded FBGs at 10 Gbps with Different Dispersion Compensation Techniques

Divya Sisodiya and Deepika Sipal, *Member, IEEE*

***Abstract*— Over long transmission distances, the use of an erbium-doped fiber amplifier (EDFA) reduces attenuation in the information signal. In addition to single-mode fiber (SMF), other dispersion reduction technologies are required today to achieve higher transmission ranges at higher data rates. Some common techniques for reducing dispersion effects in fiber-optic communications are dispersion compensated fiber (DCF) and fiber Bragg gratings (FBG). This paper describes different types of DCF techniques using cascaded uniform and chirped FBGs. The Opti system 7.0 software is used to compare the results of DCF technology for pre, post, and balanced fiber arrangement with and without cascaded FBGs at a rate of 10 Gbps on a 120 km SMF.**

Index Terms*— *EDFA, SMF, amplitude modulation, optical fiber communication, DCF.

I. Introduction

System performance of optical communication system can be improved by removing the dispersion from it. The consequence of chromatic dispersion over the execution of an optical fibre system is called inter-symbol interference (ISI). In ISI, pulse spreading takes place, due to which pulses at the output overlap with each other [1]. To reduce the dispersion, dispersion compensation techniques are adopted. Some efficient techniques are dispersion compensating fibres (DCF) and fibre Bragg gratings (FBGs) [1]. DCF is used to compensate for the dispersion loss caused by single-mode fibre (SMF). Moreover, DCF also attains negative dispersion that makes it a special kind of fibre. Depending on the location of the SMF and DCF, three compensation configurations are available: pre- DCF, post-DCF, and balanced-DCF. In pre-DCF, DCF is activated before SMF. For post-DCF, DCF is activated after SMF, and for balanced-DCF, DCF is activated before and after SMF.

Another Versatile approach for dispersion compensation is fibre Bragg grating (FBG) [2]. It is a miniature piece of optical fibre. It has a small refractive index in its core. For a uniform FBG, the spacing of these indices is equal, while for a chirped FBG, the spacing of these indices is not equal. Uniform FBG reflects one wavelength of a given bandwidth, $\Delta\lambda$, and allows to pass all other wavelengths [2]. The wavelength which gets reflected is called Bragg wavelength.

D. Sisodiya and D. Sipal are with the Department of Electronics and Communication Engineering, Delhi Technological University, Delhi, India (e-mail: {divsisnit27@gmail.com; deepikasipal@dtu.ac.in}).

Chirped FBGs reflect more wavelengths unequally from different places of the core due to which it reduces dispersion.

In this paper, dispersion compensation schemes are studied for amplitude modulated signal using four uniform cascaded FBGs at the transmitter side. Transmitter and receiver are connected with three different schemes of DCF. Chirped FGBs are used at the output to compensate for the accumulated dispersion over the fibre. Comparative results are presented with and without cascaded FBGs. The analysis of the model is in observed in bit error rate, eye-stature and quality(Q)-factor of the signal. The wavelength range of cascaded FBGs is changed according to the user-defined parameters. Results are shown for the 193 THz range of frequency. The gain of erbium-doped fibre amplifier (EDFA) is 20 dB with a noise figure (NF) of 2 dB. The bit rate of the system is set at 10 Gbps. The length of SMF is taken as 120 km and the length of DCF is 24 km. The parameter for dispersion in SMF is 16.75 ps/nm/km and parameter for dispersion in DCF is -80 ps/nm/km. The principle of dispersion compensation is shown in Fig.1, this presents that the addition of positive and negative dispersion reduces the overall impact of dispersion in the system [1].

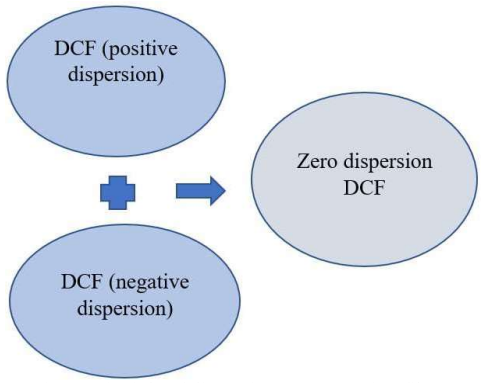

Fig.1: Principle of dispersion compensation fibre

This paper is organized into different sections. Section II discusses the dispersion compensation techniques. Section III shows the proposed system model with different techniques of DCF using Cascaded FBGs. Comparative simulation results are shown in section IV.

II. Dispersion Compensation Techniques

The generally used fibre for transmission links is a common single-mode fibre (CSMF). CSMF has a dispersion of 17 ps/nm/km in 1550 nm window [2]. For the longer distance of transmission, this dispersion becomes immense

due to which it reduces the signal-to-noise ratio and simultaneously increases bit error rate. So, the main objective with DCF is to induce the negative dispersion in the working range of wavelengths [1]. Induced negative dispersion compensates for the positive dispersion and the quality of the signal improves.

The relationship of dispersion with the second derivative of propagation constant (β) is shown in (1) [1].

$$D = \frac{-2\pi}{\lambda^2}\frac{d^2\beta}{d\omega^2} = \frac{1}{c}\left(2\frac{dn_e}{d\omega} + \omega\frac{d^2n_e}{d\omega^2}\right) \quad (1)$$

Where, c, λ, ω and n_e represents the speed of light in vacuum, wavelength, frequency and index(effective) respectively.

Equation (2) is defining the constant of propagation-

$$\beta = k_o n_e = \frac{\omega}{c}n_e = \frac{2\pi}{\lambda}n_e \quad (2)$$

Effective index number can be defined as-

$$n_e = \Delta n_e + n_o \quad (3)$$

Where, Δn_e is representing difference of effective index and n_o is representing cladding's refractive index.

Now, the dispersion is defined in (4) as-

$$D = \frac{-2\pi cd^2}{\lambda^2}\frac{k_o\Delta n_e}{d\omega^2} + \frac{-2\pi cd^2}{\lambda^2}\frac{k_o n_o}{d\omega^2} = D_{waveguide} + D_{material} \quad (4)$$

The elimination of dispersion is shown in (5) [1,4]-

$$D_{TF}L_{TF} + D_{DCF}L_{DCF} = 0 \quad (5)$$

Where, D_{TF} is coefficient of dispersion for transmission fiber, L_{TF} is representing the length of transmission fiber, D_{DCF} is coefficient of dispersion of DCF and L_{DCF} is the length of DCF.

Another discussed technique for dispersion compensation is FBG. These are very flexible in use. FBG can perform single as well as multichannel dispersion compensation modules (DCM) which is not practical with DCF [1]. FBG has a grid period defined as the distance between two vertices of the refractive index. The narrow spectrum of wavelength λ_B is mirrored by FBGs, while it passes all other wavelengths. Mirrored wavelength is Bragg wavelength shown in (6)-

$$\lambda_B = 2\Delta n_g \quad (6)$$

Where, λ_B is denoting the wavelength(nm) which got reflected, Δ is representing the grating period (nm) and n_g is the refractive index (effective).

III. System Model

DCF circuit simulations are analysed by introducing cascaded FBGs in each of the three configurations. To implement this concept, four cascaded uniform FBGs are connected after the amplitude modulator of the transmitter part. The wavelength of FBGs and continuous wave (CW) laser are matched. The signal is then transmitted to the channelpath via loop control. At the yield of the channel path, chirped FBG is connected which is used to eliminate the dispersion existing in the signal. The signal is passed through the PIN photodetector, low pass Bessel filter, and finally observed at the BER analyser. Fig.2 is showing block representation of simulated model for pre, post, and balanced techniques of DCF with cascaded FBGs.

The transmitter part of the system contains a pseudo-random bit sequence generator (PRBS), CW laser of 1550nm wavelength, amplitude modulator (AM), and non-return-to-zero (NRZ) pulse generator. The signal is sent at a bit rate of 10 Gbps. Channel path consists of SMF of length 120 km, DCF of length 24 km, and EDFA amplifiers of gain 20 dB. Channel path is connected with the loop control having number of loops equal to 1, which means a signal is getting amplified one time. The position of DCF is changed with respect to SMF so that all three techniques of dispersion compensation can be verified.

The receiver section of the system consists of a PIN photodetector to transform the optical signal of light into an electrical signal. It is further connected with a low pass Bessel filter and bit error analyser to obtain the Q-factor and bit error rate of the signal respectively. The specifications used for simulations are shown in Table I.

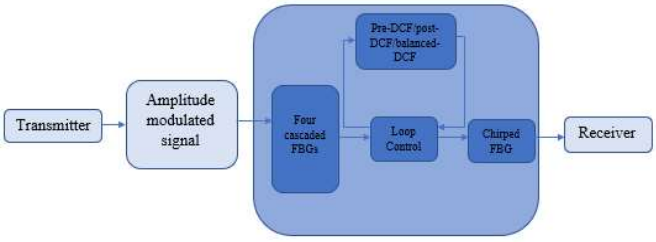

Fig.2: Block diagram for: (a) pre-DCF, (b) post-DCF, and (c) balanced-DCF cascaded FBG

Table I: Simulation specifications

Sr. No.	Parameters	Value
1.	System bit rate (Gbps)	10
2.	Frequency (THz)	193.1
3.	Length of DCF fiber(km)	24
4.	Length of fiber (km)	120
5.	DCF attenuation (dB/km)	0.3
6.	Fiber attenuation (dB/km)	0.2
7.	DCF dispersion(ps/nm/km)	-80
8.	SMF dispersion(ps/nm/km)	16.75

IV. The Results and Discussion

Comparative results are presented for each technique of the DCF system shown in Fig.2 at 1550 nm wavelength. Fig.3 is showing the comparative Q-factor plot obtained at 1550 nm

wavelength for pre, post, and balanced DCF techniques with and without the use of cascaded FBGs.

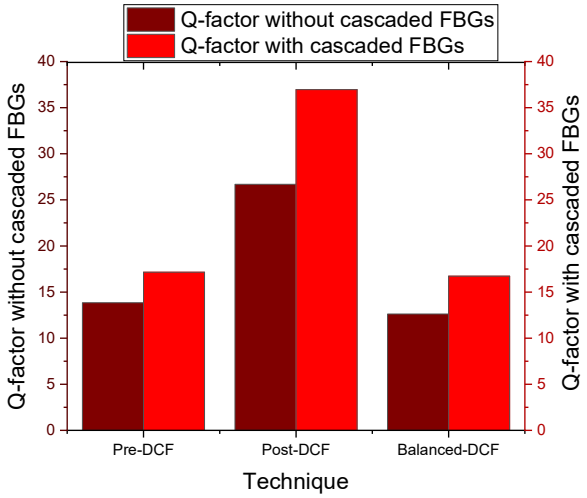

Fig.3: Comparative Q-factor plot of pre, post and balanced-DCF model with and without using cascaded FBGs at 1550nm.

The simulation of pre, post, and balanced DCF models shown in Fig.2. are observed at 1550 nm of wavelength. By changing the frequency, slight changes are observed in the quality factor and bit error rate of the received signal. Similarly, the simulation of pre, post, and balanced DCF with cascaded FBG models shown in Fig.3 are also observed at a 1550 nm wavelength. Frequencies of cascaded uniform FBGs and the chirped FBG connected at the yield are changed simultaneously according to the wavelength of the CW laser. The quality factor and bit error rate are observed on bit error analyzer and based on that, pre, post, and balanced compensation techniques of DCF model with and without cascaded FBG are differentiated [3]. Table II is showing the Q-factor of DCF techniques with and without using cascaded FBGs.

Table II: Observation table for Q-factor of DCF technique with and without using cascaded FBGs

Sr.No.	Technique	Q-factor without cascaded FBGs	Q-factor with cascaded FBGs	Percent -age change
1.	Pre-DCF	13.837	17.159	24%
2.	Post-DCF	26.692	36.961	38%
3.	Balanced-DCF	12.619	16.721	32%

Fig.4 is showing the comparative logarithmic plot of BER observed at BER analyser for pre, post and balanced DCF technique with and without cascaded FBGs

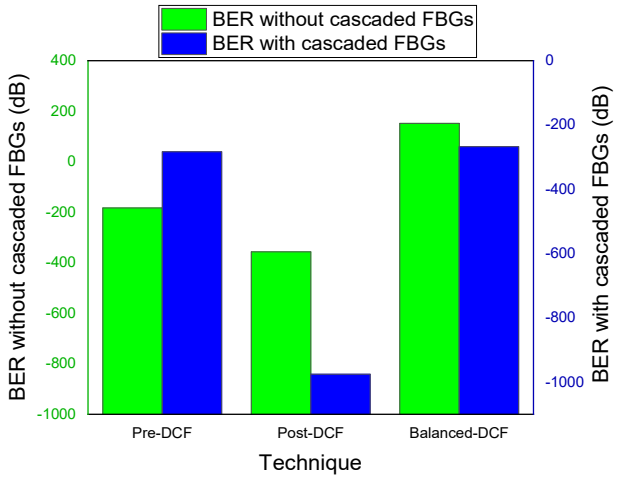

Fig.4: Comparative bit error rate (BER) plot of pre, post and balanced-DCF model with and without using cascaded FBGs at 1550nm.

The bit error rate is observed for 1550 nm of wavelength and based on that, pre, post, and balanced compensation techniques of the DCF model with and without cascaded FBGs are differentiated. Table III is showing the observations of the BER of DCF techniques with and without cascaded FBGs.

Table III: Observation table for average BER (logarithmic) of DCF techniques with and without cascaded FBGs.

Sr.No.	Technique	BER without cascaded FBGs (dB)	BER with cascaded FBGs (dB)	Percenta -ge change
1.	Pre-DCF	-183.07	-283.46	54%
2.	Post-DCF	≈-356.67	≈-975.187	≈ 98%
3.	Balanced-DCF	-151.83	-267.58	76%

As it can be clearly seen from Fig.3 that by introducing a set of cascaded FBGs at the transmitter part, the Q-factor of the signal is increased which means there is a lower rate of energy loss in the signal. From Fig.4, it is observed that cascaded FBGs have reduced the bit errors in the signal which means the transmitted bits have not been altered due to noise or distortion. The BER was observed in exponential and converted to decibels to find out the improvement in performance in terms of percentage. Among all the DCF techniques, the highest percentage change in performance of cascaded FBGs is observed with the post- DCF and balanced-DCF technique as compared to pre-DCF technique. Different eye-statures obtained from the simulations are observed through BER analyser and are shown in Fig.5 and Fig.6 for without and with cascaded FBGs for post-DCF.

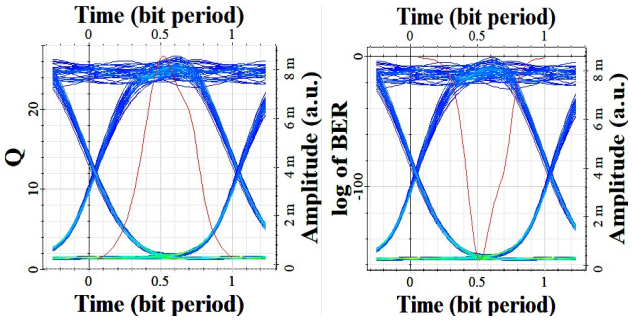

(a) Post-DCF Q-factor (b) Post-DCF BER

Fig.5: Eye-statures for (a) Q-factor and (b) BER without cascaded FBGs for post-DCF configuration

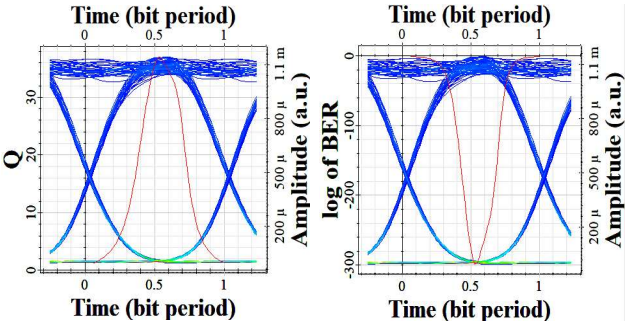

(a) Post-DCF Q-factor (b) Post-DCF BER

Fig.6: Eye-statures for (a) Q-factor and (b) BER with cascaded FBGs for post-DCF configuration

In the eye-stature of Fig.6 (a) and Fig.6 (b), the Q-factor has increased and minimum BER has decreased as compared to Fig.5 (a) and Fig. 5 (b), indicating that the DCF approach with cascaded FBGs delivers better signal than without cascaded FBGs. Through observations of Q-factor, BER and eye-stature, it has been observed that the system is working good with cascaded FBGs instead of non-cascaded FBGs. The DCF techniques using cascaded FBGs can also be implemented with wavelength division multiplexers (WDM) for large number of users [4]-[6].

V. Conclusion

The proposed model is focused on reducing the chromatic dispersion in the amplitude modulated signal by using the DCF and cascaded FBGs concept. DCF technique is used for three different configurations without cascading FBG and with cascading FBG namely pre, balanced and post configurations. Results from the different configurations are compared in terms of Q-factor, BER and eye-statures. Among different DCF techniques, the post-DCF and balanced-DCF configurations are improving the system more efficiently as compared to pre-DCF configuration. The maximum percentage change in Q-factor and BER of post-DCF is 38% and ≈98% and for balanced-DCF, it is 32% and 76% respectively. Although the bit error rate and information quality are both getting better, there exists a potential limitation of the work as the obtained power with DCF and cascaded FBGs is -32 dBm while without cascaded FBGs, the obtained output power is -15 dBm which is much closer to 0 with high signal intensity and amplified signal.

References

[1] Sharma, A,. Singh, I., Bhattacharya, S., Sharma, S. (2019), "Performance Comparison of DCF and FBG as Dispersion Compensation Techniques at 100 Gbps over 120 km using SMF," in *Nath, V., Mandal, J. (eds) Nanoelectronics, Circuits and Communication Systems. Lecture notes in Electrical Engineering,* vol 511. Springer, Singapore, doi: https://doi.org/10.1007/978-981-13-0776-8_40

[2] Sayed, A.F., Mustafa, F.M., Khalaf, A.A.M. et al, "An Enhanced WDM optical communication system using a cascaded fiber Bragg grating," Opt Quant Electron 52, 181 (2020), doi: https://doi.org/10.1007/s11082-020-02305-9.

[3] J. Karunya and P. Prakash, "Analysis of WDM system using DCF," *2017 Fourth International Conference on Signal Processing, Communication and Networking (ICSCN), 2017*, pp. 1-4, doi: 10.1109/ICSCN.2017.8085726.

[4] F. Khair, I. W. Mustika, Fahmi, D. Zulherman and F. Hario, "Comparative Analysis of Dispersion Compensating Fiber in DWDM System Using 10 Gbps and 40 Gbps Bit Rate," *2018 10th International Conference on Information Technology and Electrical Engineering (ICITEE), 2018*, pp. 412-417, doi: 10.1109/ICITEED.2018.8534851.

[5] N. M. Litchinitser, B. J. Eggleton and G. P. Agrawal, "Dispersion of cascaded fiber gratings in WDM lightwave systems," *in Journal of Lightwave Technology, vol. 16*, no. 8, pp. 1523-1529, Aug. 1998, doi: 10.1109/50.704620.

[6] Bedir Yousif, Ahmed Sh. Samrahb, and Rawan Waheed, "High quality factor and dispersion compensation based on fiber Bragg grating in dense wavelength division multiplexing," *ISSN 1060- 992X, Optical memory and neural networks, 2020, Vol. 29, No. 3, pp. 228–243. © Allerton Press, Inc., 2020.*

[7] Nath, Vijay, Mandal, J.K "Nanoelectronics, communications and circuits system," *Springer science and business media ltd, proceeding of NCCS 2019,* doi: https://doi.org/10.1007/978-981-15-7486-3.

[8] D. Sisodiya, S. Dwivedi and G. Kaur, "Multi User Optical CDMA System Utilizing Fiber Bragg Grating," *2021 Emerging Trends in Industry 4.0 (ETI 4.0),* 2021, pp. 1-5, doi: 10.1109/ETI4.051663.2021.9619369.

[9] D. Sisodiya and D. Sipal, "Long Range and Low Cost WDM OWC System Based on Hybrid Configuration of Optical Amplifiers," *2022 Second International Conference on Advances in Electrical, Computing, Communication and Sustainable Technologies (ICAECT),* 2022, pp. 1-5, doi: 10.1109/ICAECT54875.2022.9807650.

[10]D. Sisodiya, S. Dwivedi, G. Kaur, "POL-SK based WDM-FSO communication for network enhancement," *International conference on computing, power and communication technologies, IEEE GUCON, 2021, Kualalumpur* doi: https://ieeexplore.ieee.org/document/9573661.

[11]S. Dwivedi, G. Singh, D. Sisodiya, G. Kaur, "Design and performance analysis of WDM-FSO communication system using Polarization Shift Keying" *Journal of Optical Communications*, 2022, doi: https://doi.org/10.1515/joc-2021-0141.

[12]D. Sisodiya, G. Kaur, "FBG-based WDM broadcast communication system for metropolitan areas," in *Advances in VLSI, communication and signal processing, chapter 16*, pp. 177-185, doi: 10.1007/978-981-19-2631-0.

Personality Detection using Kernel-based Ensemble Model for leveraging Social Psychology in Online Networks

AKSHI KUMAR

Dept. of Computing & Mathematics, Manchester Metropolitan University, Manchester, United Kingdom

ROHIT BENIWAL

Dept. of Computer Science & Engineering, Delhi Technological University, New Delhi, India

DIPIKA JAIN*

Dept. of Computer Science & Engineering, Delhi Technological University, New Delhi, India

The Asian social networking market dominates the world landscape with the highest consumer penetration rate. Businesses and investors often look for winning strategies to attract consumers to increase revenues from sales, advertisements, and other services offered on social media platforms. Social media engagement and online relational cohesion have often been defined within the frameworks of social psychology and personality identification is a possible way in which social psychology can inform, engage, and learn from social media. Personality profiling has many real-world applications, including preference-based recommendation systems, relationship building, and career counseling. This research puts forward a novel kernel-based soft-voting ensemble model for personality detection from natural language, KBSVE-P. The KBSVE-P model is built by firstly evaluating the performance of various Support Vector Machine (SVM) kernels, namely radial basis function (RBF), linear, sigmoidal, and polynomial, to find the best-suited kernel for automatic personality detection in natural language text. Next, an ensemble of SVM kernels is implemented with a variety of voting techniques, such as soft voting, hard voting, and weighted hard voting. The model is evaluated on the publicly available Kaggle_MBTI dataset and a novel South Asian, Indian, low-resource Hindi language विशेष चरित्र_MBTI (pronounced as vishesh charitr, meaning personality in Hindi) dataset for detecting a user's personality across four personality traits, namely introvert/extrovert (IE), thinking/feeling (TF), sensing/intuitive (SI), and judging/perceiving (JP). The proposed kernel-based ensemble with soft voting, KBSVE-P, outperforms the existing models on English Kaggle-MBTI dataset with an average F-score of 85.677 and achieves an accuracy of 66.89 for the Hindi विशेष चरित्र_MBTI dataset.

CCS CONCEPTS • **Information systems** → Social networking sites; • **Computing methodologies** → Natural language processing; Machine learning

Additional Keywords and Phrases: Social Networks, Personality Psychology, Natural language, kernel-based methods

Just Accepted

Permission to make digital or hard copies of all or part of this work for personal or classroom use is granted without fee provided that copies are not made or distributed for profit or commercial advantage and that copies bear this notice and the full citation on the first page. Copyrights for components of this work owned by others than the author(s) must be honored. Abstracting with credit is permitted. To copy otherwise, or republish, to post on servers or to redistribute to lists, requires prior specific permission and/or a fee. Request permissions from permissions@acm.org.
© 2023 Copyright held by the owner/author(s). Publication rights licensed to ACM.
2375-4699/2023/1-ART1 $15.00
http://dx.doi.org/10.1145/3571584

Table.1. Taxonomy

Abbreviation	Definition
I/E	Introvert-Extrovert
N/S	iNtution – Sensing
J/P	Judging – Perceiving
T/F	Thinking – Feeling
MBTI	Myers Briggs Type Indicator
MLP	Multi-Layer Perceptron
MCC	Matthews Correlation Coefficient
NLP	Natural Language Processing
NLTK	Natural Language Tool Kit
RBF	Radial Basis Function
ROC-AUC	Area Under Receiver Operating Characteristic Curve
SVM	Support Vector Machine
TN	True Negative
TP	True Positive
FN	False Negative
FP	False Positive
TF-IDF	Term Frequency- Inverse Document Frequency

Just Accepted

1 INTRODUCTION

Personality is defined as the summation of the habits in which a person reacts and interacts with others [1, 2]. Certain determinants assist in the analysis of the personality of a person's heredity, environment, and situation. It can be characterized as psychological factors that affect the actions, thoughts, and feeling patterns of a person that distinguish characters from each other. No two individuals have the same personalities. Each of them has a unique character. The individuals might possess some identical characteristics, but not all the features can be similar. Personality profiling helps people become both self-aware and aware of how others around them think, feel, and act.

Personality is usually measured through questionnaire-based psychometric testing, in which a series of questions are asked about the respondents' behavior, thoughts, and emotions. This approach has been criticized for two reasons. First, it requires respondents to have good introspection and an accurate picture of who they are. Second, if these questionnaires are used in selection contexts, for example, in job hiring, some of the candidates could try to portray a desirable image of themselves to be hired. Recently, personality psychology can become an important tool for designing new applications, predicting the success of a new product, introducing new features to existing systems, or developing user adaptation approaches. The development of personality computing methods can be of high advantage to personality and social psychology. Computational technologies allow the processing of a larger volume of behavioral data that might be hard to analyze with techniques traditionally applied in psychology (observational methods, surveys, etc.). In this respect, personality computing might help to establish patterns of thought, emotion, and behavior" from machine measurable cues, including affective computing [3,[4] (the domain dealing with emotions), social signal processing (the area related to non-verbal communication in public interactions) and sociolinguistics (the domain that analyses traces of social phenomena in language), etc.

Social networks [5,6] define a complex global system that comprises several mathematical models and philosophies to study its behavior and to explain and predict its dynamics. Sometimes called "relationship networks," these help people and organizations connect online to share information and ideas. The benefits of using social networking [5] include market research, brand awareness, lead generation, relationship building, and customer service. Undoubtedly, social networks are a vast and growing body of research that has influenced the social, cultural [7], economic, and psychological aspects of people across the globe. In Asia, the online social networking landscape is even more dynamic. Asians are among the heaviest social media consumers in the world with the highest social media penetration rates across the globe. The most popular social network apps in the region include Facebook [8-12], WhatsApp, Messenger, Instagram, Youtube, Wechat, Line, Reddit [13], Twitter [14], and Snapchat. Fig. 1 shows the social media statistics in Asia from August 2021 to

August 2022[1]. Quite clearly, the Asian Social networks are a dominant and ongoing real-world phenomenon which have been top of mind for every investor, entrepreneur, business executive, and consumer.

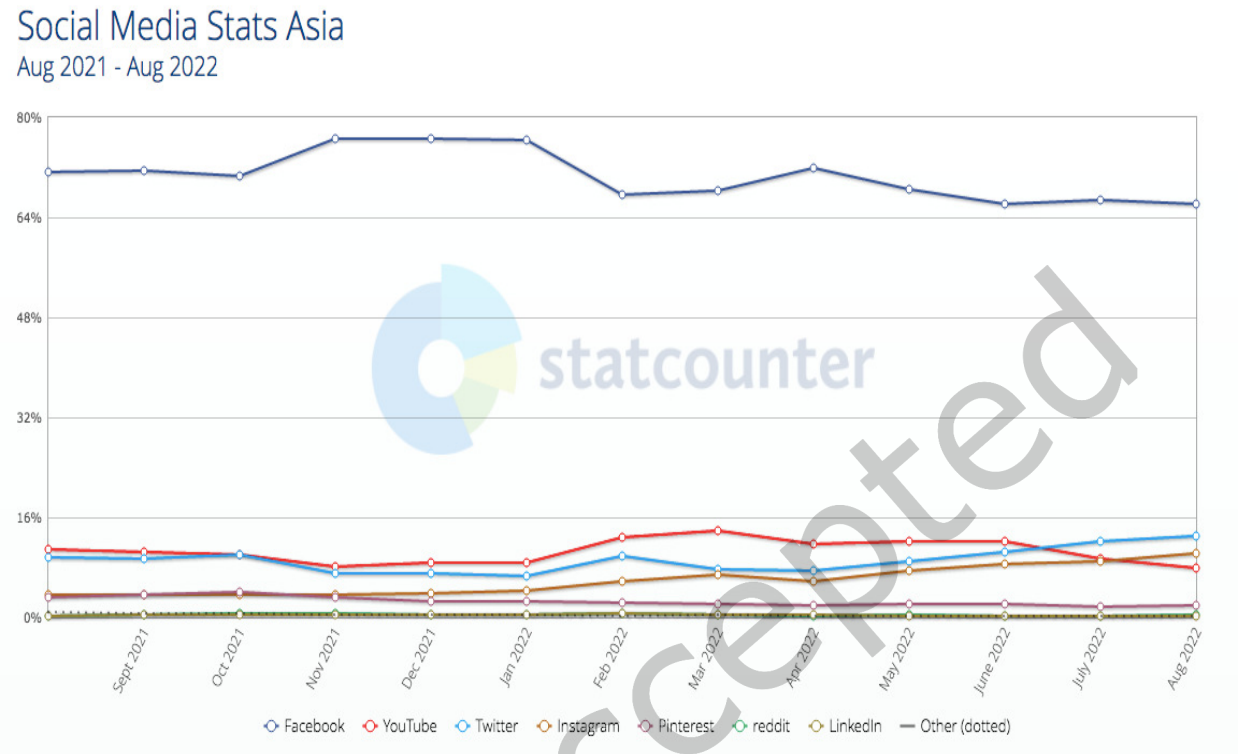

Fig. 1. Asian Social Network statistics

Social networks [15] have unequivocally brought the largest upheaval to the social context, changing the mode in which people interact and engage with each other. Understanding this context is an important aspect of social psychology which is the scientific study of how individuals think, feel and behave in social conditions and situations. Social media [16] engagement and online relational cohesion have often been defined within the frameworks of social psychology [17] and personality identification is a possible way in which social psychology can inform, engage, and learn from social media. Further, multimodal [18] affective combinations of speaking style (prosody, intonation, etc.) and body movements can serve as cue accounting as features for personality traits. Personality theorists claim that a user's personality traits are a good starting point for predicting a user's social behavior, which can have a substantial influence on his/her preferences and decisions. Recognizing personality types that can aid in understanding people's preferences and associated cognitive processes is a well-studied problem of computational psychology. Real-time analytics of personality attributes has appeared as a portion of vibrant market research and branding approaches that can facilitate the personalization of web, recommendation services, and intelligent empathetic conversational agents.

Various personality trait theories have been developed to categorize, interpret, and understand the human personality. These include Cattell's Sixteen Personality Factor [11], Hans Eysenck's psychoticism, extraversion, and neuroticism, Myers–Briggs Type Indicator, and Big-Five [27]. Further, according to the input data type, automatic personality trait recognition is categorized into unimodal and multimodal. Specifically, unimodal contains the audio only, text only, visual (static images and dynamic videos) or only physiological signals for personality trait recognition, and multimodal personality trait recognition, integrating multiple modalities of behavioral data, such as audio, visual, and text information. In recent years, several datasets with different data modalities for personality detection have been created, such as Big Five Personality Tests, Myers Briggs Type Indicator (Kaggle_MBTI), Standard Essays, First Impression-

[1] Social Media Stats Asia | Statcounter Global Stats

Just Accepted

Chalearn dataset, multimodal databaASe for impliCit pERsonaliTy and Affect recognitIoN (ASCERTAIN) [27], and the Personality and Demographics of Reddit Authors (PANDORA) dataset [13]. Fig.2 depicts the key modality features reported in the literature on automatic personality detection.

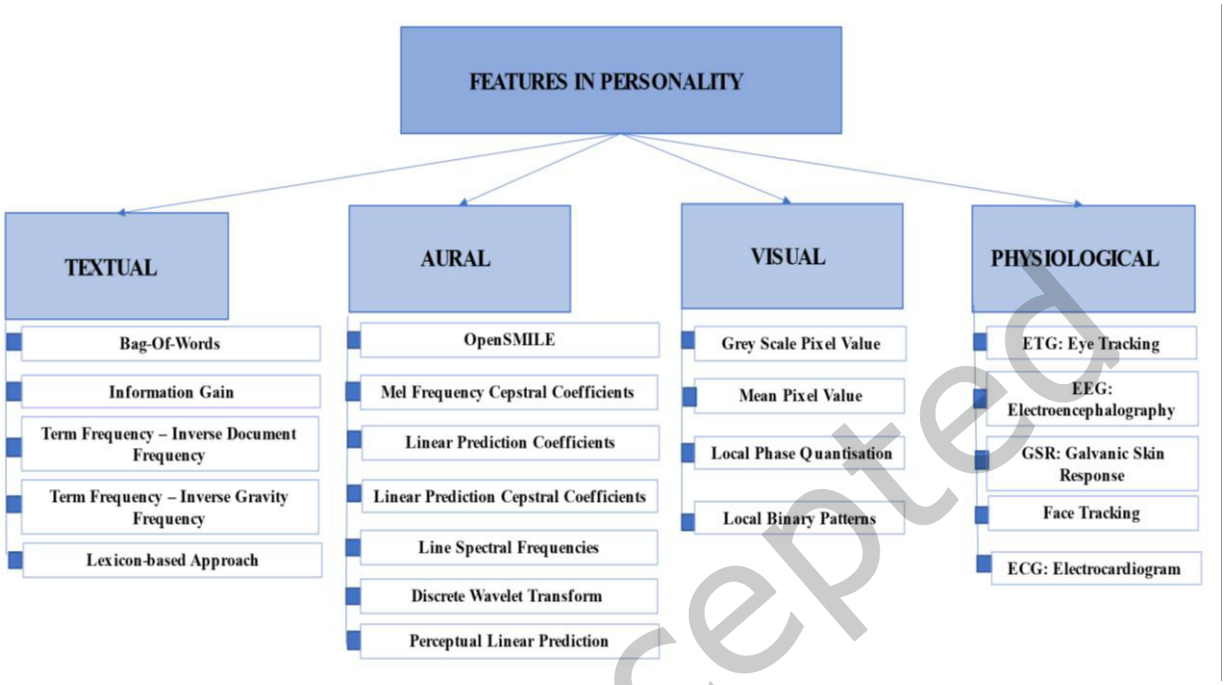

Fig. 2. Modality features for automatic personality detection

Text-based personality prediction from multiple social media data sources has gained much attention among researchers in recent years. Kaggle_MBTI is a popular text-based personality dataset that was collected using the PersonalityCafe forum. It consists of 8600 rows elaborating 8 distinct types of personality explaining the perspective of cognitive functions of Jungian [19] theory/ topology. The dataset has a four-letter code for each of the sixteen personality types distributed over four axis as shown in fig.3. These dimensions and their corresponding possibilities are Introversion (I) – Extroversion (E), Intuition (N) – Sensing (S), Thinking (T) – Feeling (F), and Judging (J) – Perceiving (P) and indicates that each person will have a personality abbreviated such as ENFJ, INFJ, ENFP, INFP, ENTJ, INTJ, ENTP, INTP, ESFJ, ISFJ, ESFP, ISFP, ESTJ, ISTJ, ESTP, and ISTP from the combination of all 4 axis.

Just Accepted

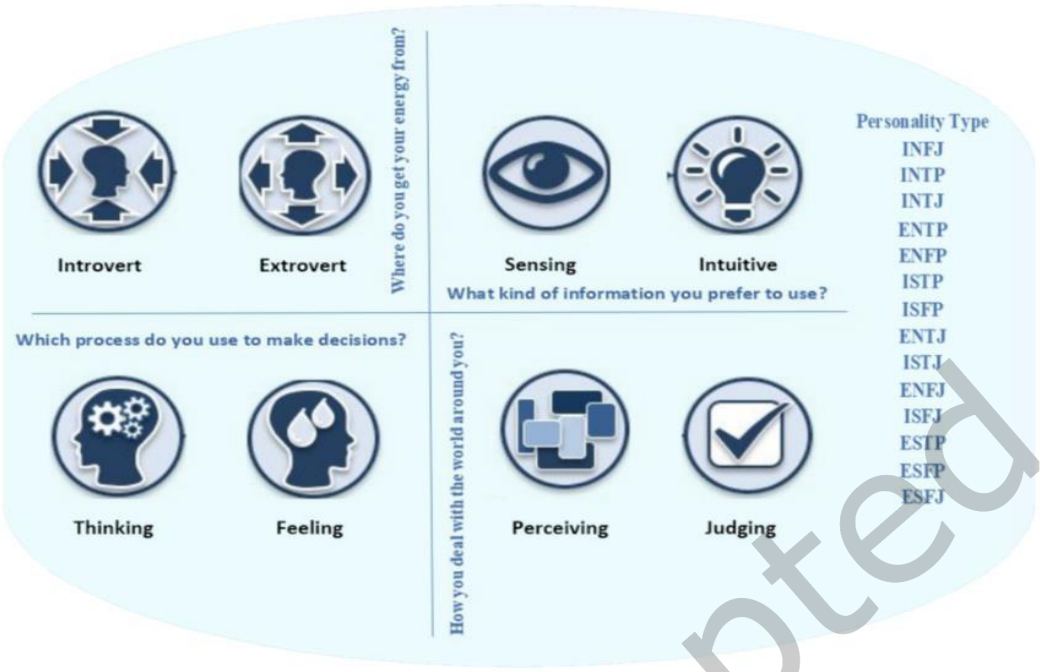

Fig. 3. MBTI personality types

Pertinent literature reports the use of deep learning techniques for text based Kaggle_MBTI personality trait recognition tasks. In real-world applications, the most common data type is tabular data, comprising samples (rows) with the same set of features (columns) but recent studies report the challenges with deep learning models when applied to tabular data such as Kaggle_MBTI. These include missing values, multimodality, and lack of locality. Moreover, the real-world datasets Kaggle_MBTI are probably never linearly separable, especially that focus on multi-class classification, and therefore higher accuracy by hyperplanes is challenging. Most of the learning models consider all the Kaggle_MBTI classes independent of each other and fail to capture the in-built relatedness of some types to other types, for example, INFP is much more like INTJ as compared to ESTJ. Moreover, with the growth of multilingual social media, the online use of local and regional languages is also rapidly expanding. However, most of the research on MBTI personality traits on social media has been restricted to the English language only. Hindi is ranked among the 3rd most spoken languages in the world, with 615 million active speakers [20] and various studies report the increased use of Hindi in social media interactions [21-25]. It will therefore be noteworthy to study and evaluate automatic personality detection in a low-resource Indian language, Hindi.

This research sets forward a kernel-based soft voting ensemble for personality detection in natural language textual data. The Support Vector Machine (SVM) [12] with soft voting ensembled kernels is used as a classifier to detect different traits of the MBTI personality type in an English and a Hindi dataset. SVM's Kernel Trick addresses non-linearly separable cases as it utilizes existing features, applies some transformations, and creates new features and these new features are the key for SVM to find the non-linear decision boundary. Simultaneously, the soft voting ensemble involves summing the predicted probabilities for class labels and predicting the class label with the largest sum probability. Thus, the primary contribution of this work is:

- To develop an efficient kernel-based ensemble model for text-based personality prediction.
- To evaluate the performance of different SVM kernels and detect the best-suited kernel for developing models for automatic personality detection in textual data, English and Low-resource South Asian language, Hindi
- To build an MBTI trait-based Hindi personality dataset, विशेष चरित्र_MBTI (pronounced as vishesh charitr, meaning personality in Hindi)

Just Accepted

- To evaluate the performance of ensembles of different SVM kernels aggregated with soft voting, hard voting, and weighted hard voting.

The organization of the paper is as follows: The next section briefs about the related work within the domain of personality detection followed by the discussion on the methodology used and the proposed model in section 3. Section 4 layout the details of model performance and the conclusion is given in section 5.

2 RELATED WORK

Overall, personality is relevant to any computing area relating to understanding, prediction, or synthesis of human behavior. Still, while being different and diverse in terms of data, technologies, and methodologies, all computing domains concerned with personality consider the following three main problems:

- identification or detection of the true personality of an individual (Automatic Personality Detection)
- estimation of the personality traits of a given individual (Automatic Personality Perception),
- fabrication of artificial personalities through embodied agents (Automatic Personality Synthesis).

This research primarily focuses on the problem of automatic personality detection. Some of the work conducted by researchers for identifying the personality of an individual is on unimodal data (text-based or video-based), whereas some are on multimodal data [6], which includes bimodal (audio-visual) and trimodal (audio-visual-textual) data. Based on the modalities, various datasets with a wide spectrum of distal cues, including written texts, nonverbal behavior, and, more recently data collected via mobile or wearable devices and online games have been available. The popular datasets include the Myers-Briggs Type Indicator (Kaggle_MBTI), Essays, myPersonality, and Chalearn.

- Big Five Personality Test is a textual dataset based on the answers for the questionnaire asked via the online platform open psychometric. It has a collection of 1,015,342 tuples concentrated over the five-factor model or the OCEAN model for personality traits.
- Kaggle_MBTI is another popular text-based personality dataset based on Carl Jung's [19] theory collected using the PersonalityCafe forum platform consisting of 8600 rows elaborating 8 distinct types of personality explaining the perspective of cognitive functions of Jungian theory/ topology. The dataset has 4 letter code for each of the 16-personality types distributed over 4 axes as explained above in figure-2.
- Essays dataset is also named as stream-of-consciousness essays or gold-standard essays is also a unimodal dataset consisting of texts. It has 2400 instances compiled by Pennebaker and King (1999) [26] from the essays written by students for the study of different linguistic styles of different individuals.
- First Impression V2 (CVPR'17) is a multimodal dataset consisting of visual and audio modalities collected from about 3000 youtube videos and converted into 10000 short clips of 15 seconds each.
- ASCERTIAN is a Big-5 personality trait dataset abbreviated for a multimodal databaASe for impliCit pERsonaliTy and Affect recognitIoN which focused on the physiological signals such as EEG, ECG, GSR, and facial activity. This shows an interrelation between emotions and personality traits for 58 users.

In 2012, Lee et al. [27] proposed a novel algorithm, namely MBTI-based-Evolutionary Algorithm for a Genetic Robot's Personality (MBTI-EAGRP), which identified the characteristics and behavior by measuring the user preference via the assessment method. This novel algorithm worked in two phases namely, Self Organizing Map-MBTI (SOMMBTI) and Evolutionary Algorithm for Genetic Robot Personality (EAGRP). The first phase mapped a user feature using Neural Networks with self-organizing maps. Thereafter, the second phase of the model precisely matched the genome of the robot. This application was designed to be used over mobile phones.

In 2017, Cui and Qi [7] used Naïve Bayes and SVM to analyze the dataset and it was found that the Naïve Bayes classifier provided 26% accuracy with overfitting data while SVM conceded 38% accuracy. Moreover, they also used the Deep Learning techniques where multi-layer LSTM was used and it yielded an accuracy of 36%. In the end, their results concluded that the performance of Deep Learning was better as compared to SVM and Naïve Bayes. Hernandez and Scott in 2017 [28] used different RNN models such as SimpleRNN, GRU, LSTM, and Bi-directional LSTM for MBTI personality traits. They concluded that the performance of LSTM was found best among all four used models. In 2019, Keh and Cheng [29] used the personality café forums dataset to deploy MBTI personality traits. They built a model after fine-tuning the BERT model to perform the classification task. At last, the model provided 49% accuracy.

Just Accepted

In 2021, Ren et al. [30] pointed out the ignorance of contextual information and polysemous words while examining different personalities and proposed a model for multi-label personality detection, which combined the pre-trained BERT model with a Neural Network to understand the text and semantics of social media. Additionally, they proposed a method to combine emotions with semantic features for detecting various personality traits. Cerkez et al. [31] also worked upon Kaggle_MBTI personality traits and proposed a technique as well as a loss function for multi-class text classification to detect personalities. They reported that the results of LSTM and CNN models were better as compared to Multi-Layer Perceptron, Naïve Bayes, and Logistic Regression. Basto C. [32] also worked upon Kaggle_MBTI and introduced data centric approach using three primary features such as sentimental, grammatical and aspects. Shafi, H. [33] worked on the MBTI framework using course tree, fine KNN, weighted KNN, ensembled bagged tree and ensembled boosted tree algorithms. A testing accuracy of 70.75% and 75.51% was respected achieved for the bagged and boosted ensemble models. In 2022, Bokishev[34] worked on Kaggle_MBTI using three models namely, multimodal logistic regression, linear support vector classifier, and XGBoost Classifier. Amongst the three models, XGBoost had the best model with a training accuracy of 92%.The existing works based on MBTI personality trait theory are restricted to the English language only. Few attempts on personality detection in other languages exists but are based on other trait theories such as Big 5 [35][36].

In 2020, Gjurkovic et al. [13] developed the first dataset, Pandora, based on the personality and demography of around 10 thousand Reddit users. This dataset supports MBTI, Big-5, and Enneagram personality models. Apart from the MBTI personality label, Pandora also had other labels such as age, gender, location, and (sociolinguistic) language. Furthermore, with Pandora, they achieved an accuracy of 45% for the MBTI personality traits. It is evident from the literature that so far, personality detection techniques address traits separately because these are supposed to be, by construction, uncorrelated and independent. However, it is imperative to capture the in-built relatedness of some types. At the same time, current studies on personality detection are based on English language sociolinguistic cues and therefore studies in local, low-resource languages such as Hindi needs further exploration. Motivated by these gaps, this research proffers a novel model for automatic personality detection

3 METHODOLOGY

The novel kernel-based soft-voting ensemble model for personality detection from natural language, KBSVE-P is built by firstly evaluating the performance of various Support Vector Machine (SVM) kernels, namely radial basis function (RBF), linear, sigmoidal, and polynomial, to find the best-suited kernel for automatic personality detection in natural language text. Next, an ensemble of SVM kernels is implemented with a variety of voting techniques such as soft voting, hard voting, and weighted hard voting. The model is evaluated on the publicly available Kaggle MBTI dataset for detecting a user's personality using various performance metrics. Simultaneously, a MBTI based Hindi personality dataset, विशेष चरित्र_MBTI (pronounced as vishesh charitr, meaning personality in Hindi) is built and the KBSVE-P model is evaluated on this dataset too. The following sub-sections expound on the details of the methodology used for personality detection in textual data.

3.1 Dataset

In this research, two textual datasets have been used, Kaggle-MBTI [38][7] and विशेष चरित्र_MBTI. The concept of Kaggle_MBTI is that every persona consists of four magnitudes, and each magnitude has 2 possibilities. These dimensions or the magnitudes and their corresponding possibilities are Introversion (I) – Extroversion (E), Intuition (N) – Sensing (S), Thinking (T) – Feeling (F), and Judging (J) – Perceiving (P). In total, this dataset has 8675 rows along with 16 combinations or personality types, which are denoted using a four-letter abbreviation. It means that each person will have a personality abbreviated such as ENFJ, INFJ, ENFP, INFP, ENTJ, INTJ, ENTP, INTP, ESFJ, ISFJ, ESFP, ISFP, ESTJ, ISTJ, ESTP, and ISTP from the permutation of all the four axis. For example, someone who is an extrovert, relies more on sensing, thinking, and perceiving rather than judging and will be labeled as an ESTP. As far as the data in the Kaggle_MBTI is concerned, in a single row, it consists of around 50 social media posts of a specific user separated by "|||". The dataset has no null or missing values neither in the type of attribute nor in the post attribute. The following fig. 4 shows the personality traits distribution in the Kaggle_MBTI dataset.

Just Accepted

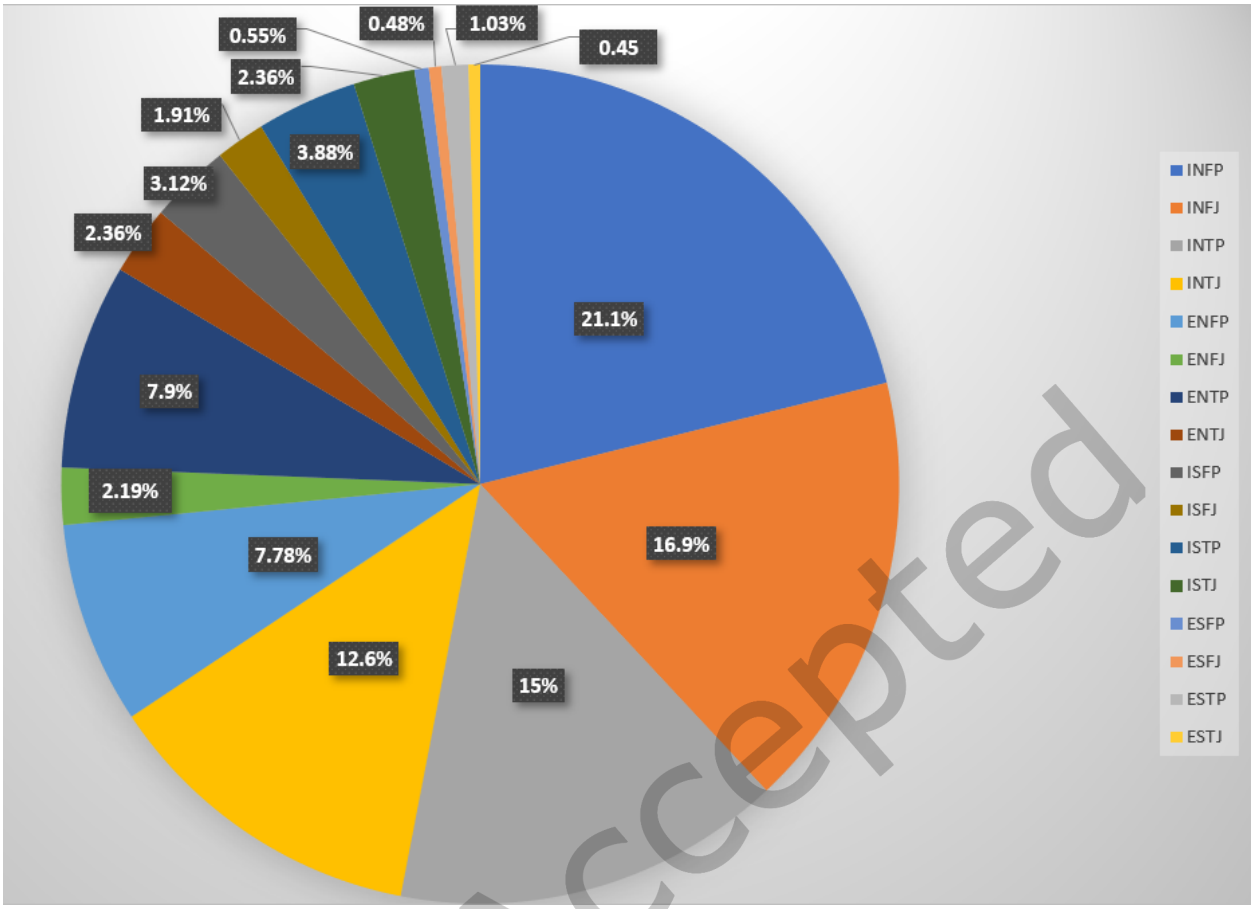

Fig. 4. Personalities distribution in the MBTI dataset

The above fig. 3 shows that the Introversion-Intuition-Feeling-Perception (INFP) trait has the maximum number of posts, while the Extroversion-Sensing-Thinker-Judgemental (ESTJ) has the least number of posts in the dataset. Moreover, the percentage share of each personality trait is clearly visible from the above figure.

We also developed a South Asian, Indian low-resource Hindi language dataset, विशेष चरित्र_MBTI by annotating the utterances (quotes) of different people on Google using Google API. The dataset has 1824 rows annotated with 16 labels out of which a four-letter abbreviation is used for each personality trait with the help of a psychology expert. Fig.5 shows the annotated example of the first five rows of the "विशेष चरित्र_MBTI dataset.

	type	posts	IE	NS	TF	JP
0	ENFJ	1. "अगर एक आदमी सब कुछ नष्ट कर सकता है, तो एक ...	0	1	0	1
1	ENFJ	2. "नुकसान की गारंटी देने का सबसे अच्छा तरीका ...	0	1	0	1
2	ENFJ	3. "आप जिस सड़क पर हैं उसे बदलने का अभी भी समय...	0	1	0	1
3	ENFJ	4. "डर से झिझक होती है, और झिझक आपके सबसे बुरे...	0	1	0	1
4	ENFJ	5. "मुझे कोई पछतावा नहीं है। यदि आप चीजों पर प...	0	1	0	1

Fig. 5. Sample of Hindi dataset विशेष चरित्र_MBTI

Just Accepted

3.2 Data Preprocessing

Data pre-processing is done to clean the data, remove unnecessary and error-prone data, and tokenize textual data to ultimately transform it from unstructured to structured data. For data cleaning, a regular expression is utilized to remove URLs, punctuations, unnecessary string marks, and numerical values. NLTK library is used to remove English stop words, which add very little meaning and are predominantly present in textual data and can cause errors in feature extraction and reduce overall model accuracy. Data cleaning also includes the lemmatization of data and converting MBTI 4 letter code to binary. Lemmatization converts all words into their original form. For example, 'playing' will be converted to 'play', and similarly, 'running' will be converted to 'run'. Converting the MBTI letter code to binary means assigning value 0 or 1 to each character so that it is easier for the model to distinguish between two characteristics. Here E, S, F, and P are all assigned with 0, whereas I, N, T, and J are all assigned with 1. Therefore, personality type INFJ will have [1,1,0,1] value. Thereafter, the data will be split randomly into train and test sets in the ratio of 75:25 (3:1), respectively as it was seen as efficient after regressive tuning of trainable dataset ratios.

3.3 Feature Extraction

The CountVectorizer transformation is used to convert tokenized textual data into a token count matrix. Term Frequency-Inverse Document Frequency (TF-IDF) [15][38] transformation is used to convert the matrix into a normalized TF-IDF representation. It is used to analyze how much a word is relevant in the collection of sentences. Here, TF is an estimate of the frequency of a word that appears in a document, while IDF represents how important a word is in a set of documents. It is calculated based on how rarely a word appears in a set of documents. The formulas used for the calculation of TF-IDF are as follows:

$$\text{TF-IDF(word,document)} = \text{TF(word,document)} * \text{IDF(word)} \quad (1)$$

$$\text{IDF(word)} = \log[n/(\text{DF(word)}+1)], \text{ if smooth_idf=False} \quad (2)$$

or

$$\text{IDF(word)} = \log[n+1/(\text{DF(word)}+1)]+1, \text{ if smooth_idf=True}$$

3.4 Proposed Kernel-Based Ensemble Model

The architectural flow of the proposed a kernel-based ensemble model for personality detection, KBSVE-P is shoen in fig. 6. The sub-sections discuss the details of the architecture.

3.4.1 Support Vector Machine (SVM)

The purpose of an SVM is to classify the given data into two classes by finding an appropriate hyperplane that can separate the classes effectively. SVM uses different linear and non-linear kernels to find the best-suited hyperplane. Support Vector machines can be used in case of non-regularly distributed data and data with unknown distribution; hence it is suitable for textual data. It efficiently finds hyperplanes to separate two classes present in any distribution due to the availability of different kernels that define equations for hyperplanes. The SVM kernel used for the classification of textual data includes the Linear Kernel, Radial Basis function kernel (RBF), Sigmoid kernel, and Polynomial Kernel. In SVM, kernel implies internal feature transformation. It is a way to compute the dot product of two vectors in a higher dimensional feature space. That is, the kernel method helps in calculating the dot product in a different space without even visiting the original space. The time taken to compute the standard dot product is $O(n^2)$, whereas the kernel takes only O(n) time to calculate the dot product. RBF is used in SVMs to help SVM to become non-linear rather than linear. A linear kernel is mainly used when we have a linearly separable set of data points. A polynomial kernel is a non-stationary kernel, which is well suited for problems where all the training data is normalized.

To find the best suited SVM kernel for classification from textual data, we train four SVM models, one model for each kernel. The Kernels mentioned above are the same kernels used for analyzing the performance of an ensemble of SVM kernels aggregated with the three voting techniques, namely soft voting, hard voting, and weighted hard voting.

Just Accepted

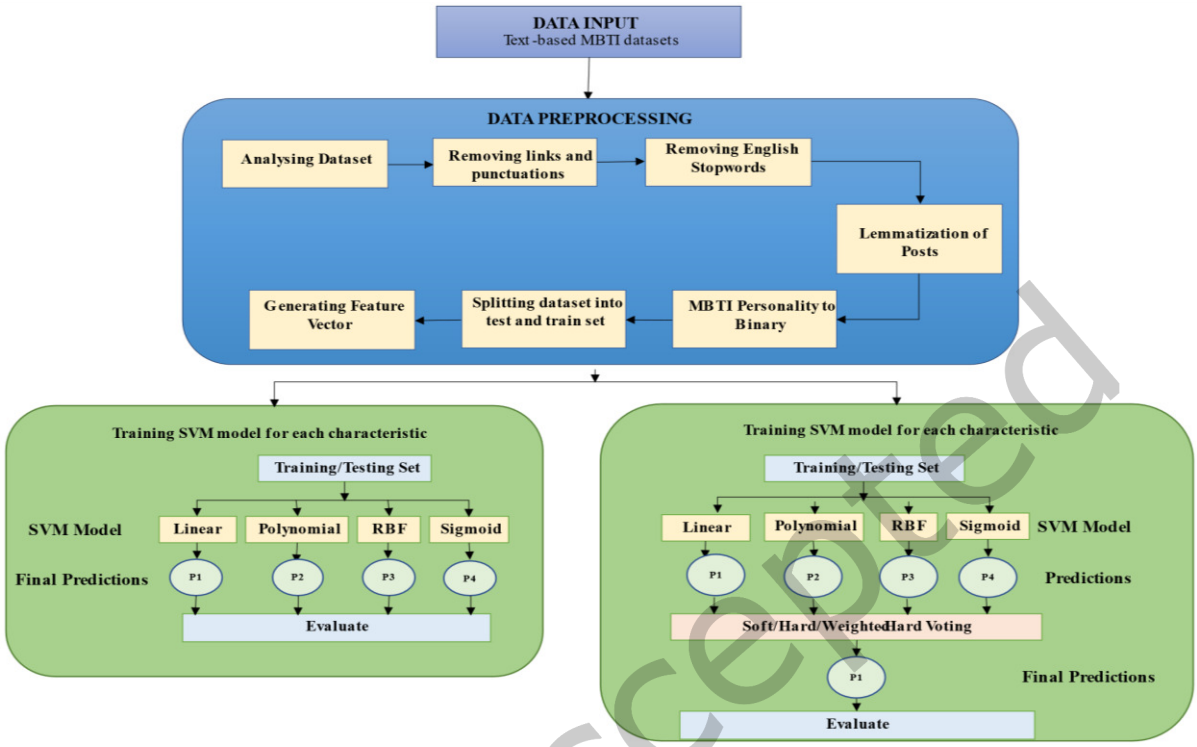

Fig. 6. Kernel-based Ensemble model (KBSVE-P)

3.4.2 *Voting*

Voting classifiers are ensemble methods for decision-making and are further divided into 2 categories: soft and hard voting. Hard voting entails picking the prediction with the highest number of votes, whereas soft voting entails combining the probabilities of each prediction in each model and picking the prediction with the highest total probability. This voting [38] classifier built by combining different classification models turns out to be a stronger meta-classifier that balances out the individual classifier's weakness on a particular dataset. It takes majority voting based on weights applied to the class or class probabilities and assigns a class label to a record based on the majority vote. A soft voting classifier is one in which the output class is predicted based on the average probability given to that class by different classifiers. The class with the highest average probability will be the final output of the ensemble. In soft voting, every individual classifier provides a probability value that a specific data point belongs to a particular target class. The predictions are weighted by the classifier's importance and summed up. Then the target label with the greatest sum of weighted probabilities wins the vote. Assume that the prediction probability of class A by 3 different classifiers is given as [0.30, 0.47, 0.53] and the prediction probability of class B is [0.20, 0.32, 0.40]. Therefore, the average prediction probability of class A is 0.43 and B is 0.306. Hence the output of the ensemble aggregated with soft voting will be class A. In hard voting classification, the output class is predicted based on the number of votes given to the concerned class. The class with the majority of votes is the output class. In hard voting, the predictions of each algorithm are considered with the ensemble selecting the class with the highest number of votes. For example, if three algorithms predict the color of a particular wine as “white,” “white,” and “red,” the ensemble will predict “red.” It is also called majority voting. Suppose that the predicted output of 3 different classifiers is class A, A, and B; it results in the majority predicted class 'A' as an output. Hence, the output of the ensemble aggregated with hard voting will be class A. Weighted hard voting is an extension of hard voting where different classifiers may have different weights. The class with the majority votes will be predicted as the output class, but every classifier may have different weights associated with them, which means the output of a particular model may be more significant than others. Fig.7 depicts diagrammatically representing these voting classifiers.

Just Accepted

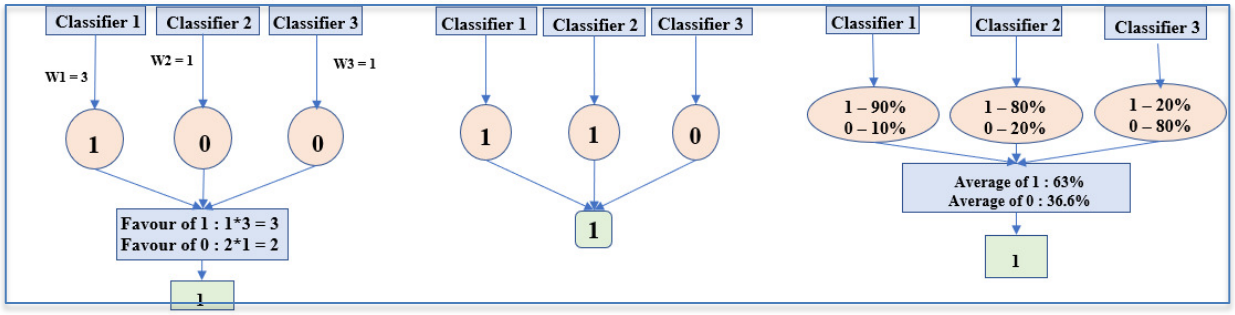

Fig.7. Voting Classifiers (Soft Voting, Hard Voting, and Weighted-Hard Voting)

4 RESULTS & DISCUSSION

The model implementation is done using Google Colab and Python libraries (TensorFlow and Keras along with the basic NumPy, Pandas, Scikit -Learn, and Matplotlib libraries). After several tests, it was found that the best ratio for weights is as follows:

Linear:Polynomial:Radial basis:Sigmoid::3:2:3:2

The following metrics are used to analyze the performance of individual kernels, voting techniques, and the proposed model:

- **Accuracy:** It is defined as the ratio of correct predictions (TP and TN) to the total number of samples (all entries of the confusion matrix summed up). Equation (4) defines the accuracy, which is as follows:

$$\textbf{Accuracy} = \frac{TP+TN}{TP+TN+FP+FN} \quad (4)$$

- **Precision:** It measures how many of the samples predicted as positive are actually positive. Thus, it is defined as the ratio of true positive (TP) values to the summation of all predicted positive values (TP and FP). Equation (5) specifies the precision, which is as follows:

$$\textbf{Precision} = \frac{TP}{TP+FP} \quad (5)$$

- **Recall:** It measures how many of the positive samples are captured by the positive predictions. Therefore, it is defined as the ratio of true positive (TP) values to the summation of all actual positive values (TP and FN). Equation (6) characterizes the recall, which is as follows:

$$\textbf{Recall} = \frac{TP}{TP+FN} \quad (6)$$

- **F1-Score:** It is also termed as F-score and is an important metric for measuring a model's performance. It is defined as the harmonic mean of precision and recall. Equation (7) defines the F1-Score, which is as follows:

$$\textbf{F1- Score} = 2 * \frac{Precision*Recall}{Precision+Recall} \quad (7)$$

- **ROC-AUC:** ROC-AUC is the Area Under Receiver Operating Characteristic Curve that summarizes the performance of a classifier over all possible thresholds. The ROC curve plots the true positive rate also known as recall on the y-axis against the false positive rate on the x-axis.

- **MCC:** MCC stands for Matthews Correlation Coefficient, which measures the correlation coefficient between the predicted values and actual values. Its values range between -1 and +1. A coefficient of +1 represents a perfect prediction, 0 an average random prediction, and -1 in an inverse prediction. Equation (8) specifies the MCC, which is as follows:

$$\textbf{MCC} = \frac{(TP*TN)-(FP*FN)}{\sqrt{(TP+FP)(TP+FN)(TN+FP)(TN+FN)}} \quad (8)$$

where; TP: True Positive, TN: True Negative, FP: False Positive, and FN: False Negative

Now, we divide this section into the following four subsections. In the first and second subsections, we discuss the performance of individual kernel models and voting techniques using the six performance matrices as mentioned above. Afterward, in the third subsection, we compare the results of the KBSVE-P model with the state-of-the-art. At last, in the

Just Accepted

fourth subsection, we evaluate and observe the results of the KBSVE-P model on the South Asia low-resource Hindi Language dataset.

4.1 **Performance of Kernel models: Kaggle_MBTI**

This subsection discusses the results obtained after training and testing four different kernels such as RBF, linear, sigmoidal, and polynomial. All the personality traits have been studied over the four kernels. The performance of all the SVM kernels is evaluated using the six metrics discussed above in the preceding subsection. The results are then tabulated in Table 2.

F1-Score is evaluated above accuracy because the accuracy metric is more delicate toward the distribution of target values; thus, it is important to capture a classifier's specificity, performance, and sensitivity on an imbalanced dataset.

Table 2. Performance of different SVM kernels: Kaggle_MBTI

Kernels	Characteristic	Accuracy (%)	Precision (%)	Recall (%)	F1- Score (%)	ROC-AUC (%)	MCC (%)	Training Time (in sec)	Confusion Matrix
RBF	I/E	85.62	86.20	96.97	91.27	71.74	54.3	132.5	[227, 261], [51, 1630]
	N/S	88.24	88.81	98.82	93.55	60.32	36.2	111.3	[65, 233], [22,1849]
	T/F	85.52	83.69	84.54	84.11	85.44	70.8	144.1	[1024,162], [152, 831]
	J/P	79.48	80.90	63.10	70.90	76.66	56.4	168.1	[1182,128], [317, 542]
LINEAR	**I/E**	86.17	87.71	95.54	91.46	74.72	56.9	82.9	[263, 225], [75, 1606]
	N/S	89.67	90.63	98.18	94.25	67.21	47.9	60.5	[108, 190], [34, 1837]
	T/F	84.42	82.87	82.71	82.79	84.27	68.5	88.1	[1018, 68], [170, 813]
	J/P	79.35	78.42	66.01	71.68	77.05	56.1	109.1	[1154,156], [292,567]
SIGMOID	I/E	86.03	87.49	95.66	91.39	74.26	56.3	81.8	[258, 230], [73, 1608]
	N/S	89.40	90.20	98.40	94.12	65.64	45.7	58.6	[98, 200], [30, 1841]
	T/F	84.56	82.93	83.01	82.97	84.42	68.8	86.4	[1018,168], [167,816]
	J/P	79.16	78.38	65.42	71.32	76.80	55.7	107.5	[1155,155], [297,562]
POLYNOMIAL	I/E	83.31	83.36	98.04	90.10	65.31	45.1	201.4	[159, 329], [33, 1648]
	N/S	87.09	87.47	99.25	92.99	54.99	23.8	190.8	[32, 266], [14, 1857]
	T/F	84.65	81.99	84.74	83.34	84.66	69.1	207.1	[1003,183], [150,833]
	J/P	78.61	85.08	55.76	67.37	74.68	55.1	209.3	[1226, 84], [380, 479]

I/E: Introvert-Extrovert; N/S: iNtution-Sensing; T/F: Thinking-Feeling; and J/P: Judgemental-Perceiving.

From Table 2, the following observations are made. First, the accuracy of the linear kernel is found to be highest in the case of I/E and N/S personality traits. Whereas in the case of T/F and J/P personality traits, the accuracy of RBF is highest.

Just Accepted

Second, the F1 score of the linear kernel turned out to be the highest in the case of I/E, N/S, and J/P personality traits. On the other hand, RBF shows the highest FI score in the case of the T/F personality trait. Third, the ROC-AUC of the linear kernel is found to be highest in the case of I/E, N/S, and J/P personality traits. Whereas in the case of T/F personality trait, the ROC -AUC of RBF is highest. Fourth, the MCC of the linear kernel turned out to be the highest in the case of I/E and N/S personality traits. On the other hand, RBF shows the highest MCC in the case of T/F and J/P personality traits. At last, from the above four observations, it can be said that the linear kernel performs better in most of the performance matrices when compared to other kernels.

The corresponding visualization of accuracies and F1-scores are shown in the following fig. 8 and 9, respectively.

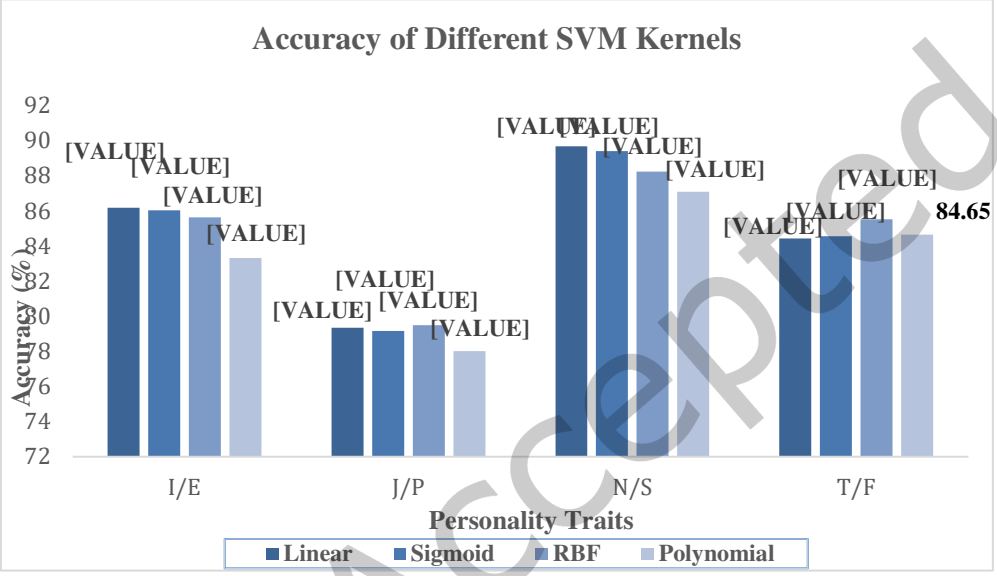

Fig. 8. Accuracies of different SVM kernels: Kaggle_MBTI

Fig.8 shows that the accuracy of the linear kernel is highest in the case of I/E (86.17) and N/S (89.67) personality traits. On the other hand, the accuracy of RBF is highest in the case of J/P (79.48) and T/F (85.52).

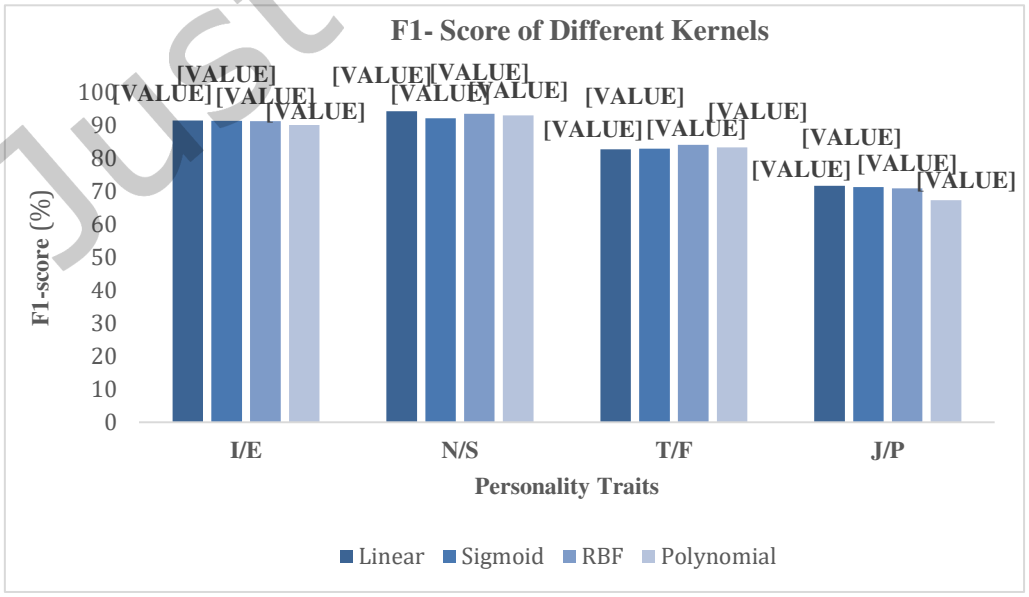

Fig. 9. F1-Score of different SVM kernels: Kaggle_MBTI

Just Accepted

Further from fig. 9, we can infer that the F1 score of the linear kernel is highest in the case of I/E (91.46), N/S (94.25), and J/P (71.68) personality traits, whereas in the case of T/F personality trait, RBF shows the highest F1 score. Hence, we conclude that the linear kernel performs better in 3 out of 4 cases as compared to the other three kernels.

The results show that the linear kernel performs best among all kernels with average accuracy and F1 score of 84.7 and 84.9, respectively for the personality traits.

4.2 **Performance of voting techniques: Kaggle_MBTI**

The results obtained after training and testing SVM kernels over the MBTI personality traits aggregated with the three different voting techniques such as soft voting, hard voting, and weighted hard voting are depicted in Table 3.

Table 3. Performance of ensemble of SVM kernels aggregated with different voting techniques

Voting	Characteristic	Accuracy (%)	Precision (%)	Recall (%)	F1-Score (%)	ROC-AUC (%)	MCC (%)	Training Time (In Second)	Confusion Matrix
SOFT VOTING	IE	86.35	88.24	95.06	91.52	75.71	57.8	2264.6	[275, 213], [83, 1598]
	NS	90.27	91.58	97.70	94.54	70.66	52.5	1884.4	[130, 168], [43, 1828]
	TF	85.38	83.70	84.13	83.92	85.28	70.5	2380.1	[1025,161], [156,827]
	JP	79.94	78.80	67.52	72.73	77.81	57.4	2695.3	[1154,156], [279,580]
HARD VOTING	IE	86.17	87.59	95.72	91.47	74.50	56.8	507.1	[260, 228], [72, 1609]
	NS	89.44	90.25	98.40	94.14	65.81	46.1	408.8	[99, 199], [30, 1841]
	TF	84.88	84.01	82.30	83.14	84.66	69.4	512.7	[1032,154], [174,809]
	JP	79.07	80.82	61.82	70.05	76.10	55.5	597.3	[1184,126], [328, 531]
WEIGH TED HARD VOTING	IE	86.17	87.59	95.72	91.47	74.50	56.8	476.2	[260, 228], [72, 1609]
	NS	89.44	90.25	98.40	94.14	65.81	46.1	395.4	[99, 199], [30, 1841]
	TF	84.88	84.01	82.30	83.14	84.66	69.4	501.8	[1032,154], [174, 809]
	JP	79.11	80.85	61.93	70.14	76.16	55.6	561.8	[1184,126], [327, 532]

I/E: Introvert-Extrovert; N/S: iNtution-Sensing; T/F: Thinking-Feeling and J/P: Judgemental-Perceiving.

From Table 3, it can be inferred that soft voting outperforms the other voting techniques, such as hard voting and weighted hard voting, while considering most of the performance matrices, such as accuracy, F1 score, ROC-AUC, and MCC. Here, another vital point to note is that hard voting and weighted hard voting perform almost identical across all performance matrices.

The corresponding visualizations of accuracy and F1-score are shown below in fig. 10 and fig. 11, respectively.

Just Accepted

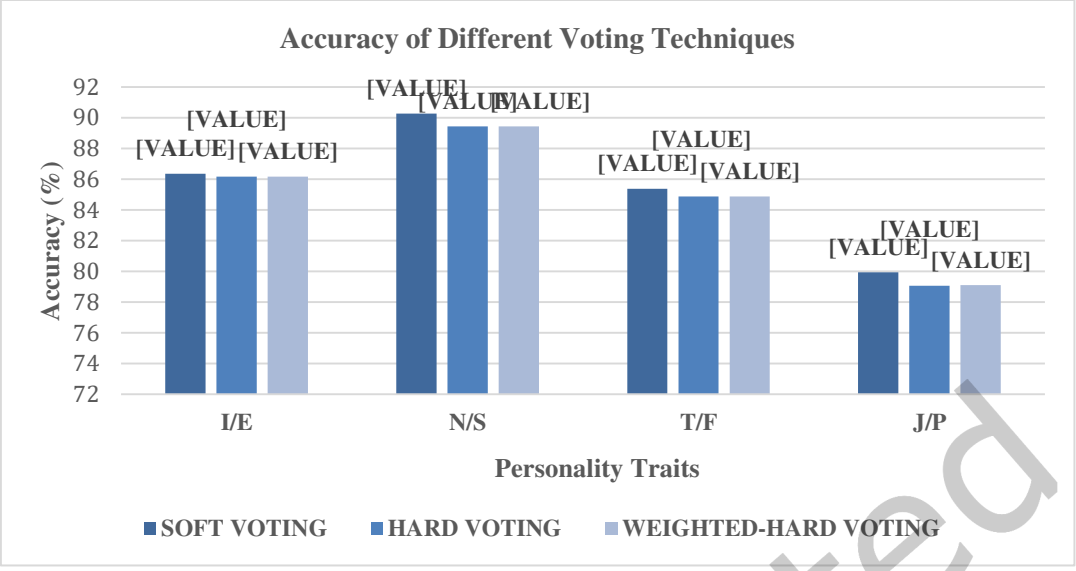

Fig. 10. Accuracies of voting techniques: Kaggle_MBTI

From fig. 10, we can conclude that the average accuracy of the soft voting classifier is 85.48, which is higher than the other voting classifiers, such as the hard voting and the weighted hard voting classifier. Here average accuracy of hard voting and weighted hard voting classifier is 84.89 and 84.9, respectively. Moreover, another critical point to note is that the accuracy of the soft voting classifier is better than other voting classifiers in the case of all personality traits.

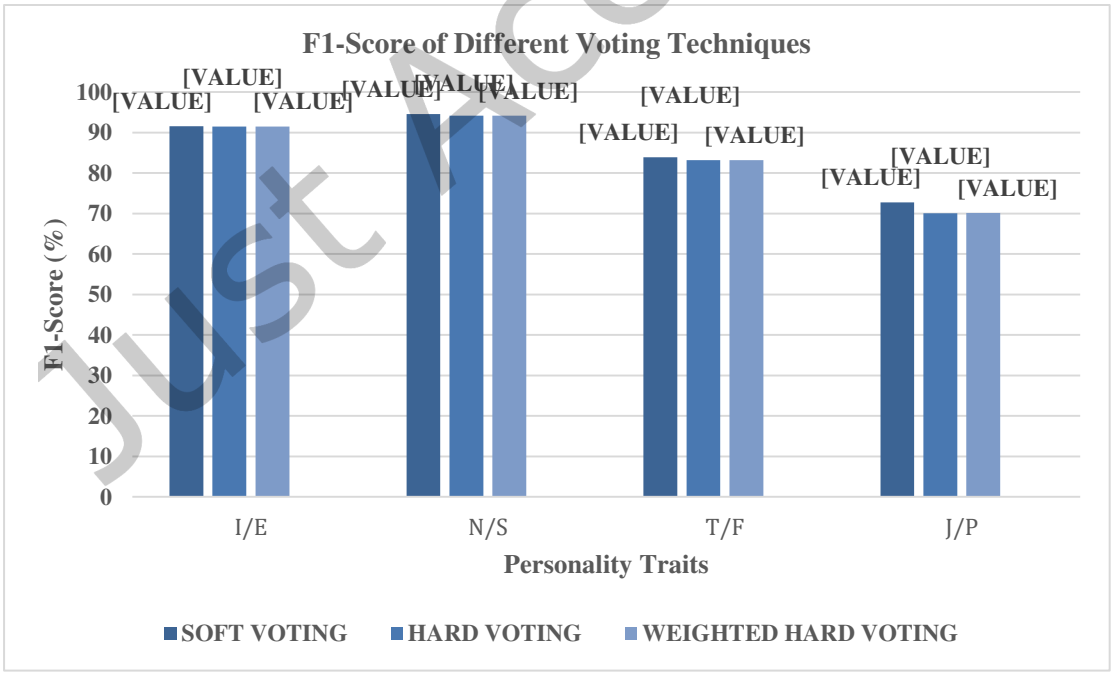

Fig. 11. F1-Score of different Voting techniques: Kaggle_MBTI

Further from fig. 11, we can infer that the F1 score of the soft voting classifier is the highest for all personality traits when compared to that for hard voting and weighted hard voting classifiers. Here average F1 score for the soft voting classifier is 85.67, while it is 84.7 and 84.72 for hard voting and weighted hard voting classifiers.

Just Accepted

4.3 Comparison with existing works: Kaggle_MBTI

The results provided by the proposed kernel-based ensemble model, KBSVE-P, are compared with the state-of-the-art on Kaggle-MBTI. The proposed model outperformed the existing works. Table 4 results show an improved performance of 9.4%, 4.6%, 12.19%, and 18.95% for I/E, N/S, T/F, and J/P MBTI personality traits, respectively.

Table 4. Comparison with the State-of-Art (Accuracy): Kaggle_MBTI

Model used	I/E	N/S	T/F	J/P
BERT + MLP [17]	78.8	86.3	76.1	67.2
BERT + SVM [17]	77.0	86.2	73.7	60.5
Proposed KBSVE-P	**86.35**	**90.27**	**85.38**	**79.94**

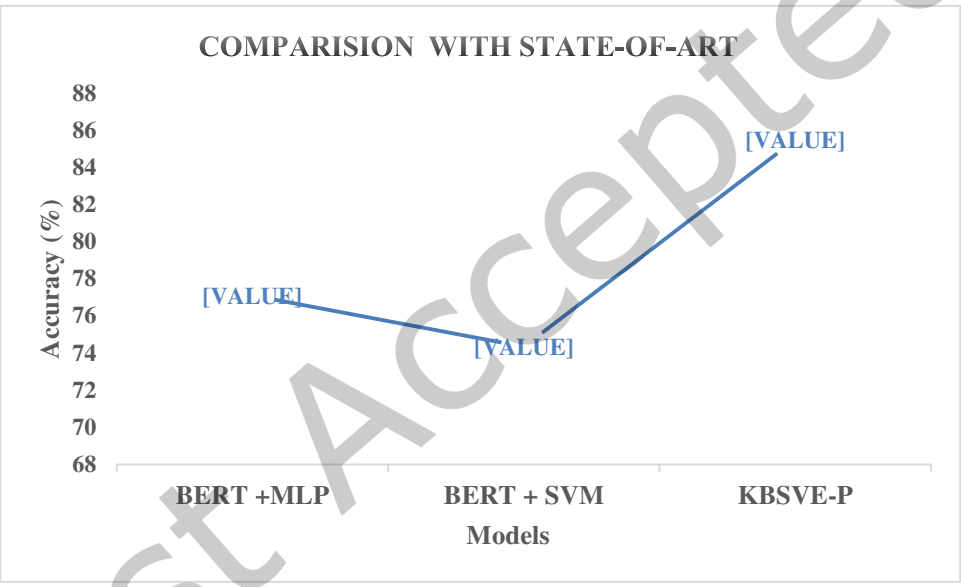

Fig. 12. Comparison with the existing work in Kaggle_MBTI

Fig. 12 shows the accuracy comparison of models, and the proposed KBSVE-P model outperforms the existing models with an average accuracy of 85.48 for the personality traits.

4.4 Evaluation of KBSVE-P on विशेष चरित्र_MBTI dataset

The proposed KBSVE-P model is also evaluated on the South Asian, Indian low-resource Hindi language dataset, विशेष चरित्र __MBTI dataset (vishesh charitr_MBTI). Table 5 shows the performance of the model.

Table 5. KBSVE-P on विशेष चरित्र_MBTI dataset

Dataset	Accuracy (%)	Precision (%)	Recall (%)	F1-Score (%)	ROC-AUC (%)	MCC (%)
विशेष चरित्र_MBTI (vishesh charitr)	66.89	67.40	70.17	67.96	64	30.09

Just Accepted

With our observations we conclude that the soft voting classifier is performing better than the hard voting and weighted hard voting classifiers. It is also observed that polynomial kernel and the radial basis function kernel performed better than linear kernel and the sigmoid kernel.

5 CONCLUSION AND FUTURE SCOPE

Personality profiling has many real-world applications, such as recruitment, team development, preference-based recommendation systems, relationship building, coaching, and development, etc. Therefore, personality detection is one of the trending research areas. However, the existing state-of-the-art lacks in efficiently determining the individual personality trait when examined using various performance matrices, especially in the low-resource textual content on social media. In this research, we proposed a novel kernel-based soft-voting ensemble model for personality detection, KBSVE-P. This model was built by firstly evaluating the performance of various Support Vector Machine (SVM) kernels such as radial basis function (RBF), linear, sigmoidal, and polynomial found the best-suited kernel for automatic personality detection in textual data. Next, an ensemble of SVM kernels was implemented with a variety of voting techniques such as soft voting, hard voting, and weighted hard voting. The model was evaluated on the publicly available Kaggle MBTI dataset for detecting a user's personality across four personality traits, namely introvert/extrovert (I/E), thinking/feeling (T/F), sensing/intuitive (S/N), and judging/perceiving (J/P). The results were evaluated on the publicly available Kaggle_MBTI dataset and a novel Hindi language personality dataset. Evidently, the linear kernel performed the best amongst kernels and the proposed kernel-based ensemble with soft voting outperformed the existing models on Kaggle-MBTI with an average F1 score of 85.677 and average accuracy of 85.48 for the personality traits. An accuracy of 66.89 is achieved by using the proposed KBSVE-P model on the novel Hindi विशेष चरित्र_MBTI dataset. Multimodal and multilingual personality detection remain some open research gaps within the domain of automatic personality detection and as a future work we intend to explore interpretable deep learning models for the same.

Just Accepted

REFERENCES

[1] Aulia, M. R., Djamal, E. C., & Bon, A. T. (2020, August). Personality Identification Based on Handwritten Signature Using Convolutional Neural Networks. In *Proceedings of the 5 th NA International Conference on Industrial Engineering and Operations Management Detroit*.

[2] Ariyanto, A., Djamal, E. C., & Ilyas, R. (2018, August). Personality Identification of Palmprint Using Convolutional Neural Networks. In *2018 International Symposium on Advanced Intelligent Informatics (SAIN)* (pp. 90-95). IEEE.

[3] Mehta, Y., Fatehi, S., Kazameini, A., Stachl, C., Cambria, E., & Eetemadi, S. (2020, November). Bottom-up and top-down: Predicting personality with psycholinguistic and language model features. In *2020 IEEE International Conference on Data Mining (ICDM)* (pp. 1184-1189). IEEE.

[4] Mehta, Y., Majumder, N., Gelbukh, A., & Cambria, E. (2020). Recent trends in deep learning based personality detection. *Artificial Intelligence Review*, *53*(4), 2313-2339.

[5] Bharadwaj, S., Sridhar, S., Choudhary, R., & Srinath, R. (2018, September). Persona traits identification based on Myers-Briggs Type Indicator (MBTI)-a text classification approach. In *2018 international conference on advances in computing, communications and informatics (ICACCI)* (pp. 1076-1082). IEEE.

[6] Bhowmick, R. S., Ganguli, I., Paul, J., & Sil, J. (2021). A multimodal deep framework for derogatory social media post identification of a recognized person. *Transactions on Asian and Low-Resource Language Information Processing*, *21*(1), 1-19.

[7] Cui, B., & Qi, C. (2017). Survey Analysis of Machine Learning Methods for Natural Language Processing for MBTI Personality Type Prediction.

[8] Furnham, A., & Stringfield, P. (1993). Personality and occupational behavior: Myers-Briggs type indicator correlates of managerial practices in two cultures. *Human Relations*, *46*(7), 827-848.

[9] Gosling, S. D., Augustine, A. A., Vazire, S., Holtzman, N., & Gaddis, S. (2011). Manifestations of personality in online social networks: Self-reported Facebook-related behaviors and observable profile information. *Cyberpsychology, Behavior, and Social Networking*, *14*(9), 483-488.

[10] Kunte, A. V., & Panicker, S. (2019, November). Using textual data for personality prediction: a machine learning approach. In *2019 4th international conference on information systems and computer networks (ISCON)* (pp. 529-533). IEEE.

[11] Ross, C., Orr, E. S., Sisic, M., Arseneault, J. M., Simmering, M. G., & Orr, R. R. (2009). Personality and motivations associated with Facebook use. *Computers in human behavior*, *25*(2), 578-586.

[12] Utami, N. A., Maharani, W., & Atastina, I. (2021). Personality classification of facebook users according to big five personality using SVM (support vector machine) method. *Procedia Computer Science*, *179*, 177-184.

[13] Giurković, M., Karan, M., Vukojević, I., Bošnjak, M., & Šnajder, J. (2020). Pandora talks: Personality and demographics on reddit. *arXiv preprint arXiv:2004.04460*.

[14] Pratama, B. Y., & Sarno, R. (2015, November). Personality classification based on Twitter text using Naive Bayes, KNN and SVM. In *2015 International Conference on Data and Software Engineering (ICoDSE)* (pp. 170-174). IEEE.

[15] Najadat, H., Alzubaidi, M. A., & Qarqaz, I. (2021). Detecting Arabic spam reviews in social networks based on classification algorithms. *Transactions on Asian and Low-Resource Language Information Processing*, *21*(1), 1-13.

[16] Sangwan, Saurabh Raj, and M. P. S. Bhatia. "Denigration bullying resolution using wolf search optimized online reputation rumour detection." Procedia Computer Science 173 (2020): 305-314.

[17] Robins, G., & Kashima, Y. (2008). Social psychology and social networks: Individuals and social systems. *Asian Journal of Social Psychology*, *11*(1), 1-12.

[18] Kumar, Akshi, Sukriti Verma, and Himanshu Mangla. "A survey of deep learning techniques in speech recognition." 2018 International Conference on Advances in Computing, Communication Control and Networking (ICACCCN). IEEE, 2018.

[19] Subramanian, R., Wache, J., Abadi, M. K., Vieriu, R. L., Winkler, S., & Sebe, N. (2016). ASCERTAIN: Emotion and personality recognition using commercial sensors. *IEEE Transactions on Affective Computing*, *9*(2), 147-160.

[20] Barbuto Jr, J. E. (1997). A critique of the Myers-Briggs Type Indicator and its operationalization of Carl Jung's psychological types. *Psychological Reports*, *80*(2), 611-625.

[21] Anna Klappenbach. 2022. The 12 most spoken languages in the world. Retrieved Jan 07, 2022 from https://blog.busuu. com/most-spoken-languages-in-the-world/

[22] Jain, D., Kumar, A., & Garg, G. (2020). Sarcasm detection in mash-up language using soft-attention based bi-directional LSTM and feature-rich CNN. *Applied Soft Computing*, *91*, 106198.

[23] Kumar, A., Sangwan, S. R., Singh, A. K., & Wadhwa, G. (2022). Hybrid deep learning model for sarcasm detection in Indian indigenous language using word-emoji embeddings. *Transactions on Asian and Low-Resource Language Information Processing*.

[24] Jain, D. K., Kumar, A., & Sangwan, S. R. (2022). TANA: The Amalgam Neural Architecture for Sarcasm Detection in Indian Indigenous Language combining LSTM and SVM with Word-Emoji Embeddings. *Pattern Recognition Letters*.

[25] Kumar, A., & Albuquerque, V. H. C. (2021). Sentiment Analysis Using XLM-R Transformer and Zero-shot Transfer Learning on Resource-poor Indian Language. *Transactions on Asian and Low-Resource Language Information Processing*, *20*(5), 1-13.

[26] Sangwan, S. R., & Bhatia, M. P. S. (2021). Denigrate comment detection in low-resource Hindi language using attention-based residual networks. *Transactions on Asian and Low-Resource Language Information Processing*, *21*(1), 1-14.

[27] Pennebaker, J. W., Boyd, R. L., Jordan, K., & Blackburn, K. (2015). *The development and psychometric properties of LIWC2015*.

[28] Lee, K. H., Choi, Y., & Stonier, D. J. (2012). Evolutionary algorithm for a genetic robot's personality based on the Myers–Briggs Type Indicator. *Robotics and Autonomous Systems*, *60*(7), 941-961.

[29] Hernandez, R. K., & Scott, I. (2017). Predicting Myers-Briggs type indicator with text. In *31st Conference on Neural Information Processing Systems (NIPS 2017)*.

[30] Keh, S. S., & Cheng, I. (2019). Myers-Briggs personality classification and personality-specific language generation using pre-trained language models. *arXiv preprint arXiv:1907.06333*.

[31] Ren, Z., Shen, Q., Diao, X., & Xu, H. (2021). A sentiment-aware deep learning approach for personality detection from text. *Information Processing & Management*, *58*(3), 102532.

[32] Cerkez, N., Vrdoljak, B., & Skansi, S. (2021). A Method for MBTI Classification Based on Impact of Class Components. *IEEE Access*, *9*, 146550-146567.

Just Accepted

[33] Basto, C. (2021). Extending the Abstraction of Personality Types based on MBTI with Machine Learning and Natural Language Processing. *arXiv preprint arXiv:2105.11798*.

[34] Shafi, H., Sikander, A., Jamal, I. M., Ahmad, J., & Aboamer, M. A. (2021). A Machine Learning Approach for Personality Type Identification using MBTI Framework. *Journal of Independent Studies and Research Computing*, *19*(2), 6-10.

[35] Adi, G. Y. N., Tandio, M. H., Ong, V., & Suhartono, D. (2018). Optimization for automatic personality recognition on Twitter in Bahasa Indonesia. *Procedia Computer Science*, *135*, 473-480.

[36] Ong V, Rahmanto ADS, Williem, Suhartono D, Nugroho AE, Andangsari EW, et al. Personality Prediction Based on Twitter Information in Bahasa Indonesia. In: Proceedings of the 2017 Federated Conference on Computer Science and Information Systems. Prague, Czech Republic; 2017. p. 367–372

[37] Choong, E. J., & Varathan, K. D. (2021). Predicting judging-perceiving of Myers-Briggs Type Indicator (MBTI) in online social forum. *PeerJ*, *9*, e11382.

[38] Yong Zhang, Hongrui Zhang, Jing Cai, and Binbin Yang, "A Weighted Voting Classifier Based on Differential Evolution".

Just Accepted

Wireless Personal Communications
https://doi.org/10.1007/s11277-022-10162-w

Post Quantum Public and Private Key Cryptography Optimized for IoT Security

Ajay Kaushik[1] · Lakshmi Sai Srikar Vadlamani[2] · Mohammed Mohsin Hussain[3] · Milind Sahay[3] · Rahul Singh[3] · Ananya Komal Singh[4] · S. Indu[3] · Puneet Goswami[1] · Nalliyanna Goundar Veerappan Kousik[5]

Accepted: 15 December 2022
© The Author(s), under exclusive licence to Springer Science+Business Media, LLC, part of Springer Nature 2022

Abstract
The number of Internet of Things devices is growing exponentially with the introduction of 5G. They are incorporated into a wide spectrum of devices ranging from our mobile phones to healthcare tracking devices. With the advent of 5G and quantum computers, traditional cryptography algorithms will be deprecated and will be prone to quantum attacks by the use of Shor's algorithm. Thus, there is a need for making Quantum Secure Cryptography Algorithms that can be utilized in 5G IoT environments. In this paper, we propose algorithms to efficiently encrypt data streams in a 5G enabled IoT environment and we establish their proof of hardness and security against quantum attacks, eavesdropping, chosen plaintext attacks, chosen ciphertext attacks, and public key attacks. The proposed algorithm is compared to leading NIST-approved post-quantum (PQ) cryptography algorithms like LWE, LIZARD, and NTRU. On the basis of the total time taken to perform operations, our symmetric algorithm is 70 times faster than the aforementioned symmetric algorithms and our asymmetric algorithm is 10 times faster than the above-stated asymmetric algorithms. Both our algorithms use 6000 times lesser memory than the algorithms mentioned above. The proposed algorithms provide a complete security framework for IoT devices against quantum attacks.

Keywords Internet of Things (IoT) · IoT security · 5G · Quantum computers · Lattice cryptography · Public-Key cryptography (PKC)

Ajay Kaushik, Lakshmi Sai Srikar Vadlamani, Mohammed Mohsin Hussain, Milind Sahay, Rahul Singh, Ananya Komal Singh, S. Indu, Puneet Goswami and Nalliyanna Goundar Veerappan Kousik have contributed equally to this work.

✉ Ajay Kaushik
ajaykw55055@gmail.com

✉ S. Indu
s.indu@dtu.ac.in

Extended author information available on the last page of the article

Published online: 28 December 2022

1 Introduction

The Internet of Things (IoT) comprises a large number of devices with sensors installed that can communicate with each other or other devices over the network for future analysis. IoT is an intelligent system that can work with or without human interaction. As the scope of growth in the IoT systems is more than ever, it is being considered the future of the internet, with the ability to connect billions of devices and information exchange through the internet instating the fact. Naturally, more connections and more applications also signify more vulnerability to threats. This extensive usage has led to a rapid increase in cyber-attacks on IoT devices. [1].

IoT devices in 5G are extensively used in various domains and have various applications such as smart homes, smart cars, smart watches, etc. [2–4]. This has increased the number of IoT connections worldwide. An increase in popularity has drawn the attention of attackers around the world and the security of systems based on IoT devices is a crucial concern that requires immediate deliberation. Many IoT systems were reported to have vulnerabilities due to lack of security considerations while developing the systems according to previous studies. These security vulnerabilities could be exploited by malicious entities and this could inflict severe damage to these systems. With the advent of Quantum Computing, traditional PKC algorithms such as RSA, Diffie-Hellman, et al. have become vulnerable to Quantum Attacks. Therefore, securing IoT devices from traditional as well as quantum attacks in the 5G era is of great significance [5].

There is a list of attacks such as eavesdropping, cloning, location tracking, replay, desynchronization, data integrity, memory probing, software tampering attacks et al. [6] which can malign both the software and hardware aspects of IoT devices. Hossain et al. [6] presented a physical unclonable function(PUF) to provide mutual authentication of the IoT devices.

In this paper, we propose two lightweight LWE-based algorithms that use Variable Length Encoding(VLE) for quantum security in IoT Devices, for symmetric key cryptography and asymmetric key cryptography respectively. Our asymmetric algorithm would use public key encryption (PKE) mechanism to transfer the symmetric secret key so that a fast and secure transfer of information may take place. Our main contributions to this paper are as follows:

- The proposed algorithm samples the public key in a deterministic manner which enables us to increase the dimension of the public key, thus providing additional security for 5G-enabled IoT devices.
- A novel Variable Length Encoding is introduced which adds additional complexity to the encryption mechanism, strengthening IoT security.
- The proposed algorithm reduces the memory requirements for the public keys from the order of $O(n^2)$ to $O(n)$.
- Deterministic sampling and Variable Length Encoding lead to a faster running time compared to existing algorithms. The proposed algorithms perform better than some of the leading NIST-approved quantum-secured algorithms as explained in the results section.

The rest of the paper is organized as follows: In Sect. 2, there is a review of the previous works done in this domain. In Sect. 3, the proposed algorithms are described in detail. In Sect. 4, conclusions and results are given.

1.1 Problem Formulation

Traditionally, communication would be secured via cryptosystem architectures such as RSA, Diffie-Hellman, Elliptic curve cryptography (ECC), etc. which would be rendered inadequate by quantum attacks [7]. Quantum computers instead of traditional bits rely on qubits for computation. An N-qubit quantum computer would be able to perform 2^N computations simultaneously.

Recent cryptography algorithms are based on either an Integer Factorization Problem, Elliptical Key Cryptography or Discrete Logarithm Problem, and it has been shown that it can be broken down by using Shor's Algorithm on a sufficiently strong Quantum Computer [8]. It is difficult for classical computers to factorize numbers with more than 2048 bits, and would take them 10,000s of years to factorize one. However, with the help of Shor's Algorithm, one can do it with relative ease using 4096 qubits. In 2012, physicists used a 4-qubit quantum computer to factor 143. Then in 2014, it used a similar setup to factorize 56,153 and in the coming few decades, it would be able to break the systems encrypted by current PKEs. In October 2019, according to a report published by Google which involved the results of their Quantum Supremacy experiment on "Sycamore", their 54-qubit processor, It targets computation in 200 seconds which would ideally take the world's fastest supercomputer about 10,000 years, thus achieving quantum supremacy [9]. Cryptosystems such as hash-based signatures, code-based cryptosystems, multivariate polynomial-based cryptosystems, and lattice-based cryptosystems are becoming widely accepted quantum-resistant public-key cryptosystems [10].

Thus, there is a need to shift the existing systems to quantum-resistant cryptography schemes to prevent sensitive data to be jeopardized. LWE is one such Lattice-Based Quantum Resistant PKE Scheme for secure key exchange. However, the sizes of the keys are large and thus, this algorithm cannot be used in places where size and computational resources are limited. IoT devices are such an example and with the rapid growth in their quantity as highlighted earlier in this text, a quantum resilient mechanism with modest key sizes and computational overhead is required.

2 Related Work

IoT networks involve data sensing through tiny sensor nodes, data aggregation, and data transmission processes, Therefore, many security algorithms have been designed in the past to safeguard the data involved in IoT networks. [11–13]. Learning with errors (LWE) [14] is a popular mathematical system and has its uses in many cryptographic schemes. It works on the concept of solving a sequence of 'approximate' randomly generated linear equations to recover the message. An error term(say $\pm 2\%$) is introduced in each equation, which is what makes the problem hard to solve. The reason for its increasing popularity is the fact that it is very flexible and at the same time as hard as worst-case lattice problems, hence facilitating the hardness of all algorithms derived from it to be secure against attacks, assuming that worst-case lattice problems are hard. The LWE problem was initially taken up to construct a Public Key Encapsulation(PKE) scheme, but its variants including itself had a major drawback which was that the parameters required were too large for practical applications and this poses an issue for them being viable for deployment in IoT environments.

Lizard, an IND-CPA Public key encryption scheme was proposed by Cheon et al. [15] along with its IND-CCA KEM version. Error sampling process in these encryptions is replaced by Lizard with deterministic rounding, thereby getting high encryption speeds. Lizard requires a 1000 KB storage size and presumably more to store a key pair in order to provide a secure arrangement. This high storage size requirement is infeasible for compact and end-to-end IoT devices.

The first iteration of NTRU was released in 1998 by Hoffstein et al. [16] whose improved version was released later in 2003 [17]. NTRU is a ring-based public key cryptosystem architecture based on the shortest vector problem(SVP) in a lattice. The operations involved are key setup, generation, encryption, and decryption. All of these operations are defined in polynomial maximal degree $(n-1)$ with ring $R = Z[X]/(X^n - 1)$ with integer coefficients in the set of $[1, 0, -1]$. The addition and multiplication of two polynomials may yield a polynomial of high degree, therefore in Ring R, the modulo function $(X^n - 1)$ is used to reduce polynomials to a certain degree.

Thus, the algorithms developed so far are quantum secure, but most of them require large key sizes, require a lot of computational power, or take a large time to execute. Our algorithm aims to solve this problem by ensuring smaller key sizes with a similar level of security against quantum attacks and it also aims to set a baseline by improving upon key generation, message encryption, and message decryption time when compared to traditional symmetric key and asymmetric key algorithms.

3 Proposed Work

3.1 Notations and Standards

The notations and standards used in the paper are shown in Table 1.

3.2 Proposed Algorithms

For enhancing the security of IoT systems, we propose two algorithms, one for Symmetric Key Cryptography and the other for Asymmetric Key Cryptography shown below.

Table 1 Notations used in the proposed work

Notation	Description
Z_q	$Z \in [0, q)$, for a positive integer q
$x \leftarrow D$	Sampling of x according to the distribution D, when D is a finite set, the sampling occurs with uniformity
G	Used to denote the Gaussian Distribution Set which generates a normal distribution from σ and μ
D^n	For an integer $n \geq 1$, denotes a positive polynomial of dimension n.
$bool(X)$	Function which converts its input into a *True* if it is ≥ 0 and 0 otherwise
$RCS(x, i)$	It is Right Circular Shift function on x shifted by i numbers of size l

3.2.1 Symmetric Key Cryptography (SymLoki-VLE)

The algorithm uses a secret key that would be shared by any two hosts/clients in an IoT network. The process is shown in Fig. 1. This process uses the hardness of the Search-LWE problem to establish secure encryption between two entities in a network.

Setup Choose positive numbers N, q, l, where q is a prime number between the range $[3 * l/4, l]$ where $l = 2^k$ and k is an integer denoting the number of bits required to store l. We choose a discrete Gaussian Distribution G_σ with a parameter σ as the error distribution. Choose another positive number M, where $M < N$.

KeyGen We generate the secret key S having N elements and size $N \times k$ bits, a random private key array with $S \leftarrow D_s^n$.

Encryption To encrypt a message bit m, we use the given technique to create variable-length encoding. We send two ciphertexts $C1$ and $C2$ of size N and L respectively, where L is a randomly chosen integer between [2, M]. First, we generate $C1$, a random polynomial with $C1 \leftarrow R_q$ having N different integers such that $1 \leq C1_i \leq q - 1$ and size $N \times k$ bits. An error polynomial E is generated having L elements and size $L \times k$ bits and values in the range $[0, q/2 - 1)$ with $E \leftarrow G_\sigma^n$. To signify encryption of $m = 1$, we encrypt bit 0 $L - 1$ times followed by the encryption of 1 at L^{th} position, or if $L = M$, we can also encrypt bit 1 M times, and to denote $m = 0$, we encrypt bit 1 $L - 1$ times, followed by an encrypted bit 0 or if $L = M$, we can also encrypt bit 0 M times. To encrypt those individual bits, the following code is used: Each bit b is embedded in the $C2$ array of size L. Elements of $C2$ are given as:

$$C2_i = (< RCS(C1, i-1), S > + E_i + b * q/2)\%q \tag{1}$$

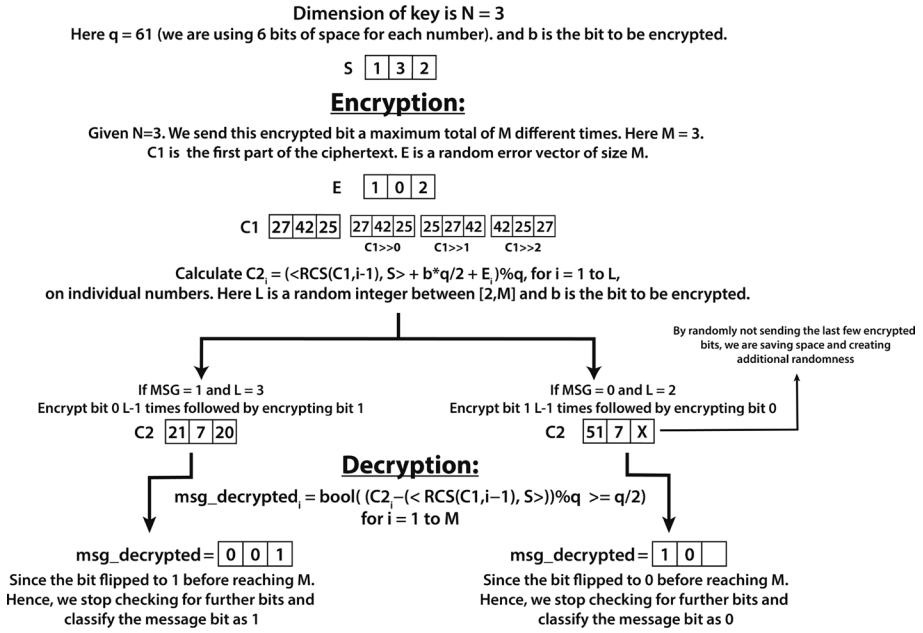

Fig. 1 Working of the Symmetric Key Algorithm

for $i = 1$ to L where $C2_i$ is the ith element in the ciphertext $C2$ and RCS is the Right Circular Shift function.

Decryption We check the given condition for each element in $C2$ to get the individual encrypted bit b.

$$b_i = bool((C2_i - < RCS(C1, i-1), S >)\%q \geq q/2) \tag{2}$$

If we get the same decrypted bit 1 for all M positions, or if we encounter less than M 0 bits followed by a flipped bit 1 at the given position, then the encrypted bit is denoted as 1. And If we get the same decrypted bit 0 for all M positions, or if we encounter less than M 1 bits followed by a flipped bit 0 at the given position, then we stop checking further and the encrypted bit is denoted as 0.

3.2.2 Asymmetric Key Cryptography(Loki-VLE)

We propose a public key encryption system that uses three keys - two public keys to be distributed to clients and a secret key that is kept safe by the host in the network. We build up on the Learning With Errors(LWE) technique and combine it with our previous work of variable length encoding as done in Symmetric Key Cryptography. The proposed algorithm reduces the required space by a function of $O(n^2)$ to $O(n)$ for the public keys, where n is the dimension of the key. This step, in turn, reduces the time complexity during the encryption process and the resulting ciphertext memory size required. The process has been described in Fig. 2.

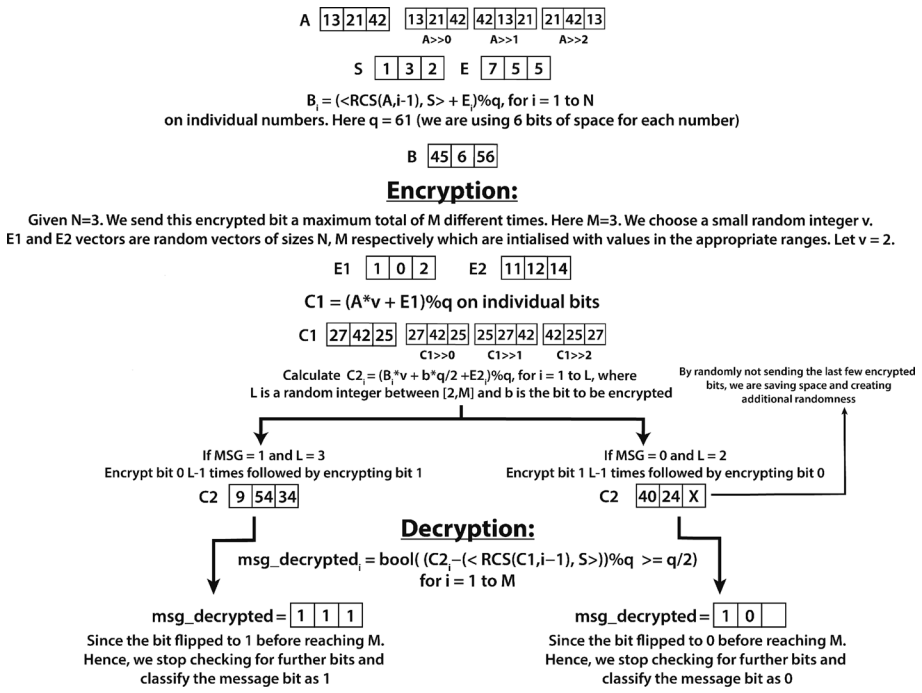

Fig. 2 Working of the asymmetric key algorithm

Setup Choose positive numbers N, q, l, where q is a a prime number between the range $[3l/4, l]$ where $l = 2^k$ and k is an integer denoting the number of bits required to store l. Choose a discrete Gaussian Distribution G_σ with a parameter σ as the error distribution. Choose another positive number M, where $M < N$.

KeyGen First, we generate A, a random public key polynomial with $A \leftarrow R_q$ having N different integers such that $1 \leq A \leq q-1$ and size $N * k$ bits. Generate a secret key S having N elements and size $N * k$ bits with $S \leftarrow D^n$, having small values, and an error polynomial E having N elements and size $N * k$ bits with $E \leftarrow G_\sigma^n$. The key B is calculated as

$$\begin{aligned} &B_i = (< RCS(A, i-1), S > + E_i)\%q, \\ &B \in R_q \end{aligned} \tag{3}$$

for $i = 1$ to N. Now we publish the public key as (A, B). The secret key vector S remains constant for the system and must be kept safe and protected at all costs.

Encryption Let the message bit be m and we send this encrypted bit a maximum total of M different times. We generate an integer v having a small random value and two other vectors $E1$ and $E2$ of size N, M respectively with random values in appropriate ranges $R1$ and $R2$ respectively.

Now, we generate two ciphertexts, $C1$ and $C2$, each having M elements and a maximum size $M * k$ bits. As done in Symmetric Key Encryption, to signify encryption of $m = 1$, we encrypt bit 1 M times or we encrypt bit 0 $L-1$ times, followed by an encrypted flipped bit 1, and to denote $m = 0$, we encrypt bit 0 M times or we encrypt bit 1 $L-1$ times, followed by an encrypted flipped bit 0, where L is a randomly chosen integer between $[2, M]$. To encrypt those individual bits, the following code is used:

$$C1_i = (A_i \times v + E1_i)\%q \tag{4}$$

$$C2_i = (B_i \times v + b \times q/2 + E2_i)\%q \tag{5}$$

from i = 1 to L, where $C1_i$, $C2_i$, $E1_i$ and $E2_i$ are *ith* elements of the vectors $C1$, $C2$, $E1$ and $E2$ respectively and b is the bit to be encrypted.

Decryption The ciphertexts $C1$ and $C2$ represent the same message bit m, encoded in a sequence of encrypted bits having varying lengths. To decrypt the ciphertexts $C1$ and $C2$ we solve the LWE problem for each element in the arrays. The decryption is done by checking the given condition for each bit

$$b_i = bool((C2_i - < RCS(C1, i-1, S >)\%q) \geq q/2) \tag{6}$$

If we get the same decrypted bit 1 for all M positions, or if we encounter less than M 0 bits followed by a flipped bit 1 at the given position, then we stop checking further and the encrypted bit is denoted as 1. And if we get the same decrypted bit 0 for all M positions, or if we encounter less than M 1 bits followed by a flipped bit 0 at the given position, the encrypted bit is denoted as 0. (Tables 2 and 3).

4 Result

The performance of the proposed algorithm is tested for hardness, security, and key efficiency. For hardness, we show that the proposed algorithm gives better IoT security than the existing algorithms in less processing time and minimized memory requirements. In

Table 2 Simulation parameters used for comparing the algorithms

Implementation Parameters			
NTRU			
p=29	q=2048		n=439
Lizard			
m=800	n=550	p=2**8	q=1021
LWE			
n=608			
SymLoki-VLE			
n=800		m=40	
Loki-VLE			
n=800		m=40	

key efficiency, the proposed work outperforms some of the famous NIST-approved IoT security algorithms such as NTRU, LWE and LIZARD in key generation, encryption, decryption, and memory requirements. The simulation parameters used are shown in Table 1.

4.1 Hardness

LWE is a problem whose best-known algorithm runs in average case exponential time. LWE is even able to ward off quantum attacks. More importantly, LWE is as hard as worst-case lattice problems. For $q = poly(n)$, LWE is as hard as GapSVP and SIVP using a quantum reduction [14]. The best-known algorithms to solve this run in 2^n time [18, 19].

In symmetric cryptography, let s be the private key shared between Alice and Bob. We have encrypted 1 as $(a, < a, s > +e)$ where e is shifted by $q/2$ and is the error polynomial. The second term is the ciphertext $C2$ having M elements and a is the ciphertext C1 having N elements, $M < N$. To provide the security it is essential to analyze whether $Enc(0)$ and $Enc(1)$ can be distinguished by an attacker who does not know the secret key s. Let the algorithm used by the attacker represented by A and P_b represent the probability that $A(Enc(b)) = 1$ for the given bit b. It is essential that P_b should be different for $b = 1$ and $b = 0$ in order for the attacker to distinguish between the two. Consider the attacker being given a tuple $E_0 = (a, < a, s > +e)$ and $e \leftarrow x_0$, that is e, the error term is not shifted by $q/2$. In this case, let $Prob(A = 1) = P_0$. Now in the case, when the attacker is given a tuple $R_0 = (a, b)$ where b is chosen randomly and is not shifted by $q/2$. In this case, let $Prob(A = 1) = q_0$. We repeat this for encoding of 1. Consider the attacker being given a tuple $E1 = (a, < a, s > +e)$ where $e \leftarrow x_0 + q/2$, that is where the error term is shifted by $q/2$. Here, let $prob(A = 1) = P_1$. Also consider the case where the attacker is given the tuple $R_1 = (a, b)$ where b is randomly chosen and then shifted by $q/2$. Let $Prob(A = 1) = q_1$ This essentially boils down to the LWE decision problem as E_1 and R_1 cannot be distinguished by any algorithm A' by adding $q/2$ to the given b and running A' on that input. Therefore $P_1 = q_1$. In R_0, b is chosen randomly whereas in R_1 b is also shifted by $q/2$. Shifting a uniformly distributed random number by constant results in a random number with the same distribution, so therefore $q_0 = q_1$. Therefore $P_0 = q_0 = q_1 = P_1$. This proves the fact that it must be impossible for an algorithm A to

exist if LWE is hard. We require at least N pairs of (A, B) to solve it but since we send N As and M Bs, therefore it becomes impossible to decrypt.

The Asymmetric algorithm generates two public keys A, and B. Ciphertexts $C1$, $C2$, where $C1 = (A * v + E1)\%q$ and $C2 = (B * v + b * q/2 + E2)\%q$ are generated. Now, if we consider A, B to be truly random then intuitively, the distribution of $C1$ and $C2$ will also be randomly making the ciphertexts almost impossible to decipher. This algorithm also essentially breaks down to be a problem based on LWE and there are no known algorithms, both classical and quantum, which can decipher it in appreciable time. It thus has the ability to evade quantum attacks.

Our work provides increased security than vanilla LWE as it allows for a higher dimension in the public key, which is directly responsible for the security level of the encryption. Thus, we can establish a much higher configuration setup without increasing the toll on computation and ciphertext size for an increased security level. We prove this by comparing the performance of algorithms on the basis of the time and memory requirements relative to the public key size that is directly proportional to the level of security. Figures 3 and 4 show how we save up on the performance parameters while simultaneously increasing the level of security thus it proves to be advantageous for IoT devices having low-level hardware specifications.

Our proposed algorithms are shown to be secure against various attacks as follows:

- *Eavesdropping* A person, Eve, when eavesdropping could only read the ciphertexts, which further need the secret key to decipher. Since Eve can't decipher the secret key as stated above, she can't eavesdrop on the transmission. On top of it, the probability of Eve knowing which bits correspond to which message becomes very low.
- *Public Key Attacks* Brute forcing the secret key from the public keys is also considered to be hard. This problem could be viewed as finding the secret key $s \in Z_q^n$ from some linear polynomials with some small errors introduced in each of them. A naive way to solve it would involve the use of the Maximum Likelihood Algorithm which would use $O(n)$ samples and would run in time $2^{O(nlog(n))}$ [20]. The works of Blum, Kalai, and Wasserman, showed the first subexponential solution for this by requiring $2^{O(n/log(n))}$) equations/time. This guarantees us safety from public key attacks.
- *CCA/CPA Security* Our asymmetric algorithm is IND-CPA secure since LWE is considered to be hard. Since the ciphertexts generated using LWE don't capture any meaning in them and can't be distinguished from random data, the probability of an adversary A finding out the actual message embedded is less. On coupling with our variable length encoding, this randomness further increases thus, making the aforementioned probability negligible. To prove it we have to make sure that the public key and the ciphertext generated are indistinguishable from random data. To do so, we define three sets of distributions:
  - $D0 = \{(pk, c1, c2) : pk \leftarrow KeyGen(), (c1, c2) \leftarrow Encrypt(m\}$
  - $D1 = \{(pk, c1, c2) : pk \leftarrow R_q^2, (c1, c2) \leftarrow Encrypt(m)\}$
  - $D2 = \{(pk, c1, c2) : pk \leftarrow R_q^{2*n}, (c1, c2) \leftarrow R_q^{2*n}\}$

  Since, $pk \leftarrow KeyGen()$ is obtained by $(A \leftarrow R_q, B_i = (< RCS(A, i-1), S > +E_i)\%q)$, and since $A \leftarrow R_q$ and similarly $B \leftarrow R_q$, thus making $pk \leftarrow R_q^2$ making $D0$, $D1$ indistinguishable. Similarly, $C1 = (A * v + E1)\%q$ and $C2 = (B * v + b * q/2 + E2)\%q$ and since, $A \leftarrow R_q$, $B \leftarrow R_q$, thus $C1, C2 \leftarrow R_q$ making $D1$ and $D2$ indistinguishable. Thus, $D0$ and $D2$ are also indistinguishable under the LWE assumption, thus making our scheme IND-CPA secure. CCA secure algorithms have been built upon LWE. If we imag-

Fig. 3 Hardness results

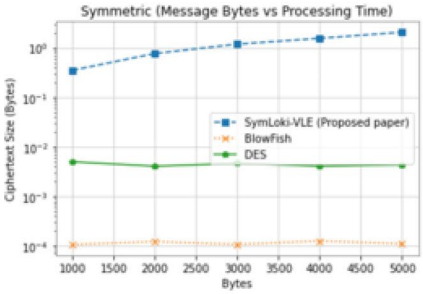

(a) Symmetric Key Algorithm Time Comparison

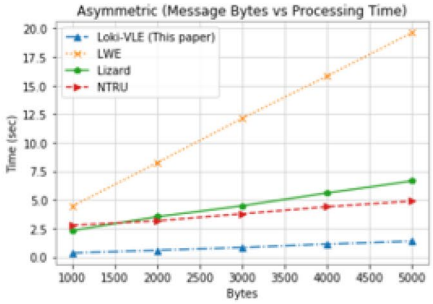

(b) Asymmetric Key Algorithm Time Comparison

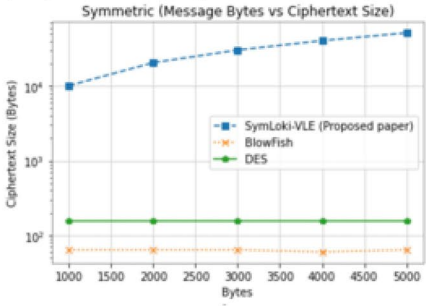

(c) Symmetric Key Algorithm Ciphertext Size Comparison

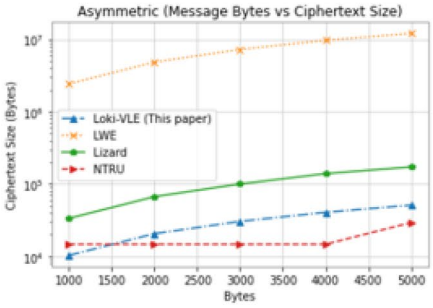

(d) Asymmetric Key Algorithm Ciphertext Size Comparison

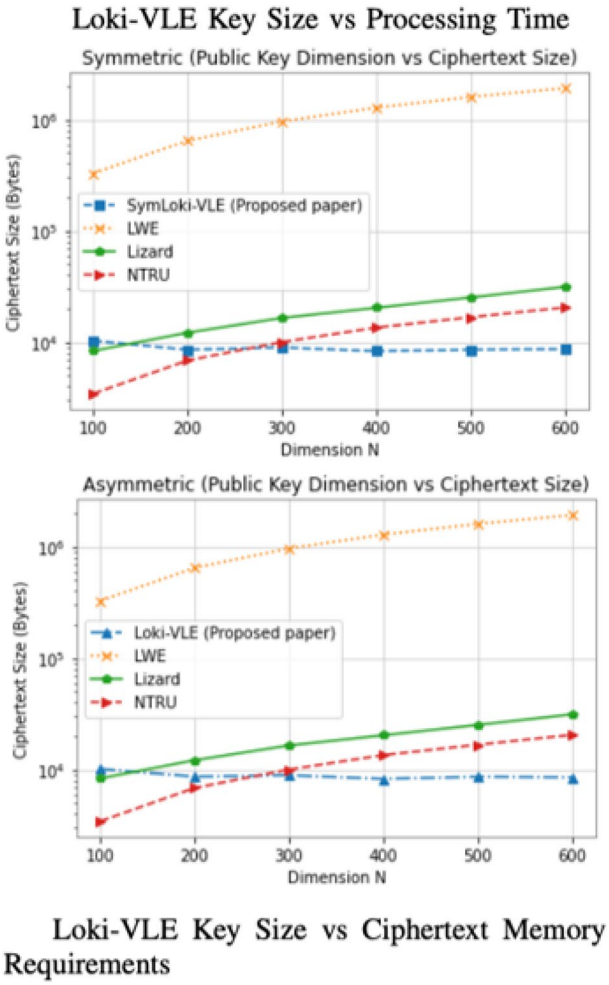

Fig. 4 Speed comparison of the algorithms

Table 3 Results of our algorithm compared to industry standards

Algorithm	Key Generation	Encryption	Decryption	Total Time
SymLoki-VLE (Proposed paper)	0.00006	0.118014	0.107934	0.226008
Loki-VLE (Proposed paper)	0.042511	0.004744	0.128058	0.175314
Lizard	0.92108	0.607547	0.006196	1.534823
LWE	0.59724	3.008443	0.007147	3.61283
NTRU	2.098819	0.003226	0.517229	2.619275

ine an encryption Oracle and decryption Oracle, for a known ciphertext and the decrypted message, to find the secret key s, it requires us to solve the Search LWE problem. CCA security is established using the random oracle and the quantum random oracle model.

4.2 Performance Evaluation

The algorithm provided is compared with existing works such as NTRU, LWE, LIZARD [16, 14, 15] Cryptography algorithms with respect to its performance in key generation, encryption, decryption and the memory required to run the algorithm as seen in Figs. 3 and 5.

The proposals, which are based on lattice-based cryptography for encryption, decryption, and authentication discussed above have been evaluated quantitatively using various performance metrics.

In comparison with the NTRU, which is the leading Post Quantum KEM algorithm submitted to NIST, we found the key generation, encryption, and decryption time to be faster by 138%, 65.76%, and 95.68% respectively as depicted in Fig. 3.

We measured the average time the processor takes to run the code for 1000, 2000, 3000, 4000, 5000 bits. We also analyzed the Memory Requirements like the size of the public key, private key, and also the size of the ciphertext. The results of the algorithm are shown in Fig. 3.

We can observe that the Symmetric key algorithm runs faster than most algorithms under consideration as evident from Fig. 3. On comparing it to Lizard, an algorithm known for its speed, previously submitted to NIST, we have found that our symmetric key algorithm is faster in key generation in order of 10^4, encryption in order of 10^3 and decryption by 44.56%.

From Fig. 4, we can observe that the Asymmetric Key Algorithm too, runs faster than most algorithms. Its performance with respect to NTRU has been discussed earlier. On comparing it to Lizard, which is another algorithm known for its speed submitted to NIST we've found that our algorithm is faster in key generation in order of 10^3, encryption in order of 10^4, and decryption by 3.26%.

The graph in Fig. 5 summarizes the public key size required by the different KEMs for the same level of security. It can be observed that although the key size required by NTRU is much lower than the one provided with our KEM, the speed benefit of our KEM is vastly superior. In addition, the key size required by our KEM is 82% times less when compared to the Lizard algorithm.

The graphs in Figs. 3 and 4 corresponding to the Symmetric key algorithm and Asymmetric key algorithm respectively, compare the cipher-text Size of various KEMs. Our symmetric and asymmetric algorithm produces a much smaller ciphertext which would aid in faster transmission of messages.

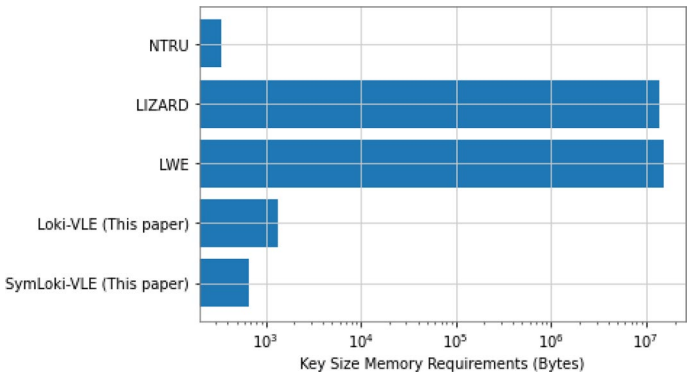

Fig. 5 Key Size comparison of various Algorithms

5 Conclusions

In this paper, we proposed a PQ-KEM as well as a new fast Symmetric Key Algorithm which can be deployed in the IoT environment. We have compared it with the leading NIST-approved PQ-KEM schemes and found out that it is superior with respect to others in terms of its computation speed. When compared with NTRU, it was found out that although the cipher text and public key size generated by NTRU was lesser than what our algorithm generated, the speed at which our algorithm was able to encrypt and decrypt was far superior to that of NTRU. It also performed better than Lizard, both in terms of speed and memory requirements. Thus, our PQ-KEM when used in conjunction with the proposed symmetric key algorithm could provide a huge boost, both in terms of computation speed as well as a decrease in memory requirements.

References

1. Kumar, P., Bagga, H., Netam, B. S., & Uduthalapally, V. (2022). Sad-iot: Security analysis of ddos attacks in iot networks. *Wireless Personal Communications, 122*(1), 87–108.
2. Abiodun, O. I., Abiodun, E. O., Alawida, M., Alkhawaldeh, R. S., & Arshad, H. (2021). A review on the security of the internet of things: Challenges and solutions. *Wireless Personal Communications, 119*(3), 2603–2637.
3. Magaia, N., Fonseca, R., Muhammad, K., Segundo, A. H. F. N., Neto, A. V. L., & de Albuquerque, V. H. C. (2020). Industrial internet-of-things security enhanced with deep learning approaches for smart cities. *IEEE Internet of Things Journal, 8*(8), 6393–6405.
4. Rezaeibagha, F., Mu, Y., Huang, K., & Chen, L. (2020). Secure and efficient data aggregation for IoT monitoring systems. *IEEE Internet of Things Journal, 8*(10), 8056–8063.
5. CA USA Symantec, Mountain View. Symantec Internet Security Threat Report. www.symantec.com/content/dam/symantec/ docs/reports/istr-23-2018-en.pdf, (2018). [Online; accessed Jun-2018].
6. Hossain, M., Noor, S., & Hasan, R. (2017). HSC-IoT: A hardware and software co-verification based authentication scheme for Internet of Things. In *2017 5th IEEE International Conference on Mobile Cloud Computing, Services, and Engineering (MobileCloud)* (pp. 109–116). IEEE.
7. Perlner, R.A., & David A Cooper, D.A. (2009). Quantum resistant public key cryptography: A survey. In *Proceedings of the 8th Symposium on Identity and Trust on the Internet*, pp. 85–93.
8. Bernstein, D. J. (2009). Introduction to post-quantum cryptography. In *Post-quantum cryptography* (pp. 1–14). Springer, Berlin, Heidelberg.
9. Google AI. Quantum supremacy using a programmable superconducting processor. https://ai.googleblog.com/2019/10/quantum-supremacy-using-programmable.html.
10. Chen, L., Chen, L., Jordan, S., Liu, Y. K., Moody, D., Peralta, R., & Smith-Tone, D. (2016). *Report on post-quantum cryptography* (Vol. 12). Gaithersburg, MD, USA: US Department of Commerce, National Institute of Standards and Technology.
11. Kaushik, A., Goswami, M., Manuja, M., Indu, S., & Gupta, D. (2020). A binary PSO approach for improving the performance of wireless sensor networks. *Wireless Personal Communications, 113*(1), 263–297.
12. Kaushik, A., Yakkali, R. T., Indu, S., Ahmed, F., Gupta, D., Nayar, R., & Yadav, S. (2019). A self-configurable event coverage approach for wireless sensor networks. *International Journal of Mobile Computing and Multimedia Communications (IJMCMC), 10*(2), 1–18.
13. Antony, S. M., Indu, S., & Pandey, R. (2020). An efficient solar energy harvesting system for wireless sensor network nodes. *Journal of Information and Optimization Sciences, 41*(1), 39–50.
14. Regev, O. (2009). On lattices, learning with errors, random linear codes, and cryptography. *Journal of the ACM (JACM), 56*(6), 1–40.
15. Cheon, J.H., Kim, D., Lee, J., & Song, Y. (2018). Lizard: Cut off the tail! a practical post-quantum public-key encryption from lwe and lwr. In *International Conference on Security and Cryptography for Networks*, (pp. 160–177). Springer.
16. Hoffstein, J., Jill Pipher, J., & Silverman, J.H. (1998). Ntru: A ring-based public key cryptosystem. In *International Algorithmic Number Theory Symposium*, (pp 267–288). Springer.
17. Hoffstein, J., Howgrave-Graham, N., Pipher, J., Silverman, J. H., & Whyte, W. Ntrusign: Digital signatures using the ntru lattice. In *Cryptographers' at the RSA Conference*, pp 122–140. Springer, (2003).

18. Ajtai, M., Kumar, R., & Sivakumar, D. (2001). A sieve algorithm for the shortest lattice vector problem. In *Proceedings of the thirty-third annual ACM symposium on Theory of computing*, (pp. 601–610).
19. Micciancio, D., & Regev, O. (2009). Lattice-based cryptography. In *Post-quantum cryptography*, (pp. 147–191). Springer.
20. Regev, O. (2010). The learning with errors problem. *Invited survey in CCC, 7,* 30.

Publisher's Note Springer Nature remains neutral with regard to jurisdictional claims in published maps and institutional affiliations.

Springer Nature or its licensor (e.g. a society or other partner) holds exclusive rights to this article under a publishing agreement with the author(s) or other rightsholder(s); author self-archiving of the accepted manuscript version of this article is solely governed by the terms of such publishing agreement and applicable law.

Dr. Ajay Kaushik received the B.Tech. and Master of Technology degrees from Kurukshetra University, India, and the Ph.D. degree from the Department of Computer Engineering, Delhi Technological University, Delhi, India. He is currently an Associate Professor at SRM University, Delhi-NCR, Sonepat, Haryana, India. He has published many journals and conference research papers in wireless sensor networks and the Internet of Things. He has received a research grant for a funded research project from the Government of India as principal investigator. His research interests include the Internet of Things, edge computing, 5G, wireless sensor networks, machine learning, neural networks, and nature-inspired intelligence. He received the Research Excellence Award for outstanding research during his Ph.D. degree. He passed the International English Language Testing System with a Band seven score in 2021. He was an Associate Member of the British Computer Society. He serve as a reviewer for reputed journals of IEEE such as IEEE Transactions on Computational Social Systems and renowned journals of Springer. He is a professional member of IEEE.

Lakshmi Sai Srikar Vadlamani is a B.Tech second-year student pursuing Computer Science Engineering from Delhi Technological University. He is constantly working to hone his skills in the field of computer science.

Mohammed Mohsin Hussain is a final year B.Tech. student from the Department of Electronics and Communication Engineering at Delhi Technological University, Delhi, India. His areas of interest are Machine Learning and Autonomous Systems.

Milind Sahay is currently pursuing his B. Tech in the discipline of Electronics and Communication Engineering from Delhi Technological University (DTU). He is a research enthusiast who aims to contribute to the field of Cryptography and Machine learning in the coming future.

Rahul Singh is a B.Tech final year student pursuing Electronics and Communications Engineering from Delhi Technological University. His areas of interest are the Internet of Things and Cryptography.

Ananya Komal Singh is B.Tech second-year student pursuing Information technology Engineering from Delhi Technological University. Her areas of interest are Deep Learning and Autonomous systems.

Prof. S. Indu is a Professor in the Department of Electronics and communication Engineering, Delhi Technological University, Delhi, and is currently the dean of student welfare there. She has done a Ph.D. in Computer Engineering from the University of Delhi and M.Tech, Post B.Tech. from the University of Kerala, Kerala. She was awarded the Best Branch Counselor award 2013 IEEE USA. Her research interests are in the field of Computer Vision, Image Processing, and wireless sensor network. She has 3 completed sponsored research projects. She published several research papers in international journals and conferences.

Dr. Puneet Goswami is a Professor in Department of Computer Science and Engineering in SRM University (NCR campus), INDIA. He has vast experience of 15 Years in teaching and his expert areas are Software Engineering, Big Data, and Cloud Computing. He has published a book titled "Big Data - A Driving Force for an Innovation". Also, he delivered a talk on "Security in Cloud Reference Models and Secure Identity Management Mechanism" at 1st International IBM Cloud Academy Conference ICA CON 2012 at the IBM Employee Activity and Fitness Center, Research Triangle Park, North Carolina USA. 6 Scholars have been awarded Ph.D. degrees and 19 Scholars have been awarded M.Tech Degree in Computer Science and Engineering under his supervision. He has published 60+ research papers in various international/National journals of repute like SCI/Scopus/WoS/UGC-Care. He is also the member of IEEE and IEANG.

Nalliyanna Goundar Veerappan Kousik was born in Tamilnadu, INDIA in 1982. He received the M.C.A., degree in Computer Applications from the Anna University, Chennai, in 2006. The M.Phil., degree in Computer Science from the PRIST University, Thangjavur, in 2010 and the Ph.D. degree in Computer Science from Bharathiar University, Coimbatore, in 2016. From 2006 to 2018,worked as an Assistant Professor in Computer Applications Department, at private engineering colleges, affiliated to Anna University, Chennai. From 2018 to 2021, worked as an associate professor, Galgotias University, Greater Nodia, Uttarpradesh, India. Now,He is doing as Data Analyst job at Corvid consulting UK Ltd., United Kingdom. He is the author of more than 20 articles. His research interests include Ad Hoc Sensor Network, Cloud Computing and Applications, Data Mining, Mobile Computing, Information processing, Wireless technology, ICT Convergence, Artificial Intelligence and Machine Learning. He is the Technical Reviewer of the various international journals.

Authors and Affiliations

Ajay Kaushik[1] · Lakshmi Sai Srikar Vadlamani[2] · Mohammed Mohsin Hussain[3] · Milind Sahay[3] · Rahul Singh[3] · Ananya Komal Singh[4] · S. Indu[3] · Puneet Goswami[1] · Nalliyanna Goundar Veerappan Kousik[5]

1 Department of Computer Science and Engineering, SRM University, Delhi-NCR, Sonepat, Haryana, India

2 Department of Computer Science and Engineering, Delhi Technological University, Delhi, India

3 Department of Electronics and Communication Engineering, Delhi Technological University, Delhi, India

4 Department of Information Technology, Delhi Technological University, Delhi, India

5 Department of Computing and IT, Stanmore College Middlesex, Stanmore, UK

2022 International Conference on Electrical, Computer, Communications and Mechatronics Engineering (ICECCME) | 978-1-6654-7095-7/22/$31.00 ©2022 IEEE | DOI: 10.1109/ICECCME55909.2022.9988575

Power Enhancement and Hotspot Reduction of a Rooftop Solar PV Array Using MOSFETs

Rahma Aman
Department of Electrical Engineering
Delhi Technological University
New Delhi,India
rahmaaman96@gmail.com

M. Rizwan
Department of Electrical Engineering
Delhi Technological University
New Delhi,India
rizwan@dce.ac.in

***Abstract*— In photovoltaic (PV) panels, the reliability issue known as "hot spots" occurs when an improperly matched cell warms up substantially, reducing the solar PV panel's output power performance. Hot areas can cause solar PV cell temperatures to rise, causing encapsulation damage and a second failure. Both of these breakdowns cause the PV panel to sustain lasting damage. Hotspots occur when there is any imperfection in solar cells, such as cracks, improper soldering, or mismatching. In this paper, hotspots that occurred due to partial shading are mainly focused on analyzing the effect of panel performance because of shading; different partial shading patterns like horizontal shape, L-shape patterns, and diagonal shape patterns are considered. A MATLAB/Simulink model for a 7x2 array size solar panel connected in series-parallel arrangements has been developed here, and all these partial shading patterns are considered. Previously, bypass diodes were connected across each module to increase the efficiency of solar panels under shading conditions. In this paper, two different arrangements are taken: in the first, MOSFETs are connected across every 14 modules, and in the second, alternate bypass diodes and MOSFETs are connected across each module. This study compares conventional hotspot mitigation techniques power–voltage characteristics with the two novel hotspot mitigation techniques.**

Keywords*— Hotspot, solar panel, partial shading, mitigation techniques, solar irradiance

I. INTRODUCTION

Solar energy systems are rapidly developing and gaining importance in response to the growing need for renewable energy sources. To reduce the cost of PV energy, the PV community and industry have achieved great strides. It depends on the system's cost, efficiency, and durability. The endurance of PV modules is crucial to the economic sustainability of installations, which will influence the pace of deployment of the technology to fulfil environmental needs. Not surprisingly, researchers are studying PV module output performance. PV hot spots arise when a cell or group of cells run at reverse bias, wasting power. This elevation in cell temperature in [1] will eventually reduce the PV module's output power. Current PV modules contain numerous hot spots, which may continue as technology progresses to finer wafers prone to micro-cracks during manufacture, transport, and installation.[2,3]. In [4] author provides a defect detection technique based on examining the theoretical curves that characterize the operation of an existing PV system. Virtual instrumentation LabVIEW software simulates voltage and power ratios for operating circumstances, solar irradiation, and PV module temperature. In addition, a polynomial function of the third order is employed to establish two detection limits for the voltage ratio and power ratios determined using the VI LabVIEW simulation tool; here, the proposed algorithm helps in hotspot detection. The hot-spot phenomenon is a reasonably common issue affecting solar producers nowadays. It poses a threat to the lifespan of the solar module and reduces its operating efficiency. Despite this, there are no commonly acknowledged strategies for managing them in practice. In [5] author describes the findings made by IES–UPM on 200 impacted solar modules. peak power rating. Electroluminescence, and operating voltage testing have also been done in addition to visual and infrared inspection. The author in [6] offers models and tests demonstrating that a new generation of bypass diodes (BPDs) may be utilized to increase the shading tolerance of traditional crystalline modules by up to one BPD per cell. We have used 0 per cent transmission cardboard and a 38 per cent transmission wire mesh (net). The greater the number of BPDs used, the greater the maximum power under shading situations. In [7], the creation of a system for detecting faulty bypassing diodes in PV modules is reported. Modern PV modules have bypass diodes to increase output power generation under partial shadowing circumstances. However, scientific research demonstrating the identification of malfunctioning bypass diodes in PV systems is lacking. Based on a Mamdani fuzzy logic system and the analysis of V_{drop}, V_{oc}, and I_{sc} achieved from the I-V curve of the investigated solar PV module; this work suggests a classification for bypass diode defect identification. The most popular method for avoiding hot spots is to connect a bypass diode in parallel with a row of PV cells. Utilizing bypass diodes across PV strings is a basic requirement for crystalline silicon PV panels [8,9]. Recent research has shown that the distributed MPPT technique proposed by the author in [10] is advantageous for minimizing the hotspot in partly shaded modules with a decreasing temperature up to 20 °C for minor shadows. This research reexamines PV hot spots using simulation and load-line analysis. Reverse bias causes hot spots in conventional panel string lengths. Several hot spot prevention strategies are described and assessed. Active bypass switches are better than passive diodes but don't prevent hotspots. Low-breakdown-voltage cells reduce power dissipation but aren't sustainable. Hot spot detection and open circuit protection solve the problem [11]. Under partial and full shadowing, a novel bypass technique for monocrystalline and polycrystalline solar panels lowers hot spot temperatures. The method uses a series-connected power MOSFET to split the shaded solar cell's reverse potential. The proposed method doesn't require control logic or power and may substitute a conventional bypass diode. The new circuit's functioning is explained using EN 61215's shading condition. Experiments on two commercial solar panels demonstrate that the shaded cell may be cooled by 24 °C compared to the usual bypass diode [12].

978-1-6654-7095-7/22/$31.00 ©2022 IEEE

Authorized licensed use limited to: DELHI TECHNICAL UNIV. Downloaded on January 04,2023 at 09:25:30 UTC from IEEE Xplore. Restrictions apply.

A high PV cell temperature resulting from hot spots may damage the cell encapsulation, leading to a second breakdown. Both failures destroy the PV panel irreversibly. The author in [13] recommends two trustworthy ways for minimizing hot zones. Solar PV hot spots were evaluated using the FLIR i5 thermal imaging camera. [14] investigates a commercial module with a rounded IV characteristic. The module's analysis includes thermography, IV response without shadow, and one-cell shadowing. Several researchers worked on active bypass diodes for hotspot reduction techniques; nowadays, MOSFETs are used instead of bypass diodes because the bypass diode mitigation technique has been less efficient. The contribution of this research is to propose a simple and efficient way to minimize the effect of solar cell hot spots. The hot spot mitigation strategy combines two more contemporary techniques: the first involves connecting MOSTEFs to panels, and the second involves 50% bypass diodes and MOSFETs. In each test, the PV module's Power-Voltage curve was examined to determine output power performance without any protection and after activating the proposed hot spot protection technique. The experiments were carried out at two different irradiances, 240 W/m^2 and 450 W/m^2, and these different shadings were given to three different shading patterns horizontal, Diagonal shape and L-shaped shading pattern. The following is the structure of this paper: The shading impact and the hotspot issue are discussed in Section 2, and a suggested hotspot mitigation strategy is discussed in Section 3 next section describes distinct shading patterns having 250 and 450 W/m^2 irradiances, further comparison of various mitigation strategy is made in Section 4. In section 5, comparisons of conventional and two new mitigation techniques results have been made with the help of the Solar Power-Voltage curve, and in the end, the paper's conclusion is done in Section 6.

II. Shading Effect and Hotspot Problem

Problems with partial shade brought on by various components of the spacecraft were initially observed in 1961 by [15]. Shadowing on PV modules has been studied extensively [16-19]. Shading is an essential design issue for solar PV modules. The primary consequence of shadow is a reduction in solar array energy production. Shadows are examined to construct mathematical models of solar cell circuit current-voltage characteristics. These models depict circuits with or without shunt or blocking diodes. The shadowing factor is designed for efficient array analysis. All models help analyze theoretical or empirical data by hand or computer [20]. The amount of power loss relies on the magnitude of the shadow and its distribution among the PV modules [21] Reverse-biased cells may overheat and lose power. If the PV module is not protected, damage due to creation of hotspot and irreversible panel damage may follow. A hotspot failure happens when a cell or PV module component overheats. In [22] Hot spots in PV panels cause damage, power loss, lower lifespan dependability, and higher production costs. Any string of cells with uneven light may cause hot spots, and the temperature rise often surpasses 100° C despite on-panel bypass diodes. Even the initial PV module application noticed hotspots [23,24]. Numerous research [25–32] have examined the hotspot mitigation technique to reduce power losses and its negative effects. Typically, a hotspot develops in a reverse-biased PV cell due to a loss of power. Hotspot mitigation techniques have been developed to improve the panel's performance comparison of traditionally used mitigation techniques with novel techniques. In [33] Uneven current production destroys a cell's protective layer, causing lasting harm. Researchers discover strategies to enhance electricity generation and reduce hot areas. The proposed technology minimizes hot spots and generates more electricity than traditional methods. In usual ways, relays/switches are linked in the PV module strings, however in the suggested methodology, they are connected in the substrings.

III. Mitigation Techniques

A. *Bypass diodes*

Bypass (BP) diodes are frequently used for a small number of series cells and are connected antiparallel to the positive and negative output terminals of a solar cell string. When bypass diodes are activated, they offer an alternate current channel and make an effort to protect PV strings from experiencing high reverse voltage bias. The widespread misunderstanding is that going around a string would keep cells from becoming hot spots. In this paper, for better solar performance to a 7 X 2 array, a bypass diode to all modules has connected the arrangement of the solar panels are made in total cross tied to improve the panels' performances as in Fig. 1.

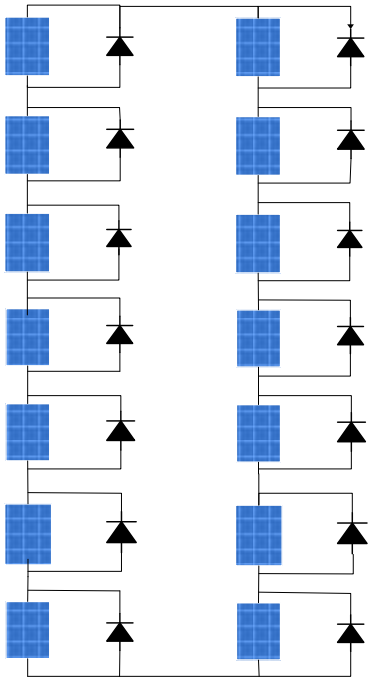

Fig.1. PV modules with bypass diodes.

B. *MOSFETs and Bypass diodes*

MOSFETs (Metal oxide conductor field effect transistor) are a type of switch instead of bypass diodes MOSFETs are incorporated over the whole of the PV module's terminals, giving an alternative path to the flow of current under partial shading conditions to reduce the effect of the hotspot. In Fig.1. only bypass diodes are connected, but its performance falls short of expectations. In this technique, Bypass diodes and MOSFET arrangements are made, as in Fig. 2. And the solar array's results have been compared for the power voltage curve. It performs much better than the use of only bypass diodes.

Authorized licensed use limited to: DELHI TECHNICAL UNIV. Downloaded on January 04,2023 at 09:25:30 UTC from IEEE Xplore. Restrictions apply.

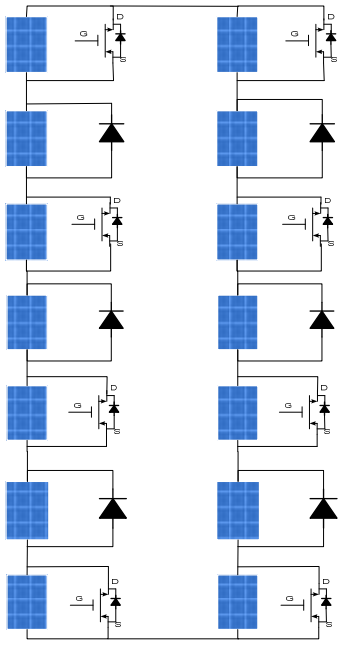

Fig.2. PV modules with Bypass Diodes and MOSFETs

C. *MOSFETs*

MOSFETs are fast-switching devices. In this technique, all the modules MOSFETs are incorporated, and then panel performance has been seen, which outperforms the above two techniques.

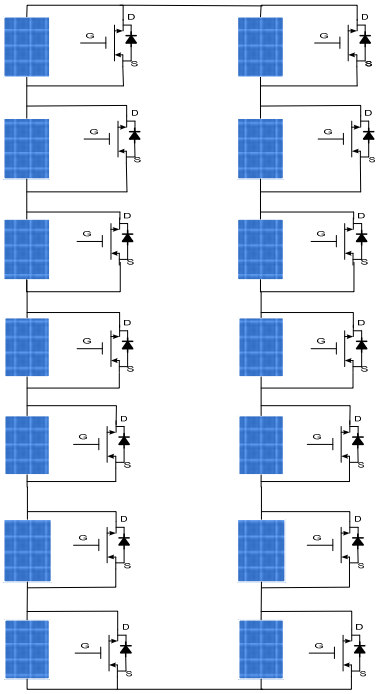

Fig.3. PV modules with MOSFETs.

IV. Shading Pattern

Partial shading causes hotspot problems here, and two partial shading conditions have different shading patterns case 1 contains 250 W/m^2 irradiances, and case 2 contains 450 W/m^2 irradiances. Both cases have different shading patterns like horizontal, Diagonal and L-shaped shading pattern. As described below in the tabular form.

Case 1 – 250 W/m^2

M11	M12
M21	M22
M31	M32
M41	M42
M51	M52
M61	M62
M71	M72

Fig.4. a) Horizontal shading

M11	M12
M21	M22
M31	M32
M41	M42
M51	M52
M61	M62
M71	M72

Fig. 4. b) L shape shading

M11	M12
M21	M22
M31	M32
M41	M42
M51	M52
M61	M62
M71	M72

Fig. 4. c) Diagonal shading

Case 2 – 450 W/m^2

M11	M12
M21	M22
M31	M32
M41	M42
M51	M52
M61	M62
M71	M72

Fig.4. a) Horizontal shading

M11	M12
M21	M22
M31	M32
M41	M42
M51	M52
M61	M62
M71	M72

Fig. 4. b) L shape shading

M11	M12
M21	M22
M31	M32
M41	M42
M51	M52
M61	M62
M71	M72

Fig. 4. c) Diagonal shading.

Case 1- 250 W/m^2

For horizontal shading patterns, Modules M11, M12, M21, M22, M31, M32, M41, M42, M51, and M52 have 1000 W/m^2 irradiance, while M61, M62, M71, and M72 have 250 W/m^2 as in Fig 4. a)

For L shape shading patterns, Modules M11, M12, M21, M22, M31, M32, M41, M42, M51, M52, and M62 have 1000 W/m^2 irradiance while M61, M71, and M72 have 250 W/m^2 as in Fig 4. b)

Authorized licensed use limited to: DELHI TECHNICAL UNIV. Downloaded on January 04,2023 at 09:25:30 UTC from IEEE Xplore. Restrictions apply.

For diagonal shading patterns, Modules M11, M12, M21, M22, M31, M32, M41, M42, M51, M52, M61, and M72. have 1000 W/m^2 irradiance, while M62, M71 have 250 W/m^2 as in Fig 4. c)

Case 2- 450 W/m^2

For horizontal shading patterns, Modules M11, M12, M21, M22, M31, M32, M41, M42, M51, and M52 have 1000 W/m^2 irradiance, while M61, M62, M71, and M72 have 450 W/m^2 as in Fig 5. a)

Modules M11, M12, M21, M22, M31, M32, M41, M42, M51, M52, and M62 have 1000 W/m^2 irradiance for L shape shading patterns, while M61, M71, and M72 have 450 W/m^2 as in Fig 5. b)

For diagonal shading patterns, Modules M11, M12, M21, M22, M31, M32, M41, M42, M51, M52, M61, and M72 have 1000 W/m^2 irradiance while M62, M71 have 450 W/m^2 as in Fig 5. c).

V. Results

Partial shading causes hotspot problems here two shading conditions; 250 and 450 W/m^2 are considered for three different shading patterns: horizontal shading, L shape shading patterns and Diagonal shading patterns. The solar panel performance has been analysed in Fig.6. and Fig.7. In case 1 for horizontal shading pattern power of hotspot reduction technique using MOSFET comes out to be 1999.23W. Hotspot reduction technique using MOSFET and diodes is coming out to be 1987.86 W primarily used hotspot reduction technique -using blocking diodes is coming out to be 1976.8 W, and without any of the mitigation technique it comes to be 800.74W, for L shape shading power of hotspot reduction technique using MOSFET is coming out to be 2090.98W, and hotspot reduction technique using MOSFET and diodes is coming out to be 1980.11 W mostly used hotspot reduction technique -using blocking diodes is coming out to be 1969.75 W. Without any of the mitigation technique it comes to be 817.393W,And for diagonal shape shading power of hotspot reduction technique using MOSFET is coming out to be 2400 W and hotspot reduction technique using MOSFET and diodes is coming out to be 2393.55 W mostly used hotspot reduction technique -using blocking diodes is coming out to be 2387.74 W and without any of the mitigation technique it comes to be 836.788 W , similarly for case 2 for horizontal shading pattern power of hotspot reduction technique using MOSFET is coming out to be 1999.95 W and hotspot reduction technique using MOSFET and diodes is coming out to be 1988.67 W mostly used hotspot reduction technique-using blocking diodes is coming out to be 1976.98 W and without any of the mitigation technique it comes to be 1442.18 W, for L shape shading power of hotspot reduction technique using MOSFET is coming out to be 2092.18W and hotspot reduction technique using MOSFET and diodes is coming out to be 1988.1 W mostly used hotspot reduction technique -using blocking diodes is coming out to be 2075.79 W and without any of the mitigation technique it comes to be 1464.13W. Furthermore, for diagonal shape shading power of the hotspot reduction technique using MOSFET comes out to be 2401.89 W and the hotspot reduction technique using MOSFET and diodes coming out to be 2248.32 W mostly used hotspot reduction technique -using blocking diodes is coming out to be 2246 W. Without any of the mitigation technique, it comes to be 2089.08 W. It is shown in the TABLE. I

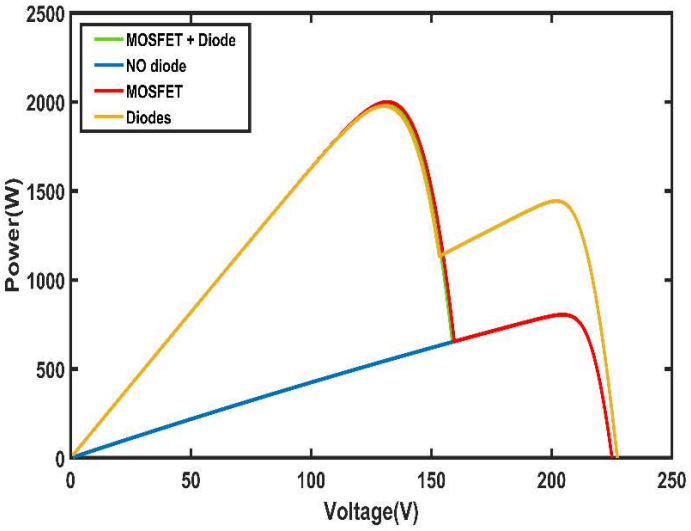

Fig. 6. a) Power – Voltage comparison curve with and without mitigation technique for horizontal shading pattern with 250 W/m^2 irradiances.

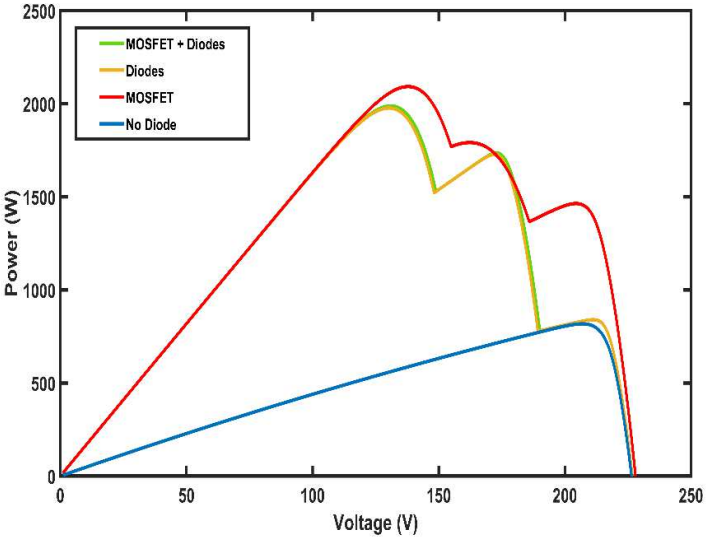

Fig. 6. b) Power – Voltage comparison curve of with and without mitigation technique for L shape shading pattern with 250 W/m^2 irradiances.

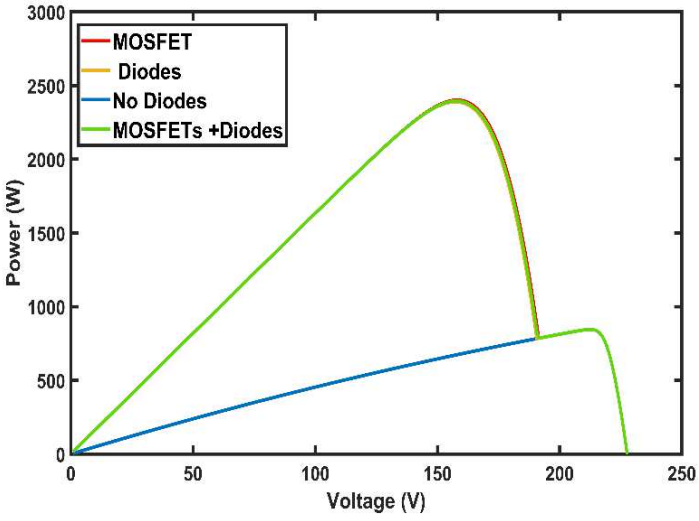

Fig. 6. c) Power – Voltage comparison curve with and without mitigation technique for diagonal shading pattern with 250 W/m^2 irradiances.

Authorized licensed use limited to: DELHI TECHNICAL UNIV. Downloaded on January 04,2023 at 09:25:30 UTC from IEEE Xplore. Restrictions apply.

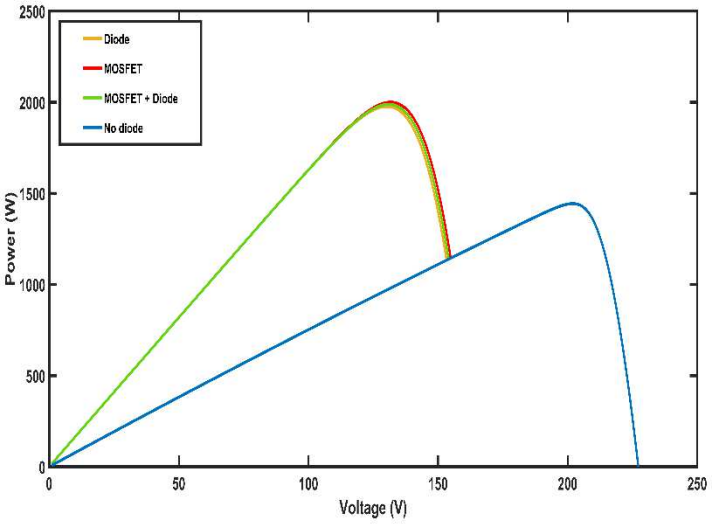

Fig. 7. a) Power – Voltage comparison curve of with and without mitigation technique for horizontal shading pattern with 450 W/m^2 irradiances.

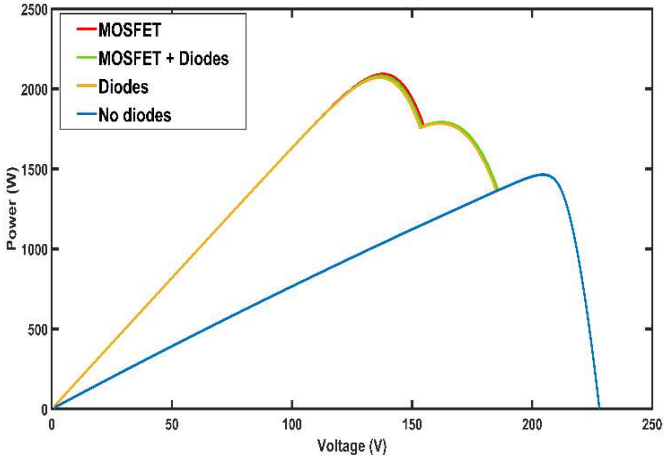

Fig. 7. b) Power – Voltage comparison curve of with and without mitigation technique for L shape shading pattern with 450 W/m^2 irradiances

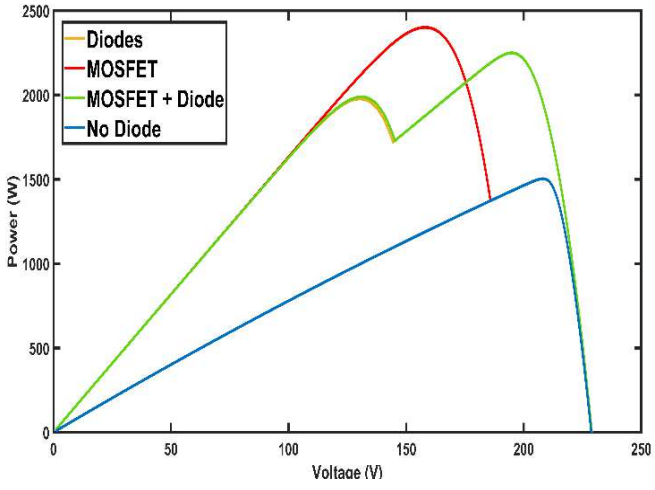

Fig. 7. c) Power – Voltage comparison curve of with and without mitigation technique for Diagonal shape shading pattern with 450 W/m^2 irradiances.

TABLE I. COMPARISON OF MAXIMUM POWER WITH DIFFERENT HOTSPOT MITIGATION TECHNIQUES FOR VARIOUS SHADING CONDITIONS

	Shading Patterns	**Mitigation Techniques**	**Maximum Power P_{max}**	**Power enhancement in %**
Case 1 – 250 W/m^2	Horizontal shading	MOSFETs	1999.23 W	1.13%
		MOSFETs + Diodes	1987.86 W	0.56%
		Bypass Diodes	1976.8 W	
	L shape shading	MOSFETs	2090.98 W	6.15%
		MOSFETs + Diodes	1980.11 W	0.53%
		Bypass Diodes	1969.75 W	
	Diagonal shading	MOSFETs	2400 W	0.51%
		MOSFETs + Diodes	2393.55 W	0.24%
		Bypass Diodes	2387.74 W	
Case 2 - 450 W/m^2	Horizontal shading	MOSFETs	1999.95 W	1.16%
		MOSFETs + Diodes	1988.67 W	1.05%
		Bypass Diodes	1976.84 W	
	L shape shading	MOSFETs	2092.19 W	0.79%
		MOSFETs + Diodes	2088.1 W	0.59%
		Bypass Diodes	2075.79 W	
	Diagonal shading	MOSFETs	2401.89 W	6.47%
		MOSFETs + Diodes	2248.32 W	0.1%
		Bypass Diodes	2246.36 W	

VI. CONCLUSION

Partial shading affects the solar panel performance, and a hotspot is created on the panel, reducing the power produced. Several mitigation techniques have been developed to improve solar panel performance, and most works are done considering bypass diodes in parallel to the solar modules. This paper discusses two mitigation techniques; the first considers MOSFET across the solar modules, and the other considers alternate MOSFET and diodes to see which mitigation outperforms under different shading conditions. A study comparing solar arrays with and without mitigation techniques showed that using MOSFETs instead of bypassing diodes is much better and gives the best results in all the cases studied in this paper. Further from TABLE. I. When the traditional approach is compared to the two hotspot mitigation strategies mentioned in this research, it can be determined that power is increased.

Authorized licensed use limited to: DELHI TECHNICAL UNIV. Downloaded on January 04,2023 at 09:25:30 UTC from IEEE Xplore. Restrictions apply.

REFERENCES

[1] M. Simon and E.L. Meyer, "Detection and analysis of hot-spot formation in solar cells", Sol. Energy Mater. Sol. Cells 94 (2), 2010, pp 106–113

[2] P. Chaturvedi, B. Hoex and T.M. Walsh, "Broken metal fingers in silicon wafer solar cells and PV modules", Sol. Energy Mater. Sol. Cells 108, 2013, pp 78–81.

[3] M. Dhimish, V. Holmes, B. Mehrdadi and M. Dales, "The impact of cracks on photovoltaic power performance", J. Sci.: Adv. Mater. Devices ,2017.

[4] M. Dhimish, V. Holmes, B. Mehrdadi, M. Dales and P. Mather, "Photovoltaic fault detection algorithm based on theoretical curves modelling and fuzzy classification system", Energy 140, 2017, pp 276–290.

[5] R. Moretón, E. Lorenzo and L. Narvarte, "Experimental observations on hot-spots and derived acceptance/rejection criteria", Sol. Energy 118, 2015, pp 28–40.

[6] B. Pannebakker, A. Waal and W.G. Sark, "Photovoltaics in the shade: One bypass diode per solar cell revisited". Prog. Photovolt. Res. Appl. ,2017, pp 836–849

[7] M. Dhimish, V. Holmes, B. Mehrdadi, M. Dales and P. Mather, "Detecting defective bypass diodes in photovoltaic modules using Mamdani fuzzy logic system", Glob. J. Res. Eng.: F Electr. Electron. Eng. 17 (5) , 2017, pp 33–44.

[8] M. Dhimish, V. Holmes, B. Mehrdadi and M. Dales, " Comparing Mamdani Sugeno fuzzy logic and RBF ANN network for PV fault detection", Renew. Energy 117, 2018 , pp 257–274.

[9] S. Silvestre, A. Boronat and A. Chouder, "Study of bypass diodes configuration on PV modules", Appl. Energy 86 , 2009, pp 1632–1640.

[10] M. Coppola, S. Daliento, P. Guerriero, D. Lauria and E. Napoli. "On the design and the control of a coupled-inductors boost dc-ac converter for an individual PV panel." In: Proceedings of the 2012 International Symposium on Power Electronics, Electrical Drives, Automation and Motion (SPEEDAM), IEEE, 2012, pp. 1154–1159.

[11] K.A. Kim and P.T. Krein, "Reexamination of photovoltaic hot spotting to show inadequacy of the bypass diode, IEEE J. Photovolt. 5, 2015 1435–1441

[12] S. Daliento, F. Di Napoli, P. Guerriero and V. dAlessandro, "A modified bypass circuit for improved hot spot reliability of solar panels subject to partial shading", Sol. Energy 134, 2016 pp 211–218.

[13] M. Dhimish, V. Holmes, B.Mehrdadi, M. Dales and P. Mather, "Output-power enhancement for hot spotted polycrystalline photovoltaic solar cells", IEEE Trans. Device Mater. Reliab. 2017, pp 37–45.

[14] V.K. Yadav, A. Yadav, R. Yadav, A.Mittal, N. H. Wazir, S. Gupta, R. K. Pachauri, and S. Ghosh. "Detection, Characterization and Modeling of Localized Defects and Thermal Breakdown in Photovoltaic Panels from Thermal Images and IV Curves." Electronic Materials, 2022,pp 154--172.

[15] W. Luft, "Partial shading of silicon solar cell converter panels". In Proceedings of the AIEE Conference, Los Angeles, CA, USA, 9–11 May 1961, pp. 62–204.

[16] A.A Conn, "Computer Computation of Shadow Effects on Solar Cell Arrays"; Eng. Rep. 9361.11-E72; TRW Systems, Inc.: Redondo Beach, CA, USA, 21 December 1966.

[17] W.R. Baron, P.F Virobik, "Solar Array Shading and a Method of Reducing the Associated Power Losses". In Proceedings of the IEEE 4th Photovoltaic Specialists Conference, Cleveland, OH, USA, 2–3 June 1964.

[18] J.Feldman, S. Singer, A. Braunstein, "Solar Cell Interconnections and the. Sol. Energy 1981, pp 419–428.

[19] P. L Jett and J. L Miller, "Analysis of effects of shadowed and open solar cells on orbital workshop solar cell array performance".In Proceedings of the 6th IECE Conference, Boston, MA. USA, 3–5 August 1971.

[20] H.S Rauschenbach, "Electrical Output of Shadowed Solar Arrays". IEEE Trans. Electron Devices 1971, pp 483–490.

[21] N.D Kaushika and A.K Rai, "An investigation of mismatch losses in solar photovoltaic cell networks" Energy 2007, 32, pp 755–759.

[22] W.P. Lamb, E.A Dallon, J. Kupfer, E. Lickey, J. Bakken, R. C. Haskell, P. N. Saeta and Qimin Yang. "Real-Time Anticipation and Prevention of Hot Spots by Monitoring the Dynamic Conductance of Photovoltaic Panels." *IEEE Journal of Photovoltaics*, 2022.

[23] F. A Blake and K.L. Hanson "The Hot-spot failure mode for Solar Arrays. In Proceedings of the 4th IECEC Conference, Washington, DC, USA, 22–26 Semptember 1969.

[24] J.C Larue and E.D Trieu "Effect of Partial Shadowing on Solar Panels Hot Spot or Breakdown", In Proceedings of the Photovoltaic Solar Energy Conference, Cannes, France, 27–31 October 1980; pp. 490–495.

[25] E.Molenbroek, D.W Waddington and K.A Emery, "Hot spot susceptibility and testing of PV modules". In Proceedings of the the Conference Record of the Twenty-Second IEEE Photovoltaic Specialists Conference, Las Vegas, NV, USA, 7–11 October 1991, pp. 547–552.

[26] H. Yoshioka, S. Nishikawa, S. Nakajima, M. Asai, S. Takeoka, T. Matsutani and A. Suzuki, "Non hot-spot PV module using solar cells with bypass diode function", In Proceedings of the Conference Record of the Twenty Fifth IEEE Photovoltaic Specialists Conference, Washington, DC, USA, 13–17 May 1996, pp. 1271–1274.

[27] W.Herrmann, W. Wiesner and W. Vaassen "Hot spot investigations on PV modules-new concepts for a test standard and consequences for module design with respect to bypass diodes", In Proceedings of the Conference Record of the Twenty Sixth IEEE Photovoltaic Specialists Conference, Anaheim, CA, USA, 29 September–3 October 1997, pp. 1129–1132.

[28] M. Danner and K. Bucher, "Reverse characteristics of commercial silicon solar cells-impact on hot spot temperatures and module integrity", In Proceedings of the Conference Record of the Twenty Sixth IEEE Photovoltaic Specialists Conference, Anaheim, CA, USA, 29 September–3 October 1997, pp. 1137–1140.

[29] D. P. Winston et al., "Solar PV's Micro Crack and Hotspots Detection Technique Using NN and SVM," in IEEE Access, vol. 9, pp. 127259-127269, 2021, doi: 10.1109/ACCESS.2021.3111904.

[30] M. Dhimish and G. Badran. "Current limiter circuit to avoid photovoltaic mismatch conditions including hot-spots and shading." *Renewable Energy* 145,2020,pp 2201-2216.

[31] S. Ghosh, V. K. Yadav and V. Mukherjee, "A Novel Hot Spot Mitigation Circuit for Improved Reliability of PV Module," in IEEE Transactions on Device and Materials Reliability, vol. 20, no. 1, March 2020, pp. 191-198.

[32] V.K Yadav, A.Yadav, R. Yadav, A. Mittal, N. H. Wazir, S. Gupta, R. K Pachauri, and S. Ghosh. "A novel reconfiguration technique for improvement of PV reliability." *Renewable Energy* 182 2022 pp 508-520.

[33] D. P. Winston, "Efficient Output Power Enhancement and Protection Technique for Hot Spotted Solar Photovoltaic Modules," in IEEE Transactions on Device and Materials Reliability, vol. 19, no. 4, Dec. 2019, pp. 664-670.

Authorized licensed use limited to: DELHI TECHNICAL UNIV. Downloaded on January 04,2023 at 09:25:30 UTC from IEEE Xplore. Restrictions apply.

Journal of Scientific & Industrial Research
Vol. 82, January 2023, pp. 63-74
DOI: 10.56042/jsir.v82i1.69939

Power Forecasting in Photovoltaic System using Hybrid ANN and Wavelet Transform based Method

Pooja Singh*, Anup Kumar Mandpura & Vinod Kumar Yadav
Department of Electrical Engineering, Delhi Technological University, Delhi 110 042, India

Received 6 May 2022; revised 15 Sep 2022; accepted 7 Oct 2022

Solar energy is a sustainable, renewable energy which is a part of latest industry standards of operation in line with industry 4.0. Solar power variability leads to fluctuation and uncertainty in Photovoltaic (PV) output power. It is a significant issue with regard to the high penetration of PV power generation. The solar irradiance is affected by weather conditions, and varies with geographical locations. Accurate PV power output forecasting is essential for the planning and scheduling alternate sources of conventional power. In this paper we propose a frequency domain approach for forecasting of short-term PV output power. The wavelet transform allows identification of periodic components with time localization, whereas the Artificial Neural Network (ANN) technique allows us to model the non-linearities in the PV time series. In this paper, PV power data for the city Bareilly, Uttar Pradesh is forecasted. Numerical simulations show that the proposed forecasting method for PV power output, shows a significant increase in accuracy over other similar methods. The root Mean Square Error, Mean Absolute Error for the proposed method are also calculated and compared with state-of-the art methods for PV power forecasting.

Keywords: Bior-orthogonal filter, Decomposition, Feed forward network, PV generation, Sustainable development

Introduction

Renewable energy has extreme importance in this modern era. It is the energy obtained from naturally restocked sources upon human timescale like- geothermal heat, sunlight, rain, wind, waves and tides. Solar energy is a primary source of abundant, clean and inexhaustible energy. In 2018 last, total Photovoltaic (PV) capacity installed at world level was 512 GW (gigawatts), from this 35% (180 GW) includes plants of utility-scale.[1] Power supplied through solar method was 3% related to electricity demand at world level in 2019.(2) Photovoltaic capacity saw an increment of 95 GW in 2017, which is about 34% growth yearly related to new installations. Capacity of cumulative installation saw an increment of 401 GW at year last, which was behaviour of PV power generation, power supply and demand does not meet.[3] Industry 4.0 plays vital role in sustainable environment. Fourth industrial revolution and digitization of supply and demand grants that implementation of industry 4.0 solution produces competitive advantages and opportunities for sustainable development.[4]

Solar power, on the other hand, has intermittent production characteristics that are dependent on meteorological conditions such as humidity, clouds, and precipitation. To ensure prediction techniques of conventional power for forecasting results precision and method convergence, an effective approach for decreasing non stationary characteristics connected to PV output power is required. In spite of these, the development of solar sector depends on digitization which entails the use of intelligent technologies that enables the automation of certain process using certain software, algorithms and Artificial Intelligence (AI) with a view of optimization. Digitization is a part of industry 4.0 which ensure higher level of sustainability. Forecasting of solar power by AI techniques is one such approach. Researchers have studied different methods for forecasting purpose which we have discussed further.[5,6]

A method is proposed by Kawasaki *et al.*[7] for estimation of the solar irradiance based on the Fourier Transform and wavelet transform. According to Ibad *et al.*[8], environmental factors such as humidity, temperature and radiation intensity, are used for PV output forecast, based upon cloud model. A Gappy Proper Orthogonal Decomposition Based Genetic Algorithm (GPOD-GA) was proposed by Jiang *et al.*[9]

*Author for Correspondence
E-mail: pooja_2k18phdee505@dtu.ac.in

to optimize the placement of smart grid based on weather information and simultaneously reduce the number of sensors. The meteorological data is utilized in forecasting two day ahead PV power using Wavelet Recurrent Neural Network (WRNN).[10] Result shows a very low Root Mean Square Error (RMSE) as compared to solar radiation prediction scheme obtained by hybrid neural network. Due to the fluctuations in solar irradiance disturbances occur in demand and supply which decreases quality of power. In this paper, LSSVM (Least Square Support Vector Machine) is used for prediction the PV power. Support Vector Machine (SVM) provides better performance upon solar irradiance with the prediction of time series for much better result normalized and appropriate parameters found by artificial intelligence algorithms. But now powerful technology is in trend such as big data and analytics due to which system responds very fast for any variation in environmental condition. Therefore, the methodology is based on sensors implementation in PV model system along with big data technology and data processing unit, which helps to find appropriate values of rout mean square error value. Hence prediction is very improved as large input parameters, are incorporated in machine learning process. Clustering of K-Means applied on meteorological data and divided in different clusters then some useful data is applied to SVM training which also allows to find the prediction error for PV power system. Also, here energy storage system is used to capture the prediction error using probability density function. This SVM regression improves the prediction accuracy.[11–13]

Several researches show that, hybrid models have effectiveness in several forecast application like- solar irradiance, global horizontal irradiance and forecast of electrical load. Normally, techniques of statistics provide better accuracy in forecast. Maximum time technique delivers better accuracy of forecast, provided the smooth input pattern in forecast model. Though, abrupt or sharp variation in metrological variables like irradiance, temperature, humidity and wind speed may cause error in forecast. Accurate forecast of PV power was shown at day ahead by using ANN. Back propagation algorithm is used with some improved technique which helps to improve forecast accuracy in weather condition. This proposed method delivers good results. Integration of power plant in to the system more accuracy of forecast is required. Therefore, ANN is used with different algorithms for hourly power output taking solar radiations, module temperature and ambient temperature as the input for artificial neural network. As solar is Variable Energy Resource (VER) so the grid output is always unpredictable at any particular time, which makes planning of grid challenging. Forecast an hour in advance PV system power output Wavelet (WT) and ANN are used for solar radiation and temperature data. WT impacts on abnormal behavior of data of time series and AI receives nonlinear distortion in PV data. PV power output includes disturbances. We are concerned with weather forecast problem related to the solar power prediction. There is a big challenge to integrate variability and uncertainty for production of PV output power. Generally, model gives picture incorporating either local weather or global weather forecast. These two are local and global changing parameters related to forecasting and are taken based on time series for obtaining forecast 18 hours before the production of PV power, data obtained from NOAA (National Ocean and Atmospheric Administration) and HRRR (High-Resolution Rapid Refresh) model. Resolution is insufficient at such scale for localized forecast over small-scale. For improving the accuracy of forecasting for local weather, a variability model based on wavelet is simulated for reduction of output change of PV power plant which takes place at upscaling from sensor of single point for whole PV system on simulated time interval. Now this is mapped with wavelet transforms of point sensor to given output of PV solar power plant and is validated on two PV plants of rooftop PV plants in Ota city, Japan of 2 Mw and 48 Mw power plants in WPPC, mountains, Nevada, United States. WVM is independent prediction model. This could be combined with forecasting methods.[14–18]

Research Methodology

In previous years, numerous studies have been studied on PV power forecasting. Power prediction method in short term related to power plants of PV contains two methods i.e., physical and statistical methods. Physical procedures containing physical parameters which is derived with forecast for process of generation of PV power as well as characteristics of system, with combination of weather data forecasting. Whereas in statistical procedures, summarization of inherent laws for forecasting output power related to plants of PV power takes place based on historical power data. Both the techniques contain

unique benefits, but non-stationary PV power characteristics output shows special effect upon properties and convergence of abovementioned methods.

Due to the non-stationary and periodic nature of PV power, previous power forecast techniques based on time series/linear models have proven to be ineffective and are currently in limited use. As a result, ANN and Wavelet Decomposition (WD) have the ability to address non-linear relationships between meteorological parameters and solar irradiance when used as a hybrid model input, depending on ANN and WD. The WD algorithm is used to extract usable data from the output of a PV power plant. ANN is used to reconstruct a model to forecast PV plant power. As a result, a forecasting model for PV power output is proposed in this study, which provides a sufficient increase in accuracy when compared to other similar modes. Model selection for forecasting, as well as PV power output and assessment metrics for economic and environmental advantages, were influenced by the following aspects. So, based on above discussion, model parameters selection of PV power estimation and forecasting are investigated in this paper.

Data Analysis

Solar radiations contain infrared, visible and ultraviolet radiations reaching to target location which depends upon certain factors i.e. time of the day, geographic location, season, local weather and land scope. Due to the earth's shape, sun rays angle varies between 0° to 90°. The surface of earth receives maximum energy for vertical sun rays. In India majority portion receives solar radiation in the range of 4–7 kWh/ square meter/ day. In one year, India gets solar energy more than 5000 trillion kWh/ year.

PV (Photovoltaic) power output forecasting is difficult for the power industry and companies that deal with PV. Solar energy has a number of issues, one of which is its inconsistency. The amount of power generated by utilizing this energy varies greatly from one site to the next, as well as due to environmental considerations. As a result, the technique to overcome this inconsistency is required. This can be done by establishing a proper prediction model to forecast the value of electricity that will be generated. Power production of solar panel is observed, and we have taken the power production output data of two years for the forecasting analysis. A Hybrid Model is used for forecasting purpose.

Our research work reflected excellent output related to prediction of solar power. So, for dealing in non-stationary and periodic applications related to output power of PV, modelling technique of hybrid nature which is depending upon ANN and WD is suggested in this paper for achieving excellent prediction results as well as convergence of better algorithm. Our work been managed as below:

- Analyses PV power generation output in frequency domain. To obtain the better frequency representation of PV output, the scalogram is used for improving localization time.
- Represents output power of PV process of decomposition using B-spline orthogonal filter.
- Represents method of hybrid prediction, combining ANN and Wavelet Transform.
- Verify and compare proposed method effectiveness.

Forecasting Analysis of PV Production Output

To forecast the PV power generation is a typical task due to environmental conditions like changing solar irradiance and weather parameter. In previous studies, various methods have been used. To overcome this problem, a method is used to analyses the data in the frequency domain is described here. The research above calculates changes in power generating output values with regard to numerous frequencies. As a result, different frequencies correspond to different lengths of time during which changes are estimated. When weather conditions are less predictable, such as cloud, fog, and so on, the output PV power is more difficult for system operators to manage. When solar irradiation reaches a high level of penetration, there is a lot of unpredictability and uncertainty. The quality and quantity of solar irradiation varies depending on geographical factors. It is extremely difficult to forecast the output of a given PV power system when the sun's position in space is dependent on the solar system's position at any given time.

In this paper, data is obtained from 2017 to 2019 at 01:00 pm from PV array which is located at a 28.367°N latitude and 79.4304°E longitude. The proposed technique aims to forecast the PV power generation output using WT and ANN. Specification of technical parameters are presented in Table 1.

Solar forecasting corresponds to environment of partial observation which represents problem of data analysis, which includes prediction and pattern completion. The power production of solar panel is

Table 1 — PV Power Plant Description

Item	Data
Longitude	79.4304°E
Latitude	28.3670°N
Altitude	268 m
Azimuth	0°
Tilt	45°
Mounting disposition	Flat roof
Field type	Fixed tilted plane
Installed capacity	100 Kw
Technology	Multi-crystalline silicon
PV module	DESERV 3M6-325

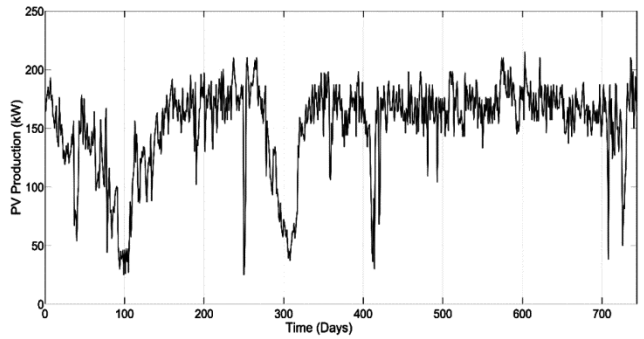

Fig. 1 — Power production curve of PV generation @ 1:00PM for two years

observed, and power production output data of two years for the forecasting analysis firstly a typical power production curve is measured by using the power output which represented as Fig. 1.

The prediction of power in PV plant keeps sufficient utilization regarding grid connection. Since PV power has characteristics of periodicity and non-stationary, traditional method of power prediction which are based upon time series or linear model have limited application. Therefore, proposed technique developed containing benefits of WD and ANN is utilized. As ANN has capability for addressing relationship of nonlinear type, theoretical values of PV power output considered like input in this hybrid model which is based upon ANN and WD.

Hybrid Forecasting Model

The model represents PV generation data for forecasting purpose. For achieving it, decomposition technique is proposed using wavelet transform, extract relevant features vectors (components) and then trained all the components, get the forecasting error. For reducing the error, artificial neural network is used. PV production is unstable and unpredictable so it may correct the stability of system. Therefore, forecasting is an alternative to attain good integration regarding PV plant output.

Wavelet Transform

The method of wavelet transform represented as tool of mathematics, similar to Fourier transform, which analyses signals in time series. The wavelet transform facilitates local replica of signal in frequency and time, which make it suitable in signal analysis having various time and frequency resolution, like output power for power plant of PV.

WT may be defined using two different categories viz- CWT (Continuous WT) and DWT (Discrete WT),

$$\text{CWT}(a, b) = \frac{1}{\sqrt{a}} \int_{-\infty}^{+\infty} x(t)\psi^*_{a,b}(t)\, dt \quad \ldots (1)$$

$$\Psi a, b(t) = \frac{1}{\sqrt{a}}\psi\left(\frac{t-b}{a}\right) \quad \ldots (2)$$

CWT may be defined using Eq. 1, which represent x(t) as signal for analyzing, Ψa , b (t) represents scaled 'mother wavelet' using factor and shifted using b as 'translated parameter', finally * represents 'complex conjugate' for chosen set wavelets. Wavelets set may be defined using Eq. 2, in which set is generated using mother wavelet "ψ" and translation special values and signal scale, using factor for energy normalization "$\frac{1}{\sqrt{a}}$.". CWT converts nonstationary signals in wavelets series using different combination of translations and scales. Further wavelet coefficients obtained may be highly redundant and CWT not contained analytical solution in majority of functions, and numerical calculation of its solution is required. For resolving these issues, DWT may be introduced. DWT is defined using Eqs 3 & 4.

$$\psi j, k(t) = \frac{1}{\sqrt{aj\,0}}\psi\left(\frac{t-kb0aj0}{aj0}\right) \quad \ldots (3)$$

where, j & k represents integers and a0 & b0 represents discretized scales and translation values.

$$\text{DWT}_x(m,n) = (2\text{^}(-m/2)) \sum_{t=0}^{T-1} x(t)\, \psi\left(\frac{t-n.2\text{^}m}{2\text{^}m}\right) \quad \ldots (4)$$

where, 'T' represents signal length x (t). Translation and Scaling parameter been integer variable function, m and n, representing $a = 2^m$ and $b = n2^m$ and t represents index in 'discrete' time.

Wavelet Decomposition

The unstable property and non-stationary nature of starting power signal of PV represents positive sign for using WT to determine frequency and temporal pattern for improving the difference in error in forecast. DWT is used in analyzing PV production signals in various bands of frequency, having several resolutions using decomposition of starting signal in detailed and coefficient value with approximation. For achieving it, DWT uses functions of two type viz scaling function attached in low pass filters and wavelet function attached in high pass filters.

Proposed Forecasting Technique of PV Power

WT signal decomposition procedure is represented by Fig. 2 and Fig. 3, represents the down sampling and up sampling process, low pass filter rejects component of higher frequency in signal and provides approximate coefficient whereas high pass filter results in signal's detailed coefficient. In this study, five level decomposition have been used. Using decomposition analysis, PV signal is splits into high pass frequency components and low- pass frequency components.

Technique of wavelet transform breaks signal in the layer of various scale having several resolution levels. This break in several scale is done due to technique of wavelet transform depends upon function with square integrable and representation of group theory.

WT-ANN Model

Data time series of PV power includes several disturbances, spike and several non-stationaries. WT may be deemed as tool of feature management for isolating above spikes. So, forecast the PV power of solar with use of WT may be utilize for improving the error in forecasting of PV power. Main concept behind this analysis in proposed model of hybrid nature as shown in Fig. 4, consist of use of artificial neural network trained with coefficient obtained from wavelet decomposition process of the PV production output signal. This hybrid network been trained for performing multistep forecasting regarding individual detailed and approximate coefficient for DWT extracted signal for PV production. It may be useful information in case of prediction based upon ANN which enables further developments in this field.

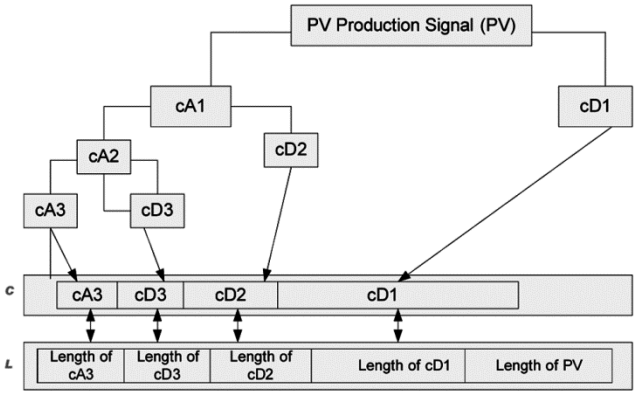

Fig. 2 — Procedure of Decomposition of DWT signal

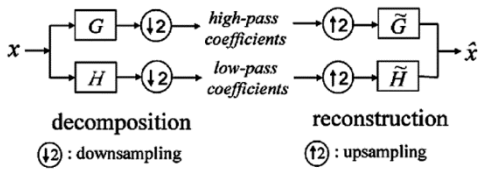

Fig. 3 — DWT signal decomposition and reconstruction process

Simulation Results

In the context of overall grid balance and planning, this propensity utility of power versus PV power is quite difficult to overcome. Solar energy integration in an efficient manner with the grid will be highly fruitful if a reliable algorithm is developed that can reduce inaccuracy in forecasting future generation of PV electricity. PV power forecasting has the potential to play a critical role in addressing the aforementioned challenge. So, using a combination of PV output data and PV system, anticipate PV system output using WT (wavelet transform) and AI (artificial intelligence) approaches. The WD breaks signal P_{pv} in its layer which are smooth and detailed. Output power signal related to power plant of PV consists sharp edge and caused jumps due to solar radiation fluctuation, having nonlinear periodicity and characteristics. Let $P_{pv}(n)$ represents signal in discrete time, in power plant of PV output power $P_{pv}(n)$ required for breaking in layer with details and a smooth layer. Using WD technique, spiltssignal on scale represented A1(n) and D1(n), also A1(n) represents input signal with smooth feature, D1(n) represents input signal x(n) detail version, represented in coefficients of wavelet transform, it can extend it until, get actual information. The approximation coefficients (A5, A4, A3, A2, A1) and detailed coefficients 'D5, D4, D3, D2, D1' from wavelet break obtained in PV production output as shown in Fig. 5. Further, for establishing the forecasting model, remove disturbances to be removed which contain frequencies.

To obtain the better frequency representation of PV generation signal, CWT (continuous wavelet transforms) is used and take the scalogram of the given signal. The scalogram represents values in absolute form

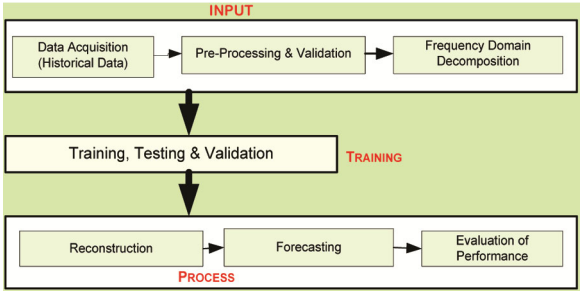

Fig. 4 — Hybrid system combined with ANN

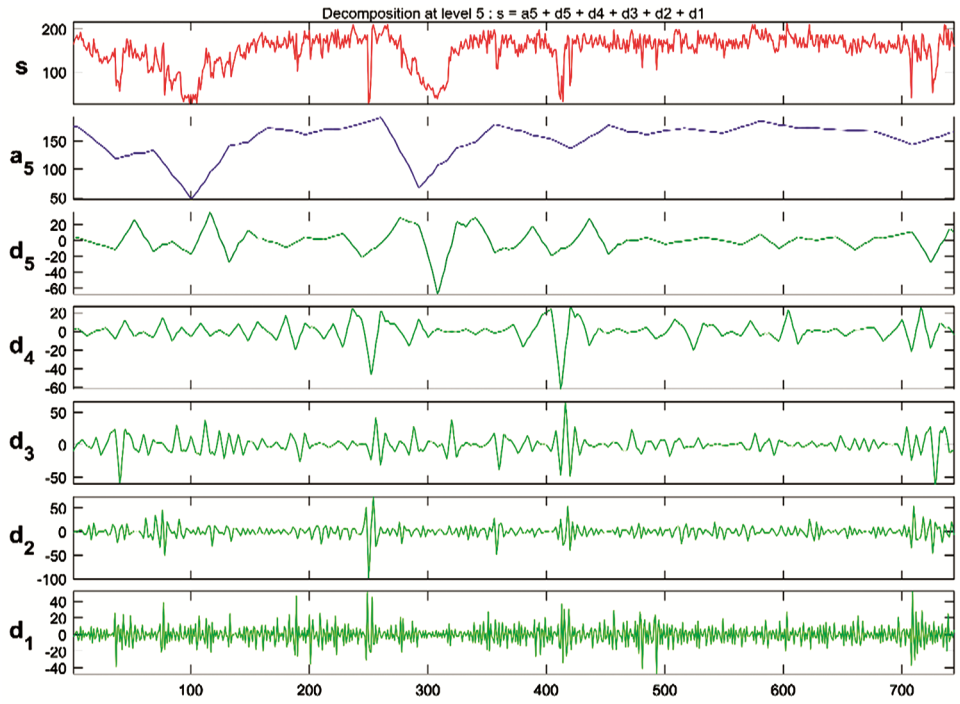

Fig. 5 — Decomposition of PV production (Fig. 1) at level 5 where x-axis represents time in days and y-axis represent decomposition of signal 's' at 5th levels

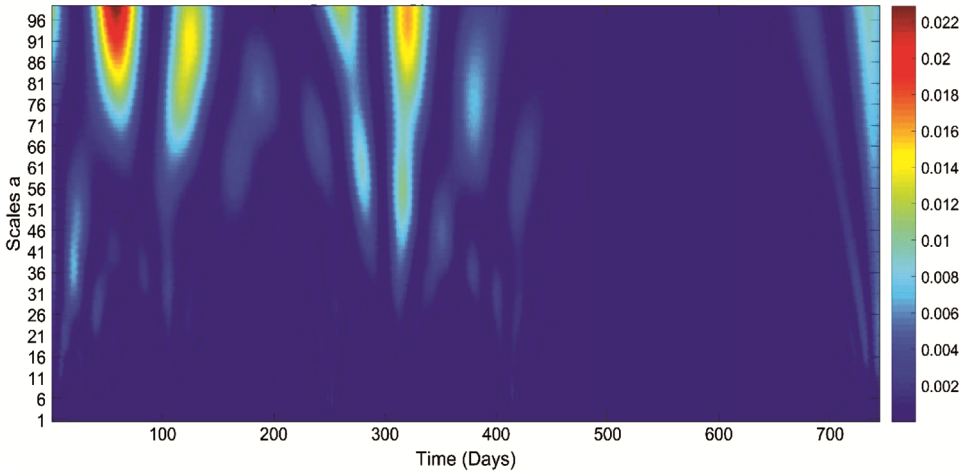

Fig. 6 — Scalogram of percentage of energy of each wavelet coefficient using continuous wavelet transform

for transform of continuous wavelet related to signal which is plotted in time & frequency function Fig. 6. The scalogram is used when we want improved localization time in case of high frequency of short duration event & improved frequency localization in events of longer duration with low frequency. Contour plot (Fig. 7) shows the wavelet spread in time and frequency preserving the energy in the analysis stage.

To improve the decomposition process (analysis and reconstruction), an orthogonal wavelet synthesis filter for the b-spline (Bior) is used, with three vanishing moments in the synthesis wavelet and five vanishing moments in the analysis wavelet as shown in Fig. 8. Hence, use of DWT has decomposed PV power production into approximation and detailed coefficient at level one as shown in Fig. 9 (a) and Fig. 9 (b) respectively. Then approximation coefficient

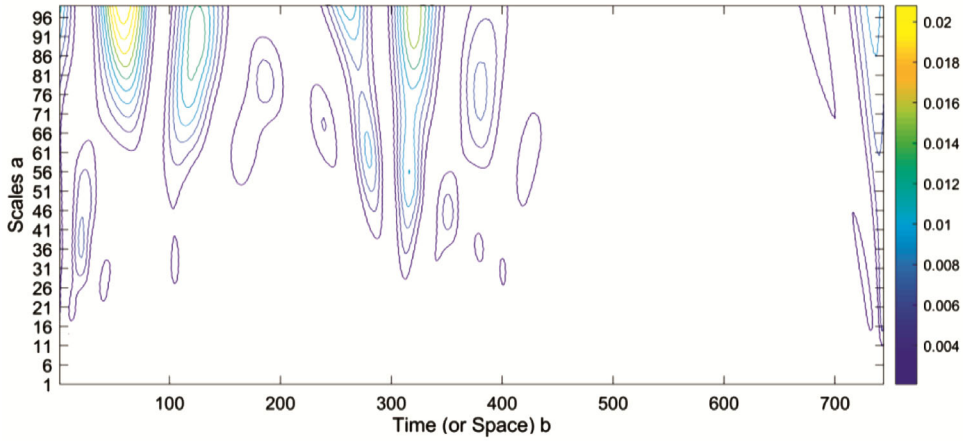

Fig. 7 — Contour of percentage energy for each wavelet coefficient

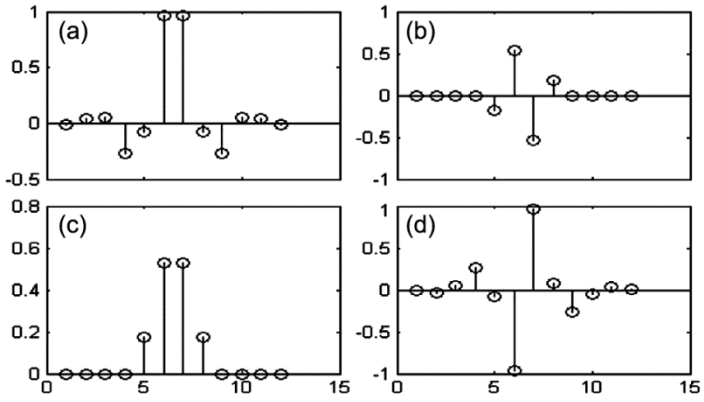

Fig. 8 — The analysis and synthesis components of continuous wavelet component of signal (Ppv)

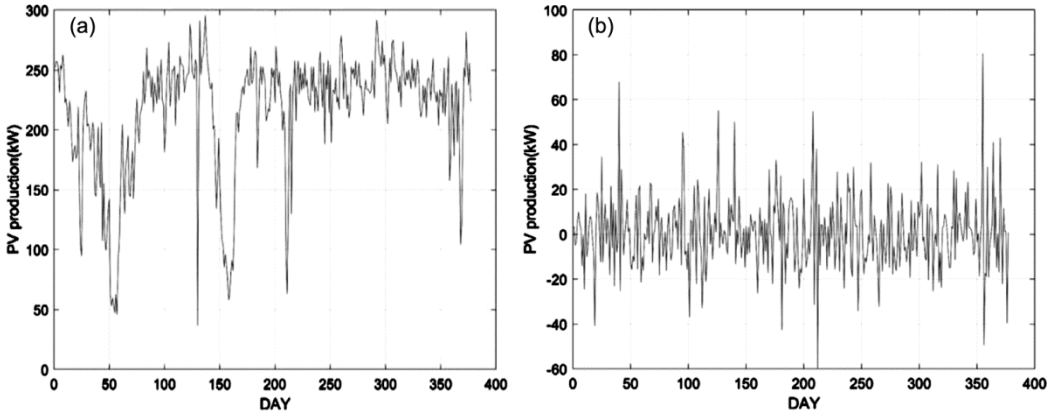

Fig. 9 (a) — Coefficient of original PV power signal at level 1: (a) Approximation, (b) Detail

and detailed coefficient will be reconstructed as shown in Fig. 10 (a) and Fig. 10 (b) respectively. By using these coefficients, the graphs are obtained as shown in Fig. 11 and Fig. 12.

In the case of signal decomposition, the observation was that introducing numerous coefficients, such as approx. 1 and 2, or further signal decomposition leads in sufficient increased complexity and training time, without increasing forecast outcomes. Many time series techniques are employed in a variety of forecasting applications, with varied model input and forecasting horizons. In

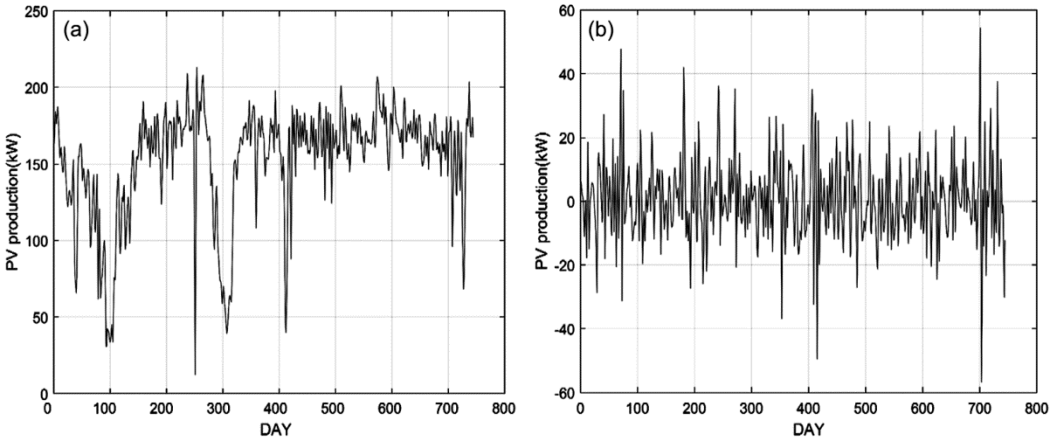

Fig. 10 — Reconstruction plots: (a) of Fig. 9(a), (b) of Fig. 9(b)

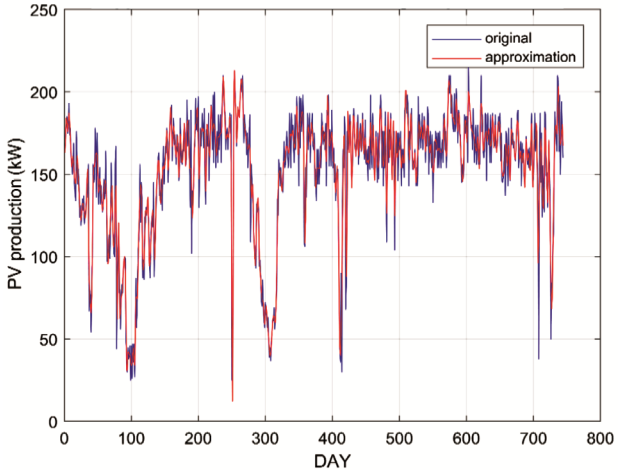

Fig. 11 — Comparison between approximation coefficient at level 1 and original PV signal

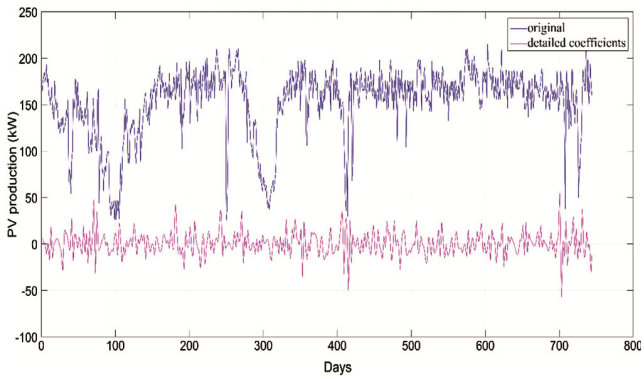

Fig. 12 — Comparison between original PV power signal and detailed coefficient D1

the application of forecasting, artificial intelligence (AI) based techniques are employed as a strong tool. The NN (neural network) gained prominence and is used as a powerful tool for computation in numerous AI techniques around 1980.

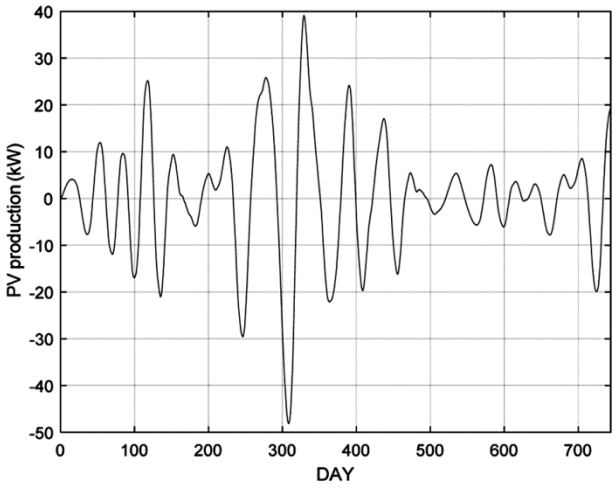

Fig. 13 — Reconstruction output of D5 coefficients

Before applying ANN, technique and performing forecasting analysis, decomposition level has to be decided. The main concept behind the operation is preprocessing of PV output data with the removing disturbances which is done by DWT. The decomposition number level depends firstly given signal under analysis. In this paper, modelutilized in other application, like forecasting of load, test is required for finding levels of optimal decomposition, in approximate and detailed level of decomposition. Thus, it is decomposed at the level 5. But it is observed that more disturbances occur at level 3 that's why B-spline by orthogonal wavelet is adopted through which the signal is analyze at 5 level and synthesized at 3 level by BiorNr.Nd. Due to this, PV production signal at the 1 evel 5 has been decomposed and then decomposition coefficient D5 can be obtained and reconstruct back this as shown in Fig. 13. According to the structure of the forecasting model. To train each coefficient

(A3, D5, D4, D3, D2, D1) and to recognize the non-liner behaviour of each component from DWT decomposition detailed coefficients 'D5, D4, D3, D2, D1' obtained from wavelet breaking our PV production output. After this process large changes occurs at level 2 as shown in Fig. 5.

Hence, Bi-orthogonal filter is used to decide decomposition level. WD with 5 layers is used in PV plant output power and further include detailed layer and approximation layer comparison. As per results, PV signal optimal level represented as level-3 of decomposition. It represents use of coefficients in this application of forecasting as A3, D1, D2, D3, D4, D5. After extracting the features vectors, trained all the coefficients by artificial neural network. In this final stage, the output of ANN reconstructed using Inverse Discrete Wavelet Transform (IDWT) as shown in Fig. 14 (a). After comparing these values with original PV signal error as shown in Fig. 14 (b). All these reconstructed obtained values are forecasted by ANN model as shown in Fig. 15, and achieved the forecasting graph as in Fig. 16 (a).

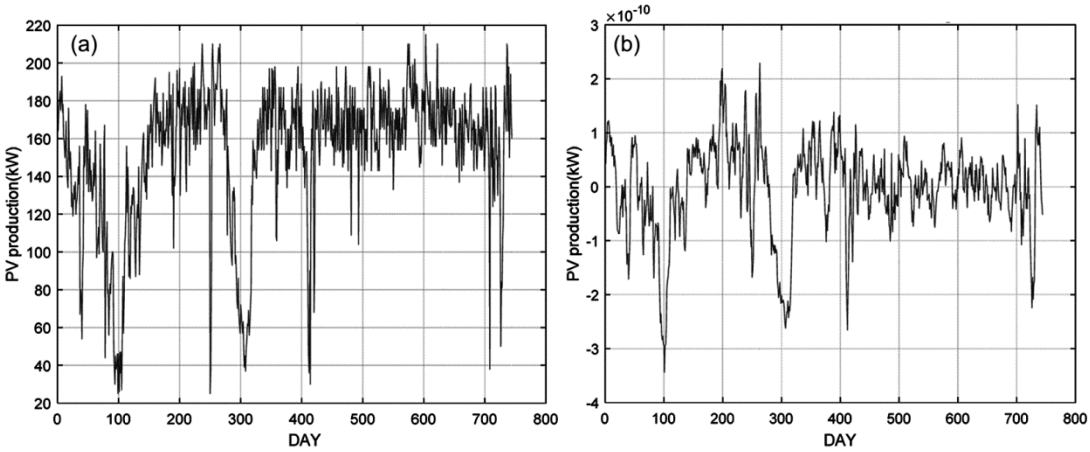

Fig. 14 (a) — Full Reconstruction output of trained coefficient Signal using IDWT, (b) — Error in Full Reconstructed output of P and original PV power signal

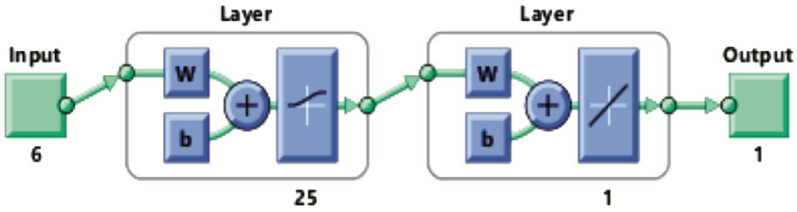

Fig. 15 — Forecasting Hybrid Model WT+ANN

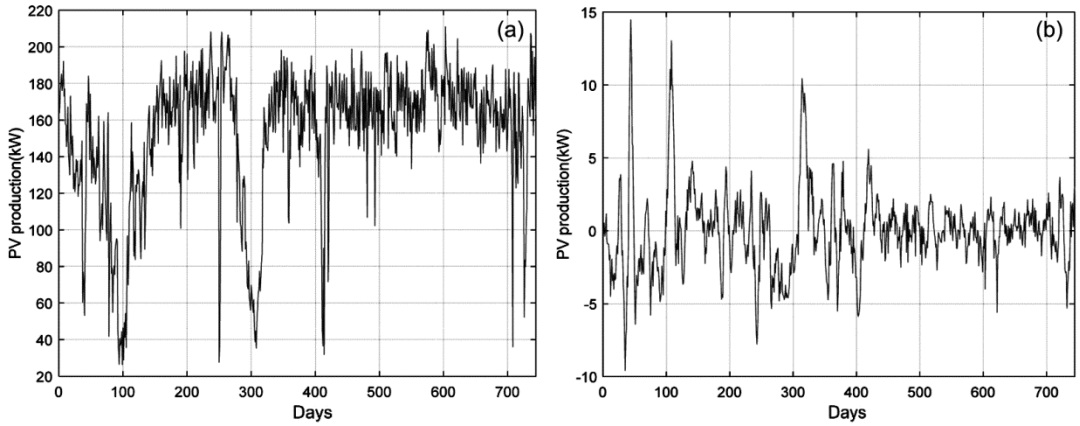

Fig. 16 — (a) Forecast output after training of reconstruct coefficients values, (b) Error in original signal PV and Forecast Output

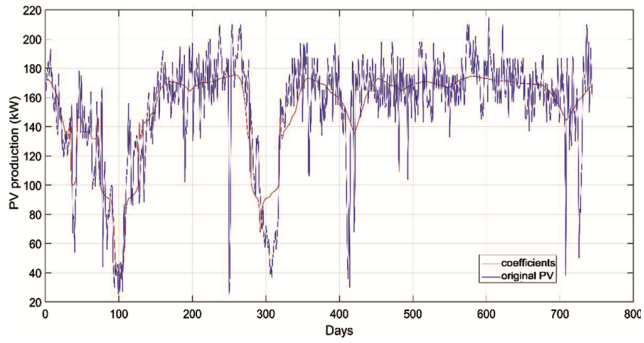

Fig. 17 — Comparison of original signal and reconstruct coefficients of PV power signal

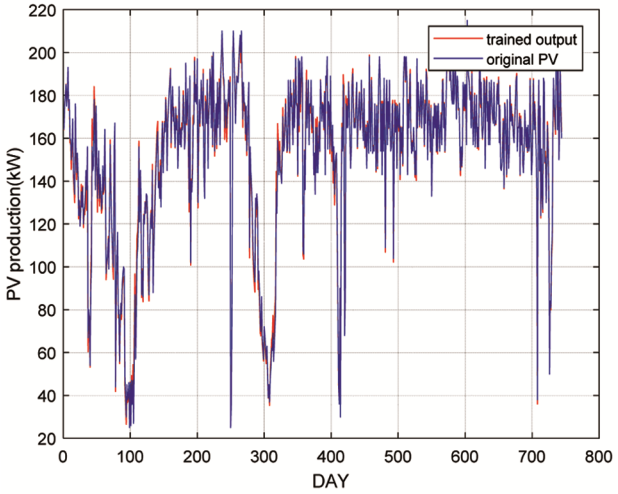

Fig. 18 — Comparison of original signal PV and forecast output

By observing the above graphs, it is predicted that graph is almost followed by the original one. For finding the error, subtract the predicted output from original PV signal. Fig. 16 (b) represents the error between predicted and original PV generation. Fig. 17 shown the comparison between reconstructed output and PV Power Generation and Fig. 18, shows comparison between forecasted output and original PV Production signal, which depicts the forecasting is well done and the accuracy is very high as compared to previous studies.

While predicting PV power, three statistical terms has been utilized for representing PV power output characteristics. The terms represented as RMSE, MAE and MAPE as shown in Table 2 and Table 3.

The PV generation data is been process for smoothness. On addendum, it is observed that missing point of input data regarding PV output data results in increment in error of forecasting. So, trained all coefficients using ANN using the process of trial and

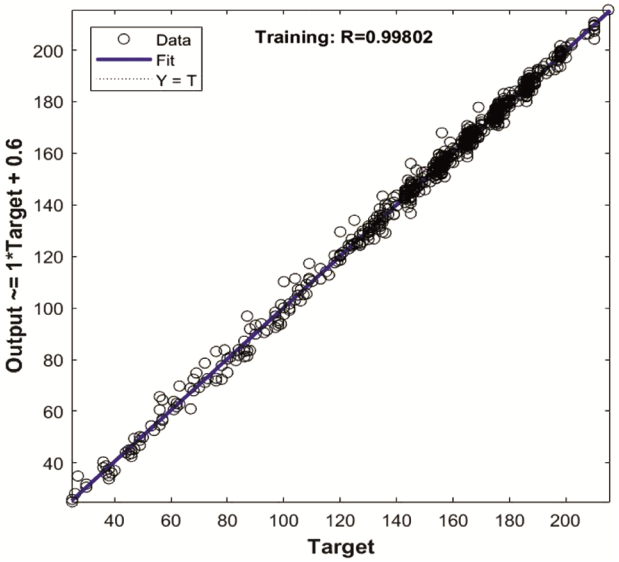

Fig. 19 — Scattered R Squared Plot for PV Power generation forecasting

Table 2 — Error in Reconstructed output signal and original PV generation Signal

Layer		Error
	RMSE (%)	8.64017e-13
	MAE (%)	6.3050e-13
	MAPE (%)	6.4969e-13
	Absolute Error	3.4417e-10

Table 3 — Forecasting Performance of Proposed hybrid model WT + ANN

Layer	Error		R	Average training time
	RMSE (%)	0.02433		
	MAE (%)	0.01725	0.99802	00:00:11
	MAPE (%)	0.01476		

error as shown in Fig. 19. Performance is based on the hidden neurons and hidden layers. From observations it was found that 25 hidden neurons gave better results. During the process of training ANN, mainly on 1st iteration, neurons weighted link are picked randomly and further optimized for minimizing in error, the process represents several minima at local level.

With reference to the period 2011–2020, a comprehensive summary of the most relevant research dealing with the applications of ML-based methods in the field of PV power forecasting is reported in this Table 4.

According to Table 4, the proposed method gives better accuracy as compared to the previous methods.

Table 4 — Machine learning (ML)-based methods for the forecast of PV power, 2011–2020

Methods	Parameters used	MAE	MAPE	RMSE	R
ANN[19]	Historical powers andmeteorological forecast	—	MAPE: 8.29% sunny day MAPE: 54.44% rainy day	—	—
ANN[20]	Historical powers andWeather forecast	—	MAPE: 0.85%	—	—
ANN[21]	Weather data and historical Measurements	MAE < 15%	—	—	—
ANN[22]	Solar radiation	MAE=1.137		RMSE=1.523	
Deep LSTM network[23]	Historical powers			RMSE = 82.15	
Hybrid WT + LSTM-DNN[24]	Historical Power generation Data	—	MAPE (%) 4.09425	RMSE=0.08225	R=0.955
WD+ANN[25]	PV power output	Clear=4.978% Cloudy=10.259% Overcat=10.220% Rainy=13.062%	Clear=13.858% Cloudy=21.550% Overcat=35.226% Rainy=30.926%	Clear=9.313 % Cloudy=18.472 % Overcast=18.511% Rainy=22.948 %	
WT+ ANN (Proposed Method)	Historical Power generation Data	MAE (%) 0.01725	MAPE (%) 0.01476	RMSE (%) 0.02433	R=0.99802

Conclusions

In this paper, data of PV production is collected at particular time, 744 samples of PV production data have been calculated. The main aim of this paper is to forecast in frequency domain, which is done with hybrid model. Wavelet Transform enables the extraction of frequency and temporal patterns. PV power output forecasting is based upon WD and ANN. Biorthogonal filter is used to choose decomposition level which is not preferably adopted in previous studies. It supports to multiresolution analysis. Smoothed signal and detailed signal related to PV output are found with application of ANN, forecasting models upon several signal layers are obtained. At last, by obtaining of forecasting results for several signal layers, PV power array forecasting results are established. By comparing with previous forecasting method, it represents that proposed forecasting method represents better precision for forecasting, as well as required convergence time for algorithm is less. These finding shows that model based upon proposed method outperform to the models of conventional mathematics in reference to forecast accuracy and adaptability in the conditions of metrological uncertainty.

References

1 Utility-scale solar in 2018 Still growing thanks to Australia and other later entrants, *W*iki-Solar (2019).

2 Snapshot (2020)-IEA-PVPS. [iea-pvps.org (2020)].

3 Transition in Energy, Transport – 10 Predictions for (2019) – 2. Solar additions rise despite China, BNEF (Bloomberg new energy finance) 2019, .

4 Nia A R, Awasthi A & Bhuiyan N, Industry 4.0 and demand forecasting of the energy supply chain: A literature review, *Comput Ind Eng*, **154** (2021) 107128.

5 Silva J L D S, Mesquita D B de, Moreira H S, Cavalcante M M, Melo K B de, Reis M V G dos, Freitas H A de & Villalva M G, Industry 4.0 approach aligned with the challenges of grid-connected photovoltaic systems, *IEEE PES ISGT Latin America* (Gramado, Brazil) 11th Nov, 2019.

6 Mihai F, Aleca O E, Steanciu A, Gheoghe M & Stan M, Digitalization-the engine of sustainability in the energy industry, *Energies*, **15** (2022) 2164.

7 Norihiro Kawasaki, Takashi Oozeki, Kenji Otani & Kosuke Kurokawa, An evaluation method of the fluctuation characteristics of photovoltaic systems by using frequency analysis, *Sol Energy Mater Sol Cells*, **90(18–19)** (2006) 3356–3363S, doi: 10.1016/j.solmat.2006.02.034.

8 Mehdi Ebad & Grady W M, A cloud shadow model for analysis of solar photovoltaic power variability in high-penetration PV distribution networks, *IEEE Pow Energy Soci Gen Meet (PESGM)* (Boston USA) 14th Nov, 2016.

9 Jiang J A, Wan J J, Zheng X Y, Chen C P, Lee C H, Su L K & Huang W C, A novelweather information-based optimization algorithm for thermal sensor placement in smart grid*, IEEE Trans*, **9(2)** (2016) 911–922.

10 Capizzi G, Napoli C & Bonanno F, Innovative second-generation wavelets construction with recurrent neural networks for solar radiation forecasting, *IEEE Trans Neu Net Learn Sys*, ***23*(11)** (2012) 1805–1815.

11 Anuwar F H & Omar A M, Future solar irradiance prediction using least square support vector machine, *Int J Adv Sci, Engg and Info Tech*, **6 (4)** (2016) 520–523.

12 Preda S, Oprea S V, Adela B & Anda B (Velicanu), PV forecasting using support vector machine learning in a big data analytics context, *Symmetry*, **10(12)** (2018) 748.

13 Bae K Y, Jang H S & Sung D K, Hourly solar irradiance prediction based on support vector machine and its error analysis, *IEEE Trans Pow Sys, **32*(2)** (2016) 935–945.

14 Ding M, Wang L & Bi R, Anann-based approach for forecasting the power output of photovoltaic system, *Proc Envil Sci*, **11** (2011) 1308–1315.

15 Konjic T, Jahic A & Pihler J, Artificial neural network approach to photovoltaic system power output forecasting, *18th Intell Sys Appl Pow Sys ISAP* (Porto, Portugal) September, 2015.

16 Mandal P, Madhira S T S & Haque A U, Forecastingpower output of solar photovoltaic system using wavelet transform and artificial intelligence techniques, *Proc Compu Sci*, **12** Dec (2012) 332–337.

17 Poolla C & Ishihara A K, Localized solar power prediction based on weather data from local history and global forecast, *45th IEEE Photovoltaic Specialists* (Waikaloa HI) 10th –15th June, 2018.

18 Lave M, Kleissl J & Stein J S, A wavelet-based variability model (WVM) for solar PV power plants, *IEEE Trans Sustene*, **4(2)** (2013) 501–509.

19 Chen C, Duan S, Cai T & Liu B, Online 24-h solar power forecasting based on weather type classification using artificial neural network, *Solar Ene*, **85(11)** (2011) 2856–2870.

20 Jimenez L A F, Jimenez A M, Falces A, Villena M M, Garrido E G, Santillan P M L, Alba E Z & Santamaria P J Z, Short-term power forecasting system for photovoltaic plants, *Renew Energy*, **44** (2012) 311–317.

21 Leva S, Dolara A, Grimaccia F, Mussetta M & Ogliari E, Analysis and validation of 24 hours ahead neural network forecasting of photovoltaic output power, *Math Comput Simul*, **131** (2017) 88–100.

22 Jogunuri S & Josh F T, Artificial intelligence methods for solar forecasting for optimum sizing of pv systems: a review, *Res J Chem Envi*, **24(SII)** June (2020) 174–180.

23 Ospin J, Newaz A & Faruque M O, Forecasting of PV plant output using hybrid wavelet-based LSTM-DNN structure model, IET *Renew Pow Gen*, **13(7)** (2019) 1087–1095, doi:10.1049/iet-rpg.2018.5779.

24 Nasser M A & Mahmoud K, Accurate photovoltaic power forecasting models using deep LSTM-RNN, *Springer Neu Compu Appl*, **31** (2017) 2727–2740.

25 Zhu H, Li Xu, Sun Q, Nie L Yao J & Zhao G et al., A power prediction method for photovoltaic power plant based on wavelet decomposition and artificial neural networks, *Energies*, **9(1)** (2016) 1–15, doi.org/10.3390/en9010011.

Robust Image Processing based Real-time Optical Mark Recognition System

Viraj Jain
Delhi Technological University
New Delhi, India
viraj.jain@hotmail.com

Siddharth Malik
Wineural Technologies Pvt. Ltd.
Gurugram, India
sidmalik@wineural.in

Vimal Bhatia
Indian Institute of Technology Indore
Indore, India
vbhatia@iiti.ac.in

2022 IEEE 6th Conference on Information and Communication Technology (CICT) | 978-1-6654-7312-5/22/$31.00 ©2022 IEEE | DOI: 10.1109/CICT56698.2022.9997878

***Abstract*—Optical mark recognition (OMR) is the process of reading marked information automatically and is globally used in automating examination marking and other forms of marking. However, the current OMR techniques are often time-consuming, expensive and require dedicated hardware for grading. Moreover, often the OMR sheets are not scanned properly due to untrained staff, sheets being damaged or put in an incorrect orientation. Therefore, to circumvent these drawbacks of existing techniques, we propose an image processing based robust model for evaluation of OMR sheets. The method is highly accurate and can identify the responses from OMR sheets with lower time and computation complexity. Robustness of the proposed model has also been tested against angle variations, blur and light imbalance. It was found that the model can handle all these artefacts efficiently, making it suitable for real-time applications. The proposed model is also low-cost and portable, as images of OMR sheets can be clicked through mobile phones without the need of scanners.**

***Index Terms*—Optical Mark Recognition, Image Processing, Edge Detection, Blur**

I. Introduction

Optical mark recognition (also called OMR) is the process of reading marked information from OMR sheets. Using OMR automates, increases efficiency, and also eliminates human marking errors. Each question is typically represented as a set of blank ovals or boxes on the optical answer sheet, wherein the user darkens these blanks. OMR is widely used to read quizzes, surveys, and examination papers. In recent years across the world, many competitive and government exams have begun to use OMR technology. Conventionally, OMR technology used traditional scanners to scan OMR sheets, and a computer extracted the information using image processing and computer vision techniques. The major drawback was that the sheets had to be scanned using dedicated hardware. In recent times, the focus has shifted towards robust models that can process camera images, eliminating scanners. Image correction is done on the input image with the model accuracy depending on light conditions, angle of rotation, skewness, and the camera.

One of OMR's early forms was developed from the punched card technology. IBM developed the "IBM 805 Test Scoring Machine", which detected the electrical conductivity of graphite pencil lead through the contact plates which read pencil marks. Chinnasarn et al. [1] proposed the first image-based OMR system based on a PC-type microcomputer connected to an image scanner. The model for each type of answer sheet is created in the learning mode by extracting all significant horizontal and vertical lines from the blank-sheet image.

The development and deployment of an OMR prototype system for automatically marking multiple-choice tests was described by Hussmann S. et al. [2]. An intelligent line scan camera was implemented with location identification and verification methods. The creation of a low-cost and high-speed OMR system prototype for marking multiple-choice questions was described by Hussmann et al. [3]. This technology is unique because it merges the entire system into a single low-cost FPGA to achieve high processing speed.

In the past, several image based OMR models have been proposed. Deng et al. [4] presented a method in which there are two types of marks on the questionnaire sheet: solid marks and hollow marks. Rectangular-shaped solid markers, termed as flag points in this study, are used to find the locations of information marks. Gupta et al. [5] proposed a low-cost OMR process solution that does not necessitate the use of a high-cost computing machine (reader) or high-quality paper for scanning. This is also an image-based strategy that can be employed in small businesses, educational institutions, and schools.

Rahul et al. [6] developed an image based system to automate the task of checking OMR response sheets. This image is preprocessed and then transmitted to the server. Following that, it is processed further, and the results are returned to the client as well as stored in the server's database. Jingyi et al. [7] proposed an algorithm to increase the accuracy of image processing OMR models having non-fixed form OMR sheets. The model finds the circular response bubble from the contours. The number of option bubbles for each question by dividing the total number of bubbles by the total darkened bubbles in the correct answer OMR template. However, this model does not account for cases when the user has not marked any option in a question. The model also cannot load high-resolution images and hence causes a decrease in accuracy when the OMR sheet has more questions.

Before any further processing, all scanned images must be registered to a fixed place, according to Rakesh et al. [8], and the corresponding position of bubbles in all scanned photos is the same. The corner square boxes are detected, and a suitable transformation matrix is used to translate all the photos such

978-1-6654-7312-5/22/$31.00 ©2022 IEEE

Authorized licensed use limited to: DELHI TECHNICAL UNIV. Downloaded on January 17,2023 at 05:29:42 UTC from IEEE Xplore. Restrictions apply.

that the position of bubbles corresponding to each question is consistent across all images. Rectangular contours of the main answer box and sub-answer boxes are identified on the OMR sheet. All the bubbles in the form are fixed in relation to these contours.

Machine learning and deep learning models can also be used in image processing, as proposed by Ray et al. [9] and Ravikumar et al. [10], but they are computationally expensive.

In this paper, we propose a low-cost and low complexity robust image processing based model that can identify responses from an OMR sheet with very high (perfect) accuracy. The model checks if the image is blurred and handles angle variations, skewness and light imbalance in the input image. It can process around 500 images in a minute with high accuracy without OMR scanners. Remainder of the paper is organised as follows; in Section 2, we introduce our OMR model by covering the details of each operation. Section 3 presents the results obtained from the model and a detailed discussion on the robustness of the model. Finally, conclusions drawn from the paper are summarised in Section 4.

II. Proposed Work

The proposed system model used for optical mark detection is shown in Fig 1. The model can detect user inputs with high accuracy in less time using image processing techniques. The model involves several operations, including edge detection, blur check, finding contours, perspective transformation and thresholding. The description of each operation performed during the OMR sheet evaluation is given below:

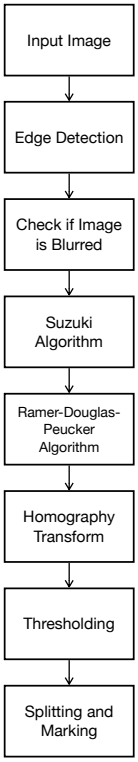

Fig. 1: System model for optical mark detection

A. Edge Detection

For edge detection, various algorithms like Sobel, Prewitt and Canny edge detection algorithms were tested on the OMR sheet. Although the Sobel and Prewitt edge detectors were able to detect edges, the number of edges detected was far lower than the Canny edge detector [11]. Canny edge detection algorithm has good localisation and works well even in the presence of noise. It also has a low error rate and detects existing edges only once. Thus, the Canny edge detection algorithm was chosen as the optimal edge detector in this model. Smoothing is done using a Gaussian filter to reduce noise from the image before detection. Image gradient is used to highlight places with high spatial derivatives. During non-maximum suppression, the algorithm moves over these zones, suppressing pixels not at maximum brightness. Hysteresis reduces the gradient array further and is used to track the remaining pixels that have not been suppressed. The following operations were performed for edge detection:

1) Gaussian Filter
   The camera-captured images are affected by noise. To handle noise many techniques were tested, as proposed by Bhatia et al. [12] and Chatterjee et al. [13]. As noise can lead to false edge detections in the image; after testing different methods, we use the Gaussian filter to smooth this noise. We filter out any noise in the input image using a 2-D convolution Gaussian filter, which is convolved with the input image.
2) Intensity Gradient
   We detect the edges where the change in grayscale intensity is maximum. We follow a procedure analogous to the Sobel kernel. For the horizontal and vertical axis, we use different matrices and then find the gradient strength and direction. Image gradient is a directional change in an image's pixel intensity or colour.
   We apply a pair of convolutional masks in x and y directions:

$$g_x = \begin{bmatrix} -1 & 0 & +1 \\ -2 & 0 & +2 \\ -1 & 0 & +1 \end{bmatrix} \quad g_y = \begin{bmatrix} -1 & -2 & -1 \\ 0 & 0 & 0 \\ +1 & +2 & +1 \end{bmatrix}$$

   Then we find the gradient strength and direction

$$G = \sqrt{g_x^2 + g_y^2} \qquad \theta = \arctan\left(\frac{g_y}{g_x}\right)$$

   The direction is rounded off to one of the four possible angles (0, 45, 90 or 135)
3) Non-maximum Suppression
   Pixels that are not considered part of an edge are removed. Based on the estimated gradient strengths and edge directions, we relate the edge direction to a direction that can be tracked along the edges. As a result, only the candidate edges with the highest probability remain.
4) Hysteresis
   The method employs two threshold values: an upper and a lower threshold. An edge is described as a pixel gradient

Authorized licensed use limited to: DELHI TECHNICAL UNIV. Downloaded on January 17,2023 at 05:29:42 UTC from IEEE Xplore. Restrictions apply.

value greater than the upper threshold. Pixel gradient values that are less than the lower threshold are rejected. If the pixel gradient is in between both thresholds, it will only be accepted if it is connected to a pixel above the upper threshold.

B. Blur Detection

Before implementing our model, we check whether the input image is blurred or not by using Discrete Fourier Transforms (DFT). For an image of size $M \times N$, the two-dimensional DFT is given by:

$$F(x,y) = \sum_{m=0}^{M-1} \sum_{n=0}^{N-1} f(m,n) e^{-j2\pi \left(x\frac{m}{M} + y\frac{n}{N}\right)}$$

where, $f(m,n)$ is the pixel at coordinates (m,n), and $F(x,y)$ is the image's frequency domain value corresponding to the x and y coordinates.

- First, we calculate the image's 2-dimensional DFT and shift the zero-frequency component to the centre for easier analysis.
- After zeroing out the centre of the Fast Fourier Transform (FFT) shift, we apply the inverse shift followed by inverse FFT.
- The mean magnitude spectrum is then calculated, which is compared to the threshold value set, to return whether the image is blurry or not. The threshold value was set after manual testing.
- If the image is blurry, we use convolution to make the image sharper. We use the sharpen kernel to increase the sharpness of the image. The kernel increases the pixel intensity of the given pixels and reduces the pixel intensity of neighbouring pixels. If the image is still blurry, we exit and prompt the user for a different image.

C. Suzuki Algorithm

To find contours in the image, we use Suzuki Algorithm [14], a border tracking algorithm. Many alternative techniques for topological structure analysis of binary images utilising raster scan and labelling have been developed, however the Suzuki algorithm is simpler and faster than the others. Border tracking algorithms are used to find the borders of images and segment different shapes. In border tracking of the inverted binary image, we find the sequence of zero pixels in the background filled with pixels larger than zero.

We input a binary rectangle image as used in the Suzuki algorithm. The Suzuki algorithm loops over the image pixels and looks for borders. When a border pixel is found, we look around the neighbourhood of that pixel to find the next border pixel. If we find a border pixel, we add it to the border and then look around its neighbours. This way, we follow border pixels sequentially and track the borders.

Using the Suzuki algorithm, we can find all the contours in the OMR sheet. We apply perspective transform on the biggest contour, the OMR sheet's outline. The desired user response box is found manually by analysing the area of all rectangular contours.

D. Ramer-Douglas-Peucker Algorithm

We only want the rectangular contours to find the biggest contour and the response box from all the contours we found using the Suzuki Algorithm. Ramer-Douglas-Peucker [15] [16] and Visvalingam–Whyatt algorithms [17] are two well-known polyline simplification techniques used to approximate the shape of the contours. As we have to analyse and evaluate OMR sheets in real-time, the Ramer-Douglas-Peucker algorithm was preferred as it is significantly faster than the Visvalingam–Whyatt algorithm.

Using the contours we find using the Suzuki Algorithm, we approximate the shape of these contours by Ramer-Douglas-Peucker Algorithm. An accuracy parameter epsilon is set, which is the maximum distance from the original contour to the approximated contour. The algorithm smooths out the polyline by reducing the number of vertices, given the value of the tolerance parameter ϵ. This way, we get a subset of the original curve point and an approximate shape similar to the input curve. Following are the steps:

- Ramer-Douglas-Peucker is an iterative algorithm – it removes the point, splits the line and starts again until there is no point that could be removed.
- The starting and endpoints of the curve are referred to as the anchor point and the floating-point. The perpendicular distance of all points from the line segment joining the anchor and floating-point is calculated. The point which is the furthest from this line segment is identified. The point is removed if the distance between the line and that point is less than ϵ, and the procedure repeats until there is no point between the endpoints.
- If the distance between the point and the line exceeds ϵ, the first and the farthest points are connected with another line, and any point closer than epsilon to this line is removed. Our original line divides in two every time a new farthest point is found, and the algorithm runs on each part separately. If a point is closer than ϵ to the line segment, then that point is discarded, and if the point is farther than ϵ, that point is kept.

E. Transformation

Perspective transformation or homography is associated with the change in the viewpoint of an image. Parallelism, length, the ratio of lengths, and angle are not preserved by this transformation, however cross-ratio and incidence are. This means that after the transformation, the straight lines will stay straight.

We use projective transformation or homography to wrap one projective plane into another projective plane. The transformation matrix is a 3x3 matrix with 8 degrees of freedom. To obtain this matrix, we take 4 points from the input image and map them to the appropriate places in the unknown output image. We apply the perspective transformation to the input image after obtaining the transformation matrix to get the final

Authorized licensed use limited to: DELHI TECHNICAL UNIV. Downloaded on January 17,2023 at 05:29:42 UTC from IEEE Xplore. Restrictions apply.

transformed image. Linear least squares estimation method is used to solve the homography linear equation.

We apply perspective transform on the response boxes. To apply homography, we convert the coordinates to homogeneous coordinates.

$$p = \begin{bmatrix} x \\ y \end{bmatrix} \Rightarrow P = \begin{bmatrix} x \\ y \\ 1 \end{bmatrix}$$

The homogeneous coordinates are multiplied by the homography matrix, and are then converted back to heterogeneous coordinates:

$$P' = H \cdot P \qquad P' = \begin{bmatrix} x' \\ y' \\ w' \end{bmatrix} \Rightarrow p' = \begin{bmatrix} x'/_{w'} \\ y'/_{w'} \end{bmatrix}$$

Now given a set of matched feature points $\{p_i, p_i'\}$, we find the best estimate of H such that $P' = H \cdot P$

F. Thresholding

In thresholding, we convert a grey image to a binary image (image with only 2 colours). By thresholding, we ensure that for an image pixel, the value is either 0 or 1.

In this paper, we use Inverted Thresholding, such that if the pixel value is greater than the threshold, it is set to 0; otherwise, it is set to 255. By using inverted thresholding, the OMR response bubbles become white and can be differentiated from the black background. This way, the grayscale image is converted to a binary image, where the pixels are either 0 or 255.

G. Splitting and Marking

a) Splitting: We split the response box horizontally by the number of questions to get rows containing each question's responses. Further, each row is split vertically by the number of options to get the individual mark response. We count the number of non-zero pixels (white pixels) for each individual response box. The box with the highest number of non-zero pixels above a given threshold is the marked answer in each row. If all the pixel values in a row are below the threshold, no option has been marked. If more than one box in a row has a number of non-zero pixels greater than the threshold value, then multiple boxes have been marked.

b) Marking: We compare the marked answers with the correct answers and output the marks scored. If no option or more than one option is marked, no marks are awarded for that question.

III. Results and Discussions

Using the proposed model and image processing techniques, OMR sheets were tested subject to three practical problems of angle variation, skew and poor lighting. The model would be helpful for examiners conducting examinations, as the model's processing time is significantly less, and it would save manual effort. It is also low cost, economical, and portable as images of OMR sheets can also be clicked through mobile phones. The OMR sheet evaluated in the proposed model is a standard OMR sheet with other information like Name, Roll Number, Date of Birth, etc., along with user response boxes. The model can precisely identify the marked responses and also determine if a question is not attempted. The model was tested 500 times on macOS running 2 GHz Quad-Core Intel Core i5-1038NG7 with 16 GB RAM. It took an average time of 0.4801 seconds per OMR sheet, scanning 200 questions. 125 images can be processed in a minute with high accuracy without the need for expensive OMR scanners. Compared to machine learning and deep learning OMR models, the proposed model uses only image processing techniques to give fast and accurate results. Fig. 2 shows the process of marking the OMR sheet.

Angle variation and skewness were introduced in the input image to check the model's robustness. As homography is used for perspective transformation, the model can handle angle variation of 44° with perfect accuracy. The model gave results with perfect accuracy and was able to handle this noise.

Progressive blur was intentionally added to the input image to check the robustness of the system in case of blur in camera images. The model was able to handle and give results with the same accuracy on low-quality images also. Images can be captured from any device without the need for high-quality scanners or special OMR sheets.

To check the robustness of the model, the accuracy was calculated at different illumination levels. The brightness factor of the image was varied from 0.5 to 1.6, and the corresponding accuracy was noted. When the illumination factor was below 0.7 or above 1.55, either rectangular contour estimation was not efficient, or the Homography matrix for perspective transformation could not be estimated. The model performed with near-perfect accuracy in the varying illumination levels.

Our proposed model has high speed and accuracy compared to previous similar works. The model proposed by Deng et al. requires high-speed scanners to acquire the images of questionnaire sheets. The average processing speed of the scanners is more than 50 pages per minute, with an average processing accuracy of 98%. The model Rakesh et al. proposed has an accuracy of up to 99.20%. The model can process over 400 forms in less than a minute, excluding scanning time, with each sheet containing more than 250 bubbles. The system proposed by Rahul et al. has an average accuracy of 97.49% for all phases, not considering partially filled bubbles. Considering errors due to partially filled bubbles, the system's accuracy is 87.41%. The average processing time was 3 seconds for every OMR sheet with 40 questions. The model proposed by Jingyi et al. has different accuracy based on the number of questions in the non-fixed OMR sheet. In our model, the accuracy is calculated for 200 questions, so we compare it to the accuracy of the OMR sheet with 120 questions, which is 99.33. Our proposed model takes an average of 0.48 seconds for every OMR sheet with 200 questions. It takes into account partially filled OMR bubbles and if the user has not marked any option or multiple options. The proposed model can handle all images and works with the same accuracy, even with low-quality mobile phone images or high-resolution images. It also doesn't require a scanner,

Authorized licensed use limited to: DELHI TECHNICAL UNIV. Downloaded on January 17,2023 at 05:29:42 UTC from IEEE Xplore. Restrictions apply.

saving cost and scanning time.

In the OMR model, we use the Canny Edge Algorithm to find the edges in the OMR sheet. Then it is checked whether the image is blurry or not. All the contours in the image are found using the Suzuki Algorithm. Using the Ramer-Douglas-Peucker algorithm, we find the rectangular contours. The sheet outline is the biggest rectangular contour. The response boxes are found by analysing the areas of the rectangular contours. Thresholding is done on the response box, and it is split horizontally to get individual rows. The rows are further split vertically to analyse each individual response mark.

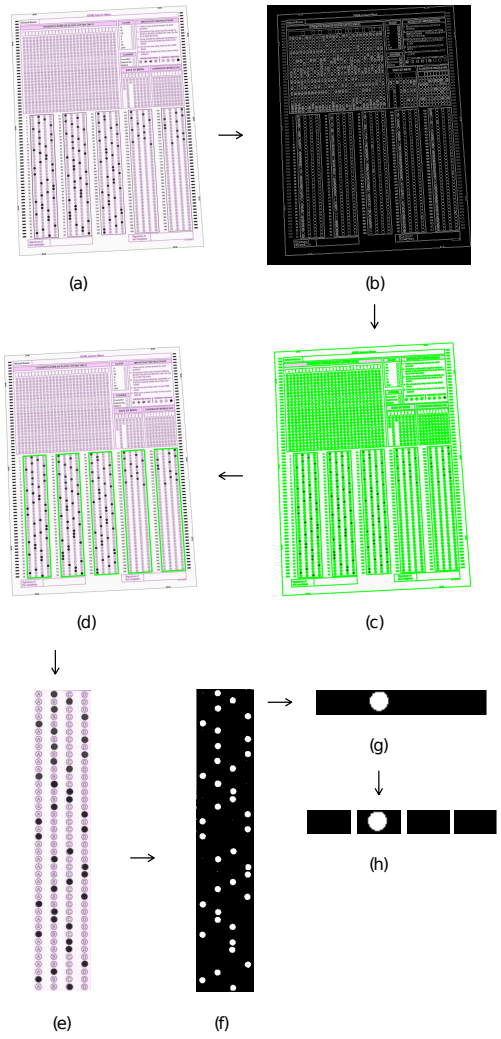

Fig. 2: (a) Input OMR sheet (b) Edge detection using Canny edge algorithm (c) Finding contours using Suzuki algorithm (d) Finding rectangular contours using Ramer-Douglas-Peucker algorithm (e) Perspective transform on the response box (f) Thresholding of response box (g) Splitting of response box into rows (h) Splitting the row to get individual mark response

IV. Conclusion

In conclusion, we proposed an image processing based optical recognition system for automatic real-time detection of marks with high accuracy. The proposed low-cost and portable model can reduce human efforts and fasten the grading procedure. Moreover, we have also found that the model is robust against various imperfections such as angle variation, poor lighting conditions, and blur. Images can also be captured through the phone, as the model can handle angle variations and low-quality images. The model can grade 500 images in a minute, making it suitable for real-time grading systems.

Acknowledgement

We gratefully acknowledge the support provided by IIT Indore and DTU for conducting this research.

References

[1] K. Chinnasarn and Y. Rangsanseri, "Image-processing-oriented optical mark reader," in *Applications of Digital Image Processing XXII*, vol. 3808. International Society for Optics and Photonics, 1999, pp. 702–708.

[2] S. Hussmann, L. Chan, C. Fung, and M. Albrecht, "Low-cost and high-speed optical mark reader based on an intelligent line camera," in *Optical Pattern Recognition XIV*, vol. 5106. SPIE, 2003, pp. 200–208.

[3] S. Hussmann and P. W. Deng, "A high-speed optical mark reader hardware implementation at low cost using programmable logic," *Real-Time Imaging*, vol. 11, no. 1, pp. 19–30, 2005.

[4] H. Deng, F. Wang, and B. Liang, "A low-cost omr solution for educational applications," in *2008 IEEE International Symposium on Parallel and Distributed Processing with Applications*, 2008, pp. 967–970.

[5] A. Gupta and S. Avasthi, "Image based low cost method to the omr process for surveys and research," *International Journal of Scientific Engineering and Applied Science (IJSEAS)–Vol.2, Issue-7*, pp. 91–95, 2016.

[6] R. Patel, S. Sanghavi, D. Gupta, and M. S. Raval, "Checkit-a low cost mobile omr system," in *TENCON 2015-2015 IEEE Region 10 Conference*. IEEE, 2015, pp. 1–5.

[7] T. Jingyi, Y. K. Hooi, and O. K. Bin, "Image processing for enhanced omr answer matching precision," in *2021 International Conference on Computer Information Sciences (ICCOINS)*, 2021, pp. 322–327.

[8] S. Rakesh, K. Atal, and A. Arora, "Cost effective optical mark reader," *International Journal of Computer Science and Artificial Intelligence*, vol. 3, no. 2, pp. 44–49, 2013.

[9] S. Ray, A. Baghel, and V. Bhatia, "Deep learning based underwater image enhancement using deep convolution neural network," in *2022 Second International Conference on Advances in Electrical, Computing, Communication and Sustainable Technologies (ICAECT)*, 2022, pp. 1–6.

[10] A. Ravikumar, R. P. Nagraj, M. K. Nair, and V. Bhatia, "Hyperspectral image classification using deep matrix capsules," in *International Conference on Signal and Information Processing (ICONSIP)*, 2022.

[11] J. Canny, "A computational approach to edge detection," *IEEE Transactions on Pattern Analysis and Machine Intelligence*, vol. PAMI-8, no. 6, pp. 679–698, 1986.

[12] V. Bhatia and B. Mulgrew, "Non-parametric likelihood based channel estimator for gaussian mixture noise," *Signal Processing*, vol. 87, no. 11, pp. 2569–2586, 2007.

[13] A. Chatterjee, P. Singh, J. Dhanotia, V. Bhatia, and S. Prakash, "Comparative analysis of image pre-filtering techniques for phase-shifted noise-affected interferograms," *Applied Optics*, vol. 59, no. 10, pp. 3227–3236, 2020.

[14] S. Suzuki *et al.*, "Topological structural analysis of digitized binary images by border following," *Computer Vision, Graphics, and Image Processing*, vol. 30, no. 1, pp. 32–46, 1985.

[15] U. Ramer, "An iterative procedure for the polygonal approximation of plane curves," *Computer Graphics and Image Processing*, vol. 1, no. 3, pp. 244–256, 1972.

[16] D. H. Douglas and T. K. Peucker, "Algorithms for the reduction of the number of points required to represent a digitized line or its caricature," *Cartographica: The International Journal for Geographic Information and Geovisualization*, vol. 10, pp. 112–122, 1973.

[17] M. Visvalingam and J. D. Whyatt, "Line generalization by repeated elimination of points," in *Landmarks in Mapping*. Routledge, 2017, pp. 144–155.

Authorized licensed use limited to: DELHI TECHNICAL UNIV. Downloaded on January 17,2023 at 05:29:42 UTC from IEEE Xplore. Restrictions apply.

Scattering Parameter Analysis of Gate Stack Gate All Around (GS-GAA) FinFET at THz for RF Applications

Bhavya Kumar
Department of Applied Physics
Delhi Technological University
Delhi, India
bhavyakumar_phd2k18@dtu.ac.in

Megha Sharma
Department of Applied Physics
Delhi Technological University
Delhi, India
meghasharma_phd2k18@dtu.ac.in

Rishu Chaujar
Department of Applied Physics
Delhi Technological University
Delhi, India
chaujar.rishu@dtu.ac.in

2022 8th International Conference on Signal Processing and Communication (ICSC) | 978-1-6654-5430-8/22/$31.00 ©2022 IEEE | DOI: 10.1109/ICSC56524.2022.10009615

***Abstract* — Within this investigation's scope, we use the Atlas device simulator to investigate how the fin width (W_{Fin}), gate electrode work function (ϕ_m), and temperature (T) influence the scattering characteristics of the gate stack gate all around (GS-GAA) FinFET while functioning within the THz frequency range. The major purpose of this research is to ascertain the W_{Fin}, ϕ_m, and T values that are ideal for use in upcoming RF applications using the proposed device. According to the findings, increasing the ϕ_m and lowering the W_{Fin} and T leads to an improvement of the leakage current of 71.83%, 98.99%, and 98.53%, respectively, which results in a significant increase in the device switching ratio. As a consequence of this, the forward/reverse transmission coefficient as well as the input/output reflection coefficient both show substantial signs of improvement. Therefore, as indicated by the results of the simulations, lowering the W_{Fin} and T while simultaneously increasing the ϕ_m makes the device presented ideal for use in microwave oscillators and amplifiers.**

Keywords* — *Fin width, gate electrode work function, GS-GAA FinFET, S-parameters, temperature, THz frequency.

I. Introduction

In recent years, the scaling of transistors has risen at an exponential pace. This has been done to improve the performance of integrated circuits as well as their density. The small size of CMOS transistors results in high short-channel effects (SCEs), which contribute significantly to the power loss in these devices [1-3]. The semiconductor industry has made significant progress in recent years, which has paved the way for the creation of FinFETs and other innovative designs. The modern integrated circuit business is powered by FinFET technology, which optimizes SCEs by allowing for high scalability, longer battery life, and decreased power consumption [4, 5]. This technology is also the driving force behind the integrated circuit industry. The Gate All Around (GAA) architecture, which encloses and protects the gate on all four sides, is another way in which the functionality of FinFET may be improved [6, 7]. As CMOS technology is continually scaled down, a new challenge presents itself in the form of an increase in the off-state leakage current (I_{off}) in parallel with a drop in the gate oxide thickness [8]. Despite the major drawbacks associated with their direct deposition on silicon substrates, the dielectrics with a high dielectric constant are the most practical choice [9]. By placing a passivated SiO_2 layer between a silicon substrate and high-dielectrics, the Gate Stack (GS) arrangement eliminates the need to alter the effective oxide thickness [10, 11].

The GaAs material is considered because it has numerous high-caliber electrical features, such as strong electron mobility, huge energy bandgap, etc., compared to Silicon [12]. The main challenge with GaAs-based devices is the lack of thermodynamically stable, high-quality insulators on GaAs that can supplement device standards such as SiO_2 on Silicon. However, after years of effort, high-quality dielectrics on III-V semiconductors have been formed using molecular beam epitaxy (MBE) and atomic layer deposition (ALD). Because of its excellent thermal stability, huge energy bandgap of 9 eV, good interface quality on GaAs, and ability to stay amorphous under typical processing circumstances, aluminum oxide (Al_2O_3) is a widely preferred gate dielectric [13].

The small-signal behavior of a transistor may be precisely characterized by utilizing the transistor's scattering (S), which can be reliably calculated using a vector network analyzer (VNA). Fig. 1 depicts a generalized two-port network for S-parameter measurement. Assuming that each port is terminated at the reference impedance, the four S-parameters of the 2-port can be calculated using Eq. (1-4). The equations mentioned for S_{11} and S_{21} are obtained by making the incident signal a_2 equal to zero. Similarly, S_{12} and S_{22} are obtained by setting a_1 equal to zero.

$$S_{11} = \frac{\text{Reflected Signal}}{\text{Incident Signal}} = \frac{b_1}{a_1} \quad (1)$$

$$S_{12} = \frac{\text{Reflected Signal}}{\text{Incident Signal}} = \frac{b_1}{a_2} \quad (2)$$

$$S_{21} = \frac{\text{Transmitted Signal}}{\text{Incident Signal}} = \frac{b_2}{a_1} \quad (3)$$

$$S_{22} = \frac{\text{Transmitted Signal}}{\text{Incident Signal}} = \frac{b_2}{a_2} \quad (4)$$

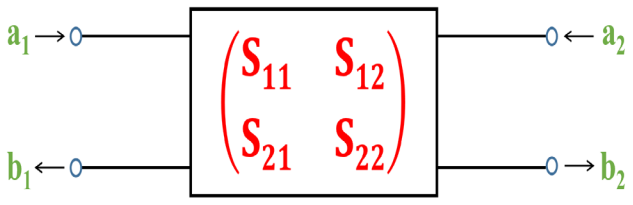

Fig. 1. Generalized two-port network for S-parameter measurement.

978-1-6654-5430-8/22/$31.00 ©2022 IEEE

Authorized licensed use limited to: DELHI TECHNICAL UNIV. Downloaded on January 17,2023 at 05:01:31 UTC from IEEE Xplore. Restrictions apply.

The above basic conversion formulae make it feasible to derive additional analogous characteristics such as hybrid (H), admittance (Y), and impedance (Z) parameters [14, 15]. When performed at high frequencies, measurements of MOSFET S-parameters are the approach that proves to be the most fruitful in terms of learning about the device. S-parameters are typically used for networks that operate at radio and microwave frequencies because it is extremely difficult to predict the current and the voltage compared to signal power and energy analysis when the frequency is high. It isn't easy to produce open and short circuits at high frequencies, which are important for defining the majority of n-port characteristics. This indicates that waves and matching terminations play a significant influence on the way that microwave engineers deal with S-parameters. This strategy also contributes to mitigating the unfavorable consequences of reflection [16].

As the size of the gadget become smaller, more and more higher-order effects become apparent. Because of these effects, the gadget's performance is drastically altered when exposed to high frequencies. As a result, an accurate evaluation of the relevant characteristics is necessary to correctly estimate how the device will react in various environmental circumstances. Thus, in this research, a comprehensive analysis of the S-parameters of GS-GAA FinFET has been conducted across the terahertz (THz) frequency range. To begin, the drain current (I_{on}), switching (I_{on}/I_{off}) ratio, and transconductance (g_m) of the proposed device are examined with fin width (W_{Fin}), gate electrode work function (ϕ_m), and temperature (T). After that, the effect that W_{Fin}, ϕ_m, and T have on the scattering parameters was carried out with the help of the ATLAS 3D tool [17].

II. Device Structure

Fig. 2(a-b) labels the systematic three-dimensional and horizontally sliced two-dimensional designs of the proposed device. The structure's fin portion is comprised of Gallium Arsenide (GaAs) material. The parameters of the device are as follows: fin height (H_{Fin} = 10 nm), source/drain length ($L_{S/D}$ = 10 nm), gate length (L_g = 7 nm), and oxide thickness (t_{ox} = 1 nm). The gate oxide is coated with a combination of Al_2O_3 and HfO_2 in equal quantities. The whole fin region has N-type doping. Doping is 5×10^{18} cm^{-3} in source/drain areas ($N_{S/D}$) and 1×10^{16} cm^{-3} in channel regions (N_{Ch}). In order to study the effect that W_{Fin}, ϕ_m, and T have on the S-parameters, the W_{Fin} is studied in the range of 3 to 7 nm, ϕ_m is altered from 4.55 eV to 4.75 eV, and T varies from 250 K to 450 K.

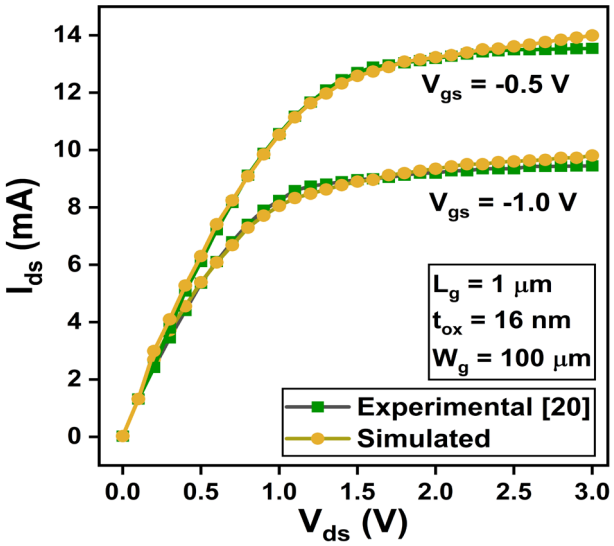

Fig. 3. Calibration plot of the Al_2O_3/GaAs MOSFET.

TABLE I. Influence of Fin Width, Gate Electrode Work Function, and Temperature on Different Parameters

Parameters		I_{on} (μA)	I_{off} (pA)	I_{on}/I_{off} ratio ($\times10^7$)	Peak g_m (μS)
W_{Fin} (nm)	**3**	151.75	0.16	94.25	228.42
	4	197.23	0.71	27.58	288.82
	5	241.36	2.45	9.85	346.15
	6	284.38	7.05	4.03	400.98
	7	326.80	15.98	2.04	454.09
ϕ_m (eV)	**4.55**	256.54	3.87	6.62	346.22
	4.6	249.13	2.95	8.45	345.59
	4.65	241.36	2.45	9.85	346.15
	4.7	233.21	1.68	13.88	345.58
	4.75	224.59	1.09	20.60	346.26
T (K)	**250**	286.99	1.02	28.13	419.35
	300	241.36	2.45	9.85	346.15
	350	208.79	2.99	6.98	292.61
	400	184.37	11.88	1.55	251.71
	450	165.38	69.61	0.23	220.75

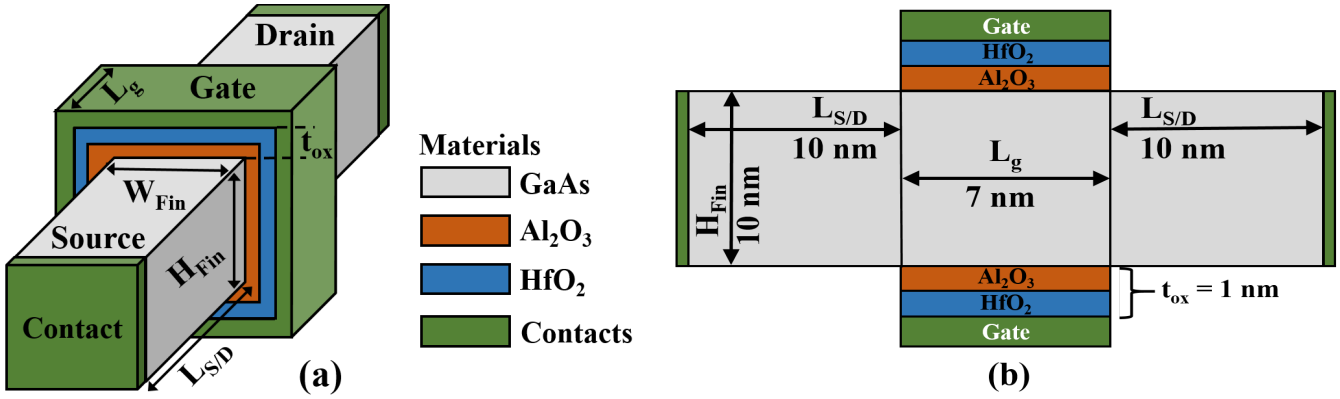

Fig. 2. (a) 3D and (b) 2D horizontally chopped architectures of the proposed device.

Authorized licensed use limited to: DELHI TECHNICAL UNIV. Downloaded on January 17,2023 at 05:01:31 UTC from IEEE Xplore. Restrictions apply.

III. Models and Experimental Calibration

The Continuity and Poisson equations provide the backbone of the device simulation, but supplementary physical models and equations are necessary to get more correct findings. Consequently, several different physical models are integrated into the simulations. The effects of quantum confinement cannot be disregarded in the devices that have been rapidly scaled; this makes them a critical parameter. In rapidly scaled systems, the effects of quantum confinement are a crucial parameter that cannot be ignored. The Bohm Quantum Potential (BQP) model includes a position-dependent quantum potential (Q) [18, 19]. The SRH recombination model is used to account for generation and recombination effects. The band-to-band Klaassen tunneling model explores both direct and indirect tunneling of electrons between the conduction and valence bands. The concentration-dependent mobility model can link low-field carrier mobility at 300 K to impurity concentration. Fermi-Dirac statistics are used to account for the characteristics of heavily doped materials. In addition, the bandgap narrowing and Crowell-Sze impact ionization models are used. Furthermore, all the mathematical issues associated with the carrier motions are solved using Newton and Block iteration methods [17].

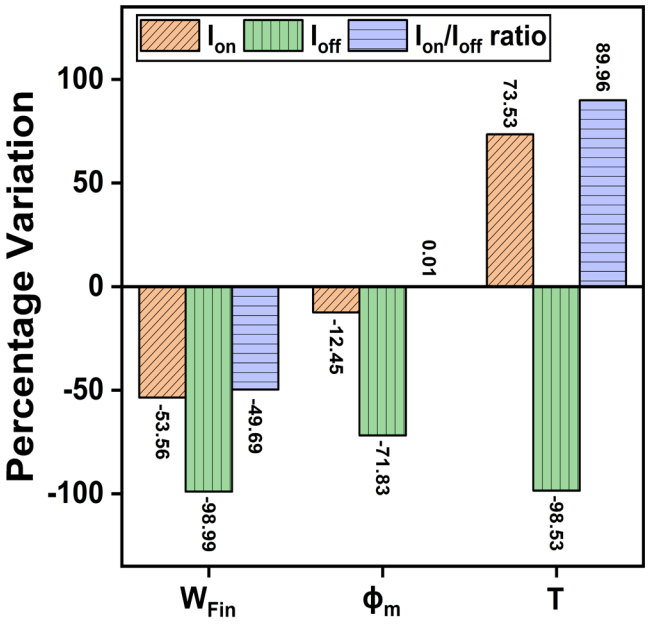

Fig. 4. DC performance parameters in terms of percentage change for the extremum values of W_{Fin}, ϕ_m, and T.

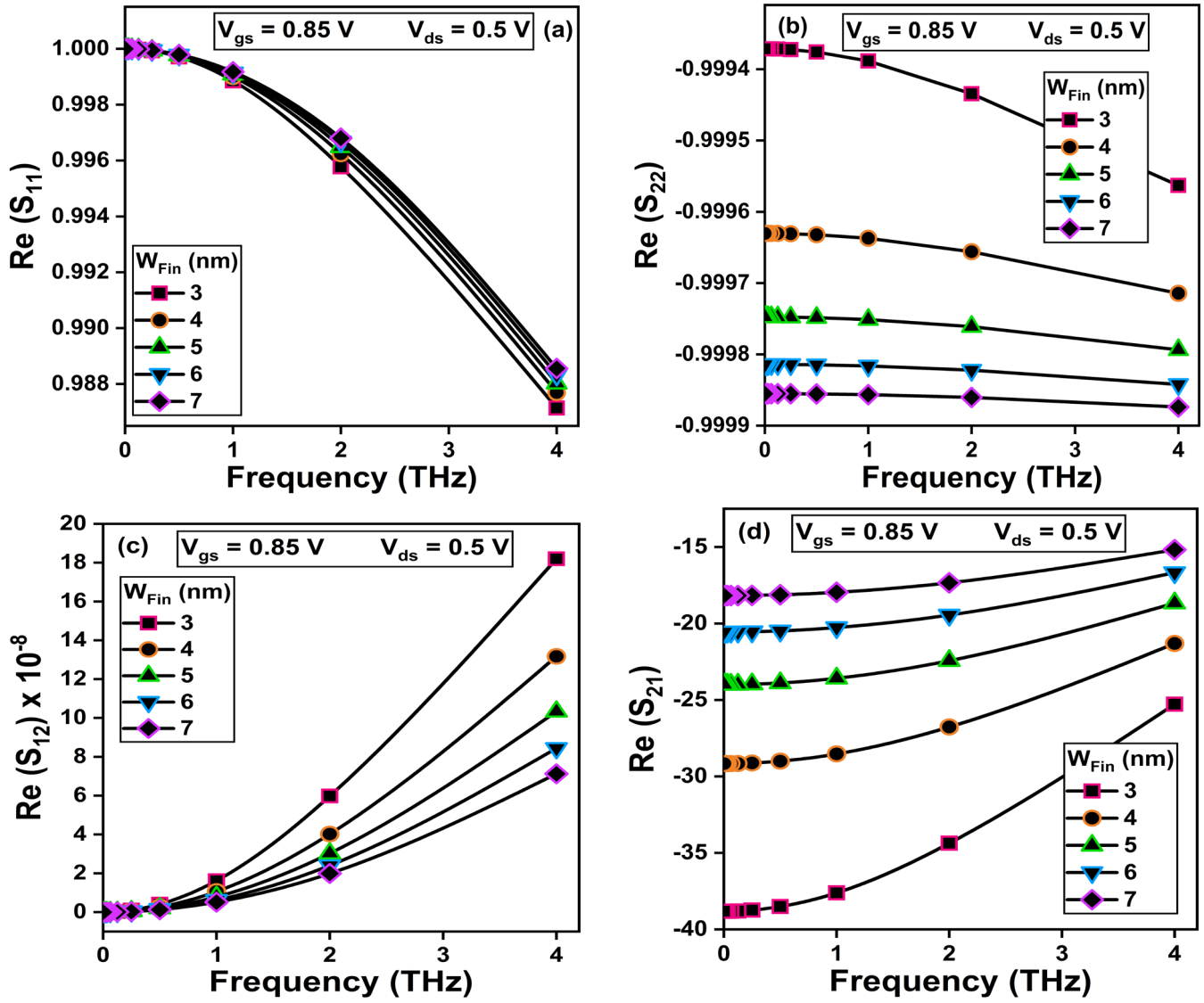

Fig. 5. The S-parameters of the GS-GAA FinFET have been examined at THz frequencies for different fin widths.

Authorized licensed use limited to: DELHI TECHNICAL UNIV. Downloaded on January 17,2023 at 05:01:31 UTC from IEEE Xplore. Restrictions apply.

We have taken the published results of Ye et al. [20] to validate the aforementioned physical models. Fig. 3 displays the experimental and simulated output characteristics of an Al_2O_3/GaAs MOSFET operating at V_{gs} = -0.5 V and V_{gs} = -1.0 V. The fact that the simulated and experimental data sets coincide closely lends credence to the models chosen for use in the simulations. A detailed flowchart of the fabrication process of GS-GAA FinFET was already covered in our published paper [21].

IV. Results and Discussion

In this part, we will explore the influence that W_{Fin}, ϕ_m, and T have on the values of the metrics, such as the leakage current, drain current, switching ratio, and transconductance. In addition, we will study the effect of W_{Fin}, ϕ_m, and T on the S-parameters (reflection and transmission coefficients) of the proposed GS-GAA FinFET.

When describing the high-frequency small-signal behavior of an active device, input and output reflection coefficients (S_{11} and S_{22}) are the most popular parameter to use because they are used to quantify the degree to which a port's impedance matches the terminating load [22]. In most RF circuits, matching is essential. The reflection coefficient is zero at a perfect match, and no waves are reflected. The high-frequency stability of an amplifier is determined by the value of the reverse transmission coefficient (S_{12}), which specifies the amount of transmission of information from the output to the input [23]. The forward transmission coefficient (S_{21}) is also known as a two-port device's forward gain.

Table I illustrates the detailed comparison of W_{Fin}, ϕ_m, and T effects on the parameters like drain current, leakage current, switching ratio, and transconductance. In Fig. 4, the change in the fundamental DC performance parameters is plotted in terms of percentage change for the extremum values of W_{Fin} (7 nm → 3 nm), ϕ_m (4.55 eV → 4.75 eV), T (450 K → 250 K). When the W_{Fin} is decreased from 7 nm to 3 nm, the drain current is reduced by 53.56% and the transconductance by 49.69%. Despite this, it achieves a large improvement in the leakage current of 98.99%, which in turn increases the switching ratio by more than 46 times. Fig. 5(a-b) depicts the variation of the real S_{11} and S_{22} at THz frequencies with fin widths ranging from 3 nm to 7 nm. The considerable increase in the I_{on}/I_{off} ratio improves the reflection coefficients (S_{11} and S_{22}) at ports 1 and 2. The transmission coefficients in the real form are shown as a function of fin width for the THz frequency range in Fig. 5(c-d). As the W_{Fin} is reduced, the reverse transmission coefficient (S_{12}) increases and moves toward a more positive value. It can be seen in Fig. 5(d) that the forward transmission coefficient (S_{21}) improves with the reduction in the W_{Fin}. Therefore, reducing the W_{Fin} makes the device suitable for microwave oscillators and amplifiers.

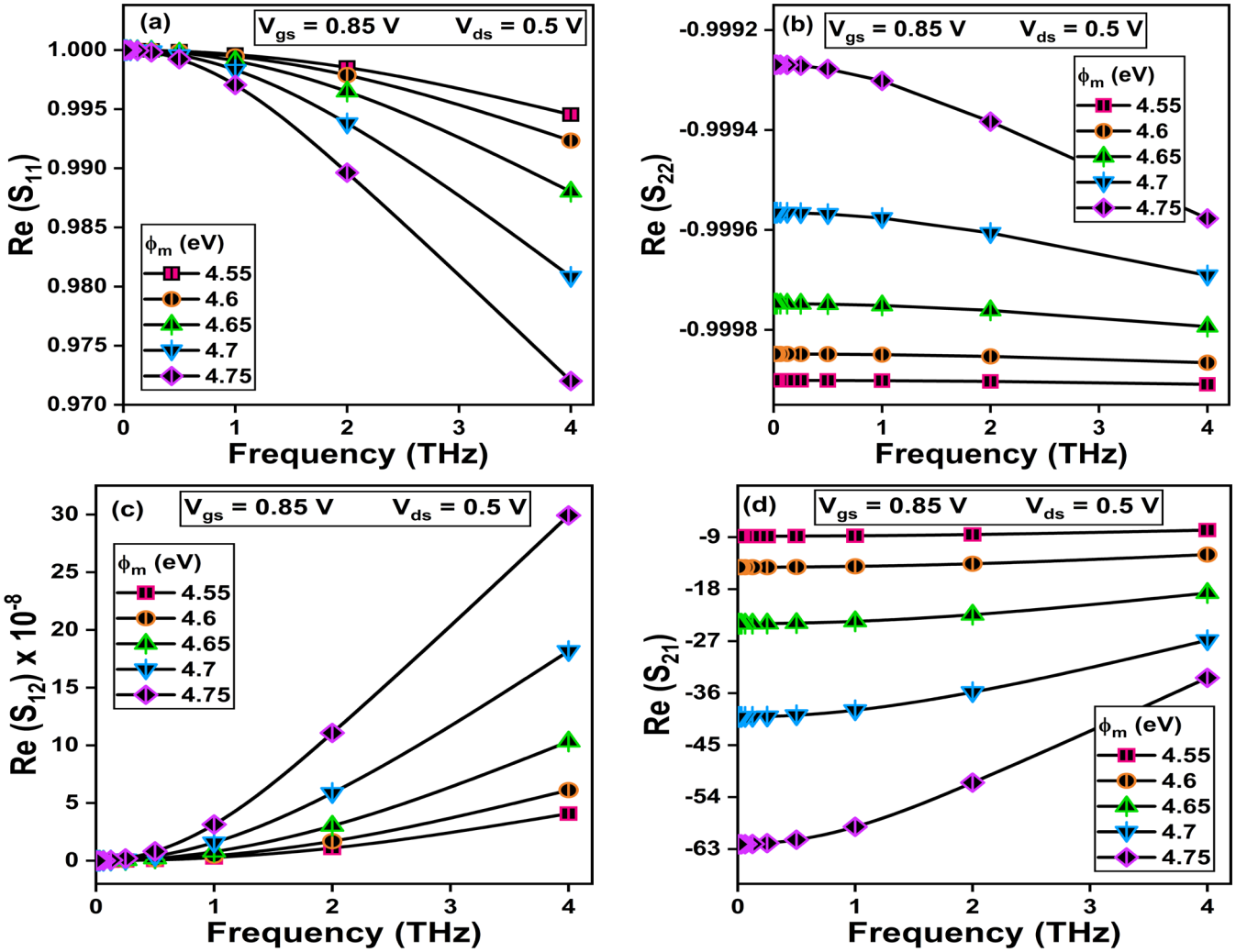

Fig. 6. The S-parameters of the GS-GAA FinFET have been examined at THz frequencies for different gate electrode work functions.

Authorized licensed use limited to: DELHI TECHNICAL UNIV. Downloaded on January 17,2023 at 05:01:31 UTC from IEEE Xplore. Restrictions apply.

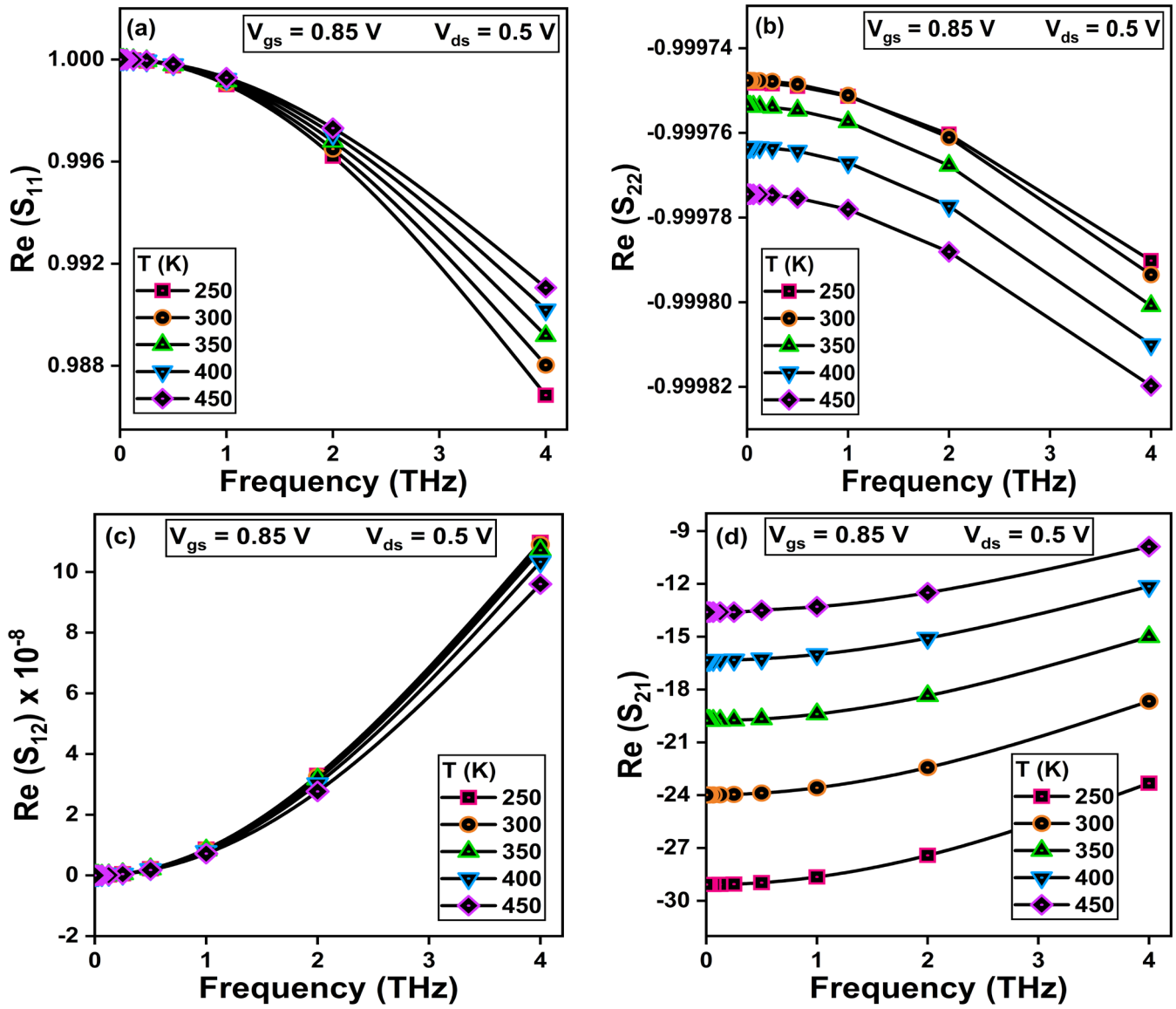

Fig. 7. The S-parameters of the GS-GAA FinFET have been examined at THz frequencies for different temperatures.

The drain current dropped by 12.45% and the leakage current improved by 71.83% (Fig. 4) due to increased band bending when the ϕ_m escalated from 4.55 eV to 4.75 eV. Since the fall in I_{off} current is more pronounced and bigger than I_{on} current, the switching ratio upgrades by a substantial 211.17% with a minimal improvement in the transconductance. Changing the ϕ_m from 4.55 eV to 4.75 eV in Fig. 6(a-b) shows how the real S_{11} and S_{22} change at THz frequencies. The S_{11} and S_{22} at ports 1 and 2 improve with the rise in the ϕ_m due to the increment in the switching ratio. Fig. 6(c-d) displays the real form transmission coefficients as a function of ϕ_m over the THz frequency range, showing that escalating the ϕ_m improves the transmission scattering coefficients. The reduction in the temperature improves the drain and leakage currents of the device due to the enhanced energy bandgap and mobility [24, 25]. Consequently, in Fig. 4, we can see that when the temperature was lowered from 450 K to 250 K, the drain current was raised by 73.53%, and the leakage current improved by 98.53%. Thereby increasing the switching ratio by more than 1200 times and transconductance by 89.96%. The S_{11} and S_{22} shift in the real form at THz frequencies for mentioned temperature is portrayed in Fig. 7(a-b). The S_{11} and S_{22} at ports 1 and 2 improve with the temperature reduction due to the enhanced transconductance. Real form S_{12} and S_{21} as a T function are shown in Fig. 7(c-d) over the THz frequency range, demonstrating that reducing T improves the transmission scattering coefficients.

V. Conclusion

In this research, we use the Atlas device simulator to evaluate the effect of fin width, gate electrode work function, and temperature on the scattering parameters of the GS-GAA FinFET operating in the THz frequency range. The study's primary objective is to determine the proposed device's optimum W_{Fin}, ϕ_m, and T for future RF applications. The results disclose that enhancing the ϕ_m and reducing the W_{Fin} and T improves the leakage current and substantially upgrades the device switching ratio. Due to this, the forward/reverse transmission coefficient and the input/output reflection coefficient both improve significantly. Thus, as shown by the simulated results reducing the W_{Fin} (7 nm → 3 nm) and T (450 K → 250 K) and raising the ϕ_m (4.55 eV → 4.75 eV) make the proposed device suitable for microwave oscillators and amplifiers.

Authorized licensed use limited to: DELHI TECHNICAL UNIV. Downloaded on January 17,2023 at 05:01:31 UTC from IEEE Xplore. Restrictions apply.

REFERENCES

[1] A. Chaudhary and M. J. Kumar, "Controlling short-channel effects in deep-submicron SOI MOSFETs for improved reliability: A review," *IEEE Trans. Device Mater. Reliab.*, vol. 4, no. 1, pp. 99–109, 2004.

[2] M. Sharma and R. Chaujar, "Ultrascaled 10 nm T-gate E-mode InAlN/AlN HEMT with polarized doped buffer for high power microwave applications," *Int. J. RF Microw. Comput. Eng.*, vol. 32, no. 4, pp. 1–10, 2022.

[3] R. Mann and R. Chaujar, "TCAD investigation of ferroelectric based substrate MOSFET for digital application," *Silicon*, vol. 14, pp. 5075-5084, 2022.

[4] V. B. Sreenivasulu and V. Narendar, "Junctionless SOI FinFET with advanced spacer techniques for sub-3 nm technology nodes," *Int. J. Electron. Commun. (AEÜ)*, vol. 145, pp. 154069, 2022.

[5] B. Kumar and R. Chaujar, "Numerical Study of JAM-GS-GAA FinFET: A Fin Aspect Ratio Optimization for Upgraded Analog and Intermodulation Distortion Performance," *Silicon*, vol. 14, pp. 309–321, 2022.

[6] Y. C. Huang, M. H. Chiang, S. J. Wang, and J. G. Fossum, "GAAFET versus pragmatic FinFET at the 5nm Si-based CMOS technology node," *IEEE J. Electron Devices Soc.*, vol. 5, no. 3, pp. 164–169, 2017.

[7] B. Kumar, A. Kumar, and R. Chaujar, "The Effect of Gate Stack and High-K Spacer on Device Performance of a Junctionless GAA FinFET," in IEEE VLSI Device, Circuit and System Conference (VLSI-DCS), pp. 159–163, 2020.

[8] S.-H. Lo, D. A. Buchanan, Y. Taur, and W. Wang, "Quantum-mechanical modeling of electron tunneling current from the inversion layer of ultra-thin-oxide nMOSFET's," *IEEE Electron Device Lett.*, vol. 18, no. 5, pp. 209–211, 1997.

[9] G. Ribes, J. Mitard, M. Denais, S. Bruyere, F. Monsieur, C. Parthasarathy, E. Vincent, and G. Ghibaudo, "Review on high-k dielectrics reliability issues," *IEEE Trans. Device Mater. Reliab.*, vol. 5, no. 1, pp. 5–19, 2005.

[10] N. Gupta and R. Chaujar, "Optimization of high-k and gate metal work function for improved analog and intermodulation performance of gate stack (GS)-GEWE-SiNW MOSFET," *Superlattices Microstruct.*, vol. 97, pp. 630–641, 2016.

[11] B. Kumar and R. Chaujar, "Analog and RF performance evaluation of junctionless accumulation mode (JAM) gate stack gate all around (GS-GAA) FinFET," *Silicon*, vol. 13, pp. 919–927, 2021.

[12] S. H. Chen, W. S. Liao, H. C. Yang, S. J. Wang, Y. G. Liaw, H. Wang, H. Gu, and M. C. Wang, "High-performance III-V MOSFET with nano-stacked high-k gate dielectric and 3D fin-shaped structure," *Nanoscale Res. Lett.*, vol. 7, pp. 1–5, 2012.

[13] H. C. Lin, P. D. Ye, and G. D. Wilk, "Leakage current and breakdown electric-field studies on ultrathin atomic layer-deposited Al_2O_3 on GaAs," *Appl. Phys. Lett.*, vol. 87, no. 18, pp. 1–3, 2005.

[14] D. M. Pozar, Microwave Engineering, 4th ed., Wiley, 2011.

[15] G. A. Botero, R. Torres, and R. M. Arteaga, "Using S-parameter measurements to determine the threshold voltage, gain factor, and mobility degradation factor for microwave bulk-MOSFETs," *Microelectronics Reliability*, vol. 51, pp. 342–349, 2011.

[16] J. J. Liou and F. Schwierz, "RF MOSFET: recent advances, current status and future trends," *Solid-State Electronics*, vol. 47, pp. 1881–1895, 2011.

[17] ATLAS User's Manual, SILVACO International, CA, USA, 2016.

[18] G. Iannaccone, G. Curatola, and G. Fiori, "Effective Bohm Quantum Potential for device simulators based on drift-diffusion and energy transport," *Simul. Semicond. Process Devices*, vol. 1, pp. 275-278, 2004.

[19] B. Kumar and R. Chaujar, "TCAD temperature analysis of gate stack gate all around (GS-GAA) FinFET for improved RF and wireless performance," *Silicon*, vol. 13, pp. 3741–3753, 2021.

[20] P. D. Ye, G. D. Wilk, J. Kwo, B. Yang, H.-J. L. Gossmann, M. Frei, S. N. G. Chu, J. P. Mannaerts, M. Sergent, M. Hong, K. K. Ng, and J. Bude, "GaAs MOSFET with oxide gate dielectric grown by atomic layer deposition," *IEEE Electron Device Lett.*, vol. 24, no. 4, pp. 209–211, 2003.

[21] B. Kumar and R. Chaujar, "Numerical simulation of analog metrics and parasitic capacitances of GaAs GS-GAA FinFET for ULSI switching applications," *Eur. Phys. J. Plus*, vol. 137, pp. 110, 2022.

[22] N. Gupta and R. Chaujar, "Influence of gate metal engineering on small-signal and noise behaviour of silicon nanowire MOSFET for low-noise amplifiers," *Appl. Phys. A*, vol. 122, pp. 1-9, 2016.

[23] A. Kumar, N. Gupta, and R. Chaujar, "TCAD RF performance investigation of transparent gate recessed channel MOSFET," *Microelectronics J.*, vol. 49, pp. 36-42, 2016.

[24] R. Saha, R. Goswami, B. Bhowmick, and S. Baishya, "Dependence of RF/analog and linearity figure of merits on temperature in ferroelectric FinFET: a simulation study," *IEEE Transactions on Ultrasonics, Ferroelectrics, and Frequency Control*, vol. 67, no. 11, pp. 2433-2439, 2020.

[25] Y. Pathak, B. D. Malhotra, and R. Chaujar, "Analog/RF Performance and Effect of Temperature on Ferroelectric Layer Improved FET device with Spacer," *Silicon*, 2022.

Authorized licensed use limited to: DELHI TECHNICAL UNIV. Downloaded on January 17,2023 at 05:01:31 UTC from IEEE Xplore. Restrictions apply.

Computers and Electrical Engineering 106 (2023) 108585

Contents lists available at ScienceDirect

Computers and Electrical Engineering

journal homepage: www.elsevier.com/locate/compeleceng

Secured healthcare monitoring for remote patient using energy-efficient IoT sensors☆

Bhaskar Kapoor [a,*], Bharti Nagpal [b], Meshal Alharbi [c]

[a] AIACT&R, Guru Gobind Singh Indraprastha University, Delhi, India
[b] NSUT (East Campus) (Formerly AIACT&R), Delhi, India
[c] Department of Computer Science, College of Computer Engineering and Sciences, Prince Sattam Bin Abdulaziz University, P.O. Box 151, Alkharj 11942, Saudi Arabia

ARTICLE INFO

Keywords:
Internet of Things
Cloud computing
Security
Clustering
Nature inspired algorithm
Fog devices

ABSTRACT

The Internet of Things (IoT) and cloud computing are found to be effective in providing on-time medical support for patients by storing and accessing their clinical data on servers. There are some issues, such as communication delay, security, and energy loss in IoT sensors, that affect the quality of the service. In this research, a remote patient monitoring system using energy-efficient IoT sensors is proposed to meet security demands. The optimization of network clustering and cluster head selection is performed based on trust, inter- and intra-cluster distance, and energy level by the proposed SS-ROW algorithm, which is formulated by integrating the characteristics of the squirrel and sparrow with Ciphertext Key 2 Policy (CK2P) encryption on data. Further, an effective trust mechanism based on CP-ABE (Ciphertext-Policy Attribute-Based Encryption) and KP-ABE (Key-Policy Attribute-Based Encryption) is established to attain better results in terms of the number of alive nodes, energy left, and throughput.

1. Introduction

The Internet of Things (IoT) is crucial in transforming the transportation sector into IoT-enabled transportation, the ordinary city into a smart city, and hospital administration into an e-healthcare-based system. Because IoT technology can monitor the condition of patients in remote areas in real time, the earliest preventive measures are possible [1]. During the last few decades, the most interesting and trending technology has been IoT healthcare, which is incorporated with the cloud computing programme. The patient's data is updated in the cloud that is related to the IoT-dependant medical sensor for future analysis and computation. The most progressive methods for maintaining the patient's life are Internet and cloud computing, sensor networks, and sensing. It provides accurate healthcare in remote areas using IoT-based systems, with data collected being uploaded to a cloud server. Therefore, there is a requirement for an IoT-based health monitoring system for high blood pressure and phycological disorders, i.e., seizures, in order to provide health services in remote areas in real time. When cloud computing and the Internet of Things are interconnected, the performance in monitoring patients can be very efficient even in remote areas, which tends to provide persistent health data to physicians and caregivers. Carrying the cloud with IoT technology improves performance in terms of storage, high resource utilization, computational ability, and energy [2].

☆ This paper is for special section VSI-siot. Reviews were processed by Guest Editor Dr. Deepak Gupta and recommended for publication.

* Corresponding author: AIACT&R, Guru Gobind Singh Indraprastha University, Delhi, India.
E-mail addresses: bhaskerkapoor@mait.ac.in (B. Kapoor), bharti.nagpal@nsut.ac.in (B. Nagpal), mg.alharbi@psau.edu.sa (M. Alharbi).

https://doi.org/10.1016/j.compeleceng.2023.108585
Received 29 October 2022; Received in revised form 4 January 2023; Accepted 5 January 2023
Available online 20 January 2023
0045-7906/© 2023 Elsevier Ltd. All rights reserved.

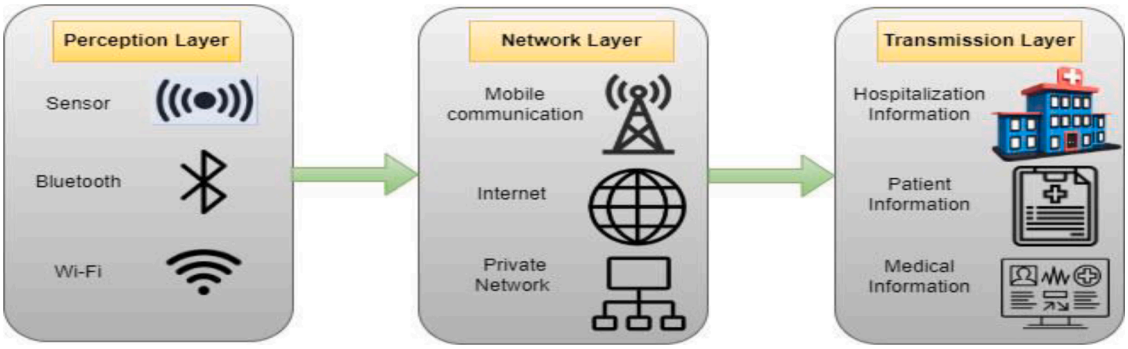

Fig. 1. IoT technology in the medical industry.

Energy efficiency is one of the most significant characteristics for IoT healthcare. The accuracy of the diagnosis of disease is reduced by the insufficient energy in the sensor node, which may lead to an interruption in the service. The depletion of energy is high due to the loss of energy in the data transmission between the IoT devices and the cloud server. The powered nodes in batteries are interfaced with sensors, transceivers, and microcontrollers that are involved in the wearable devices of the IoT. The energy efficiency of fog-based and other techniques is greatly improved; additionally, they tend to preserve the interlink between the smart gateway and sensor node. The IoT devices, which are grouped together as a cluster, monitor the healthcare data, and the appropriate channel is selected for transferring the data to the IoT devices' cloud server via the Fog gadget. The use of IoT technology in the medical profession enables the digital administration of medical data, allowing medical staff to devote more time to patients in order to deliver better medical care. It adheres to the standard 3-tier IoT application architecture. The IoT's architecture for the medical industry is shown in Fig. 1.

i) *Perception layer*: It uses a variety of signal acquisition techniques and multiple types of sensors, including physical signal sensors, physiological signal sensors, and chemical sensors, to transmit all network participants' information. Short-range data transmission technologies like ZigBee, Wi-Fi, Bluetooth, etc. are used by the data access sublayer to connect the data gathered by the data acquisition sublayer to the network layer. *ii) Network layer*: The network transmission and service layer make up the network layer, which is the backbone of the IoT. It uses the mobile communication network, the Internet, and other specialised networks to convey the data information obtained by the perception layer in a real-time, accurate, dependable, and barrier-free manner. *iii) Transmission layer*: The medical information application and the medical information decision-making application are the two levels that make up the transmission layer, also known as the application layer. Applications for managing medical information include managing patient information, inpatient and outpatient treatment information management, etc. Applications of medical information decision-making include analysing patient information, disease information, pharmaceutical information, diagnosis and therapy information, and others.

The processes of computation and processing are the major difficulties faced by the conventional health care industry, whereas security, privacy, insufficient physical storage, and error are some of the intrinsic difficulties. The fog device ensures security by encrypting data at the sensor node before implementing decryption and processing via fog-based smart gateways. Securing data during transmission is a vital process, which can be done by adding a Secure Socket Layer to the channel to ensure privacy and security. The patient's health record is protected by the cloud server, and its cost is much less expensive than the need for storage capacity in the server and the equipment materials [3]. The advantages of the cloud server, such as security, flexibility, and scalability, provide a motive to develop the IoT-cloud-based patient monitoring system with an enhanced encryption algorithm for fast and secure clinical data transmission. The main novelty of the research lies in the proposed Cipher Text Key 2 Policy (CK2P) encryption scheme and SS-ROW cluster optimization, which provides secure and fast clinical data transactions on hospital servers. Furthermore, a new secured storage algorithm is being developed to ensure security and overcome cloud-based challenges.

The goal of this study is to design and develop a disease diagnosis strategy for patients in remote locations. Patients in remote areas are thus monitored using smart units known as IoT sensors, which collect patient health information in the form of medical images and signals. This health care information is communicated to the base station through the IoT cluster head. In order to ensure the effective communication of the data with the base station, the network clustering is using the optimization approach, which engages in clustering the network based on the trust factor, distance, inter- and intra-cluster distance, and energy level of the IoT sensor nodes. The optimization for the network clustering is done based on the SS-ROW optimization algorithm. The collected data is stored on the hospital server or in the cloud, from which the diagnoses are suggested to the patients. Further, the patient data is sensitive and should be protected from outsiders. Hence, an effective trust mechanism called Cipher Text Key 2 Policy (CK2P) is incorporated at the data collection and storage end. The encryption schemes are employed for data protection at the collection and storage ends, which allow access only to the authorised doctors, who suggest a decision based on the collected patient data. The main contributions of the research are as follows:

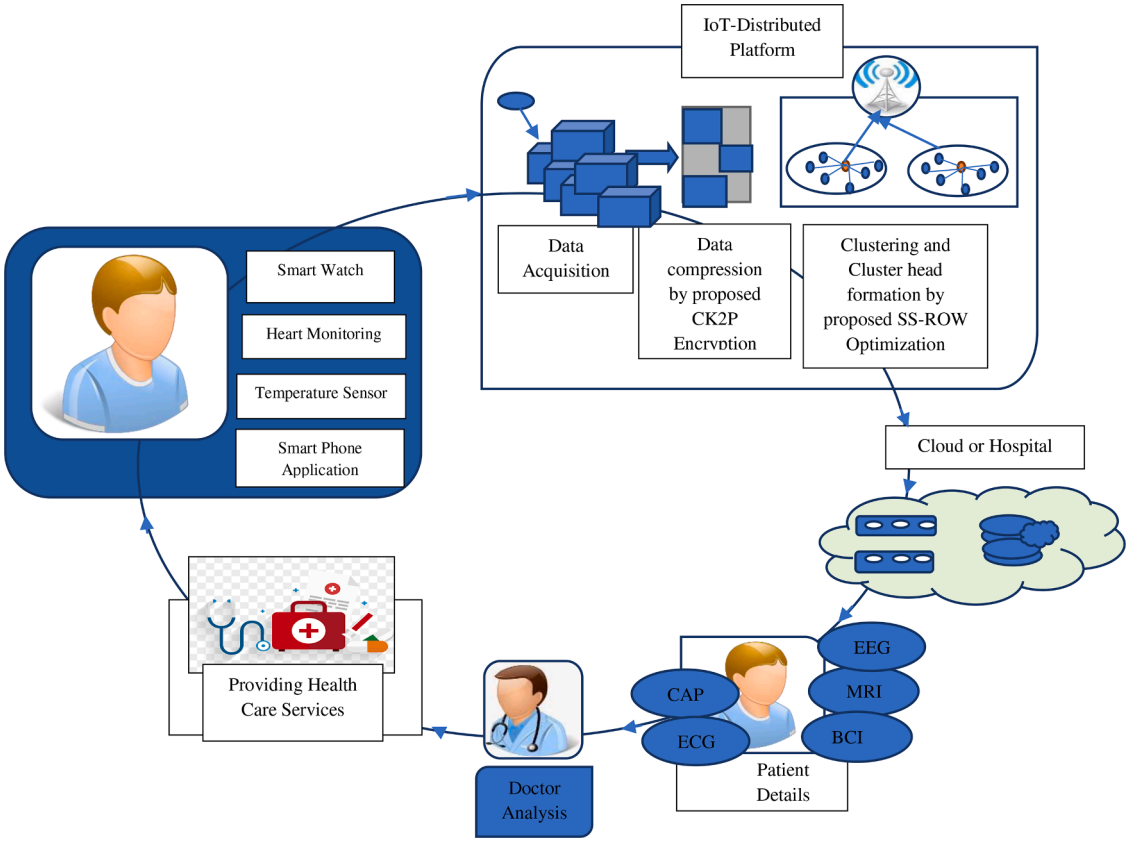

Fig. 2. Diagrammatic representation of the proposed methodology.

- The proposed SS-ROW algorithm is a biologically inspired algorithm that is developed by integrating the foraging characteristics of squirrels and the competing characteristics of sparrows.
- Through SS-ROW optimization-based cluster formation, large data sets are broken up into many subsets. This cuts down on the time it takes to process the data.
- SS-ROW optimisation is used to choose the cluster head so that data can be sent quickly and safely.
- The proposed CK2P encryption scheme is used for data compression to establish secure communication.

The manuscript is organised as follows: the literature review with the need for The remote patient monitoring model is enumerated in Section 2. The proposed remote patient monitoring model is described in Section 3. The mathematical design of the new biologically inspired SS-ROW optimization algorithm is explained in Section 4. The preliminary and comparative result analyses are explained in Section 5. Finally, the manuscript is concluded in Section 6.

2. Related works

In this section, the most common techniques for monitoring patients in remote areas via IoT devices are reviewed, along with their benefits and limitations. The challenges faced by the various researchers are also discussed in this section.

2.1. Literature review

The review of the conventional methods related to secure data transfer is revealed in this section. Anuradha et al. [4] applied both IoT and cloud computing to the prediction of cancer disease. The data related to cancer patients were collected and processed in the IoT which is encrypted by the developed Advanced Encryption Standards (AES) algorithm. Raj [5] presented an effective method for monitoring ECG signals, and the features are extracted by the fast Fourier transform-dependant Discrete Wavelet Transform (DWT). In terms of higher-order filter length, the difficulties involved in mathematical operation computations are minimized. Sood and Mahajan et al. [6] introduced an IoT-Fog-dependant healthcare monitoring scheme for continuous analysis and to predict the blood pressure data related to hypertension patients. The main aim is to consistently update the status of the blood pressure level variations on their respective mobile phones. Nguyen Gia et al. [7] presented a fog-based system for health monitoring in remote areas with accurate prediction and that is more energy efficient. The accuracy is greatly improved, even though they continuously monitor the different

types of signals. Bharathi et al. [8] used an energy-efficient clustering technique named as Particle Swarm Optimization for selecting the suitable cluster heads from various IoT devices. The sensed data is transmitted to the cloud server, where the disease can be diagnosed based on the illness and produce an alert signal. Kumar et al. [9] employed IoT and cloud-based mobile healthcare techniques for observing and diagnosing diabetes diseases. For continuous monitoring and analysing the severity of disease, a fuzzy rule-based neural classifier is utilized. Singh and Malhotra [10] presented an early and automatic detection of epileptic seizure disease using cloud computing and machine learning methods. By utilising a random forest algorithm with Higher Order Statistics (HOS) features, the model is adaptable for real-time monitoring with high accuracy. Amudha and Murali [11] developed a renovated WORN-DEAR algorithm in terms of Body Area Networks (BAN)-IoT networks for obtaining better energy efficiency with the basic principle of deep learning. It is well suited for emergency situations in remote healthcare monitoring systems. Ramesh et al. [12] developed a model for calculating risk prediction for diabetic patients using SVM and a 10-fold cross validation method with 83.20% accuracy that can be used with wireless technologies, and the remote monitoring device can become one of the most cutting-edge technologies. Nancy et al. [13] proposed a smart heart disease prediction system based on Bi-LSTM that collects electronic clinical data from IoT devices and stores it in the cloud for predictive analysis, with a 98.86% accuracy. Muneer and Raza [14] coupled cloud computing and IoT, which tend to give doctors and carers persistent health data, and found that the performance is highly effective in monitoring patients even in remote places. Ahmed and Kannan [15] proposed a secure RFID-based end-to-end authentication system with high privacy protection that employs a smart wearable sensor smart watch to detect falls, blood pressure, and heart rate. Akram et al. [16] created innovative methods for asset management, remote monitoring, autonomous assistive solutions, medication delivery, early warning systems, proactive treatment plans, and equipment maintenance. Karunarathne et al. [17] find that the Internet of Things, which enables machines and items to connect and communicate with one another in the presence of the Internet, is a new industry that is expanding with the aid of the Internet.

3. Proposed patient monitoring using energy-efficient IoT sensors

This section provides a detailed description of the steps involved in the patient monitoring system, and Fig. 2 depicts the proposed patient monitoring system. Most of the people are suffering from deadly diseases such as brain and heart disease, which require immediate health care assistance. On-time monitoring of the patients is a crucial factor that enhances their life expectancy by rendering on-time medical service.

In such cases, the patients in the remote area are monitored using smart units known as IoT sensors, which collect the information of the patient in the form of signals and medical images, such as EEG, ECG, MRI, and other medical data. The physiological data collected from the patients through wearable IoT devices, such as smart watches, smart phones, and electrodes, is encrypted by the proposed CK2P encryption scheme, which is an effective trust mechanism based on Cipher text-Policy Attribute-Based Encryption (CP-ABE) and Key-Policy Attribute-Based Encryption (KP-ABE). The encrypted data is transmitted to hospital server through the IoT cluster head, which is formed by proposed SS-ROW optimization. Finally, the cluster head formed by the SS-ROW will be engaged in the communication of the collected patient data with the base station or the hospital server. The physician thus obtains the clinical information, such as EEG, ECG, MRI, BCI, and CAP, that enables them to provide appropriate health care services to the patient. The encryption schemes are employed for data protection at the collection and storage ends, which provide access only to the authorised doctors, who suggest a decision on the collected patient data.

3.1. Distributed platform

The IoT platform enables the continuous monitoring of the patients with the help of sensors, which have the ability to estimate physiological signals such as electroencephalograms (EEG), heart rates, electrocardiograms (ECG), and electromyograms (EMG). The aforementioned health care data related to the heart and brain are gathered from the patients, and these data are transmitted to the base station through the cluster heads at a regular interval. The indicators, which resemble the health care condition of the patient, are quickly transmitted to the hospital server (the cloud). By using the data, the health care assistants evaluate the patient's condition and provide on-time healthcare services without any delay. Let us assume that there are n number of patients in the remote monitoring network as represented as,

$$P = \{P_1, P_2, \ldots..P_i, \ldots...P_n\} \tag{1}$$

Patient monitoring is performed through the incorporation of IoT sensors in the patients. The patient data are collected by the IoT sensors and the data generated is given as,$D = \{D_1,D_2,\ldots..D_i\ldots..D_n\}$(2)

The data records Dincluded EEG [18], ECG [19], MRI [20], BCI (Brain Computer interface) [21] and CAP [22]. The data is compressed and transmitted to the hospital server based on the proposed Ciphertext Key 2 Policy (CK2P) approach developed by combining KP-ABE and CP-ABE.

3.2. Data compression using proposed encryption scheme

The data compression is the crucial task to be performed after the data collection, in order to minimize the utilization of the storage size, maximize the access speed. The data compression further enhances the transmission capacity and minimises the bandwidth requirement. The data is compressed without losing important information. In this research, the data compression is carried out using

the proposed CK2P encryption scheme. In the proposed CK2P encryption scheme, the cipher text is related to the access framework over the subsets of the *n*elements in the space of elements. The decryption process works if the element set *Es* is related to the security key legitimated in the access frameworkA. The key to policy-based encryption is the access framework, and the attributes perform dual functions. Let the element space is denoted as ξ and the collection of the access framework is denoted asΛf overξ, such that$\Lambda f \in$ A. The subsets ofB$\subset\xi$, in which $|B| \leq n$and the minimal set *Es*of Asatisfies that*Es*⊂B. The Ciphertext policy for $\Lambda f$is the functional encryption of $\rho^{ct} : 2^{\xi} \times A \rightarrow \{0,1\}$ that is determined by $\rho^{ct}(Es,\Lambda f) = 1$if $Es \in \Lambda f$(for $Es \subseteq \xi$and$\Lambda f \in$ A). The description consists of the elements universe ξ and bound*n*, whereas $\sum_{K}^{ct} = 2^{\xi}$and$\sum_{encrypt}^{ct} =$ A. The key policy of Aover ξis the functional encryption for $\rho^{ct} : A \times \binom{\xi}{< n} \rightarrow \{0,1\}$ and it is defined as$\rho^{ct}(\Lambda f,Es) = 1$. The description consists of the elements universe ξ and bound*n*, whereas $\sum_{K}^{kpol} =$ Aand$\sum_{encrypt}^{ct} = \binom{\xi}{< n}$. In the CK2P encryption scheme, the ciphertext and the key policies are integrated, and the description consists of the elements universe ξ and bound*n*, whereas $\sum_{K}^{ck2p} = 2^{\xi}$Aand$\sum_{encrypt}^{ck2p} = \left(A.\binom{\xi}{< n}\right)$.

3.3. Secured data storage in hospital web server

The data of the patients is stored in the cloud storage framework, which enables the users, whether they are doctors or patients, to store and access the medical data from anywhere and at any time. The accessibility of the data increases its convenience for the users. Yet, the patients are more concerned about the security and privacy of the data because it contains more sensitive information. The user data is categorised into two main parts, such as the private data and the shared part of the data. The users can store their sensitive or private data in the private data part, which is only accessible by the users themselves, and they can share it with numerous authenticated users through the shared data part. The operation performed by the users is described as follows:

1) *Authentication of users to hospital authorities:* Users must authenticate to the Healthcare Assistant (HCA) and register for the patient token, which the hospital authority provides in the cloud interface. The public key of the registered or enrolled users is provided in the token list.
2) *Authentication of the user to the cloud interface:* After obtaining the patient token from hospital authorities, the user can utilise his password or his identity to login to the cloud interface. The cloud validates the patient token with respect to the token list created by hospital authorities, and then the user can provide two parts of the cloud service.
3) *Operations in the Private Data Section:* In the Private Data Section, the user needs to encrypt their confidential data at the customer's side using the proposed encryption algorithm. The information is uploaded to the private data section of the hospital server. When the consumer or the doctors needs the data, he/she has to download the data and need to decrypt the data with the aid of the session key.
4) *Operations in the shared data section:* In the shared data section, the users first need to store the data, which then needs to be shared with authenticated users. The data that needs to be shared is first encrypted with the section key, and the section key is further encrypted with the private key of the key pair. It is then certificated with HCA, which is an upload key management order type of base64-encoded.

After the encryption process, the user needs to upload the concatenation of the encryption included in the two sections, which is shared with the hospital server. The authenticated user validates the public key of users, who upload the data from the certificate list and utilise the public key to decrypt the session key encrypted by the uploader. The session key is now utilised to decrypt the data that is encrypted by the data provider. For both the shared and private data sections, the user encrypts their data using the proposed encryption algorithm with distinct session keys. In the shared data section, the data provider encrypts the session key utilising the proposed encryption algorithm to obtain the private key. The users can control all the operations with the help of the hospital server and the HCA through the proposed encryption algorithm. This data storage framework allows users to not only access and store their data, but also securely share it with other multi-authenticated users. In the proposed data storage framework, the user is initially authenticated to HCA so as to establish that the user consists of authentic private data in accordance with a public key. If the certificate is provided by the HCA, then mutual authentication between the user and the cloud provider is established.

Step-1 sending request message to HCA: The users use the new optimization algorithm to create the key pair which consists of the public key $Pu_k$and private keyPr_k. The user can generate the request message by concatenating the public key and the user identity. This request message is now being transmitted to HCA.

Step-2: Validation of user identity by HCA and transmission of the request to the user: After obtaining the request message, the HCA obtains the identity of the user and also obtains the public key of the user, who sent the request. The HCA now confirms that the user generated the private key in correspondence with the public key.

Step-3 User authentication to HCA: The HCA decrypts the message and compares it with the hash function; if both are found to be equivalent, then the user is authenticated with the HCA.

Step-4: Sending the Acknowledgement Message: The HCA now sends the acknowledgement to the user and generates the public key certificates.

Step-5: Certificate distribution: After the authentication of the user and the HCA, the certificate is published in a directory and sends the URL of the certificates to its servers. The authenticated users validate the certificate from the hospital server.

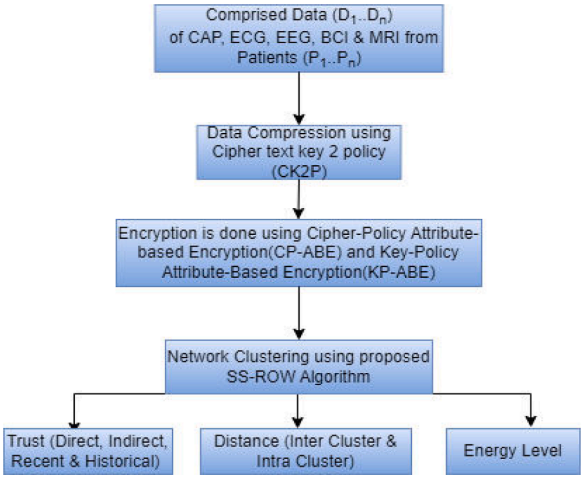

Fig. 3. Network clustering in the SS-ROW optimisation algorithm based on objectives.

3.4. Network clustering using the proposed SS-row algorithm

The cluster is a significant component in the unsupervised learning task because it reduces the processing time by grouping the data instance into numerous subsets. The main objective is to divide the entire clinical data into different subsets, in which the elements present in each subset are similar to each other and different subsets are dissimilar to each other. The clustering is established based on the objectives, such as trust, inter- and intra-cluster distance, distance, and energy level. Fig. 3 represents the block diagram of network clustering in the SS-ROW optimisation algorithm based on objectives.

1) ***Trust:*** This research concentrates on evaluating the feasible solutions to estimate the available data requirement by the quality of the clinical data. Hence, the trust-aware clustering scheme is utilised to enhance the security of the clinical data. A brief description of the trust *T*utilised in this research, such as direct trust, indirect trust, recent trust and historical trust, is given below.

a) ***Direct Trust:*** Direct Trust, which is also called "local trust," determines the part of the agent calculated from its own experience about the target representative. Let us assume $Td^t_N(a_1, a_2)$ determines the direct trust, in which the representative$a_1$has on the representative $a_2$within N transaction within time interval *t*.The satisfaction measure is utilised to determine the direct trust, and it is defined as follows:

$$Td^t_N(a_1, a_2) = sat^t_N(a_{1,}a_2) \tag{3}$$

The representative's own experience is used to estimate satisfaction, which is then used as local trust. If the representative $a_2$provides better services then the $a_1$rate it with high satisfaction value. Hence, $a_2$attains high level of local trust in the perspective of agenta_2.

b) ***Indirect trust:*** The indirect trust is also called the recommendation, is estimated from the experience gained by the other representatives. The representative requests the other agents so as to provide recommendations about the target representative. The estimating representative then accumulates the recommendations from the other representatives along with the feedback credibility of the recommender. Let us assume that $TI^t_N(a_1, a_2)$ denotes the indirect trust that the representative $a_1$estimates ona_2.

$$TI^t_N(a_1, a_2) = \begin{cases} \dfrac{\sum\limits_{x \in SR-\{a_1\}} FC^t_N(a_1, x) \times Td^t_N(x, a_2)'}{\sum\limits_{x \in SR-\{a_1\}} FC^t_N(a_1, x)} \\ 0, \ |SR - \{a_1\}| \geq 0. \end{cases} \tag{4}$$

In the above equation, it is demonstrated that the indirect trust is estimated as the weighted average of the recommendations obtained from the various recommenders, where the weights denote the feedback credibility of the recommenders. Where *SR* denotes the set of representative, who interacted with the representative a_1 and FC^t_N represents the feedback credibility.

c) ***Recent Trust:*** The recent trust is utilised to reflect the recent behaviour, and it is characterised as a weighted amalgamation of indirect and direct trust. Direct trust obtains higher weights as the analysing representatives perform more interfaces with the target representative. The analyser has more confidence in its own experience than it does in the recommendations from the other targets. Let us consider $TR_N^t(a_1, a_2)$ as the recent trust, and which is mathematically represented as,

$$TR_N^t(a_1, a_2) = W \times Td_N^t(a_1, a_2) + (1 - W) \times TI_N^t(a_1, a_2) \tag{5}$$

where, Wdenotes the weight of the direct trust and it is estimated from the following equation

$$W = \frac{IN^t(a_1, a_2)}{IN^t(a_1, a_2) + \mu^t(a_1, a_2)} \tag{6}$$

$$\mu^t(a_1, a_2) = \frac{\sum_{x \in SR - \{a_1\}} FC_N^t(a_1, x) \times IN^t(x, a_2)}{|SR - \{a_1\}|} \tag{7}$$

Where SRdenotes the set of representatives, who is ever interacted with the agent a_2 and $IN^t(x, a_2)$ denotes the number of interactions representative $a_1$conducted with the representative a_2 at t^{th} interval. The mean of iterations conducted by the other representatives on a_2 is indicated by $\mu^t(a_1, a_2)$. The iteration count $IN^t$is weighted with feedback credibility FC of the recommenders in evaluating $\mu^t(a_1, a_2)$. It is shown that the $IN^t(a_1, a_2)$increases with respect to $\mu^t(a_1, a_2)$, in which the value of Walso increases. It signifies that the analyser is more experienced and depends on its own judgement.

d) ***Historical Trust:*** The historical trust is developed from previous experiences, and the historical trust considers the behavioural pattern over the long term. The historical trust is determined by utilising the exponential averaging update function. The storage overhead related in storing the former recent trusts is significantly reduced by utilizing exponential averaging update function. Let us assume, $TH_N^t(a_1, a_2)$ as the historical trust that the representative a_1 consists about a_2.

$$TH_N^t(a_1, a_2) = \frac{fr \times TH_N^t(a_1, a_2) + TR_{N-1}^t(a_1, a_2)}{2} \tag{8}$$

Where fr denotes the forgetting factor. For the representative to be characterised as good, the representative has to act in a collaborative manner for a huge number of transactions. Hence, the recent trends are replaced with the historical trend.

These trusts are combined by the fusion parameter αas per the following equation:

$$T_N^t = \alpha * dT_N^t + \alpha(1-\alpha)IT_N^t + \alpha(1-\alpha)(1-\beta)TR_N^t + \alpha(1-\alpha)\beta(1-\beta)TH_N^t \tag{9}$$

2) ***Distance:*** The distance is the main function utilized in clustering so as to determine similarity between the two data. If the distance between the two data points is higher, then the data should be kept in a different cluster; otherwise, it should be kept within the cluster. The Euclidean distance is commonly utilised for distance estimation. The mathematical model of the Euclidean distance is given as

$$D_N^t = \sqrt{\sum_{j=1}^{N} \left(a_j - a_{j-1}\right)^2} \tag{10}$$

Here a_j and $a_{j\ -\ 1}$denotes the two consecutive frames and Nrepresents the total number of frame.

1) Inter cluster distance: The inter-cluster distance DI_N^t measure is defined as the measurements of distance between all the pairs of the centroid of different cluster.
2) Intra cluster distance: The intra-cluster distance Da_N^t is the distance between the members of the cluster, and the intra-cluster distance will be minimised as compared to inter-cluster distance.
3) Energy level: The energy level E_N^t is also considered an objective function for cluster formation. Hence, these objectives are considered for cluster formation, and the multi-objective function is mathematically represented as,

$$MF = \alpha \times T_N^t + \beta \times D_N^t + \chi \times DI_N^t + \delta Da_N^t + \varepsilon E_N^t \tag{11}$$

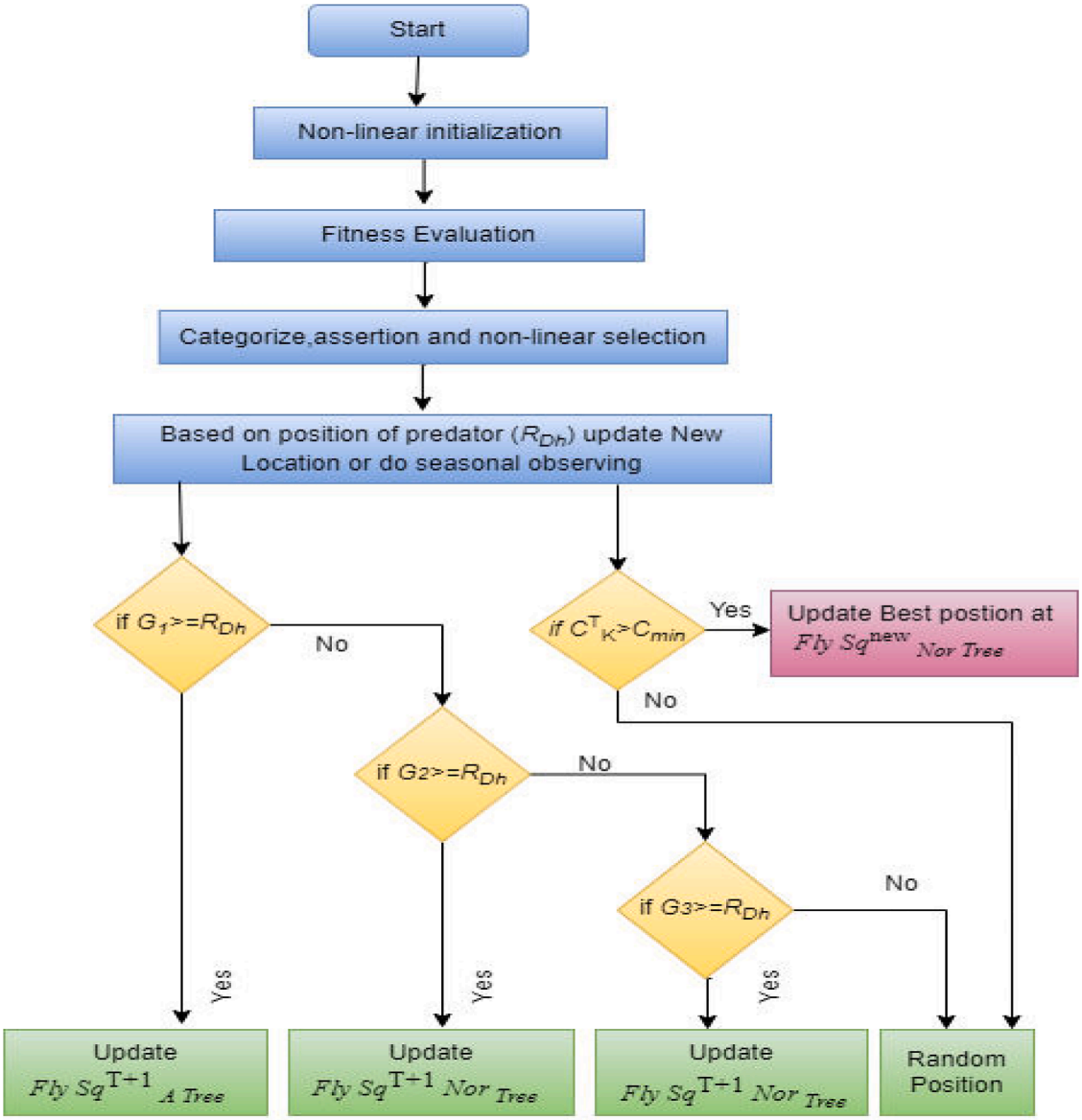

Fig. 4. The Procedure of the SS-ROW Optimization Method.

where, α,β, χ, δ and ε are the fusion parameters, which is evaluated by proposed SS-ROW optimization algorithm. Thus, the cluster head selection is established in the wireless communication network to ensure a fast and safe channel for data communication. Further, the data transfer through the cluster heads minimises the energy consumption of the network. In this research the SS-ROW optimisation is utilised to select the cluster heads for every group of nodes that is facilitated using the clustering approach for which the multi-objective function is designed as per Eq. (11).

4. Proposed SS-row optimization-new biological inspired optimization algorithm

The proposed SS-ROW optimization holds the characteristics of Squirrels and Sparrows due to their intelligent foraging behaviour. The Squirrel Search Optimization involves the interesting fact that the flying squirrel prefers a "sliding" movement for locomotion without flying. Thus, the loss of energy is less, it is more efficient and it has the capability to forage a large area within a short time. The avoidance of hunting, the search for better food, and the foraging cost are the primary reasons for the evolution of sliding movements. Squirrel search possess some limitations depending on the variation in climate; in autumn, the availability of food sources is abundant, and it is eaten by the squirrel searches while the remaining food is collected to store in their own nests, in the ground, or in other

cavities. The demand for food is high during the winter; they prefer to eat the food at the site where it was found, but sometimes the foraging is difficult and the squirrels become less active due to the inadequate amount of food. The convergence speed is low and the convergence accuracy is low for the squirrel search method, which is overcome by the group foraging and anti-predating behaviour of sparrows.

4.1. Mathematical design of the proposed SS-row optimization

In the transient forest, a total of one flying squirrel is allowed to stay in one tree. They individually explore food, and the availability of their energetic food-searching behaviour makes the available food sources optimal. Food sources are typically found in three trees: the hickory tree, the oak tree, and the normal tree, with hickory nuts and acorn nuts. The best optimal solution is obtained by performing the initialization, evaluating fitness, performing the selection process, and updating the new location based on the flying squirrel position of the tree. The flow chart of the complete procedure of the SS-ROW optimization method is represented in Fig. 4.

i) *Non-linear initialization:* The flying squirrel with k number is initialised initially based on their location in the forest. The position of m^{th} flying squirrel is described by the vector and is determined by the given matrix as:

$$Fly\,Sq = \begin{bmatrix} Fly\,Sq_{1,1} & Fly\,Sq_{1,2} & \dots & \dots & Fly\,Sq_{1,D} \\ Fly\,Sq_{2,1} & Fly\,Sq_{2,2} & \dots & \dots & Fly\,Sq_{2,D} \\ \vdots & \vdots & \vdots & \vdots & \vdots \\ \vdots & \vdots & \vdots & \vdots & \vdots \\ Fly\,Sq_{k,1} & Fly\,Sq_{k,2} & \dots & \dots & Fly\,Sq_{k,D} \end{bmatrix} \tag{12}$$

where the n^{th} dimension of m^{th} flying squirrel is denoted as $FlySq_{m,n}$.

The initial position of the flying squirrel in the forest is allocated by uniform distribution as follows:

$$Fly\,Sq_m = Fly\,Sq_{low} + \mathrm{N}(0,1) \times \left(Fly\,Sq_{up} - Fly\,Sq_{low}\right) \tag{13}$$

where the flying squirrel $m$with n^{th}space dimension for upper and lower bounds are represented as $FlySq_{up}$ and $FlySq_{low}$. The random number is uniformly distributed $\mathrm{N}(0,1)$within the range of [0, 1].

ii) *Evaluating fitness:* The decision variable, which is the solution vector values, is involved in the user-defined fitness function for calculating the flying squirrel's best fittest position individually, and the related values are stored in the form of an array given in Eq. (14). The quality of the explored food source is depicted by the fitness value of the location of each flying squirrel. The flying squirrels that are in acorn trees are considered a normal food source, the hickory tree provides an optimal food source, and there is an absence of food in the normal tree.

$$F = \begin{bmatrix} F_1\left(\left[Fly\,Sq_{1,1} \;\; Fly\,Sq_{1,2}, \dots\dots, Fly\,Sq_{1,D}\right]\right) \\ F_2\left(\left[Fly\,Sq_{2,1} \;\; Fly\,Sq_{2,2}, \dots\dots, Fly\,Sq_{2,D}\right]\right) \\ \vdots \\ \vdots \\ F_k\left(\left[Fly\,Sq_{k,1} \;\; Fly\,Sq_{k,2}, \dots\dots, Fly\,Sq_{k,D}\right]\right) \end{bmatrix} \tag{14}$$

iii) *Categorize, assertion and non-linear selection: After classifying the individual flying squirrel position based on its fitness value, the array is arranged from low to high value. It is decided that the flying squirrel with a low fitness value will be placed in the hickory nut tree. The acorn nut trees are occupied by the next three finest value of flying squirrel, and it has the tendency to climb towards the hickory nut tree. The rest of the flying squirrel has a lower fitness value, and the next three finest are located on the normal trees. The fitness value is evaluated by the average of the metrics such as alive nodes, average energy, and throughput in the network. The flying squirrel's exploratory characteristics are influenced mainly by the presence of predators. Thus, the location renovation takes place by modelling the natural behaviour with respect to the position of the predator(R_{Dh}).*

iv) *New location update: During the energetic exploration of the flying squirrel, there is the occurrence of varying situations in three categories. In all three conditions, the flying squirrel slides and explores the food efficiently throughout the area to eat their favourite food in the absence of predators. It prefers to walk randomly in the presence of predators and hide in a safe location nearby. The energetic food seeking behaviour is depicted below.*

Illustration 1: The new updated position of the flying squirrel as it skates the hickory nut tree from the acorn nut trees $Fly\,Sq_{\mathrm{ATree}}$is obtained as follows:

$$Fly\,Sq_{\mathrm{ATree}}^{\mathrm{T}+1} = \begin{cases} Fly\,Sq_{\mathrm{ATree}}^{\mathrm{T}} + D_s \times S_{\mathrm{K}} \times \left(Fly\,Sq_{\mathrm{HTree}}^{\mathrm{T}} - Fly\,Sq_{\mathrm{ATree}}^{\mathrm{T}}\right) & G_1 \geq R_{Dh} \\ Random\,location \quad otherwise \end{cases} \tag{15}$$

Algorithm 1
Pseudocode of proposed SS-ROW Algorithm.

Input: $Flysq_{m,n}$; $(1 < m < U_n)$
Output: $Fly\,Sq^{new}_{NorTree}$
1: Set initial position of flying squirrel in the forest is allocated by uniform distribution using Eq. (13) as $Fly\,Sq_m = Fly\,Sq_{low} + \mathrm{N}(0,1) \times (Fly\,Sq_{up} - Fly\,Sq_{low})$
2: **Evaluating fitness:** Calculate the flying squirrel best fittest position using array (Eq. (14))
3: **Categorize, Assertion, Non-linear selection:** The fitness value is evaluated by the metrics such as alive nodes, average energy and throughput in the network.
4: **While**($F_m > F_B$)
5: Based on position of predator (R_{Dh})update new location.
6: *Illustration 1*: The new updated position of flying squirrel skate towards the hickory nut tree from the acorn nut trees $Fly\,Sq_{ATree}$are obtained as
7: **if** $G_1 \geq R_{Dh}$
8: $Fly\,Sq^{T+1}_{ATree} = Fly\,Sq^{T}_{ATree} + D_s \times S_K \times (Fly\,Sq^{T}_{HTree} - Fly\,Sq^{T}_{ATree})$
9: **else**
10: $Fly\,Sq^{T+1}_{ATree} = Random\,position$
11: **end**
12: *Illustration 2*: The new location of flying squirrel which may move from the normal trees to the acorn nut trees and it is obtained as
13: **if** $G_2 \geq R_{Dh}$
14: $Fly\,Sq^{T+1}_{NorTree} = Fly\,Sq^{T}_{NorTree} + D_s \times S_K \times (Fly\,Sq^{T}_{ATree} - Fly\,Sq^{T}_{NorTree})$
15: **else**
16: $Fly\,Sq^{T+1}_{NorTree} = Random\,position$
17: **end**
18: *Illustration 3*: The flying squirrel which are already consumed enough food move towards skate towards the hickory nut trees for storing food, the updated location is obtained as
19: **if** $G_3 \geq R_{Dh}$
20: $Fly\,Sq^{T+1}_{NorTree} = Fly\,Sq^{T}_{NorTree} + D_s \times S_K \times (Fly\,Sq^{T}_{HTree} - Fly\,Sq^{T}_{NorTree})$
21: **else**
22: $Fly\,Sq^{T+1}_{NorTree} = Random\,position$
23: **end**
24: *Seasonal observing condition:* The seasonal constant $C_K$is calculated and check
25: **if** $C^T_K < C_{min}$ then Repositioned randomly
26: **if** $C^T_K > C_{min}$ then Reposition at best position using
$Fly\,Sq^{new}_{NorTree} = Fly\,Sq_{low} + Y^{T+1}_{m,n} \times (Fly\,Sq_{upper} - Fly\,Sq_{low})$
27: **End while**

where the random sliding distance is denoted as D_s, the random number G_1 is assigned within the range of [0, 1], the position of the flying squirrel after reaching the hickory nut tree is$Fly\,Sq^{T}_{HTree}$and the current iteration is denoted as T. The exploration and exploitation are balanced by the sliding constantS_K.

Illustration 2: The new location of the flying squirrel, which may move from the normal trees to the acorn nut trees, is obtained as follows:

$$Fly\,Sq^{T+1}_{NorTree} = \begin{cases} Fly\,Sq^{T}_{NorTree} + D_s \times S_K \times \left(Fly\,Sq^{T}_{ATree} - Fly\,Sq^{T}_{NorTree}\right) & G_2 \geq R_{Dh} \\ Random\,location \qquad otherwise \end{cases} \tag{16}$$

The random number G_2 is in the range of [0, 1]

Illustration 3: The preservation and storage of food for consumption when there is a high demand is done in the third case, where the flying squirrels, who have already consumed enough food in the acorn nut trees, are skating towards the hickory nut trees from the normal tree, and the updated location is obtained as follows:

$$Fly\,Sq^{T+1}_{NorTree} = \begin{cases} Fly\,Sq^{T}_{NorTree} + D_s \times S_K \times \left(Fly\,Sq^{T}_{HTree} - Fly\,Sq^{T}_{NorTree}\right) & G_3 \geq R_{Dh} \\ Random\,location \qquad otherwise \end{cases} \tag{17}$$

where the random number G_3 within the range of [0, 1].

v) *Seasonal observing condition:* The flying squirrel locomotion is affected by varying weather conditions, and it causes the algorithm to get trapped in the local solutions. The seasonal constant C_K can be evaluated as follows:

$$C^T_K = \sqrt{\sum_{l=1}^{D} \left(Fly\,Sq^{T}_{ATree,l} - Fly\,Sq_{HTree,l}\right)^2} \tag{18}$$

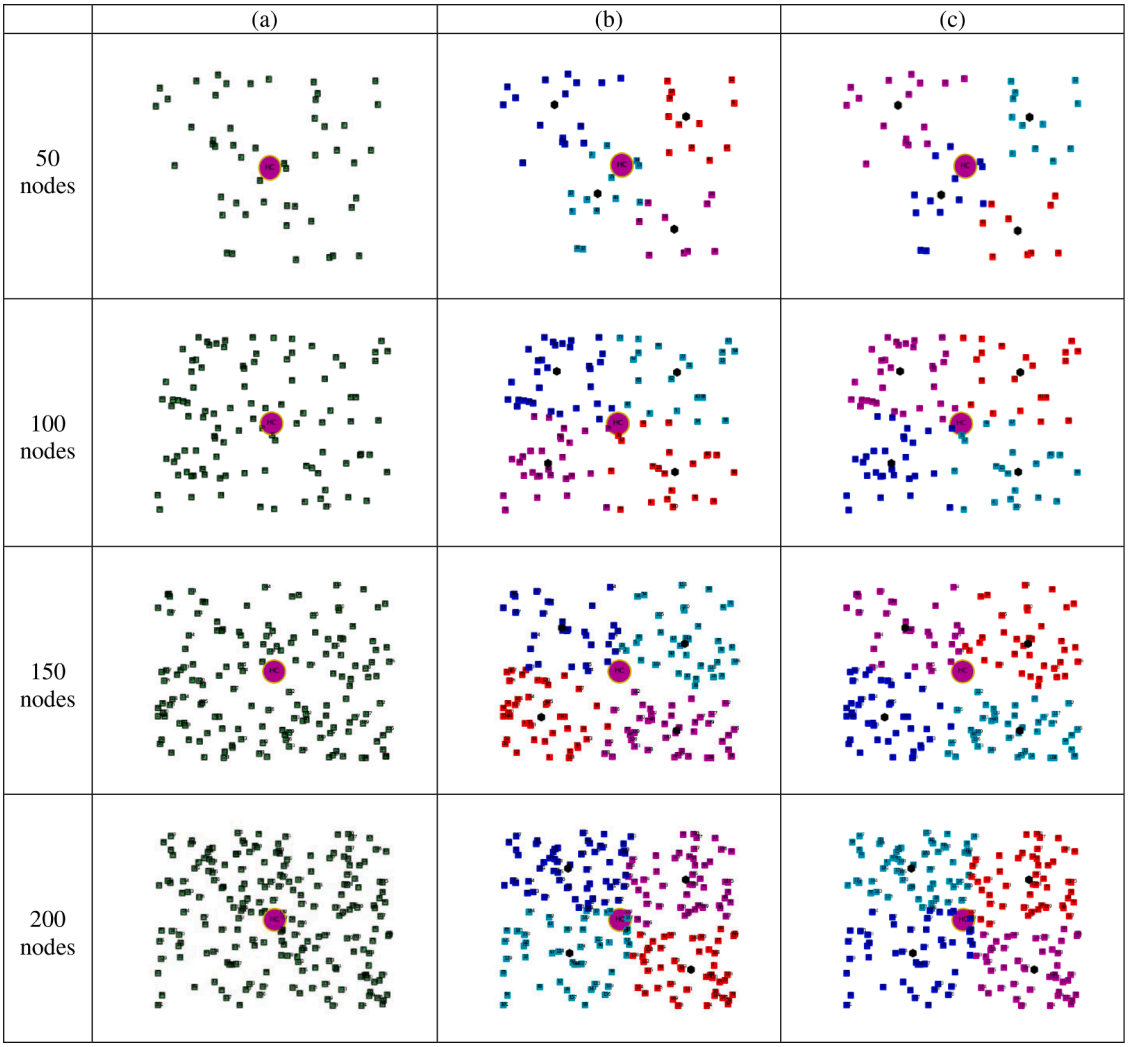

Fig. 5. Preliminary results of simulation area for various nodes.

where T = 1, 2, 3. The seasonal observing condition is evaluated as, $C_K^T < C_{min}$, where $C_{min}$is the seasonal constant minimum value, and it is estimated as,

$$C_{min} = \frac{10I^{-6}}{(365)^{T/(T_{max}/2.5)}} \tag{19}$$

where present and maximum iteration values are represented as T and T_{max}. If the value of $C_{min}$is large, it helps to develop the exploration phase, while the $C_{min}$is small it helps to improve the exploitation phase of the algorithm.

vi) *Random repositioning at the end of the winter season:* During the winter, flying squirrels do not search for food in the forest, but rather move in a different direction in search of a better food source. Thus, the random repositioning of the flying squirrel cage is enhanced by the excellent behaviour of sparrows, and it is modelled as,

$$Fly\,Sq_{NorTree}^{new} = Fly\,Sq_{low} + Y_{m,n}^{T+1} \times \left(Fly\,Sq_{upper} - Fly\,Sq_{low}\right) \tag{20}$$

If $F_m > F_B$,

$$Y_{m,n}^{T+1} = Y_{best}^{T} + \alpha.\left|Y_{m,n}^{T} - Y_{best}^{T}\right| \tag{21}$$

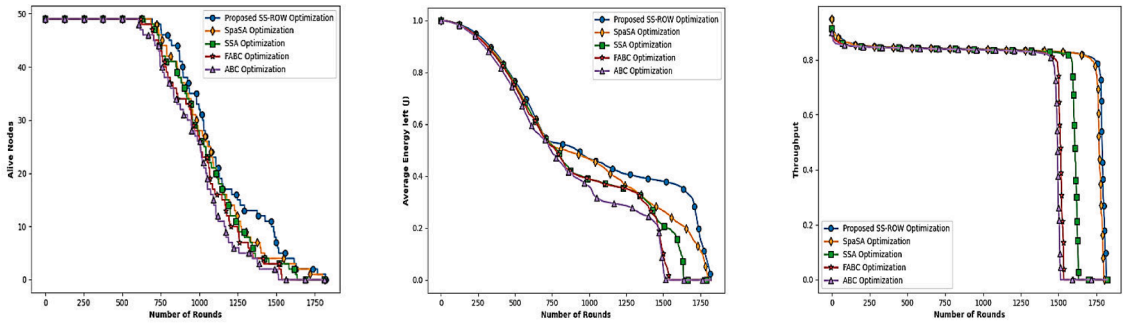

Fig. 6. Comparative analysis based on 50 nodes in terms of a) Alive Nodes b) Average energy left c) Throughput.

The global search for food resources is enhanced by the best solution obtained by the sparrow's exploration behaviour. This is done by choosing a place that is better than the last one and making sure that the area around it is safe for foraging. Y_{best} is the best possible current position, and the control parameter for the step size is denoted as α. The location is preferred mostly at the edge of the group, which may easily escape from the predator. They move forward to occupy the safe area when they satisfy the condition$F_m > F_B$. Thus, in the winter season, Eq. (20) represents the repositioning of the flying squirrel, which is done by the excellent foraging behaviour of sparrows with an awareness of predators, whereas the exploring characteristic of the flying squirrel is enhanced efficiently. The pseudocode for the proposed SS-ROW algorithm is described in Algorithm 1.

5. Results and discussion

In this section, the results and discussion of the proposed SS-ROW optimization to design and develop the monitoring system for disease diagnosis in remote locations are described. The efficiency of the proposed optimization is verified by considering the performance measures based on the number of a*live nodes,* which remain in the cluster after the transmission process at the last stage, *average energy,* which remains in each sensor node for the process of communication, and *throughput*, which is defined by the total amount of transferred packets reached at the receiver side with security. The proposed SS-ROW optimization mathematical expressions are tested in a MATLAB tool running in Windows 10 with 8GB RAM to reveal their real effectiveness.

5.1. Preliminary results

In the preliminary results section, the proposed SS-ROW optimization simulation results are enumerated. The performance of the proposed optimization with various nodes such as 50, 100, 150, and 200 is illustrated in Fig. 5.

The collected data are modified into varying cluster based on their affected diseases and again transmitted to the hospital cloud. Figure (a) represents the distribution of IoT nodes that gather the data from the patients in different locations. Figure (b) represents the cluster head formation, in which the four different clusters are denoted by four different colors. Figure (c) illustrates the transmission of data from the cluster head to the hospital server or the cloud.

5.3. Comparative methods

The developed SS-ROW optimization method is compared with the most existing four prevalent techniques, such as SpaSA optimization, Salp Swarm Algorithm (SSA) optimization [23], Fractional Artificial Bee Colony Algorithm (FABC) optimization [24], and Artificial Bee Colony (ABC) optimization [25].

5.4. Comparative analysis based on the proposed SS-row optimization

The network is simulated with the various nodes (such as 50, 100, 150 and 200 nodes) for analysing the performance of the proposed method. The efficiency of proposed method is revealed by considering the performance metrics based on the number of alive nodes, network energy, and throughput in the network cluster.

i) *Analysis based on 50 nodes*: The performance of the developed methods is initially done with 50 alive nodes. The proposed method shows better performance in the transmission process with a maximum number of active nodes of 8 up to the 698th round, as shown in Fig. 6(a). It has the maximum average energy of 0.3799 J until the completion of one round in the network shown in Fig. 6(b), and it has the maximum throughput of 0.8331 bps until the completion of one round in the network, which is revealed in Fig. 6(c). The high throughput reveals that the proposed SS-ROW model satisfies the security concerns, as the optimization algorithm clusters the nodes based on the trust factor.

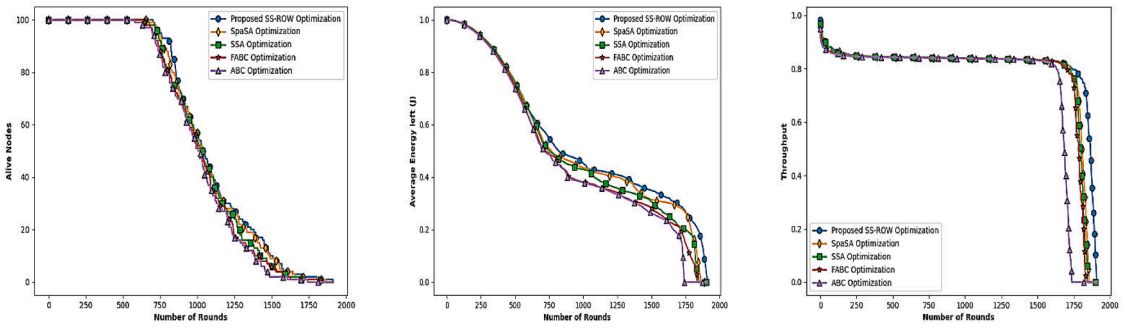

Fig. 7. Comparative analysis based on 100 nodes in terms of a) Alive Nodes b) Average energy left c) Throughput.

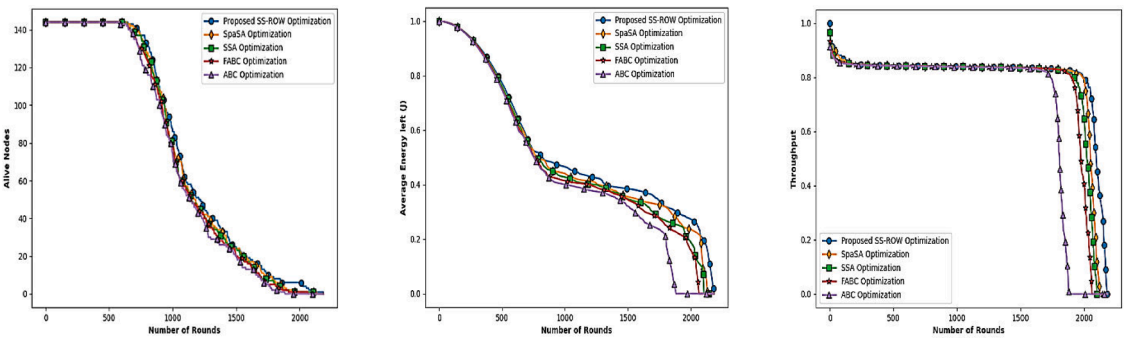

Fig. 8. Comparative analysis based on 150 nodes in terms of a) Alive Nodes b) Average energy left c) Throughput.

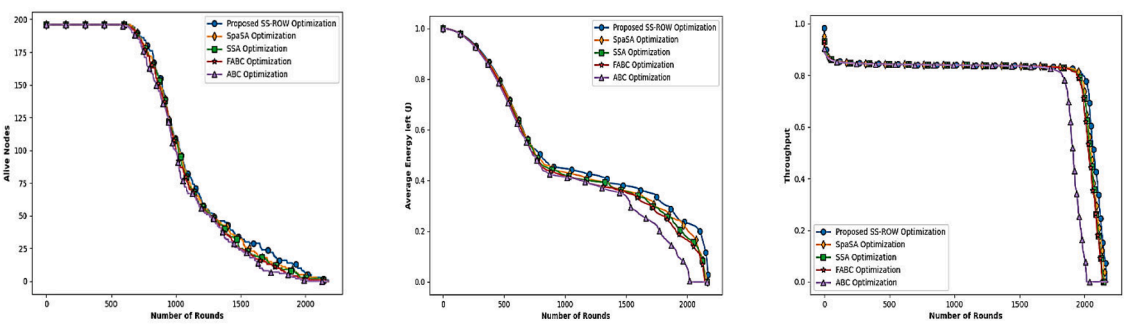

Fig. 9. Comparative analysis based on 200 nodes in terms of a) Alive Nodes b) Average energy left c) Throughput.

ii) *Analysis based on 100 nodes*: Subsequently, the performance of the developed methods is done with the 100 number of alive nodes. The proposed SS-ROW optimization exhibits the highest performance with maximum active nodes up to 10 at the 1510th round, as revealed in Fig. 7(a). Fig. 7(b) illustrates that the proposed method possesses the maximum average energy of 0.3502 J until the completion of the 1500th round. Fig. 7(c) reveals the productiveness of the proposed SS-ROW model in terms of throughput at 0.8349 bps till the completion of a round.

iii) *Analysis based on 150 nodes*: Further, the performance of the developed and prevalent methods is analysed by counting 150 alive nodes. Thus, the proposed optimization shows better performance in the transmission process with a maximum number of alive nodes of 25 up to the 1767th round, as revealed in Fig. 8(a).

The average network energy of the proposed SS-ROW optimization remains at 0.3851 J at the round of 1500 in the network, as shown in Fig. 8(b). The proposed method has a maximum throughput of 0.8374 bps until the completion of round 1400 in the network,

Table 1
Comparative discussion of the proposed method with the prevalent methods based on the alive nodes, average energy left, and the throughput with varying rounds.

Method	Alive nodes at 1500 rounds				Energy left at 1500 rounds				Throughput at 1400 rounds			
	With 50 nodes	With 100 nodes	With 150 nodes	With 200 nodes	With 50 nodes	With 100 nodes	With 150 nodes	With 200 nodes	With 50 nodes	With 100 nodes	With 150 nodes	With 200 nodes
SpaSA optimization	4	9	24	32	0.2657	0.3147	0.3557	0.3591	0.8329	0.8349	0.8371	0.8373
SSA optimization	3	7	24	25	0.2093	0.3077	0.3475	0.3567	0.8306	0.8345	0.8370	0.8370
FABC optimization	3	6	20	25	0.1022	0.2837	0.3457	0.3536	0.8265	0.8343	0.8369	0.8369
ABC optimization	2	2	20	24	0.0519	0.2629	0.3216	0.3383	0.8233	0.8338	0.8357	0.8364
Proposed SS-ROW optimization	**8**	**10**	**25**	**33**	**0.3799**	**0.3502**	**0.3851**	**0.3798**	**0.8331**	**0.8349**	**0.8374**	**0.8375**

as revealed in Fig. 8(c).

iv) *Analysis based on 200 nodes*: Finally, the developed and prevalent methods are tested with the 200 active nodes. Fig. 9(a) demonstrates that the proposed optimization provides better performance in the transmission process with a maximum number of active nodes of 33 up to the 1767th round. The proposed method has a maximum average energy of 0.3798 J until the completion of round 1500 in the network, as shown in Fig. 9(b). At round 1400, the maximum throughput of the proposed SS-ROW optimization is 0.8375 bps until the completion of the round in the network, as revealed in Fig. 9(c).

5.5. Comparative discussion

This research ensures smart monitoring through remote data access and the suggestion of the diagnostic steps, thereby ensuring secure data transfer. The performance analysis is done based on the remaining alive nodes, energy, and throughput for various rounds. Table 1 discusses the efficacy of the proposed smart system in terms of its performance measures.

6. Conclusion and future scope

IoT is found to be effective in remote patient monitoring when it is utilised with cloud computing technology. This research focuses on enhancing the e-healthcare system by incorporating both the IoT and cloud computing technologies. The clinical data of the patients are collected and processes in cloud server, in which the sensitive information of the patient are secured by the incorporation of trust mechanisms such, as CP-ABE (Ciphertext-Policy Attribute-Based Encryption) and KP-ABE (Key-Policy Attribute-Based Encryption). The network clustering is established by considering factors like trust, distance (inter-cluster distance and intra-cluster distance), and the energy level of sensor nodes. The optimization for the network clustering is carried out by the proposed SS-ROW optimization algorithm. The cluster head is selected using the SS-ROW optimization algorithm to ensure fast and efficient communication. From the experimental analysis, it is demonstrated that the proposed SS-ROW optimization exceeds all the conventional methods in terms of alive nodes, energy left, and throughput with 8, 0.3799, and 0.8331, respectively. The SS-ROW optimization algorithm reveal better performance when compared to the several existing methods and it will be very helpful in data processing using IoT sensors for such type of disease management. We have seen that COVID-19-affected patients have a high chance of getting seizures, so in the future, if we collect physiological data from COVID-19 patients through wearable IoT devices, prediction could be performed more efficiently.

Declarations

Author contribution

idea and implementation by Bhaskar Kapoor; original manuscript preparation by Bhaskar Kapoor and Bharti Nagpal; results analysis by Bhaskar Kapoor and Meshal Alharbi; manuscript editing by Bhaskar Kapoor, Bharti Nagpal, and Meshal Alharbi. The entire work has been done under the supervision of Bharti Nagpal.

Data availability statement

Datasets used for experimental analysis in this study are publically available and cited within the article.

Code availability

Not applicable

Declaration of Competing Interest

All authors declare that they do not have any conflict of interest.

Data availability

Data will be made available on request.

References

[1] Li Y, Orgerie A-C, Rodero I, Amersho BL, Parashar M, Menaud J-M. End-to-end energy models for Edge Cloud-based IoT platforms: application to data stream analysis in IoT. Fut Gener Comput Syst 2018;87:667–78. https://doi.org/10.1016/j.future.2017.12.048.
[2] Wu T, Wu F, Redouté J, Yuce MR. An Autonomous Wireless Body Area Network Implementation Towards IoT Connected Healthcare Applications. IEEE Access 2017;5:11413–22. https://doi.org/10.1109/ACCESS.2017.2716344.
[3] Stergiou C, Psannis KE, Gupta BB, Ishibashi Y. Security, privacy & efficiency of sustainable Cloud Computing for Big Data & IoT. Sustain Comput 2018;19:174–84. https://doi.org/10.1016/j.suscom.2018.06.003.

[4] Anuradha M, Jayasankar T, Prakash NB, Sikkandar MY, Hemalakshmi GR, Bharatiraja C, et al. IoT enabled cancer prediction system to enhance the authentication and security using cloud computing. Microprocess Microsyst 2021;80(1):103301. https://doi.org/10.1016/j.micpro.2020.103301.
[5] Raj S. An efficient IoT-based platform for remote real-time cardiac activity monitoring. IEEE Trans Consumer Electron 2020;66(2):106–14. https://doi.org/10.1109/TCE.2020.2981511.
[6] Sood SK, Mahajan I. IoT-Fog-based healthcare framework to identify and control hypertension attack. IEEE IoT J 2019;6(2):1920–7. https://doi.org/10.1109/JIOT.2018.2871630.
[7] Gia TN, Dhaou IB, Ali M, Rahmani AM, Westerlund T, Liljeberg P, et al. Energy efficient fog-assisted IoT system for monitoring diabetic patients with cardiovascular disease 2019. Fut Gener Comput Syst 2019;93:198–211. https://doi.org/10.1016/j.future.2018.10.029.
[8] Bharathi R, Abirami T, Dhanasekaran S, Gupta D, Khanna A, Elhoseny M, et al. Energy efficient clustering with disease diagnosis model for IoT based sustainable healthcare systems. Sustain Comput 2020;28(5):100453. https://doi.org/10.1016/j.suscom.2020.100453.
[9] Kumar PM, Lokesh S, Varatharajan R, Babu GC, Parthasarathy P. Cloud and IoT based disease prediction and diagnosis system for healthcare using Fuzzy neural classifier. Fut Gener Comput Syst 2018;86(3):527–34. https://doi.org/10.1016/j.future.2018.04.036.
[10] Singh K, Malhotra J. IoT and cloud computing based automatic epileptic seizure detection using HOS features based random forest classification. J Ambient Intell Humaniz Comput 2019:1–16. https://doi.org/10.1007/s12652-019-01613-7.
[11] Amudha S, Murali M. Deep learning-based energy efficient novel scheduling algorithms for body-fog-cloud in smart hospital. J Ambient Intell Humaniz Comput 2021;12(7):7441–60. https://doi.org/10.1007/s12652-020-02421-0.
[12] Ramesh J, Aburukba R, Sagahyroon A. A remote healthcare monitoring framework for diabetes prediction using machine learning. Healthc Technol Lett 2021;8:45–57. https://doi.org/10.1049/htl2.12010.
[13] Nancy AA, Ravindran D, Raj Vincent PMD, Srinivasan K, Gutierrez Reina D. IoT-cloud-based smart healthcare monitoring system for heart disease prediction via deep learning. Electronics (Basel) 2022;11(15):2292. https://doi.org/10.3390/electronics11152292.
[14] Muneer S, Raza H. An IoMT enabled smart healthcare model to monitor elderly people using Explainable Artificial Intelligence (EAI). J NCBAE 2022;1(2):16–22. no.
[15] Ahmed MI, Kannan G. Secure and lightweight privacy preserving Internet of things integration for remote patient monitoring. J King Saud Univ.-Comput. Inf. Sci. 2022;34(9):6895–908. no.
[16] Akram PS, Ramesha M, Valiveti SAS, Sohail S, Rao KTSS. IoT based Remote Patient Health Monitoring system. In: 2021 7th International Conference on Advanced Computing and Communication Systems (ICACCS); 2021. p. 1519–24. https://doi.org/10.1109/ICACCS51430.2021.9441874.
[17] Karunarathne SM, Saxena N, Khan MK. Security and privacy in IoT smart healthcare. In: IEEE Internet Computing. 25; 2021. p. 37–48. https://doi.org/10.1109/MIC.2021.3051675. 1 July-Aug.
[18] EEG dataset https://physionet.org/content/eegmmidb/1.0.0/(Accessed on 3 July 2022).
[19] ECG database https://physionet.org/content/mitdb/1.0.0/(Accessed on 12 August 2022).
[20] MRI dataset https://www.med.upenn.edu/sbia/brats2018/data.html (Accessed on 3 July 2022).
[21] BCI datset https://bbci.de/competition/iv/(accessed on 12 August 2022).
[22] CAP Sleep database https://physionet.org/content/capslpdb/1.0.0/(Accessed on 12 August 2022).
[23] Bairathi D., Gopalani D., Salp Swarm Algorithm (SSA) for training feed-forward neural networks. In: Bansal J., Das K., Nagar A., Deep K., Ojha A. (eds) Soft computing for problem solving. advances in intelligent systems and computing, vol 816, pp. 521–34, 2019 Springer, Singapore.doi:10.1007/978-981-13-1592-3_41.
[24] Kumar R, Kumar D. Multi-objective fractional artificial bee colony algorithm to energy aware routing protocol in wireless sensor network. Wirel Netw 2016;22:1461–74. https://doi.org/10.1007/s11276-015-1039-4.
[25] Karaboga D, Basturk B. On the performance of artificial bee colony (ABC) algorithm. Appl Soft Comput 2008;8(1):687–97. https://doi.org/10.1016/j.asoc.2007.05.007.

Bhaskar Kapoor is PhD Scholar of AIACT&R, G.G.S. Indraprastha University Delhi. He has done ME (CTA) from Delhi College of Engineering (Delhi University). He has 18 years of Experience in Teaching/Research,/Industry. His research interests lie in EEG Signal Processing, Machine and Deep Learning and Brain Computer Interface Devices. He has published various research papers in International Journals (Springer, IEEE & IET).

Bharti Nagpal is currently working as Assistant Professor in CSE Department at Netaji Subhas University of Technology East Campus, Delhi, India. She has 21 years of teaching experience. Her areas of interest are Machine Learning, Information Security and Data Science.

Meshal Alharbi is an Assistant Professor of A.I. in Computer Science Department at Prince Sattam Bin Abdulaziz University (Saudi Arabia). He is PhD (Computer Science) from Durham University (UK) & MSc (Computer Science) from Wayne State University (USA). He has 10 years of Experience in Teaching/Research,/Industry. His research interests lie in the Artificial Intelligence Applications and Algorithms, Agent-Based Modelling and Simulation Applications, Disaster/Emergency Management and Resilience, Optimization Applications, and Machine Learning.

How to Cite:
Ajaz, F., Prince, P., & Seniaray, S. (2022). Sentiment classification and analysis of twitter data on distance learning using ML classifiers. *International Journal of Health Sciences*, *6*(S3), 5750–5759. https://doi.org/10.53730/ijhs.v6nS3.7231

Sentiment classification and analysis of twitter data on distance learning using ML classifiers

Farheen Ajaz
Department of Applied Mathematics, Delhi Technological University, New Delhi 110042, India
*Corresponding author email: farheenhanna92@gmail.com

Prince
Department of Applied Mathematics, Delhi Technological University, New Delhi 110042, India
Email: sharma18.prince@gmail.com

Sumedha Seniaray
Department of Applied Mathematics, Delhi Technological University, New Delhi 110042, India
Email: sumedhaeniaray@dtu.ac.in

***Abstract*---**Online education comes in shades of grey. We analyze public view on the pandemic in regards with mental stress, interrupted power supply, affordability and access to internet, flexibility of schedule, reduction of long-distance commute, risk of covid and other such consequences of online learning and Government's take on the need for inclusive education policies. In this paper, we qualitatively inspect the consequences of COVID-19 pandemic on education of the students. This study primarily focuses on the response of students of all age groups, educators, college professors, school teachers and also parents of young students towards the approach of distance learning or Online education in the past two years. We have taken two datasets, first being the Twitter dataset comprising of tweets from around the whole world and second, dataset which is specific to tweets from India. The data has been extracted from twitter with the aid of twitter API and then two sentiment analysis approaches have been implemented, first Machine learning classifiers namely, Naïve Bayes, SVM, Random Forest, Logistic Regression, KNN, XG-Boost and secondly, Lexicon Based algorithms, VADER and TEXTBLOB. Upon performing the said approaches, the maximum accuracy achieved is 94%.

***Keywords*---**COVID-19, distance learning, online education, twitter.

Introduction

The novel Coronavirus (COVID-19) is a communicable ailment which is caused by the SARS-CoV-2 virus. Mild to moderate symptoms are experienced by people who fall victim to COVID-19, and they usually recover without any kind of special treatment. Although, for some people it becomes fatal and leads to the requirement of immediate medical attention and therefore this disease should not be taken lightly by any means. The first case of novel corona virus was encountered in Wuhan, China and within a span of three months it spread all across the world. COVID-19 is not only a global pandemic and public-health emergency; It has also had a significant impact on the global economy and financial industry. Significant reductions in income, an upsurge in unemployment, and disturbances in the transportation services and manufacturing industries are among the consequences of the disease vindication measures that have been executed in many countries.[1]

Along with these impacts, one of the biggest hit sectors is the sector of education. The Government all over the world has been encouraging online mode to impart education ever since the beginning of COVID-19, in order to achieve academic steadiness. These measures need to be taken to protect children from COVID-19 as well as to ensure that their studies remain unhampered. While few educational establishments find online education a staggering task, many have already made the switch from offline to online mode through platforms like Microsoft teams, Google meet, Zoom etc. There are various challenges of online education which occur at different levels. The first and the foremost being reliable internet access. According to a study conducted by the National Center for Education Statistics that over twenty three percent Indian students, including those from urban areas, do not have access to the internet for online studies while 6 percent of them have access only through smartphone.

The next prime challenge is the consistency of the students. Change has always been tough to embrace, let alone adapting oneself amidst a pandemic. It is hard to move from an organized day at school to a completely unstructured routine at home. It mostly affects younger children since for them, it is challenging to sit still in front of a camera to watch a lesson their teacher recorded or taught live online. It makes them miss important concepts from the class, mainly the reason being distraction. Through this research we aim to establish what is the common man's opinion concerning the online mode of education. Although Online education has been present in the form of distance learning (which is offered by institutes like IGNOU) as well for past few years but now it has become predominant and essential since the beginning of the pandemic. There are various machine learning algorithms generally used for sentiment analysis namely Convolutional Neural Network (CNN), Naïve Bayes, Support Vector Machine (SVM), Recurrent Neural Network (RNN), etc.

Naive Bayes is an elementary collection of algorithms of probabilistic kind which, for sentiment analysis classification, assigns to every word, a probability that the given word or phrase should be accepted as positive or negative. Sentiment analysis, also popularly known as opinion mining, is an approach to natural language processing that identifies the emotional tone behind a given sentence or

collection of words. It is a common technique utilized by various businesses to determine peoples' sentiments regarding any new product, service or concept. This method makes use of artificial intelligence and machine learning simultaneously to extract subjective information for text mining. As discussed in [2], E-Learning is an approach which combines distance learning and education within the classroom. Using modern means of communication, like smartphones, internet, graphics, and digital libraries, the motive of E-learning is to reach the student in the shortest time, with minimum effort and producing maximum benefit. It is expected that this pattern of imparting education will prevail in most teaching institutions around the world in near future.

Related work

Malak Aljabri et al. [3] proposed a model to analyze the distance learning in Saudi Arabia with the help of Twitter Dataset during COVID-19 pandemic period. All the tweets collected are written in Arabic language and geographic location is set to Saudi Arabia. The tweets are classified into the educational stages i.e., primary school and kindergarten, intermediate and high schools, or university. Then 6 Machine Learning Algorithms (LR, NB, KNN, XGB, SVM, RF) done on the dataset. The Logistic Regression ML technique has achieved the best accuracy of 89.9%. Filiz Angay Kutluk et al. [4] has proposed a model to analyze the student's satisfaction on distance education. In the model, Dataset is collected with the help of first degree data collection method from the two universities of Turkey, and with the help of T-test and One Way Anova the analysis is performed on it.

Usame Omer OSMANOGLU et al. [5] has proposed a model to measure the satisfaction for distance education course materials of Anadolu University. Overall, 6059 feedbacks were received, scaling was processed with the help of the triple Likert method and finally, Machine learning techniques were performed on the dataset. In which, 77.5% accuracy was achieved using Logistic Regression algorithm. Nimasha Arambepola [6] has proposed a model to analyse the effectiveness of the distance learning. Twitter Dataset is collected consisted 202,645 tweets during the lockdown period during the pandemic. The model gives out the result of 54% sentiments as positive, while 30% tweets are negative and 16% tweets comes out to be neutral. Imatitikua D. Aiyanyo et al. [7] has proposed a model to analyze the impact of COVID-19 pandemic on the educational sector of South Korea. Twitter dataset is collected during the COVID-19 period with the geographical boundaries set to South Korea. Pretrained sentiment Textblob and VADER were used and the result are analysed comparatively.

Methodology

The methodology can be broadly classified in three phases, namely Data collection and preprocessing, Tweet Classification and sentiment analysis using machine learning classifiers.

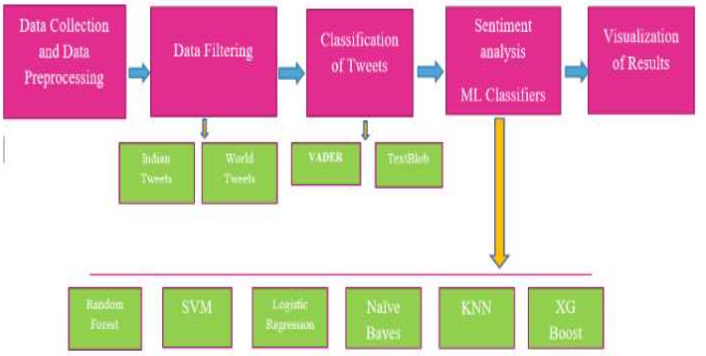

Figure 1. Represents the logical flow of our approach

Phase I
Data Collection

The twitter API allows a user to stream and download real time tweets. The process involves setting up a twitter developer platform. A user may apply for the same and the confirmation comes within a week. After that the user is provided with two keys including Consumer key and a secret key which has to be incorporated in the python program in order to stream and download real time tweets. In this paper we have extracted tweets in two phases:

- Extraction of tweets using hashtags
  The first phase of data collection was carried out by inputting particular hashtags in the code. These hashtags include 'Elearning', 'distanceeducation', 'googleclassroom', 'onlineclass', 'onlineexam', 'openschool', 'onlinelearning', 'eschool' and so on.
- Extraction of tweets using keywords
  The next phase is carried out in the same way as the phase 1 but the only difference is that the tweets are extracted by inserting a list of keywords in the search query instead of particular hashtags. These keywords are similar to the hashtags used in phase 1 of data collection. The tweets post extraction are represented in the Figure below

{"created_at": "Sat Nov 20 11:40:52 +0000 2021", "id": 1462023113985075208, "id_str": "1462023113985075208", "full_text": "RT @NehaSahni810: @PriyaMaryMathew @IvyRoseMathew Change is the END Result of all true learning.\n\n#Amityglobalconference #AmityOnline #AGOE\u2026", "truncated": false, "display_text_range": [0, 140], "entities": {"hashtags": [{"text": "Amityglobalconference", "indices": [98, 120]}, {"text": "AmityOnline", "indices": [121, 133]}], "symbols": [], "user_mentions": [{"screen_name": "NehaSahni810", "name": "Neha Sharma Sahni", "id": 2408521946, "id_str": "2408521946", "indices": [3, 16]}, {"screen_name": "PriyaMaryMathew", "name": "Dr Priya Mary Mathew", "id": 72035535, "id_str": "72035535", "indices": [18, 34]}, {"screen_name": "IvyRoseMathew", "name": "Ivy Rose Mathew", "id": 2406850579, "id_str": "2406850579", "indices": [35, 49]}], "urls": []}, "metadata": {"iso_language_code": "en", "result_type": "recent"}, "source": "Twitter Web App", "in_reply_to_status_id": null, "in_reply_to_status_id_str": null, "in_reply_to_user_id": null, "in_reply_to_user_id_str": null, "in_reply_to_screen_name": null,

Figure 2

Segregation of Indian tweets from original dataset

In this proposed approach, we have focused on the sentiment analysis of twitter data from India. Since most of the tweets have location mentioned in the description, we have made use of the location to filter the Indian tweets from the

world tweets dataset. Apart from this method, Geolocation has also been incorporated to directly extract the tweets specific to India. The geolocation aids in sieving tweets as per the wish of the user. It works by adding the 'geocode' parameter in the search query. The geocode parameter expects three values namely the latitude, longitude and the radius (which can either be in kilometers or miles). For example, if a user wants tweets from Delhi within 10 miles the code is illustrated below

```
new_tweets = api.search(q=search_query,
    count=tweetsPerQuery,
geocode=['28.5120' '77.3290' '10mi'],
lang="en",tweet_mode='extended')
```

Data preprocessing

The extracted tweets contain a lot of gibberish which is of no utility to the user. Further the tweets are in the form of a large paragraph filled with URLs and other such attributes which need to be eliminated for efficient of the text analysis. Following are the attributes of the extracted tweets.

Here, created at: determines the date and time of the tweet creation.
Data obtained from twitter usually contains a lot of HTML entities, for example < > & which get embedded in the original data. As a result, it is vital to eliminate these entities. This process is collectively known as Data cleaning or Data preprocessing. Significant steps for Data cleaning:

- Removal of duplicate tweets: For this, the tweets were extracted at the gap of at least 7-10 days.
- Removing unwanted URLs
- Inserting the key attributes of the tweet in a CSV file
- Conversion of the CSV file to a dataframe in python

Phase II
Sentiment classification
VADER

VADER (Valence Aware Dictionary and sentiment Reasoner) is a lexicon and rule-based tool for performing sentiment analysis that is specifically dedicated to sentiments expressed on social media. For the implementation of VADER (lexicon-based model for performing sentiment analysis), which has already been discussed formerly, we added classification attributes to the dataframe comprising the tweets. These attributes determine the polarity of the tweet and

assign sentiment score to every tweet. The columns are 'positive', 'negative', 'neutral' and 'compound' which signify the score as the name of the column suggests. VADER is implemented by incorporating the SentimentIntensityAnalyzer from the class Vadersentiment. Following the prescribed method, we have obtained positive, negative, neutral and compound score of corresponding to every tweet. Based on the compound score the tweet can be classified as positive, negative or neutral.

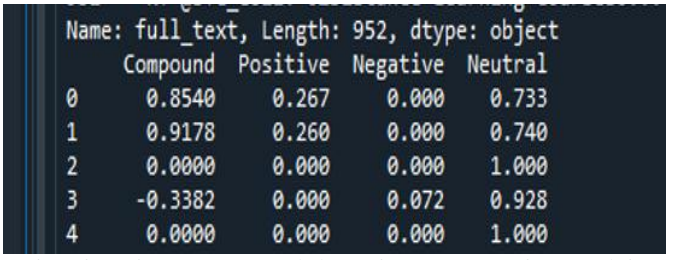

Name: full_text, Length: 952, dtype: object

	Compound	Positive	Negative	Neutral
0	0.8540	0.267	0.000	0.733
1	0.9178	0.260	0.000	0.740
2	0.0000	0.000	0.000	1.000
3	-0.3382	0.000	0.072	0.928
4	0.0000	0.000	0.000	1.000

Fig 3. Illustrates the dataframe comprising the tweets along with sentiment score.

Textblob

TextBlob is a very useful Python library which is used to process textual data. Textblob helps API to do the common natural processing tasks. With the help of Textblob, the following tasks were performed: Noun phrase extraction, Part of speech tagging, Sentiment Analysis, Classification, Tokenization.

Phase III
Machine Learning Techniques and Sentimental Analysis

Machine learning is a data analytic technique which teaches computers to think like humans, means to approach to a problem from its experience. Machine learning algorithms uses computational methods to learn from data.Usually there are 3 basic approaches of Machine learning: Supervised learning, Unsupervised learning and Semi-supervised learning. In this model, we apply supervised machine learning algorithms for the sentiment analysis i.e., Naïve bayes, Support Vector Machine, Logistic Regression, XG-Boost, Random Forest.

Results

Sentiment Classification
Vader

For world tweets, we obtain that 29% are positive, 7.5% negative and 64% neutral tweets.

	Positive	***Negative***	***Neutral***
World	29%	7.5%	64%
India	56.5%	14.8%	28.6%

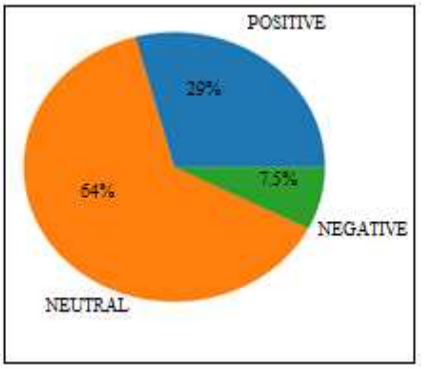

For Indian tweets we obtain 56% positive, 14.8% negative and 28.6% are neutral tweets.

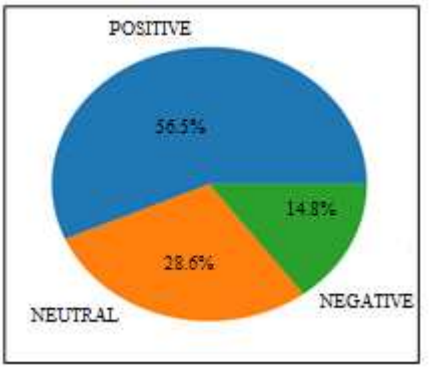

Textblob

With the help of pretrained sentiment Textblob. For world tweets, we obtain that 27.1% are positive, 4.5% negative and 68.4% neutral tweets.

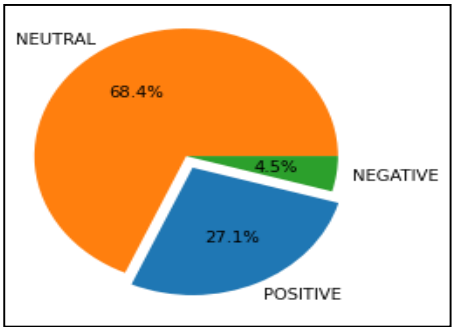

For Indian tweets, we obtain 56.2% positive, 11.4% negative and 32.4% neutral tweets.

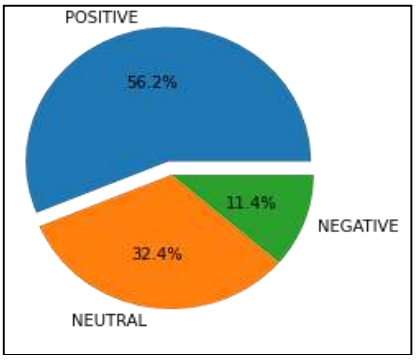

	Positive	Negative	Neutral
World	27.1%	4.5%	68.4%
India	56.2%	11.4%	32.4%

With the help of TextBlob, figure 4 illustrated below are the Top 10 positive hashtags

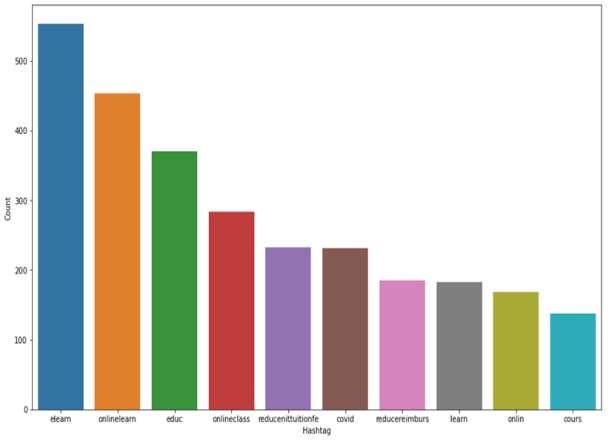

Figure 4

A Wordcloud is illustrated in figure 5 which displays the most prominent words in the dataset.

Figure 5

Experimental Setup

All experiments were conducting using Windows 10 operating machine having 2.1 GHz 12 CPUs AMD Ryzen 5 5500U processor with 8192 MB 3200Mhz DDR5 memory. With the help of 6 Machine Algorithms (NB, SVM, LR, XGB, RF, KNN), We get the following result where maximum accuracy achieved using XGBOOST to be 0.94

Classifier	Accuracy	F-Score	Precision	Recall
NB	0.92	0.96	0.92	1.00
SVM	0.93	0.96	0.94	0.99
LR	0.93	0.96	0.93	1.00
XGB	0.94	0.97	0.95	0.99
RF	0.92	0.96	0.92	1.00
KNN	0.92	0.96	0.93	0.99

Figure 6. Result

Conclusion

As the pandemic takes over, Distance learning comes into the play as students are not able to go school physically, classrooms are now taken to the home of students. In this work, we have examined how the distance learning plays a vital role in building the future of students in India and globally. It is observed that there are some areas of improvement to make distance learning more efficient and accessible to the students of the country. There are many plus points of distance learning in India, Now, Students are now getting quality education also in remote areas and they also do not have to travel to attend school far from their home. The biggest problem in distance learning is the screen time facing by the students which is affecting the mental and physical health of student. One way to reduce screen time is to have limited number of classes in a day and there should be break between each class which may help the students to understand easily and they will also refresh after taking their classes. Since the cases are now declining in India, schools are now open in offline mode but we can apply the positive outcomes of distance learning in offline mode like submitting the assignments online or having quizzes from the home which will help students as they don't have to bring load kgs of school bag daily. Finally, With the help of distance learning we can make the education for students more accessible which help them to make their future bright and make themselves assets in the development of the country.

Future scope

In this study, we analyze the effect of COVID-19 pandemic on the life of students and educators in India by summarizing the dataset collected from Twitter API and analyze it with the help of pretrained python package (i.e., TextBlob, Vader) and Machine learning techniques (i.e., Naïve bayes, Support Vector Machine, Logistic

Regression, XG-Boost, Random Forest). There are also some extra scopes of research is to analyze how distance learning playing role specifically in school going children and college going children and how the difference is there in between two. The study can also be further expanded and should compare the distance learning before the Covid-19 period and during the Covid-19 period. The results should also be done on the developing countries and the results should compare with the developed countries so the required steps should be taken to make distance learning better across the world.

References

1. AntonPak, Oyelola A.Adegboye,,"Economic consequences of the covid-19 outbreak: The need for epidemic preparedness"
2. Yahya Almurtadha , Sentiment Analysis to Measure Public Response to Online Education During Coronavirus Pandemic
3. Aljabri, M.; Chrouf, S.M.B.; Alzahrani, N.A.; Alghamdi, L.; Alfehaid, R.; Alqarawi, R.; Alhuthayfi, J.; Alduhailan, N. Sentiment Analysis of Arabic Tweets Regarding Distance Learning in Saudi Arabia during the COVID-19 Pandemic. Sensors 2021, 21, 5431. Doi: 10.3390/s21165431
4. Filiz Angay Kutluk, Mustafa Gulmez, "A research about distance education students' satisfaction with education quality at an accounting program" Published by Elsevier Ltd. Selection and/or peer review under responsibility of Prof. Dr. Hüseyin Uzunboylu
5. doi: 10.1016/j.sbspro.2012.05.556
6. Osmanoglu,U.O., Atak,O.N., Caglar,K., Kayhan, H. &Can, T.C. (2020). Sentiment Analysis for Distance Education, Doi: 10.31681/jetol.663733
7. Nimasha Arambepola, Analysing the Tweets about Distance Learning during COVID-19 Pandemic using Sentiment Analysis, ISSN 2756-9160 / November 2020.
8. Aiyanyo, I.D.; Samuel, H.; Lim, H. Effects of the COVID-19 Pandemic on Classrooms: A Case Study on Foreigners in South Korea Using Applied Machine Learning. Sustainability 2021, 13, 4986. Doi:10.3390/su13094986

Education and Information Technologies
https://doi.org/10.1007/s10639-022-11568-6

Shifting from traditional engineering education towards competency-based approach: The most recommended approach-review

Ruchika Malhotra[1] · **Massoud Massoudi**[1] · **Rajni Jindal**[2]

Received: 30 August 2022 / Accepted: 28 December 2022
© The Author(s), under exclusive licence to Springer Science+Business Media, LLC, part of Springer Nature 2023

Abstract

In recent years, universities have been developing more robust competency-based classes for students in Science, Technology, Engineering, and Mathematics (STEM). Competency-based education (CBE) is based on outcomes and is student-centred, creating a better learning experience. This paper provides context for competency-based education over a knowledge area (KA), knowledge unit (KU), and learning outcome (LO) mindset. Additionally, we compared the traditional educational approaches and CBE using a software engineering competency list as assessment criteria. This study provides a thorough review, emphasizing the transition toward competency-based approach in software engineering education and training. The five main reasons education institutes turn toward CBE are: Firstly, CBE supports lifelong learning. Second, it fosters an empowered and inclusive learning culture. Thirdly, it provides appropriate teaching and support on a timely and individualized basis. Fourth, it employs instructional ideas that are matched with students' needs and objectives. Finally, CBE places a premium on transparency and sets out explicit expectations. Our findings indicate that competency-based education is the outcome-driven approach in today's engineering education. It encourages students to know what to do upon graduation rather than what they know.

Keywords Competency-based education · Engineering education · Learning outcomes · Learning assessment

✉ Massoud Massoudi
massoud.massoudi@hotmail.com

Ruchika Malhotra
ruchikamalhotra2004@yahoo.com

Rajni Jindal
rajnijindal@dce.ac.in

[1] Software Engineering Department, Delhi Technological University, Delhi, India

[2] Computer Science & Engineering, Delhi Technological University, Delhi, India

Published online: 07 January 2023

1 Introduction

Competency-based education is a general term that refers to an educational approach that concentrates on learners' knowledge of a particular topic (Hoogveld et al., 2005). Learners have to develop their progress in CBE by assessing their competency, which means they must demonstrate that they have mastered the skills and knowledge necessary to complete the subject (Passow & Passow, 2017). CBE often called mastery-based, performance-based, or proficiency-based education, is gaining momentum. A growing number of districts and universities have implemented competency-based curriculum in recent years. Educational institutions adopt competency-based education for a variety of purposes: including the development of internationally competitive learners, the design of schools that prioritize what works best to help students succeed, the achievement of greater equality, the establishment of a method of quality growth and learning, and the promotion of effective teaching (Sturgis & Casey, 2018). There are many problems facing engineering education presently, and there is a need to upgrade them. The diversity of US higher educational institutions' student population is growing, with over 90% of the student body made up of the non-traditional student body (Roe & Bartelt, 2015). Over the previous decade, there has been a move in science, innovation, engineering, and math instruction, particularly in engineering, towards a competency-based teaching method. CBE is a result-based, student-based type of learning where understudies progress to further developed work after acing the fundamental essential substance and abilities (Henri et al., 2017). A competent person has the power and skills to perform the assigned activities and work at a required level of competency.

Hence, in the competency model, the knowledge is different from the skilled term, i.e., knowledge is what one knows, while skill is what one can do (C. Society & SWECOM, 2014). Competencies result from integrative learning encounters in which aptitudes, capacities, and information are communicated to shape education and learning packs identified with the errand for which they are amassed. Moreover, enthusiasm within competency is quickening worldwide, competencies and abilities examined from the exciting side of work and thought offered principally to workers' necessities. Additionally, competency models can be utilized by the graceful side of the job market too. For example, a student, labourer, cheerful and hopeful new representatives are going after a situation to accomplish job dependability. Hence, competency-based methods benefit from a strong correlation with optimistic student learning explanations, as they shift the emphasis from instructional delivery to student achievability (Baughman et al., 2012).

As a result, software engineering education must go beyond curriculum knowledge acquisition to include a more extensive portfolio of knowledge and skills. The term competence can acquire this concept. Ethical concerns, business and society relevance are part of the overall competent-centred curriculum. However, successful software engineering education and training must include what individuals know, how they know, and why they learn (ACM/IEEE, 2020). This article seeks to encourage lecturers who are backers of CBE to understand how their courses can be updated with game design elements. In brief, the implementation of game dynamics is tailored to competency growth. The association is defined at the top level of abstract objectives of learning strategies by

using dynamics (Bartel et al., 2015). Our studies find the major robust points in transitioning into a competency-based software engineering education and training mindset. In addition, we pinpoint the advantages and role of competency-based learning over knowledge-based learning concerning software engineering education. Consequently, we formulated some research questions, and we are trying to address the response to the following research questions: 1. What are competency levels, and how do they impact a student with poor skills? 2. What is the type of assessment in competency-based education? 3. What are the advantages and disadvantages of competency-based education in the field of software engineering? 4. What are the primary distinctions between competency-based and knowledge-based education and reasons academia transitioning towards competency learning approach? The remainder of the article is structured as follows: Section II summarizes competency-based education. Section III discusses the methodology; section IV illustrates the findings and results of the study; section V explores the discussion, and section VI wraps up the conclusion.

2 Background

2.1 Competency-based education

The terms' competence' and 'competency' are used interchangeably in the literature and are described differently by various scholars. The bulk of these concepts is based on "descriptions of work tasks," or what a person must do in their career, and "descriptions of behaviour," or how an individual performs their task (Boahin, 2018). According to different studies, there are multiple views on competency. Hene, the CBE's main aim is on a student's ability what she can do rather than what they know (Klink et al., 2007). Although, there is no normalized and acceptable description of the term CBE. As per Weinert, "*competency refers to an individually or inter-individually available collection of prerequisites for successful action in meaningful task domains*" (Weinert, 1999). This concept encompasses an individual's potentiality, skill, way of thinking, comprehension, and the ability to use these self-composed solutions to problems in defined contexts (Bartel et al., 2015). Consequently, considering the critical principle of CBE, based on the premise that courses do not transmit information but rather concentrate on comprehensive skills that allow understudies to resolve issues in diverse and complex contexts. Indeed, conveying knowledge is more convenient and straightforward than transferring competencies to pupils, i.e., competencies require various types of educating approaches than knowledge, where the view on competencies lead to a determined view on learning (Ehlers, 2010).

a. Learning is considered a constructive and engaged process; it occurs in the proper contexts which consider problems from an expert practice.
b. Learning results are defined absolutely and straightforward; the spotlight doesn't lie on knowledge yet in addition to course-specific-methodological, social, individual, and action-related abilities.

c. Understudies are self-liable for learning and assume a functioning job in the learning circumstance; on the other hand, teachers primarily act as coaches and guides.
d. Inspiration and feelings are establishments for fruitful competency advancement.

Additionally, (Thurner et al., 2014) stated: based on our previous observations, we firmly believe that sometimes the impediments to gaining new knowledge in the STEM fields are not due to a lack of intellectual capacity, but rather due to a lack of base competencies (self-competency, practical and cognitive just as social competencies). Furthermore, according to past experiences, to identify gaps in each student's competencies, we come across to put an endpoint to those gaps effectively. We find out that students with transfigured succeeded in the exam that was almost-dropouts. Thus, we pinpoint specific base competencies that must be prerequisites to acquire new and complex knowledge (Thurner & Böttcher, 2012). Additionally, Fig. 1 illustrates the competency needed for obtaining technical abilities. Self-competencies are the most central viewpoint, framing a reason for progressively complex skills and aptitudes. Practical and cognitive competencies include required structured work methods and various capacities that help work correctly in an objective-oriented way.

Lastly, the social competencies reflect the ability to see and regard others' needs and desires, communicate with them and support them effectively (Thurner & Böttcher, 2012). There are no universal alternatives to competency-based instruction, and there is no well-defined concept. Accordingly, the distinction between competency-based and competence-oriented approaches is meaningless. A competency-based curriculum would cater to students involved in addressing challenges creatively. The primary view obtained by reflecting on competencies profoundly impacts how learners get information (Bartel et al., 2015; Ehlers, 2010). The focus of CBE is on "Output" than just "Learning" and is now most widely found in education programs and ongoing training (Bechtel et al., 1999). Many modes of education are correlated with the actual existential danger. A genocide theory is merely an anti-theistic notion. There are alternative methods of education than using only adults as

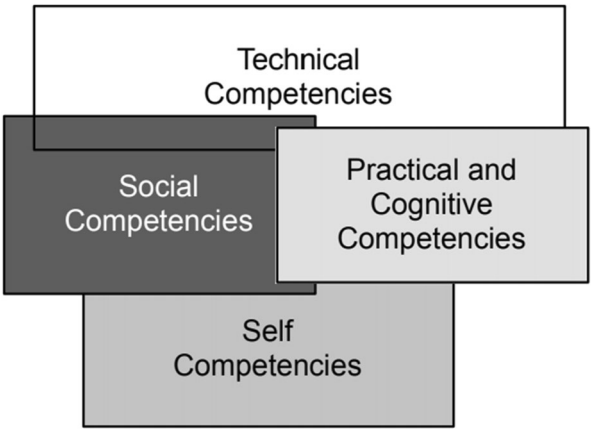

Fig. 1 Competency call for acquiring technical competencies

subjects. So it could result in a final tragedy and the destruction of humanity. Also, the individual is simple merchandise subject to creation utilizing the labour force with little respect to consciousness or resistance. It is very similar to the practice of human trafficking. Educators would not implement competency-based education and training for control and mass destruction but rather for the people's welfare, the economy, and culture (Preston, 2017).

3 Methodology

This study analyzed relevant literature to determine the strengths, impacts, and limitations of CBE and knowledge based learning. The existing literature and this qualitative research data were analyzed to determine the best strategies for highlighting the efficacy and benefits of competency-based education in engineering education and training.

We also used meta-analysis research to compare the two educational approaches and to demonstrate the strengths and weaknesses of competency-based education in the context of STEM education, specifically software engineering education and training. The purpose of this study is to determine which of these approaches has the best chance of benefiting and succeeding in engineering education and training. Additionally, encourage institutions to migrate from the existing system to one based on CBE.

3.1 Research questions

In this study, the main focus is on transitioning from knowledge-based learning to competency-based software engineering education. Table 1 summarizes the research questions (RQs) we formulated and the motivations behind each research question.

3.2 Search process

Articles on engineering education were extracted from a variety of resources. For example, ACM, IEEE, Taylor & Francis, and other computer-related journals were reviewed and analyzed. The process was supported by a search of scientific databases conducted automatically. The relevant papers were extracted using keywords such as competency-based learning in software engineering, competency-based education in engineering education, lifelong learning, proficiency learning, mastery-based learning, and knowledge-based learning. Thus, Taylor & Francis Online, IEEE Xplore Digital Library, ACM/IEEE Computing Curricula 2020, Springer Link, and ACM Digital Library were employed for the automatic search. Peer-reviewed academic publications addressing the application of CBE in engineering education met the inclusion criteria.

Overall, we identified various publications: journal publications, conference proceeding publications, web publications, and books related to the CBE approach. Among these, 78 studies were finalized for completion of this study. Two criteria for inclusion to our sample considered: 1) the study had to be conducted on competency-based learning impacts on engineering education; 2) studies conducted mostly since 2010; Additionally, we set standards to maximize study independence and avoid

Table 1 Research questions and their motivations

RQs	Research questions	Motivations
1	What are competency levels, and how do they impact a student with poor skills?	RQ 1 aims to ascertain the five primary competency levels and their effect on limited ability and skill students.
2	What is the type of assessment in competency-based education?	The RQ 2 will examine the many forms of assessments used in competency-based education and state of the art in software engineering competency assessment.
3	What are the advantages and disadvantages of competency-based education in the field of software engineering?	There are strengths and weaknesses to competency-based education, which the RQ 3 addresses in software engineering education.
4	What are the primary distinctions between competency-based and knowledge-based education and reasons academia transitioning towards competency learning approach?	RQ 4 identifies the fundamental distinctions between competency-based education and knowledge-based education, and the reason academia changing their learning methodology towards CBE.

counting the same study twice in the analysis. When many articles reported the same comparison, we analyzed the most comprehensive report (Kulik et al., 1979).

Finally, we discovered a few further publications on CBE education and training in recent issues of prominent academic and multidisciplinary publications. Table 2 summarizes the number of publications for this work from various journals, conferences, and other resources.

The preceding Table 2 summarizes 57 per cent of the articles published in reputable journals such as Engineering education, the European journal of education, and STEM education. In addition, 15 per cent of the papers in this study were published at various IEEE, ACM, and other conferences. Furthermore, the remaining research, which totals 28 per cent, was gathered from multiple sources, including symposiums, books, and online resources.

4 Results and findings

Our findings indicate that competency-based education is one of the most successful and fruitful approaches available in engineering. This scheme is more concerned with the student's skills and competence. In this scheme, teachers play a different role than in conventional systems. Teachers primarily act as guides, mentors, and facilitators. Our study's findings also show that assessment place is central and assessment-driven in CBE.

Additionally, CBE (Clear et al., 2020) systems value transparency by laying down clear and explicit expectations from teachers and students; students know what is to be learned, the level of performance they need to demonstrate for mastery, and how they progress throughout a course. Students feel motivated and enthusiastic when learning targets are clear to them. The following sections address the research questions formulated in Table 1. We responded to each RQ in detail.

4.1 Software engineering competency-based model

4.1.1 What are competency levels, and how do they impact a student with poor skills?

The software engineering competency model defines the competencies required by software engineers who design and update software-intensive systems. There are listed

Table 2 Summary of studies for this review

Type	Number	Percentages
Journal	44	57
Conferences	12	15
Others	22	28
Total	78	100

skill areas, abilities inside skill areas, and job tasks for each skill. Activities are listed on a five-tiered competency scale in Fig. 2 (I. C. ACMJIEEE-CS Joint as Force Computing Curricula, 2014).

In particular, a technician obeys directions. An entry-level practitioner aids in executing an operation or conducts an activity with oversight; a practitioner performs tasks with minimal or no supervision; a technical leader directs individuals and teams in operations performance; and a senior software developer modifies develops new methods and tools. Some companies may decide to combine the technician and entry-level practitioner levels. A senior software engineer may act as the "chief engineer" for a software company. Specific senior software engineers may be industry experts who define and promote the software engineering profession. An example of competency from subsequent areas of the requirements management is in Table 3; Generally, notations represent the five stages of competency. In some instances, a person with lower ability can be capable of specific tasks, but not all of them. For example, entry-level performers can conduct traceability analysis (C. Society & SWECOM, 2014).

It should be noted that in certain situations (for example, the practitioner level in Table 3), a person must be qualified to engage in or lead a job operation, such as executing a requirements management plan. The project's scale, scope, and sophistication can influence whether they participate or lead.

There is a general understanding in training that accomplishment in school and vocation preparation requires that understudies build up several qualities and characteristics (Kennedy, 2007). Regularly sorted out within three terms, i.e., knowledge, skills, and dispositions. Hence, we tend to focus on a working description of competency that associates the above three dimensions. Figure 3 (captured from (Council of Chief State School Officers, 2013)) illustrates these interrelated elements of competency.

Simultaneously, (ACM/IEEE, 2020) refines the expertise, ability, and disposition system popularized in (*Information Technology Curricula 2017*, 2017). Although the knowledge dimensions of computing have been very well addressed in most computing curricula, the sense of ability and temperament have had a substantially lesser emphasis. To expand previous work, we find that competencies are based on K-S-D dimensions and use the task as a component as per the below Fig. 4:

The above figure explains the four components of the competency model (knowledge, skills, dispositions, and task) with the following meanings.

Knowledge It is a conceptual and theoretical understanding; it is a visible characteristic developed through excellent competency-based education with a coefficient of 35 per cent.

Skills Skill is a measurable and observable proficiency learned through good training and learning (Diksha, 2021). The skills aspect of competency points out the ability to execute different skills competently in a task. Therefore, "skills" reflect the

Fig. 2 Competency levels

Table 3 Competency levels work activities

Proficiency levels for work activities related to software requirements management					
Skill Area: Software Requirements					
Skill: Requirements Management					
Competency Levels	Technician Activities	Entry Level Practitioner	Practitioner	Team Leader	Senior Software Engineer
Activities	Follows established procedures to assist with requirements management.	Utilizes relevant tools to assist with requirements management.	Requirements management plans are put into effect.	Ensures project requirements management plans	Modifies current instructions, models, methods, and approaches for standards management and develops new ones

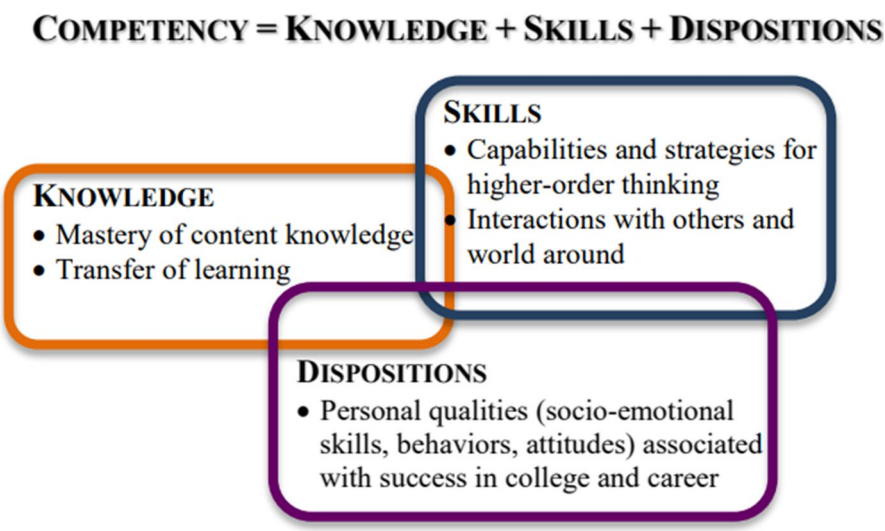

Fig. 3 KSD framework

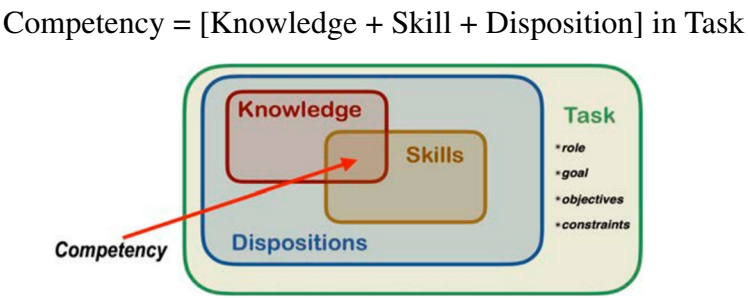

Fig. 4 Conceptual Structure of the CC2020 Competency Model. Competency = [Knowledge + Skill + Disposition] in Task

knowledge portion of competency that requires applying knowledge. Experience and expertise are built through continuous practice over time. The combination of 'know-what,' 'know-how,' and 'know-why,' altogether, used to cause 'know-what.' For using any aspect of knowledge in a competency specification to be intelligible, it must be interpreted as a degree of proficiency with the coefficient of 30 per cent. The competency model is implemented in this way due to learning that is skill-based (ACM/IEEE, 2020).

Dispositions The Disposition component of competency frames the required core know-why quality of task completion. It exemplifies the value of the occupation. Hence, the dispositions component shapes the perception of skilful commitment of "know-what" and "know-how." It also preserves knowledge and skill elements to the

extent that they correspond to the relationship between the indicator and criterion (Baron & Kenny, 1986). Since dispositions attach the 'better' or 'correct' application of knowledge and skill to the sense, they are applied. Indeed, dispositions moderate a professional's proficiency in how they carry out their duties (ACM/IEEE, 2020). with the coefficient of 20 per cent.

Task The task specifies the talented use of knowledge and how the talent is expressed in the disposition dimension. The task was communicated as a conversational declaration which provides a setting to demonstrate disposition. In this context, the assignment integrates a systematic theory of competency, which includes all competency areas (knowledge, skills, and disposition). Therefore, mission representations help develop a teaching method that enables learners to attain true proficiency in computing with a coefficient of 15 per cent.

4.2 The potential of competency-based education

4.2.1 What are the advantages and disadvantages of competency-based education in the field of software engineering?

Studies say that engineering students are academically qualified but lack the abilities essential for quality success and individual development (Evans et al., 2015). While CBE has many strengths, it also has weaknesses and challenges. There is concern on whether CBE is helpful for teaching understudies dedicated skills such as communication, prioritizing, teamwork, and strong communication skills (Felder et al., 2015; Gharaibeh et al., 2013; Walther et al., 2011). The strengths of CBE are listed in Table 4.

Even though CBE offers several advantages, there are also known weaknesses and uncertainties. While it is undisputed that the CBE has been shown to improve teamwork, leadership skills, there is debate in the literature about how successful it is in teaching students such as leadership, promoting constructive argumentation, and working under pressure (Felder et al., 2011; Gharaibeh et al., 2013; Walther et al., 2011). Research suggests engineering graduates are often well-rounded, but they aren't well qualified for quality jobs due to a lack of professional skills (Evans et al., 2015). Table 5 depicts the weakness of CBE in engineering education.

4.3 Transitioning towards competency-based education

4.3.1 What are the primary distinctions between competency-based and knowledge-based education and reasons academia transitioning towards competency learning approach?

Competence means acquiring adequate knowledge, communication, decision-making skills, and attitudes to accredit the performance of activities and explicit tasks to a certain level of efficiency (Chacko, 2014). Hence, (Epstein & Hundert, 2002)

Table 4 Strengths of competency-based learning

Authors	Strengths	Descriptions
(Silva et al., 2013; Witt et al., 2006; Henri et al., 2017)	Master prerequisite materials, Positive learning experience, lower dropout, and high attendance	CBE allows students to practice foundational material regardless of the present course continually. Success improves when students are used to checking prerequisites, and retention decreases. Preventing students from falling behind, although some CBE initiatives are predicting reduced dropout and increased enrolment.
(Hsu & Ho, 2012)	Facilitates student-centred and individualized learning paths	A more creative approach to meet this atypical student population's needs is to incorporate various delivery systems like remote, electronic, or online learning Integrating these strategies is both possible and critical in the CBE design.
(Henri et al., 2017)	The appropriate strategy for today's diverse student body	Working several jobs along with college is commonplace for young adults. Stopping students from falling behind and learning at their speed is suitable for them. CBE can educate non-traditional students in engineering programs. CBE is a practical approach in today's diverse student body
(Khoumsi & Gonzalez-Rubio, 2006; Sutcliffe et al., 2005; Nelson, 2013; Dinsmore et al., 2008; Canaleta et al., 2014)	Positive student attitudes regarding the courses and curriculum, Better performance than the traditional approach, knowledge, and performance improvement	Some evidence indicates that student grades are enhanced, and students in CBE courses succeeded considerably more than their conventional courses counterparts. Additionally, research has shown that general information is improved in CBE students.

Table 4 (continued)

Authors	Strengths	Descriptions
(Sutcliffe et al., 2005)	Fulfil industrial expectations for more skilled professionals	CBE could be the best way to fulfil the industry's desires for better-qualified engineers. The competency and work market is getting more complex, and CBE systems will quickly adapt to meet those requirements.
(Bensah et al., 2011; Dinsmore et al., 2008; Hernandez et al., 2009; Spelt et al., 2015; Woodrow et al., 2013; Henri et al., 2017)	Improves knowledge-based and professional competencies	The exciting thing about studying while on the job is that you keep being forced to learn. CBE can help develop technical skills as well as general knowledge.
(Witt et al., 2006; Silva et al., 2013)	Easy internship placement and employment	Studies have shown that those who have completed CBE courses can secure employment quickly.
(Baughman et al., 2012)	Fosters mutual comprehension between the educators and learners	CBE contributes to shared understanding between students and teachers and aids in the preparation of instructional materials design. In CBE, teachers have well-defined learning objectives and assessment standards. Students know what to do if they want to be competitive in their courses. When students see the learning objectives and expectations from the outset, there is less student frustration or disappointment.
(Abdulaal et al., 2011; Dinsmore et al., 2008; Veldman et al., 2008; Woodrow et al., 2013; Bensah et al., 2011; Di Trapani and Clarke, 2012a, b; May et al., 2015; Lin et al., 2013; Tang, 2014; Oladiran et al., 2011; Evans et al., 2015)	Enriches implementation of additional pedagogies in students such as project-based learning, problem-based learning, experiential learning, virtual reality, team-based learning, and scaffolding	CBE is designed to allow for other pedagogical practices, including project-based learning, enhanced learning outcomes, problem-based learning, scaffolding, team-based learning, and experiential learning.

Table 5 Weakness of CBE system

Authors	Weakness	Descriptions
(Ro et al., 2015; Henri et al., 2017)	Lack of professional, contextual competence, and confidence	Engineering students often excel academically but struggle with success and professional development. One of the main factors of success in the workforce is aptitude and proficiency in using creative and contextual skills. Lack of discretization of academic competencies coupled with their inclusion in all other educational systems makes it hard to deliver skills in the CBE fashion.
(Walther et al., 2011)	Categorization	The main weakness of CBE is that the material and expertise are distributed into discrete competencies. Therefore students can only see a small portion of the project at a time. Thus, students have a firm understanding of each unit of knowledge but can't combine ideas. Alternatively, since CBE categorizes information, students can find it challenging to learn how to implement it. As CBE became more common in education in the 1970s, it considered each capability to be just a set of separate components. This was one of its significant challenges as well.
(Rikakis et al., 2013)	Application/Implementation of CBE	Educators also face many issues transitioning an engineering curriculum from a standard educational method to a competency-based model. The more time and commitment it would be to introduce a different educational approach, the more difficult it would have for educators and pupils accustomed to conventional classroom and setting courses.
(Tony Bates, n.d.)	It does not address the needs of most students' learning styles	A competency-based approach is being used by managers and an incentive to re-skill or pursue mid-level work skills. It's not suitable for all types of pupils, and it cannot improve higher-order abilities such as problem-solving and logical reasoning. Educators should prepare the syllabus so that learners who fall behind can progress rather than simply submit to those who step forward independently. Educators have to stick to a timetable and cover all the course materials within the coursework.
(Fedena, n.d.)	Increased chances of procrastination	Unmotivated students may be a drawback in competency-based instruction. As there is no set timetable or due date, it can result in sloppiness between the students. For a competency-based curriculum to be effective, students must be self-disciplined and self-motivated. This does not apply to everyone.
(Fedena, n.d.)	It does not take social learning into account	Social learning is where students benefit by seeing someone do things and practice. Since competency learning, students usually lose out on social learning rewards.

illustrated this as "the habitual and judicious use of communication, knowledge, technical skills, clinical reasoning, emotions, values and reflection in daily practice for the benefit of the individual, and the community being served." Although the words competence and competence are utilized mostly interchangeably in the literature, the idiom competency is used for skill and competence as an attribute of the doer's capability to fulfil the required skill. The definition of "competence" is based on the subject's experience, ability, strength, and judgment. It is important to remember that this term often appears similar to the concept: being competent in law does not equal competence in medicine (Webster, 2020). In the European Qualifications Framework context, competence is described as responsibility and autonomy (European Parliament & Council of the European Union, 2008). The below Fig. 5 states that in the KSD framework, knowledge, skill, and disposition can be acquired by a learner, but the task is not guaranteed.

Whereas in the competency model, task depictions give an unequivocal setting to the program to create a teaching method that empowers graduates to exhibit competency as computing proficient.

On the one side, (Carraccio et al., 2002; Chacko, 2014) stated the essence of the differences between the two learning approaches, namely competency-based Education and knowledge-based Education (Table 6).

On the other side, (Chacko, 2014; Gruppen et al., 2012) highlighted other unique features of the competency-based education paradigm as:

a) Competency generally centres concerning the performance of the final result
b) The CBE uses a capability-based evaluation procedure that is not contingent on the success of others.
c) CBE informs its competitors and other stakeholders regarding product quality and relevant results.
d) CBE is self-regulated and offers versatile learning opportunities, such as learning in different ways for different ages.

Furthermore, Fig. 6 summarizes the components of both methods, competency-based Education and knowledge-based Education.

Knowledge-based learning relies on the subject to be taught. It places more emphasis on the test than on competency. In the learning process, the only instructor-based pedagogy is used in the KBL, and the teacher plays the primary role in transmitting information to students. The instructor is in charge of

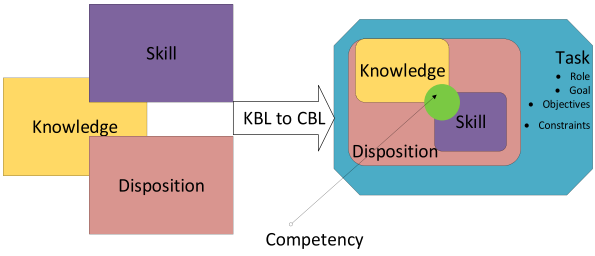

Fig. 5 Integration of KSD & Competency framework

Table 6 CBE and KA-KU-LO differences

Variables	Knowledge-based Education	Competency-Based Education
Curriculum driving force	Content, i.e., knowledge acquisition	Outcome, i.e., knowledge application
Process driving force	Teacher	Learner
Responsibility for content	Teacher	Teacher and learner
Assessment tool	Proxy, mostly subjective	Authentic, i.e., mimic actual professional tasks
Timing of appraisal	affirmation on summative	Emphasis on formative
Completion of program	Stable time	Variable time till attainment of competency

choosing the materials based on her preferences and availability. Finally, there are significant difficulties in incorporating new technology into a knowledge-based learning environment (Huili, 2010).

On the other hand, the critical focus of competency-based education is developing each student's abilities to do their tasks. CBE creates and educates students to learn distinctively. It also boasts a candidate's trust in their ability to complete a given job. Rather than receiving pre-packaged content, trained staff learn more effectively and efficiently with the assistance of an instructor in CBE (Sullivan, 1995).

Table 7 summarizes the contrast between traditional knowledge-based learning and the competency-based learning approach (Diksha, 2021).

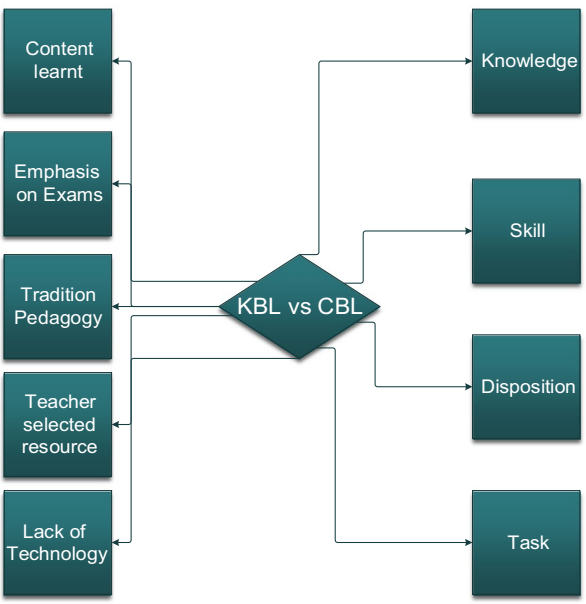

Fig. 6 Knowledge-based learning vs competency-based learning

Based on the outcome, the traditional education system focuses on memorization and understanding of the content, whereas CBE focuses on demonstrating learned knowledge and skill. The conventional education system is based on a fixed mindset ideology. At the same time, a CBE system is based on a growth mindset ideology. The traditional approach believes in encouraging a culture of compliance. But the CBE fosters the culture of empowerment. The support system in the conventional method is need-based for a few students. At the same time, it is a differentiated instruction support system for all the students in CBE. Concerning pedagogy, the traditional strategy has a single curriculum for all students.

Furthermore, CBE offers an individual learning pathway for each student. The standard educational system uses a one-size-fits-all evaluation technique, whereas CBE uses a tailored learning assessment approach. In old systems, competence criteria have varying meanings for various persons. However, proficiency criteria have a similar purpose for everyone in the CBE. Lastly, the traditional system's advancement is time-based, whereas, in the CBE, it is learning-based.

4.3.2 Reasons academia turning toward competency-based education

The traditional system is not structured to achieve the goals we have set for it or to deliver the results that our students, families, and country so desperately need and deserve. The traditional system has ten major flaws that foster inequity and poor achievement. Table 8 compares the conventional and CBE methods in terms of equity. They can be remedied by redesigning a curriculum for success that ensures mastery for all students (Sturgis & Casey, 2018).

Finally, there is a strong motivation for moving towards competency-based education because it's outcome-oriented and efficiency-driven. Five main strengths in Fig. 7 explain the need for competency-based education in today's education ecosystem.

CBE supports lifelong learning (Demetriades & Jacobs, 2006; Meincke & Tavangarian, 2011) by focusing on academic knowledge and transferable skills. It ensures that students become problem solvers, independent learners, and successful in new contexts. It also focuses on student agency which means that students can choose their learning pace and act as independent and self-regulating learners. CBE creates cultures that emphasize growth, inclusion and empowerment for students and educators. It aims to foster a growth mindset in students to take ownership of their learning. Educators are also empowered and given the flexibility to make decisions in the best interests of students.

Additionally, equity lies at the heart of competency education to ensure that all students grow and benefit, not just some. The CBE is a timely based instruction and support to students. Support in CBE is not a reactive measure when a student fails. Support is offered proactively throughout the learning process. More emphasis on the process than the result, remedial learning opportunities, formative assessment, and effective feedback are provided regularly to continue learning and building knowledge and skills. The pedagogical principles of CBE are aligned to meet students' actual learning needs and goals. Educators do not seek and teach students based on their age and grade, but they begin meeting students where they are and their learning needs?

Table 7 The contrast between the traditional approach and CBE

Distinguishing parameter	Traditional approach	Competency-based Education
Outcome	Memorization and understanding of academic content	Demonstration of learned knowledge and skill
Mindset	Fixed mindset	Growth mindset
Culture	Culture of compliance	Culture of empowerment
Support system	Need-based support to some students	Differentiated instruction and support to all the students
Pedagogy	Single curriculum for all students	Individual learning pathway for each student
Assessment	One size fits all approach	Personalized learning approach
Proficiency standards	Different meanings for different people	Consistent meaning for everyone
Advancement	Time-based	Learning-based

Table 8 Comparing traditional and CBE approaches with equity

	The traditional system's weakness	Characteristics in competency-based education	Hallmarks of high-quality competency-based education with equity
Mindset	The traditional system is based on a fixed mindset: Students are ranked and classified, resulting in winners and losers.	It is based on a development mindset, which holds that learning and success can be improved with commitment.	Ensures the experience and ability holes are filled to qualify students for further advanced studies adequately. Seeks out and eliminates unfair and unjust patterns and biases.
Outcome	Concentrates on a small number of learning results, emphasizing academic skills, memorization, and language comprehension. Fails to understand that student achievement is contingent upon a diverse set of foundational qualities, including social and emotional abilities and applying those abilities.	Concentrates on a comprehensive and holistic range of student achievement outcomes, including a firm grasp of subject awareness and ability displayed by practice, as well as competencies that educate students for education, career, and lifelong learning.	Emphasizes students' innate strengths and motivates them to explore their interests and abilities while broadening their academic experience, competence, and proficiencies.
Support	Assists students whose educational or psychological demands are slightly above or below the standards (i.e., special education, gifted and talented).	They are designed to provide instruction and service on a timely and differentiated basis.	Supports and instructs in a culturally sensitive manner. Academic pathways are provided for students who cannot graduate by 18 to finish their secondary education.
Culture	Instils a sense of compliance and order in the educational setting. It relies on a centralized, hierarchical structure to maintain established positions, societal values, and power structures.	Promotes empowering, collaborative learning environments. With distributed government, values student and adult organization. Recognizes the critical role of protection and belonging in learning.	At all levels of the system, the school system embraces cultural responsiveness. Students are engaged in school governance.
Pedagogy	Delivers a consistent program to all students regardless of their age. Per year, emphasis is placed on covering the curriculum.	Incorporates learning sciences into the creation of pedagogical values for students and adults. Considers the pupil pathway when developing teaching. Utilizes research-based techniques to increase inspiration, commitment, and initiative.	Education is grounded in intimate relationships, and the program is purposefully analyzed to overcome bias and foster an inclusive society. Incorporates methods from Universal Design for Learning.

Table 8 (continued)

	The traditional system's weakness	Characteristics in competency-based education	Hallmarks of high-quality competency-based education with equity
Assessment	Assessment is emphasized for summative reasons to validate what students learned. One-size-fits-all tests are given to all students simultaneously and in the same manner on the same content at fixed points in time or after the unit.	Assessment is embedded in a customized learning loop and aligned to information and competence transfer results.	Maintains quality standards and rigour for all students. Provides ongoing opportunities to apply or pass a learning goal in novel ways and includes documentation.
Reliability	Allows for a great deal of flexibility in how educators, colleges, and districts assess proficiency. Students are kept to various requirements through classes, colleges, and communities.	Guarantees the standards and meanings of what it takes to learn knowledge and skills are explicit. Creates a moderated assessment of student mastery when holding all students to the exact high expectations. Ensures the grading procedures are standardized.	Formulates mechanisms for moderation and calibration through schools and districts to minimize inconsistency and varying sets of expectations for different students and populations.
Learning infrastructure	Provides ambiguous learning outcomes and success goals and scant knowledge on the learning period for students Students earn marks and no direction about how to revise.	Transparency with complete, realistic standards of what is to be accomplished and the student's level of achievement is valued. Provides quantifiable learning objectives which make proficiency visible to pupils.	Enriches and motivates students by making options available to feel their voice in the curriculum.
Grading	Student evaluations are often challenging to interpret and include mixed signals about what students know.	Is connected to the students' learning experience and performance Carefully monitor students' development and success according to their level of learning.	The measurement of success ensures that all students reach their target degree of rigour. Provides relevant and accurate information about student academic performance to support professional growth for teachers and students.
Advancement	The conventional approach is chronological. Classrooms should be constructed for students' ages, keeping them progressing through material and classes simultaneously.	This advances students by basing their education on learning goals (mastery) and follows a creative approach. Students need to learn principles and knowledge before they can use them. Not only is that required, but that additional assistance is also required.	To better plan for student success and improve performance, design their learning paths around students' characteristics. Offers instructional help simulates a degree and level of academic advancement that results in college and career readiness through college and career completion.

Fig. 7 CBE strengths

This means that learning tasks are designed based on students' academic foundations. The support systems offered to help students learn and achieve their goals are determined by students' social, emotional, and cognitive development.

Additionally, CBE (Clear et al., 2020) systems value transparency by laying down clear and explicit expectations from teachers and students; students know exactly what is to be learned, the level of performance they need to demonstrate for mastery, and how they progress throughout a course. Students feel motivated and enthusiastic when learning targets are clear to them. Finally, students feel empowered when they have a say in learning and demonstrating proficiency. What is unique about CBE is that it focuses on what students learned and not on time spent in the classroom completing the syllabus.

In a nutshell, a list of competencies for software engineering courses is shown in Table 9. Based on the list, students have the opportunity to learn software engineering skills.

4.4 Assessment in competency-based education

4.4.1 What is the type of assessment in competency-based education?

Over the last two decades, accreditation bodies and educational professionals throughout the world have underlined the significant importance of integrating transdisciplinary competencies into engineering education programs in preparing learners for employment in engineering (Cruz et al., 2020). The place of assessment in competency learning is central. It is assessment-driven (Ravet, 2013). The vital step to ensure that students learn the courses is to create sufficient success tasks to determine and task's mastery. Since CBE is industry-driven, the appraisal is based on verifiable results and demonstrated expertise, ensuring that the assessment instruments have the evidence. You can utilize a portfolio. A portfolio is an excellent tool for collecting, organizing, and presenting evidence (Ravet, 2013).

In the sense of CBE, assessment is the method of comparing expertise to predefined success levels. The CBE evaluation method is both formative and summative. However, formative assessment increases the consistency of teaching and student learning. Likewise, summative assessment measures the achievement of results (Boahin, 2018). Consequently, assessment affects how students understand and remember what they've learned. Since, this indicates a change from knowledge-based to competency-based learning, which effectively incorporates information and attitude facets (Van Merriënboer & Kirschner, 2007). Students' willingness to meet job specifications is the primary objective of CBE assessment (Gulikers et al., 2010). Particularly for students in the early stages of their learning who wants to know what subjects to include

Table 9 Competency list for software engineering courses

Competency list in SE	Outcome
Computer programming and coding	Students demonstrate their ability to write and execute different programs using the required programming languages and implement algorithms.
Software development	Students will analyze users' needs and then design, test, and develop software to meet those requirements. They will be able to work with natural systems.
Object-oriented design	Students will understand the four critical components of object orient, namely: a. Abstraction b. Encapsulation c. Inheritance d. Polymorphism
Software testing and debugging	Students will understand and generate different testing tools to test software. Students will also think analytically about how a system is put together.
Problem-solving and logical thinking	Students will demonstrate their ability to identify technical challenges and use deductive logic to solve problems and improve software for commercial use.
Written and verbal communication	Students will illustrate the most appropriate strategies for developing their verbal and written communication abilities. They would be able to clarify to a customer something technical or complicated.
Teamwork	Students may show their interpersonal qualities, such as empathy for others, listening capacity, taking feedback, and empathizing.

in their study program (Sadler, 1985). Students should be provided with appropriate assessment requirements before learning activities to assist in decision-making (Fastré et al., 2014). Often, competencies are assessed continually rather than being completed with extra funding. According to this theory, these shortcomings seem to be rectified in colleges in competency-based learning. Whether a student fails an exam or a section of an exam, they need further support. CBE means that students and teachers know just what they need to know. Students have the opportunity to make their own choices and tackle the issues, even though the task is challenging for them. In competency-based education assessment, the criterion is also set as competencies that the learner is willing to demonstrate (Gre'goire, 1997). A tangible example is knowing how to communicate correctly and applying wisdom, skills, and disposition.

The purpose and type of assessment differ across the educational systems. Table 10 lists the number of assessments in both the methods, namely CBE and the traditional approach.

In CBE, the assessment relies on students' learning outcomes and is primarily formative; in knowledge-based learning, the evaluation is predominantly summative since students show their knowledge of the topic. With CBE, each student is measured on their success and the group's Progress and proficiency of the learning outcomes.

Assessment is incorporated into every phase of the learning process to provide students with coaching and assistance in attaining competence (Soares, 2012). This level

Table 10 The assessment in CBE and traditional approaches

Competency-based assessment	Traditional based assessment
Assessment for learning and assessment as learning	Assessment of learning
Formative, ongoing, diagnostic	Summative in nature
Aligned to learning outcomes	Checks what students know
Individual pathway	One-size-fits-all approach

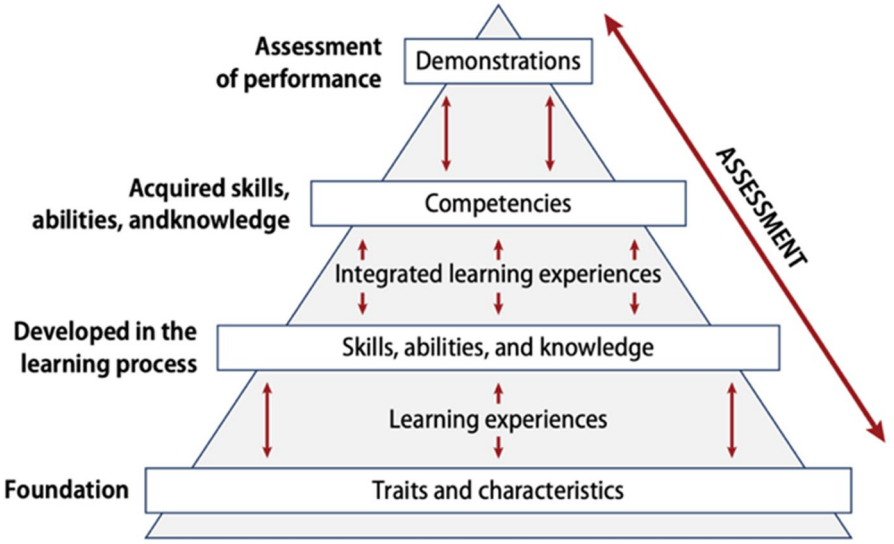

Fig. 8 Conceptual learning model

of scrutiny is meant to hone real-time expertise. Figure 8, taken from the National Postsecondary Education Cooperative's study "Defining and Assessing Learning," offers a straightforward but robust visual of the competency-based model.

As defined in the figure, the first stage consists of attributes and characteristics; basic understandings and learned skills reside. Skills, talent, and knowledge gained by learning are often involved. The third row, the competencies, are about understanding and capabilities. Finally, competencies are shown by presentations at the highest rung. In all points of this learning process, assessment is imperative and ongoing. There are two main methods to assess learning in CBE.

a) Norm-referenced assessment
b) Criterion-referenced assessment

The concept criterion-referenced assessment was coined in education and educational psychology in 1962 to describe assessments of proficiency based on academic achievement. Criterion referencing highlight higher-order cognitive abilities like logical

reasoning and concise and incisive writing (Lok et al., 2016). Table 11 summarizes the distinctions and correlations between criterion-referenced and norm-referenced evaluations.

In CBE, most universities assess students using rubrics (Learning, 2010), which are highly dependent on the extent to which data, documents, or objects demonstrate students meeting the stated quality, criteria, or rubric. Additionally, some universities have developed their standard-based report cards (Newell, 2016). Rather than just listing subject areas, that lists expectations that students must follow for each content area. Similarly, input on the report card is an "A" or anything similar, outlining the degree to which the learner applied those standards. Figure 9 illustrates the comparison between the traditional education approaches and CBE approaches using software engineering competency lists as assessment criteria. Students are required to be able not only to understand, write, and explain concepts and algorithms but also to design their algorithms. As a result, students are expected to develop algorithms to address issues they confront. Goldman discussed the importance of demonstrating this ability to imagine and develop solutions (Goldman et al., 2008). CBE follows the formative and summative assessments; they assess throughout the learning process and teaching. Students proceed at the teacher's pace, regardless of whether they have mastered the material or require additional time. In the traditional approach, the students are expected to read, write and explain the algorithms for the given problem and know how to program and code. The summative assessment is primarily used in this approach. Within conventional education, learners must meet grade-level criteria for college and career readiness. The typical approach to assessment is to provide exams, tests, and quizzes to ascertain students' level of comprehension of the course material. There is, however, little emphasis on what the learner can accomplish or how she may apply her knowledge to develop real-world systems. One of the initial stages in sustaining an object-oriented approach is periodically evaluating its design during the system's development lifespan (Serban, 2010).

5 Discussion

The current study investigates the strengths of CBE over knowledge-based learning. It contributes to software engineering education and training. CBE is industry-driven and equips students to address real-world challenges and grow into lifelong learners. In an era where much technological progress and many transitions and changes occur, the world becomes a small village where the sights are mingled. Cultures are blended with technological evolution.

Additionally, schools and universities are no longer the only sources of information nowadays. Students can find information quickly and conveniently through the internet and modern technology. To keep up with the rapid development of educational systems, it may access information beyond what is required to know during its study years. As a result, the educational system requires more flexible and innovative action. Competency-based education is an essential characteristic of this flexibility because it measures learning rather than time.

Table 11 Distinction and correlations between CRA and NRA

	Criterion-referenced assessment	Norm-referenced assessment
Purpose	Exemplify the developmental performance of the individual learners	Create a rating system for students about a group.
Design of assessment tasks	Consistent with the contents and anticipated results	Distinguishes between high and low achievers
Unit of score interpretation	Individual	Group
Score presentation	Grades assigned by criteria	Grades are calculated from raw scores and are often displayed in a normal distribution. They are often coarse-grained to the grading scale.
Advantages	• Capable of reflecting each student's real success and development • Allows overt inclusion of higher-order cognitive capabilities so that evaluation will properly reflect these abilities	• Capable of comparing individuals within a population • It can be scientifically calibrated to have a defined width (standard deviation) • Capable of avoiding grade inflation
Disadvantages	• There is no regulation over grade allocation, resulting in grade inflation • Less likely to compare with their counterparts	• Group efforts may affect individual scores, resulting in inequitable treatment for the students in the group • Can understate the extent to which factual discrepancies exist between individual students

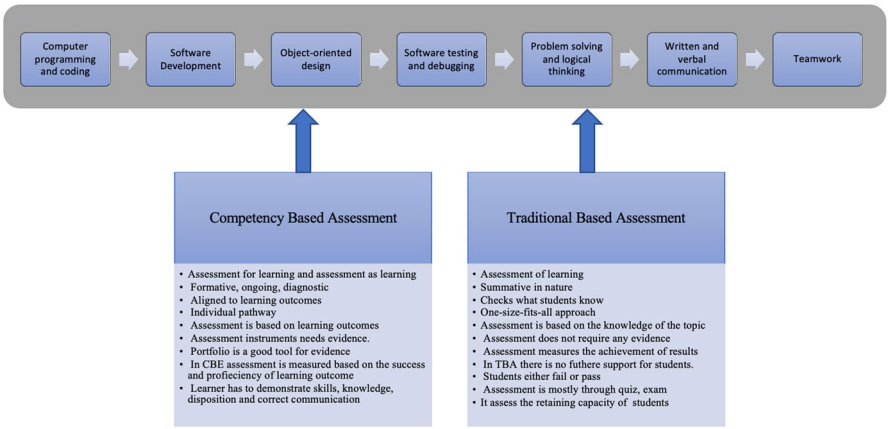

Fig. 9 Comparison between the traditional education approaches and CBE approaches using software engineering competency list

Moreover, a competency-based curriculum could play a significant role in higher education, providing accessible opportunities that contribute to proven competence (Soares, 2012). It can be inferred that the CBE is rapidly making inroads in engineering education, fulfilling various student needs, and satisfying business and career demands for qualified engineers (Henri et al., 2017). CBE focuses more on the skills, ability, and talents to perform a task in a standardized way. Hence, it identifies the technical skills of a student and focuses on behavioural competencies.

In CBE, the role of teachers is different from that of the traditional approach. Here, the teacher acts as a guide, mentor, and facilitator. The learning outcomes are explicit, rigorous, and shared. The measurement of learning is based on mastery but not time or participation. The instructional approaches and support in CBE are individualized, relevant, varied, and offer students independence and responsibility. At the same time, the assessment process provides flexibility and choice in showing what they know.

Consequently, assessment plays a critical role in CBE; it is assessment-driven. There are two primary methods for assessing learning in CBE (Lok et al., 2016): norm reference assessment and criterion reference assessment. Norm reference assessment aims to determine what constitutes outstanding, decent, and lousy performance on tasks by learners; the purpose of norm reference assessment is to evaluate learners within a cohort. While, in criterion reference assessment, students are defined either as competent or not yet competent, there is no in-between. The goal is to compare learners within standards. The traditional system is not designed to achieve goals or deliver the results that students, communities, and society deserve.

Meanwhile, the traditional system's flaws contribute to inequity and failure. The conventional system categorizes and rates students, resulting in winners and losers. In the end, there is no focus on building students' capability and competency—failure to comprehend that student growth depends on social and emotional abilities and the

ability to employ them. Consequently, assistance is intended to help students who have educational or psychological requirements that are unusual.

Most importantly, traditional methods emphasized summative evaluation to validate student learning. During or after the semester, all students take the same test on the same topic (Sturgis & Casey, 2018). Enrolled students in CBE courses that include practical educational activities, including lab work, are better suited to develop research projects and other higher-order skills and knowledge needed for employment or further education (di Trapani & Clarke, 2012a, b). The number of studies on CBE in engineering education focuses on non-content-based competencies that all students should acquire before graduation. A far more extensive body of literature examines how to determine which professional or contextual competencies engineering students should possess and improve students' achievement and assessment of those competencies. Any engineering education methodology, including CBE, should successfully deliver engineers who are skilled in technical knowledge and skills and capable of competing in a global market by effectively collaborating with broad categories of people in diverse circumstances. The most effective pedagogy is ineffective unless it teaches the required skills. While knowledge-based capabilities vary by speciality, all engineers should possess a core set of professional competencies upon completing their undergraduate degrees. Hence, these professional abilities are critical for students to succeed as competitive and competent engineers in the engineering field. a) Ability to lead, b) Capacity for collaboration, c) Effective communication abilities, d) Practice of reflective behaviour, e) Multidisciplinary abilities, f) Taking a disciplinary viewpoint into account, g) Contextuality, h) Design abilities (Henri et al., 2017). To summarize, CBE assures students' happiness and the ease with which they will complete the course.

6 Conclusion

Although competency-based education demands a considerable initial investment, it can reposition instructors as facilitators and promoters of education rather than enforcers. Despite this possibility, higher education has not yet reached a position where competency-based models may be entirely adopted without requiring a commitment to transform mindsets. The shift from traditional learning modes to CBE is examined in detail in this paper. The conventional method of education in this era is a waste of time and money for the learners. They invest time yet ultimately receive less than they invested. The competency objective is to transmit knowledge and focus on extensive skills that enable students to find solutions to difficult problems and complex contexts. Hence, we specified competency is composed of knowledge, skills, and dimensions within a task's performance.

Moreover, we have designed a model for integrating the KSD framework, and a learner can acquire a competency framework wherein the KSD framework knowledge, skill, and disposition. Still, the task is not guaranteed. In the competency model, task depictions give an unequivocal setting to the program to create a teaching method that empowers graduates to exhibit competency as computing proficient. On the one hand, we have pinpointed the essence of the differences between the two

learning approaches, namely knowledge-based Education and competency-based Education.

On the other hand, we enlisted both learning approaches' focus and found that competency-based learning is more recommended and required for teaching software engineering courses. The software engineering course's competency list is constructed to demonstrate their ability to succeed in the course. The competence assessment approach is assessment-driven, and it is a continuous evaluation that accelerates students' acquisition of information, skills, and value as they progress through the course. Lastly, Future studies should emphasize the advantages of CBE over alternative techniques in engineering education.

Data availability Data sharing is not applicable to this study as no dataset is used.

Declarations

Conflict of interest None.

References

Abdulaal, R., Al-Bahi, A., Soliman, A., & Iskanderani, F. (2011). Design and implementa- tion of a project-based active/cooperative engineering design course for freshmen. *European Journal of Engineering Education, 36*((4)), 391–402. https://doi.org/10.1080/03043797.2011.598498

ACMJIEEE-CS Joint as Force Computing Curricula. (2014) Software l engineering 2014: Curriculum curricula, guidelines for undergraduate degree programs in software engineering

ACM/IEEE. (2020). Computing Curricula 2020 CC2020. *ACM/IEEE*, 1–207. https://doi.org/10.0000/0000000

Baron, R. M., & Kenny, D. A. (1986). The moderator-mediator variable distinction in social psychological research: Conceptual, strategic, and statistical considerations. *Journal of Pe~nality and Social Psychology, 51*, 1173–1182.

Bartel, A., Figas, P., & Hagel, G. (2015). Towards a competency-based education with gamification design elements. *CHI PLAY 2015 - Proceedings of the 2015 Annual Symposium on Computer-Human Interaction in Play*, 457–462. https://doi.org/10.1145/2793107.2810325

Baughman, J. A., Brumm, T. J., & Mickelson, S. K. (2012). Student professional development: Competency based learning and assessment. *Agricultural and Biosystems Engineering Publications*, *38*(2), 1–15. https://doi.org/10.21061/jots.v38i2.a.6

Bechtel, G. A., Davidhizar, R., & Bradshaw, M. J. (1999). Problem-based learning in a competency-based world. *Nurse Education Today, 19*(3), 182–187

Bensah, E. C., Ahiekpor, J. C., & Boateng, C. D. (2011). Migrating from subject-based to competency-based training in Higher National Diploma Chemical Engineering: The case of Kumasi Polytechnic. *Education for Chemical Engineers., 6*((3)), 71–82. https://doi.org/10.1016/j.ece.2011.04.001

Boahin, P. (2018). Competency -based curriculum: A Framework for bridging the gap in teaching, assessement and the world of work. *International Journal of Vocational and Technical Education Research, 4*(3), 121.

Canaleta, X., Vernet, D., Vicent, L., & Montero, J. A. (2014). Master in teacher training: A real implementation of active learning. *Computers in Human Behavior, 31*, 651–658. https://doi.org/10.1016/j.chb.2013.09.020

Carraccio, C., Wolfsthal, S. D., Englander, R., Ferentz Kevin, M. P. H., & Martin, C. (2002). Shifting paradigms: From flexner to competencies. *ACADEM I C MEDIC INE, 77*, 361–367.

Chacko, T. (2014). Moving toward competency-based Education: Challenges and the way forward. *Archives of Medicine and Health Sciences, 2*(2), 247. https://doi.org/10.4103/2321-4848.144365

Clear, A., Clear, T., Impagliazzo, J., & Wang, P. (2020). From knowledge-based to competency-based computing education: Future directions. *Proceedings - Frontiers in Education Conference, FIE, 2020-Octob*. https://doi.org/10.1109/FIE44824.2020.9274288

Council of Chief State School Officers. (2013). Knowledge, skills, and dispositions: The innovation lab network state framework for college, career, and citizenship readiness, and implications for state policy council of chief state school officers. pp. 2–13

Cruz, M. L., Saunders-Smits, G. N., & Groen, P. (2020). Evaluation of competency methods in engineering education: A systematic review. *European Journal of Engineering Education, 45*(5), 729–757. https://doi.org/10.1080/03043797.2019.1671810

Demetriades, L., & Jacobs, K. (2006). 386 Managing' normality' and CF during adolescence: A qualitative study. *Journal of Cystic Fibrosis, 5*, S85. https://doi.org/10.1016/s1569-1993(06)80326-7

Di Trapani, G., & Clarke, F. (2012a). Biotechniques laboratory: An enabling course in the biological sciences. *Biochemistry and Molecular Biology Education, 40*((1)), 29–36. https://doi.org/10.1002/bmb.20573

di Trapani, G., & Clarke, F. (2012b). Biotechniques laboratory: An enabling course in the biological sciences. *Biochemistry and Molecular Biology Education, 40*(1), 29–36. https://doi.org/10.1002/bmb.20573

Diksha. (2021). *How CBE differes from traditional approach*. https://diksha.gov.in/resources?

Dinsmore, D. L., Alexander, P. A., & Loughlin, S. M. (2008). The impact of new learning environments in an engineering design course. *Instructional Science, 36*(5/6), 375–393. https://doi.org/10.1007/s11251-008-9061-x

Ehlers, U.-D. (2010). Changing cultures in higher education moving ahead to future learning. *Springer Heidelberg Dordrecht London New York*, pp. 1–533. https://doi.org/10.1007/978-3-642-03582-1

Epstein, R. M., & Hundert, E. M. (2002). *Defining and Assessing Professional Competence*. *287*(2), 226–235. www.jama.com

European Parliament and Council of the European Union. (2008). Recommendations of the European Parliament and of the council of 23 April 2008 on the establishment of the European Qualifications Framework for lifelong learning - (2008/C 111/01). *Official Journal of the European Union, C111*, 1–7. https://doi.org/10.2766/14352

Evans, J. J., Garcia, E., Smith, M., Van Epps, A., Fosmire, M., & Matei, S. (2015). An assessment architecture for competency-based learning: Version 1.0. *Proceedings - Frontiers in Education Conference, FIE, 2015*. https://doi.org/10.1109/FIE.2015.7344340

Fastré, G. M. J., van der Klink, M. R., Amsing-Smit, P., & van Merriënboer, J. J. G. (2014). Assessment criteria for competency-based education: A study in nursing education. *Instructional Science, 42*(6), 971–994. https://doi.org/10.1007/s11251-014-9326-5

Fedena. (n.d.). *Competency-Based Learning: Pros & Cons*. Retrieved March 12, 2021, from https://fedena.com/blog/2019/09/competency-based-learning-pros-cons.html

Felder, R. M., Brent, R., & Prince, M. J. (2011). Engineering instructional development: Programs, best practices, and recommendations. *Journal OfEngineering Education, 100*((1)), 89–122. https://doi.org/10.1002/j.2168-9830.2011.tb00005.x

Felder, R. M., Brent, R., & Prince, M. J. (2015). Engineering instructional development: Programs, best practices, and recommendations. *Cambridge Handbook of Engineering Education Research, 100*(1), 409–436. https://doi.org/10.1017/CBO9781139013451.027

Gharaibeh, K., Harb, B., BanySalameh, H., Zoubi, A., Shamali, A., Murphy, N., & Brennan, C. (2013). Review and redesign of the curriculum of a Masters programme in telecommunications engineering - Towards an outcome-based approach. *European Journal of Engineering Education, 38*(2), 194–210. https://doi.org/10.1080/03043797.2013.766674

Goldman, K., Gross, P., Heeren, C., Herman, G., Kaczmarczyk, L., Loui, M. C., & Zilles, C. (2008). Identifying important and difficult concepts in introductory computing courses using a delphi process. *SIGCSE'08 - Proceedings of the 39th ACM Technical Symposium on Computer Science Education*, 256–260. https://doi.org/10.1145/1352135.1352226

Gre'goire, J. (1997). Diagnostic assessment of learning disabilities: From assessment of performance to assessment of competence. *European Journal of Psychological Assessment, 13*((1)), 10–20.

Gruppen, L. D., Mangrulkar, R. S., & Kolars, J. C. (2012). The promise of competency-based education in the health professions for improving global health. *Human Resources for Health, 10*(1), 1–7

Gulikers, J. T. M., Baartman, L. K. J., & Biemans, H. J. A. (2010). Facilitating evaluations of innovative, competence-based assessments: Creating understanding and involving multiple stakeholders. *Evaluation and Program Planning, 33*, 120–127.

Henri, M., Johnson, M. D., & Nepal, B. (2017). A review of competency-based learning: Tools, assessments, and recommendations. *Journal of Engineering Education, 106*(4), 607–638. https://doi.org/10.1002/jee.20180

Hernandez, W., Palmero, J., Labrador, M., Alvarez-Vellisco, A., & Bonache, J. (2009). Analysis of results of application of a student-centered learning system to improve perfor- mance of first-year students. *International Journal of Engineering Education, 25*((1)), 161–172.

Hoogveld, A. W. M., Paas, F., & Jochems, W. M. G. (2005). Training higher education teachers for instructional design of competency-based Education: Product-oriented versus process-oriented worked examples. *Teaching and Teacher Education, 21*(3), 287–297. https://doi.org/10.1016/j.tate.2005.01.002

Hsu, & Ho, C.-C. (2012). The design and implementation of a competency-based intelli- gent mobile learning system. *Expert Systems with Applications, 39*(9), 8030–8043. https://doi.org/10.1016/j.eswa.2012.01.130

Huili, Z. (2010). Knowledge-based design of the open-learning process. *IEEE,2010 International Conference on Networking and Digital Society*, 302–305.

Kennedy, D. (2006). Writing and using learning outcomes: A practical guide. University College Cork

Khoumsi, A., & Gonzalez-Rubio, R. (2006). Applying a competency- and problem-based approach for learning compiler design. *Journal of STEM Education: Innovations and Research, 7*(1–2), 24–33.

Kulik, J. A., Kulik, C. L. C., & Cohen, P. A. (1979). Research on audio-tutorial instruction: A meta-analysis of comparative studies. *Research in Higher Education, 11*(4), 321–341. https://doi.org/10.1007/BF00975623

Learning, C. for the E. of T. and. (2010). Rubrics for Engineering Education. *Hong Kong Engineering Education Enhancement and Research*, *i*. http://hke3r.cetl.hku.hk

Lin, T.-J., Duh, H.B.-L., Li, N., Wang, H.-Y., & Tsai, C.-C. (2013). An investigation of learners' collaborative knowledge construction performances and behavior patterns in an augmented reality simulation system. *Computers and Education, 68*, 314–321. https://doi.org/10.1016/j.compedu.2013.05.011

Lok, B., McNaught, C., & Young, K. (2016). Criterion-referenced and norm-referenced assessments: Compatibility and complementarity. *Assessment and Evaluation in Higher Education, 41*(3), 450–465. https://doi.org/10.1080/02602938.2015.1022136

May, D., Wold, K., & Moore, S. (2015). Using interactive online role-playing simulations to develop global competency and to prepare engineering students for a globalized world. *European Journal of Engineering Education, 40*((5)), 522–545. https://doi.org/10.1080/03043797.2014.960511

Meincke, F., & Tavangarian, D. (2011, September). Computer engineering online-Best practice in long distance approaches for lifelong learning. *In 2011 14th International Conference on Interactive Collaborative Learning, IEEE*, (pp. 161–164)

Nelson, B. (2013). Using a competency-based instructional approach in thermodynamics. *Frontiers in Education Conference, 2013 IEEE, Oklahoma City, OK.*

Newell, S. P. (2016). The impact of standards-based report cards on reading development of primary grade students. *Dissertation Abstracts International Section A: Humanities and Social Sciences*, *76*(8-A(E)). http://search.ebscohost.com/login.aspx?direct=true&db=psyh&AN=2016-17336-119&site=ehost-live

Oladiran, M., Uziak, J., Eisenberg, M., & Scheffer, C. (2011). Global engineering teams–A programme promoting teamwork in engineering design and manufacturing. *European Journal of Engineering Education, 36*((2)), 173–186. https://doi.org/10.1080/03043797.2011.573534

Passow, H. J., & Passow, C. H. (2017). What Competencies should undergraduate engineering programs emphasize? A systematic review. *Journal of Engineering Education, 106*(3), 475–526. https://doi.org/10.1002/jee.20171

Preston, J. (2017). Competence based education and training (CBET) and the end of human learning: The existential threat of competency. Springer

Ravet, S. (2013). *Competency based learning: What is the place of assessment?* Transit.Ea/Gr.

Rikakis, T., Tinapple, D., & Olson, L. (2013). The digital culture degree: A competency-based interdisciplinary program spanning engineering and the arts. *Frontiers in Education Conference, 2013 IEEE, Oklahoma City, OK.*

Ro, H. K., Merson, D., Lattuca, L. R., & Terenzini, P. T. (2015). Validity of the contextual competence scale for engineering students. *Journal of Engineering Education, 104*((1)), 35–54. https://doi.org/10.1002/jee.20062

Roe, E. A., & Bartelt, T. (2015). Converting a traditional engineering technology program to a competency-based, self-paced, open-entry/open-exit format. *ASEE Annual Conference and Exposition, Conference Proceedings*, *122nd ASEE*(122nd ASEE Annual Conference and Exposition: Making Value for Society). https://doi.org/10.18260/p.23747

Sadler, D. R. (1985). The origins and functions of evaluative criteria. *Educational Theory, 35*((3)), 285–297.

Serban, C. (2010). A conceptual framework for object-oriented design assessment. *Proceedings - UKSim 4th European Modelling Symposium on Computer Modelling and Simulation, EMS2010*, 90–95. https://doi.org/10.1109/EMS.2010.26

Silva, E., Almeida, J., Martins, A., Baptista, J. P., & Campos Neves, B. (2013). Master's in autonomous systems: An overview of the robotics curriculum and outcomes at ISEP, Portugal. *IEEE Transactions on Education, 56*(1), 98–102. https://doi.org/10.1109/TE.2012.2220360

Soares, L. (2012). A 'Disruptive' Look at Competency-Based Education | Center for American Progress. *Center for American Progress*, 1–12. http://www.americanprogress.org/issues/higher-education/report/2012/06/07/11680/a-disruptive-look-at-competency-based-education/

Society, I. C. (2014). Software Engineering Competency Model. *SWECOM A Project of the IEEE Computer Society*, pp. 1–168

Spelt, E. J. H., Luning, P. A., van Boekel, M. A. J. S., & Mulder, M. (2015). Constructively aligned teaching and learning in higher education in engineering: What do students per- ceive as contributing to the learning of interdisciplinary thinking? *European Journal of Engineering Education, 40*((5)), 459–475. https://doi.org/10.1080/03043797.2014.987647

Sturgis, C. and Casey, K. Quality principles for competency based education. Vienna: INACOL, 2018

Sullivan, R., & McIntosh, N. (1996). The competency-based approach to training. *Medical Journal of Indonesia, 5*(2), 95–8

Sutcliffe, N., Chan, S. S., & Nakayama, M. (2005). A competency based MSIS curriculum. *Journal of Information Systems Education, 16*(3), 301–310.

Tang, S. (2014). An interactive simulator-based pedagogical (ISP) approach for teaching microcontrollers in engineering programs. *Advances in Engineering Education, 4*((2)), 1–18.

Task Group on Information Technology Curricula. (2017). Information technology curricula 2017: Curriculum guidelines for baccalaureate degree programs in information technology. Association for Computing Machinery, New York, NY, USA

Thurner, V., & Böttcher, A. (2012, April). Expectations and deficiencies in soft skills. In Proceedings of the 2012 IEEE global engineering education conference (EDUCON), IEEE, (pp. 1–7)

Thurner, V., Ottcher, A., & Kämper, A. (2014). Identifying Base Competencies as Prerequisites for Software Engineering Education. *IEEE Global Engineering Education Conference (EDUCON)*, 1069–1076

Tony Bates. (n.d.). *The strengths and weaknesses of competency-based learning in a digital age*. Retrieved March 12, 2021, from https://www.tonybates.ca/2014/09/15/the-strengths-and-weaknesses-of-competency-based-learning-in-a-digital-age/

Van der Klink, M., Boon, J., & Schlusmans, K. (2007). Competences and vocational higher education: Now and in future. *European journal of vocational training, 40*(1), 67–82

Van Merriënboer, J. J. G., & Kirschner, P. A. (2007). *Ten steps to complex learning*. Erlbaum/ Taylor and Francis.

Veldman, F. J., De Wet, M. A., Mokhele, N. E. I., & Bouwer, W. A. J. (2008). Can engineer- ing education in South Africa afford to avoid problem-based learning as a didactic approach? *European Journal OfEngineering Education, 33*((5–6)), 551–559. https://doi.org/10.1080/03043790802564152

Walther, J., Kellam, N., Sochacka, N., & Radcliffe, D. (2011). Engineering competence? An interpretive investigation of engineering students' professional formation. *Journal of Engineering Education, 100*(4), 703–740. https://doi.org/10.1002/j.2168-9830.2011.tb00033.x

Webster, M. (2020). https://www.merriam-webster.com/dictionary/competency

Weinert, F. E. (2013). Max planck institute for psychological research, Munich. Memory development: Universal changes and individual differences, pp. 381

Witt, H.-J., Alabart, J., Giralt, F., Herrero, J., Vernis, L., & Medir, M. (2006). A competency-based educational model in a chemical engineering school. *International Journal of Engineering Education, 22*(2), 218–235.

Woodrow, M., Bisby, L., & Torero, J. L. (2013). A nascent educational framework for fire safety engineering. *Fire Safety Journal, 58*, 180–194. https://doi.org/10.1016/j.firesaf.2013.02.004

Publisher's note Springer Nature remains neutral with regard to jurisdictional claims in published maps and institutional affiliations.

Springer Nature or its licensor (e.g. a society or other partner) holds exclusive rights to this article under a publishing agreement with the author(s) or other rightsholder(s); author self-archiving of the accepted manuscript version of this article is solely governed by the terms of such publishing agreement and applicable law.

Single DXCCTA based Charge Controlled Floating Incremental/Decremental Memristor Emulator

2022 8th International Conference on Signal Processing and Communication (ICSC) | 978-1-6654-5430-8/22/$31.00 ©2022 IEEE | DOI: 10.1109/ICSC56524.2022.10009249

Navnit Kumar
Department of Electronics and Communication Engineering, Delhi Technological University,
Delhi, India.
navnitnitmanipur@gmail.com

Manjeet Kumar
Department of Electronics and Communication Engineering, Delhi Technological University,
Delhi, India.
manjeetchhillar@gmail.com

Neeta Pandey
Department of Electronics and Communication Engineering, Delhi Technological University,
Delhi, India.
n66pandey@rediffmail.com

***Abstract* - This article offers a charge controlled floating incremental/decremental memristor emulator using Dual-X Current Conveyor Transconductance Amplifier (DXCCTA). The proposed circuit includes one DXCCTA, four resistors, one grounded capacitor and two MOS switches. Incremental and decremental mode of operation depends upon setting of MOS switch. This paper avoids the utilization of analog multiplier circuit. Pinch hysteresis curves of proposed circuit are hold up to 60 MHz. Moreover, two memristor combinations are connected in series and parallel to examine the functionality of the proposed memristor emulator, and the intended results are acquired. Performance of the designed circuit is evaluated, at schematic level 90 CMOS process technology, are presented.**

Keywords- Memristor Emulator, Mem-immittance Circuit, Pinch Hysteresis loop, DXCCTA.

I. INTRODUCTION

Memristor is two terminal passive component that provides connection between electric charge (q) and magnetic flux (φ). It is known as fourth element [1,2] after inductor, capacitor, and resistor. Non-volatile nature of memristor provides various applications such as programmable gate array [3], programmable analog circuit [4], neuromorphic computing circuit [5], adaptive filter [6], hyperchaotic oscillator [7], relaxation oscillator [8,9] and many more. Memristor is conceived by L. O. Chua in 1971.First solid state memristor is fabricated by Hewlett-Packard (H. P.) lab in 2008. This solid state memristor is designed by sandwiching titanium dioxide between two platinum plates. Due to its exorbitant price and challenging fabrication method, this solid state memristor is not easily obtainable. This limitation motivates to researcher to develop active building block (ABB) based memristor circuits. Literature survey of ABB based memristor emulator is given below.

Sozen and cam [10] proposed flux controlled floating memristor circuit. It includes four second generation current conveyor (CCII), three operational transconductance amplifier (OTA), six resistors and one grounded capacitor. 10 kHz is maximum operating frequency of the circuit. Tahir and khalifa [11] introduced a floating memristor circuit. This circuit consist of four AD844 IC, two diodes, four resistors and four capacitors. Lopez et al. [12] designed charge control grounded memristor emulator. This circuit uses two ADD844N IC (integrated circuit), one AD633JN IC, four resistors and three capacitors. Pinch hysteresis curve of the designed circuit maintained up to 160 kHz. Lopez et al. [13] introduced flux controlled floating memristor circuit. This circuit uses four ADD844N IC, one AD633JN IC, five resistor and one capacitor. 20.2 kHz is operating frequency of the designed circuit. Kanyal et al. [14] proposed flux controlled floating memristor emulator. This circuit uses two OTAs and one grounded capacitor. Maximum operating frequency of designed circuit is 400 kHz. Ranjan et al. [15] introduced charge controlled floating memristor emulator. The proposed circuit includes one current conveyor transconductance amplifier (CCTA), three resistors and one capacitor. 10 MHz is maximum frequency of operation of this circuit. A Charge controlled grounded memristor emulator was proposed by Ranjan et al. [16]. One differential voltage current conveyor transconductance amplifier (DVCCTA), three passive resistors, and one capacitor are used in the designed circuit. Operating frequency of this circuit is 1MHz. Yesil et al. [17] designed floating memristor emulator established on differential difference current conveyor (DDCC). This circuit consist of one DDCC, two resistors, one multiplier circuit and one grounded capacitor. Maximum operating frequency of the designed circuit is 1 MHz. Vista and Ranjan [18] proposed flux controlled floating memristor emulator. Proposed circuit includes one voltage difference transconductance amplifier (VDTA), one passive resistor and one grounded capacitor. Operating frequency of designed emulator is reported as 50 MHz. Petrovic [19] introduced flux controlled floating memristor emulator circuit. This circuit is designed with help of one VDTA, one analog multiplier circuit, two passive resistors, one grounded capacitor. Output range of frequency of proposed circuit is 2 MHz. Yadav et al. [20] designed flux controlled floating memristor emulator circuit. This circuit includes one voltage differencing buffered amplifier (VDBA) as an ABB and one capacitor as passive component. 1 MHz is operating frequency of the designed circuit. Yesil et al. [21] introduced flux controlled grounded memristor circuit. This circuit is designed using one voltage differencing current conveyor (VDCC), one grounded capacitor and two MOS resistor. Maximum operating frequency of designed circuit is 2 MHz. Raj et al. [22] introduced flux controlled grounded memristor emulator circuit. This circuit includes one CCII, one OTA, one resistor and one grounded capacitor. 26.3 MHz is maximum operating frequency of this circuit. A grounded memristor circuit is introduced by Ayten et al. [23]. One current backward transconductance amplifier (CBTA), two passive resistors, one analogue multiplier circuit, and one capacitor are used.460 kHz is maximum operating frequency of the designed circuit.

In this study we present charge controlled floating incremental/decremental memristor emulator circuit. The designed circuit consists of one DXCCTA as active

978-1-6654-5430-8/22/$31.00 ©2022 IEEE

Authorized licensed use limited to: DELHI TECHNICAL UNIV. Downloaded on January 17,2023 at 05:02:15 UTC from IEEE Xplore. Restrictions apply.

components, four resistors and one grounded capacitor as passive components. Incremental and decremental modes of operation is achieved by appropriate setting of MOS switch. Additional circuit such as analog multiplier circuit is not required to design the proposed circuit. 60 MHz frequency is maximum operating frequency of the designed circuit. Remaining paper is organized as follow: Circuit description of proposed circuit is discussed in section 2. Fingerprints and nonvolatile nature of proposed circuit is discussed in section 3. Section 4 shows application of proposed emulator. Finally, section 5 concludes the research article.

II. CIRCUIT DESCRIPTION

DXCCTA is advance analog active building block. It is designed using CCII, ICCII and OTA. The block symbol and its MOS based internal realization is depicted in Fig.1. Voltage and current relationship of DXCCTA is given in equation (1) as:

$$I_Y = 0; \varsigma_{\Xi+} = +V_Y; \varsigma_{\Xi-} = -V_Y; I_{\Xi+} = I_{Z+}; I_{\Xi-} = I_{Z-};$$

$$I_{0+} = g_m V_{Z-};\ I_{0-} = -g_m V_{Z-} \quad (1)$$

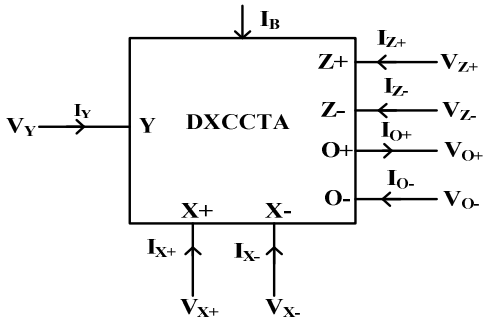

(a)

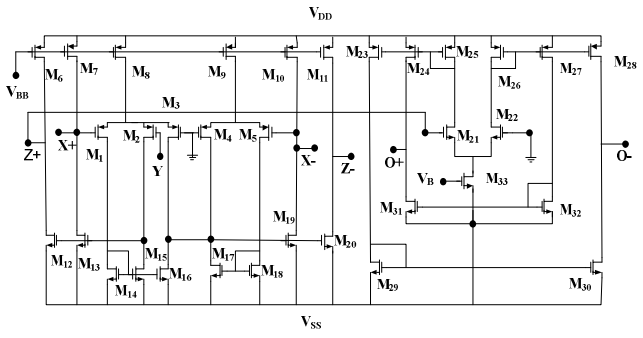

(b)

Fig. 1. DXCCTA (a) Block symbol (b) MOS based internal design [24].

A charge controlled floating incremental/decremental memristor emulator using DXCCTA is proposed in Fig.2. This circuit includes one active building block (DXCCTA), two MOS switches, four resistors and one grounded capacitor. Incremental and decremental mode of operation may be achieved by high and low gate voltage (V_A) of MOS switch respectively.

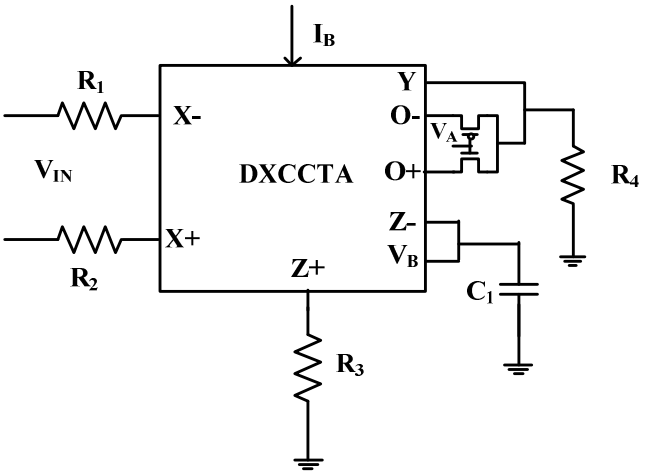

Fig. 2. Proposed memristor emulator using DXCCTA.

Current passing through the terminals I_{X+} and I_{X-} terminal of proposed circuit may be expressed as:

$$I_{X+} = \frac{V_{in1} - V_Y}{R_1}\ ; I_{X-} = \frac{V_{in2} + V_Y}{R_2} \quad (2)$$

Voltage at Y terminal of proposed circuit using characteristic equation of DXCCTA, we get

$$V_Y = \pm 2k(V_B + V_{ss} - V_T) I_{X+} R_3 R_4 \quad (3)$$

Where $k = \mu_n C_{ox} \frac{W}{L}$. Here, μ_n, C_{ox} and $\frac{W}{L}$ having their usual meaning. The input voltage across the memristor circuit may be given by

$$V_{in} = V_{in1} - V_{in2} = I_{X+} R_1 - R_2 I_{X-} \pm 4k(V_B + V_{ss} - V_T) I_{X+} R_3 R_4 \quad (4)$$

Substitute $V_{in1} = V_{in}(t)$ and $V_{in2} = \frac{V_{in}(t)}{2}$ in above expression, then above equation may be written as:

$$V_{in}(t) = I_{in}(t)(R_1 - R_2) \pm 4k(V_B + V_{ss} - V_T) I_{in}(t) R_3 R_4 \quad (5)$$

Substitute $V_B = \frac{q_c(t)}{C}$ in above equation, we get memristance of proposed memristor emulator as:

$$M(q_C(t)) = \frac{V_{in}(t)}{I_{in}(t)} = (R_1 - R_2) \pm 4k\left(\frac{q_c(t)}{C} + V_{ss} - V_T\right) R_3 R_4 \quad (6)$$

If $R_1 = R_2 = R$, then memristance of floating memristor emulator may be rewritten as:

$$M(q_C(t)) = \frac{V_{in}(t)}{I_{in}(t)} = \pm 2k(V_{ss} - V_T) R_3 R_4 \pm 4k \frac{q_c(t)}{C} R_3 R_4 \quad (7)$$

Frequency response of proposed circuit may be obtained by connecting ac voltage source Vin=$A_m sin(\omega_m t)$ at input terminal. Where, A_m and ω_m are known as amplitude and angular frequency. Now, memristance may be obtained as:

Authorized licensed use limited to: DELHI TECHNICAL UNIV. Downloaded on January 17,2023 at 05:02:15 UTC from IEEE Xplore. Restrictions apply.

$$M(q_C(t)) = \frac{V_{in}(t)}{I_{in}(t)} = \pm 2k(V_{ss} - V_T)R_3R_4 \pm 4k\frac{A_m cos(\omega t - \pi)}{C\omega_m(2k(V_{ss}-V_T))} \quad (8)$$

III. Simulation Results

Theoretical aspects of proposed floating memristor emulator are verified by PSPICE simulation using Microwind 90 nm process technology (Level-3). Supply voltage and bias voltage (V_{BB}) of DXCCTA are ±1.2 V and 0.42 V respectively. The size of transistors of DXCCTA are mentioned in ref. [24]. Investigation of the transient response of proposed floating memristor, the components value selected as R_1=R_2=2.2 kΩ, R_3=5 kΩ, R_4=2.6 kΩ, and C_1=5 pF and differential input voltage Vin=120 mV at 10 MHz input frequency. The transient response and corresponding pinch hysteresis curve are illustrated in Fig.3, which conforms first fingerprint [25] of designed memristor circuit.

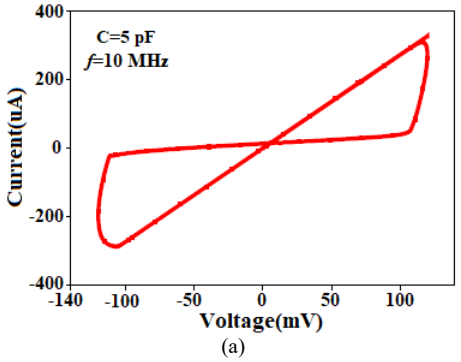

(a)

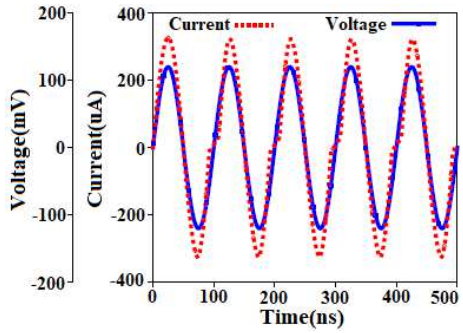

(b)

Fig. 3. Characteristic of proposed memristor emulator. (a) Pinch hysteresis curve and (b)Transient response.

Moreover, Fig. 4 shows pinch hysteresis curve of floating memristor emulator at different capacitance value of 5 pF, 10 pF, and 30 pF while making frequency f=10 MHz and amplitude of differential input signal Vin=120 mV constant. It is seen from Fig.4 that linear time invariant part of equation (8) is dominating at capacitance value of 30 pF. Fig. 5(a) to 5(c) show pinch hysteresis curve of proposed memristor emulator at different input frequency of 10 MHz, 20 MHz, and 60 MHz while making capacitance C=10 pF and amplitude of input differential signal Vin=120 mV constant. It is seen from the Fig. 5(a-c) that area of lobe of pinch hysteresis curves start to decrease as input frequency increase, and finally the proposed memristor emulator changes its nonlinear resistor behavior to a linear resistor at 60 MHz input frequency, these are commonly known as 2nd and 3rd fingerprints [25] of memristor, which conform that the proposed nonlinear circuit is memristor. In addition, effect of variation of bias voltage (V_{BB}) of DXCCTA is illustrated in Fig.6, which shows that pinch hysteresis curve of memristor is decreased as bias voltage of DXCCTA is increased. Non-volatile characteristic of proposed circuit is shown in Fig. 7. Power consumption of the proposed circuit is 4.7 mW. Comparison between active block based published memristor circuit and proposed memristor emulator is mentioned in Table1.

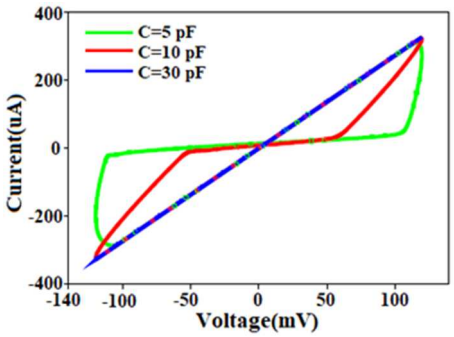

Fig. 4. Pinch hysteresis curve of proposed memristor emulator for C=5 pF to 30 pF

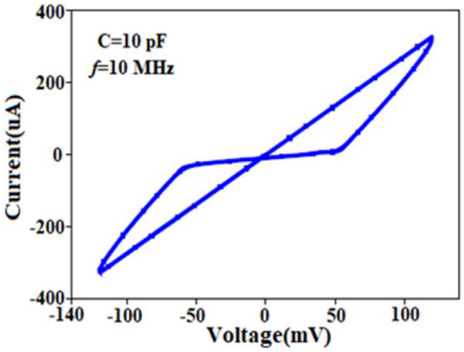

(a)

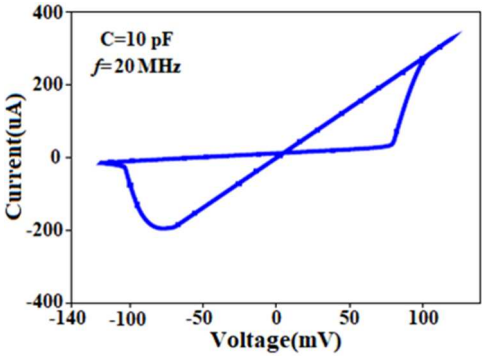

(b)

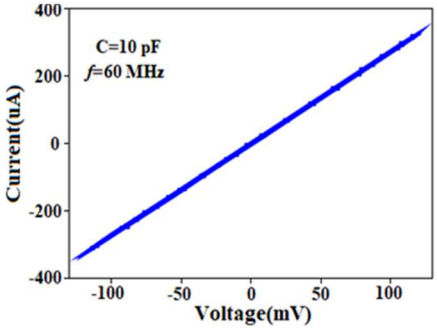

(c)

Authorized licensed use limited to: DELHI TECHNICAL UNIV. Downloaded on January 17,2023 at 05:02:15 UTC from IEEE Xplore. Restrictions apply.

Fig. 5. Pinch hysteresis curve of proposed memristor emulator for (a) f=10 MHz, (b) f=20 MHz and (c) f= 60 MHz.

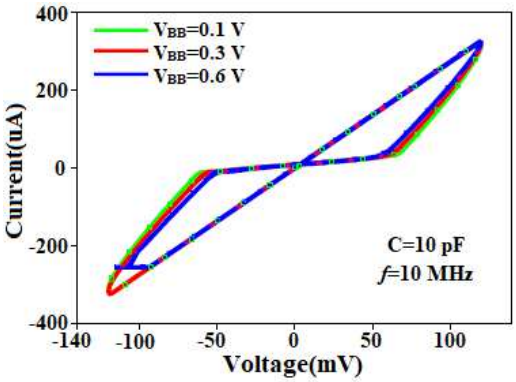

Fig. 6. Pinch hysteresis curve of proposed memristor emulator for different bias voltage of DXCCTA.

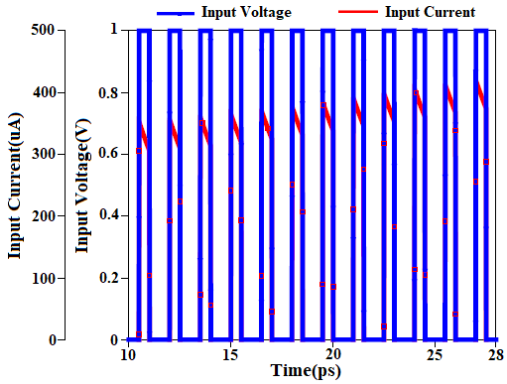

Fig. 7. Non-Volatile nature of proposed memristor emulator.

TABLE I. COMPARISON OF ACTIVE BLOCK BASED PUBLISHED MEMRISTOR CIRCUIT WITH PROPOSED MEMRISTOR EMULATOR

Reference	No. of Active Block	No. of Resistors(R) / Capacitors (C)	Parameter	Power supply	Floating/ Grounded	Tunability	Max. Operating Freq.
[14]	OTA-2	0/1	180 nm	±1.2 V	Floating	YES	400 kHz
[15]	CCTA-1	3/1	180 nm	±1.5 V	Floating	YES	10 MHz
[16]	DVCCTA-1	3/1	250 nm	±1.25 V	Grounded	YES	1 MHz
[17]	DDCC-1 Multiplier-1	2/1	250 nm	±1.5 V	Floating	NO	1 MHz
[21]	VDCC-1	2/1	180 nm	±0.9 V	Grounded	YES	2 MHz
[22]	CCII-1 OTA-1	1/1	180 nm	±1.2 V	Grounded	YES	26.3 MHz
[23]	CBTA-1 Multiplier-1	2/1	180 nm	±0.9 V	Grounded	YES	460 kHz
Proposed	DXCCTA-1	4/1	90 nm	±1.2 V	Floating	YES	60 MHz

IV. APPLICATION

Performance of proposed memristor emulator can be verified through different configurations of connection of proposed circuit. Parallel configuration and series configuration of proposed circuit are displayed in Figs. 8(a) and 8(b) respectively. Fig. 9(a) shows that pinch hysteresis curve of proposed memristor circuit for parallel configuration in which memristance becomes half, therefore amount of current across the memristor will increase. Thus, area of lobe of pinch hysteresis curve in parallel connection is larger than area of lobe of pinch hysteresis curve in single configuration. Fig. 8(b) shows that pinch hysteresis loop of proposed memristor circuit in series configuration in which memristance becomes double, therefore current across the memristor will decrease. Hence, the area of lobe of pinch hysteresis curve in series configuration is smaller than area of lobe of pinch hysteresis curve in single configuration.

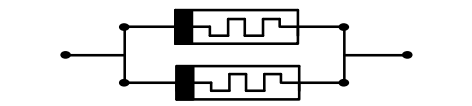

(a)

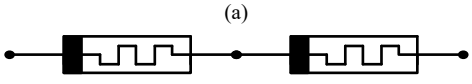

(b)

Fig. 8. Memristor connected in different configurations (a) Parallel and (b) Series.

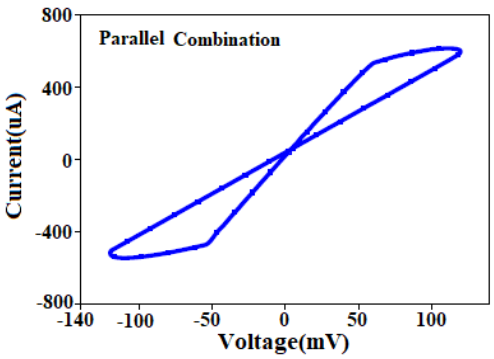

(a)

Authorized licensed use limited to: DELHI TECHNICAL UNIV. Downloaded on January 17,2023 at 05:02:15 UTC from IEEE Xplore. Restrictions apply.

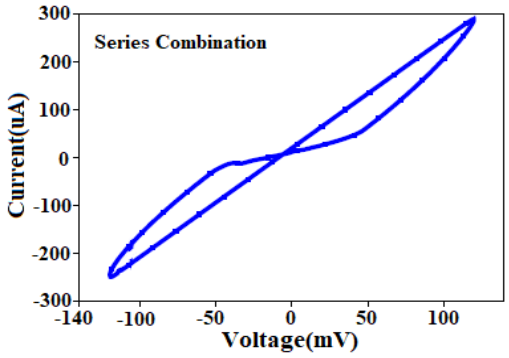

(b)

Fig. 9. Pinch hysteresis curve of proposed memristor emulator for(a) parallel configuration and (b) series configuration.

A first order low pass filter circuit may be used to show the workability of proposed memristor circuit. The first order MC_L and RC based low filter is shown in Fig. 10(a) and Fig. 10(b) respectively. Cut off frequency of memristor based high pass filter can be expressed as.

$$f = \frac{1}{2\pi C_L R_M} \tag{9}$$

Where R_M and C_L are memristance and capacitance respectively of the memristor based low pass filter. Resistance and capacitance value of RC based low pass filter are 2.2 kΩ, and 1 pF respectively. Whereas components selection for memristor based low pass filter are R_1=R_2=2.2 kΩ, R_3=5 kΩ, R_4=2.6 kΩ, C_1=5 pF and C_L=1 pF. Frequency response of RC based low pass filter and memristor based low pass filter are illustrated in Fig.11. It is seen from Fig.11 that the cut off frequency of the low pass filter is 72.38 MHz.

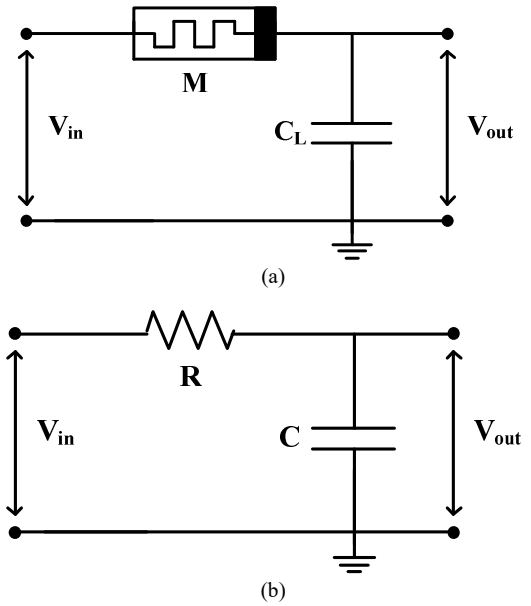

Fig. 10. (a) Memristor based low pass filter and (b) RC based low pass filter.

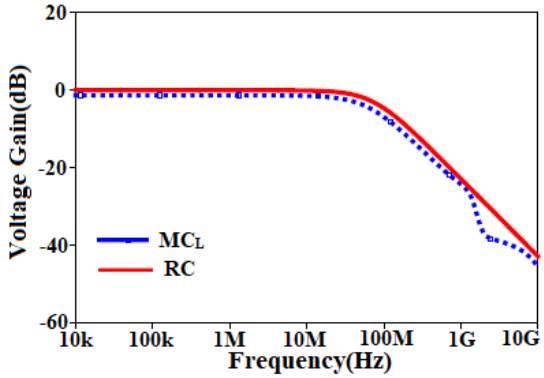

Fig. 11. Frequency response of RC and MC_L based low pass filter circuit

V. Conclusion

This paper presented charge controlled floating incremental/decremental memristor emulator. This circuit consist of one DXCCTA, two MOS switches, four resistors and one grounded capacitor. Incremental mode of operation to decremental mode of operation or vice-versa is achieved by appropriate setting of MOS switches. The designed circuit is free from additional circuit such as analog multiplier circuit, analog to digital convertor circuit and digital to analog converter circuit. Fingerprints and non-volatile nature of proposed emulator are demonstrated through corresponding results. Moreover, pinch hysteresis loop of proposed memristor is maintained up to 60 MHz. Finally, functionality of proposed emulator is examined by memristor based low pass filter circuits.

References

[1] J. M. Tour, and T. He, "Electronics: The fourth element," Nature, vol. 453, pp. 42-43, 2008.

[2] L. O. Chua, "Memristor: the missing circuit element." IEEE Transactions on Circuit Theory, vol. 18, no. 5, pp. 507-512, 1971.

[3] H. A. F. Almurib, T.N. Kumar, and F. Lombardi, "Design and evaluation of a memristor-based look-up table for non-volatile field programmable gate arrays," IET Circuits, Device System, vol. 10, no.4, pp.292-300, 2016.

[4] Y.V. Pershin, and M. Di Ventra, "Practical approach to programable analog circuits with memristors", IEEE Trans. Circuits System I, Reg. paper, vol. 57, no. 8, pp. 1857-1864, 2010.

[5] G. C. Adam, B. D. Hoskins, M. Prezioso, F. Merrikh-Bayat, B. Chakrabarti, and D. B. Strukov, "3-D memristor crossbars for analog and neuromorphic computing applications" IEEE Transaction Electron Devices, vol.64, no.1, pp.312-318, 2017.

[6] T. Driscoll et al., "Memristive adaptive filters," Applied phys. Letter, vol.97, no. 9, p. 093502, 2010.

[7] M.E.Sahin, A. S. Demirkol, H. Guler and S. E. Hamamci, "Design of a hyperchaotic memristive circuit based on wien bridge oscillator," Computers and Electrical Engineering, 88 (2020) 106826.

[8] D. Yu, H. H. C. Iu, "A Floating Memristor Emulator Based Relaxation Oscillator," IEEE Transaction on Circuits and System I: Regular Papers, vol. 61, no. 10, pp.2888-2896, Oct. 2014.

[9] M. E. Fouda, and A. G. Radwan, "Memristor-based voltage-controlled relaxation oscillators." International journal of circuit theory and applications, vol. 42, no. 10, pp. 1092-1102, 2014.

[10] H. Sozen and U. Cam, "Electronically tunable memristor emulator circuit," Analog Integrated Circuits Signal Processor, vol. 89, no. 3, pp. 655-663, 2016.

[11] M. T. Abuelama'atti and Z. J. Khalifa, "A new floating memristor emulator and its application in frequency-to-voltage conversion," Analog Integrated Circuit and Signal Processing. Vol. 86, pp. 141-147, 2016.

Authorized licensed use limited to: DELHI TECHNICAL UNIV. Downloaded on January 17,2023 at 05:02:15 UTC from IEEE Xplore. Restrictions apply.

[12] C. S. Lopez, M. A. C. Aguilar and C. M. Montero, “A 16 Hz-160kHz memristor emulator circuit,” International Journal of Electronics and Communications, vol. 69, no. 9, pp. 1208-1219, 2015.

[13] C. S. Lopez, M. A. C. Aguilar and C. M. Montero, “A Floating Analog Memristor Emulator Circuit,” IEEE Transactions on Circuits and System II, vol. 61, no. 5, pp. 309-313, May 2014.

[14] G. Kanyal, P. Kumar, S. K. Paul, and A. Kumar, “OTA based high frequency tunable resistorless grounded and floating memristor emulators,” International Journal of Electronics and Communications, vol. 92, pp. 124-145, Aug. 2018.

[15] R. K. Ranjan, N. Rani, R. Pal, S. K. Paul, and G. Kanyal, “Single CCTA based high frequency floating and grounded type of incremental/decremental memristor emulator and its application,” Microelectronics Journal, vol. 60, pp. 119-128, Feb. 2017.

[16] R.K. Ranjan, N. Bhuwal, N. Raj and F. Khateb, “Single DVCCTA based High frequency incremental/decremental Memristor Emulator and its Application,” International Journal of Electronics and Communications, vol. 82, pp. 177-190, Dec.2017.

[17] A. Yesil, Y. Babacan and F. Kacar, “A new DDCC based memristor emulator circuit and its applications.,” Microelectronics Journal, vol. 45, no. 3, pp. 282-287, 2014.

[18] J. Vista and A. Ranjan, “Flux Controlled Floating Memristor Employing VDTA: Incremental or Decremental Operation,” IEEE Transactions on Computer Aided Design of Integrated Circuits and System, vol. 40, no. 2, pp. 364-372, Feb. 2021.

[19] P. B. Petrovic, “Floating incremental/decremental flux-controlled memristor emulator circuit based on single VDTA,” Analog integrated circuits and signal processing, no. 96, pp. 417-433, March 2018.

[20] N. Yadav, S. K. Rai, and R. Pandey, “Novel Memristor using Fully Balanced VDBA and Grounded Capacitor,” Iranian Journal of Science and Technology Transactions of Electrical Engineering, vol. 45, pp. 229-245, June 2021.

[21] A. Yesil, Y. Babacan, F. Kacar, “Electronically tunable memristor based on VDCC,” AEU-International Journal of Electronics and Communications, vol. 107, pp. 282-290, 2019.

[22] N. Raj, R. K. Ranjan, F. Khateb, “Flux-controlled Memristor Emulator and its Experimental result,” IEEE Transactions on Very Large Scale Integration (VLSI) System, vol. 28, no. 4, pp. 1050-1061, April 2020 .

[23] U. E. Ayten, S. Minaei and M. Sagbas, “Memristor emulator circuits using single CBTA,” International Journal of Electronics and Communications, vol. 82, pp. 109-118, 2017.

[24] A. Kumar, and B. Chaturvedi, “Novel CMOS dual-X current conveyor transconductance amplifier realization with current mode multifunction filter and quadrature oscillator”, Circuit System Signal Processing, vol. 37, pp. 1-11, 2019.

[25] S. P. Adhikari, M. P. Sah, H. Kim and L. O. Chua, “Three Fingerprints of Memristor,” IEEE Trans Circuits System I Regular Paper, vol. 60, no. 11, pp. 3008-3021, Nov.2013.

Authorized licensed use limited to: DELHI TECHNICAL UNIV. Downloaded on January 17,2023 at 05:02:15 UTC from IEEE Xplore. Restrictions apply.

Soft Computing
https://doi.org/10.1007/s00500-022-07738-w

APPLICATION OF SOFT COMPUTING

Software defect prediction using hybrid techniques: a systematic literature review

Ruchika Malhotra[1] · Sonali Chawla[1] · Anjali Sharma[2]

Accepted: 8 December 2022
© The Author(s), under exclusive licence to Springer-Verlag GmbH Germany, part of Springer Nature 2023

Abstract
Software defect prediction is the process of developing predictive models that helps in the early identification of defect-prone modules based on software metrics and defect data. It enables the project managers to allocate resources optimally. Recently search-based techniques have been widely adopted for providing optimal solutions to develop effective software defect prediction models. When merged with statistical or machine learning techniques, these techniques give rise to hybridization. Hybrid techniques significantly improve the performance of search-based techniques and the quality of solutions produced by them. In this systematic review, we have investigated 72 papers published from January 2000 to December 2021 that ascertain the use of hybrid techniques and their effectiveness in predicting software defects. The review identifies and evaluates various techniques, experimental design, fitness functions, performance measures, threats to validity, and well-known statistical tests in the studies that apply these hybrid techniques. We also compared the performance of hybrid techniques among themselves and statistical and machine learning techniques present in the literature. According to the findings, the predictive capability of hybrid techniques is encouraging. The results of this review paper will serve as guidelines for the researchers and practitioners, allowing them to make appropriate choices for applying hybrid techniques in the software defect prediction process.

Keywords Search-based techniques · Machine learning techniques · Hybrid techniques · Software defect prediction · Systematic review · Statistical validation

1 Introduction

A software defect is a fault or bug in the program that creates a deficiency in the software product, producing incorrect and unexpected results (Mcdonald et al. 2007). As software grows in size and complexity, more rigorous and effective testing is required to capture software defects to maintain product quality, efficiency, and reliability. A software testing team is involved in defect identification and prevention, but it consumes a lot of time and workforce; hence allocating the resources judiciously to the areas of the system with a higher probability of defects would be reasonable (D'Ambros et al. 2012).

Software defect prediction (SDP) is the process of creating a predictive model that helps identify the defect-prone software modules before the testing phase begins (Li et al. 2018). The classifier must be trained using historical data to create an effective predictive model. Software metrics are used as independent variables to develop the prediction models. These metrics quantitatively analyze and control the functional characteristics of software projects, such as their reliability, maintainability, testability, and fault-proneness (Rathore and Kumar 2019) (Kalsoom et al. 2018). Traditional or static code metrics like Halstead (1977) and McCabe and Butler (1989) are derived from the source code automatically (Turhan and Bener 2009). Some

✉ Anjali Sharma
anjali1007@gmail.com

Ruchika Malhotra
ruchikamalhotra2004@yahoo.com

Sonali Chawla
sonalichwl@gmail.com

[1] Department of Software Engineering, Delhi Technological University, Bawana Road, New Delhi, Delhi 110042, India

[2] Department of Planning Monitoring and Evaluation, CSIR-National Physical Laboratory, Dr. KS Krishnan Marg, Pusa, New Delhi, Delhi 110012, India

Published online: 17 January 2023

researchers also use the object-oriented (OO) metrics suite by Chidamber and Kemerer (1994) in creating SDP models.

Over the last three decades, statistical and machine learning (ML) techniques have been extensively applied to solve SDP problems. The most frequently used algorithms include support vector machines (Singh et al. 2009), naïve Bayes (Turhan and Bener 2009), random forest (Ibrahim et al. 2017), decision trees (Rathore and Kumar 2016), and neural networks (Jayanthi and Florence 2018; Arora and Saha 2016). Lately, researchers have discovered that search-based techniques have received considerable attention in several software engineering tasks such as effort estimation, change prediction, project management, test case generation, and defect prediction also (Ferrucci et al. 2014; Lakshminarayana and Sureshkumar 2020; Rhmann et al. 2021; Malhotra and Khanna 2021). However, using the hybridized version of search-based techniques can alter the perspective of applying these techniques in SDP modeling.

Search-based techniques are metaheuristic procedures that use the fitness function to find the optimized solution in a vast input search space of possible candidate solutions. The operators like selection, mutation, crossover, and replacement are used for finding the set of candidate solutions. This procedure continues until an optimal or near-optimal solution is identified or when the iterations are over (Harman 2010a). The current solution is continuously improved by optimizing the fitness function until the best solution is reached. Search-based techniques help balance the conflicts and constraints of the incomplete, noisy, and partially accurate input search space (Harman 2010a). Moreover, search-based algorithms' flexible, robust, and fast converging nature has led to their tremendous applications in software engineering (Grosan and Abraham 2007; Harman 2010a, b).

When search-based and ML techniques are combined, hybridized techniques are created. We have used these terms interchangeably throughout this review. Hybrid techniques typically integrate the strengths of both search-based and ML techniques into a single approach. The hybrid techniques may use a search-based technique for either hyperparameter tuning, feature selection, or deciding the structure for another technique to achieve optimal results (Malhotra et al. 2017). Hybrid techniques provide a global optimum solution without getting trapped into local minima (Khoshgoftaar et al. 2003). Some of the advantages of these techniques are: that they are well suited for projects with different properties and characteristics (Harman et al. 2012); they undergo a simplified, automated search process requiring fewer parameters (Hochman et al. 1996; Kayarvizhy et al. 2013); their fast convergence speed leads to optimal quality solutions (Hochman et al. 1996; Grosan and Abraham 2007; Jin and Jin 2015). Harman and Clark (2004) explained how the relationship between metrics and fitness function could be a guiding force in the search for optimal or suboptimal solutions to a software engineering problem.

Researchers use various search-based techniques for SDP, such as particle swarm optimization (PSO), firefly algorithm (FA), genetic algorithms (GA), salp swarm optimization (SSO), whale optimization algorithm (WOA), etc. Various interesting combinations of search-based techniques with ML or statistical techniques are introduced in the literature, which shows an effective improvement in the SDP modeling like PSO-ANN (Jin and Jin 2015), FA-SVM (Anbu and Anandha Mala 2019), GA-Decision Tree (Khari and Kumar 2018), WOA-KNN (Hassouneh et al. 2021). Although many studies are conducted in this domain, additional research is needed. Studying these previous works systematically and extracting meaningful information from them is crucial. In the recent past, there have been some efforts made in this direction. Rhmann et al. (2020) explored the use of hybrid algorithms in fault prediction using change metrics and compared their performance with ML techniques. They found that different techniques are statistically the same. The usefulness of search-based and hybrid strategies was demonstrated by Malhotra (2018) using a framework that addressed the stochastic nature of these techniques and statistical analysis to prove the results. Khari and Kumar (2018) evaluated the relationship between defect prediction and OO metrics using search-based and hybrid techniques to conclude that the predictive capability of these techniques is highly effective. The objectives of existing review articles addressed different research questions (Malhotra 2014, 2015; Wahono 2015; Malhotra et al. 2017; Son et al. 2019) on ML, search-based, and hybrid techniques. But as per our knowledge, there is no comprehensive study that describes in a unified way how hybrid techniques can be helpful in defect predictive modeling. Hence, it is essential to identify, analyze and evaluate the effectiveness of various hybrid techniques in classifying the defect and non-defect-prone modules.

This systematic review primarily focuses on the use of hybrid techniques in the field of SDP modeling that covers the literature studies of the past two decades, i.e., from January 2000 to December 2021. We restrict our search from 2000 to 2021 since the term Search-Based Software Engineering was introduced in 2001 (Harman and Jones 2001), which caused a subsequent rise in the number of studies. Seventy-two primary studies have been investigated in this review after an extensive search through seven digital libraries to address all the research questions. This review describes and evaluates the empirical evidence of different hybridized techniques and their performance

comparison with ML techniques. The main objective of this systematic review is to present a comprehensive analysis of hybridized techniques covering various dimensions that include:

- commonly used search-based and ML techniques that form hybrid techniques.
- datasets, metrics, feature/parameter optimization, and validation methods found in the literature.
- various fitness functions employed in search-based techniques (part of hybrid techniques),
- performance measures used for the evaluation of hybrid techniques,
- overall and comparative performance of various hybrid techniques with statistical and ML techniques,
- different statistical tests used to validate the results,
- strengths and weaknesses of these techniques, as discussed in the literature,
- potential threats to validity as reported by the studies.

This review paper also gives future guidance to software researchers and the industrial community by presenting a body of knowledge that wants to use and implement new hybrid techniques for SDP modeling. The paper is structured as follows: Sect. 2 discusses related works and the motivation behind our study. Section 3 describes the review methodology process followed in this paper. Section 4 contains the primary studies' sources and their quality ratings. Section 5 presents the results in the form of answers to the research questions. Section 6 discusses the limitations of the review. Section 7 outlines the conclusion of this review and presents future directions.

2 Background and motivation

Several studies in the literature have effectively applied ML and search-based techniques for SDP. This section describes some similar work done in this area as well as how our study differs from past studies.

Malhotra (2014) compiled eight primary studies between January 1991 and October 2013 to provide an overview of search-based techniques utilized in software fault prediction. It stated how preliminary results from these studies were positive but that further research is required to determine their effectiveness compared to statistical and ML techniques.

Malhotra (2015) performed a systematic review of the applications of ML techniques in software fault prediction from 1991 to 2013. They investigated 64 primary studies that identified the different categories of ML techniques, datasets, and metrics, analyzed the predictive capability of ML techniques, and compared these techniques with statistical ones.

Wahono (2015) reviewed 71 primary studies from 2000 to 2013 that identified and analyzed the five research topics and trends—estimation, classification, association, clustering, dataset analysis, datasets, and methods. This study also identified the most cited and important frameworks used in SDP models.

Malhotra et al. (2017) conducted a systematic review from January 1992 to December 2015 on four dimensions of software engineering, i.e., effort estimation, maintainability, defect prediction, and change-proneness. They analyzed 78 research papers that use search-based algorithms by assessment of appropriate specifications of parameter settings, fitness functions, validation techniques, etc.

Malhotra (2018) extensively compared and assessed 20 search-based, 16 hybrid, and 10 ML techniques for developing SDP models using OO metrics on 17 input datasets. The statistical results proved the predictive capability of search-based and hybrid techniques for classifying software defects.

Son et al. (2019) performed a systematic review of 98 studies from 1995 to 2018, where they addressed nine research questions that covered all the aspects of an SDP model—data collection, pre-processing, techniques for building SDP models, performance evaluation methods, security-related defects, number of studies performing cross-project SDP and addressing defects of severity levels.

Pandey et al. (2021) investigated various characteristics of ML algorithms for SDP in a study of 154 articles published between 1990 and June 2019. They summarized different ML techniques, datasets, feature reduction techniques, software metrics, strengths and weaknesses of ML techniques, and performance comparison of ML with statistical techniques used in SDP. They also examined different threats and challenges faced in this domain using ML techniques.

Our current review paper strives more on the use and applicability of hybrid techniques for SDP. It offers a taxonomical classification of search-based and ML techniques for building hybrid-based SDP models. We identify and analyze all important aspects of hybrid-based SDP models that have not been explored earlier, such as—the distribution of hybrid techniques according to the search-based and ML techniques, datasets and metrics, feature selection/parameter optimization techniques used, validation methods, fitness functions employed, performance evaluation of hybrid techniques and statistical validation to compare the results of hybrid techniques with statistical and ML techniques. We also mention the strengths and weaknesses of different hybrid techniques and validity threats, as reported by the studies.

3 Review methodology

The systematic review is carried out as per Kitchenham and Charters' (2007) guidelines. Figure 1 depicts the process followed in the literature review. The three primary activities involved are—planning, conducting, and reporting the review. The first step determines the need for review, identifies the research questions to be addressed, the development of the review protocol and its evaluation. The review methodology is driven by the research questions, as these are the objectives that a literature review is intended to address. The primary studies are explored on the basis of research questions developed at this step. The review protocol development consists of various stages. In the first stage, a search strategy involves identifying the search terms and choosing suitable sources for collecting the relevant studies. The next stage forms the inclusion and exclusion criteria that filter the candidate studies based on relevance. After that, quality assessment criteria are prepared to ensure the quality of each candidate's study. The last step involves the procedure for defining the data extraction and synthesis part of all the primary research studies collected in the previous step.

The next step is conducting the review, which requires executing the steps described in the review protocol. The search strategy is implemented, and the inclusion/exclusion criteria are applied to extract the relevant primary studies. Their data is collected, analyzed, and synthesized in the forms of tables, graphs, figures, boxplots, etc., to draw conclusions about the results. The last stage is reporting the results, where the answers to each research question are addressed. The review protocol established in our work is thoroughly evaluated by all three researchers independently. Any inconsistencies found were resolved after comprehensive discussions.

3.1 Research questions

In this systematic literature review, we aim to investigate the answers to the below research questions:

RQ1: What are the commonly used search-based and ML techniques in forming hybridized techniques for SDP?

RQ2: What is the year-wise distribution of studies using hybridized techniques for SDP?

RQ3: Which prominent journals and conferences have published studies using hybridized techniques for SDP?

RQ4: Which datasets and techniques are used in the experimental design of hybridized techniques for SDP?

- RQ4.1: Which datasets are used?
- RQ4.2: Which software metrics are used as independent variables?
- RQ4.3: What are the feature selection techniques used?
- RQ4.4: What are the parameter tuning techniques used?
- RQ4.5: Which performance measures are used?
- RQ4.6: Which validation techniques are used?

RQ5: Which fitness functions are employed in search-based techniques (part of hybridized techniques) for SDP?

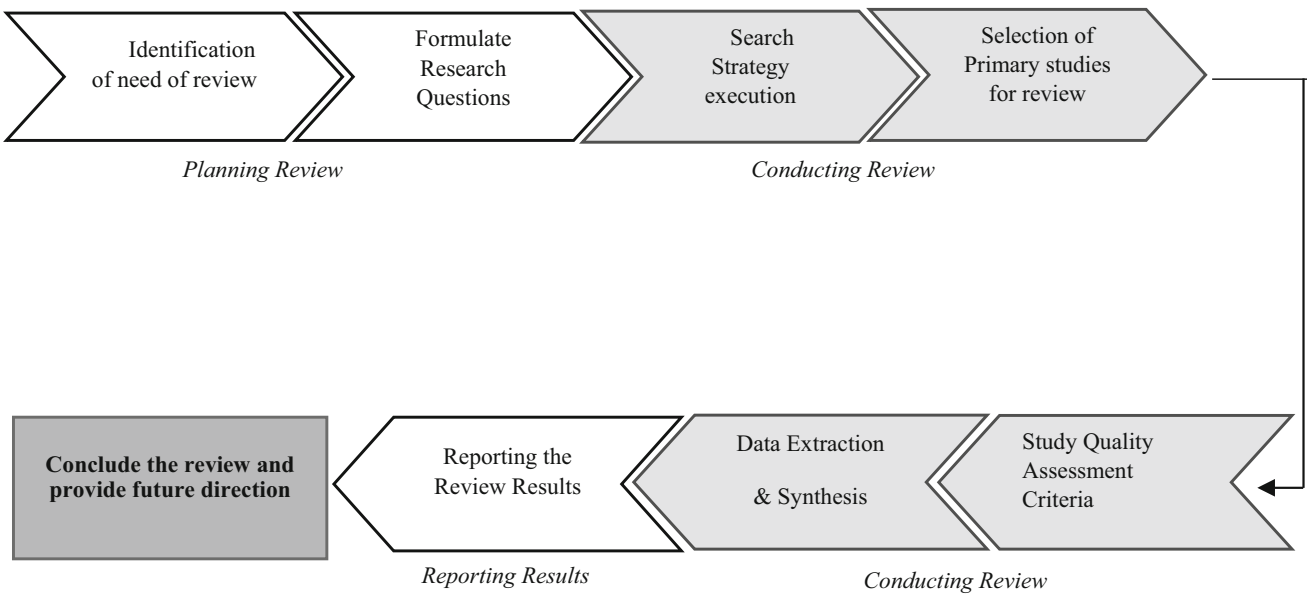

Fig. 1 Process of systematic literature review

RQ6: What is the performance of hybridized techniques for SDP?

RQ6.1: What is the overall performance of hybridized techniques?
RQ6.2: What is the comparative performance of hybridized techniques with traditional ML and statistical techniques?

RQ7: What are the different statistical tests used to study hybridized techniques in SDP?
RQ8: What are the strengths and weaknesses of hybridized techniques for SDP?
RQ9: What are the threats to validity in studies using hybridized techniques for SDP?

RQ1 provides the major categorization of search-based and ML techniques for building hybrid-based SDP models. RQ2 and RQ3 provide the year-wise distribution and the list of prominent journals/conferences where primary studies are published. RQ4 identifies various datasets, metrics, validation methods, pre-processing techniques, and performance analyzers used in hybrid techniques. RQ5 identifies the different fitness functions employed in the hybrid techniques. RQ6 assesses the predictive capability of the hybrid-based models and compares their performance with statistical and ML techniques. RQ7 reports different statistical tests applied to validate the comparative performance in primary studies. RQ8 discusses the strengths and weaknesses of the models built using hybridized techniques. RQ9 reports various threats to the validity as mentioned by the primary studies.

3.1.1 Search strategy and study selection criteria

The review process involved selecting relevant and significant studies from the literature using the appropriate search terms. The preliminary search was initiated by scanning keywords such as "software defect prediction." Specific search keywords were formed by using the research questions (Sect. 3.1) and existing literature studies (Malhotra 2014; Malhotra et al. 2017; Pandey et al. 2021). The synonyms and alternate terms for those keywords were concatenated using the Boolean expressions "OR", "AND", and "NOT" to form a complete search string.

Software AND (Defect OR Error OR Fault) AND (Prediction OR Proneness OR Tendency) AND (Hybrid OR Hybridized) AND (Search-Based OR Search Based OR Heuristic OR Meta-Heuristic) AND (Machine Learning OR Statistical) AND (Evolutionary OR Swarm Intelligence OR Bio-Inspired OR Optimization OR Genetic Algorithm OR Wolf Pack Algorithm OR Particle Swarm Optimization OR Cuckoo Search OR Ant Colony Optimization OR Firefly Search OR Artificial Bee Colony OR Genetic Programming OR Tabu Search OR Simulated Annealing OR Harmony Search OR Bat Search OR Evolutionary Programming OR Differential Evolution OR Artificial Immune System) AND (Decision Tree OR Support Vector Machine OR Naïve Bayes OR Neural Network OR Logistic Regression OR Nearest Neighbor OR Random Forest).

Once the search string was formulated, it was required to select the most prominent and appropriate digital databases to extract relevant primary studies. The below digital libraries were chosen as per the author's researcher expertise and criteria outlined by Chen et al. (2010).

- IEEE Explore (https://ieeexplore.ieee.org).
- Springer (www.springer.com).
- Wiley Online Library (www.wiley.com).
- ACM Library (https://dl.acm.org).
- Google Scholar (https://scholar.google.com/).
- Science Direct (https://www.sciencedirect.com/).

Different online databases have different mechanisms for searching the papers, and we modified the search string accordingly. An initial search began by executing the search string, and we focused on the studies between January 2000 and December 2021. This list got reduced after discarding the studies based on titles, abstracts, and duplicate studies. After browsing through many articles, the inclusion and exclusion criteria were applied to select the most relevant studies. A final list of 72 primary studies was selected, satisfying the quality assessment criteria. We performed the snowballing procedure by scanning the references of the chosen studies and including them in our studies (Wohlin 2014). We found some review articles similar to our domain during our search process and extracted candidate studies from their reference sections. However, these review articles were not included as they don't possess empirical results.

The inclusion and exclusion criteria applied to the candidate studies were defined as follows:

3.1.2 Inclusion criteria

- Empirical studies use "defects" (defective/non-defective classes) as the independent variable.
- Empirical studies that use hybridized techniques for developing SDP models.
- Empirical studies that compare the performance of hybridized techniques with statistical or ML models.
- Empirical studies that apply hybridized techniques for feature selection or parameter optimization.

3.1.3 Exclusion criteria

- Studies in which "defect count/number of defects" is the dependent variable.
- Studies in which there is no empirical evidence for SDP.
- Studies that do not discuss the application of any hybridized techniques in SDP models
- Studies in which defect prediction models are based on expert judgment.
- Similar studies include those presented by the same author at a conference and an expanded version published in a journal. However, if the results in both studies were different, they were retained.
- Studies not in the English language.
- Review studies.

3.1.4 Study quality assessment criteria

The quality evaluation score helps to exclude studies that may be essential for the literature review but are of lower quality than other studies. Low quality here signifies that the study scored low according to our set quality criteria even though the study is good and the results are valid. We formed a questionnaire consisting of 14 questions to evaluate the significance of each study according to the suggestions provided by Wen et al. (2012). For every study, a quality score of 0 (poor rating/No), 0.5 (adequate rating/Partly), or 1 (very good rating/Yes) was given for each question. Table 1 contains the list of all quality assessment questions and the total count of studies that were assigned 1, 0.5, and 0 scores for each question.

3.1.5 Data extraction and synthesis

We extracted and synthesized the data collected from 72 primary studies. We used a data extraction form that contains the relevant data required to answer all the research questions. Different data items were extracted:

- Title of the study.
- Publisher.
- Year.
- Authors.
- Publication type-conference/journal/book chapter/symposium.
- Research methodology adopted.
- Search-based techniques and ML techniques.
- Hybrid techniques.
- Datasets.
- Metrics.
- Performance measures.
- Parameter tuning techniques.
- Feature selection techniques.
- Validation methods.
- Statistical tests.
- Fitness functions.
- Strengths and weaknesses.
- Limitations of the study.

After the data extraction was complete, we performed data synthesis to compile the answers for each research

Table 1 Quality assessment questions

S. no	Quality questions	Yes (1)	Partly (0.5)	No (0)
1	Whether the aims/objectives of the research are clearly stated?	35	37	0
2	Whether the study clearly states the defect prediction	72	0	0
3	Whether the data collection procedure is clearly defined?	66	3	3
4	Whether the predictor variables clearly stated and defined?	41	13	18
5	Whether the study evaluation parameters clearly defined?	65	6	1
6	Whether validation techniques are clearly defined?	59	0	13
7	Whether the study clearly defines and describes the search-based techniques used	59	8	5
8	Whether the study conduct any comparative analysis between search-based techniques, ML, or statistical techniques?	54	3	15
9	Whether fitness functions are clearly stated?	50	4	18
10	Whether the results and findings are reported clearly?	64	8	0
11	Whether any statistical tests are applied in the research to verify the results	33	0	39
12	Are the limitations of the review specified?	20	1	51
13	Whether the study is repeatable?	24	23	25
14	Whether the study's average citation count per year adequate?	56	0	16

question. The other two authors cross-checked the above-extracted data, and if any consistencies were found, it was resolved through discussions and consensus meetings. The final answers were prepared for each RQ after in-depth analysis—both quantitative and qualitative. Quantitative analysis collects and evaluates the data from various sources and draws a conclusion about its effects/outcomes. The qualitative analysis produces new insights and understanding after a comprehensive review of the methods and processes used in the study. Under quantitative analysis, we evaluated the performance of various algorithms dataset-wise. Under qualitative analysis, we identified and analyzed the different types of search-based and ML techniques, datasets, metrics, validation methods, fitness functions, performance measures, strengths and weaknesses, threats to validity, and statistical tests for validation. The results are presented in the form of tables, bar charts, pie charts, figures, and box plots.

4 Description of primary studies and quality assessment

A total of 72 primary studies were chosen only after thoroughly applying the inclusion/exclusion criteria (Sect. 3.2) and meeting all the quality standards (Sect. 3.3). As discussed in Sect. 3.3, we analyzed the quality of the candidate studies based on 14 quality assessment questions mentioned in Table 1. A study can acquire the lowest score of 0 and the highest score of 14. We decided to keep those studies that scored equal to or above 50% of the quality criteria. Therefore, we accepted a primary study only if its quality score is greater than or equal to 7. The significance of a study on a particular topic is directly correlated with the quality score. Table 2 presents the lists of all primary studies and their quality scores. Each primary study is referred to by a unique identifier which will be used throughout the following sections of the paper. Three studies (HS17, HS20, and HS51) achieved the highest score of 14, followed by one study that achieved the next highest score of 13.5(HS36).

5 Results

5.1 RQ1: What are the commonly used search-based and ML techniques in forming hybridized techniques for SDP?

Over the years, researchers have employed various techniques for accurately predicting software defects. Initially, only statistical and ML techniques were used for SDP modeling. These techniques establish the relationship between software metrics and defect data. It became significantly more efficient with the introduction of search-based approaches. Hybrid approaches are now being employed, integrating ML/statistical and search-based techniques. Based on the primary studies selected for this systematic review, we grouped search-based and ML techniques used to form hybrid techniques as follows.

- Search-Based Techniques:

(a) Local Search
(b) Evolutionary
(c) Swarm Intelligence
(d) Bio-Inspired
(e) Nature-inspired

- ML Techniques:

(a) Decision Trees
(b) Ensemble Learners
(c) Support Vector Machines
(d) Neural Networks
(e) Other Techniques

Figure 2 describes the taxonomy of different search-based and ML techniques used in hybridized techniques for SDP. The table presenting hybridized techniques with respect to study no. is presented in Appendix 8.1 (Table 18). Figure 3 shows the percentage of the studies that use a specific category (search-based and ML techniques) in hybridized techniques for defect prediction.

Figure 3a depicts evolutionary algorithms as the most frequently used category in search-based techniques. These algorithms are explored in 54% of the primary studies forming hybrid techniques like GA-ANN, GP-NB, DE-RF, GA-ELM, etc. GA is the most popular algorithm in this category. Swarm intelligence algorithms are the next frequently used techniques, found in 42% of the total studies, forming hybrid techniques like PSO-LDA, ACO-LRNN, ABC-ANN, WOA-KNN, etc. PSO is the most popular algorithm in this category. Nature-inspired, local, and bio-inspired search categories comprise 18%, 13%, and 1% of the total primary studies forming hybrid techniques like Firefly-SVM, HS-Bagging-DT, WSO-SVM, etc.

Figure 3b depicts that SVM and neural networks are the most popular algorithms in the category of ML approaches explored in 33% and 33% of the studies, respectively. Decision tree algorithms account for 24% of the total studies. KNN, Ensemble learners, and Naïve Bayes are used in 19%, 17%, and 11% of the studies. Other techniques like K*, IDN, Fuzzy Mutual Information, Fuzzy Logic, and Rule-Based Learning comprise 11% of the primary studies. Statistical Techniques (LR and LDA) are also used to form hybrid techniques and account for 17% of

Table 2 Primary studies

Study#	References	Quality score	Study#	References	Quality score
HS1	(Khoshgoftaar et al. 2003)	9	HS37	(Niu et al. 2018)	7
HS2	(Gao et al. 2011)	11.5	HS38	(Geng 2018)	12
HS3	(Pendharkar 2010)	8	HS39	(Khari and Kumar 2018)	12.5
HS4	(Chiu 2011)	11	HS40	(Rhmann 2020)	11.5
HS5	(Sarro et al. 2012)	13	HS41	(Arora and Saha 2018)	11.5
HS6	(Yu 2012)	11.5	HS42	(Manjula and Florence 2018)	7
HS7	(Wahono and Suryana 2013)	12	HS43	(Malhotra et al. 2018)	11
HS8	(He et al. 2013)	10.5	HS44	(Manivasagam and Gunasundari 2018)	7
HS9	(Shuai et al. 2013)	9.5	HS45	(Brezočnik and Podgorelec 2019)	8.5
HS10	(Kayarvizhy et al. 2013)	12.5	HS46	(Cai et al. 2020)	10
HS11	(Wahono et al. 2014)	11.5	HS47	(Manjula and Florence 2019)	10.5
HS12	(Li et al. 2014)	9	HS48	(Tumar et al. 2020)	10.5
HS13	(Arar and Ayan 2015)	12.5	HS49	(Mabayoje et al. 2019)	7.5
HS14	(Jin and Jin 2015)	11.5	HS50	(Ayon 2019)	8.5
HS15	(Dhanalaxmi et al. 2015)	7.5	HS51	(Ni et al. 2019)	14
HS16	(Xia et al. 2016)	13	HS52	(Matloob et al. 2019)	8.5
HS17	(Ryu and Baik 2016)	14	HS53	(Arora and Saha 2019)	10.5
HS18	(Afzal and Torkar 2016)	10.5	HS54	(Alsghaier and Akour 2020)	11
HS19	(Hosseini et al. 2016)	13	HS55	(Thaher and Arman 2020)	11.5
HS20	(Shukla et al. 2018)	14	HS56	(Rhmann et al. 2020)	12
HS21	(Li et al. 2016)	10	HS57	(Zhang et al. 2020)	12
HS22	(Fazel 2016)	8	HS58	(Alsghaier and Akour 2021)	13
HS23	(Kumar and Rath 2017)	12	HS59	(Oloduowo et al. 2020)	8
HS24	(Jin and Dong 2016)	9	HS60	(Bahaweres et al. 2020)	8.5
HS25	(Jayaraj and Raman 2016)	7.5	HS61	(Banga et al. 2020)	10.5
HS26	(Ibrahim et al. 2017)	9.5	HS62	(Yang et al. 2020)	10.5
HS27	(Moussa and Azar 2017)	11	HS63	(Balogun et al. 2020)	7.5
HS28	(Hosseini et al. 2018)	13	HS64	(Wu et al. 2020)	8
HS29	(Haveri and Suresh 2018)	8.5	HS65	(Hassouneh et al. 2021)	12.5
HS30	(Anbu and Anandha Mala 2019)	10	HS66	(Kassaymeh et al. 2021)	12
HS31	(Rong and Cui 2017)	8	HS67	(Malhotra et al. 2021)	7
HS32	(Pal et al. 2017)	10	HS68	(Zhu et al. 2021)	11.5
HS33	(Thangavel and Pugazendi 2017)	8.5	HS69	(Zhang et al. 2021)	11.5
HS34	(Turabieh et al. 2019)	12.5	HS70	(Kang et al. 2021)	11
HS35	(Cao et al. 2018)	9	HS71	(Jin 2021)	11
HS36	(Rhmann 2018)	13.5	HS72	(Li et al. 2021)	9

the total primary studies. We also noted that there had been an increase in the use of neural networks—CNNs and DNNs in software engineering domains in recent years. They operate on vast amounts of data to identify complex relationships between independent variables and improve various tasks to boost the performance of defect prediction models (Yang et al. 2015) (Wang et al. 2016).

Hybrid techniques have become popular for predictive modeling, as they combine the benefits of search-based and ML/statistical techniques in a specific approach. These techniques offer globally optimum solutions, which is a feature of search-based techniques, and faster convergence power, a feature of the ML technique (Grosan and Abraham 2007). These techniques are also better for handling noise and data uncertainty (Ting et al. 2015). They have a simple automated search process with fewer parameters required for training (Hochman et al. 1996; Kayarvizhy et al. 2013). Hence, they improve the performance of a search-based technique by providing better quality solutions. We note that different variants of each category of

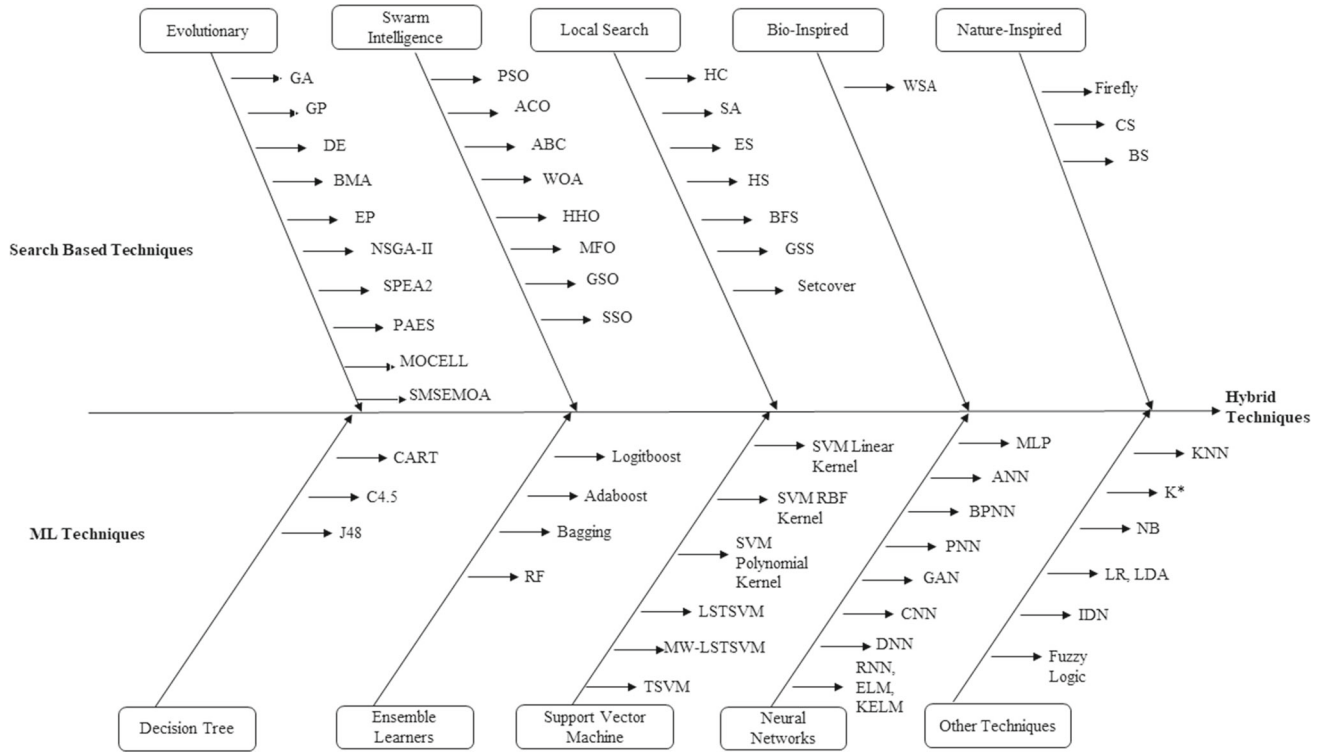

Fig. 2 Classification of Search-based and ML techniques. GA*:* Genetic Algorithm, PSO*:* Particle Swarm Optimization, GP*:* Genetic Programming, BMA*:* Bird Mating Algorithm, EP*:* Evolutionary Programming, NSGA-II*:* Nondominated sorting genetic algorithm, SPEA2*:* Improved strength Pareto evolutionary algorithm, MO-Cell*:* Multi-Objective Cellular, PAES*:* Pareto archived evolution strategy, ACO*:* Ant Colony Optimization, MFO*:* Moth Flame Optimization, HHO*:* Harris hawks Optimization, SSO*:* Salp Swarm Optimization, GSO*:* Glowworm Swarm Optimization, DE*:* Differential Evolution, ABC*:* Artificial Bee Colony, WOA*:* Whale Optimization Algorithm, HC*:* Hill Climbing, ES*:* Exhaustive Search, HS*:* Heuristic Search, AHS*:* Automatic Hybrid Search, GSS*:* Greedy Stepwise Search, BFS*:* Best First Search, SA*:* Simulated Annealing, WSA*:* Wolf Search algorithm, CS*:* Cuckoo search, BS*:* Bat search, SVM*:* Support vector machine, TSVM*:* Twin support vector machine, LSTSVM*:* Least Squares Twin Support Vector Machines, MW-LSTSVM-Mean Weighted Least Squares Twin Support Vector Machine, RBF*:* Radial Basis Function, RF*:* Random Forest, CART*:* Classification And Regression Trees, MLP*:* Multilayer Perceptron, ANN*:* Artificial Neural Network, BPNN*:* Back-propagation Neural Network, PNN*:* Probabilistic Neural Network, CNN-Convolutional Neural Network, DNN*:* Deep Neural Network, GAN*:* Generative Adversarial Network, RNN*:* Recurrent neural network, ELM*:* Extreme Learning Machine, KELM*:* Kernel Extreme Learning Machine, KNN*:* K Nearest Neighbor, IDN*:* Integrated Decision Network, NB*:* Naïve Bayes, LR*:* Logistic regression, LDA*:* Linear Discriminant Analysis

Fig. 3 Distribution of studies by search-based and ML techniques used

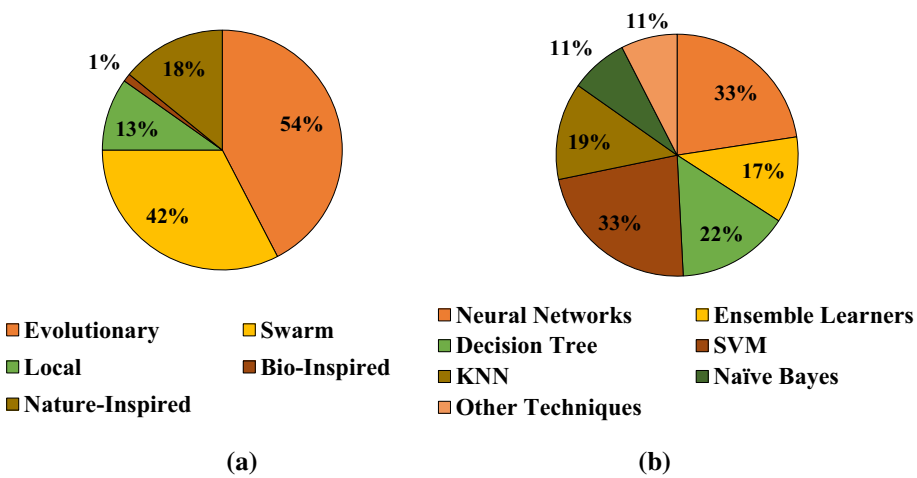

techniques are applied to form interesting combinations, which are presented in Appendix 8.1.

5.2 RQ2: What is the year-wise distribution of studies using hybridized techniques for SDP?

The primary studies are classified based on year and type of publication, as depicted in Fig. 4. It shows that before 2013, only six studies applied hybrid techniques in SDP. The majority of primary studies—roughly 92% of the overall studies-were published between 2013 and 2021.

In 2001, Harman and Jones (2001) introduced the word "Search-Based Software Engineering". In 2010, Harman (2010b) argued that we could apply metaheuristic search techniques in the software engineering domain. Since then, the interest of the researchers and practitioners has increased significantly, allowing them to discuss, review and identify significant challenges posed by SBSE on the current state of software engineering. The number of studies has increased after 2016 because of the application of deep learning techniques with search-based techniques in the SDP domain, which is relatively new and shows improved performance over ML and statistical techniques with search-based techniques.

5.3 RQ3: Which prominent journals and conferences have published studies using hybridized techniques for SDP?

This section describes the publication sources of the primary studies that use hybridized techniques for developing SDP models. According to Fig. 5, 71% of primary studies were published in journals, 22% in conferences, and 7% in book chapters. Hence, the count of studies in journals (51) is a lot higher than that of conferences (16) and book chapters (5).

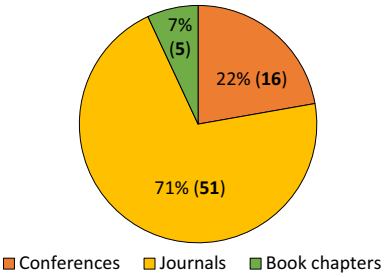

Fig. 5 Distribution of primary studies according to their type

Table 3 describes the details of the prominent journals and conferences, with their impact factors (current date) and the count of studies in each publication. These journals and conferences are influential, high in impact factor, and contain relevant previously published articles related to software engineering (Chulani et al. 1999; Xue et al. 2016). Three papers have been published in the Journal of Systems and Software (HS27, HS51, HS68), Software—Practice and Experience (HS2, HS54, HS58), Applied Soft Computing (HS13, HS14, HS17), and Expert Systems with Applications (HS4, HS34, HS71). One journal paper is published in IEEE Transactions on Software Engineering (HS16) and Information and Software Technology (HS28). All other research articles are also from other well-known publications. The top five highly cited studies are HS2, HS16, HS13, HS46, and HS1. We also list the top fifteen highly cited studies in Appendix 8.2 (Table 19).

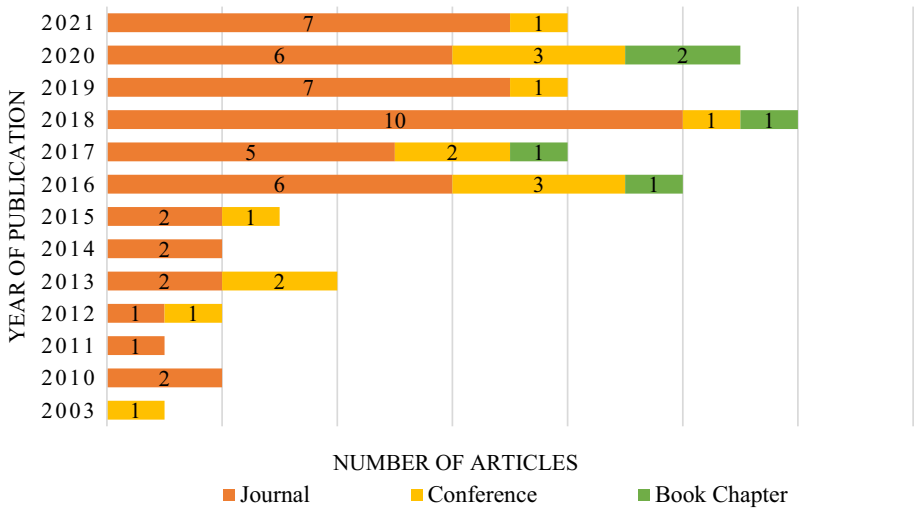

Fig. 4 Classification of primary studies by year and publication

Table 3 Top publication venues

Publication name	Type	Number of studies	Impact factor
Journal of Systems and Software	Journal	3	2.829
Software: Practice and Experience	Journal	3	2.028
Applied Soft Computing	Journal	3	6.725
Expert Systems with Applications	Journal	3	6.954
Information Sciences	Journal	2	6.795
Information and Software Technology	Journal	1	2.73
IEEE Transactions on Software Engineering	Journal	1	3.331
IEEE International Conference on Tools with Artificial Intelligence	Conference	1	–
ACM Symposium on Applied Computing	Conference	1	–
International Conference on Predictive Models and Data Analytics in Software Engineering	Conference	1	–

5.4 RQ4: Which datasets and techniques are used in the experimental design of hybridized techniques for SDP?

This section determines the most commonly used datasets, software metrics, feature selection techniques, parameter tuning techniques, validation methods, and performance measures used to develop an SDP model using hybridized techniques.

5.4.1 RQ4.1: Which datasets are used?

A variety of datasets are used in primary studies that apply hybridized techniques for SDP models. There are two kinds of datasets—public and private. Public datasets are publically available for free, whereas private datasets are private in nature and hence not open to the public easily. Figure 6 represents the percentage of studies against the different types of datasets used. Datasets of our domain can be categorized as below:

1. *PROMISE Repository Dataset*: This kind of dataset is available for free and accessible in the PROMISE repository. About 38% of the selected studies (HS3, HS5, HS10, HS16, HS17, HS18, HS19, HS20, HS23, HS27, HS28, HS29, HS34, HS39, HS43, HS45, HS48, HS51, HS54, HS55, HS58, HS63, HS65, HS66, HS68, HS69, HS71) use this kind of dataset. Java datasets like Apache POI, Apache Xalan, jEdit version, etc., are all available in the PROMISE repository (Jureczko and Madeyski 2010).
2. *NASA Dataset*: The most commonly used datasets for SDP come from the NASA Metrics Data Program, providing open-source software data to the public. About 64% of the studies (HS3, HS4, HS6, HS7, HS8, HS9, HS11, HS15, HS12, HS13, HS14, HS18, HS21, HS22, HS24, HS25, HS26, HS30, HS31, HS32, HS33, HS35, HS36, HS37, HS38, HS40, HS41, HS42, HS44, HS45, HS46, HS47, HS49, HS50, HS52, HS53, HS54, HS57, HS58, HS59, HS60, HS61, HS63, HS64, HS66, HS69) include NASA datasets for model development. JM1, KC1, PC1, MW1, etc., all these datasets are available in a public NASA repository (Menzies et al. 2007).
3. *Open-source Software Datasets*: Repositories like GitHub and Sourceforge.net provide open-source software projects from which researchers can download free data for their use. Eight studies (HS56, HS62, HS63, HS67, HS68, HS70, HS71, HS72) acquire data from open-source libraries. Some commonly used open-source benchmark datasets include AEEEM (D'Ambros et al. 2012) and ReLink (Wu et al. 2011).
4. *Academic Dataset*: This dataset includes student research projects developed as a part of their course or degree. Only one study, HS17, has used 17 academic projects as a single merged academic dataset in their research.
5. *Industrial Dataset*: This kind of dataset is proprietary in nature and belongs to some industries or private organizations, like the telecommunication dataset. About 7% of the total studies include industrial datasets.

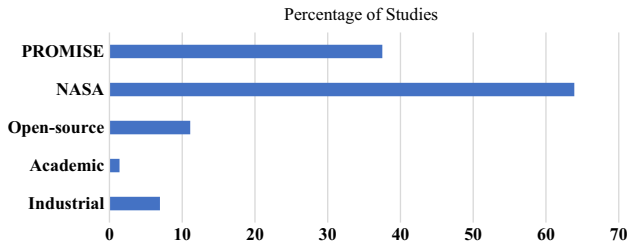

Fig. 6 Distribution of studies according to the type of datasets

Table 4 Attribute details of the most commonly used public datasets

Source	Datasets	Granularity level	Language	# of instances	# of attributes	# of defective instances	Defective ratio (%)
NASA	JM1	Method	C	7783	22	1672	21.48
	CM1	Method	C	498	22	49	9.84
	MW1	Method	C	403	40	61	15.14
	MC1	Method	C + +	1988	39	46	2.31
	MC2	Method	C + +	161	40	52	32.30
	KC1	Method	C + +	2109	22	326	15.46
	KC2	Method	C + +	522	22	105	20.11
	KC3	Method	Java	458	40	43	9.39
	KC4	Method	Perl	125	40	61	48.80
	PC1	Method	C	1107	40	76	6.87
	PC2	Method	C	5589	40	23	0.41
	PC3	Method	C	1077	38	134	12.44
	PC4	Method	C	1458	38	178	12.21
	PC5	Method	C + +	1711	39	471	27.53
AEEEM	Eclipse JDT Core	Class	Java	997	62	206	20.66
	Eclipse PDE	Class	Java	1492	62	209	14.01
	Equinox	Class	Java	324	62	129	39.81
	Lucene	Class	Java	691	62	64	9.26
	Mylyn	Class	Java	1862	62	245	13.16
PROMISE	ant-1.3	Class	Java	125	21	20	16.00
	ant 1.4	Class	Java	178	21	40	22.47
	ant 1.5	Class	Java	293	21	32	10.92
	ant 1.6	Class	Java	351	21	92	26.21
	ant 1.7	Class	Java	745	21	166	22.28
	camel-1.0	Class	Java	339	21	13	3.83
	camel-1.2	Class	Java	608	21	216	35.53
	camel-1.4	Class	Java	872	21	145	16.63
	camel-1.6	Class	Java	965	21	188	19.48
	ivy-1.1	Class	Java	111	21	63	56.76
	ivy-1.4	Class	Java	241	21	16	6.64
	ivy-2.0	Class	Java	352	21	40	11.36
	jedit-3.2	Class	Java	272	21	90	33.09
	jedit-4.0	Class	Java	306	21	75	24.51
	jedit-4.2	Class	Java	367	21	48	13.08
	jedit-4.3	Class	Java	492	21	11	2.24
	log4j-1.0	Class	Java	135	21	34	25.19
	log4j-1.1	Class	Java	109	21	37	33.94
	log4j-1.2	Class	Java	205	21	189	92.20
	poi-1.5	Class	Java	237	21	141	59.49
	poi-2.0	Class	Java	314	21	37	11.78
	poi-2.5	Class	Java	385	21	248	64.42
	poi-3.0	Class	Java	442	21	281	63.57
	lucene-2.0	Class	Java	195	21	91	46.67
	lucene-2.2	Class	Java	247	21	144	58.30
	lucene-2.4	Class	Java	340	21	203	59.71
	synapse-1.0	Class	Java	157	21	16	10.19
	synapse-1.1	Class	Java	222	21	60	27.03
	synapse-1.2	Class	Java	257	21	86	33.46

Table 4 continued

Source	Datasets	Granularity level	Language	# of instances	# of attributes	# of defective instances	Defective ratio (%)
	velocity-1.4	Class	Java	196	21	147	75.00
	velocity-1.5	Class	Java	214	21	142	66.36
	velocity-1.6	Class	Java	229	21	78	34.06
	xalan-2.4	Class	Java	723	21	110	15.21
	xalan-2.5	Class	Java	803	21	387	48.19
	xalan-2.6	Class	Java	885	21	411	46.44
	xalan-2.7	Class	Java	909	21	898	98.79
	xerces-1.2	Class	Java	440	21	71	16.14
	xerces-1.3	Class	Java	453	21	69	15.23
	xerces-init	Class	Java	162	21	77	47.53
	xerces-1.4	Class	Java	588	21	437	74.32
Relink	Apache	File	Java	194	27	98	50.52
	Safe	File	Java	56	27	22	39.29
	Zxing	File	Java	399	27	118	29.57

Table 4 describes the most commonly used public software projects available in NASA, PROMISE, AEEEM, and RELINK datasets, with details such as granularity level, programming language, total instances, attributes, no. of defective instances, and defective ratio. All these datasets have independent numeric variables and one categorical dependent variable—defect (yes—for one or more defects /no—for 0 defects). NASA datasets contain fourteen projects that use static code metrics like—size, Mccabe (1976)'s complexity, and Halstead (1977)'s metrics. AEEEM datasets have five projects that include 61 source code metrics, such as static code, previous defect metrics, the entropy of source code and change metrics, and churn of source code metrics (D'Ambros et al. 2012). PROMISE datasets have 40 projects, all containing 20 metrics that include—Mccabe (1976)'s complexity, Chidamber and Kemerer (1994)'s metrics, and other OO metrics (Jureczko and Madeyski 2010). Relink Datasets have three projects that include 26 metrics based on code complexity derived from Understand Tool (Wu et al. 2011).

5.4.2 RQ4.2: Which software metrics are used as independent variables?

Software metrics quantitatively analyze and describe the characteristics of the software projects like size, complexity cohesion, coupling, inheritance, etc. These metrics act as significant predictors or independent variables in defect prediction modeling. We define the classification based on the metrics used in the primary studies that apply hybridized techniques. Figure 7 depicts the percentage of studies according to the metrics used.

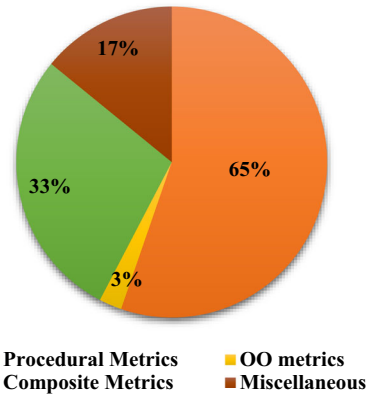

Fig. 7 Percentage of studies according to software metrics

1. *Traditional/procedural metrics* These are also known as static code metrics as they measure software attributes extracted directly from the source code without requiring any execution. Metrics like McCabe and Butler (1989) Mccabe (1976) (cyclomatic complexity, essential complexity, etc.), Halstead (1977) (program length, volume, effort, etc.) and size metrics like LOC have been used by about 65% of the primary studies namely HS3, HS4, HS6, HS7, HS8, HS9, HS11, HS12, HS13, HS14, HS15, HS18, HS21, HS22, HS24, HS25, HS26, HS27, HS30, HS31, HS32, HS33, HS35, HS36, HS37, HS38, HS40, HS41, HS42, HS44, HS46, HS47, HS49, HS50, HS52, HS53, HS54, HS57, HS58, HS59, HS60, HS61, HS63, HS64, HS66, HS69.

2. *Object-oriented metrics* OO metrics could capture various key aspects of the software that static code metrics couldn't. These metrics could measure OO paradigms like—encapsulation, inheritance, coupling, cohesion, polymorphism, etc. Various researchers also consider the size metric LOC an OO metric; hence we have included this metric in both categories (static and OO). About 3% of the total studies, i.e., only 2, use only OO metrics, namely HS39 and HS67.
3. *Composite metrics* OO and static metrics, together as independent variables, have been grouped in this category of composite metrics. 33% of the total studies HS5, HS10, HS16, HS17, HS18, HS19, HS20, HS23, HS28, HS29, HS34, HS43, HS45, HS48, HS51, HS54, HS55, HS58, HS63, HS65, HS66, HS68, HS69, HS71) use combination of both OO and static metrics together for defect prediction.
4. *Miscellaneous metrics* Studies that do not use OO or static metrics fall under this category. 12 primary studies use different types of metrics—HS56, HS62, and HS70 include change metrics; HS1 includes one LOC-based process metric and 4 product metrics; HS2 includes 24 product metrics; HS51, HS68, and HS71 use a combination of complexity and size metrics and HS63, HS68, and HS71 use 61 variety of metrics like defect metrics, the entropy of change, source code metrics, etc. HS72 includes metrics related to procedure information, dataflow information, and other code coverage metrics.

5.4.3 RQ4.3: What are the feature selection techniques used?

Feature selection is a data pre-processing technique that reduces the original features set to form a smaller optimal subset by eliminating redundant and irrelevant features. It helps remove noise in the dataset and increases the efficiency of a predictive model. There are three feature selection techniques—Filter, Wrapper, and Embedded methods. Filter methods measure the relevance of the attributes by finding a correlation with dependent variables, whereas wrapper methods measure the usefulness of attributes by training a model on them. Search-based techniques act as wrapper feature selection methods that require a learning algorithm to select optimal attributes of a dataset. Embedded methods combine the features of both filter and wrapper methods. Tables 5 and 6 show the different feature selection techniques used by primary studies.

Among 72 primary studies, 46% of studies use feature selection techniques in developing SDP models. In Table 5, we can observe that Information Gain is the most frequently used filter technique. Information gain for each attribute is calculated, and those with a higher value are selected. In Table 6, we can observe that GA is the more commonly used wrapper technique. It has a strong ability to perform a global search and explore the search space using various crossover techniques (Manjula and Florence 2018; Ayon 2019; Turabieh et al. 2019). Several authors (Arora and Saha 2019) (Ni et al. 2019) (Matloob et al. 2019) (Mabayoje et al. 2019) (Afzal and Torkar 2016) have also compared different search-based techniques with other filter methods (Information Gain, Gain Ratio, Correlation method) and wrapper (best first search, greedy stepwise, linear forward selection). It is concluded that search-based techniques outperform the conventional feature selection methods because of their stochastic nature, efficient search space exploration, and avoidance of getting trapped in local optima.

Table 5 Filter feature selection techniques

Primary studies	Filter techniques	Count of studies
HS13, HS18, HS26	Correlation-Based Feature Selection	3
HS2, HS18, HS28, HS53	Information Gain	4
HS2, HS53	Chi-Square Statistic	2
HS2, HS53	Gain Ratio	2
HS2	Kolmogorov–Smirnov Statistic	1
HS2, HS18, HS53	Relief Algorithm	3
HS2, HS53	Symmetrical Uncertainty	2
HS18	Principal Component Analysis	1
HS57	Kernel Principal Component Analysis	1
HS18	Consistency-Based Subset Evaluation	1
HS53	Probabilistic Significance	1
HS33	Mutual Information	1

Table 6 Wrapper feature selection techniques

Primary studies	Wrapper techniques	Count of studies
HS2	ES, HS, AHS	1
HS7, HS11, HS14, HS27, HS34, HS36, HS38, HS52, HS53, HS54, HS61, HS63, HS67	PSO	13
HS11, HS22, HS23, HS27, HS32, HS34, HS36, HS42, HS47, HS49, HS50, HS52, HS53, HS54, HS56, HS58, HS60, HS61, HS63	GA	19
HS18	GP	1
HS26, HS63	Bat Search	2
HS30, HS53, HS59, HS63	Firefly Search	4
HS34, HS44, HS63	ACO	3
HS49	Multi-Objective Evolutionary search	1
HS48	Binary Moth Flame Optimization	1
HS58, HS65, HS68	Whale Optimization	3
HS59	Wolf Search	1
HS55	Harris Hawks Optimization	1
HS51, HS63, HS69	MOFES-NSGA-II, NSGA-III	3
HS68	Simulated Annealing	1
HS63	Bee Colony Optimization	1
HS63	Cuckoo Search Optimization	1
HS63	Elephant Search	1
HS63	Flower Search	1
HS63	Rhinoceros Search	1

Table 7 Parameter optimization techniques

Primary studies	Techniques used for parameter optimization	Count of studies
HS4, HS8, HS10, HS36, HS41, HS71, HS72	PSO	6
HS5, HS16, HS29, HS36, HS41, HS57	GA	6
HS13	ABC	1
HS21, HS64	Bat search	2
HS31, HS35, HS37, HS46	Multi-Objective Cuckoo search	4
HS33, HS41	Firefly Search Algorithm	2
HS43, HS62	Differential Evolution	2
HS32	Bird Mating	1
HS66	Salp Swarm Optimization	1
HS70	Harmony Search	1
HS43	Simulated Annealing	1
HS72	Wolf Pack Algorithm	1

5.4.4 RQ4.4: What are the parameter tuning techniques used?

The values of parameters in a model control its learning process and influence its performance. When building hybrid-based models, the optimal configuration/parameter settings of classification algorithms must be determined to achieve the optimum classification performance of the model. Since search-based techniques explore different possible configurations in their search space, they are best suitable for this problem. Table 7 represents search-based techniques found in the primary studies used for parameter optimization of different classification algorithms.

GA(HS5), PSO(HS8) and, Bat algorithm (HS21), MOCS (HS31, HS35, HS37, HS46), Firefly Algorithm (HS33) are used to optimize parameters of SVM. PSO

(HS4, HS10) is used to obtain connection weights of integrated decision networks and ANN, respectively. ABC(HS13), GA (HS29, HS41), PSO(HS41), and Bird Mating Algorithm (HS32) are used to optimize weights for ANN. GA(HS16) is used to optimize source project weights and build a GA classifier. DE and SA(HS43) for optimizing parameters of CART and Random Forest. GA (HS57) is used to optimize the weights and bias of the ELM algorithm. DE (HS62) determines the coefficients of the LR model according to the metric Density percentile average. An improved version of PSO (HS71) is used for parameter tuning of Kernel Twin SVM. A multi-objective Bat algorithm (HS64) addresses the problem of imbalance and synchronous parameter optimization of SVM. A hybrid of the Wolf Pack algorithm and PSO(HS72) optimizes the hyperparameters of the DNN.

5.4.5 RQ4.5: Which performance measures are used?

The predictive capability of various SDP models developed using hybridized techniques should be evaluated as different authors consider different performance measures. Table 8 lists all the performance metrics along with the studies in which they are used.

Figure 8 depicts the distribution of studies based on these performance metrics. The most commonly utilized performance metrics while evaluating hybrid-based SDP models were recall and accuracy, which appeared in about 53% and 50% of the selected primary studies. F-measure

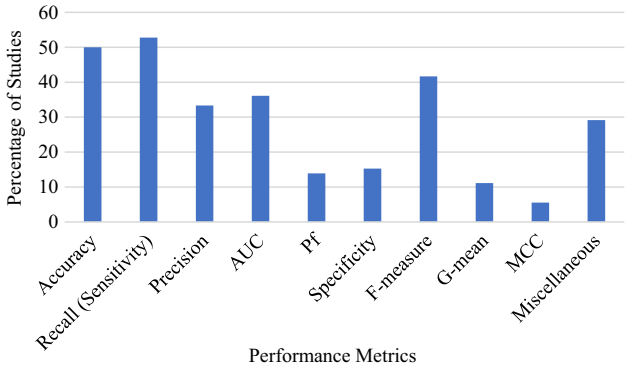

Fig. 8 Distribution of primary studies based on performance metrics

was used to assess around 42% of the studies and AUC in about 36% of the studies. Accuracy though widely used is not recommended and may be misleading while evaluating the model's performance on imbalanced datasets (He and Garcia 2009). Instead, the AUC measure is considered more effective while handling imbalanced and noisy datasets with respect to class distribution (de Carvalho et al. 2010). Researchers should employ a suitable performance metric that would produce valid and reliable results and improve the study's conclusion validity. Other studies use Precision (33%), Probability of False alarm (14%), Specificity (15%), G-mean (11%), and MCC (6%). Some miscellaneous metrics (29%) like Type I error, Type II error, Defect density, Balance, Error rate, Mean Absolute Error, False Positive rate, Misclassification rate, mean

Table 8 Performance measures used by primary studies

Primary studies	Performance measures
HS3, HS4, HS5, HS6, HS8, HS10, HS12, HS13, HS15, HS21, HS22, HS23, HS24, HS25, HS26, HS27, HS29, HS30, HS31, HS32, HS33, HS36, HS41, HS42, HS45, HS47, HS49, HS50, HS52, HS53, HS54, HS58, HS59, HS61, HS63, HS66	Accuracy
HS4, HS5, HS6, HS12, HS13, HS15, HS17, HS19, HS20, HS21, HS24, HS25, HS30, HS31, HS33, HS39, HS35, HS37, HS40, HS41, HS42, HS44, HS46, HS47, HS49, HS48, HS50, HS54, HS55, HS56, HS57, HS58, HS59, HS61, HS66, HS67, HS70, HS72	Recall (sensitivity)
HS4, HS5, HS12, HS19, HS21, HS24, HS25, HS30, HS31, HS33, HS39, HS40, HS43, HS44, HS47, HS49, HS50, HS54, HS56, HS57, HS58, HS59, HS61, HS72	Precision
HS2, HS6, HS7, HS9, HS11, HS13, HS14, HS17, HS18, HS26, HS32, HS34, HS38, HS47, HS48, HS51, HS52, HS55, HS60, HS63, HS65, HS66, HS67, HS68, HS71, HS72	AUC
HS13, HS17, HS31, HS33, HS35, HS37, HS46, HS59, HS69, HS70	Probability of false alarm (pf)
HS6, HS15, HS41, HS42, HS47, HS48, HS50, HS54, HS55, HS58, HS66	Specificity
HS4, HS5, HS12, HS16, HS19, HS20, HS21, HS23, HS24, HS25, HS28, HS30, HS31, HS39, HS43, HS44, HS45, HS47, HS50, HS52, HS54, HS57, HS58, HS59, HS61, HS67, HS68, HS69, HS71, HS72	F-measure
HS19, HS28, HS36, HS46, HS60, HS64, HS68, HS69,	G-mean
HS50, HS52, HS68, HS69	Mathews correlation coefficient (MCC)
HS1, HS4, HS13, HS15, HS16, HS17, HS20, HS27, HS29, HS33, HS41, HS44, HS49, HS50, HS51, HS52, HS54, HS58, HS66, HS62, HS70	Miscellaneous

absolute relative error, R-square, Standard error of the mean, mean square error, Root mean square error, Hypervolume are also used in very few studies.

5.4.6 RQ4.6 Which validation techniques are used?

An efficient validation method can increase the reliability of the results produced by a predictive model. Fifty-nine primary studies reported using validation methods categorized as Hold-out, K-Fold cross-validation, and Cross-project validation. Table 9 contains all the validation methods utilized in the studies, a brief description of each, and the study identifiers that use a specific method. Figure 9 shows the study based on the validation methods used.

We discovered that the most common validation approach is K-fold cross-validation, which gives the mean values of all the partitions of the training dataset, reducing variability. Unlike hold-out validation, the dataset is unaffected by the created partitions. But one disadvantage is that this method requires more computational cost as the model training needs to be done K times.

5.5 RQ5: Which fitness functions are employed in search-based techniques (part of hybridized techniques) for SDP?

A population comprises multiple candidate solutions that are evaluated for goodness using a fitness function to arrive at an optimal or suboptimal solution. The fitness function should be able to quantify how well a given solution fits the problem. According to Harman and Clark (2004), software metrics can act as fitness functions in search-based techniques and, therefore, can be used for the creation of software predictive models. Studies have employed various performance measures, such as fitness functions like accuracy, F-measure, etc., and their variants in search-based techniques. Around 81% of the primary studies specify fitness functions explicitly. Table 10 lists the various fitness functions used in different studies.

According to Table 10, accuracy and its variants are the most commonly utilized fitness functions, accounting for 24% of all primary studies. Pd and pf are used as a multi-objective fitness function in 10% of the studies with the objective of maximizing recall and minimizing pf values. The misclassification cost and its variants are found in 6% of the studies. F-measure and its variants are used in 4% of the studies. AUC is considered an objective function in 6% of the total studies. Other fitness functions include G-mean, Balance, the sum of absolute error, mean square error, etc., which are considered miscellaneous functions. A total of 14 studies have not explicitly stated the fitness functions used in their studies.

However, it is necessary to explore different fitness functions as they form a key factor in any optimization technique. It influences the classification performance, computational time, and the input search space for solutions. The kind of learning algorithm also determines the performance of a fitness function (Xue et al. 2016). Multi-objective fitness functions should also be studied because they balance multiple objective functions while giving a stable predictive model.

5.6 RQ6: What is the performance of hybridized techniques for SDP?

Various primary studies have proposed numerous hybridized techniques, and their performance must be evaluated to ensure their relevance in SDP modeling. Therefore, we present the predictive capabilities of these techniques by

Table 9 Description of validation methods

Validation techniques	Brief description	Study#
K-Fold Cross-Validation	The dataset is split into K equal-sized partitions in this procedure. K-1 partitions are used to train the model in each iteration, whereas 1 out of K partitions is used to test the model. This procedure is repeated K times. The commonly used K values are 5 and 10	HS2, HS4, HS7, HS8, HS9, HS11, HS13, HS17, HS18, HS19, HS23, HS26, H27, HS28, HS31, HS34, HS35, HS36, HS37, HS39, HS41, HS45, HS48, HS49, HS50, HS53, HS54, HS55, HS56, HS57, HS58, HS59, HS60, HS61, HS62, HS63, HS66, HS70
Hold-out Validation	The dataset is split randomly into two parts—one is used for training a model, and another is used for testing a model. The datasets are divided into specific ratios. The commonly used ratios are 80:20 and 70:30	HS1, HS3, HS5, HS6, HS10, HS12, HS14, HS21, HS22, HS24, HS32, HS33, HS34, HS38, HS40, HS51, HS52, HS65
Cross-project Validation	The model is trained using a dataset from a specific project (X) and is validated using a dataset from another project (Y)	HS16, HS20, HS69, HS71

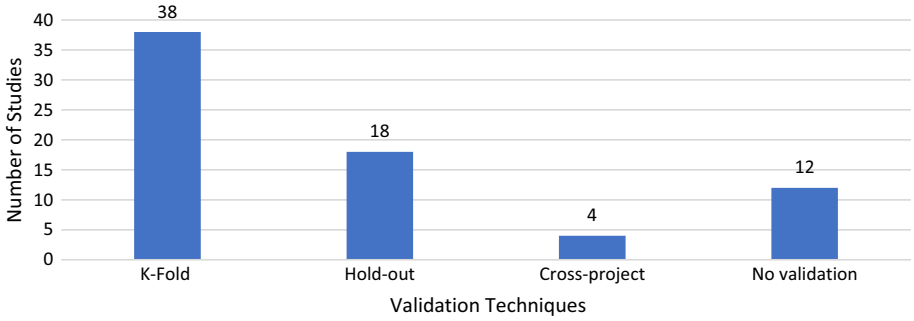

Fig. 9 Distribution of studies based on validation methods used

Table 10 Fitness functions employed by search-based techniques in hybrid-based models

Fitness functions	Study#
Misclassification Cost	HS1, HS20, HS24, HS26
Accuracy	HS3, HS4, HS7, HS10, HS11, HS23, HS27, HS34, HS36, HS42, HS44, HS45, HS47, HS48, HS55, HS61, HS68
F-measure	HS5, HS16, HS30
Multi-objective: Specificity and Sensitivity	HS6
Mean absolute error	HS18, HS29
F1 Score * G-mean	HS19, HS28
Multi-Objective: Probability of detection(Pd) and probability of false alarm (pf)	HS17, HS20, HS31, HS35, HS37, HS46, HS64
AUC	HS51, HS65, HS66, HS60
Miscellaneous	HS8, HS9, HS12, HS13, HS14, HS15, HS17, HS21, HS22, HS32, HS38, HS50, HS51, HS57, HS62, HS67, HS69, HS70, HS71, HS72
Not Clearly stated	HS25, HS33, HS39, HS40, HS41, HS43, HS49, HS52, HS53, HS54, HS56, HS58, HS59, HS63

reporting the performance measures analyzed in Sect. **5.4.5**. The results of only those techniques are recorded and examined on a minimum of three different data sets and used in at least two primary studies to generalize the findings. It is necessary to avoid bias caused by a technique's superior performance in research or on specific datasets.

5.6.1 RQ6.1: What is the overall performance of hybridized techniques used for SDP models?

We record the values of accuracy, recall, and F-measure for hybridized techniques on different datasets to examine their performance. These metrics were chosen for evaluation because they are the most frequently used performance metrics, as mentioned in Sect. 5.4.5. We present the descriptive statistics of performance measures after removing the outliers in Table 11. The outliers were removed because some techniques may produce biased predictions when applied to specific datasets. Therefore, outlier analysis was essential and done with the help of boxplots for the performance measures dataset-wise. Figure 10 Dataset-wise Recall outliers for Hybridized Techniques represent the recall outliers reported on different datasets. We can observe that, in total, there are nine recall outliers. MC2 is an outlier for GA-KNN and GA-NB algorithms with low recall values. Xalan-2.5, poi-2.5, poi-3.0, KC4, and Lucene-2.2 observe low recall values and are outliers for the PSO-SVM algorithm. PC2 and PC4 are outliers for PSO-ANN and GA-NB algorithms with higher recall values. Figure 11 represents the F-measure outliers reported on different datasets. According to the figure, GA-DT and GA-ANN have one outlier each for the Log4j dataset. Lucene-2.2 is an outlier for the PSO-SVM algorithm. Figure 12 represents the accuracy of outliers reported on different datasets. We observe three outliers in the GA-NB algorithm where MC2 and EQ have lower accuracy values, and PC2 has high accuracy values.

A good SDP model should possess results with high values in the recall, F-measure, and accuracy. Table 11 describes the descriptive statistics for the performance measures: recall, F-measure, and accuracy, including the

Table 11 Descriptive statistics of performance measures for hybrid-based SDP models

Algorithm	Count	Performance measure	Minimum	Maximum	Mean	Median	SD
HIDER	7	Recall	0.14	1	0.66	0.74	0.35
	7	F-measure	0.22	0.94	0.65	0.7	0.25
	3	Accuracy	88.1	97.38	94.14	96.93	5.23
GA-ANN	14	Recall	0.02	1	0.64	0.83	0.4
	6	F-measure	0.41	0.94	0.73	0.72	0.18
	18	Accuracy	76.72	100	89.5	88.07	7.65
GA-DT	10	Recall	0.14	1	0.65	0.63	0.28
	6	F-measure	0.5	0.94	0.74	0.72	0.16
	3	Accuracy	91.68	93.36	92.37	92.09	0.88
PSO-ANN	6	Recall	0	0.1944	0.048	0.03	0.073
	13	Accuracy	80.27	99.79	89.41	87.55	6.03
Firefly-SVM	4	Recall	0.807	0.993	0.92	0.94	0.08
	4	F-measure	0.72	0.99	0.88	0.91	0.12
	4	Accuracy	80.7	99.3	91.9	93.82	8.32
GFS-AB	6	Recall	0.738	1	0.91	0.98	0.12
	3	Accuracy	96.9	97.9	97.57	97.9	0.58
GA-KNN	4	Recall	0.8	s0.97	0.87	0.86	0.074
	5	Accuracy	64.52	96.81	84.99	87.6	13.38
GA-SVM	30	Recall	0.3	1	0.84	0.967	0.227
	30	F-measure	0.46	0.997	0.818	0.876	0.166
	30	Accuracy	35	99.59	77.83	79.76	16.47
GA-Fuzzy Logic	3	Recall	0.48	0.78	0.65	0.68	0.15
	3	F-measure	0.6	0.75	0.69	0.73	0.08
	3	Accuracy	68	74.17	72.02	73.91	3.49
PSO-SVM	20	Recall	0.859	1	0.97	0.99	0.045
	24	F-measure	0.63	0.99	0.87	0.92	0.12
	25	Accuracy	58.75	99.59	82.58	85.87	11.29
GFS-LB	3	Accuracy	94.9	98.9	97.23	97.89	2.08
Firefly-NB	8	Accuracy	72.8	88	81.95	83.64	5.77
GA-NB	3	Recall	0.81	0.86	0.84	0.86	0.028
	6	Accuracy	81.44	86.8	84.55	84.93	2.025

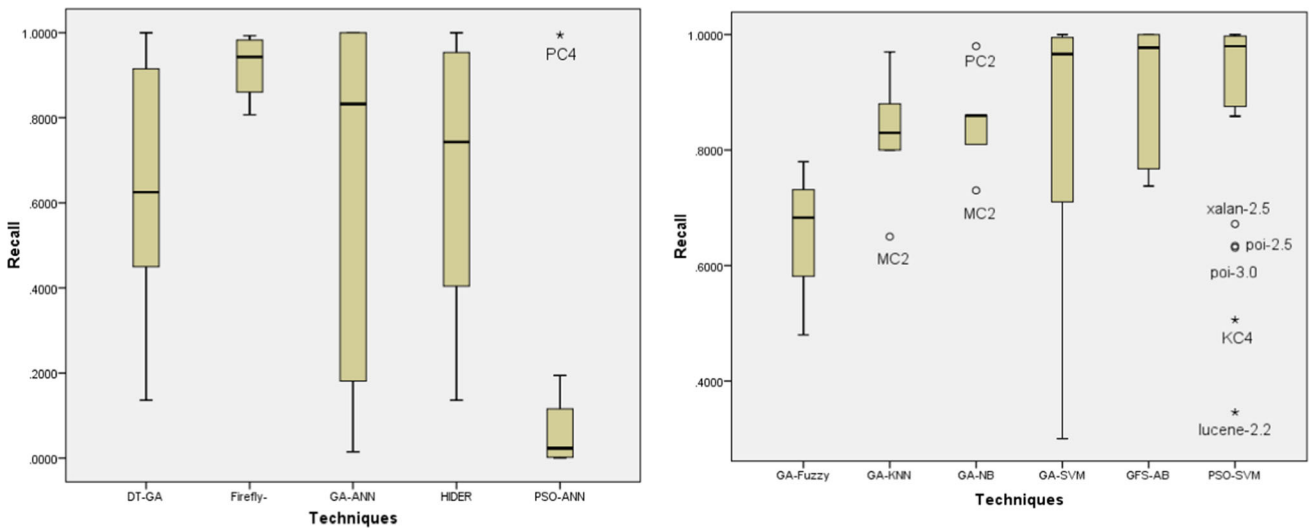

Fig. 10 Dataset-wise recall outliers for hybridized techniques

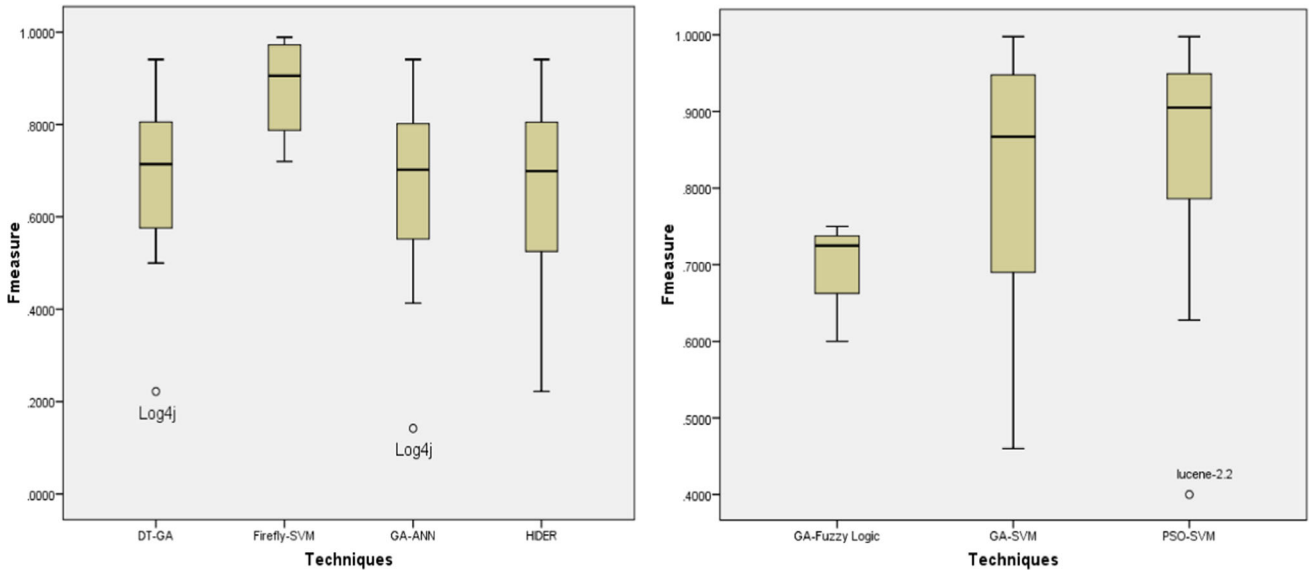

Fig. 11 Dataset-wise F-measure outliers for hybridized techniques

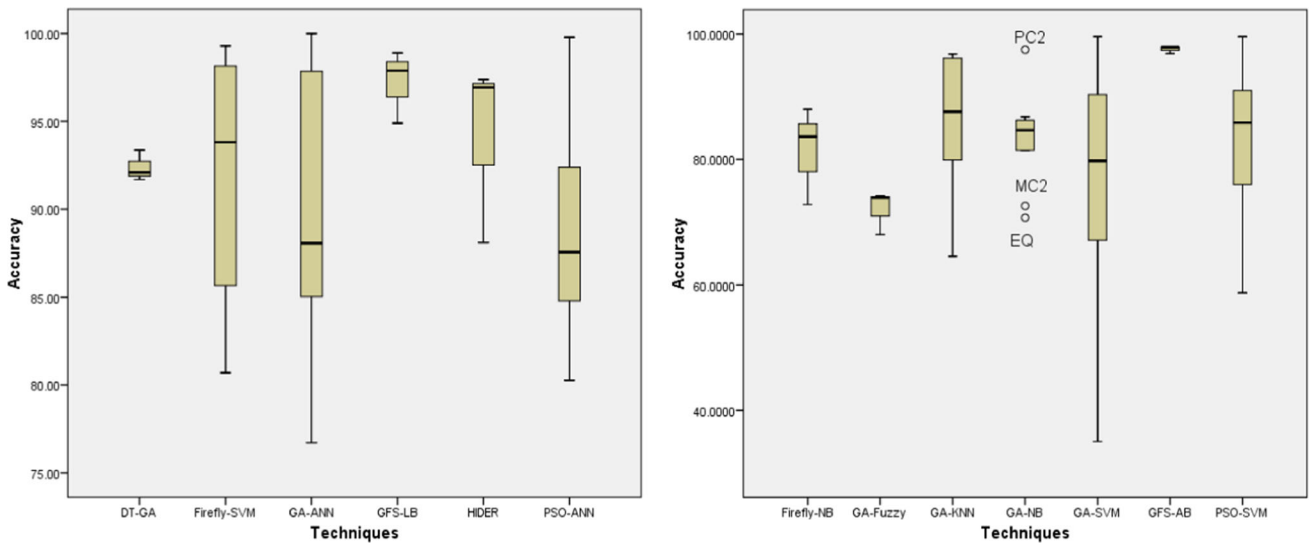

Fig. 12 Dataset-wise accuracy outliers for hybridized techniques

minimum, maximum, mean, median, and standard deviation values, as well as the count of studies from which these values are extracted dataset-wise. It is depicted in Table 11 that the majority of the hybrid techniques show mean values of recall in the range of 0.64–0.92. PSO-SVM represented the best mean recall value of 0.97, followed by Firefly-SVM and GFS-AB, with mean recall values of 0.92 and 0.91, respectively. With respect to the median recall values, PSO-SVM scored the best median recall value of 0.99. PSO-ANN scored the worst mean and median recall values of 0.048 and 0.03, which can be attributed to the fact that these recall values are obtained from only one study. With respect to the F-measure values, the hybrid algorithms show mean values in the range of 0.65–0.88, where the maximum mean value is attained by Firefly-SVM with a value of 0.88, followed by the next best PSO-SVM with the mean F-measure value of 0.87. Again, PSO-SVM obtains the highest median F-measure value of 0.92. With respect to the accuracy values, GFS-AB scores the best mean and median accuracy values of 97.57 and 97.9, followed by the next best GFS-LB with mean and median accuracy values of 97.23 and 97.89. Also, the mean accuracy values of a majority of the hybrid algorithms range from 82.58 to 97.57, which is quite acceptable. The

statistics in Table 11 show the effectiveness of using hybridized techniques in SDP models.

5.6.2 RQ6.2: What is the comparative performance of hybridized techniques with traditional ML and statistical techniques?

This section investigates the comparative performance of hybridized techniques with statistical and ML techniques used in the literature for the development of SDP models. We analyzed the performance of 13 hybrid algorithms, namely, HIDER, GFS-LB, GA-ANN, GA-DT, PSO-ANN, Firefly-SVM, GFS-AB, GA-KNN, PSO-SVM, GA-SVM, GA-Fuzzy Logic, Firefly-NB, and GA-NB among each other and seven ML techniques, namely Support Vector Machines (SVM), Random Forest (RF), K Nearest Neighbor (KNN), J48, Artificial Neural Network (ANN), Naïve Bayes (NB), C4.5, and two statistical techniques Linear Discriminant Analysis (LDA) and Logistic Regression (LR). These ML/statistical techniques were selected for comparison on the basis that we could extract enough data from at least two primary studies and evaluate them on at least three datasets. We followed the two rules for analyzing the results while comparing the performance of hybridized techniques.

- If any study builds SDP models on the same dataset multiple times, but with different parameter settings, the best performance measure value is chosen for that technique.
- In the case of multiple studies, building the model using the same technique and dataset, the best performance measure values of all the studies are chosen for that technique.

For statistical validation of comparative performance between several hybrid, ML, and statistical techniques, we used the Wilcoxon signed-rank test with a significance level of 0.05. Tables 12, 13, and 14 show the results for recall, F-measure, and accuracy values, respectively. We use different symbols to represent if the algorithm's performance in the row is superior, inferior, or equivalent to the performance of another algorithm in the column.

- If performance measure value is significantly superior—(↑*)
- If performance measure value is significantly inferior—(↓*)
- If performance measure value is superior but is not significant—(↑)
- If performance measure value is inferior but is not significant—(↓)
- If an equal number of positive and negative ranks are obtained—(=)

Table 12 Wilcoxon test results for recall values

	HIDER	GA-ANN	GA-DT	PSO-ANN	Firefly-SVM	GFS-AB	GA-KNN	PSO-SVM	GA-SVM	GA-Fuzzy	GA-NB	SVM	RF	KNN	NB	J48	ANN	LR	C4.5	LDA
HIDER	–	(↑)	(↑)	#	#	#	#	#	#	#	#	#	#	#	#	#	#	#	#	#
GA-ANN	(↓)	–	(↑)	(↑*)	#	#	#	(↓)	(↓)	#	#	(↓)	#	#	#	#	#	#	#	#
GA-DT	(↑)	(↓)	–	#	#	#	#	(↑)	(↓)	#	#	(↓)	#	(↑)	(↑)	#	#	#	#	#
PSO-ANN	#	(↓*)	#	–	#	#	#	(↓*)	(↓*)	#	#	(↓*)	#	#	#	#	#	#	#	#
Firefly-SVM	#	#	#	#	–	#	#	(↓)	(↓)	#	#	(↓)	=	#	#	#	#	#	#	#
GFS-AB	#	#	#	#	#	–	#	=	=	#	#	(↓)	#	#	(↑)	#	(↑)	(↑)	(↑)	(↑)
GA-KNN	#	#	#	#	#	#	–	(↓)	(↓)	#	(↓)	(↓)	#	(↑)	(↑)	=	#	#	#	#
PSO-SVM	#	(↑)	(↓)	(↑*)	(↑)	=	(↑)	–	=	(↓)	(↑)	(↑*)	(↑)	(↑*)	(↑*)	(↑*)	#	#	#	#
GA-SVM	#	(↑)	(↑)	(↑*)	(↑)	=	(↑)	=	–	(↑)	(↑)	(↑)	(↑*)	(↑*)	(↑*)	(↑*)	(↑*)	(↑*)	(↑*)	(↑)
GA-Fuzzy	#	#	#	#	#	#	#	(↑)	(↓)	–	#	(↓)	#	#	(↓)	#	#	(↑)	#	#
GA-NB	#	#	#	#	#	#	(↑)	(↓)	(↓)	#	–	(↓*)	#	(↑)	(↑*)	(↑)	#	#	#	#

Table 13 Wilcoxon test results for F-measure values

	HIDER	GA-ANN	GA-DT	Firefly-SVM	PSO-SVM	GA-SVM	GA-Fuzzy	SVM	RF	KNN	NB	ANN	LR	C4.5	LDA
HIDER	–	(↑)	(↓)	#	#	#	#	#	#	#	#	#	#	#	#
GA-ANN	(↓)	–	(↓)	#	#	#	#	#	#	#	#	#	#	#	#
GA-DT	(↑)	(↑)	–	#	#	#	#	#	#	#	#	#	#	#	#
Firefly-SVM	#	#	#	–	(↓)	(↓)	#	(↓)	(↓)	#	#	#	#	#	#
PSO-SVM	#	#	#	(↑)	–	(↓*)	(↑)	(↑*)	(↑)	#	(↑*)	(↑*)	(↑)	(↑)	(↑)
GA-SVM	#	#	#	(↑)	(↑*)	–	(↑)	(↑*)	(↑*)	(↑*)	(↑*)	(↑*)	(↑*)	(↑*)	(↑)
GA-Fuzzy	#	#	#	#	(↓)	(↓)	–	(↓)	#	#	(↑)	(↓)	(↑)	#	#

Table 14 Wilcoxon test results for accuracy values

	HIDER	GFS-LB	GA-ANN	GA-DT	PSO-ANN	Firefly-SVM	GFS-AB	GA-KNN	PSO-SVM	GA-SVM	GA-Fuzzy
HIDER	–	(↓)	(↑)	#	#	#	(↓)	#	(↑)	(↑)	#
GFS-LB	(↑)	–	(↑)	#	#	#	(↑)	#	(↑)	(↑)	#
GA-ANN	(↓)	(↓)	–	(↑)	=	(↓)	(↓)	(↑)	(↑)	(↓)	#
GA-DT	#	#	(↓)	–	(↑)	#	#	#	(↑)	(↑)	#
PSO-ANN	#	#	=	(↓)	–	#	#	#	(↓)	(↓)	#
Firefly-SVM	#	#	(↑)	#	#	–	#	#	(↓)	(↓)	#
GFS-AB	(↑)	(↓)	(↑)	#	#	#	–	#	(↑)	(↑)	#
GA-KNN	#	#	(↓)	#	#	#	#	–	(↓)	(↓)	#
PSO-SVM	(↓)	(↓)	(↓)	(↓)	(↑)	(↑)	(↓)	(↑)	–	(↓*)	(↑)
GA-SVM	(↓)	(↓)	(↑)	(↓)	(↑)	(↑)	(↓)	(↑)	(↑*)	–	(↑)
GA-Fuzzy	#	#	#	#	#	#	#	#	(↓)	(↓)	–
Firefly-NB	#	#	#	#	#	#	#	#	(↓)	(↓)	#
GA-NB	#	#	#	#	#	#	#	(↓)	(↑)	(↑)	#

	Firefly-NB	GA-NB	SVM	RF	KNN	NB	J48	ANN	LR	C4.5	LDA
HIDER	#	#	(↑)	#	#	(↑)	#	#	#	(↑)	#
GFS-LB	#	#	(↑)	#	#	(↑)	#	#	#	(↑)	#
GA-ANN	#	#	=	(↑*)	(↑)	(↑*)	(↑)	=	(↑)	(↑)	(↑)
GA-DT	#	#	(↑)	(↑)	#	#	#	#	#	#	#
PSO-ANN	#	#	(↓)	(↑*)	(↑)	(↑)	#	(↑)	#	(↑)	#
Firefly-SVM	#	#	(↓)	=	#	#	#	#	#	#	#
GFS-AB	#	#	(↑)	#	#	(↑)	#	#	#	(↑)	#
GA-KNN	#	(↑)	(↓)	(↑)	(↑)	(↑)	(↑)	(↓)	#	#	#
PSO-SVM	(↑)	(↑)	(↑*)	(↑*)	(↑*)	(↑)	(↑*)	(↑)	(↑*)	(↑*)	(↑)
GA-SVM	(↑)	(↑)	(↑*)	(↑*)	(↑*)	(↑*)	(↑*)	(↑*)	(↑*)	(↑*)	(↑)
GA-Fuzzy	#	#	(↓)	#	#	(↓)	#	(↓)	(↑)	#	#
Firefly-NB	–	=	(↓)	(↑)	(↓)	=	(↑)	(↓)	(↑)	(↑)	#
GA-NB	=	–	(↓)	#	(↓)	(↑)	(↑)	(↓)	#	#	#

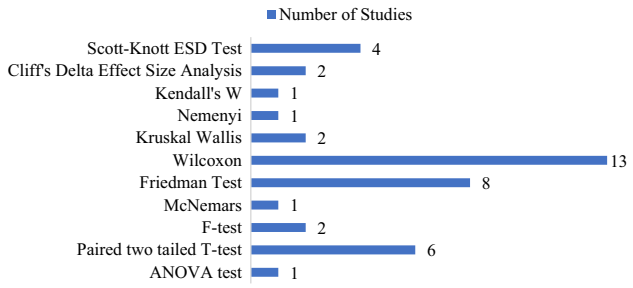

Fig. 13 Distribution of studies according to statistical analysis

- If there is not sufficient data to compare between two techniques—(#)

As observed in Table 12, GA-SVM outperforms all other algorithms in terms of recall, with significant superior values over PSO-ANN, RF, KNN, NB, J48, ANN, LR, and C4.5 algorithms and non-significantly superior values over other algorithms. PSO-SVM is considered equivalent to GA-SVM and performs better than most algorithms except for GA-DT and GA-Fuzzy Logic. GA-SVM, GFS-AB, and GA-Fuzzy show superior performance over the LR technique. Table 13 again indicates that GA-SVM depicted better F-measure results than other algorithms. With respect to accuracy values, GA-SVM gave significantly better results than PSO-SVM, LR, and all ML algorithms, as shown in Table 14. For all other algorithms, it gave better accuracy values but was not significant except for HIDER, GFS-LB, GA-DT, and GFS-AB. Five hybrid algorithms, GA-ANN, PSO-SVM, GA-SVM, GA-Fuzzy, and Firefly-NB, performed better than the LR technique in terms of accuracy. Among all the ML algorithms, SVM gave better performance than five hybrid algorithms (PSO-ANN, Firefly-SVM, GA-KNN, GA-Fuzzy, GA-NB) in terms of accuracy and recall values. In Table 13 and Table 14, we can observe that GA-SVM gave the best performance measure values out of all the algorithms and hence can be considered the best hybrid algorithm for developing SDP models. Overall, all the hybrid algorithms show superior results over LR and ML techniques. It proves the effectiveness of the hybridized techniques compared to statistical and ML techniques. However, there is a need to collect more studies due to the unavailability of sufficient data for all the performance measures, a more comprehensive comparison is required between the various algorithms.

5.7 RQ7: What are the different statistical tests used to study hybridized techniques in SDP?

Statistical tests are essential to obtain quantifiable and statistically verifiable results regarding the predictions produced by a predictive model. These tests provide adequate support to validate the comparisons between different hybridized techniques for building defect prediction models. Out of 72 primary studies, only 41 studies (around 57%) use statistical tests to give evidence of their conclusive results. Parametric and non-parametric tests are the two types of statistical tests used.

Figure 13 describes the distribution of studies based on statistical tests. Non-parametric tests are used in 78% of studies that include statistical analysis, while parametric

Table 15 Statistical tests used by primary studies

Statistical test	Type	Primary studies
ANOVA	Parametric	HS2
F-test	Parametric	HS55, HS65
Paired two-tailed T-test	Parametric	HS6, HS7, HS11, HS23, HS61, HS66
McNemar's	Non-Parametric	HS4
Friedman	Non-Parametric	HS13, HS28, HS39, HS36, HS40, HS45, HS51, HS56
Wilcoxon	Non-Parametric	HS16, HS17, HS19, HS20, HS28, HS34, HS45, HS43, HS54, HS58, HS65, HS68, HS71
Kruskal–Wallis	Non-Parametric	HS18, HS28
Nemenyi	Non-Parametric	HS28
Kendall's W	Non-Parametric	HS39
Scott-Knott ESD	Non-Parametric	HS68, HS69, HS62, HS63
Cliff's Delta Effect Size Analysis	Non-Parametric	HS68, HS69

Table 16 Strengths and weaknesses of hybridized techniques for SDP

Study#	Technique	Strengths	Weaknesses
HS36, HS56	GFS-LB	(1) Multiple weak classifiers combined to form a strong classifier resulting in higher performance (2) Learning rate is fast	It requires high interaction between the rules, resulting in a poor–quality rule base
HS36, HS40, HS56	GFS-AB	(1) Multiple weak classifiers combined to form a strong classifier resulting in higher performance (2) Learning rate is fast	It requires high interaction between the rules resulting in a poor–quality rule base
HS10, HS29, HS32, HS39, HS41	GA-ANN	(1) GA has a parallel search method and global optimization properties that enable the ANN to have a higher prediction accuracy and faster convergence (2) GA has interesting searching patterns that select the best weight for a neural network	(1) Crossover and mutation operators are inherently complex in GA (2) Computational cost is increased
HS39, HS42	DT-GA	It selects features better than other greedy algorithms	Suffers from pre–mature convergence problem of local optima when applied on huge datasets and complex problems
HS10, HS41	PSO-ANN	(1) PSO is known to have a strong ability in training ANN (2) No special requirement for encoding and decoding operators for training the ANN 3) Requires very few parameters and produces a robust model	–
HS30, HS33, HS59	Firefly-SVM	Computationally faster and more efficient than GA or PSO	–
HS8, HS21, HS54	PSO-SVM	The model is robust as it is not affected by individual particle error	–
HS12, HS24	GA-Fuzzy Logic	It does not return to the local minima	–

tests are used in 22%. The wide use of nonparametric tests is supported because they don't require any assumptions about data normality. They are simple to understand and easy to use. Whereas parametric tests require complete knowledge of population distribution, data normality should be true before applying these tests. Some studies have performed parametric tests such as F-test, Paired two-tailed t-test, and ANOVA tests. Some studies have performed nonparametric tests, such as Kendall's W, Nemenyi, Kruskal–Wallis, Friedman, Wilcoxon, McNemars, Scott-Knott ESD, and Cliff's Delta Effect Size analysis tests. The Wilcoxon test is the most popular of all the studies, which can be used individually for the pairwise comparison of different techniques. It is also generally applied as a post hoc analysis test after the Friedman test (Demšar 2006). All the statistical tests used by various primary studies are listed in Table 15.

5.8 RQ8: What are the strengths and weaknesses of hybridized techniques for SDP?

The strengths and weaknesses of various hybridized techniques, as stated in the primary studies, are highlighted in this section. Hybridized techniques are formed by combining different ML/statistical and search-based techniques for developing SDP models. Few authors have tried replicating the techniques on other datasets like GA-ANN, GA-DT, Firefly-SVM, PSO-SVM, etc. The focus is primarily on creating new hybrid-based models to find interesting results and compare them with the previous works. We present the strengths and weaknesses of these techniques as supported by studies in Table 16. It is observed that the characteristics of various hybridized techniques may only be valid within the study's context. As a result, it is hard to determine whether the application of a particular hybrid technique fits a specific domain. However, to avoid study bias, we only report those characteristics supported by a minimum of two studies.

5.9 RQ9: What are the threats to validity in studies using hybridized techniques for SDP?

This section describes all the threats analyzed in the primary studies using the hybridized techniques for SDP. A researcher must examine all the potential threats at the early stages of the experiment to ensure that the results are valid and reliable. It would ensure that proper experiments

Table 17 Threats to validity reported by primary studies

Study#	Threats to Validity	Threat Description
HS29	Internal Threat	Obtained results don't take into account the severity of the faults
HS36, HS39, HS56	Internal Threat	The size of the software can affect the independent variables, and hence results can be affected
HS27, HS29	Internal Threat	Confounding effect of independent variables and influence of other human factors -developer's experience, familiarity with code
HS2, HS16, HS17, HS18, HS20, HS51, HS57, HS69	Internal Threat	Experimental setting errors and errors in model selection
HS5, HS28, HS36, HS39, HS40, HS56	External Threat	Obtained results are validated on datasets written in a specific language and cannot be generalized
HS2, HS16, HS17, HS19, HS27, HS28, HS29, HS51, HS57, HS58, HS62 HS70,	External Threat	Obtained results are validated on specific datasets, which leads to generalizability issues
HS17, HS20, HS27, HS29	External Threat	Obtained results validated based on specific independent variables used
HS2, HS18, HS27, HS51, HS58, HS70	External Threat	Obtained results are validated based on specific algorithms/techniques used
HS16, HS27	External Threat	Obtained results cannot be replicated
HS19, HS20	External Threat	Obtained results are not validated on proprietary datasets
HS2, HS5, HS16, HS18, HS19, HS20, HS28, HS36, HS39, HS40, HS62	Construct Validity	Independent and dependent variables may not be correctly collected
HS2, HS18	Construct Validity	Outliers and noise may not be removed from the training dataset
HS17, HS18, HS20, HS51	Construct Validity	Misinterpretation of concepts and measures
HS16, HS17, HS19, HS20, HS28, HS51	Conclusion Validity	Appropriate statistical tests and significance levels may not be chosen correctly
HS16, HS19, HS28	Conclusion Validity	Performance measures may not be appropriately chosen

are conducted so that majority of the threats can be reduced. Additionally, the authors should mention potential threats to inform readers about the study's limitations. We extracted the validity threats from the study sections titled "Limitations" or "Threats to validity." The threats described in the primary studies are classified into internal, external, construct, and conclusion threats. Table 17 shows the different categories of threats along with its brief description with respect to study identifiers.

28% of the primary studies (HS2, HS5, HS16, HS17, HS18, HS19, HS20, HS27, HS28, HS29, HS36, HS39, HS40, HS51, HS56, HS57, HS58, HS62, HS69, HS70) have mentioned the threats in their studies. Only a few studies (HS5, HS17, HS20, HS27, HS39, HS40, HS51) have discussed some threat mitigation strategies. HS5, HS17, and HS20 reduced the randomness of the algorithms GA and HS by executing them 30 times. HS51 used pair programming to cross-check all the programming and experimental errors. HS27 generalized the results by selecting balanced and unbalanced datasets of different sizes. HS39 also eliminated this threat of generalizability by experimenting with varying distributions of defective classes in datasets. HS40 mitigated the external threat by using the hold-out validation method.

6 Limitations of review

Our systematic review consists of several primary studies available in the literature that evaluates the efficiency and effectiveness of SDP models built using hybrid algorithms. We conducted an exhaustive search in all the digital libraries and selected 72 primary studies, but there can be a threat that some relevant studies are excluded in this review. We also assume that the primary studies are impartial and non-biased, but if this is false, there is a threat of validity in our review results (Jorgensen and Shepperd 2007).

SDP models developed using hybrid, statistical, and ML algorithms are evaluated using only three performance measures—recall, F-measure, and accuracy. These metrics were chosen since most primary studies use these measures

to assess model performance. AUC, a more stable measure, could be used to analyze the performance of the models. Still, some studies did not mention those values, hence contributing to the insufficient data; there is a threat that if the models are analyzed using other performance metrics like AUC, the results may vary. Also, the performance of the models may vary depending on different experimental configurations like datasets, independent variables, fitness functions, learning algorithms in feature selection, cross-validation, etc. It can pose a threat to our study; however, to reduce it, an outlier analysis was performed, and median values were reported (Malhotra and Lata 2020).

Most primary studies apply a different hybrid technique for developing SDP models. Therefore we could not evaluate all the hybrid techniques for performance comparison. We included only those studies where the hybrid technique was used in at least two primary studies and validated on at least three different datasets.

7 Conclusion and future directions

This review studies and examines the SDP models predicted using hybridized techniques from various viewpoints, like the techniques used in the studies, datasets and metrics used, fitness functions employed, performance metrics, validation methods, and statistical tests for validation. This review also helps determine the pre-processing feature selection/parameter optimization techniques to develop these predictive models. We analyze the effectiveness of hybridized techniques and show how they are better in prediction capability than statistical and ML techniques using statistical tests. We investigated a total of 72 primary studies after successful refinement based on the quality assessment criteria and inclusion/exclusion factors. The studies are published between January 2000 and December 2021. This process included snowballing, where we scanned the references of the selected papers, and as a result, more relevant studies were found and passed the quality criteria. The information gained from this rigorous systematic review will help the researchers and industrial community to carefully select the hybridized techniques in proposing new SDP models. The significant findings as a result of this systematic review are stated below:

RQ1 Hybrid techniques are formed by merging the search-based and ML techniques or search-based and statistical techniques. Search-based techniques are classified into six categories: Local Search, Swarm Intelligence, Nature-Inspired, Bio-inspired, and Evolutionary algorithms. ML techniques are classified into five major categories—Decision Trees, Ensemble Learners, Support Vector Machines, Neural Networks, and other techniques. Statistical techniques such as LR and LDA are also combined with search-based techniques to form hybrid techniques. The most frequently used category in search-based and ML techniques are the evolutionary techniques (54% of the studies) and the SVM technique (33% of the studies) used to form hybrid-based models.

RQ2 The primary studies included in this systematic review are published between 2000 and 2021. 92% of the primary studies are published between 2013 and 2021. After 2016, we noticed a rise in the number of studies as a result of the application of deep learning techniques such as CNN, LRNN, DNN, ELM, and KELM.

RQ3 This systematic review includes 72 papers, with 72% of the primary studies (51) published in journals, 23% of the studies (16) published in conferences, and 7% of the studies (5) published as book chapters.

RQ4 SDP models using hybridized techniques are developed on various datasets—NASA, Promise, Open-source, academic and industrial datasets. Most studies use traditional or static metrics (65%) as the predictor variables. Composite metrics that include static and OO metrics are used in 33% of the studies, OO metrics alone are used in 3% of the studies, and 17% use miscellaneous metrics like change metrics, process, and product metrics, etc. For data pre-processing, 46% of the studies use search-based techniques for selecting features, and 33% use search-based techniques for parameter optimization. F-measure, accuracy, and recall are the widely used performance metrics in primary studies for evaluating SDP models. K-Fold validation is employed in most studies, whereas hold-out validation is used in some studies where the dataset size is huge.

RQ5 The most frequently used fitness functions are accuracy and its variants and the multi-objective function of maximizing the recall and minimizing the false positive rate. It becomes crucial for researchers to choose the correct fitness function to achieve the best results because the fitness function impacts the efficiency of the overall model prediction.

RQ6 The predictive capability of hybridized techniques in terms of recall ranged between mean values of 0.64 and 0.97, mean F-measure values ranged from 0.65 to 0.88, and mean accuracy values ranged from 72.02 to 97.57. The Wilcoxon sign test results show that GA-SVM outperforms the majority of other hybrid approaches and ML and statistical techniques with respect to all three performance measures. GA is the most widely used evolutionary algorithm, and PSO is more commonly used in the category of swarm intelligence. Overall, the performance of hybrid techniques is superior in comparison with ML and statistical-based models.

RQ7 57% of the primary studies use statistical tests. Friedman and Wilcoxon's tests are the most commonly used nonparametric tests, as they don't require any assumptions about data distribution.

RQ8 Only a few papers have looked into the strengths and weaknesses of the hybridized techniques used to develop SDP models. Generally, a hybrid technique may have specific properties suitable for a particular predictive modeling task, which can affect the predictive capability of a model. Therefore, it is necessary to thoroughly examine a technique before using it in any predictive model.

RQ9 Only 33% of the studies have mentioned threats to validity in their research works. We classified these threats into internal, external, construct, and conclusion. It is observed that there are more generalizability issues in terms of the specific datasets used, programming language, techniques used, etc., in all the experiments conducted by the studies. Very few studies mitigated these threats to yield valid and reliable results.

We provide the future guidelines below for the researchers and industrial community who want to pursue this field of research.

- Most studies using hybrid techniques obtain data from public or open-source repositories. Only a few studies among them used industrial datasets. Therefore, industrial datasets should be made freely available to the research community so that more research experiments can be conducted and generalizable results are obtained.
- We noticed that various hybrid-based models were built, each introducing a novel hybrid approach with a specific input dataset. Future studies should also test those models on different defect datasets and compare the results with other hybrid and ML techniques to ensure these models' generalizability, accountability, and effectiveness.
- While implementing hybrid techniques, it is required that the researchers specify all the parameter settings, fitness functions, and learning algorithms clearly so that it becomes easy for researchers to repeat the experiments.
- We found that 43% of the studies that use hybrid techniques did not conduct any statistical test. Future studies must incorporate statistical tests for proper validation of their results.
- The computational complexity should be evaluated for all the hybrid techniques used for developing models or for feature/parameter selection, and alternate ways, like parallel processing or cloud computing-based techniques, can be introduced to enhance the computational efficiency of the model.
- Search-based techniques suffer from issues like premature convergence, being stuck in local optima, poor computation speed, etc. Similarly, ML techniques also suffer from issues like feature correlation, overfitting, class imbalance, higher training time, etc. Therefore, an in-depth analysis should be performed before selecting any search-based or ML technique, as it may impact the prediction capability of the new hybrid model.
- Search-based techniques are perfectly suitable for solving multi-objective optimization problems due to their population-based nature. However, only 11% of the studies use multi-objective fitness functions. More studies should be conducted where researchers can simultaneously balance other objectives like cost, predictive quality, scalability, etc.
- In conjunction with search-based techniques, deep learning techniques produce outstanding results when the dataset is huge. The use of search-based techniques and hyperparameter tuning should be carefully considered by researchers. More studies should be conducted that utilize the application of deep neural networks in the implementation of complex SDP models.

Appendix

Hybridized techniques used in primary studies

Table 18 lists all the search-based and ML algorithms used in the hybridized techniques for making SDP models.

Table 18 Algorithms used in primary studies

Study#	Algorithms used
HS1	MOGP-DT
HS2	ES/HS/AHS-NB/MLP/SVM/LR/KNN
HS3	ES-PNN, SA-PNN
HS4	PSO-Integrated Decision Network
HS6	Evolutionary Programming with Least Square SVM
HS7	PSO-Bagging-LDA/LR/NB/KNN/K*/BPNN/SVM/LibSVM/CART/C4.5/Random Forest
HS11	GA/PSO-Bagging-LR/LDA/NB/KNN/K*/BPNN/SVM/C4.5/CART/RF
HS13	ABC-ANN
HS14	Quantum PSO-ANN
HS15	Adaptive PSO-ANN
HS16	GA-Ensemble Learning
HS17	Harmony Search-NB/LR/DT
HS18	GP-NB, GP-C4.5
HS20	MOGA-NSGA-II
HS21	CRBA-SVM
HS23	GA-LR
HS25	Glowworm Swarm Optimization-GA-MLPNN
HS26	BA-RF
HS27	PSO-GA-C4.5
HS30	Firefly-KNN
HS31	MOCS-SVM
HS32	Bird Mating Algorithm—ANN
HS34	LRNN-BGA-BPSO-BACO
HS35	MOCSTSVM
HS36	GFS-MaxLB, PSO-LDA
HS37	Adaptive Two SVM-MOCS
HS38	Bound PSO-DNN
HS39	Neural network evolutionary programming, Hybrid fuzzy GBML, ADI, INT
HS40	CamNN, PSO_ACO-C, BNGE_C, Linear LMS-C
HS41	Firefly-ANN
HS43	DE-CART/RF, SA-CART/RF
HS44	Fuzzy Mutual Information ACO
HS45	Weighted PSO-C4.5, Weighted PSO-NB
HS46	HMOCSSVM
HS47	GA-DNN
HS48	MFO-KNN/DT/LDA
HS49	MOES-J48, MOES-NB, MOES-KNN, GA-J48
HS50	GA-PSO-Feedforward Neural Network/RNN/ANN/DNN
HS51	MOFES-NSGA-II, MOFES—MO-Cell, MOFES-SPEA2, MOFES-PAES, MOFES-SMSEMOA
HS52	GA/PSO-Stacking-MLP-DT/RF/SVM/KNN/BN
HS53	PSO-ELM, PSO-KELM, Firefly-ELM, Firefly-KELM
HS54	GA-PSO-SVM
HS55	Binary Harris Hawk Optimization-KNN/DT/LDA
HS57	KAEA
HS58	WO-SVM, GA-WO-SVM
HS59	Firefly-RF/SVM, WSA-RF/SVM
HS60	GA-Bagging-KNN/LR/SVM/NB/DT
HS61	PSO-Modified GA-Bagging—KNN/RF/SVM/LSTSVM/MW-LSTSVM

Table 18 (continued)

Study#	Algorithms used
HS62	DE-LR
HS63	ACO/ABC/BA/CS/Elephant Search/Flower Search/NSGA-II/PSO/Rhinoceros Search-NB
HS64	Multi-Objective BA-SVM
HS65	WOA-KNN/DT
HS66	SSO-BPNN
HS67	PSO-SMOTE-SVM
HS68	WOA-SA-DNN-KELM
HS69	NSGA-III-CNN-SVM
HS70	Harmony Search-Bagging-DT
HS71	Improved QPSO-KTSVM
HS72	PSO-WPA—DNN
HS12, HS24	GA-Fuzzy Logic
HS49, HS22	GA-KNN
HS49, HS63	GA-NB
HS39, HS36	HIDER
HS29, HS32, HS39, HS41	GA-ANN
HS39, HS42	DT-GA
HS36, HS56	GFS-LB
HS36, HS56, HS40	GFS-AB
HS8, HS54	PSO-SVM
HS58, HS5, HS9, HS23, HS54	GA-SVM
HS41, HS10	PSO-ANN
HS30, HS33, HS59	Firefly-SVM
HS30, HS63	Firefly-NB
HS53, HS23	GA-ELM
HS28, HS19	GA-Nearest Neighbor Filter

INT: Genetic algorithm-based classifier with intervalar rules, HIDER: hierarchical decision rules, ADI: Genetic algorithm-based classifier XCS: X classifier system, UCS: Supervised classifier System, MOGP: Multi-Objective Genetic Programming, SHO: Spotted Hyena Optimizer, AIRS: Artificial Immune Recognition System, GFS-LB: Genetic Fuzzy System-Logitboost, GFS-AB: Genetic Fuzzy System-Adaboost, GFS-MaxLB: Genetic Fuzzy System—Logitboost with Single Winner Inference, PSOLDA–PSO Linear Discriminant Analysis, HMOCSSVM: Hybrid multi-objective cuckoo algorithm under sampling algorithm with SVM, CRBA: Changing Range Bat Algorithm, KAEA: Kernel principal component analysis—ADAPTIVE Genetic Algorithm-Extreme Learning Machine-Adaboost, MOFES: Multi-objective Feature Selection, CamNN: Nearest neighbor classification using the cam weighted distance, BNGE_C: Batch Nested Generalized Exemplar Classifier, LinearLMS: Least Mean Square Linear Classifier, BACO: Binary Ant Colony Optimization, BPSO: Binary Particle Swarm Optimization, LRNN: layered recurrent neural network, BGA: Binary Genetic Algorithm, MOES: Multi-Objective Evolutionary Search, MOCS: Multi-Objective Cuckoo Search, GSO: Group Search Optimization, MOGA: Multi-objective Genetic Algorithm, MFO: Moth Flame Optimization, MLPNN: Multilayer Perceptron Neural Network, GBML: Genetics based ML (Pittsburgh and Michigan), WPA: Wolf Pack Algorithm

Highly cited journals/conferences

Table 19 presents the list of the top 15 highly cited journals/conferences.

Table 19 List of top 15 highly cited journals/conferences

Study#	Year	Type	Journal/Conference Name	Title	No. of citations
HS2	2010	Journal	Software: Practice And Experience	Choosing software metrics for defect prediction: an investigation on feature selection techniques	266
HS16	2016	Journal	IEEE Transactions on Software engineering	HYDRA: Massively Compositional Model for Cross-Project Defect Prediction	175
HS13	2015	Journal	Applied Soft Computing	Software defect prediction using cost-sensitive neural network	142
HS46	2019	Journal	Concurrency and Computation: Practice and Experience	An under-sampled software defect prediction method based on hybrid multi-objective cuckoo search	104
HS1	2003	Conference	Proceedings. 15th IEEE International Conference on Tools with Artificial Intelligence	Genetic Programming-Based Decision Trees for Software Quality Classification	60
HS47	2019	Journal	Cluster Computing	Deep neural network-based hybrid approach for software defect prediction using software metrics	58
HS14	2015	Journal	Applied Soft Computing	Prediction approach of software fault-proneness based on hybrid artificial neural network and quantum particle swarm optimization	56
HS17	2016	Journal	Applied Soft Computing	Effective multi-objective naïve Bayes learning for cross-project defect prediction	56
HS28	2017	Journal	Information and Software Technology	A benchmark study on the effectiveness of search-based data selection and feature selection for cross-project defect prediction	55
HS7	2013	Journal	International Journal of Software Engineering and Its Applications	Combining Particle Swarm Optimization based Feature Selection and Bagging Technique for Software Defect Prediction	52
HS5	2012	Conference	SAC '12: Proceedings of the 27th Annual ACM Symposium on Applied Computing	A Further Analysis on the Use of Genetic Algorithm to configure SVM for inter-release Fault Prediction	45
HS11	2014	Journal	JOURNAL OF SOFTWARE	Metaheuristic Optimization based Feature Selection for Software Defect Prediction	39
HS34	2018	Journal	Expert Systems with Applications	Iterated feature selection algorithms with layered recurrent neural network for software fault prediction	39
HS3	2010	Journal	Engineering Applications of Artificial Intelligence	Exhaustive and heuristic search approaches for learning a software defect prediction model	38
HS6	2012	Journal	Information Sciences	An evolutionary programming based asymmetric weighted least squares support vector machine ensemble learning methodology for software repository mining	35

Author contributions RM conceived the presented idea. The literature search was done by SC. The initial draft was written by SC. AS and RM commented on the previous versions of the manuscript. All the authors contributed to the final manuscript.

Funding The authors declare that no funds, grants, or other support were received during the preparation of this manuscript.

Data availability The datasets used for analysis are available at the following links http://promise.site.uottawa.ca/SERepository/, http://purl.org/MarianJureczko/MetricsRepo, https://bug.inf.usi.ch/index.php, https://cse.hkust.edu.hk/~scc/ReLink.htm. Other datasets are either industrial or academic and private in nature.

Declarations

Conflict of interests The authors have no competing interests to declare that are relevant to the content of this article. This article does not contain any studies with human participants or animals performed by any of the authors.

References

Afzal W, Torkar R (2016) Towards benchmarking feature subset selection methods for software fault prediction. In: Studies in computational intelligence. Springer, Berlin, pp 33–58

Alsghaier H, Akour M (2020) Software fault prediction using particle swarm algorithm with genetic algorithm and support vector machine classifier. Softw Pract Exp 50:407–427. https://doi.org/10.1002/spe.2784

Alsghaier H, Akour M (2021) Software fault prediction using Whale algorithm with genetics algorithm. Softw Pract Exp 51:1121–1146. https://doi.org/10.1002/spe.2941

Anbu M, Anandha Mala GS (2019) Feature selection using firefly algorithm in software defect prediction. Cluster Comput 22:10925–10934. https://doi.org/10.1007/s10586-017-1235-3

Arar ÖF, Ayan K (2015) Software defect prediction using cost-sensitive neural network. Appl Soft Comput J 33:263–277. https://doi.org/10.1016/j.asoc.2015.04.045

Arora I, Saha A (2019) ELM and KELM based software defect prediction using feature selection techniques. J Inf Optim Sci 40:1025–1045. https://doi.org/10.1080/02522667.2019.1637999

Arora I, Saha A (2016) Comparison of back propagation training algorithms for software defect prediction. In: Proceedings of the 2016 2nd international conference on contemporary computing and informatics, IC3I 2016. Institute of Electrical and Electronics Engineers Inc., pp 51–58

Arora I, Saha A (2018) Software fault prediction using firefly algorithm. Int J Intell Eng Inform 6:356–377. https://doi.org/10.5555/3271870.3271878

Ayon SI (2019) Neural network based software defect prediction using genetic algorithm and particle swarm optimization. In: 2019 1st international conference on advances in science, engineering and robotics technology, ICASERT. Institute of Electrical and Electronics Engineers Inc., Dhaka, Bangladesh

Bahaweres RB, Imam Suroso A, Wahyu Hutomo A et al (2020) Tackling feature selection problems with genetic algorithms in software defect prediction for optimization. In: 2020 international conference on informatics, multimedia, cyber and information system (ICIMCIS). IEEE, Jakarta, Indonesia, pp 64–69

Balogun AO, Basri S, Jadid SA et al (2020) Search-based wrapper feature selection methods in software defect prediction: an empirical analysis. In: Intelligent algorithms in software engineering. Springer, Berlin, pp 492–503

Banga M, Bansal A, Singh A (2020) Proposed approach to predict software faults detection using entropy. Int J Syst Assur Eng Manag 11:301–312. https://doi.org/10.1007/s13198-019-00934-2

Brezočnik L, Podgorelec V (2019) Applying weighted particle swarm optimization to imbalanced data in software defect prediction. In: Lecture notes in networks and systems. Springer, Berlin, pp 289–296

Cai X, Niu Y, Geng S et al (2020) An under-sampled software defect prediction method based on hybrid multi-objective cuckoo search. Concurr Comput. https://doi.org/10.1002/cpe.5478

Cao Y, Ding Z, Xue F, Rong X (2018) An improved twin support vector machine based on multi-objective cuckoo search for software defect prediction. Int J Bio-Inspir Comput 11:282–291. https://doi.org/10.1504/IJBIC.2018.092808

de Carvalho AB, Pozo A, Vergilio SR (2010) A symbolic fault-prediction model based on multiobjective particle swarm optimization. J Syst Softw 83:868–882. https://doi.org/10.1016/j.jss.2009.12.023

Chen L, Babar MA, Zhang HN (2010) Towards an evidence-based understanding of electronic data sources. In: 14th international conference on evaluation and assessment in software engineering (EASE). BCS Learning and Development, Keele, UK

Chidamber SR, Kemerer CF (1994) A metrics suite for object oriented design. IEEE Trans Softw Eng 20:476–493. https://doi.org/10.1109/32.295895

Chiu NH (2011) Combining techniques for software quality classification: an integrated decision network approach. Expert Syst Appl 38:4618–4625. https://doi.org/10.1016/j.eswa.2010.09.136

Chulani S, Boehm B, Steece B (1999) Bayesian analysis of empirical software engineering cost models. IEEE Trans Softw Eng 25:573–583. https://doi.org/10.1109/32.799958

Demšar J (2006) Statistical comparisons of classifiers over multiple data sets. J Mach Learn Res 7:1–30. https://doi.org/10.5555/1248547.1248548

Dhanalaxmi B, Apparao Naidu G, Anuradha K (2015) Adaptive PSO based association rule mining technique for software defect classification using ANN. In: Procedia computer science. Elsevier, Amsterdam, pp 432–442

D'Ambros M, Lanza M, Robbes R (2012) Evaluating defect prediction approaches: a benchmark and an extensive comparison. Empir Softw Eng 17:531–577. https://doi.org/10.1007/s10664-011-9173-9

Fazel FS (2016) A new method to predict the software fault using improved genetic algorithm. Bull Soc Roy Sci Liège 85:187–202. https://doi.org/10.25518/0037-9565.5275

Ferrucci F, Harman M, Sarro F (2014) Search-based software project management. In: Software project management in a changing world. Springer, Berlin, pp 373–399

Gao K, Khoshgoftaar TM, Wang H, Seliya N (2011) Choosing software metrics for defect prediction: an investigation on feature selection techniques. Softw Pract Exp 41:579–606. https://doi.org/10.1002/spe.1043

Geng W (2018) Cognitive deep neural networks prediction method for software fault tendency module based on bound particle swarm optimization. Cogn Syst Res 52:12–20. https://doi.org/10.1016/j.cogsys.2018.06.001

Grosan C, Abraham A (2007) Hybrid evolutionary algorithms: methodologies, architectures, and reviews. In: Hybrid evolutionary algorithms. Springer, Berlin pp 1–17

Halstead MH (1977) Elements of software science. Elsevier Science Ltd., New York

Harman M, Jones BF (2001) Search-based software engineering. Inf Softw Technol 43:833–839. https://doi.org/10.1016/S0950-5849(01)00189-6

Harman M, Mansouri SA, Zhang Y (2012) Search-based software engineering: trends, techniques, and applications. ACM Comput Surv (CSUR) 45:1–61. https://doi.org/10.1145/2379776.2379787

Harman M, Clark J (2004) Metrics are fitness functions too. In: Proceedings—international software metrics symposium. IEEE, Chicago, IL, USA, pp 58–69

Harman M (2010a) The relationship between search based software engineering and predictive modeling. In: PROMISE '10: Proceedings of the 6th international conference on predictive models in software engineering. Timişoara Romania, pp 1–13

Harman M (2010b) Why the virtual nature of software makes it ideal for search based optimization. In: FASE'10: Proceedings of the 13th international conference on fundamental approaches to software engineering. Springer, Berlin, pp 1–12

Hassouneh Y, Turabieh H, Thaher T et al (2021) Boosted whale optimization algorithm with natural selection operators for software fault prediction. IEEE Access 9:14239–14258. https://doi.org/10.1109/ACCESS.2021.3052149

Haveri A, Suresh Y (2018) Software fault prediction using artificial intelligence techniques. In: 2nd international conference on computational systems and information technology for sustainable solutions, CSITSS 2017. Institute of Electrical and Electronics Engineers Inc.

He H, Garcia EA (2009) Learning from imbalanced data. IEEE Trans Knowl Data Eng 21:1263–1284

He C, Xing J, Zhu R, et al (2013) A new model for software defect prediction using Particle Swarm Optimization and support vector machine. In: 2013 25th Chinese control and decision conference, CCDC 2013. Guiyang, China, pp 4106–4110

Hochman R, Khoshgoftaar TM, Allen EB, Hudepohl JP (1996) Using the genetic algorithm to build optimal neural networks for fault-prone module detection. In: Proceedings of the international

symposium on software reliability engineering, ISSRE. IEEE, White Plains, NY, USA, pp 152–162
Hosseini S, Turhan B, Mäntylä M (2018) A benchmark study on the effectiveness of search-based data selection and feature selection for cross project defect prediction. Inf Softw Technol 95:296–312. https://doi.org/10.1016/j.infsof.2017.06.004
Hosseini S, Turhan B, Mantyl M (2016) Search based training data selection for cross project defect prediction. In: ACM international conference proceeding series. Association for Computing Machinery
Ibrahim DR, Ghnemat R, Hudaib A (2017) Software defect prediction using feature selection and random forest algorithm. In: Proceedings—2017 international conference on new trends in computing sciences, ICTCS 2017. Institute of Electrical and Electronics Engineers Inc., pp 252–257
Jayanthi R, Florence L (2018) Software defect prediction techniques using metrics based on neural network classifier. Cluster Comput 22:77–88. https://doi.org/10.1007/S10586-018-1730-1
Jayaraj V, Raman NS (2016) An hybrid multilayer perceptron using GSO-GA for software defect prediction. Int J Adv Res Sci Eng 5:129–142
Jin C (2021) Cross-project software defect prediction based on domain adaptation learning and optimization. Expert Syst Appl 171:114637. https://doi.org/10.1016/J.ESWA.2021.114637
Jin C, Jin SW (2015) Prediction approach of software fault-proneness based on hybrid artificial neural network and quantum particle swarm optimization. Appl Soft Comput J 35:717–725. https://doi.org/10.1016/j.asoc.2015.07.006
Jin C, Dong EM (2016) Software defect prediction using fuzzy integral and genetic algorithm. In: Software engineering and information technology 2015. World Scientific Pub Co Pte Lt, Guilin, pp 334–340
Jorgensen M, Shepperd M (2007) A systematic review of software development cost estimation studies. IEEE Trans Softw Eng 33:33–53. https://doi.org/10.1109/TSE.2007.256943
Jureczko M, Madeyski L (2010) Towards identifying software project clusters with regard to defect prediction. In: ACM international conference proceeding series. pp 1–10
Kalsoom A, Maqsood M, Ghazanfar MA et al (2018) A dimensionality reduction-based efficient software fault prediction using Fisher linear discriminant analysis (FLDA). J Supercomput 74:4568–4602. https://doi.org/10.1007/S11227-018-2326-5/TABLES/17
Kang J, Kwon S, Ryu D, Baik J (2021) HASPO: harmony search-based parameter optimization for just-in-time software defect prediction in maritime software. Appl Sci. https://doi.org/10.3390/app11052002
Kassaymeh S, Abdullah S, Al-Betar MA, Alweshah M (2021) Salp swarm optimizer for modeling the software fault prediction problem. J King Saud Univ Comput Inf Sci 34:3365–3378. https://doi.org/10.1016/J.JKSUCI.2021.01.015
Kayarvizhy N, Kanmani S, Rhymend Uthariaraj V (2013) Improving Fault Prediction using ANN-PSO in Object Oriented Systems. Int J Comput Appl 73:18–25. https://doi.org/10.5120/12721-9556
Khari M, Kumar P (2018) Evolutionary computation-based techniques over multiple data sets: an empirical assessment. Arab J Sci Eng 43:3875–3885. https://doi.org/10.1007/s13369-017-2653-5
Khoshgoftaar TM, Liu Y, Seliya N, Khosh Goftaar M (2003) Genetic programming-based decision trees for software quality classification. IEEE, Sacramento, CA, USA
Kitchenham B, Charters MS (2007) Guidelines for performing systematic literature reviews in software engineering. Technical report EBSE-2007-01, UK
Kumar L, Rath SK (2017) Application of genetic algorithm as feature selection technique in development of effective fault prediction model. In: 2016 IEEE Uttar Pradesh Section international conference on electrical, computer and electronics engineering, UPCON 2016. Institute of Electrical and Electronics Engineers Inc., Varanasi, India, pp 432–437
Lakshminarayana P, Sureshkumar Tv (2020) Automatic generation and optimization of test case using hybrid Cuckoo search and bee colony algorithm. J Intell Syst 30:59–72. https://doi.org/10.1515/JISYS-2019-0051/MACHINEREADABLECITATION/RIS
Li K, Chen C, Liu W et al (2014) Software defect prediction using fuzzy integral fusion based on GA-FM. Wuhan Univ J Nat Sci 19:405–408. https://doi.org/10.1007/s11859-014-1032-2
Li Z, Jing XY, Zhu X (2018) Progress on approaches to software defect prediction. IET Software 12:161–175. https://doi.org/10.1049/IET-SEN.2017.0148
Li Z, Li T, Wu Y et al (2021) Software defect prediction based on hybrid swarm intelligence and deep learning. Comput Intell Neurosci. https://doi.org/10.1155/2021/4997459
Li F, Rong X, Cui Z (2016) A hybrid CRBA-SVM model for software defect prediction. Int J Wireless Mobile Comput 10:191–196. https://doi.org/10.1504/IJWMC.2016.076145
Mabayoje MA, Balogun A, Mojeed H et al (2019) Wrapper feature selection based heterogeneous classifiers for software defect prediction. Adeleke Univ J Eng Technol 2:1–11
Malhotra R (2015) A systematic review of machine learning techniques for software fault prediction. Appl Soft Comput 27:504–518. https://doi.org/10.1016/J.ASOC.2014.11.023
Malhotra R (2018) An extensive analysis of search-based techniques for predicting defective classes. Comput Electr Eng 71:611–626. https://doi.org/10.1016/j.compeleceng.2018.08.017
Malhotra R, Khanna M (2021) On the applicability of search-based algorithms for software change prediction. Int J Syst Assur Eng Manag. https://doi.org/10.1007/S13198-021-01099-7/FIGURES/6
Malhotra R, Khanna M, Raje RR (2017) On the application of search-based techniques for software engineering predictive modeling: a systematic review and future directions. Swarm Evol Comput 32:85–109. https://doi.org/10.1016/j.swevo.2016.10.002
Malhotra R, Lata K (2020) A systematic literature review on empirical studies towards prediction of software maintainability. Soft Comput 24:16655–16677. https://doi.org/10.1007/S00500-020-05005-4/TABLES/15
Malhotra R, Rajpal A, Rathore D (2018) Parameter tuning on software defect prediction using differential evolution & simulated annealing. Int Conf Big Data Artif Intell BDAI 2018:97–106. https://doi.org/10.1109/BDAI.2018.8546671
Malhotra R, Nishant, Gurha S, Rathi V (2021) Application of particle swarm optimization for software defect prediction using object oriented metrics. In: 2021 11th international conference on cloud computing, data science and engineering. Institute of Electrical and Electronics Engineers Inc., Noida, India, pp 88–93
Malhotra R (2014) Search based techniques for software fault prediction: current trends and future directions. In: SBST 2014: Proceedings of the 7th international workshop on search-based software testing. association for computing machinery, Hyderabad, India, pp 35–36
Manivasagam G, Gunasundari R (2018) An optimized feature selection using fuzzy mutual information based ant colony optimization for software defect prediction. Int J Eng Technol 7:456–460. https://doi.org/10.14419/ijet.v7i1.1.9954
Manjula C, Florence L (2019) Deep neural network based hybrid approach for software defect prediction using software metrics. Cluster Comput 22:9847–9863. https://doi.org/10.1007/s10586-018-1696-z

Manjula C, Florence L (2018) Hybrid approach for software defect prediction using machine learning with optimization technique. Int J Comput Inform Eng 12:28–32https://doi.org/10.5281/zenodo.1315961

Matloob F, Aftab S, Iqbal A (2019) A Framework for software defect prediction using feature selection and ensemble learning techniques. IJ Modern Educ Comput Sci 12:14–20. https://doi.org/10.5815/ijmecs.2019.12.02

McCabe TJ, Butler CW (1989) Design complexity measurement and testing. Commun ACM 32:1415–1425. https://doi.org/10.1145/76380.76382

Mccabe TJ (1976) A complexity measure. IEEE Trans Softw Eng SE 2:308–320. https://doi.org/10.1109/TSE.1976.233837

Mcdonald M, Musson R, Smith R (2007) The practical guide to defect prevention. Microsoft Press, Redmond

Menzies T, Greenwald J, Frank A (2007) Data mining static code attributes to learn defect predictors. IEEE Trans Softw Eng 33:2–13. https://doi.org/10.1109/TSE.2007.256941

Moussa R, Azar D (2017) A PSO-GA approach targeting fault-prone software modules. J Syst Softw 132:41–49. https://doi.org/10.1016/j.jss.2017.06.059

Ni C, Chen X, Wu F et al (2019) An empirical study on pareto based multi-objective feature selection for software defect prediction. J Syst Softw 152:215–238. https://doi.org/10.1016/j.jss.2019.03.012

Niu Y, Tian Z, Zhang M et al (2018) Adaptive two-SVM multi-objective cuckoo search algorithm for software defect prediction. Int J Comput Sci Math 9:547–554. https://doi.org/10.1504/IJCSM.2018.096327

Oloduowo AA, Raheem MO, Ayinla FB, Ayeyemi BM (2020) Software defect prediction using metaheuristic-based feature selection and classification algorithms. Ilorin J Comput Sci Inf Technol 3:23–39

Pal A, Jain H, Kumar M (2017) Optimizing software error proneness prediction using bird mating algorithm. Springer, Cham, pp 257–287

Pandey SK, Mishra RB, Tripathi AK (2021) Machine learning based methods for software fault prediction: a survey. Expert Syst Appl 172:114595. https://doi.org/10.1016/J.ESWA.2021.114595

Pendharkar PC (2010) Exhaustive and heuristic search approaches for learning a software defect prediction model. Eng Appl Artif Intell 23:34–40. https://doi.org/10.1016/j.engappai.2009.10.001

Rathore SS, Kumar S (2016) A decision tree logic based recommendation system to select software fault prediction techniques. Computing 99:255–285. https://doi.org/10.1007/S00607-016-0489-6

Rathore SS, Kumar S (2019) A study on software fault prediction techniques. Artif Intell Rev 51:255–327. https://doi.org/10.1007/S10462-017-9563-5/FIGURES/8

Rhmann W (2018) Application of hybrid search based algorithms for software defect prediction. Int J f Modern Educ Comput Sci 10:51–62. https://doi.org/10.5815/ijmecs.2018.04.07

Rhmann W (2020) Cross project defect prediction using hybrid search based algorithms. Int J Inf Technol (singapore) 12:531–538. https://doi.org/10.1007/s41870-018-0244-7

Rhmann W, Pandey B, Ansari GA (2021) Software effort estimation using ensemble of hybrid search-based algorithms based on metaheuristic algorithms. Innov Syst Softw Eng. https://doi.org/10.1007/S11334-020-00377-0/FIGURES/5

Rhmann W, Pandey B, Ansari G, Pandey DK (2020) Software fault prediction based on change metrics using hybrid algorithms: an empirical study. J King Saud Univ Comput Inf Sci 32:419–424. https://doi.org/10.1016/j.jksuci.2019.03.006

Rong X, Cui Z (2017) Hybrid algorithm for two-objective software defect prediction problem. Int J Innov Comput Appl 8:207–212

Ryu D, Baik J (2016) Effective multi-objective naïve Bayes learning for cross-project defect prediction. Appl Soft Comput J 49:1062–1077. https://doi.org/10.1016/j.asoc.2016.04.009

Sarro F, Martino S di, Ferrucci F, Gravino C (2012) A further analysis on the use of genetic algorithm to configure support vector machines for inter-release fault prediction. In: SAC '12: proceedings of the 27th annual ACM symposium on applied computing. ACM Press, New York, pp 1215–1220

Shuai B, Li H, Li M, et al (2013) Software defect prediction using dynamic support vector machine. In: Proceedings—9th international conference on computational intelligence and security, CIS 2013. pp 260–263

Shukla S, Radhakrishnan T, Muthukumaran K, Neti LBM (2018) Multi-objective cross-version defect prediction. Soft Comput 22:1959–1980. https://doi.org/10.1007/s00500-016-2456-8

Singh Y, Kaur A, Malhotra R (2009) Software fault proneness prediction using support vector machines. In: Proceedings of the world congress on engineering 2009. London, UK

Son LH, Pritam N, Khari M et al (2019) Empirical study of software defect prediction: a systematic mapping. Symmetry 11:212. https://doi.org/10.3390/SYM11020212

Thaher T, Arman N (2020) Efficient multi-swarm binary Harris Hawks optimization as a feature selection approach for software fault prediction. In: 2020 11th international conference on information and communication systems, ICICS 2020. Institute of Electrical and Electronics Engineers Inc., pp 249–254

Thangavel M, Pugazendi DR (2017) Optimized support vector machine for software defect prediction. Int J Eng Res Dev 13:1–11

Ting TO, Yang XS, Cheng S, Huang K (2015) Hybrid metaheuristic algorithms: past, present, and future. In: recent advances in swarm intelligence and evolutionary computation. Springer, Cham, pp 71–83

Tumar I, Hassouneh Y, Turabieh H, Thaher T (2020) Enhanced binary moth flame optimization as a feature selection algorithm to predict software fault prediction. IEEE Access 8:8041–8055. https://doi.org/10.1109/ACCESS.2020.2964321

Turabieh H, Mafarja M, Li X (2019) Iterated feature selection algorithms with layered recurrent neural network for software fault prediction. Expert Syst Appl 122:27–42. https://doi.org/10.1016/j.eswa.2018.12.033

Turhan B, Bener A (2009) Analysis of Naive Bayes' assumptions on software fault data: an empirical study. Data Knowl Eng 68:278–290. https://doi.org/10.1016/J.DATAK.2008.10.005

Wahono RS, Suryana N (2013) Combining particle swarm optimization based feature selection and bagging technique for software defect prediction. Int J Softw Eng Appl 7:153–166. https://doi.org/10.14257/ijseia.2013.7.5.16

Wahono RS, Suryana N, Ahmad S (2014) Metaheuristic optimization based feature selection for software defect prediction. J Softw. https://doi.org/10.4304/jsw.9.5.1324-1333

Wahono RS (2015) A systematic literature review of software defect prediction: research trends, datasets, methods and frameworks. J Softw Eng 1:1–16

Wang S, Liu T, Tan L (2016) Automatically learning semantic features for defect prediction. In: ICSE '16: proceedings of the 38th international conference on software engineering. IEEE Computer Society, pp 297–308

Wen J, Li S, Lin Z et al (2012) Systematic literature review of machine learning based software development effort estimation models. Inf Softw Technol 54:41–59. https://doi.org/10.1016/J.INFSOF.2011.09.002

Wohlin C (2014) Guidelines for snowballing in systematic literature studies and a replication in software engineering. In: EASE '14: proceedings of the 18th international conference on evaluation

and assessment in software engineering, May 2014. Association for Computing Machinery

Wu R, Zhang H, Kim S, Cheung SC (2011) ReLink: recovering links between bugs and changes. In: Proceedings of the joint meeting of the European Software En—gineering conference and the symposium on the foundations of software engineering. pp 15–25

Wu D, Zhang J, Geng S et al (2020) A Multi-objective bat algorithm for software defect prediction. In: Bio-inspired computing: theories and applications. Springer, Berlin, pp 269–283

Xia X, Lo D, Pan SJ et al (2016) HYDRA: Massively compositional model for cross-project defect prediction. IEEE Trans Softw Eng 42:977–998. https://doi.org/10.1109/TSE.2016.2543218

Xue B, Zhang M, Browne WN, Yao X (2016) A survey on evolutionary computation approaches to feature selection. IEEE Trans Evol Comput 20:606–626. https://doi.org/10.1109/TEVC.2015.2504420

Yang X, Yu H, Fan G, Yang K (2020) A differential evolution-based approach for effort-aware just-in-Time software defect prediction. In: Proceedings of the 1st ACM SIGSOFT international workshop on representation learning for software engineering and program languages. Association for Computing Machinery, Inc, pp 13–16

Yang X, Lo D, Xia X et al (2015) Deep learning for just-in-time defect prediction. In: Proceedings—2015 IEEE International Conference on Software Quality, Reliability and Security, QRS 2015. Institute of Electrical and Electronics Engineers Inc., Vancouver, BC, Canada, pp 17–26

Yu L (2012) An evolutionary programming based asymmetric weighted least squares support vector machine ensemble learning methodology for software repository mining. Inf Sci (n Y) 191:31–46. https://doi.org/10.1016/j.ins.2011.09.034

Zhang N, Ying S, Ding W et al (2021) WGNCS: A robust hybrid cross-version defect model via multi-objective optimization and deep enhanced feature representation. Inf Sci (n Y) 570:545–576. https://doi.org/10.1016/J.INS.2021.05.008

Zhang N, Zhu K, Ying S, Wang X (2020) KAEA: A novel three-stage ensemble model for software defect prediction. Comput Mater Contin 64:471–499. https://doi.org/10.32604/CMC.2020.010117

Zhu K, Ying S, Zhang N, Zhu D (2021) Software defect prediction based on enhanced metaheuristic feature selection optimization and a hybrid deep neural network. J Syst Softw. https://doi.org/10.1016/j.jss.2021.111026

Publisher's Note Springer Nature remains neutral with regard to jurisdictional claims in published maps and institutional affiliations.

Springer Nature or its licensor (e.g. a society or other partner) holds exclusive rights to this article under a publishing agreement with the author(s) or other rightsholder(s); author self-archiving of the accepted manuscript version of this article is solely governed by the terms of such publishing agreement and applicable law.

sensors

MDPI

Article

SONG: A Multi-Objective Evolutionary Algorithm for Delay and Energy Aware Facility Location in Vehicular Fog Networks

Md. Muzakkir Hussain [1], Ahmad Taher Azar [2,3,*], Rafeeq Ahmed [4], Syed Umar Amin [2], Basit Qureshi [2], V. Dinesh Reddy [1], Irfan Alam [5] and Zafar Iqbal Khan [2]

1 Department of Computer Science and Engineering, SRM University, Amaravati 522502, India
2 College of Computer and Information Sciences, Prince Sultan University, Riyadh 11586, Saudi Arabia
3 Faculty of Computers and Artificial Intelligence, Benha University, Benha 13511, Egypt
4 Department of CSE, Koneru Lakshmaiah Education Foundation, Vaddeswaram 522302, India
5 Department of Computer Science and Engineering, Delhi Technological University, Delhi 110042, India
* Correspondence: aazar@psu.edu.sa or ahmad.azar@fci.bu.edu.eg or ahmad_t_azar@ieee.org

Abstract: With the emergence of delay- and energy-critical vehicular applications, forwarding sense-actuate data from vehicles to the cloud became practically infeasible. Therefore, a new computational model called Vehicular Fog Computing (VFC) was proposed. It offloads the computation workload from passenger devices (PDs) to transportation infrastructures such as roadside units (RSUs) and base stations (BSs), called static fog nodes. It can also exploit the underutilized computation resources of nearby vehicles that can act as vehicular fog nodes (VFNs) and provide delay- and energy-aware computing services. However, the capacity planning and dimensioning of VFC, which come under a class of facility location problems (FLPs), is a challenging issue. The complexity arises from the spatio-temporal dynamics of vehicular traffic, varying resource demand from PD applications, and the mobility of VFNs. This paper proposes a multi-objective optimization model to investigate the facility location in VFC networks. The solutions to this model generate optimal VFC topologies pertaining to an optimized trade-off (Pareto front) between the service delay and energy consumption. Thus, to solve this model, we propose a hybrid Evolutionary Multi-Objective (EMO) algorithm called **S**warm **O**ptimized **N**on-dominated sorting **G**enetic algorithm (SONG). It combines the convergence and search efficiency of two popular EMO algorithms: the Non-dominated Sorting Genetic Algorithm (NSGA-II) and Speed-constrained Particle Swarm Optimization (SMPSO). First, we solve an example problem using the SONG algorithm to illustrate the delay–energy solution frontiers and plotted the corresponding layout topology. Subsequently, we evaluate the evolutionary performance of the SONG algorithm on real-world vehicular traces against three quality indicators: Hyper-Volume (HV), Inverted Generational Distance (IGD) and CPU delay gap. The empirical results show that SONG exhibits improved solution quality over the NSGA-II and SMPSO algorithms and hence can be utilized as a potential tool by the service providers for the planning and design of VFC networks.

Keywords: intelligent transportation systems; vehicular fog computing; Genetic Algorithm; vehicular ad hoc network; SDG7; SDG9; SDG11; SDG12

check for updates

Citation: Hussain, M.M.; Azar, A.T. ; Ahmed, R.; Umar Amin, S.; Qureshi, B.; Dinesh Reddy, V.; Alam, I.; Khan, Z.I. SONG: A Multi-Objective Evolutionary Algorithm for Delay and Energy Aware Facility Location in Vehicular Fog Networks. *Sensors* **2023**, *23*, 667. https://doi.org/10.3390/s23020667

Academic Editors: Zhiheng Li, Hailong Zhu, Yilong Ren and Jiyuan Tan

Received: 21 November 2022
Revised: 26 December 2022
Accepted: 27 December 2022
Published: 6 January 2023

Copyright: © 2023 by the authors. Licensee MDPI, Basel, Switzerland. This article is an open access article distributed under the terms and conditions of the Creative Commons Attribution (CC BY) license (https://creativecommons.org/licenses/by/4.0/).

1. Introduction

The integration of Internet of Things (IoT) systems with heterogeneous vehicular ad hoc networks (VANETs) has revitalized new capabilities in intelligent transportation systems (ITSs) [1]. Through machine-to-machine (M2M) communication protocols and standards, facilities such as RFID, WSN, GPS, etc., the IoT complements the evolution of ITS applications [2]. In fact, the future ITS is revolutionizing the transport system and autonomous mobility by the introduction of connected and autonomous vehicles (CAVs) with each vehicle having enormous capabilities in terms of storing, computing and networking (SCN). According to the worldwide CAV forecast from the International Data

Corporation (IDC), the global market size of CAVs that are at upper levels of autonomy ($L1\geq$) will rise from 31.4 million units during the period 2019–2020 to 54.2 million units during the period 2024–2025, reflecting a five-year Compound Annual Growth Rate (CAGR) of 11.5% https://www.idc.com/research/viewtoc.jsp?containerId=CA49221622, accessed on 20 October 2022). Feature by feature, the IoT adds novel capabilities for the smart, safe and secure operation of an incoming CAV fleet, a dramatic shift towards an increasingly autonomous future [3].

However, as a curse of volume, vast amounts of data are generated, prompting a delay- and energy-critical analysis and processing. Each CAV is to be equipped with at least 200 on-board sensor units (OBUs) for gathering the ambient information; hence, a galactic volume of sensed data is generated when it is running on the road [1]. According to preliminary estimates, a CAV generates approximately 30 terabytes of data every day. Furthermore, there will be a growing need for new services and frameworks that keep them connected while on the move for the rapid growth of connected mobility [4]. In such a scenario, efficiently processing the quality of service (QoS)-intensive CAV workload, extracting valuable information and making the correct decisions become critical issues.

Although cloud computing employs high-end servers called cloud data centers (CDCs) for processing vehicular data streams, they cause an intolerable delay and have a huge energy footprint [5]. Moreover, the presence of unstable connections in multi-user CAV environments degrades the overall quality of experience. For instance, many ITS applications need interactivity requiring a low response time and service delay for providing instant feedback [6]. In such scenarios, the control nodes must provide accurate signals for the steering system in milliseconds. In the case of a queuing delay or networking failure in cloud server, a vehicle may loose its intelligence, which may even lead to a crash. As a result, a fog computing (FC) model is proposed. Contrary to the cloud computing, fog deploys SCN capabilities into the intermediary in-network devices as well as in the CDCs, making a cloud-to-edge continuum. As a result, FC reduces the overall service delay for the VANET applications [7]. Moreover, since the data are processed and stored in the edge devices, the volume of data traffic transmitted through the network is also reduced [8].

VFC is proposed as a special case of fog computing in VANETs [9]. It is an emerging paradigm that can potentially provide real-time and location-aware SCN services for a wide range of ITS applications [10]. The main idea of VFC is to employ the underutilized vehicular resources as active components of fog infrastructures and at the same time, enable the practical and effective use of conventional cloud resources [9,11]. VFC offers a context-aware, low latency, and energy-efficient SCN framework that leverages VANET users with a wide range of ITS applications [8]. It also enables on-road vehicles to make intelligent offloading decisions, instantly reacting and attuning to rapid changes in the ITS supply chain [12]. An overall architecture of VFC is given in Figure 1.

Because of its peculiar properties, the VFC has been attracting significant dedicated attention from the transportation industry and research communities in recent years [9]. The VFC infrastructure comprises fog nodes, both static (RSUs, BSs, etc.) and dynamic (heavy vehicles, taxis and buses) deployed at appropriate locations to provide computing services to the ITS users [12]. Although VFC architecture can provide ultra-low latency communications and a very low response time, deploying the architecture in the real world is a complex task [13]. The naive strategy to blindly place more and more resources is not practical because the corresponding cost will be very high. Thus, we need a mathematical framework to define the assignment of available resources across various architectural layers. In operation research, this is called an FLP. To be specific, a facility location model for VFC will deal with selecting optimal locations for installing a set of fog nodes, and the available channels for transferring vehicular data, by minimizing or maximizing some objectives. The solutions should satisfy the workload requirements with respect to a set of constraints defined over a given space [14]. The formal definition of a VFC FLP is given as [15]:

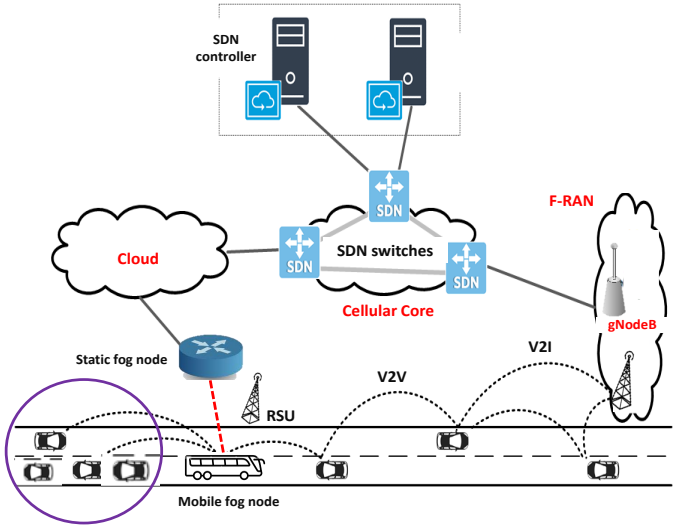

Figure 1. The hierarchical system architecture of VFC.

Definition 1. *Facility Location Problem (FLP): Consider a bipartite graph with a bi-partition* (F, V)*, where F and V represent the set of fog nodes and set of client vehicles, respectively. Suppose that the set* $F = \{f_1, f_2 \ldots .\}$ *denotes the potential facility locations,* $c_f \geq 0$ *denotes the deployment cost of a facility at location for* $f \in F$ *with capacity* $X_f^{max} \geq 0$*,* $c_{fl} \geq 0$ *denotes the communication cost for each link between* $f \in F$ *and* $v \in V$*, and* $d_v \geq 0$ *denotes a demand function for each client* $v \in V$*. Then, the goal of FLP is to find a subset* $F_1 \subseteq F$ *and an assignment vector* $\Phi : V \rightarrow F_1$ *that maps requests from each client's* $v \in V$ *to appropriate facilities* $f \in F$*, such that the total communicating and processing cost is minimized. Note that this is the simplified definition sometimes known as simple FLP. However, we can generalize the depth of partition and make it a multi-level FLP [16].*

EMO algorithms are a class of algorithms inspired by a mechanism of natural evolution. They apply intelligent and approximate heuristics in order to search the optimal Pareto trade-off fronts. Compared to classical methods, preference-based algorithms include weighted sum methods [17], ϵ-constraint methods [18], and hierarchical methods [19], etc. The EMO algorithms offer a good balance between the Pareto optimality and search time efficiency. Hence, the EMO algorithms are becoming increasingly popular in the modeling and optimization of complex systems. A study reveals that a significant number of studies have used EMO algorithms to find the solution to resource management problems. These are commonly used to study the structural complexity of decentralized computing models such as cloud or fog computing [20], vehicular fog computing [12], etc. In fact, the survey performed by the authors of [21] found that, in approximately 18% of related studies, EMO algorithms were used to solve optimization problems such as VM allocation, VM migration, service placement, task offloading, and capacity planning, among others.

In this work, we present a multi-objective optimization model to formulate the FLP in VFC networks. The key objective of this model was to generate an optimal VFC topology that satisfies the service requirements of low-power and low-latency ITS applications. The objective function minimizes the average response delay and system energy consumption. The solutions to this model generate optimal decisions on where to install the fog nodes, how vehicle-generated requests are routed to these nodes, and the amount of storage–computation resources to be installed in each fog node. Essentially, we examine the suitability of different EMO algorithms to solve the FLP in VFC. The model is solved through one exact algorithm-weighted sum method in CPLEX solver, and two EMO algorithms; non-dominated sorting genetic algorithm-II (NSGA-II); and speed-constrained particle swarm optimization (SMPSO) algorithm. Motivated by the nature of solutions generated by these algorithms, we proposed a hybrid EMO algorithm called Swarm Opti-

mized Non-dominated sorting Genetic Algorithm (SONG). Basically, SONG combines the convergence efficiency of NSGA-II [22] and search efficiency of SMPSO [23], and it gives better results in terms of solution quality. We measure the performance of the SONG algorithm by comparing with the baseline EMO algorithms against three baseline indicators, namely; hyper-volume (HV), inverted generational distance (IGD) and delay gap. The empirical results on real-world vehicular traces show that SONG exhibits better solution quality than the counterpart algorithms, and hence can be adapted as an efficient planning tool for planning and design of VFC networks. **The key highlights of this paper are given as follows:**

1. We formulate the FLP in VFC as a multi-objective optimization model combining two sub-problems: fog node placement (FNP) and fog node dimensioning (FND). The objective of this model is to minimize the average response delay and overall energy consumption, with an effort to attain Pareto-optimality.
2. We solve the model using an exact weighted-sum scalarization algorithm in the IBM ILOG CPLEX solver. The results obtained in this step are used as the baseline for EMO analysis. We also solved the model using two popular EMO algorithms: the NSGA-II and SMPSO algorithms. The nature of Pareto-fronts obtained in this step is the key driver for the development of a hybrid EMO algorithm.
3. We proposed a hybrid EMO algorithm called the Swarm Optimized Non-dominated Sorting Genetic algorithm (SONG) that combines the convergence efficiency of NSGA-II and the solution diversity of SMPSO. We compared and evaluated the efficiency of the SONG algorithm with that of weighted sum (CPLEX), NSGA-II, and SMPSO algorithms against three quality indicators; Hyper-Volume (HV), Inverted Generational Distance (IGD), and delay gap.
4. Through evaluation with real-world datasets, we showed that SONG exhibits a better solution quality than the three baseline algorithms, and can hence be utilized as an efficient planning tool for the planning and design of VFC networks.

The remainder of this paper is organized as follows. Section 2 gives a brief overview of the FLP and the motivation for conducting this research. Related works are given in Section 3. The system description and model formulations are provided in Section 4. Section 5 summarizes the exact and EMO algorithms for facility location in VFC. The proposed SONG algorithm is explained in Section 6. The evolutionary parameters of SONG algorithms are discussed in Section 7. Experimental and simulation setups are explained in Section 8. The results and discussions are given in Section 9. Finally, Section 10 concludes the paper.

2. Motivation

In distributed network environments, FLP refers to the identification of facilities for the deployment of storage and computing services [14]. The outputs of a facility location problem are: placement decisions regarding facilities that are placed at the potential locations; the links to be selected from an available set, and the amount of client workload that is to be transmitted across different architectural layers. It is a rational process that encompasses the topology design, network synthesis, and network realization [24]. The facility location model in VFC deals with selecting the optimal locations for installing a set of fog nodes, and the available channels for transferring vehicular data by minimizing or maximizing some objectives. The solutions should satisfy the workload requirements with respect to a set of constraints defined over a given space [25]. The constraints can be defined on available hardware, the fog node type and orientation, the channel bandwidth, etc. To be specific, it deals with the dimensioning and layout planning of VFC architectural components and generates a topology that optimizes parameters such as the response time, energy consumption, and cost of infrastructure, etc. [13]. Often, these parameters are conflicting, so the resulting topology must give an optimal balance (trade-off) between the network and equipment power consumption, interference and performance (e.g., in terms of throughput or latency).

However, due to the highly decentralized and mobile nature of fog nodes and context-aware computational demands of vehicular applications, the facility location in VFC is a complex task [6]. Here, the FLP can be partitioned into three sub-problems. The first sub-problem is an FNP that deals with selecting a subset of candidate nodes to act as fog nodes. FND is another sub-problem where the capacity levels of resources such as fog nodes, links and channels are estimated. The optimizing attributes for both these sub-problems are: the cost of the fog node, the weight (bandwidth) of communication links, the vehicular workload (# req/s) and other QoS parameters. The third sub-problem is computation offloading, i.e., the process of forwarding client requests to the appropriate nodes for execution. It is noteworthy that all these sub-problems are inter-dependent and are equally significant towards facility location in VFC networks. It has been theoretically proven that finding optimal solution for each of these individual sub-problems is NP-hard [26]. Obviously, a model that integrates all these sub-problems will also be NP-hard [16]. For an in-depth analysis of how facility location works in VFC, please refer to [25].

As mentioned above, generating an optimal solution to facility location in VFC is a complex task due to many factors, e.g., the decentralized nature of VANETs, vehicle mobility, network size, the number and heterogeneous nature of the VFC hardware equipment(s), cloud–fog cooperation, etc. Therefore, it is critical for VFC network designers to adopt a structured methodology while formulating, designing, and planning VFC infrastructures [27]. Figure 2 shows a comprehensive framework for facility location in VFC networks. In the definition phase, the input data from the VANET environment are collected to conduct a requirement analysis. The information, for instance, the vehicular traffic patterns and traffic density, can be used to estimate the hardware type and cost, network capacity and QoS requirements. Obtaining real-world vehicular data is often complex and time-consuming. In that case, the inputs can be synthetically generated and then validated against a real-world ITS scenario [28].

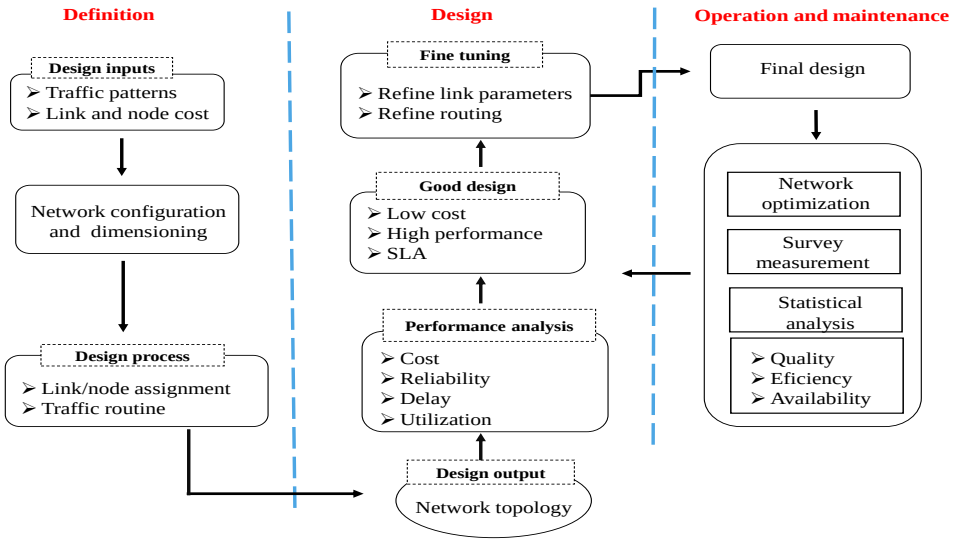

Figure 2. Steps involved in facility location in VFC.

In the network design phase, efficient dimensioning and layout planning algorithms are employed [29]. These involve activities such as the selection of various processing nodes, potential locations, the sizing and costing, etc. Depending on the design constraints, the output of this phase can be a routing topology guaranteeing optimal QoS requirements. Furthermore, these outputs are selectively fed as input to the optimization model. This generates optimal solutions that correspond to minimized service delay, network traffic, deployment cost and energy consumption. The final step is a performance evaluation that involves the sensitivity and statistical analysis of model outputs. From a designer's

perspective, the overall facility location framework must deliver the maximum network performance to ITS users, which can be targeted to meet the following key objectives:

- **Minimizing service delay:** Minimizing the service delay is persuaded to be the key performance objective in almost all networked architectures because a slight increase in the user-perceived delay might lead to a substantial revenue loss for the service providers. Since VFC services mainly target decentralized IoT devices and vehicles, an effective facility location framework should rigorously consider the latency requirements of ITS applications.
- **Minimizing energy consumption:** With a huge volume of service requests, the power consumption of powering up (and cooling down) CDC is soaring. It is thus necessary to study the energy management aspects of VFC design.
- **Minimizing capital expenditure (CAPEX):** Budgetary and monetary factors have always been a major concern for network designers. Therefore, it is crucial to minimize the total CAPEX involved in hardware purchasing, facility rental, link installation, etc.

It is observed that each of these objectives define sub-problems that are both inter-dependent as well as mutually conflicting [30]. For example, to minimize the service delay, a large number of fog nodes might be deployed, but this will increase the CAPEX. The energy consumption also gears-up proportionally. On the contrary, the CAPEX can be kept within budget by selecting fewer locations for fog placement. However, in that case, the client requests might not be served in the fog layer, but rather offloaded to distant cloud servers leading to a degradation in network performance and QoS. Considering all these factors, we formulate the FLP as a multi-objective optimization model where the objective function minimizes the average response time as well as system energy consumption. The optimal solutions called Pareto Fronts seek for the best compromise between the response time and energy consumption [31]. This leverages the VFC service providers as well as the network designers to assess the abilities of possible trade-off solutions, leading to intelligent network planning and design decisions.

3. Related Work

VFC extends fog computing to mobile VANETs, where the vehicles and RSU can both act as mobile fog nodes, thereby leveraging the full utilization of storage and computation resources. Considering the mobility of VANET infrastructures, the facility location and capacity planning in VFC recently received considerable attention. For example, in some papers, the VFC is studied from the viewpoint of delay optimization [9], energy optimization [32], utility maximization [33], cost minimization [6], etc.

The authors in [34] investigated the scenario wherein multiple vehicles formed a community and jointly shared computing resources to maximize their utility. The RSU acts as an orchestrator and takes charge of decision making for community formation and workload scheduling. According to [10], the RSU acts as both as a gateway to the remote CDC as well as a task scheduler.

Moreover, the use of EMO algorithms is becoming an emerging trend and has been widely adopted for resource management in decentralized architectures such as cloud, edge–fog computing, VFC, etc. EMO provides intelligent heuristics to solve a wide range of optimization problems such as VM allocation [20], data replica placement [35], federated clouds [36], among others. Studies that address the facility location in fog environments can be broadly categorized from numerous perspectives. We exhaustively reviewed the existing literature in fog server placement, identified the key highlights and presented the motivation for carrying out similar research, which is equally adaptive to the vehicular fog computing environments.

The first set of works minimizes network delays which are approximated through geospatial distant metrics between generation nodes and fog servers. For instance, the authors in [37], proposed an integer linear programming (ILP)-based service placement model that minimizes the hop-count between communicating nodes, thus reducing the communication latency and eventually the service latency. The bandwidth consumption

between communicating services is implemented through a flow matrix. The goal of the architecture is to place the services in convenient for servers and allow these services to dynamically migrate according to the changing conditions of the network and status of the users. In [38], the authors proposed an semi-Markov decision process (SMDP)-based task offloading model for VFC considering the transmission delay, processing delay, available RSUs, and the variability feature of tasks and vehicle mobility into account. The model is solved using an iterative Bellman method where the objective is to maximize the long-term reward.

Souza et al. [39] proposed a QoS-aware service placement technique for cloud–fog scenarios in smart city environment. The model that minimizes the latency experienced by the services while guaranteeing the fulfillment of the capacity constraints. In [40], the authors employed priced timed Petri nets (PTPNs) models that allow the user to choose the available resources from a pre-allocated resource pool. The algorithm dynamically allocates the fog resources based on the predicted value of price-time weighted cost and credibility evaluation scheme. The authors in [8] have proposed a dynamic task allocation scheme that finds an optimal trade-off between service delay and quality loss constraints in VFC. The event-triggered task allocation problem is solved using a binary PSO algorithm and simulated in real-world vehicular mobility traces for video streaming and real-time object recognition tasks [41]. Considering the distributed capacity, the range and types of user applications and the mobility of IoT devices, Bittencourt et al. [42] analyzed the significance of concurrent, first-come first-served (FCFS), and delay-priority scheduling policies to improve the execution time in fog environments.

The authors in [43] employed modified NSGA-II to propose a multi-level resource scheduling model in the fog environment. To address the uneven distribution of the solution in the Pareto fronts in the standard NSGA, a modified crowding distance expression is defined that minimizes the service latency and improve the task execution stability. In [44], the authors employed the Tabu search for the joint optimization of data blocks placement and task scheduling in edge computing, with reduced computation delay and response time. Various parameters such as data block popularity, data storage capacity and replacement costs for data blocks, as well as replacement ratios of edge servers, are considered to calculate the value of each data block. Considering the containers as the lightweight resource unit for user services, an optimal placement scheme is presented that can avoid the repeated replacement of data blocks, thereby reducing the overall bandwidth overhead. Wang et al. [45] employed M/M/1 waiting queues to develop a latency-minimum offloading decision- and resource-allocation scheme for fog-enabled IoT networks. The optimization problem is solved using genetic simulated annealing-based algorithm to generate offloading decisions with improved convergence speed and quality.

The next thread of the literature focuses on minimizing the deployment costs of the servers while limiting maximal latency. For instance, the authors in [46] considered the client association, resource provisioning, task distribution, and VM placement as decision variables to develop a cost-effective optimization model for fog computing. The same set of variables were investigated in [47] to propose a cost optimal placement model fog-computing-supported medical cyber-physical system (MCPS). Urgaonkar et al. [48] modeled the dynamic service migration and workload scheduling in fog placement as a sequential Markov decision problem. The objective was to optimize operational costs while providing rigorous QoS guarantees. The same research group in [49] simulated the fog nodes as mobile micro-clouds and proposed a placement scheme based on an online approximation algorithm. The algorithm minimizes the average cost over time, and converges in polynomial time, leveraging the ability of predicting the future cost parameters with known accuracy. González et al. [50] employed the considered fog locations and their capacities, the user-to-fog association, and the number of deployed fog nodes as decision variables to model the fog placement as a mixed-integer linear programming (MILP) problem. The model is further solved using a hybrid simulated annealing algorithm, evaluated on a 5G desktop application leveraged with network function virtualization

(NFV). A cost efficient data-driven VFC framework was proposed in a very recent work [6] where authors used both heuristic and integer linear programming (ILP) to solve the data-driven capacity planning problem. The objective is to minimize installation and operational expenses considering spatio-temporal variations in vehicular traffic and QoS constraints. A similar work was proposed in [31] that finds the optimal location of fog nodes in a green field scenario.

The third category of papers studies the impact of task and service placement strategies on the energy consumption of fog infrastructures. For example, the authors in [51] presented a placement scheme that minimizes the total energy consumption of the network, keeping the access delay within an acceptable threshold. The multi-objective optimization problem was solved using the particle swarm optimization (PSO) algorithm and the performance was evaluated on the real-world dataset of Shanghai Telecom's base stations. In [52], the energy-sentient scheme for deploying flow-based IoT applications is proposed and formulated as a quadratic programming problem. The complexity of this model was handled by transforming it into to an MWIS problem via a co-location graph. Here, the mapping strategy seeks to minimize the total communication energy cost by merging the services and the co-locating neighboring services on the same node. In a recent work [53], the authors used reinforcement leaning to implement an energy-efficient vehicle scheduling scheme that ensures task offloading to stationary as well as mobile fog nodes.

Another perspective for fog placement is to optimize the trade-off between latency and energy consumption. Deng et al. [20] investigated the trade-off between power consumption and transmission delay in the fog–cloud computing system. A framework that obtains the optimal workload allocation is solved through sub-problem approximation approach. It demonstrates that, by sacrificing modest computation resources, fog computing can give a substantially improved performance over cloud computing. Mebrek et al. [54] studied the optimization problem of an energy-delay trade-off in fog-based IoT architectures using the Genetic Algorithm (GA) and Broadcast Incremental Power (BIP) algorithm. In [55], a computation offloading scheme was proposed that aimed to minimize the energy consumption and the task processing delay in the fog layer while increasing the network lifetime. The notion serves to distribute high computational tasks among several fog nodes and access points, such that the network lifetime increased, especially in mission-critical scenarios that consume much more network resources. Sarker et al. [56] employed multiple parallel deep neural networks to propose an delay-energy-optimized binary offloading scheme in fog computing. The decision outputs are then placed in a relay memory system to train and test all neural networks. A similar algorithm was proposed in [12], wherein task offloading in VFC was modeled as a Multi-Hop Computation Offloading (MHCO) framework. The model was solved using a modified differential evolution algorithm that optimizes both service delay and average energy consumption, and facilitates the allocation of tasks for both static (RSU) and vehicular fog nodes. Table 1 presents a summary of the literature in facility location or service placement in VFC and related architectures.

Synthesis

From an extensive study of the recent literature, we concluded that the algorithms to solve FLPs can be categorized as: exact methods and approximate or EMO methods. Most exact algorithms combine multiple objectives into one single objective. A common advantage of such methods is that, for every weight assigned to the objectives, the translated problem is as difficult as a single-objective optimization problem. This makes the exact methods simple to implement. However, due to the presence of discrete structures in the instances of FLP, it is not sufficient to aggregate multiple objectives using a weight vector. Because of NP-hardness, there will be solution called non-supported efficient (NE) solutions which are not optimal for any weighted sum of objectives.

Table 1. Summary of the literature in facility location or service placement problem in VFC or fog architectures.

Ref.	Objective Function	Decision Outputs	Algorithm	Mobility Support
[8]	Delay	Task offloading	Binary PSO	Yes
[37]	Delay	Service placement	ILP	No
[38]	Delay minimization	Task offloading	SMDP/Bellman equation	Yes
[39]	Delay	Service placement	ILP	No
[40]	Delay	Service placement	Petri nets	No
[43]	Delay	Task scheduling	NSGA-II	No
[44]	Delay	Task scheduling	Tabu Search	No
[45]	Delay	Task offloading	Simulated annealing	No
[46]	Cost	Service placement	ILP	No
[47]	Cost	Service placement	Heuristics	No
[48]	Cost	Service migration	MDP	No
[49]	Cost	Service placement	MDP	No
[6]	Cost	Service placement	MILP	Yes
[51]	Energy consumption	Service placement	Monte Carlo	No
[52]	Energy consumption	Service placement	ILP	No
[53]	Energy consumption	Task scheduling	Fuzzy reinforcement learning	No
[20]	Delay and energy consumption	Task offloading	Hungarian algorithm	No
[54]	Delay and energy consumption	Task offloading	Genetic algorithm	No
[55]	Delay and energy consumption	Task offloading	Heuristics	No
[56]	Delay and energy consumption	Task scheduling	Deep neural network	No
[12]	Delay and energy consumption	Task offloading	Differential evolution	Yes
Our work	Delay and energy consumption	Service placement	SONG	Yes

EMO algorithms come under approximate resolution methods, commonly termed meta-heuristic algorithms. These algorithms yield a good trade-off between the solution set quality, CPU time, and memory [22]. They can be classified based on the principle of search directions and principle of dominance, where they take advantage of the information carried by a population of solutions using the notion of dominance. On the contrary to exact algorithms where only one individual is attracted to the non-dominated frontier, in EMO, all the population contributes to the evolution process. Thus, by maintaining a solution pool, then these methods can search for multiple efficient solution points in parallel via self-adaptation and cooperation. Such characteristics make EMO algorithms suitable for solving FLP in VFC [26]. Driven by this motivation, in what follows, we discuss the popular EMO algorithms that solve the multi-objective versions of an FLP. We also propose a new EMO algorithm named SONG, which is characteristically a hybrid version of NSGA-II and SMPSO. We performed extensive experimentation on a wide set of inputs to demonstrate the efficiency of SONG. In particular, we compared the performance of SONG with that of NSGA-II and SMPSO, and showed that SONG offers a better balance between the Pareto optimality and computation time efficiency.

4. System Description and Problem Formulation

The system model is explained in detail in this section. We first introduced the scenario and then described the procedure of offloading a task in VFC according to the 802.11p standard [38]. The VANET scenario considered in this paper is modeled as a connected undirected graph $G\{V(.), E(w)\}$. The vertices in set $V(.)$ include a set of vehicles $\{v_1, v_2, \ldots v_V\}$, a set of fog nodes $F = \{f_1, f_2, \ldots f_F\}$ and a cloud server (C). The vehicles moving on highway lanes form a VFC system equipped with seamless connectivity to an upper fog–cloud layer via BS or RSU. The function $E(w)$ denotes the set of edges having weights $w = \{w_1, w_2, \ldots\}$. Here, each weight w_i represents the network usage descriptor (NUD) between each pair of vertices in $V(.)$. In our analysis, we model w_i by a triple $(r_{n2n}, \omega_{n2n}, \tau_{n2n})$, where r_{n2n} denotes the transmission rate between two nodes, ω_{n2n} denotes the link bandwidth between two nodes and τ_{n2n} denotes the end-to-end delay. The number of passengers residing inside each vehicle v varies randomly between 0 and P_v, with one PD per person. Hence, the total number of PDs in a VFC system (cluster) can be given as $N = \sum_{v=1}^{V} P_v$.

A vehicle joining or leaving the VFC system according to a Poisson process with an arrival and departure rate λ_v and μ_v, respectively. The vehicles adopted the 802.11p

communication standard to transfer data/request through one-hop communication [8]. Each vehicle knows the availability fog nodes by communicating with each other through handshaking [12]. When the PD has a task to offload, the task offloading module makes a decision to offload it onto appropriate fog nodes. On the basis of the estimation of available resources, e.g., memory, vCPU, VM, bandwidth, etc., the host vehicle will either accept the task with a probability Π_v or offload to a nearby fog node or to remote CDC. For the sake of simplicity, it is assumed that fog nodes, i.e., taxis as well as RSU are connected through a strong backhaul network [27].

On the basis of the assumptions discussed above, we formulated the model for average response delay τ_{sys}^{avg} and average energy consumption e_{sys}^{avg} per vehicular application, for the different scenarios of facility location in VFC. The overall framework is given in Figure 3. The key symbols and notations used for the model are summarized in Table 2.

Table 2. Acronyms and symbols used in this paper.

Acronym	Description
PDs	Passenger devices
BSs	Base stations
HV	Hyper-volume
VFC	Vehicular fog computing
RSUs	Roadside units
VFN	Vehicular fog node
IGD	Inverted generational distance
IoT	Internet of Things
SCN	Storage, computing and networking
IDC	International Data Corporation
FLP	Facility location problem
QoS	Quality of service
ITSs	Intelligent transportation systems
CAVs	Connected and autonomous vehicles
EMO	Evolutionary multi-objective optimization
CAGR	Compound annual growth rate
NSGA	Non-Dominated Sorting Genetic Algorithm
VANET	Vehicular ad hoc network
SMPSO	Speed-constrained particle swarm optimization
Symbol	**Description**
v, V	Index for set of vehicles
f, F	Index for set of vehicles fog nodes
c, C	Index for set of vehicles cloud servers
r_v^a	Workload for vehicle v (bytes/s.)
r_f^a	Traffic arrival rate for fog node f
r_c^a	Traffic arrival rate for cloud server c
r_f^s	Service rate of fog node f
r_c^s	Service rate of cloud server c
σ_v	Task size (bytes) v
$\mathcal{E}_f$	Energy consumption per CPU cycle of fog node f
$\mathcal{C}_f$	Computing capacity of fog node f
$\Re_v$	Up-link data rate for vehicle v
$\mathcal{P}_p^{tran}$	Transmission power of PD p
POF_v	Processor occupancy factor of vehicle v

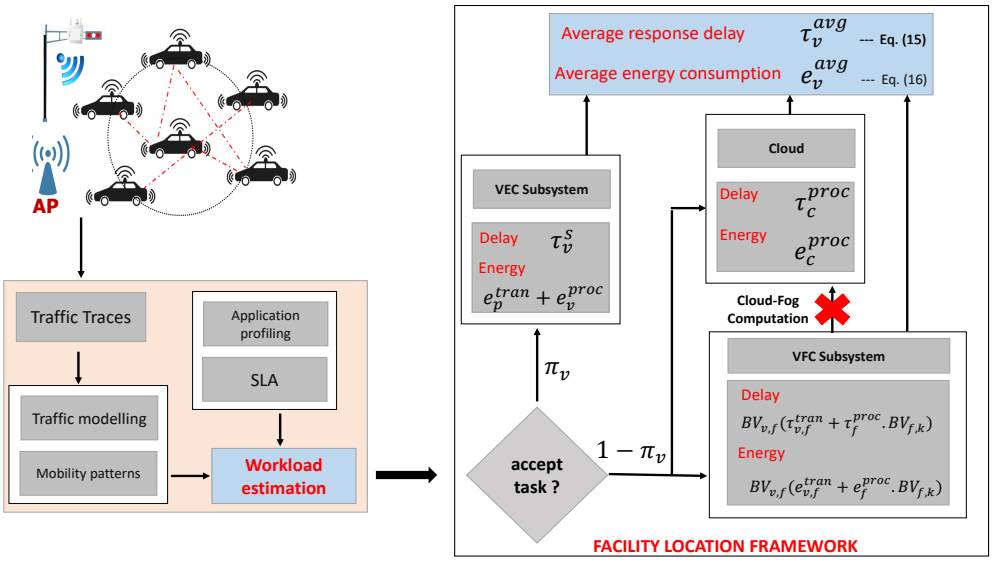

Figure 3. An overall framework of power consumption-delay trade-off in a VFC system.

Decision Variables:

- A probabilistic variable Π_v representing whether the host vehicle v accepts the PD request.
- Binary variable $BV_{v,f}$ representing cloud–fog offloading decision (*where* to offload), i.e.,

$$BV_{v,f} = \begin{cases} 1 & task\ from\ vehicle\ v\ is\ offloaded\ to\ fog\ node\ f \\ 0 & to\ \ cloud \end{cases} \quad (1)$$

- The RSUs or taxis/buses are both potential candidates to act as a fog node. For a time interval, a subset of these nodes will be selected for processing the PD workloads. The binary variable $BV_{f,k}$ denotes whether an RSU or a taxi/bus k is selected as a fog node f.

$$BV_{f,k} = \begin{cases} 1 & if\ RSU\ or\ taxi/bus\ k\ is\ selected\ as\ fog\ node\ f \\ 0 & not\ \ selected \end{cases} \quad (2)$$

Definition 2. *Task: A task $\mathcal{T}_v$ generated from a vehicle v can be defined by a triplet $\langle \sigma_v, \mathcal{F}_v, \tau_v^{max} \rangle$, where σ_v is the size of task in bytes, $\mathcal{F}_v$ denotes the number of CPU cycles needed to process the task $\mathcal{T}_v$ [27] and τ_v^{max} denotes the delay constraint for the vehicular application that generates the task $\mathcal{T}_v$.*

Definition 3. *Response delay: The response delay τ_v^{avg} for a task $\mathcal{T}_v$ is the time required to serve it, i.e., the time interval between the moment when a client vehicle makes a service request and when it receives the response (result) for that request.*

4.1. Delay and Energy Formulation

- **Case I: When vehicle v accepts the PD request:** Generally, a vehicle pools requests from its resident PDs, and each task is assumed to be computationally intensive and mutually independent. In case a vehicle v accepts the request coming from PD $p \in P$ with an arrival rate r_p^a, the overall workload r_v^a for vehicle v can be given as:

$$r_v^a = \sum_{p=1}^{P} r_p^a \quad \forall p \in P \quad \forall vs. \in V \quad (3)$$

Modeling the vehicular edge computation as an $M/M/1$ queue, the service time when v processes a task from a PD p can be expressed as:

$$\tau_v^s = \frac{\sum_{p \in P} \tau_p^s}{|V|} = \frac{1}{|V|} \sum_{p=1}^{N} \frac{1}{r_v^{cap}(1 - POF_v) - \Pi_v \cdot r_v^a} \tag{4}$$

where r_v^{cap} denotes the processing capability of the vehicle v, and POF_v denotes the normalized workload on vehicle v, i.e., the fraction of processing a resource that is currently involved in serving other tasks. If $POF_v = 1$, then the CPU is fully occupied and hence the requests are offloaded either onto fog nodes or the cloud. Every time a vehicle is on the highway, it is processing some kernel tasks, therefore,

$$0 \leq POF_v^V < 1 \tag{5}$$

In our VFC framework, the client requests are forwarded via dedicated short-range communication (DSRC) or cellular V2X (C-V2X [8], hence the energy required by PD p to transmit a task of size σ_v over a channel bandwidth $\omega_{p,v}$ is given by [57]:

$$e_p^{tran} = \frac{\mathcal{P}_p^{tran} \cdot \sigma_v}{\omega_{p,v}} \tag{6}$$

where $\mathcal{P}_p^{tran}$ is the transmission power of PD p. The corresponding energy required by vehicle v to execute this task is given by [27]:

$$e_v^{proc} = \mathcal{F}_v \cdot \beta_v \tag{7}$$

where β_v denotes the energy consumption (in energy units) per unit CPU cycle of task $\mathcal{T}_v$.

- **Case II: When the vehicle v offloads the PD request to the fog node:** Because of a limited processing capability, the host vehicle frequently fails to execute concurrent PD requests; hence, it is forwarded to a proximate fog node. Considering a reliable communication link of bandwidth $\omega_{v,f}$, the time required to offload the input request of size σ_v into fog node f is given by:

$$\tau_v^{tran} = \frac{r_f^a \cdot \sigma_v}{\omega_{v,f}} \tag{8}$$

Similarly, the processing delay due to processing at fog node f with computing capacity $\mathcal{C}_f$ is given by:

$$\tau_f^{proc} = \lceil \frac{\mathcal{F}_v}{\mathcal{C}_f} \rceil \tag{9}$$

The energy consumed while forwarding a task of size σ_v is given by:

$$e_{v,f}^{tran} = \frac{\alpha_v \cdot \sigma_v}{\omega_{v,f}} \tag{10}$$

where α_v depends on the communication channel over which the task is offloaded. For 5G-enabled V2X communication, we consider $\alpha_v = 2605$ mJ/s [58]. The energy consumed by fog node f to process task σ_v can be expressed as:

$$e_f^{proc} = \mathcal{E}_f \cdot r_f^a \cdot \sigma_v \tag{11}$$

where $\mathcal{E}_f$ and r_f^a represents the energy consumption per CPU cycle of fog node f, and the number of CPU cycles required to process one bit of task $\mathcal{T}_f$, respectively.

- **Case III: When vehicle v offloads the PD request to CDC:** The time for the cloud layer consists of two parts. First, the transmission time for dispatching and processing time at the cloud server. Assuming the vehicle-cloud channel has infinite bandwidth, the transmission time can be considered constant [30]. Realizing the cloud servers as an $M/M/\infty$ queue with a service rate r_c^s, the processing time is given by:

$$\tau_c^{proc} = \frac{1}{r_c^s} \tag{12}$$

Assuming that each server c hosts a homogeneous VM with an identical CPU frequency, then the energy consumption can be approximated by a nonlinear function of CPU frequency [20], i.e.,

$$\eta_c = A_c \cdot \eta_c^u + B_c \tag{13}$$

where u lies between 2.5 and 3 [20]. In order to cope with the workload surge, the CDCs are enabled with power-saving modes wherein more servers are either powered ON or switched OFF dynamically. In that case, the energy consumption is given as:

$$e_c^{proc} = BV_c \cdot n_c \cdot \eta_c \tag{14}$$

where the binary decision variable BV_c reflects the ON/OFF state of the server c (0-OFF, 1-ON), and n_c denotes the number of machines that are currently turned ON. For the sake of keeping the model simple, we assume that the cloud servers are always ON (i.e., $BV_c = 1$).

Integrating Equations (4), (8), (9) and (12), we obtain the average response delay τ_v^{avg} as:

$$\tau_v^{avg} = \frac{\sum_{v \in V} \sum_{p \in P} \tau_v}{|V|} = \frac{1}{|V|} \cdot \left\{ \overbrace{\Pi_v \cdot \tau_v^s}^{\text{PD to vehicle}} + \overbrace{(1 - \Pi_v) \cdot [BV_{v,f}(\tau_{v,f}^{tran} + \tau_f^{proc} \cdot BV_{f,k})}^{\text{vehicle to fog}} + \underbrace{(1 - BV_{v,f}) \cdot \tau_c^{proc}\}]}_{\text{vehicle to cloud}} \right\} \quad \forall p \in P \tag{15}$$

Similarly, from Equations (6), (7), (10), (11) and (14),

$$e_v^{avg} = \frac{\sum_{v \in V} \sum_{p \in P} e_{sys}}{|V|} = \frac{1}{|V|} \cdot \left\{ \overbrace{\Pi_v \cdot (e_p^{tran} + e_p^{proc})}^{\text{PD to vehicle}} + \overbrace{(1 - \Pi_v) \cdot [BV_{v,f} \cdot (e_{v,f}^{tran} + e_f^{proc} \cdot BV_{f,k})}^{\text{vehicle to fog}} + \underbrace{(1 - BV_{v,f}) \cdot e_c^{proc}]}_{\text{vehicle to cloud}} \right\} \quad \forall p \in P \tag{16}$$

4.2. Optimization Model

The overall goal of the proposed facility location model is to minimize the average response delay τ_v^{avg} and energy consumption e_v^{avg} of the VFC components. Hence, the optimization problem can be formulated as:

$$\textbf{P1} \qquad \underset{\forall vs., \forall f, \forall l}{\text{minimize}} \quad F(\tau_v^{avg}, e_v^{avg}) \tag{17}$$

Subject to constraints:

$$r_v^{cap}(1 - POF_v) > \Pi_v \cdot r_v^a \tag{18}$$

$$r_c^s > r_f^s \tag{19}$$

$$\tau_{avg} < \tau_v^{max} \tag{20}$$

$$\sum_{f \in F} BV_{v,f} = 1 \quad \forall v \in V \tag{21}$$

$$\sum_{v \in V} BV_{v,f} = BV_{f,k} \quad \forall f \in F \tag{22}$$

$$\sum_{f \in F} BV_{v,f} \cdot r_f^a < \mathcal{C}_f \quad \forall v \in V \tag{23}$$

$$\sum_{f \in F} BV_{f,k} \leq 1 \quad \forall k \in K \tag{24}$$

$$BV_{v,f} - \sum_{f \in F} BV_{f,k} \leq 0 \quad \forall k \in K \tag{25}$$

Constraint (18) says that the workload at vehicle v must not exceed its maximum processing capacity. Constraint (19) is an integrity constraint that keeps the service rate of CDCs much higher than that of fog nodes. Constraint (20) is a QoS constraint which the response delay for any task must not exceed the delay threshold specified for that vehicular application. Equation (21) is a vehicular assignment constraint that assumes the workload generated from each vehicle $v \in V$ to be atomic. At every time-slot, a task is either offloaded for fog level processing or to the cloud, but not to both. Likewise, constraint (22) says that the vehicle v should send its workload to one and only fog node. Constraint (23) ensures that the total workload of a fog node should not exceed its processing capacity. For simplicity, we use the constraint (24) as a node uniqueness constraint that limits each location $k \in K$ to accommodate at most one fog node $f \in F$. This is realistic because an RSU can act as a single fog node only. However, it is also possible to install additional servers at the RSU site, when it will be hosting multiple fog nodes. Moreover, it also means that a VFN will not be selected in the range exclusive for RSU. Finally, constraint (25) guarantees that each vehicle v can only offload to a location k iff a fog node f is installed there.

Remark 1. *As mentioned in the system description, we abstract the weight vector $E(w)$ through an NUD. It represents the resource usage between each facility in the VFC facility location. Since NUD is transparent to the mathematical solver and algorithms, it can be modified beforehand to meet specific design and dimensioning requirements. For example, if a specific passenger does not want to upload their data to a specific node due to security concerns or policy issues, then we may label the corresponding PD-fog node link as infinite. In that case, their data will never be forwarded to this adverse fog node and hence, a security requirement will be safeguarded.*

4.3. Complexity Analysis

It can be observed that the multi-optimization model P1 has two conflicting objectives. A trivial strategy is to handle each objective sequentially by translating them into independent single objective sub-problems. However, this approach does not explore the interconnections and overlaps between sub-problems, and hence the solutions may suffer from a local optimum. Thus, it is preferable to employ a global approach, i.e., solve all sub-problems simultaneously.

For complexity analysis, let us relax and make three versions of P1: SP1, SP2 and SP3, from three perspectives. SP1 aims to minimize the response time and SP2 aims to minimize the energy consumption, while SP3 is a weighted combination of both SP1 and SP2, i.e.,

$$\textbf{SP1} \qquad \underset{\forall v,\forall f,\forall l}{\text{minimize}} \quad F_1(\tau_{avg}) \tag{26}$$
$$\textbf{Subject to constraints:} \quad e_{sys} \leq e_{min}$$

$$\textbf{SP2} \qquad \underset{\forall v,\forall f,\forall l}{\text{minimize}} \quad F_2(e_{sys}) \tag{27}$$
$$\textbf{Subject to constraints:} \quad \tau_{sys} \leq \tau_{min}$$

$$\textbf{SP3}$$
$$\min_{\forall v,\forall f,\forall l} \quad F(\tau_{avg}, e_{sys}) = C_1 \cdot \sum_{f \in F} e_{sys} + C_2 \cdot \sum_{v \in V} \tau_{avg} \tag{28}$$
$$\textbf{Subject to constraints:} \quad 18\text{–}25$$

Definition 4. *k-median clustering problem: Consider a bipartite graph with a bi-partition* (F, V) *where F represents a set of fog nodes and V is a set of clients. Let k be a positive integer that specifies the number of nodes that are allowed to be deployed (e.g., may be limited by budgetary constraints). Suppose that the set* w_{vf} *denotes the cost (weight) of connection(s) between vehicle* $v \in V$ *to fog node* $f \in F$*. Then, the goal of the k-median clustering problem is to select k representatives of F to minimize the total connecting cost. Mathematically,*

k-MEDIAN CLUSTERING
Input: Finite set F and integer k
Output: $F^* \subset F$ with $|F^*| = k$
Objective: minimum cost$(F^*) = \sum_{x \in F} \rho(x, F^*)$

Theorem 1. *SP1 is NP-hard.*

Proof. To approximate the hardness of SP1, we relax certain constraints. For instance, assume that we have prior information about the number of fog nodes f that can be deployed and are available. We also relax the capacity constraint for nodes at each location $l \in L$. In that case, the decision problem SP1 of finding an assignment vector from vehicle $v \in V$ to fog node $f \in F$ that minimizes the total response delay can be reduced to a k-median clustering problem. It is well known that the k-median clustering problem is NP-complete [16]. Since an instance of SP1 can be reduced to a k-median clustering problem (by definition 5.1), it is therefore also NP-hard. □

Theorem 2. *SP2 is NP-hard.*

Proof. Upon adopting a relaxation strategy similar to that for SP1, SP2 becomes an instance of the traveling salesman problem (TSP) with pre-determined initial and final locations. Since, TSP is known to be NP-hard, SP2 is also NP-hard. □

Theorem 3. *SP3 is NP-hard.*

Proof. If we carefully observe the SP3 and the definition of FLP in Section I, we will find that FLP is an instance of SP3 (provided with some relaxation). Since finding an optimal solution to FLP on general graphs is NP-hard, then SP3 is also NP-hard. □

5. Algorithms for Facility Location in VFC

5.1. Exact Algorithms

It can be observed from Equations (15) and (16) that the optimization model P1 is a mixed-integer nonlinear programming (MINLP) problem with two conflicting objectives, which is NP-hard [59]. Different categories of algorithms have been proposed in the literature to solve such problems, e.g., exact methods and approximate or heuristics, nature-

inspired EMO, etc. The exact methods can be further categorized into several classes, viz. labeling algorithms, greedy algorithm, scalarization methods, two phase methods, and branch and bound algorithms. Most of the algorithms in this class combine multiple objectives into one single objective. A common advantage of such methods is that for every weight combinations of α_1 and α_2, defined for the objectives, the translated problem is as difficult as a single-objective FLP.

The weighted sum is a popular scalarization method that has been widely adopted for facility location problems. In the weighted sum approach, multiple objective functions are combined into a single objective function, where individual objectives are assigned a certain weight between 0 and 1. In other words, multiple objectives $F_1(x)$, $F_2(x)$, $F_3(x)$,..... $F_n(x)$ in a multi-objective decision problem are translated into a weighted single objective function given as [60]:

$$\begin{aligned} &\text{minimize}\{\alpha_1 F_1(x) + +\alpha_2 F_2(x) + \ldots\ldots + \alpha_n F_n(x)\} \\ &\textbf{Such that:} \\ &0 \leq \alpha_i \leq 1 \\ &\sum_{i=1}^{n} \alpha_i = 1 \end{aligned} \tag{29}$$

where α_i is the weight factor assigned to each objective to capturing the relative importance of a given objective $F_i(x)$. Assigning a higher (lower) weight places more or (less) emphasis on a specific objective. Formula (29) is used to minimize or maximize the parametric sum of all objective functions. By varying the weight vector, all supported efficient (SE) solutions can be found.

However, the success of exact algorithms to solve FLPs entirely depends on the availability of good lower and upper bounds ℓ and u, respectively, i.e., $\ell \leq X^* \leq u$. Here, X^* is the optimal value (solution) of the optimization problem. Often, it is not sufficient to aggregate multiple objectives through weighted sum methods due to the presence of discrete and conflicting structures in the FLPs. Furthermore, due to their NP-hard nature, there will be solutions called Non-supported efficient (NE) solutions which are not optimal for any combination of weight factors. For a non-convex function, it is difficult to obtain the weight vectors α_i that will generate Pareto-fronts lying in a desired region of objective space. Additionally, it is unrealistic to extend the exact methods to a multi-objective scenario or have more than a few hundred variables.

5.2. Evolutionary Multi-Objective (EMO) Algorithms

Evolutionary or meta-heuristic algorithms are a class of algorithms inspired by natural evolution mechanisms. Compared to exact and simple heuristics, they provide a more efficient search for larger and complicated problems, and yield a good trade-off between solution set quality, time and memory [22]. In general, evolutionary algorithms are broadly categorized based on the principle of search directions and principle of dominance, i.e., information is carried forward by a population (swarm) of solutions [61]. In contrast to exact methods where only a single individual is attracted to the non-dominated frontier, all the population in the solution pool contributes to the evolution process. Essentially, by maintaining a solution pool, the meta-heuristics methods can search for multiple efficient solution points in parallel via self-adaptation (independent evolution and assortment) and cooperation (the exchange of information between individuals) to improve the solution quality [26]. Such characteristics make population-based approximation algorithms suitable for multi-objective FLPs in VFC [26,59].

5.2.1. Genetic Algorithm

Genetic Algorithm (GA) [62] is the first class of population-based optimization algorithms proposed to solve FLPs. GA iteratively evolves a set of encoded solutions using three key operations, viz. *reproduction*, *crossover* and *mutation* in order to converge to an optimal solution [22]. At each iteration, a fitness function is defined to quantify the

optimality of solutions where the parent/child selection is based on individual fitness. The *fitness function* ensures that better solutions persist in future generations and weaker solutions are eliminated. In other words, the higher the fitness level (value), the greater the chance is that the solution contributes to creating solutions in the subsequent generation. This process halts when the predefined conditions (e.g., maximum number of iterations) are met.

Normally, a single-objective variant of GA [62] combines the multiple objective functions into a single-composite function. It does so by weighting the objectives with a weight vector, as in the case of an exact algorithm discussed in Section 5.1. An alternate strategy is to keep only one among them as the main objective in the optimization model and keeping rest as varying constraints. To obtain Pareto-optimal solutions, both of these techniques require several runs. However, because of its ability to concurrently search for the different regions of a solution space, a single-objective GA can be transformed into a multi-objective GA (MOGA), which finds a set of Pareto optimal solutions in a single run. Since most multi-objective GA algorithms do not require the user to prioritize, scale, or weight any of the objective(s), they are among the most frequently used meta-heuristics scheme for solving FLPs, even with conflicting objectives [26].

5.2.2. Non-Dominated Sorting Genetic Algorithm (NSGA-II)

The key objectives in the design of MOGA algorithms are:

- Guiding the search process towards the Pareto set through fitness assignment and offspring selection.
- Preserving the diversity of Pareto fronts.
- Retaining the best chromosomes for subsequent generations (elitism).
- Decreasing the computational time (e.g., CPU time).

The NSGA algorithm was among the first algorithms of the class of multi-objective GA [22]. The earliest version of this algorithm received numerous criticisms because it has high computational complexity $[O(AB^3)]$ for a non-dominated sorting procedure (where A denotes the number of objectives and B represents the size of the population). Another prominent issue with NSGA is the lack of elitism which leads to the loss of quality solutions. Additionally, NSGA requires specifically sharing the parameter explicitly to ensure diversity preservation. In order to address all such shortcomings, Deb et al. [22] proposed an improvement over NSGA which is faster than NSGA, which is termed NSGA-II. NSGA-II has the computational complexity of $[O(AB^2)]$. NSGA-II uses the identical method as the generic GA with the distinction that the latter makes use of an elitist ranking procedure (i.e., the non-dominated sorting procedure). The NSGA-II preserves the best population inside the latest solution pool utilizing the fast ranking procedure. In Algorithm 1, we explain the steps for the locate the facility using the NSGA-II algorithm.

Although NSGA-II efficiently handles continuous multi-objective problems, it does not appear to be ideal for service placement problems due to its characteristic discrete nature [25]. For instance, in some specific FLPs, as shown in Figure 4, we found that although NSGA-II converges quickly towards the Pareto fronts, the search space is irregularly distributed. Nonetheless, in many iterations, the NSGA-II struggles to cover the whole Pareto front. Actually, this shortcoming stems from the ranking process (between line 5 and 7) employed in NSGA-II, where the concentrated effect of a non-dominated sorting procedure harms the diversity in NSGA-II's solution fronts. Even if the mutation index or crossover index are varied, no meaningful improvement is achieved. Additionally, the non-dominated sorting procedure also affects the diversity of solutions in NSGA-II. Although such shortcomings can be overcome by an elitism strategy, the temporal complexity of evaluating the elitist sets is extremely high, which might be a major issue for large-scale FLPs.

Algorithm 1 NSGA-II Algorithm for facility location in VFC

Input: Vehicular demand $|V|$, number of fog node $|F|$, number of iterations gen_{max}, Mutation Distribution Index, Mutation Probability, Crossover Distribution Index, crossover rate CR
Output: Set of non-dominated Pareto fronts minimizes Equation (17)

Extract the client vehicle set V, fog node set F, set of CDCs C
Initialize $gen = 1$, Parent population $P_i = Random_Initialization(N)$ using MCPE encoding
FP_i = return_first_front (P_i)
while $gen \leq gen_{max}$ **do**
    $Q_i \leftarrow \emptyset$
    for *i=1 to N* **do**
        Select parent P1 using greedy selection process
        Select parent P2 using greedy selection process
        Create child C1, child C2 through knowledge_based_crossover $(P1, P2)$
        C = Uniform_Mutation(C1, C2)
        Compute $fitness_(C)$ (according to (17))
        $Q_i = Q_i \cup C$
    end
    while *non stop criteria* **do**
        $CP_i = P_i \cup EC_i$
        /* Create a combined population CP of size 2N
        Sort CP_i using *non_dominated_Sort*
        /* Generate a set containing all non-dominated fronts $(front_1, front_2, ...front_m)$ of CP_i
        $P_{i+1} = \emptyset, j = 1$
        while $Len(P_{i+1}) + Len(CP_j) \leq N$ **do**
            CD_i = Crowding_Distance_Assignment ($CP[j]$)
            /* Calculate crowding distance for all members $\in front_i$
            $P_{i+1} = P_{i+1} \cup CP[j]$
            /* Add members from $front_i$ to P_{i+1}
            $j = j + 1$
        end
        $CP[j] \leftarrow sort(CP[j], CD_i, non_increasing)$
        $P_{i+1} = P_{i+1} \cup CP[j]\{1 : (N - len(P_{i+1}))\}$
        Q_{i+1} = make_new_offspring (P_{i+1}, N)
        /* Generate new solution pool by greedy selection
        Q_{i+1} = crossover(Q_{i+1})
        Q_{i+1} = Standard_Uniform_Mutation(Q_{i+1})
        $i = i + 1$
        FP_i = return_first_front ($P_i \cup Q_i$)
    end
end
return *Optimal facility location scheme that minimizes (17)*

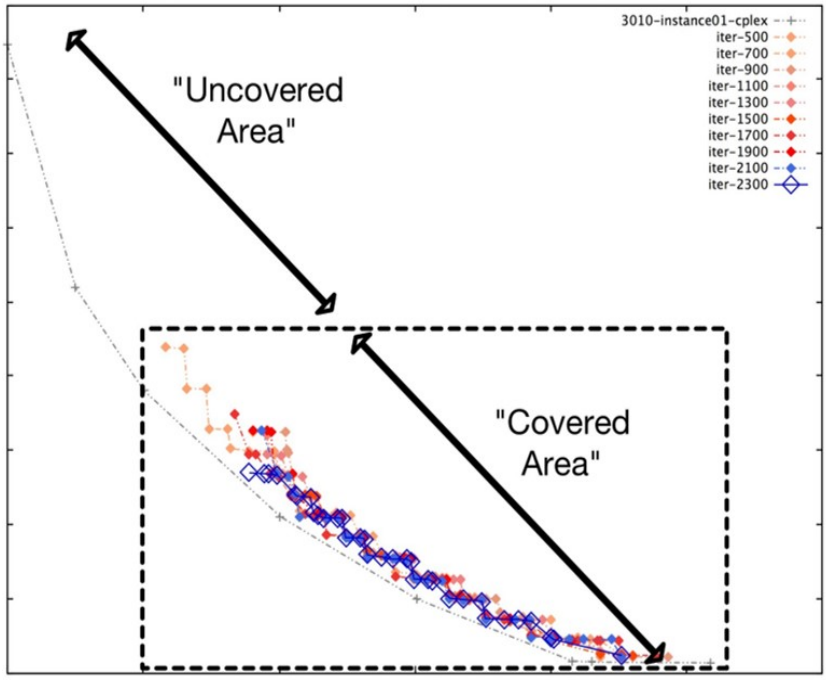

Figure 4. NSGA-II algorithm struggles to cover the whole Pareto front.

5.2.3. Particle Swarm Optimization (PSO)

Another class of evolutionary algorithms given by Kennedy et al. called particle swarm optimization (PSO) imitates the social behavior of bird flocking or fish schooling [61]. Basically, the PSO imitates a swarm of S potential solutions called particles which move through a D-dimensional solution space, as they hunt for a global optimum.

PSO is a stochastic population-based algorithm that is easier to implement than GA, as this latter requires excessive effort to tune a large number of parameters. Additionally, PSO exploits a larger search space than GA [63]. Moreover, the particles in PSO have a memory term which is important for the algorithm. In PSO, each particle p is allocated a random position x_p and a velocity $v_p(p = 1, 2 \ldots |S|)$. In every iteration, the particle adjusts its velocity according to the previous best (x_{pp}) and global best solution (leader, x_{gp}). The position vector of the particle p is updated at time-step t according to the equation:

$$x_p^t = x_p^{t-1} + v_p^t \tag{30}$$

where the velocity function v_p^t is given by Equation (28), where C1 and C2 are two positive learning factors (also referred to as trust parameters), r_1, r_2 are random vectors.

$$v_p^t = \overbrace{w \cdot v_p^{t-1}}^{\text{Inertia}} + \underbrace{C_1 \cdot r_1 \cdot (x_{pp} - x_p)}_{\text{Personal influence}} + \underbrace{C_2 \cdot r_2 \cdot (x_{gp} - x_p)}_{\text{Social influence}} \tag{31}$$

However, for MOCO problems, the constrained-based fitness function for two solutions Y_i and Y_j need to be redefined, so that it fits in the multi-objective context. Here, a solution Y_i is said to "*constrain-dominate*" over a solution (particle) Y_j (i.e., $Y_i \prec Y_j$), if any of the following conditions are true:

- Solution Y_i is feasible and solution Y_j is not.
- Solution Y_i and Y_j are both infeasible, but solution Y_i might have a smaller constraint violation (which can be computed by adding the normalized violation of all constraints).
- Both solutions Y_i and Y_j are feasible and solution Y_i dominates solution Y_j in the sense of Pareto dominance.

5.2.4. Speed-Constrained Multi-Objective PSO (SMPSO)

As the name suggests, SMPSO is an improved version of the PSO algorithm [23], which is distinguished by its use of a velocity-limiting procedure, for generating new effective particle positions in cases where the velocity exceeds a limit. Additionally, SMPSO employs a turbulence factor over γ percent of the particles (in place of polynomial mutation) and an external ranked list to store the non-dominated Pareto fronts obtained during the search process. This makes SMPSO fast and more accurate than generic PSO. The pseudo code of SMPSO-based facility location is given in Algorithm 2. The key difference between the SMPSO and generic PSO is that, instead of controlling the velocity step size with upper- and lower-valued parameters, SMPSO adopts a constriction coefficient $\aleph$ on the resulting velocity given as:

$$\aleph = \frac{2}{2 - \varphi - \sqrt{\varphi^2 - 4\varphi}} \tag{32}$$

where

$$\partial = \begin{cases} C_1 + C_2 & if \quad C_1 + C_2 > 4 \\ 0 & if \quad C_1 + C_2 \leq 4 \end{cases}$$

Algorithm 2 SMPSO Algorithm for facility location in VFC

Input: Number of vehicles $|V|$, number of fog node $|F|$, Vehicular demand vector D[V], number of iterations gen_{max}, size of particle swarm $|PS|$
Output: An optimal facility location vector that minimizes objective function (17)

```
Extract the client vehicle set V, fog node set F, set of CDCs C
Initialize gen = 1, p = 1, target population ( Random facility location strategy) N as swarm set S, crossover rate
  CR, EA = InitializeEliteArchive(ϕ), Randomize Search Velocity v_p, number of iterations max_iter, p = 0.01
Compute the fitness of population p ∈ S
EA ← non-dominated local optimal solutions
while gen ≤ gen_max or stopping criteria do
    for each p ∈ S do
        Select solutions A from EA using constrained greedy selection strategy
        for each solution q ∈ A do
            x_gp ← q
            Compute the speed of p according to (28)
            Update position of p according to (27)
        end
    end
    Perform polynomial mutation (γ) // with turbulence factor γ
    Compute the fitness value of p ∈ S /* Evaluation
    Update EA with non-dominated solutions from S
    gen++
end
return Set of Pareto optimal solutions in set EA
```

Furthermore, the accumulated particle velocity (resulting value) of each particle p is further bounded by constriction equation.

$$v_p^t = \begin{cases} \partial & v_p^t > \partial \\ -\partial & if \quad v_p^t \leq \partial \\ v_p^t & otherwise \end{cases}$$

where

$$\partial = \frac{upper_lim_p - lower_lim_p}{2}$$

On the other hand, SMPSO shows different characteristics. For the same problem set considered for NSGA-II, it can be observed from Figure 5 that SMPSO produces better results that comprehensively examine the entire front. This conserves the diversity in the solution set and produces Pareto fronts that are always evenly distributed. SMPSO, on the other hand, struggles to obtain the solution set converged into a true optimal front. However, for the same initial population size, SMPSO performs better than NSGA-II in terms of the coverage of Pareto fronts, but after a certain number of iterations, it still searches a different solution space instead of converging the solution towards the true optimal front. Whilst the solution quality can be substantially improved after an increased number of iterations, it results in a significant increase in computation time.

As a concluding remark, it can be said that NSGA-II achieves a better performance in terms of closeness to optimal solutions, while SMPSO performs better in terms of preserving the diversity in Pareto frontiers. However, none of these algorithms perform efficiently with regard to the diversity of solutions and the convergence gap towards the optimal front. Motivated by these drawbacks, in the next section, we propose a hybrid version of NSGA-II and SMPSO called a swarm-optimized non-dominated sorting Genetic Algorithm (SONG). The key objective of SONG is to exploit the searching efficiency of GA and PSO. In particular, the proposed SONG algorithm inherits the convergence and the diversity quality from NSGA-II and SMPSO, respectively.

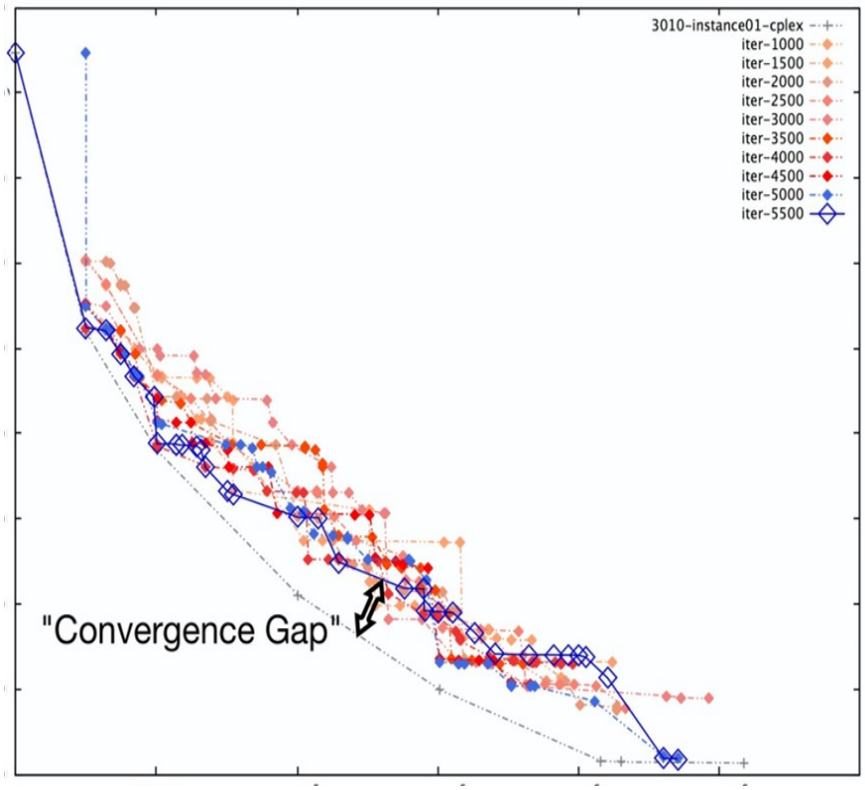

Figure 5. SMPSO algorithm struggles to converge into a true Pareto front.

6. Swarm Optimized Non-Dominated Sorting Genetic (SONG) Algorithm

The motivation of developing the SONG algorithm is to address the drawback of NSGA-II and SMPSO algorithms, which is also to combine the advantages of both these EMO algorithms. SONG is actually a hybrid version of these two algorithms wherein SMPSO precedes the NSGA phase in order to pre-process the Pareto optimal solution set. By embedding the NSGA operators in SMPSO, the balance between exploration and exploitation is significantly improved. To summarize, the SONG algorithm combines the ability of social thinking in the swarm algorithm with the local search capability of the NSGA-II algorithm. Because SMPSO and NSGA-II both are population-based algorithms, the SONG algorithm is also a population-based algorithm and is hence guaranteed to find the global solution.

The proposed SONG algorithm is given in Algorithm 3. In the initialization phase, the particles of the swarm and corresponding velocities are randomly generated over the search space. Thereafter, the position of each particle is updated according to Equation (27). After creating a new generation in the SMPSO phase, some particles of a new population are selected and NSGA-II is applied to each of them separately (line 18). Because the swarm size is often very large, it is not time efficient to employ NSGA over an entire population. Hence, out of the total swarm population, the number of swarm ($\mathcal{N}_{nsga}$) that should evolve into a SMPSO renewal process is defined by:

$$\mathcal{N}_{nsga} = \mathcal{N}_{nsga}^{max} - \left(\frac{SMPSO_i}{SMPSO_{maxit}}\right)^{\gamma} \cdot \left(\mathcal{N}_{nsga}^{max} - \mathcal{N}_{nsga}^{min}\right) \tag{33}$$

where $SMPSO_i$ and $SMPSO_{maxit}$ denote the maximum number of generations in SMPSO, respectively. After selecting the individual with the highest fitness (greedy selection), SONG creates a new population by replacing the individuals with improved fitness via selection, crossover, and mutation operators. Once a new population is evaluated, the population size $\mathcal{N}_{nsga}^{pop}$ and maximum number of iterations $NSGA_{maxit}$ for the NSGA-II phase are updated with respect to each SMPSO iteration according to the following equations:

$$\mathcal{N}_{nsga}^{pop.} = \mathcal{N}_{nsga}^{minpop} + (\frac{SMPSO_i}{SMPSO_{maxit}})^{\gamma} \cdot (\mathcal{N}_{nsga}^{maxpop} - \mathcal{N}_{nsga}^{minpop}) \tag{34}$$

$$NSGA_{maxit} = \mathcal{N}_{nsga}^{minit} + (\frac{SMPSO_i}{SMPSO_{maxit}})^{\beta} \cdot (\mathcal{N}_{nsga}^{maxit} - \mathcal{N}_{nsga}^{minit}) \tag{35}$$

Algorithm 3 SONG Algorithm for facility location in VFC

Input: Number of vehicles $|V|$, number of fog node $|F|$, Vehicular demand vector D[V], number of iterations gen_{max}, size of particle swarm $|PS|$
Output: An optimal facility location vector that minimizes objective function (17)

```
Extract the client vehicle set V, fog node set F, set of CDCs C
Initialize gen = 1, i = 1, index for SMPSO iteration i = 0, crossover rate CR, EA = InitializeEliteArchive(ϕ),
  Randomize Search Velocity v_p, number of iterations maxit, p = 0.01
Generate target population ( Random facility location strategy) N as swarm set S
for SMPSO_i = 0 : SMPSO_maxit do
    CreateNewGeneration ():
    for each p ∈ S do
        x_gp ← p
        Initialize position x_p and velocity v
        Update velocity v_p^t according to (28)
        Update positions x_pp and x_gp according to (27)
        Perform uniform mutation (γ)
        Compute the fitness value of p ∈ S /* Evaluation
        Update EA with non-dominated solutions from S
    end
    return Updated swarm set EA
     Evolve ():
    Select solution X_s from EA using constrained greedy selection strategy
    Procedure NSGA-II (X_s):
    if i ≤ N_nsga then
        i=i+1
    end
    else
        Update NSGA-II parameters N_nsga^pop. and NSGA_maxit according to (31) and (32), respectively.
    end
    SMPSO_i = SMPSO_i + 1
end
return Set of Pareto optimal solutions in set EA
```

Complexity Analysis

Denoting $\mathcal{K}$ = initial population size, x = mutation probability, $\mathcal{N}$ = number of objective functions, $\mathcal{I}$ = Max. Iterations. For each iteration, the SMPSO algorithm includes three key operations:

Particle speed computation: $\mathcal{O}(\mathcal{K})$
Uniform mutation operation: $\mathcal{O}(x\% \cdot \mathcal{K})$
Polling for elite set: $\mathcal{O}(\mathcal{N}\mathcal{K}^2)$

Thus, for $\mathcal{I}$ iterations, the complexity of the SMPSO procedure is $\mathcal{O}(\mathcal{I}\mathcal{N}\mathcal{K}^2)$. Similarly, for each iteration, the NSGA-II algorithm includes three operations:

Non-dominated sorting: $\mathcal{O}(\mathcal{N}(2\mathcal{K})^2)$
Crowding distance assignment: $\mathcal{O}(\mathcal{N}(2\mathcal{K})log(2\mathcal{K}))$
Sorting and polling: $\mathcal{O}(2\mathcal{K}log(2\mathcal{K}))$

Thus, for $\mathcal{I}$ iterations, the complexity of the NSGA-II procedure is $\mathcal{O}(\mathcal{N}(2\mathcal{K})^2)$. Combining both phases, the overall complexity of the SONG algorithm becomes $\mathcal{O}(\mathcal{I}\mathcal{N}\mathcal{K}^2)$.

7. Evolutionary Algorithms Parametrization

7.1. Encoding Scheme for SONG

Generally, the EMO algorithm starts the reproduction process by generating an initial population pool. Each member in the initial population pool represents a potential solution to the optimization problem. In order to obtain a fitness value, these members are evaluated

against a given objective and constraint function. Following this, different EMO algorithms apply different evolving processes to improve the fitness value of each member in the population. The whole process terminates when the predefined conditions are met. A solution will be selected as output only if it is not dominated by any members in the population (also known as non-dominated solutions) and do not violate any environment-specific (explicit) constraints.

While generating an initial population pool, the first step is to design a representative encoding scheme for the decision variables. The encoding scheme transfers multiple variables from a goal problem into a string of binary or integer values. The encoding technique has a significant effect on the EMO's performance. The count-preserving encoding (CPE) [26] solves the problem arising in random encoding through a bit-count tracking scheme. In this work, we proposed a modified version of CPE (named as MCPE) where the same bit-count tracking scheme is employed but added with a novel facility capacity guarantee scheme. The facility capacity guarantee is enforced by applying the constraints (23) and (25) on each chromosome.

For a VFC network with a $|V|$ number of vehicles, the number of fog node $|F|$ and $|L|$ number of links, the dimension of chromosome (G) is $(|V| + |F| + |L|)$. We assume that each fog node is connected to the remote CDCs through a single link of virtually infinite bandwidth, i.e., $|F| = |L|$. Hence, the overall dimension of chromosome (G) becomes $(|V| + 2|F|)$. In Figure 6, we illustrate an encoding string for the gth chromosome/particle in an FLP with 10 vehicles and 5 fog node locations. Suppose that C_g is the gth particle of the population denoted by $C_g = [Z_{g,1}, Z_{g,2} \ldots Z_{g,G}]$. Each component (gene) $Z_{g,h}(h \in G)$ of encoding string C_g is defined as:

- For $1 \leq h \leq |F|$, $Z_{g,h}$ denotes whether an fog node is deployed at location l. Specifically, $Z_{g,h} = x$ indicates a fog node of type x is selected for location $l_h \in L$.

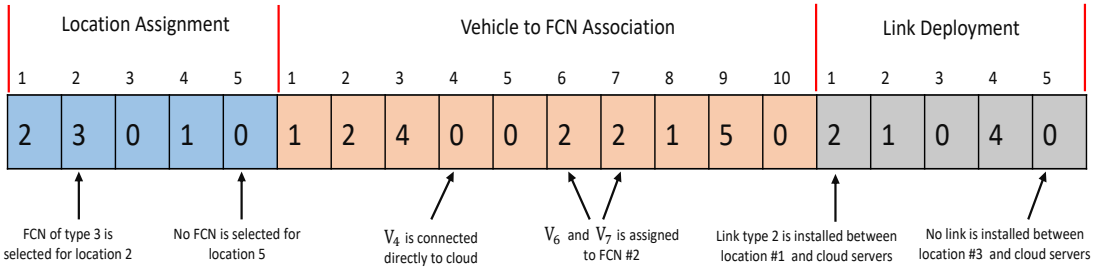

Figure 6. Proposed MCPE-based encoding string for gth chromosome.

- For $|F| + 1 \leq h \leq |F| + |V|$, $Z_{g,h}$ denotes to which fog node type the workload from vehicle $v_h \in V$ is offloaded. Specifically, $Z_{g,h} = y$ indicates that v_h is assigned to fog node y $(y \in F)$, and $Z_{gh} = 0$ indicates that v_h is directly connected to the cloud.
- For $|F| + |V| + 1 \leq h \leq 2 \cdot |F| + |V|$, $Z_{g,h}$ denotes the link decisions for the location l. Specifically, $Z_{g,h} = z$ indicates that a link of type z is installed at location l, whereas $Z_{g,h} = 0$ indicates no link is placed for this location.

7.2. Operators

- **Selection:** The SONG algorithm employs an aggressive selection process in the NSGA-II phase, which states that a child is selected for reproduction only if it is non-dominated or upgrades one fitness value achieved thus far. Because the SMPSO procedure preserves the population diversity, a harsh fitness process will not harm the solutions' spread.
- **Crossover:** Generally, the population-based meta-heuristic algorithms employ a crossover operation for combining two parent chromosomes, with the hope of generating better-quality offspring. Unlike the standard crossover operator (viz. single point, binomial, and polynomial crossover), we define a knowledge-based crossover

operator for NSGA-II phase in SONG. Here, the knowledge-based crossover operator selects two parents π_1 and π_2 according to an aggressive selection process described above in order to generate one offspring. To be specific, the local fitness of each gene is compared with the weighted combination of the average response time τ_{avg} and system energy consumption e_{sys}, given by Equation (17). The gene with better local fitness is copied to the offspring. The knowledge-based crossover operation is better depicted in Figure 7. Here, the genes marked in 'red' represent smaller local fitness values compared with their parents. Hence, the genes at indexes 1, 4, 7, 13, 17, and 20 are copied from parent 1, and the rest genes are copied from parent 2.

- **Mutation:** The mutation operators modify chromosomes so as to improve the fitness values and avoid early convergence (i.e., to abstain from struck in local minima). It is a momentum variable which keeps the diversity of the population and avoids premature convergence. The SONG algorithm employs a uniform mutation where a binary mutation vector $\mathcal{M} = (m_1, m_2 \ldots m_L)$ is randomly generated. For each $m_h = 1$, the value of gene $Z_{g,h}$ is flipped to a different value $Z_{g,h/}$ where $h \neq h/$. Figure 8 illustrates the uniform mutation for the mutation vector $\mathcal{M} = (0,0,1,0,1,0,0,1,0,0,0,1,1,0,1,0,0,1,1,1)$.

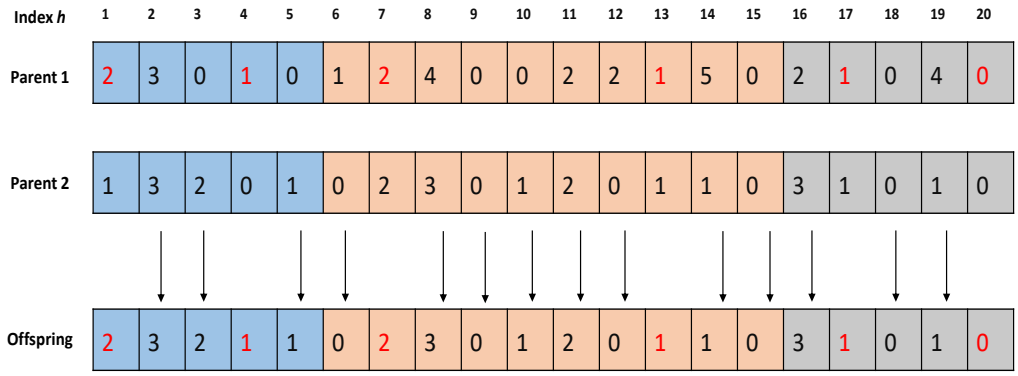

Figure 7. Knowledge-based crossover.

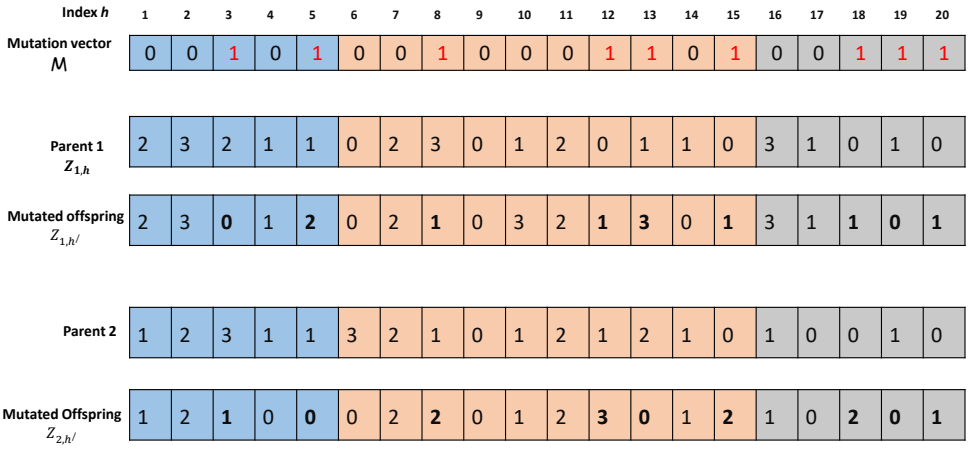

Figure 8. Uniform mutation.

Each heuristic algorithm has several tunable hyperparameters, which can eventually have an impact on the quality of the final solution. Before running experiments on the generated datasets, the parameters of NSGA-II and SMPSO were tuned so that the best results can be obtained. For the NSGA-II algorithm, we compare the volume of the dominated space (HV) for four different parameters: the mutation distribution index, the crossover distribution index, mutation probability, and crossover probability. For tuning purposes, a population size of 100 according to [64] and 3000 iterations were used following

the method in [29]. The basic idea is to test the number of iterations for EMO algorithms to reach 98% of the HV of the CPLEX's Pareto front. We observed that all three EMOs can reach the 98% HV of CPLEX within 3000 iterations. Therefore, in parameter tuning tests, a population size of 100 with a number of iterations of 3000 is used for different settings.

Mutation probability is the probability to randomly change each decision variable. In our experiment, the value of MP takes a value in the range of [0,1] with a step size 0.1. Crossover probability (CP) is the probability of producing offspring from parent solutions. In our experiment, the value of CP takes value in the range of [0,1] with a step size of 0.1. We performed preliminary experiments on sample problems and observed that keeping a mutation probability as 0.1 shows the best performance. Similarly, setting the value of CP as 0.9 gives the best performance. We did not present the whole experiment since, as shown in Table 3, the value of 0.1 shows overall best performance.

Table 3. Parameter selection for different phases of the SONG algorithm.

Parameters	NSGA II	SMPSO
C_1, C_2	-	1.5, 1.5
Inertia (w)	-	
$\mathcal{N}_{nsga}^{max}$, $\mathcal{N}_{nsga}^{min}$	20, 1	-
γ, β	10, 15	-
$\mathcal{N}_{nsga}^{minpop}$, $\mathcal{N}_{nsga}^{minit}$	10, 10	-
Mutation distribution index	18	14
Mutation probability	0.02	-
Crossover distribution index	18	-
Crossover probability	0.9	-

The set of experiments similar to SMPSO parameter tuning were also performed to compare the volume of dominated space for two parameters: the mutation distribution index and mutation probability. The complete list of selected parameters for the NSGA II and SMPSO algorithm is presented in Table 3. The source codes for the NSGA-II, SMPSO, and SONG-based solutions are implemented in PYOMO (http://www.pyomo.org/, accessed on 21 November 2022), a Python-based open source package for solving multi-objective optimization problems. To perform the experiments, an Intel(R) Core (TM) workstation with i5-4590 CPU, 3.30 GHz internal clock and 8 GB RAM is used.

7.3. Settings for the Weighted Sum Method in ILOG CPLEX

We used the linearization technique to convert the problem P1 into a mixed integer linear programming (MILP) model. For creating baselines, we solved the model in an IBM ILOG CPLEX solver with default parameter settings (https://www.ibm.com/products/ilog-cplex-optimization-studio, accessed on 22 November 2022). For each problem instance, we generate 11 pair of weights with steps of size 0.1, the weight factors α_1 and α_2, where $\alpha_1 + \alpha_2 = 1$ and the model is executed for 100 min. The weights factors α_1 and α_2, respectively, reflect the relative importance of an average response delay τ_{avg} and system energy consumption e_{sys} on the overall optimization problem. For instance, in latency critical vehicular applications α_1 will be relatively larger (or vice versa for a low power green computation models). The results obtained from the CPLEX solver are saved for to later be used as a reference for performance evaluation during EMO analysis.

8. Simulation Setup

In this section, we define the traffic scenario on which a case study is performed, followed by VANET configuration and other simulation parameterization for facility location in VFC, i.e., fog node characteristics, network topology, application characteristics and workload distribution, etc.

8.1. Traffic Simulation

In the proposed VFC architecture, each vehicle is considered to act either as a client node or a VFN. Hence, to simulate the mobility of mobile fog nodes, we used a set of real-world taxi and bus traces. Basically, we performed a case study of the data (traffic) management on a real-world city topology generated from the taxi and bus traces of Cologne [65]. Cologne is the third largest city of Germany by area and the fourth largest city by population density after Berlin, Hamburg and Munich. The mobility traces were created as part of the TAPASCologne project, an initiative of the ITS at the German Aerospace Center (ITS-DLR) [66]. The goal of this project is to simulate vehicular traffic in the greater urban area of Cologne, Germany, as realistically as possible. The dataset covers 4500 kilometers of roads in a 400-square-kilometer area and spans 24 h during a normal workday. It gives per-second information on the geographical coordinates and the speed of vehicles involved in 688,536 individual car trips. This is one of the most comprehensive mobility datasets to date that has been made freely available. The traces were obtained by integrating state-of-the-art tools devoted to VFC-specific attributes for traffic modeling in VANET. For VFC experiments, we retrieved the traces of only 1500 taxis/bus that include the longitude and latitude coordinates of GPS locations, heading directions, moving speeds, and record time-stamp. Because the vehicular distribution varies by zone, we consider one section of size 64 km^2 from each of dense and sparse zone in Leverkusen (latitude 51.0603° N, longitude 6.97332° E). The output topology generated in SUMO (https://www.eclipse.org/sumo/, accessed on 21 November 2022) is shown in Figure 9, the where red encircled zone is considered for our study. In two time frames of 15 min (6.00–6.15 a.m. IST, 8.30–8.45 a.m. IST, 22 February 2022), 189 and 481 vehicles are observed in the rush hour and idle hour, respectively. To discover the locations of RSU, we considered the deployment of cellular BSs in Cologne, retrieved from public German databases in 2012 [65]. We used the same format for the RSU location information as we used for the vehicle positions, and is available at the same repository.

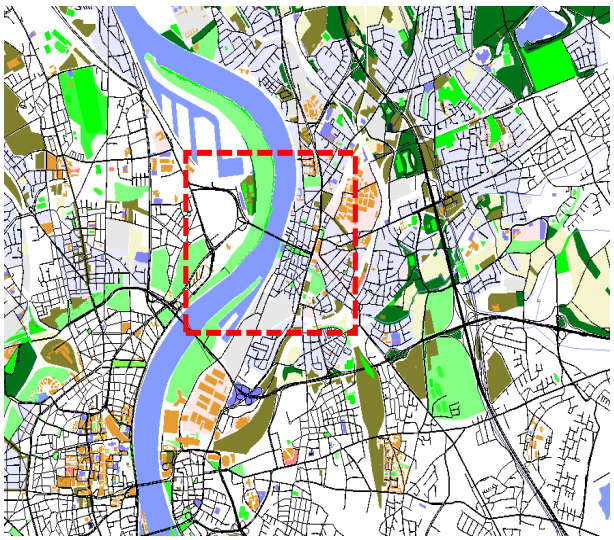

Figure 9. Map of Cologne considered for mobility generation. The bordered region contains 481 (rush hour) and 189 (idle hour) taxis and buses (VFN) and 67 RSUs.

For solving the proposed facility location model using different EMO algorithms, we used a Python-based optimization package called PYOMO. We simulated the above-mentioned VANET scenario using Veins (https://veins.car2x.org/, accessed on 21 November 2022), an open source inter-vehicle communication (IVC) simulator. Basically, Veins connects the microscopic SUMO topology with an event-based network simulation framework called OMNET++ via Traffic Control Interface (TraCI) (https://sumo.dlr.de/docs/TraCI.html, accessed on 21 November 2022). DSRC and 5G communication are realized in

SimuLTE (https://simulte.com/ accessed on 21 November 2022), an extension over the INET model library. It is an advanced simulation tool that enables a complex system-level performance evaluation of LTE and LTE advanced networks (3GPP Release 8 onwards). In our model, SimuLTE enables vehicles to either exchange data with vehicles or BS through IEEE 802.11p or IEEE 802.11bd, respectively. The overall simulation tools and the network configuration parameters are summarized in Table 4.

For modeling client vehicles, 150 vehicle routes are generated in SUMO using jtrouter (https://sumo.dlr.de/docs/jtrrouter.html, accessed on 21 November 2022), between times of 0 and 900 s. The vehicle flow density is maintained following Manhattan traffic model [67]. For each direction, the flow parameters are the maximum number of vehicles, the starting road and the destination of the flow, the time to start and end the flow and the probabilities of turning to different directions at each junction (0.3 to go straight, 0.25 to turn right and 0.25 to turn left). For each scenario, the workload (request/s) is generated by a constant bit rate (CBR) generator that lasts for 60 s. Each vehicle is assumed to be of same computing power. The processing power of fog nodes and vehicles are estimated to be 50 and 10 times more than that of PDs. Similarly, the cloud servers are assumed to be at least 200 times faster than that of FCN [32].

Table 4. Network specification and simulation parameters.

Parameters	Specifications
Π_v	0.1
POF_v	0.3
r_p^a	U[1, 2] MIPS
r_v^{cap}	5 MIPS
$\|F\|$	481 (dense), 189 (sparse)
$\|V\|$	150
Speed of VFN	[2, 5] km/h
Client Vehicle speed	[20, 40] km/h
σ_v	U[32, 128] bytes
τ_v^{max}	50–700 ms
$\mathcal{C}_f$ (MIPS)	50 (cars) & 100 (bus)
$\omega_{v,f}$	20 MHz (802.11p, WAVE)
	410 MHz (802.11bd, 5G NR (FR1))
r_c^s	10^5 MIPS
$\mathcal{P}_p^{tran}$	23 dBm
α_v	2605 mJ/s
A_c	{3.2, 4.4, 2.3}
B_c	{68, 53, 70}
u	U[2.5, 3]
n_c	U[200, 500]
OMNET++ Simulation time	60 s

8.2. VANET System Configuration

For simulating inter-vehicular communication in the sparse zone, the IEEE 802.11p DSRC standard is used with a maximum data rate of 27 Mbps and approximately 300 m of coverage [12]. For dense vehicular zones, IEEE 802.11bd and 5G NR V2X are assumed to be the mode of communication among vehicles. The neighboring vehicles communicate with each other by broadcasting beacon messages through DSRC. However, vehicle-to-BS communication needs high mobility for the vehicles going at high speed. Thus, we use 5G NR V2X for high-speed vehicles moving at 350 km/h [8].

Based on the topology analysis in Section 8.1, we generated 25 problem instances to be used in EMO experimentation. The problem instances are generated by a program written in Python and are specified in Table 5. The task profile for each PD is specified according to Definition 1.

For the example problem $\Pi(10, 30, 5, \infty)$, we handle the uncertainty in location and velocity using fluid traffic model (FTM) [38] for modeling vehicular mobility. The FTM

describes the output velocity v_s of vehicle v as a monotonically decreasing function of vehicular density and enforces a lower bound on vehicle velocity when the traffic congestion reaches a critical state, guided by Equation (34).

$$v_s = \min\{v_s^{min}, v_s^{max}(1 - \frac{k}{k_{jam}})\} \tag{36}$$

where v_s^{min} and v_s^{max} are the minimum and maximum speed, respectively, k_{jam} is the vehicular density for which a traffic jam is detected, and k is the current vehicular density of the road. We assume that the maximum speed v_s^{max} of the vehicle is 40 km/h, and correspondingly, we randomly generate four instances for each problem size, over a location range (−100 and +100 m). This gives rise to a total of 100 problems. Each algorithm is then executed for four instances of each problem index/size. Finally, the values averaged over these four instances are presented. This goal here is to produce a better performance for each algorithm considering the randomness of each problem instance.

Table 5. Problem instances for SONG experiments.

Problem No.	# Fog Nodes	# Vehicles	# RSU	Cloud
1	5	10	1	∞
2	5	15	1	∞
3	5	20	2	∞
4	5	25	2	∞
5	10	30	2	∞
6	10	40	2	∞
7	10	50	5	∞
8	10	60	5	∞
9	10	70	5	∞
10	10	80	5	∞
11	15	70	8	∞
12	15	80	8	∞
13	15	90	8	∞
14	15	100	8	∞
15	15	100	10	∞
16	15	100	10	∞
17	15	120	10	∞
18	15	140	10	∞
19	15	160	10	∞
20	15	180	10	∞
21	20	200	10	∞
22	20	250	10	∞
23	20	300	10	∞
24	20	350	10	∞
25	20	400	10	∞

Definition 5. *FLP Instance: In order to explain the working of a proposed FLP model, we defined an FLP instance by a quadruple* $\Pi(f, v, r, \infty)$*, where* f *indicates the number of fog locations,* r *represents the number of RSUs installed in that segment,* v *is the number of vehicles, and* ∞ *is for the remote cloud. For example,* $\Pi(6, 12, 4, \infty)$ *indicates that tasks from twelve vehicles need to be routed to six fog locations, in a road segment installed with fur RSUs.*

9. Results and Discussions

9.1. An Illustrative FLP Problem Π (10, 30, 5, ∞)

To demonstrate the effectiveness of the proposed algorithm, we first evaluate the proposed SONG algorithm on an example problem $\Pi(10, 30, 5, \infty)$. We used this example to have a thorough analysis of the results to examine how a typical facility location model works for VFC. Here, one instance of $\Pi(10, 30, 5, \infty)$ is solved with the weighted sum

method (CPLEX), NSGA-II, SMPSO and SONG algorithms. The nodes are assumed to be uniformly distributed in a $(100 \times 100\ \text{km}^2)$ area. The progress against the varying number of iterations and Pareto frontiers generated using CPLEX, NSGA-II, SMPSO, SONG, are plotted in Figure 10. It can be observed that, compared to NSGA-II which could not completely explore the solution space, the Pareto fronts in the SONG algorithm are uniformly distributed and are more extended along both axes. Similarly, compared to SMPSO where the solutions are far away from the optimal, the SONG solutions are sticking (nearest) to the optimal curve.

Each optimal solution indicates a different planning and routing scheme for the VFC network designers leading to trade-off between delay and energy.

For the problem $\Pi(10, 30, 5, \infty)$, it is also noteworthy that the multi-objective model gives several optimal solutions where different solution indices may converge to same objective function values. Each optimal solution indicates a different planning and routing scheme for the VFC network designers leading to a trade-off between delay and energy. For this example, we explained one solution where the optimal solution obtained from the CPLEX has a delay (τ_{avg}) of 7.023 milliseconds and energy consumption (e_{sys}) value 2.32 unit. Basically, we plotted the topology layout generated for all four algorithms, corresponding to a fixed value of energy consumption of 77.31 units. In this case, we observed roughly identical solutions in each iteration as the search space is very small.

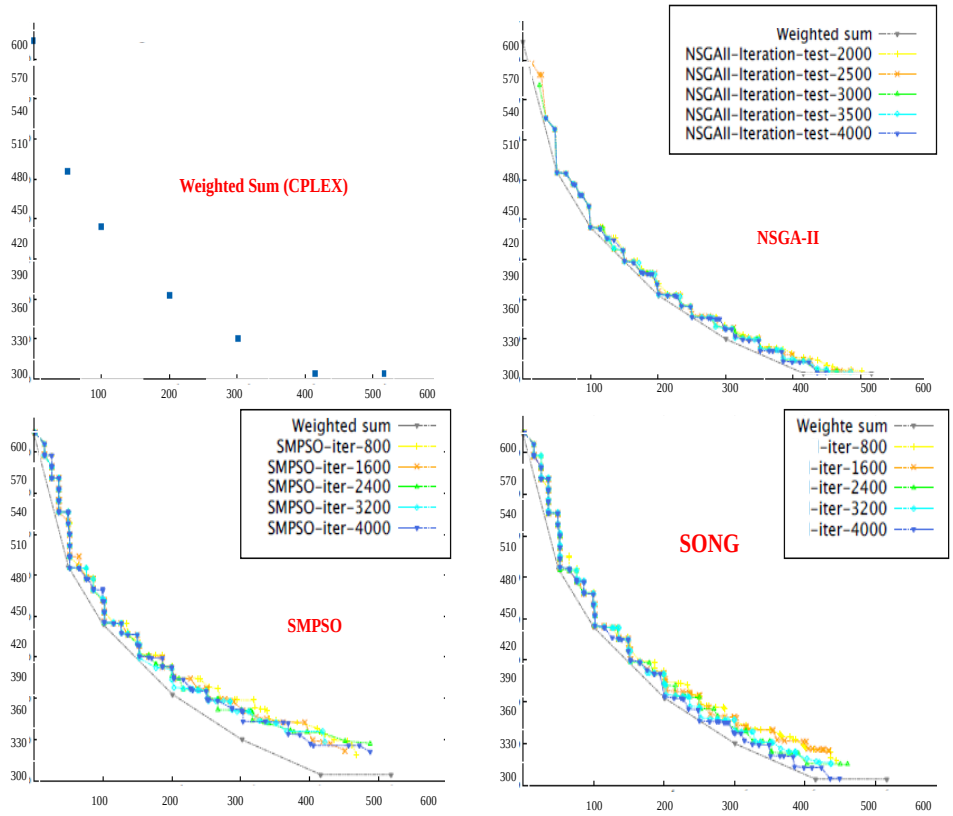

Figure 10. Solution frontiers for $\Pi(10, 30, 5, \infty)$.

It can be observed from Figures 11–14 that both NSGA-II and SONG generate nearly the same topologies as that of the weighted sum (CPLEX). For the same energy consumption (77.31 units), the delay for CPLEX, NSGA-II, SMPSO and SONG are 321.9 ms, 322.4 ms, 324.1 ms and 322.3 ms, respectively. The slight differences in delay are due to the variation in placement of a small number of vehicles (i.e., E11 and E12), and can be resolved through the efficient reallocation and load-balancing strategies.

Moreover, as the problem size increases, the solution time for CPLEX increases steeply. This is because CPLEX uses the branch and bound (B&B) algorithm which first splits

the search space into smaller search spaces called *branching*. Then, it explores the sets of a smaller search space to obtain the minimum value of the objective function. The B&B strategy avoids the brute force search and testing by keeping track of bounds on the minimum value of the objective function. The bounds are then utilized to prune the search space by eliminating the candidate solutions that cannot give an optimal solution. In fact, the randomness in the nonlinear increase in the average solution time for a large problem size can also be related to the theory that the combinatorial solution points are pruned by the CPLEX solver during B&B heuristics. However, it is found that there is a wider gap for two different placement locations in the solution time. This is due to the NP-hardness of FLPs.

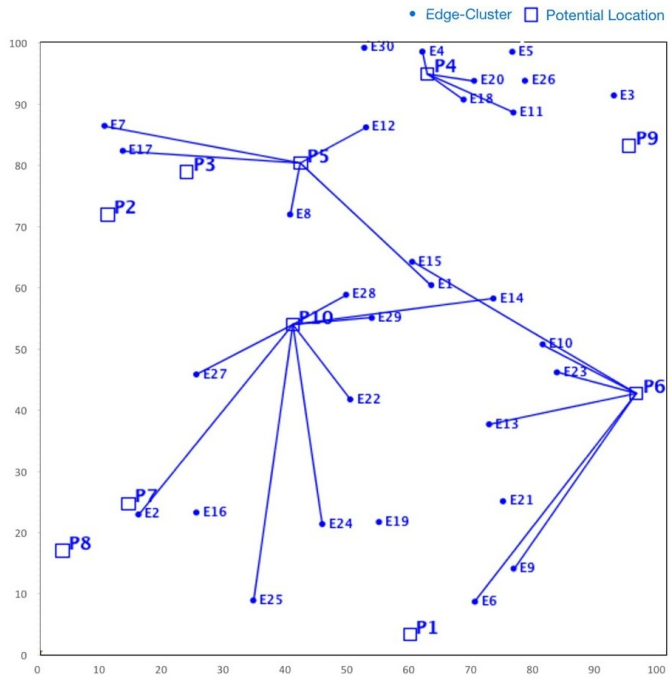

Figure 11. Output layout for CPLEX at $e_v^{avg} = 77.31$ units, τ_v^{avg} 321.9 ms.

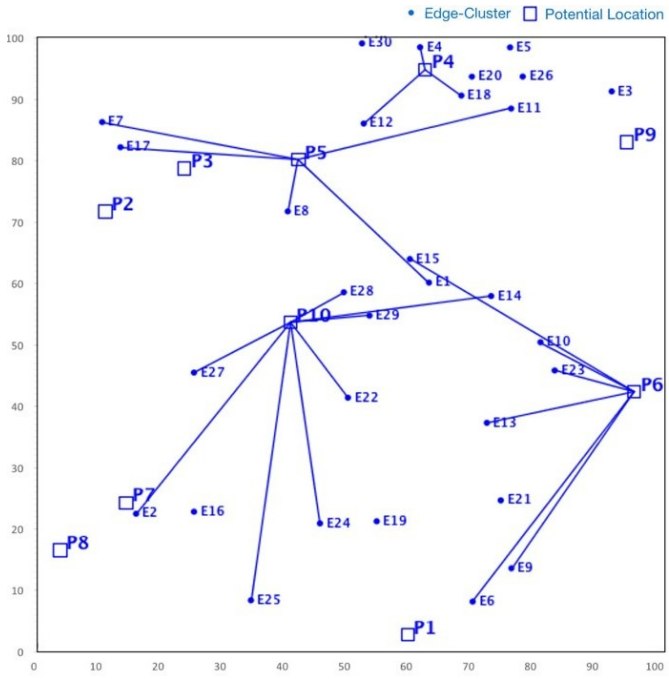

Figure 12. Output layout for NSGA-II at $e_v^{avg} = 77.31$ units, 322.4 ms.

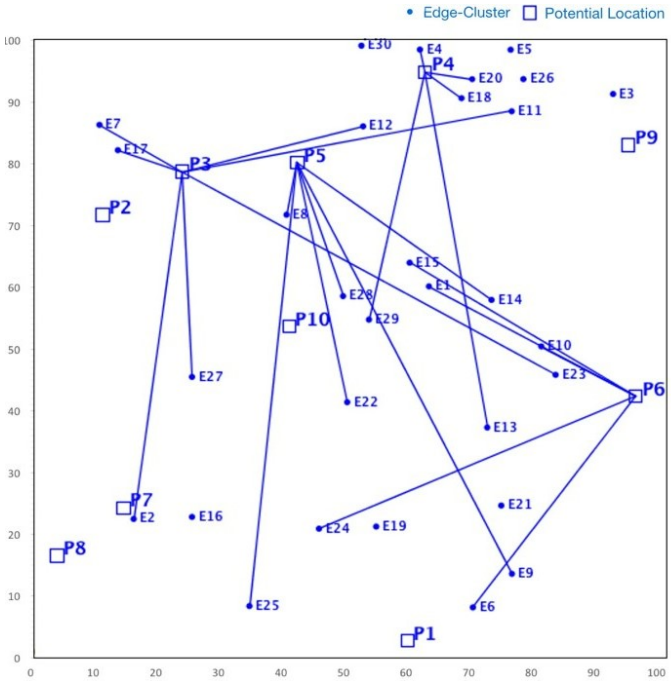

Figure 13. Output layout for SMPSO at $e_v^{avg} = 77.31$ units, τ_v^{avg} 324.4 ms.

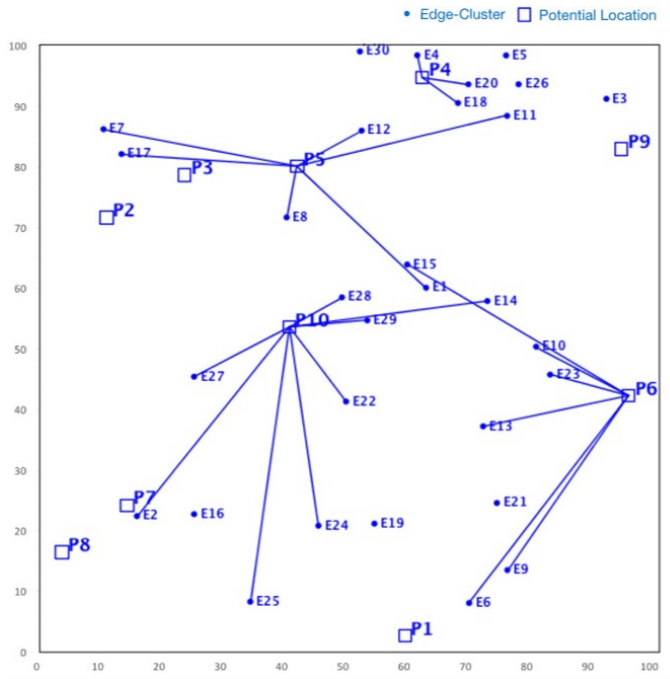

Figure 14. Output layout for SONG at $e_v^{avg} = 77.31$ units, τ_v^{avg} 323.1 ms.

9.2. Performance Analysis on Real-World Transportation Datasets

An important issue in EMO is the qualitative analysis of the performance of different algorithms. There are numerous methods of measuring the quality of the solution for any optimization problem. The most common and simplest technique to measure the solution quality is to keep track of the objective functions and the time taken by the solver to reach an optimal solution. Generally, the time taken to reach an optimal solution must increase proportionally to the fleet size as the solver must consider a lot of combinations of where to install the fog nodes, what type of fog node needs to be installed, and which vehicle should be assigned to it. Usually, the outcome of an EMO algorithm is an approximation of the Pareto-optimal front, denoted as an approximation set. Hence, the question arises of how to

evaluate the quality of those approximation sets. In this work, we performed a comparative analysis of SONG with the results obtained by a weighted sum method (CPLEX), NSGA-II and SMPSO in terms of three comparison metrics, namely hyper-volume (HV) indicator [33], delay gap, and inverted generational distance (IGD) [29]. For performance evaluation, we solved the facility location model for 25 different problems defined in Table 5.

EMO algorithms tend to create a set of non-dominated solutions to form Pareto fronts, which introduces uncertainty into decision makers' preference. To deal with the uncertainty, a compromised solution on the Pareto fronts of each problem using fuzzy systems is used [68], which models the fuzziness in the goal of each objective function. The contribution of Pareto fronts to each objective is modeled as a fuzzy membership function which has values in the range of [0, 1]. The best compromising solution is found when the solutions in a Pareto front are very close to each other. The membership value for the jth solution for the ith objective in the Pareto front is calculated using the membership function:

$$\mu_i^j = \begin{cases} 1 & if \quad F_i \leq F_i^{min} \\ \frac{F_i^{max} - F_i}{F_i^{max} - F_i^{min}} & if \quad F_i^{min} < F_i < F_i^{max} \\ 0 & F_i \geq F_i^{max} \end{cases} \tag{37}$$

where μ_i^j indicates how well the jth solution is able to satisfy the ith objective in a Pareto optimal set. The sum of all the membership values for all objectives of the jth solution indicates how well it satisfies all the objectives. Given Y solutions in a Pareto front and χ objective functions for each solution, the achievement of each solution with respect to all the Y solutions can be calculated by:

$$\mu^j = \frac{\sum_{i=1}^{\chi} \mu_i^j}{\sum_{j=1}^{Y} \sum_{i=1}^{\chi} \mu_i^j} \tag{38}$$

The best compromise solution accepted by the decision maker is the solution which has a maximum value of μ^j.

9.2.1. Comparison of Hyper-Volume (HV) Indicator

The volume enclosed by a Pareto approximation and a reference set is called the HV indicator, which is also called Nadir point. The reference point usually represents the worst possible point in the solution set. It explores both the convergence and diversity properties of a solution set. Search strategies in EMO are usually evaluated using reference points because it helps reduce complexity in density-based EMO and also follows strict monotonicity in Pareto dominance [22]. *A set with a large HV is always desirable as it presents a better set of trade-offs*.

From Figure 15, it can be observed that the SONG algorithm achieves superior results over other algorithms for the majority of problem sizes. We noticed that among the 100 solved problems, SONG gives the highest HV value for 89 problems (89%). The performance of the weighted sum from CPLEX is poor due to the fact that a branch and bound search can only generate a single solution. It is also to be noted that the performance of NSGA-II decreases as the problem size increases. This is due to two reasons. First, the search space is large in large-scale problems. Second, the non-dominated sorting in the NSGA-II algorithm has a concentrated effect. Basically, the SONG algorithm exhibits improved results because of the cooperative optimization between the SMPSO phase and the NSGA-II phase. It exploits the advantages of both SMPSO as well as NSGA-II, i.e., the former explores the decision space and preserves the diversity in the solution frontiers whereas the latter gives emphasis to the convergence of the solution pool towards the optimal Pareto fronts.

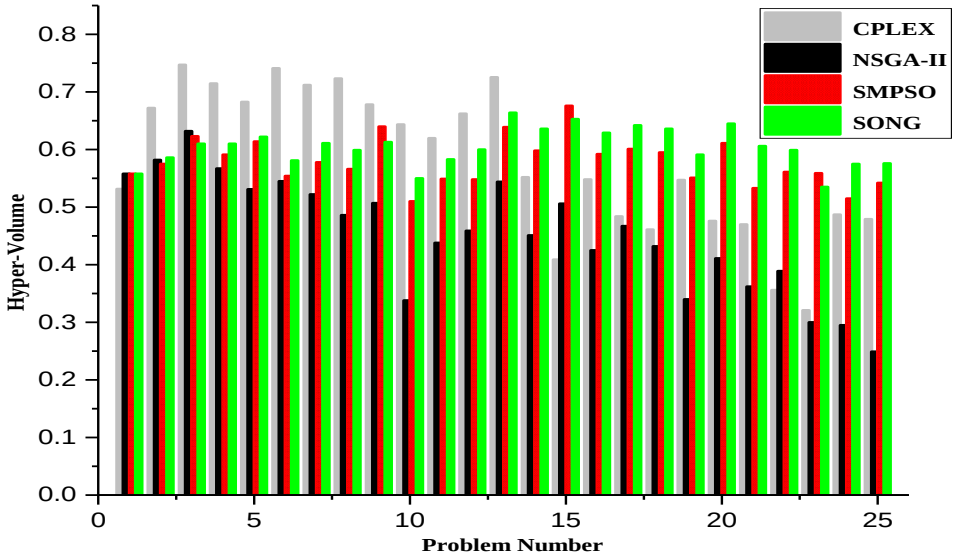

Figure 15. Comparison of HV indicators.

9.2.2. Comparison for IGD Indicators

The notion of generational distance (GD) was introduced in [69] as a metric to estimate how far the elements obtained in the Pareto front are from those in the true Pareto front of the problem. The IGD is an "inverted" version of GD that utilizes the true Pareto front as a reference set and compares each of its elements with respect to the front produced by an algorithm. For a non-dominated vector $X = \{x_1, x_2, \ldots x_{|X|}\}$ and reference vector $Y = \{y_1, y_2, \ldots y_{|Y|}\}$, the IGD is defined as:

$$IGD(X) = \frac{1}{|Y|}\sqrt{(\sum_{i=1}^{|Y|} d_i^2)} \tag{39}$$

where d_i is the Euclidean distance (measured in objective space) between each member of the solution set x_i and the nearest member of the reference set Y. Since the IGD is a measure of distance, *the lower the value of IGD, the better the quality of solution set is*. In our analysis, the best non-dominated solutions returned by all three methods (NSGA-II, SMPSO, SONG $\{P = 50\}$) are used as a reference set.

In Table 6, we provide the values of the IGD quality indicator obtained for the weighted sum (CPLEX), NSGA-II, SMPSO and SONG algorithms. It can be seen that the SONG algorithm gives better solution quality (lower IGD values) over other three algorithms for more than 90% of problems. Such an improvement over NSGA-II and SMPSO can be defined by the information exchange between the PSO and GA phases in the SONG algorithm. Smaller values of IGD values shown by the SONG algorithm for the majority of FLP problem instances proves that the Pareto fronts obtained are better than the other three algorithms.

9.2.3. Delay Gap Comparison

As discussed in Section 7.3, for each problem, with a scale of 0.1, we generate 11 different weight combinations for the WS method. Correspondingly, we obtain the decision output for the link type and the fog type at each location. We also calculate the relative mixed-integer programming (MIP) gap, i.e., the percentage gap between the solution frontier obtained by CPLEX and the value of the optimum for each problem instance. Without loss of generality, it can be concluded that all solutions provided by the CPLEX solver are optimal solutions. In other words, given a fixed value of energy consumption, the delay produced by the weighted sum and CPLEX can obtain the optimum solution.

Now, considering CPLEX solutions as the reference, we compute the average delay gaps between CPLEX vs. NSGA II, SMPSO and SONG. It is noteworthy that the delay gaps were calculated only if the weighted sum solution frontiers has the same fitness and CPLEX obtained the optimal solutions, i.e., the relative MIP is equal to 0. It can be observed from Figure 16 that NSGA-II provides the minimal delay gap to optimal solutions because of the non-dominated sorting procedure that concentrates the solution sets on the optimal front. Interestingly, the delay gap for SONG is the second minimum (best) for the majority of problems.

Table 6. Comparison of IGD values.

Prob. No.	CPLEX	NSGA-II	SMPSO	SONG
1	0.294	0.0201	0.0024	0.0013
2	0.147	0.00922	0.0026	0.0012
3	0.0958	0.00594	0.0019	0.00096
4	0.0372	0.0124	0.0026	0.00146
5	0.0411	0.013	0.0021	0.00291
6	0.03572	0.0135	0.0035	0.00315
7	0.0743	0.0121	0.0053	0.00613
8	0.0992	0.224	0.00498	0.00448
9	0.0843	0.0168	0.00259	0.00229
10	0.112	0.0173	0.00554	0.00454
11	0.134	0.0208	0.00444	0.00344
12	0.0391	0.0157	0.00532	0.00502
13	0.0521	0.00178	0.00355	0.00325
14	0.0705	0.0176	0.0024	0.00194
15	0.0427	0.0151	0.00237	0.00167
16	0.124	0.017	0.00311	0.002311
17	0.112	0.0152	0.00353	0.003153
18	0.179	0.0176	0.00351	0.00321
19	0.181	0.0164	0.00343	0.003043
20	0.297	0.0192	0.00386	0.00426
21	0.353	0.0153	0.00259	0.00289
22	0.303	0.0179	0.00334	0.00304
23	0.438	0.0197	0.00355	0.002955
24	0.403	0.0156	0.00459	0.003459
25	0.683	0.0198	0.00641	0.00681

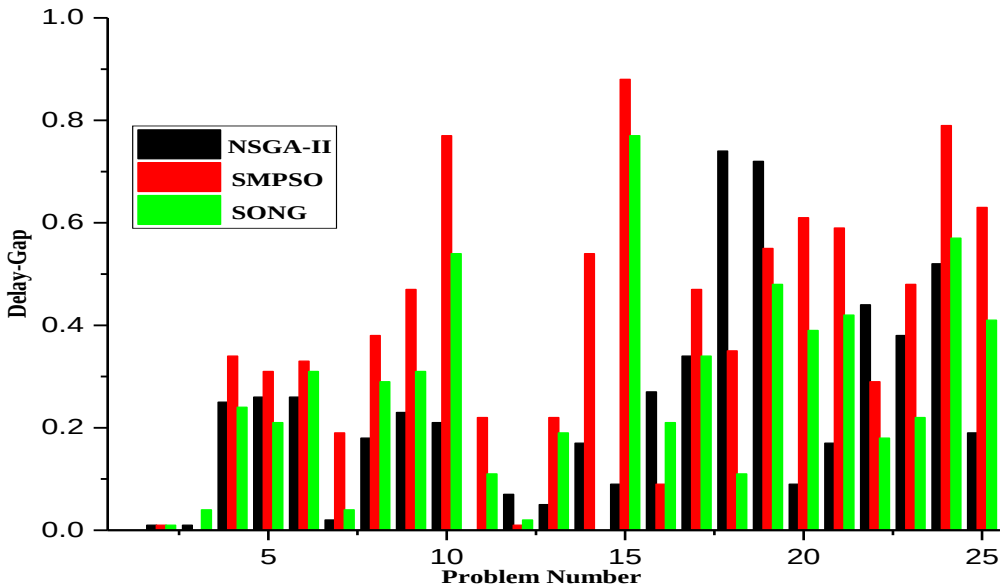

Figure 16. Delay Gap Comparison with reference to CPLEX.

10. Conclusions

In this paper, we studied the FLP in VFC networks. Specifically, we provided a multi-objective formulation of the FLP to minimize the service delay and system energy consumption. To solve this problem, we developed a hybrid EMO algorithm called SONG, which combines the convergence speed of NSGA-II, and the diversity efficiency of SMPSO algorithm. We show that, although the SONG algorithm theoretically has the same complexity as NSGA-II and SMPSO, for a facility location in VFC, it gives improved results. Furthermore, to evaluate its empirical performance, we computed the values of three quality indicators, namely: HV, IGD, and delay gap, for each of these algorithms. We execute the SONG algorithm on an example problem as well as on real-world mobility datasets and observed that SONG exhibits a better solution quality than the NSGA-II and SMPSO algorithm. In particular, the SONG-based facility location framework will enable the VFC service providers as well as transportation planners to evaluate the pros and cons of each of the trade-off solutions, leading to informed network planning and design decisions. Moreover, because we consider the mobility of fog nodes through topology generation from real-world vehicular traces, the proposed framework will provide more flexibility, especially when there is uncertainty in the traffic demand.

The peculiar property of VFC to integrate the Internet of Vehicles (IoT), sensor fusion, and V2X communication is attributed to its wide application in the transportation industry. We believed that the analytical studies conducted in this work will pave better ways for researchers and ITS planners to develop VFC services for future connected and autonomous vehicle (CAV) driving beyond 5G networks. However, the current formulation is an offline model, i.e., it assumes all the workloads are known in advance. Although such a model can be extremely useful for benchmarking, it cannot be used in a real-time environment because some of the information, e.g., the start time, end time, task duration, etc., are not available at the time to make the decision. One possible approach to address such an issue is to develop online heuristics that dynamically assign tasks to fog nodes whenever they arrive, and simultaneously manage the status of all fog nodes. We keep this as a scope of our future study.

Author Contributions: Conceptualization, M.M.H.; Data curation, M.M.H., A.T.A., R.A., S.U.A., B.Q., V.D.R., I.A. and Z.I.K.; Formal analysis, M.M.H., A.T.A., R.A., S.U.A. and B.Q.; Funding acquisition, S.U.A.; Investigation, B.Q., V.D.R., I.A. and Z.I.K.; Methodology, M.M.H., A.T.A., R.A. and S.U.A.; Resources, A.T.A., R.A., S.U.A., B.Q., V.D.R., I.A. and Z.I.K.; Software, M.M.H., R.A., V.D.R., I.A. and Z.I.K.; Supervision, A.T.A. and B.Q.; Validation, A.T.A., B.Q., V.D.R., I.A. and Z.I.K.; Visualization, R.A., S.U.A., V.D.R., I.A. and Z.I.K.; Writing—original draft, M.M.H.; Writing—review & editing, M.M.H., A.T.A., R.A., S.U.A., B.Q., V.D.R., I.A. and Z.I.K. All authors have read and agreed to the published version of the manuscript.

Funding: This research was funded by Prince Sultan University, Riyadh, Saudi Arabia.

Institutional Review Board Statement: Not applicable.

Informed Consent Statement: Not applicable.

Data Availability Statement: The datasets used for the research work can be provided on request.

Acknowledgments: The authors would like to thank Prince Sultan University, Riyadh, Saudi Arabia for funding the Article Processing Charges (APCs) of this publication. Special acknowledgments are given to Automated Systems & Soft Computing Lab (ASSCL), Prince Sultan University, Riyadh, Saudi Arabia.

Conflicts of Interest: The authors declare no conflict of interest.

References

1. Zhou, Z.; Liao, H.; Wang, X.; Mumtaz, S.; Rodriguez, J. When vehicular fog computing meets autonomous driving: Computational resource management and task offloading. *IEEE Netw.* **2020**, *34*, 70–76. [CrossRef]
2. Manoharan, H. An operative constellation rate for smart safety units using Internet of Things. *Concurr. Comput. Pract. Exp.* **2021**, *33*, e6085. [CrossRef]

3. Hamdi, A.M.A.; Hussain, F.K.; Hussain, O.K. Task offloading in vehicular fog computing: State-of-the-art and open issues. *Future Gener. Comput. Syst.* **2022,** *133*, 201–212. [CrossRef]
4. Xu, X.; Xue, Y.; Qi, L.; Yuan, Y.; Zhang, X.; Umer, T.; Wan, S. An edge computing-enabled computation offloading method with privacy preservation for internet of connected vehicles. *Future Gener. Comput. Syst.* **2019**, *96*, 89–100. [CrossRef]
5. Qian, Y.; Jiang, Y.; Hossain, M.S.; Hu, L.; Muhammad, G.; Amin, S.U. Privacy-preserving based task allocation with mobile edge clouds. *Inf. Sci.* **2020**, *507*, 288–297. [CrossRef]
6. Mao, W.; Akgul, O.U.; Mehrabi, A.; Cho, B.; Xiao, Y.; Ylä-Jääski, A. Data-Driven Capacity Planning for Vehicular Fog Computing. *IEEE Internet Things J.* **2022**, *9*, 13179–13194. [CrossRef]
7. Ahmad, R.; Asim, M.A.; Khan, S.Z.; Singh, B. Green IoT—issues and challenges. In Proceedings of the 2nd International Conference on Advanced Computing and Software Engineering (ICACSE), Sultanpur, India, 8–9 February 2019.
8. Zhu, C.; Tao, J.; Pastor, G.; Xiao, Y.; Ji, Y.; Zhou, Q.; Ylä-Jääski, A. Folo: Latency and quality optimized task allocation in vehicular fog computing. *IEEE Internet Things J.* **2018**, *6*, 4150–4161. [CrossRef]
9. Ning, Z.; Huang, J.; Wang, X. Vehicular fog computing: Enabling real-time traffic management for smart cities. *IEEE Wirel. Commun.* **2019**, *26*, 87–93. [CrossRef]
10. Tang, C.; Wei, X.; Zhu, C.; Wang, Y.; Jia, W. Mobile vehicles as fog nodes for latency optimization in smart cities. *IEEE Trans. Veh. Technol.* **2020**, *69*, 9364–9375. [CrossRef]
11. Hou, X.; Li, Y.; Chen, M.; Wu, D.; Jin, D.; Chen, S. Vehicular fog computing: A viewpoint of vehicles as the infrastructures. *IEEE Trans. Veh. Technol.* **2016**, *65*, 3860–3873. [CrossRef]
12. Hussain, M.M.; Beg, M.S. CODE-V: Multi-hop computation offloading in Vehicular Fog Computing. *Future Gener. Comput. Syst.* **2021**, *116*, 86–102. [CrossRef]
13. Lin, B.; Zhou, X.; Duan, J. Dimensioning and layout planning of 5G-based vehicular edge computing networks towards intelligent transportation. *IEEE Open J. Veh. Technol.* **2020**, *1*, 146–155. [CrossRef]
14. Alves de Queiroz, T.; Canali, C.; Iori, M.; Lancellotti, R. A Variable Neighborhood Heuristic for Facility Locations in Fog Computing. In Proceedings of the International Conference on Variable Neighborhood Search, Abu Dhabi, United Arab Emirates, 21–25 March 2021; Springer: Cham, Switzerland, 2021; pp. 28–42.
15. Farahani, R.Z.; Hekmatfar, M. (Eds.) *Facility Location: Concepts, Models, Algorithms and Case Studies*; Springer Science & Business Media: Berlin/Heidelberg, Germany, 2009.
16. Ortiz-Astorquiza, C.; Contreras, I.; Laporte, G. Multi-level facility location problems. *Eur. J. Oper. Res.* **2018**, *267*, 791–805. [CrossRef]
17. Eichfelder, G. *Adaptive Scalarization Methods in Multiobjective Optimization*; Springer: Berlin, Germany, 2008; Volume 436.
18. Chalmet, L.G.; Lemonidis, L.; Elzinga, D.J. An algorithm for the bi-criterion integer programming problem. *Eur. J. Oper. Res.* **1986**, *25*, 292–300. [CrossRef]
19. Grodzevich, O.; Romanko, O. Normalization and other topics in multi-objective optimization. In Proceedings of the Fields–MITACS Industrial Problems Workshop, Toronto, ON, Canada, 14–18 August 2006.
20. Deng, R.; Lu, R.; Lai, C.; Luan, T.H.; Liang, H. Optimal workload allocation in fog-cloud computing toward balanced delay and power consumption. *IEEE Internet Things J.* **2016**, *3*, 1171–1181. [CrossRef]
21. Mukherjee, M.; Shu, L.; Wang, D. Survey of fog computing: Fundamental, network applications, and research challenges. *IEEE Commun. Surv. Tutor.* **2018**, *20*, 1826–1857. [CrossRef]
22. Deb, K.; Pratap, A.; Agarwal, S.; Meyarivan, T.A.M.T. A fast and elitist multiobjective genetic algorithm: NSGA-II. *IEEE Trans. Evol. Comput.* **2002**, *6*, 182–197. [CrossRef]
23. Nebro, A.J.; Durillo, J.J.; Garcia-Nieto, J.; Coello, C.C.; Luna, F.; Alba, E. SMPSO: A new PSO-based metaheuristic for multi-objective optimization. In Proceedings of the 2009 IEEE Symposium on Computational Intelligence in Multi-criteria Decision-Making (MCDM), Nashville, TN, USA, 30 March–2 April 2009; pp. 66–73.
24. Piliouras, T.C. *Network Design: Management and Technical Perspectives*; CRC Press: Boca Raton, FL, USA; Elsevier: Amsterdam, The Netherlands, 2004.
25. Hussain, M.M.; Alam, M.S.; Beg, M.S. Vehicular Fog Computing-Planning and Design. *Procedia Comput. Sci.* **2019**, *167*, 2570–2580. [CrossRef]
26. Ehrgott, M. *Multicriteria Optimization*; Springer Science & Business Media: Berlin/Heidelberg, Germany, 2005; Volume 491.
27. Deb, P.K.; Roy, C.; Roy, A.; Misra, S. DEFT: Decentralized Multiuser Computation Offloading in a Fog-Enabled IoV Environment. *IEEE Trans. Veh. Technol.* **2020**, *69*, 15978–15987. [CrossRef]
28. Celes, C.; Boukerche, A.; Loureiro, A.A. Mobility Trace Analysis for Intelligent Vehicular Networks: Methods, Models, and Applications. *ACM Comput. Surv. (CSUR)* **2021**, *54*, 1–38. [CrossRef]
29. Guerrero, C.; Lera, I.; Juiz, C. Evaluation and efficiency comparison of evolutionary algorithms for service placement optimization in fog architectures. *Future Gener. Comput. Syst.* **2019**, *97*, 131–144. [CrossRef]
30. Liu, L.; Chang, Z.; Guo, X.; Mao, S.; Ristaniemi, T. Multiobjective optimization for computation offloading in fog computing. *IEEE Internet Things J.* **2017**, *5*, 283–294. [CrossRef]
31. Haider, F.; Zhang, D.; St-Hilaire, M.; Makaya, C. On the planning and design problem of fog computing networks. *IEEE Trans. Cloud Comput.* **2018**, *9*, 724–736. [CrossRef]

32. Hussain, M.; Saad Alam, M.; Sufyan Beg, M.M.; Akhtar, N. Towards Minimizing Delay and Energy Consumption in Vehicular Fog Computing (VFC). *J. Intell. Fuzzy Syst.* **2020**, *38*, 6549–6560. [CrossRef]
33. Daigneault, J.; St-Hilaire, M. Real-Time Task Assignment in Fog/Cloud Network Environments for Profit Maximization. In Proceedings of the 2022 International Wireless Communications and Mobile Computing (IWCMC), Dubrovnik, Croatia, 30 May–3 June 2022; pp. 1094–1100.
34. Tang, C.; Zhu, C.; Wei, X.; Chen, W.; Rodrigues, J.J. Rsu-empowered resource pooling for task scheduling in vehicular fog computing. In Proceedings of the 2020 International Wireless Communications and Mobile Computing (IWCMC), Limassol, Cyprus, 15–19 June 2020; pp. 1758–1763.
35. Huang, T.; Lin, W.; Li, Y.; He, L.; Peng, S. A latency-aware multiple data replicas placement strategy for fog computing. *J. Signal Process. Syst.* **2019**, *91*, 1191–1204. [CrossRef]
36. Chikhaoui, A.; Lemarch, L.; Boukhalfa, K.; Boukhobza, J. StorNIR, a multi-objective replica placement strategy for cloud federations. In Proceedings of the 36th Annual ACM Symposium on Applied Computing, Virtual, 22–26 March 2021; pp. 50–59.
37. Velasquez, K.; Abreu, D.P.; Curado, M.; Monteiro, E. Service placement for latency reduction in the internet of things. *Ann. Telecommun.* **2017**, *72*, 105–115. [CrossRef]
38. Wu, Q.; Liu, H.; Wang, R.; Fan, P.; Fan, Q.; Li, Z. Delay-sensitive task offloading in the 802.11 p-based vehicular fog computing systems. *IEEE Internet Things J.* **2019**, *7*, 773–785. [CrossRef]
39. Souza, V.B.C.; Ramírez, W.; Masip-Bruin, X.; Marín-Tordera, E.; Ren, G.; Tashakor, G. Handling service allocation in combined fog-cloud scenarios. In Proceedings of the 2016 IEEE International Conference on Communications (ICC), Kuala Lumpur, Malaysia, 22–27 May 2016; pp. 1–5.
40. Ni, L.; Zhang, J.; Jiang, C.; Yan, C.; Yu, K. Resource allocation strategy in fog computing based on priced timed petri nets. *IEEE Internet Things J.* **2017**, *4*, 1216–1228. [CrossRef]
41. Hao, Y.; Jiang, Y.; Hossain, M.S.; Alhamid, M.F.; Amin, S.U. Learning for smart edge: Cognitive learning-based computation offloading. *Mob. Netw. Appl.* **2020**, *25*, 1016–1022. [CrossRef]
42. Bittencourt, L.F.; Diaz-Montes, J.; Buyya, R.; Rana, O.F.; Parashar, M. Mobility-aware application scheduling in fog computing. *IEEE Cloud Comput.* **2017**, *4*, 26–35. [CrossRef]
43. Sun, Y.; Lin, F.; Xu, H. Multi-objective optimization of resource scheduling in fog computing using an improved NSGA-II. *Wirel. Pers. Commun.* **2018**, *102*, 1369–1385. [CrossRef]
44. Li, C.; Bai, J.; Tang, J. Joint optimization of data placement and scheduling for improving user experience in edge computing. *J. Parallel Distrib. Comput.* **2019**, *125*, 93–105. [CrossRef]
45. Wang, Q.; Chen, S. Latency-minimum offloading decision and resource allocation for fog-enabled Internet of Things networks. *Trans. Emerg. Telecommun. Technol.* **2020**, *31*, e3880. [CrossRef]
46. Arkian, H.R.; Diyanat, A.; Pourkhalili, A. MIST: Fog-based data analytics scheme with cost-efficient resource provisioning for IoT crowdsensing applications. *J. Netw. Comput. Appl.* **2017**, *82*, 152–165. [CrossRef]
47. Gu, L.; Zeng, D.; Guo, S.; Barnawi, A.; Xiang, Y. Cost efficient resource management in fog computing supported medical cyber-physical system. *IEEE Trans. Emerg. Top. Comput.* **2015**, *5*, 108–119. [CrossRef]
48. Urgaonkar, R.; Wang, S.; He, T.; Zafer, M.; Chan, K.; Leung, K.K. Dynamic service migration and workload scheduling in edge-clouds. *Perform. Eval.* **2015**, *91*, 205–228. [CrossRef]
49. Wang, S.; Urgaonkar, R.; He, T.; Chan, K.; Zafer, M.; Leung, K.K. Dynamic service placement for mobile micro-clouds with predicted future costs. *IEEE Trans. Parallel Distrib. Syst.* **2016**, *28*, 1002–1016. [CrossRef]
50. Santoyo-González, A.; Cervelló-Pastor, C. Latency-aware cost optimization of the service infrastructure placement in 5G networks. *J. Netw. Comput. Appl.* **2018**, *114*, 29–37. [CrossRef]
51. Li, Y.; Wang, S. An energy-aware edge server placement algorithm in mobile edge computing. In Proceedings of the 2018 IEEE International Conference on Edge Computing (EDGE), San Francisco, CA, USA, 2–7 July 2018; pp. 66–73.
52. Huang, Z.; Lin, K.J.; Yu, S.Y.; Hsu, J.Y.J. Co-locating services in IoT systems to minimize the communication energy cost. *J. Innov. Digit. Ecosyst.* **2014**, *1*, 47–57. [CrossRef]
53. Vemireddy, S.; Rout, R.R. Fuzzy Reinforcement Learning for energy efficient task offloading in Vehicular Fog Computing. *Comput. Netw.* **2021**, *199*, 108463. [CrossRef]
54. Mebrek, A.; Merghem-Boulahia, L.; Esseghir, M. Efficient green solution for a balanced energy consumption and delay in the IoT-Fog-Cloud computing. In Proceedings of the 2017 IEEE 16th International Symposium on Network Computing and Applications (NCA), Cambridge, MA, USA, 30 October–1 November 2017; pp. 1–4.
55. Bozorgchenani, A.; Tarchi, D.; Corazza, G.E. An energy and delay-efficient partial offloading technique for fog computing architectures. In Proceedings of the GLOBECOM 2017-2017 IEEE Global Communications Conference, Singapore, 4–8 December 2017; pp. 1–6.
56. Sarkar, I.; Kumar, S. Deep learning-based energy-efficient computational offloading strategy in heterogeneous fog computing networks. *J. Supercomput.* **2022**, *78*, 15089–15106. [CrossRef]
57. Misra, S.; Saha, N. Detour: Dynamic task offloading in software-defined fog for IoT applications. *IEEE J. Sel. Areas Commun.* **2019**, *37*, 1159–1166. [CrossRef]
58. Shah-Mansouri, H.; Wong, V.W. Hierarchical fog-cloud computing for IoT systems: A computation offloading game. *IEEE Internet Things J.* **2018**, *5*, 3246–3257. [CrossRef]

59. Hussain, M.; Beg, M.M.; Alam, M.S. Fog computing for big data analytics in IoT aided smart grid networks. *Wirel. Pers. Commun.* **2020**, *114*, 3395–3418. [CrossRef]
60. Marler, R.T.; Arora, J.S. The weighted sum method for multi-objective optimization: New insights. *Struct. Multidiscip. Optim.* **2010**, *41*, 853–862. [CrossRef]
61. Kennedy, J.; Eberhart, R. Particle swarm optimization (PSO). In Proceedings of the IEEE International Conference on Neural Networks, Perth, Australia, 27 November–1 December 1995; pp. 1942–1948.
62. Holland, J.H. *Adaptation in Natural and Artificial Systems: An Introductory Analysis with Applications to Biology, Control, and Artificial Intelligence*; MIT press: Cambridge, MA, USA, 1992.
63. Liu, Y.; Dai, J.; Zhao, S.; Zhang, J.; Shang, W.; Li, T.; Zheng, Y.; Lan, T.; Wang, Z. Optimization of five-parameter BRDF model based on hybrid GA-PSO algorithm. *Optik* **2020**, *219*, 164978. [CrossRef]
64. Reeves, C.R. (Ed.) *Modern Heuristic Techniques for Combinatorial Problems*; John Wiley Sons, Inc.: New York, NY, USA, 1993.
65. Available online: https://sourceforge.net/projects/sumo/files/traffic_data/scenarios/TAPASCologne/ (accessed on 4 October 2022).
66. Noori, H.; Valkama, M. Impact of VANET-based V2X communication using IEEE 802.11 p on reducing vehicles travelling time in realistic large scale urban area. In Proceedings of the 2013 International Conference on Connected Vehicles and Expo (ICCVE), Las Vegas, NV, USA, 2–6 December 2013; pp. 654–661.
67. Spaho, E.; Ikeda, M.; Barolli, L.; Xhafa, F.; Kolici, V.; Takizawa, M. Performance evaluation of olsr protocol in a grid manhattan vanet scenario for different applications. In Proceedings of the 2013 Seventh International Conference on Complex, Intelligent, and Software Intensive Systems, Taichung, Taiwan, 3–5 July 2013; pp. 47–52.
68. Sakawa, M.; Yano, H.; Yumine, T. An interactive fuzzy satisficing method for multiobjective linear-programming problems and its application. *IEEE Trans. Syst. Man Cybern.* **1987**, *17*, 654–661. [CrossRef]
69. Ishibuchi, H.; Masuda, H.; Nojima, Y. A study on performance evaluation ability of a modified inverted generational distance indicator. In Proceedings of the 2015 Annual Conference on Genetic and Evolutionary Computation, Madrid, Spain, 11–15 July 2015; pp. 695–702.

Disclaimer/Publisher's Note: The statements, opinions and data contained in all publications are solely those of the individual author(s) and contributor(s) and not of MDPI and/or the editor(s). MDPI and/or the editor(s) disclaim responsibility for any injury to people or property resulting from any ideas, methods, instructions or products referred to in the content.

International Journal of Advances in Engineering and Management (IJAEM)
Volume 5, Issue 1 Jan. 2023, pp: 39-45 www.ijaem.net ISSN: 2395-5252

Stopwatch Method For Assembly Line Production

S. Wangchuk, A.K Madan

[1]*Production and Industrial Engineering (PIE), Delhi Technological University (DTU), New Delhi 110042, India.*

[2]*Professor, Department of Mechanical Engineering (ME), Delhi Technological University (DTU), New Delhi, 110042, India.*

Date of Submission: 01-01-2023 Date of Acceptance: 08-01-2023

ABSTRACT

Work measurement is one of the most crucial factors in determining how productive a service or product organisation is. The methods used evaluate the strategy adopted and the amount of time required to finish a task. It makes it easier to cut back on spending and waste. This study includes a few direct observational stopwatch time study strategies. The discussion of various time concepts, such as observed time, normal time, and standard time, will provide opportunity to more clearly conceptualise the concept of work measurement. The assembly line used to make plastics on this study's assembly line had a computed standard time of 767.96 seconds and a normal time of 599.0 seconds.

Key words: Work measurement, Stopwatch method, normal time, observed time, standard time, assembly line

I. INTRODUCTION

Through a variety of scientific methodologies, changes and progress are brought to the industrial and business fields that are both practically and economically beneficial. Productivity is one of the key factors that determines whether a firm will succeed. The ratio of output to input often serves as a quantitative measure of productivity. The cost of the goods or services produced, as well as the resources used to make it, including labour, capital, raw materials, and energy, are included in the output. Partial and total production are two ways to describe it [1].

One of the most important strategies for increasing productivity is work measurement. The method entails calculating the work in terms of standard time. The standard time is mainly established using methods like time study, work sample predetermined motion time study (PMTS), and the standard data technique. This method and time study were first created by F.W. Taylor and were titled "Scientific task and job rating" [12].

Time study is the most widely used method to determine standard time. It is a technique of finding out the standard time to do a given job, based upon the method of measurement of work, with consideration of allowances such as fatigue, and unavoidable delays [2].

Time studies are carried out through job analysis, technique standardisation, and time study combined, respectively [3]. Numerous manufacturing processes can make use of work measures. This study is carried out based on plastic industry where resin, raw material, is being produced into a wide variety of shapes. Weighing, dissolving, mixing, injecting, finishing, assembling, and packaging are further processes used in the above manufacturing process. The procedure is carried out using both automatic and manual methods. Because they frequently happen at assembly workspaces, bottlenecks cannot be avoided.The primary goals of standard time determination are process standardisation, waste reduction, movement elimination, capital investment reduction, and quantitative systematisation of work using acknowledged standards [6].The objective of this study is to determine the standard time of assembly process and study various time study methods used to evaluate it.

II. LITERATURE REVIEW

Time Study Concept

Time study is the skill of watching and keeping track of how long it takes to complete each specific task in an industrial operation [7]. Time study is referred to as a work measurement technique by the ILO (International Labor Organization) for recording the times and work

International Journal of Advances in Engineering and Management (IJAEM)
Volume 5, Issue 1 Jan. 2023, pp: 39-45 www.ijaem.net ISSN: 2395-5252

rates for the specified job carried out in the specified environment and for obtaining data on the amount of time required to complete the job at a specified level of performance [5]. In other words, it is the calculation of the amount of time needed for a skilled and well-trained individual to do a certain work in a typical setting [4]. There are several time study methodologies, including the stopwatch approach and traditional data analytical estimation [8].

Standard time is the end product of time studies [2]. The collection of diverse jobs' standard times results in the standard data catalogue [8].

Major reason for studying time

Time study and work measuring techniques are used for a variety of tasks, such as (1) planning and scheduling work, (2) determining standard operating costs, (3) creating budgets, estimating product costs, calculating machine efficiency, (5) establishing the foundation for a payment control of labour costs [2], (6) making purchases or decisions, (7) balancing the work of group of operators, (8) estimating delivery dates, and (9) calculating the amount of time needed to generate a certain inventory level [8].

III. RESEARCH METHODS

The quantitative approach used to address research problems is known as research methodology. Here, stopwatch time study is being utilised to determine the time. The above-mentioned plastic manufacturing firm are the source of the study which is carried based on. The information is gathered and examined using various stopwatch method techniques. Both secondary and primary data are being used in this study. While secondary data were gathered through textbooks, charters, numerous periodicals, and prior study articles, primary data were acquired through firsthand observations and exclusive interviews. Data analysis was done after data collection in a number of processes.The methods listed below were used to determine standard time:

1. performed a stopwatch study,
2. documented the findings,
3. timed each element,
4. computed the normal time, established allowances, and
5. established the standard time

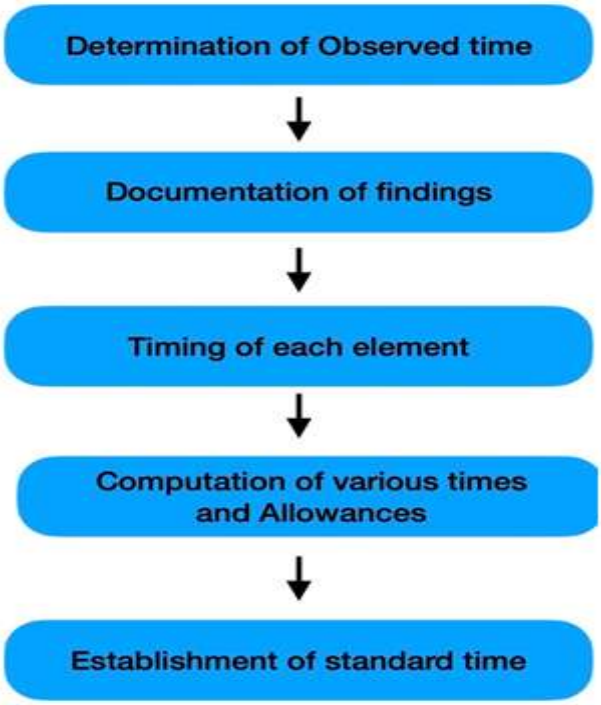

Fig 1: Research Methods

International Journal of Advances in Engineering and Management (IJAEM)
Volume 5, Issue 1 Jan. 2023, pp: 39-45 www.ijaem.net ISSN: 2395-5252

IV. DATA ANALYSIS AND DISCUSSION

1. Observed time

The stopwatch method is the work measurement approach employed in this investigation. There are 5 different production procedures in the assembly line. Every time, a stopwatch has been used to record how long it takes to complete activities. To quickly determine the average trial duration, data are taken for subgroups.

Sub groups	**Time recorded(s)**					**Average**
Tasks	1	2	3	4	5	
1	600	400	450	460	560	494
2	570	500	670	450	650	568
3	432	569	478	459	560	499.6
4	590	590	567	670	568	597

Table 1: Observed time

$$n = \left(\frac{40\sqrt{\Sigma t^2 - (\Sigma t)^2}}{\Sigma t}\right)^2$$

Here, to determine the sample size, by theory of work sampling, the equation below is used.

Where, ′t′ is observation time in seconds. The sample size decision depends on the confidence level of the result. In motion time study, 2σ (standard deviations) are used which ensures 95.45±5% success rate [9]. The confidence level with standard deviations is given below:

Confidence level	**Level of Significance**	$Z_{\alpha/2}$
99%	1%	2.575
95%	5%	1.96
90%	10%	1.645

Table 2: The confidence level with standard deviations [10].

2. Control Charts

Control charts are the instruments used to assess the statistical control of a manufacturing or business process [11]. Control is used to evaluate the data's consistency. It is a tool for quality assurance. It displays a situation of normal distribution. Control limit determinations often employ the 3σ limit (99.7% confidence). Accordingly, there are only three chances in a thousand $(1:1000)$ that a point will go outside its bounds [3].

International Journal of Advances in Engineering and Management (IJAEM)
Volume 5, Issue 1 Jan. 2023, pp: 39-45 www.ijaem.net ISSN: 2395-5252

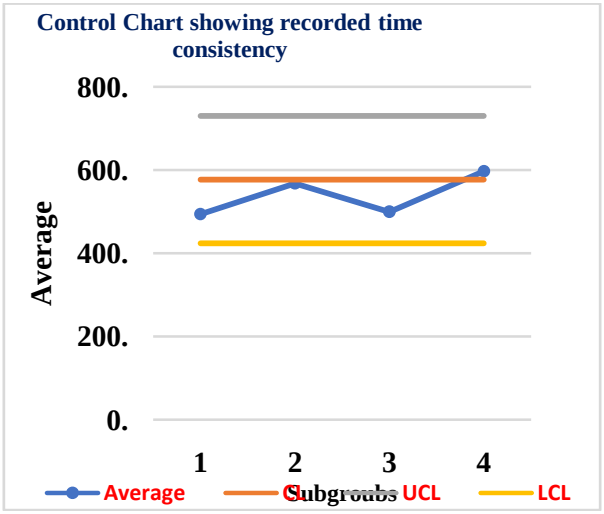

Fig 2: Control Chart showing recorded time consistency.

3. **Normal Time**

Utilizing the performance rating factor [7], it needs to be normalised. The ratio of a worker's performance level to the standard performance expected determines their performance rating [8].

Good Skill(C1)	**+0.06**
Good Effort(C2)	**+0.05**
Average Condition(D)	**0.00**
Average Consistency(D)	**0.00**
Total	**+0.11**

Table 1: Selected performance rating criteria for the assembly line.

Westinghouse system is one of rating performance scheme. There is skill, effort, condition, and consistency. In the Westinghouse method, there are six classes of each factor as shown in above table.

Based on observation and Westinghouse table, performance rating of operator at assembly line was observed. Then the normal time is calculated using the relation:

$$normal \quad time = Observed \quad time\left(\frac{Rating \quad in \quad percent}{100}\right)$$

International Journal of Advances in Engineering and Management (IJAEM)
Volume 5, Issue 1 Jan. 2023, pp: 39-45 www.ijaem.net ISSN: 2395-5252

SKILL			EFFORT		
+ 0.15	A1	Super skill	+ 0.13	A1	Super skill
+ 0.13	A2		+ 0.12	A2	
+ 0.11	B1	Excellent	+ 0.1	B1	Excellent
+ 0.08	B2		+ 0.08	B2	
+ 0.06	C1	Good	+ 0.05	C1	Good
+ 0.03	C2		+ 0.02	C2	
0.00	D	Average	0.00	D	Average
- 0.05	E1	Fair	- 0.04	E1	Fair
- 0.10	E2		- 0.08	E2	
- 0.16	F1	Poor	- 0.12	F1	Poor
- 0.22	F2		- 0.17	F2	
CONDITION			**CONSISTENCY**		
+ 0.06	A	Ideal	+ 0.04	A	Ideal
+ 0.04	B	Excellent	+ 0.03	B	Excellent
+ 0.02	C	Good	+ 0.01	C	Good
0.00	D	Average	0.00	D	Average
- 0.03	E	Fair	- 0.02	E	Fair
- 0.07	F	Poor	- 0.04	F	Poor

Table 2: Westinghouse table [10]

From the above data, the normal time is calculated to be 599.01s.

4. Standard Time

To the normal time determined above, several allowances are added to determine standard time. Allowances are added to compensate idle time because employees are incapable of working continuously [8]. It provides flexibilities to employees for taking breaks and to engage in other activities. There are several various kinds of allowance, including personal, fatigue, and delay allowances [7].

$$Standard\ \ time = Normal\ \ time\left(\frac{100}{100 - Allowance\ \ in\ \ \%}\right)$$

The ILO divides allowances into two categories: variable allowances and constant allowances. In table 4, various allowance types that the ILO recommends are listed. Following careful inspection, some considerations for allowances for assembly line workers that need to be made include:

Basic fatigue allowance	**4%**
Standing allowance	**2%**
Muscular energy	**0%**
Bad light	**2%**
Atmospheric conditions	**10%**
Near/close attention	**0%**
Noise level	**2%**
Mental Strain	**1%**
Monotony	**1%**
Tediousness	**0%**
Total	**22%**

Table 3: Selected allowance criteria for assembly line(with reference to table 4)

International Journal of Advances in Engineering and Management (IJAEM)
Volume 5, Issue 1 Jan. 2023, pp: 39-45 www.ijaem.net ISSN: 2395-5252

With the above calculated allowance, the standard time of the operation is 767.96s per product.

Variable	Allowance (%)	Factor	Allowance (%)
A. Constant allowances		Atmospheric conditions (heat and humdityi- variable	0-100
Personal allowance	5	Close attention:	
Basic fatigue allowance	4	Fairly fine work	0
B. Variable allowances:		Fine or exact ng	2
Standing allowance	2	Very fine or very exacting	5
Ad tional position allowance:		Noise level:	
Slightly awkward	0	Continuous	0
Awkward (bendirg)	2	Intermittent - lcud	2
Very awkward (lying, stretching)	7	Intermittent - very loud	5
70	22		
Bad light			
Slightly be ow recommended	0		
Well below	2		
Quite inadequate	5		

Table 4: ILO recommended allowances[9]

V. CONCLUSION

One of the methods for measuring work is the stopwatch method. It entails keeping track of the amount of time needed to complete a certain task before figuring out normal and standard time from the directly observed time. When determining standard time, performance rating is taken into account together with the inclusion of allowances. The average time for the aforementioned data set was determined to be 599.01 and 767.96 seconds, respectively. Each of the three different time periods has a distinct meaning. The stopwatch time study is recommended because it is easier and less expensive than other techniques.

REFERENCES

- Ishwar Bhiradi , B.K.Singh, "Work Measurement Approach For Productivity Improvement In A Heavy Machine Shop", 5 th International & 26th All India Manufacturing Technology, Design and Research Conference (AIMTDR 2014) December 12th–14th, 2014, IIT Guwahati, Assam, India, 2014.
- A. Freivalds, "Niebel's Methods, Standard, and Work Design," McGraw-Hill, 2009.
- A. Karanjkar, "Manufacturing and Operations Management", Nıralı Prakashan, 2008. [4] Ralph M. Barnes, "Motion and Time Study Design And Measurement Of Work," John Wiley & Sons, Inc, 1980 [5] International Labour Organisation (ILO), "Introduction to Work Study," Universal Publishing Corp., India. , Third Revised Edition, 1986.
- Ralph M. Barnes, "Motion and Time Study Design And Measurement Of Work," John Wiley & Sons, Inc, 1980
- International Labour Organisation (ILO), "Introduction to Work Study," Universal Publishing Corp., India. , Third Revised Edition, 1986.
- Prakash C, Prakash Rao B, Shetty DV, Vaibhava
- S. Application of time and motion study to increase the productivity and efficiency. Journal of Physics: Conference Series. 2020;1706(1):012126.

- Jain M. Time Study: Definition, objectives and advantages (with formula) [Internet]. Your Article Library. The Next Generation Library; 2016 [cited 2022Nov16]. Available from: https://www.yourarticlelibrary.com/cost-accounting/time-study/time-study-definition-objectives-and-advantages-with-formula/90524
- Khana OP. Industrial Engineering and Management. 1st ed Dhanpat Rai Publishers, INDIA; 2017.
- Hartanti L. Work measurement approach to determine standard time in assembly line [Internet]. Academia.edu. IRAJ International Journals; 2016 [cited 2022Nov16]. Available from: https://www.academia.edu/86985671/Work_Measurement_Approach_to_Determine_Standard_Time_in_Assembly_Line
- Kiernan D. Natural Resources Biometrics [Internet]. Chapter 2: Sampling Distributions and Confidence Intervals | Natural Resources Biometrics. Open SUNY Textbooks; 2020 [cited 2022Nov16]. Available from: https://courses.lumenlearning.com/suny-natural-resources-biometrics/chapter/chapter-2-sampling-distributions-and-confidence-intervals/
- Admin. Control charts: Types of Control Charts and features [Internet]. BYJUS. BYJU'S; 2021 [cited 2022Nov16]. Available from: https://byjus.com/maths/control-charts/
- 2 BAB. Bab 2 kajian literatur 2.1 Pengenalan - Universiti malaya [Internet]. Udemy. [cited 2022Nov16]. Available from: http://studentsrepo.um.edu.my/1708/3/BAB_2.pdf

Super Ultra-Wideband Planar Antenna with Parasitic Notch and Frequency Selective Surface for Gain Enhancement

Pankaj Jha[1], Anubhav Kumar[1], Asok De[2], and Rakesh Kumar Jain[1]

[1]Department of Electronics and Communication Engineering
Shobhit Institute of Engineering and Technology (Deemed to be University), Meerut 250110, India

[2]Department of Electronics and Communication Engineering
Delhi Technological University (DTU), New Delhi 110042, India
pankaj.maahi@gmail.com; asok.de@gmail.com

Abstract **–** A compact Super ultra-wideband (SUW) antenna is discussed in this work. A rectangular radiator is modified into a tree-shaped structure with the defected partial ground to enhance the operating bandwidth. The novel rectangular parasitic with the circular slot is used as a notch in the ground plane which prevents the WLAN frequency. The proposed SUW antenna is achieving the 10 dB impedance bandwidth (IBW) from 3.5 GHz to 66.5 GHz frequency with a notched band varying from 5.0 GHz to 5.4 GHz. The bandwidth ratio (BDR) of the proposed SUW antenna is 1773.4 whereas the obtained bandwidth percentage (BW %) is 180. A modified SRR frequency selective surface (FSS) is designed for UWB application to improve the gain of the antenna. The compact unit cell of FSS is having electrical dimensions of $0.16\lambda_0 \times 0.16\lambda_0$. The antenna achieves the maximum realized gain 9.46 dB when FSS is loaded as a superstrate and up to 5.2 dB gain enhancement is observed in the UWB frequency.

Index Terms **–** SUW, BDR, FSS, gain enhancement, notch band.

I. INTRODUCTION

The present scenario of wireless communication demands a compact antenna design with improved data rate, large capacity and secure communication. The standard bandwidth of UWB communication is varying from 3.1 GHz to 10.6 GHz, it is preferred in short range applications [1]. To enhance the functionality of the communication system, the SUW antenna can be a better design option for long-range, short-range and many wireless applications. Further due to the large bandwidth (at least 10:1 bandwidth ratio [2]) of antenna it provides high channel capacity with higher data rate which can be advantageous for ISM band, GPS, GSM, and WLAN, defense, satellite communication, aeronautical navigation and radio astronomy [3]. Researchers proposed different structures and technologies for SUW antenna and they focused upon compactness, bandwidth % and BDR of the antenna. In [2], a monopole SUW antenna having 10 dB IBW from 2.59 – 31.14 GHz was designed in which a rectangular stub is accomplished for the improvement of impedance matching. In [3], three elliptical structures are used to design a tree-shaped radiator to obtained SUW characteristics from 0.65 – 35.61 GHz frequency. Sierpinski-shaped [4], the octagonal fractal antenna [5] with defects in the ground is used to design a SUW antenna with 1414.5 and 3015 BDR value respectively. In [6], an elliptical monopole SUW antenna is designed where a tapered feed is used for bandwidth improvement. In [7], CPW fed, Propeller-shaped radiator is designed to obtain the SUW characteristics from 3.15–32 GHz frequency. In [8], a transparent antenna is designed for SUW application obtaining BW % of 191. In [9], a gap is created between the ground plane and radiator to achieve SUW characteristics from 2.5–110 GHz frequency.

The gain of the antenna is an essential requirement in wireless communication and the EM signals can be transmitted as well as received effectively with a high gain antenna therefore to fulfil this many gain enhancement technologies are presented in the literature in which AMC [10–12], Metamaterial [13–15] and FSS [16–21] are the major techniques introduced by researchers. The Metamaterial techniques depends upon the characteristics of permittivity and permeability for the gain enhancement whereas the AMC and FSS control the grating lobes introduced by the antenna, reflect the radiations in a specific direction and increase the overall gain of the antenna. In [10], AMC technology is used in multi-band antenna where gain enhancement depends upon the reflection phase angle. In [11], rectangular loop fractal AMC is positioned parallel to the ground plane in a wideband antenna for gain enhancement. In [12], modified circular loop AMC loaded on the CPW antenna

Submitted On: January 28, 2022
Accepted On: July 13, 2022

1054-4887 © ACES

https://doi.org/10.13052/2022.ACES.J.370702

where it is working as a reflector. In [13], the dielectric superstrate is used the gain improvement and the radius of slots in the superstrate altered the effective permittivity. In [14], a metamaterial unit cell in the ground plane placed diagonally enhances the gain of a dual-band antenna. In [15], two hexagonal metamaterial cells are placed behind the antenna having double Negative metamaterial (DNG) property increases the antenna gain. In [16], a single layer FSS with the modification in loop structure is designed for the antenna operating in sub-6 GHz frequency. In [17], an FSS is designed using four asymmetric rectangular conducting elements with circular slots in one unit cell for the UWB antenna. In [18], a dual-layer FSS is designed for ISM band gain enhancement. In [19], two-layer FSS is developed accomplished with an air gap between the arrays for umbrella-shaped antenna where the UWB antenna achieved up to 4 dB gain enhancement with the FSS arrangement. In [20], FSS is accomplished with four interconnected square loop metallic paths demonstrating the stopband characteristics in the entire operating band. In [21], two layers of thin FSS are designed accomplished with cross-shape and circular-shape design in the top and bottom layer.

According to the literature analysis, the SUW antenna and FSS are designed in the proposed work with the following technical contributions and novelties.

(i) The proposed antenna is designed with a simple structure and compact electric length of $0.29\lambda_0 \times 0.35\lambda_0$ where λ_0 is a wavelength of the lowest operating frequency. A very high value of BDR (1773.4) validates the compactness of discussed antenna.
(ii) A parasitic rectangular stub with a circular slot demonstrates stopband characteristics and a novel WLAN notch is achieved due to formation of parallel LC circuit.
(iii) A modified SRR structure is used to design the compact FSS unit cell with the electric dimension of $0.16\lambda_0 \times 0.16\lambda_0$ and the stopband characteristics associated in FSS superstrate are diminished from the antenna notch band.
(iv) FSS superstrate significantly enhances the realized gain up of antenna up to 5.22 dB in the UWB frequency range.

II. ANTENNA DESIGN AND EVOLUTION

The SUW antenna and FSS is designed with FR4 substrate having dielectric constant (ε_r) 4.4 and 1.6 mm substrate thickness. The proposed SUW antenna design is depicted in Figs. 1 (a) and (b), and hardware is illustrated in Fig. 1 (c). The antenna acquires a physical space of 25 (U1) × 30 (U2) mm2. The SUW antenna is ensuring the dimensions details as follows, P1 = 9.5 mm, U3 = 8.5 mm, G1 = 7.1 mm, P2 = 9 mm, G2 = 11 mm, U4 = 3 mm, P3 = 5.5 mm, G3 = 11 mm, U5 = 5.5 mm, G5 = 3 mm, P4 = 5.5 mm, U6 = 5.5 mm, G6 = 2 mm, P5 = 9 mm, G4 = 4 mm, G7 = 4 mm, G8 = 3.1 mm, R = 2.75 mm and U7 = 7.5 mm.

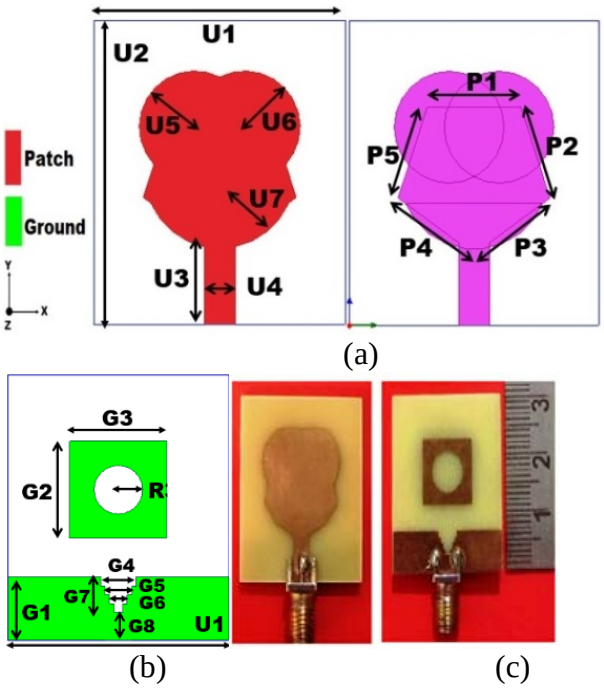

Fig. 1. (a) Dimensions of top plane. (b) Dimensions of bottom plane. (c) Prototype hardware of SUW antenna.

The proposed SUW antenna with parasitic stub is developed in five successive steps as depicted in Fig. 2. In step 1, a rectangular radiating patch is designed using eqn (1) [22] given below.

$$W_P = \frac{c}{2f}\sqrt{\frac{2}{\varepsilon_r+1}}, \quad (1)$$

where W_P is the patch width of the antenna, c represents light velocity and f is the minimum operating frequency. Using above equation the obtained width of patch is 25 mm for 3.5 GHz frequency validating the antenna dimensions.

To obtain and validate 50 Ω impedance matching of proposed work eqn (2) [22] is utilized as given below.

$$Z_0 = \frac{120\pi}{\sqrt{\varepsilon_{re}}\left[\frac{W_p}{h}+1.393+0.667\ln\left(\frac{W_p}{h}+1.444\right)\right]}, \quad (2)$$

where W_P and h is the dimension of proposed antenna and ε_{re} is effective permittivity.

Further the micro-strip feed is designed with a 3 mm width and 7.5 mm length where partial groundconductor height is 7 mm. The feed is also matched with 50 Ω impedance matching. The rectangular-shaped radiator's

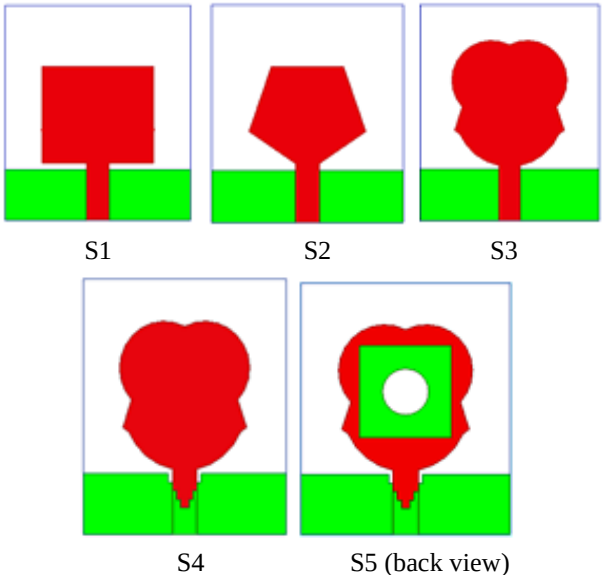

Fig. 2. Development steps of SUW antenna.

$|S_{11}|$ varies from 4.3 GHz to 22.7 GHz. The radiator is modified into a polygon shape in step 2, to enhance the 10 dB IBW and improved impedance matching where $|S_{11}|$ varies from 3.7-23.6 GHz. Three circular stubs are consummated with the polygon-shape radiator in step 3, to convert into a tree-shape structure which increases the electric length and smoothen the current movement in the radiator and 10 dB IBW is obtained from 3.6 - 15.5 GHz and 18.1 - 24.1 GHz. Figure 3 (a) depicts the variations in $|S_{11}|$ of step 1 to step 3. To advance the impedance matching the stair-shaped defects are created in the bottom plane in step 4 to obtain the characteristics of SUW and 10 dB IBW is obtained from 3.5 - 66.5 GHz. In step 5, a parasitic stub with a circular slot is embedded in the ground that acts as a stopband and creates a notch from 5.0 GHz to 5.4 GHz. Figure 3 (b) depicts the variations in $|S_{11}|$ of step 4 & 5 and Fig. 3 (c) shows the final 10 dB IBW of SUW antenna. The presence of a circular defect in the parasitic stubs creates perturbation of current distribution and the electric current flowing on the ground has to face a longer path. This perturbation of the path creates a change in inductance (L). Similarly, the second effect of aperture in the ground plane is due to the gap located below the strip conductor. The thin gap determines an accumulation of charge and consequently can be investigated as series capacitance (C). The combination of these two singularities creates an equivalent parallel LC circuit which results in a notch band from 5.0 GHz to 5.4 GHz frequency which can prevent the WLAN frequencies in UWB applications. Figure 3 (d) is demonstrating the current circulation in the antenna with the parasitic stub.

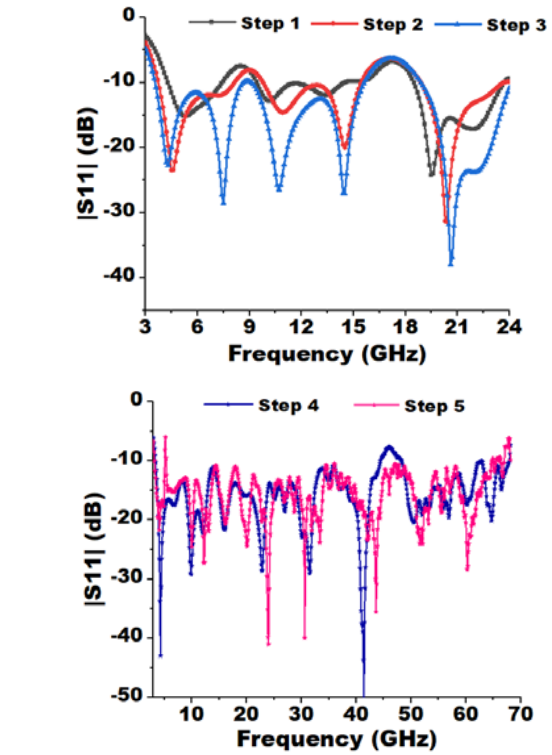

(a) and (b)

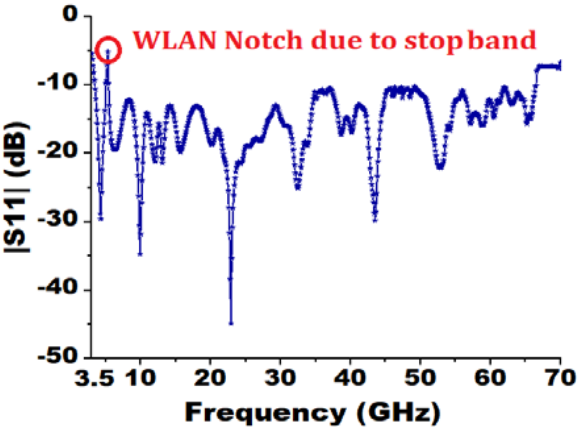

(c)

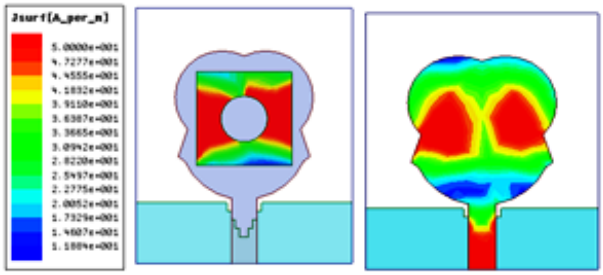

(d)

Fig. 3. (a) and (b) Variation in $|S_{11}|$ for Step 1 to Step 5. (c) Obtained $|S_{11}|$ of proposed SUW antenna with notch. (d) Surface current distribution in the presence of parasitic stub and a circular slot at 5.1 GHz frequency.

Table 1: Comparative study of proposed SUW antenna with the recent works

Ref.	Size $(\lambda_0)^2$	10 dB IBW (GHz)	BW %	BDR
2	0.345 × 0.345	2.59-31.14	169	1419.86
3	0.325 × 0.368	0.65-35.61	193	1613.7
4	0.347 × 0.358	1.68-26	175.72	1414.5
5	0.32 × 0.34	3.8-68	179	3015
6	0.37 × 0.42	1.02-24.1	183	1167
7	0.55 × 0.38	3.0-35.0	168	805
8	0.31 × 0.46	3.15-32	164	1102.9
9	0.33 × 0.416	2.5-110	191	1391
Proposed work	0.29 × 0.35	3.5-66.5	180	1773.4

III. SUW ANTENNA PARAMETERS

SUW antenna should have a BDR of 10:1, and with this BDR antenna can be designed without the restriction of predefined bandwidth. SUW antenna is used in long and short-range of communication, the parameters like BW % and BDR determines the performance of the antenna with realized gain, radiation efficiency and far-field analysis. BDR reflects the compactness as well as measures fractional usable bandwidth in SUW antenna. A higher value of BDR assures the wideband characteristics and the compactness of the antenna. It can be calculated with given eqn (3) [1].

$$\mathrm{BDR} = \frac{\mathrm{BW}\ \%}{\lambda_{\mathrm{L}} \times \lambda_{\mathrm{W}}}, \tag{3}$$

where λ_L represents the electrical length and λ_W represents the electrical width of the antenna and BW% can be estimated with the given eqn (4) [1].

$$\mathrm{BW}\% = \frac{\mathrm{f_H} - \mathrm{f_L}}{\mathrm{f_C}} \times 100, \tag{4}$$

where f_H and f_L are the lower and higher frequency in operating bandwidth and center frequency f_C is calculated by arithmetical mean. The calculated value of BW% and BDR are 180 and 1773.4 respectively.

IV. FSS EVOLUTION AND ANALYSIS

The proposed FSS is designed for UWB frequency application where the FSS superstrate is positioned below the antenna. The gain enhancement in the antenna is obtained maximum when the reflection of EM waves from the FSS superstrate and radiation of the antenna is in the same direction. The FSS unit cell is designed for frequency 3.5 to 10 GHz with a modified SRR structure. The FSS evolution and FSS analysis as discussed below.

A. FSS evolution

To determine the dimensions of the FSS superstrate eqn (5) [16] is used as given below.

$$\mathrm{Pr} < \frac{\lambda p}{(1 + Sin\theta)}, \tag{5}$$

where Pr is the periodicity of the unit cell, wavelength λ_p is obtained from the maximum frequency in the operating band and incident wave angle is θ. At $\theta = 0^\circ$ and for frequency 10 GHz, the obtained λ_p is 30 mm, therefore the dimensions of the unit cell is considered only 14 mm x 14 mm with the electric length of $0.16\lambda_0 \times 0.16\lambda_0$. The FSS unit cell is developed in four stages as depicted in Fig. 4 (a). The FSS unit cell dimensions are as follows, W2 = 4 mm, L4 = 6 mm, W1 = 14 mm, L3 = 7 mm, W4 = 2 mm, L2 = 6 mm, W3 = 10 mm and L1 = 14 mm as illustrated in Fig. 4 (b). The fabricated FSS and the s-parameters of evolution steps of the FSS superstrate are shown in Figs. 4 (c) and (d). A square shape FSS is designed in step(S)-1, to obtain stopband characteristics in UBW frequency. The $|S_{12}|$ is varying from 3 GHz to 10 GHz, demonstrating weak stopband characteristics. In step 2, SRR is introduced with 1 mm uniform width (Fw) in the FSS unit cell to improve the stopband charac-

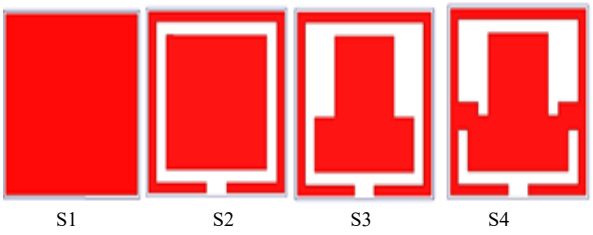

(a)

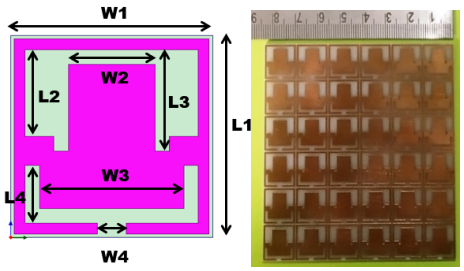

(b) (c)

Fig. 4. *Continued.*

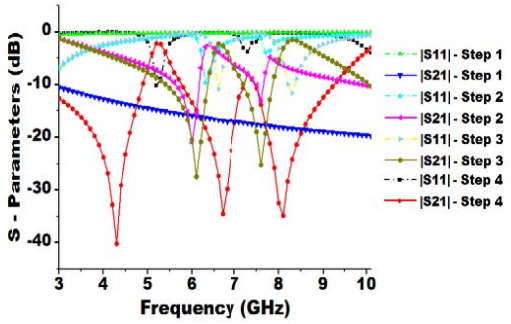

(d)

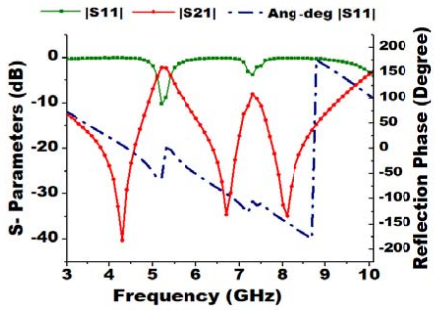

(e)

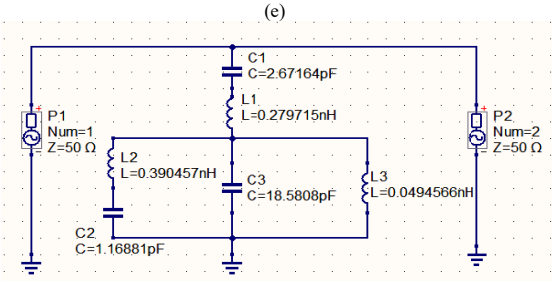

(f)

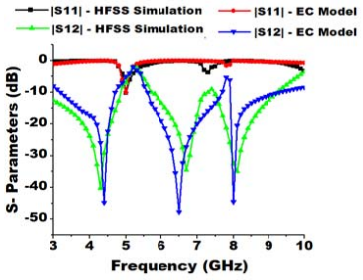

(g)

Fig. 4. (a) FSS evolution steps. (b) FSS unit cell dimensions. (c) Hardware prototype of FSS. (d) S-parameters associated with evolution steps. (e) Extracted EC model of unit cell. (f) FSS s-parameters with variation in reflection phase angle. (g) S-parameters of the proposed unit cell using HFSS simulation and EC model.

teristics where $|S_{12}|$ is varying from 5.6 GHz to 7.2 GHz. In step 3, the structure of SRR is modified and improved $|S_{12}|$ bands are obtained which are varying from 5.6 GHz 7.8 GHz but still, the stopband characteristics are not obtained in the lower operating band. Finally in step-4, the FSS unit cell is further modified which increase the electric length and improves the stopband characteristics but keeping in the mind the notch characteristics of the antenna, the stopband characteristics mitigate from the unit cell. The final $|S_{12}|$ is varying from 3.0 GHz to 10 GHz except notch band where it reveals that stopband characteristics are diminished from the results where the antenna demonstrates the notch band. The phase angle of $|S_{11}|$ varies linearly in entier frequency range and decreases when the frequency is increasing except the notch band as shown in Fig. 4 (e).

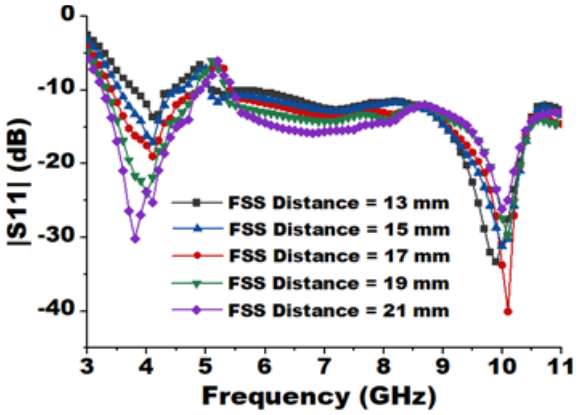

(a)

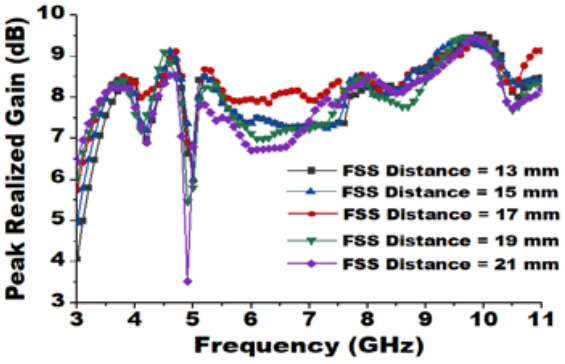

(b)

Fig. 5. (a) $|S_{11}|$. (b) Realized gain at different distance between FSS and proposed antenna.

The equivalent circuit (EC) model of the FSS unit cell is designed using QUCS software with lumped components as depicted in Fig. 4 (f). The lumped elements of the circuit are determined from the eqn (6) and (7) [16] where three capacitive elements C1, C2 and C3 have values of 2.67 pF, 1.16 pF and 18.58 pF along with three inductive elements L1, L2 and L3 with values of 0.276 nH, 0.39 nH and 0.049 nH.

Table 2: Comparative analysis of proposed gain enhancement technology with the other recent works

Ref.	Antenna Size (mm^2)	Technology used	Operating Band (GHz)	Gain Enhancement (dB)
11	64 × 64	AMC	3.36, 5.96, 9.09	3.58
12	70 × 70	AMC	1.9–6.95	3.06
14	38 × 38	Metamaterial	2.4–5.82	3.69
16	35 × 25	Metamaterial	5.6–10.3	3.2
17	30 × 30	Single layer FSS	3.6–6.1	4.0
18	20 × 27	Single layer FSS	4.7–14.9	4.5
19	63.65 × 51.16	Single/dual layer FSS	2.4	4.4
20	35 × 30	Single layer FSS	3.0–13.4	4
21	40 × 30	Dual-layer FSS	8.1–13.2	3.3
Proposed work	25 × 30	Single layer FSS	3.5–11.0	5.2

$$\frac{X_L}{Z_0} = \omega L = \frac{w_1}{L_1}\,\mathrm{Cos}\theta\; F(L_1, 2F_w, \theta, \lambda). \quad (6)$$

$$\frac{B_C}{Y_0} = \omega C = 4\varepsilon_r \frac{w_1}{L_1}\,\mathrm{Sec}\theta\; F(L_1, h, \theta, \lambda), \quad (7)$$

where w_1, L_1, the FSS width, length, h is the and θ is the incidence angle. The extracted s-parameters from EC model are compared with the simulated values using HFSS-13 simulator as depicted in Fig. 3 (g) where both are having similar variations. The advance simulation techniques as a prospective are used to extract the solution for nonconformal meshes of EM wave [24], To solve anisotropic Maxwell's equations [25] and Phase Synthesis of Beam-Scanning in Deep Learning Technique [26].

B. FSS analysis

The separation of FSS superstrate from the antenna is the vital parameter for gain enhancement and it can be calculated with eqn (8) [16] as given below.

$$\varphi_{FSS} - 2KF_d = 2N\pi. \quad (8)$$

In the equation, F_d is the distance of the antenna from FSS and K is constant which is equal to $2\pi/\lambda$. The value of N can be chosen for any integer value and λ is the wavelength at which the reflection phase is zero. The reflection phase is 0° at 4.4 GHz frequency as depicted in Fig. 4 (e) and at this frequency, the value of $\lambda/4$ is 17.02 mm. Keeping this in mind that the position of FSS is varied from 13 mm to 21mm and the variation in

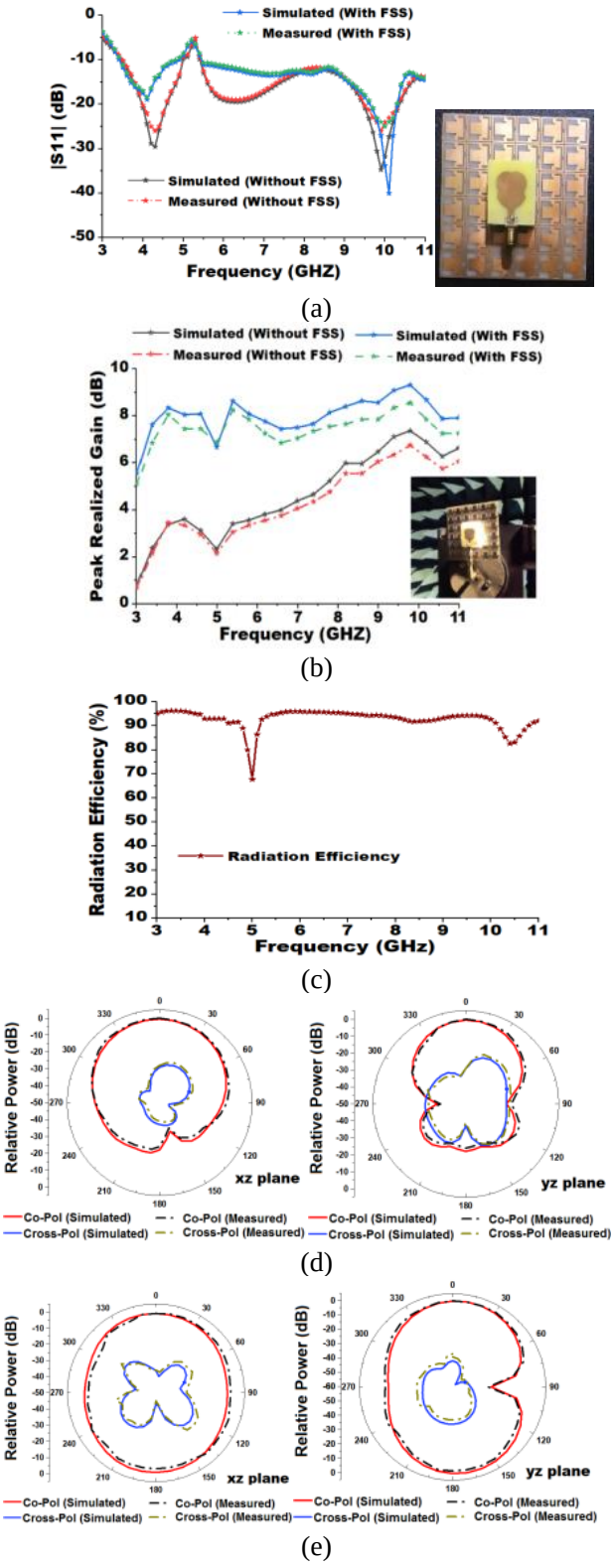

Fig. 6. (a) Measured $|S_{11}|$ with simulated values. (b) Measured peak gain. (c) Radiation efficiency. (d) and (e) Radiation patterns at frequency 4.1 GHz and 7.50 GHz in x-z and y-z coordinates with FSS superstrate.

|S11| and peak gain are observed. The |S11| of antenna is having minor variations after the notch band irrespective of the FSS superstrate position but the lower operating bandwidth reduces when FSS distance behind the antenna decreases as depicted in Fig. 5 (a). The peak gain with the FSS superstrate at different placement is illustrated in Fig. 5 (b) where at the 17 mm distance, the minimum variations are observed and maximum gain enhancement is achieved 5.2 dB. Therefore 17 mm optimum distance is finalized between FSS superstrate and antenna where the 10 dB IBW is varying from 3.5 GHz to 11 GHz and the peak gain is having a maximum value of 9.46 dB.

V. RESULT AND DISCUSSION

HFSS-13 software is used to simulate the proposed antenna and FSS design whereas experimental results of $|S_{11}|$ are obtained by Anritsu-MS2038C VNA and the far-field analysis is done in the anechoic chamber. The simulated $|S_{11}|$ of the antenna is varying from 3.5 GHz to 66.5 GHz with a WLAN notch band from 5 GHz to 5.4 GHz. As per VNA availability the $|S_{11}|$ measurement is carried out up to 11 GHz with and without FSS and the measured results have similarities with the simulated values as shown in Fig. 6 (a). The measured gain of the discussed antenna is shown in Fig. 6 (b) where the measured gain is having minor deviations which are less than 0.5 dB in the presence of FSS also. The gain enhancement is achieved up to 5.2 dB using a single layer FSS. The simulation radiation efficiency is found more than 85 % except for the notch band as illustrated in Fig. 6 (c). The measured and simulated radiation pattern with FSS are illustrated in Figures 5 (e) and 6 (d), at two centre frequencies in the x-z and y-z coordinate system which are demonstrating the omnidirectional radiation pattern. The comparative analysis with related work of SUW antenna is given in Table 1, which authorizes that the presented tree-shaped antenna is compact having an electrical length of $0.29\lambda_0 \times 0.35\lambda_0$. The BW % of the SUW antenna is 180 with a high value of BDR which is 1773.4. The gain enhancement with a single layer and single-sided FSS superstrate is compared with gain improvement existing technology in Table 2; it reveals that the proposed FSS enhances the gain effectively in the entire operating band up to 5.2 dB.

VI. CONCLUSION

The tree-shaped SUW antenna is designed with a novel parasitic stub in the ground demonstrating notch characteristics. The tree-shaped radiator is improving the operating bandwidth whereas defected ground enhances the impedance matching in the antenna. The parasitic stub with a circular slot in the bottom plane creates a WLAN notch in the antenna. The high value of BDR confirms the compactness of the proposed SUW antenna. The modified SRR based single-layer FSS superstrate is placed below the antenna which reflects the grating lobes and enhances the antenna gain up to 5.2 dB.

REFERENCES

[1] W. Balani, M. Sarvagya, T. Ali, M. M., Manohara Pai, J. Anguera, A. Andujar, and S. Das, "Design techniques of super-wideband antenna–existing and future prospective," *IEEE Access*, vol. 7, 2019.

[2] T. Okan, "A compact octagonal ring monopole antenna for super wideband applications," *Microw. Opt. Technol. Lett.*, vol. 62, no. 3, pp. 1237-1244, 2020.

[3] S. Singhal and A. K. Singh, "Elliptical monopole based super wideband fractal antenna," *Microw. Opt. Technol. Lett.*, vol. 62, no. 3, pp. 1324-1328, 2020.

[4] C. Á. Figueroa Torres, J. L. Medina Monroy, H. Lobato Morales, R. A. Chávez Pérez, and A. Calvillo Téllez, "A novel fractal antenna based on the Sierpinski structure for super wide band applications," *Microw. Opt. Technol. Lett.*, vol. 59, no. 5, pp. 1148-1153, 2017.

[5] S. Singhal and A. K. Singh, "CPW-fed hexagonal Sierpinski super wideband fractal antenna," *IET Microw. Antennas Propag.*, vol. 10, no. 15, pp. 1701-1707, 2016.

[6] J. Liu, S. Zhong, and K. P. Esselle, "A printed elliptical monopole antenna with modified feeding structure for bandwidth enhancement," *IEEE Trans. Antennas Propag.*, vol. 59, no. 2, pp. 667-670, 2010.

[7] A. Gorai, A. Karmakar, M. Pal, and R. Ghatak, "A CPW-fed propeller shaped monopole antenna with super wideband characteristics," *Progress Electromagn. Res. C*, vol. 45, pp. 125-135, 2013.

[8] S. Hakimi, S. K. A. Rahim, M. Abedian, S. M. Noghabaei, and M. Khalily, "CPW-fed transparent antenna for extended ultrawideband applications," *IEEE Antennas Wireless Propag. Lett.*, vol. 13, pp. 1251-1254, 2014.

[9] A. Seyfollahi and J. Bornemann, "Printed-circuit monopole antenna for super-wideband applications," pp. 654-655, 2018.

[10] A. Ghosh, "Gain enhancement of triple-band patch antenna by using triple-band artificial magnetic conductor," *IET Microwaves, Antennas Propag.*, vol. 12, no. 8, Art. no. 1400, 2018.

[11] B. Zhang, P. Yao, and J. Duan. "Gain-enhanced antenna backed with the fractal artificial magnetic conductor," *IET Microw. Antennas Propag.*, vol. 12, no. 9, Art. no. 1457, 2018.

[12] K. N. Paracha, "A dual band stub-loaded AMC design for the gain enhancement of a planar monopole antenna," *Microw. Opt. Technol. Lett.*, vol. 60, no. 9, 2018.

[13] J. H. Kim, C.-H. Ahn, and J.-K. Bang, "Antenna gain enhancement using a holey superstrate," *IEEE Trans. Antennas Propag.*, vol. 64, no. 3, Art. no. 1164, 2016.

[14] S. Roy and U. Chakraborty, "Gain enhancement of a dual-band WLAN microstrip antenna loaded with diagonal pattern metamaterials," *IET Commun*., vol. 12, no. 12, Art. no. 1448, 2018.

[15] N. Rajak, N. Chattoraj, and R. Mark, "Metamaterial cell inspired high gain multiband antenna for wireless applications," *AEU-Int. J. Electron. Commun*., vol. 109, pp. 23, 2019.

[16] A. Kumar, A. De, and R. K. Jain, "Gain enhancement using modified circular loop FSS loaded with slot antenna for sub-6 GHz 5G application," *Progress Electromagn. Res. Lett*., vol. 98, pp. 41-48, 2021.

[17] P. Das and K. Mandal, "Modelling of ultra-wide stop-band frequency-selective surface to enhance the gain of a UWB antenna," *IET Microw. Antennas Propag.*, vol. 13, no. 3, pp. 269-277, 2019.

[18] M. A. Belen, "Performance enhancement of a microstrip patch antenna using dual-layer frequency-selective surface for ISM band applications," *Microw. Opt. Technol. Lett*., vol. 60, no. 11, pp. 2730-2734, 2018.

[19] S. Kundu, A. Chatterjee, S. K. Jana, and S. K. Parui, "A compact umbrella-shaped UWB antenna with gain augmentation using frequency selective surface," *Radio Eng*., vol. 27, no. 2, pp. 448-454, 2018.

[20] G. S. Paul, K. Mandal, and A. Lalbakhsh, "Single-layer ultra-wide stop-band frequency selective surface using interconnected square rings," *AEU-Int. J. Electron. Commun.*, vol. 132, 2021.

[21] A. Bhattacharya, B. Dasgupta, and R. Jyoti, "Design and analysis of ultrathin X-band frequency selective surface structure for gain enhancement of hybrid antenna," *Int. J. RF Microw. Comput.-Aided Eng.*, 2020.

[22] A. F. Alsager, *Design and Analysis of Microstrip Patch Antenna Arrays*, 2011.

[23] Q. Y. F. Zhan, M. Zhuang, M. Yuan, and Q. H. Liu, "Stabilized DG-PSTD method with nonconformal meshes for electromagnetic waves," *IEEE Trans. Antennas Propag*., vol. 68, no. 6, pp. 4714-4726, 2020.

[24] Q. Zhan, Y. Wang, Y. Fang, Q. Ren, S. Yang, W.-Y. Yin, and Q. H. Liu, "An adaptive high-order transient algorithm to solve large-scale anisotropic Maxwell's equations," *IEEE Trans. Antennas Propag.*, vol. 70, no. 3, pp. 2082-2092, 2022.

[25] T. Shan, M. Li, S. Xu, and F. Yang, "Phase synthesis of beam-scanning reflectarray antenna based on deep learning technique," *Progress Electromagn. Res.*, vol. 172, pp. 41-49, 2021.

Pankaj Jha received B. Tech and M. Tech degree from Uttar Pradesh Technical University (Now AKTU), Lucknow, UP, India, He is currently pursuing Ph.D from Shobhit Institute of Engineering and Technology, (Deemed to be University) Meerut, UP, India. His research area includes micro strip antenna, Metamaterial inspired antenna, MIMO, FSS and wearable antenna.

Anubhav Kumar received B. Tech and M.Tech from Uttar Pradesh Technical University (Now AKTU), Lucknow, UP, India. He is currently pursuing Ph.D from Shobhit Institute of Engineering and Technology, (Deemed to be University) Meerut, UP, India. He has published many SCIE/ESCI and Scopus indexed research papers. His research interests include microstrip antenna, metamaterial, FSS, MIMO, Wearable antenna, EBG and Image processing.

Asok De did his Ph.D from Indian Institute of Technology, Kharagpur. He served as faculty at University of Delhi, University of Kolkata from 1984 to 1997. He was the founder Principal of Ambedkar Institute of Advanced Communication Technology and Research (2005-2012). He served National Institute of Technology Patna and Durgapur as a Director from 2012 to 2017. Professor De has published more than 200 research papers in International Journals and International conferences. He supervised 16 Ph.D scholars till now.

Journal of Molecular Modeling (2023) 29:55
https://doi.org/10.1007/s00894-023-05454-2

ORIGINAL PAPER

Targeting Y220C mutated p53 by *Foeniculum vulgare*-derived phytochemicals as cancer therapeutics

Saksham Garg[1] · Japneet Singh[1] · Smita Rastogi Verma[1]

Received: 2 June 2022 / Accepted: 16 January 2023
© The Author(s), under exclusive licence to Springer-Verlag GmbH Germany, part of Springer Nature 2023

Abstract

Context The mutations in the *TP53* gene are the most frequent (50–60% of human cancer) genetic alterations in cancer cells, indicating the critical role of wild-type p53 in the regulation of cell proliferation and apoptosis upon oncogenic stress. Most missense mutations are clustered in the DNA-binding core domain, disrupting DNA binding ability. However, some mutations like Y220C occur outside the DNA binding domain and are associated with p53 structure destabilization. Overall, the results of these mutations are single amino acid substitutions in p53 and the production of dysfunctional p53 protein in large amounts, consequently allowing the escape of apoptosis and rapid progression of tumor growth. Thus, therapeutic targeting of mutant p53 in tumors to restore its wild-type tumor suppression activity has immense potential for translational cancer research. Various molecules have been discovered with modern scientific techniques to reactivate mutant p53 by reverting structural changes and/or DNA binding ability. These compounds include small molecules, various peptides, and phytochemicals. TP53 protein is long thought of as a potential target; however, its translation for therapeutic purposes is still in its infancy. The study comprehensively analyzed the therapeutic potential of small phytochemicals from *Foeniculum vulgare* (Fennel) with drug-likeness and capability to reactivate mutant p53 (Y220C) through molecular docking simulation. The docking study and the stable molecular dynamic simulations revealed juglalin (− 8.6 kcal/mol), retinol (− 9.14 kcal/mol), and 3-nitrofluoranthene (− 8.43 kcal/mol) significantly bind to the mutated site suggesting the possibility of drug designing against the Y220C mutp53. The study supports these compounds for further animal based in vivo and in vitro research to validate their efficacy.

Methods For the purposes of drug repurposing, recently in-silico methods have presented with opportunity to rule out many compounds which have less probability to act as a drug based on their structural moiety and interaction with the target macromolecule. The study here utilizes molecular docking via Autodock 4.2.6 and molecular dynamics using Schrodinger 2021 to find potential therapeutic options which are capable to reactive the mutated TP53 protein.

Keywords *Foeniculum vulgare* · Juglalin · mutp53 · 3-Nitrofluoranthene · Retinol · Y220C mutated p53

Introduction

Tumor protein p53, commonly known as the guardian of the genome, is one of the most crucial protectors of the human genome [1]. It is activated after various stress factors, including oxidative stress, DNA damage, and oncogenic signaling. Activated p53 acts as a sequence-specific transcription factor that stimulates the expression of proteins implicated in DNA repair, cell cycle arrest, apoptosis, and senescence to protect cells from genomic instability, replicative stress, and consequently carcinogenesis.

Mutations in the p53-encoding *TP53* gene or any other gene of the pathway that results in the inactivation of wild-type p53 are crucially associated with cancer development. This exemplifies the formation of mutated p53 protein (mutp53) with either loss of tumor suppressor function of the wild-type p53 or gain of new oncogenic functions. With the advancement of massively parallel sequencing of tumor genomes, different ways of altering *TP53* locus in tumors have become evident [2]. The resultant *TP53* mutant translates into functional effects such as loss of control of p53 on the regulation of cell cycle proliferation or apoptosis upon oncogenic stress, consequently promoting more aggressive tumorigenesis.

✉ Smita Rastogi Verma
smitar@dtu.ac.in

[1] Department of Biotechnology, Delhi Technological University, Delhi 110042, India

Published online: 26 January 2023

The most prevalent mutations in *TP53* in various cancers are missense mutations, although truncations, deletions, and frameshift mutations also occur [3]. These mutations are distributed in all exons with a prominent preference for the DNA-binding domain (DBD), affecting p53's DNA binding ability [4]. Missense mutations result in single amino acid substitutions and six hotspots in DBD are R175, G245, R248, R249, R273, and R282 [5]. Such mutations in *TP53* result in the mutp53 with local or global conformational changes in its structure, distorted core domain folding, disrupted DNA binding, transcriptional transactivation of p53 target genes, and aberrant modulation of various signaling pathways [6, 7]. R273H, R248Q, and R248W are contact mutants derived from missense mutations in amino acid residues responsible for direct contact with the DNA sequences. On the other hand, R175H, G245S, R249S, and R282H are conformational residues involved in structure maintenance [4]. Nevertheless, this bipartite mutation classification is somewhat arbitrary. Outside the DBD of p53, Y220C (Tp53C) is the most common cancerous mutation. It does not affect DNA binding ability but instead leads to p53 structure destabilization involving the creation of a surface cavity. Due to the Y220C mutation, electrostatic interactions of Tyr 220 with Val 147, Pro 151, Pro 153, and Pro 223 located in S3/S4 and S7/S8 loops are lost, resulting in structural fluctuation and displacement of the S7/S8 loop from its original position [8]. These amino acid residues are mutational hotspots lying within the β-sheet of p53. This Y220C missense mutation cause mutp53 structure destabilization, denaturation at room temperature, local loss of hydrophobicity, and water network, and hence, functionally inactive conformation are responsible for approximately 100,000 cancer cases [9].

In comparison to the wild type, mutant p53 exhibits a longer half-life; thus, it accumulates in the nucleus, interacting with oncogenes to promote carcinogenesis. The altered functions of mutp53 as compared to wild-type p53 owe to the interactions of conformationally altered mutp53 with many transcription factors, such as NF-Y, E2Fs, NRF2, YAP, VDR, SREBP, p63, p73, Sp1, ETS1/2, NF-κB, ATM, and SMADs as well as specific mutp53 protein–protein interactions [10]. These changes alter transcription, leading to enhanced cell proliferation, cholesterol synthesis, and cell survival, inhibited DNA repair machinery and autophagy, and accumulated reactive oxygen species. There is a result of genetic instability and new oncogenic properties such as uncontrolled cellular proliferation, enhanced migration, tissue invasion, metastasis, and chemo-/radio-resistance to specific therapies and others [11]. Cancerous cells become tolerable to challenging conditions originating during tumorigeneses, such as DNA damage related to profuse proliferation, proteotoxic and oxidative stress, stromal cues, physical constraints, nutrient fluctuations, hypoxic conditions, and the anti-tumor immune response [12]. All these present formidable challenges in developing cancer therapeutics, and specific TP53 mutations in human cancers are associated with poor prognosis.

As revealed by structural studies, unfolding the mutp53 core domain is not irreversible. Several studies on mouse models have demonstrated that the wild-type p53 tumor suppression functions can be restored upon genetic reconstitution, thereby preventing tumor growth. This strongly suggests the possibility of treating human cancers by restoring wild-type p53 activity or inhibiting mutp53 oncogenic activity [10]. An opportunity to selectively target mutp53 harboring cancer cells is attributable to the structural differences between the wild-type p53 and mutp53 [13, 14]. Thus, new therapeutic strategies involving small molecules, peptides, and phytochemicals that revert the structural changes and subvert the oncogenic activities of mutp53 into wild-type p53 tumor suppressor functions have been devised to treat human cancers [15, 16]. Promising results have been obtained with small compounds and peptides targeting mutp53, for example, PK083, PK5174, NSC319726, PRIMA-1, APR-246, CP-31398, SCH529074, PK7088, C-terminal peptide of p53, and peptide CDB3 [9]. Furthermore, targeting mutp53, high selectivity to cancer cells in contrast to normal cells is provided, as the latter lack mutp53. Furthermore, small molecules and peptides may be designed to selectively target a particular type of mutp53 in specificity and efficacy. The application of phytochemicals for the synthesis of various therapeutic agents in order to target mutp53 is gaining impetus for natural medicine nowadays [9, 17]. These include coumarins, isoflavones, monoterpenes, and terpenoids. *Foeniculum vulgare* has been evaluated for its various medicinal activities, including anti-inflammatory, anti-anxiety, antioxidant, hepato-protection, and anti-diabetic [18]. A few studies have also evaluated anticancer properties. Ethanol extract of the plant showed apoptotic potential on leukemic cells [19]. Other studies found the methanol extract of fennel to be effective against breast cancer cells and liver cancer. The study aimed to identify a natural and possibly safer chemotherapeutic agent to target mutp53 protein [20]. Keeping in mind the vital role of protein–ligand interactions in drug design, the therapeutic potential of several small natural phytocompounds from *Foeniculum vulgare* (Fennel) to target Y220Cp53 through molecular docking simulation was investigated after confirming their drug-likeness.

Material and methods

The methodology involved the following steps: (i) selection and retrieval of protein and ligands (i.e., small phytochemicals from *F. vulgare*, (ii) comparison of structures of

wild-type p53 and mutp53, (iii) determination of drug-likeness of phytochemicals, and (iv) molecular docking analysis of phytochemicals with Y220Cmutp53 and molecular dynamics of the filtered docked complex.

Macromolecule/protein

The monomeric 3-dimensional structure of Y220Cmutp53 protein (PDB Id: 5O1C) was obtained from the RCSB PDB database and was used as a macromolecule. The protein structure was based on X-ray crystallography with a resolution of 1.32 Å. It was in a complex with compound MB184 (native ligand), bound at the mutated site Y220C.

Ligands

Indian Medicinal Plants, Phytochemistry, and Therapeutics (IMPPAT) repository [21] was used to identify the phytochemicals present in *Foeniculum vulgare* (Fennel). A total of 65 phytochemicals were identified. The 3D structures of the compounds were retrieved from the PubChem database [22] in SDF. They were later converted into.pdb using Biovia Discovery Studio for molecular docking analysis.

Drug-likeness analysis

All 65 compounds were subjected to Lipinski's rule of five [23] to rule out the less potential druggable candidates. Lipinski's four parameters were employed: molecular weight should be less than 500 Da, lipophilicity, i.e., LogP should be less than 5, number of hydrogen bond acceptors should be less than 10, and hydrogen bond donors no more than 5. To measure these parameters, the SMILES of the individual ligand were fed into the SwissADME webserver [24].

Molecular docking

Molecular docking simulation was done with Autodock 4.2.6 interface [25], and 57 phytocompounds from fennel with drug-likeness were docked with Y220Cmutp53, and their binding affinities were evaluated. The residues interacting with the native ligand were considered active site residues, including Thr150, Pro153, Cys220, Pro151, Pro152, Pro222, Thr230, Glu221, Leu145, Pro223, and Val147. Protein was prepared by removing water molecules, adding polar hydrogen, incorporating charges, and removing native ligands (from the protein). Gasteiger charges were computed for ligands, polar hydrogens were added, and rotatable bonds were detected and allowed to show torsion. A grid of dimensions 40*42*51 with a spacing of 0.375 Å was defined at the center of the native ligand coordinates to accommodate all the residues interacting with it. The genetic algorithm was used for the docking process, and output was obtained in Lamarckian GA. Ten conformations were obtained, out of which the one with the least binding energy was built and saved as a protein databank file to analyze in Biovia Discovery Studio.

Molecular dynamics

The potential hits obtained from molecular docking were analyzed using all-atom molecular dynamic simulation for 100 ns utilizing the Desmond Module's [26] novel parallel algorithm of Schrodinger 2021. Before dynamics, the protein–ligand complexed were prepared and optimized: the maestro module, as per default, uses the most efficient and accurate result-producing algorithms. A solvent system was built around the complexes in the TIP3P water model and under the influence of the OPLS-AA 2005 force field. The solvent was also provided with either sodium or chlorine ions at 0.15 M to neutralize the overall model. The SHAKE/RATTLE algorithm limited the movement of the covalent bonds, and NPT ensemble class relaxed the whole system. A dynamic simulation after relaxing the system was done at 300 K and 1 bar pressure. The thermostat method was set on the Nose–Hoover chain with a relaxation time of 1 ps and Martyna – Tuckerman – Tobias – Klein (MTTK) barostat method was employed with 2 ps relaxation time to maintain temperature and pressure. The parameters are given as input as compiled by the RESPA integrator to produce the results. The 100 ns simulation was divided into 1000 frame trajectory as the output of the simulation, and the plots were derivatives of the trajectory file.

Results and discussion

Drug-likeness analysis

The molecular properties of 65 phytocompounds from *F. vulgare* (Fennel) were evaluated to fit into the Lipinski rule of five. This rule is a crucial way to satisfy the rational drug design and determine the bioactivity score for drugs meant for oral consumption. This preliminary analysis eliminated the weaker drug candidates. This filtration process did not necessarily guarantee a ligand to be a potential drug molecule, rather just signified their drug-likeness. 57 out of 65 phytocompounds did not show the violation of Lipinski's rule of 5, i.e., molecular weight < 500 Da, Log*P* (lipophilicity) < 5, number of hydrogen bond acceptors < 10, and number of hydrogen bond donors < 5. The results of ADME analysis of 65 compounds from *F. vulgare* are presented in Table 1.

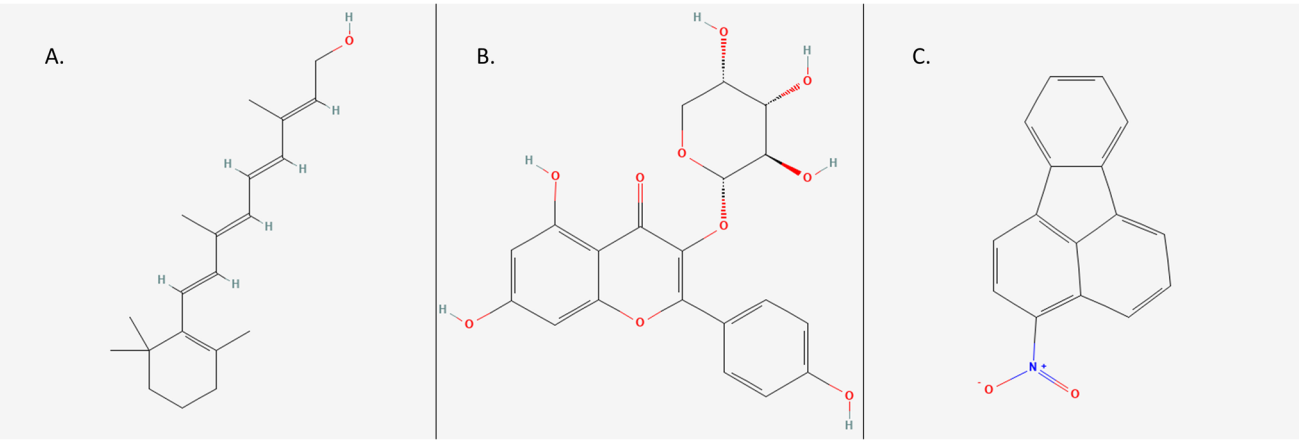

Fig. 1 Structures of ligands. **A** Retinol. **B** Juglalin. **C** 3-Nitrofluoranthene

Molecular docking

Structurally, p53 protein is a homotetramer that has an affinity to bind to DNA sequences and form a stable folded structure. Y220C mutation disrupts the protein folding, thus causing a loss of function of the protein and destabilizing its structure. Although cysteine accommodates exact space as tyrosine residue, the mutation leads to the loss of the hydrophobic group offered by tyrosine. This affects the packing of the binding site residues and forms a solvent-accessible opening, causing an influx of the surrounding water. The mutation exposes the buried residues like Leu 145 to solvent molecules. These contribute to its volatile nature. However, the binding of the small molecule can reactivate the protein and hence its tumor suppressor function. Hence, molecular docking analysis of phytocompounds from *F. vulgare* with Y220Cmutp53 was performed. Out of 4 parameters, violation of more than one parameter in ADME analysis led to the omission of that particular phytocompound from further molecular docking study. Following the same, 8 compounds were eliminated from the molecular docking studies. The top seven phytocompounds from *F. vulgare* that exhibited high binding affinities towards Y220Cmutp53 were retinol, juglalin, 3-nitrofluoranthene, AC1N75QA, O-geranyl vanillin, CID 20055979 and CID 20055976. The results of molecular docking studies are tabulated in Table 2. All these 7 phytocompounds also exhibited good drug-likeness, as shown in Table 1. The structures of the top three phytocompounds listed in Table 2 exhibiting high binding affinities towards Y220Cmutp53 (i.e., ligands) are presented in Fig. 1.

Out of these 7 phytocompounds, the retinol-mutp53 complex showed the best docking conformation with the minimum binding energy of − 9.14 kcal/mol. The interactions of mutp53 protein with retinol are shown in Fig. 2. Cumulative 19 residues contributed to the minimum binding energy. Pro 219 and Asn 200 showed strong hydrogen bond formation with the terminal hydroxyl group, probably anchoring the ligand in the binding site. The mutated residue and Cys 220 formed 3 alkyl bonds with different groups of retinol. Other residues like Val 157, Ile 232, Cys 229, Pro 222, Pro 151, Val 147, Phe 109, Leu 257, Leu 154, and Val 218 formed numerous pi-alkyl and alkyl bonds which stabilized the docked complex.

The second best-docked phytocompound was juglalin. Figure 3 represents the 2D diagram of bond formations between the mutp53 protein mutated site and juglalin. Out of 10 conformations obtained, the best conformation showed the least binding energy of − 8.6 kcal/mol. Due to numerous functional groups and ring structures, the compound interacted with the surrounding protein residues in various fashions. Val 147 and Leu 145 showed a conventional hydrogen bond with a hydroxyl group and pi-alkyl interaction with the ring. Glu 221 formed two amide-pi stacking interactions. Pro 151, Leu 257, and Pro 220 also showed numerous pi-alkyl bonds. The residue of interest Cys 220 formed two types of bonds, pi-donor hydrogen bond, and pi-sulfur interaction, thus actively participating in the protein–ligand complex formation. Unfavorable donor–donor interaction was formed by THR230 as well.

The best-docked conformation had the minimum binding energy of − 8.43 kcal/mol of the 5O1C-3-nitrofluoranthene complex (Fig. 4). The ligand interacted and formed multiple types of bonds. Mutation spot residue, Cys 220 interacted with pi-sulfur bond with two 6-member rings while Glu 221 stacked itself, forming two amide-pi interactions with both 5 and 6-membered aromatic rings. Val 147 acted as the anchor, forming a hydrogen bond with the nitro group and 2 pi-sigma bonds along with Thr 230. Pro 222, Pro 151, and Pro 223 all had multiple pi-alkyl bonds. Trp 146 showed a carbon-hydrogen bond with the nitro group, and Leu 145 unfavorably interacted with nitro group electrons.

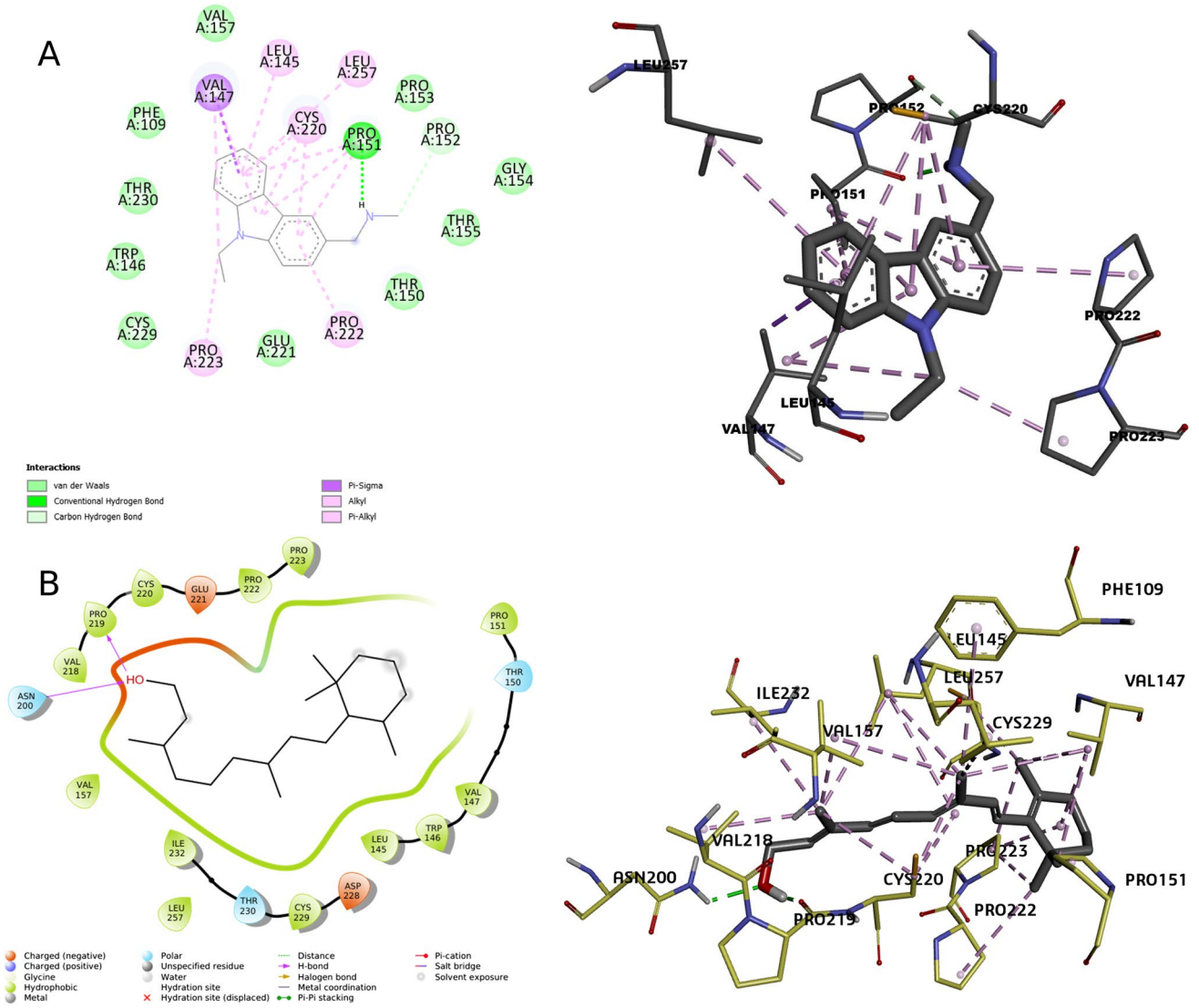

Fig. 2 Interactions between Y220C mutated p53 protein and (**A**) PhiKan083 (PK083) and (**B**) retinol

To summarize, certain residues, including Leu145, Val147, Pro223, Pro222, Pro151, and Cys220, interacted with the ligand in all three proposed complexes. They were also the key residues to interact with PK083. Although, their nature of bonding in all three best-docked complexes and PK083 might differ. Pro151 formed H-bond with PK083 while with other ligands was involved in hydrophobic interactions. Cys220 was engaged by all the ligands in a similar fashion as it interacted with PK083. Val147 altered the interaction type to H-bond with Juglalin and 3-nitrofluoranthene making it a key stabilizing residue for the complex formation. Pro222 and Pro223 along with Leu145 provided hydrophobic pocket to all the ligands and PK083. Overall, the novel ligands studied bound increased number of residues. The binding energies of the three compounds were significantly low [retinol (−9.14 kcal/mol), juglalin (−8.6 kcal/mol), and 3-nitrofluoranthene (−8.43 kcal/mol)] and hence higher binding affinity to the Y220Cmutp53 protein. Structural docking simulation of PK083, a known drug molecule specifically for the Y220Cmutp53 reactivation, predicted lower binding affinity with Y220Cmutp53 with a binding energy of −7.93 kcal/mol (Table 2).

Molecular dynamics

All-atom simulation analysis was carried out post molecular docking studies. The three best hit complexes were subjected to 100 ns dynamic simulation. The trajectory analysis revealed total energy as −72,828.791 kcal/mol, −78,823.521 kcal/mol, and −72,838.982 kcal/mol for 5O1C-retinol complex, 5O1C-3-nitrofluoranthene, and 5O1C-juglalin complexes, respectively. The structural

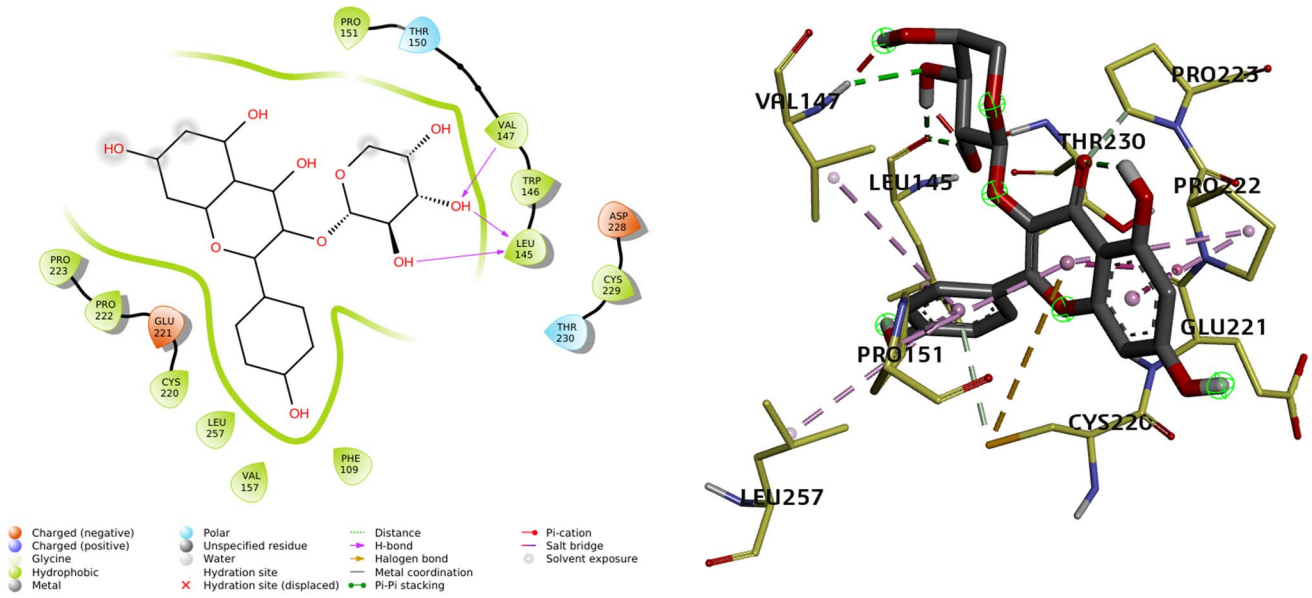

Fig. 3 Interactions between Y220C mutated p53 protein and juglalin

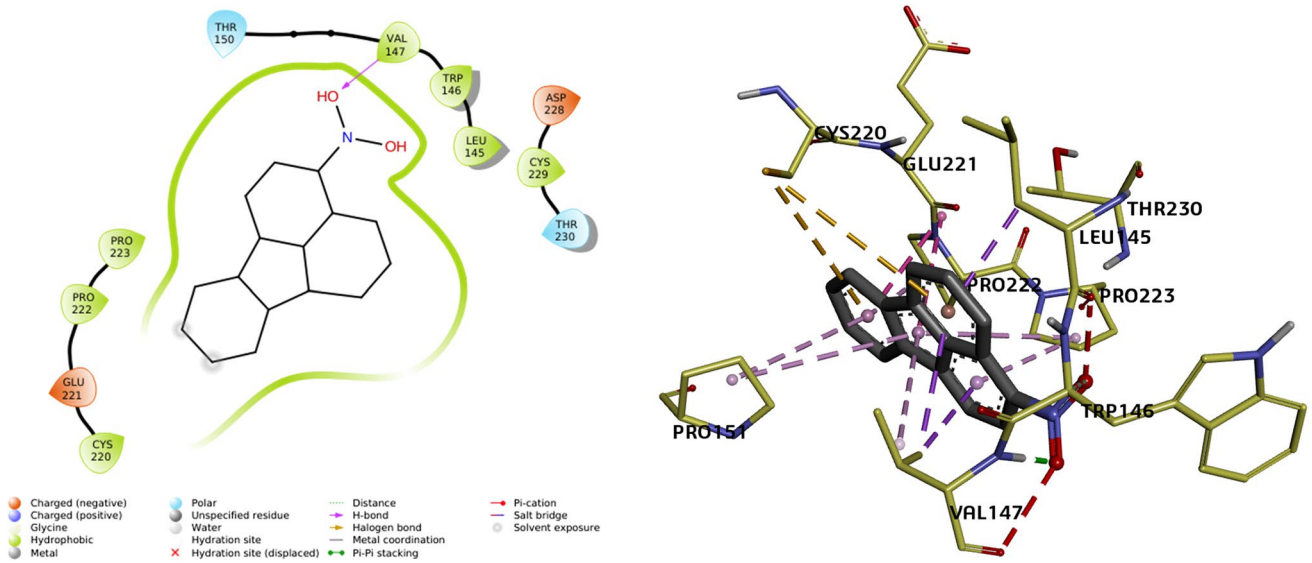

Fig. 4 Interactions between Y220C mutated p53 protein and 3-nitrofluoranthene

analysis at different time stamps further deepened the molecular dynamics study. Y220C mutation in p53 protein exposes a broader and deeper cavity near the mutation site. During simulation, due to binding with retinol (Fig. 5A, a–c), the cavity can be observed to obtain its wild-type conformation. The interaction timeline plot reveals the changing state of protein residues interacting with the ligands. Glu 198 and His 233 acted as the anchor for the binding of retinol, while other residues like Leu 145, Asn 200, Pro 151, Val 157, and Ile 232 are in the supporting the binding intermittently throughout the 100 ns simulation (Fig. 5B). The binding pattern of juglalin was entirely different from retinol. Due to the presence of multiple hydroxyl groups, the potency of bond formation increases; however, the steric hindrance affects the penetration of the ligand into the cavity. Val 147, Thr 230, and Asp 228 maintain contact with Juglalin throughout the 100 ns (Fig. 5C). Pro 151, Leu 145, and Cys 220 majorly impacted the binding during the initial half of the simulation, while residues such as Ser 227, Pro 223, and Glu 224 upheld their contacts during the latter 50 ns simulation. Compared

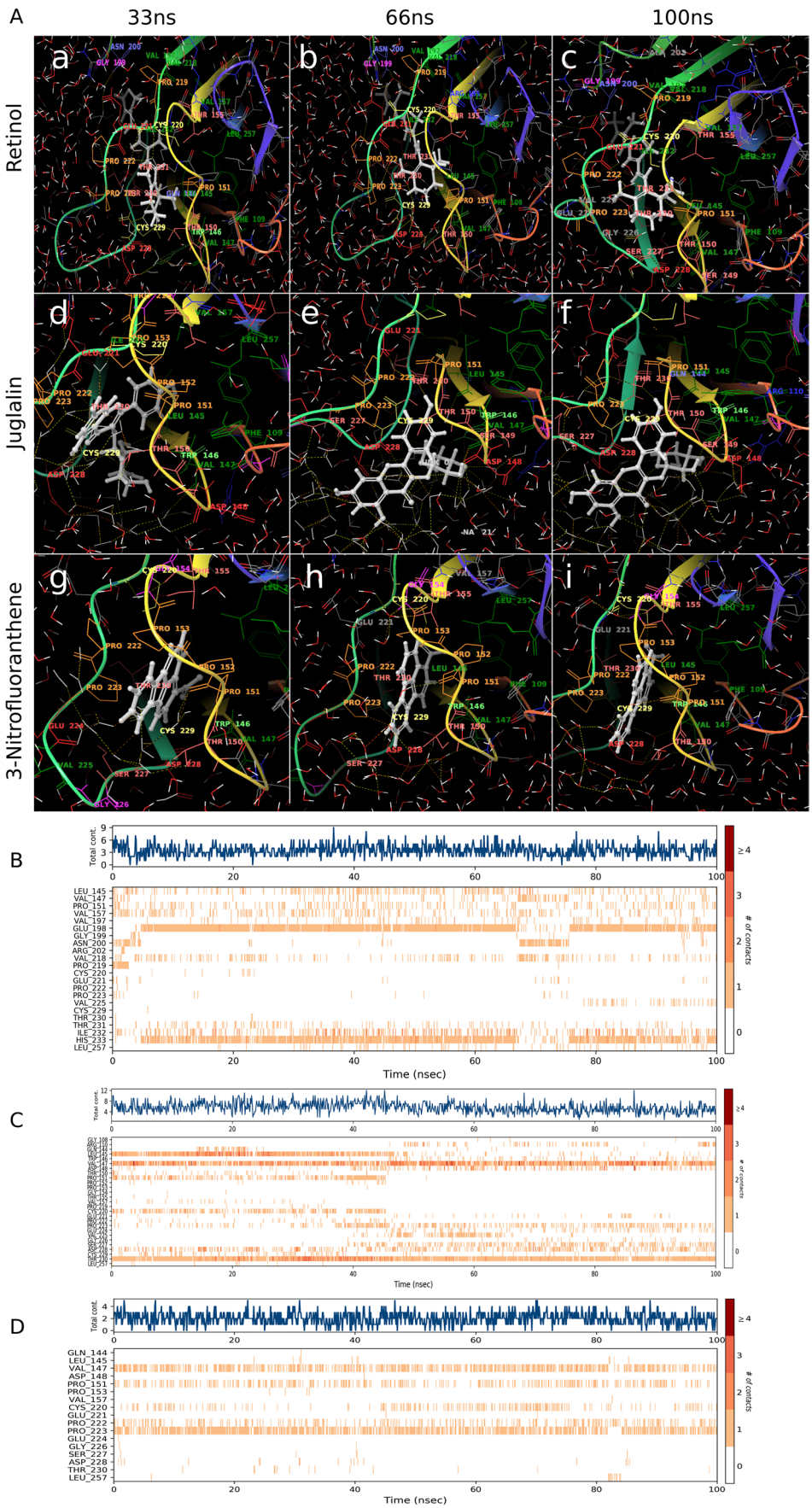

Fig. 5 **A** Protein–Ligand complexes during the course of molecular dynamics. (a), (d), (g) represents the snapshot at 33 ns, (b), (e), (h) represents the snapshot at 66 ns, and (c), (f), (i) represent the final state of protein with retinol, juglalin, and 3-nitrofluoranthene respectively. The dynamic state of protein–ligand contact can be further visualized using the Interaction timeline plot of (**B**) mutp53-retinol, (**C**) mutp53-juglalin, and (**D**) mutp53-3-nitrofluoranthene

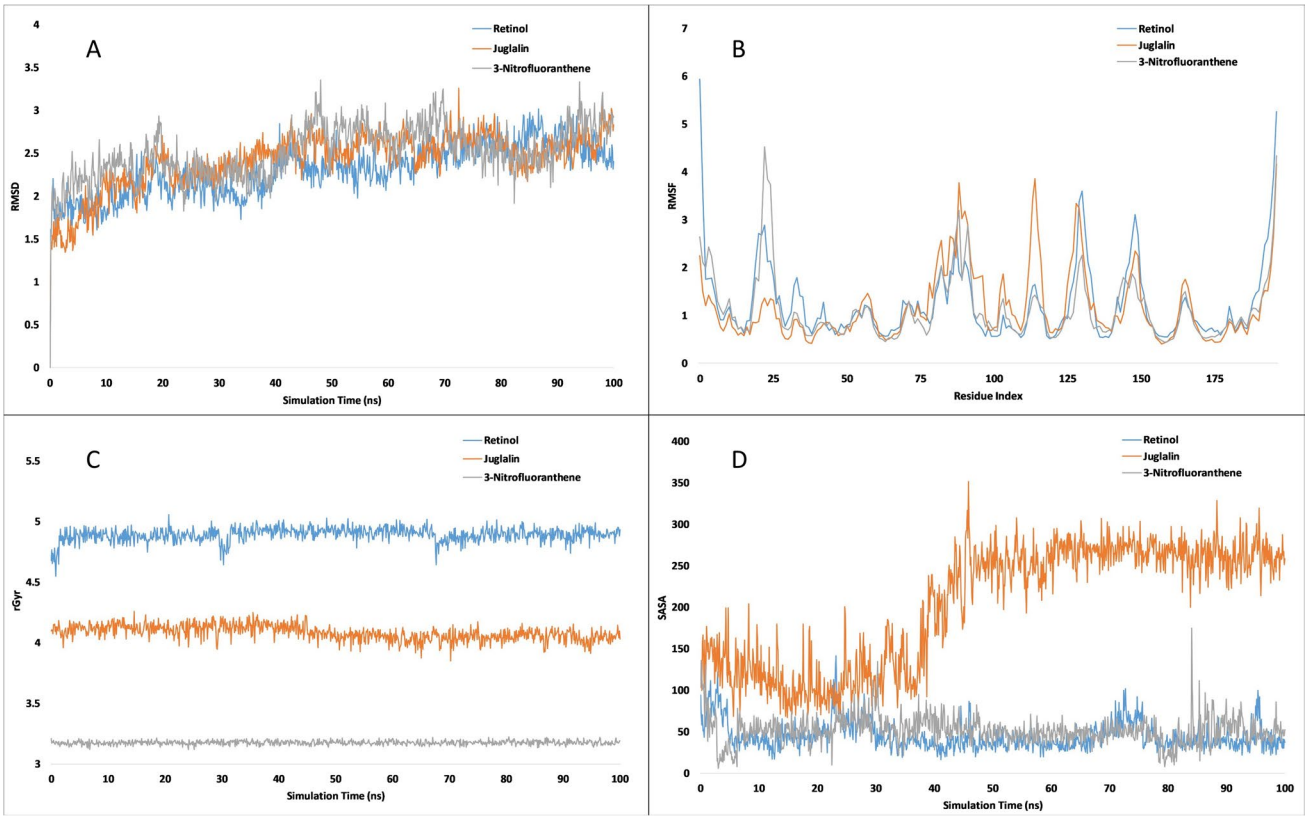

Fig. 6 Structural dynamics of three complexes: (**A**) RMSD, (**B**) RMSF, (**C**) rGyr, and (**D**) SASA (blue: retinol; orange: juglalin; and gray: 3-nitrofluoranthene)

to others, there were the least binding contacts with 3-nitrofluoranthene. Overall, Val 14, Pro 151, Pro 222, and Pro 223 anchored the ligand binding while other residues played the supporting role in a spread-out manner (Fig. 5D).

Analysis of structural stability and compactness

To establish the conformational stability and the compactness of the protein–ligand complexes, root mean square deviation (RMSD), root mean square fluctuation (RMSF), the radius of gyration (rGyr), and solvent accessible surface area (SASA) were calculated and compared (Fig. 6).

The binding of any ligand to the protein can result in a change in structure and compactness of the protein. RMSD helps analyze the deviation in structure and its stability over the simulation. Mean values derived from the primary data of mutp53-retinol, mutp53-juglalin, and mutp53-3-nitrofluoranthene were 2.29 Å, 2.41 Å, and 2.50 Å, respectively. A comparison of the visual plots (Fig. 6A) of RMSD was suggestive of the complex with retinol as the most stable among the three. Towards the end of the simulation, only retinol retained the stable plateau around its mean value, while complexes with juglalin and 3-nitrofluoranthene were frequently undergoing conformational changes. The mean and the graph of mutp53-retinol implicated a sustainable binding in the protein–ligand complex.

The RMSF plot (Fig. 6B) was analyzed upon binding all three ligands with protein to assess the vibrations and fluctuations on the residue level. All the peaks formed in the plot corresponded to either the loop or straight chain residues, while the lower spectrum of the graph consisted of residues actively forming secondary structures, i.e., α-helix and β-sheets of the protein. Secondary structures are comparatively more rigid; thus, they tend to fluctuate less, while the terminal or non-secondary structured residues are relatively free to deviate. This convention is confirmed by the RMSF plot of all three complexes. Mean values calculated were 1.24 Å, 1.18 Å, and 1.14 Å for mutp53-retinol, mutp53-juglalin, and mutp53-3-nitrofluoranthene, respectively. The higher RMSF of the retinol complex could be traced back to a docking study where several interactions were formed, resulting in a local adjustment in protein.

rGyr, another parameter measured in the analysis, was suggestive of the extent of folding nature and compactness of the protein–ligand complex. The mean values for mutp53-retinol, mutp53-juglalin, and mutp53-3-nitrofluoranthene were 4.89 Å, 4.08 Å, and 3.17 Å, respectively. The lower value of

mutp53-3-nitrofluoranthene indicated high compactness of the structure. While complex with retinol exhibited lower compactness. This variation was also a direct result of the binding of the ligand with protein and suggested the adjustment of protein to accommodate the ligand in the active site (Fig. 6C).

SASA, a measure of surface area exposed to the surrounding solvent of the complex, was another parameter analyzed. As the nature of solvent is dynamic regarding conditions provided to the system, the study computed the values and the SASA plots (Fig. 6D). Average of the SASA offered to the ligand in three complexes was computed as 44.99 $Å^2$, 203.373 $Å^2$ and 51.36 $Å^2$, respectively. A higher value of mutp53-juglalin resulted from the higher number of internal residues in contact with the solvent. At the same time, retinol and 3-nitrofluoranthene fluctuated at the start but stabilized towards the end of the simulation around a fixed average value. The result signified the structural stability of the binding pocket of mutp53-retinol and mutp53-3-nitrofluoranthene.

Interaction between protein and ligand complexes

The trajectory was computed for the interactions between protein and the ligands. The bar plot gave an estimate of the

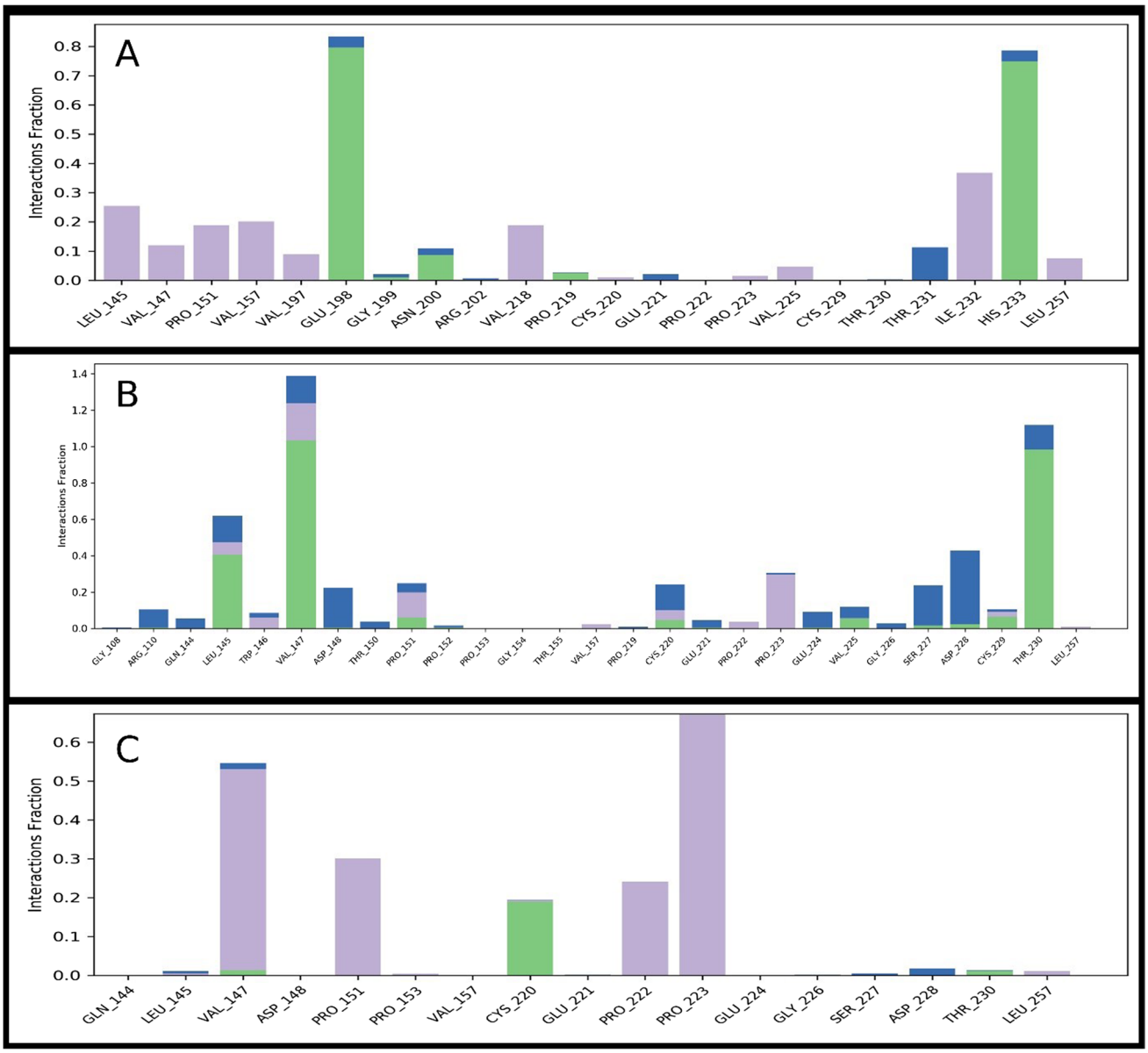

Fig. 7 Interaction bar plots: (**A**) mutp53-retinol (**B**) mutp53-juglalin, and (**C**) mutp53-3-nitrofluoranthene. Protein interactions with the ligand can be monitored throughout the simulation. These interactions can be categorized by type (green: H-bond; purple: hydrophobic bonds; and blue: water bridges)

binding of the residues with ligand along the relative nature of the bond formation.

An appreciable binding was observed with retinol which was consistent with the docking study (Fig. 7A). Glu 198 and His 233 complemented each other's binding to the ligand molecule throughout the simulation time with a strong H-bond while also showing water bridge formation at particular instances. These two bonds were assisted with other hydrophobic interactions majorly facilitated by Leu 145, Val 147, Pro 151, Val 157, Val 218, and Ile 238. In addition, 13 other residues also interacted with the ligand very briefly.

Juglalin retention in the binding site of the protein could be attributed to Leu 145, Val 147, and Thr 230 as they anchored the ligand with a significant hydrogen bond during the 100 ns simulation. The remaining 23 residues complemented these three interactions owing to the binding and structural stability of the complex (Fig. 7B).

Relative to the other two complexes, the binding was significantly lower quantitatively and qualitatively for the 3-nitrofluoranthene. A total of 17 residues interacted with only Cys 220, forming a hydrogen bond, only for 1/5th fraction of the simulation. Val 147, Pro 151, Pro 222, and Pro 223 formed hydrophobic interactions that facilitate ligands' retention in the binding site (Fig. 7C).

Conclusion

Over the years, several small molecules-based and peptide-based therapeutic options have been formulated against p53 mutation in cancer. Targeting mutant p53 protein offers significant advantages, such as developing molecules or peptides specific to a particular mutation and conferring high specificity to cancer cells as mutant protein is absent from healthy cells. Plants are a reserved house of endless small molecules which in traditional therapy gave fruitful remedies; thus, exploring plant compounds in a highly specific manner can lead to modern-day therapies. We evaluate the compounds in *Foeniculum vulgare* against the Y220C mutation in TP53. Overall, the results showed that retinol, juglalin, and 3-nitrofluoranthene could significantly bind to the mutated site. Retinol also reversed the structural deformation and restoration of wild-type conformation. Hence, they can be considered as leads for drug designing against the Y220C mutated p53 protein. However, the efficacy of these phytocompounds in cancer treatment and management strategies needs to be validated through wet-lab experiments.

Supplementary Information The online version contains supplementary material available at https://doi.org/10.1007/s00894-023-05454-2.

Author contribution Saksham Garg and Japneet Singh contributed to the study conception and design and performed molecular docking. The first draft of the manuscript was written by Saksham Garg and Japneet Singh and critical review was done by Dr. Smita Rastogi Verma. All authors read and approved the final manuscript.

Data availability The datasets generated and analyzed during the current study are available from the corresponding author upon reasonable request.

Declarations

Ethics approval This is not applicable.

Consent to participate This is not applicable.

Consent to publish This is not applicable.

Competing interests The authors declare no competing interests.

References

1. Mantovani F, Collavin L, Del Sal G (2019) Mutant p53 as a guardian of the cancer cell. Cell Death Differ 26(2):199–212. https://doi.org/10.1038/s41418-018-0246-9. (Nature Publishing Group)
2. Di Agostino S, Fontemaggi G, Strano S, Blandino G, D'Orazi G (2019) Targeting mutant p53 in cancer: the latest insights. J Exp Clin Cancer Res 38(1):290. https://doi.org/10.1186/s13046-019-1302-0
3. Pavlakis E, Stiewe T (2020) p53's extended reach: the mutant p53 secretome. Biomolecules 10(2):307. https://doi.org/10.3390/biom10020307
4. Brosh R, Rotter V (2009) When mutants gain new powers: news from the mutant p53 field. Nat Rev Cancer. 9(10):701–713. https://doi.org/10.1038/nrc2693
5. Zhu G, Pan C, Bei J-X, Li B, Liang C, Xu Y, Fu X (2020) Mutant p53 in cancer progression and targeted therapies. Front Oncol, 10. https://doi.org/10.3389/fonc.2020.595187
6. Joerger AC, Fersht AR (2008) Structural biology of the tumor suppressor p53. Annu Rev Biochem 77(1):557–582. https://doi.org/10.1146/annurev.biochem.77.060806.091238
7. Walerych D, Lisek K, Del Sal G (2015) Mutant p53: one, no one, and one hundred thousand. Front Oncol 5. https://doi.org/10.3389/fonc.2015.00289
8. Rauf SMA, Endou A, Takaba H, Miyamoto A (2013) Effect of Y220C mutation on p53 and its rescue mechanism: a computer chemistry approach. Protein J 32(1):68–74. https://doi.org/10.1007/s10930-012-9458-x
9. Sundar D, Yu Y, Katiyar SP, Putri JF, Dhanjal JK, Wang J, Sari AN, Kolettas E, Kaul SC, Wadhwa R (2019) Wild type p53 function in p53Y220C mutant harboring cells by treatment with Ashwagandha derived anticancer withanolides: bioinformatics and experimental evidence. J Exp Clin Cancer Res 38(1):103. https://doi.org/10.1186/s13046-019-1099-x
10. Blandino G, Di Agostino S (2018) New therapeutic strategies to treat human cancers expressing mutant p53 proteins. J Exp Clin Cancer Res 37(1):30. https://doi.org/10.1186/s13046-018-0705-7
11. D'Orazi G, Cirone M (2019) Mutant p53 and cellular stress pathways: a criminal alliance that promotes cancer progression. Cancers 11(5):614. https://doi.org/10.3390/cancers11050614

12. Senft D, Ronai ZA (2016) Adaptive stress responses during tumor metastasis and dormancy. Trends in Cancer 2(8):429–442. https://doi.org/10.1016/j.trecan.2016.06.004
13. Bykov VJN, Eriksson SE, Bianchi J, Wiman KG (2018) Targeting mutant p53 for efficient cancer therapy. Nat Rev Cancer 18(2):89–102. https://doi.org/10.1038/nrc.2017.109
14. Parrales A, Iwakuma T (2015) Targeting oncogenic mutant p53 for cancer therapy. Front Oncol 5. https://doi.org/10.3389/fonc.2015.00288
15. Binayke A, Mishra S, Suman P, Das S, Chander H (2019) Awakening the "guardian of genome": reactivation of mutant p53. Cancer Chemother Pharmacol 83(1):1–15. https://doi.org/10.1007/s00280-018-3701-x
16. Tal P, Eizenberger S, Cohen E, Goldfinger N, Pietrokovski S, Oren M, Rotter V (2016) Cancer therapeutic approach based on conformational stabilization of mutant p53 protein by small peptides. Oncotarget 7(11):11817–11837. https://doi.org/10.18632/oncotarget.7857
17. Garufi A, Pistritto G, Cirone M, D'Orazi G (2016) Reactivation of mutant p53 by capsaicin, the major constituent of peppers. J Exp Clin Cancer Res 35(1):136. https://doi.org/10.1186/s13046-016-0417-9
18. Badgujar SB, Patel VV, Bandivdekar AH (2014) Foeniculum vulgare Mill: a review of its botany, phytochemistry, pharmacology, contemporary application, and toxicology. Biomed Res Int 2014:1–32. https://doi.org/10.1155/2014/842674
19. Bogucka-Kocka A, Smolarz HD, Kocki J (2008) Apoptotic activities of ethanol extracts from some Apiaceae on human leukaemia cell lines. Fitoterapia 79(7–8):487–497. https://doi.org/10.1016/j.fitote.2008.07.002
20. Mohamad RH, El-Bastawesy AM, Abdel-Monem MG, Noor AM, Al-Mehdar HAR, Sharawy SM, El-Merzabani MM (2011) Antioxidant and anticarcinogenic effects of methanolic extract and volatile oil of fennel seeds (Foeniculum vulgare). J Med Food 14(9):986–1001. https://doi.org/10.1089/jmf.2008.0255
21. Mohanraj K, Karthikeyan BS, Vivek-Ananth RP, Chand RPB, Aparna SR, Mangalapandi P, Samal A (2018) IMPPAT: a curated database of Indian medicinal plants, phytochemistry and therapeutics. Sci Rep 8(1):4329. https://doi.org/10.1038/s41598-018-22631-z
22. Kim S, Thiessen PA, Bolton EE, Chen J, Fu G, Gindulyte A, Han L, He J, He S, Shoemaker BA, Wang J, Yu B, Zhang J, Bryant SH (2016) PubChem substance and compound databases. Nucleic Acids Res 44(D1):D1202–D1213. https://doi.org/10.1093/nar/gkv951
23. Lipinski CA (2004) Lead- and drug-like compounds: the rule-of-five revolution. Drug Discov Today Technol 1(4):337–341. https://doi.org/10.1016/j.ddtec.2004.11.007
24. Daina A, Michielin O, Zoete V (2017) SwissADME: a free web tool to evaluate pharmacokinetics, drug-likeness and medicinal chemistry friendliness of small molecules. Sci Rep 7(1):42717. https://doi.org/10.1038/srep42717
25. Morris GM, Huey R, Lindstrom W, Sanner MF, Belew RK, Goodsell DS, Olson AJ (2009) AutoDock4 and AutoDockTools4: automated docking with selective receptor flexibility. J Comput Chem 30(16):2785–2791. https://doi.org/10.1002/jcc.21256
26. Bowers KJ, Chow DE, Xu H, Dror RO, Eastwood MP, Gregersen BA, Klepeis JL, Kolossvary I, Moraes MA, Sacerdoti FD, Salmon JK, Shan Y, Shaw DE (2006) Scalable algorithms for molecular dynamics simulations on commodity clusters. ACM/IEEE SC 2006 Conference (SC'06), 43–43. https://doi.org/10.1109/SC.2006.54

Publisher's note Springer Nature remains neutral with regard to jurisdictional claims in published maps and institutional affiliations.

Springer Nature or its licensor (e.g. a society or other partner) holds exclusive rights to this article under a publishing agreement with the author(s) or other rightsholder(s); author self-archiving of the accepted manuscript version of this article is solely governed by the terms of such publishing agreement and applicable law.

The Scientific Temper
Vol. 13, No. 2, July-December, 2022:pp 110-117
ISSN 0976-8653, E-ISSN 2231-6396
A Web of Science Journal
DOI: https://doi.org/10.58414/SCIENTIFICTEMPER.13.2.2022.110-117
Doc ID: https://connectjournals.com/03960.2022.13.2.110

The Problematics of Parenthood in the *Shiva Trilogy* by Amish

Saroj Bala and Rajiv Ranjan Dwivedi
Department of Humanities, Delhi Technological University, Delhi-42, India
Corresponding author: sarojbala@dtu.ac.in

ABSTRACT

The paper attempts to analyze the perennial issue of parenthood through a psychoanalytical perspective, in a mythical context for making it relevant for the present generation which is more inclined towards western cultural values. Myths have been used as a tool by authors to discuss contemporary issues and challenges in society. The representation of child-parent relationships has always been one of the most coveted subjects for writers in general and new-age writers in particular. Kahlil Gibran, renowned Lebanese American poet advocates detached individuality in the relationship between parents and children. In this context *Shiva Trilogy*, one of the most popular works by Amish is relevant to refer to. The psychoanalytical lens probes the conceptual framework of the text for endorsing responsible parenting as a must for rearing children for the greater good of society in general by citing examples from the *Shiva Trilogy*.

Keywords: Parenthood, child-parent relationship, Shiva Trilogy, Contemporary Indian English Literature, Amish Tripathi, Social Psychology, Psychoanalysis

INTRODUCTION

CHILDREN BEGIN BY LOVING THEIR PARENTS. AFTER A TIME, THEY JUDGE THEM. RARELY, IF EVER, DO THEY FORGIVE THEM.

–Oscar Wilde, *A Woman of No Importance*

According to the *Oxford Advanced Learner's Dictionary of Current English* (ISBN 0194311015, 9780194311014), Parenthood is the state of being a parent. It is a process of bearing or adopting, and rearing children. This can be called the most difficult unpaid job in the world which demands patience, tolerance, and never-ending expectations from both sides. From British essayist Francis Bacon to an expert on parenting, Sudha Murthy of India, many writers have given advice on parenting. A unique piece of advice on successful parenting is given by Kahlil Gibran who very smartly explains how some amount of detached individuality needs to reform the relationship between parents and children. With the increasing suicide rate among students and teenagers, it is imperative to study the reasons behind it. The first reason that comes to mind is insufficient quality time spent with the parents. In this context psychoanalytic theory comes to the rescue for analyzing and providing solutions to the problem. The sharing of ideas, feelings, and problems on a regular basis creates a caring and healthy attitude between both parties for a secure future. This foundation helps a sound emotional and physical growth of a family. So, parenthood is an essential aspect of life that needs to be discussed and explored. This issue has been a substantial part of literature, psychology, films, mythology, and folklore. It has been a recurring theme in the works of many writers at a global level. The focus of the paper places this aspect in the *Shiva Trilogy* for proving its perpetual significance in the world. Although this theme is shared by the mythology of many cultures, the current study will concentrate on Indian mythology as the *Shiva Trilogy* has its roots in the same. Throughout centuries Indian mythology has contained a myriad of stories associated with parent-child relationships. For instance, the story of Shravan Kumar, who carried his blind parents for the pilgrimage on his shoulders, is a part of the Indian psyche. The mythology

of different civilizations and writers of English and other languages have raised the issue of parenthood in their works. Dickens's novels have the recurring theme of the parent-child relationship in many shades. Shakespeare's dramas also have this theme with the subtle treatment of the problem to highlight the crises. The heterogeneous representation of the child-parent relationship has a textual narrative feature in Amish's works where allegiance to values in the relationship and the violation of the same prevail juxtaposed against each other. Many sets of parents and children leave their mark on his works. The current study speculates reasons and social dynamics of parenting as relevant problems. The styles of parenting spelled out in literary works may be endless and unique to every household, yet a balanced mix of some common principles undergird responsible parenting, as exemplified by Shiva and Sati which stem from their uncorrupted, pure and mindful state of being. *The Immortals of Meluha* is the first book of the *Shiva Trilogy*, which introduces Daksha and Veerini who are Sati's parents. At the surface level, everything seems fine but in the course of time, it is revealed that Sati has a twin sister Kali, who was Naga as she had outgrowths on her body. King Daksha abandoned her at the time of birth against the wishes of his wife, Veerini who wanted to accept fate and requested Daksha to go to Panchavati where their abandoned child and grandchild were staying but Daksha remained stubborn and decided otherwise. Even in their grey years, she requests him to leave the kingdom for the sake of expiation for the sins they committed against their daughter and grandson. The story has psychological significance as well as it calls for the inner turmoil that might be unnerving for the abandoned child in this context:

> I AM SAYING ONCE AGAIN, DAKSHA, LET'S FORGET EVERYTHING,' SAID VEERINI. 'YOU HAVE ACHIEVED ALL YOU WANTED TO. YOU ARE THE EMPEROR OF INDIA. WE CANNOT LIVE IN PANCHAWATI ANYMORE. WE LOST OPPORTUNITIES LONG AGO. KALI AND GANESH DESPISE US. AND I DON'T BLAME THEM FOR IT. LET US TAKE SANYAS, RETREAT TO THE HIMALAYAS, AND LIVE OUT THE REST OF OUR LIVES IN PEACE AND MEDITATION. WE WILL DIE WITH THE NAME OF THE LORD ON OUR LIPS (AMISH, 2013, P. 82).

The pivotal role played by the politics of cultural supremacy has a deep impact on relationships. A royal ambition apparently seems to prevail over filial affection and acceptability. That is why he does not follow Veerini's well-meant advice. His deep-rooted colonial aspirations and excessive attachment to Sati do not allow him to take the righteous path. When Sati gave birth to a Naga child, he threw it away without the mother's consent and got his first son-in-law killed. His obsession with his daughter Sati's safety leads him to plan to get his second son-in-law killed by mercenaries but his plans get foiled. In contrast to Daksha, Sati is a devout Suryavanshi who follows all the rules made by the great Lord Rama. Despite being a royal she follows all the rituals to be performed as a Vikarma woman who is discriminated against in society. She is overjoyed to meet her estranged son Ganesh and twin sister Kali who are not acceptable in Meluhan society due to their physical deformities. In Swadeep, the Chandravanshi kingdom also, it is the power structure that rules private life. Swadeepan king Dilipa is yet another case of abused parenting. He does not trust his own son Bhagirath and keeps him away from matters of administration. Although Bhagirath, the Swadeepan prince is a virtuous person, Dilipa's insecurity as an old person keeps his son at bay. After the attack on the convoy of the Neelkanth, Bhagirath has suspicion that it might have been the work of king Daksha and his father:

> *"YES! IT LOOKS LIKE EMPEROR DAKSHA AND MY WEAKLING FATHER HAVE FORMED AN ALLIANCE AGAINST THE NEELKANTH" (AMISH, 2013, P. 8).*

Neelkanth recognizes his worth and supports him in his endeavors. There is yet another mythical character Renuka who has also been given a makeover for presenting the problems of parenting. The extraordinary relationship of Renuka with her son Parshuram is rather touching. The dreaded outlaw Parshuram's plight in obeying his mother's order to behead her sets a benchmark in obedience. Society could not accept the inter-caste marriage of his parents and his mother's kinsmen killed his father in front of her eyes. This devastated her and forced her to think of her own end which led to her beheading. Parshuram's parents were responsible parents but unfortunately due to oppressive societal pressure could not lead a peaceful life.

The guiding principle of parenthood is a cosmopolitan concern that extends beyond time and space represented through the critical and creative endeavor of the writers for instance one of the most profound English essayist Francis Bacon in his essay '*Of Parents and Children'* opines:

> "LET PARENTS CHOOSE BETIMES THE VOCATIONS AND COURSES THEY MEAN THEIR CHILDREN SHOULD TAKE, FOR THEN THEY ARE MOST FLEXIBLE; AND LET THEM NOT TOO MUCH APPLY THEMSELVES TO THE DISPOSITION OF THEIR CHILDREN, AS THINKING THEY

WILL TAKE BEST TO THAT WHICH THEY HAVE THE MOST MIND TO" (BACON 2001, P. 30).

Most of the epical works of art have laid down ethical discourses on parenthood illustrating the lives of the characters. The Ramayana and the Mahabharata in Indian and Greek cultural epics are some of the radiant examples to refer to. Telemachus, the son of the great Greek warrior Ulysses, is altogether different from his father in ideology. For him, the comforts of his palace, country, and terrain are preferable to travel and adventure. After his return from the great war of Troy Ulysses finds life very dull and adventureless for lack of action and challenges. Therefore, Ulysses decides that his son can govern Ithaca and he himself can go outside his kingdom and lead an adventurous life according to his whims and fancies. The following excerpt from Tennyson's well-known poem 'Ulysses' is observable in this context:

MOST BLAMELESS IS HE, CENTERED IN THE SPHERE OF COMMON DUTIES, DECENT NOT TO FAIL IN OFFICES OF TENDERNESS, AND PAY MEET ADORATION TO MY HOUSEHOLD GODS, WHEN I AM GONE. HE WORKS HIS WORK, I MINE (Tennyson, 2008, p. 408).

As a good parent Ulysses does not criticize Telemachus' different temperament and priorities. He describes his son as a perfect heir who can rule Ithaca successfully after he is gone as Telemachus possesses the competence, right attitude, and ability to handle political matters.

As for the *Shiva Trilogy,* a superior moral order dictates the maintenance of a child-parent relationship. As such taking the 'elixir' or *Somras* as referred to in the text is an apparent cause of parental aversion and dislike towards their own children for the fact that the Nagas are associated with the elixir and the resultant Naga offspring is bound by an irony where parents are at fault by drinking *Somras* in excess. Daksha as a Meluhan has easy access to *Somras* which empowers him with longevity. This makes him think about more and more power over other provinces of Sapt Sindhu. For him, parenthood means greater access to security through normal and able-bodied Sati and Shiva, who is the Neelkanth. Anyone who is a hindrance in his path to power is an enemy even if it is his own child (Kali) and grandson (Ganesh). He does not even think of Sati's grief over the death of her first husband Chandradhwaj, who gets killed by Daksha himself. Daksha's irresponsible parenting is of the worst kind that leads to the death of Sati and the destruction of his own kingdom, Meluha itself. Paul, Sandeep (2020) argues that "Tripathi's treatment of mythology is more a frame of reference to contemporary issues of the twenty-first century than a historical retelling" (Paul, p.1). The cultural and psychological dimensions of parenting manifested in the text explore the inner recesses of the human mind. This paper demonstrates a psychoanalytical perspective of the literary representation of parenthood in the *Shiva Trilogy.*

Materials and Methods:

The critical analysis of the three texts of the Shiva Trilogy:

1. THE IMMORTALS OF MELUHA (ISBN 978-93-80658-74-2)
2. THE SECRET OF THE NAGAS (ISBN 978-93-8065-879-7)
3. THE OATH OF THE VAYUPUTRAS (ISBN 9789382618348)

The current study has employed an eclectic methodology which consists of a close reading of the text. The psychoanalysis theory propounded by Freud is applied to analyze the text, characters, and ideologies. The methodology adopted in the paper involves a comprehensive study of the psychological ramifications of parenting in the text. The text is simultaneously placed within the socio-cultural and socio-historical contexts to understand the psychoanalytical perspective of the author. Along with textual analysis of the main text, parallels are drawn from the literature of the past. Since it is a qualitative study, data was not collected and analyzed.

RESULTS

The prime importance given to dynamic, unconscious, and psychological conflicts by the Freudian theory is applied to the text for understanding the problematics of parenthood in the *Shiva Trilogy.* The rapid advancements in science and technology have changed the course of life and aggravated many existing problems due to the generation gap. Current crises of the parent-child relationship are due to the apathy of children towards parents who are less proficient in the use of ever-growing advancements in technology. Moreover, easy access to the internet has resulted in enhanced exposure to western culture which has brought a radical decline in moral values. In fact, the problem of parenthood has been an ancient phenomenon that has changed/evolved at every age according to the culture and traditions of society. The ancient example from the *Bible* is Abraham's obedience in accepting God's will and sacrifice of his son Isaac. The symbolic meaning of this sacrifice is that God is our parent and human beings must obey in order to reap benefits from the Lord. In Shakespeare, different hues of parenthood can be observed in plays like *Hamlet, The Tempest, Macbeth, Romeo and Juliet, King Lear*, etc. The history of humankind is replete with diverse instances of parenthood

that are either exemplary/moderate or shamefully startling. Parenting is exemplary when the moments of pride, joy, and inexplicable satisfaction are balanced with a mindful execution of responsibilities. At the same time, an abdication of responsibility and mutual hostility makes for an unhealthy parent-child relationship. Amish has cleverly discussed many such contemporary problems through his fictional account of Shiva's adventures. "Amish Tripathi's *Shiva Trilogy* is an epic fantasy that treats the life of God Shiva from a humanistic point of view in an odd blend of fantasy, reality, and speculative history" (Chatterjee Abhinaba, 2017, p. 75).

Among other issues like environmental pollution, marginalization, and power politics, parenthood is also woven into the tale. With working mothers, nuclear families, and a lack of a healthy support system, the problem of parenting is surmounting in cities. Parents splurge money as if to show their parental care and concern which gets misappropriated with adverse impacts with a resultant rise in cases of suicides, mental depression, and loneliness in children. Insecurity among children/ youth is increasing as parents throw money instead of giving them quality time and attention. A child today has become more of a necessity and a liability to bear. Some couples decide to remain childless for the sheer sake of their career and pleasure. What Hindi poet Surdas rejoiced in (Krishna's childhood pranks) has become a servant's privilege in the current era. Very few parents enjoy the childhood activities of their children. Most parents invest/ believe in earning and spending money on their children through good schools, expensive clothes, and gadgets. Money is the mantra and hedonism is the philosophy of life. Parenting is a social burden for some couples as they are career oriented and keep running after promotion and pleasures. Amish has contemporized this phenomenon through his work based on Hindu mythology where the mythical character of Daksha has been given a new persona that is obsessed with power. As the emperor of Meluha, he is selfish and self-centered and his primary interest in colonizing the other provinces of the Sapt Sindhu region leads him to manipulate Suryavanshi's principles. He breaks rules made by the great Lord Rama but expects others to follow the same rules. Sati gets shocked when she discovers the secrets of her twin sister Kali and her son Ganesh's abandonment and the murder of her first husband by her father. Daksha holds Shiva responsible for his soured relations with his beloved daughter Sati. Exasperated Daksha tries to attack Shiva with his knife but Nandi saves him with the shield in his hand. Sati puts her sword at her father's neck to force him to acknowledge the truth:

> *"DAKSHA'S EYES WERE GLUED ON A TEARY-EYED SATI, WHO HAD HER SWORD INCHES AWAY FROM HER FATHER'S THROAT. HIS FACE EXHIBITED THE SENSE OF BETRAYAL AND LOSS HE FELT. SATI WAS THE ONLY PERSON HE HAD EVER TRULY LOVED" (AMISH, 2011, 329).*
>
> *SHE ADMITS LATER ON THAT SHE WAS "ASHAMED" THAT DAKSHA'S "BLOOD" RAN IN HER "VEINS," (AMISH, 2011, P. 330).*

Parental responsibility as a duty comes in the way of blind love for the child which reminds us of King Dhritrashtra's obsession with his evil-minded son Duryodhan in the epic Mahabharata. The irrational decisions taken by Dhritrashtra to please his son Duryodhan led to the great war that annihilated the Kuru clan. Although Daksha is a doting father, but he is not a responsible parent who can think of her welfare in the long run. His plan for a peace conference which is actually a guise to kill his second son-in-law Neelkanth turns the table on him. Instead of Neelkanth, his own daughter gets killed by the mercenaries and Daksha's dream of keeping Sati in close vicinity gets shattered by his own conspiracy. On the other hand, in contrast to her father Sati is righteous and compassionate toward the needy. Her goodness brings joy and comfort to the helpless residents of Ichhawar village where she fights with the man-eater ligers and saves their lives. It is rightly said that an intelligent child brings joy to all the people around him/ her. It is a blessing to have such a child who can excel/ outwit its own parents. Thiruvalluvar, a Tamil saint-poet has expressed the same thoughts in *Thirukkural*. Kural-68 says "If the children's intelligence is more than that of parents, it will be a joy to all the living beings of the earth" (Chakravarti, A. 1953, p. 56).

He means to say that it will be a joy to the entire living beings including parents if the children excel their parents in intelligence.' Children by virtue of their behavior, attitude, knowledge, nobility, obedience, duty towards parents, compassion towards the poor and needy, broader human outlook, etc. can make this world a beautiful place. The case of the famous Raghuvanshi king Dashrath and his sons can be cited in this context. In the famous Indian epic Ramayana parenthood and children's obedience to parents, are both exemplary. The Raghuvanshi kings like Lord Rama made the earth a better place to inhabit where there was no fear of anti-social elements like Asuras and Rakshasas. Lebanese American poet Kahlil Gibran (2017) a great name in the world of prose poems has very wisely explained the status of parents and children in his book *'The Prophet'*:

"YOUR CHILDREN ARE NOT YOUR CHILDREN.
THEY ARE SONS AND DAUGHTERS OF LIFE'S LONGING FOR ITSELF.
THEY COME THROUGH YOU BUT NOT FROM YOU.
AND THOUGH THEY ARE WITH YOU YET THEY BELONG NOT TO YOU." (GIBRAN, P. 17)

Literature is full of examples of parenthood, be it Hamlet's mother, King Lear's relationship with his daughters, Jane Austen's portrayal of parents, Migrant parents in Diaspora literature, and parenthood in Dystopian novels to name a few. Dickens is famous for the theme of the parent-child relationship in his works. Kr. Dombey's love for Paul is an example of oppressive and destructive love. *Pickwick Papers* is the only novel where Dickens adds humor and a healthy understanding of parental affection. In his later novels negativity is more visible in child-parent relationships. In the 18th century, didactic books were written for parents and children to educate them on the right conduct. *The Family Instructor* (1715) by Defoe, *Parent's Assistant* (1796) by Edgeworth, and *Early Lessons* (1798) by A L Barbauld are a few examples of such books. Even now the market is flooded with books on parenting to help young/old parents. Famous scientist Nicola Tesla recommended that only deserving couples should get the right to become parents and others should be deprived of this responsibility. The overpopulated countries can find a solution in this personal opinion of the scientist. Georgieva, M. (2009) concludes in her paper on Parenthood in literature:

"Through diverse forms of literature, society gradually came to conceptualize parenthood, often without making direct reference to the word itself. However, the ramifications of the theme are numerous and provide a rich background for innovative academic research" (Georgieva, p. 6).

In contrast to Daksha's ambition to get respect from the Meluhan society, Shiva and Sati as ideal parents don't care for society's opinion of them. Not only for their own children but for others' children also they give their best to help them. Her desperation to save the villagers of Ichhawar brings out her extraordinary courage and martial skills which help her fight the pride of ligers that have turned man-eaters. In contrast to her bravery, father Daksha is weak in mind and body. Mishra, Lata (2013) in her paper 'Ethical Wisdom and Philosophical judgment in Amish's *The Oath of the Vayuputras'* states about Sati:

> HER IDENTITY, NATURE, AND ACTIONS ARE DEFINED AND ACTED OUT VIS-A-VIS HER FATHER, DAKSHA. MUCH DOTING FATHER BUT EQUALLY MANIPULATIVE, KING DAKSHA KEEPS SATI IGNORANT OF THE TRUTH THAT SHE HAS GIVEN BIRTH TO A DEFORMED SON AND MISINFORMS HER OF A STILLBORN BIRTH, (MISHRA, P. 28).

Sati's acceptance of Kali and Ganesh despite having their stigma of being Nagas resonates with the discourse of disability studies. The hegemonic tyrant Daksha expects submission and subordination from the Nagas for proving his authority over them. His weak-mindedness is reflected in his decisions to destroy the convoy of the Neelkanth in alliance with the sage Bhrigu. This gives a clear picture of the dictum- 'power corrupts and absolute power corrupts absolutely'. Thus, the study explores the psychological reasons and negative consequences of unhealthy parenthood exemplified through the character of King Daksha detailed in the *Shiva Trilogy.*

DISCUSSION

The *Trilogy,* in the garb of mythology, carries many important issues of the contemporary world. The humanized character of Shiva gives solutions to many problems which are relevant in the present time. Karthic & Immanuel (2018) observe in this context:

We affirm that Tripathi actually endeavors to give an account of contemporary society in the guise of Meluha. (Karthic & Immanuel, p. 207)

Like contemporary society, the social structure of Meluha is under influence of the power structure owned by Daksha. This influence is visible in the parenting style of Daksha who is not ready to mend ways in spite of the immense pressure of his beloved daughter Sati. He flaunts his desire to impress his over-dominating father Brahmanayak:

"It is his intense desire to impress the person he loves the most,' expounded Daksha. "Look at me. I have always loved my father. My desire to impress him is what is driving me even today. Even after his death, I still want to make him proud of me. It is driving me to my destiny as the king who will re-establish the pure Suryavanshi way of life across India" (Amish, 2010, p. 154).

The conflict between the strong-minded and the weak-minded has been a part of mythical narratives. This struggle gets reflected in his father Brahamanayak's impossible standards of courage versus the shameful weaknesses of his son. The narrator goes on to state the obsessiveness "about the honor and respect that his empire should garner his son's lack of courage and character was a source of anger and dismay." (Amish, 2011, p. 337)

Roman emperor Marcus Aurelius in the first book

of *Meditations* shares qualities he inherited from his grandfather and mother saying "Of my grandfather Verus I have learned to be gentle and meek and to refrain from all anger and passion. Of my mother I have, I learned to be religious, and bountiful" (2016, p. 28). In the *Trilogy,* Sati inherited bravery from her grandfather and the layering in the nuances of courage is glorified in the case of Sati many times over in the *Trilogy* for instance when she tries to save an immigrant woman from a pack of wild dogs at the age of sixteen. During the war, she accepts the responsibility of defeat as a leader which proves her exceptional moral standards. Nothing can beat her fight with Swuth, the Egyptian killer that forces him to accept her greatness as a warrior. Unlike her cowardly father, she shows her gallantry as a brave Kshatriya and a true Suryavanshi.

The apprehensions, turmoil, and dilemmas shape the characters of people as Daksha's faulty and selfish concern for his emperor hood forces him to oppose the Neelkanth who is the prophesied savior. As an opportunist, he is very humble to Shiva when he marries Sati after abolishing Vikarma law. In *The Immortals of Meluha*, the narrator mentions Daksha turning "to Shiva with a grateful smile" saying "I have one more thing to thank you, my Lord. My daughter is part of my soul. I wouldn't have been able to survive without her" (Amish, 2010, p. 278).

But when Shiva discovers that he was misguided in considering Chandravanshis as evil and *Somras* as the actual evil, Daksha takes the help of Egyptian mercenaries to get the prophesied savior Shiva killed.

Amish has resurrected the ancient mythical character of Daksha of Hindu mythology in a new avatar. As an emperor of Meluha, his colonial aspirations are over and above the relationships. Opposite to Daksha Sati's virtues as a good parent, daughter and Kshatriya are exceptional. Her virtues are shared by her both sons who follow the right path guided by Shiva and Sati. Ganesh and Kartik are obedient sons who excel in martial arts as true Kshatriyas. Sati's pride in Shiva's greatness as a large-hearted father is beautiful and is revealed when she says "You are my son. You are his son. He will accept you. You don't know the size of your father's heart. The entire world can live in it" (Amish, 2011, p. 259).

Sati is right in her assumption when she expresses her faith in Shiva's role as a parent to her Naga child Ganesh from her first husband. After discovering Ganesh's virtues as a chivalrous person Shiva does not hesitate to show his approval and happiness:

"Shiva breathed deeply. Ganesh had once again shown tremendous character, fighting injustice even at the risk of his own life. Shiva was proud of his son. 'You did the right thing." (Amish, 2013, p. 140)

Not only Ganesh and Kartik but the son of Swadeepan king Dilipa also finds a place in Shiva's heart. Prince Bhagirath is betrayed by his army during the war with the Suryavanshis as King Dilipa does not trust his own son for war tactics. He wanted to strike from the rear but Chandravanshi generals did not listen to Bhagirath's advice. This resulted in their defeat in the war with the Suryavanshis. Shiva also comes to know about it that Bhagirath "is not trusted by his father. And therefore, not by most Swadeepans kings or generals either. They believed he would have taken the soldiers, escaped to Ayodhya, and declared himself Emperor" (Amish, 2011, p. 19-20).

Even after the defeat in the war king Dilipa, the Swadeepan king is happy as for all practical purposes, he would retain his empire and his independence. He feels at least safe from his son who might appropriate the throne.

The ideological difference is stark in the parenting style of Suryavanshis and Chandravanshis as parenthood is not a matter of choice in Meluha where birth children are not allowed to live with their parents except in the case of the royals. Kusugal (2015) highlights this aspect: "Shiva is not with the Maika system also". He questions, 'But this is about flexibility. What about stability?' (p. 37). Maika the hospital city of Meluha decides the future of the children where they are born and brought up. The freedom of parenting is not given to Meluhan parents as they can adopt a child by putting in an application. All pregnant women have to travel to Maika for delivery. Husbands and relatives of the pregnant woman are not allowed to enter. After the birth of a child, he or she is kept in Maika for a few weeks but the mother is sent back to Meluha. The Meluhan Gurukul is a massive school established by the empire that takes care of the child. Every child gets equal opportunities in this education system. As they enter adolescence, they are given the *Somras*. They all can follow their vocation according to their abilities to become successful in life. When children turn sixteen, they are allotted to the parents who are applicants for adoption. Children born with deformed bodies are sent to Panchawati. The third book, *The Oath of the Vayuputras* states:

> "ACTUALLY, TENETS OF MELUHAN LAW REQUIRE PARENTS TO ACCOMPANY THEIR NAGA CHILDREN TO PANCHAWATI. IN DOING SO, THEY ARE FOLLOWING THEIR LAW. BUT OTHERS REFUSED TO DO SO. THEY ABANDON THEIR CHILDREN

AND RETURN TO THEIR COMFORTABLE LIFE IN MELUHA. IN SUCH CASES, ONLY THE CHILD IS HANDED OVER. THE MAIKA GOVERNOR PRETENDS NOT TO NOTICE THIS BREACH OF LAW" (AMISH, 2013, P. 67).

The parenting style of Meluhan society is juxtaposed against the rival Swadeepan kingdom which gives enough liberty to parents and children. Oscar Wilde's quote fits the Meluhan princess's upbringing as she respects her parents till the day, she discovers the secret of her twin sister and sons' abandonment. She questions her father's integrity and expresses her grief over having his blood in her veins. She leaves him for good and never forgives him for his faults. Thus, Amish's indirect reference to contemporary problems like parenting is successfully done through the myth of Shiva. Paul, Ritika (2013) also writes the same thing in her paper on Amish's *The Immortals of Meluha* when she states, "Amish Tripathi through this novel tries to address the social reality of the contemporary society." (p. 427) The world is witnessing a crucial phase these days when children's loneliness is increasing across the globe due to many reasons. The citizens/government must rectify this problem according to the cultural norms of society.

CONCLUSION

Amish has psychoanalytically investigated the multiple dimensions of the problem of child-parent relationships in his three books of the *Shiva Trilogy* which comes under the genre of mythological fiction. King Daksha's illogical parenting style is attachment driven which begets doom for himself and everyone around him both within the family and society at large. His lack of guilt in disowning his Naga progeny speaks volumes about his callousness and eventually leads to his punishment through Sati's assassination by the mercenaries hired by him to get the Neelkanth killed. The irony of losing his beloved daughter has been coupled with the annihilation of the Meluhan capital Devgiri also. However, Sati prefers to protect both her long-lost sibling and the child even if it means abandonment by the Meluhan society. We have witnessed alleged stark examples in contemporary times of parents' apparent indifference to their children, which is painful and shameful as well. Parenting is a pious responsibility that sanctifies one's own life and one's children's lives, which eventually furthers nation-building as future citizens are healthily groomed and develop meaningful, mutually reinforcing bonds of love and respect. This is no less than patriotism because it creates social capital within the nation at large, where citizens grounded in healthy relationships within families also manifest mutual trust and respect in flourishing democratic states. Though Amish has been successful in highlighting the problem of parenting by citing many examples in his *Shiva Trilogy* based on mythical characters, the juxtaposition of their cases paves the way for further research in other mythological works.

ACKNOWLEDGEMENTS:

Authors are grateful to the Vice Chancellor, Delhi Technological University, New Delhi, for the moral support and critical suggestions received during the preparation of the manuscript.

Conflict of Interest: There is no conflict of interest among authors for the present work. We also declare that all academic ethical guidelines have been followed in this study.

REFERENCES:

Books:

Amish (2010). *The Immortals of Meluha*, Westland Ltd. New Delhi.

Amish (2011). *The Secret of the Nagas,* Westland Ltd, New Delhi.

Amish (2013). *The Oath of the Vayuputras,* Westland Ltd, New Delhi.

Aurelius, M. (2016). *Meditations*, Grapevine India, New Delhi.

Bacon, F. (2001). *Of Parents and Children*, *The Essays.* Mozambook.

Chakravarti, A. (1953) *Thirukkural: With English Translation and Commentary and an Introduction*, Madras: Diocesan Press.

Freud, Sigmund. (2012) *A General Introduction to Psychoanalysis*, Wordsworth eds. Ltd., UK.

Georgieva, M. (2009). *Parenthood in English Literature*. HAL- 00476206.

Gibran K. (2017). *Collected Works of Kahlil Gibran*, Maple Press Private Limited, Noida.

Hornby A. S. (2015). *Oxford Advanced Learner's Dictionary of Current English*, Oxford University Press.

Tennyson, A. L. (2008). "Ulysses." *Fifteen Poets.* Oxford University Press.

Wilde, O. (2013). *A Woman of No Importance.* Duke Classics.

PAPERS:

Chatterjee, Abhinaba. (2017) *Humanizing Theography through Mystical Mythology: Amish Tripathi's Shiva Trilogy*. Research and Criticism, Vol. 1, No 1, Banaras Hindu University, pp. 72-86.

Karthic, R. & S. Garret Raja Immanuel. (2018) *Deformed bodies and Posthuman Alterity: A Foucauldian Critique of Social Constructions in The Immortals*

of Meluha by Amish. Research Journal of English Language and Literature, Vol.6. Issue-3. (July-Sept) pp. 205-208.

Mishra, Lata. (2013) *Ethical Wisdom and Philosophical Judgment in Amish Tripathi's The Oath of the Vayuputras.* Linguistics and Literature Studies. 1(1), 28-31.
DOI: 10.13189/IIs.2013.010104

Paul, Ritika. (2017) *Shiva for all times: A Study of Amish Tripathi's The Immortals of Meluha.* Research Journal of English Language and Literature, Vol.5. Issue 1. (Jan-Mar), pp. 425-428

Paul, Sandip. (2020) *Twentieth -first Century Imagination in Amish Tripathi's Shiva Trilogy*. Dialog, Issue no-36, Autumn, pp.1-18.

Kusugal, S. Kavita. (2015) *Deconstructing the Myth in Amish Tripathi's Shiva Trilogy- A Review*. Journal of Innovative Research and Solutions, Vol.1, Issue 1, (Jan-June), pp. 33-34

Journal Pre-proof

Unwinding the modalities of necrosome activation and necroptosis machinery in neurological diseases

Rohan Gupta, Smita Kumari, Rahul Tripathi, Rashmi K Ambasta, Pravir Kumar

PII: S1568-1637(23)00014-4

DOI: https://doi.org/10.1016/j.arr.2023.101855

Reference: ARR101855

To appear in: *Ageing Research Reviews*

Received date: 30 September 2022
Revised date: 9 December 2022
Accepted date: 15 January 2023

Please cite this article as: Rohan Gupta, Smita Kumari, Rahul Tripathi, Rashmi K Ambasta and Pravir Kumar, Unwinding the modalities of necrosome activation and necroptosis machinery in neurological diseases, *Ageing Research Reviews,* (2022) doi:https://doi.org/10.1016/j.arr.2023.101855

This is a PDF file of an article that has undergone enhancements after acceptance, such as the addition of a cover page and metadata, and formatting for readability, but it is not yet the definitive version of record. This version will undergo additional copyediting, typesetting and review before it is published in its final form, but we are providing this version to give early visibility of the article. Please note that, during the production process, errors may be discovered which could affect the content, and all legal disclaimers that apply to the journal pertain.

© 2022 Published by Elsevier.

Journal Pre-proof

Unwinding the modalities of necrosome activation and necroptosis machinery in neurological diseases

Rohan Gupta[1], Smita Kumari[1], Rahul Tripathi[1], Rashmi K Ambasta[1], Pravir Kumar[$]

1: Molecular Neuroscience and Functional Genomics Laboratory, Department of Biotechnology, Delhi Technological University (Formerly Delhi College of Engineering)

$Author to whom correspondence should be addressed:
Prof Pravir Kumar, PhD
Professor and Head, Department of Biotechnology
Dean (International Affairs)
Molecular Neuroscience and Functional Genomics Laboratory
*Former Dean***,** Delhi Technological University (Formerly Delhi College of Engineering)
Room# FW4TF3, Mechanical Engineering Building
Shahbad Daulatpur, Bawana Road, Delhi 110042; Phone: +91- 9818898622
Email: pravirkumar@dtu.ac.in; kpravir@gmail.com
ORCID ID: 0000-0001-7444-2344; **Scopus ID:** 14831447800; **ISI Research ID:** B-2164-2015

Abstract

Necroptosis, a regulated form of cell death, is involved in the genesis and development of various life-threatening diseases, including cancer, neurological disorders, cardiac myopathy, and diabetes. Necroptosis initiates with the formation and activation of a necrosome complex, which consists of RIPK1, RIPK2, RIPK3, and MLKL. Emerging studies has demonstrated the regulation of the necroptosis cell death pathway through the implication of numerous post-translational modifications, namely ubiquitination, acetylation, methylation, SUMOylation, hydroxylation, and others. In addition, the negative regulation of the necroptosis pathway has been shown to interfere with brain homeostasis through the regulation of axonal degeneration, mitochondrial dynamics, lysosomal defects, and inflammatory response. Necroptosis is controlled by the activity and expression of signaling molecules, namely VEGF/VEGFR, PI3K/Akt/GSK-3β, c-Jun N-terminal kinases (JNK), ERK/MAPK, and Wnt/β-catenin. Herein, we briefly discussed the implication and potential of necrosome activation in the pathogenesis and progression of neurological manifestations, such as Alzheimer's disease, Parkinson's disease, multiple sclerosis, traumatic brain injury, and others. Further, we present a detailed picture of natural compounds, micro-RNAs, and chemical compounds as therapeutic agents for treating neurological manifestations.

Keywords: **Necroptosis; Post-translational modification; neurodegenerative disease; Neurological disease; Axonal degeneration; Natural compounds**

List of Abbreviations

PCD: programmed cell death; TLRs: toll-like receptors; RIPK1: receptor-interacting protein kinase 1; RIPK2: receptor-interacting protein kinase 2; MLKL: mixed lineage kinase domain-like; RIPK3: receptor-interacting protein kinase 3; AD: Alzheimer's disease; PD: Parkinson's diseases; ALS: Amyotrop; hic lateral sclerosis; HD: Huntington's disease; MS: multiple sclerosis; TNF-α: tumor necrosis factor-alpha; PTMs: post-translational modifications; TRADD: tumor necrosis factor receptor type 1-associated DEATH domain protein; FADD: Fas-associated via death domain; TRAF 2/5: TNF receptor-associated factor 2/5; cIAPs: cellular inhibitor of apoptosis proteins; NF-κB: nuclear factor kappa B; MAPK: mitogen-activated protein kinase; TRIF: TIR-domain-containing adapter-inducing interferon-β; TBI: traumatic brain injury; IL-1β: interleukin-1β; IL-6: interleukin-6; Bcl-2: B-cell lymphoma 2; TGF-β: transforming growth factor-β; TAK1: TGF-β-activated kinase 1; CNS: central nervous system; SCI: spinal cord injury; mTORC1: mammalian targets of rapamycin complex 1; TNFR1: TNF-receptor I; Ca^{2+}: calcium ions; ROS: reactive oxygen species; mPTP: mitochondrial permeability transition pores; iPSC: pluripotent stem cell; Nec-1: Necrostatin-1; MPTP: 1-methyl-4-phenyl-1,2,3,6-tetrahydropyridine; MPP^{+}: 1-Methyl-4-phenylpyridinium; Aβ: β-amyloid; AMPK: AMP-activated protein kinase; DAMPs: damage-associated molecular patterns; HMGB1: high-mobility group box 1; BBB: blood-brain barrier; IL-1: interleukin-1; IFN: interferon; TRAIL: TNF-related apoptosis-inducing ligand; LUBAC: linear ubiquitin chain assembly complex; IKK: I-κB

Journal Pre-proof

kinase; SARM1: sterile alpha and Toll/interleukin-1 receptor motif-containing 1; JNK: c-Jun N-terminal kinases; CaMK: calcium-calmodulin kinase; TRPM7: transient receptor potential melastatin related 7; PARP1: Poly(ADP-ribose) polymerase-1; GSK-3β: Glycogen synthase kinase 3 beta; KLF8: Krüppel-like factor 8; VEGF: vascular endothelial growth factor; VEGFR: vascular endothelial growth factor receptor; NLRs: nucleotide-binding domain and leucine-rich repeat-containing molecules; Myd88: myeloid differentiation protein; GLUL: glutamate-ammonia ligase; PYGL: glycogen phosphorylase; GLUD1: glutamate dehydrogenase 1; GVD: granulovacuolar degeneration; TDP-43: TAR DNA-binding protein 43; OPA1: optic atrophy protein 1; NPCs: neural progenitor cells; Htt: Huntingtin; TRIAD: transcriptional repression-induced atypical cell death of neuron; LATS: large tumor suppressor kinase 1; SOD1: superoxide dismutase 1; hMSC: human mesenchymal stem cells; CHMP4B: charged multivesicular body protein 4b; PGAM5: phosphoglycerate mutase 5; BiP/GRP78: immunoglobulin-binding protein; c-FLIP: (FADD-like IL-1β-converting enzyme)-inhibitory protein; GD: Gaucher's disease; ICH: intracerebral hemorrhage; AIF: apoptosis-inducing factor; ATF4: activating transcription factor; SE: status epilepticus; NMDA: N-methyl-D-aspartate receptor; LDH: lactate dehydrogenase; miR: micro RNA;

Journal Pre-proof

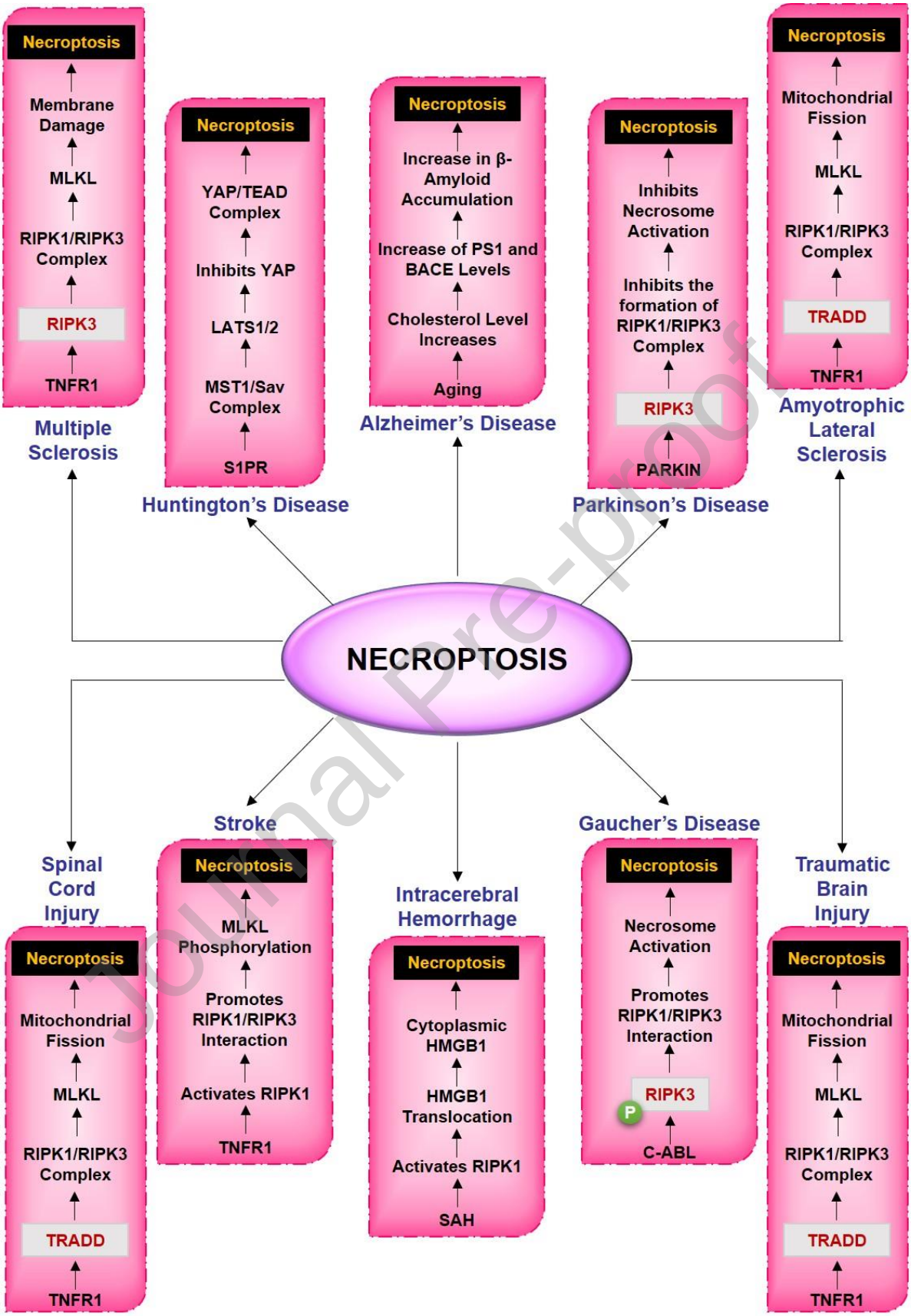

Graphical Abstract: Activation of necrosome through upregulation of RIPK1, RIPK2, RIPK3, and MLKL causes dysregulation in several biological processes, namely cell death activation that is involved in the progression and pathogenesis of numerous neurological manifestations, such as Alzheimer's disease,

Parkinson's disease, Huntington's disease, traumatic brain injury, spinal cord injury, stroke, Gaucher's disease, and others.

1. Introduction

Emerging evidence suggests the implementation of programmed cell death (PCD), namely apoptosis and necroptosis, in embryonic development and tissue homeostasis (Dhuriya and Sharma, 2018a). Apoptosis is a cell death mechanism regulated by the caspases and involved in the regulation of neuronal development, whereas necroptosis is a form of cell death activated by the deficiency of apoptosis (J. Yuan et al., 2019). Many studies have been performed that characterized necroptosis as an alternative form of cell death that mimics the features of necrosis and apoptosis and hence termed as necroptosis (Degterev et al., 2005). Necroptosis machinery is highly controlled by the activity and expression of toll-like receptors (TLRs), death receptors, interferons, receptor-interacting protein kinase 1 (RIPK1), receptor-interacting protein kinase 2 (RIPK2), and mixed lineage kinase domain-like (MLKL), which are found to be associated with various pathological conditions, namely neurological diseases, cancer, obesity, myocardial infarction, and inflammatory diseases (Jing Chen et al., 2019; Gong et al., 2019; Yan et al., 2022; Zhuang and Chen, 2020). Additionally, the genetic modulation of RIPK1 controls its activation and interaction with downstream mediators, such as caspase-8 and RIPK3, to promote apoptosis and necroptosis (D. Xu et al., 2021). Further, different necroptosis inhibitors, namely Necrostatin-1 (Nec-1), GSK-872, and Necrosulfonamide, have been identified to inhibit the activity of RIPK1 and receptor-interacting protein kinase 3 (RIPK3), which leads to the inhibition of necrosome (Cao and Mu, 2021; Chen et al., 2018; Ueda et al., 2022). The last decade witnessed the development and prosecution of different necroptosis inhibitors (Kopalli et al., 2016). For example, Zharp-99, PK68, AMG-47a, AP24534, 1-Benzyl-1H-pyrazole derivatives, aminoisoquinolines, pyrrolo[2,3-b]pyridines, furo[2,3-d]pyrimidines, GSK2982772, and GSK'074 have been developed and implemented for the inhibition of RIPK1, RIPK3, and MLKL activity, which causes inhibition of necrosome activity (Hou et al., 2019; Jacobsen et al., 2022; Khoury et al., 2020; Kopalli et al., 2016; Xia et al., 2020). However, despite the advancements in the development of necrosome inhibitions, the complexity associated with the necroptosis inhibitors made it challenging to target the proteins that regulate the necroptosis pathway (Choi et al., 2019).

Although based on their morphological features, various forms of regulated cell death have been characterized, such as apoptosis, necroptosis, autophagy, ferroptosis, pyroptosis, NETosis, and others, but the implication of necroptotic cell death in the progression and pathogenesis of neurological diseases have gained attention from the last one decade (Moujalled et al., 2021; Tower, 2015; Yan et al., 2020). Neurological diseases, namely Alzheimer's disease (AD), Parkinson's diseases (PD), Amyotrophic lateral sclerosis (ALS), Huntington's disease (HD), multiple sclerosis (MS), ischemic stroke, epilepsy, and others, involve the degeneration of neuronal cells, rupture of the blood-brain barrier, axonal degeneration, disruption of RNA metabolism, and defective axonal trafficking that leads to the death of nervous system (Gil-Martins et al., 2020; Küpeli Akkol et al., 2021; Lee et al., 2022; Nussbacher et al., 2019; Sleigh et al., 2019). For instance, in AD pathogenesis, tumor necrosis factor-alpha (TNF-α)-induced necroptosis is involved in neuronal loss, whereas, in PD, inhibition of RIPK3/MLKL with Nec-1 blocks necrosome activation that enhances the dopamine levels and rescues neuronal loss (Jayaraman et al., 2021; Lin et al., 2019). In addition, mounting evidence sheds light on the role of different post-translational modifications (PTMs), such as acetylation, ubiquitination, hydroxylation, SUMOylation, phosphorylation, and others in the regulation of necroptosis pathways (Douglas and Saleh, 2019; Meng et al., 2021; Q. Wang et al., 2021). For instance, loss of ubiquitin-specific peptidase 22 expressions significantly decreases the TNF-α-induced necroptosis cell death

(Roedig et al., 2021), whereas, administration of pterostilbene inhibits the RIPK3-induced necrosome activation by reducing sirtuin 2-mediated nuclear factor of activated T-cells 4 deacetylation (Shao et al., 2021). Herein, we review the current molecular mechanism and therapeutic interventions of necrosome activation in the pathophysiology of neurological diseases. We also shed light on the role of various PTMs in regulating necroptosis machinery, followed by the mechanistic implication of necrosome activation in the regulation of brain homeostasis. Further, based on our current knowledge, we highlighted the role of different signaling molecules in regulating the necroptosis pathway in the context of neurological diseases. Lately, we briefly discussed the implementation of necroptosis cell death in the pathophysiology of various neurological disorders and their current therapeutic intervention based on natural compounds, synthetic drug molecules, and RNA interference. **(Figure 1)**

Journal Pre-proof

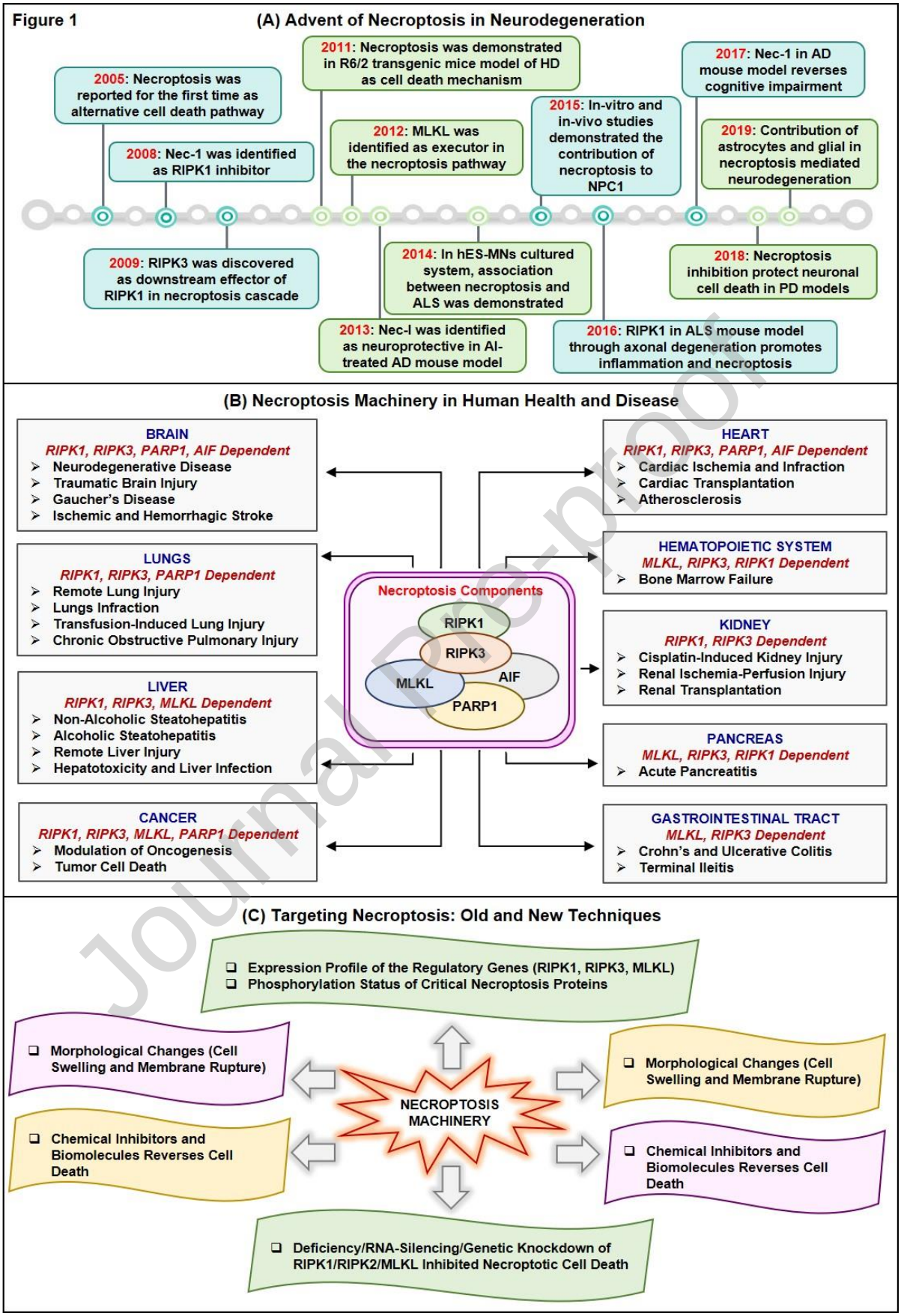

Figure 1: (A) Advent of necroptosis in neurodegeneration: the discovery of necroptosis cell death in the pathogenesis of neurodegenerative diseases occurs with the development of Nec-1 as a specific

inhibitor of RIPK1. Afterward, in 2009, RIPK3 was found to be a downstream target of the necroptosis pathway. In 2011, necroptosis cell death was first demonstrated in the R6/2 transgenic mice model of HD and in 2012, MLKL was found to be an effector in the necroptosis cell death pathway. Later on, in 2013, the potential of Nec-1 was demonstrated in an AD transgenic mice model, whereas in 2015 demonstrated the *in vitro* and *in vivo* of necroptosis pathways. In 2018, inhibition of necroptosis was shown to protect from neuronal cell death, whereas, in 2019, the contribution of astrocytes and glial cells in necroptotic-mediated neurodegeneration was proved. (B) The necroptosis cell death pathway is involved in different body organs through the activation of necrosome complexes, such as the brain, lungs, liver, heart, kidney, cancer, and others. (C) till now, different techniques and methods have been proved to target necroptosis pathways, namely morphological changes, the expression profile of the regulatory genes, phosphorylation status, siRNA-silencing, and chemical inhibitors.

2. Necroptosis machinery: An overview

Necroptosis, a controlled cell death pathway, is regulated by the expression of RIPK1, RIPK2, RIPK3, and MLKL, which collectively form a complex called as necrosome (Dhuriya and Sharma, 2018a). However, current studies and advancements in molecular research have focused on the activity and expression levels of RIPK3, TNF-α, and caspase-8 to understand the molecular mechanism of necroptosis (Choi et al., 2019). Necroptosis is characterized by the presence of dying cells clustering together, disrupted membranes, swollen cell bodies and organelles, and inflammasomes. It is hypothesized that necroptotic bodies passively move through the ruptured membrane into the extracellular matrix (Del Re et al., 2019). At a molecular level, necroptosis can be commenced by TNF superfamily receptors, TLRs, and interferon receptors, which are categorized into three categories, namely extrinsic necroptosis, intrinsic necroptosis, and ischemic-mediated intrinsic necroptosis (Tang et al., 2019). Extrinsic necroptosis is defined as classical necroptosis, which initiates with TNF-α that binds with the complementary receptor and leads to the formation of complex 1 consisting of tumor necrosis factor receptor type 1-associated DEATH domain protein (TRADD), Fas-associated via death domain (FADD), RIPK1, TNF receptor-associated factor 2/5 (TRAF 2/5), and cellular inhibitor of apoptosis proteins (cIAP 1/2) (Del Re et al., 2019). TRADD helps in the recruitment of RIPK1 to TNF-receptor I (TNFR1), followed by recruitment of cIAP 1/2 and TRAF 2/3/5 to complex I. Afterward, on activation, cIAP 1/2 and TRAF 2/5 cause RIPK1 ubiquitination that lead to the formation of stable complex I, which activates the signaling pathways, namely nuclear factor kappa B (NF-κB) and mitogen-activated protein kinase (MAPK) pathway that leads to the cell death (Santagostino et al., 2021). Further, studies have shown that caspase-8 deactivates necroptosis by inhibiting the activity of RIPK1 and RIPK3, whereas, inhibition of caspase-8 leads to activate RIPK1 through deubiquitination (Newton et al., 2019). Thus, removing ubiquitin molecules from RIPK1 leads to its interaction with FADD, TRADD, RIPK3, and caspase-8, which leads to the formation of complex II (Shan et al., 2018). Lately, RIPK1 has interacted with the RIPK3, leading to necrosome formation, which initiates the necroptotic cell death pathway (Xie et al., 2013). As compared with the classical necroptosis signaling, in non-classical signaling proteins, namely TLR 3/4, TIR-domain-containing adapter-inducing interferon-β (TRIF), and DNA activator of interferon initiates the formation of the necrosome complex to activate cell death (He et al., 2011; Kaiser et al., 2013a). TRIF is considered as a potential substrate for proteolytic cleavage mediated through caspase-8, where interaction between RIPK3 and TRIF is crucial for initiating the necroptosis pathway (Chan Kenta Moriwaki et al., 2022). Further, several studies have demonstrated that both RIPK1 and RIPK3 are substrates for caspase-8 mediated cleavage, which plays a crucial role in necroptosis cell death. For instance, Lalaoui *et al*., 2019 demonstrated that heterozygous missense mutations D324N, D324H and D324Y prevent caspase cleavage of RIPK1, whereas, Newton *et al*., 2019 showed that cleavage of RIPK1 by caspase-8 is crucial for limiting apoptosis and necroptosis (Lalaoui et al., 2019; Newton et al., 2019). Likewise, Zhang *et al*., 2019 concluded that

RIPK1 could mediate apoptosis as well as necroptosis through caspase activation (X. Zhang et al., 2019). Additionally, Tao *et al*., 2019 demonstrated that impaired cleavage of RIPK1 D324 variants by caspase-8 sensitized patients' peripheral-blood mononuclear cells to RIPK1 activation, apoptosis and necroptosis induced by TNF (Tao et al., 2019). (**Figure 2a)**

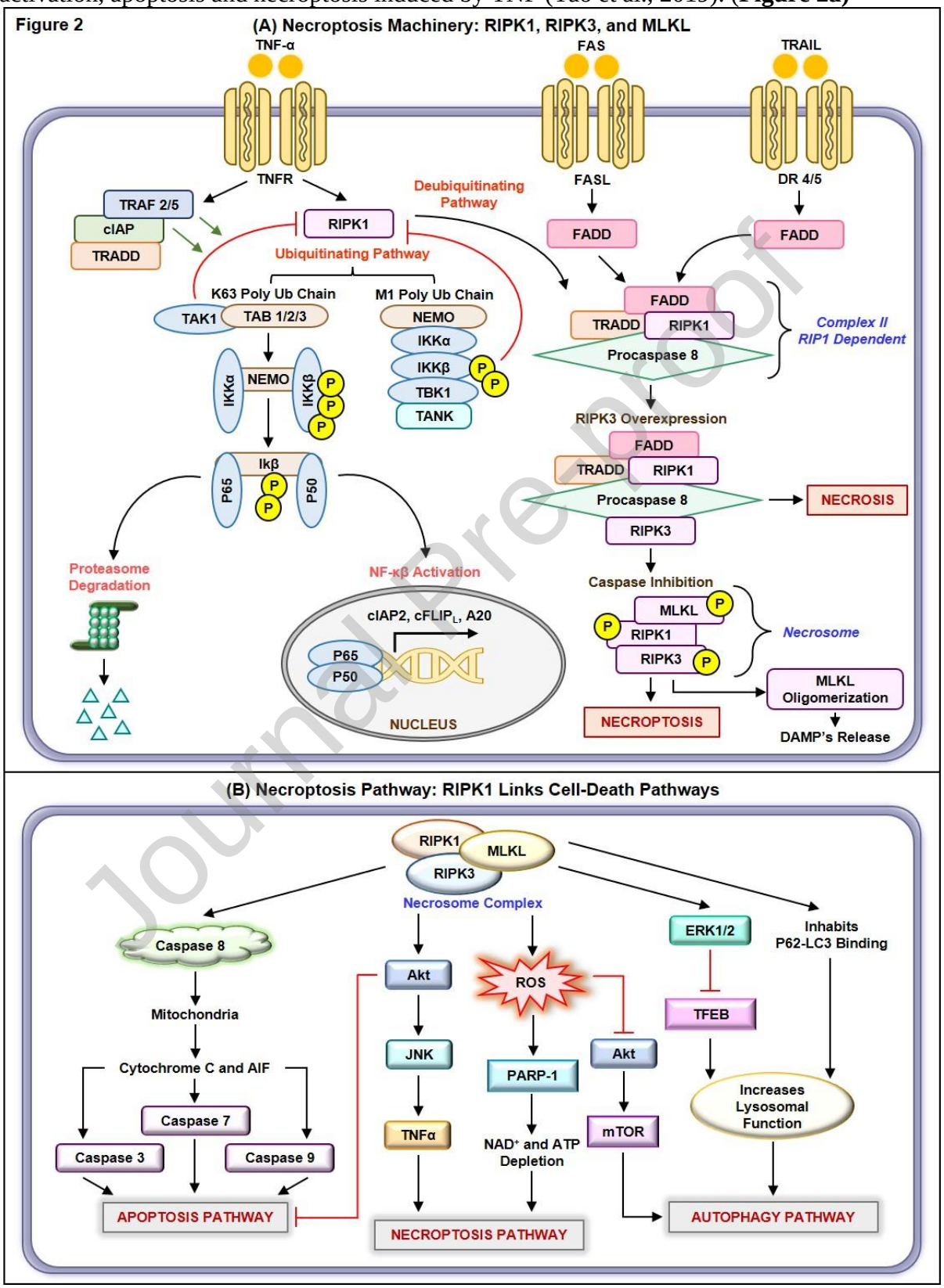

Figure 2: (A) Necroptosis machinery: RIPK1, RIPK3, and MLKL: necroptosis pathway initiates with the activation of death receptor ligands, namely TNFR1, FASL, and DR4/5. Activation of TNFR1 causes the

formation of a complex between TRAF2/5, cIAP, and TRADD, which activates the ubiquitination pathway. RIPK1 is a ubiquitination pathway that causes proteasome degradation and NF-κB activation. Similarly, FASL and DR 4/5 cause activation of FADD, which forms a complex with TRADD, RIPK1, and procaspase 8 that leads to RIPK3 overexpression. Overexpression of RIPK3 leads to caspase inactivation that causes necroptosis cell death. (B) Necroptosis pathway: RIPK1 links cell-death pathways: overexpression of RIPK1 causes necrosome activation, which targets caspase-8, Akt, and ERK1/2. Activation of caspase-8 on activation of caspase-3/7/9 leads to apoptosis cell death. In addition, the activation of Akt enhances the activity of JNK and TNF-α, which are involved in the regulation of necroptosis. In contrast, overexpression of ERK1/2 increases the lysosomal function and increasess the activity of the autophagic pathway.

3. RIPK1: A potential connection between necroptosis, apoptosis, and autophagy

Mounting evidence highlighted the potential involvement of RIPK1 and RIPK3 at the edge of necroptosis and apoptosis signaling events (Dillon et al., 2014; Kaiser et al., 2014; Lalaoui et al., 2019; Newton et al., 2019; Rickard et al., 2014; Tao et al., 2019; X. Zhang et al., 2019). For instance, in a rat model of traumatic brain injury (TBI), silencing of RIPK1 and inhibition of the NF-κB pathway, the protein expression levels of Interleukin-1β (IL-1β), Interleukin-6 (IL-6), TNF-α, Bax, and cleaved-caspase-3 was downregulated. The same study concluded that the expression of B-cell lymphoma 2 (Bcl-2), ATG5, and LC3II/LC3I was upregulated. The same study concluded the reduction in neuron injury, neuronal apoptosis, and enhanced neuronal autophagic degradation through RIPK1 downregulation (Liu et al., 2020). Likewise, inhibition of histone methyltransferase, namely Dot1L, rescued from RIPK1-dependent neuronal apoptosis through enhanced RIPK1 K63-ubiquitylation and decreased formation of RIPK1/caspase-8 complex. In addition, decreasing the H3K73me3 levels in the promoter region of ubiquitin-modifying enzyme cIAP 1 contributes to enhanced K63-deubiquitination (J. Wang et al., 2021). Further, under ischemic conditions, activation of RIPK1 rapidly activates necroptosis followed by apoptosis through the reduction in transforming growth factor-β (TGF-β)-activated kinase 1 (TAK1) in microglial/infiltrated macrophages (Naito et al., 2020). Subsequently, Xu *et al*., 2018 demonstrated that TAK1, a RIPK1 kinase inhibitor, enhances axonal degeneration, neuronal loss, and neuronal apoptosis (Xu et al., 2018). Recently, Qi *et al*., 2020 Elevated miR-494 and repressed the expression of RIPK1 to rescue the hippocampal neuron injury, accelerate neuronal proliferation, and restrain neuronal apoptosis by inactivating the NF-κB signaling pathway (Qi et al., 2020). Moreover, RIPK1 activity mediates the crosstalk between necroptosis and autophagic degradation in the central nervous system (CNS) (Saleem, 2021). For example, Xu *et al*., 2021 demonstrated that stimulation of TNF-α cause the formation of the p62/RIPK1 complex, which induces RIPK1 self-oligomerization and leads to necroptosis cell death and impaired autophagic pathway (C. Xu et al., 2021). Likewise, Liu *et al*., 2018 concluded that stimulation of autophagy and lysosomal function with rapamycin treatment led to decreased accumulation of RIPK1 and attenuated cell death after spinal cord injury (SCI) (Liu et al., 2018). Another study found that DRD1 signaling promotes RIPK1 ubiquitination via the E3 ubiquitin ligase Chip and degradation through autophagy. The same concluded that DRD1 signaling prevented neuronal death, suppressed neuroinflammation, and restored many TBI-related functional sequelae through an autophagy-dependent mechanism (Lin et al., 2022). Additionally, growth differentiation factor 11 protects the traumatically injured spinal cord by suppressing pyroptosis and necroptosis via transcription factor E3-mediated autophagy augmentation (Yu Xu et al., 2021). Thus, the evidence mentioned above demonstrated the potential link between cell death pathways through the mechanistic involvement of RIPK1. Necroptosis is similar to another cell-death pathway, namely pyroptosis, through membrane damage that leads to be distinct signaling pathways (Frank and Vince, 2018). However, further studies were required to extract the molecular mechanism in different experimental models, namely *in vitro* and *in vivo.* **(Figure 2b)**

4. Mechanistic implementation of post-translational modification in necroptosis

Journal Pre-proof

In recent years, insight into the PTMs associated with RIPK1, RIPK3 and MLKL activity, structure, stability, interactions and localization has increased immensely. PTMs are vital in modulating RIPK1 to either engage in or get excluded from cell death signaling. At the same time, most of the identified PTMs in RIPK3 and MLKL promote their necroptotic activity (Meng et al., 2021). PTMs promoting necroptotic cell death are an attractive target for treating various diseases. Currently, the effort to target these PTMs is mainly directed at RIPK1, and multiple inhibitors are under clinical trials (Jensen et al., 2020). RIPK1 contains 86 Ser/Thr, where PTMs such as phosphorylation can occur, but some are not activated, and others do not change RIPK1 activity upon phosphorylation (Degterev et al., 2008; Delanghe et al., 2020). Ser161 and Ser166, in particular, are given more attention as their phosphorylation has been reported to activate numerous signaling pathways and are commonly used as necroptotic markers in several diseases (Najjar et al., 2016; Sun et al., 2002). It has been reported that RIPK1 phosphorylation at Ser166, due to ischemic/traumatic brain injury, activates R1PK1 kinase and results in necroptosis [64]. The mammalian targets of rapamycin complex 1 (mTORC1) inhibitors (rapamycin or Ku-0063794) and a p70s6 inhibitor (PF-4708671) decreased Ser166 phosphorylation (Abe et al., 2019). It has been reported that the site of ubiquitinylation of RIPK1 is vital for its activity (Feltham and Silke, 2017). Lys11, Lys48 and Lys63 are three major sites of ubiquitinylation in RIPK1 as identified by mass spectrometry (Simpson et al., 2021). The activation of NF-κB occurs after cIAP-mediated Lys63 ubiquitination of RIPK1 associated with the intracellular domain of TNFR1 called complex I. The non-ubiquitinated or deubiquitinated RIPK1 transitions to complex II and necrosome formation to cause cell death (Aksentijevich and Zhou, 2017). Various E3 ligases and deubiquitinases, such as A20, linear ubiquitin chain assembly complex (LUBAC), cIAP 1/2 and CYLD, have been suggested to modulate ubiquitin modifications in RIPK1 (Zou et al., 2021). Caspase-8 suppresses necroptosis, and its inhibitors and substrates modulate necroptosis. Downregulation of Caspase-8 or its associated protein FADD allows necroptosis to occur (Kaiser et al., 2011; Zhang et al., 2011). Caspase-8 activity is modulated by two cFLIP isoforms (Irmler et al., 1997; Scaffidi et al., 1999). cFLIPL forms a heterodimer with Caspase-8 and inhibits its autoprocessing leading to apoptosis inhibition (Oberst et al., 2011). While cFLIPS inhibits cleavage of RIPK1 and RIPK3 besides preventing Caspase-8 auto-processing (Feoktistova et al., 2011). CYLD has been reported as a Caspase-8 substrate, and its cleavage was shown to reduce TNF-induced necroptosis (O'Donnell et al., 2011). Protein phosphatase 1B (Ppm1b) has been reported to dephosphorylate RIPK3 at T231 and S232, which are observed to increase RIPK3 catalytic activity (Chen et al., 2015, 2013). RIPK3 is also regulated by E3 ubiquitin ligases, such as A20, PELI1 and CHIP, that also ubiquitylate RIPK1 and inhibit necroptosis (Choi et al., 2018; Seo et al., 2016). Like RIPK1, Caspase-8-mediated cleavage of RIPK3 at D328 inhibits necroptosis, leading to non-death outcomes via TNF signaling (Feng et al., 2007). MLKL is activated by phosphorylation of its pseudokinase domain by RIPK3, causing a conformational change in its structure, leading to the translocation of MLKL to the plasma membrane and causing necroptotic death in both human and mouse cell lines (Murphy et al., 2013; Sun et al., 2012). Studies have suggested that molecules or compounds that can target multiple effectors of necroptosis, such as RIPK1, RIPK3 and MLKL, at the same time could help in the effective treatment of necroptotic diseases (Pierotti et al., 2020). **(Figure 3)**

Journal Pre-proof

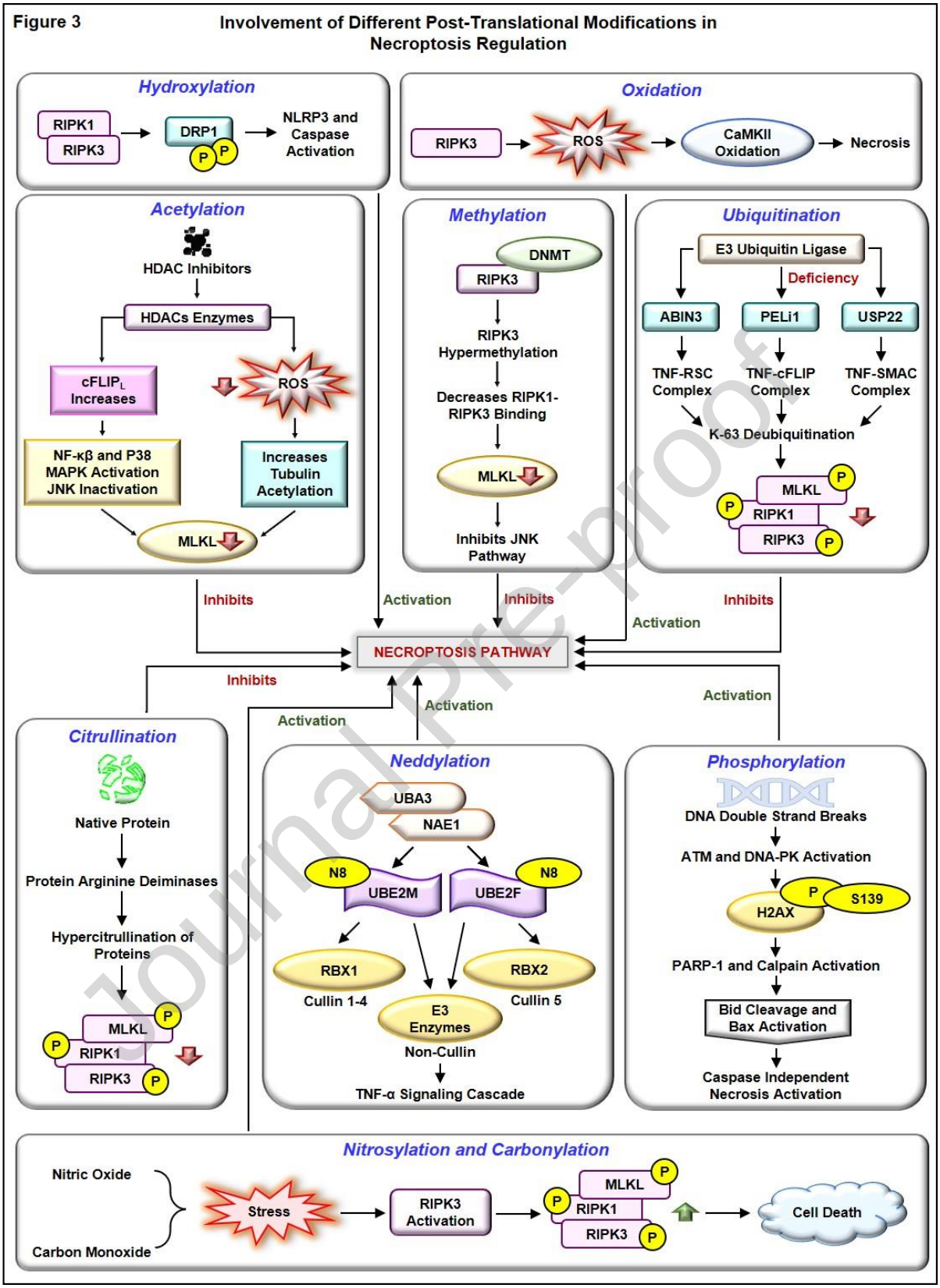

Figure 3: Involvement of Different Post-Translational Modifications in Necroptosis Regulation: mounting evidence suggests post-translational modifications' involvement in activating or inhibiting the necroptosis pathway. For example, acetylation, methylation, ubiquitination, and citrullination inhibit the necroptosis pathway, whereas hydroxylation, oxidation, neddylation, phosphorylation, nitrosylation, and carbonylation inhibit activates the necroptosis pathway.

Journal Pre-proof

Table 1: Post-translational modifying enzymes as a therapeutic target against necroptosis machinery in the pathogenesis of various neurological diseases

PTM	Enzyme	Experimental model	Target	Signaling molecules	Mechanism	References
Acetylation	HDAC6	OGD model	Tubulin	ROS	Inhibiting ROS activity reversed the OGD-induced increase of ROS and the decrease in acetylated tubulin.	(Yuan et al., 2015)
	HDAC	L929 cells	$cFLIP_L$	JNK, mTOR, Akt, p38 MAPK	Promotes anti-inflammatory and neuroprotective activity.	(Wang et al., 2013)
Ubiquitination	USP22	HT-29 cells	RIPK3	TNF-α, H2A, H2B	Ubiquitination of RIPK3 at K518 increases necroptosis cell death.	(Roedig et al., 2021)
	____	PC12 cells	RIPK1	MLKL and RIPK3	Ubiquitination of RIPK1 promotes necroptosis cell death.	(Y. Y. Zhang et al., 2021)
	Triad3A	Mouse model with MCAO	TNF-α	iNOS, CD32, CD68, IL-6, IL-1β	Regulate necroptotic cell death to mediate the progression of cerebral I/R injury.	(Z. Yuan et al., 2020)
	Smurf1	Pc12 cells	RIPK1	RIPK3 and inflammatory cytokines	It promotes neuronal necroptosis and enhances neuroinflammation.	(Shao et al., 2018)
SUMOylation	SUMO2	HEK-293T	FADD	Drp1, Caspase 10	SUMOylation at K120, K125, and K149 regulates necroptosis cell death.	(Choi et al., 2017)
Neddylation	Cullin	----	CSN	CNS1, CNS8	Promotes necroptotic cell death.	(Lewno et al., 2021)
Methylation	DNMT1	Mesothelioma cells	RIPK3	Caspase-8, FADD, and MLKL	Epigenetic silencing of RIPK3 by DNA methylation impairs necroptosis.	(Tan et al., 2021)
	DNMT1	Mouse embryonic fibroblast	RIPK3	IDH1	2-HG-induces DNA hypermethylation and suggests impaired necroptosis.	(Z. Yang et al., 2017)
	SMYD2	$Apc^{Min/+}$ mice, B6 /J mice and $Rag1^{-/-}$ mice	RIPK1	TNF-α	Inhibits TNF-induced apoptosis and necroptosis.	(Yu et al., 2022)
	----	HEK293T, MEFs, L929, and BMDM cell	RIPK1	IκBα, p38, caspase-8, caspase-3, caspase-8	RIPK1-DD in mediating RIPK1dimerization and activation of its kinase activity during necroptosis.	(Meng et al., 2018)
Hydroxylation	PHD1/2/3	THP-1 cells and primary human monocytes	HIF	IL-1β, NF-κB, TLR, caspase-3/7	Inhibition of the HIF-hydroxylases selectively targets monocytes for cell death.	(Crifo et al., 2019)
Citrullination	____	C57BL/6N mice	H3	RIPK1, MLKL	Promotes necroptosis cell death.	(Nakazawa et al., 2018)
	PAD-4	RSV A2 strain	Histone protein	PI3K/AKT, ERK and p38 MAPK	Induces ROS-dependent necroptosis through enhanced histone citrullination.	(Muraro et al., 2018)
	PAD-4	Synovial tissue of patients	14-3-3η	TNF-α, RIPK1, RIPK2, MLKL, IL-6	Promotes necroptosis cell death through increased citrullination by PAD-4.	(Trimova et al., 2019)
Nitrosylation	SNO	Patients sample	LIM protein	TLR3, RIPK3, NLRP3	SNO-MLP also increased the complex formation between TLR3 and RIP3, enhancing necroptosis.	(Tang et al., 2020)
	SNO	HEK293 cells	RIPK3	NO, nNOS, GSNO	Induces cerebral ischemic injury through enhanced necroptosis cell death.	(Miao et al., 2015)
Carbonylation	CO	HEK293 cells	RIPK1, IDO	ROS	Promotes necroptosis cell death.	(Teixeira et al., 2018)
	CO	Ischemia-reperfusion injury in animal models	MLKL	IL-8, p21	Carbonylation induces necroptosis.	(Lewinska et al., 2020)
	____	MPTP-treated neurons	OPA1	ROS levels, mtDNA	Carbonylation through CO causes enhanced necroptosis cell death.	(Iannielli et al., 2018)

HDAC6: Histone deacetylase 6; ROS: Reactive oxygen species; OGD: Oxygen-glucose deprivation; mTOR: Mammalian target of rapamycin; JNK: c-Jun N-terminal kinase; Akt: Protein kinase C; p38 MAPK: p38 mitogen-activated protein kinases; $cFLIP_L$: Cellular FLICE-inhibitory protein; USP22: Ubiquitin specific peptidase 22; RIPK3: Receptor-interacting serine/threonine-protein kinase 3; TNF-α: Tumour necrosis factor alpha; RIPK1: Receptor-interacting serine/threonine-protein kinase 1; MLKL: Mixed lineage kinase domain-like; MCAO: Middle cerebral artery occlusion; iNOS: Inducible nitric oxide synthetase; CD32: Cluster of differentiation 32; CD68: Cluster of differentiation 68; IL-6: Interleukin 6; IL-1β: Interleukin-1β; I/R: Ischemia-reperfusion; FADD: Fas associated via death domain; Drp1: Dynamin-related protein 1; CSN: COP9 signalosome; IDH1: Isocitrate dehydrogenase 1; SMYD2: SET And MYND Domain Containing 2; IκBα: Nuclear factor of kappa light polypeptide gene enhancer in B-cells inhibitor, alpha; HIF: Hypoxia-inducible factor; NF-κB: Nuclear factor kappa B; TLR: Toll-like receptor; PI3K: Phosphoinositide 3-kinases; PHD: Hypoxia-inducible

Journal Pre-proof

factor prolyl hydroxylase; PAD-4: Protein arginine deiminases 4; RIPK2: Receptor Interacting Serine/Threonine Kinase 2; NLRP3: NLR family pyrin domain containing 3; NO: Nitric oxide; nNOS: Neuronal nitric oxide synthase; GSNO: S-Nitrosoglutathione; IL-8: Interleukin 8; mtDNA: Mitochondrial DNA

5. Necroptosis interferes with biological processes in the brain

5.1. Mitochondrial dysfunction and lysosomal defects

Mitochondrial dysfunction and neuroinflammation aggravate neurodegenerative diseases. Mitochondrial malfunction can cause inflammation by activating the NLR family pyrin domain containing 3 inflammasomes (Manini et al., 2022). Unlike apoptosis, the involvement of mitochondria in necroptosis is complicated, and it appears that mitochondrial malfunction plays a crucial role in necroptosis, depending on the underlying cellular circumstances, various physiological and pathological states, and cell type. Necroptosis, like apoptosis, is carried out without the need of the Death Receptor by using cell-intrinsic components such as increased calcium ions (Ca^{2+}) and reactive oxygen species (ROS). Mitochondrial dysfunction is caused by increased ROS, mitochondrial swelling, decreased ATP synthesis, and the development of mitochondrial permeability transition pores (mPTP). Interestingly, ROS production during mitochondrial failure was correlated to the stability of necrosome proteins, creating a positive feedback loop that aided necroptosis. RIPK3 is thought to be essential for generating ROS in mitochondria during necroptosis activation (Faizan and Ahmad, 2021). The gradual loss of dopaminergic neurons in the substantia nigra is a hallmark of PD, and mitochondrial dysfunction plays a key role (Exner et al., 2012). Optic atrophy protein 1 (OPA1) being a vital resident protein of the inner mitochondrial membrane that regulates both mitochondrial shape and dynamics (MacVicar and Langer, 2016). In neural cells, OPA1 mutations alter mitochondria function. In one of the studies, researchers showed that PD-associated OPA1 mutations in patients activate induced pluripotent stem cell (iPSC)-derived neural cells, resulting in significant mitochondrial dysfunctions, reduced oxidative phosphorylation, and elevated oxidative stress levels, causing neuronal cell loss Nec-1 inhibited RIPK1 kinase activity, protecting PC12 cells (pheochromocytoma of the rat adrenal medulla) against cell death induced by 6-hydroxydopamine, a mitochondrial respiration inhibitor used to produce PD (J. R. Wu et al., 2015). Additionally, according to Lannielli *et al*., 2018 necroptosis suppression restored cells' ability to develop and successfully protected nigral DA neurons in mice treated with the 1-methyl-4-phenyl-1,2,3,6-tetrahydropyridine (MPTP) neurotoxin. mPTP is a precursor of the neurotoxin 1-Methyl-4-phenylpyridinium (MPP^{+}), which causes PD by killing dopaminergic neurons inside the brain's substantia nigra (Iannielli et al., 2018). Similarly, the functioning of mitochondria is critical in β-amyloid (Aβ)-mediated neuronal damage. Aβ oligomers cause an increase in ROS levels *in vivo* and are susceptible to various mitochondrial enzymes, including α-ketoglutarate dehydrogenase and aconitase. Therefore, Aβ-oligomers may disrupt mitochondrial function, leading to a loss of mitochondrial membrane potential and increased ROS levels (Wang et al., 2007). Furthermore, Death receptor-signaling causes necroptosis directly by 1) or can incorporate mitochondrial signaling in a cell-type-specific way 2) MLKL and RIPK3 (activated necrosome complex proteins) have been demonstrated to translocate to the mitochondria and promote mPTP opening, resulting in lower ATP levels, mitochondrial collapse, and higher mitochondrial ROS generation The mitochondrial ROS generated activates several proteins, perhaps amplifying the necroptosis signal. RIPK1 is one such protein that has been demonstrated to be auto-phosphorylated by mitochondrial ROS and stimulate necrosome production in a feedback mechanism (Shili Zhang et al., 2019). Wang *et al*., 2014 reported that RIPK3 kinase promotes MLKL phosphorylation at T357/S358, causing oligomerization. Afterward, MLKL oligomer travels from the cytoplasm to intracellular and plasma membranes. During necroptosis, the MLKL oligomer compromises membrane integrity directly (H. Wang et al., 2014). Similar to the pathology observed in PD and AD, the protein levels of RIPK1, RIPK3 and MLKL in various indications, such as ALS, MS, and others.

The lysosome is another crucial acidic organelle essential for the turnover of undesirable cellular components, particles, and organelles (Gómez-Sintes et al., 2016). The importance of the lysosome in cell death regulation is currently receiving much attention. The lysosome, being a multifunctional organelle, is responsible for the majority of controlled necrosis, including necroptosis, ferroptosis, and pyroptosis (Alu et al., 2020). For instance, according to Liu *et al*., 2018 lysosomal disruption following spinal cord injury induces an increase in RIPK1 and RIPK3 protein levels, which potentiates necroptosis. Another study reported that CHIP (carboxyl terminus of Hsp70-interacting protein; also known as STUB1), E3 ligase-mediated ubiquitylation negatively regulates RIPK3 expression level and leads to its lysosomal degradation. Interestingly, lysosomal protease inhibitors, like E64d and pepstatin A (E64d/PepA), blocked RIPK1 and RIPK3 Expression, but not by proteasomal inhibitor MG132 (Liu et al., 2018; Seo et al., 2016). Further, the scientists discovered that RIPK1 deletion causes increased mTORC1 activity, which leads to lysosomal dysfunction. Moreover, RIPK1, through targeting AMP-activated protein kinase (AMPK), regulates mTORC1 inhibition (Najafov et al., 2021). Consequently, several studies have proposed that targeting the lysosome might improve the prognosis of relevant illnesses by managing the controlled necrosis process. **(Figure 4)**

5.2. Inflammatory response and microglial activation

Inflammatory pathways may be regulated directly by necroptosis signaling kinases. Necroptosis is a lytic form of cell death that leads to damage-associated molecular patterns (DAMPs) production and the progression of inflammation (Pasparakis and Vandenabeele, 2015). Necroptosis includes several events, such as loss of membrane integrity, cell swelling and leaking, and the release of energy and DAMPs that causes cell death and neuroinflammation, which has a role in the pathogenesis of MS, ALS, PD, and AD (Weinlich et al., 2017). It has the ability to significantly elicit the local microenvironment and causes CNS pathology (J. Yuan et al., 2019). DAMPs-dependent Inflammation cases due to necroptosis are referred to as "Necroinflammation" (Sarhan et al., 2018). Many necrosis-associated DAMPs have been discovered, namely high-mobility group box 1 (HMGB1), S100 proteins, heat shock proteins, receptors for advanced glycation end-products, exRNAs, cfDNA and ATP (Kaczmarek et al., 2013; Murao et al., 2021). In neurodegenerative disease, HMGB1 and thrombin also serve as neuroinflammation biomarkers by activating inflammation and blood-brain barrier (BBB) dysfunction (Jeon et al., 2021). In AD patients, higher levels of HMGB1 and soluble receptors for advanced glycation end-products are associated with amyloid-beta formation, whereas S100B and neuron-specific enolase levels relate to disease severity (Chaves et al., 2010; Festoff et al., 2016). Similarly, In PD patients, serum HMGB1 and TLR4 protein levels were dramatically raised and corresponded with PD stages (Y. Yang et al., 2018). Further research suggested that inflammasome activation and cell lysis by necroptosis can also result in proinflammatory cytokines and chemokines released into the bloodstream circulation. Moreover, recent research shows that under proinflammatory conditions, mitochondrial DNA may act as a cellular DAMP following release from the mitochondria (Nakahira et al., 2011). Lin *et al*., 2017 investigated the feasible relationship between shikonin (quinone-containing natural product)-induced autophagy and shikonin-induced necroptosis to understand the immune response. Here they have also studied the mechanism by which Shikonin-induced autophagy can directly contribute to DAMPs upregulation which could be critical for immunogenicity in cells undergoing necroptosis (Lin et al., 2017). Further, extensive research is still ongoing to understand the regulation of inflammation by necroptosis-associated proteins in neurological diseases. Different types of proinflammatory cytokines, interleukin-1 (IL-1), interferon (IFN), and TNF, were reported to be upregulated. These, including other ligands, such as Fas ligand and TNF-related apoptosis-inducing ligand (TRAIL), can cause extrinsic apoptosis and

necroptosis by acting on death receptors in numerous CNS cell types such as neurons and oligodendrocytes. TNF activates genes involved in inflammation by binding to TNFR1. TNF-stimulated TNFR1 has three possible impacts, each reliant on regulatory protein assembly. These distinct routes lead to NF-κB-dependent inflammation, caspase-8-dependent apoptosis, or alternate activation of the necroptosis pathway in the presence of caspase-8 suppression (Choi et al., 2019). Here we will discuss NF-κB-mediated inflammatory signaling. When TNFR1 is activated, a complex between RIPK1 and the TRADD protein and several accessory proteins form. cIAPs or LUBAC Ubiquinate RIPK1, which causes engagement of the inhibitor of I-κB kinase (IKK) complex, leading to NF-κB activation and nuclear translocation, which further activates transcription of genes involved in cell survival, proinflammatory cytokines (Ofengeim and Yuan, 2013). Hence, targeting RIPK1 kinase or NF-κB for the treatment of human disorders characterized by necrosis and inflammation might be beneficial.

Microglia are macrophage-like cells resident in the CNS. These can cause neuronal death in response to infectious or tissue damage, ischemic, traumatic, and neurodegenerative diseases, generating proinflammatory cytokines (e.g., TNF-α) and eventually becoming phagocytic in nature. These cells participate in immunosurveillance by propagating inflammatory signals in response to stimuli (such as cytokines, chemokines, PGE2, lipopolysaccharides (LPS), IFNs, and nitric oxide) that activate the proinflammatory pathway (Bachiller et al., 2018). Microglial activation has traditionally been divided into two categories: classic (M1) and alternative (M2). The M1 phenotype is characterized as pro-inflammatory, which produces and secretes ROS, reactive nitrogen species and cytokines (TNF-α, IL-1β, or IL-12). In contrast, the M2 microglial phenotype is referred to as an anti-inflammatory and is implicated in the generation and release of trophic factors, such as TGF-β and brain-derived neurotrophic factors (Tang and Le, 2015). DAMPs likewise activate microglial cells in the CNS. DAMPs, such as HMGB1, bind to pattern recognition receptors on innate immunity cells in the central nervous system (e.g., microglia), causing the activation and production of pro-inflammatory cytokines (Thadathil et al., 2021). Microglial activation is also regarded as a crucial driver for AD pathogenesis. Salvadores et al. have shown that Aβ oligomers colocalize with the phosphorylated MLKL, a necroptosis effector. Aβ oligomers-stimulated microglia activate necroptosis in neurons through TNF-α signaling, resulting in substantial neurodegeneration. Inhibition of necroptosis signaling provides neuronal protection (Salvadores et al., 2022) **(Figure 4)**. Additionally, Fricker *et al*., 2013 demonstrated the relevance of caspase-8 suppression in primary neuronal/glial cultures by utilizing a caspase inhibitor that eliminates inflammatory stimulated microglia. Most notably, we discovered that Nec-1, which prohibits microglia necroptosis, completely reversed the neuronal loss caused by caspase inhibition (Fricker et al., 2013). Further ischemia research reveals a unique function for necroptotic neurons in microglia M1/M2 balance modulation via the myeloid differentiation protein (Myd88) pathway. In the ischemic brain, suppressing RIPK3 or MLKL might alter microglia/macrophage activity from M1 to M2 type (J. Yang et al., 2018). Consequently, increased RIPK1 protein levels in microglia and astrocytes elicit a deleterious neuroinflammatory response that adds to the neurodegenerative environment in progressive MS. However, the microglial is the most abundant immune cell in MS. In microglia, RIPK1 signaling is pro-inflammatory and harmful, but in astrocytes, it is pro-inflammatory but does not cause cell death. NF-kB signaling regulates inflammatory transcriptional programs in microglia and astrocytes (Zelic et al., 2021). Thus, studies show that therapeutic RIPK1 inhibition (such as nec1) reduces symptoms in patients with a degenerative neurological condition.

5.3. Axonal degeneration

Axonal degeneration is activated by various stimuli that intervene in the induction of a necroptotic programmed cell-death program via a cell-autonomous process is a crucial target for neuroprotection since it leads to functional impairment in a variety of nervous system diseases. Axonal degeneration has been linked to several specific factors and subcellular processes. However, researchers have yet to discover an integrative signaling system that triggers a self-destructive process in the pathogenesis of axonal degeneration. It is induced by mitochondrial dysfunction, activation of the mPTP, calcium release from the endoplasmic reticulum, and ROS production (Court and Coleman, 2012). Necroptosis has a role in nervous-system diseases characterized by prominent axonal degeneration, such as ALS, MS, neuroinflammation, AD and PD. A plethora of studies reported in both the peripheral nervous system and the CNS models of Wallerian degeneration that pharmacological inhibition (by Nec-1) and genetic suppression or knock-down of RIPK3 significantly slowdown morphological and functional loss of axons (Arrázola et al., 2019a). In the PD model, Onate et al. proposed the notion of "necroaxoptosis" as a new process of axonal degeneration driven by necroptosis machinery components. Inhibition of necroaxoptosis appears to be an effective therapeutic target for preserving the function and structure of axons and terminals in PD indication and other neurodegenerative conditions. Here data showed that in a mouse model of PD, genetic deletion of RIPK3 and MLKL, or treatment of Nec-1, reduced axonal degeneration, resulting in improved motor function (Oñate et al., 2019). In addition, Hernaández *et al*., 2018 describe that axonal degeneration post glutamate excitotoxicity is also regulated by necroptosis. They discovered that inhibiting RIPK1, RIPK3 or MLKL prevents activities in axonal degeneration, such as Ca^{2+} instability in the axonal compartment, mPTP opening and mitochondrial dysfunction. Interestingly, the same excitotoxic stimuli cause apoptosis in the cell soma, revealing the co-activation of two distinct mechanisms in separate compartments of the same cell (Hernández et al., 2018). Additionally, with aging, necroptosis is induced in the hippocampus, particularly in axonal tracts. MLKL, the major necroptotic effector, was enough to prevent age-related axonal degeneration. Studies show that inhibition of RIPK3 can reverse axonal degeneration and hippocampus-dependent functional decline in elderly mice (Arrázola et al., 2021). Furthermore, a specialized form of axonal necroptosis event happens. Sterile alpha and Toll/interleukin-1 receptor motif-containing 1 (SARM1) is an inducible NAD^+ cleavage enzyme whose activation induces axon degeneration in both classic injury-induced Wallerian degeneration and the dying back axon loss of peripheral neuropathy. SARM1-dependent axon degeneration, oligodendrocyte loss, and subsequent retinal ganglion cell death can occur when neuroinflammatory signals and necroptosis operate locally in the axon (Ko et al., 2020). However, investigations have indicated that SARM1 is essential in innate immunity regulation because its structure contains the TIR (Toll/interleukin-1 receptor) domain, which is found in TLRs, potentially connecting axon degeneration to pathogen response and intercellular communication. SARM1 is an excellent candidate for treatment since it slows axon degeneration (Hopkins et al., 2021). Progressive axonal degeneration has been related to Aβ and tau accumulation in the early stages of AD (Salvadores et al., 2020). ALS is caused by the Optineurin (Optn) gene mutation by modulating RIPK1 turnover, and optineurin actively reduces RIPK1-dependent signaling. By activating necroptotic machinery in the CNS, such as RIPK1, RIPK3, and MLKL, loss of Optn led to gradual dysmyelination and axonal degeneration. As a result, RIPK1/RIPK3 is essential in causing progressive axonal degeneration (Ito et al., 2016). Hence, findings suggest necroptosis as a promising target for the future development of treatments for age-related impairments, ALS, AD, PD, and other axonal degenerative illnesses in humans. **(Figure 4)**

Journal Pre-proof

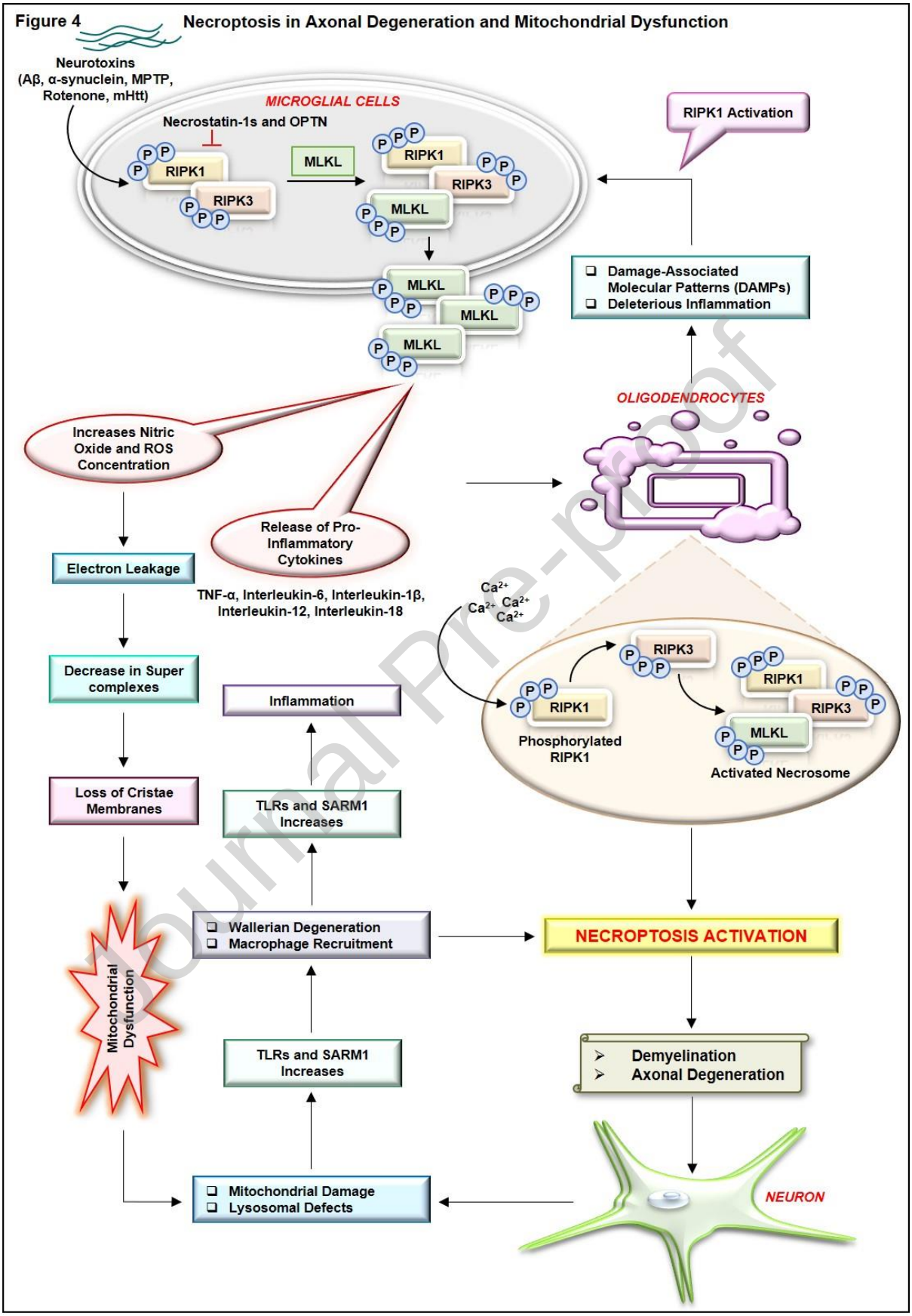

Figure 4: Necroptosis in Axonal Degeneration and Mitochondrial Dysfunction: activation of necrosome complex inside the microglial cell through administration of neurotoxins hampers the oligodendrocytes, which leads to necroptosis activation and causes demyelination and axonal degeneration. Further,

mitochondrial damage and lysosomal defects lead to an increase in the activity of TLRs and SARM1 and cause inflammatory response-mediated necroptosis cell death.

6. Necroptosis impedes cellular signaling events that alter brain homeostasis

6.1. Calcium signaling and ERK/MAPK cascade

Ca^{2+} signaling is critical for the implementation of apoptosis-induced cell death. Recent research suggests that increased cytosolic Ca^{2+} can also cause necroptotic cell death. Ca^{2+}-induced necroptosis can indeed be DR-dependent or DR-independent, depending on the cell type and necroptosis-inducing agents present. During DR-induced necroptosis, a rise in cytosolic Ca^{2+} has been seen as a downstream consequence of necrosome formation. Ca^{2+} signaling is an upstream regulator of necrosome complex proteins during DR-independent necroptosis (Faizan and Ahmad, 2021). A natural compound such as 2-methoxy-6-acetyl-7-methyljuglone causes necroptotic cell death vis a death receptor-independent manner was attributed to increased ROS level, RIPK1/RIPK3 activation, and an elevated cytosolic Ca^{2+} levels (Sun et al., 2016). In addition, one research found that the RIPK1/RIPK3 complex or the formation of necrosomes promotes downstream processes such as c-Jun N-terminal kinases (JNK) pathway activation, mitochondrial ROS generation, and calcium build-up in the cytosol (Sun et al., 2017). Another study demonstrated that increased cytoplasmic calcium levels induced necroptosis via activating calcium-calmodulin kinase (CaMK) II. Finally, it was discovered that CaMKII activation was responsible for RIPK1 phosphorylation (Nomura et al., 2014). In recent years, a plethora of studies showed that calcium malfunction has been linked with neurodegenerative diseases, such as PD, AD, ALS, and related dementias (Verma et al., 2018). By activating oxygenase enzymes or increasing electron leakage from the mitochondria, dysregulation of Ca^{2+} homeostasis in neurons can cause ROS overproduction, destabilizing Ca^{2+} homeostasis (Khodorov et al., 1999). Of note, it is known that Aβ aggregation disrupts Ca^{2+} homeostasis and ramps up Aβ aggregation by enabling the formation of early protofibrillar structures and fibrils, along with more adverse downstream effects, such as mitochondrial dysfunction and apoptosis (Isaacs et al., 2006). During the physiological state, mitochondrial calcium handling is crucial for controlling intracellular signaling cascades. Mitochondrial Ca^{2+} absorption via the mitochondrial calcium uniporter complex has a high capacity but low affinity, which helps buffer intracellular calcium levels. The action of sodium/calcium antiporters like NCLX, which release calcium back into the cytosol, balances mitochondrial Ca^{2+} absorption (Palty et al., 2010). Elevation of mitochondrial Ca^{2+} causes mitochondrial ROS to be produced either independently of mPTP opening or by activating mPTP first, which inhibits the electron transport chain. Mitochondrial ROS can start mPTP in both a mitochondrial Ca^{2+} dependent and independent manner. Although active mPTP is a key element in necroptosis, it is unclear how mPTP opening affects the necrosome complex. The constraint is provided by the simultaneous rise in mitochondrial ROS and mPTP opening, despite the fact that the involvement of mitochondrial ROS in necrosome induction is well established (Faizan and Ahmad, 2021). Other studies suggested that MLKL may interact with the cation channel transient receptor potential melastatin related 7 (TRPM7), causing aberrant calcium influx, cell swelling, and plasma membrane rupture (Gong et al., 2017). Blocking of TRPM7 reduced the increase of Ca^{2+} and reduced necroptosis (Nomura et al., 2014). In the PD condition, mitochondrial Ca^{2+} homeostasis was disrupted, resulting in Ca^{2+} overload, which increases ROS production and cell death by opening the mPTP. Mitochondrial Ca^{2+} transporters are used as a therapeutic target in PD (Dey et al., 2020). The mammalian MAPK signaling family consists majorly three subfamilies: the extracellular signal-regulated kinases (ERKs), the p38-MAPK and the

JNKs. The ERK/MAPK signaling pathway is associated with cell proliferation, migration, and survival. It has a long history of tumorigenesis and is dysregulated in various malignancies (Lee et al., 2020). Despite cancer, deviation from the rigorous regulation of MAPK signaling pathways has been linked to the development of neurodegenerative diseases, including AD, PD, and ALS. In AD, PD, and ALS, prolonged activation of the JNK or p38 signaling pathways has been proposed to mediate neuronal apoptosis. For instance, In the AD brain, the microtubule-associated protein tau, present in neurofibrillary tangles, has been hyperphosphorylated by multiple kinases, including JNK, p38, and ERK. PD-901, an ERK inhibitor, has been found by Siano *et al*., 2019 as a potential medicinal chemical since it decreases and inhibits Tau aggregation (Siano et al., 2019). Whereas, in the case of PD, α-synuclein aggregates stimulate and upregulate MAPK signaling, which elevates the production of the pro-inflammatory cytokines, including IL-1β and TNF-α in microglia. In addition, it also promotes astrocytes to produce IL-6, resulting in chronic inflammation. These expressed cytokines have the potential to kill neighboring dopaminergic neurons. Thus, neuronal death, a common occurrence in all neurodegenerative illnesses, including PD, is linked to ERK1/2 signaling. Phosphorylated ERK1/2 was discovered in the mitochondria of degenerating neurons in PD and Lewy body dementia patients. Other research supports the hypothesis that ERK1/2 inhibition stimulates apoptotic and necrotic cell death-inducing pathways (Bohush et al., 2018). In addition, studies also showed in dopaminergic neurons, α-Synuclein aggregates promote ROS production by mitochondria, and the release of cytochrome *C* from these organelles into the cytosol, culminating in the caspase cascade activation and induction of apoptosis (Kim and Choi, 2010). Likewise, Veereshwarayya *et al*., 2006 found that Hsp70, Hsp90, and Hsp60 decreases free-radical burden and cytochrome c release that prevents caspase-9 activation, and thus, decreases β-amyloid toxicity (Veereshwarayya et al., 2006). Further, Hsp70 interacts with cyclins, namely Cyclin D and Cyclin E1 to promote cell cycle re-entry in neurodegeneration (Kwon et al., 2014). The initiation and activity of necroptosis signals are the primary components of necroptosis signaling pathways. TNF family cytokines such as TNF-α, Fas/CD95, and TRAIL bind to membrane receptors and activate intracellular RIP family kinases, triggering necroptosis. TNF-α signaling activates MAPK, which is a pro-survival pathway. Depending on the cell type, TNF-α starts a variety of signaling pathways, including extracellular signal-regulated protein kinase, JNK, p38MAPK, NF-κB, and caspase cascades. TNF signaling is activated by MAP kinases both upstream and downstream (Sabio and Davis, 2014; Zhang et al., 2015). Moreover, TLR-stimulated MAPK signaling involves interesting crosstalk with the IKK/NF-κB pathway. TLR3 and TLR4 activate TRIF-dependent NF-κB and MAPK via RIPK1. RIPK1 is recruited to TLR3 and TLR4 signaling complexes on endosomes via the adaptor protein TRIF, which possesses an RHIM. It activates TAK1 and the IKK complex but appears non essentially for TRIF-dependent activation of IRF3 and the IFN-1 expression, along with TRIF-dependent activation of RIPK3/MLKL-dependent necroptosis. However, blocking of RIPK1 can leads to inhibiting TRIF-dependent necroptosis (Newton, 2020). Furthermore, the NF-κB1 precursor protein p105 tends to form a stable complex with the MAP3K Tpl2 protein, stabilizing Tpl2 and prohibiting phosphorylation of MKK1/2 (downstream kinases). Upon activation by the TLR signal, IKK phosphorylates p105 to trigger its ubiquitin-dependent degradation, allowing Tpl2 to phosphorylate MKK1/2, resulting in ERK1/2 activation (Shi and Sun, 2018). Interestingly, ROS is an essential and common messenger created in response to diverse environmental conditions and is known to

Journal Pre-proof

activate numerous MAPKs (Jalmi and Sinha, 2015). These results showed the importance of Calcium signaling and MAPK pathways concerning necroptosis. **(Figure 5)**

6.2. PI3K/Akt/GSK-3β and JNK signaling pathway

JNK pathways involve many protein kinases in stress signaling pathways, gene expression, neuronal plasticity, renewal, cell death, and cellular senescence regulation. JNKs have been implicated in apoptotic and non-apoptotic PCD mechanisms such as necroptosis, ferroptosis, pyroptosis, and autophagy (Dhanasekaran and Premkumar Reddy, 2017). Both *in vitro* and *in vivo* studies reported that dysregulation of the JNK signaling pathway is highly active in CNS and linked with neurodegenerative diseases such as PD, AD, and many more (Corrales et al., 2021). JNK's, notably JNK3, are involved in the maturation and formation of neurofibrillary tangles and increases Aβ production. Overexpression of phosphorylated JNK along with co-localized with Aβ was observed in human post-mortem brain samples from AD patients (Yarza et al., 2016). Similarly, In a PD model, activation of JNK3 in dopaminergic neurons occurs after injection of neurotoxins such as paraquat and rotenone (Choi et al., 2010). JNK upregulation leads to hippocampal cell necrosis through the inflammatory niche. Thus, JNK emerges as a potential biomarker and could be considered a potential therapeutic target for AD and PD (Peng and Andersen, 2003; Rehfeldt et al., 2020). Recent studies showed that upregulated RIPK1 promotes necrosis, inflammation response, mitochondrial dysfunction, and ROS production via activation of the JNK pathway in both AD and PD. However, RIPK1 mediates the necroptosis and is highly expressed in the microglial cells of human AD brains, accelerating the inflammation response and the accumulation of β-amyloid in AD and MPP^+-treated SHSY5Y cells and MPTP-induced PD mice. Liu *et al*., 2021 found that the RIPK1 inhibitor Nec-1 inhibited the activation of the Apoptosis-signaling kinase-1 (ASK1)/JNK pathway, alleviating PD mice's behavioral impairment (J. Liu et al., 2021). Moreover, Nec-5, and Nec-7, are thought to inhibit the necroptotic signaling pathway (Fuji et al., 2018; González-Juarbe et al., 2015). Another study showed that the combination of flavone and bilobalide chemicals in Ginkgo biloba extract 761 (EGb761) inhibited JNK-STAT3 activation, which caused cell stress (ROS generation) and necrosis in cells (Tu et al., 2020). Various neurotoxicants such as rotenone, MPP^+, manganese, dieldrin, and salsolinol cause a rise in H_2O_2 and ROS production, which leads to activation of the JNK1/2 pathway (Chun et al., 2001). According to Hu *et al*., 2020 RIPK3-mediated necroptosis engages with JNK-mediated inflammatory signaling to contribute to widespread cerebral I/R injury. Inflammatory mediators controlled by JNK may enhance necroptosis initiation (W. Hu et al., 2020). A study reported that PARKIN, an E3 ubiquitin ligase, regulates inflammation and necroptosis in microglia cells, representing unanticipated PD pathogenesis function. Loss of PARKIN leads to LPS-driven inflammatory response by over-activation of JNK and NF-κB pathways (P. E. A. Dionísio et al., 2019). Recent research has also looked at Poly(ADP-ribose) polymerase-1 (PARP1), a nuclear enzyme that can cause caspase-independent necrosis and is dependent on JNK activation (Douglas and Baines, n.d.). ROS production is responsible for the executioner of necroptosis. ROS serve as an oxidant and affects different JNK pathway via TNF/NF-κB (Tansey et al., 2007). Hence, it's critical to look at JNKs as a possible target for treating neurodegenerative diseases like AD and PD. Apoptotic neuronal cell death is known to be inhibited by the Akt protein (Lee et al., 2009). The mechanistic mTOR signaling is an Akt downstream effector that regulates protein synthesis. Through phosphorylation on Thr308 during necroptosis, Akt is activated in a RIPK1-dependent manner. Through phosphorylation on Thr308 during necroptosis, Akt is activated in a

RIPK1-dependent manner. Akt regulates necroptosis by targeting mTORC1. Akt activity, which is mediated in part by mTORC1, connects RIP1 to JNK activation and autocrine TNF-α generation (McNamara et al., 2013). On the contrary, Akt/mTOR inhibition did not affect the necrosome complex formation, although it did reduce oxidative stress and cell death. TNF/zVAD promoted Akt and mTOR phosphorylation on Thr-308 and Ser-473, along with phosphorylation of Akt's direct substrates, glycogen synthase kinase 3 beta (GSK-3β), FOXO-1 and mTOR S6 ribosomal protein. Nec-1, a powerful and highly selective RIPK1 inhibitor, prevented these phosphorylation events. According to immunoprecipitation experiments data, in one such study, TNF/ZVAD induced RIPK1/Akt and RIPK1/pAkt/473 association. Nec-1 inhibits Akt-RIPK1 binding. Inhibition of Akt/mTOR did not affect the RIPK1/RIPK3 interaction, although it did reduce ROS generation and cell death. Moreover, genetic suppression of Akt and mTOR combined decreased cell mortality by a magnitude comparable to pharmacological inhibitors, indicating that specific role for Akt and mTOR (Degterev et al., 2008; Q. Liu et al., 2014). Another study reported that TNF-induced necroptosis was mediated by the PI3K-AKT signaling pathway, although how PI3K induces necroptosis is unknown. Interestingly, researchers discovered that knocking down p110α, the catalytic subunit of PI3K, decreased RIPK1, RIPK3, and MLKL phosphorylation and oligomerization in response to TNF treatment. Finally, they discovered that in the mechanism of TNF-induced necroptosis, p110α bound to RIPK3, but not RIPK1, to form a protein complex and that p110α mediated TNF-induced necroptosis in the lack of RIPK1 (S. Hu et al., 2020). Hence, these studies showed the importance of targeting the JNK signaling pathway and PI3K/Akt/GSK-3β for discovering new therapies targeting neurological diseases. **(Figure 5)**

Journal Pre-proof

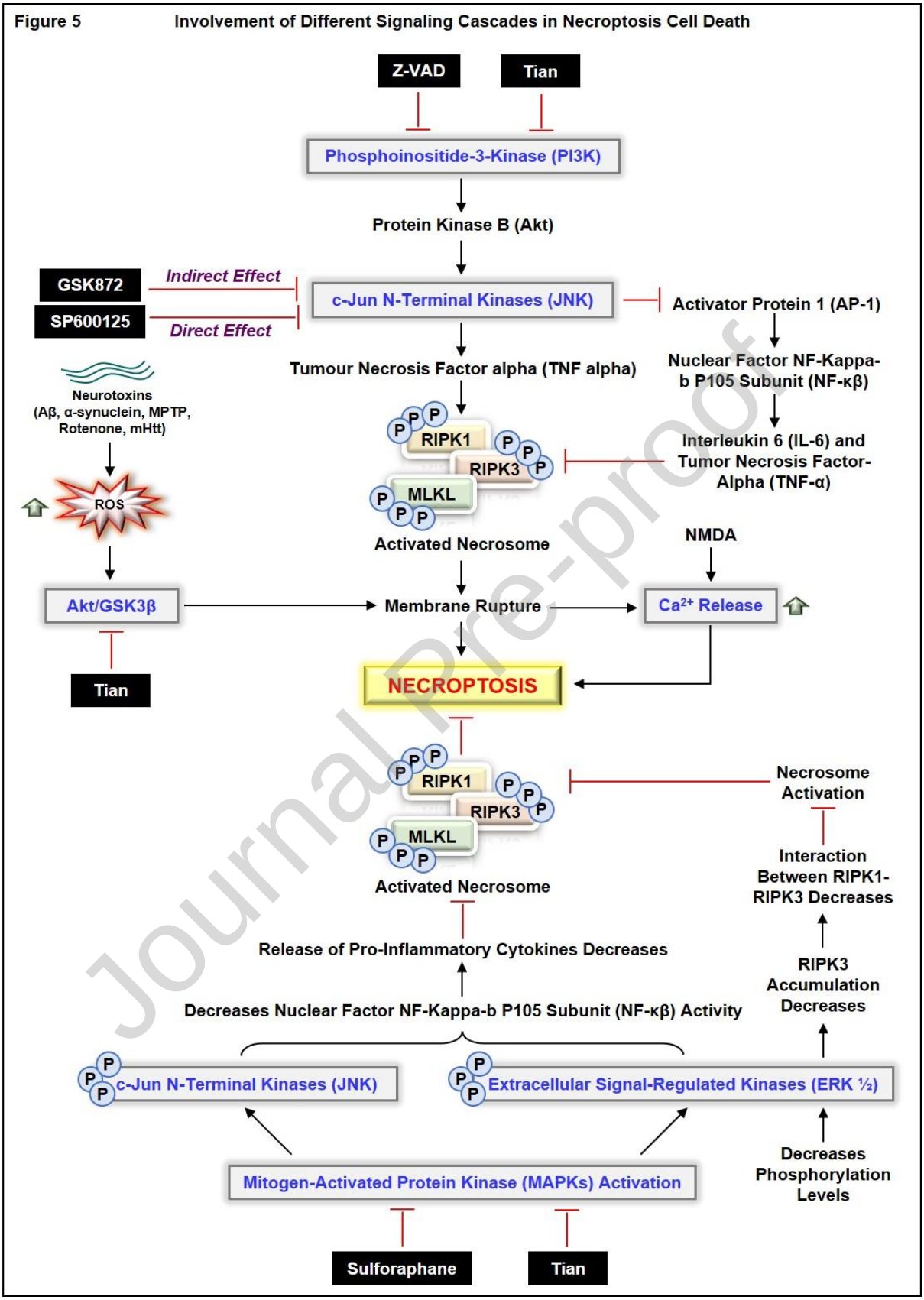

Figure 5: Inhibition of PI3K with Z-VAD and Tian inhibits the activity of Akt and Jnk, which inhibits the activation of necrosome, and ultimately inhibits necroptosis. In addition, administration of GSK872 and SP600125 causes downregulation of JNK that inhibits the necroptosis pathway, whereas, inhibition of sulforaphane and tian causes downregulation of MAPK that decreases the release of pro-inflammatory cytokines that inhibits the necroptosis pathway.

Journal Pre-proof

6.3. VEGF/VEGFR and Wnt/β-catenin

A plethora of evidence suggests perturbations of the Wnt/β-catenin pathway have been linked to the etiology of neurodegenerative diseases, including AD, PD and others. The wnt/β-catenin pathway has a pivotal role in synaptic stability and BBB integrity. Dysregulation of the Wnt/β-catenin signaling cascade has been linked with AD initiation and progression. Presenilin 1 restricts GSK-3β (a Wnt signaling protein) activity in normal circumstances, increasing β-catenin stability by inducing Akt protein (Libro et al., 2016). On the other hand, in the case of AD patients, a mutation in Presenilin 1 is related to increased GSK-3β levels and decreased β-catenin levels, which leads to the suppression of the Wnt/β-catenin pathway. In one study, researchers have shown that increased β-catenin levels were associated with decreased NF-κB activity, overexpression of β-catenin targeted transcription factor Krüppel-like factor 8 (KLF8) and together with results in activation of Wnt signaling in primary neuronal cells derived from AD models (Yi et al., 2014). A study by Ferrari *et al.*, 2003 showed that Lithium chloride, which mimics Wnt signaling by suppressing GSK-3β, restored β-catenin levels to control levels and helped the survival of post-mitotic neurons against Aβ. This suggests the therapeutic potential of the Wnt/β-catenin pathway in AD patients (De Ferrari et al., 2003). However, in PD, upregulation of Dickkopf-1, an endogenous antagonist of Wnt signaling, is associated with enhanced GSK-3β activity and reduced Wnt/β-catenin signaling. Dysregulation of this pathway has also been linked to LRRK2 and Parkin mutations (Lin et al., 2010). Regarding necroptosis in neurodegenerative disease, this signaling has received little attention. GSK-3β regulates inflammation and apoptosis, regulating the appropriate balance between immunological tolerance/inflammation and neuronal survival/neurodegeneration (Libro et al., 2016). Other indications for necroptosis have been investigated concerning Wnt signalings, such as cancer (Bozec et al., 2016), alcoholic fatty liver disease (Qian et al., 2022) and Tuberculosis (X. Wu et al., 2015). For instance, vascular peroxidase 1, which plays a significant role in regulating cardiovascular oxidative damage, also promotes endothelial programmed necrosis under hyperlipidemic circumstances by activating β-catenin signaling. It may serve as a novel therapeutic target for preventing endothelial dysfunction in hyperlipidemia (Zhang et al., 2018).

Angiogenesis, vasculogenesis, migration of neurons and neuroprotectants are mediated by mainly a potent growth factor, namely vascular endothelial growth factor (VEGF). Apart from neuronal function, possible functions of VEGF have been demonstrated in other diseases, namely cancer and diabetes. For instance, curcumin administration enhanced VEGF/PECAM expression and decreased caspase expression level, leading to decreased apoptotic cell death (Arivazhagan et al., 2015). Likewise, luteolin has been found to be better in inhibiting angiogenesis through downregulating VEGF activity (Ambasta et al., 2015). However, enhanced expression of VEGF destroys intracellular barriers, increases leakage of the choroid plexus endothelia, and causes edema and activation of inflammatory pathways. According to some studies, VEGF levels are known to decline with age and to affect BBB by the production of endothelial hyperpermeability and BBB impairment is linked to neurogenerative diseases such as AD, PD, ALS etc. (Shim and Madsen, 2018). The VEGF family's seven different homologous members are VEGF-A, VEGF-B, VEGF-C, VEGF-D, VEGF-E, VEGF-F, and placental growth factor (PGF). Among them, the VEGF-D function is carried out by a high-affinity tyrosine kinase. Vascular endothelial growth factor receptor (VEGFR)-3. VEGFR-3 is primarily expressed in reactive astrocytes in the peri-infarction penumbra area, indicating that VEGFR-3 is implicated in the glial response to ischemic insults.

Reactive astrocytes have been shown to increase damage by releasing neurotoxic amounts of ROS, magnify inflammation by producing cytokines, undermine BBB integrity by producing VEGF, and enhance cytotoxic edema by stimulating AQP4 (aquaporin-4). It plays a vital

function in glymphatic solute transport and brain water balance (Zhu et al., 2021). Kim *et al*., 2012 discovered a relationship between angiogenin, VEGF growth factor and their receptors, such as VEGFR levels in the blood and AD. In comparison to 18 healthy controls, data indicated that 20 AD patients had higher VEGF levels and lower angiogenin levels in their blood (YN and DH, 2012). Moreover, previous research has also revealed a strong relationship between necroptosis and ROS; both necroptosis and ROS play essential roles in human physiological states, such as inflammation regulation and cancer biology, according to mounting evidence (Hsu et al., 2020). Furthermore, Hanghi *et al*., 2017 found that RIPK1 and RIPK3 kinase activity has a physiological significance in the tumor microenvironment, namely tumor cell extravasation and remodeling, through changing permeability factor downstream signaling cascades. In addition to its role in necroptosis regulation, the kinase activity of RIPK1/RIPK3 has a novel function (Hänggi et al., 2017).

6.4. Toll-like receptors and reactive oxygen species

Cell death mediated by signal transduction from receptor-interacting serine/threonine kinase (RIPK 1 to RIPK3 is known as necroptosis. Under certain conditions, the removal of RIPK1 perhaps encourages RIPK3-mediated necroptosis. The emergence of neurodegenerative disorders has been associated with nonapoptotic cell death. It is noteworthy because it plays a role in many human diseases, including ischemic brain damage, immune system problems, and cancer. Thus, targeting and suppressing necroptosis has the potential to be exploited therapeutically. Necroptosis involves rapid permeabilization of the plasma membrane, resulting in the discharge of cell contents and the exposure of DAMPs (Khan et al., 2021). Pattern recognition receptors recognize DAMPs and pathogen-associated molecular patterns. The pattern recognition receptors family includes TLRs, C-type lectin receptors, RIG-I-like receptors, and nucleotide-binding domain and leucine-rich repeat-containing molecules (NLRs) (Takeuchi and Akira, 2010). The well-known chemokines/cytokine-driven pathways activate TLRs signaling, which stimulates NF-κB together with IRF3/IRF7 (F. Zhang et al., 2017). In contrast to TLR3, which communicates through the TRIF adaptor, other TLRs recruit downstream the MyD88 adaptor. TRIF, which is downstream of TLR3 and TLR4 implicated in the activation of necroptosis response to a large amount of double-stranded RNA or LPS (Kaiser et al., 2013b). TLRs can also recognize bacterial, viral, or self-nucleic acid. Additionally, DAMPs generated by inadvertently necrotic cells have also been observed to interact with receptors that do not identify particular pathogen-associated molecular patterns (CD24 and P2X/Y receptors, IL-1R) (Kaczmarek et al., 2013). TLRs are present in various brain cell types, including astrocytes, microglia, neurons, oligodendrocytes, and immune cell types, including macrophages and dendritic cells. Microglia, for example, express all TLR subtypes, neurons TLR3, TLR7, TLR8, TLR9, astrocytes TLR2, TLR3, TLR9, and oligodendrocytes only TLR2 and TLR3 (Hanke and Kielian, 2011). The misfolded Aβ plaques trigger an inflammatory response in AD patients via TLR2, TLR4, and TLR6 and their co-receptors, including their co-receptors CD36, CD14, and CD47 (Zolezzi et al., 2019). In PD, aggregated α-synuclein can activate the TLRs, such as TLR2 and TLR4 (Kim et al., 2013). A study by Griffioen *et al*., 2018 suggested that homozygous TLRs 2 and 3 and heterozygous TLR4 deficiency significantly extends the life expectancy of HD mice (Griffioen et al., 2018). A recent study reported that Nec-1 administration in a transgenic R6/2 mouse model, which develops a spontaneous HD-like disease, delayed the disease onset (Zhu et al., 2011). Thus, TLR's relation with necroptosis mediates the development of neurodegenerative pathological conditions.

In addition to MLKL, mitochondrial ROS induces necroptosis through RIP autophosphorylation, which is essential for RIPK3 recruitment into the necrosome. Hence, it acts as a positive feedback mechanism for necrosome assembly (Y. Zhang et al., 2017). There are two primary pathways that contribute to increased mitochondrial ROS generation. The

first is RIP1 phosphorylation-dependent integration of STAT3 and GRIM-19 (mitochondrial electron transport chain complex I component), and the second is physical interactions between RIP3 and the enzymes glutamate-ammonia ligase (GLUL), glycogen phosphorylase (PYGL) and glutamate dehydrogenase 1 (GLUD1), which may improve energy metabolism and mitochondrial ROS production (Dixon and Stockwell, 2013). Concurrently, ROS is responsible for decreasing levels and activation of executioner caspases 3, caspases 6, and caspases 7. As a result of the change from apoptosis to necroptosis, mitochondrial ROS enhanced neonatal hypoxia-ischemia-brain damage in hyperglycemic mice. TNF-α plays a role in neurodegeneration by stimulating ROS production in neurons and neurodegeneration by promoting ROS creation in neurons and glia via Cdk5 activation (Sandoval et al., 2018). Similarly, Schenk *et al*., 2015 studied insights into the redox reaction of necroptosis by finding ROS as an essential driver of BV6/TNF-α-induced necroptotic signaling and cell death (Schenk and Fulda, 2015). In the context of caspase inhibitor Z-VAD-FMK therapy, data supports the function of ROS as a crucial regulator of necroptosis and the considerable reduction of intracellular ROS by pre-treatment with necroptosis antagonists corresponds with enhanced cell survival (Jayaraman et al., 2021). Genes such as PARKIN, DJ-1, PINK1, α -synuclein, and LRRK2 cause PD to have complicated effects on mitochondrial function, resulting in exacerbation of ROS generation oxidative stress susceptibility (Dias et al., 2013). Moreover, in the PD model, MPP^+, a neurotoxin, can accumulate within mitochondria. It suppresses electron transport chain complex I, interrupting electron flow and resulting in reduced ATP synthesis and increased ROS production, particularly superoxide. Furthermore, while mitochondria being an essential source of ROS, data suggests that other prominent producers of cellular ROS, such as NADPH oxidases, cytochrome P450, and lipoxygenases, may play a significant role in PD. A transversal PD trait, ROS generation by activated inflammatory glial cells during neuroinflammation, may also be substantial for forming an oxidative environment in the disease (Dionísio et al., 2021; Iannielli et al., 2018). ROS generation affects necroptosis in diverse ways, depending on cell type, insulting stimuli, and metabolic activity.

Table 2: Therapeutic potential of different signaling molecules in the necroptosis pathway

Signaling molecule	Signaling event	Interactors	Experimental model	Mechanism	References
cIAP1/2	TNF-α/RIPK1/TAK1 survival pathway	TLR3/4, calcium flux, caspase-3/7, IKK1/2	NIH 3T3 cells	Inhibition of Smac mimetic reduces cell damage in an *in vivo* necroptosis model of ischemia-reperfusion injury	(Ros et al., 2017)
RIPK1	TNF-α receptor pathway	CaMKII	SK-N-SH and SK-N-AS cells	An increased concentration of cytoplasmic calcium triggered necroptosis by activating CaMKII	(Nomura et al., 2014)
NMDA	Excitotoxicity pathway	LDH	Wistar rats	Necroptosis contributes to NMDA-induced excitotoxicity, and the elevation of intracellular Ca^{2+} may be one of the potential mechanisms underlying NMDA-induced necroptosis	(Li et al., 2008)
RIPK1	Calcium pathway	____	C57BL mice	Inhibition of RIPK1 preserved the viability of cells and calcium activity.	(Mitroshina et al., 2022)
MLKL	Calcium signaling pathway	IL-1R1, RIPK3, Ca^{2+}	Adult male Wistar rats	inhibition of MLKL-dependent neuronal necroptosis through downregulating IL-1R1 contributes to neuroprotection of hypoxic preconditioning against tGCI	(Zhan et al., 2021)
CaMK-II	Calcium signaling pathway	RIPK1, RIPK3, MLKL	Sprague-Dawley rat	Heliox preconditioning may alleviate cytoplasmic Ca^{2+} overload by regulating p-RyR2, which inhibits the necroptosis in the brain, exerting neuroprotective effects on hypoxic-ischemic encephalopathy	(Zhong et al., 2022)
PDEIII	Akt/GSK-3β/CREB pathway	SOCS3, IL-6, JAK-2, STAT-3, TLR4	Adult male Wistar rats	Administration of cilostazol inhibits neuronal necroptosis through Akt/GSK-3β/CREB pathway modulating	(El-Abhar et al., 2018)
AMPA	Akt/GSK-3β	LDH, RIPK1,	Traumatic Neuronal	The AMPAR Antagonist Perampanel Regulates	(Chen et

	Signaling	RIPK3, caspase-3	Injury model in primary cultured cortical neurons	Neuronal Necroptosis via Akt/GSK-3β Signaling After Acute Traumatic Injury in Cortical Neurons	al., 2020a)
RIPK1	JNK signaling pathway	ROS, NCLX, MCUB, MICU1, MICU2, VADC	BV2 microglial cells	EGb761 ameliorates cell necroptosis by attenuating RIPK1-mediated mitochondrial dysfunction and ROS production in both *in vivo* and *in vitro* models of Alzheimer's disease	(Tu et al., 2020)
RIPK3-AIF	JNK signaling pathway	IL-6	Sprague-Dawley rat	Inhibitor GSK872 attenuates RIPK3-AIF complex enrichment in the nucleus, and regulation of RIPK3 affects the JNK and IL-6-induced inflammation.	(W. Hu et al., 2020)
ET-1	JNK signaling pathway	IL-6, NMDA	Yorkshire pigs	Inhibition of ET-1 reduces the release of IL-6 that inhibits the necroptosis cell death by modulating the JNK/MAPK pathway	(Armstead et al., 2019)
IL-1Ra	IL-1β/JNK signaling pathway	TNFR1, caspase-3, RIPK1, RIPK3 and MLKL	Male Wistar rats	$AlCl_3$ induced hippocampal neural cells death and depression-like behavior in rats by activating IL-1β/JNK signaling pathway	(H. Zhang et al., 2020)
MAPKs	MAPK/NF-κB signaling pathways	RIPK3, MLKL, TNF-α, IL-1β, IL-6 and iNOS	LPS-activated BV-2 microglia	SFN attenuates LPS-induced pro-inflammatory responses through down-regulation of MAPK/NF-κB signaling pathway in BV-2 microglia and thus indirectly suppresses microglia-mediated neuronal necroptosis	(Qin et al., 2018)
p38	p-38 MAPK signaling pathway	TNF-α, RIPK1, RIPK3, MLKL	The mouse hippocampal neuronal HT-22 cells and murine microglial N9 cells	Necroptosis induced by microglia-derived TNF-α upon arsenite exposure partially played a role in arsenic-induced cell death through p38/MAPK signaling pathway	(H. Wang et al., 2022)
RIPK3	ERK1/2 and p38 signaling pathways	RIPK1, RIPK3, MLKL, TNF-α, IL-1β, IL-6	The human THP-1 cell line	DHA attenuates Aβ-induced necroptosis through the RIPK1/RIPK3 signaling pathway in THP-1 monocytes	(S. Yuan et al., 2020)
VEGF	VEGFR signaling event	RIPK1, RIPK3, MLKL, connexin 43, caspase 9, caspase-8, Beclin 1	$SOD1^{G93A}$ Rats	The combination of repeated intrathecal and intramuscular hMSC applications protects motor neurons and neuromuscular junctions, not only through a reduction of apoptosis and autophagy but also through the necroptosis pathway, which is significantly involved in cell death in rodent $SOD1^{G93A}$ model of ALS	(Řehořová et al., 2019)
VEGF and GDNF	VEGFR signaling event	RIPK3 and Iba 1	PC12 cells	Enhanced motor function and behavioral characteristics due to the ability of stem cells to suppress necroptosis and consequently extend cell survival	(Saeidikhoo et al., 2020)
RIPK1	VEGF-D/VEGFR-3 signaling pathways	RIPK3 and MLKL	transient middle cerebral artery occlusion rat model	RIP1K participates in the formation of astrogliosis and glial scar via impairment of normal astrocyte responses and enhancing the astrocytic VEGF-D/VEGFR-3 signaling pathways	(Zhu et al., 2021)
ROS accumulation and calcium influx	CYLD-RIPK1-RIPK3-MLKL signaling pathway	TNF-α	HT-22 hippocampal neuronal cells	RIPK3 in TNF-α-induced toxicity of hippocampal neurons but also demonstrates that TNF-α promotes CYLD-RIP1-RIP3-MLKL-mediated necroptosis of hippocampal neurons, largely bypassing ROS accumulation and calcium influx	(S. Liu et al., 2014)
SOD	MAPK signaling pathways	AIF and Endo G	HT-22 Hippocampal neuronal cells	Menadione-induced cell death is caspase-independent due to the rapid depletion of ATP. The release of AIF and Endo G contributes significantly to cell death. Alterations of SOD1 or SOD2 levels alter menadione-induced neuronal cytotoxicity	(Fukui et al., 2012)
MLKL	Oxidative stress	ROS	C57BL/6J mice *in vivo* and HT-22 cell lines	ketamine may have neuroprotective effects as a potent inhibitor of necroptosis by decreasing ROS concentration	(L. Wang et al., 2021)
HO-1	ROS/HO-1 signaling	NF-κB, TNF-α, IL-6,	C57BL/6 mouse model	Hydrogen-rich saline enhanced neurological outcomes in mice and minimized neuronal	(Y. Hu et al., 2022)

Journal Pre-proof

		IL-1β, RIPK1, RIPK3, Nrf2		death by inducing protective effects against neural necroptosis as well as neuroinflammation	
ROS	ROS/iNOS/NF-κB Pathway	iNOS, RIPK1, RIPK3, MLKL, NF-κB, TNF-α, COX-2, iNOS, PTGEs, and IL-1β	Isa hens	Quercetin had an alleviative effect on cadmium-induced necroptosis in the chicken brain through inhibition of ROS/iNOS/NF-κB pathway	(L. Liu et al., 2021)
Caspase	TLR signaling event	TNF-α, TNFR, RIPK1 and RIPK3	Wild-type B6.129SF2/J and C57BL/6J mice	RIPK3-dependent necroptosis signaling pathway in TLR-activated microglia upon caspase blockade and suggests that TLR signaling and programmed cell death pathways are closely linked in microglia, which could contribute to neuropathology and neuroinflammation when dysregulated	(Kim and Li, 2013)
HMGB1	TLR4 signaling pathway	aquaporin-4, IL-6	Adult male CD-1, C3H/OuJ, C3H/HeJ	HMGB1 promotes cerebral edema after traumatic brain injury via activation of TLR4	(Laird et al., 2014)

*** cIAP: cellular inhibitor of apoptosis proteins; TNF-α: tumour necrosis factor α; RIPK1: Receptor-interacting serine/threonine-protein kinase 1; TAK1: transforming growth factor-β (TGF-β)-activated kinase 1; TLR: toll-like receptor; IKK: IκB kinase; CaMKII: calcium/calmodulin-dependent protein kinase II; LDH: lactate dehydrogenase; NMDA: N-methyl-D-aspartate receptor; IL-1R1: interleukin 1 receptor type 1; RIPK3: receptor-interacting serine/threonine-protein kinase 3; Ca^{2+}: calcium ions; MLKL: mixed lineage kinase domain-like; tGCI: transient global cerebral ischemia; p-RyR2: ryanodine receptor 2; SOCS3: suppressor of cytokine signaling 3; IL-6: interleukin 6; JAK-2: janus kinase 2; STAT-3: signal transducer and activator of transcription 3; Akt: protein kinase B; GSK-3β: Glycogen synthase kinase 3 beta; CREB: cAMP response element-binding protein; AMPAR: α-amino-3-hydroxy-5-methyl-4-isoxazolepropionic acid receptor; ROS: reactive oxygen species; PDEIII: phosphodiesterase; AMPA: α-amino-3-hydroxy-5-methyl-4-isoxazole propionic acid; JNK: c-Jun N-terminal kinases; NCLX: mitochondrial sodium/calcium exchanger protein; MCUB: Mitochondrial calcium uniporter dominant negative subunit beta; MICU1: mitochondrial calcium uptake 1; MICU2: mitochondrial calcium uptake 1; VADC: voltage-dependent anion channel; AIF: apoptosis inducing factors; ET-1: Endothelin 1; MAPK: mitogen-activated protein kinase; IL-1Ra: interleukin-1 receptor antagonist; IL-1β: interleukin-1β; TNFR1: tumor necrosis factor receptor 1; $AlCl_3$: Aluminum trichloride; iNOS: inducible nitric oxide synthase; SFN: Stratifin; ERK1/2: serine/threonine protein kinase; Aβ: β-amyloid; VEGF: vascular endothelial growth factor; VEGFR: vascular endothelial growth factor receptor; SOD1: Superoxide dismutase 1; ALS: Amyotrophic lateral sclerosis; hMSC: human mesenchymal stem cells; GDNF: glial cell line-derived neurotrophic factor; Iba1: ionized calcium binding adaptor molecule 1; VEGF-D: vascular endothelial growth factor-D; CYLD: lysine 63 deubiquitinas; ATP: adenosine triphosphate; HO-1: heme oxygenase; NF-κB: nuclear factor kappa B; Nrf2: nuclear factor-erythroid factor 2-related factor 2; COX-2: cyclooxygenase-2; PTGEs: prostaglandin E synthase; HMGB1: High mobility group box protein 1**

7. Role of necroptosis in neurological disorders

7.1. Alzheimer's disease and Parkinson's disease

AD is the most prevalent form of dementia caused by tau hyperphosphorylation and accumulation of Aβ fragments (Habib et al., 2020). Excessive autophagy and apoptosis are considered significant contributors to cell death in AD pathogenesis. Still, mounting evidence demonstrated the involvement of necroptosis machinery in the pathogenesis and progression of AD (Shan et al., 2018; Zhao et al., 2022). For instance, a study observed that RIPK1-regulated genes were significantly expressed in correlation with AD transcriptomics signatures, where reduced necroptosis activation inhibits neuronal cell loss. The study indicated the positive role of necroptosis activation in cognitive loss-induced AD pathology (Caccamo et al., 2017a). TNF-α is an important pro-inflammatory cytokine that is linked with necroptosis-mediated neuronal loss in the progression of AD. It was demonstrated that HT-22 hippocampal neuronal cells are sensitive to TNF-α in the presence of caspase inhibition that further undergoes necroptosis cell death through cylindromatosis lysine 63 deubiquitinase (CYLD)/RIPK1/RIPK3/MLKL signaling cascade (S. Liu et al., 2014). In AD, phosphorylation of RIPK3 and MLKL in the CA1 pyramidal region of post-mortem brain samples leads to increased expression of TNF-α and TNFR1, which causes induction of necroptosis cell death (Jayaraman et al., 2021). In addition, Xu *et al*., 2021 in neuronal cell culture and AD mouse models concluded that TNF-α-induced necroptosis is through RIPK1 recruitment and oligomerization through p62 accumulation on TNF-α activation, which activates RIPK1/RIPK3/MLKL pathway (C. Xu et al., 2021). Similarly, another study on the

AD rat model confirmed the presence of human adipose-derived stem cells in AD rats, which decreases the expression of necroptosis markers, namely RIPK1, RIPK3, and MLKL (Eftekharzadeh et al., 2020). The presence of necroptosis markers is associated with granulovacuolar degeneration (GVD) as in neurons, and necrosome components are actively found in GVD lesions, which colocalize with phosphorylated TAR DNA-binding protein 43 (TDP-43) and casein kinase I isoform delta (Koper et al., 2019). Further, the expression level of the brain-derived neurotrophic factor also plays a vital role in necroptosis activation, where the low level of brain-derived neurotrophic factor causes Aβ aggregation and induction of necroptosis machinery (Tagai et al., 1073). Recently, Pang *et al*., 2021 observed that the App knock-in rat model exhibited neuronal necroptosis and tau pathologies, which are rarely seen in other APP models (Pang et al., 2021). In the subsequent year, Dong *et al*., 2022 concluded that hyperphosphorylated tau could induce necroptosis in neuronal cells by promoting the formation of the RIPK1/RIPK3/MLKL necrosome. In addition, pTau significantly stimulated cell-autonomous overexpression of cytokines and chemokine (Dong et al., 2022). Further, mNat1 deficiency in $Nat1^{-/-}$ mice and two AD mouse models promote blood-brain barrier (BBB) damage and endothelial necroptosis (Zou et al., 2020). (**Figure 6)**

PD is the second most prevalent neurodegenerative disease, characterized by loss of dopaminergic neurons, mitochondrial dysfunction, and metabolism imbalance (Iannielli et al., 2018). Different biomolecules, namely sesamol and naringenin, have been demonstrated to be neuroprotective against PD pathogenesis through reduced caspase activation and ubiquitin expression (Sonia Angeline et al., 2013). Mounting evidence demonstrated that the downstream target of necroptosis, that is, autophagy, caspase-3, and caspase-9, is involved in neuronal cell death in the pathogenesis of PD (Arduíno et al., 2012; Pan and Yue, 2014; Sonia Angeline et al., 2012; S. Zhang et al., 2017). For instance, Lannielli *et al*., 2018 demonstrated that mutation in OPA1 mutant iPSC-derived neural progenitor cells (NPCs) presents high levels of oxidative stress that causes mitochondrial dysfunction, where Nec-1 can improve the survival of OPA1 mutant in MPTP-treated neurons (Iannielli et al., 2018). Parkin is the most common cause of familial and sporadic PD that regulates necroptosis and neuroinflammation through modulation of necrosome formation (Dawson and Dawson, 2010; Wong, 2019). Parkin, which is phosphorylated and activated by AMPK, prevents the formation of the RIPK1/RIPK3 complex by enhancing the polyubiquitination of RIPK3. Parkin deficiency enhances the interaction between RIPK1 and RIPK3, which accelerates necroptotic cell death (Lee et al., 2019). However, the ablation of RIPK3 protects against neuronal cell death in the MPTP-induced mice model of PD (P. A. Dionísio et al., 2019). Likewise, Lin *et al*., 2019 concluded that the activity of RIPK1/RIPK3/MLKL was enhanced after MPTP administration, which causes increased activity of pro-inflammatory cytokines and leads to necroptotic cell death. However, the authors also concluded that the administration of Nec-1 and deletion of RIPK3 or MLKL reduces the expression of pro-inflammatory cytokines and inhibits necroptotic cell death (Lin et al., 2019). Nec-1 is a necroptosis inhibitor, which protects dopaminergic neurons from necroptotic cell death through mitochondrial membrane potential stabilization, inhibition of excessive autophagy, reduced expression of cathepsin B, and increased expression of Bcl-2 (J. R. Wu et al., 2015). Despite having the potential for necrosome inhibition, Nec-1 is considered a neurotoxin that affects mitochondrial morphology and fails to protect mitochondria against rotenone toxicity in the SH-SY5Y cell culture model of PD (Alegre-Cortés et al., 2020). Recently, Oliveira *et al.*, 2021 discovered Oxa12 as a potential compound that inhibits necrosome activation and protects from necroptotic cell death in the MPTP-induced mouse model of PD (Oliveira et al., 2021a).

7.2. Huntington's disease and amyotrophic lateral sclerosis

HD is characterized by the presence of polyQ (glutamine) repeats in mutant Huntingtin (Htt) protein, which causes neuronal abnormalities and cell death (Ross and Tabrizi, 2011). Studies demonstrated that enhanced neuronal cell death is due to necrosome activation, which leads to necroptotic cell death (Han et al., 2009; Mangiarini et al., 1996; Prakash G. Jagtap et al., 2007; S. Zhang et al., 2017). For instance, Mao *et al*., 2016 demonstrated that viral vector-mediated delivery of sphingosine 1-phosphate rescues the endoplasmic reticulum instability and necrosis in the HD mice model, where Yes-associated protein phosphorylation at Thr77 causes changes in YAP interacting partner from TEA domain family member to p73 (Mao et al., 2016). Similarly, Yamanishi *et al*., 2017 demonstrated that a novel form of necroptotic cell death that is transcriptional repression-induced atypical cell death of neurons (TRIAD), is responsible for cell death in HD. The authors demonstrated that large tumor suppressor kinase 1 (LATS1) kinase, an important regulator and marker of TRIAD, is activated in cortical neurons of post-mortem human HD and Htt-KI mouse brains. Further, in the same study, they reported the enlargement of the endoplasmic reticulum, which characterizes TRIAD, in cortical neurons of the HD brain sample (Yamanishi et al., 2017). Recently, it was concluded that human olfactory stem cells rescue motor functions and prevent necroptosis-induced cell death in the HD rat model. In this study, the authors demonstrated that striatal transplantation of olfactory ecto-mesenchymal stem cells, which are characterized by the presence of CD73, CD90, and CD105, causes a reduction in microglial inflammatory factor, TNF-α, and RIPK3 expression, which rescues from necroptosis cell death (Bayat et al., 2021).

ALS is another neurodegenerative disease that is characterized by the progressive loss of both upper and lower motor neurons (Masrori and Damme, 2020). Earlier, it was believed that neuronal cell death in ALS is a dichotomy between apoptosis and necrosis. However, recently necroptosis cell death has been characterized as the primary reason for motor neuron loss in ALS pathogenesis (Morrice et al., 2017). For instance, TAK1 is a significant genetic cause of ALS and leads to age-dependent neurodegeneration and acts as an endogenous inhibitor of RIPK1 kinase activity. However, in $Tbk^{+/-}$ mice model of ALS, the activity of myeloid TAK1 expression decreases and promotes the key features of ALS, such as neuroinflammation, TDP-43 aggregation, axonal degeneration, and neuronal loss (Xu et al., 2018). Another study concluded the critical role of RIPK3 deletion in the pathogenesis of ALS, where deletion of *Ripk3* prevents motor neuron death. In mutant superoxide dismutase-1 (SOD1) transgenic mice model of ALS, *Ripk3* silencing prevents motor neurons from neurotoxicity and protects them from myelin decomposition *in vitro* but not *in vivo* (Dermentzaki et al., 2019). In 2019, Rehorova *et al*., in the $SOD1^{G93A}$ mice model of ALS, demonstrated neuroprotective effects of intrathecal applications of human mesenchymal stem cells (hMSC) or their conditioned medium through lumbar puncture or injection into the muscles. The study concluded that hMSC treatment successfully improves life span, increases motor activity, and decreases the number of terminal deoxynucleotidyl transferase dUTP nick end labeling positive cells. The same study also demonstrated that hMSC combined treatment causes increased motor neuron survival and reduces the activity of RIPK1 (Řehořová et al., 2019). In addition, Schoor *et al*., 2020 concluded that necrosome-positive granulovacuolar degeneration was associated with TDP-43 pathological lesion in the hippocampus of ALS, whereas, Chevin *et al*., 2020 demonstrated the upregulation of critical markers of necroptosis activation in lower motor neurons of the spinal cord (Chevin et al., 2020; Van Schoor et al., 2021). Despite having the potential evidence that preferentially concluded the implication of necroptosis in ALS as mentioned above, some evidence demonstrated that necroptosis is dispensable for motor neuron degeneration in ALS pathogenesis. For instance, Wang *et al*., 2020 in a mouse model of ALS, demonstrated that disease progression does not affect in $SOD1^{G93A}$ mice lacking MLKL. Thus, motor neuron

degeneration and neuroinflammation are independent of MLKL expression. However, RIPK1 accumulation was observed in the late stage of disease progression, but no significant changes were observed in the expression of RIPK3 and MLKL at any stage of disease progression (Wang et al., 2020). Similarly, another study concluded that genetic inactivation of RIPK1 kinase does not rescue motor neuron degeneration in a mouse model of ALS (Dominguez et al., 2021). Thus, the role of necroptotic machinery in the pathogenesis of ALS is debateable and more studies are required to underpinning the exact relationship between ALS and necroptosis cell death. **(Figure 6)**

7.3. Traumatic brain injury and spinal cord injury

Mounting evidence has demonstrated that TBI and SCI are capable of causing several aberrant brain pathologies, such as sensory and motor dysfunction (X. Hu et al., 2022). Necrosome activation has been characterized in the pathogenesis of brain injuries, namely traumatic brain injury and spinal cord injury. For instance, overexpression of the charged multivesicular body protein 4b (CHMP4B) decreases the necrosome activation in the microglia through the increased activity of forkhead transcription factor O1 (FOXO1) that enhances the CHMP4B binding to its promoter region (P. Zhao et al., 2020). Additionally, Bao *et al*., 2019 concluded that in a rat model of TBI, translocation of HMGB1 to cytoplasm causes upregulation of receptors for advanced glycation end-products, NF-κB, and IL-6. Further, the authors in the same study demonstrated that silencing of A20 enhanced the necroptosis and reversed the protective effects of Nec-1 and melatonin (Bao et al., 2019). Genetic deletion of necrosome components, namely RIPK1 and RIPK3, prevents neuronal cell death through necroptosis inhibition, resulting in improved memory and cognitive functions (Wehn et al., 2021). For example, Wu *et* al., 2021 demonstrated that the genetic knockdown of RIPK3 rescued from functional outcomes in TBI injury is independent of necroptosis (Wu et al., 2021). Different compounds, namely 2-(2-Benzofuranyl)-2-imidazoline, perampanel, and hydrogen-rich saline, have been identified that provide neuroprotection against necroptosis through the inhibition of necrosome components (Chen et al., 2020a; Y. Hu et al., 2022; Ni et al., 2019; Yang et al., 2021). Recently, controlled decompression has been identified as a potential therapeutic strategy against TBI through necroptosis inhibition, where controlled decompression causes the downregulation of inflammatory cytokines, namely TNF-α, IL-6, and others (T. Chen et al., 2021; C. Zhang et al., 2021). Chen *et al*., 2021 have concluded that activation of phosphoglycerate mutase 5 (PGAM5), a mitochondrial protein, regulates Asc oligomerization, which worsens inflammatory outcomes post-TBI and could be a possible therapeutic target in the TBI model (Y. Chen et al., 2021). Likewise, Chen *et al*., 2020 demonstrated that the genetic knockdown of Arc activates the metabotropic glutamate receptor 1 and intracellular Ca^{2+} release in neurons, which increases neuronal cell death through enhanced necroptosis (Chen et al., 2020b).

SCI has been categorized into primary and secondary injuries, where the primary injury is the strong prognostic marker, whereas, secondary injury is related to overall morbidity and mortality (Alizadeh et al., 2019). Recent times have demonstrated the potential implication of neuroinflammatory mechanism-induced necroptosis cell death in the progression of SCI (Liu et al., 2015). For instance, upregulated expression of RIPK1 was observed in cultured neurons, astrocytes, and oligodendrocytes, followed by SCI (Kanno et al., 2020). Likewise, RIPK3 inhibition with GSK872 and Nec-1 prevents mitochondrial dysfunction and decreases antioxidative capacity after SCI (Yang Wang et al., 2019c). Recently, Wang *et al*., 2019 demonstrated the upregulation of micro-RNA-223-3p rescued from RIPK3-induced necroptosis cell death by reducing inflammatory response after SCI (Yang Wang et al., 2019a). Additionally, Liu *et al*., 2018 concluded that impaired lysosomal degradation causes the accumulation of RIPK1 and RIPK3 that leads to the initiation of necroptosis, and thus,

demonstrated the potential of the lysosomal pathway in necroptosis (Liu et al., 2018). Further, several necroptosis inhibitors and techniques to inhibit necroptosis machinery have been applied to reverse the memory impairment and cognitive decline in the progression of SCI (Fiani et al., 2021; X. Wang et al., 2021; Y. Wang et al., 2014; Yongxiang Wang et al., 2018). For instance, astragalin and growth differentiation factor 11 protect the impaired spinal cord through the inhibition of necrosome via modulating oxidative stress and autophagic degradation (Sun et al., 2021; Yu Xu et al., 2021). Similarly, Wang *et al*., 2017 demonstrated that administration of Nec-1 rescues mitochondrial and endoplasmic reticulum damage that inhibits the necrosome activation and thus inhibits necroptosis through downregulating the immunoglobulin-binding protein (BiP/GRP78) and X box-binding protein-1 activity (S. Wang et al., 2017). Quercetin, a natural compound, ameliorates the necroptosis of oligodendrocytes through the inhibition of microglial polarization via decreasing ROS (Fan et al., 2019). Additionally, quercetin administration significantly reduces hypoxia-inducible factor 1α (HIF1α), VEGFA, caspase-3 and ubiquitin levels in hypoxic conditions (Sarkar et al., 2012). **(Figure 6)**

Journal Pre-proof

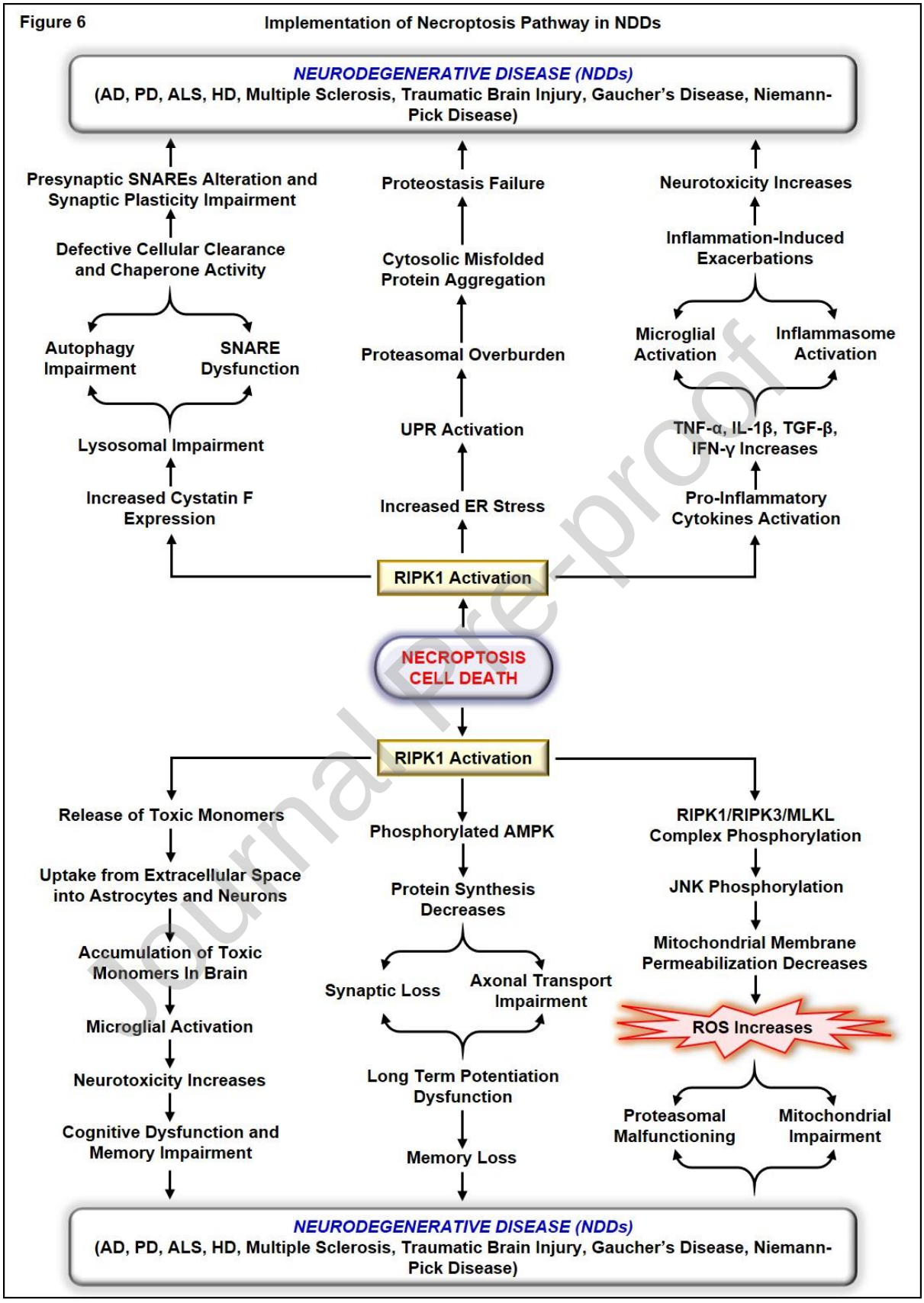

Figure 6: Necroptosis cell death is involved in the pathogenesis of neurological manifestation, including neurodegenerative disease and neurological diseases. Activation of RIPK1 increases cystatin F expression, ER stress, and release of pro-inflammatory cytokines that simultaneously causes lysosomal defects, UPR activation, and microglial activation. Lysosomal impairment leads to autophagic degradation and SNARE dysfunction that causes chaperone activity and is involved in the pathogenesis

of AD. Similarly, failure of proteasomal overburden and activation of microglial increases neurotoxicity +that is involved in the pathogenesis of neurodegenerative diseases. Further, the Activation of RIPK1 increases the release of toxic monomers, AMPK phosphorylation, and necrosome phosphorylation, causing axonal degeneration and synaptic loss. In addition, RIPK1 activation causes microglial activation and inflammasome activation that increases neurotoxicity, leading to neurological disease progression.

7.4. Multiple sclerosis and Gaucher's disease

MS is a type of neurodegenerative disease characterized by the loss of oligodendrocytes and demyelination in the CNS (Dobson and Giovannoni, 2019). However, the exact pathology and mechanism of disease progression are still unclear. TNF-α is considered to be implemented in the progression of MS, which can activate the necroptosis pathway through the activation of RIPK1 and RIPK3 during caspase-8 deficiency (Ofengeim et al., 2015). The necroptosis cell death pathway in the pathology of MS is a multi-step process with the increased expression of FADD, RIPK1, RIPK3, MLKL, and TNFR1. The increased expression and phosphorylation of RIPK3 and MLKL lead to the necroptosis pathway activation by forming protein oligomers in the necrosome. A simultaneous decrease in caspase-8-dependent apoptosis signaling was observed during necroptosis activation in MS progression (Magliozzi et al., 2019; Picon et al., 2021). Further, defective/inactive caspase-8 expression was also observed in MS lesions by activating pro-inflammatory cytokines. Thus, it may be concluded that caspase-8 deficiency promotes necroptosis cell death through an inflammatory signaling cascade (Dhib-Jalbut and Kalvakolanu, 2015). An experimental study performed by Zhang *et al*., 2019 on the immune and chemical-induced mouse model demonstrated that RIPK1-MLKL dependent cell death has no role in the process of demyelination, whereas, RIPK3 independent function of MLKL leads to demyelination in the peripheral nervous system and CNS (Sitao Zhang et al., 2019). Further, studies found the possible role of IFN-γ in the progression of MS, where TNF + IFN-γ induced animals demonstrated elevated expression of phosphoRIPK3 and phosphoMLKL indicating the activation of necroptosis pathway (James et al., 2020). Thus, it may be concluded that inflammatory process and microglial activation plays an important role in the pathogenesis of MS through activation of necrosome complex (RIPK1, RIPK3, and MLKL) under reduced caspase-8 activation and increased (FADD-like IL-1β-converting enzyme)-inhibitory protein (c-FLIP) expression. Thus, inhibition of necroptosis pathway might provide a great avenue for the treatment of MS. **(Figure 6)**

Gaucher's disease (GD) is characterized by mutations in the glucocerebrosidase gene, which is the most occurring lysosomal storage disease. The possible reason for GD etiology is the accumulation of sphingolipid glucosylceramide due to impaired glucocerebrosidase activity (Futerman and van Meer, 2004). However, the exact mechanism of GD is still unknown. Further, numerous studies observed enhanced cell death in the pathogenesis of GD (Linari and Castaman, 2015). However, the activity of caspase-3, caspase-7, and caspase-9 was not elevated. The studies also found the absence of proteolytic cleavage of caspase-8. Thus, the results concluded that cell death in GD progression is nonapoptotic and independent of caspase activity (Enquist et al., 2007; Vitner et al., 2014). The evidence comes from the study conducted by Vinter *et al*., 2014, where the authors demonstrated increased expression levels of RIPK1 and RIPK3 in the brain samples of symptomatic $Gba^{flox/flox}$ nestin-cre mice. Further, they observed high activity of c-FLIP in the brain samples, which suggests the presence of caspase-8/c-FLIP heterodimer in nestin-cre mice. The authors also concluded that the presence of caspase-8/c-FLIP heterodimer is responsible for the absence of caspase-8 activity. In addition, the expression level of RIPK1 was also found to be increased in the patients treated with type 2 GD compared to age-matched control samples. Thus, the results concluded the involvement of the necroptosis pathway in nGD brain samples. Similarly, RIPK3 was found in the nuclei of neurons of $Gba^{flox/flox}$ mice, suggesting the possible function of RIPK3 in necroptosis cell death (Hughes et al., 2016;

Vitner et al., 2014). Moreover, Yanez *et al*., 2021 concluded that the active and phosphorylated form of c-Abl was increased several times in different GD experimental models, which acts as the upstream target of RIPK3. The authors observed that increased phosphorylation activity of c-Abl caused increased phosphorylation of RIPK3 at tyrosine. However, the pharmacological inhibition or genetic ablation of c-Abl decreased the RIPK3 phosphorylation. Thus, suggesting the crucial role of c-Abl phosphorylation in RIPK3-induced necroptosis cell death in the pathogenesis of GD (Yañez et al., 2021).

7.5. Stroke and intracerebral hemorrhage

Ischemic stroke is a complex disease that causes neuronal cell mortality and leads to neurological dysfunction (Jayaraj et al., 2019). Mounting evidence suggests the connection between necroptosis cell death in the pathogenesis and progression of neuronal stroke. For instance, TRIAD3A and TRAF2 inhibit the progression of necroptotic cell death. Li *et al*., 2019 demonstrated that deletion of TRAF2 leads to an increase in infraction size and cell death, whereas, Yuan *et al*., 2020 concluded that Trad3A knockdown increased microglial-induced neuronal cell death through increased expression of pro-inflammatory cytokines (Li et al., 2019; Z. Yuan et al., 2020). Further, the knockdown of the critical regulator of necroptosis that is RIPK1 promotes neural regeneration and inhibits neuronal proliferation. In addition, the knockdown of RIPK1 leads to a decrease in VEGF-D expression, which causes impairment in astrocyte function (Zhu et al., 2021). Moreover, inactivation of RIPK1/RIPK3/MLKL signaling through deletion of either RIPK1, RIPK3, and MLKL rescued from cerebral ischemic injury. Zhang *et al*., 2020 concluded that RIPK1 mutant mice showed decreased brain infarct volume, whereas, RIPK3 and MLKL deficient mice were protected from ischemic damage by inhibiting inflammatory response in the infarct area (Y. Zhang et al., 2020). Additionally, overexpression of RIPK1 leads to an increase in perivascular M1-like microglia-induced endothelial necroptosis, which ultimately leads to BBB disruption and eventually causes neuronal loss. Thus, inhibition of RIPK1 with Nec-1 reversed neuronal damage after cerebral stroke by inhibiting neuroinflammatory response (A.-Q. Chen et al., 2019). In addition, recent evidence suggests the involvement of mitochondria in necroptosis-induced cell death in the pathogenesis of ischemic stroke. For instance, Lu *et al*., 2016 demonstrated that deficiency of mitochondrial PGAM5 exacerbated the necroptosis cell death through the accumulation of damaged mitochondria, which increases ROS (Lu et al., 2016). Further, mitochondrial ROS leads to RIPK1 oxidation, which regulates the activity of executioner caspases and necrosome activation (Deragon et al., 2020). Thus, it can be concluded that activation of RIPK1 triggers RIPK3 and MLKL activity, which causes necroptosis cell death through a different mechanism, including accumulation of ROS in the mitochondria in the pathogenesis of ischemic stroke. **(Figure 6)**

Further, necrosome-activated necroptosis was observed in experimental models of intracerebral hemorrhage (ICH). For instance, Yuan *et* al., 2019 demonstrated that in an experimental rat model, the activity level of RIPK3 was significantly increased after subarachnoid hemorrhage, where inhibition of RIPK3 expression promotes neuroprotection against subarachnoid hemorrhage. The study also concluded that an increase in RIPK3 activity causes a loss of blood-brain permeability and an increase in brain lesions (S. Yuan et al., 2019). In addition, RIPK3 exacerbated necroptosis cell death by activating CaMKII and apoptosis-inducing factor (AIF) after ICH through the phosphorylation of MLKL. AIF forms a complex with RIPK3 in the cytoplasm, where it causes brain edema and brain lesion (Yang Xu et al., 2021). Apart from RIPK3, studies demonstrated the cell-specific activation of RIPK1 and MLKL after ICH (Lule et al., 2020). For instance, inhibition or genetic breakdown of RIPK1 inhibits brain injury in a rat model of ICH through inhibition of TNF-α activity. In the same study, the authors also demonstrated that mutation in serine/threonine sites of RIPK1 decreases the phosphorylation of RIPK1, which partially diminishes the

induction of necroptosis. Thus, phosphorylation is crucial for medium-induced necroptosis cell death (Shen et al., 2017). Furthermore, hemin, a breakdown product of hemoglobin, is vital for necroptosis cell death in ICH. For example, Chu *et al*., 2018 concluded that hemin causes necroptosis cell death in C57BL/6 mice and IL-1R1$^{-/-}$ mice through an association between Interleukin-1R1 and necrosome (Chu et al., 2018). Similarly, Su *et al*., 2018 demonstrated that hemin causes the activation of RIPK1 and RIPK3 to activate necrosome, which causes necroptosis cell death in HT22 hippocampal neuronal cells (Su et al., 2018). Recently, a study conducted by Wei *et al*., 2021 demonstrated that overexpression of miR-383-3p promotes neuronal necroptosis through inhibition of activating transcription factor 4 (ATF4) levels in the ICH-induced Sprague–Dawley rats experimental model (Wei et al., 2021). Moreover, Cai *et al*., 2020 demonstrated the neuroprotective function of electroacupuncture in cerebral hemorrhage. The authors concluded that the application of electropuncture inhibits the activation of RIPK1, which decreases the interaction between RIPK1 and RIPK3. Further, the authors demonstrated that electropuncture reduced the expression of interleukin-6, interleukin-8, and TNF-α in the rat model of cerebral hemorrhage (Cai et al., 2020).

7.6. Epilepsy

Epilepsy is a chronic disease of CNS characterized by seizures such as predisposition, focal, and generate (Beghi, 2020). Hippocampal neurons exhibit a variety of cell-death pathways after the occurrence of status epilepticus (SE). Experimental studies suggested that prolonged seizures cause neuronal cell death in the brain contributing to cognitive impairment. In the lithium-pilocarpine-induced epilepsy rat model, necroptosis-like morphological changes were observed with the formation of autophagosomes and loss of ribosomes (Phelan et al., 2015). Further, the expression of RIPK1 and p-MLKL were increased after 24 hours and peaked at 72 hours in the amygdala and piriform cortex (Cai et al., 2017). The increased expression of MLKL results in the movement of MLKL from the cytosol to the plasma and intracellular membrane, which increases Na^+ and Ca^{2+} influx. Moreover, an experimental study conducted on cortical neurons isolated from ketamine-induced Wistar rats suggested that inhibition of necroptosis with its selective inhibitor that is Nec-1, at 100 μmol/L inhibited the N-methyl-D-aspartate receptor (NMDA)-induces cell death and leakage of lactate dehydrogenase (LDH). The results also concluded that inhibition of necroptosis with Nec-1 decreases the intracellular Ca^{2+} level, which is the major contributing factor in NMDA-induced necroptosis (Li et al., 2008). Mounting evidence suggests that activation of the RIPK1/RIPK3/MLKL complex leads to mitochondrial impairment through altering ROS concentration (Mao et al., 2019). An experimental study performed by Jia *et al*., on the lithium-pilocarpine model of SE observed that hydrogen reverses spatial learning and memory deficits. Treatment with hydrogen downregulates the expression of the necroptosis-related proteins such as MLKL, RIPK3, and phosphoMLKL in the hippocampus. Hydrogen treatment also prevents neuronal cell death caused by SE by inhibiting caspase-8-dependent apoptosis (Jia et al., 2019).

8. Therapeutic treatment targeting necroptosis-related proteins

8.1. Natural and chemical compounds as therapeutic agents

Modulation of necrosis was first studied in ischemic brain injury in 2005 (Degterev et al., 2005) and afterward in liver injury (Afonso et al., 2015). Necroptosis has also been found to be associated with neurodegenerative diseases such as AD (Caccamo et al., 2017b), PD (Iannielli et al., 2018), HD (Vandenabeele et al., 2010) and MS (Ofengeim et al., 2015). Various natural and chemical compounds have been discovered to target RIPK1, RIPK3, and MLKL, which are significant components of necroptosis (Zhuang and Chen, 2020). Pharmacological intervention to inhibit necroptosis was first studied using Nec-1, an ATP-competitive allosteric inhibitor of RIPK1 (Takahashi et al., 2012). Nec-1 has been reported to

protect retinal pigment epithelial from degradation through anti-oxidation (Hanus et al., 2016), anti-inflammation (Murakami et al., 2013), and possibly restoring lysosomal function (Cao and Mu, 2021). Thus, it has therapeutic potential in treating RPE degradation-related diseases such as age-related macular degeneration (Cao and Mu, 2021). It has also been reported to be protective in other neurodegenerative disease models, such as axonal degeneration (Arrázola et al., 2019b) and PD (Alegre-Cortés et al., 2020). It has also been shown to alleviate neuronal cell damage induced by aluminum, a metal typically transported to the brain, where it can contribute to AD pathology (Qinli et al., 2013). Structure-activity relationship analysis of Nec-1 analogs identified 7-Cl-O-Nec-1 that was more potent and metabolically stable than the original Nec-1 (Degterev et al., 2008; Teng et al., 2005). Oxa12, an oxazolone identified through phenotypic screening, was reported to act as a potent necroptosis inhibitor in two cellular models (BV2 microglial and L929 fibrosarcoma cells) with no associated cytotoxicity (Oliveira et al., 2018b). It inhibited MLKL S358 phosphorylation and necrosome assembly, important necroptosis markers, in BV2 cells. It strongly reduced the necroptosis-mediated activation of JNK and p38 MAPK signaling pathways associated with the pathogenesis of neurodegenerative diseases, such as AD and PD (Oliveira et al., 2018a). Necrosulfonamide has been reported to inhibit MLKL-dependent necroptosis and ameliorate neurological impairment in the SCI mouse model (Jiao et al., 2019). NSA was also reported to reduce spatial learning and memory deficits by targeting MLKL in a rat model of AD induced by the administration of $AlCl_3$ (Tarek M.K. Motawi et al., 2020). Curcumin, a polyphenol extracted from the Curcuma longa plant, has been shown to protect the neuronal cell from status-epilepticus-induced damage to hippocampal neurons by inducing autophagy and inhibiting necroptosis in lithium–pilocarpine-induced status epilepticus rat model (Wang et al., 2016). Further, curcumin administration improved hepatocellular architecture through downregulating VEGF, Hsp90 and p-Akt (Anand et al., 2012).

Table 3: Role of different drug molecules and natural biomolecules in the prevention of necroptosis-induced neurological defects

Compound	Disease	Experimental Model	Effect	References
β-Caryophyllene	Cerebral Ischemia	Primary neurons induced oxygen-glucose deprivation and re-oxygenation	Reduced neuronal cell death and MLKL protein expression	(M. Yang et al., 2017)
		Mice model	Decreased RIPK1 and RIPk3 expression, decreased neuronal necrosis, decreased interleukin-1β and toll-like receptor 4 levels.	
Nec-1	Ischemic stroke	Middle cerebral artery occlusion-induced cerebral ischemia rats' model	Prevented RIPK1 phosphorylation and its downstream signaling activation	(Xu-Xu Deng Feng-Yan Sun, n.d.)
		12-week-old C57BL/6 mice model	Inhibition of necroptosis decreased inflammatory response and reversed cognitive dysfunction	(Zhang et al., 2016)
		Murine endothelin-1 model of ischemia-reperfusion injury	Inhibition of RIPK1 leads to downregulating the activity of caspase-3 and caspase 7, which leads to a decrease in neuronal cell apoptosis.	(Dojo Soeandy et al., 2020)
	Intracerebral hemorrhage	Collagenase-induced intracerebral hemorrhage in mice	Reduced cell death and prevented blood-brain barrier opening. Administration of Nec-1 also inhibited edema development.	(King et al., 2014)
	Subarachnoid hemorrhage	Subarachnoid hemorrhage rat model	Reduced the lesion volume, inhibited brain swelling, prevented blood-brain barrier disruption through inhibition of RIPK3 expression	(Jingsen Chen et al., 2019)
	Multiple sclerosis	C57BL/6 mice	Decreases the number of lesions and production of pro-inflammatory cytokines.	(Ying Wang et al., 2019)
	Intracerebral hemorrhage	Collagenase-induced intracerebral hemorrhage in mice	Inhibits RIPK1/RIPK3 activation, which leads to inactivation of necrosome, and thus results in a decrease in necroptosis	(Su et al., 2015)
	Traumatic	Sprague-Dawley rats	Prevented integration of BNIP3 into	(Mu et al.,

	brain injury		mitochondria, which promotes the protection of neurons and oligodendrocytes by inhibiting the necroptosis pathway	2021)
	Spinal cord injury	neuropathic pain rat model	Reduces neuroinflammation and inhibits necroptosis cell death	(Liang et al., 2019)
AATF core peptide SAP-12	Ischemic stroke	Middle cerebral artery occlusion-induced cerebral ischemia	Decreases TNF-α levels, reduces brain infarct size, decreases RIPK3 and MLKL expression	(Guo and Xie, 2019)
Dabrafenib	Ischemic brain injury	C57BL6 mice	Inhibits necroptosis cell death, reduced TNF-α levels, and reduces brain infarct size	(Cruz et al., 2018)
	Spinal cord injury	Mouse model of thoracic spinal cord contusion injury	Decreases neuronal loss, demyelination, axonal damage, and tissue damage through inhibition of RIPK3-induced necroptosis cell death	(Sugaya et al., 2019)
Salubrinal	Ischemic stroke	Transient global cerebral ischemia in the rat model	Decreased the necroptotic marker levels and reduced the areas of selective neuronal loss	(Font-Belmonte et al., 2019)
Caspofungin	Ischemic stroke	Sprague-Dawley rat brains	Improved neurological functions through upregulation of Pellino3, increased ubiquitination of RIPK1, and downregulation of necroptosis	(Y.-Y. Zhang et al., 2021)
Melatonin	Intracerebral hemorrhage	Intracerebral hemorrhage in C57 mice	Inhibits RIPK3 activity through regulation of A20, which decreases necroptotic cell death	(Lu et al., 2019)
Deferoxamine	Intracerebral hemorrhage	Piglet model of intracerebral hemorrhage	It reduced white matter necrosis through decreased TNF-α and RIPK1 levels.	(Xie et al., 2014)
Perampanel	Intracerebral hemorrhage	C57BL/6 mice and in a hemin-induced neuron damage cell culture model	Inhibits the activation of pro-inflammatory cytokines. Promotes neuroprotection through reduced neuroinflammation and activation of the PTEN pathway	(Yang et al., 2021)
GSK'872	Subarachnoid hemorrhage	Sprague-Dawley rats	Attenuate brain edema, decrease RIPK3 expression and MLKL expression, and reduce brain edema. Further, decreased HMGB1 expression and cytoplasmic translocation	(Chen et al., 2018)
ex-527	Cerebral ischemia-reperfusion injury	Animal model of focal cerebral ischemia	ex-527 microinjection reduces the infarction volume of ischemic brains and improves the survival rate	(Nikseresht et al., 2019)
Necrosulfonamide	Alzheimer's disease	Alzheimer's disease rat model	Decreases the expression of TNF-α and BACE1. Further, Necrosulfonamide administration reduces β-amyloid accumulation and tau hyperphosphorylation by inhibiting MLKL-dependent necroptosis	(Tarek M. K. Motawi et al., 2020)
	Spinal cord injury	Oxygen-glucose deprivation-induced cell damage and SCI-mice	Improves antioxidant capacity and inhibits necrosome activation	(Jiao et al., 2019)
Apelin	Alzheimer's disease	Hippocampus of streptozotocin-induced Alzheimer's disease rat model	Administration of apelin reduces RIPK1, RIPK2, and TNF-α expression in the hippocampus, which attenuates dementia	(Nasseri et al., 2020)
Docosahexaenoic acid	Alzheimer's disease	Human THP-1 monocytes	Administration of docosahexaenoic acid prevents neuronal loss through the prevention of β-amyloid-induced necroptosis cell death through the RIPK1/RIPK3 signaling cascade	(S. Yuan et al., 2020)
EGb761	Alzheimer's disease	β-amyloid treated cultured BV2 microglial cells and β-amyloid injected Alzheimer's disease rat model	Inhibits necroptosis signaling pathway and improves cognitive function by decreasing ROS production and mitochondrial dysfunction	(Tu et al., 2020)
Oxa12	Parkinson's disease	1-methyl-1-4-phenyl-1,2,3,6-tetrahydropyridine hydrochloride Parkinson's disease mouse model	Inhibits necroptosis machinery and prevents dopaminergic neuronal loss	(Oliveira et al., 2021a)
Baicalein	Parkinson's disease	Acrolein-induced rat model	Baicalein inhibits apoptosis and necroptosis through the reduction in oxidative damage and neuroinflammation	(Zhao et al., 2017)
Butylphthalide	Multiple sclerosis	spinal cord tissues	Inhibition of microglial inflammation through decreasing PGAM5 activity, which rescued from necroptosis	(Ying Wang et al., 2018)
P110	Multiple sclerosis	EAE-immunized and cuprizone toxicity-induced demyelinating mouse models	Inhibition of dynamin-related protein 1, which is rescued from neuroinflammation by decreasing necroptosis	(Luo et al., 2017)

Journal Pre-proof

Vigabatrin	Epilepsy	Sprague-Dawley adult male rats	Vigabatrin activates necroptosis and apoptosis pathways, which may be rescued with the administration of Vigabatrin in the combination of B12 and Omega 3	(El-kader et al., 2021)
Aucubin	Epilepsy	Lithium-pilocarpine-induced status epilepticus rat model	Decreases the number of dying neurons and increases the number of surviving neurons through enhanced autophagy and reduced necroptosis in the hippocampus	(J. Wang et al., 2017)
Curcumin	Epilepsy	Lithium-pilocarpine-induced status epilepticus rat model	Protects neuronal cell damage through inhibition of necroptosis and induction of autophagic degradation	(Wang et al., 2016)
2-hydroxypropyl-β-cyclodextrin	Niemann-Pick disease	$Npc1^{-/-}$: $Ripk1^{kd/kd}$ double mutant mice	Inhibition of necrosome and thus inhibits necroptosis machinery through the reduction in neuroinflammation	(Cougnoux et al., 2018)
2-(2-Benzofuranyl)-2-imidazoline	Traumatic brain injury	Traumatic brain injury-induced rat model	Reduced microglial activation and pro-inflammatory cytokines released through inhibition of necroptosis machinery	(Ni et al., 2019)
Quercetin	Spinal cord injury	Spinal cord injury-induced rat model	Reduction in myelin loss and axonal damage through inhibition of necroptosis and suppression of microglia M1 phenotypes by inhibiting STAT3 and NFκβ	(Fan et al., 2019)

RIPK1: Receptor-interacting serine/threonine-protein kinase 1; MLKL: Mixed lineage kinase domain-like pseudokinase; TNF-α: Tumour necrosis factor α; AATF: Apoptosis antagonizing transcription factor; SAP-12: Stress-associated protein 12; RIPK3: Receptor interacting serine/threonine kinase 3; PGAM5: Phosphoglycerate mutase 5; PTEN: Phosphatase and tensin homolog; NFκβ: Nuclear factor kappa-light-chain-enhancer of activated B cells; STAT3: Signal transducer and activator of transcription 3;

8.2. RNA interference as a potential therapeutic agent against necrosome activation

Micro RNAs (miRNAs) are small non-coding RNA molecules involved in post-transcriptional regulation of various biological processes, including PCD through intrinsic Bcl-2, extrinsic cell surface receptors, p53 and ER stress-induced apoptosis and necroptotic apoptosis cell death (Shirjang et al., 2019). Recent studies have given insight into the mechanism of necroptosis regulation by miRNAs (X. Hu et al., 2022). After H_2O_2 stimulation, miR-155 was reported to be overexpressed and prevent necrotic cell death by targeting RIP1 in cardiomyocyte progenitor cells (Liu et al., 2011). Reduced levels of two miRNAs (miR-27a-3p and miR-221-3p) were observed in football players in sub-acute stages after a sports-related concussion, and an inverse relationship could be seen with SRC symptom severity (Shultz et al., 2022). Increased expression of miR-21 was observed in extracellular vesicles in simian immunodeficiency virus encephalitic brains. MiR-21-induced neurotoxicity was not affected by apoptosis inhibition but was prevented by Nec-1, a necroptotic inhibitor, signifying its involvement in the necroptotic cell death pathway (Yelamanchili et al., 2015). miR-383-3p has been reported to promote neuronal necroptosis by negatively regulating the ATF4 expression in intracerebral hemorrhage (Wei et al., 2021). In MPTP-treated mice, necroptosis activation and miR-425 deficiency were reported. Supplementation of miR-425 mimics (AgomiR-425) decreased RIPK1 expression, and the dopaminergic system was significantly protected from MPTP toxicity (Y. B. Hu et al., 2019). In the microglia cell lines (BV2 and N6), miR-335 directly targeted LRRK2 mRNA, reduced LPS-induced pro-inflammatory gene expression and negatively regulated the expression of receptor-interacting proteins 1 and 3 (RIPK1 and RIPK3) that are associated with necroptotic and inflammatory signaling pathways (Oliveira et al., 2021b). miR-223-3p was noted to be downregulated in H2O2-induced spinal cord injury, where it was attached to 3′-UTR of RIPK3 mRNA and inhibited the RIPK3 necroptotic signaling pathway (Yang Wang et al., 2019a). MiRNA-103/107 was reported to regulate programmed necrosis by targeting FADD in H_2O_2-induced myocardial ischemia/reperfusion injury but is not involved in TNF-α-induced necrosis (Wang et al., 2015). The expression of miR-183-5p has been reported to be induced by stress conditions such as using hydrogen peroxide, tunicamycin or TNF-α. Furthermore, its overexpression increased cell survival by regulating apoptosis and necroptosis pathways by targeting PDCD4 and RIPK3, while its knockdown resulted in cell

death. MiR-183-5p is consistently reduced in ALS patients and mouse models, suggesting its involvement in the survival of motor neurons in stress conditions observed in ALS (Li et al., 2020).

Table 4: Micro RNAs, circular RNAs, and long non-coding RNAs as potential therapeutic agents against necroptosis activation in the progression and pathogenesis of neurological diseases

RNAs	Experimental model	Disease	Targets	Signaling affected	Outcomes	References
miR-383-3p	Sprague–Dawley rats	Intracerebral hemorrhage	RIPK1, RIPK2, MLKL, ATF4	Microglial activation	Necroptosis of neurons was increased in intracerebral hemorrhage rats by detecting the expression of RIP1 and RIP3	(Wei et al., 2021)
miR-223-3p	H_2O_2-induced mice spinal cord injury model	Spinal cord injury	RIPK3	Neuronal inflammation	Rescue from RIPK3-induced inflammatory response and necroptosis cell death	(Yang Wang et al., 2019b)
miR-425	C57BL/6 mice	Parkinson's disease	RIPK1	Neuronal inflammation	miR-425 deficiency promotes necroptosis and dopaminergic neurodegeneration in Parkinson's disease	(Y.-B. Hu et al., 2019)
miR-183-5p	Neuro2a cells	Amyotrophic lateral sclerosis	PDCD4 and RIPK3	Neuronal inflammation	Overexpression protects neuronal cells from necroptosis cell death	(Li et al., 2020)
miR-335	BV2 and N9 microglial cell lines	Parkinson's disease	LRRK2	ERK1/2 signaling event and neuronal inflammation	Overexpression of miR-335 mitigates neuroinflammation signaling through downregulating RIPK1 and RIPK3 expression and thus prevents neuronal necroptosis cell death	(Oliveira et al., 2021b)
H19	C57BL/6 mice	Neurogenesis	NLRP3	lncRNA-H19/miR-423-5p/NLRP3 axis	Enhanced neurogenesis following OGD	(Ye et al., 2022)
XIST	Sprague-Dawley rats and Wistar rats	Spinal cord injury	Smurf1 and miR-27a	XIST/miR-27a/Smurf1 pathway	Smurf1 mediates the protective role of XIST deletion in SCI via miR-27a	(Q. Zhao et al., 2020)
MEG3	App^{NL-G-F}	Alzheimer's disease	RIPK1 and RIPK3	Neuronal Inflammation	Overexpression of MEG3 activates neuronal necroptosis in the pathogenesis of Alzheimer's disease	(Balusu et al., 2022)
GAS5	Sprague–Dawley rats	Transient focal ischemia	miRNA-221	Hypoxia pathway	Promotes neuronal cell death through enhanced expression of PUMA	(Zhou et al., 2019)

RIPK1: Receptor-interacting serine/threonine-protein kinase 1; RIPK2: Receptor-interacting serine/threonine-protein kinase 2; MLKL: Mixed lineage kinase domain-like pseudokinase; ATF4: Activating transcription factor 4; H_2O_2: Hydrogen peroxide; PDCD4: Programmed cell death protein 4; LRRK2: Leucine-rich repeat kinase 2; NLRP3: NLR family pyrin domain containing 3;

Conclusion and Future Perspectives

Necroptosis is a novel form of regulated necrosis controlled by the activation of numerous extracellular and intracellular stimuli, namely TNF-α, TNFR, TLRs, and others. With the advancements in biological research, the underlying molecular phenomenon and biological functions of necroptosis have revealed the therapeutic opportunities of necrosome activation in treating neurological manifestations (Dai et al., 2021). Necroptosis achieves the pathophysiological effects by activating either the TNF or TLR pathway involved in the formation of complex IIb consisting of RIPK1, RIPK2, RIPK3, and MLKL, which further activates necroptotic cell death (Wegner et al., 2017). However, the mechanism of necroptotic cell death through the activation of TLR3 and TLR4 pathways is still unclear (He et al., 2011). For instance, In AD, inhibition of IKKβ could promote the RIPK1-induced necroptosis caused by Aβ accumulation, whereas, in TBI, administration of celastrol leads to a decrease in the expression of RIPK3 and MLKL, which rescue from necroptosis cell death (Lu et al., 2022; W. Wang et al., 2022). Although the implication of necroptosis in inflammatory or apoptotic-related pathologies has been appreciated in the past many years, the exact mechanism has not been identified yet (Yang et al., 2015). Studies have also made it abundantly evident that RIPK3 serves a variety of functions in cells. Numerous

investigations have validated the function of RIPK3 in conditions other than necroptosis. In particular, TLR4 is necessary for the activation of the NLRP3 inflammasome by the caspase-8 enzyme, as well as RIPK3 and ROS (Morgan and Kim, 2022). In addition, RIPK3 may have an alternative function in regulating metabolic enzymes, such as GLUD1, isocitrate dehydrogenase 1 (IDH1), glutamate-ammonia ligase (GLUL), glycogen phosphorylase (PYGL) associated with glycolysis (aerobic respiration) and the mitochondria (Z. Yang et al., 2018). A promising therapeutic target is suggested by mounting evidence that indicates inhibiting necroptosis may have neuroprotective effects in NDDs.

Different necroptosis inhibitors targeting RIPK1, RIPK3, and MLKL have been identified and tested across different experimental models to establish their potential in treating neurological manifestations (Dhuriya and Sharma, 2018b). For example, inhibition of RIPK1 through dose-dependent administration of necrostatin 1 significantly prevents neuronal injury that deactivates the necroptosis pathway (Dojo Soeandy et al., 2020). In the PD model, on the other hand, necrostatin 1's inhibition of necroptosis is mitochondria-independent, and Nec-1 was unable to repair rotenone-induced oxidative stress and mitochondrial changes by directly acting on the necrosome. Rotenone promotes ROS generation while inhibiting the mitochondrial complex I, and that in turn triggers necroptosis through RIPK1. Necrostatin 1 also suppresses mitophagy and worsens the rotenone's toxicity (Alegre-Cortés et al., 2020). Moreover, necrostatin 1 has been verified in numerous disease models, such as for cardiovascular, chronic pulmonary diseases, cancer, neurology, and renal conditions. (Cao and Mu, 2021). The use of necrostatin 1 has significant downsides due to its short half-life (approx. 1hr) and off-target effects caused by its targeting of indoleamine 2,3-dioxygenase (IDO) (Muller et al., 2005). This increases the difficulty for researchers to define RIPK1 kinase function using Nec-1 and restricts the therapeutic use of directly targeting RIPK1. The off-target effect, however, allows necrostatin 1 to prevent inflammatory diseases by reducing both necroptosis-induced and IDO-mediated inflammation because IDO has a substantial impact on inflammation (Prendergast et al., 2014). Combination therapy will be important to align the various active cell death pathways in order to stop the death of neurons since necroptosis may combine with other damaging mechanisms including apoptosis and inflammation in neurodegenerative disorders. Recent advances in cell death research show interconnection and crosstalk amongst apoptosis, autophagy, and necrosis signaling pathways in other diseases. The complexity of cell death programs is implicated by the occurrence of numerous controlled cell death pathways, which also offer new therapeutic avenues. Additional research is necessary to understand the connections between various cell death programmes and to pinpoint the crucial molecular elements that, under particular clinical circumstances, govern cell death and can be controlled pharmacologically. Another major issue related to necroptosis inhibitors is the application of Necrosulfonamide. Till date, there is no genetic proof that confirms that administration of Necrosulfonamide inhibits the human MLKL in the pathogenesis of neurological diseases, such as AD, PD, ICH, stroke, epilepsy, and others. However, different studies have been published that demonstrated the potential implication of Necrosulfonamide to inhibit human MLKL in other diseases (Yang et al., 2022). For instance, Sun *et al*., 2012 concluded that Necrosulfonamide specifically blocks necrosis downstream of RIP3 activation, namely MLKL in HeLa cells and HT29 cells through genetic knockdown by specific siRNA (Sun et al., 2012). Likewise, Zhang *et al*., 2020 demonstrated that Necrosulfonamide could reverse the effects of IL-1β through MLKL inhibition (Q. X. Zhang et al., 2020). Thus, more studies were required to validate the relationship between Necrosulfonamide and human MLKL *in vivo* and *in vitro*.

Thus, the focus has been shifted towards identifying combined therapies to target multiple cell death pathways to prevent neuronal loss. Emerging studies has confirmed that RIPK1, RIPK3, and MLKL are not unique biomarkers of necroptosis cell death pathways but are also

involved in other biological process, namely inflammatory response (S. Zhang et al., 2017). Thus, the development and prosecution of necroptosis inhibitors might be a potential therapeutic strategy for the treatment of various neurological diseases and inflammation-related diseases. This comprehensive review has open several avenues for the reseachers to unravel *(i) Issues related to the use of necrostatin inhibitors, such as necrostatin while inhibiting necroptosis, suppress other positive biological events that accelerate neurotoxicity. (ii) to fill up the research gap in the relationship between apoptosis, autophagy, and necroptosis and how targeting RIPK1 or RIPK2 activates apoptosis and autophagy pathways. (iii) exact mechanism of necrosulfonamide as an MLKL inhibitor in neurological disorders. (iv) attention is required to show the combination therapy that targets multiple cell death pathways to prevent neuronal loss (v) to find unique biomarkers of necroptosis apart from necrosome (iv) apart from the necroptosis, RIPK3 has been involved in other biological functions, and thus more studies were required to prove RIPK3 as a specific necroptosis biomarker.*

Author's Contribution

Conceived and designed by P.K. Materials collected and art work done by R.G., S.K., R.T. Critical evaluation and analysis of data done by R.K.A and PK. Manuscript written by R.G., S.K., R.T., R.K.A., and P.K. All authors read the manuscript and agreed to submit.

Conflict of Interest

The authors declare that there is no conflict of interest.

Acknowledgment

We would like to thank the senior management of Delhi Technological University for their constant support and guidance.

References

Abe, K., Yano, T., Tanno, M., Miki, T., Kuno, A., Sato, T., Kouzu, H., Nakata, K., Ohwada, W., Kimura, Y., Sugawara, H., Shibata, S., Igaki, Y., Ino, S., Miura, T., 2019. mTORC1 inhibition attenuates necroptosis through RIP1 inhibition-mediated TFEB activation. Biochim. Biophys. Acta - Mol. Basis Dis. 1865, 165552. https://doi.org/10.1016/J.BBADIS.2019.165552

Afonso, M.B., Rodrigues, P.M., Carvalho, T., Caridade, M., Borralho, P., Cortez-Pinto, H., Castro, R.E., Rodrigues, C.M.P., 2015. Necroptosis is a key pathogenic event in human and experimental murine models of non-alcoholic steatohepatitis. Clin. Sci. 129, 721–739. https://doi.org/10.1042/CS20140732

Aksentijevich, I., Zhou, Q., 2017. NF-κB pathway in autoinflammatory diseases: Dysregulation of protein modifications by ubiquitin defines a new category of autoinflammatory diseases. Front. Immunol. 8, 399. https://doi.org/10.3389/FIMMU.2017.00399/PDF

Alegre-Cortés, E., Muriel-González, A., Canales-Cortés, S., Uribe-Carretero, E., Martínez-Chacón, G., Aiastui, A., Munain, A.L. de, Niso-Santano, M., Gonzalez-Polo, R.A., Fuentes, J.M., Yakhine-Diop, S.M.S., 2020. Toxicity of Necrostatin-1 in Parkinson's Disease Models. Antioxidants 2020, Vol. 9, Page 524 9, 524. https://doi.org/10.3390/ANTIOX9060524

Alizadeh, A., Dyck, S.M., Karimi-Abdolrezaee, S., 2019. Traumatic spinal cord injury: An overview of pathophysiology, models and acute injury mechanisms. Front. Neurol. 10, 282. https://doi.org/10.3389/FNEUR.2019.00282/BIBTEX

Alu, A., Han, X., Ma, X., Wu, M., Wei, Y., Wei, X., 2020. The role of lysosome in regulated necrosis. Acta Pharm. Sin. B 10, 1880–1903. https://doi.org/10.1016/J.APSB.2020.07.003

Ambasta, R.K., Jha, S.K., Kumar, D., Sharma, R., Jha, N.K., Kumar, P., 2015. Comparative

study of anti-angiogenic activities of luteolin, lectin and lupeol biomolecules. J. Transl. Med. 13, 1–10. https://doi.org/10.1186/S12967-015-0665-Z/FIGURES/4

Anand, K., Sarkar, A., Kumar, A., Ambasta, R.K., Kumar, P., 2012. Combinatorial Antitumor Effect of Naringenin and Curcumin Elicit Angioinhibitory Activities In Vivo. http://dx.doi.org/10.1080/01635581.2012.686648 64, 714–724. https://doi.org/10.1080/01635581.2012.686648

Arduíno, D.M., Esteves, A.R., Cardoso, S.M., 2012. Mitochondria drive autophagy pathology via microtubule disassembly. https://doi.org/10.4161/auto.22443 9, 112–114. https://doi.org/10.4161/AUTO.22443

Arivazhagan, A., Krishna, S., Yadav, S., Shah, H.R., Kumar, P., Ambasta, R.K., 2015. Synergy of bone marrow transplantation and curcumin ensue protective effects at early onset of diabetes in mice 在早期发病的糖尿病小鼠中使用骨髓移植和姜黄素联合治疗具有协同保护作用. J. Diabetes 7, 473–484. https://doi.org/10.1111/1753-0407.12204

Armstead, W.M., Hekierski, H., Pastor, P., Yarovoi, S., Higazi, A.A.R., Cines, D.B., 2019. Release of IL-6 After Stroke Contributes to Impaired Cerebral Autoregulation and Hippocampal Neuronal Necrosis Through NMDA Receptor Activation and Upregulation of ET-1 and JNK. Transl. Stroke Res. 10, 104–111. https://doi.org/10.1007/S12975-018-0617-Z/FIGURES/5

Arrázola, M.S., Lira, M., Quiroz, G., Iqbal, S., Eaton, S.L., Kline, R.A., Lamont, D.J., Huerta, H., Ureta, G., Bernales, S., Cárdenas, J.C., Cerpa, W., Wishart, T.M., Court, F.A., 2021. Necroptosis inhibition counteracts axonal degeneration, cognitive decline and key hallmarks of aging, promoting brain rejuvenation. bioRxiv 2021.11.10.468052. https://doi.org/10.1101/2021.11.10.468052

Arrázola, M.S., Saquel, C., Catalán, R.J., Barrientos, S.A., Hernandez, D.E., Martínez, N.W., Catenaccio, A., Court, F.A., 2019a. Axonal Degeneration Is Mediated by Necroptosis Activation. J. Neurosci. 39, 3832. https://doi.org/10.1523/JNEUROSCI.0881-18.2019

Arrázola, M.S., Saquel, C., Catalán, R.J., Barrientos, S.A., Hernandez, D.E., Martínez, N.W., Catenaccio, A., Court, F.A., 2019b. Axonal Degeneration Is Mediated by Necroptosis Activation. J. Neurosci. 39, 3832–3844. https://doi.org/10.1523/JNEUROSCI.0881-18.2019

Bachiller, S., Jiménez-Ferrer, I., Paulus, A., Yang, Y., Swanberg, M., Deierborg, T., Boza-Serrano, A., 2018. Microglia in neurological diseases: A road map to brain-disease dependent-inflammatory response. Front. Cell. Neurosci. 12, 488. https://doi.org/10.3389/FNCEL.2018.00488/BIBTEX

Balusu, S., Horré, K., Thrupp, N., Snellinx, A., Serneels, L., Chrysidou, I., Arranz, A.M., Sierksma, A., Simrén, J., Karikari, T.K., Zetterberg, H., Chen, W.-T., Thal, D.R., Salta, E., Fiers, M., Strooper, B. De, 2022. Long noncoding RNA MEG3 activates neuronal necroptosis in Alzheimer's disease. bioRxiv 2022.02.18.480849. https://doi.org/10.1101/2022.02.18.480849

Bao, Z., Fan, L., Zhao, L., Xu, X., Liu, Yinlong, Chao, H., Liu, N., You, Y., Liu, Yan, Wang, X., Ji, J., 2019. Silencing of A20 Aggravates Neuronal Death and Inflammation After Traumatic Brain Injury: A Potential Trigger of Necroptosis. Front. Mol. Neurosci. 12. https://doi.org/10.3389/FNMOL.2019.00222/FULL

Bayat, A.H., Saeidikhoo, S., Ebrahimi, V., Mesgar, S., Joneidi, M., Soltani, R., Aghajanpour, F., Mohammadzadeh, I., Torabi, A., Abdollahifar, M. amin, Bagher, Z., Alizadeh, R., Aliaghaei, A., 2021. Bilateral striatal transplantation of human olfactory stem cells ameliorates motor function, prevents necroptosis-induced cell death and improves striatal volume in the rat model of Huntington's disease. J. Chem. Neuroanat. 112,

101903. https://doi.org/10.1016/J.JCHEMNEU.2020.101903
Beghi, E., 2020. The Epidemiology of Epilepsy. Neuroepidemiology 54, 185–191. https://doi.org/10.1159/000503831
Bohush, A., Niewiadomska, G., Filipek, A., 2018. Role of Mitogen Activated Protein Kinase Signaling in Parkinson's Disease. Int. J. Mol. Sci. 2018, Vol. 19, Page 2973 19, 2973. https://doi.org/10.3390/IJMS19102973
Bozec, D., Iuga, A.C., Roda, G., Dahan, S., Yeretssian, G., 2016. Critical function of the necroptosis adaptor RIPK3 in protecting from intestinal tumorigenesis. Oncotarget 7, 46384. https://doi.org/10.18632/ONCOTARGET.10135
Caccamo, A., Branca, C., Piras, I.S., Ferreira, E., Huentelman, M.J., Liang, W.S., Readhead, B., Dudley, J.T., Spangenberg, E.E., Green, K.N., Belfiore, R., Winslow, W., Oddo, S., 2017a. Necroptosis activation in Alzheimer's disease. Nat. Neurosci. 20, 1236–1246. https://doi.org/10.1038/NN.4608
Caccamo, A., Branca, C., Piras, I.S., Ferreira, E., Huentelman, M.J., Liang, W.S., Readhead, B., Dudley, J.T., Spangenberg, E.E., Green, K.N., Belfiore, R., Winslow, W., Oddo, S., 2017b. Necroptosis activation in Alzheimer's disease. Nat. Neurosci. 2017 209 20, 1236–1246. https://doi.org/10.1038/nn.4608
Cai, G.F., Sun, Z.R., Zhuang, Z., Zhou, H.C., Gao, S., Liu, K., Shang, L.L., Jia, K.P., Wang, X.Z., Zhao, H., Cai, G.L., Song, W.L., Xu, S.N., 2020. Cross electro-nape-acupuncture ameliorates cerebral hemorrhageinduced brain damage by inhibiting necroptosis. World J. Clin. Cases 8, 1848–1858. https://doi.org/10.12998/wjcc.v8.i10.1848
Cai, Q., Gan, J., Luo, R., Qu, Y., Li, S., Wan, C., Mu, D., 2017. The role of necroptosis in status epilepticus-induced brain injury in juvenile rats. Epilepsy Behav. 75, 134–142. https://doi.org/https://doi.org/10.1016/j.yebeh.2017.05.025
Cao, L., Mu, W., 2021. Necrostatin-1 and necroptosis inhibition: Pathophysiology and therapeutic implications. Pharmacol. Res. 163, 105297. https://doi.org/10.1016/J.PHRS.2020.105297
Chan Kenta Moriwaki, K.-M., Bertin, J., Gough, P.J., 2022. Processing β IL-1 − Atypical Pro Caspase 8 Complex Mediates − A RIPK3. https://doi.org/10.4049/jimmunol.1402167
Chaves, M.L., Camozzato, A.L., Ferreira, E.D., Piazenski, I., Kochhann, R., Dall'Igna, O., Mazzini, G.S., Souza, D.O., Portela, L. V., 2010. Serum levels of S100B and NSE proteins in Alzheimer's disease patients. J. Neuroinflammation 7. https://doi.org/10.1186/1742-2094-7-6
Chen, A.-Q., Fang, Z., Chen, X.-L., Yang, S., Zhou, Y.-F., Mao, L., Xia, Y.-P., Jin, H.-J., Li, Y.-N., You, M.-F., Wang, X.-X., Lei, H., He, Q.-W., Hu, B., 2019. Microglia-derived TNF-α mediates endothelial necroptosis aggravating blood brain–barrier disruption after ischemic stroke. Cell Death Dis. 10, 487. https://doi.org/10.1038/s41419-019-1716-9
Chen, Jingsen, Jin, H., Xu, H., Peng, Y., Jie, L., Xu, D., Chen, L., Li, T., Fan, L., He, P., Ying, G., Gu, C., Wang, C., Wang, L., Chen, G., 2019. The Neuroprotective Effects of Necrostatin-1 on Subarachnoid Hemorrhage in Rats Are Possibly Mediated by Preventing Blood–Brain Barrier Disruption and RIP3-Mediated Necroptosis. Cell Transplant. 28, 1358–1372. https://doi.org/10.1177/0963689719867285
Chen, Jing, Kos, R., Garssen, J., Redegeld, F., 2019. Molecular Insights into the Mechanism of Necroptosis: The Necrosome as a Potential Therapeutic Target. Cells 2019, Vol. 8, Page 1486 8, 1486. https://doi.org/10.3390/CELLS8121486
Chen, T., Pan, H., Li, J., Xu, H., Jin, H., Qian, C., Yan, F., Chen, Jingyin, Wang, C., Chen, Jingsen, Wang, L., Chen, G., 2018. Inhibiting of RIPK3 attenuates early brain injury following subarachnoid hemorrhage: Possibly through alleviating necroptosis. Biomed. Pharmacother. 107, 563–570. https://doi.org/10.1016/j.biopha.2018.08.056
Chen, T., Qian, X., Zhu, J., Yang, L.K., Wang, Y.H., 2021. Controlled Decompression

Journal Pre-proof

Attenuates Compressive Injury following Traumatic Brain Injury via TREK-1-Mediated Inhibition of Necroptosis and Neuroinflammation. Oxid. Med. Cell. Longev. 2021. https://doi.org/10.1155/2021/4280951

Chen, T., Yang, L.-K., Zhu, J., Hang, C.-H., Wang, Y.-H., 2020a. The AMPAR Antagonist Perampanel Regulates Neuronal Necroptosis via Akt/GSK3β Signaling After Acute Traumatic Injury in Cortical Neurons. CNS Neurol. Disord. - Drug Targets 20, 266–272. https://doi.org/10.2174/1871527319666201001110937

Chen, T., Zhu, J., Wang, Y.H., Hang, C.H., 2020b. Arc silence aggravates traumatic neuronal injury via mGluR1-mediated ER stress and necroptosis. Cell Death Dis. 11. https://doi.org/10.1038/S41419-019-2198-5

Chen, W., Wu, J., Li, L., Zhang, Zhengmao, Ren, J., Liang, Y., Chen, F., Yang, C., Zhou, Z., Sean Su, S., Zheng, X., Zhang, Zhirong, Zhong, C.Q., Wan, H., Xiao, M., Lin, X., Feng, X.H., Han, J., 2015. Ppm1b negatively regulates necroptosis through dephosphorylating Rip3. Nat. Cell Biol. 2014 174 17, 434–444. https://doi.org/10.1038/ncb3120

Chen, W., Zhou, Z., Li, S., Zhong, C.Q., Zheng, X., Wu, X., Zhang, Y., Ma, H., Huang, D., Li, W., Xia, Z., Han, J., 2013. Diverse Sequence Determinants Control Human and Mouse Receptor Interacting Protein 3 (RIP3) and Mixed Lineage Kinase domain-Like (MLKL) Interaction in Necroptotic Signaling *. J. Biol. Chem. 288, 16247–16261. https://doi.org/10.1074/JBC.M112.435545

Chen, Y., Gong, K., Guo, L., Zhang, B., Chen, S., Li, Z., Quanhua, X., Liu, W., Wang, Z., 2021. Downregulation of phosphoglycerate mutase 5 improves microglial inflammasome activation after traumatic brain injury. Cell Death Discov. 7. https://doi.org/10.1038/S41420-021-00686-8

Chevin, M., Sébire, G., Deltenre, P., Kadhim, H., 2020. Necroptotic neuronal cell death in amyotrophic lateral sclerosis: A relevant hypothesis with potential therapeutic implication? Med. Hypotheses 144, 110295. https://doi.org/10.1016/J.MEHY.2020.110295

Choi, M.E., Price, D.R., Ryter, S.W., Choi, A.M.K., 2019. Necroptosis: a crucial pathogenic mediator of human disease. JCI Insight 4. https://doi.org/10.1172/JCI.INSIGHT.128834

Choi, S.-G., Kim, H., Jeong, E. Il, Lee, Ho-June, Park, S., Lee, S.-Y., Lee, Hyeon-Jeong, Lee, S.W., Chung, C.H., Jung, Y.-K., 2017. SUMO-Modified FADD Recruits Cytosolic Drp1 and Caspase-10 to Mitochondria for Regulated Necrosis. Mol. Cell. Biol. 37. https://doi.org/10.1128/MCB.00254-16/SUPPL_FILE/ZMB999101390S1.PDF

Choi, S.W., Park, H.H., Kim, S., Chung, J.M., Noh, H.J., Kim, S.K., Song, H.K., Lee, C.W., Morgan, M.J., Kang, H.C., Kim, Y.S., 2018. PELI1 Selectively Targets Kinase-Active RIP3 for Ubiquitylation-Dependent Proteasomal Degradation. Mol. Cell 70, 920-935.e7. https://doi.org/10.1016/J.MOLCEL.2018.05.016

Choi, W.S., Abel, G., Klintworth, H., Flavell, R.A., Xia, Z., 2010. JNK3 mediates paraquat- and rotenone-induced dopaminergic neuron death. J. Neuropathol. Exp. Neurol. 69, 511–520. https://doi.org/10.1097/NEN.0B013E3181DB8100

Chu, X., Wu, X., Feng, H., Zhao, H., Tan, Y., Wang, L., Ran, H., Yi, L., Peng, Y., Tong, H., Liu, R., Bai, W., Shi, H., Li, L., Huo, D., 2018. Coupling between interleukin-1R1 and necrosome complex involves in hemin-induced neuronal necroptosis after intracranial hemorrhage. Stroke 49, 2473–2482. https://doi.org/10.1161/STROKEAHA.117.019253

Chun, H.S., Gibson, G.E., Degiorgio, L.A., Zhang, H., Kidd, V.J., Son, J.H., 2001. Dopaminergic cell death induced by MPP(+), oxidant and specific neurotoxicants shares the common molecular mechanism. J. Neurochem. 76, 1010–1021. https://doi.org/10.1046/J.1471-4159.2001.00096.X

Corrales, T. de los R., Losada-Pérez, M., Casas-Tintó, S., 2021. JNK Pathway in CNS Pathologies. Int. J. Mol. Sci. 22. https://doi.org/10.3390/IJMS22083883

Journal Pre-proof

Cougnoux, A., Clifford, S., Salman, A., Ng, S.-L., Bertin, J., Porter, F.D., 2018. Necroptosis inhibition as a therapy for Niemann-Pick disease, type C1: inhibition of RIP kinases and combination therapy with 2-hydroxypropyl-β-cyclodextrin. Mol. Genet. Metab. 125, 345. https://doi.org/10.1016/J.YMGME.2018.10.009

Court, F.A., Coleman, M.P., 2012. Mitochondria as a central sensor for axonal degenerative stimuli. Trends Neurosci. 35, 364–372. https://doi.org/10.1016/J.TINS.2012.04.001

Crifo, B., Schaible, B., Brown, E., Halligan, D.N., Scholz, C.C., Fitzpatrick, S.F., Kirwan, A., Roche, H.M., Criscuoli, M., Naldini, A., Giffney, H., Crean, D., Blanco, A., Cavadas, M.A., Cummins, E.P., Fabian, Z., Taylor, C.T., 2019. Hydroxylase Inhibition Selectively Induces Cell Death in Monocytes. J. Immunol. 202, 1521–1530. https://doi.org/10.4049/JIMMUNOL.1800912/-/DCSUPPLEMENTAL

Cruz, S.A., Qin, Z., Stewart, A.F.R., Chen, H.-H., 2018. Dabrafenib, an inhibitor of RIP3 kinase-dependent necroptosis, reduces ischemic brain injury. Neural Regen. Res. 13, 252–256. https://doi.org/10.4103/1673-5374.226394

Dai, W., Cheng, J., Leng, X., Hu, X., Ao, Y., 2021. The potential role of necroptosis in clinical diseases (Review). Int. J. Mol. Med. 47, 1–16. https://doi.org/10.3892/IJMM.2021.4922/HTML

Dawson, T.M., Dawson, V.L., 2010. The Role of Parkin in Familial and Sporadic Parkinson's Disease. Mov. Disord. 25, S32. https://doi.org/10.1002/MDS.22798

De Ferrari, G. V., Chacón, M.A., Barría, M.I., Garrido, J.L., Godoy, J.A., Olivares, G., Reyes, A.E., Alvarez, A., Bronfman, M., Inestrosa, N.C., 2003. Activation of Wnt signaling rescues neurodegeneration and behavioral impairments induced by β-amyloid fibrils. Mol. Psychiatry 2003 82 8, 195–208. https://doi.org/10.1038/sj.mp.4001208

Degterev, A., Hitomi, J., Germscheid, M., Ch'en, I.L., Korkina, O., Teng, X., Abbott, D., Cuny, G.D., Yuan, C., Wagner, G., Hedrick, S.M., Gerber, S.A., Lugovskoy, A., Yuan, J., 2008. Identification of RIP1 kinase as a specific cellular target of necrostatins. Nat. Chem. Biol. 4, 313. https://doi.org/10.1038/NCHEMBIO.83

Degterev, A., Huang, Z., Boyce, M., Li, Y., Jagtap, P., Mizushima, N., Cuny, G.D., Mitchison, T.J., Moskowitz, M.A., Yuan, J., 2005. Chemical inhibitor of nonapoptotic cell death with therapeutic potential for ischemic brain injury. Nat. Chem. Biol. 2005 12 1, 112–119. https://doi.org/10.1038/nchembio711

Del Re, D.P., Amgalan, D., Linkermann, A., Liu, Q., Kitsis, R.N., 2019. Fundamental Mechanisms of Regulated Cell Death and Implications for Heart Disease. Physiol. Rev. 99, 1765. https://doi.org/10.1152/PHYSREV.00022.2018

Delanghe, T., Dondelinger, Y., Bertrand, M.J.M., 2020. RIPK1 Kinase-Dependent Death: A Symphony of Phosphorylation Events. Trends Cell Biol. 30, 189–200. https://doi.org/10.1016/J.TCB.2019.12.009

Deragon, M.A., McCaig, W.D., Patel, P.S., Haluska, R.J., Hodges, A.L., Sosunov, S.A., Murphy, M.P., Ten, V.S., LaRocca, T.J., 2020. Mitochondrial ROS prime the hyperglycemic shift from apoptosis to necroptosis. Cell death Discov. 6, 132. https://doi.org/10.1038/s41420-020-00370-3

Dermentzaki, G., Politi, K.A., Lu, L., Mishra, V., Pérez-Torres, E.J., Sosunov, A.A., McKhann, G.M., II, Lotti, F., Shneider, N.A., Przedborski, S., 2019. Deletion of Ripk3 Prevents Motor Neuron Death In Vitro but not In Vivo. eNeuro 6. https://doi.org/10.1523/ENEURO.0308-18.2018

Dey, K., Bazala, M.A., Kuznicki, J., 2020. Targeting mitochondrial calcium pathways as a potential treatment against Parkinson's disease. Cell Calcium 89, 102216. https://doi.org/10.1016/J.CECA.2020.102216

Dhanasekaran, D.N., Premkumar Reddy, E., 2017. JNK-signaling: A multiplexing hub in programmed cell death. Genes and Cancer 8, 682–694.

https://doi.org/10.18632/GENESANDCANCER.155
Dhib-Jalbut, S., Kalvakolanu, D. V, 2015. Microglia and necroptosis: The culprits of neuronal cell death in multiple sclerosis. Cytokine 76, 583–584. https://doi.org/https://doi.org/10.1016/j.cyto.2015.06.004
Dhuriya, Y.K., Sharma, D., 2018a. Necroptosis: a regulated inflammatory mode of cell death. J. Neuroinflammation 2018 151 15, 1–9. https://doi.org/10.1186/S12974-018-1235-0
Dhuriya, Y.K., Sharma, D., 2018b. Necroptosis: a regulated inflammatory mode of cell death. J. Neuroinflammation 15. https://doi.org/10.1186/S12974-018-1235-0
Dias, V., Junn, E., Mouradian, M.M., 2013. The Role of Oxidative Stress in Parkinson's Disease. J. Parkinsons. Dis. 3, 461. https://doi.org/10.3233/JPD-130230
Dillon, C.P., Weinlich, R., Rodriguez, D.A., Cripps, J.G., Quarato, G., Gurung, P., Verbist, K.C., Brewer, T.L., Llambi, F., Gong, Y.N., Janke, L.J., Kelliher, M.A., Kanneganti, T.D., Green, D.R., 2014. RIPK1 blocks early postnatal lethality mediated by caspase-8 and RIPK3. Cell 157, 1189–1202. https://doi.org/10.1016/j.cell.2014.04.018
Dionísio, P.A., Amaral, J.D., Rodrigues, C.M.P., 2021. Oxidative stress and regulated cell death in Parkinson's disease. Ageing Res. Rev. 67, 101263. https://doi.org/10.1016/J.ARR.2021.101263
Dionísio, P.A., Oliveira, S.R., Gaspar, M.M., Gama, M.J., Castro-Caldas, M., Amaral, J.D., Rodrigues, C.M.P., 2019. Ablation of RIP3 protects from dopaminergic neurodegeneration in experimental Parkinson's disease. Cell Death Dis. 2019 1011 10, 1–14. https://doi.org/10.1038/s41419-019-2078-z
Dionísio, P.E.A., Oliveira, S.R., Amaral, J.S.J.D., Rodrigues, C.M.P., 2019. Loss of Microglial Parkin Inhibits Necroptosis and Contributes to Neuroinflammation. Mol. Neurobiol. 56, 2990–3004. https://doi.org/10.1007/S12035-018-1264-9/FIGURES/8
Dixon, S.J., Stockwell, B.R., 2013. The role of iron and reactive oxygen species in cell death. Nat. Chem. Biol. 2014 101 10, 9–17. https://doi.org/10.1038/nchembio.1416
Dobson, R., Giovannoni, G., 2019. Multiple sclerosis – a review. Eur. J. Neurol. https://doi.org/10.1111/ene.13819
Dojo Soeandy, C., Elia, A.J., Cao, Y., Rodgers, C., Huang, S., Elia, A.C., Henderson, J.T., 2020. Necroptotic-Apoptotic Regulation in an Endothelin-1 Model of Cerebral Ischemia. Cell. Mol. Neurobiol. https://doi.org/10.1007/s10571-020-00942-y
Dominguez, S., Varfolomeev, E., Brendza, R., Stark, K., Tea, J., Imperio, J., Ngu, H., Earr, T., Foreman, O., Webster, J.D., Easton, A., Vucic, D., Bingol, B., 2021. Genetic inactivation of RIP1 kinase does not ameliorate disease in a mouse model of ALS. Cell Death Differ. 28, 915–931. https://doi.org/10.1038/S41418-020-00625-7
Dong, Y., Yu, H., Li, X., Bian, K., Zheng, Y., Dai, M., Feng, X., Sun, Y., He, Y., Yu, B., Zhang, H., Wu, J., Yu, X., Wu, H., Kong, W., 2022. Hyperphosphorylated tau mediates neuronal death by inducing necroptosis and inflammation in Alzheimer's disease. J. Neuroinflammation 19, 1–18. https://doi.org/10.1186/S12974-022-02567-Y/FIGURES/7
Douglas, D.L., Baines, C.P., n.d. PARP1-mediated necrosis is dependent on parallel JNK and Ca 2+ /calpain pathways. J. Cell Sci. https://doi.org/10.1242/jcs.128009
Douglas, T., Saleh, M., 2019. Post-translational Modification of OTULIN Regulates Ubiquitin Dynamics and Cell Death. Cell Rep. 29, 3652-3663.e5. https://doi.org/10.1016/J.CELREP.2019.11.014
Eftekharzadeh, M., Simorgh, S., Doshmanziari, M., Hassanzadeh, L., Shariatpanahi, M., 2020. Human adipose-derived stem cells reduce receptor-interacting protein 1, receptor-interacting protein 3, and mixed lineage kinase domain-like pseudokinase as necroptotic markers in rat model of Alzheimer's disease. Indian J. Pharmacol. 52, 392. https://doi.org/10.4103/IJP.IJP_545_19
El-Abhar, H., Abd El Fattah, M.A., Wadie, W., El-Tanbouly, D.M., 2018. Cilostazol disrupts

TLR-4, Akt/GSK-3β/CREB, and IL-6/JAK-2/STAT-3/SOCS-3 crosstalk in a rat model of Huntington's disease. PLoS One 13, e0203837. https://doi.org/10.1371/JOURNAL.PONE.0203837

El-kader, M.A., Hamza, E., El-Gamal, R., Eladl, A.S.R., Nashar, E.M. El, Alghamdi, M.A., Erfan, O.S., 2021. Modulation of vigabatrin induced cerebellar injury: the role of caspase-3 and RIPK1/RIPK3-regulated cell death pathways. J. Mol. Histol. 2021 1–18. https://doi.org/10.1007/S10735-021-09984-Y

Enquist, I.B., Lo Bianco, C., Ooka, A., Nilsson, E., Månsson, J.-E., Ehinger, M., Richter, J., Brady, R.O., Kirik, D., Karlsson, S., 2007. Murine models of acute neuronopathic Gaucher disease. Proc. Natl. Acad. Sci. U. S. A. 104, 17483–17488. https://doi.org/10.1073/pnas.0708086104

Exner, N., Lutz, A.K., Haass, C., Winklhofer, K.F., 2012. Mitochondrial dysfunction in Parkinson's disease: molecular mechanisms and pathophysiological consequences. EMBO J. 31, 3038–3062. https://doi.org/10.1038/EMBOJ.2012.170

Faizan, M.I., Ahmad, T., 2021. Altered mitochondrial calcium handling and cell death by necroptosis: An emerging paradigm. Mitochondrion 57, 47–62. https://doi.org/10.1016/J.MITO.2020.12.004

Fan, H., Tang, H.-B., Shan, L.-Q., Liu, S.-C., Huang, D.-G., Chen, X., Chen, Z., Yang, M., Yin, X.-H., Yang, H., Hao, D.-J., 2019. Quercetin prevents necroptosis of oligodendrocytes by inhibiting macrophages/microglia polarization to M1 phenotype after spinal cord injury in rats. J. Neuroinflammation 16. https://doi.org/10.1186/S12974-019-1613-2

Feltham, R., Silke, J., 2017. The small molecule that packs a punch: ubiquitin-mediated regulation of RIPK1/FADD/caspase-8 complexes. Cell Death Differ. 2017 247 24, 1196–1204. https://doi.org/10.1038/cdd.2017.67

Feng, S., Yang, Y., Mei, Y., Ma, L., Zhu, D. e., Hoti, N., Castanares, M., Wu, M., 2007. Cleavage of RIP3 inactivates its caspase-independent apoptosis pathway by removal of kinase domain. Cell. Signal. 19, 2056–2067. https://doi.org/10.1016/J.CELLSIG.2007.05.016

Feoktistova, M., Geserick, P., Kellert, B., Dimitrova, D.P., Langlais, C., Hupe, M., Cain, K., MacFarlane, M., Häcker, G., Leverkus, M., 2011. cIAPs Block Ripoptosome Formation, a RIP1/Caspase-8 Containing Intracellular Cell Death Complex Differentially Regulated by cFLIP Isoforms. Mol. Cell 43, 449. https://doi.org/10.1016/J.MOLCEL.2011.06.011

Festoff, B.W., Sajja, R.K., van Dreden, P., Cucullo, L., 2016. HMGB1 and thrombin mediate the blood-brain barrier dysfunction acting as biomarkers of neuroinflammation and progression to neurodegeneration in Alzheimer's disease. J. Neuroinflammation 13. https://doi.org/10.1186/S12974-016-0670-Z

Fiani, B., Kondilis, A., Soula, M., Tao, A., Alvi, M., 2021. Novel Methods of Necroptosis Inhibition for Spinal Cord Injury Using Translational Research to Limit Secondary Injury and Enhance Endogenous Repair and Regeneration. Neurospine 18, 261. https://doi.org/10.14245/NS.2040722.361

Font-Belmonte, E., Ugidos, I.F., Santos-Galdiano, M., González-Rodríguez, P., Anuncibay-Soto, B., Pérez-Rodríguez, D., Gonzalo-Orden, J.M., Fernández-López, A., 2019. Post-ischemic salubrinal administration reduces necroptosis in a rat model of global cerebral ischemia. J. Neurochem. 151, 777–794. https://doi.org/10.1111/jnc.14789

Frank, D., Vince, J.E., 2018. Pyroptosis versus necroptosis: similarities, differences, and crosstalk. Cell Death Differ. 2018 261 26, 99–114. https://doi.org/10.1038/s41418-018-0212-6

Fricker, M., Vilalta, A., Tolkovsky, A.M., Brown, G.C., 2013. Caspase Inhibitors Protect Neurons by Enabling Selective Necroptosis of Inflamed Microglia *. J. Biol. Chem. 288,

9145–9152. https://doi.org/10.1074/JBC.M112.427880

Fuji, H., Ohmae, S., Noma, N., Takeiri, M., Yasutomi, H., Izumi, K., Ito, M., Toyomoto, M., Iwaki, S., Takemoto, K., Seo, S., Taura, K., Hida, S., Aoyama, M., Ishihama, Y., Hagiwara, M., Takeda, N., Hatano, E., Iwaisako, K., Uemoto, S., Asagiri, M., 2018. Necrostatin-7 suppresses RANK-NFATc1 signaling and attenuates macrophage to osteoclast differentiation. Biochem. Biophys. Res. Commun. 503, 544–549. https://doi.org/10.1016/J.BBRC.2018.05.153

Fukui, M., Choi, H.J., Zhu, B.T., 2012. Rapid generation of mitochondrial superoxide induces mitochondrion-dependent but caspase-independent cell death in hippocampal neuronal cells that morphologically resembles necroptosis. Toxicol. Appl. Pharmacol. 262, 156–166. https://doi.org/10.1016/J.TAAP.2012.04.030

Futerman, A.H., van Meer, G., 2004. The cell biology of lysosomal storage disorders. Nat. Rev. Mol. Cell Biol. 5, 554–565. https://doi.org/10.1038/nrm1423

Gil-Martins, E., Barbosa, D.J., Silva, V., Remião, F., Silva, R., 2020. Dysfunction of ABC transporters at the blood-brain barrier: Role in neurological disorders. Pharmacol. Ther. 213, 107554. https://doi.org/10.1016/J.PHARMTHERA.2020.107554

Gómez-Sintes, R., Ledesma, M.D., Boya, P., 2016. Lysosomal cell death mechanisms in aging. Ageing Res. Rev. 32, 150–168. https://doi.org/10.1016/J.ARR.2016.02.009

Gong, Y., Fan, Z., Luo, G., Yang, C., Huang, Q., Fan, K., Cheng, H., Jin, K., Ni, Q., Yu, X., Liu, C., 2019. The role of necroptosis in cancer biology and therapy. Mol. Cancer 2019 181 18, 1–17. https://doi.org/10.1186/S12943-019-1029-8

Gong, Y.N., Guy, C., Crawford, J.C., Green, D.R., 2017. Biological events and molecular signaling following MLKL activation during necroptosis. Cell Cycle 16, 1748–1760. https://doi.org/10.1080/15384101.2017.1371889

González-Juarbe, N., Gilley, R.P., Hinojosa, C.A., Bradley, K.M., Kamei, A., Gao, G., Dube, P.H., Bergman, M.A., Orihuela, C.J., 2015. Pore-Forming Toxins Induce Macrophage Necroptosis during Acute Bacterial Pneumonia. PLOS Pathog. 11, e1005337. https://doi.org/10.1371/JOURNAL.PPAT.1005337

Griffioen, K., Mattson, M.P., Okun, E., 2018. Deficiency of Toll-like receptors 2, 3 or 4 extends life expectancy in Huntington's disease mice. Heliyon 4. https://doi.org/10.1016/J.HELIYON.2018.E00508

Guo, Q., Xie, J., 2019. Abstract 426: Inhibition of RIPK3/MLKL-dependent Necroptosis by SAP-12 in Ischemic Brain. Arterioscler. Thromb. Vasc. Biol. 39, A426–A426. https://doi.org/10.1161/atvb.39.suppl_1.426

Habib, N., McCabe, C., Medina, S., Varshavsky, M., Kitsberg, D., Dvir-Szternfeld, R., Green, G., Dionne, D., Nguyen, L., Marshall, J.L., Chen, F., Zhang, F., Kaplan, T., Regev, A., Schwartz, M., 2020. Disease-associated astrocytes in Alzheimer's disease and aging. Nat. Neurosci. 2020 236 23, 701–706. https://doi.org/10.1038/s41593-020-0624-8

Han, W., Xie, J., Li, L., Liu, Z., Hu, X., 2009. Necrostatin-1 reverts shikonin-induced necroptosis to apoptosis. Apoptosis 2009 145 14, 674–686. https://doi.org/10.1007/S10495-009-0334-X

Hänggi, K., Vasilikos, L., Valls, A.F., Yerbes, R., Knop, J., Spilgies, L.M., Rieck, K., Misra, T., Bertin, J., Gough, P.J., Schmidt, T., De Almodòvar, C.R., Wong, W.W.L., 2017. RIPK1/RIPK3 promotes vascular permeability to allow tumor cell extravasation independent of its necroptotic function. Cell Death Dis. 8, e2588. https://doi.org/10.1038/CDDIS.2017.20

Hanke, M.L., Kielian, T., 2011. Toll-like receptors in health and disease in the brain: mechanisms and therapeutic potential. Clin. Sci. (Lond). 121, 367. https://doi.org/10.1042/CS20110164

Journal Pre-proof

Hanus, J., Anderson, C., Sarraf, D., Ma, J., Wang, S., 2016. Retinal pigment epithelial cell necroptosis in response to sodium iodate. Cell Death Discov. 2016 21 2, 1–9. https://doi.org/10.1038/cddiscovery.2016.54

He, S., Liang, Y., Shao, F., Wang, X., 2011. Toll-like receptors activate programmed necrosis in macrophages through a receptor-interacting kinase-3-mediated pathway. Proc. Natl. Acad. Sci. U. S. A. 108, 20054–20059. https://doi.org/10.1073/PNAS.1116302108

Hernández, D.E., Salvadores, N.A., Moya-Alvarado, G., Catalán, R.J., Bronfman, F.C., Court, F.A., 2018. Axonal degeneration induced by glutamate excitotoxicity is mediated by necroptosis. J. Cell Sci. 131. https://doi.org/10.1242/JCS.214684/265656/AM/AXONAL-DEGENERATION-INDUCED-BY-GLUTAMATE

Hopkins, E.L., Gu, W., Kobe, B., Coleman, M.P., 2021. A Novel NAD Signaling Mechanism in Axon Degeneration and its Relationship to Innate Immunity. Front. Mol. Biosci. 8, 662. https://doi.org/10.3389/FMOLB.2021.703532/BIBTEX

Hou, J., Ju, J., Zhang, Z., Zhao, C., Li, Z., Zheng, J., Sheng, T., Zhang, H., Hu, L., Yu, X., Zhang, W., Li, Y., Wu, M., Ma, H., Zhang, X., He, S., 2019. Discovery of potent necroptosis inhibitors targeting RIPK1 kinase activity for the treatment of inflammatory disorder and cancer metastasis. Cell Death Dis. 2019 107 10, 1–13. https://doi.org/10.1038/s41419-019-1735-6

Hsu, S.K., Chang, W.T., Lin, I.L., Chen, Y.F., Padalwar, N.B., Cheng, K.C., Teng, Y.N., Wang, C.H., Chiu, C.C., 2020. The Role of Necroptosis in ROS-Mediated Cancer Therapies and Its Promising Applications. Cancers 2020, Vol. 12, Page 2185 12, 2185. https://doi.org/10.3390/CANCERS12082185

Hu, S., Chang, X., Zhu, H., Wang, D., Chen, G., 2020. PI3K mediates tumor necrosis factor induced-necroptosis through initiating RIP1-RIP3-MLKL signaling pathway activation. Cytokine 129, 155046. https://doi.org/10.1016/J.CYTO.2020.155046

Hu, W., Wu, X., Yu, D., Zhao, L., Zhu, X., Li, X., Huang, T., Chu, Z., Xu, Y., 2020. Regulation of JNK signaling pathway and RIPK3/AIF in necroptosis-mediated global cerebral ischemia/reperfusion injury in rats. Exp. Neurol. 331, 113374. https://doi.org/10.1016/J.EXPNEUROL.2020.113374

Hu, X., Xu, Y., Zhang, H., Li, Y., Wang, X., Xu, C., Ni, W., Zhou, K., 2022. Role of necroptosis in traumatic brain and spinal cord injuries. J. Adv. Res. https://doi.org/10.1016/J.JARE.2021.12.002

Hu, Y.-B., Zhang, Y.-F., Wang, H., Ren, R.-J., Cui, H.-L., Huang, W.-Y., Cheng, Q., Chen, H.-Z., Wang, G., 2019. miR-425 deficiency promotes necroptosis and dopaminergic neurodegeneration in Parkinson's disease. Cell Death Dis. 2019 108 10, 1–15. https://doi.org/10.1038/s41419-019-1809-5

Hu, Y., Feng, X., Chen, J., Wu, Y., Shen, L., 2022. Hydrogen-rich saline alleviates early brain injury through inhibition of necroptosis and neuroinflammation via the ROS/HO-1 signaling pathway after traumatic brain injury. Exp. Ther. Med. 23. https://doi.org/10.3892/ETM.2021.11049

Hu, Y.B., Zhang, Y.F., Wang, H., Ren, R.J., Cui, H.L., Huang, W.Y., Cheng, Q., Chen, H.Z., Wang, G., 2019. miR-425 deficiency promotes necroptosis and dopaminergic neurodegeneration in Parkinson's disease. Cell Death Dis. 10. https://doi.org/10.1038/S41419-019-1809-5

Hughes, M.A., Powley, I.R., Jukes-Jones, R., Horn, S., Feoktistova, M., Fairall, L., Schwabe, J.W.R., Leverkus, M., Cain, K., MacFarlane, M., 2016. Co-operative and Hierarchical Binding of c-FLIP and Caspase-8: A Unified Model Defines How c-FLIP Isoforms Differentially Control Cell Fate. Mol. Cell 61, 834–849. https://doi.org/10.1016/j.molcel.2016.02.023

Journal Pre-proof

Iannielli, A., Bido, S., Folladori, L., Segnali, A., Cancellieri, C., Maresca, A., Massimino, L., Rubio, A., Morabito, G., Caporali, L., Tagliavini, F., Musumeci, O., Gregato, G., Bezard, E., Carelli, V., Tiranti, V., Broccoli, V., 2018. Pharmacological Inhibition of Necroptosis Protects from Dopaminergic Neuronal Cell Death in Parkinson's Disease Models. Cell Rep. 22, 2066–2079. https://doi.org/10.1016/J.CELREP.2018.01.089

Irmler, M., Thome, M., Hahne, M., Schneider, P., Hofmann, K., Steiner, V., Bodmer, J.L., Schröter, M., Burns, K., Mattmann, C., Rimoldi, D., French, L.E., Tschopp, J., 1997. Inhibition of death receptor signals by cellular FLIP. Nature 388, 190–195. https://doi.org/10.1038/40657

Isaacs, A.M., Senn, D.B., Yuan, M., Shine, J.P., Yankner, B.A., 2006. Acceleration of Amyloid β-Peptide Aggregation by Physiological Concentrations of Calcium. J. Biol. Chem. 281, 27916–27923. https://doi.org/10.1074/JBC.M602061200

Ito, Y., Ofengeim, D., Najafov, A., Das, S., Saberi, S., Li, Y., Hitomi, J., Zhu, H., Chen, H., Mayo, L., Geng, J., Amin, P., DeWitt, J.P., Mookhtiar, A.K., Florez, M., Ouchida, A.T., Fan, J.B., Pasparakis, M., Kelliher, M.A., Ravits, J., Yuan, J., 2016. RIPK1 Mediates Axonal Degeneration By Promoting Inflammation and Necroptosis in ALS. Science 353, 603. https://doi.org/10.1126/SCIENCE.AAF6803

Jacobsen, A. V., Pierotti, C.L., Lowes, K.N., Au, A.E., Zhang, Y., Etemadi, N., Fitzgibbon, C., Kersten, W.J.A., Samson, A.L., van Delft, M.F., Huang, D.C.S., Sabroux, H.J., Lessene, G., Silke, J., Murphy, J.M., 2022. The Lck inhibitor, AMG-47a, blocks necroptosis and implicates RIPK1 in signalling downstream of MLKL. Cell Death Dis. 2022 134 13, 1–13. https://doi.org/10.1038/s41419-022-04740-w

Jalmi, S.K., Sinha, A.K., 2015. ROS mediated MAPK signaling in abiotic and biotic stress-striking similarities and differences. Front. Plant Sci. 6, 769. https://doi.org/10.3389/FPLS.2015.00769/BIBTEX

James, R.E., Schalks, R., Browne, E., Eleftheriadou, I., Munoz, C.P., Mazarakis, N.D., Reynolds, R., 2020. Persistent elevation of intrathecal pro-inflammatory cytokines leads to multiple sclerosis-like cortical demyelination and neurodegeneration. Acta Neuropathol. Commun. 8, 66. https://doi.org/10.1186/s40478-020-00938-1

Jayaraj, R.L., Azimullah, S., Beiram, R., Jalal, F.Y., Rosenberg, G.A., 2019. Neuroinflammation: friend and foe for ischemic stroke. J. Neuroinflammation 16, 142. https://doi.org/10.1186/s12974-019-1516-2

Jayaraman, A., Htike, T.T., James, R., Picon, C., Reynolds, R., 2021. TNF-mediated neuroinflammation is linked to neuronal necroptosis in Alzheimer's disease hippocampus. bioRxiv 2021.07.09.451781. https://doi.org/10.1101/2021.07.09.451781

Jensen, S., Seidelin, J.B., LaCasse, E.C., Nielsen, O.H., 2020. SMAC mimetics and RIPK inhibitors as therapeutics for chronic inflammatory diseases. Sci. Signal. 13. https://doi.org/10.1126/SCISIGNAL.AAX8295

Jeon, M.T., Kim, K.S., Kim, E.S., Lee, S., Kim, J., Hoe, H.S., Kim, D.G., 2021. Emerging pathogenic role of peripheral blood factors following BBB disruption in neurodegenerative disease. Ageing Res. Rev. 68, 101333. https://doi.org/10.1016/J.ARR.2021.101333

Jia, R., Jia, N., Yang, F., Liu, Z., Li, R., Jiang, Y., Zhao, J., Wang, L., Zhang, S., Zhang, Z., Zhang, H., Wu, S., Gao, F., Jiang, W., 2019. Hydrogen Alleviates Necroptosis and Cognitive Deficits in Lithium–Pilocarpine Model of Status Epilepticus. Cell. Mol. Neurobiol. 39, 857–869. https://doi.org/10.1007/s10571-019-00685-5

Jiao, J., Wang, Y., Ren, P., Sun, S., Wu, M., 2019. Necrosulfonamide Ameliorates Neurological Impairment in Spinal Cord Injury by Improving Antioxidative Capacity. Front. Pharmacol. 10, 1. https://doi.org/10.3389/FPHAR.2019.01538

Kaczmarek, A., Vandenabeele, P., Krysko, D. V., 2013. Necroptosis: The Release of

Journal Pre-proof

Damage-Associated Molecular Patterns and Its Physiological Relevance. Immunity 38, 209–223. https://doi.org/10.1016/J.IMMUNI.2013.02.003

Kaiser, W.J., Daley-Bauer, L.P., Thapa, R.J., Mandal, P., Berger, S.B., Huang, C., Sundararajan, A., Guo, H., Roback, L., Speck, S.H., Bertin, J., Gough, P.J., Balachandran, S., Mocarski, E.S., 2014. RIP1 suppresses innate immune necrotic as well as apoptotic cell death during mammalian parturition. Proc. Natl. Acad. Sci. U. S. A. 111, 7753–7758. https://doi.org/10.1073/PNAS.1401857111/SUPPL_FILE/PNAS.201401857SI.PDF

Kaiser, W.J., Sridharan, H., Huang, C., Mandal, P., Upton, J.W., Gough, P.J., Sehon, C.A., Marquis, R.W., Bertin, J., Mocarski, E.S., 2013a. Toll-like Receptor 3-mediated Necrosis via TRIF, RIP3, and MLKL *. J. Biol. Chem. 288, 31268–31279. https://doi.org/10.1074/JBC.M113.462341

Kaiser, W.J., Sridharan, H., Huang, C., Mandal, P., Upton, J.W., Gough, P.J., Sehon, C.A., Marquis, R.W., Bertin, J., Mocarski, E.S., 2013b. Toll-like Receptor 3-mediated Necrosis via TRIF, RIP3, and MLKL. J. Biol. Chem. 288, 31268. https://doi.org/10.1074/JBC.M113.462341

Kaiser, W.J., Upton, J.W., Long, A.B., Livingston-Rosanoff, D., Daley-Bauer, L.P., Hakem, R., Caspary, T., Mocarski, E.S., 2011. RIP3 mediates the embryonic lethality of caspase-8-deficient mice. Nature 471, 368. https://doi.org/10.1038/NATURE09857

Kanno, H., Ozawa, H., Handa, K., Murakami, T., Itoi, E., 2020. Changes in Expression of Receptor-Interacting Protein Kinase 1 in Secondary Neural Tissue Damage Following Spinal Cord Injury. Neurosci. Insights 15. https://doi.org/10.1177/2633105520906402

Khan, I., Yousif, A., Chesnokov, M., Hong, L., Chefetz, Ii.I., 2021. A decade of cell death studies: Breathing new life into necroptosis. Pharmacol. Ther. 220, 107717. https://doi.org/10.1016/J.PHARMTHERA.2020.107717

Khodorov, B., Pinelis, V., Storozhevykh, T., Yuravichus, A., Khaspekhov, L., 1999. Blockade of mitochondrial Ca2+ uptake by mitochondrial inhibitors amplifies the glutamate-induced calcium response in cultured cerebellar granule cells. FEBS Lett. 458, 162–166. https://doi.org/10.1016/S0014-5793(99)01130-8

Khoury, M.K., Gupta, K., Franco, S.R., Liu, B., 2020. Necroptosis in the Pathophysiology of Disease. Am. J. Pathol. 190, 272–285. https://doi.org/10.1016/J.AJPATH.2019.10.012

Kim, C., Ho, D.H., Suk, J.E., You, S., Michael, S., Kang, J., Lee, Sung Joong, Masliah, E., Hwang, D., Lee, H.J., Lee, Seung Jae, 2013. Neuron-released oligomeric α-synuclein is an endogenous agonist of TLR2 for paracrine activation of microglia. Nat. Commun. 4. https://doi.org/10.1038/NCOMMS2534

Kim, E.K., Choi, E.J., 2010. Pathological roles of MAPK signaling pathways in human diseases. Biochim. Biophys. Acta - Mol. Basis Dis. 1802, 396–405. https://doi.org/10.1016/J.BBADIS.2009.12.009

Kim, S.J., Li, J., 2013. Caspase blockade induces RIP3-mediated programmed necrosis in Toll-like receptor-activated microglia. Cell Death Dis. 2013 47 4, e716–e716. https://doi.org/10.1038/cddis.2013.238

King, M.D., Whitaker-Lea, W.A., Campbell, J.M., Alleyne, C.H.J., Dhandapani, K.M., 2014. Necrostatin-1 reduces neurovascular injury after intracerebral hemorrhage. Int. J. Cell Biol. 2014, 495817. https://doi.org/10.1155/2014/495817

Ko, K.W., Milbrandt, J., DiAntonio, A., 2020. SARM1 acts downstream of neuroinflammatory and necroptotic signaling to induce axon degeneration. J. Cell Biol. 219. https://doi.org/10.1083/JCB.201912047/151915

Kopalli, S.R., Kang, T.B., Koppula, S., 2016. Necroptosis inhibitors as therapeutic targets in inflammation mediated disorders - a review of the current literature and patents. http://dx.doi.org/10.1080/13543776.2016.1230201 26, 1239–1256.

https://doi.org/10.1080/13543776.2016.1230201

Koper, M.J., Schoor, E. Van, Ospitalieri, S., Vandenberghe, R., Vandenbulcke, M., Arnim, C.A.F. von, Tousseyn, T., Balusu, S., Strooper, B. De, Thal, D.R., 2019. Necrosome complex detected in granulovacuolar degeneration is associated with neuronal loss in Alzheimer's disease. Acta Neuropathol. 2019 1393 139, 463–484. https://doi.org/10.1007/S00401-019-02103-Y

Küpeli Akkol, E., Tatlı Çankaya, I., Şeker Karatoprak, G., Carpar, E., Sobarzo-Sánchez, E., Capasso, R., 2021. Natural Compounds as Medical Strategies in the Prevention and Treatment of Psychiatric Disorders Seen in Neurological Diseases. Front. Pharmacol. 12. https://doi.org/10.3389/FPHAR.2021.669638/FULL

Kwon, B., Kumar, P., Lee, H.K., Zeng, L., Walsh, K., Fu, Q., Barakat, A., Querfurth, H.W., 2014. Aberrant cell cycle reentry in human and experimental inclusion body myositis and polymyositis. Hum. Mol. Genet. 23, 3681–3694. https://doi.org/10.1093/HMG/DDU077

Laird, M.D., Shields, J.S., Sukumari-Ramesh, S., Kimbler, D.E., Fessler, R.D., Shakir, B., Youssef, P., Yanasak, N., Vender, J.R., Dhandapani, K.M., 2014. High mobility group box protein-1 promotes cerebral edema after traumatic brain injury via activation of toll-like receptor 4. Glia 62, 26–38. https://doi.org/10.1002/GLIA.22581

Lalaoui, N., Boyden, S.E., Oda, H., Wood, G.M., Stone, D.L., Chau, D., Liu, L., Stoffels, M., Kratina, T., Lawlor, K.E., Zaal, K.J.M., Hoffmann, P.M., Etemadi, N., Shield-Artin, K., Biben, C., Tsai, W.L., Blake, M.D., Kuehn, H.S., Yang, D., Anderton, H., Silke, N., Wachsmuth, L., Zheng, L., Moura, N.S., Beck, D.B., Gutierrez-Cruz, G., Ombrello, A.K., Pinto-Patarroyo, G.P., Kueh, A.J., Herold, M.J., Hall, C., Wang, H., Chae, J.J., Dmitrieva, N.I., McKenzie, M., Light, A., Barham, B.K., Jones, A., Romeo, T.M., Zhou, Q., Aksentijevich, I., Mullikin, J.C., Gross, A.J., Shum, A.K., Hawkins, E.D., Masters, S.L., Lenardo, M.J., Boehm, M., Rosenzweig, S.D., Pasparakis, M., Voss, A.K., Gadina, M., Kastner, D.L., Silke, J., 2019. Mutations that prevent caspase cleavage of RIPK1 cause autoinflammatory disease. Nat. 2019 5777788 577, 103–108. https://doi.org/10.1038/s41586-019-1828-5

Lee, H.G., Wheeler, M.A., Quintana, F.J., 2022. Function and therapeutic value of astrocytes in neurological diseases. Nat. Rev. Drug Discov. 2022 215 21, 339–358. https://doi.org/10.1038/s41573-022-00390-x

Lee, H.K., Kumar, P., Fu, Q., Rosen, K.M., Querfurth, H.W., 2009. The insulin/Akt signaling pathway is targeted by intracellular β-amyloid. Mol. Biol. Cell 20, 1533–1544. https://doi.org/10.1091/MBC.E08-07-0777/ASSET/IMAGES/LARGE/ZMK0050989590008.JPEG

Lee, S., Rauch, J., Kolch, W., 2020. Targeting MAPK Signaling in Cancer: Mechanisms of Drug Resistance and Sensitivity. Int. J. Mol. Sci. 21. https://doi.org/10.3390/IJMS21031102

Lee, S.B., Kim, J.J., Han, S.-A., Fan, Y., Guo, L.-S., Aziz, K., Nowsheen, S., Kim, S.S., Park, S.-Y., Luo, Q., Chung, J.O., Choi, S. Il, Aziz, A., Yin, P., Tong, S.-Y., Fiesel, F.C., Springer, W., Zhang, J.-S., Lou, Z., 2019. The AMPK–Parkin axis negatively regulates necroptosis and tumorigenesis by inhibiting the necrosome. Nat. Cell Biol. 2019 218 21, 940–951. https://doi.org/10.1038/s41556-019-0356-8

Lewinska, A., Adamczyk-Grochala, J., Bloniarz, D., Horeczy, B., Zurek, S., Kurowicki, A., Woloszczuk-Gebicka, B., Widenka, K., Wnuk, M., 2020. Remifentanil preconditioning protects against hypoxia-induced senescence and necroptosis in human cardiac myocytes in vitro. Aging (Albany NY) 12, 13924. https://doi.org/10.18632/AGING.103604

Lewno, M.T., Cui, T., Wang, X., 2021. Cullin Deneddylation Suppresses the Necroptotic

Journal Pre-proof

Pathway in Cardiomyocytes. Front. Physiol. 12, 690423. https://doi.org/10.3389/FPHYS.2021.690423

Li, C., Chen, Y., Chen, X., Wei, Q., Ou, R., Gu, X., Cao, B., Shang, H., 2020. MicroRNA-183-5p is stress-inducible and protects neurons against cell death in amyotrophic lateral sclerosis. J. Cell. Mol. Med. 24, 8614–8622. https://doi.org/10.1111/JCMM.15490

Li, J., Zhang, J., Zhang, Y., Wang, Z., Song, Y., Wei, S., He, M., You, S., Jia, J., Cheng, J., 2019. TRAF2 protects against cerebral ischemia-induced brain injury by suppressing necroptosis. Cell Death Dis. 10, 328. https://doi.org/10.1038/s41419-019-1558-5

Li, Y., Yang, X., Ma, C., Qiao, J., Zhang, C., 2008. Necroptosis contributes to the NMDA-induced excitotoxicity in rat's cultured cortical neurons. Neurosci. Lett. 447, 120–123. https://doi.org/https://doi.org/10.1016/j.neulet.2008.08.037

Liang, Y.-X., Wang, N.-N., Zhang, Z.-Y., Juan, Z.-D., Zhang, C., 2019. Necrostatin-1 Ameliorates Peripheral Nerve Injury-Induced Neuropathic Pain by Inhibiting the RIP1/RIP3 Pathway. Front. Cell. Neurosci. 13. https://doi.org/10.3389/FNCEL.2019.00211

Libro, R., Bramanti, P., Mazzon, E., 2016. The role of the Wnt canonical signaling in neurodegenerative diseases. Life Sci. 158, 78–88. https://doi.org/10.1016/J.LFS.2016.06.024

Lin, C., Chang, H., Bao, Z., Luo, H., Xu, L., Wu, W., Liu, N., Ji, J., 2022. DRD1 signaling enhances recovery after traumatic brain injury via an autophagy dependent pathway. https://doi.org/10.21203/rs.3.rs-1598118/v1

Lin, C.H., Tsai, P.I., Wu, R.M., Chien, C.T., 2010. LRRK2 G2019S Mutation Induces Dendrite Degeneration through Mislocalization and Phosphorylation of Tau by Recruiting Autoactivated GSK3β. J. Neurosci. 30, 13138. https://doi.org/10.1523/JNEUROSCI.1737-10.2010

Lin, Q.-S., Chen, P., Wang, W.-X., Lin, C.-C., Zhou, Y., Yu, L.-H., Lin, Y.-X., Xu, Y.-F., Kang, D.-Z., 2019. RIP1/RIP3/MLKL mediates dopaminergic neuron necroptosis in a mouse model of Parkinson disease. Lab. Investig. 2019 1003 100, 503–511. https://doi.org/10.1038/s41374-019-0319-5

Lin, S.Y., Hsieh, S.Y., Fan, Y.T., Wei, W.C., Hsiao, P.W., Tsai, D.H., Wu, T.S., Yang, N.S., 2017. Necroptosis promotes autophagy-dependent upregulation of DAMP and results in immunosurveillance. https://doi.org/10.1080/15548627.2017.1386359 14, 778–795. https://doi.org/10.1080/15548627.2017.1386359

Linari, S., Castaman, G., 2015. Clinical manifestations and management of Gaucher disease. Clin. Cases Miner. Bone Metab. 12, 157–164. https://doi.org/10.11138/ccmbm/2015.12.2.157

Liu, J., Hu, H., Wu, B., 2021. RIPK1 inhibitor ameliorates the MPP+/MPTP-induced Parkinson's disease through the ASK1/JNK signalling pathway. Brain Res. 1757, 147310. https://doi.org/10.1016/J.BRAINRES.2021.147310

Liu, J., van Mil, A., Vrijsen, K., Zhao, J., Gao, L., Metz, C.H.G., Goumans, M.J., Doevendans, P.A., Sluijter, J.P.G., 2011. MicroRNA-155 prevents necrotic cell death in human cardiomyocyte progenitor cells via targeting RIP1. J. Cell. Mol. Med. 15, 1474. https://doi.org/10.1111/J.1582-4934.2010.01104.X

Liu, J., Zhu, Z., Wang, L., Du, J., Zhang, B., Feng, X., Zhang, G., 2020. Functional suppression of Ripk1 blocks the NF-κB signaling pathway and induces neuron autophagy after traumatic brain injury. Mol. Cell. Biochem. 472, 105–114. https://doi.org/10.1007/S11010-020-03789-5/FIGURES/4

Liu, L., Liu, Y., Cheng, X., Qiao, X., 2021. The Alleviative Effects of Quercetin on Cadmium-Induced Necroptosis via Inhibition ROS/iNOS/NF-κB Pathway in the Chicken Brain. Biol. Trace Elem. Res. 199, 1584–1594. https://doi.org/10.1007/S12011-

Journal Pre-proof

020-02563-4/FIGURES/6

Liu, M., Wu, W., Li, H., Li, S., Huang, L.T., Yang, Y.Q., Sun, Q., Wang, C.X., Yu, Z., Hang, C.H., 2015. Necroptosis, a novel type of programmed cell death, contributes to early neural cells damage after spinal cord injury in adult mice. J. Spinal Cord Med. 38, 745. https://doi.org/10.1179/2045772314Y.0000000224

Liu, Q., Qiu, J., Liang, M., Golinski, J., Van Leyen, K., Jung, J.E., You, Z., Lo, E.H., Degterev, A., Whalen, M.J., 2014. Akt and mTOR mediate programmed necrosis in neurons. Cell Death Dis. 5, e1084. https://doi.org/10.1038/CDDIS.2014.69

Liu, S., Li, Y., Choi, H.M.C., Sarkar, C., Koh, E.Y., Wu, J., Lipinski, M.M., 2018. Lysosomal damage after spinal cord injury causes accumulation of RIPK1 and RIPK3 proteins and potentiation of necroptosis. Cell Death Dis. 9. https://doi.org/10.1038/S41419-018-0469-1

Liu, S., Wang, X., Li, Y., Xu, L., Yu, X., Ge, L., Li, J., Zhu, Y., He, S., 2014. Necroptosis mediates TNF-induced toxicity of hippocampal neurons. Biomed Res. Int. 2014. https://doi.org/10.1155/2014/290182

Lu, J., Sun, Z., Fang, Y., Zheng, J., Xu, S., Xu, W., Shi, L., Mei, S., Wu, H., Liang, F., Zhang, J., 2019. Melatonin Suppresses Microglial Necroptosis by Regulating Deubiquitinating Enzyme A20 After Intracerebral Hemorrhage. Front. Immunol. 10, 1360. https://doi.org/10.3389/fimmu.2019.01360

Lu, W., Sun, J., Yoon, J.S., Zhang, Y., Zheng, L., Murphy, E., Mattson, M.P., Lenardo, M.J., 2016. Mitochondrial Protein PGAM5 Regulates Mitophagic Protection against Cell Necroptosis. PLoS One 11, e0147792. https://doi.org/10.1371/journal.pone.0147792

Lu, Z., Wei, M., Feng, D., Li, Y., Wang, Xiaodong, Yan, Z., Wang, Xingdong, Pei, Y., Wang, G., Dong, L., Zhang, H., 2022. Celastrol Exerts Neuroprotective Effects by Inhibiting Necroptosis and Inflammation in Intracerebral Hemorrhage-Induced Brain Injury. SSRN Electron. J. https://doi.org/10.2139/SSRN.4001301

Lule, S., Wu, L., Sarro-Schwartz, A., Edmiston, W.J., Izzy, S., Songtachalert, T., Ahn, S.H., Fernandes, N.D., Jin, G., Chung, J.Y., Balachandran, S., Lo, E.H., Kaplan, D., Degterev, A., Whalen, M.J., 2020. Cell-specific activation of RIPK1 and MLKL after intracerebral hemorrhage in mice. J. Cereb. Blood Flow Metab. https://doi.org/10.1177/0271678X20973609

Luo, F., Herrup, K., Qi, X., Yang, Y., 2017. Inhibition of Drp1 hyper-activation is protective in animal models of experimental multiple sclerosis. Exp. Neurol. 292, 21. https://doi.org/10.1016/J.EXPNEUROL.2017.02.015

MacVicar, T., Langer, T., 2016. OPA1 processing in cell death and disease - the long and short of it. J. Cell Sci. 129, 2297–2306. https://doi.org/10.1242/JCS.159186

Magliozzi, R., Howell, O.W., Durrenberger, P., Aricò, E., James, R., Cruciani, C., Reeves, C., Roncaroli, F., Nicholas, R., Reynolds, R., 2019. Meningeal inflammation changes the balance of TNF signalling in cortical grey matter in multiple sclerosis. J. Neuroinflammation 16, 259. https://doi.org/10.1186/s12974-019-1650-x

Mangiarini, L., Sathasivam, K., Seller, M., Cozens, B., Harper, A., Hetherington, C., Lawton, M., Trottier, Y., Lehrach, H., Davies, S.W., Bates, G.P., 1996. Exon 1 of the HD Gene with an Expanded CAG Repeat Is Sufficient to Cause a Progressive Neurological Phenotype in Transgenic Mice. Cell 87, 493–506. https://doi.org/10.1016/S0092-8674(00)81369-0

Manini, A., Abati, E., Comi, G. Pietro, Corti, S., Ronchi, D., 2022. Mitochondrial DNA homeostasis impairment and dopaminergic dysfunction: A trembling balance. Ageing Res. Rev. 76, 101578. https://doi.org/10.1016/J.ARR.2022.101578

Mao, X.-Y., Zhou, H.-H., Jin, W.-L., 2019. Redox-Related Neuronal Death and Crosstalk as Drug Targets: Focus on Epilepsy. Front. Neurosci. 13, 512.

https://doi.org/10.3389/fnins.2019.00512

Mao, Y., Chen, X., Xu, M., Fujita, K., Motoki, K., Sasabe, T., Homma, H., Murata, M., Tagawa, K., Tamura, T., Kaye, J., Finkbeiner, S., Blandino, G., Sudol, M., Okazawa, H., 2016. Targeting TEAD/YAP-transcription-dependent necrosis, TRIAD, ameliorates Huntington's disease pathology. Hum. Mol. Genet. 25, 4749–4770. https://doi.org/10.1093/HMG/DDW303

Masrori, P., Damme, P. Van, 2020. Amyotrophic lateral sclerosis: a clinical review. Eur. J. Neurol. 27, 1918–1929. https://doi.org/10.1111/ENE.14393

McNamara, C.R., Ahuja, R., Osafo-Addo, A.D., Barrows, D., Kettenbach, A., Skidan, I., Teng, X., Cuny, G.D., Gerber, S., Degterev, A., 2013. Akt Regulates TNFα Synthesis Downstream of RIP1 Kinase Activation during Necroptosis. PLoS One. https://doi.org/10.1371/journal.pone.0056576

Meng, H., Liu, Z., Li, X., Wang, H., Jin, T., Wu, G., Shan, B., Christofferson, D.E., Qi, C., Yu, Q., Li, Y., Yuan, J., 2018. Death-domain dimerization-mediated activation of RIPK1 controls necroptosis and RIPK1-dependent apoptosis. Proc. Natl. Acad. Sci. U. S. A. 115, E2001–E2009. https://doi.org/10.1073/PNAS.1722013115/-/DCSUPPLEMENTAL

Meng, Y., Sandow, J.J., Czabotar, P.E., Murphy, J.M., 2021. The regulation of necroptosis by post-translational modifications. Cell Death Differ. 2021 283 28, 861–883. https://doi.org/10.1038/s41418-020-00722-7

Miao, W., Qu, Z., Shi, K., Zhang, D., Zong, Y., Zhang, Gongliang, Zhang, Guangyi, Hu, S., 2015. RIP3 S-nitrosylation contributes to cerebral ischemic neuronal injury. Brain Res. 1627, 165–176. https://doi.org/10.1016/J.BRAINRES.2015.08.020

Mitroshina, E. V., Loginova, M.M., Yarkov, R.S., Urazov, M.D., Novozhilova, M.O., Krivonosov, M.I., Ivanchenko, M. V., Vedunova, M. V., 2022. Inhibition of Neuronal Necroptosis Mediated by RIPK1 Provides Neuroprotective Effects on Hypoxia and Ischemia In Vitro and In Vivo. Int. J. Mol. Sci. 2022, Vol. 23, Page 735 23, 735. https://doi.org/10.3390/IJMS23020735

Morgan, M.J., Kim, Y.S., 2022. Roles of RIPK3 in necroptosis, cell signaling, and disease. Exp. Mol. Med. 54, 1695–1704. https://doi.org/10.1038/s12276-022-00868-z

Morrice, J.R., Gregory-Evans, C.Y., Shaw, C.A., 2017. Necroptosis in amyotrophic lateral sclerosis and other neurological disorders. Biochim. Biophys. Acta - Mol. Basis Dis. 1863, 347–353. https://doi.org/10.1016/J.BBADIS.2016.11.025

Motawi, Tarek M.K., Abdel-Nasser, Z.M., Shahin, N.N., 2020. Ameliorative Effect of Necrosulfonamide in a Rat Model of Alzheimer's Disease: Targeting Mixed Lineage Kinase Domain-like Protein-Mediated Necroptosis. ACS Chem. Neurosci. 11, 3386–3397. https://doi.org/10.1021/ACSCHEMNEURO.0C00516/SUPPL_FILE/CN0C00516_SI_001.PDF

Motawi, Tarek M. K., Abdel-Nasser, Z.M., Shahin, N.N., 2020. Ameliorative Effect of Necrosulfonamide in a Rat Model of Alzheimer's Disease: Targeting Mixed Lineage Kinase Domain-like Protein-Mediated Necroptosis. ACS Chem. Neurosci. 11, 3386–3397. https://doi.org/10.1021/ACSCHEMNEURO.0C00516

Moujalled, D., Strasser, A., Liddell, J.R., 2021. Molecular mechanisms of cell death in neurological diseases. Cell Death Differ. 2021 287 28, 2029–2044. https://doi.org/10.1038/s41418-021-00814-y

Mu, J., Weng, J., Yang, C., Guan, T., Deng, L., Li, M., Zhang, G., Kong, J., 2021. Necrostatin-1 prevents the proapoptotic protein Bcl-2/adenovirus E1B 19-kDa interacting protein 3 from integration into mitochondria. J. Neurochem. 156, 929–942. https://doi.org/10.1111/JNC.14993

Journal Pre-proof

Muller, A.J., DuHadaway, J.B., Donover, P.S., Sutanto-Ward, E., Prendergast, G.C., 2005. Inhibition of indoleamine 2,3-dioxygenase, an immunoregulatory target of the cancer suppression gene Bin1, potentiates cancer chemotherapy. Nat. Med. 11, 312–319. https://doi.org/10.1038/NM1196

Murakami, Y., Matsumoto, H., Roh, M., Giani, A., Kataoka, K., Morizane, Y., Kayama, M., Thanos, A., Nakatake, S., Notomi, S., Hisatomi, T., Ikeda, Y., Ishibashi, T., Connor, K.M., Miller, J.W., Vavvas, D.G., 2013. Programmed necrosis, not apoptosis, is a key mediator of cell loss and DAMP-mediated inflammation in dsRNA-induced retinal degeneration. Cell Death Differ. 2014 212 21, 270–277. https://doi.org/10.1038/cdd.2013.109

Murao, A., Aziz, M., Wang, H., Brenner, M., Wang, P., 2021. Release mechanisms of major DAMPs. Apoptosis 26, 152–162. https://doi.org/10.1007/S10495-021-01663-3/TABLES/1

Muraro, S.P., De Souza, G.F., Gallo, S.W., Da Silva, B.K., De Oliveira, S.D., Vinolo, M.A.R., Saraiva, E.M., Porto, B.N., 2018. Respiratory Syncytial Virus induces the classical ROS-dependent NETosis through PAD-4 and necroptosis pathways activation. Sci. Reports 2018 81 8, 1–12. https://doi.org/10.1038/s41598-018-32576-y

Murphy, J.M., Czabotar, P.E., Hildebrand, J.M., Lucet, I.S., Zhang, J.G., Alvarez-Diaz, S., Lewis, R., Lalaoui, N., Metcalf, D., Webb, A.I., Young, S.N., Varghese, L.N., Tannahill, G.M., Hatchell, E.C., Majewski, I.J., Okamoto, T., Dobson, R.C.J., Hilton, D.J., Babon, J.J., Nicola, N.A., Strasser, A., Silke, J., Alexander, W.S., 2013. The pseudokinase MLKL mediates necroptosis via a molecular switch mechanism. Immunity 39, 443–453. https://doi.org/10.1016/J.IMMUNI.2013.06.018

Naito, M.G., Xu, D., Amin, P., Lee, J., Wang, H., Li, W., Kelliher, M., Pasparakis, M., Yuan, J., 2020. Sequential activation of necroptosis and apoptosis cooperates to mediate vascular and neural pathology in stroke. Proc. Natl. Acad. Sci. U. S. A. 117, 4959–4970. https://doi.org/10.1073/PNAS.1916427117

Najafov, A., Luu, H.S., Mookhtiar, A.K., Mifflin, L., Xia, H. guang, Amin, P.P., Ordureau, A., Wang, H., Yuan, J., 2021. RIPK1 Promotes Energy Sensing by the mTORC1 Pathway. Mol. Cell 81, 370-385.e7. https://doi.org/10.1016/J.MOLCEL.2020.11.008

Najjar, M., Saleh, D., Zelic, M., Nogusa, S., Shah, S., Tai, A., Finger, J.N., Polykratis, A., Gough, P.J., Bertin, J., Whalen, M.J., Pasparakis, M., Balachandran, S., Kelliher, M., Poltorak, A., Degterev, A., 2016. RIPK1 and RIPK3 Kinases Promote Cell-Death-Independent Inflammation by Toll-like Receptor 4. Immunity 45, 46–59. https://doi.org/10.1016/J.IMMUNI.2016.06.007

Nakahira, K., Haspel, J.A., Rathinam, V.A.K., Lee, S.J., Dolinay, T., Lam, H.C., Englert, J.A., Rabinovitch, M., Cernadas, M., Kim, H.P., Fitzgerald, K.A., Ryter, S.W., Choi, A.M.K., 2011. Autophagy proteins regulate innate immune responses by inhibiting the release of mitochondrial DNA mediated by the NALP3 inflammasome. Nat. Immunol. 12, 222–230. https://doi.org/10.1038/NI.1980

Nakazawa, D., Desai, J., Steiger, S., Müller, S., Devarapu, S.K., Mulay, S.R., Iwakura, T., Anders, H.J., 2018. Activated platelets induce MLKL-driven neutrophil necroptosis and release of neutrophil extracellular traps in venous thrombosis. Cell Death Discov. 2018 41 4, 1–11. https://doi.org/10.1038/s41420-018-0073-2

Nasseri, B., Zareian, P., Alizade, H., 2020. Apelin attenuates streptozotocin-induced learning and memory impairment by modulating necroptosis signaling pathway. Int. Immunopharmacol. 84, 106546. https://doi.org/10.1016/J.INTIMP.2020.106546

Newton, K., 2020. Multitasking Kinase RIPK1 Regulates Cell Death and Inflammation. Cold Spring Harb. Perspect. Biol. 12. https://doi.org/10.1101/CSHPERSPECT.A036368

Newton, K., Wickliffe, K.E., Dugger, D.L., Maltzman, A., Roose-Girma, M., Dohse, M.,

Journal Pre-proof

Kőműves, L., Webster, J.D., Dixit, V.M., 2019. Cleavage of RIPK1 by caspase-8 is crucial for limiting apoptosis and necroptosis. Nat. 2019 5747778 574, 428–431. https://doi.org/10.1038/s41586-019-1548-x

Ni, H., Rui, Q., Lin, X., Li, D., Liu, H., Chen, G., 2019. 2-BFI Provides Neuroprotection Against Inflammation and Necroptosis in a Rat Model of Traumatic Brain Injury. Front. Neurosci. 13. https://doi.org/10.3389/FNINS.2019.00674

Nikseresht, S., Khodagholi, F., Ahmadiani, A., 2019. Protective effects of ex-527 on cerebral ischemia–reperfusion injury through necroptosis signaling pathway attenuation. J. Cell. Physiol. 234, 1816–1826. https://doi.org/10.1002/jcp.27055

Nomura, M., Ueno, A., Saga, K., Fukuzawa, M., Kaneda, Y., 2014. Accumulation of cytosolic calcium induces necroptotic cell death in human neuroblastoma. Cancer Res. 74, 1056–1066. https://doi.org/10.1158/0008-5472.CAN-13-1283/651285/AM/ACCUMULATION-OF-CYTOSOLIC-CALCIUM-INDUCES

Nussbacher, J.K., Tabet, R., Yeo, G.W., Lagier-Tourenne, C., 2019. Disruption of RNA Metabolism in Neurological Diseases and Emerging Therapeutic Interventions. Neuron 102, 294–320. https://doi.org/10.1016/J.NEURON.2019.03.014

O'Donnell, M.A., Perez-Jimenez, E., Oberst, A., Ng, A., Massoumi, R., Xavier, R., Green, D.R., Ting, A.T., 2011. CASPASE 8 inhibits programmed necrosis by processing CYLD. Nat. Cell Biol. 13, 1437. https://doi.org/10.1038/NCB2362

Oberst, A., Dillon, C.P., Weinlich, R., McCormick, L.L., Fitzgerald, P., Pop, C., Hakem, R., Salvesen, G.S., Green, D.R., 2011. Catalytic activity of the caspase-8-FLIPL complex inhibits RIPK3-dependent necrosis. Nature 471, 363. https://doi.org/10.1038/NATURE09852

Ofengeim, D., Ito, Y., Najafov, A., Zhang, Y., Shan, B., DeWitt, J.P., Ye, J., Zhang, X., Chang, A., Vakifahmetoglu-Norberg, H., Geng, J., Py, B., Zhou, W., Amin, P., Berlink Lima, J., Qi, C., Yu, Q., Trapp, B., Yuan, J., 2015. Activation of necroptosis in multiple sclerosis. Cell Rep. 10, 1836–1849. https://doi.org/10.1016/j.celrep.2015.02.051

Ofengeim, D., Yuan, J., 2013. Regulation of RIP1 kinase signalling at the crossroads of inflammation and cell death. Nat. Rev. Mol. Cell Biol. 14, 727–736. https://doi.org/10.1038/NRM3683

Oliveira, S.R., Amaral, J.D., Rodrigues, C.M.P., 2018a. Mechanism and disease implications of necroptosis and neuronal inflammation. Cell Death Dis. 2018 99 9, 1–3. https://doi.org/10.1038/s41419-018-0872-7

Oliveira, S.R., Dionísio, P.A., Brito, H., Franco, L., Rodrigues, C.A.B., Guedes, R.C., Afonso, C.A.M., Amaral, J.D., Rodrigues, C.M.P., 2018b. Phenotypic screening identifies a new oxazolone inhibitor of necroptosis and neuroinflammation. Cell Death Discov. 2018 41 4, 1–14. https://doi.org/10.1038/s41420-018-0067-0

Oliveira, S.R., Dionísio, P.A., Gaspar, M.M., Ferreira, M.B.T., Rodrigues, C.A.B., Pereira, R.G., Estevão, M.S., Perry, M.J., Moreira, R., Afonso, C.A.M., Amaral, J.D., Rodrigues, C.M.P., 2021a. Discovery of a Necroptosis Inhibitor Improving Dopaminergic Neuronal Loss after MPTP Exposure in Mice. Int. J. Mol. Sci. 2021, Vol. 22, Page 5289 22, 5289. https://doi.org/10.3390/IJMS22105289

Oliveira, S.R., Dionísio, P.A., Gaspar, M.M., Guedes, L.C., Coelho, M., Rosa, M.M., Ferreira, J.J., Amaral, J.D., Rodrigues, C.M.P., 2021b. miR-335 Targets LRRK2 and Mitigates Inflammation in Parkinson's Disease. Front. Cell Dev. Biol. 9. https://doi.org/10.3389/FCELL.2021.661461

Oñate, M., Catenaccio, A., Salvadores, N., Saquel, C., Martinez, A., Moreno-Gonzalez, I., Gamez, N., Soto, P., Soto, C., Hetz, C., Court, F.A., 2019. The necroptosis machinery mediates axonal degeneration in a model of Parkinson disease. Cell Death Differ. 2019 274 27, 1169–1185. https://doi.org/10.1038/s41418-019-0408-4

Journal Pre-proof

Palty, R., Silverman, W.F., Hershfinkel, M., Caporale, T., Sensi, S.L., Parnis, J., Nolte, C., Fishman, D., Shoshan-Barmatz, V., Herrmann, S., Khananshvili, D., Sekler, I., 2010. NCLX is an essential component of mitochondrial Na+/Ca2+ exchange. Proc. Natl. Acad. Sci. U. S. A. 107, 436–441. https://doi.org/10.1073/PNAS.0908099107

Pan, P.-Y., Yue, Z., 2014. Genetic causes of Parkinson's disease and their links to autophagy regulation. Parkinsonism Relat. Disord. 20, S154–S157. https://doi.org/10.1016/S1353-8020(13)70037-3

Pang, K., Jiang, R., Zhang, W., Yang, Z., Li, L.L., Shimozawa, M., Tambaro, S., Mayer, J., Zhang, B., Li, M., Wang, J., Liu, H., Yang, A., Chen, X., Liu, J., Winblad, B., Han, H., Jiang, T., Wang, W., Nilsson, P., Guo, W., Lu, B., 2021. An App knock-in rat model for Alzheimer's disease exhibiting Aβ and tau pathologies, neuronal death and cognitive impairments. Cell Res. 2021 322 32, 157–175. https://doi.org/10.1038/s41422-021-00582-x

Pasparakis, M., Vandenabeele, P., 2015. Necroptosis and its role in inflammation. Nat. 2015 5177534 517, 311–320. https://doi.org/10.1038/nature14191

Peng, J., Andersen, J.K., 2003. The Role of c-Jun N-Terminal Kinase (JNK) in Parkinson's Disease. IUBMB Life 55, 267–271. https://doi.org/10.1080/1521654031000121666

Phelan, K.D., Shwe, U.T., Williams, D.K., Greenfield, L.J., Zheng, F., 2015. Pilocarpine-induced status epilepticus in mice: A comparison of spectral analysis of electroencephalogram and behavioral grading using the Racine scale. Epilepsy Res. 117, 90–96. https://doi.org/10.1016/j.eplepsyres.2015.09.008

Picon, C., Jayaraman, A., James, R., Beck, C., Gallego, P., Witte, M.E., van Horssen, J., Mazarakis, N.D., Reynolds, R., 2021. Neuron-specific activation of necroptosis signaling in multiple sclerosis cortical grey matter. Acta Neuropathol. https://doi.org/10.1007/s00401-021-02274-7

Pierotti, C.L., Tanzer, M.C., Jacobsen, A. V., Hildebrand, J.M., Garnier, J.M., Sharma, P., Lucet, I.S., Cowan, A.D., Kersten, W.J.A., Luo, M.X., Liang, L.Y., Fitzgibbon, C., Garnish, S.E., Hempel, A., Nachbur, U., Huang, D.C.S., Czabotar, P.E., Silke, J., Van Delft, M.F., Murphy, J.M., Lessene, G., 2020. Potent Inhibition of Necroptosis by Simultaneously Targeting Multiple Effectors of the Pathway. ACS Chem. Biol. 15, 2702–2713. https://doi.org/10.1021/ACSCHEMBIO.0C00482

Prakash G. Jagtap, †, Alexei Degterev, ‡,§, Sungwoon Choi, †, Heather Keys, §, Junying Yuan, ‡ and, Gregory D. Cuny*, †, 2007. Structure−Activity Relationship Study of Tricyclic Necroptosis Inhibitors. J. Med. Chem. 50, 1886–1895. https://doi.org/10.1021/JM061016O

Prendergast, G.C., Smith, C., Thomas, S., Mandik-Nayak, L., Laury-Kleintop, L., Metz, R., Muller, A.J., 2014. Indoleamine 2,3-dioxygenase pathways of pathogenic inflammation and immune escape in cancer. Cancer Immunol. Immunother. https://doi.org/10.1007/s00262-014-1549-4

Qi, Y., Qian, R., Jia, L., Fei, X., Zhang, D., Zhang, Y., Jiang, S., Fu, X., 2020. Overexpressed microRNA-494 represses RIPK1 to attenuate hippocampal neuron injury in epilepsy rats by inactivating the NF-κB signaling pathway. https://doi.org/10.1080/15384101.2020.1749472 19, 1298–1313. https://doi.org/10.1080/15384101.2020.1749472

Qian, L.L., Ji, J.J., Jiang, Y., Guo, J.Q., Wu, Y., Yang, Z., Ma, G.S., Yao, Y.Y., 2022. Serpina3c deficiency induced necroptosis promotes non-alcoholic fatty liver disease through β-catenin/Foxo1/TLR4 signaling. FASEB J. 36, e22316. https://doi.org/10.1096/FJ.202101345RRR

Qin, S., Yang, C., Huang, W., Du, S., Mai, H., Xiao, J., Lü, T., 2018. Sulforaphane attenuates microglia-mediated neuronal necroptosis through down-regulation of MAPK/NF-κB

signaling pathways in LPS-activated BV-2 microglia. Pharmacol. Res. 133, 218–235. https://doi.org/10.1016/J.PHRS.2018.01.014

Qinli, Z., Meiqing, L., Xia, J., Li, X., Weili, G., Xiuliang, J., Junwei, J., Hailan, Y., Ce, Z., Qiao, N., 2013. Necrostatin-1 inhibits the degeneration of neural cells induced by aluminum exposure. Restor. Neurol. Neurosci. https://doi.org/10.3233/RNN-120304

Rehfeldt, S.C.H., Majolo, F., Goettert, M.I., Laufer, S., 2020. c-Jun N-Terminal Kinase Inhibitors as Potential Leads for New Therapeutics for Alzheimer's Diseases. Int. J. Mol. Sci. 21, 1–33. https://doi.org/10.3390/IJMS21249677

Řehořová, M., Vargová, I., Forostyak, S., Vacková, I., Turnovcová, K., Skalníková, H.K., Vodička, P., Kubinová, Š., Syková, E., Jendelová, P., 2019. A Combination of Intrathecal and Intramuscular Application of Human Mesenchymal Stem Cells Partly Reduces the Activation of Necroptosis in the Spinal Cord of SOD1G93A Rats. Stem Cells Transl. Med. 8, 535. https://doi.org/10.1002/SCTM.18-0223

Rickard, J.A., O'Donnell, J.A., Evans, J.M., Lalaoui, N., Poh, A.R., Rogers, T., Vince, J.E., Lawlor, K.E., Ninnis, R.L., Anderton, H., Hall, C., Spall, S.K., Phesse, T.J., Abud, H.E., Cengia, L.H., Corbin, J., Mifsud, S., Di Rago, L., Metcalf, D., Ernst, M., Dewson, G., Roberts, A.W., Alexander, W.S., Murphy, J.M., Ekert, P.G., Masters, S.L., Vaux, D.L., Croker, B.A., Gerlic, M., Silke, J., 2014. RIPK1 regulates RIPK3-MLKL-driven systemic inflammation and emergency hematopoiesis. Cell 157, 1175–1188. https://doi.org/10.1016/j.cell.2014.04.019

Roedig, J., Kowald, L., Juretschke, T., Karlowitz, R., Abhari, B.A., Roedig, H., Fulda, S., Beli, P., Wijk, S.J. van, 2021. USP22 controls necroptosis by regulating receptor-interacting protein kinase 3 ubiquitination. EMBO Rep. 22, e50163. https://doi.org/10.15252/EMBR.202050163

Ros, U., Peña-Blanco, A., Hänggi, K., Kunzendorf, U., Krautwald, S., Wong, W.W.L., García-Sáez, A.J., 2017. Necroptosis Execution Is Mediated by Plasma Membrane Nanopores Independent of Calcium. Cell Rep. 19, 175–187. https://doi.org/10.1016/J.CELREP.2017.03.024

Ross, C.A., Tabrizi, S.J., 2011. Huntington's disease: from molecular pathogenesis to clinical treatment. Lancet Neurol. 10, 83–98. https://doi.org/10.1016/S1474-4422(10)70245-3

Sabio, G., Davis, R.J., 2014. TNF and MAP kinase signaling pathways. Semin. Immunol. 26, 237. https://doi.org/10.1016/J.SMIM.2014.02.009

Saeidikhoo, S., Ezi, S., Khatmi, A., Aghajanpour, F., Soltani, R., Abdollahifar, M.A., Jahanian, A., Aliaghaei, A., 2020. Effect of Sertoli Cell Transplantation on Reducing Neuroinflammation-Induced Necroptosis and Improving Motor Coordination in the Rat Model of Cerebellar Ataxia Induced by 3-Acetylpyridine. J. Mol. Neurosci. 70, 1153–1163. https://doi.org/10.1007/S12031-020-01522-X/FIGURES/9

Saleem, S., 2021. Apoptosis, Autophagy, Necrosis and Their Multi Galore Crosstalk in Neurodegeneration. Neuroscience 469, 162–174. https://doi.org/10.1016/J.NEUROSCIENCE.2021.06.023

Salvadores, N., Gerónimo-Olvera, C., Court, F.A., 2020. Axonal Degeneration in AD: The Contribution of Aβ and Tau. Front. Aging Neurosci. 12, 319. https://doi.org/10.3389/FNAGI.2020.581767/BIBTEX

Salvadores, N., Moreno-Gonzalez, I., Gamez, N., Quiroz, G., Vegas-Gomez, L., Escandón, M., Jimenez, S., Vitorica, J., Gutierrez, A., Soto, C., Court, F.A., 2022. Aβ oligomers trigger necroptosis-mediated neurodegeneration via microglia activation in Alzheimer's disease. Acta Neuropathol. Commun. 10, 1–18. https://doi.org/10.1186/S40478-022-01332-9/FIGURES/5

Sandoval, R., Lazcano, P., Ferrari, F., Pinto-Pardo, N., González-Billault, C., Utreras, E., 2018. TNF-α Increases Production of Reactive Oxygen Species through Cdk5

Activation in Nociceptive Neurons. Front. Physiol. 9. https://doi.org/10.3389/FPHYS.2018.00065

Santagostino, S.F., Assenmacher, C.A., Tarrant, J.C., Adedeji, A.O., Radaelli, E., 2021. Mechanisms of Regulated Cell Death: Current Perspectives. Vet. Pathol. 58, 596–623. https://doi.org/10.1177/03009858211005537

Sarhan, M., Land, W.G., Tonnus, W., Hugo, C.P., Linkermann, A., 2018. Origin and Consequences of Necroinflammation. Physiol. Rev. 98, 727–780. https://doi.org/10.1152/PHYSREV.00041.2016

Sarkar, A., Angeline, M.S., Anand, K., Ambasta, R.K., Kumar, P., 2012. Naringenin and quercetin reverse the effect of hypobaric hypoxia and elicit neuroprotective response in the murine model. Brain Res. 1481, 59–70. https://doi.org/10.1016/J.BRAINRES.2012.08.036

Scaffidi, C., Schmitz, I., Krammer, P.H., Peter, M.E., 1999. The role of c-FLIP in modulation of CD95-induced apoptosis. J. Biol. Chem. 274, 1541–1548. https://doi.org/10.1074/JBC.274.3.1541

Schenk, B., Fulda, S., 2015. Reactive oxygen species regulate Smac mimetic/TNFα-induced necroptotic signaling and cell death. Oncogene 2015 3447 34, 5796–5806. https://doi.org/10.1038/onc.2015.35

Seo, J., Lee, E.W., Sung, H., Seong, D., Dondelinger, Y., Shin, J., Jeong, M., Lee, H.K., Kim, J.H., Han, S.Y., Lee, C., Seong, J.K., Vandenabeele, P., Song, J., 2016. CHIP controls necroptosis through ubiquitylation- and lysosome-dependent degradation of RIPK3. Nat. Cell Biol. 2016 183 18, 291–302. https://doi.org/10.1038/ncb3314

Shan, B., Pan, H., Najafov, A., Yuan, J., 2018. Necroptosis in development and diseases. Genes Dev. 32, 327–340. https://doi.org/10.1101/GAD.312561.118

Shao, L., Liu, X., Zhu, S., Liu, C., Gao, Y., Xu, X., 2018. The Role of Smurf1 in Neuronal Necroptosis after Lipopolysaccharide-Induced Neuroinflammation. Cell. Mol. Neurobiol. 38, 809–816. https://doi.org/10.1007/S10571-017-0553-6/FIGURES/4

Shao, Y., Wang, X., Zhou, Y., Jiang, Y., Wu, R., Lu, C., 2021. Pterostilbene attenuates RIPK3-dependent hepatocyte necroptosis in alcoholic liver disease via SIRT2-mediated NFATc4 deacetylation. Toxicology 461, 152923. https://doi.org/10.1016/J.TOX.2021.152923

Shen, H., Liu, C., Zhang, D., Yao, X., Zhang, K., Li, H., Chen, G., 2017. Role for RIP1 in mediating necroptosis in experimental intracerebral hemorrhage model both in vivo and in vitro. Cell Death Dis. 8, e2641. https://doi.org/10.1038/cddis.2017.58

Shi, J.H., Sun, S.C., 2018. Tumor necrosis factor receptor-associated factor regulation of nuclear factor κB and mitogen-activated protein kinase pathways. Front. Immunol. 9, 1849. https://doi.org/10.3389/FIMMU.2018.01849/BIBTEX

Shim, J.W., Madsen, J.R., 2018. VEGF Signaling in Neurological Disorders. Int. J. Mol. Sci. 19. https://doi.org/10.3390/IJMS19010275

Shirjang, S., Mansoori, B., Asghari, S., Duijf, P.H.G., Mohammadi, A., Gjerstorff, M., Baradaran, B., 2019. MicroRNAs in cancer cell death pathways: Apoptosis and necroptosis. Free Radic. Biol. Med. 139, 1–15. https://doi.org/10.1016/J.FREERADBIOMED.2019.05.017

Shultz, S.R., Taylor, C.J., Aggio-Bruce, R., O'Brien, W.T., Sun, M., Cioanca, A. V., Neocleous, G., Symons, G.F., Brady, R.D., Hardikar, A.A., Joglekar, M. V., Costello, D.M., O'Brien, T.J., Natoli, R., McDonald, S.J., 2022. Decrease in Plasma miR-27a and miR-221 After Concussion in Australian Football Players: https://doi.org/10.1177/11772719221081318 17. https://doi.org/10.1177/11772719221081318

Siano, G., Caiazza, M.C., Ollà, I., Varisco, M., Madaro, G., Quercioli, V., Calvello, M.,

Cattaneo, A., Di Primio, C., 2019. Identification of an ERK Inhibitor as a Therapeutic Drug Against Tau Aggregation in a New Cell-Based Assay. Front. Cell. Neurosci. 13, 386. https://doi.org/10.3389/FNCEL.2019.00386/BIBTEX

Simpson, D.S., Gabrielyan, A., Feltham, R., 2021. RIPK1 ubiquitination: Evidence, correlations and the undefined. Semin. Cell Dev. Biol. 109, 76–85. https://doi.org/10.1016/J.SEMCDB.2020.08.008

Sleigh, J.N., Rossor, A.M., Fellows, A.D., Tosolini, A.P., Schiavo, G., 2019. Axonal transport and neurological disease. Nat. Rev. Neurol. 2019 1512 15, 691–703. https://doi.org/10.1038/s41582-019-0257-2

Sonia Angeline, M., Chaterjee, P., Anand, K., Ambasta, R.K., Kumar, P., 2012. Rotenone-induced parkinsonism elicits behavioral impairments and differential expression of parkin, heat shock proteins and caspases in the rat. Neuroscience 220, 291–301. https://doi.org/10.1016/J.NEUROSCIENCE.2012.06.021

Sonia Angeline, M., Sarkar, A., Anand, K., Ambasta, R.K., Kumar, P., 2013. Sesamol and naringenin reverse the effect of rotenone-induced PD rat model. Neuroscience 254, 379–394. https://doi.org/10.1016/J.NEUROSCIENCE.2013.09.029

Su, X., Wang, H., Kang, D., Zhu, J., Sun, Q., Li, T., Ding, K., 2015. Necrostatin-1 Ameliorates Intracerebral Hemorrhage-Induced Brain Injury in Mice Through Inhibiting RIP1/RIP3 Pathway. Neurochem. Res. 40, 643–650. https://doi.org/10.1007/s11064-014-1510-0

Su, X., Wang, H., Lin, Y., Chen, F., 2018. RIP1 and RIP3 mediate hemin-induced cell death in HT22 hippocampal neuronal cells. Neuropsychiatr. Dis. Treat. 14, 3111–3119. https://doi.org/10.2147/NDT.S181074

Sugaya, T., Kanno, H., Matsuda, M., Handa, K., Tateda, S., Murakami, T., Ozawa, H., Itoi, E., 2019. B-RAFV600E Inhibitor Dabrafenib Attenuates RIPK3-Mediated Necroptosis and Promotes Functional Recovery after Spinal Cord Injury. Cells 8. https://doi.org/10.3390/CELLS8121582

Sun, F., Zhang, H., Shi, J., Huang, T., Wang, Y., 2021. Astragalin Protects against Spinal Cord Ischemia Reperfusion Injury through Attenuating Oxidative Stress-Induced Necroptosis. Biomed Res. Int. 2021. https://doi.org/10.1155/2021/7254708

Sun, L., Wang, H., Wang, Z., He, S., Chen, S., Liao, D., Wang, L., Yan, J., Liu, W., Lei, X., Wang, X., 2012. Mixed lineage kinase domain-like protein mediates necrosis signaling downstream of RIP3 kinase. Cell 148, 213–227. https://doi.org/10.1016/J.CELL.2011.11.031

Sun, W., Bao, J., Lin, W., Gao, H., Zhao, W., Zhang, Q., Leung, C.H., Ma, D.L., Lu, J., Chen, X., 2016. 2-Methoxy-6-acetyl-7-methyljuglone (MAM), a natural naphthoquinone, induces NO-dependent apoptosis and necroptosis by H2O2-dependent JNK activation in cancer cells. Free Radic. Biol. Med. 92, 61–77. https://doi.org/10.1016/J.FREERADBIOMED.2016.01.014

Sun, W., Wu, X., Gao, H., Yu, J., Zhao, W., Lu, J.J., Wang, J., Du, G., Chen, X., 2017. Cytosolic calcium mediates RIP1/RIP3 complex-dependent necroptosis through JNK activation and mitochondrial ROS production in human colon cancer cells. Free Radic. Biol. Med. 108, 433–444. https://doi.org/10.1016/J.FREERADBIOMED.2017.04.010

Sun, X., Yin, J., Starovasnik, M.A., Fairbrother, W.J., Dixit, V.M., 2002. Identification of a Novel Homotypic Interaction Motif Required for the Phosphorylation of Receptor-interacting Protein (RIP) by RIP3. J. Biol. Chem. 277, 9505–9511. https://doi.org/10.1074/JBC.M109488200

Tagai, N., Tanaka, A., Sato, A., Uchiumi, F., Tanuma, S.-I., 1073. Low Levels of Brain-Derived Neurotrophic Factor Trigger Self-aggregated Amyloid β-Induced Neuronal Cell Death in an Alzheimer's Cell Model. Biol. Pharm. Bull 43, 1073–1080.

Journal Pre-proof

Takahashi, N., Duprez, L., Grootjans, S., Cauwels, A., Nerinckx, W., Duhadaway, J.B., Goossens, V., Roelandt, R., Van Hauwermeiren, F., Libert, C., Declercq, W., Callewaert, N., Prendergast, G.C., Degterev, A., Yuan, J., Vandenabeele, P., 2012. Necrostatin-1 analogues: critical issues on the specificity, activity and in vivo use in experimental disease models. Cell Death Dis. 2012 311 3, e437–e437. https://doi.org/10.1038/cddis.2012.176

Takeuchi, O., Akira, S., 2010. Pattern Recognition Receptors and Inflammation. Cell 140, 805–820. https://doi.org/10.1016/J.CELL.2010.01.022

Tan, Y., Sementino, E., Cheung, M., Peri, S., Menges, C.W., Kukuyan, A.M., Zhang, T., Khazak, V., Fox, L.A., Ross, E.A., Ramanathan, S., Jhanwar, S.C., Flores, R.M., Balachandran, S., Testa, J.R., 2021. Somatic Epigenetic Silencing of RIPK3 Inactivates Necroptosis and Contributes to Chemoresistance in Malignant Mesothelioma. Clin. Cancer Res. 27, 1200–1213. https://doi.org/10.1158/1078-0432.CCR-18-3683/74187/AM/SOMATIC-EPIGENETIC-SILENCING-OF-RIPK3-INACTIVATES

Tang, D., Kang, R., Berghe, T. Vanden, Vandenabeele, P., Kroemer, G., 2019. The molecular machinery of regulated cell death. Cell Res. 2019 295 29, 347–364. https://doi.org/10.1038/s41422-019-0164-5

Tang, X., Pan, L., Zhao, S., Dai, F., Chao, M., Jiang, H., Li, X., Lin, Z., Huang, Z., Meng, G., Wang, C., Chen, C., Liu, J., Wang, X., Ferro, A., Wang, H., Chen, H., Gao, Y., Lu, Q., Xie, L., Han, Y., Ji, Y., 2020. SNO-MLP (S-Nitrosylation of Muscle LIM Protein) Facilitates Myocardial Hypertrophy through TLR3 (Toll-Like Receptor 3)-Mediated RIP3 (Receptor-Interacting Protein Kinase 3) and NLRP3 (NOD-Like Receptor Pyrin Domain Containing 3) Inflammasome Activation. Circulation 984–1000. https://doi.org/10.1161/CIRCULATIONAHA.119.042336

Tang, Y., Le, W., 2015. Differential Roles of M1 and M2 Microglia in Neurodegenerative Diseases. Mol. Neurobiol. 2015 532 53, 1181–1194. https://doi.org/10.1007/S12035-014-9070-5

Tansey, M.G., McCoy, M.K., Frank-Cannon, T.C., 2007. Neuroinflammatory mechanisms in Parkinson's disease: Potential environmental triggers, pathways, and targets for early therapeutic intervention. Exp. Neurol. 208, 1–25. https://doi.org/10.1016/J.EXPNEUROL.2007.07.004

Tao, P., Sun, J., Wu, Z., Wang, S., Wang, J., Li, W., Pan, H., Bai, R., Zhang, J., Wang, Y., Lee, P.Y., Ying, W., Zhou, Qinhua, Hou, J., Wang, W., Sun, B., Yang, M., Liu, D., Fang, R., Han, H., Yang, Z., Huang, X., Li, H., Deuitch, N., Zhang, Y., Dissanayake, D., Haude, K., McWalter, K., Roadhouse, C., MacKenzie, J.J., Laxer, R.M., Aksentijevich, I., Yu, X., Wang, X., Yuan, J., Zhou, Qing, 2019. A dominant autoinflammatory disease caused by non-cleavable variants of RIPK1. Nat. 2019 5777788 577, 109–114. https://doi.org/10.1038/s41586-019-1830-y

Teixeira, J., Basit, F., Swarts, H.G., Forkink, M., Oliveira, P.J., Willems, P.H.G.M., Koopman, W.J.H., 2018. Extracellular acidification induces ROS- and mPTP-mediated death in HEK293 cells. Redox Biol. 15, 394–404. https://doi.org/10.1016/J.REDOX.2017.12.018

Teng, X., Degterev, A., Jagtap, P., Xing, X., Choi, S., Denu, R., Yuan, J., Cuny, G.D., 2005. Structure–activity relationship study of novel necroptosis inhibitors. Bioorg. Med. Chem. Lett. 15, 5039–5044. https://doi.org/10.1016/J.BMCL.2005.07.077

Thadathil, N., Nicklas, E.H., Mohammed, S., Lewis, T.L., Richardson, A., Deepa, S.S., 2021. Necroptosis increases with age in the brain and contributes to age-related neuroinflammation. GeroScience 43, 2345–2361. https://doi.org/10.1007/S11357-021-00448-5/FIGURES/8

Tower, J., 2015. Programmed cell death in aging. Ageing Res. Rev. 23, 90–100.

https://doi.org/10.1016/J.ARR.2015.04.002

Trimova, G., Yamagata, K., Iwata, S., Zhang, T., Uemura, F., Satoh, M., Zaharik, M., Biln, N., Hirata, S., Nakayamada, S., Tanaka, Y., 2019. THU0057B TNF-ALPHA INDUCES NECROPTOSIS-LIKE DEATH OF MACROPHAGES AND PROMOTES EXTRACELLULAR RELEASE OF 14–3–3ETA. Ann. Rheum. Dis. 78, 296–296. https://doi.org/10.1136/ANNRHEUMDIS-2019-EULAR.3886

Tu, J.L., Chen, W.P., Cheng, Z.J., Zhang, G., Luo, Q.H., Li, M., Liu, X., 2020. EGb761 ameliorates cell necroptosis by attenuating RIP1-mediated mitochondrial dysfunction and ROS production in both in vivo and in vitro models of Alzheimer's disease. Brain Res. 1736, 146730. https://doi.org/10.1016/J.BRAINRES.2020.146730

Ueda, S., Chen-Yoshikawa, T.F., Tanaka, S., Yamada, Y., Nakajima, D., Ohsumi, A., Date, H., 2022. Protective effect of necrosulfonamide on rat pulmonary ischemia-reperfusion injury via inhibition of necroptosis. J. Thorac. Cardiovasc. Surg. 163, e113–e122. https://doi.org/10.1016/J.JTCVS.2021.01.037

Van Schoor, E., Koper, M.J., Ospitalieri, S., Dedeene, L., Tomé, S.O., Vandenberghe, R., Brenner, D., Otto, M., Weishaupt, J., Ludolph, A.C., Van Damme, P., Van Den Bosch, L., Thal, D.R., 2021. Necrosome-positive granulovacuolar degeneration is associated with TDP-43 pathological lesions in the hippocampus of ALS/FTLD cases. Neuropathol. Appl. Neurobiol. 47, 328–345. https://doi.org/10.1111/NAN.12668

Vandenabeele, P., Galluzzi, L., Vanden Berghe, T., Kroemer, G., 2010. Molecular mechanisms of necroptosis: an ordered cellular explosion. Nat. Rev. Mol. Cell Biol. 2010 1110 11, 700–714. https://doi.org/10.1038/nrm2970

Veereshwarayya, V., Kumar, P., Rosen, K.M., Mestril, R., Querfurth, H.W., 2006. Differential Effects of Mitochondrial Heat Shock Protein 60 and Related Molecular Chaperones to Prevent Intracellular Î²-Amyloid-induced Inhibition of Complex IV and Limit Apoptosis*. J. Biol. Chem. 281, 29468–29478. https://doi.org/10.1074/jbc.M602533200

Verma, M., Wills, Z., Chu, C.T., 2018. Excitatory Dendritic Mitochondrial Calcium Toxicity: Implications for Parkinson's and Other Neurodegenerative Diseases. Front. Neurosci. 12. https://doi.org/10.3389/FNINS.2018.00523

Vitner, E.B., Salomon, R., Farfel-Becker, T., Meshcheriakova, A., Ali, M., Klein, A.D., Platt, F.M., Cox, T.M., Futerman, A.H., 2014. RIPK3 as a potential therapeutic target for Gaucher's disease. Nat. Med. 20, 204–208. https://doi.org/10.1038/nm.3449

Wang, D., Zhao, M., Chen, G., Cheng, X., Han, X., Lin, S., Zhang, X., Yu, X., 2013. The histone deacetylase inhibitor vorinostat prevents TNFα-induced necroptosis by regulating multiple signaling pathways. Apoptosis 18, 1348–1362. https://doi.org/10.1007/S10495-013-0866-Y/FIGURES/7

Wang, H., Chen, Y., Liu, X., Zhang, R., Wang, X., Zhang, Q., Wei, Y., Fang, F., Yuan, Y., Zhou, Q., Dong, Y., Shi, S., Jiang, X., Li, X., 2022. TNF-α derived from arsenite-induced microglia activation mediated neuronal necroptosis. Ecotoxicol. Environ. Saf. 236, 113468. https://doi.org/10.1016/J.ECOENV.2022.113468

Wang, H., Sun, L., Su, L., Rizo, J., Liu, L., Wang, L.F., Wang, F.S., Wang, X., 2014. Mixed Lineage Kinase Domain-like Protein MLKL Causes Necrotic Membrane Disruption upon Phosphorylation by RIP3. Mol. Cell 54, 133–146. https://doi.org/10.1016/J.MOLCEL.2014.03.003

Wang, J., Li, Y., Huang, W.-H., Zeng, X.-C., Li, X.-H., Li, J., Zhou, J., Xiao, J., Xiao, B., Ouyang, D.-S., Hu, K., 2017. The Protective Effect of Aucubin from Eucommia ulmoides Against Status Epilepticus by Inducing Autophagy and Inhibiting Necroptosis. http://dx.doi.org/10.1142/S0192415X17500331 45, 557–573. https://doi.org/10.1142/S0192415X17500331

Journal Pre-proof

Wang, J., Liu, Y., Li, X.-H., Zeng, X.-C., Li, J., Zhou, J., Xiao, B., Hu, K., 2016. Curcumin protects neuronal cells against status-epilepticus-induced hippocampal damage through induction of autophagy and inhibition of necroptosis. https://doi.org/10.1139/cjpp-2016-0154 95, 501–509. https://doi.org/10.1139/CJPP-2016-0154

Wang, J., Zhong, W., Su, H., Xu, J., Yang, D., Liu, X., Zhu, Y.Z., 2021. Histone methyltransferase dot1L contributes to RIPK1 kinase-dependent apoptosis in cerebral ischemia/reperfusion. J. Am. Heart Assoc. 10, 22791. https://doi.org/10.1161/JAHA.121.022791

Wang, J.X., Zhang, X.J., Li, Q., Wang, K., Wang, Y., Jiao, J.Q., Feng, C., Teng, S., Zhou, L.Y., Gong, Y., Zhou, Z.X., Liu, J., Wang, J.L., Li, P.F., 2015. MicroRNA-103/107 regulate programmed necrosis and myocardial ischemia/reperfusion injury through targeting FADD. Circ. Res. 117, 352–363. https://doi.org/10.1161/CIRCRESAHA.117.305781

Wang, L., Deng, B., Yan, P., Wu, H., Li, C., Zhu, H., Du, J., Hou, L., 2021. Neuroprotective effect of ketamine against TNF-α-induced necroptosis in hippocampal neurons. J. Cell. Mol. Med. 25, 3449–3459. https://doi.org/10.1111/JCMM.16426

Wang, Q., Fan, D., Xia, Y., Ye, Q., Xi, X., Zhang, G., Xiao, C., 2021. The latest information on the RIPK1 post-translational modifications and functions. Biomed. Pharmacother. 142, 112082. https://doi.org/10.1016/J.BIOPHA.2021.112082

Wang, S., Wu, J., Zeng, Y.Z., Wu, S.S., Deng, G.R., Chen, Z. Da, Lin, B., 2017. Necrostatin-1 Mitigates Endoplasmic Reticulum Stress After Spinal Cord Injury. Neurochem. Res. 42, 3548–3558. https://doi.org/10.1007/S11064-017-2402-X/FIGURES/7

Wang, T., Perera, N.D., Chiam, M.D.F., Cuic, B., Wanniarachchillage, N., Tomas, D., Samson, A.L., Cawthorne, W., Valor, E.N., Murphy, J.M., Turner, B.J., 2020. Necroptosis is dispensable for motor neuron degeneration in a mouse model of ALS. Cell Death Differ. 27, 1728. https://doi.org/10.1038/S41418-019-0457-8

Wang, W., Gu, X., Cheng, Z., Lu, X., Xie, S., Liu, X., 2022. IKKβ Alleviates Neuron Injury in Alzheimer's Disease via Regulating Autophagy and RIPK1-Mediated Necroptosis. Mol. Neurobiol. 59, 2407–2423. https://doi.org/10.1007/S12035-021-02652-Y/FIGURES/7

Wang, X., Kuang, N., Chen, Y., Liu, G., Wang, N., Kong, F., Yue, S., Zheng, Z., 2021. Transplantation of olfactory ensheathing cells promotes the therapeutic effect of neural stem cells on spinal cord injury by inhibiting necrioptosis. Aging (Albany NY) 13, 9056. https://doi.org/10.18632/AGING.202758

Wang, X., Su, B., Perry, G., Smith, M.A., Zhu, X., 2007. Insights into amyloid-β-induced mitochondrial dysfunction in Alzheimer disease. Free Radic. Biol. Med. 43, 1569–1573. https://doi.org/10.1016/J.FREERADBIOMED.2007.09.007

Wang, Ying, Bi, Y., Xia, Z., Shi, W., Li, Bo, Li, Bin, Chen, L., Guo, L., 2018. Butylphthalide ameliorates experimental autoimmune encephalomyelitis by suppressing PGAM5-induced necroptosis and inflammation in microglia. Biochem. Biophys. Res. Commun. 497, 80–86. https://doi.org/10.1016/J.BBRC.2018.02.024

Wang, Ying, Guo, L., Wang, J., Shi, W., Xia, Z., Li, B., 2019. Necrostatin-1 ameliorates the pathogenesis of experimental autoimmune encephalomyelitis by suppressing apoptosis and necroptosis of oligodendrocyte precursor cells. Exp. Ther. Med. 18, 4113. https://doi.org/10.3892/ETM.2019.8005

Wang, Yang, Jiao, J., Ren, P., Wu, M., 2019a. Upregulation of miRNA-223-3p ameliorates RIP3-mediated necroptosis and inflammatory responses via targeting RIP3 after spinal cord injury. J. Cell. Biochem. 120, 11582–11592. https://doi.org/10.1002/JCB.28438

Wang, Yang, Jiao, J., Ren, P., Wu, M., 2019b. Upregulation of miRNA-223-3p ameliorates RIP3-mediated necroptosis and inflammatory responses via targeting RIP3 after spinal

Journal Pre-proof

cord injury. J. Cell. Biochem. 120, 11582–11592. https://doi.org/10.1002/JCB.28438
Wang, Yang, Jiao, J., Zhang, S., Zheng, C., Wu, M., 2019c. RIP3 inhibition protects locomotion function through ameliorating mitochondrial antioxidative capacity after spinal cord injury. Biomed. Pharmacother. 116, 109019. https://doi.org/10.1016/J.BIOPHA.2019.109019
Wang, Y., Wang, H., Tao, Y., Zhang, S., Wang, J., Feng, X., 2014. Necroptosis inhibitor necrostatin-1 promotes cell protection and physiological function in traumatic spinal cord injury. Neuroscience 266, 91–101. https://doi.org/10.1016/J.NEUROSCIENCE.2014.02.007
Wang, Yongxiang, Wang, J., Wang, H., Feng, X., Tao, Y., Yang, J., Cai, J., 2018. Necrosulfonamide Attenuates Spinal Cord Injury via Necroptosis Inhibition. World Neurosurg. 114, e1186–e1191. https://doi.org/10.1016/J.WNEU.2018.03.174
Wegner, K.W., Saleh, D., Degterev, A., 2017. Complex Pathologic Roles of RIPK1 and RIPK3: Moving Beyond Necroptosis. Trends Pharmacol. Sci. 38, 202. https://doi.org/10.1016/J.TIPS.2016.12.005
Wehn, A.C., Khalin, I., Duering, M., Hellal, F., Culmsee, C., Vandenabeele, P., Plesnila, N., Terpolilli, N.A., 2021. RIPK1 or RIPK3 deletion prevents progressive neuronal cell death and improves memory function after traumatic brain injury. Acta Neuropathol. Commun. 9. https://doi.org/10.1186/S40478-021-01236-0
Wei, M., Li, C., Yan, Z., Hu, Z., Dong, L., Zhang, J., Wang, X., Li, Y., Zhang, H., 2021. Activated Microglia Exosomes Mediated miR-383-3p Promotes Neuronal Necroptosis Through Inhibiting ATF4 Expression in Intracerebral Hemorrhage. Neurochem. Res. 46, 1337–1349. https://doi.org/10.1007/s11064-021-03268-3
Weinlich, R., Oberst, A., Beere, H.M., Green, D.R., 2017. Necroptosis in development, inflammation and disease. Nat. Rev. Mol. Cell Biol. 18, 127–136. https://doi.org/10.1038/NRM.2016.149
Wong, W., 2019. Parkin protects against necroptosis. Sci. Signal. 12. https://doi.org/10.1126/SCISIGNAL.AAZ1464
Wu, J.R., Wang, J., Zhou, S.K., Yang, L., Yin, J. Le, Cao, J.P., Cheng, Y.B., 2015. Necrostatin-1 protection of dopaminergic neurons. Neural Regen. Res. https://doi.org/10.4103/1673-5374.160108
Wu, L., Chung, J.Y., Cao, T., Jin, G., Edmiston, W.J., Hickman, S., Levy, E.S., Whalen, J.A., Abrams, E.S.L.R., Degterev, A., Lo, E.H., Tozzi, L., Kaplan, D.L., El Khoury, J., Whalen, M.J., 2021. Genetic inhibition of RIPK3 ameliorates functional outcome in controlled cortical impact independent of necroptosis. Cell Death Dis. 12. https://doi.org/10.1038/S41419-021-04333-Z
Wu, X., Deng, G., Li, M., Li, Y., Ma, C., Wang, Y., Liu, X., 2015. Wnt/β-Catenin signaling reduces Bacillus Calmette-Guerin-induced macrophage necrosis through a ROS - mediated PARP/AIF-dependent pathway. BMC Immunol. 16. https://doi.org/10.1186/S12865-015-0080-5
Xia, K., Zhu, F., Yang, C., Wu, S., Lin, Y., Ma, H., Yu, X., Zhao, C., Ji, Y., Ge, W., Wang, J., Du, Y., Zhang, W., Yang, T., Zhang, X., He, S., 2020. Discovery of a Potent RIPK3 Inhibitor for the Amelioration of Necroptosis-Associated Inflammatory Injury. Front. Cell Dev. Biol. 8, 1507. https://doi.org/10.3389/FCELL.2020.606119/BIBTEX
Xie, Q., Gu, Y., Hua, Y., Liu, W., Keep, R.F., Xi, G., 2014. Deferoxamine attenuates white matter injury in a piglet intracerebral hemorrhage model. Stroke 45, 290–292. https://doi.org/10.1161/strokeaha.113.003033
Xie, T., Peng, W., Yan, C., Wu, J., Gong, X., Shi, Y., 2013. Structural Insights into RIP3-Mediated Necroptotic Signaling. Cell Rep. 5, 70–78. https://doi.org/10.1016/J.CELREP.2013.08.044

Journal Pre-proof

Xu-Xu Deng Feng-Yan Sun, S.-S.L., n.d. Necrostatin-1 Prevents Necroptosis in Brains after Ischemic Stroke via Inhibition of RIPK1-Mediated RIPK3/MLKL Signaling. Aging Dis.

Xu, C., Wu, J., Wu, Y., Ren, Z., Yao, Y., Chen, G., Fang, E.F., Noh, J.H., Liu, Y.U., Wei, L., Chen, X., Sima, J., 2021. TNF-α-dependent neuronal necroptosis regulated in Alzheimer's disease by coordination of RIPK1-p62 complex with autophagic UVRAG. Theranostics 11, 9452. https://doi.org/10.7150/THNO.62376

Xu, D., Jin, T., Zhu, H., Chen, H., Ofengeim, D., Zou, C., Mifflin, L., Pan, L., Amin, P., Li, W., Shan, B., Naito, M.G., Meng, H., Li, Y., Pan, H., Aron, L., Adiconis, X., Levin, J.Z., Yankner, B.A., Yuan, J., 2018. TBK1 suppresses RIPK1-driven apoptosis and inflammation during development and in aging. Cell 174, 1477. https://doi.org/10.1016/J.CELL.2018.07.041

Xu, D., Zou, C., Yuan, J., 2021. Genetic Regulation of RIPK1 and Necroptosis. https://doi.org/10.1146/annurev-genet-071719-022748 55, 235–263. https://doi.org/10.1146/ANNUREV-GENET-071719-022748

Xu, Yu, Hu, X., Li, F., Zhang, H., Lou, J., Wang, Xingyu, Wang, H., Yin, L., Ni, W., Kong, J., Wang, Xiangyang, Li, Y., Zhou, K., Xu, H., 2021. GDF-11 Protects the Traumatically Injured Spinal Cord by Suppressing Pyroptosis and Necroptosis via TFE3-Mediated Autophagy Augmentation. Oxid. Med. Cell. Longev. 2021. https://doi.org/10.1155/2021/8186877

Xu, Yang, Wu, X., Hu, W., Yu, D., Shao, Z., Li, W., Huang, T., Zhang, J., Zhu, X., Li, X., Yang, H., Chu, Z., Lv, K., 2021. RIP3 facilitates necroptosis through CaMKII and AIF after intracerebral hemorrhage in mice. Neurosci. Lett. 749, 135699. https://doi.org/10.1016/j.neulet.2021.135699

Yamanishi, E., Hasegawa, K., Fujita, K., Ichinose, S., Yagishita, S., Murata, M., Tagawa, K., Akashi, T., Eishi, Y., Okazawa, H., 2017. A novel form of necrosis, TRIAD, occurs in human Huntington's disease. Acta Neuropathol. Commun. 5, 19. https://doi.org/10.1186/S40478-017-0420-1

Yan, G., Elbadawi, M., Efferth, T., 2020. Multiple cell death modalities and their key features (Review). World Acad. Sci. J. 2, 39–48. https://doi.org/10.3892/WASJ.2020.40/HTML

Yan, J., Wan, P., Choksi, S., Liu, Z.G., 2022. Necroptosis and tumor progression. Trends in Cancer 8, 21–27. https://doi.org/10.1016/j.trecan.2021.09.003

Yañez, M.J., Campos, F., Marín, T., Klein, A.D., Futerman, A.H., Alvarez, A.R., Zanlungo, S., 2021. c-Abl activates RIPK3 signaling in Gaucher disease. Biochim. Biophys. Acta - Mol. Basis Dis. 1867, 166089. https://doi.org/https://doi.org/10.1016/j.bbadis.2021.166089

Yang, J., Zhao, Y., Zhang, L., Fan, H., Qi, C., Zhang, K., Liu, X., Fei, L., Chen, S., Wang, M., Kuang, F., Wang, Y., Wu, S., 2018. RIPK3/MLKL-Mediated Neuronal Necroptosis Modulates the M1/M2 Polarization of Microglia/Macrophages in the Ischemic Cortex. Cereb. Cortex 28, 2622–2635. https://doi.org/10.1093/CERCOR/BHY089

Yang, L., Wang, Y., Zhang, C., Chen, T., Cheng, H., 2021. Perampanel, an AMPAR antagonist, alleviates experimental intracerebral hemorrhage-induced brain injury via necroptosis and neuroinflammation. Mol. Med. Rep. 24. https://doi.org/10.3892/MMR.2021.12183

Yang, M., Lv, Y., Tian, X., Lou, J., An, R., Zhang, Q., Li, M., Xu, L., Dong, Z., 2017. Neuroprotective Effect of β-Caryophyllene on Cerebral Ischemia-Reperfusion Injury via Regulation of Necroptotic Neuronal Death and Inflammation: In Vivo and in Vitro. Front. Neurosci. 11, 583. https://doi.org/10.3389/fnins.2017.00583

Yang, W., Tao, K., Wang, Y., Huang, Y., Duan, C., Wang, T., Li, C., Zhang, P., Yin, Y., Gao, J., Li, R., 2022. Necrosulfonamide ameliorates intestinal inflammation via inhibiting GSDMD-medicated pyroptosis and MLKL-mediated necroptosis. Biochem.

Journal Pre-proof

Pharmacol. 206, 115338. https://doi.org/10.1016/J.BCP.2022.115338
Yang, Y., Han, C., Guo, L., Guan, Q., 2018. High expression of the HMGB1-TLR4 axis and its downstream signaling factors in patients with Parkinson's disease and the relationship of pathological staging. Brain Behav. 8. https://doi.org/10.1002/BRB3.948
Yang, Y., Jiang, G., Zhang, P., Fan, J., 2015. Programmed cell death and its role in inflammation. Mil. Med. Res. 2, 1–12. https://doi.org/10.1186/S40779-015-0039-0/FIGURES/2
Yang, Z., Jiang, B., Wang, Y., Ni, H., Zhang, J., Xia, J., Shi, M., Hung, L.M., Ruan, J., Mak, T.W., Li, Q., Han, J., 2017. 2-HG Inhibits Necroptosis by Stimulating DNMT1-Dependent Hypermethylation of the RIP3 Promoter. Cell Rep. 19, 1846–1857. https://doi.org/10.1016/J.CELREP.2017.05.012
Yang, Z., Wang, Y., Zhang, Y., He, X., Zhong, C.Q., Ni, H., Chen, X., Liang, Y., Wu, J., Zhao, S., Zhou, D., Han, J., 2018. RIP3 targets pyruvate dehydrogenase complex to increase aerobic respiration in TNF-induced necroptosis. Nat. Cell Biol. 20, 186–197. https://doi.org/10.1038/S41556-017-0022-Y
Yarza, R., Vela, S., Solas, M., Ramirez, M.J., 2016. c-Jun N-terminal kinase (JNK) signaling as a therapeutic target for Alzheimer's disease. Front. Pharmacol. 6, 321. https://doi.org/10.3389/FPHAR.2015.00321/BIBTEX
Ye, Y., Feng, Z., Tian, S., Yang, Y., Jia, Y., Wang, G., Wang, J., Bai, W., Li, J., He, X., 2022. HBO Alleviates Neural Stem Cell Pyroptosis via lncRNA-H19/miR-423-5p/NLRP3 Axis and Improves Neurogenesis after Oxygen Glucose Deprivation. Oxid. Med. Cell. Longev. 2022. https://doi.org/10.1155/2022/9030771
Yelamanchili, S. V., Lamberty, B.G., Rennard, D.A., Morsey, B.M., Hochfelder, C.G., Meays, B.M., Levy, E., Fox, H.S., 2015. MiR-21 in Extracellular Vesicles Leads to Neurotoxicity via TLR7 Signaling in SIV Neurological Disease. PLOS Pathog. 11, e1005032. https://doi.org/10.1371/JOURNAL.PPAT.1005032
Yi, R., Chen, B., Zhao, J., Zhan, X., Zhang, L., Liu, X., Dong, Q., 2014. Krüppel-like factor 8 ameliorates Alzheimer's disease by activating β-catenin. J. Mol. Neurosci. 52, 231–241. https://doi.org/10.1007/S12031-013-0131-4
YN, K., DH, K., 2012. Decreased serum angiogenin level in Alzheimer's disease. Prog. Neuropsychopharmacol. Biol. Psychiatry 38. https://doi.org/10.1016/J.PNPBP.2012.02.010
Yu, Y. qiang, Thonn, V., Patankar, J. V., Thoma, O.M., Waldner, M., Zielinska, M., Bao, L. li, Gonzalez-Acera, M., Wallmüller, S., Engel, F.B., Stürzl, M., Neurath, M.F., Liebing, E., Becker, C., 2022. SMYD2 targets RIPK1 and restricts TNF-induced apoptosis and necroptosis to support colon tumor growth. Cell Death Dis. 2022 131 13, 1–10. https://doi.org/10.1038/s41419-021-04483-0
Yuan, J., Amin, P., Ofengeim, D., 2019. Necroptosis and RIPK1-mediated neuroinflammation in CNS diseases. Nat. Rev. Neurosci. 20, 19. https://doi.org/10.1038/S41583-018-0093-1
Yuan, L., Wang, Z., Liu, L., Jian, X., 2015. Inhibiting histone deacetylase 6 partly protects cultured rat cortical neurons from oxygen-glucose deprivation-induced necroptosis. Mol. Med. Rep. 12, 2661–2667. https://doi.org/10.3892/MMR.2015.3779/HTML
Yuan, S., Li, H., Yang, C., Xie, Wenyi, Wang, Y., Zhang, J., cai, Z., Mao, Z., Xie, Weibing, Lü, T., 2020. DHA attenuates Aβ-induced necroptosis through the RIPK1/RIPK3 signaling pathway in THP-1 monocytes. Biomed. Pharmacother. 126, 110102. https://doi.org/10.1016/J.BIOPHA.2020.110102
Yuan, S., Yu, Z., Zhang, Z., Zhang, J., Zhang, P., Li, X., Li, H., Shen, H., Chen, G., 2019. RIP3 participates in early brain injury after experimental subarachnoid hemorrhage in rats by inducing necroptosis. Neurobiol. Dis. 129, 144–158.

https://doi.org/10.1016/j.nbd.2019.05.004
Yuan, Z., Yi-Yun, S., Hai-Yan, Y., 2020. Triad3A displays a critical role in suppression of cerebral ischemic/reperfusion (I/R) injury by regulating necroptosis. Biomed. Pharmacother. 128, 110045. https://doi.org/10.1016/j.biopha.2020.110045
Zelic, M., Pontarelli, F., Woodworth, L., Zhu, C., Mahan, A., Ren, Y., LaMorte, M., Gruber, R., Keane, A., Loring, P., Guo, L., Xia, T. he, Zhang, B., Orning, P., Lien, E., Degterev, A., Hammond, T., Ofengeim, D., 2021. RIPK1 activation mediates neuroinflammation and disease progression in multiple sclerosis. Cell Rep. 35, 109112. https://doi.org/10.1016/j.celrep.2021.109112
Zhan, L., Lu, X., Xu, W., Sun, W., Xu, E., 2021. Inhibition of MLKL-dependent necroptosis via downregulating interleukin-1R1 contributes to neuroprotection of hypoxic preconditioning in transient global cerebral ischemic rats. J. Neuroinflammation 18, 1–15. https://doi.org/10.1186/S12974-021-02141-Y/FIGURES/6
Zhang, B., Wu, T., Wang, Z., Zhang, Y., Wang, J., Yang, B., Zhao, Y., Rao, Z., Gao, J., 2015. p38MAPK activation mediates tumor necrosis factor-α-induced apoptosis in glioma cells. Mol. Med. Rep. 11, 3101–3107. https://doi.org/10.3892/MMR.2014.3002/HTML
Zhang, C., Wang, Yue, Chen, J., Yang, S., Wang, Yuhai, 2021. Controlled decompression alleviates early brain injury in rabbitintracranial hypertension model by regulatingapoptosis/necroptosis. Acta Cirúrgica Bras. 36. https://doi.org/10.1590/ACB360406
Zhang, F., Zhong, R., Li, S., Fu, Z., Cheng, C., Cai, H., Le, W., 2017. Acute hypoxia induced an imbalanced M1/M2 activation of microglia through NF-κB signaling in Alzheimer's disease mice and wild-type littermates. Front. Aging Neurosci. 9, 282. https://doi.org/10.3389/FNAGI.2017.00282/BIBTEX
Zhang, H., Wei, M., Lu, X., Sun, Q., Wang, C., Zhang, J., Fan, H., 2020. Aluminum trichloride caused hippocampal neural cells death and subsequent depression-like behavior in rats via the activation of IL-1β/JNK signaling pathway. Sci. Total Environ. 715, 136942. https://doi.org/10.1016/J.SCITOTENV.2020.136942
Zhang, H., Zhou, X., McQuade, T., Li, J., Chan, F.K.M., Zhang, J., 2011. Functional complementation between FADD and RIP1 in embryos and lymphocytes. Nature 471, 373. https://doi.org/10.1038/NATURE09878
Zhang, Q.X., Guo, D., Wang, F.C., Ding, W.Y., 2020. Necrosulfonamide (NSA) protects intervertebral disc degeneration via necroptosis and apoptosis inhibition. Eur. Rev. Med. Pharmacol. Sci. 24, 2683–2691. https://doi.org/10.26355/EURREV_202003_20538
Zhang, Shili, Che, L., He, C., Huang, J., Guo, N., Shi, J., Lin, Y., Lin, Z., 2019. Drp1 and RB interaction to mediate mitochondria-dependent necroptosis induced by cadmium in hepatocytes. Cell Death Dis. 2019 107 10, 1–17. https://doi.org/10.1038/s41419-019-1730-y
Zhang, Sitao, Su, Y., Ying, Z., Guo, D., Pan, C., Guo, J., Zou, Z., Wang, L., Zhang, Ze, Jiang, Z., Zhang, Zhiyuan, Wang, X., 2019. RIP1 kinase inhibitor halts the progression of an immune-induced demyelination disease at the stage of monocyte elevation. Proc. Natl. Acad. Sci. U. S. A. 116, 5675–5680. https://doi.org/10.1073/pnas.1819917116
Zhang, S., Tang, M.B., Luo, H.Y., Shi, C.H., Xu, Y.M., 2017. Necroptosis in neurodegenerative diseases: A potential therapeutic target. Cell Death Dis. 8. https://doi.org/10.1038/CDDIS.2017.286
Zhang, S., Wang, Y., Li, D., Wu, J., Si, W., Wu, Y., 2016. Necrostatin-1 Attenuates Inflammatory Response and Improves Cognitive Function in Chronic Ischemic Stroke Mice. Med. (Basel, Switzerland) 3. https://doi.org/10.3390/medicines3030016
Zhang, X., Dowling, J.P., Zhang, J., 2019. RIPK1 can mediate apoptosis in addition to

Journal Pre-proof

necroptosis during embryonic development. Cell Death Dis. 2019 103 10, 1–11. https://doi.org/10.1038/s41419-019-1490-8

Zhang, Y.-Y., Tian, J., Peng, Z.-M., Peng, Y.-W., Zhang, X.-J., Hu, Z.-Y., Luo, X.-J., Peng, J., 2021. Caspofungin suppresses brain cell necroptosis in the ischemic stroke rat via up-regulation of Pellino3. https://doi.org/10.21203/rs.3.rs-358513/v1

Zhang, Y., Li, M., Li, X., Zhang, Haiwei, Wang, L., Wu, X., Zhang, Haibing, Luo, Y., 2020. Catalytically inactive RIP1 and RIP3 deficiency protect against acute ischemic stroke by inhibiting necroptosis and neuroinflammation. Cell Death Dis. 11, 565. https://doi.org/10.1038/s41419-020-02770-w

Zhang, Y., Su, S.S., Zhao, S., Yang, Z., Zhong, C.Q., Chen, X., Cai, Q., Yang, Z.H., Huang, D., Wu, R., Han, J., 2017. RIP1 autophosphorylation is promoted by mitochondrial ROS and is essential for RIP3 recruitment into necrosome. Nat. Commun. 8. https://doi.org/10.1038/NCOMMS14329

Zhang, Y.Y., Tian, J., Peng, Z.M., Liu, B., Peng, Y.W., Zhang, X.J., Hu, Z.Y., Luo, X.J., Peng, J., 2021. Caspofungin Suppresses Brain Cell Necroptosis in Ischemic Stroke Rats via Up-Regulation of Pellino3. Cardiovasc. Drugs Ther. 1–15. https://doi.org/10.1007/S10557-021-07231-W/FIGURES/8

Zhang, Y.Z., Wang, L., Zhang, J.J., Xiong, X.M., Zhang, D., Tang, X.M., Luo, X.J., Ma, Q.L., Peng, J., 2018. Vascular peroxide 1 promotes ox-LDL-induced programmed necrosis in endothelial cells through a mechanism involving β-catenin signaling. Atherosclerosis 274, 128–138. https://doi.org/10.1016/J.ATHEROSCLEROSIS.2018.04.031

Zhao, P., Li, C., Chen, B., Sun, G., Chao, H., Tu, Y., Bao, Z., Fan, L., Du, X., Ji, J., 2020. Up-regulation of CHMP4B alleviates microglial necroptosis induced by traumatic brain injury. J. Cell. Mol. Med. 24, 8466. https://doi.org/10.1111/JCMM.15406

Zhao, Q., Lu, F., Su, Q., Liu, Z., Xia, X., Yan, Z., Zhou, F., Qin, R., 2020. Knockdown of long noncoding RNA XIST mitigates the apoptosis and inflammatory injury of microglia cells after spinal cord injury through miR-27a/Smurf1 axis. Neurosci. Lett. 715, 134649. https://doi.org/10.1016/J.NEULET.2019.134649

Zhao, W.-Z., Wang, H.-T., Huang, H.-J., Lo, Y.-L., Lin, A.M.-Y., 2017. Neuroprotective Effects of Baicalein on Acrolein-induced Neurotoxicity in the Nigrostriatal Dopaminergic System of Rat Brain. Mol. Neurobiol. 2017 551 55, 130–137. https://doi.org/10.1007/S12035-017-0725-X

Zhao, W., Liu, Y., Xu, L., He, Y., Cai, Z., Yu, J., Zhang, W., Xing, C., Zhuang, C., Qu, Z., 2022. Targeting Necroptosis as a Promising Therapy for Alzheimer's Disease. ACS Chem. Neurosci. 13, 1697–1713. https://doi.org/10.1021/ACSCHEMNEURO.2C00172/ASSET/IMAGES/MEDIUM/CN2C00172_0008.GIF

Zhong, W., Cheng, J., Yang, · Xiaosheng, Liu, W., Li, Y., 2022. Heliox Preconditioning Exerts Neuroprotective Effects on Neonatal Ischemia/Hypoxia Injury by Inhibiting Necroptosis Induced by Ca2+ Elevation. Transl. Stroke Res. 2022 1, 1–16. https://doi.org/10.1007/S12975-022-01021-8

Zhou, X.B., Lai, L.F., Xie, G. Bin, Ding, C., Xu, X., Wang, Y., 2019. LncRNAGAS5 sponges miRNA-221 to promote neurons apoptosis by up-regulated PUMA under hypoxia condition. https://doi.org/10.1080/01616412.2019.1672382 42, 8–16. https://doi.org/10.1080/01616412.2019.1672382

Zhu, S., Zhang, Y., Bai, G., Li, H., 2011. Necrostatin-1 ameliorates symptoms in R6/2 transgenic mouse model of Huntington's disease. Cell Death Dis. 2011 21 2, e115–e115. https://doi.org/10.1038/cddis.2010.94

Zhu, Y.-M., Lin, L., Wei, C., Guo, Y., Qin, Y., Li, Z.-S., Kent, T.A., McCoy, C.E., Wang, Z.-

Journal Pre-proof

X., Ni, Y., Zhou, X.-Y., Zhang, H.-L., 2021. The Key Regulator of Necroptosis, RIP1 Kinase, Contributes to the Formation of Astrogliosis and Glial Scar in Ischemic Stroke. Transl. Stroke Res. https://doi.org/10.1007/s12975-021-00888-3

Zhuang, C., Chen, F., 2020. Small-Molecule Inhibitors of Necroptosis: Current Status and Perspectives. J. Med. Chem. 63, 1490–1510. https://doi.org/10.1021/ACS.JMEDCHEM.9B01317/SUPPL_FILE/JM9B01317_SI_001.CSV

Zolezzi, J.M., Bastías-Candia, S., Inestrosa, N.C., 2019. Toll-Like Receptors (TLRs) in Neurodegeneration: Integrative Approach to TLR Cascades in Alzheimer's and Parkinson's Diseases. Toll-like Recept. https://doi.org/10.5772/INTECHOPEN.86167

Zou, C., Mifflin, L., Hu, Z., Zhang, T., Shan, B., Wang, H., Xing, X., Zhu, H., Adiconis, X., Levin, J.Z., Li, F., Liu, C.F., Liu, J.S., Yuan, J., 2020. Reduction of mNAT1/hNAT2 Contributes to Cerebral Endothelial Necroptosis and Aβ Accumulation in Alzheimer's Disease. Cell Rep. 33, 108447. https://doi.org/10.1016/j.celrep.2020.108447

Zou, M., Zeng, Q.S., Nie, J., Yang, J.H., Luo, Z.Y., Gan, H.T., 2021. The Role of E3 Ubiquitin Ligases and Deubiquitinases in Inflammatory Bowel Disease: Friend or Foe? Front. Immunol. 12. https://doi.org/10.3389/FIMMU.2021.769167

Highlights

- Downstream targets and effectors of necrosome that leads to neuronal cell death.
- Post-translational modifications regulate the necrosome activation.
- RIPK1 in establishing the connection between necroptosis, apoptosis, and autophagy pathway.
- Impact of necrosome activation on different biological processes in the brain.
- Different signaling molecules and pathways modulation necroptosis machinery.
- Therapeutic applications of natural compounds, small chemical inhibitors, micro-RNAs, circular-RNAs, and long non-coding RNAs.

Journal Pre-proof